MALAYSIAN JOURNAL OF ANALYTICAL SCIENCES

Published by The Malaysian Analytical Sciences Society

ISSN 1394 - 2506

Vol 22 No 1 (2018)

Vol 22 No 2 (2018)

Vol 22 No 3 (2018)

Vol 22 No 4 (2018)

Vol 22 No 5 (2018)

Vol 22 No 6 (2018)

2018

Malaysian Journal of Analytical Sciences Vol 22 No 1 2018

Articles 13 - 20 are selected papers from the "Regional Conference on Sciences, Technology and Sosial Sciences 2016 (RCSTSS 2016), 4 - 6 December 2016, Copthorne Hotel, Cameron Highlands, Malaysia; organised by Universiti Teknologi MARA (UiTM) Cawangan Pahang Kampus Jengka, 26400 Bandar Tun Abdul Razak Jengka, Pahang Darul Makmur, Malaysia."

Guest Editor: Azhan Hashim@Ismail

		Page
1.	SIMPLE µ-SOLID PHASE EXTRACTION USING C18 FILM FOR THE EXTRACTION OF POLYCYCLIC AROMATIC HYDROCARBONS IN COFFEE BEVERAGE (Pengekstrakan µ-Fasa Pepejal yang Mudah Menggunakan Filem C18 untuk Pengekstrakan Hidrokarbon Aromatik Polisiklik dalam Minuman Kopi) *Saw Hong Loh, Pei Ee Neoh, Chee Tung Tai, Sazlinda Kamaruzaman*	1
2.	CATALYTIC CRACKING OF USED VEGETABLE OIL TO GREEN FUEL WITH METAL FUNCTIONALIZED ZSM-5 CATALYSTS (Pemecahan Bermangkin Minyak Sayur Terpakai kepada Bahan Api Hijau dengan Pemangkin ZSM-5 Berfungsi Logam) *Mohamed Azeem Abdul Majed and Ching Thian Tye*	8
3.	SYNTHESIS AND CHARACTERIZATION OF MESOPOROUS POLYMER-SILICA HYBRID MONOLITH USING CONVENTIONAL SOL-GEL METHOD FOR ENZYME SUPPORT (Sintesis dan Pencirian Monolit Hibrid Polimer-Silika Berliang-Meso Menggunakan Kaedah Konvensional Sol-Gel Untuk Bertindak Sebagai Sokongan Enzim) *Noor Hidayah Idrohani, Samuel M. Mugo, Sabiqah Tuan Anuar*	17
4.	COMPLEXATION OF 5,5,7,12,12,14-HEXAMETHYL-1,4,8,11-TETRAAZACYCLOTETRADECA-7,14-DIENIUM DIPERCHLORATE WITH COPPER(II) ACETATE MONOHYDRATE IN IONIC LIQUID (Pengkompleksan 5,5,7,12,12,14-Heksametil-1,4,8,11-Tetraazasiklo tetraazadeka-7,14-Dienium Diperklorat dengan Kuprum(II) Asetat Monohidrat dalam Cecair Ionik) *Noorhanani M. Ali, Nurzati Amani M. Zaid, Nurul Huda Abd. Karim, Bohari M. Yamin, Nur Hasyareeda Hassan*	27
5.	PHYSICOCHEMICAL AND SENSORIAL PROPERTIES OF OPTIMISED ROSELLE-PINEAPPLE LEATHER (Ciri-Ciri Fizikokimia dan Sensori Snek Rozel-Nenas yang Dioptimumkan) *Noorlaila Ahmad, Siti Nadiah Shafi'i, Nor Hasanah Hassan, Asmeda Rajab, Azizah Othman*	35
6.	ASSESSING STIR BAR SORPTIVE EXTRACTION FOR TRIAZINE HERBICIDES EXTRACTION BY USING A CENTRAL COMPOSITE DESIGN APPROACH (Penilaian Pengekstrakan Erapan Bar untuk Pengekstrakan Herbisid Triazin Menggunakan Pendekatan Reka Bentuk Komposit Berpusat) *Nurul Auni Zainal Abidin, Md Pauzi Abdullah, Fouad Fadhil Al-Qaim, Wan Mohd Afiq Wan Mohd Khalik, Mohamed Rozali Othman*	45

7. MICROEMULSION ELECTROKINETIC CHROMATOGRAPHY COUPLED WITH DISPERSIVE MICRO-SOLID PHASE EXTRACTION FOR DETERMINATION OF ISOFLAVONES IN SOYBEAN PRODUCTS 54
(Kromatografi Elektrokinetik Mikro-Emulsi Berganding dengan Pengekstrakan Fasa Pepejal Mikro Serakan bagi Pengenalpastian Isoflavon di dalam Produk Kacang Soya)
Khaulah Ab Rahim, Mohd Marsin Sanagi, Dadan Hermawan, Wan Aini Wan Ibrahim, Aemi Syazwani Abdul Keyon

8. NEW DITERPENOIDS FROM THE ROOTS OF *Croton hirtus* (EUPHORBIACEAE) 64
(Diterpenoid-Diterpenoid Terbaharu Daripada Akar *Croton hirtus* (Euphorbiaceae))
Andi Rifki Rosandy, Anis Asmi Azman, Rozida Mohd Khalid, Rizafizah Othaman, Azwan Mat Lazim, Iqbal M. Choudary, Yana Maulana Syah, Jalifah Latip, Ikram Md. Said, Muntaz Abu Bakar

9. FORENSIC GAS CHROMATOGRAPHY ANALYSIS OF TIME ELAPSED GASOLINE IN FIRE SCENE INVESTIGATION 72
(Analisis Kromatografi Gas Forensik bagi Gasolin yang Masanya Berlalu dalam Penyiasatan Tempat Kebakaran)
Pei Wen Lim, Ahmad Fahmi Lim Abdullah, Kah Haw Chang

10. EFFECTS OF DEPOSITION TIME ON OF COBALT SULFIDE THIN FILM ELECTRODE FORMATION 80
(Kesan Tempoh Masa Enapan Terhadap Pembentukan Elektrod Filem Nipis Kobalt Sulfida)
Norshazlinah Abdul Karim, Norasikin Ahmad Ludin, Mohd Asri Mat-Teridi, Suhaila Sepeai, Mohd Adib Ibrahim, M. Kouhnavard, Kamaruzzaman Sopian, Hironori Arakawa

11. EFFECT OF EXTRACTION METHODS ON THE YIELD, FUCOSE CONTENT AND PURITY OF FUCOIDAN FROM *Sargassum* sp. OBTAINED FROM PULAU LANGKAWI, MALAYSIA 87
(Kesan Kaedah Pengekstrakan Fukoidan Terhadap Hasil, Kandungan Fukosa dan Ketulenan Fukoidan daripada *Sargassum* sp. dari Pulau Langkawi, Malaysia)
Bibi Marliana Baba, Wan Aida Wan Mustapha, Lim Seng Joe

12. CO-SENSITIZATION OF NATURAL SENSITIZERS EXTRACTED FROM RENGAS (*Gluta* spp.) AND MENGKULANG (*Heritiera elata*) WOOD WITH RUTHENIUM DYE (N719) TO ENHANCE THE PERFORMANCE OF DYE-SENSITIZED SOLAR CELLS 95
(Ko-Pemekaan Pemeka Semulajadi Disari daripada Kayu Rengas (*Gluta* Spp.) dan Mengkulang (*Heritiera Elata*) dengan Pewarna Rutenium (N719) untuk Meningkatkan Prestasi Sel Solar Terpeka Pewarna)
Nur Ezyanie Safie, Norasikin Ahmad Ludin, Norul Hisham Hamid, Mohd Sukor Suait, Mohd Asri Mat-Teridi, Suhaila Sepeai, Mohd Adib Ibrahim, Kamaruzzaman Sopian, Hironori Arakawa

13. CLAMSHELL AND SEA SAND AS HETEROGENEOUS CATALYSTS FOR WASTE COOKING OIL BASED BIODIESEL PRODUCTION VIA TRANSESTERIFICATION REACTION 107
(Kulit Kerang dan Pasir Pantai Sebagai Mangkin Heterogen untuk Penghasilan Biodiesel Berasaskan Minyak Masak Sawit Terpakai Melalui Tindakbalas Transesterifikasi)
Arsyad Ismail Sanuzi, Syuhada Mohd Tahir, Siti Norhafiza Mohd Khazaai

14. REMOVAL OF CRYSTAL VIOLET AND ACID GREEN DYE IN AQUEOUS SOLUTION USING BANANA PLANT-DERIVED SORBENTS 115
(Penyingkiran Pewarna Crystal Violet Dan Acid Green Dalam Larutan Akues Menggunakan Penjerap Berasaskan Pokok Pisang)
Siti Kartina Abdul Karim, Soh-Fong Lim, David Chua, Shanti Faridah Salleh, Puong Ling Law

15. PHYTOCHEMICAL AND ANTIMICROBIAL EVALUATION OF *Pithecellobium jiringa* STEM BARKS 123

EXTRACTS
(Penyaringan Fitokimia dan Antimikrob ke atas Ekstrak Kulit Kayu Batang *Pithecellobium jiringa*)
Zurhana Mat Hussin, Nurul Anasuhah Osman, Aiza Harun, Shaari Daud

16. SEPARATION OF Pb(II) FROM WASTEWATER USING UNTREATED COCONUT (*Cocos nucifera*) FROND POWDER 128
(Pengasingan Pb(II) daripada Air Buangan Menggunakan Serbuk Pelepah Kelapa (*Cocos nucifera*) yang Tidak Dirawat)
Nur Fatin Adlina Mohd Fouzi, Mardhiah Ismail, Zurhana Mat Hussin, Sarah Laila Mohd Jan

17. DESALINATION OF SEAWATER USING NEWLY FABRICATED NANOFILTRATION FLAT SHEET MEMBRANE 136
(Penyahgaraman Air Laut Menggunakan Rekaan Baru Membran Kepingan Rata Penapisan Nano)
Wan Syarizawani Wan Chik, Mohd Johan Mohamed Ibrahim, Ramlah Mohd Tajuddin

18. INFLUENCE OF ALKALI TREATMENT ON PHYSICO-CHEMICAL PROPERTIES OF MALAYSIAN BAMBOO FIBER: A PRELIMINARY STUDY 143
(Pengaruh Rawatan Alkali terhadap Sifat-sifat Fizikal-Kimia Serat Buluh Malaysia: Satu Kajian Awal)
Foo Sheng Tong, Siew Choo Chin, Mohd Tamizi Mustafa, Huei Ruey Ong, Md. Maksudur Rahman Khan, Jolius Gimbun, Shu Ing Doh

19. STUDIES ON PHYTOCHEMICAL CONSTITUENTS AND ANTIMICROBIAL PROPERTIES OF *Citrullus lanatus* PEELS 151
(Kajian Jujukan Fitokimia dan Antimikrob Kulit *Citrullus lanatus*)
Siti Suhaila Harith, Muhd Harith Mazlun, Marlina Mohd Mydin, Liliwirianis Nawi, Rohaiza Saat

20. TRANSESTERIFICATION OF WASTE COOKING OIL IN BIODIESEL PRODUCTION UTILIZING CaO/Al_2O_3 HETEROGENEOUS CATALYST 157
(Transesterifikasi Sisa Minyak Masak dalam Pengeluaran Biodiesel Menggunakan CaO/Al_2O_3 Mangkin Heterogenus)
Norshahidatul Akmar Mohd Shohaimi and Fatin Nur Syahirah Marodzi

Malaysian Journal of Analytical Sciences, Vol 22 No 1 (2018): 1 - 7
DOI: https://doi.org/10.17576/mjas-2018-2201-01

MALAYSIAN JOURNAL OF ANALYTICAL SCIENCES
Published by The Malaysian Analytical Sciences Society
ISSN 1394 - 2506

SIMPLE μ-SOLID PHASE EXTRACTION USING C_{18} FILM FOR THE EXTRACTION OF POLYCYCLIC AROMATIC HYDROCARBONS IN COFFEE BEVERAGE

(Pengekstrakan μ-Fasa Pepejal yang Mudah Menggunakan Filem C_{18} untuk Pengekstrakan Hidrokarbon Aromatik Polisiklik dalam Minuman Kopi)

Saw Hong Loh[1]*, Pei Ee Neoh[1], Chee Tung Tai[1], Sazlinda Kamaruzaman[2]

[1]*School of Marine and Environmental Sciences,*
Universiti Malaysia Terengganu, 21030 Kuala Nerus, Terengganu, Malaysia
[2]*Department of Chemistry, Faculty of Science,*
Universiti Putra Malaysia, 43400 Serdang, Selangor, Malaysia

**Corresponding author: lohsh@umt.edu.my*

Received: 6 July 2017; Accepted: 15 August 2017

Abstract

Polycyclic aromatic hydrocarbons (PAHs) are produced as by-products in the coffee roasting process. A simple and efficient micro-solid phase extraction (μ-SPE) procedure coupled with high performance liquid chromatography and fluorescence detection has been developed for the simultaneous analysis of selected PAHs, namely phenanthrene (PHE) and benzo[a]pyrene (BaP) in coffee beverage. The method offered trace detection limits in the range of 0.003 to 0.1 μg/L and good relative recovery average in the range of 88.3 to 95.7%. The μ-SPE procedure has been simplified by employing C_{18} film as an adsorbent. The method is beneficial in terms of rapidity, simple operation, in-expensive, consumption of micro volumes of solvent and biodegradable agarose film as the adsorbent holder. The method was then applied to analyse five coffee beverage samples and the results indicated the presence of BaP in the range of 1.0 to 1.9 μg/L.

Keywords: agarose, polycyclic aromatic hydrocarbons, coffee, C_{18}, micro-solid phase extraction

Abstrak

Hidrokarbon aromatik polisiklik (PAHs) dihasilkan sebagai produk sampingan dalam proses memanggang kopi. Suatu prosedur pengekstrakan mikro-fasa pepejal (μ-SPE) yang mudah dan cekap bergabung dengan kromatografi cecair berprestasi tinggi dan pengesanan pendarfluor telah dibangunkan untuk analisis serentak PAHs terpilih, iaitu fenanterena (PHE) dan benzo[a]pirena (BaP) dalam minuman kopi. Kaedah ini menawarkan had pengesanan surih dalam julat 0.003 hingga 0.1 μg/L dan purata perolehan semula relatif yang baik dalam julat 88.3 hingga 95.7%. Prosedur μ-SPE ini telah diringkaskan dengan menggunakan filem C_{18} sebagai penjerap. Kaedah ini berfaedah daripada aspek ianya cepat, beroperasi mudah, tidak mahal, penggunaan isipadu pelarut yang mikro dan filem agarosa yang terdegradasi-bio sebagai pemegang penjerap. Kaedah ini kemudian diaplikasikan untuk menganalisa lima sampel minuman kopi dan keputusan menunjukkan kehadiran BaP dalam julat 1.0 hingga 1.9 μg/L.

Kata kunci: agarosa, hidrokarbon aromatik polisiklik, kopi, C_{18}, pengekstrakan mikro-fasa pepejal

Introduction

Polycyclic aromatic hydrocarbons (PAHs) are classified as relatively persistent organic environmental contaminants. Several PAHs, including benzo[a]pyrene (BaP) are classified as carcinogen and mutagen [1]. Human

are usually exposed to PAHs via intake of food. Heat processing of food such as roasting, charcoal grilling and smoking are factors which cause the food contaminated with PAHs. PAHs are non-desirable by-products produced by incomplete combustion during the roasting step in coffee production [2]. The 1971 World Health Organisation International Standards has recommended a guideline for six representative PAH compounds namely fluoranthene, 3,4-benzfluoranthene, 11,12-benzfluoranthene, 3,4-benzpyrene, 1,12-benzpyrene and indeno[1,2,3-cd]pyrene as not exceeding 0.0002 mg L^{-1} in drinking water [3]. To the best of our knowledge, there is no specific maximum residue guideline established for beverage.

Classic techniques such as liquid-liquid extraction (LLE) and solid phase extraction (SPE) are frequently used to extract PAHs in various matrices [4-7]. However, these techniques are not eco-friendly as they applied large amounts of organic solvent during extraction. Therefore, micro-scale sample preparation techniques that work towards green chemistry are developed.

Membrane-assisted solvent extraction (MASE) required shorter extraction time (30 min) as compared to stir bar sorptive extraction (SBSE) (3 hours) for the analysis of pesticide and BaP residues in Brazilian sugarcane juice. MASE offered a faster and better analyte recovery technique whereas SBSE has greater sensitivity, repeatability and required lower amounts of sample [8]. Dispersive liquid-liquid microextraction (DLLME) is simple, sensitive and rapid for the extraction and pre-concentration of PAHs from beverage samples because it applies dispersive concept throughout the extraction [9]. Magnetic solid phase extraction simplified the collection of adsorbent disperse in the sample solution and offered ultra-trace analysis of PAHs in both coffee and tea samples [10]. Ishizaki and co-researchers demonstrated online in-tube solid phase microextraction (SPME) that was simple, selective, sensitive and rapid to extract PAHs from food samples [11]. These techniques minimize solvent usage and has gained significant attention.

This study employs agarose as adsorbent holder, which is made up of natural polymer extracted from seaweed. It is a toxic-free and inert material. The proposed approach in this study displays a double "green chemistry" nature due to its micro-extraction format and the biodegradability of the adsorbent holder.

Materials and Methods

Chemicals and materials

Phenanthrene (PHE) and benzo[a]pyrene (BaP) were purchased from Sigma-Aldrich (Missouri, United States). HPLC grade isopropyl alcohol, methanol and acetonitrile were obtained from Merck (New Jersey, United States). Agarose and C_{18} adsorbent were purchased from Sigma-Aldrich (Missouri, United States).

Preparation of standards and samples

Standard stock solutions of PHE and BaP (500 mg/L) were prepared individually by weighing 0.005 g of each analyte in 10 mL of volumetric flask and diluted to volume with acetonitrile, respectively. A series of working mixture standard solutions were prepared by diluting the stock solutions with methanol. The solutions were stored at 0 ˚C in refrigerator when not in use.

Coffee beverage samples were obtained from selected local enterprise shops. Samples selections were more preferred with different brands. Samples were extracted using optimized micro-solid phase extraction (μ-SPE) technique without pre-treatment.

Preparation of C_{18} film

C_{18} (0.1 g) was dispersed and sonicated in 5 mL of ethanol. The C_{18} solution (1 mL) was pipetted into a petri dish (5 cm diameter). Agarose (0.1 g) was added into 10 mL of deionized water and the solution was heated to boil. The resulting hot agarose solution (3.5 mL) was pipetted into the petri dish containing the C_{18} solution. The mixture was allowed to cool and form a C_{18}-impregnated agarose gel. The gel was dried at room temperature for 2 days to form a C_{18} film. The film was cut into a small piece of square sheet (1.5 cm x 1.5 cm) to function as an adsorbent film.

Micro-solid phase extraction procedure

The C_{18} film was dipped into methanol for 2 minutes and followed by deionized water for 30 s to activate and condition the C_{18}, respectively. Sample solution (15 mL) was pipetted into a 25-mL sample vial and the C_{18} film was tumbled into the sample solution for extraction. The sample vial was capped and sonicated for 10 minutes. After sonication, the film was withdrawn and added into a safe-lock screw vial containing 100 µL of acetonitrile. The desorption of target analytes from the C_{18} film was performed by sonicating the screw vial for 10 minutes. The acetonitrile extract was then filtered through 0.2 µm nylon syringe filter prior to quantification using high performance liquid chromatography coupled with fluorescence detection (HPLC-FD). Figure 1 shows the schematic diagram of the proposed µ-SPE.

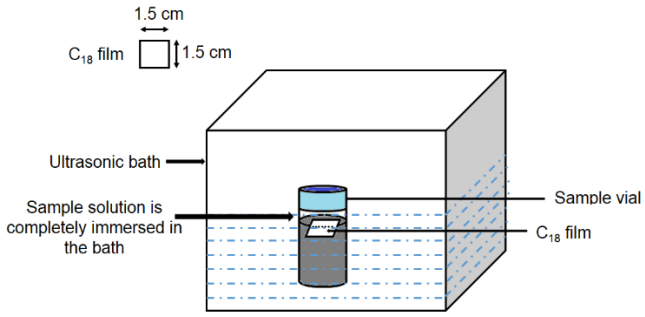


Figure 1. Schematic diagram of µ-SPE

Chromatographic conditions

Analytes quantification was performed using high performance liquid chromatography (Shimadzu, Kyoto, Japan) coupled with fluorescence detection (Shimadzu, Kyoto, Japan). The chromatographic separation of polycyclic aromatic hydrocarbons (PAHs) was carried out on a reversed phase Platinum EPS C_{18} column (4.6 × 250 mm, 5 µm). The separation was performed using isocratic mobile phase acetonitrile-water (80:20) (v/v) at column temperature of 30 ˚C. The flow rate, injection volume and detection wavelengths were fixed at 1.0 mL/min, 10 µL and 250/400 nm of excitation/emission wavelengths, respectively.

Optimization and validation of micro-solid phase extraction

In this study, several extraction parameters were thoroughly investigated to enhance the analytes enrichment. Sample volume, extraction time, types of desorption solvents, desorption time and volume of desorption solvent were optimized before the application of the proposed method for the analysis of coffee beverage samples. Minimal validation was carried out to assess the viability of method and these included linearity, repeatability, relative recovery, limit of detection (LOD) and limit of quantification (LOQ), which were determined based on signal to noise 3:1 and 10:1, respectively.

Results and Discussion

Optimization of micro-solid phase extraction

Five parameters which influenced the extraction efficiency of micro-solid phase extraction (µ-SPE) were optimized and these included sample volume, extraction time, type of desorption solvent, desorption time and desorption solvent volume. Optimization was carried out using deionized water sample spiked with 10 µg/L each of phenanthrene (PHE) and benzo[a]pyrene (BaP), respectively. Triplicate extractions were carried out for each parameter optimized in this study.

Sample volume

Sample volume was examined as it influenced the adsorption capacity of the C_{18} film. Sample volume in the range of 10 to 20 mL was studied. Figure 2a shows that the C_{18} film adsorbed lesser PAHs when smaller sample volume

(10 mL) was extracted. The amount of analytes extracted increased as the sample volume increased and reached optimum at 15 mL and the extraction efficiency did not increase significantly with further increase in sample volume. This was due to the C_{18} film was saturated with the PAHs and further increase in sample volume would not result in the increment of the peak areas [12]. Therefore, 15 mL sample solution was applied for next parameter study.

Extraction time

Extraction time ranging from 5 to 15 minutes was examined to identify the equilibrium time required for the analytes to adsorb onto C_{18} film. PAHs are hydrophobic compound. The octanol-water partition coefficient (K_{ow}) increases from PHE to BaP with the increasing of their molecular weight. The hydrophobic PAHs required some time to diffuse through the static layer of water to be adsorbed onto the C_{18} film [13]. The extraction efficiency increased gradually when the extraction time increased as indicated in Figure 2b. Extraction time of 10 minutes was chosen over 15 minutes even though the extraction efficiency showed an increase at 15 minutes. Both PHE and BaP increased for 10.9 and 8.4%, respectively. However, the increment was not significant according to ANOVA-Tukey test, $P > 0.05$. Therefore 10 minutes extraction time was chosen for the subsequent study as it was sufficient to obtain a better extraction efficiency and save time for the extraction process.

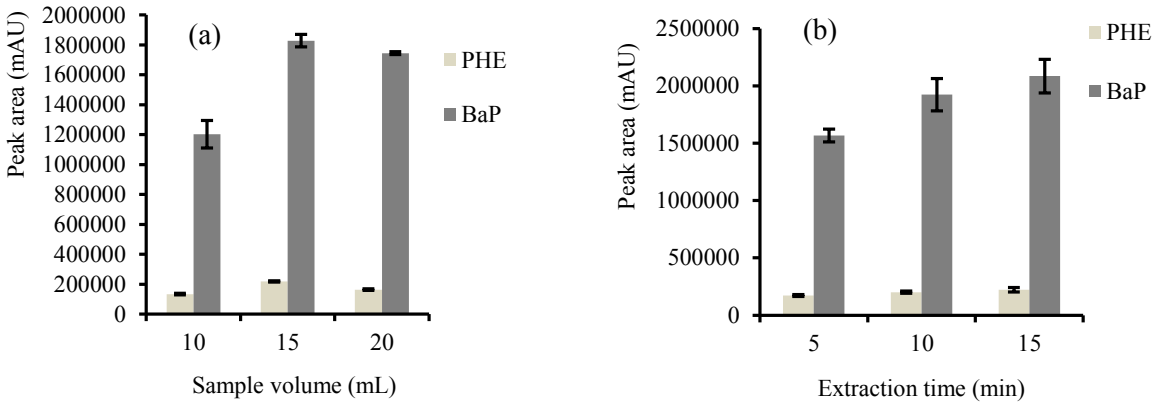


Figure 2. Effect of sample volume (a) and extraction time (b) on the μ-SPE for the extraction of PHE and BaP in the spiked deionized water samples

Type of desorption solvent

Desorption solvent was used to desorb the PAHs from the C_{18} film. The desorption solvents investigated were acetonitrile (ACN), methanol (MEOH) and isopropanol (IPA). PAHs are lipophilic and non-polar compounds, thus it will adsorb strongly on C_{18} film. Therefore, a stronger solvent which is relatively non-polar is required to desorb the PAHs from the film. Among the solvents, the elution strength of IPA is the strongest, it was then followed by ACN and MEOH. The results showed that ACN was a better choice as a desorption solvent for PHE, a PAH with lower molecular weight, as compared with MEOH and IPA. On the other hand, the IPA showed greater affinity to the BaP, a PAH with higher molecular weight. The desorption was less efficient when MEOH was applied. The desorption strengths of both ACN and IPA were comparable and no significant different. The ACN was chosen in subsequent studies as it was also applied as the mobile phase.

Desorption Time

Desorption time in the range of 5 to 15 minutes was investigated. Figure 3a shows the peak area of PHE increased as the desorption time increased and became stagnant at 10 minutes. However, the peak area of BaP was the highest at 5 minutes and decreased gradually when the desorption time was extended. Prolonged desorption time might lead to re-adsorption of the BaP onto the C_{18} film and caused the drop in peak area [14]. The desorption time at 10

minutes was chosen because greater peak area for PHE (increased 30%) was obtained while extraction efficiency for BaP decreased only slightly (declined for 20%).

Volume of desorption solvent

A range of 100 µL to 200 µL of acetonitrile was investigated in this study. Figure 3b indicates that when a lower volume of desorption solvent was used, the greater the peak areas. This is due to the lower volume enhanced the analyte enrichment [15]. In addition, the amount of solvent used should be as minimal as possible in order to obtain a greater sensitivity and the volume of the solvent must be sufficient to completely immerse the entire film [16]. A volume of 100 µL desorption solvent was chosen because it gave higher extraction efficiency for all of the analytes.

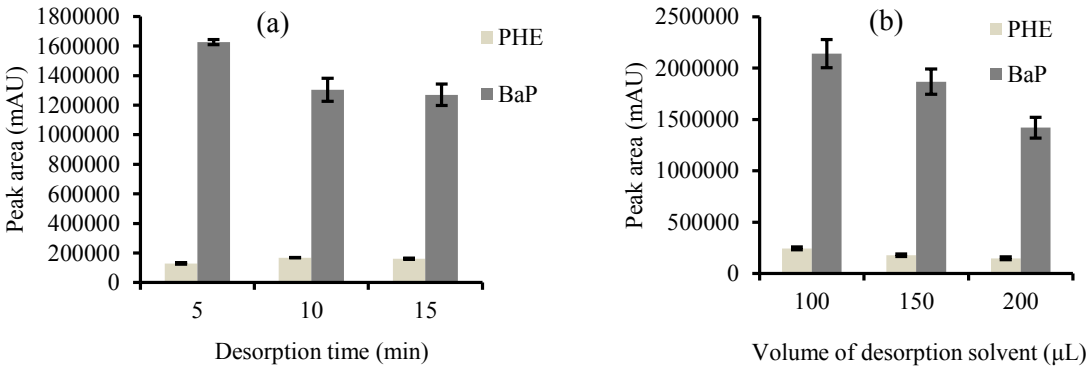


Figure 3. Effect of desorption time (a) and volume of desorption solvent (b) on the µ-SPE for the extraction of PHE and BaP in the spiked deionized water samples

Validation of micro-solid phase extraction

Linearity of an analytical procedure is its ability (within a given range) to obtain test results that are directly proportional to the concentration (amount) of analyte in the sample [17]. Relative calibration for the two analytes of interest, namely PHE and BaP were performed because µ-SPE technique is a non-exhaustive extraction. Five deionized water samples spiked in a specified range were extracted and quantitated using optimized µ-SPE-HPLC-FD. The results indicated that a good linearity was obtained for both PHE and BaP in the range of 5 to 200 µg/L and 1 to 25 µg/L, respectively with correlation of coefficients, $r \geq 0.996$.

Limit of detection (LOD) is defined as the lowest amount of analyte in the sample which can be detected but not necessarily quantitated under stated experimental conditions. Whereas limit of quantification (LOQ) is defined as the lowest amount of analyte in a sample which can be quantitatively determined with suitable precision and accuracy [18]. LOD and LOQ can be determined by visual inspection, signal-to-noise ratio or the standard deviation of the response and the slope [19]. In this study, a signal-to-noise ratio of 3:1 and 10:1 were used to establish the LOD and LOQ, respectively. The results showed that the proposed µ-SPE-HPLC-FD was able to offer LODs in the range of 0.003 to 0.1 µg/L and LOQs in the range of 0.01 to 0.4 µg/L. This revealed that µ-SPE-HPLC-FD method using C_{18} film as the adsorbent film was sensitive to analyse the ultra-trace PAHs in coffee beverage samples.

Relative recovery study was performed by spiking the coffee beverage samples to give a final concentration of 30 µg/L of PHE and 25 µg/L of BaP. Table 1 shows that the µ-SPE was capable to recover PAHs from the spiked coffee beverage samples with relative recovery average ranging from 88.3 to 95.7% coupled with good repeatability with relative standard deviations (RSDs) of ≤ 7.6%. This revealed that matrix effect was not significant and thus the µ-SPE combined with C_{18} film can be employed in the analysis of PAHs residues in the coffee beverage samples.

Table 1. Validation data of the μ-SPE-HPLC-FD for the determination of PAHs in coffee beverage samples

PAH	Linearity range, μg/L	r	LOD, μg/L	LOQ, μg/L	Average relative recovery ± RSD, % (n=3)
PHE	5-200	0.9961	0.1	0.4	88.3±7.6
BaP	1-25	0.9985	0.003	0.01	95.7±0.8

Analysis of selected PAHs in coffee beverage samples

The optimized and validated μ-SPE technique was applied to extract the PAHs from five coffee beverage samples that were obtained from retail shops. The results show that BaP was detected in four out of five coffee beverage samples. The BaP concentration was detected in the range of 1.0 to 1.9 μg/L while PHE was not detected. Currently, there is no regulation that set a maximum limit for BaP level in coffee beverage.

Conclusion

The micro-solid phase extraction using C_{18} film as the adsorbent is a sensitive, simple and green technique. The agarose used is a biodegradable material that makes it environmental friendly coupled with the reduction in the consumption of solvent due its micro-scale format. This technique fulfils the green chemistry concept that is widely approached these days. The technique shall then be applied for the extraction of 16 PAHs to examine the competition among the PAHs for the minute amounts of adsorption sites.

Acknowledgement

The authors would like to thank Universiti Malaysia Terengganu and Ministry of Higher Education Malaysia for the financial supports through research grants with vote number: 68006/INSENTIF/57 and 59367, respectively.

References

1. Public Health England. (2008). Polycyclic aromatic hydrocarbons (benzo[a]pyrene). General information https://www.gov.uk/government/uploads/system/uploads/attachment_data/file/341369/PAHs_General_Information_phe_v1.pdf [Accessed online on 5 July 2017].
2. Oosterveld, A., Voragen, A. G. J. and Schols, H. A. (2003). Effect of roasting on the carbohydrate composition of Coffea arabica beans. *Carbohydrates Polymers,* 54: 83-192.
3. World Health Organization. (2003). Polynuclear aromatic hydrocarbons in drinking-water. Background document for preparation of WHO Guidelines for drinking-water quality.Geneva, World Health Organization (WHO/SDE/WSH/03.04/59). http://www.who.int/water_sanitation_health/dwq/chemicals/pahsum.pdf [Accessed online on 5 July 2017].
4. Lin, D., Tu, Y. and Zhu, L. (2005). Concentrations and health risk of polycyclic aromatic hydrocarbons in tea. *Food and Chemical Toxicology,* 43(1): 41-48.
5. Kayali-Sayadi, M. N., Rubio-Barroso, S., Cuesta-Jimenez, M. P. and Polo-Díez, L. M. (1998). Rapid determination of polycyclic aromatic hydrocarbons in tea infusion samples by high-performance liquid chromatography and fluorimetric detection based on solid-phase extraction. *Analyst,* 123: 2145-2148.
6. Bishnoi, N. R., Mehta, U., Sain, U. and Pandit, G. G. (2005). Quantification of polycyclic aromatic hydrocarbons in coffee and tea samples of Mumbai city (India) by high performance liquid chromatography. *Environmental Monitoring and Assessment,* 107: 399-406.
7. Luo, D., Yu, Q., Yin, H. and Feng, Y. (2007). Humic acid-bonded silica as a novel sorbent for solid-phase extraction of benzo[a]pyrene in edible oils. *Analytica Chimica Acta,* 588(2): 261-267.
8. Zuin, V. G., Schellin, M., Montero, L., Yariwake, J. H., Augusto, F. and Popp, P. (2006). Comparison of stir bar sorptive extraction and membrane assisted solvent extraction as enrichment techniques for the determination of pesticide and benzo[a]pyrene residues in Brazilian sugarcane juice. *Journal of Chromatography A,* 1114(2): 180-187.
9. Loh, S. H., Chong, Y. T., Nor Afindi, K. N. and Kamaruddin, N. A. (2016). Determination of polycyclic aromatic hydrocarbons in beverage by low density solvent based-dispersive liquid-liquid microextraction-high performance liquid chromatography-fluorescence detection. *Sains Malaysiana*, 45(10): 1453-1459.

10. Shi, Y., Wu, H., Wang, C., Guo, X., Du, J. and Du, L. (2016). Determination of polycyclic aromatic hydrocarbons in coffee and tea samples by magnetic solid-phase extraction coupled with HPLC–FLD. *Food Chemistry*, 199: 75-80.
11. Ishizaki, A., Saito, K., Hanioka, N., Narimatsu, S. and Kataoka, H. (2010). Determination of polycyclic aromatic hydrocarbons in food samples by automated on-line in-tube solid-phase microextraction coupled with high-performance liquid chromatography-fluorescence detection. *Journal of Chromatography A*, 1217(35): 5555-5563.
12. Loh, S. H., Sanagi, M. M., Wan Ibrahim, W. A. and Hasan, M. N. (2013). Multi-walled carbon nanotube-impregnated agarose film microextraction of polycyclic aromatic hydrocarbons in green tea beverage. *Talanta*, 106: 200-205.
13. Risticevic, S., Lord, H., Górecki, T., Arthur, C. L. and Pawliszyn, J. (2010). Protocol for solid phase microextraction method development. *Nature Protocols,* 5(1): 122-139.
14. Ge, D. and Lee, H. K. (2001). Water stability of zeolite imidazolate framework 8 and application to porous membrane-protected micro-solid-phase extraction of polycyclic aromatic hydrocarbons from environmental water samples. *Journal of Chromatography A*, 1218(47): 8490-8495.
15. Barcelo, D. (2000). Sample handling and trace analysis of pollutants: Techniques, applications and quality assurance. Elsevier, Amsterdam: pp. 26.
16. Pawliszyn, J. (2012). Handbook of solid phase microextraction. Elsevier, London: pp. 156.
17. Ahuja, S and Rasmussen, H. (2007). HPLC method development for pharmaceuticals. Elsevier, USA: pp. 448.
18. Shrivastava, A. and Gupta, V. B. (2011). Methods for the determination of limit of detection and limit of quantitation of the analytical methods. *Chronicles of Young Scientists,* 2(1): 21-25.
19. Krause, S. O. (2003). Good analytical method validation practice deriving acceptance criteria for the AMV protocol: Part II. *Journal of Validation Technology,* 9(2): 162-178.

Malaysian Journal of Analytical Sciences, Vol 22 No 1 (2018): 8 - 16
DOI: https://doi.org/10.17576/mjas-2018-2201-02

MALAYSIAN JOURNAL OF ANALYTICAL SCIENCES
Published by The Malaysian Analytical Sciences Society
ISSN 1394 - 2506

CATALYTIC CRACKING OF USED VEGETABLE OIL TO GREEN FUEL WITH METAL FUNCTIONALIZED ZSM-5 CATALYSTS

(Pemecahan Bermangkin Minyak Sayur Terpakai kepada Bahan Api Hijau dengan Pemangkin ZSM-5 Berfungsi Logam)

Mohamed Azeem Abdul Majed and Ching Thian Tye*

School of Chemical Engineering, Engineering Campus
Universiti Sains Malaysia, 14300 Nibong Tebal, Penang, Malaysia

**Corresponding author: chcttye@usm.my*

Received: 6 September 2017; Accepted: 8 January 2018

Abstract

Depletion of fossil fuel reserves and environmental issue have led to the development of biofuels. Plant derived oil, such as palm oil, has been claimed as one of the promising source of renewable energy. However, high oxygen content in palm oil makes it unsuitable to be directly used as fuel. In the present study, the performance of Ni/ZSM-5, Mo/ZSM-5 and NiMo/ZSM-5 catalysts was investigated in catalytic cracking of used vegetable oil (UVO) into green fuel. The catalytic cracking reactions were carried out in a fixed bed reactor at 4 $hour^{-1}$(WHSV), continuously for 3 hours. Conversions of the two major fatty acids: palmitic acid (84.72%) and stearic acid (74.10%) were found highest at 350 °C with Mo/ZSM-5. The optimum palmitic acid and stearic acid conversion with Mo/ZSM-5 were found at 400 °C. Comparison study was also done with Pd/Al_2O_3 at 400 °C for its performance in catalytic cracking of UVO. Similar conversion for palmitic acid was obtained for Mo/ZSM-5 (84.72%) and Pd/Al_2O_3 (86.37%) at steady state. However, system with Mo/ZSM-5 as catalyst approached steady state earlier at 60 mins compared to that of Pd/Al_2O_3 at 120 minutes.

Keywords: catalytic cracking, used vegetable oil, green fuel, ZSM-5

Abstrak

Penurunan rizab bahan api fosil dan isu alam sekitar telah membawa kepada pembangunan bahan api bio. Minyak daripada tumbuhan, seperti minyak kelapa sawit telah dituntut sebagai salah satu sumber tenaga boleh diperbaharui yang menjanjikan. Namun, kandungan oksigen yang tinggi dalam minyak kelapa sawit menjadikannya tidak sesuai digunakan secara terus sebagai bahan bakar. Dalam kajian ini, prestasi pemangkin Ni/ZSM-5, Mo/ZSM-5 dan NiMo/ZSM-5 telah diuji dalam pemecahan bermangkin minyak sayuran terpakai (UVO) kepada bahan api hijau. Tindak balas pemecahan bermangkin tersebut adalah dijalankan dalam reaktor lapisan tetap pada 4 jam^{-1} (WHSV), secara berterusan selama 3 jam. Penukaran kedua-dua asid lemak utama: asid palmitik (84.72%) dan asid stearik (74.10%) didapati paling tinggi pada 350 °C dengan Mo/ZSM-5. Penukaran optimum asid palmitik dan asid stearik dengan Mo/ZSM-5 didapati pada 400 °C. Kajian perbandingan juga dilakukan dengan Pd/Al_2O_3 pada suhu 400 °C untuk prestasinya dalam pemecahan bermangkin UVO. Penukaran yang sama telah diperolehi untuk asid palmitik dengan Mo/ZSM-5 (84.72%) dan Pd/Al_2O_3 (86.37%) pada keadaan mantap. Namun begitu, sistem yang menggunakan Mo/ZSM-5 sebagai pemangkin mencecah keadaan mantap lebih awal pada 60 minit berbanding dengan Pd/Al_2O_3 pada 120 minit.

Kata kunci: pemecahan bermangkin, minyak sayuran terpakai, bahan api hijau, ZSM-5

Introduction

It is reported that biofuel leads to greenhouse gas reductions, on a well-to-wheel basis, of 40–60% when compared with conventional petroleum diesel [1]. In the USA alone, over 1.5 billion gallons of biofuel was produced from vegetable oils in year 2016 [2]. Meanwhile, global biodiesel production and consumption is forecast to rise by 14% from 2016 to 2020, driven by the fulfillment of current biofuel policies in the US, Argentina, Brazil, Indonesia and the EU. At the meantime, the biodiesel from waste-based production was forecast to grow to 4.4 billion liters [3].

Catalytic cracking is a process widely used in petroleum refining for converting heavy portion into lighter products. Catalytic cracking of vegetable oil into green fuel is favorable as it does not require additional infrastructure to be build [4]. The process can be carried out in the catalytic cracker in the conventional petroleum refinery. Further, green fuel derived from it has the similar chemical properties as the conventional petroleum fuel and can be used directly as the fossil derived fuel. This is attractive as compared to biofuel produced from transesterification of vegetable oil with ethanol or methanol that being converted to fatty acid methyl ester (FAME). Unlike green diesel, biodiesel can only be used in diesel engines blended (<20%) with diesel in order to avoid excessive buildup of carbon in diesel engines. Another major issue with the biodiesel is the tendency to freeze at low temperature, which makes it not suitable to be used in winter or other cold period of the year [5]. Therefore, production of green fuel from catalytic cracking is getting more attention. Zeolite is one of the most common catalysts used in catalytic cracking reaction [6, 7, 8]. Its tunable acid-basic properties, easy modification by ion exchange and molecular sieving properties make it widely favorable [8].

There are a few common types of zeolites, such as ZSM-5, β zeolite, γ zeolite, Mordenite, silico alumino phosphate and several mesoporous materials, were studied in converting vegetable oil into biofuels [9, 10]. Several studies reported catalytic cracking of pure vegetable oils, like cottonseed [11], sunflower [12] and palm oils [10, 13] with the yields of gasoline being about 30% in all the cases. Some reported catalytic cracking of mixture of 5-10% vegetable oil with vacuum gas oil [4, 12]. Most studies were carried out with commercial zeolite catalyst. Snåre et al. [14] studied a series of metals of high selectivity performance: palladium (Pd), platinum (Pt), nickel (Ni), ruthenium (Ru), rhodium (Rh) and Osmium (Os) towards conversion or deoxygenation of stearic acid in vegetable oil. Pd and Pt metal catalyst was reported to give a promising performance [14-17]. Later, there were several studies on Pd base catalysts such as Pd/ZSM-5 [18] and Pd/SiO_2 [19] on cracking or deoxygenation in biofuel production and derivatives. Recently, TiO_2 has also been tested as potential catalyst for deoxygenation of triglyceride to hydrocarbon-like biofuel [20]. Although these noble metals gave promising performance, the price is very expensive. Catalyst with similar performance and lower price is essential for an economic process.

Nickel (Ni) and molybdenum (Mo) are transition metals of group 10 and group 6 elements in periodic table, respectively. These two transition metals were chosen in this study for zeolite functionalization. Ni was chosen due to its properties similar with other group 10 element such as Pd and Pt [21]. On the other hand, Mo is a transition metal which is commonly used as catalyst in various cracking and treating of petroleum products. The main objective of the present study is to study the performance of a series of metal functionalized zeolite in catalytic cracking of UVO in order to explore for a more efficient and cheaper catalyst.

Materials and Methods

Materials

The feedstock, waste cooking oil used in the reaction was collected from the Universiti Sains Malaysia's engineering campus cafeteria. For catalyst preparation, ammonium molybdate tetrahydrate, $(NH_4)_6Mo_7O_{24}.4H_2O$ (≥ 99%) and 5 wt% palladium on alumina, Pd/Al_2O_3 were from Aldrich. ZSM-5 zeolite (CV2314) was from Zeolyst International and nickel (II) nitrate, $Ni(NO_3)_2.6H_2O$ (99%) used was from Acros. Palmitic acid, as the model compound was from Merck.

Catalyst preparation

Zeolite based catalysts prepared in the present study were functionalized with different metals. Incipient wetness impregnation method was applied to load different type of metals at 5 wt% on ZSM-5 zeolite. Firstly, the desired amount of zeolite (95 wt%) and metal precursor (5 wt% metal equivalent), such as $Ni(NO_3)_2.6H_2O$ was dissolved in deionized water. Then, the mixture was stirred at room temperature for 8 hours to enhance the distribution of metal

precursor on ZSM-5. Next, the mixture was dried in the oven at 120°C for 16 hours. The dried material was then calcined at 550 °C for 2 hours in a furnace. The formed catalyst is termed Ni/ZSM-5. The procedure was repeated by replacing nickel precursor with $(NH_4)_6Mo_7O_{24}.4H_2O$ as molybdenum precursor at metal loading of 5 wt% to obtain Mo/ZSM-5 catalyst. Catalyst prepared after calcinations is in oxide form. In order to obtain ZSM-5 with reduced metal, a reduction step would be performed *in-situ* prior to the catalytic cracking reaction.

Catalyst characterization

The metal functionalized zeolites prepared were characterized by using *x*-ray diffraction (XRD), scanning electron microscopy (SEM) and energy dispersive *x*-ray (EDX) spectroscopy. XRD was carried out using a Philips *x*-ray diffractometer (generator: PW 1729, Goniometer: PW 1820, diffraction controller: PW 1710). The diffractometer was used with monochromatized Cu-K_α radiation at $\lambda = 0.15418$ nm and taken in the range of 10^o to 90^o (2θ). The *x*-ray tube was operated at 40kV and 120mA. SEM was carried out by using a Scanning Electron Microscope model Leo Supra 50 VP Field Emission. The SEM unit was equipped with an INCA 400 Energy Dispersive X-ray (EDX) microanalyser with an operating voltage in the range of 0.1kV to 30kV. The EDX analysis used Mn K_α as the energy source operated at 15kV of accelerating voltage, 155eV resolution with 22.4° take off angle.

Catalyst activity test

The catalytic cracking reactions of UVO were conducted in a fixed-bed reactor system with reactor outer diameter of ½ inch as shown in Figure 1. First, 1 g of catalyst was loaded on top of the flattened quartz wool. The reactor's temperature was raised to the desired reaction temperature in a tube furnace (Nabertherm B170). A mass flow controller (model M100B by MKS Instrument) was used to control the flow of hydrogen or nitrogen gas into the reactor. Prior to a reaction, whenever necessary, a catalyst reduction step was carried out by flowing through hydrogen ($100cm^3$(STP) min^{-1}) for 2 hours at 200°C with starting heating rate at 10 °C min^{-1}. Then, the reactor system was switched to 10 ml/min of N_2 flow. N_2 gas was used as the carrier gas in the reaction. The reactant, UVO in a volumetric flask with magnetic stirrer stirring continuously, was charged into the reactor from the top using a Series I high performance metering pump by Lab Alliance. The feed rate was set at 4 $hour^{-1}$ (weight hourly space velocity, WHSV). The reaction time was considered to start once the metering pump was started. The liquid product samples were collected from the bottom of the reactor via outlet tubing every half an hour interval continuously for 3 hrs.

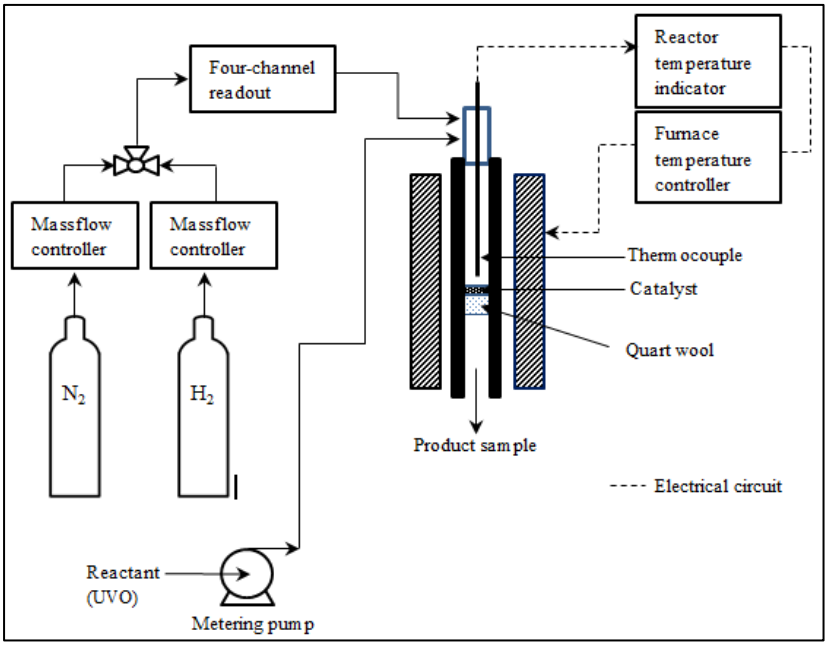


Figure 1. Schematic diagram of fixed bed reactor system

Product analysis

Possible components of liquid products were identified by gas chromatograph-mass spectrometer (GC-MS). The liquid products were analyzed by using gas chromatography (GC-FID) equipped with a flame ionization detector (FID) and a NUKOL column with dimension of 15m x 0.53mm x 0.5 µm. The gas chromatography oven temperature program was set at: initial oven temperature at 110 °C and hold it for 0.5 minutes, heating from 110 °C to 220 °C at 10 °C/min and finally hold 220 °C for 10 minutes.

Results and Discussion

Catalyst characterization

ZSM-5 used was the aluminosilicate zeolite with SiO_2/Al_2O_3 mole ratio of 23 and Na_2O of 0.05 wt%. It has large surface area of 425 m^2/g. Elements such as Al, C, O, Si, and Na are present in ZSM-5 [22]. However, EDX spectroscopy did not detect Al and Na. According to Danilina et al. [23], aluminum in ZSM-5 crystallized structure was preferentially located in the rim, while silicon and oxygen were well distributed. Because of its limited penetration, EDX could have failed to detect the enrichment.

Anyhow, the EDX Spectroscopy does show that the metal has successfully loaded onto the zeolite. EDX results are shown in Figure 2. If any foreign element or impurity presents in the catalyst, it can be identified. EDX showed there is no impurity in all three tested catalysts.

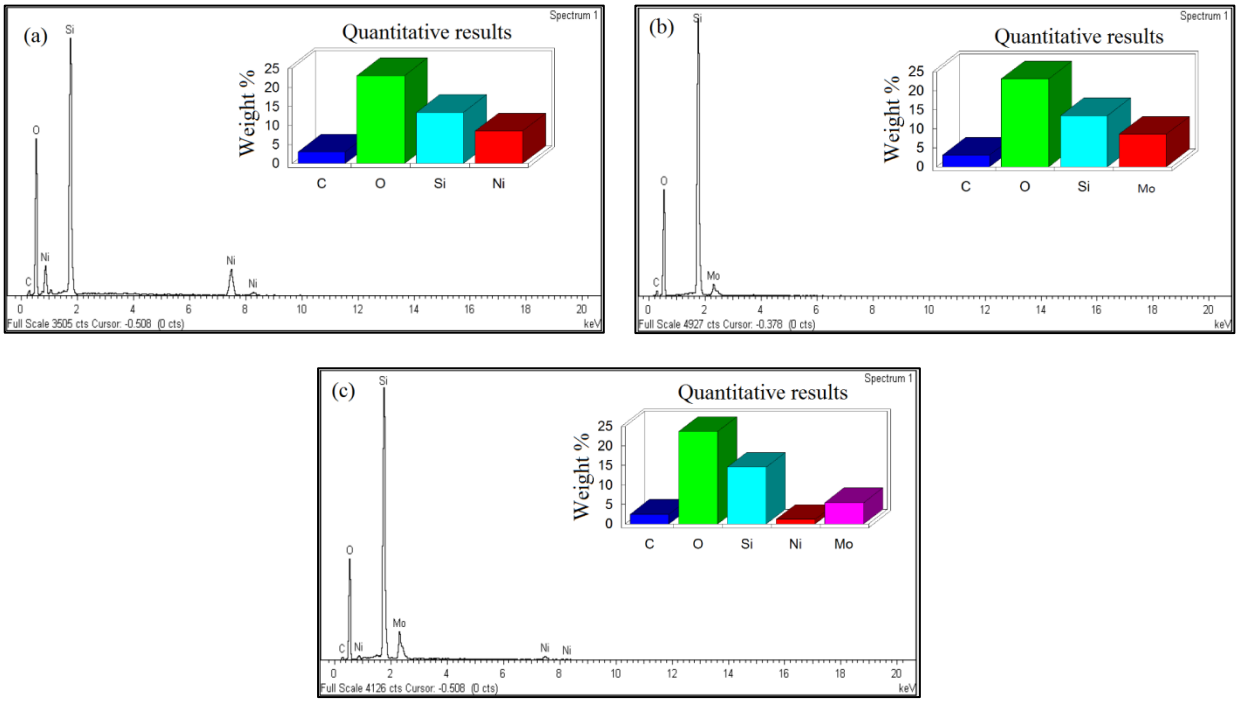


Figure 2. EDX Spectroscopy of (a) Ni/ZSM-5, (b) Mo/ZSM-5 and (c) NiMo/ZSM-5

The SEM images of Ni/ZSM-5, Mo/ZSM-5 and NiMo/ZSM-5 at magnification of 10 000x are shown in Figure 3. The figure shows that all three catalysts are porous with well-formed particle of sphere-like-structure. These porous structure make the material possessed a large surface area. However, the particles are non-uniform due to different metals were impregnated on ZSM-5.

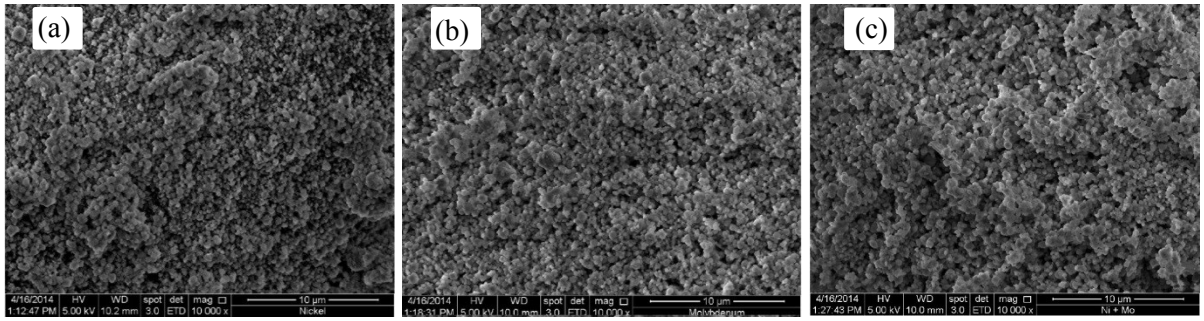


Figure 3. SEM images of (a) Ni/ZSM-5, (b) Mo/ZSM-5, (c) NiMo/ZSM-5 at magnification of 10000x

From XRD analysis (XRD spectra not shown), nickel and molybdenum oxides as expected were formed. Oxide formed on Ni/ZSM-5 was identified as monoclinic nickel oxide, NiO, while crystalline structure of orthorhombic molybdenum trioxide, MoO_3 was formed on Mo/ZSM-5. For NiMo/ZSM-5, in addition to nickel oxide and molybdenum trioxide, crystalline monoclinic nickel molybdenum oxide, $NiMoO_4$ had also been identified.

Different metal functionalized ZSM-5 catalyst in catalytic cracking of UVO

In the current study, two major types of fatty acids, namely palmitic acid, $C_{16}H_{32}O_2$ (86.9%) and stearic acid, $C_{18}H_{36}O_2$ (13.1%), were identified from the UVO composition. This is different from the other studies using palm oil as feedstock, where significant oleic acid (40-53%) and linoleic acid (6-14%) were found [24, 25]. This could be due to the different compositions of the fresh cooking oil used, the different cooking conditions and the food cooked.

From previous study by Chiam and Tye [26], a significant amount of alkane and alkene had been found in the liquid product after a non-catalytic thermal reaction of the UVO. It can tell that cracking and deoxygenation of fatty acids to alkane and alkene occurred during the reaction at high temperature (>300 ^oC). Therefore, it can be deduced that higher conversion of fatty acid leads to higher production of lighter oil in the system. Due to the complex mixture of different types of cracking fatty acid products formed in the liquid such as decanoic acid ($C_{10}H_{20}O_{2)}$, lauric acid, ($C_{12}H_{24}O_2$), tetradecanoic acid ($C_{14}H_{28}O_2$), oleic acid ($C_{18}H_{34}O_2$) etc. in the present study, the catalyst cracking activities were compared in terms of the conversion of palmitic acid and stearic acid.

ZSM-5 and ZSM-5 functionalized with different reduced metals: Ni, Mo and NiMo were tested for their catalytic cracking activities of UVO. As shown in Figure 4(a), generally the conversion of palmitic acid reached steady state after 60 minutes of the catalytic cracking reaction of UVO except for the reaction using pure ZSM-5 zeolite as catalyst. The conversion of the palmitic acid for different catalyst used is in increasing order of ZSM-5 (50.66%) < Ni/ZSM-5 (60.84%) < NiMo/ZSM-5 (76.75%) < Mo/ZSM-5 (84.72%) after 150 minutes. Similar trend was observed for conversion of stearic acid: ZSM-5 (48.02%) < Ni/ZSM-5 (60.43%) < NiMo/ZSM-5 (67.01%) < Mo/ZSM-5 (74.10%). This clearly shows that the Mo/ZSM-5 gives the highest conversion of both palmitic acid and stearic acid in catalytic cracking of UVO.

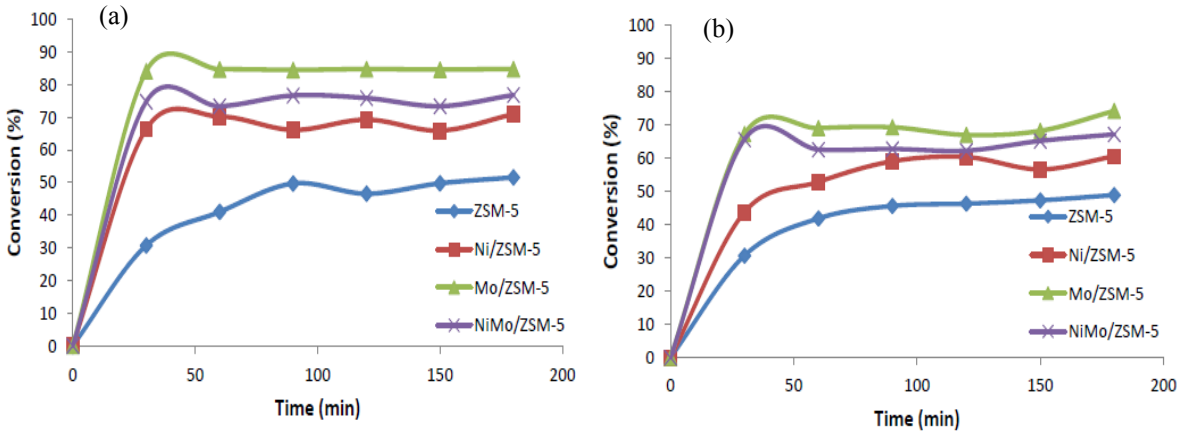


Figure 4. Conversion profiles of UVO with respect to (a) palmitic acid, and (b) stearic acid with different catalyst (Temperature = 350 °C, UVO feed WHSV = 4 hour^{-1})

Effect of oxidation state of Metal/ZSM-5 catalyst for catalytic cracking of UVO

Since Mo/ZSM-5 catalyst towards catalytic cracking reactions of UVO was found to be the best performing catalyst in the present study, Mo/ZSM-5 was then tested with different oxidation states: oxide state and reduced state to study the influence of oxidation state of the metal on zeolite catalyst in catalytic cracking reactions of UVO. The conversion of both palmitic acid and stearic acid over reduced state (Mo/ZSM-5) and oxide phase (MoO_x/ZSM-5) catalyst was shown in Figure 5.

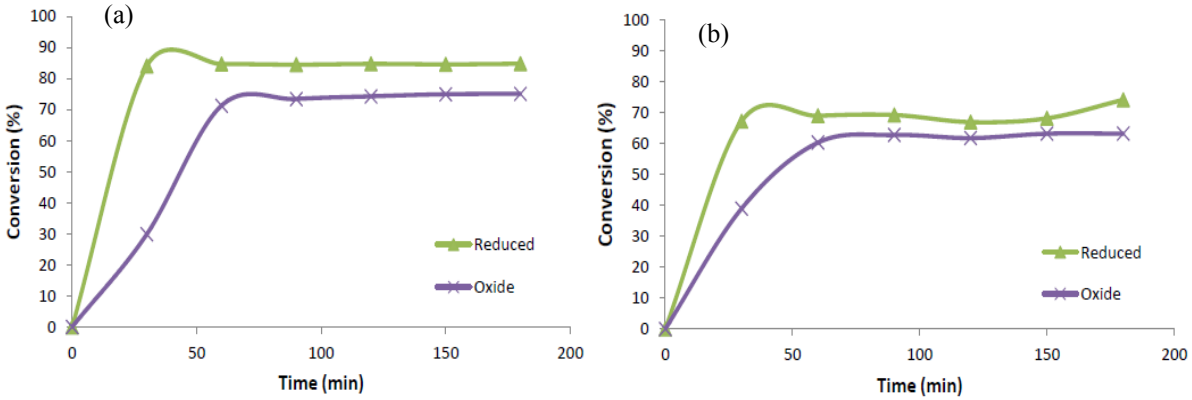


Figure 5. Conversion profiles of UVO with respect to (a) palmitic acid, (b) stearic acid with reduced Mo/ZSM-5 and oxide Mo/ZSM-5 catalyst (Temperature = 350 °C, UVO feed WHSV = 4 hour^{-1})

From the conversion profile in Figure 5, it was shown that the steady state of the catalytic cracking reaction of UVO was achieved around 90 minutes. It is clear that the conversion profile of reduced molybdenum is better compared to that of the molybdenum oxide. The highest conversion found for reduced Mo/ZSM-5 catalyst was 84.72% for palmitic acid and 74.10% for stearic acid. The highest conversion obtained for oxide Mo/ZSM-5 was 75.00% for palmitic acid and 63.18% for stearic acid. The catalytic cracking reaction of reduced Mo/ZSM-5 gave better results compared to oxide Mo/ZSM-5. Reduced catalyst would be used in the next section to test the operating temperature in catalytic cracking of UVO.

Effect of operating temperature for the catalytic cracking of UVO

The effect of operating temperature for the catalytic cracking reaction of UVO was carried out using the best catalyst with the highest conversion of palmitic acid, reduced Mo/ZSM-5. Effect of temperatures for the catalytic cracking reaction of UVO was carried out at 350 °C, 400 °C, and 450 °C. The conversion profile for the palmitic acid was found to be no significant difference in the range of temperature studied. However, slightly higher than average conversion (73.50%) was observed for stearic acid at 400 ^{o}C in the catalytic cracking of UVO at steady state compared to temperature at 350 ^{o}C (69.44%) and 450 ^{o}C (68.12%).

Theoretically, the conversion increases with the temperature due to higher kinetic energy possessed by the molecules in the system. In the present case, optimum temperature for conversion of palmitic acid and steric acid is found to be around 350-400 ^{o}C. These can be deduced that unwanted reactions start to be significant at temperature higher than 400 ^{o}C.

Comparison to catalytic cracking with palladium catalyst

In the present studies, the highest conversion for palmitic acid and stearic acid over catalytic cracking reaction of UVO was obtained by using Mo/ZSM-5 catalyst at temperature 400 °C. The performance this catalyst was then compared with a promising catalyst, Pd/Al_2O_3 in catalytic cracking of UVO. The commercially obtained Pd/Al_2O_3 was used directly in the reaction. The results obtained from the test were plotted in Figure 6.

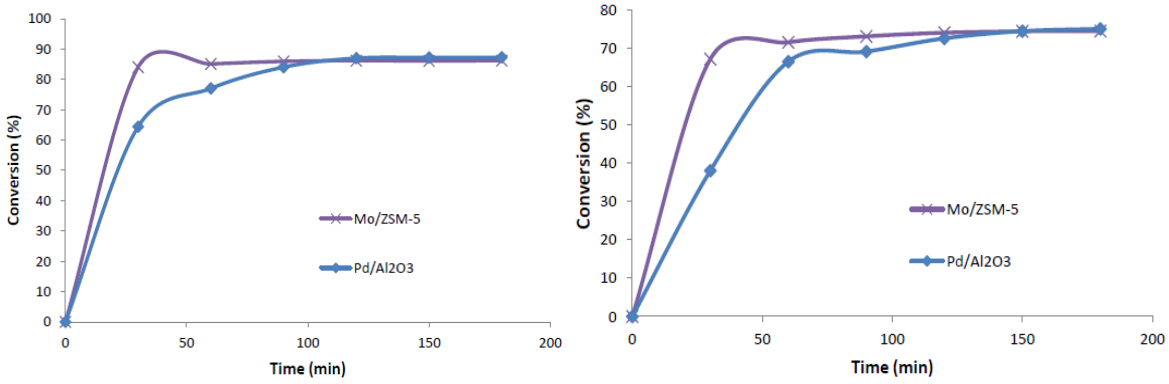


Figure 6. Conversion profiles of UVO with respect to (a) palmitic acid, (b) stearic acid (Temperature = 400 °C, UVO feed WHSV = 4 hour^{-1})

The conversion profile shows that there is no significant difference in terms of the conversion of both palmitic acid and stearic acid for both catalysts after the system reached steady state. However, Mo/ZSM-5 approaches steady state faster at 60 minutes than Pd/Al_2O_3 which is after 120 minutes. In the present study, the conversion remained stable even after 3 hours of operation which showed the catalyst remained active. There is still further study needed to be carried out to have better understanding of the Mo/ZSM-5 catalyst in catalytic cracking of UVO since coking is commonly reported as an issue in catalytic cracking. Anyhow, Mo/ZSM-5 is found to be an effective catalyst which is much cheaper compared to Pd/Al_2O_3 as catalyst used in catalytic cracking of UVO.

Conclusion

Catalytic cracking reaction of UVO with Ni, Mo or NiMo functionalized zeolite as catalyst into conventional fuel-like hydrocarbons or green fuels was investigated. The two major components in UVO used, palmitic acid and stearic acid, were analysed for their conversions in the reaction. The conversion of the palmitic acid and stearic acid for different catalysts used is in increasing order of ZSM-5< Ni/ZSM-5 < NiMo/ZSM-5 < Mo/ZSM-5. Mo/ZSM-5 outperformed the other catalysts in the conversion of palmitic acid (84.72%) and stearic acid (74.10%). As expected, reduced Mo/ZSM-5 was found to be more effective than MoO_x/ZSM-5 in the reaction. Among the studied temperature, conducting catalytic cracking of UVO with Mo/ZSM-5 at 400°C gives the best results. When

comparing to Pd/Al_2O_3, a promising catalyst in catalytic cracking of UVO, system with Mo/ZSM-5 is not only giving similar conversion at steady state but also approaches steady state much earlier than Pd/Al_2O_3. Cheaper Mo/ZSM-5 can be deduced a potential favorable catalyst for catalytic cracking of UVO. Nevertheless, further investigation is needed in order to optimize the final product, hydrocarbon yield as there were significant intermediates or side products in the liquid product.

Acknowledgement

The authors acknowledge the RUI grant (814220) from Universiti Sains Malaysia for carried out the project.

References

1. Dos Anjos, J. S., De Araujo, G. W, Lam, Y. L. and Frety, R. (1983). Catalytic decomposition of vegetable oil. *Applied Catalysis*, 5(3): 299-308.
2. Kaplan, S. (2017). Section 10 renewable energy. In: Monthly energy review July 2017, U.S. Energy Information Administration, Office of Energy Statistics, U.S. Department of Energy, Publication number DOE/EIA-0035(2017/7), Washington, DC: pp 156.
3. Fox, J. (2016). World biodiesel production/consumption to rise 14% by 2020: OECD/FAO. S&P Global Platts. https://www.platts.com/latest-news/agriculture/london/world-biodiesel-productionconsumption-to-rise 26485632. [Access online 1 August 2017].
4. Abbasov, V., Mammadova, T., Aliyeva, N., Abbasov, M., Movsumov, N., Joshi A., Lvov Y. and Abdullayev, E. (2016). Catalytic cracking of vegetable oils and vacuum gasoil with commercial high alumina zeolite and halloysite nanotubes for biofuel production. *Fuel*, 181: 55–63.
5. Natural Fuel (2017). What is the difference between biodiesel and green diesel? http://naturalfuel. com.au/difference-biodiesel-green-diesel/[Acessonline 28 December 2017].
6. Rigutto, M. S., Van Veen, R. and Huve, L. (2007). Chapter 24: Zeolites in hydrocarbon processing. *Studies in Surface Science and Catalysis*, 168: 855-913.
7. Corma, A. and Martínez, A. (2005). Zeolites in refining and petrochemistry. *Studies in Surface Science and Catalysis*, 157: 337-366.
8. Di Renzo, F. and Fajula, F. (2005). Introduction to molecular sieves: trends of evolution of the zeolite community. *Studies in Surface Science and Catalysis*, 157: 1-12.
9. Adjaye, J. D., Katikaneni, S. P. and Bakhshi, N. N. (1996). Catalytic conversion of a biofuel to hydrocarbons: Effect of mixtures of HZSM-5 and silica-alumina catalysts on product distribution. *Fuel Processing Technology*, 48(2): 115-143.
10. Twaiq, F.A., Zabidi, N.A. and Bhatia, S. (1999). Catalytic conversion of palm oil to hydrocarbons: Performance of various zeolite catalysts. *Industrial and Engineering Chemistry Research,* 38(9): 3230-3237.
11. Li, H., Shen, B., Kabalu, J. C. and Nchare, M. (2009). Enhancing the production of biofuels from cottonseed oil by fixed-fluidized bed catalytic cracking. *Renew Energy,* 34(4):1033–1039.
12. Doronin, V. P., Potapenko, O. V., Lipin, P. V. and Sorokina, T. P. (2013). Catalytic cracking of vegetable oils and vacuum gas oil. *Fuel,* 106: 757–765.
13. Twaiq, F. A., Mohamed, A. R. and Bhatia, S. (2003). Liquid hydrocarbon fuels from palm oil by catalytic cracking over aluminosilicate mesoporous catalysts with various Si/Al ratios. *Microporous and Mesoporous Materials*, 64(1-3): 95-107.
14. Snåre, M., Kubičková, I., Mäki-Arvela, P., Eränen, K. and Murzin, D. Y. (2006). Heterogeneous catalytic deoxygenation of stearic acid for production of biodiesel. *Industrial and Engineering Chemistry Research*, 45(16): 5708-5715.
15. Lestari, S., Maki-Arvela, P., Bernas, H., Simakova, O., Sjöholm, R., Beltramini, J., Max Lu, G. Q., Myllyoja, J., Simakova, I. and Murzin D.Y. (2009). Catalytic deoxygenation of stearic acid in a continuous reactor over a mesoporous carbon-supported Pd catalyst. *Energy & Fuels,* 23(8): 3842-3845.
16. Mäki-Arvela, P., Kubickova, I., Snåre, M., Eränen, K. and Murzin, D.Y. (2007). Catalytic deoxygenation of fatty acids and their derivatives. *Energy & Fuels,* 21(1): 30-41.
17. Kubičková, I., Snåre, M., Eränen, K., Mäki-Arvela, P. and Murzin, D. Y. (2005). Hydrocarbons for diesel fuel via decarboxylation of vegetable oils. *Catalysis Today*, 106(1-4): 197-200.

18. Hunns, J. A., Arroyo, M., Lee, A. F., Escola, J. M., Serrano, D. and Wilson, K. (2016). Hierarchical mesoporous Pd/ZSM-5 for the selective catalytic hydrodeoxygenation of m-cresol to methylcyclohexane. Catalysis Science and Technology, 6: 2560-2564.
19. Raut, R., Banakar, V. V. and Darbha, S. (2016). Catalytic decarboxylation of non-edible oils over three-dimensional mesoporous silica supported Pd. *Journal of Molecular Catalysis A: Chemical*, 417: 126-134.
20. Oi, L. E., Choo, M-Y., Suraya, Z., Lee, H.V. and Juan, J. C. (2017). Mesoporous TiO_2: Potential catalyst for deoxygenation of triglyceride to hydrocarbon-like biofuel. *Malaysian Journal of Catalysis,* 2(2): 53-56.
21. Kordulis, C., Bourikas, K., Gousi, M., Kordouli, E. and Lycourghiotis, A. (2016). Development of nickel based catalysts for the transformation of natural triglycerides and related compounds into green diesel: a critical review. *Applied Catalysis B.,* 181: 156-196.
22. Cejka, J. (2005). Zeolites and ordered mesoporous materials: progress and prospects: the 1st FEZA School on Zeolites, August 20-21, 2005, Gulf Professional Publishing, Prague, Czech Republic.
23. Danilina, N., Krumeich, F., Castelanelli, S. A. and van Bokhoven, J. A. (2010). Where are the active sites in zeolites? origin of aluminum zoning in ZSM-5. *Journal of Physical Chemistry C*, 114 (14): 6640–6645.
24. Chhetri, A. B., Watts, K. C. and Islam M. R. (2008). Waste cooking oil as an alternate feedstock for biodiesel production. Energies, 1(1): 3-18.
25. Canakci, M., Van Gerpen, J. (2001). Biodiesel production from oils and fats with high free fatty acids. Transactions-American Society of Agricultural Engineers, 44(6):1429-1436.
26. Chiam, L. T. and Tye, C. T. (2013). Deoxygenation of plant fatty acid using $NiSnK/SiO_2$ as catalyst. *Malaysian Journal of Analytical Sciences*, 17(1): 129 – 138.

Malaysian Journal of Analytical Sciences, Vol 22 No 1 (2018): 17 - 26
DOI: https://doi.org/10.17576/mjas-2018-2201-03

MALAYSIAN JOURNAL OF ANALYTICAL SCIENCES
Published by The Malaysian Analytical Sciences Society
ISSN 1394 - 2506

SYNTHESIS AND CHARACTERIZATION OF MESOPOROUS POLYMER-SILICA HYBRID MONOLITH USING CONVENTIONAL SOL-GEL METHOD FOR ENZYME SUPPORT

(Sintesis dan Pencirian Monolit Hibrid Polimer-Silika Berliang-Meso Menggunakan Kaedah Konvensional Sol-Gel Untuk Bertindak Sebagai Sokongan Enzim)

Noor Hidayah Idrohani[1], Samuel M. Mugo[2], Sabiqah Tuan Anuar[1]*

[1]*School of Marine and Environmental Sciences,*
Universiti Malaysia Terengganu, 21030 Kuala Nerus, Terengganu, Malaysia
[2]*Department of Physical Sciences,*
Mac Ewan University, Edmonton, Alberta, T5J 4S2, Canada

[*]*Corresponding author: sabiqahanuar@umt.edu.my*

Received: 26 August 2017; Accepted: 2 January 2018

Abstract

This research involved developing a novel solid support for an enzyme attachment, focusing on synthesizing a polymer-silica hybrid monolith *via in-situ* sol-gel polymerization method. The fabrication of a very large surface area of the monolith was done using a cold mixture of poly(ethylene-glycol) (PEG) with tetraethyl-orthosilicate (TEOS) and acetic acid with different ratios of PEG amount and molecular weights, namely PEG-0.1, PEG-0.2, and PEG-0.3. The experiments were conducted at a very low temperature of 0 °C, followed by overnight gelification and aging. The sol then underwent calcination at 200 °C forming a hybrid monolith. The characterizations of hybrid monoliths were performed by Attenuated-Total Reflection–Fourier Transformed Infrared Spectroscopy (ATR-FTIR), Scanning Electron Microscope (SEM), and Surface Area and Porosity Analyzer using both Brunauer-Emmett-Teller (BET) and Barrett-Joyner-Halenda (BJH) methods to describe the developed monoliths. FTIR shows the presence of Si-O-Si stretching associated with the monolith network due to the polymerization process together with the presence of silanol functional group (Si-OH) that can be exploited further for covalent attachment with the enzyme. Results also showed that the optimum ratios for the hybrid polymer-silica synthesis were PEG-0.1with 10,000 M_n surface area of mesoporous network recorded for 494.121 m^2/g and pore volume of 0.265 cm^3/g. These findings showed that the synthesized hybrid monolith on fused silica capillary will provide a vast surface area with desirable functional groups; thus, very promising for lipase immobilization support that can be used in future small-scale lipid transformation.

Keywords: hybrid monolith, fused silica capillary, sol-gel polymerization, enzyme support, mesoporous monolith

Abstrak

Penyelidikan ini melibatkan penghasilan satu sokongan baru untuk tautan enzim yang mana berfokuskan kepada sintesis monolit hibrid polimer-silika melalui kaedah pempolimeran sol-gel secara *in-situ*. Pemfabrikatan monolit yang mempunyai luas permukaan yang sangat besar telah dilakukan menggunakan campuran sejuk daripada poli(etilina-glikol)(PEG) dengan tetraetil-ortosilikat (TEOS) dan asid asetik pada nisbah bagi jumlah dan berat molekular PEG yang berbeza, dan dinamakan PEG-0.1, PEG-0.2 dan PEG-0.3. Eksperimen telah dijalankan dalam suhu yang sangat rendah pada 0°C diikuti dengan pengegelan dan penuaan untuk semalaman. Sol tersebut kemudiannya melalui proses kalsinasi pada suhu 200 °C lalu membentuk hibrid monolit. Hibrid monolit yang dihasilkan telah dicirikan melalui inframerah transformasi Fourier (FTIR), mikroskop pengimbas elektron (SEM) dan penganalisa rongga dan luas permukaan menggunakan kaedah Brunauer-Emmett-Teller (BET) dan Barrett-Joyner-Halenda (BJH) untuk menggambarkan monolit yang telah terbentuk. Keputusan dari FTIR menunjukkan kehadiran regangan Si-O-Si daripada jaringan monolit disebabkan proses pempolimeran, bersama-sama dengan kehadiran kumpulan berfungsi silanol

(Si-OH) yang boleh dieksplotasi untuk digunakan di dalam tautan kovalen dengan enzim. Didapati bahawa nisbah optima bagi sintesis polimer-silika hibrid adalah PEG-0.1 dengan berat molekul 10,000 M_n, yang mempunyai luas permukaan bagi jaringan liang-meso sebanyak 494.121 m^2/g dan isipadu liang 0.265 cm^3/g. Keputusan tersebut menunjukkan hibrid monolit yang disintesis di dalam kapilari silika kosong boleh menghasilkan luas permukaan yang sangat besar, dan berpotensi sebagai sokongan untuk pemegunan lipase bagi transformasi lipid berskala kecil di masa hadapan.

Kata kunci: campuran monolit, kapilari silika kosong, pempolimeran sol-gel, sokongan enzim, monolit berliang-meso

Introduction

To date, there are great interests in monolith fabrications for various analytical applications, especially in chromatography and catalysis. The wide range of monoliths has been developed with a variety and versatile class of materials as they can be easily prepared with varying porosity, pore size, and various chemical functionalities during the polymerization process [1]. Generally, monolith can be defined as a column or capillary that consists of a single large block of stone, particularly derived from the Greek word *monolithos* with *monos* meaning "single" and *lithos*, "stone", respectively [2]. A monolith can be described as a continuously interconnected skeleton with large through-pores [3]. Meanwhile, according to IUPAC, a monolith is a shaped and intractable network with a homogenous fabricated microstructure in which it does not show any structural components discernible by optical microscopy [4, 5]. Fundamentally, the monolith structures comprise of a honeycomb-like structure accompanied by many thin, vertical, and parallel channels of layers of a continuous uniform porous support material [6]. Monoliths are broadly categorized but the organic- and inorganic-based monoliths are widely used for their classification purpose. Most of the monoliths are made by a combination of several monomers or can simply be one monomer being transformed with certain modifications [2]. For an organic monolith, the pre-polymerization mixture of monolith can contain monomers or porogen, crosslinkers, initiators, and porogenic solvents in a mold before polymerization takes place [7].

Common materials being utilized in the polymeric monolith include styrene and methacrylate together with other acrylamide-based monomers where the polymerizable vinyl groups can be prepared in-situ within the capillary or column by radical polymerization using heat or UV reaction [2, 7, 8]. To date, a vast variety of organic polymer based-monoliths have been prepared, for instance, poly(glycidyl methacrylate-co-ethylene dimethacrylate) [9, 10], poly(N-acryloyltris (hydroxymethyl)aminomethane-co-pentaerythritol triacrylate) (NAHAM- co-PETA) [11], poly(butyl methacrylate-co-ethylene glycol dimethacrylate) [12], 3-(trimethoxysilyl)propylmethacrylate modified graphene oxide [13], and palladium-Schiff-base functionalized methyl methacrylate-glycidyl methacrylate (MMA-GMA) [14]. The monoliths prepared with this technique can still maintain their stability and have even gone through very high pH conditions. However, in the major scenarios, shrinkage and swelling cannot be avoided, especially when they were exposed to other mobile phases such as organic solvents, hence resulting in the low mechanical stability [15] that limits their application.

Thus, the modification of this type of monolith with an inorganic material such as silica is needed in order to increase their application. Previously, silica-based (inorganic) monoliths were generally prepared by the process of sol-gel and their surface eventually underwent silanization modifications [16]. On the contrary to the polymer monoliths that are easily swelled and undergone decomposition under solvent or temperature changes, silica monoliths are sufficiently great, even under extreme conditions [16, 17]. However, the drawbacks that cannot be fully neglected in preparing silica monolith are the shrinkage and cracking of the monolith itself [2, 16, 18, 19]. Therefore, the sol-gel hybrid materials have attracted huge attentions and proven to be promising since they have the merits from both earlier types of monolith, especially their outstanding mechanical strength and stability, as well as excellent pH stability [2, 20]. Nevertheless, the fabrication of polymer-silica hybrid monolith presented herein showed the improvements of this type of support due to the ease of preparation with the higher surface area and minimal shrinkage as the major benefits. Moreover, it was demonstrated in this study that the mesoporous networks of the monolith could be tailored differently with different ratios of monomer or porogen.

Materials and Methods

Polyethylene glycol (PEG; M_n = 10,000 and 20,000), tetraethylorthosilicate (TEOS, 98%), acetic acid glacial, sodium hydroxide, hydrochloric acid, and methanol were purchased from Fluka/Sigma-Aldrich (Sigma-Aldrich,

Missouri, USA). The fused-silica capillary of 530-µm I.D and 700-µm O.D was purchased from Polymicro Technologies (Molex Singapore Pte. Ltd., Singapore). A precise NE-300 infusion syringe pump (New Era Pump System Inc., New York, USA) was used to infuse the substrates through capillaries.

Preparation of polymer-silica hybrid monolith capillary

The preparation conditions of the monolithic silica-hybrid columns were similar to those reported previously but with some modification [19, 21, 22]. Prior to use, a fused-silica capillary was cut into 15 – 20 cm in length and treated with 0.1 mol HCl for 2 hours, water for 0.5 hour, 0.1 mol NaOH for 2 hours, water for 0.5 hour, and methanol for 0.5 hour, respectively. The resultant capillary was dried by a flow of nitrogen. The polymerization mixture was prepared by mixing 0.45 ml TEOS and 1 ml 0.01 M acetic acid with either 0.1 g PEG (PEG-0.1), 0.2 g PEG (PEG-0.2) or 0.3 g PEG (PEG-0.3). The optimum PEG weight (PEG-0.1) was later evaluated for different molecular weights (PEG-0.1 at 10,000 M_n and 20,000 M_n). The mixture was then agitated using a vortex mixer to promote the hydrolytic reaction in an ice that was maintained at 0 °C for 40 minutes. The pretreated fused silica capillary was then filled with the transparent cold sol using a flow infusion pump at a flow rate of 5 µl/min for 1.5 hour. Both ends of the capillary were then sealed with septum before being submerged into the thermostatic bath at 42 °C for 24 hours. Lastly, calcination was carried out at 200 °C for 24 hours in a furnace oven, resulting in the decomposition of organic moieties in the capillary. After this, the polymer-silica hybrid monolith was ready for characterizations.

Evaluation of the hybrid monolithic capillary

Attenuated-Total Reflection (ATR) Fourier Transform Infrared (FTIR) spectroscopy (IR Tracer-100 SHIMADZU, Kyoto, Japan) was used to characterize the surface functional groups of the monolith. Before the characterization, the diamond ATR crystal was solvent washed and dried, then an infrared background was collected. A small amount of monolith sample was prepared and loaded onto the ATR crystal and scanned to acquire the IR spectra. The scan rate was set to 20 spectra per seconds.

The surface morphology of monolith was determined using SEM (JOEL JSM-6360LA, Massachusetts, USA). Samples were prepared by cutting the fused silica capillary to a length of 1-2 mm and mounted on stainless steel stub. The mounted samples were coated with a thin layer of gold before being placed into a holder. Subsequently, all the samples were transferred into the SEM chamber. SEM was operated at 16kV with magnifications of 3000 magnification and 5000 magnifications.

The Surface Area and Porosity Analyzer (Micromeritics, Georgia, USA) was used for evaluating the monoliths. Nitrogen adsorption/desorption isotherms were measured by ASAP 2020 Micromeritics surface area analyzer at -196 °C. The specific surface areas of monoliths were assessed according to the standard Brunauer- Emmett-Teller (BET) method. The pore size distributions and total pore volume were also determined from the adsorption branches of isotherms by the Barrett-Joyner-Halenda (BJH) method.

Results and Discussion

In this paper, the synthesis and characterization of polymer-silica hybrid monolith support prepared *in-situ* and rapidly in fused silica capillary tubing were demonstrated. The monolith was synthesized using poly(ethylene-glycol) (PEG) as an organic sol-gel precursor and monomer into the sol-gel solution which consisted of tetraethyl orthosilicate (TEOS) and acetic acid (AA). The PEG that also acted as a porogen in the synthesis monomers where the polymerizable vinyl groups from PEG were utilized to make mesopore networks with the TEOS. In this process, the incorporation of the precursor was proven to be vital as it possessed an octadecyl moiety [23]. The effects of adding different types and weights of PEG (PEG with molecular weights of 10,000 M_n and 20,000 M_n at 0.1 g, 0.2 g, and 0.3 g) to a pre-polymerization mixture were studied in order to understand the effect of porogen addition for the purpose of making very porous monolith that can still provide a higher surface area. The introduction of PEG as a porogen material will eventually provide the mesoporous structure of a monolithic network. To evaluate this, ATR-FTIR, SEM, and Surface Area and Porosity Analyzer using BET and BJH methods were all used in the characterization.

The surface functional groups presented on the polymer-silica hybrid monolith were depicted by ATR-FTIR analysis. Similar spectral peaks were observed for all samples, revealing no significant contribution of difference in the weight and type of PEG content on the type of functional groups. Figure 1 exhibits FTIR spectra for monoliths with different ratios of the amount and molecular weight for PEG used, with respect to Figure 1(a) for hybrid monolith with PEG 10,000 M_n while Figure 1(b) for hybrid monolith with PEG 20,000 M_n, both in different amounts of 0.1 g, 0.2 g, and 0.3 g. All samples of monoliths showed strong peaks at around 790 – 800 cm^{-1} ascribed to the Si-O-Si symmetric stretching vibrations, similar to the previously described silica nanostructure gel and microstructure capillary prepared by sol-gel synthesis [18, 24].

The vibrational bands around 945 – 955 cm^{-1} showed the presence of Si-OH groups from the silanol functionality of the hybrid monolith, where this is the band that strongly represented the mesoporous structure of silica monolith. This finding is also similar to those reported previously for the mesoporous silica with with alkoxysilane groups [25]. This silanol group is significant to the monolith formation in order to provide a hydroxyl functional group which is important in the subsequent covalent attachment of enzyme by means of a crosslinker [19]. Intense peaks were observed around 1050 – 1080 cm^{-1} showing the Si-O-Si asymmetric stretching vibrations. Previously, Nocuń et al. [26] suggested that the hybrid monolith will transmit a strong absorption band for Si-O-Si as a characteristic after the modification of pure silica gel [26]. List of functional groups in polymer-silica hybrid monolith tabulated in Table 1.

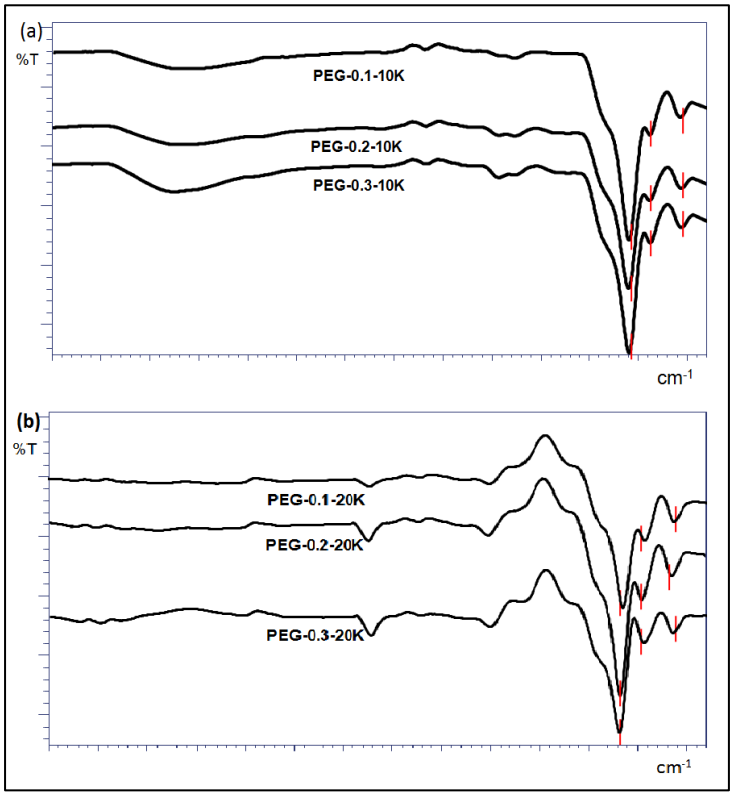


Figure 1. FTIR spectrum of polymer-silica hybrid monolith (a) PEG (M_n = 10,000) with different weight used, (b) PEG (M_n = 20,000) with different weight used

Table 1. List of functional groups in polymer-silica hybrid monolith

Functional Group	Type of Vibration	Frequency (cm^{-1})					
		PEG (M_n = 10,000)			PEG (M_n = 20,000)		
		0.1g	0.2g	0.3g	0.1g	0.2g	0.3g
Si-O-Si	Symmetric stretching vibrations	790.81	790.81	792.74	796.60	796.6	798.53
Si-OH	Bond vibration	947.81	952.84	952.84	941.26	945.12	945.12
Si-O-Si	Asymmetric stretching vibrations	1053.13	1060.85	1060.85	1049.28	1053.13	1068.56

Effect of variation in the PEG porogen concentrations

The effect of porogen concentrations onto monolithic textural properties was investigated with varying amounts of PEG (M_n = 10,000) from 0.1g to 0.3 g. The samples were denoted as PEG-0.1 10 K, PEG-0.2 10 K, and PEG-0.3 10 K, respectively. Figures 2(a) and (b) show that a mesoporous structure can be seen for the hybrid monolith with 0.1 g and 0. 2 g of PEG added while for Figure 2(c), the increasing amount of porogen to 0.3 g PEG will make the hybrid monolith to become a homogeneous and porous monolithic structure. The addition of different amounts of PEG acted as an organic porogen will provide higher porosity to the monolithic network, where the then organic modifier will make the structure less compact [26]. However, our findings also show that this structure will eventually become agglomerated when the concentration of porogen increased.

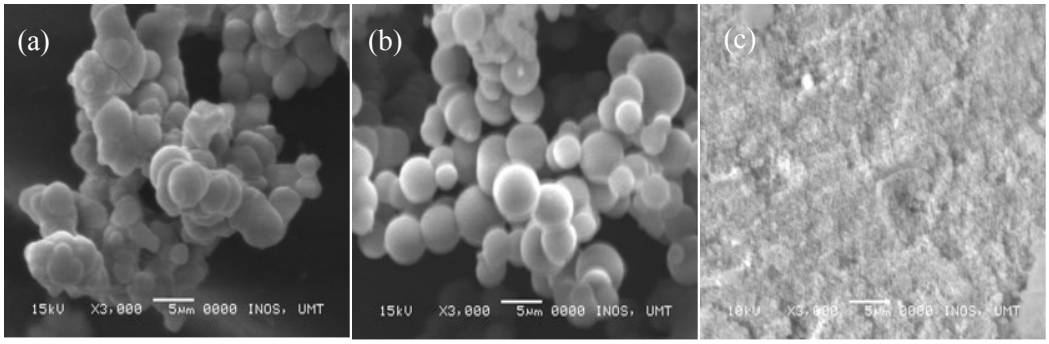


Figure 2. SEM images of polymer-silica hybrid monolith made with different amount of PEG 10,000 M_n used: (a) PEG-0.1, (b) PEG-0.2, (c) PEG-0.3, at 3000x magnification

Figure 3 shows the isothermal linear plots for all the monolith samples made from PEG 10,000 M_n for 0.1 g to 0.3 g. The nitrogen gas adsorption/desorption isotherm study from Brunauer–Emmett–Teller (BET) method of the hybrid monoliths presented the applicability of H_3-type hysteresis loop with well-defined Type IV(a) isotherm for all the synthesized samples, which confirmed the presence of mesopore structures in the monolith. In the case of Type IV(a) isotherm, the capillary condensation might occur when the pore width exceeded to a certain critical width, depending on the adsorption system and temperature [27]. These findings were supported by the measurement of BET surface area as shown in Table 2. The specific surface determined by BET method was related to the total surface area (reactive surface) as all porous structures adsorb the small gas molecules. The results showed that increased amount of porogen used made the monolith surface area became smaller, for instance, the use of 0.1 g PEG 10,000 Mn showed a significant amount of 494.121 m^2/g surface area, compared to when using 0.2 g (457.586 m^2/g) and 0.3 g (431.102 m^2/g) of PEG. This might be due to the reactive surface that decreased as the surface area became smaller. Additionally, the results measured for the pore volume and size that were obtained by the Barrett-Joyner-Halenda (BJH) method showed that as the amount of PEG used increased, the pore size for each monolith also increased where the 0.1 g PEG of 10,000 M_n resulted with 2.797 nm, 0.2 g PEG of 10,000 M_n resulted with 3.49 nm, and 0.3 g PEG of 10,000 M_n resulted in 9.348 nm in pore diameters. On the other hand, the pore volume of each monolith also became bigger, as described in Table 2.

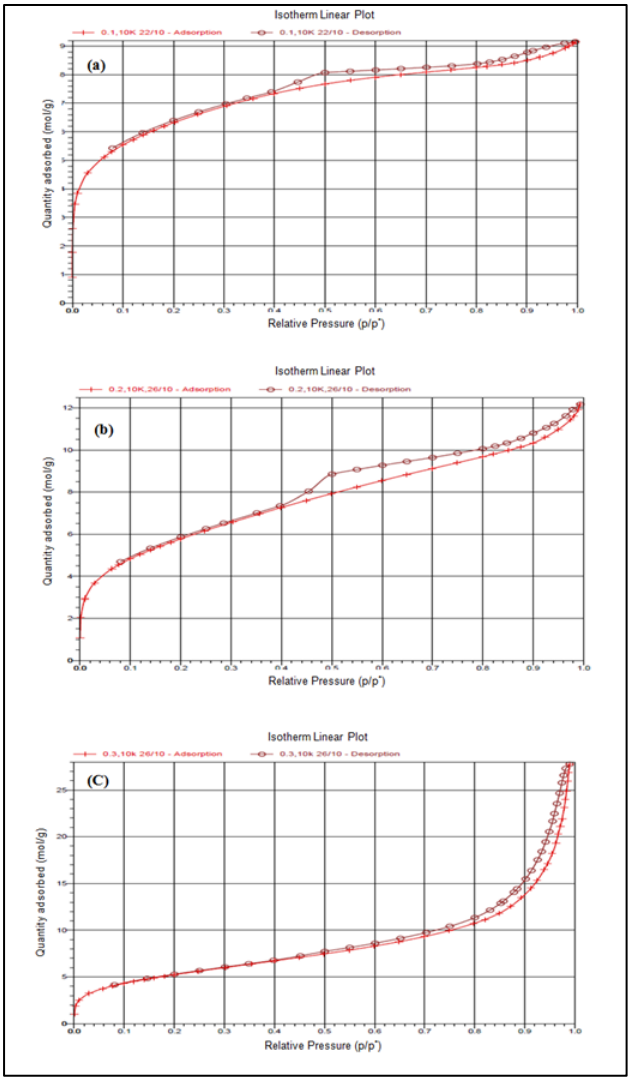


Figure 3. N_2 adsorption–desorption isotherm of polymer-silica hybrid monoliths with PEG 10,000 M_n for (a) PEG-0.1, (b) PEG-0.2, (c) PEG-0.3

Table 2. Surface area, pore size and pore volume measurement for PEG of 10,000 M_n using BET and BJH methods

Weight (g)	Brunauer- Emmett-Teller (BET) Surface Area (m^2/g)	Barrett-Joyner-Halenda (BJH)	
		Pore Volume (cm^3/g)	Pore size (nm)
0.1	494.121	0.265	2.797
0.2	457.586	0.467	3.549
0.3	431.102	0.949	9.348

Effect of variations in porogen type

The effect of different porogen types onto monolithic textural properties was also assessed by using different molecular weights for 0.1 g of poly(ethylene-glycol)(PEG) with M_n of 10,000 and 20,000. The samples were

denoted as PEG-0.1-10K and PEG-0.1-20K, respectively. Figure 4 shows the SEM images with different magnifications, verifying that very porous structure and interconnecting network are visible for both PEG-0.1-10K and PEG-0.1-20K synthesized in TEOS, that yielded to a continuous skeleton structure monolith. This result is consistent with the previous study that used 3-mercaptopropyltrimethoxysilane (MPTMS) as a porogen precursor for silica monolith synthesis in the presence of TEOS where the addition of organic monomer helped in introducing the organic moiety to the silica backbone during the preparation of monolith [15, 20, 28]. In Figure 4, the higher magnification images for 5000x magnification (inset) displayed that the skeleton of the monolithic network joined together, building up interconnected spheres in globules form (Figure 4(a)) and also in very homogenous spheres form (Figure 4(b)). The SEM images show that both types of PEG resulted in different characteristics of mesoporous structures. Therefore, the surface area and porosity of each monolith were analyzed using the BET and BJH method, respectively in order to determine the porosity and surface area of the monoliths.

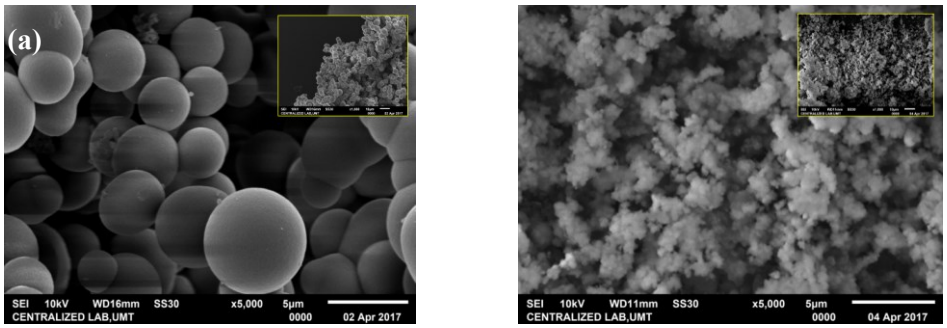


Figure 4. SEM images of polymer silica-hybrid monolith with different molecular weight (a) PEG-0.1-10K for 5000x magnification (inset: 1000x), (b) PEG-0.1-20K for 5000 x magnification (inset: 1000x)

The nitrogen gas adsorption-desorption isotherm of the hybrid monoliths with 0.1g PEG with10,000 M_n (PEG-0.1-10K) and 0.1g PEG with 20,000M_n (PEG-0.1-20K) are tabulated in Figures 5(a) and (b). The isothermal linear plots for both samples revealed a H_3-type hysteresis loop with well-defined type IV isotherms. The surface area calculated using the BET method gave a value of 494.121 m^2/g for hybrid monolith PEG-0.1-10K used and 468.830 m^2/g for hybrid monolith PEG-0.1-20K. This shows that the lower molecular weight of porogen is more desirable for the synthesis of the higher surface value of support. The volume of nitrogen gas adsorbed for the isotherms increased sharply, starting from 0.5 of relative pressure (p=p0) (Figure 5(a)). This behavior might signify the capillary condensation of nitrogen gas within the continuous mesoporous structures [29, 30]. Additionally, based on the BJH report for the porosity study (report not included), for the sample with 0.1g of PEG with 10,000 molecular weight (PEG-0.1-10K), the pore volume and size appeared to be 0.265 cm^3/g and 2.797 nm, respectively while the same amount of PEG with 20,000 molecular weight ((PEG-0.1-20K) only gave a slightly different pore value of 0.264 cm^3/g pore volume and 2.762 nm pore size. Therefore, while the surface area can be different for both types of the monolith, it can be agreed that there is not much different in the monolith porosity of using different molecular weights of PEG as porogen as compared to the different amounts of PEG used in each hybrid monolith sample preparation.

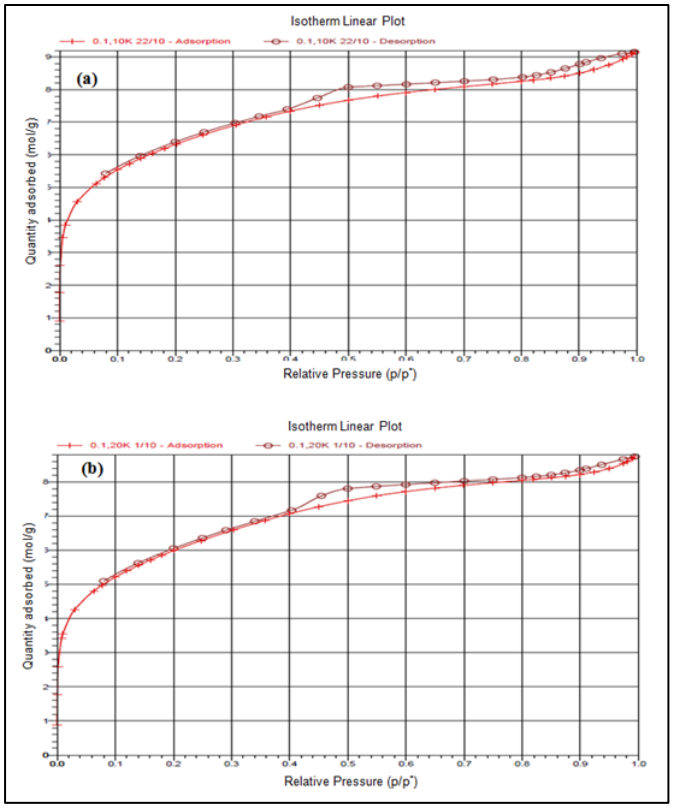


Figure 5. The Nitrogen gas adsorption-desorption isotherm of the hybrid monoliths with (a) PEG-0.1-10K and (b) PEG-0.1-20K

Conclusion

The fabrications of the hybrid monolith as a precursor for manufacturing enzyme support were accomplished by employing *in-situ* conventional sol gel method as described. All the synthesized monoliths were found to be having a porous structure. It was proven that diversified mesoporous structures can be tuned using different amounts and types of the porogen. Results showed that the most optimum condition for hybrid monolith synthesis was using PEG-0.1-10K. It can be concluded that the synthesized polymer-silica hybrid monolith permits a great surface area with a desirable functional group of silanol for further enzyme immobilization support. In future, this kind of support will be such a good platform for lipid modification and rapid lipid analysis, especially in a small scale analytical reaction.

Acknowledgements

The authors would like to thank the Malaysian Ministry of Higher Education (MOHE) for FRGS Research grant given to Dr. Sabiqah T. Anuar (59327) and MOHE MyBrain15 for providing graduate student funding (Noor Hidayah Idrohani). The authors also acknowledge the analytical and technical supports from Dr. Alyza A. Azmi for technical advice and Dr. Mohd Hasmizam Bin Razali from the School of Fundamental Sciences, UMT for providing technical help on the BET and BJH analyses.

References

1. Vázquez, M. and Paull, B. (2010). Review on recent and advanced applications of monoliths and related porous polymer gels in micro-fluidic devices. *Analytica Chimica Acta*, 668(2): 100 – 113.
2. Nema, T., Chan, E. C. Y. and Ho, P. C. (2014). Applications of monolithic materials for sample preparation. *Journal of Pharmaceutical and Biomedical Analysis*, 87: 130 – 141.

3. Bakry, R., Huck, C. W. and Bonn, G. K. (2009). Recent applications of organic monoliths in capillary liquid chromatographic separation of biomolecules. *Journal of Chromatographic Science*, 47(6): 418 – 431.
4. Gaweł, B., Gaweł, K. and Øye, G. (2010). Sol-gel synthesis of non-silica monolithic materials. *Materials,* 3(4): 2815 – 2833.
5. Nic, M., Jirat, J., and Kosata, B. (2012). IUPAC gold book. http://goldbook.iupac.org/MT07559.html. [Access online 02 April 2016].
6. Svec, F. (2002). Advances in biochemical engineering/biotechnology: Modern advances in chromatography. Springer-Verlag Berlin Heidelberg, New York. 76*:* pp. 1 – 47.
7. Rieux, L., Niederländer, H., Verpoorte, E. and Bischoff, R. (2005). Silica monolithic columns: Synthesis, characterisation and applications to the analysis of biological molecules. *Journal of Separation Science*, 28(14): 1628 – 1641.
8. Nordborg, A. and Hilder, E. F. (2009). Recent advances in polymer monoliths for ion-exchange chromatography. *Analytical and Bioanalytical Chemistry*, 394(1): 71 – 84.
9. Xu, Y., Cao, Q., Svec, F. and Fréchet, J. M. J. (2010). Porous polymer monolithic column with surface-bound gold nanoparticles for the capture and separation of cysteine-containing peptides. *Analytical Chemistry*, 82(8): 3352 – 3358.
10. Lv, Y.-Q., Fu, D.-Y., Tan, T.-W. and Wang, M.-Y. (2010). One-step purification of YLLIP2 isoforms from *Candida* sp. 99–125 by polyethyleneimine modified poly(glycidyl methacrylate-co-ethylene glycol dimethacrylate) monolith. *Journal of Molecular Catalysis B: Enzymatic*, 62(2): 149 – 154.
11. Chen, M. L., Wei, S. S., Yuan, B. F. and Feng, Y. Q. (2012). Preparation of methacrylate-based monolith for capillary hydrophilic interaction chromatography and its application in determination of nucleosides in urine. *J ournal of Chromatography A,* 1228: 183 – 192.
12. Liu, W., Qi, J., Yan, L., Jia, Q. and Yu, C. (2011). Application of poly(butyl methacrylate-co-ethylene glycol dimethacrylate) monolith microextraction coupled with high performance liquid chromatography to the determination of polycyclic aromatic hydrocarbons in smoked meat products. *Journal of Chromatography B*, 879 (28): 3012 – 3016.
13. Li, Y., Qi, L. and Ma, H. (2013). Preparation of porous polymer monolithic column using functionalized graphene oxide as a functional crosslinker for high performance liquid chromatography separation of small molecules. *The Analyst*, 138(18): 5470 – 5478.
14. Nandi, M. and Uyama, H. (2014). Porous acrylate monolith supported Pd nanoparticles: Highly active and reusable catalyst for Suzuki–Miyaura reaction in water. *RSC Advances*, 4(40): 20847 – 20855.
15. Ou, J., Lin, H., Zhang, Z., Huang, G., Dong, J. and Zou, H. (2013). Recent advances in preparation and application of hybrid organic-silica monolithic capillary columns. *Electrophoresis*, 34(1): 126 – 140.
16. Yuan, H., Zhang, L. and Zhang, Y. (2012). Comprehensive sampling and sample preparation: Analytical techniques for scientists. Academic Press, Elsevier Inc, Amsterdam. 2: pp. 345 – 358.
17. Xu, L. and Lee, H. K. (2008). Preparation, characterization and analytical application of a hybrid organic-inorganic silica-based monolith. *Journal of Chromatography A*, 1195 (1–2): 78 – 84.
18. Anuar, S. T., Zhao, Y-Y., Mugo, S. M. and Curtis, J. M. (2013). The development of a capillary microreactor for transesterification reactions using lipase immobilized onto a silica monolith. *Journal of Molecular Catalysis B: Enzymatic,* 92: 62 – 70.
19. Anuar, S. T., Mugo, S. M. and Curtis, J. M. (2015). A flow-through enzymatic microreactor for the rapid conversion of triacylglycerols into fatty acid ethyl ester and fatty acid methyl ester derivatives for GC analysis. *Analytical Methods*, 7(14): 5898 – 5906.
20. Wu, M., Wu, R., Zhang, Z. and Zou, H. (2011). Preparation and application of organic-silica hybrid monolithic capillary columns. *Electrophoresis*, 32(1): 105 – 115.
21. Wang, J., Wu, F., Xia, R., Zhao, Q., Lin, X. and Xie, Z. (2016). Rapid fabrication of ionic liquid-functionalized monolithic column via in-situ urea-formaldehyde polycondensation for pressurized capillary electrochromatography. *Journal of Chromatography A*, 1449: 100 – 108.
22. Xie, C., Ye, M., Jiang, X., Jin, W. and Zou, H. (2006). Octadecylated silica monolith capillary column with integrated nanoelectrospray ionization emitter for highly efficient proteome analysis. *Molecular and Cellular Proteomics*, 454 – 461.
23. Hayes, J. and Malik, A. (2000). Sol-gel monolithic columns with reversed electroosmotic flow for capillary electrochromatography. *Analytical Chemistry*, 72(17): 4090 – 4099.

24. Battisha, I. K., El Beyally, A., Abd El Mongy, S. and Nahrawi, A. M. (2007). Development of the FTIR properties of nano-structure silica gel doped with different rare earth elements, prepared by sol-gel route. *Journal of Sol-Gel Science and Technology*, 41 (2): 129 – 137.
25. Andrade, G. F., Soares, D. C. F., Almeida, R. K. D. S. and Sousa, E. M. B. (2012). Mesoporous silica SBA-16 functionalized with alkoxysilane groups: preparation, characterization, and release profile study. *Journal of Nanomaterials*, 2012: 1 – 10.
26. Nocuń, M., Siwulski, S., Leja, E. and Jedliński, J. (2005). Structural studies of TEOS-tetraethoxytitanate based hybrids. *Optical Materials*, 27(9): 1523 – 1528.
27. Thommes, M., Kaneko, K., Neimark, A. V., Olivier, J. P., Rodriguez-reinoso, F., Rouquerol, J. and Sing, K. S. W. (2015). Physisorption of gases, with special reference to the evaluation of surface area and pore size distribution (IUPAC Technical Report), *Pure and Applied Chemistry,* 87(9-10): 1051 – 1069.
28. Zheng, M. M., Ruan, G. D. and Feng, Y. Q. (2009). Hybrid organic-inorganic silica monolith with hydrophobic /strong cation-exchange functional groups as a sorbent for micro-solid phase extraction. *Journal of Chromatography A*, 1216(45): 7739 – 7746.
29. Thejaswini, T. V. L., Prabhakaran, D. and Maheswari, M. A. (2017). Structurally engineered TiO_2–SiO_2 monolithic designs for the enhanced photocatalytic degradation of organic textile dye pollutants. *Functional Materials Letters*, 10(2): 2 – 5.
30. Ahmad, A., Razali, M.H., Kassim, K. and Mat Amin, K.A. (2017). Synthesis of multiwalled carbon nanotubes supported on M/MCM-41 (M = Ni, Co and Fe) mesoporous catalyst by chemical vapour deposition method. *Journal of Porous Materials*, 1-9.

Malaysian Journal of Analytical Sciences, Vol 22 No 1 (2018): 27 - 34
DOI: https://doi.org/10.17576/mjas-2018-2201-04

MALAYSIAN JOURNAL OF ANALYTICAL SCIENCES
Published by The Malaysian Analytical Sciences Society
ISSN 1394 - 2506

COMPLEXATION OF 5,5,7,12,12,14-HEXAMETHYL-1,4,8,11-TETRAAZACYCLOTETRADECA-7,14-DIENIUM DIPERCHLORATE WITH COPPER(II) ACETATE MONOHYDRATE IN IONIC LIQUID

(Pengkompleksan 5,5,7,12,12,14-Heksametil-1,4,8,11-Tetraazasiklo tetraazadeka-7,14-Dienium Diperklorat dengan Kuprum(II) Asetat Monohidrat dalam Cecair Ionik)

Noorhanani M. Ali, Nurzati Amani M. Zaid, Nurul Huda Abd. Karim, Bohari M. Yamin, Nur Hasyareeda Hassan*

School of Chemical Sciences and Food Technology,
Faculty of Science and Technology,
Universiti Kebangsaan Malaysia, 43600 UKM Bangi, Selangor, Malaysia

Corresponding author: syareeda@ukm.edu.my

Received: 4 September 2017; Accepted: 19 December 2017

Abstract

In the previous study, 5,5,7,12,12,14–hexamethyl–1,4,8,11–tetraazacyclotetradeca–7,14–dienium diperchlorate, $[Me_6C_{10}H_{16}N_4](ClO_4)_2$ formed complex of $C_{16}H_{34}N_4OCu(ClO_4)_2$ and $C_{16}H_{32}N_4Cu(ClO_4)_2$ when reacted with copper(II) acetate monohydrate in acetonitrile and aqueous solutions, respectively. However, when the same reaction carried out in 1–butyl–3–methylimidazolium hexafluorophosphate ionic liquid, [Bmim][PF_6], disproportionation took place to give bis(ethylenediamine) bis(perchlorato-O) copper(II) complex, $C_4H_{16}N_4Cu(ClO_4)_2$. X-ray study showed that the central copper atom was coordinated to two ethylenediamine ligands and two oxygen atoms of perchlorate ions in a distorted octahedral environment. Thermogravimetric Analysis (TGA) study showed the complex decomposition in one spontaneous mass loss at 260 ºC due to the explosive nature of the perchlorate.

Keywords: ionic liquid, disproportionation, copper(II) complex

Abstrak

Dalam kajian yang lepas, 5,5,7,12,12,14-heksametil-1,4,8,11-tetraazasiklotetradeka-7,14-dienium diperklorat, $[Me_6C_{10}H_{16}N_4](ClO_4)_2$ membentuk kompleks $C_{16}H_{32}N_4OCu(ClO_4)_2$ dan $C_{16}H_{32}N_4Cu(ClO_4)_2$ apabila masing-masing bertindak balas dengan kuprum(II) asetat monohidrat dalam larutan asetonitril dan akues. Walaubagaimanapun, apabila tindak balas yang sama dilakukan dalam cecair ionik 1-butil-3-metilimidazolium heksaflorofosfat, [Bmim][PF_6], keperkadaran tidak seimbang berlaku dan menghasilkan kompleks kuprum(II) bis(etilenadiamina) bis(perklorato-O), $C_4H_{16}N_4Cu(ClO_4)_2$. Kajian X-ray menunjukkan atom kuprum berkoordinasi dengan dua ligan etilenadiamina dan dua atom oksigen ion perklorat dalam keadaan oktahedron terherot. Analisis termogravimetri (TGA) menunjukkan kompleks terurai dengan mengalami kehilangan jisim mendadak pada 260 ºC disebabkan oleh sifat perklorat yang mudah meletup.

Kata kunci: cecair ionik, keperkadaran tidak seimbang, kompleks kuprum(II)

Introduction

5,5,7,12,12,14–hexamethyl–1,4,8,11 – tetraazacyclotetradeca – 7,14 – dienium diperchlorate, $[Me_6C_{10}H_{16}N_4](ClO_4)_2$ is a special macrocyclic tetraaza because it was obtained by templation when Curtis recrystallized bis(ethylenediamine) nickel in acetone [1]. Since then, many such complexes were synthesised by templation

method. Very few reports were on the interaction or mechanism for the reaction between the ligand and metals. However, there were some studies on the stability of the complexes in basic and acidic solutions in which isomerisation or decomposition may have taken place [2-4]. The discovery of a deprotonated Curtis salt $(Me_6C_{10}H_{16}N_4)X_2$ where X= halogen has opened up a new scope to study the reaction from both synthetic and reaction point of view [5-7]. The complexation product is influenced by the type of tetraaza ligands, metal salts, and the solvents. For example, $(Me_6C_{10}H_{16}N_4)Br_2$ reacted with $CuBr_2$ and NH_4CuCl_4 was found to give $[(Me_6C_{10}H_{16}N_4)BrCu]Br.2H_2O$ and $[(Me_6C_{10}H_{16}N_4)Cu][Cl_4Cu]$ [8-9]. In our previous work on the reaction of $[Me_6C_{10}H_{16}N_4](ClO_4)_2$ with copper(II) acetate monohydrate, the same complex, $[(Me_6C_{10}H_{16}N_4)Cu](ClO_4)_2$ reported by Curtis was obtained [10].

Ionic liquid is a molten salt composed of ions and exist as liquid at ambient temperature. Its non-volatility, low vapor pressure and broad range of anion combination render them as well-known green solvent for many reactions and as an attractive alternative to conventional organic solvents [11]. Besides an ability to provide easy reaction medium, it may also involve in the reaction. The first report of synthesis in coordination chemistry using an ionic liquid was reported by Zhang et al. in 2013 where the reaction was carried out by using templation method [12]. To look at the role that ionic liquids can play in the complexation of tetraaza macrocyclic ligand with copper(II) acetate monohydrate, we decided to use $[Bmim][PF_6]$ as solvent for the reaction without using templation method. It was anticipated that the basic nature of ionic liquid will have an influence at least on the stability of the complex.

Materials and Methods

Chemicals

Ammonium perchlorate, ethylenediamine, copper(II) acetate monohydrate, 1–butyl–3–methylimidazolium hexafluorophosphate ionic liquid, $[Bmim][PF_6]$, methanol and acetone were purchased from Sigma-Aldrich and Friedemann Schmidt. All chemicals were of the analytical reagent grade (AR) and used without purification.

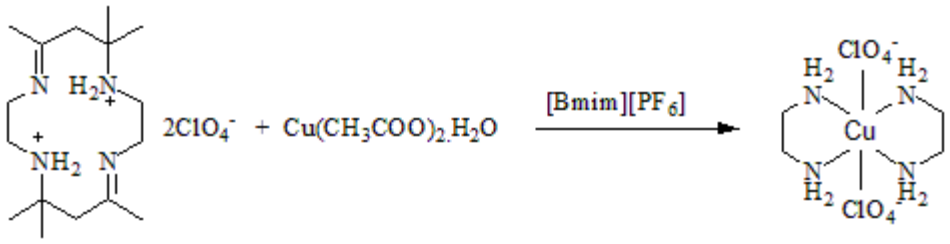
Physical measurement

Melting point was measured by using Barnstead Electrothermal Melting Point IA9100 series. Microelemental analyses were conducted using Thermo-Finnigan Flash EA 1112 Elemental Analyser. The metal content of the copper(II) complex was determined by atomic absorption technique using Perkin-Elmer AAnalyst 800 AA spectrometer. IR spectrum was recorded using FTIR Perkin-Elmer GX model with compound dispersed in KBr disks with the spectral range of 4000-400cm^{-1}. The electronic spectrum of the complex in water was recorded on Shimadzu UV-2450 and mass spectrometry was carried out using Bruker MicroTof Q Mass Spectrometer. Magnetic susceptibility was measured using Sherwood Magnetic Susceptibility Balance (Auto) at room temperature. Thermogram was obtained by using a Mettler Toledo TGA/SDTA 851 instrument under N_2 atmosphere with a flow rate of 20 mL min^{-1}, in the temperature range of 27 to 600 ºC at the heating rate of 10 ºC min^{-1}.

A single-crystal X-ray diffraction investigation was performed on Bruker D8 QUEST fitted with CCD area detectors (graphite monochromator, Mo Kα radiation). Cell constant and an orientation matrix for data collection was obtained by least-squares refinement of diffraction data from 8144 unique reflections. The structure was solved by direct methods and refined by full-matrix least-squares techniques on $\boldsymbol{F}^2$ using the solution program SHELXS-97 and refined using SHELXL-97 [13, 14]. Non-hydrogen atoms were refined with anisotropic thermal parameters and hydrogen atoms were included from the difference Fourier maps and refined with isotropic thermal parameters. Molecular drawing was obtained using MERCURY software.

Syntheses

$[Me_6C_{10}H_{16}N_4](ClO_4)_2$ was prepared by the same method described in the previous paper [7]. A solution of $Cu(CH_3COO)_2.H_2O$ (0.1 g, 0.0005 mol) in $[Bmim][PF_6]$ (5 mL) and $[Me_6C_{10}H_{16}N_4](ClO_4)_2$ (0.24 g, 0.0005 mol) in $[Bmim][PF_6]$ (5 mL) were mixed in round bottom flask. The mixture was then refluxed for 3 hours under constant stirring at 70 ºC. The solution was filtered using 150 mm filter paper and extracted with water in a separating funnel. The aqueous layer was left to evaporate at room temperature. Purple crystals were obtained after one week. The crystals were washed with cold methanol, dried, and kept in a desiccator. The synthetic route of copper(II) complex is shown in Scheme 1.



Scheme 1. Synthetic route of copper(II) complex

Results and Discussion

Physical and microelemental analysis (C, H, N)

The complex was synthesised in the form of a purple solid in 79% yield. The microelemental analysis data showed an agreement with the formula of $C_4H_{16}N_4Cu(ClO_4)_2$ which was different from previous reported [7]. The yield, melting point, colour, and microelemental analysis data are shown in Table 1.

Table 1. Analytical data and physical properties of copper(II) complex

Compound	Colour	Yield (%)	Melting Point (ºC)	Elemental Analysis			
				C	H	N	Cu
$C_4H_{16}N_4Cu(ClO_4)_2$	Purple	79	268.5-268.9	14.16	4.41	14.92	16.23
				12.55	**4.21**	**14.64**	**16.62**

*****Bold value = Theoretical value*

Infrared spectroscopy

IR spectrum of the complex exhibited stretching frequency for NH_2, C-H, and C-N of 3308, 3217 cm^{-1}, 2965 cm^{-1}, and 1088 cm^{-1}, respectively as shown in Figure 1. The absence of a band at 1670 cm^{-1} which corresponded to the ν(C=N) stretch indicated the breaking of macrocyclic ring. The stretching bands at 627 cm^{-1} and 524 cm^{-1} were assigned for O-Cl-O bond of perchlorate and Cu-O bond, respectively [15,16]. The band at 476 cm^{-1} was assigned for ν(Cu-N) according to Nakamoto and Carthy [17].

Table 2. IR spectral data of Curtis ligand and copper(II) complex

Compound	ν(NH_2)	FTIR wavenumbers (cm^{-1})						
		ν(N-H)	ν(C-H)	ν(C=N)	ν(C-N)	ν(Cl-O)	ν(Cu-N)	ν(Cu-O)
$C_{16}H_{34}N_4(ClO_4)_2$ (Ligand)	-	3466-3407 (stretch)	2981	1667	1079	623	-	-
$C_4H_{16}N_4Cu(ClO_4)_2$ (Complex)	3308, 3217	1580 (bend)	2965	-	1088	627	476	524

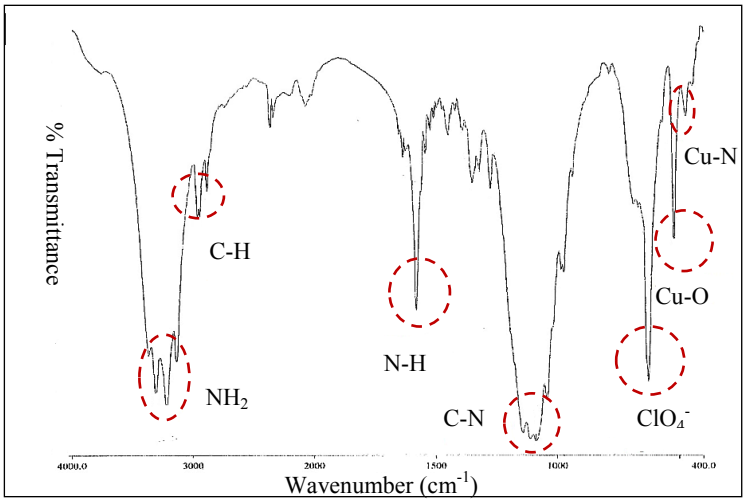


Figure 1. The FTIR spectrum of copper(II) complex

Mass spectrometry

The ESI–mass spectrum was measured to confirm the composition and purity of the complex under investigation. Representative mass spectrum of a solution containing copper(II) complex in the positive ion mode is shown in Figure 2. The ESI mass spectrum that contained molecular ion peak at m/z 381.18 was attributable to $[M\text{-}H]^+$. The molecular ion peak was in good agreement with the expected value of the copper(II) complex molecular weight. The peaks at m/z 281.24, 343.15 and 643.37 were assigned to $[M^+ - ClO_4^- - H^+]$, $[M^+ - ClO_4^- + Na^+ + K^+ - H^+]$, and $[M^+ - 2ClO_4^- - Na^+ + K^+]$, respectively. These assignments were based on ^{63}Cu.

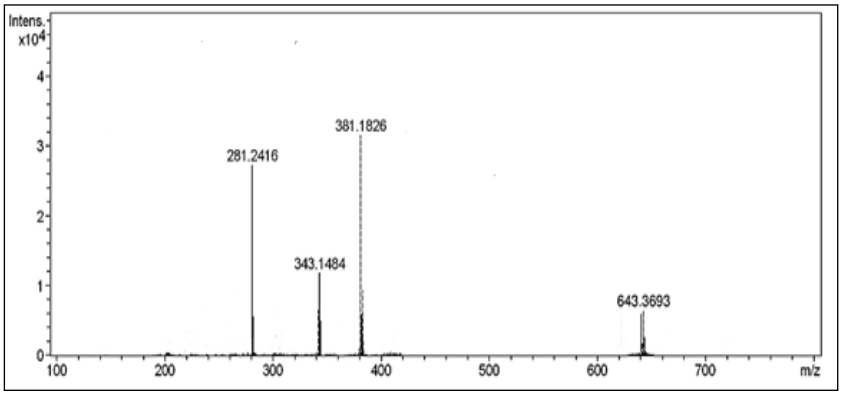


Figure 2. ESI mass spectrum in positive ion mode of copper(II) complex

Electronic spectral analysis

The UV-Vis spectrum of the complex is shown in Figure 3. The electronic spectra showed two characteristic absorption peaks at 229 nm (ε = 1370.0 $Lmol^{-1}cm^{-1}$) and 547 nm (ε = 1.7 $Lmol^{-1}cm^{-1}$) which were assigned for $\pi \rightarrow \pi^*$ and *d-d* transition, respectively [6]. However, the maximum absorption at 547 nm was obtained at high concentration because of low extinction coefficient.

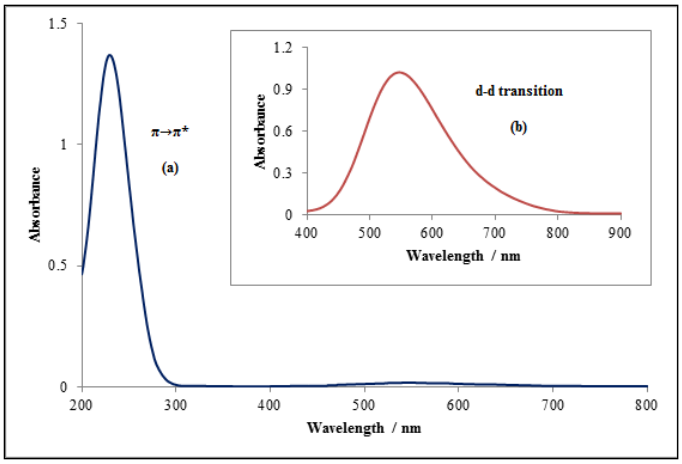


Figure 3. Absorption spectra of copper(II) complex (a) at 0.001 mol.L^{-1} and (b) at 0.01 mol.L^{-1}

Magnetic susceptibility determination

The magnetic susceptibility measurement in the solid state showed that the present complex was paramagnetic at room temperature. The magnetic moment value ($\mu_{eff.}$) of the complex was 1.82 B.M. for paramagnetic copper with octahedral geometry and lies within the range normally found for other copper(II) complexes [18].

Thermal analysis

Thermogram of the complex (Figure 4) showed its stability up to 260 °C followed by spontaneous mass loss with residual amount of 5.46%. Such behaviour corresponded to the loss of organic moiety in the complex [7].

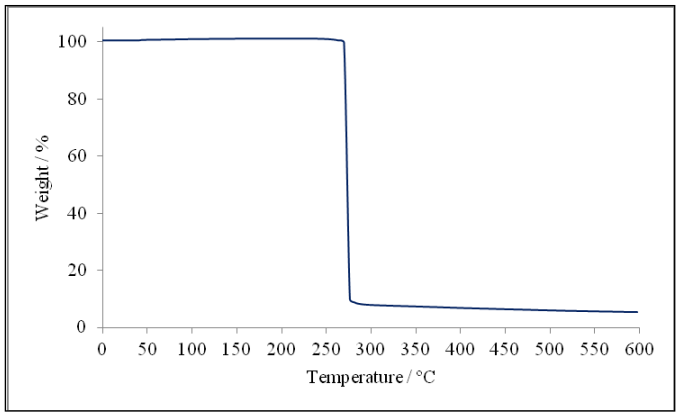


Figure 4. TGA curve of copper(II) complex

X-ray crystallography

Crystal structure of copper(II) complex, $C_4H_{16}N_4Cu(ClO_4)_2$ as shown in Figure 5 agreed with the data obtained from the physicochemical and the spectral studies. The structure of copper(II) complex was determined in a single crystal X-ray diffraction study. The X-ray of the single crystal structure for this copper(II) complex showed that the complex has a monoclinic system with a space group C 2/m, unit cell dimension with a = 12.4825(13) Å, b = 9.6470(11) Å and c = 5.7256(6) Å; α = 90º, β = 104.31º and γ = 90º. The crystallographic data, conditions for the collection of intensity data, and some features of the structure refinements are listed in Table 3. This complex formed an octahedral coordination with four nitrogen atoms in the basal plane and a definite coordination of two oxygen atoms from the perchlorate anion on the axial sites of the complex. The two Cu-O bonds (2.587 Å) were

considerably shorter than the Van der Waals radii of copper and oxygen which was 2.92 Å and therefore proved that there was a definite coordination of oxygen to the copper centre. The selected bond lengths and bond angles are shown in Tables 4 and 5.

Table 3. Details of crystallographic data collection and structure refinement parameters

State	**Data**
Empirical formula	C4 H16 Cl2 Cu N4 O8
Formula weight	382.65
Temperature	300(2) K
Wavelength	0.71073 Å
Crystal system	Monoclinic
Space group	C 2/m
Unit cell dimensions	a = 12.4825(13) Å α= 90°
	b = 9.6470(11) Å β= 104.309(3)°
	c = 5.7256(6) Å γ = 90°
Volume	668.08(12) Å3
Z	2
Density (calculated)	1.902 Mg/m3
Absorption coefficient	2.075 mm-1
F(000)	390
Crystal size	0.500 x 0.170 x 0.160 mm3
Theta range for data collection	3.369 to 28.316°.
Index ranges	-16<=h<=15, -12<=k<=12, -6<=l<=7
Reflections collected/unique	8144, 882 [R(int) = 0.0437]
Completeness to theta=28.32	99.8%
Refinement method	Full-matrix least-squares on F2
Data / restraints / parameters	882 / 4 / 65
Goodness-of-fit on F^2	1.159
Final R indices [I>2sigma(I)]	R1 = 0.0384, wR2 = 0.0890
R indices (all data)	R1 = 0.0446, wR2 = 0.0921
Largest diff. peak and hole	0.437 and -0.555 e.Å^{-3}

Table 4. Selected bond lengths [Å] for the copper(II) complex

Bond	**Bond length/[Å]**
Cu(1)-N(1)	2.011(3)
Cu(1)-N(1)	2.011(3)
Cu(1)-N(1)	2.011(3)
Cu(1)-N(1)	2.011(3)
Cu(1)-O(1)	2.587(3)
Cu(1)-O(1)	2.587(3)

Table 5. Selected bond angles [°] for the copper(II) complex

Bond	Bond angle/[°]
N(1)-Cu(1)-N(1)	180.0
N(1)-Cu(1)-N(1)	95.30(18)
N(1)-Cu(1)-N(1)	84.70(18)
N(1)-Cu(1)-N(1)	84.70(18)
N(1)-Cu(1)-N(1)	95.30(18)
N(1)-Cu(1)-N(1)	180.0

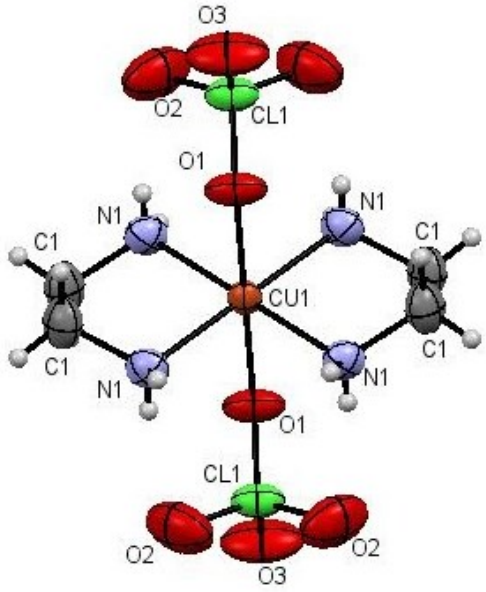


Figure 5. The ORTEP drawing of $C_4H_{16}N_4Cu(ClO_4)_2$ drawn at 50% probability ellipsoid

Conclusion

In the present communication, we have successfully synthesised and characterised copper(II) complex, $C_4H_{16}N_4Cu(ClO_4)_2$ in ionic liquid, [Bmim][PF_6]. Mass spectrum under ESI-condition was in line with the microelemental analysis, confirming the composition of the Cu(II) complex. Based on the analytical and spectral data, we assumed that the Cu(II) complex exhibited an octahedral geometry. TGA studies suggested that the complex was thermally stable up to 260 ºC before the major decomposition due to the loss of the organic moiety in the complex. X-ray crystallography also showed that copper ion was bound to two ethylene diamine ligands and two oxygen atoms of perchlorate ion forming an octahedral coordination. The full mechanism of this reaction is still under investigation as we are looking at the effect of using different types of ionic liquids in this reaction. We believe ionic liquid does not act only as a solvent but is also involved in this reaction.

Acknowledgement

The authors would like to thank the Faculty of Sciences and Technology, Universiti Kebangsaan Malaysia for providing necessary laboratory facilities and the lab assistants who were equally helpful in making this work. The authors also gratefully acknowledged the research grant from FRGS/1/2014/ST01/UKM/02/1 and GGPM2013-038 for financial support.

References

1. Curtis, N. F. and House, D. A. (1961). Structure of some aliphatic Schiff base complexes of nickel(II) and copper(II). *Chemistry and Industry*, 6: 1708 – 1709.
2. Chen, F. T., Lee, C. S. and Chung, C. S. (1983). Steric effects in the complexation kinetics of copper (II) with Rac-5,7,12,12,14-hexamethyl-1,4,8,11-tetraazacyclotetradecane in basic aqueous media. *Polyhedron*, 12(2): 1301 – 1306.
3. Kou, F., Zhu, S., Lin, H., Chen, W., Chen, Y. and Lin, M. (1997). Kinetics and mechanism of the acid dissociation of copper(II) complex of novel c-functionalized macrocyclic dioxotetraamines. *Polyhedron*, 12(16): 2021 – 2028.
4. Hay, R. W. and Pujari, M. P. (1985). The dissociation of $[Cu(cyclen)]^{2+}$ in acid solution. A kinetic study. *Inorganica Chimica Acta*, 100(2): 1 – 3.
5. Yusoff, L. M., Yusoff, S. F. M., Ismail, W. and Yamin, B. M. (2013). Synthesis and characterization of Ni(II) complex with 5,5,7,12,12,14-hexamethyl-1,4,8,11-tetraazacyclotetradeca-7,14-dienium bromide. *AIP Conference Proceedings*, (1614): 358 – 361.
6. Huddin, A. A. S, Yamin, B. M. and Yusoff, S. F. M. (2014). Complexation of 5,5,7,12,12,14- hexamethyl-1,4,8,11-tetraazacyclotetradeca-7,14-dienium Bromide with copper Salts. *AIP Conference Proceedings*, (1614): 371 – 374.
7. Ali. N. M., Hassan, N. H., Yamin, B. M., Karim, N. H. A. and Ghani, N. A. A. (2014). Synthesis and characterization of 5,5,7,12,12,14–hexamethyl -1,4,8,11-tetraazacyclotetradeca-7,14-dienium diperchlorate copper(II) complex. *Malaysian Journal of Analytical Sciences*, 18(3): 562 – 571.
8. Shi, F. F. and He, X. L. (2011). Bromido(meso-5,5,7,12,12,14-hexamethyl-1,4,8,11-tetraazacyclotetradeca-1,7-diene)copper(II) bromide dehydrate. *Acta Crystallographica Section E Structure Report Online*, 67(5): 607.
9. Yamin, B. M., Ismail, W. and Daran, J. C. (2012). Catena - Poly[[(5,5,7,12,12,14 – hexamethyl - 1,4,8,11 – tetraazacyclotetradeca -1,7- diene) copper(II)] –μ– chloride - [dichlorocuprate(II)] -μ- chlorido]. *Acta Crystallographica Section E Structure Report Online*, 68(7): 886 – 887.
10. Curtis, N. F. (2003). Fundamentals: Ligands, complexes, synthesis, purification and structure. *Comprehensive Coordination Chemistry II*: pp. 447 – 474.
11. Szefczyk, B. and Sokalski, W. A. (2014). Physical nature of intermolecular interactions in [Bmim][PF6] ionic liquid. *The Journal of Physical Chemistry B*, 118: 2147 – 2156.
12. Zhang, J., Luo, S., McCluskey, A. and Lawrance, G. A. (2013). Metal-templated macrocycle synthesis in an ionic liquid: A comparison with reaction in protic solvents. *Synthesis and Reactivity in Inorganic, Metal-Organic, and Nano-Metal Chemistry*. 43(1): 1 – 5.
13. Sheldrick, G. M. (2008). A short history of SHELX. *Acta Crystallographica Section A: Foundations of Crystallography*, 64(1): 112 – 122.
14. Sheldrick, G. M. (1993) SHELX-97, Program for the refinement of crystal structure. University of Göttingen.
15. Gu, B. and Coates, J. D. (2006). Perchlorate: Environmental occurrence, interactions and treatment. *Springer Science & Business Media*: pp. 137.
16. Saif, M., Mashaly, M. M., Eid, M. F. and Fouad, R. (2011). Synthesis and thermal studies of tetraaza macrocylic ligand and its transition metal complexes. DNA binding affinity of copper complex. *Spectrochimica Acta Part A*, 79: 1849 – 1855.
17. Nakamoto, K. and Carthy, M. (1968). Spectroscopy and structure of metal chelate compound. *John Wiley, New York*.
18. Procter, I. M., Hathaway, B. J. and Nicholls, P. (1968). The electronic properties and stereochemistry of the copper(II) ion. Part I. bis(ethylenediamine)copper(II) complexes. *Journal of the Chemical Society A: Inorganic, Physical, Theoretical*: 1678 – 1684.

Malaysian Journal of Analytical Sciences, Vol 22 No 1 (2018): 35 - 44
DOI: https://doi.org/10.17576/mjas-2018-2201-05

MALAYSIAN JOURNAL OF ANALYTICAL SCIENCES
Published by The Malaysian Analytical Sciences Society
ISSN 1394 - 2506

PHYSICOCHEMICAL AND SENSORIAL PROPERTIES OF OPTIMISED ROSELLE-PINEAPPLE LEATHER

(Ciri-Ciri Fizikokimia dan Sensori Snek Rozel-Nenas yang Dioptimumkan)

Noorlaila Ahmad*, Siti Nadiah Shafi'i, Nor Hasanah Hassan, Asmeda Rajab, Azizah Othman

Faculty of Applied Sciences,
Universiti Teknologi MARA, 40450 Shah Alam, Selangor, Malaysia

**Corresponding author: dnoorlaila@salam.uitm.edu.my*

Received: 4 September 2017; Accepted: 11 January 2018

Abstract

Roselle-pineapple leathers added with maltodextrin and hydrocolloids (locust bean gum and xanthan gum) were formulated to develop a new healthy-functional snack. The optimisation was carried out by the response surface methodology using a 5-level central composite rotatable design. The optimised fruit leather (pH= 3.2, TSS= 75°Brix) were dehydrated and subjected to physicochemical and antioxidant analyses as well as sensorial evaluation. The combination of 0.2% xanthan gum – 0.2% locust bean gum – 1.0% maltodextrin significantly maintained the fruit leather's colour and increased its extensibility. However, it significantly had lower ($p < 0.05$) total phenolic, total flavonoid, ferric reducing ability of plasma and 2,2-diphenyl-1-picrylhydrazyl radical-scavenging activity of the optimised fruit leather as compared to the control sample. Untrained panellists have assessed the sensory acceptability of the formulated snack food. They preferred the optimised roselle-pineapple leather added with maltodextrin and hydrocolloids as compared to the control roselle-pineapple leather.

Keywords: roselle-pineapple leather, antioxidant, hydrocolloid, extensibility, sensorial properties

Abstrak

Snek rozel-nenas yang ditambah maltodekstrin dan hidrokoloid (gam kacang lokus dan gam xantan) di formulasi untuk menghasilkan snek baru yang berkhasiat. Proses pengoptimuman dijalankan menggunakan kaedah gerak balas permukaan. Snek buah-buahan yang terhasil (pH= 3.2, jumlah pepejal larut= 75°Brix) dinyahhidrasi dan analisis fizikokimia, antioksida dan ciri-ciri sensori telah dijalankan. Kombinasi 0.2% gam xantan – 0.2% gam kacang lokus – 1.0% maltodekstrin mempunyai kesan signifikan terhadap warna snek rozel-nenas dan ekstensibilitinya berjaya ditingkatkan. Walau bagaimanapun, ia mempunyai kandungan fenolik, flavonoid, keupayaan penurunan ferik dan aktiviti pemerangkapan radikal bebas 2, 2-difenil-1-pikrilhidrazil yang rendah ($p < 0.05$) berbanding snek kawalan. Panel tidak terlatih telah membuat penilaian sensori ke atas snek yang di formulasi. Panel sensori lebih menggemari snek rozel-nenas yang ditambahkan maltodekstrin dan hidrokoloid berbanding snek kawalan.

Kata kunci: snek rozel-nenas, antioksida, hidrokoloid, ekstensibiliti, ciri-ciri sensori

Introduction

Roselle (*Hibiscus sabdariffa* Linn.) has vivid red colour and contains various polyphenols, including anthocyanins, proanthocyanidins and flavonols [1]. It also contains various organic acids such as oxalic, malic, citric, stearic and tartaric [2]. Each part of roselle plants (seed, calyx, leaf and stem) contains antioxidant properties that can be extracted using water and ethanol extraction [3].

The importance of antioxidant properties in roselle plant has attracted the food researchers to produce roselle-based products. Fruit leather is one of the food products which is produced through dehydration of fruit puree by using the red acid calyx of roselle [4, 5]. The drying of fruit to make rolls or leathers offers a convenient method for fruits' marketing. In addition, the drying process can enhance their shelf life to avoid any losses when there is an overproduction of the fruit. Fruit leather can be made from a variety of fruits such as apple [6, 7], roselle [8], pineapple [9] and pomegranate [10]. Typically, the fruit leather produced from roselle puree is mixed with other ingredients to improve consumer acceptance.

Various drying methods and conditions that affect the quality of fruit leathers have been previously studied [11]. The addition of various additives in fruit leathers leads to the improvement in extensibility of the finished products. A good combination of hydrocolloids should be able to maximise the extensibility of the fruit leather. One or more hydrocolloids (xanthan gum, locust bean gum, gellan gum, agar, Arabic gum, pectin, gelatine, modified or unmodified starch) may be present together with carrageenan in the hydrocolloid confectionery product [12]; it is reported to enable the creation of desirable gelling and textural properties [13]. Thus, the objective of this study is to develop new formulations of fruit leathers from roselle-pineapple and to assess its physicochemical and sensorial properties of the fruit leathers.

Materials and Methods

Raw materials

Fresh roselle fruit from Sudan cultivar (*Hibiscus sabdariffa* Linn.) of the red variety was purchased from Roselle Farms, Klang, Selangor. Pineapple of Morris variety was purchased from local market in Klang, Selangor. Xanthan gum, locust bean gum and carrageenan were purchased from Sigma-Aldrich, Malaysia while maltodextrin was purchased from Meilun Food Chemical Sdn. Bhd., Selangor, Malaysia.

Preparations of roselle-pineapple leather

In the production of fruit leather, the roselle and pineapple were initially washed with water to remove dirt, leaves and foreign materials. Then, the pineapple was sliced into small pieces, blended and filtered through muslin cloth. The pineapple juice was blended together with roselle (2:1 ratio) (w/w) as well as hydrocolloids and maltodextrin to produce mixed fruit puree. The function of these hydrocolloids and maltodextrin was to improve the extensibility and chewiness of the fruit leather. The optimised formulation of roselle-pineapple leather was generated by response surface methodology (RSM) software. For control sample, there was no addition of hydrocolloids (locust bean gum and xanthan gum) and maltodextrin in the fruit leathers' formulation. Sugar and glucose syrup (dextrose equivalent = 42%) were added into the fruit puree mixture until 50^{o} Brix was achieved in these mixtures. Sodium citrate was added to adjust the mixture to pH 3.2. These mixtures were then boiled and left to cool for about 60 minutes. Each treatment batch was poured into a 22.9 x 22.9 cm plastic mould to a depth of 3 mm and dried in the cabinet dryer at 55°C for 12 hours [14]. The roselle-pineapple leather was displayed in Figure 1.

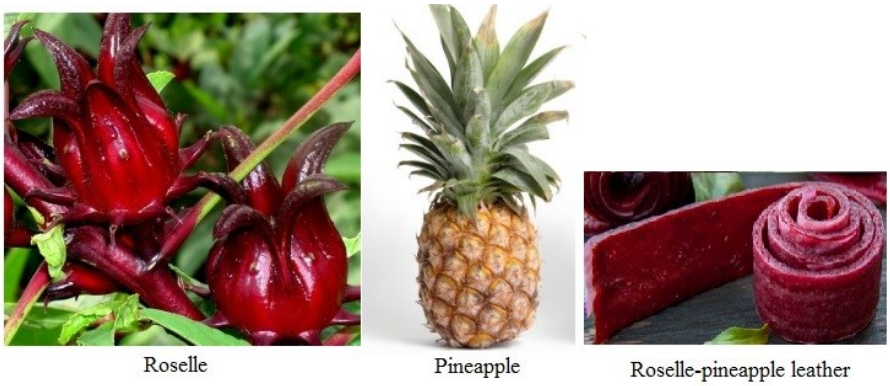


Figure 1. Roselle (*Hibiscus sabdariffa* Linn.), pineapple and roselle-pineapple leather

Optimisation of hydrocolloids and maltodextrin using CCRD

Design Expert Software version 6.0.4 (Stat-Ease Inc., USA) was used to generate the experimental designs, statistical analysis and regression model. The optimisation was carried out by employing the RSM using a 5-level CCRD. Table 1 shows the standard arrangement for three factors and the observed response. Three independent variables namely as xanthan gum (X_1), locust bean gum (X_2) and maltodextrin (X_3) were varied over five different levels ($-\alpha$, -1, 0, +1 and $+\alpha$). The response measured was the extensibility of the roselle-pineapple leather. A total of 20 experiments run (8 factorial points, 6 axial points and 6 replicated of the centre points) were unblocked and performed in random order to minimise the effects of unexpected variability in the observed response.

Table 1. Experimental design with actual levels for a 3-factors central composite rotatable design and the response values

Exp. Run[a]	Independent Variable			Response
	Xanthan Gum (%), X_1	Locust Bean Gum (%), X_2	Maltodextrin (%), X_3	Extensibility (g), Y_1
1	0.20	0.20	1.00	860.15
2	0.50	0.20	1.00	1109.74
3	0.20	0.50	1.00	390.13
4	0.50	0.50	1.00	860.34
5	0.20	0.20	3.00	690.44
6	0.50	0.20	3.00	801.20
7	0.20	0.50	3.00	795.50
8	0.10	0.35	3.00	871.31
9	0.60	0.35	2.00	520.69
10	0.35	0.10	2.00	950.14
11	0.35	0.60	2.00	1050.57
12	0.35	0.35	2.00	790.21
13	0.35	0.35	0.32	850.63
14	0.35	0.35	3.68	798.59
15	0.35	0.35	2.00	1032.30
16	0.35	0.35	2.00	1061.68
17	0.35	0.35	2.00	1127.69
18	0.35	0.35	2.00	1116.15
19	0.35	0.35	2.00	1049.05
20	0.35	0.35	2.00	1047.48

[a] Experiments were conducted in random order.

Determination of extensibility

Extensibility of roselle-pineapple fruit leathers with and without hydrocolloids was performed by using a TA.XT2i® Texture Analyser (Stable Micro Systems Ltd., Godalming, Surrey, U.K.) programmed with the Texture Exponent software. The samples were cut into uniform strips of 2.5 × 5.0 cm. A probe labelled Tensile Grips (A/TG) was used to extend each sample until it breaks. The measurement for extensibility was done in triplicate for each sample [15].

Preparation of fruit leather extracts for antioxidant assays
The extracts were prepared according to the method of Mohd-Esa et al. [3]. The fruit leathers were extracted with distilled water for 2 hours at room temperature, using an orbital shaker (Unimax 1010, Heidolph, Germany). The ratio of sample to extraction medium was 1:1000 (w/v). The mixture was filtered through a filter paper (Whatman no. 4). The filtrate was used for the antioxidant assays.

Antioxidant properties of roselle-pineapple leather: Total phenolic content
0.5 g gallic acid was dissolved in 10 ml ethanol (stock solution). From the stock solution, the standards with 50, 100, 250, 500 mg/litre concentration were prepared. 1 ml of sample extracts, gallic acid calibration standard, or blank (deionized or distilled water) was placed in a 100-ml volumetric flask. Approximately 70 ml of deionized water was added, followed by 5 ml Folin Ciocalteu reagent. The sample was incubated for about 1 to 8 minutes at room temperature. Next, about 15 ml of sodium carbonate solution was added to the sample. The sample was made up to 100 ml with distilled water and incubated for 2 hours at room temperature and the absorbance was measured at 765 nm with UV-Vis spectrophotometer. The calibration curve from the standards was created. This curve was used to determine the corresponding gallic acid concentration of the samples. The values were reported in gallic acid equivalents (GAE) using units of mg/litre [16].

Total flavonoid content
The total flavonoid content was measured using an aluminium chloride colorimetric assay. An aliquot (1 ml) of extracts or a standard solution of (+)-catechin (20, 40, 60, 80 and 100 mg/L) was added to a volumetric flask, containing 4 ml of distilled deionized water (ddH_2O). About 0.3 ml 5% sodium nitrite ($NaNO_3$) was added into these flasks. After 5 minutes, 0.3 ml 10% aluminium chloride ($AlCl_3$) was added and at the 6 minutes mark, 2 ml 1M sodium hydroxide (NaOH) was added. The sample was made up to 10 ml with ddH_2O. The sample was mixed, and the absorbance was measured against reagent blank at 510 nm with UV-Vis spectrophotometer. The total flavonoid contents of the fruit leather were expressed as milligrams of (+)-catechin equivalents (CE) per 100 g dry mass (mg CE/100 g dwb) [17].

Ferric reducing ability of plasma (FRAP)
The antioxidant capability of the extract based on ferric reducing power was determined according to the method described in Benzie and Strain [18] with some modifications. The stock solutions contained 300 mM acetate buffer (pH 3.6), 10 mM of 2,4,6-tripyridyl-s-triazine (TPTZ) solution in 40 mM HCl and 20 mM ferric chloride ($Fe_2Cl_3.6H_2O$) solution. The working solution was freshly prepared by mixing the acetate buffer, TPTZ solution and $Fe_2Cl_3.6H_2O$ solution in 10:1:1 ratio and then incubated at 37 ^oC for 10 minutes prior to the analysis. 0.1 ml of sample extracts were allowed to react with 2.9 ml of the FRAP solution for 30 minutes in the dark condition. The readings of the blue (ferrous tripyridyl triazine) complex were measured using UV-Vis spectrophotometer at 593 nm. The linear standard calibration curve ranging from 0-100 mM Trolox was established. The final results were expressed in mM TE/g of fresh extract weight.

2,2-diphenyl-1-picrylhydrazyl (DPPH) radical-scavenging activity
Radical scavenging activity of the sample extracts was conducted based on the method developed by Brand-Williams et al. [19] with slight modifications. About 600 µL of a various concentration of standards and samples ranging from 0-0.1 mg/ml were prepared. 4.5 ml of 60 µM DPPH solution in 95% ethanol was added to the sample solutions. The reaction was allowed to take place in the dark for 30 minutes and the absorbance reading at λ_{max} = 517 nm was recorded to determine the concentration of remaining DPPH. The results were expressed as EC_{50} (Efficient Concentration at 50% scavenging activity). Ascorbic acid and the mixture of synthetic antioxidant BHA/BHT were used as standards in comparison with the extracts.

Colour measurement
The colour of roselle-pineapple leathers was measured with a Minolta CR-300 Chroma meter, using illuminant C (6774K) attached to a DP-100 Data Processor and a standard white reflection plate (Minolta Corp, Ramsey, NJ). The results were expressed as L* value (colour intensity changing from light to dark), chroma (intensity of colour) and hue angle (actual colour). The instrument was positioned with minimal pressure perpendicular to the sample

surface and acquires CIELAB measurements over the 8-mm diameter interrogation area. The measurement of colour for each sample was run for at least three times [20].

Sensory evaluation
About 16 g of the samples (control and optimised fruit leather) were placed on coded plate accordingly. Sensory evaluation, using a 9-point hedonic scale (1=dislike extremely, 5=neither like nor dislike, 9=like extremely) was used to evaluate the samples [21] by 50 untrained panellists. The products were evaluated according to the degree of liking towards the appearance, colour, taste, texture and overall acceptability of roselle-pineapple leathers.

Statistical analysis
All data were expressed as a mean ± standard deviation from triplicate values. Data were analysed using SPSS 15.0.

Results and Discussion

Optimisation of hydrocolloids and maltodextrin using CCRD
The concentration of xanthan gum (X_1), locust bean gum (X_2) and maltodextrin (X_3) were selected using the CCRD as shown in Table 1 to investigate the effect of these hydrocolloids on the extensibility of roselle-pineapple leather. The concentration for XG (0.20-0.50%), LBG (0.20-0.50%) and maltodextrin (1.00-3.00%) were fixed accordingly to the previous study using two-level full factorial design [14].

Based on Table 1, the range values of extensibility for roselle-pineapple leathers were between 390.12 g to 1127.69 g. To analyse the data, the quadratic model ($p<0.05$) was suggested by CCRD because it has insignificant lack of fit (LOF) ($p>0.05$) and high R-squared (0.9762), which indicates a good fit of a model and there were good correlations between response and independent variables [9]. The effects and interaction between hydrocolloids and maltodextrin were observed in Equation 1, where X_1, X_2 and X_3 were coded for XG, LBG and maltodextrin, respectively. A positive sign for the coefficient estimated in the fitted model equation may indicate the tendency of the hydrocolloids and maltodextrin to increase the extensibility and vice versa.

$$\text{Extensibility (g)} = 1072.86 + 119.25\,\mathbf{X_1} - 71.91\,\mathbf{X_2} - 10.94\,\mathbf{X_3} - 112.21\,\mathbf{X_1}^2 - 56.81\,\mathbf{X_2}^2 - 90.68\,\mathbf{X_3}^2 + 23.21\,\mathbf{X_1X_2} - 66.65\,\mathbf{X_1X_3} + 111.82\,\mathbf{X_2X_3} \quad (1)$$

Three different effects were determined through this equation, which are single effects, multiple effects and combination effects. For single effects, only addition of XG (X_1= +119.25) had the highest coefficient, indicating its major contribution on the extensibility of roselle-pineapple leather compared to LBG and maltodextrin. In contrast, LBG (X_2= -71.91) and maltodextrin (X_3= -10.94) had negative coefficient values, which indicate that these two factors tend to decrease the extensibility of roselle-pineapple leather. Also, in multiple additions, the different effects of hydrocolloid and maltodextrin were observed to have the tendency in reducing the extensibility of roselle-pineapple leather. In combination, the mixture of LBG-maltodextrin (X_2X_3= +111.82) had a more positive effect which tends to increase the value of extensibility compared to the mixture of XG-LBG (X_1X_2= +23.21) and XG-maltodextrin (X_1X_3= – 66.65). From this equation, it can be concluded that single addition of XG and mixtures of LBG-maltodextrin and XG-LBG are sufficient to increase the extensibility of roselle-pineapple leather compared to other treatments.

Figure 2 depicts the relationship of the mixture (XG-LBG-maltodextrin) with the extensibility of roselle-pineapple leather. At the concentration of 1% maltodextrin, the extensibility of roselle-pineapple leather increased with the presence of high concentration of XG and LBG. This indicated that the increased concentration of hydrocolloids resulted in an increased extensibility of the dried roselle-pineapple leather. For optimisation process, only response (extensibility) was fixed as maximum while hydrocolloids (0.2 - 0.5%) and maltodextrin (1 - 3%) were fixed in their concentrations' range.

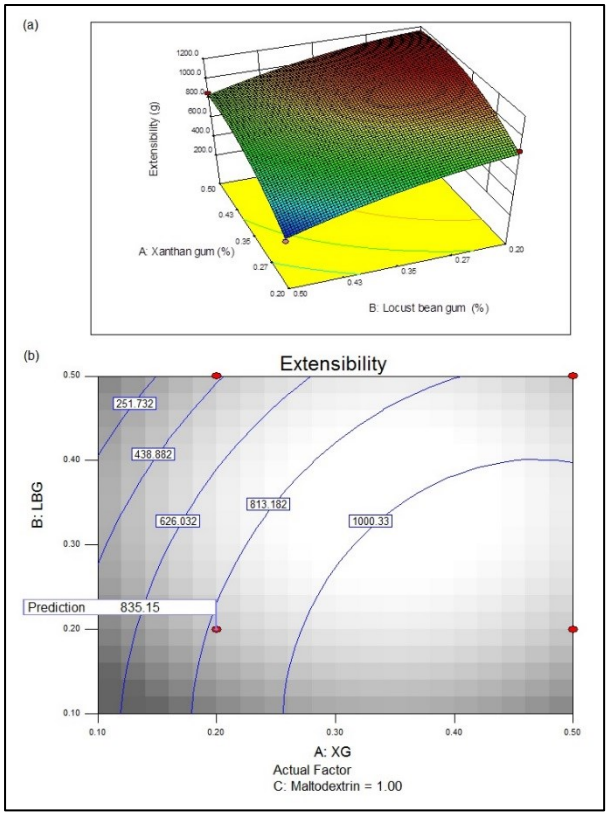


Figure 2. (a) Three-dimensional plot (3D), and (b) Two-dimensional plot (2D) showing the relationship between the extensibility, xanthan gum and locust bean gum at low level of maltodextrin (1% w/w)

The optimised hydrocolloids and maltodextrin composition obtained from the reduced factorial model was 0.2% XG - 0.2% LBG - 1% maltodextrin. The observed values from the experimental runs were used to evaluate the validity of the optimum point using Root Mean Squared Deviation (RMSD). The predicted value for the extensibility (835.15 g) has small RMSD value (0.94) with the verified values (836.09 g) which indicated the validity of the model. Jueanville and Badrie [22] and Dangkrajang et al. [23] also selected low concentration of hydrocolloids (0.15% and 0.20%) in their roselle leather formulations. It was also demonstrated that roselle leather containing a higher concentration of XG (0.30% and 0.60%) and guar gum (0.40% and 0.60%) exhibited greater extensibility which lowers their sensory acceptability.

Extensibility of roselle-pineapple leather

Referring to Table 2, there was significant difference between control and optimised leathers, which were 396.16 g and 836.09 g, respectively. High extensibility is desired to retain the shape of fruit leather, especially after drying. The addition of hydrocolloids (XG and LBG) at 0.20% as well as maltodextrin at 1.00% concentration promotes desirable extensibility of roselle-pineapple leather as described in sensory evaluation as the optimised fruit leather's texture was preferred over the control fruit leather (Figure 3). It is associated that the increase in extensibility of optimised fruit leather requires a high force to break it as compared to the control sample [11].

Table 2. Physicochemical and antioxidant properties of roselle-pineapple leathers as well as correlations of antioxidant parameters

	Control Leather	**Optimised Leather**
Initial pH	2.80±0.08[a]	2.80±0.08[a]
*Final pH	3.20±0.08[a]	3.20±0.08[a]
Extensibility (g)	396.16±25.49[b]	836.09±29.93[a]
Colour		
• *L**	22.84±0.51[a]	23.39±0.71[a]
• *a**	1.93±0.39[b]	9.43±0.47[a]
• *b**	1.10±0.12[a]	2.71±0.99[a]
Total phenolic (mg GAE/g)	0.53±0.03[a]	0.50±0.02[b]
Total flavonoid (mg QE/g)	0.46±0.01[a]	0.35±0.02[b]
FRAP (mM TE/g)	0.71±0.01[a]	0.69±0.01[b]
DPPH (**%**)	33.91[a]	29.90[b]
Correlations (r)		
• Total phenolic x FRAP	0.232; p<0.05	
• Total phenolic x DPPH	0.400; p<0.05	
• Total flavonoid x FRAP	0.858; p<0.05	
• Total flavonoid x DPPH	0.969; p<0.05	

*Sodium citrate was added until the pH value reached 3.2.
Values are means ± standard deviation (n=3).
Means within the same row with different letters are significantly different at p<0.05.

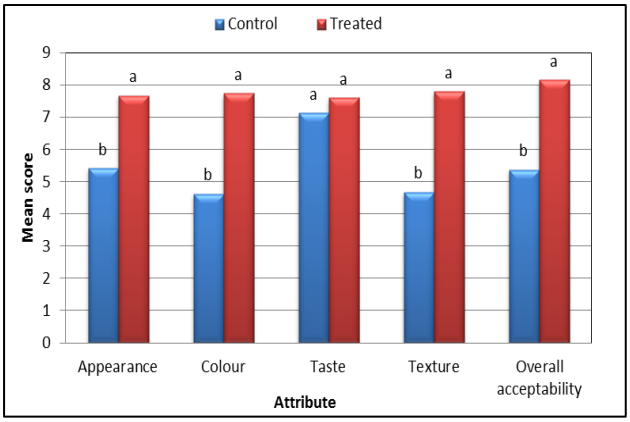


Figure 3. Acceptability scores of sensory attributes of control (left) and treated (right) roselle-pineapple leathers

Antioxidant properties of roselle-pineapple leather

Total phenolic content

As shown in Table 2, the total phenolic compound of control fruit leather (0.53 mg/GAE g) and optimised fruit leather (0.50 mg/GAE g) were lower than roselle leather (2.59 mg GAE/g) [8]. The roselle-pineapple leathers produced has lower phenolic content than roselle fruits itself, which is 1.85 mg of GAE/g [3]. The phenolic

compounds in roselle include organic and phenolic acids, such as citric acid, hydroxycitric acid, hibiscus acid and protocatechuic acid [24]. The reduction of total phenolic content in the fruit leathers might be due to its losses during the heating process (100 °C). Sharma et al. [9] observed the decrease in total phenolic content of fruit leather with the increasing temperature and this is due to the decarboxylation of phenolic acids. In their study, the experimental values of total phenolic content, ascorbic acid content, flavonoid content and antioxidant activity were 46.91 mg GAE/100 g, 51.97 mg/100 g, 48.75 μg of quercetin/g and 95.95%, respectively. Heating process caused an increment in the concentration of mixtures containing maltodextrin and hydrocolloids; in which the reacting molecules becomes closer once the mixture is concentrated, accelerating the degradation of the compounds [25].

Total flavonoid content

Total flavonoid content (Table 2) of control fruit leather (0.46 mg QE/g) was significantly higher ($p<0.05$) than the optimised fruit leather (0.35 mg QE/g). Roselle contain polyphenols of the flavonol and flavanol type in simple or polymerised form. The following flavonoids have been described in roselle extracts: hibiscitrin (hibiscetin-3-glucoside), sabdaritrin, gossypitrin, gossytrin and other gossypetin glucosides, quercetin, luteolin chlorogenic acid, protocatechuic acid, pelargonidic acid, eugenol, quercetin, luteolin and the sterols b-sitosterol and ergosterol [26]. Flavonoids such as quercetin, luteolin or gossipetin, and their respective glycosides are also present [24]. Sharma et al. [9] also reported that flavonoid content of pineapple fruit leather was decreased up to 37% after extrusion cooking with increasing temperature.

Ferric reducing ability of plasma

The potential of the antioxidants component present in roselle-pineapple leathers to reduce ferric ion (Fe^{3+}-TPTZ to a blue coloured Fe^{2+}-TPTZ) was determined using FRAP assay [27, 28]. As shown in Table 2, the antioxidant potential for the control fruit leather (0.71) was significantly higher ($p<0.05$) than optimised fruit leather (0.69). Although there is only low correlation of total phenolic content with FRAP value ($r = 0.232$, $p<0.05$) in optimised fruit leather, it is previously claimed that low FRAP values was related with the low phenolic content in the fruit leather [27]. Without the presence of hydrocolloids and maltodextrin, antioxidant compounds were easily reachable to the ferric ion, which causes the redox reaction to occur faster, leading to higher antioxidant potential in the control fruit leather. Meanwhile, strong and positive correlation were observed between total flavonoid content and FRAP ($r = 0.858$, $p<0.05$) as well as with DPPH activity ($r= 0.969$, $p<0.05$) (Table 2); which indicate that the flavonoid content in these optimised roselle-pineapple leather has a strong relation to its antioxidant activity.

Scavenging activity on 2, 2-diphenyl-1-picrylhydrazyl

The scavenging of 2,2-diphenyl-1-picrylhydrazyl (DPPH) radical by hydrogen-donating antioxidant is characterised by a rapid decline in the absorbance at 515 nm followed by a slow step where the absorbance depreciates more gradually [29]. When DPPH encounters proton radical scavengers, its purple colour fades rapidly [27]. As shown in Table 2, DPPH of control fruit leather (33.91%) was significantly higher ($p<0.05$) than optimised fruit leather (29.90%). This result was quite similar to Mohd-Esa et al. [3], in which the scavenging activity for roselle calyx was 30.8% in water extracts. Lower scavenging ability on DPPH radicals in optimised roselle-pineapple leather extracts might be due to its low content of flavonoid. As shown through correlation analysis, there is a strong positive correlation between DPPH and total flavonoid content ($r = 0.969$).

Colour analysis

Based on Table 2, the lightness (L*) and yellowness (+b*) of control and optimised fruit leathers were similar ($p>0.05$), but for redness (+a*), optimised fruit leather (9.43) showed significantly higher ($p<0.05$) compared to control fruit leather (1.93). It signified that the reddish colour of roselle dominates over the yellowish colour of pineapples in roselle-pineapple leather. As reported by Dangkrajang et al. [23], roselle leather containing guar gum (4.17) which possessed higher thickening properties was more reddish compared to roselle leather containing pectin; with a* values of 4.17 and 3.81, respectively. In this study, the combination of hydrocolloids mixture (xanthan gum and locust bean gum) was able to preserve the original colour of roselle puree in its viscous mixture.

Sensory evaluation

Results from the sensory evaluation revealed that the appearance, colour, texture and overall acceptability (Figure 3) of optimised fruit leather had significantly higher ($p<0.05$) mean scores as compared to the control fruit leather,

indicating its superior quality and preference to the panellists. Meanwhile, the sensory score of taste showed no significant difference between the tastes of optimised roselle-pineapple leather with the control roselle-pineapple leather. Both types of fruit leather had similar taste acceptability ($p>0.05$).

Conclusion

The panellists preferred the optimised roselle-pineapple leather added with maltodextrin and hydrocolloids compared to the control roselle-pineapple leather. The addition of maltodextrin and hydrocolloids significantly retained the fruit leather's colour, but it has also significantly lowered the total phenolic content, total flavonoid content, DPPH and FRAP values as compared to the control fruit leather. Optimised roselle-pineapple leather had significantly improved extensibility than the control leather. Further study on preserving the fruit leather's antioxidant properties shall be conducted in complement with its commercial added value.

Acknowledgement

This work was supported by Universiti Teknologi MARA, Ministry of Higher Education (MOHE) for the FRGS grant, FRGS FASA 02/2010, Reference: 600-RMI/ST/FRGS 5/3/Fst (215/2009) and Research Management Institute for Excellent Funds 11/2010, Reference: 600-RMI/ST/DANA 5/3/Dst (122/2010).

References

1. Formagio, A. S. N., Ramos, D. D., Vieira, M. C., Ramalho, S. R., Silva, M. M., Zárate, N. A. H., Foglio, M. A. and Carvalho, J. E. (2015). Phenolic compounds of *Hibiscus sabdariffa* and influence of organic residues on its antioxidant and antitumoral properties. *Brazilian Journal of Biology,* 75(1): 69 – 70.
2. Ali, B. H., Al Wabel, N. and Blunden, G. (2005). Phytochemical pharmacological and toxicological aspects of *Hibiscus sabdariffa L*: A review. *Phytotherapy Research,* 19(5): 369 – 375.
3. Mohd-Esa, N. Hern, F. S., Ismail, A. and Yee, C. L. (2010). Antioxidant activity in different parts of roselle (*Hibiscus sabdariffa L*) extracts and potential exploitation of the seeds. *Food Chemistry,* 122(4): 1055 – 1060.
4. D'Heureux-Calix, F. and Badrie, N. (2004). Consumer acceptance and physicochemical quality of processed red sorrel/roselle (*Hibiscus sabdariffa* L) sauces from enzymatic extracted calyces. *Food Service Technology,* 4: 141 – 148.
5. Sirichote, A., Ruangsri, P., Chumsri, P. and Itharat, A. (2008). Changes in quality and bioactive properties of concentrated Roselle (*Hibiscus sabdariffa* Linn) extract. *Journal of Food Agriculture Industrial,* 1(2): 62 – 67.
6. Demarchi, S. M., Ruiz, N. A. Q., Concellon, A. and Giner, S. A. (2013). Effect of temperature on hot-air drying rate and on retention of antioxidant capacity in apple leathers. *Food and Bioproducts Processing*, 9: 310 – 318.
7. Valenzuela, C. and Aguilera, J. M. (2015). Effects of maltodextrin on hygroscopicity and crispiness of apple leathers. *Journal of Food Engineering,* 144: 1 – 9.
8. Dangkrajang, S. (2011). Development of roselle leather from roselle (*Hibiscus sabdariffa* L.) by-product. Thesis of Master Degree, Prince of Songkhla University.
9. Sharma, P., Ramchiary, M., Samyor, D. and Das, A. B. (2016). Study on the phytochemical properties of pineapple fruit leather processed by extrusion cooking. Original Research Article *LWT - Food Science and Technology,* 72: 534 – 543.
10. Yilmaz, F. M., Yüksekkaya, S., Vardin, H. and Karaaslan, M. (2017). The effects of drying conditions on moisture transfer and quality of pomegranate fruit leather (pestil). *Journal of the Saudi Society of Agricultural Sciences,* 16(1): 33 – 40.
11. Gujral, H. S. and Brar, S. S. (2003). Effect of hydrocolloids on the dehydration kinetics colour and texture of mango leather. *International Journal of Food Properties,* 6(2): 269 – 279.
12. Saha, D. and Bhattacharya, S. (2010). Hydrocolloids as thickening and gelling agents in food: A critical review. *Journal of Food Science and Technology,* 47(6): 587 – 597.
13. Ong, M. H. and Whitehouse, A. S. (2003). United States Patent 20110256271. http://patentsjustiacom/inventor/mei-horng-ong. [Access online 12 March 2017].
14. Siti-Nadiah, S., Noorlaila, A., Mohd Zahid, A., Norziah, M. H. and Normah, I. (2013). Optimization of hydrocolloids and maltodextrin addition on roselle-based fruit leather using two-level full factorial design. *International Journal of Bioscience Biochemistry and Bioinformatics,* 3(4): 387 – 391.
15. Phimpharian, C., Jangchud, A., Jangchud, K., Therdthai, N., Prinyawiwatkul, W. and No, H. K. (2011). Physico chemical characteristics and sensory optimisation of pineapple leather snack as affected by glucose syrup and

pectin concentrations. *International Journal of Food Science and Technology,* 46: 972 – 981.
16. Stoica, R., Ion, R. M., Bunghez, I. R., Senin, R. and Bajenaru, I. G. (2011). Assessing the total phenolics of romanian wine varieties. *The Scientific Bulletin of Valahia University – Materials and Mechanics,* 6 (9): 101 – 103.
17. Sulaiman, C. T. and Balachandran, I. (2012). Total phenolics and total flavonoids in selected Indian medicinal plants. *Indian Journal of Pharmaceutical Sciences,* 74(3): 258 – 260.
18. Benzie, I. F. F. and Strain, J. J. (1996). The ferric reducing ability of plasma (FRAP) as a measure of 'anti-oxidant power': The FRAP assay. *Analytical Biochemistry,* 239: 70 – 76.
19. Brand-williams, W., Cuvelier, M. E. and Berset, C. (1995). Use of free radical method to evaluate antioxidant activity. *LWT - Food Science and Technology,* 28 (1): 25 – 30.
20. McGuire, R. G. (1992). Reporting of objective colour measurements. *Hort-Science,* 27(12): 1254 – 1255.
21. Larmond, E. (1977). Laboratory methods for sensory evaluation of foods Ottawa: Canada Department of Agriculture. http://www.archive.org/details/laboratorymethodOOotta. [Access online 20 January 2017].
22. Jueanville, M. and Badrie, N. (2007). Processed sorrel/roselle (*Hibiscus sabdariffa L*) leather from pectolase-treated alyces: Effects of xanthan gum on physicochemical quality and sensory acceptance. *Journal of Food Technology,* 5(2): 98 – 104.
23. Dangkrajang, S., Sirichote, A. and Suwansichon, T. (2009). Development of roselle leather from roselle (*Hibiscus sabdariffa* L) by-product. *Asian Journal of Food and Agro-industry,* 2(4): 788 – 795.
24. Borrás-Linares, I. S., Arráez-Roman, D. P. A., Palmeros-Suárez, P. A., Del Val-Díaz, R., Andrade-Gonzáles, I., Fernández-Gutiérrez, A. Gómez-Leyva, J. F. and Segura-Carretero A. (2015). Characterization of phenolic compounds anthocyanidin antioxidant and antimicrobial activity of 25 varieties of Mexican Roselle (*Hibiscus sabdariffa*). *Industrial Crops and Products,* 69: 385 – 394.
25. Patras, A., Brunton, N. P., O'Donell, C. P. and Kumar, T. B. (2010). Effect of thermal processing on antho-cyanin stability in foods; mechanisms and kinetics of degradation. *Trends in Food Science and Technology,* 21: 3 – 11.
26. Da-Costa-Rocha, I., Bonnlaender, B. Sievers, H., Pischel, I. and Heinrich, M. (2014). *Hibiscus sabdariffa* L.– A phytochemical and pharmacological review. *Food Chemistry,* 165: 424 – 443.
27. Azizah, O., Amin, I., Nawalyah, A. G. and Ilham, A. (2007). Antioxidant capacity and phenolic content of cocoa beans. *Food Chemistry,* 100: 1523 – 1530.
28. Hajimahmoodi, M., Oveisi, M. R., Sadeghi, N., Jannat, B., Hadjibabaie, M., Farahani, E., Akrami, M. R. and Namdar, R. (2008). Antioxidant properties of peel and pulp hydro-extract in ten Persian pomegranate cultivars. *Pakistan Journal of Biological Sciences,* 11: 1600 – 1604.
29. Balasundram, N. Ai, T. Y., Sambanthamurthi, R., Sundram, K. and Samman, S. (2005). Antioxidant properties of palm fruit extracts. *Asia Pacific Journal of Clinic Nutrition,* 4(4): 319 - 324.

Malaysian Journal of Analytical Sciences, Vol 22 No 1 (2018): 45 - 53
DOI: https://doi.org/10.17576/mjas-2018-2201-06

MALAYSIAN JOURNAL OF ANALYTICAL SCIENCES
Published by The Malaysian Analytical Sciences Society
ISSN 1394 - 2506

ASSESSING STIR BAR SORPTIVE EXTRACTION FOR TRIAZINE HERBICIDES EXTRACTION BY USING A CENTRAL COMPOSITE DESIGN APPROACH

(Penilaian Pengekstrakan Erapan Bar untuk Pengekstrakan Herbisid Triazin Menggunakan Pendekatan Reka Bentuk Komposit Berpusat)

Nurul Auni Zainal Abidin[1, 2]*, Md Pauzi Abdullah[1, 3], Fouad Fadhil Al-Qaim[1, 4, 5], Wan Mohd Afiq Wan Mohd Khalik[3, 6], Mohamed Rozali Othman[1, 3]

[1]*School of Chemical Sciences and Food Technology, Faculty of Science and Technology, Universiti Kebangsaan Malaysia, 43600 UKM Bangi, Selangor, Malaysia*
[2]*Faculty of Applied Sciences, Universiti Teknologi MARA Negeri Sembilan, Kuala Pilah Campus, 72000 Kuala Pilah, Negeri Sembilan, Malaysia*
[3]*Centre for Water Research and Analysis (ALIR), Faculty of Science and Technology, Universiti Kebangsaan Malaysia, 43600 UKM Bangi, Selangor, Malaysia*
[4]*Department of Chemistry, Faculty of Science for Women, University of Babylon, PO Box 4, Hilla, Iraq*
[5]*Department of Environmental Engineering and Green Technology, Malaysia–Japan International Institute of Technology, Universiti Teknologi Malaysia, 54100 Kuala Lumpur, Malaysia.*
[6]*School of Marine and Environmental Sciences, Universiti Malaysia Terengganu, 21030 Kuala Nerus, Terengganu, Malaysia*

Corresponding author: nurulauni@ns.uitm.edu.my

Received: 24 October 2017; Accepted: 4 January 2018

Abstract

A (PDMS)-coated stir bar was prepared for a glass jacket-free stir bar sorptive extraction (SBSE) configuration by adhesion technique for the extraction of triazine herbicides prior to quantification using a gas chromatography-flame ionization detector (GC-FID). A central composite design (CCD) was used in the optimization of extraction and desorption conditions. At optimum conditions, values of factors were set as pH 8.5, with no addition of NaCl, for 25 minutes of extraction time, and 24 minutes of desorption time. Under optimal experimental conditions, the proposed method has linear ranges at 0.1 – 100 μgL^{-1} with correlation of determination (R^2), ranging from 0.9991 – 0.9995, respectively. The limit of detection (LODs) and limit of quantification (LOQs) of three triazines were found to be ranging from 0.015 – 0.023 μgL^{-1} and 0.047 – 0.060 μgL^{-1}, respectively.

Keywords: stir bar sorptive extraction, triazine herbicides, central composite design, partition coefficient

Abstrak

Bar berputar yang disalut dengan polidimetilsiloksana (PDMS) telah disediakan untuk pengekstrakan erapan bar berputar (SBSE) tanpa jaket kaca melalui teknik lekatan untuk dianalisa sebelum kuantifikasi racun herbisid triazin dengan menggunakan kromatografi gas-pengesan ionisasi nyala (GC-FID). Reka bentuk komposit berpusat (CCD) telah digunakan untuk proses pengoptimuman keadaan pengekstrakan dan nyahjerapan. Pada keadaan optimum, nilai faktor adalah pH 8.5, tanpa penambahan NaCl, 25 minit masa pengekstrakan, dan masa nyahjerapan 24 minit. Kajian berdasarkan julat kelinearan antara 0.1 – 100 μgL^{-1}

telah mencapai kelinearan yang baik dengan pekali R^2 di rekod antara 0.9991 – 0.9995. Had pengesanan (LODs) dan kuantifikasi (LOQs) bagi tiga jenis triazin tersebut masing- masing dihitung antara 0.015 – 0.023 μgL^{-1} dan 0.047 – 0.060 μgL^{-1}.

Kata kunci: pengekstrakan erapan bar berputar, herbisid triazin, reka bentuk komposit berpusat, pemalar pemisahan

Introduction

Since their introduction, triazine herbicides have been widely used in agriculture as selective herbicides in many parts of world. These herbicides and their degradation products are highly persistent and hence their analysis in environmental samples is important [1]. The concentration of triazines in aquatic environments like ground water, rivers and estuaries is often found to be close to the lower detection limits of most elaborate analytical procedures [2]. Therefore, in order to protect human health and the environment, it is significantly important to monitor their levels in environmental waters. This has increased the demand for the development of simple, reliable, sensitive and rapid analytical methods. Sample preparation is considered as the most critical step in the overall analytical process since it plays a key role in analyte extraction, pre-concentration, and cleanup [3].

Conventional liquid–liquid extraction (LLE) and solid-phase extraction (SPE) have been used for pre-concentration and cleanup before analysis. LLE is time-consuming and hazardous to health due to the high volume of toxic solvents used [4]. SPE needs less solvent but it is still time consuming, and often requires a concentration stage that presents disadvantages such as loss in the evaporation step [5].

However, modern trends in analytical chemistry are moving towards the simplification and miniaturization of sample preparation, as well as the minimization of organic solvent used. Stir bar sorptive extraction (SBSE), as a microextraction method, was first introduced by Baltussen et al. in 1999 [6]. This technique has gained wide acceptance as a highly efficient sample preparation method for enrichment of solutes from aqueous samples [7]. The extraction is controlled by the solutes partitioning coefficient between the polymer coating and the sample matrix and by the phase ratio between the polymer coating and the sample volume. For a polydimethylsiloxane coating and aqueous samples, this partitioning coefficient resembles the octanol-water partitioning coefficient. In comparison to solid phase micro-extraction, a larger amount of sorptive extraction phase is used, and consequently, very high sensitivities in environmental, food and biomedical fields trace analysis. SPME and SBSE have been compared for the analysis of different compounds, as organochlorine pesticides [8] and organophosphorus insecticides [9]. All the studies reached the same conclusion, whereby the SBSE concentration capability was better than those presented by SPME because of polydimethylsiloxane (PDMS) film phase that covers the bar is thicker.

In the SBSE technique, the sample is stirred with a glass enclosed magnetic stir bar coated with a layer of PDMS, resulting in a distribution of analytes between the aqueous sample matrix and the PDMS layer [3]. The glass jacket is useful to immobilize sorbents onto the stir bar but it may lead to low stability and reproducibility because the glass jacket is relatively fragile. In this work, we introduced a glass jacket-free SBSE configuration by introducing a low cost hollow glass cylinder as a template for coating the SBSE polymeric phase. This template is important for reproducing the same bar characteristics from batch to batch.

Thus, this work aims to develop the prepared homemade glass jacket-free SBSE using PDMS sorbent for the determination of the selected triazine herbicides at trace levels from water samples prior to their determination by gas chromatography-flame ionization detector (GC-FID). An experimental design was used to investigate the influence of the principal parameters affecting glass jacket-free SBSE extraction of triazines. Thus, for determining the best experimental conditions, a central composite design (CCD) was applied. The developed method was then tested using different quality control approaches including detection limit and recovery assay.

Materials and Methods

Chemicals and reagents

Triazines namely atrazine, cyanazine, and ametryn, were purchased from Dr. Ehrenstorfer (GmBH, Germany). A standard compound solution at 1000 mgL^{-1} each were prepared in methanol. The mixture of all the compounds was prepared by diluting the standard solution in ultrapure water. All standard stock solutions were kept in a refrigerator

at 4 °C. HPLC-grade methanol, acetonitrile, acetic acid and hydrochloric acid were purchased from Merck (Darmstadt, Germany). Sodium chloride and sodium hydroxide were of analytical grade and obtained from R & M (Essex, UK). Ultrapure water was purified by Milli-Q EasypureRodi system (Barnstead, USA). PDMS Sylgard 184 silicone elastomer kit, which comprised base/curing agent to be mixed in a ratio of 10 (base) to 1 (curing agent) was obtained from Sigma Aldrich (St. Louis, USA).

Gas chromatographic analysis

A gas chromatography (GC) model HP 5890 Series II system equipped with a flame ionization detector (FID) (Hewlett-Packard) was used in this work. An Agilent DB-5 capillary column (30 m x 0.32 mm i.d. x 1.50 µm film thickness) was employed for the chromatographic separation. Helium was used as carrier gas at a flow rate of 1.0 mL min^{-1}. The GC oven temperature was programmed as follows: initial temperature was held at 120 °C for 1 min, programmed at 30 °C min^{-1} to 180 °C and kept at this temperature for 1 min, then 10 °C min^{-1} to 250 °C and kept at this temperature for 3 min. The total run time was 15.00 min. The injection port and detector temperature were both set at 250 °C and 280 °C, respectively. Sample (1 µL) was manually injected into the injection port under the splitless mode.

Experimental design of PDMS stir bar sorptive extraction procedure

The glass jacket-free SBSE conditions were optimized by using a CCD (with α = 2.000), based on 2^4 factorial design plus eight axial points plus six replicates in the centre of the design. The variables chosen for SBSE optimization were pH of the sample solution, ionic strength, extraction time, and desorption time. The factors, their levels, and symbols that were investigated by CCD are shown in Table 1. 30 experiments were generated by CCD and executed in a randomized order. The data were processed using Minitab version 17 (Minitab Inc. USA).

Table 1. Design matrix for central composite design

Factors	Levels				
	-α (-2)	Low (-1)	Central (0)	High (+1)	+α (+2)
(A) pH of sample solution	3.5	5.0	6.5	8.0	9.5
(B) Ionic strength (NaCl % (w/v))	0.0	1.0	2.0	3.0	4.0
(C) Extraction time (min)	5.0	10.0	15.0	20.0	25.0
(D) Desorption time (min)	10.0	15.0	20.0	25.0	30.0

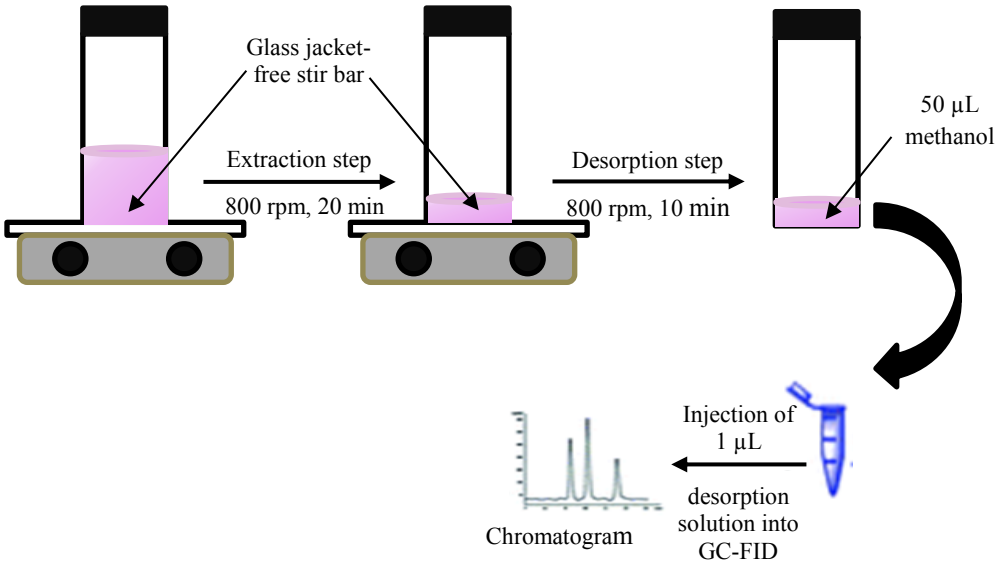


Figure 1. Schematic illustration of glass jacket-free SBSE process

In principle, the extractions were carried out with the homemade PDMS stir bar in a 25-mL amber glass vial, containing 10 mL standard solution of three selected triazines, and according to the experimental factorial design matrix. The vial was placed on the constant temperature magnetic stirrer. The stir bar was immersed into the standard solution and stirred at 800 rpm for 20 minutes. After extraction, the modified stir bar was removed, dried on a clean lint-tissue and transferred into a cylindrical glass desorption vial containing 50 µL methanol to desorb the targeted triazines under a magnetic stirring rate of 800 rpm for 10 minutes. Then, 1 µL of desorption solution was injected to the GC-FID injection port for analysis. The stir bar was regenerated in 0.5 µL methanol under ultrasonication for 15 minutes before the next use. Finally, a numerical data analysis resulting from CCD suggested that the optimum conditions were set as: 8.5 (pH), no addition of NaCl, 25 min (extraction time), and 24 min (desorption time).

Method validation

Analytical performance of the proposed stir bar was validated in terms of repeatability, linearity, limit of detection (LOD), and limit of quantification (LOQ) using the optimized extraction conditions. The linearity was obtained from the construction of calibration curve from 0.1 – 100 μgL^{-1} with triplicate measurements. LOD was determined at signal-to-noise ratio (S/N = 3) whilst the LOQ was determined at signal-to-noise ratio (S/N = 10). Repeatability of the methods was evaluated by performing nine measurements (three concentrations/three replicates) encompassing the concentration range, and calculating the relative standard deviations (RSD).

Quantification of partition coefficient and enrichment factor

At equilibrium, the partition coefficient for the analyte is dependent upon the phase ratio, and thus on the amount of extraction phase used as shown in equation 1.

$$K = \frac{C_{e,eq}}{C_{s,eq}} = \frac{m_e}{m_s} \times \frac{V_s}{V_e} = \frac{m_e}{m_s} \times \beta \quad (1)$$

The distribution coefficient between the extraction phase used and the sample is defined as the ratio between the analyte concentrations in the extraction phase ($C_{e,eq}$) over the concentration of the analyte in the sample ($C_{s,eq}$) at equilibrium. This ratio is equal to the ratio of the mass of the analyte in the extraction phase (m_e) over the mass of the analyte in the sample (m_s) times the phase ratio β, which is defined as the ratio between the volume of the sample (V_s) over the volume of the extraction phase (V_e). According to the mass balance relationship (equation 2):

$$C_t.V_s = C_{e,eq}.V_e + C_{s,eq}.V_s \quad (2)$$

where C_t is the original concentration of analytes. The enrichment factor, EF, can be defined as the ratio of the equilibrium concentration of analytes in the extraction phase to the original concentration of analytes in the sample. EF can be calculated from equation 3:

$$EF = \frac{C_{e,eq}}{C_t} = \frac{1}{\left(\frac{Ve}{V_s} + \frac{1}{K}\right)} \quad (3)$$

Results and Discussion

Central composite design

Based on the above results, a 2^4 of CCD was performed at five levels to optimize the factors pH, ionic strength, extraction time, and desorption time in order to improve the extraction recovery (ER%) percentage of of triazines. The stirring speed and volume of desorption solvent were held constant at 800 rpm and 300 µL. The CCD was used not only to evaluate the variables significance, but also to analyze the interaction among them. A quadratic regression model, on the basis of a multiple linear regression (MLR), should be applied to relate the responses and the variables. The second order polynomial equation obtained using coded value is given in regression in Equation 4:

$$ER = 66.44 + 6.865\ A - 5.512\ B + 10.674\ C + 5.396\ D - 6.880\ A^2 - 1.768\ B^2 - 3.568\ C^2 - 4.226\ D^2 + 4.12\ AB + 6.07\ AC - 5.49\ BC \quad (4)$$

where, A, B, C and D are the pH, ionic strength, extraction time and desorption time, respectively. As shown in the equation, the developed model consisted of four main effects, four curvature effects, and three interaction effects. Variables A, C, D, and interaction effects of AB and AC had positive linearity toward the fitted model.

To evaluate the significance of each factor and interaction terms, analysis of variance (ANOVA) was used and the obtained results are presented in Table 2. The quality of fit of the model equation was represented by the coefficient of determination (R^2 and adjusted-R^2). R^2 of 0.9651 and adjusted-R^2 of 0.9538 showed a good relationship between the experimental data and fitted model, as well as the high potential of model in prediction of response. The P-values were used to check the statistical significance of each coefficient, which in turn was necessary to understand the pattern of the mutual interactions between the test variables. Furthermore, P-value lower than 0.05 indicates the statistical significance of an effect at 95% confidence level. In this study, all individual experimental factors were significant with P-value < 0.05.

The other criterion for evaluating the model is the lack of fit (LOF) test which was performed by comparing the residual with the pure error achieved from the replicated design points at the central level of variables. In this case, if the P-value was greater than 0.05 (at the significance level of 95%), the regression will be significant. Considering the ANOVA results from Table 2, the P-value of the LOF test was 0.799, which confirms the lack of fit insignificance.

Table 2. Analysis of variance (ANOVA) for the developed models

Source	**Df**[a]	**Sum of Square**	**Mean Square**	**F-value**	**P-value**
Model	11	8365.69	760.52	45.25	0.000
Blocks	1	64.0	64.0	4.77	0.043
A	1	1131.17	1131.17	67.30	0.001
B	1	729.30	729.30	43.39	0.000
C	1	2734.22	2734.22	162.67	0.002
D	1	698.76	698.76	41.57	0.000
A^2	1	1298.39	1298.39	77.25	0.001
B^2	1	85.71	85.71	5.10	0.037
C^2	1	349.13	349.13	20.77	0.003
D^2	1	489.86	489.86	29.14	0.000
AB	1	271.43	271.43	16.15	0.001
AC	1	590.09	590.09	35.11	0.000
BC	1	482.17	482.17	28.69	0.000
LOF[b]	13	202.86	14.49	0.58	0.799
Pure error	4	99.69	24.92		
Total	29	8668.24			

[a] Degree of freedom, [b] Lack of fit, and bold value is significant at $p < 0.05$

Effect of variables on extraction efficiency

The matrix pH and ionic strength variables affect the extraction thermodynamics, so influencing the interaction between the analytes and the PDMS phase. The pH of the sample solution plays an important role for ionizable compounds such as triazines. Triazines are basic herbicides, and it is assumed that at a basic pH condition, better extraction recovery will be obtained.

In this work, pH values ranging from 3.5 to 9.5 were investigated. Triazine compounds contain amino groups and their existing forms will be affected by medium pH. It can be seen from the figure that at low pH values, the extraction efficiencies are low because the nitrogen atoms of triazines were protonated. Therefore, the molecules of trizaines were in ionic form, resulting in only π-π interaction that contributed to the extraction. With the increase of pH value, hydrophobic interaction also contributed to the extraction because triazines existed in a neutral form. According to the polynomial equation (equation 1) and response surface plot (Figure 2 (a)), the pH variables were significant with a positive sign, showing an increase of extraction recovery due to the increase in pH value, reaching the maximum at pH 8.5 and then decreasing after that. Lei et al. [10] applied polydimethylsiloxane (PDMS)/MIL-100(Fe) coated stir bar for the determination of six triazines (simazine, atrazine, prometon, ametryn, prometryne and prebane) and observed that pH 8 was the optimum pH for their study.

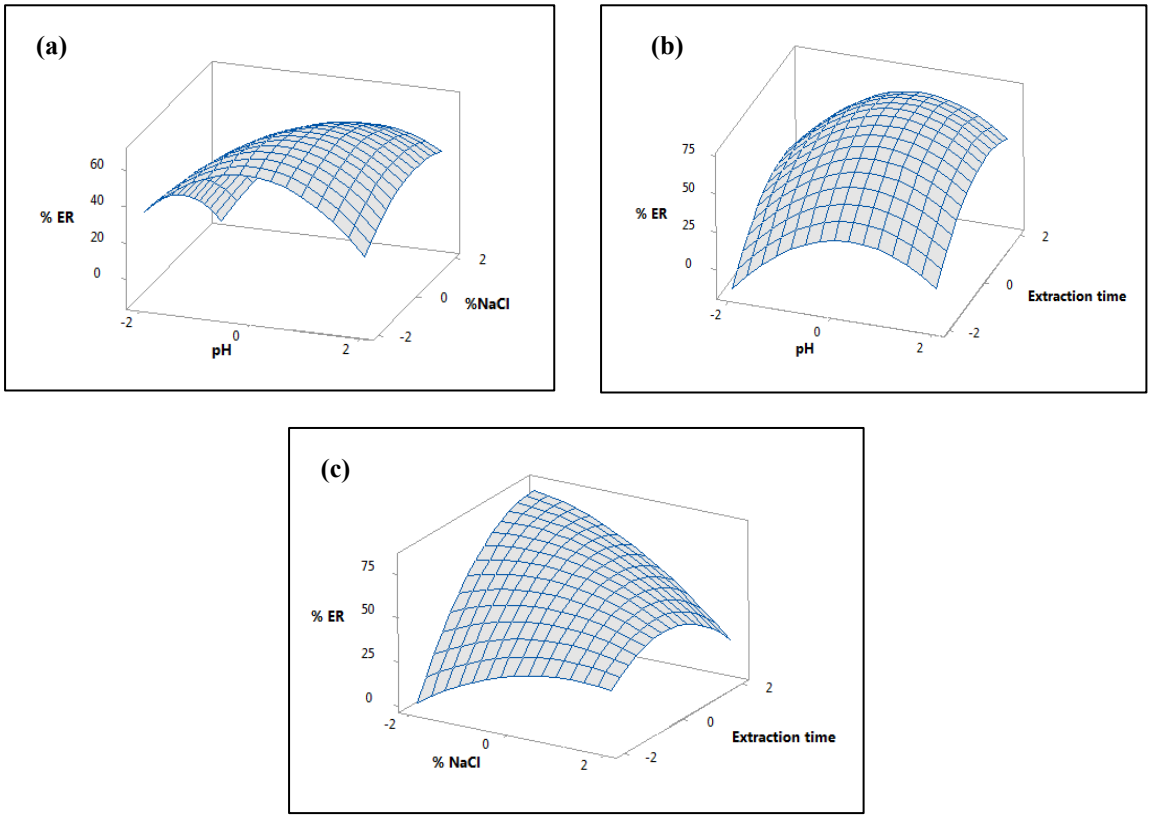


Figure 2. Response surface plots of total extraction recovery as a function of (a) pH *vs* NaCl, (b) pH *vs* extraction time and (c) extraction time *vs* NaCl

However, inert salts, such as sodium chloride, were added during SBSE in order to modify the ionic strength of the sample solution. It has been observed that the addition of inert salt does not improve, but even reduce, the extraction efficiency for hydrophobic analytes (log $K_{o/w} > 3$) [11]. In contrast, for polar analytes (log $K_{o/w} < 3$), the extraction efficiency increased with the addition of salts. Since the log $K_{o/w}$ for atrazine, ametryn, and cyanazine was 2.61, 2.98, and 2.22, respectively, they can be considered as semi polar analytes and the addition of the inert salt was

investigated. Apart from pH adjustment, salt addition showed a significant effect ($P < 0.05$) with a negative sign which indicated the reduction of extraction efficiency with an increase of salt content.

Extraction time is one of the parameters that impact the extraction efficiency. A range of extraction time varying from 5 – 25 min has been studied in this SBSE and the results are shown in Figure 2 (b) and Figure 2 (c). The extraction time has a positive effect upon extraction and increasing the extraction time caused the increase of the extraction recovery of the target triazines.

The multi-response optimization process was done by selecting the Minitab software profile for the selection of optimum conditions of the SBSE. Based on the optimization plot in Figure 3, the suggested optimum conditions suggested were set as: 8.5 (pH), no addition of NaCl, 25 min (extraction time), and 24 min (desorption time). Three additional experiments were carried out under the optimal conditions, in which a good agreement between the calculated and experimental responses was obtained (97.5 % ER) with 3.8% of RSD value.

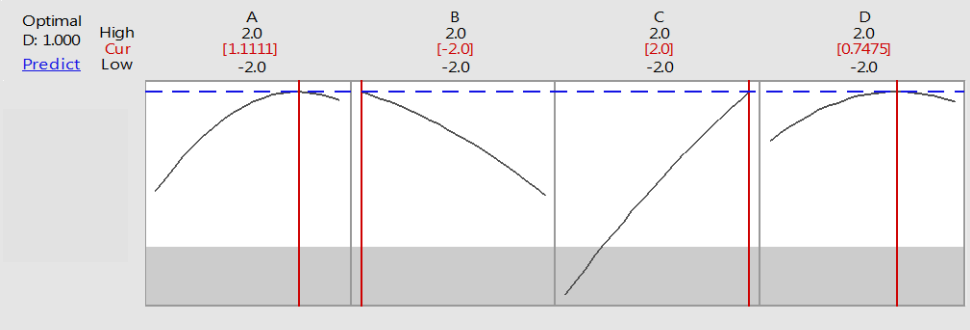


Figure 3. The optimization plots for the central composite design.

Method validation

Under the optimized conditions, analytical performance of the proposed method was evaluated and the results are summarized in Table 3. A good linearity was obtained in a concentration range of 0.10 – 100 μgL^{-1} with correlation of determination (R^2) ranging from 0.9991 – 0.9995. The LODs and LOQs were calculated as the concentration corresponding to signal-to-noise ratios of 3 and 10 respectively. The LODs and LOQs of three triazines were found to be ranging from 0.015 – 0.023 μgL^{-1} and 0.047 - 0.060 $\mu g\ L^{-1}$, respectively, which were lower than the maximum residue limit (MRL) set by European Union (EU) for triazines (a maximum level of 0.10 μgL^{-1} of a pesticide in water samples). The RSDs for three target analytes were in the range of 4.1 – 7.5% (c = 10 μgL^{-1}).

Pan et al. [1] used stir bar sorptive extraction (SBSE) coupled with pulse glow discharge-ion mobility spectrometry (PGD-IMS) for the analysis of triazine herbicides in water samples. The LODs ranged from 0.006 to 0.015 μgL^{-1}. Wu et al. [12] used solid-phase microextraction with graphene-coated fiber for the analysis of triazine herbicides in water samples. The LODs ranged from 0.05 to 0.2 μgL^{-1}. Liu et al. [13] used effervescent tablet assisted on-site liquid phase microextraction for the determination of five triazine herbicides in water by an ultra-high pressure liquid chromatography tandem mass spectrometer. The LODs ranged from 0.002 to 0.008 μgL^{-1}. It is important to note that the detection limits achieved by the proposed method are better than or comparable to those reported previously using different extraction techniques.

Table 3. Analytical performance of the proposed PDMS coated stir bar for the analysis of triazines

Analytes	Linear Equation	Linear Range ($\mu g L^{-1}$)	Correlation Coefficient (R^2)	Limit of Detection ($\mu g\ L^{-1}$)	Limit of Quantification ($\mu g\ L^{-1}$)	Repeatability (%RSD)
Atrazine	y = 2.34x + 3.24	0.1 - 100	0.9991	0.015	0.047	7.5
Ametryn	y = 1.05x + 3.50	0.1 - 100	0.9995	0.023	0.060	4.1
Cyanazine	y = 1.23x + 8.01	0.1 - 100	0.9993	0.018	0.055	5.0

Quantification of partition coefficient and enrichment factor

SBSE is a sample preparation technique based on sorptive extraction. The sorptive extraction process is by nature an equilibrium technique, where the extraction of solutes from the liquid sample phase into the extraction medium is controlled by the partition coefficient (***K***). This coefficient is dependent upon the phase ratio, and thus on the amount of extraction phase used.

The coefficient, *K* shows that to obtain high EF, a low V_e/V_s ratio and high partition coefficient are required. SBSE may be applied to medium polarity and non-polar analytes and to those whose polarities can be reduced before extraction. The major factor affecting EF was the partition coefficient. The EF was directly related to *K*.

In the present study, the amount of atrazine, cyanazine, and ametryn in the PDMS sorbent were calculated using the peak area ratio measurements and the calibration curves of the standards only. Data of the enrichment factor for the target analytes were determined and presented in Table 4 which indicates the correlations between the enrichment factor and partition coefficient. The enrichment factor of cyanazinne was slightly lower as compared to atrazine and ametryn. This was due to the higher solubility of cyanazine in the sample aqueous phase thus reducing its partition into the extraction phase.

Table 4. Analytical performance in term of enrichment factor and partition coefficient

Triazines	Enrichment factor, EF[a]	Partition coefficient, *K*
Ametryn	334	614
Atrazine	316	581
Cyanazine	281	511

[a] Enrichment was determined at concentration of 5.0 $\mu g\ L^{-1}$ for all analytes

Analysis of real samples

In most microextraction techniques, the efficiency of extraction by SBSE can be affected by the composition of the matrix. High levels of dissolved or suspended organic matter contained in real water samples may disrupt analytes from extraction to the stir bar, thus the extraction performance changes from sample to sample.

The relative recovery (RR) was investigated to study the matrix effect towards the extraction efficiency of respective devices [14]. To further evaluate the practical applicability of the proposed method, extraction and analysis were performed on six water samples that were collected from paddy fields (three stations from organic plots and three stations from conventional plots). In order to identify the influence of matrix, the extraction recovery of triazines from real samples were compared with the extraction recovery from ultrapure water sample. The proposed method achieved relative recoveries in the range of 95–98% with RSD values between 3% and 6%.

Conclusion

A study on the extraction of triazines by using a homemade PDMS-coated stir bar was successfully carried out. By applying the experimental design, behaviour of each variable and their interaction during the extraction and

desorption procedures were discriminated using the ANOVA test. In this study, the SBSE parameters affecting the extraction recovery have been optimized as follows: sample at pH 8.5, no addition of NaCl, 25 minutes of extraction time, and 24 minutes of desorption time. A low V_E/V_S ratio and high partition coefficient offered a high enrichment factor. The enrichment factor was directly related to the partition coefficient. Overall, the proposed procedure was proven to be a good alternative methodology for the determination of selected triazine residues in environmental samples, being a simple, fast, reproducible, effective and an environmentally-friendly analytical method.

Acknowledgments

We highly express our sincere gratitude to Universiti Kebangsaan Malaysia for the research facilities and the Ministry of Education (MOE) for the funding this work under the SLAB/SLAI scheme.

References

1. Pan, C., Zou, N., Yuan, C., Liu, S., Han, Y., Li, Y. and Zhang, J. (2016). Coupling of multi-walled carbon nanotubes/polydimethylsiloxane coated stir bar sorptive extraction with pulse glow discharge-ion mobility spectrometry for analysis of triazine herbicides in water and soil samples. *Journal of Chromatography A*, 1457: 14-21.
2. Chen, L., Wen, Y., Chen, L., Li, J. and Liu, D. (2014). Recent advances in solid-phase sorbents for sample preparation prior to chromatographic analysis. *Trends in Analytical Chemistry*, 59: 26-41.
3. Sharif, M., Khodadoust, S., Mousavi, A. and Mahmoudi, R. (2017). Preconcentration of carbamate insecticides in water samples by using modified stir bar with ZnS nanoparticles loaded on activated carbon and their HPLC determination : Response surface methodology. *Microchemical Journal*, 130: 64-70.
4. Lei, Y., He, M., Chen, B. and Hu, B. (2016). Polyaniline / cyclodextrin composite coated stir bar sorptive extraction combined with high performance liquid chromatography-ultraviolet detection for the analysis of trace polychlorinated biphenyls in environmental waters. *Talanta*, 150: 310-318.
5. Zhang, H., Low, W. P. and Lee, H. K. (2012). Evaluation of sulfonated graphene sheets as sorbent for micro-solid-phase extraction combined with gas chromatography–mass spectrometry. *Journal of Chromatography A*, 1233, 16-21.
6. Baltussen, E., Sandra, P., David, F. and Cramers, C. (1999). Stir bar sorptive extraction (SBSE), a novel extraction technique for aqueous samples: Theory and principles. *Journal of Microcolumn Separations*, 11(10): 737-747.
7. Ayazi, Z. and Matin, A. A. (2016). Development of carbon nanotube–polyamide nanocomposite-based stir bar sorptive extraction coupled to HPLC-UV applying response surface methodology for the analysis of bisphenol a in aqueous samples. *Journal of Chromatographic Science*, 4: 1-10.
8. Manuel, J. and Nogueira, F. (2015). Stir-bar sorptive extraction : 15 years making sample preparation. *Trends in Analytical Chemistry*, 71: 214-223.
9. Blasco, C., Fernández, M., Picó, Y. and Font, G. (2004). Comparison of solid-phase microextraction and stir bar sorptive extraction for determining six organophosphorus insecticides in honey by liquid chromatography – mass spectrometry. *Journal of Chromatography A*, 1030: 77-85.
10. Lei, Y., Chen, B., You, L., He, M. and Hu, B. (2017). Polydimethylsiloxane / MIL-100 (Fe) coated stir bar sorptive extraction-high performance liquid chromatography for the determination of triazines in environmental water samples. *Talanta*, 175: 158-167.
11. Ayazi, Z. and Rafighi, P. (2015). Preparation and application of a carbon nanotube reinforced polyamide-based stir bar for sorptive extraction of naproxen from biological samples prior to its spectrofluorometric determination. *Analytical Methods*, 7: 3200-3210.
12. Wu, Q., Feng, C., Zhao, G., Wang, C. and Wang, Z. (2012). Graphene-coated fiber for solid-phase microextraction of triazine herbicides in water samples. *Journal of Separation Sciences*, 35: 193-199.
13. Liu, D., Liu, X., Shen, Z., Wang, P., Liu, C. and Zhou, Z. (2014). Effervescence assisted on-site liquid phase microextraction for the determination of five triazine herbicides in water. *Journal of Chromatography A*, 1371: 58-64.
14. Sanagi, M. M., See, H. H., Ibrahim, W. A.W. and Naim, A. A. (2010). Determination of triazine herbicides using membrane-protected carbon nanotubes solid phase membrane tip extraction prior to micro-liquid chromatography. *Journal of Chromatography A*, 1217: 1767-1772.

Malaysian Journal of Analytical Sciences, Vol 22 No 1 (2018): 54 - 63
DOI: https://doi.org/10.17576/mjas-2018-2201-07

MALAYSIAN JOURNAL OF ANALYTICAL SCIENCES
Published by The Malaysian Analytical Sciences Society
ISSN 1394 - 2506

MICROEMULSION ELECTROKINETIC CHROMATOGRAPHY COUPLED WITH DISPERSIVE MICRO-SOLID PHASE EXTRACTION FOR DETERMINATION OF ISOFLAVONES IN SOYBEAN PRODUCTS

(Kromatografi Elektrokinetik Mikro-Emulsi Berganding dengan Pengekstrakan Fasa Pepejal Mikro Serakan bagi Pengenalpastian Isoflavon di dalam Produk Kacang Soya)

Khaulah Ab Rahim[1], Mohd Marsin Sanagi[1,2]*, Dadan Hermawan[3], Wan Aini Wan Ibrahim[1,2], Aemi Syazwani Abdul Keyon[1]

[1]*Department of Chemistry, Faculty of Science*
[2]*Centre for Sustainable Nanomaterials, Ibnu Sina Institute for Scientific and Industrial Research*
Universiti Teknologi Malaysia, 81310 UTM Johor Bahru, Johor, Malaysia
[3]*Department of Chemistry, Faculty of Science and Engineering,*
Universitas Jenderal Soedirman (UNSOED), Purwokerto, Indonesia

**Corresponding author: marsin@kimia.fs.utm.my*

Received: 26 August 2017; Accepted: 27 December 2017

Abstract

A new method based on microemulsion electrokinetic chromatography (MEEKC) coupled with dispersive micro solid phase extraction (D-µ-SPE) was developed for the determination of isoflavones in soy products. D-µ-SPEs of real samples were carried out using multi-walled carbon nanotubes (MWCNTs) as adsorbent prior to MEEKC. Separations of selected isoflavones namely daidzein, genistein and formononetin by MEEKC were carried out using fresh daily-prepared microemulsion background electrolyte (BGE). The optimized MEEKC conditions for the separation of isoflavones were 4 mM borate buffer pH 8.5, 6.6% (w/v) 1-butanol, 0.9% (w/v) sodium dodecyl sulphate, 0.75% (w/v) ethyl acetate, 3% (w/v) acetonitrile at 3 s injection time, 27 kV and 35 °C. Meanwhile, the optimum D-µ-SPE conditions were 5 mg of MWCNTs and 300 µL of methanol as desorption solvent. Under the optimized conditions, the developed D-µ-SPE-MEEKC method showed good linearity in the concentration range of 1-10 mg/L with coefficients of determination (r^2) > 0.99 and limits of detection of 0.27-0.95 mg/L. The method was successfully applied to the determination of isoflavones in five soybean products namely soy supplement, tofu, tempeh, egg tofu and fujook and good recoveries were obtained in the range of 74.5-112.5% with RSDs of < 3%. The method has proved to be simple and offers low consumption of organic solvent and relatively short analysis time, thus it is a potentially viable green alternative method for extraction and determination of isoflavones in soybean products.

Keywords: microemulsion electrokinetic chromatography, background electrolyte, dispersive micro solid phase extraction, isoflavones, soybean products

Abstrak

Satu kaedah baharu berasaskan kromatografi elektrokinetik mikroemulsi (MEEKC) berganding dengan pengekstrakan fasa pepejal mikro serakan (D-µ-SPE) telah dibangunkan bagi menentukan isoflavon di dalam produk kacang soya. D-µ-SPE sampel sebenar telah dijalankan menggunakan tiub nano karbon dinding berganda (MWCNT) sebagai penjerap sebelum MEEKC. Pemisahan isoflavon terpilih iaitu daidzein, genistein dan formononetin dengan MEEKC telah dijalankan menggunakan mikroemulsi elektrolit latar belakang (BGE) baharu yang disediakan setiap hari. Keadaan optimum MEEKC untuk pemisahan isoflavon ialah 4 mM penimbal borat pH 8.5, 6.6% (w/v) 1-butanol, 0.9% (w/v) natrium dodekil sulfat, 0.75% (w/v) etil asetat, 3% (w/v) asetonitril pada masa suntikan 3 s, 27 kV dan 35°C. Sementara itu, keadaan optimum untuk pengekstrakan ialah 5 mg

MWCNT dan 300 µL metanol sebagai pelarut penyaherapan. Di bawah keadaan optimum, kaedah D-µ-SPE-MEEKC yang dibangunkan menunjukkan kelinearan yang baik dalam julat 1-10 mg/L dengan pekali penentuan (r^2) > 0.99 dan had pengesanan 0.27-0.95 mg/L. Kaedah D-µ-SPE-MEEKC telah berjaya digunakan dalam penentuan isoflavon di dalam lima produk soya iaitu makanan tambahan soya, tofu, tempe, tauhu telur dan kulit tauhu dengan kadar pengembalian 74.5 – 112.5% dan sisihan piawai relatif (RSD) < 3%. Kaedah ini terbukti mudah dan ia menggunakan pelarut organik yang sedikit dan memberi masa analisis yang cepat, justeru berpotensi sebagai kaedah hijau berdaya saing bagi pengekstrakan dan penentuan isoflavon di dalam produk kacang soya.

Keywords: Kromatografi elektrokinetik mikroemulsi, elektrolit latar belakang, pengekstrakan fasa pepejal mikro serakan, isoflavon, produk kacang soya

Introduction

Nutritional supplements based on soy extract are rapidly growing segment in the food and health care market. Due to their content of phytoestrogens, these supplements are especially offered for postmenopausal women as an alternative to the traditional hormone replacement therapy [1, 2]. Phytoestrogens are found in plants and food products as glycosidic conjugate. In fermented food, they are deconjugated to aglycones. Based on the structural similarity to the mammalian estrogen, isoflavones can bind to the receptors and show weak estrogenic activities [3]. Isoflavones is a class of organic compound and biomolecules related to the flavonoids and classified to four major subgroups according to their functional groups namely aglycones, glucosides, malonylglucosides and acetyl glucosides.

Isoflavones have been investigated in a number of clinical and in animal studies to determine their health protective effects. Isoflavones were reported to reduce the risk of cardiovascular disease, prostate, breast and colon cancer. In addition, isoflavones improve bone health by alleviating symptoms of osteoporosis which occurs after menopause. To date, 12 chemical forms of isoflavones have been found in soybeans [4], including 4-aglycones (major isoflavones in soybean) namely daidzein, genistein, glycitein and formononetin, 3 glucosides which are daidzin, genistin and glycitin [5]. The other forms of isoflavones are in malonylglucoside and acetyl glucoside groups. The basic characteristic isoflavone structure is a flavones nucleus, composed of two benzene rings linked to heterocyclic ring. The structure of some isoflavones component is shown in Figure 1.

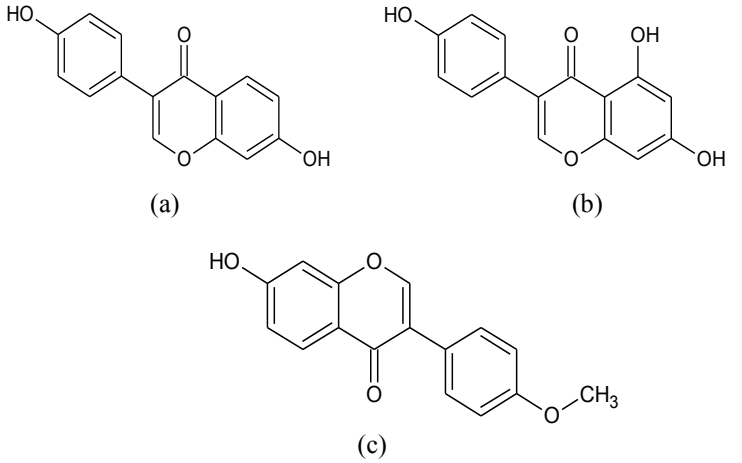


Figure 1. Structures of (a) daidzein, (b) genistein, and (c) formononetin

Several analytical methods to determine the isoflavones have been reported in the last few years including the high performance liquid chromatography (HPLC) with UV [6], gas chromatography (GC) coupled to mass spectrometry [7], and electrophoresis [8]. Among these methods, capillary electrophoresis has a great potential for the determination of isoflavones in soybean because it offers interesting advantages such as ease of automation, low solvent consumption, small sample volume, reproducible and high separation efficiency.

Microemulsion electrokinetic chromatography (MEEKC) is a mode of capillary electrophoresis (CE). It is a technique that separates solutes based on their hydrophobicities and electrophoretic mobilities [9] which offers highly efficient separation of both charged and neutral solutes covering wide range of water solubility. It has been demonstrate as a reliable separation for both highly hydrophobic and hydrophilic compounds [10, 11, 12]. This technique uses an aqueous buffer containing droplet of oil, surfactant and co-surfactant to form a microemulsion background electrolyte (BGE) solution [13]. The most frequently used microemulsion BGE solution uses a water-immiscible solvent (oil), such as *n*-heptane or *n*-octane and a surfactant such as sodium dodecyl sulfate (SDS) in an aqueous buffer such as borate or phosphate. A co-surfactant such as butanol is often added to improve the microemulsion stability.

Microemulsions are solution containing nano-meter size droplets of immiscible liquids dispersed in an aqueous buffer. Normally, the microemulsion droplets contain buffer, surfactant, co-surfactant, organic modifier and oil (ethyl acetate or *n*-octane) [14, 15]. The droplets are coated with surfactant to reduce the surface tension between the two liquid layers allowing an emulsion to form. The surface tension of the droplet is further lowered by the addition of short-chain alcohol, such as butanol, which stabilizes the system. The diameter of the oil droplets is below 10 nm giving an optically transparent emulsion; larger droplets would scatter light making an opaque emulsion [16].

A microemulsion containing ionic surfactant allows chromatographic separation to be obtained as solutes can partition between the charged oil droplets and the aqueous buffer phase. Water-insoluble compounds will favour inclusion into the oil droplets rather than into the buffer phase. The more hydrophobic the solute is, the more it will partition into the microemulsion droplet and the longer it will migrate to the detector.

Sample preparation is the most important part in chemical analysis. Extensive sample cleanup procedures are usually required to remove matrix components which may interfere the analysis. Dispersive micro solid phase extraction (D- µ-SPE) allows the direct contact between the analytes with the sorbents because of the homogenous dispersion of the solid in the extract. In the present study, the applicability of D-µ-SPE using carbon nanotube (CNT) as sorbents for the first time to simply extract daidzein, genistein and formononetin in soybean supplement and soybean food was investigated. The advantages of this technique are its easy miniaturization: small sample volume, less organic solvent and sorbent needed, short time requirement and convenience for efficiency of recovery.

This work was set out to develop an environmental friendly for analysis of isoflavones namely daidzein, genistein and formononetin using water in oil microemulsion electrokinetic chromatography (MEEKC) coupled with (D-µ-SPE). The method was validated and applied to the determination of isoflavones in soybean supplement and fermented soybean meal.

Materials and Methods

Materials, method and instruments

Standard of isoflavones (daidzein, genestein and formononetin) were purchased from Sigma-Aldrich (St. Louis, MO, USA). Sodium dodecyl sulfate (SDS) was purchased from Fischer Chemicals (Loughborough, Leics, UK) while sodium hydroxide, boric acid and sodium tetraborate anhydrous were purchased from Merck (Darmstadt, Germany). Methanol, 1-butanol, ethyl acetate and acetonitrile purchased from J.T Baker (Pennsylvania, USA). Deionized water was purified by Millipore Simplicity (Simpak©2).

Stock solutions of 1000 mg/L isoflavones (daidzein, genistein, formononetin) were prepared with methanol as solvent. Standard working solutions of 25, 50, 100 and 200 mg/L were prepared by diluting the stock solution with methanol. The stock solutions and all standards working solutions prepared were labelled and sealed to avoid evaporation of solution and stored in refrigerator until use.

An Agilent Technology Capillary Electrophoresis System (Wald-Bronn, Germany) equipped with diode array detection (DAD) operating at 254 nm was used. An uncoated fused-silica capillary of 50 µm inner diameter (I.D) with a total length of 64.5 cm (56 cm to detector) was used for the separation process. Each new capillary used was

conditioned for 10 min with 1.0 N NaOH and then equilibrated with Milli-Q water for 30 min, followed by 0.1 N NaOH for 30 min, after that Milli-Q water for 30 min, and finally with background electrolyte (BGE) for 30 min. The capillary was pre-conditioned for 2 min with BGE and post-conditioned with 0.1 N NaOH and Milli-Q water for 2 min between analyses. When the capillary was not in use, it was flushed using air for 5 min and stored.

Preparation of microemulsions

Sodium tetraborate buffer (4 mM) was prepared by dissolving 0.9534 g of sodium tetraborate anhydrous using deionized water in a 250-mL volumetric flask.The buffer solution was diluted to the mark after the solution was adjusted to pH 8.5 using 2 M boric acid. Microemulsions (ME) were prepared as follows: 17.75 g of buffer and 0.18 g surfactant (SDS) were mixed. Subsequently, 0.15 g of oil (ethyl acetate), 1.32 g co-surfactant (1-butanol) and 0.6 g of organic modifier (acetonitrile) were added. The solution obtained was sonicated for 20 minutes to aid the dissolution. The ME solution was filtered through 0.22 μm nylon syringe to remove impurities. All of the ME solutions used in this research were prepared using similar method daily.

Sample pretreatment and extraction procedure

The dispersive-μ-solid phase extraction (D-μ-SPE) procedure used in this study was adopted from a previous study [17] with some modifications. The proteins and fats in 10 mL samples were precipitated by shaking vigorously with 3 mL of a mixture of acetone and acetonitrile (2:1, v/v). The solution was then centrifuge at 4000 rpm for 5 minutes. The supernatant was evaporated in a nitrogen atmosphere to eliminate the organic solvents. The D-μ-SPE procedure involved immersing 5 mg of carbon nanotube (CNT) in a 10 mL of the deproteinized sample in a centrifuge tube. After 10 minutes of extraction by vigorous shaking using vortex and centrifuge at maximum speed, the adsorbents were collected and desorbed with 300 μL of methanol. After incubation for 5 minutes, the adsorbent were filtered and easily removed by filter device (0.45 μm) from the desorption solvent. The extract was then directly injected to CE for analysis.

Results and Discussion

Optimization of MEEKC system

A microemulsion composed of SDS, 1-butanol, ethyl acetate and aqueous buffer has been the most frequently used electrophoretic medium in MEEKC [10]. Therefore, this mixture was selected to explore the potential of MEEKC to determine the isoflavones in soybean. The influence of specific parameters such as surfactant concentration, co-surfactant, organic modifier and oil, applied voltage, pH buffer, injection time and temperature were systematically investigated.

Effect of applied voltage, temperature and injection time

The capillary temperature can affect solute stability which is related to the partitioning coefficient. The electrophoretic mobility of an ion is also affected by temperature [3]. The temperature leads to a reduction of migration times by decreasing the buffer viscosity. This phenomenon can be explained with the increasing of EOF when higher temperature is applied into the microemulsion system. When the EOF was increased, the migration time of the analyte decreased due to the strong sweeping process of the analyte towards the cathode by the EOF. However, higher temperature could enhance the band broadening and decrease the peak efficiency [18]. Considering the migration time, temperature of 35°C was selected as the best condition for the determination of isoflavones using MEEKC method.

Meanwhile, the effect of applied voltage in the range of 25-30 kV was studied. Application of higher voltage (30 kV) has resulted in obvious decrease in the resolution due to the increased Joule heating. However, use of lower voltage (25 kV) resulted in longer migration times. Therefore, the optimum voltage for analysis was chosen at 27 kV as it gave faster analysis time and greater peak area. Figure 1 shows the effect of applied voltage to peak area. Higher applied voltage may damage the capillary used due to Joule heating.

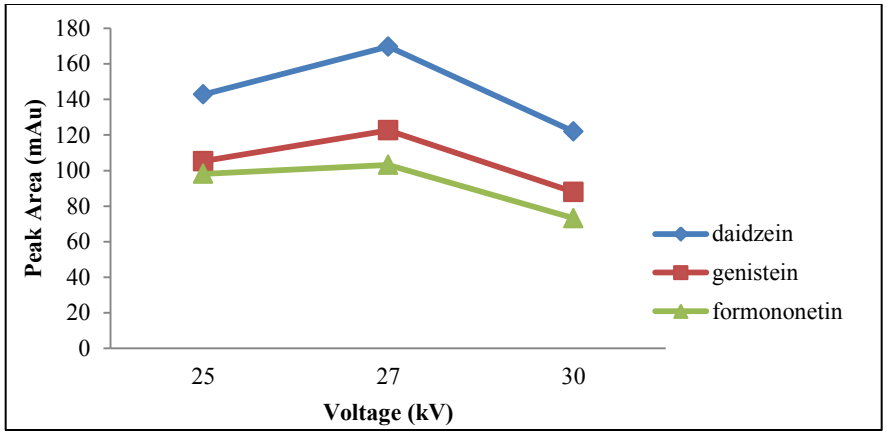


Figure 1. Effect of voltage on peak area on MEEKC (n = 3 in each case)

A small sample zone and short injection time reduce band broadening and maintain efficient peaks with high plate numbers. This improves injection volume precision but only works well if the injection time is at least 3 s. In this study, the injection time was varied in the range of 2-5 s. Apparently; shorter injection time resulted in improved resolution of the peaks. At higher injection time, the isoflavones were not well-separated because of the excessive amounts of analyte per injection. Thus, 3 s was selected to be the optimum injection time.

Effect of composition in background electrolyte: **Effect of buffer pH, buffer, surfactant and co-surfactant concentration**

Buffer pH influences the degree of capillary ionization and hence the EOF velocity. At high pH, the EOF may be so rapid that incomplete separations may occur. However, at lower pH where the EOF is greatly reduced, both cations and anions can be measured [19]. In this work, with the concentration of 10 mM borate buffer unchanged, different pH values ranging from 8-9 were tested. Taking into account the resolution, peak area and migration time, pH 8.5 was chosen for subsequent experiments.

Generally, MEEKC was performed using low ionic strength of borate or phosphate buffer. These generate relatively low currents and a reasonably fast EOF. Higher buffer concentrations suppress the EOF and generate high currents which may limit the level of voltage that can be applied. In optimizing the MEEKC of isoflavones, the buffer concentration in the range of 3-5 mM was investigated. Taking into account the migration time and the peak area, 4mM buffer concentration was chosen as the optimum and used in subsequent experiments.

Surfactant plays main role in lowering the surface tension between the oil and aqueous phase of ME. SDS is anionic surfactant which penetrates into the oil droplet. The choice of surfactant has a marked effect on the separation achieved in MEEKC as it affects the oil droplet charge and size, the level and direction of EOF [3]. Increasing the surfactant concentration will increases the ionic strength of the buffer which reduces the EOF level and increase analysis time. SDS concentrations ranging of 0.8-1.0 % w/w were investigated for optimization study. Figure 2 shows the effect of SDS concentration towards migration time. The fastest migration time was obtained at concentration of SDS of 0.9.

The size of oil droplet increases with increased co-surfactant concentration that will affect the charge density of the droplet. Studies have shown that the separation selectivity is unaltered [9] by variation of 1-butanol concentration. Higher 1-butanol concentration reduces migration times for water insoluble solute but do not alter the capacity factors. The migration times are altered with varying co-surfactant concentration as it affects the solution viscosity which in turns affects the EOF rate. Even though 3.3% 1-butanol concentration gave the fastest migration time, the peak area and peak height is the lowest. The optimum condition for separation of isoflavones was achieved using 6.6% 1-butanol concentration. Table 1 summarizes the MEEKC parameters optimized in this work.

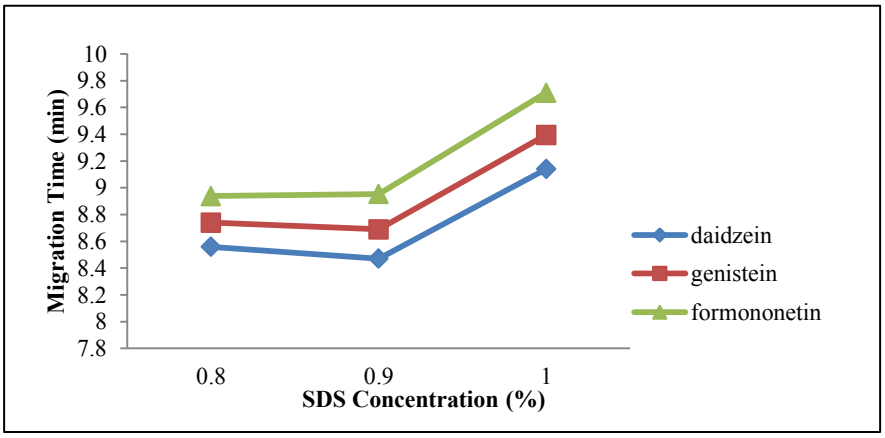


Figure 2. Effect of SDS concentration on migration time

Table 1. Parameters evaluated in the MEEKC system

Parameters	Optimized Condition
Applied voltage (kV)	27
Temperature (°C)	35
Injection time (s)	3
pH buffer	8.5
Buffer concentration (%)	88.75
SDS concentration (%)	0.9
1-butanol concentration (%)	6.6
Acetonitrile concentration (%)	3
Ethyl acetate concentration (%)	0.75

Optimization of D-μ-SPE

According to previous studies [20, 17], there are three important parameters that affect the extraction efficiency of D-μ-SPE: type of adsorbent, amount of adsorbent and type of desorption solvent. Optimization was carried out in triplicate using spiked deionized water spiked with daidzein, genistein and formononetin at a concentration of 1 μg mL^{-1}.

The first parameter studied was the type of adsorbent. For this purpose, three different adsorbents namely multi-walled carbon nanotubes (MWCNT), primary secondary amine (PSA) and octadecyl-silylsilica (C18) were evaluated. Ideal carbonaceous adsorbent should have large surface area to enhance the adsorption efficiency and extraction characteristics of the organic compounds from aqueous solutions. CNT offered the best peak area after extraction of isoflavones as it has high surface area, chemical stability and mechanical strength [21]. The ability of CNT to establish π–π interactions as well as excellent Van der Waals interaction with hydrophobic molecules (existence of aromatic ring) make them suitable for the extraction of isoflavones. Many applications of CNT as sorbent have been reported for extraction such as herbicide in tobacco [22], pesticide from water [20] and nitrosamines in meat products [17]. To our best knowledge, no work has been reported on the use of MWCNT as sorbent for the extraction of isoflavones from soybean products.

Amount of sorbent was studied in this work. The quantity of CNT added into the sample was varied between 1 and 7 mg. As expected, the peak area increased as the amount of adsorbent increased up to 5 mg. However, when 7 mg

MWCNT was added, the peak area of daidzein, genistein and formononetin decrease. Therefore, 5 mg of MWCNT was chosen as optimum amount of adsorbent as the recovery values are acceptable (104-117 %).

Once the analytes have been extracted, they should be eluted for the analysis. Four commonly used desorption solvent (methanol, acetonitrile, isopropanol and ethanol) were evaluated in this work. Methanol provides the best and more reproducible recovery values and the relative standard deviations were acceptable in all assays with values lower than 2.1 %. The effect of desorption solvent to the peak area is shown in Figure 3. 300 µL of methanol provided the best elution in terms of precision and sensitivity. Although isopropanol showed the highest peak area, it was not chosen because it resulted in noisy baselines that became worse with repeated injections probably due to interferences from impurities.

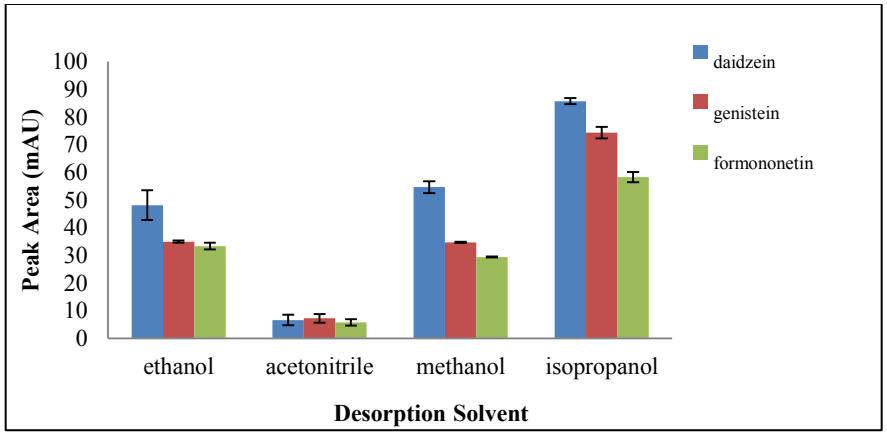


Figure 3. Effect of desorption solvent on peak area

Method validation

In order to determine the linearity and precision of the method, a series of standard solutions of the three isoflavones at concentrations in the range of 1-10 µg/mL were analyzed. In general, the three targeted analytes were successfully separated with good resolution. Results from regression analysis of three calibration curves and detection limits are presented in Table 2. The RSD values were < 3.35%, which indicated that the method enabled the accurate simultaneous determination of the three analytes.

The detection limits were evaluated on the basis of a single-to-noise ratio of 3:1. Under the optimized conditions, the calibration curves of the isoflavones showed good linearity in the concentration range of 10-100 µg/mL with coefficients of determination (r^2) > 0.99 and limit of detections range from 0.27µg/mL to 0.95 µg/mL.

A standard mixture solution of three isoflavones was determined in triplicate in order to determine the reproducibility of the peak area and migration time for all analytes under optimum conditions.

Table 2. Parameters for the extraction standard curves for isoflavones

Compound	Regression Equation	Correlation Coefficient	Linear Range (µg/mL)	Detection Limit (µg/mL)	RSD (%)
Daidzein	y = 10.056x	0.9922	1-10	0.95	1.49
Genistein	y = 7.7467x – 6.0181	0.9969	1-10	0.58	3.35
Formononetin	y = 6.8084x – 4.8344	0.9995	1-10	0.27	1.67

Analyte recovery

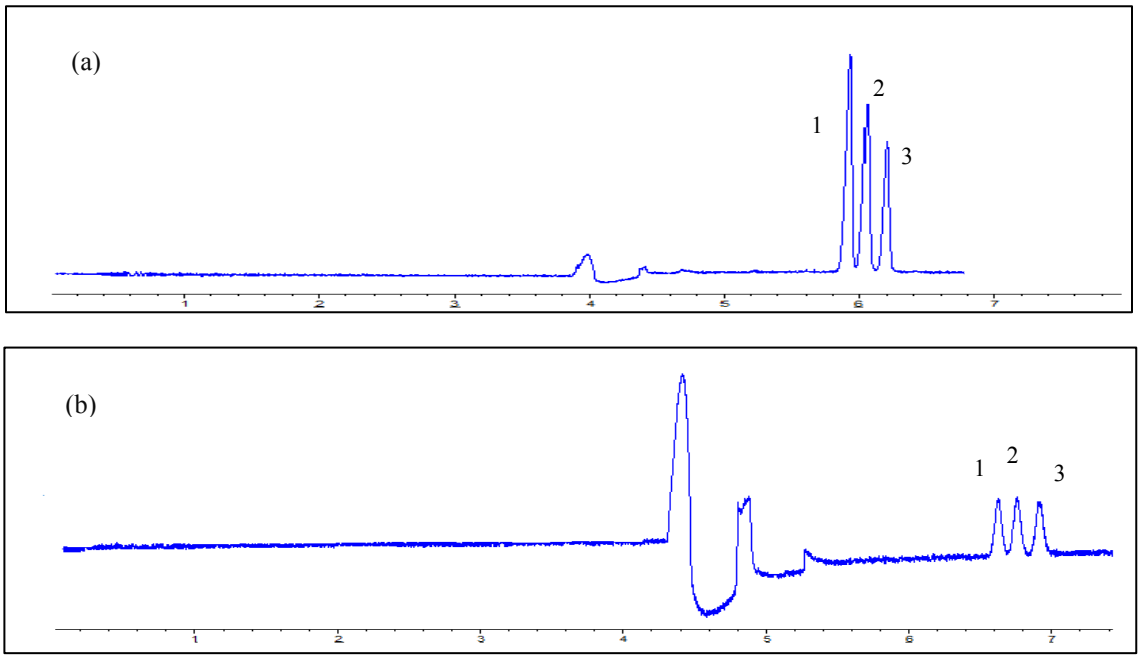
Accurate amounts of three standards were added into the real soybean meal samples with known contents of the desired compounds. The mixtures prepared using the same method as described in the sample pretreatment and extraction procedure section were analyzed using the developed MEEKC method. The percentage analyte recoveries are shown in Table 3. Under the optimized conditions, the recoveries of the investigated compounds ranged from 104.6-120.0%, with RSDs < 2.2% which indicated that the method enabled the accurate simultaneous determination of the three analytes.

Table 3. Recoveries of three isoflavones (n = 3)

Sample	Compound	Recovery (%)	RSD (%)
Tempeh	Daidzein	120.0	1.25
	Genistein	119.0	2.11
	Formononetin	112.9	0.96
Soy supplement	Daidzein	107	1.23
	Genistein	117.7	1.42
	Formononetin	104.6	0.91

Application of D-μ-SPE-MEEKC to soybean products

The develop method was applied to two samples namely tempeh and soy supplement. Both samples were purchased from local market in Johor, Malaysia. The three target isoflavones were all successfully baseline-separated within 8 minutes. Typical electropherograms of the separation of standard isoflavones and extracted isoflavones from samples are shown in Figure 4. It was found that higher amount of genistein, daidzein and formononetin extracted in soy supplement than tempeh. This might be due to the fermentation process and heat supply during the process [23]. Higher recoveries of extraction of the aglycones in tempeh (112.9-120%) and soy supplement (104.6-117.7%) showing that this technique has a lot of potential in the determination of isoflavones in other soy food.



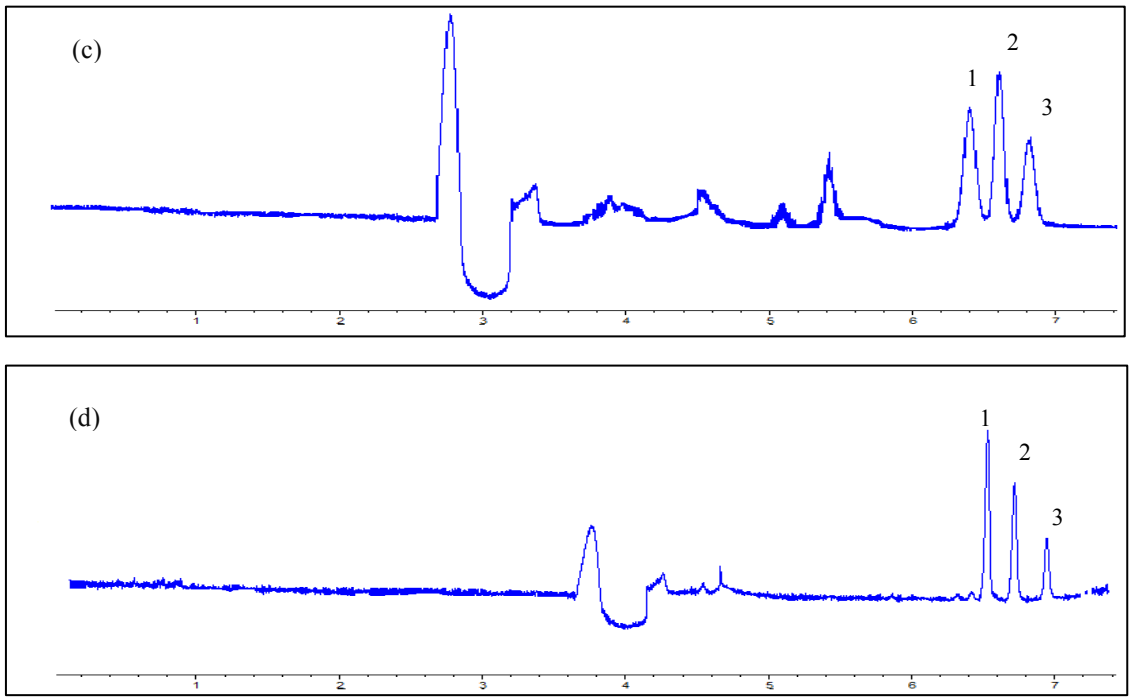


Figure 4. Electropherograms for isoflavones (a) standard mixture solution (100 µg/mL), (b) standard mixture solution after extraction (10 µg/mL), (c) soy supplement and (d) tempeh. Running buffer: 4 mM borate buffer pH 8.5, 6.6% 1-butanol, 0.9% sodium dodecyl sulpahate, 0.75% ethyl acetate, 3% acetonitrile at 3s injection time, 27 kV and 35 °C. Peak identities: 1 = genistein, 2 = daidzein, 3 = formononetin

Conclusion

A newly developed MEEKC method combine with D-µ-SPE was applicable for the determination of isoflavones in soybean meal and supplement. Three isoflavones were successfully separated within 8 minutes, which is three times faster than reported work by Xiao et al. [8]. Minimum usage of organic solvent and small sample volume make this method environmental friendly. The high recoveries and low RSD values demonstrated in this study proved that MEEKC-D-µ-SPE is capable to become a new technique for determination of isoflavones.

Acknowledgement

The authors would like to thank Universiti Teknologi Malaysia and the Ministry of Higher Education Malaysia (MOHE) for financial supports through research grants number Q.J130000.2526.03H79 and R.J130000.7809.4F177 and studentship for Khaulah Ab Rahim.

References

1. Rangel, M. B., Zamarreno, M. M. D., Martinez, R. C. and Alvarez, J. D. (2012). Analysis of isoflavones in soy drink by capillary electrophoresis coupled with electrospray ionization mass spectrometry. *Analytica Chimica Acta,* 709: 113 – 119.
2. Achouri, A., Boye, J. I. and Belanger, D. (2005). Soybean isoflavones: Efficiency of extraction conditions and effect of food type on extractability. *Food Research International*, 38: 1199 – 1204.
3. Sturtz, M., Lander, V., Schimd, W. and Winhalter, P. (2008). Quantitative determination of isoflavones in soy based nutritional supplements by high-performance liquid chromatography. *Journal of Consumer Protection and Food Safety,* 3: 127 – 136.

4. Taku, K., Melby, K. M., Takebayashi, J., Mizuno, S., Ishimi, Y., Omori. T. and Watanabe, S. (2010). Effect of soy isoflavone extract supplements on bone mineral density in menopausal women: meta-analysis of randomized controlled trials. *Asia Pacific Journal of Clinical Nutrition,* 19: 33 – 42.
5. Ming, S. J., Li, S. B., Rong, Y. S, Hua. Y. and Kikuchi, A. (2011). Rapid HPLC method for determination of 12 isoflavone components in soybean seeds. *Agricultural Sciences in China,* 1: 70 – 77.
6. Garc′ia, M. C., Marina, M. L. and Torre, M. (2000). Determination by perfusion reversed-phase high-performance liquid chromatography of the soybean protein content of commercial soybean products prepared directly from whole soybeans. *Journal of Chromatography A*, 880: 37 – 46.
7. Magiera, S., Uhlschmied, C., Rainerb, M., Huck, C. W., Baranowska, I. and Bonn, G. K. (2011). GC-MS method for the simultaneous determination of blockers, flavonoids, isoflavones and their metabolites in human urine. *Journal of Pharmaceutical and Biomedical Analysis,* 56: 93 – 102.
8. Xiao, M., Ye, J., Tang, X. and Huang, Y. (2011). Determination of soybean isoflavones in soybean meal and fermented soybean meal by micellar electrokinetic capillary chromatography. *Food Chemistry,* 126: 1488 – 1492.
9. Altria, K. D. (2000). Background theory and applications of microemulsion electrokinetic chromatography. *Journal of Chromatography A,* 892: 171 – 186.
10. Mahuzier, P. E., Aurora, M. S., Clark, B. J., Hackmann, E. R. M. and Altria, K. D. (2003). An introduction to the theory and application of microemulsion electrokinetic chromatography. *LC-GC Europe,* 16(1): 22 – 29.
11. Jandera, P., Fischer, J., Jebava, J. and Effenberger, H. (2001). Characterization of retention in micellar high performance liquid chromatography and in micellar electrokinetic chromatography with reduced flow. *Journal of Chromatography,* 914: 233 – 244
12. Nakamura, H., Sano, A. and Matsuura, K. (1998). Determination of micelle concentration of anionic surfactant by capillary electrophoresis using 2-naphthalenemethanol as a marker for micelle formation. *Journal of Analytical Science,* 14, 379-372
13. Puyana, M. C., Crego, A. L. and Marina, M. L. (2008). Recent advances in the analysis of antibiotics by CE and CEC. *Electrophoresis*, 29: 274 – 293.
14. McEvoy, E., Marsh, A., Altria, K., Donegan, S. and Power, J. (2007). Recent advances in the development and application of microemulsion EKC. *Electrophoresis,* 28: 193 – 207.
15. Ryan, R., Altria, K.D., Donegan, S. and Power, J. (2013). Developments in the methodology and application of microemulsion electrokinetic chromatography. *Electrophoresis,* 34: 154 – 177.
16. Chuerkaoui, S. and Veuthey, J. L. (2002). Micellar and microemulsion electrokinetic chromatography of selected anesthetic drugs. *Journal of Separation Science,* 25: 1073 – 1078.
17. Huang, M. C., Chen, H. C., Fu, S. C. and Ding, W. H. (2013). Determination of volatile *n*-nitrosamines in meat products by microwave-assisted extraction coupled with dispersive micro solid-phase extraction and gas chromatography- chemical ionization mass spectrometry. *Food Chemistry,* 138: 227 – 233.
18. Miola, F. M., Snowden, M. J. and Altria, K. D. (1998). The use of microemulsion electrokinetic chromatography in pharmaceutical analysis. *Journal of Pharmaceutical and Biomedical Analysis,* 18: 785 – 797.
19. Himmelsbach, M., Haunschmidt, M., Buchberger, W. and Klampfl, C. W. (2007). Microemulsion electrokinetic chromatography with on-line atmospheric pressure. *Analytical Chemistry,* 79: 1564 – 1568.
20. Soto, J. M. J., Cardenas, S. and Valcarcel, M. (2012). Dispersive micro solid-phase extraction of triazines from waters using oxidized single-walled carbon nanohorns as sorbent. *Journal of Chromatography A,* 1245: 17 – 23.
21. Zhou, Y. G., Chen, X. H., Pan. S. D., Zhu, H. and Shen, H. Y. (2013). Simultaneous analysis of eight phenolic environmental estrogens in blood using dispersive micro-solid-phase extraction combined with ultra-fast liquid chromatography-tandem mass spectrometry. *Talanta*, 115: 787 – 797.
22. Liao, Q. G., Zhou, Y. M., Luo L. G., Wang, L. B. and Feng, H. X. (2014). Determination of twelve herbicides in tobacco by a combination of solid–liquid–solid dispersive extraction using multi-walled carbon nanotubes, dispersive liquid-liquid micro-extraction, and detection by GC with triple quadrupole mass spectrometry. *Microchimica Acta,* 181: 163 – 169.
23. Murphy, P. A., Barua, K. and Hauck, C. C. (2002). Solvent extraction selection in the determination of isoflavones in soy foods. *Journal of Chromatography B*, 777: 129 – 138.

Malaysian Journal of Analytical Sciences, Vol 22 No 1 (2018): 64 - 71
DOI: https://doi.org/10.17576/mjas-2018-2201-08

MALAYSIAN JOURNAL OF ANALYTICAL SCIENCES
Published by The Malaysian Analytical Sciences Society
ISSN 1394 - 2506

NEW DITERPENOIDS FROM THE ROOTS OF *Croton hirtus* (EUPHORBIACEAE)

(Diterpenoid-Diterpenoid Terbaharu Daripada Akar *Croton hirtus* (Euphorbiaceae))

Andi Rifki Rosandy[1], Anis Asmi Azman[1], Rozida Mohd Khalid[1], Rizafizah Othaman[1], Azwan Mat Lazim[1], Iqbal M. Choudary[2], Yana Maulana Syah[3], Jalifah Latip[1], Ikram Md. Said[1], Muntaz Abu Bakar[1]*

[1]*School of Chemical Sciences and Food Technology, Faculty of Science and Technology, Universiti Kebangsaan Malaysia,43600 UKM Bangi, Selangor, Malaysia*
[2]*Hussain Ebrahim Jamal Research Institute of Chemistry, University of Karachi, Karachi, 75270, Pakistan*
[3]*Organic Chemistry Division, Faculty of Mathematics and Natural Sciences, Institut Teknologi Bandung, Jalan Ganesha 10, Bandung 40132, Indonesia*

[*]*Corresponding author: muntaz@ukm.edu.my*

Received: 14 February 2017; Accepted: 28 December 2017

Abstract

The root of *Croton hirtus* was collected at Tanjung Sepat, Banting for study of its chemical compounds. This sample was dried before being ground and extracted using the methanol solvent at room temperature for three days yielding 18.25 gram of crude extract. The crude extracts obtained were analysed using thin layer chromatography (TLC) then fractionated *via* vacuum column chromatography (VLC) and proceed the isolation using radial chromatography (RC) to get the pure compounds. The pure compounds obtained were elucidated by nuclear magnetic resonance (NMR), Fourier Transform Infrared (FT-IR) and mass spectroscopy to confirm their structures and from that analysis, the compounds were identified as two new compounds naming (-)-5,8-dihydroxyjatrophan-3-one (**1**) and (+)-14,16,17-trihydroxykauran-1-on (**2**) with total weight 4.9 mg and 4.5 mg respectively. This two compound were reported for this time on this genus.

Keywords: *Croton hirtus*, diterpenoid, euphorbiaceae

Abstrak

Akar *Croton hirtus* dikumpulkan di Tanjung Sepat, Banting untuk mengkaji sebatian kimianya. Sampel ini dikeringkan sebelum dikisar dan diekstrak dengan menggunakan pelarut metanol pada suhu bilik selama tiga hari dan ia menghasilkan 18.25 g ekstrak mentah. Ekstrak mentah yang diperoleh dianalisis dengan menggunakan kromatografi lapisan nipis (TLC) kemudian difraksikan melalui kromatografi cecair vakum (VLC) dan pengasingan diteruskan dengan menggunakan kromatografi radial (RC) untuk mendapatkan sebatian tulen. Sebatian tulen yang diperoleh ditentukan oleh resonan magnetik nuklear (RMN), inframerah transformasi Fourier (FTIR) dan spektroskopi jisim untuk mengesahkan struktur mereka dan dari analisis itu, sebatian telah dikenal pasti sebagai dua sebatian baru yang diberi nama (-)-5,8- dihidroksijatrophan-3-one (**1**) dan (+)-14,16,17-trihidroksikauran-1-on (**2**) dengan jumlah berat masing-masing sebanyak 4.9 mg dan 4.5 mg. Kedua-dua sebatian ini dilaporkan buat kali pertama bagi genus ini.

Kata kunci: *Croton hirtus*, diterpenoid, euphorbiaceae

Introduction

Croton hirtus, also known as *Croton glandulosus*, is a shrub belonging to genus *Croton* and family Euphorbiaceae. They were distributed widespread around the world as trees, shrubs and herbs with about 1300 species. Croton is widely found in Malaysia and in several areas of Indonesia except Kalimantan, Sulawesi and the Sunda Islands [1]. Extensive work has been carried out on various species of Croton, resulting in the isolation of mainly terpenoid class of compounds, namely sesquiterpenoids [2 – 5], diterpenoids [6 – 13], and triterpenoids [14 – 17]. Non-terpenoid was isolated such as alkaloids, flavonoids, lignans and megastigmane glycosides [18]. Work on Brazilian *C. hirtus* has mainly concentrated on diterpenes [19] and essential oils [20]. So, with this background information, the aim of this present study are to analyse and characterize two new diterpenoid that have been isolated from root of genus using the spectroscopy NMR (1D and 2D), FT-IR and mass spectroscopy.

Materials and Methods

Raw materials

The roots of *C. hirtus* were collected in Tanjung Sepat, Banting, Selangor, Malaysia and herbarium specimen (SM-461) was deposited in the Herbarium of Universiti Kebangsaan Malaysia.

Extraction and isolation

Dried and ground roots of *C. hirtus* (415 g) were extracted with methanol to give a dark green extract (18.25 g). The crude extract (18.25 g) was partitioned between chloroform and water (1:1) after which the chloroform extract was further extracted with 10% *n*-hexane and 90% methanol to give methanol sub-extract. The sub-extract (3.52 g) was fractionated by using silica gel vacuum liquid chromatography eluted with increasing polarity of *n*-hexane- ethyl acetate to give ten fractions. The eluents that showed the same profile on thin layer chromatography (TLC) were combined to give four fractions (I-IV). Purification of fraction II (0.2027 g) was carried out using radial chromatography (RC) with silica gel plate of 1 mm thickness eluted with 60:40 *n*-hexane-ethyl acetate in 5% polarity increment to yield compound 1 (4.9 mg). Purification of fraction III (0.3163 g) was also carried out in a similar manner eluting with 1:1 *n*-hexane-ethyl acetate producing sub-fractions III^a-III^f. Sub-fraction (III^c= 0.0221 g) was further purified using RC with silica gel plate of 1 mm, eluting with 30:70 *n*-hexane-ethyl acetate, which resulted in the isolation of compound 2 (4.5 mg).

Results and Discussion

(-)-5,8-dihydroxyjatrophan-3-one (**1**), $[\alpha]_D^{25}$-102.50 (*c* 0.40, $CHCl_3$), was isolated as a pinkish oily material with molecular formula $C_{20}H_{30}O_3$, obtained by HR-CI–MS $[M+1]^+$ 319.2276 m/z. The IR spectra exhibited absorptions for hydroxyl groups (3402 cm^{-1}), cyclic aliphatic group (2922 cm^{-1}), and α,β-unsaturated carbonyl group (1709 and 1647 cm^{-1}) (Figure 1).

The ^{13}C spectrum indicated the presence of 20 carbons consisting of five methyls, three methylenes, seven methines and five quaternary carbons. The most highly deshielded signal at δ_C 199.7 (C-3) integrated for carbon attributed to a carbonyl group, three signals for methane carbon at δ_C 145.3 (C-1), 125.7 (C-7) and 119.4 (C-12) indicating the presence of olefinic carbons that are linked with olefinic-quaternary carbons at δ_c 134.6 (C-2), 143.7 (C-6) and 137.7 (C-13), while the other two shielded methine carbons at δ_c 77.4 (C-5) and 67.7 (C-8) belongs to two carbinol groups in the molecule, while the other three carbons at δ_c 25.5 (C- 9), 31.6 (C-11) and 39.9 (C-14) is indicative of the aliphatic component of the cyclic system, which also contains five methyl carbons from C-16 to C-20. The DBE value of $C_{20}H_{30}O_3$ is 6, indicating that the compound consists of four double bonds (three olefinics and one carbonyl) and two rings of aliphatic group. The ^1H-NMR spectrum showed 18 proton resonance signals representing 30 protons. Eighteen of the signals came from the three signals, three each from methyl group at H-16 (δ_H 1.95, s), H-17 (δ_H 1.72, s), and H-20 (δ_H 1.61, s) bonded to an olefinic carbon while the other two protons at H-18 (δ_H 1.03, s) and H-19 (δ_H 1.17, s) represent the two non- equivalent methyl protons. Furthermore, six signals of methylene protons and seven signals of methine protons are from a cyclic aliphatic or jatrophane skeleton as the main structure in the molecule (Figure 2).

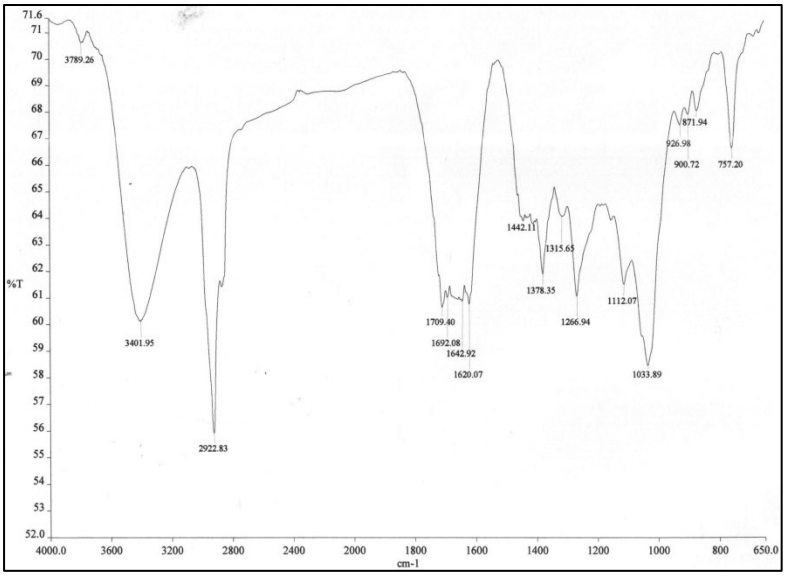


Figure 1. FTIR spectrum of (-)-5,8-dihydroxyjatrophan-3-one

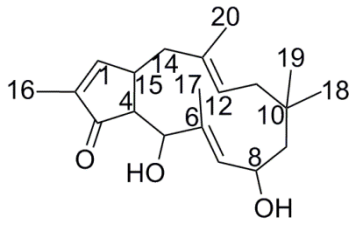


Figure 2. Chemical structure of (-)-5,8-dihydroxyjatrophan-3-one

The structure was confirmed by using 2D NMR. The HMBC experiment showed H-16 in correlation with C-1 and C-3, confirming the position of this methyl group bonded to C-2 at the cyclopentane ring and also C-20 with methylene (C-14) and olefinic-methine (C-12), confirming C-20 as the methyl carbon attached to the quaternary carbon at C-13. Meanwhile, non-equivalent dimethyl protons at H-18 and H-19 show ^{2}J interaction with each other and the quaternary carbon at C-10. Each of the carbinol protons at H-5 and H-8 correlated with the carbonyl group at C-3 and the olefinic methine at C-7 respectively (Figure 3).

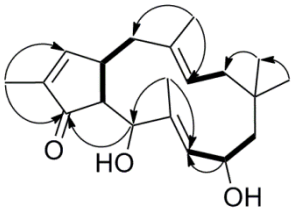


Figure 3. Significant ^{1}H-^{1}H COSY (-) and HMBC (→) correlations of (-)-5,8-dihydroxyjatrophan-3-one

(+)-14,16,17-trihydroxykauran-1-on (**2**), $[\alpha]_D^{25}$+30.00 (*c* 0.40, $CHCl_3$) is a white needle crystal. The IR spectrum showed characteristic absorptions for hydroxyl (3244 cm^{-1}), and carbonyl (1696 cm^{-1}) (Figure 4).

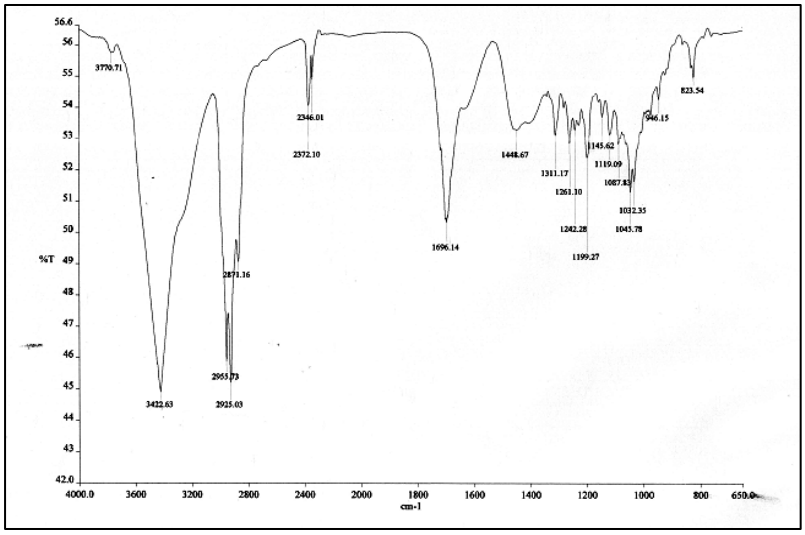


Figure 4. FTIR spectrum of (+)-14,16,17-trihydroxykauran-1-on

This compound contains 20 carbons observed from the ^{13}C NMR spectra, which shows that the compound is made up of three methyls, eight methylenes, four methines and five quaternary carbons (Table 1). The DBE value of five indicates that this compound have four cyclic systems with only one double bond. The highly deshielded carbon at δC 212.4 is a carbonyl. Meanwhile, three carbinol carbons appear δ_C at 76.5 (C-14), 89.5 (C-16) and 65.7 (C-17). Overlapping carbon signals with a significantly high intensity at δ_C 17.5-59.4 suggest that there is a long chain of cyclic aliphatic carbons. The appearance of a towering signal of protons indicates the presence of a series of long chain methylene groups forming the alkyl of the cyclic aliphatic group along with three hydroxyl groups and three methyls at the terminal of the chain. To determine methylene groups in the alkyl part, mass spectrometer was used. The MS spectral data shows that molecular weight of this compound is 336 m/z ($[M^+$+H - H2O] = 319.2259). Based on the discussion, this compound is identified as (+)-14,16,17-trihydroxykauran-1-on (Figure 5) with molecular formula of $C_{20}H_{32}O_4$.

Table 1. ^1H and ^{13}C NMR data (500 and 125 MHz, $CDCl_3$) for compounds **1** and **2**

Position	^{13}C (ppm)		^1H (ΣH, *mult.*, J in Hz))	
	1	**2**	**1**	**2**
1	145.3	212.4	6.30 (1H, *dd*, J_1 = 9.5 Hz, J_2 = 1.1Hz)	-
2	134.6	37.8	-	2.40 (1H, *s*)
				2.38 (1H, *d*, *J* = 3.5 Hz)
3	199.7	41.4	-	1.47 (1H, *m*)
				1.19 (1H, *d*, *J* = 4.0 Hz)
4	28.1	33.2	1.53 (1H, *d*, *J* = 6.2 Hz)	-
5	77.4	53.2	4.13 (1H, *d*, *J* = 6.2 Hz)	1.27 (1H, *dd*, J_1 = 10.2 Hz, J_2 = 6.9Hz)
6	143.7	40.2	-	1.87 (1H, *m*)
				1.12 (1H, *dd*, J_1 = 12.8 Hz, J_2 = 3.3 Hz)

Table 1 (cont'd). ^{1}H and ^{13}C NMR data (500 and 125 MHz, $CDCl_3$) for compounds **1** and **2**

Position	^{13}C (ppm)		^{1}H (ΣH, *mult.*, J in Hz))	
	1	**2**	**1**	**2**
7	125.7	41.1	5.20 (1H, *dd*, J_1 = 8.0 Hz, J_2 = 1.1 Hz)	2.09 (1H, *dd*, J_1 = 11.6 Hz, J_2 = 3.5 Hz) 1.90 (1H, *m*)
8	67.7	56.0	5.26 (1H, *dd*, J_1 = 8.0 Hz, J_2 = 6.6 Hz)	-
9	25.5	59.4	2.09 (1H, *m*) 0.78 (1H, *m*)	1.86 (1H, *m*)
10	29.8	36.9	-	-
11	31.6	18.2	2.31 (1H, *m*) 2.25 (1H, *m*)	1.66 (1H, *dd*, J_1 = 11.6 Hz, J_2 = 3.5 Hz) 1.50 (1H, *m*)
12	119.4	43.4	4.70 (1H, *ddd*, J_1 = 9.5 Hz, J_2 = 4.0 Hz, J_3 = 1.1 Hz)	2.14 (1H, *d*, *J* = 11.6 Hz) 1.57 (1H, *m*)
13	137.7	41.5	-	2.61 (1H, *t*, *J* = 6.5 Hz)
14	39.9	76.5	2.23 (1H, *m*) 1.70 (1H, *m*)	4.48 (1H, *s*)
15	35.8	46.4	1.19 (1H, *d*, *J* = 9.5 Hz)	2.04 (1H, *d*, *J* = 12.0 Hz) 1.69 (1H, *m*)
16	12.1	89.5	1.95 (3H, *d*, *J* = 1.1 Hz)	-
17	10.3	65.7	1.72 (3H, *d*, *J* =1.5 H)	3.83 (1H, *d*, *J* = 12.0 Hz) 3.64 (1H, *d*, *J* = 12.0 Hz)
18	16.1	21.3	1.03 (3H, *s*)	0.85 (3H, *s*)
19	29.3	33.3	1.17 (3H, *s*)	0.87 (3H, *s*)
20	15.4	17.5	1.61 (3H, *d*, *J* = 1.1 Hz)	1.25 (3H, *s*)

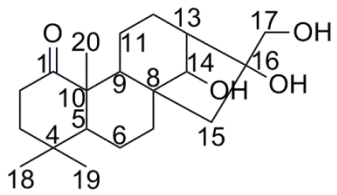


Figure 5. Chemical structure of (+)-14,16,17-trihydroxykauran-1-on

The structure of the compound was further confirmed using 2D NMR experiments including HMBC and COSY. From the HMBC experiments, the position of carbonyl carbon (C-1) was proven by correlations of C-2, C-5 and C-20 toward C-1. The proton H-14 in correlation with C-9 confirmed the position of this carbinol group bonded to C-8 and C-13 as branches to the other two carbinol groups at C-16 and C-17. COSY spectrum shows correlations between four proton methylene (H-2, H-3, H-6, H-7, H-11 and H-12) that forms the unsubstituted aliphatic component of the main ring skeleton in the molecule (Figure 6).

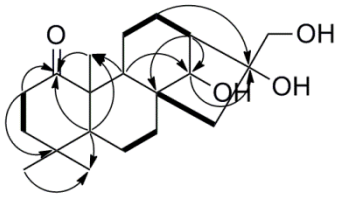


Figure 6. Significant ^{1}H-^{1}H COSY (-) and HMBC (→) correlations of (+)-14,16,17-trihydroxykauran-1-on

Chemotaxonomic significance

The genus *Croton* is the second largest genus of Euphorbiaceae with over 1300 species, and over 100 species from this genus have been studied phytochemically, resulting in the isolation and identification of more than 200 various types of diterpenoids) [21,22] comprising of different skeleton types such as clerodane (most common), kaurane, cembranoid, halimane, isopimarane, labdane, phorbol and trachylobane [23].

In this study, a new jatrophane and kaurane-type diterpenoid, (-)-5,8-dihydroxyjatrophan-3-one (**1**) and (+)-14,16,17-trihydroxykauran-1-on (**2**) respectively, was obtained from the roots of *C. hirtus*. The occurrence of diterpenoids in Euphorbiaceae is not unusual. Compounds with jatrophane-type skeleton was isolated from the genus Jatropha for the first time, and widely identified in the other genera (Euphorbiaceae) as well. The roots and rhizomes of several *Jatropha* species was reported to contain jatrophone, hydroxyjatrophone A-C, 9β-hydroxyisabellione, 9β-13α-hydroxyisabellione, citlalitrione, jatrophenone, and japodagrone [24 – 32]. Meanwhile, four jatrophane polyesters were isolated from the aerial parts of the East Asian weed *Euphorbia mongolica* Prokh [33].

In 2010, Hegazy et al. [34] identified the new guyonianin E and F from the aerial parts of *Euphorbia guyoniana*. Meanwhile, euphodendrophane A (Euph A) and euphodendrophane B (Euph B) were isolated from the jatrophane fraction of Euphorbia dendroidesn L. [35]. Since only these two genera were reported to biologically synthesize diterpenoid, thus chemotaxonomically, it can be assumed that the genus *Croton* is related to genera *Jatropha* and *Euphorbia*. Despite the large number of kaurane-type diterpenoids isolated from this genus, some species from other families also show the presence of this diterpenoid subclass. Four ent-kaurane diterpenoid glycosides, cussovantosides A–D were isolated with other known compounds from the dried leaves of *Cussonia vantsilana* Baker (Araliaceae) [36]. Other ent-kaurane derivatives such as ent-16- kauren-19-oic acid (kaurenoic acid) methyl ester, grandiflorenic acid methyl ester, ent-16-kauren-19-al, 16α,17- epoxy-15α-angeloyloxykauran-19-oic acid methyl. Grandiflorenic acid and 15-α-angeloyloxy-16,17-α-epoxy- ent-16-kauren-19-oic acid were present only in the Asteraceae plant *Smallanthus sonchifolius* and *Smallanthus siegesbeckius* [37].

Conclusion

Two diterpenoids; (-)-5,8-dihydroxyjatrophan-3-one (**1**) and (+)-14,16,17-trihydroxykauran-1-on (**2**) were successfully isolated from the methanolic extract of Croton hirtus. To the best of our knowledge, this is the first report for both compounds from this species. Both of compounds can be used to carry out biological activities because this species was known as many useful in traditional medicine.

Acknowledgement

We would like to thank the School of Chemical Sciences and Food Technology, Faculty of Science and Technology, Universiti Kebangsaan Malaysia (UKM) and Malaysia Genome Institute for providing research facilities. Authors also would like to express our gratitude to the LPDP (Indonesia Endowment Fund for Education), DIKTI and the Ministry of Science and Technology and Universiti Kebangsaan Malaysia for financial support through research grant of IRPA 09-02-02-0086-EA227, GGPM-2013-076 and FRGS-1-2014-SG01-UKM-02-5, respectively.

References

1. Soernaji, M., Kostermans, A. J. G. H. and Tjittrosoepomo, G. (1976). Weed of rice in Indonesia. Balai Pustaka. Jakarta.

2. Boonyarathanakornkit, L., Che, C., Fong, H. H. S. and Farnsworth, N. R. (1987). Constituents of *Croton crassifolius* roots. *Planta Medica*, 54: 61-62.
3. Siems, K., Dominguez, X. A. and Jakupovic, J. (1992). Diterpenes and other constituents from *Croton cortesianus*. *Phytochemistry*, 40: 4363-4365.
4. Ngadui, B. T., Abegaz, B. M., Keumedjio, F., Folefoc, G. N. and Kapche, G. W. F. (2002). Diterpenoids from the stem bark of *Croton zambesicus. Phytochemistry*, 60: 345-349.
5. Aguilar-Guadarrama, A. B. and Rios, M. Y. (2004). Three new sesquiterpenes from *Croton arboreous*. *Journal of Natural Products*, 67: 914-917.
6. Chatterjee, A., Banerjee, A. and Bohlman, F. (1977). Crotocaudin: A rearranged labdane type nor-diterpene from *Croton caudatus* Geisel. *Tetrahedron*, 33: 2407-2414.
7. Craveiro, A. and Silveira, E. R. (1982). Two cleistanthane type diterpenes from *Croton sonderianus*. *Phytochemistry*, 21: 2571-2574.
8. Monte, F. J. R., Dante, E. M. G. and Braz, R. (1988). New diterpenoids from *Croton argyarophylloides*. *Phytochemistry*, 27: 3209-3212.
9. Ichihara, Y., Takeya, K., Hitotsuyanagi, Y., Morita, H. and Itokawa, H. (1992). Cajucarinolide and isocajucarinolide: Anti-inflammatory diterpenes from *Croton cajucara*. *Planta Medica*, 58: 549-551.
10. Babili, F. E., Moulis, C., Bon, M., Respaud, M. J. and Fouraste, I. (1998). Three furano-diterpenes from the bark of *Croton campestris*. *Phytochemistry*, 48: 165-169.
11. Farias, A. C. G., Melo, P. S., Aoyama, H., Haun, M., Duran, N. and Ferreira, C. V. (2002). Cytotoxic effect of the diterpene lactone dehydrocrotonin from *Croton cajucara* on human promyelocytic leukemia cells. *Planta Medica*, 69: 67-69.
12. Puebla, P., Correa, S. X., Guerrero, M., Carron, R. and San Feliciano, A. (2005). New cis-clerodane diterpenoids from *Croton schiedeanus*. *Chemical Pharma Bulletin (Tokyo)*, 53: 328-329.
13. Norizan Ahmat, A. H., Ikram M. S., Jalifah Latip, Laily B. D., Syah Y. M. and Euis H. H. (2007). Styryldehydropyrone and clerodane-type diterpene from *Croton argyratus*. *Malaysian Journal of Analytical Sciences*, 11(1): 189-192.
14. Maciel, M. A. (2000). Ethnopharmacology, phytochemistry and pharmacology a successful combination in the study of *Croton cajucara*. *Journal of Ethnnopharmacology*, 70: 41-45.
15. Barbosa, P. R., Fascio, M., Martins, D., Maria, L., Guedes, S. and Roque, N. F. (2003). Triterpenes of *Croton betulaster* (Euphorbiaceae). *Biochemical Systematics and Ecology*, 31: 307-308.
16. Mulholland, D. A., Langat, M. K., Crouch, N. R., Coley, H. M., Mutambi, E. M. and Nuzillard, J. (2010). Cembranolides from the stem bark of the southern African medicinal plant, *Croton gratissimus* (Euphorbiaceae). *Phytochemistry*, 71: 1381–1386.
17. Gelaw, H., Adane, L., Tariku, Y. and Hailu, A. (2012). Isolation of Crotepoxide From Berries of *Croton macrostachyus* and Evaluation of Its Anti-Leishmanial Activity. *Journal of Pharmacognosy and Phytochemistry*, 1(4):15-24.
18. Kawakami, S., Matsunami, K., Otsuka, H., Shinzato, T. and Takeda, H. (2011). Crotonionosides A–G: Megastigmane glycosides from leaves of *Croton cascarilloides* Räuschel. *Phytochemistry*, 72: 147–153.
19. Fuentes, J. C., Castro, V., Jakupovic, J. and Murillo, R. (2004). Diterpenos y otros constituyentes de *Croton hirtus* (Euphorbiaceae). *Revista de Biología Tropical*, 52(1): 269-285.
20. de Lima, S. G., Medeiros, L. B. P., Cunha, C. N. L. C., da Silva, D., de Andrade, N. C., Moita Neto, J. M., Lopes, J. A.D., Steffen, R. A., Araújo, B. Q. and Reis, F. de A. M. (2012). Chemical composition of essential oils of Croton hirtusL'Her from Piauí (Brazil). *Journal of Essential oil Research*, 24(4): 371-376.
21. Puebla, P., Lopez, J. L., Guerrero, M., Carron, R., Martin, M. L., Roman, L. S. and Feliciano, A. S. (2003). Neo-Clerodane diterpenoids from Croton Schiedeanus. *Phytochemistry*, 62: 551-555.
22. Barbosa, P. S., Abreu, A. S., Batista, E. F., Guilhon, G. M. S. P., Müller, A. H., Arruda, M. S. P., Santos, L. S., Arruda, A. C. and Secco, R. S. (2007). Glutarimide alkaloids and terpenoids *from Croton pullei* var. glabrior Lanj. *Biochemical Systematics and Ecology*, 35: 887-890.
23. Yang, X. D., Chen, W., Zhao, J. F., Yang, L. J., Zhang, H. B., Li, L. (2009). Ent-kaurane diterpenes and phenolic compounds from *Croton kongensis* (Euphorbiaceae). *Biochemical Systematics and Ecology*, 37: 237–240.

24. Kupchan, S. M., Sigel, C. W., Matz, M. J., Saenz Renauld, J. A., Haltiwanger, R. C. and Bryan, R.F. (1970). Jatrophone, a novel macrocyclic diterpenoid tumor inhibitor from *Jatropha gossypiifolia*. *Journal of American Chemical Society*, 92(14:, 4476-4477.
25. Kupchan, S. M., Sigel, C. W., Matz, M. J., Gilmore, C. J. and Bryan, R. F. (1976). Structure and stereochemistry of jatrophone, a novel macrocyclic diterpenoid tumor inhibitor. *Journal of American Chemical Society*, 98(8): 2295-2300.
26. Taylor, M. D., Smith, A. B., Furst, G. T., Gunasekara, S. P., Bevelle, C. A., Cordell, G. A., Farnsworth, N. R., Kupchan, S. M., Uchida, H., Branfman, A. R., Daily, R. G. and Sneden, A. T. (1983). Plant anticancer agents. 28. New antileukemic jatrophone derivatives from Jatropha gossypiifolia: structural and stereochemical assignment through nuclear magnetic resonance spectroscopy. *Journal of American Chemical Society*, 105: 3177-3183.
27. Goulart Marilla, O. F., Sant'Ana, Antonio Euzebio G., De Lima, Roberto A., Cavalcante Sergio, H., De Carvalho, Mario G., Braz Filho and Raimundo .(1993). Fitoconstituintes Químicos Isolados de ***Jatropha elliptica***. Atribuição dos Deslocamentos Químicos dos Átomos de Carbono e Hidrogênio dos Diterpenos Jatrofolonas A e B. *Química Nova*, 16(2): 95–100.
28. Das, B. and Venkataiah, B. (1999). A rare diterpene from *Jatropha gossypiifolia*. *Biochemical Systematics and Ecology*, 27: 759–760.
29. Ravindranath, N., Venkataiah, B., Ramesh, C., Jayaprakash, P. and Das, B. (2003). Jatrophenone, a Novel Macrocyclic Bioactive Diterpene from *Jatropha gossypifolia. Chemical and Pharmaceutical Bulletin*, 51(7): 870-971.
30. Aiyelaagbe, O. O., Adesogan, E. K., Ekundayo, O. and Gloer, J. B. (2007). Antibacterial diterpenoids from *Jatropha podagrica* Hook. *Phytochemistry*, 68: 2420–2425.
31. Pertino, M., Schmeda-Hirschmann, G., Rodríguez, J. A. and Theoduloz, C. (2007). Gastroprotective effect and cytotoxicity of terpenes from the Paraguayan crude drug "yagua rova" (Jatropha isabelli). *Journal of Ethnopharmacology*, 111: 553-559.
32. Das, B., Laxminarayana, K., Krishnaiah, M., Srinivas, Y. and Raju, T. V. (2009). Multidione, a novel diterpenoid from *Jatropha multifida*. *Tetrahedron Letters*, 50: 4885-4887
33. Rédei, D., Forgo, P., Molnár, J., Szabó, P., Zorig, T. and Hohmann, J. (2012). Jatrophane diterpenoids with multidrug resistance-modulating activity from *Euphorbia mongolica* Prokh. *Tetrahedron*, 68: 8403-8407.
34. Hegazy, M. E. F., Mohamed, A. E. H., Aoki, N., Ikeuchi, Ohta, E. and Ohta, S. (2010). Bioactive jatrophane diterpenes from *Euphorbia guyoniana*. *Phytochemistry*, 71: 249-253.
35. Pešić, M., Banković, J., Aljančić, I. S., Todorović, N. M., Jadranin, M., Vajs, V. E., Tešević, V. V., Vučković, I., Momčilović, M., Marković, I. D., Tanić, N. and Ruždijić, S. (2011). New anti-cancer characteristics of jatrophane diterpenes from *Euphorbia dendroides*. *Food and Chemical Toxicology*, 49: 3165–3173.
36. Harinantenaina, L., Kasai, R. and Yamasaki, K. (2002). Ent-kaurane diterpenoid glycosides from a Malagasy endemic plant, *Cussonia vantsilana*. *Phytochemistry*, 61: 367–372.
37. Aráoz, M. V. C., Mercado, M. I., Grau, A. and Catalán, C. A. N. (2010). Ent-kaurane derivatives from the root cortex of yacon and other three Smallanthus species (Heliantheae, Asteraceae). *Biochemical Systematics and Ecology*, 38: 1042–1048.

Malaysian Journal of Analytical Sciences, Vol 22 No 1 (2018): 72 - 79
DOI: https://doi.org/10.17576/mjas-2018-2201-09

MALAYSIAN JOURNAL OF ANALYTICAL SCIENCES
Published by The Malaysian Analytical Sciences Society
ISSN 1394 - 2506

FORENSIC GAS CHROMATOGRAPHY ANALYSIS OF TIME ELAPSED GASOLINE IN FIRE SCENE INVESTIGATION

(Analisis Kromatografi Gas Forensik bagi Gasolin yang Masanya Berlalu dalam Penyiasatan Tempat Kebakaran)

Pei Wen Lim, Ahmad Fahmi Lim Abdullah, Kah Haw Chang*

Forensic Science Programme, School of Health Sciences,
Universiti Sains Malaysia, 16150 Kubang Kerian, Kelantan, Malaysia

Corresponding author: changkh@usm.my

Received: 25 September 2017; Accepted: 29 January 2018

Abstract

Gasoline residues present in fire debris serves as important evidence in arson investigation. In view of safety considerations, fire investigators do not enter fire scene immediately after fire extinguishing activity. In this perspective, gasoline residue in burnt carpet was analysed in relation to time elapsed after a fire to evaluate the influence of evaporative weathering process on the detection of gasoline traces from fire debris. Simulating fire condition, carpet samples poured with gasoline were burned, and the fire was extinguished with water before exposure to varying evaporation time at room temperature. All burnt carpet samples were then extracted by hexane and analysed using gas chromatography-flame ionisation detector. Selected peaks were then subjected to principal component analysis (PCA) for clustering. Experimental results revealed rapid evaporation of gasoline during the first 30 minutes, followed by continuous but non-linear decrease up to one-month interval. Four clusters were found in the PCA plots wherein samples that were subjected to less than nine hours exposure were located close to positive control and could be distinguished from the rest. Hence, it is recommended that safety measures should be completed within nine hours.

Keywords: forensic science, fire scene, gasoline detection, gas chromatography, time elapsed

Abstrak

Kehadiran sisa-sisa gasolin pada serpihan kebakaran ialah bukti penting dalam penyiasatan arson. Oleh kerana pertimbangan keselamatan, penyiasat-penyiasat kebakaran tidak memasuki tempat kejadian kebakaran sejurus selepas aktiviti pemadaman api. Dalam perspektif ini, sisa gasolin pada permaidani terbakar telah dianalisis untuk dikaitkan dengan masa berlalu selepas suatu kebakaran, bertujuan untuk menilai kesan proses sejatan terhadap pengesanan gasolin surih daripada serpihan kebakaran. Menerusi simulasi keadaan kebakaran sebenar, sampel permaidani yang dicurahkan dengan gasolin telah dibakar, dan api tersebut dipadamkan dengan air sebelum didedahkan kepada pelbagai tempoh penyejatan pada suhu bilik. Kesemua sampel permaidani terbakar kemudian tertakluk kepada pengekstrakan heksana dan dianalisis menggunakan kromatografi gas-pengesan pengionan nyalaan. Puncak-puncak terpilih kemudiannya tertakluk kepada analisis komponen utama (PCA) untuk tujuan pengelompokan. Keputusan eksperimen telah menunjukkan penyejatan pesat gasolin pada 30 minit pertama, diikuti dengan penurunan secara berterusan tidak linear sehingga tempoh satu bulan. Empat kelompok telah diperolehi dalam plot PCA dan sampel yang didedahkan pada jangka masa kurang daripada sembilan jam terletak berdekatan dengan kawalan positif dan boleh dibezakan daripada yang lain. Justeru, adalah disyorkan bahawa langkah keselamatan perlu diselesaikan dalam jangka masa sembilan jam.

Kata kunci: sains forensik, tempat kejadian kebakaran, pengesanan gasolin, kromatografi gas, masa berlalu

Introduction

Arson is a willful and malicious burning of property [1]. Statistics from the Fire and Rescue Department Malaysia revealed an annual upward trend of fire breakouts from 2012 to 2016 in which arson was the second major culprit with 5,000 to 10,000 cases annually [2]. Recently, a recent school arson case in Kuala Lumpur that caused 23 deaths shocked the entire nation [3]. This blatant criminal act needs greater investigative effort, particularly in determining the origin and cause of the fire.

Ignitable liquids were frequently used in arson not only to initiate instant burning but also to accelerate burning rate and fire spread. Low cost, widely available and easy to handle hydrocarbon based fuel, such as gasoline was frequently used [4]. Hence, the detection of ignitable liquid residues at the fire scene could serve as an investigative lead to support the hypothesis on the occurrence of arson crime [5-7]. Identifying an arsonist is also closely related with the possibility of collecting and analysing any ignitable liquid in the possession of the suspect [8].

Due to rapid progression and destructive nature of a fire, determination of an arson crime is often difficult. Massive damage from heat commonly leaves only small traces of valuable evidence at a fire scene, particularly the volatile ignitable liquid, such as gasoline [9]. Apart from that, such residues, if recoverable, could have been altered through evaporative weathering accelerated by heat and time elapsed [9]. Theoretically, forensic investigation should start as soon as possible upon fire suppression to recover any remaining residues prior to subsequent loss, but this could be delayed since forensic investigators must ensure that the investigation site is structurally safe or free of lethal toxic gas and heat.

The above situation delineates that there is a time gap between the onset of fire, its suppression and fire scene investigation. It is uncertain on the degree of subsequent loss of volatile ignitable liquid residues upon suppression. In view of this, this study focuses on the analysis of gasoline residues and the influences of time elapsed after a fire on the recovery and detection of gasoline from burnt carpets using gas chromatography technique. This approach could provide additional information to fire investigators even on negative results of ignitable liquid recovered from fire debris; either due to true absence of ignitable liquid used or because of severe evaporative weathering that has rendered the accelerant undetectable. It would also be interesting to estimate the maximum time persistence of gasoline on exposed fire debris at room temperature to allow the fire investigator in planning an appropriate sampling strategy and evidence preservation method prior to laboratory analysis.

Materials and Methods

Materials and chemicals

Gasoline (RON 95, Petronas, Kota Bharu) was obtained from a petrol service station near our research laboratory. A common household cotton type carpet purchased from a carpet shop was used as substrate. As this study focused on the comparison of the effect of varying time elapsed towards gasoline profiles, only one type of substrate was used, which was the household carpet that could be found in many residential structures. Distilled water was used to extinguish the simulated fire. Analytical grade hexane used to extract the burnt samples was purchased from Merck (Kenilworth, NJ).

Preparation of carpet samples

The carpets were cut into square of 5 cm × 5 cm and placed on the center of a square metal can of 15 cm × 15 cm. Then, 20 mL of gasoline was spread evenly on the surface of the carpet. Fire was ignited using matches and allowed the gasoline-soaked carpet to burn for 30 seconds followed by extinguishment of fire by spraying 500 mL distilled water. Unburnt carpet samples with gasoline were used as positive control while a piece of new carpet without gasoline was used as negative control.

In triplicate, the burnt carpets could evaporate at different time interval up to a month at room temperature (≈ 25 °C), giving a total of 36 simulated fire conditions in this study. Immediately upon the exposure time, three strips of 1 cm × 1 cm were cut from randomly selected region of each burnt sample and placed in separate 10 mL glass vial (Supelco, Bellefonte, PA). Solvent extraction, adapted from ASTM E-1386, was performed by adding 5 mL hexane as organic solvent into the vials with samples and allowing it to stand for one hour [10]. All samples were then transferred and filtered into glass vials for GC analysis.

GC-FID analysis

Analysis of gasoline was carried out using a 7890A gas chromatography-flame ionisation detector (GC-FID) equipped with G4513A series autosampler (Agilent Technologies, Santa Clara, CA). Chromatography was achieved using a HP-5 capillary column (30 m × 0.25 mm × 0.25 µm film thickness) purchased from Agilent Technologies. Purified nitrogen gas (99.9%) was used as carrier gas with constant flow rate of 1.2 mL/min. Split mode (10:1) injection technique and the inlet temperature was set at 300 °C. Oven was set at 50 °C as initial temperature for 2.5 mins, ramp at 15 °C/min to 250 °C, and held for 5.83 mins. Detector temperature was set at 300 °C. Hydrogen flow, air flow and make up gas flow were set at 30, 300 and 15 mL/min, respectively. Chemstation software (Rev. B.04.02, Agilent Technologies, Santa Clara, CA) was used for GC automation and data analysis. All extracted samples including positive and negative controls were analysed. Prior to analysis of burnt samples, neat gasoline was diluted with hexane (1:4, v/v) and analysed to obtain its reference chromatogram. Note that blank was run between the samples to avoid carry-over. Gas chromatogram of each sample was compared and evaluated.

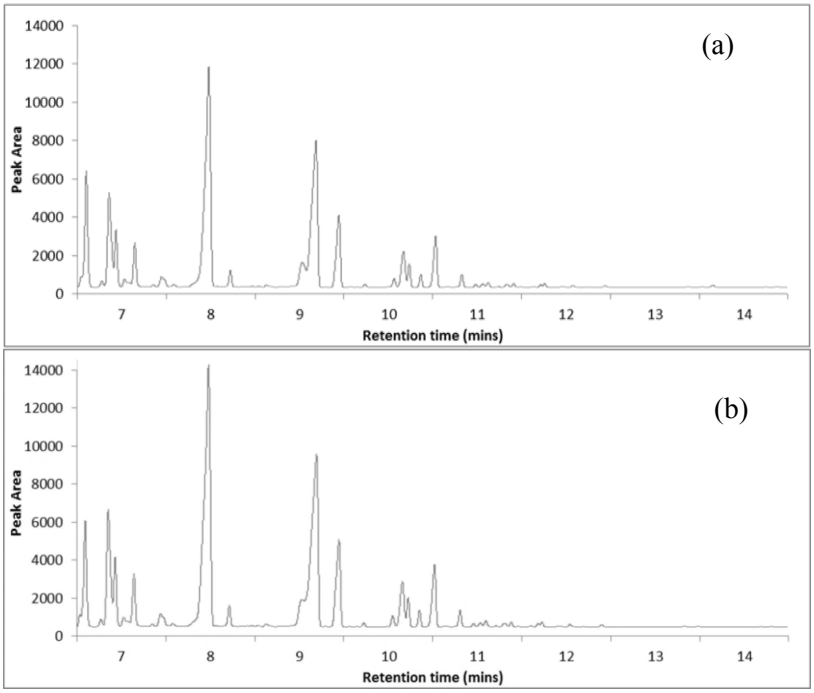
Data analysis

Using reference chromatogram of neat gasoline, the peak areas of 52 peaks with sufficient chromatographic features and intensity of the burnt samples were selected and integrated before being transferred to Microsoft Excel® Spread sheet (Microsoft office, Demond, WA). A bar chart was used to investigate the behaviour of gasoline peaks loss with time elapsed. For statistical analysis, two data pre-treatment procedures were considered in this study, namely by normalisation of each peak to the sum of peak areas in the respective regions that lied between 6 and 15 minutes [11, 12] and normalisation of each peak to the total sum of peak areas in a chromatogram [13]. Normalised peaks were then served as variables to Principle Component Analysis (PCA) for multivariate analysis using Minitab 16 software (Minitab Inc., State College, PA).

Results and Discussion

GC-FID analysis

Representative chromatogram profiles of neat gasoline, positive and negative controls were demonstrated in Figure 1. The chromatogram of positive control showed very similar profile as compared to the chromatogram profiles of neat gasoline, illustrated in respective Figures 1(a) and 1(b). Under our experimental condition, the carpet substrate showed no observable interference peaks additional to the profile of positive control, as demonstrated in Figure 1(c).



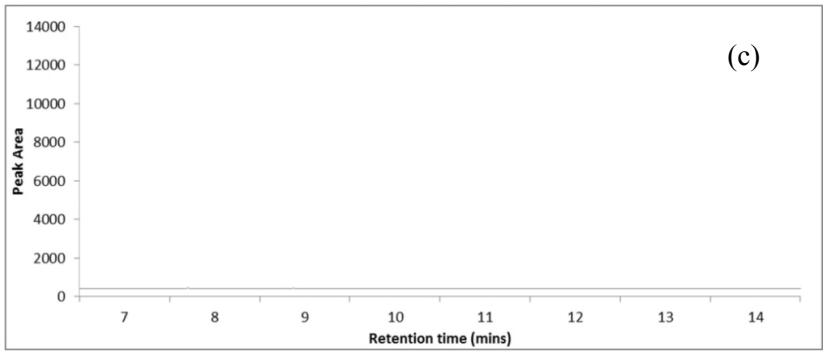


Figure 1. Representative chromatograms of (a) neat gasoline, (b) positive control and (c) negative control

The analytical parameters used in this study were adopted from ASTM E1618-06 method [14]. Due to complex features of gasoline, only well separated and symmetrical peaks were selected for data analysis. In our experiment, the same gasoline sample was used throughout the study to prevent any variation in chromatographic profile due to different gasoline samples. It is worth noting that no attempt was made to identify the identity of respective compounds of a particular retention time, since our aim is to make a relative comparison of the 52 selected peaks and their respective peak areas in relation to the varying time elapsed after a fire.

Investigation of gasoline profile with time elapsed after a fire

A chromatographic profile of gasoline contains mixture of alkanes, cycloalkanes, aromatic and condensed ring aromatic compounds [14, 15]. These compounds carry different characteristics, which ranged from very low to relatively high volatilities. In our study, it was observed that lighter compounds in gasoline of lower retention times disappeared more rapidly than those heavier compounds. Lighter compounds, being more volatile, evaporated off faster from the burnt carpet samples and this observation was supported by review of Martín-Alberca et al. [16]. The tendency of losing more volatile or lighter weight compounds when ignitable liquids were subjected to evaporation alter their GC chromatographic features, making chromatogram comparison challenging.

Figure 2 shows a bar chart illustrating the percentage of selected peak remained in respective chromatogram based on time elapsed after a fire. At a glance, the decrease in the number of peaks that could be recovered from the burnt carpets was evident as compared to reference gasoline profile. An elapsed of nine hours after a fire dies out, almost 20% of peak loss was observed. Subsequently, approximately 50% loss in the number of selected peaks was seen after 24 hours. As a result, many peaks delineating the profile of gasoline were no longer detectable under the experimental condition. Results suggest that if a chromatographic profile showed only 20% of indicative peaks of gasoline, or upon exposure to room condition exposure for seven days (168 hours) upon suppression, it is difficult to confidently confirm the potential presence of gasoline to initiate arson.

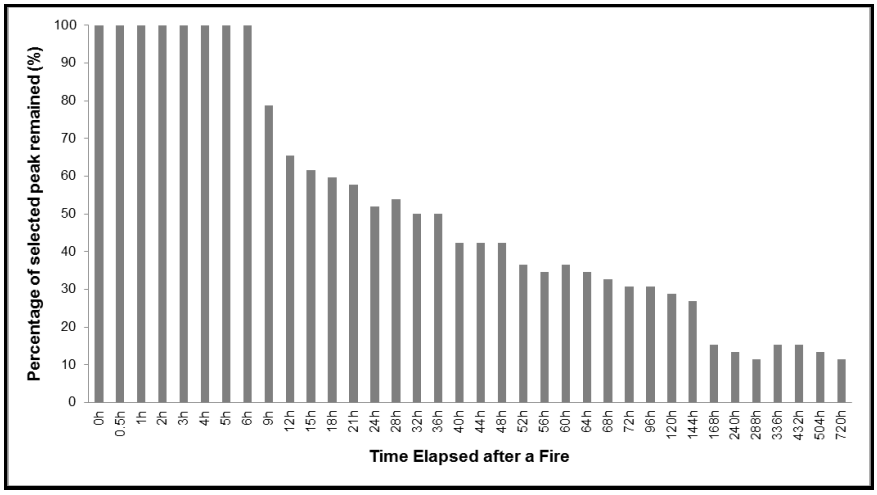


Figure 2. Bar chart illustrating the percentage of selected peak remained in respective chromatogram against the time elapsed after a fire

The amount of gasoline that could be recovered from burnt carpet samples at each time interval was further investigated by examining the abundance of respective compounds in nine separate regions. Figure 3 shows line graphs taken by slicing the normalised peaks into different regions of increasing retention times as represented by Regions A to I, depicting the relationship between the normalised peak areas of each region and the time elapsed after a fire. The Region A consisted of peaks which lie between retention times of 6 to 7 minutes, followed by different regions with consecutive retention time interval of one minute until Region I that spanned from the retention time of 14 to 15 minutes.

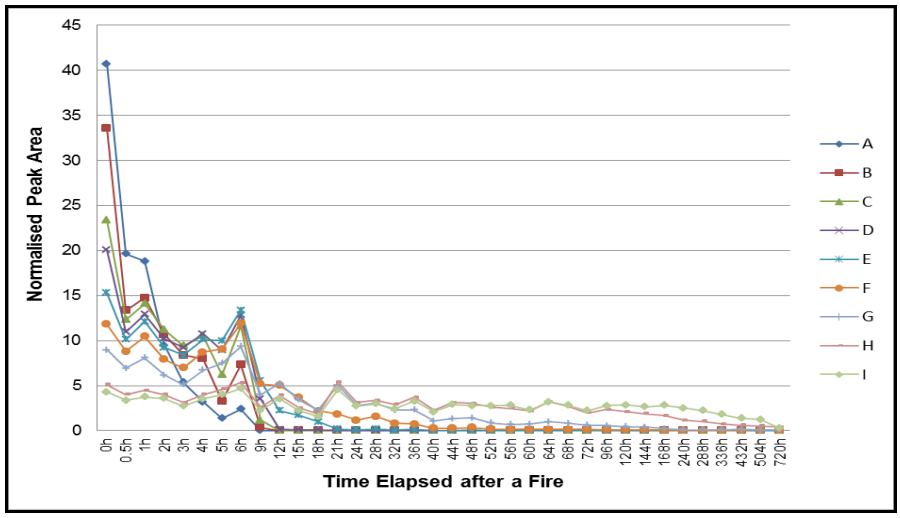


Figure 3. Line graphs of normalised peak area versus time elapsed after a fire

In general, all the line graphs in Figure 3 demonstrated downward trends where the peak areas decreased with time elapsed upon combustion. Generally, significant drop of peak areas during the first 30 minutes was evident and a continuous but non-linear decrease along with different time intervals up to one month of elapsed after a simulated fire. Similar observation was also reported by several previous studies evaluating the persistence of gasoline on

various substrates, including Folkman et al. [17] on clothing, shoes, carpet and wood, Darrer et al. [18] on PVC gloves, Tan et al. [10] on various types of woods, as well as Dhabbah et al. [19] on carpet.

The lower retention times from Regions A to E were found to approach X-axis faster than those indicating higher retention times from Regions F to I (Figure 3), which supports the finding where lighter compounds in gasoline evaporated more rapidly than relatively heavier compounds. Based on our experimental results, longer exposure time of gasoline to the surrounding was shown to potentially lead to greater difficulty in recovering gasoline residues from the burnt samples. However, in real case scenario, a fire could produce different outcomes on a gasoline profile due to uncontrollable factors, such as unequal distribution of gasoline throughout the carpet sample, burning rate, fire intensity, air flow and spread of fire which could directly or indirectly influenced the recovered amount of accelerant residues from fire debris [20].

Principal component analysis

The chromatographic profiles of burnt samples in relation to time elapsed were also subjected to multivariate analysis. Prior to PCA analysis, the experimental data was pre-treated by two different data normalisation to minimise the effect of highly abundance compounds. Figure 4 illustrates the score plot upon normalisation of selected peaks to the sum of peak areas in respective regions while Figure 5 exhibits the score plot subjected to normalisation of selected peaks to the total peak areas. Note that these score plots used the normalised abundance of selected peaks as 52 variables for PCA input data. PC and NC in the score plots indicate positive and negative controls, respectively.

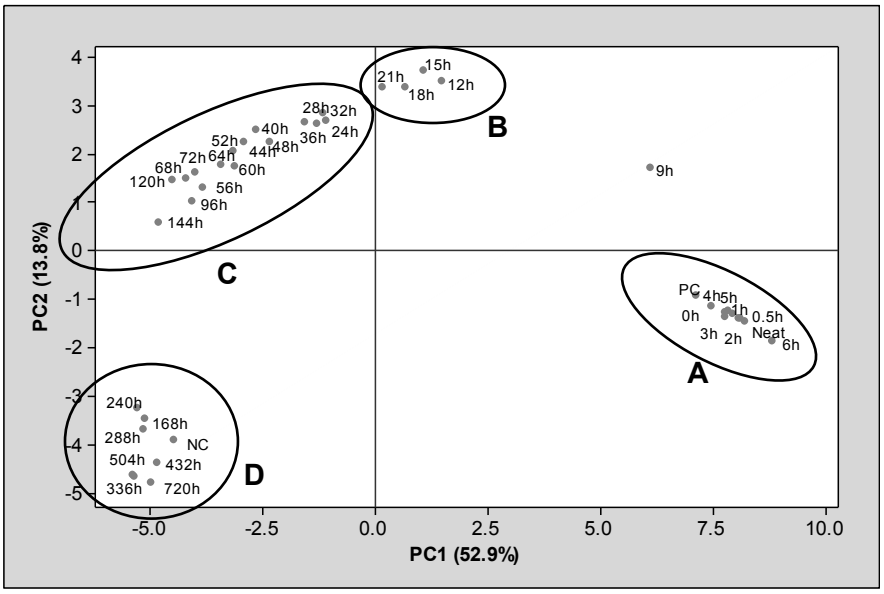


Figure 4. Score plot of burnt samples subjected to normalisation to the sum of peak areas in respective regions

Samples composing of very similar profiles tend to cluster together upon PCA. In both score plots, four different clusters were observed, namely clusters A, B, C and D, respectively. Visual comparison also showed that normalisation procedure based on different regions (Figure 4) has demonstrated better clustering of the samples into four distinctive clusters as shown in circles. As opposed to Figure 4, normalising the respective peak area to the total sum of peak areas in a chromatogram formed more loose clusters, particularly Cluster B and C, as shown in Figure 5. In our study, it was notable that different results could be obtained by the choice of data pre-treatment procedure prior to PCA. Both score plots have indicated the formation of four distinct clusters, but the members located in each cluster were found to vary suggesting the importance in utilising suitable data pre-treatment procedure to make data comparable. For our classification, normalisation according to different regions by

comparison has shown with more distinctive clustering where the grouping of peak areas within desirable ranges has aided in trimming down the complexity and huge number of response [11, 12].

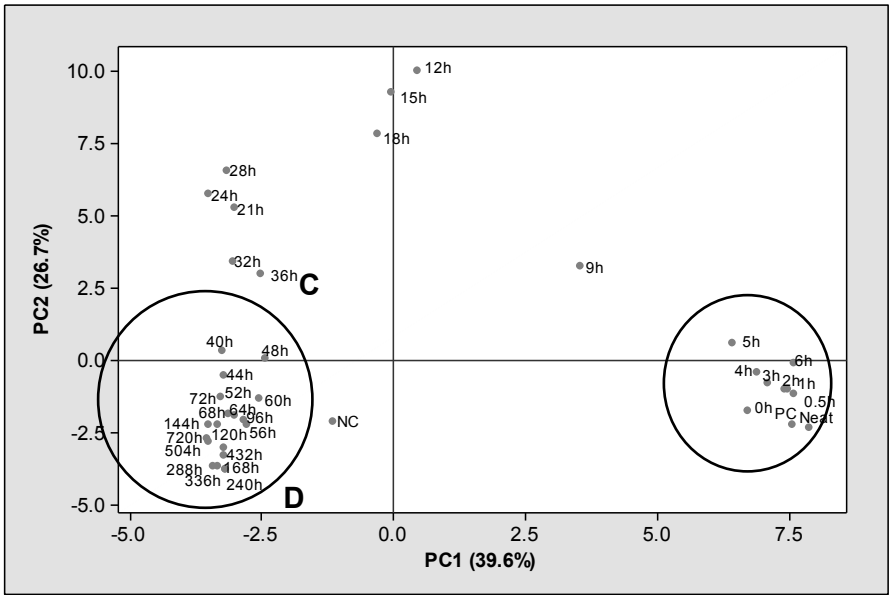


Figure 5. Score plot of burnt samples subjected to normalisation treatment to the total peak areas

Using peaks normalised based on regions as the variables for PCA, the result shows that the first two PCs accounted for 66.7% of the explained variance that distinguishing the burnt samples. PC1 (52.9%) allowed the discrimination of burnt samples as a function of gasoline content. Samples in Cluster A showed positive score together with positive control, whereas those in Cluster D, including the negative control, showed negative score on PC1. It was also evident that data points were shifted from the right to left with exposure time elapsed. Examination on PC2 (13.8%) shows that data points trajected downward to the left bottom of the score plot and assembled in Cluster D. After seven days of exposure upon combustion, the characteristic chromatographic profiles of a gasoline diminished making them be clustered closed to the negative control.

Generally, most samples in this study were clustered into four distinct clusters based on the two peak normalisation treatments, presuming that these samples could have different chromatographic profiles due to evaporative weathering process. For forensic intelligence, our findings suggested that the maximum recoverable time of gasoline residing within burnt carpet samples could remain recognisable up to nine hours under our experimental settings, retaining approximately 80% of the reference chromatographic peaks. However, the confirmation on the presence of gasoline from burnt samples could be difficult if the time elapsed was too long as seen in the samples exposed to seven days. In other words, the possibility to recover gasoline residues could be restricted, for instance in scenario where a re-sampling or re-analysing becomes necessary, it must be performed as soon as possible. This study suggests that a fire investigation and evidence collection should be started as soon as after fire suppression, preferably within nine hours and not more than seven days.

Conclusion

In contrast to our perception that accelerant residues could be protected in the substrate materials from environment insults, the study shows that immediate recovery of ignitable liquid residues upon fire suppression is important, as rapid sample loss occurred to have led to non-detection if the fire debris were left at the environment over an extended period. Therefore, in an event where a re-sampling or re-analysing is necessary, it should be performed as soon as possible. Collected samples should also be secured for further weathering if sample analysis could not be

performed immediately. For future study, the factors such as the types of substrates and ignitable liquid used, duration of burning time, as well as the surrounding conditions during a fire, which could affect the recovery of ignitable liquid residues from fire debris should be investigated.

Acknowledgement

The authors thank Universiti Sains Malaysia for the financial support via the USM Short Term grant (304/PPSK/61313147). Special thanks to Associate Professor Lim Boon Huat and Associate Professor P.T. Jayaprakash for their editorial assistance.

References

1. De Haan, J. D. and Icove, D. J. (2011). Kirk's fire investigation. Pearson Higher Ed.
2. Fire and Rescue Department Malaysia. (2016). State/District Social Statistics Malaysia 2016. Department of Statistics Malaysia.
3. The Star. (2017). Fire department confirms tahfiz school fire deliberately ignited. http://www.thestar.com.my/videos/2017/09/21/fire-department-confirms-tahfiz-school-fire-deliberately-ignited/. [Access online 23 December 2017].
4. Redsicker, D. R. and O'Connor, J. J. (1996). Practical fire and arson investigation. CRC Press.
5. Thomson N. (2001). Technology & engineering fire hazards in industry. Elsevier, Salford.
6. Stauffer, E., Dolan, J. A. and Newman, R. (2007). Fire debris analysis. Academic Press.
7. Baechler S., Comment S., and Delemont O. (2010). Extraction and concentration of vapors from fire debris for forensic purposes: evaluation of the use of radiello passive air sampler. *Talanta*, 82(4):1247 - 1253.
8. Cacho, J. I., Campillo, N., Aliste, M., Vinas, P. and Hernandez-Cordoba, M. (2014). Headspace sorptive extraction for the detection of combustion accelerants in fire debris. *Forensic Science International*, 238: 26 - 32.
9. Almirall, J. R. and Furton, K. G. (2016). Analysis and interpretation of fire scene evidence. CRC Press.
10. ASTM. (2015). E1386-15 Standard practice for separation of ignitable liquid residues from fire debris samples by solvent extraction. ASTM International, West Conshohocken.
11. Tan, B., Hardy, J. K. and Snavely, R. E. (2000). Accelerant classification by gas chromatography/mass spectrometry and multivariate pattern recognition. *Analytica Chimica Acta*, 422: 37 - 46.
12. Ribeiro, J., Teófilo, R., Augusto, F. and Ferreira, M. (2010). Simultaneous optimization of the microextraction of coffee volatiles using response surface methodology and principal component analysis. *Chemometrics and Intelligent Laboratory Systems*, 102: 45 - 52.
13. Samri, M. A. S. and Chang K. H. (2016). Gas chromatography based forensic analysis of gasoline from burnt carpets retrieved using different fire extinguishing methods. *Malaysian Journal of Forensic Sciences*, 7(1): 39 - 44.
14. ASTM. (2014). E1618-06 standard test methods for ignitable liquid residues in extracts from fire debris samples by gas chromatography-mass spectrometry. ASTM International, West Conshohocken.
15. Prather, K. R., McGuffin, V. L. and Waddell Smith, R. (2012). Effect of evaporation and matrix interferences on the association of simulated ignitable liquid residues to the corresponding liquid standard. *Forensic Science International,* 222(1-3): 242 - 251.
16. Martín-Alberca, C., Ortega-Ojeda, F. E. and Garcia-Ruiz, C. (2016). Analytical tools for the analysis of fire debris: A review: 2008–2015. *Analytica Chimica Acta*, 928: 1 - 19.
17. Folkman, T., Kuehl, A., Groves, R. and Beveridge, A. (1990). Evaporation rate of gasoline from shoes, clothing, wood and carpet materials and kerosene from shoes and clothing. *Canadian Society of Forensic Science Journal,* 23: 49 - 59.
18. Darrer, M., Jacquemet-Papilloud, J. and Delémont, O. (2008). Gasoline on hands: Preliminary study on collection and persistence. *Forensic Science International*, 175: 171 - 178.
19. Dhabbah, A. M., Al-Jaber, S. S., Al-Ghamdi, A. H. and Aqel, A. (2014). Determination of gasoline residues on carpets by SPME–GC-MS technique. *Arabian Journal for Science and Engineering*, 39: 6749 - 6756.
20. Mach, M. (1977). Gas chromatography-mass spectrometry of simulated arson residue using gasoline as an accelerant. *Journal of Forensic Sciences*, 22: 348 - 357.

Malaysian Journal of Analytical Sciences, Vol 22 No 1 (2018): 80 - 86
DOI: https://doi.org/10.17576/mjas-2018-2201-10

MALAYSIAN JOURNAL OF ANALYTICAL SCIENCES
Published by The Malaysian Analytical Sciences Society
ISSN 1394 - 2506

EFFECTS OF DEPOSITION TIME ON OF COBALT SULFIDE THIN FILM ELECTRODE FORMATION

(Kesan Tempoh Masa Enapan Terhadap Pembentukan Elektrod Filem Nipis Kobalt Sulfida)

Norshazlinah Abdul Karim[1], Norasikin Ahmad Ludin[1]*, Mohd Asri Mat-Teridi[1], Suhaila Sepeai[1], Mohd Adib Ibrahim[1], M. Kouhnavard[2], Kamaruzzaman Sopian[1], Hironori Arakawa[3]

[1]*Solar Energy Research Institute (SERI),*
Universiti Kebangsaan Malaysia, 43600 UKM, Bangi, Selangor, Malaysia
[2]*Malaysia-Japan International Institute of Technology (MJIT),*
Universiti Teknologi Malaysia, 54100 Kuala Lumpur, Malaysia
[3]*Department of Industrial Chemistry, Faculty of Engineering,*
Tokyo University of Science, 1-3 Kagurazaka, Shinjuku, Tokyo 162-0825, Japan

**Corresponding author: sheekeen@ukm.edu.my*

Received: 12 April 2017; Accepted: 1 September 2017

Abstract

Cobalt sulfide counter electrodes (CE) were prepared using the electrodeposition and ionic exchange deposition method on the fluorine doped tin oxide (FTO). Time deposition effect of thin film were analyzed by using a field emission scanning X-ray diffraction (XRD), field emission electron microscope (FESEM), atomic force microscopic (AFM), and profilometry. The electrocatalytic activities of electrode were measured using cyclic voltammetry (CV) analysis. The growth of cobalt sulfide structure was confirmed by XRD. Therefore, the optimum deposition time of cobalt sulfide thin film electrode at 10 min was exhibiting the higher electrocatalytic activity with cathodic current and surface roughness of -3.36 mA.cm^{-2} and 34 nm, respectively.

Keywords: cobalt sulfide, surface roughness, electrocatalytic activity, electrodeposition, ion exchange deposition

Abstrak

Elektrod lawan (CE) kobalt sulfida telah disediakan menggunakan teknik elektroenapan dan enapan pertukaran ion pada permukaan substrat fluorin terdop-timah oksida (FTO). Kesan tempoh masa enapan terhadap filem nipis telah di analisis menggunakan pembelauan sinar-X (XRD), analisis elektron imbasan pancaran medan (FESEM), mikroskop daya atom (AFM) dan profilometer. Keaktifan bermangkin bagi elektrod telah dianalisis menggunakan teknik kitaran voltamogram (CV). Elektrod kobalt sulfida pada tempoh masa enapan 10 min mempunyai keaktifan elektrobermangkin yang tinggi dengan nilai arus katod dan kekasaran permukaan, masing-masing adalah iaitu -3.36 mA.cm^{-2} dan 34 nm.

Kata kunci: kobalt sulfida, kekasaran permukaan, keaktifan elektrobermangkin, elektroenapan, enapan pertukaran ion

Introduction

Cobalt sulfide is a metal sulfide group from inorganic material with formula Co_xS_y which has higher catalytic activity and is the one most preferred material for counter electrode (CE), due to its electrocatalytic activity towards I_3^- reduction [1, 2]. Cobalt sulfide exists in several type metal chalcogenide phases such as Co_9S_8, Co_3S_4, CoS_2 and CoS [3, 4]. In 2009, cobalt sulfide was used as counter electrode in dye sensitized solar cell (DSSC) for the first time to replace platinum as counter electrode and shows the good catalytic activity for tri-iodide reduction then

achieved 6.5% of efficiency [1]. The main role of counter electrode is to shift electrons arriving from the external circuit and catalyzes the reduction of tri-iodide and redox couple in electrolyte and then supplied back to the dye molecules [5]. Criteria for CE material for DSSC which are should have higher surface roughness, porous structure, and large active area for electrolyte to penetrate through the film easily [6, 7]. Cobalt sulfide electrodes are produced via different techniques – electrodeposition [8], chemical bath deposition [9], and spray pyrolysis [10].

In this study, cobalt sulfide is coated onto fluorine-doped tin oxide (FTO) substrate by using electrodeposition and ionic exchange deposition method at different deposition time. It was expected that the deposition time of thin film subsequently effected the surface roughness and the electrocatalytic activity of cobalt sulfide thin film electrode in iodine-based electrolyte.

Materials and Methods

The CEs were prepared by using electrodeposition and ion exchange deposition methods were followed as previous report [11]. The electrodeposition of cobalt hydroxide ($Co(OH)_2$) was carried out in an aqueous deposition bath containing 5 mM cobalt chloride hexahydrate ($CoCl_2.6H_2O$) at ambient temperature. The electrodeposition had three electrode systems - an FTO substrate as the working electrodes (WE), platinum as a counter electrode (CE) and an Ag/AgCl electrode as reference. The film was prepared by using equipment ModuLab, Solatron. The voltage used was fixed at -0.8 V for different deposition time which were 5, 10, and 15 minutes. After the formation of the $Co(OH)_2$ film, it was rinsed with deionized water, blown with flowing nitrogen gas and immersed in 100 mM of Na_2S solution at 60 ºC for 2 minutes to facilitate ionic exchange reaction. Finally, the cobalt sulfide/FTO film was rinsed with deionized water and dried using nitrogen gas. The compositions of the films were characterized by an X-ray diffraction (XRD, model Bruker D8 Advance). The surface roughness of the film was characterized using atomic force microscopic (AFM, model Nanosurf easyScan2) and the film thickness was measured by using profilometry (Model Dektak 150, Bruker). The morphology structures were characterized by field emission scanning electron microscope (FESEM, Carl Zeiss Supra 55VP). The electrocatalytic activities of thin films were analyzed by cyclic voltammetry (CV) techniques using potentiostats (ModuLab Solatron).

Results and Discussion

Figure 1 shows the surface roughness of cobalt sulfide films on FTO glass substrate measured using AFM. The average film thickness for 5, 10, and 15 minutes were measured by using profilometry were 141 nm, 266 nm, and 341 nm, respectively as listed in Table 1. The average surface roughness is found to increase from 17 nm to 34 nm with the increase of deposition time up to 10 minutes and then decreased at 15 minutes with average surface roughness of 30 nm. The thin film at 10 minutes time deposition formed higher surface roughness compared to other samples which is 34 nm. For film at 15 minutes deposition time has lower surface roughness and due to the increase of film and flake thickness. According to Hsu et al., the surface roughness of the counter electrode will reflect the effective activity area for tri-iodide reduction and the large surface area of the thin film which contributed to more active site for electrolyte diffusion [12].

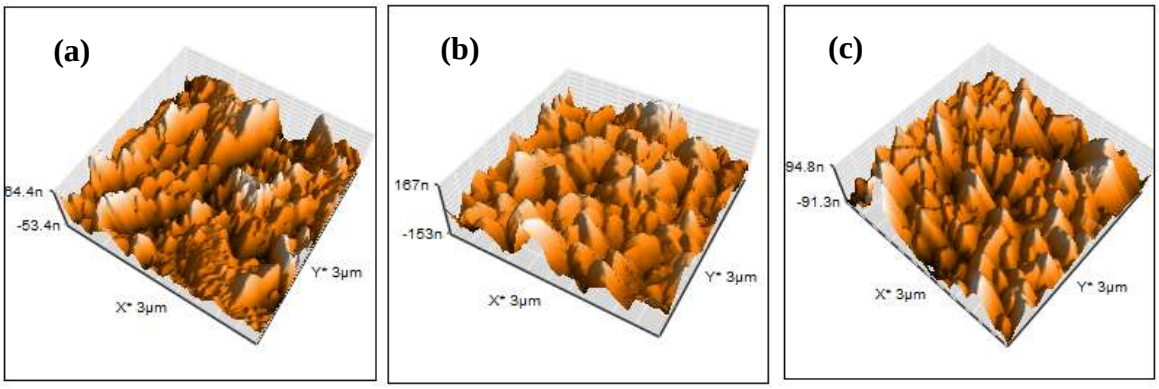


Figure 1. AFM topography images of cobalt sulfide thin film at (a) 5 min, (b) 10 min, and (c) 15 minutes

The early formation of $Co(OH)_2$ thin film using electrochemical deposition produces transparent and colorless film. After $Co(OH)_2$ film was immersed in the Na_2S solution bath, the color of thin film changed to the black color. The color changed provides a preliminary indication of the formation of cobalt sulfide thin film as reported from previous literature [10]. Figure 2 shows the morphological structure the growth of cobalt sulfide mesoporous nanoflakes. The similar structure was reported by the previous literature [11, 13]. At the first 5 minutes time deposition, mesoporous nanoflakes is starting to grow but in small amount and not fully covered on FTO surface as shown by Figure 2(a). Whereas, Figure 2(b) indicates the growth of cobalt sulfide nanoflakes and covered the FTO surface. In Figure 2(c), the growth of cobalt sulfide is found to be increased and more compact in comparison to the 10 minutes time electrodeposition. The average thicknesses of flakes also found to be increased from 5 to 15 minutes of deposition time; which are 16 nm, 17 nm and 18 nm. The distribution of cobalt and sulfur elements in the deposited cobalt sulfide thin film is illustrated in SEM images of Figure 2(d). The weight percentage (wt.%) of Co and S were quantified by using energy dispersive X-ray spectroscopy (EDAX). It was found that, when the time deposition increased, the wt. % of Co and S also increased as listed in the Table 2. From the calculated empirical formula, the deposited cobalt sulfide was found to have higher cobalt elements contents. This fact is most probably due to the uncompleted formation of cobalt sulfide deposited.

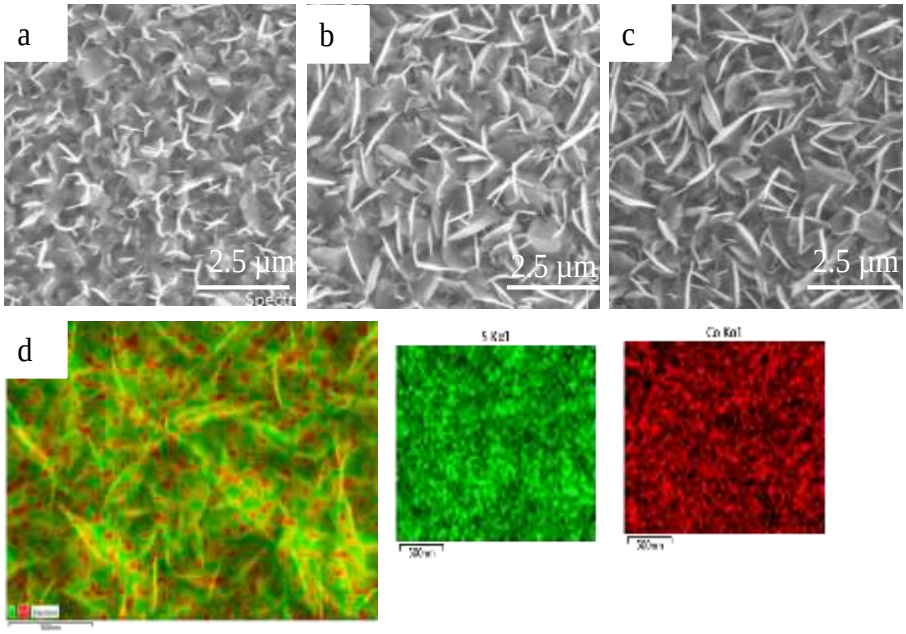


Figure 2. FESEM images of cobalt sulfide thin film deposited at (a) 5 (b) 10 (c) 15 minutes and d) is mapping picture to show the Co and S distribution (green color for sulfur and red color for cobalt)

Figure 3 shows the XRD pattern on the formation of cobalt sulfide analyzed by using X'pert HighScore software. Based on the diffraction pattern, diffraction of hexagonal CoS was obtained, and the structures were confirmed with JCPDS, PDF no. 00-001-1279. The CoS formation were existed for 5 minutes at 2θ = 44.42˚ and 47.40˚, for 10 minutes at 2θ = 44.42˚ and 47.46˚, and for 15 minutes at 2θ = 44.50˚ and 47.48˚. The formation of CoS from $Co(OH)_2$ is due to removal of $(OH)_2$ ion by replacing with sulfur sources, Na_2S, then converted to the CoS thin film [14,15]. Cobalt (Co) was also identified at (100) with JCPDS, PDF no. 00-001-1277, confirming our previous speculation on EDX analysis. The intensity peak of CoS film increased due to the increment of thickness on FTO as deposition time increased. The stronger peaks of growth CoS is preferred orientation at plane (100) and (102). The peaks of FTO slightly reduced when the time deposition was increased due to the increment of film thickness. No changes were observed in the position of the CoS peaks when the time deposition was increased. The average crystallite size of CoS thin films has been calculated by using the equation Scherrer's formula in equation (1) [9].

$$D = \frac{0.9\lambda}{\beta cos\theta} \quad (1)$$

where λ is the wavelength X-ray (0.15406 nm), β is full-width at the half maximum (FWMH) of diffraction peak and θ is diffraction angle. The result has given in Table 1. The average crystallite size of CoS was estimated from Scherrer equation in between 20 nm to 47 nm.

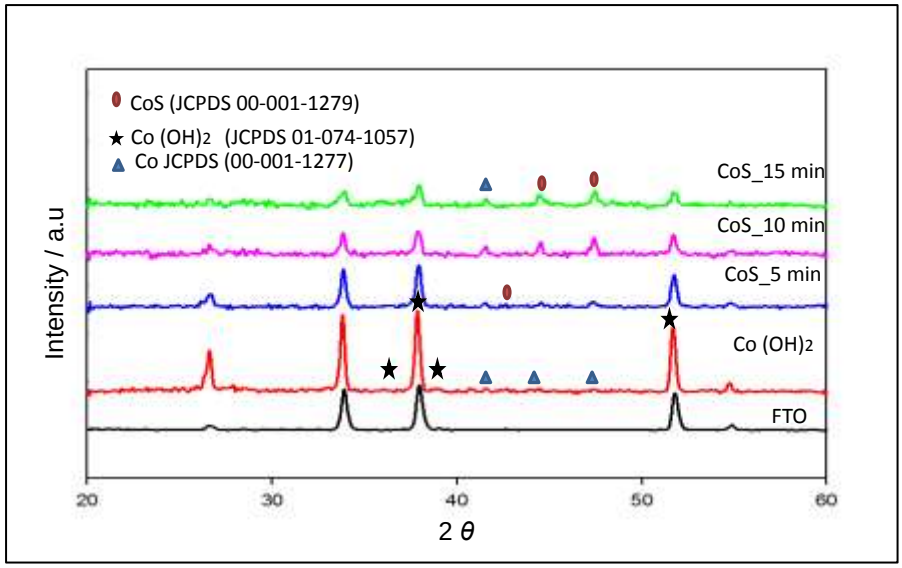


Figure 3. XRD pattern of FTO, $Co(OH)_2$ and as-deposited and CoS thin films for different deposition time

Table 1. The average crystallite size, flakes thickness, film thickness, and surface roughness of as-deposited cobalt sulfide thin film at 5, 10 and 15 minutes of time deposition

Deposition Time (minutes)	**Average Surface Roughness (R_a) (nm)**	**Average Film Thickness (nm)**	**Average Crystallite Size (D) (nm)**	**Average Flakes Thickness (nm)**
5	17	141	47	16
10	34	266	26	17
15	30	341	20	18

Table 2. The average of weight percentage (wt. %) for Co and S element from EDAX

Deposition Time (minutes)	**Co (wt. %)**	**S (wt. %)**	**Calculated Empirical Formula**
0 min	100	-	Co
5 min	75.55	24.44	$Co_{1.7}S$
10 min	72.58	27.42	$Co_{1.4}S$
15 min	71.43	28.57	$Co_{1.4}S$

The cyclic voltammetry is used to evaluate the catalytic activity of cobalt sulfide thin film on FTO substrate in iodide-based electrolyte. The deposited CoS electrode was analyzed by cyclic voltammetry (CV) using a three-electrode configuration in acetonitrile solution contains of 10 mM LiI, 1.0 mM I_2 and 0.1 M $LiClO_4$. Figure 4, shows two pairs of reversible redox peaks were observed for cobalt sulfide electrodes and the results are listed in Table 3. The left pair is represented by reduction equation (2) and right pair is represented by reduction equation (3) [16].

$$I^-_3 + 2e^- \rightleftharpoons 3I^- \quad (2)$$

$$3I_2 + 2e^- \rightleftharpoons 2I^-_3 \quad (3)$$

The left position at cathodic peak is related to catalytic activity of CoS electrode to reduce tri-iodide (I^-_3) to iodide (I^-) ion which attributed by the redox reaction of equation 2 [17]. The film electrode without sulfurization showed the poor electrocatalytic activity in designated electrolyte by showing an oxidation peak only. This is due to non-catalytic behavior of $Co(OH)_2$ film. The reduction peak appeared only after sulfurization and the formation of CoS after sulfurization is proved by the increased in catalytic activity of electrochemical reaction of I^-_3 to I^-. The highest electrocatalytic activity was obtained by CoS film electrode at 10 minutes of deposition time when the cathodic peak potential towards positive value (-0.144 mV) and cathodic peak current towards a negative value (-3.36 $mA.cm^{-2}$) in comparison to others deposition time. Thus, the increasing of cathodic current density is determined a faster rate for the reduction of I^-_3 as indicated by Wu et al. [17]. The increased in catalytic activity might be due to the increases of surface roughness and smaller crystallite size of CoS film electrode. According to previous report, the higher surface roughness and smaller CoS nanoflake crystallite size can promotes more active surfaces area for tri-iodide reduction, thus enhancing the catalytic activity of the CoS electrode [12, 18].

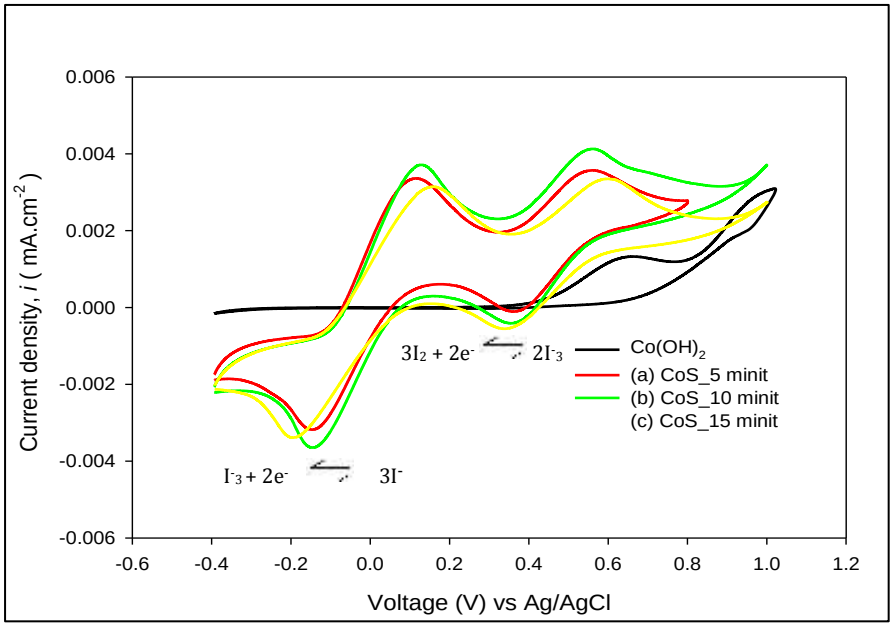


Figure 4. Cyclic voltammetry (CV) graphs of thin film before and after sulfurization, at 5, 10, and 15 minutes of deposition time

Table 3. Cathodic current density and potential of cobalt sulfide electrode for different time deposition

Deposition Time (minutes)	Cathodic Current Density ($mA.cm^{-2}$)	Cathodic Potential (mV)
0	-	-
5	-3.18	-0.15
10	-3.65	-0.15
15	-3.39	-0.19

Conclusion

Cobalt sulfide was successfully deposited via electrodeposition and ionic exchange deposition. cobalt sulfide formed are found to be in nanoflakes architectural with porous structure and also gives high surface roughness. The highest surface roughness and smaller crystallite size was obtained at 10 min of deposition time showed higher electrocatalytic activity of I^-_3 to I^- reduction. These preliminary result shows that the cobalt sulfide thin film electrode is promising to be used as counter electrode in electrochemical cells, especially dye sensitized solar cell (DSSC).

Acknowledgement

This research was supported by Ministry of Education (MOE) Malaysia under Exploratory Research Grant Scheme (ERGS/1/2012/TK07/UKM/03/5) and Look East Policy Grant (LEP 2.0/14/UKM/NT/03/1). This paper was presented in UKM-UCA international joint seminar on Science and Technology 2016.

References

1. Wang, M., Anghel, A. M., Marsan, B., Cevey Ha, N.-L., Pootrakulchote, N. Zakeeruddin, S. M. and Grätzel, M. (2009). CoS supersedes Pt as efficient electrocatalyst for triiodide reduction in dye-sensitized solar cells. *Journal of the American Chemical Society*, 131(44): 15976–15977.
2. Lin, J.-Y., Liao, J.-H. and Wei, T.-C. (2011). Honeycomb-like CoS counter electrodes for transparent dye-sensitized solar cells. *Electrochemical and Solid-State Letters*, 14(4): 41.
3. Ramasamy, K., Malik, M. A., Raftery, J., Tuna, F. and O'Brien, P. (2010). Selective deposition of cobalt sulfide nanostructured thin films from single-source precursors. *Chemistry of Materials*, 22(17): 4919–4930.
4. Eze, F. C. and Okeke, C. E. (1997). Chemical-bath-deposited cobalt sulphide films: Preparation effects. *Materials Chemistry and Physics*, 47, 31–36.
5. Lee, K. S., Lee, H. K., Wang, D. H., Park, N.-G., Lee, J. Y., Park, O. O. and Park, J. H. (2010). Dye-sensitized solar cells with Pt- and TCO-free counter electrodes. *Chemical Communications*, 46(25): 4505-4507.
6. Hauch, A. and Georg, A. (2001). Diffusion in the electrolyte and charge-transfer reaction at the platinum electrode in dye-sensitized solar cells. *Electrochimica Acta*, *46*(22), 3457–3466.
7. Papageorgiou, N. (2004). Counter-electrode function in nanocrystalline photoelectrochemical cell configurations. *Coordination Chemistry Reviews*, 248, 1421–1446.
8. Lin, J., Liao, J. and Chou, S. (2011). Cathodic electrodeposition of highly porous cobalt sulfide counter electrodes for dye-sensitized solar cells. *Electrochimica Acta*, 56(24): 8818–8826.
9. Kamble, S. S., Sikora, A., Pawar, S. T., Maldar, N. N. and Deshmukh, L. P. (2015). Cobalt sulfide thin films: Chemical growth, reaction kinetics and microstructural analysis. *Journal of Alloys and Compounds*, 623: 466–472.
10. Chang, S. H., Lu, M. De, Tung, Y. L. and Tuan, H. Y. (2013). Gram-scale synthesis of catalytic Co_9S_8 nanocrystal ink as a cathode material for spray-deposited, large-area dye-sensitized solar cells. *ACS Nano*, *7*, 9443–9451.
11. Tai, S.-Y., Chang, C.-F., Liu, W.-C., Liao, J.-H. and Lin, J.-Y. (2013). Optically transparent counter electrode for dye-sensitized solar cells based on cobalt sulfide nanosheet arrays. *Electrochimica Acta*, 107: 66–70.
12. Hsu, S., Li, C., Chien, H., Salunkhe, R. R., Suzuki, N., Yamauchi, Y. and Ho, K. –C. (2014). Platinum-free counter electrode nanoparticles for efficient. *Scientific Report*, 4:1-6.

13. Chae, S. Y., Hwang, Y. J., Choi, J.-H. and Joo, O.-S. (2013). Cobalt sulfide thin films for counter electrodes of dye-sensitized solar cells with cobalt complex based electrolytes. *Electrochimica Acta*, 114: 745-749.
14. Rao, S. S., Gopi, C. V. V. M., Kim, S., Son, M., Jeong, M., Savariraj, A. D., Prabakar, K. (2014). Cobalt sulfide thin film as an efficient counter electrode for dye-sensitized solar cells. *Electrochimica Acta*, 133: 174-179.
15. Hu, G., Orkoulas, G. and Christofides, P. D. (2009). Regulation of film thickness, surface roughness and porosity in thin film growth using deposition rate. *Chemical Engineering Science*, 64: 3903-3913.
16. Hauch, A. and Georg, A. (2001). Diffusion in the electrolyte and charge-transfer reaction at the platinum electrode in dye-sensitized solar cells. *Electrochimica Acta*, 46(22): 3457-3466.
17. Wu, M., Wang, Y., Lin, X., Yu, N., Wang, L., Wang, L., Hagfeldt, A. (2011). Economical and effective sulfide catalysts for dye-sensitized solar cells as counter electrodes. *Physical chemistry chemical physics*, 13(43): 19298–19301.
18. Yang, J., Bao, C., Zhu, K., Yu, T., Li, F., Liu, J., Li, Z. (2014). High catalytic activity and stability of nickel sulfide and cobalt sulfide hierarchical nanospheres on the counter electrodes for dye-sensitized solar cells. *Chemical Communications*, 50(37): 4824–4826.

Malaysian Journal of Analytical Sciences, Vol 22 No 1 (2018): 87 - 94
DOI: https://doi.org/10.17576/mjas-2018-2201-11

MALAYSIAN JOURNAL OF ANALYTICAL SCIENCES
Published by The Malaysian Analytical Sciences Society
ISSN 1394 - 2506

EFFECT OF EXTRACTION METHODS ON THE YIELD, FUCOSE CONTENT AND PURITY OF FUCOIDAN FROM *Sargassum* sp. OBTAINED FROM PULAU LANGKAWI, MALAYSIA

(Kesan Kaedah Pengekstrakan Fukoidan Terhadap Hasil, Kandungan Fukosa dan Ketulenan Fukoidan daripada *Sargassum* sp. dari Pulau Langkawi, Malaysia)

Bibi Marliana Baba, Wan Aida Wan Mustapha*, Lim Seng Joe

School of Chemical Sciences & Food Technology,
Faculty of Science and Technology,
Universiti Kebangsaan Malaysia, 43600 UKM Bangi, Selangor, Malaysia

**Corresponding author: wanaidawm@ukm.edu.my*

Received: 12 April 2017; Accepted: 1 September 2017

Abstract

The objective of this study was to determine the effect of extraction methods on the yield, fucose content and purity of fucoidan that had been isolated from brown seaweed, *Sargassum* sp. The extraction of fucoidan was carried out based on the factorial design assigned, which involved three different parameters including two types of extraction (acid and alkaline), three different extraction temperatures (45, 65 and 85 °C) and three different extraction time (1, 3 and 5 hours). Results obtained showed that the best extraction parameter that gave the highest yield of fucoidan extract was the alkaline extraction at 65 °C for 3 hours. Alkaline extraction also produced higher purity and better quality of fucoidan compared to the fucoidan extracted by hydrochloric acidic.

Keywords: acidic extraction, alkaline extraction, fucoidan, fucose content

Abstrak

Objektif kajian adalah untuk mengkaji kesan kaedah-kaedah pengekstrakan terhadap hasil, kandungan fukosa dan ketulenan ekstrak fukoidan yang diperoleh daripada rumpai laut perang, *Sargassum* sp. Pengekstrakan fukoidan dilakukan berdasarkan reka bentuk eksperimen berfaktor, di mana tiga parameter yang berbeza telah ditetapkan termasuklah dua jenis pengekstrakan (berasid dan beralkali), tiga suhu pengekstrakan (45, 65 dan 85 °C) dan tiga masa pengekstrakan (1, 3 dan 5 jam). Keputusan kajian menunjukkan bahawa kaedah pengekstrakan terbaik yang memberi hasil fukoidan paling tinggi adalah melalui pengekstrakan beralkali pada suhu 65 °C selama 3 jam. Pengekstrakan beralkali juga menghasilkan ekstrak yang lebih tulen dan berkualiti berbanding dengan fukoidan yang diekstrak menggunakan asid hidroklorik.

Kata kunci: pengekstrakan berasid, pengekstrakan beralkali, fukoidan, kandungan fukosa

Introduction

Seaweeds are usually classified into three groups including brown (Phaeophyceae), red (Rhodophyceae) and green seaweeds (Chlorophyceae). Red algae is the most abundant group (6000 species), followed by brown (2000 species) and green (1200 species) [1]. They are excellent sources of various bioactive compounds such as polyphenols, carotenoids and polysaccharides [2-5]. These seaweeds have traditionally formed part of the oriental diet, especially in Japan, China and Korea [6]. The major use in Western countries has mainly focused on the extraction of active

compounds used by pharmaceutical, cosmetics and food industries as the source of phycocolloids (polysaccharides extracted from both fresh and marine algae), thickening and gelling agents.

In Malaysia, there is an abundant supply of seaweeds consisting of the three groups. Brown and red seaweeds are mainly used as the sources of phycocolloids, i.e. carrageenan and alginate while green seaweed is normally consumed fresh. According to Phang [7], Malaysia is rich in wild species of brown seaweed such as *Sargassum, Laurencia, Fucus, Ascophyllum* and many others. Among these brown seaweeds, *Sargassum* contributes the highest amount of phytocolloids. There are 21 species of *Sargassum* recorded in Malaysia as reported in literature [7]. *Sargassum binderi* is a type of brown seaweed (Phaeophyceae) that is commonly found in Malaysia. Phang [7] also reported that the phytocolloids extracted from *Sargassum binderi* consist of fucoidan, alginate and laminaran.

Ponce et al. [8] claimed that fucoidan is the major bioactive compound found in *Sargassum*. Fucoidan is a water soluble polysaccharide containing mainly L-fucose and sulphate, together with minor amount of glucuronic acid and xylose. It is a high molecular weight (approximately about 20000 Da) water soluble dietary fibre or polysaccharide. It comes from a family of sulphated homo and heteropolysaccharides composed mainly of α-(1/2)-, α-(1/3)- and/or α-(1/4)-linked α-L-fucose pyranose residues [9]. The main monomer for bioactive components is the fucose, which is one of the eight essential biological sugars. In addition, fucoidan also contains galactose, mannose, xylose, and glucoronic acid residue [10]. The chemical structures of fucoidans from different brown seaweeds vary in terms of types of population species, level of maturity, geographical location and climate [11]. Besides, these particular factors also exhibit different biological activities of fucoidan. Biological activities of fucoidan mainly occur due to its degree of sulphation, structural peculiarities and molecular weight [12]. Fucoidan has a variety of biological functions such as antibacterial, antiviral, antioxidant, anti-cancer, anti-tumour as developed in nutraceutical products and dietary supplements [13]. Lim et al. [9] reported that fucoidan extracted from *Sargassum sp*. that was harvested in Semporna Sabah, Malaysia gave some different characteristics compared to other species of brown seaweeds such as *Padina sp*.

There are many extraction methods that can be used to extract fucoidan from seaweeds. Most of the extraction methods tend to extract fucoidan as a multicomponent crude form of fucoidan, commonly referred as the crude fucoidan [14]. Ion-exchange chromatography or filtration process can be performed to obtain a purified fucoidan. Initially, pre-treatment of the seaweed is commonly performed using a mixture of methanol/chloroform/water (4:2:1 v/v/v) to remove lipids, terpenes and phenols [15]. Raw seaweeds are usually extracted with acid or base solutions as the solvent [13, 16]. Each method of extraction gives different yield and purity of the extracted fucoidan. Hence, this study was carried out to determine the effects of extraction methods (types of extraction, time and temperature) on the fucoidan yield and its fucose content.

Materials and Methods

Chemicals and reagents

Absolute ethanol, methanol and chloroform were obtained from Merck, Germany. Hydrochloric acid (HCl), sulphuric acid (H_2SO_4), calcium chloride ($CaCl_2$), sodium hydroxide (NaOH), sodium iodide (NaI) and Cetavlon were acquired from Fischer Scientific, USA, whereas L-cysteine was obtained from Sigma Aldrich, USA.

Sample preparation

Brown seaweed, *Sargassum* sp. from Pulau Langkawi, Kedah, Malaysia was collected to be used as the study sample. The sample was intentionally planted in an isolated coastal area which did not mix with other genus of seaweeds. The seaweed sample was cleaned and washed with filtered water to remove the sand, debris, epiphytes and other foreign matters prior to storage of sample in an ice cooler box (4 °C). This was to done to ensure low temperature and to preserve the structure of the sample throughout the transportation to the laboratory in UKM, Malaysia. Upon arrival, the sample was again rinsed with distilled water for several times to ensure that it was free from sand and debris. The cleaned seaweed sample was oven-dried at 60 ºC for three days, until the sample achieved a constant weight. The dried sample was ground into powder form by using a high power grinder (C7104, Panasonic, Japan) before being tightly-packed in a glass jar and stored at -18 ºC until further analyses.

Experimental design
The design of this study was a factorial, consisting of three factors that represent the type of extraction, extraction temperature and time. There were two types of fucoidan extraction i.e. acid and alkaline extraction using both 0.15 M of HCl and $CaCl_2$ respectively, at 45, 65 and 85°C for 1, 3 and 5 hours.

Extraction of fucoidan: Acid extraction
The extraction of fucoidan using acid solution, HCl was performed according to the procedures as described [17]. Pre-treatment of the sample was initially conducted to remove lipids, coloured matter and low molecular weight components by refluxing approximately 20 g of the ground sample in 200 mL absolute ethanol at 80 °C for 2 hours. The sample solution was then centrifuged at 18,500×*g* for 10 minutes and the supernatant was removed. The defatted sample was then left to dry overnight at room temperature before being weighed again. Sample was extracted with 200 mL of 0.15 M HCl solution at 45 °C for 1 hour with continuous mechanical stirring (350 rpm). This step was consecutively repeated four times to ensure a complete fucoidan extraction. The sample was centrifuged at 18,500×*g* for 10 minutes after extraction and 3 M sodium hydroxide, NaOH was slowly added into the collected supernatant while being slowly stirred to neutralize the extract solution. The neutralized extract solution was stored overnight at 4 °C. Four volume of absolute ethanol was added into the extract solution and was left to stay overnight at 4 °C to precipitate the fucoidan, prior to centrifugation at 18,500×*g* for 10 minutes to recover fucoidan. The fucoidan obtained was then washed with ethanol and dried at room temperature until constant weight was achieved, and kept in an air tight sample bottle. These procedures were repeated by following different parameters i.e. extraction temperature (65 and 85 °C) and extraction time (3 and 5 hours).

Alkaline extraction
Alkaline extraction of fucoidan was conducted by referring to the method reported in literature [18]. Approximately 20 g of ground seaweed sample was pre-treated with 200 mL of mixture solvent consisting of methanol, chloroform and distilled water (4:2:1; v/v/v) with continuous mechanical stirring at 350 rpm overnight. This was to remove lipids, coloured matter and low molecular weight components from the sample. The suspension was then filtered, and the sample residue was collected. This step was repeated several times until clear solution was obtained to ensure the removal of unwanted components. The defatted seaweed was re-weighed prior to drying using a vacuum oven (Vacucell MMM, Munich, Germany) at 50 °C for 24 hours. Sample was then heated with 200 mL of 0.15 M $CaCl_2$ solution at 45 °C for 1 hour to extract water-soluble polysaccharides. This step was consecutively repeated four times to ensure a complete fucoidan extraction.

Sample solution was mixed thoroughly with 30 mL of 10% hexadecyltrimethylammonium bromide/Cetavlon solution (in excess) and left overnight at 4 °C after being filtered. The solution was centrifuged at 18,500×*g* for 10 minutes using an *Eppendorf 5810R* centrifuge and the supernatant was removed. The precipitate obtained was washed with distilled water and mechanically stirred with 50 mL of 20% ethanolic sodium iodide, NaI (Fischer Scientific) solution overnight at room temperature. This step was repeated for four consecutive days. The mixture solution was rinsed with ethanol to remove excess sodium iodide and dissolved in water. The fucoidan solution was then dialysed against distilled water for several days using a Visking tube with a molecular weight cut-off (MWCO) of 2000 Da, before being lyophilised to obtain crude fucoidan and kept in an air tight sample bottle. These procedures were repeated by following different parameters i.e. extraction temperature (65 and 85 °C) and extraction time (3 and 5 hours).

Quantitative analyses: Determination of extraction yield
The collected fucoidan extract was weighed and the extraction yield was calculated as the following equation 1:

$$\text{Yield of fucoidan (\% of dry weight)} = \frac{\text{Weight of fucoidan (g)}}{\text{Weight of ground seaweed (g)}} \times 100\% \quad (1)$$

Determination of fucose content
Approximately 1 mL of fucoidan extract and 4.5 mL of diluted sulphuric acid, H_2SO_4 solution (1:6, H_2O:H_2SO_4) were pipetted into respective test tubes that had been placed in an ice-water bath. All test tubes were placed into a

boiling water bath for 10 minutes after 1 minute of cooling in the ice-water bath. Aliquots in the test tubes were then left to cool to room temperature prior to the addition of 0.1 mL of 3% L-cysteine (Sigma Aldrich) solution and the solutions were allowed to stand for 30mins to ensure thorough mixing as reported by Lim et al. [9]. Absorbance reading of all the samples was measured in a 96-well plate at 396 nm and 427 nm by using a BioTek Epoch microplate spectrophotometer (Vermont, USA) [19]. Calibration curve ranging from 0.002-0.02% (w/v) of a commercial fucoidan (F_{ysk}) was used to determine the content of fucoidan in the sample extracts. This spectrophotometric analysis was also used in order to calculate the purity of fucoidan based on its content and the initial concentration of sample used (0.02%). n =3 replication was conducted to ensure more accurate results.

Statistical analysis

All analyses were conducted in triplicates (n=3) and collected data were expressed in terms of mean and standard deviation. The statistical analysis was performed using both t-test and one-way ANOVA followed by Duncan's multiple range test (DMRT) using SPSS software for Windows Version 22. Difference in values of mean was considered significant when $p < 0.05$.

Results and Discussion

Yield of fucoidan extract

Techniques of extraction greatly influenced the yield of fucoidan extract. Different mechanical and chemical processes such as the solvent extraction and steam distillation are normally used for the extraction of some bio-compounds from plant sources. The selection of methods differs according to the nature of soluble polysaccharides to be extracted (fucoidan) to obtain its maximum yield. Based on the study that has been conducted, it showed that the acid extraction (fucoidan extracted by HCl) of all parameters gave lower yield in terms of its dry weight percentage (% w/w) compared to that of the alkaline extraction (Figure 1). The alkaline extraction of fucoidan at 65 °C for 3 hours yielded statistically the highest amount of fucoidan, 3.81±0.73% compared to other extraction parameters. In contrast, the least yield of fucoidan extracted by HCl at 85 °C for 5 hours was 0.13±0.05%. Similar result was reported by Ale that the alkaline extraction yielded a significant higher amount of fucoidan compared to acidic extraction [20].

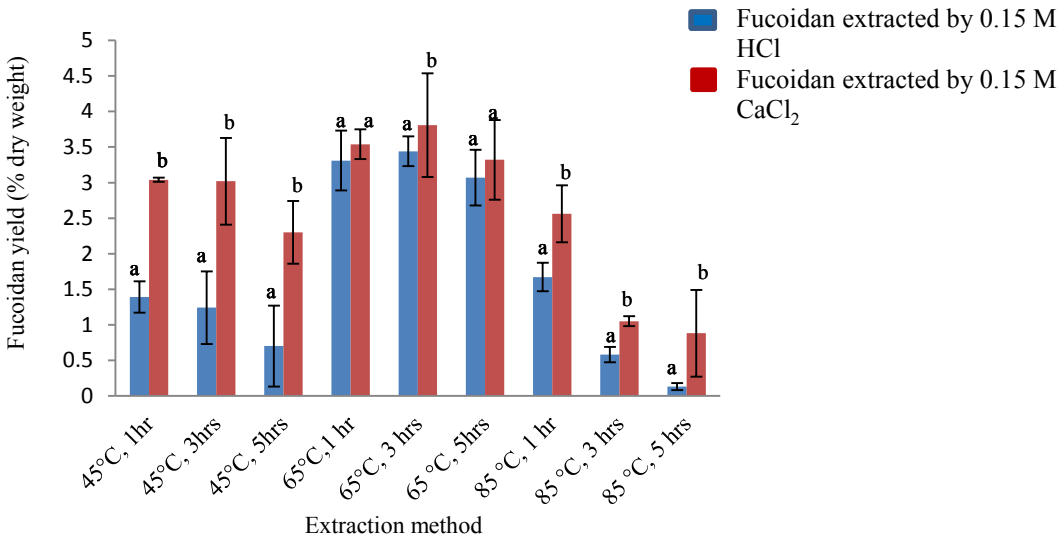


Figure 1. Graph of fucoidan yield (dry weight percentage) against the extraction method. [a-b] Different letters on fucoidan yield indicate a statistically significant difference ($p< 0.05$)

Both acid and alkaline extraction methods showed a significant difference in the fucoidan yield due to its chemical properties. Both solvents used during the process influenced the yield of fucoidan due to their pH values. Protons or hydroxide ions interfere with the hydrogen bonds between the various polysaccharides, releasing them into the solution resulted in an increased yield of extract [15]. The acidic properties of HCl during the extraction of fucoidan might cause the breaking of chemical bonds between the structures of fucose, resulted in the failure of fucose detection [21]. In addition, the extraction of fucoidan at higher temperature (more than 70 °C) and longer extraction time might lead to a degradation of fucose chain. Lower temperature tends to provide slightly low yield of fucoidan as the extraction process might be less efficient than that of the intermediate temperature (65 °C) used (Figure 1). Theoretically, temperature of a substrate or solvent affects the rate/kinetics of a chemical reaction [11]. The higher the temperature applied, the rate and kinetic become higher and faster. In this study, the extraction temperature of 45 °C might not be suitable to extract fucoidan from the seaweed. This explained the result obtained where the yield of fucoidan at 85 °C was lower although longer extraction time was used.

Fucose content of fucoidan extract

Screening of fucoidan content from the raw seaweed sample played the role as the pre-confirmatory analysis in this study. The method used was defined as the colorimetric method in which specific colour reactions occur between fucose with the mixture of L-cysteine and sulphuric acid. This colorimetric method was applied with two different wavelengths, 396 nm and 427 nm. Both absorbance readings were recorded and the change in absorbance between those wavelengths (396 nm and 427 nm respectively) differentiates the presence of fucose content from that of other hexoses [9]. Usov et al. claimed that the absorbance of other hexoses remains the same at both wavelengths at a point of time [22].

Based on the analysis done, fucoidan extracted by 0.15 M $CaCl_2$ at 65 °C for 3 hours showed the significantly highest ($p< 0.05$) fucose content compared to that of all extraction methods that was 3.80±0.91%. Figure 2 also showed the significantly lowest ($p< 0.05$) fucose content was found to be in the fucoidan extracted by 0.15 M HCl at 85 °C for 5 hours which was 0.22±0.7%. The result obtained was reliable as brown seaweeds do not contain other 6-deoxyhexoses which may be found in other seaweeds [22]. Hence, the colour reaction was due to fucose from the brown seaweed sample itself, excluding other sugars by the colour measurement at two wavelengths.

According to recent studies by Rioux et al. [11], fucoidan content in various seaweed species ranges from 0.4% to 21%. This showed that the fucoidan content highly depends on the species of seaweed itself. In addition, he claimed that the fucoidan content in seaweed is also influenced several other factors including season, geographic location, chemical composition of fucoidan as well as the maturity of the plant [11]. Recent study on the fucoidan content in brown seaweed samples collected from several regions in Japan stated that they contain fucoidan ranging from 2.2% to 10.4% [23]. Therefore, it is clearly observed that the fucoidan content in brown seaweed (*Sargassum sp.*) from Pulau Langkawi, Malaysia is within the range. Studies also reported that the fucose composition also varies among species of seaweeds as well as its technique of fucoidan extraction [12]. As Ponce et al. reported, fucoidan been extracted at room temperature and at 70°C possessed completely different chemical compositions [8].

Structure of the plant itself also affects the fucose content in the brown seaweed. Scientifically, it is determined that fucose can highly be contained in the holdfast of the seaweed [24]. Blade-derived fucoidan tend to possess lower fucose content compared to that obtained from the holdfast part. Previous research proved that the sporophyll part of the seaweed plant contains higher quantity fucoidan than that from the blade [25]. Moreover, Chopin and Sawhney [26] claimed that maturity of the seaweed plants also relates positively with the fucose content. The more mature is the seaweed plant, the higher is its fucose content. Hence, there are many internal and external factors which will influence the fucose content in brown seaweeds. Several related factors will be taken into account and discussed in the further analyses of this study.

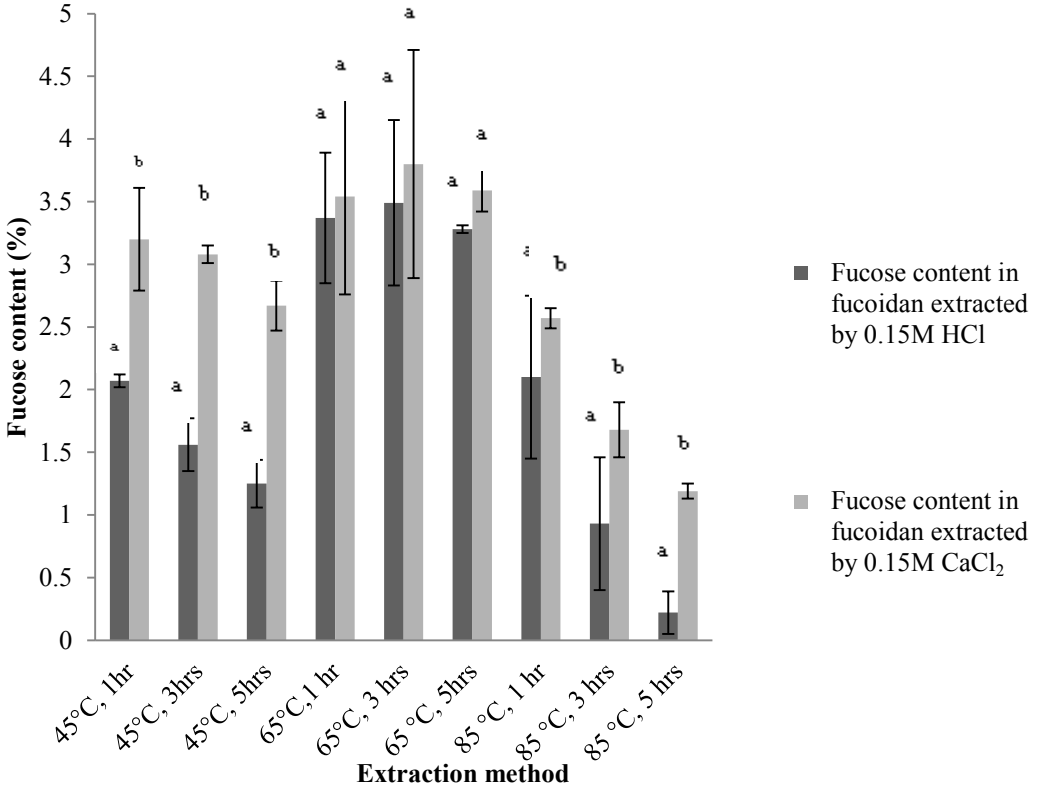


Figure 2. Graph of fucose content (%) against the extraction method. [a-b] Different letters on fucoidan yield indicate a statistically significant difference ($p < 0.05$)

Fucoidan purity

The quality of the extracted fucoidan is normally determined by its purity. The colour of fucoidan also affects the quality of fucoidan in terms of its purity [27]. Purity of the fucoidan extract can be determined visually as lighter colour of fucoidan indicates that it tends to have higher purity, thus higher quality. On the contrary, darker colour of fucoidan extract shows that the extract has a low purity. However, the purity of fucoidan can be measured more accurately by using the colorimetric method as described [19].

In this study, fucoidan obtained from both extraction methods were compared in terms of their purity by using colorimetric method, followed with *t*-test analysis. Based on the results shown in Table 1 below, fucoidan obtained from alkaline extraction (using $CaCl_2$) had a significantly higher purity ($p< 0.05$) than the fucoidan obtained from acidic extraction. This might be due to the existence of other soluble polysaccharides especially alginate that contained in the extract from acidic extraction. During the extraction of fucoidan by HCl, simultaneous extraction of alginate occurred, causing the alginate to be present as the alginic acid. Presence of alginic acid in the fucoidan extract significantly affected the purity of fucoidan when tested. On the contrary, the presence of alginic acid in the fucoidan extracted by alkaline solvent, $CaCl_2$ was determined to be in the form of alginate (insoluble).

Table 1. Percentage of purity of the fucoidan extract

Type of extraction	Purity (%)
Acidic extraction	36.5[a]
Alkaline extraction	82.7[b]

[a-b] Different letters on fucoidan yield indicate a statistically significant difference ($p < 0.05$)

Conclusion

The best parameter for fucoidan extraction was at 65 °C for 3 hours, as it produced the highest yield experimentally. However, there was no significant difference when extracted for 5 hours at lower temperature (45 and 65 °C). Alkaline extraction exhibited higher purity and better quality of fucoidan obtained compared to that of the acid extraction.

Acknowledgement

This research was funded by DPP-2014-035 and GGPM-2015-025 grants together with the MyBrain15 (MyMasters) Scholarship by the Ministry of Higher Education, Malaysia. The authors would like to thank Yaizu Suisankagaku Industry Co., Ltd., Yaizu City, Japan for providing commercial food-grade fucoidan and the School of Chemical Sciences and Food Technology, Faculty of Science and Technology, Universiti Kebangsaan Malaysia which provided all the facilities necessary for this research. Authors would like to thank the organizing committee of UKM-UCA international joint seminar on Science and Technology 2016 for their efforts during this scientific event.

References

1. Venugopal, V. (2011). Polysaccharides from Seaweed and Microalgae Marine Polysaccharides Food Applications. Boca Raton, USA: CRC Press. pp. 89-129.
2. Diplock, A. T., Charleux, J. L., Crozier, W. G., Kok, F. J., Rice, E. C., Stahl, W., Roberfroid M. and Vina, R. J. (1998). Functional food science and defense against reactive oxidative species. *British Journal of Nutrition*, 80: 77-112.
3. Lahaye, M. (1991). Marine algae as sources of fibres: Determination of soluble and insoluble dietary fibre contents in some sea vegetables. *Journal of the Science of Food and Agriculture,* 54(4): 587-594.
4. Fisal, A., Mohd Rosni, S., Welzan, S., Chye, F. Y. and Patricia, M. (2012). Proximate compositions and total phenolic contents of selected edible seaweeds from Semporna, Sabah, Malaysia. *Borneo Science*, 31: 74-83.
5. Wijesinghe, W. A. J. P. and Jeon, Y. J. (2011). Biological activities and potential industrial application of fucose rich sulphated polysaccharides and fucoidans isolated from brown seaweed: A review. *Carbohydrate Polymers,* 88: 13-20.
6. Food and Agriculture Organization (2012). FAO yearbook 2010: Fishery and aquaculture statistics. Rome: Food and Agriculture Organization of the United Nations.
7. Phang, S. M. (1998). Potential products from tropical algae and seaweeds, especially with reference to Malaysia. *Malaysian Journal of Science,* 29(2): 160-166.
8. Ponce, N. M., Pujol, C. A., Damonte, E. B., Flores, M. L. and Stortz, C. A. (2003). Fucoidans from the brown seaweed *Adenocystisutricularis*: Extraction methods, antiviral activity and structural studies. *Carbohydrate Research*, 338: 153-165.
9. Lim, S. J., Wan Aida, W. M., Mohamad Yusof, M., Mamot, S., Jokiman R. and Diah Mazita, M. (2014). Isolation and antioxidant capacity of fucoidan from selected Malaysian seaweeds. *Food Hydrocolloids*, 42: 280-288.
10. Bilan, M. I., Grachev, A. A., Shashkov, A. S., Kelly, M., Sanderson, C. J. and Nifantiev, N. E. (2010). Further studies on the composition and structure of a fucoidan preparation from the brown alga *Saccharinalatissima*. *Carbohydrate Research,* 345: 2038-2047.
11. Rioux, L. E., Turgeon, S. L. and Beaulieu, M. (2007). Characterization of polysaccharides extracted from brown seaweeds. *Carbohydrate Polymers,* 69: 530-537.

12. Nagumo, T. and Nishino, T. (1996). Fucan sulfates and their anticoagulant activities. Polysaccharides in medical applications. Special edition. Marcel Dekker Publisher, New York. pp. 545-574.
13. Bilan, M. I., Grachev, A. A., Ustuzhanina, N. E., Shashkov, A. S., Kelly, M., Sanderson, C. J., Nifantiev, N. E. and Usov, A. I. (2002). Structure of fucoidan from the brown seaweed *Fucus evanescens*. *Carbohydrate Research,* 337: 719-730.
14. Eluvakkal, T., Sivakumar, S. R. and Arunkumar, K. (2010). Fucoidan in some Indian brown seaweed found along the Coast Gulf of Mannar. *International Journal of Botany,* 6(2): 176-181.
15. Hahn, T., Lang, S., Roland, U. and Kai, M. (2012). Novel procedures for the extraction of fucoidan from brown algae. *Process Biochemistry,* 47: 1691-1698.
16. Shin, S. Y., Bajpai, V. K., Kim, H. R. and Kang, S.C. (2007). Antibacterial activity of eicosapentaenoic acid (EPA) against food borne and food spoilage microorganisms. *LWT- Food Science and Technology*, 40(9): 1515-1519.
17. Lee, B., Wei, X. J. and Xu, S. Y. (2004). Structural investigation of a fucoidan containing a fucose free core from the brown seaweed. *Carbohydrate Research,* 341: 1135-1146.
18. Bilan, M. I., Grachev, A. A., Ustuzhanina, N. E., Shashkov, A. S., Kelly, M., Sanderson, C. J., Nifantiev, N. E. and Usov, A. I. (2004). A highly regular fraction of a fucoidan from the brown seaweed *Fucus distichus* L. *Carbohydrate Research,* 339: 511-517.
19. Hellebust, J. A. and Craigie, J. S. (1978). Physiological & biochemical methods: Handbook of plants' phycological methods. Cambridge University Press, London. pp. 382-397.
20. Ale, M. T., Meyer, A. S. and Mikkelsen, J. D. (2013). Fucoidans from brown seaweeds: An update on structures, extraction techniques and use of enzymes as tools for structural elucidation. *RSC Advances*, 22(3): 8131-8141.
21. Umeda, Y., Kihara, H., Ikai, K. and Kato, I. (2003). Food or beverage additives containing fucoidan and food and beverage containing fucoidan. *US Patents*: 6573250.
22. Usov, A. I., Smrnova, G. P. and Klochkova, N. G. (2001). Polysaccharides of algae: Polysachharide composition of several brown algae from Kamchatka. *Russian Journal of Bioorganic Chemistry,* 27(6): 395-399.
23. Wijesinghe, A. P. and Jeon, Y. J. (2011). Effects of fucoidan extraction using different solvents. *Carbohydrate Polymers,* 88: 13-20.
24. Verlaque, M., Flagella, M. M. and Soria, A. (2007). Macroalgal survival in ballast water tanks. *Marine Pollution Bulletin,* 54(9): 1395-1401.
25. Usov, A. I., Smrnova, G. P. and Klochkova, N. G. (2005). Soluble polysaccharides extraction from different types of algae. *Russian Journal of Bioorganic Chemistry,* 32(2): 321-333.
26. Chopin, T. and Sawhney, M. (2008). Seaweeds and their maricultures. *The Encyclopedia of Ocean Sciences*. Elsevier, Oxford, U.K., London.
27. Mak, W. F., Wang, S. K., & Liu, T. (2012). Extraction, Characterization and Antioxidant Activity of Fucoidan from New Zealand *Undaria pinnatifida* (Harvey) Suringar. *Carbohydrate Polymer*, 87: 123-131.

Malaysian Journal of Analytical Sciences, Vol 22 No 1 (2018): 95 - 106
DOI: https://doi.org/10.17576/mjas-2018-2201-12

MALAYSIAN JOURNAL OF ANALYTICAL SCIENCES
Published by The Malaysian Analytical Sciences Society
ISSN 1394 - 2506

CO-SENSITIZATION OF NATURAL SENSITIZERS EXTRACTED FROM RENGAS (*Gluta spp.*) AND MENGKULANG (*Heritiera elata*) WOOD WITH RUTHENIUM DYE (N719) TO ENHANCE THE PERFORMANCE OF DYE-SENSITIZED SOLAR CELLS

(Ko-Pemekaan Pemeka Semulajadi Disari daripada Kayu Rengas (*Gluta Spp.*) dan Mengkulang (*Heritiera Elata*) dengan Pewarna Rutenium (N719) untuk Meningkatkan Prestasi Sel Solar Terpeka Pewarna)

Nur Ezyanie Safie[1], Norasikin Ahmad Ludin[1]*, Norul Hisham Hamid[2], Mohd Sukor Suait[1], Mohd Asri Mat-Teridi[1], Suhaila Sepeai[1], Mohd Adib Ibrahim[1], Kamaruzzaman Sopian[1], Hironori Arakawa[3]

[1]*Solar Energy Research Institute (SERI),*
Universiti Kebangsaan Malaysia, 43600 UKM Bangi, Selangor, Malaysia
[2] *Faculty of Forestry,*
Universiti Putra Malaysia, 43400 Serdang, Selangor, Malaysia
[3] *Department of Industrial Chemistry, Faculty of Engineering,*
Tokyo University of Science, 162-0826, Japan

**Corresponding author: sheekeen@ukm.edu.my*

Received: 12 April 2017; Accepted: 1 September 2017

Abstract

In this study, photovoltaic performance was improved when two natural sensitizers, namely, rengas (*Gluta spp.*) and mengkulang (*Heritiera elata*), were mixed with ruthenium (N719) sensitizer. Five different ratios were prepared and their performances were compared with individual sensitizers. The components of the sensitizers were analyzed via ultraviolet–visible spectrophotometry and Fourier transform infrared spectroscopy. The band gap values and the highest occupied molecular orbital–lowest unoccupied molecular orbital (HOMO-LUMO) levels were calculated using data obtained from photoluminescence analysis and cyclic voltammetry. The mengkulang: N719 (80%:20%) sensitizer exhibits the highest conversion efficiency (η), which is 0.58% with an open circuit voltage (V_{oc}) of 0.63 V, a short circuit photocurrent density (J_{sc}) of 2.1 mA/cm^2, and a fill factor (ff) of 0.44. By contrast, the individual mengkulang sensitizer presents a poor conversion efficiency (η) of 0.16%.

Keywords: natural sensitizer, mixed sensitizer, band gap, HOMO–LUMO level

Abstrak

Dalam kajian ini, prestasi fotovoltik telah bertambah baik apabila dua pemeka yang semula jadi, iaitu, rengas (*Gluta spp*.) dan mengkulang (*Heritiera elata*), telah di campur dengan pemeka rutenium (N719). Lima nisbah yang berbeza telah disediakan dan prestasi mereka dibandingkan dengan pemeka individu. Komponen pemeka dianalisis melalui spektrofotometri ultralembayung cahaya nampak dan spektroskopi inframerah transformasi Fourier. Nilai jurang jalur dan aras orbit molekul tertinggi yang diduduki - orbit molekul terendah yang diduduki (HOMO-LUMO) dikira menggunakan data yang diperolehi daripada analisis kefotopendarcahayaan dan voltammetri berkitar. Pemeka mengkulang:N719 (80%: 20%) mempamerkan kecekapan penukaran tertinggi (η), iaitu 0.58% dengan voltan litar terbuka (V_{oc}) 0.63 V, kepadatan fotoarus litar pintas (J_{sc}) sebanyak 2.1 mA/cm^2 dan faktor isi (ff) daripada 0.44. Sebaliknya, pemeka individu mengkulang memberikan kecekapan penukaran terendah (η) 0.16%.

Kata kunci: pemeka semula jadi, pemeka campuran, jurang jalur, aras HOMO-LUMO

Introduction

Dye sensitized solar cells (DSSCs) becomes reliable solar cells device as it is reported to promote low cost for material and simple synthesis method in achieving efficient conversion efficiency [1-4]. Basically, DSSCs consists of four components to convert light into electricity which are porous semiconductor, sensitizer, electrolyte and counter electrode. A lot of explorations have been made for each of the components to enhance the effectiveness of DSSCs [5, 6]. Since sensitizer plays important key roles to absorb light and supply electron for the mechanism in DSSCs, an intense attract to introduce effective sensitizer have led to few types of sensitizer such as metal complexes, metal-free, organic, inorganic, synthetic and natural sensitizers. Each type of sensitizers has their own potential to enhance the conversion efficiency as well as drawbacks that limit their performance [7-10]. A sensitizer that works as a light harvester in dye-sensitized solar cells (DSSCs) is the key to improving the performance of such cells.

Recently, natural dyes have become reliable alternatives for expensive organic, inorganic, or synthetic dyes. Several studies have found that using natural sensitizers have several possible advantages. For example, natural materials can be easily extracted from fruits, flowers, and leaves with minimal procedures; hence, they have attracted considerable interest to produce low-cost and biodegradable sensitizers [11, 12]. Furthermore, such sensitizers are effective because they provide charge carriers and the model cells exhibit similarities to the photosynthetic mechanism [13, 14]. Natural dyes, which are abundant, provide reasonable light harvesting efficiency; they are also sustainable, low cost, and non-toxic [15, 16]. The most efficient photosensitizer for DSSCs is obtained from ruthenium polypyridyl complexes, such as N719, which exhibits conversion efficiency (η) of over 10% [17]. This characteristic is attributed to metal-to-ligand charge transfer, which produces excited states with long lifetimes, and thus, provides N719 with a broad photon absorption band in the visible spectrum range [18-20]. However, a few drawbacks exhibited by N719 have prompted researchers to seek for another alternative photosensitizer. Although ruthenium exhibits high thermal and chemical stabilities, as well as provides a relatively high efficiency, this trace element is extremely expensive and the demand for it is high; moreover, its sophisticated synthesis and purification processes lead to a high production cost [9]. In addition, ruthenium is a heavy metal, and thus, is a threat to the environment that can pose potential risks even to future generations.

This study aims to investigate experimentally the photovoltaic performance of natural sensitizers extracted from rengas (*Gluta spp*.) and mengkulang (*Heritiera elata*) wood. These natural sensitizers are mixed with a low percentage of N719 sensitizer to enhance their cell performances and optical characteristics.

Materials and Methods

Plants materials and wood extraction

Rengas and mengkulang wood samples were collected from a local sawmill in Kuala Lumpur, Malaysia. A wood chipper machine and a knife ring chipper were used to obtain fine particles from the wood samples. The particles were then dried in an oven at 60 °C for 24 hours before they underwent a segregation process according to particle size. The large particles were ground further using a ball mill. The obtained sawdust was then dried in an oven at 130 °C for 24 hours to decrease its moisture content. To extract dye from the sawdust, methanol was used as the organic solvent in a cold extraction technique. The sawdust was soaked in methanol (1:10 w/v ratio) and left overnight at room temperature. All extraction procedures were performed under dim condition. The glassware that contained the dyes were covered with aluminum foil to minimize photoxidation. Then, the mixture was made to undergo Soxhlet extraction to obtain the extractive compound. The crude extract was stored in a refrigerator (4 °C) until further used.

Subsequently, 0.3 mM N719 sensitizer was prepared by mixing 50 mL acetonitrile (J.T. Baker® Chemicals, PA, USA) and 50 mL 4 *tert*-butyl alcohol (99.7%, Sigma-Aldrich Corporation, MO, USA) with 0.036 g B2 (N719) dye (Dyesol, NSW, Australia). The mixture was left overnight at room temperature before it was ready for use. Apart from the individual sensitizers, we also prepared mixtures of both natural sensitizers with N719 for further analysis. Five different v/v ratios were prepared and denoted as mengkulang: N719 (80%:20%), mengkulang: N719 (90%:10%), mengkulang: rengas: N719 (40%:40%:20%), rengas: N719 (80%:20%), and rengas: N719 (90%:10%).

Fabricating DSSCs

Photoelectrodes were prepared by depositing titanium dioxide (TiO_2) paste (WER 2-0, Dyesol, NSW, Australia) onto fluorine-doped conducting tin oxide (FTO) glasses (~15 Ω sq^{-1}, Solaronix SA, Aubonne, Switzerland) as conductive glass plates via the doctor-blading technique. The electrodes were then sintered at 450 °C for 30 minutes. The photoelectrodes were subsequently dipped into their respective sensitizers, namely, mengkulang, rengas, and their mixtures [mengkulang: N719 (80%:20%), mengkulang: N719 (90%:10%), mengkulang: rengas: N719 (40%:40%:20%), rengas: N719 (80%:20%), and rengas: N719 (90%:10%)], for 24 hours at room temperature to allow sufficient time for the dye molecules to be absorbed onto TiO_2 surface. Then, the TiO_2 electrodes were removed and rinsed with methanol before being dried with nitrogen gas. The DSSCs were assembled by introducing the redox electrolyte (iodolyte AN-50, Solaronix SA, Aubonne, Switzerland) between the dyed TiO_2 electrode and the platinum counter electrode. The platinum paste purchased from Solaronix was deposited onto FTO glasses (~8 Ω sq^{-1}, Solaronix SA, Aubonne, Switzerland) and heated at 450 °C for 30 minutes. Surlyn® (60 μm, Meltonix 1170-60, Solaronix SA, Aubonne, Switzerland) was used to assemble the photo electrode and the counter electrode of the cell.

Characterization and device performance

The absorption spectra were obtained using an ultraviolet–visible (UV–Vis) absorption spectrophotometer (UV-1800, Shimadzu Corporation, Kyoto, Japan). The functional groups of the sensitizers were determined via Fourier transformed infrared spectroscopy (FTIR) using the Spectrum 400 FTIR Imaging System (PerkinElmer, Inc., MA, USA). The highest occupied molecular orbital (HOMO) and the lowest unoccupied molecular orbital (LUMO) were determined by photoluminescence (PL) analysis using FLSP920 fluorescence spectrometer (Edinburgh Instruments, Ltd., Livingston, UK) and cyclic voltammetry (CV) using the ModuLab system (Solartron Analytical, PA, USA). The CV measurements consist of three electrodes, namely, glassy carbon working electrode, platinum counter electrode, and silver/silver chloride (Ag/AgCl) reference electrode, at a scan rate of 100 mV/s. In this study, 0.1 M lithium perchlorate ($LiClO_4$) is used as the supporting electrolyte. Current–voltage (*I–V*) measurement was conducted using a class AAA solar simulator (XES-40S1, San-Ei Electric Co., Ltd., Osaka, Japan) under an irradiation of 1000 W/m^2. The maximum power conversion efficiency (η) was calculated using the following formula in equation 1:

$$\eta = ff \times I_{sc} \times V_{oc}/P \quad (1)$$

where *ff* is the fill factor, I_{sc} is the short circuit photo current density (A/cm^2), V_{oc} is the open circuit voltage (V), and P is the intensity of the incident light (W/cm^2) of the DSSC. The fill factor (*ff*) was defined using the following equation 2:

$$FF = (I_{max} \times V_{max})/(I_{sc} \times V_{oc}) \quad (2)$$

where I_{max} and V_{max} represent the maximum output value of the current and voltage, respectively; while I_{sc} and V_{oc} represent the short-circuit current and open-circuit voltage, respectively. Incident photon-to-current efficiency (IPCE) was also measured using a spectral response measurement system (IVT Solar PVE-300, Bentham Instruments, Ltd., Berkshire, UK).

Results and Discussion

UV–Vis analysis

The extracted crude sensitizers from rengas and mengkulang wood were examined under a UV–Vis spectrophotometer with methanol as the solvent reference. The absorption spectra of the crude sensitizers are shown in Figure 1. The intense peaks were found at 400 nm and 512 nm, which were observed in the rengas sensitizer. However, a broad shoulder appeared between 420 nm to 550 nm, which represented the mengkulang sensitizer. Based on these data, the rengas sensitizer can exhibit strong absorption at low wavelengths. Moreover, Figure 2 illustrates the absorption spectra of the mengkulang and rengas mixtures with the N719 sensitizer at five different percentage ratios. As shown in the figure, the absorption spectra of mengkulang: rengas: N719 (40%:40%:20%), rengas: N719 (80%:20%), and rengas: N719 (90%:10%) exhibit similarity to that of the individual rengas sensitizer. This finding may be attributed to the chemical characteristic of the rengas sensitizer, which is more dominantly

absorbed onto TiO_2 surface compared with the other sensitizers. Moreover, the absorption spectra of mengkulang: N719 (80%:20%) and mengkulang: N719 (90%:10%) also exhibit similarity to that of the individual mengkulang sensitizer because of the dominant effect of this sensitizer over the N719 sensitizer.

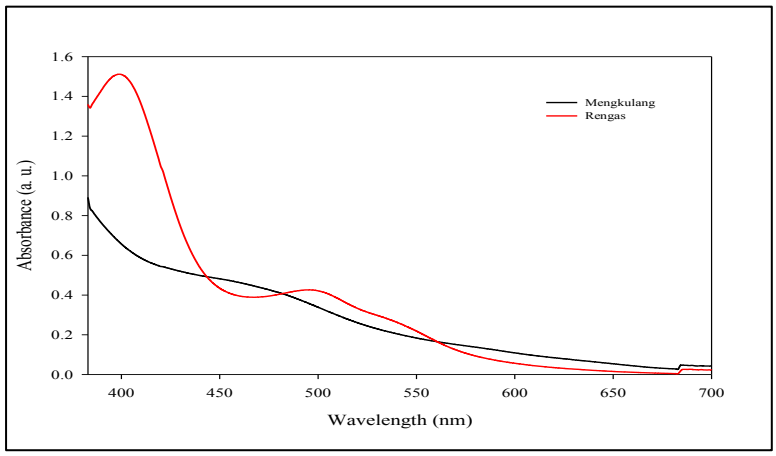


Figure 1: UV–Vis absorption spectra of the mengkulang and rengas sensitizers

In addition, the absorption spectra of the mixed sensitizers absorbed onto TiO_2 are also shown in Figure 2. Upon absorbed onto TiO_2, the spectra did not present an obvious peak although wide shoulders were observed between 400 nm and 450 nm and between 500 nm and 550 nm for mengkulang: rengas: N719 (40%:40%:20%), rengas: N719 (80%:20%), and rengas: N719 (90%:10%), as well as between 500 nm and 550 nm for mengkulang: N719 (80%:20%) and mengkulang: N719 (90%:10%). The UV–Vis absorption of TiO_2 without a sensitizer is also shown to compare it with those with absorbed sensitizers. Based on the comparison results, the absorption spectra of the sensitizers absorbed onto TiO_2 exhibit a more stable and broader shoulder than that of TiO_2 without a sensitizer; this characteristic enables the photoelectrode to harvest light from a broad spectrum of solar energy, which causes a device to generate high photocurrent [21]. Another important finding is that dye concentration also affects absorption value.

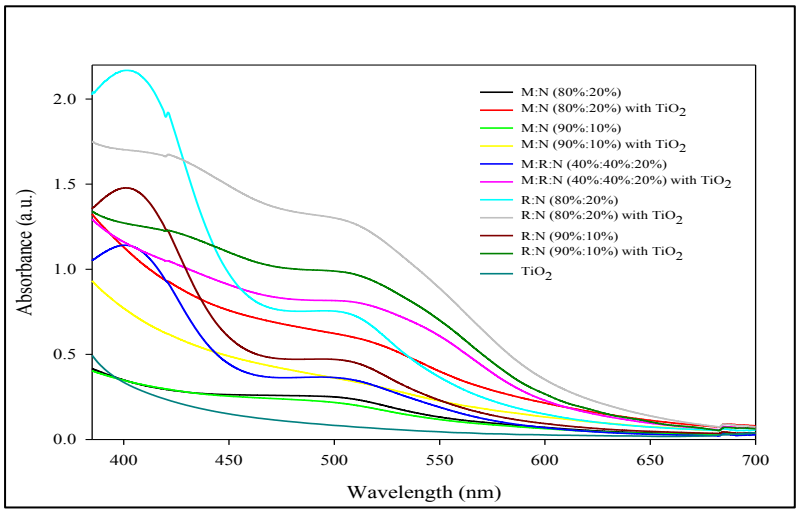


Figure 2. UV–Vis absorption of the mixed sensitizers, the TiO_2 electrode, and the sensitizers absorbed onto TiO_2 (M stands for mengkulang; N denotes N719; and R indicates rengas).

FTIR analysis

The functional groups of the sensitizers were analyzed via FTIR spectroscopy, with potassium bromide as the background reference. Figure 3 shows that the patterns of the infrared spectra are similar for all samples probably because the functional groups present in all the investigated sensitizers are the same. The broad bands observed at 3323, 3309, 3340, 3352, and 3320 cm^{-1} were attributed to the vibrations of the free hydroxyl group (Ar–O–H) of phenols. The intense peaks observed at 2832 cm^{-1} and 2944 cm^{-1} were attributed to the stretching of the sp^3 C–H bond. Moreover, the small shoulder that appeared at 1449 cm^{-1} was ascribed to the presence of aromatic C=C stretching, whereas the one observed at 1650 cm^{-1} was attributed to the presence of a C=N bond. The intense and long peak at 1023 cm^{-1} was ascribed to the presence of a C–O bond. Based on the collected information, the carboxyl and carbonyl functional groups do not exist in the studied natural sensitizers. Previous literature has reported that the functional group that is required to interact with TiO_2 surface is either a carboxylic group or other peripheral acidic anchoring groups [22].

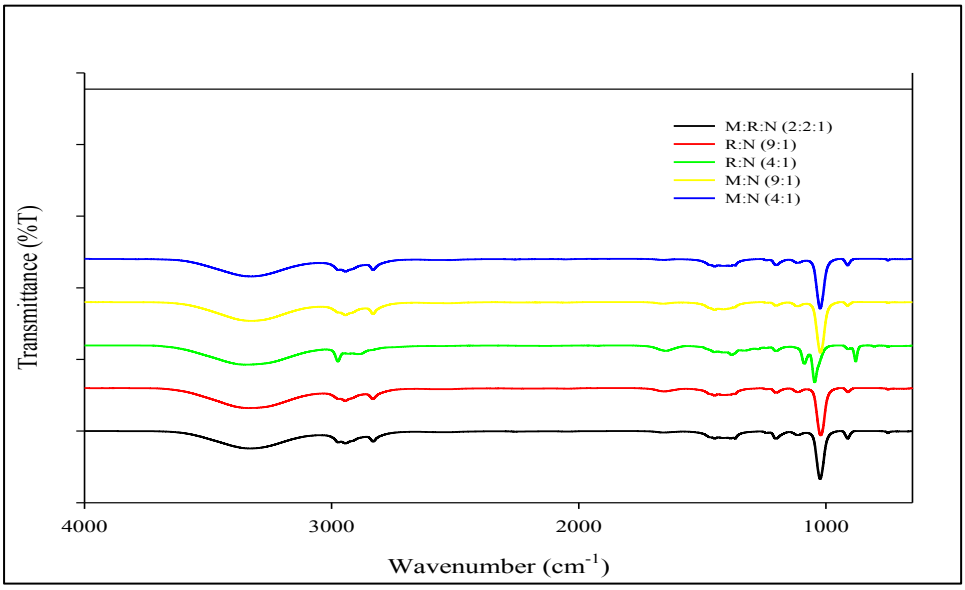


Figure 3. FTIR analyses of the individual and mixed sensitizers (M stands for mengkulang; N denotes N719; and R indicates rengas)

PL Analysis

Band gap measurement was performed via PL analysis. The optical band gaps of the sensitizers were obtained from the relation $E_g = hc/\lambda$, where h is Planck's constant, c is the speed of light, and λ is the emission peak obtained from the PL emission spectra. Table 1 provides the band gap measurements of all types of samples used in this study. Based on the data, the mengkulang and mengkulang: N719 (80%:20%) sensitizers exhibit the highest band gap value, that is, 2.38 eV, at the emission peaks of 522 nm and 520 nm, respectively. Furthermore, the mengkulang: N719 (90%:10%) sensitizer presents a slightly lower band gap value, that is, 2.36 eV at the emission peak of 525 nm. The remaining samples exhibit close band gap value of 2.15 eV for both the rengas sensitizer at the emission peak of 576 nm and the rengas: N719 (80%:20%) sensitizer at the emission peak of 578 nm. The band gap value of 2.16 eV was obtained for both the mengkulang: N719 (80%:20%) and mengkulang: rengas: N719 (40%:40%:20%) sensitizers at the same emission peak of 575 nm. As shown in Figure 4, the mengkulang, mengkulang: N719 (80%:20%), and mengkulang: N719 (90%:10%) sensitizers have broad emission peaks, whereas the other sensitizers exhibit similar emission peak patterns. In addition, 90% and 80% mengkulang present higher intensity than 90% and 80% rengas in the mixed sensitizers. Moreover, the mixed sensitizers with 10% N719 have higher intensities than those with 20% N719.

Table 1. Summary of optical band gap measurement

Sensitizer	**λ max (nm)**	$E_g = hc/\lambda$ **(eV)**
Mengkulang (M)	522	2.38
Rengas (R)	576	2.15
M:R:N (40%:40%:20%)	575	2.16
M:N (90%:10%)	525	2.36
M:N (80%:20%)	520	2.38
R:N (90%:10%)	575	2.16
R:N (80%:20%)	578	2.15

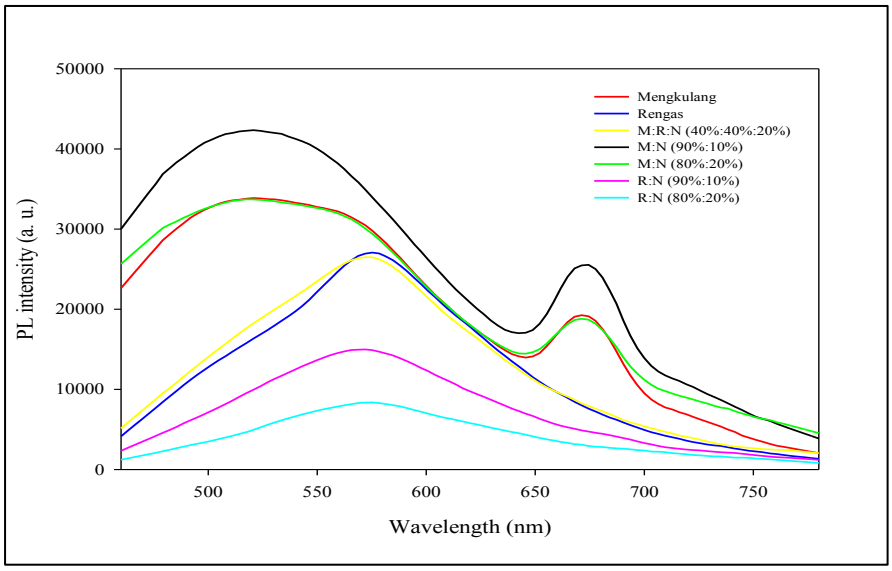


Figure 4. Emission spectra of the individual and mixed sensitizers (M stands for mengkulang; N denotes N719; and R indicates rengas

Cyclic voltammetry analysis

The HOMO–LUMO was calculated via CV [23]. The cyclic voltammograms of mengkulang, rengas, mengkulang: N719 (80%:20%), mengkulang: N719 (90%:10%), mengkulang: rengas: N719 (40%:40%:20%), rengas: N719 (80%:20%), and rengas: N719 (90%:10%) are presented in Figure 5. The calculated positions of the HOMO and LUMO levels are presented in Table 2 with respect to their individual reduction potential onset extrapolated from the voltammograms of the sensitizers [24]. Based on the HOMO–LUMO levels presented in Table 2, schematics were illustrated in Figures 6 and 7 to compare the energy levels of the investigated sensitizers in terms of vacuum level and normal hydrogen electrode (NHE).

Table 2. Calculated HOMO–LUMO energy levels and band gap measurements

Sensitizer	**Band Gap, E_g(eV)**	**E_{ox}^{onset} vs Ag/AgCl (V)**	**LUMO Level (eV)**	**HOMO Level (eV)**
Mengkulang (M)	2.38	0.29	-2.31	-4.69
Rengas (R)	2.15	0.26	-2.51	-4.66
M:N (80%:20%)	2.38	0.27	-2.29	-4.67
M:N (90%:10%)	2.36	0.32	-2.36	-4.72
M:R:N (40%:40%:20%)	2.16	0.32	-2.56	-4.72
R:N (80%:20%)	2.15	0.27	-2.52	-4.67
R:N (90%:10%)	2.16	0.31	-2.55	-4.71

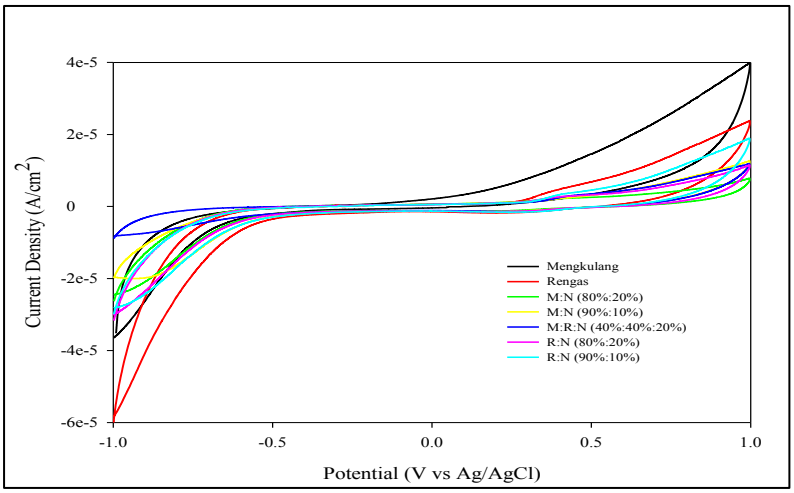


Figure 5. Cyclic voltammograms of the individual and mixed sensitizers (M stands for mengkulang; N denotes N719; and R indicates rengas)

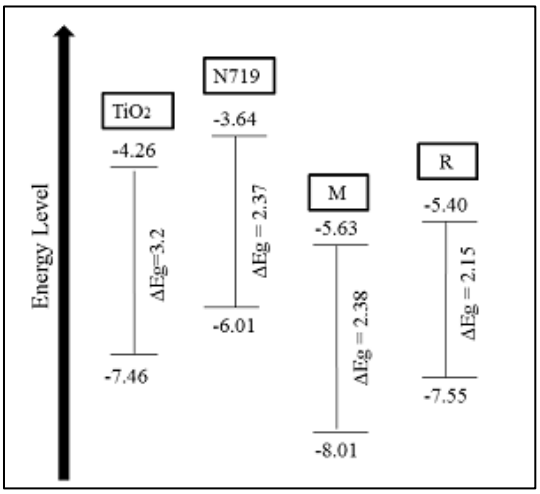


Figure 6. Schematic of the energy levels of TiO_2 and the N719, mengkulang, and rengas sensitizers with respect to vacuum level and NHE (M stands for mengkulang and R denotes rengas)

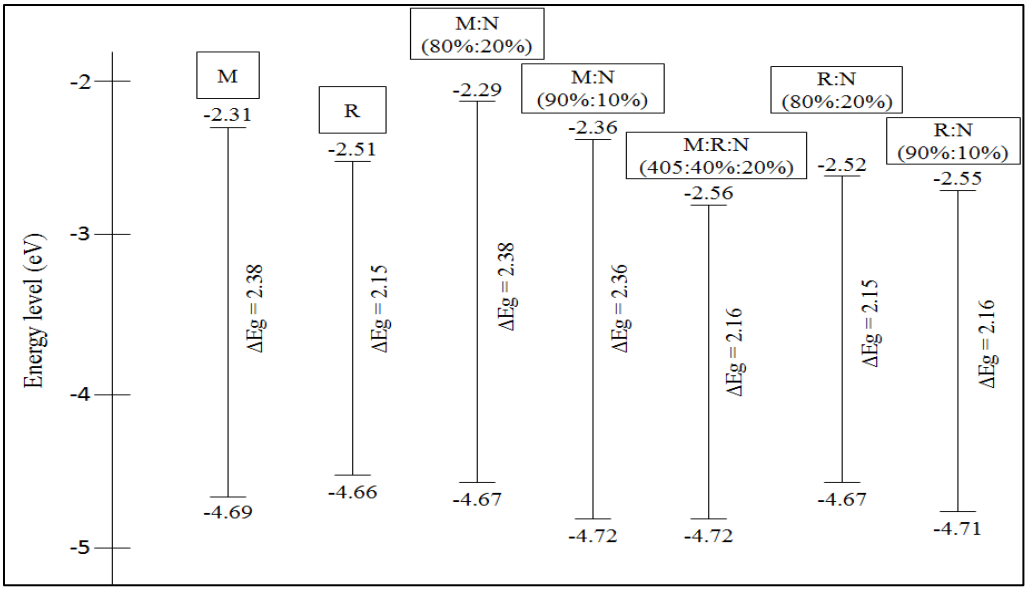


Figure 7. Schematic of the comparison of the energy levels of the investigated sensitizers with respect to vacuum level and NHE (M stands for mengkulang; N denotes N719; and R indicates rengas)

As shown in Figures 6 and 7, the LUMO levels of mengkulang, rengas, mengkulang: N719 (80%:20%), mengkulang: N719 (90%:10%), mengkulang: rengas: N719 (40%:40%:20%), rengas: N719 (80%:20%), and rengas: N719 (90%:10%) were located below the conduction band (CB) of TiO_2. By contrast, the LUMO level of a sensitizer must be located slightly above the energy level of a semiconductor to enable the sensitizer to inject electrons into the conduction band of TiO_2 with high quantum yields [25]. Given that the LUMO levels of the investigated sensitizers obtained in this study are lower than the CB level of TiO_2, the performance of the cells is predicted to be poor.

I–V characteristics

Figure 8 shows the *I–V* curve of the mengkulang, rengas, mengkulang: N719 (80%:20%), mengkulang: N719 (90%:10%), mengkulang: rengas: N719 (40%:40%:20%), rengas: N719 (80%:20%), and rengas: N719 (90%:10%) sensitizers evaluated under the illumination of AM 1.5 global simulated solar light. The performances of the DSSCs are calculated and the results are presented in Table 3. The best performance is exhibited by the mengkulang: N719 (80%:20%) sensitizer, which presents a conversion efficiency (η) of 0.58%, with an open circuit voltage (V_{oc}) of 0.63 V, a short circuit photocurrent density (J_{sc}) of 2.1 mA/cm^2, and a fill factor (*ff*) of 0.44. The mengkulang: N719 (90%:10%) sensitizer follows with a conversion efficiency (η) of 0.45%, V_{oc} of 0.606 V, J_{sc} of 1.7 mA/cm^2, and *ff* of 0.44 under an irradiance of 1000 W/m^2. Moreover, the other mixed sensitizers exhibit lower conversion efficiencies than the two synthesizers but still higher than those of the individual sensitizers, namely, mengkulang and rengas. Between these two, mengkulang achieves higher conversion efficiency (η) of 0.16%, with V_{oc} of 0.53 V, J_{sc} of 0.4 mA/cm^2, and *ff* of 0.76. Meanwhile, rengas has conversion efficiency (η) of 0.11%, V_{oc} of 0.5 V, J_{sc} of 0.3 mA/cm^2, and *ff* of 0.73. Based on the obtained data, the J_{sc} value is directly proportional to conversion efficiency (η). Ooyama et al. [26] reported that the J_{sc} value is dependent on the interaction between TiO_2 and the dye sensitizer. A high J_{sc} value directly indicates strong light-absorption capability and high electron-injection efficiency for a photoexcited dye. Hence, a high J_{sc} value will contribute to increasing conversion efficiency (η).

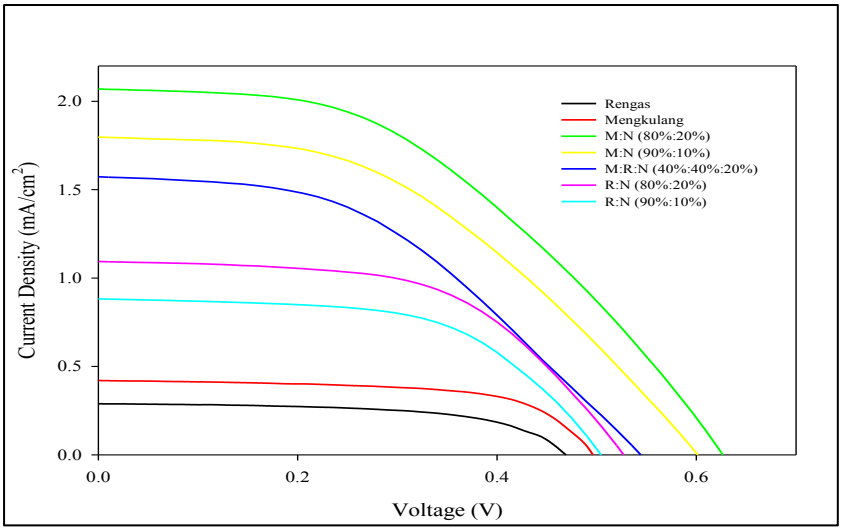


Figure 8. Comparison of the *I–V* characteristics of the individual and mixed sensitizers (M stands for mengkulang; N denotes N719; and R indicates rengas)

Table 3. *I–V* characteristics and power conversion efficiencies (η) of DSSCs with different type of sensitizers

Sensitizer	V_{oc} **(V)**	J_{sc} **(mA cm^{-2})**	***ff***	η**/%**
Mengkulang (M)	0.53	0.40	75.98	0.16
Rengas (R)	0.50	0.30	72.88	0.11
M:N (80%:20%)	0.63	2.10	44.00	0.58
M:N (90%:10%)	0.61	1.70	44.41	0.46
M:R:N (40%:40%:20%)	0.55	1.60	45.23	0.39
R:N (80%:20%)	0.53	1.10	57.07	0.33
R:N (90%:10%)	0.56	0.70	65.03	0.25

IPCE spectra

Figure 9 shows the IPCE spectra of all the investigated sensitizers. As shown in the figure, the mengkulang: N719 (80%:20%) and mengkulang: N719 (90%:10%) sensitizers exhibit the highest efficiency with two similar intense peaks at 354 nm and 540 nm, respectively. Meanwhile, the mengkulang: rengas: N719 (40%:40%:20%), rengas: N719 (80%:20%), and rengas: N719 (90%:10%) sensitizers present similar curve patterns, where mengkulang: rengas: N719 (40%:40%:20%) has the highest efficiency, followed by rengas: N719 (80%:20%) and rengas: N719 (90%:10%). Both the individual sensitizers, namely, mengkulang and rengas, exhibit lower efficiencies compared with the mixed sensitizers, which are parallel to their lower efficiency in *I–V* characteristics. The results in IPCE percentage agree with the *I–V* data collected in this study. They are consistent with the findings of Kumara et al. [23], wherein low IPCE contributes to the low energy conversion efficiency (η) of a DSSC.

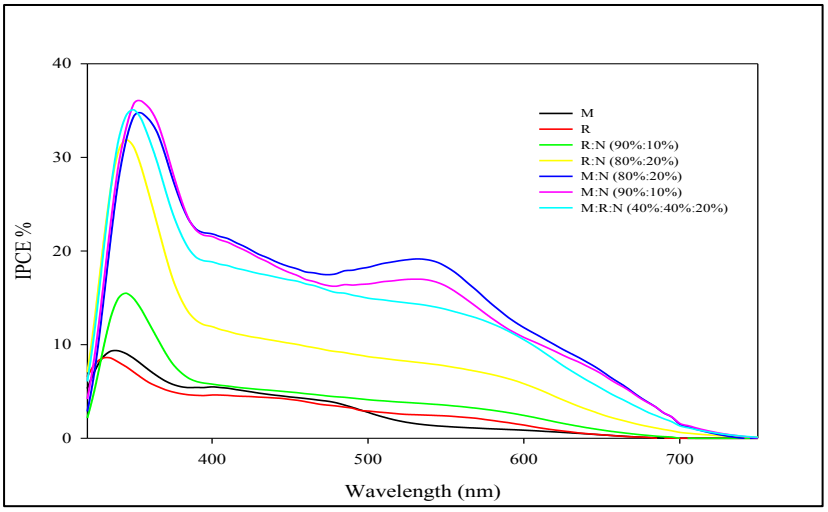


Figure 9. IPCE spectra of the individual and mixed sensitizers (M stands for mengkulang; N denotes N719; and R indicates rengas)

Conclusion

This study reveals the enhanced performance of DSSCs with natural sensitizers extracted from rengas and mengkulang mixed with N719 sensitizer. The best performance is exhibited by the mengkulang: N719 (80%:20%) sensitizer, with a conversion efficiency (η) of 0.584%. This conversion efficiency shows an increment compared with the individual mengkulang sensitizer (0.161%). The mixed sensitizers present better photovoltaic performance than the individual sensitizers across all analyses. Their IPCE and *I–V* curves demonstrate parallel results. For example, mengkulang and rengas have low IPCE percentages, which contribute to low conversion efficiency. The HOMO and LUMO levels of all the investigated sensitizers have been calculated to determine their capability to inject electrons into the CB of TiO_2. The LUMO levels of all the investigated sensitizers are located below the Fermi level of TiO_2, which results in low conversion efficiency (ŋ). Although the efficiencies obtained using these natural sensitizers remain too low for large-scale practical applications, the obtained results may motivate researchers to conduct studies to explore these natural sensitizers further.

Acknowledgements

This research was supported by Universiti Kebangsaan Malaysia under Iconic Collaboration Grant (ICONIC-2013-006) and presented in UKM-UCA international joint seminar on Science and Technology 2016.

References

1. Hua, Y., Chang, S., Wang, H., Huang, D., Zhao, J., Chen, T. and Zhu, X. (2013). New phenothiazine-based dyes for efficient dye-sensitized solar cells: Positioning effect of a donor group on the cell performance. *Journal of Power Sources*, 243: 253-259.
2. Chang, J., Lee, C., Kumar, D., Chen, P., Lin, L., Thomas, K. R. J. and Ho, K. (2013). Co-sensitization promoted light harvesting for organic dye-sensitized solar cells using unsymmetrical squaraine dye and novel. *Journal of Power Sources*, 240: 779-785.
3. Namuangruk, S., Fukuda, R., Ehara, M., Meeprasert, J., Khanasa, T., Morada, S., Kaewin, T., Jungsuttiwong, S., Sudyoadsuk, T. and Promarak, V. (2012). D–D− π–A-Type organic dyes for dye-sensitized solar cells with a potential for direct electron injection and a high extinction coefficient: synthesis, characterization, and theoretical investigation. *The Journal of Physical Chemistry C*, 116(49): 25653-25663.
4. Pei, K., Wu, Y., Islam, A., Zhu, S., Han, L., Geng, Z. and Zhu, W. (2014). Dye-sensitized solar cells based on quinoxaline dyes: effect of π – linker on absorption, energy levels, and photovoltaic performances, *The Journal of Physical Chemistry C,* 118(30): 16552-16561.

5. Hamadanian, M., Jabbari, V. and Gravand, A. (2012). Materials science in semiconductor processing dependence of energy conversion efficiency of dye-sensitized solar cells on the annealing temperature of TiO_2 nanoparticles. *Materials Science in Semiconductor Processing*, 15(4): 371-379.
6. Lee, J. P., Yoo, B., Suresh, T., Kang, M. S., Vital, R. and Kim, K. J. (2009). Novel silane-substituted benzimidazolium iodide as gel electrolyte for dye-sensitized solar cells. *Electrochimica Acta*, 54(18): 4365-4370.
7. Torchani, A., Saadaoui, S., Gharbi, R. and Fathallah, M. (2015). Sensitized solar cells based on natural dyes. *Current Applied Physics*, 15(3): 307-312.
8. Ludin, N. A., Al-Alwani Mahmoud, A. M., Bakar Mohamad, A., Kadhum, A. A. H., Sopian, K. and Abdul Karim, N. S. (2014). Review on the development of natural dye photosensitizer for dye-sensitized solar cells. *Renewable and Sustainable Energy Reviews*, 31: 386-396.
9. Gong, J., Liang, J. and Sumathy, K. (2012). Review on dye-sensitized solar cells (DSSCs): Fundamental concepts and novel materials. *Renewable and Sustainable Energy Reviews*, 16(8), 5848-5860.
10. Polo, A. S., Itokazu, M. K. and Murakami Iha, N. Y. (2004). Metal complex sensitizers in dye-sensitized solar cells. *Coordination Chemistry Reviews*, 248(13-14), 1343-1361.
11. Richhariya, G., Kumar, A., Tekasakul, P. and Gupta, B. (2017). Natural dyes for dye-sensitized solar cell: A review. *Renewable and Sustainable Energy Reviews*, 69: 705-718.
12. Hamadanian, M., Safaei-Ghomi, J., Hosseinpour, M., Masoomi, R. and Jabbari, V. (2014). Uses of new natural dye photosensitizers in fabrication of high potential dye-sensitized solar cells (DSSCs). *Materials Science in Semiconductor Processing*, 27: 733-739.
13. Koyama, Y., Miki, T., Wang, X. F. and Nagae, H. (2009). Dye-sensitized solar cells based on the principles and materials of photosynthesis: Mechanisms of suppression and enhancement of photocurrent and conversion efficiency. *International Journal of Molecular Sciences*, 10(11): 4575-4622.
14. Kalyanasundaram, K. and Graetzel, M. (2010). Artificial photosynthesis: Biomimetic approaches to solar energy conversion and storage. *Current Opinion in Biotechnology*, 21(3): 298-310.
15. Shahid, M., Shahid-Ul-Islam and Mohammad, F. (2013). Recent advancements in natural dye applications: A review. *Journal of Cleaner Production*, 53: 310-331.
16. Hao, S., Wu, J., Huang, Y. and Lin, J. (2006). Natural dyes as photosensitizers for dye-sensitized solar cell. *Solar Energy*, 80(2): 209-216.
17. Nazeeruddin, M. K., Péchy, P., Renouard, T., Zakeeruddin, S. M., Humphry-Baker, R., Comte, P., Liska, P., Cevey, L., Costa, E., Shklover, V. and Spiccia, L. (2001). Engineering of efficient panchromatic sensitizers for nanocrystalline TiO_2-based solar cells. *Journal of the American Chemical Society*, 123(8): 1613-1624.
18. Nwanya, A. C., Ezema, F. I. and Ejikeme, P. M. (2011). Dyed sensitized solar cells: A technically and economically alternative concept to p-n junction photovoltaic devices. *International Journal of the Physical Sciences*, 6(22): 5190-5201.
19. Ahn, J., Lee, K.C., Kim, D., Lee, C., Lee, S., Cho, D.W., Kyung, S. and Im, C. (2013). Synthesis of novel ruthenium dyes with thiophene or thienothiophene substituted terpyridyl ligands and their characterization. *Molecular Crystals and Liquid Crystals*, 581(1): 45-51.
20. Zhang, J., Yu, C., Wang, L., Li, Y., Ren, Y. and Shum, K. (2014). Energy barrier at the N719-dye/$CsSnI_3$ interface for photogenerated holes in dye-sensitized solar cells. *Scientific Reports,* 4: 6954.
21. Lim, A., Manaf, N., Tennakoon, K., Chandrakanthi, R. L. N., Lim, L. B. L., Bandara, J. M. R. and Ekanayake, P. (2015). Higher performance of DSSC with dyes from *Cladophora sp*. as mixed co-sensitizer through synergistic effect. *Journal of Biophysics*: 1-8.
22. Galoppini, E. (2004). Linkers for anchoring sensitizers to semiconductor nanoparticles. *Coordination Chemistry Reviews*, 248(13-14): 1283-1297.
23. Kumara, N. T. R. N., Ekanayake, P., Lim, A., Iskandar, M. and Ming, L. C. (2013). Study of the enhancement of cell performance of dye sensitized solar cells sensitized with *Nephelium lappaceum* (*F: Sapindaceae*). *Journal of Solar Energy Engineering*, 135: 031014.
24. Leonat, L., Sbârcea, G. and Braňzoi, I. V. (2013). Cyclic voltammetry for energy levels estimation of organic materials. *UPB Scientific Bulletin, Series B: Chemistry and Materials Science*, 75: 111-118.
25. Kumara, N. T. R. N., Ekanayake, P., Lim, A., Liew, L. Y. C., Iskandar, M., Ming, L. C. and Senadeera, G. K. R. (2013). Layered co-sensitization for enhancement of conversion efficiency of natural dye sensitized solar cells. *Journal of Alloys and Compounds*, 581: 186-191.

26. Ooyama, Y. and Harima, Y. (2012). Photophysical and electrochemical properties, and molecular structures of organic dyes for dye-sensitized solar cells. *ChemPhysChem*, 13(18): 4032-4080.

Malaysian Journal of Analytical Sciences, Vol 22 No 1 (2018): 107 - 114
DOI: https://doi.org/10.17576/mjas-2018-2201-13

MALAYSIAN JOURNAL OF ANALYTICAL SCIENCES
Published by The Malaysian Analytical Sciences Society
ISSN 1394 - 2506

CLAMSHELL AND SEA SAND AS HETEROGENEOUS CATALYSTS FOR WASTE COOKING OIL BASED BIODIESEL PRODUCTION VIA TRANSESTERIFICATION REACTION

(Kulit Kerang dan Pasir Pantai Sebagai Mangkin Heterogen untuk Penghasilan Biodiesel Berasaskan Minyak Masak Sawit Terpakai Melalui Tindakbalas Transesterifikasi)

Arsyad Ismail Sanuzi, Syuhada Mohd Tahir*, Siti Norhafiza Mohd Khazaai

Faculty of Applied Sciences,
Universiti Teknologi MARA Cawangan Pahang, 26400 Bandar Tun Abdul Razak Jengka, Pahang, Malaysia

**Corresponding author: syuhadamohdtahir@pahang.uitm.edu.my*

Received: 4 December 2016; Accepted: 1 December 2017

Abstract

This study was carried out to study the effectiveness of clamshell and sea sand as heterogeneous catalyst to produce biodiesel via transesterification of waste cooking oil (WCO). WCO was first pre-treated to discard water and impurities. Clamshell and sea sand were crushed into fine powder, sieved to 500 µm particles and calcined. Next, the pre-treated WCO was used to obtain fatty acid methyl ester (FAME) via transesterification reaction. FTIR and XRD results of calcined clamshell confirmed the formation of CaO and $Ca(OH)_2$ while sea sand contains SiO_2 before and after calcination. 2:1 clamshell-to-sea sand ratio produced highest FAME yield. This ratio was used to study the effect of catalyst loading amount. 7 wt% catalyst produced highest FAME yield. Increasing catalyst to 10 wt% reduced the FAME yield due to the soap formation. Analysis of FAME using GC-MS showed the presence of myristic acid, palmitic acid and oleic acid. This study shows that combination of clamshell and sea sand is good potential catalyst for transesterification reaction to produce biodiesel.

Keywords: biodiesel, heterogeneous catalyst, transesterification, waste cooking oil

Abstrak

Kajian ini dijalankan untuk mengkaji keberkesanan kulit kerang dan pasir pantai sebagai mangkin heterogen untuk menghasilkan biodiesel melalui transesterifikasi minyak masak sawit terpakai (WCO). WCO dirawat terlebih dahulu untuk membuang air dan kekotoran. Kulit kerang dan pasir pantai dihancurkan menjadi serbuk halus, ditapis kepada 500 µm dan dikalsinasi. Tindakbalas transesterifikasi WCO dijalankan untuk menghasilkan metil ester (FAME). Data daripada FTIR dan XRD untuk kulit kerang terkalsinasi mengesahkan pembentukan CaO dan $Ca(OH)_2$ manakala pasir pantai pula mengandungi SiO_2 sebelum dan selepas kalsinasi. Nisbah 2:1 kulit kerang terhadap pasir pantai menghasilkan FAME yang paling tinggi dan nisbah ini digunakan dalam kajian seterusnya untuk melihat kesan jumlah pemangkin terhadap jumlah FAME yang dihasilkan. Mangkin sebanyak 7 wt% menghasilkan jumlah FAME yang paling tinggi. Penggunaan mangkin sebanyak 10 wt% mengurangkan jumlah FAME yang diperoleh disebabkan pembentukan sabun. Analisis FAME menggunakan GC-MS menunjukkan kehadiran asid miristik, asid palmitik dan asid oleik. Kajian ini menunjukkan campuran kulit kerang dan pasir pantai adalah mangkin yang berpotensi baik untuk tindakbalas transesterifikasi untuk menghasilkan biodiesel.

Kata kunci: biodiesel, mangkin heterogen, transesterifikasi, minyak masak sawit terpakai

Introduction

Biodiesel is an attractive alternative for conservative petroleum-based fuel and can be used directly in commercial diesel engines. Biodiesel is made of natural and renewable sources such as new and used vegetable oils and animal fats. Biodiesel made from edible vegetable oils have undesirable impact to the environment as they require a large amount of farmland [1]. Waste cooking oil (WCO) is an abundant, readily available and cheap raw material for biodiesel. The use of WCO can minimize biodiesel production costs up to 60-90% [2].

Biodiesel can be produced by two methods: acid esterification and alkaline transesterification. The common catalysts for acid esterification are H_2SO_4 and $Fe_2(SO_4)_3$. Unfortunately, this method produced water along with the desired ester and inhibits transesterification of glyceride. Alkaline transesterification is more prefered method because it is 4000 times faster than acid esterification method. Two types of catalyst in alkaline transesterification are homogeneous and heterogeneous catalysts. Homogeneous catalyst (NaOH and KOH) is effective and affordable but highly sensitive to water and free fatty acid content and require high energy consumption for purification [2]. Researchers have found various types of heterogeneous catalysts such as ion exchange resins, sulfated oxides, transition metal oxide, boron group, alkaline earth metal oxide, mixed metal oxide, alkali metal oxides, waste material, carbon based and enzyme based [2]. Heterogeneous catalysts are environmentally friendly, economical and have high chance for heat integration [3].

CaO, an alkaline earth metal oxides is an ionic crystal and is an established heterogeneous catalyst. The Lewis acidity of the metal cation due to its modest electronegativity makes it a good heterogeneous catalyst [4]. The conjugated oxygen anions in the crystal structure posses strong basic property. In this study, clamshell was chosen as the renewable resource for CaO. Clamshell has high content of calcium carbonate ($CaCO_3$), when calcined at proper temperature, will be converted into CaO. In this study, CaO from clamshell will be combined with SiO_2 from seasand in order to increase the catalytic effectiveness.

Materials and Methods

The clamshells were cleaned and dried in oven at 105 ºC for 24 hours and crushed into a fine powder. Next, the powder was sieved through 500 µm. The powder obtained was then calcined in a furnace at 900 ºC for 3.5 hours [5]. The sea sand was rinsed, dried, screened to extract larger particles and sieved through 500 µm. Then, sea sand was calcined at 800 ºC for 2 hours [6]. The catalysts were characterized by using FTIR and XRD.

WCO sample was collected from a restaurant at Bandar Pusat Jengka, Pahang. WCO was first filtered to remove suspended solid particles and heated at 80 ºC. Then, the oil was washed with water (approximately 10% of the oil volume) and centrifuged at 600 rpm for 10 minutes to remove water soluble salt impurities. Lastly, the organic phase collected and kept under vacuum at 80 ºC for 30 minutes to remove water [6].

Transesterification process carried out in three-necked round bottom flask equipped with reflux, thermometer and magnetic stirrer. WCO and methanol with a molar ratio of 1:12 were mixed with catalyst and refluxed at 60 °C for 6 hours at 600 rpm. The solid catalyst was separated by filtration afterwards. The resulting liquid was placed in a separatory funnel and left for 24 hours at room temperature, until two layers were formed. The top layer was FAME in methanol and the bottom layer was glycerol. The methanol layer was collected and evaporated in a rotary evaporator to obtain the biodiesel (FAME). Table 1 shows the catalysts composition used in this study to observe the effect of catalyst ratio for 5 wt% weight of catalyst over weight of WCO. The optimum ratio with highest yield of biodiesel was used to further study on the effect of loading amount of the catalyst at 7 and 10 wt%. All temperature and time taken for transesterification reaction were kept constant.

FTIR spectra were recorded using Spectrum 100, Perkin Elmer, in the range of 450-4000 cm^{-1} wavenumbers. The catalysts were characterized before and after calcined using XRD model D-5000 Siemen. The data was collected at diffraction angle 2θ from 3° to 80° at the rate of 0.04 s^{-1}. The FAME was analyzed with gas chromatography-mass spectrometry (GC-MS) using Agilent 5977A MSD Mass Spectrometer/Data System at initial temperature of 125 °C for 4 min 15 °C per minute temperature increment until reaching final temperature at 275 °C [7].

Table 1. Catalysts composition used for 5 wt% weight of catalyst over weight of WCO

Weight of Catalyst Over Weight of WCO (%)	Clamshell-to-Sea Sand Ratio	Clamshell (g)	Sea Sand (g)
5	1:0	0.50	0
	0:1	0	0.50
	1:1	0.25	0.25
	1:2	0.17	0.33
	2:1	0.33	0.17

Results and Discussion

Figure 1 shows the FTIR spectrum and the absorption peaks of uncalcined and calcined clamshell, respectively. Uncalcined clamshell showed three main absorption peaks belongs to three vibration modes for CO_3^{2-} molecule; asymmetric stretch, out-of plane bend and in-plane bend. During calcination, $CaCO_3$ will decompose into CaO and CO_2, as shown in equation 1 [8]. Exposure of CaO to atmospheric air cause the formation of $Ca(OH)_2$ as shown in equation 2, hence a sharp OH bond stretching band observed at 3640 cm^{-1} [5]. The presence of CaO and OH absorption peaks prove the complete decomposition of $CaCO_3$ at the chosen calcination temperature.

$$CaCO_3 \rightarrow CaO + CO_2 \quad (1)$$

$$CaO + H_2O \rightarrow Ca(OH)_2 \quad (2)$$

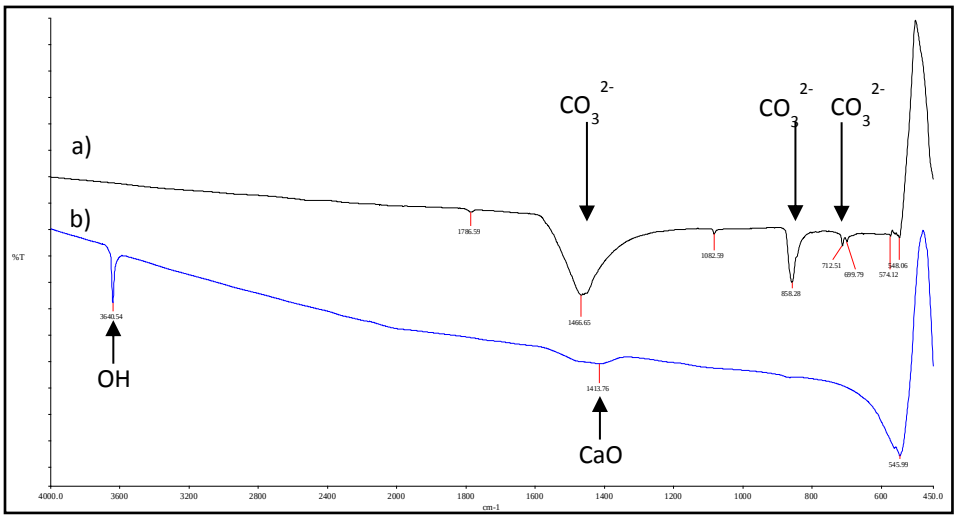


Figure 1. FTIR spectra of clamshell; (a) uncalcined and (b) calcined

FTIR spectrum of uncalcined and calcined sea sand in Figure 2 shows an almost similar absorption peaks, means calcination did not change the chemical structure of sea sand and calcination was not necessary. The four major absorption peaks observed were classified as quartz or silicon dioxide, SiO_2. The peaks at 778.84 cm^{-1} and 777.95 cm^{-1} refers to Si-O symmetrical stretching vibration while 1086.93 cm^{-1} and 1084.92 cm^{-1} refers to Si-O asymmetrical stretching [9].

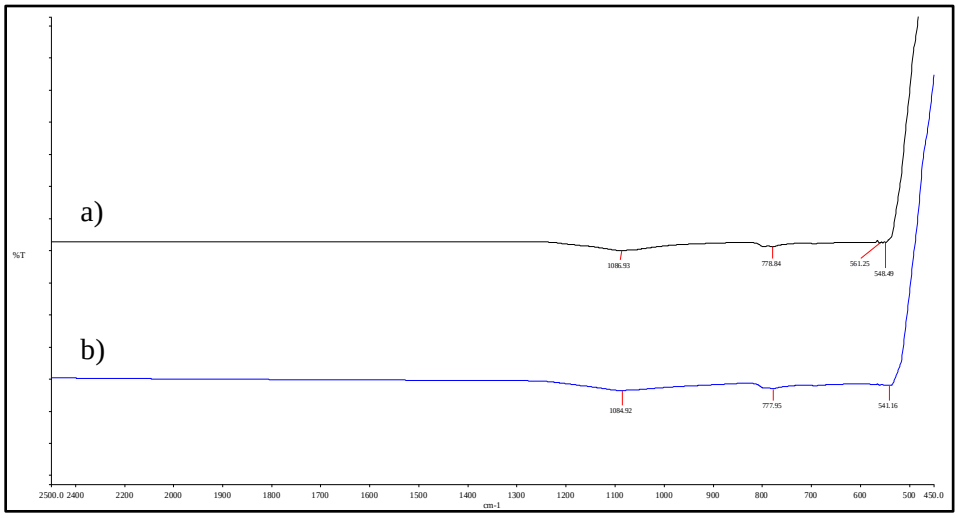


Figure 2. The FTIR spectra of sea sand; a) uncalcined and b) calcined

Figure 3 represents the XRD diffractograms for uncalcined and calcined clamshell. The result revealed that the composition of uncalcined clamshell dominantly consists of $CaCO_3$ (aragonite). The diffraction peaks for $CaCO_3$ can be observed at $2\theta = 26.34°$, $33.24°$ and $45.93°$. After calcination at 900 °C, $CaCO_3$ completely transformed into CaO by releasing CO_2. The peaks of CaO (lime syn) appeared at $2\theta = 32.38°$, $37.52°$, and $53.98°$ with (111), (200) and (220) orientations. In addition, $Ca(OH)_2$ (portlandite) also observed at $2\theta = 18.16°$ and $34.26°$ due to hydration of CaO by atmospheric moisture [10]. These XRD result proves the calcination temperature of clamshell, 900 °C for 3.5 hours was suitable to completely decompose $CaCO_3$ into CaO.

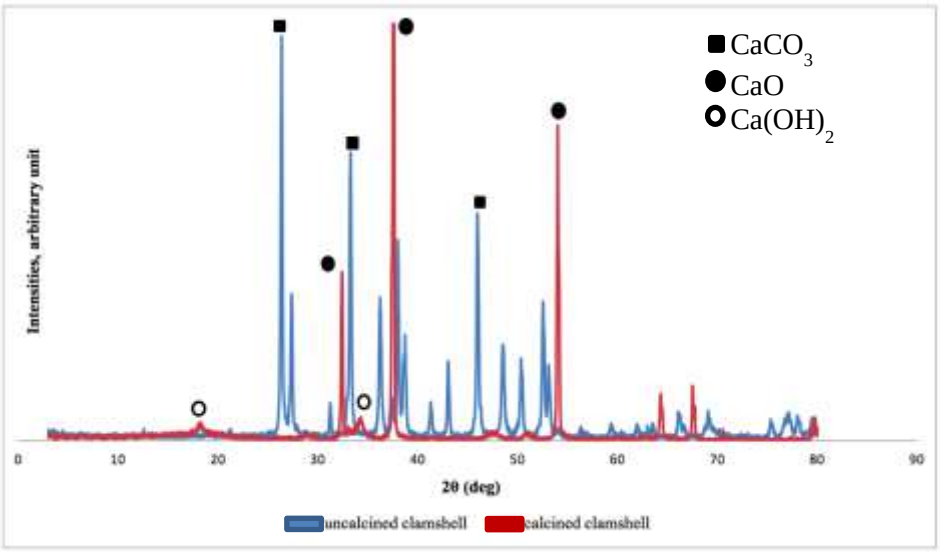


Figure 3. XRD diffractograms of uncalcined and calcined clamshell

Figure 4 represents the XRD patterns for uncalcined and calcined sea sand. The result revealed that the composition of uncalcined sea sand dominantly consists of SiO_2. These intensity diffraction peaks can be observed at $2\theta = 20.89°$ and 26.84°. Meanwhile, the peaks of SiO_2 for calcined sea sand were observed at $2\theta = 20.94°$ and 26.70°. SiO_2 was the major constituent due to high quartz content rather than any mineral in the sea sand. The JCPDS standard pattern number 46-1045 values for SiO_2 (quartz) are $2\theta = 20.82°$ and 26.62°.

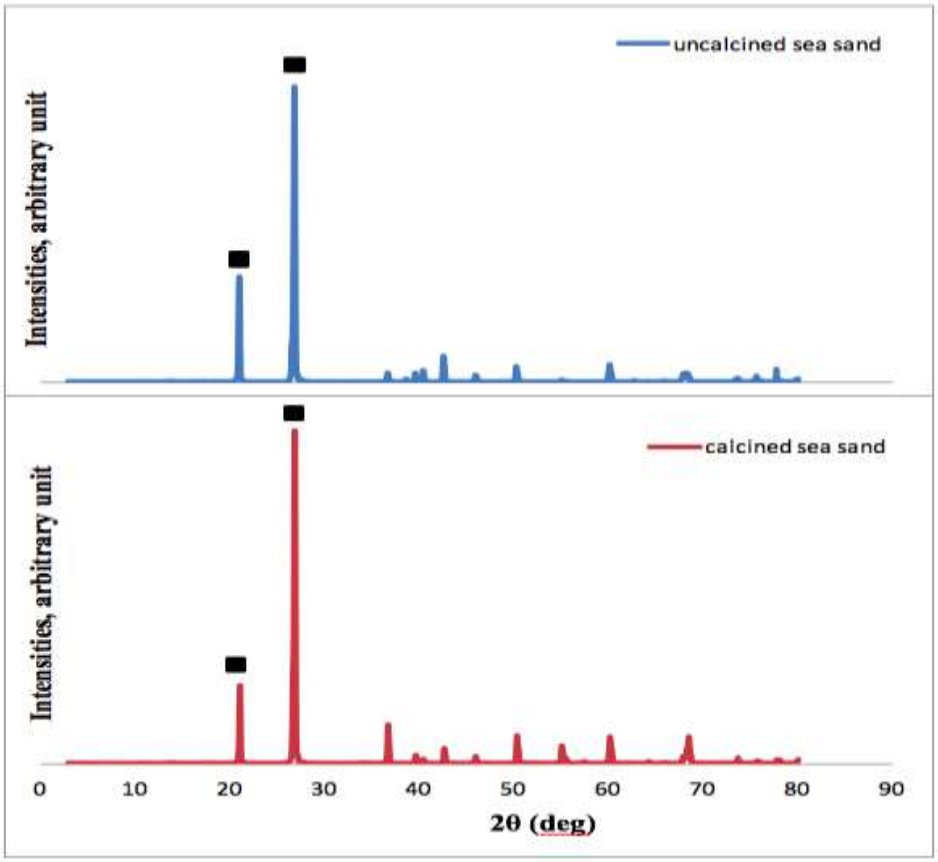


Figure 4. XRD diffractograms of uncalcined sea sand and calcined sea sand (■:SiO_2)

According to GC-MS result, each samples of FAME produced contain palmitin. Their peak ranges between 10.00 – 12.00 minutes. Uzun et al. [11] stated that five properties of WCO-based FAME is myristic acid, palmitic acid, oleic acid, linolenic acid, and linoleic acid. However, the column for GC-MS instrument used in this study only capable to detect three of them; myristic acid, palmitic acid and oleic acid. Figure 5 shows the GC-MS spectra of FAME obtained and detailed in Table 2.

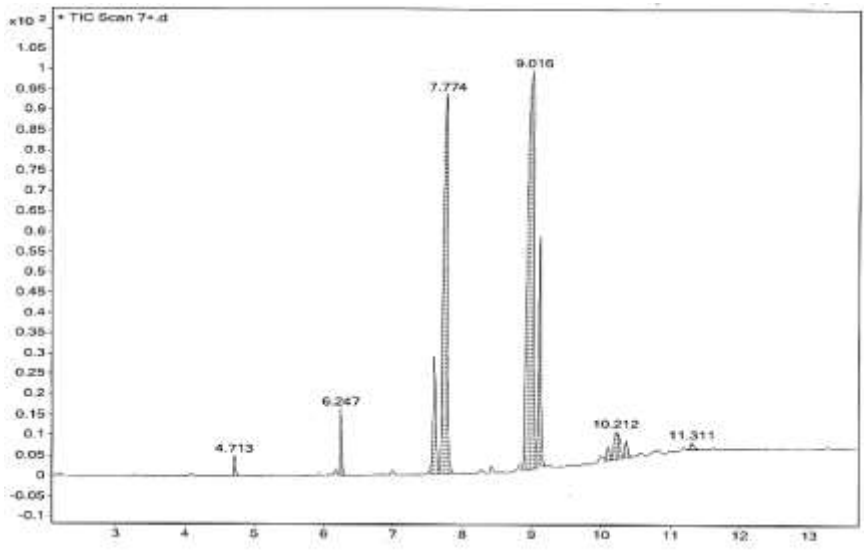


Figure 5. GC-MS spectrum of FAME using 7 wt% loading amount with 2:1 clamshell-to-sea sand ratio

Table 2. The scan range of FAME properties 2:1 clamshell-to-sea sand ratio

Properties	Scan Range (minutes)		
	5 wt%	7 wt%	10 wt%
Palmitic acid	7.774	7.774	7.775
Oleic acid	9.016, 9.113	9.016, 9.101	9.011, 9.112
Stearic acid	-	-	-
Myristic acid	6.247	6.247	6.247
Lauric acid	4.713	4.713	4.714
Palmitoleic acid	7.597	7.597	7.592
Ascorbic acid	-	-	-
Palmitin	10.224, 11.317	10.212, 11.311	10.212, 11.317
Glycidyl palmitate	-	-	-
Glycidyl oleate	-	-	-
Cyclopropanebutanoic acid	-	-	-

To observe the effect of clamshell-to-sea sand ratio on FAME production, five ratios were chosen; 1:0, 0:1, 1:1, 1:2, and 2:1. Loading amount used was fixed at 5 wt%. The result shown in Figure 6. It was found that the highest percentage FAME yield obtained was 71.1% with clamshell-to-sea sand ratio of 2:1. This result shows that the combination of two catalysts increase the percentage yield significantly and the greater amount of clamshell in the catalyst ratio gave higher biodiesel yield. The presence of CaO and $Ca(OH)_2$ in the calcined clamshell was believed as the factor. O^{2-} in CaO and OH^- in $Ca(OH)_2$ are the adsorptive sites that will extract H^+ from methanol to form methoxide anions that will then react with the fatty acid in triglyceride molecules to form FAME.

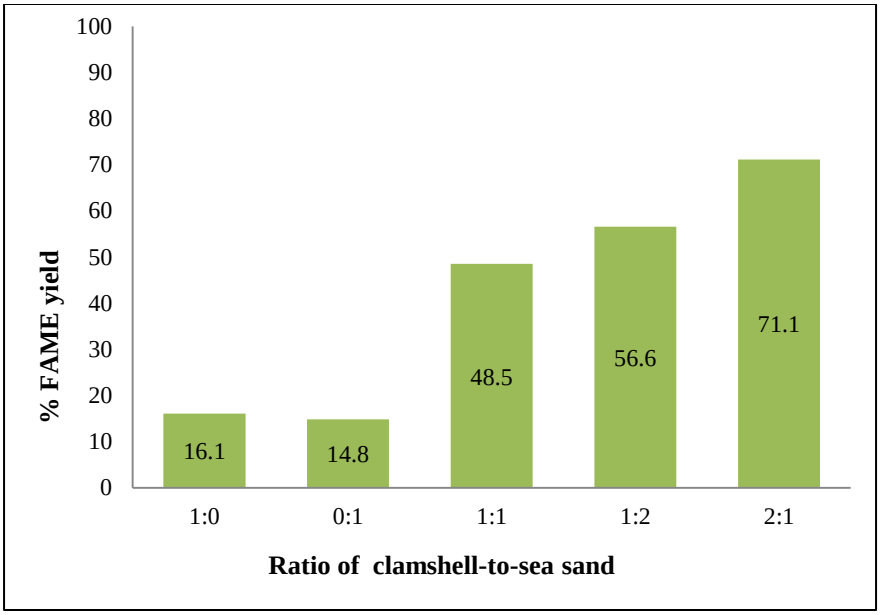


Figure 6. Effect of clamshell-to-sea sand ratio on FAME yield using 5 wt% catalyst loading

The clamshell-to-sea sand ratio of 2:1 was used to further study the effect of catalyst loading on FAME production. As shown in Figure 7, 7 wt% loading amount of the catalysts produced highest FAME yield of 75.3%. Increasing the loading amount from 5 to 7 wt% increase the percentage yield but further increase to 10 wt% reduced the yield. High basicity in CaO and $Ca(OH)_2$ helps in breaking the bond of free fatty acid chain with glycerol in producing FAME. Insufficient catalyst dosage will reduce the breaking process results in incomplete transesterification and reduce the FAME yield. FAME yield increased with the increase in the catalyst loading amount since more triglyceride molecules will be broken. However, excess alkaline catalyst loading could results in more triglyceride participation leading to soap formation and thus decrease biodiesel yield especially in a longer retention time [12].

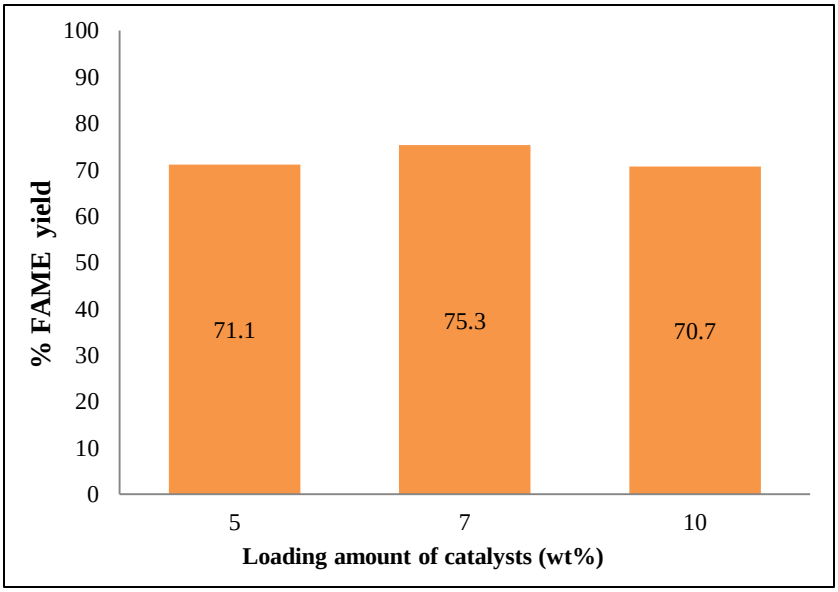


Figure **7**. Effect of loading amount of catalyst on FAME yield using 2:1 clamshell-to-sea sand ratio

Conclusion

Waste cooking oil-based biodiesel (FAME) was produced via transesterification reaction. The effect of ratio and loading amount of combination of alkaline heterogeneous catalyst; clamshell as source of CaO and sea sand as source of SiO_2 was studied. FTIR and XRD results showed the calcination of clamshell at 900 °C for 3.5 hours were suitable to completely decompose $CaCO_3$ into CaO. Presence $Ca(OH)_2$ also observed as the result of reaction of CaO with atmospheric moisture. Combination of two catalysts was found to increase the percentage yield significantly and the greater amount of clamshell in the catalysts ratio gave higher FAME yield. The optimum ratio for clamshell-to-sea sand was 2:1 and this ratio was used to study the effect of loading amount of the catalysts in FAME percentage yield. Increasing the loading amount from 5 to 7 wt% increase the percentage yield but further increase to 10 wt% loading amount reduced the yield due to the soap formation especially in a longer retention time. 7 wt% loading amount of the catalysts produced highest FAME yield of 75.3%. In conclusion, combination of clamshell and sea sand possesses good potential as heterogeneous catalyst in WCO-based FAME production.

Acknowledgements

The authors would like to thank Universiti Teknologi MARA and Ministry of Higher Education, Malaysia for research grant no RAGS/1/2014/SG01/UITM//3.

References

1. Mandolesi de Araújo, C. D., de Andrade, C. C., de Souza, E., Silva, E. and Dupas, F. A. (2013). Biodiesel production from used cooking oil: A review. *Renewable and Sustainable Energy Reviews*, 27: 445-452.
2. Talebian-Kiakalaieh, A., Amin, N. A. S. and Mazaheri, H. (2013). A review on novel processes of biodiesel production from waste cooking oil. *Applied Energy*, 104: 683-710.
3. Aransiola, E. F., Ojumu, T. V., Oyekola, O. O., Madzimbamuto, T. F. and Ikhu-Omoregbe, D. I. O. (2014). A review of current technology for biodiesel production: State of the art. *Biomass and Bioenergy*, 61: 276-297.
4. Kouzu, M. and Hidaka, J. S. (2012). Transesterification of vegetable oil into biodiesel catalyzed by CaO: A review. *Fuel*, 93: 1-12.
5. Nair, P., Singh, B., Upadhyay, S. N. and Sharma, Y. C. (2012). Synthesis of biodiesel from low FFA waste frying oil using calcium oxide derived from Mereterix mereterix as a heterogeneous catalyst. *Journal of Cleaner Production*, 29-30: 82-90.
6. Muciño, G. G., Romero, R., Ramírez, A., Martínez, S. L., Baeza-Jiménez, R. and Natividad, R. (2014). Biodiesel production from used cooking oil and sea sand as heterogeneous catalyst. *Fuel*, 138: 143-148.
7. Nyoman, P. A., Santi, D. S., Suprapto Kusno, B. and Achmad, R. (2012). Development of heterogeneous alumina supported base catalyst for biodiesel production. 3rd international conference on biology, environment and chemistry, *IACSIT Press*, Singapore, V46. 25, 117-120.
8. El-Gendy, N. S., Deriase, S. F., Hamdy, A. and Abdallah, R. I. (2015). Statistical optimization of biodiesel production from sunflower waste cooking oil using basic heterogeneous biocatalyst prepared from eggshells. *Egyptian Journal of Petroleum*, 24: 37-48.
9. Sivakumar, S., Ravisankar, R., Raghu, Y., Chandrasekaran, A. and Chandramohan, J. (2012). FTIR spectroscopic studies on coastal sediment samples from cuddalore district, Tamilnadu, India. *Indian Journal of Advances in Chemical Science*, 1: 40-46.
10. Jaiyen, S., Naree, T. and Ngamcharussrivichai, C. (2015). Comparative study of natural dolomitic rock and waste mixed seashells as heterogeneous catalysts for the methanolysis of palm oil to biodiesel. *Renewable Energy*, 74: 433-440.
11. Uzun, B. B., Kılıç, M., Özbay, N., Pütün, A. E. and Pütün, E. (2012). Biodiesel production from waste frying oils: Optimization of reaction parameters and determination of fuel properties. *Energy*, 44(1): 347-351.
12. Sirisomboonchai, S., Abuduwayiti, M. and Guan, G. (2015). Biodiesel production from waste cooking oil using calcined scallop shell as catalyst. *Energy Conversion and Management*, 95: 242-247.

Malaysian Journal of Analytical Sciences, Vol 22 No 1 (2018): 115 - 122
DOI: https://doi.org/10.17576/mjas-2018-2201-14

MALAYSIAN JOURNAL OF ANALYTICAL SCIENCES
Published by The Malaysian Analytical Sciences Society
ISSN 1394 - 2506

REMOVAL OF CRYSTAL VIOLET AND ACID GREEN DYE IN AQUEOUS SOLUTION USING BANANA PLANT-DERIVED SORBENTS

(Penyingkiran Pewarna Crystal Violet Dan Acid Green Dalam Larutan Akues Menggunakan Penjerap Berasaskan Pokok Pisang)

Siti Kartina Abdul Karim[1]*, Soh-Fong Lim[2], David Chua[2], Shanti Faridah Salleh[2], Puong Ling Law[2]

[1]*Faculty of Applied Science,*
Universiti Teknologi MARA Cawangan Sarawak, Samarahan 2 Campus, 94300 Kota Samarahan, Sarawak, Malaysia
[2]*Faculty of Engineering,*
Universiti Malaysia Sarawak, 94300 Kota Samarahan, Sarawak, Malaysia

[*]*Corresponding author: sitik094@sarawak.uitm.edu.my*

Received: 4 December 2016; Accepted: 1 December 2017

Abstract

In this study, the sorption of crystal violet (CV) and acid green (AG) dyes from aqueous solution was performed using banana plant-derived sorbents. Kinetics for both dyes showed that percentage removal increased with a contact time until equilibrium, where it stays almost constant. For CV dye, the percentage removal was above 90% at equilibrium. On the other hand, the percentage removal of AG dye was between 44-54% for the three sorbents. To study the effect of sorbent dose, the dose of the sorbents used was varied from 1 to 100 g/L. From the results, it was observed that an increase in sorbent dose would result in an increase of percentage removal of both dyes. However, for CV dye, the percentage removal became constant after 10 g/L. The effect of pH was also determined for both dye removal, where it was found that CV dye was unaffected by pH change. However, the AG dye can be removed more in highly acidic conditions.

Keywords: acid green dye, crystal violet dye, banana plant-derived sorbents, sorption

Abstrak

Dalam kajian ini, penjerapan pewarna Crystal Violet (CV) dan Acid Green (AG) dari larutan akues dilakukan dengan menggunakan penjerap berasaskan pokok pisang. Eksperimen kinetik menunjukkan bahawa peratus penyingkiran meningkat dengan masa sehingga keseimbangan, di mana peratus ini akan kekal sama. Untuk pewarna CV, lebih 90% pewarna disingkirkan untuk ketiga-tiga penjerap yang digunakan. Peratus penyingkiran pewarna AG hanya antara 44-54% sahaja. Selain itu, eksperimen kesan dos penjerap untuk pewarna menggunakan dos penjerap dari 1 ke 100 g/L. Untuk kedua-dua pewarna, peningkatan dalam dos penjerap meningkatkan peratus penyingkiran. Namun begitu, untuk pewarna CV, dos yang lebih tinggi dari 10 g/L tidak meningkatkan peratus penyingkiran. Kesan pH terhadap penyingkiran pewarna menunjukkan yang pewarna CV tidak dipengaruhi oleh pH. Sebaliknya, pewarna AG hanya boleh disingkirkan dengan baik pada keadaan yang sangat berasid.

Kata kunci: pewarna acid green, pewarna crystal violet, penjerap berasaskan pokok pisang, penjerapan

Introduction

Banana residues are an abundant source from agricultural waste. Banana is cultivated for its fruits, and the rest of the plant becomes waste once the fruits are harvested. Several parts of banana commonly used for water treatment are banana pith [1, 2], banana stalk [3], banana frond [4], and pseudo stem [5]. The production of banana in

Malaysia had been consistent at an average of 300,000 tonnes per year for the last ten years [6]. Therefore, it is essential that the agriculture wastes produced from banana plantation to be disposed or reused to minimize the environmental impact.

Recently, application of cellulosic fibers as adsorbent has attracted scientists and researchers due to its massive usage as non-renewable sources and poor management of agricultural wastes which lead to environmental problems [7]. The natural cellulosic fibers are emerging as the novel low cost materials for environmental and industrial applications [8].

This study focuses on the use of three parts of banana plant fibers. They are the fibers from banana leaves, stem, and stalk that act as sorbents in removing the CV and AG dyes from water. Both dyes are triarylmethane dyes, with CV as cationic dye and AG as anionic dye. Dye is considered one of major pollutants in water [9]. The experiments were performed in batch mode. The adsorption kinetics, the effect of sorbent dose and the effect of pH were studied to determine the effectiveness of banana plant derived fibers as sorbents in removing the CV and AG dyes.

Materials and Methods

Materials

The dyes used were anhydrous CV dye (90.0%, Sigma, US) and AG dye (pure, Acros Organics). The sodium hydroxide (Systerm, Malaysia) and nitric acid (69-70%, Merck, Germany) were prepared as 0.1M solution to adjust the pH of the dyes prior to experiment. The banana plants taken to prepare the sorbents were collected from Kota Samarahan, Sarawak area.

Preparation of sorbent

The banana sorbents used in this study were taken from three parts of the banana plant, which are the stem, stalk, and leaves. All three parts were cut into uneven shapes, about 2 cm in length. Then, the banana fibers were washed with deionized water several times before they were dried at room temperature for three days. The final drying was done in the oven at 60 °C for 24 hours. The dried sorbents were then grinded and sieved to particle size less than 500 µm. The prepared sorbents were kept in air tight containers prior to use.

Preparation of dye solution

The dye solutions of CV and AG were prepared similarly. A known quantity of dye was dissolved in 1000 mL of deionized water to prepare the desired concentration of 1000 ppm.

Batch sorption study

The kinetics of adsorption was studied at 25 °C, agitation speed of 200 rpm, initial pH 7, initial concentration of 1000 ppm, and sorbent dose of 10 g/L for CV dye and 60 g/L for AG dye. For the first ten minutes, the samples were taken every minute. After 10 minutes, the samples were taken every 5 minutes until the 30^{th} minute. Afterwards, the samples were taken every 30 minutes until three hours. After the samples were taken, they were filtered and the residual solutions were analyzed using UV-Vis spectrophotometer (Thermo Scientific, model Evolution 201).

The effect of sorbent dose was studied at 25 °C, agitation speed of 200 rpm, initial pH 7, initial concentration of 1000 ppm, and contact time of 3 hours. The sorbent doses were varied 1 to 100 g/L. After three hours, the samples were filtered and the residual solutions were analyzed using UV-Vis spectrophotometer (Thermo Scientific, model Evolution 201).

The effect of pH was studied at 25°C, agitation speed of 200 rpm, initial concentration of 1000 ppm, sorbent dose of 10 g/L for CV dye and 60 g/L for AG dye, and contact time of 3 hours. The initial pH of solution were varied from 2 to 12. After three hours, the samples were filtered and the residual solutions were analyzed using UV-Vis spectrophotometer (Thermo Scientific, model Evolution 201).

Results and Discussion

Sorption kinetics

The study of kinetics is to determine the characteristics of sorption with respect to time. Figure 1 and Figure 2 show the percent removal of CV and AG dyes over time. The removal of both dyes exhibit similar trends. The percent removal increases sharply during the early part of sorption (in part I) of the graph. This is where the sorption occurs very fast because of the availability of sorption sites and sorbates. As the sorption sites are gradually filled and sorbates become less, the sorption of dye onto sorbents become slower, as shown in part II of the graph. In the last part of the graph, this indicates equilibrium of sorption, where there are no further sorption occurring due to saturation of sorption sites. For CV dye, the equilibrium time is faster than AG dye. The equilibrium time for CV dye is 60 minutes, whereas 120 minutes is needed to achieve equilibrium for AG dye. Previous works on sorption of CV dye demonstrated wide range of equilibrium time, from 120 minutes using modified spirulina [10] to 8 hours using modified rice husk [11]. For AG dye, there are little works done on sorption using natural fibers. Comparison of sorption time with other method such as photoelectrocatalytic process [12], showed similar equilibrium time with the ones used in this study.

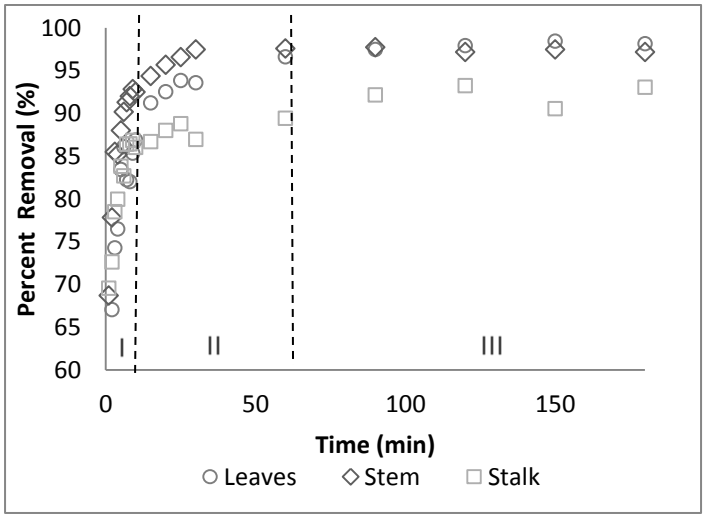


Figure 1. Percent removal of CV dye over time

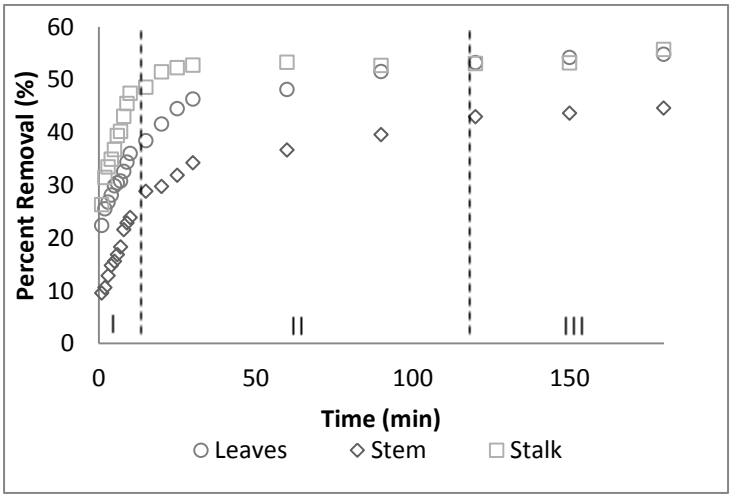


Figure 2. Percent removal of AG dye over time

The sorption of CV and AG dyes was fitted to 4 kinetics model, namely pseudo first order, pseudo second order, intraparticle diffusion, and Elovich, to determine the rate controlling step(s). The linear forms of these models were used to calculate the rate constants and coefficient of correlation. The linear forms for pseudo first order, pseudo second order, intraparticle diffusion, and Elovich are given as equations (1) to (4) below:

$$ln\ (q_e - q_t) = ln\ q_e - k_1 t \quad (1)$$

$$\frac{t}{q_t} = \frac{1}{k_2 q_e^2} + \frac{1}{q_e} t \quad (2)$$

$$q_t = k_{id} t^{0.5} \quad (3)$$

$$q_t = \frac{1}{\beta} \ln(\alpha\beta) + \frac{1}{\beta} \ln t \quad (4)$$

where q_e is the equilibrium adsorption capacity in mg/g, q_t is the adsorption capacity(mg/g) at time t, k_1 is the rate constant for pseudo first order (min^{-1}), k_2 is the rate constant for pseudo second order (g/mg min), k_{id} is the rate constant for intraparticle diffusion ($mg/g \cdot min^{0.5}$), t is time in minutes, α (mg/g·min) is the initial adsorption rate and β (g/mg) is the desorption constant.

The linearization fitting results are presented in Tables 1 and 2. For the CV dye removal, the sorption seems to fit very well with pseudo second order, with $R^2 > 0.999$, followed by Elovich>pseudo first order>intraparticle diffusion. The inclination towards pseudo second order indicates that the sorbate (CV dye) might be interacting with 2 sorption sites at one time. For the AG dye removal, however, all the kinetic models conform well to the sorption of the AG dye with $R^2 > 0.800$. Nevertheless, the pseudo second order model shows the best fit, followed by intraparticle diffusion > Elovich >pseudo first order. This indicates that there might be several rate controlling steps in the sorption of AG dye onto the banana fibers of the leaves, stem, and stalk which act as sorbents.

Table 1. Kinetics parameters for adsorption of CV dye onto banana leaves, stem, and stalk sorbents

	$q_{e,\ exp}$	$q_{e,\ cal}$	Pseudo first order		Pseudo second order		Intraparticle diffusion		Elovich		
			k_1	R^2	k_2	R^2	k_{id}	R^2	α	β	R^2
Banana leaves	93.7	21.0	0.09	0.8815	1.17×10^{-6}	0.9995	7.63	0.7075	1.536×10^{3}	0.095	0.8864
Banana stem	95.4	27.3	0.14	0.9453	6.73×10^{-7}	0.9999	4.86	0.7215	9.197×10^{5}	0.13	0.9045
Banana stalk	95.2	11.2	0.09	0.6567	3.93×10^{-7}	0.9997	3.79	0.6443	2.150×10^{6}	0.17	0.8442

Table 2. Kinetics parameters for adsorption of AG dye onto banana leaves, stem, and stalk sorbents

	$q_{e,\ exp}$	$q_{e,\ cal}$	Pseudo first order		Pseudo second order		Intraparticle diffusion		Elovich		
			k_1	R^2	k_2	R^2	k_{id}	R^2	α	β	R^2
Banana leaves	7.31	6.95	0.24	0.9356	4.08×10^{-4}	0.9962	1.80	0.9823	210.9	0.62	0.9832
Banana stem	12.1	5.28	0.27	0.8000	4.62×10^{-3}	0.9384	1.93	0.9542	8.201	0.60	0.8901
Banana stalk	14.3	8.32	0.26	0.9256	3.33×10^{-4}	0.9900	2.65	0.9848	75.78	0.43	0.9679

The effect of sorbent dose

The effect of sorbent dose is presented in Figure 3 (CV dye) and Figure 4 (AG dye). For CV dye, the increase in sorbent dose increases the percent removal of dye until saturation, where further increase in sorbent dose does not affect the percent removal. This is similar for all three sorbents, where the sorbent dose increase up to 10 g/L has positive effect on the percent removal of CV dye. As can be seen in Figure 3, the percent removal of CV dye using 10 g/L is already >90%, therefore further increase in sorbent dose results in constant percent removal.

The banana leaves, stem, and stalk sorbents does not remove a high percentage of AG dye, compared to CV dye. Increasing the sorbent dose up to 100 g/L only removes slightly more than 50 percent of AG dye. The sorbent dose cannot be increased further, as there will be little solution left for the analysis to proceed.

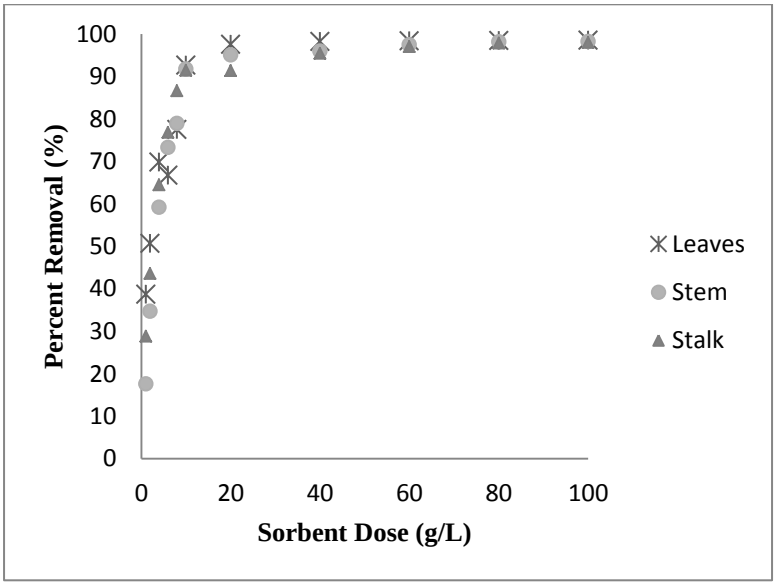


Figure 3. Percent removal of CV dye over sorbent dose

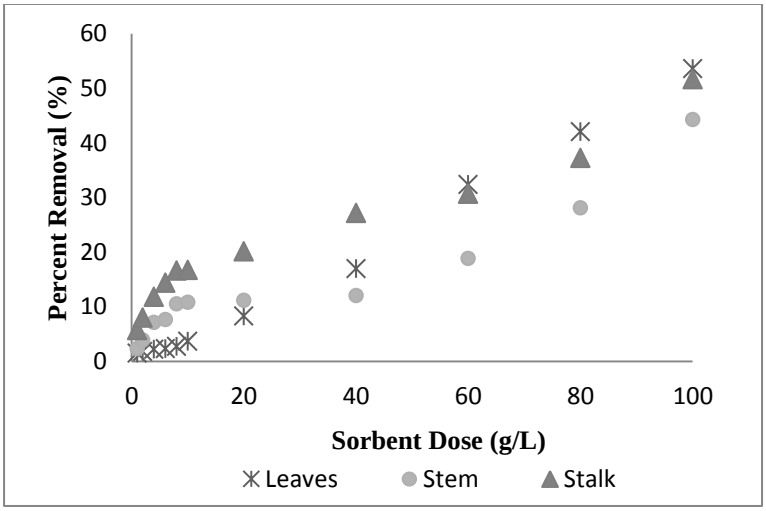


Figure 4. Percent removal of AG dye over sorbent dose

The effect of pH

The effects of solution pH on the CV and AG dye removal are presented in Figure 5 and Figure 7, respectively. The solution pH is an important factor in sorption process, as it affects the surface charge of an sorbent and therefore the interaction between the sorbent and sorbates is greatly affected. From Fig 5, it is shown that the initial solution pH does not affect the sorption of the CV dye onto the banana leaves, stem, and stalk sorbents. The percent removal remains almost constant with the increase of initial solution pH. The initial vs final pH from CV dye removal in Figure 6 shows that the final pH of 6 is attained when the initial pH is from 4-7. This finding is consistent with a study reported in literature. The CV dye adsorption using *Bacillus amyloliquefaciens* biofilm showed that at solution pH > 4, the solution pH did not affect the adsorption capacity [13]. In another study using modified rice husk, however, the increase in solution pH has a positive effect on adsorption, up until pH 10 [11]. The difference in solution pH effect towards adsorption capacity is due to the characteristic of the sorbents used. This is due to the difference of pH potential zero charge (pH_{pzc}) in each sorbent. A lower pH_{pzc} means that the surface charge of sorbent becomes negative at a lower pH, therefore can attract more adsorbate, which is cationic.

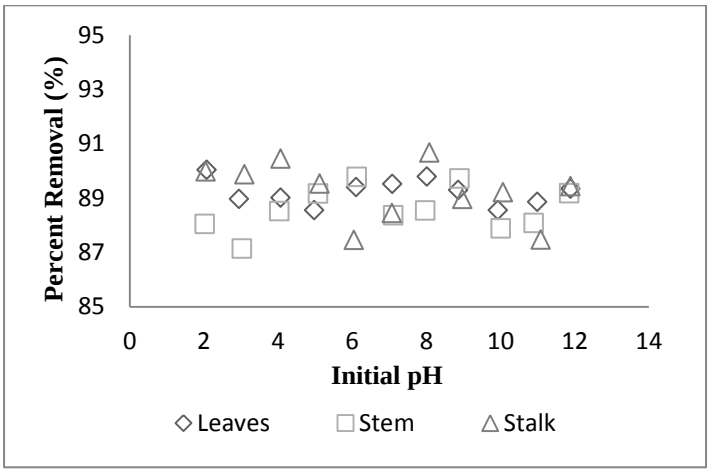


Figure 5. Percent removal of CV dye over initial pH

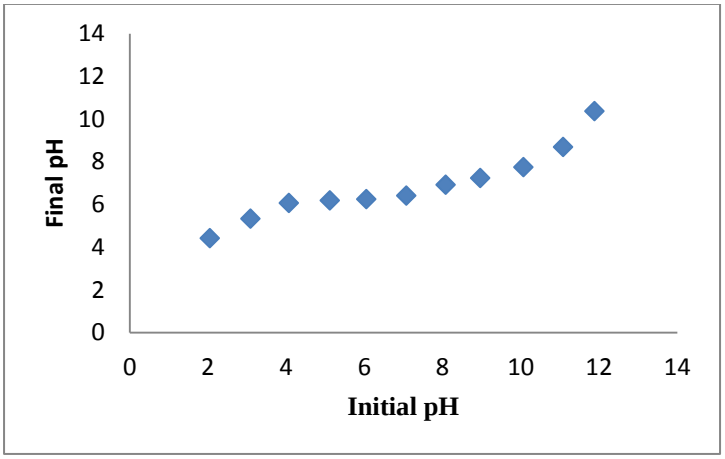


Figure 6. Initial vs final pH for CV dye removal

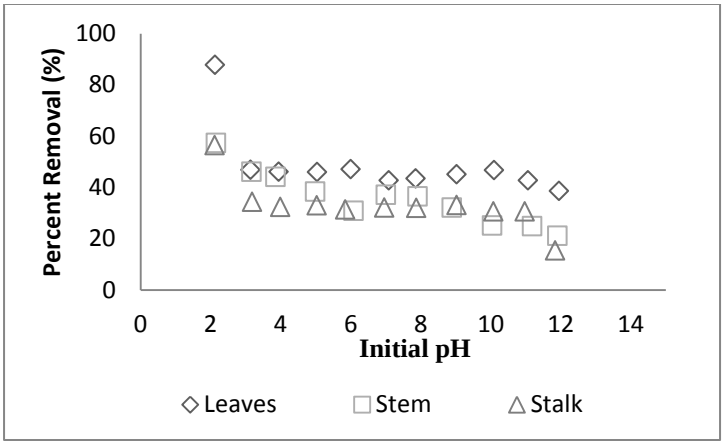


Figure 7. Percent removal of AG dye over initial pH

For the AG dye removal, only at high acidic condition (initial solution pH 2) the adsorption produces more than 50 percent removal. At higher the solution pH, the percent removal remains constant, and drops when starting from initial solution pH of 12. This finding is in line with the characteristic of the AG dye which is an anionic dye (negatively charged material). The AG dye compound will interact with the sorbent surface that is positively charged. For AG dye removal, most of its solution has a final pH 6 (for initial pH 3-8). At this buffer zone, the percent removal also remains constant. At final pH of 4, the percent removal is the highest, whereas the percent removal drops when the final pH is higher than 8.

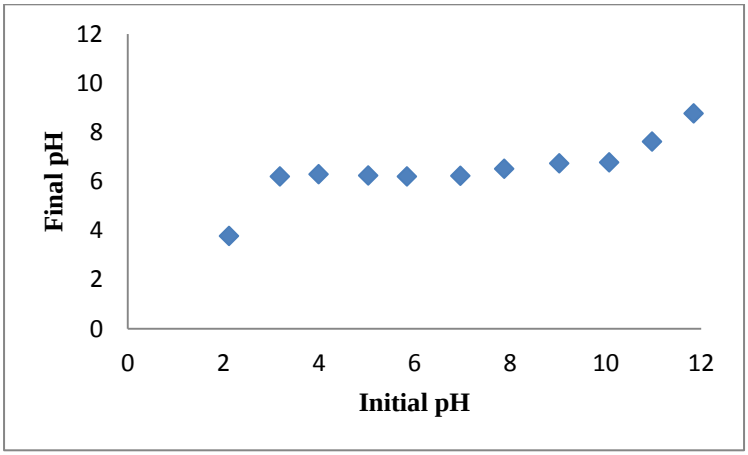


Figure 8. Initial vs final pH for AG dye removal

Conclusion

The removal of CV dye and AG dye can be performed using the banana leaves, stem and stalk sorbents. The percent removal of CV dye is more than 90% at equilibrium time of 60 minutes, whereas the AG dye can be removed up to 55% at equilibrium time of 120 minutes. The removal of both dyes fits closely to pseudo second order kinetics model. For CV dye, the increase of sorbent dose increases the percent removal of dye, until saturation. After 10 g/L sorbent dose, there is no further increase of percent removal. On the other hand, the percent removal of AG dye keeps increasing with increase in sorbent dose, up to 100 g/L. Further increase of sorbent dose is not possible due to limited solution available for analysis. The effect of pH is also determined for both dyes. For CV dye, the pH does not affect the percent removal whereas the AG dye can be removed better at initial pH of 2.

Acknowledgement

The authors thank the staffs of Fac. of Engineering, UNIMAS and Centre of Applied Sciences, UiTM for their technical help.

References

1. Kadirvelu, K., Kavipriya, M., Karthika, C., Radhika, M., Vennilamani, N. and Pattabhi, S. (2003). Utilization of various agricultural wastes for activated carbon preparation and application for the removal of dyes and metal ions from aqueous solutions. *Bioresource Technology,* 87(1): 129-132.
2. Namasivayam, C., Prabha, D. and Kumutha, M. (1998). Removal of direct red and acid brilliant blue by adsorption on to banana pith. *Bioresource Technology,* 64(1): 77-79.
3. Hameed, B. H., Mahmoud, D. K. and Ahmad, A. L. (2008). Sorption equilibrium and kinetics of basic dye from aqueous solution using banana stalk waste. *Journal of Hazardous Materials,* 158(2–3): 499-506.
4. Foo, K. Y., Lee, L. K. and Hameed, B. H. (2013). Preparation of banana frond activated carbon by microwave induced activation for the removal of boron and total iron from landfill leachate. *Chemical Engineering Journal,* 223: 604-610.
5. Becker, H., Matos, R. F., Souza, J. A. D., Lima, D. D. A., Souza, F. T. C. D. and Longhinotti, E. (2013). Pseudo-stem banana fibers: Characterization and chromium removal. *Orbital: The Electronic Journal of Chemistry,* 5(3): 164-170.
6. Food and Agriculture Organization of the United Nations Statistics Division (2015). *Faostat: For a World without Hunger*. Available from: http://faostat3.fao.org/home/E. /.[Access online 20 January 2017].
7. Pappu, A., Patil, V., Jain, S., Mahindrakar, A., Haque, R. and Thakur, V. K. (2015). Advances in industrial prospective of cellulosic macromolecules enriched banana biofibre resources: A review. *International Journal of Biological Macromolecules,* 79: 449-458.
8. Wondraczek, H. and Heinze, T. (2015). Cellulosic biomaterials, in polysaccharides: Bioactivity and biotechnology. Springer International Publishing: pp. 289-328.
9. Pure Earth and Green Cross Switzerland (2016). The world's worst pollution problems 2016: Toxics beneath our feet. Available from: http://www.worstpolluted.org/.[Access online 20 January 2017].
10. Guler, U. A., Ersan, M., Tuncel, E. and Dügenci, F. (2016). Mono and simultaneous removal of crystal violet and safranin dyes from aqueous solutions by hdtma-modified *Spirulina* sp. *Process Safety and Environmental Protection,* 99: 194-206.
11. Masoumi, A., Hemmati, K. and Ghaemy, M. (2016). Low-cost nanoparticles sorbent from modified rice husk and a copolymer for efficient removal of Pb(II) and crystal violet from water. *Chemosphere,* 146: 253-262.
12. Ramírez, R. J., Arellano, C. A. P., Gallegos, A. A. Á., González, A. E. J. and Martínez, S. S. (2015). H_2O_2-assisted TiO_2 generation during the photoelectrocatalytic process to decompose the acid green textile dye by fenton reaction. *Journal of Photochemistry and Photobiology A: Chemistry,* 305: 51-59.
13. Sun, P., Hui, C., Wang, S., Wan, L., Zhang, X. and Zhao, Y. (2016). *Bacillus amyloliquefaciens* biofilm as a novel biosorbent for the removal of crystal violet from solution. *Colloids and Surfaces B: Biointerfaces,* 139: 164-170.

Malaysian Journal of Analytical Sciences, Vol 22 No 1 (2018): 123 - 127
DOI: https://doi.org/10.17576/mjas-2018-2201-15

MALAYSIAN JOURNAL OF ANALYTICAL SCIENCES
Published by The Malaysian Analytical Sciences Society
ISSN 1394 - 2506

PHYTOCHEMICAL AND ANTIMICROBIAL EVALUATION OF *Pithecellobium jiringa* STEM BARKS EXTRACTS

(Penyaringan Fitokimia dan Antimikrob ke atas Ekstrak Kulit Kayu Batang *Pithecellobium jiringa)*

Zurhana Mat Hussin*, Nurul Anasuhah Osman, Aiza Harun, Shaari Daud

Faculty of Applied Sciences,
Universiti Teknologi MARA Pahang, 26400 Bandar Tun Abdul Razak, Jengka, Pahang, Malaysia

**Corresponding author: zurhana_mhussin@pahang.uitm.edu.my*

Received: 4 December 2016; Accepted: 1 December 2017

Abstract

Pithecellobium jiringa (*P. jiringa*) is economically important due to its various traditional uses in treating hypertension and diabetes (seeds), medicine (leaves) and source of dye for silk (pods). This is a pioneer study that reports its effectiveness as antimicrobial agent from stem bark of *P. jiringa.* The present study was carried out to detect preliminary phytochemicals and antimicrobial of solvent extracts from *P. jiringa* stem bark. Qualitative phytochemical analysis was performed on ethanol and ethyl acetate extracts. These extracts were investigated for their antimicrobial activity of different microorganism tests including bacteria and fungi by using agar disc diffusion technique. Tannins, flavonoids, terpenoids and saponins were the main metabolites found in phytochemical screenings. Both ethanol and ethyl acetate extracts exhibited marked antimicrobial activity against skin disease caused-microbes *Staphylococcus aureus, Staphylococcus epidermidis* and *Trychophyton mentagrophytes* with highest inhibition zone (IZ) of 23 mm at 200 mg/mL ethyl acetate extracts. The current study confirmed that the stem bark of *P. jiringa* has a potential source of active antimicrobial agent. Further analysis on the isolation and characterization of compound form *P. jiringa* stem bark, responsible for antimicrobial properties is in progress.

Keywords: antifungal activity, antimicrobial activity, inhibition zone, *Pithecellobium jiringa*

Abstrak

Pithecellobium jiringa (*P. jiringa*) adalah penting dari segi ekonomi dengan kegunaan tradisional pelbagai dalam merawat tekanan darah tinggi dan kencing manis (biji), perubatan (daun) dan sumber pewarna untuk sutera (buah). Melalui kajian ini, melaporkan kali pertama, keberkesanannya sebagai agen antimikrob daripada kulit kayu batang *P. jiringa*. Kajian ini telah dijalankan untuk mengesan fitokimia awal dan antimikrob ekstrak pelarut dari kulit kayu batang *P. jiringa*. Analisis fitokimia kualitatif telah dilakukan ke atas ekstrak etanol dan etil asetat. Ekstrak ini telah dikaji untuk aktiviti antimikrob dengan ujian mikroorganisma yang berbeza termasuk bakteria dan kulat menggunakan teknik resapan cakera agar. Tanin, flavonoid, terpenoid dan saponin adalah metabolit utama yang diperolehi dari saringan fitokimia. Kedua-dua etanol dan etil asetat ekstrak mempamerkan tanda aktiviti antimikrob terhadap penyakit kulit yang disebabkan oleh mikrob *Staphylococcus aureus*, *Staphylococcus epidermidis* dan *Trychophyton mentagrophytes* dengan zon perencatan tertinggi (IZ) 23 mm pada 200 mg/mL ekstrak etil asetat. Kajian ini mengesahkan bahawa kulit kayu batang *P. jiringa* mempunyai sumber potensi antimikrob aktif. Analisis lanjut mengenai pengasingan dan pencirian komponen kulit kayu batang *P. jiringa*, bertanggungjawab untuk ciri-ciri antimikrob sedang dijalankan.

Kata kunci: aktiviti antikulat, aktiviti antimikrob, zon perencatan, *Pithecellobium jiringa*

Introduction

Pithecellobium jiringa (Jack) Prain is a traditional medicinal plant belongs to the family of Leguminosae which originated from the Southeast Asia [1]. *P. Jiringa* is known as *jering* in Malaysia, *djengkol* in Indonesia and *Luk-nieng* in Thailand. *P. jiringa* is commonly consumed in Malaysia, Indonesia and Thailand. The fruit has been used to eliminate bladder stones when taken as a drink that is mixed with ginger. Traditionally, the plant is also used to treat hypertension and diabetes. The fruit rinds have been identified to be used as ingredients to make traditional soaps, shampoos and detergents. The leaves of *P. jiringa* is used to cure the itchy parts of the human body [2]. In the present day, *P. jiringa* is also being used in the production of organic pesticide as a replacement for synthetic pesticide; since the plant contains djenkolic acid that could kill and inhibit pests. Old folk has also been using its pounded leaves and bark for chest pains, skin ailments, gum pains and toothache [3].

The previous research on the extraction of leaves, pods and seeds of *P. jiringa* using methanol revealed the antimicrobial and antifungal activities against the microorganisms such as *Staphylococcus aureus* and *Staphylococcus epidermidis* from bacteria group while *Microsporum gypsum* from fungi [4]. According to Charungchitraka et al., *Archidendron jiringa* Nielsen lectin had shown low concentration antifungal activity against *Exserohilum turcicum*, *Fusarium oxysporum* and *Colletotrichum cassiicola* while *Bacilus subtilis*, *Staphylococcus aureus* and *Candida albicans* were observed by minimal inhibitory concentration (MIC) determination [5]. The extraction of *P. Jiringa* seed using methanol had inhibited the bacteria even at low concentration against *Exserohilum turcicum*, *Fusarium oxysporum* and *Colletotrichum cassiicola*. Moreover, the leaves of *P. jiringa* had showed an inhibition zone of fungi that mostly active against *Staphylococcus aureus*, *Staphylococcus epidermidis* and *Microsporum gypsum* at 100 mg/mL [1].

Nowadays, the high cost and non-availability of new generation antibiotics with limited effective span have encouraged the increasing in morbidity and death. Thus, a new solution must be produced from other sources with proven antimicrobial properties. As a result, this has led to the new research about the materials of plant origin to find out more effective antimicrobial agents other than to discover the potential useful active ingredients that can be used as source for the synthesis of new antimicrobial drugs and baseline to identify the active compounds that involve in this activity. The scientific value of *P. jiringa* stem bark on the antimicrobial activity under this study can be used to extend its use to the community.

Materials and Methods

Plant extraction

Pithecellobium jiringa (*P. jiringa*) stem bark was washed and kept air-dried for one week. The dried plant material was cut into small pieces, and ground twice to produce fine particles. The stem bark of *P. jiringa* was weighed and soaked with ethyl acetate in ratio 1:5 (w/v) for 72 hours. The same stem bark was soaked again with ethanol with same ratio and time of extraction. The mixtures were filtrated and concentrated by using rotary evaporator at 40 °C.

Test microorganisms

For antimicrobial and antifungal studies, *Staphylococcus aureus*, *Staphylococcus epidermidis*, *Trychophyton mentagrohytes* and *Candida albicans* were obtained from Biological Laboratory 3, Universiti Teknologi MARA (Pahang).

Agar preparation

Nutrient agar and Potato dextrose agar (PDA) were used for the microbiological analysis; antimicrobial and antifungal activities of the crude extract in stem bark of *P. jiringa* on the two pure cultures of bacterial and two cultures of dermatophytes. All media were prepared and sterilized on different petri dish that followed the manufacturer's specifications [6].

Microbiological assay

The fungal suspension was standardized spectrophotometrically to an absorbance optical density (OD) of 0.1 at 450 nm by using UV-VIS. This adjusted suspension corresponded to 0.5 - 2.5 x 10^3 cells/mL and used as inoculums for antifungal susceptibility testing. Potato Dextrose Agar (PDA) was inoculated with *Trychophyton mentagrohytes* and *Candida albicans* by using cotton buds. Then, all discs with different concentration of ethyl acetate and ethanol

extracts (25, 50, 100 and 200 mg/mL) were aseptically transferred to the inoculated agar plates and later all the plates were incubated for two days at 37 °C [6].

The bacterial suspension was standardized spectrophotometrically to final optical densities (OD) of 0.1 was achieved using UV-VIS at 600 nm. These standardized OD values of inoculums were corresponding to the concentration of 1.5 x 10^6 CFU/mL. Nutrient Agar (NA) was inoculated with *Staphylococcus aureus* and *Staphylococcus epidermidis* by using cotton buds and the plates were allowed to dry for five minutes. Then, all discs with different concentration of extracts (25, 50, 100 and 200 mg/mL) were aseptically transferred to the inoculated agar plates and all the plates were incubated for 24 hours at 37 °C [7].

The activity of microbes was determined by the presence of clear zones of inhibition around the discs. The diameter of the zone of inhibition was recorded in millimetre (mm). Nystatin was used as standard antifungal, ampicillin (10 µg) as standard antibacterial and solvent as a negative control. All determinations were carried out in triplicate [8].

Phytochemical analysis

Test for alkaloids: 1 mL of each filtrate of extracts was added with a few drops of the Mayer's reagent. The formation of greenish colour or cream precipitate indicates the presence of alkaloids. Test for saponins: 1 mL of each filtrate of extracts was mixed with 10 mL of distilled water. Then, the mixture was shaken vigorously for 30 seconds. The honey comb froth formation indicated the presence of saponins. Test for flavonoids: 1 mL of each filtrate of extracts was mixed with few pieces of magnesium strips and a few drops of concentrated HCl. An orange faint colour of effervescence solution indicated the presence of flavonoids. Test for tannins: 1 mL of each filtrate of extracts was added with three drops of ferric chloride solution. A blue black or blue green precipitate was taken as evidence for the presence of tannins. Test for terpenoids: 1 mL of each filtrate of extracts was added with 2 mL of chloroform. 3 mL of concentrated H_2SO_4 was carefully added to form a layer. A reddish brown colouration of the interface indicates the presence of terpenoids.

Results and Discussion

Antimicrobial assays of ethanol and ethyl acetate extracts of *P. jiringa* stem bark were screened against bacteria and fungi. Antifungal activity was investigated using two fungal strains *Trichophyton mentagrophytes* and *Candida albicans* as shown in Table 1. The ethanol and ethyl acetate extract showed the maximum diameter of inhibition zone 18.0 and 23.0 mm against *Trichophyton mentagrophytes* at 200 mg/mL and showed no inhibition against *Candida albicans*. The results of both the extracts were correlated with the standard drug thus showed that the ethyl acetate extracts had performed good activity against *Trichophyton mentagrophyte*.

Table 1. Antifungal activity of extracts of *P. jiringa* stem bark on two fungal strains at various concentrations

Fungi	Concentration (mg/mL)	Extracts (Diameter of Inhibition Zone, mm)		
		Ethanol	Ethyl Acetate	Nystatin (Control)
Trychophyton mentagrophytes	25	8.0±0.58	12.0±0.58	12.0±0.1
	50	9.0±1.00	13.0±1.53	
	100	13.0±1.00	19.0±1.53	
	200	18.0±1.00	23.0±1.00	
*Candida albican*s	25	-	-	30.0±0.05
	50	-	-	
	100	-	-	
	200	-	-	

- sign no inhibition

The antibacterial activity of the ethanol and ethyl acetate extracts of *P. jiringa* stem bark against two standard gram-positive bacterial strains; *Staphylococcus aureus* and *Staphylococcus epidermidis* was investigated. Both of bacteria were the causative bacterium of skin disease in community acquired pneumonia and blood sepsis [9]. The result shown in Table 2 revealed the diameter of zone inhibition was dependent manner with concentration. It means, the higher the concentration of the extract, the larger diameter inhibition zone against microorganisms.

Table 2. Antibacterial activities of extracts of *P. jiringa* stem bark on two strains of bacteria at various concentrations

Bacteria	**Concentration (mg/mL)**	**Extracts (Diameter of Inhibition Zone, mm)**		
		Ethanol	**Ethyl Acetate**	**Ampicilin (Control)**
Staphylococcus aureus	25	8.0±0.58	7.7±0.00	18.0±0.1
	50	7.5±0.00	8.2±0.58	
	100	8.2±0.53	9.5±0.58	
	200	9.0±1.53	11.7±1.53	
Staphylococcus epidermidis	25	6.0±1.00	7.0±0.00	37.0±0.05
	50	7.0±1.53	12.0±0.58	
	100	9.0±0.58	11.0±1.53	
	200	9.5±0.58	13.0±0.58	

The microbial activity of *Staphylococcus epidermidis* had more efficiently inhibited towards the extracts than *Staphylococcus aureus*. This was revealed by the diameter of zone inhibition for all extracts. At highest concentration (200 mg/mL), 13.0 mm was the largest inhibition zone of ethyl acetate extract was inhibited against *Staphylococcus epidermidis* compared to *Staphylococcus aureus* with 11.7 mm of zone inhibition. For the control activity, all solvents extract used as the negative control did not inhibit the bacteria. Meanwhile, the positive control, Ampicilin had strongly inhibited both bacteria; *Staphylococcus aureus* with 18.0 mm inhibition zone and *Staphylococcus epidermidis*, 37.0 mm inhibition zone. This means the extracts were active towards bacteria.

The phytochemical screening of the ethyl acetate and ethanol extracts studies on the stem bark of *P. jiringa* revealed that both crude extracts were rich in saponins, flavonoids, tannins and terpenoids but alkaloids does not present as shown in Table 3. These compounds have been known to be biologically active and therefore aid the antimicrobial activities of *P. jiringa* stem bark.

Table 3. Phytochemical screening test for *P. jiringa* stem bark extracts

	Alkaloids	**Saponins**	**Flavonoids**	**Tannins**	**Terpenoids**
Ethyl acetate	-	++	+	++	++
Ethanol	-	++	+	++	++

++: strongly presence, +: presence, -: absence

Saponins were reported as a major components acting as antifungal secondary metabolite [10, 11]. Therefore, saponins that found in stem bark of *P. jiringa* extracts have supported the usefulness of this plant in managing inflammation. Parekh and Chanda were reported that tannins are known to react with proteins to provide the typical tanning effect which is important for the treatment of inflamed or ulcerated tissues [12]. The presence of tannins in stem bark of *P. jiringa* shows its potential for treatment of different ailments. Flavonoids in *P. jiringa* stem bark extracts can exhibit a wide range of biological activities like antimicrobial, anti-inflammatory, anti-angionic,

analgesic, anti-allergic, cytostatic and antioxidant properties [13]. Study done by Quinlan et al. revealed that some medicinal plants which exhibited antibacterial activities contained terpenoids compound [14]. Terpenoids are also responsible for the diverse pharmacological actions of the crude extract used.

Conclusion

Stem bark of *P. jiringa* contains important secondary metabolites (tannins, flavonoids, terpenoids, and saponins) thus has proven the therapeutic potentials of the plant. The screening of ethyl acetate crude extract of *P. jiringa* stem bark showed active activities against *Staphylococcus aureus, Staphylococcus epidermidis* and *Trychophyton mentagrohytes*. The largest diameter of inhibition zone for antibacterial is 13 mm which is moderately inhibited while for antifungal is 23 mm which indicates strongly inhibited. Therefore, it can be concluded that *P. jiringa* stem bark can be a potential source of active antimicrobial agents, and a detailed assessment of its in-vivo potencies and toxicological profile should be perfomed. This plant also appears to be the clinical, scientific, and pharmacologic basis for the use of herbal preparations. Further study on isolation and characterization of the active compounds from the crude *P. jiringa* stem bark extract is important for drug synthesis.

Acknowledgements

The authors would like to gratefully acknowledge the Biological Laboratory 3 of Universiti Teknologi MARA (Pahang) for their kind assistance in providing the strains of bacteria.

References

1. Bunawan, H., Dusik, L., Bunawan, S. N., M. and Amin, N. (2013). Botany, traditional uses, phytochemistry and pharmacology of *Archidendron jiringa*: A Review. *Global Journal of Pharmacology*, 7(4): 474-478.
2. Nahdzatul, S. M., Zeyad, D. N., Abdalrahim, F. A. A., Shafaei, A., Norshirin, I., Amin, M. S. A. M. and Zhari, I. (2012). Antiangiogenesis and antioxidant activity of ethanol extracts of *Pithecellobium jiringa. BMC Complementary and Alternative Medicine*, 12(1): 210.
3. Muslim, N. and Majid, A. (2010). *Pithecellobium jiringa*: A traditional medicinal herb. *Webmed Central Complementary Medicine,* 1 (12): 1371.
4. Ruzilawati, A. B., Imran, A. and Shaida, F. S. (2012). Effect of *Pithecellobium jiringa* as antimicrobial agent. *Bangladesh Journal of Pharmacology*, 7(2): 131-134.
5. Charungchitraka, S., Petsoma, A., Sangvanicha, P. and Karnchanatat, A. (2011). Antifungal and antibacterial activities of lectin from the seeds of *Archidendron jiringa* Nielsen. *Food Chemistry*, 126 (3): 1025–1032.
6. Sule, W. F., Okonko, I. O., Omo-Ogun, S., Nwanze, J. C., Ojezele, M. O., Ojezele, O. J., Alli, J. A., Soyemi, E. T. and Olaonipekun, T. O. (2011). Phytochemical properties and *in-vitro* antifungal activity of *Senna Alata* Linn. crude stem bark extract. *Journal of Medicinal Plants Research,* 5(2): 176-183.
7. Ncube, B., Finnie, J. F. and Staden, J. V. (2012). *In vitro* antimicrobial synergism within plant extracts combinations from there South African medicinal bulbs**.** *Journal of Ethnopharmacology*, 139: 81–89.
8. Mutai, C., Bii, C., Rukunga, G., Ondicho, J., Mwitari, P., Abatis, D., Vagias, C., Roussis, V. and Kirui, J. (2009). Antimicrobial activity of pentacyclic triterpenes isolated from acacia mellifera. *African Journal of Traditional, Complementary and Alternatives Medicines,* 6(1): 42–48.
9. Sujana, P., Sridhar, T. M., Josthna, P. and Naidu, C. V. (2013). Antibacterial activity and phytochemical analysis of *Mentha piperita* L. (peppermint)—an important multipurpose medicinal plant. *American Journal of Plant Sciences*, 4: 77-83.
10. Onwuliri, F. C. and Wonang, D. L. (2003). Biochemical and antimicrobial studies of *Zingiber officiale* and *Allium sativum* on the selected microorganisms. B.Sc. Thesis, Department of Botany, University of Jos: 59.
11. Onwuliri, F. C. and Wonang, D. L. (2005). Studies on the combined antibacterial action of ginger (*Zingiber officinale* L) and garlic (*Allium sativum* L) on some bacteria. *Nigerian Journal of Botany,* 18: 224-228
12. Parekh, J. and Chanda, S. (2007). *In vitro* antibacterial activity of crude methanol extract of *Woodfordia fruticosa* Kurz flower (Lythacease). *Brazilian Journal of Microbiology,* 38(2): 204-207.
13. Hodek, P., Trefil, P. and Stiborova, M. (2002). Flavonoids - potent and versatile biologically active compounds interacting with cytochrome P450. *Chemico-Biological Interactions,* 139(1): 1-21.
14. Quinlan, M. B., Quinlan, R. J. and Nolan, J. M. (2002). Ethnophysiology and herbal treatments of intestinal worms in Dominica, West Indies. *Journal of Ethnopharmacology,* 80(1): 75-83.

Malaysian Journal of Analytical Sciences, Vol 22 No 1 (2018): 128 - 135
DOI: https://doi.org/10.17576/mjas-2018-2201-16

MALAYSIAN JOURNAL OF ANALYTICAL SCIENCES
Published by The Malaysian Analytical Sciences Society
ISSN 1394 - 2506

SEPARATION OF Pb(II) FROM WASTEWATER USING UNTREATED COCONUT (*Cocos nucifera*) FROND POWDER

(Pengasingan Pb(II) daripada Air Buangan Menggunakan Serbuk Pelepah Kelapa (*Cocos nucifera*) yang Tidak Dirawat)

Nur Fatin Adlina Mohd Fouzi, Mardhiah Ismail*, Zurhana Mat Hussin, Sarah Laila Mohd Jan

Faculty of Applied Sciences,
Universiti Teknologi MARA Pahang, 26400 Bandar Tun Abdul Razak Jengka, Pahang, Malaysia

**Corresponding author: marismael@pahang.uitm.edu.my*

Received: 4 December 2016; Accepted: 1 December 2017

Abstract

The adsorption of Pb(II) ion from wastewater by coconut frond powder was evaluated in the batch adsorption process. Characteristic of the coconut frond powder (CFP) was determined by performing a pH_{zpc} analysis and also infra-red spectroscopy analysis for the investigation of the functional group on CFP surface. The batch adsorption study was carried out using five parameters including the effect of pH, the effect of adsorbent dosage, the effect of initial concentration and contact time, the kinetic and isotherm study. The optimum dosage used in this study was 0.0.4 g while the optimum pH for the adsorption of lead ions was pH 4. The adsorption capacities depended on lead concentration and contact time. It required a relatively short period of time to reach an equilibrium which is less than 60 minutes. Two kinetics models; pseudo first order and pseudo second order were used to analyze the lead adsorption process. Pseudo second order model was found to fit well enough the experimental data compared to pseudo first order.

Keywords: adsorption, *Cocos nucifera*, kinetic, lead

Abstrak

Penjerapan Pb(II) ion daripada sisa air oleh serbuk pelepah kelapa telah dinilai menggunakan proses penjerapan secara berkelompok. Ciri-ciri serbuk pelepah kelapa (CFP) telah ditentukan dengan menjalankan analisa pH_{zpc} dan juga spektroskopi infra-merah untuk mengkaji kumpulan-kumpulan berfungsi pada permukaan CFP. Kajian penjerapan berkelompok telah dijalankan dengan menilai lima parameter termasuk kesan pH, kesan dos penjerap, kesan kepekatan awal dan masa penjerapan, kajian kinetic dan kajian isoterma. Dos penjerap yang optimum diperolehi adalah 0.04 g sementara pH optima adalah pH 4. Kapasiti penjerapan bergantung kepada kepekatan larutan plumbum dan masa tindak balas. Proses penjerapan memerlukan masa yang pendek untuk mencapai keseimbangan iaitu kurang daripada 60 minit. Dua model kinetik; pseudo peringkat pertama dan pseudo peringkat kedua telah digunakan untuk menilai proses penjerapan plumbum. Model pseudo peringkat kedua didapati lebih sesuai untuk membincangkan data kinetic berbanding model pseudo peringkat pertama.

Kata kunci: penjerapan, *Cocos nucifera*, kinetik, plumbum

Introduction

The presence of heavy metal in the aquatic environment has become a great concern to scientist and also world community due to the toxic nature and negative effect on the receiving water. The major sources of the heavy metal come from industries such as metal electroplating, mining, painting, plumbing, battery manufacturing and many other industries [1,2].

The word heavy metal attribute to any metallic element that has a relatively high density, specific gravity or atomic weight. The heavy metal is toxic and poisonous even at low concentration. Heavy metals exist naturally in the Earth's crust and also being released into surrounding due to human activities. It can be found in water, sediment, soil, microorganism and rock with natural background concentration. Heavy metals cannot be degraded and destroyed; hence, it will persist in the environment [3]. An example of heavy metals includes mercury, lead, cadmium, arsenic, copper, iron, and thallium. When absorbed by human body, it can cause the physiological and neurological disorder. Heavy metal can enter human bodies via food, air, and drinking. Some heavy metals such as copper, selenium, and zinc are fundamental to maintain the metabolism of the human body. However, at higher concentration, heavy metal can lead to poisoning through high ambient air concentration near emission sources or via the food chain.

Lead can be considered as a hazardous metal due to its negative effect on the human nervous system, blood circulation system, kidneys and reproductive system[4,5]. Usually, the common victim of lead poisoning is children and it can cause mental retardation and semi-permanent brain damage. Due to its toxicity and carcinogenic properties, it causes a serious threat to the human population and also flora and fauna when the lead discharged into wastewater. Lead get into the human body via inhalation, ingestion, and skin adsorption. It can affect organ and system in human body. It is necessary to discard this toxic heavy metal from wastewater before it is disposed of as this will avoid and reduce health hazard to both mankind and another living organism. Hence, lead from industrial wastewater must be properly treated to avoid it from reaching the water bodies. There are a few physicochemical methods that have been introduced in the removing of heavy metals from wastewater such as chemical precipitation, chemical coagulation, ultrafiltration, using natural zeolite ion exchange, adsorption, and electrochemical deposition. Many researchers have focused on untreated plant waste such as papaya wood [6], garlic peel [7], cotton [8, 9]. There are many advantages of using plant waste as an adsorbent in the treatment of wastewater such as it is a simple technique, low operation cost, great adsorption capacity, can be regenerate and the ability to adsorb heavy metal ions. However, besides the advantages of untreated plant waste, they also bring some problems such as low adsorption capacity, high in chemical oxygen demand (COD), biological chemical demand (BOD), and total organic carbon (TOC). This happened due to the release of the soluble organic compound in the plant materials [10, 11]. Plant material can be divided into a few parts such as fruit, flower, bark, leaf and others. All part of the plant has been studied as an adsorbent.

A coconut tree, known as (*Cocos nucifera*) is a member of the *Arecaceae* (palm family). It is also known as "the tree of life" since it gives many benefits to the human and living organisms such as sources of food and medicine. Normally, *Cocos nucifera* grows up to 30 meters tall. It has pinnate leaves with 4-6 meter long, and pinnae 60-90 cm long [12]. The leaves will break away when it old and leave the trunk smooth. The coconut is very nutritious and highly in fiber, vitamins, and minerals. The coconut oil is used in traditional medicine among Asian and pacific population since it contains healing properties compared to any other dietary oil. This tree consists of a few parts which are a shell, fruit, coconut frond and others. The various part of the coconut has been extensively studied as bio-sorbents for removal of pollutants from water [13]. Coconut frond was first used [14] in removing carbofuran insecticides by mesoporous activated carbon from coconut frond. The treated spent grated coconut shows high adsorption capacity compared to the untreated spent grated coconut which is 366.50 mg/g. Treatment of spent grated coconut with acid increased the adsorption capacity due to the increasing of surface area and pores. Previous research [15] were performed a research on sulphuric acid treated coconut (*Cocos nucifera*) frond powder in removing methylene blue from aqueous solution. In this study, untreated coconut frond powder will be used for removing Pb(II) from aqueous solution. Literature also has shown that untreated coconut frond in removing Pb(II) never been conducted as well.

Materials and Methods

Adsorbent preparation

Coconut frond was collected from Kelantan, Malaysia. The frond was washed to remove soluble impurities before rinsing with deionized water and was dried in an oven at 333 K to avoid any sample degradation overnight before being ground and sieved by using a mechanical grinder to obtain a particle size of 125-250 μm. The newly prepared

coconut frond powder was labeled as CFP (coconut frond powder). The CFP was used as adsorbent without any chemical treatment.

Adsorbent characterization

The determination of pH_{ZPC} of CFP was performed according to the solid addition method as reported by Balistrieri and Murray [16]. A 50 mL of 0.01 M KNO_3 solution was placed into 8 different 100 mL conical flasks. The initial pH of the solutions was adjusted to a value between pH 2-9 by adding 0.1 M HCl or NaOH solutions. Then, 1 g of CFP was added to each flask, stirred and the final pH of the solutions was measured after 24 hours. The value of pH_{ZPC} can be determined from the curve that cuts the pH line of the plot ΔpH versus initial pH. The type of functional groups presents in the CFP was determined by using a Fourier transform infrared spectrometer (FTIR) (Perkin Elmer, Spectrum 100, USA).

Adsorption experiment

Lead nitrate ($Pb(NO_3)_2$, MW = 331.2 g mol^{-1}) was purchased from MERCK, Malaysia. The stock solution of 1000 mg L^{-1} Pb(II) was prepared and diluted to the preferred concentrations with deionized water. The effect of dosage was performed by mixing 0.02, 0.04, 0.06, 0.08 and 0.1 g CFP with 50 mL (10 mg L^{-1}) Pb(II) and stirred at 120 strokes per minute at 298±1 K for 90 min to achieved equilibrium. The effect of pH was studied in the pH range between 2 to 4. Adsorption kinetic study was conducted using three different Pb(II) concentrations (10, 20 and 30 mg L^{-1}) at various contact times (0-90 minutes). After adsorption, the CFP was filtered and the final concentration of Pb(II) was determined by using Atomic Absorption Spectrometer (PinAAcle 900T, Perkin Elmer, USA). All experiments were conducted in duplicate and the RSD values for all analyses were less than 5%. The amount of Pb(II) ion adsorbed (q_e, mg g^{-1}) and percentage removal (%) was calculated by using equations (1) and (2), respectively:

$$q_e = \frac{C_i - C_e}{m} V \quad (1)$$

$$\text{Removal}(\%) = \frac{C_i - C_e}{C_i} x100 \quad (2)$$

where C_i and C_e are the initial and final concentrations (mg L^{-1}) of Pb(II) and m is the weight of CFP (g).

Results and Discussion

Adsorbent characterization

The pH_{zpc} is important to determine the pH where the surfaces of the adsorbent exhibit zero electrical charges. It also gives important information on the electrostatic interaction between the adsorbent and the adsorbate. The pH_{zpc} for coconut frond powder (CFP) was determined at 5.45. At this point, the functional group of the adsorbent is no longer contributed to the pH of the solution. At the point where the pH is lower than pH_{zpc} value, the adsorbent surface will carry a positive charge (attract anion) while when the pH is higher than pH_{zpc} value, the adsorbent will carry negative charge ion (attract cation).

FTIR analysis was carried out in order to reveal the active functional on the surface of the CFP that might be involved in the adsorption process. The FTIR spectra of CFP before and after adsorption were shown in Fig. 1 below. The spectra display a number of adsorption peak, indicate the nature of a functional group of CFP that consist of complex functional groups such as amino, hydroxyl, and carbonyl. All these groups have possibility can have a chemical interaction with Pb(II) ion. After adsorption with Pb(II) ion, many functional groups shifted to a different wavenumber which can be a confirmation that CFP has chemical or physical interaction with Pb(II) ion. The strong and broad peak at 3331 cm^{-1} indicates the presence of O-H stretching vibration due to the alcohol, phenols and carboxylic acid [17]. However, after the adsorption, the peak slightly shifted to a lower band of 3289 cm^{-1}. The peak that observed at 2922 cm^{-1} can be appointed to asymmetric and symmetric $–CH_2$ group [18].

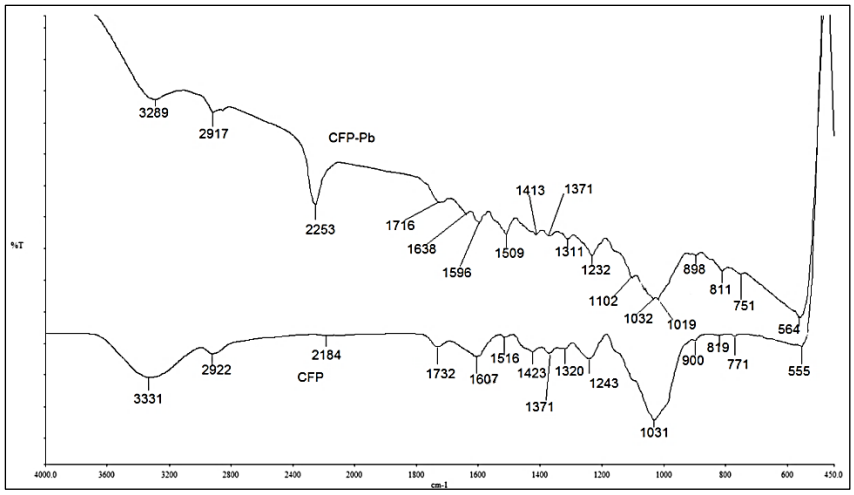


Figure 1. FTIR spectra for CFP and CFP-Pb after adsorption

The minor peak at 2184 before adsorption shifted to a higher frequency of 2253 cm^{-1} after the adsorption. The peak corresponds to the alkene group C=C. The peak at 1732 cm^{-1} before adsorption shifted to the lower band at 1716 indicate the presence of carbonyl group C=O. N-H bond for primary and secondary amines and amide appear at peak 1607 cm^{-1} before adsorption and slightly increase after adsorption to 1637.64 cm^{-1}. Besides that, the C-O group (alcohols, ether, esters, carboxylic acids, anhydrides) appeared at peak ranging from 1300-1000 cm^{-1}. The small peak observed at 1517 cm^{-1} is due to $–NH_2$ group [19], the frequency decrease after the adsorption of lead Pb(II) to 1509 cm^{-1}. Based on spectroscopy analysis, it can be concluded that the functional group responsible for the adsorption of Pb(II) onto CFP are carbonyl and amine groups which have a partial negative of oxygen and nitrogen that attracted toward a positive charged of Pb(II) ions.

Study of pH

The effect of pH on adsorption of Pb by CFP (Fig. 2) was studied in the pH ranges from 2 to 5 with an adsorbent dosage of 0.04 g and adsorbate concentration of 10 mg L^{-1}. pH 5 and above were not chosen because precipitation of $Pb(OH)_2$ will occur and to ensure that only Pb(II) involved in the adsorption studies [20]. The result of the effect of pH is illustrated in Fig. 2 below. From the result, the amount of Pb(II) ion adsorbed increased with the increasing of pH value. At pH 2, the amount of Pb(II) adsorbed was the lowest amount among the others which was 1.71 mg g^{-1}. The highest adsorption of Pb(II) occurs at pH 5 (11.79 mg g^{-1}). The adsorption capacity of Pb(II) lows at pH 2 because Pb(II) ion need to compete with H_3O^+ for adsorption site. When the pH increased, the competing effect of H_3O^+ decreased and more adsorbent surface were revealed, the positive Pb(II) ions could easily adsorbed on the available adsorption sites of the adsorbents. The Pb(II) ion carried a positive charge and result in less repulsion of Pb(II) ion with the negative adsorption pH at high pH value contribute to high adsorption at higher pH (between pH 3-5). Pb(II) ion usually present at pH less than 5 and it is suitable to use in adsorption study. The pH adsorption edge in this experiment was between 2 to 4. At pH higher than 5, Pb(II) ion adsorbed will decrease due to the formation of $Pb(OH)_2$. Hence, the applicable pH for adsorption of Pb(II) ion in this experiment was pH 4.

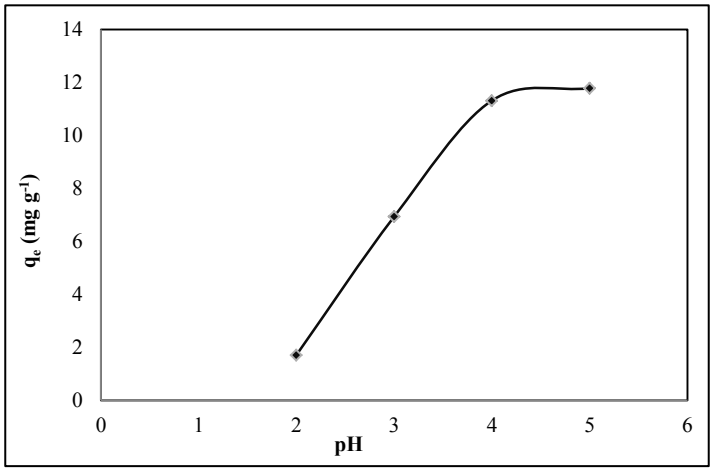


Figure 2. Effect of pH on adsorption of Pb onto CFP

Study of dosage

Fig 3 shows the removal of Pb(II) as a function of CFP dosage. Based on the result obtained, when the dosage increased from 0.02 g to 0.1 g, the percentage removal increased from 52.3 to 93.26% but inversely the adsorption capacity decreased gradually from 13.08 to 4.66 g mg^{-1}. This might happen due to the availability of more binding sites as there is more adsorbent is added with the same amount of Pb(II) [21]. The amount of Pb(II) adsorbed remains constant above 0.06 g. As the number of adsorption site increased and heavy metal concentration was fixed at a similar concentration (10 mg L^{-1}), there will be a lot of un-adsorbed adsorption sites. According to the result obtained, the adsorbent dosage of 0.04 g showed both relatively high percentage removal and high adsorption capacity. As a result, 0.04 g was used for further adsorption parameter in this study.

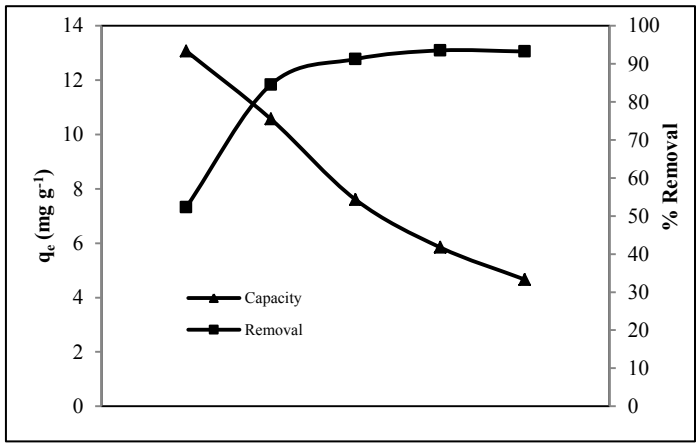


Figure 3. Effect of CFP dosage on the Pb adsorption onto CFP

Study of initial Pb(II) ion concentration and contact time

The effect of lead concentration and contact time are important factors to determine the kinetic of adsorption. The adsorption data at different initial Pb(II) concentrations and contact time are shown in Fig 4. The adsorption process was carried out at different contact times and initial concentration of Pb(II) with constant adsorbent dose (0.04 g) at room temperature. Based on the graph, the adsorption capacity and equilibrium time depended on the concentration of Pb(II). The adsorption reached equilibrium within 10 minutes for the lead concentration of 10 and 20 mg L^{-1} and

30 minutes for 30 mg L^{-1}. The amount of Pb(II) adsorbed at equilibrium were 11.06 mg L^{-1}, 19.51 mg L^{-1} and 34.96 mg L^{-1} for the concentration of 10, 20 and 30 mg L^{-1} respectively. At the initial stage, large capacity of the available bare surface area of the adsorbent was favorable for the adsorption of the Pb(II) and after an equilibrium time, the pores of the coconut frond (CFP) are fully saturated with the Pb(II) molecules and adsorption process becomes constant. This is happening because the remaining available sites of the CFP compete among the Pb(II) molecules due to the steric effect as well as repulsive forces, and as the number of empty adsorption site decrease compare with the number of lead ion available, the rate of the adsorption slowing down [22]. From the result obtain in this study, we can see that the amount of the Pb(II) molecules adsorbed per unit mass of CFP increase with an increase in the initial concentration of Pb(II) which caused by the high concentration gradient at high concentration that acts as a driving force for the adsorption process.

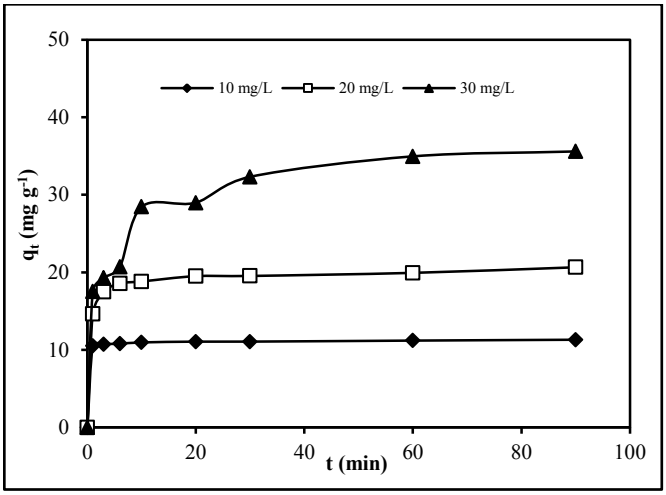


Figure 4. Effect of initial concentration and contact time on adsorption of Pb onto CFP

Adsorption kinetic model

The kinetic data for the adsorption of Pb(II) were further analyzed by using the pseudo first order and pseudo second order kinetic models. The equations for both kinetic models were expressed in equation (3) and (4) respectively:

$$\log(q_e - q_t) = \log q_e - \frac{K_1}{2.303} t \quad (3)$$

$$\frac{t}{q_t} = \frac{1}{K_2 q_e^2} + \frac{1}{q_e} t \quad (4)$$

where q_e is the amount (mg g^{-1}) of Pb(II) adsorbed onto CFP at equilibrium and q_t is the amount (mg g^{-1}) of Pb(II) adsorbed at any time t (min) while K_1 and K_2 are the rate constants of pseudo-first-order and second-order models, respectively. While $K_2 q_e^2$ will give the value of h.

Based on the kinetic parameter in Table 1, the pseudo second order kinetic model has accurately explained the experimental data. Both q_e calculated and the q_e experiments for pseudo second order are almost closed to each other compared to the pseudo first order. For pseudo second order, the value of q_e calculated for 10, 20 and 30 mg L^{-1} were 11.99, 23.42 and 36.77 mg g^{-1} respectively. These values are in good agreement with the value of the q_e experiment, 11.30, 20.65 and 35.59 mg g^{-1} for 10, 20 and 30 mg L^{-1} respectively. The R^2 value for the pseudo second order also close to the unity compared to the pseudo first which is very far from the unity. Hence, we can conclude that the pseudo second order kinetic model fitted well with all the experimental data which mean that the rate-limiting step for this adsorption process might be the chemisorption process. [23]. A similar finding was observed in the adsorption of Pb(II) ions from aqueous solution onto pine cone activated carbon [24].

Table 1. Adsorption kinetic parameters for Pb(II) adsorption on CFP

[Pb] mg L^{-1}	$q_{e,exp}$ (mg g^{-1})	Pseudo-First-Order			Pseudo-Second-Order			
		$q_{e,cal}$ (mg g^{-1})	K_1 (min^{-1})	R^2	h (mg/(g.min))	K_2 (g/(mg.min))	$q_{e,cal}$ (mg g^{-1})	R^2
10	11.30	1.57	0.005	0.799	8.40	0.058	11.99	0.997
20	20.65	7.27	0.007	0.631	6.72	0.012	23.42	0.983
30	35.59	17.36	0.050	0.989	10.96	0.008	36.76	0.999

Conclusion

In this study, untreated CPF was characterized and tested as a potential new adsorbent for removal of Pb(II) ion from aqueous solution. It can be summarized that FTIR spectra analysis suggested that the CFP have a functional group that suits for Pb(II) ion adsorption. From the kinetic study, it can be confirmed that Pb(II) adsorption onto CFP is determined by chemisorption. The adsorption is very fast where the equilibrium was attained in less than 60 minutes. While, from the value of pH_{ZPC} and pH study, the adsorption can be carried out at pH 4 for optimum removal of Pb(II) ion from aqueous solution.

Acknowledgement

Authors are thankful to those who are directly or indirectly involved in this research, especially those from Chemistry Department of Applied Sciences Faculty, UiTM Jengka for providing chemical and laboratory facility in completing this research. Special thanks for Mr. Fauzi Ismail, Laboratory assistant who's committedly helping final year project's students for FSG 661.

References

1. Nguyen, T. H., Ngo, H. H., Guo, W. S., Zhang, J., Liang, S., Yue, Q. Y., Li, Q. and Nguyen, T. V. (2013). Applicability of agricultural waste and by-products for adsorptive removal of heavy metals from wastewater. *Bioresource Technology,* 148: 574–85.
2. Kadirvelu, K., Thamaraiselvi, K. and Namasivayam, C. (2001). Removal of heavy metals from industrial wastewaters by adsorption onto activated carbon prepared from an agricultural solid waste. *Bioresource Technology,* 76(1): 63–65.
3. Duruibe, J. O., Ogwuegbu, M. O. C. and Egwurugwu, J. N. (2001). Heavy metal pollution and human biotoxic effects. *International Journal of Physical Sciences,* 2(5): 112–118.
4. Jalali Heravi M. and Sereshti, H. (2007). Determination of essential oil components of *Artemisia haussknechtii Boiss*. using simultaneous hydrodistillation-static headspace liquid phase microextraction-gas chromatography mass spectrometry. *Journal of Chromatography A*, 1160(1): 81–9.
5. Li, Q., Chai, L., Yang, Z. and Wang, Q. (2009). Kinetics and thermodynamics of Pb(II) adsorption onto modified spent grain from aqueous solutions. *Applied Surface Science*, 255 (7): 4298–4303.
6. Saeed, A., Akhter, M. W. and Iqbal, M. (2005) Removal and recovery of heavy metals from aqueous solution using papaya wood as a new biosorbent. *Separation and Purification Technology,* 45(1): 25–31.
7. Hameed, B. and Ahmad, A. (2009). Batch adsorption of methylene blue from aqueous solution by garlic peel, an agricultural waste biomass. *Journal of Hazardous Materials*, 164: 870–875.
8. Deng, H., Lu, J., Li, G., Zhang, G. and Wang, X. (2011) Adsorption of methylene blue on adsorbent materials produced from cotton stalk. *Chemical Engineering Journal*, 172 (1): 326–334.
9. Ertaş, M., Acemioğlu, B., Alma, M. and Usta, M. (2010). Removal of methylene blue from aqueous solution using cotton stalk, cotton waste and cotton dust. *Journal of Hazardous Materials*, 183: 421–427.
10. Gaballah, I. and Kilbertus, G. (1998). Recovery of heavy metal ions through decontamination of synthetic solutions and industrial effluents using modified barks. *Journal of Geochemical Exploration*, 62 (1–3): 241–286.
11. Nakajima, A.and Sakaguchi, T. (1990). Recovery and removal of uranium by using plant wastes. *Biomass*, 21(1): 55–63.

12. Fatombi, J. K., Lartiges, B., Aminou, T., Barres, O. and Caillet, C. (2013). A natural coagulant protein from copra (*Cocos nucifera*): Isolation, characterization, and potential for water purification. *Separation and Purification Technology*, 116: 35–40.
13. Bhatnagar, A. and Sillanpää, M. (2010). Utilization of agro-industrial and municipal waste materials as potential adsorbents for water treatment-A review. *Chemical Engineering Journal*, 157(2–3): 277–296.
14. Njoku, V. O., Islam, M. A., Asif, M. and Hameed, B. H. (2014). Preparation of mesoporous activated carbon from coconut frond for the adsorption of carbofuran insecticide. *Journal of Analytical and Applied Pyrolysis*, 110(1): 172–180.
15. Ismail, M., Megat Hanafiah, M. A. K., Zainal Abidin, M. S., Mat Hussin, Z. and Khalid, K. (2015) Kinetics of methylene blue adsorption on sulphuric acid treated coconut (*Cocos nucifiera*) frond powder. *American Journal of Engineering and Applied Sciences,* 5(3): 33-37
16. Balistrieri, L. and Murray, J. W. (1981). The surface chemistry of goethite (alpha FeOOH) in major ion seawater. *American Journal of Science*, 281(6): 788–806,.
17. Mwangi, I. W. and Ngila, J. C. (2012). Removal of heavy metals from contaminated water using ethylenediamine-modified green seaweed (*Caulerpa serrulata*). *Physics and Chemistry of the Earth*, 50–52: 111–120.
18. Khambhaty, Y., Mody, K., Basha, S. and Jha, B. (2009). Biosorption of Cr(VI) onto marine *Aspergillus niger*: Experimental studies and pseudo-second order kinetics. *World Journal of Microbiology and Biotechnology*, 25(8): 1413–1421.
19. Ncibi, M. C., Mahjoub, B. and Seffen, M. (2007). Kinetic and equilibrium studies of methylene blue biosorption by *Posidonia oceanica (L.)* fibres. *Journal of Hazardous Materials*, 139(2): 280–285.
20. Lee, S. H., Shon, J. S., Chung, H., Lee, M.-Y. and Yang, J.-W. (1999). Effect of chemical modification of carboxyl groups in apple residues on metal ion binding. *Korean Journal of Chemical Engineering*, 16(5): 576–580.
21. Vijayaraghavan, K., Palanivelu, K. and Velan, M. (2006). Biosorption of copper(II) and cobalt(II) from aqueous solutions by crab shell particles. *Bioresource Technology*, 97(12): 1411–1419.
22. Bhattacharyya, K. G. and Gupta, S. S. (2006). Adsorption of chromium (VI) from water by clays. *Industrial & Engineering Chemistry Research*, 45: 7232–7240.
23. Kumar, P. S. and Kirthika, K. (2009). Equilibrium and kinetic study of adsorption of nickel from aqueous solution onto bael tree leaf powder. *Journal of Engineering Science and Technology*, 4(4): 351–363.
24. Momčilović, M., Purenović, M., Bojić, A., Zarubica, A. and Ranđelović, M. (2011). Removal of lead(II) ions from aqueous solutions by adsorption onto pine cone activated carbon. *Desalination*, 276 (1–3): 53–59.

Malaysian Journal of Analytical Sciences, Vol 22 No 1 (2018): 136 - 142
DOI: https://doi.org/10.17576/mjas-2018-2201-17

MALAYSIAN JOURNAL OF ANALYTICAL SCIENCES
Published by The Malaysian Analytical Sciences Society
ISSN 1394 - 2506

DESALINATION OF SEAWATER USING NEWLY FABRICATED NANOFILTRATION FLAT SHEET MEMBRANE

(Penyahgaraman Air Laut Menggunakan Rekaan Baru Membran Kepingan Rata Penapisan Nano)

Wan Syarizawani Wan Chik[1]*, Mohd Johan Mohamed Ibrahim[1], Ramlah Mohd Tajuddin[2]

[1]*Faculty of Civil Engineering,*
Universiti Teknologi MARA Cawangan Johor, Kampus Pasir Gudang, 85000 Segamat, Johor, Malaysia
[2]*Faculty of Civil Engineering,*
Universiti Teknologi MARA, 40450 Shah Alam, Selangor, Malaysia.

**Corresponding author: zawani9681@johor.uitm.edu.my*

Received: 4 December 2016; Accepted: 1 December 2017

Abstract

Desalination is one of the technologies to produce clean water for drinking, irrigation, industrial and development. Generally desalination can be classified based on their separation mechanisms which are thermal and membrane based desalination. In this study the newly fabricated nanofiltration membrane was used to identify their performance in desalination process. The material chosen in this study is polysulfone (PSf), N-methyl-2-pyrolidon (NMP) and polyvinylpyrrolidone (PVP). The dope solution composition was determined by using titration method. The membrane compositions are 20:1:79, 20:2:78, 20:3:77 and 20:4:76 (weight ratio) for PSf/PVP-1%, PSf/PVP-2%, PSf/PVP-3% and PSf/PVP-4% respectively. The polysulfone membrane was fabricated by wet phase inversion method. The aims of this research are to investigate the effect of different PVP concentrations in material composition on membrane morphology, membrane fluxes and seawater rejection. The results observed by SEM show the membrane composition PSf/PVP-1% has lower pore size with average pore size 8.4 nm while PSf/PVP-4% has highest pore size. Membrane PSf/PVP-1% has highest rejection (5.7%) and lower flux (2.43 L/cm^2.hr) while PSf/PVP-4% has highest flux (6.44 L/cm^2.hr) and lower rejection (0.87%). It is related with PVP contents in the membrane solution. In conclusion, increase PVP concentration will increase pore size, therefore it will increase flux while the rejection will decrease.

Keywords: membrane based desalination, nanofiltration, polysulfone, polyvinylpyrrolidone

Abstrak

Penyahgaraman adalah salah satu teknologi untuk menghasilkan air bersih untuk minuman, pengairan, perindustrian dan pembangunan. Secara umumnya penyahgaraman boleh dikelaskan berdasarkan mekanisme pengasingan iaitu penyahgaraman berdasarkan terma dan membran. Dalam kajian ini membran penapisan nano yang baru direka telah digunakan untuk mengenal pasti prestasi dalam proses penyahgaraman. Bahan dipilih dalam kajian ini adalah polisulfon (PSf), N-metil-2-pirolidon (NMP) dan polivinilpirolidon (PVP). Komposisi cecair larutan yang telah ditentukan adalah menggunakan kaedah titratan. Komposisi membran yang digunakan ialah 20:1:79, 20:2:78, 20:3:77 dan 20:4:76 (nisbah berat) untuk PSf/PVP-1%, PSf/PVP-2%, PSf/PVP-3% dan PSf/PVP-4%. Membran polisulfon dihasilkan melalui kaedah fasa penyongsangan basah. Tujuan kajian ini adalah untuk mengkaji kesan kepekatan PVP berbeza dalam komposisi bahan morfologi membran, fluks membran dan penyingkiran air laut. Keputusan dipatuhi oleh SEM menunjukkan membran komposisi PSF/PVP-1% mempunyai saiz liang yang lebih kecil dengan purata saiz liang 8.4 nm manakala PSF/PVP-4% mempunyai saiz liang terbesar. Membran PSF/PVP-1% mempunyai penyingkiran tertinggi (5.7%) dan fluks yang lebih rendah (2.43 L/cm2.hr) manakala PSF/PVP-4% mempunyai fluks tertinggi (6.44 L/cm2.hr) dan penyingkiran yang lebih rendah (0.87%). Ia berhubungkait dengan kandungan PVP dalam larutan membran. Kesimpulannya, peningkatan kepekatan PVP akan meningkatkan saiz liang, oleh itu ia akan meningkatkan fluks manakala penyingkiran akan berkurangan.

Kata kunci: penyahgaraman berdasarkan membran, penapisan nano, polisulfon, polivinilpirolidon

Introduction

Water is an important component in our daily life besides water is a natural resource that covers 75% of the earth's surface. However from all the water resources only 3% is for potable usage [1]. Nowadays the most serious problem affecting people around the world is global water crisis. The increasing of population and development will increase the demand on the quantity and quality of drinking water. It is projected that by year 2030, the global demand of water would increase from 4500 billion m^3 to 6900 billion m^3 [2]. Therefore, the future needs of water resources are higher than the current surface water resources available. Nowadays membrane desalination technology such as reverse osmosis (RO), nanofiltration (NF) and membrane distillation (MD) are the most popular membrane based technology used for saline water treatment. At present more than 50% of the world's desalination water is produced by membrane technology [3]. Respect to that NF has potential in the desalination process due to development of new membrane material and novel process, furthermore NF will enhanced flux, lower operational pressure and energy saving compare with RO system [4]. Membrane materials with high permeability and selectivity, and advanced of fabrication technologies to produce membrane with a defect free ultrathin dense selective layer are the primary focuses for most membrane technologist. Significant progresses have been made in membrane materials, dope preparation, fabrication technique and fundamental understanding of membrane formation. Choosing appropriate membrane materials is one of the key factors to the success of membrane performance. Basically, for producing asymmetric membrane structure, components that must consist in the dope formulation are polymer, solvent and additive. Introduced second polymer in the solution will improve the properties of polymer and produced high porous membrane. In this study the polyvinylpyrrolidone (PVP) was chosen as additional polymer in the membrane material solutions because of their characteristics. The PVP will control morphology from both thermodynamics and kinetics aspects [5]. Study of Chakrabarty et al. showed that the additional PVP in the solution increase the pore number as well as porosity of the prepared membrane [6].

Materials and Methods

Materials

Membranes material used in this study consists of polymer, solvent and additive. Polymer used in this study to fabricate nanofiltration flat sheet membrane is polysulfone (PSf). Polysulfone was chosen as main component because of their characteristics and advantages. PSf is widely used as a component in the fabrication of membrane because of its excellent balance of chemical, thermal and mechanical properties [7]. Besides it has good chemical and temperature stability up to 80 ^{o}C and pH range from 1.5 to 12 for cleaning [8]. Although it shows some tolerance to oxidizing agents such as chlorine and ability to retain their mechanical properties in hot and wet environments. The solvent used to prepare dope solution was N-methyl-2-pyrolidon (NMP). NMP was used because this solvent able to dissolved in several types of polymers. The casting solution based on this solvent can precipitate rapidly when immersed in the water and resulting porous and very anisotropic membranes [9]. Additive is introduced in the polymer solution to improve the properties of polymer membranes. Additive used in this study was polyvinylpyrrolidone (PVP). According to Yoo et al. adding the second polymer in the solution produced high porous membranes, well interconnected pores and surface properties [10]. PVP was chosen because of their benefits. The PVP will control morphology from both thermodynamics and the kinetics aspects [11]. Thus in the thermodynamics, it makes the system unstable and prone to phase separation. Then in kinetics, the high viscosity of the polymer solution after the addition of PVP will delay the phase separation and slow down the demixing process. The final result was the trade-off between two effects [12, 13].

Methods

Membrane fabrications have several processes to complete, firstly the dope formulation was determined and specified formulation was recorded. The dope solution was mixed before the casting process. After the casting process the flat sheet membrane was immersed in the coagulation bath and finally membrane was stored in the water bath for a day before dry at room temperature.

Seawater (25 L) was prepared in the feed tank as feed solution. The physical and chemical characteristics of seawater were tested in the environmental laboratory. The physical parameter tested were color, temperature, turbidity, conductivity, total dissolved solid and total suspended solid while chemical parameter tested were pH and dissolved oxygen (DO).

Membrane separation process was conducted using laboratory scale cross flow filtration system. The seawater was prepared as feed solution. Pure water also prepared as feed solution to compare their membrane performance. Membrane sample was fractured into small size to fix the flat sheet membrane. Then the pressure was setup at 2 bar or 30 psi to pump so that the feed solution will pass through the membrane. The feed solution was maintained at room temperature which is 25 – 30 ^{o}C. After that permeate and rejection concentration was determined. Permeate and rejection concentration was tested by using conductivity meter in order to determine the concentration after the filtration process.

Results and Discussion

Membrane dope formulation

The PVP concentration used in this study is the range 1to 4 (wt%) as show in Table 1. Based on Han et al. studied, by adding PVP in PSf casting solution the thermodynamic and rheological properties will varies [14]. The result indicated that when adding low content PVP (below 5 wt%), the variation in thermodynamic property controlled the demixing process and led to the enhancement of phase separation. With further increment of PVP content, the demixing process was delayed due to high viscosity of the casting solution. Based on the four membrane prepared with different percentage of PVP in the material solution. The result show membrane PSf/PVP-1% give highest performance compared to other membrane. This because, PVP will affect the membrane morphology thus it will influence the membrane flux and seawater rejection.

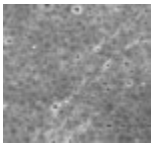
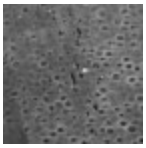
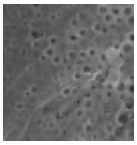
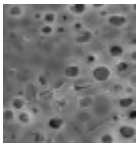
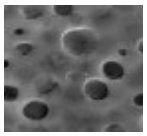
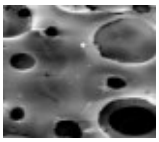
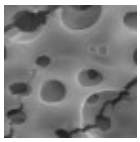
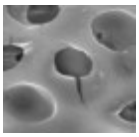
Table 1. Membrane dope formulation

Membrane	Solution Composition (wt%)		
	PSf	PVP	NMP
PSf 1	20	1	79
PSf 2	20	2	78
PSf 3	20	3	77
PSf 4	20	4	76

Effect of membrane composition on membrane morphology

Four membrane PSf prepared by different amount of PVP was observed by Scanning Electron Microscope (SEM) to identify their morphology. Table 2 shows the images observed by SEM at magnification 7000x and 25000x. The images show pore size of the membrane was increase with increase the percentage of PVP in the material compositions. From the Table 2 highest percentage of PVP in the material composition (4%) give highest pore size (18.6±2.1 nm) while lowest percentage of PVP (1%) give lowest pore size (8.4±1.2 nm). Increase the PVP content in the membrane solution will increase the surface membrane pore size, it happened because of, after the casting film on a glass plate, pre evaporation began and water intake occurred at the top layer of the casting film [15]. Water soluble PVP could migrate and aggregate to the casting film/water interface in order to minimize the interfacial energy. The aggregation of PVP formed polymer lean phase, which might be the rudiment of pore structure on membrane surface and top layer. After immersing the casting film into the coagulation bath, it could induce the formation and growth of pore structure [16, 17]

Table 2. Surface pore size of PSf membrane with different amount of additive

% PVP	Membrane Surface Pore Size (nm)			
	1	2	3	4
7000x				
25000x				
	8.4±1.2	11.2±1.5	15.5±1.9	18.6±2.1

Membrane cross section

The prepared four membrane samples were characterized using Scanning Electron Microscope. SEM analysis showed the images of cross section structure of asymmetric nanofiltration membrane PSf/PVP at different composition of PVP as show in Figure 1 and 2. It was found that all the membrane exhibits typical morphological structure of asymmetric membrane which consists of dense top layer and porous sub layer containing macro voids, pores and micro voids. This sub layer formation is controlled by variable of polymer dope solution such as compositions, coagulant temperature and additives [18]. Based on Table 2 the increasing of PVP concentrations in the solution increase the pore size while the cross section for all membranes prepared have same typical asymmetric membrane morphology.

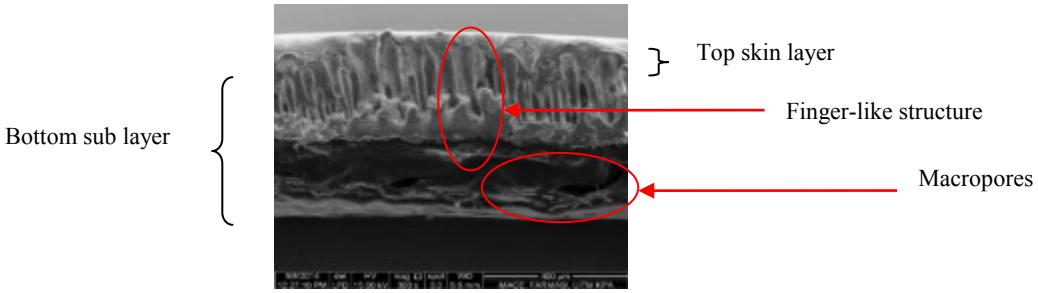
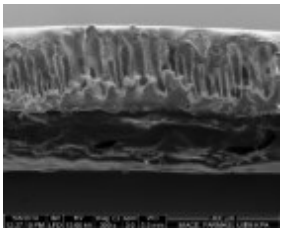
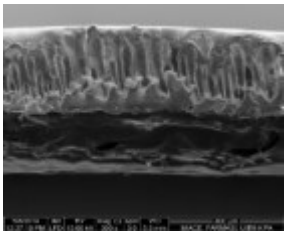


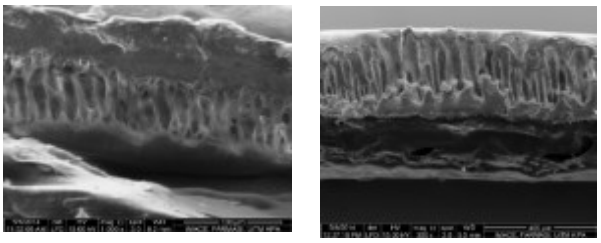
Figure 1. Morphology of PSf/PVP – 4%



(a) PSf/NMP/PVP- 1%



(b) PSf/NMP/PVP- 2%



(c) PSf/NMP/PVP- 3% (d) PSf/NMP/PVP- 4%

Figure 2. SEM micrograph of cross sectional view of PSf/NMP/PVP membrane; (a) PSf/NMP/PVP- 1%; (b) PSf/NMP/PVP- 2%; (c) PSf/NMP/PVP- 3%; (d) PSf/NMP/PVP- 4%

Effect of PVP concentration in membrane composition on membrane flux

Figure 3 shows the membrane flux for different percentage of the PVP content. Pure water fluxes of PSf/PVP membranes increase gradually with increasing PVP content, which is probably due to increase of surface hydrophilicity, surface pore size, porosity, acicular pores and macrovoids. It clearly shows that membrane with highest percentage of PVP content (4%) will give highest flux (6.44 L/cm^2.hr) while membrane with lowest percentage of PVP (1%) give lowest flux (2.43 L/cm^2.hr). Based on the discussion on membrane morphology membrane with more percentage of PVP content will increase the membrane pore size, therefore the increase of pore size will increase the membrane flux, hence it will increase the membrane performance. This is related with the aggregation of PVP in the casting film interface during pre evaporation and the pore forming effect of PVP after immersing the casting film into coagulation bath. It has been accepted worldwide that PVP other than its hydrophilic characteristic that able to attract water, it also known as a pore forming agent which in this case is responsible to produce bigger pore in membrane structure.

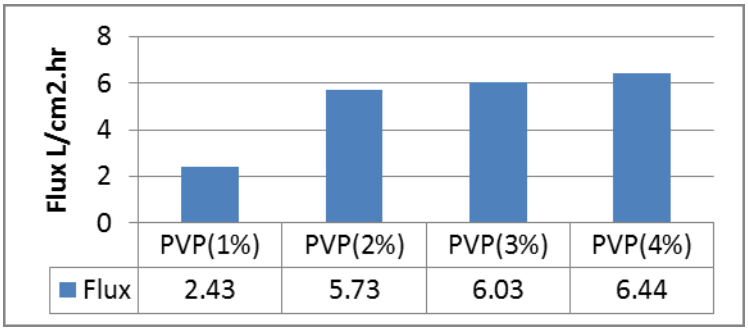


Figure 3. Membrane flux with different % PVP concentration.

Effect of PVP concentration in membrane composition on seawater rejection

Table 3 shows the concentration before and after membrane separation process. Based on the result, the concentration of seawater was decrease after separation process for all membrane types. Figure 4 shows membrane with lowest percentage of PVP (1%) gives highest rejection (5.7 %) while membrane with highest percentage of PVP (4%) gives lowest rejection (0.87%). These results are consistent with the SEM characteristics. Membrane morphology show increase percentage of PVP in the material composition will increase the pore size while decrease the percentage of PVP will decrease the pore size. It can be seen that pure water fluxes of membranes increased while seawater rejection decrease obviously, which probably due to the increase of the surface pore size.

Table 3. Concentrations of seawater before and after membrane separation process

	Pressure (bar)	Feed (Cf) g/l	Permeate (Cp) g/l	Rejection %
PSf/PVP-1%	2	23	21.7	5.7
PSf/PVP-2%	2	23	22	4.3
PSf/PVP-3%	2	23	22.2	3.5
PSf/PVP-4%	2	23	22.8	0.87

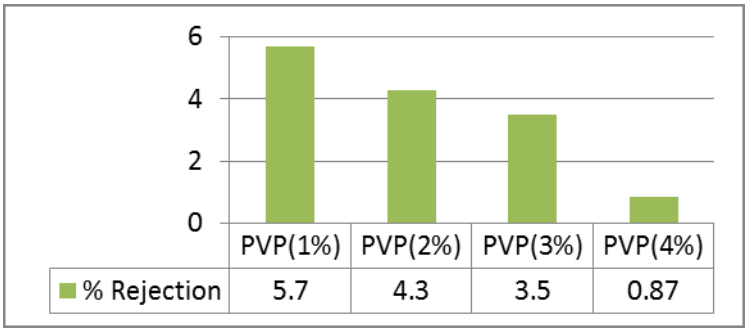


Figure 4. Percentage of seawater rejection with different % PVP content

Conclusion

The morphology of the membrane was observed by SEM. The top surface of the membrane was imaged at 7000x and 25000x magnification for all membrane. The result show the pore size was increase with increase of PVP content in the membrane solution. The cross section of all type of membranes show typical asymmetric membrane structure which consist of dense top layer and porous sub layer containing macro voids, pores and micro voids. The membrane composition PSf/PVP-1% with composition 20:1:79 (weight ratio) PSf/PVP/NMP has lower pore size with average pore size of 8.4 nm. Compared with PSf/PVP-4% with composition 20:4:76 (weight ratio) that have the highest pore size. Membrane PSf/PVP-1% has the highest rejection (5.7%) and lower flux (2.43 L/cm^2.hr) while PSf/PVP-4% has the highest flux (6.44 L/cm^2.hr) and lower rejection (0.87%). It is related with PVP content in the membrane solution. Increase PVP content will increase pore size, therefore it will increase flux while decrease the PVP content will decrease the pore size, therefore it will decrease flux but increase rejection

References

1. Ioannis, C., Karagiannis, P. and Soldatos, G. (2008). Water desalination cost literature: Review and assessment. *Desalination*, 223: 448-456.
2. Misdan, N., Lau, W. J. and Ismail, A. F. (2012). Seawater reverse osmosis (SWRO) desalination by thin-film composite membrane-current development, challenges and future prospects. *Desalination*, 287: 228-237.
3. Altaee, A., Zaragoza, G. and Tonningen, H. R. V. (2014). Comparison between forward osmosis-reverse osmosis and reverse osmosis processes for seawater desalination. *Desalination*, 336: 50-57.
4. Fang, Y., Bian, L., Bi, Q., Li, Q. and Wang, X. (2014). Evaluation of the pore size distribution of a forward osmosis membrane in three different ways. *Journal of Membrane Science,* 454: 390-397.
5. Zhao, S., Wang, Z., Wei, X., Tian, X., Wang, J., Yang, S. and Wang, S. (2011). Comparison study of the effect of PVP and PANI nanofiber additives on membrane formation mechanism, structure and performance. *Journal of Membrane Science*, 385-386: 110-122.
6. Chakrabarty, B., Ghoshal, A. K. and Purkait, M. K. (2008). Preparation, characterization and performance studies of polysulfone membranes using PVP as an additive. *Journal of Membrane Science*, 315: 36-47.

7. Song, H. J. and Kim, C. K. (2013). Fabrication and properties of ultrafiltration membranes composed of polysulfone and poly (1-vinypyrrolidone) grated silica nanoparticles. *Journal of Membrane Science*, 444: 318-326.
8. Derya, Y. and Koseoglu, L. (2013). The determination of performances of polysulfone (PS) ultrafiltration membranes fabricated at different evaporation temperatures for the pretreatment of textile wastewater. *Desalination*, 316: 110-119.
9. Sener, T., Okumus, E., Gurkan, T. and Yilmaz, T. (2010). The effect of different solvents on the performance of zeolite filled composite prvaporation membranes. *Desalination*, 261: 181-1185.
10. Yoo, S. H., Kim, J. K., Jho, J. Y., Won, J. and Kang, Y. S. (2004). Influence of the addition of PVP on the morphology of asymmetric polyimide phase inversion membranes: effect of PVP molecular weight. *Journal of Membrane Science*, 236: 203-207.
11. Zhao, S., Wang, Z., Wei, X., Tian, X., Wang, J., Yang, S. and Wang, S. (2011). Comparison study of the effect of PVP and PANI nanofiber additives on membrane formation mechanism, structure and performance. *Journal of Membrane Science*, 385-386: 110-122.
12. Zhang, P. Y., Wang, Y. L., Xu, Z. L. and Yang, H. (2011). Preparation of poly(vinybutyral) hollow fiber ultrafiltration membrane via wet spinning method using PVP as additive. *Desalination*, 278: 186-193.
13. Dieling, Z., Jian, Z., Kang, L. and Tai, S. (2017). Fluorographite modified PVDF membranes for seawater desalination via direct contact membrane distillation. *Desalination*, 413: 119-126.
14. Han, J., Yang, D., Zhang, S. and Jian, X. (2009). Effect of dope compositions on the structure and performance of PPES hollow fiber ultrafiltration membranes. *Journal of Membranes Science*, 345: 257-266.
15. Guan, R., Dai, H., Li, C., Liu, J. H. and Xu, J. (2006*).* Effect of casting solvent on the morphology and performance of sulfonated polyethersulfone membranes. *Journal of Membrane Science*, 277: 148-156.
16. Hu, D., Xu, Z. L., Wei, Y. M. and Liu, Y. F. (2014). Poly(styrene sulfonic acid) sodium modified nanofiltration membranes with improved permeability for the softening of highly concentrated seawater. *Desalination*, 336: 179-186.
17. Alireza, Z., Ahmad, R. and Mathias, U. (2017). Nano-sized metal organic framework to improve the structural properties and desalination performance of thin film composite forward osmosis membrane. *Journal of Membrane Science,* 531: 59-67.
18. Baker, R.W. (2004). Membrane technology and application. Membrane technology and research. John Wiley & Son Inc.: pp. 17-81.

Malaysian Journal of Analytical Sciences, Vol 22 No 1 (2018): 143 - 150
DOI: https://doi.org/10.17576/mjas-2018-2201-18

MALAYSIAN JOURNAL OF ANALYTICAL SCIENCES
Published by The Malaysian Analytical Sciences Society
ISSN 1394 - 2506

INFLUENCE OF ALKALI TREATMENT ON PHYSICO-CHEMICAL PROPERTIES OF MALAYSIAN BAMBOO FIBER: A PRELIMINARY STUDY

(Pengaruh Rawatan Alkali terhadap Sifat-sifat Fizikal-Kimia Serat Buluh Malaysia: Satu Kajian Awal)

Foo Sheng Tong[1]*, Siew Choo Chin[1, 2], Mohd Tamizi Mustafa[4], Huei Ruey Ong[3], Md. Maksudur Rahman Khan[2, 3], Jolius Gimbun[2, 3], Shu Ing Doh[1]

[1]Faculty of Civil Engineering & Earth Resources
[2]Centre of Excellence for Advanced Research in Fluid Flow (CARIFF)
[3]Faculty of Chemical & Natural Resources Engineering
University Malaysia Pahang, 26300 Gambang, Pahang, Malaysia
[4]Kualiti Kayu dan Hasil Bukan Kayu, Bahagian Keluaran Hutan,
Forest Research Institute of Malaysia, 52109 Kuala Lumpur, Malaysia

[*]Corresponding author: tongfoosheng@hotmail.com

Received: 4 December 2016; Accepted: 1 December 2017

Abstract

In the present study, the effect of alkaline treatment on the morphology and physico-chemical properties of Malaysian bamboo fibers was elucidated. The fibers were extracted from raw bamboo culm using alkaline solution with concentrations of 0 and 10 wt% at 24 hours and followed by roller milling techniques. The treated and untreated fibers were characterized by Fourier transform infrared spectroscopy (FTIR), thermogravimetric analysis (TGA) and scanning electron microscope (SEM). Apart from that, the mechanical properties of single fiber were also investigated. It was found that the tensile strength and modulus of the alkali-treated fiber were improved by 45.6 and 72%, respectively, compared to the untreated fiber. The surface morphology of the treated fiber was improved in which the surface roughness has been reduced significantly as proven in SEM. The FTIR and TGA data suggested that alkaline treatment gradually removed the lignin and hemicellulose. These findings highly recommended that, local bamboo fiber could be used as a reinforcement agent for composite making.

Keywords: alkaline treatment, bamboo fiber, natural fiber, natural fiber composite, roller milling techniques

Abstrak

Dalam kajian ini, kesan rawatan alkali terhadap sifat morfologi dan fizikokimia gentian buluh Malaysia telah dijelaskan. Serat telah diambil dari laras buluh mentah dengan menggunakan larutan alkali dengan kepekatan 0 dan 10% pada 24 jam dan diikuti dengan teknik penggilingan roller. Serat yang dirawat dan tidak dirawat dicirikan oleh spektroskopi transformasi Fourier (FTIR), analisis termogravimetrik (TGA) and mikroskop imbasan elektron (SEM). Selain itu, sifat mekanik serat tunggal juga disiasat. Keputusan telah didapati bahawa kekuatan tegangan dan modulus serat yang dirawat alkali telah meningkat sebanyak 45.6 dan 72%, berbanding dengan serat yang tidak dirawat. Morfologi permukaan serat yang dirawat telah diperbaiki dengan kekasaran permukaan berkurangan dengan nyata, seperti yang dibuktikan oleh SEM. Data FTIR dan TGA mencadangkan rawatan alkali telah menghilangkan lignin dan hemiselulosa secara beransur-ansur. Penemuan ini sangat disyorkan bahawa, serat buluh tempatan boleh digunakan sebagai ejen tetulang untuk pembuatan komposit.

Kata kunci: rawatan alkali, serat buluh, serat semulajadi, komposit gentian semulajadi, teknik penggilingan roller

Introduction

Synthetic fiber reinforced polymer (FRP) composite is an advanced external strengthening material which used to address the structurally deficient reinforced concrete (RC) member in the building industry. The most common type of artificial fibers in practice nowadays are made of glass, nylon, aramid, or carbon fiber. The efficient performance of a composite material of RC component has been witnessed by a number of researchers and practicing engineers. However, the production process of artificial fiber is adversely affecting the environment by consuming huge amount of fossil fuel as energy, releasing enormous carbon dioxide, causing heavy environmental loads, in addition to the high production cost. In order to achieve the economical, eco-friendly and renewable natural resource requirements, the investigation of various natural fibers as a potential substitution to the artificial fiber have been conducted tremendously [1]. It was found that the introduction of the natural fiber as reinforcement in polymer matrix composites (PMCs) is capable to enhance the mechanical properties and performance of virgin materials [2].

The benefits of natural fiber are renewable, recyclable and biodegradable in nature, low cost, light in weight and density, high specific stiffness and mechanical properties as well as low abrasion to manufacturing equipment [3]. The applications of cellulose are diverse, for instance, civilian construction, paper and pulp, furniture, packaging and storage, and automotive industry [3 – 6]. Nonetheless, it was found that not all the natural fibers are suitable to be utilized as reinforcement in composites. The development of agriculture is one of the greatest threat to the tropical forests. By considering the context of preserving the biodiversity, the plants that can be harvested several times in a growing cycle are the most favorable [7].

Bamboo fiber has been identified as the most attractive reinforcement material [8, 9]. The function of bamboo ranged for household goods (furniture, chopsticks, handicraft, and textiles) and industrial applications. Bamboo is a common construction material that is utilized by mankind. In China, it is usually employed as a temporary exterior structural member such as scaffolding and housing. Bamboo sticks were added to concrete to improve the flexural and compressive strength [10]. Bamboo fibers were distributed into concrete to upgrade the concrete strength [11]. Bamboo fiber is also recognized as a typical natural composite material which offering extraordinary benefits over other natural fibers [12]. It is one of the fastest growing woody plants due to its unique rhizome-dependent system. The complete recovery growth period of bamboo can be done within two to three years prior to utilize. Moreover, the productivity of an acre of bamboo is greater than cotton about 10 times [13]. In Malaysia, where a tropical rainforest climate is all year round apparently, the accessibility and abundant availability of economical bamboo fibers are addressing the sustainable technology which can solve the disadvantages of the synthetic fibers. The mechanical properties of bamboo fiber are advantageous primarily because of its unidirectional fiber arrangement in the tissue and cellulose being its major constituent [14]. The unidirectional fiber consisting of parallel and long cellulose that embedded in ground tissues in ligneous matrix form [1].

All of the aspects of bamboo fiber have fulfil the latest material of structural upgradation criterion [11]. Yet, there were not enough studies had been conducted on the use of bamboo fiber as reinforcement to enhance the behaviour of the RC members externally. Most of the investigation of natural fibers as structural reinforcement is focused on kenaf, jute and sisal fibers [15 – 17]. The present study aims to study the influence of the alkaline treatment on physical-chemical properties of local bamboo fiber. Besides that, the effect of alkaline treatment on the mechanical properties of fibers was also elucidated.

Materials and Methods

Materials

The local bamboo species, *Gigantochloa scortechinii Gamble* of age range from three to five years old were used due to its commercialized viable and high strength feature. The raw bamboo culms were harvested by the laborers at the tropical forest in Raub district, Pahang, Malaysia. The obtained bamboo culms were delivered and stored in the shade at Non-wood Product Workshop at Forest Research Institute Malaysia (FRIM) which situated at Kepong, Selangor Darul Ehsan.

Extraction of fibers

The bamboo culms were cleaved using heavy-duty bamboo splitters into strips in approximately 30 x 15 x 1500 mm. The aqueous NaOH solution was prepared by dissolving the NaOH pellets in distilled water. The bamboo

strips were treated with 10% NaOH solution for 24 hours at ambient temperature. On the other hand, another batch of bamboo strips was immersed under the distilled water for 24 hours, served as control specimens. The alkali-treated bamboo strips were washed and immersed in the distilled water for 12 hours. Then the bamboo strips were placed into the mill roller machine to obtain the fibers and remove the impurities. The bamboo fibers were produced during the milling process. Then, the bamboo fibers were rinsed with distilled water several times to remove the alkaline content followed by examining using Universal Indicator Paper. The fiber with a pH of 6 was dried in an electrical oven at 60 °C for 24 hours. The fibers were stored in a desiccator with silica gel prior to characterization after drying in the oven. Figure 1 depicts macroscopic photographs of alkali treated bamboo fibers.



Figure 1. Macroscopic photograph of alkali treated bamboo fibers

Characterization: Single fiber tensile test

Ten (10) single fiber specimens were prepared according to ASTM C1557-14 standard. The determination of tensile strength and modulus of bamboo fibers was carried out at an ambient temperature of 24.9 °C with a relative humidity of 55%. The specimens for testing were prepared by mounting a single fiber on a paper frame with a span length of 25.4 mm. A vicinity in diamond shape of length equivalent to the gauge length was cut out in the middle of the mounting tab. Both ends of the fiber were glued on the paper with epoxy based adhesives. The tests were conducted using an Instron 50 kN Blue Hill 3369 Universal Testing Machine (UTM). The crosshead speed was recorded at 0.48 mm/min. Both sides of the mounting tab had been cut at mid-gauge to release the fiber specimen before testing. The average diameter of the bamboo fiber was measured directly from the images on projection screen using an optical microscope MarVision MM 320. A total of three measuring points was taken at different locations along the gauge length of each fiber specimen. The average diameter was used to calculate the average cross-sectional area of the bamboo fiber by assuming that the fibers are in cylindrical shape. The diameters of the alkali treated bamboo fibers were in the ranged of 90-580 μm. In contrast, the diameter of the untreated fibers was ranged from 120-650 μm.

Scanning electron microscope

The surface morphology and microstructure of alkali-treated and raw bamboo fibers were examined using Hitachi (Japan) TM3030 Plus Benchtop Scanning Electron Microscope (SEM).

Fourier transform infrared spectroscopy

The Fourier transformed infrared spectrum of the bamboo fibers were performed using a Thermo Scientific Model Smart Performer attenuated total reflectance (ATR) accessory of Ge crystal, attach to a Thermo Scientific spectrophotometer (Model Nicolet iS50) with a single bounce. The wavenumber range of 500 – 4000 cm^{-1} with a resolution of 4 cm^{-1} and an average of 32 scans per minute were adopted. The bamboo fibers were ground into powder form before use in this characterization.

Thermogravimetric analysis

The thermal stability of alkali-treated and untreated bamboo fibers were examined by the thermogravimetric analyzer (STA7000, Hitachi). The equipment was programmed under nitrogen atmosphere in the temperature range of 30 to 800°C at a heating rate of 10°C/min and purge rate of 60 mL/min. The percentage of weight loss of the sample was calculated as follows:

$$\text{Percentage of weight loss} = (W_1 - W_2)/W_1 \times 100\% \quad (1)$$

where, W_1 = Sample weight before testing and W_2 = Sample weight at any given temperature.

Results and Discussion

Tensile properties

The tensile properties of raw and alkali-treated bamboo fibers are summarized in Table 1. It can be seen that, all the tested fibers failed. Bamboo fiber possessed a comparable strength to that of the artificial glass fibers as reported in the previous study [18]. Both tensile strength and modulus of the bamboo fibers were improved after the alkaline treatment. The highest tensile strength of the alkali-treated fiber was 368.33 MPa in contrast to the raw fiber of 252.93 MPa. On the other hand, the average tensile modulus of raw and alkali-treated bamboo fibers was 10.89 and 27.93 GPa, respectively. A maximum enhancement of tensile strength was obtained approximately 115.4 MPa or 45.6% is accomplished by NaOH treatment. Besides that, an increased in tensile modulus (23.14 GPa or 72%) was also established by the alkaline treatment. The improvements of the tensile properties had agreed with the previous study [3], due to the cementing materials like lignin and hemicellulose were eliminated during the alkaline treatment, which leads to an increment of the effective fiber surface area and roughness.

Table 1. Tensile properties of tested bamboo fibers

Properties	Bamboo Fibers	
	Untreated	Treated
Ultimate Tensile Strength (MPa)	252.93	368.33
Average Tensile strength (MPa)	140.10±22.26	267.44±51.89
Ultimate Tensile Modulus (GPa)	32.10	55.24
Average Tensile Modulus (GPa)	10.89±2.6	27.93±5.97

Surface morphology analysis

The surface morphology of alkali-treated and untreated bamboo fibers are presented in Figure 2. Referring to Figure 2(a), the surface of the untreated fiber was covered by a superficial layer of impurities, which may include lignin, pectin, and other debris. On the contrary, most of the hemicellulose, lignin and other extractives were removed from the alkali-treated fiber surface (Figure 2(b)), which led to the formation of effective fiber surface attached with some tiny fissures and joints [1]. The increased in the cleanness and the smoothness of the fiber surface promotes the bonding reaction and interlocking adhesion which increased the adhesion of fiber–matrix due to the hydroxyl groups' exposure to the matrix. Furthermore, the separation of cemented fibers reduced the fiber diameter, resulting to a higher aspect ratio [1].

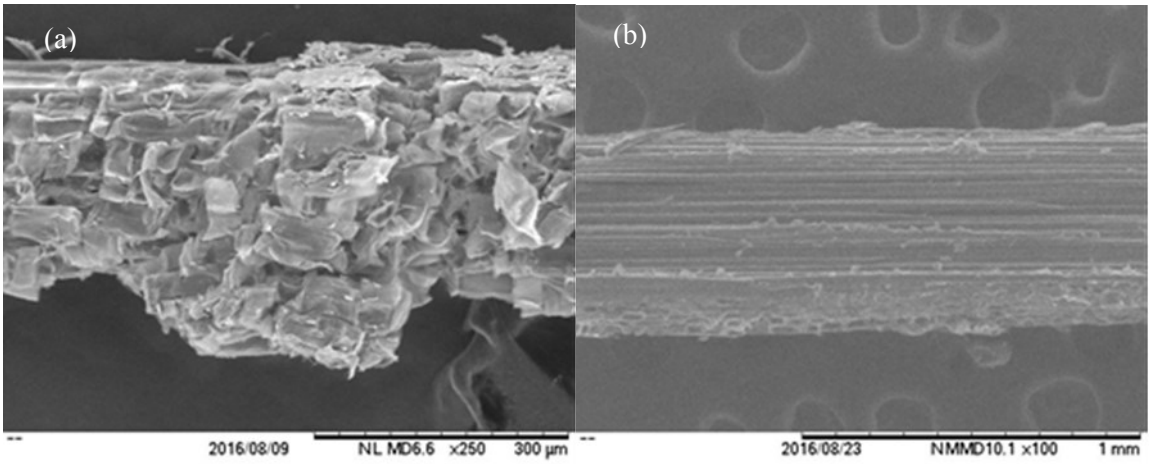


Figure 2. SEM images for longitudinal-section of (a) raw and (b) alkali-treated bamboo fiber

FTIR analysis

A comparison of the FTIR spectra of the alkali-untreated and treated bamboo fibers are illustrated in Figure 3. Multi part of the samples were represented by a number of absorption peaks. The comparison between the spectra were established on the relative intensity of the peaks, taking as the band at 897 cm^{-1}, which attributed to C-O stretching vibration of amorphous cellulose, which indicates the β-glycosidic linkage between the monosaccharides [1, 19]. The absorption peak at 1403 and 1140 cm^{-1} were the typical peak of cellulose in the natural fiber. The broad characteristics band of hydrogen bonded (O-H) stretching vibration can be seen from the wavenumber ranged from 3665 – 3013 cm^{-1} [3], the peak occurred at 3338.42 cm^{-1}. While this peak was shifted to 3338.38 cm^{-1} after NaOH treatment. This phenomenon could be explained by the rising of hydroxyl group due to alkali-sensitive material is wiped off during treatment. The vibration peak at approximate of 1513.05 cm^{-1} was attributed to the stretching vibrational of pectin and hemicellulose and 2987.14 cm^{-1} was corresponding to the stretching of aromatic rings and alkane (C-H) stretching vibration in methyl and methylene, whereas for the alkali-treated fiber, this peak was decreased and moved to 2985.14 cm^{-1}, caused by the removal of cementing materials. The raised peak at 1604 cm^{-1} could be defined by the presence of lignin. The absorption band from the range of 1765 - 1612 cm^{-1} was derived from the vibrational stretching of unconjugated carbonyl stretching (C=O) of pectin and hemicellulose. This band was decreased in the alkali-treated fiber IR spectrum, which could be due to the partial removal of lignin and hemicelluloses. Additionally, the vibrational stretching at the range of 1267 – 1239 cm^{-1} which attributed to the C-O of acetyl functional groups in the hemicelluloses and lignin was reduced during the NaOH treatment. The ester bond of raw fiber at 1033.27 cm^{-1} also showed the high C-O or C-C stretching of lignin and hemicellulose for raw bamboo fiber. The remarkable reduction in the intensity of the bamboo fiber after alkaline treatment indicates that the impurities and hemicellulose of the fiber surface were partially eliminated by the NaOH treatment, with no new functional groups are introduced in the cellulose molecules. These improvements are consistent with the observation of the alkali-treated fiber surface from the SEM micrographs, which indicated a reduction of cementing materials as reported by previous studies [1, 2, 7].

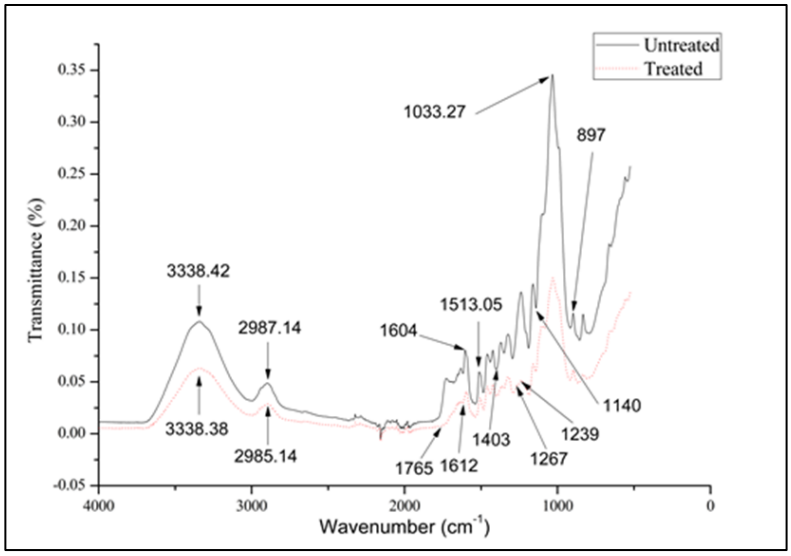


Figure 3. FTIR-ATR spectra of the alkali untreated and treated bamboo fiber

Thermal analysis

The TGA curve of raw and alkali-treated fiber is depicted in Figure 4. As can be seen from the weight loss curve, the degradation profiles of the both fibers are defined by three thermal decomposition stages. The alkalized bamboo fiber experienced minor weight loss as compared to the raw fiber. The first weight loss existed between 30 and 100 °C, which were the moisture evaporation of the fiber. The corresponding weight loss was approximately 7%. Meanwhile, the evaporation of moisture was found to be reduced in the alkali-treated fiber due to NaOH treatment caused a reduction in hydrophilicity of the fiber. The next degradation, so called initial degradation or onset temperature (T_{onset}) of the decomposition commenced in the range of 235 – 342 °C was mainly caused by the decomposition of the cellulose.

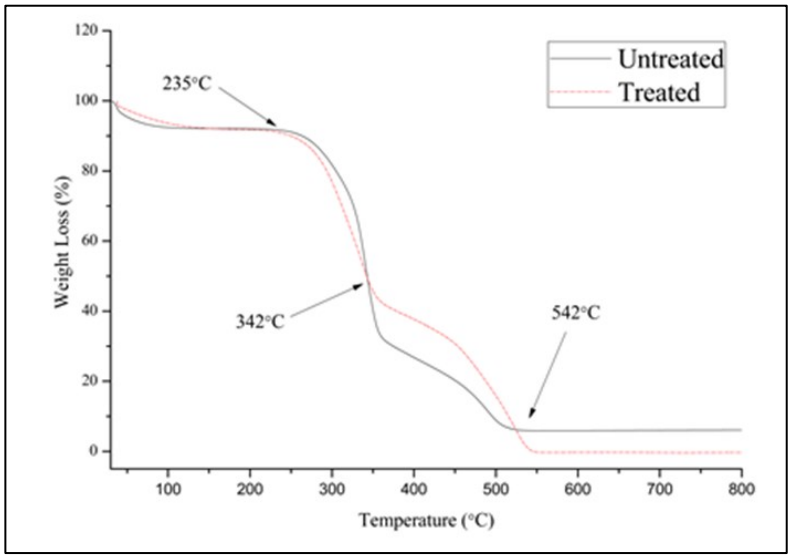


Figure 4. TGA curve of untreated and alkali treated bamboo fibers

The degradation temperature (T_d) for both raw and treated fibers was similar, which recorded at 343 °C. In the following weight loss step, the decomposition of non-cellulosic materials (lignin) occurred at the lower decomposition rate and broad temperature range, from 356 to 542 °C, due to lignin being difficult to decompose. The bamboo fibers were completely degraded at the temperature of approximately 542 °C. The distinction in weight loss indicated the partial removal of lignin and hemicellulose materials. The overall degradation temperature of the NaOH treated fibers possessed a higher thermal stability. These results are almost identical to those reported elsewhere [1, 2, 20].

Conclusion

The alkaline treatment has been identified as a significant factor for the reinforcement agent properties. FTIR analysis confirmed the removal of extractives, hemicellulose and lignin. Furthermore, no new functional group was noticed for the alkali-treated fiber. The alkaline treated fiber exhibited better thermal stability than untreated fiber, as the cementing material was removed via the alkaline treatment. Moreover, it can be associated with SEM images, where the surface smoothness of the treated fiber was better than untreated fiber. The tensile strength and modulus of the bamboo fiber were significantly improved after treated with 10% NaOH treatment for 24 hours. In comparison with raw fiber, the increment in tensile strength and modulus were about 45.6 and 72%, respectively. From the findings, the local abundant and economic bamboo fiber has the potential to be used as a reinforcement agent in developing composite materials for the construction industry.

Acknowledgement

This research is assisted by the Ministry of Higher Education (MOHE), Malaysia under the Research Acculturation Grant Scheme (RAGS) RDU 151409. The authors would like to express their gratitude to the Forest Research Institute of Malaysia (FRIM), Center of Excellence for Advanced Research in Fluid Flow (CARIFF), and laboratory of Faculty of Civil Engineering and Earth Resources (FKASA), University Malaysia Pahang (UMP) for the facilities and testing equipment provided.

References

1. Zhang, X., Wang, F. and Keer, L. M., (2015). Influence of surface modification on the microstructure and thermo-mechanical properties of bamboo fibers. *Materials,* 8: 6597 - 6608.
2. Simão, J.A., Carmona, V.B., Marconcin, J.M., Mattoso, L.H.C., Barsberg, S.T. and Sanadi, A.R. (2016). Effect of fiber treatment condition and coupling agent on the mechanical and thermal properties in highly filled composites of sugarcane bagasse fiber/pp. *Materials Research,* 19(4): 746 - 751.
3. Hossain, S. I., Hasan, M., Hasan, M. N. and Hassan, A. (2013). Effect of chemical treatment on physical, mechanical and thermal properties of ladies finger natural fiber. *Advances in Materials Science and Engineering,* 2013: 1- 7.
4. Dalbehera, S. and Acharya, S. K. (2014). Study on mechanical properties of natural fiber reinforced woven jute -glass hybrid epoxy composites. *Advances in Polymer Science and Technology: An International Journal,* 4(1): 1 - 6.
5. Alves, C., Ferrão, P. M. C., Silva, A. J., Reis, L. G., Freitas, M., Rodrigues, L. B. and Alves, D. E. (2010).Eco design of automotive components making use of natural jute fiber composites. *Journal of Cleaner Production,* 18(4): 313 - 327.
6. Summerscales, J., Dissanayake, N. P. J., Virk, A. S. and Hall, W. (2010). A review of bast fibres and their composites. Part 1 - Fibres as reinforcements. *Composites Part A: Applied Science and Manufacturing,* 41(10): 1329 – 1335.
7. Elenga, R. G., Djemia, P., Tingaud, D., Chauveau, T., Maniongui, J. G. and Dirras, G. (2013). Effects of alkali treatment on the microstructure, composition, and properties of the raffia textiles fiber. *BioResources,* 8(2): 2934 - 2949.
8. Zakikhani, P., Zahari, R., Sultan, M. H. and Majid, D. L. (2014). Bamboo fibre extraction and its reinforced polymer composite material. *International Journal of Chemical, Nuclear, Materials and Metallurgical Engineering,* 8(4): 287 – 290.
9. Biswas, S., Shahinur, S., Hasan, M. and Ahsan, Q. (2015). Physical, mechanical and thermal properties of jute and bamboo fiber reinforced unidirectional epoxy composites. *Procedia Engineering,* 105: 933 - 939.

10. Ahmad, S., Raza, A. and Gipta, H. (2014). Mechanical properties of bamboo fibre reinforced concrete. In: 2nd *I nternational conference on research in science, engineering and technology (ICRSET 2014).* Dubai (UAE): pp 162 - 166.
11. Vajje, S. and Murthym N. R. K. (2013) Study on addition of the natural fibers into concrete. *International Jour nal of Scientific & Technology Research,* 2 (11): 213 – 218.
12. Zakikhani, P., Zahari, R., Sultan, M. T. H. and Majid, D. L. (2014). Extraction and preparation of bamboo fibre -reinforced composites. *Materials and Design,* 63: 820 - 828.
13. Afrin, T., Tsuzuki, T. and Wang, X. (2009). Bamboo fibres and their unique properties. *Bamboo Bulletin,* 11(1): 36 - 39.
14. Liu, H., Huang, Y., Yuan, L., He, P., Cai, Z., Shen, Y., Xu, Y., Yu, Y. and Xiong, H. (2010). Isothermal crystallization kinetics of modified bamboo cellulose/PCL composites. *Carbohydrate Polymer,* 79(3): 513 – 519.
15. Alam, M. A., Nouri, K. and Jumaat, M. Z. (2015). Flexural strengthening of reinforced concrete beam using jute rope composite plate. *In: The 3rd national Graduate conference (NatGrad2015)*: pp. 8 - 9.
16. Hafizah, N. A. K., Bhutta, M. A. R., Hamaludin, M. Y., Warid, M. H., Ismail, M., Rahman, M. S., Yunus, I. and Azman, M. (2014). Kenaf fiber reinforced polymer composites for strengthening RC beams. *Journal of Advanced Concrete Technology,* 12(6): 167 - 177.
17. Sen, T. and Jagannatha Reddy, H. N. (2014). Flexural strengthening of RC beams using natural sisal and artificial carbon and glass fabric reinforced composite system. *Sustainable Cities and Society,* 10: 195 - 206.
18. Okubo, K., Fujii, T. and Yamamoto, Y. (2004). Development of bamboo-based polymer composites and their mechanical properties. *Composites: Part A: Applied Science and Manufacturing,* 35(3): 377 - 383.
19. Ramli, R., Khan, M. M. R., Yunus, R. M., Ong, H. R., Halim, R. M., Aziz, A. A., Ibrahim, Z. and Zainal, N. H. (2014). In-situ impregnation of copper nanoparticles on palm empty fruit bunch powder. *Advances in Nano-particles,* 3: 65 - 71.
20. Chowdhury, M. N. K., Beg, M. D. H., Khan, M. R. and Mina, M. F. (2013). Modification of oil palm empty fruit bunch fibers by nanoparticle impregnation and alkali treatment. *Cellulose,* 20(3): 1477 - 1490.

Malaysian Journal of Analytical Sciences, Vol 22 No 1 (2018): 151 - 156
DOI: https://doi.org/10.17576/mjas-2018-2201-19

MALAYSIAN JOURNAL OF ANALYTICAL SCIENCES
Published by The Malaysian Analytical Sciences Society
ISSN 1394 - 2506

STUDIES ON PHYTOCHEMICAL CONSTITUENTS AND ANTIMICROBIAL PROPERTIES OF *Citrullus lanatus* PEELS

(Kajian Jujukan Fitokimia dan Antimikrob Kulit C*itrullus lanatus)*

Siti Suhaila Harith[1]*, Muhd Harith Mazlun[1], Marlina Mohd Mydin[2], Liliwirianis Nawi[1], Rohaiza Saat[3]

[1]*Faculty of Applied Sciences,*
Universiti Teknologi MARA Pahang, 26400 Jengka, Pahang, Malaysia
[2]*Faculty of Applied Sciences,*
Universiti Teknologi MARA Perak, 35400 Tapah, Perak, Malaysia
[3]*Faculty of Applied Sciences,*
Universiti Teknologi MARA Negeri Sembilan, 72000, Kuala Pilah, Negeri Sembilan, Malaysia

**Corresponding author: ssuhaila@pahang.uitm.edu.my*

Received: 4 December 2016; Accepted: 1 December 2017

Abstract

Citrullus lanatus is one of many species that are categorized under the genus *Citrullus,* which originates from Family Cucurbitaceae, the gourd family. It has been scientifically proven that many members of this family possessed pharmaceutical and medicinal values such as *Cucurbit pepo* (pumpkin), *Citrullus colocynthis* (bitter cucumber) and *Citrullus lanatus* (watermelon) is one of them. The aim of this study is to determine its phytochemical constituents and potential antimicrobial activity of *C. lanatus*, particularly in its peels. The peels were put under sequential extraction process involving two types of solvents, namely, methanol and hexane. *Citrullus lanatus* extracts were then evaluated in terms of its phytochemical constituents, by six qualitative phytochemical screening tests. In assessing *C. lanatus* potential antimicrobial activity, the peels extract were tested on two types of microorganisms, which are *Staphylococcus epidermidis* and *Trichophyton mentagrophytes* by using disk-diffusion method. For both solvents used, phytochemical screening tests verified the presence of alkaloid, flavonoid, saponin, tannin and terpenoid, except for phenolic compounds in the fruit peels. Result of antimicrobial activity revealed that *C. lanatus* peels extract impeded growth to both tested microorganisms. In conclusion, present study suggested that *C. lanatus* can be further developed to utilize its medicinal and pharmaceutical values.

Keywords: antimicrobial, *Citrullus lanatus*, disk-diffusion, phytochemical, sequential extraction

Abstrak

Citrullus lanatus merupakan salah satu daripada banyak spesies di bawah genus *Citrullus* yang berasal dari keluarga Cucurbitaceae, keluarga labu. Ia telah terbukti secara saintifik bahawa banyak ahli keluarga ini memiliki nilai farmaseutikal dan nilai perubatan dan tidak terkecuali *Cucurbit pepo* (labu), *Citrullus colocynthis* (timun pahit) dan *Citrullus lanatus* (tembikai). Tujuan kajian ini adalah untuk menentukan juzuk fitokimia dan potensi aktiviti antimikrob *C. lanatus*, terutamanya kulit. Kulit diekstrak secara berperingkat yang melibatkan dua jenis pelarut iaitu, metanol dan heksana. Ekstrak *C. lanatus* kemudiannya dinilai dari segi juzuk fitokimia, oleh enam ujian saringan fitokimia kualitatif. Dalam menilai *C. lanatus* aktiviti antimikrob yang berpotensi, ekstrak kulit yang telah diuji ke atas dua jenis mikroorganisma iaitu *Staphylococcus epidermidis* dan *Trichophyton mentagrophytes* menggunakan kaedah cakera resapan. Bagi kedua-dua pelarut yang digunakan, ujian saringan fitokimia mengesahkan kehadiran alkaloid, flavonoid, saponin, tanin dan terpenoid kecuali sebatian fenolik dalam kulit buah. Keputusan aktiviti antimikrob mendedahkan bahawa ekstrak kulit *C. lanatus* merencat pertumbuhan kedua-dua mikroorganisma yang diuji. Kesimpulannya, kajian ini mencadangkan bahawa *C. lanatus* mempunyai nilai-nilai perubatan dan farmaseutikal yang boleh dibangunkan.

Keywords: antimikrob, *Citrullus lanatus*, cakera resapan, fitokimia, pengekstrakan secara berperingkat.

Introduction

Medicinal plants or also known as natural remedies have been used since earliest times of mankind history. Although scientifically proven details about the chemical compounds in the plants were not yet discovered at those times, people had widely gained benefits from using the plants as medication. In fact, people from either developed or developing countries around the world are still consuming natural medications until today. In Malaysia, some of the serious ill-inflicted patients have turned to plant-based medications instead of common drugs in the hospital, such as using grape seed extracts to suppress cancer cells. The effectiveness of those extracts against cancer was stated by Sravanthi et al. [1].

Watermelon or scientifically known as *Citrullus lanatus* is among the favourite fruits for many people in the world. It is mainly composed of water, which is about 6% sugar and 92% water by weight. Watermelon belongs to Cucurbitaceae Family under Genus *Citrullus* [2]. Cucurbitaceae is a family that comprises of approximately 120 genera and over 900 species which is vastly distributed in tropical and subtropical regions of, Asia, Australia, Africa and America [3]. Genus *Citrullus* consists of basically four species; *C. colocynthis*, *C. ecirrhosus*, *C. rehnii* and *C. lanatus*. The fruits are usually oblong, ovoid or ellipsoid in shape with elliptical, flattened seeds that are commonly brown or black in colour,and uncommonly white in colour.

Phytochemical constituents or also known as secondary plant metabolites can be defined as non-nutritive chemicals naturally produced by plants. There are thousands of known and unknown phytochemical compounds such as alkaloids, anthocyanins, carotenoids, flavonoids, alkaloids, tannins, monoterpenes, phenolic acids, saponin and terpenoid. These chemicals are responsible in determining their characteristics; the aroma, colour and flavour. However, the main role of these chemicals is as protection and defence for the plants against diseases and damage. Phytochemical compound can be classify into its different bioactive and anti-diseases properties; antibacterial properties are demonstrate by terpenoids, alkaloids and phenolic while anticancer properties are exhibit by carotenoids and flavonoids [4].

Referring to past researches, several members from this family do possessed positive antimicrobial, antifungal and anti-parasite properties. *Cucumis melo* are capable in suppressing both bacteria and fungus [5]. Result from the study has shown that *C. melo* extracts exhibited resistance against several bacteria and fungus. In separate study by Gurudeeban et al. [6], *C. colocynthis* has shown broad-spectrum antimicrobial activity against 16 clinical microorganisms isolated from HIV positive patients. *Cucurbit pepo* seeds extracts, also known as pumpkin, are useful against intestinal parasites [7, 8]. The positive antimicrobial, antifungal and anti-parasite properties are shown in all three representatives sp chosen. Thus, *C. lanatus* which comes from the same family may have the potential to exhibit one of the stated properties.

Citrullus lanatus is one of the species originated from genus *Citrullus*. In Malaysia, it is locally known as "Tembikai Air". *Citrullus lanatus* is being widely studied in previous researches particularly on its fruits and leaves, but only a small scale of them explored into its peels. Thus, this study was aimed to determine the phytochemical constituents and potential antimicrobial activity of *C. lanatus* peels.

Materials and Methods

Plant sample collection

Citrullus lanatus fruits were bought from the nearby fruit stalls and the peels were collected and kept in sterilized container.

Plant sample extraction

The fruit peels were chopped into small pieces so that its surface area can be increased. The fruit peels were then dried in the oven for 4 days. Once dried, they were grounded into powder by using a grinder. The ground material were mixed thoroughly and left soaked in methanol. After that, the solution was filtered by using cloth strainer and paper filter. Later, the filtrate was evaporated using rotary evaporator. Evaporation from rotary evaporator yielded methanol crude extract. The crude extract was collected and stored in a beaker that had first been autoclaved and

was sealed using aluminium foil and parafilm at the cool room to prevent contamination of other microorganism [9]. The peel powder that previously soaked with methanol was then soaked in hexane, a process that is called as sequential extraction. Steps in collecting crude methanol extract were repeated to obtain crude hexane extract.

Qualitative phytochemical screening: Alkaloid determination
Alkaloids presence was determined through Meyer's and Wagner's test. 1 g of powdered sample was mixed with 5 ml methanol and 5 ml of 2M HCl. Then, the filtrate was treated with Meyer's and Wagner's reagent. The presence of alkaloid was denoted by the formation of precipitate [10].

Flavonoid determination
Methanol and hexane extract of *C. lanatus* peels were added with a small piece of magnesium ribbon. Concentrated hydrochloric acid was added to the solution. Changes of colour from orange to red, crimson or magenta indicated the presence of flavonoid [11].

Saponin determination
Saponin presence was determined through froth test. 2 g of powdered sample was boiled in 20 ml of distilled water for 30 minutes. The boiled solution was allowed to cool and then was filtered. 10 ml of the filtrate was added with 5 ml of distilled water. The solution was vigorously shaken for 15 minutes to detect any appearance of froth [12].

Phenolic compounds determination
Phenolic compounds were determined through ferric chloride test. 1.0 g of extract powder was added with 2 ml water and few drops of 10% ferric chloride. Blue and green coloration indicated the presence of phenolic compounds.

Tannin determination
Tannin presence was determined through ferric chloride test. An amount 0.5g of the crude powder extract of sample was boiled in 20 ml of water in a test tube. The solution was then filtered. The filtrate was then added with a few drops of 0.1% ferric chloride. Development of brownish-green and blue-black coloration indicated the presence of tannin.

Terpenoid determination
Terpenoid presence was determined through Salkowski test. An amount 2 ml of chloroform was mixed thoroughly with the sample extract solution. Next, 3 ml of concentrated sulfuric acid was carefully added to form a layer. A reddish brown coloration of the interface indicated the presence of terpenoids.

Antimicrobial assays: Disk-diffusion method
To test the antimicrobial activity, disk-diffusion method was applied. Firstly, nutrient agar and petri plates were sterilized through autoclaving. An amount 20 ml of agar medium was dispensed into petri plate in sterile conditions in a laminar flow to obtain plates of a uniform depth of 4 mm. The overnight inoculums containing *S. epidermidis* and *T. mentagrophytes* cells/ml were spread onto the surface of the solidified nutrient agar plates. Due to limited crude extract availability, crude extract was measured and used on mg of extract solute per ml of solvent basis.

For methanol crude, antimicrobial discs were impregnated into *C. lanatus* extracts of different concentrations namely 20, 40, 60, 80, 100 mg/ml. For hexane crude extract, only concentration of 20, 40, 60, 80 mg/ml were applied. By using sterile forceps, the discs containing the plant extracts were laid down on the surface of inoculated agar plate. The plates were incubated at 37 °C for 24 hours and the diameter of the zone of inhibition was measured in millimeter. Minimum inhibitory concentration (MIC) can be understood as the lowest concentration of antimicrobial agent at which a microorganism fails to exhibit visible growth on agar plate. Positive control for fungus and bacteria was nystatin and commercial ampicillin respectively. The negative control for fungus and bacteria was methanol and hexane themselves.

Results and Discussion

Qualitative phytochemical screening of *Citrullus lanatus*

Phytochemical test of *C. lanatus* peels, as illustrated in Table 1, shows methanol extract, *C. lanatus* peel yielded positive result to five out of six phytochemical namely alkaloid, flavonoid, saponin, phenolic compounds, tannin and terpenoid. The result also revealed that hexane extract of *C. lanatus,* in general, only yielded positive result from three out of six phytochemicals tests, where all remaining tests had shown negative result. Hexane extract contained alkaloid, saponin, terpenoid but flavonoid, phenolic compounds and tannins were not detected in it. For both methanol and hexane extracts of *C. lanatus*, it can be seen that phenolic compounds were absent in both type of extract.

Table 1. Qualitative phytochemical screening test of *C. lanatus* peel sample

Test	Methanol peel extract	Hexane peel extract
Alkaloid	+	+
Flavonoid	+	-
Saponin	+	+
Phenolic	-	-
Tannin	+	-
Terpenoid	+	+

Note: - = absent; + = present

According to Saxena et al. [4], three phytochemicals that were crucial in combating microorganisms including bacteria and fungus are terpenoids, phenols and alkaloids. Referring to Table 1, though phenols were absent, terpenoids and alkaloids were present in both type of extract. Thus, the presence of antimicrobial activity and positive test for phytochemical in the *C. lanatus* peels were responsible in the emergence of its antifungal and antibacterial property. Flavonoid was mainly functioned in antioxidants [13]. As flavonoid was present in *C. lanatus* peels, it can be expected then that these peels would make antioxidants remedy. Saponins were present in both of the peels extracts hold a pivotal role in killing insects particularly pests [14]. Thus, *C. lanatus* peels may have potential in serving as insecticide. Apart from that, the positive result of tannin as shown in the table may indicate that *C. lanatus* peels can be further explored and studied in terms of the tannin content as the phytochemical is beneficial in antidiarrheal, haemostatic and antihemorrhoidal [15].

Antimicrobial activity test

As depicted in the Table 2, it was generally revealed that both methanol and hexane extracts exhibited antibacterial and antifungal properties [16]. This was relevant as the anti-microorganisms phytochemicals (terpenoids, alkaloids) were present in either of the extract. However, the table has obviously shown that methanol extract of *C. lanatus* exhibited slightly stronger anti-microorganisms properties than hexane extract. The higher concentration of terpenoids and alkaloids in methanol as compared to hexane may possibly explain this situation.

Methanol extract displayed the strongest inhibition zone to *S. epidermidis* under 20 mg/ml of its concentration. The inhibition zone decreased to moderate level of inhibition and was maintained for the next three consecutive concentrations. At the highest concentration, zone of inhibition ceased. It can be therefore stated that the minimum inhibitory concentration (MIC) of methanol extract on *S. epidermidis* was at 20 mg/ml. Meanwhile, in *T. mentagrophytes,* the table exhibited that the zone of inhibition resulted by methanol extract was increasing through applying increasing concentrations of the extract. The MIC of methanol extract on *T. mentagrophytes* was also at 20 mg/ml.

Table 2. Antimicrobial activity of the *C. lanatus* peel extracts

Extract	Concentration (mg/ml)	Zone of Inhibition (mm)	
		SE	TM
Methanol	20	+++	++
	40	++	++
	60	++	++
	80	++	+++
	100	-	+++
Nystatin		-	++
Ampicillin		+++	-
Hexane	20	+	++
	40	+	++
	60	++	-
	80	-	-
Nystatin		-	+++
Ampicillin		++	-

SE: *Staphylococcus epidermidis*;
TM: *Trichophyton mentagrophytes*;
- = no inhibition zone;
+ = weak inhibition zone (≤ 4 mm);
++ = moderate inhibition zone (5-9 mm);
+++ = strong inhibition zone (≥10 mm)

Table 2 also portrayed that, for testing upon *S. epidermidis*, hexane extract generally resulted weak inhibition zone when using first two concentrations; 20 mg/ml and 40 mg/ml. At the concentration of 80 mg/ml), the zone of inhibition was absent. It can also be observed on the table that the MIC of hexane extract on the bacteria was 20 mg/ml. When tested on dermatophyte *T. mentagrophytes*, it can be seen from the Table 2 that the zone of inhibition had shown a decreasing trend through increasing of concentration used. The diameter of inhibition zone started at a moderate size and was consistent on the first two concentrations and then ceased for the last two concentrations. The MIC was 20 mg/ml. The antimicrobial properties of both extract suggested to concentration independent which is in others word time dependent. The percentage of time larger than MIC is associated with concentration-independent killing and short post-antifungal effect [17].

Previous study on antimicrobial activity of ethanol (polar solvent) and hexane (non-polar solvent) extracts of *C. lanatus* leaves, stems, fruits and seeds by Rahman et al. [18] can be used as reference point. Methanolic extracts exhibit strong antibacterial and antifungal property compare to hexane extracts. This explains that the phytochemical constituents in the fruits have similarities to that of peels.

Conclusion

Bactericidal and antifungal effects shown by two different extracts of *C. lanatus* peels on two types of microorganisms; a bacteria and a fungal, suggest that *C. lanatus* peels may provide opportunity for utilizing its potential as new herbal drug. Other phytochemicals that present in the peels beside the ones responsible for anti-microorganisms activities may open up a new ground for further studies to explore its other possible potential medicinal values and importance. Apart from stems, leaves, seeds and fruits of *C. lanatus* that displayed therapeutic actions which had been observed in previous studies, it can be concluded from this study that *C. lanatus* peels also possess the same capability.

Acknowledgement

The authors would like to acknowledge Suhairi bin Suib, Nor Hafidzan bin Mahbob, Fauzie bin Idrus, Azman bin Mohd Nor, Zairus binti Ismail and Nur Hanis binti Mohd Yasim for their help to grant the success of this research.

References

1. Sravanthi, K. N., Unissa, R., Prashanth, Y. and Sudhakar, M. (2013). Grape seed extract-a therapeutic review. *International Journal of Pharmacy and Pharmaceutical Sciences*, 3(2): 323-327.
2. Erhirhie, E. O. and Ekene, N. E. (2013). Medicinal values on *Citrullus lanatus* (watermelon) pharmacological review. *International Journal of Research in Pharmaceutical and Biomedical Sciences,* 4(4): 1305-1312.
3. Rubatzky, V. E. and Yamaguchi-Mas. (1997). World vegetables, principles, production and nutritive value. 2nd Edition, Chapman and Hall, U.S.A: pp. 577–639.
4. Saxena, M., Saxena, J., Nema, R., Singh, D. and Gupta, A. (2013). Phytochemistry of medicinal plants. *Journal of Pharmcognosy and Phytochemistry*, 1(6): 168-182.
5. Thakur, H. A. (2014). Antimicrobial and antifungal activity of *Cucumis melo* L. (cucurbitacae) and *Pergularia daemia* (asclepiadaceae) an ethnomedicinal plants. *International Journal of Bioassays*, 4(1), 3661-3665.
6. Gurudeeban, S., Ramanathan, T., Satyavani, K. and Dhinesh, T. (2011). Antimicrobial effect of coastal medicinal plant-*Citrullus colocynthis* against pathogenic microorganisms. *African Journal of Pure and Applied Chemistry,* 5(5): 199-122.
7. Elhadi, I. M., Koko, W. S., Dahab, M. M., Imam, Y. M. E. and Mageed, M. A. E. A. (2013). Antigiardial activity of some *Cucurbita* species and *Lagenaria siceraria*. *Journal of Forest Products and Industries*, 2(4): 43-47.
8. Jadhav, V. D., Bhanuwanshe, S. M., Patil, S. P., Chaudhari, D. V. and Adke, M. B. (2013). Antibacterial activity of different plant and callus extracts a comparative study. *International Journal of Scientific and Technology*, 2(10): 285-288.
9. Tiwari, P., Kumar, B., Kaur, M., Kaur, G. and Kaur, H. (2011). Phytochemical screening and extraction: A review. *Internationale Pharmaceutica Sciencia,* 1(1): 98-106.
10. Yadav, R. and Agarwala, M. (2011). Phytochemical analysis of some medicinal plants. *Journal of Phytology*, 3(12): 10-14.
11. Benmehdi, H., Hasnaoui, O., Benali, O. and Salhi, F. (2012). Phytochemical investigation of leaves and fruits extracts of *Chamaerops humilis* L. *Journal of Material and Environment Science*, 3(2): 320-327.
12. Sheikh, N., Kumar, Y., Misra, A. K. and Pfoze, L. (2013). Phytochemical screening to validate the ethnobotanical importance of root tubers of *Diosorea* species of Meghalaya, North East India. *Journal of Medicinal Plants Studies*, 1(6): 62-69.
13. Tyagi, S., Singh, G., Sharma, A. and Aggarwal, G. (2012). Phytochemicals as candidate therapeutics: An overview. *International Journal of Pharmaceutical Sciences Review and Research*, 3(1):53-55.
14. Chaieb, I. (2010). Saponins as insecticides: A review. *Tunisian Journal of Plant Protection,* 5(1): 39-50.
15. Ashok, P. K. and Upadhyaya, K. (2012). Tannins are astringent. *Journal of Pharmacognosy and Phytochemistry*, 1(3): 45-50.
16. Kabera, J. N., Semana, E., Mussa, A. R. and He, X. (2014). Plant secondary metabolites: Biosynthesis, classification, function and pharmacological properties. *Journal of Pharmacy and Pharmacology*, 2: 377-392.
17. David, A. M. D. (2006). Pharmacokinetics and pharmacodynamics of antifungals. *Infect Disease Clinics of North America,* 20: 679–697.
18. Rahman, H., Priyanka, P., Lavanya, T., Srilakshmi, N. and Kumar, P. R. (2013). A review on the ethnobotany, phytochemistry and pharmacology of *Citrullus lanatus*. *International Research Journal of Pharmaceutical and Applied Sciences,* 3(2): 77-81.

Malaysian Journal of Analytical Sciences, Vol 22 No 1 (2018): 157 - 165
DOI: https://doi.org/10.17576/mjas-2018-2201-20

MALAYSIAN JOURNAL OF ANALYTICAL SCIENCES
Published by The Malaysian Analytical Sciences Society
ISSN 1394 - 2506

TRANSESTERIFICATION OF WASTE COOKING OIL IN BIODIESEL PRODUCTION UTILIZING CaO/Al_2O_3 HETEROGENEOUS CATALYST

(Transesterifikasi Sisa Minyak Masak dalam Pengeluaran Biodiesel Menggunakan CaO/Al_2O_3 Mangkin Heterogenus)

Norshahidatul Akmar Mohd Shohaimi* and Fatin Nur Syahirah Marodzi

Faculty of Applied Sciences,
Universiti Teknologi MARA Pahang, 26400 Bandar Tun Abdul Razak Jengka, Pahang, Malaysia

Corresponding author: akmarshohaimi@pahang.uitm.edu.my

Received: 4 December 2016; Accepted: 1 December 2017

Abstract

The increasing demand for fossil fuel brings a great concern as it is natural and non-renewable sources. There are several studies on biodiesel using renewable sources such as waste cooking oil. The process of transforming waste cooking oil into biodiesel is called transesterification reaction which involved one step (esterification) and two step (esterification-transesterification) reaction. The performance of the CaO/Al_2O_3 catalyst was investigated. The parameters studied were reaction time and catalyst loading. In this study, it was found that the highest yield was obtained from the two step transesterification reaction, 30.91% with optimum condition of 3 wt.% of Ca/Al_2O_3 catalyst, 12:1 methanol to oil ratio, reaction temperature of 65 ºC for 3 hours. Esterification reaction reduce the FFA content in the feedstock, because, in order to achieve high biodiesel yield, the acid value of feed stock should below than 1 mg KOH/g oil. GC-MS results showed that six methyl ester species was found in the product and this finding reveals that the free fatty acid had successfully converted to methyl ester by using two step esterification-tranesterification reaction.

Keywords: biodiesel, heterogeneous catalyst, transesterification, waste cooking oil

Abstrak

Permintaan yang semakin meningkat bagi bahan api fosil membawa kebimbangan besar kerana ia adalah sumber semula jadi dan tidak boleh diperbaharui. Terdapat beberapa kajian mengenai biodiesel menggunakan sumber yang boleh diperbaharui seperti sisa minyak masak. Proses mengubah sisa minyak masak kepada biodiesel dipanggil reaksi transesterifikasi yang melibatkan reaksi satu langkah (pengesteran) dan dua langkah (pengesteran- transesterifikasi). Prestasi pemangkin CaO/Al_2O_3 dikaji. Parameter yang dikaji ialah masa tindak balas dan jumlah pemangkin. Dalam kajian ini, didapati bahawa hasil tertinggi diperoleh daripada tindak balas transesterifikasi dua langkah, 30.91% dengan keadaan optimum daripada 3% berat pemangkin Ca/Al_2O_3, 12:1 metanol kepada nisbah minyak, suhu tindak balas 65 ºC selama 3 jam. Tindak balas pengesteran mengurangkan kandungan FFA dalam bahan mentah, kerana untuk mencapai hasil biodiesel tinggi, nilai asid stok suapan sepatutnya kurang dari 1 mg KOH/g minyak. Keputusan GC-MS menunjukkan bahawa enam spesis metil ester ditemui dalam produk dan penemuan ini mendedahkan bahawa asid lemak bebas telah berjaya ditukar kepada metil ester dengan menggunakan dua langkah tindak balas pengesteran- transesterifikasi.

Kata kunci: biodiesel, mangkin heterogenus, transesterifikasi, sisa minyak masak

Introduction

The widespread use of diesel fuel in the world and the rapid reduction of crude oil reservoir has spurred interest and extensive research into an alternative fuels. Biodiesel as an alternative fuel is an eco-friendly and proven to be environmentally safe. Biodiesel mainly consisting of alkyl esters of fatty acid and can be generated from renewable sources such as animal fat, vegetable oils and waste cooking oils [1]. The advantage of biodiesel over diesel is less carbon dioxide was produced and emits to the atmosphere. Meanwhile, biodiesel contains no sulfur or aromatics compounds and its combustion will results in reducing the unburned hydrocarbons, carbon monoxide and particulate matter. Moreover, the reducing amount of carbon released to the atmosphere will overcome the global warming emission including air toxic [2]. In the year of 2000, biodiesel had became the only alternative fuel in the country which have successfully completed and fulfilled the severe health effects testing under the Clean Air Act [2, 3].

There are several studies on alternative diesel as an initiative to reduce the usage of the natural sources. Transesterification is the common technique used for biodiesel production in order to reduce the viscosity of triglycerides [1]. The transesterification also called alcoholysis, where the displacement of alkyl alcohol group with alkyl from the ester thus produces different ester and alcohol. The mechanism of transesterification involve three steps, where at first, the triglycerides from feedstock is reduced to form diglycerides and a fatty-acid-methyl-ester and repeated stepwise until the monoglyceride is converted to glycerine [1]. Acidic, basic, enzyme, solid metal catalyst and solid super base are the most common catalyst used in biodiesel production.

In this study, heterogeneous base catalyst, calcium oxide with alumina support, Ca/Al_2O_3, was studied. The heterogeneous base catalyst is neither being consumed nor dissolved in the reaction which easier for the catalyst separation. Besides, it produce high biodiesel yield, high glycerol purity [4,5], low cost and environmental friendly as it does not required large amount of solvent in the washing step of crude ester [6]. In addition, the heterogeneous catalyst poses large surface area compared to homogeneous catalyst [1]. Waste Cooking Oil (WCO) was chosen as a feedstock material due to its low viscosity [1] and easily to be obtain. In addition, the cost of raw vegetable oils is higher compared to the edible vegetable oils.

Materials and Methods

Material and feedstock

The important ingredients to ensure successful reaction were calcium nitrate ($Ca(NO_3).4H_2O$), alumina beads (Al_2O_3), methanol and waste cooking oil (WCO), Saji Brand. All the solvents and chemicals were purchased and directly used without any purification except for WCO. Ethanol, potassium hydroxide and potassium hydrogen phthalate, were used in the titration process to determine acid value. Lastly, hexane was used to dilute the biodiesel obtained for biodiesel analysis.

Sample pre-treatment

The solid particles and other impurities were removed from the WCO obtained by filtration technique. The filtered WCO then was heated at 120 ºC while stirred for 2 hours to remove water content. Then, the pre-treatment WCO was stored in a clean container.

Catalyst preparation

In this study, an alkaline earth metal which is calcium with alumina support has been used in the transesterification reaction. For screening purpose, three different catalyst concentration were used which are 3, 5 and 8 M. The 5 mm diameter of alumina, Al_2O_3 beads was used in this study. The catalyst has been prepared using aqueous Incipient Wet Impregnation (IWI) method. Firstly, 5.90 g of calcium nitrate has been weighed and dissolved in 5 ml of distilled water in a 50 mL-beaker to obtain 5 M concentration. The mixture was stirred for 30 minutes at room temperature.

Next, the alumina support was submerged in the catalyst solution for 20 to 30 minutes to ensure it is fully coated by the catalyst. The fully coated alumina support was then transferred onto a glass wool on an evaporating dish to ensure homogeneity and was ripened in an oven at 80 to 90 for 24 hours to remove excess water and to guarantee for a good coating metal onto the surface of the alumina support [7]. This alumina supported catalyst was then

calcined at temperature of 1000 for 5 hours using carbolite chamber furnace to produce a metal oxide and remove any impurities left. The catalyst was then stored in the closed-tight vials to avoid any contact with the atmosphere and to be used in next analysis. Similar procedure was repeated for 3 and 8 M catalyst concentration.

One step transesterification reaction

WCO, methanol and catalyst were the main ingredient in this transesterification process. The parameters selected in this study were catalyst loading, reaction time and catalyst concentration. The reaction process has been carried out in the 250 mL of three-necked round-bottom flask fitted with a reflux condenser, heating mantle with stirrer and a thermometer. Firstly, the catalyst was activated by dispersing it in the 120 g methanol at 50 with a constant stirring speed for 20 minutes. After the catalyst activation, 10 g of waste cooking oil (pre-heated again for 20 minutes) was introduced into the three-necked round-bottom flask. The mixture was then reflux at reaction temperature of 65 with continuous stirring [8] for various reaction time.

After the transesterification reaction complete, the reaction mixture was filtered through a filter paper to separate the solid catalyst and other residual. The solution was poured into separatory funnel and left overnight to separate the glycerol compound and biodiesel. The biodiesel obtained as the top layer and glycerol at the bottom [8]. The biodiesel then was purified using distillation technique to remove the excess methanol present [9]. The purified biodiesel was stored in a closed-tight vial. The quality of biodiesel produce was analyzed by using Agilent Technologies 7890B GC system–5977A MSD (GC-MS) and Perkin Elmer Spectrum TM 100 FTIR spectroscopy to determine the composition of methyl ester.

Two-step reaction (esterification-transesterification)

Two step reactions consist of acid esterification and base transesterification process. Acid esterification utilized sulphuric acid as a catalyst with 0.35 wt.% based on 10 g of oil. Firstly, the catalyst with 120 g of methanol and 10 g of WCO were poured into 250 mL of three necked round bottom flask. The mixture was heated using water bath technique and continued stirred at 65ºC for various reaction times. After the reaction was completed, the reaction mixture was poured into a separatory funnel and left overnight. On the next day, the bottom phase was collected and purified by using rotator evaporator before proceed to the next step. The upper phase which contained catalyst and water were discarded [10].

Transesterification reaction was begun with activation of the catalyst with methanol for 20 minutes. The catalyst was weighed for 3 wt.% based on 5 g oil and the methanol to oil ratio was set to be constant 12:1. The reaction was heated at 65ºC and continuous stirred for various reaction times (3, 4, and 5 hours). The reaction mixture was then transferred into the separatory funnel and left overnight to allow the separation of glycerol and FAME. The upper phase was obtained and purified using distillation technique. The purified biodiesel was stored in a closed-tight vial to be used for biodiesel characterization using Agilent Technologies 7890B GC system–5977A MSD (GC-MS) and Perkin Elmer Spectrum ^{TM} 100 FTIR spectroscopy.

The conversion of acylglycerols into biodiesel was calculated by using equation 1 below:

$$\text{Yield}(\%) = \frac{\text{Weight of biodiesel produced}}{\text{Weight of oil used}} \text{ x } 100\% \quad (1)$$

Blank sample

The one step reaction and two step reaction for a blank sample were conducted. The blank sample is a sample that only contains of WCO and methanol. The reaction condition of these blank were followed the highest biodiesel yield. The biodiesel produced was analyzed by using GC-MS and FTIR.

Biodiesel analysis: Fourier transform infrared spectroscopy

The crystal and plate was clean and background scanning was performed before sample analysis. The instrument spectrum was set up from 4000 to 400 cm^{-1}. A little of biodiesel sample was drops on the crystal plate. By using the spectrum data, the chemical constituent of the compound could be determined and the formation of the fatty acid methyl ester could be confirmed.

Gas chromatography-mass spectroscopy

The GC-MS is an instrument build with a library that will provide a complete list of components detected in the sample. The instrument was set up as follow: Injection port: Split; injection port temperature; 250 °C, oven temperature; 100 °C to 290 °C at 40 °C min^{-1}, column flow rate; 40 mL/s and detector temperature is 250 °C. The 1 µL of sample was introduced to the GC. The sample was repeatedly injected to get reproducible peak areas. The structure and chemical constituent present in the biodiesel was determined from the chromatograph.

Results and Discussion

One step transesterification reaction

In the transesterification reaction, the methanol to oil ratio, catalyst loading, reaction temperature and reaction time were crucial variables because each of these variables influence the amount of FFA converted to FAME. Two variables were set constant from the references [11] were reaction temperature and methanol to oil ratio, 65 ºC and 12:1 while another two variables were applied for screening process to find optimum condition for the reaction.

Effect of catalyst concentration

To determine the optimal catalyst concentration to be used, an experiment was performed with reaction condition, 3 wt.% catalyst loading and 12:1 methanol to oil ratio at temperature of 65 ºC for 3 hours. The result was exemplified in the Figure 1 where lower catalyst concentration of 3 M offer lower biodiesel yield of 18.6%. Increasing the catalyst concentration to 5 M will also increased the FAME yield and the yield was maintained when the catalyst concentration further increased to 8 M. This is due to at lower concentration, there is less presence of active site for reaction to take place while, at high concentration the reaction mixture become too viscous thus increase mass transfer resistance [8]. Thus, 5 M was the optimum catalyst concentration to be applied in the one step reaction which gave the FAME yield of 28.5%.

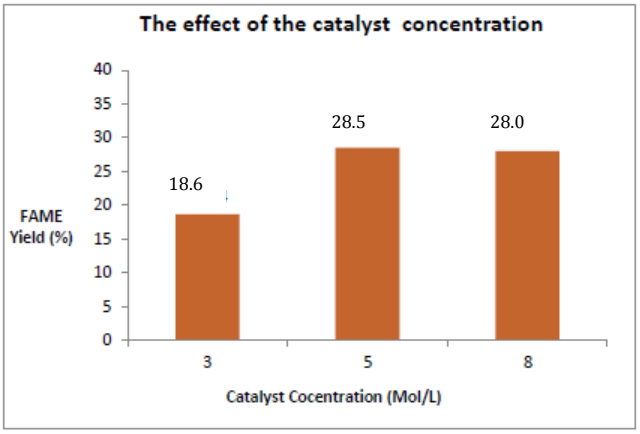


Figure 1. The effect of the catalyst concentration on the FAME yield (3 wt.%, 12:1 MeOH:oil, 65 ºC and 3 hours)

Optimization of reaction conditions

The optimum reaction condition of one step transesterification was obtained for further investigation. The experimental results illustrated in Figure 2 indicate the trend for catalyst loading to the biodiesel yield in relation with the reaction time. Firstly, the effect of catalyst loading was investigated prior to the FAME yield obtained. The addition of catalyst proved its significance in the biodiesel production. The highest biodiesel recorded was 28.5% utilizing 3 wt.% of CaO/Al_2O_3 with 3 h reaction time. As for blank reaction, the FAME yield obtained was only 13.0% without addition of catalyst for the same reaction condition. The trend of yield produced was slightly declined as catalyst loading increased. The excess catalyst loading lowering the conversion of FFA to FAME as it reacts with triglyceride to produce soap and emulsion [12]. In addition, a high dosage of catalyst increased the viscosity of reaction mixture which will resist the mass transfer in the multiphase system (liquid-liquid-solid) [13].

During the experimental process, an emulsion was observed at 5 h using 4 wt.% of catalyst during the separation process.

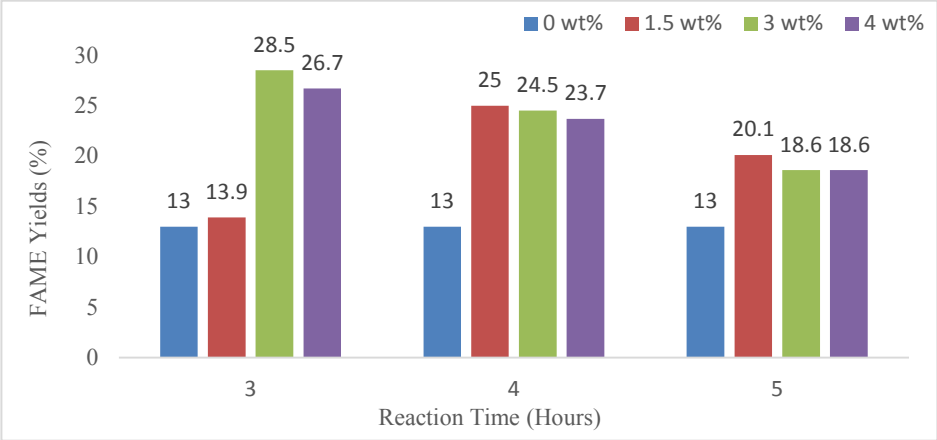


Figure 2. The effect of catalyst loading in relation with reaction time (12:1 MeOH:oil and 65 ºC)

Next, the effect of reaction time was also studied because it affect the trend of biodiesel yield produced. The reaction time of 3, 4 and 5 hours was tested employing 12:1 methanol to oil ratio, 3 wt.% catalyst loading at 65ºC. From Figure 3 we can see the trend of biodiesel produced decreased as time increased. In longer reaction time, the methyl ester favors to undergo backward reaction producing more glycerol than methyl ester [14].

In addition, the presence of emulsion was observed at 5 hours reaction time and this also lowering the yield of FAME [15]. Furthermore, the optimum reaction time was interrelated with methanol ratio used. As reported by Ramadhas et al. [16], high molar ratio required shorter time because it has sufficient methanol to driven the reaction to completion with high yield. Hence, the reaction time of 3 hours was chosen for the optimum reaction time which offers high biodiesel yield.

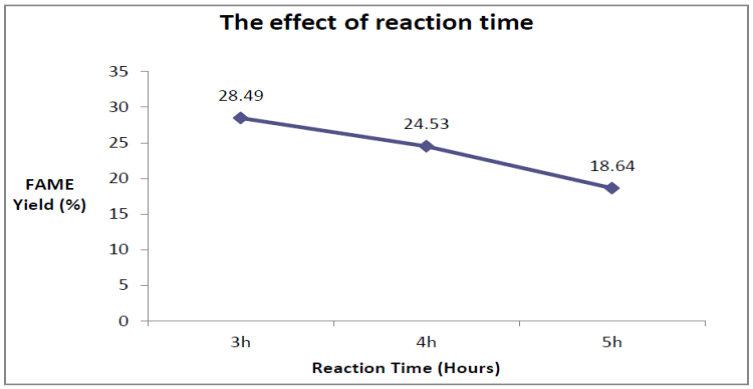


Figure 3. The effect of reaction time (3 wt.%, 12:1 MeOH:oil and 65 ºC)

Two step reaction

Due to lower biodiesel yield obtained in the one step reaction, the WCO was treated with sulphuric acid to reduce the level of FFA. The only manipulated variable in the acid-esterification was esterification time. Other parameters were taken from Muciño et al. [13] in which, 12:1 methanol to oil ratio, 0.35 wt.% of H_2SO_4 at 50 ºC were employed. As for the transesterification reaction, the optimum condition obtained from the earlier investigation was

employed (3 wt.% of CaO/Al_2O_3, 12:1 methanol to oil ratio, 65ºC and 3 h reaction time). The results of esterified oil and its corresponding FAME were illustrated in the Figure 4.

The conversion of FFA to FAME was increased from 75.29% at 0.5 hour to 77.65 at 1 hour. After 2 hours, the trend was declined to 74.67%. The same result was obtained by Ullah et al. [17] where after 2 hours reaction, the yield of FFA conversion was declined. Therefore, 1 hour was chosen as the optimum reaction time of esterification reaction. Although, from the GC-MS analysis the WCO was completely converted to biodiesel, acid catalyst was not recommended to use as it gave drawbacks to the environment. Acid catalyst was corrosive and unable to recover thus will increase the cost of operation process.

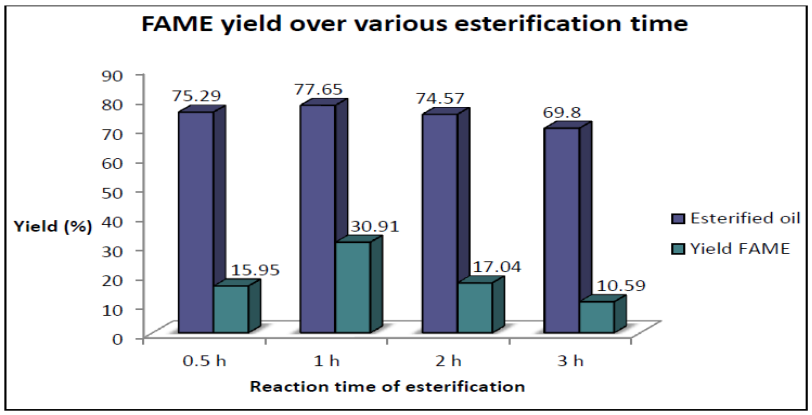


Figure 4. FAME yield over various esterification time (0.5, 1, 2 and 3 hour).

In this study, the effect of reaction time of transesterification to esterified oil was also investigated, the results was illustrated in Figure 5. The highest biodiesel yield from the reaction was 30.91% at 3 hours of reaction time. As compared to blank, transesterification utilized metal alkali catalyst offers higher yield, in which blank only offers 18.55%. Thus, CaO/Al_2O_3 was added in the production biodiesel from esterified oil.

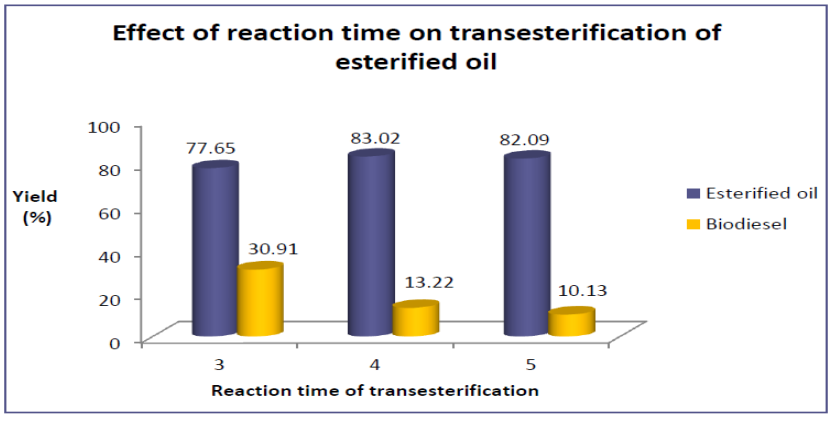


Figure 5. Effect of reaction time on transesterification of esterified oil

Confirmation of ester group using FTIR

FTIR is an instrument that can only give information of compound that has dipole moment and functional group. In this study, the information on the shifted of carbonyl group of carboxylic acid to ester was investigated. This information proved that the FFA was fully converted into FAME. However, the absorption peak of carbonyl group

for feedstock and biodiesel showed no significant different. Figure 6 showed the overlay spectra of different type of oil which were WCO, esterified oil and the FAME of two step reaction.

The assignation peak for C=O observed for all oil samples was belong to the ester group. The peak region for C=O carboxylic acid as state in Pavia et al. [18] was in the region 1725 cm^{-1} to 1700 cm^{-1}, which means the peak appeared for feedstock should shifted slightly to the right. This situation has been report by Rabelo et al. [19] in which the reason was because of the WCO and the biodiesel was chemically similar. Because of that, it is difficult to prove the FFA was completely converted into FAME by running FTIR analysis only. Thus, GC-MS was performed to support the result.

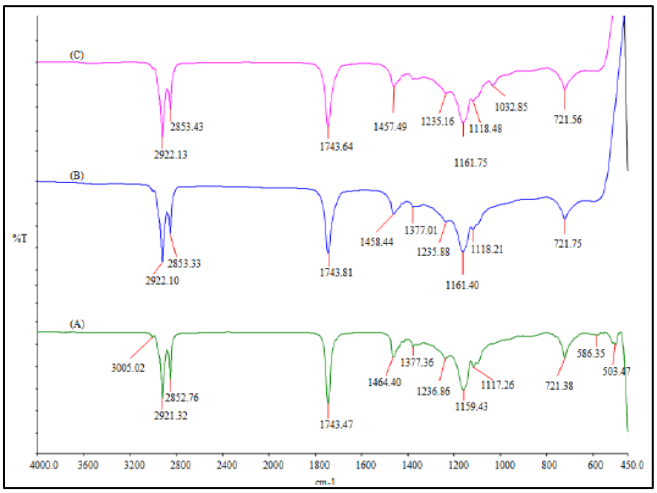


Figure 6. FTIR spectra of (a) WCO, (b) Esterified oil and (c) FAME

Confirmation of FAME using GC-MS

Figure 7 clearly showed the entire compound present in the biodiesel. There were nine major peaks observed and six peaks were corresponds to the ester group. The identified FAME were dodecanoic acid methyl ester, methyl tetradecanoate, hexadecanoic acid methyl ester, 9-octadecenoic acid methyl ester, 9,12-octadecadienoic acid methyl ester and 10-octadecenoic acid methyl ester. All peaks appeared were corresponds to different type of ester and were confirmed using MS-NIST program. The details of the composition were tabulated in the Table 1.

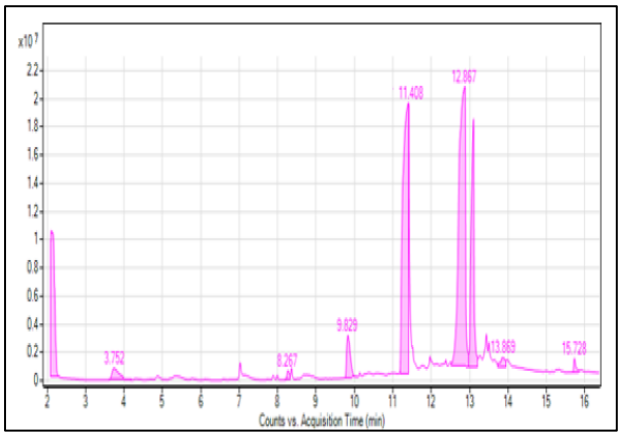


Figure 7. GC-MS chromatogram of FAME yield

Table 1. FAME composition in biodiesel

Retention Time (min)	Identified Compound	Common Name	Chemical Formula
8.267	Dodecanoic acid methyl ester	Lauric acid ME	$C_{13}H2_6O_2$
9.829	Methyl tetradecanoate	-	$C_{15}H_{30}O_2$
11.408	Hexadecanoic acid methyl ester	Palmitic acid ME	$C_{17}H_{34}O_2$
12.867	9-octadecenoicacid(Z), methyl ester	Oleic acid ME	$C_{19}H_{36}O_2$
13.102	9,12-octadecadienoic acid (Z,Z), methyl ester	Linoleic acid ME	$C_{19}H_{34}O_2$
13.869	10-octadecenoic acid methyl ester	-	$C_{19}H_{36}O_2$

Conclusion

As for conclusion, two step reaction processes offers high FAME yield than one step process. The FAME yield for two step process was 30.91% with transesterification reaction condition of 3 hours of reaction time, 12:1 methanol to oil ratio, and temperature of 65 ºC with the best CaO/Al_2O_3 loading, 3 wt.%. Although the yield is low, the FFA content in the sample was verified had been converted into FAME using GCMS and FTIR. Even though, there are subtle differences observed in the FTIR spectra since the biodiesel is chemically similar to WCO, the GCMS gave positive results as few common groups of methyl esters were present.

Acknowledgement

Authors gratefully acknowledged the financial support by the Research Grant, iRAGS (Vote no.: 600RMI/IRAGS 5/3 (14/2015)) and UiTM Pahang for providing facilities in order to complete this work.

References

1. Lan, J. C-W., Tsui, A., Wang, S. S. and Wu, H-S. (2009). A review of biodiesel as renewable energy. In Biochemical Engineering. Dumont, F. E. and Sacco. J. A. (eds.). Nova Science Publisher, Inc., New York: pp. 1-40.
2. Srinivasan, S. P., Malliga, P. and Murugan, S. (2008). Supply chain network of jatropha oil for biodiesel. In Bio-Fuels: Marketing stratergies and impact on rural development. Mehla., S.K. (eds.). Aavishkar Publiser, Distributors., India: pp. 29-40.
3. Sastry, G. R. (2008). Biodiesel: biodegradable alternative fuel for diesel engine. New Delhi: Readworthy Publications (P) Ltd, India.
4. Wen, Z., Yu, X., Tu, S-T., Yan, J. and Dahlquist, E. (2010). Biodiesel production from waste cooking oil catalyzed by TiO_2-MgO mixed oxides. *Bioresource Technology*, 101(24): 9570-9576.
5. Lam, M. K., and Lee, K. T. (2011). Production of biodiesel using palm oil. In Biofuels: Alternative feedstocks and conversion process. Elsevier Inc, USA: pp. 353-374.
6. Agarwal, M., Chauhan, G., Chaurasia, S. and Singh, K. (2012). Study of catalytic behaviour of KOH as homogeneous and heterogeneous alkali catalyst for biodiesel production. *Journal of the Taiwan Institute of Chemical Engineers*, 43(1): 89-94.
7. Shohaimi, N. A. M., Bakar, W. A. W. A. and Jaafar, J. (2014). Catalytic neutralization of acidic crude oil utilizing ammonia in ethylene glycol basic solution. *Journal of Industrial and Engineering Chemistry*, 20(4): 2086–2094.
8. Farooq, M., Ramli, A. and Naeem, A. (2015). Biodiesel production from low FFA waste cooking oil using heterogeneous catalyst derived from chicken bones. *Renewable Energy*, 76: 362-368.
9. Mahesh, S. E., Ramanathan, A., Begum, K. M. M. S. and Narayanan, A. (2015). Biodiesel production from waste cooking oil using KBr impregnated CaO as catalyst. *Energy Conversion and Management*, 91: 442–450.

10. Chongkhong, S. Ã., Tongurai, C., Chetpattananondh, P. and Bunyakan, C. (2007). Biodiesel production by esterification of palm fatty acid distillate. *Biomass and Bioenergy*, 31: 563-568.
11. Liu, X., He, H., Wang, Y., Zhu, S. and Piao, X. (2008). Transesterification of soybean oil to biodiesel using CaO as a solid base catalyst. *Fuel,* 87: 216-221.
12. Sirisomboonchai, S., Abuduwayiti, M., Guan, G., Samart, C., Abliz, S., Hao, X. and Abudula, A. (2015). Biodiesel production from waste cooking oil using calcined scallop shell as catalyst. *Energy Conversion and Management*, 95: 242–247.
13. Muciño, G. G., Romero, R., Ramírez, A., Luz Martínez, S., Baeza-Jiménez, R. and Natividad, R. (2014). Biodiesel production from used cooking oil and sea sand as heterogeneous catalyst. *Fuel*, 138: 143-148.
14. Leung, D. Y. C., Wu, X. and Leung, M. K. H. (2010). A review on biodiesel production using catalyzed transesterification. *Applied Energy*, 87(4): 1083-1095.
15. Lee, S. L., Wong, Y. C., Tan, Y. P. and Yew, S. Y. (2015). Transesterification of palm oil to biodiesel by using waste obtuse horn shell-derived CaO catalyst. *Energy Conversion and Management*, 93: 282–288.
16. Ramadhas, A. S., Jayaraj, S and Muraleedharan, C. (2004). Biodiesel production from high FFA rubber seed oil. *Fuel*, 84: 335-340.
17. Ullah, Z., Bustam, M. A. and Man, Z. (2015). Biodiesel production from waste cooking oil by acidic ionic liquid as a catalyst. *Renewable Energy*, 77: 521-526.
18. Pavia, D. L., Lampman, G. M., Kriz, G. S. and Vyvyan, J. R. (2015). Introduction to Spectroscopy (5th edition). Cengage Learning, Washington.
19. Rabelo, S. N., Ferraz, V. P., Oliveira, L. S. and Franca, A. S. (2015). FTIR analysis for quantification of fatty acid methyl esters in biodiesel produced by microwave-assisted transesterification. *International Journal of Environmental Science and Development*, 6(12): 964-969.

Malaysian Journal of Analytical Sciences Vol 22 No 2 2018

Articles 10-16 are selected papers from the "Regional Conference on Sciences, Technology and Sosial Sciences 2016 (RCSTSS 2016), 4-6 December 2016, Copthorne Hotel, Cameron Highlands, Malaysia; organised by Universiti Teknologi MARA (UiTM) Cawangan Pahang Kampus Jengka, 26400 Bandar Tun Abdul Razak Jengka, Pahang Darul Makmur, Malaysia."

Guest Editor: Azhan Hashim@Ismail

Articles 17-24 are selected papers from the "3rd International Conference on Global Sustainability and Chemical Engineering (ICGSCE 2017), 15-16 February 2017, Marriott Hotel, Putrajaya, Malaysia; organised by Faculty of Chemical Engineering, Universiti Teknologi MARA, Shah Alam, Selangor, Malaysia."

Guest Editor: Fazlena Hamzah

Page

1. A REVIEW ON EXTRACTION SOLVENTS IN THE DISPERSIVE LIQUID-LIQUID MICROEXTRACTION 166
(Sebuah Ulasan Terhadap Pelarut Pengekstrakan dalam Pengekstrakan Mikro Cecair-Cecair Serakan)
Tan Yeong Hwang, Chai Mee Kin, Wong Ling Shing

2. RECENT ADVANCES IN THE PREPARATION OF OIL PALM WASTE-BASED ADSORBENTS FOR REMOVAL OF ENVIRONMENTAL POLLUTANTS - A REVIEW 175
(Kemajuan Terkini dalam Penyediaan Penjerap Berasaskan Sisa Kelapa Sawit untuk Penyingkiran Bahan Pencemar Alam Sekitar - Sebuah Ulasan)
Faridah M. Marsin, Wan Aini Wan Ibrahim, Hamid Rashidi Nodeh, Zetty Azalea Sutirman, Ng Nyuk Ting, Mohd Marsin Sanagi

3. DETERMINATION OF POLYPHENOL CONTENTS IN *Hevea brasiliensis* AND RUBBER-PROCESSING EFFLUENT 185
(Penentuan Kandungan Polifenol dalam *Hevea brasiliensis* dan Sisa Pemprosesan Getah)
Azmi Ismun, Marinah Mohd Ariffin, Shamsul Bahri Abd Razak, Chin Wei Ong, Fauziah Tufail Ahmad, Aidilla Mubarak

4. VALIDATION METHOD FOR EXTRACTION AND DETERMINATION OF MARBOFLOXACIN IN PLASMA AND EDIBLE CHICKEN TISSUES 197
(Kaedah Validasi bagi Pengesktrakan dan Penentuan Marbofloxacin di dalam Plasma dan Tisu Ayam yang Boleh Di Makan)
Natalia Francisca Urzúa, Guillermo Fermín Prieto, Carlos Fernando Lüders, Maria Paula Tonini, Eduardo Jesús Picco, Carlos Alberto Errecalde

5. RESPONSE SURFACE METHODOLOGY ON THE EFFECTS OF SODA – ANTHRAQUINONE PULPING CONDITIONS ON OIL PALM EMPTY FRUIT BUNCHES PULP PROPERTIES 203
(Kaedah Gerak Balas Permukaan Terhadap Kesan Faktor-Faktor Pemulpaan Soda-Antrakuinon Ke Atas Sifat-sifat Gentian Tandan Buah Kosong Kelapa Sawit)
Nurul Husna Mohd Hassan, Mazlan Ibrahim, Nor Yuziah Mohd Yunus

6. VALIDATED RP-HPLC METHOD FOR QUANTIFICATION OF GASTRODIN IN ETHANOLIC EXTRACT FROM THE PSEUDOBULBS OF *Grammatophyllum speciosum* Blume 219
(Validasi Kaedah FT-KCPT bagi Kuantifikasi Gastrodin di dalam Ekstrak Etanolik dari Pseudobulbs *Grammatophyllum speciosum* Blume)
Verisa Chowjarean, Apirada Sucontphunt, Saowapak Vchirawongkwin, Tossaton Charoonratana,Thanapat Songsak, Saraporn Harikarnpakdee, Parkpoom Tengamnuay

7. THE ELECTROCHEMICAL BEHAVIOR OF ZINC OXIDE/REDUCED GRAPHENE OXIDE COMPOSITE ELECTRODE IN DOPAMINE 227
(Sifat Elektrokimia Elektrod Komposit Zink Oksida/Grafin Oksida Terturun dalam Dopamin)
Farhanini Yusoff, Ngai Tze Khing, Chai Chee Hao, Lee Pak Sang, Nurul'ain Basyirah Muhamad, Noorashikin Md Saleh

8. ION-CONDUCTING POLYMER ELECTROLYTE FILMS BASED ON POLY (SODIUM 4-STYRENESULFONATE) COMPLEXED WITH AMMONIUM NITRATE: STUDIES BASED ON MORPHOLOGY, STRUCTURAL AND ELECTRICAL SPECTROSCOPY 238
(Filem Elektrolit Polimer Pengaliran Ion Berasaskan Kompleks Poli(sodium 4-stirenasulfonat) dengan Amonium Nitrat: Kajian ke atas Morfologi, Struktur dan Spektroskopi Elektrik)
Mohd Faiz Hassan, Siti Khalijah Zainuddin, Khadijah Hilmun Kamarudin, Chan Kok Sheng, Mohd Aidil Adha Abdullah

9. OPTIMIZATION OF SELECTED CHARCOAL POWDER COMPOSITE ELECTRODE FOR ELECTROCHEMICAL TREATMENT OF LANDFILL LEACHATE 249
(Pengoptimuman Komposit Elektrod daripada Serbuk Arang Terpilih untuk Rawatan Elektrokimia Bahan Larut Lesap Tapak Pelupusan)
Majd Ahmed Jumaah, Mohamed Rozali Othman, Jumat Salimon, Baydaa Khalaf, Wan Mohd Afiq Wan Mohd Khalik

10. PRENYLATED DIHYDROSTILBENES FROM *Macaranga heynei* (EUPHORBIACEAE) 258
(Dihidrostilbena Terprenil daripada *Macaranga heynei* (Euphorbiaceae))
Aisyah Salihah Kamarozaman, Norizan Ahmat, Nur Fariza Abd Rahman, Khong Heng Yen

11. SUGARS, MINERALS COMPOSITION AND METAL ION CHELATING ACTIVITY OF *Arenga pinnata* SYRUP USING VACUUM EVAPORATION 264
(Komposisi Gula, Mineral dan Aktiviti Ion Logam Pengkelat daripada Sirap *Arenga pinnata* Mengunakan Proses Vakum Penyejatan)
Nurul Janah Yunos, Alawi Sulaiman, Nor Azma Yusuf, Dzil Razman Ghazali

12. PHOTOCATALYTIC DEGRADATION OF METHYLENE BLUE WITH SILVER DOPED ZnO NANOPARTICLES GROWN ON MICROSCOPIC SAND PARTICLES 270
(Degradasi Metilena Biru Menggunakan Nanopartikel ZnO Sebagai Fotomangkin yang Didopkan dengan Perak Tumbuh di atas Pasir Bersaiz Mikro)
Nur Azmina Mohamed Safian, Roslan Md Nor, Hartini Ahmad Rafaie, Siti Fairus Abdul Sani, Zurina Osman

13. SYNTHESIS OF ALUMINA-CaO-KI CATALYST FOR THE PRODUCTION OF BIODIESEL FROM RUBBER SEED OIL 279
(Sintesis Mangkin Alumina-CaO-KI untuk Penghasilan Biodiesel daripada Minyak Biji Getah)
Zainal Kifli Abdul Razak, Shahida Hanum Kamarullah, Siti Norhafiza Mohd Khazaai, Gaanty Pragas Maniam

14. APPLICATION OF PROTEOLYTIC ENZYME IN HIGH AMMONIATED NATURAL RUBBER LATEX 286
(Aplikasi Enzim Proteolitik dalam Lateks Getah Asli Berammonia Tinggi)

Aziana Abu Hassan, Norazreen Abd Rahman, Nurulhuda Abdullah, Roslinda Sajari, Mok Kok Lang

15. EFFECT OF SILVER ON THE PHYSICAL AND STRUCTURAL PROPERTIES OF LEAD NEODYMIUM BOROTELLURITE GLASS SYSTEM 296
(Kesan Perak atas Sifat Fizikal dan Struktur Sistem Kaca Plumbum Neodimium Borotelurit)
Norihan Yahya, Azman Kasim, Azhan Hashim, Siti Nasuha Rafien, Wan Aizuddin Wan Razali, Syamsyir Akmal Senawi, Ruziana Mohamed, Mardhiah Abdullah

16. EVALUATION OF DOSE SENSITIVITY RESPONSE VIA OPTICAL CHARACTERISTICS FOR CRESOL RED-DYED POLYHYDROXYETHYLMETHACRYLATE GEL (PHEMAG) 303
(Penilaian Respons Kepekaan Dos Melalui Ciri Optikal Bagi Kresol Merah-Dicelup Polihidrosietilmetakrilik Gel (PHEMAG))
Nur Sha'adah Zainuddin, Fairuzdzah Ahmad Lothfy, Hartini Ahmad Rafaie, Mazlini Mazlan, Iskandar Shahrim Mustafa, Azhar Abdul Rahman

17. MORPHOLOGY AND CHEMICAL STRUCTURE OF $Sn(Oct)_2$ THIN LAYER ADDED BINDER VIA SOL GEL METHOD 311
(Morfologi dan Struktur Kimia bagi Lapisan Nipis $Sn(Oct)_2$ ditambah Bahan Pengikat Melalui Kaedah Sol Gel)
Rafizah Zaiton, Nor Afifah Omar, Norliza Ibrahim

18. GRANULATION OF MEFENAMIC ACID AND POLY-ETHYLENE GLYCOL (PEG) USING PRESSURE SWING GRANULATION (PSG) TECHNIQUE IN FLUIDIZED BED 318
(Pembentukan Granul Berasaskan Asid Mefenamik dan Polietilena Glikol (PEG) Menggunakan Teknik Pengranulan Tekanan Terayun dalam Turus Terbendalir)
Salinda Ab Ghani, Noor Fitrah Abu Bakar, Mohd Rushdi Abu Bakar, Yus Aniza Yusof, Norazah Abd Rahman

19. CHARACTERISTICS OF RICE HUSK BIOCHAR BLENDED WITH COAL FLY ASH FOR POTENTIAL SORPTION MATERIAL 326
(Ciri-Ciri Gabungan Biochar dari Sekam Padi dengan Abu Terbang Arang Batu Sebagai Potensi Bahan Penjerab)
Nurul Farhana Ahmad, Azil Bahari Alias, Norhayati Talib, Zulkifli Abd Rashid , Wan Azlina Wan Ab Karim Ghani

20. CHARACTERIZATION OF TiO_2 THIN FILMS DERIVED USING ACETIC ACID AND NITRIC ACID 333
(Pencirian Filem Nipis TiO_2 yang Dihasilkan Menggunakan Asid Asetik dan Asid Nitrik)
Nur Munirah Safiay, Syahman Shamsuddin, Nur Najwa Yunus, Fazlena Hamzah

21. SELF-ASSEMBLIES BEHAVIOUR OF PALM OIL-BASED GALACTOSIDE 339
(Sifat Swapenyusunan Galaktosida Berasaskan Minyak Sawit)
Marina Yusoff , Nurul Fadhilah Kamalul Aripin, Nurfatin Inani Aznan, Ruzitah Mohd Salleh

22. BIOLOGICAL REMOVAL OF AMMONIA BY NATURALLY GROWN BACTERIA IN SAND BIOFILTER (Penyingkiran Ammonia Secara Biologi Menggunakan Bakteria Semulajadi dalam Biopenuras Pasir) 346
Fuzieah Subari, Siti Rozaimah Sheikh Abdullah, Hassimi Abu Hasan, Norliza Abd. Rahman

23. ANALYSIS OF *Sesquiterpenes* IN AGARWOOD ESSENTIAL OIL FROM HYDRODISTILLATION PROCESS 353
(Analisis *Sesquiterpenes* di dalam Pati Minyak Gaharu daripada Proses Penyulingan Air)
Nurhaslina Che Radzi, Mohamad Khir Zahari Harip, Mohibah Musa, Nurul Asyikin Md Zaki, Habsah Alwi, Miradatul Najwa Muhd Rodhi, Ku Halim Ku Hamid

24. THE DETECTION OF FATTY ACID METHYL ESTER IN STERCULIACEAE 358
(Pengesanan Asid Lemak Metil Ester dalam Sterculiaceae)
Fathin Nurizati Samsul, Ibtisam Abdul Wahab, Hannis Fadzillah Mohsin

Malaysian Journal of Analytical Sciences, Vol 22 No 2 (2018): 166 - 174
DOI: https://doi.org/10.17576/mjas-2018-2202-01

MALAYSIAN JOURNAL OF ANALYTICAL SCIENCES
Published by The Malaysian Analytical Sciences Society
ISSN 1394 - 2506

A REVIEW ON EXTRACTION SOLVENTS IN THE DISPERSIVE LIQUID-LIQUID MICROEXTRACTION

(Sebuah Ulasan Terhadap Pelarut Pengekstrakan dalam Pengekstrakan Mikro Cecair-Cecair Serakan)

Tan Yeong Hwang[1]*, Chai Mee Kin[1], Wong Ling Shing[2]

[1]*College of Engineering,*
Universiti Tenaga Nasional, Jalan Ikram-Uniten, 43000 Kajang, Selangor, Malaysia
[2]*Faculty of Science, Technology, Engineering and Mathematics (FOSTEM),*
INTI International University, Persiaran Perdana BBN, Putra Nilai, 71800 Nilai, Negeri Sembilan, Malaysia

**Corresponding author: yeonghwang_113@hotmail.com*

Received: 26 August 2017; Accepted: 29 January 2018

Abstract

Dispersive liquid-liquid microextraction (DLLME) is a novel sample preparation technique that has higher level of extraction efficiency by means of relying on microvolumes of solvents. It has gained considerable attention from researchers owing to several advantages such as its simplicity, shorter extraction time, lower cost and higher enrichment factor. In conventional DLLME, chlorinated solvents are widely used as the extraction solvents. Notwithstanding, most of these solvents are reportedly toxic and environmentally-unfriendly. Many related studies in recent years have focused on the use of nontoxic or low toxic extraction solvents and better practical procedures, which have helped improve the extraction efficiency. The aim of this review is to discuss the development of low toxic extraction solvent used recently in the DLLME. The possible improvement of extraction solvent from the green analytical chemistry perspectives is also discussed.

Keywords: extraction solvents, dispersive liquid-liquid microextraction, green analytical chemistry

Abstrak

Pengekstrakan mikro cecair-cecair serakan (DLLME) merupakan teknik penyediaan sampel novel yang mempunyai lebih tinggi kecekapan pengekstrakan dengan menggunakan mikroliter pelarut. Teknik ini telah mendapat perhatian daripada penyelidik kerana beberapa kelebihan seperti ringkas, masa pengekstrakan yang lebih pendek, kos yang lebih rendah dan faktor pengayaan yang lebih tinggi. Dalam DLLME konvensional, pelarut berklorin digunakan secara meluas sebagai pelarut pengekstrakan. Namun, kebanyakan pelarut ini dilaporkan toksik dan tidak mesra alam. Dalam tahun kebelakangan ini, banyak kajian yang berkaitan telah fokus kepada penggunaan pelarut pengekstrakan yang tidak bertoksik atau rendah toksik dan praktikal prosedur yang lebih baik telah meningkatkan kecekapan pengekstrakan. Tujuan kajian ini adalah untuk membincangkan perkembangan pelarut pengekstrakan rendah toksik yang digunakan dalam DLLME terkini. Penambahbaikan pelarut pengekstrakan dari perspektif kimia analisis hijau juga dibincangkan.

Kata kunci: pelarut pengekstrakan, pengekstrakan mikro cecair-cecair serakan, kimia analitik hijau

Introduction

The step involving the sample preparation is the most important one in analytical process as most of the samples are not capable of being injected directly into the analytical instruments for analysis. The main aim of sample pre-treatment is to both clean up and enrich the analytes of interest from the sample, and execute the analytes into forms that are considered suitable for instrument of analytical measurement [1].

As far as sample pre-treatment and separation are concerned, traditional methods for sample preparation such as liquid-liquid extraction (LLE) and solid-phase extraction (SPE) have mostly been used for many years. Nonetheless, some weaknesses were associated with these traditional methods such as the usage of large amount of organic solvents, which are toxic and environmentally-unfriendly, time-consuming and labour-intensive [2]. For this reason, many researchers have attempted towards better development of sample pre-treatment step that involves relatively lower solvent consumption, economic and rapid.

In the year of 2006, the dispersive liquid-liquid microextraction (DLLME), which is now one of the powerful sample pre-treatment techniques, was invented by Rezaee and his co-workers [3]. The advantages of DLLME method are inter alia simplicity, short extraction time, low cost, high enrichment factor, and high-recovery. As a result of such favourable characteristics, it has drawn considerable attention from analytical chemists. A significant number of research articles relating to DLLME having been published since its introduction bears testimony to the attention it has gained. Originally, the DLLME was established for preparation from water samples. Subsequently, it was developed for other matrices including food [4], soil [5], cosmetic products [6] and biological samples [7]. In relation to the types of analytes, they are not only limited to numerous organic compounds, but inorganic analytes were also successfully extracted from the sample using DLLME [8].

A comprehensive review of literature has pointed to many excellent reviews discussing the development and applications of DLLME [9-12]. Some of the reviews were found to summarise various strategies for improving dispersion liquid-liquid microextraction [13, 14] and application with different analytical instruments [15, 16]. Notwithstanding such reviews, none of the reviews meticulously discussed the different types of extraction solvents used in DLLME. The present study therefore fills such a gap in the literature. Specifically, it presents the review of extraction solvents used in the conventional DLLME and modified DLLME. In addition, future trend of extraction solvents used in DLLME is also discussed from the perspective of green analytical chemistry.

Principle of DLLME

It has to be noted that the DLLME is based on the ternary solvent system, in which miniaturized volume of solvents are used. In a typical procedure, extraction solvent is mostly used to extract the analytes of interest from the samples. In the event of promoting the rapid transfer of analytes of interest from the samples, dispersion solvent is used. Upon injecting the mixture of extraction solvent and dispersion solvent into the sample solution, microdroplets of extraction solvent is rapidly dispersed into the aqueous sample and a cloudy solution is formed. As a large surface area is formed between extraction solvent and the aqueous sample in the cloudy solution, the transfer of analytes of interest to extraction phase is therefore rapid. As the extraction equilibrium is rapidly achieved, the extraction time is therefore relatively shorter. The mixture is then separated by centrifugation and the extraction solvent containing analytes of interest is collected by means of using microsyringe. This is followed by the identification of analytes in the extraction solvent, which can be performed using analytical instrument [3].

In order to obtain high extraction efficiency, several parameters have to be looked into. In such processes, the selection of appropriate extraction solvent is considered very important. In the DLLME, extraction solvent should have the following requirements: the extraction solvent is required to have low solubility with water and miscible with the dispersive solvent. In addition, it is also required to have the potential for extracting analytes of interest and suitable chromatographic behaviour. Besides, the extraction solvent must have different densities with the water so that it can be phase separated. In the conventional DLLME, the extraction solvent usually have relatively higher density than water. As a result, it is able to form sedimented phase in the bottom of the tube after phase separation [3]. Chlorinated solvents such as chloroform, chlorobenzene, carbon tetrachloride, and tetrachloroethylene are commonly selected as extraction solvent as they fulfil such requirements [17]. These chlorinated solvents show the advantages in DLLME such as producing high enrichment factor, short extraction time, ease of operation and high

sensitivity [18-20]. However, these solvents are highly toxic. Most of them have low lethal dose and carcinogenic [21].

Extraction solvents used in DLLME

With the aim of minimizing the drawbacks associated with using chlorinated solvents, other types of solvents including heavy-density, low density and ionic liquid were introduced. Table 1 shows a summary of these extraction solvents. Heavy-density solvents including brominated and iodinated solvents have been introduced. The results revealed that extraction efficiencies of these solvents were comparable and higher than using the chlorinated solvents. Good sensitivity with relatively lower limit of detection was also obtained [22-26]. Compared to chlorinated solvents, some of the brominated and iodinated solvents have lower toxicity [22, 26, 27]. In addition, higher recovery efficiency with lower relative standard deviation can also be achieved by means of using only 1-methyl-3-bromobutane as extraction solvent without having to rely on dispersive solvent, which is capable of reducing the use of organic solvent [28]. Nevertheless, not all brominated and iodinated solvents have lower toxicity. In this regard, some solvents such as 2-iodopropane [29] and 1, 2-dibromoethane [21] are as toxic as chlorinated solvents. Furthermore, there are only limited number of brominated or iodinated solvents with low toxicity [30].

Table 1. Summary of advantages and disadvantages of heavy-density, low density and ionic liquid

Type of Extraction Solvent	Advantages	Disadvantages
Heavy-density solvent	High extraction recovery Some solvents can extract analytes without dispersive solvents	Limited choice of solvent. Some solvents are as toxic as chlorinated solvents.
Low-density solvent	Higher extraction recovery Lower toxicity extraction solvent Choices of solvent are broader than heavy density solvent Extract is cleaner Some methods do not required centrifugation	Some require specially designed tools to collect organic phase It can be difficult to differentiate the interphase between the floating organic phase and the aqueous phase Choice of solvents for DLLME-SFO is limited
Ionic liquid	Lower melting point, lower vapor pressure, higher thermal stability and good solubility in organic and inorganic compounds Higher extraction recovery and sensitivity Choices of solvent are broader than low-density and high-density solvents	Not suitable for analysis with GC Toxicity to environment is not well understood

*DLLME-SFO: Dispersive liquid liquid microextraction based on solidification of floating drop
GC: gas chromatography

Low-density solvents were used recently as extraction solvent in DLLME. The choice of lower-density organic solvent is more popular than high-density solvents [31]. The low-density solvents such as n-hexane [30], toluene [32], 2-ethyl-1-hexanol [31], 1-heptanol [34], 1-octanol [35], isooctane [36], and 1-dodecanol [37] and 1-undecanol [38] have been used as extraction solvents in low-density solvents (LDS) DLLME. In addition, they have been proven to possess low LOD and LOQ, high recovery and higher linearity. Unlike in the conventional DLLME, the low-density solvents do not sediment at the bottom of the tubes as the low-density extraction solvent floats on the top of the aqueous phase after phase separation is carried out. The floated extraction solvent is much easier to collect and the extract is cleaner since any matrix components will be sedimented at the bottom of the extraction vessel [4]. Therefore, a good chromatogram can be easily achieved. It is also worthy of note that some methods do

not require centrifugation for phase separation and thus extraction time is relatively shorter. Low-density extraction solvent droplets float on the surface of the aqueous phase after the samples and solvents are mixed and shaken [35]. Then, the floating extraction phase was collected by means of employing different techniques. This method is useful for preventing analytes from being degraded by excessive centrifugation or ultrasonic energy [39]. However, to draw off the floating solvents, some required the use of specially designed devices [40].

Leong & Huang [41] and Xu et al. [42] developed the new DLLME method based on solidification of a floating organic drop (DLLME-SFO). Specifically, the mixture of low-density extraction solvent and dispersive solvent are injected into aqueous samples and as a result, a cloudy solution is formed. The mixture is then centrifuged and placed in the ice bath to solidify the floated extraction solvent. Following the solidification stage, the solidified solvent is taken by spatula and melted prior to sending it for analysis. In DLLME-SFO, extraction solvent must fulfil several requirements, namely low melting point below room temperature, low solubility in water, lower density than water, and high affinity towards analytes of interest and compatible for instrument analysis. Good extraction efficiencies such as low LOQ, LOD and high recovery were successfully obtained by means of using the DLLME-SFO [37, 43-45]. In comparison with the conventional DLLME, this method uses low-toxic extraction solvents. The drawbacks of this method are limited to the solvent selected, which must have low melting point of below room temperature. This method may not be considered as suitable for use if the laboratory is not air conditioned and located in warm climate [13]. Apart from that, spatula is used for transfer solidified solvent, which may result in the loss of analytes. Guiñez and his teammates [45] tried using Hamilton syringe to collect floating or solidified extraction solvent but the efficiency was low since the interphase between the floating organic phase and the aqueous phase was rather hard to differentiate. Besides, Nojavan and his colleagues [46] indicated that high-density solvents had revealed better performance and reproducibility than lower-density solvents in extraction of seven basic pharmaceutical compounds.

Room temperature ionic liquids or ionic liquids (ILs, not all ILs are room temperature ILs.) are one of the extraction solvents that have been widely discussed in the literature. ILs are the salts that are made of substituted organic cation with an organic or inorganic anion that exist in liquid state at room temperature [47]. They possess outstanding physical properties such as low melting point, low vapour pressure, high thermal stability and good solubility in organic and inorganic compounds. As ILs are non-flammable and non-volatile, they are therefore classified as green solvent [9, 48]. Quite a number of studies related to IL-DLLME and a few review pieces have been published since IL-DLLME was first introduced in the year of 2008 [9, 47, 48]. Based on cation segment, ILs can be categorized into four types, which are alkylammonium-based, dialkylimidazolium-based, phosphonium-based and N-alkylpyridinium-based [49]. Most of the works have been found to have used dialkylimidazolium-based ILs as extraction solvents. In this regard, Hu et al. [50] employed three different dialkylimidazolium-based ILs as extraction solvent for determination of urinary 3-hydroxybenzo [a] pyrene. The recovery was found to be much higher than chlorinated solvents. IL-DLLME revealed excellent sensitivity with relatively lower LOD within a range of pg/mL [50, 51] or ng/mL [52-54] was obtained. Moreover, the types of ionic liquid are broader as many kinds of cations and anions can be combined [55]. By means of changing the structure and interaction of ions, their chemical and physical properties can vary and thus, ILs can be designed to exhibit target-selective [47]. Nonetheless, ILs have several drawbacks. Low volatility of ILs make them not suitable for gas chromatography. Hence, most IL-DLLME reported in related studies were coupled with high performance liquid chromatography (HPLC). However, ILs will be retained in the column or injector, which can result in distorted chromatograms [56, 57]. In order to overcome such problems, special design of injectors are required such as the combination of programmed temperature vaporization injector and thermal desorption unit, which can directly inject the analytes and prevent the entering of ILs into GC system [51].

Future trend based on green analytical chemistry

As a result of the limitless and almost never-ending human activities, there have been growing concerns about the potential negative influences on the environment. The side effects of the environment must be taken into consideration in the chemistry activities. The ideas of “green analytical chemistry” was originally proposed in the year of 2008 [58]. Green analytical chemistry can be applied in many forms, one of the segments is the reduction of the amount and toxicity of the solvents and reagent used. Thus, high toxicity solvents especially halogenated solvents have to be avoided from being used in sample preparation. Some interesting alternatives such as ILs, agro-

solvents and lipid structures could be greener solution for replacement of high toxicity solvents [59]. Nevertheless, their strengths, weaknesses, threats to the environment and compatibility to the analytical instruments should be explicitly identified due to the fact that their detrimental effects are not well understood.

The concept of three Rs (reduce, replace, recycle) has often been mentioned in the green analytical chemistry [60]. The reuse of chemicals or materials in process with minimum interferences from extraction efficiency is considered necessary. For instance, Wang and colleagues [61] applied such concepts in their attempts to extract three endocrine disrupting compounds from food packaging. Specifically, IL used as extraction solvent, was successfully recovered by modifying the pH and it can be reused three times without any significant loss of extraction efficiencies. In addition, Sheikhian and Shirafkan [62] also successfully separated ILs from analytes by changing pH and reused ILs at least four times. These methods are capable of minimizing the cost of extraction solvents and the environment and safety issues. In addition, recycle of ILs can help prevent the problem of ILs remaining in the column of HPLC. Hence, future works may have to zoom in on identifying ways to recycle and reuse the solvents.

One of the growing trends in analytical chemistry is the automation of extraction and analytical procedures. Automation is capable of minimizing the operator risks, waste generation, energy and solvent consumption [59]. In this regard, many innovative ideas for automated DLLME including automated agitation-assisted demulsification DLLME [63], effervescence assisted DLLME [64] and DLLME-switchable polarity dispersive solvent (DLLME-SPDS) [65] have over the years been introduced. The former method used agitation for the phase separation and the whole automated process requires only a total of 160 µL of solvents. The latter two approaches are automated and they have also excluded the negative impact of dispersive solvents on the solubility of analytes in aqueous sample. However, DLLME-SPDS has some limitations; it is only able to extract analytes in neutral and alkaline medium. Other automated techniques including flow, batch, flow-batch and in-syringe modes were also reported in the literature [66].

Conclusion

DLLME is considered as a powerful sample preparation for extraction of analytes from aqueous samples. It is worthy of note that the selection of appropriate extraction solvent is a critical parameter with the aim of acquiring a good extraction efficiency. Several types of extraction solvents such as the heavy-density solvents, low-density solvent and ionic liquids are discussed in the paper. In addition, the future trend for development of extraction solvents based on green chemistry was also intensively discussed. Overall, the exploitation of new extraction solvents and improvement of extraction performance in DLLME based on green analytical chemistry can be the main focus in future.

Acknowledgement

The authors would like to express special thanks to the Ministry of Higher Education of Malaysia ‘’Fundamental Research Grand no. “FRGS/1/2016/STG01/UNITEN/02/1” for the financial supports, and Institute of Sustainable Energy of UNITEN for the laboratory analysis.

References

1. Saraji, M. and Boroujeni, M. K. (2013). Recent developments in dispersive liquid–liquid microextraction. *Analytical and Bioanalytical Chemistry*, 406(8): 2027 - 2066.
2. Sarafraz-Yazdi, A. and Amiri, A. (2010). Liquid-phase microextraction. *Trends in Analytical Chemistry*, 29(1): 1 – 14.
3. Rezaee, M., Assadi, Y., Hosseini, M. R. M., Aghaee, E., Ahmadi, F. and Berijani, S. (2006). Determination of organic compounds in water using dispersive liquid–liquid microextraction. *Journal of Chromatography A*, 1116(1): 1 – 9.
4. Habibi, H., Mohammadi, A. and Kamankesh, M. (2017). Application and optimization of dispersive liquid-liquid microextraction coupled with high-performance liquid chromatography for sensitive determination of furfural and hydroxymethyl furfural in jarred and canned baby-foods. *Nutrition and Food Sciences Research*, 4(1): 25 – 32.

5. Pastor-Belda, M., Garrido, I., Campillo, N., Viñasa, P., Hellín, P., Flores, P. and Fenoll, J. (2015). Dispersive liquid-liquid microextraction for the determination of new generation pesticides in soils by liquid chromatography and tandem mass spectrometry. *Journal of Chromatography A*, 1394: 1 – 8.
6. Chisvert, A., Benedé, J. L., Peiró, M., Pedrón, I. and Salvador, A. (2017). Determination of N-nitrosodiethanolamine in cosmetic products by reversed-phase dispersive liquid-liquid microextraction followed by liquid chromatography. *Talanta*, 166: 81 – 86.
7. Asghari, A., Saffarzadeh, Z., Bazregar, M., Rajabi, M. and Boutorabi, L. (2017). Low-toxic air-agitated liquid-liquid microextraction using a solidifiable organic solvent followed by gas chromatography for analysis of amitriptyline and imipramine in human plasma and wastewater samples. *Microchemical Journal*, 130: 122 – 128.
8. Liang, P. and Sang, H. B. (2008). Determination of trace lead in biological and water samples with dispersive liquid–liquid microextraction preconcentration. *Analytical Biochemistry*, 380(1): 21 – 25.
9. Zang, H. X. Wu, Q. H., Zhang, M. Y., Xi, G. H. and Zhi, W. (2009). Developments of dispersive liquid-liquid microextraction technique. *Chinese Journal of Analytical Chemistry*, 37(2): 161 – 168.
10. Zgoła-Grzeskowiak, A. and Grzeskowiak, T. (2011). Dispersive liquid-liquid microextraction. *Trends in Analytical Chemistry*, 30(9): 1382 – 1399.
11. Viñas, P., Campillo, N., López-García, I. and Hernández-Córdoba, M. (2013). Dispersive liquid–liquid microextraction in food analysis: A critical review. *Analytical and Bioanalytical Chemistry*, 406(8): 2067 – 2099.
12. Campillo, N., Viñas, P., Šandrejová, J. and Andruch, V. (2016). Ten years of dispersive liquid-liquid microextraction and derived techniques. *Applied Spectroscopy Reviews,* 52(4): 267 – 415.
13. Leong, M. I., Fuh, M. R. and Huang, S. D. (2014). Beyond dispersive liquid–liquid microextraction. *Journal of Chromatography A*, 1335: 2 – 14.
14. Li, M. J. Zhang, H. Y., Liu, X. Z., Chui, C. Y. and Shi, Z. H. (2015). Progress of extraction solvent dispersion strategies for dispersive liquid-liquid microextraction. *Chinese Journal of Analytical Chemistry*, 43(8): 1231 – 1240.
15. Al-Saidi, H. M. and Emara, A. A. A. (2014). The recent developments in dispersive liquid–liquid microextraction for preconcentration and determination of inorganic analytes. *Journal of Saudi Chemical Society*, 18(6): 745 – 761.
16. Ahmad, W., Al-Sibaai, A. A., Bashammakh, A. S., Alwael, H. and El-Shahawi, M. S. (2015). Recent advances in dispersive liquid-liquid microextraction for pesticide analysis. *Trends in Analytical Chemistry*, 72: 181 – 192.
17. Alcantara, G. S. K., Calixto, L. A., de Moraes, L. A. B., Queiroz, R. H. C., de Oliveira, A. R. M. and de Gaitani, C. M. (2016). Determination of levetiracetam in human plasma by dispersive liquid-liquid microextraction followed by gas chromatography-mass spectrometry. *Journal of Analytical Methods in Chemistry*, 2016: 1 – 12.
18. Tobiszewski, M., Bigus, P. and Namiesnik, J. (2014). Determination of parent and methylated polycyclic aromatic hydrocarbons in water samples by dispersive liquid–liquid microextraction two-dimensional gas chromatography–time-of-flight mass spectrometry. *Analytical Method*, 6(17): 6678 – 6687.
19. Liu, J. Y., Lu, W. H. Liu, H. T., Wu, X. Q., Li, J. H. and Chen, L. X. (2016). Dispersive liquid-liquidmicroextraction for four phenolic environmental estrogens in water samples followed by determination using capillary electrophoresis. *Electrophoresis*, 37(19): 2502 – 2508.
20. Larki, A. (2017). A novel application of carbon dots for colorimetric determination of fenitrothion insecticide based on the microextraction method. *Spectrochimica Acta Part A: Molecular and Biomolecular Spectroscopy*, 173: 1 – 5.
21. U. S. National Library of Medicine (2016). Hazardous Substances Data Bank. https://toxnet.nlm.nih.gov/newtoxnet/hsdb.htm. [Access online 2 July 2017].
22. Hu, X. Z., Wu, J. H. and Feng, Y. Q. (2010). Molecular complex-based dispersive liquid–liquid microextraction: Analysis of polar compounds in aqueous solution. *Journal of Chromatography A*, 1217(45): 7010 – 7016.
23. Farajzadeh, M. A. Djozan, D., Afshar, M. R. and Norouzi, J. (2012). Determination of phthalate esters in cow milk samples using dispersive liquid–liquid microextraction coupled with gas chromatography followed by flame ionization and mass spectrometric detection. *Journal of Separation Science*, 35(5-6): 742 – 749.

24. Pena, M. T., Vecino-Bello, X., Casais, M. C., Mejuto, M. C. and Cela, R. (2012). Optimization of a dispersive liquid–liquid microextraction method for the analysis of benzotriazoles and benzothiazoles in water samples. *Analytical and Bioanalytical Chemistry*, 402(4): 1679 – 1695.
25. Emídio, E. S., da Silva, C. P. and de Marchi, M. R. R. (2015). Determination of estrogenic mycotoxins in environmental water samples by low-toxicity dispersive liquid-liquid microextraction and liquid chromatography-tandem mass spectrometry. *Journal of Chromatography A*: 1391(1): 1 – 8.
26. Peng, G. L. Lu, Y. He, Q., Mmereki, D., Zhou, G. M., Chen, J. H. and Tang, X. H. (2016). Dispersive liquid–liquid microextraction using low-toxic solvent for the determination of heavy metals in water samples by inductively coupled plasma–mass spectrometry. *Journal of AOAC International*, 99(1): 260 – 266.
27. Leong, M. I., Chang, C. C., Fuh, M. R. and Huang, S. D. (2010). Low toxic dispersive liquid–liquid microextraction using halosolvents for extraction of polycyclic aromatic hydrocarbons in water samples. *Journal of Chromatography A*, 1217(34): 5455 – 5461.
28. Chai, M. K., Premla, D. C. and Wong, L. S. (2016). Modified dispersive liquid-liquid microextraction using green solvent for determination of polycyclic aromatic hydrocarbons (PAHs) in vegetable samples. *Malaysian Journal of Analytical Sciences*, 20(1): 14 – 20.
29. Chemical Book (2016). http://www.chemicalbook.com/CAS_75-30-9.htm. [Access online 2 July 2017].
30. Guo, L. and Lee, H. K. (2011). Low-density solvent-based solvent demulsification dispersive liquid–liquid microextraction for the fast determination of trace levels of sixteen priority polycyclic aromatic hydrocarbons in environmental water samples. *Journal of Chromatography A*, 1218(31): 5040 – 5046.
31. Chen, X. C., You, X. W., Liu, F. M. and Zhang, X. (2015). Low-density solvent based vortex-assisted surfactant enhanced emulsification microextraction with a home-made extraction device for the determination of four herbicide residues in river water. *Analytical Method*, 7(22): 9513 – 9519.
32. Barrett, C. A., Orban, D. A., Seebeck, S. E., Lowe, L. E. and Owens, J. E. (2015). Development of a low-density-solvent dispersive liquid–liquid microextraction with gas chromatography and mass spectrometry method for the quantitation of tetrabromobisphenol-A from dust. *Journal of Separation Science*, 38: 2500 – 2509.
33. Fatemi, M. H., Hadjmohammadi, M. E. and Shakeri, P. (2014). Evaluation of alcoholic-assisted dispersive liquid–liquid microextraction of bisphenol A in water samples using an experimental design. *Acta Chromatographica*, 26 (3): 401 – 412.
34. Aghamohammadi, M., Shahdousti, P. and Harooni, B. (2016). Ultrasound-assisted emulsification microextraction followed by gas chromatography–flame ionization detection for urinary methylmalonic acid determination. *Microchemical Journal*, 124: 188 – 194.
35. Çabuk, H. and Köktürk, M. (2013). Low density solvent-based dispersive liquid-liquid microextraction for the determination of synthetic antioxidants in beverages by high-performance liquid chromatography. *The Scientific World Journal*, 2013: 1 – 8.
36. Bai, X. Z. Zhang, T., Li, H. P. and Yang, Z. G. (2016). Simultaneous dispersive liquid–liquid microextraction based on a low-density solvent and derivatization followed by gas chromatography for the simultaneous determination of chloroanisoles and the precursor 2,4,6-trichlorophenol in water samples. *Journal of Separation Science*, 39: 2146 – 2155.
37. Xu, H., Ding, Z. Q., Lv, L. L., Song, D. D. and Feng, Y. Q. (2009). A novel dispersive liquid–liquid microextraction based on solidification of floating organic droplet method for determination of polycyclic aromatic hydrocarbons in aqueous samples. *Analytica Chimica Acta*, 636: 28 – 33.
38. Rezaee, M., Yamini, Y., Khanchi, A., Faraji, M. and Saleh, A. (2010). A simple and rapid new dispersive liquid–liquid microextraction based on solidification of floating organic drop combined with inductively coupled plasma-optical emission spectrometry for preconcentration and determination of aluminium in water samples. *Journal of Hazardous Materials*, 178: 766 – 770.
39. Peng, G. L., He, Q., Mmereki, D., Zhou, G. M., Pan, W. L., Gu, L., Fan, L. L. and Mao, Y. F. (2015). Vortex-assisted liquid–liquid microextraction using a low-toxicity solvent for the determination of five organophosphorus pesticides in water samples by high-performance liquid chromatography. *Journal of Separation Science*, 38 (20): 3487 – 3493.
40. Kocúrová, L., Balogh, I. S., Šandrejová, J. and Andruch, V. (2012). Recent advances in dispersive liquid–liquid microextraction using organic solvents lighter than water. A review. *Microchemical Journal*, 102: 11 – 17.

41. Leong, M. I. and Huang, S. D. (2008). Dispersive liquid–liquid microextraction method based on solidification of floating organic drop combined with gas chromatography with electron-capture or mass spectrometry detection. *Journal of Chromatography A*, 1211: 8 – 12.
42. Xu, H., Ding, Z. Q., Lv, L. L., Song, D. D. and Feng, Y. Q. (2009). A novel dispersive liquid–liquid microextraction based on solidification of floating organic droplet method for determination of polycyclic aromatic hydrocarbons in aqueous samples. *Analytica Chimica Acta*, 636(1): 28 – 33.
43. Asadollahi, T., Dadfarnia, S., Shabani, A. M. H. and Amirkavei, M. (2015). Separation/preconcentration and determination of quercetin in food samples by dispersive liquid–liquid microextraction based on solidification of floating organic drop -flow injection spectrophotometry. *Journal of Food Science and Technology*, 52(2): 1103 – 1109.
44. Bolzan, C. M. Caldas, S. S., Guimarães, B. S., and Primel, E. G. (2016). Dispersive liquid–liquid microextraction based on solidification of floating organic droplet for the determination of triazine and triazoles in mineral water samples. *Journal of Separation Science*, 39(17): 3410 – 3417.
45. Guiñez, M., Martinez, L. D., Fernandez, L. and Cerutti, S. (2017). Dispersive liquid–liquid microextraction based on solidification of floating organic drop and fluorescence detection for the determination of nitrated polycyclic aromatic hydrocarbons in aqueous samples. *Microchemical Journal*, 131: 1 – 8.
46. Nojavan, S., Gorji, T., Davarani, S. S. H. and Morteza-Najarian, A. (2014). Solvent selection in ultrasonic-assisted emulsification microextraction: Comparison between high- and low-density solvents by means of novel type of extraction vessel. *Analytica Chimica Acta*, 838: 51 – 57.
47. Ho, T. D., Zhang, C., Hantao, L. W., and Anderson, J. L. (2014). Ionic liquids in analytical chemistry: Fundamentals, advances, and perspectives. *Analytical Chemistry*, 86: 262 – 285.
48. Vekariya, R. L. (2017). A review of ionic liquids: Applications towards catalytic organic transformations. *Journal of Molecular Liquids*, 227: 44 – 60.
49. Ghandi, K. (2014). A review of ionic liquids, their limits and applications. *Green and Sustainable Chemistry*, 4: 44 – 53.
50. Hu, H., Liu, B. Z., Yang, J., Lin, Z. M. and Gan, W. (2016). Sensitive determination of trace urinary 3-hydroxybenzo[a]pyrene using ionic liquids-based dispersive liquid–liquid microextraction followed by chemical derivatization and high performance liquid chromatography–high resolution tandem mass spectrometry. *Journal of Chromatography B*, 1027: 200 – 206.
51. Cacho, J. I., Campillo, N., Viñas, P. and Hernández-Córdoba, M. (2016). Improved sensitivity gas chromatography–mass spectrometry determination of parabens in waters using ionic liquids. *Talanta*, 146: 568 – 574.
52. Peng, B., Zhang, J. H., Wu, C. H., Li, S. Q., Li, Y. B., Gao, H. X., Lu R. H. and Zhou W. F. (2014). Use of ionic liquid-based dispersive liquid–liquid microextraction and high-performance liquid chromatography to detect formaldehyde in air, water, and soil samples. *Journal of Liquid Chromatography & Related Technologies*, 37(6): 815 – 828.
53. Gong, A. Q. and Zhu, X. S. (2015). Dispersive solvent-free ultrasound-assisted ionic liquid dispersive liquid–liquid microextraction coupled with HPLC for determination of ulipristal acetate. *Talanta*, 131: 603 – 608.
54. Albishri, H. M., Aldawsari, H. A. M. and El-Hady, D. A. (2016). Ultrasound-assisted temperature-controlled ionic liquid dispersive liquid phase microextraction combined with reversed phase liquid chromatography for determination of organophosphorus pesticides in water samples. *Electrophoresis*, 37 (39): 2462 – 2469.
55. Trujillo-Rodríguez M. J., Rocío-Bautista, P., Pino, V. and Afonso, A. M. (2013). Ionic liquids in dispersive liquid-liquid microextraction. *Trends in Analytical Chemistry*, 51: 87 – 106.
56. Poole, C. F. and Poole, S. K. (2010). Extraction of organic compounds with room temperature ionic liquids. *Journal of Chromatography A*, 1217 (16): 2268 – 2286.
57. Ma, X. G., Huang, M. H., Li, Z. H. and Wu, J. M. (2011). Hollow fiber supported liquid-phase microextraction using ionic liquid as extractant for preconcentration of benzene, toluene, ethylbenzene and xylenes from water sample with gas chromatography-hydrogen flame ionization detection. *Journal of Hazardous Materials*, 194: 24 –29.
58. Armenta, S. Garrigues, S. and de la Guardia, M. (2008). Green analytical chemistry. *Trends in Analytical Chemistry*, 27(6): 497 – 511.
59. Armenta, S., Garrigues, S. and de la Guardia, M. (2015). The role of green extraction techniques in Green analytical chemistry. *Trends in Analytical Chemistry*, 71: 2 – 8.

60. Welch, C. J. Wu, N. J. M., Biba, M., Hartman, R., Brkovic, T., Gong. X. Y., Helmy, R., Schafer, W., Cuff, J., Pirzada, Z. and Zhou, L. L. (2010). Greening analytical chromatography. *Trends in Analytical Chemistry*, 29 (7): 667 – 680.
61. Wang, L. L., Zhang, D. F., Xu, X. and Zhang, L. (2016). Application of ionic liquid-based dispersive liquid phase microextraction for highly sensitive simultaneous determination of three endocrine disrupting compounds in food packaging. *Food Chemistry*, 197: 754 – 760.
62. Sheikhian, L. and Shirafkan, M. (2016). Temperature-assisted ionic liquid-based dispersive liquid–liquid microextraction with following back-extraction for HPLC/UV–Vis determination of 3-indole acetic acid in pea plants. *Journal of Iranian Chemical Society*, 13(5): 903 – 911.
63. Guo, L., Chia, S. S. and Lee, H. K. (2016). Automated agitation-assisted demulsification dispersive liquid-liquid microextraction. *Analytical Chemistry*, 88 (5): 2548 – 2552.
64. Medinskaia, K., Vakh, C., Aseeva, D., Andruch, V., Moskvin, L. and Bulatov, A. (2016). A fully automated effervescence assisted dispersive liquid–liquid microextraction based on a stepwise injection system. Determination of antipyrine in saliva samples. *Analytica Chimica Acta*, 902: 129 – 134.
65. Timofeeva, I., Timofeev, S., Moskvin, L. and Bulatov, A. (2017). A dispersive liquid-liquid microextraction using a switchable polarity dispersive solvent. Automated HPLC-FLD determination of ofloxacin in chicken meat. *Analytica Chimica Acta*, 949: 35 – 42.
66. Alexovič, M., Horstkotte, N., Šrámková, I. Solich, P. and Sabo, S. (2017). Automation of dispersive liquid-liquid microextraction and related techniques. Approaches based on flow, batch, flowbatch and in-syringe modes. *Trends in Analytical Chemistry*, 86: 39 – 55.

Malaysian Journal of Analytical Sciences, Vol 22 No 2 (2018): 175 - 184
DOI: https://doi.org/10.17576/mjas-2018-2202-02

MALAYSIAN JOURNAL OF ANALYTICAL SCIENCES
Published by The Malaysian Analytical Sciences Society
ISSN 1394 - 2506

RECENT ADVANCES IN THE PREPARATION OF OIL PALM WASTE-BASED ADSORBENTS FOR REMOVAL OF ENVIRONMENTAL POLLUTANTS - A REVIEW

(Kemajuan Terkini dalam Penyediaan Penjerap Berasaskan Sisa Kelapa Sawit untuk Penyingkiran Bahan Pencemar Alam Sekitar - Sebuah Ulasan)

Faridah M. Marsin[1, 2], Wan Aini Wan Ibrahim[1, 3], Hamid Rashidi Nodeh[4], Zetty Azalea Sutirman[1], Ng Nyuk Ting[1], Mohd Marsin Sanagi[1,3]*

[1]*Department of Chemistry, Faculty of Science,*
Universiti Teknologi Malaysia, 81310 UTM Johor Bahru, Johor, Malaysia
[2]*Malaysia Department of Chemistry (Southern Branch), 80100 Johor Bahru, Johor, Malaysia*
[3]*Centre for Sustainable Nanomaterials, Ibnu Sina Institute for Scientific and Industrial Research,*
Universiti Teknologi Malaysia, 81310 Johor Bahru, Johor, Malaysia
[4]*Department of Chemistry, Faculty of Science,*
University of Tehran, Tehran, Iran

**Corresponding author: marsin@kimia.fs.utm.my*

Received: 10 November 2017; Accepted: 28 February 2018

Abstract

The palm oil industry is an excellent source for huge quantities of highly useful biomass. Utilization of oil palm biomass-based materials for the removal of environmental pollutants appears to be a viable solution in the lights of promoting sustainable development. This article aims to review recent advances in the preparation of adsorbent from different parts of oil palm biomass for the removal of heavy metal and organic environmental pollutants from water. Physical and chemical factors that enhance the applicability of oil palm waste as adsorbents are also discussed. It is clear that each part of the oil palm biomass is potentially applicable as biosorbents for most environmental pollutants and the capability could be further enhanced through modifications in accordance with its intended pollutants. Modifications by chemical treatments such as acidic, basic or drying agent treatments under optimum dosages have been found to have significant effects on the selectivity of the analyte absorption. In general, basic treatment is more suitable for common pollutants such as metals, pesticide and basic dyes. Meanwhile, the acidic treatment is more suitable for non-polar organic pollutants such as phenols. Recent trends in the application of oil palm biomass as biosorbents are also discussed that together open new doors to sustainable development.

Keywords: oil palm biomass, adsorbent, activated carbon, environmental pollutants

Abstrak

Industri minyak kelapa sawit merupakan sumber yang baik untuk mendapatkan biojisim bermanfaat dalam kuantiti yang besar. Penggunaan bahan berasaskan biojisim minyak kelapa sawit bagi penyingkiran pencemar alam sekitar merupakan salah satu penyelesaian berdaya maju dalam mempromosi pembangunan mampan. Artikel ini bertujuan untuk mengulas kemajuan dalam penyediaan penjerap daripada pelbagai bahagian biojisim kelapa sawit bagi penyingkiran ion logam berat dan pencemar organik alam sekitar daripada air. Faktor fizikal dan kimia bagi meningkatkan kebolehgunaan sisa kelapa sawit sebagai penjerap juga dibincangkan. Ianya jelas bahawa setiap bahagian biojisim kelapa sawit berpotensi untuk digunakan sebagai bio-pengerap bagi kebanyakan bahan pencemar, dan keupayaannya dapat dipertingkatkan melalui pengubahsuaian sesuai dengan bahan pencemar yang digunakan. Pengubahsuaian dengan rawatan kimia misalnya rawatan asid, alkali dan ejen pengeringan dengan dos yang optimum didapati memberi kesan terhadap pemilihan penjerapan analit. Secara keseluruhan, rawatan alkali lebih sesuai bagi

bahan pencemar lazim misalnya logam, racun mahluk perosak, dan pewarna alkali. Sementara itu, rawatan asid lebih sesuai untuk bahan pencemar organik yang tidak berkutub misalnya fenol. Aliran terkini dalam aplikasi biojisim kelapa sawit sebagai bio-pengerap juga dibincangkan bagi membuka laluan baharu untuk pembangunan mampan.

Kata kunci: biojisim kelapa sawit, penjerap, karbon teraktif, pencemar alam sekitar

Introduction

In recent years, increasing costs and environmental considerations have led to the use of new low-cost adsorbents derived from renewable resources. Numerous researches have expanded the idea of utilizing inexpensive adsorbents from natural materials, such as agricultural waste and minerals for removal of environmental pollutants. We have dedicated time in search towards a greener and sustainable alternative adsorbents for removal of pollutants using biomaterials such as starch [1], alginate [2], agarose [3], and chitosan [4, 5]. The booming of the *Elais guineensis*, or generally known as oil palm, triggered the massive increase in oil palm plantation area of more than 5.74 million hectares in Malaysia in 2016 [6]. With the rapid growth of palm oil production, the amount of waste generated also shows a corresponding increase. An approximate 85.5% of agricultural wastes in Malaysia came from palm oil plantations [7]. The oil palm biomass waste consists of mainly empty fruit bunches (EFB), shell and kernels, fronds, leaves and trunks. The huge amount of waste generated has to be utilized efficiently to promote sustainability.

Currently, various technologies have been applied to convert palm oil waste to renewable energy, value-added products and bio-based products such as pellet for feedstock, fertilizers, fillers, bioplastics and adsorbent (Figure 1). Limited work has been made to retrieve valuable components such as carotene, tocopherols and tocotrienols in residue oil from palm pressed fibers [8]. However, there have been considerable developments where oil palm waste is turned into adsorbents via activated carbon, char, ash and combination with other suitable material to enhance its ability and selectivity for adsorption. This article reviews current trends in physical and chemical preparation treatments of different parts of palm oil waste as adsorbent to maximize its potential for selective removal of assorted environmental pollutants such as dyes, pesticides, metals and other organic pollutants.

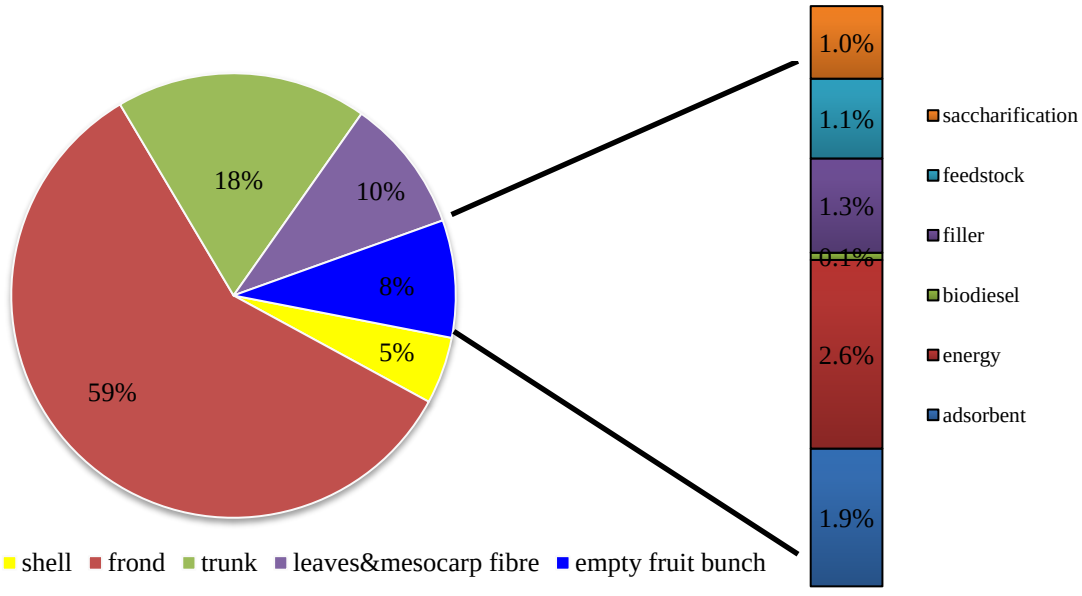


Figure 1. Oil palm biomass percentage in 2009 [9] and percentage of work towards recyclability of oil palm empty fruit bunch in recent years (2013-2016) [10]

Oil palm waste as adsorbent

In general, oil palm mills generate a number of biomass wastes. The amount of biomass produced by an oil palm tree, inclusive of the oil and lignocellulose materials is on the average of 231.5 kg dry weight/year [7]. EFB and mesocarp fiber is the highest contributor of oil palm waste, with approximately 15.8 and 9.6 million tonnes, respectively [11]. EFB, mesocarp fiber and shells are collected during the pressing of sterilized fruits whilst oil palm fronds are available daily throughout the year when the palms are pruned during the harvesting of fresh fruit bunch for the production of oil. Oil palm trunk is obtained during the replantation of the oil palm trees that occurred every 15-20 years. Recent research output proved that each part of oil palm waste could be converted into value added products such as oil palm activated carbon that has been used to treat air toxics such as carbon monoxide (CO) and sulphur oxides (SO_x) [12, 13].

The adsorbent obtained from different parts of oil palm biomass show different morphology in accordance to its composition (Table 1) as it was turned to activated carbon for the enhancement of adsorption process. Biomass with higher cellulose composition will produce low molecular weight products comprising anhydro-sugar, aldehyde, hydroxyl, furan, acetic acid and the carbonaceous chars. On the other hand, when lignin decomposes under elevated temperature, unsaturated chain and phenolic compounds with higher molecular weight, such as eugenol, styrene, alcohols, and carbonaceous chars will be produced [14]. This occurrence will in turn have an effect on selectivity of the analytes towards the carbon produced.

Table 1: Basic composition percentage of oil palm waste

Oil Palm Waste	Cellulose (%)	Hemicellulose (%)	Lignin (%)	Inorganic Compounds (%)	Waste Percentage Generated from Palm Oil Industry (%)	References
Empty fruit bunch	25	28	27	16	22	[15]
Frond	35	36	29	n.a.	14	[16]
Shell	28	22	44	n.a.	5	[17]
Trunk	50	70	20	n.a.	n.a.	[18]
Leaves/mesocarp fiber	45	48	27	n.a.	n.a.	[19]

* n.a. – not available

The adsorption characteristics of activated carbons are generally governed by the surface area pores formation on the surface, and surface functional groups. It is believed that mesopores are more suitable for adsorption as compared to micropores and macropores [18]. Surface functional groups play an important role during cationic and anionic adsorbate removal. Thus the specific treatment of each part of oil palm waste is a crucial step in the advancement of oil palm waste based adsorbent.

The difference in thermal treatment gave a significant impact on the textural properties of the oil palm-based adsorbent. This was proven by Hamza et al. [20] who reported that the pore networks in oil palm shell increased with increase of up to 700 °C. Nomanbhay et al. [15] found that microwave assisted extraction followed by basic treatment of oil palm EFB significantly improved the saccarification of EFB by removing more lignin and hemicellulose, and increasing the accessibility to hydrolytic enzymes. Furthermore, a recent study also concluded that the increment of activation temperature on oil palm empty fruit bunch will noticeable decrease the pore size, increase the surface area and the amount of carbonyl groups, thus increasing the probability of phenolic analyte adsorption [21].

The use of dehydrating agent can be categorized into either acid or basic treatment, whereby both treatments are efficient methods used to produce adsorbents with high surface area and porosity. Wirasnita et al. [22] found that

the evaporation of the chemicals impregnated on the surface of the precursor-EFB, formed smaller cavities during activation process, and at the same time restricts the formation of tar.

Other impregnation treatments such as chitosan coating-oil palm waste – based adsorbent was also studied to improve the structure and surface area of the adsorbent [23]. The coating was found to increase its hydroxyl groups for more adsorption of polar pollutants. Such treatment onto different parts of oil palm waste to develop suitable adsorbent was discussed in accordance to the type of pollutants generally common in water matrices.

Removal of dyes using oil palm adsorbents

Dyes are a major source of pollution that is generally present in effluents from textile industries. These dye effluents are considered toxic as they reduce photosynthetic activity due to the coloration of water, and in turn affects the symbiotic process in the aqueous system. Palm oil mill effluents derived from bleaching process can cause coloration of streams. Thus, adsorption studies have been carried out using oil palm biomass-based adsorbents for the removal of dyes in streams.

The procedure of turning waste into adsorbents generally requires physical treatment. This was evident from recent studies on the removal of dyes (Table 2). Hameed et al. [24] postulated that pyrolysis at an optimum temperature of 862 °C can change the characteristics of oil palm EFB-based carbon for maximum removal of targeted dye, methylene blue. They also applied the same procedure to prepare adsorbent from oil palm trunks without treatment and found high malachite green uptake of 149.35 mg/g [25]. Meanwhile, Montoya-Suarez et al. [26] studied the physical treatment of oil palm shell at 600-800°C and obtained adsorbent with high surface area of 1268 m^2/g.

Sajab et al. used oil palm EFB for the removal of anionic and cationic dyes [27]. They noticed changes in selectivity when using different types of treatments. The EFB-citric acid treated is more selective towards targeted cationic dye (methylene blue) with an uptake of 450.4 mg/g of adsorbent, whilst EFB-polyethylene imine has higher tendency to adsorb the targeted anionic dye (phenyl red) with 555.4 mg/g [28]. When combined in a continuous column bed, EFB-polyethylene imine was more dominant compared to EFB-citric acid, which influenced the simultaneous adsorption of methylene blue and phenyl red.

The ability of oil palm fiber-based adsorbent was investigated by Kietkwanboot [29] for the decolorization of highly alkaline palm oil mill effluent (POME). With the combination of oil palm fibers and *Trameters hirsuta* AK4 microorganism embedded onto the fiber, up to 82.4% POME decolorization was achieved. Meanwhile, Hussin et al. [30] successfully treated oil palm fronds with mixtures of acid and basic treatment to extract microcrystalline cellulose and tested the adsorption of methylene blue with a mild uptake of 51.81 mg/g.

The oil palm ash from oil palm waste was tested for its adsorption ability by Khanday et al. [25]. To compensate for the loss of lignocellulose in oil palm ash, it was added with chitosan and treated using sodium hydroxide for the removal of methylene blue and acid blue 29 dyes. They noticed that both acid blue 29 and methylene blue were able to be absorbed by the oil palm ash-chitosan adsorbent with and uptake of 270 mg/g and 199.2 mg/g, respectively. This was due to the presence of more anionic sites from the oil palm ash and cationic sites from amino and hydroxyl groups from chitosan.

Wong et al. took it one step further by using oil palm shell activated carbon with the addition of magnetic nanoparticles for easier separation of adsorbents from water samples [31]. They tested and found that it has the ability to adsorb methylene blue with a good uptake of 163.3 mg/g due to hydrophobic interactions between oil palm shell and analytes, and the presence of magnetite that contributes via ionic interaction between metal and analytes.

Table 2. Literature studies on preparation of oil palm waste-based adsorbent for removal of dyes

Oil Palm Waste Part	Activation Temperature	Treatment	Dyes	Removal Percentage / Uptake	Ref.
Oil palm EFB	862 °C	Potassium hydroxide	Methylene blue	400 mg/g	[24]
	120 °C	Citric acid and polyethylene imine	Methylene blue and phenyl red	130 mg/g and 170 mg/g	[28]
Oil palm fibers	Nil	*Trameters hirsuta* fungus	Decolorization POME*	82.4%	[29]
Oil palm fronds	Room temperature	Acetic acid and sodium hypochlorite, followed by sodium hydroxide	Methylene blue	51.81 mg/g	[30]
Oil palm fronds and leaves	80-100 °C	Nil	Methylene blue	88.72%	[32]
Oil palm trunks	Nil	Nil.	Malachite green	149.35 mg/g	[25]
Oil palm shell	Microwave	Zinc chloride	Methylene blue	0.73 mg/g	[33]
	600-800 °C	Nil	Methylene blue	110 mg/g	[26]
		Magnetic nanoparticle	Methylene blue	163.3 mg/g	[31]
Oil palm ash	Nil	Nil	Bleaching palm oil	97.3%	[34]
	Nil	Sodium hydroxide and chitosan addition	Methylene blue and acid blue 29	192.2 mg/g and 270.3 mg/g	[35]

POME – palm oil mill effluent, Nil – no treatment reported.

Removal of pesticides using oil palm adsorbents

Pesticides are one of the sought-after environmental pollutants for their carcinogenic effects and accumulation into aquatic life that will cause dire effects to human health. The chosen oil palm waste-biosorbents need to have the chemical affinity towards these polar pesticides for successful adsorption.

Oil palm EFB-based adsorbent was chemically treated with basic solution of ammonia solution for the removal of 2,4,6-trichlorophenol with an impressive uptake of 168.89 mg/g [36]. Salman et al. [37] used similar KOH treatment on oil palm fronds for successful removal of bentazon. Oil palm shell treated with NaOH reported by Hamad et al. [38] gave a maximum uptake of 454.5 mg/g of 4-chloroguiacol. Hamad et al. [39] also found that with the use of K_2CO_3 as activating agent, the oil palm shell based adsorbent is able to successfully remove 2,4-dichlorophenol with an uptake of 323.62 mg/g. The use of alkaline treatment was found to effectively remove the hemicellulose part of oil palm EFB [40], leaving the lignin and cellulose part as an active adsorption sites.

Yavari et al. [41] worked on oil palm EFB using low temperature pyrolysis at 300-700 °C for the synthesis of biosorbents for the removal of imazapyr and imazapic herbicides and concluded that the reduction of pyrolysis temperature increased the adsorption of polar analytes. Similar results were reported by Salman et al. [42] who prepared oil palm fronds-based adsorbents using pyrolysis and used it for the removal of glyphosate with an uptake of 104.2 mg/g. Beforehand, most of the studies used a temperature of above 800°C for the preparation of the adsorbent [43, 44]. Tan et al. [45] described an ineffective adsorption using oil palm shell-based adsorbent that was treated with a solution of HNO_3 for atrazine removal with uptake of a mere 0.046 mg/g. This showed that basic treatment is preferred for the adsorption of pesticides, as it provided basic sites for the adsorption of pesticides to occur. The maximum uptake levels of various pesticides using oil palm biomass-based adsorbents are listed in Table 3.

Table 3. Literature studies on preparation of oil palm waste-based adsorbents for removal of pesticides

Oil Palm Waste Part	Activation Temperature	Treatment	Pesticides	Removal Percentage / Uptake	Ref.
Oil palm EFB	814 °C	Potassium hydroxide	2,4,6-tricholorophenol	168.89 mg/g	[43]
	814 °C	Ammonia	2,4-dichlorophenol	285.71 mg/g	[36]
	300-700 °C	Nil	Imazapyr, imazapic	24 mg/kg	[41]
Oil palm fronds	850 °C	Potassium hydroxide	Bentazon	99.85%	[37]
	700 °C	Potassium hydroxide	Dichlorophenoxy acetic acid	353 mg/g	[44]
	700 °C	Potassium hydroxide	Glyphosate	104.2 mg/g	[42]
Oil palm shell	800 °C	Sodium hydroxide	4-chloroguiacal	454.5 mg/g	[38]
		Nitric acid	Atrazine	0.046 mg/g	[45]

Removal of metal using oil palm adsorbents

Metal pollution is one of the most important environmental concerns due to their toxicity and accumulation in the food chain. Wastewaters from various industries such as mining, metallurgical and electronics may contain one or more toxic metals. Oil palm biomass waste has been investigated for the removal of diverse metals from water. Salamantinia et al. [46] investigated copper and zinc uptake using oil palm fronds-based adsorbents. Oil palm EFB-based biosorbents were thoroughly investigated by Wahi et al. [47]. They used chemical treatment with NaOH at activation temperature of 400-700 °C to prepare the adsorbent. The removal uptake for copper, lead and mercury were at a high of 52.5 mg/g. Meanwhile, Montoya-Suarez et al. [26] found that adsorbent obtained from pyrolysis of oil palm shell at 600-800 °C was able to remove only 0.37 mg/g of chromium ions. Similar findings were reported by Rehman et al. [48] who studied oil palm clinker sand as adsorbents and obtained an arsenic uptake of 9 mg/g. However, a recent work by Daneshfozoun et al. [49] who used grinded oil palm EFB without any treatment for removal of lead in water and found that the lead uptake is at par with alkaline-treated based adsorbent with an uptake of 47.49 mg/g. It was observed that the metal ion adsorption occurs onto the lignocellulose sites in the adsorbent. With pyrolysis, the disappearances of cellulose sites decrease the uptake of metals onto the adsorbent.

Table 4. Literature studies on preparation of oil palm waste-based adsorbent for removal of heavy metal

Oil Palm Waste Parts	Activation Temperature	Treatment	Metal Ions	Removal Percentage / Uptake	Ref.
Oil palm EFB	400-700 °C	Sodium hydroxide	Cu, Pb, Hg	52.5 mg/g	[47]
	Nil	Grinded	Pb	47.49 mg/g	[49]
	Nil	Magnetic nanoparticle	Pb	93.7%	[50]
Oil palm fronds	70 °C	Sodium hydroxide	Zn, Cu	90%	[46]
Oil palm shell	600-800 °C	Nil	Cr	0.37 mg/g	[26]
Oil palm ash	Nil	Nil	As	9 mg/g	[48]

Removal of phenolic compounds using oil palm adsorbents

Oil palm waste-based adsorbents have also been applied in the removal of other phenolic compounds (Table 5). Lua and Jia [51] used oil palm shell treated at steam activation temperature of 675 °C to produce the adsorbents for phenol removal. They reported a successful removal of phenol with an uptake of 166 mg/g. Alam et al. [52] also used steam activation for the preparation of oil palm EFB-based adsorbent obtained at a temperature of 800 °C with an uptake of 300 mg/L water. This indicates that the uptake of phenolic compounds increases with higher activation temperature. Al-Aoh et al. [53] examined oil palm ash that has been treated with acid and found that the uptake of 4-nitrophenol was high (1000 mg/g). Hamad et al. [38, 39] reported the removal of chlorinated phenolic compounds using oil palm shell activated at a high temperature of 800 °C with potassium carbonate treatment to attract the anion site of the analyte. Thus, it is apparent that high activation temperature serves as the main factor in increasing the phenolic compound adsorption capacity. Elevated activation temperatures and further acidic treatment tend to decrease the amount of oxygen groups from cellulose, thus helping in the formation of more non-polar sites on the adsorbent that in turn increases the adsorption ability of the adsorbent towards organic pollutants.

Table 5. Literature studies on preparation of oil palm waste-based adsorbent for removal of phenol

Oil Palm Waste Parts	Activation Temperature	Treatment	Analyte	Removal Percentage / Uptake	Ref.
Oil palm EFB	800 °C	Nil	Phenol	200-300 mg/L	[52]
Oil palm shell	Steam 675 °C	Nil	Phenol	166 mg/g	[51]
	800 °C	Potassium carbonate	4-Cl-2-methyoxyphenol	323.62 mg/g	[39]
Oil palm ash	Nil	Sulfuric acid	4-nitrophenol	1000 mg/g	[53]

* nil – no further treatment

Conclusion

To uphold sustainability in the expanding palm oil industry, oil palm waste was proven a viable alternative source of adsorbent for various types of pollutants. Surface modification by physicochemical methods directs an alternative approach for the improvement of each oil palm waste-based adsorbents towards the pollutant uptake from aqueous solution. Therefore, the technique of choice could be attuned in accordance to the analytes of interest. It was also observed that for different part of oil palm waste, different activation treatment is needed for optimum removal of targeted pollutants. In general, physical activation at high temperatures was needed for all parts of oil palm bio-waste for the adsorption of organic pollutants as more covalent and hydrophobic interactions may occur on the surface of the activated carbon. Chemical treatment of the adsorbent is to improve the selectivity of the adsorbent towards the analyte. Basic treatment is more suitable for anionic dyes such as acid blue 29 and phenyl red compared to cationic dyes. The addition of dehydrating agents such as zinc chloride affects the physical type of pore produced on the adsorbent.

Most of the studies reported on the removal of pesticides utilized basic treatment (ammonia, potassium hydroxide and sodium hydroxide) for enhanced chemisorption of the pesticides onto the oil palm waste-based adsorbents. The use of acid treatment reduces the uptake of pesticides, as they are repelled from the active sites of the adsorbent. It is noteworthy that adsorbents obtained from oil palm waste via basic treatment are favorable for the removal of metal ions. This preparation technique generates more hydroxyl active sites on the surface of the oil palm waste-based adsorbents for more efficient removal of metal ions. The trends also show that most organic pollutants studied favor adsorbent prepared using acid treatment and higher temperature. This is because less oxygenated active sites are produced, thus more non-polar interactions occur, increasing the uptake of organic pollutants such as phenols and glyphosate. Despite numerous works on oil palm waste-based adsorbents, there seem to be the lacking of studies on the addition and combination of other compounds with oil palm waste-based adsorbents in pursue of improved adsorbents. Thus, there is ample opportunity for future investigations such as combining palm oil waste-based adsorbents with compounds such as molecular orbital framework compounds or polymers. Such innovations might

increase the chances of these low-cost adsorbents to be used as greener and more sustainable alternatives to more conventional adsorbents.

Acknowledgement

The authors acknowledge the Organization Prohibition of Chemical Weapon Research Grants R.J130000.7309.4B222 and R.J130000.7836.4B219 for financial supports. Faridah M.M. is a recipient of HLP scholarship under Public Service Department, Malaysia. The authors declared no conflict of interest.

References

1. Umar, A., Sanagi, M. M., Salisu, A., Wan Ibrahim, W. A., Abd Karim, K. J. and Abdul Keyon, A. S. (2016). Preparation and characterization of starch grafted with methacrylamide using ammonium persulphate initiator. *Materials Letters*, 185:173–176.
2. Salisu, A., Sanagi, M. M., Naim, A. A. and Karim, K. J. (2015). Removal of methylene blue dye from aqueous solution using alginate grafted polyacrylonitrile beads. *Der Pharma Chemica*, 7(2): 237–242.
3. Sanagi, M. M., Muzakkir Mat Jais, M. N., Kamaruzaman, S., Wan Ibrahim, W. A. and Baig, U. (2015). Multi-walled carbon nanotubes-agarose gel micro-solid phase extraction for the determination of triazine herbicides in water samples. *Analytical Methods*, 7(6): 2862–2868.
4. Umar, A., Abu Naim, A. and Sanagi, M. M. (2014). Synthesis and characterization of chitosan grafted with polystyrene using ammonium persulfate initiator. *Materials Letters*, 124: 12–14.
5. Sutirman, Z. A., Sanagi, M. M., Abd Karim, K. J. and Wan Ibrahim, W. A. (2016). Preparation of methacrylamide-functionalized crosslinked chitosan by free radical polymerization for the removal of lead ions. *Carbohydrate Polymers*, 151: 1091–1099.
6. Malaysia Palm Oil Board. (2016). Overview of the malaysian oil palm industry. http://bepi.mpob.gov.my/images/overview/Overview_of_Industry_2016.pdf [Accessed online May 2017].
7. Sumathi, S., Chai, S. P. and Mohamed, A. R. (2008). Utilization of oil palm as a source of renewable energy in Malaysia. *Renewable and Sustainable Energy Reviews*, 12(9): 2404–2421.
8. Sanagi, M. M., See, H. H., Wan Ibrahim, W. A. and Naim, A. A. (2005). Determination of carotene, tocopherols and tocotrienols in residue oil from palm pressed fiber using pressurized liquid extraction-normal phase liquid chromatography. *Analytica Chimica Acta*, 538(1–2): 71–76.
9. Ng, F. Y., Yew, F. K. and Basiron, K. Y. (2011). A renewable future driven with malaysian palm oil-based green technology. *Journal of Oil Palm and The Environment*, 2: 1–7.
10. Web of Science Core Collection (2017). Oil palm biowaste. https://apps.webofknowledge.com, [Access online 7 November 2017].
11. Malaysian Palm Oil Board (2016). Oil palm statistics. fact sheets on malaysian palm oil. http://bepi.mpob.gov.my/images/overview/Overview_of_Industry_2016.pdf [Access online May 2017].
12. Guo, J. and Lua, A. C. (2002). Characterization of adsorbent prepared from oil-palm shell by CO_2 activation for removal of gaseous pollutants. *Materials Letters*, 55(5): 334–339.
13. Guo, J., Xu, W. S., Chen, Y. L. and Lua, A. C. (2005). Adsorption of NH_3 onto activated carbon prepared from palm shells impregnated with H_2SO_4. *Journal of Colloid and Interface Science*, 281(2): 285–290.
14. Meier, D., Andersons, B., Irbe, I., Chirkova, J. and Faix, O. (2008). Preliminary study on fungicide and sorption effects of fast pyrolysis liquids used as wood preservative. In A. V. Bridgwater (Ed.), *Progress in Thermochemical Biomass Conversion*. Oxford: Blackwell Science: 1550–1563.
15. Nomanbhay, S. M., Hussain, R. and Palanisamy, K. (2013). Microwave-Assisted alkaline pretreatment and microwave assisted enzymatic saccharification of oil palm empty fruit bunch fiber for enhanced fermentable sugar yield. *Journal of Sustainable Bioenergy Systems*, 3(1): 7–17.
16. Ofori-Boateng, C. and Lee, K. T. (2013). Sustainable utilization of oil palm wastes for bioactive phytochemicals for the benefit of the oil palm and nutraceutical industries. *Phytochemistry Reviews*, 12(1): 173–190.
17. Rugayah, A. F., Astimar, A. A. and Norzita, N. (2014). Preparation and characterisation of activated carbon from palm kernel shell by physical activation with steam. *Journal of Oil Palm Research*, 26(3): 251–264.
18. Ahmad, T., Danish, M., Rafatullah, M., Ghazali, A., Sulaiman, O., Hashim, R., and Ibrahim, M. N. M. (2012). The use of date palm as a potential adsorbent for wastewater treatment: A review. *Environmental Science and Pollution Research*, 19(5): 1464–1484.

19. Sidik, S. M., Jalil, A. A., Triwahyono, S., Adam, S. H., Satar, M. A. H. and Hameed, B. H. (2012). Modified oil palm leaves adsorbent with enhanced hydrophobicity for crude oil removal. *Chemical Engineering Journal*, 203: 9–18.
20. Hamza, U. D., Nasri, N. S., Amin, N. S., Mohammed, J. and Zain, H. M. (2016). Characteristics of oil palm shell biochar and activated carbon prepared at different carbonization times. *Desalination and Water Treatment*, 15(17): 7999–8006.
21. Sutrisno, B. and Hidayat, A. (2015). The effects of activation temperature on physico-chemical characteristics of activated carbons derived from biomass wastes. *AIP Conference Proceedings*, 1699: 060016.
22. Wirasnita, R., Hadibarata, T., Mohd Yusoff, A. R. and Mat Lazim, Z. (2015). Preparation and characterization of activated carbon from oil palm empty fruit bunch wastes using zinc chloride. *Jurnal Teknologi*, 74(11): 77–81.
23. Nomanbhay, S. M. and Palanisamy, K. (2005). Removal of heavy metal from industrial wastewater using chitosan coated oil palm shell charcoal. *Electronic Journal of Biotechnology*, 8(1): 43–53.
24. Hameed, B. H., Tan, I. A. W. and Ahmad, A. L. (2008). Optimization of basic dye removal by oil palm fibre-based activated carbon using response surface methodology. *Journal of Hazardous Materials*, 158: 324–332.
25. Hameed, B. H. and El-Khaiary, M. I. (2008). Batch removal of malachite green from aqueous solutions by adsorption on oil palm trunk fibre: Equilibrium isotherms and kinetic studies. *Journal of Hazardous Materials*, 154(1–3): 237–244.
26. Montoya-Suarez, S., Colpas-Castillo, F., Meza-Fuentes, E., Rodríguez-Ruiz, J. and Fernandez-Maestre, R. (2016). Activated carbons from waste of oil-palm kernel shells, sawdust and tannery leather scraps and application to chromium(VI), phenol, and methylene blue dye adsorption. *Water Science and Technology*, 73(1): 21–27.
27. Sajab, M. S., Chia, C. H., Zakaria, S. and Sillanpää, M. (2015). Fixed-bed column studies for the removal of cationic and anionic dyes by chemically modified oil palm empty fruit bunch fibers : Single- and multi-solute systems. *Desalination and Water Treatment*, 55(5): 1372–1379.
28. Sajab, M. S., Chia, C. H., Zakaria, S. and Khiew, P. S. (2013). Cationic and anionic modifications of oil palm empty fruit bunch fibers for the removal of dyes from aqueous solutions. *Bioresource Technology*, 128: 571–577.
29. Kietkwanboot, A., Tran, H. T. M. and Suttinun, O. (2015). Simultaneous dephenolization and decolorization of treated palm oil mill effluent by oil palm fiber-immobilized trametes hirsuta strain AK 04. *Water, Air, and Soil Pollution*, 226: 345.
30. Hussin, M. H., Pohan, N. A., Garba, Z. N., Kassim, M. J., Rahim, A. A., Brosse, N. and Haafiz, M. K. M. (2016). Physicochemical of microcrystalline cellulose from oil palm fronds as potential methylene blue adsorbents. *International Journal of Biological Macromolecules*, 92: 11–19.
31. Wong, K. T., Eu, N. C., Ibrahim, S., Kim, H., Yoon, Y. and Jang, M. (2015). Recyclable magnetite-loaded palm shell-waste based activated carbon for the effective removal of methylene blue from aqueous solution. *Journal of Cleaner Production*, 115: 337–342.
32. Setiabudi, H. D., Jusoh, R., Suhaimi, S. F. R. M. and Masrur, S. F. (2015). Adsorption of methylene blue onto oil palm (*Elaeis guineensis*) leaves: Process optimization, isotherm, kinetics and thermodynamic studies. *Journal of the Taiwan Institute of Chemical Engineers*, 63: 363–370.
33. Zaini, M. A. A., Meng, T. W., Kamaruddin, M. J., Setapar, S. H. M. and Yunus, M. A. C. (2014). Microwave-induced zinc chloride activated palm kernel shell for dye removal. *Sains Malaysiana*, 43(9): 1421–1428.
34. Acquah, C., Sie Yon, L., Tuah, Z., Ling Ngee, N. and Danquah, M. K. (2016). Synthesis and performance analysis of oil palm ash (OPA) based adsorbent as a palm oil bleaching material. *Journal of Cleaner Production*, 139: 1098–1104.
35. Khanday, W. A., Asif, M. and Hameed, B. H. (2016). Cross-linked beads of activated oil palm ash zeolite/chitosan composite as a bio-adsorbent for the removal of methylene blue and acid blue 29 dyes. *International Journal of Biological Macromolecules*, 95: 895–902.
36. Shaarani, F. W. and Hameed, B. H. (2011). Ammonia-modified activated carbon for the adsorption of 2,4-dichlorophenol. *Chemical Engineering Journal*, 169(1–3): 180–185.
37. Salman, J. M. and Hameed, B. H. (2010). Effect of preparation conditions of oil palm fronds activated carbon on adsorption of bentazon from aqueous solutions. *Journal of Hazardous Materials*, 175(1–3), 133–137.

38. Hamad, B. K., Noor, A. M., Afida, A. R. and Mohd Asri, M. N. (2010). High removal of 4-chloroguaiacol by high surface area of oil palm shell-activated carbon activated with NaOH from aqueous solution. *Desalination*, 257(1–3): 1–7.
39. Hamad, B. K., Noor, A. M. and Rahim, A. A. (2011). Removal of 4-chloro-2-methoxyphenol from aqueous solution by adsorption to oil palm shell activated carbon activated with K_2CO_3. *Journal of Physical Science*, 22(1): 39–55.
40. Nasir, M. A. M. and Saleh, S. H. (2016). Characterization of hemicelluloses from oil palm empty fruit bunches obtained by alkaline extraction and ethanol precipitation. *Malaysian Journal of Analytical Sciences*, 20(4), 849–855.
41. Yavari, S., Malakahmad, A., Sapari, N. B. and Yavari, S. (2016). Sorption-desorption mechanisms of imazapic and imazapyr herbicides on biochars produced from agricultural wastes. *Journal of Environmental Chemical Engineering*, 4(4): 3981–3989.
42. Salman, J. M., Abid, F. M. and Muhammed, A. A. (2012). Batch study for pesticide glyphosate adsorption onto palm oil fronds activated carbon. *Asian Journal of Chemistry*, 24(12): 5646–5648.
43. Hameed, B. H., Tan, I. A. W. and Ahmad, A. L. (2009). Preparation of oil palm empty fruit bunch-based activated carbon for removal of 2,4,6-trichlorophenol: Optimization using response surface methodology. *Journal of Hazardous Materials*, 164(2–3): 1316–1324.
44. Salman, J. M., Njoku, V. O. and Hameed, B. H. (2011). Batch and fixed-bed adsorption of 2,4-dichlorophenoxyacetic acid onto oil palm frond activated carbon. *Chemical Engineering Journal*, 174(1): 33–40.
45. Tan, I., Lim, L. and Lim, K. (2013). Removal of atrazine from aqueous solutions using HNO_3 treated oil palm shell-based adsorbent. *Unimas e-Journal of Civil Engineering*, 4(3): 17–22.
46. Salamatinia, B., Kamaruddin, A. H. and Abdullah, A. Z. (2008). Modeling of the continuous copper and zinc removal by sorption onto sodium hydroxide-modified oil palm frond in a fixed-bed column. *Chemical Engineering Journal*, 145(2): 259–266.
47. Wahi, R., Ngaini, Z. and Jok, V. (2009). Removal of mercury, lead and copper from aqueous solution by activated carbon of palm oil empty fruit bunch. *World Applied Sciences Journal*, 5: 84–91.
48. Rehman, M. A., Yusoff, I., Ahmmad, R. and Alias, Y. (2015). Arsenic Adsorption using palm oil waste clinker sand biotechnology: an experimental and optimization approach. *Water, Air, and Soil Pollution*, 226(5): 149.
49. Daneshfozoun, S., Abdullah, B. and Abdullah, M. A. (2016). The effects of oil palm empty fruit bunch sorbent sizes on plumbum (II) ion sorption. *Advanced Materials Research*, 1133: 542–546.
50. Daneshfozoun, S., Redza, R., Vo, D.-V. N., Ramli, N. M., Abdullah, M. A. and Abdullah, B. (2017). Adsorption kinetics of Pb(II) ions from aqueous solution using modified magnetic nano-composite of OPEFB. *Indian Journal of Science and Technology*, 10(11), 1–5.
51. Lua, A. C. and Jia, Q. (2009). Adsorption of phenol by oil-palm-shell activated carbons in a fixed bed. *Chemical Engineering Journal*, 150(2–3): 455–461.
52. Alam, M. Z., Muyibi, S. A., Mansor, M. F. and Wahid, R. (2007). Activated carbons derived from oil palm empty-fruit bunches: Application to environmental problems. *Journal of Environmental Sciences*, 19(1): 103–108.
53. AL-Aoh, H. A., Maah, M. J., Ahmad, A. A., and Abas, M. R. (2012). Adsorption of 4-nitrophenol on palm oil fuel ash activated by amino silane coupling agent. *Desalination and Water Treatment*, 40(1–3), 159–167.

Malaysian Journal of Analytical Sciences, Vol 22 No 2 (2018): 185 - 196
DOI: https://doi.org/10.17576/mjas-2018-2202-03

MALAYSIAN JOURNAL OF ANALYTICAL SCIENCES
Published by The Malaysian Analytical Sciences Society
ISSN 1394 - 2506

DETERMINATION OF POLYPHENOL CONTENTS IN *Hevea brasiliensis* AND RUBBER-PROCESSING EFFLUENT

(Penentuan Kandungan Polifenol dalam *Hevea brasiliensis* dan Sisa Pemprosesan Getah)

Azmi Ismun[1], Marinah Mohd Ariffin[2], Shamsul Bahri Abd Razak[1], Ong Chin Wei[3], Fauziah Tufail Ahmad[1], Aidilla Mubarak[1]*

[1]*School of Food Science and Technology*
[2]*School of Marine and Environmental Science*
Universiti Malaysia Terengganu, 21030 Kuala Nerus, Terengganu, Malaysia
[3]*Crop Improvement and Protection Unit,*
Rubber Research Institute of Malaysia, 47000 Sungai Buloh, Selangor, Malaysia

**Corresponding author: aidilla@umt.edu.my*

Received: 26 August 2017; Accepted: 29 January 2018

Abstract

The information on polyphenol composition of *Hevea brasiliensis* is limited despite the importance of understanding the value of this phytochemical, especially in terms of plant protection. There are also no reports available on the polyphenols content of rubber-processing effluent. The objective of this study is to determine the presence of polyphenol compounds in latex C-serum and effluent using Fourier-transform infrared spectroscopy (FTIR) analysis. This study also aims to profile specific phenolics using High Performance Liquid Chromatography (HPLC). Results from the FTIR analysis showed the presence of polyphenols in both latex and effluent. The optimal method for determining polyphenol by HPLC was determined which uses methanol and 0.5% acetic acid as the mobile phases. Several polyphenol peaks, including gallic acid, naphtoic acid, quercetin, chlorogenic acid and rutin, were detected in both latex and effluent when compared to authentic polyphenol standards. Optimization of the solid phase extraction using weak anion-exchange reversed-phase (WAX + C18) chromatography was shown to yield a higher recovery percentage compared to a C18-E cartridge. The results of this study show the potential for understanding polyphenol composition in latex of *H. brasiliensis* and effluent from rubber processing which has not been explored before.

Keywords: *Hevea brasiliensis,* polyphenols, latex, effluent, solid phase extraction

Abstrak

Maklumat mengenai komposisi polifenol di dalam *Hevea brasiliensis* adalah terhad walaupun kefahaman ke atas fitokimia ini penting, terutama bagi aspek perlindungan tanaman. Kandungan polifenol di dalam sisa buangan pemprosesan getah juga masih belum dilaporkan. Objektif kajian ini adalah untuk menentukan kehadiran sebatian polifenol di dalam C-serum lateks dan sisa buangan menggunakan analisis spektroskopi inframerah transformasi Fourier (FTIR). Kajian ini juga mensasarkan untuk mencirikan fenolik yang spesifik di dalam kedua-dua sampel lateks dan sisa buangan menggunakan analisis kromatografi cecair prestasi tinggi (HPLC). Analisis menggunakan FTIR telah membuktikan kehadiran sebatian polifenol di dalam kedua-dua sampel lateks dan sisa buangan. Kaedah optimum untuk menentukan kandungan polifenol menggunakan HPLC telah dapat dibangunkan dengan penggunaan metanol dan 0.5% asid asetik sebagai fasa bergerak. Analisis HPLC mengenalpasti beberapa puncak polifenol telah dikenalpasti di dalam sampel lateks dan sisa buangan yang sepadan dengan piawai polifenol termasuk asid galik, asid naftoik, kuersetin, asid klorogenik dan rutin. Pengoptimuman pengekstrakan fasa pepejal menggunakan kromatografi gabungan pertukaran anion lemah bersama C18 (WAX+C18) telah menunjukkan hasil peratus perolehan kembali yang lebih tinggi berbanding katrij C18-E. Hasil kajian ini menunjukkan potensi bagi memahami komposisi polifenol di dalam lateks *H. brasiliensis* dan sisa buangan pemprosesan getah yang masih belum diterokai.

Kata kunci: *Hevea brasiliensis,* polifenol, lateks, sisa buangan, pengekstrakan fasa pepejal

Introduction

Hevea brasiliensis is the common rubber tree grown in tropical regions for the commercial production of rubber latex. Rubber is one of the world's important commodities and Malaysia is one producer and contributed RM 16.5 billion to the nation's income in 2016 [1]. The valuable latex yielded by the rubber tree contains several components including 36% as the rubber fraction, 5% as non-rubber components such as C-serum and B-serum proteins, sugars and lipids and 59% as water [2]. C-serum protein, a clear serum corresponding to latex cytosol [3], has been reported to have anti-fungal effects on *Aspergillus niger* [4] and is a rich source of protein, nucleic acid and multitude of organic compounds [5].

Polyphenols, also known as polyhydroxyphenols, are a structural class of compounds characterized by the presence of multiple phenol structural units. Many studies have explored the pharmacological benefits of polyphenols, including their potential as antioxidants [6,7], anti-cancer agents [8] and other health-promoting properties [9,10]. They are also considered crucial in regulating plant defenses and have been reported for their role in plant defense mechanisms in tapping wounds of rubber plants, specifically of *H. brasiliensis* [11].

In addition to latex from *Hevea*, the effluent from rubber processing is another output from the rubber industry that attracted our attention. The effluent from rubber processing has possible deteriorating effects on surface water quality. It may contain high concentrations of organic matter, suspended solids and nitrogen, besides generating malodor when discharged into the environment [12]. The effluent has the potential to increase the biochemical oxygen demand (BOD) index of the water if the waste is released untreated. Higher BOD number determines the consumption of oxygen by microorganisms for oxidation [13]. Polyphenols in rubber may be passed into the aqueous phase of waste effluent. These valuable natural antioxidants may be utilized to optimize resources from the rubber industry. Such utilization has been explored in other studies of other industrial effluents [14,15]. Thus, understanding the polyphenol composition of the effluent from rubber processing is valuable knowledge that can generate possible financial benefits through its isolation, rather than otherwise being a waste product.

Solid phase extraction (SPE) is considered to be a convenient technique, demonstrating better chromatographic separation and its use is common in environmental, pharmaceutical and food laboratories for isolating organic compounds from a variety of matrices [16]. Many studies have reported the application of SPE for the purpose of polyphenol extraction from various samples [17-20]. To date, SPE has never been reported in the literature with regard to polyphenol extraction from *H. brasiliensis* latex or its processing effluent.

This study aims to contribute towards a fundamental understanding of rubber plant secondary metabolites and to increase the information available on rubber plants. In addition, the study aims to assess the potential purification of polyphenol, which is important in terms of waste management from the processing industry. This study also aims to determine the accuracy of the SPE method for extracting the major polyphenols in latex serum of *H. brasiliensis* and its rubber-processing effluent that can be measured using HPLC analysis. The method and conditions for HPLC analysis are also optimized to obtain the best separation.

Materials and Methods

Sample collection and preparation

Latex from *H. brasiliensis* was freshly obtained from a rubber plantation in Setiu, Terengganu, Malaysia and placed on ice without any additive to avoid coagulation. The latex was then centrifuged at 19,000 rpm for 60 minutes at 4 °C to separate it into a three-layer form, containing latex at the top, followed by C-serum and B-serum at the bottom layer. Then C-serum was obtained and freeze-dried for further analysis. The rubber-processing effluent sample was obtained from Pond 1, MARDEC factory in Kuala Berang, Terengganu, Malaysia. The effluent was then filtered through Whatman No. 1 filter paper to remove the suspended debris and centrifuged at 9,000 rpm at 4 °C. The supernatant was then freeze-dried before further analysis.

Fourier-transform infrared spectroscopy (FTIR) analysis

The ATR-FTIR screening was carried out by placing a small amount of concentrated crude extract directly on the surface of a diamond crystal of a Nicolet iS10 infrared spectrometer (Thermo Fisher Scientific, USA). Subsequently, a constant pressure was applied to the sample [21]. Spectra were obtained with the aid of an OMNI-sampler ATR accessory with a wavenumber range of 400–4000 cm^{-1} with 32 scans. The reference spectra were acquired from the cleaned blank diamond crystal. Detection was based on the peak value in the region of the infrared spectrum and compared results of the study by Coates [22].

Total phenolic content analysis

Total phenolic content was determined using the Folin-Ciocalteu assay [23] in order to quantify the value of the total phenolic concentration. Total phenolic concentration was measured in C-serum of latex using a UV-Vis spectrophotometer. Gallic acid with a range of concentration between 0 to 100 mg/L was used as phenolic standard in this assay. 1 mL of 70% ethanol was added to 20 mg of the dried C-serum and effluent sample and heated at 70 °C. The mixture was then centrifuged at 200 *g* for 10 min. The supernatant was collected and diluted up to a 20-mL volume with distilled water. 1 mL of standards, blank and samples extracts were loaded into each cuvette and 5 mL of diluted Folin-Ciocalteu reagent (1:10 v/v with ultrapurified water) was added and mixed. The mixtures were incubated at room temperature for five minutes. Then, 80 µL of 7.5% sodium carbonate was added to each mixture to stop the reaction and incubated at 45 °C for 30 minutes in the dark. The mixtures were then read at 765 nm using the UV-Vis spectrophotometer. The area under the curve was calculated against the gallic acid standard curve and results expressed as gallic acid equivalent (GAE).

Optimization of High Performance Liquid Chromatography (HPLC) methods

Polyphenol analysis was carried out using an Agilent® HPLC 1260 system with UV detector at 280 nm using a flow rate of 1.0 mL/min and a sample injection volume of 20 µL. The stationary phase used was Agilent® Zorbax C-18 Eclipse Plus. Method development for HPLC analysis was performed by optimizing each of the HPLC parameters, including solvent systems, solvent ratios, gradient programme and ion-pairing agents. Four methods were tested to determine the best separation of the polyphenols standard mixture. Methanol and 0.5% acetic acid were used as mobile phases for Method A and B, while for Method C and D, acetonitrile and phosphoric acid were used at different gradient ratios, according to Mradu et al. [24] with a slight modification of acid concentrations in the mobile phase. Table 1 shows the specifications of the four HPLC methods that were tested.

Table 1. Four tested HPLC method with different conditions of running time, mobile phases and gradient elution

Method	Running Time (minute)	Mobile Phase		Gradient Elution	
		Solvent A	Solvent B		
A	22	Methanol	0.5% acetic acid	0-4 min	100 % solvent B
				4-10 min	50 % solvent A, 50 % solvent B
				10-20 min	80 % solvent A, 20 % solvent B
				20-22 min	50 % solvent A, 50 % solvent B
B	25	Methanol	0.5% acetic acid	0-5 min	60 % solvent A, 40 % solvent B
				5-10 min	35 % solvent A, 65 % solvent B
				10-25 min	60 % solvent A, 40 % solvent B
C	30	Acetonitrile	0.1% phosphoric acid	0-12 min	15 % solvent A, 85 % solvent B
				12-22 min	25 % solvent A, 75 % solvent B
				22-30 min	15 % solvent A, 85 % solvent B
D	45	Acetonitrile	0.1% phosphoric acid	0-35 min	8 % solvent A, 92 % solvent B
				35-45 min	22 % solvent A, 78 % solvent B
				45 min	8 % solvent A, 92 % solvent B

Five standards were used, including chlorogenic acid, gallic acid, naphthoic acid, quercetin and rutin. All the standards were prepared at 400 ppm. The best separation of the standards mixture was used on the C-serum latex and effluent samples. HPLC was chosen to further the analysis of polyphenol profiling due to the capacity of polyphenols to completely dissolve in solvents and their characteristic of high polarity [25].The polyphenols of C-serum latex and effluent were determined using HPLC with the best optimized method.

Optimization of solid phase extraction

Two types of SPE cartridges were tested in the study: C18-E (silica-based sorbent) and the combination of weak anion-exchange and C18 (WAX + C18, polymer-based sorbent) from Phenomenex®. Every equilibration, washing and elution were done separately with regard to the SPE cartridges. All cartridges were activated with 3 mL methanol. The polyphenol with the highest concentration that was demonstrated in the sample was chosen for the optimization of SPE.

The C18-E cartridge was equilibrated with 3 mL deionised water before 1 mL of 10 ppm gallic acid standard was loaded. Washing was then carried out using 3 mL of 25 mM sulphuric acid and, finally, elution with 3 mL methanol. The procedure was conducted according to de Villiers et al. [26]. The WAX+C18 cartridge was equilibrated with deionised water pH 6.5 before 10 ppm gallic standard was loaded, followed by washing using ammonium acetate buffer pH 6.5 and elution with a mixture of 6 mL methanol and 5% formic acid. All the sample eluents were dried in a nitrogen gas concentrator prior to being re-dissolved in 1 mL of HPLC-grade methanol. The extracts were then filtered through a 0.45-µL pore-size syringe filter, and subsequently analyzed by HPLC using the optimized method described in the previous section. The percentage of end-product from the eluent of both cartridges was calculated by comparing the area values of the HPLC chromatogram of the eluent with the gallic acid standard to determine the concentration of specific polyphenol compounds present in the samples.

Results and Discussion

Identification of polyphenol content using FTIR analysis

The peak values and probable functional groups present in the C-serum and effluent crude samples are presented in Figure 1a and 1b, respectively. The peaks were analyzed and correlated according to Coates [22].

The FTIR spectrum for C-serum shows the following characteristic peaks: 3272.56 cm^{-1}, 2912.72 cm^{-1}, 2161.11 cm^{-1}, 1567.77 cm^{-1}, 1394.16 cm^{-1}, 1013.09 cm^{-1} and 653.25 cm^{-1}. The polyphenol was detected by the peak at wavenumber 3272.56 cm^{-1} which represents the O-H phenolic group and supported by the presence of C-O group peak at wavenumber 1394.16 cm^{-1}. The 2912.72 cm^{-1} peak is specific for aldehyde group, 2161.11 cm^{-1} for alkene group, 1567.77 cm^{-1} for amine group, 1013.09 cm-1 for halogen group.

For the effluent, the FTIR spectrum detected the two same peaks at wavenumber 3273.56 cm^{-1} and 1394.16 cm^{-1}, which represent O-H phenolic group. The other peaks that were also present were 1553.56 cm^{-1} for amine group and 985.00 cm^{-1} for C-X halogen and fluoride group, which are the main groups to generate an odor. Aromatic C=C groups were also present in the both crude samples.

This study successfully determined the O-H group as the main indicator of the polyphenol present in both C-serum and rubber-processing effluent. Several studies have used FTIR as a tool for analyzing and determining polyphenols in plants and crops [27,28]. However, the results of the FTIR analysis were insufficient and have been supported by other analyses including HPLC.

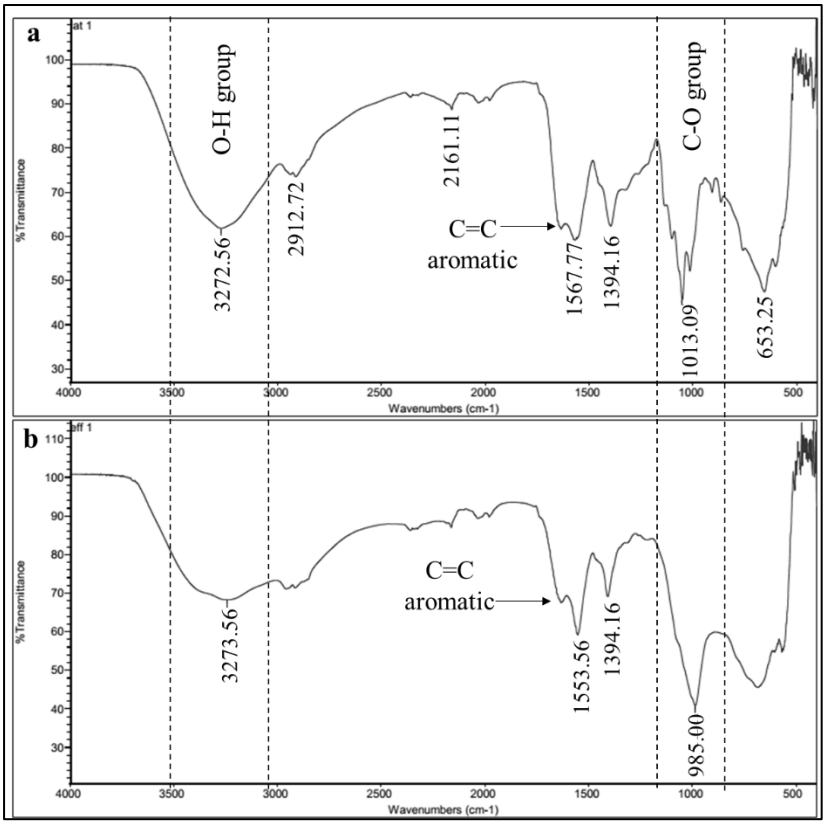


Figure 1. The FTIR spectrum for a) C-serum of latex and b) rubber-processing effluent, both of which are crude samples

Quantification of total phenolic content

The total polyphenol content of C-serum and effluent were expressed as GAE (standard equation of the curve: y = 0.0116x; R^2 = 0.9921). Figure 2 illustrates the polyphenol content quantified in C-serum which was 0.0393 GAE/mL, and in effluent which was 0.0099 GAE/mL. Total polyphenol content of C-serum latex were higher (p<0.05) by approximately 75% than in rubber-processing effluent. However, considering effluent as a waste product of rubber processing, the phenolic quantified is considered to be valuable. Previously, polyphenols, including rutin, luteolin and tyrosol, were detected in olive oil wastewater [29]. Identification of polyphenols in such waste sources can present a valuable element for gaining optimal profit and minimizing loss from waste reprocessing. In addition, polyphenols in olive-mill wastewater were reported to contribute to the phytotoxic effects that cause ecological problems when released to the environment [14]. Thus, knowing the composition of polyphenols in effluent from rubber processing may therefore indicate the importance of removing these compounds from the effluent to reduce risks to the environment.

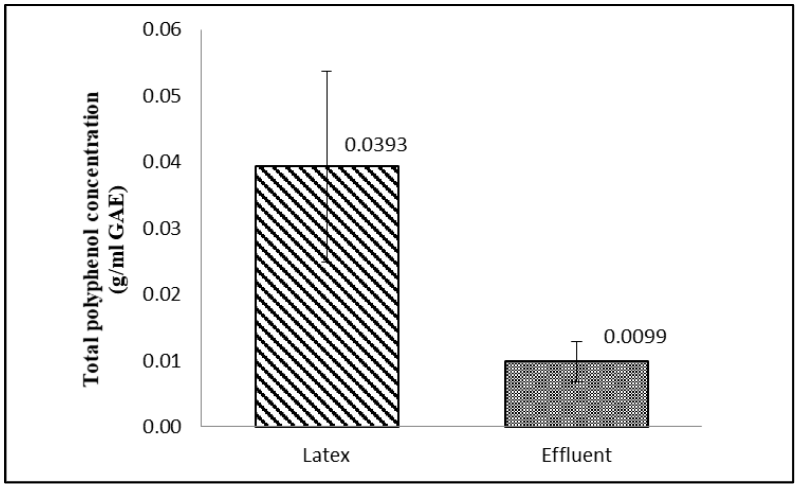
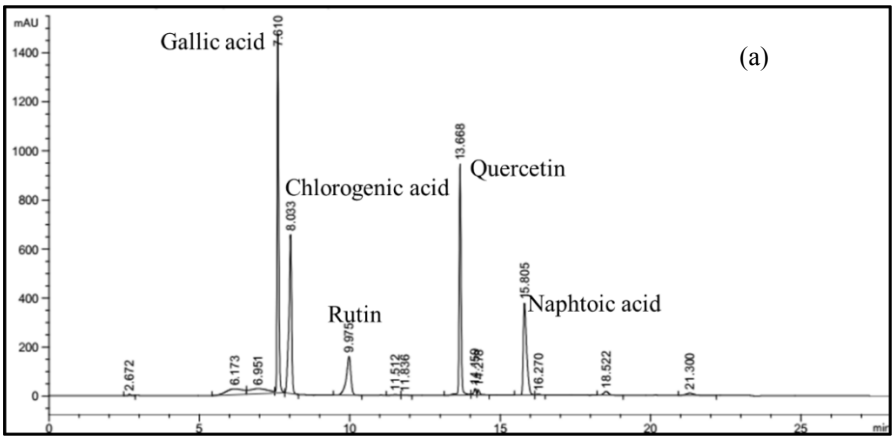


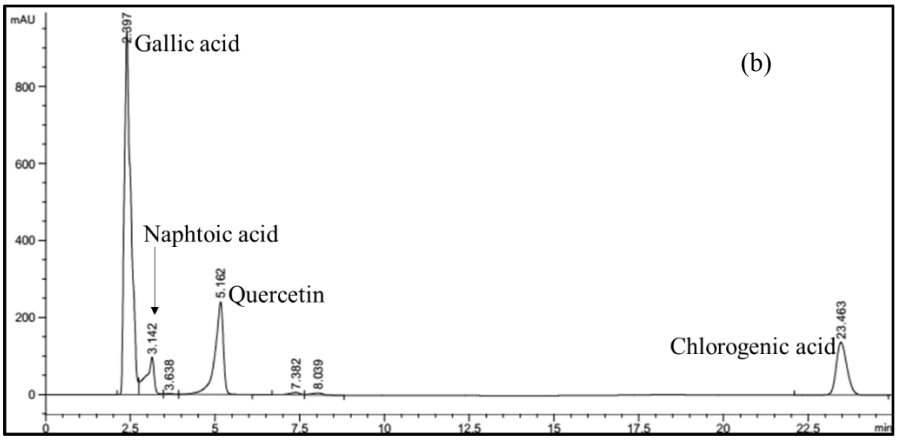
Figure 2. Total polyphenol content of C-serum of latex and effluent expressed as g/mL gallic acid equivalents. Data are mean values of triplicate extractions from pooled latex samples from five trees; and triplicate extractions of the effluent

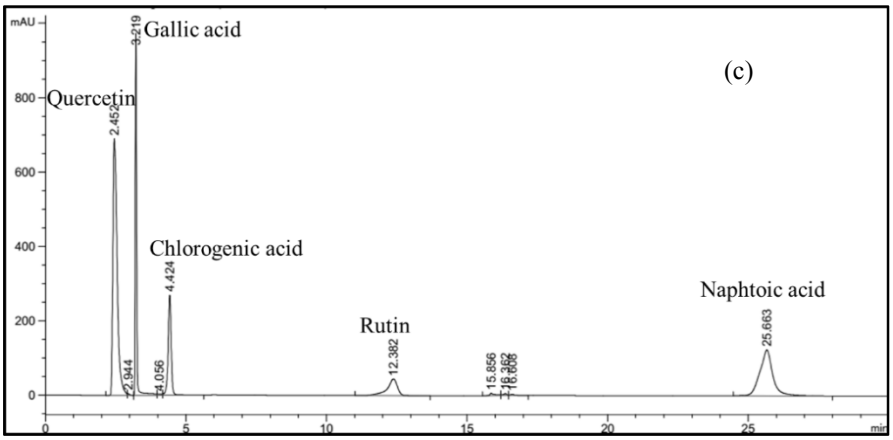
Optimized HPLC method for identification of polyphenols

Method A (Figure 3a) possessed the best separation for the polyphenol mixture compared to the other methods. All the peaks that represented gallic acid, cholorogenic acid, rutin, quercetin and naphtoic acid were well separated when compared to the other tested methods.

The presence of acetic acid in the mobile phase facilitated the increased chromatogram resolution of a compound that possessed a carboxyl and hydroxyl group in their structures [26]. Acetic acid concentration, which was higher with method A than method B (Figure 3b), contributed to the better resolution of the chromatograms.







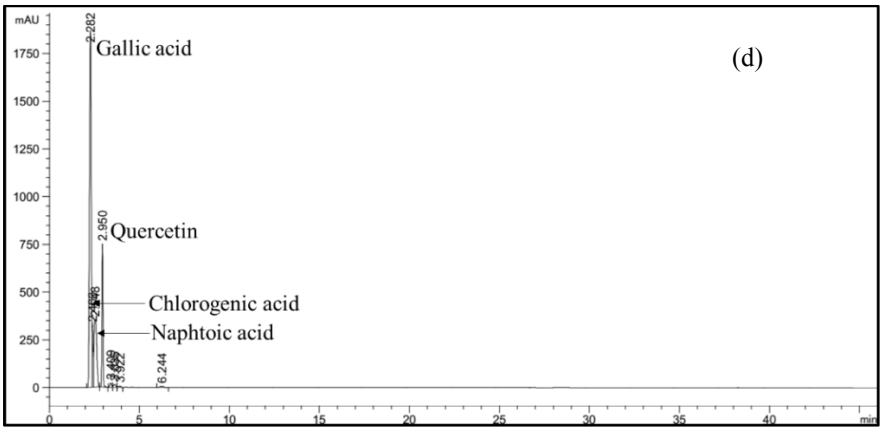


Figure 3. Chromatogram of HPLC from method A (a), method B (b), method C (c) and method D (d): the peaks represent gallic acid, cholorogenic acid, rutin, quercetin and naphtoic acid

The chromatograms obtained from analysis using method C (Figure 3c) and D (Figure 3d) show that the addition of phosphoric acid to the mobile phase also conveyed a good resolution of the chromatograms with method C and D. However, the run time of 30 min was considered as inefficient in terms of solvent usage compared to method A and B. The peaks that spiked from analysis using method D were considered sharp, but the retention time between the

peaks was too close to each other. Addition of formic acid to the mobile phase has been previously reported to contribute to the good resolution of peaks for a compound, but it decreased the retention time due to its co-solvent effect in the mobile phase [30].

Figure 4a and Figure 4b show the separation of polyphenols using HPLC analysis of C-serum of latex and the effluent, respectively. There were two major peaks present in the C-serum of latex, representing gallic acid and naphthoic acid (Figure 4a), while the presence of gallic acid, naphtoic acid and quercetin was detected in the effluent from rubber processing (Figure 4b). Identity of the peaks was verified by comparing the retention times with those of authentic standards. Unknown peaks were observed in both samples at a similar retention time. The unknown peaks found in both C-serum of latex and the rubber-processing effluent will be analysed and identified using Liquid Chromatography Mass Spectrometry (LCMS).

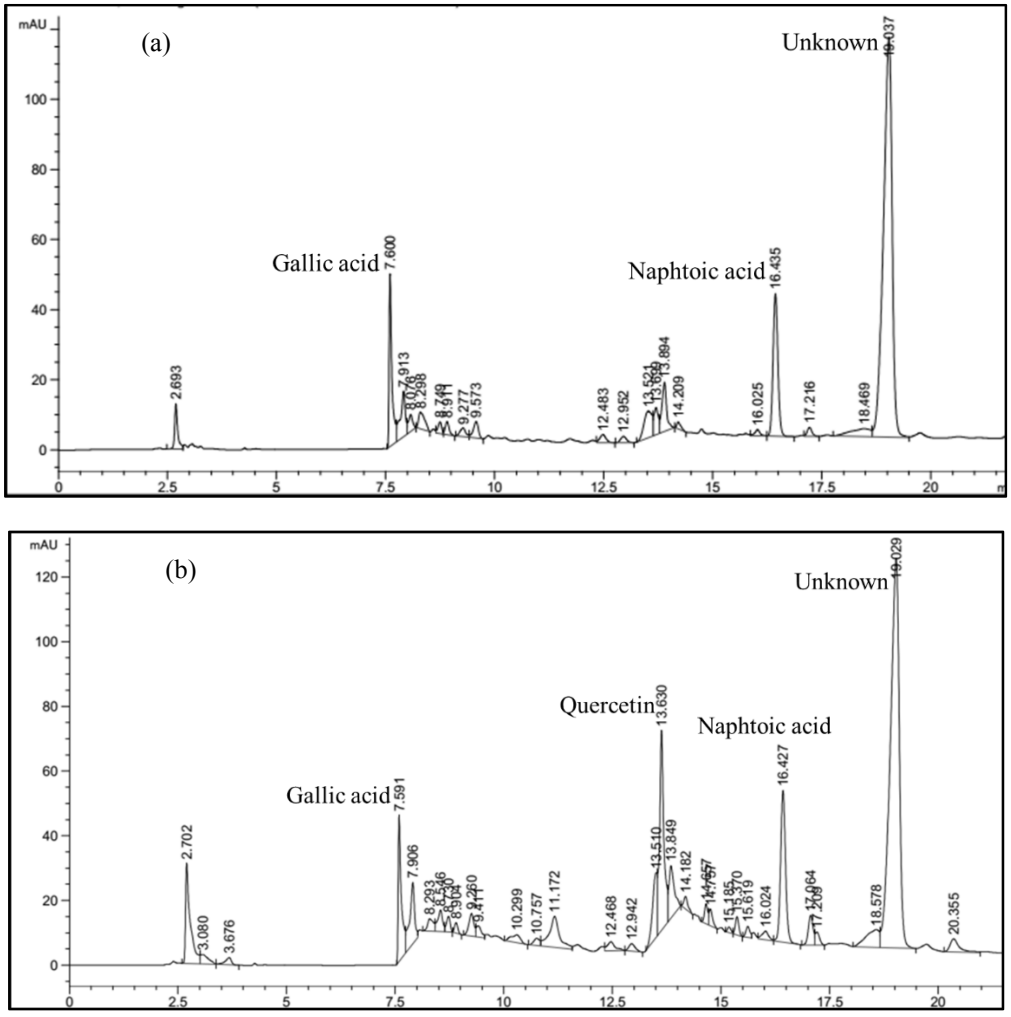


Figure 4. HPLC chromatogram of (a) C-serum from latex and (b) rubber-processing effluent

Previous studies have suggested that latex plays a role in fighting diseases and pests [31-34]. Several studies have discovered certain compound of interest and defense activity in the C-serum of latex. This includes the discovery of hevein, a single chain serine protease that has been described as an antifungal protein [35]. Daruliza et al. [4] also successfully determined the presence of antifungal activity of C-serum of latex towards *Aspergillus niger*.

Polyphenols have been associated with resistance mechanisms in plants [36]. Previous studies have reported antifungal activities of phenolics, including gallic acid, quercetin and naphthoic acid, isolated from various plants [37-39]. In addition, plants with high content of phenolics were reported to be less infested by crop aphids, suggesting a natural insecticide activity of phenolics [40]. Furthermore, polyphenols in rubber plants were reported to protect the tapping wound from pathogens, which supports the suggestion that polyphenols may play an important role in plant defense systems [11].

To our knowledge, information on the composition of polyphenols in latex is scarce. It is therefore important to study the composition of phenolics in latex which may also contribute to activities concerning rubber plant defense systems, and C-serum of the latex is a good target for analysing these bioactive compounds. Our study successfully determined the presence of polyphenols in the C-serum of latex by spectrophotometry, FTIR and HPLC analysis. This information could provide a foundation for further research on the determination of specific polyphenol compounds that could be related to resistance activities in rubber plants.

Profiling of polyphenols in many crops provides valuable knowledge which could be used to indicate potential markers for breeding in horticultural sectors. This has mainly been an effort to produce polyphenol-enriched plants due to interest in the pharmacological benefits of polyphenols. However, information obtained from profiling can also be useful for producing elite lines of Hevea species that may have profitable potential, such as pest resistance. Metabolic engineering of some crops has been performed via secondary metabolism pathways in an attempt to improve their tolerance to stress and productivity [41].

To date, there are no reports of investigations of polyphenol content of the effluent from processing of rubber latex. There have been studies conducted on the effluent, but these have focused only on the waste management aspect [42-44]. This study is therefore an initial attempt to determine the existence of polyphenols in the effluent using spectrophotometry, infrared analysis and HPLC. We found that the effluent contains valuable polyphenol compounds that have the potential to be extracted and isolated before being discarded as waste into the environment.

Solid phase extraction (SPE)

For the purpose of optimizing the extraction technique for polyphenols from latex and effluent using SPE, gallic acid standard was used and tested due to the consistency of its appearance in both samples. 10 ppm of gallic acid dissolved in methanol was loaded into both tested SPE cartridges, C18-E and WAX+C18. As shown in Table 2, extraction using the WAX+C18 cartridge showed output with a higher percentage of gallic acid recovery (61.2%, equivalent to 6.12 ppm) than using the C18-E cartridge. There was a small leakage which occurred during gallic acid loading and washing with ammonium acetate buffer [45]. Extraction using the C18-E cartridge had a very low recovery of gallic acid (0.99 %, equivalent to 0.099 ppm).

Table 2. Comparison of area and percentage values of SPE output as analysed by HPLC

Solid Phase Extraction Cartridge	Area±SD			Percentage Recovery From Eluent (%)
	Loading	Wash	Eluent	
C18-E	68.2±0.7	90.6±0.5	11.65±0.6	0.99
WAX+C18	60.7±0.5	90.6±0.4	719.43±0.5	61.2

The SPE cartridge is considered the most convenient method for extracting the desired analytes and compounds from various samples from the environment, pharmaceutical sector and food industries [16]. It has the capacity to operate with smaller elution volumes and yield cleaner extracts with lower interferences due to the optimization of the bed mass to reduce non-specific matrix adsorption [46]. Furthermore, it is also able to retain organic compounds, even when high flow rates are used. However, it also has some limitations including the loss of the sample volume during the elution process [47], restricted flow rates and plugging of the top frit for samples containing suspended solids [48]. SPE has been used for polyphenols extraction from various samples, including

wine [26], beer [18] and vegetables [49, 50]. The approach could save sample preparation time and disposal costs, and can be used with very small volumes of sample [51], proving it to be a promising technique for extracting polyphenols from our sample of interest.

Conclusion

This study has successfully demonstrated that both C-serum of the latex and effluent from rubber processing contained polyphenols, assessed using Fourier-transform infrared spectroscopy (FTIR) and HPLC analysis. The results obtained fulfilled the research objective which was to determine the polyphenols in the C-serum latex and rubber-processing effluent through optimized analytical and extraction techniques. We are currently analysing the C-serum and rubber-processing effluent using LCMS to further identify the unknown peaks that were detected by HPLC analysis. We are also attempting to complete the method development by means of method validation process. These findings present a promising prospect for further investigation of specific polyphenols which may possess important plant defense activities in *H. brasiliensis.*

Acknowledgement

We would like to thank the Malaysian Ministry of Higher Education (FRGS: 59328) for funding this project.

References

1. Malaysia External Trade (MATRADE) Statistics (2016). Top 10 Major Export Products 2016. MATRADE. http://www.matrade.gov.my/en/malaysia-exporters-section/33-trade-statistics/4554-top-10-major-export-products-2016. [Access online 27 November 2016].
2. Sansatsadeekul, J., Sakdapipanich, J. and Rojruthai, P. (2011) Characterization of associated proteins and phospholipids in natural rubber latex. *Journal of Bioscience and Bioengineering,* 111(6): 628-934.
3. Kongsawadworakul, P. and Chrestin, H. (2003). Laser diffraction: a new tool for identification and studies of physiological effectors involved in aggregation coagulation of the rubber particles from *Hevea* latex. *Journal of Plant and Cell Physiology,* 44(7): 707-717.
4. Daruliza, K. M. A. Lam, K. L. Yang, K. L. Priscilla, J. T. Sunderasan, E. and Ong, M. T. (2011). Anti-fungal effect of *Hevea brasiliensis* latex C-serum on *Aspergillus niger*. *Journal of European Review for Medical and Pharmalogical Sciences,* 15(9): 1027-1033.
5. Lam, K. L., Yang, K. L., Sunderasan E. and Ong, M. T. (2012). Latex C-serum from *Hevea brasiliensis* induces non-apoptic cell death in hepatocellular carcinoma cell line HepG2. *Cell Proliferation,* 45(6): 577- 585.
6. Abeywickrama, G., Debnath, S. C., Ambigaipalan, P. and Shahidi, F. (2016). Phenolics of selected cranberry genotypes *(Vaccinium macrocarpon* Ait.*)* and their antioxidant efficacy. *Journal of Agricultural and Food Chemistry,* 64(49): 9342-9351.
7. Rouphael, Y., Bernardi, J., Cardarelli, M., Bernardo, L., Kane, D., Colla, G. and Lucini, L. (2016). Phenolic compounds and sesquiterpene lactones profile in leaves of nineteen artichoke cultivars anticancer *Journal of Agricultural and Food Chem*istry, 64(45): 8540-8548.
8. Manach, C., Scalbert, A., Morand, C., Rémésy, C. and Jiménez, L. (2004). Polyphenols: Food sources and bioavailability. *American Journal of Clinical Nutrition,* 79(5): 727-747.
9. Boudet, A. M. (2007). Evolution and current status of research in phenolic compounds. *Journal of Phytochemistry,* 68(22): 2722-2735.
10. Feng, J., Wang, Y., Yi, X., Yang, W. and He, X. (2016). Phenolics from durian exert pronounced no inhibitory and antioxidant activities. *Journal of Agricultural and Food Chemistry,* 64(21): 4273-4279.
11. Wititsuwannakul, D., Chareonthiphakornb, N., Pacec, M. and Wititsuwannakul, R. (2002). Polyphenol oxidases from latex of *Hevea brasiliensis*: Purification and characterization. *Phytochemistry,* 61(61): 115-121.
12. Kumlanghan, A., Kanatharana, P. and Asawatreratanakul, P. (2008). Microbial BOD sensor for monitoring treatment of wastewater. *Enzyme and Microbial Technology,* 42(6): 483-491.
13. Arimoro, F. O., Iwegbue, C. M. A. and Osiobe, O. (2008). Effects of industrial wastewater on the physical and chemical characteristics of a tropical coastal river. *Research Journal of Environmental Sciences,* 2(3): 209-220.
14. Casa, R., Annibale, A. D., Pieruccetti, F., Stazi, S. R., Sermanni, G. and Cascio, B. L. (2003). Reduction of the phenolic components in olive-mill wastewater by an enzymatic treatment and its impact on durum wheat (*Triticum durum* Desf.) germinability. *Chemosphere,* 50: 959-966.

15. Achak, M., Hafidi, A., Ouazzani, N., Sayadi, S. and Mandi, L. (2009). Low cost biosorbent "banana peel" for the removal of phenolic compounds from olive mill wastewater: Kinetic and equilibrium studies. *Journal of Hazardous Materials,* 166(1): 117-125.
16. Brenneman, C. and Ebeler, S. E. (1999). Chromatographic separations using solid-phase extraction cartridges: Separation of wine phenolics. *Journal of Chemical Education,* 76(12): 1710-1711.
17. Papagiannopoulos, M., Wollseifen, H. R., Mellenthin, A., Haber, B. and Galensa, R. (2004). Identification and quantification of polyphenols in carob fruits (*Ceratonia siliqua* L.) and derived products by HPLC-UV-ESI/MS. *Journal of Agricultural and Food Chemistry*, 52(12): 3784-3791.
18. Dvořáková, M., Hulín, P., Karabín, M. and Dostálek, P. (2007). Determination of polyphenols in beer by an effective method based on solid-phase extraction and high performance liquid chromatography with diode-array detection. *Czech Journal of Food Sciences,* 25(4): 182-188.
19. Šeruga, M., Novak, I. and Jakobek, L. (2011). Determination of polyphenols content and antioxidant activity of some red wines by differential pulse voltammetry, HPLC and spectrophotometric methods. *Food Chemistry,* 124(3): 1208-1216.
20. Xie, F. (2011). Rapid and sensitive analysis of eight polyphenols in tobacco by rapid resolution liquid chromatography. *American Journal of Analytical Chemistry,* 2(8): 929-933.
21. Das, A. J., Khawas, P., Miyaji, T. and Deka, S. C. (2015). Phytochemical constituents, ATR-FTIR analysis and antimicrobial activity of four plant leaves used for preparing rice beer in Assam, India. *International Journal of Food Properties,* 19(9): 2087-2101.
22. Coates, J. (2006). Interpretation of infrared spectra, a practical approach. In *Encyclopedia of Analytical Chemistry*, Meyers, R.A., Ed; John Wiley and Sons, Inc., Hoboken, New Jersey, USA: pp.10815- 10837.
23. Folin, O. and Ciocalteu, V. (1927). On tyrosine and trytophane determination in protein. *Journal of Biological Chemistry,* 27: 627-650.
24. Mradu, G., Saumyakanti, S., Sohini, M. and Arup, M. (2012). HPLC profiles of standard phenolic compounds present in medicinal plants. *International Journal of Pharmacognosy and Phytochemical Research,* 4(3): 162-167.
25. Yu, J., Ahmedna, M. and Goktepe, I. (2005). Effects of processing methods and extraction solvents on concentration and antioxidant activity of peanut skin phenolics. *Food Chemistry,* 90(1): 199-206.
26. de Villiers, A., Lynen, F., Crouch, A., and Sandra, P. (2004). Development of a solid-phase extraction Procedure for the simultaneous determination of polyphenols, organic acids and sugars in wine. *Chromatographia,* 59 (7-8): 403-409.
27. Loeser, E. (2009). Peculiarities of mobile phases containing formic acid. *Chromatographia,* 69(9-10): 807-811.
28. Singh, R. and Mendhulkar, V. D. (2015). FTIR studies and spectrophotometric analysis of natural antioxidants, polyphenols and flavonoids in *Abutilon indicum* (Linn) sweet leaf extract. *Journal of Chemical and Pharmaceutical Research,* 7(6): 205-211.
29. Trifunschi, S., Munteanu, M. F., Agotici, V., Ardelean, S. P., and Gligor, R. (2015). Determination of flavonoid and polyphenol compounds in *Viscum album* and *Allium sativum* extracts. *International Current Pharmaceutical Journal,* 4(5): 382-385.
30. Li, S., Tian, M. and Row, K. (2010). Effect of mobile phase additives on the resolution of four bioactive compounds by RP-HPLC. *International Journal of Molecular Sciences,* 11(5): 2229-2240.
31. Mulinnaci, N., Romani, A., Galardi, C., Pinelli, P., Giaccherini, C. and Vincieri, F. F. (2001). Polyphenolic content in olive oil waste waters and related olive samples. *Journal of Agriculture and Food Chemistry,* 49(8): 3509-3515.
32. Dussourd, D. E. and Eisner, T. (1987). Vein-cutting behavior: insect counterploy to the latex defense of plants. *Science,* 237(4817): 898-901.
33. Farrell, B. D., Dussourd, D. E. and Mitter, C. (1991). Escalation of plant defenses: Do latex and resin canals spur plant diversification? *American Naturalist,* 138(4): 881-900.
34. Sangsil, P., Nualsri, C., Woraathasin, N. and Nakkanong, K. (2016). Characterization of the phenylalanine ammonia lyase gene from the rubber tree (*Hevea brasiliensis* Mull. Arg.) and differential response during *Rigidoporus microporus* infection. *Journal of Plant Protection Research,* 56(4): 380-388.
35. Ko, J. H., Chow, K. S. and Han, K. H. (2003). Transcriptome analysis reveals novel features of the molecular events occurring in the laticifers of *Hevea brasiliensis* (para rubber tree). *Journal of Plant Molecular Biology,* 53(4): 479-492.

36. Lattanzio, V., Kroon, P. A., Quideau, S., and Treutter, D. (2008). Plant phenolics – secondary metabolites with diverse functions. In Recent Advances in Polyphenol Research, Daayf, F.; Lattanzio, V., Eds; Wiley-Blackwell, Oxford, UK: pp. 1-386.
37. Aziz, N. H., Farag, S. E., Mousa, L. A. and Abo-Zaid, M. A. (1998). Comparative antibacterial and antifungal effects of some phenolic compounds. *Microbiology,* 93(374): 43-54.
38. Tempesti, T. C., Alvarez, M. G., de Araújo, M. F., Catunda Júnior, F. E. A., de Carvalho, M. G. and Durantini, E. N. (2012). Antifungal activity of a novel quercetin derivative bearing a trifluoromethyl group on *Candida albicans*. *Medicinal Chemistry Research,* 21(9): 2217-2222.
39. Nguyen, D. M. C., Seo, D. J., Lee, H. B., Kim, I. S., Kim, K. Y., Park, R. D. and Jung, W. J. (2013). Antifungal activity of gallic acid purified from *Terminalia nigrovenulosa* bark against *Fusarium solani*. *Microbial Pathogenesis,* 56: 8-15.
40. Leszczyński, B., Warchoł, J. and Niraz, S. (1985). The influence of phenolic compounds on the preference of winter wheat cultivars by cereal aphids. *International Journal of Tropical Insect Science,* 6(2): 157-158.
41. Verpoorte, R., van der Heijden, R., ten Hoopen, H. J. G. and Memelink, J. (1999). Metabolic engineering of plant secondary metabolite pathways for the production of fine chemicals. *Biotechnology Letters,* 21(6): 467-479.
42. Nguyen, N. H. and Luong, T. T. (2012). Situation of wastewater treatment of natural rubber latex processing in the Southeastern region, Vietnam. *Journal of Vietnamese Environment,* 2(2): 58-64.
43. Mohammadi, M., Man, H., Hassan, M. and Yee, P. (2013). Treatment of wastewater from rubber industry in Malaysia. *African Journal of Biotechnology,* 9(38): 6233-6243.
44. Owamah, H. I., Enaboifo, M. A. and Izinyon, O. C. (2015). Treatment of wastewater from raw rubber processing industry using water lettuce macrophyte pond and the reuse of its effluent as biofertilizer. *Agricultural Water Management,* 146: 262-269.
45. Andersson, L. I., Paprica, A. and Arvidsson, T. (1997). A highly selective solid phase extraction sorbent for pre-concentration of sameridine made by molecular imprinting. *Chromatographia,* 46(1-2): 57-62.
46. Abd-Talib, N., Mohd-Setapar, S. H. and Khamis, A. K. (2014). The benefits and limitations of methods development in solid phase extraction: Mini review. *Jurnal Teknologi (Sciences and Engineering)*, 69(4): 69-72.
47. Thurman, E. M. and Snavely, K. (2000). Advances in solid-phase extraction disks for environmental chemistry. *TrAC - Trends in Analytical Chemistry,* 19(1): 18-26.
48. Nema, T., Chan, E. C. Y. and Ho, P. C. (2010). Application of silica-based monolith as solid phase extraction cartridge for extracting polar compounds from urine. *Talanta,* 82(2): 488-494.
49. Garcia-Salas, P., Morales-Soto, A., Segura-Carretero, A. and Fernández-Gutiérrez, A. (2010). Phenolic-compound-extraction systems for fruit and vegetable samples. *Molecules,* 15(12):8813-8826.
50. Rosa, L., Alvarez-Parrilla, E. and Gonz, G. A. (2010). Fruit and vegetable phytochemicals fruit and vegetable phytochemicals. Wiley-Blackwell, Iowa, USA: pp. 53-88.
51. Kumar, A., Malik, A. K. and Tewary, D. K. (2009). A new method for determination of myricetin and quercetin using solid phase microextraction-high performance liquid chromatography-ultra violet/visible system in grapes, vegetables and red wine samples. *Analytica Chimica Acta,* 631(2): 177-181.

Malaysian Journal of Analytical Sciences, Vol 22 No 2 (2018): 197 - 202
DOI: https://doi.org/10.17576/mjas-2018-2202-04

MALAYSIAN JOURNAL OF ANALYTICAL SCIENCES
Published by The Malaysian Analytical Sciences Society
ISSN 1394 - 2506

VALIDATION METHOD FOR EXTRACTION AND DETERMINATION OF MARBOFLOXACIN IN PLASMA AND EDIBLE CHICKEN TISSUES

(Kaedah Validasi bagi Pengesktrakan dan Penentuan Marbofloxacin di dalam Plasma dan Tisu Ayam yang Boleh Di Makan)

Natalia Francisca Urzúa[1]*, Guillermo Fermín Prieto[1], Carlos Fernando Lüders[2], Maria Paula Tonini[1], Eduardo Jesús Picco[3], Carlos Alberto Errecalde[1]

[1] *Department of Animal Clinic, Faculty of Agronomy and Veterinary Medicine, University National of Rio Cuarto, Route 36 Km 601, Rio Cuarto, Argentina*
[2] *School of Veterinary Medicine, Catholic University of Temuco, Casilla 15D, Temuco, Chile*
[3] *Chair of Pharmacology, Faculty of Veterinary Sciences, University National of the Litoral, Kreder 2805, Esperanza, Argentina*

**Corresponding author: nurzuapizarro@ayv.unrc.edu.ar*

Received: 16 December 2017; Accepted: 16 February 2018

Abstract

Marbofloxacin (MBX) is an antimicrobial for exclusive veterinary use, relatively new and of which there are few analytical methods for the extraction, identification and quantification in plasma and edible tissues (muscle, liver, kidney, lung, skin) in broiler chickens. The objective of developing a simple, sensitive and efficient extraction and detection method through high-performance liquid chromatography (HPLC) with fluorescence detection. For the preparation of the samples, known concentrations of MBX, enrofloxacin (ENX) as internal standard, methanol, water and perchloric acid, were added to plasma or tissues. Chromatographic conditions were: fluorescence detector at λex 295 and λem 490 nm, mobile phase composed of deionized water, acetonitrile and triethylamine adjusted to pH 3.0. For all matrices, the method was linear (r^2= 0.99) for MAR concentrations (0.039 to 2.5 µg/ml or gr), with an average retention time for MBX in the different matrices of 3.97 ± 0.144 minutes, and 4.99 ± 0.24 minutes for the internal standard (enrofloxacin). Detection limit in all matrices was less than 0.006 µg/ml, while recoverability percentage was 89 ± 4.65% and variation coefficients in intraday-interday assay ≤ 1.4%, determining the accuracy of the study. The analytical method applied is efficient, sensitive and reliable for future residue determinations or pharmacokinetic studies of marbofloxacin in plasma, muscle, liver, kidney, skin and lung in broiler chickens.

Keywords: marbofloxacin, high-performance liquid chromatography, chicken

Abstrak

Marbofloxacin (MBX) ialah antimikrob yang digunakan secara eksklusif bagi veterinar, secara relatifnya adalah baru dan hanya beberapa kaedah analisis bagi pengekstrakan, pengenalpastian dan kuantifikasi di dalam plasma dan tisu yang boleh di makan (otot, hati, buah pinggang, paru-paru dan kulit) di dalam ayam daging telah di perkenal. Objektif kajian adalah pembangunan kaedah pengesanan yang mudah, sensitif dan berkesan menggunakan kromatografi cecair berprestasi tinggi (HPLC) dengan pengesan pendaflour. Bagi penyediaan sampel, kepekatan MBX, enrofloxacin (ENX) sebagai piawai dalam, metanol, air dan asid perklorik ditambah ke dalam tisu plasma. Tetapan kromatografi adalah: pengesan pendaflour pada λex 295 dan λem 490 nm, fasa bergerak terdiri daripada air ternyahion, asetonitril, dan trietilamina yang diselaraskan pada pH 3.0. Bagi semua matriks sampel, kaedah adalah bersifat linear (r^2= 0.99) bagi kepekatan MBX (0.039 hingga 2.5 µg/ml atau µg/g), dengan purata masa tahanan di dalam matriks berbeza ialah 3.97 ± 0.144 minit, dan 4.99 ± 0.24 minit bagi piawai (enrofloxacin). Had pengesan di dalam semua matriks adalah lebih rendah dari nilai 0.006 µg/ml, manakala peratus perolehan semula ialah 89 ± 4.65% dan pekali variasi bagi ujian intra-hari dan inter-hari ≤ 1.4%, menjelaskan kejituan kaedah. Kaedah analisis yang digunapakai adalah

efisien, sensitif, dan dipercayai bagi tujuan penentuan sisa atau kajian farmakokinetik marbofloxacin di dalam plasma, otot, hati, buah pinggang, kulit dan paru-paru ayam daging.

Kata kunci: marbofloxacin, kromatografi cecair berprestasi tinggi, ayam

Introduction

Currently, the search of simple, reliable, efficient and selective analytical methods for determination and quantification of antimicrobial residues in animals for human consumption is important to provide safe foods [1]. Liquid chromatography is the most widely used, specific and selective method for fluoroquinolones determination, antimicrobial agents widely used in infections in animals and humans, but their improper use can lead to development of bacterial resistance, or even, cause allergies in antibiotics sensitive individuals [2-4].

Fluoroquinolones are synthetic antimicrobial agents widely used for their efficacy against pathogens with importance in commercial poultry [5], with their activity being the inhibitor the enzyme gyrase, preventing bacterial replication [6]. Marbofloxacin (MBX) belongs to second-generation fluoroquinolones with Gram-negative antimicrobial activity, some Gram-positive and mycoplasmas [7], including bird pathogens such as *Mycoplasma gallisepticum*, *Escherichia coli* [8, 9] and *Pasteurella multocida* [10].

For MBX identification and quantification, some chromatographic analytical methods have been developed for plasma and edible tissues of chickens, including high performance liquid chromatography (HPLC) with UV detector [6, 9, 11-13]. HPLC with fluorescence detector [14], HPLC with photodiode-array detector [15] and HPLC with MS/MS tandem detector [16, 17]. The method has an extensive extraction and sample preparation processes, especially in complex matrices (skin, liver or lung). The aim of this work was to validate a new analytical method for the extraction, identification, and quantification of MBX by HPLC with fluorescence detector in plasma and edible broiler chickens tissues. This is because MBX is one of the last quinolones approved for use in food animals such as cows and pigs [18-19], due to its high efficiency in bacterial respiratory infections, which determines MBX as a potential therapeutic tool in poultry farming.

The importance of this research is to propose an optimization of the analytical method for the determination of MBX, promoting food safety, avoiding the presence of harmful pharmaceutical residues in food, one of the causes of bacterial resistance.

Materials and Methods

Reagents and instrument

Antimicrobials namely MBX (Guobang Pharma 99.9%) and enrofloxacin (Laboratory Chile 99.38%) were used as internal standard. Acetonitrile (Applichem Panreac 99.9%), triethylamine (Sintorgan 99%), deionized water, methanol (Applichem Panreac 99.9%), 70% perchloric acid (Lab. Cicarelli) and 85% orthophosphoric acid, were used to carry out the study.

A Hewlett-Packard 1050 liquid chromatography, equipped with quaternary pump, in-line mobile phase degasser, manual injector, was achieved on an Agilent octadecylsilane C18 column (25cm x 4.6 mm, 5 μm) (Agilent Technologies, Wald-bronn, Germany), Phenomenex precolumn, Hamilton injection syringes 100 μl, Hewlett-Packard fluorescence detector series 1046-A adjustable wavelength and personal computer with plate and program for equipment control, acquisition, data processing and printing of chromatograms.

HPLC analysis

The mobile phase was composed of deionized water, acetonitrile and triethylamine (790: 200: 10 v/v/v) adjusted to pH 3.0 with orthophosphoric acid, filtered with vacuum pump an 0.22 μm nylon membrane. The determination was performed at room temperature by reverse phase isocratic elution at flow rate of 0.8 ml/min, with a fluorescence detector set at 295 nm excitation and 490 nm emission [17] and an injection volume of 50 μl.

Sample pre-treatment and extraction procedure
Samples were processed according to Böttcher et al. method with modification [20]. For plasma, a liquid-liquid extraction was carried out by incorporating 150 µl of chicken plasma, 150 µl of a known MBX concentration, 600 µl of methanol and 40 µl of the internal standard (enrofloxacin 2.5 µg/ml) into an Eppendorf tube of 1.5 ml. For the tissue samples, 150 µg of the tissue, 150 µl of known MBX concentration, 600 µL of a homogenization solution, composed of deionized water, methanol and 70% perchloric acid (50: 48: 2) and 40 µl of the internal standard was added to an Eppendorf, proceeding to homogenize the whole for one minute with a homogenizer (Dremel 3000®). Then, samples were stirred in vortex for 30 seconds, held for 1 hours at room temperature 22 °C and then 12 hours at 4 °C; at the end of this time, were centrifuged at 13,500 rpm at 4 °C for 25 minutes. The supernatant was filtered through a 0.22 µm nylon membrane, obtaining the sample to be eluted.

Method validation
The validation of the chromatographic methodology was performed according to the *Codex Committee on Residues of Veterinary Drugs in Foods* (CCRVDF), proposed by the European Medicines Agency (EMEA) [21].

Calibration curve
The calibration curve was performed with different concentrations of MBX in the range of 0.0097 - 2.5 µg/ml (plasma), 0.0048 - 1.25 µg/g (muscle) and 0.0195 - 2.5 µg/g (skin, lung, liver and kidney); concentrations were incorporated into the sample preparation as described previously dependent on the tissue used. Determination was performed by linear regression, linearity, regression coefficient, slope, intercept, detection limit (LOD) and quantification limit (LOQ). The intercept and slope values of the calibration curve were used for a linear function to obtain the ratio of the peak of marbofloxacin and internal standard (enrofloxacin), determining the final concentration of the analyte.

Precision and recoverability assays
For precision, intra-day tests were employed, which refers to the dilution of calibration standards (0.039 to 1.250 µg/ml or µg/g) of plasma and muscle; meanwhile in tissues, concentrations from 0.078 to 2.5 µg/g were used, by six-fold. Test was considered acceptable when the coefficient of variation (CV%) between elution, as the area index of the chromatograms was achieved ≤ 1.5%.

Finally, inter-day test consisted in the dilution of the calibration standards from 0.039 to 1.25 µg/ml or µg/g of plasma and muscle and 0.078 to 2.5 µg/g in tissues performed in 6 different days. It was considered acceptable when the CV% of the area indices of the chromatograms was ≤ 3%. For recoverability (plasma and muscle) MBX calibration standards were used in the same concentration of 0.039 to 1.250 µg/ml or µg/g, whereas in the other tissues (liver, kidney, lung, skin) it was 0.078 to 2.5 µg/g with fortified samples, observing differences between standard versus fortified samples calculating the recoverability percentage.

Results and Discussion

Table 1 shows results of the intercept, slope and the adjustment coefficient for each matrix studied. Table 2 shows variation coefficients of intraday and inter-day assays and the percentages of relative recovery of marbofloxacin in all matrices studied. Table 3 indicates the different detection and quantification limits for marbofloxacin in the different biological matrices studied. Retention time for MBX in the different matrices studied was 3.97±0.144 minutes, and 4.99±0.24 minutes for internal standard (enrofloxacin) without interferences in the chromatogram.

The coefficient of adjustment of linearity (Table 1) in the range of concentrations studied, shows that this analytical method is efficient and sensitive for the determination of MBX in different tissues of chickens, for pharmacokinetic behavior studies and for residues monitoring of this drug in broiler chickens (plasma, muscle, liver, lung, kidney, skin) [21].

Table 1. Linearity of marbofloxacin in plasma and chicken tissues

Matrix	Ranges of Concentrations (*)	A	B	r^2
Plasma	0.0097-2.50	0.008128	0.4154	0.9928
Muscle	0.0048-1.25	0.01456	0.7084	0.9999
Liver	0.0097-2.50	0.1087	0.8059	0.9908
Kidney	0.0097-2.50	-0.01264	0.4973	0.9993
Lung	0.0097-2.50	0.01509	0.4398	0.9986
Skin	0.0097-2.50	0.01264	0.5294	0.9992

(*) µg/ml o µg/g. **A**: intercept **B**: slope r^2: coefficient of adjustment

Intra-day and inter-day precision tests (Table 2), coefficients variation (%CV) obtained in plasma and tissues tested were ≤1.73 and ≤ 2.14%, respectively; being less than those obtained by other authors ranging from 5.7 to 15.5%, [6, 8, 11-17] after the application of more complex extraction methods, with amount of reagents and a large procedures such as evaporation with nitrogen at 30 °C, confirm the accuracy of the analytical method implemented. The results obtained in the validation tests confirm the sufficiency of the procedures destined to extract the analyte from the plasma, using in the extraction methanol as a polar solvent followed by centrifugation [22].

Table 2. Recovery and precision assay of marbofloxacin in plasma and chicken tissues

Matrix	Ranges of Concentrations (µg/ml or µg/gr)	Recovery (%)	Precision (%CV)	
			Intra-day	Inter-day
Plasma	0.039 – 1.25	86.2 ± 3.75	1.39 ± 0.61	1.73 ± 0.65
Muscle	0.039 – 1.25	87.6 ± 6.91	1.47 ± 0.34	1.54 ± 0.50
Liver	0.078 – 2.50	86.5 ± 5.17	0.91 ± 0.11	2.16 ± 0.62
Kidney	0.078 – 2.50	93.7 ± 7.17	1.02 ± 0.42	1.21± 0.13
Lung	0.0078 – 2.50	92.8 ±4.44	0.74 ± 0.07	1.54 ± 0.39
Skin	0.0078 – 2.50	89.0 ± 2.17	1.16 ± 0.22	2.14 ± 0.63

CV: Coefficient of variation

Moreover, recoverability percentages in this study were 89 ± 4.65% (Table 2) among all matrices studied, higher than 64% to 75% observed with methods developed by other authors ranging for plasma and different tissues [6, 11, 14]. Yu et al. [16] and Rocha et al. [17] obtained percentages of MBX recovery similar to this work, between 78 and 95% in the different tissues (muscle, kidney and liver), Rocha et al. [17] performed two different extraction methods and with an HPLC coupled to tandem MS/MS, their percentages in muscle were 88 and 89%, while in the kidney they were greater between 95 to 96%.

Zhao et al. [12] obtained between 90 to 95% in muscle while Yang et al. [13] in plasma obtained between 88 to 95% and in tissues (lung, muscle, kidney and liver) between 81 to 89%. These data corroborate that the results obtained are in the acceptable ranges, promoting the greater recovery of the analyte in the study sample, in complex matrices such as lung, kidney or liver, validating the extraction method.

On the other hand, LOQ for MBX matrices (Table 3) are lower than those observed in extraction methods performed by Anadón et al. [6] and Ding et al. [8] in plasma obtained at 0.01 µg/ml and 0.02 µg/ml, respectively. In tissues samples, where Ding et al. [8] determined to LOQ of 0.05 µg/g (liver, kidney and muscle). Yorke and Forc

[14] reported LOQ 0.75 µg/g for muscle and Anadón et al. [6] recorded 0.01 µg/g (muscle, liver and kidney). A study performed by Anadón et al. [6] is similar to the one obtained in our research, although the previous studies are much higher, but the high sensitivity of our analytical method still considerable for the drug studied, in the different chicken tissues.

Table 3. Limits of detection (LOD) and limits of quantification (LOQ) in chicken tissue (µg/g)

Matrix	LOD	LOQ
Plasma	0.002	0.006
Muscule	0.003	0.009
Liver	0.003	0.009
Kidney	0.006	0.018
Lung	0.005	0.017
Skin	0.006	0.018

Considering the complexity of determining fluoroquinolones for their amphoteric character [22], added to the complexity of the matrices worked (muscle, kidney, lung, liver and skin), the processes of sample preparation and analyte extraction are complicated, with great quantity of organic solvents, for dilution and cleaning of the sample, removing macromolecules that interfere with the correct determination of the analyte. The above shows that our study by optimizing the process of sample preparation and extraction of the analyte, in addition to the validation of the analytical method, demonstrates the reliability of routine studies for marbofloxacin in the edible tissues of broiler chickens.

Conclusion

The optimization method developed in this study for the determination and quantification of MBX in plasma and edible tissues of broiler chickens (muscle, lung, kidney, liver and skin) could be considered as reliable, efficient, fast, precise, and also economical procedure due to the low amount of solvents used, being a useful tool for the monitoring of the pharmacokinetics and/or residues of MBX in broiler chickens, since it has been determined in previous studies as a potential therapeutic tool in poultry farming.

References

1. Hermo, M. P., Barrón, D. and Barbosa, J. (2006). Development of analytical methods for multiresidue determination of quinolones in pig muscle samples by liquid chromatography with ultraviolet detection, liquid chromatography–mass spectrometry and liquid chromagraphy–tandem mass spectrometry. *Journal of Chromatography A*, 1104(1): 132-139.
2. Garcia, M. A., Solans, C., Aramayona, J. J., Rueda, S. and Bregante, M. A. (1999). Determination of marbofloxacin in plasma samples by high-performance liquid chromatography using fluorescence detection. *Journal of Chromatography B: Biomedical Sciences and Applications*, 729(1): 157-161.
3. Talero-Pérez, Y. V., Medina, O. J. and Rozo-Núñez, W. (2014). Técnicas analíticas contemporáneas para la identificación de residuos de sulfonamidas, quinolonas y cloranfenicol. *Universitas Scientiarum*, 19(1):11-29.
4. Teixeira, A. M. (2009). Determinação de resíduos de fluoroquinolonas em amostras de tecido muscular de frangos e respectivo impacto na saúde humana. Tesis doctorado de Universidade de Coimbra. Portugal: pp. 44-45.
5. Landoni, M. F. and Albarellos, G. (2015). The use of antimicrobial agents in broiler chickens. *The Veterinary Journal*, 205(1): 21-27.
6. Anadón A., Martínez-Larragaña, M. R. Días, M. J., Martínez, M. A., Frejo, M. T. Martínez, M., Tafur, M. and Castellano, V. J. (2002). Pharmacokinetic characteristics and tissue residues for marbofloxacin and its metabolite N-desmethyl-marbofloxacin in broiler chickens. *American Journal of Veterinary Research*, 63(7): 927-933.

7. Spreng, M., Deleforge, J., Thomas, V., Boisrame, B. and Drugeon, H. (1995). Antibacterial activity of marbofloxacin. A new fluoroquinolone for veterinary use against canine and feline isolates. *Journal of Veterinary Pharmacology and Therapeutics*, 18(4): 284-289.
8. Ding, H., Wang, L., Shen, X., Gu, X., Zeng, D. and Zeng, Z. (2013). Plasma and tissue pharmacokinetics of marbofloxacin in experimentally infected chickens with *Mycoplasma gallisepticum* and *Escherichia coli*. *Journal of Veterinary Pharmacology and Therapeutics*, 36(5): 511-515.
9. El-Komy, A., Attia, T., El Latif, A. A. and Fathy, H. (2016). Bioavailability pharmacokinetics and residues of marbofloxacin in normal and E. coli infected broiler chicken. *International Journal of Pharmacology and Toxicology*, 4(2): 144-149.
10. Huang, X. H., Chen, Z. L. and Zhang, S. T. (2003). Influence of experimentally *Pasteurella multocida* infection on the pharmacokinetics of marbofloxacin in broiler chickens. *Acta Veterinaria et Zootechnica Sinica*, 34(1): 98-102.
11. Verdon, E., Couëdor, P. and Sanders, P. (2004). Validation of a multi-quinolone, multi-matrix, multi-species method for the determination of quinolone residues by HPLC with fluorescence detection. CRL AFSSA LERMVD. Posters.
12. Zhao, S. Jiang, H. Li, X. Mi, T. Li, C. and Shen, J. (2007). Simultaneous determination of trace levels of 10 quinolones in swine, chicken, and shrimp muscle tissues using HPLC with programmable fluorescence detection. *Journal of Agricultural and Food Chemistry*, 55(10): 3829-3834.
13. Yang, F., Yang, Y. R., Wang, L., Huang, X. H., Qiao, G. and Zeng, Z. L. (2014). Estimating marbofloxacin withdrawal time in broiler chickens using a population physiologically based pharmacokinetics model. *Journal of Veterinary Pharmacology and Therapeutics*, 37(6): 579-588.
14. Yorke, J. C. and Froc, P. (2000). Quantitation of nine quinolones in chicken tissues by high-performance liquid chromatography with fluorescence detection. *Journal of Chromatography A*, 882(1): 63-77.
15. Gigosos, P. G., Revesado, P. R., Cadahıa, O., Fente, C. A., Vazquez, B. I., Franco, C. M. and Cepeda, A. (2000). Determination of quinolones in animal tissues and eggs by high-performance liquid chromatography with photodiode-array detection. *Journal of Chromatography A*, 871(1): 31-36.
16. Yu, H., Tao, Y., Chen, D., Pan, Y., Liu, Z., Wang, Y. and Yuan, Z. (2012). Simultaneous determination of fluoroquinolones in foods of animal origin by a high performance liquid chromatography and a liquid chromatography tandem mass spectrometry with accelerated solvent extraction. *Journal of Chromatography B*, 885: 150-159.
17. Rocha, D. G., Santos, F. A., da Silva, J. C. C., Augusti, R. and Faria, A. F. (2015). Multiresidue determination of fluoroquinolones in poultry muscle and kidney according to the regulation 2002/657/EC. A systematic comparison of two different approaches: Liquid chromatography coupled to high-resolution mass spectrometry or tandem mass spectrometry. *Journal of Chromatography A*, 1379: 83-91.
18. Valle, M., Schneider, M., Galland, D., Giboin, H. and Woehrle, F. (2012). Pharmacokinetic and pharmacodynamic testing of marbofloxacin administered as a single injection for the treatment of bovine respiratory disease. *Journal of Veterinary Pharmacology And Therapeutics*, 35(6): 519-528.
19. Silva, N. and Sousa, M. (2017). Is marbofloxacin a good candidate for treating pigs in Europe?. *Veterinary Record*, 180(24): 588-590.
20. Böttcher, S., Baum, H. V., Hoppe-Tichy, T., Benz, C. and Sonntag, H. G. (2001). An HPLC assay and a microbiological assay to determine levofloxacin in soft tissue, bone, bile and serum. *Journal of Pharmaceutical and Biomedical Analysis*, 25(2): 197-203.
21. EMEA. 2002, 2002/657/EC: Commission Decision of 12 August 2002 implementing Council Directive 96/23/EC concerning the performance of analytical methods and the interpretation of results (Text with EEA relevance) (notified under document number C (3044), European Medicines Agency.
22. Bailac, S., Ballesteros, O., Jiménez-Lozano, E., Barrón, D., Sanz-Nebot, V., Navalón A. and Barbosa, J. (2004). Determination of quinolones in chicken tissues by liquid chromatography with ultraviolet absorbance detection. *Journal Chromatography. A*, 1029 (1):145-151.

Malaysian Journal of Analytical Sciences, Vol 22 No 2 (2018): 203 - 218
DOI: https://doi.org/10.17576/mjas-2018-2202-05

MALAYSIAN JOURNAL OF ANALYTICAL SCIENCES
Published by The Malaysian Analytical Sciences Society
ISSN 1394 - 2506

RESPONSE SURFACE METHODOLOGY ON THE EFFECTS OF SODA – ANTHRAQUINONE PULPING CONDITIONS ON OIL PALM EMPTY FRUIT BUNCHES PULP PROPERTIES

(Kaedah Gerak Balas Permukaan Terhadap Kesan Faktor-Faktor Pemulpaan Soda-Antrakuinon Ke Atas Sifat-sifat Gentian Tandan Buah Kosong Kelapa Sawit)

Nurul Husna Mohd Hassan[1]*, Mazlan Ibrahim[2], Nor Yuziah Mohd Yunus[1]

[1]*School of Wood Industry, Faculty of Applied Sciences,*
Universiti Teknologi MARA, Cawangan Pahang, Kampus Jengka, 26400 Bandar Tun Abdul Razak, Pahang
[2]*School of Industrial Technology,*
Universiti Sains Malaysia, 11800 USM Pulau Pinang, Malaysia

**Corresponding author: nurulhusna@uitm.edu.my*

Received: 15 November 2016; Accepted: 29 January 2018

Abstract

Effects of soda–antrhraquinone (soda-AQ) pulping conditions on pulp properties of oil palm empty fruit bunches were studied by using response surface methodology (RSM) based on central composite design (CCD). Alkali charge (A), pulping temperature (T) and pulping time (t) were the pulping factors studied, with their ranges between 20 - 30%, 160 - 180 °C and 60 - 120 minutes, respectively. Pulp properties evaluated based on total yield (35.37 - 58.87%), screened yield (30.37 - 56.07%), Kappa number (6 – 16) and viscosity (5.43 - 16.02 cP). The effect of soda-AQ pulping conditions on oil palm empty fruit bunches fibers was clearly elucidated by the regression model obtained. The generated mathematical relationship showed that the optimum pulping condition was 27.30% alkali charge, temperature 160 ^{o}C at 60 minutes. This combination of mild pulping conditions level produced: total yield (55.54%), screened yield (53.20%), Kappa number (10) and viscosity (12.02 cP).

Keywords: oil palm empty fruit bunches, pulp properties, response surface methodology

Abstrak

Kesan faktor-faktor pemulpaan soda-antrakuinon ke atas sifat-sifat gentian tandan buah kosong kelapa sawit telah dikaji dengan menggunakan kaedah gerak balas permukaan (RSM) berasaskan rekabentuk komposit berpusat (CCD). Julat faktor-faktor pemulpaan iaitu cas alkali (A), suhu pemulpaan (T) dan masa pemulpaan (t) adalah antara 20 – 30%, 160 – 180 ^{o}C dan 60 – 120 minit. Sifat-sifat gentian yang dinilai adalah berdasarkan jumlah keseluruhan (35.37 - 58.87%), hasil saringan (30.37 - 56.07%), nombor Kappa (6 – 16) dan kelikatan (5.43 - 16.02 cP). Pengaruh faktor-faktor pemulpaan soda-AQ ke atas gentian tandan buah kosong kelapa sawit dapat dijelaskan berdasarkan model regrasi yang diperolehi. Melalui persamaan matematik yang terhasil, pemulpaan optimum berlaku apabila faktor-faktor pemulpaan iaitu cas alkali, suhu pemulpaan dan masa pemulpaan diselaraskan pada 27.3%, 160 ^{o}C dan 60 minit. Penggunaan kombinasi aras faktor pemulpaan yang rendah ini dapat menghasilkan hasil keseluruhan (55.54%), hasil penskrinan (53.20%), nombor Kappa (10) dan kelikatan (12.02 cP).

Kata kunci: tandan buah kosong kelapa sawit, sifat-sifat gentian, kaedah gerak balas permukaan

Introduction

Oil Palm Industry

Oil palm tree was first introduced for aesthetic and decorative nature at Botanical Garden of Singapore in 1870 and soon has created interest for its commercial exploits. The first two chosen plantation locations were Tenamaran and Elmina Estate, in Kuala Selangor, Malaysia. Subsequently, early 90's had shown the establishment of large plantation areas in Sumatera and Malaysia, by using the palm oil seeds brought over by commercial labourer from Southern America. Today, oil palms are planted commercially in Africa, South East Asia, Pacific Island and Southern America. This industry has many vital roles and the planting activities increase after World War II resulting from world demand and world's fats and oils price stabilization [1].

In Malaysia, the development of oil palm industry is slower, as more emphasis is given towards rubberwood plantation as major export product.The situation changes in 1960's, as the price of the rubber dropped due to the synthetic rubber introduction [2]. Subsequently, Malaysian Government had initiated a major agricultural development program in order to reduce dependency on singular commodity rubber as export income contributor. This led to the opening of newland for oil palm planting and when a rubber estate reached maturity, it was replanted with oil palm.This activities had contributed to rapid increase in oil palm hectarage in a short time. The plantation area surpassed 2 million hectares in 1990 and currently reached 3.8 million hectares, which capable of delivering more than 18.6 million tons crude palm oil. Entering the new millennium era, Malaysia was covered by 3.38 million hectares of oil palm plantations [3, 4, 5]. By 2014, Malaysia has recorded a staggering 5.39 million hectares of oil palm plantations [6], an increase of 11.0% from the previous 4.85 million hectares in 2010 [7]. Malaysia's total land mass is 32.98 million hectares [8], which equivalent to 16% of the land that is occupied with oil palm plantation. Mohd Fahmi et al. [7] reported the current situation related to the oil palm industry in Malaysia; the availability of oil palm waste and its utilization through thermochemical conversion, with specific regards to the liquefaction process.

Oil palm lignocellulosic

Oil palm, *Elaeis guineensis*, is originated from South Africa and was introduced to South East Asian countries especially Malaysia and Indonesia and the oil is obtained from its fruits [9]. Malaysia is the largest palm oil producer by covering 51% of world oil palm production [10]. However, in 2007, Indonesia had overtaken Malaysia due to the rapid expansion of oil palm plantations in the region. Nevertheless, Malaysia still held the title as the world's largest crude palm oil exporter [11]. When combined, these neighboring countries had accounted for more than 80% of the global palm oil supply annually [12, 13]

After 20 to 25 years, the palm oil fruit production will reduce and need to be cut down for re-planting. Re-planting activities lead to the increase of the abundance of palm oil trunks (OPT) and oil palm frond (OPF). As more plantations reached the limit of its economic production cycle, re-planting activities are expected to increase in the near future. Thus, the disposal of huge volume of palm oil trunks and fronds will become a serious matter as activities during harvering also yield fronds.

In oil palm mills, by-products of oil extraction activities generate palm kernel shell (PKS), empty fruit bunches (EFB), pressed fruit fibers (PFF) and palm oil mill effluent (POME). The oil palm mills waste by-product amount was quoted to be in the range of 70–80 million tons per annum, where only 10% of the total biomass was utilized and the rest was discarded as wastes [14].These by-products could and have been re-routed to various agronomic uses and mills.These wastes ended up in low value-added activities such as being supplement in ruminant feed, burning material, or would be burnt in the plantation area [4]. The fronds obtained from continuous pruning in plantation are used as interrows coverage [1].Except for POME, the rest of the wastes have high content of fibers [7] and are suitable to be used as the raw material for pulp and paper industry.

Soda-anthraquinone pulping

According to Eckett et al. [15], soda pulping without AQ gave lower yield and lower viscosity compared to kraft pulping. It utilized 40% more alkali and 100% higher H factor to attain the targeted kappa number. The addition of 0.1% AQ during soda cooking had reduced H factor to kraft level, but only with the use of higher alkali percentage. Further AQ addition to 0.15% will reduce alkali usage and improve yield and viscosity. In both instances, the soda

usage is still higher than kraft. With AQ addition above 0.35%, soda reduction is no longer proportional to AQ dosage and the reaction level approached an equilibium state.

The application of anthraquinone (AQ) as a pulping catalyst has been well documented in scientific studies and mill applications. AQ is known to increase the rate of delignification, enabling a reduction in pulping time, temperature, or chemical charge and an increase in pulp yield. However, Hart & Rudie also highlighted that due to unknown health risk, recently, many pulp and paper companies had decided to stop using AQ in the production of direct food contact products [16].

This study aims to focus on EFB as the raw material for pulp and paper production based on the abundant availability of oil palm waste material produced from the oil palm harvesting. The usage of more environmentally chemical pulping process by using soda pulping with AQ was chosen for EFB pulp production, due to its low lignin content as compared to wood materials. With the aid of Response Surface Methology (RSM) Experimental Design, three pulping parameters (alkali percentage, pulping temperature and pulping time) were optimized to find the best pulping conditions combination for EFB fibers. The pulping conditions model can be used to predict the most suitable pulping conditions to be used based on the desired pulp properties.

Materials and Methods

Raw material preparation

The raw material used in this study is empty fruit bunches (EFB) obtained from SABUTEK Sdn. Bhd., Teluk Intan, Perak in the form of fibers. The EFB was soaked overnight and washed with water to remove debris such as soil and dust. The fibres were then sun-dried until constant moisture content between 11 – 12%.

Soda-anthraquinone pulping: Experimental design by response surface methodology

Sodium hydroxide (NaOH) solution, water and AQ were added to 300g of EFB fiber placed in a Rotary Digester. The digester temperature was increased from room temperature to pulping temperature within 90 minutes. This was done to evenly mix NaOH solution and EFB fiber prior to the delignification process. Then, the mixture underwent pulping reaction for the selected duration (Table 1). Upon pulping process completion, the pulp was washed under running water to remove all the black liquor. The washed pulp was screened to remove uncooked EFB and any debris. Measurements were taken and recorded throughout the process to determine the pulp moisture content, screened yield, rejected and total yield.

Response surface methodology (RSM**)** was used in the research to identify the optimum pulping factors. The evaluated factors were pulping temperature (160 – 180 ^{o}C), pulping time (60 – 120 minutes) and active alkali (20 – 30%).The fixed factors were time of 90 minutes to reach pulping temperature, AQ percentage of 0.1% with respect to oven dried EFB and EFB fiber of 300g for each pulping batch.The pulping process followed combinations stated in Table 1. Based on this program design, 20 experiments were done by following the experimental sequencing. This sequencing allows completely randomized pulping process.

Table 1. Sequencing of soda-anthraquinone pulping

Run	Experiment	Pulping Parameters		
		Temperature (T), ^{o}C	Time (t), min	Alkali (A), %
1	4	160	60	20
2	19	180	60	20
3	6	160	120	20
4	8	180	120	20
5	2	160	60	30
6	7	180	60	30
7	1	160	120	30
8	18	180	120	30

Table 1 (cont'd). Sequencing of soda-anthraquinone pulping

Run	Experiment	Pulping Parameters		
		Temperature (T), ^{o}C	Time (t), min	Alkali (A), %
9	9	153	90	25
10	5	187	90	25
11	20	170	40	25
12	15	170	141	25
13	17	170	90	16.6
14	3	170	90	33.4
15	12	170	90	25
16	13	170	90	25
17	14	170	90	25
18	16	170	90	25
19	11	170	90	25
20	10	170	90	25

Pulp properties determination: Yield determination

Washed pulp was wringed, weighted and the moisture content was determined with a moisture content analyser. Total yield percentage was calculated using equation 1 [17].

$$\text{Total yield, \%} = \frac{\text{Weight of oven dried (o.d.) pulp, g}}{\text{Weight of o.d. raw material, g}} \times 100 \quad (1)$$

Then, the pulp was screened by using Sommerville Fractionator screener. After screening, screened pulp was spin dried, weighted and moisture content was determined. Total screened yield percentage was calculated using equation 2 [18].

$$\text{Screened yield, \%} = \frac{\text{Weight of o.d. screened pulp, g}}{\text{Weight of o.d. raw material, g}} \times 100 \quad (2)$$

Reject yield was determined from collected rejects on screener plate. They were oven dried at 105 ± 3^{o}C to a constant weight. Reject percentage was calculated based on equation 3 [19].

$$\text{Reject yield, \%} = \frac{\text{Weight of o.d. rejects, g}}{\text{Weight of o.d. raw material, g}} \times 100 \quad (3)$$

Kappa number

Kappa number qualitatively or indirectly determines the lignin content in pulp. It was verified according to TAPPI T236 cm-85[18]. Potassium permanganate (0.02M) and sodium thiosulphate (0.2M) solutions were standardized before used.

Viscosity

Prior to viscosity determination, the pulp that was delignified as unbleach pulp was used. This was done to remove lignins and prevent clogging of capillary viscometer. Holocellulosic delignification process was based on the procedure developed by Browning [19], with some modifications. Oven dried (o.d.) pulp (2.5g) was mixed with required buffer solution in a 250 ml elenmeyer flask, so that the combined pulp and solution weight equals to 83g.

Viscosity determinations involved the technique of pulp dissolution and measurement of the resulting solution. The experiment was conducted according to TAPPI T230 om-89 [20] and the method used was mixing pulp and liquid in an open tube with a copper rod.

Results and Discussion

Total yield determination

Total yield is the percentage o.d. pulp weight compared to the o.d. EFB used during pulping. Total yield comprised of reject material, including uncooked EFB or undissolved substances in pulping liquor. Rejects will be collected on top of the screen plate with slots measuring 0.15 mm. Pulp that could not pass through the screen plate were considered coarse and unsuitable for paper making. Rejected yield is the percentages of o.d. reject compared to the o.d. EFB weight before pulping. With reference to Table 2, it can be seen that the screened yield and reject yield is not equivalent to the total yield. There were areas of potential losses during washing, container transfer and pulp lodged at screen slots.

Table 2. Percentage of the pulping yield

Pulping Yield	Percentage (%)*
Total yield	52.47
Screened yield	44.41
Reject yield	2.96
Loss yield	5.10

*Average of 20 pulping batches

Table 3 shows the total yield, screened yield, Kappa number and viscosity responses. Total yield ranges from 35.70% to 58.87%. These have given initial indication on how the total yield is dependent on the pulping procedures. For Experiment 6, the total yield is the lowest as two pulping factors namely temperature and alkali percent dosage were at the maximum value. High temperature and high alkali content caused more pulp degradation which lead to lower yield.

Table 3. Total yield, screened yield, Kappa number and viscosity responses

No. of Exp	Pulping Factors Combination						Total Yield, %	Screened Yield, %	Kappa Number	Viscosity, cP
	Code			Actual Value						
	T	t	A	T, ^{o}C	t, min	A, %				
1	-1	-1	-1	160	60	20	58.83	37.44	14.9	15.34
2	+1	-1	-1	180	60	20	56.88	44.70	10.8	10.47
3	-1	+1	-1	160	120	20	50.62	42.34	13.5	15.48
4	+1	+1	-1	180	120	20	53.09	49.99	9.6	9.13
5	-1	-1	+1	160	60	30	57.23	56.07	7.3	9.30
6	+1	-1	+1	180	60	30	35.70	34.57	7.7	9.19
7	-1	+1	+1	160	120	30	52.94	42.83	7.5	9.24
8	+1	+1	+1	180	120	30	39.17	37.73	5.8	5.43
9	-1.682	0	0	153	90	25	55.43	51.00	9.4	10.74
10	+1.682	0	0	187	90	25	55.91	42.09	7.9	7.11

Table 3 (cont'd). Total yield, screened yield, Kappa number and viscosity responses

No. of Exp	Pulping Factors Combination						Total Yield, %	Screened Yield, %	Kappa Number	Viscosity, cP
	Code			Actual Value						
	T	t	A	T, °C	t, min	A, %				
11	0	-1.682	0	170	40	25	58.87	40.98	12.4	16.02
12	0	+1.682	0	170	141	25	49.88	48.77	7.2	7.95
13	0	0	-1.682	170	90	16.6	58.82	30.37	15.6	14.34
14	0	0	+1.682	170	90	33.4	53.44	37.17	6.7	7.90
15	0	0	0	170	90	25	52.27	47.94	9.1	7.67
16	0	0	0	170	90	25	51.06	49.62	8.7	9.02
17	0	0	0	170	90	25	53.80	50.52	7.9	8.51
18	0	0	0	170	90	25	56.37	49.20	8.1	9.74
19	0	0	0	170	90	25	50.02	49.13	8.4	8.73
20	0	0	0	170	90	25	48.99	45.65	9.4	9.80

Total yield ANOVA analysis

Exprimental data obtained was statisticaly analysed by RSM to ascertain the suitable model selection for each surface response. Analysis of variance (ANOVA) evaluation included Sequential Model Sum of Squares (SMSS), Lack of Fit (LOF) and Model Summary Statistic (MSS) [21].

Through RSM, the linear and quadratic models are the most probably suitable models. The models were chosen based on the Probability of a larger F (Prob. F.), which in SMSS is significant with Prob. $F < 0.05$ and not significant in LOF with Prob. $F > 0.10$. In MSS, a model was chosen based on the minimum Predicted Residual Sum of Squares, (PRESS) and maximum Multiple Correlation Coefficient, R^2.

Table 4 shows the ANOVA analysis for total yield. From SMSS total yield, F-value for quadratic model is highly significant at 0.0091 compared to 0.0361 for the linear model. LOF Prob. F value for quadratic model shows insignificant value (0.1129) as opposed to linear model (0.0499). Based on MSS, the most suitable model is quadratic, with higher R^2 of 0.6861 as compared to -0.0650 for linear model. The correlation between the quadratic model and soda-AQ pulping conditions showed that the total yield increased with the increasing of the pulping conditions. However, at a certain stage of pulping conditions, the total yield can be decreased due to high severity in pulping conditions especially at high temperature and high alkali percentage. Quadratic regression model for total yield is represented by equation 4 for the surface response for total yield.

Table 4. Total yield ANOVA analysis

Pulping Yield	Model	Sequential Model Sum of Squares (SMSS)*	Lack of Fit Test (LOF)#	Model Summary Statistic (MSS)‡
Total Yield, %	Linear	F-value = 3.63 Prob. F = 0.0361	F-value = 4.71 Prob. F = 0.0499	R^2 = -0.0650 PRESS = 736.27
	Quadratic	F-value = 4.74 Prob. F = 0.0091	F-value = 3.12 Prob. F = 0.1129	R^2 = 0.6861 PRESS = 793.31

* Choose model with significant Prob. F (Prob. $F < 0.05$).
# Choose model with insignificant Prob. F (Prob. $F > 0.10$).
‡ Choose model with high R^2 and low PRESS.

$$\text{Total yield, \%} = -165.19 + 1.53\mathbf{T} - 1.16\mathbf{t} + 13.75x10^{-3}\mathbf{Tt} - 0.09\ \mathbf{TA} + 9.317x10^{-3}\mathbf{tA} \quad (4)$$

Effect of pulping conditions on total yield

Effect of pulping conditions on total yield could not be clearly seen if the analysis is done only through ANOVA and best-fit-model. To explain a model easier, a three dimensional (3D) graph plot was used. However, the 3D plot could only show the effect of two factors and one response at a time. Therefore, one of the factors must be kept constant. Through pertubation plot, factors that have the highest effect on a response were represented by X and Y axis while the Z axis represented the lowest effect response of pulping factors.

Figure 1 shows the pertubation plot for total yield. Temperature and alkali factors showed more impact on total yield compared to time factor and will be represented by the X and Y axis. Figure 2 shows the 3D plot for total yield of alkali and temperature at 60 min time. Total yield decreased when time increased to 90 min and 120 min. This was expected as more lignin, hemicellulose and cellulose were dissolved with the increase of pulping time.

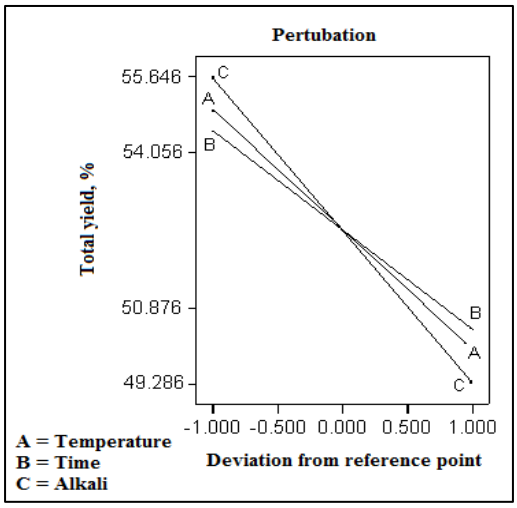


Figure 1. Total yield perturbation plot

According to Smook [22], if pulping was done at range of 155 – 175 ^{o}C, the delignification rate will be doubled for every 10 ^{o}C increment. Since the temperature used in this study was 160 – 180 ^{o}C, it was not a surprise if the total yield decreased with the increase of temperature. Pulping at high temperature encouraged dissolution of lignin and carbohydrate. This finding is supported by Mimms et al. [23] where small increment in temperature was shown to have large effect on delignification rate. When temperature above 175 ^{o}C was used, lignin selection became lower and more cellulose degredation occurred, causing lower yield. High temperature would cause more degradation of hemicellulose and cellulose. Thus, total yield decreased as temperature increased.

Increasing alkali contents also decreases total yield. Soda easily interacts with the phenolic functionality of the lignins by rendering it to be soluble in aqueous solution. Subsequently, delignification rate increases with increasing of alkali percentage. The amount of dissolved hemicellulose will also increase as the amorphous structure opens and the hydroxyl functionality reacts leading to yield reduction. Hydroxyl ion (OH^-) is an active component in pulping.Hydroxyl ions concentration plays a major role during pulping for lignin solubilization and unwanted reaction such as cellulose degradation [24].

Temperature and alkali factors have interactions that affect the total yield. With reference to Figure 2, total yield only increased at either high alkali dosage with low temperature, or at high temperature with low alkali dosage.

High alkali dosage and high temperature combination caused yield reduction. Degradation of cellulose, hemicellulose and lignin desolubilization is high in these conditions.

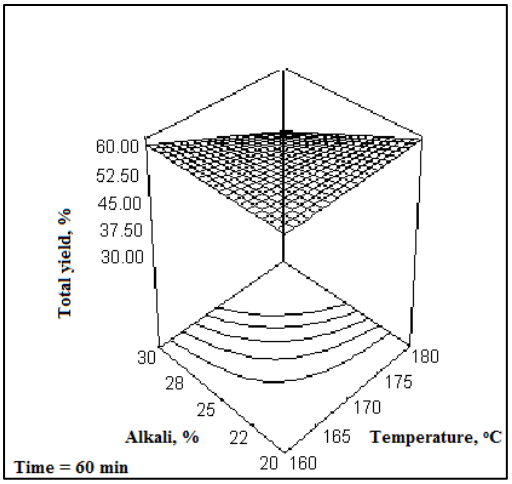


Figure 2. 3D plot on effect of alkali (A) and temperature (T) on total yield variation at time (t) = 60 minutes

In conclusion, temperature and alkali factors give stronger effects toward total yield, compared to time factor. To obtain high total yield, level of temperature, alkali and time has to be used at the lower value. However, it should be noted that, total yield still includes rejects from coarse undissolved EFB during pulping which adds on to total yield weight during yield determination process.

Screened yield determination

Screened yield was obtained after the total yield pulp had undergone screening process and pulp had passed the screen slot plates routed to astrainer. Screened yield percentage is the screened pulp o.d. weight over the o.d. weight of EFB used. Based on Table 3, the screened yield ranged between 30.37% and 56.07% experiment 5 showed the highest percentage of screened yield. It is believed that the pulping factors were at optimum level, namely low temperature with short time and high alkali dosage. This was proven by optimum factors level suggested by RSM during optimization process in which the pulping factors were at 160 ^{o}C temperature, 60 minutes time and 27.3% of alkali percentage.

Screened yield ANOVA analysis

ANOVA of screened yield (Table 5) showed SMSS quadratic model with highly significant F-value 0.0007 compared to linear model with insignificant F-value 0.6888. Both models are significant for LOF but quadratic model has higher insignificant value at 0.0369, compared to linear model at 0.0014. Observation of MSS strengthens the choice of quadratic model with high R^2 and low PRESS of 0.1194 and 719.28 as compared to -0.5783 and 1289.18 for linear model respectively. Equation 5 gives the response surface representing quadratic model for screened yield.

Table 5. Screened yield ANOVA analysis

Pulping Yield	Model	Sequential Model Sum of Squares (SMSS)*	Lack of Fit Test (LOF)#	Model Summary Statistic (MSS)‡
Screened yield, %	Linear	F-value = 0.05 Prob. F = 0.6888	F-value = 23.01 Prob. F = 0.0014	R^2 = -0.5783 PRESS = 1289.18
	Quadratic	F-value = 10.80 Prob. F = 0.0007	F-value = 5.90 Prob. F = 0.0369	R^2 = 0.1194 PRESS = 719.28

* Choose model with significant Prob. F (Prob. F < 0.05).
# Choose model with insignificant Prob. F (Prob. F > 0.10).
‡ Choose model with high $R^2$and low PRESS values.

$$\text{Screened yield, \%} = -528.223 + 2.97\mathbf{T} - 0.55\mathbf{t} + 29.02\mathbf{A} - 3.527\text{x}10^{-3}\mathbf{T^2} - 1.048\text{x}10^{-3}\mathbf{t^2} - 0.19\mathbf{A^2} + 6.996\text{x}10^{-3}\mathbf{Tt} - 0.10\mathbf{TA} - 0.017\text{t}\mathbf{A} \quad (5)$$

Effect of pulping conditions on screened yield

Screened yield perturbation plot is shown in Figure 3. From all the three factors tested, temperature and alkali factors gave higher impact on the screen yield compared to time. Thus, the X-axis represents temperature and Y-axis represents alkali.

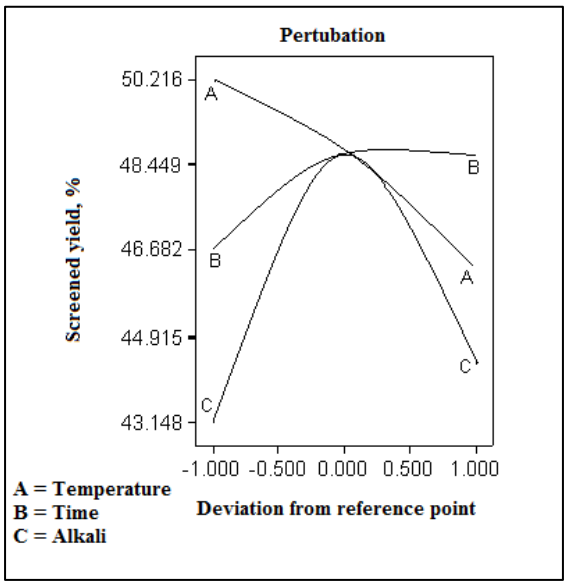


Figure 3. Screened yield perturbation plot

Figure 4 shows the 3D illustration of screened yield affected by temperature and alkali factors. Time factor was kept constant at 60 minutes as it has less impact on screened yield. However, the effect of time can be seen on screened yield when quadratic model on the surface response of Figure 4 shows changes in screened yield reduction as time increases. This is due to the cellulose degradation which occurs at longer pulping time.

As the alkali percentage increased, screened yield also increased as more lignin can be dissolved. This is similarly reported by Khairunisak et al. [24] where as active alkali increased, pulping yield increased. On the other hand, if alkali percentage is too low, incomplete EFB pulping process will produced high rejects yield and thus decreased

the screened yield. The same could be said for temperature factor. Screened yield increased with the increasing in temperature as at range of 150 – 170 ^{o}C, and at lower temperature delignification was incomplete [23]. At higher temperature, more lignin could be dissolved at faster rate.

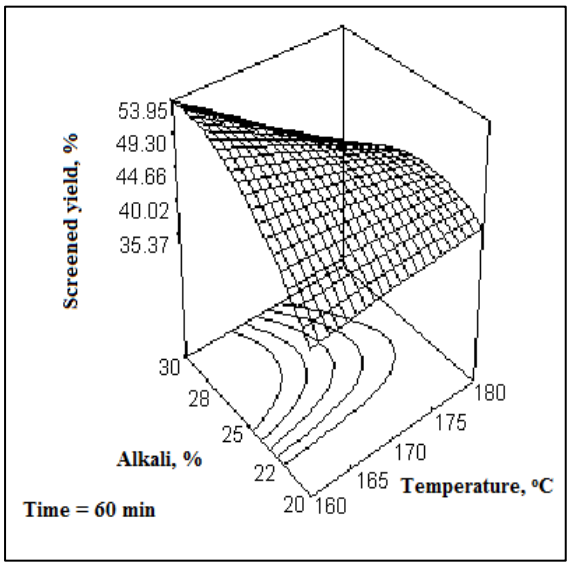


Figure 4. 3D plot on effect of alkali (A) and temperature (T) on screened yield variation at time (t) = 60 minutes

Alkali concentration has stronger impact on lignin dissolution compared to both temperature and time. The alkali impact become more important as temperature increased [25]. The combination of these factors has resulted in more efficient pulping digestion.There is an interaction between temperature and alkali factor which resulted in screened yield quantum. With reference to Figure 4, increase in screened yield with respect to temperature increase will only occur at low alkali percentage (< 25%). This is because, at low alkali percentage, high pulping temperature can increase delignification rate resulting in higher screened yield. When alkali percentage is at high level (> 25%), rising pulping temperature will cause screened yield reduction as some of the carbohydrate also dissolved instead of just lignin.

Thus, it could not be denied that the used of too high alkali percentage and high temperature, would cause fibres to undergo severe degradation and produced lower yield. The effect intensifies with longer time used. These conditions could be seen in Figure 4 as the screened yield dropped when the pulping time was increased. At this point, the cellulose and hemicellulose undergo degradation causing formation of fines which flushed through the screening wire mesh, leading to screened yield reduction.

Kappa number

Kappa number is defined as volume (ml) of 0.1N aqueous potassium permanganate used by 1g of o.d. pulp under specified conditions. This is an indirect method to identify the lignin content via oxidation of lignin through reaction with aqueous potassium permanganate. Kappa number has a relationship to lignin for pulp with yield lower than 70%. Percentage of lignin is estimated and factored at K x 0.15 [22].Within the industry, Kappa number test is used to check the degree of delignification during pulping and to determine chemical requirement for bleaching.Table 3 shows the Kappa number at various pulping conditions. Kappa number ranges from 5.8 to 15.6. This values neccessitate bleaching process to be done, if the pulp is needed for dissolving pulp experiments.

Kappa number ANOVA Analysis

Table 6 shows the ANOVA on resultant Kappa number. With reference to SMSS, both linear and quadratic model are significant with Prob F <0.0001. At LOF, only quadratic model shows insignificant value of 0.1229. MSS

observations strengthen the choice of quadratic model due to higher R^2 and lower PRESS (0.9446 and 42.28 respectively) compared to linear model (0.6944 and 42.87 respectively). Equation 6 represents surface acceptance for Kappa number quadratic model.

Table 6. Kappa number ANOVA Analysis.

Pulp Properties	Model	Sequential Model Sum of Squares (SMSS)*	Lack of Fit Test (LOF)#	Model Summary Statistic (MSS)‡
Kappa number	Linear	F-value = 24.05 Prob. F < 0.0001	F-value = 6.43 Prob. F = 0.0261	R^2 = 0.6944 PRESS = 42.87
	Quadratic	F-value = 23.46 Prob. F < 0.0001	F-value = 3.20 Prob. F = 0.1229	R^2 = 0.9446 PRESS = 42.28

* Choose model with significant Prob. F (Prob. F < 0.05).
# Choose model with insignificant Prob. F (Prob. F > 0.10).
‡ Choose model with high R^2 and low PRESS values.

$$\text{Kappa Number} = +124.22 - 0.43\mathbf{T} + 0.011\mathbf{t} - 5.12\mathbf{A} + 4.04\text{x}10^{-4}\mathbf{t^2} + 0.034\mathbf{A^2} - 7.917\text{x}10^{-4}\mathbf{Tt} + 0.017\mathbf{TA} + 7.5\text{x}10^{-4}\mathbf{tA} \quad (6)$$

Effect of pulping conditions on Kappa number

Figure 5 shows the pertubation plot for Kappa number. The alkali factor gives the highest effect on Kappa number compared to other pulping factors. Percentage difference of alkali at constant temperature and pulping time will yield significant Kappa number change.

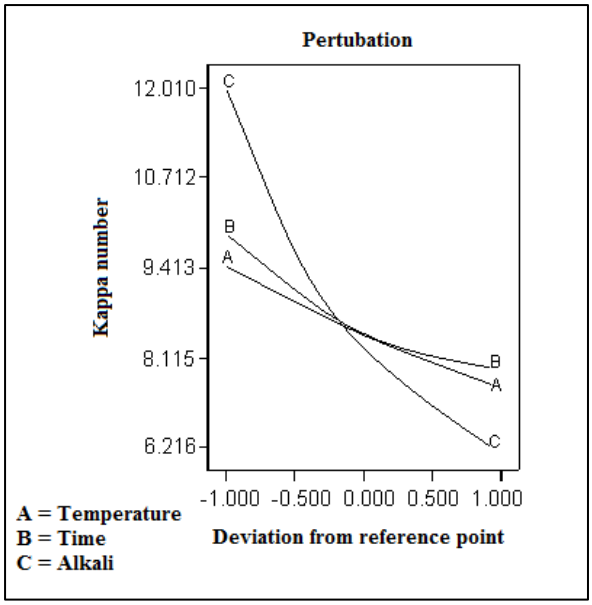


Figure 5. Kappa number perturbation plot

Examples of observation; Experiment 13 which used the lowest alkali percentage (16.6%) and Experiment 14 which used the highest alkali percentage (33.4%) were done at same pulping temperature and time. Experiment 13 gave high Kappa number reading while Experiment 14 gave low Kappa number reading.The Kappa number was

determined through observation of reaction of potassium permanganate with any lignin presence in pulp. Difference in effects of alkali factor can be directly seen by the colour variation in resultant pulp.

X-axis represents temperature and Y-axis represents alkali percentage. When temperature increase, the Kappa number will decrease as lignin dissolves faster at higher temperature. Kappa number value is closely linked to lignin content in pulp. High Kappa number shows high lignin content in pulp while low Kappa number shows low lignin content [26].

When alkali percentage increased, Kappa number decreased. This happened as more lignin dissolved and only small amount of lignin is still left in the pulp. High alkali percentage will dissolve more lignin component and decrease the Kappa number. Figure 6 shows the effects of Kappa number with alkali and temperature at constant time. Lengthening of time will remove more lignin and thus reduced Kappa number. According to Kleppe [27] high lignin content in pulp will control strength quality and optical quality of paper. High lignin content in paper will reduce paper strength and optical characteristic. Thus, the function of pulping is to maximize the removal of lignin into the pulping liquor.

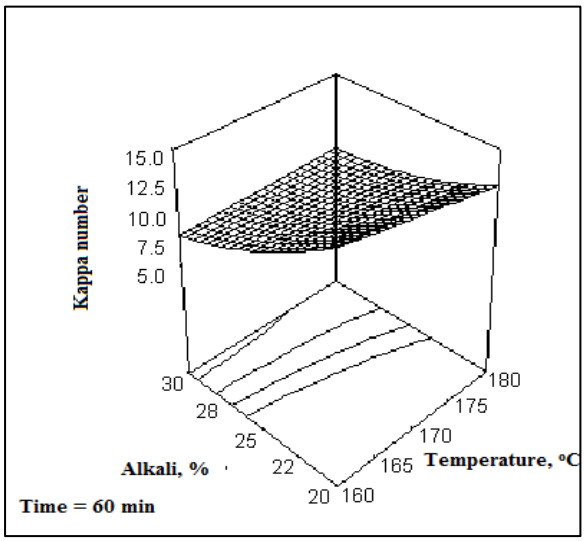


Figure 6. 3D plot on effect of alkali (A) and temperature (T) on Kappa number variation at time (t) = 60 minutes

Viscosity

Viscosity of a pulp solution indicates the average degree of cellulose polymerization. This test gives a relative indication on the reduction of cellulose molecule weight caused by the pulping process. Among the methods used to confirm the average cellulose degree of polymerization (dp) is by measuring the cellulose solution viscosity with known concentration in solvent such as cupriethylene diamine (CED), as CED can dissolve cellulose faster and has good chemical stability [22]. Table 3 shows the viscosity response which varies according to the pulping treament. Viscosity obtained ranges from 5.43 – 16.06 cP.

Viscosity ANOVA analysis

Table 7 shows the ANOVA analysis for viscosity response with quadratic model. F probability value at SMSS clearly shows the appropriate choice of quadratic model even though both linear and quadratic model give significant SMSS. Quadratic model was chosen as it has lower value that of $p<0.0001$. However, observation at LOF shows insignificant value for quadratic model than linear model at 0.1061 and 0.0261 respectively. With reference to MSS, the choice of using quadratic model is stronger as it has high R^2 and lower PRESS compared to linear model. Equation 7 describes the surface response plot for reducing quadratic model for viscosity.

Table 7. Viscosity ANOVA analysis

Pulp Properties	Model	Sequential Model Sum of Squares (SMSS)*	Lack of Fit Test (LOF)#	Model Summary Statistic (MSS)‡
Viscosity, cP	Linear	F-value = 12.70 Prob. F = 0.0002	F-value = 6.44 Prob. F = 0.0261	R^2 = 0.5042 PRESS = 81.76
	Quadratic	F-value = 14.10 Prob. F < 0.0001	F-value = 3.26 Prob. F = 0.1061	R^2 = 0.8916 PRESS = 76.74

* Choose model with significant Prob. F (Prob. F < 0.05).
# Choose model with insignificant Prob. F (Prob. F > 0.10).
‡ Choose model with high $R^2$and low PRESS values.

$$\text{Viscosity, cP} = +121.32 - 0.42\mathbf{T} + 0.21\mathbf{t} - 4.94\mathbf{A} + 1.136\text{x}10^{-3}\mathbf{t}^2 + 0.029\,\mathbf{A}^2 - 2.158\text{x}10^{-3}\mathbf{Tt} + 0.018\mathbf{TA} \quad (7)$$

Effect of pulping conditions on viscosity

Figure 7 shows the perturbation plot for viscosity response. It can be seen that time and alkali percentage gave higher influence than temperature. Therefore, X–axis represented time and Y–axis represented alkali. In the meantime, the temperature was kept constant at 160°C as in Figure 8. Temperature had minimal effect on viscosity as the response surface plot only moved slighty downwards as temperature was increased from 160 °C to 170 °C and from 170 °C to 180 °C.

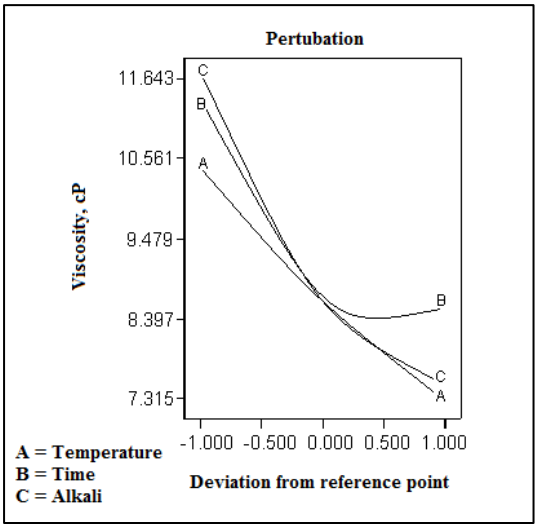


Figure 7. Viscosity pertubation plot

At long pulping duration, the viscosity value dropped at less than 11cP. Similarly, when alkali percentages increased, viscosity decreased. Viscosity reduction was caused by the degradation of cellulose chain during pulping process especially at high temperature and high alkali percentage. Moreover, soda can act as a surface tension reduction agent which had lowered the viscosity as solution.

In conclusion, pulp sample that undergoes extreme severity during pulping process has low viscosity while pulp which undergoes less severity has high viscosity. This is due to longer cellulose chain having stronger internal interactions and being easily tangled thus becoming more viscous. As consequence, it will take longer time to pass through viscometer capillary tube.

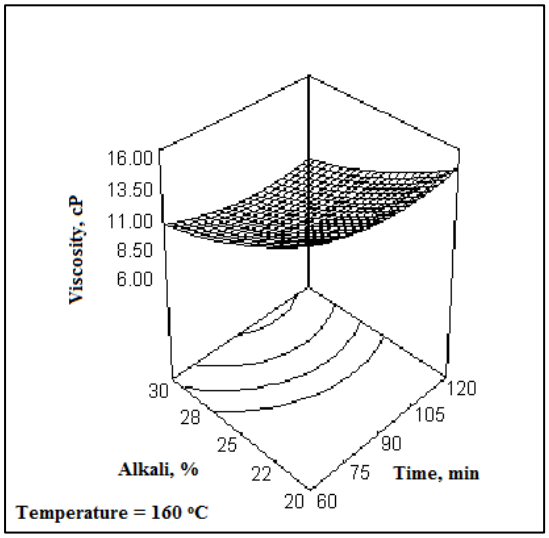


Figure 8. 3D plot on effect of alkali (A) and time (t) on viscosity variation at temperature (T) = 160 ^{o}C

Optimization of pulping parameters

To get the desired pulp quality, the pulp criteria were set to a fixed value. A few pulping level factors were suggested by the Design-Expert software as listed in Table 8. An experiment was done by using the solution factors at solution number 1 to obtain the nearest values according to predicted values for pulp properties.

Table 8. Pulping factors level suggested by Design Expert software for optimum pulp properties

Solution	Pulping Parameters			Pulp Properties				
	T, ^{o}C	t, min	A, %	*TY*	*SY*	*KN*	*V*	Achievability
1	160.00	60.00	27.30	55.53	53.20	9.85	12.02	0.713
2	160.21	60.10	27.28	55.48	53.06	9.83	11.99	0.711

TY=total yield, *SY*=screened yield, *KN*=Kappa number, *V*=viscosity

Conclusion

With reference to RSM usage, it can be concluded that alkali and temperature factors give the highest influence to most of pulp properties (total yield, screened yield and Kappa number). The combination of alkali and time factors gives more influence to viscosity response. The research objective to investigate the effects of pulping factors on pulp properties on total yield, screened yield, Kappa number and viscosity, was achieved. Total yield decreases with the increase of temperature, time and alkali. Screened yield increases with the increase of pulping factors up to 58.83% and then drops to 35.70% with extreme pulping condition usage. Kappa number and viscosity decrease with the increase of pulping factors. The optimum pulping conditions are temperature at 160 ^{o}C, pulping time at 60 minutes and alkali percentage at 27.3%. This is achievable at 71% to obtain 55.53% of total yield, 53.20% of screened yield, 9.85 of Kappa number and 12.02 cP of pulp viscosity.

Acknowledgement

The authors would like to express their appreciation to SABUTEK Sdn. Bhd., Teluk Intan, Perak, for providing the raw material for this study.

References

1. Khozirah, S. and Khoo, K. C. (1991). Oil palm utilisation-review of research, Forest Research Institute (FRIM), Kepong, Selangor. *Research Pamphlet* No.107: 1-7
2. Moll, H. A. J. (1987). The economics of oil palm. economics of crops in developing Countries No.2. Pudoc Wageningen, Netherlands.
3. Sulaiman, O., Salim, N., Nordin, N.A., Hashim, R., Ibrahim, M. and Sato, M. (2012). The potential of oil palm trunk biomass as an alternative source for compressed wood. *BioResearch,* 7(2):688-706.
4. Jalani, B. S. (2002). Prospects of elevating national oil palm productivity: A Malaysian perspective. *Oil Palm Industry Economic Journal*, 2: 1–9.
5. Abdullah, R. (2003). Short-term and long-term projection of Malaysian palm oil production. *Oil Palm Industry Economic Journal,* 3:32–36.
6. MPOB (2015). Economic & industry development devision. oil palm planted area. Retrieved from: http://bepi.mpob.gov.my/index.php/statistics/area.html.
7. Mohd-Fahmi, A., Othman, S., Rokiah, H. and Wan Noor Aidawati, W. N. (2015). An overview of the oil palm industry in Malaysia and its waste utilization through thermochemical conversion specifically via liquefaction. *Renewable and Sustainable Energy Reviews,* 50:1469-1484.
8. Shafie, S., Mahlia, T., Masjuki, H. and Andriyana, A. (2011). Current energy usage and sustainable energy in Malaysia: A review. *Renewable and Sustainable Energy Reviews*, 15(9): 4370-4377.
9. Wan Rosli, W. D., Leh, C. P., Zainuddin, Z. and Tanaka, R. (2003). Optimisation of soda pulping variables for preparation of dissolving pulps from oil palm fibre, Holzforschung, Walter de Gruyter, 57 (1), 106-113.
10. MPOPC (2004). Malaysian palm oil promotion council, Kuala Lumpur, Malaysia. Retrieved from:http://www.mpopc.org.my.
11. AIM (2013). National biomass strategy (2020): New wealth creation for Malaysia's biomass industry: Version 2.0, 2013. Agensi Inovasi Malaysia, Kuala Lumpur.
12. Amiruddin, M. N., Abrahman, A. K. and Shariff, F. (2005). Market potential and challenges for the Malaysian palm oil industry in facing competition from other vegetable oils. *Oil Palm Industry Economic Journal,* 5: 17–27.
13. FAOSTAT (2015). Food and Agriculture Organization of the United Nations for a world without hunger. Retrieved from: http://faostat.fao.org/site/339/default. aspx.=
14. Faizi, M. K., Shahriman, A.B, Abdul Majid, M. S., Shamsul, B. M. T., Ng, Y. G., Basah, S. N., Cheng, E. M., Afendi, M., Zuradzman, M. R., Khairunizam, W. A. N. and Hazry, D. (2017). An overview of the oil palm empty fruit bunch (OPEFB) potential as reinforcing fibre in polymer composite for energy absorption applications MATEC Web of Conferences 90: 01064.
15. Eckert, R. C., Pfeiffer, G. O., Gupta, M. K. and Lower, C. R. (1984). Soda anthraquinone pulping of *Douglas fir*. *TAPPI: Journal of the Technical Association of the Pulp and Paper Industry,* 67(11): 104-108.
16. Hart, P. W and Rudie, A. W. (2014). Anthraquinone-A review of the rise and fall of a pulping catalyst. *TAPPI: Journal of the Technical Association of the Pulp and Paper Industry,* 13(10): 23-31.
17. TAPPI test methods 1994 – 1995 (1994). T211 Ash in wood, pulp, paper and paperboard: combustion at 525°C. Vol. I, Atlanta, Georgia, Tappi Press.
18. TAPPI test methods 1994 – 1995 (1994). T236 Kappa Number of Pulp. Vol. I, Atlanta, Georgia, Tappi Press.
19. Browning, B. L. (1967). Methods of wood chemistry, Vol. II, Interscience Publishers, John Wiley & Sons, Inc.
20. TAPPI test methods 1994 – 1995 (1994). T230 Viscosity of pulp (Capillary Viscometer Method). Vol. I, Atlanta, Georgia, Tappi Press.
21. Kraber, S. (1997). Handbook for experimenters, Minneapolis: Stat-Ease Inc.
22. Smook, G. A. (1992). Handbook for pulp & paper technologist, 2nd Edition, Vancouver, Angus Wilde Publications.
23. Mimms, A., Kocurek, M. J., Pyatte, J. A. and Wright, E. E. (1989). Kraft Pulping: A compilation of notes, United State of America: Atlanta, Tappi Press.
24. Khairunisak, A. R., Hong, O. B., Zakaria, S., Ahmad, S. and Mohd Yussof, M. N. (2002). Effect of Kraft pulping with anthraquinone and methanol on oil palm empty fruit bunches. Proceeding 5th national seminar on utilization of oil palm tree – oil palm biomass: opportunities and challenges in commercial exploitation, Kuala Lumpur, oil palm tree utilization committee of Malaysia: pp. 205-210.

25. Iglesias, G., Bao, M., Lamas, J. and Vega, A. (1996). Soda pulping of *Miscanthus sinensis*. Effects of operational variables on pulp yield and lignin solubilization, Elsevier Science Ltd., Great Britain, *Bioresource Technology*, 58: 17-23.
26. Casey, J. P. (1980). Pulp and paper: Chemistry and chemical technology, Vol. I, 3rd Edition, New York, John Wiley & Sons.
27. Kleppe, P. J. (1970). Kraft pulping (feature review). *TAPPI: Journal of the Technical Association of the Pulp and Paper Industry,* 53(1): 35-47.

Malaysian Journal of Analytical Sciences, Vol 22 No 2 (2018): 219 - 226
DOI: https://doi.org/10.17576/mjas-2018-2202-06

MALAYSIAN JOURNAL OF ANALYTICAL SCIENCES
Published by The Malaysian Analytical Sciences Society
ISSN 1394 - 2506

VALIDATED RP-HPLC METHOD FOR QUANTIFICATION OF GASTRODIN IN ETHANOLIC EXTRACT FROM THE PSEUDOBULBS OF *Grammatophyllum speciosum* Blume

(Validasi Kaedah FT-KCPT bagi Kuantifikasi Gastrodin di dalam Ekstrak Etanolik dari Pseudobulbs *Grammatophyllum speciosum* Blume)

Verisa Chowjarean[1, 2], Apirada Sucontphunt[2], Saowapak Vchirawongkwin[3], Tossaton Charoonratana[4], Thanapat Songsak[4], Saraporn Harikarnpakdee[2, 5], Parkpoom Tengamnuay[6]*

[1]*Department of Pharmaceutical Technology Faculty of Pharmacy*
[2]*Cosmeceutical Research, Development and Testing Center, Faculty of Pharmacy*
[3]*Department of Pharmaceutical Chemistry, Faculty of Pharmacy*
[4]*Department of Pharmacognosy, Faculty of Pharmacy*
[5]*Department of Industrial Pharmacy, Faculty of Pharmacy*
Rangsit University, Pathumthani 12000, Thailand
[6]*Department of Pharmaceutics and Industrial Pharmacy, Faculty of Pharmaceutical Sciences,*
Chulalongkorn University, Bangkok 10330, Thailand

**Corresponding author: parkpoom.t@chula.ac.th*

Received: 7 September 2017; Accepted: 7 February 2018

Abstract

A reversed phase-high performance liquid chromatography-diode array detector (RP-HPLC-DAD) method was developed to determine the amount of gastrodin, the major active component of *Grammatophyllum speciosum* pseudobulbs. A previous study suggested that the ethanolic extract of *G. speciosum* had a potential to encourage stemness of keratinocytes. Therefore, in order to determine the quality of *G. speciosum* ethanolic extract, the quantitative analysis of gastrodin should be validated. The optimized RP-HPLC condition was achieved within 18 min, using a column, Inertsil ODS-3 (4.6 x 150 mm, 5 µm). The mobile phase consisted of a mixture of water: acetonitrile with a gradient from 1:99 to 100:0 in 14 minutes and keep constant at 1:99 for 4 minutes. The flow rate was 1.7 mL/min with the monitored UV wavelength of 220 nm. Gastrodin was eluted at the retention time of 6.5 minutes. The calibration curve of gastrodin at the concentration of 10 - 100 µg/mL showed good linearity (r^2 = 0.999). In addition, the intraday and interday precisions of gastrodin were 1.05 and 0.38%, respectively. The percentage recovery was within 99.3 - 101.5%. Average gastrodin contents in 3 samples were 55.52 - 58.12 mg/g. The results indicate that this method can be utilized to control the quality of *G. speciosum* extract.

Keywords: gastrodin, *Grammatophyllum speciosum*, reversed-phase high performance liquid chromatography, quantification

Abstrak

Kaedah fasa terbalik-kromatografi cecair berprestasi tinggi-pengesan susunan diod (FT-KPCT-PSD) telah dibangunkan untuk menentukan jumlah kandungan gastrodin, komponen aktif utama bagi pseudobulbs *Grammatophyllum speciosum*. Kajian sebelumnya mencadangkan ekstrak etanolik terhadap *G. speciosum* mempunyai potensi menguatkan stem keratinocytes. Oleh demikian, bagi menentukan kualiti ekstrak etanolik *G. speciosum,* analisis kuantitatif terhadap gastrodin perlu ditentusahkan. Keadaan optimum FT-KCPT telah dicapai pada minit ke 18, mengunakan turus Inertsil ODS-3 (4.6 x 150 mm, 5 µm). Fasa bergerak mengandungi campuran air:asetonitril dengan cerunan dari 1:99 hingga 100:0 bagi tempoh 14 minit dan kekal malar pada 1:99 selama 4 minit. Kadar aliran ialah 1.7 mL/min dengan pemerhatian panjang gelombang UV pada 220 nm. Gastrodin terelusi pada masa tahanan ialah minit ke 6.5. Lengkung kalibrasi gastrodin pada aras kepekatan 10 - 100 µg/mL telah

menunjukkan kelinearan yang baik (r^2 = 0.999). Kejituan intra-hari dan inter-hari telah dicapai masing-masing pada 1.05 dan 0.38%. Peratusan perolehan semula berada di dalam julat 99.3 - 101.5%. Purata kandungan gastrodin di dalam 3 sampel adalah 55.52 - 58.12 mg/g. Keputusan ini menunjukkan kaedah boleh digunapakai untuk mengawal kualiti *G. speciosum* yang diekstrak.

Kata kunci: gastrodin, *Grammatophyllum speciosum*, fasa terbalik kromatografi cecair berprestasi tinggi, kuantifikasi

Introduction

Grammatophyllum speciosum Blume or Waan-Phet-Cha-hueng (Thai name) is a plant in Orchidaceae family. It is also known as giant orchid, tiger orchid, sugar cane orchid or queen of the orchid. This gigantic orchid is typically found in the tropical rainforests of Southeast Asia such as Thailand, Malaysia, Indonesia, and Philippines [1, 2]. In Thai traditional medicine, its root is utilized as a treatment for centipede and scorpion venom, while its trunk, when blended with alcohol, is utilized to treat sores. The previous research found that the liquid extract of *G. speciosum* at the concentration of 0.706 mg/mL was effective in treating scorpion venom (*Heterometrus laoticus*) with a 23% cure rate [3]. Phytochemical investigation by Sahakitpichan et al. [2], reported new compounds isolated from the methanolic extract of the fresh pseudobulbs of *G. speciosum* which included glucosyloxybenzyl derivatives of (R)-2-benzylmalic acid and of (R)-eucomic acid, grammatophyllosides A-C, and a new phenolic glucoside, grammatophylloside D, cronupapine, vandateroside II, gastrodin, vanilloloside, orcinolglucoside, and isovitexin.

Gastrodin (Figure 1), a phenolic glycoside [p-hydroxymethylphenyl-β-D-glucopyranoside] found as a major active component in *G. speciosum*, is a potent antioxidant. Gastrodin was also found to function as anti-apoptotic activities in brain areas [4], a memory enhancer [5, 6], as well as having anti-convulsant [7], anti-cell death [8], anti-Alzheimer's disease [9], anti-Parkinson's disease activities [10], as well as protective effects against osteoporosis linking to a reduction in reactive oxygen species [11]. In addition, *G. speciosum* ethanolic extract was reported to have a potential to increase stem cell phenotypes of human keratinocytes. Moreover, the extract also had an ability to protect the cells against superoxide anion-induced cell death [12]. As gastrodin is a major active compound in the *G. speciosum* ethanolic extract, this study selected gastrodin as an analytical marker to control the quality of *G. speciosum* ethanolic extract. It was also used as an analytical marker for quality evaluation of *Gastrodiae rhizoma* extracts using RP-HPLC [13, 14, 15].

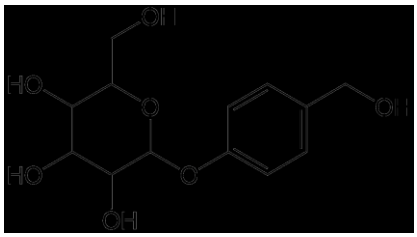


Figure 1. Basic structure of gastrodin

Therefore, in this study, RP-HPLC technique was developed to analyze the quantity of gastrodin in *G. speciosum* extract. The method was developed and validated according to the AOAC Guidelines for Single Laboratory Validation of Chemical Methods for Dietary Supplements and Botanicals [16]. The quantitative analysis of gastrodin, the analytical marker in *G. speciosum* extract by RP-HPLC technique can be utilized to monitor the quality of the plant's raw materials and may also be applied to analyze *G. speciosum* extract in future cosmetic formulations.

Materials and Methods

Extract preparation

Fresh pseudobulbs of *G. speciosum* were collected from the Khao Hin Sorn Royal Development Study Center's Area, Chachoengsao province. Dry pseudobulbs of *G. speciosum* were ground up and macerated 3 times for 3 days in ethanol (1:9 w/v), at 25 ºC. The extract was then filtered and evaporated under vacuum pressure at a temperature

below 40 ºC. The extract of *G. speciosum* were prepared in 3 different batches (batch 1: January, batch 2: May, and batch 3: September, year 2016). Each batch was collected 4 months apart.

LC-MS analysis

The *G. speciosum* extract was analyzed using a Dionex Ultimate TM 3000 HPLC (Germering, Germany) coupling with Bruker Amazon SL mass spectrometer (Bremen, Germany). Acclaim 120-C18 column (2.1 x 150 mm, 3 µm, Thermo Fisher Scientific, Germany) was used as a stationary phase. Analysis was performed in a gradient mode using 0.1% formic acid-acetonitrile ratio at 99:1 (0-3 minutes), gradient from 99:1 to 90:10 (3-5 minutes), gradient from 90:10 to 75:25 (5-8 minutes), gradient from 75:25 to 50:50 (8-10 minutes), gradient from 50:50 to 1:99 (10-11 minutes), isocratic at 1:99 (11-16 minutes), and re-equilibrate at 99:1 for 5 minutes. The column was maintained at 25 ^{o}C with a flow rate of 0.15 mL/min and the injection volume was 5 µL. The mass spectrometer was equipped with an ESI ion source and a quadrupole-ion trap. LC-MS evaluation was performed using full scan in negative mode recorded on a mass range of m/z 100-1,000. Capillary voltage was set at 4,500 V, and drying gas temperature was 200 ^{o}C with a flow rate of 7.0 L/min. Nebulizer pressure was set at 2 bars. Gastrodin was recognized by comparing the parent and fragment ions with the reference standard using the multiple reactions monitoring (MRM) method. Data were processed by Compass 1.3 SR2 program.

Instrumentation and chromatographic conditions

Chromatographic analysis was performed using Agilent high performance liquid chromatographic system (Agilent Technologies, California, United States of America) with a quaternary pump (G1311A). An auto-sampler (Agilent G1313A) and column oven (G1316A) were used with a photodiode array detector (G 1315A). Results were acquired and evaluated by ChemStation software (Agilent Technologies, California, United States of America). Chromatography was performed under gradient conditions with a total run time of 18 minutes. The mobile phase was filtered through a 0.22-µm membrane filter prior to use. The mobile phase consisted of solvent A (water) and solvent B (acetonitrile). The gradient started with 99% solvent A for 3 minutes, was adjusted to 90% solvent A for 2 minutes, to 75% solvent A for 3 minutes, to 50% solvent A for 2 minutes, to 100% solvent B for 4 minutes, and finally to 99% solvent A for 4 minutes. The flow rate of the system was 1.7 mL/min with the column temperature controlled at 25 °C. The injection volume was set at 20 µl. DAD was adjusted at 200-380 nm with a monitoring wavelength of 220 nm. The RP-HPLC column used was an Inertsil ODS-3 C18 (4.6 x150 mm, 5 µm) column. Gastrodin was found to elute at the retention time of 6.5 minutes. Gastrodin was identified by comparing the chromatogram and retention time of *G. speciosum* extract with gastrodin standard (% purity > 98%) (Chengdu Biopurify Phytochemicals, Sichuan, China).

Calibration and method validation

An amount 5 mg of gastrodin standard was dissolved in 5 mL of ethanol (20% w/w) and diluted with ethanol (20% w/w) corresponding to test ranges. Gastrodin standard solution was diluted with ethanol (20% w/w) to obtain final concentrations of 10, 20, 30, 40, 50, 70 and 100 µg/mL. After filtering through a 0.22-µm syringe filter, 20 µL of each standard solution was injected into the RP-HPLC system. The calibration curve was constructed by plotting peak areas against the corresponding concentration of gastrodin. Each concentration was analysed in triplicate. The slope, y-intercept and r^2 were calculated using the least squares regression method. Limits of detection (LOD) and quantification (LOQ) were calculated from the calibration line at the low concentration. LOD and LOQ were calculated from the following formulas in equation 1 and 2 [17]:

$$LOD = 3.3\ Sy/S \quad (1)$$

$$LOQ = 10\ Sy/S \quad (2)$$

where Sy is the standard deviation of the response curve and S is the slope of the calibration curve.

Specificity was examined by separately injecting the gastrodin standard solution at concentration of 50 µg/mL and *G. speciosum* extract solution using RP-HPLC to obtain gastrodin peak response.

The precision of the developed method was evaluated through intraday and interday variations of gastrodin at concentration of 50 µg/mL. The intraday precision analysis was performed in 6 replicates on samples prepared on a single day, while interday precision analysis was performed in 6 replicates on 3 different days. Accuracy was evaluated by determining the average % recovery of analytes. Three different concentrations were prepared by accurately weighing 50 mg of *G. speciosum* extract solution into well-sealed glass containers, after which 80 ml of ethanol (20% w/w) was added and the solution was sonicated for 5 minutes. A gastrodin standard solution was added to each *G. speciosum* extract solution sample to obtain final concentrations of 45, 50 and 55 µg/mL. Ethanol (20% w/w) was then added to acquire a volume of 100 ml. Each concentration was analyzed in triplicate. Average % recovery and % relative standard deviation (%RSD) values were calculated to determine the accuracy and precision of the system.

Sample analysis

An amount 5 mg of *G. speciosum* extract was dissolved in 5 mL of ethanol (20% w/w). The extract mixture was then filtered through 0.22-µm syringe filter, and 20 µL of the resulting filtrate was injected into the RP-HPLC system. Every sample solution was analyzed in triplicate**.**

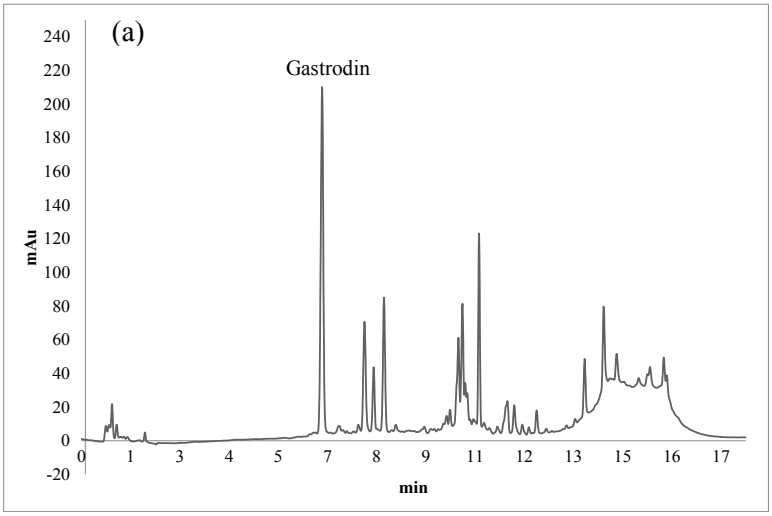
Statistical analysis

Results were expressed as the mean values ± standard deviation (SD) from at least three independent experiments. The statistical comparisons were carried out using one-way ANOVA with post hoc test (SPSS, SPSS Inc., Chicago, IL, USA). Statistical significance was accepted within the 95% confidence limit ($p < 0.05$).

Results and Discussion

To optimize the RP-HPLC condition, the tests were done under various conditions. The mobile phases were prepared using multiple proportions including water-acetonitrile or water-methanol. Among several C-18 reversed-phase columns, column Inertsil ODS-3 (4.6 x 150 mm, 5 µm) was selected as the most suitable condition because of its relatively shorter running time.

For specificity, gastrodin peaks were identified with retention times comparable with the gastrodin standard and confirmed for its characteristic spectra by diode array detection (range 200-380 nm). The retention time of *G. speciosum* extract samples and standard solutions were found to elute at 6.483 and 6.494 minutes, respectively (Figure 2). In addition, the UV pattern of the extract at the retention time of 6.483 minutes was similar to the gastrodin standard (Figure 3).



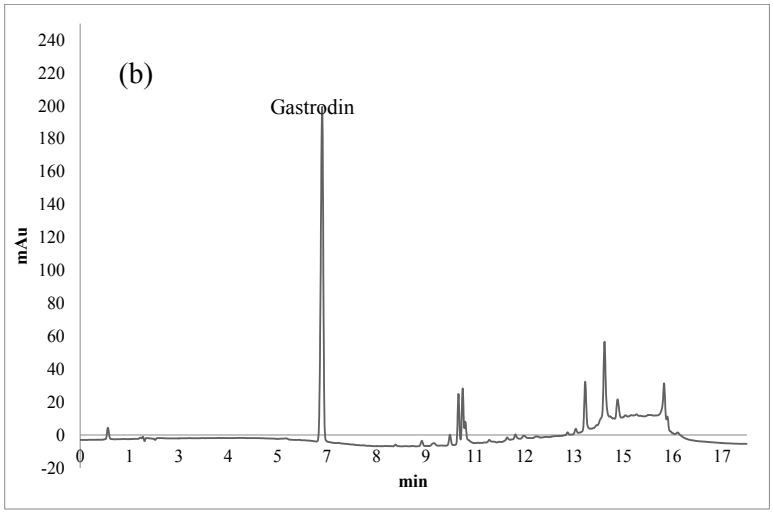


Figure 2. (a) A typical HPLC chromatogram of the *G. speciosum* pseudobulb ethanolic extract and (b) gastrodin standard HPLC chromatogram

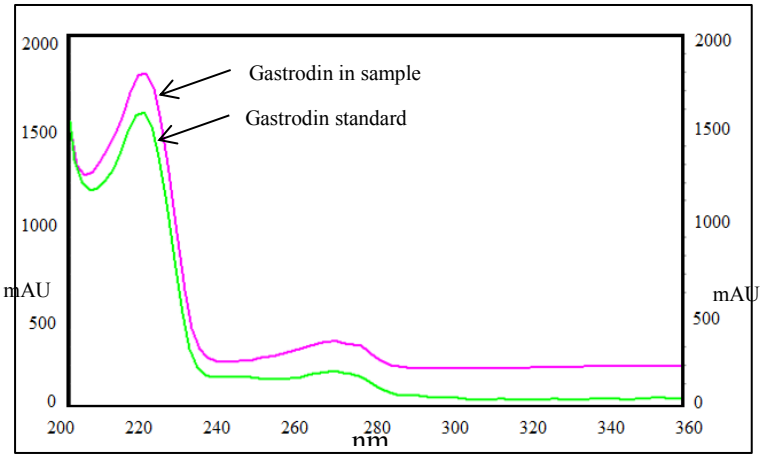


Figure 3. LC-UV absorption patterns of gastrodin in the *G. speciosum* Pseudobulb ethanolic extract (upper line) and gastrodin standard (lower line)

Moreover, the identification of gastrodin, an analytical marker of *G. speciosum* ethanolic extract, was confirmed using LC-MS technique. The mass transition was monitored in the reference and sample solutions to guarantee specificity. The molecular mass at 331.1 *m/z* ($[M-H]^-$ 331.1) of the *G. speciosum* extract was comparable to the gastrodin standard using formic acid addition in negative ion mode. The fragmentation pattern mass spectrum was found at 285.0, 206.8, 160.8 and 122.9 *m/z* which was consistent with the previous study [14] (Figure 4). Linearity parameters of the system are shown in Table 1. The results showed that gastrodin exhibited good linearity within specified ranges with coefficient of determination (r^2) of 0.9999. These results complied with the AOAC Guidelines, which stated that the coefficient of determination should be >0.99 for acceptable linearity. The regression equation was y = 20.0029x + 0.9758, where y is the peak area and x is the corresponding concentration of gastrodin standard. The linear range was 10 - 100 µg/mL. The calculated LOD and LOQ of gastrodin were 0.1244 and 0.3769 µg/mL, respectively.

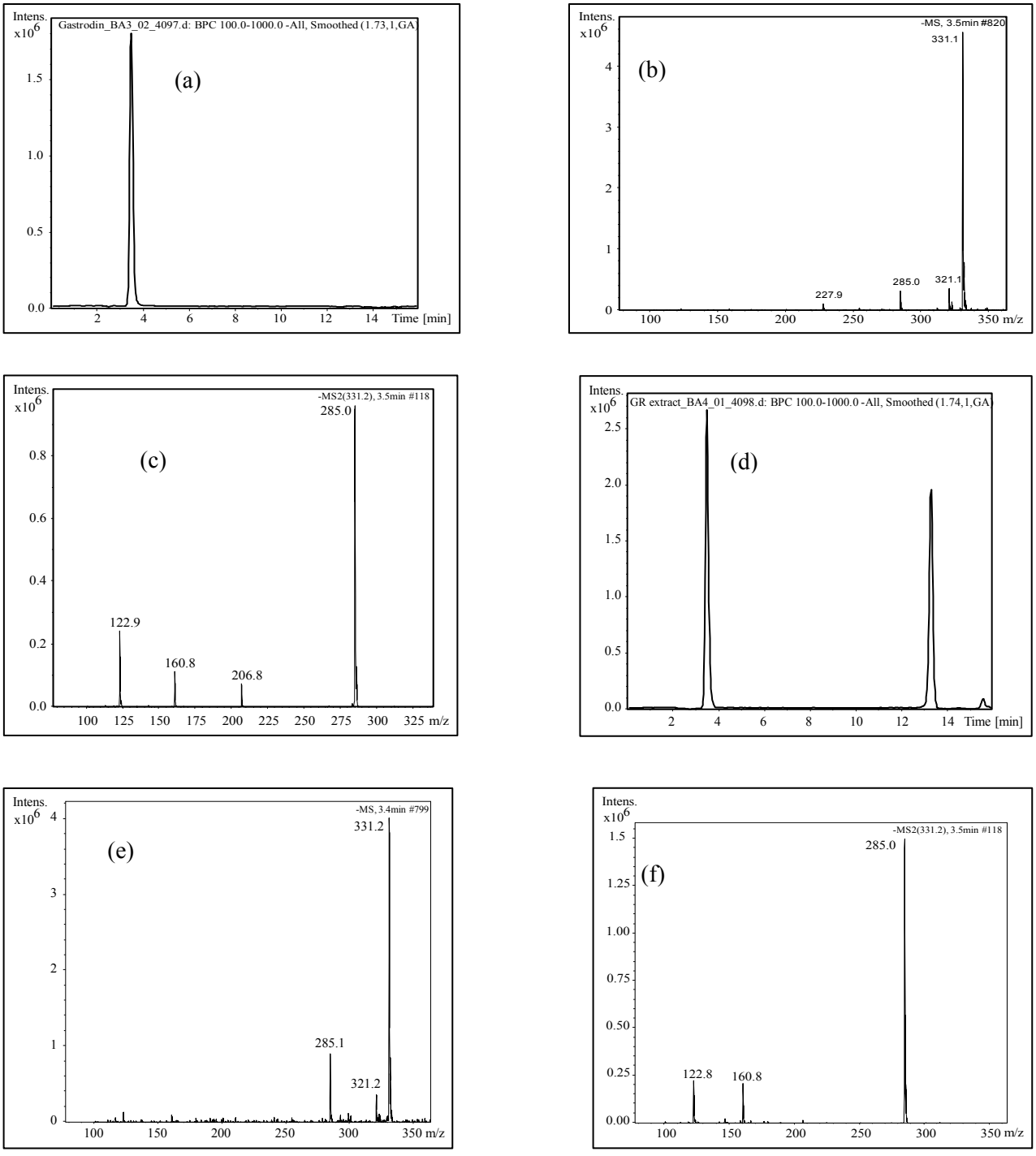


Figure 4. Typical chromatogram and MS spectra of the gastrodin (a) Base peak chromatogram of gastrodin standard (Rt = 3.5 min) (b) MS spectra of gastrodin standard ion [M+HCOOH-H]- (c) MS2 spectra of gastrodin standard ion [M+HCOOH-H]- at m/z 331.1 (d) Base peak chromatogram of *G. speciosum* extract (e) MS spectra of *G. speciosum* extract ion at 3.5 min (f) MS2 spectra of *G. speciosum* extract ion at m/z 331.2

Repeatability precision of the system is shown as a %RSD values in Table 1. The intraday and interday precisions were 1.05 and 0.38%, respectively. The repeatability results for gastrodin analytical markers showed %RSD values of <1.5, which complied with the AOAC Guidelines [16]. The accuracy of the system is shown in Table 1. The average % recovery was found 100.14, 100.54 and 101.25 for 80%, 100% and 120% concentrations of gastrodin, respectively. The average %recovery of gastrodin complied with the AOAC Guidelines, which stated that this value should be between 95-102%. These results indicate that the developed HPLC method was accurate and precise in the determination of gastrodin in ethanolic extracts of *G. speciosum*.

Table 1. Validation data of gastrodin

Parameters	**Gastrodin**
Linearity	
Range (µg/mL)	10 - 100
Coefficient of determination (r^2)	0.9999
Equation	
Intercept	0.9758
Slope	20.0029
Precision (50 µg/mL)	
Intra-day (%RSD)	1.05
Inter-day (%RSD)	0.38
Accuracy (%Recovery)	
80% (45 µg/mL)	100.14
100% (50 µg/mL)	100.54
120% (55 µg/mL)	101.25
Limit of quantitation (µg/mL)	0.3769
Limit of detection (µg/mL)	0.1244

The amount of gastrodin in 3 different batches of *G. speciosum* ethanolic extract was analyzed using a validated method. The results showed that the amount of gastrodin from batch 1, batch 2, and batch 3 contained 58.12±4.6, 57.24±2.5, and 55.50±1.4 mg/g, respectively (Table 2), which was considered to be not significantly different from one another ($p>0.05$). The result thus suggested that gastrodin levels were not significantly different among batches.

Table 2. Gastrodin contents of *G. speciosum* pseudobulb at different batches (n = 5)

Batch	**1**	**2**	**3**
Gastrodin (mg/g)	58.12±4.6	57.24±2.5	55.50±1.4

Conclusion

This developed HPLC method agreed well with AOAC Guidelines for Single-Laboratory Validation of Chemical Methods for Dietary Supplements and Botanicals which can be effectively used for the quality control of *G. speciosum* extracts and can be applied for quantification of gastrodin in future cosmetic products. Further studies on the determinations of gastrodin contents from all varieties and sources of *G. speciosum* will be worthwhile in establishing a quality control database.

Acknowledgement

This research was supported by grant no. CDRT-1600-01-2016 from supported by Cosmeceutical Research, Development and Testing Center, Faculty of Pharmacy, Rangsit University, Thailand. The authors wish to thank the Faculty of Pharmacy of Rangsit University for providing the research facilities.

References

1. Nontachaiyapoom, S., Sasirat, S. and Manoch, L. (2011). Symbiotic seed germination of *Grammatophyllum speciosum* Blume and *Dendrobium draconis* Rchb. f., native orchids of Thailand. *Scienta Horticultuae,* 130(1): 303 - 308.
2. Sahakitpichan, P., Mahidol, C., Disadee, W., Chimnoi, N., Ruchirawat, S. and Kanchanapoom, T. (2013). Glucopyranosyloxybenzyl derivatives of (R)-2-benzylmalic acid and (R)-eucomic acid, and an aromatic glucoside from the pseudobulbs of *Grammatophyllum speciosum*. *Tetrahedron,* 69(3): 1031 - 1037.
3. Uawonggul, N., Chaveerach, A., Thammasirirak, S., Arkaravichien, T., Chuachan, C. and Daduang, S. (2006). Screening of plants acting against *Heterometrus laoticus* scorpion venom activity on fibroblast cell lysis. *Journal of Ethnopharmacology,* 103 (2): 201 - 207.
4. Kumar, H., Kim, I. S., More, S. V., Kim, B. W., Bahk, Y. Y. and Choi, D. K. (2013). Gastrodin protects apoptotic dopaminergic neurons in a toxin-induced Parkinson's disease model. *Journal of Evidence-Based Complementary and Alternative Medicine*, 2013: 1 - 14.
5. Hsieh, M. T., Wu, C. R. and Chen, C. F. (1997). Gastrodin and p-hydroxybenzyl alcohol facilitate memory consolidation and retrieval, but not acquisition, on the passive avoidance task in rats. *Journal of Ethnopharmacology*, 56(1): 45 - 54.
6. Wu, C. R., Hsieh, M. T., Huang, S. C., Peng, W. H., Chang, Y. S. and Chen, C. F. (1996). Effects of *Gastrodia elata* and its active constituents on scopolamine-induced amnesia in rats. *Planta Medica*, 62 (4): 317 - 321.
7. An, S. J., Park, S. K., Hwang, I. K., Choi, S. Y., Kim, S. K., Kwon, O. S., Jung, S. J., Baek, N. I., Lee, H. Y. and Won, M. H. (2003). Gastrodin decreases immunoreactivities of γ-aminobutyric acid shunt enzymes in the hippocampus of seizure-sensitive gerbils. *Journal of Neuroscience Research*, 71(4): 534 - 543.
8. Kim, H. J., Moon, K. D., Lee, D. S. and Lee, S. H. (2003). Ethyl ether fraction of *Gastrodia elata* Blume protects amyloid β peptide-induced cell death. *Journal of Ethnopharmacology*, 84(1): 95 - 98.
9. Hu, Y., Li, C. and Shen, W. (2014). Gastrodin alleviates memory deficits and reduces neuropathology in a mouse model of Alzheimer's disease. *Neuropathology,* 34(4): 370 - 377.
10. Wang, X. L., Xing, G. H., Hong, B., Li, X. M., Zou, Y., Zhang, X. J. and Dong, M. X. (2014). Gastrodin prevents motor deficits and oxidative stress in the MPTP mouse model of Parkinson's disease: Involvement of ERK1/2–Nrf2 signaling pathway. *Life Sciences*, 114(2): 77 - 85.
11. Huang, Q., Shi, J., Gao, B., Zhang, H. Y., Fan, J., Li, X. J., Fan, J. Z., Han, Y. H., Zhang, J. K. and Yang, L. (2015). Gastrodin: an ancient Chinese herbal medicine as a source for anti-osteoporosis agents via reducing reactive oxygen species. *Bone,* 73: 132 - 144.
12. Chowjarean, V., Nimmannit, U., Chaotham, C., Eaknai, W., Sucontphunt, A., Plaimee, P. P., Tengamnuay, P. and Chanvorachote, P. (2017). *Grammatophyllum speciosum* extract potentiates stemness in keratinocyte cells. *Chiang Mai Journal of Science,* 45 (1): 237 - 248.
13. Chen, W. C., Lai, Y. S., Lu, K. H., Lin, S. H., Liao, L. Y., Ho, C. T. and Sheen, L. Y. (2015). Method development and validation for the high-performance liquid chromatography assay of gastrodin in water extracts from different sources of *Gastrodia elata* Blume. *Journal of Food and Drug Analysis*, 23 (4): 803 - 810.
14. Jia, Y., L,i X., Xie, H., Shen, J., Luo, J., Wang, J., Wang, K. D., Liu, Q. and Kong, L. (2014). Analysis and pharmacokinetics studies of gastrodin and *p*-hydroxybenzyl alcohol in dogs using ultra fast liquid chromatography–tandem mass spectrometry method. *Journal of Pharmaceutical and Biomedical Analysis*, 99: 83 - 88.
15. Lee, J-G., Moon, S-O., Kim, S-Y., Yang, E-J., Min, J-S., An, J-H., Choi, E-A., Liu, K-H., Park, E. J. and Lee, H-D. (2015). Rapid HPLC determination of gastrodin in Gastrodiae Rhizoma. *Applied Biological Chemistry*, 58 (3): 409 - 413.
16. AOAC Official Methods of Analysis (2013). Appendix K: Guideline for dietary supplements and botanicals. http://www.eoma.aoac.org/app_k.pdf. [Accessed online 29 June 2017].
17. Shrivastava, A. and Gupta, V. B. (2011). Methods for the determination of limit of detection and limit of quantitation of the analytical methods. *Chronicles of Young Scientists,* 2(1): 21 - 21.

Malaysian Journal of Analytical Sciences, Vol 22 No 2 (2018): 227 - 237
DOI: https://doi.org/10.17576/mjas-2018-2202-07

MALAYSIAN JOURNAL OF ANALYTICAL SCIENCES
Published by The Malaysian Analytical Sciences Society
ISSN 1394 - 2506

THE ELECTROCHEMICAL BEHAVIOR OF ZINC OXIDE/REDUCED GRAPHENE OXIDE COMPOSITE ELECTRODE IN DOPAMINE

(Sifat Elektrokimia Elektrod Komposit Zink Oksida/Grafin Oksida Terturun dalam Dopamin)

Farhanini Yusoff[1]*, Ngai Tze Khing[1], Chai Chee Hao[1], Lee Pak Sang[1], Nurul'ain Basyirah Muhamad[1], Noorashikin Md Saleh[2]

[1]School of Marine and Environmental Sciences,
Universiti Malaysia Terengganu, 21030 Kuala Nerus, Terengganu, Malaysia
[2]Research Centre for Sustainable Process Technology,
Department of Chemical Engineering, Faculty of Engineering and Built Environment,
Universiti Kebangsaan Malaysia, 43600 UKM Bangi, Selangor, Malaysia

**Corresponding author: farhanini@umt.edu.my*

Received: 2 January 2018; Accepted: 6 March 2018

Abstract

Zinc oxide/reduced graphene oxide (ZnO/rGO) composite was synthesized via the modified Hummers' method. The presence of ZnO composite on the rGO sheets was confirmed by Scanning Electron Microscope (SEM), X-Ray Diffractometer (XRD) and Fourier Transform Infrared (FTIR) spectrometer. FTIR result showed the formation of ZnO/rGO with the presence ZnO stretching peak and the surface of ZnO/rGO was found to have better morphology with functionalized groups attached to it. XRD analysis also confirms the formation of ZnO/rGO composite by wurtzite structured indexed peak of the diffractogram. The ZnO/rGO composite was drop on the surface of GCE by drop casting method to increase the electrocatalytic activities of bare GCE. The electrochemical behaviour of ZnO/rGO modified electrode shows the enhancement in electron transfer and the system is diffusion-controlled. The electrochemical studies also revealed that the ZnO/rGO/GCE dramatically increased the current response against the dopamine (DA), due to the synergistic effect emerged between ZnO and rGO. This attributed that ZnO/rGO/GCE could exhibit excellent electrocatalytic activity and effective electron transfer kinetics towards the oxidation of DA. Therefore, the ZnO/rGO/GCE could be used to determine the DA concentration and provide an ideal matrix for clinical applications.

Keywords: zinc oxide, reduced graphene oxide, composite materials, dopamine, electrocatalysis

Abstrak

Komposit zink oksida/grafin oksida terturun (ZnO/rGO) telah disintesis melalui kaedah Hummer terubahsuai. Kehadiran komposit ZnO pada lapisan rGO telah diujikan oleh mikroskop imbasan elektron (SEM), Pembelauan sinar X (XRD) dan Inframerah transformasi Fourier (FTIR). Keputusan FTIR menunjukkan pembentukan ZnO/rGO dengan kehadiran puncak ZnO dan permukaan ZnO/rGO didapati mempunyai morfologi yang lebih baik dengan kumpulan berfungsi melekat padanya. Analisis XRD juga menunjukkan pembentukan komposit ZnO/rGO melalui diffraktogram indeks puncak struktrur wurtzit. Komposit ZnO/rGO telah diubahsuai dengan elektrod karbon berkaca (GCE) dengan menggunakan kaedah alas titis. Perlakuan elektrokimia ZnO/rGO/GCE menunjukkan peningkatan dalam pemindahan elektron dan sistem adalah proses serapan terkawal. Kajian elektrokimia mendedahkan bahawa respon arus ZnO/rGO/GCE meningkat terhadap DA, disebabkan kesan sinergi antara ZnO dan rGO. Ini disebabkan respon arus ZnO/rGO/GCE boleh mempamerkan aktiviti elektropemangkin yang berkesan terhadap kinetik pemindahan elektron DA. Oleh itu, ZnO/rGO/GCE boleh digunakan untuk menentukan kepekatan DA dan menjadi pemangkin sesuai untuk aplikasi klinikal.

Kata kunci: zink oksida, grafin oksida terturun, bahan komposit, dopamin, elektropemangkin

Introduction

Dopamine (DA) is the most significant catecholamines, belongs to the excitatory neurotransmitter family which consists of an amine group linked to a catechol structure. It has great influence on central nervous, endocrine, and cardiovascular system [1]. Moreover, DA plays a vital role in brain pleasure centers, emotional response and help to regulate movement for human. Abnormal level of dopamine in human body can lead to central nervous system disorders such as Parkinson's, Alzheimer's, Huntington's disease and schizophrenia diseases are cause by. Recent studies show that low dopaminergic activity, as indicated by high DA/metabolite ratios, was positively correlated with addiction [2]. Therefore, the development of an accurate and sensitive method for DA determination is necessary for the clinical diagnostic purposes.

Numerous analytical techniques are available for the detection of DA level such as UV-vis spectrometry, capillary electrophoresis, chemiluminescence and electrochemical analysis. Among these methods, electrochemical method are favorable owing to their advantages such fast speed, low cost, low detection limits and also high in accuracy [3]. However, uric acid (UA) and ascorbic acid (AA) are usually coexisted with DA in the extracellular fluids of the central nervous system in mammals or the biological fluid such as urine, blood and human breast milk [4]. Thus, AA and UA will become the interfering species that will result in poor selectivity and sensitivity towards DA detection.

In order to overcome this problem, two fundamental approaches were often performed; improve the electrocatalytic performance on the electrode surface to separate their oxidation potentials, and selective interaction with DA on the electrode surface without interferences [5]. From the strategies, various chemically modified electrodes have been fabricated using polymers [6], metal oxides [7], nanoparticles [8], and carbon based materials [9]. A great deal of attention has been given to the use of multiwall carbon nanotubes (MWNTs), and more recently to graphene, as modification materials on the surface of electrodes [10].

Graphene, a two-dimensional sheet of sp^2-hybridized carbon, has receive a lot of attention in the electrochemical field due to its unexpected stability, exotic band structure and unique electronic properties, especially the high specific surface area and excellent electric conductivity low mass density. Graphene was obtained so far by several techniques including mechanical exfoliation of graphite [11], chemical vapor deposition [12], electrochemical reduction of exfoliated graphite oxide precursor [13] and chemical reduction of graphene oxide [14]. Among the various methods reported for reduction of GO, the chemical reduction of GO sheets pre-deposited on electrode surfaces seems to be a promising route for preparing reduced graphene oxide (rGO)-modified electrode surfaces because it is simple, high surface to volume ratio, abundant defect sites, and fast electron transfer rate [15]. One major drawback of rGO is the natural tendency of agglomeration and restacking due to van der Waals interactions, which lower the surface area of product [16]. To overcome this problem, modification of rGO with different functional molecules would have to be introduced to improve their electrochemical activity. Studies have shown that fabricating metal/metal oxide-nanocarbon hybrid have increased the catalysts properties by utilizing both the advantages of metal and nanocarbon [17,18].

In this research, the zinc oxide/reduced graphene oxide composite (ZnO/rGO) electrode has been developed to investigate its performance towards oxidation of DA. It was then used to determine the concentration of DA in human urine samples.

Materials and Methods

Chemicals and Materials

3-hydroxytyramine hydrochloride (DA), natural graphite powder, concentrated sulfuric acid (H_2SO_4, 95 - 98%), hydrochloric acid (HCl), sodium nitrite ($NaNO_3$), potassium permanganate ($KMnO_4$), hydrogen peroxide (H_2O_2, 30%), zinc nitrate ($Zn(NO_3)_2$), potassium hydroxide (KOH), potassium ferrocyanide ($[Fe(CN)_6]^{4-}$), potassium chloride (KCl), disodium hydrogen phosphate dodecahydrate ($Na_2HPO_4 \cdot 12H_2O$), and sodium dihydrogen phosphate dehydrate ($NaH_2PO_4 \cdot 2H_2O$) were purchased from Sigma Aldrich, USA. The stock solution of DA was prepared in the 0.1M of phosphate buffer solution. All reagents are of analytical grade and were used without any further purification.

Instrumentation
The electrochemical experiment was performed using Potentiostat/Galvanostat module PGSTAT30 (Metrohm AUTOLAB, Nertherlands), three electrode systems consist of platinum wire counter electrode, glassy carbon electrode (BASi MF-2012 3.0 mm diameter), with or without modification of ZnO-decorated rGO as working electrode, and Ag/AgCl (Methrom, with 3 M of KCl) as reference electrode. Physical characterization of ZnO/rGO were performed using Scanning electron microscope (SEM, JEOL JSM-6360LA), X-Ray Diffractometer (XRD, Rigaku MiniFlex II), and Fourier Transform Infrared Spectrometer (FTIR, PerkinElmer Spectrum 100).

Preparation of ZnO/rGO
The GO which synthesized from the graphite powder via the modified Hummers method [19] was reduced to reduced graphene oxide (rGO) by zinc nitrate as reduced precursors. Firstly, 0.01 mol of $Zn(NO_3)_2$ and 50 mL of distilled water were added to the conical flask and stirred vigorously with magnetic bar in the ice water bath for 1 hours. Next, 0.0904 g of GO was treated with 100 mL of distilled water to form GO solution. The GO solution was separated in to two centrifuge tubes (50 mL) with equal amount and ultrasonic for 1 hours. After 1 hours, the GO solution was added to the of $Zn(NO_3)_2$ mixture solution and stirred homogenously for 10 minutes. Then, 5.6 g of potassium hydroxide was added to the mixture solution and left for overnight. In this time, the pH for mixture solution is pH 8.5. After that, the mixture solution was centrifuged and filter by suction filtration. The distilled water was added during the filtration process to neutralize the rGO to pH 7. The rGO was dried at oven for 1 hour to obtain the ZnO/rGO precursors.

Fabrication of ZnO/rGO/GCE
The working electrode was prepared by dropping the ZnO/rGO solution onto a glassy carbon electrode. First, glassy carbon electrode (GCE) was polished by alumina oxide followed by rinsing with water, ethanol and water, in turn. To modify the ZnO/rGO/GCE, 1 mg ZnO/rGO powder was ultrasonic dispersed into 10 mL of distilled water for 20 minutes. Then, 8 µL of ZnO/rGO was dropped onto a clean GCE with a micropipette and dried at room temperature. The electrocatalytic ability of the ZnO/rGO modified electrode was investigated by cyclic voltammetry in 0.1 M of phosphate buffer solution (pH 7.0) as electrolyte.

Electrochemical characterization ZnO/rGO/GCE
The cyclic voltammetry of 5.0 mM $K_3[Fe(CN)^6]$ in 0.1 M KCl on all electrodes were carried out at potential window of −0.2 to 0.8 V at room temperature with different scan rates using an electrochemical cell with three electrodes system. The electrolyte solution was purged with nitrogen gas to eliminate oxygen before use.

Results and Discussion

Characterization of ZnO/rGO: Fourier transform infrared (FTIR) analysis
FT-IR spectroscopy is known to be an important tool to characterize the graphene-based hybrid materials. In the FT-IR spectra of the pure graphite powder (Figure 1a), there is no significant peak observed in raw graphite. This attributed to that the graphite powder was pure and do not contain any functional groups on the graphite molecules. In the FT-IR spectra of GO samples (Figure 1b), there is a strong broad peak presence at 3390 cm^{-1} and several weak ones at 1728, 1622 and 1053 cm^{-1}, which are attributed to the stretching vibration of O–H groups (carboxyl and hydroxyl), stretching of C=O, skeletal vibration of C=C (carboxyl or carbonyl), and stretching vibrations of C–O (epoxy or alkoxy), respectively.

The strong characteristics of C=O stretch at 1728 cm^{-1} indicating the present of oxygen-containing group in GO surface. After the GO is chemically reduced, the spectrum (Figure 1c) resulted in significant reduction of hydroxyl, carbonyl, and epoxide group. The C=O vibration band which located at 1728 cm^{-1} was disappeared, while the board O-H, C=C and C-O stretching bands remain. These results demonstrate that the functional oxygen-containing group on the GO surface were almost reduced after the reduction by $Zn(NO_3)_2$. Additionally, the spectrum for ZnO/rGO showed the distinct peak at around 507 cm^{-1}, which corresponds to ZnO [20]. Based on the analysis, one can conclude that GO was both reduced and functionalized by $Zn(NO_3)_2$.

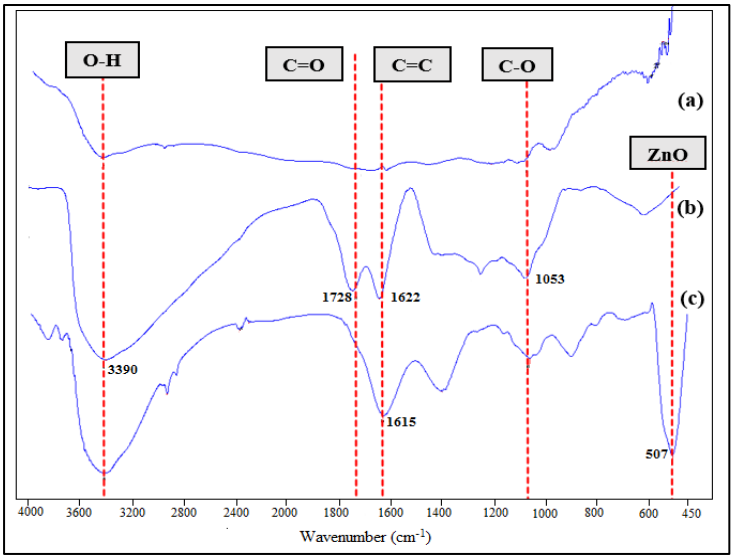


Figure 1. FT-IR Spectra of (a) Graphite, (b) GO, and (c) ZnO/rGO

Consequently, the purpose for reduction of GO was to eliminated the epoxy and hydroxyl groups on the plane, while other functional groups, such as carboxyl, carbonyl and ester groups which present at the edges of the carbon plane only have a minor influence on the conductivity of an rGO sheet. Moreover, the strong sharp peak of ZnO shown in FTIR spectra indicated that the ZnO were anchoring on the surface of rGO layer. Therefore, the electrochemical properties of ZnO/rGO composite is expected to enhance due to the wide band gap particles of ZnO and large surface area of graphene compared to those of pristine graphene oxide and ZnO particles alone.

X-ray diffractometry analysis (XRD)

The XRD analysis is used to verify the formation of the ZnO crystal on the surface of GO. The XRD pattern (Figure 2a) of graphite shows an intensive diffraction peak at 2θ = 26.5°, reflecting the crystal form of graphite. If compare to GO spectra, the characteristic peak of GO at 10.25º was observed that indicates the presence of the larger interlayer distance between GO due to the oxidation of graphite and formation of the functional groups such as carboxyl, hydroxyl and epoxy, as indicated in the FT-IR results. While in the XRD pattern of ZnO/rGO, there are 8 peaks appearing at 2θ values of 31.7, 34.3, 36.1, 47.3, 56.4, 62.6, 67.7, and 68.8 º corresponding to the crystal planes of (100), (101), (102), (110), (103), (112), and (201) respectively. These peaks are indexed as wurtzite structured (crystal structure) of ZnO, which are consistent to the value in the standard card. Theoretically (002) peak of rGO is expected to appear in the XRD diffractogram of ZnO/rGO. However, it cannot be observed in the corresponding compositions (Figure 2b), indicating that the surfaces of rGO are fully covered by ZnO [21]. Hence, the diffraction peaks are mainly from the up-layer ZnO phase in the ZnO/rGO compositions. Moreover, the peak disappearance at 10.25º also indicating the surface of rGO is fully covered by ZnO. Therefore, it can be concluded that there is the formation of ZnO/rGO after the GO was reduced by zinc nitrate.

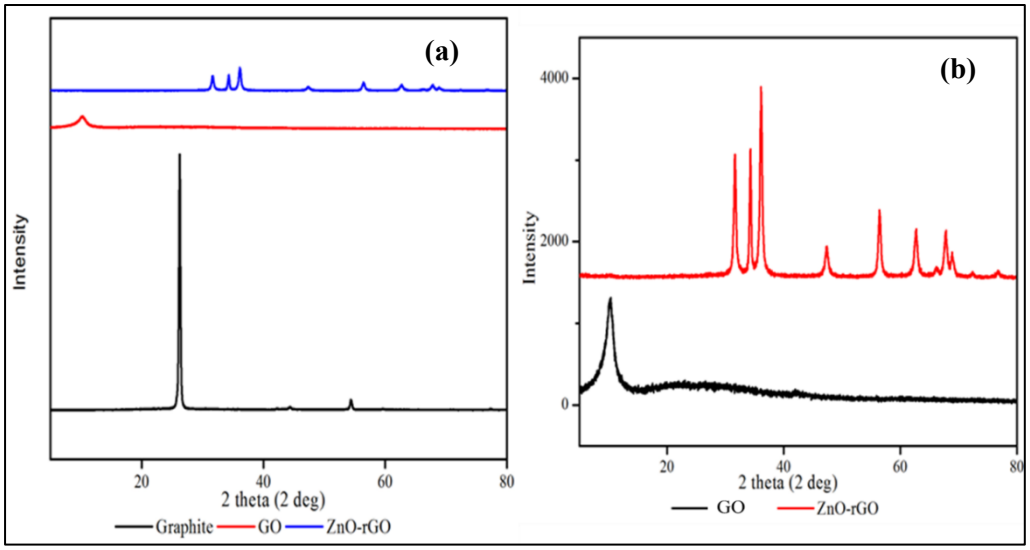


Figure 2. (a) XRD patterns for graphite, GO and ZnO/rGO composite and (b) Enlarge XRD patterns for GO and ZnO/rGO composite

Scanning electron microscopy analysis (SEM)

The morphology of the graphite, GO, and ZnO/rGO (Figure 3) was physically characterized by SEM. From the SEM image of pure graphite, the individual needle shaped particles are made up of graphite having intrinsic flake morphology. Graphite arranged in agglomerates and presented a typical multilayer structure. The SEM image of GO showing that the oxidation of graphite after treated with modified Hummers' method caused a visible change in their morphology, or it has a wrinkled appearance with multiple folds. This wrinkled aspect can be explained by the oxidation process to promote the admission of hydroxyl groups and epoxy groups, known as functional groups [21].

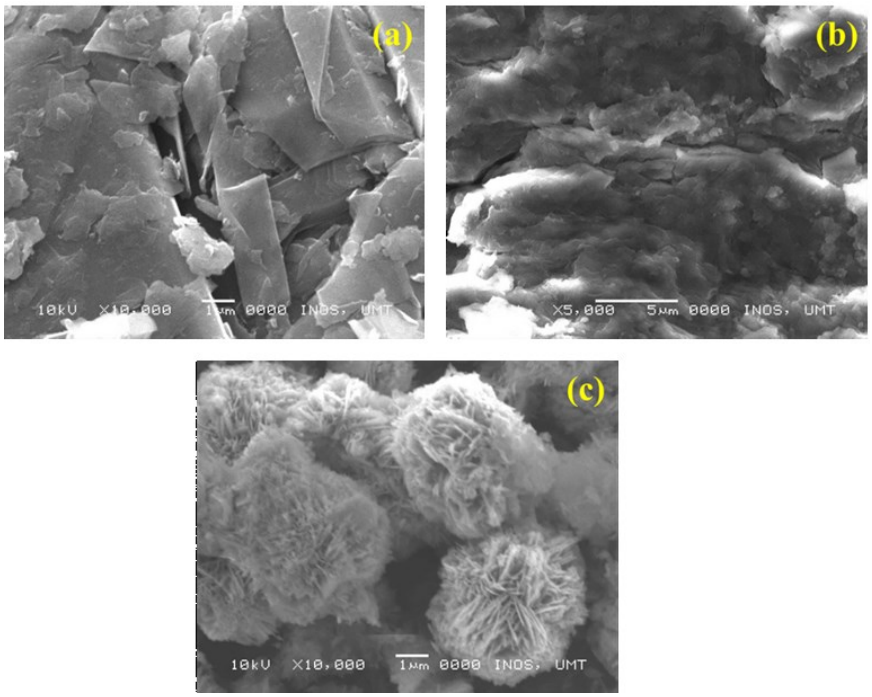


Figure 3. SEM image of (a) pure graphite; (b) GO and (c) ZnO/rGO composite

The formation of ZnO on the surface of graphene layer is indicated by the microsphere-like hierarchical structures after the GO is undergoes reduction by $Zn(NO_3)_2$. The ZnO composite with an average size of 5 µm were horizontally and randomly stacked between or on the RGO layers, in other words, graphene sheets are homogeneously incorporated in a ZnO matrix which clearly shown in Figure 3c. This result is also supported by XRD analysis. It may be due to the restriction of full length extension of ZnO in the space within the graphene layers. The results also indicated that the functional groups in GO were significantly reduced during $Zn(NO_3)_2$ reduction.

The electrochemical behavior of ZnO/rGO modified electrode

The electrochemical behavior of bare GCE, GO and ZnO/rGO/GCE was investigated by cyclic voltammetry (Figure 4a). Cyclic voltammetry (CV) is frequently used in analytical field due to it offers a wealth of experimental information and insights into both the kinetic and thermodynamic details of many chemical systems. The electrochemical behavior of bare GCE and ZnO/rGO/GCE is investigated by CV to elucidate their electron transfer behavior in the presence of 0.1 M KCl and 0.05 M $K_4[Fe(CN)_6]$ at scan rate 50 mVs^{-1} and potential range in -0.2 V to 0.8 V. Curve of the bare GCE and ZnO/rGO/GCE showed a pair of well-defined quasi-reversible peaks with the anodic and cathodic peaks for bare GCE is at 348 mV and 200 mV, respectively. Meanwhile, the anodic and cathodic potential of ZnO/rGO/GCE are 298 mV and 190 mV, respectively.

The voltammogram shows the oxidation peak on ZnO/rGO/GCE was negatively shifted to 298 mV with remarkably enhanced of oxidation peak current. The ZnO/rGO/GCE present the largest background current and the peak current compared with the bare electrode. For the modified electrode (ZnO/rGO/GCE), the oxidation peak current was dramatically enhanced to 0.32 mA compare to GO and bare GCE. The decreased in peak potential separation ($\Delta E_p = E_{Anodic\ Peak} - E_{Cathodic\ peak}$) are observed for ZnO/rGO/GCE (ΔE_p = 99.8 mV) than that on GO and bare GCE electrode (ΔE_p = 150 mV).

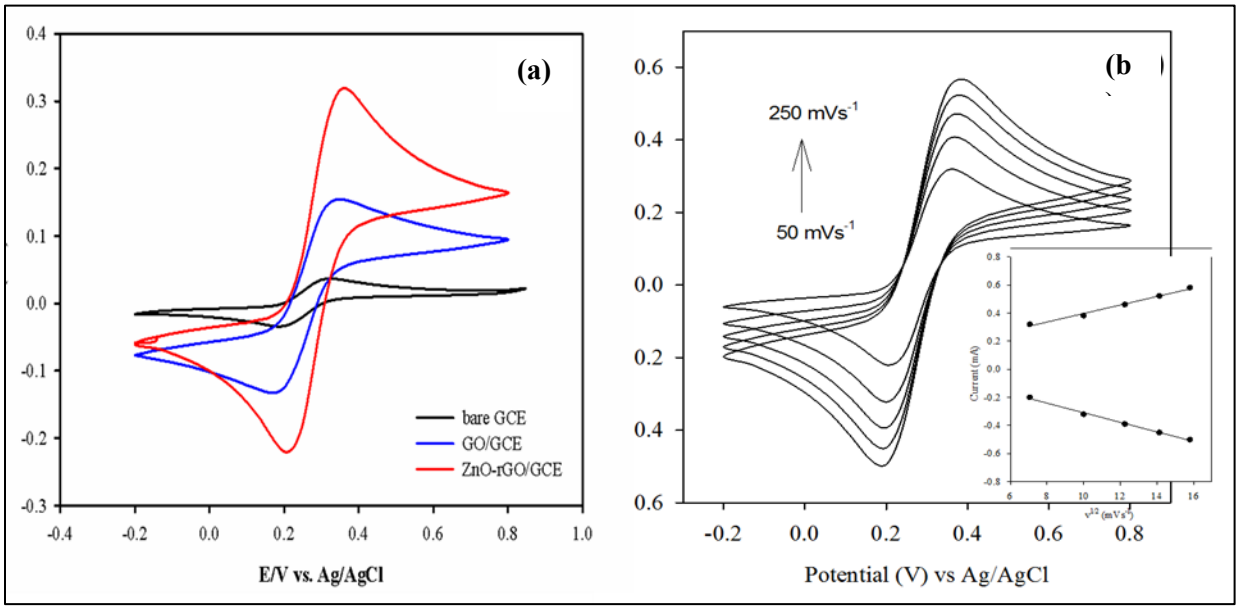


Figure 4. (a) Cyclic voltammograms obtained at the bare GCE, GO and ZnO/rGO/GCE in 0.1 M of KCl and 0.05 M of $K_4[Fe(CN)_6]$ at a scan rate of 250 mVs^{-1} and (b) Cyclic voltammograms of ZnO/rGO/GCE at different scan rate. (Inset: The plot of square root of scan rate vs. current)

The response with smaller peak potential separation on ZnO/rGO/GCE was nearly reversible as a fully reversible system is ΔE_p = 59.2 mV at all scan rate, which suggested a rapid electron transfer occurring at the interface of

ZnO/rGO/GCE. Besides, the redox peak currents increased obviously after the ZnO/rGO solution was drop-casted on the surface of bare GCE surface, which can be attributed to the synergistic effect of rGO and ZnO, promoting the electron transfer between the redox probe and the electrode surface.

The improved electrochemical behavior can be attributed to the excellent electrical conductivity of the ZnO/rGO present on the electrode surface. The carbon atoms in GO is decorated by oxygen-containing groups, which can expand the interlayer distance of graphene layer but also make the atomic-thick layers became hydrophilic. These properties will result the low electrochemical properties of synthesized GO [12]. Thus, the chemical reduction of GO should be carry out to reduce the oxygen-containing group which anchor on the surface of GO. Zn/rGO composite was produced after the GO was treated with $Zn(NO_3)_2$ as reduce precursors. The conductivity of monolayer graphene mainly relies on carrier transport within the carbon plane. Thus, various functional groups anchored to the plane are the main factor that influencing its conductivity.

The graphene with superior electrical conductivity and unique electron transport property could accelerate the electron transfer rate at the electrode/electrolyte interface. This shows that the electrical conductivity of ZnO is greatly enhanced the bare electrode. KCl and $K_4[Fe(CN)_6]$ was used as the electrolyte to determine the electrochemical behavior for both electrode due to KCl is the inert supporting electrolyte which ensure that the ionic strength of the solution is high and hence that the electric field is homogeneous and near-zero and is not perturbed by the oxidation or reduction of the analyte concerned. While $K_4[Fe(CN)_6]$ act as the redox species that present the reduction peak in cyclic voltammogram.

To investigate the reaction kinetics, the influence of scan rates on the electrocatalytic response of ZnO/rGO/GCE in $K_4[Fe(CN)_6]$ was examined and the results are shown in Figure 4b. The scan cycles and potential range were standardized at value of 0.10 mM, 6 scan cycles, and -0.2 V to 0.8 V respectively. It can be clearly observed that the oxidation peak currents are increased linearly while the oxidation peak potential is shifted positively as the scan rate increasing from 50 mVs^{-1} to 250 mVs^{-1}, accompanied with an enlargement of the peak separation. Moreover, the increased of cathodic and anodic peak currents as the scan rate increased from 50 mVs^{-1} to 250 mVs^{-1} attributed that the electro-redox of ferrocyanide ion on ZnO/rGO/GCE is a typical diffusion controlled process [22]. In addition, at higher scan rates, the anode (E_{pa}) and cathode (E_{pc}) peak potential have a linear relationship with the square root of scan rate (Figure 4b: Inset). This is due to no stirring process was performed during CV test. Thus, the thickness of diffusion layer is increased as the time passes through and the concentration of ferrocyanide at the electrode surface had further diffused from the bulk solution. The faster the scan rate, the shorter the diffusion layer; hence greater the electron transfer [23]. Besides, the flux to the electrode is smaller at lower scan rate compare with the higher scan rate and the current is directly proportional to flux toward the electrode. Thus, scan rate 50 mVs^{-1} is selected as the optimize scan rate for further electrochemical study of DA at ZnO/rGO/GCE.

Electrocatalytic response of towards the oxidation of dopamine (DA)

Figure 5a shows the CV responses obtained for the bare GCE and ZnO/rGO/GCE in the presence of 0.1 mM DA in 0.1 M PBS by scan rate of 50 mVs^{-1} at pH 7. At a bare GCE, a well-defined redox peak is observed 347 mV and 243 mV with the anodic current of 3.39 µA. However, at ZnO/rGO/GCE the oxidation peak current is dramatically increased to 20.0 µA which can be attributed to the enhanced electrochemical performance towards the oxidation of DA. This might be contributed from the excellent electrical conductivity of the ZnO/rGO presented on the electrode surface that can act as an effective electron promoter for electrocatalytic oxidation of DA. As the voltage increasing from -0.2 V, DA is attracted to the surface of ZnO/rGO/GCE. This situation lead the diffusion layer become greater as voltage increase, large amount of DA molecule adsorbed over the electrode surface.

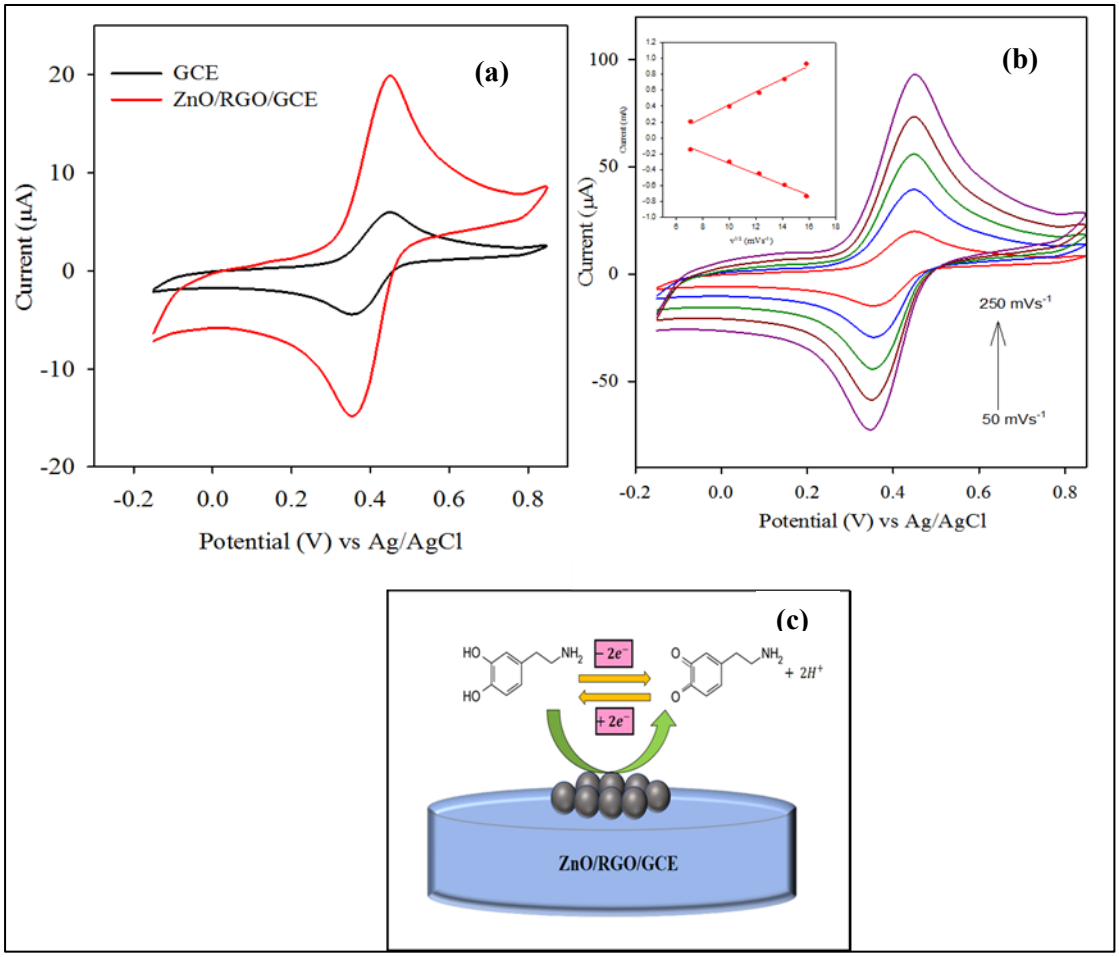


Figure 5. (a) Cyclic voltammograms obtained at the bare GCE and ZnO/rGO/GCE in 0.1 M of PBS (pH 7) containing 1.0 mM of DA, (b) Cyclic voltammograms obtained at ZnO/rGO/GCE in 0.1 M of PBS (pH 7) containing 1.0 mM of DA at different scan rate (50, 100, 150, 200, and 250 mVs^{-1}). (Inset: the plot of peak current vs. square root of scan rate) and (c) Electrocatalytic oxidation of dopamine at ZnO/rGO/GCE

The effect of potential scan rate was studied on the electrocatalytic properties of the ZnO/rGO/GCE toward oxidation of DA. As can be seen in Figure 5b, increase in scan rate potential, resulted in non-shifted potential value for the catalytic oxidation of DA. This result suggesting a stable kinetic in the reaction between the redox sites of the ZnO/rGO/GCE and DA. The result also shows that anodic and cathodic current increases with increasing of square root of scan rate indicating diffusion process. Redox reaction process of DA occurred at ZnO/rGO/GCE by two electrons transferred (Figure 5c). DA is oxidized during the positive sweep to form dopamine-o-quinone which is reduced back to dopamine in the negative sweep.

Effect of pH

The electrochemical behaviour of DA is strongly dependent on the pH value of electrolyte solution. Phosphate buffer solution (PBS) with different pH value (pH 3 to pH 11) at the surface of ZnO/rGO/GCE was prepared to investigate the optimum condition for the best electroactivity of DA standard solution. Figure 6 shows the characterizing of 0.10 mM of DA standard solution in 0.1 M of PBS with different pH at constant scan cycle (6 scan) and scan rate (50 mVs^{-1}) at ZnO/rGO/GCE. Cyclic voltammograms obtained with the ZnO/rGO/GCE for electrolyte containing DA in higher pH condition shows that DA did not couple with the ZnO/rGO/GCE and show

the lowest current peak compare to others. At pH 3 and 7 the oxidation peak current (I_{pa}) shows the maximum and obvious current. This indicated that the DA oxidized efficiency in both acidic and neutral condition. In this study, the redox reaction process of DA involves the transfer of two protons and two electrons. This phenomenon indicates that the uptake of electrons is accompanied by the same protons [24]. Therefore, considering the sensitive determination for DA, 0.10 M of PBS (pH 7) can be selected for further electrochemical investigation of DA at ZnO/rGO/GCE.

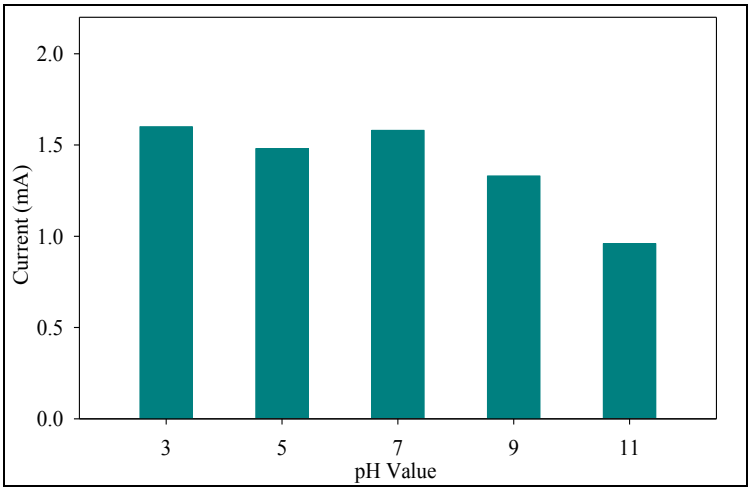


Figure 6. Chart of current *vs.* pH at the ZnO/rGO/GCE in 0.1 M of PBS with different pH value (pH 3, pH 5, pH 7, pH9 and pH 11) at scan rate 50 mVs^{-1} which containing 1.0 mM of DA

Conclusion

The modified electrode ZnO/rGO/GCE composite had been successfully synthesized via a simple, cost-effective and green approach method. The ZnO/rGO/GCE showed significantly improved peaks currents towards the redox reaction of DA compared with the bare GCE. Modified Hummers' method was proposed in this research to synthesized graphene oxide from raw graphite powder. Chemical reduction was carried out to reduce GO to ZnO/rGO. Chemical reduction was choosing due to the rGO which synthesize by this method is has a substandard surface area and electrically conductivity. The functional groups that anchor on the surface of graphene layer were characterized by Fourier transform infrared spectroscopy (FTIR). In addition, the morphology of ZnO/rGO was physical characterized by X-Ray diffractometer (XRD) and Scanning Electron Microscope (SEM). The FTIR results obtained indicate that the oxygen containing groups were almost reduced when the GO treat with ZnO/rGO as reduced precursor. Besides, the results from XRD and SEM proved that the ZnO composite were successfully covered on the graphene layer when the GO was chemical reduced. The ZnO composite which anchor on the surface of graphene layer will enhance the electrochemical behavior of GCE toward the redox reaction of DA. The ZnO/rGO/GCE displayed excellent electrocatalytic activity towards the DA oxidation. These results attribute that the ZnO/rGO/GCE could be a candidate for clinical, electrochemical and biosensor applications due to its excellent electrical performance.

Acknowledgements

The authors gratefully acknowledge to Ministry of Education for financial support from the Research Acculturation Grant Scheme (RAGS) RAGS/1/2015/ST0/UMT/03/2, Fundamental Research Grant Scheme (FRGS) FRGS/1/2017/STG01/UMT/02/2 and Central Lab UMT for providing facilities for undertaking this research.

References

1. Hu, X., Qi, R., Zhu, J., Luo, Y., Jin, J. and Jiang, P. (2014). Preparation and properties of dopamine reduced graphene oxide and its composites of epoxy. *Journal of Applied Polymer Science,* 131(2): 39754.

2. Siciliano, C. A., Locke, J. L., Mathews, T. A., Lopez, M. F., Becker, H. C. and Jones, S. R. (2017). Dopamine synthesis in alcohol drinking-prone and -resistant mouse strains. *Alcohol,* 58: 25 – 32.
3. Kim, D., Lee. S. and Piao Y. (2017). Electrochemical determination of dopamine and acetaminophen using activated graphene-nafion modified glassy carbon electrode. *Journal of Electroanalytical Chemistry,* 794: 221 - 228.
4. Quan, D. P., Tuyen, D. P., Lam, T. D., Tram, P. T. N., Binh, N. H. and Viet, P. H. (2011). Electrochemically selective determination of dopamine in the presence of ascorbic and uric acids on the surface of the modified nafion/single wall carbon nanotube/poly(3-methylthiophene) glassy carbon electrodes. *Colloids and Surfaces B: Bionterfaces,* 88(2): 764 - 770.
5. Wilson, G. S. and Johnson, M. A. (2008). In-vivo electrochemistry: What can we learn about living systems? *Chemical Review,* 108 (7): 2462 - 2481.
6. Lakshmi, D., Bossi, A., Whitcombe, M. J., Chianella, I., Fowler, S. A., Subrahmanyam, S., Piletska, E. V. and Piletsky, S. A. (2009). Electrochemical sensor for catechol and dopamine based on a catalytic molecularly imprinted polymer-conducting polymer hybrid recognition element. *Analytical Chemistry,* 81(9): 3578 - 3584.
7. Mahshid, S., Li, C., Mahshid, S. S., Askari, M., Dolati, A., Yang, L., Luo, S. and Cai, Q. (2011). Sensitive determination of dopamine in the presence of uric acid and ascorbic acid using TiO_2 nanotubes modified with Pd, Pt and Au nanoparticles. *Analyst,* 136(11): 2322 - 2329.
8. Fang, B., Wang, G., Zhang, W., Li, M. and Kan, X. (2005). Fabrication of Fe_3O_4 nanoparticles modified electrode and its application for voltammetric sensing of dopamine. *Electroanalysis,* 17(9): 744 - 748.
9. Wang, W., Xu, G., Cui, X. T., Sheng, G. and Luo, X. (2014). Enhanced catalytic and dopamine sensing properties of electrochemically reduced conducting polymer nanocomposite doped with pure graphene oxide. *Biosensors and Bioelectronics,* 58: 153 - 156.
10. Liu, X., Peng, Y., Qu, X., Ai, S., Han, R. and Zhu, X. (2011). Multi-walled carbon nanotube-chitosan/poly(amidoamine)/DNA nanocomposite modified gold electrode for determination of dopamine and uric acid under coexistence of ascorbic acid. *Journal of Electroanalytical Chemistry,* 654 (1-2): 72 - 78.
11. Hernandez, Y., Nicolosi, V., Lotya, M., Blighe, F. M., Sun, Z., De, S., McGovern, I. T., Holland, B., Byrne, M., Gun'ko, Y., Boland, J., Niraj, P., Duesberg, G., Krishnamurti, S., Goodhue, R., Hutchison, J., Scardaci, V., Ferrari, A. C. and Coleman, J. N. (2008). High-yield production of graphene by liquid-phase exfoliation of graphite. *Nature Nanotechnology,* 3(9): 563 - 568.
12. Shan, C., Tang, H., Wong, T., He, L. and Lee, S-T. (2012). Facile synthesis of a large quantity of graphene by chemical vapor deposition: an advanced catalyst carrier. *Advanced Materials*, 24(18): 2491 - 2495.
13. Fan, Z. J., Kai, W., Yan, J., Wei, T., Zhi, L. J., Feng, J., Ren, Y. M., Song, L. P. and Wei, F. (2011). Facile synthesis of graphene nanosheets via fe reduction of exfoliated graphite oxide. *ACS Nano,* 5(1): 191 - 198.
14. Ling, Y. Y., Huang, Q. A., Zhu, M. S., Feng, D. X., Li, X. Z. and Wei, Y. (2013). A facile one-step electrochemical fabrication of reduced graphene oxide–multiwall carbon nanotubes–phospotungstic acid composite for dopamine sensing. *Journal of Electroanalytical Chemistry*, 693: 9 - 15.
15. Zhang, F., Wang, Z., Zhang, Y., Zheng, Z., Wang, C., Du, Y. and Ye, W. (2012). Simultaneous electrochemical determination of uric acid, xanthine and hypoxanthine based on poly(l-arginine)/graphene composite film modified electrode. *Talanta,* 93: 320 - 325.
16. Wang, G., Shen, X., Wang, B., Yao, J. and Park, J. (2009). Synthesis and characterization of hydrophilic and organophilic graphene nanosheets. *Carbon,* 47(5): 1359 - 1364.
17. Cui, X., Fang, X., Zhao, H., Li, Z. and Ren, H. (2017). An electrochemical sensor for dopamine based on polydopamine modified reduced graphene oxide anchored with tin dioxide and gold nanoparticles. *Analytical Methods,* 36(9): 5322 - 5332.
18. Chang, Z., Zhou, Y., Hao, L., Hao, Y., Zhu, X. and Xu, M. (2017). Simultaneous determination of dopamine and ascorbic acid using β-cyclodextrin/au nanopaerticles/graphene-modifie electrodes. *Analytical Methods*, 9(4): 664 - 671.
19. Tang, L., Li, X., Ji, R., Teng, K. S., Tai, G., Ye, J., Wei, C. and Lau, S. P. (2012). Bottom-up synthesis of large-scale graphene oxide nanosheets. *Journal of Materials Chemistry,* 22(12): 24981 - 24982.
20. Babu K. S., Reddy, R., Sujatha, C., Reddy, K. V. and Mallika, A. N. (2013). Synthesis and optical characterization of porous ZnO. *Journal of Advanced Ceramic,* 2(3): 260 - 265.

21. Chen, Y. L., Hu, Z. A., Wang, H. W., Zhang, Z, Y., Yang, Y. Y. and Wu, H. Y. (2011). Zinc oxide/reduced graphene oxide composites and electrochemical capacitance enhanced by homogeneous incorporation of reduced graphene oxide sheets in zinc oxide matrix. *The Journal of Physical Chemistry,* 115(5): 2563 - 2571.
22. Yusoff, F., Aziz, A., Mohamed, N. and Ghani, S. A. (2013). Synthesis and characterizations of BSCF at different pH as future cathode materials of fuel cells. *International Journal of Electrochemical Science,* 8(8): 10672 - 10687.
23. Fritea, L., Goff, A. L., Putaux, J. L., Tertis, M., Cristea, C., Săndulescu, R. and Cosnier, S. (2015). Design of a reduced-graphene-oxide composite electrode from an electropolymerizable graphene aqueous dispersion using a cyclodextrin-pyrrole monomer. Application to dopamine biosensing. *Electrochimica Acta,* 178: 108 - 112.
24. Avendańo S. C., Angeles, G. A., Silva, M. T. R., Pina, G. R., Romo, M. R. and Pardavě, M. P. (2007). On the electrochemistry of dopamine in aqueous solution. Part 1: The role of [SDS] on the voltammetric behavior of dopamine on a carbon paste electrode. *Journal of Electroanalytical Chemistry,* 609(1): 17 - 26.

Malaysian Journal of Analytical Sciences, Vol 22 No 2 (2018): 238 - 248
DOI: https://doi.org/10.17576/mjas-2018-2202-08

MALAYSIAN JOURNAL OF ANALYTICAL SCIENCES
Published by The Malaysian Analytical Sciences Society
ISSN 1394 - 2506

ION-CONDUCTING POLYMER ELECTROLYTE FILMS BASED ON POLY (SODIUM 4-STYRENESULFONATE) COMPLEXED WITH AMMONIUM NITRATE: STUDIES BASED ON MORPHOLOGY, STRUCTURAL AND ELECTRICAL SPECTROSCOPY

(Filem Elektrolit Polimer Pengaliran Ion Berasaskan Kompleks Poli(sodium 4-stirenasulfonat) dengan Amonium Nitrat: Kajian ke atas Morfologi, Struktur dan Spektroskopi Elektrik)

Mohd Faiz Hassan*, Siti Khalijah Zainuddin, Khadijah Hilmun Kamarudin, Chan Kok Sheng, Mohd Aidil Adha Abdullah

School of Fundamental Sciences
Universiti Malaysia Terengganu, 21030 Kuala Nerus, Terengganu, Malaysia

**Corresponding author: mfhassan@umt.edu.my*

Received: 10 July 2017; Accepted: 12 March 2018

Abstract

Solid polymer electrolytes of poly(sodium 4-styrenesulfonate) as a polymer host and ammonium nitrate as an ionic dopant were prepared using a single-solvent via solution casting technique. According to the X-ray diffractogram and Fourier transmission infrared analyses, the solid electrolyte films were in an amorphous state and the coexistence of interaction between cation NH_4^+ and the polymer structure agrees that the complex film was successfully prepared. The scanning electron microscope observations revealed that the films appeared to be rough, flat, and irregularly shaped surface. The highest ionic conductivity (σ) of 3.16×10^{-4} Scm^{-1} was achieved at room temperature (303K) for the sample containing 30 wt.% ammonium nitrate.

Keywords: solution cast technique, solid polymer electrolyte, complexation, ionic conductivity

Abstrak

Elektrolit polimer pepejal poli(sodium 4-stirenasulfonat) sebagai polimer perumah dan ammonium nitrat sebagai dopan ionik telah dihasilkan menggunakan pelarut tunggal melalui teknik tuangan larutan. Merujuk kepada analisa difraktogram sinar-X dan inframerah transformasi Fourier, filem-filem elektrolit pepejal dihasilkan dalam keadaan amorfus dan pengkompleksan di antara kation NH^{4+} dan struktur polimer mengesahkan filem tersebut berjaya dihasilkan. Pemerhatian mikroskopi elektron imbasan mendedahkan filem-filem tersebut mempunyai permukaan yang kasar, rata dan wujudnya bentuk-bentuk yang tidak seragam pada permukaannya. Nilai tertinggi konduktiviti ionik (σ) of 3.16×10^{-4} Scm^{-1} telah diperolehi pada suhu bilik (303K) bagi sampel yang mengandungi 30 wt.% ammonium nitrat.

Kata kunci: teknik tuangan larutan, elektrolit polimer pepejal, pengkompleksan, konduktiviti ionik

Introduction

Polymer electrolytes are the topic of exhaustive studies, to a certain extent because of their opportunity to be utilized as the electrolyte in all-solid-state batteries [1]. Briefly, an ionic salt (for example, ammonium nitrate (NH)) is dissolved in a solid host polymer like poly(sodium 4-styrenesulfonate) (PSS) to form the polymer electrolyte and may be prepared as crystalline, amorphous, and/or in both phases. Wright proposed the first documented idea to prepare the solid polymer electrolyte [2]. Since then, studies of this subject have been continuously performed until

today, aiming to discover the potential material of SPEs especially for energy storage applications. In general, SPE is known to have insufficient performance at ambient temperature, which could be one of the drawbacks to their usefulness compared to the existing conventional liquid/hybrid electrolytes [3]. To this extent, numerous studies have been conducted to overcome this disadvantage and to enhance their room-temperature conductivity as well as mechanical properties through blending a variety of polymers [2-4], crosslinking [5], insertion of ceramic fillers [6], plasticization [7], and doping with ionic salts [8-14]. The result from these studies indicated that the utilization of doping salts, which formed at low-temperature eutectics with polymers, is one of the significant approaches to gain SPE with high ionic conductivity and at the same time could preserve their flexibility by controlling the amount of salt in the polymer.

PSS is used as a host polymer and NH as an ionic dopant in SPEs preparation. PSS is well known as an anionic polyelectrolyte [15]. It is obtained by the polymerization of an anionic surfactant, sodium styrene sulfonate. This polyelectrolyte can be dissolved in polar solvents as listed in Zoghlami et al. [15]. PSS gets exclusive awareness by many researchers because of its advantages as an agent of dispersion of graphene in water for sensor application [16], as filler for coating thin mercury film electrode, and as a detector to trace metal in water [17-20]. PSS also can act as an effective binder for graphene sheet, increase the specific capacitance, and improve the rate capability of capacitance [21]. It is universally used as a host polymer and, experimentally proven by some researchers, can boost the ionic conductivity in electrolyte systems [22-25].

NH, the chemical compound with the formula NH_4NO_3, came with white crystalline solids at room temperature. It is odourless, easily soluble in hot and cold water, and highly soluble in acetone, partially soluble in methanol, and insoluble in diethyl ether. It is useful reagents in agriculture and military fields [26, 27]. Previous studies show that the polymers-based complex with NH possess high ionic conductivity, making these hybrids' membranes attractive for further exploration [28, 29].

In this current work, the authors attempt to study the effect of NH on the morphology, structural, and electrical properties of PSS. To examine the evolution of the morphology on the surface of doped-SPE, the SEM technique was used with high and low magnification configurations. The structure modifications of SPE were investigated through FTIR spectroscopy and X-ray diffraction, respectively. Their electrical properties were determined by electrochemical impedance spectroscopy.

Materials and Methods

Preparation

Membranes were prepared using a solution casting technique. The details of the compositions of the PSS (Aldrich, molecular weight ~ 5 x 10^6) doped with NH (Sigma-Aldrich, 99.99%) follow. Briefly, the solutions were obtained by diluting 1g of PSS powder into 100 ml of distilled water. Subsequently, different amounts of NH (varied from 0 to 30 in weight percentage, wt.%) were added to the solutions, as listed in Table 1.

Table 1. The compositions of PSS and NH powders.

	Solvent (ml)	Polymer (g)	Ionic Salt (wt.%)	Ionic Salt (g)
Pure	100	1	0	0
A	100	1	5	0.053
B	100	1	10	0.111
C	100	1	15	0.177
D	100	1	20	0.250
E	100	1	25	0.333
F	100	1	30	0.429

The mixtures were stirred continuously with the magnetic stirrer until homogenous solutions were achieved. Next, the solutions were poured into different plastic Petri dishes and left for the evaporation process to form thin films. The films were then kept in desiccators (with silica gel) for a certain period to reduce water content. All the experimental steps were carried out at room temperature.

Characterization

The amorphous or crystal phase of a sample was determined by X-ray diffraction technique. XRD is also used to analyse the atomic arrangements of the materials, because inter-planar spacing (*d*-spacing) of the diffracting planes is the same order of X-ray wavelength. A MiniFlex II diffractometer equipped with an X'celerator using CuKα radiation was used to record the XRD pattern in the range of $2\theta = 10^o$ to 80^o.

The composition and complex formation in the sample was analysed by a Thermo Nicolet Avatar 380 FT-IR spectrometer. It simultaneously collects spectral data in a wide spectral range from 4000 to 675 cm^{-1} with spectra resolution of 4 cm^{-1}. The spectrometer is equipped with an attenuated total reflection (ATR) accessory with a germanium crystal. The sample was put on the germanium crystal and infrared light was passed through the sample; the graph is sketched.

The surface morphology of the prepared sample was investigated by scanning electron microscopy. It was carried out using the Model JEOL JSM-6360LA device with an acceleration voltage of 20kV. The samples were observed under the magnifications of 300x to 5000x, accordingly. Through this technique, the crystalline or amorphous nature of the sample can be directly observed. Impedance spectroscopes for room temperature (30 $^{\circ}$C) were measured by using the HIOKI 3532-02 LCR Hi-Tester, which is interfaced to a computer. It is used to determine the electrical properties over a wide range of frequencies from 50 Hz to 1 MHz. The prepared samples were cut into two-centimetre diameter size and placed between two stainless steel electrodes on a sample holder connected via leads to a computer. The imaginary impedance (Z_i) versus the real impedance (Z_r) was plotted using the same scale for both vertical and horizontal axes to obtain the bulk resistance, R_b. A micrometre-screw gauge was used to measure the sample thickness, employed to calculate conductivity of the sample using the equation (1):

$$\sigma = \frac{t}{R_b A} \tag{1}$$

where t = thickness of the thin film (in cm) and A = area of the contact and R_b= bulk resistance.

Results and Discussion

The results of XRD analysis at room temperature recorded from $2\theta = 10^o$ to 80^o for NH, pure PSS, and PSS-NH complexes systems are shown in Figure 1. Several sharp peaks, located at 22.2, 24.1, 28.6, 32.7, 35.9, 37.6, 39.9, 45.6, 49.3, 50.8, 51.5, and 58.4^o, were clearly visible in the NH pattern, indicating that it is rich with crystalline moieties. A hump (very broad) peak can be observed in between 25^o and 35^o, which also corresponds to an amorphous phase of NH; however, its portion is quite low compared to the crystalline phase, although these structures of NH are similarly reported in literature [30-34]. As the comparison for all XRD patterns of PSS-NH samples reveal that they have a certain similarity and subsist in an amorphous state. Specifically, a very broadened peak in between $2\theta = 15^o$ and 25^o can be identified in PSS diffraction pattern, which refers to naturally amorphous phases of polymer. By adding 10 to 30 wt.% NH into the polymer, two hump peaks are observed in the patterns located at 15^o to 25^o and 23^o to 33^o, which match the broaden peaks of PSS and NH, respectively, and confirm the complex processes taking place in these materials. The result also reveals that the complex films tend to be highly amorphous rather than crystalline phase, and, significantly, the presence of NH does not have much influence on the formation of peaks in the complex samples. The coexistence of XRD peaks belongs to these two materials, validating their appearance in solid polymer electrolyte film [35, 36].

The FTIR spectra for ammonium nitrate and polymer-ionic dopant complexes are shown in Figure 2. In the spectrum of NH (Figure 2(a)), the strong and medium bands of NH at 1380 and 832 cm^{-1} correspond to the nitrate functional group [37, 38]. Another band in the nitrate group is 1630 cm^{-1}, where the water molecule is bound symmetrically or asymmetrically to the nitrate ion, according to Goebbert et al. [39]. The spectrum also contains a band at 3030 cm^{-1} that is due to the N-H stretching in the ammonium group. From observation on the complexed

spectra, there are significant changes for all prepared samples, especially within their intensity and spectrum patterns. Ordinarily, the peak intensities increase as the used amount of NH in PSS increases, and, specifically, the characteristic peaks of NH peaks obviously appear in the whole of the PSS spectra. Coates and John mentioned that if an IR spectrum has the functional group of two different materials (in this case, ammonium nitrate and PSS), it can confirm that the chain-reaction (or addition) polymerization process is successfully achieved due to the existence of each chain in that spectrum [37].

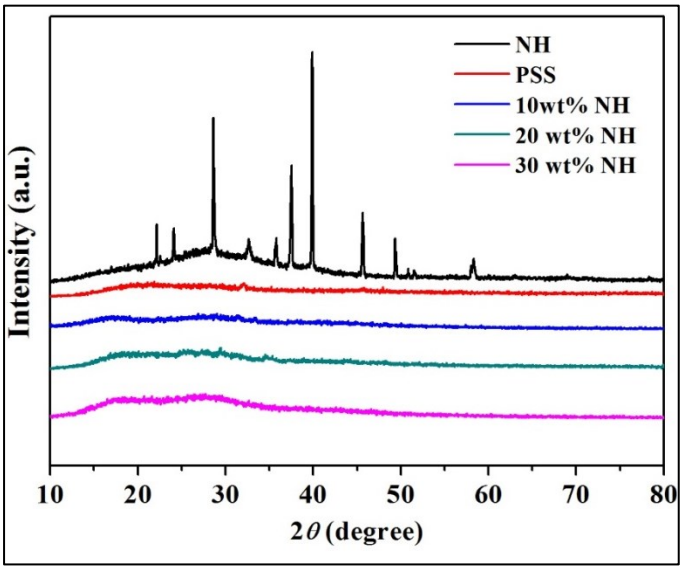


Figure 1. XRD pattern for PSS, NH, and hybrid PSS-NH films

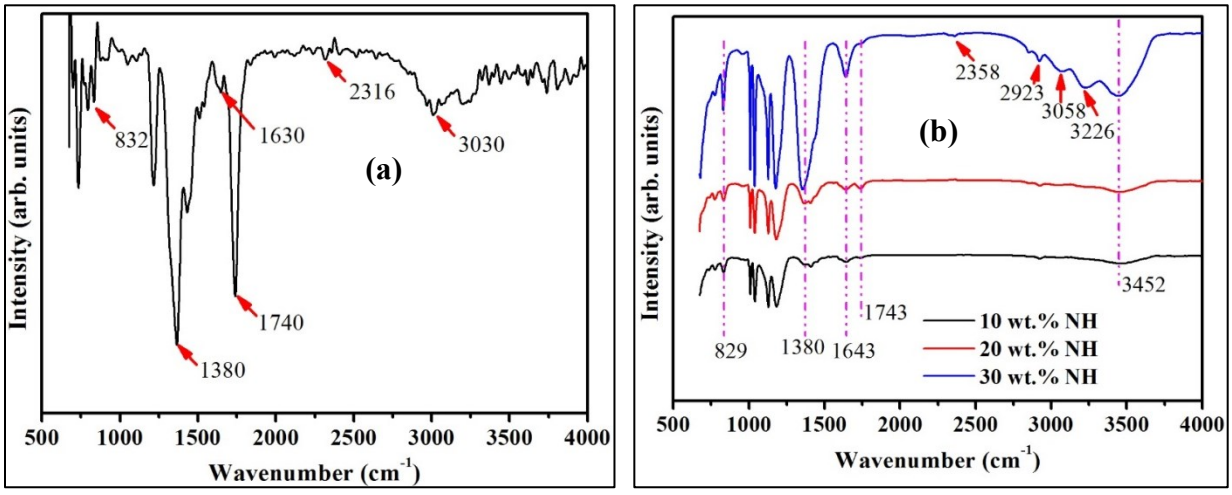


Figure 2. FTIR analysis of (a) NH and (b) different weight % of NH in PSS

Figure 3 shows the scanning electron micrographs of pure PSS and PSS-NH complex films. Typically, all prepared samples were transparent films with no separation. They were in a solid form while analysed at different magnifications (×300; ×500; ×5,000) and regions, as shown in Figures 3(a) to 3(f). In Figure 3(a), the morphology of NH powder appeared to be uneven, rough, and contain some irregular shapes with varied sizes, whereas Figure

3(b) is the morphology of PSS powder, indicating that PSS particles have the most regular shape and smoothest surface texture (closer to spheres with a smoother surface). Figure 3(c) illustrates the SEM image for the pure PSS film with some of wave shape observed on its surface. The wave shape, together with some small grains contour (x5000 magnification image), were also observed on the whole SEM image for 10 wt.% NH sample (Figure 3(d)). The surface contour of the sample with 20 wt.% NH changed to have a bigger and thicker wave shape, as depicted in Figure 3(e). Taken in a selected area of the image, the morphology tended to have some mixed small and large square plate grain shapes. These square plate grains appeared in a larger size (compared to Figure 3(d)) and presented in a different directional orientation. Figure 3(f) demonstrates the SEM image of the sample containing 30 wt. % NH. Adding a stated amount of NH shows that the morphology surface has changed a little bit with the existence of many smaller diameters of wave contours covering the whole area of the SEM image. Interestingly, the zooming SEM image at 5000x magnification reveals that this surface morphology has similar grains shapes as observed in Figure 3(d), but with most them at a smaller size, and their directional orientation is more arranged.

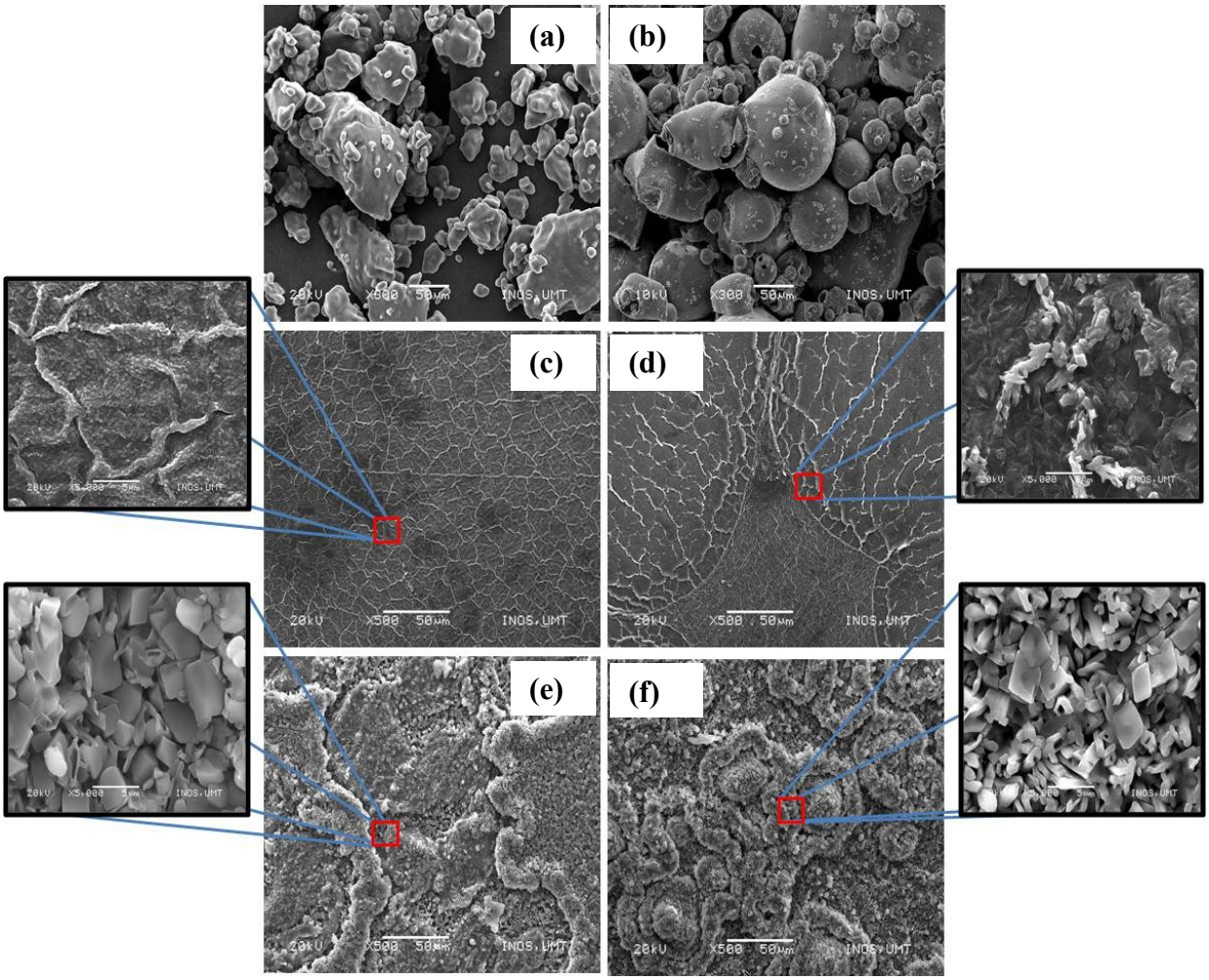


Figure 3. SEM micrographs for (a) NH powder, (b) PSS powder, (c) PSS film (pure), (d) 10 wt.% NH (sample B), (e) 20 wt.% NH (sample D) and (f) 30 wt.% NH (sample F). (Note: □: the selected image in x5000 magnification)

The specific size of surface area for selected grains for Figure 3(e) and Figure 3(f) was calculated using imaging software and depicted in Figure 4. The measured data were transformed to the graph of area versus the grain number

(Figure 4b and Figure 4d). As observed, the mixed grains with the biggest and average area sizes in 20 wt.% NH are 19.8 and 5.1 μm^2, whereas for the sample with 30 wt.% NH, the values are 9.7 and 3.8 μm^2, respectively. A group of researchers have proven that the size of particle can provide a significant effect on the electrical properties of materials when employed in the closed system [40-42].

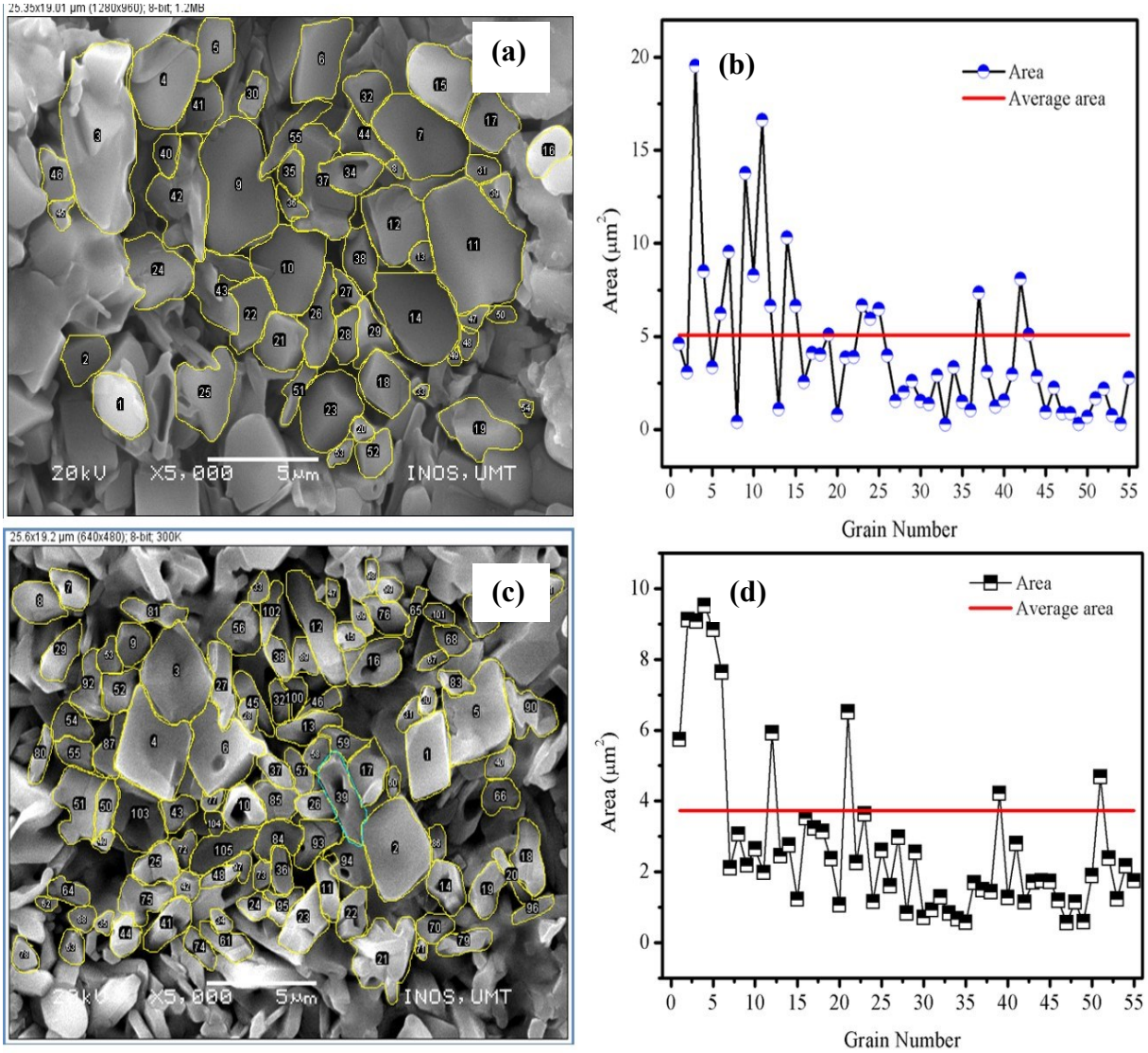


Figure 4. The area size of grain for (a, b) sample e and (c, d) sample f

Figure 5 shows the SEM image for the sample of 30 wt.% NH, with red circles of pores detected in the whole image. There are two differences of images in Figure 4 and Figure 5: first, the area size of grains, and second, the structure, which came together with the pores distinguished in the specific area of the image. These pores have the diameter size in range of 14 to 38 nm, as tabulated in Table 2, and have special characteristics which could contribute to enhancing the electrical properties of the studied materials [43, 44].

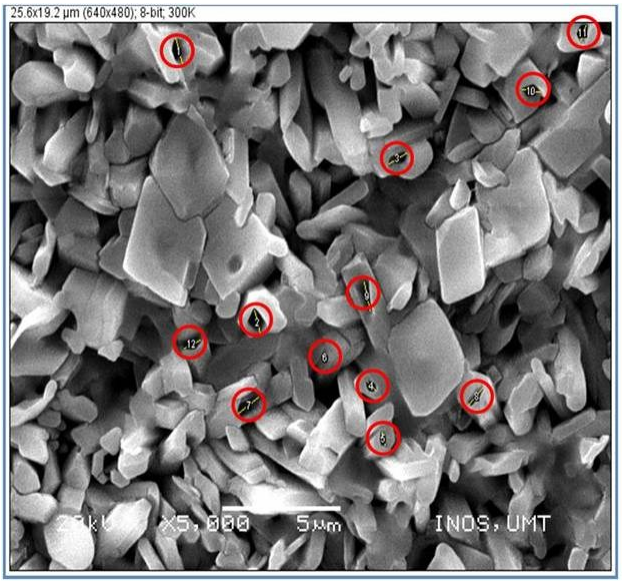


Figure 5. The SEM image of pore in the specific location in the whole SEM image for the highest conductivity sample

Table 2. The diameter of pore in nanometre

No. of Pore	Pore Diameter (nm)
1	38
2	35
3	35
4	21
5	21
6	14
7	38
8	35
9	35
10	21
11	21
12	14

The values of bulk resistance, R_b, and the conductivity, σ, of the samples are tabulated in Table 3. The measured thicknesses of the samples were between 0.009 and 0.016 cm. The bulk resistance of pure PSS in the film form is about 1.01 x 10^3 Ω, with an ionic conductivity of approximately 2.83 x 10^{-6} S cm^{-1}. By adding 5 wt.% of NH in the polymer, the bulk resistance increases to 1.21 x 10^3 Ω and the ionic conductivity increases to 3.68 x 10^{-6} S cm^{-1}. The bulk resistance (1.08 x 10^2 Ω) decreases after adding 15 wt.% NH and gives the ionic conductivity of 1.85 x 10^{-5} S cm^{-1}. Further adding 20 wt.% NH, the bulk resistance increases to 1.82 x 10^3 Ω and gives the lowest ionic conductivity (8.05 x 10^{-6} S cm^{-1}). At 25 wt.% NH, the measured resistance decreases (3.48 x 10^3 Ω), offering an increase in ionic conductivity to 1.46 x 10^{-5} S cm^{-1}. The increase trend of ionic conductivity continues in the 30 wt.% NH sample, with the value of 3.16 x 10^{-4} S cm^{-1}. Additional NH in the polymer solution experimentally reduces rigidity of the mixture; as a result, the complex film cannot be formed, and its ionic conductivity is difficult

to measure using the current equipment. The overall trend of conductivity variation as a function of salt content at room temperature is depicted in Figure 6. In general, the increasing trend of ionic conductivity is probably due to the amorphous state of film and the increase in the number of mobile charge carriers, as the NH concentration increases in the samples. The decreasing pattern here is possibly due to the decrease in carrier mobility and the crystallites affecting ionic conductivity. The boundary between the crystallites and the amorphous area could function as a barrier for the ionic migration. The crystallites also sterically hinder the ionic migration. These effects may be answerable for the lower ionic conductivity for the film at 20 wt.% concentration [45-48]. The low crystalline phase and the presence of porosity structure should contribute more to enhancing the ionic conductivity by allowing the larger group of ions to flow through it [1, 45, 48].

Table 3. The ionic conductivity of PSS–NH at room temperature

	Bulk resistance, R_b (Ω)	**Conductivity, σ (Scm^{-1})**
Pure	1.01×10^{3}	2.83×10^{-6}
A	1.21×10^{3}	3.68×10^{-6}
B	1.08×10^{2}	2.35×10^{-5}
C	1.03×10^{2}	1.85×10^{-5}
D	1.82×10^{3}	8.05×10^{-6}
E	3.48×10^{2}	1.46×10^{-5}
F	1.61×10^{1}	3.16×10^{-4}

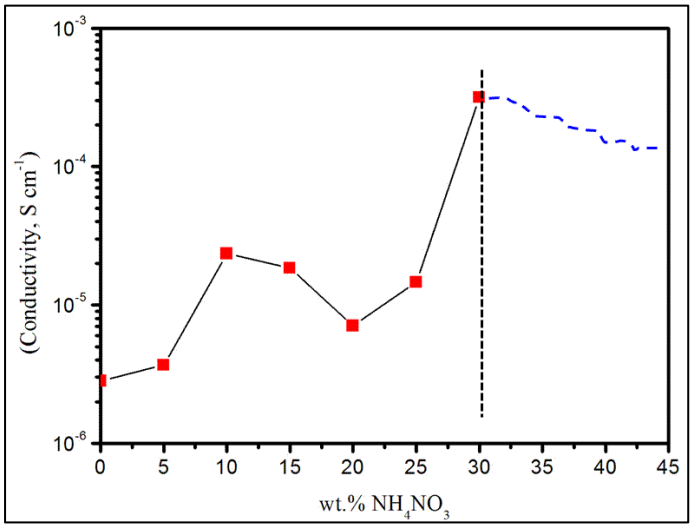


Figure 6. The conductivity variation as a function of salt content at room temperature

Conclusion

In this study, the ion-conducting polymer electrolytes based on PSS-NH have been successfully prepared via a solution casting technique. The effects of NH on the PPS structure were investigated based on X-ray diffraction, infrared spectroscopy, and scanning electron microscope. To current knowledge, this is the first time that the film based on PSS complex with NH has been discussed, particularly regarding its structure and ionic conductivity. This information is crucial for further studies on thin film electrolytes as one of the key components in solid state battery application.

In summary, it can be concluded that the complex films were in the amorphous rather than the crystalline phase. The FTIR analysis can be described as coexistence bands from both materials, which confirmed the successful polymerization process occurring in this study. According to the morphology observations, the addition of NH can appreciably change the surface morphology of the film, with the highest conducting sample containing 30 wt.% NH (1.82×10^{-5} S cm^{-1}) tending to have mixed small and large square uneven shapes that attached together. Also observed, with an addition of 30 wt.% NH to PSS film, the pore structures can be clearly seen, which the authors strongly believe contributed in enhancing the ionic conductivity of the PSS-NH hybrids film.

Acknowledgement

The authors would like to thank the School of Fundamental Science and School of Ocean Engineering, Universiti Malaysia Terengganu for financial supports on this study.

References

1. Gadjourova, Z., Andreev, Y. G., Tunstall, D. P. and Bruce, P. G. (2001). Ionic conductivity in crystalline polymer electrolytes. *Nature,* 412: 520-523.
2. Wright, P. V. (1975). Electrical conductivity in ionic complexes of poly(ethylene oxide). *British Polymer Journal,* 7:319–324.
3. Dillip, K. P., Choudhary, R. N. P. and Samantaray, B. K. (2008). Studies of dielectric relaxation and AC conductivity behaviour of plasticized polymer nanocomposite electrolyte. *International Journal Electrochemistry Science,* 3: 597-608.
4. Kim, D. W., Park, J. R. and Rhee, H. W. (1996). Conductivity and thermal studies of solid polymer electrolytes prepared by blending poly(ethylene oxide), poly(oligo[oxyethylene]oxysebacoyl) and lithium perchlorate. *Solid State Ionics,* 83(1-2): 49-56.
5. Wieckzorek, W. and Stevens, J. R. (1997). Impedance spectroscopy and phase structure of polyether-poly(methyl methaacrylate)-$LiCF_3SO_3$ blend-based electrolytes. *Journal of Physical Chemistry B,* 101(9):1529-1534.
6. Przyluski, J. and Wieczorek, W. (1989). Increasing the conductivity of polymer solid electrolytes: A review. *Solid State Ionics,* 36(3-4): 165-169.
7. Cherng, J. Y., Munshi, M. Z. A., Owens, B. B. and Smyrl, W. H. (1988). Applications of multivalent ionic conductors to polymeric electrolyte batteries. *Solid State Ionics,* 28-30: 857-861.
8. Hassan, M. F. and Arof, A. K. (2005). Ionic conductivity in PEO-KOH polymer electrolytes and electrochemical cell performance. *Physica Status Solidi-A,* 202(13): 2494-2500.
9. Rajendran, S., Sivakumar, M. and Subadevi, R. (2004). Investigations on the effect of various plasticizers in PVA-PMMA solid polymer blend electrolytes. *Materials Letters, 58*(5), 641-649.
10. Choi, N. S. and Park, J. K. (2001). New polymer electrolytes based on PVC/PMMA blend for plastic lithium-ion batteries. *Electrochimica Acta,* 46(10-11): 1453-1459.
11. Pandey, K., Dwivedi, M. M., Asthana, N., Singh, M. and Agrawal, S. L. (2011). Structural and ion transport studies in (100-x)PVdF + xNH4SCN gel Electrolyte. *Materials Sciences and Application,* 2: 721-728.
12. Zhang, J., Huang, X., Fu, J., Huang, Y., Liu, W. and Tang, X. (2010). Novel PEO-based composite solid polymer electrolytes incorporated with active inorganic-organic hybrid polyphosphazene microspheres. *Materials Chemistry and Physics,* 121(3): 511-518.
13. Feng, W., Wang, J. and Wu, Q. (2005). Preparation and conductivity of PVA films composited with decatungstomolybdovanadogermanic heteropoly acid. *Materials Chemistry and Physics,* 93(1): 31-34.
14. Ramesh, S. and Ng, H. M. (2011). An investigation on PAN-PVC-LiTFSI based polymer electrolytes system. *Solid State Ionics,* 192(1): 2-5.
15. Zoghlami, O., Guettari, M. and Tajouri, T. (2017). Study of poly(sodium-4-styrenesulfonate) behavior in water/non-solvent mixtures by conductivity and refractive index measurements. *Colloid and Polymer Science*, 295(9): 1729-1739.
16. Li, J., Miao, D., Yang, R., Qu, L. and Harrington, P. B. (2014). Synthesis of poly(sodium 4-styrenesulfonate) functionalized graphene/cetyltrimethylammonium bromide (CTAB) nanocomposite and its application in electrochemical oxidation of 2,4-dichlorophenol. *Electrochimica Acta*, 125: 1-8.

17. Monterroso, S. C., Carapuca, H. M. and Dearte, A. C. (2003). Performance of poly(styrenesulfonate)-coated thin mercury film electrodes in the determination of lead and copper in estuarine water samples of high salinity. *Electroanalysis,* 15(23-24): 1878-1883.
18. Jia, J., Cao, L., Wang, Z. and Wang, T. (2007). Properties of poly(sodium 4-styrenesulfonate)-ionic liquid composite film and its application in the determination of trace metals combined with bismuth film electrode. *Electroanalysis,* 20: 542-549.
19. Rocha, L. S., Pinheiro, J. P. and Carapuca, H. M. (2006). Ion-exchange voltammetry with nafion/poly(sodium 4-styrenesulfonate) mixed coatings on mercury film electrodes: characterization studies and application to the determination of trace metals. *Langmuir,* 22(19): 8241-8247.
20. Du, F. P., Wang, J. J., Tang, C. Y., Tsui, C. P., Zhou, X. P., Xie, X. L. and Liao, Y. G. (2012). Water-soluble graphene grafted by poly(sodium 4-styrenesulfonate) for enhancement of electric capacitance. *Nanotechnology,* 23: 475704.
21. Imrea, A. W., Schönhoff, M. and Cramer, C. (2008). A conductivity study and calorimetric analysis of dried poly(sodium 4-styrene sulfonate)/poly(diallyldimethylammonium chloride) polyelectrolyte complexes. *The Journal of Chemical Physics,* 128: 134905.
22. Wesp, V., Hermann, M., Schäfer, M., Hühn, J., Parak, W. J. and Weitzel, K. M. (2016). Bombardment induced ion transport – part IV: Ionic conductivity of ultra-thin polyelectrolyte multilayer films. *Physical Chemistry Chemical Physics,* 18(6): 4345-4351.
23. Kolling, T., Schlemmer, A., Pietzonka, C., Harbrecht, B. and Weitzel, K. M. (2010). Field effects in alkali ion emitters: Transition from Langmuir-Child to Schottky regime. *Journal of Applied Physics,* 107: 014105.
24. Schulze, S., Zakel, J., Schäfer, M. and Weitzel, K. M. (2012). Potassium ion transport through poly-para-xylylene films. *IEEE Transactions on Dielectrics and Electrical Insulation,* 19: 1167-1174.
25. Overberger, C. G. and Sannes, K. N. (1974). Polymere als reagentien fur organische synthesen. *Angewandte Chemie,* 86: 139-145.
26. Cook, M. A. and Talbot, E. L. (1951). Explosive sensitivity of ammonium nitrate-hydrocarbon mixtures. *Industrial and Engineering Chemistry,* 43(5): 1098-1102.
27. Majid, S. R. and Arof, A. K. (2005). Proton-conducting polymer electrolyte films based on acetate complexed with NH_4NO_3 salt. *Physica B,* 355(1-4): 78-82.
28. Kamarudin, K. H. and Isa, M. I. N. (2013). Structural and DC ionic conductivity studies of carboxy methylcellulose doped with ammonium nitrate as solid polymer electrolytes. *International Journal of Physical Sciences,* 8(31): 1581-1587.
29. Hendricks, S. B., Posnjak, E. and Kracek, F. C. (1932). Molecular rotation in the solid state. The variation of the crystal structure of ammonium nitrate with temperature. *Journal of American Chemical Society,* 54: 2766-2786.
30. Ferg, E. E., Levendis, D. C. and Schoening, F. R. L. (1993). X-ray diffraction study of the orientational relation between the IV and III phases of ammonium nitrate. *Chemistry of Materials,* 5(9): 1293-1298.
31. Sorescu, D. C. and Thompson, D. L. (2001). Quantum mechanical studies of pressure effects in crystalline ammonium dinitramide. *Journal of Physical Chemistry A,* 105(31): 7413-7422.
32. Wu, H. B., Chan, M. N. and Chan, C. K. (2007). FTIR characterization of polymorphic transformation of ammonium nitrate. *Aerosol Science and Technology,* 41(6): 581-588.
33. Golovina, N., Nechiporrenko, G., Nemtsev, G., Zyuzin, I., Manelis, G. B. and Lempert, D. (2009). Ammonium nitrate phase state stabilization with small amounts of some organic compounds. *Central European Journal of Energetic Materials,* 6: 45-56.
34. Joshi, J. M. and Sinha, V. K. (2006). Synthesis and characterization of carboxymethyls chitosan grafted methacrylic acid initiated by ceric ammonium nitrate. *Journal of Polymer Research,* 13: 387-395.
35. Parvathy, P. C. and Jyothi, A. N. (2012). Synthesis, characterization and swelling behavior of superabsorbent polymers from cassava starch-graft-poly(acrylamide). *Starch,* 64: 207-218.
36. Coates, J. (2000). Interpretation of infrared spectra, a practical approach. in encyclopedia of analytical chemistry, Meyers, R. A., Editor. Chichester: John Wiley & Sons Ltd.
37. Miller, F. A. and Wilkins, C. H. (1952). Infrared spectra and characteristic frequencies of inorganic ions. *Analytical Chemistry,* 24: 1253-1294.

38. Goebbert, D. J., Garand, E., Wende, T., Bergmann, R., Meijer, G., Asmis, K. R. and Neumark, D. M. (2009). Infrared spectroscopy of the microhydrated nitrate ions $NO_3^-(H_2O)_{1-6}$. *Journal of Physical Chemistry A,* 113(26): 7584-7592.
39. Suherman, H., Duskiardi and Irmayani. (2015). Effect of particle size and graphite loading concentration on the electrical conductivity of graphite/epoxy composites. Paper presented at the International Conference on Chemical, Metallurgy and Material Science Engineering (CMMSE-2015), Pataya, Thailand.
40. Tsujimoto, Y., Matsushita, Y., Yu, S., Yamaura, K. and Uchikoshi, T. (2015). Size dependence of structural, magnetic, and electrical properties in corundum-type Ti_2O_3 nanoparticles showing insulator-metal transition. *Journal of Asian Ceramic Societies,* 3(3): 325-333.
41. Supmak, W., Petchsukand, A. and Thanaboonsombut, A. (2008). Influence of ceramic particle sizes on electrical properties of lead zirconate titanate (pzt)/nylon57 composites. *Journal of Metals, Materials and Minerals,* 18: 147-151.
42. Li, B. Q. and Lu, X. (2011). The effect of pore structure on the electrical conductivity of Ti. *Transport in Porous Media,* 87(1): 179-189.
43. Li, Y., Samad, Y. A., Polychronopoulou, K., Alhassan, S. M. and Liao, K. (2014). Highly electrically conductive nanocomposites based on polymer-infused graphene sponges. *Scientific Reports,* 4: 4652.
44. Angell, C. A. (1992). Mobile ions in amorphous solids. *Annual Reviews of Physics Chemistry,* 43: 693-717.
45. Tuller, H. (2007). Ionic conductivity and applications. Springer Handbook of Electronic and Photonic Materials.
46. Feng S, Greenblatt M. (1992). Preparation, characterization and ionic conductivity of novel crystalline, microporous germanates, $M_3HGe_7O_{16}.xH_2O$, M = NH^{4+}, Li^+, K^+, Rb^+, Cs^+; x = 4-6. II. *Chemistry of Materials,* 4(2):462-468.
47. Kim, D. W., Ryoo, B. K., Park, J. K., Maeng, K. S. and Hwang, T. S. (1992). Study on the ionic conductivity and mobility of liquid polymer electrolytes containing lithium salts. *Polymer Journal,* 24: 509-518.
48. Braga, M. H., Murchison, A. J., Ferreira, J. A., Singh, P., & Goodenough, J. B. (2016). Glass-Amorphous Alkali-Ion Solid Electrolytes and Their Performance in Symmetrical Cells, In: Energy and Environmental Science. *Energy and Environmental Science,* 9(3): 948-954.

Malaysian Journal of Analytical Sciences, Vol 22 No 2 (2018): 249 - 257
DOI: https://doi.org/10.17576/mjas-2018-2202-09

MALAYSIAN JOURNAL OF ANALYTICAL SCIENCES
Published by The Malaysian Analytical Sciences Society
ISSN 1394 - 2506

OPTIMIZATION OF SELECTED CHARCOAL POWDER COMPOSITE ELECTRODE FOR ELECTROCHEMICAL TREATMENT OF LANDFILL LEACHATE

(Pengoptimuman Komposit Elektrod daripada Serbuk Arang Terpilih untuk Rawatan Elektrokimia Bahan Larut Lesap Tapak Pelupusan)

Majd Ahmed Jumaah[1]*, Mohamed Rozali Othman[1, 2], Jumat Salimon[1], Baydaa Khalaf[1], Wan Mohd Afiq Wan Mohd Khalik[2, 3]

[1]*School of Chemical Sciences and Food Technology, Faculty of Science and Technology*
[2]*Centre for Water Research and Analysis, Faculty of Science and Technology*
Universiti Kebangsaan Malaysia, 43600 UKM Bangi, Selangor, Malaysia
[3]*School of Marine and Environmental Sciences,*
Universiti Malaysia Terengganu, 21030 Kuala Nerus, Terengganu, Malaysia

**Corresponding author: majd.ahmed88@yahoo.com*

Received: 19 October 2017; Accepted: 29 January 2018

Abstract

Charcoal powders obtained from commercially available charcoal and the open burning of palm oil, rubber, coconut, and mangrove trees were used to fabricate composite electrodes in this study. A weight portion of charcoal powder, graphite, cobalt, and polyvinyl chloride (C-C^{G}-Co-PVC) were mixed in tetrahydrofuran (THF). The fabricated composite electrodes were then used as working electrodes for the electrochemical treatment of landfill leachate samples. A variable pressure scanning electron microscope (VPSEM) was used to examine the appearance of the charcoal powder. The results showed that rubber tree charcoal powder is the best charcoal powder for fabricating the composite electrodes, as it has various pore sizes and more surface area available for adsorption and reaction. Field emission scanning electron microscopy (FESEM) was performed before and after electrolysis of the landfill leachate. The results revealed that the presence of voids on the electrode surface before and after electrolysis improved the electrochemical oxidation of the landfill leachate, and yielded removal percentages in colour, COD, NH_3-N, and total P of not less than 80%, 91%, 73%, and 84%, respectively.

Keywords: landfill leachate, charcoal powder, composite electrode, electrochemical method

Abstrak

Serbuk arang yang diperoleh dari arang komersil dan pembakaran terbuka batang-batang pokok kelapa sawit, pokok getah, pokok kelapa, dan pokok bakau telah digunakan untuk membina elektrod komposit berasaskan arang hasil gabungan serbuk arang, grafit, kobalt dan polivinil klorida (C-C^{G}-Co-PVC) yang telah dicampurkan mengikut komposisi berat tertentu dalam pelarut tetrahidrofuran (THF). Elektrod komposit yang telah dibina kemudiannya digunakan sebagai elektrod kerja untuk merawat sampel air bahan larut lesap melalui kaedah elektrokimia. Mikroskop elektron imbasan tekanan boleh ubah (VPSEM) telah digunakan untuk mengkaji sifat fizikal serbuk arang. Keputusan menunjukkan bahawa serbuk arang pokok getah merupakan serbuk arang terbaik untuk membina elektrod komposit dalam kajian ini kerana ia mempunyai banyak liang dan luas permukaan yang lebih tinggi untuk penjerapan dan tindak balas berlaku. Mikroskop imbasan elektron medan pancaran (FESEM) telah digunakan untuk memerhati permukaan elektrod yang telah disediakan sebelum dan selepas elektrolisis bahan larut lesap. Keputusan menunjukkan bahawa terdapat kehadiran lohong pada permukaan elektrod sebelum dan selepas elektrolisis. Hal ini

membantu memperbaiki proses pengoksidaan elektrokimia bahan larut lesap yang telah menyebabkan peratus pengurangan warna, COD, NH_3-N, dan total P masing-masingnya tidak kurang daripada 80%, 91%, 73%, dan 84%.

Kata kunci: bahan larut lesap tapak pelupusan, serbuk arang, elektrod komposit, kaedah elektrokimia

Introduction

Municipal councils and cities around the world commonly use sanitary landfills to manage solid waste [1]. The increased growth in population, urbanisation, and industrialisation has resulted in a high amount of solid wastes being generated. The generation of municipal solid waste is increasing day-by-day due to the rapid development of urban areas and rural-urban migration. After landfilling, solid waste undergoes physico-chemical and biological changes. Consequently, the degradation of the organic fraction of the wastes in combination with percolating rainwater leads to the production of a dark-coloured, highly polluted liquid called "leachate" [2]. Landfill leachate contains high concentrations of pollutants such as ammonia, phosphorus, and total dissolved solid as well as high chemical oxygen demand (COD). Leachates are fast becoming an issue in wastewater sources since it can cause serious pollution to the ecosystem [3]. Humid substances represent more than 60% of the total organic carbon found in anaerobic landfill leachates.

In an effort to control the pollution caused by landfill leachate, various treatment processes have been studied, including biological treatment [4], photocatalysis [5], adsorption [6], chemical precipitation [7], Fenton's oxidative treatment [8], coagulation/flocculation [9], advanced oxidation processes, and membrane processes [10]. However these methods still have disadvantages such as decreased treatment efficiencies and increased cost. Up until now, the electrochemical oxidation process has been proven to be the more promising wastewater treatment method mainly due to its high effectiveness, ease of operation, and economy. This method is particularly suited for landfill leachate treatment because the rich chloride ions and good conductivity of the leachates enhance the benefits of the electrochemical method. The electrochemical oxidation technique is an effective method not only for colour removal but also for COD removal. The pollutants are destroyed through a direct or indirect oxidation process [11].

The choice of anode material is critical and considered a major experimental concern because the anode serves as the site for oxidation reaction and electrochemical catalysis. Therefore, the selection of materials for fabricating a working electrode (anode) is crucial, so as to produce high oxidation efficiency and high electrochemical catalysis. Meanwhile, the effect of cathode materials has not been extensively investigated, although it may have a considerable influence on the electro-oxidation of organic compounds [12]. However, the electrode material must have the following properties: high physical and chemical stability, high electrical conductivity, rapid electron transfer kinetics in a wide range of redirections, ease of setup as well as inexpensive and durable [13]. Different types of anode materials such as Pt, PbO_2, Al, and graphite have been investigated for electrochemical treatment [14, 15].

In the present study, a novel charcoal-based metallic composite electrode is proposed as an electrode material to treat landfill leachate. Out of the several types of carbon, charcoal was selected because other carbon types such as diamond and graphite are expensive. The study also investigates different types of charcoal prepared from palm oil, rubber, coconut, and mangrove trees as well as available commercial charcoal to determine the best type for treating landfill leachate. The efficiency of charcoal carbon in wastewater treatment is due to its low cost compared to other materials as well as its ability to absorb organic compounds and other pollutants from the leachate [16].

Materials and Methods

Sampling and analysis

Leachate samples were collected from Jeram Sanitary Landfill, which is located in an oil palm plantation near Mukim Jeram, Kuala Selangor, Malaysia. The samples were collected in 1 L amber glass bottles with Teflon-lined caps to ensure sample integrity, using a stainless steel bucket previously rinsed with distilled water and methanol. The bottle headspace was kept to a minimum by filling the bottles until the top. The bottles were rinsed in the field with the sample and filled to the top on the second sampling. Disposable gloves were used to prevent any contamination. The samples were transported to the laboratory in an ice-cooled container and stored at 4 ºC in order to retain the leachate characteristics. Finally, all samples were characterised based on selected parameters such as

pH, colour, and COD. The tests were conducted according to the Standard Methods for the Examination of Water and Wastewater [17]. COD and colour were measured using a HACH DR2400 spectrophotometer. The pH was measured using a pH meter (EUTECH pH 2700).

Preparation of electrodes

Composite electrodes at a composition of C:C^G:Co:PVC were fabricated accordingly as per a previous study, by mixing together a weighed portion of charcoal powder 0.5 mm graphite and Co with PVC in 4 ml THF solvent and swirled flatly into a homogeneous composition, followed by drying in an oven at 100 ºC for 3 hours [3, 18].The mixture was then placed in a 1-cm diameter stainless steel mould and pressed at 10 ton/cm^2. A typical pellet contains approximately 60% (w/w) charcoal powder, 15% (w/w) graphite, 10% (w/w) Co, and 15% (w/w) PVC powder. The total weight of the pellet obtained was approximately 0.5 g. The pellets were connected to a silver wire with silver conducting paint prior to being covered with epoxy gum. A weight ratio of C:C^G:Co:PVC was used for the prepared electrodes, as summarised in Table 1.

Table 1. Weight ratio and composition of charcoals, graphite, metal, and PVC powders for the prepared electrodes

Electrode	Ratio C:C^G:Co:PVC	C (g)	C^G (g)	Co (g)	PVC (g)
$C^{coconut}C^G{}_{15}Co_{10}PVC_{15}$	60:15:10:15	0.3	0.075	0.05	0.075
$C^{rubber\ tree}{}_{60}C^G{}_{15}Co_{10}$-$PVC_{15}$	60:15:10:15	0.3	0.075	0.05	0.075
$C^{mangrove}{}_{60}\ C^G{}_{15}Co_{10}$-$PVC_{15}$	60:15:10:15	0.3	0.075	0.05	0.075
$C^{palm\ oil}{}_{60}\ C^G{}_{15}Co_{10}$-$PVC_{15}$	60:15:10:15	0.3	0.075	0.05	0.075
$C^{commercial}{}_{60}C^G{}_{15}Co_{10}$-$PVC_{15}$	60:15:10:15	0.3	0.075	0.05	0.075

Note* C = charcoal, C^G= graphite

The surface morphology of the five charcoal powders used in this work was analysed using VP-SEM (LEO model 1450VP), while the surface morphology of the composite electrodes before and after the electrochemical oxidation process was analysed using SEM (ZEISS, merlin compact model, Germany).

The experimental setup

The electrochemical cell setup consists of a DC power supply (CP x 200 DUAL, 35 V 10 A PSU) and a glass beaker (250 ml) complete with a $C_{60}C^G{}_{15}Co_{10}PVC_{15}$ composite electrode as the anode and a stainless steel rod (d = 10 mm) as the cathode (Figure 1). The electrodes were placed parallel to each other in the electrolytic reactor, with a distance of approximately 1 cm between the cathode and anode. Stirrers were used throughout to maintain homogeneity of the sample.

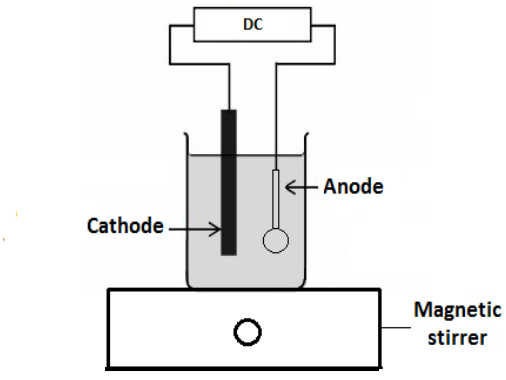
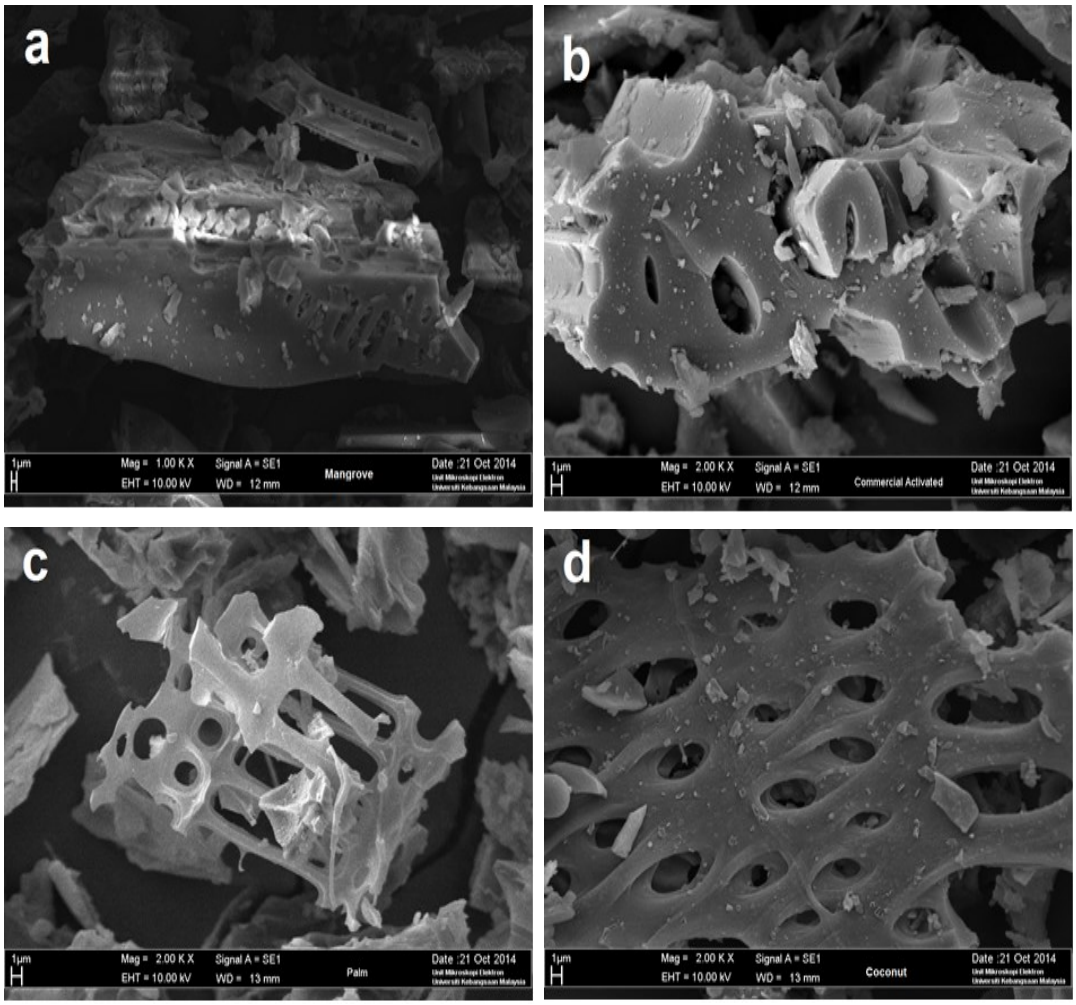


Figure 1. Schematic experimental setup

Results and Discussion

Study on the surface morphology of the five charcoal powders

VPSEM was used to examine the appearance of the charcoal powder obtained from five types of charcoal (Figures 2). Results of the VPSEM analysis show that charcoal powder particles are irregularly shaped, with different sizes [19]. Mangrove charcoal appears to have a smooth surface and a few holes. Meanwhile, some holes were also observed on the surface of commercially available charcoal. The palm oil charcoal has a structural shape and is non-coherent. This structure is not effective for absorbing pollutants. Coconut and rubber charcoal clearly have a wide variety of pores present along with a fibrous structure. Many holes are also found, which would contribute to more surface area available for adsorption and reaction [20]. The rubber tree charcoal powder was finally chosen as the best charcoal type for fabricating the electrode to treat the landfill leachate in this study, based on the two types of adsorptions that occur between organic compounds and the anode: (1) the physical adsorption involving Van der Waals forces; and (2) the chemical adsorption involving the formation of chemical bonds between the anode surface and organic compounds [21].



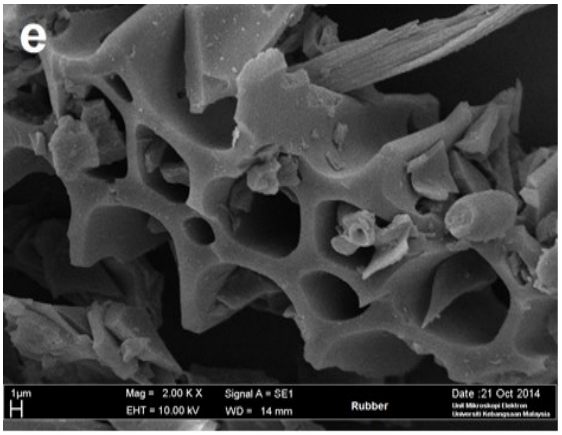


Figure 2. VPSEM of charcoal powder for: (a) Mangrove; (b) commercial charcoal; (c) palm oil; (d) coconut; and (e) rubber tree, using an accelerating voltage of 10 kV

Colour removal

Colour removal is of great interest in this study because colour is not just a parameter; it is also a good anthropogenic indicator [22, 23]. The colour removal efficiency of different types of charcoal for fabricating the electrodes in this study is therefore investigated. The results obtained are summarised in Table 2.

Table 2. Electrochemical oxidation of landfill leachate using different charcoal composite electrodes

Electrode composition	Decolouring percentage (%)	Observation	
		Electrolysis product	Anode
$C^{coconut}C^{G}_{15}Co_{10}PVC_{15}$	83	Yellowish solution	Unchanged
$C^{rubber\ tree}{}_{60}C^{G}_{15}Co_{10}$-$PVC_{15}$	80	Yellowish solution	Unchanged
$C^{mangrove\ tree}{}_{60}\ C^{G}_{15}Co_{10}$-$PVC_{15}$	57	Yellowish solution	Slightly corroded
$C^{palm\ oil}{}_{60}C^{G}_{15}Co$-$PVC_{15}$	65	Yellowish solution	Unchanged
$C^{commercially\ available}{}_{60}C^{G}15$	59	Yellowish solution	Slightly corroded

Majd and Othman [14] used optimum operating conditions such as 120 min electrolysis time, an applied voltage of 10 V, a sodium chloride concentration of 1.5% (w/v) and pH 4, with electrode compositions of $C^{coconut\ tree}C^{G}_{15}Co_{10}PVC_{15}$ and $C^{rubber\ tree}{}_{60}C^{G}_{15}Co_{10}PVC_{15,}$ which yielded the best colour removal via the electrochemical treatment of landfill leachate, with a colour removal percentage of 83% and 80%, respectively. However, the colour removal efficiencies for charcoal obtained from palm oil and mangrove trees and commercially available charcoal, were only 65%, 57%, and 59%, respectively. Therefore, it is clear that coconut and rubber electrode yield high colour removal and do not undergo any change in physical properties. The electrode used in any electrochemical process should be stable chemically and physically [24]. Therefore, based on these criteria, the best electrode must not only be able to remove colour, but also have the appropriate chemical and physically stability.

The results obtained for the electrodes fabricated from Mangrove tree charcoal and commercially available charcoal yielded the lowest colour removal percentages. Not only that, the electrodes also became slightly corroded. Although the charcoal obtained from palm oil has good chemical and physically stability, its colour removal efficiency is lower than the electrodes fabricated from coconut and rubber tree charcoal. These results correspond with the results of the SEM micrograph, which show the effectiveness of the electrodes fabricated from coconut and rubber trees in electrochemically treating landfill leachates. Although the electrode fabricated from coconut tree charcoal gave the highest colour removal efficiency, this charcoal type is difficult to obtain and is usually

unavailable in the market. Therefore, the rubber charcoal composite electrode was selected as the best type of electrode in this case due to its effectiveness in removing colour and wide availability, especially in Malaysia [25].

SEM of rubber tree charcoal-graphite- Co-PVC electrode

The surface morphology of $C^{rubber\ tree}C^{G}$CoPVC electrode was investigated using SEM. The SEM micrographs were obtained using an accelerating voltage of 15 kV to evaluate the effectiveness of electrochemical oxidation before and after treatment (Figure 3).

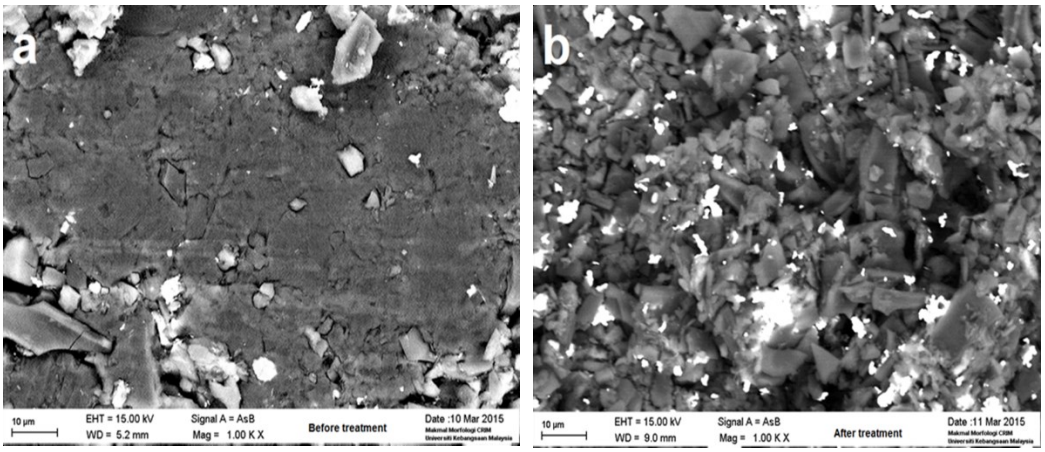


Figure 3. SEM micrograph of: (a) $C^{rubber\ tree}{}_{60}C^{G}{}_{15}Co_{10}PVC_{15}$ electrode before (a) and after (b) treatment of leachate

Figure 3(a) before electrolysis shows a smooth-surfaced electrode. There are no free holes on the surface of the $C^{rubber\ tree}{}_{60}C^{G}{}_{15}Co_{10}PVC_{15}$ electrode since it did not undergo electrochemical oxidation. Once electrochemical oxidation occurs, as shown in Figure 3(b), the process clearly affects the electrode surface, creating many pores that allow pollutants to enter; thus leading to an electrochemical oxidation reaction occurring inside the electrode [26, 27] and resulting in a working electrode for landfill leachate treatment.

Characterisation of landfill leachate after electrochemical treatment

Selected values of water quality parameter (colour, COD, NH_3-N, and total P) on landfill leachate before and after electrolysis were analysed in optimum operating conditions, as previously mentioned. The results obtained show that the electrochemical oxidation process was able to reduce the colour, COD, NH_3-N and total P values in the landfill leachate. The removal percentages in colour, COD, NH_3-N, and total P were not less than 80%, 91%, 73%, and 84%, respectively (Figure 4).

Reduction in COD value was due to the breaking down of large molecules into small molecules, which chemically and/or biologically eases the oxidisation process in the electrochemical oxidation technique [28, 29]. This breakdown process is supported by the existence of self-generated hypochlorite ions, which can reduce the concentration of organic compounds [30, 31]. The measurement of pH of the landfill leachate showed that all samples were in alkaline conditions, changing to neutral upon completion of electrochemical oxidation duration due to the formation of a carbonate buffer from the CO_2 produced at the end of the electrolysis process.

Colour is known as an important pollutant indicator in leachates. Therefore, besides testing the organic and nitrogen compound pollutants, colour removal was also investigated. Together with the electro-oxidation process, a strong oxidation process also occurred, to ensure the removal of colour-causing pollutants. This study achieved satisfactory findings for highly-coloured landfill leachates. This could be due to the increased generation of OCl^- species that can oxidise coloured substances. During electrochemical oxidation, OCl^- was produced due to the presence of chloride ions responsible for making hypochlorite ions, which then degrade the pollutants in leachate [32]. High

NH_3-N removal efficiencies can be achieved *via* the electro-oxidation process. Removal of nitrogen compounds can be explained by the mechanism used in this process.

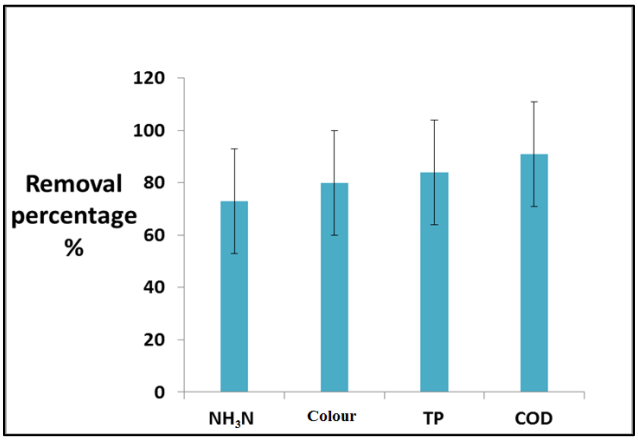


Figure 4. Removal efficiency of $C^{rubber\ tree}{}_{60}C^{G}{}_{15}Co_{10}PVC_{15}$ anode in the electrochemical oxidation process with 10 V, 1.5% (w/v) NaCl, and pH 4

Conclusion

Charcoal powders obtained from commercially available charcoal and charcoal prepared from palm oil, rubber, coconut, and mangrove trees were used to fabricate composite electrodes in this study. The results showed that the best electrode was fabricated from rubber tree charcoal according to the composition of $C_{60}C^{G}{}_{15}Co_{10}$-$PVC_{15}$, yielding removal percentages in colour, COD, NH_3N, and total P of 80%, 91%, 73%, and 84%, respectively, under optimum operating conditions of sodium chloride (NaCl) concentration of 1.5% (w/v) as the supporting electrolyte, an applied voltage of 10 V, an operating time of 120 min, and a pH of 4, using stainless steel as the cathode.

The variable pressure scanning electron microscope (VPSEM) analysis showed that rubber tree charcoal powder is the best type of charcoal for fabricating the composite electrode in this study due to its many holes and more surface area available for adsorption and reaction. The field emission scanning electron microscopy (FESEM) shows the presence of voids on the electrode surface before and after the electrolysis of the leachate sample, which improves the electrochemical oxidation of landfill leachates. Hence, the charcoal-based metallic composite electrode used in this study has proven efficient in the electrochemical treatment of landfill leachates.

Acknowledgement

The authors gratefully acknowledge the funding provided by Universiti Kebangsaan Malaysia and the Ministry of Higher Education, Malaysia, through grant number FRGS/2/2013/SG01/UKM/01/1.

References

1. Wu, J. J., Wu, C. C., Ma, H. W. and Chang, C. C. (2004). Treatment of landfill leachate by ozone-based advanced oxidation processes. *Chemosphere*, 54(7): 997-1003.
2. Kurniawan, T. A., Lo, W. H. and Chan, G. Y. (2006). Physico-chemical treatments for removal of recalcitrant contaminants from landfill leachate. *Journal of hazardous materials*, 129(1): 80-100.
3. Jumaah, M. A., Othman, M. R. and Yusop, M. R. (2016). Characterization of leachate from Jeram sanitary landfill-Malaysia. *International Journal of ChemTech Research*, 9(8): 571-574.
4. Xu, Z. Y., Zeng, G. M., Yang, Z. H., Xiao, Y., Cao, M., Sun, H. S., Ji, L. L. and Chen, Y. (2010). Biological treatment of landfill leachate with the integration of partial nitrification, anaerobic ammonium oxidation and heterotrophic denitrification. *Bioresource Technology*, 101(1): 79-86.
5. Cho, S. P., Hong, S. C. and Hong, S. I. (2002). Photocatalytic degradation of the landfill leachate containing refractory matters and nitrogen compounds. *Applied Catalysis B: Environmental*, 39(2): 125-133.

6. Lim, Y. N., Shaaban, M. G. and Yin, C. Y. (2009). Treatment of landfill leachate using palm shell-activated carbon column: Axial dispersion modeling and treatment profile. *Chemical Engineering Journal*, 146(1): 86-89.
7. Neczaj, E., Okoniewska, E. and Kacprzak, M. (2005). Treatment of landfill leachate by sequencing batch reactor. *Desalination*, 185(1): 357-362.
8. Galeano, L. A., Vicente, M. Á. and Gil, A. (2011). Treatment of municipal leachate of landfill by Fenton-like heterogeneous catalytic wet peroxide oxidation using an Al/Fe-pillared montmorillonite as active catalyst. *Chemical Engineering Journal*, 178(15): 146-153.
9. Li, W., Hua, T., Zhou, Q., Zhang, S. and Li, F. (2010). Treatment of stabilized landfill leachate by the combined process of coagulation/flocculation and powder activated carbon adsorption. *Desalination*, 264(1): 56-62.
10. Hasar, H., Unsal, S. A., Ipek, U., Karatas, S., Cınar, O., Yaman, C. and Kınacı, C. (2009). Stripping/flocculation/membrane bioreactor/reverse osmosis treatment of municipal landfill leachate. *Journal of Hazardous Materials*, 171(1): 309-317.
11. Tabet, K., Moulin, P., Vilomet, J. D., Amberto, A. and Charbit, F. (2002). Purification of landfill leachate with membrane processes: Preliminary studies for an industrial plant. *Separation Science and Technology*, 37(5): 1041-1063.
12. Bashir, M. J., Isa, M. H., Kutty, S. R. M., Awang, Z. B., Aziz, H. A., Mohajeri, S. and Farooqi, I. H. (2009). Landfill leachate treatment by electrochemical oxidation. *Waste Management*, 29(9): 2534-2541.
13. Jumaah, M. A. and Othman, M. R. (2015). Decolorization of landfill leachate using electrochemical oxidation technique. In *AIP Conference Proceedings,* 1678(1): 050032.
14. Jumaah, M. A. and Othman, M. R. (2015). Study the efficiency of various metal powder composition electrodes based on landfill leachate treatment. *International Journal of ChemTech Research*, 8(12): 559-563.
15. Martínez-Huitle, C. A. and Brillas, E. (2009). Decontamination of wastewaters containing synthetic organic dyes by electrochemical methods: A general review. *Applied Catalysis B: Environmental*, 87(3): 105-145.
16. Jumaah, M. A., Othman, M. R. and Yusop, M. R. (2016). Batch method treatment of landfill leachate using charcoal composite. *International Journal of ChemTech Research*, 9(8): 583-586.
17. American Public Health Association (2005). Standard methods for the examination of water and wastewater, 21st edition; American Public Health Association: Washington, D.C.
18. Hamdan, M. S., Nordin, N. and Amir, S. F. M. (2011). Electrochemical behaviour of Ni and Ni-PVC electrodes for the electroxidation of ethanol. *Sains Malaysiana*, 40(12): 1421-1427.
19. Gubernat, M., Tomala, J., Frohs, W., Fraczek-Szczypta, A. and Blazewicz, S. (2016). De-agglomeration and homogenisation of nanoparticles in coal tar pitch-based carbon materials. *Journal of Nanoparticle Research*, 18(3): 56-69.
20. Shendkar, C. D., Torane, R. C., Mundhe, K. S., Lavate, S. M., Pawar, A. B. and Deshpande, N. R. (2013). Characterization and application of activated carbon prepared from waste weed. *International Journal of Pharmacy and Pharmaceutical Sciences*, 5(2): 527-529.
21. Jumaah, M. A., Othman, M. R. and Yusop, M. R. (2016). Electrochemical treatment of landfill leachate: Optimization of COD removal using charcoal-graphite-cobalt-polyvinyl chloride electrode. *Research Journal of Pharmaceutical, Biological and Chemical Sciences*, 7(5): 2812-2816.
22. Blanco, J., Torrades, F., De la Varga, M. and García-Montaño, J. (2012). Fenton and biological-Fenton coupled processes for textile wastewater treatment and reuse. *Desalination*, 286: 394-399.
23. Zakaria, Z., Nordin, N., Hasan, S. Z., Baharuddin, N. A., Jumaah, M. A. and Othman, M. R. (2015). Decolorization of reactive orange 16 dye using fabricated charcoal base metallic composite electrode. *Malaysian Journal of Analytical Sciences*, 19(3): 493-502.
24. Zhang, L. L. and Zhao, X. S. (2009). Carbon-based materials as supercapacitor electrodes. *Chemical Society Reviews*, 38(9): 2520-2531.
25. Ratnasingam, J., Ioras, F. and Wenming, L. (2011). Sustainability of the rubber wood sector in Malaysia. *Notulae Botanicae Horti Agrobotanici Cluj-Napoca*, 39(2): 305-311.
26. Sanroman, M. A., Pazos, M., Ricart, M. T. and Cameselle, C. (2004). Electrochemical decolourisation of structurally different dyes. *Chemosphere*, 57(3): 233-239.
27. Chang, X., Thind, S. S. and Chen, A. (2014). Electrocatalytic enhancement of salicylic acid oxidation at electrochemically reduced TiO_2 nanotubes. *ACS Catalysis*, 4(8): 2616-2622.

28. Jumaah, M. A. and Othman, M. R. (2015). Optimization of operating conditions for landfill leachate treatment using electrochemical oxidation technique. *International Journal of ChemTech Research*, 8(2): 783-787.
29. Chen, G. (2004). Electrochemical technologies in wastewater treatment. *Separation and Purification Technology*, 38(1): 11-41.
30. Jumaah, M. A. and Othman, M. R. (2015). COD removal from landfill leachate by electrochemical method using charcoal-PVC electrode. *International Journal of ChemTech Research*, 8(12): 604-609.
31. Jumaah, M. A., Othman, M. R. and Zakaria, Z. (2015). Fabrication of selected metal powder composite electrode for landfill leachate treatment using electrochemical method. *International Journal of Chemical Sciences*, 13(2): 943-954.
32. Jumaah, M. A., Othman, M. R., Yusop, M. R., Salimon, J., Khalaf, B. and Khalik, W. M. A. W. M. (2017). Charcoal base metallic composite electrode for wastewater treatment. *Malaysian Journal of Analytical Sciences*, 21(6): 1432-1437.

Malaysian Journal of Analytical Sciences, Vol 22 No 2 (2018): 258 - 263
DOI: https://doi.org/10.17576/mjas-2018-2202-10

MALAYSIAN JOURNAL OF ANALYTICAL SCIENCES
Published by The Malaysian Analytical Sciences Society
ISSN 1394 - 2506

PRENYLATED DIHYDROSTILBENES FROM *Macaranga heynei* (EUPHORBIACEAE)

(Dihidrostilbena Terprenil daripada *Macaranga heynei* (Euphorbiaceae))

Aisyah Salihah Kamarozaman[1,2,3]*, Norizan Ahmat[2,3], Nur Fariza Abd Rahman[1], Khong Heng Yen[4]

[1]*Centre of Foundation Studies,*
Universiti Teknologi MARA, Selangor Branch, Dengkil Campus, 43800 Dengkil, Selangor, Malaysia
[2]*Faculty of Applied Sciences,*
Universiti Teknologi MARA, 40450 Shah Alam, Selangor, Malaysia
[3]*Atta-ur-Rahman Institute for Natural Product Discovery,*
Universiti Teknologi MARA, Puncak Alam Campus, 42300 Bandar Puncak Alam, Selangor, Malaysia
[4]*Faculty of Applied Sciences,*
Universiti Teknologi MARA, Sarawak Branch, Samarahan Campus, 94300 Kota Samarahan, Sarawak, Malaysia

**Corresponding author: aisyah2910@puncakalam.uitm.edu.my*

Received: 4 December 2016; Accepted: 1 December 2017

Abstract

Macaranga is the largest genus in Euphorbiaceae which consists of approximately 300 species and are widely distributed in New Guinea, Borneo and from West Africa to the south Pacific islands. Phytochemical study on the leaves of *Macaranga heynei* has been conducted. The powder of the leaves of *M. heynei* was macerated in methanol at room temperature for 24 hours and repeated three times. The crude extract obtained was dissolved in aqueous methanol (80:20) and partitioned with hexane and ethyl acetate. The ethyl acetate crude extract was fractionated by vacuum liquid chromatography (VLC) with hexane:ethyl acetate in increasing polarity to give seven combined fractions (MH 1-7). Fraction MH 2 (1000 mg) was further purified by radial chromatography (RC) with hexane:ethyl acetate in increasing polarity to give six combined subfractions (MH 21-26). Fraction MH 23 (693.7 mg) was further purified by the same chromatographic technique but with different eluent which was chloroform:ethyl acetate in increasing polarity to afford two pure compounds **(1)** (10 mg) and **(2)** (12 mg). Based on spectroscopy analysis, the pure compounds were characterized as laevifolins A **(1)** and B **(2)**.

Keywords: Laevifolin A, laevifolin B, leaves, *Macaranga heynei*

Abstrak

Macaranga merupakan genus terbesar dalam famili Euphorbiaceae yang mengandungi kira-kira 300 spesies dan taburannya meliputi New Guinea, Borneo dan dari Afrika Selatan ke utara kepulauan Pasifik. Kajian fitokimia ke atas daun *Macaranga heynei* telah dijalankan. Serbuk daun *M. heynei* direndam dalam metanol pada suhu bilik selama 24 jam dan pengesktrakan diulang sebanyak tiga kali. Ekstrak mentah yang diperolehi telah dilarutkan dalam larutan metanol (80:20) dan dipisahkan dengan heksana dan etil asetat. Etil asetat mentah difraksinasi menggunakan kromatografi cecair vakum (KCV) dengan heksana:etil asetat mengikut peningkatan kekutuban menghasilkan tujuh fraksi gabungan (MH 1-7). Fraksi MH 2 (1000 mg) selanjutnya ditulenkan dengan menggunakan kromatografi radial (RC) dengan heksana:etil asetat mengikut peningkatan kekutuban menghasilkan enam subfraksi gabungan (MH 21-26). Fraksi MH 23 (693.7 mg) seterusnya ditulenkan dengan menggunakan teknik kromatografi yang sama tetapi menggunakan eluen yang berbeza iaitu kloroform:etil asetat mengikut peningkatan kekutuban menghasilkan dua sebatian tulen **(1)** (10 mg) dan **(2)** (12 mg). Berdasarkan analisis spektroskopi, sebatian tulen tersebut dicirikan sebagai laevifolin A **(1)** dan B **(2)**.

Kata kunci: Laevifolin A, laevifolin B, daun, *Macaranga heynei*

Introduction

Macaranga which comprises a large genus with 300 species [1] is widely distributed in New Guinea, Borneo and from West Africa to the south Pacific islands [2]. Generally, these species are found in village-thickets, wastelands and swampy forests [3]. These species are commonly distributed in the forests as well as in disturbed areas. However, most of the species are found to be well-flourished in developed or disturbed vegetation areas compared to the natural forest [4]. Apart from being exploited as plywood and match splints, this genus is widely used for traditional remedies by the old folks. The decoction root of *M. tanarius* has been used to treat fever and as antitusive for coughing. In addition, the dried root is used as emetic agent while the fresh leaves have been used to cover wounds which act as an anti-inflammatory [5]. In Sumatra, the fruit of this species was used to improve the quality of the sugar produced while in Philippines, the bark and leaves are used in the preparation of fermented drink made from sugarcane [6].

Phytochemical studies on the species from *Macaranga* have shown that this genus has abundant sources of flavonoids especially prenylated flavonoids [7, 8]. In addition, this genus does contain stilbenoids, tannins, as well as terpenoids [9, 10, 11]. The flavonoid compounds isolated from *Macaranga* species possessed broad spectrum of pharmacological properties such as cytotoxicity, antiviral, antimicrobial as well as acetylcholinesterase activities [12, 13, 14]. Similarly, flavonoids displayed significant role in dietary antioxidant by reducing the oxidative stress in the body [15]. Meanwhile, the stilbenoids namely laevifolins A and B which were isolated from *M. javanica* possessed significant activities against *S. aureus* with MIC values 35 μM [16].

M. heynei or being called as mahang biru by the locals is widely distributed in Peninsular Malaysia and Thailand. This species was found to occur on open places up to 1000 metres height as well as on exposed subsoil. *M. heynei* is classified by the folks as medicinal plants due to its potential in treating several illness [17]. Due to the promising bioactivities of compounds isolated from *Macaranga* species, *M. heynei* was selected for the phytochemical study.

Materials and Methods

The leaves of *M. heynei* was collected from Kuala Kangsar, Perak in December 2015 and the voucher specimen SK2875/15 was deposited at the herbarium of Universiti Putra Malaysia. The plant was identified by Dr. Shamsul Khamis, a botanist from Universiti Putra Malaysia.

Extraction and isolation

The leaves of *M. heynei* was dried and ground to form powder. The powder of the leaves (2 kg) was then macerated in methanol at room temperature. The extraction was done for 24 hours and repeated for three times. The extract was dried by using rotary evaporator to give methanolic crude extract (300 g). The methanolic crude extract was dissolved in the mixture of 80% methanol: 20% water followed by partition with hexane and ethyl acetate. The ethyl acetate crude extract (150 g) was fractionated by using vacuum liquid chromatography (VLC) with a mixture of hexane-ethyl acetate in increasing polarity to give seven combined fraction (MH 1-7). Fraction MH 2 (1000 mg) was further purified by radial chromatography (RC) with hexane: ethyl acetate in increasing polarity to give six combined subfractions (MH 21-26). Fraction MH 23 (693.7 mg) was further purified by the same chromatographic technique but with different eluent which was chloroform:ethyl acetate in increasing polarity to afford two pure compounds **(1)** (10 mg) and **(2)** (12 mg).

Analysis

The isolated compounds (MH 233 and MH 235) were elucidated by means of ultraviolet-visible (UV-VIS), infrared (IR), mass (MS) and one and two dimensioned nuclear magnetic resonance (NMR) spectroscopy, as well as comparison with literature data. The proton NMR was recorded in 600 MHz while the carbon-APT NMR in 150 MHz. Chemical shift, δ, ppm recorded in $CDCl_3$.

Results and Discussion

Compound **(1)** as shown in Figure 1 was obtained as brownish viscous oil from the isolation of the leaves of *M. heynei*. The TOFMS in positive mode recorded a pseudo-molecular ion $[M+H]^+$ peak indicated the molecular formula of $C_{29}H_{38}O_4$. The UV absorptions (λ 208, 257 nm) showed the characteristic of typical aromatic and

phenol. It is supported by the IR absorptions at 3447 (O-H); 2923(alkyl); 1606 (C=C aromatic) and 1216, 1012 (ether) cm^{-1}.The ^{1}H NMR spectrum of **(1)** exhibited three aromatic protons at δ_H 6.75 – 6.31. One singlet signal at δ_H 6.31 of aromatic proton, a doublet signal at δ_H 3.34 (4H), a triplet of multiplet signal at δ_H 5.10 (2H) as well as two broad singlet signals at δ_H 1.80 (6H) and 1.73 (6H) showed that the aromatic proton of ring A pairs with two prenyl groups which is in symmetrical structure. Meanwhile, there are two doublet signals at δ_H 6.75 and 6.68 indicated the presence of *ortho*-coupled aromatic protons which pair with a prenyl group at δ_H 5.12, 3.39, 1.80 and 1.74 of ring B. In addition, there are two multiplet signals at δ_H 2.86 and 2.73 exhibited the presence of methylene protons which are connected to ring A and B which suggested that the compound is a dihydrostibene derivative.

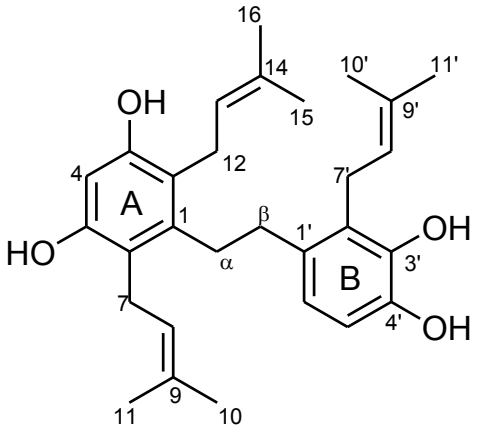


Figure 1. Chemical structure of compound **(1)**

The ^{13}C – APT NMR spectrum of **(1)** exhibited twenty two signals which represent twenty seven carbons suggested that the dihydrostilbene structure contains of four hydroxyl substituents and three phenyl groups. It was displayed by the oxyaril signals at δ_C 153.5, 142.4 and 142.3 while the signals at δ_C 139.7, 134.6, 133.8, 132.2, 125.9 and 118.2 represents eight quartenary carbons. The signals at δ_C 123.0, 122.1, 121.1, 112.8 and 102.0 represents six methine carbons while five methylene carbons were represented by the signals at δ_C 33.9, 31.5, 26.6, 25.7 and 25.6. Three methyl carbon was exhibited by the signals at δ_C 25.8 and 17.9.

The long range correlations between proton and carbon could be observed from HMBC spectrum .The doublet signal at δ_H 3.34 (4H) showed correlation with carbon signals at δ_C 139.7 (C-1), 118.2 (C-2/6) and 153.5 (C-3/5) which confirmed the position of two prenyl groups at C-2 and C-6 at ring A. Meanwhile, another correlation was observed between the doublet signal at δ_H 3.39 (2H) with carbon signals at δ_C 132.2 (C-1'), 125.9 (C-2') and 142.3 (C-3'), confirming the position of one prenyl group at C-2' at ring B (Figure 2). The signals shown in ^{1}H, ^{13}C – APT and HMBC NMR spectra are consistent with the literature [18] and characterised as laevifolin A **(1)**.

Compound **(2)** as shown in Figure 3 was obtained as brownish viscous oil from the isolation of the leaves of *M. heynei*. The pseudo-molecular ion $[M+H]^+$ peak indicated the molecular formula of $C_{29}H_{38}O_4$. The UV absorptions (λ 208, 260 nm) exhibited the presence of phenol and aromatic system. The IR absorptions at 3412 (O-H); 2923(alkyl); 1599 (C=C aromatic) and 1217, 1017 (ether) cm^{-1} supported the presence of phenolic system in the structure . The ^{1}H NMR spectrum of **(2)** is close to the compound **(1)** except for two doublet signal at δ_H 6.61 and 6.54 which showed the presence of *meta*-coupled aromatic protons in ring B. A broad singlet signal at δ_H 6.31 indicated the presence of aromatic proton in ring A. The presence of three prenyl groups was displayed by the signals at δ_H 5.35 – 1.74 which two of them are attached to ring A while the remaining is attached to ring B.

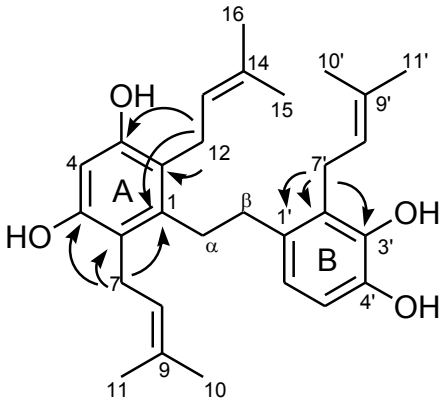


Figure 2. Selected ^{1}H – ^{13}C HMBC found in compound **(1)**

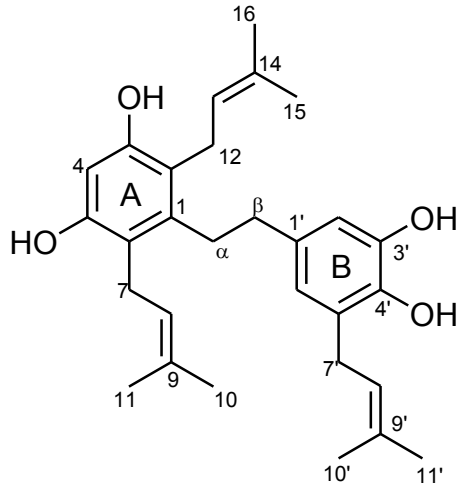


Figure 3. Chemical structure of compound **(2)**

The ^{13}C – APT NMR spectrum of **(2)** exhibited twenty two signals which represent twenty seven carbons which are similar to those shown in the spectrum of compound **(1)**. There are four signals representing oxyaril carbons at δ_C 153.4, 153.1, 143.8 and 140.4 while five signals indicating the presence of eight quartenary carbons at δ_C 139.6, 134.2, 133.1, 127.6 and 118.2. Meanwhile, six methyne carbons were exhibited by the presence of five signals at δ_C 123.5, 122.1, 121.4, 113.0 and 102.8. The methylene carbons were represented by the signals at δ_C 35.7, 31.7, 29.5 and 25.2 while six methyl carbons were displayed at δ_C 26.7, 26.6, 18.0 and 17.9.

The long range correlations between proton and carbon could be observed from HMBC spectrum. A doublet signal of methylene protons at δ_H 3.37 (2H) exhibited correlation with 140.4 (C-4'), 127.6 (C-5') and 122.1 (C-6') confirming the location of one prenyl group at C-5' at ring B (Figure 4). Meanwhile, the position of two prenyl groups at ring A are similar to that of laevifolin A **(1)**. Based on the comparison of ^{1}H, ^{13}C – APT and HMBC NMR spectra with the literature [18], the compound was characterised as laevifolin B **(2)**.

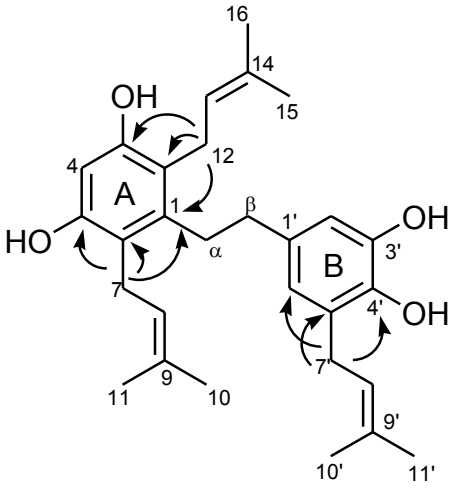


Figure 4. Selected $^{1}H - ^{13}C$ HMBC found in compound **(2)**

Conclusion

In conclusion, the phytochemical study on the leaves of *M. heynei* has successfully isolated two prenylated dihydrostilbenes namely laevifolins A **(1)** and B **(2)**. This is the first report of the compounds in this species.

Acknowledgement

I would like to express my greatest appreciation to the Ministry of Education, Malaysia for the financial support (RAGS/1/2014/SG01/UITM/4), Universiti Teknologi MARA, UiTM for providing the equipments and laboratory as well as Dr. Shamsul Khamis, a botanist from Universiti Putra Malaysia for the identification and plant collection.

References

1. Lim, T. Y., Lim, Y. Y. and Yule, C. M. (2009). Evaluation of antioxidant, antibacterial and anti-tyrosinase activities of four *Macaranga* species. *Food Chemistry*, 114: 594-599.
2. Whitmore, T. C. (1967). Studies in *Macaranga*, an easy genus of Malayan wayside trees. *Malayan Nature Journal,* 20(3): 89–99.
3. Corner, E. J. H. (1988). Wayside trees of Malaya. Malayan Nature Society, 1: pp 296–304.
4. Zakaria, R., Rosley, N. F. N., Mansor, M. and Zakaria, M. Y. (2008). The distribution of *Macaranga*, genus (family euphorbiaceae) in Penang Island, Peninsular Malaysia. *Journal of Bioscience*, 19(2): 91-99.
5. Phupattanapong, L. and Wongprasert, T. (1987) Thai medicinal plants. Part 5. Chutima: Bangkok.
6. Orwa, C., Mutua, A., Kindt, R., Jamnadass, R. and Anthony, S. (2009) Agroforestree Database: A tree reference and selection guide version 4.0 from http://www.worldagroforestry.org/sites/treedbs/ treedatabases.asp. [Access online 22nd July 2016].
7. Sutthivaiyakit, S., Unganon,t S., Sutthivaiyaki,t P. and Suksamrarn, A. (2002). Diterpenylated and prenylated flavonoids from *Macaranga denticulata*. *Tetrahedron*, 58: 3619-3622.
8. Kumazawa, S., Murase, M., Momose, N. and Fukumoto, S. (2014). Analysis of antioxidant prenylflavonoids in different parts of *Macaranga tanarius*, the plant origin of Okinawan propolis. *Asian Pacific Journal of Tropical Medicine,* 7(1): 16-20.
9. Lin, J. H., Ishmatsu, M., Tanaka, T., Nonaka, G. and Nishioka, I. (1990). Tannins and related compounds. XCVI. Structures of macaranins and macarinins, new hydrolyzable tannis possessing macaranoyl and tergalloy ester groups from the leaves of *Macaranga sinensis* (BAILL.) Muell.-Arg. *Chemical and. Pharmaceutical Bulletin,* 3: 1844-1851.
10. Beutler, J. A., Shoemaker, R. H., Johnson, T. and Boyd, M. R. (1998). Cytotoxic geranyl stilbenes from *Macaranga schweinfurthii*. *Journal Natural Product,* 61: 1509-1512.

11. Salah, M. A., Bedir, E., Toyang, N. J., Khan, I. A., Harries, M. D. and Wedge, D. E. (2003). Antifungal clerodane diterpenes from *Macaranga monandra* (L) Muell. et Arg. (Euphorbiaceae). *Journal of Agricultural and Food Chemistry,* 51(26): 7607-7610.
12. Shinji, F., Kanki, K., Yukinori, M., Tsuyoshi, T. and Shigeo, N. (1995). Cytocidal and antimicrobial activities of flavonoids. *Natural Medicines*, 49(3): 322-328.
13. Orhan, D. D., Ozcelik, B., Ozgen, S. and Ergun, F. (2010). Antibacterial, antifungal and antiviral activities of some flavonoids. *Microbiological Research*, 165: 496-504.
14. Jianguo, C., Xian, X., Xiling, D., Jianbo, X., Quanxi, W., Andrae-Marobela, K. and Okatch, H. (2013). Flavonoids profiles, antioxidant, acetylcholinesterase inhibition activities of extract from Dryoathyrium boryanum (Willd.) Ching. *Food and Chemical Toxicology*, 55: 121-128.
15. Das, S., Mitra, I., Batuta, S., Alam, M. N., Roy, K. and Begum, N. A. (2014). Design, synthesis and exploring the quantitative structure–activity relationship of some antioxidant flavonoid analogues. *Bioorganic & Medicinal Chemistry Letters,* 24(21): 5050-5054.
16. Ilmiawati, A., Hakim, E. H. and Syah, Y. M. (2015). Prenylated 9,10-dihydrophenanthrenes from *Macaranga javanica*. *Zeitschrift für Naturforschung B*, 70(9): 659-663.
17. Jansen, P. C. M., Westphal, E. and Wulijarni-Soetjipto, N. (1997). PROSEA: Plant resources of south-east asia 11, Auxiliary Plants. LIPI Press: Jakarta.
18. Ahmat, N., Said, I. M., Latip, J., Din, L. B., Syah, Y. M. and Hakim, E. H. (2007). New prenylated dihydrostilbenes from *Croton laevifolius*. *Natural Product Communications*, 2(11): 1137-1140.

Malaysian Journal of Analytical Sciences, Vol 22 No 2 (2018): 264 - 269
DOI: https://doi.org/10.17576/mjas-2018-2202-11

MALAYSIAN JOURNAL OF ANALYTICAL SCIENCES
Published by The Malaysian Analytical Sciences Society
ISSN 1394 - 2506

SUGARS, MINERALS COMPOSITION AND METAL ION CHELATING ACTIVITY OF *Arenga pinnata* SYRUP USING VACUUM EVAPORATION

(Komposisi Gula, Mineral dan Aktiviti Ion Logam Pengkelat daripada Sirap *Arenga pinnata* Mengunakan Proses Vakum Penyejatan)

Nurul Janah Yunos[1]*, Alawi Sulaiman[1], Nor Azma Yusuf[1], Dzil Razman Ghazali[2]

[1]Faculty of Plantation and Agrotechnology,
Universiti Teknologi MARA, 40450 Shah Alam, Selangor Darul Ehsan, Malaysia
[2]Balung Plantation
Wisma Sabah, Jalan Tun Razak, 88817 Kota Kinabalu, Malaysia

**Corresponding author: janahyunos23@gmail.com*

Received: 4 December 2016; Accepted: 1December 2017

Abstract

Palm saps harvested from *Arenga pinnata* tree which typically known as sweet natural beverage were produced into palm sugars using three different production methods of open pan cooking, freeze dry and vacuum evaporation. Sugars and minerals composition such as sucrose, glucose, fructose, magnesium, potassium, sodium and phosphorus were determined. An iron chelating activity was performed to determine the antioxidant activity of different production methods of palm sugars which related to the ability of chelating the transition metal ions. Results showed that all production methods of palm sugars obtained significantly ($p<0.05$) different amounts of sugars and minerals. There were significantly ($p<0.05$) different in ion chelating activity in different production methods of palm sugars. Vacuum evaporated palm syrup exhibited the highest ability in chelating ferrous ion and the vacuum evaporator dominated the highest percentage of chelating ions at 28.20% followed by freeze dryer at 26.31% and open pan at 12.75%, respectively. From the results, slow and controlled temperature by vacuum evaporation could be a promising approach that capable to preserve the ion binding capacity of palm syrup which related in antioxidant activity.

Keywords: antioxidant, *Arenga pinnata*, freeze dry, open pan cooking, vacuum evaporation

Abstrak

Air nira yang dituai daripada pokok *Arenga pinnata* yang dikenali sebagai air manisan semulajadi telah dijadikan sebagai produk gula kabung dengan menggunakan tiga kaedah iaitu secara tradisi menggunakan kayu api diatas kuali terbuka, dan dua teknologi moden iaitu pembekuan kering dan vakum penyejatan. Komposisi gula dan mineral seperti sukrosa, glukosa, fruktosa, magnesium, potassium, sodium dan fosforus telah ditentukan. Aktiviti ion logam pengkelat telah dikaji untuk menentukan aktiviti antioksidan kepada ketiga-tiga pengeluaran gula kabung yang berkaitan dengan keupayaan peralihan ion logam pengkelat. Hasil kajian mendapati ketiga-tiga pengeluaran gula kabung adalah signifikan ($p<0.05$). Gula kabung dari pengeluaran vakum penyejatan menunjukkan hasil paling tinggi iaitu pada 28.20% diikuti oleh pembekuan kering pada 26.31% dan pengeluaran secara tradisi iaitu 12.75%. Oleh yang demikian, hasil menunjukkan pengeluaran gula kabung yang menggunakan vakum penyejatan secara perlahan dan suhu terkawal boleh menjadi pendekatan yang mampu memelihara kapasiti mengikat ion yang berkaitan dengan ketinggian aktiviti antioksidan.

Kata kunci: antioksidan, *Arenga pinnata*, pembekuan kering, kuali terbuka, vakum penyejatan

Introduction

Palm sap or commonly known as *Nira Kabun*g is harvested from *Arenga pinnata* tree which widely grown in tropical region and humid climate. This palm tree belongs to family Arecaceae, which originated from the tropical south Asia and South-east Asia. Some studies showed that *A. pinnata* could reach altitude from 20 meters to 1400 meters above sea level with a diameter trunk of 65 cm approximately [1]. In fact, a single tree of *A. pinnata* could yield up to 6 litres of saps per day. It is widely reported that the environment conditions where *A. pinnata* grows affects sugar, protein, and mineral contents in the tree [2].

In Malaysia, *A. Pinnata* tree is commonly grown in the forest by some local entrepreneurs for economic purposes. Local community usually collect the palm saps by tapping process using bamboo cut collectors before being cooked and turn to palm sugar block. Many studies reported that the production of palm saps from *A. pinnata* tree could contribute to the socioeconomic growth in local areas for extra household income. According to Schoneman [3], the palm sugar is the first palm that used to be the one of the economic purposes in trading process. The community of West Java Indonesia has utilized this tree to produce to produce palm sugar block as a household income. Research study showed that that crucial of palm sugar products is capable four to eight times more productive compared to sugar cane product [4].

Normally, the concentrated palm sugar was produced by traditional cooking method using firewood before being moulded into sugar blocks using bamboo fragments. However, the cooking temperature could be associated with loss of nutrients in the palm sugar. Other study reported that the heating temperature was the most influential factor for determining the palm sugar quality [5]. Moreover, the non enzymatic browning reaction which resulted from reducing sugars and amino acids reaction also contributed to the changes of palm sugar quality. Therefore, the three different production methods of palm sugars were evaluated for their chemical compositions.

The present study discusses the sugars properties (sucrose, glucose and fructose) and mineral properties (magnesium, potassium, sodium and phosphorus) of open pan cook, freeze dried and vacuum evaporated palm sugars. Currently, there is no research has been reported regarding the metal ion chelating activity of *A. pinnata* sugar. Hence this study revealed the effects of different production methods of palm sugars towards chelating ability that relate to the antioxidant activity.

Materials and Methods

Sample preparation

Three different production methods of palm sugars by open pan cooking, freeze drying and vacuum evaporation which were obtained from Balung Plantation, Sabah. Respectively, the palm sugars were formed into concentrated palm sugar block by open pan cooking, powder formed by freeze dryer and syrup formed by vacuum evaporator.

Determination of sugars

High Performance Liquid Chromatography (HPLC) (1200 Series, Agilent Technologies, United States) was used to determine the type of sugars content in palm sugars. Data was obtained at 195 nm by using refractive index detector. The system was maintained in controlled room temperature. Mobile phase of pure water and acetonitrile (50:50) was freshly prepared and sonicated under ultrasonic bath for 30 minutes prior to HPLC analysis. A flow rate of 1.5 ml/min and injection volume of 20 µL was used. Sample analysis was performed using C-18 column.The samples solution was made up with 50 mL using pure water and acetonitrile (50:50) for every 5.0 g of palm sugar samples. All samples must be filtered through a 0.45 µm filter prior to injection. Sugar standards were diluted using 100 mL using pure water and acetonitrile (50:50) for every 3.0 g of D-glucose, 3.8 g of D-fructose and 0.6 g sucrose. The prepared standard solutions were sonicated for 30 minutes in ultrasonic bath to remove all the air bubbles.

Determination of minerals

Calcium, phosphorus, sodium and potassium content were analyzed using inductively coupled plasma mass spectrometry (ICP-MS) (7300 DV, Agilent Technologies, United States). The method was modified as described by Ajai et al. [6]. All the palm sugar samples were weighed about 5 g and dissolved in 10 mL 0.1 M HNO_3. The

samples mixtures were cautiously heated under fume hood. After that, the samples solutions were filtered using Whatman No.1 filter paper. The samples filtrates were diluted using 50 mL of pure water.

Determination of metal ion chelating activity

Metal chelating activity was determined using modified method [7]. Palm sugar samples were diluted using 10 mL of pure water. An amount 500 µL of diluted samples were mixed with 500 µL of 2mM $FeCl_2$ and 0.2 mL of 5 mM ferrozine solution. After 10 minutes, the absorbance reading was measured spectrophotometrically at 562 nm using UV-Vis spectrophotometer (ST-UV8000, Sastec, Germany). The percentage of inhibition of ferrozine–$Fe2^+$ complex formation was expressed by using the equation: by [1-(test sample absorbance/blank sample absorbance)] x 100.

Statistical analysis

Data were analyzed to analysis of variance (ANOVA) using Statistical Package for Social Science (SPSS version 19.0). Results were performed in triplicate and the results were expressed as the mean values and standard deviation. The results of significance differences were determined by Tukey's (HSD) post hoc test ($p<0.05$).

Results and Discussion

Tabulated results were obtained in determining the sugar and mineral compositions in three different production methods of palm sugars. Sucrose, glucose and fructose content of palm sugars are shown in Table 1 and the results showed significance difference ($p<0.05$) in sugars content. The major sugar present in all palm sugars was sucrose. Freeze dry production method showed the highest sucrose content followed by open pan and vacuum evaporator production methods. As shown in Table 1 the freeze dried palm sugar exhibited the highest sugars content of sucrose, glucose and fructose compared to vacuum evaporated palm sugar. Food and Nutrition Research Institute-Department of Science and Technology of Philippines had conducted the study on the sugar composition of palm sugar block (Kaong sugar). The data revealed that the palm sugar had the highest sucrose content at 95.80%, 0.37% of glucose and 0.80% of fructose. This is in contrast to the results obtained for this study for open pan cooking production method. However, these findings may be due to the different techniques used for open pan cooking during the making of palm sugars. Besides, the time storage of palm sugars also could contribute to the various sugars content. With respect to the results obtained, the vacuum evaporation production method which was maintained at low and controlled-temperature showed low inversion of sucrose during the production process. It is interesting to note that as the temperature increases the sucrose content in the palm sugar will break down into glucose and fructose. This present study is similar to other researcher where the palm sugar syrup heated by vacuum evaporator could retain more sucrose content from further inverted compared to palm syrup heated by open pan [5].

Table 1. Types of sugar content of palm sugar samples

Production Methods	Sucrose (%)	Glucose (%)	Fructose (%)
Open pan	60.23 ± 0.26^a	3.83 ± 0.05^a	4.67 ± 0.05^a
Freeze dry	61.20 ± 0.17^b	6.53 ± 0.05^b	6.77 ± 0.05^b
Vacuum evaporation	50.37 ± 0.13^c	3.50 ± 0.09^c	3.27 ± 0.05^c

Data presented as mean ± SD of triplicate results. The different superscript letters represented the significant different ($p<0.05$)

Table 2 represents the results of minerals composition in three different production methods of palm sugars. The mineral elements have been evaluated using inductively coupled plasma spectrometry (ICP-MS). Generally, ICP-MS application is a powerful tool in detection of metals and non-metals especially in solution. This tool uses Argon gas to move the sample vapour into a chamber under high vacuum condition where both of the samples and gas are heated such that elements will give off a characteristic wavelength of light [8].

Table 2. Types of mineral content of palm sugar sample

Production Methods	Magnesium (mg/kg)	Potassium (mg/kg)	Calcium (mg/kg)	Phosphorus (mg/kg)
Open pan	289.22 ± 0.88[a]	6412.8 ± 56.41[a]	77.76 ± 0.60[a]	1536.60 ± 15.62[a]
Freeze dry	264.02 ± 0.64[b]	5569.70 ±141.39[b]	68.83 ± 0.56[b]	1381.30 ± 21.90[b]
Vacuum evaporator	207.82 ± 0.67[c]	4315.30 ± 104.54[c]	108.65± 0.36[c]	8645.20 ± 15.72[c]

Data presented as mean ± SD of triplicate results. The different superscript letters represented the significant different ($p<0.05$)

The above data shows that there were significance differences ($p<0.05$) in magnesium, potassium, calcium and phosphorus content in all palm sugar samples. The vacuum evaporated palm sugar exhibited the lowest magnesium and potassium content. However, the vacuum evaporated palm sugar showed the highest content in phosphorus content compared to other production methods. Previous study of maple syrup showed the most of common minerals found were potassium and calcium but low amount in magnesium and phosphorus [9]. All the mentioned minerals definitely play the vital roles in regulating the physiological and biochemical in human body. Other reseacher reported that the influence of other factors such as geographical environment, soil chemistry, viticulture practices and processing methods need to be understood [10]. Other study revealed that the seasons and altitudes had contributed a significant effects on magnesium, potassium and calcium content in *A. pinnata* sap from North Sulawesi Province, Indonesia [2]. Comparing with the study obtained by this author, there were substantial increases in the concentration of minerals elements in the palm sugars after being applied to different production methods. During the process, the palm saps were concentrated gradually into browning palm sugar due to increase in sugar content as well as increased in minerals and others chemicals composition in the palm sugar that reflects from the heating processes.

Other study showed that, the distinctive mineral composition of the date palm heart could be because of the bioaccumulation capabilities in assimilating and accumulating minerals from the soil tree [11,12]. Also, the various results acquired between the three production methods of palm sugars might be attributed from the environmental factors such as pedoclimatic and atmospheric conditions. The varied in extraction technique could also affluent the results obtained.

Figure 1 represents the chelating Fe^{2+} ions ability in three different production methods of palm sugars. Undoubtedly, the results obtained showed that all production methods of palm sugars were significantly ($p<0.05$) different and the vacuum evaporator dominated the highest percentage of chelating ions at 28.20% followed by freeze dryer at 26.31% and open pan at 12.75%, respectively. Similar results were found in the palm dates syrup at 250 µg acquired about 28.70% in chelating Fe^{2+} ions [13] . In recent study, the metal chelating agents function as inactivate metal ions (Fe^{2+}) besides can reduce the redox potential where the agents are classified as effective secondary antioxidants [14].

In general, antioxidants can be described as reductants which reduced the oxidation reaction by inactivated the oxidant [15]. Complementary to this, an iron commonly act as an initiator of unwanted oxidative reactions in lipids, proteins and other cellular components which can be simplified as free radicals generator [13]. According to Gulcin et al., Fe^{2+} ions are able to create the formation and propagation of radical reactions and non-reactive radicals by transferring the single electrons [16]. Therefore, the results obtained declared that the presence of active compounds in the palm sugars could inhibit the metal ions (Fe^{2+}). In regards to this, the results signify the vacuum evaporation production method could preserve the active compounds that represent the capability to chelate the Fe^{2+} ions compared to the other production methods. This is might be related with slow and controlled-temperature of heating method that slows down the rapid loss of active compounds in the palm sugars during the processes. It was also confirmed that the results obtained from ion chelating activity of *A. pinnata* palm sugar was the first being reported.

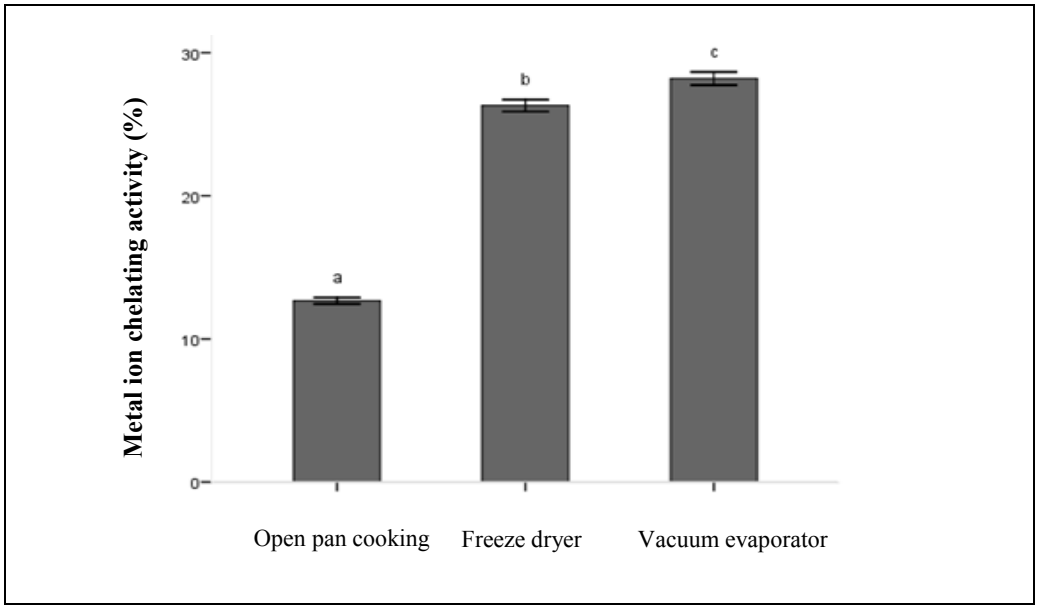


Figure 1. Metal ion chelating activity of different production methods of palm sugar. Data presented as mean ± SD of triplicate results. The different letters represented the significant different ($p<0.05$)

Conclusion

The present study showed that the different production methods of palm sugars demonstrated the results variability in sugars and minerals content. Also, this study suggested that the ion chelating activity of the palm sugar was largely influenced by the heating method. The slow and controlled temperature of vacuum evaporation could retain the higher antioxidant activity in their palm syrups. It is expected that the findings of this study will be useful in determining the optimum heating temperature in palm syrup of vacuum evaporation production method for optimum antioxidant preservation.

Acknowledgement

The authors would like to thank the Universiti Teknologi MARA (UiTM) for the grant of Research Entity Initiative (REI): 600-RMI/DANA 513/REI (8/2013), Fundamental Research Grant Scheme (FRGS): 600-RMI/FRGS 5/3(84/2015) and Postgraduate Supporting Fellowship (ZAMALAH): 600-RMI/DANA 5/3/PSF (10/2015). Also, we would like to thank the Balung Plantation, Sabah for providing the palm sugars samples.

References

1. Safari, A. (1995). Making techniques palm sugar. http://docsdrive.com/pdfs/ansinet/pjn/2015/531-534.pdf. [Access online 13 February 2016].
2. Lantemona, H., Abadi, A. L., Rachmansyah, A. and Pontoh, J. (2013). Impact of altitude and seasons to volume, brix content, and chemical composition of aren sap in north Sulawesi. *IOSR Journal of Environmental Science, Toxicology and Food Technology*, 4: 42-48.
3. Schoneman, J. P. (2010). Overview of uses of palms with an emphasis on old world and Australasian medicinal uses. Doctoral dissertation, University of Texas, USA.
4. Ismail, L. (2012). Acoustic and durability performances of *Arenga Pinnata* panel. Doctoral dissertation, Universiti Tun Hussein Onn Malaysia, Malaysia.
5. Naknean, P., Meenune, M. and Roudaut, G. (2009). Changes in physical and chemical properties during the production of palm sugar syrup by open pan and vacuum evaporator. *Asian Journal of Food and Agro-industry*, 2(4): 448-456.
6. Ajai, A. I., Ochigbo, S. S., Abdullahi, Z. and Anigboro, P. I. (2014). Determination of trace metals and essential minerals in selected fruit juices in Minna, Nigeria. *International Journal of Food Science*, 2014: 1-5.

7. Decker, E. A., and Welch, B. (1990). Role of ferritin as a lipid oxidation catalyst in muscle food. *Journal of Agricultural and Food Chemistry*, 38(3): 674-677.
8. University of Massachusetts Amherst (2011). Chemical analysis of mineral analysis. http://www.geo.umass.edu/courses/geo311/min%20chem%20anal ysis%20lecture.pdf. [Access online 23 February 2016].
9. Heiligmann, R. B., Koelling, M. R. and Perkins, T. D. (2006). North American maple syrup producers manual. *Ohio State University Extension Bulletin,* 856: 298-299.
10. Rupasinghe, H. P. V. and Clegg, S. (2007). Total antioxidant capacity, total phenolic content, mineral elements, and histamine concentrations in wines of different fruit sources. *Journal of Food Composition and Analysis*, 20(2): 133–137.
11. Damodaran, D., Shatty, K.V. and Mohan, B.R. (2013). Effect of Chelaters on Bioaccumulation of Cd (II), Cu(II), Cr(VI), Ph(II) and Zn(II) in *Galerina vittiformis* from Soil. *International Biodeterioration and Biodegradation*, 85: 182-188.
12. Kumaravel, S. and Alagusundaram, K. (2014). Determination of mineral content in Indian spices by ICP-OES. *Oriental Journal of Chemistry*, 30(2): 631-636.
13. Al-Mamary, M., Al-Habori, M. and Al-Zubairi, A. S. (2014). The *in vitro* antioxidant activity of different types of palm dates (Phoenix dactylifera) syrups. *Arabian Journal of Chemistry*, 7(6): 964–971.
14. Kchaou, W., Abbès, F., Blecker, C., Attia, H. and Besbes, S. (2013). Effects of extraction solvents on phenolic contents and antioxidant activities of Tunisian date varieties (Phoenix dactylifera L.). *Industrial Crops and Products*, 45: 262-269.
15. Phisut, N. and Jiraporn, B. (2013). Characteristics and antioxidant activity of Maillard reaction products derived from chitosan-sugar solution. *International Food Research Journal*, 20(3): 1077-1085.
16. Gulcin, I., Elmastas, M. and Aboul-Enein, H. Y. (2007). Determination of antioxidant and radical scavenging activity of Basil (*Ocimum basilicum* L. Family Lamiaceae) assayed by different methodologies. *Phytotherapy Research*, 21(4): 354-361.

Malaysian Journal of Analytical Sciences, Vol 22 No 2 (2018): 270 - 278
DOI: https://doi.org/10.17576/mjas-2018-2202-12

MALAYSIAN JOURNAL OF ANALYTICAL SCIENCES
Published by The Malaysian Analytical Sciences Society
ISSN 1394 - 2506

PHOTOCATALYTIC DEGRADATION OF METHYLENE BLUE WITH SILVER DOPED ZnO NANOPARTICLES GROWN ON MICROSCOPIC SAND PARTICLES

(Degradasi Metilena Biru Menggunakan Nanopartikel ZnO Sebagai Fotomangkin yang Didopkan dengan Perak Tumbuh di atas Pasir Bersaiz Mikro)

Nur Azmina Mohamed Safian[1]*, Roslan Md Nor[1], Hartini Ahmad Rafaie[2], Siti Fairus Abdul Sani[1], Zurina Osman[1]

[1]*Department of Physics, Faculty of Sciences,*
University of Malaya, 50603 Kuala Lumpur, Malaysia
[2]*Unit of Physics, School of Science,*
Universiti Teknologi MARA Pahang, Jengka, 26400 Bandar Tun Abdul Razak, Jengka Pahang, Malaysia

**Corresponding author: nurazminasafian@siswa.um.edu.my*

Received: 4 December 2016; Accepted: 1 December 2017

Abstract

Pure and Ag doped ZnO nanoparticles were synthesized on microscopic sand particles by sol-gel method. Silver nitrate was used as the doping precursor, Ag doping levels of 1.3 to 7.7 of Ag/Zn ratios were obtained based on energy dispersive X-ray spectroscopy analysis. X-ray diffraction results show that a ZnO (101) peak of Ag doped samples are shifted towards lower degree which around 0.17º compared to pure ZnO NPs, indicating the existence of doping in the Ag doped samples. The pure and Ag doped ZnO samples were used as photocatalysts in the degradation of methylene blue under UV irradiation. Photodegradation efficiency based on the pseudo-first kinetics model gave measured values of the photodegradation rate, k of 8.9, 11.8, 12.7, 14.8 and 17.4 x 10^{-3} min^{-1} for pure, 1.3, 1.6, 1.7 and 2.4 of Ag/Zn ratios, respectively. At higher doping levels of 3.3 and 7.7 of Ag/Zn ratios, the k values receded to 12.7 and 12.0 x 10^{-3} min^{-1}, respectively. The increasing trend on k values can be due to the doping defect levels which trapped the recombining electrons, thus lengthening the lifetime of the electron hole pairs.

Keywords: photocatalysis, Ag doped ZnO, nanoparticles

Abstrak

Nanopartikel ZnO tulen dan nanopartikel ZnO yang didopkan dengan perak (Ag) telah disintesiskan di atas pasir bersaiz mikro menggunakan kaedah sol-gel. Argentum nitrat digunakan sebagai sumber Ag, dapatan tahap pendopan adalah 1.3 sehingga 7.7 nisbah Ag kepada Zn (Ag/Zn). Berdasarkan keputusan spektroskopi sinar-X, terdapat peralihan kedudukan puncak ZnO (101) sebanyak 0.17º jika dibandingkan antara ZnO tulen dan sampel ZnO yang didopkan dengan Ag. Ini menunjukkan berlaku pendopan di dalam sampel nanopartikel ZnO yang didopkan dengan Ag. Semua sampel diuji sebagai fotomangkin di dalam degradasi metilena biru di bawah sinar UV. Kecekapan degradasi dikira menggunakan model kinetik pseudo-pertama dan memberikan nilai kadar degradasi, k iaitu masing-masing 8.9, 11.8, 12.7, 14.8 dan 17.4 x 10^{-3} min^{-1} untuk sampel ZnO tulen, 1.3, 1.6, 1.7 dan 2.4 untuk nisbah Ag/Zn. Pada tahap pendopan yang tinggi iaitu 3.3 dan 7.7 Ag/Zn, nilai k berkurangan kepada 12.7 dan 12.0 x 10^{-3} min^{-1}. Peningkatan nilai k adalah disebabkan oleh kesan pendopan di mana elektron terperangkap untuk pergabungan semula dan memangjangkan jangka hayat pasangan elektron dan lubang.

Kata kunci: fotomangkin, perak didopkan ZnO, nanopartikel

Introduction

Since 1972, the capability of ZnO in the degradation of wastewater has been studied [1]. Due to its remarkable features which has wide band gap (3.37 eV) at room temperature and high exciton binding energy of approximately 60 meV has made ZnO as a perfect candidate in photocatalyst application. To achieve high photocatalytic degradation efficiency of wastewater, ZnO photocatalyst must offer large specific surface area and a high efficiency for segregation photogenerated electron and holes. The most efficient way to accelerate the charge carrier separation by dope with noble metals. Silver (Ag) has been reported as the best element to dope with ZnO due to its high solubility [2] and can act as a sink to collect photogenerated electrons from the conduction band of ZnO [3]. Furthermore, Ag 4d and oxygen 2p states were overlapped to form impurity band. This lead to the Fermi level shifted toward valence band and induced properties in ZnO [4].

Although there have ***many*** reports on the properties and photocatalysis efficiency of Ag doped ZnO, there is still lack of understanding in details about photodegradation mechanism using Ag doped ZnO. In this work, the differences of the photocatalytic degradation between ZnO and Ag doped ZnO on microscopic sand has been studied. Also, the effect of Ag ions on the morphology, defect and photocatalytic efficiency of all samples were investigated in detailed.

Materials and Methods

Synthesis of Ag doped ZnO Nanoparticles on microscopic sand

ZnO NPs growth on microscopic sand by simple seeded solution process using zinc acetate, $Zn(O_2CCH_3)_2$ which was prepared in absolute ethanol at 0.0005 mol concentration. The sand were soaked for 5 minutes and then dry at 300 ^oC for 10 minutes. The process were repeated for three times before calcination process. Zinc nitrate hexahydrate ($Zn(NO_3)_2 \cdot 6H_2O$) and hexamethylenetetramine (HMTA) were initially combined at the molar ratio of 1:1 in deionized water for growth solution. Then, silver nitrate hexahydrate ($AgNO_3$) were added in mixture solution at 1.0 to 3.5 mol % with 0.5 mol % increment. 5g of the seeded sand were added in the doping solution and stirred continuously at 100 ^oC for 6 hours. After completing the growth process, the Ag doped ZnO NPs grown on sand were wash and rinsed several times thoroughly in DI water and calcined at 300 ^oC for 2 hours.

Characterization of Ag doped ZnO Nanoparticles

The as-prepared Ag doped ZnO NPs grown on sand were examined by several characterization techniques. The elemental of as-prepared nanomaterials were characterized by energy dispersive spectroscopy (EDX - JSM 7600-F). The morphologies were examined by field emission scanning electron microscopy (FESEM – JSM 7600-F). The crystallinity and optical properties of ZnO NPs samples were studied by X-ray diffractometer (XRD - EMPYREAN, PANalytical) and photoluminescence (PL-In-Via Raman Microscope) spectroscopy, respectively.

Photocatalytic degradation of methylene blue using Ag doped ZnO nanoparticles

The photocatalytic performances of the samples were evaluated by the decomposition of 0.5 mg/ 100 ml methylene blue solution under UV light at 254 nm wavelength. An amount 1g of samples were added in the MB solution and placed in the dark mood for 30 minutes before switching the UV lamp (6 Watt, UVGL-58). Afterwards, absorption spectra of the MB solutions were taken and analyzed by ultraviolet-visible (UV-Vis - EVOLUTION 201, Thermo Scientific) spectroscopy.

Results and Discussion

The present of Ag element in the ZnO samples grown on microscopic sand were evidenced by EDX spectra as shown in Figure 1. The amount of Ag doped ZnO were calculated by atomic percent (at. %) which leads to 1.3, 1.6, 1.7, 2.4, 3.3 and 7.7 of Ag/Zn ratios for 1.0, 1.5, 2.0, 2.5, 3.0 and 3.5 mol %, respectively as tabulated in Table 1. As the amount of Ag doped increases, a strong peak of $Ag_{L\alpha}$ and $Ag_{L\beta}$ appeared in ZnO samples at 2.97 and 2.98 KeV especially for ZnO 3.3 and 7.7 of Ag/Zn ratio samples.

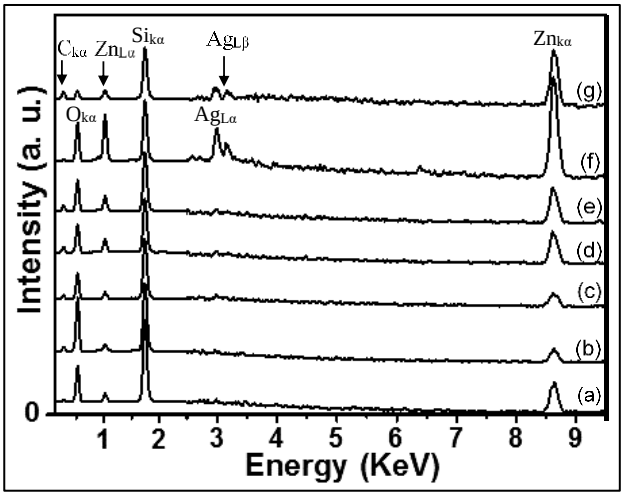


Figure 1. EDX spectra of (a) pure ZnO NPs and Ag doped ZnO NPs grown on microscopic sand at (b) 1.0, (c) 1.5, (d) 2.0, (e) 2.5, (f) 3.0 and (g) 3.5 mol% of $AgNO_3$

Table 1. The summary of elements composition of pure and Ag doped ZnO NPs grown on microscopic sand based on EDX analysis

Samples		**At. %**				**[Ag]/[Zn] x 100**
		O	Si	Zn	Ag	
(a)	pure ZnO NPs	36.39	43.54	7.13	-	0
(b)	1.0 mol% $AgNO_3$	59.54	26.90	1.55	0.02	1.3
(c)	1.5 mol% $AgNO_3$	45.22	36.65	3.72	0.06	1.6
(d)	2.0 mol% $AgNO_3$	54.53	24.85	7.05	0.12	1.7
(e)	2.5 mol% $AgNO_3$	48.48	28.03	2.09	0.05	2.4
(f)	3.0 mol% $AgNO_3$	53.92	21.68	11.84	0.39	3.3
(g)	3.5 mol % $AgNO_3$	22.90	18.93	2.60	0.20	7.7

The images of surface morphology, particles sizes and shape of the ZnO and Ag doped ZnO NPs grown on sand were obtained by FESEM as shown in Figure 2. High density of the ZnO and Ag doped ZnO NPs were observed throughout the sand surface with the sizes of particles in the range of tens to hundreds of nanometers. From the observation, most of the particles in the ZnO and Ag doped ZnO NPs samples were exhibited spindles-like shape which has wide in the middle and tapers at both ends. The particles sizes were found to be mixed between small and large particles in the 2.4 of Ag/Zn ratio sample as shown in Figure 2(e). These small particles might increase the surface area of Ag doped ZnO samples which will enhance its light absorption and improve its photocatalytic activity. The images also show that the particles sizes of Ag doped ZnO seem like become bigger at high Ag content. The changes in particles sizes was believed due to the aggregation of Ag and Zn particle into bigger cluster. This can cause decreased light utilization rate and led to low photocatalytic activity. The biggest particles diameters were measured in the Ag doped ZnO at 7.7 of Ag/Zn ratio which around 223 to 225 nm.

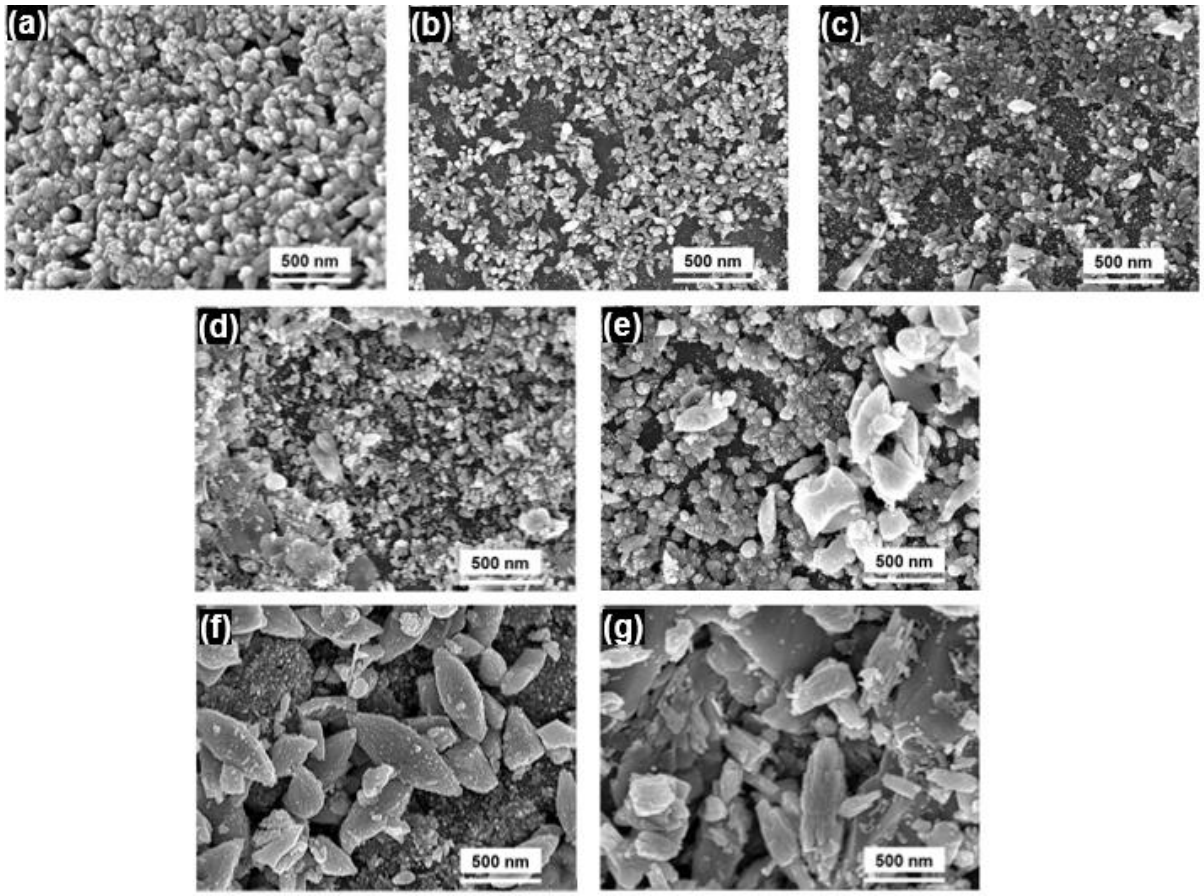


Figure 2. FESEM images of as-synthesized (a) pure ZnO NPs, (b) 1.3, (c) 1.6, (d) 1.7, (e) 2.4, (f) 3.3 and (g) 7.7 of Ag/Zn ratios

The typical XRD patterns of pure ZnO nanoparticles and Ag doped ZnO grown on sand are illustrated in Figure 3(a). Clearly, all samples showed common ZnO peaks at 31.8º, 34.4º, 36.3º, 47.6º, 56.7º, 62.9º, 66.4º and 69.2º. The peaks position can be indexed to the wurtzite crystal ZnO structure (JCPDS File No. 01-79-2205) and correspond to (100), (002), (101), (102), (110), (103), (200) and (201), respectively. The others peaks at 39.7º, 40.4º, 42.6º, 45.9º, 50.4º, 55.1º and 60.1º can be indexed to the (012), (111), (200), (201), (134), (022) and (211) reflection planes of quartz based on the JCPDS file no. 46-1045. Figure 3(b) shows an enlarged view of XRD patterns of ZnO and Ag doped ZnO grown on microscopic sand. Noting that the peak position of (101) reflection peak had shifted toward lower values as the Ag dopant increases. The shift might be due to the partial substitution of Ag^{+} in the ZnO lattice and causes the increases of lattice constant a and c [5, 6]. This occurred probably related to the differentiation of ionic radii between Ag^{+} and Zn^{2+} ions which 1.22 Å and 0.74 Å, respectively.

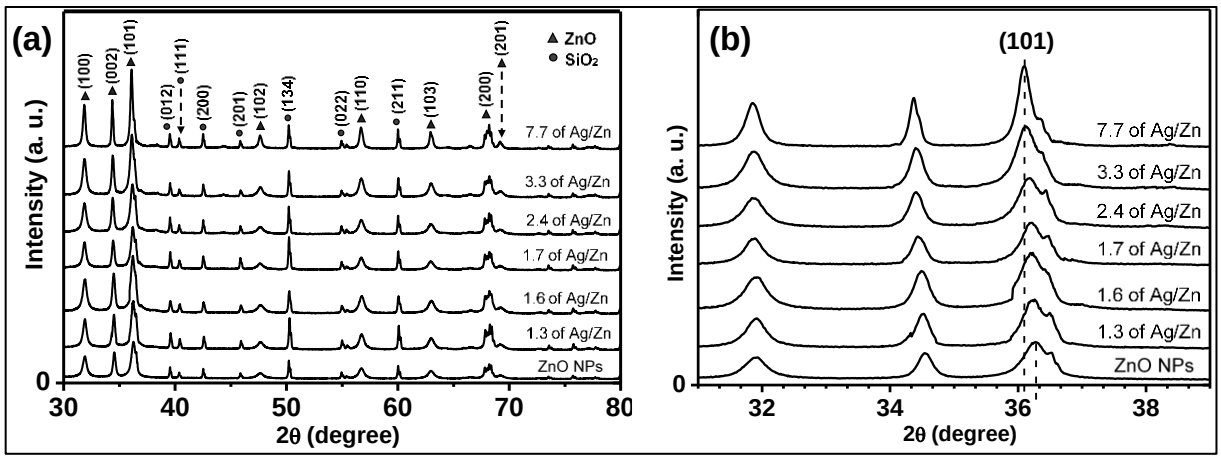


Figure 3. (a) Full range of XRD patterns and (b) shift detail of ZnO (101) peak of ZnO and Ag doped ZnO grown on sand

Figure 4 shows the photoluminescence spectra of pure and Ag doped ZnO sample in the range of 200 to 900 nm. There are two peaks showed in PL spectra which the obvious and broad peak was appeared at 500 to 800 nm and small peak was appeared at round 350 to 420 nm as shown in inset graph in Figure 4. The small peaks below 420 nm were indicated as near-band-edge (NBE) emission which associated with exciton emission which obtained in ZnO and 2.4 of Ag/Zn ratio sample. The NBE emission usually caused by band structural deformation resulting from lattice deformation [7]. This peak which are attributed to the reduction of oxygen interstitials at ZnO surface [8]. By reducing the defect of oxygen interstitials, it might enhanced the photocatalytic activity of ZnO as photocatalyst. The center of these peaks position were obtained at 394 nm for ZnO NPs and 404 nm for 2.4 of Ag/Zn ratio sample.

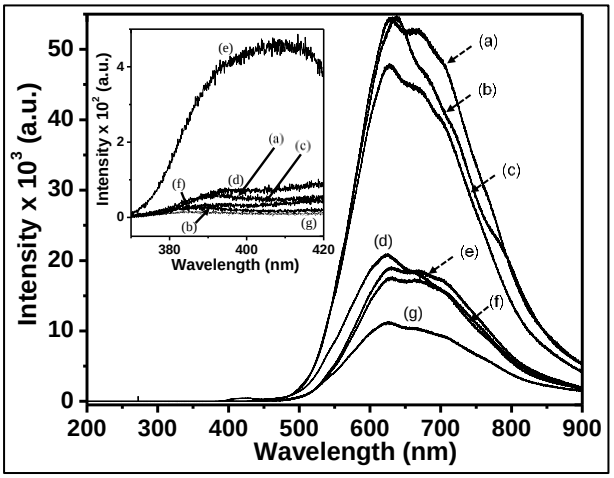


Figure 4. Full range PL spectra from 300 to 900 nm. The inset graph shows enlargement PL spectra at range 370 to 490 nm of (a) pure ZnO NPs, (b) 1.3, (c) 1.6, (d) 1.7, (e) 2.4, (f) 3.3 and (g) 7.7 of Ag/Zn ratios

The broad peak at range 500 to 800 nm in the PL spectra was called as deep level emission. The deep level emission is usually related to the structural defect and impurities of samples [7]. Figure 5 (a) to (g) show the deep level emission for pure ZnO NPs, 1.3, 1.6, 1.7, 2.4, 3.3 and 7.7 of Ag/Zn ratio samples, respectively. The fitting of broad spectrum was done using Gaussian distribution which shows four major peaks around 553 to 567 nm, 608 to 614 nm, 653 to 684 and 713 to 780 nm. The peak around 553 to 567 nm was believed attributed to the transition of zinc

interstitial to zinc vacancies. While two peaks at range 608-614nm and 653-674 nm were known as orange-yellow and orange-red emission respectively, obtained due to the structural defect and single ionized vacancy [9, 10] as well as oxygen interstitial [11]. The single negatively charged interstitial oxygen ion inside the lattice occurs due to the loss of oxygen ions within the crystal lattice [12]. The last peak around 713 to 780 nm was appeared which corresponding to the oxygen vacancies and zinc interstitials [13].

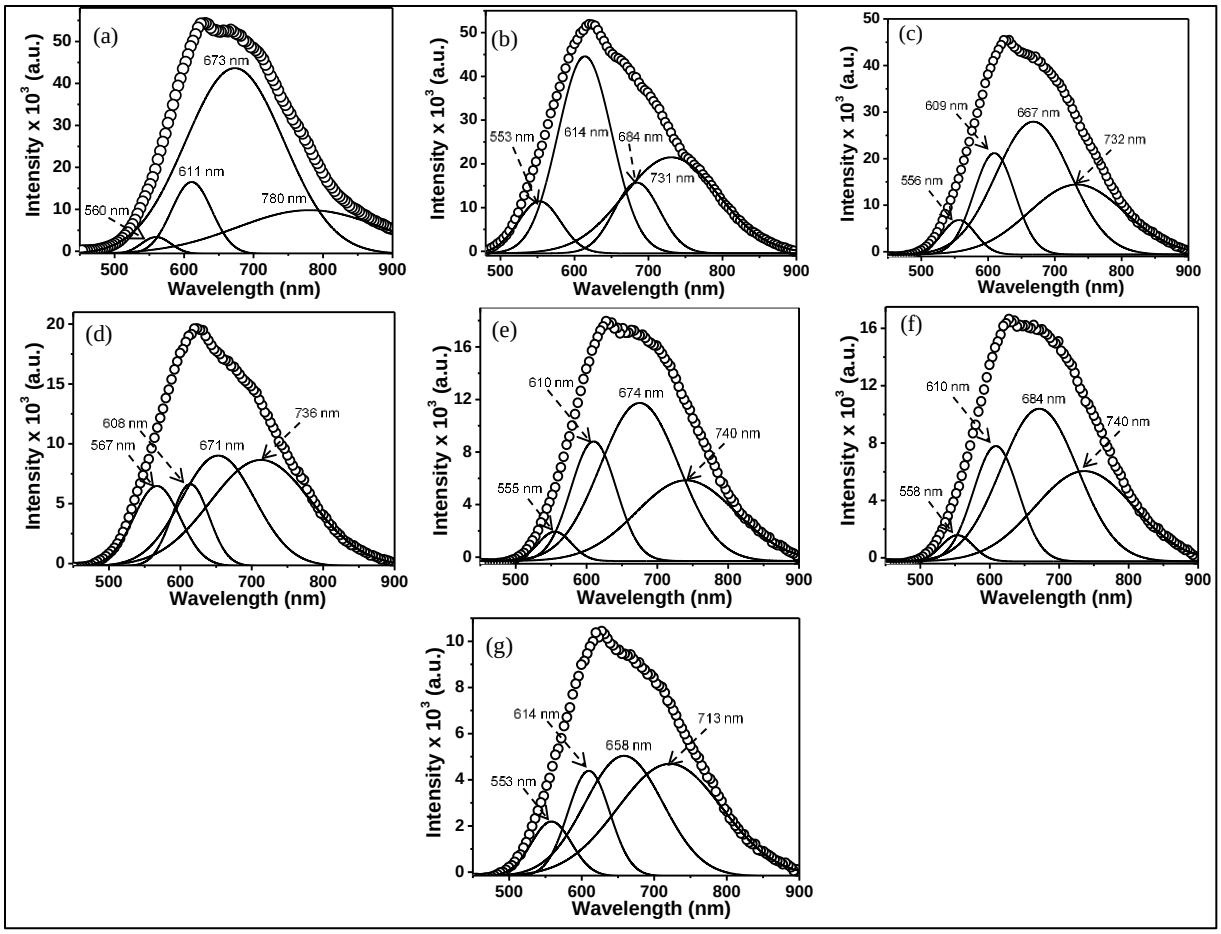


Figure 5. Gaussian fitted PL spectrum of (a) pure ZnO NPs, (b) 1.3 (c) 1.6, (d) 1.7, (e) 2.4, (f) 3.3 and (g) 7.7 of Ag/Zn ratios

The absorption spectra of photodegradation 100 ml MB solution using (a) pure ZnO and Ag doped ZnO at (b) 1.3, (c) 1.6, (d) 1.7, (e) 2.4, (f) 3.3 and (g) 7.7 of Ag/Zn ratios under UV light irradiation for 150 mins are shown in Figure 6. The UV-vis spectra was seen to be similar for all samples which is the tremendous peak of MB dye was appeared at 664 nm. The intensity of peak at 664 nm were gradually decreased with each 15 minutes increment irradiation time. The curve of absorption for 2.4 of Ag/Zn ratio of Ag doped ZnO photocatalyst at 150 minutes irradiation time was shows nearly horizontal meaning the MB solution was almost completely degrade.

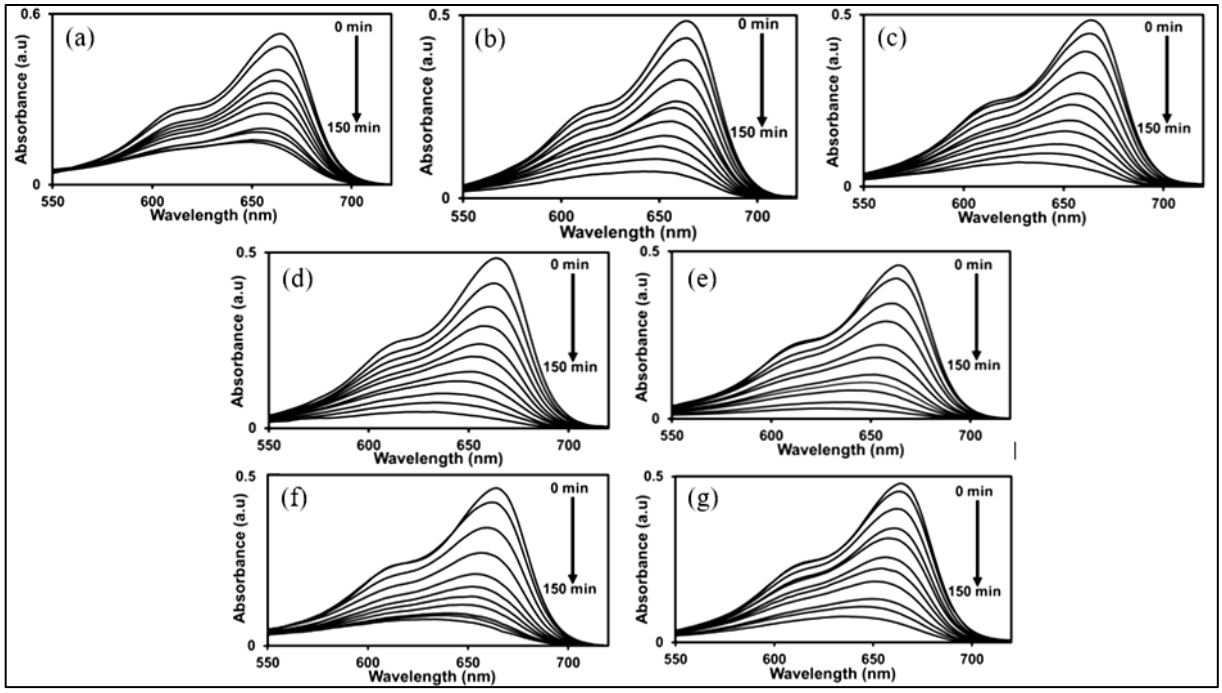


Figure 6. UV-vis absorption spectra of photodegradation 100 ml of 5 mg/l MB solution under UV lamp irradiation using: (a) pure ZnO NPs, (b) 1.3 (c) 1.6, (d) 1.7, (e) 2.4, (f) 3.3 and (g) 7.7 of Ag/Zn ratios as photocatalysts

Figure 7(a) shows the photodegradation efficiency (%) for 150 minutes irradiation time for all samples. The highest photodegradation efficiency was calculated at 2.4 of Ag/Zn ratio sample which was 93.3%. Then followed by 1.7, 1.6, 1.3, 7.7 and 3.3 of Ag/Zn ratio samples which were 90.4%, 85.3%. 84.8%, 83.6% and 83.1%, respectively. The lowest photodegradation efficiency was obtained from pure ZnO sample which around 71.7%. Based on results, it clearly demonstrated that ZnO doped with Ag degrades dye more efficiently than pure ZnO. It is evident that doping of ZnO with transition metals like Ag enhances photocatalytic activities of ZnO. However, further increasing the Ag content in the ZnO samples show decreases of photocatalytic activity as obtained at 3.3 and 7.7 of Ag/Zn ratio samples. It was believed due to the existence of bulk defects which the only ones have bad effects on the photocatalytic activity [14]. The agglomeration of small particles into bigger clusters has formed impurities or bulk defect as confirmed by FESEM analysis. Consequently, decreased the surface area of photocatalyst and decelerates the oxidation and reduction process of MB solution.

The photodegradation rate constant, k of pure ZnO and Ag doped ZnO NPs samples were obtained by plotting ln (C/C_o) against irradiation time as shown in Figure 7(b). The linear plots revealed that the photodegradation of MB has follow pseudo-first order reaction kinetics. The lowest value of k was calculated at pure ZnO NPs sample which 8.9 x 10^{-3} min^{-1} then as dopant increase from 1.3 to 2.4 of Ag/Zn ratio, the value of k has been increased from 11.8 to 17.4 x 10^{-3} min^{-1} as shown in Figure 7(c). The value of k then decreases as increase the Ag content in ZnO sample which around 12.7 to 12.0 x 10^{-3} min^{-1} at 3.3 and 7.7 of Ag/Zn ratio sample, respectively. At the optimum Ag content which was 2.4 of Ag/Zn ratio, the Ag particles that deposited with the ZnO can act as electron-hole separation center. The electron might be transfer from the ZnO conduction band to metallic silver particles at interface. In contrast, high Ag dopant is detrimental to the photodegradation efficiency which the Ag particles can act as electron hole recombination center, thereby decreasing the photocatalytic activity of ZnO.

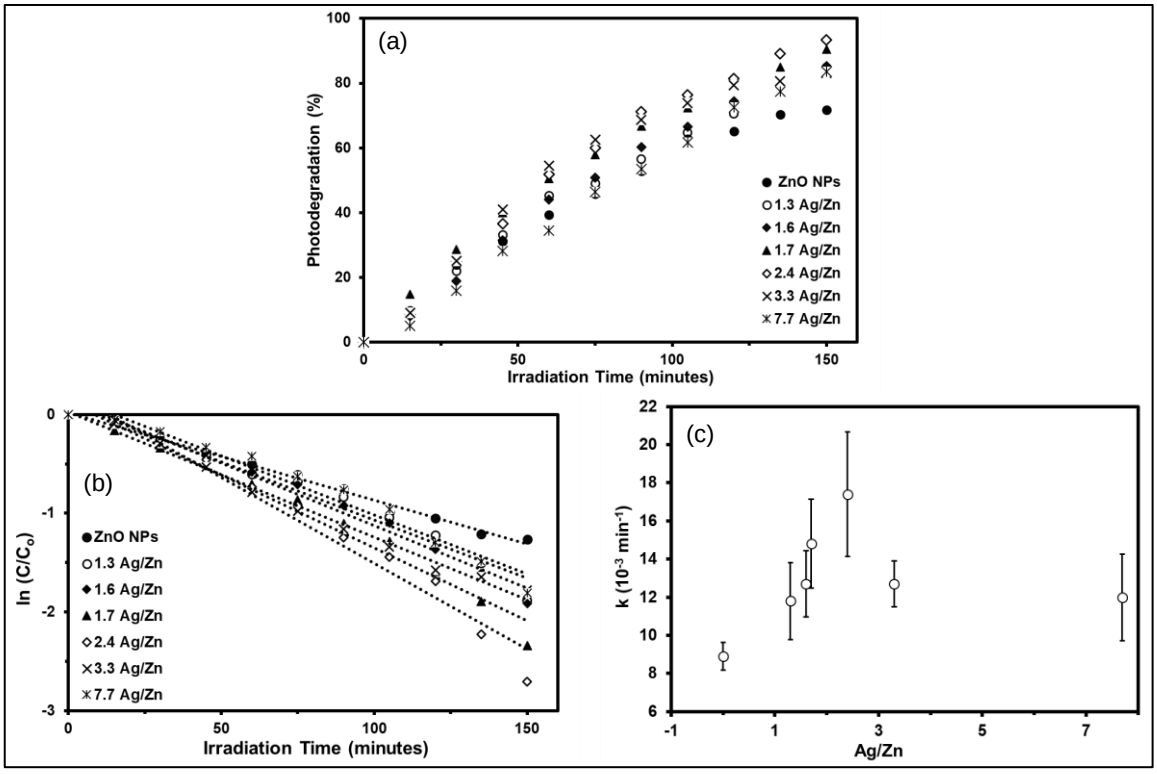


Figure 7. (a) The percentage of photodegradation MB solution for 150 minutes. (b) Linear plots of ln (C/C_o) for the photodegradation of MB in the presence of sand-ZnO and Ag doped ZnO samples and (c) the changes of k values as a function of Ag content.

Conclusion

Ag doped ZnO with varied Ag content from 1.3 to 7.7 of Ag/Zn ratios has been successfully synthesized on the microscopic sand. The EDX has shown the existence of Ag element in the samples and the shifted ZnO [101] peak of XRD has proven that the Ag particles has been doped in the ZnO samples. The FESEM images show that the diameters and structures of ZnO were slightly change to bigger sizes as increases of Ag dopant. The defects introduce additional states in the band gap of ZnO which act as electron trapping centers and contributed in the prolonging a lifetime of charge carriers. The photocatalytic activity for Ag doped ZnO at 2.4 of Ag/Zn ratio has increase was almost twice compared to the pure ZnO which from 8.9 to 17.4 x 10^{-3} min^{-1}. Therefore, the Ag doped ZnO samples grown on sand had shown very interesting characteristics and promising as good photocatalytic agent as well as has good potential for application on the water purification especially in industrial sector.

Acknowledgement

The authors are grateful to the Institute of Research Management and Monitoring, University of Malaya for providing a postgraduate research grant (Project Code: PG110-2015A) and Department of Physics, University of Malaya for financial and facilities support of this work.

References

1. Tanaka, K. and Blyholder, G. (1972). Photocatalytic reactions on zinc oxide. III. Hydrogenation of ethylene. *The Journal of Physical Chemistry*, 76(10): 1394-1397.
2. Yan, Y., Al-Jassim, M. M. and Wei, S. H. (2006). Doping of ZnO by Group-IB elements. *Applied physics letters*, 89(18): 181912.
3. Ren, C., Yang, B., Wu, M., Xu, J., Fu, Z., Guo, T., Zhao, Y. and Zhu, C. (2010). Synthesis of Ag/ZnO nanorods array with enhanced photocatalytic performance. *Journal of Hazardous materials*, 182(1): 123-129.

4. Hosseini, S. M., Sarsari, I. A., Kameli, P. and Salamati, H. (2015). Effect of Ag doping on structural, optical, and photocatalytic properties of ZnO nanoparticles. *Journal of Alloys and Compounds*, 640: 408-415.
5. Karunakaran, C., Rajeswari, V. and Gomathisankar, P. (2011). Combustion synthesis of ZnO and Ag-doped ZnO and their bactericidal and photocatalytic activities. *Superlattices and Microstructures*, 50(3): 234-241.
6. Amornpitoksuk, P., Suwanboon, S., Sangkanu, S., Sukhoom, A., Muensit, N. and Baltrusaitis, J. (2012). Synthesis, characterization, photocatalytic and antibacterial activities of Ag-doped ZnO powders modified with a diblock copolymer. *Powder Technology*, 219: 158-164.
7. Tamargo, M. C. (2002). II-VI semiconductor materials and their applications (Vol. 12). CRC Press.
8. Sun, W. C., Yeh, Y. C., Ko, C. T., He, J. H. and Chen, M. J. (2011). Improved characteristics of near-band-edge and deep-level emissions from ZnO nanorod arrays by atomic-layer-deposited Al_2O_3 and ZnO shell layers. *Nanoscale Research Letters*, 6(1): 556.
9. Vanheusden, K., Warren, W. L., Seager, C. H., Tallant, D. R., Voigt, J. A. and Gnade, B. E. (1996). Mechanisms behind green photoluminescence in ZnO phosphor powders. *Journal of Applied Physics*, 79 (10): 7983-7990.
10. Wu, J. J. and Liu, S. C. (2002). Low-temperature growth of well-aligned ZnO nanorods by chemical vapor deposition. *Advanced Materials*, 14(3): 215-218.
11. Liu, M., Kitai, A. H. and Mascher, P. (1992). Point defects and luminescence centres in zinc oxide and zinc oxide doped with manganese. *Journal of Luminescence*, 54(1): 35-42.
12. Wu, X. L., Siu, G. G., Fu, C. L. and Ong, H. C. (2001). Photoluminescence and cathodoluminescence studies of stoichiometric and oxygen-deficient ZnO films. *Applied Physics Letters*, 78(16): 2285-2287.
13. Djurišić, A. B., Leung, Y. H., Tam, K. H., Hsu, Y. F., Ding, L., Ge, W. K., Zhong, Y. C., Wong, K. S., Chan, W. K., Tam, H. L. and Cheah, K. W. (2007). Defect emissions in ZnO nanostructures. *Nanotechnology*, 18(9): 095702.
14. Kong, M., Li, Y., Chen, X., Tian, T., Fang, P., Zheng, F. and Zhao, X. (2011). Tuning the relative concentration ratio of bulk defects to surface defects in TiO_2 nanocrystals leads to high photocatalytic efficiency. *Journal of the American Chemical Society*, 133(41): 16414-16417.

Malaysian Journal of Analytical Sciences, Vol 22 No 2 (2018): 279 - 285
DOI: https://doi.org/10.17576/mjas-2018-2202-13

MALAYSIAN JOURNAL OF ANALYTICAL SCIENCES
Published by The Malaysian Analytical Sciences Society
ISSN 1394 - 2506

SYNTHESIS OF ALUMINA-CaO-KI CATALYST FOR THE PRODUCTION OF BIODIESEL FROM RUBBER SEED OIL

(Sintesis Mangkin Alumina-CaO-KI untuk Penghasilan Biodiesel daripada Minyak Biji Getah)

Zainal Kifli Abdul Razak[1]*, Shahida Hanum Kamarullah [1], Siti Norhafiza Mohd Khazaai [1,2], Gaanty Pragas Maniam [2]

[1]*Faculty of Applied Sciences,*
Universiti Teknologi MARA Pahang, 26400 Bandar Tun Abdul Razak, Jengka, Pahang, Malaysia
[2]*Faculty of Industrial Sciences & Technology,*
Universiti Malaysia Pahang, Lebuhraya Tun Razak, 26300 Gambang, Pahang, Malaysia

**Corresponding author: zainalk@uitm.edu.my*

Received: 4 December 2016; Accepted: 1 December 2017

Abstract

In this research, biodiesel was produced by transesterification of rubber seed oil with methanol catalyzed by three types of alumina-supported catalyst. The catalysts were Al_2O_3-CaO, Al_2O_3-KI, and Al_2O_3-CaO-KI. The catalysts were prepared by heating a mixture of alumina and the corresponding salt in a furnace at 700 ^oC. Transesterification reactions were carried out at 65 °C using a mixture of rubber seed oil: methanol of mass ratio 1:9 with different catalyst loadings between 0 and 3.5%. The optimum catalyst loading was at 2.0% for all types of catalyst and Al_2O_3-CaO-KI gave the highest yield (91.6%) followed by Al_2O_3-KI (90.7%) and Al_2O_3-CaO (63.5%). The catalyst Al_2O_3-CaO-KI also gave high biodiesel yields over a wider range of catalyst loadings compared to the other two catalysts. Reactions were also carried out at different temperatures (25, 40 and 65°C). It was observed that the yield increased drastically with increasing reaction temperature. At all temperatures the Al_2O_3-CaO-KI catalyst gave the highest yield. Therefore, the study showed that among these three catalysts the most productive was Al_2O_3-CaO-KI, (100:30:35).

Keywords: alumina-supported catalyst, biodiesel, rubber seed oil, transesterification

Abstrak

Dalam kajian ini, biodiesel dihasilkan melalui tindak balas transesterifikasi minyak biji getah dengan metanol menggunakan tiga jenis mangkin tersokong alumina. Mangkin-mangkin tersebut adalah Al_2O_3-CaO, Al_2O_3-KI dan Al_2O_3-CaO-KI. Mangkin-mangkin itu disediakan dengan pemanasan campuran alumina dan garam yang berkaitan di dalam relau pada suhu 700 °C. Tindak balas transesterifikasi dijalankan pada suhu 65 °C dengan menggunakan campuran minyak biji getah: metanol dengan nisbah jisim 1:9 dengan beban mangkin yang berbeza di antara 0 hingga 3.5%. Beban mangkin yang optimum adalah 2.0% untuk semua jenis mangkin dan mangkin Al_2O_3-CaO-KI memberikan peratus hasil yang paling tinggi (91.6%) diikuti oleh Al_2O_3-KI (90.7%) dan Al_2O_3-CaO (63.5%). Mangkin Al_2O_3-CaO-KI juga memberikan peratus hasil biodiesel yang tinggi pada julat beban mangkin yang lebih besar berbanding dengan dua mangkin yang lain. Tindak balas juga dijalankan pada suhu-suhu yang berbeza (25, 40 dan 65 °C). Didapati bahawa peratus hasil meningkat secara mendadak dengan peningkatan suhu tindak balas. Pada sebarang suhu mangkin Al_2O_3-CaO-KI memberikan peratus hasil yang paling tinggi. Oleh itu, kajian ini menunjukkan bahawa di antara ketiga-tiga jenis mangkin ini Al_2O_3-CaO-KI, (100:30:35) adalah yang paling produktif.

Kata kunci: mangkin tersokong alumina, biodiesel, minyak biji getah, transesterifikasi

Introduction

The excessive use of fossil fuels has stirred environmental concern due to their non-renewable nature. Therefore, as an alternative biodiesel is becoming a popular choice of renewable fuel. Biodiesels are fatty acid methyl esters that can be produced from fats or oils from plants or animals. There are two chemical reactions which can be used to produce biodiesel, namely esterification, and transesterification. The more commonly applied reaction is transesterification since it involves only a single step reaction between oil and methanol. Transesterification reaction can be carried out with or without the presence of a catalyst [1]. However, the use of a catalyst can reduce the production time by speeding up the reaction. There are three types of catalysts which are acid, base and enzyme. Acids catalysed transesterification is a slow reaction, therefore is not favourable [2]. On the other hand, enzymes are too costly. The cost of enzyme-catalyzed production of biodiesel is about twice that of the alkali-catalyzed process [3]. Therefore, this research focuses on the application of a base catalyst to produce biodiesel from rubber seed oil. Base catalysts can be in the form of a homogeneous catalyst which is soluble in the reaction medium or heterogeneous catalyst which are insoluble. However, the homogeneous base catalyst is sensitive to water and free fatty acid content in the feedstock where it will cause the formation of soap. This will cause difficulty in the purification of the biodiesel because soap will lead to the formation of oil-water emulsion [4].

Currently, the use of heterogeneous catalysts is gaining attention among researchers since they are reusable and therefore could save the production cost. These catalysts are in the form of metal oxides such as alkaline earth metal oxides, MnO and TiO [5, 6]. Even though these catalysts are reusable, but some studies have shown that they are subjected to leachate where part of the solid dissolves in the reaction medium and thus limiting the reusability [7]. An approach to overcome this problem is to bind the catalyst to a solid support. One of the materials that have been studied extensively as a support is an alumina.

As to evaluate the catalytic activity of alumina supported, they were used KI, CaO, and CaO-KI to transesterify palm oil into biodiesel. The alumina supported-KI showed the highest conversion [8-10]. However, since palm oil is edible oil, then there is an issue of competition with the food supply. Moreover, there was reported, 925 million people were facing with malnutrition [11]. As such, in this research, we are utilizing rubber seed oil, which is a non-edible oil to produce biodiesel. The aim of this research is to compare the catalytic activity of alumina-CaO, alumina-KI, and alumina-CaO-KI in the transesterification of rubber seed oil with methanol.

Materials and Methods

Rubber seeds were collected from local rubber plantations. Aluminium oxide powder, potassium iodide and calcium acetate were purchased from R&M Chemicals. Methanol (99%) was from HmbG Chemicals. The chromatographic standards used were methyl heptadecanoate as internal standard and the FAME standard mixture GLC-10. Both were from Sigma-Aldrich. GLC-10 consists of methyl palmitate, methyl stearate, methyl oleate, methyl linoleate and methyl linolenate.

Rubber seeds were crushed, and the kernel was separated from the shell. The kernel was dried in the oven at 60 $^{\circ}$C overnight and then milled by using a household blender. Rubber seed oil was extracted from the kernel by a Soxhlet extractor using petroleum ether for 6 hours. The solvent was evaporated in a rotary evaporator. The oil was then kept in a refrigerator.

Three types of catalysts were prepared. They are alumina-CaO-KI, alumina-CaO, and alumina-KI. The alumina-CaO-KI catalyst was prepared as follows. A 33.8 g of calcium acetate and 14 g of potassium iodide were dissolved in 100 mL water in a beaker. Then 40 g of alumina was added to the mixture. The mixture was stirred for 4 hours at room temperature. Then it was dried in an oven at 100 $^{\circ}$C overnight. The dried mixture was then calcined at 700 $^{\circ}$C for 5 hours. The mass ratio of alumina: CaO: KI in the catalyst is 100: 30: 35. The mass of CaO produced from calcium acetate was calculated based on TGA data. The alumina-CaO was prepared with the same method but without adding potassium iodide. Alumina-KI was also prepared with the method but without adding calcium acetate.

The Brunauer-Emmett-Teller (BET) surface area analysis of porous properties of the catalysts was determined by Micromeritis ASAP 2000. Adsorption N_2 gas within 6 hours at 250 $^{\circ}$C (de-gassed). Investigation of the chemical

composition and morphology of the catalysts done by using FESEM-EDX (JSM 7800F). While, X-Ray Diffraction analysis (XRD) was achieved by using Rigaku with Cu Kα X-ray as a source, 2θ range from 2° to 80° with step sizes of 0.02°, at a scanning speed of 1° min^{-1}.

Transesterification reaction was carried out in a three-neck flask equipped with a thermometer, a condenser, and a magnetic stirrer. 10 g of rubber seed oil was mixed with 90 g methanol and various amounts of the catalyst. The amount of catalyst used were between 0 and 3.5% (weight percent to total reactants). The reactions were carried out at 65 °C and stirred at 600 rpm for 5 hours. After the reaction was completed, the catalyst was removed by filtration, and the reaction mixture was poured into a separatory funnel. Two layers formed where the lower layer is glycerol, and the upper layer is biodiesel (FAME) solution in methanol. The glycerol layer was discarded, and biodiesel was obtained from the upper layer by evaporation with a rotary evaporator. Reactions were also carried out at 25 °C and 40 °C using 2% catalyst loading to study the effect of temperature on the biodiesel yield.

Quantification of biodiesel was done by Agilent 7890B gas chromatographer equipped with 5977A MSD and Zebron ZB-Wax column (30 m x 0.25 mm x 0.25 μm). The injector and MS transfer-line temperatures were set at 240 °C and 280 °C, respectively. The column temperature was held at 110 °C for 2 minutes and then programmed to 240 °C at 6 °C/min. The methyl esters were quantified by an internal standard method using methyl heptadecanoate as internal standard and compared against GLC-10 FAME standards (Supelco).

Results and Discussion

The BET surface area, pore volume and pore size of different catalysts from the previous and currently studies are reported in Table 1. Referring the table, the surface area of the catalysts is ranging from 4.9283 – 48.8130 m^2/g. The literature data of Al_2O_3 act as a catalyst showed ranging 120 – 265 m^2/g of the surface area. The decreasing in surface area was considering the sequence of catalyst displacement on the metal oxide, Al_2O_3. During the impregnation and calcination method, the reduction of BET surface area also occurred and reflecting the pore volume and pore size. The phenomena were apparently due to the insertion of CaO or KI into pores and surface of Al_2O_3. An identical measurement has been discussed by several researchers [9, 10, 12-14]. Referring to this range of pore size (2 to 50 nm = mesopore), the average pore size of the catalysts ranged from 10.9 to 18.6 nm categorize as mesoporous type. Meanwhile, the pore diameter less than 2 nm is microporous and on top of 50 nm is macroporous.

Table 1. BET characterization of the catalysts.

	Asri et al. [10]		**Zabeti et al. [9]**	**Present Study**		
Samples	Al_2O_3/CaO	Al_2O_3/KI/CaO	Al_2O_3/CaO	Al_2O_3/CaO	Al_2O_3/KI	Al_2O_3/KI/CaO
Surface area (m^2/g)	83.77	54.551	83.74	48.813	4.928	21.246
Pore volume (cm^3/g)	0.135	0.083	0.223	0.148	0.022	0.058
Pore size (x 10^{-8}m)	3.421	3.821	63.37	1.212	1.860	1.092

The crystal morphology exposes through the micrograph of the catalyst. The CaO and KI on the surface of amorphous Al_2O_3 create porous materials. The impregnation and calcination method, made spherical crystals on the surface become obvious needle-shaped spicules of Al_2O_3 with a porous apparent in all of the catalysts. As can be seen in Figure 1, no distinct different between KI and KI/CaO samples thus propose highly dispersed on the surface of support catalyst. Also, notified the sustained structure of Al_2O_3 after impregnation with another compound was important. Almost similar observation reported by [8]. The composition of catalysts is displayed in EDX analysis. The result showed the existence of Al (29.55%), O (18.69%) and Ca (7.04%) for Al_2O_3/CaO. Meanwhile for Al_2O_3/KI, confirms the composition of O (23.77%), I (23.48%), Al (13.48%) and K (9.25%). Also, the EDX

analysis showed the composition of O (34.94%), Al (21.28%), I (9.54%), K (4.11%) and Ca (3.32%) for Al_2O_3/KI/CaO.

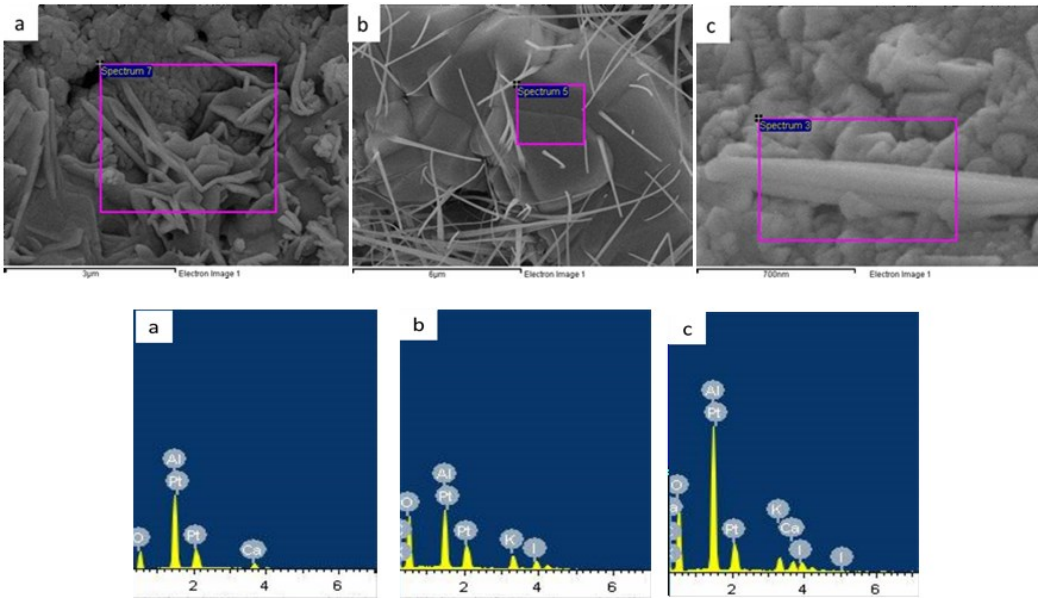


Figure 1. FESEM-EDX micrographs of (a) Al_2O_3/CaO, (b) Al_2O_3/KI and (c) Al_2O_3/KI/CaO

The XRD profile of the catalysts is presented in Figure 2. The result demonstrated the characteristic peaks at 2θ ranging from 20° to 70°. It showed large reflection at 29.66°, 25.62° and 25.46°, respectively and confirmed to be Al_2O_3. This is recommended that the structure of Al_2O_3 undefiled although loading with other compound. Meanwhile, small reflection of diffraction peaks from KI and CaO suggesting it was well dispersed on the surface of the support catalyst [15].

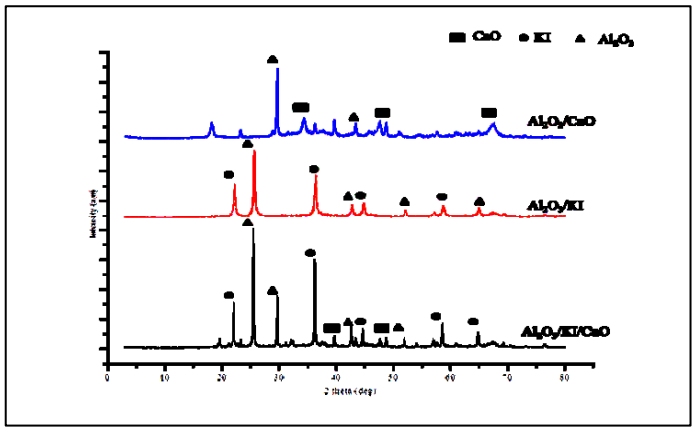


Figure 2. XRD patterns for the catalysts calcined at 700 ℃ for 2 hours

Production of biodiesel by transesterification of rubber seed oil refluxed with methanol was carried out by using three alumina-supported catalysts. Biodiesel yield was observed by varying the catalyst loading between 0 to 3.5 %. As shown in Figure 3, the yield increased with increasing catalyst loading from 0 to 2% loading for all of the

catalysts. The highest yield of biodiesel with alumina CaO-KI, alumina-KI and alumina-CaO were 91.6%, 90.7% and 63.5% respectively. It was found that the optimal catalyst loading was at 2.0% but decreasing yield of biodiesel was observed with further increasing amount of catalyst. As expected, alumina-CaO-KI gave the highest yield of biodiesel probably due to the combination of factors; the high basicity of alumina-KI catalyst [16] and higher activity in the mild reaction condition of CaO catalyst [17]. Similarly, high biodiesel yield (95%) was also observed from palm oil using same catalyst [10].

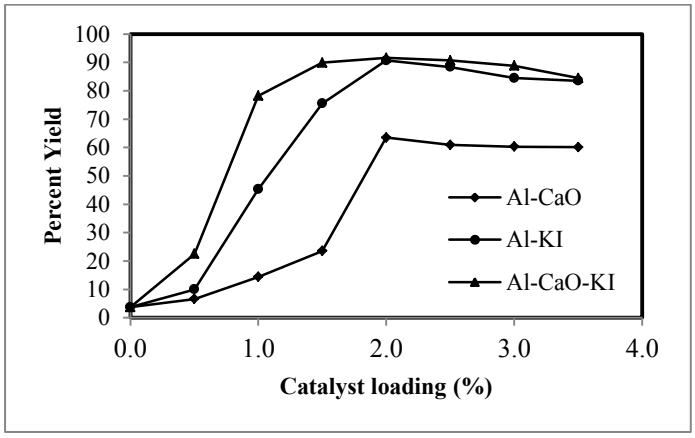


Figure 3. Effect of the catalyst loading on the biodiesel yield

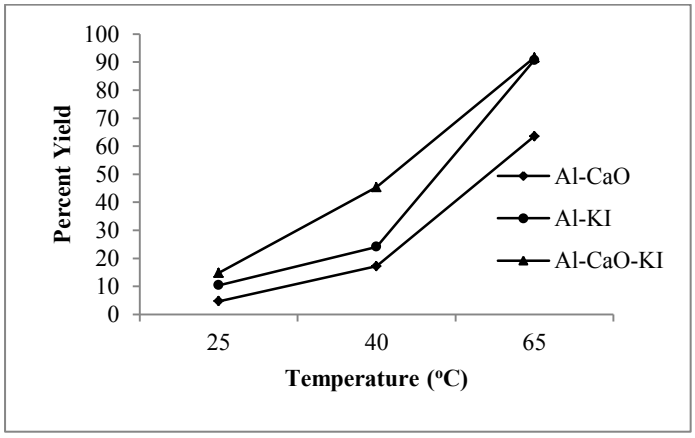


Figure 4. Effect of temperature on the biodiesel yield

The decline of biodiesel yield when the catalyst loading exceeded 2.0% was due to the mixing effectiveness of the reaction mixture. Beyond the optimum catalyst loading, there is a mass transfer limitation of the reactants. Previous studies by other researchers also showed the same trend [18, 19].

Calcium oxide is a popular heterogeneous catalyst because of its availability. However, the activity of this catalyst will decline after multiple uses due to leachate into the reaction medium. An approach to overcome this problem is to bind the calcium oxide onto a catalyst support such as alumina [9]. Other than calcium oxide, some potassium salts supported on alumina also showed high catalytic activity. Previously, it was discovered that alumina-supported potassium iodide with 35% KI loading gave the highest catalytic activity among several alumina-supported potassium salts [8]. It was also observed that when CaO was combined with this catalyst the optimum loading of

CaO was 30% as used in our study [10]. In this study, we tried to investigate whether a combination of CaO and KI supported onto alumina gives a higher catalytic activity compared to when any of them are used separately. Amazingly, the alumina-CaO-KI catalyst was capable of producing higher biodiesel yields compared to alumina-CaO or alumina-KI.

According to Figure 4, the yield increased drastically when the temperature was raised from 25°C to 65°C. At 25°C the yield for all catalysts was only between 4.7% and 14.8%, whereas at 65^{o}C it was between 63.5% and 91.6%. At all temperatures, Alumina-CaO-KI gave the highest yield. The study was done only up to a maximum reaction temperature of 65°C because it is the boiling temperature of methanol and thus, the highest temperature that can be achieved by refluxing. Moreover, to increase the temperature beyond that, special equipment is required. Previously, a study using alumina-supported CaO as a catalyst also showed a drastic increase in biodiesel yield between 55 °C and 65 °C [9]. Similarly, the same trend was also observed using a catalyst made of a mixture of calcium oxide and manganese oxide [20].

Conclusion

Biodiesel was successfully produced from rubber seed oil by transesterification with methanol using alumina-supported CaO-KI as the catalyst. In this research, we have studied the activity of three types of alumina-supported catalysts, namely alumina-supported CaO, alumina-supported KI and alumina-supported CaO-KI. It was proven that a combination of CaO and KI supported onto alumina had a higher catalytic activity than any of the salts supported separately onto alumina. The highest biodiesel yield achieved was 91.6% using alumina-CaO-KI (100:30:35) with a 2.0% catalyst loading.

Acknowledgement

The authors acknowledge the Ministry of Higher Education Malaysia and Universiti Teknologi MARA, Pahang for funding the work through RAGS Grant (011000150004), UMP PGRS (170311) and for scholarship (Khazaai, S.N.M).

References

1. Patel, A., Brahmkhatri, V. and Singh, N. (2013). Biodiesel production by esterification of free fatty acid over sulfated zirconia. *Renewable Energy*, 51: 227–233.
2. Lee, D., Park, Y. and Lee, K. (2009). Heterogeneous base catalysts for transesterification in biodiesel synthesis. *Catalysis Surveys from Asia*, 13: 63-77.
3. Jegannathan, K. R., Eng-Seng, C. and Ravindra, P. (2011). Economic assessment of biodiesel production: Comparison of alkali and biocatalyst processes. *Renewable and Sustainable Energy Reviews*, 15: 745–751.
4. Talebian-Kiakalaieh, A., Amin, N. A. S. and Mazaheri, H. (2013). A review on novel processes of biodiesel production from waste cooking oil. *Applied Energy*, 104: 683–710.
5. Helwani, Z., Othman, M. R., Aziz, N. and Kim, J. (2009). Solid heterogeneous catalysts for transesterification of triglycerides with methanol: A review. *Applied Catalysis A: General*, 363: 1–10.
6. Gombotz, K., Parette, R., Austic, G., Kannan, D. and Matson, J. V. (2012). MnO and TiO solid catalysts with low-grade feedstocks for biodiesel production. *Fuel,* 92: 9–15.
7. Kouzu, M., Hidaka, J., Komichi, Y., Nakano, H. and Yamamoto, M. (2009). A process to transesterify vegetable oil with methanol in the presence of quicklime bit functioning as solid base catalyst. *Fuel,* 88: 1983–1990.
8. Xie, W. and Li, H. (2006). Alumina-supported potassium iodide as a heterogeneous catalyst for biodiesel production from soybean oil. *Journal of Molecular Catalysis A: Chemical*, 255: 1-9.
9. Zabeti, M., Daud, W. M. A. W. and Aroua, M. K. (2010). Biodiesel production using alumina-supported calcium oxide: An optimization study. *Fuel Processing Technology*, 91: 243–248.
10. Asri, N. P., Savitri, S. D., Suprapto, B. K. and Roesyadi, A. (2012). Development of heterogeneous alumina supported base catalyst for biodiesel production. *Environment and Chemistry*, 46: 116-121.
11. Maniam, G. P., Hindryawati, N., Nurfitria, I., Manaf, I. S. A., Ramachandran, N. and Rahim, M. H. A. (2015). Utilization of waste fat from cat fish (*Pangasius*) in methyl esters preparation using CaO derived from waste marine barnacle and bivalve clam as solid catalysts. *Journal of the Taiwan Institute of Chemical Engineers*, 49: 58–66.

12. Umdu, E. S. and Seker, E. (2012). Transesterification of sunflower oil on single step sol-gel made Al_2O_3 supported CaO catalysts: Effect of basic strength and basicity on turnover frequency. *Bioresource Technology,* 106: 178-181.
13. Pasupuletey, N. Gunda, K., Liu, Y., Rempel, G. L. and Ng, F. T. T. (2013). Production of biodiesel from soybean oil on CaO/Al_2O_3 solid base catalyst. *Applied Catalysis: A General*, 452: 189-202.
14. Islam, A., Taufiq-Yap, Y. H., Chu, C. M., Ravindra, P. and Chan, E. S. (2013). Transesterification of palm oil using KF and $NaNO_3$ catalysts supported on spherical millimetric γ-Al_2O_3. *Renewable Energy*. 59: 23–29.
15. Farooq, M. and Ramli, A., Subbarao, D. (2013). Biodiesel production from waste cooking oil using bifunctional heterogeneous solid catalysts. *Journal of Cleaner Production*. 59: 131–140.
16. Evangelista, J. P. D. C., Gondim, A. D., Souza, D. L. and Araujo, A. S. (2016). Alumina-supported potassium compounds as heterogeneous catalysts for biodiesel production: A review. *Renewable and Sustainable Energy Reviews*, 59: 887-894.
17. Boey, P.-L., Maniam, G. P. and Hamid, S. A. (2009). Biodiesel production via transesterification of palm olein using waste mud crab (*Scylla serrata*) shell as a heterogeneous catalyst. *Bioresource Technology*, 100 (24): 6362-6368.
18. Nur, Z. A. S., Taufiq-Yap, Y. H., Nizah, M. F. R. , Teo, S. H., Syazwani, O. N. and Islam, A. (2014). Production of biodiesel from palm oil using modified Malaysian natural dolomites. *Energy Conversion and Management*, 78: 738-744.
19. Xie, W. and Zhao, L. (2013). Production of biodiesel by transesterification of soybean oil using calcium supported tin oxides as heterogeneous catalysts. *Energy Conversion and Management,* 76: 55–62.
20. Dias, M. J., Alvim-Ferraz, M. C. M., Almeida, M. F., Diaz, J. D. M., Polo, M. S. and Utrilla, J. R. (2012). Selection of heterogeneous catalysts for biodiesel production from animal fat. *Fuel*, 94: 418-425.

Malaysian Journal of Analytical Sciences, Vol 22 No 2 (2018): 286 - 295
DOI: https://doi.org/10.17576/mjas-2018-2202-14

MALAYSIAN JOURNAL OF ANALYTICAL SCIENCES
Published by The Malaysian Analytical Sciences Society
ISSN 1394 - 2506

APPLICATION OF PROTEOLYTIC ENZYME IN HIGH AMMONIATED NATURAL RUBBER LATEX

(Aplikasi Enzim Proteolitik dalam Lateks Getah Asli Berammonia Tinggi)

Aziana Abu Hassan[1]*, Norazreen Abd Rahman[2], Nurulhuda Abdullah[1], Roslinda Sajari[3], Mok Kok Lang[1]

[1]*Technology and Engineering Division*
[2]*Production Development Division*
[3]*Genomics and Bioinformatics Centre*
Malaysian Rubber Board, 47000 Sg. Buloh, Selangor, Malaysia

**Corresponding author: aziana@lgm.gov.my*

Received: 4 December 2016; Accepted: 1 December 2017

Abstract

Natural rubber latex (NRL) with 'low protein content' is regarded as alternative raw material for less allergenic latex. However, these 'low protein latexes' have been reported to give uncertain and at times poorer mechanical properties in which could be due to its method of preparation. Therefore this study was conducted to strengthen the fundamental approach of making 'low protein latex' via enzymatic treatment. Proteolytic enzymes were employed to digest the proteins and inactivate some of the proteins function. The aim was to study the effect of enzymatic treatment towards the nitrogen content in NRL that is mainly contributed by the presence of proteins. Impact on the mechanical properties due to changes in the native proteins was also evaluated. Results show that proteolytic enzyme at low concentration effectively hydrolysed the protein molecules. However, nitrogen content in NRL serum was simultaneously increased with increasing enzyme concentration. This could be due to the tendency of enzyme to form new peptides bonds known also as aminolysis. Interestingly, the amount of allergenic proteins was observed to decrease proportionally with the upsurge of enzyme concentration, suggesting deactivation of allergenicity by the enzyme. These preliminary results indicate a potential approach to produce low allergenic risk NRL products.

Keywords: low protein latex, proteolytic enzyme, protein allergy, mechanical properties

Abstrak

Lateks getah asli (LGA) dengan 'kandungan protein rendah' dianggap sebagai bahan mentah alternatif untuk mengurangkan risiko alahan terhadap protein LGA. Walau bagaimanapun, 'lateks protein rendah' menyebabkan sifat mekanikal lateks tersebut terjejas dan bergantung juga kepada kaedah penyediaannya. Oleh itu kajian ini dijalankan untuk mengukuhkan pendekatan asas dalam membuat 'lateks protein rendah' melalui rawatan enzimatik. Enzim proteolitik digunakan untuk mencerna protein dan menyahaktifkan beberapa fungsi protein. Tujuannya adalah untuk mengkaji kesan rawatan enzimatik ke atas kandungan nitrogen dalam LGA yang secara tidak langsung dapat mengesan kehadiran protein. Perubahan secara mekanikal akibat perubahan protein juga dinilai. Keputusan menunjukkan bahawa enzim proteolitik pada kepekatan rendah berupaya menghidrolisis molekul protein. Walau bagaimanapun, kandungan nitrogen dalam serum LGA meningkat dengan peningkatan kepekatan enzim. Ini mungkin disebabkan oleh kecenderungan enzim untuk membentuk jaringan peptida baru yang dikenali juga sebagai aminolisis. Menariknya, jumlah protein penyebab alahan berkurangan secara berkadar dengan peningkatan kepekatan enzim. Ini menunjukkan rawatan enzim berkemungkinan berupaya untuk menyahaktifan aktiviti protein penyebab alahan tersebut. Keputusan awal ini menunjukkan pendekatan berpotensi untuk menghasilkan produk LGA dengan risiko alahan yang rendah.

Kata kunci: lateks protein rendah, enzim proteolitik, alahan protein, sifat mekanikal

Introduction

Natural rubber latex (NRL) is a stable dispersion of cis-1,4-polyisoprene rubber encapsulated in mostly spherical particles with average size of 0.15 μm to 3 μm, in an aqueous phase [1]. The dispersed phase of NRL is mainly rubber hydrocarbon and the dispersion medium is water. Freshly-tapped NRL as obtained from the tree is a whitish fluid of density 0.975 - 0.980 g/ml and with a pH from 6.0 - 7.0 [2]. Being a natural product, its composition varies between a wide range. Typically NRL consists of 36% of total solid content including dry rubber content of 33%, proteinaceous substances about 1%, resinous substances 1-2.5%, ash and sugar 1% respectively, and 60% content of water [3].

These substances are distributed between three principal phases namely, rubber particles (35% of latex by weight), the aqueous phase (55%) and the remaining lutoid phase (10%) [4]. The aqueous non-rubber phase is made up of carbohydrates (quebrachitol, sucrose, glucose, fructose and raffinose), proteins and amino acids (α-globulin and hevein) and other serum constituents (free nitrogenous bases, lipids, organic acids, inorganic anions and metallic ions) and a range of enzymes [5]. According to Tata, fresh NRL contains 0.95% proteins of which 27.2% is in the rubber fraction, 47.5% in the serum fraction and 25.3% on the bottom fraction. Technically, about 60% of the protein content is dissolved in the aqueous phase, approximately 20% is adsorbed on the surface of rubber particles and the remaining 20% is associated with the larger particulate bodies such as lutoids and Frey-Wyssling particles [6].

NRL proteins are commonly related to allergenic issues associated with the usage of latex-based products. In 1986, researches had revealed that the allergic reactions to latex products were instead IgE-mediated and that the allergens were latex proteins which still remained in the finished products [7, 8]. Since then, most of research studies were conducted as precaution measures to minimize the latex proteins allergenic risk. Currently, low protein latexes are widely available in the market with various methods employed to deplete the proteins. Generally, low protein latex can be prepared via few approaches namely mechanical, chemical or biological treatment [9, 10, 11]. The mechanical process usually involves multiple centrifugation or membrane filtration of diluted latex. In chemical treatment, chemicals such as urea are used to remove proteins while biological approach usually involves combination of proteolytic enzymes.

Non-rubber components especially proteins are important in maintaining latex colloidal stability. Due to their solubility behaviour, proteins are found abundantly in the serum fraction upon centrifugation while the rest are surface-bound to rubber particles. Additionally, the process of concentrating the latex to about 60% rubber content also significantly reduces the protein content. In the technological aspect, proteins are regarded as an essential component that any alteration towards its composition can implicate on the products' properties [12, 13]. A study by Gazeley had shown that overall rate of crosslink insertion during prevulcanization reaction is reduced for low protein NRL [14]. This finding was also supported by Yatim [15] that claimed the presence of non-rubbers accelerates prevulcanization rate during latex stage. However until now, it is unclear which non-rubber substituents are important in determining the rate at which the reaction occurs. The rate of prevulcanization could be a consequence of synergism between the non-rubber substances in NRL [12].

In this study, high ammoniated NRL (HA-NRL) was treated with a proteolytic enzyme known as alcalase in order to determine its digestive effects on the native proteins. To investigate this, HA-NRL was mixed with alcalase in various concentrations from 1% to 4% and incubated for two hours. Changes on the native proteins in HA-NRL were determined by measurement of total protein content (N%) and protein molecular weight using SDS - Polyacrylamide Gel Electrophoresis (SDS-PAGE). Presence of allergenic protein and colloidal stability of the mixture were also evaluated.

Materials and Methods

High ammoniated latex

High ammoniated natural rubber latex (HA-NRL) preserved with 0.7% ammonia was obtained from a local supplier. The dry rubber content (DRC) of HA-NRL was 60%.

Alcalase
Alcalase was obtained from Novozyme Sdn Bhd. The alcalase solution was diluted to several concentrations in the range of 2% to 8% to get the final concentration of 1-4% when mixed with HA-NRL.

Preparation of high ammoniated natural rubber latex with alcalase
The initial concentration of 300 mL HA-NRL was diluted to 30% DRC after it was mixed with alcalase in different concentrations from 1% to 4%. The mixture was stirred continuously for two hours at 100 rpm at ambient temperature.

Measurement of total protein content
Samples of unleached and leached latex films were prepared by casting the treated HA-NRL on glass plates. For leaching, latex films from each treatment were immersed in water bath at 60 ^{o}C for 5 minutes. Rubber phase from the latex was obtained by centrifugation (Beckman Coulter Optima L-100K Ultracentrifuge) at 30,000 *x g* for 1 hour to separate the rubber from the serum phase. The total protein content in the rubber phase as well as the leached and unleached latex films were determined by measuring their nitrogen contents (N %) using the Kjedhal method based on AOAC International [16].

Determination of protein molecular weight and detection of allergenic proteins
The treated latex was firstly centrifuged at 30,000 *x g* for 1 hr (T=5^{o}C) to obtain a clear serum fraction. The serum fraction was then subjected to SDS - Polyacrylamide Gel Electrophoresis (SDS-PAGE). The SDS-PAGE analysis was conducted at a constant current of 0.25A for 1 hour. The reference marker was run concurrently in all experiments. The SDS-PAGE gels were stained with silver staining method followed by destained in destaining solution. Meanwhile, presences of allergenic proteins in the serum and rubber samples were detected by using Latex-T Test Kit.

Zeta potential analysis
The zeta potential of the alcalase treated HA-NRL was measured using the 90Plus/BI-MAS and ZetaPlus from Brookhaven Instrument Corporation. Sample was diluted to 0.01 wt% with distilled water and pH of the sample in a range from 2 to 12 was adjusted with 0.1M H_2SO_4 and 0.1M KOH prior to the test.

Statistical analysis
The data obtained was analyzed by using IBM SPSS Statistic 20, subjected to Compare Means procedure using one way ANOVA.

Results and Discussion

Effect of alcalase on protein content of high ammoniated–natural rubber latex
Leaching process removes water soluble proteins from the latex. Latex is an emulsion that comprises a stable dispersion of rubber particles in an aqueous phase [12]. The aqueous phase is made up of water, non-rubber compounds such as carbohydrates (quebrachitol, sucrose, glucose, fructose and raffinose), proteins and amino acids (α-globulin and hevein), other serum constituents (free nitrogenous bases, lipids, organic acids, inorganic anions and metallic ions) and a range of enzymes [5]. These constituents including proteins that dissolved in the aqueous phase are commonly water soluble and can be removed by washing with water.

Figure 1 shows the effect of leaching on films prepared from HA-NRL treated with varying concentrations of alcalase. The nitrogen content (N%) of unleached latex film in the absence of alcalase was referred as the initial protein content in the HA-NRL. After two hours incubation time, protein content in the unleached latex films increased proportionally with increasing alcalase concentration. This shows that the total protein content in the treated HA-NRL was influenced by the presence of alcalase.

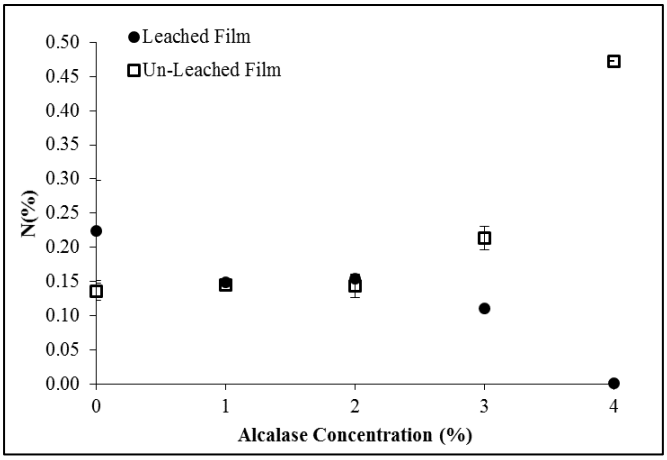


Figure 1. Total nitrogen content of the unleached and leached HA-NRL films in the presence of alcalase

The extent of protein removal from HA-NRL in the presence of alcalase showed two different trends. In the first trend, the amount of N% in leached films was not significantly different than the unleached films in the presence of low concentration of alcalase (1% and 2%). Contrary in the second trend, when alcalase concentration was increased to 3% and 4%, the total amount of proteins in leached HA-NRL film was significantly lower than the unleached film. At this condition, it is possible that most of the accumulated proteins on the latex film surface have been extracted into the leaching water and hence the nitrogen content dropped significantly. Therefore, more water soluble proteins were removed from HA-NRL in the presence of alcalase above 3% with two hours incubation time.

When the treated HA-NRL was casted on glass plates to make films, drying process of the latex caused water inside the serum to evaporate, along which the non-rubbers components especially proteins, would be drawn to the surface of the latex film eventually. Alcalase is a proteolytic enzyme under the group of serine proteases which belong to subtilases. Subtilisin is a non-specific protease that was initially obtained from certain types of soil bacteria such as *Bacillus amyloliquefaciens* [3, 16]. This protein-digestive enzyme attacks the peptide bonds that covalently link the amino acids through a serine residue at the active site of the enzyme. Treating the HA-NRL with alcalase causes proteins digestion or hydrolysis whereby the proteins molecules are cleaved into more smaller sizes. At higher concentration of alcalase, more proteins are truncated by the enzyme. The truncated proteins being of smaller molecular fragments, would be easily moved to the film surface during the drying process. When the films were leached in water subsequently, these proteins would be easily solubilized in water.

The degree of protein hydrolysis by proteolytic enzyme is influenced by the enzyme and substrates concentration [17]. As described by James et al. [18] enzyme concentration generally had a greater effect on accelerating hydrolysis reaction thus able to shorten the reaction time when compared with temperature increment. Generally, the rate of reaction is simultaneuosly increased when more enzyme is added, provided that the substrate concentration is high and kept at constant rate. On the other hand, there is usually a hyperbolic relation between the rate of reaction and the concentration of substrate. The rate of reaction is increased with increasing substrate concentration until a point is reached whereby the active sites of the enzyme molecules are saturated with substrates. As a consequence, any further increment in substrate concentration will not have any affect to the reaction rate.

In this study, the rate of reaction or the degree of protein hydrolysis in the treated HA-NRL could be visualized by looking at the fractionation of proteins in HA-NRL serum based on the difference in molecular weights as shown in Figure 2. Results from SDS-PAGE also confirmed that more proteins were being digested at high concentration of alcalase (4%). Based on Figure 2, faint bands were observed at the higher molecular weight region, indicating that most of the proteins have been degraded into small molecular weights. As the alcalase concentration increased, there was increased bands at the lower molecular weight region, suggesting that the innate high molecular weight proteins were digested by alcalase into smaller molecular weight protein fragments.

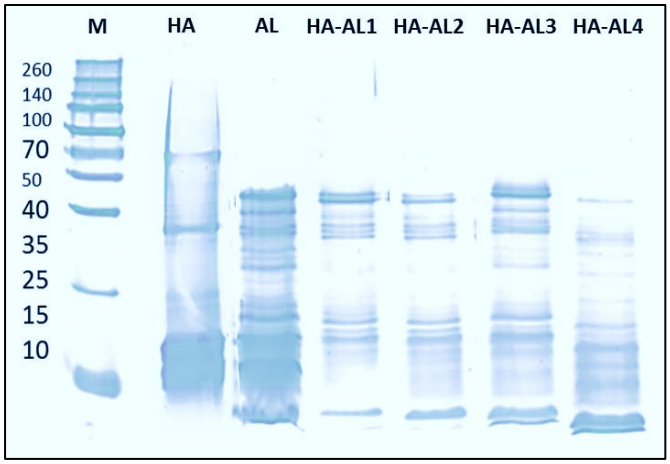


Figure 2. SDS-PAGE of HA-NRL serum after 2-hour incubation with enzymatic treatment; M; protein marker, HA; control (HA-NRL without alcalase), AL; control (alcalase blank), HA-ALx (x-alcalase concentration of 1%, 2%, 3% and 4%)

Effect of alcalase on protein content in white rubber phase of high ammoniated–natural rubber latex

In this experiment, the HA-NRL was subjected to high speed centrifugation in order to purify the rubber phase from proteins and other non-rubber substances. Presence of nitrogen (N) in the white rubber phase after this process would measure the efficiency of the enzyme in removing the non-rubber substances from the rubber particles surfaces. As discussed earlier in this study, more proteins were digested at higher enzyme concentration. Presumably, after centrifugation process the amount of proteins in the white rubber phase from HA-NRL with high alcalase concentration should as well being reduced. This is due to gravitational forces that would have separated and removed the small protein peptides during centrifugation process.

The relationship between N% and alcalase concentration in white rubber phase could be interpreted by dividing the graph into three different parts as shown in Figure 3. In the absence of alcalase, the level of protein content in the white rubber phase of HA-NRL was recorded at 0.07%, which was higher than that of treated HA-NRL. This might be attributed to proteins that were tightly bound to the rubber particles. Interestingly, the protein content in white rubber phase from HA-NRL treated with 1% of alcalase showed significant reduction of 91%, decreasing from 0.07% to 0.006% (Part a). These findings showed that proteins were hydrolysed and cleaved into smaller molecules. The cleaved and lighter molecular weight proteins then entered into the latex serum hence reducing the amount of proteins still locked on to the rubber particle surfaces. The serum proteins were subsequently removed upon centrifugation.

However, as concentration of alcalase was increased (Part b), the amount of proteins in the white rubber phase was proportionally increased up to 3% of alcalase. This shows that the total protein content in the treated HA-NRL was influenced by the presence of alcalase. Alcalase which is a proteolytic enzyme, digested the native proteins in the latex by cutting the peptide bonds that covalently linked the amino acids, turning the proteins into low molecular weight molecules. Consequently, the proteins could be easily removed by centrifugation or solubilisation with water. However, alcalase itself is a long polypeptide chain of proteins. Therefore, increment of protein content in the white rubber phase of the treated HA-NRL was probably contributed by the peptide chains of alcalase. Meanwhile, in the third part (Part c), no significant changes in protein content was observed.

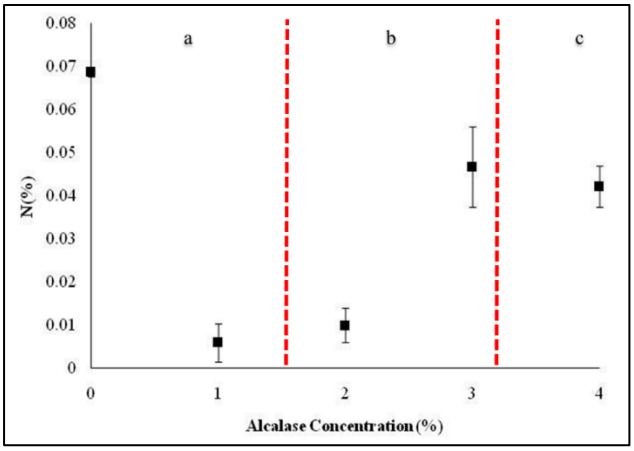


Figure 3. Total nitrogen content from white rubber phase of HA-NRL after centrifugation in different concentration of alcalase

Based on the findings above, there are two hypothetical theories that could likely explain the increase in N% content in the white rubber phase of HA-NRL in the presence of alcalase after centrifugation process. The first theory is the occurence of adsorption and desorption of protein molecules on the surface of rubber particles. The absorption of other protein peptides on the rubber particles surface could be due to ionic (elecrostatic) bonding or hydrophobic interaction [19]. As described previously by Stoker [20], electrostatic interaction can occur with small peptides and amino acids. Commonly, alcalase consists of a single peptide chain with 274 amino acid residues in the absence of disulfide bonds [21]. A study by Tangboriboonrat et al. [22] implied that certain proteins and other non-rubber substances still have the possibilities to remain intact on the rubber particle surfaces after deprotenization process. The small peptides resulted from hydrolysed proteins in HA-NRL that might still be bound on the rubber particles surface could electrostatically interact with amino acids derived from the alcalase. Subsequently, amide bond between amine and carboxylic acid functional groups in the small peptide and the amino acids would be formed and resulted in new chains of amino acids. An empty space left by the digested protein might be replaced by the free floating protein peptides of alcalase. The weakly modified rubber particle surface due to reduction in negatively charged protein provides a hydrophobic surface that other protein molecules could adsorb to. Concentration gradient is one of the factors that influences the transport of proteins to a solid surface [23]. Therefore, the tendancy of non-polar hydrophobic region in alcalase to interact with the rubber particles surface will eventually increase when the concentration of alcalase is increased.

Meanwhile in the second theory, increment or reduction of proteins in the white rubber phase might be influenced by the rate of hydrolysis and aminolysis reaction. In the presence of large amount of substrates and limited amount of water, there is a tendency of the proteolytic enzyme to act in the opposite direction, leading to the formation of new peptides bonds also known as aminolysis [24]. As enzyme concentration increases, competition between hydrolysis and aminolysis reaction might occur. Thus, under this circumstance the carboxy terminal modified amino acid ethyl ester of the protein from the substrate will act as nucleophile and binds to the active site of the proteolytic enzyme to initiate chain length propagation [25]. This reaction could happen on rubber particles surface as shown in Figure 4. As a result, the total nitrogen content on the rubber particles increased as indicated by the total nitrogen content in the white rubber phase of treated HA-NRL.

Study by Tangpakdee and Tanaka [26] found that insignificant change in the molecular weight of rubber was observed which showed proteolytic enzyme broke down proteins selectively at certain sites of the amino acids chain and remained as oligopeptide groups that form branched molecules. Furthermore, enzymatic treatment in latex could not remove the free fatty acid components although there was reduction in the amount of phosphorus after the treatment. The remaining free fatty acid components after proteolysis reaction were believed to be derived from phospholipids, a main component that could also form branched molecules [27].

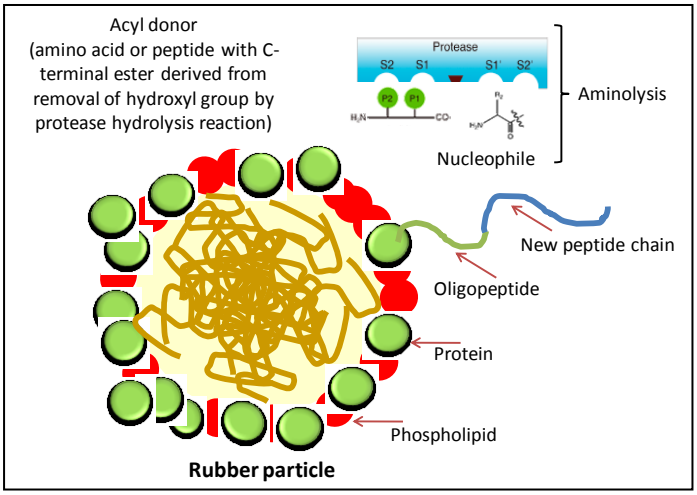


Figure 4. Schematic representation of hypothesize aminolysis reaction on the rubber particle surfaces

Effect of alcalase on allergenic protein in high ammoniated–natural rubber latex

The Latex-T Diagnostic Kit detected the presence of two major types of allergenic proteins that represented as Blue allergen and Red allergen. In the absence of alcalase the concentration of Red allergen was significantly higher than Blue allergen (Figure 5). Interestingly, the concentration of Red allergen in HA-NRL treated with 1% of alcalase was significantly reduced and continue to drop until at 4% alcalase concentration. In the contrary, insignificant changes of Blue allergen in the treated HA-NRL was observed. The results indicated that the proteolytic enzyme is effectively reduce the amount of Red allergen compared to Blue allergen. Therefore, the proteolytic enzyme has the potential to act as deproteinizing agent that could assist in reducing the allergenic risk from NRL.

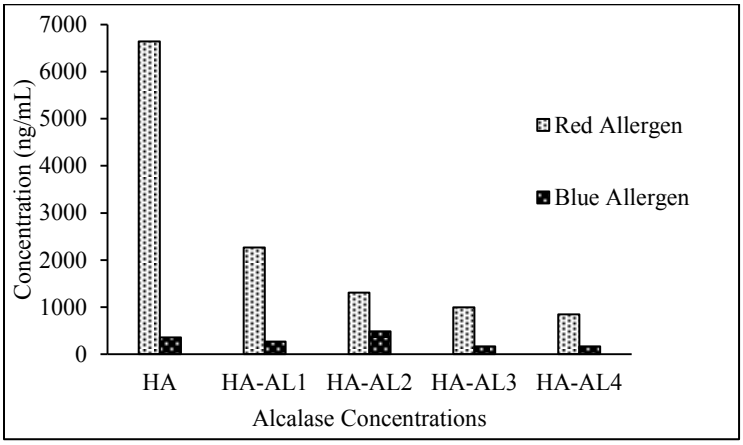


Figure 5. Concentration of major allergenic proteins in HA-NRL in different concentration of alcalase

Effect of alcalase on the colloidal stability of high ammoniated–natural rubber latex

According to Salopek et al. [28] zeta potential or also known as electrokinetic is used to observe the behaviour of dispersive systems in liquids. The potential stability of a colloidal system can be represented by the magnitude of the zeta potential. Whenever a particle is disperses in a liquid medium, it will forms an interfacial region on the particle surface. The interfacial region consists of ions of opposite charge to that of particle that closely located to the particle surface (Stern layer), and counter ions that loosely associated with the particle (diffuse layer). These

layers are referred as the electrical double layer. The potential magnitude of zeta potential is measured at the boundary of the diffuse layer that adjacent to the bulk dispersant or known as surface of hydrodynamic shear [29].

The potential stability of the colloidal systems as indicated by the zeta potential is depending on the concentration of ions. High concentration of ions with positive or negative charges will resulted in stable colloidal systems in which coagulation between the particles will be absence. Charges on the particles also contribute to the electrostatic repulsion that caused the particles to repel from each other. Absence of any positive or negative ion charges will reduce the electrostatic repulsion and thus there will be no force to prevent the particles coming together and agglomerate. Changes on the concentration of ions on the particles surface that influence the stability of a suspension can be observed from a graph plotted with zeta potential (mV) versus pH. In aqueous media, the pH of the sample is one of the most important factors that affect zeta potential of the particles [30]. Balance between the positive and negative charges presence in a suspension is influence by the pH. At a specific pH the positive and negative charges will be equal and the net charge will be zero. The pH where a colloidal system reaches its neutralization state is called the isoelectric point (IEP). At this point the suspension is at the least stable condition due to absence of inter-particle repulsive forces. As a rule of thumb, stability of the particles in a colloidal system is generally taken at either above +30 or -30 mV [31].

Figure 6 shows the zeta potential analysis for treated HA-NRL samples recorded over pH range from pH 2 to pH 10. Based on the graph, the IEP for all samples were below than pH4. HA-NRL consists of latex particles with more negative charges as shown by the IEP value. As pH decreases, abundant presence of H^+ ions caused the latex particles to lose their negative charges until they reach the neutralization state at pH 2 and eventually became more stable as the pH increased (above pH 4). However, the HA-NRL treated samples showed a different trend in which more OH^- were needed in order to reach the IE point as shown by the increasing in pH (above pH 2). Thus indicate that the latex particles in the treated HA-NRL were having less negative ions concentration when compared with HA-NRL in the absence of alcalase. This result could be implied with previous finding by Salgin et al. [32] mentioned that, the difference in the IEP can be due to different in ionic environment such as ionic strength, pH and ion type. Different in ions concentration could possibly influence by the presence of alcalase that also carried charges proteins. The isoelectric point for alcalase is 9.4 which is near to 12. Protein with isoelectric point of 12 or more, are most likely having side chains of amino acid that positively charges [33].

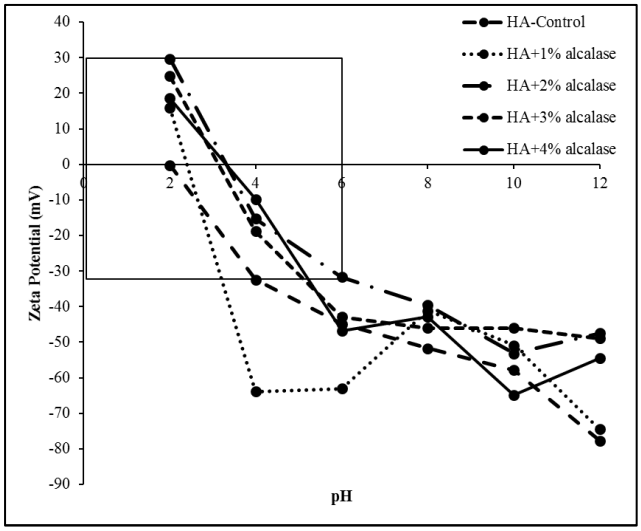


Figure 6. Zeta potential behaviour in a function of pH

Conclusion

Enzymatic treatment of HA-NRL effectively hydrolysed the protein molecules in the serum and increased the amount of water-soluble proteins in which could be removed easily by water leaching process. Hydrolysis reaction in the serum increased steadily proportional to the increment in proteolytic enzyme concentration. This finding was also supported by the results from SDS-PAGE analysis which showed most of the protein bands were located at the low molecular weight region in the presence of 4% alcalase concentration. Nevertheless, instead of reducing the protein content in the white rubber phase of HA-NRL, different proteolytic enzyme concentrations triggered different reactions. The ratio of enzyme and substrate (*i.e.* latex in this study) concentration significantly influenced the proteolytic enzyme activity. It was found that at 1% of alcalase concentration, drastic reduction of N% in white rubber phase was observed. Further investigation is needed on the effect of proteolytic enzyme on mechanical and colloidal stability of treated HA-NRL. Nevertheless, results from this study indicates that low concentration of alcalase is sufficient to reduce the protein content with the possibility to produce HA-NRL that has low allergenicity risk.

Acknowledgements

The authors wish to thank the Director General of the Malaysian Rubber Board for the permission to publish this paper and the support given for technical and financial assistances for the project. We appreciate the advices and comments made by the Panel of the Scientific Economic and Advisory Committee (SEAC) during the proposal and monitoring stage of the study. Not to be forgotten are the capable technical work and support rendered by Mr. Hanipiah Basri.

References

1. Kroschwitz, J. (1990). Concise encyclopedia of polymer science and engineering. Wiley InterScience of John Wiley & Sons, Inc., Hoboken, pp. 24-64.
2. Blomfield, G. F. (1951). The rubber hydrocarbon in freshly tapped Hevea latex. *Rubber Chemistry and Technology*. 24(4): 737–749.
3. Blackley, D. C. (1997). Types of latices. Polymer latices: Science and technology Volume 2: Springer Science and Business Media.
4. Angrove, S. N. (1964). Preservation of NR latex concentrate; Part I—method of evaluation and evaluation of existing preservative systems. *Transactions of the Institution of the Rubber* Industry: 40.
5. Hasma, H. and Subramaniam, A. (1986). Composition of lipids in latex of Hevea brasiliensis clone RRIM 501 [Malaysia]. *Journal of Natural Rubber Research,* 1: 30–40.
6. Tata, S. J. (1980). Distribution of proteins between the fractions of Hevea latex separated by ultracentrifugation. *Journal of Rubber Research Institute of Malaysia,* 28: 77–85.
7. Archer, B. L., Barnard, E.G., Cockbain, J.W., Cornforth, R.H. and Popjak, G. (1966). The stereochemistry of rubber biosynthesis. *Proceedings of the Royal Society B: Biological Sciences,* 163: 519–523.
8. Yeang, H. Y., Arif, S. A. M., Yusof, F. and Sunderasan, E. (2002). Allergenic proteins of natural rubber latex. *Methods,* 27: 32–45.
9. Sussman, G. L., Beezhold, D. H. and Kurup, V. P. (2002). Allergens and natural rubber proteins. *Journal of Allergy and Clinical Immunology,* 110: S33–S39.
10. Aprem A. B. and Satyendra N. P. (2002). Latex allergy and recent developments in deproteinisation of natural rubber latex. *Journal of Rubber Research Institute of Malaysia,* 5: 94–134
11. Perrella, F. W. and Gaspari, A. A. (2002). Natural rubber latex protein reduction with an emphasis on enzyme treatment. *Methods*, 27: 77–86.
12. Manroshan, S., Asrul Mustafa, Mok, K. L., Kawahara, S., Amir-Hashim M. Y. and Booten, K. (2009). Comparison between sodium dodecyl sulfate and polyfructose surfactant systems in urea deproteinisation of natural rubber latex. *Journal of Rubber Research Institute of Malaysia,* 12: 1–11.
13. Gazeley, K. F., Gorton, A. D. T. and Pendle, T. D. (1988). Natural rubber science and technology in ed. by A. D. Roberts (England: Oxford University Press): 63–98.
14. Yatim, A. H. M. (1997). Effect of natural latex non-rubbers on the vulcanisation and physical behaviour of natural rubber latex films. PhD Dissertation. University of North London, England.
15. AOAC (2000). Official methods of analysis. AOAC International.

16. Priest, F. G., Goodfellow, M., Shute, L. A. and Berkeley, R. C. W. (1987). *Bacillus amyloliquefaciens* sp. nov., nom. rev. *International Journal of Systematic Bacteriology,* 37: 69–71.
17. Salwanee, S., Wan Aida, W. M., Mamot, S., Askat, M. Y. M. and Im, S. I. (2013). Effects of enzyme concentration, temperature, pH and time on the degree of hydrolysis of protein extract from viscera of tuna (Euthynnus affinis) by using alcalase. *Sains Malaysiana,* 42: 279–287.
18. James, I. T., Philip, B. G. and Sheila, A. B. (2005). Optimization of conditions for the enzymatic hydrolysis of phytoestrogen conjugates in urine and plasma. *Analytical Biochemistry,* 341(2): 220-229
19. Kim, J. (2002). Protein adsorption on polymer particles. *Journal of Biomedical Materials Research,* 21: 4373–4381.
20. Stoker, H. S. (2015). *General, Organic, and Biological Chemistry*. Cengage Learning.
21. Cowan, D., Daniel, R. and Morgan, H. (1985). Thermophilic proteases: Properties and potential applications. *Trends in Biotechnology,* 3: 68–72.
22. Tangboriboonrat, P., Tiyapiboonchaiya, C. and Lerthititrakul, C. (1998). New evidence of the surface morphology of deproteinized natural rubber particles. *Polymer Bulletin,* 41: 601–608.
23. Dee, K. C., Puleo, D. A. and Bizios, R. (2003). An introduction to tissue-biomaterial interactions. John Wiley & Sons.
24. Yazawa, K. and Numata, K. (2014). Recent advances in chemoenzymatic peptide syntheses. *Molecules,* 19: 13755–74.
25. Baker, P. J., Patwardhan, S. V and Numata, K. (2014). Synthesis of homopolypeptides by aminolysis mediated by proteases encapsulated in silica nanospheres. *Macromolecular Bioscience,* 14: 1619–1626.
26. Tangpakdee, J. and Tanaka, Y. (1997). Characterization of sol and gel in hevea natural rubber. *Rubber Chemistry and Technology,* 70: 707–713.
27. Sakdapipanich, J. T. (2007). Structural characterization of natural rubber based on recent evidence from selective enzymatic treatments. *Journal of Bioscience and Bioengineering,* 103: 287–292.
28. Salopek, B., Krasic, D. and Filipovic, S. (1992). Measurement and application of zeta-potential. *Rudarsko-geoloiko-naftni zbornik,* 4: 147–151.
29. Kaszuba, M., Corbett, J., Watson, F. M.and Jones, A. (2010). High-concentration zeta potential measurements using light-scattering techniques. *Philosophical Transactions of The Royal Society A Mathematical Physical and Engineering Sciences,* 368: 4439–4451.
30. Prabhu, S. and Murugan, K. (2015). Zeta potential measurements in colloidal suspensions. *International Conference on Systems, Science, Control, Communication, Engineering and Technology*: pp. 221–224.
31. Honary, S. and Zahir, F. (2013). Effect of zeta potential on the properties of nano-drug delivery systems -A review (Part 2). *Tropical Journal of Pharmaceutical Research,* 12(2): 265–265.
32. Salgın, S., Salgın, U. and Bahadır, S. (2012). Zeta potentials and isoelectric points of biomolecules: the effects of ion types and ionic strengths. *International Journal of Electrochemical Science,* 7: 12404–12414.
33. Gençkal, H. (2004). Studies on alkaline protease production from *Bacillus* sp. Master Dissertation. Izmir Institute of Technology, Turkey.

Malaysian Journal of Analytical Sciences, Vol 22 No 2 (2018): 296 - 302
DOI: https://doi.org/10.17576/mjas-2018-2202-15

MALAYSIAN JOURNAL OF ANALYTICAL SCIENCES
Published by The Malaysian Analytical Sciences Society
ISSN 1394 - 2506

EFFECT OF SILVER ON THE PHYSICAL AND STRUCTURAL PROPERTIES OF LEAD NEODYMIUM BOROTELLURITE GLASS SYSTEM

(Kesan Perak atas Sifat Fizikal dan Struktur Sistem Kaca Plumbum Neodimium Borotelurit)

Norihan Yahya[1]*, Azman Kasim[1], Azhan Hashim[1], Siti Nasuha Rafien[1], Wan Aizuddin Wan Razali[1], Syamsyir Akmal Senawi[1], Ruziana Mohamed[1], Mardhiah Abdullah[2]

[1]*Faculty of Applied Sciences,*
Universiti Teknologi MARA Cawangan Pahang, 26400 Bandar Tun Abdul Razak Jengka, Pahang, Malaysia
[2]*Faculty of Applied Sciences,*
Universiti Teknologi MARA Cawangan Terengganu, Kampus Bukit Besi, 23200 Dungun,Terengganu, Malaysia

**Corresponding author: norihan@pahang.uitm.edu.my*

Received: 4 December 2016; Accepted: 1 December 2017

Abstract

Neodymium doped borotellurite glass is well known to be one of the most promising candidate due to it various applications. Nd^{3+} doped lead borotellurite glasses containing silver were successfully been prepared by conventional melt-quenching method with the chemical composition (69.5-*x*)TeO_2-20B_2O_3-10PbO-0.5Nd_2O_3-*x*$AgNO_3$ (where *x* = 0, 0.5, 1.0, 1.5, 2.0 and 2.5 mol %). The physical properties such as density, molar volume and oxygen packing density were measured. Their structural properties of the glass system were studied via X-Ray Diffraction (XRD) analysis and Fourier Transform Infrared (FTIR) spectroscopy. From the result, the amorphous nature of the prepared glass samples have been confirmed through X-ray diffraction spectral analysis. The presence of Te-O-Te or O-Te-O, Ag-O, Te-O-Pb and B-O and characteristic of the hydrogen bond in the prepared glasses were explored through the FTIR spectral studies recorded in the 400-4000 cm^{-1} wave number range at room temperature. Meanwhile, the results of physical properties are found to vary with respect to concentration of $AgNO_3$ content. Some other results will be reported and discussed.

Keywords: neodymium, borotellurite, silver, physical properties, structural properties

Abstrak

Kaca borotelurit di dop neodimium merupakan salah satu bahan yang diyakini disebabkan oleh kepelbagaian aplikasinya. Kaca borotelurit di dop Nd^{3+} mengandungi perak telah berjaya disediakan dengan kaedah konvensional sepuh lindap dengan komposisi kimia (69.5-*x*)TeO_2-20B_2O_3-10PbO-0.5Nd_2O_3-*x*$AgNO_3$ (di mana x = 0, 0.5, 1.0, 1.5, 2.0 dan 2.5 mol%). Sifat-sifat fizikal seperti ketumpatan, isipadu molar dan ketumpatan padat oksigen telah diukur. Sifat-sifat struktur sistem kaca ini telah dikaji melalui analisis pembelauan sinar-X (XRD) dan spektroskopi inframerah transformasi Fourier (FTIR). Dari hasil kajian, sifat semulajadi amorfus sampel kaca yang disediakan telah disahkan melalui analisis spektra pembelauan sinar-X. Kehadiran Te-O-Te atau O-Te-O, Ag-O, Te-O-Pb, B-O dan ciri-ciri ikatan hidrogen dalam kaca yang disediakan telah diterokai melalui kajian spektra FTIR yang direkodkan dalam julat gelombang 400-4000 cm^{-1} pada suhu bilik. Sementara itu, hasil kajian bagi sifat fizikal didapati berubah mengikut kepekatan kandungan $AgNO_3$. Beberapa keputusan lain akan dilaporkan dan dibincangkan.

Kata kunci: neodimium, borotelurit, perak, sifat fizikal, sifat struktur

Introduction

The physical and structural studies of glass oxide incorporated with various rare earth (RE) draw much attention due to their important role in the development of many optical devices such as infrared laser, colour display devices, optical detectors, light converters and sensors [1]. Among the oxide glass, lead borotellurite glass systems were much attractive due to their high density, high refractive index [2], low phonon energies (~700 cm^{-1}), extended infrared transmittance (0.35-6.0 μm), large corrosion resistance, high mechanical strength and relatively high thermal stability [3, 4]. The glass hosts are excellent candidate for laser applications due to their low cost as well as ease to fabricate in various geometries [5]. In the literature there are relatively few reports on the structural properties of glass doped with Nd^{3+} ions [6, 7]. Recently study reported on the effects produced by the codoping with silver nitrate of glasses doped with various RE ions on the structural properties [8] that confer potential applications for these material. In this work, we prepared some Nd^{3+} doped lead borotellurite glass containing silver. The sample have a fixed Nd^{3+} and PbO content whereas the TeO_2:$AgNO_3$ content are varied. The physical properties by mean of their density, molar volume as well as the oxygen packing density (OPD) will be determined. Meanwhile, their structural study will be identify using the X-ray diffraction (XRD) and Fourier transform infrared (FTIR) spectroscopy. However, the aim of this study was to investigate the influence of silver on the physical and structural properties of the investigated materials.

Materials and Methods

Glasses with chemical composition (69.5-*x*)TeO_2-20B_2O_3-10PbO-0.5Nd_2O_3-*x*$AgNO_3$ (*x* = 0.0, 0.5, 1.0, 1.5, 2.0 and 2.5 mol%) were prepared by a conventional melt-quenching method using reagents of analytical grade. The chemicals of the required compositions of approximately 10g batches were weighed in an electrical balance and mixed thoroughly in milling process about 1 hour in order to obtain homogeneous mixtures. The mixture was melted at 1000 °C for 30 minutes in an electric box furnace. The mixture was then poured into stainless steel plate and immediately transferred into a preheated furnace for annealing process at temperature 400 °C for 3 hours before allowed to cool down gradually to room temperature. The glass samples of each composition were prepared and polished to obtain a planar faces for structural analysis. The composition of the investigated glasses are listed in Table 1.

Table 1. Chemical Composition of (69.5-*x*)TeO_2-20B_2O_3-10PbO-0.5Nd_2O_3-*x*$AgNO_3$ glass system

Sample No	Composition (mol%)				
	TeO_2	B_2O_3	PbO	Nd_2O_3	$AgNO_3$
S1	69.5	20	10	0.5	0.0
S2	69.0	20	10	0.5	0.5
S3	68.5	20	10	0.5	1.0
S4	68.0	20	10	0.5	1.5
S5	67.5	20	10	0.5	2.0
S6	67.0	20	10	0.5	2.5

The density of the glass samples was measured using distilled water as an immersion liquid by Archimedes' principle on a Electronic Densimeter MD-300S balance. Formula for calculating density, molar volume and oxygen packing density is given in Table 2. The structural properties of the glass samples were analyzed using X-Ray Diffraction (XRD) analysis which is performed at room temperature to confirmed its amorphous nature. The Fourier Transform Infrared (FTIR) spectroscopy absorption spectra of the glass samples were recorded on Perkin-Elmer Spectrum 100 FT-IR Spectrometer at room temperature in the wavenumber range 400-4000 cm^{-1} with a resolution of 4 cm^{-1}.

Table 2. Formulas for calculating physical properties of silver addition of lead borotellurite glass.

Eq. No.	Parameter	Formula	Description
1	Density (ρ)	$\rho = \left(\frac{W_a}{W_a - W_{dw}} \right) \rho_{dw}$	W_a - Weight of sample in air W_{dw} - Weight of sample in distilled water ρ_{dw} - Density of distilled water
2	Molar volume (V_m)	$V_m = \frac{M_{ave}}{\rho}$	M_{ave} - Average molecular weight ρ - Density
3	Oxygen packing density (OPD)	$1000n \times \frac{\rho}{M_{ave}}$	n - Number of oxygen atoms per formula ρ - Density M_{ave} - Average molecular weight

Results and Discussion

Physical properties

Table 3 shows the result of density and molar volume of Nd^{3+} doped lead borotellurite glass containing silver and Figure 1 shows the variation of density and molar volume with respect to silver content. As tabulated in the Table 3, the density of glass was found to increase from 4.969 gcm^{-3} to 5.053 gcm^{-3} with the increasing concentration of $AgNO_3$ from 0.0 mol% to 1.0 mol% before it start to decrease to 5.028 gcm^{-3} at 1.5 mol% of $AgNO_3$. By increasing of some amount of $AgNO_3$, the formation of non-bridging oxygen (NBO) take place and caused the modification of glass network brought extra compactness with higher density but shrinkage in free volume [9]. However, the density of glass seem to decreases slightly at the 1.0 mol% of $AgNO_3$. This may be due to the fact that an occupation of Ag between 1.0 to 1.5 mol% in the free space region in the network structure cause the compactness reduction of the glass network [10]. Meanwhile, the result of molar volume of the glass sample decrease from 29.642 cm^3/mol to 29.169 cm^3/mol with the increasing concentration of $AgNO_3$ from 0.0 mol% to 1.0 mol% before it start to increase to 29.324 cm^3/mol at 1.5 mol%. This trend of results are expected due to incorporation of Ag of radii 1.65 pm to replace Te of radii 1.23 pm tend to alter the glass network. This trend results has been observed by Yusof et al. [11].

Table 3. Physical properties of silver addition of lead borotellurite glass.

Physical Parameters	Unit	Glass Name					
		S1	S2	S3	S4	S5	S6
Density (ρ)	(g/cm^3)	4.969	4.980	5.053	5.028	5.031	5.071
Average molecular weight (M_{ave})	(g)	147.289	147.340	147.392	147.443	147.494	147.546
Molar volume (V_m)	(cm^3/mol)	29.642	29.586	29.169	29.324	29.317	29.096
Oxygen packing density (OPD)	(g.atom/L)	71.015	71.317	72.508	72.295	72.483	73.206

Meanwhile, the oxygen packing density (OPD) is the important parameter to explain the compactness of glass structure [12] and to measure of the tightness of the oxide network [13]. OPD measurements of all glass samples can be calculated using equation 3 from Table 2 and the results are listed in Table 3. As depicted in Figure 2, the OPD seen to vary with respect to silver content. From Figure 2 the OPD are found to increase from 71.015 g.atom/L to 72.508 g.atom/L with the increasing of $AgNO_3$ content from 0.0 mol% to 1.0 mol%. However, the values of oxygen packing density drop slightly to 72.295 g.atom/L as the $AgNO_3$ increased to 1.5 mol%. The results are then start to increase again from 72.483 g.atom/L to 73.206 g.atom/L as the $AgNO_3$ increase from 1.5 mol% to 2.5 mol%. This results show the similar trends to the density with respect to silver content [14].

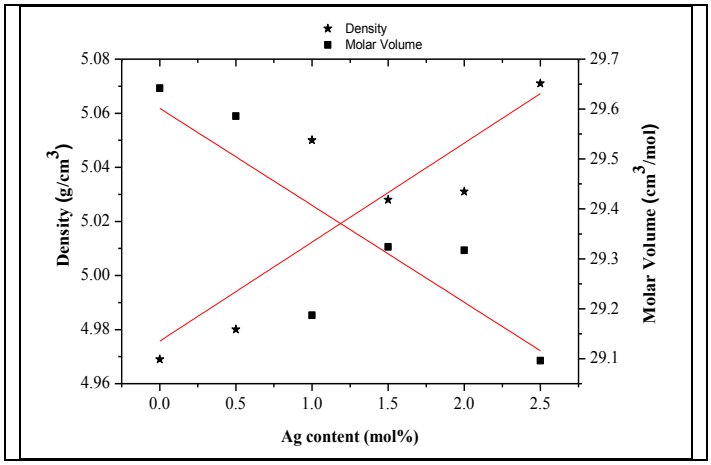


Figure 1. Variation of density and molar volume of silver addition of lead borotellurite glass

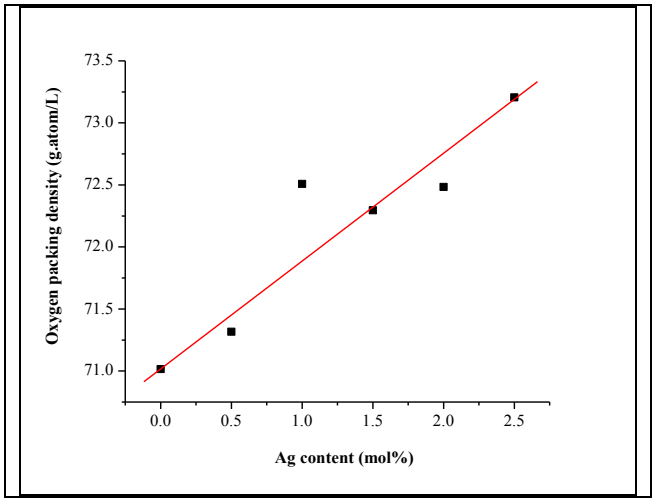


Figure 2. Variation of OPD of silver addition of lead borotellurite glass

Structural properties

The amorphous nature of the glass system (69.5-x)TeO_2-20B_2O_3-10PbO-0.5Nd_2O_3-$x$$AgNO_3$ with x varying from 0.0 to 2.5 mol% of $AgNO_3$ were confirmed through the x-ray diffraction pattern recorded in the range $10° \leq \theta \leq 90°$ as shown in Figure 3. As in Figure 3, there are no sharp peaks but broad hump diffusion been observed. This confirm the amorphous nature of the glass samples [15]. It can also be observed that the intensity of pattern in all glass samples is slightly different, thus indicating that the glass samples have a different degree of amorphousity. This result shows a good agreement with previous study [16].

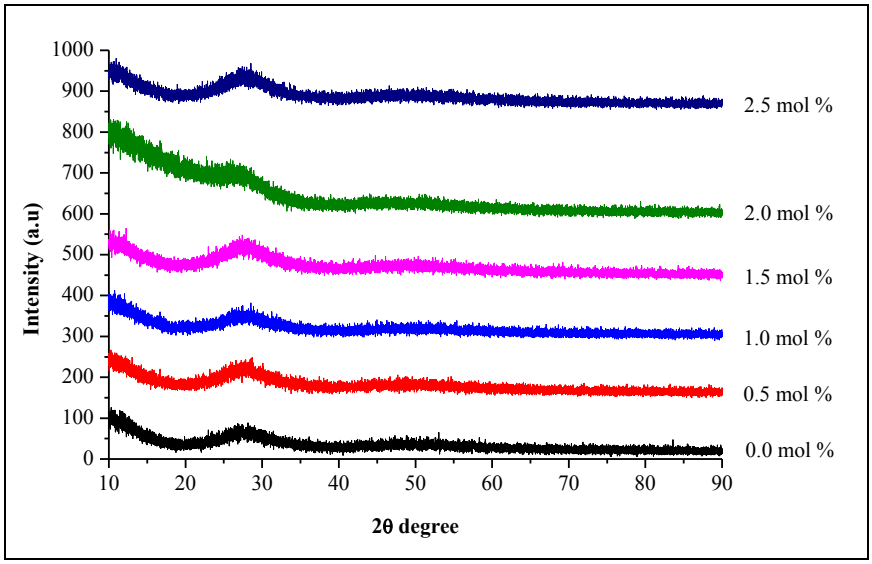


Figure 3. XRD pattern of silver addition of lead borotellurite glass.

In this work, FTIR spectroscopy was carried out in order to identify the existing functional groups peak in the glass networks. Therefore, Figure 4 shows the FTIR spectra of lead borotellurite glass in the range between 400-4000 cm^{-1} for different glass compositions. From Figure 4, the FTIR spectra of the borotellurite glasses show six significant IR absorptions bands respectively. Their peak assignments of these glasses are listed in Table 4 based on the literature data on the wavenumber ranges that related to the corresponding vibrations of the structural units in various glassy system.

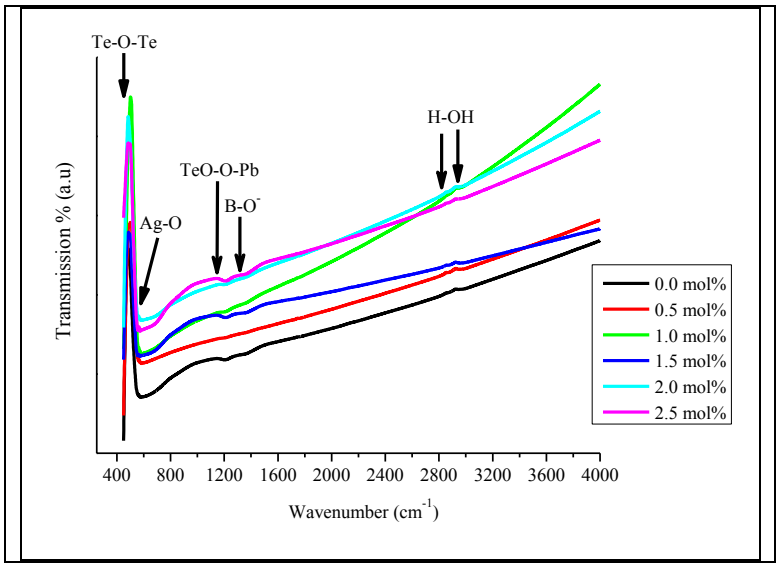


Figure 4. IR spectra of silver addition of lead borotellurite glass

As can be seen from Table 4, the bands are found in the regions around 460-476 cm^{-1}, 552-575 cm^{-1}, 1177-1209 cm^{-1}, 1350-1371 cm^{-1}, 2872-2880 cm^{-1} and 2940-2960 cm^{-1} wavelength respectively. The spectra bands observed between 460 cm^{-1} and 476 cm^{-1} are belongs to the Te-O-Te or O-Te-O symmetric stretching vibrations mode at corner sharing sites. This indicates that the vibrations of Te-O-Te or O-Te-O linkage in these glasses are corresponding to the transformation of TeO_4 group into TeO_3 groups [17]. Meanwhile, the bands around 552-575 cm^{-1} are assigned to symmetrical bending vibrations of Ag-O bond [18]. The IR absorption at around 1177-1209 cm^{-1} are attributed to the Te-O-Pb streching vibrations. This result indicates that the addition of PbO into the glass network could cause a change to the Te coordination polyhedron from TeO_4 trigonal bipyramid (tbp) to TeO_3 trigonalpyramid (tp) thus creating more non-bridging oxygen's (NBOs) [19]. The bands occurring in the spectral range 1350-1371 cm^{-1} are attributed to the B-O stretching vibration in BO_3 units. These bands are similar reported by Pawar et al. [20]. Finally, the absorption bands located around 2872-2880 cm^{-1} and 2940-2960 cm^{-1} are due to the characteristic of the hydrogen bond in the glass samples [21].

Table 4. IR band assignments of silver addition of lead borotellurite glass.

Characteristic Bands (cm^{-1})	**Assignment**
460 - 476	Stretching vibrations modes of Te-O-Te or O-Te-O
552 - 575	Bending vibrations of Ag-O
1177 - 1209	Streching vibrations of Te-O-Pb
1350 - 1371	B-O stretching vibration in BO_3
2872 - 2880	Hydrogen bond
2940 - 2960	Hydrogen bond

Conclusion

A series of glass of the system of $(69.5\text{-}x)TeO_2\text{-}20B_2O_3\text{-}10PbO\text{-}0.5Nd_2O_3\text{-}xAgNO_3$ where x = 0.0, 0.5, 1.0, 1.5, 2.0 and 2.5 mol% have been well fabricated as they are in a good quality as visualized. The density of the glasses increased from 4.969 gcm^{-3} to 5.053 gcm^{-3} while their molar volume values decreases from 29.642 cm^3/mol to 29.169 cm^3/mol with respect to $AgNO_3$ content. The oxygen packing density (OPD) show the same trend to the density as they vary from 71.015 g.atom/L to 73.206 g.atom/L with respect to $AgNO_3$ content. The XRD results confirmed fact the glasses obtained are amorphous in nature. The FTIR spectra indicated the presence of Te-O-Te or O-Te-O, Ag-O, Te-O-Pb and B-O functional group of the glass network.

Acknowledgements

The author wishes to thanks Ministry of Education (MOE), Malaysia for the Research Acculturation Grant Scheme (RAGS) research grant and UiTM Pahang for the encouragement and support.

References

1. Selvi, S., Venkataiah, G., Arunkumar, S., Muralidharan, G. and Marimuthu, K. (2014). Structural and luminescence studies on Dy^{3+} doped lead boro-telluro-phosphate glasses. *Physica B*, 454: 72-81.
2. Karthikeyan, P., Vijayakumar, R. and Marimuthu, K. (2017). Luminescence studies on Dy^{3+} doped calcium boro-tellurite glasses for White light application.. *Physica B*, 521: 347-354.
3. Selvaraju, K. and Marimuthu, K. (2012). Structural and spectroscopic studies on concentration dependent Er^{3+} doped boro-tellurite glasses. *Journal of Luminescence*, 132: 1171-1178.
4. Sasikala, T., Rama Moorthy, L. and Mohan Babu, A. (2013). Optical and luminescent properties of Sm^{3+} doped tellurite glasses. *Spectrochimica Acta Part A: Molecular and Biomolecular Spectroscopy*, 104: 445-450.
5. Maheshvaran, K., Linganna, K. and Marimuthu, K.. (2011). Composition dependent structural and optical properties of Sm^{3+} doped boro-tellurite glasses. *Journal of Luminescence*, 131: 2746-2753.
6. Hasim, N., Rohani, M. S. and Sahar, M. R. (2016). Structural Characteristics of Er^{3+} and Nd^{3+} doped Lithium Niobate Tellurite Glass. *Materials Science Forum*, 846: 126-130.

7. Linganna, K., Narro-García, R., Desirena, H., De la Rosa, E., Basavapoornima, Ch., Venkatramu, V. and Jayasankar, C. K. (2016). Effect of P_2O_5 addition on structural and luminescence properties of Nd^{3+}-doped tellurite glasses. *Journal of Alloys and Compounds*, 684: 322-327.
8. Reza Dousti, M. and Raheleh Hosseinian, S. (2014). Enhanced upconversion emission of Dy^{3+}-doped tellurite glass by heat-treated silver nanoparticles. *Journal of Luminescence*, 154: 218-223.
9. Ashur, Z., Mahraz, S., Sahar, M. R. and Ghoshal, S. K. (2015). Enhanced luminescence from silver nanoparticles integrated Er^{3+}-doped boro-tellurite glasses: Impact of annealing temperature. *Journal of Alloys and Compounds*, 649: 1102-1109.
10. Huang, B., Zhou, Y., Cheng, P., Zhou, Z., Li, J. and Yang, G. (2016). The 1.85 μm spectroscopic properties of Er^{3+}/Tm^{3+} co-doped tellurite glasses containing silver nanoparticles. *Journal of Alloys and Compounds*, 686: 785-792.
11. Yusoff, N. M. and Sahar, M. R. (2015). Effect of silver nanoparticles incorporated with samarium-doped magnesium tellurite glasses. *Physica B*, 456: 191-196.
12. Terny, S., De la Rubia, M.A., Alonso, R. E., J. de Frutos and Frechero, M. A. (2015). Structure and electrical behavior relationship of a magnesium-tellurite glass using Raman and impedance spectroscopy. *Journal of Non-Crystalline Solids*, 411: 13-18.
13. Farouk, M., Samir, A., Metawe, F. and Elokr, M. (2013). Optical absorption and structural studies of bismuth borate glasses containing Er^{3+} ions. *Journal of Non-Crystalline Solids*, 371-372: 14-21.
14. Farag, M. A., Abd-Allah, K., Turky, G. and Alokr, M. M. (2015). Optical and Upconversion properties of Nd^{3+} doped lead borate barium glass system. *Nature and Science*, 13(5): 123-129.
15. Ratnakaram, Y. C., Babu, S., Krishna Bharat, L. and Nayak, C. (2016). Fluorescence characteristics of Nd^{3+} doped multicomponent fluoro-phosphate glasses for potential solid-state laser applications. *Journal of Luminescence*, 175: 57-66.
16. Azevedo, J., Coelho, J., Hungerford, G. and Sooraj Hussain, N. (2010). Lasing transition ($^4F_{3/2}$-$^4I_{11/2}$) at 1.06 μm in neodymium oxide doped lithium boro tellurite glass. *Physica B*, 405: 4696-4701.
17. Surendra, B. S., Rajeswari, R., Kiwan, J. Cho, E. J., Kyoung, H. J., Hyo, J. S. and Jayasankar, C. K. (2010). Spectroscopic investigations of 1.06 μm emission in Nd^{3+}-doped alkali niobium zinc tellurite glasses. *Journal of Luminescence*, 130: 1021-1025.
18. Bolundut, L., Culea, E., Borodi, G., Stefan, R., Munteanu, C. and Pascuta, P. (2015). Influence of Sm^{3+}:Ag codoping on structural and spectroscopic properties of lead tellurite glass ceramics. *Ceramics International*, 41: 2931-2939.
19. Nurbaisyatula, E. S., Azman, K., Azhan, H., Razali, W. A. W. and Noranizah, A. (2014). The structural properties of trivalent rare earth ions (Er^{3+}) doped borotellurite glass. *Jurnal Teknologi*, 69(2): 97-100.
20. Pawar, P. P., Munishwar, S. R. and Gedam, R. S. (2016). Physical and optical properties of Dy^{3+}/Pr^{3+} Co-doped lithium borate glasses for W-LED. *Journal of Alloys and Compounds*, 660: 347-355.
21. Vijayalakshmi, L., Naveen, K. and Vijayalakshmi, R. P. (2016). Energy transfer based photoluminescence spectra of co-doped (Dy^{3+}+Sm^{3+}): Li_2O-LiF-B_2O_3-ZnO glasses for orange emission. *Optical Materials*, 57: 125-133.

Malaysian Journal of Analytical Sciences, Vol 22 No 2 (2018): 303 - 310
DOI: https://doi.org/10.17576/mjas-2018-2202-16

MALAYSIAN JOURNAL OF ANALYTICAL SCIENCES
Published by The Malaysian Analytical Sciences Society
ISSN 1394 - 2506

EVALUATION OF DOSE SENSITIVITY RESPONSE VIA OPTICAL CHARACTERISTICS FOR CRESOL RED-DYED POLYHYDROXYETHYLMETHACRYLATE GEL (PHEMAG)

(Penilaian Respons Kepekaan Dos Melalui Ciri Optikal Bagi Kresol Merah-Dicelup Polihidrosietilmetakrilik Gel (PHEMAG))

Nur Sha'adah Zainuddin[1]*, Fairuzdzah Ahmad Lothfy[1], Hartini Ahmad Rafaie[1], Mazlini Mazlan[2], Iskandar Shahrim Mustafa[3], Azhar Abdul Rahman[3]

[1]*Faculty of Applied Sciences,*
Universiti Teknologi MARA Pahang, 26400 Bandar Tun Abdul Razak Jengka, Pahang, Malaysia
[2]*Faculty of Applied Sciences,*
Universiti Teknologi MARA Tapah, 35400 Tapah, Perak, Malaysia
[3]*School of Physics,*
Universiti Sains Malaysia, 11800 Minden, Pinang, Malaysia

**Corresponding author: nsz@pahang.uitm.edu.my*

Received: 4 December 2016; Accepted: 1 December 2017

Abstract

A new polymer gel blended with the acid base indicator of cresol red were prepared consisted of 4%, 5% and 6% of monomer (2-Hydroxyethyl Methacrylate; HEMA) in order to characterize the radiation induced changes known as cresol red Polyhydroxyethylmethacrylate Gel (PHEMAG). Cresol red-dyed PHEMAG were prepared consisted of gelatin, deionized water, HEMA, cresol red sodium salt stock solution and ascorbic acid. The polymerization Cresol red-PHEMAG was studied with 6 MV photon beam rates 300 Gy/min which received doses up to 40 Gy for the reveletion sensitivity as a function of absorbed dose based on the physical properties by using UV-Vis spectroscopy. It is indicated that 4% of HEMA exhibited a greater sensitivity of the polymer gel dosimeter based on a mathematical model of the fitting equation of the dose response curve. The value of $\boldsymbol{D}_o$ (sensitivity parameter) for 4% of HEMA is the lowest about 42.373 Gy. The lower value of $\boldsymbol{D}_o$ would cause the higher radiosensitive of the matter which was actively reacted at the time of exposure.

Keywords: absorbed dose, cresol red, photon beam, polymer gel

Abstrak

Gel polimer baru dicampur dengan penunjuk asas asid kresol merah telah disediakan yang terdiri daripada 4%, 5% dan 6% daripada monomer (2- hidrosietilmetakrilik; HEMA) untuk mencirikan radiasi mendorong perubahan yang dikenali sebagai Kresol merah-dicelup Polihidrosietilmetakrilik Gel (PHEMAG). Kresol merah – dicelup PHEMAG telah dihasilkan terdiri daripada gelatin, air nyah ion, HEMA, stok larutan kresol merah natrium garam dan asid askobik. Pempolimeran kresol merah PHEMAG telah dikaji dengan pancaran foton 6 MV pada kadar yang berterusan 300 Gy/min yang menerima dos sehingga 40 Gy untuk mendedahkan kepekaan sebagai fungsi dos terserap berdasarkan sifat-sifat fizikal dengan menggunakan spektroskopi UV-Vis. Ia menunjukkan bahawa 4% daripada HEMA menghasilkan kepekaan polimer gel dosimeter yang lebih tinggi berdasarkan model persamaan matematik sesuai tindak balas dos keluk. Nilai $\boldsymbol{D}_o$ (parameter sensitiviti) untuk 4% daripada HEMA adalah yang paling rendah kira-kira 42.37 Gy. Nilai yang lebih rendah daripada $\boldsymbol{D}_o$ akan menyebabkan radiosensitif jisim yang bertindak balas secara aktif pada masa pendedahan.

Kata kunci: dos terserap, kresol merah, pancaran foton, gel polimer

Introduction

Dosimeter is a device that would able to measure quantitatively such as absorbed dose, equivalent dose or other related radiation quantities. This variation of dosimeter is mostly required to exhibit an ideal dosimeter based on the energy deposited in term of absorbed dose for the detection limit from exceeding the dose required during the treatment either from radiology or industry modalities. Polymer gel dosimeter promises a great response of the absorbed dose in three dimensions that able to overcome the limitation of the common dosimeter such as absolute dosimeter and ionization chamber. These responses based on retaining of 3D spatial dose distribution mostly in the application of radiology and radiotherapy treatment [1, 2]. Basically, the radiological treatment is mostly targeted on the carcinogenic tissue of the patient by considering the limitation of the surrounding tissue. The integrated of absorbed dose in 3D of polymer gel, raises great interest amongst the researcher in order to improve their accuracy, sensitivity, reproducibility and stability of the dosimeter. The first polymer gel created by Fricke and Morse in 1927 is according to the radiation-induced ferrosulphate solution until a further development with the addition of the monomer and then blend with the gel matrix. This revolution of the polymer gel dosimeter has been exposed by a different type of radiation modality that has either low or high energy, and characterizes absorbed dose in terms of physical, and structural characterization [3-5]. The solid polymer blends with the dyes that have a great response to transition of visual color and acts as a radiation-sensitive indicator that could be the prior requirement to ascertain the absorbed dose displayed once it is introduced to the ionizing radiation [6, 7]. Thus by this concept of this solid polymer blend cresol red dye, it shows a great response of optical properties and optical transitions which leads to the use of the gelatins compared of the solid polymer as a gelling agent in order to maintain the polymer aggregated for the post irradiation. The main objective of this project was to fabricate and characterized the optical properties and dosimetric parameter of radiation-induced cresol red-dyed PHEMAG as a dosimeter according to the various of the concentration of monomer (HEMA). The high energy of photon beam that induced the color transition of cresol red-dyed PHEMAG was being measured quantitatively and qualitatively according to its pH, visible absorption dose response and structural characterization.

Materials and Methods

Stock solution of cresol red

The stock solution of Cresol Red as an acid-base indicator is synthesised based on the formulation introduced by Ebraheem et al. [7] and was modified in terms of controlling its pH level in a basic form for cresol red-dyed PHEMAG before irradiated [6, 8]. A purple form of basic cresol red dye which is alkaline in the range of pH > 8.8 whereas in the acidic form in the range of 2.8 < pH < 7.2 [6]. For that purpose, 0.08 g of cresol red (product of R&M chemicals) was dissolved in 15 ml of aqueous NaOH solution ([NaOH]=1.0 mol/l) and completed its final volume with ethanol in 50 ml volumetric flask. This stock solution was stirred for 5 minutes at room temperature to ensure a homogenous cresol red dye stock solution.This stock solution was stored in a refrigerator (4 $^{\circ}$C) overnight and covered withopaque ziplock bags prior to minimize the degradation of the the dye from direct sunlight since the dye is a photosensitizer [9].

Synthesis of Cresol red-dyed Polyhydroxyethylmethacrylate(PHEMAG) gel dosimeter

The PHEMAG gel dosimeter formulation, introduced by Rozlan et al. [10], was used as a foundation to study a new polymer gel dosimeter with a different concentration of monomer (HEMA) and doped with the cresol red dye. This new synthesis of polymer gel was named as Cresol red-dyed PHEMAG polymer gel dosimeter. Cresol red-dyed PHEMAG were prepared consisted of 8% (w/w) gelatine (bovine skin, Type B, Sigma Chemical Co), 88 % (w/w) of deionized water, (4%, 5% and 6% (w/w) of 2-Hydroxyethyl Methacrylate, HEMA 96% stabilized from ACROS Organics), 5 mL of cresol red sodium salt stock solution and 4mM of antioxidant (AA) (CalbioChem) under normal atmospheric conditions [11]. The antioxidant was used in order to inhibit free radical copolymerization reactions for normoxic polymer gel dosimeter [12, 13]. The gelatine was dissolved with deionized water, allowed to swell and stirred with magnetic stirrer by heating up to 50^{O}C in the water bath until a clear solution is shown. Then the gelatin solution was cooled down until reached it reach of 40 °C. An amount of 5 ml cresol red sodium salt stock solution is added in the mixture. The mixture solution show the changes in colour from purple to red-orange which was correlated to its pH transition in basic form around pH > 8 [10]. Lastly, HEMA and AA were added and stirred at a room temperature for half an hour. Throughout the cooling process of the mixed solution, the beakers were covered

with the aluminium foils and covered with the opaque wrapper in order to minimize the polymer gel from light-induced polymerization.It was then filled into the 4 ml cuvette and sealed with parafilm tape [9]. The gels were stored in a refrigerator (4^{O}C) overnight in order to solidify the cresol red dye polymer gel for pre and post irradiation process.

pH measurement and UV absorbance

After the fabrication of the polymer gel (before stored in the freezer), the pH for each batch of cresol red-dyed PHEMAG in aqueous solution was measured by using a digital pH meter pen respectively. Before taking the measurement, the pH meter was calibrated by using a buffer solution of pH 7 right after the electrode was rinsed with the distilled water. In addition, the UV-1800 Shimadzu spectrophotometer was used to analyze the absorption spectra of cresol red-dyed PHEMAG pre and post irradiated in the range of 200 nm and 800 nm by using the double beam photometric system and air as reference.

Irradiation of cresol red-dyed PHEMAG

All the samples were studied for their characteristics based on physical properties such absorption response curve and sensitivity according to the radiation-induced of the polymer gels. After solidify for overnight all the batches of the polymer gels were irradiated using Siemens Mevatron Linear Accelerator (LINAC) at Mount Miriam Cancer Hospital (MMCH) with parallel opposed 15 cm x 15 cm beams. This was so that the uniform dose distribution between 25 Gy up to 40 Gy of accumulated dose could be received. Also, the unirradiated bathces were left as background reading. The Perspex slab 30 cm width x 30 cm length) with the total thickness around 1.2 cm is used as cuvettes holder. The cuvettes is placed in the middle of the separation distance of 10 cm of solid water phantom slabs. The source-surface distance (SSD) was set at 95 cm so that the samples were irradiated isocentrically at 5 cm depth from the surfaces of the phantom with equally weighted. Then, 4.4 cm of solid water phantoms were placed on top of the polymer gels to give adequate build-up of the region of irradiation dose. It also minimizes backscatter radiation for maximum absorbed dose once the photon beam interacts with the polymer gel [5, 14].

Results and Discussion

Indicator basicity of Cresol red-dyed PHEMAG

The mixture of the gelatine with water created the acidity of pH 5.5, meanwhile a stock solution of cresol red with pH 13.10 is made in high concentration of basicity with optimum molarity of 1.0M NaOH. The molarity of NaOH is crucial in order to control the final basicity of cresol red-dyed PHEMAG before irradiated based on the physical changes of color as shown in Figure 1. As illustrated in Figure 1, the colour variation of polymer gel and the pH value shows that the optimum molarity of 1.0M NaOH is the most suitable concentration to be used during the fabrication process which acts as colour indicator. The pH value in Figure 1(a) is 7 whereas in Figure 1(b) is 8.9 that can be correlated to the color transition based on research work done by Susilawati in 2005 [15] as depicted in Figure 3(a).

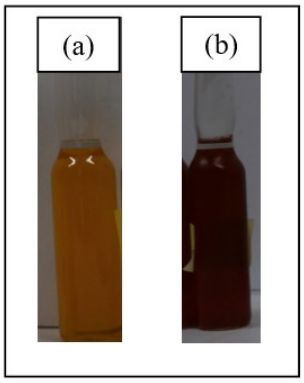
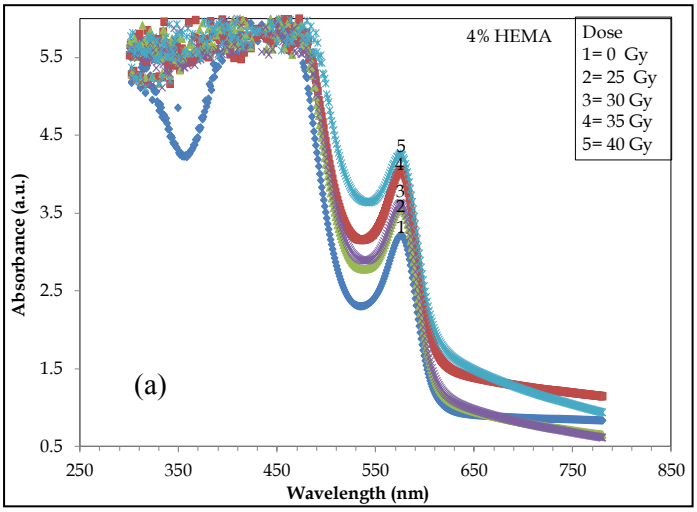


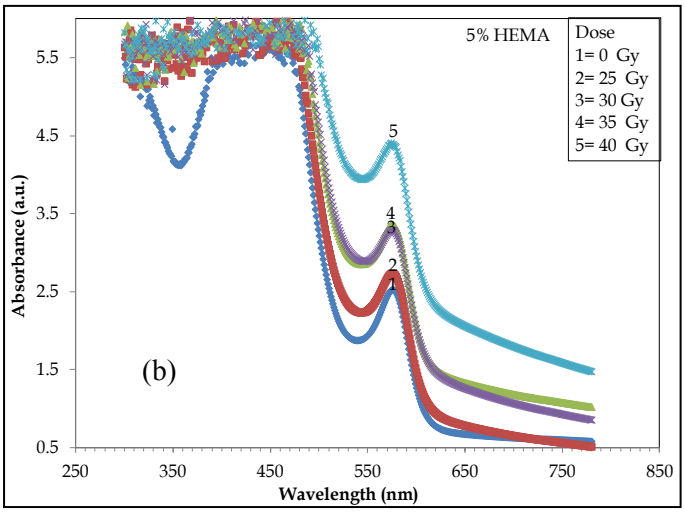
Figure 1. The physical changes of cresol red-dyed PHEMAG before irradiated (a) cresol red-dyed PHEMAG consist of 0.1 M of NaOH and (b) cresol red-dyed PHEMAG consist of 1.0 M of NaOH

Visible absorption spectra

The effect of ionizing radiation on cresol red-dyed PHEMAG was measured by using UV-Vis spectroscopy for the absorbance spectra corresponding to the absorbed dose 25 Gy up to 40 Gy respectively for 4%, 5% and 6% of HEMA as shown in Figure 2.

The maximum absorbance at wavelength 575 nm was chosen, and it is indicated that the dosimetric properties for the visual red orange color of the cresol red-dyed PHEMAG [8, 16]. The pH value for pre-irradiation of cresol red-dyed PHEMAG was around 8.33±0.15 as the basic visual color of red-orange before it is changed into orange after irradiation. From the Figure 2 (c), 575 nm band showed a gradually increment as compared to Figure 2(a) and (b) which illustrate slight increament with the increased of the absorbed dose. It was mainly due to the radiolysis of water molecules of polymer gel. It also caused the slightly dissociations of cresol red dye into acidic but still in basic solution [16]. Indirectly, the free radicals that were formed reacted with the cresol red dye hence slightly contributed to the formation of H^+ in volume interest of cresol red-dyed PHEMAG. With the highest absorbed dose (40 Gy), the absorption band increased at 575 nm due to the disorder defect in the amorphous nature in the polymer chain of PHEMAG. Hence, it induced more degradation and discoloration of cresol red-dyed PHEMAG. It attributed to the formation of acidic form in the reaction further with cresol red dye which changing the colour from red-orange towards orange as illustrated in Figure 3(b) [8].





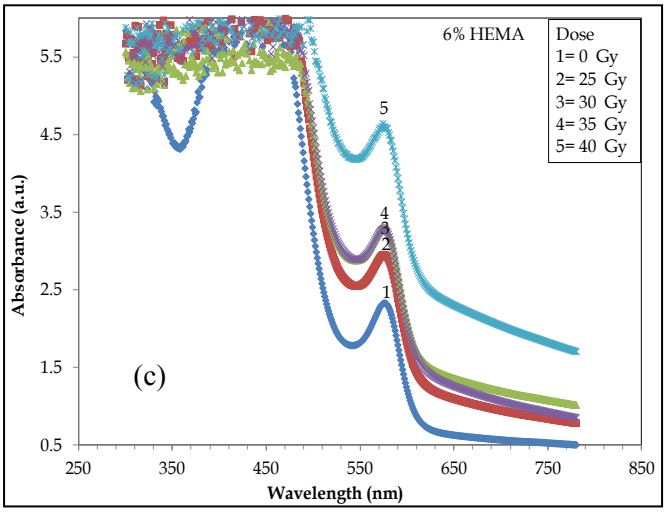


Figure 2. Absorption spectra of the cresol red-dyed PHEMAG pre and post irradiation for (a) 4% of HEMA, (b) 5% of HEMA and (c) 6% of HEMA

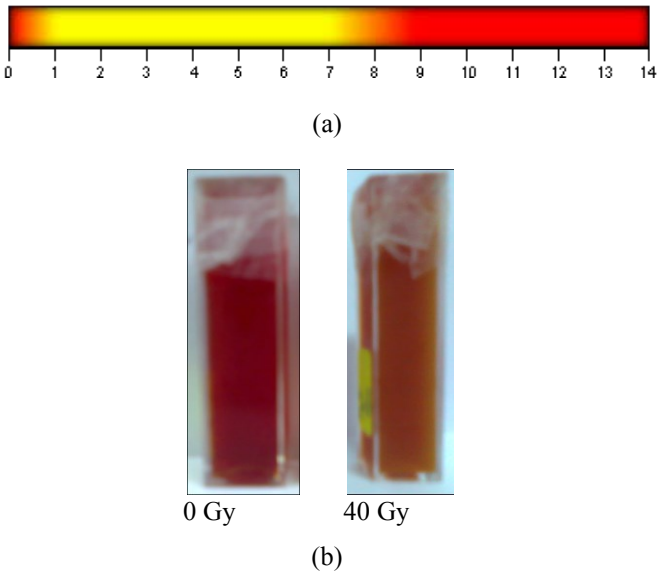


Figure 3. The visual color transition of (a) cresol red in basic solution, (b) cresol red-dyed PHEMAG for 4 % HEMA

Dose response curves

Dose response is defined as the dose range over defined energy that is proportional to the amount of incident radiation [17]. The dose response curve of cresol red-dyed PHEMAG consisted of varying concentrations of HEMA is shown in Figure 4 was established in terms of change in absorbance per unit length cuvette at 575 nm wavelength against the absorbed dose respectively in relation formulated by Abdel-Fatteh [18]. Equation (1) was used as followed:

$$\Delta A = | A_o - A_i | \quad (1)$$

where A_o is the absorbance of the unirradiated and A_i refer for the absorbance of irradiated cresol red-dyed PHEMAG.

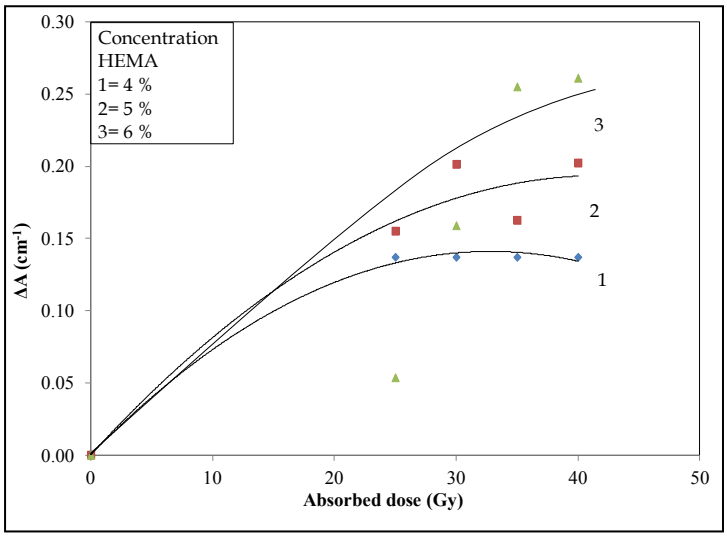


Figure 4. The change in absorbance, ΔA as a function of absorbed dose of cresol red-dyed PHEMAG at 575 nm with different concentration of monomer

Obviously in Figure 4, the dose response curve of maximum absorbance at 575 nm shows a minor increament with the increased of the concentration HEMA and absorbed dose. Thus, radiation-induced cresol red-dyed PHEMAG led to the yield of acidic form is due to the water radiolysis which indicate the presence of H^+ [16], hence more chain polymerization would occur between HEMA and cresol red dye. In addition, maximum absorbance at 575 nm showed a slightly exponential increment with absorbed dose that is fully parallel to the mathemathically model of the fitting equation as follows:

$$y = y_o e^{-D/D_o} \quad (2)$$

where y_o is the unirradiated absorbance, *D* is referred as the absorbed dose and *Do* is referred as 'sensitivity parameter' that also known as the dose sensitivity which refer to minimum amount of dose required to reduce the fraction of molecules for breaking down the monomer to 37% of the cresol red-dye PHEMAG. In other words, 37% of the absorbed dose is required for the consumption of HEMA in order to degrade the chemical bond during the chain polymerization of cresol red-dyed PHEMAG. Fitting equation curve to the concentration of HEMA showing a linear relationship with *Do* as shown in Figure 5.

Eventually, the lower concentration of HEMA for 4% ,5% and 6% of cresol red-dyed PHEMAG would exhibit greater sensitive reaction upon irradiation. As depicted for, 4 % of HEMA is having the lowest sensitivity which is 42.37 Gy, whereas 5% and 6 % of HEMA having 59.52 Gy and 97.09 Gy respesctively. Thus, the value of *Do* for 4% of HEMA exhibited a greater sensitivity in order to consume 37% of monomer in the propagation of chain polymerization.

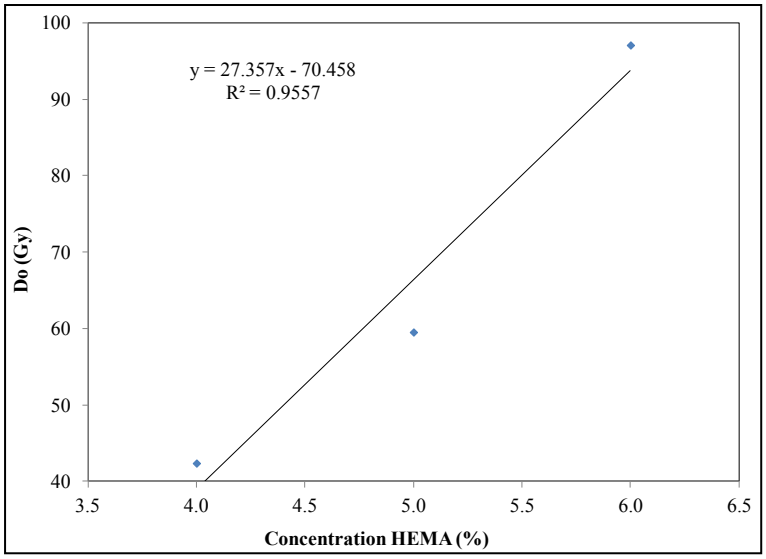


Figure 5. The variation values of the sensitive dose Do as derived at the band 575 nm as the function of concentration of HEMA for cresol red-dyed PHEMAG

Conclusion

Cresol red-dyed PHEMAG with different of the monomer concentrations of 2-Hydroxyethyl Methacrylate doped with cresol red dye as polymer gel dosimeter were developed. The optical properties and dosimetric parameter of the Cresol red-dyed PHEMAG were successfully analyzed using UV-VIS spectroscopy based on the variations of absorption spectra. The remarkable of the peak absorbance at 575 nm illustrate the increasing trend as the increament of absorbed dose shows that the higher radiation dose will induced polymerization. The sensitivity of the Cresol red-dyed PHEMAG showed the significant sensitivity as the monomer concentration decrease. Lastly, the study of the novel polymer gel based on the radiation induced color transition of the dye could be a starting point for further discovery based on the optical properties and structural characterization.

Acknowledgement

The author would like to acknowledge the financial support by the grant RUi USM 811301and UiTM training budget in finding throughout this work.

References

1. Schreiner, L. J., Olding, T. and McAuley, K. B. (2010). Polymer gel dosimetry. *Journal of Physics: Conference Series,* 250(1): 1-5.
2. Mattea, F., Romero, M. R, Vedelago, J., Quiroga, A., Valente, M. and Strumia, M. C. (2015). Molecular structure effects on the post irradiation diffusion in polymer gel dosimeters. *Applied Radiation and Isotopes*, 100: 101-107.
3. Vandescasteele, J. and De Deene, Y. (2013). Evaluation of radiochromic gel dosimetry and polymer gel dosimetry in a clinical dose verification. *Physics in Medicine and Biology*, 58(18): 6241-6262.
4. MacDougall, N. D., Miquel, M. E. and Keevil, S. F. (2014). Effects of phantom volume and shape on the accuracy of MRI BANG gel dosimetry using BANG3^{TM}. *The British Journal of Radiology,* 81(986): 46-50.
5. Mattea, F., Chacon, D., Vedelago, J., Valente, M. and Strumia, M. C. (2015). Polymer gel dosimeter based on itaconic acid. *Applied Radiation and Isotopes*, 105: 98-104.
6. Doyan, A. (2009). Dose response and optical properties of dyed poly vinyl alcohol-trichloroacetic acid polymeric blends irradiated with gamma-rays. *American Journal of Applied Sciences*, 6(12): 2071.
7. Beshir, W. B. (2013). Radiation sensitive indicator based on tetrabromophenol blue dyed poly (vinyl alcohol). *Radiation Phycis and Chemistry,* 86: 129-135.

8. Saion, E., Doyan, A., Zainal Abidin, S., Azmi, Z., Zulkifli, A., Mohd Zaki, A. and Karni, T. (2005). Changes in the optical band gap and absorption edge of gamma-irradiated polymer blends. *Journal of Applied Sciences,* 5: 1825-1829.
9. Chanda, M. (2000). *Advanced polymer chemistry*: *A problem solving guide*. Marcel Dekker: pp. 462-475.
10. Rozlan, A. A., Jaafar, M. S. and Rahman, A. A. (2011). A study of normoxic polymer gel dosimeter using raman spectroscopy analysis. *International Conference on Biomedical Engineering and Technology*, 11(2011): 19-23.
11. Ab Razak, N. N. A. N., Rahman, A. A., Kandaiya, S., Mustafa, I. S., Yahaya, N. Z. and Mahmoud, A. A. J. (2015). Accuracy and precision of magat gel as a dosimeter. *Material Science Research India,* 12(1): 01-08.
12. Vergote, K. (2005). Development of polymer gel dosimetry for applications in intensity-modulated radiotherapy. Department of Radiotherapy and Nuclear Medicine, Faculty of Medicine and Health Sciences, Gent, Belgium: pp. 20-21.
13. MacAuley, K. B. (2006). Fundamentals of polymer gel dosimeters. *Journal of Physics: Conference Series*, 56(1): 35.
14. Attix, F. H. (2008). Introduction to radiological physics and radiation dosimetry. John Wiley & Sons: pp. 34-36.
15. Susilawati (2005). Radiation and temperature effects on optical and electrical properties of dyed poly (vinyl alcohol) organic composite containing chlorine. PhD dissertation, Universiti Putra Malaysia.
16. Ebraheem, S., Eid, S. and Kovacs, A. (2002). A new dyed poly (vinyl alcohol) film for high-dose applications. *Radiation Physics and Chemistry,* 63(3): 807-811.
17. Morris, S. and Williams, A. (2001). Radiotherapy physics and equipment. Churchill Livingstone: pp. 28-30.
18. Abdel-Fattah, A. A., Hegazy, E. S. A. and El-Din, H. E. (2002). Radiation-chemical formation of HCl in poly (vinyl butyral) films containing chloral hydrate for use in radiation dosimetry. *International Journal of Polymeric Materials,* 51(9): 851-874.

Malaysian Journal of Analytical Sciences, Vol 22 No 2 (2018): 311 - 317
DOI: https://doi.org/10.17576/mjas-2018-2202-17

MALAYSIAN JOURNAL OF ANALYTICAL SCIENCES
Published by The Malaysian Analytical Sciences Society
ISSN 1394 - 2506

MORPHOLOGY AND CHEMICAL STRUCTURE OF $Sn(Oct)_2$ THIN LAYER ADDED BINDER VIA SOL GEL METHOD

(Morfologi dan Struktur Kimia bagi Lapisan Nipis $Sn(Oct)_2$ ditambah Bahan Pengikat Melalui Kaedah Sol Gel)

Rafizah Zaiton*, Nor Afifah Omar, Norliza Ibrahim

Faculty of Chemical Engineering,
Universiti Teknologi MARA, 40450 Shah Alam, Selangor, Malaysia

**Corresponding author: rafizah_fiezah@yahoo.com*

Received: 15 February 2017; Accepted: 2 January 2018

Abstract

This paper contains a selection of parameters in sol gel synthesis to produce thin layer tin octoate, $Sn(Oct)_2$. The main purpose is to discuss the effect of binder on morphology and chemical structure in order to produce high quality coating. The sol-gel method gives better control of the texture, composition homogeneity and structural properties of the final product. However, the disadvantages of this process is the formation of cracks during drying of gels. Binder is one of the compounds help to prevent cracking. In this research, $Sn(Oct)_2$ was synthesized through sol-gel method with the addition of binders which are polyvinyl alcohol (PVA) and polyethylene glycol (PEG) to enhance mechanical strength of sol gel coating on glass substrate. Different concentration of binder were varied to produce $Sn(Oct)_2$ thin film. The paper first describes the effect of binder on spectral characteristic from chemical bonding. Then, the effect of binders toward membrane features also studied. The characteristic of thin layer with binders were also discussed. FTIR characterization used to determine the chemical compound and crystalline structure was confirmed by XRD analysis. It has been shown that, added binder into the solution is an effective method to improve the strength of thin layer.

Keywords: sol gel, binder, thin layer, polyvinyl alcohol, polyethylene glycol

Abstrak

Kertas ini membincangkan pilihan parameter dalam sintesis sol gel untuk menghasilkan lapisan nipis bagi Sn $(Oct)_2$. Tujuan utama adalah untuk membincangkan kesan pengikat ke atas morfologi dan struktur kimia bagi menghasilkan salutan berkualiti tinggi. Kaedah sol-gel memberikan kawalan yang lebih baik terhadap tekstur,homogeniti komposisi dan struktur produk. Walau bagaimanapun, kelemahan proses ini adalah pembentukan keretakan semasa pengeringan gel. Bahan pengikat adalah salah satu daripada sebatian yang dapat membantu mencegah keretakan. Dalam penyelidikan ini, Sn $(Oct)_2$ telah disintesis melalui kaedah sol-gel dengan penambahan pengikat seperti polivinil alkohol (PVA) dan polietilena glikol (PEG) untuk meningkatkan kekuatan mekanik salutan sol gel pada substrat kaca. Kepekatan yang berbeza dari pengikat diubah untuk menghasilkan $Sn(Oct)_2$ lapisan nipis. Kajian ini adalah yang pertama menerangkan kesan pengikat pada ciri spektral dari ikatan kimia. Kemudian kajian itu menerangkan kesan pengikat ke atas ciri-ciri membran. Ciri-ciri lapisan nipis dengan pengikat juga dibincangkan. Analisis FTIR digunakan untuk menentukan sebatian kimia dan struktur kristal telah disahkan oleh analisis XRD. Telah ditunjukkan bahawa, penambahan pengikat ke dalam sebatian adalah kaedah penyelesaian yang berkesan untuk menambahbaik lapisan nipis.

Kata kunci: sol gel, pengikat, lapisan nipis, polivinil alkohol, polietilena glikol

Introduction

Tin(II) octoate, or stannous octoate, $Sn(Oct)_2$, is applied as glass coating, PVC heat stabilizer, biocides and agrochemicals. $Sn(Oct)_2$ also used as catalyst for glycolysis of polyurethane waste [1] and as Lewis catalyst for esterification and transesterification of acid vegetables oil [2]. It also prefer for biomedical application because of its low toxicity, FDA approval,and high catalytic activity [3, 4]. Besides that, it has high efficiency and solubility in most of organic solvent [5, 6].

Sol-gel synthesis may be used to prepare materials with a variety of shapes, such as porous structures, thin fibers, dense powders and thin films [7]. Sol-gel method is specialized in mixing organic and inorganic materials in one process [8]. In this process, an organometallic compound solution was hydrolysed to create a "sol" which is a colloidal suspension of a solid in a liquid and the sol will undergo further process to form a gel that will produce a ceramic object with required shape [9]. It is one of the favourable methods in making thin, and homogenous at low cost and yield excellent attachment between metallic substrate and the top coat other than provide an efficient, and economic method to produce coatings with high quality [7].

It is generally essential for ceramic powder to be added with binder because binder is a material that enhance the green ceramic mechanical strength in order to get through the production steps so cracking can be prevented or minimized [9]. Binder provides the necessary plasticity for shaping technique and also dry (green) shape with enough strength that can bear the shaping and sintering process. There are two types of binder, organic and inorganic. The most well-known organic binders for ceramic dry-pressing are polyethylene glycol (PEG) and polyvinyl alcohol (PVA) which provide high green strength and high green density for ceramic respectively [10].

In the presence work, the $Sn(Oct)_2$ thin films with different binders were prepared on glass substrate by sol-gel method. Thin films deposition on glass substrate by dip coating technique was used due to low cost of preparation, homogeneity and uniformity of the final products. The influence on morphology, and chemical structure also studied by varying binder concentrations and characterizations of thin film were carried out using Fourier Transform Infrared Spectroscopy (FTIR), X-ray Diffraction (XRD), Optical Microscope, and also Scanning Electron Microscope (SEM) [11].

Materials and Methods

Materials

Tin octoate (95 % Sigma Aldrich), nitric acid, ethylene glycol (EG), polyvinyl alcohol (PVA), and polyethylene glycol (PEG).

Film preparation and characterization

The $Sn(Oct)_2$ thin film was prepared by sol gel method. Reagent grade of tin octoate as the precursor and Ethylene Glycol as organic solvent were used. One mole of $Sn(Oct)_2$ was added into 10 mol of ethylene glycol and stirred for 30 minutes. Then, diluted HNO_3 was added to peptize the sol and molar ratio of H^+ to Sn^{2+} in the ratio of 0.1:1. The solution was stirred for 6 hours at 90 ^oC under reflux condition to ensure complete mixing and hydrolysis. The binder in different concentration was diluted in deionized water at 60 ^oC and stirred to dissolve it completely. In this study, PEG and PVA were used as binders. Binder was added in initial solution followed by 6 hours peptization period. After aging of solutions for 24 hours, deposition of thin films on glass substrates was performed by dip coating technique at room temperature. The coated substrates was calcined in an oven at 200 ^oC for 2 hours. Fourier Transform Infrared (FTIR) characterization was carried out to investigate the spectral characteristic indicating the chemical bonding of tin octoate thin film. Hence, crystalline phase of resulted powder were identified using X-ray diffraction (XRD). The optical microscope was used to determine the macroscopic appearance and the microstructure of the $Sn(Oct)_2$ coatings on the glass substrate while Scanning Electron Microscope (SEM) is used to determine the surface morphology of $Sn(Oct)_2$ film.

Results and Discussion

Effect of binder on spectral characteristic from chemical bonding

FTIR spectroscopy gives qualitative information about the way in which the adsorbed PVA and PEG molecules are bonded to the surface of the Sn $(Oct)_2$ particles. Figure 1a, and 1b compares the IR spectra of Sn $(Oct)_2$ particles with the presence of adsorbed PVA and PEG after calcination temperature of 200 °C.
The FTIR analysis was recorded using an FTIR spectrometer in a range between 4000 cm^{-1} to 500 cm^{-1}. The absorption peaks between 700 cm^{-1} to 500 cm^{-1} are assigned to Sn-O and Sn-O-Sn vibrations of SnO_2. Small peaks between 1900 cm^{-1} to 1600 cm^{-1} are attributed to Sn-OH vibrational mode. Since the precursor solution contains water, Sn-OH vibrational mode appears in the spectrum. The absorption peak in the 2850 cm^{-1} in the spectrum corresponds to the CH group stretching vibration of PEG and also PVA [12]. It proves that the molecules of PVA and PEG were absorbed by the Sn $(Oct)_2$ particles while typical rutile type Sn $(Oct)_2$ peak 615 cm^{-1}[13]. This result supported by Attia and El-Kader [12] proving that the addition of binders does not affect the spectral structure of sample.

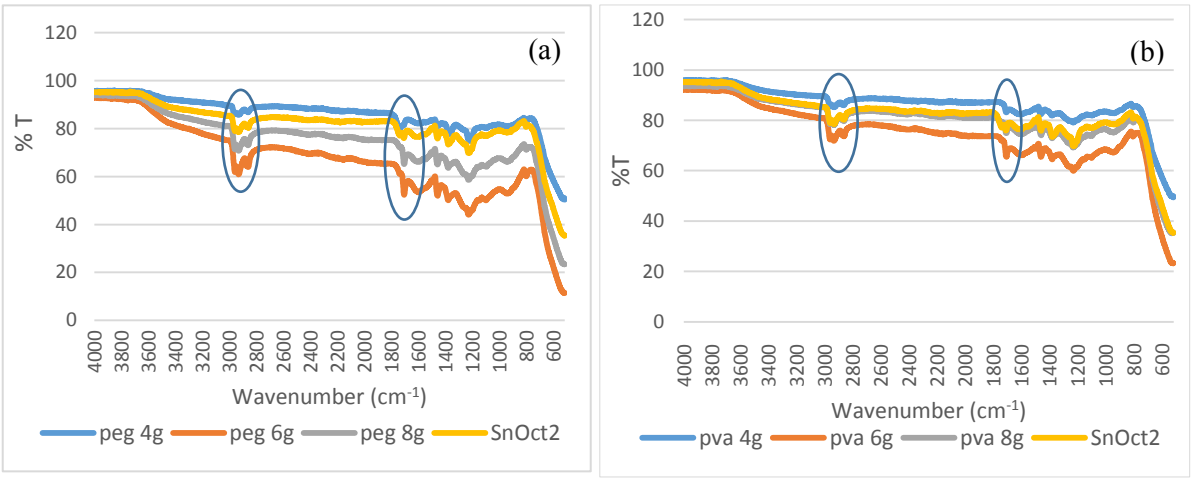


Figure 1. FTIR Spectra of (a) PEG and (b) PVA after drying at 200 °C

Figure 2a and 2b shows the XRD patterns of Sn $(Oct)_2$ with PEG 1500 and PVA. XRD is a technique used to identify the crystalline species in material. Therefore, this analysis is done in order to characterize the crystalline species in $Sn(Oct)_2$ powder with different concentration of binders addition. The structure of the $Sn(Oct)_2$ and binders were studied using X-ray diffraction with angle of 20–80◦, 40V and 30A with speed time of 1min/s with radiation of CuKα in wavelength λ=1.5406 Å [14].

From the XRD measurements of $Sn(Oct)_2$ with binder addition as shown in Figure 2a and 2b, it can be seen that the gel is X-ray amorphous where it only shows broad humps in every diagrams. This is because most tin ions are bonded with oxygen in the xerogel and they are still in an amorphous state when dried at temperature below 250 °C. It clearly shows that the XRD patterns of $Sn(Oct)_2$ coated with PVA and PEG in Figure 2a and 2b have same patterns for all different concentration of binders which are 4g, 6g and 8g. This fact shows that adsorption of PVA and PEG and with different concentrations on $Sn(Oct)_2$ particles does not gives any effect towards the crystallinity of $Sn(Oct)_2$ particles since sharp peaks on the pattern indicated the crystalline structure of material. All coated samples revealed the same sharp peaks at the same wavelength range.

When comparing the XRD patterns of $Sn(Oct)_2$ with PVA binder of different concentration shown in Figure 2a, it can be clearly seen that the intensity of diffraction peaks increased as the concentration of PVA increased. Same goes to XRD patterns of $Sn(Oct)_2$ with PEG binder. The intensity of diffraction peaks also increased as the concentration of PEG increased. However, the intensity of PEG is higher compared with PVA. It is clearly shown

at the first peak from wavelength range 25 to 29. This proved that $Sn(Oct)_2$ coated with PEG is more crystalline compared to PVA since the intensity peaks indicates the crystalline structure of material.

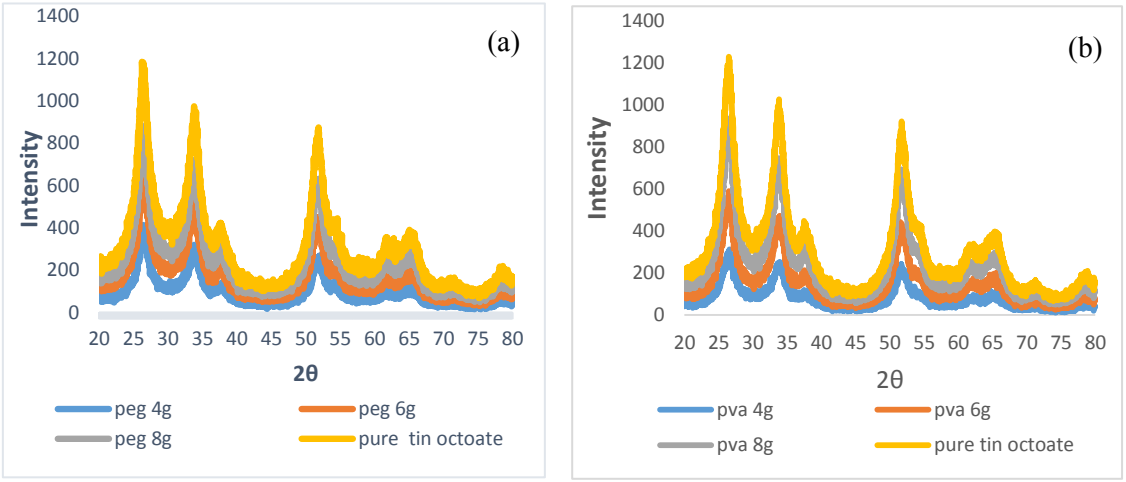


Figure 2. XRD patterns of (a) PEG and (b) PVA in powder form

Optical microscope is used to characterize the macroscopic appearance and the microstructure of the $Sn(Oct)_2$ coatings on the glass substrate. In this test, $Sn(Oct)_2$ sol gel was coated on a glass slide. The structure of coated $Sn(Oct)_2$ with PVA and PEG binders were characterized by using optical microscope at magnification of 10x as displayed in Figure 3. The result shows that with an increment in the amount of binder, the porosity of the coatings decreased because the compactness and density of coating particles increased. For PVA images, it can be seen that as PVA concentration increased, the binder images that coated on glass slide can be seen more clearly. The binder look strongly attached to each other as the concentration of binder increased since the function of binder is to enhance the strength of coating on substrate.

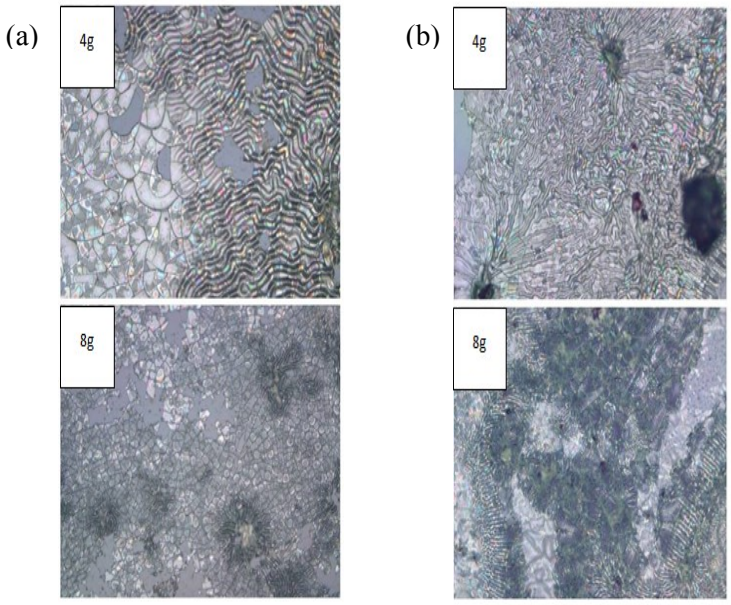


Figure 3. Optical imagesof $Sn(Oct)_2$ with (a) PVA and (b) PEG 1500 binder coated after drying at 200 ^oC

Scanning Electron Microscope (SEM) is used to characterize the surface morphology of $Sn(Oct)_2$ after calcination temperature of 200 °C for 2 hours. In this analysis, the cracking formation were observed for each sample that consists of Sn(Oct)2 with PVA and PEG binders under different concentration of binders. The magnification used in this test was 500x.

Based from the result obtained in Figure 4 and Figure 5, crack formation can be seen throughout the powder particles for both PVA and PEG binders. This is because the drying process that take place up until 200°C had caused densification of the whole gel structure which pulled all the colloid particles close to each other. It formed surface tension and internal stress in the structure of gel which water was actually needed to bind the colloid particles and prevent constant crack after the coating [15].

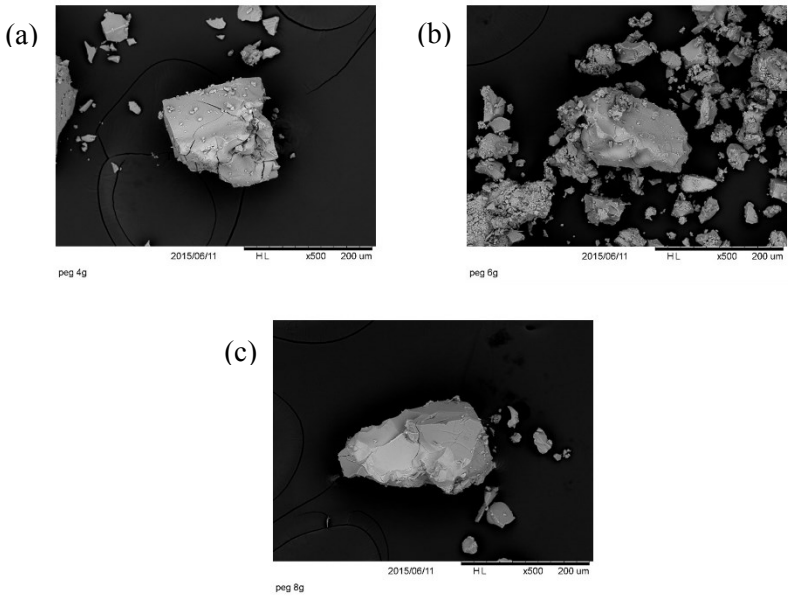


Figure 4. The SEM micrographs of cross-sectional view of $Sn(Oct)_2$ with a) 4g PVA b) 6g PVA and c) 8g PVA

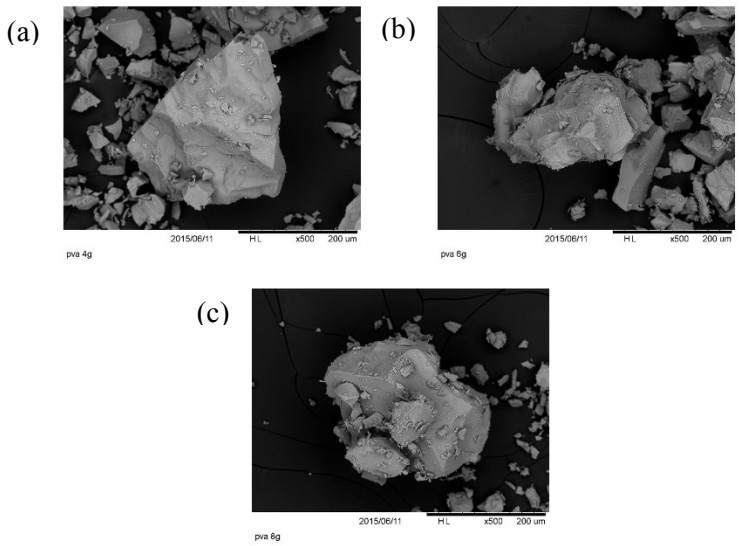


Figure 5. The SEM micrographs of cross-sectional view of $Sn(Oct)_2$ with a) 4g PEG b) 6g PEG and c) 8g PEG

However, as concentration of both binders increased, the crack formations were reduced. This is because the binders had begun to crystallize and necking process starts to occur causing the particles to connect towards each other through the atomic diffusion. Despite that, drying process that involved binders must be done at lowest heating rate in order to avoid the membrane microstructure layer from having micro cracks because binders can be totally decomposed at temperature near 400 °C [15].

Conclusion

In conclusion, as the binder concentration increased, the formation of crack on $Sn(Oct)_2$ coatings will be decreased. The coating attachment on glass slide are stronger with the addition of binder amount. It was due to the increment of density and also viscosity of binders for both PVA and PEG since the function of binder is to enhance the mechanical strength of coating on substrate. However, in comparison of PVA and PEG binder, PEG is better compared to PVA because it has more tendencies to have crystalline structure compared to PVA, other than it shows much stronger attachment of $Sn(Oct)_2$ sol coating on glass slide compared to PVA.

Acknowledgement

The authors would like to thank the Ministry of Education Malaysia for financial support via Fundamental Research Grant Scheme (600-IRMI/FRGS 5/3 (93/2016)). The authors also gratefully acknowledged use of services and research facilities available at the Faculty of Chemical Engineering, Universiti Teknologi MARA, Malaysia.

References

1. Batt, J. M. and Stewardship, D. P. (2004). The world of organotin chemicals: applications, substitutes, and the environment. *ATOFINA Chemicals*, Inc, 6.
2. Casas, A., Ramos, M. J., Rodríguez, J. F. and Pérez, Á. (2013). Tin compounds as Lewis acid catalysts for esterification and transesterification of acid vegetable oils. *Fuel Processing Technology*, 106: 321-325.
3. Molero, C., de Lucas, A. and Rodriguez, J. F. (2009). Activities of octoate salts as novel catalysts for the transesterification of flexible polyurethane foams with diethylene glycol. *Polymer Degradation and Stability*, 94(4): 533-539.
4. Sobczak, M. (2012). Ring opening polymerization of cyclic esters in the presence of choline/$SnOct_2$ catalytic system. *Journal of the Polymer Bulletin*, 68: 2219-2228.
5. Wheaton, C. A. and Hayes, P. G. (2011). Designing cationic zinc and magnesium catalyst for coordination-insertion polymerization of lactide. *Comments on Inorganic Chemistry,* 32: 127-162.

6. Torres, T. and Bottari, G. (2013). Organic nanomaterials: synthesis, characterization, and device applications. John Wiley & Sons.
7. Znaidi, L., Touam, T., Vrel, D., Souded, N., Ben Yahia, S., Brinza, O., and Boudrioua, A. (2012). ZnO thin films synthesized by sol-gel process for photonic applications. *Acta Physica Polonica-Series A General Physics*, 121(1): 165-168.
8. Wright, J. D. and Sommerdijk, N. A. (2014). Sol-gel materials: chemistry and applications. CRC press.
9. Binders for Ceramic Bodies. (2008). Digitalfire Reference Database: http://digitalfire.com/4sight/ education/ binders_for_ceramic_bodies_345.html [Access online July 15, 2014].
10. Carter, C. B. and Norton, M. G. (2007). Ceramic materials: science and engineering. Springer Science & Business Media.
11. Ceramic Materials Analysis. (2014). Anderson Materials Evaluation, Inc.: http://www.anderson materials.com/ceramics.html [Acess online Retrieved July 1, 2014].
12. Attia, G. and El-Kader, M. A. (2013). Structural, optical and thermal characterization of PVA/2HEC polyblend films. *International Journal of Electrochemical Sciences*, 8: 5672-5687.
13. Nabiyouni, G., Barati, A. and Saadat, M. (2011). Surface adsorption of polyethylene glycol and polyvinyl alcohol with variable molecular weights on zinc oxide nanoparticles. *Iranian Journal of Chemical Engineering*, 8(1): 20-30.
14. Liu, Y. C., Lu, Y. F., Zeng, Y. Z., Liao, C. H., Chung, J. C. and Wei, T. Y. (2011). Nanostructured mesoporous titanium dioxide thin film prepared by sol-gel method for dye-sensitized solar cell. *International Journal of Photoenergy*, 2011: 1-9.
15. Ahmad, A. L., Jaya, M. A. T. and Chieh, D. C. J. (2011). Effect of binder concentration on titania sol turbidity and palladium-titania membrane. *Journal of Materials Science and Engineering,* 5(5): 534-540.

Malaysian Journal of Analytical Sciences, Vol 22 No 2 (2018): 318 - 325
DOI: https://doi.org/10.17576/mjas-2018-2202-18

MALAYSIAN JOURNAL OF ANALYTICAL SCIENCES
Published by The Malaysian Analytical Sciences Society
ISSN 1394 - 2506

GRANULATION OF MEFENAMIC ACID AND POLY-ETHYLENE GLYCOL (PEG) USING PRESSURE SWING GRANULATION (PSG) TECHNIQUE IN FLUIDIZED BED

(Pembentukan Granul Berasaskan Asid Mefenamik dan Polietilena Glikol (PEG) Menggunakan Teknik Pengranulan Tekanan Terayun dalam Turus Terbendalir)

Salinda Ab Ghani [1], Noor Fitrah Abu Bakar [1]*, Mohd Rushdi Abu Bakar [2], Yus Aniza Yusof [3], Norazah Abd Rahman[1]

[1]*Faculty of Chemical Engineering,*
Universiti Teknologi MARA, 40450 Shah Alam, Selangor, Malaysia
[2]*Department of Pharmaceutical Technology, Kulliyyah of Pharmacy,*
International Islamic University Malaysia, Bandar Indera Mahkota, 25200 Kuantan, Pahang, Malaysia
[3]*Department of Process and Food Engineering, Faculty of Engineering,*
Universiti Putra Malaysia, 43400 Serdang, Selangor, Malaysia

**Corresponding author: fitrah@salam.uitm.edu.my*

Received: 15 February 2017; Accepted: 2 January 2018

Abstract

Granulation of mefenamic acid particles was conducted to produce spherical shape, narrow size distribution of granules, high granule strength and good content uniformity by using Pressure Swing Granulation (PSG) technique in a fluidized bed. Two types (binderless and with binder) of granules namely lactose-mefenamic acid (MA) and lactose-polyethylene glycol (PEG)-(MA) with mass ratio of 30:70 and 25:5:70 were produced respectively. The later type of granules was heated for 80 ˚C, above the PEG melting point. Results indicated that all granules were uniform, spherical and narrow size distribution with the average granules size was less than 500 µm. The tensile strength of the lactose-PEG-MA was higher than the lactose-MA due to heating process. The tensile strength of lactose-PEG-MA and lactose-MA with average granules size of 500 µm were 0.42 MPa and 0.33 MPa, respectively. The drug contents in both types of granules were uniform i.e. around 70 ± 0.3 wt.%.

Keywords: mefenamic acid, lactose, polyethylene glycol, pressure swing granulation

Abstrak

Pembentukan granul zarah asid mefenamik telah dijalankan untuk menghasilkan bentuk bulat, taburan saiz granul yang kecil, kekuatan granul dan keseragaman kandungan yang baik dengan menggunakan teknik pengranulan terbendalir (PSG). Dua jenis granul (tanpa perekat dan dengan perekat) iaitu laktosa-asid mefenamik (MA) dan laktosa-polietilena glikol (PEG)-(MA) dengan nisbah jisim masing-masing adalah 30:70 dan 25:5:70. Granul kemudian dipanaskan pada 80 °C, melebihi takat lebur PEG. Keputusan menunjukkan bahawa semua granul yang terhasil adalah seragam, taburan saiz granul adalah sempit dengan saiz purata granul adalah kurang daripada 500 µm. Kekuatan tegangan laktosa-PEG-MA adalah lebih tinggi daripada laktosa-MA disebabkan oleh proses pemanasan semasa pengranulan. Kekuatan tegangan laktosa PEG-MA dan laktosa-MA dengan saiz granul purata 500 mikron masing-masing adalah 0.42 MPa dan 0.33 MPa. Kandungan MA dalam kedua-dua jenis granul adalah seragam iaitu sekitar peratusan jisim 70 ± 0.3 wt.%.

Kata kunci: acid mefenamik, laktosa, polietilena glikol, pengranulan tekanan terayun

Introduction

In the pharmaceutical industry, approximately more than 80% of all dosage forms are supplied in the forms of tablet [1]. The advantages of supplying the drugs powders in tablet form are low production cost, convenience in dosing and drug stability due to dry condition compared with liquid semi-solid presentation. Particle properties such as shape and size are important in increasing the bioavailability of active pharmaceutical ingredients (APIs). Most APIs used these days are fine powders 100 µm or less which typically having a wide size distribution. Further, particles size smaller than 30 µm are extremely difficult to handle and are generic problem for the industry [2].

Mefenamic acid is a non-stereoidal anti inflammatory drug (NSAIDs) that belongs to a group of fenamate medicines. Mefenamic acid is used to treat pain such as headache, dental pain and fever. It is also used to treat menstrual pain. The usual oral dosage is 250 to 500 mg, being administered three times daily [3]. Mefenamic acid works by decreases the inflammation and uterine contractions and stopping the body's production of a substance that cause pain [4]. Mefenamic acid is a poorly soluble drug in aqueous media [5], tendency to stick to surfaces and it is not easy to handle in granulation and tabletting processes.

Understanding the deformation behavior of powder under compaction or compression [7, 9, 10] it can minimize its sticking tendency during tableting. Small/irregular particles deformed more plastically at high compression pressure and had higher tendency for friction and sticking [7]. Nano- or micrometer size range for particulate drug powders is an obstacle during manufacturing of the dosage forms containing them, particularly if the form is a conventional solid (tablet, capsule) [11]. Particle size and shape could completely change the compaction behavior of materials, which would finally affect the physical characters of the final compact (tablet) [7, 12]. Therefore, granulation is a possible method in reducing the sticking problem without changing the original size and shape of the mefenamic acid crystal.

Granulation is often added as unit operation before the compaction step to enlarge particle size and to form spherical agglomerates [6, 20] of the starting material but also to improve the mechanical properties under pressure [7, 8]. Improvement of sticking tendency during tableting through granulation of APIs such as ibuprofen up to 70 wt.% with 30 wt.% lactose was successfully conducted through pressure swing granulation (PSG) technique in fluidized bed [6].

Thus, PSG technique can be applied for granulation of small size particles of high dosage mefenamic acid and low dosage of excipient without any binder prior to the tableting process. In this study, a binderless granulation method that is known as pressure swing granulation (PSG) technique will be used for enlarging the particle size and forming into spherical and narrow size granules prior to the tableting process.

Materials and Methods

Materials and preparation of mefenamic acid

The materials used were lactose, polyethylene glycol (PEG) and mefenamic acid (MA) powder. 5 grams of as received MA was milled by using ball mill for 60 minutes (Mixer mill, MM400) to obtain a particle size of ~5 µm. The particle size distribution of mefenamic acid before and after milling process was measured by using a laser diffraction particle size analyzer (Malvern Mastersizer 2000).

Preparation of granules

A batch of 120 g of well mixed samples was fed into the PSG granulator as illustrated in Figure 1. The column was made of stainless steel consists of two part which are lower part with internal diameter of 108 mm and the upper part with a diameter of 151 mm. A filter bag with a diameter of 70 mm and 157 mm in length was suspended from the top flange. Two types of granules namely lactose-MA and lactose-PEG-MA with mass ratio of 30:70 and 25:5:70 were produced respectively under operating conditions as listed in Table 1. Both types of granules were granulated for 120 minutes.

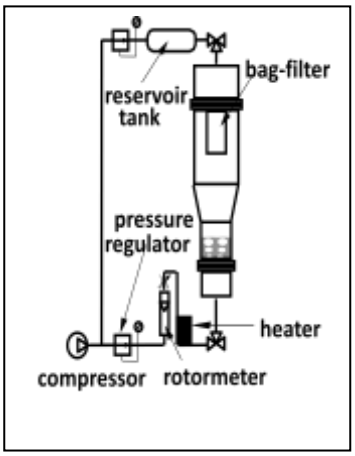


Figure 1. Experimental setup for Pressure Swing Granulation (PSG) technique [14]

Table 1. Granulation Condition

Type of Granules	**Lactose:MA**	**Lactose: PEG:MA**
Temperature	25 °C	80 °C
Powder batch mass	120 g	
Gas velocity	0.364 m/s	
Duration of fluidization	15 s	
Duration of compaction	1 s	
Compaction pressure	0.03 MPa	
Total granulation time	120 min	

Characterization of granules

The size distribution of the product granules was determined by using sieving method. The morphology of the granules was measured using Scanning Electron Microscopy (SEM). The density and pore volume of the granules range of 250 to 800 µm were measured using pycnometer density (AccuPyc 1340, Micromeritics). Compression strength of granules was measured by using micro compression tester (Shimadzu MCT-511) for granules size range between 250 to 800 µm. From the measured fracture force (F_f), the tensile strength (σ), for brittle material can be calculated using equation from Hiramatsu and Oka [15],

$$\sigma = \frac{2.8\, F_f}{\pi d^2} \quad (1)$$

where d is granule diameter. MA concentration in the granulated products were determined by following the standard procedure as proposed in US pharmacopeia. The dissolution tests for the product granules were determined using United States Pharmacopeia dissolution apparatus XXIV-Type II (paddle-37 °C) (Electro Lab, Mumbai, India). The dissolution medium was a 900 mL phosphate buffer with pH 7.4. The amount of dissolved drug was determined using UV spectrophotometric method (UV 1601 A, Shimadzu, Japan) at 260 nm.

Results and Discussion

Scanning electron microscopy

The average size of MA particles (as received) before milling was approximately 500 µm whereas the average size of MA particles after milling was about 10 to 15 µm. Figure 2 shows the SEM images of the core granules with addition of mefenamic acid (MA) after granulation process. Figure 2(a) shows morphology of the granules that consist of 30 wt.% lactose and 70 wt.% MA whereby the granulation process was conducted at ambient temperature. The same morphology was observed for other type of granules that consist of lactose, PEG and MA with 25, 5 and 70 wt.% respectively as in Figure 2 (b). The shape of the granules is spherical but it is not smooth on the surface. This might due to the size of the milled MA used in the granulation process that is slightly bigger than 5 µm whereby to have spherical and smoothness product granules, the size of the powder introduced in the fluidized bed must be less than 5 µm [6, 13, 14].

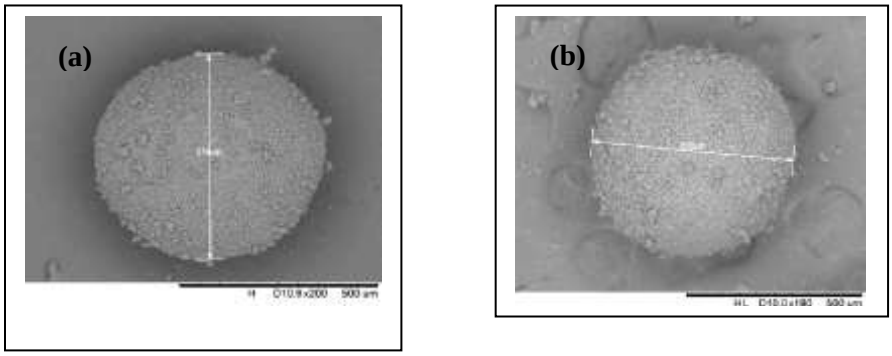


Figure 2. SEM images of (a) lactose-MA granules and (b) lactose-PEG-MA granules

Granule size distribution

Figure 3 shows the granule size distribution for all types of product granules of lactose-MA and lactose-PEG-MA. The graph shows the narrow size distribution because almost 80% of the granule size is less than 500 µm [6, 13, 14]. According to Takano et al. [16], over 80% of the granules size must be in the range of 355 µm to 1410 µm for the preparation of pharmaceutical process. The sizes of the lactose-PEG-MA granules are slightly larger than the lactose-MA granules due to heating whereby PEG melted and adhered more particles on the granules.

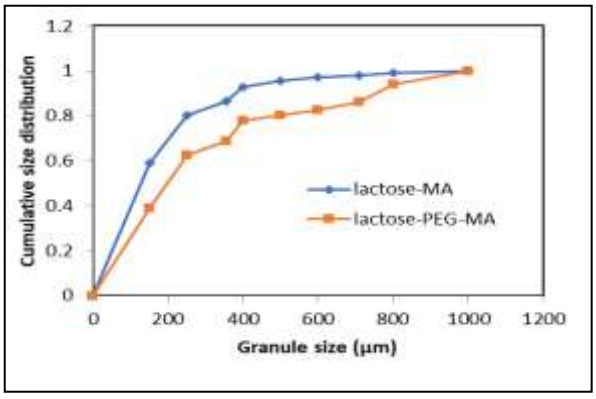


Figure 3. Granule size distributions of lactose-MA and lactose-PEG-MA

Pore volume and granules density

Table 2 shows the total pore volume and density for each size of granules for lactose-MA and lactose-PEG-MA that was measured using a pycnometer. The pore volume of granules for lactose-PEG-MA was smaller than the lactose-

MA granules. This was due to solid bridge formation between lactose and mefenamic acid particles, when melted PEG filled and solidified in the void area inside the granules. From Table 2, it clearly shows that the pore volume for the granules increased with increasing granule size from 250 to 600 µm and followed by decreasing trend for 710 and 800 µm. The smallest size of granules shows the lowest pore volume. The density of the lactose-MA granules was slightly higher than the lactose-PEG-MA that might due to higher amount of lactose in the lactose-MA granules although the total pore volume of the lactose-MA was higher than the lactose-PEG-MA. As the granule size increased, the porosity first increased and then decreased, and there was a maximum value of the porosity in Table 2. Summarizing Table 2, the minimum and maximum values of the porosity with increasing the granule size may be owing to the deformation created in the wet granule while melting during granulation [17]. Since all granules in PSG process normally experienced dry granulation condition, deformation [18, 20] was the main reason that created such pore volume, density and strength of the product granules.

Table 2. Pore volume and density for each granule size of Lactose-MA and Lactose-PEG-MA

Granule Size (µm)	Lactose-MA		Lactose-PEG-MA	
	Pore Volume (cm^3/g)	Density (g/cm^3)	Pore Volume (cm^3/g)	Density (g/cm^3)
250	0.2451 ± 0.005	1.3248 ± 0.009	0.2299 ± 0.004	1.3013 ± 0.007
355	0.2587 ± 0.004	1.3489 ± 0.007	0.2464 ± 0.001	1.3276 ± 0.002
400	0.2658 ± 0.004	1.3621 ± 0.007	0.2591 ± 0.003	1.3516 ± 0.005
500	0.2743 ± 0.234	1.3761 ± 0.013	0.2721 ± 0.003	1.3740 ± 0.006
600	0.2767 ± 0.003	1.3932 ± 0.005	0.2632 ± 0.003	1.3573 ± 0.006
710	0.2277 ± 0.003	1.3948 ± 0.004	0.2114 ± 0.003	1.3729 ± 0.005
800	0.2224 ± 0.003	1.2960 ± 0.004	0.2222 ± 0.003	1.2929 ± 0.004

Tensile strength

Figure 4 shows the tensile strength of the product granules for different sizes.The tensile strength for lactose-PEG-MA granules was higher than lactose-MA granules due to the melting of the PEG particles during heating which later formed a solid bridging inside the granule after cooling down. The tensile strength increased with decreasing granules sizes whereby small granules has less porosity, thus the number of contact points (coordination number) of primary particles can be increased by which the strength of the granules increase according to the Rumpf micromodels [19].

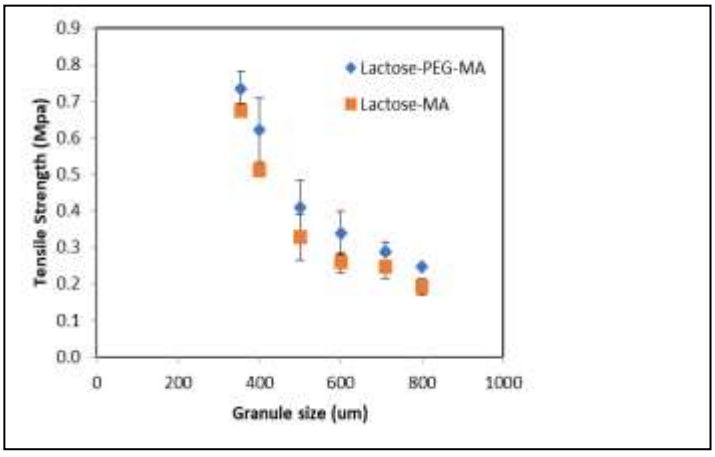


Figure 4. Tensile strength for Lactose-MA and Lactose-PEG-MA granules

Uniformity of mefenamic acid concentration

Table 3 shows the summary of the MA concentration of the product granule for different granules sizes. The content of MA in the selected granules size was approximately similar to the feed mixture introduced before granulation process which was 70 wt.% for both types of granules. Although the average size of the milled MA particles was larger than other materials i.e. lactose and PEG particles, granulation using PSG can produce uniform concentration of MA regardless the size of the produced granules. As stated in [16], the uniformity of drug content in PSG granules may be related to the growth mechanism of granules in PSG as discussed by [18], where granule growth takes place by recapturing the attrited fines that are returned to the bed from the bag filter.

Table 3. Concentration of Lactose-MA and Lactose-PEG-MA in granules

Granule Size (μm)	MA Concentration	
	Lactose-MA Granules	Lactose-PEG-MA Granules
355	61.7 ± 18.7	61.8 ± 6.5
500	68.1 ± 2.9	67 ± 1.8
800	68.3 ± 7.4	66.3 ± 5.1
1000	82.9 ± 3.77	76.5 ± 4.6

Dissolution test

Dissolution test for 500 μm and 800 μm of granule was performed with the aim to assess the effective size of granule to be used for the tablet formulation. Figure 5 shows the dissolution profile for both of the product granules. The as-received MA particles was reported to achieve less than 80% drug released at 35 minutes [21]. The granule size of 500 μm indicated a comparable dissolution rate within 30 minutes i.e. as good as milled MA of average particles size of 15 μm regardless the granules were formed with or without binder. The dissolution rate of 500 μm was higher compared to the size 800 μm for both types of granules due to higher ratio of surface area per volume. Previous works observed that the dissolution rate of MA incresead by producing smaller size of MA particles than the as received MA particles [21, 22] which emphasized on the importance of high surface per volume ratio. By referring to the same granules size, lactose-PEG-MA granules dissolved slightly better than lactose-MA granules due to existence of PEG that highly dissolve in water.

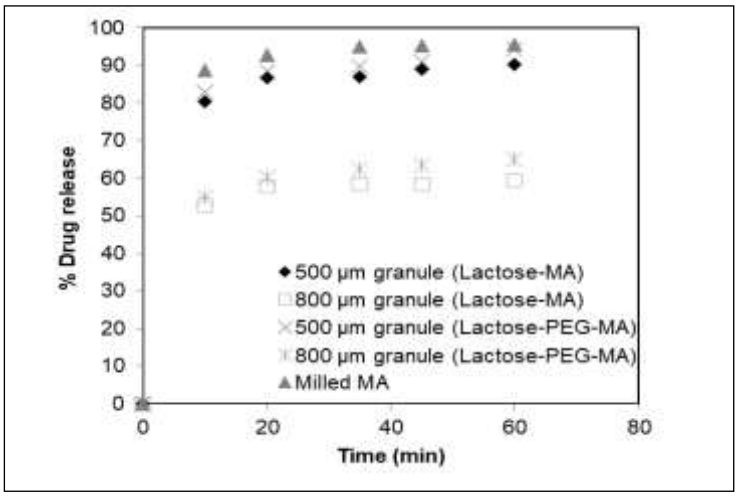


Figure 5. Dissolution test for Lactose-MA and Lactose-PEG-MA granules

Conclusion

From the present study, both types of granules show narrow size distribution as almost 80% of the granules size was less than 500 µm. Tensile strength of the granules of lactose-PEG-MA was higher than the granules of lactose-MA due to heating process. The drug contents in both types of granules were uniform and almost similar to the drug content introduced before granulation which was approximately 70wt.%. It can be concluded that by using PSG technique, granules with uniform size less than 500 µm, spherical shape, higher strength and high content uniformity can be achieved with and without the usage of binder. This technique is effective to be further applied for tableting formation as the drug can be dispensed effectively.

Acknowledegment

The authors would like to express their gratitude to Universiti Teknologi MARA (UiTM) Shah Alam, Malaysia for funding this work. This study was supported by Research Entity Initiative grant 600-RMI/DANA 5/3/REI (2/2013) from UiTM, Fundamental Research Grant Scheme (FRGS) 600-RMI/ST/FRGS 5/3/Fst (111/2010) and Race Acculturation Colloborative Efforts grant 600-RMI/RACE 16/6/2(6/2012) from Ministry of Education Malaysia.

References

1. Jivraj, M., Martini, L. G. and Thomson, C.M. (2000). An overview of the different excipients useful for the direct compression of tablets. *Pharmaceutical Science and Technology Today*, 3: 58-63.
2. Yang, J., Sliva, A., Banerjee, A., Dave, R. and Pfeffer, R. (2005). Dry particle coating for improving the flowability of cohesive powders. *Powder Technology*, 158: 21-33.
3. Martindale (1998). The extra pharmacopeia. *The Pharmaceutical Press, London*, 31th edition: pp. 58-59.
4. Hezave, A. Z., Khademi, M. H. and Esmaelizadeh, F. (2012). Measurement and modelling of mefenamic acid solubility in supercritical carbon dioxide. *Fluid Phase Equilibria*, 313: 140-147.
5. James E. F. R. and Anne B. P. (1982). The extra pharmacopeia. *The Pharmaceutical Press, London*, 28th edition: pp. 262-263.
6. Abu Bakar, N. F., Mujumdar, A., Urabe, S., Takano, K., Nishii, K. and Horio, M. (2007). Improvement of sticking tendency of granules during tabletting process by pressure swing granulation. *Powder Technology*, 176: 137-147.
7. Abdel-Hamid, S., Alshihabi, F. and Betz, G. (2011). Investigating the effect of particle size and shape on high speed tabletting through radial die-wall pressure monitoring. *International Journal of Pharmaceutics*, 413: 29-35.
8. Leuenberger, H., Puchkov, M., Krausbauer, E. and Betz, G. (2009). Manufacturing pharmaceutical granules: is the granulation end-point a myth?. *Powder Technology*, 189: 141-148.
9. Gentis, N. D. and Betz, G. (2012). Compressibility of binary powder formulations: Investigation and evaluation with compaction equations. *Journal of Pharmaceutical Sciences*, 101: 777–793.
10. Siiriä, S. M, Antikainen, O., Heinämäki. J. and Yliruusi, J. (2011). 3D simulation of internal tablet strength during tabletin. *AAPS PharmSciTech*, 12: 593-603.
11. Lin, X., Chyi, C. W., Ruan, K. F., Feng, Y. and Heng, P. W. (2011). Development of potential novel cushioning agents for the compaction of coated multi-particulates by co-processing micronized lactose with polymers. *Europe Journal Pharmacy Biopharm*, 79: 406–415.
12. Adam, A., Schrimpl, L. and Schmidt, P. C. (2000). Some physicochemical properties of mefenamic acid. *Drug Development and Industrial Pharmacy*, 26(5): 477–487.
13. Takano, K., Nishii, K., Mukoyama, A., Iwadate, Y., Kamiya, H. and Horio, M. (2002). Binderless granulation of pharmaceutical lactose powders. *Powder Technology*, 122: 212-221.
14. Nishii, K., Itoh, Y., Kawakami, N. and Horio, M. (1993). Pressure swing granulation, a novel binderless granulation by cyclic fluidization and gas flow compaction. *Powder Technology*, 74: 1-6.
15. Hiramatsu, Y. and Oka, Y. (1966). Determination of the tensile strength of rock by a compression test of an irregular test piece. *International Journal of Rock Mechanics and Mining Science*, 3: 89-90.
16. Takano, K., Maruyama, N., Mukoyama, A., Nishii, K., Kamiya, H. and Horio, M. (2003). Fluidized bed binderless granulation of hydrophobic drugs with fine lactose powder. *Advanced Powder Technology*,14(3): 369-381.
17. Shu-hua, D., Feng-man, S. and Ai-bing, Y. (2008). Granule size distribution and porosity of granule packing. *Journal of Iron and Steel Research*,15(5): 1-5.

18. Abu Bakar, N. F., Anzai, R. and Horio, M. (2009). Direct measurement of particle-particle interaction using micro particle interaction analyzer (MPIA). *Advanced Powder Technology,* 20(5): 455-463
19. Horio, M., Mukouyama, A., Maruyama, M., Takano, K. and Nishii, K. (2001). The mechanism of fluidized bed dry granulation of fine powders. *Fluidization,* 10: 485-491.
20. Abu Bakar, N. F., Anzai, R. and Horio, M. (2013). Microscopic evaluation of binderless granulation in a pressure swing granulation fluidized bed. *Chemical Engineering Science,* 98: 51-58/
21. Zolkepali, N. K., Abu bakar, N. F., Naim, M. N., Anuar, N., Kamalul Aripin, N. F., Abu Bakar, M. R., Lenggoro, I. W. and Kamiya, H. (2016). Formation of fine and encapsulated mefenamic acid form I particles for dissolution improvement via electrospray method. *Particulate Science and Technology*, 36(3): 298-307.
22. Zolkepali, N. K., Abu Bakar, N. F., Naim, M. N., Anuar, N. and Abu Bakar, M. R. (2014). Nanoparticle preparation of mefenamic acid by electrospray drying. *AIP Conference Proceedings***,** 1586: 113-118

Malaysian Journal of Analytical Sciences, Vol 22 No 2 (2018): 326 - 332
DOI: https://doi.org/10.17576/mjas-2018-2202-19

MALAYSIAN JOURNAL OF ANALYTICAL SCIENCES
Published by The Malaysian Analytical Sciences Society
ISSN 1394 - 2506

CHARACTERISTICS OF RICE HUSK BIOCHAR BLENDED WITH COAL FLY ASH FOR POTENTIAL SORPTION MATERIAL

(Ciri-Ciri Gabungan Biochar dari Sekam Padi dengan Abu Terbang Arang Batu Sebagai Potensi Bahan Penjerab)

Nurul Farhana Ahmad[1], Azil Bahari Alias[1]*, Norhayati Talib[1], Zulkifli Abd Rashid [1], Wan Azlina Wan Ab Karim Ghani[2]

[1]*Faculty of Chemical Engineering,*
Universiti Teknologi MARA, 40450 Shah Alam, Selangor Darul Ehsan, Malaysia
[2]*Department of Chemical and Environmental Engineering,*
Universiti Putra Malaysia, 43400 Serdang, Selangor Darul Ehsan, Malaysia

**Corresponding author: azilbahari@salam.uitm.edu.my*

Received: 15 February 2017; Accepted: 2 January 2018

Abstract

Biochar has received a great attention recently due to abundant biomass left in Malaysia. Besides that, the application of biochar in environmental aspects widely used in the world to improvise soil fertility and water quality. In this research, biochar is produced from rice husk (RH) by pyrolysis at 500 °C using fixed-bed tube reactor. Then the biochar will be blended with coal fly ash (CFA) using the ratio of rice husk biochar (RHB) to CFA (0.2:0.8, 0.5:0.5, and 0.8:0.2) to be further analyzed on their characteristics. From proximate analysis, the ash content is increasing while moisture content, volatile matter, and fixed carbon decrease as the ratio are decrease. For determination of carbon, hydrogen, oxygen, nitrogen and sulphur, the result from ultimate analysis indicates that hydrogen, carbon and nitrogen increase as the ratio increases. Based on the BET result, the surface area is increase proportionally to the ratio (0.2:0.8, 0.5:0.5, 0.8:0.2). Based on this research, RHB has a great potential to be applied as an adsorbent. However, blended RH with CFA are not giving desire result to be used an adsorbent. It is believed that introduction of CFA will offer some magnetic effect to the sorbant to attract pollutants.

Keywords: biochar, biomass, coal fly ash, pyrolysis, rice husk

Abstrak

Biochar telah diberi perhatian besar baru-baru ini disebabkan kuantiti biojisim terbuang ini yang amat banyak di Malaysia. Selain itu, biochar ini banyak digunakan di dalam aspek alam sekitar iaitu secara meluas untuk penambahbaikkan kesuburan tanah dan kualiti air. Dalam penyelidikan ini, biochar dihasilkan dari sekam padi (RH) oleh proses pirolisis pada 500 °C menggunakan reaktor tiub lapisan tetap. Kemudian biochar akan dicampurkan dengan abu terbang (CFA) batu arang menggunakan nisbah sekam padi biochar (RHB) kepada CFA (0.2:0.8, 0.5:0.5 dan 0.8:0.2) seterusnya dianalisis ciri-ciri mereka. Dari analisis proksimat, kandungan abu bertambah manakala kandungan lembapan, jirim meruap dan karbon tetap berkurang dengan pengurangan nisbah RHB kepada CFA. Untuk nilai karbon, hidrogen, oksigen, nitrogen dan sulfur, keputusan dari analisis muktamad menunjukkan kadar hidrogen, karbon dan nitrogen dan sulfur meningkat dengan peningkatan nisbah RHB kepada CFA. Berdasarkan keputusan BET, luas permukaan meningkat secara berkadaran kepada nisbah (0.2:0.8, 0.5:0.5, 0.8:0.2) RHB kepada CFA. Berdasarkan penyelidikan ini, RHB mempunyai potensi besar untuk digunakan sebagai satu bahan penjerap. Walaubagaimanapun, dengan mencampurkan RH dengan CFA tidak memberi keputusan positif untuk diguna pakai sebagai bahan penjerap. Penambahan CFA dipercayai akan memberi kesan magnet kepada bahan penjerab bagi menarik bahan pencemar.

Kata kunci: biochar, biojisim, abu terbang arang batu, pirolisis, sekam padi

Introduction

Biomass can be defined as a biological material derived from living thing or organisms. Biomass is a renewable resource since it often comes from plant-based material but can be applied to animal source as well [1]. Biomass can be categorized into five main groups which are virgin wood, energy crops, agricultural residues, food waste and industrial waste and co-products [2]. Scope of biomass as renewable energy can be derived into a new product by undergoes a few processes. Biomass will undergo some processes to turn as bio-product, bio-fuel and bio-power.

Biochar is applicable to control the environment pollution. Biochar acted as adsorbent to filter all the contaminants in the polluted water. Adsorption is a process whereby the surface interaction between dissolved materials and char. The difference between adsorption and absorption is based on the concept "to soak up" or "to take into". The contaminants will diffuse into char pores (absorption) where they bind to char surfaces (adsorption). A large area of porosity content in the char provides many reactive sites for the attachment of dissolved compounds. Hence, heavy metal content can be removed by using biochar during water treatment [3]. Bio-fuel or known as biochar needs to be excess in order to maintain forest and agricultural cropland health. Biomass turns to biochar by thermal conversion process. Biochar is produced during pyrolysis and gasification whereby superheating of the biomass with limited oxygen and presence of nitrogen gas. By pyrolysis, all the volatile gases such as methane and carbon monoxide are burned and only carbon-enriched biochar left.

Pyrolysis is a thermal decomposition of materials in the absence or less presence of oxygen as compared to complete combustion. From the ancient philosophy, the product from pyrolysis is a carbonization of biomass or called as char. Nowadays, the pyrolysis will produce different product according to the principal of pyrolysis (temperature, heating rate and vapor residence time).

Rice husk (RH) is a waste product from paddy field after the harvesting season. The disposal of RH can cause a problem due to bulky volume because of its lower density. RH contains approximately 38% of cellulose, 18% of hemicellulose and 22% of lignin [4]. The application of RHB comes in many ways such construction material to produce concrete and adsorbent of organic dye and inorganic metal in wastewater treatment.

Coal fly ash (CFA) is a waste product from coal combustion from anthracite to lignite. In Malaysia, coal is widely used in generating electricity of power plant. CFA can be considered as high contamination since it is by-product from coal combustion and consist of toxic trace element condenses from the flue gas. Most of CFA is disposed as a landfill or became a source in cement industry as a raw material for concrete production. CFA has a spherical size within range 0.5 to 300 μm and pozzolanic properties. Pozzolans can be defined as a siliceous and aluminous material stick together and form as cementations products when it react with water and calcium hydroxide at ambient temperature. Common fly ash consists of SiO_2 (57.82%), Al_2O_3 (22.10%), Fe_2O_3 (8.33%) [4].

The RHB and CFA have potential to be used in environmental aspect as an adsorbent to save the environment. Therefore, this study is to determine the characteristics of single RHB and blend biochar with CFA.

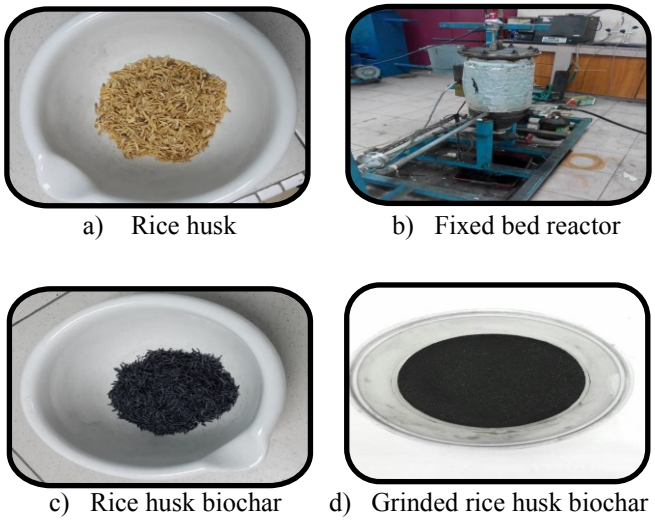
Materials and Method

Materials

RH samples were collected from BERNAS Rice Factory, Sekinchan and CFA samples originated from low rank coal (Mukah Balingian), Sarawak Biomass are crushed and leave them dry for 24 hours at 100^{o}C.

Production of biochar

A laboratory scale fixed-bed tube reactor slow pyrolysis was developed to pyrolyse the feedstock. The dried biomass is placed in cylindrical stainless steel fixed bed reactor. The sample placed in crucible and covered with aluminum foil. Pyrolysis was undergoing at constant temperature at 500^{o}C for 60 minutes. The nitrogen as carrier gas was fed at flowrate 30 mL/min into the reactor. Biochar was collected and weighed after cooling session for 3 hours [5]. The production steps of biochar are illustrated in Figure 1.



a) Rice husk b) Fixed bed reactor

c) Rice husk biochar d) Grinded rice husk biochar

Figure 1. Preparation of biochar

Preparation of sample single and blended biochar

RHB undergo leaching process with 0.1 mol/L of until pH 6 is obtained to remove ash increase the porosity. Then RHB will be neutralized and dried for 1 day at 40 ^{o}C. Then, the samples were prepared by 4 sample by the blended ratio RHB to CFA are 1.0:0.0, 0.2:0.8, 0.5:0.5, 0.8:0.2 and 0.0:1.0 by wt%.

Characterization of RHB and blended RHB

To analyze proximate analysis, the samples were measured by Thermogravimentric Analyzer (Model: Thermobalance TGA/SDRA51e, Mettler Toledo). Ultimate analysis was performed by Elemental Analyzer CHNO-S (Model: Thermo Finnigan FlashEA 1112 Series). Proximate and ultimate analysis of the samples is shown in Table 1 and Table 2, respectively. Scanning Electron Microscope was performed to observe the surface morphology changes in the RHB and blended RHB. To measure the surface area, pore volume and porosity size samples, Brunauer-Emmett-Teller (BET) with nitrogen was performed.

Table 1. Proximate analysis

Proximate (db) (wt.%)	**Sample Ratio (RHB: CFA)**				
	1.0:0	**0.8:0.2**	**0.5:0.5**	**0.2:0.8**	**0.0:1.0**
Moisture	3.9	4.8	2.6	0.9	0.3
Volatile matter	10.8	10.0	9.6	3.4	1.4
Fixed carbon	62.1	52.4	41.2	11.3	3.7
Ash	23.3	23.3	46.6	84.4	94.6

Table 2. Ultimate analysis

Ultimate (daf) (wt.%)	Sample Ratio (RHB: CFA)				
	1.0:0	**0.8:0.2**	**0.5:0.5**	**0.2:0.8**	**0.0:1.0**
Nitrogen	0.2	0.18	0.10	0.08	0.05
Carbon	18.32	21.99	15.13	13.65	21.34
Hydrogen	1.35	1.22	0.62	0.27	0.18
Sulphur	0.00	0.00	0.00	0.00	0.00
Oxygen[a]	80.09	76.61	84.15	86.00	78.43

[*]a = Calculate by differences (100-N-C-H-S)

Results and Discussion

Proximate analysis

Proximate analysis is performed to measure the moisture content, volatile matter, ash content and fixed carbon of the blended biochar. The moisture content of single RHB and CFA is 3.9 and 0.3. While the moisture content of blended biochar of 0.8:0.2, 0.5:0.5 and 0.2:0.8 is 4.8, 2.6 and 0.9 respectively according to the increment of ratio. The percentage of ash in CFA is seem to be the highest which is 94.6% since it is already in ash form. The percentage of ash for single biochar is the lowest compared to the blended RHB with CFA. The percentage of ash is increasing from 23% to 84% which from single biochar to the blended biochar from low to high ratio biochar to CFA. Effect of cellulose and silicon content give difference result on char. If the char contains high cellulose and hemicellulose, therefore the components will reduce to carbon which forms as a fixed carbon. Meanwhile, for silicon and mineral factor, the higher silicon contents, the higher the ash content. The RH contained high silicon and mineral concentration and convert it to ash composition during pyrolysis [7]. Besides, the temperature also affected the composition of ash. The higher the temperature during pyrolysis, the higher the ash composition due to the releasing of volatile matter is increases [6]. Therefore, the increment of composition ash can be varying by ratio of biochar to blended biochar due to the chemical composition of RHB: CFA at constant temperature of 500 ^{o}C in this study.

Ultimate analysis

Determination the amount of nitrogen, carbon, hydrogen, sulphur and oxygen is performed by ultimate analysis. Nitrogen is an inert gas and it does not give any significance usage and generally found as low as 1%. Composition of carbon and hydrogen is related which means the greater the percentage, the higher the quality and calorific value. However, the hydrogen is related to the volatile matter which when it combines with oxygen (O) and form as water, the calorific value reduces. Therefore, a less amount of hydrogen is more preferable. Meanwhile, the lesser the sulphur is the best. This is because oxidation from sulphur form sulphur dioxide or sulphur trioxide which may lead to acid rain and environmental pollution [7]. From the result, it can be inferred that the composition of nitrogen, hydrogen and carbon increase when the ratio of RHB to the CFA increases. Composition of nitrogen of single biochar is 0.24% and increase from 0.08% to 0.18% from the ratio 0.2:0.8. For carbon composition of single biochar is 18.32%. The same trending is shown by carbon which the compositions raise proportionally to the ratio. The composition of carbon is increase from 13.65% to 21.99% by 0.2:0.8. In this study, there is no sulphur content either in single biochar or blended biochar. According to the result, these materials have no impact on sulphur oxidation.

Surface morphology

Figure 2 to 5 show the scanning electron microscopy (SEM) images of CFA, RHB by the ratio 0.2, 0.5 and 0.8 of RHD to CFA. The result for surface morphology will be varies due to the evaporation of volatile matter of biochar. From Figure 2, it depicts that the particles are comes from various sized and shapes. The sizes are varying from smaller to larger sizes of particle. Moreover, the shape comes in varies from regular spherical shapes to completely irregular shape. Figure 2 shows the image of CFA from SEM.

From Figure 3, the SEM image showed the micro porous structure. The shape is honeycomb-like with formation of porosity cylindrically. It shows that the RHB has various size of porosity on the tip side while on the body the porosity is hardly to form as viewed from 600 magnifications. Based on the size of porosity, it has the potential to act as an absorbent. The formation of pores is due to creation of numerous micropores when de-volatilization [8]. A similar observation is also reported in literature [9].

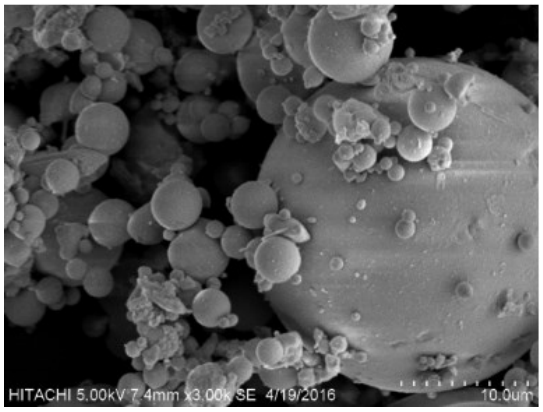


Figure 2. SEM image of CFA (0.0:1.0)

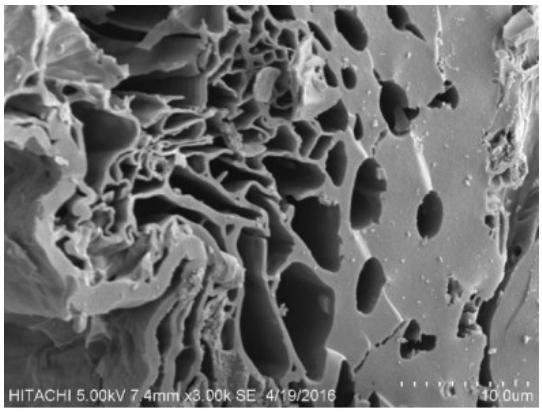


Figure 3. SEM image of RHB (1.0:0.0)

Figure 4, 5 and 6 are the images for blended biochar with coal fly ash by different ration. From the result, it can be observed that the particle of coal fly ash is attached over the biochar surface. For the ratio 0.2:0.8 from Figure 4, the pores and surface are mostly covered by the coal fly ash. Ratio of 0.5:0.5 that shown in Figure 5, the particles of coal fly ash is less cover the pores and surface area of biochar. Figure 6 shown the result for the ratio 0.8:0.2 the pores have more surface and most of the coal fly ash are attached on body's surface area.

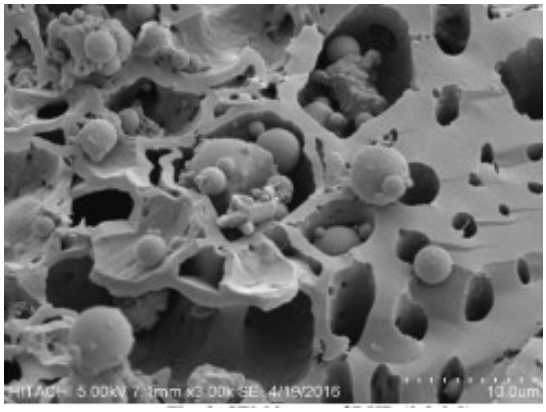


Figure 4. SEM image of RHB (0.2:0.8)

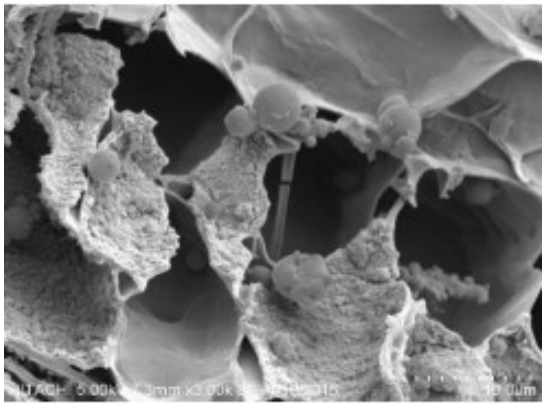


Figure 5. SEM image of RHB (0.5:0.5)

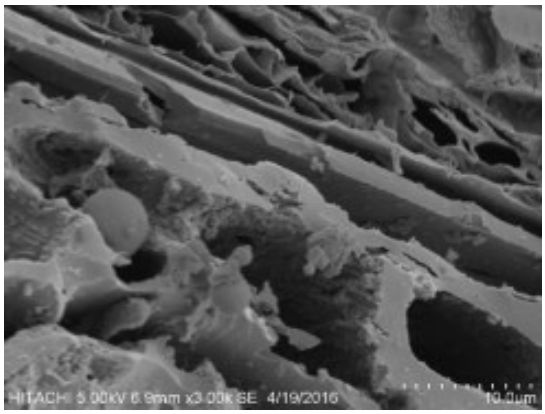


Figure 6. SEM image of RHB (0.8:0.2)

Surface area, pore volume and pore size

From the SEM image above, it can be related to the BET result to discuss about the BET surface area, pore volume and pore size. The result of BET surface area, pore volume and pore size shown in Table 3. Based on the result, the surface area is decreasing from 3.8661 to 3.3769 m^2/g as well as pore volume and pore size. For the pore volume, the volume reduced from 0.00908 to 0.00726 cm^3/g. While for the pore size, the size is decreasing from 93.9042 to 79.0427 Å. This is because the surface area of biochar is depending on the amount of inorganic material which is CFA (ash content) due to the fusion of the molten ash covered up pores in the biochar hence reducing the accessible surface area, [10]. It can be inferred that the higher the amount of ash content, the smaller the surface area of biochar as resulting from proximate analysis. By referring to Table 1, the ash content of samples is increasing from ratio 1.0:0.0 to 0.0:1.0 (RHB: CFA)

Table 3. BET surface area, pore volume and pore size

Sample Ratio (RHB: CFA)	BET Surface Area (m^2/g)	Pore Volume (cm^3/g)	Pore Size (Å)
1.0:0.0	3.866	0.0090	93.904
0.8:0.2	3.539	0.0084	90.566
0.5:0.5	3.430	0.0079	85.593
0.2:0.8	3.376	0.0072	79.042
0.0:1.0	4.301	0.0064	60.116

Even though the results seem not giving a desire result however based on the pozzolanic criteria on coal fly ash, it has high potential to adsorb heavy metal. As mentioned, pozzolans can be defined as siliceous or aluminous material stick together and form as cementitious products when it reacts with water at ambient temperature [8]. Therefore, by adding coal fly ash it may become as a medium to aid biochar in adsorbing contaminant in wastewater.

Conclusion

Blended ratio of RHB and CFA resulting different data and observation. From proximate analysis, the ash content is increasing while moisture content, volatile matter and fixed carbon decrease. For determination of C, H, O, N and S the result from ultimate analysis indicates that hydrogen, carbon and nitrogen increase as the ratio increases. Referring to surface morphology, the shape and pore size is varying by difference ratio. Based on the BET result, the surface area is increase proportionally to the ratio of RHB: CFA 0.2:0.8, 0.5:0.5, 0.8:0.2.

Acknowledgments

The authors gratefully acknowledge the financial support received from Education Ministry of Malaysia through 'Dana Kecemerlangan Pendidikan UiTM Geran Inisiatif Penyeliaan' (GIP) (600-IRMI/GIP 5/3 (0040/2016)), Institute of Graduate Studies (IPSIS) Research Management Centre (RMC), Faculty of Chemical Engineering and Universiti Teknologi MARA, Selangor, Malaysia.

References

1. Mekhilef, S., Saidur, R. and Mustaffa, W. E. S. B. (2011). Biomass energy in Malaysia: Current state and prospects. *Renewable and Sustainable Energy Reviews*, 15(7): 3360-3370.
2. Moghtaderi, B., Meesri, C. and Wall, T. F. (2004). Pyrolytic characteristics of blended coal and woody biomass. *Fuel*, 83(6), 745-750.
3. Frederik, R., Sven, V., Dane, D. and Wolter, P. (2013). Production and characterization of slow pyrolysis biochar: Influence of feedsstock type and pyrolysis conditions, *GCB Bioenergy*, 5: 104-115,
4. Windeatt, J. H., Ross, A. B., Williams, P. T., Forster, P. M., Nahil, M. A. and Singh, S. (2014). Characteristics of biochars from crop residues: Potential for carbon sequestration and soil amendment. *Journal of Environmental Management*, 146: 189-197.
5. Mahmoud, D. K., Salleh, M. A. M., Karim, W. A. W. A., Idris, A. and Abidin, Z. Z. (2012). Batch adsorption of basic dye using acid treated kenaf fibre char: Equilibrium, kinetic and thermodynamic studies. *Chemical Engineering Journal*, 181, 449-457.
6. Crombie, K., Mašek, O., Sohi, S. P., Brownsort, P. and Cross, A. (2013). The effect of pyrolysis conditions on biochar stability as determined by three methods. *GCB Bioenergy*, 5(2), 122-131.
7. Kizito, S., Wu, S., Kirui, W. K., Lei, M., Lu, Q., Bah, H. and Dong, R. (2015). Evaluation of slow pyrolyzed wood and rice husks biochar for adsorption of ammonium nitrogen from piggery manure anaerobic digestate slurry. *Science of the Total Environment*, 505: 102-112.
8. Masto, R. E., Ansari, M. A., George, J., Selvi, V. A. and Ram, L. C. (2013). Co-application of biochar and lignite fly ash on soil nutrients and biological parameters at different crop growth stages of Zea mays. *Ecological Engineering*, 58: 314-322.
9. Claoston, N., Samsuri, A. W., Ahmad Husni, M. H. and Mohd Amran, M. S. (2014). Effects of pyrolysis temperature on the physicochemical properties of empty fruit bunch and rice husk biochars. *Waste Management & Research*, 32(4): 331-339.
10. Ronsse, F., Van Hecke, S., Dickinson, D., & Prins, W. (2013). Production and characterization of slow pyrolysis biochar: influence of feedstock type and pyrolysis conditions. *GCB Bioenergy*, 5(2): 104-115.

Malaysian Journal of Analytical Sciences, Vol 22 No 2 (2018): 333 - 338
DOI: https://doi.org/10.17576/mjas-2018-2202-20

MALAYSIAN JOURNAL OF ANALYTICAL SCIENCES
Published by The Malaysian Analytical Sciences Society
ISSN 1394 - 2506

CHARACTERIZATION OF TiO_2 THIN FILMS DERIVED USING ACETIC ACID AND NITRIC ACID

(Pencirian Filem Nipis TiO_2 yang Dihasilkan Menggunakan Asid Asetik dan Asid Nitrik)

Nur Munirah Safiay[1], Syahman Shamsuddin[2], Nur Najwa Yunus[2], Fazlena Hamzah[2]*

[1]*Centre of Nanoscience and Nonaotechnology, Institute of Science*
[2]*Biocatalysis and Biobased Material Research Group, CoRe of Green Technology & Sustainable Development, Faculty of Chemical Engineering*
Universiti Teknologi MARA, Shah Alam Campus, 40450 Shah Alam, Selangor, Malaysia

**Corresponding author: fazlena@salam.uitm.edu.my*

Received: 15 February 2017; Accepted: 2 January 2018

Abstract

Titanium dioxide (TiO_2) thin films were prepared *via* sol gel method using different concentration of glacial acetic acid and nitric acid. The deposition of TiO_2 gel on the ITO substrate was conducted using spin coating techniques at a rate of 3,000 rpm for 30 s and was calcinated at 500 ^oC for 10 minutes. The study was conducted to determine the surface morphology and characteristic of the TiO_2 thin film based on the different acid precursor. The GAA – TiO_2 and HNO_3 - TiO_2 thin film were analyzed using Contact Angle Goniometer for absorption property study and Scanning Electron Microscope (SEM) for surface topography study. The result indicated that different acid and different concentration influence wettability of the synthesized TiO_2 thin film. Higher concentration of GAA results in higher contact angle of TiO_2 thin film whereas higher concentration of HNO_3 reduced the contact angle of TiO_2 thin film. However, the contact angle obtained through this study was in a range of 27.55^o – 67.55^o for the concentration acid of 8 – 10 mmol which represent hydrophilic characteristic of the TiO_2 thin film. For surface analysis, uneven and not uniform surface of thin film was detected for the entire sample. This might be due to the several factors such as temperature and particle size that limited the adhesion of the TiO_2 sol gel to the ITO substrate. Transform Infrared Spectroscopy (FTIR) analysis was used to validate the present of the Ti-O bond vibrations in the sample and it was observed in ranges of 515–800 cm^{-1}. On the other hand, the crystallinity structure of the synthesized TiO_2 was validated using X-ray Diffraction (XRD). The results indicated that both GAA - TiO_2 and HNO_3 - TiO_2 mixtures gave a strong anatase crystal structure. The major XRD diffraction peaks can be attributed to (101), (004), (200), (211), (204) and (116) plane of the tetragonal TiO_2-anatase phase.

Keywords: characterization, acid, thin films, titanium dioxide, titanium isopropoxide

Abstrak

Titanium dioksida (TiO_2) filem nipis telah dihasilkan melalui kaedah sol gel dengan menggunakan kepekatan asid asetik glasial dan asid nitrik yang berbeza. Pemendakan gel TiO_2 pada substrat ITO dilakukan menggunakan teknik salutan berputar pada kadar 3,000 rpm selama 30 s dan dikalsinasi pada 500 ^oC selama 10 minit. Kajian ini dijalankan untuk menentukan morfologi permukaan dan ciri-ciri filem TiO_2 nipis berdasarkan kepekatan asid yang berbeza. Filem nipis GAA - TiO_2 dan HNO_3 - TiO_2 dianalisis dengan menggunakan goniometer sudut sentuh untuk kajian ciri-ciri penyerapan dan mikroskop imbasan elektron (SEM) untuk kajian topografi permukaan. Hasil kajian menunjukkan bahawa asid yang berbeza dan kepekatan yang berbeza mempengaruhi kelembapan TiO_2 filem nipis yang dihasilkan. Kepekatan GAA yang tinggi menghasilkan sudut sentuh yang lebih tinggi pada TiO_2 filem nipis manakala kepekatan HNO_3 yang lebih tinggi mengurangkan sudut sentuh TiO_2 filem nipis. Walau bagaimanapun, sudut hubungan yang diperolehi melalui kajian ini adalah dalam lingkungan 27.55^o - 67.55^o untuk kepekatan asid 8 - 10 mmol yang mewakili ciri hidrofilik TiO_2 filem nipis. Untuk analisis permukaan, permukaan filem nipis adalah tidak rata dan tidak seragam dikesan untuk semua sampel. Hal ini mungkin disebabkan beberapa faktor seperti suhu dan saiz zarah yang menghadkan pelekatan sol gel TiO_2 kepada substrat ITO. Analisis Spektroskopi Inframerah (FTIR) digunakan

untuk mengesahkan kehadiran getaran Ti-O di dalam sampel dan keputusan menunjukkan kehadiran getaran Ti-O di dalam lingkungan 515-800 cm^{-1}. Manakala struktur kristal TiO_2 yang disintesis telah disahkan dengan menggunakan pembelauan sinar-X (XRD). Keputusan menunjukkan bahawa campuran GAA - TiO_2 dan HNO_3 - TiO_2 memberikan struktur kristal anatase yang kuat. Puncak pembelauan XRD yang utama boleh dikaitkan dengan fasa TiO_2-anatase tetragonal pada (101), (004), (200), (211), (204) dan (116).

Kata kunci: pencirian, asid, filem nipis, titanium dioksida, titanium isopropoksida

Introduction

Titanium dioxide, also known as titanium (IV) oxide or titania, is the naturally occurring oxide of titanium with chemical formula of TiO2. It is sourced from ilmenite, rutile and anatase [1]. It has been explored in a widen industrial application due to its unique physical, chemical and electro-optic characteristic such as low cost, easy handling, non-toxicity, and resistance to photochemical and chemical erosion. TiO_2 has been used as a material in solar cells, chemical sensors, for hydrogen gas evolution, as pigments, self-cleaning surfaces, and environmental purification applications [2]. Another potential of TiO_2 is in form of thin film. The research of the thin film TiO_2 has been explored by Kajitvichyanukul et al. [3] for photocatalytic reduction of chromium(VI) in photocatalysis process. The photocatalytic reactivity of the obtained thin film is at a par with the reactivity using powder TiO_2. The results indicate that the differences in photocatalytic reduction of Chromium(VI) could be correlated with the structural morphology of the thin film. As indicated by Qiu et al. [4], TiO_2 nanostructured thin films possess a large surface area and show unique chemical, physical and electronic properties that are different from those bulk materials. These characteristics make it a potential material in in constructing a novel sensing device such as electrochemical sensors and biosensors. However, the characteristic of the thin film TiO_2 might be varies based on the method used to fabricate it. Several methods have been employed to fabricate TiO_2 films, including sputtering, chemical vapor deposition, and sol-gel process [5, 6, 7]. However, the sol-gel process is one of the most appropriate technologies to prepare thin oxide coating. The interest in application of sol-gel method is due to several advantages including; good homogeneity, ease of composition control, low processing temperature, large area coatings, low equipment cost, and good photocatalytic properties [8].

This paper, aims to investigate effects of the preparation conditions on the surface morphology and properties of TiO_2 thin film. Titanium dioxide (TiO_2) thin film was prepared by glacial acetic acid- sol-gel method and nitric acid -sol-gel method. The phase transformation was investigated by an X-ray diffractometer (XRD) and the microstructure was characterized by a scanning electron microscope (SEM).

Materials and Methods

Preparation of sol-gel solution

The preparation of titanium dioxide solutions had been performed by sol-gel method. Fifty milliliter of absolute Ethanol (99% Merck) was mixed with 5 ml glacial acetic acid (99.5% GCC), 6.6 ml titanium tetra isopropoxide TTIP (99%, sigma-Aldrich). Then, these liquids were continuously stirred by using a magnetic stirrer on a hot plate. Acetylacetone, glacial acetic acid (GAA), distilled water and polyethylene glycol (PEG) were added and these solutions were stirred vigorously for 2 hours at temperature 50 °C and 300-500 rpm. After 2 hours, the solution was sonicated inside the ultrasonic cleaner for 30 minutes. ITO glass slides (25 mm x 25 mm x 2 mm) were used as substrate after cleaned with acetone, ethanol, and deionized water in an ultrasonic bath. Thereafter, the slides were dried with filter paper. Spin coating method was used for deposition of TiO_2 gel on the substrate at a rate of 3,000 rpm for 30 s. Then, the samples was dried at 150 °C for 5 minutes and calcined at 500 °C for 10 minutes. Reagents were used as we received from supplier without more purification. Similar procedure was repeated for nitric acid - sol-gel solution.

Characterization of TiO_2 film

The crystal structure of the TiO_2 coated on ITO was characterized by $\theta/2\theta$ X-ray diffractometer (Seifert, PTS 3000, USA) using Cu Kα radiation (λ=0.154 nm) (45 kV at 200 mA). The XRD pattern was obtained at 2θ angle range of 20–80° with a scanning step of 0.02°/step and a scanning speed of 5°/min. Scanning electron microscopy (SEM – EFI Company) was used to investigate the surface morphology of the thin films. The Fourier Transform Infrared Spectroscopy (FTIR) (Thermo Fisher, Nicolet iG50, USA) was used to evaluate the functional group present in the

synthesized TiO_2 and Contact Angle (AST, VCA 3000S, USA) analysis was used to evaluate the absorption property of the TiO_2 thin film. The method used is according to Miao et al. [9].

Results and Discussion

Absorption properties of the TiO_2 thin films

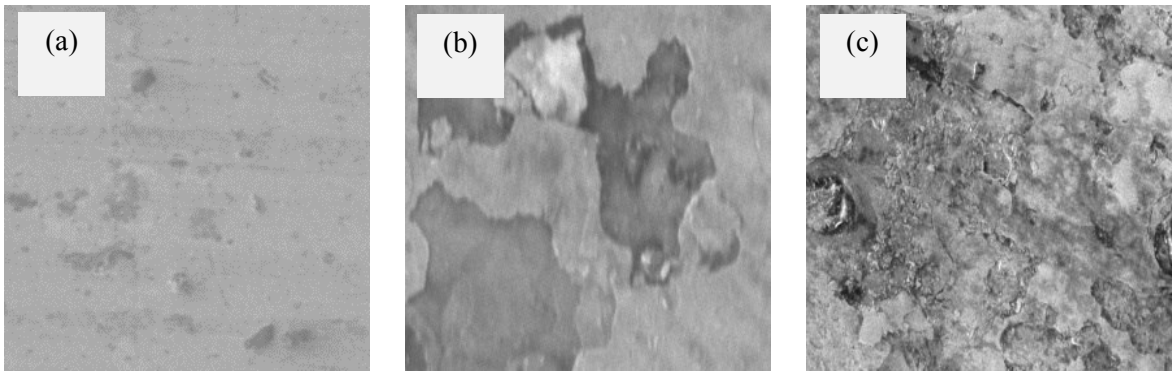
To evaluate the surface properties of the thin films, contact angle analysis was carried out in order to determine the hydrophilicity of the sample. The contact angle is the angle, conventionally measured through the liquid, where a liquid–vapor interface meets a solid surface. It quantifies the wettability of a solid surface by a liquid. Table 1 shows the result of contact angle analysis of the TiO_2 thin films. From the results, it was found that the contact angles for synthesizing TiO_2 thin films was less than 90^o which consider that the solid surface of TiO_2 thin films is hydrophilic. Two different acids were used in the preparation of TiO_2 thin film and the results indicated that nitric acid (HNO_3) gave higher contact angle value as compared to glacial acetic acid (GAA) thin film. However, increment of acid concentration reduced contact angle of the TiO_2 thin film to 34.86^o at 10 mmol HNO_3 instead of 67.6^o at 8mmol HNO_3. On the other hand, increment of GAA concentration up to 10 mmol, increased contact angle of TiO2 thin film to 39.95^o from 27.55^o at 8mmol GAA. However, all of the samples were hydrophilic film and it is suitable to be used in application of bio-liquid detection system. According to Li et al. [10], hydrophilic characteristic of thin film gave a great application potential on serving as biosensor. The finding indicated that SiN thin film surface is hydrophilic with contact angle of 45^o. Similar finding had been reported by Miao et al. [9] which indicated that the deposited porous and amorphous TiO_2 thin films enable an increase of the surface tension of the material, thereby improving absorption property of the composite structure.

Table 1. Contact angle of TiO_2 thin films with different concentration of GAA and HNO_3

Concentration GAA (mmol)	Contact Angle (°)	Concentration HNO_3 (mmol)	Contact Angle (°)
8	27.55	8	67.60
9	39.35	9	52.40
10	39.95	10	34.85

Surface morphology and surface area of the TiO_2 thin films

The surface morphology of the TiO_2 films was examined using SEM and is revealed in Figure 1. SEM images of different films derived from GAA and HNO_3 catalyst was very similar to each other. The adhesion of the TiO_2 thin film was observed for both sample but the surface was not smooth with irregularities. SEM image of GAA – TiO_2 and HNO_3 – TiO_2 at 9 mmol had shown a crack surface and not uniform structure (Figure 1b and e).



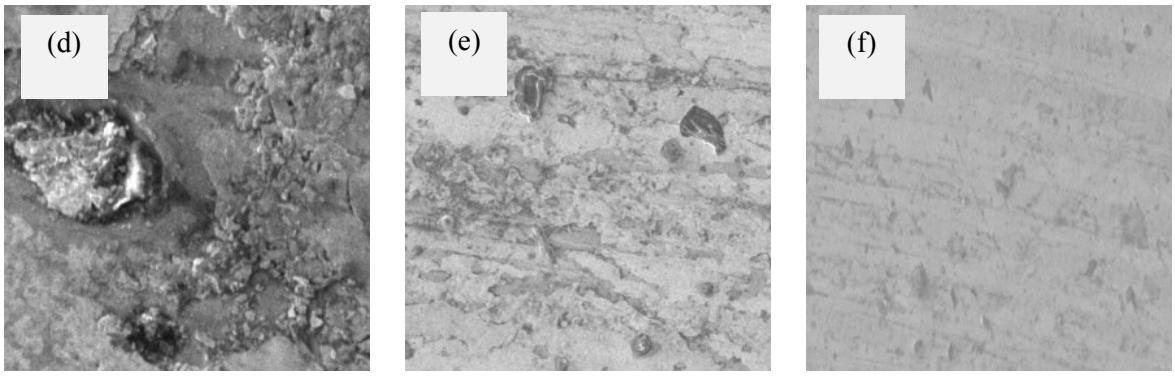


Figure 1. FE-SEM images of TiO_2 thin films (a) 8 mmol GAA (b) 9 mmol GAA and (c) 10 mmol GAA (d) 8 mmol HNO_3 (e) 9 mmol HNO_3 (f) 10 mmol HNO_3

The surface was almost plain for all sample with some agglomerations were detected at 8 mmol GAA – TiO_2 and 10 mmol HNO_3 – TiO_2 thin film (Figure 1a and f). The tendency of particle agglomeration might happen which is directly related to the increase in crystallite size. On the other hand, the temperature might influent the surface morphology of the thin film. Higher temperature during annealing may lead to non-uniform and cracked coating and reduce coating lucidity and transparency. According to Alzamani et al. [11], this is due to substrate plasticity and softening or crystalline size increase or film structure variation. In a sol-gel process of transition metal alkoxides, hydrolysis and condensation reactions occur very rapidly, so uniform and ultrafine products are difficult to obtain. With the use of bulky, branched alkoxy groups (i.e. isopropoxides), the hydrolysis and condensation rates can be reduced to favor the formation of nanometric clusters, yielding a more uniform particle size.

Fourier transform infrared spectroscopy analysis of TiO_2 powder

Figure 2 shows the FTIR pattern of TiO_2 synthesized from sol-gel method with glacial acetic acid and nitric acid in range of 515-4000 cm^{-1}. Both graph shown a similar trend and intensity of the spectrum. In all spectra measured, the bands assigned to the stretching vibrations of OH groups (at about 3400-3437 cm^{-1}) together with the bending vibrations in H_2O molecules (at about 1529 cm^{-1}) were observed, which relates to the sol-gel synthesis. The intensity of all those bands will decreases during an annealing process. While, bands connected with Ti-O bond vibrations occur in the ranges of 515-800 cm^{-1}. Similar finding was recorded by Fatma et al. [12] and Adamczyk and Dlugon [13]. Moreover, the bands at 1050, 1089, and 1138 cm^{-1} were ascribed to stretching of Ti-O-C while lower mode of amorphous TiO_2 appeared at 932 cm^{-1} [14-15]. While the peak appeared at 1249-1250 cm^{-1} and 1285 cm^{-1} was the vibration mood of C-O-O group. The doublet in 1349-1350 cm^{-1} and 1443-1445 cm^{-1} designated the symmetric and asymmetric stretching vibration of the carboxylic group coordinated to Ti as a bidentate ligand [16].

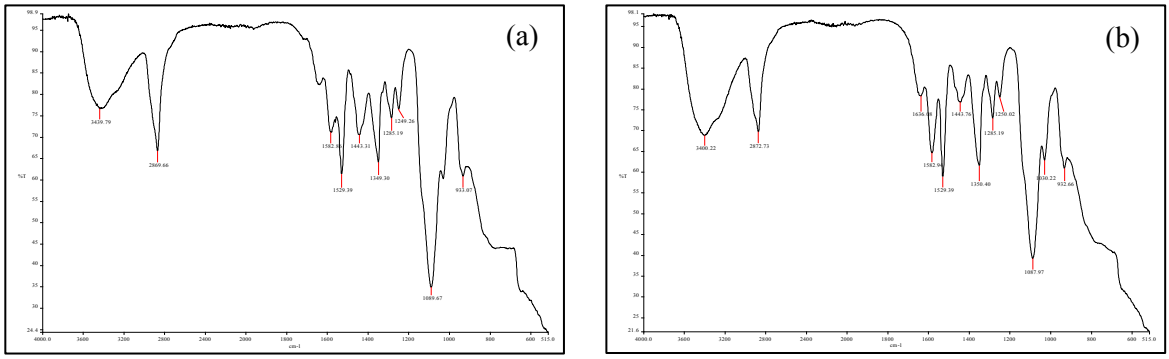


Figure 2. (a) FTIR pattern of TiO_2-GAA powder, (b) FTIR pattern of TiO_2-HNO_3 powder

X-Ray diffraction analysis of TiO_2 powder

Figure 3 shows the XRD images of GAA-TiO_2 and HNO_3-TiO2. The GAA-TiO_2 and HNO_3-TiO_2 diffraction peaks showing similar crystallinity properties. On diffractograms, the dominant peaks were associated with anatase (A), rutile (R) and brookite (B) phases. It can be seen that both samples showed the anatase TiO_2 crystal structure. The major XRD diffraction peaks can be attributed to (101), (004), (200), (211), (204) and (116) plane of the tetragonal TiO2-anatase phase. Theoretically, all the TiO_2 samples are polycrystalline in nature with most intense peak corresponding to (110) plane. Similar result was obtained by Tsegaa and Dejeneb [17], Yu et al. [18] and Thamaphat et al. [19]. The results show that low concentration of GAA results in higher intensity of the anatase phase at (101) plane.

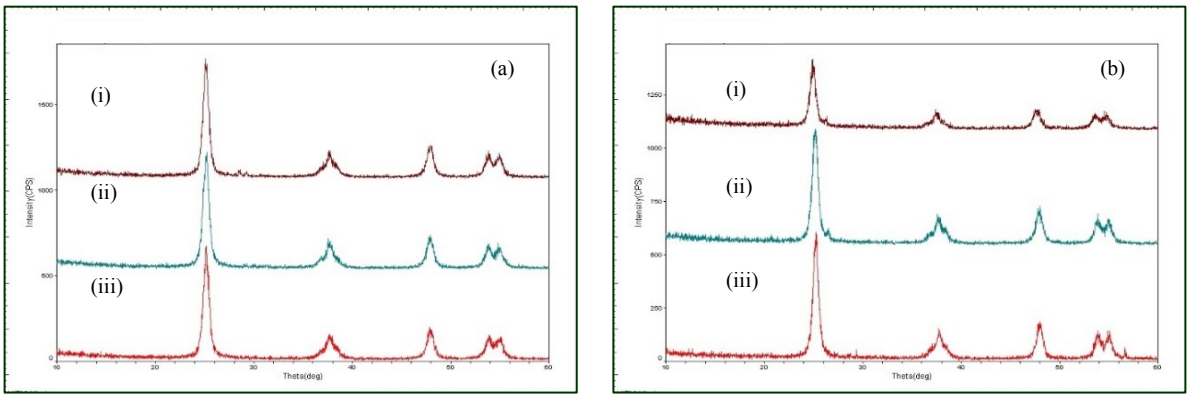


Figure 3. (a) XRD pattern of (i) 8 mmol GAA (ii) 9 mmol GAA (iii) 10 mmol GAA of TiO_2 powder, (b) XRD pattern of (i) 8 mmol HNO_3 (ii) 9 mmol HNO_3 (iii) 10 mmol HNO_3 of TiO_2 powder

On the other hand, higher concentration of HNO_3 was leaded for higher intensity of the anatase peak in HNO_3-TiO_2 sample at (101) plane. This might occurred due to the different kinds of strain such as tensile and compressive in the TiO_2 particle. In the study by Tsegaa and Dejeneb [17], the diffraction peaks of the TiO_2 were shifted slightly to the higher angle side with the increase of acid concentration. While, Serrano et al. [20] claim that nitric acids lead to the development of TiO_2 photocatalysts with convenient textural properties which produce the selective crystallization into anatase with small nanocrystals being present within the pore walls. This shown that concentration of the acid will influence the crystallinity polymorphs of the material.

Conclusion

Titanium dioxide (TiO_2) thin films was developed using 2 different acid which is GAA and HNO_3 gave different characteristic and properties of TiO_2 thin film. Both acid results in hydrophilic characteristic of thin film with contact angle value less than 90^o. However, increasing the concentration of GAA reduced hydrophilicity value of TiO_2 thin film. On the other hand, higher concentration of HNO_3 results in higher hydrophilicity value of TiO_2 thin film. On the other hand, different acid and its concentration results in similar topography image of the thin film. Deposition of TiO_2 sol gel was observed on ITO substrate but uneven and not uniform layer of TiO_2 was presented. While for FTIR and XRD analysis of the both sample, the present of Ti-O group was observed at the absorbance range of 515-800 cm^{-1} and the crystal peak observed for both sample were associated with anatase (A), rutile (R) and brookite (B) phases which represents the nature characteristic of TiO_2.

Acknowledgement

The present study was made possible through funding from Faculty of Chemical Engineering and Universiti Teknologi MARA - 600-RMI/GIP 5/3(0041/2016), and continuous support from Research Management Institute (RMI) of University Technology MARA is gratefully acknowledged. Authors also like to show gratitude to the facilities and constant encouragement from Faculty of Chemical Engineering, Universiti Teknologi MARA.

References

1. Titanium dioxide definition, https://en.wikipedia.org/wiki/Titanium_dioxide [Access online 20 October 2016].
2. Hoffmann, M. R., Martin, S. T., Choi, W. and Bahnemann, D.W. (1995). Environmental applications of semiconductor photocatalysis. *Chemical Reviews*, 95: 69-96.
3. Kajitvichyanukula P., Ananpattarachaia J. and Pongpom S. (2005). Sol–gel preparation and properties study of TiO_2 thin film for photocatalytic reduction of chromium(VI) in photocatalysis process. *Science and Technology of Advanced Materials*, 6: 352-358.
4. Qiu J., Zhang S. and Zhao H. (2011). Recent applications of TiO_2 nanomaterials in chemical sensing in aqueous media. *Sensors & Actuators: B. Chemical,* 160: 875-890.
5. Ding Z., Hu X., Yue P. L., Lu G. Q. and Greenfield P. F. (2001). Synthesis of anatase TiO_2 supported on porous solids by chemical vapor deposition. *Catalysis Today*, 68: 173-182.
6. Pecchi G., Reyes P. and Sanhueza, J. P. (2001). Photocatalytic degradation of pentachlorophenol on TiO_2 sol–gel catalysts. *Chemosphere*, 43: 141–146.
7. Sonawane, R. S., Hegde, S. G. and Dongare, M. K. (2002). Preparation of titanium (IV) oxide thin film photocatalyst by sol–gel dip coating. *Materials Chemistry and Physics,* 77: 744–750.
8. Sakka, S., Yoko, T. in: Jørgenson, J. C. and Reisfield, R. (Eds.) (1991). Chemistry, spectroscopy, and application of sol–gel glasses, *Springer,* Heidelberg: 89–91.
9. Miao, D., Hu, H., Li, A., Jiang, S. and Shang, S. (2015). Fabrication of porous and amorphous TiO_2 thin films on flexible textile substrates. *Ceramics International*, 41: 9177-9182.
10. Li, Y. G., Ma, L. X., Sarro, P. M., Du, D. X. and Liu, X. F. (2016). Mass sensitivity of aluminum nitride thin film based surface acoustic wave sensors prepared for biosensing application. *Symposium on Piezoelectricity, Acoustic Waves, and Device Applications*, 21-24 Oct. 2016.
11. Alzamani, M., Shokuhfar, A., Eghdam, E. and Mastali, S. (2013). Influence of catalyst on structural and morphological properties of TiO_2 nanostructured films prepared by sol–gel on glass. *Progress in Natural Science: Materials International*, 23(1):77–84.
12. Parra, R., Góes, M. S., Castro, M. S., Longo, E., Bueno, P. R. and Varela, J. A. (2008). Reaction pathway to the synthesis of anatase via the chemical modification of titanium isopropoxide with acetic acid. *Chemistry of Materials*, 20: 143-150.
13. Gonzalez, R. J., Zallen, R. and Berger, H. (1997). Infrared reflectivity and lattice fundamentals in anatase TiO_2s. *Physic Review B,* 55: 7014-7017.
14. Nolan, N. T., Seery, M. K. and Pillai, S. C. (2009). Spectroscopic investigation of the anatase-to-rutile transformation of sol-gel-synthesized TiO_2 photocatalysts. *Journal of Physical Chemistry C*, 2113: 16151-16157.
15. Gökdemir, F. P., Yüzbaşıoğlu, V. E., Keskin, B., Özdemir O. and Kutlu, K. (2014). Formation of TiO_2 thin films by a modified sol gel route and characterization of structural, optical and electrochromic properties. *Advance Materials Letter,* 5(7): 367-371.
16. Adamczyk, A. and Długoń E. (2012). The FTIR studies of gels and thin films of Al_2O_3 – TiO_2 and Al_2O_3 – TiO_2 – SiO_2 systems. *Spectrochimica Acta Part A: Molecular and Biomolecular Spectroscopy*, 89: 11-17.
17. Tsegaa, M. and Dejeneb, F. B. (2017). Influence of acidic pH on the formulation of TiO_2 nanocrystalline powders with enhanced photoluminescence property. *Heliyon*, 3:246.
18. Yu, J. C., Yu, J., Ho, W. K, Jiang, Z. and Zhang, L. Z (2002). Effects of F- doping on the photocatalytic activity and microstructures of nanocrystalline TiO_2 powders. *Chemistry of Materials*, 14: 3808-3816.
19. Serrano, D. P., Calleja, G., Sanz, R. and Pizarro, P. (2007). Development of crystallinity and photocatalytic properties in porous TiO_2 by mild acid treatment. *Journal of Materials Chemistry*, 17(12): 1178-1187.
20. Thamaphat, K., Limsuwan, P. and Ngotawornchai, B. (2008). Phase characterization of TiO_2 powder by XRD and TEM *Kasetsart Journal (Natural Science)*, 42: 357-361.

Malaysian Journal of Analytical Sciences, Vol 22 No 2 (2018): 339 - 345
DOI: https://doi.org/10.17576/mjas-2018-2202-21

MALAYSIAN JOURNAL OF ANALYTICAL SCIENCES
Published by The Malaysian Analytical Sciences Society
ISSN 1394 - 2506

SELF-ASSEMBLIES BEHAVIOUR OF PALM OIL-BASED GALACTOSIDE

(Sifat Swapenyusunan Galaktosida Berasaskan Minyak Sawit)

Marina Yusoff, Nurul Fadhilah Kamalul Aripin*, Nurfatin Inani Aznan, Ruzitah Mohd Salleh

School of Chemical Engineering,
Universiti Teknologi MARA, 40450 Shah Alam, Selangor, Malaysia

**Corresponding author: fadhilah9413@salam.uitm.edu.my*

Received: 25 February 2017; Accepted: 2 January 2018

Abstract

Analyses of palm kernel oil-based galactosides self-assemblies are important to determine their applications in pharmaceutical products. The palm kernel oil-based galactosides (GalPKO) are synthesized by adopting Fischer glycosylation method with minor modification. A birefringent fan-shaped texture was observed upon cooling using optical polarizing microscope (OPM) indicates formation of a smectic phase. The galactosides form isotropic phase completely at 137 °C. Water contact penetration showed that GalPKO does not form other lyotropic system except hydrated smectic phase. Based on its lyotropic behavior, critical aggregation concentration (CAC) is determined at value 0.11 mM indicating low solubility of the galactosides in water. Based on finding, galactoside can form a special class of liquid crystal mesophases and give a variety interesting application.

Keywords: galactoside, thermotropic, lyotropic, liquid crystal, mesophase

Abstrak

Analisa swapenyusunan galaktosida berasaskan minyak kernel sawit penting bagi menentukan aplikasinya dalam produk farmaseutikal. Galaktosida berasaskan minyak kernel sawit (GalPKO) disintesis menggunakan kaedah Fischer glikosilasi yang diubahsuai. Tekstur birefringen berbentuk seperti kipas diperhatikan menggunakan mikroskop polarisasi optik (OPM) semasa proses penyejukan sampel, menunjukkan pembentukan fasa smektik. Galaktosida membentuk fasa isotropik sepenuhnya pada 137 °C. Penyerapan air menunjukkan bahawa GalPKO hanya membentuk sistem liatropik fasa smektik terhidrat. Berdasarkan sifat liotropik itu, kepekatan gumpalan kritikal (CAC) ditentukan pada 0.11 mM menunjukkan keterlarutan galaktosida dalam air yang memuaskan. Hasil penyelidikan menunjukkan galatoksida ini bakal membentuk satu kelas khas fasameso cecair hablur serta kemungkinan dalam pelbagai aplikasi menarik.

Kata kunci: galaktosida, termotropik, liotropik, cecair hablur, fasameso

Introduction

Glycolipids or glycosides being one of important component in membrane exhibit liquid crystals behavior of both thermotropic and lyotropic properties because of its amphiphilic structure [1]. Interestingly, glycolipids form a special class of liquid crystal mesogens capable of giving variety of interesting applications [2]. Glycolipids are produced by connecting carbohydrates with lipids through covalent bond [3]. They consist of a sugar head group and an alkyl chain attached to an anomeric carbon *via* the glycosidic bond. The head group could be a monosaccharide or several sugar units whereas the attached alkyl chain could be a single or a branched chain [4]. Commonly, glycosylation takes place when hydrogen of OH group C1 of the sugar is being replaced by a hydrophobic chain [5]. Galactoside is one type of glycoside which consists of galactose head group. For this work, the galactosides are made from reduced palm kernel oil (PKO) fatty acids. PKO was selected as the alkyl chain

since it composed of mostly saturated fatty acids. Although, there are no data on this galactosides toxicity and biocompatibility, they are assumed to be non-toxic and biocompatible since these glycosides are made from food materials [6].

Currently, there are more than 300 natural glycolipids have been isolated. For some cases, structural features of glycolipids were modified by additional functional groups such as phosphates, sulfates, glycerol, etc. to fulfill certain applications [7]. However, to obtain natural glycolipids in large quantities is a problem because they are difficult to extract in sufficient quantities. Moreover, purification for biophysical experiments and total synthesis of these lipids often proves challenging [8]. In order to overcome these problems, researchers are more encouraged to develop synthetic glycolipids [9]. Current awareness that prefers environmental friendly technology leads to high demand for biodegradable materials that can be synthesized from renewable resources also low in cost. Some studies have shown that these synthetic glycolipids structurally mimicking natural glycosides which will be used to replace the natural glycolipids in certain biological functions [7, 10].

Synthetic glycosides are prepared through enzymatic synthesis, chemical processes, or a combination of both methods [11]. The common glycosylation strategy is using 'Fisher glycosidation' [12]. In this paper, galactoside was synthesized *via* modified version of this method which is described in details at methodology section. The objectives of this research are to investigate the thermotropic and lyotropic properties of palm kernel oil based galactoside in order to determine the types of self -assembly formation. This research only focuses on glycosides which contains of galactose as sugar head and PKO alcohol as their tail. Thermotropic properties are determined by studying phase transitions stimulated thermally using calorimetric and microscopic techniques. Lyotropic behavior is commonly observed in amphiphilic molecules where the molecules have at least two different solubility capacities towards a solvent (usually water) within itself [13]. The lyotropic properties are determined using microscopic technique and surface tension measurements to obtain the critical aggregation concentration (CAC).

Materials and Methods

Materials

Palm kernel oil (PKO) obtained from Golden Jomalina Food Industries Sdn. Bhd. (Malaysia) was reduced to PKO alcohol by using lithium aluminum hydride. D-galactose and boron trifluoride (BF_3) required for glycosides syntheses were purchased from Sigma Aldrich (USA).

Synthesis of galactoside

The glycolipids were synthesized using glycosylation procedure by Hashim et al. with minor modifications [14]. Synthesis method consists of three major steps, i.e. protection and activation of the sugars (acetylation), glycosylation and deprotection of the sugars (deacetylation). The alcohol mixtures were produced from the reduction of palm kernel oil (PKO) using a general reduction method [15]. Acetylation is a protection strategy for selective glycosylation at galactose anomeric carbon as well as for activation was prepared by a known method [16].

For glycosylation, peracetylated sugar (15 mmol) and the PKO alcohol (17 mmol) were dissolved in 60 ml dichloromethane and stirred in a closed apparatus at room temperature. Boron trifluoride (18.2 mmol) that act as catalyst was slowly injected into the solution and the glycosylation reaction took 24 hours to complete for a 2:1 ratio of alpha and beta anomeric mixture. After that, the reaction was stopped by neutralizing the solution with saturated sodium bicarbonate solution and the organic layer was washed two times with water. Dichloromethane was evaporated and acetonitrile was added later to the product. Hexane extractions were done a few times to completely remove the excess alcohol before organic solvent was evaporated.

Finally, deacetylation (removal protection group) step was performed by adding a catalytic amount of sodium methoxide to induce a basic medium into a methanolic solution of peracetylated glycosides (50 ml). The solution was stirred overnight. After the reaction was completed, Amberlite-IR-120 in methanol was added to neutralize the excess sodium methoxide. Then methanol was evaporated and product was purified from unreacted sugar with n-butanol and water extractions. N-butanol was evaporated and the product was dried in a vacuum oven at 50 ºC for 48 hours before will be characterized by Nuclear Magnetic Resonance (NMR) spectra ^{1}H NMR.

Nuclear magnetic resonance analysis
Structure elucidation of the synthesized galactosides and its starting materials were determined through NMR technique using Varian NMR Systems spectrometer at 500MHz. NMR samples were prepared in methanol-d4 (CD_3OD) solutions and recorded at room temperature. 1H NMR: δ = 5.35 (m, 0.3H, CH), 5.15 (m, 1H, H-1"), 4.81 (d, αH-1, J = 3.6 Hz), 4.22 (d, βH-1, J = 8.0 Hz), 3.40–3.90 (m, bulk sugar signals), 2.02–2.07 (m, 0.6H, CH_2), 1.62–1.67 (m, 2H, CH_2), 1.31 (m, 20H, CH_2), 0.92 (t, 3H, CH_3).

Optical polarizing microscope analysis
The instrument used in the investigation is an Olympus BX52 optical polarizing microscope equipped with a Mettler FP82 Hotstage (heating stage). Sample preparation for OPM measurement for thermotropic and lyotropic study was same. A thin layer of sample was placed sandwiched between slip cover and the glass slide. The sample was heated from room temperature to 130-140 ºC. The end temperature depends on the clearing point of the sample, therefore every sample has a different end temperature. For thermotropic study, phase transition temperatures were recorded at 5 °C/min for both heating and cooling rate. Mesophases exhibited by samples were identified based on the texture. The melting and clearing temperatures were confirmed by differential scanning calorimetry (DSC).

For lyotropic study, a sample was heated until its melting point then cooled to room temperature. Then solvent was introduced at the edge of covered slide. The solvent slowly moved towards the sample in a capillary action surrounding the sample before any contact occurred. The lyotropic phase was observed by OPM and identified based on texture and time. The images were captured for every 5-10 minutes. Water was used as the solvent in this investigation due to the application task of the material as surfactant. All experiments were performed at room temperature.

Differential scanning calorimetric analysis
Samples were measured based on a heating-cooling-heating cycle. The temperature range applied was based on data obtained from OPM studies. Samples, weighing around 4-8 mg, were placed in standard aluminum pans (crucibles) of 40µl size and sealed tightly. Then, heated to isotropic state, cooled down to the initial temperature (25 °C) and followed by second heating to isotropic temperature. A heating and cooling rate of 10°C/min and 5°C/min was applied respectively.

Critical aggregation concentrations measurements
CAC was determined through surface tension measurements of galactoside solutions using Du Nuoy ring method [17]. A series of solutions of various concentrations were prepared from stock solution containing 10 mg of palm kernel oil based galactoside in 250 ml of deionised water. 10ml series of concentration is then derived from the stock solution was measured.

Results and Discussion

Synthesis
GalPKO (Figure 1) for this study was prepared by 24-hour glycosylation process to produce an α dominant mixture. Glycosylation time determines the amount of α and β anomers produced since each anomer has different stability factor; α anomer is thermodynamically favored whereas the latter is more kinetically favored. For this work, a slightly α dominant mixture (2:1 α/β ratio) was selected because it showed to be a better topical drug carrier in terms of providing flexibility to vesicle membrane which increase drug delivery [18]. GalPKO contains a mixture of 48% Dodecyl galactosides ($GalC_{12}$), 16% Oleyl galactosides ($GalC_{18:1}$) and other saturated and unsaturated chains galactosides of α and β configurations based on the fatty acids content of palm kernel oil.

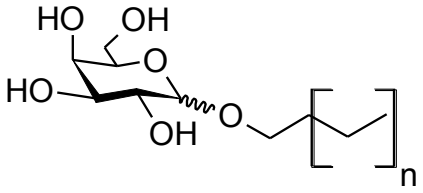


Figure 1. Structure of palm oil galactosides (GalPKO). Sample consists of stereoisomers of various alkyl chains mixture

Thermotropic study

GalPKO, like its pure components forms smectic A phase above ambient temperature [19]. It displays a bâtonnet texture immediately after temperature went below its clearing temperature, 140 °C (observed by OPM) (Figure 2(a)). However, this texture disappeared as temperature decreased to room temperature which at this point, only an isotropic with birefringence defects was observed (Figure 2 (b)). The observed birefringence defects are the shape of Maltese cross.

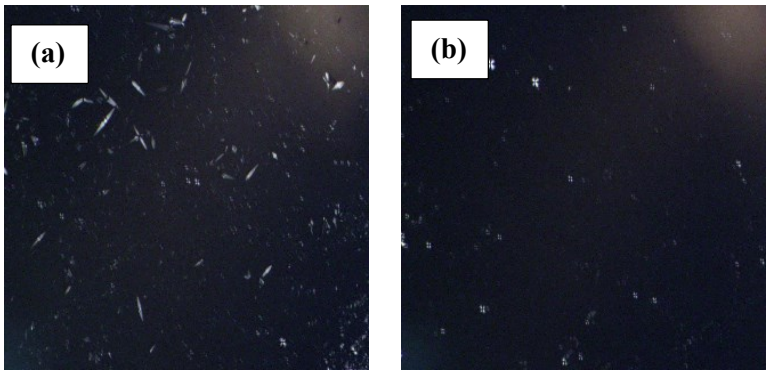


Figure 2. OPM images captured upon cooling at 137 ºC showing a bâtonnet texture immediately after isotropic point (a) and at 30 ºC where a Maltese cross texture was observed (b). All textures were observed under magnification of x10

Table 1 shows the transition temperatures of GalPKO based on DSC measurements. From four cycles of heating and cooling, the clearing temperatures are consistently observed at 137 °C. Generally, clearing temperature of a liquid crystal compound is when an isotropic phase or more commonly known as liquid phase is formed from a liquid crystalline phase. When comparing clearing temperature of GalPKO and its pure components, $GalC_{12}$ and $GalC_{18:1}$, the transition temperature is considerably low. $Gal\beta C_{12}$ and $Gal\beta C_{18:1}$ are reported to have isotropic temperatures of 166 °C and 145 °C, respectively [19]. Presence of unsaturated glycosides would lower transition temperature because double bond prevents close packing assemblies due to bending alkyl chain [20]. Thus, we could say that 16% of $GalC_{18:1}$ in GalPKO mixture attributes to lowering the clearing temperature of the mixture. However, to further explain low clearing temperature of GalPKO is caused by stereochemistry factor would be objectionable. Pertaining to a previous work, α anomer of galatosides was reported to be more stable than its β counterpart with difference in transition temperatures to be almost 16 °C, which is significantly higher compared to glucosides anomers [19]. Thus, it is conjectured the low clearing point of GalPKO is due to synergistic effect of the components.

Table 1. Thermotropic transition temperature and enthalpies based on DSC measurements

	First Heating	Second Heating	First Cooling	Second Cooling
T_{iso} range (°C)	133 – 149	131 – 147	127 – 139	125 – 139
T_{iso} peak (°C)	138	137	137	137
ΔH_{iso} (kJ mol^{-1})	-5.58	-3.64	3.04	3.43

From DSC thermogram, only one phase transition (smectic → isotropic) was observed for monoalkylated GalPKO (Figure 3) while pure $GalC_{12}$ and $GalC_{18:1}$, showed two transitions: crystal → smectic and smectic → isotropic. The absence of crystal to smectic phase transition also could be attributed to synergistic effect which probably diminished intermolecular interactions to form a more ordered crystal phase. The enthalpy change for the transition from smectic liquid crystal to liquid (ΔH_{iso}) is substantially larger compared to pure components (the difference is approximately 2 kJ mol^{-1}) showing that more energy is required to break molecular interactions in the mixture than in pure compounds [19]. Enthalpies of isotropic clearing are consistent for three cycles of heating and cooling except for the first heating which shows a larger enthalpy value. This may be due to a small amount of crystals formed during storage. It is a common practice to neglect any observation from first sample heating. It is confirmed no degradation towards the sample as observed by the microscope.

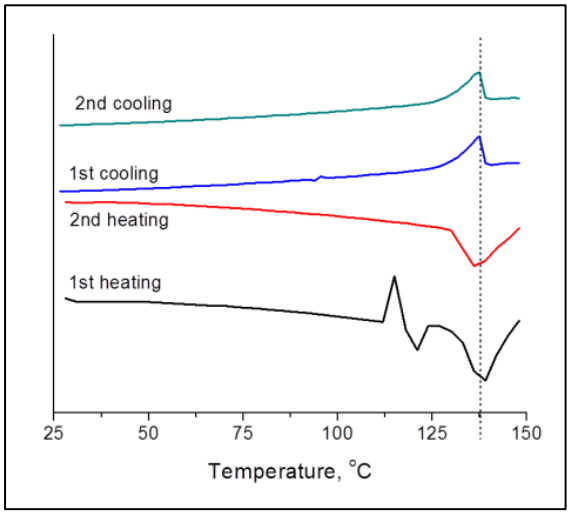


Figure 3. DSC curves obtained at heating and cooling rate of 10 °C/min and 5 °C/min of GalPKO

Lyotropic study

Lyotropic properties of GalPKO were determined using contact penetration method. This method provides a qualitative phase diagram with increasing water concentration. To acquire concentrations at phase boundaries, a quantitative method is required though is not within the scope of this work. Figure 4 shows water penetration of GalPKO at room temperature. When water penetrated dry GalPKO sample, a probable lamellar phase hydration was observed considering lack of birefringence at the penetrated region. At higher water content, GalPKO slightly dissolved as micellar solution. On contrary, similar observation was not observed in pure galactoside components as they only exhibited myelin figures [19]. These observations further support the conjecture of synergistic effect in GalPKO.

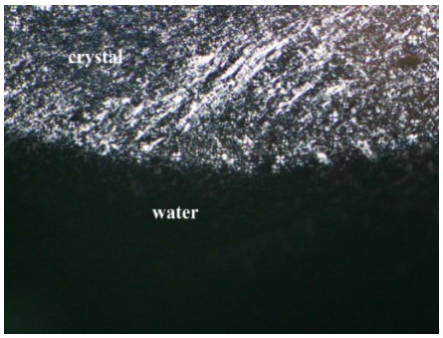


Figure 4. Contact penetration of water into GalPKO at room temperature under x10 magnification

Critical aggregation concentration (CAC) measurements grant quantitative values towards the improved water solubility of GalPKO. Typically, low CAC value indicates high hydrophobicity of an amphiphile [21]. Table 2 shows surface tension data of GalPKO and pure galactosides. Comparing GalPKO and these galactosides it is easy to notice that GalPKO has a higher CAC and capable of reducing surface tension of water by ca. 3 mNm^{-1} and ca. 7.5 mNm^{-1} more than $GalC_{18:1}$ and $GalC_{14}$ respectively.

Table 2. Surface tension data of GalPKO and pure galactosides

Compound	**CAC (mM)**	**γ_{CAC} (mNm^{-1})**
GalPKO	0.110	28.0
$GalC_{14}$*	0.020	35.5
$GalC_{18:1}$*	0.023	31.0

*pure galactosides data was taken from Garofalakis [22]

Conclusion

GalPKO, a galactosides mixture produced from glycosylation of galactose sugar with fatty alcohols from palm kernel oil has been studied with respect to its thermotropic and lyotropic behavior. The palm kernel oil-based galactoside was found to have different behavior compared to its pure galactoside components. It is believed that a synergistic effect is an important determinant of changes in GalPKO liquid crystalline properties.

Acknowledgement

This work was supported by the Ministry of Education under Research Acculturation Grant Scheme (RAGS) 600 RMI/RAGS 5/3 (140/2014).

References

1. Rodzi, N. Z. B. M., Heidelberg, T., Hashim, R., Sugimura, A. and Minamikawa, H. (2011). Synthesis and liquid crystals properties of α-methylated galactosides. *Physics Procedia*, 14: 91–95.
2. Jeffrey, G. A. and Wingert, L.W. (1992). Carbohydrate liquid crystal. *Liquid Crystal*, 12: 179–202.
3. Allen, H. J. and Kisailus, E.C. (1992). Glycoconjugates: composition, structure and function. Marcel Dekker Inc USA.
4. Kwong, W. L., Gan, W. C., Abd. Majid, W. H., Hashim, R. and Heidelberg, T. (2010). Pyroelectric detection in glycolipid thin film. *Thin Solid Films*, 518: 4412–4416.
5. Long, F. A. (1975). The Priestley heritage: Prospects for chemistry in its third 100 years. *Journal of Chemistry Education*, 52 (1): 12-14.
6. De Vries, R. J. (1984). Utilization of Malaysian palm oil and palm kernel oil for fatty acids and derivatives. *Journal of American Oil Chemical Society*, 61: 404–407.

7. Wakao, M. and Suda, Y. (2008). Synthesis of glycolipids. Glycoscience. Berlin Heidelberg: Springer-Verlag Berlin Heidelberg.
8. Van Boeckel, C. A. A. and van Boom, J. H. (1980). Synthesis of phosphatidyl-α-glucosyl-diacylglycerol containing palmitic and oleic acid esters. *Tetrahedron Letters,* 21: 3705–3708.
9. Ruiz, C. C. (2008). Sugar-Based Surfactants: Fundamentals and Applications. Paper presented at the CRC Press.
10. Tyman, J. H. P. (1992). Surfactants in lipid chemistry: Recent synthetic, physical, and biodegradative studies. Royal Society of Chemistry.
11. Holmberg, K. (2001). Natural surfactants. *Current Opinion in Colloid Interface Science*, 6: 148-159.
12. Fischer, E. (1895). Ber. Dtsch. *Chemische Berichte*, 28: 1973–1974.
13. Ahmadi, S., Achari, V. M., Nguan, H. S. and Hashim, R. (2014). Atomistic simulation studies of the α/β-glucoside and galactoside in anhydrous bilayers: Effect of the anomeric and epimeric configurations. *Journal of Molecular Modelling*, 20: 1-12.
14. Hashim, R., Abdalla Hashim, H. H., Mohd. Rodzi, N. Z., Duali Hussen, R. S. and Heidelberg, T. (2006). Branched chain glycosides: Enhanced diversity for phase behavior of easily accessible synthetic glycolipids. *Thin Solid Films*, 509: 27–35.
15. Nystrom, R. F. and Brown, W. G. (1947). Reduction of organic compounds by lithium aluminum hydride. I. aldehydes, ketones, esters, acid chlorides and acid anhydrides. *Journal of American Chemical Society*, 69: 1197–1199.
16. Vogel, A. (1989). Textbook of quantitative chemical analysis (5th edition). New York: Longman and John Wiley and Sons.
17. Ferrer, F., Comelles, F., Plou, F. J., Cruces, M. A., Fuentes, G., Parra, J. L. and Ballesteros, A. (2002). Comparative surface activities of di- and trisaccharide fatty acid esters. *Langmuir*, 47(6): 1517-1520.
18. Aripin, N. F. K., Park, J. W. and Park, H. J. (2012). Preparation of vesicle drug carrier from palm oil- and palm kernel oil-based glycosides. *Colloids Surface B*, 95: 144-153.
19. Vill, V., von Minden, H. M., Koch, M. H. J., Seydel, U. and Brandesburg, K. (2000). Thermotropic and lyotropic properties of long chain alkyl glycopyranosides. Part I: Monosaccharide headgroups. *Chemistry and Physics of Lipids,* 104: 75–91.
20. Von Minden, H. M., Brandenburg, K., Seydel, U., Koch, M. H. J., Garamus, V., Willumeit, R. and Vill, V. (2000). Thermotropic and lyotropic properties of long chain alkyl glycopyranosides. Part II. Disaccharide headgroups. *Chemistry and Physics of Lipids*, 106: 157–179.
21. Ducret, A., Giroux, A., Trani, M. and Lortie, R. (1996). Characterization of enzymatically prepared biosurfactants. *Journal of American Oil Chemistry Society*, 73: 109-113.
22. Garofalakis, G., Murray, B. S. and Sarney, D. B. (2000). Surface activity and critical aggregation concentration of pure sugar esters with different sugar headgroups. *Journal of Colloid Interface Science*, 229: 391-398.

Malaysian Journal of Analytical Sciences, Vol 22 No 2 (2018): 346 - 352
DOI: https://doi.org/10.17576/mjas-2018-2202-22

MALAYSIAN JOURNAL OF ANALYTICAL SCIENCES
Published by The Malaysian Analytical Sciences Society
ISSN 1394 - 2506

BIOLOGICAL REMOVAL OF AMMONIA BY NATURALLY GROWN BACTERIA IN SAND BIOFILTER

(Penyingkiran Ammonia Secara Biologi Menggunakan Bakteria Semulajadi dalam Biopenuras Pasir)

Fuzieah Subari[1, 2]*, Siti Rozaimah Sheikh Abdullah[1], Hassimi Abu Hasan[1], Norliza Abd. Rahman[1]

[1]*Department of Chemical and Process Engineering, Faculty of Engineering and Built Environment*
Universiti Kebangsaan Malaysia, 43600 UKM Bangi, Selangor, Malaysia
[2]*Faculty of Chemical Engineering,*
Universiti Teknologi MARA, 40450 Shah Alam, Selangor, Malaysia

**Corresponding author: fuzieahs@gmail.com*

Received: 15 February 2017; Accepted: 2 January 2018

Abstract

Drinking water treatment through biological process is commonly applied in developed countries, but not yet in developing countries such as Malaysia. The non-existence of biological treatment has urged drinking water treatment plant operator in Malaysia to shut down the plants whenever there are ammonia contaminations. This is to avoid the formation of disinfection byproducts (DBPs), which are toxic and carcinogenic, when ammonia reacts with chlorine as the disinfectant. The study aims to develop a biological drinking water treatment for to remove ammonia in a biological sand filter column. The derived biofilm, a mixed bacterial consortium is naturally cultured from surface lake water, hence eliminating the potential of pathogenic microorganism occurrence, which is not suitable for drinking water application. The biofilm was inoculated in the batch down flow column consisting of heterogeneous fine sand with diameter of 1.2 mm (top layer) and 6.7 mm (bottom layer). The study was conducted by varying the flowrate (0.09, 0.13, and 0.18 m^3/h) and hydraulic retention time (HRT) (5 and 24 hours). The water sample was taken at different depths of 0.05 m (SP4), 0.1 m (SP3) and 0.2 m (SP2) from the column base for the ammonia analysis. Significant reduction of ammonia with 96-98% was observed at 0.09 m^3/h and 24 hours and the final treated effluent had complied with the stringent regulation stipulated by the Malaysia, Ministry of Health that is lower than 1.5 mg/L.

Keywords: ammonium removal, biological treatment, drinking water treatment plant, sand biofilter

Abstrak

Rawatan air minuman menggunakan proses biologi telah lama digunakan di negara maju tetapi belum lagi di negara membangun seperti Malaysia. Ketiadaan teknologi rawatan air secara biologi ini telah memaksa operator di loji rawatan air minuman menutup loji rawatan air minuman setiap kali berlakunya pencemaran ammonia. Ianya dilakukan untuk mengelakkan pembentukan hasil sampingan disinfektan (DBP) yang toksik dan karsinogen apabila ammonia bertindak dengan klorin yang digunakan sebagai disinfektan. Objektif kajian ini dijalankan adalah untuk membangunkan satu rawatan air secara biologi untuk menyingkir ammonia dalam biopenuras pasir. Biofilem yang digunakan, merupakan konsortium bakteria campuran, di inokulasi secara semula jadi daripada air tasik untuk mengurangkan kebarangkalian kehadiran bakteria patogen memandangkan aplikasi sistem ini dibangunkan untuk rawatan air minuman. Biofilem di inolukasi dalam kelompok turus dengan aliran ke bawah yang menempatkan pasir bersaiz berbeza dengan garis pusat 1.2mm (lapisan atas) dan 6.7mm (lapisan bawah). Kajian dilakukan dengan mengubah kadar aliran (0.09, 0.13 dan 0.18 m^3/jam) dan masa penahanan hidraulik (HRT) (5 dan 24 jam). Sampel air di ambil pada ketinggian berbeza iaitu 0.05 m (SP4), 0.1 m (SP3) dan 0.2 m (SP2) dari tapak turus untuk analisis kandungan ammonia. Pengurangan ammonia sebanyak 96-98% di 0.09 m^3/jam and 24 jam dengan air terawat telah mematuhi had kawalan yang telah ditetapkan oleh kemeterian kesihatan Malaysia iaitu dibawah 1.5 mg/L.

Kata kunci: penyingkiran ammonia, rawatan biologi, loji rawatan air minuman, biopenuras pasir

Introduction

Depletion in water quality should not be taken lightly especially when it deals with survival needs of human life for drinking water. In Malaysia, sources of drinking water mainly collected from surface water while remaining 1% from groundwater [1]. Surface and groundwater naturally consist of ammonia and manganese but in very low level. However, the level may increase due to human activities such as agricultural activity and rapid development nearby the water intake [2]. Rapid development with improper planning may cause surface water polluted with heavy metal, dissolved organic carbon, dissolved organic nitrogen and many other harmful that consequently give adverse impact to human health.

In drinking water treatment plant (DWTP), ammonia needs to be removed before water being disinfected with the chlorine. Ammonia naturally may reacts with chlorine to produce chloramines, which is known to be carcinogenic [3]. The presence of ammonia in water system leads to oxygen depletion, eutrophication of surface water and toxicity for fish. A study showed that occasionally high level of ammonia was found at the water intake than of regulated one which 1.5 mg/L for ammonia in treated water [4]. As a result treatment plant need to be shut off until ammonia level reduced to its allowable limit. Water disruption not only cause interruption to the household, business premises and factories activities but it is also a signal to improvise current treatment method to prevent such cases repeated.

Removal of ammonia can be achieved via physico-chemical treatment and biological treatment. Chlorination, ion exchange and membrane filtration known as common physiochemical treatment method apply in DWTP [5-7]. However biological approach has gain much attention nowadays and consider as a future technology for drinking water production. This is due to rapid filtration rates, low operation and maintenance cost, single stage filtration and no chemical required [8]. In biological treatment, ammonia will undergo oxidation process to form nitrite by the ammonia oxidizing bacteria (AOB) or ammonia oxidizing archae (AOA) and further oxidized to nitrate by nitrite oxidizing bacteria (NOB). Most of the microorganisms detected are *Nitrosomonas* and *Nitrobacter* type of bacteria [9-11]. Sand filter column can be operated at different hydraulic loading rates, which then differentiate the operation of slow sand filter (SSF) and rapid sand filter column (RSF). Normally RSF was used in drinking water treatment plant rather than SSF mainly to produce large volume of treated water with high capacity of flowrate that is 5-30 m^3/h. Unfortunately, least biological impacts was observed on treated water flowing through RSF [12]. Furthermore, hydrodynamic conditions such as flow rate, velocity and residence time significantly affect the stability of biofilm developed which majority of the microorganism involve in ammonia degradation attached to subsequently made the RSF not suitable for biological treatment [13]. Hence, SSF with flowrate slower than RSF will be used in this study to determine the removal of ammonia at different flowrate using naturally grown bacteria in slow sand filter column and finally microbial community will be microscopically observed under scanning electron microscope.

Materials and Methods

Lake water from Universiti Kebangsaan Malaysia (UKM), Malaysia was used throughout the study. The collection point of the lake water was surface water at the downstream of the lake where it is situated 300 m away from the laboratory. A 5 L plastic bottle was placed on the surface of flowing water to collect the water sample and brought to the laboratory for immediate analyses. The physiochemical properties of water such as turbidity, total suspended solid, color, COD, phosphate, nitrate, and ammonium nitrogen were measured using spectrophotometric measurement. Standard analytical method of the water properties is presented in Table 1. The biofilm was observed using E100 LED Trinocular microscope (Nikon, Japan) and the morphology of the bacteria colony was observed using the High-resolution Field Emission Scanning Microscope Electron (FESEM) (Merlin Compact, USA). Sand was taken at different heights (top surface water, 10cm and 5cm above the biofilter base) to represent the biofilm development in accordance to height.

Table 1. Standard analytical method for water characterization

Parameter	Equipment /Wavelength	Method
Turbidity	HACH 2100 AN Turbiditimeter	DOC022.52.80205
Suspended Solid	HACH DR 3900 (USA), 630 nm	Method 8006
Phosphate	HACH DR 3900 (USA), 490 nm	Method 8048
COD	DRB 200 reactor, HACH DR 3900 (USA), 430 nm	Method 8000 (HACH, 1999)
NH_4^+-N	HACH DR 3900 (USA), 425 nm	Method 8038 (HACH 1999)
NO_3^--N	HACH DR 3900 (USA), 355 nm	Method 8039 (HACH 1999).

Set-up of sand biofilter

The experimental set up of the sand biofilter is illustrated in Figure 1. Column is made of PVC with a diameter of 0.25 m and 0.3 m in height. Two sizes of grain sand were used such that the grain sand has an average diameter of 1.2 mm stacked at the upper layer of the column while the sand filled at the bottom layer has an average particle diameter of 6.7 mm. The sand was initially rinsed with tap water and oven dried to remove fine particulate matter prior to load in the filter. Bacteria used in this study were naturally grown from the surface lake water to minimize the occurrence of pathogenic bacteria. Future investigation will be conducted to determine pathogenic characteristic of the grown bacteria. The biofilm was inoculated for about 3 months prior to the experiment. During innoculation period, no additional nutrients were added to the system except continuously aerated at a rate of 0.36 m^3/hr via an air pump to ensure sufficient oxygen supplied for bacteria growth. Column temperature measured in between 28±1 °C. The sand biofilter operated batchwise in downward flow. In this study, the filtration rate was varied at 0.18 (Run 1), 0.13 (Run 2) and 0.09 (Run 3) m^3/h. Hydraulic retention time (HRT) was set up at 5hr and 24 hr to monitor the reduction of ammonia and manganese level. Sampling point was taken at three different sampling ports that are 0.05 m (SP4), 0.1 m (SP3) and 0.2 m (SP2) from the column base.

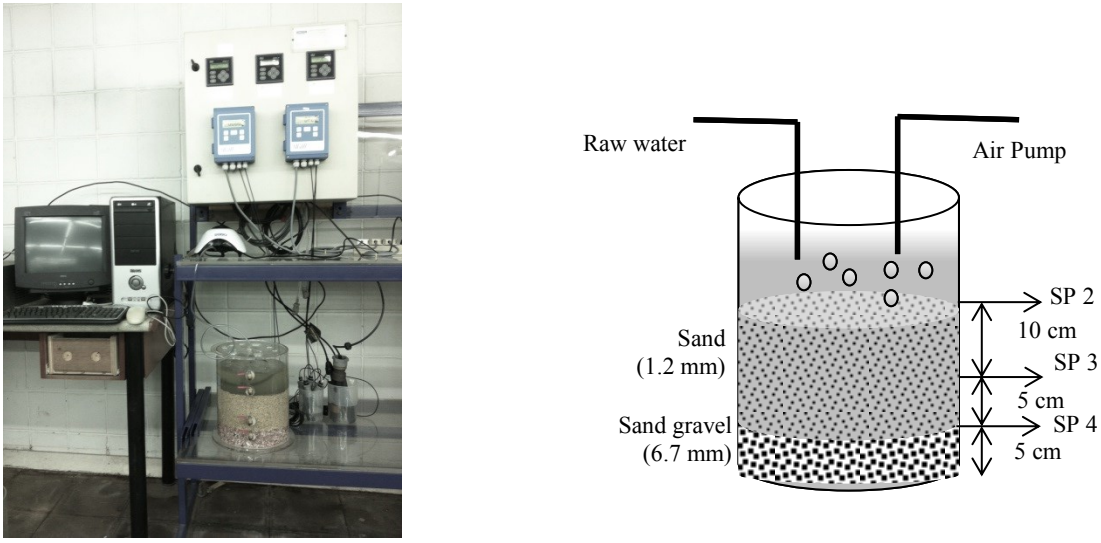


Figure 1. Schematic diagram of biological slow sand filter

Results and Discussion

Characterization of lake water

Lake water quality was monitored throughout the study both physically and chemically. Physiochemical properties of the surface lake water during the study are depicted in Table 2.

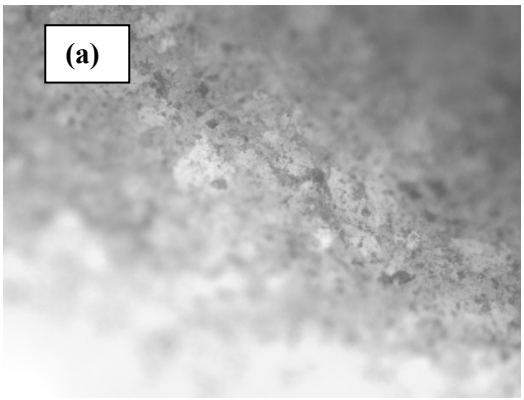
Table 2. Characterization of surface water

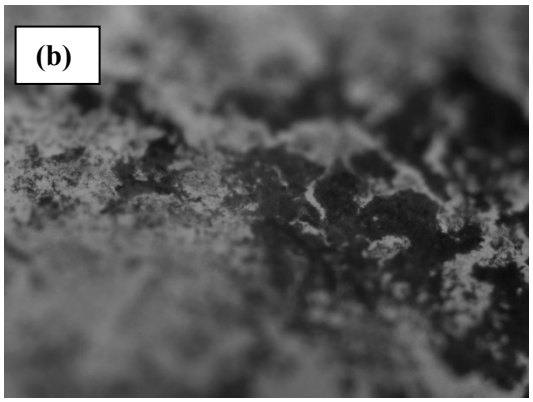
Parameter	Standard Ministry of Health	Run 1 (12/4/16)	Run 2 (19/4/16)	Run 3 (26/4/16)
Turbidity (NTU)	100	39.2 ± 0.2	42.4 ± 1.1	26.6 ± 0.3
Suspended solid (mg/L)	-	53.3 ± 0.7	42.0 ± 1	22.3 ± 1
pH	5.5-9.0	7.1 ± 0.04	7.9 ± 0.25	7.6 ± 0.01
Color (Pt co)	300	408.7 ± 1.3	337.0 ± 2	269.7 ± 1
Ammonia Nitrogen (mg/L)	1.5	4.7 ± 0.02	6.3± 0.0	3.5± 0.01
Chemical Oxygen Demand (COD) (mg/L)	10	27.3 ± 0.7	48.7 ± 1	17.0 ± 0.0
Phosphate (mg/L)	-	0.18 ± 0.01	0.65 ± 0.15	0.97 ± 0.01
Nitrate (mg/L)	10	0.17 ± 0.1	0.20 ± 0.00	0.70 ± 0.0

Water quality parameters of ammonia, color and Chemical Oxygen Demand (COD) exceeded the allowable limit set by the Ministry of Health (MOH), Malaysia [14] for surface lake water. The maximum color level and COD was observed during Run 1 while the ammonia reached its maximum value by 6.3 mg/L during Run 2. High level of ammonia during Run 2 can cause eutrophication process to the sampling area, supported by higher COD content than usual sampling. In overall, other measured properties show normal trend and within stipulated standard.

Analysis of biofilm morphology

Sand particles were sampled from biofilter at different height to monitor biofilm development in according to the column height. Figure 2(a) shown the sand morphology before innoculation while Figure 2(b) shown biofilm attached on the media after 3 month innoculation period. Microbial biomass increased generally with time and decreased with depth and most biomass development occurred in the upper layer of the filter [15]. Figure 2(c) shows the sand before inoculation while Figure 2(d) to (f) showed sands after three months of inoculation stage at different depth in the sand biofilter. The presence of microorganism was observed attached on the fine sand located at the top surface (Figure 2(d)) of the sand biofilter and none was observed on the sand located at the bottom of biofilter (10cm from the surface).





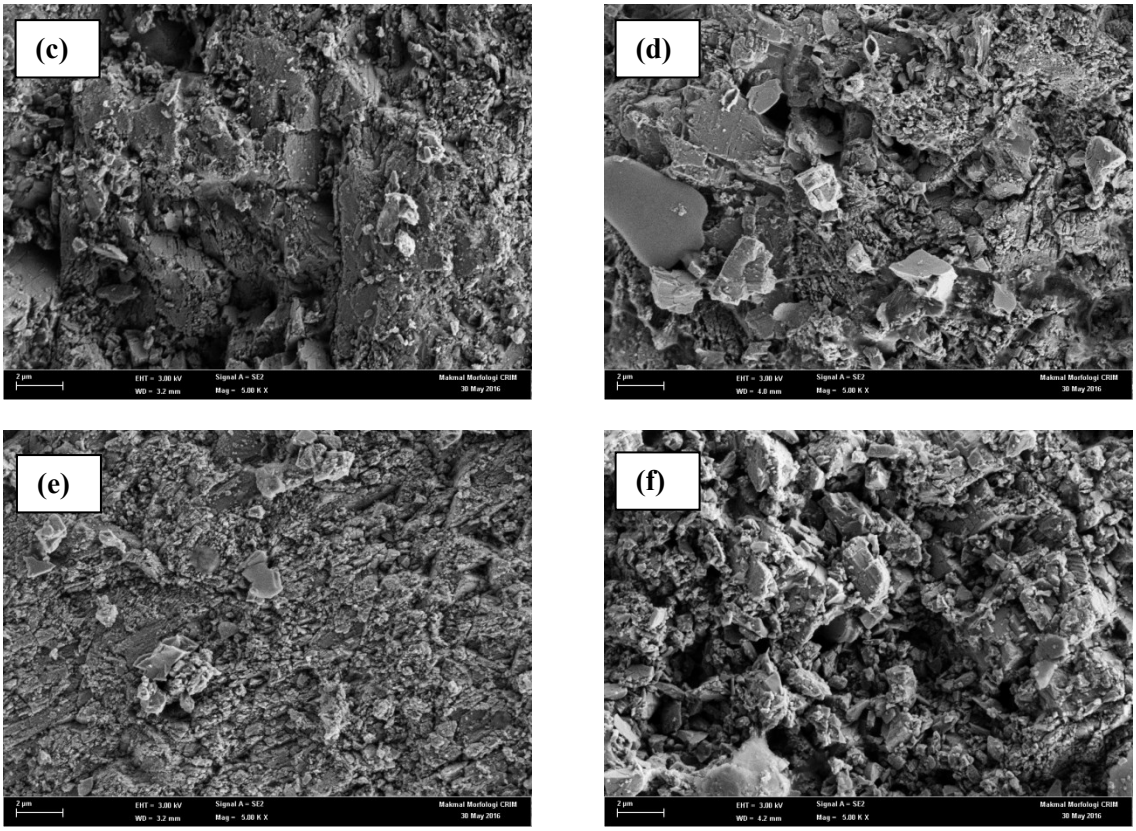


Figure 2. Sand morphology (a) Sand before innoculation (b) biofilm attached on the media after innoculation using Trinocular microscope under 4X magnification (c) Control (d) Biofilter surface (e) 5cm under biofilter surface (f) 10cm under biofilter surface under 5000X magnification using FESEM

Removal efficiency of ammonia in biofilter

Ammonia removal observed at all conditions in all runs shows the presence of AOB in the sand biofilter. Figure 3 depicts the surface water profile at different HRT, sampling point and filtration rate. Initial concentration of ammonium was varied at 3.5 to 6.3 mg/L. Generally, the ammonia removal trend shows an increment as the flowrate reduces. Hydrodynamic conditions such as flowrate and velocity have an adverse impact on the biofilm stability. Higher flowrate could interrupt microorganism colonies (AOB) responsible to reduce ammonia directly and hence decreasing the removal efficiency at higher flow rate [12, 13]. The ammonium concentration both at 5 and 24 HRT at 0.19 and 0.13 m^3/h as shown in Figure 3(a) and (b) respectively, was still unsatisfactorily removed with the values are still above the water quality standard. On the other hand, the removal rate of ammonium reached 98 and 97% respectively at sampling point 2 after 24 hr HRT at a slower flowrate of 0.09 m^3/h (Figure 3(c)).

At 5 hr HRT only 58% reduction was observed at the same flowrate and the concentration of ammonium still above the drinking water standard of 1 mg/L. Samples were taken at different height in the sand biofilter with ammonium concentration at all runs was observed reduced remarkably at sampling point 4 which is located at 5cm from the column base. Even though the microorganism colonies were observed available only on the sand located at the top column, it may have entrapped between void spaces of the sand at the bottom layer. Under the influence of liquid flow velocity and at its maturation time, biofilm may have been detached from the media to recolonization to the other places [16].

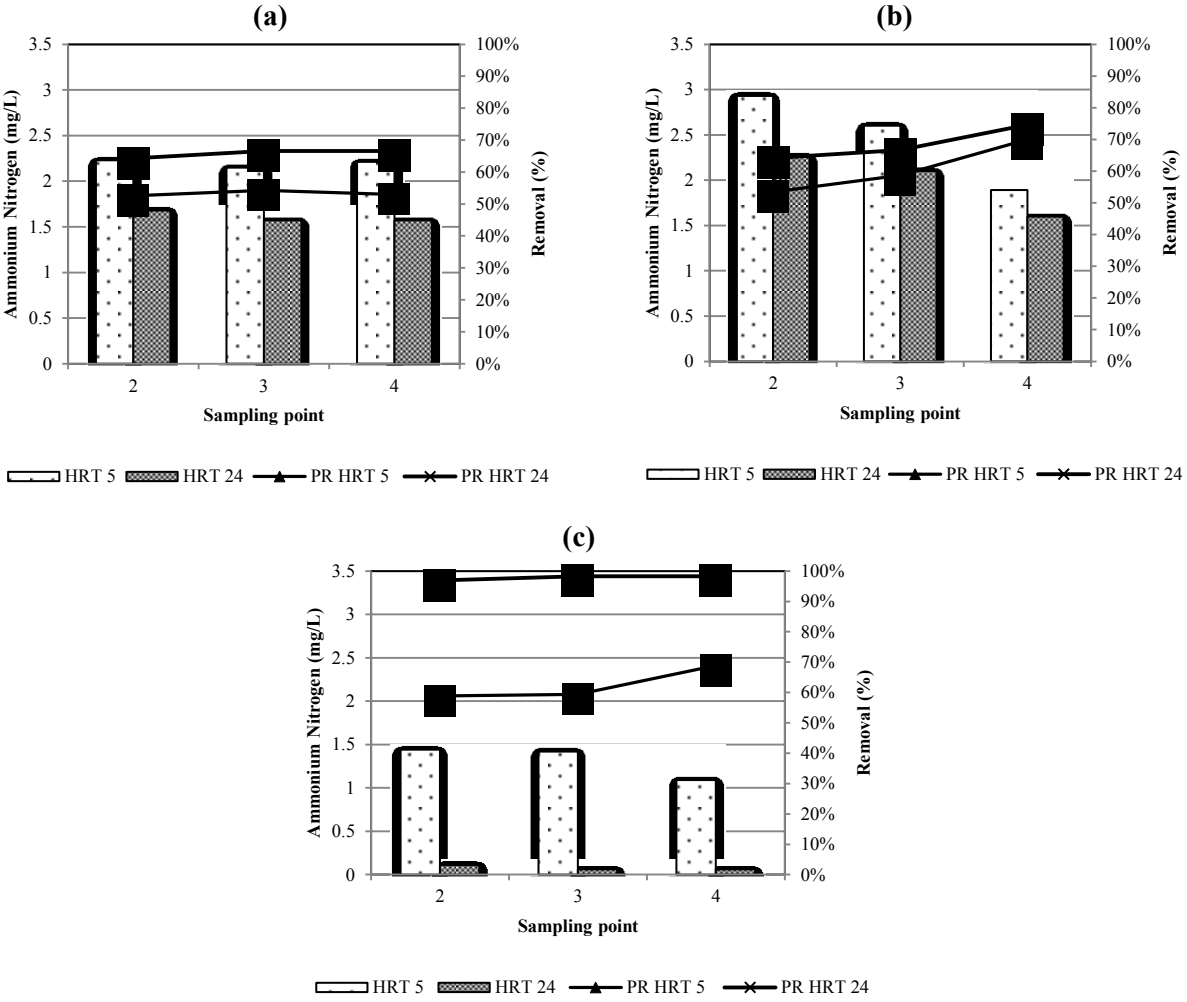


Figure 3. Concentration and percent reduction of ammonia nitrogen at vary flowrate (a) 0.18 m^3/h (b) 0.13 m^3/h (c) 0.09 m^3/h

Conclusion

Natural biofilm, a mixed bacterial consortium, cultured from a surface water lake in UKM had shown great potential in ammonia removal through biological pathway. The high removal of more than 90% removal efficiency was achieved after 24 hr HRT. It is flexible and very cost effective to be adapted in any conventional water treatment plant system since it is naturally grown from the water source eliminating any concern of the presence of pathogenic microorganism coming from biomass derived from wastewater treatment plant to be applied in drinking water treatment plant. The presence of the microbial colony and biofilm matrix were clearly captured under scanning electron microscope under 5000x magnification. Identification of microbial colony responsible for ammonia removal using molecular technique will be conducted for future study.

Acknowledgement

The authors would like to acknowledge Universiti Kebangsaan Malaysia (UKM) for providing research grants of DIP-2016-030 and AP-2015-013 to accomplish this study. The first author would also like to acknowledge the Ministry of Higher Education (MOHE) Malaysia and Universiti Teknologi MARA (UiTM) for granting the PhD scholarship.

References

1. Ab Razak, N. H., Praveena, S. M., Aris, A. Z. and Hashim, Z. (2015). Drinking water studies: A review on heavy metal, application of biomarker and health risk assessment (a special focus in Malaysia). *Journal of Epidemiology and Global Health*, 5(4): 297-310.
2. Aslan, S. and Cakici, H. (2007). Biological denitrification of drinking water in a slow sand filter. *Journal of Hazardous Materials*, 148(1–2): 253–258.
3. Sadiq, R. and Rodriguez, M. (2004). Disinfection by-products (DBPs) in drinking water and predictive models for their occurrence: a review. *Science of The Total Environment,* 321(1–3): 21–46.
4. Abu Hasan, H., Sheikh Abdullah, S. R., Kamarudin, S. K. and Tan Kofli, N. (2011). Ammonia and manganese problems in Malaysian drinking water treatment. *World Applied Sciences Journal,* 12: 1890–1896.
5. Ersahin, M. E., Ozgun, H., Dereli, R. K., Ozturk, I., Roest, K. and van Lier, J. B. (2012). A review on dynamic membrane filtration: Materials, applications and future perspectives. *Bioresource Technology*, 122: 196–206.
6. Kulkarni, P. and Chellam, S. (2010). Disinfection by-product formation following chlorination of drinking water: Artificial neural network models and changes in speciation with treatment. *Science of The Total Environment*, 408(19): 4202–4210.
7. Primo, O., Rivero, M. J., Urtiaga, A. M. and Ortiz, I. (2009). Nitrate removal from electro-oxidized landfill leachate by ion exchange. *Journal of Hazardous Materials,* 164(1), 389–393.
8. Sahabi, D. M., Takeda, M., Suzuki, I. and Koizumi, J. (2009). Removal of Mn^{2+} from water by "aged" biofilter media: The role of catalytic oxides layers. *Journal of Bioscience and Bioengineering*, 107(2): 151–157.
9. Jun, Y. and Wenfeng, X. (2009). Ammonia biofiltration and community analysis of ammonia-oxidizing bacteria in biofilters. *Bioresource Technology,* 100(17): 3869–3876.
10. Leyva-Díaz, J. C., González-Martínez., A., González-López, J., Muñío, M. M. and Poyatos, J. M. (2015). Kinetic modeling and microbiological study of two-step nitrification in a membrane bioreactor and hybrid moving bed biofilm reactor-membrane bioreactor for wastewater treatment. *Chemical Engineering Journal,* 259: 692–702.
11. Nicolaisen, M. H. and Ramsing, N. B. (2002). Denaturing gradient gel electrophoresis (DGGE) approaches to study the diversity of ammonia-oxidizing bacteria. *Journal Microbiol Methods*, 50(2): 189–203.
12. Bar-Zeev, E., Belkin, N., Liberman, B., Berman, T. and Berman-Frank, I. (2012). Rapid sand filtration pretreatment for SWRO: Microbial maturation dynamics and filtration efficiency of organic matter. *Desalination,* 286: 120–130.
13. Gomes, I. B., Simões, M. and Simões, L. C. (2014). An overview on the reactors to study drinking water biofilms. *Water Research,* 62: 63–87.
14. Ministry of Health (2012). Drinking water quality standard. http://kmam.moh.gov.my/public-user/drinking-water-quality-standard.html [Access online 1 December 2015].
15. Campos, L. C., Su, M. F. J., Graham, N. J. D. and Smith, S. R. (2002). Biomass development in slow sand filters. *Water Research,* 36(18): 4543–4551.
16. Codony, F., Morató, J. and Mas, J. (2005). Role of discontinuous chlorination on microbial production by drinking water biofilms. *Water Research,* 39(9): 1896–1906.

Malaysian Journal of Analytical Sciences, Vol 22 No 2 (2018): 353 - 357
DOI: https://doi.org/10.17576/mjas-2018-2202-23

MALAYSIAN JOURNAL OF ANALYTICAL SCIENCES
Published by The Malaysian Analytical Sciences Society
ISSN 1394 - 2506

ANALYSIS OF *Sesquiterpenes* IN AGARWOOD ESSENTIAL OIL FROM HYDRODISTILLATION PROCESS

(Analisis S*esquiterpenes* di dalam Pati Minyak Gaharu daripada Proses Penyulingan Air)

Nurhaslina Che Radzi*, Mohamad Khir Zahari Harip, Mohibah Musa, Nurul Asyikin Md Zaki, Habsah Alwi, Miradatul Najwa Muhd Rodhi, Ku Halim Ku Hamid

Faculty of Chemical Engineering,
Universiti Teknologi MARA, 40450 Shah Alam, Selangor, Malaysia

**Corresponding author: nurhaslina483@salam.uitm.edu.my*

Received: 15 February 2017; Accepted: 2 January 2018

Abstract

Agarwood or its specific named, *Aquilaria spp.* is a precious tree in the world. It has been used widely in pharmaceutical industry, production of perfumes and incense raw material. In this study, the agarwood essential oil, species of *Aquilaria maleccensis* is being extracted by using hydrodistillation method. This study aims to analyse the present of chemical compound named *sesquiterpenes* in the agarwood essential oil. The effect of pre-treatment using soaking process on the agarwood within 7 days, 14 days and 21 days before proceed for hydrodistillation process had been done. The hydrodistillation process took 3 days before the sample of essential oil is collected. The sample is being analysed by using gas chromatography mass spectrometry (GC-MS). The result showed the existence of s*esquiterpenes* had been identified from all sample of three batches. However, different types of *sesquiterpenes* were identified for different batch. The highest *sesquiterpenes* content for 1st batch is *α-gurjunene* with 2.95%, the 2nd batch is *ç-Himachalene* with 0.292% and the 3rd batch is same with the 1st batch which is α-gurjunene with 0.356%.

Keywords: agarwood, *Aquilaria maleccensis*, *Sesquiterpenes*, hydrodistillation, gas chromatography mass spectrometry

Abstrak

Gaharu atau nama spesifiknya, *Aquilaria spp.* adalah pokok yang sangat berharga di dunia. Ia banyak digunakan di dalam industri farmaseutikal, penghasilan minyak wangi dan bahan asas kemenyan. Dalam kajian ini, pati minyak gaharu, jenis *Aquilaria maleccensis* di ekstrak melalui kaedah penyulingan air. Tujuan kajian ini adalah untuk menganalisis kehadiran komponen kimia yang dinamakan sebagai *sesquiterpenes* di dalam pati minyak gaharu. Kesan pra rawatan menggunakan proses rendaman ke atas gaharu dilakukan antara 7 hari, 14 hari dan 21 hari sebelum dilanjutkan ke proses penyulingan air. Proses penyulingan air mengambil masa 3 hari sebelum sampel pati minyak gaharu diambil. Sampel tersebut tersebut seterusnya dianalisis menggunakan kromatografi gas spektrometri jisim (GC-MS). Keputusan menunjukkan kehadiran s*esquiterpenes* daripada ketiga-tiga kumpulan. Walau bagaimanapun, jenis s*esquiterpenes* berbeza dikenalpasti bagi setiap kumpulan. Kuantiti s*esquiterpenes* paling tinggi dalam kumpulan pertama ialah *α-gurjunene* iaitu 2.95%, kumpulan kedua ialah *ç-Himachalene* iaitu sebanyak 0.292% dan kumpulan ketiga adalah bersamaan dengan kumpulan pertama iaitu 0.356%.

Kata kunci: gaharu, *Aquilaria maleccensis*, *Sesquiterpenes*, penyulingan air, kromatografi gas spektrometri jisim

Introduction

Agarwood has been known and used a long time ago as medicinal properties in pharmaceutical, incense, in religious practices and mostly perfume [1]. In Malaysia, agarwood commonly known as gaharu, is a tree of the genus *Aquilaria* spp. belongs taxonomically to the *Thymelaeaceae* family. It has various known species which is more than 15 species and can be categorized into 4 grades; A, B, C and D referring to its physical properties, formation and scent. Most previous study about agarwood is focused on the extraction of essential oil [2]. There are many ways to extract the essential oil from agarwood such as supercritical fluid extraction, solvent extraction, hydrodistillation and others. In this study, hydrodistillation method has been used because it is commonly used in industry to extract essential oils. Hydrodistillation method also is low cost, simplest and easy to construct. However, using this method, the oil yield is very low [1].

Therefore, the pre-treatment process had been introduced in order to enhance the essentials oil yield. There are several methods to pre-treat plant sample from previous study before extraction such as chemical treatment, soaking in water and sonication. Some studies focused on the pre-treatment process in order to increase the oil yield which is similarly to this study. For this pre-treatment process, agarwood was soaked by tap water. Previous study by Veronica et. al [1] on the effects of soaking time showed different quality of essential oils yield. There are many studies about pharmacological properties on the agarwood essential oil especially in anti-inflammatory [3], antioxidant [4], antibacterial [5], anti-hyperglycemic [6] and anti-ischemic [7]. However, only few research had been done for the identification of *sesquiterpenes* which believe have a potential to cure cancer. Hence, this study will be focused on pharmacological properties which had been identified as a secondary compound in the agarwood essential oil called *sesquiterpenes.* This *sesquiterpenes* is believed can act as anti-cancer agent. The presence of *sesquiterpenes* in the agarwood essential oil will be analysed using gas chromatography mass spectrometry GC-MS. Therefore, this study aim to analyze an effect of pre treatment towards types of *sesquiterpenes* exist in agarwood essential oil.

Materials and Methods

Sample collection and preparation

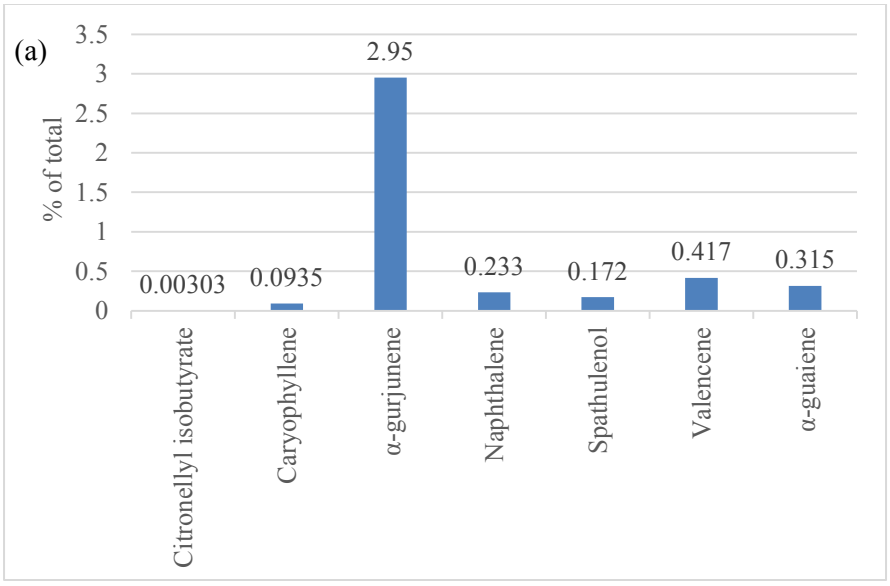
The raw agarwood species of *Aquilaria Maleccensis* were obtained from Taiping, Perak. Pretreatment process which is soaking the 25 kg agarwood chips with tap water was run within 7 days (1st batch), 14 days (2nd batch) and 21 days (3rd batch). Before proceed to hydrodistillation process, the agarwood chips need to be drying first by using solar (sun). Then, every batch of agarwood chips is fully immersed into the water for hydrodistillation process. The essential oils of agarwood were collected once after the oils have been extracted via hydrodistillation process that will undergo for 3 days. The sample of oils were analysed to determine the existence of *sesquiterpenes* properties.

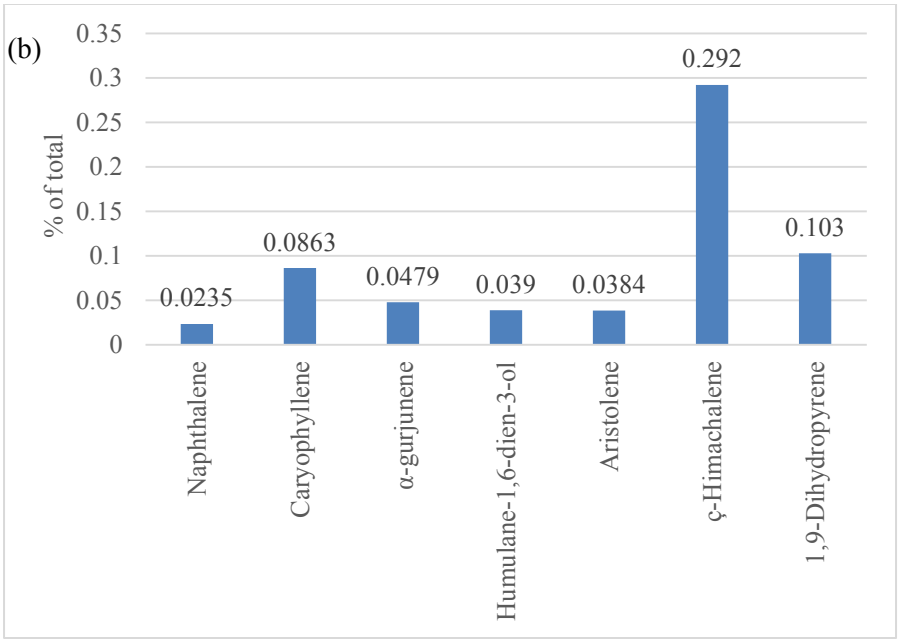
Gas chromatography mass spectrometry analysis

The *sesquiterpenes* properties in the sample of agarwood essential oils were identified by using GC-MS (Varian Inc.). Separation of analytes by gas chromatography was carried by using silica DB-1 capillary column (30 m x 0.25 mm x 0.25 mm). The oven temperature was programmed to 80 ˚C for 2 minutes. Then, the temperature increased 10 ˚C/min until 250˚C. The retention time selected was 50 minutes. Helium was used as carrier gas with a constant gas flow rate of 2 ml/min. Electron impact were measured at acceleration energy of 70 eV. Injection volume of 1 µl of the sample was performed in the split mode used at a 50:1 split ratio [8, 9].

Results and Discussion

The results of existence compound *sesquiterpenes* from all sample among 3 batches were obtained after being analysed by using GC-MS. Figure 1(a) - (c) show the result of chemical compound of agarwood oil from 1st, 2nd and 3rd batch, respectively.


(a)
% of total
3.5
3
2.5
2
1.5
1
0.5
0
0.00303
0.0935
2.95
0.233
0.172
0.417
0.315
Citronellyl isobutyrate
Caryophyllene
α-gurjunene
Naphthalene
Spathulenol
Valencene
α-guaiene


(b)
% of total
0.35
0.3
0.25
0.2
0.15
0.1
0.05
0
0.0235
0.0863
0.0479
0.039
0.0384
0.292
0.103
Naphthalene
Caryophyllene
α-gurjunene
Humulane-1,6-dien-3-ol
Aristolene
ç-Himachalene
1,9-Dihydropyrene

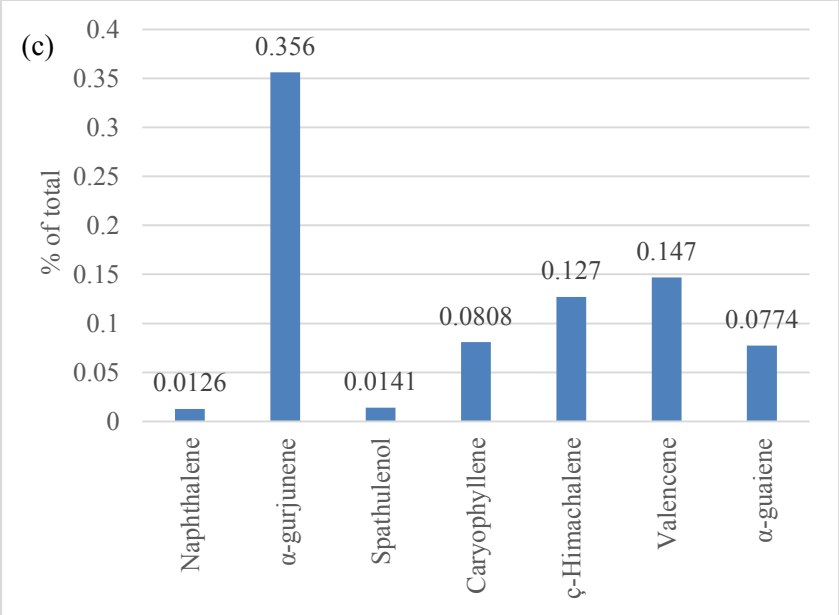


Figure 1. Chemical compound of agarwood oil in (a) 1st batch, (b) 2nd batch and (c) 3rd batch

The results show that there were several major types of *sesquiterpenes* obtained from the agarwood oil from all three batches such as *α-gurjunene, α-guaiene, aristolene, ç-Himachalene, caryophyllene* and others. The average percentage content of *sesquiterpenes* found in all three batch were about 2%. The chemical composition of the agarwood essential oil may result in difference composition by several factors which are species of the agarwood tree, pre-treatment and extraction method used for agarwood essential oil [10]. This can be proved by Figure 1(a) - (c) that showed different types of *sesquiterpenes* were identified among three batches. The 1st batch obtained *sesquiterpenes* of *Citronellyl isobutyrate* which is not identified in the 2nd batch and 3rd batch. Then, the 2nd batch obtained *sesquiterpenes* of *Humulane-1,6-dien-3-ol, Aristolene* and *1,9-Dihydropyrene* which are not identified in the 1st batch and 3rd batch. Besides that, this also can be proved in the previous study which is several different types of *sesquiterpenes* were found in agarwood of *Aquilaria Sinensis* species [11]. The soaking activity for pre-treatment also shows the effect towards the quality of agarwood oil. Soaking process was conducted during agar wood essential oil extraction, which contributes to the opening and enlargement of pore size on agar wood structure as well as the oil yield percentage. Soaking in water should then be one of the unit operations to extract essential oil from agar wood. To disturb the structure of the cell wall, the environment and surrounding condition need to be changed or altered by introducing to acidic or alkali solvent to allow the movement desired compounds from high to low concentration. By altering the external and internal factors, it can contribute the secretion of compound to the soaked water environment [1]. During soaking process, the cell has expanded and finally burst, thus releasing the content out to the soaking medium. The solvent enters cell wall by simple diffusion and increase the turgor pressure. The solvent becomes more acidic along the time due to the released compounds and corrodes the cell wall. It damages the structure of the cell wall. However, too long soaking time causes more compounds content wasted to the solvent. The soaked agarwood give higher yield of essential oil compared to non-soaked agarwood [12].

Hence, the results for this study from GC-MS analysis showed different types of *sesquiterpenes* were found among three batches. However, further study need to be done to confirm the presence of the *sesquiterpenes* content in agarwood oil such as by using other analysis method namely high performance liquid chromatography (HPLC) and Fourier transform infrared (FTIR).

Conclusion

The analysis of *sesquiterpenes* from agarwood essential oil using GC-MS is successfully carried out. The results show that several types of *sesquiterpenes* compound were identified. The quality of essential oil also may varies based on the chemical compound. Pre-treatment by soaking activity at optimum time prove to produce higher yield and more compound extracted compared to non-soaking activity. Further studies are needed to refine the results which later can be used to assist and improve pharmaceutical industry especially for curing cancer.

.

Acknowledgement

The authors want to express special gratitude to Universiti Teknologi MARA, UiTM Shah Alam, specifically to Faculty of Chemical Engineering for allowing the usage of facilities especially for all the laboratory instrument. Many thanks to all who have been directly and indirectly assisted this research.

References

1. Jok, V. A., Che Radzi, N. and Ku Hamid, K. H. (2015). Agarwood oil yield as a result of changes in cell morphology due to soaking process. *Procedia-Social and Behavioral Sciences,* 195: 2443-2450.
2. Zainuddin, N. A. S., Ismail, K. N., Ku hamid, K. H., Muhd Rodhi, M. N. and Musa, M. (2013). Analysis of agarwood waste at different pre-treatment for silica xerogel production. *Advanced Materials Research* 709: 915-918.
3. Zhou, M., H. Wang, S., Kou, J. and Yu, B. (2008). Antinociceptive and anti-inflammatory activities of *Aquilaria sinensis* (Lour.) Gilg. leaves extract. *Journal of Ethnopharmacology,* 117: 345-350.
4. Sattayasai, J., Bantadkit, J., Aromdee, C., Lattmann, E. and Airarat, W. (2012). Antipyretic, analgesic and anti-oxidative activities of *Aquilaria crasnna* leaves extract in rodents. *Journal of Ayurveda and Integrative Medicine,* 3(4): 175-179.
5. Kamonwannasit, S., Nantapong, N., Kumkrai, P., Luecha, P., Kupittayanant, S. and Chudapongse, N. (2013). Antibacterial activity of *Aquilaria crasnna* leaf extract against *Staphylococcus* epidermidis by disruption of cell wall. *Annals of Clinical Microbiology and Antimicrobials,* 12(1): 20.
6. Pranakhon, R., Pannangpetch, P. and Aromdee, C. (2011). Antihyperglycemic activity of agarwood leaf extracts in STZ-induced diabetic rats and glucose uptake enhancement activity in rat adipocytes. *Songklanakarin Journal of Science & Technology*, 33(4):405-410.
7. Suwannasing, C., Paiyabhroma, N. and Kumphune, S. (2012). Anti-ischemic effect of ethyl acetate extract of *Aquilaria crasnna* by attenuation of p38-MAPK activation. *Journal of Applied Pharmaceutical Science* 2(10): 026-030.
8. Chen, Y., Wu, Y-G., Xu, Y., Zhang, J-F., Song, X-Q., Zhu, G-P. and Hu, X-W. (2014). Dynamic ccumulation of sesquiterpenes in essential oil of Pogostemon cablin. *Revista Brasileira De Farmacognosia-Brazilian Journal of Pharmacognosy* 24(6): 626-634.
9. Yumi Z., Hashim, H-Y., Ismail, N. I. and Abbas, P. (2014). Analysis of chemical compounds of agarwood oil from different species by gas chromatography mass spectrometry (GCMS). *IIUM Engineering Journal* 15: 55-60.
10. Mohd Ali, N. A., Ismail, N. and Taib, M. N. (2012). Analysis of agarwood oil (*Aquilaria malaccensis*) based on GC-MS data. *IEEE 8th International Colloquium on Signal Processing and its Applications*: 470-473.
11. Li, W., Cai, C-H., Guo, Z-K., Wang, H., Zuo, W-J.,Dong, W-H., Mei, W-L. & Dai, H-F. (2015). Five new eudesmane-type sesquiterpenoids from Chinese agarwood induced by artificial holing. Fitoterapia 100: 44-49.
12. Muhammad Fadzil, A. H., Ku Halim, K. H. and Muhd Rodhi, M. N. (2013). Extraction of essential oil from biologically inoculated agarwood. *IEEE Business Engineering and Industrial Applications Colloquium*: 889-892.

Malaysian Journal of Analytical Sciences, Vol 22 No 2 (2018): 358 - 364
DOI: https://doi.org/10.17576/mjas-2018-2202-24

MALAYSIAN JOURNAL OF ANALYTICAL SCIENCES
Published by The Malaysian Analytical Sciences Society
ISSN 1394 - 2506

THE DETECTION OF FATTY ACID METHYL ESTER IN STERCULIACEAE

(Pengesanan Asid Lemak Metil Ester dalam Sterculiaceae)

Fathin Nurizati Samsul, Ibtisam Abdul Wahab*, Hannis Fadzillah Mohsin

Department of Pharmacology & Chemistry, Faculty of Pharmacy,
Universiti Teknologi MARA, 42300 Puncak Alam, Selangor, Malaysia

**Corresponding author: ibtisam@puncakalam.uitm.edu.my*

Received: 15 February 2017; Accepted: 2 January 2018

Abstract

This study introduces the Sterculiaceae plant family which are also called as malva nuts. They are utilised as the remedy against pharyngitis, tussis and constipation. Malva nut is a well-known plant, used in Thai traditional medicine as a cooling agent to treat fever, coughing and sore throats. The literatures mentioned that the Sterculiaceae extracts could function as antioxidative, antiulcer and would help in reducing body weight. The objective of this study is to investigate the constituents in the seeds extracts by using chromatography and Nuclear Magnetic Resonance (NMR) spectroscopy. The NMR spectrum revealed that the isolated compound from the chloroform extract was a mixture of an aromatic aldehyde and a fatty acid methyl ester (FAME) component. Future work is encouraged to reinvestigate the extract and establish more extensive NMR data. It is hoped that this study could increase the knowledge about the phytochemistry of Sterculiaceae family which then could be added as the line of today's drug.

Keywords: chromatography, fatty acid, spectroscopy, Sterculiaceae

Abstrak

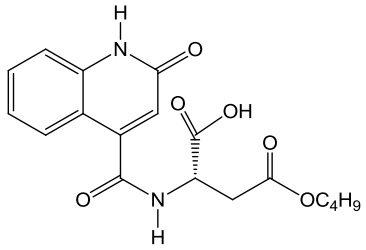
Kajian ini mempersembahkan keluarga tumbuhan Sterkuliaceae yang turut dikenali sebagai kacang malva. Ia digunakan sebagai rawatan faringitis, tussis dan konstipasi. Kacang malva merupakan pokok yang dikenali, digunakan dalam perubatan tradisional Thai sebagai agen penyejuk untuk menyembuh dari demam, batuk dan sakit tekak. Literatur menerangkan bahawa ekstrak Sterkuliaceae boleh berfungsi sebagai anti oksidatif, anti ulser dan mampu membantu pengurangan berat badan. Objektif kajian ini adalah untuk menyiasat kandungan ekstrak biji melalui kromatografi dan spektroskopi resonan magnetik nukleus (RMN). Spektrum RMN menunjukkan sebatian yang terasing dari ekstrak klorofom merupakan satu campuran aldehid aromatik dan komponen asid lemak metil ester. Lebih usaha digalakkan untuk mengkaji semula ekstrak dan mendapatkan lebih data RMN secara ekstensif. Adalah diharapkan agar penyelidikan ini mampu meningkatkan pengetahuan mengenai fitokimia keluarga Sterkuliaceae yang boleh dijadikan bahan perubatan masa kini.

Kata kunci: kromatografi, asid lemak, spektroskopi, Sterkuliaceae

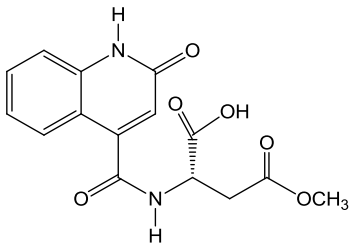
Introduction

This study is parallel to a report that was launched by local researchers on the medicinal, phytochemistry and pharmacology of the Sterculiaceae [1]. These plants are called as malva nuts that can provide health benefits to human kinds. In Peninsular Malaysia, they are also known as "kembang semangkuk jantung" [1]. The uses of this species include as the remedy against pharyngitis, tussis and constipation. Malva nuts are well known plants, used in Thai traditional medicine as a cooling agent to treat fever, coughing and sore throats [2]. From the review, the

medicinal property of Sterculiaceae was reported as antioxidative [3] and antiulcer [4]. The secondary metabolites that were previously isolated include the alkaloids [5] (Figure 1).



Sterculinine I



Sterculinine II

Figure 1. The chemical structures of Sterculinine I and Sterculinine II, which are the alkaloids, previously isolated from ethanol extract of the seed of *Sterculia lychnophora*

The objective of this study is to investigate the constituents in the Sterculiaceae seeds. The organic extraction was conducted to examine the natural compounds. The extracts are examined by using Thin Layer Chromatography (TLC). Nuclear Magnetic Resonance (NMR) spectroscopy are performed to examine the natural compounds.

Materials and Methods

The dried malva nuts were purchased from retails. The solvents such as hexane, chloroform ($CHCl_3$), ethyl acetate (EtOAc), ethanol (EtOH) and methanol (MeOH) (analytical reagent grade) were purchased from Merck (Germany). The plant material was grinded by using Waring commercial blender, single-speed, with a stainless steel jar. Then, the sample was extracted via maceration, in room temperature. The solvent was evaporated under reduced pressure, to obtain the dried crude extracts. The screening of natural compounds in the extract was perfomed by using TLC. The extract was separated by using commercially produced analytical silica gel chromatographic plates (Merck, 60G F_{254}, 0.25 mm). The plates were later developed in a TLC glass chamber by using mixtures of hexane:ethyl acetate (2:1 v/v) as the mobile phase.The spots were visualized under both short and long wavelength ultraviolet (UV) light, λ = 254 nm and 366 nm, respectively. Bosch heat gun was used to heat the plate (250 ± 2 ^{o}C) after spraying with the staining reagent (e.g. sulphuric anisaldehyde). Preparative silica gel chromatographic plates were utilized in order to fractionate and isolate the constituents. The NMR spectrum was obtained from the Bruker spectrometer (500 MHz, $CDCl_3$).

Results and Discussion

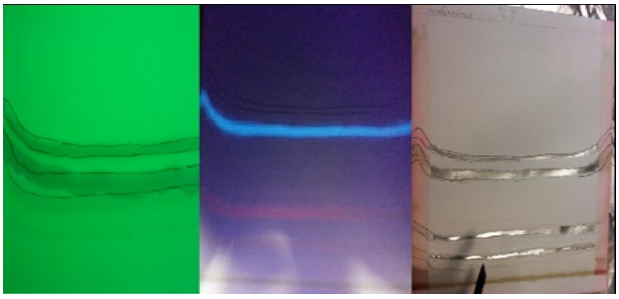
The dried malva nuts were conveniently obtained from retails. It was noted that some product distributors labelled the seed part as the flower bowl. Figure 2(a). Figure (2b) displayed the TLC profiles of the organic crude extracts, showing separated and coloured spots.

From the preparative TLC (Figure 3), it was found that this technique was able to isolate the compounds from the chloroform extract, using a developing solvent system, which was hexane: ethyl acetate (7:1). The bands showed in Figure 3 were visualized under ultraviolet light (λ=254 and 360 nm). Figure 3(a) shows that under UV light (λ=254 nm), two bands were observed. A blue band also can be seen (λ=360 nm, Figure 3(b)). Both left and right sides of the plate were sprayed with anisaldehyde (Figure 3(c)). There were two bands at the bottom of the plate in Figure 3(c). However the distance between them were quite close, it was recorded after the plate edges were coloured with anisaldehyde. All four bands or compounds were scrapped. They were subjected to NMR experiments (500 MHz, $CDCl_3$) for structural elucidation.



(a) (b)

Figure 2. (a) The dry seeds of malva nut fruit, and (b) the TLC profiles of EtOAc, $CHCl_3$, EtOH and MeOH crude extracts, developed with hexane:ethyl acetate (7:1 v/v) as the mobile phase

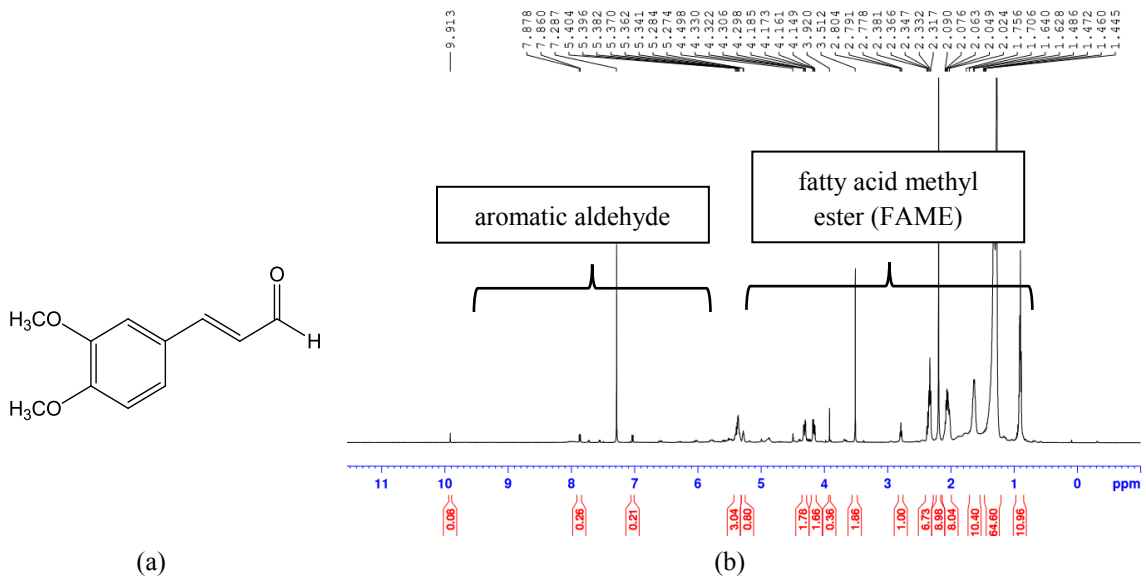


(a) (b) (c)

Figure 3. The preparative plate:- (a,b) observed under UV light and (c) after spraying with anisaldehyde.

Unfortunately, only Compound A (band 2 from the top of the plate, isolated from the chloroform extract, Rf = 0.4) shows significant ^{1}H-NMR signals compared, with the other bands. From the ^{1}H-NMR analysis, an aldehyde moiety (Figure 4(a)) was detected from the spectrum in Figure 4(b), at δ_H 9.91 ppm. This finding would be in in line with an evidence [6] that identified an aldehyde named 3-(3,4-dimethoxyphenyl) 2-propenal. The aldehyde was recorded from *Helicteres angustifolia* (L.), which also belongs to the Sterculiaceae family. It was noted that the olefinic-type of protons (δ_H 6 - 7 ppm) were absent. Nevertheless, the rest of the peaks still require further investigation. This is due to the occurrence of centrosymmetrical multiplets at the chemical shifts of δ_H 4.16 and 4.30 ppm (doublet of doublets, J = 12, 4 Hz, 2H).

It is believed that a mixture of both aromatic aldehyde (δ_H 7 - 10 ppm) and fatty acid (δ_H 0 – 5.5 ppm) compounds could present in current study (Figure 3b). Hence, a cross-referencing of other *Sterculia*'s composition is performed. It was mentioned that oils from *Sterculia* seeds, collected from the tropical rain forests of south eastern Mexico, are commonly used for human and animal nutrition. These oils contain cyclopropene fatty acids, whose consumption is related with beneficial, as well as detrimental physiological effects [7]. In a following report, *Sterculia* species might contain fatty acids with branched ester derivatives [7] (Figure 5). It is also confirmed that the uniqueness of *Sterculia*'s fatty acid, sets in the presence of a cyclopropene unit. It may contribute to up to 70%, in the form of sterculic acid [(9,10-methylene-9-octadecenoic acid, Figure 5(a) and malvalic acid (8,9-methylene-8-heptadecenoic acid, Figure (5b).



(a) (b)

Figure 4. (a) 3-(3,4-dimethoxyphenyl)2-propenal was identified from *Helicteres angustifolia* (L.) (Sterculiaceae) and (b) the ^{1}H-NMR spectrum (500 MHz, $CDCl_3$) of the chemical composition of the malva nut

The total ion current gas chromatograms of *Sterculia* hexanoic seed extracts were established, in order to determine the fatty acids profile [7]. This is followed by the determination of mass spectra of sterculic acid (Figure 5a). It was demonstrated that cyclopropene fatty acids (CPFA) are unusual fatty acids, which contain a three member carbocyclic ring, forming the center of their 18 and 17 carbon chains.



(a) (b)

Figure 5. The chemical structure of (a) sterculic acid (9,10-methylene-9-octadecenoic acid) and (b) malvalic acid (8,9-methylene-8-heptadecenoic acid)

In this current study, the assignment of the protons in the fatty acid methyl ester (FAME) is possible, as shown in Table 1 and Figure 6 [8].

Table 1. The comparison of ^{1}H-NMR (500 MHz, $CDCl_3$) data of compound A with ^{1}H-NMR (400 MHz, $CDCl_3$) data of FAME from the literature [8]

^{1}H-NMR chemical shift, δ_H in ppm (multiplicity)		
Compound A (500 MHz, $CDCl_3$)	**FAME from *S. foetida* L. Oil [8] (400 MHz, $CDCl_3$)**	**Types of protons**
0.87 (t, J = 6.5 Hz)	0.85 (t, J = 6.8 Hz)	CH_3CH_2-
0.91 (s)	0.73 (s)	-C-CH_2-C-,cylopropene (2H)
1.32-1.48 (m)	1.17 - 1.40 (m)	-CH_2-

Table 1 (cont'd). The comparison of ^{1}H-NMR (500 MHz, $CDCl_3$) data of compound A with ^{1}H-NMR (400 MHz, $CDCl_3$) data of FAME from the literature [8]

^{1}H-NMR chemical shift, δ_H in ppm (multiplicity)		**Types of protons**
Compound A (500 MHz, $CDCl_3$)	**FAME from *S. foetida* L. Oil [8] (400 MHz, $CDCl_3$)**	
0.87 (t, J = 6.5 Hz)	0.85 (t, J = 6.8 Hz)	C**H**$_3$CH$_2$-
0.91 (s)	0.73 (s)	-C-C**H**$_2$-C-,cylopropene (2H)
1.32-1.48 (m)	1.17 - 1.40 (m)	-CH$_2$-
1.64 (m)	1.59 (m)	-CH$_2$-
2.06 (m)	2.27 (m)	Allylic -CH$_2$- of cyclopropene (2H)
2.33 (t, J = 7.5 Hz)	2.00 (m, J = 7.0 Hz)	C**H**$_2$COO- (4H)
2.36 (m)	2.27 (t, J = 7.0 Hz)	Allylic -CH$_2$- of cyclopropene (2H)
2.79 (t,J = 6.5 Hz)	2.74 (t,J = 6.0 Hz)	= CH-C**H**$_2$-CH= (2H)
3.51 (s)	3.63 (m)	-OC**H**$_3$
4.16 (dd, J = 12, 4 Hz)	4. 14 (dd, J= 11.9, 6.0 Hz)	-OCH(C**H**$_2$)$_2$ (2H)
4.30 (dd, J = 12, 4 Hz)	4.29 (dd, J= 11.9, 4.3 Hz)	-OCH(C**H**$_2$)$_2$ (2H)
5.28 (m)	5.26 (m)	-OCH(C**H**$_2$)$_2$ (1H)
5.39 (m)	5.30 (m)	-C**H**=C**H**- (4H)

dd = double of doublet, m = multiplet, s = singlet, t = triplet

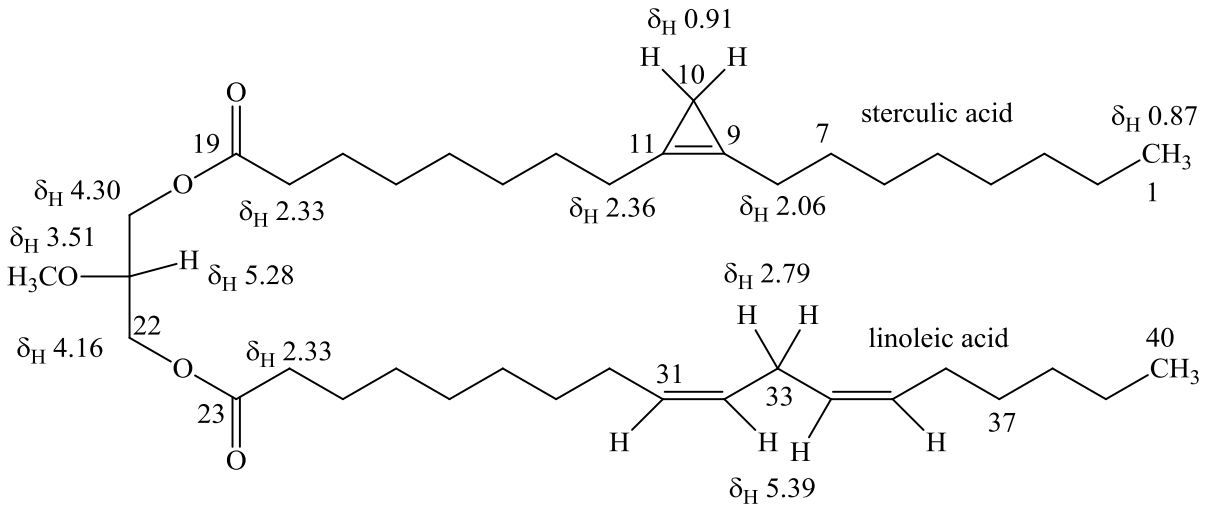


Figure 6. The structure of fatty acid methyl ester (FAME), from the malva nut showing the major ^{1}H-NMR chemical shift (ppm). The carbons are numbered accordingly

According to Table 1 and Figure 6, ^{1}H-NMR δ (ppm) values, in $CDCl_3$ are 5.39 (4H,*m*,-CH=CH-), 5.28(1H,*m*,-$OCH(CH_2)_2$), 4.30 (2H, *dd*,J=12,4 Hz,-$OCH(CH_2)_2$), 4.16 (2H, dd,J = 12,4 Hz,-$OCH(CH_2)_2$, 3.51 (s,-OCH_3), 2.79 (2H, t, J = 6.5, =CH-CH_2-CH=), 2.36 (2H, m, Allylic -CH_2- of cyclopropene), 2.33 (4H, t, J = 7.5 Hz, CH_2COO-), 2.06 (2H, m, Allylic -CH_2- of cyclopropene), 1.64 (m,-CH_2-), 1.32-1.48 (m,-CH2-), 0.91(2H, s,-C-CH_2-C-,cylopropene), 0.87 (t, J = 6.5 Hz, CH_3CH_2-).

Both Figure 4 and 6, plus the chemical shifts in Table 1, presented the protons of *Sterculia*'s fatty acid methyl ester (FAME) that could were characterized by using ^{1}H-NMR spectroscopy. ^{1}H NMR spectrum of compound A showed a diagnostic peak as fatty acid with branched ester derivatives appearing as singlet at δ_H 0.91 (C-CH_2-C), indicating two hydrogen of the cyclopropene ring at C10. The carbon at C8/C12 appeared as multiplet signals at δ_H 2.36 and 2.06 ppm respectively, indicate the allylic -CH_2- of cyclopropene while a triplet at δ_H 0.87 ppm due to terminal methyl hydrogen groups of all fatty acids or the methyl esters which compose the triacylglycerol (C1). The occurrences of double of doublet at the chemical shifts of δ_H 4.16 and 4.30 ppm, in addition to the multiplet at δ_H 5.28 ppm were contributed by the –CH_2 and –CH resonances from the glycerol backbone. The presence of proton at C34, the conjugated double bonds of linoleic acid, was assigned as the multiplet at δ_H 5.39 ppm. Since the hydrogen atoms of the linoleic acid are on the same side the molecule, the likely arrangement of the linoleic acid is the *cis*-isomer. It could be deduced that, both sterculic and linoleic acids could construct the chemical structure. Therefore, compound A in this *Sterculia* sample is suggested as a FAME molecule, (9Z,12Z)-,methoxy-3-((8-(2,octylcyclo prop-1-en-1-yl)octanoyl)oxy)propyloctadeca-9,12-dieoate (Figure 6) with proposed molecular formula of $C_{41}H_{72}0_5$, (MW=645.01 g/mol). These results agreed with the assignment with the chemical shifts of the FAME from *Sterculia foetida* L. oil, reported by Manurung et al. shown in Table 1 [8].

Conclusion

This research could increase the knowledge on the pharmacochemistry of the Sterculiaceae. The ^{1}H-NMR spectroscopic analysis suggested that compound A from the chloroform extract, was a mixture of an aromatic aldehyde and a fatty acid methyl ester (FAME). The FAME in this Sterculia sample consists of sterculic and linoleic acids. Sterculic acid is composed of around 55%, which is the highest content, as reported in Sterculia foetida seeds oil [7]. Though compound A might not be a secondary metabolite, its primary activity correlates with its benefits in reducing the body weight and improving the hepatic inflammation [9]. Further study is needed to re-investigate a higher purity of FAME. It is hoped to provide evidence in order to support the traditional uses of malva nut in folklore medicine.

Acknowledgement

The authors wish to thank Faculty of Pharmacy, UiTM for the support. The authors would also like to acknowledge Mr. Mohd Syukri Baharudin, Assistant Science Officer, Atta-ur-Rahman Institute for Natural Products Discovery (AuRIns), UiTM, Puncak Alam Campus, Selangor Darul Ehsan.

References

1. Al Muqarrabun, L. M. R. and Ahmat, N. (2015). Medicinal uses, phytochemistry and pharmacology of family Sterculiaceae: A review. *European Journal of Medicinal Chemistry*, 92: 514–530.
2. Palve, A., Shetty, P., Pimpliskar, M. and Jadhav, R. N. (2015). HPTL method for qualitative determination of phytochemical compunds in extract of *Sterculia lychnophora*. *International Journal Research Ayurveda Pharmaceutical*, 6: 358 – 365.
3. Petchlert, C., Boonsala, P., Payon, V., Kitcharoen, K. and Promsopa, S. (2012). *Proceeding of the 4th International Conference on Natural Products for Health and Beauty*, 28th – 30th November 2012, Thailand.
4. Ogale, S. C., Kasture, S. B., Kasture, V. S., Tiwari, R. and Temrikar, Z. (2014). Screening of methanolic extract of *sterculia scaphigera* wall seeds for ulcerprotective & antioxidant activity. *World Journal of Pharmacy and Pharmaceutical Sciences*, 4: 1332-1346.
5. Wang, R.-F., Yang, X.-W., Ma, C.-M., Shang, M.-Y., Liang, J.-Y., Wang, X., Cai, S. Q. and Shoyama, Y. (2003). Alkaloids from the seeds of *Sterculia lychnophora* (Pangdahai). *Phytochemistry*, 63: 475–478.
6. Chen, W., Tang, W., Lou, L. and Zhao, W. (2006). *Phytochemistry*, 67: 1041-1047.

7. Herrera-Meza, S., Martínez, A. J., Sánchez-Otero, M. G., Mendoza-López, M. R., García-Barradas, O., Ortiz-Viveros, G. R. and Oliart-Ros, R. M. (2014). Fatty acid composition and some physicochemical characteristics of *Sterculia apetala* seed oils. *Grasas Y Aceites*, 65: e039.
8. Manurung, R., Daniel, L., van de Bovenkamp, H. H., Buntara, T., Maemunah, S., Kraai, G., Makertihartha, I. G. B. N., Broekhuis, A. A. and Heeres, H. J. (2012). *European Journal of Lipid Science and Technology,* 114: 31–48.
9. Phlicharoenphon, W., Gritsanapan, W. and Sithisarn, P. (2013). *Thai Journal of Pharmaceutical Sciences*, 38: 58 – 60.

Malaysian Journal of Analytical Sciences Vol 22 No 3 2018

Articles 7-19 are selected papers from the "Regional Conference on Sciences, Technology and Sosial Sciences 2016 (RCSTSS 2016), 4-6 December 2016, Copthorne Hotel, Cameron Highlands, Malaysia; organised by Universiti Teknologi MARA (UiTM) Cawangan Pahang Kampus Jengka, 26400 Bandar Tun Abdul Razak Jengka, Pahang Darul Makmur, Malaysia."

Guest Editor: Azhan Hashim@Ismail

Articles 20-25 are selected papers from the "2nd International Conference on Separation Technology (ICOST 2017), 15 & 16 April 2017, Pulai Springs Resort, Johor Bahru, Malaysia; organised by Centre of Lipids Engineering and Applied Research, Universiti Teknologi Malaysia."

Guest Editor: Norasikin Othman

Page

1. AN ENVIRONMENTALLY FRIENDLY METHOD FOR EXTRACTION OF PARABENS IN VARIOUS SAMPLES USING LOW VISCOSITY AND LOW CLOUD POINT TEMPERATURE SURFACTANT 365
(Satu Kaedah Mesra Alam untuk Pengekstrakan Paraben dalam Pelbagai Sampel Menggunakan Surfaktan yang Rendah Kelikatan dan Rendah Suhu Titik Awan)
Norseyrihan Mohd Sohaimi, Noorashikin Mohd Saleh, Marinah Mohd Ariffin, Shiuan Yih Beh, Ruzita Ahmad

2. A-NOR STEROIDS FROM THE MARINE SPONGE, *Clathria* SPECIES 375
(Steroid A-nor daripada Span Laut, Spesies *Clathria*)
Idin Sahidin, Carla Wulandari Sabandar, Wahyuni, Rini Hamsidi, Muhammad Hajrul Malaka, Baru Sadarun, La Ode Aslan

3. EXTRACTION OF BISPHENOL A IN ENVIRONMENTAL WATER AND SOFT DRINK BY C_{18}-IMPREGNATED CELLULOSE TRIACETATE COMPOSITE FILM 383
(Pengekstrakan Bisfenol A dalam Air Alam Sekitar dan Minuman Ringan Menggunakan Filem Komposit Selulosa Triasetat Berimpregnasikan C_{18})
Saw Hong Loh, Ee Ling Aw, Seok Wen Lee

4. KAJIAN KELIKATAN PELARUT EUTEKTIK RELINA TERHADAP PENGEKSTRAKAN α-TOKOFEROL DARIPADA MINYAK SAWIT MENTAH 391
(Study on Viscosity of Reline Deep Eutectic Solvent on The α-Tocopherol Extraction From Crude Palm Oil)
Noor Hasyimah Hussain, Zetty Shafiqa Othman, Edison Eukun Sage, Rozida Mohd Khalid, Nur Hasyareeda Hassan

5. ROOM TEMPERATURE SYNTHESIS OF CERIA BY THE ASSISTED OF CATIONIC SURFACTANT AND AGING TIME 404
(Sintesis Ceria Pada Suhu Bilik Dengan Bantuan Surfaktan Kation Dan Masa Penuaan)
Nor Aqilah Mohd Fadzil, Mohd Hasbi Ab. Rahim, Gaanty Pragas Maniam

6. QUANTIFICATION OF GROUNDWATER-DERIVED NUTRIENTS INTO BEACH RIDGE DRAINAGE USING RADON MASS BALANCE MODEL 416

(Kuantifikasi Nutrien Air Bawah Tanah ke Saluran Pematang Pasir dengan Model Keseimbangan Jisim Radon)
Nicholas Chia Wei Ng and Seng-Chee Poh

7. MECHANICAL PROPERTIES OF BIOPLASTIC FROM JACKFRUIT SEED FLOUR AND POLYPROPYLENE 429
(Sifat Mekanikal Bioplastik daripada Tepung Biji Nangka dan Polipropelina)
Fairuzdzah Ahmad Lothfy, Asiah Mohd Nor, Syamsyir Akmal Senawi, Nur Sha'adah Zainuddin, Ermadasila Mohmad, Nur Aina Shuhada Norzeri, Nur Yasmin Sahira Saifful Bahri, Puteri Elyana Natasa Mohmad Azmi, Aliya Nuharissa Kamaruzaman

8. PREPARATION AND CHARACTERIZATION OF Ag NANOPARTICLES DECORATED WITH ZnO MICROSTRUCTURES FOR THE CATALYTIC PHOTODEGRADATION OF METHYLENE BLUE DYE UNDER UV LIGHT IRRADIATION 435
(Penyediaan dan Pencirian Ag Berstruktur Nanopartikel Diubahsuai dengan ZnO Berstruktur Mikro untuk Penurunan Fotokatalisis Pewarna Metilena Biru di bawah Sinar UV)
Hartini Ahmad Rafaie, Nur Azmina Mohemaed Safian, Roslan Md Nor, Yusof Mohd Amin

9. SUPERCONDUCTING PROPERTIES OF $Y_2Ba_5Cu_8O_\delta$ (Y258) POROUS AND NON- POROUS STRUCTURE 441
(Sifat Superkonduktor $Y_2Ba_5Cu_8O_\delta$ (Y258) Struktur Berliang dan Tidak Berliang)
Suazlina Mat Ali, Syamsyir Akmal Senawi, Azhan Hashim, Azman Kasim, Wan Aizuddin Wan Razali, Hartini Ahmad Rafaie, Norihan Yahya

10. VENTILATION EFFECT ON THE RADON-222 ANNUAL EFFECTIVE DOSE INSIDE GUA GAJAH AND GUA PENYU CAVES, KOMPLEKS GUA KOTA GELANGGI, PAHANG, MALAYSIA 446
(Kesan Pengudaraan Kepada Dos Berkesan Tahunan Radon-222 dalam Gua Gajah dan Gua Penyu, Kompleks Gua Kota Gelanggi, Pahang, Malaysia)
Nazree Ahmad, Junaidah Md Sani, Nur Hafilah Muslim, Nur Amirah Alias, Ahmad Saat

11. PHYTOCHEMICAL SCREENING, ANTIFUNGAL AND ANTIBACTERIAL ACTIVITIES OF *Musa acuminata* PLANT 452
(Saringan Fitokimia, Antikulat dan Aktiviti Antibakteria Pokok *Musa acuminata*)
Siti Suhaila Harith, Nur Hanis Mohd Yasim, Aiza Harun, Wan Siti Atikah Wan Omar, Mohd Supi Musa

12. FABRICATION AND CHARACTERIZATION OF RUBY NANOPARTICLES 458
(Fabrikasi dan Pencirian Partikel Nano Delima)
Wan Aizuddin Wan Razali, Azman Kasim , Syamsyir Akmal Senawi, Azhan Hashim, Norihan Yahya, Hartini Ahmad Rafaie

13. SYNTHESIZED AND CHARACTERIZATION OF SODIUM COBALT OXIDE AS SODIUM-ION CATHODE BATTERIES USING SOL-GEL METHOD 465
(Sintesis dan Pencirian Sodium Kobalt Oksida Sebagai katod Bateri Ion-Sodium Menggunakan Kaedah Sol-Gel)
Sarah Laila Mohd Jan, Nur Athirah Mohd Azhar, Musfiroh Jani

14. PHYTOCHEMICAL SCREENING AND LARVICIDAL ACTIVITY OF *Murraya koenigii* LEAVES EXTRACTS AGAINST MOSQUITO LARVAE 471
(Saringan Fitokimia dan Aktiviti Larvisid Ekstrak Daun *Murraya koenigii* Terhadap Larva Nyamuk)
Siti Suhaila Harith, Syarifah Nurul Akma Syed Mohd, Noorshilawati Abdul Aziz, Marlina Mohd Mydin, Nur Thabitah Shaikh Nasir

15. THE EFFECTS OF FE-DOPING ON MECHANICAL PROPERTIES IN $Bi_{1.6}Pb_{0.4}Sr_2Ca_2Cu_{3-X}Fe_XO_Y$ SUPERCONDUCTOR 477
(Kesan Dop Ferum Terhadap Sifat Superkonduktor $Bi_{1.6}Pb_{0.4}Sr_2Ca_2Cu_{3-X}Fe_XO_Y$)
Suazlina Mat Ali, Azhan Hashim, Syamsyir Akmal Senawi, Azman Kasim, Wan Aizuddin Wan Razali, Ruziana Mohamed, Fairuzdzah Ahmad Lothfy

16. THE ASSESSMENT OF INDOOR RADON-222 CONCENTRATION AND EMANATION RATE AT GUA PENYU, PAHANG 483
(Penilaian Kepekatan dan Kadar Pancaran Dalaman Radon-222 di Gua Penyu, Pahang)
Junaidah Md Sani, Nuramirah Alias, Nazree Ahmad, Ahmad Saat

17. ELECTROCHEMICAL PROPERTIES OF POLYMER ELECTROLYTES TREATED WITH 6PPD ON 30% POLY(METHYL METHACRYLATE) GRAFTED NATURAL RUBBER 491
(Sifat Elektrokimia Elektrolit Polimer 30% Poli(Metil Metakrilat) Cangkutan Getah Asli Terawat Dengan 6PPD)
Ahmad Fairoz Aziz, Khuzaimah Nazir. Siti Fadzilah Ayub, Nurul Ilham Adam, Muhd Zu Azhan Yahya, Ab Malik Marwan Ali

18. COMPARATIVE STUDY OF MICROBIAL FUEL CELL'S PERFORMANCE USING THREE DIFFERENT ELECTRODES 499
(Kajian Perbandingan Bagi Prestasi Sel Bahan Bakar Mikrob Menggunakan Tiga Elektrod yang Berbeza)
Khairul Baqir Alkhair, Oskar Hasdinor Hassan, Sharifah Aminah Syed Mohamed,Yap Kian Chung Andrew, Zulkifli Ab. Rahman, Tunku Ishak Tunku Kudin,Ab. Malik Marwan Ali, Mohd Zu Azhan Yahya, Muhammad Haikal Zainal

19. VARIATION OF PM_{10} AND HEAVY METALS CONCENTRATION OF SUB-URBAN AREA CAUSED BY HAZE EPISODE 508
(Variasi PM_{10} dan Kepekatan Logam Berat di Kawasan Separa-Bandar disebabkan oleh Episod Jerebu)
Mohd Zahari Abdullah and Nurul Afirah Alias

20. PREPARATION, CHARACTERIZATION AND PERFORMANCE OF POLYVINYLIDENE FLUORIDE/TETRAOCTYL PHOSPHONIUM BROMIDE NANOCOMPOSITE ULTRAFILTRATION MEMBRANE 514
(Penyediaan, Pencirian dan Prestasi Membran Ultraturasan Nanokomposit Polivinilidena Flourida/Tetraoktil Fosfonium Bromida)
Asmadi Ali, Connie Ling Mee Yu, Nur Alyaa Mohd Sani, Mohd Aidil Adha Abdullah, Mohamad Awang, Nor Shalihan Mohamed, Mohd Azizi Che Yunus

21. ALGINATE AEROGELS DRIED BY SUPERCRITICAL CO_2 AS HERBAL DELIVERY CARRIER 522
(Pengeringan Gel Aero Alginat oleh CO_2 Supergenting Sebagai Pembawa Penghantaran Herba)
Ana Najwa Mustapa, Ángel Martín, María José Cocero

22. MONOETHANOLAMINE WASTEWATER TREATMENT VIA ADSORPTION USING WOOD SAWDUST BASED ACTIVATED CARBON 532
(Rawatan Air Sisa Monoetanolamina Melalui Kaedah Penjerapan Menggunakan Karbon Habuk Kayu Yang Diaktifkan)
Azry Borhan, Tong Yeong Yit, Suzana Yusup, Normawati Mohd Yunus

23. SURFACE MODIFICATION OF POLYETHERSULFONE MEMBRANE VIA UV-GRAFTING FOR FORWARD OSMOSIS TECHNOLOGY 542
(Modifikasi Permukaan Membran Polyetersulfon Melalui Cantuman-UV untuk Teknologi Osmosis ke Hadapan)

Ahmad Fikri Hadi Abdul Rahman and Mazrul Nizam Abu Seman

24. RAPID SYNTHESIS AND CHARACTERIZATION OF LEAF-LIKE ZEOLITIC IMIDAZOLATE FRAMEWORK 553
(Sintesis Cepat dan Pencirian Kerangka Seperti Daun Imidazolat Zeolitik)
Imran Ullah Khan, Mohd Hafiz Dzarfan Othman, Juhana Jaafar, Haslenda Hashim, Ahmad Fauzi Ismail, Mukhlis A Rahman, Norafiqah Ismail

25. SEPARATION OF FATTY ACIDS FROM PALM OIL USING ORGANIC SOLVENT NANOFILTRATION 561
(Pemisahan Asid Lemak daripada Minyak Kelapa Sawit Menggunakan Penuras Nano Pelarut Organik)
Dayang Nur Fitrah Awang Ismail and Nazlee Faisal Ghazali

Malaysian Journal of Analytical Sciences, Vol 22 No 3 (2018): 365 - 374
DOI: https://doi.org/10.17576/mjas-2018-2203-01

MALAYSIAN JOURNAL OF ANALYTICAL SCIENCES
Published by The Malaysian Analytical Sciences Society
ISSN 1394 - 2506

AN ENVIRONMENTALLY FRIENDLY METHOD FOR EXTRACTION OF PARABENS IN VARIOUS SAMPLES USING LOW VISCOSITY AND LOW CLOUD POINT TEMPERATURE SURFACTANT

(Satu Kaedah Mesra Alam untuk Pengekstrakan Paraben dalam Pelbagai Sampel Menggunakan Surfaktan yang Rendah Kelikatan dan Rendah Suhu Titik Awan)

Norseyrihan Mohd Sohaimi[1], Noorashikin Mohd Saleh[2]*, Marinah Mohd Ariffin[1], Shiuan Yih Beh[2], Ruzita Ahmad[1]

[1]*School of Marine Science and Environment, Universiti Malaysia Terengganu, 21030 Kuala Nerus, Terengganu, Malaysia*
[2]*Chemical Engineering Programme, Research Centre for Sustainable Process Technology (CESPRO), Universiti Kebangsaan Malaysia, 43600 UKM Bangi, Selangor, Malaysia*

**Corresponding author: noorashikin@ukm.edu.my*

Received: 8 January 2018; Accepted: 21 March 2018

Abstract

Cloud point extraction is developed using a low viscosity surfactant (Sylgard 309) coupled with HPLC-UV. It is a simple method for extraction of parabens in various samples. At the optimum conditions, the method developed achieves limit of detection and extraction recoveries in the range of 0.01 ppm – 0.02 ppm and 68.5% -119.3%, respectively. Linearity of the calibration curves in the range of 0.2-1.0 mg/L. The correlation coefficient are achieved between 0.9995-0.9999. Each replicated samples are spiked with 1 mg/L of parabens. The results indicate that surfactant Sylgard 309 has a great potential for the extraction of organic pollutant in various samples.

Keywords: cloud point extraction, parabens, sylgard 309, simple method for extraction

Abstrak

Pengekstrakan titik awan dibangunkan menggunakan surfaktan yang mempunyai kelikatan yang rendah (Sylgard 309) digabungkan dengan KCPT-UV. Ini merupakan satu kaedah yang mudah untuk pemisahan paraben dalam pelbagai jenis sampel. Pada keadaan yang optimum, kaedah yang dibangunkan ini boleh mencapai had pengesanan dan perolehan semula pengekstrakan dalam julat 0.01 ppm – 0.02 ppm dan 68.5% -119.3%. Pekali korelasi yang dicapai adalah dalam julat 0.9995-0.9999. Larutan piawai yang ditambahkan dalam sampel iaitu 1mg/l paraben dalam setiap sampel replikat. Keputusan kajian menunjukkan bahawa surfaktan Sylgard 309 mempunyai potensi yang besar untuk diterokai bagi pengekstrakan pencemar 365rganic dalam pelbagai sampel.

Kata kunci: pengekstrakan titik awan, paraben, sylgard 309, kaedah ringkas untuk pengekstrakan

Introduction

Based on the study by Darbre and Harvey [1], the presence of free parabens (the formation of unconjugated forms and it considered as biological active) in human body tissues demonstrates that parabens are able to penetrate human skin intact without breakdown by esterase. Darbre et al. [2] measured concentrations of esters of paraben in human breast tumor and suggested that at least a proportion of the parabens present in daily used products such as cosmetic, food and pharmaceutical products can be absorbed and retained in the body tissue without undergo

hydrolysis [2]. Darbre and Harvey [1] reported that the estrogenic activity of ArP is higher than linear alkyl paraben which can promote breast cancer development. In fact, parabens are considered as endocrine disrupting chemicals (EDC) due to estrogens mimicker which increases the expression of genes and can cause human breast tumor cell [3]. It is suggested that more studies should be carried out for detailed evaluation of the potential of parabens. Concentration of parabens seldom exceeds 1% in products but it varies in different products [4]. Parabens do not persist in the environment since they will be degraded by photolysis in the air and biodegraded in water. The existence of the paraben are spread widely in the aquatic environment which it cannot easily be removed from the incoming water [5]. These phenomena occurs from swimmers using sunscreens and from sewage treatment plant [6].

There are a few methods that have been introduced to determine the parabens in water samples. The methods namely solid phase extraction [7], QuEChERS [8], dispersive liquid-liquid micro-extraction (DLLME) [9] and ionic liquid-based single-drop liquid phase micro-extraction (IL-based SDLME) [10]. Based on a study by Han et al. [11], these methods have their own specific disadvantages and not very suitable for determination of parabens in water samples. For example, due to high viscosity of surfactants, they cannot directly injected into CPE and dilution with solvent or water is necessary to complete the process of decreasing the viscosity. Each method has its own drawback such as QuEChERS has determination interference in the measurement; DLLME has poor reproducibility in extraction process due to its matrix where only the method only applicable for the simultaneous separation for intra-day repeatability [12], SDLPME is not very robust, and the droplets may be lost from the needle tip of the microsyringe during extraction.

As reported by Andersen [13], the available data of parabens are currently insufficient compared to other antimicrobial preservative compounds to support the assessment of their study. The concerns of the presence of paraben in human body tissue which develop to human breast cancer tissues become major interest in this research study [14]. With the continued use of paraben in the most of skincare cosmetics, foods and the residue from the industrial waste discharged to water, there is a need to carry out detailed evaluation regarding the potential of parabens. In fact, the information on the concentration of paraben in water samples could be helpful for risk assessment. In relation to this, the method of CPE is suitable method to extract parabens as it has a lot of advantages. It is simple, easy to carry out and rapid, low cost, environmental friendly and high sensitivity method of extraction in determining parabens from various samples without disturbing the neutrality of the environment [15].

Materials and Methods

Reagents and solutions

Sylgard 309 (3-(3-Hydroxypropyl)-heptamethyltrisiloxane ethoxylated acetate (>60%) were purchased from Dow Corning (Shanghai, China). Sylgard 309 has the properties which are viscosity of 40 cST, cloud point temperature of 3˚C and surface tension of 23 dynes/cm. The structure of Sylgard 309 is shown in Figure 1. Methylparaben (MeP, 99%), Ethylparaben (EtP, 99%), Propylparaben (PrP, 99.5%) and Benzylparaben (ArP, 99%) were purchased from Sigma Aldrich (USA). Sodium hydroxide (NaOH, 99%), hydrochloric acid (HCl, 37%), and acetonitrile (ACN, 99.9%) used are analytical grade and were purchased from Merck (Germany). Deionized water was prepared through Millipore Milli-Q Plus water purification system. Stock standard solution of parabens (MeP, EtP, PrP, ArP) (1000 mg/L) were prepared in HPLC grade acetonitrile and stored at 4 ˚C. The stock solutions were brought to ambient temperature prior to use.

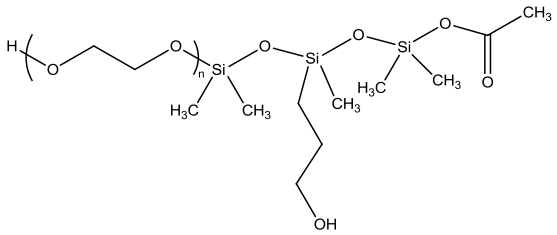


Figure 1. Structure of Sylgard 309 non-ionic surfactant

Instrumentations
Extracted samples after undergo CPE were injected into Agilent Technologies with ultraviolet detector to test the presence of parabens. The HPLC-UV system is made up of pump, deggaser, auto injector, column oven, guard column, SUPELCO Ascentis and C_{18} column (15 cm × 4.6 mm, 0.5 µm, Sigma-Aldrich). Conditions of HPLC used for this separation are mobile phase was deionized water: acetonitrile (50:50, v/v) with flow rate of 1.00 mL/min and detection of 254 nm.

Cloud point extraction procedure
A total of 2.5 mL of sample or standard solution containing the analyte (1 mg/L), 0.2 mL of 20% surfactant (Sylgard 309) concentration (w/v), 0.5 mL of 1.5 M of sodium sulphate (Na_2SO_4), and 0.2 mL of water samples is mixed in a 10 mL centrifuge tube. The phase separation is placed in the sonicator for 5 minutes to induce separation into two phases. The cloud point temperature is determined by measuring the temperature of the solution when it became turbid after sonication. The upper layer of surfactant rich phase of the two layers formed is extracted using a long needle syringe and filtered with 0.45 µm nylon filter membrane before injected into the HPLC-UV for analysis.

Optimization of parameters for paraben extraction
The extraction of paraben was conducted under one variable parameter with other parameter fixed as constant to obtain the optimum condition for the extraction. The parameters optimization include effect of pH, water weight loss in the surfactant rich phase and interference ions.

For parameter effect of pH, a series of sample at different pH (2, 4, 6, 7, 8, 9, 10, 11, 12 and 14) was adjusted using dilute acid (hydrochloric acid) or dilute alkaline solution (sodium hydroxide) to obtain the desired pH solution with other parameters kept constant. For parameter water weight loss in the surfactant rich phase, a series of non-ionic surfactant Sylgard-309 were prepared at various concentrations of 10% (w/v), 20% (w/v), 30% (w/v), 40% (w/v) and 50% (w/v) using deionized water with other parameters kept constant.

For parameter interference ions, a series of sample at different type of ions (Li^{2+}, Mg^{2+}, Br^-, Cl^-, SO_4^{2-}, NO_2^-, NH_4^+, PO_4^{3-}, F^-, K^+, NO_3^-, Na^+, Ca^{2+}) were prepared in 500 ppm concentration in order to investigate selectivity with other parameters kept constant.

Real sample preparation
The pharmaceutical, personal care products such as shower cream, moisturizer, cleanser, make-up remover, body lotion, shampoo, mouth rinse, toothpaste, cough drop and herbal lotion and beverage samples such as drinking water, mineral water, mango juice, syrup cordial and carbonated drink were brought from local market in area of Terengganu, Malaysia. The pharmaceutical and personal care products were prepared in such way that 1 mg of the sample was added into 100 ml volumetric flask and top up with deionized water until it reaches the mark. For beverage sample, 1 ml of sample is taken and dilute with deionized water with the ratio of 1:100. Then, all samples are filtered using a 0.45 µm nylon membrane filter to remove suspended particulate matters and placed at 4 ˚C in the dark for storage. The samples are brought to ambient temperature when ready for analysis and 0.2 mL of each prepared samples is added to the CPE method preparation.

Results and Discussion

Optimization of parameters: Effects of pH
pH plays an important factor in the CPE method to determine the extraction of an acidic or alkaline analyte in the aqueous solution. In order to determine the influence of the sample pH on the recovery of the studied analyte, an experiment was conducted over the range of pH 2-13. The results are illustrated in Figure 2 which shown that the highest level extraction at pH 7 for all studied parabens. The change in the extraction recoveries can be explained by considering the change in the charged of the parabens. At below pH 3, paraben is in the protonated form, the extraction recovery of parabens in this form is low. This is because protonation of paraben may greatly weaken the hydrophobic interaction between paraben and the surfactant [16].

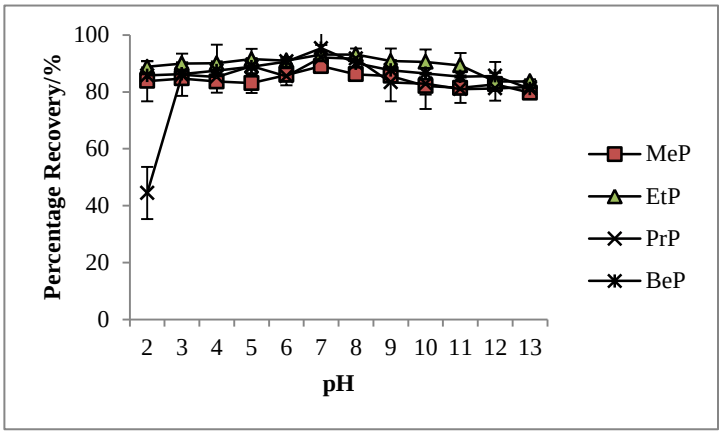


Figure 2. Effect of pH on the extraction recovery of parabens

Meanwhile, at pH 4-6, paraben exists mainly in the neutral form. There is slight increase in extraction recovery of paraben in this region as paraben loses its net positive charge due to the hydroxyl group becoming deprotonated. At pH 7, paraben exists mostly in a negatively charged form because the hydroxyl group is now fully deprotonated. In this region, percentage recovery for all parabens increase. In CPE method, the hydrogen bonding, electrostatic attraction, and π-π interaction could be the main interaction when paraben start to be deprotonated with the surfactant Sylgard 309.

From Figure 2, the decreasing trend of percentage recovery shown from pH 8-13. This might be the reason that the percentage recovery of parabens is decreased at pH 8 because all paraben compounds are fully transformed into alcohol and hydroxybenzoic acid [17]. Based on the previous research on the investigated of the parabens in water samples [18], the extraction performance reached a better level at pH 9 for all the studied paraben. Thus, it can be concluding that pH plays an important role in determining the optimum conditions for paraben extraction [19, 20]. Therefore, based on this optimization, we decide to use pH 7 as the optimal condition in this study.

Water weight loss in the surfactant rich phase

Referring to Figure 3, the extraction of MeP shows the highest amount of water content at most 28% at low concentration of surfactant-rich phase of 10% (w/v) surfactant concentration. This percentage of water content was reduced to almost 2% of water content at 50% (w/v) surfactant concentration. This show a reduction of 26% from MeP when the surfactant concentration was increased from 10% (w/v) to 50% (w/v). The overall reduction for EtP is slightly lower than that of MeP which is 21% followed by 15% for ArP and then 12% for PrP.

Percentage of water content in the surfactant-rich phase is an important parameter as it will affect the pre-concentration factor and the recovery of the analyte extracted. A high amount of water in the surfactant-rich phase will causes lower concentration of analytes to be extracted [21]. Thus, to have satisfactory extraction of analytes, the percentage of water content of in the surfactant-rich phase should be low. According to Yao and Yang [22], the performance of CPE is limited by the water content in the surfactant-rich phase. The lower amount of water content in the surfactant-rich phase will affect the concentration of analyte [19].

The trend that was shown in Figure 3 is increasing of surfactant concentration leads to decreasing of percentage water content. According to Sadeghi et al. [23], solute-solute interaction was greater than the interaction between surfactant with salt and water. When there is more hydrophilic surfactant in the solution, the solute-solute interaction will be more favorable and molecule of surfactant will interact with the surfactant than interacting with water molecules. This may give results of less percentage of water content in the surfactant-rich phase as less amount of water was detected. It is a good trend of water content corresponding to the surfactant concentration. This is because lesser water content in the surfactant-rich phase leading to a better performance of the surfactant in the

CPE method. Thus, high percentage recovery of parabens will be extracted in the surfactant-rich phase. The presence of salt may be causes low water content in the surfactant-rich phase [24].

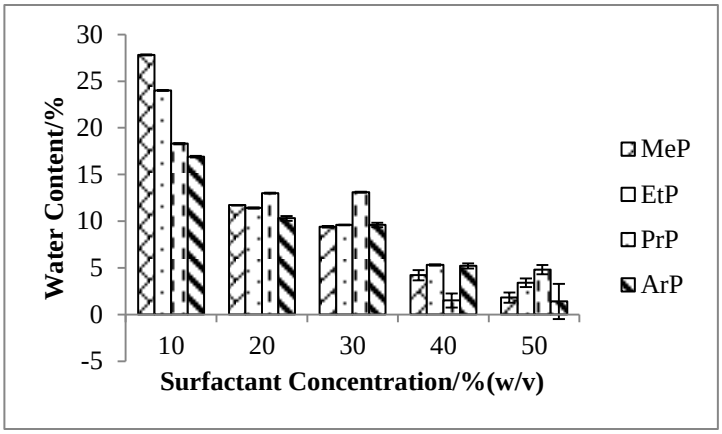


Figure 3. Water content in surfactant-rich phase using CPE method

Interferences Study

The efficiency of the proposed method in the extraction and pre-concentration of the parabens (MeP, EtP, PrP and ArP) ions in the presence of various cations and anions was examined by using solution containing 1.0 mg/L of parabens with addition of various concentrations of potential interferences. The tolerance levels of each potentially interfering ion species was tested, and if interferences occurred, the ratio was reduced until it ceased. As can be seen from Table 1, several species did not interfere, showing that the method described is applicable to the analysis of parabens ions in different samples.

Table 1. Interferences of ions to the extraction recovery

Ion	MeP	EtP	PrP	BeP
Li^+	81.6	87.9	81.1	95.1
Mg^{2+}	80.9	83.9	82.4	98.7
Br^-	80.8	84.9	81.6	98.4
Cl^-	80.2	87.9	82.4	98.8
SO_4^{2-}	80.3	88.6	81.6	92.7
NO_2^-	80.4	87.9	82.1	95.3
NH_4^+	80.7	87.0	84.5	96.9
PO_4^{3-}	81.1	85.9	82.6	98.1
F^-	80.8	85.3	82.0	94.7
K^+	80.1	84.7	80.8	93.2
NO_3^-	81.9	87.3	80.7	89.1
Na^+	80.5	84.1	88.1	94.6
Ca^{2+}	80.3	84.8	85.8	96.7

Analytical performance

Quantitative parameters of CPE method such as linear range, correlation coefficients, limit of detection (LODs), limit of quantitation (LOQs) and regression equation were evaluated and summarized in Table 2. For the

quantification of the target analytes, an external standard calibration with five different concentration levels was used such as 0.2, 0.4, 0.6, 0.8 and 1.0 mg/L for all parabens MeP, EtP, PrP and ArP. For each level, three replicate extractions were performed under the optimal conditions. Linearity of the calibration curves was determined in the range of 0.2-1.0 mg/L. the correlation coefficients are between 0.9995-0.9999 respectively, suggesting that the linearity is satisfactory in the linear range of the analytes. The LODs and LOQs, based on signal-to-noise ratio (S/N) of 3:1 and 10:1, were obtained in the range of 0.01-0.02 mg/L and 0.04-0.07 mg/L, respectively.

Table 2. Analytical performance of proposed method

Method	Paraben	Regression Equation[a]	R^2	LOD (mg/L)	LOQ (mg/L)
	MeP	y= 20.489x – 0.2173	0.9995	0.02	0.07
	EtP	y= 21.179x – 0.4411	0.9999	0.02	0.06
	PrP	y= 17.728x – 0.4771	0.9997	0.01	0.04
CPE	ArP	y= 16.151x – 0.5682	0.9999	0.02	0.07

[a] Peak area = slope x [paraben concentration (mg/L)] + intercept

Application of CPE in real samples

Based on the optimized conditions, the performance of CPE method is tested on the pharmaceutical and personal care product samples in order to evaluate the accuracy and precision. To validate the method, three replicated samples are prepared. Each replicated samples are spiked with 1.0 mg/L of parabens. The relative standard deviation (RSD) and extraction recoveries of the spiked samples are shown in Table 3. As is obvious from Table 3, the recoveries for the spiked samples were found to be in the range of 68.5-119% with RSDs ranging from 0.10% to 5.11% in personal care product samples, the percentage recoveries are higher in MeP and PrP especially in moisturizer are 108.8% and 112.5%, respectively. These result concluded that, the MeP and PrP are most commonly compounds are used in personal care product to increase preservative effect. The chromatogram of the pharmaceutical and personal care products is shown in Figure 4.

Table 3. Relative recoveries of parabens from various samples with spiked concentration 1 ppm for each analyte

Matrix	Found (µg mL^{-1},± RSD, n=3)				% Relative Recovery			
	MeP	EtP	PrP	ArP	MeP	EtP	PrP	ArP
Shower Cream	Nd	Nd	Nd	Nd	83.6	76.5	84.6	90.4
Moisturizer	0.34(±0.40)	Nd	0.46(±4.45)	Nd	108.8	80.1	112.5	95.7
Cleanser	0.33(±1.04)	0.02(±0.24)	Nd	Nd	86.3	82.1	86.2	91.9
Make-up Remover	0.11(±0.58)	Nd	Nd	Nd	89.7	76.5	84.7	91.3
Body Lotion	0.75(±5.11)	Nd	0.20(±0.30)	Nd	108.4	68.5	96.3	81.0
Shampoo	0.15(±1.13)	0.02(±0.42)	Nd	Nd	80.3	75.1	82.6	89.8
Mouth Rinse	Nd	Nd	Nd	Nd	83.3	76.1	86.1	91.6
Toothpaste	0.45(±1.13)	0.01(±1.42)	Nd	Nd	80.4	72.8	80.9	88.7
Cough Drop	Nd	Nd	0.001(±0.10)	Nd	81.6	73.0	81.7	87.9
Herbal Lotion	Nd	0.18(±0.58)	Nd	Nd	81.0	74.5	80.9	119.3
Drinking Water	Nd	Nd	Nd	Nd	85.3	77.0	85.0	88.3
Mineral Water	Nd	Nd	1.07(±0.78)	Nd	85.3	78.1	89.6	99.2
Mango Juice	Nd	Nd	Nd	Nd	84.6	75.8	85.5	90.3
Syrup Cordial	Nd	Nd	Nd	Nd	87.5	78.8	85.5	89.2
Carbonated Drinking	Nd	Nd	Nd	Nd	83.1	76.7	88.4	91.3

RSD: Relative Standard Deviation, Nd: Non detected

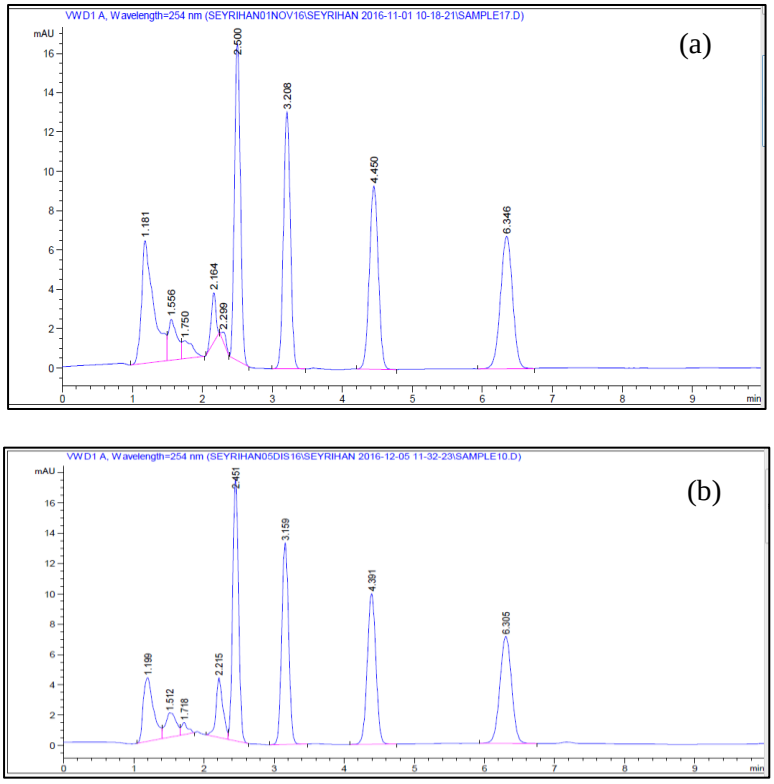


Figure 4. HPLC chromatograms of pharmaceutical and personal care products (a) shampoo (retention time; 2.50 (MeP); 3.209 (EtP); 4.450 (PrP) and 6.346 (ArP) and (b) shower cream (retention time; 2.451 (MeP); 3.159 (EtP); 4.391 (PrP) and 6.305 (ArP)).

From the chromatogram, the recoveries of pharmaceutical and personal care product have high peak intensity for all tested parabens, using these developed method also can separate the peaks easily without contaminated with other sample matrix. The peak area showed at high intensity, it is considered the presence of parabens compounds in pharmaceutical and personal care products can enter into the aquatic ecosystem via multiple pathways, including human excretion, unused drugs and products agricultural [25].

As can be seen, all the investigated compounds were found in the pharmaceutical and personal care products samples. The presence of parabens in greater amount in the pharmaceutical samples is due to the presence of chemicals substances in products. All the analytical results indicated that the simple CPE method proposed was very suitable for the simultaneous and rapid determination of parabens in pharmaceutical and personal care products samples without derivatization.

Nowadays, a variety of pharmaceuticals and personal care products (PPCPs) persist in natural freshwater resources [26].

Comparison study

The proposed method was compared with a variety of methods that have been reported recently in the literature for pre-concentration and determination of parabens in cosmetic products. Table 4 summarizes the main analytical information of the comparable methods reported for this type of samples. On the other hand, the percentage recoveries for proposed method achieved are higher compared with some of the method [27]. Besides that, the cost of acquision and maintenance of the system presented in this study are lower. The complexity of the analytical systems employed [28, 29] and sample pre-treatment requiring several steps [29, 30] of other methods described, can be compared with the ease of operation and low cost of CPE-HPLC-UV performance. Apparently, presented

method has low LODs, higher percentage recoveries, good RSD and these characteristics are comparable or even better than most of the other methods in Table 4.

Table 4. Comparison of the proposed method with other developed alternative for the determination of parabens in cosmetics

Method	Cosmetics Products	LOD	RSD (%)	Recovery (%)	Ref
SFE[a]/HPLC-MS	Lanoline cream, Skin milk	4.7-19.3 μgL^{-1}	< 18.6	-	[27]
HPLC-CL[b]	Wash-off cosmetics	1.9-5.33 μgL^{-1}	< 3.1	93-106	[28]
HPLC-UV	Foam shampoo	0.02-0.05 μgL^{-1}	< 3.2	98-105	[30]
FIA[c]–SPE-MEKC	Gel, Lotions, water/oil based Creams	0.07-0.1 mgL^{-1}	< 2.3	93-102	[29]
SPE-HPLC-CAD	Cream, Shampoo, Make-up, Lotions	0.5-2.1 mgL^{-1}	< 3.8	90-104	[7]
CPE-HPLC-UV	Shower Cream, Moisturizer, Cleanser, Make-up Remover, Lotions	0.01-0.02 mgL^{-1}	< 6.0	68-112	This work

[a]SFE: supercritical fluid extraction, [b]CL: chemiluminescene and [c]FIA: flow injection analysis

Conclusion

In this study, it shows that the method of CPE paired with non-ionic surfactant Sylgard 309 is an effective extraction method of parabens in various types of samples. Under the optimal conditions, the determination of four widely used parabens (MeP, EtP, PrP and ArP) using the combination of CPE and HPLC-UV indicates excellent LOD as low as 0.01-0.02 ppm. This CPE method have advantages such as simple, easy to carry out and fast as the extraction time is just 5 minutes. This method uses a minimum amount of organic solvents consequently leads to less organic waste, lower cost and even more environmental friendly as the surfactant used are less toxic. It also produces a high sensitivity method of extraction if compared with other proposed methods. CPE application to a wide range of pharmaceutical and personal care products and beverages samples matrices analysis without a significant variation in the sample preparation and extraction procedures shows that this method could be applied for the determination of parabens in various samples in laboratories analysis.

Acknowledgement

The authors wish to thank Department of Analytical and Environmental Chemistry, School of Marine and Environmental Sciences, Universiti Malaysia Terengganu for the facilities provided.

References

1. Darbre, P. D. and Harvey, P. W. (2008). Paraben esters: Review of recent studies of endocrine toxicity, absorption, esterase and human exposure, and discussion of potential human health risks. *Journal Applied Toxicology*, 28(5): 561-578.
2. Darbre, P. D., Aljarrah, A., Miller, W. R., Coldham, N. G., Sauer, M. J. and Pope, G. S. (2004). Concentrations of parabens in human breast tumours. *Journal of Applied Toxicology*, 24(1): 5-13.
3. Calafat, A. M., Ye, X., Wong, L.Y., Bishop, A. M. and Needham, L. L. (2010). Urinary concentrations of four parabens in the us population: Nhanes 2005-2006. *Environmental Health Perspective*, 118(5): 679.
4. Soni, M., Carabin, I., and Burdock, G. (2005). Safety assessment of esters of p-hydroxybenzoic acid (parabens). *Food and Chemical Toxicology*, 43 (7): 985-1015.
5. Jonkers, N., Kohler, H. P. E., Dammshäuser, A. and Giger, W. (2009). Mass flows of endocrine disruptors in the glatt river during varying weather conditions. *Environmental Pollution*, 157(3): 714-723.

6. Peng, X., Yu, Y., Tang, C., Tan, J., Huang, Q., and Wang, Z. (2008). Occurrence of steroid estrogens, endocrine-disrupting phenols, and acid pharmaceutical residues in urban riverine water of the pearl river delta, south china. *Science of the Total Environment*, 397 (1): 158-166.
7. Márquez-Sillero, I., Aguilera-Herrador, E., Cárdenas, S. and Valcárcel, M. (2010). Determination of parabens in cosmetic products using multi-walled carbon nanotubes as solid phase extraction sorbent and corona-charged aerosol detection system. *Journal of Chromatography A*, 1217(1):1-6.
8. Plassmann, M. M., Schmidt, M., Brack, W. and Krauss, M. (2015). Detecting a wide range of environmental contaminants in human blood samples—combining quechers with LC-MS and GC-MS methods. *Analytical Bioanaytical Chemistry*, 407 (23): 7047-7054.
9. Jain, R., Mudiam, M. K. R., Chauhan, A., Ch, R., Murthy, R., and Khan, H. A. (2013). Simultaneous derivatisation and preconcentration of parabens in food and other matrices by isobutyl chloroformate and dispersive liquid–liquid microextraction followed by gas chromatographic analysis. *Food Chemistry*, 141(1): 436-443.
10. Guo, X., Yin, D., Peng, J. and Hu, X. (2012). Ionic liquid-based single-drop liquid-phase microextraction combined with high-performance liquid chromatography for the determination of sulfonamides in environmental water. *Journal of Separation Science*, 35(3): 452-458.
11. Han, J., Wang, Y., Liu, Y., Li, Y., Lu, Y., Yan, Y. and Ni, L. (2013). Ionic liquid-salt aqueous two-phase extraction based on salting-out coupled with high-performance liquid chromatography for the determination of sulfonamides in water and food. *Analytical and Bioanaytical Chemistry*, 405(4): 1245-1255.
12. Wen, Y., Li, J., Zhang, W., and Chen, L. (2011). Dispersive liquid–liquid microextraction coupled with capillary electrophoresis for simultaneous determination of sulfonamides with the aid of experimental design. *Electrophoresis*, 32 (16): 2131-2138.
13. Andersen, F. A. (2008). Final amended report on the safety assessment of methylparaben, ethylparaben, propylparaben, isopropylparaben, butylparaben, isobutylparaben, and benzylparaben as used in cosmetic products. *International Journal Toxicology*, 27: 1-82.
14. Noorashikin, M. S., Farhanini, Y., Karthi, S. and Ruzita, A. (2017). Detecting parabens in environmental water samples. *International News on Fats, Oils and Related Materials*, 28: 16-17.
15. Norseyrihan, M. S., Noorashikin, M. S. and Hasrina, H. Z. (2017). Cloud point extraction of parabens from water samples. Advances in medicine and biology. Nova Science Publisher, Inc., New York: pp. 259-276.
16. Yin, X.-B., Guo, J.-M. and Wei, W. (2010). Dual-cloud point extraction and tertiary amine labeling for selective and sensitive capillary electrophoresis-electrochemiluminescent detection of auxins. *Journal Chromatography A*, 1217 (8): 1399-1406.
17. Angelov, T., Vlasenko, A. and Tashkov, W. (2008). HPLC determination of pka of parabens and investigation on their lipophilicity parameters. *Journal of Liquid Chromatography & Related Technologies*, 31: 188-197.
18. Noorashikin, M. S., Raoov, M., Mohamad, S. and Abas, M. R. (2013). Cloud point extraction of parabens using non-ionic surfactant with cylodextrin functionalized ionic liquid as a modifier. *International Journal of Molecular Sciences*, 14(12): 24531-24548.
19. Noorashikin, M. S., Nur Nadiah, A. B., Nurain, I., Siti Aisyah, A. A., and Siti Zulaika, M. R. (2016). Determination of phenol in water samples using cloud point extraction and uv spectrophotometry. *Desalination and Water Treatment*, 57(33): 15486-15494.
20. Noorashikin, M. S., Mohamad, S. and Abas, M. R. (2016). Determination of parabens in water samples by cloud point extraction and aqueous two-phase extraction using high-performance liquid chromatography. *Desalination and Water Treatment*, 57(47): 22353-22361.
21. Norseyrihan, M. S., Noorashikin, M. S., Adibah, M. S. N. and Yusoff, F. (2016). Cloud point extraction of methylphenol in water samples with low viscosity of non-ionic surfactant sylgard 309 coupled with high-performance liquid chromatography. *Separation Science and Technology*, 51(14): 2386-2393.
22. Yao, B. and Yang, L. (2008). Equilibrium partition of polycyclic aromatic hydrocarbons in cloud point extraction with a silicone surfactant. *Journal of Colloid and Interface Science*, 319(1): 316-321.
23. Sadeghi, R., Ebrahimi, N. and Mahdavi, A. (2012). Thermodynamic studies of the ionic liquid 1-hexyl-3-methylimidazolium chloride [c 6 mim][cl] in polyethylene glycol aqueous solutions. *The Journal of Chemical Thermodynamics*, 47: 48-55.
24. Noorashikin, M. S., Mohamad, S. and Abas, M. R. B. (2013). Cloud point extraction (CPE) of parabens using nonionic surfactant phase sepration. *Separation Science and Technology*, 48: 1675-1681.

25. Rosi-Marshall, E. J. and Royer, T. V. (2012). Pharmaceutical compounds and ecosystem function: An emerging research challenge for aquatic ecologists. *Ecosystems*, 15(6): 867-880.
26. Zhang, J., and Ma, P. X. (2013). Cyclodextrin-based supramolecular systems for drug delivery: Recent progress and future perspective. *Advanced Drug Delivery Reviews*, 65(9): 1215-1233.
27. Lee, M.-R., Lin, C.-Y., Li, Z.-G. and Tsai, T.-F. (2006). Simultaneous analysis of antioxidants and preservatives in cosmetics by supercritical fluid extraction combined with liquid chromatography–mass spectrometry. *Journal of Chromatography A*, 1120 (1–2): 244-251.
28. Zhang, Q., Lian, M., Liu, L. and Cui, H. (2005). High-performance liquid chromatographic assay of parabens in wash-off cosmetic products and foods using chemiluminescence detection. *Analytica Chimica Acta*, 537(1): 31-39.
29. Han, F., He, Y.-Z. and Yu, C.-Z. (2008). On-line pretreatment and determination of parabens in cosmetic products by combination of flow injection analysis, solid-phase extraction and micellar electrokinetic chromatography. *Talanta*, 74(5): 1371-1377.
30. Labat, L., Kummer, E., Dallet, P. and Dubost, J. P. (2000). Comparison of high-performance liquid chromatography and capillary zone electrophoresis for the determination of parabens in a cosmetic product. *Journal of Pharmaceutical and Biomedical Analysis*, 23(4): 763-769.

Malaysian Journal of Analytical Sciences, Vol 22 No 3 (2018): 375 - 382
DOI: https://doi.org/10.17576/mjas-2018-2203-02

MALAYSIAN JOURNAL OF ANALYTICAL SCIENCES
Published by The Malaysian Analytical Sciences Society
ISSN 1394 - 2506

A-NOR STEROIDS FROM THE MARINE SPONGE, *Clathria* SPECIES

(Steroid *A*-nor daripada Span Laut, Spesies *Clathria*)

Idin Sahidin[1]*, Carla Wulandari Sabandar[1], Wahyuni[1], Rini Hamsidi[1], Muhammad Hajrul Malaka[1], Baru Sadarun[2], La Ode Aslan[2]

[1]*Faculty of Pharmacy*
[2]*Faculty of Fisheries and Marine Science*
Universitas Halu Oleo, Kendari 93232, Indonesia

**Corresponding author: sahidin02@yahoo.com*

Received: 22 August 2017; Accepted: 20 March 2018

Abstract

Chemical compounds classified as *A*-nor steroids (**1**–**4**) were isolated from a marine sponge of the *Clathria* sp., collected from Southeast Sulawesi, Indonesia. Of these, one new compound, clathruhoate (**1**) was elucidated as 3*β*-(butyryloxymethyl)-*A*-nor-5*α*-cholestane. All compounds were obtained using silica gel chromatography techniques and their structures were determined based on 1D and 2D NMR spectroscopic measurements and comparison with values from literature. Meanwhile, all compounds were inactive for antimicrobial activity.

Keywords: *Clathria* sp., marine sponge, *A*-nor steroid, 3*β*-(Butyryloxymethyl)-*A*-nor-5*α*-cholestane

Abstrak

Sebatian kimia diklasifikasikan sebagai steroid *A*-nor (**1**–**4**) telah diasingkan daripada span laut *Clathria* yang dikumpul dari Sulawesi Tenggara, Indonesia. Satu sebatian baharu, klathruhoat (**1**) telah ditentukan sebagai 3*β*-(butiriloksimetil)-*A*-nor-5*α*-kolestan. Semua sebatian diperoleh dengan menggunakan teknik kromatografi gel silika dan struktur sebatian-sebatian ini telah ditentukan menggunakan spektroskopi 1D dan 2D NMR dan dengan perbandingan nilai dari kajian literatur. Sementara itu, semua sebatian didapati tidak aktif terhadap aktiviti antimikrob.

Kata kunci: *Clahtria* sp., span laut, steroid *A*-nor, 3*β*-(Butiriloksimetil)-*A*-nor-5*α*-kolestan

Introduction

The diversity of marine species in the Indonesian Archipelago has been recognized worldwide [1, 2], and various species of sponges have been discovered in east Indonesia [3, 4]. The genus *Clathria* from the family Microcionidae is classified as Demospongia and contains approximately 544 accepted species worldwide [5]. Of these, some species from the marine regions of Australia, Argentina, Indo-Pacific, Korea, Panama, Philippines and New Zealand have been phytochemically investigated and found to contain alkaloids [6–12], amides [13], peptides [14, 15], anthraquinones [16], and terpenoids [17–23]. Meanwhile, biological activities including antibacterial [7, 11, 21, 22], anti-HIV [18], cytotoxicity towards cancer cell lines [9, 10, 13, 14, 22], anti-inflammatory [19], and antiplasmodial [24] have been attributed to the species in the genus *Clathria*.

In our extensive study on the diversity and chemistry of Indonesian marine sponges, we investigated the chemical constituents of *Clathria* sp. from the Southeast Sulawesi marine region. The investigation resulted in the isolation and elucidation of one new *A*-nor steroid (**1**), together with three known *A*-nor steroids (**2**–**4**). The isolated compounds (**1**–**4**) were also evaluated for their antimicrobial activity.

Materials and Methods

Chemicals

Solvents used were distilled technical grades. Aluminium sheets kieselgel 60 PF_{254} 0.25 mm (Merck 1.05554), silica gel 60 HF_{254} 5-40 μm (Merck 1.07747), and silica gel 60 GF_{254} 5-40 μm containing gypsum (Merck 1.07749) were used to perform thin layer chromatography (TLC), vacuum liquid chromatography (VLC), and radial chromatography (RC), respectively. Nutrient agar (NA), nutrient broth (NB), potato dextrose agar (PDA), potato dextrose broth (PDB), chloramphenicol, ketoconazole, and DMSO were used for antimicrobial assays.

Animal material

Samples of *Clathria* sp. (Figure 1) were collected by hand using SCUBA (Self Contained Underwater Breathing Apparatus) from the reef slope area (70°) of the Bintang Samudra Marine Education Park, Southeast Sulawesi, Indonesia, at a depth of 2–10 m, in May 2015. Samples (6.5 kg) were stored in ice and brought back shortly afterwards to the laboratory for further analysis. A sponge specimen was identified by the staffs of the Faculty of Fisheries and Marine Science of Universitas Halu Oleo with the registration number UHO-2015-03.



Figure 1. A photograph of the investigated *Clathria* sp.

Extraction and isolation

The dried powdered sponge (4 kg) was macerated with MeOH (3 x 8 L, 24 h each time) at room temperature and filtered. The solvent was evaporated under reduced pressure to yield the MeOH extract in the form of a brownish-yellow gum (300 g). A portion of this extract (30 g) was fractionated using silica gel vacuum liquid chromatography (VLC) (13 x 5 cm) with a gradient elution of *n*-hexane/EtOAc (9:1, 8:2, 7:3, 5:5, v/v) to produce five main fractions (F1-F5). Fraction F1 (2 g) was subjected to a silica gel radial chromatography (RC) and eluted isocratically with *n*-hexane/EtOAc (9.5:0.5, v/v) to yield nine subfractions ($F1_1$-$F1_9$). The combined subfractions $F1_1$-$F1_3$ (1.36 g) were further separated on a silica gel RC with an elution of *n*-hexane/$CHCl_3$ (9.5:0.5, v/v) to afford compound **1** (30 mg). Purification of subfraction $F1_4$ (0.14 g) using a silica gel RC with *n*-hexane/CH_2Cl_2 (6:4, v/v) as its mobile phase yielded compound **2** (23 mg). Fraction F2 (10 g) was subjected to a silica gel VLC (10 x 5 cm), eluted with *n*-hexane/EtOAc (9:1-0:10, v/v), and given eight subfractions ($F2_1$-$F2_8$). Subfraction $F2_4$ (0.8 g) was purified using silica gel RC with *n*-hexane/EtOAc/acetone (7:1:0.5, v/v) as its mobile phase to give compound **3** (200 mg). Purification of subfraction $F2_6$ (1.1 g) on a silica gel RC with the elution of *n*-hexane/EtOAc/acetone (7:1:0.5, v/v) yielded compound **4** (120 mg).

Characterization study

The infrared (IR) analysis of compounds was performed using a Nicolet iS5 spectrophotometer with iD5 ATR (Thermo Scientific, Waltham, MA, USA). The HRESI-MS spectra were measured using a Waters QTOF mass spectrometer (Milford, MA, USA). Meanwhile, the ^{1}H, ^{13}C, and 2D NMR spectra were recorded using a JEOL ECP 500 MHz (Tokyo, Japan) or an Agilent DD2 500 MHz (Agilent Technologies, Inc., Santa Clara, California, USA) spectrometers.

***In vitro* antimicrobial assay**

Antimicrobial assay for the isolated compounds was performed using an agar well diffusion method towards *E. coli* ATCC 35218, *S. aureus* ATCC 25923, and *C. albicans* ATCC 10231 according to the previous method [30]. The development of microbial growth in a Petri dish was assisted using semisolid media. For bacterial growth, a semisolid medium containing sterilized nutrient agar (NA) (20 g/L) and nutrient broth (NB) (0.8 g/0.1 L) was prepared. Meanwhile, a semisolid medium for fungal growth was prepared with sterilized potato dextrose agar (PDA) (65 g/L) and potato dextrose broth (PDB) (2.4 g/0.1 L). One mL of microbial suspension (turbidity of 0.5 McFarland at 600 nm) was added into NB (5 mL) or PDB (5 mL) and mixed. Solutions of tested compounds were prepared with concentrations of 0.1, 0.2, and 0.3% in DMSO (10%, v/v). Chloramphenicol and ketoconazole each in 0.1% (v/v) were used as respective positive controls for bacteria and fungi, while DMSO was used as a negative control. The solid medium (10 mL) was poured into Petri dishes and allowed to solidify. Onto the solid medium, holes for samples were punched aseptically with tips. After that, the liquid medium-containing microbial suspension was evenly spread onto the surface of the solid medium. Samples (100 μL) were then added to their respective holes and the Petri dishes were incubated at 37 °C for 24 hours (bacteria) and 72 hours (fungi). Antimicrobial activity was evaluated by measuring the diameter of the clear zone around the hole. The inhibition zone of compounds and positive controls is categorized as strong (10-20 mm), moderate (5-10 mm), and weak (<5 mm).

Results and Discussion

Characterization of isolated compounds

Purification of the methanol extract of the dried powdered *Clathria* sp. using silica gel vacuum liquid chromatography (VLC) and radial chromatography (RC) techniques yielded one new *A*-nor steroid, clathruhoate (**1**) and other known *A*-nor steroids (**2**–**4**). Structures of these compounds are displayed in Figure 2.

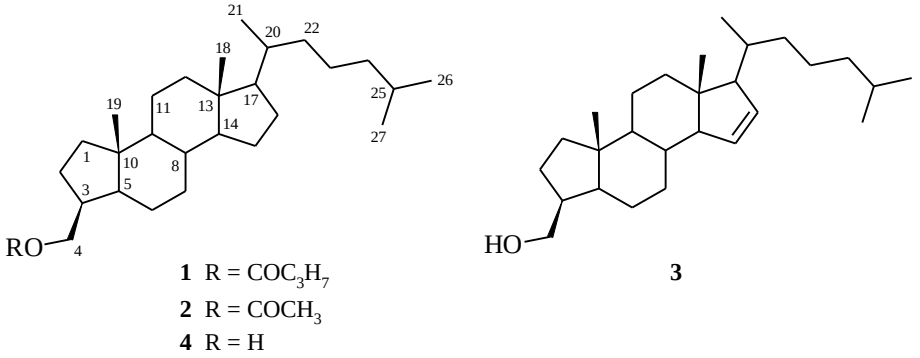


Figure 2. Chemical structures of compounds **1**–**4**

By comparing the values between spectroscopic measurements and literatures data, compounds **2**–**4** were identified as 3*β*-(acetoxymethyl)-*A*-nor-5*α*-cholestane (**2**) [25], 3*β*-(hydroxymethyl)-*A*-nor-5α-cholest-15-ene (**3**) [25, 26], and 3*β*-(hydroxymethyl)-*A*-nor-5*α*-cholestane (**4**) [25]. *A*-nor sterols are produced by marine Demosponges (e.g *Axinella* sp., *Homoaxinella* sp., *Phakellia* sp.) [25–28] via conversion of dietary sterols [29]. The occurrence of compounds **3** and **4** have been described in species *Axinella* [27, 28] and *Homoaxinella* [25], while the acetylation of compound **4** produced compound **2** [25]. Herein we report compound **2** as a natural product of the investigated *Clathria* sp. To our knowledge, the occurrence of these compounds in the genus *Clathria* is firstly reported in this work.

3*β*-(butyryloxymethyl)-*A*-nor-5*α*-cholestane (1)
White solid. HRMS-ESI: *m/z* 459.4112 $[M+H]^+$ (calculated for $C_{31}H_{55}O_2^+$: 459.4197). ATR-FTIR (ν_{max}, cm^{-1}): 2922, 2853, 1734, 1464, 1379, 1173, 968, 723. ^1H and ^{13}C NMR data are listed in Table 1.

Table 1. NMR data of compounds **1–4** (125 MHz for ^{13}C and 500 MHz for ^1H, in $CDCl_3$, δ, ppm, J/Hz)

C atom	1		2	3	4
	δ_C	δ_H	δ_C	δ_C	δ_C
1	39.0	1.08 (1H, m), 1.61 (1H, m)	39.1	39.9	39.1
2	27.3	1.44 (1H, m), 1.94 (1H, m)	22.8	22.9	24.6
3	38.5	2.31 (1H, m)	38.6	39.7	42.9
4	68.3	3.94 (1H, dd, J=10.27, 6.85), 4.09 (1H, dd, J=10.27, 6.85)	68.5	67.2	66.7
5	52.4	1.44 (1H, m)	52.6	52.7	52.6
6	24.4	1.04 (1H, m), 1.55 (1H, m)	27.5	27.4	27.4
7	32.7	0.83 (1H, m), 1.74 m (1H, m)	32.8	32.9	32.8
8	35.8	1.36 (1H, m)	35.7	35.7	35.6
9	55.4	0.73 m (1H, m)	55.6	55.6	55.5
10	44.1	–	44.3	44.2	44.1
11	22.8	1.31 (2H, m)	23.4	24.6	22.8
12	39.5	1.14 (2H, m)	39.5	36.3	39.9
13	43.1	–	43.1	43.1	43.1
14	56.3	0.99 (1H, m)	56.4	56.5	56.5
15	23.8	1.14 (1H, m), 1.34 (1H, m)	24.6	130.0	24.6
16	29.3	1.26 (2H, m)	28.3	131.1	28.3
17	56.2	1.00 (1H, m)	56.4	56.4	56.4
18	12.2	0.66 (3H, s)	12.3	12.3	12.1
19	14.5	0.78 (3H, s)	14.6	14.7	14.4
20	35.5	1.29 ((1H, m)	35.9	29.8	35.8
21	18.7	0.91 (3H, m)	18.9	18.9	18.7
22	36.2	0.99 (2H, m)	36.3	35.9	36.2
23	23.2	1.33 (1H, m), 1.44 (1H, m)	23.0	24.6	23.9
24	39.9	1.14 (1H, m), 1.95 (1H, m)	40.0	40.0	39.5
25	28.2	1.24 (1H, m), 1.81 (1H, m)	28.2	28.2	28.0
26	22.7	0.86 (3H, m)	22.7	22.7	22.7
27	22.6	0.86 (3H, m)	22.6	23.0	22.7
1’	174.1	–	171.5		
2’	34.5	2.27 (2H, t, J=7.83)	21.2		
3’	22.5	1.63 (2H, m)			
4’	14.1	0.89 (3H, m)			

Compound **1** was isolated as a white solid and was found to have a molecular formula of $C_{31}H_{55}O_2$ (MW 458.41238) based on a HRESI-MS analysis at *m/z* 459.4112 $[M + H]^+$, requiring five degrees of unsaturation. Of

these, one degree of unsaturation could be attributable to a carbonyl resonance (δ 174.1), while the remaining degrees were denoted by four rings. The IR spectrum showed absorption bands of methyl and methylene groups at 2922 cm^{-1} (CH_3 stretching), 2853 cm^{-1} (CH_2 stretching), 1464 cm^{-1} and 1379 cm^{-1} (CH_3 and CH_2 deformation) and an ester group at 1734 cm^{-1} (C=O stretching) and 1173 cm^{-1} (C–O stretching). The ^{1}H NMR spectrum showed signals representing five resonances of methyl protons at δ 0.66 (H-18), 0.78 (H-19), 0.86 (H-26, H-27) and 0.91 (H-21) and two double doublet (dd) resonances of oxymethylene protons (H-4) at δ 3.94 (J=10.27, 6.85) and 4.09 (J=10.27, 6.85), indicating a typical 3*β*-(hydroxymethyl)-*A*-nor cholestane [25, 26]. In addition, a methyl group at δ 0.89 (H-4') and two methylenes at δ 1.63 (H-3') and 2.27 (H-2') were observed in the spectrum, suggesting a butyryl group of an ester functionality in the structure as inferred in the IR analysis. In the ^{13}C NMR spectrum, thirty-one carbon signals were observed, thus supporting the results from the mass analysis. The carbon of oxymethylene of the *A*-nor steroid was resonanced at δ 68.3 (C-4) and one carbonyl of ester functionality was resonanced at δ 174.1 (C-1'). The assignments of these protons and carbons in the skeleton of compound **1** were based on a HSQC analysis and are given in Table 1.

The presence of cholestane skeleton in compound **1** was verified using 2D NMR analyses, in particular, the HMBC measurement. Using this analysis, all carbons with the exception of C-2 (δ 27.3), C-6 (δ 24.4), C-11 (δ 22.8), and C-15 (δ 23.8) could be associated with one or more of the methyl groups based on $^2J_{CH}$ and $^3J_{CH}$ correlations (Figure 3). The patterns of these correlations were similar to the known compounds **2** and **4**, which confirmed **1** as an *A*-nor cholestane. The oxymethylene protons at C-4 and methine proton at C-3 showed $^3J_{CH}$ and $^4J_{CH}$ correlations to a carbonyl carbon (δ 174.1) of an ester functionality, respectively, confirming the position of this carbonyl at C-1'. The presence of a butyryloxy group (C_3H_7COO–) was confirmed using the observed correlations of the methyl (H-4') and methylenes (H-2', H-3') protons toward the carbonyl carbon C-1'. In addition, protons H-2' also showed $^4J_{CH}$ correlation to the oxymethylene carbon (C-4). Hence, this side group was attached to C-4. Based on these evidences, compound **1** was established as 3*β*-(butyryloxymethyl)-*A*-nor-5*α*-cholestane for which clathruhoate as a trivial name is proposed.

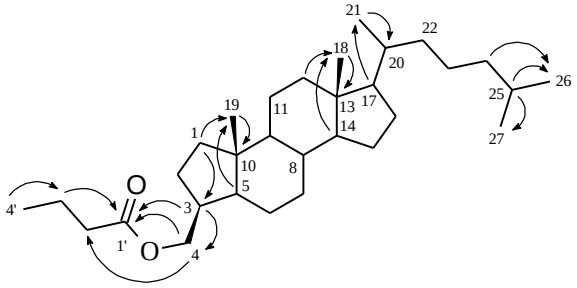


Figure 3. HMBC correlations (H→C) of compound **1**

3*β*-(acetoxymethyl)-*A*-nor-5*α*-cholestane (2)
Yellow crystal. MW: 430.7061 ($C_{29}H_{50}O_2$). ATR-FTIR (ν_{max}, cm^{-1}): 2926, 2858, 1740, 1455, 1370, 1164, 969, 721; ^{1}H NMR ($CDCl_3$, 500 MHz, δ/ppm, J/Hz): 4.09 (1H, dd, J=10.27, 7.15, H-4a)), 3.95 (1H, t, J=8.4, H-4b), 2.33 (1H, m, H-3), 2.03 (3H, s, H-2'), 0.91 (3H, m, H-21), 0.86 (3H, m, H-27), 0.85 (3H, m, H-26), 0.75 (3H, s, H-19), 0.65 (3H, s, H-18). ^{13}C NMR data are given in Table 1.

Compound **2** was obtained as a yellow crystal and gave a molecular formula of $C_{29}H_{50}O_2$ (MW 430.7061) based on analyses using ^{1}H and ^{13}C NMR spectra. According to this formula, five degrees of unsaturation were calculated as denoted by a carbonyl resonance (δ 171.5) and four rings of the cholestane skeleton. The IR spectrum of compound **2** showed the presence of methyl and methylene groups (2926, 2858, 1455, 1370 cm^{-1}) and an ester group (1740, 1164 cm^{-1}), which was similar to compound **1**. The ^{1}H NMR spectrum exhibited six resonances of methyl protons at δ 0.65 (s, H-18), 0.75 (s, H-19), 0.85 (m, H-26), 0.86 (m, H-27), 0.91 (m, H-21) and 2.03 (s, H-2') and multiplet resonances of typical cholestane protons ranging from δ 0.83 to 2.33. The oxymethylene protons (H-4) were

observed as a double doublet at δ 4.09 (J=10.27, 7.15, H-4a) and a triplet at δ 3.95 (J=8.14, H-4b). Meanwhile, the ^{13}C NMR spectra showed twenty-nine carbons in the skeleton of compound **2** (Table 1), and their values were identical to those given in [25]. Hence, compound **2** was deduced as 3*β*-(acetoxymethyl)-*A*-nor-5*α*-cholestane.

3*β*-(hydroxymethyl)-*A*-nor-5*α*-cholest-15-ene (3)
White solid. MW: 386.6535 ($C_{27}H_{46}O$). ATR-FTIR (ν_{max}, cm^{-1}): 3334, 2918, 2853, 1594, 1508, 1454, 1376, 1265, 1035, 977. ^{1}H NMR ($CDCl_3$, 500 MHz, δ/ppm, J/Hz): 5.15 (1H, m, H-15), 5.13 (1H, m, H-16), 3.71 (1H, dd, J=10.45, 6.50, H-4a), 3.47 (1H, t, J=9.72, H-4b), 2.22 (1H, m, H-3), 1.95 (2H, m), 1.82 (1H, m), 0.90 (3H, m, H-21), 0.89 (3H, m, H-27), 0.85 (3H, m, H-26), 0.74 (3H, s, H-19), 0.65 (3H, s, H-18). ^{13}C NMR data are given in Table 1.

Compound **3** was obtained as a white solid. The compound has a molecular formula of $C_{27}H_{46}O$ (MW 386.6535) based on ^{1}H and ^{13}C NMR spectral analyses and required five degrees of unsaturation, originating from one olefinic group (δ 130.0, 131.1) and four rings of the cholestane structure. The IR spectrum displayed absorption bands of a hydroxyl group (3334 cm^{-1}, OH stretching), methyl and methylenes groups (2918, 2853, 1454, 1376 cm^{-1}), and an alkene group (1594 cm^{-1}, C=C stretching). The ^{1}H NMR spectrum of compound **3** exhibited resonances of olefinic protons at δ 5.15 (m, H-15) and 5.13 (m, H-16), oxymethylene protons at δ 3.71 (dd, J=10.45, 6.50, H-4a) and 3.47 (t, J=9.72, H-4b), and methyl protons at δ 0.65 (s, H-18), 0.74 (s, H-19), 0.85 (m, H-26), 0.89 (m, H-27) and 0.90 (m, H-21). The presence of a hydroxyl group in the IR spectrum and oxymethylene protons (δ 3.71, 3.47) in the ^{1}H NMR spectrum suggested an alcohol functionality in compound **3**. The ^{13}C NMR spectrum consisted of twenty-seven carbons including two olefinic carbons (δ 130.0, 131.1) and one oxymethylene carbon (δ 67.2) (Table 1). The NMR data of compound **3** were identical with those assigned for 3*β*-(hydroxymethyl)-*A*-nor-5*α*-cholest-15-ene [25, 26]. This compound was previously reported from *Homoaxinella trachys* [25], *Phakellia aruensis* [26], and *Axinella proliferans* [27].

3*β*-(hydroxymethyl)-*A*-nor-5*α*-cholestane (4)
White solid. MW: 388.6694 ($C_{27}H_{48}O_2$). ATR-IR (ν_{max}, cm^{-1}): 3357, 2915, 2820, 1454, 1378, 1276, 1196, 740; ^{1}H NMR ($CDCl_3$, 500 MHz, δ/ppm, J/Hz): 3.70 (1H, dd, J=10.3, 6.3, H-4a), 3.46 (1H, t, J=9.6, H-4b), 2.23 (1H, m, H-3), 1.93 (2H, m), 1.82 (1H, m), 0.91 (3H, m, H-21), 0.86 (3H, m, H-27), 0.84 (3H, m, H-26), 0.73 (3H, s, H-19), 0.64 (3H, s, H-18). ^{13}C NMR data are given in Table 1.

Compound **4** was isolated as a white solid and have a molecular formula of $C_{27}H_{48}O_2$ (MW 388.6694). Four degrees of unsaturation calculated from this formula was attributed by four rings of the cholestane structure. The IR spectrum suggested a hydroxyl group (3357 cm^{-1}) and methyl and methylenes groups (2918, 2853, 1454, 1376 cm^{-1}). The ^{1}H NMR spectrum showed two coupled peaks at δ 3.70 (dd, J=10.3, 6.3) and 3.46 (t, J=9.6), indicating the mutual oxymethylene protons as previously observed in compounds **1**–**3**. Similarly, five methyl groups of typical cholestane skeleton were observed at δ 0.64 (s, H-18), 0.73 (s, H-19), 0.84 (m, H-26), 0.86 (m, H-27) and 0.91 (m, H-21). Meanwhile, as many as twenty-seven carbons were obtained from the ^{13}C NMR spectrum and their values were identical to compounds **1**–**2** with the exception of butyryloxy and acetoxy carbons. Hence, compound **4** was determined as 3*β*-(hydroxymethyl)-*A*-nor-5*α*-cholestane [25]. This compound was previously reported from *Axinella verrucosa* [28].

Antimicrobial activity of isolated compounds
The isolated compounds were evaluated for antibacterial activity against *E. coli*, *S. aureus*, and antifungal activity against *C. albicans*. However, none of the tested compounds exhibited antibacterial and antifungal activities as compared to chloramphenicol and ketoconazole, respectively. To our knowledge, the antimicrobial activity of these compounds is reported for the first time in this study.

Conclusion

Four *A*-nor steroids were isolated and identified from the methanol extract of the marine sponge *Clathria* sp. in the genus *Clathria* for the first time, which are 3*β*-(butyryloxymethyl)-*A*-nor-5*α*-cholestane (**1**), 3*β*-(acetoxymethyl)-*A*-nor-5*α*-cholestane (**2**), 3*β*-(hydroxymethyl)-*A*-nor-5α-cholest-15-ene (**3**), and 3*β*-(hydroxymethyl)-*A*-nor-5*α*-cholestane (**4**). Compound **1** named as clathruhoate was established as a new compound from this species. The

presence of these compounds could enrich the chemical diversity of the genus *Clathria*. Despite their inactive properties towards *E. coli*, *S. aureus*, and *C. albicans*, further studies are still required to explore more about the potent antimicrobial compounds from this species as well as other biological activities.

Acknowledgment

The authors thank the Ministry of Research, Technology, and Higher Education of the Republic of Indonesia for a research grant scheme (Hibah Kompetensi 2016) for financial support.

References

1. Spalding, M. D., Ravilious, C. and Green, E. P. (2001). World atlas of coral reefs. University of California Press, Berkeley, Los Angeles, CA: pp. 21 – 22.
2. Mora, C., Chittaro, P. M., Sale, P. F., Kritzer, J.P. and Ludsin, S.A. (2003). Patterns and processes in reef fish diversity. *Nature*, 421: 933 – 936.
3. van Soest, R. W. M. (1989). The Indonesia sponge fauna: a status report. *Netherlands Journal of Sea Research*, 23: 223 – 230.
4. Soekarno, R. (1989). Comparative studies on the status of Indonesia coral reefs. *Netherlands Journal of Sea Research*, 23: 215 – 222.
5. van Soest, R. (2017). *Clathria* Schmidt, 1982. In *Wold Porifera Database*. van Soest, R. W. M., Boury-Esnault, N., Hooper, J. N. A., Rützler, K., de Voogd, N. J., Alvarez de Glasby, B., Pisera, A. B., Manconi, R., Schoenberg, C., Klautau, M., Picton, B., Kelly, M., Vacelet, J., Dohrmann, M., Díaz, M. C., Cárdenas, P., Carballo, J. L. and Rios Lopez, P. (Eds). Accessed through: World Register of Marine Species (http://www.marinespecies.org/aphia.php?p=taxdetails&id=131868 on 2017-07-23).
6. Sperry, S. and Crews, P. (1996). A novel alkaloid from the Indo-Pacific sponge *Clathria basilana*. *Tetrahedron Letters*, 37: 2389 – 2390.
7. Capon, R. J., Miller, M. and Rooney, F. (2001). Mirabilin G: a new alkaloid from a southern Australian marine sponge, *Clathria* species. *Journal of Natural Products*, 64: 643 – 644.
8. Zuleta, I. A., Vitelli, M. L., Baggio, R., Garland, M. T., Seldes, A. M. and Palermo, J. A. (2002). Novel pteridine alkaloids from the sponge *Clathria* sp. *Tetrahedron*, 58: 4481 – 4486.
9. El-Naggar, M., Conte, M. and Capon, R. J. (2010). Mirabilins revisited: polyketide alkaloids from a southern Australian marine sponge, *Clathria* sp. *Organic & Biomolecular Chemistry*, 8: 407 – 412.
10. Laville, R., Thomas, O. P., Berrué, F., Marquez, D., Vacelet, J. and Amade, P. (2009). Bioactive guanidine alkaloids from two Carribean marine sponges. *Journal of Natural Products*, 72: 1589 – 1594.
11. Sun, X., Sun, S., Ference, C., Zhu, W., Zhou, N., Zhang, Y. and Zhou, K. (2015). A potent antimicrobial compound isolated from *Clathria cervicornis*. *Bioorganic & Medicinal Chemistry Letters*, 25: 67 – 69.
12. Wei, X., Henriksen, N. M., Skalicky, J. J., Harper, M. K., Cheatham, T. E., III, Ireland, C. M. and Van Wagoner, R. M. (2011). Araiosamines A-D: tris-bromoindole cyclic guanidine alkaloids from the marine sponge *Clathria (Thalysias) araiosa*. *The Journal of Organic Chemistry*, 76: 5515 – 5523.
13. Ohta, S., Okada, H., Kobayashi, H., Oclarit, J. M. and Ikegami, S. (1993). Clathrynamides A, B, and C: novel amides from a marine sponge *Clathria* sp. that inhibit cell division of fertilized starfish eggs. *Tetrahedron Letters*, 34: 5935 – 5938.
14. Davis, R. A., Mangalindan, G. C., Bojo, Z. P., Antemano, R. R., Rodriguez, N. O., Concepcion, G. P., Samson, S. C., de Guzman, D., Cruz, L. J., Tasdemir, D., Harper, M. K., Feng, X., Carter, G. T. and Ireland, C. M. (2004). Microcionamides A and B, bioactive peptides from the Philippine sponge *Clathria (Thalysias) abietina*. *The Journal of Organic Chemistry*, 69: 4170 – 4176.
15. Woo, J. –K., Jeon, J., Kim, C. –K., Sim, C. J., Oh, D. –C., Oh, K. –B. and Shin, J. (2013). Gombamide A, a cyclic thiopeptide from the sponge *Clathria gombawuiensis*. *Journal of Natural Products*, 76: 1380 – 1383.
16. Khokhar, S., Pierens, G. K., Hooper, J. N. A., Ekins, M. G., Feng, Y. and Davis, R. A. (2016). Rhodocomatulin-type anthraquinones from the Australian marine invertebrates *Clathria hirsuta* and *Comatula rotalaria*. *Journal of Natural Products*, 79: 946 – 953.
17. Capon, R. J., Miller, M. and Rooney, F. (2000). Clathrins A-C: metabolites from a southern Australian marine sponge, *Clathria* species. *Journal of Natural Products*, 63: 821 – 824.
18. Rudi, A., Yosief, T., Loya, S., Hizi, A., Schleyer, M. and Kashman, Y. (2001). Clathsterol, a novel anti-HIV-1 RT sulfated sterol from the sponge *Clathria* species. *Journal of Natural Products*, 64: 1451 – 1453.

19. Keyzers, R. A., Northcote, P. T. and Webb, V. (2002). Clathriol, a novel polyoxygenated 14*β* steroid isolated from the New Zealand marine sponge *Clathria lissosclera*. *Journal of Natural Products*, 65: 598 – 600.
20. Santalova, E. A., Makarieva, T. N., Gorshkova, I. A., Dmitrenok, A. S., Krasokhin, V. B. and Stonik, V. A. (2004). Sterols from six marine sponges. *Biochemical Systematics and Ecology*, 32: 153 – 167.
21. Gupta, P., Sharma, U., Schulz, T. C., McLean, A. B., Robins, A. J. and West, L. M. (2012). Bicyclic C21 terpenoids from the marine sponge *Clathria compressa*. *Journal of Natural Products*, 75: 1223 – 1227.
22. Woo, J. –K., Kim, C. –K., Kim, S. –H., Kim, H., Oh, D. –C., Oh, K. –B. and Shin, J. (2014). Gombaspiroketals A-C, sesterterpenes from the sponge *Clathria gombawuiensis*. *Organic Letters*, 16: 2826 – 2829.
23. Woo, J. –K., Kim, C. –K., Ahn, C. –H., Oh, D. –C., Oh, K. –B. and Shin, J. (2015). Additional sesterterpenes and a nortriterpene saponin from the sponge *Clathria gombawuiensis*. *Journal of Natural Products*, 78: 218 – 224.
24. Inbaneson, S. J. and Ravikumar, S. (2012). *In vitro* antiplasmodial activity of *Clathria vulpina* sponge associated bacteria against *Plasmodium falciparum*. *Asian Pacific Journal of Tropical Disease*, 2012: 319 – 323.
25. Eggersdorfer, M. L., Kokke, W. C. M. C., Crandell, C. W., Hochlowski, J. E. and Djerassi, C. (1982). Sterols in marine invertebrates. 32.[1] Isolation of 3*β*-(hydroxymethyl)-A-nor-5*α*-cholest-15-ene, the first naturally occurring sterol with a 15-16 double bond. *The Journal of Organic Chemistry*, 47: 5304 – 5309.
26. Malik, S. and Djerassi, C. (1989). Minor and trace sterols in marine invertebrates. 61. Isolation and structure elucidation of new A-nor sterols from the marine sponge *Phakellia aruensis*. *Steroids*, 53: 271 – 284.
27. Aknin, M., Gaydou, E. M., Boury-Esnault, N., Constantino, V., Fattorusso, E. and Mangoni, A. (1996). Nor-sterols in *Axinella proliferans*, sponge from the Indian Ocean. *Comparative Biochemistry and Physiology*, 113: 845 – 848.
28. Minale, L. and Sodano, G. (1974). Marine sterols: unique 3*β*-hydroxymethyl-A-nor-5*α*-steranes from the sponge *Axinella verrucosa*. *Journal of the Chemical Society, Perkin Transactions I*: 2380 – 2384.
29. Bibolini, L., Minale, L. and Sodano, G. (1978). Investigations on the ring contraction step in the biosynthesis of A-nor-stanols by the marine sponge *Axinella verrucosa*. *Journal of the Chemical Society, Chemistry Communications*: 524 – 525.
30. Ngajow, M., Abidjulua, J. and Kamu, VS. (2013). Pengaruh antibakteri ekstrak kulit batang Matoa (*Pometia pinnata*) terhadap bakteri *Staphylococcus aureus* secara *in vitro*. *Jurnal Mipa Unsrat Online*, 2(2): 128 – 132.

Malaysian Journal of Analytical Sciences, Vol 22 No 3 (2018): 383 - 390
DOI: https://doi.org/10.17576/mjas-2018-2203-03

MALAYSIAN JOURNAL OF ANALYTICAL SCIENCES
Published by The Malaysian Analytical Sciences Society
ISSN 1394 - 2506

EXTRACTION OF BISPHENOL A IN ENVIRONMENTAL WATER AND SOFT DRINK BY C_{18}-IMPREGNATED CELLULOSE TRIACETATE COMPOSITE FILM

(Pengekstrakan Bisfenol A dalam Air Alam Sekitar dan Minuman Ringan Menggunakan Filem Komposit Selulosa Triasetat Berimpregnasikan C_{18})

Saw Hong Loh*, Ee Ling Aw, Seok Wen Lee

School of Marine and Environmental Sciences,
Universiti Malaysia Terengganu, 21030 Kuala Nerus, Terengganu, Malaysia

**Corresponding author: lohsh@umt.edu.my*

Received: 12 February 2018; Accepted: 29 April 2018

Abstract

Bisphenol A (BPA) is an industrial chemical applied in making polycarbonate and epoxy resin that commonly used as food containers, beverage cans and baby bottles. BPA could be discharged into the environment from industrial waste and sewage treatment plant which then causing adverse effects to aquatic organism and consumers. Micro-solid phase extraction (µ-SPE) using C_{18}-impregnated cellulose triacetate (C_{18}-CTA) composite film as the adsorbent films coupled with high performance liquid chromatography–fluorescence detection (HPLC-FD) has been developed for the determination of BPA in environmental water and soft drink samples. Under the optimum extraction conditions, the method showed excellent linearity in the range of 0.1 to 500 ppb with correlation coefficient, r = 0.992. This method provided ultra-trace detection limit of 0.004 ppb, trace quantification limit of 0.01 ppb and acceptable relative recovery average in the range of 80.9 to 102.6% with relative standard deviation ≤ 9.7%. The proposed microextraction method is simple, rapid and eco-friendly as it consumes less amount of non-hazardous organic solvent.

Keywords: bisphenol A, C_{18}, cellulose triacetate, film, micro-solid phase extraction, high performance liquid chromatography

Abstrak

Bisfenol A (BPA) ialah suatu bahan kimia industri yang digunakan dalam pembuatan polikarbonat dan resin epoksi yang biasa digunakan sebagai bekas makanan, tin minuman dan botol bayi. BPA boleh dilepaskan ke dalam alam sekitar daripada sisa industri dan loji rawatan kumbahan yang kemudiannya menyebabkan kesan buruk kepada organisma akuatik dan pengguna. Pengekstrakan mikro fasa pepejal (µ-SPE) menggunakan filem komposit selulosa triasetat berimpregnasi C_{18} (C_{18}-CTA) sebagai filem penjerap berpasangan kromatografi cecair prestasi tinggi-pengesanan pendarfluor (HPLC-FD) telah dibangunkan untuk penentuan BPA dalam sampel air alam sekitar dan minuman ringan. Di bawah keadaan pengekstrakan optimum, kaedah ini menunjukkan kelinearan yang cemerlang daripada kepekatan 0.1 hingga 500 ppb dengan pekali korelasi, r = 0.992. Kaedah ini memberi had pengesanan ultra rendah iaitu 0.004 ppb, had kuantifikasi rendah iaitu 0.01 ppb dan purata pemulihan relatif yang boleh diterima dalam lingkungan 80.9 hingga 102.6% dengan sisihan piawai relatif ≤ 9.7%. Pengekstrakan mikro yang dicadangkan adalah bermanfaat daripada segi operasi mudah, cepat dan mesra alam kerana ia menggunakan sedikit pelarut organik yang tidak berbahaya.

Kata kunci: bisfenol A, C_{18}, selulosa triasetat, filem, pengekstrakan mikro fasa pepejal, kromatografi cecair prestasi tinggi

Introduction

Bisphenol A (BPA) is a strong endocrine disrupter with widespread application, mainly as a monomer in making polycarbonate (PC) plastic used as food and drink containers. BPA is also found in epoxy resins where it is used to coat the lining of some metal-based beverage and food cans to prevent corrosion. BPA can be found in the environment mainly from the industrial wastewater and through food that was kept in the PC containers. In January 2010, FDA agreed with National Toxicology Program (NTP)'s scientific assessment of BPA, and thus stopped using the BPA in food supply [1]. Nowadays, many countries regulated BPA since it is widely used in consumer products and the residues of BPA can lead to health problem like diabetes, breast cancer and heart disease.

The common methods such as liquid-liquid extraction (LLE) and solid phase extraction (SPE) have been regularly applied to extract BPA in environmental water. Both methods provide adequate sensitivity that fulfil the requirement of laboratory analysis. However, LLE and SPE require relatively large volumes of organic solvent and both are involving evaporation step to pre-concentrate the extract for trace analyses. Besides, large amount of solvent exerted from both LLE and SPE cause environmental pollution, hazard to health and require extra costs for waste treatment. For example, LLE was applied to extract BPA in various brands of drinking bottled water in Riyadh, Saudi Arabia. This research acquired a good recovery which was in the range of 79 to 94% [2]. Besides, SPE was employed to determine the BPA in water and milk and the results achieved ultra-trace detection limit [3, 4]. The great sensitivity shown by SPE is one of the main causes of its popularity, especially when the complicated sample matrices are analysed.

Lately, microextraction techniques have been applied to replace the LLE and SPE in order to meet the green chemistry requirement. These new methods have some advantages such as low cost, minimal solvent consumption, ease of employment and high analytes enrichment compared to both LLE and SPE. Liu and co-researchers demonstrated solid phase microextraction (SPME) coupled with high performance liquid chromatography (HPLC) to determine the BPA in milk and water samples in 2008. This research obtained ultra-trace detection limit and satisfactory relative recoveries which were in the range of 93.1 to 101%, 93.9 to 102% and 100.2 to 104.9% for milk, soybean milk and tap water samples, respectively [5,6]. The SPME is fast, simple, sensitive, and environmentally friendly. De Coensel and co-researchers studied the migration of BPA from baby bottles in 2009. In this research, stir bar sorptive extraction (SBSE) was applied to extract BPA before running through the gas chromatography-mass spectrometry (GC-MS). They also concluded that larger amount of BPA was released at high water temperature [7]. The SBSE simplifies the extraction as it does not require special skill and greatly minimizes the extraction solvent.

Gao and co-researchers demonstrated single drop microextraction (SDME) coupled with HPLC to determine BPA in thermal printing papers in 2013 [8]. Although the SDME is sensitive due to the extractant in a droplet, the slow kinetics of extraction and instability of the drop cause a longer equilibrium time and higher uncertainty. Loh et al. demonstrated dispersive liquid-liquid microextraction based on solidification of floating organic (DLLME-SFO) to extract BPA from water and soft drink samples [9]. The DLLME-SFO successfully extracted the bisphenol A from samples within a minute applying dispersive concept and simplified the collection of extractant by cooling the extractant with low melting point.

This study embeds the C_{18} adsorbent within the cellulose triacetate film to function as an adsorbent film in the µ-SPE technique. The technique simplifies the procedures and stands as a potential on-site extraction tool to minimize the analytes degradation throughout the transportation from sampling sites to laboratory for analysis.

Materials and Methods

Chemicals and materials

HPLC grade reagents like methanol (MeOH) and acetonitrile (ACN), ethanol, isopropanol and chloroform were obtained from Merck (Darmstadt, Germany). Cellulose triacetate (CTA) and octadecylsilane (C_{18}) were obtained from Sigma (St. Louis, Missouri, United States). Bisphenol A (BPA) reference standard was purchased from Dr. Ehrenstorfer GmbH (Augsburg, German).

Preparation of standard solutions
A standard stock solution of BPA (500 ppm) was prepared by dissolving 0.005 g of bisphenol A (BPA) reference standard in a 10 mL of volumetric flask and then diluted to volume with methanol. A series of working standard solutions were prepared by diluting the stock solution with methanol. All of the solutions were stored at 0˚C in darkness when not in use.

Preparation of samples
Three type of environmental water samples were collected from areas around Universiti Malaysia Terengganu which included river water, lake water, and sea water. In addition, soft drink samples that supplied in epoxy can were purchased from retailed shop in Kuala Terengganu. The samples were kept in freezer prior to extraction.

Preparation of C_{18}-impregnated cellulose triacetate composite film
Approximately, 0.04 g of cellulose triacetate (CTA) was weighed in a vial and 2 mL of chloroform was added into the same vial. The solution was then left for at least 5 hours at room temperature to make sure the dissolution was complete. Then, C_{18} (0.01 g) was weighed into a petri dish (5 cm diameter). The resulting CTA solution was added into the petri dish containing C_{18}. The solution was sonicated for 2 minutes to ensure even distribution of C_{18} in the CTA solution. The mixture was allowed to cool and dry in the fume hood at room temperature for 2 hours. C_{18} impregnated cellulose triacetate (C_{18}-CTA) composite film was then formed. The film was cut into small pieces (5mm) to function as an adsorbent film.

Micro-solid phase extraction procedure
The C_{18}-CTA composite film was conditioned by immersing the film in methanol for 30 seconds to wet and activate the sorbent surface. The sample was adjusted to pH 7 using either 0.1 M sodium hydroxide (NaOH) or 0.1 M hydrochloric acid (HCl). Sample (40 mL) was added into a sample vial and the films (7 pieces) were placed into the vial. The sample solution was then sonicated for 5 minutes. After 5 minutes of extraction, the films were removed from the sample solution and transferred to a safe-lock vial. The analytes were desorbed from the film using 50 µL of acetonitrile (ACN) under ultra-sonication for 10 min. The extract was filtered *via* 0.45 µm nylon syringe filter and injected into HPLC-fluorescence detection (FD) for quantification.

High performance liquid chromatography chromatographic conditions
All analyses were performed using HPLC (Shimazu, Kyoto, Japan) coupled with FD (Shimazu, Kyoto, Japan). The chromatographic determination of BPA was carried out on a reversed phase C_{18} column (4.6 x 250 mm, 5 µm). The determination was performed using isocratic mobile phase, acetonitrile-deionized water (60:40) (v/v) at column temperature of 30˚C. The flow rate, injection volume and detection wavelength were fixed at 1.0 mL/ min, 10 µL and 275/305 nm of excitation/emission wavelengths, respectively.

Optimization and validation of µ-SPE HPLC-FD
Several extraction parameters were thoroughly investigated to improve the extraction efficiency of the µ-SPE using C_{18}-impregnated CTA composite film as an adsorbent film. The parameters included amount of C_{18}-CTA films, sample pH, extraction time, volume of desorption solvent, desorption time, salt addition and type of desorption solvent. The µ-SPE coupled with HPLC-FD was then assessed for linearity, relative recovery, limit of detection (LOD), limit of quantification (LOQ) and precision before sample analysis. The LOD and LOQ were determined using signal-to-noise ratio. The peak-to-peak noise around the analyte retention time is measured by using this method. A signal-to-noise ratio (S/N) of three is used for measuring LOD and signal-to-noise ratio of ten is applied for measuring LOQ.

Results and Discussion

Optimization of micro-solid phase extraction procedure

Seven parameters which included amount of C_{18}-CTA composite film, extraction time, type of desorption solvent, volume of desorption solvent, desorption time, sample pH and salt addition were examined to increase the analyte enrichment when the µ-SPE technique was applied to extract BPA. The optimization was carried out using deionized water spiked with 20 ppb of BPA. Triplicate extractions were performed for each parameter to ensure the consistency of the results. The relative standard deviation (%RSD) was controlled in less than 10% to ensure precision and repeatability of the result [10].

The C_{18} which was immobilized within CTA acts as an adsorbent to extract the target analyte, BPA. The amount of C_{18}-CTA composite films vary from 4 to 8 pieces were investigated when extracting the BPA from 40 mL sample solution to determine the adsorption capacity of the C_{18}-CTA composite film. Figure 1(a) shows that the extraction efficiency increased when the amount of C_{18}-CTA composite film was increased from 4 pieces to 8 pieces. In this study, t-test (paired two sample for means) was used to determine the significant difference between 7 and 8 pieces. The result showed that the p-value for this statistics was 0.09 ($p > 0.05$). This mean that there was evidence that there was no significant difference between 7 pieces and 8 pieces. Although the 8 pieces of C_{18}-CTA film have the highest peak area among others, but there was no significant difference ($p > 0.05$) between 7 and 8 pieces. Therefore, 7 pieces of C_{18}-CTA film was applied in the subsequent experiments because the slightly higher peak area obtained by 8 pieces was due to random error.

Extraction time is one of the important factor in the extraction procedures. The microextraction technique is time-dependent since the target analyte mass transfer is the time-dependent process [11]. In this study, the extraction time in the range of 2 to 15 minutes was investigated with other optimized parameters remained unchanged. Figure 1(b) indicates the peak area of BPA increased from 2 to 5 minutes and then dropped from 5 to 15 minutes. The result shows that 5 min was effective to enrich the BPA. Thus, 5 minutes was chosen as optimum extraction time.

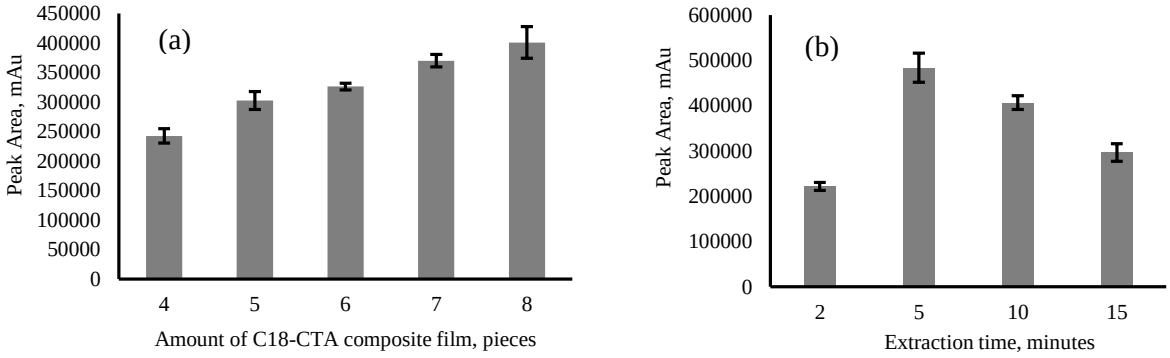


Figure 1. Effect of amounts of composite film (a) and extraction time (b) on µ-SPE for the extraction of BPA from spike deionized water samples. Each error bar indicates the standard deviation of triplicate extractions

The desorption solvent was applied to desorb the target analyte from the adsorbent. The affinity of analyte to the desorption solvent must be stronger as compared to the adsorbent to succeed the desorption process. The acetonitrile (ACN), isopropanol (IPA), ethanol (EtOH) and methanol (MeOH) were investigated as desorption solvents. As summarized in Figure 2(a), the highest peak area was obtained while using the ACN as desorption solvent which exhibited higher extraction efficiency. The higher the value of the polarity index, the more polar the molecule. Although ACN has higher polarity index among IPA, EtOH and MeOH. BPA is a polar compound and it tended to dissolve in polar solvent which depended on the concept of "like dissolve like". Consequently, ACN was chosen as the optimum desorption solvent.

Generally, the volume of desorption solvent should be kept low to increase the analyte enrichment factor because high volume of desorption solvent tends to dilute the analytes [12]. The volume of desorption solvent in the range of 50 to 200 µL was investigated. Figure 2(b) shows that the peak area dropped significantly from 50 µL to 200 µL. A suitable desorption solvent can effectively desorb the target analyte from the C_{18}-CTA films with a minimum volume [13]. The highest peak area was obtained when 50 µL of desorption volume was used. The desorption solvent which was less than 50 µL was not examined in this study because the volume was insufficient to submerge the films. Besides, the peak area decreased from 100 to 200 µL was due to the dilution of analytes. Therefore, 50 µL desorption solvent was chosen as the optimum volume of desorption solvent in the subsequent experiments.

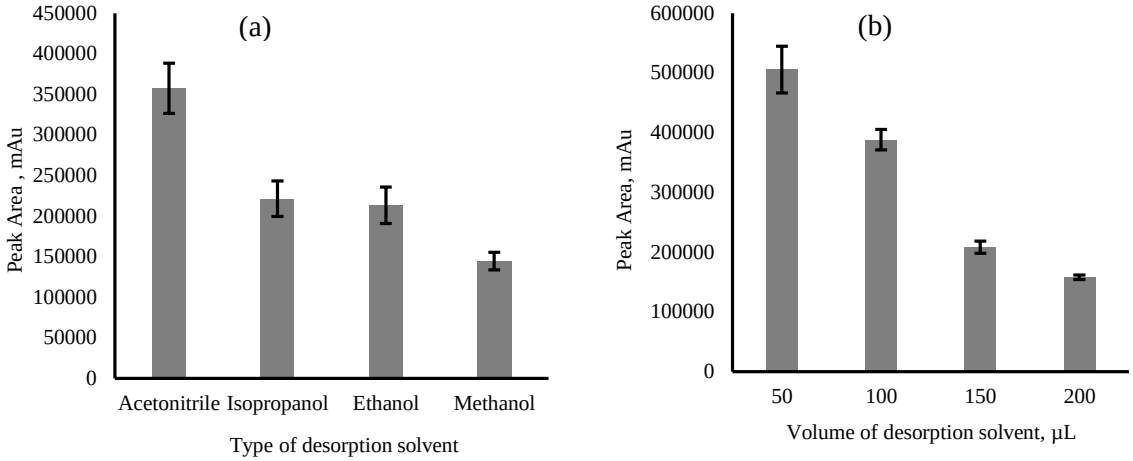


Figure 2. Effect of type of desorption solvent (a) and volume of desorption solvent (b) on µ-SPE for the extraction of BPA from spike deionized water samples. Each error bar indicates the standard deviation of triplicate extractions

Desorption time in the range of 2 to 20 minutes was investigated with other experimental conditions remained unchanged in order to achieve the maximum recovery of BPA. The microextraction technique is time-dependent and the analyte transfer from the C_{18}-CTA composite films to the solvent is also a time-dependent process [11]. Figure 3(a) indicates the peak area increased from 2 to 10 minutes and then dropped significantly from 10 to 20 minutes. Since 10 minutes of desorption time have the highest peak area, thus 10 minutes was applied for next experiment.

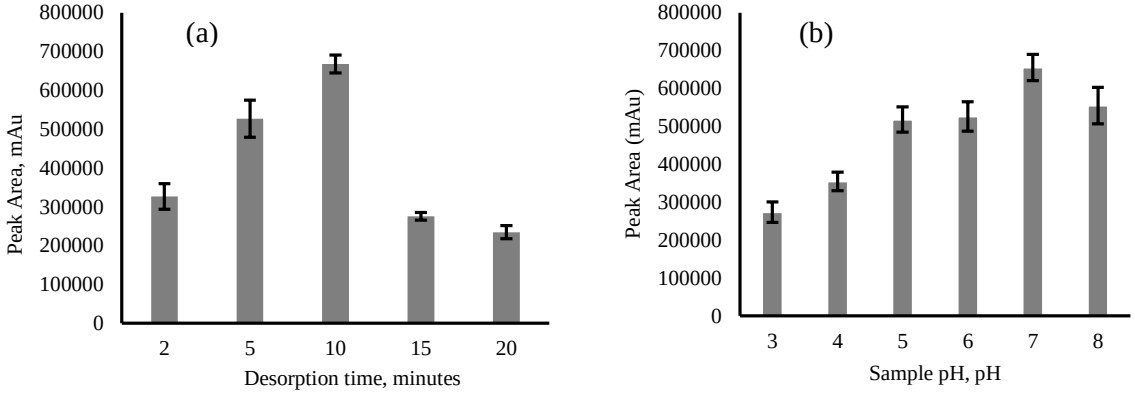


Figure 3. Effect of desorption time (a) and sample pH (b) on µ-SPE for the extraction of BPA from spike deionized water samples. Each error bar indicates the standard deviation of triplicate extractions

At different value of pH, the BPA will be present at different forms [12]. In general, the BPA in molecular form is easier to be extracted using organic solvent [14]. Therefore, the sample pH was fixed to assure the BPA was in molecular form. The BPA is a weak acid compound with pK_a value in the range of 9.6 to 10.2 [15].Various pH of sample solution ranging from 3 to 8 were investigated in this study where the pH was adjusted using either 0.1 M hydrochloric acid or 0.1 M sodium hydroxide. As shown in Figure 3(b), the best extraction efficiency was achieved at pH 7. When the pH of the sample less than the pK_a value of BPA, the BPA existed in molecular form. On the other hand, the BPA existed in ionic form which was more soluble in water when the sample pH over the pK_a value of BPA. The BPA existed in molecular form at pH 3 to 7. Besides, the decreasing peak area was obtained at pH 8. The BPA was protonated when the sample pH was made alkaline. Therefore, pH 7 was used as the optimum sample pH for the following analysis.

The addition of salt was applied to reduce the solubility of the analyte by increasing the ionic strength of sample because the salting-out effect could improve the analyte enrichment [13]. To study the effect of salt addition, this experiment was performed by spiking different concentrations of sodium chloride, NaCl into the sample solution which ranging from 0 to 7.5%, while other experimental conditions were kept constant. The sample without the addition of NaCl gave the highest peak area as compared to other samples with NaCl. Therefore, the factor of salt addition was not considered in the µ-SPE technique due to the salting-in effect.

Validation of micro-solid phase extraction procedure

The validation was carried out to verify the applicable of optimized µ-SPE technique using C_{18}-CTA composite films as the adsorbent films coupled with HPLC-FD in the analysis of BPA in environmental water and soft drink samples. Calibration was performed using deionized water spiked with target analyte, BPA in the range of 0.1 to 500 ppb. The results showed good linearity in the specified concentration with the correlation coefficient, r = 0.992.

The limit of detection (LOD) and limit of quantification (LOQ) are important characteristics applied in the method validation. The LOD and LOQ were 0.004 and 0.01 ppb, calculated based on the signal-to-noise ratio (S/N) of 3 and 10, respectively. The LOQ calculated was at levels lower than the maximum residue limit (MRL) of 0.25 ppb established by the European Union [16]. This revealed that the µ-SPE technique developed in this study was able to perform ultra-trace quantification of BPA in environmental water and soft drink samples.

Relative recovery was conducted by spiking the sea water, lake water, river water and soft drink samples each at 1 and 10 ppb of BPA, respectively. The sample blanks and spiked samples were then extracted using the optimized µ-SPE technique. All samples were free from BPA and Table 1 shows that the good relative recovery average ranging from 80.9% to 102.6% were obtained. Good repeatability was indicated by relative standard deviation (RSDs) of ≤ 9.7%. Thus, the matrix effect was insignificant and µ-SPE techniques can be employed in the analysis of these environmental water and soft drink samples.

Table 1. Relative recovery study using µ-SPE for the extraction of BPA in environmental water and soft drink samples

Sample	**Average of relative recovery ± relative standard deviation, % (n=3)**	
	Spiked at 1 ppb	**Spiked at 10 ppb**
Sea water	84.1 ± 2.4	81.2 ± 1.0
Lake water	90.3 ± 0.8	84.0 ± 2.9
River water	80.9 ± 2.4	92.5 ± 2.3
Isotonic soft drink	102.6 ± 2.7	87.6 ± 9.7
Carbonated orange juice	98.8 ± 8.8	98.7 ± 7.2

Conclusion

The µ-SPE technique has minimized the consumption of organic solvent and also amount of adsorbent throughout the extraction process. This technique applied cellulose triacetate (CTA) as a medium to hold the C_{18} which acts as adsorbent for the extraction of BPA. In addition, the optimization and validation results indicated that this technique gives sensitive extraction within a short analysis time. The µ-SPE technique is simple and easy to operate since it has low requirement of technical skill as compared to other microextraction technique. This technique is fulfilling the basis green analytical chemistry.

Acknowledgement

The authors would like to thank Universiti Malaysia Terengganu for facilitations and Ministry of Higher Education Malaysia for the financial supports through research grants with vote number 59367, respectively.

References

1. National Toxicology Program (2010). Bisphenol A (BPA). https://www.niehs.nih.gov/research/supported/assets/docs/a_c/bpa_fact_sheet_508.pdf. [Access online 12 February 2018].
2. Elobeid, M. A., Almarhoon, Z. M., Virk, P., Hassan, Z. K., Omer, S. O., EIamin, M., Daghestani, M. H. and AIOIayan, E. M. (2012). Bisphenol A detection in various brands of drinking bottled water in Riyadh, Saudi Arabia using gas chromatography/mass spectrometer. *Tropical Journal of Pharmaceutical Research*, 11(3): 455-459.
3. Omer, L., Ahmed, H. and Elbashir, A. (2016). Determination of bisphenol A in exposed bottled water samples to direct sunlight using multi walled carbon nanotubes as solid phase extraction sorbent. *Journal of Environmental Chemistry and Ecotoxicology,* 8(7): 51-57.
4. Szymanski, A., Rykowska, I. and Wasiak, W. (2006). Determination of bisphenol A in water and milk by micellar liquid chromatography. *Acta Chromatographica*, 17: 161-172.
5. Liu, X. Y., Ji, Y. S., Zhang, H. X. and Liu, M. C. (2008). Elimination of matrix effects in the determination of bisphenol A in milk by solid-phase microextraction-high-performance liquid chromatography. *Food Additives & Contamination*, 25(6): 772-778.
6. Liu, X. Y., Ji, Y. S., Zhang, H. X. and Liu, M. C. (2008). A chemometric strategy for optimization of solid-phase microextraction: Determination of bisphenol A and 4-nonylphenol with HPLC. *Journal of Chromatographic Science*, 46: 590-600.
7. De Coensel, N., David, F. and Sandra, P. (2009). Study on the migration of bisphenol A from baby bottles by stir bar sorptive extraction-thermal desorption-capillary GC-MS. *Journal of Separation Science*, 32(21): 3829-3836.
8. Gao, L., Zou, J., Liu, H., Zeng, J., Wang, Y. and Chen, X. (2013). Determination of Bisphenol A in thermal printing papers treated by alkaline aqueous solution using the combination of single-drop microextraction and HPLC. *Journal of Separation Science*, 36(7): 1298-1303.
9. Loh, S. H., Ong, S. T., Ngu, M. L. and Mohd Ariffin, M. (2017). Rapid extraction of bisphenol A by dispersive liquid-liquid microextraction based on solidification of floating organic. *Sains Malaysiana*, 46 (4): 615-621.
10. Kocourek, V. (2012). Method validation and quality control procedure. *Institute of Chemical Technology Prague.* https://web.vscht.cz/~kocourev/en_GB/files/Method%20validation%202012.pdf. [Access online 12 February 2018].
11. Yohannes, A., Tolesa, T., Merdassa, Y. and Megersa, N. (2016). Single drop microextraction analytical technique for simultaneous separation and trace enrichment of atrazine and its major degradation products from environmental waters followed by liquid chromatographic determination. *Journal of Analytical & Bioanalytical Techniques*, 7(5): 1-8.
12. Sadeghi, M., Nematifar, Z., Fattahi, N., Piraheb, M. and Shamsipur, M. (2016). Determination of Bisphenol A in food and environmental samples using combined solid-phase extraction-dispersive liquid-liquid microextraction with solidification of floating organic drop followed by HPLC. *Food Analysis Methods*, 9(6): 1814-1824.
13. Wang, L., Zhang, Z., Zhang, J. and Zhang, L. (2016). Magnetic solid-phase extraction using nanoporous three dimensional graphene hybrid materials for high-capacity enrichment and simultaneous detection of nine bisphenol analogs from water sample. *Journal of Chromatography A*, 1463: 1-10.

14. Wang, L., Liang, N., Sun, Z., Liu, D. and Hou, X. (2013). Development of dispersive liquid-liquid microextraction method based on solidification of floating organic drops combined with high performance liquid chromatography for the determination of curcumin in rat plasma. *Asian Journal*, 8(6): 147-158.
15. Yoon, Y., Westerhoff, P., Snyder, S. A. and Esparza, M. (2003). HPLC-fluorescence detection and adsorption of bisphenol A, 17β-estradiol, and 17α-ethynyl estradiol on powdered activated carbon. *Water Research*, 37(14): 3530-3537.
16. Rudel, R. A., Gray, J. M., Engel, C. L., Rawsthorne, T. W., Dodson, R. E., Ackerman, J. M., Rizzo, J., Nudelman, J. L. and Brody, J. G. (2011). Food packaging and bisphenol A and bis(2-ethyhexyl) phthalate exposure: Findings from a dietary intervention. *Environmental Health Perspective*, 119(7): 914-920.

Malaysian Journal of Analytical Sciences, Vol 22No 3 (2018): 391- 403
DOI: https://doi.org/10.17576/mjas-2018-2203-04

MALAYSIANJOURNAL OF ANALYTICAL SCIENCES
Published by The Malaysian Analytical Sciences Society
ISSN 1394 - 2506

KAJIAN KELIKATAN PELARUT EUTEKTIK RELINA TERHADAP PENGEKSTRAKAN α-TOKOFEROL DARIPADA MINYAK SAWIT MENTAH

(Study on Viscosity of Reline Deep Eutectic Solvent on The α-Tocopherol Extraction From Crude Palm Oil)

Noor Hasyimah Hussain, Zetty Shafiqa Othman, Edison Eukun Sage, Rozida Mohd Khalid, Nur Hasyareeda Hassan*

Pusat Pengajian Sains Kimia dan Teknologi Makanan,
Fakulti Sains dan Teknologi,
Universiti Kebangsaan Malaysia, 43600 UKM Bangi, Selangor, Malaysia

**Pengarang utama: syareeda@ukm.edu.my*

Received: 7 June 2017; Accepted: 14 March 2018

Abstrak

DES Relina diklasifikasikan sebagai pelarut hijau dan serasi untuk digunakan bagi pengekstrakan α-tokoferol (α-T) daripada minyak sawit mentah (CPO) kerana kemampuannya untuk membentuk ikatan hidrogen yang kuat dengan molekul α-T. Kepekatan dan hasil α-T dikuantifikasi menggunakan kromatografi cecair prestasi tinggi fasa berbalik (RP-HPLC). Dua parameter dikaji melalui penggunaan lima siri nisbah CPO: DES relina (1: 1, 1: 2, 1: 3, 1: 4 dan 1: 5) pada 2 dan 3 jam masa pengekstrakan untuk mengenalpasti keadaan optimum bagi pengekstrakan α-T. Kepekatan α-T untuk semua sampel yang diekstrak dibandingkan dengan kawalan (tanpa DES relina) memberikan nisbah 1: 2 (CPO: DES relina) dengan kelikatan pelarut 5.7 ± 0:58 cP pada 3 jam masa pengekstrakan sebagai keadaan pengekstrakan terbaik bagi mendapatkan kepekatan α-T tertinggi iaitu 825.321 ± 74.27 mg / L dengan keberhasilan 0.1554 ± 0.0156 (%). Perkara ini menunjukkan bahawa keadaan tersebut merupakan keadaan yang paling kondusif bagi penyerapan molekul *α*-T ke dalam ruang kosong dalam struktur pelarut di mana molekul *α*-T dan DES relina berinteraksi melalui ikatan hidrogen. Ikatan hidrogen yang kuat terbentuk antara kumpulan –OH *α*-T dengan kumpulan amina –NH_2 DES relina merupakan faktor peningkatan keupayaan DES relina untuk mengekstrak sebatian *α*-T yang tinggi daripada CPO.

Kata kunci: penderma ikatan hidrogen, pelarut eutektik dalam relina, tokoferol, kelikatan

Abstract

Reline DES was classified as a green solvent and compatible to be used for *α*-tocopherol (*α*-T) extraction from crude palm oil (CPO) due to its ability to form strong hydrogen bond with *α*-T molecule. The *α*-T concentration and yield was quantified using reverse phase high performance liquid chromatography (RP-HPLC). Two parameters were studied through utilization of five CPO: Reline DES ratio series (1:1, 1:2, 1:3, 1:4 and 1:5) at 2 and 3 hours extraction time in determining optimize *α*-T extraction condition. Concentration of *α*-T for all extracted samples was compared to the control (without reline DES) resulted towards CPO: Reline DES ratio of 1:2 with solvent viscosity of 5.7 ± 0.58 cP at 3 hours extraction time as the best condition to obtain the highest *α*-T concentration of 825.321 ± 74.27 mg/L with the yield of 0.1554 ± 0.0156 (%). It can be concluded that this condition is the most conducive for *α*-T molecules diffusion into free space of solvent structure in which molecules of *α*-T and reline DES interact through hydrogen bond. The strong hydrogen bond formed between –OH group of *α*-T and -NH_2 group of reline DES is the factor enhancing the capability of reline DES to extract higher *α*-T compound from CPO.

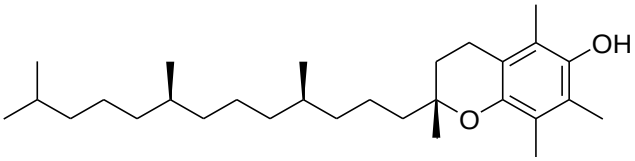
Keywords: hydrogen bond donor, reline deep eutectic solvent, tocopherol, viscosity

Pengenalan

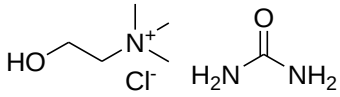
Sebatian α-tokoferol (Rajah 1(a)) merupakan salah satu terbitan vitamin E yang berupaya bertindak sebagai agen anti pengoksidaan dalam merawat penyakit kanser. Selain itu, sebatian vitamin E juga dikatakan sebagai terapi yang berpotensi merawat penyakit neurodegenaratif seperti Alzheimer dan Sindrom down [1]. Sebatian alfa tokoferol sering digunakan dalam bidang penyelidikan dan bidang perubatan. Kepentingan sebatian ini dalam pelbagai bidang menjadikan sebatian tokoferol mendapat permintaan yang tinggi [2]. Sebatian tokoferol boleh diperoleh daripada sumber asli seperti minyak sawit mentah (CPO) dan minyak ini mengandungi lima jenis isomer vitamin E iaitu α-tokoferol (α-T), α-tokotrienol ($\alpha-T_3$), γ-tokoferol (γ-T), γ-tokotrienol ($\gamma-T_3$) dan δ-tokotrienol ($\delta-T_3$) [3-6].

Pada tahun 2011, Goossens dan Marion [7] telah menjalankan kajian mengenai pengekstrakan sebatian α- dan δ- T daripada minyak *Canola* dan minyak kacang soya melalui kaedah emparan dan pusaran pada kelajuan 3000 rpm selama lima minit. Walaubagaimanapun, menurut Goossens dan Marion [7], kaedah pengekstrakan yang digunakan adalah tidak sempurna kerana menyebabkan degradasi sebatian tokoferol. Penyimpanan sebatian yang tidak mengikut keadaan yang sesuai juga (-20 °C) merupakan faktor sebatian ini teroksida dan terdegradasi. Oleh yang demikian, kajian yang melibatkan sebatian seperti tokoferol memerlukan pengendalian yang teliti bagi mengurangkan degradasi sebatian ini memandangkan sifatnya yang sensitif terhadap, haba, cahaya dan udara [8].

Sebatian vitamin E juga boleh diperoleh melalui kaedah pengekstrakan dengan menggunakan pelarut organik sebagai medium pengekstrakan. Kajian sebelum ini oleh Sanagi et al. [9] menggunakan pelarut organik heksana dalam kaedah pengekstrakan cecair bertekanan (PLE) memberikan pengekstrakan kandungan vitamin E yang tinggi. Walaubagaimanapun, penggunaan pelarut organik heksana pada suhu dan tekanan yang tinggi adalah berbahaya kerana pelarut ini mudah terbakar [10]. Secara konvensional pelarut organik sering digunakan bagi pengekstrakan sebatian α-T daripada sumber semula jadi. Namun, penggunaan pelarut organik menghasilkan kepekatan dan keberhasilan pengekstrakan yang rendah selain sifatnya yang toksik dan mudah meruap adalah berbahaya kepada pengguna.



(a)



(b)

Rajah 1. (a) Struktur kimia α-tokoferol (B) DES relina

Oleh yang demikian, pelarut hijau seperti pelarut eutektik dalam (DES) semakin giat dikaji oleh penyelidik masa kini dalam pelbagai bidang penyelidikan. Hal ini kerana ia merupakan pelarut yang mesra alam, murah dan tidak bertoksik [11]. Di samping itu, ciri-ciri pensolvatan yang luar biasa oleh pelarut hijau DES [12] menjadikan pelarut ini sesuai digunakan sebagai pelarut hijau alternatif dalam pengekstrakan sebatian α-T. DES merupakan campuran dua atau tiga komponen yang murah dan selamat di mana kesemua komponen ini berupaya untuk bercampur antara satu sama lain melalui pembentukan ikatan hidrogen sehingga menghasilkan campuran eutektik [13]. Secara umumnya, DES terdiri daripada kombinasi garam pepejal dan kumpulan penderma ikatan hidrogen pada perkadaran yang berbeza.

DES mempunyai ciri-ciri yang sama seperti cecair ionik bahkan ia mempunyai beberapa kelebihan lain [14] seperti proses penyediaan yang mudah dalam keadaan tulen, tidak reaktif terhadap air dan sebahagiannya bersifat biodegradasi. Selain itu, DES merupakan pelarut hijau yang larut dalam air, tidak mudah terbakar dan tidak mudah meruap. Ciri-ciri ini menjadikan DES berpotensi sebagai pelarut yang efektif untuk proses pelarutan sempurna dan pelarut pengekstrakan sebatian berkutub dan tidak berkutub. Nu'man et al. [15] telah mengkaji penggunaan DES terbitan tiga jenis asid karboksilik sebagai pelarut pengekstrakan sebatian vitamin E melalui kaedah pengekstrakan cecair-cecair (LLE). Penggunaan DES menunjukkan kecekapan pengekstrakan yang lebih baik berbanding pelarut organik konvensional. Tambahan pelarut ini juga boleh di kitar dan diguna semula dalam proses pengekstrakan.

Dalam kajian ini, DES relina digunakan sebagai pelarut pengekstrakan sebatian *α*-T. Rajah 1 (a) dan 1(b) menunjukkan struktur *α*-T dan DES relina. DES relina merupakan pelarut homogen yang terdiri daripada campuran garam ammonium kuarterner (kolin klorida, ChCl) dan penderma ikatan hidrogen (urea) yang dihasilkan pada nisbah 1:2 dengan pengacauan dan pemanasan pada suhu 85 ºC.

Walaubagaimanapun, kelikatan DES relina yang tinggi merupakan halangan untuk sebatian *α*-T berinteraksi dengan molekul pelarut ini. Oleh itu, kajian ini dijalankan bagi menentukan keadaan pengekstrakan terbaik bagi mengekstrak sebatian *α*-T secara optimum dengan mengkaji kesan kelikatan DES relina pada lima nisbah DES relina yang berbeza dengan masa pengekstrakan (2 dan 3 jam) terhadap kepekatan ekstrak sebatian *α*-T.

Bahan dan Kaedah

Bahan kimia

Minyak sawit mentah diperoleh daripada Sime Darby Berhad Malaysia manakala bahan kimia yang digunakan dalam kajian ini merupakan kolin klorida, asetonitril gred HPLC dan gred analisis, heksana, metanol, urea dan piawai *α*-T (95.5%). Kesemua bahan kimia diperoleh daripada R&M kecuali piawai *α*-Tyang diperoleh daripada Sigma Aldrich.

Penyediaan DES relina

DES relina disediakan dengan mencampurkan kolin klorida (ChCl) dan urea pada nisbah molar 1:2. Campuran ini dipanaskan pada suhu 85 °C sambil dikacau menggunakan pengacau magnet sehingga larutan menjadi homogen dan tidak berwarna terbentuk [16].

Pengekstrakan α-Tokoferol

Bagi nisbah 1:1 CPO kepada DES relina, 10 g CPO dilarutkan dalam 100 mL heksana manakala 10 g DES dilarutkan dalam 100 mL metanol. Kedua-dua bahan ini dicampurkan dalam kelalang kon 250 mL yang dibalut dengan kerajang aluminium dan dikacau selama 2 jam. Campuran ini seterusnya dipindahkan ke dalam corong pemisah dan dibiarkan seketika untuk membentuk dua lapisan. Lapisan DES kemudian dicampurkan dengan campuran heksana-air (1:4) sebelum fasa tokol-heksana dipisahkan daripada pelarut DES. Isi padu fasa tokol-heksana diukur dan dipindahkan ke dalam vial yang dibalut dengan kerajang aluminium dan produk disimpan pada suhu -4°C sebelum dianalisis menggunakan kromatografi cecair prestasi tinggi fasa berbalik (RP-HPLC). Pengekstrakan diulang dengan menggunakan nisbah CPO kepada DES yang berbeza iaitu 1:2, 1:3, 1:4 dan 1:5. Kelima-lima nisbah ini dikaji pada masa pengekstrakan 2 dan 3 jam. Setiap pengekstrakan yang dilakukan mestilah dalam keadaan terhindar daripada cahaya. Langkah ini penting bagi mengelakkan degradasi sebatian *α*-T kerana sifatnya yang sensitif terhadap cahaya dan udara. Eksperimen bagi kawalan pengekstrakan diulang tanpa penggunaan DES relina.

Analisis struktur DES relina

Elusidasi dan analisis DES relina dilakukan dengan menggunakan kaedah spektroskopi resonans magnetik nukleus (NMR) dan spektroskopi inframerah transformasi Fourier (FTIR). Sampel urea dan DES relina dilarutkan dengan pelarut dimetilsulfoksida (DMSO) yang terdeuterat- d_6 bagi analisis NMR satu dimensi (1D), (^{1}H dan ^{13}C). Selain itu, struktur DES relina juga ditentukan melalui mod dua dimensi (2D) iaitu NOESY dan HMQC. Analisis melalui spektroskopi FTIR adalah melalui mod ATR. Spektrum DES relina daripada kedua-dua kaedah spektroskopi dibandingkan dengan spektrum penderma ikatan hidrogen urea.

Analisis kelikatan DES relina

DES relina 10 g, 20 g, 30 g, 40 g dan 50 g mengikut nisbah 1,2,3,4 dan 5 masing-masing disediakan di dalam bikar. Kelima-lima sampel pelarut ini masing-masing dilarutkan ke dalam 100 mL metanol. Kemudian, kelikatan kelima-lima sampel larutan ini dikaji menggunakan viskometer (spindel bernombor 3 selama 1 minit dengan kelajuan 100 rpm). Kelikatan setiap sampel dicatat dalam unit cP dan setiap kelikatan sampel diukur sebanyak 3 kali.

Analisis kandungan α-T

Sistem HPLC Agilent yang terdiri daripada autosampel dan pisahan C_{18} Waters berdiameter 4.6μm dengan panjang 250 mm. Pengesan UV digunakan pada panjang gelombang 292 nm bagi mengesan pemisahan sampel. Asetonitril: air digunakan dalam sistem ini sebagai fasa bergerak pada nisbah 95:5 dengan kadar alir 1.0 $mLmin^{-1}$ pada suhu bilik (30 °C). Graf kalibrasi sebatian *α*-T diplotkan menggunakan lima siri larutan piawai α-T (2.5, 10, 30, 40 dan 80 ppm). Kepekatan sebatian *α*-T dihitung melalui persamaan (1) dan (2) yang dilaporkan oleh Nu'man et al. [15] manakala bagi peratus hasil ekstrak (%) dihitung melalui persamaan (3).

$$C_i = 1/G \times A_i \times D_i \qquad (1)$$

di mana, C_i = kepekatan tokoferol (mg/L), G = faktor gerak balas daripada regrasi plot linear, A_i = keluasan sampel, D_i = faktor pencairan, ditakrifkan sebagai berat sampel per isi padu pencairan.

$$D_i = v_i/v_f, \qquad (2)$$

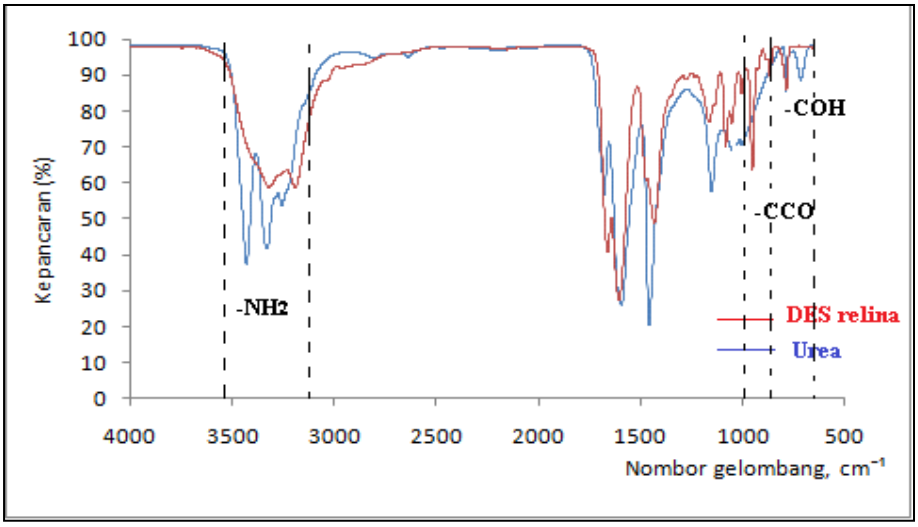
di mana, v_i = isi padu sampel (mL), v_f = isipadu sampel esktrak (mL)

$$\text{Peratus hasil ekstrak (\%)} = \frac{[\text{Kepekatan tokoferol } C_i \times \text{ Isi padu akhir ekstrak (L)}]}{10000 \text{ mg}} \times 100\ \% \qquad (3)$$

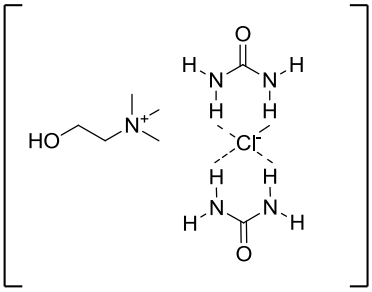
Hasil dan Perbincangan

Ikatan hidrogen dalam Struktur DES relina

DES relina yang disediakan dalam kajian ini menunjukkan bahawa terdapat interaksi antara kolin klorida (ChCl) dan urea melalui ikatan hidrogen. Daripada spektrum perbandingan FTIR (Rajah 2), tiga jalur serapan –NH dalam spektrum urea lebih tajam berbanding dua jalur serapan –NH dalam sampel DES relina. Menurut Pavia et al. [17], amina primer –NH dalam keadaan pepejal menghasilkan jalur getaran yang kuat disebabkan oleh perubahan fasa pepejal urea kepada fasa cecair DES relina. Spektrum FTIR DES relina menunjukkan jalur serapan yang lebih lebar kerana jalur serapan –OH dalam struktur ion kolin, Ch^+ bertindih dengan puncak serapan $–NH_2$. Pertindihan ini disebabkan oleh kumpulan -OH dan –NH berada pada julat nombor gelombang yang sama iaitu sekitar 2500 cm^{-1} hingga 4000 cm^{-1} [17]. Selain itu, kewujudan ikatan hidrogen antara ion klorida Cl^- dan $–NH_2$ dalam struktur DES relina seperti Rajah 3 menyebabkan jalur serapan teranjak kepada julat nombor gelombang yang lebih kecil [18]. Kewujudan ikatan ini disokong kajian oleh Zaira [19] yang menyatakan bahawa pembinaan ikatan hidrogen antara dua komponen ini adalah melalui proton amina sekunder dengan anion Cl^-. Kesemua jalur serapan yang ditunjukkan oleh spektrum FTIR urea wujud dalam spektrum FTIR DES relina. Namun, bentuk dan intensiti jalur serapan yang ditunjukkan bagi kedua-dua spektrum adalah berbeza. Perbezaan ini menunjukkan berlakunya interaksi melalui percampuran kolin klorida dan urea bagi penghasilan DES relina.

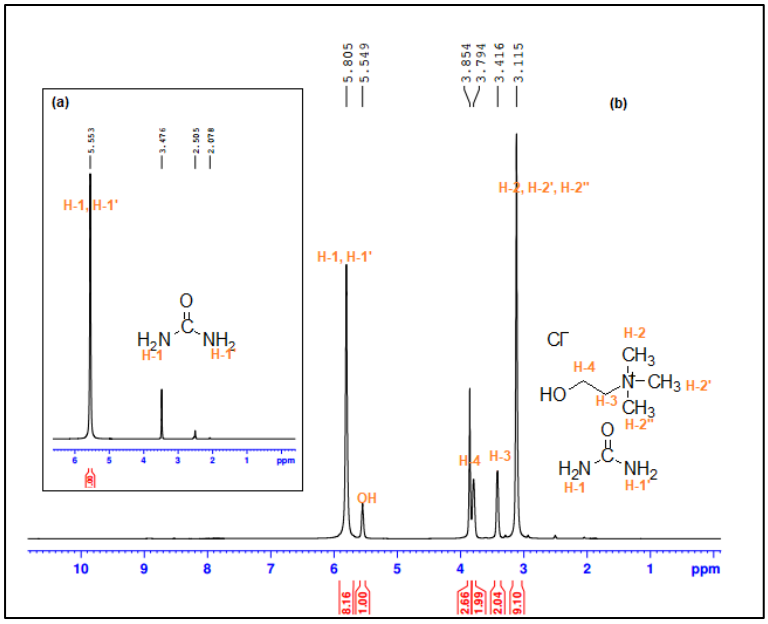


Rajah 2. Perbandingan spektrum FTIR-ATR antara urea dan DES relina

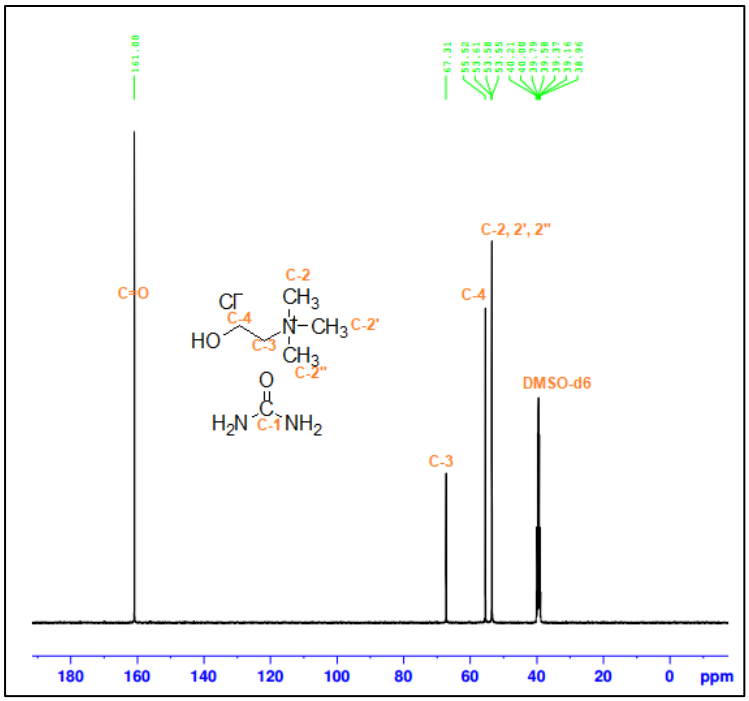


Rajah 3. Ikatan hidrogen yang terbentuk dalam struktur DES relina

Struktur DES relina juga disokong melalui spektrum ^{1}H-NMR (Rajah 4(b)) di mana terdapat lapan proton sekitar anjakan kimia 3.15 ppm sehingga 5.81 ppm yang mewakili proton urea dan kolin klorida. Anjakan kimia pada 5.81 ppm (Rajah 4 (a)) mewakili proton amina bagi dua molekul urea dan selebihnya mewakili proton kolin klorida. Selain itu, DES relina yang dihasilkan dalam kajian ini juga menunjukkan spektrum DES relina yang sama seperti kajian yang dilakukan oleh Lobo dan Rennet [20]. Tambahan, kelebaran bentuk puncak spektrum ^{1}H-NMR bagi sampel DES relina ini sama seperti kajian yang dilakukan oleh D'Agostino et al. [21] dan kelebaran puncak proton ini adalah disebabkan oleh kelikatan DES relina yang tinggi [21]. Rajah 5 menunjukkan ^{13}C-NMR DES relina dan didapati empat karbon sekitar anjakan 53 ppm sehingga 161 ppm, dimana anjakan kimia pada 161 ppm mewakili karbon pada urea dan anjakan kimia selebihnya (53.58 ppm, 55.52 ppm, 67.31 ppm) mewakili karbon dalam kolin klorida.



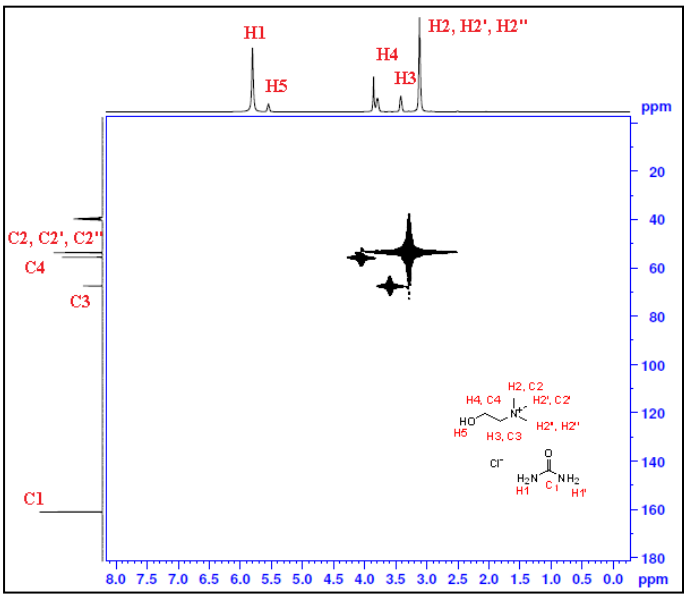
Rajah 4. Spektrum ^{1}H-NMR (a) urea dan (b) DES relina



Rajah 5. Spektrum ^{13}C-NMR DES relina

Daripada perbandingan spektrum FTIR-ATR, ^{1}H-NMR dan ^{13}C-NMR urea dan DES relina, didapati bahawa tiada kemusnahan bagi struktur urea. Analisis 2D HMQC juga menunjukkan interaksi langsung antara proton dan karbon yang terdapat pada struktur DES relina (Rajah 6). Berdasarkan spektrum NMR 2D, interaksi atom karbon dan hidrogen pada struktur ion kolin, Ch^{+} menunjukkan molekul ini tidak musnah semasa proses penghasilan DES

relina [22]. Selain itu, spektrum yang ditunjukkan menepati struktur DES relina di mana hanya terdapat interaksi langsung antara atom karbon dan hidrogen bagi ion Ch^+ manakala bagi molekul penderma ikatan hidrogen urea tiada interaksi yang ditunjukkan kerana atom karbon tidak terikat kepada hidrogen secara langsung (C1 dan H1).



Rajah 6. Spektrum HMQC bagi DES relina

Kesan kelikatan DES relina ke atas pengekstrakan α-Tokoferol

Pengekstrakan cecair-cecair (LLE) memerlukan pembentukan dua fasa bagi membolehkan pemisahan berlaku. DES relina merupakan sebatian hidrofilik kerana ciri pensolvatan yang baik dengan pelarut air. Salah satu ciri pelarut yang digunakan dalam pengekstrakan bagi penghasilan produk yang optimum adalah kelikatan [23]. Oleh sebab kelikatan DES lebih tinggi berbanding pelarut konvensional organik [24], proses pelarutan DES relina ke dalam pelarut metanol dilakukan sebelum pengekstrakan. Proses pelarutan ini bertujuan bagi mengurangkan kelikatan pelarut dan memperbaiki pekali taburan dalam kedua-dua komponen [25]. Proses ini penting bagi membolehkan molekul *α*-T tersebar ke dalam pelarut DES relina ini.

Menurut Duran et al. [24], kelikatan suatu DES terhasil daripada rangkaian ikatan hidrogen, Van der Waals dan juga interaksi elektrostatik. Kelikatan DES adalah disebabkan oleh kehadiran rangkaian ikatan hidrogen yang tinggi antara komponen DES sehingga mengurangkan pergerakan spesies ion bebas dalam struktur pelarut DES sendiri [13, 26]. Menurut Zhang et al. [13], saiz ion yang besar dan isi padu bebas yang kecil juga salah merupakan satu faktor peningkatan kelikatan pelarut DES. Oleh itu, penyelidik menggunakan teori kelompangan bagi mengurangkan kelikatan DES melalui penggunaan komponen DES yang mempunyai saiz spesies ion bebas yang lebih kecil bagi meningkat isi padu bebas yang diperlukan untuk spesies ion bebas ini bergerak dalam struktur DES sendiri [27].

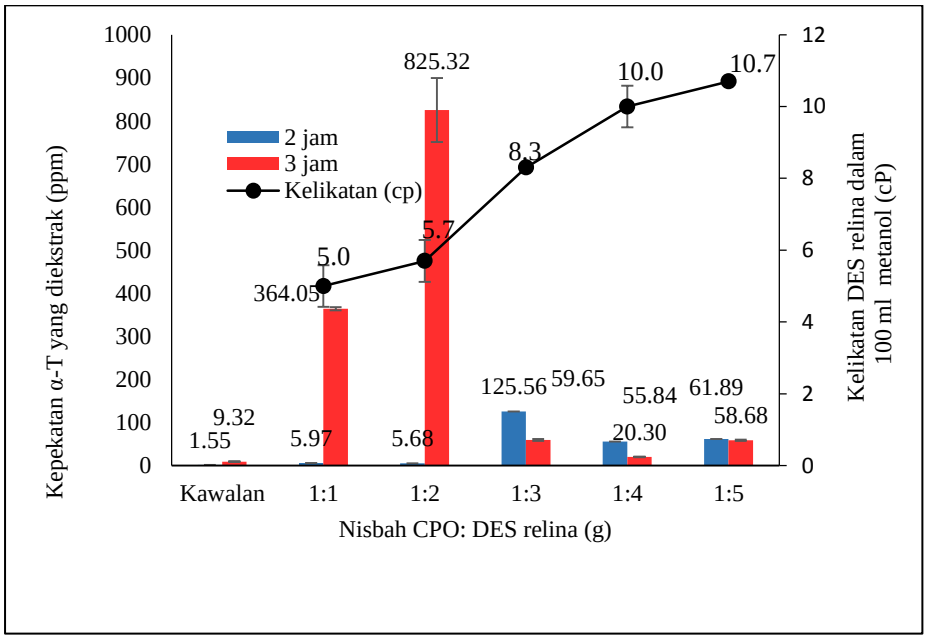
Ujian kelikatan bagi setiap nisbah DES relina yang digunakan dalam pengekstrakan dilakukan bagi mengetahui kesan kelikatan DES relina ke atas kepekatan dan peratus hasil ekstrak *α*-T. Kelikatan DES relina yang dihasilkan pada nisbah 1:2 (kolin klorida: urea) adalah 169 cP [27]. Berdasarkan Jadual 1, kelikatan bagi semua nisbah DES yang dikaji menunjukkan bacaan jauh lebih rendah iaitu <<<169 cP. Penurunan bacaan kelikatan DES relina ini disebabkan oleh pelarutan pelarut ini ke dalam 100 mL metanol. Proses pelarutan DES relina telah meningkatkan isi padu bebas dan meningkatkan pergerakan spesies ion bebas dalam struktur pelarut ini.

Jadual 1.Kelikatan bagi lima nisbah DES relina yang digunakan dalam pengekstrakan α- T

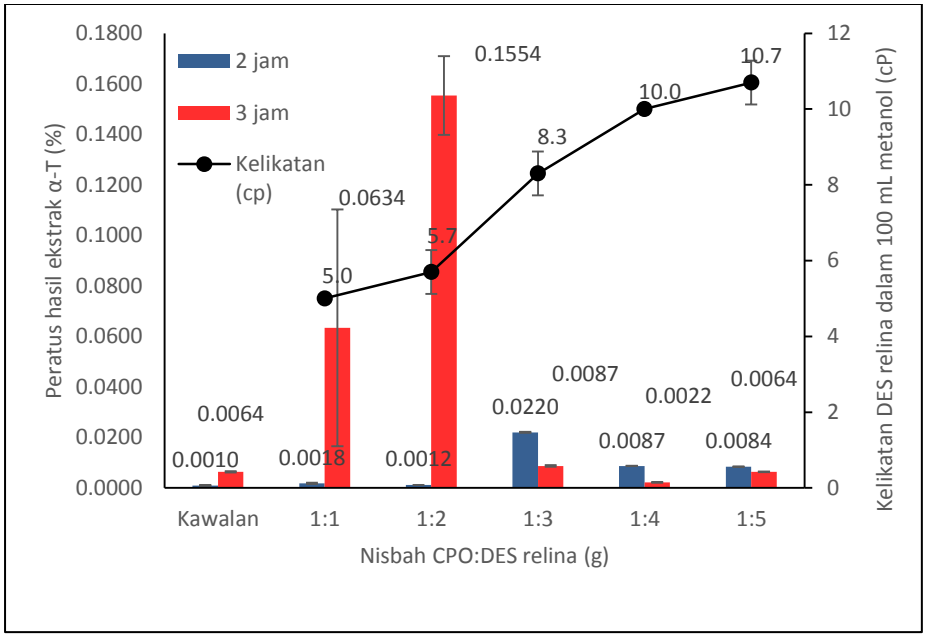
Nisbah DES Relina (g)	**Bacaan Kelikatan Viskometer (cP)**			**Kelikatan DES Relina dalam 100 mL Pelarut Metanol (cP)**
	Replikat 1	**Replikat 2**	**Replikat 3**	
1	5.0	5.0	5.0	5.0 ± 0.00
2	5.0	6.0	6.0	5.7 ± 0.58
3	8.0	8.0	9.0	8.3 ± 0.58
4	10.0	10.0	10.0	10.0 ± 0.00
5	10.0	11.0	11.0	10.7 ± 0.58

Merujuk Jadual 1, kelikatan pelarut semakin meningkat apabila nisbah DES relina ditingkatkan. Hasil kajian kelikatan menunjukkan peningkatan dalam kuantiti DES relina yang dilarutkan ke dalam 100 mL pelarut metanol menyebabkan semakin banyak molekul DES relina di dalam struktur pelarut metanol. Kelikatan pelarut berkait rapat dengan isi padu teori kelompangan, penyebaran atau pergerakan ion dan perubahan intermolekul [21, 27]. Selain itu, setiap nisbah DES relina dengan kelikatan yang berbeza menunjukkan kepekatan (mg/ml) *α*-T dan peratus hasil ekstrak (%) *α*-T yang berbeza-beza.

Merujuk Rajah 7 dan Rajah 8, nisbah 2 DES relina dengan kelikatan 5.7 ± 0.58 cP merupakan nisbah yang menunjukkan kandungan *α*-T (825.321 ± 74.27 mg/L) dan peratus hasil ekstrak (0.1554 ± 0.0156%) yang optimum pada masa pengekstrakan 3 jam. Bagi masa pengekstrakan 2 jam, nisbah 3 DES relina dengan kepekatan 8.3 ± 0.58 cP menunjukkan kepekatan *α*-T yang paling tinggi. Ini menunjukkan, pemerolehan sebatian *α*-T optimum bagi kedua-dua masa pengekstrakan adalah pada nisbah DES relina yang berbeza. Perbezaan yang ditunjukkan mungkin disebabkan oleh faktor penyebaran molekul *α*-T ke dalam struktur pelarut dan tempoh bagi menghasilkan interaksi yang optimum dengan molekul pelarut DES relina.



Rajah 7. Kepekatan *α*-T yang diekstrak menggunakan nisbah DES relina dan kelikatan yang berbeza

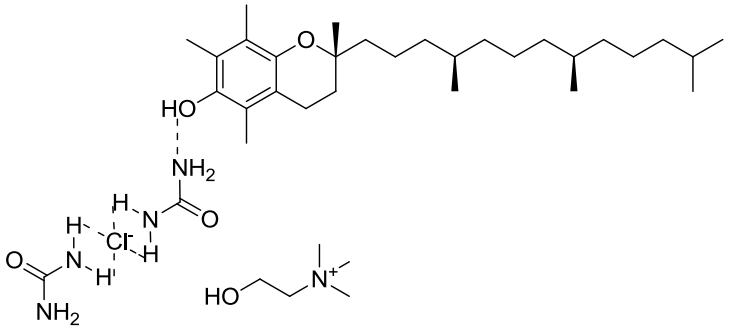


Rajah 8. Peratus hasil ekstrak sebatian α-T (%) menggunakan nisbah DES relina dan kelikatan yang berbeza

Selain itu, Rajah 7 dan Rajah 8 juga menunjukkan pola graf yang sama sekitar nisbah 3 DES relina hingga 5 di mana berlakunya pengurangan kepekatan α-T dan hasil ekstrak pada nisbah 3 DES relina kepada 4 dan seterusnya berlaku peningkatan semula pada nisbah 5 DES relina bagi kedua-dua masa pengekstrakan. Di samping itu juga terdapat perbezaan yang ketara pada nisbah 3 hingga 5 DES relina apabila membandingkan kedua-dua masa pengekstrakan. Perbezaan ini dapat dilihat melalui pengurangan kepekatan sebatian α-T yang diekstrak dari 2 jam kepada 3 jam masa pengekstrakan.

Pengurangan sebatian α-T yang berlaku ini jelas menunjukkan bahawa sebatian ini lebih cenderung untuk terperangkap dalam fasa minyak. Ini adalah disebabkan oleh struktur sebatian α-T dengan rantai yang panjang dan tahap kekutuban yang lemah [28]. Pengurangan kepekatan α-T yang ditunjukkan juga disebabkan oleh isi padu bebas dalam struktur pelarut yang terhad bagi membolehkan lebih banyak molekul α-T tersebar dan berinteraksi dengan pelarut DES relina. Isi padu bebas dalam struktur pelarut DES relina adalah penting kerana saiz molekul α-T yang besar memerlukan ruang yang sesuai untuk molekul ini dan molekul pelarut berinteraksi. Selain itu, pada nisbah 3 DES relina kepada 5 menunjukkan masa pengekstrakan 2 jam lebih sesuai berbanding 3 jam. Walaubagaimanapun, masa pengekstrakan 3 jam dengan nisbah 2 DES relina menghasilkan kepekatan sebatian α-T yang paling maksimum.

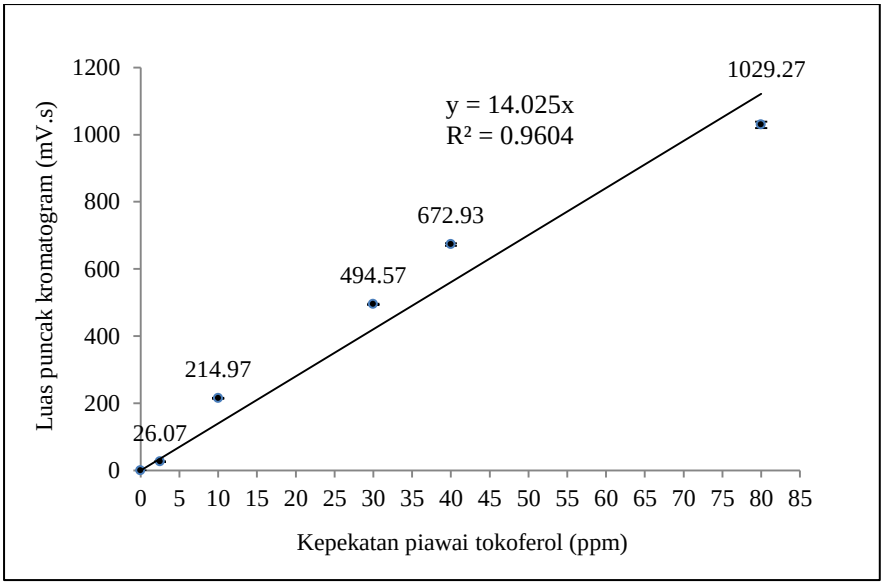
Masa pengekstrakan 3 jam menunjukkan masa ideal bagi menghasilkan interaksi maksimum antara sebatian α-T dan molekul pelarut pada nisbah 2 DES relina. Keadaan DES relina pada nisbah 2 membolehkan lebih banyak molekul α-T tersebar ke dalam ruang-ruang kosong pelarut dan berinteraksi antara satu sama lain melalui ikatan hidrogen yang ditunjukkan seperti dalam Rajah 9. Ikatan hidrogen yang terhasil ini merupakan analog daripada kajian yang telah dilakukan oleh Xiaolei et al. [25]. Kajian oleh Dai et al. [29] juga menunjukkan bahawa anion Cl^- pada struktur DES relina berpotensi untuk berinteraksi dengan sebatian α-T [29] melalui ikatan hidrogen. Walaubagaimanapun, pembentukan ikatan hidrogen yang kuat lebih cenderung berlaku pada kumpulan hidroksil, -OH bagi molekul α-T kerana kumpulan ini memberikan keasidan ikatan hidrogen yang tinggi [25] untuk berinteraksi dengan pelarut DES relina (kebesan ikatan hidrogen). Pembentukan ikatan hidrogen yang kuat antara molekul α-T dan DES relina ini membolehkan pemisahan sebatian α-T daripada fasa minyak.



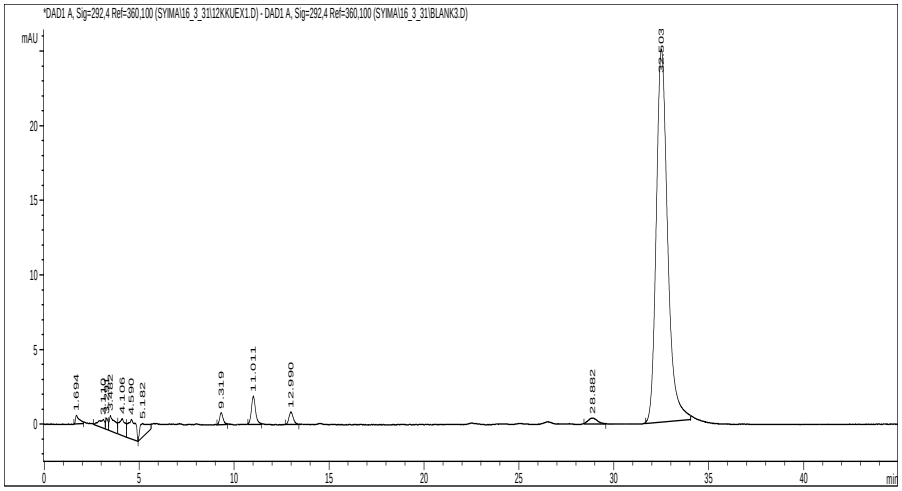
Rajah 9. Analog ikatan hidrogen yang terhasil antara sebatian α- T dan DES relina yang dirujuk daripada kajian Xiaolei et al [25]

Melalui kajian ini, jelas menunjukkan bahawa kelikatan bagi setiap nisbah DES relina dan masa pengekstrakan mempengaruhi kandungan α-T yang diekstrak. Walaubagaimanapun, nisbah DES relina yang tinggi menunjukkan kepekatan α-T yang rendah. Ini disebabkan oleh pergerakan dan penyebaran molekul α-T ke dalam struktur pelarut adalah terbatas. Jadi, interaksi antara kedua-dua molekul ini semakin sukar.

Kepekatan sebatian α-T yang diekstrak bagi kesemua sampel dihitung dengan menggunakan kaedah yang telah dilaporkan oleh Nu'man et al. [15] dengan merujuk graf kalibrasi bagi lima siri kepekatan piawai α-T yang telah disuntik ke dalam HPLC seperti Rajah 10. Kesemua sampel piawai menunjukkan masa penahanan sekitar 32.503 ± 2.00 min. Berdasarkan kromatogram yang ditunjukkan dalam Rajah 11, masa penahanan sebatian α-T menunjukkan bahawa sebatian α-T merupakan sebatian yang mempunyai tahap kekutuban yang rendah kerana tempoh penahanan sebatian α-T adalah lama. Masa penahanan sebatian terelusi daripada kolum adalah bergantung pada sifat kekutubannya. Sebatian yang mempunyai kekutuban yang tinggi akan mudah dielusi dan masa penahanannya pada fasa pegun adalah lebih singkat.



Rajah 10. Graf kalibrasi piawai α-T dengan pekali penentuan, R^2 = 0.960 dan faktor gerak balas, G = 14.02 mV.s $mg^{-1}L$



Rajah 11. Kromatogram bagi sampel ekstrak menunjukkan sebatian α-T terelusi pada 32.503 minit

Kesimpulan

DES berpotensi sebagai pelarut pengekstrakan hijau alternatif kerana keupayaannya untuk berinteraksi dengan sebatian dan membentuk sistem dwifasa. Melalui kajian ini, kecekapan DES relina (ChCl-urea) sebagai pelarut pengekstrakan sebatian *α*-T dikaji dengan menggunakan lima siri nisbah CPO: DES relina pada masa pengekstrakan 2 dan 3 jam. Melalui hasil kajian ini, kelikatan DES relina sangat memberi kesan ke atas kecekapan pengekstrakan dan kandungan *α*-T yang diekstrak. Kecekapan pengekstrakan yang ditunjukkan oleh pelarut ini menjadikan DES relina sesuai sebagai pelarut alternatif dalam pengekstrakan sebatian *α*-T. Penggunaan pelarut ini selama 3 jam pengekstrakan pada nisbah CPO:DES relina (1:2) dengan kelikatan DES relina dalam 100 mL metanol 5.7 ± 0.58 cP memberikan hasil kandungan *α*-T yang optimum iaitu sebanyak 825.321 ± 74.27 mg/L dengan peratus hasil ekstrak 0.1554 ± 0.0156% (w/w). Keupayaan sebatian ini membentuk ikatan hidrogen dengan kumpulan –OH dan $–NH_2$ pada molekul DES relina membolehkan pemisahan *α*-T daripada fasa tidak berkutub CPO ke fasa berkutub DES berlaku.

Penghargaan

Ribuan terima kasih ditujukan kepada Universiti Kebangsaan Malaysia dan Kementerian Pendidikan Tinggi, Malaysia atas kemudahan dan geran penyelidikan (FRGS/1/2014/ST01/UKM/02/1, GUP-2017-014) yang disalurkan. Selain itu, ribuan terima kasih diucapkan kepada Pusat Pengajian Sains Kimia dan Teknologi Makanan Fakulti Sains dan Teknologi, UKM dalam menyediakan kemudahan dan alat instrumen bagi memudahkan penyelidikan ini dijalankan.

Rujukan

1. Mazlan, M., Wan Ngah, W. Z., Mat Top, G. and Then, S. M. (2010). Comparison of the effects of *A*-tocopherol and *Γ*-tocotrienol against oxidative stress in two different neuronal cultures. *Sains Malaysiana*,39:145-56.
2. Top, N. M. H. G. M., Ngan, C. Y. M. M. A., Ma, N. M. H. Y. M. and Wahid, A. N. M. B. (2006). Palm tocols (tocopherols and tocotrienols) as a standard reference materials (MRM 3). Bangi: Malaysian Palm Oil Board, Ministry of Plantation Industries and Commodities, Malaysia.
3. Goh, S. H., Choo, Y. M. and Ong, S. H. (1985). Minor constituents of palm oil. *Journal of the American Oil Chemists' Society,* 62(2): 237-240.
4. Ng, M. H, Choo, Y. M., Ma, A. N., Chuah, C. H. and Hashim, M. A. (2004). Separation of vitamin E (tocopherol, tocotrienol, and tocomonoenol) in palm oil. *Lipids*, 39(10): 1031-1035.
5. Ng, M. H., Choo Y. M., Ma A. N., Chuah C. H. and Hashim, M. A. (2004). Isolation of palm tocols using supercritical fluid chromatography. *Journal of Chromatographic Science,* 42(10):1031-1035.

6. Choo, Y. M., Ng, M. H., Ma, A. N., Chuah, C. H. and Hashim, M. A. (2005). Application of supercritical fluid chromatography in the quantitative analysis of minor components (carotenes, vitamin e, sterols, and squalene) from palm oil. *Lipids*,40(4): 429-432.
7. Goossens, B. and Marion, J. (2011). Quantifying vitamin E in vegetable oils with reversed-phase high performance liquid chromatography. *Journal of Analytical Chemistry*, 2: 44-50.
8. Ruperez, F. J., Martın, D., Herrera, E. and Barbas, C. (2001). Chromatographic Analysis of Alpha-Tocopherol and Related Compounds in Various Matrices. *Journal of chromatography A,935*(1): 45-69.
9. Sanagi, M. M., See, H. H., Ibrahim, W. A. W., and Naim, A. A. (2005). Determination of carotene, tocopherols and tocotrienols in residue oil from palm pressed fiber using pressurized liquid extraction-normal phase liquid chromatography. *Analytica Chimica Acta*, 538(1–2): 71-76.
10. Johnson, L. A. and Lusas, E. W. (1983). Comparison of alternative solvents for oils extraction. *Journal of the American Oil Chemists' Society*, 60(2): 229-242.
11. Nam, M. W., Zhao, J., Lee, M. S., Jeong, J. H. and Lee, J. (2015). Enhanced extraction of bioactive natural products using tailor-made deep eutectic solvents: application to flavonoid extraction from *FlosSophorae*. *Green Chemistry*, *17*(3):1718-1727.
12. Hayyan, M., Mjalli, F. S., Hashim, M. A. and AlNashef, I. M. (2010). A novel technique for separating glycerine from palm oil-based biodiesel using ionic liquids. *Fuel Process Technology*, 91: 116-120.
13. Zhang, Q., Vigier, D. O., Royer, K., S. and Jerome, F. (2012). Deep eutectic solvents: Syntheses, properties and applications. *Chemical Society Reviews*, 41(21): 7108-7146.
14. Abbott, A. P., Cullis, P. M., Gibson, M. J. Harris R. C. and Raven E. (2007). Extraction of gylcerine from biodiesel into eutectic based ionic liquid. *Green Chem*istry, 9: 868-872.
15. Nu'man, A. H., Ng, M., Choo, Y., Hashim, M. and Jayakumar, N. (2015). Performance of choline-based deep eutectic solvents in the extraction of tocols from crude palm oil. *Journal of American Oil Chemical Society*, 92(11-12): 1709-1716.
16. Cvjetko, B. M., Ćurko, N., Tomašević, M., Kovačević Ganić, K. and Radojčić Redovniković, I. (2016). Green extraction of grape skin phenolics by using deep eutectic solvents. *Food Chemistry*, 200: 159-166.
17. Pavia, L. D., Lampman, M. G., Kriz, S. G. and Vyvyan, R. J. (2009). Introduction to spectroscopy. Brooks/Cole Cengage Learning, 4rd Ed. Canada: Lisa Lockwood.
18. Qamar, A. and Leo, B. (2011). Anodic dissolution of refractory metals in choline chloride based binary mixtures. *The Electrochemical Society ECS Transactions*, 33(30): 57-67.
19. Zaira, M. (2014). Deep eutectic solvents: Properties and biocatalytic applications. Thesis PhD, University (Rheinisch-Westfälische Technische Hochschule Aachen), Germany.
20. Lobo, R. H. (2013). Synthesis of novel colorants for dye-sensitized solar cells and use of greener protocols for heterocyclic synthesis. Thesis PhD. Institute of Chemical Technology, India.
21. D'Agostino, C., Gladden, L. F., Mantle, M. D., Abbott, A. P., Essa, I. A., Al-Murshedi, A. Y. and Harris, R. C. (2015). Molecular and ionic diffusion in aqueous–deep eutectic solvent mixtures: Probing inter-molecular interactions using PFG NMR. *Physical Chemistry Chemical Physics*, 17(23): 15297-15304.
22. Yue, D., Jia, Y., Yao, Y., Sun, J. and Jing, Y. (2012). Structure and electrochemical behavior of ionic liquid analogue based on choline chloride and urea. *Electrochimica Acta*, 65: 30-36.
23. Dai, Y., Van S., J., Witkamp, G.-J., Verpoorte, R. and Choi, Y. H. (2013). Ionic liquids and deep eutectic solvents in natural products research: Mixtures of solids as extraction solvents. *Journal of Natural Products*, 76(11): 2162-2173.
24. Durand, E., Lecomte, J. and Villeneuve, P. (2013). Deep eutectic solvents: Synthesis, application, and focus on lipase-catalyzed reactions. *European Journal of Lipid Science and Technology*, 115(4): 379-385.
25. Xiaolei, N., Xing, H., Yang, Q., Wang, J., Su, B., Bao, Z. and Ren, Q. (2012). Selective liquid–liquid extraction of natural phenolic compounds using amino acid ionic liquids: a case of α-tocopherol and methyl linoleate separation. *Industrial & Engineering Chemistry Research*, 51(18): 6480-6488.
26. Haiying, D. (2013). Low transition- temperature mixtures (LTTMs): New generation of designer solvents. Acess from http://ism2.univ-amu.fr/fichiers_pdf/seminaires-stereo/2013-07-15-biblio-2013-04-08-haiying-DU.pdf [23 March 2016].
27. Abbott, A. P., Glen, C. and Stephen, G. (2006). Design of improved deep eutectic solvents using hole theory. *European Journal of Chemical Physics and Physical Chemistry*, 7(4): 803-806.

28. Dubbs, M. D. and Gupta, R. B. (1998). Solubility of vitamin E (α-tocopherol) and vitamin K3 (menadione) in ethanol− water mixture. *Journal of Chemical & Engineering Data*, 43(4): 590-591.
29. Dai, Y, Van Spronsen, J., Witkamp, G. J., Verpoorte, R. and Choi, Y. H. (2013). Natural deep eutectic solvents as new potential media for green technology. *Analytica Chimica Acta*, 766: 61-68.

Malaysian Journal of Analytical Sciences, Vol 22 No 3 (2018): 404 - 415
DOI: https://doi.org/10.17576/mjas-2018-2203-05

MALAYSIAN JOURNAL OF ANALYTICAL SCIENCES
Published by The Malaysian Analytical Sciences Society
ISSN 1394 - 2506

ROOM TEMPERATURE SYNTHESIS OF CERIA BY THE ASSISTED OF CATIONIC SURFACTANT AND AGING TIME

(Sintesis Ceria Pada Suhu Bilik Dengan Bantuan Surfaktan Kation Dan Masa Penuaan)

Nor Aqilah Mohd Fadzil[1]*, Mohd Hasbi Ab. Rahim[1], Gaanty Pragas Maniam[2]

[1]*Faculty of Industrial Science & Technology*
[2]*Central Laboratory*
Universiti Malaysia Pahang, Lebuhraya Tun Razak,26300 Gambang, Kuantan, Pahang, Malaysia

**Corresponding author: Aqilah_mawaddah@yahoo.com*

Received: 14 January 2018; Accepted: 8 May 2018

Abstract

This paper presents the synthesis of rare earth cerium(IV) oxide (ceria) via simple precipitation method under room temperature. The two aims of this research are to: (i) synthesise a ceria-based material using simple process and chemicals and (ii) modify the ceria-based material with environmentally friendly elements. In this study, cerium nitrate hexahydrate and sodium hydroxide were utilised as the precursor and precipitant, respectively, to attain desired crystallite size and shape, at a fixed reaction pH of 12. Besides that, common cationic surfactant, cetyl-tri-methyl-ammonium bromide (CTAB), was used to enhance ceria-based material's coveted properties. Furthermore, addition of surfactant and aging time (30 minutes, and 5, 10, 20, and 30 days) were also examined. Findings showed that as aging time increased, crystallite size decreased and production of large agglomerations were not observed. Then, optimum aging time was applied for synthesis of ceria material and modified ceria material, Fe-CeO_2/TiO_2, *via* impregnation method. These materials were subjected to X-ray diffraction (XRD), CO_2-Temperature-Programmed Desorption (CO_2-TPD), and Field Emission Scanning Electron Microscopy (FESEM) to investigate the mutual effect of surfactant addition and aging time.

Keywords: cationic, ceria, crystallite, precipitating, surfactant

Abstrak

Kajian ini menggambarkan sintesis salah satu unsur nadir bumi iaitu cerium(IV) oksida (ceria), melalui kaedah pemendakan pada suhu bilik. Matlamat kajian ini ialah: (i) sintesis bahan berasaskan ceria menggunakan proses dan bahan kimia yang mudah dan (ii) mengubahsuai bahan berasaskan ceria dengan penambahan unsur-unsur mesra alam. Dalam kajian ini, cerium nitrat heksahidrat dan natrium hidroksida telah digunakan sebagai bahan pemula dan agen pemendakan, supaya saiz dan bentuk yang dikehendaki dapat diperolehi pada pH yang telah ditetapkan iaitu pH 12. Selain itu, bahan tipikal surfaktan kation, cetil-tri-metil-ammonium bromida (CTAB), telah digunakan untuk memudahkan penghasilan bahan berasakan ceria dengan sifat-sifat yang dikehendaki. Di samping itu, penambahan surfaktan dan kadar masa penuaan (30 minit, dan 5, 10, 20, dan 30 hari) turut dikaji. Hasil penemuan menunjukkan bahawa, apabila kadar masa penuaan ditingkatkan, saiz kristal berkurangan dan penghasilan gumpalan besar tidak ditemui. Justeru, kadar masa penuaan optima dipilih untuk sintesis bahan ceria dan bahan ceria yang diubah suai, Fe-CeO_2/TiO_2, melalui kaedah impregnasi. Seterusnya, bahan-bahan ini dianalisis melalui sistem pembelauan sinar-X (XRD), program penjerap bersuhu-CO_2 (CO_2-TPD), dan mikroskop elektron pengimbas pancaran medan (FESEM) untuk mengkaji kesan penambahan surfaktan dan kadar masa penuaan.

Kata kunci: kation, ceria, kristal, pemendakan, surfaktan

Introduction

Rare earth elements are an interesting prospect for research due to its potential of application in many areas, including catalysis, UV absorbance, medical/bio-sensing, and gas and solar sensors [1, 2]. Cerium is one such element, possessing great prospects in the chemical-based industry. Its electronic configuration's versatility (Xe 4f1 5d1 6s2) is a unique feature that allows electrons to move freely from similar energy level orbitals between 4f1 and 5d1. This results in positive contributions, especially in catalytic reactions.

Moreover, upon combination with oxygen, cerium oxide (CeO_2; ceria) is formed, with a composition ratio of 1:2 (cerium; oxygen). This attributes for its oxygen storage capacity (OSC). Ceria can oxidise and/or reduce any material that comes into contact with its surface. Oxygen vacancy defects will immediately form, which is a necessity, especially during catalytic processes. A faster and increased formation of oxygen vacancy defects results in high OSC, making ceria a superior material for oxidation/reduction processes [3].

Ceria can be synthesised via various techniques, including ones involving surfactant media. By applying surfactant during synthesis, good properties pertaining to ceria's crystallite size and morphology can be facilitated, resulting in better performance in certain applications. Ceria prepared in a surfactant media forms a clear shape (e.g. sphere, nanorods) and possesses a significantly larger surface area (>130 m^2/g) compared to an analogue sample devoid of surfactant [4]. Thus, in the absence of surfactant during synthesis, an irregularly shaped ceria with a small surface area (≈50 m^2/g) was formed. Additionally, ceria preparation in a surfactant media is typically combined with specific aging time (<30 days). Generally, nanoparticle formation occurs in a short time, but application of aging time extends its growth. The particles will stack among themselves to grow directionally [5].

The formation of 1-D nanostructured ceria could be easily performed in the presence of a surfactant. This situation is termed soft template assisted. Apart from cetyl-tri-methyl-ammonium bromide (CTAB), other surfactants that can be used as a soft template are alkyltrimethylammonium salts, octadcylamine, and ethylenediamine. In the primary stage, addition of cerium precursor salts into a basic condition will form hydrous cerium oxide. Then, due to presence of the template, hydrous cerium oxide will react with organic molecules through exchange of OH^- group on the surface. Next, hydrous cerium oxide may undergo an exchange with either a cation or anion. Nevertheless, this process is pH dependent. Hence, if the pH is higher than the isoelectric point of hydrous cerium oxide (pH: 6.75 to 8.00), exchange of OH^- group with the surfactant's cation will take place [6, 7]. The higher surface area of Ce(IV) will result in a smaller nanoparticle size. Furthermore, presence of surfactant will also assist in oxidation of cerium(III) to cerium(IV) [8].

Surfactant addition can also manipulate the shape of 1-D ceria produced. Specifically, by controlling ratio of surfactant to cerium precursor, from 1.0:1.0 to 1.5:1.0, shape of ceria nanoparticles might change from spherical to nanorod. Nonetheless, this effort must be accompanied by well-controlled temperature, pH, and effective reaction time [9]. At a lower temperature, i.e. <150 °C, nanorod morphology cannot be formed. This is because temperature of <150 °C could not assist in nucleation growth of particles. Moreover, previous studies [10–12] that demonstrated the single step of producing ceria nanorod structure, revealed that it involves a complicated and non-environmentally friendly approach. This is due to high temperature (>150 °C) and long reaction time needed to yield ceria's nanorod structure.

In general, the morphology of 1-D nanostructured ceria could be briefly explained as follows. First, under a basic condition, cerium will be oxidised into hydrated Ce^{4+}. Then, this hydrated molecule readily reacts with CTAB surfactant, producing polymeric hydrous oxide. If the reaction pH is above the isoelectric point of ceria, i.e. above pH 8, polymeric hydrous oxide will react with alkylammonium salt. During this reaction, surfactant and deprotonated hydroxyl group will generate an inorganic/organic composite [13]. This composite is the primary cause for cerium oxide's high surface area (>100 m^2/g). Typically, products with a high surface area are formed due to efficient drying or calcination process. Therefore, during drying or calcination process, surfactant will play a key role in formation of nanostructured ceria. For example, a lower surfactant amount will usually result in a shorter length for ceria nanostructure [14].

The main role of a surfactant is to facilitate a favourable site for growth of particulate assemblies between cerium cation and surfactant micelle. This influences the morphology and formation processes like nucleation, growth, and coagulation. However, presence of surfactant alone is futile. Instead, it should be accompanied by aging time factor. Aging time varies from an hour up to a couple of weeks. Yang and Guo [15] suggested that a short aging time (30 minutes to 7 days) will induce the colloidal solution to predominantly contain Ce^{4+}. Meanwhile, for a long aging time (8 to 30 days), the colloidal solution will contain ceria nanoparticles and Ce^{4+}. Nevertheless, this situation may change based on different surfactant and reaction conditions applied.

As previously mentioned, with a long aging time, the oxidation state of cerium will change along with its particle size. Changes in oxidation state will modify adsorption capability and band gap measurement, resulting in different electrochemistry properties of ceria [16]. Nonetheless, an overlong aging time is undesirable, since the particles will start to disappear due to unstable condition. Besides that, if the colloidal solution is left too long for aging time purpose, the pH of the solution will turn acidic because of slow adsorption of CO_2 gas into it.

On the other hand, generation of ceria nanorod structure could still be achieved without addition of surfactants. Lin and Chowdhury [17] demonstrated the application of a well-known hydrothermal synthesis technique at a higher concentration of sodium hydroxide (pH >10). This method was conducted for 24 hours and successfully produced 1-D nanorod structure with 20–40 nm and 200–300 nm of diameter and length, respectively. Furthermore, this ceria nanorod structure was obtained through drying overnight in an oven at 60 °C followed by calcination at 300 °C for 3 hours, in the presence of air.

As such, this study incorporates both surfactant application and aging time for modification of ceria into Fe-CeO_2/TiO_2 nanoparticle. Ceria is typically used for active support, as numerous research findings have indicated that such a characteristic is due to strong metal-ceria surface defects bonding, which stabilises the metal catalyst [18–22]. In this situation, ceria-metal interface will exist through oxygen migration from the support to the metal and vice versa, resulting in an enhanced surface reaction (e.g. catalysis). Thus, applying ceria as the main element in Fe-CeO_2/TiO_2 nanoparticle is expected to boost oxygen migration and display excellent catalytic performance. However, this work will only focus on characteristics of the developed Fe-CeO_2/TiO_2 nanoparticles.

Materials and Methods

Cerium nitrate hexahydrate (Sigma-Aldrich, Missouri, USA) and sodium hydroxide (Sigma-Aldrich, Missouri, USA) were utilised as the precursor and precipitant agent, respectively. In settings requiring surfactant media, cationic surfactant CTAB (Sigma-Aldrich, Missouri, USA) was utilised, whereas metal loading and catalyst support were provided by iron nitrate hexahydrate (Sigma-Aldrich, Missouri, USA) and titanium dioxide (Sigma-Aldrich, Missouri, USA), respectively.

Synthesis of ceria nanoparticles *via* simple precipitation method

Simple precipitation technique was used to produce ceria nanoparticles. The concentration ratio of 3:1 (CTAB: cerium precursor) was prepared in 100 mL deionised water (DI), at pH 12 and at room temperature. Firstly, 6.5 g of CTAB was dissolved in 100 mL DI water, and then 2.6 g of cerium precursor was added with vigorous stirring. After the solution became homogeneous, precipitant sodium hydroxide solution (0.5 M) was added drop by drop until pH 12 was achieved. Subsequently, the solution was kept under vigorous stirring for 2 hours and left for aging (at t = 30 minutes and 3, 5, 10, 20, and 30 days). Finally, the solution was filtered and washed thrice using DI water, followed by drying in the oven for 3 hours at 70 °C.

Synthesis of Fe-CeO_2/TiO_2 nanoparticle *via* impregnation method

The modified ceria material, Fe-CeO_2/TiO_2, was synthesised using impregnation method, in which different total metal loadings of 0.5, 1.0, 3.0, and 5.0 wt.% were applied. First, 0.25 g of $FeCI_2.4H_2O$ was added to 30 mL DI water, with the solution being kept under vigorous stirring and mild heating (40 °C). Then, 1.9 g TiO_2 and ceria mixture were physically mixed and grinded before being added into the iron solution under vigorous stirring. Next, the reaction mixture was covered using an aluminium foil with many small holes and dried overnight in an oven at 100 °C. Before sending the sample for characterisation, it was first calcined using a horizontal furnace for 3 hours at 400 °C, with a heating rate of 40 °C/min.

Characterisation

The sample powder's crystallite size was obtained using Rigaku Miniflex X-ray Diffractometer (XRD). The X-ray of the Cu Kα radiation was filtered by a Ni filter with λ=1.54 Å, whereas Scherrer's formula (equation (1)) was utilised to determine crystallite size [22]. In Scherrer's formula, C indicates a numerical constant (≈0.9). The wavelength of X-ray was 1.5418 Å for Cu Kα radiation. Meanwhile, β and θ were the full width at half maximum (FWHM) in radians and diffraction angle for the peak, respectively.

$$\text{Crystallite size} = C\lambda / \beta\cos\theta \quad (1)$$

Morphological studies for the prepared sample were done using Field Emission Scanning Electron Microscope (FESEM), model JSM-8700F. The sample was coated with platinum and/or gold. Besides that, elemental analysis was conducted using Energy Dispersive X-ray Analysis (EDX) FEI Quanta 450, while CO_2-Temperature Programmed Desorption (CO_2-TPD) was carried out to examine the sample's surface basicity. TPDRO 1100 Series Thermo Finnigan was purged with helium gas before commencing analysis.

Results and Discussion

Percentage yield

Reaction time under vigorous stirring was set for 2 hours, however, no significant advantage in percentage yield was observed when time was extended to 4, 8, 24, and 48 hours. As shown in Table 1, reaction time did not greatly influence percentage yield of ceria nanoparticles, indicating that 2 hours is the optimum reaction time for the process. Results also indicated that stirring rate was proportional to percentage yield. A slow stirring rate showed a low percentage yield, while as it increased up to 1200 rpm, percentage yield increased twofold. Moreover, at the high stirring rate, the solution turned yellowish in colour. High stirring rate could have induced air circulation, which aided oxidation of Ce^{3+} to Ce^{4+} and subsequently led to formation of CeO_2 nanoparticles [23].

In contrast, a purple coloured solution was observed for slow stirring rate (450 rpm) regardless of reaction time, suggesting that less oxidation occurred. Oxidation typically occurs once air produced from strong agitation during stirring process converts Ce^{3+} to Ce^{4+}. Therefore, a higher stirring rate caused rigorous agitation of the solution, thus producing more air for consumption during oxidation process, allowing more conversion of Ce^{4+} from Ce^{3+}. Then, available Ce^{4+} combined with oxygen to form the yellow solid CeO_2 ceria. Equations (2)–(5) suggest several mechanisms for ceria nanoparticle formation, as follows:

$$4NaOH(s) \rightarrow 4Na^{+}(aq) + 4OH^{-}(aq) \quad (2)$$

$$Ce(NO_3)_3{\cdot}6H_2O(s) \rightarrow Ce^{3+}(aq) + 3NO^{3-}(aq) + 6H_2O(aq) \quad (3)$$

$$Ce^{3+}(aq) + 4OH^{-}(aq) + 6H_2O(aq) \rightarrow Ce(OH)_4{\cdot}6H_2O(s) \quad (4)$$

$$Ce(OH)_4.6H_2O \rightarrow CeO_2(s) + 2H_2O(g) + 2H_2(g) \quad (5)$$

Table 1. Effect of reaction time and stirring rate towards percentage yield of ceria nanoparticle synthesis.

Reaction Time (hours)	Stirring Rate (rpm)	Percentage Yield	Physical Observation
0.5	1200	39	NA
1.0	1200	43	NA
2.0	450	30	Purple solution after approximately 30 minutes of stirring
2.0	1200	81	Cloudy to yellowish solution formed after approximately 30–45 minutes of stirring
2.0	1500	82	Cloudy to yellowish solution formed after approximately 30–45 minutes of stirring

Table 1 (cont'd). Effect of reaction time and stirring rate towards percentage yield of ceria nanoparticle synthesis.

Reaction Time (hours)	Stirring Rate (rpm)	Percentage Yield	Physical Observation
4.0	1200	83	Cloudy to yellowish solution formed after approximately 30–45 minutes of stirring
8.0	1200	84	Cloudy to yellowish solution formed after approximately 30–45 minutes of stirring
24.0	450	38	Purple solution at the beginning and thin yellowish layer formed on top of solution after overnight stirring
24.0	1200	79	Cloudy to yellowish solution formed after approximately 30–45 minutes of stirring
48.0	450	24	Cloudy to yellowish solution formed after approximately 30–45 minutes of stirring
48.0	1200	34	Purple solution at the beginning and thin yellowish layer formed on top of solution after overnight stirring

NA: Not Available

X-ray diffraction

Figure 1 illustrates XRD pattern of ceria nanoparticles at different aging time, i.e. t = 0 (S2), t = 30 minutes (S6), and t = 5 days (S3). All peaks exhibited in Figure 1 can be indexed to a pure cubic phase of CeO_2 according to The Joint Committee on Powder Diffraction Standards (JCPDS file No. 34-0394). Furthermore, the XRD pattern has shown four main reflections of (111), (200), (220), and (311) of CeO_2 in the cubic phase with fluorite structure. In addition, the calculated lattice constant for the synthesised sample, a = 0.511 nm, matched the value from literature, namely a = 0.514 nm, calculated using equation $1/d^2 = h^2+k^2+l^2/a^2$ [24]. All displayed peaks have shown that the synthesised ceria nanoparticles were clean from the surfactant as no additional peaks due to other phases or impurity were detected. This resulted in a CeO_2 cubic phase of high purity.

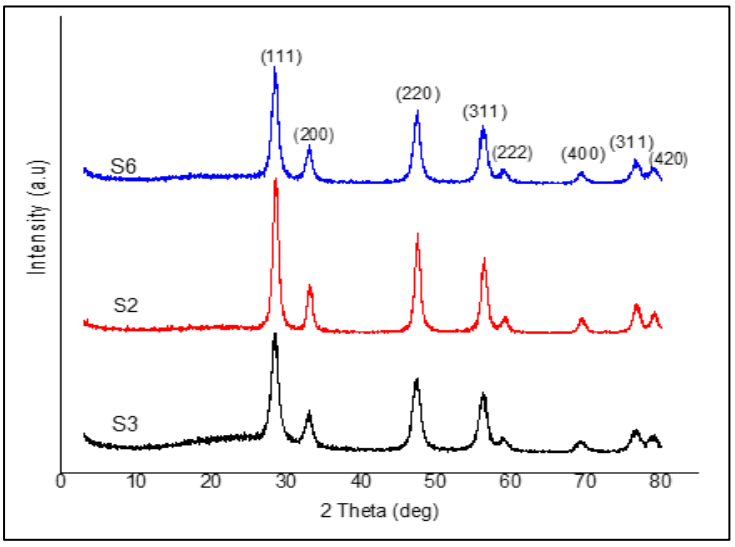


Figure 1. XRD pattern for S2, S3, and S6 samples

Findings have highlighted that at (200): (111), synthesised ceria displayed a higher intensity ratio (0.315) compared to bulk ceria (0.260). A similar trend was observed for (220): (111), whereby synthesised ceria nanoparticles' intensity ratio was 0.689, while bulk ceria's was 0.550. Thus, this trend suggests that there was better exposure for the active (100) and (110) surfaces relative to (111) surface of the synthesised ceria nanoparticles, in comparison to bulk ceria [24].

On the other hand, as tabulated in Table 2, crystallite size was between 4–12 nm, with a slight difference observed when CTAB surfactant was added. Nevertheless, aging time application is crucial for samples added with surfactant. For instance, an aging time of less than 20 days did not show any noticeable difference in crystallite size. This may be due to less or slow conversion of Ce^{4+} from Ce^{3+}, resulting in reduced CeO_2 formation and directional growth.

Table 2. Crystallite size of synthesised ceria and modified ceria (Fe-CeO_2/TiO_2) nanoparticles

Sample	Surfactant	Aging Time (days)	Crystallite Size (nm)
CeO_2 (S2)	No	NA	9.0
CeO_2 (S3)	Yes	<1 (0.5 hours)	8.7
CeO_2 (S6)	Yes	5	7.5
CeO_2	Yes	10	7.1
CeO_2	Yes	20	5.3
CeO_2 (S7)	Yes	30	4.5
Fe-CeO_2/TiO_2 (S10)	NA	NA	11.3

NA: Not Available

Importance of aging time towards nanoparticle/structure formation (Figure 2) has been reported in the literature [25]. For aging time of less than a week, no enhancement in crystallite size was noted, and this is attributable to the reaction mixture containing uniform amount of Ce^{3+} and Ce^{4+} ions. When aging time was extended to a month, significant results were observed, implying the dominance of Ce^{4+} in the reaction mixture. Therefore, CeO_2 grew directionally in the presence of surfactant.

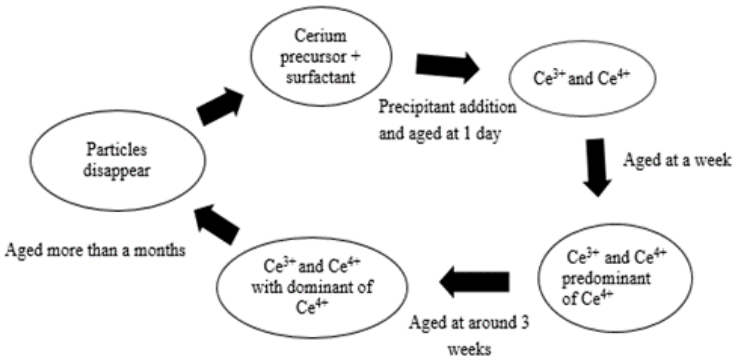


Figure 2. The proposed oxidation-reduction cycle [25]

The role played by cationic CTAB surfactant was studied by comparing samples containing and devoid of it. Sample without CTAB exhibited an unclear shape, compared to sample containing CTAB, which displayed a

sphere-like shape (Figure 3 (a) and (b)). This observation implies the influential role of CTAB in tuning the nano-shape formation. The mechanisms proposed for this observation are as follows: (i) oxidation of Ce^{3+} to Ce^{4+}; (ii) incorporation of Ce^{4+} with cetyl-tri-methyl ammonium ion (CTA^+); and (iii) simultaneously, exchange between H^+ and alkylammonium cation (from CTAB surfactant) occurs, as per the equilibrium shown in Figure 4.

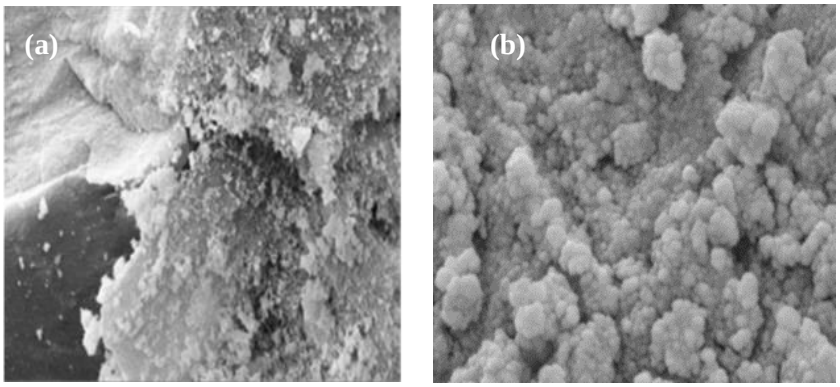


Figure 3. (a) CeO_2 sample prepared without assistance of CTAB surfactant; and (b) CeO_2 sample prepared with assistance of CTAB surfactant

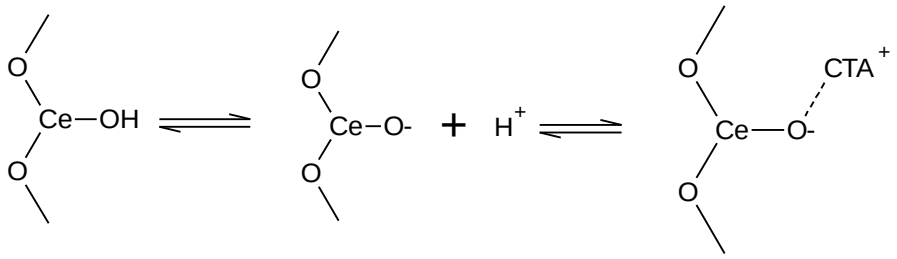


Figure 4. Reaction between alkylammonium cation (from CTAB surfactant) and cerium(IV) hydroxide

Electrostatic interaction of Ce-O----CTA^+ will then initiate polymerisation, which causes micellization. Excess surfactant species were expected to be adsorbed on ceria nanoparticle surface and colloidal ceria nanoparticles with surfactant would have then generated CTA^+ surfactant capsule. Next, ceria/surfactant bilayers were formed due to coalescence of both organic and inorganic nanocomposites. This occurred due to inter-chain interaction between surfactant and colloidal ceria nanoparticles. Such processes enhance ceria nano-shape growth orientation [25]. Moreover, CTA^+ surfactant capsule is attributable to ceria nano-shape size regulation. Finally, excess surfactant was eliminated after synthesis process via washing, to ensure the obtained sample is pure.

Hammet test and CO_2-TPD

Before conducting CO_2-TPD, a simple acidity and basicity analysis was performed, i.e. Hammett test (Table 3). This test is a simple analysis used to roughly describe the acidity and basicity of samples. As presented in Table 3, all samples changed the colour of phenolphthalein (pH indicator; pH 8.2) from colourless to pink. In addition, two other pH indicators were also used; 4-nitroaniline (pH 18.4) and 2,4-dinitroaniline (pH 15.0); however, no colour changes were observed. Therefore, these preliminary results suggest that all the samples were not acidic in nature while the basicity was in the range of 8.2< pH <15.0. Since Hammett test provided the basicity range for all the samples, TPD analysis was continued with CO_2-TPD.

Table 3. Hammet test analysis for S2, S3, and S6

Catalyst	Phenolphthalein	2,4-dinitroaniline	4-nitroaniline
S2	Colourless to pink	No colour changes	No colour changes
S3	Colourless to pink	No colour changes	No colour changes
S6	Colourless to pink	No colour changes	No colour changes

CO_2-TPD was conducted on S2, S3, and S6 samples and the total CO_2 gas desorbed were 18.56, 2211.19, and 2076.00 µmol/g, respectively. Figure 5 and Table 4 both depict the peaks exhibited by all three samples. The CO_2-TPD technique can be classified according to type, as follows:

peaks at <200°C : weak basic sites;
peaks at 200°C–400°C : medium basic sites; and
peaks >400°C : strong basic sites.

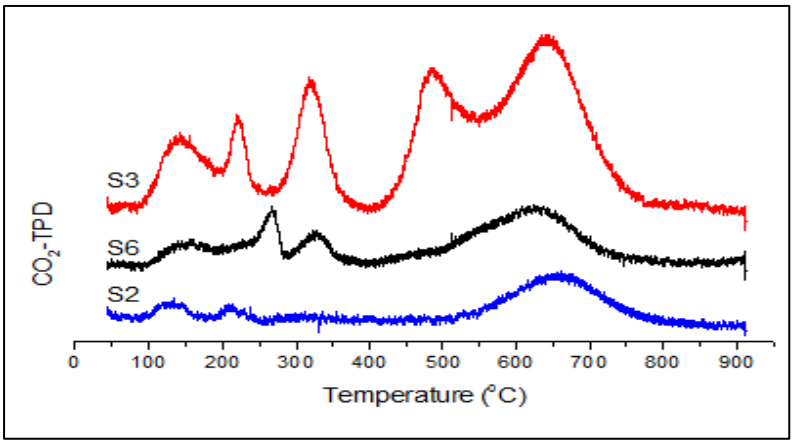


Figure 5. CO_2-TPD for S2, S3, and S6

Table 4. Total CO_2 desorption for S2, S3, and S6

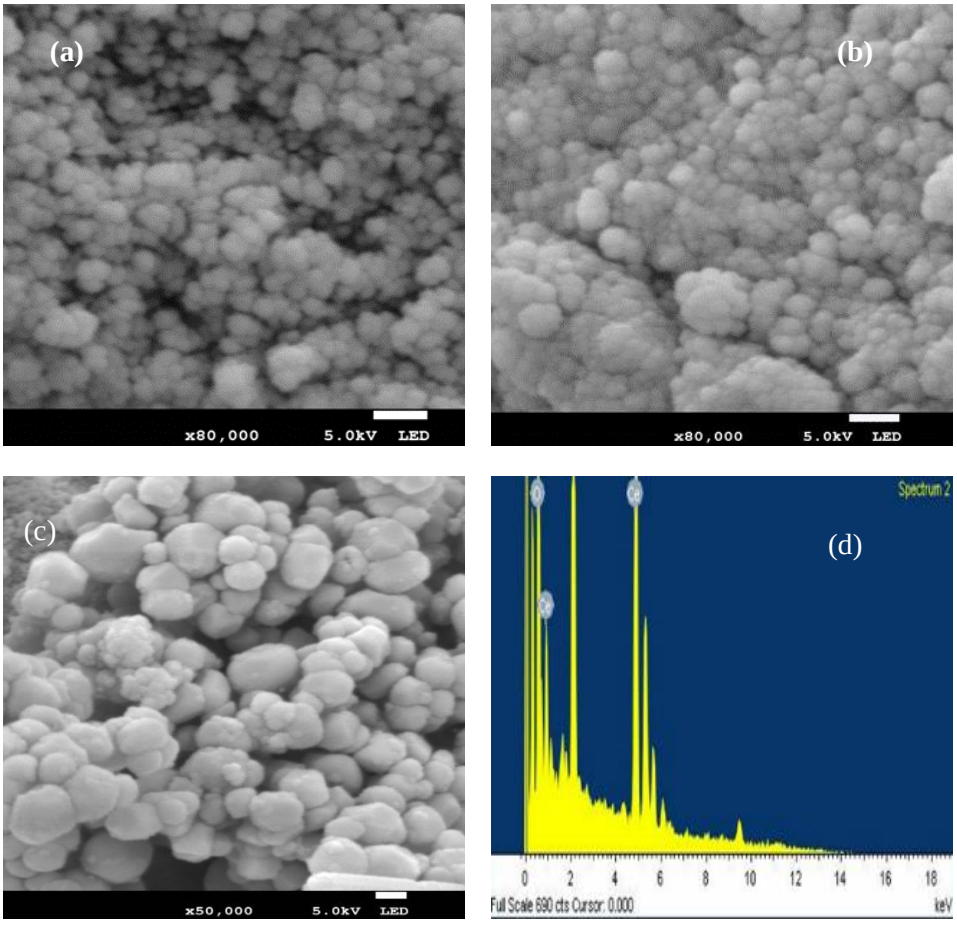
Sample	Peak (°C)	Total CO_2 Desorption (%)
S2	662	100
S3	145	6
	223	6
	321	13
	491	18
	645	57
S6	162	2
	267	58
	624	40

Sample S3 exhibited peaks at 145°C, 223°C, 321°C, 491°C, and 645°C, indicating the presence of strong basic sites. Nonetheless, additional mild basic site peaks observed at 223°C and 491°C may also imply formation of inorganic and/or organic species, causing reaction between surfactant and deprotonated OH^- group [26]. As such, this preliminary result suggests that longer aging time may have influenced the sample's basic sites, as it led to stronger interface interaction between cationic surfactant and ceria surface nanoparticles. Hence, the cationic part of surfactant may have acted as a Lewis acid and altered the basic sites.

Field emission scanning electron microscopy

High resolution FESEM analysis was carried out to study the morphology and elemental composition of synthesised ceria and modified ceria, Fe-CeO_2/TiO_2, nanoparticles. Figure 6 (a–c) shows that both samples did not agglomerate and form a sphere-like structure. On the other hand, Figure 6(d) reveals that synthesised ceria nanoparticles contained only Ce and O elements, which concur with XRD results. Meanwhile, Figure 6(e) exhibits the EDX spectrum of Fe-CeO_2/TiO_2 that proves the presence of Fe and Ti elements in the sample.

Nevertheless, due to technique-related limitations, presence of other ions originating from the surfactant cannot be ruled out. The ions were expected to be adsorbed at the surface, but its adsorption effect on ceria surface was weak and negligible [27]. In addition, Figure 6(c) illustrates the clear sphere-like shape observed. This indicates the interaction between Fe ion with the basic surface of CeO_2, contributing towards CeO_2 nanoparticles tuning shape process. Thus, CeO_2 surface's mild to high range of basicity was expected to enhance the electrostatic interaction occurring between Fe ion and CeO_2 surface.



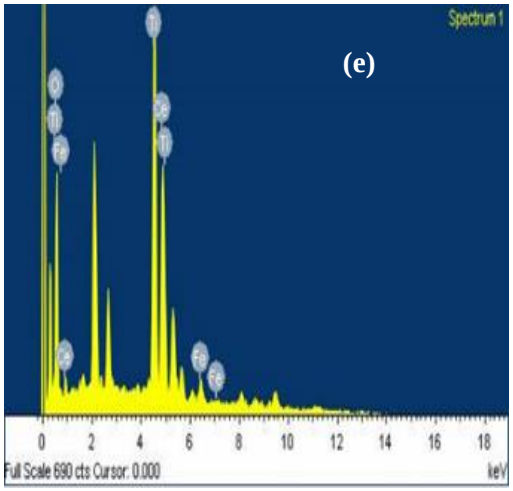


Figure 6. FESEM images of ceria and modified ceria nanoparticles: (a) S3 sample; (b) S7 sample; (c) S10 sample; (d) EDX spectrum of synthesised CeO_2 sample from different areas; and (e) EDX spectrum of Fe-CeO_2/TiO_2 particle sample

Conclusion

CeO_2 nanoparticles and modified CeO_2, Fe-CeO_2/TiO_2, were successfully synthesised using precipitation and impregnation methods, respectively. Synthesised CeO_2 nanoparticles produced crystallite sized between 4–18 nm and showed no agglomeration in FESEM images. Meanwhile, modified CeO_2 nanoparticles with iron metal loading and titania (TiO_2) as support formed a sphere-like shape, with the presence of Fe and Ti confirmed by EDX spectrum. Additionally, synthesis of ceria hybrid and CeO_2 using other surfactants and substrates like polyvinyl alcohol (PVA) could be an interesting prospective study. Other than that, previous research reported on synthesis of a particular material hybrid nanoparticle, which provided significant enhancement for properties like hardness and heat resistance [28–30]. Therefore, in future, comprehensive study on CeO_2 hybrid nanoparticle synthesis with PVA surfactant will be considered.

Acknowledgement

This work is supported by Universiti Malaysia Pahang, the Ministry of Education, Malaysia for Exploratory Research Grant Scheme (ERGS) (RDU 120605), and Malaysia Toray Science Foundation (RDU 141501). The first author would like to thank the Ministry of Education, Malaysia for their support *via* MyPhD funding.

References

1. Sayyed, S. A., Beedri, N. I., Kadam, V. S. and Pathan, H. M. (2016). Rose bengal-sensitized nanocrystalline ceria photoanode for dye-sensitized solar cell application. *Bulletin of Materials Science*, 39(6): 1381-1387.
2. Namjesnik, D., Mutka, S., Iveković, D., Gajović, A., Willinger, M. and Preočanin, T. (2016). Application of the surface potential data to elucidate interfacial equilibrium at ceria/aqueous electrolyte interface. *Adsorption*, 22(4-6): 825-837.
3. Eltayeb, A., Vijayaraghavan, R. K., McCoy, A., Venkatanarayanan, A., Yaremchenko, A. A., Surendran, R. and Daniels, S. (2015). Control and enhancement of the oxygen storage capacity of ceria films by variation of the deposition gas atmosphere during pulsed DC magnetron sputtering. *Journal of Power Sources*, 279: 94-99.
4. Li, H., Hu, T., Liu, J., Song, S., Du, N., Zhang, R. and Hou, W. (2016). Thickness-dependent photocatalytic activity of bismuth oxybromide nanosheets with highly exposed (010) facets. *Applied Catalysis B: Environmental*, 182: 431-438.
5. Gao, G.-M., Zou, H.-F., Liu, D.-R., Miao, L.-N., Ji, G.-J. and Gan, S.-C. (2009). Influence of surfactant surface coverage and aging time on physical properties of silica nanoparticles. *Colloids and Surfaces A: Physicochemical and Engineering Aspects*, 350(1): 33-37.

6. Das, D., Llorca, J., Dominguez, M., Colussi, S., Trovarelli, A. and Gayen, A. (2015). Methanol steam reforming behavior of copper impregnated over CeO_2–ZrO_2 derived from a surfactant assisted coprecipitation route. *International Journal of Hydrogen Energy,* 40(33): 10463-10479.
7. Vantomme, A., Yuan, Z.-Y., Du, G. and Su, B.-L. (2005). Surfactant-assisted large-scale preparation of crystalline CeO_2 nanorods. *Langmuir,* 21(3): 1132-1135.
8. Pan, C., Zhang, D. and Shi, L. (2008). CTAB assisted hydrothermal synthesis, controlled conversion and CO oxidation properties of CeO_2 nanoplates, nanotubes, and nanorods. *Journal of Solid State Chemistry,* 181(6): 1298-1306.
9. Ebadi, M., Amiri, O. and Sabet, M. (2018). Synthesis of CeO_2/Au/Ho nanostructures as novel and highly efficient visible light driven photocatalyst. *Separation and Purification Technology,* 190: 117-122.
10. Liu, Q., Ding, Y., Yang, Y., Zhang, L., Sun, L., Chen, P. and Gao, C. (2016). Enhanced peroxidase-like activity of porphyrin functionalized ceria nanorods for sensitive and selective colorimetric detection of glucose. *Materials Science and Engineering: C,* 59: 445-453.
11. Younis, A., Chu, D., Kaneti, Y. V. and Li, S. (2016). Tuning the surface oxygen concentration of {111} surrounded ceria nanocrystals for enhanced photocatalytic activities. *Nanoscale,* 8(1): 378-387.
12. Zhang, D., Fu, H., Shi, L., Pan, C., Li, Q., Chu, Y. and Yu, W. (2007). Synthesis of CeO_2 nanorods via ultrasonication assisted by polyethylene glycol. *Inorganic Chemistry,* 46(7): 2446-2451.
13. Terribile, D., Trovarelli, A., Llorca, J., de Leitenburg, C. and Dolcetti, G. (1998). The synthesis and characterization of mesoporous high-surface area ceria prepared using a hybrid organic/inorganic route. *Journal of Catalysis,* 178(1): 299-308.
14. Ramasamy, V. and Vijayalakshmi, G. (2016). Synthesis and characterization of ceria quantum dots using effective surfactants. *Materials Science in Semiconductor Processing,* 42: 334-343.
15. Yang, R. and Guo, L. (2005). Synthesis of cubic fluorite CeO_2 nanowires. *Journal of Materials Science,* 40(5): 1305-1307.
16. Choi, M., Na, K., Kim, J., Sakamoto, Y., Terasaki, O. and Ryoo, R. (2009). Stable single-unit-cell nanosheets of zeolite MFI as active and long-lived catalysts. *Nature,* 461 (7261): 246-249.
17. Lin, K.-S. and Chowdhury, S. (2010). Synthesis, characterization, and application of 1-D cerium oxide nanomaterials: A review. *International Journal of Molecular Sciences,* 11(9): 3226-3251.
18. Torrente-Murciano, L., Chapman, R. S., Narvaez-Dinamarca, A., Mattia, D. and Jones, M. D. (2016). Effect of nanostructured ceria as support for the iron catalysed hydrogenation of CO_2 into hydrocarbons. *Physical Chemistry Chemical Physics,* 18(23): 15496-15500.
19. Laosiripojana, N., Assabumrungrat, S. and Charojrochkul, S. (2007). Steam reforming of ethanol with Co-Fed oxygen and hydrogen over Ni on high surface area ceria support. *Applied Catalysis A: General,* 327(2): 180-188.
20. Yao, S., Xu, W., Johnston-Peck, A., Zhao, F., Liu, Z., Luo, S. and Rodriguez, J. (2014). Morphological effects of the nanostructured ceria support on the activity and stability of CuO/CeO_2 catalysts for the water-gas shift reaction. *Physical Chemistry Chemical Physics,* 16(32): 17183-17195.
21. Yoshida, T., Murachi, M., Tsuji, S. and Taguchi, N. (1999). High heat-resistant catalyst with a porous ceria support. U.S. Patent and Trademark Office, Washington, DC.
22. Li, H., Wang, G., Zhang, F., Cai, Y., Wang, Y. and Djerdj, I. (2012). Surfactant-assisted synthesis of CeO_2 nanoparticles and their application in wastewater treatment. *RSC Advances,* 2(32): 12413-12423.
23. Wang, J., Liu, Q. and Liu, Q. (2008). Ceria-and Cu-doped ceria nanocrystals synthesized by the hydrothermal methods. *Journal of the American Ceramic Society,* 91(8): 2706-2708.
24. Deori, K., Gupta, D., Saha, B., Awasthi, S. K. and Deka, S. (2013). Introducing nanocrystalline CeO_2 as heterogeneous environmental friendly catalyst for the aerobic oxidation of para-xylene to terephthalic acid in water. *Journal of Materials Chemistry A,* 1(24): 7091-7099.
25. Karakoti, A. S., Munusamy, P., Hostetler, K., Kodali, V., Kuchibhatla, S., Orr, G. and Baer, D. R. (2012). Preparation and characterization challenges to understanding environmental and biological impacts of ceria nanoparticles. *Surface and Interface Analysis,* 44(8): 882-889.
26. Indran, V. P., Zuhaimi, N. A. S., Deraman, M. A., Maniam, G. P., Yusoff, M. M., Hin, T.-Y. Y. and Rahim, M. H. A. (2014). An accelerated route of glycerol carbonate formation from glycerol using waste boiler ash as catalyst. *RSC Advances,* 4(48): 25257-25267.

27. Huang, X.-S., Sun, H., Wang, L.-C., Liu, Y.-M., Fan, K.-N. and Cao, Y. (2009). Morphology effects of nanoscale ceria on the activity of Au/CeO_2 catalysts for low-temperature CO oxidation. *Applied Catalysis B: Environmental*, 90(1): 224-232.
28. Aziz, R. C. A., Ab Rahman, I. and Mohamad, D. (2012). Synthesis of silica hybrid nanoparticles and the effect of their addition on the hardness of the dental nanocomposites. *International Journal on Advanced Science, Engineering and Information Technology*, 2(3): 211-214.
29. Yunus, M., Suharyadi, E. and Triyana, K. (2016). Effect of stirring rate on the synthesis silver nanowires using polyvinyl alcohol as a capping agent by polyol process. *International Journal on Advanced Science, Engineering and Information Technology*, 6(3): 365-369.
30. Zain, N. M., Rashdi, N. M., Ubaidillah, N. K. A. N. and Azmi, M. S. (2016). The effect of carbon nanotube loading on wettability of solder paste SAC 237 and different substrates. *International Journal on Advanced Science, Engineering and Information Technology*, 6(4): 540-543.

Malaysian Journal of Analytical Sciences, Vol 22 No 3 (2018): 416 - 428
DOI: https://doi.org/10.17576/mjas-2018-2203-06

MALAYSIAN JOURNAL OF ANALYTICAL SCIENCES
Published by The Malaysian Analytical Sciences Society
ISSN 1394 - 2506

QUANTIFICATION OF GROUNDWATER-DERIVED NUTRIENTS INTO BEACH RIDGE DRAINAGE USING RADON MASS BALANCE MODEL

(Kuantifikasi Nutrien Air Bawah Tanah ke Saluran Pematang Pasir dengan Model Keseimbangan Jisim Radon)

Nicholas Chia Wei Ng and Seng-Chee Poh*

School of Marine and Environmental Sciences,
Universiti Malaysia Terengganu, 21030 Kuala Nerus, Terengganu, Malaysia

**Corresponding author: poh@umt.edu.my*

Received: 10 November 2017; Accepted: 22 May 2018

Abstract

Groundwater discharge can be a significant pathway for dissolved nutrients to surface water and thus can bring forth important implications to the coastal biogeochemical cycles. Discrete sampling of radon concentrations at several locations along an inter-ridge drainage off Setiu Wetlands were carried out to estimate the fluxes of groundwater discharge. The ^{222}Rn mass balance results show that groundwater discharge in the drainage is estimated to be 6649 m^3day^{-1}, made up of ~33% of total water discharge and has contributed 2.88×10^2 $molday^{-1}$, 1.23×10^2 $molday^{-1}$ and $0.75molday^{-1}$ of ammonium-nitrogen, nitrate-nitrogen and nitrite-nitrogen, respectively into the surface water drainage. Strong correlation between radon and ammonium suggested that the source of nutrient in drainage is groundwater-based, derived probably from the nearby damaged or leaking residential septic tanks and from agricultural practices of oil palm plantation.

Keywords: groundwater-surface water interaction, water quality, beach ridge drainage, Setiu, Malaysia

Abstrak

Pelepasan air bawah tanah merupakan satu laluan penting untuk nutrien ke air permukaan. Proses ini mampu membawa implikasi yang penting terhadap kitaran biogeokimia di pesisiran pantai. Pensampelan radon di sepanjang saluran pematang pasir telah dijalankan untuk menentukan kadar pelepasan air bawah tanah. Hasil model keseimbangan jisim ^{222}Rn telah menunjukkan kadar pelepasan air bawah tanah di saluran adalah sebanyak 6649 m^3hari^{-1} dan nilai ini merangkumi ~33% daripada jumlah pelepasan air. Pelepasan air bawah tanah juga menyumbang sebanyak 2.88×10^2 mol $hari^{-1}$ amonium-nitrogen, 1.23×10^2 mol $hari^{-1}$ nitrit-nitrogen dan 0.75 mol $hari^{-1}$ dan nitrit-nitrogen ke air permukaan saluran. Kolerasi antara kepekatan radon dan ammonium di saluran juga mencadangkan sumber nutrien berasal dari air bawah tanah yang kemungkinan tercemar oleh sisa pembuangan kumbahan dari kawasan kediaman berdekatan dan rembesan pertanian dari ladang kelapa sawit di sekitarnya.

Kata kunci: interaksi air bawah tanah-air permukaan, kualiti air, saluran pematang pasir, Setiu, Malaysia

Introduction

Importance of groundwater discharge as a nutrient source to the river and estuaries are often overlooked. Several studies have demonstrated that groundwater discharge can be a significant contributor of nutrients to the coastal environment and being recognized as a potential pathway for non-point pollution, especially when agricultural practices or urban activities had impacted the groundwater quality [1-4]. Previous studies have shown that radon is a great tool to study groundwater-surface water interaction in different environmental settings [5, 6, 7]. Radon has

relatively short halve-lives (3.8 days) and low solubility in water, 0.01 $molkg^{-1}$ bar^{-1} at 293 K [8]. Radon concentration tend to be higher in groundwater compared to the surface water i.e. lake, river, estuary and ocean. In aquifer, radon concentration in groundwater is proportional to radium-bearing rocks and soils. On contrary, radon concentration in surface water tends to be low due to natural decay, degassing and dilution processes. The large difference in radon concentration between surface and groundwater can be used as a proxy to determine groundwater discharge hotspots [9, 10].

Numerous studies have applied ^{222}Rn mass model to assess groundwater discharge in rivers and estuaries [11, 12]. Other studies also incorporate geophysical technique such as seepage meters with ^{222}Rn measurement to examine groundwater discharge into the river [13]. Most of the groundwater discharge studies were carried out *in-situ* by a portable radon gas detector [14, 15]. In general, the radon measurement required a headspace equilibrator attached to the radon detector. The equilibrator allows radon gas in water to exchange rapidly with gases in the headspace. The radon activities in headspace will then determine by a semiconductor detector e.g. RAD7, the electronic radon detector (Durridge, USA). The detector convert the alpha radiation from the radon decay products (primarily ^{218}Po) into electrical signals and have a measurement range of 4 to 400, 000 Bq/m^3 [17].

Longitudinal and time-series radon samplings are two common approaches used to trace and quantify groundwater discharge in a system. The former sampling technique involved collection of discrete water samples followed by *in-situ* sample analysis is convenient and provides instantaneous values of radon activity in the water. Sometimes, radon samples were measured in laboratory within 24 hours of sampling time if the *in-situ* measurement is not accessible. This sampling strategy provides a fast and cost-effective way to locate the groundwater discharge hotspots within a large scale study area [18]. Time-series sampling technique on the other hand, provides a near real-time concentration of radon activities in a single sampling point. This sampling strategy is normally applied in area where the groundwater hotspots was found and a high-resolution radon measurements are needed to better quantify the exchange fluxes between groundwater-surface water [10, 15, 19].

Setiu Wetlands is located in the eastern coast of Peninsular Malaysia. The entire coastal zone of Setiu is characterized by wide sandy undulating landscape, consists a series of shore-parallel beach ridges and sandy swales. Setiu wetland is located on the low-lying sandy swales surrounded by elevated paleo-beach ridges. Since 1980s, the natural drainage system in this area was heavily modified to support local agricultural and aquaculture activities. Some of the natural streams were straightened and widened to facilitate the water supply. Additional artificial channels cutting perpendicular through the ridges were built to fulfil the water demands associated to agricultural practices. Besides agricultural and aquaculture activities, local communities' livelihood in this area is highly dependent on the natural resources found in the wetlands. Fish and shrimp farming, molluscan shellfish (e.g. gastropods and bivalves) aquaculture and harvesting, and commercial fishing are the major economic activities of the local populations in the area.

Setiu Wetlands has been subjected to increasing environmental pressures due to rapid growth of aquaculture and agricultural activities [20]. The excess nutrients from the pond could potentially leak into the groundwater. The polluted groundwater is non-point source pollution which may cause additional environmental pressure to Setiu Wetlands. In addition, the intensive farming activities on the beach ridges adjacent to lagoon may also contribute nutrients into the lagoon [21].

Previous study shows that Berombak Lake has contributed significant nutrients to Setiu Wetlands lagoon [22]. However, there has been no study on groundwater discharge as parts of the nutrient budget of drainage channel that connecting the lake and lagoon. Hence, this study is conducted to (i) identify the groundwater discharge hotspots along the drainage channels (hereinafter refer as Ular River) and (ii) quantify the groundwater fluxes and its associated nutrients to the surface water.

Materials and Methods

Study area

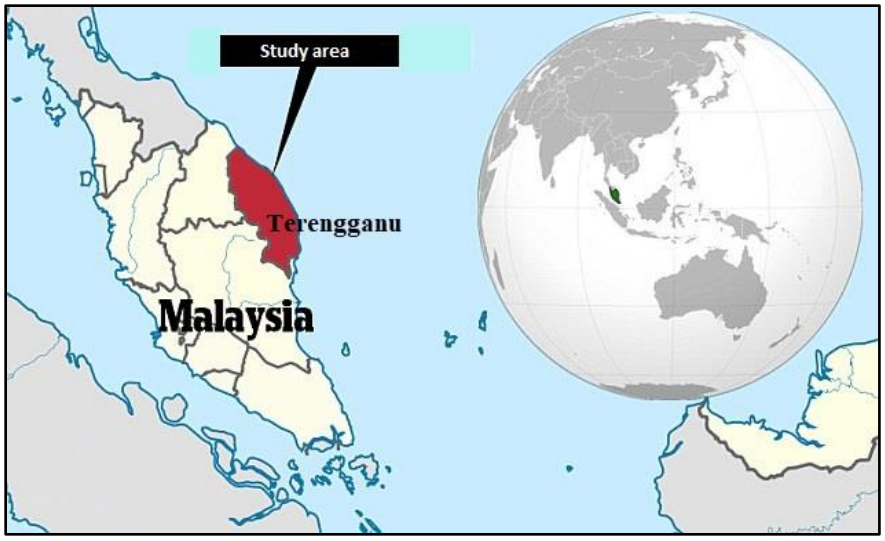
Ular River is a tributary of the Setiu Wetlands Lagoon, Terengganu, Malaysia. The river stretch between the coordinates 5°40'05.06" N to 5°40'45.04" N and 102°41'40.51" E to 102°42'54.04" E. The river is approximately 4

km in length, connected to its headwaters the Berombak Lake by two channels branches split about 2km from the river mouth. The total size of river catchment is approximately 48,000 m^2 and the average river depth is ranging from 0.1-1.8 m. The river receives freshwater input primarily from the Berombak Lake but one-fourth of the river from the downstream is subjected to saline water intrusion (Figure 1). The riverbed materials of upper part river, approximately 1.5 km from the river mouth is dominated by the fluvial deposits, followed by the middle part of river is dominated by the fluvial sand and marine mud. The lower part of river is dominated by the estuarine deposits. This estuarine deposits mainly consists of cohesive sediments with the combination of clay, silt and organic matter [23].

Surface water and groundwater sampling

Three longitudinal surface and groundwater sampling were conducted in Ular River in 2015. The first sampling is carried out in January 2015, followed by second and third samplings in March 2015 and May 2016. The first sampling was conducted during wet season, where the studied area received 152 mm of rain in the week prior to sampling in January 2015. On the other hand, March was the driest month of 2015 with less than 30 mm monthly rainfall while May 2016 recorded less than 35 mm of rainfall a week prior the sampling, making it a perfect timing to obtain the representative samples for dry season base-flow condition [24]. A total of 40 surface water and 19 groundwater samples were collected for radon and nutrient analysis.

For groundwater sampling, three piezometers were installed in riparian zone along Ular River (P1-P3, Figure 1). The boreholes were dug using a vibracorer to the depth of ~3m. Slotted PVC pipes (drilled with 0.5cm diameter holes, extended from the base of the pipe for ~30cm) were placed into borehole and backfilled with the excavated materials. A cement grout was installed at the top of borehole to prevent surface water from moving via a preferential pathway into the piezometer. After installation, the piezometers were developed using a peristaltic pump until the discharge groundwater was clear. Besides piezometers, five addition groundwater samples were also collected from the nearby private groundwater wells (B1-B5, Figure 1). The depth of these groundwater wells ranges from 5 to 7 m below ground, and the groundwater samples were collected from water tap attached to the automatic submersible pumps.



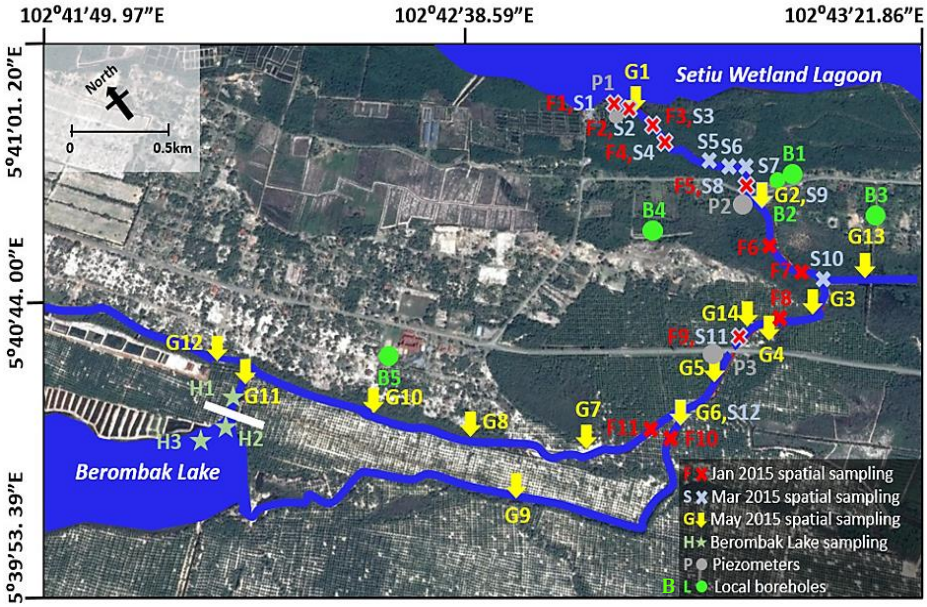


Figure 1. Location of Ular River and its sampling sites

Radon analysis

Surface water and groundwater samples for the radon concentration were collected using a Schott gas-tight glass bottle (500 ml, Duran, Germany) and stored under 10 °C prior to the analysis. The measurement of radon in water was conducted as proposed by Lee and Kim [25]. In general, the radon water sample was transferred to a gas-washing bottle with fitted disc (500 ml, Duran, Germany). The bottle was then connected to a desiccant column and RAD7 with a closed air loop circulation system. A desiccant column was installed between the gas washing bottle and RAD7 to reduce the moisture content in the radon detector. The internal pump in the RAD7 was set to ~1L/min to provide a continuous air flow within the experimental setup. The equilibrium time for radon concentration equilibrium between water and recirculating air take approximately 15 minutes. Each radon sample was counted for two hours in order to yield good counting statistics. For actual radon concentration report, data reduction was performed by taking account of the radon decay activities during the time lapse between sample collection and analysis.

Nutrient analysis and physico-chemical parameters measurement

One liter of groundwater and surface water samples were collected and filtered through 0.45 mm cellulose acetate membrane. The filtrate was stored in acid prewashed HDPE bottle, chilled with ice and transported back to the lab for nutrients analyses. The measurement of ammonium, NH_4^+-N (Phenate Method, 4500-NH_4^+-G), nitrite, NO_2^--N (Colorimetric Method, 4500- NO_2^--B), nitrate NO_3^--N (Automated Cadmium Reduction Method, 4500-NO_3^--F) and phosphate PO_4^{3-}-P (Ascorbic Acid Method, 4500-P-E) concentrations were conducted by standard spectrophotometric techniques [26]. pH, dissolved oxygen, salinity and water temperature of the surface water and groundwater were measured *in-situ* using a pre-calibrated YSI Professional Plus multiparameter Sonde (Xylem Inc. USA).

Radon mass balance model

In this study, radon mass balance method was used to estimate groundwater discharge rate. This method could provide an excellent time-integrated estimation of groundwater flux [20]. Figure 2 shows that the net radon concentration in a system can be inferred through the quantification of its sources and sink. The radon sources in surface water include the groundwater discharge, diffusive benthic flux and radioactive decay from the radon parental isotope, ^{226}Ra in the water column while atmospheric evasion or outgassing is the only sink for radon in surface water.

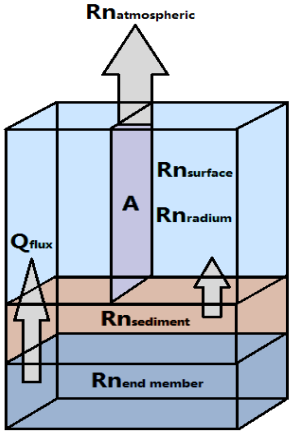


Figure 2. Radon mass balance model

Changes in groundwater flux (Q_{flux}) within a river can be expressed as:

$$Q_{flux} = \frac{\mathrm{Rn}_{surface} + Rn_{atmospheric} - Rn_{radium} - Rn_{sediment}}{Rn_{end-member}} \times D_v \quad (1)$$

Q_{flux} is the groundwater flux, expressed as $m^3 d^{-1}$; $\mathrm{Rn}_{surface}$ is the radon concentration in the surface water of Ular River (Bq/m^3); $\mathrm{Rn}_{atmospheric}$ is the radon loss to the atmosphere ($Bq/m^2 day$); Rn_{radium} is the radon contributed by radium-226 in the surface water (Bq/m^3); $\mathrm{Rn}_{sediment}$ is the radon contributed by the sediment diffusion in the water column ($Bq/m^2 day$); $\mathrm{Rn}_{end\text{-}member}$ is the radon concentration in the groundwater end-member (Bq/m^3) and D_v is the total riverine discharge rate (m^3/day) in Ular River.

Total riverine discharge rate (D_v) was obtained by the multiply the average current velocity (ms^{-1}) with the average cross-sections of the river (m^2). The velocity distribution in the river was measured by a handheld velocity flowmeter (Hach Co. USA), while the cross-sections and the average water depth of the river was measured using a measuring tape.

Fourteen surface water samples (40L each) were brought back to the lab for radium (Rn_{radium}) measurement. The measurement of Rn_{radium} followed method as described in [16, 27]. In general, the radium samples were first pre-concentrated by passing the water samples through the manganese oxide impregnated fiber inside a PVC cartridge (Figure 3). The cartridge was 250 mm in length, 50 mm in diameter clear PVC tube coupled with a 50 mm PVC end cap and Union at both ends. Two brass ball valves with thread tape were then installed on the end cap and Union. The loaded manganese cartridge after the pre-concentration step was sealed inside the air-tight cartridge and left for 14 days in order to achieve ^{226}Ra and ^{222}Rn secular equilibrium [27]. The measurement of radon contributed by ^{226}Ra in the surface water was completed by RAD7.

The measurement of diffused radon rate from the sediment ($\mathrm{Rn}_{sediment}$) was carried at G1, G2 and G5 (represent upstream, middle and downstream of Ular River, respectively, see Figure 1). At each sampling site, three 50 mm-diameter PVC corers were hand-pushed into the riverbed and the corer was retrieve and transfer into glass Erlenmeyer flask. The flask was capped with rubber bunks after filling up with overlying river water. The sediment cores were then transported back to lab and incubated at room temperature for three weeks. The incubation allowed the radon in overlying water to achieve equilibrium with the diffusive inputs from the underlying sediments. The overlaying water was carefully transferred from each core into a gas washing bottle and analyzed by RAD7 at the end of the incubation period. Additional sediment core samples were collected by using 20mm-diameter HDPE tubes for both bulk density and sediment porosity test as described in previous study [28].



Figure 3. Design of Manganese Oxide cartridges; The brass valves (A), the PVC plug (B), the union with O-ring (C), the clear PVC pipe (D), and the end cap (E)

Radon diffusive flux from the sediment ($Rn_{sediment}$) was calculated based on [6, 28]:

$$Rn_{sediment} = (\lambda D_s)^{\frac{1}{2}}(C_{eq} - C_0) \quad (2)$$

$$D_s = D_m/(1\text{-}ln(\emptyset^2) \quad (3)$$

$$-logD_m = (980/T) + 1.59] \quad (4)$$

where $Rn_{sediment}$ is the radon contributed by sediment diffusion, expressed as Bq/m^2day; λ represents the radon decay constant (0.181 day^{-1}); C_{eq} is the radon released by radium in the sediments during sediment incubation experiments describe above, C_0 is the radon concentration detected in the overlying water before incubation experiment, D_s represents the effective wet bulk sediment diffusion coefficient (m^{2}day^{-1}), T is the water temperature and ø is the sediment porosity.

Porosity of the sediment can be calculated using equation 5 below:

$$\emptyset = \frac{(\frac{W_D}{\rho_w})}{(W_D/\rho_w)+(1-W_D/\rho_{dry})} \quad (5)$$

where W_D represents the water fraction presents in the sediments; ρ_w (g/cm^3) represents the water density of the surface water and ρ_{dry} (g/cm^3) represents the dry grain density measured by dividing oven-dry soil weight with the volume of soil solids.

Atmospheric evasion

A seven-hour continuous measurement of radon-in-air by two units of RAD7s next to downstream (G1) and upstream (G5) sites was conducted to estimate the radon loss from the river through atmospheric evasion. The radon loss due to atmospheric evasion was calculated by using the following equation 6:

$$Rn_{atmophere} = k(C_w - \propto C_{atm}) \quad (6)$$

where $Rn_{atmosphere}$ represents radon atmospheric evasion flux; C_w is the radon concentration in river; C_{atm} represents radon concentration in the air; $\propto$ is the Ostwald's solubility coefficient (0.2 at 30 °C) [29]; *k* is the piston velocity or gas transfer velocity at water-air boundary. The piston velocity of radon can be inferred from wind and current velocity as mentioned in [30]. The *k* value is calculated using equation 7:

$$k = 1 + 1.719w^{(0.5)}h^{-0.5} + 2.58u_{10} \quad (7)$$

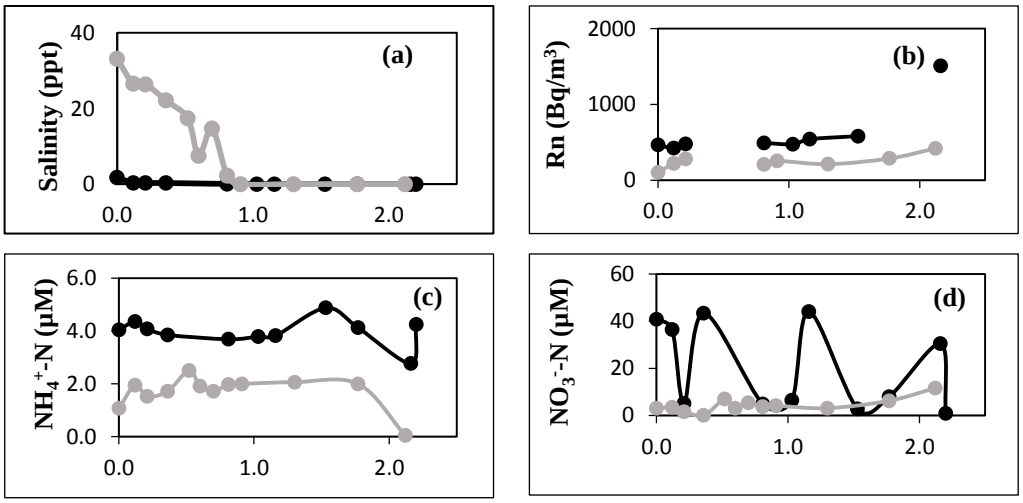
where w is the water current velocity (cms^{-1}) in river measured by a handheld flowmeter (Hach, USA), h is the effective depth of water exchanging with the atmosphere (m), in this case, the average water depth of Ular River was adopted. u_{10} is the wind speed (ms^{-1}) recorded by a portable digital anemometer (Kanomax, USA) on hourly basis during the radon-in-air sampling.

Results and Discussion

Variations of the water quality in Ular River during base flow and post-storm conditions

The physicochemical and nutrients data for all water samples are presented in Table 1. Figure 4a displays a clear seasonal variation of salt water intrusion in Ular River. During the dry period (March 2015), salt-wedge reached its maximum of ~700m from river mouth with the salinity ranged from 0.02 to 33.12 psu. In contrast, the water salinity stayed relatively fresh (< 2ppt) during the post-storm period (January 2015) in Ular River.

Figure 4b shows higher radon concentration (average: 620 Bq/m^3, n=8) observed after the storm event as compared to the dry period (average: 248 Bq/m^3, n=8). Higher radon concentration during the post-storm event could be the result of increased groundwater influx from the shallow aquifer into the river basin [34]. Rapid increase of groundwater table during the storm period could increase the hydrostatic pressure thus increase the lateral groundwater discharge into adjacent river [31, 32]. Level of radon recorded during post-storm was at least one magnitude higher compared to the dry period, indicates high portion of groundwater contributing to storm flow generated in Ular River.



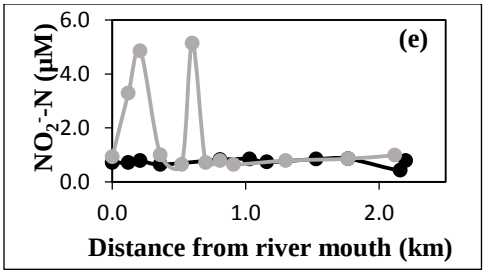


Figure 4. Longitudinal variation of salinity, radon and nutrient parameters in Ular River against distance from the river mouth; post-storm period (Jan 2015) in black and dry period (March 2015) in grey

Table 1. Physicochemical and nutrient data for both surface and groundwater

	Site	Latitude °	Longitude °	DO mg/L	pH	°C	Salinity ppt	Phosphate µM	Ammonia µM	Nitrate µM	Nitrite µM	Radon Bq/L
Ular River, January 2015	F1	5.67878	102.71206	4.67	7.51	26.9	1.75	0.02	4.05	40.9	0.71	0.47
	F2	5.67789	102.71294	4.02	6.10	27.1	0.34	<LOD	4.35	36.4	0.71	0.42
	F3	5.67647	102.71317	3.73	5.99	27.3	0.31	<LOD	4.08	5.01	0.79	0.48
	F4	5.67600	102.71314	3.66	5.97	27.6	0.32	<LOD	3.85	43.4	0.64	N/A
	F5	5.67306	102.71472	3.68	5.91	28.6	0.08	<LOD	3.69	4.75	0.82	0.49
	F6	5.67092	102.71472	3.53	5.59	29.2	0.02	0.03	3.78	6.44	0.85	0.47
	F7	5.66933	102.71397	3.35	5.57	29.7	0.02	<LOD	3.82	44.1	0.74	0.54
	F8	5.66881	102.71383	3.39	5.65	29.6	0.02	<LOD	4.87	2.73	0.84	0.58
	F9	5.66903	102.71106	3.43	5.57	29.6	0.02	<LOD	4.13	7.93	0.86	N/A
	F10	5.66792	102.70772	3.42	5.40	27.1	0.02	<LOD	2.77	30.43	0.43	1.51
	F11	5.66825	102.70769	3.34	5.49	30.0	0.01	<LOD	4.25	0.86	0.79	N/A
Ular River, March 2015	S1	5.67875	102.71257	5.96	6.80	31.8	33.1	0.06	1.07	3.00	0.93	0.10
	S2	5.67788	102.71298	2.81	7.94	33.9	26.5	0.03	1.95	3.43	3.29	0.22
	S3	5.67647	102.71317	4.25	7.66	32.1	26.4	<LOD	1.52	1.57	4.86	0.28
	S4	5.67573	102.71342	3.55	7.58	33.2	22.2	<LOD	1.72	<LOD	1.00	N/A
	S5	5.67418	102.71457	5.46	7.90	33.5	17.4	<LOD	2.50	7.00	0.64	N/A
	S6	5.67367	102.71500	4.43	7.49	33.5	7.53	<LOD	1.91	3.00	5.14	N/A
	S7	5.67343	102.71485	4.65	7.48	33.3	14.7	<LOD	1.72	5.36	0.71	N/A
	S8	5.67306	102.71472	5.30	7.84	32.8	2.27	<LOD	1.97	3.64	0.79	0.21
	S9	5.67248	102.71477	6.62	7.71	33.3	0.02	<LOD	2.00	4.07	0.64	0.26
	S10	5.66908	102.71472	6.00	8.47	35.3	0.03	<LOD	2.06	3.07	0.79	0.21
	S11	5.66903	102.71106	7.06	9.32	35.4	0.03	<LOD	2.00	6.21	0.86	0.29
	S12	5.66758	102.70770	6.91	8.12	33.0	0.03	<LOD	0.04	11.6	0.99	0.42
Ular River, May 2016	G1	5.67852	102.71234	1.79	7.22	33.1	27.7	<LOD	8.43	1.39	0.04	0.09
	G2	5.67228	102.71456	5.34	6.86	31.1	5.27	<LOD	4.03	0.66	0.03	0.05
	G3	5.66834	102.71395	4.31	7.42	33.6	21.1	<LOD	3.40	0.54	0.09	0.05
	G4	5.66806	102.71206	2.47	5.86	31.1	0.21	<LOD	4.53	2.69	0.08	0.09
	G5	5.66828	102.70960	6.06	5.90	31.6	0.03	<LOD	4.25	0.84	0.15	0.11
	G6	5.66754	102.70719	3.48	5.16	30.3	0.03	<LOD	0.29	0.14	0.11	0.19
	G7	5.66857	102.70468	7.46	6.39	34.0	0.03	<LOD	12.3	0.39	0.13	0.12
	G8	5.67118	102.70133	6.67	5.81	34.2	0.03	<LOD	14.2	1.99	0.07	0.21
	G9	5.66888	102.70164	2.55	4.16	30.8	0.03	<LOD	3.93	1.27	0.09	0.20
	G10	5.67400	102.69916	5.05	5.27	32.8	0.03	<LOD	15.6	0.12	0.05	0.20
	G11	5.67659	102.69529	3.30	4.56	32.2	0.03	<LOD	16.1	0.93	0.07	0.37
	G12	5.67782	102.69531	3.20	5.34	30.8	0.05	<LOD	27.2	0.09	0.03	0.13
	G13	5.66819	102.71607	1.89	6.88	33.3	0.02	<LOD	9.96	0.65	0.10	N/A
	G14	5.66941	102.71164	7.13	6.06	31.2	0.03	<LOD	N/A	0.93	0.15	0.07
Lake	H1	5.67581	102.69409	2.51	5.33	27.7	0.01	N/A	<LOD	1.69	0.26	1.90
	H2	5.67614	102.69494	4.48	5.66	29.0	0.01	N/A	<LOD	5.86	0.23	0.35
	H3	5.67581	102.69409	4.30	5.78	29.6	0.01	N/A	16.0	0.72	0.26	0.11

Table 1 (cont'd). Physicochemical and nutrient data for both surface and groundwater

	Site	Latitude °	Longitude °	DO mg/L	pH	°C	Salinity ppt	Phosphate µM	Ammonia µM	Nitrate µM	Nitrite µM	Radon Bq/L
Groundwater	P1_1	5.678597	102.712228	1.38	6.82	29.0	21.1	N/A	162	5.57	0.07	0.64
	P1_2	5.678597	102.712228	0.39	6.72	29.0	25.9	N/A	<LOD	6.71	0.07	1.23
	P2_1	5.672889	102.714317	0.45	3.74	28.4	3.84	N/A	34.7	2.93	0.21	0.23
	P2_2	5.672889	102.714317	0.55	5.26	28.6	4.83	N/A	83.1	2.36	0.21	0.32
	P2_3	5.672889	102.714317	0.63	5.55	28.5	4.86	N/A	119	5.29	0.14	1.48
	P2_4	5.672889	102.714317	0.57	5.44	28.8	5.01	N/A	148	12.4	0.14	1.56
	P3_1	5.668772	102.710153	0.66	5.52	29.5	0.02	N/A	47.6	4.07	0.07	1.16
	P3_2	5.668772	102.710153	0.34	5.12	29.3	0.03	N/A	37.8	4.36	0.07	1.09
	P3_3	5.668772	102.710153	0.57	5.44	28.8	5.01	N/A	118	54.4	0.36	1.27
	B1_1	5.672200	102.716781	0.66	5.52	29.5	0.02	N/A	26.3	9.43	0.14	N/A
	B1_2	5.672200	102.716781	0.43	5.64	28.5	0.07	N/A	19.4	7.29	0.14	1.35
	B2	5.672308	102.716236	0.45	3.74	28.4	3.84	N/A	38.1	22.1	0.14	N/A
	B3	5.669511	102.717411	0.77	4.35	29.7	0.02	N/A	17.0	81.0	0.14	1.26
	B4_1	5.673775	102.710578	2.38	5.37	30.1	0.02	N/A	11.5	7.64	0.07	2.78
	B4_2	5.673775	102.710578	0.52	5.52	30.1	0.02	N/A	13.1	8.64	0.07	2.46
	B4_3	5.673775	102.710578	3.30	6.88	29.8	0.02	N/A	10.2	16.0	<LOD	2.21
	B5_1	5.674797	102.700203	3.70	4.60	29.3	0.01	N/A	15.1	35.7	<LOD	1.28
	B5_2	5.674797	102.700203	3.99	3.78	29.5	0.01	N/A	3.36	36.0	0.07	1.47
	B5_3	5.674797	102.700203	3.77	4.95	29.6	0.01	N/A	6.57	67.6	0.07	1.34

<LOD: below detection limit; N/A: no measurement

The radon level was found higher at the upstream (Figure 4b and 5) and decreasing in concentration as the water flows downstream. This trend is probably due to significant dilution of radon concentration by the lagoon water at the river mouth, coupled with addition radioactive decay loss of the short half-life of radon during its transport down the river.

Ammonium and nitrate concentrations were higher in the post-storm sampling with an average of 3.97 NH_4^+-N µM and 20.3 NO_3^--N µM than to the dry season condition with 1.71 NH_4^+-N µM and 4.33 NO_3^--N µM recorded, respectively. However, both parameters showed no clear distribution trends in Ular River. Sources of nitrogen in the water body can be derived from agricultural runoff and sewage discharge from the residential area. Since groundwater often contains higher nitrogen concentrations than the surface water.

The average of NO_2^--N and PO_4^{3-}-P during both dry period and post-storm sampling were 1.72 NO_2^--N µM and 0.01 PO_4^{3-}-P µM, and 0.74 NO_2^--N µM and below detection limit (PO_4^{3-}P: <0.01 µM), respectively. Nitrite and phosphate concentrations were found higher at downstream sites (Figure 3e, f). Higher nutrient concentrations observed at the downstream suggested possible input from the lagoon water. In contrary to most of the parameters studied, the concentrations of these nutrients were also higher during dry period.

Radon inventory and groundwater discharge in Ular River

The inventories for radon sources, sink, groundwater discharge rate and its associated nutrient fluxes are presented in Table 2. The average groundwater radon concentration obtained is 1061±665 Bq/m^3; this value is approximately three times higher than the average radon concentration of 358±246 Bq/m^3 observed in the surface water. Figure 5 shows that the groundwater discharge hotspots occur at upper and middle part of Ular River (G7-G12).

The radon loss through atmospheric evasion was calculated to be 4198±259 Bq/m^2day^{-1}, which accounted for only about 0.01% of the total radon inventories studied in the model. Radon input contributed from the dissolved radium and sediment diffusion was also not insignificant. The radon inventories for both product of radium decay and sediment diffusion are 1.92±0.47 Bq/m^3 and 0.75±0.33 Bq/m^2day, respectively.

With the assumption of the river flow is steady and uniform, groundwater discharge rate in Ular River could account up to 6649±6178 m^3day^{-1} (Table 2). Since the total riverine flow is a sum of surface water flow and the groundwater flow into the river, the percentage of groundwater flow contributed to the surface water can be calculated. the groundwater flow is equivalent to ~33% of the total riverine flow in Ular River. This value is higher than most of the values reported elsewhere; where most estimation of the fresh groundwater fluxes into the river ranged from 0.6%-16% of the total riverine flow [12, 14, 33].

Table 2. Radon inventories and mass balance input for radon box model

Inventory	**Symbol and Unit**	**Concentration ± SD (n)**
^{222}Rn in the surface water	$Rn_{surface}$ (Bqm^{-3})	358±246 (14)
^{222}Rn in the groundwater	$Rn_{end\text{-}member}$ (Bqm^{-3})	1061±665 (17)
Radon sources		
^{222}Rn from the radium in water	Rn_{radium} (Bqm^{-3})	1.92±0.47 (6)
^{222}Rn diffused from the sediment	$Rn_{sediment}$ ($Bqm^{-2}day^{-1}$)	0.75±0.33 (6)
Radon sinks		
Atmospheric evasion	$Rn_{atmospheric}$ ($Bqm^{-2}day^{-1}$)	4198±259 (2)
Box model		
River cross sections	m^2	5.31±5.78 (14)
Current velocity	ms^{-1}	0.11±0.13 (13)
Total riverine discharge	D_v (m^3day^{-1})	20355±19109 (13)
Groundwater discharge from aquifer	Q_{flux} (m^3day^{-1})	6649±6178 (13)
Dissolved inorganic nutrient fluxes		
Groundwater-derived NH_4^+-N flux	$moldays^{-1}$	$2.88\times10^2\pm2.67\times10^2$ (13)
Groundwater-derived NO_3^--N flux	$moldays^{-1}$	$1.23\times10^2\pm1.14\times10^2$ (13)
Groundwater-derived NO_2^--N flux	$moldays^{-1}$	0.75±0.69 (13)
Total riverine NH_4^+-N flux	$moldays^{-1}$	$1.93\times10^2\pm1.74\times10^2$ (13)
Total riverine NO_3^--N flux	$moldays^{-1}$	18.7±16.9 (13)
Total riverine NO_2^--N flux	$moldays^{-1}$	1.60±1.44 (13)

Higher groundwater discharge rate in Ular River could be attributed to both geomorphological setting and aquifer's properties. The underlying material in study area is highly permeable. Lithological examination on borehole core samples suggests that the aquifer material throughout the river composed of generally fine sand with thin sandy silt (~10cm) found at the top layer while the rest of the aquifer materials (~300cm) are composed of coarse and fine sands with the porosity percentage between 17%-26% throughout the river bed. Figure 5 shows that high groundwater discharge rate (radon concentration) near G11 could be driven by topographic-gradients. G11 received water from Berombak Lake flow southward through a narrow beach ridges valley with high and steep riverbank (+4m) created steep hydraulic gradient which induce more groundwater input to surface water. Furthermore, almost 90% of the Ular River catchment is occupied by oil palm plantation, the elevation of water table during irrigation may increase the hydraulic head pressure, intensify the groundwater discharge rate into the river basin. A combination of above mention factors resulted in a higher percentage of groundwater flow over the total riverine flow in Ular River.

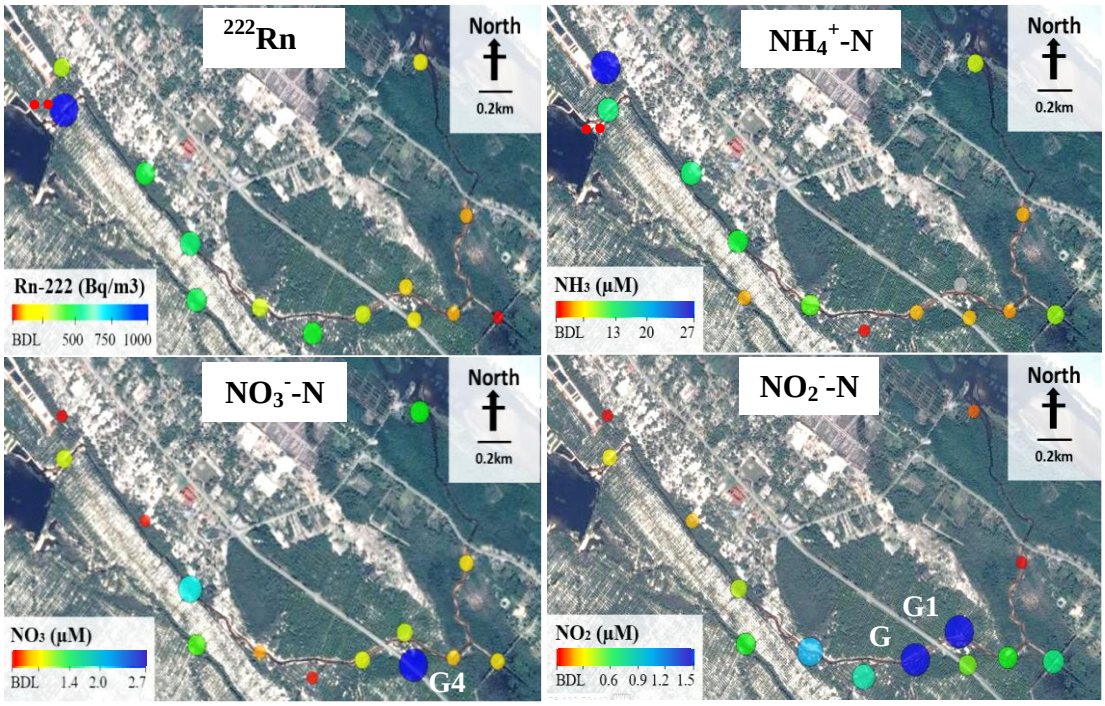


Figure 5. Radon and nitrogen-based nutrients distribution patterns in Ular River during May 2016 sampling. BDL = below detection limit: NH_4^+-N: <0.30µM; NO_3^--N: <0.10µM; NO_2^--N: <0.14µM.

Groundwater-derived nutrient fluxes

Groundwater sampling on May 2015 revealed a strong correlation between NH_4^+-N and radon concentrations in Ular surface water (Pearson correlation coefficient, r: 0.82, $p<0.05$). Figure 5 illustrates that both NH_4^+-N and radon concentrations peaked approximately 4km upstream from the estuary, decrease gradually to the downstream. We first suspect Berombak Lake to be the major source of ammonium however, NH_4^+-N concentration in Berombak Lake (H2, H3; Figure 5 & Table 1) was below detection limit, suggesting that the contamination input was derived from the groundwater source rather than from the Berombak Lake. One of the plausible NH_4^+-N contamination source could be came from the leakage of underground sewage septic tank located near to a residential area next to the oil palm plantation. Figure 5 also shows the concentration of NO_3^--N and NO_2^--N reaching their maximum in G4, G5 and G14, respectively; suggesting that the surface runoff from oil palm plantation would be more likely to be the source of these nutrients.

Groundwater nutrient fluxes to Ular River can be calculated by multiply the groundwater discharge rate in the river with the nutrient concentrations of the groundwater end-member [4, 33]. Calculation from the radon mass balance model showed that the groundwater contributes an average of 2.88×10^2 molday^{-1} NH_4^+-N, 1.23×10^2 molday^{-1} NO_3^--N and 0.75 molday^{-1} NO_2^--N into the Ular River, respectively (Table 2). These nitrogen species in the groundwater are probably derived from the agricultural seepage from the surrounding oil palm plantation. Ammonium sources could also be derived from the sewage discharge from the nearby residential area located nearby the upstream of the Ular River. Underground storage tank leakage, septic system failure resulted in clogging and malfunction of the septic drain field could also lead to soil and groundwater contamination when the untreated wastewater recharge to the shallow aquifer.

Conclusion

This study successfully identified the groundwater discharge hotspots and its relationship with nutrients distribution in Ular River. The radon mass balance model results show that groundwater discharge

represents a significant component of surface water balance accounted for about 33% of the total riverine flow. The strong correlation between radon and NH_4^+-N suggested that the source of ammonium in Ular River is groundwater-derived. However, nitrate and nitrite showed insignificant correlation with radon indicating that the origin of these nutrients could be derived from the surface runoff. However, this study is only tracing the effects of groundwater-derived nutrient from one of the freshwater-fed drainage channel or tributaries connected to the Setiu lagoon and its nutrients contribution percentage. There are large portions of unaccounted groundwater-derived nutrients inputs from the other tributaries from the lagoon itself which are yet to be studied as part of the nutrient budget in Setiu Wetlands which may warrant further investigation by future studies. In overall, this investigation would allow coastal manager to assess the magnitude of groundwater discharge and its nutrients contribution into the Setiu Wetlands and highlighted significance of groundwater-based nutrients in riverine and estuarine nutrient budgets.

Acknowledgement

This work was also made possible through the funding from Ministry of Higher Education of Malaysia, Niche Research Grant Scheme (NRGS-53131). NCW wished to thank Malaysian Government for MyBrian15 scholarship.

References

1. Buddemeier, R. W. (1996). Groundwater discharge in the coastal zone. *Ecological Economics*, 35(200): 25–33. Burnett, W. C. Taniguchi, M. and Oberdorfer, J. (2001). Measurement and significance of the direct discharge of groundwater into the coastal zone. *Journal of Sea Research*, 46(2), 109–116.
2. Johnson, A. G., Glenn, C. R., Burnett, W. C., Peterson, R. N. and Lucey, P. G. (2008). Aerial infrared imaging reveals large nutrient-rich groundwater inputs to the ocean. *Geophysical Research Letters*, 35 (15): 1–6.
3. Lee, Y. W., Hwang, D. W., Kim, G., Lee, W. C. and Oh, H. T. (2009). Nutrient input from submarine groundwater discharge (SGD) in Masan Bay, an embayment surrounded by heavily industrialized cities, Korea. *Science of the Total Environment*, 407: 3181–3188.
4. Burnett, W. C., Aggarwal, P. K., Aureli, A., Bokuniewicz, H., Cable, J. E., Charette, M. A., Kontar, E., Krupa, S., Kulkarni, K. M. and Loveless, A. (2006). Quantifying submarine groundwater discharge in the coastal zone *via* multiple methods. *Science of the Total Environment*, 367: 498–543.
5. Cable, J. E., Burnett, W. C., Chanton, J. P. and Weatherly, G. L. (1996). Estimating groundwater discharge into the northeastern Gulf of Mexico using radon-222. *Earth Planetary Science Letters*, 144: 591-604.
6. Dulaiova, H., Gonneea, M. E., Henderson, P. B. and Charette, M. A. (2008). Geochemical and physical sources of radon variation in a subterranean estuary–implication for groundwater radon activities in submarine groundwater discharge studies. *Marine Chemistry*, 110, 120–127.
7. Lerman, A. (1979). Geochemical processes. Wiley-Interscience. New York: p. 481.
8. Schubert, M., Knoeller, K., Treutler, H.-C., Weiss, H. and Dehnert, J. (2006). ^{222}Rn as a tracer for the estimation of infiltration of surface waters into aquifers, in Radionuclides in the environment Povinec, P. P. and Sanchez-Cabeza,
9. J. A. (Editor). *Radioactivity in the Environment*, 8: 326–334.
10. Burnett, W. C. and Dulaiova, H. (2003). Estimating the dynamics of groundwater input into the coastal zone *via* continuous radon-222 measurements. *Journal of Environmental Radioactivity*, 69 (1-2): 21–35.
11. Mullinger, N. J., Binley, A. M., Pates, J. M. and Crook, N. P. (2007). Radon in Chalk streams: Spatial and temporal variation of groundwater sources in the Pang and Lambourn catchments, UK. *Journal of Hydrology*, 339: 172–182.
12. Schwartz, M. C. (2003). Significant groundwater input to a coastal plain estuary: Assessment from excess radon. *Estuarine, Coastal and Shelf Science*, 56: 31–42.
13. Swarzenski, P.W., Orem, W.H., McPherson, B.F., Baskaran, M. and Wan, Y. (2006). Biogeochemical transport in the Loxahatchee river estuary: the role of submarine groundwater discharge. *Marine Chemistry*, 101: 248–265.
14. Santos, I. R. and Eyre, B. D. (2011). Radon tracing of groundwater discharge into an Australian estuary surrounded by coastal acid sulphate soils. *Journal Hydrology*, 396: 246-257.

15. Burnett, W. C., Peterson, R. N., Santos, I. R. and Hicks, R. W. (2010). Use of automated radon measurements for rapid assessment of groundwater flow into Florida streams. *Journal of Hydrology*. 380: 298–304.
16. Peterson, R. N., Burnett, W. C., Dimova, N. and Santos, I. R. (2009). Comparing measurement methods for radium-226 on manganese-fiber. *Limnology and Oceanography*. 7: 196–205.
17. Durridge Company Inc. (2014). RAD H2O user manual radon in water accessory.
18. Baskaran, M. (2016). Radon measurement techniques in: Radon: A tracer for geological, geophysical and geochemical studies. *Springer Geochemistry*: pp. 15-35.
19. Dulaiova, H., Peterson, R. N., Burnett, W. C. and Lane-Smith, D. (2005). A multi-detector continuous monitor for assessment of ^{222}Rn in the coastal ocean. *Journal of Radioanalytical and Nuclear Chemistry*, 263, 361–365.
20. Najilah, M., Nadirah, M., Sakri, I. and Shaharom-Harrison, F. (2010). Bacteria associated with wild mud crab (*Scylla serrata*) from Setiu Malaysia with emphasis on antibiotic resistance. *Pakistan Journal of Biological Sciences*, 13(6): 293–297.
21. Suratman, S., Mohd Tahir, N., Jusoh, S. R. and Ariffin, M. M. (2005). Assessment of anthropogenic effects on water quality in Setiu Wetland, Terengganu. *Sains Malaysiana*, 34: 87–92.
22. Suratman, S., Hussein, A. N. A. R., Mohd Tahir, N., Latif, M. T., Mostapa, R. and Weston, K. (2016). Seasonal and spatial variability of selected surface water quality parameters in Setiu Wetlands, Terengganu, Malaysia. *Sains Malaysiana*, 45(4): 551–558.
23. Rosnan, Y., Mohd, L.H. and Noor, A. M. S. (1995). Grain-size distribution of sediment in the vicinity of Setiu lagoon-estuary system. *Pertanika Journal of Tropical Agricultural Science*, 18(1): 71–76.
24. Department of Irrigation and Drainage Malaysia (2016). Flood information. Access from http://infobanjir.water.gov.my/. [Access date on 10 October 2016].
25. Lee, J-M. and Kim, G. (2006). A simple and rapid method for analyzing radon in coastal and groundwaters using a radon-in-air monitor. *Journal of Environmental Radioactivity*, 89(3): 219–228.
26. APHA. (2005). Standard methods for the examination of water and wastewater, 21st edition. American Public Health Association, Washington, DC.
27. Kim, G., Burnett, W. C., Dulaiova, H., Swarzenski, P. W., Moore, W. S. (2001). Measurement of ^{224}Ra and ^{226}Ra activities in natural waters using a radon-in-air monitor. *Environmental Science and Technology*, 35: 4680–4683.
28. Corbett, D., Burnett, W., Cable, J. E. and Clark, S. B. (1998). A multiple approach to the determination of radon fluxes from sediments. *Journal of Radioanalytical and Nuclear Chemistry*, 236: 247–252.
29. Clever, H. L. (1979). Solubility Data Series. Krypton, Xenon & Radon-Gas solubilities. Pergamon Press, Oxford.
30. Dulaiova, H., and Burnett, W. C. (2006). Radon loss across the water–air interface (Gulf of Thailand) estimated experimentally from ^{222}Rn-^{224}Ra. *Geophysical Research Letters*, 33(5): 1–4.
31. Hamada, H., Sukchan, S. and Putiso, M. (2005). Measurement of ^{222}Rn concentrations in surface water in northern Thailand. *Radioisotopes*, 54: 315–320.
32. Fetter, C. W. (1994). Applied hydrogeology (3rd Edition). McMillian, New York.
33. Charette, M. A. and Buesseler, K.O. (2004). Submarine groundwater discharge of nutrients and copper to an urban sub estuary of Chesapeake Bay (Elizabeth River). *Limnology and Oceanography*, 49(2), 376–385.

Malaysian Journal of Analytical Sciences, Vol 22 No 3 (2018): 429 - 434
DOI: https://doi.org/10.17576/mjas-2018-2203-07

MALAYSIAN JOURNAL OF ANALYTICAL SCIENCES
Published by The Malaysian Analytical Sciences Society
ISSN 1394 - 2506

MECHANICAL PROPERTIES OF BIOPLASTIC FROM JACKFRUIT SEED FLOUR AND POLYPROPYLENE

(Sifat Mekanikal Bioplastik daripada Tepung Biji Nangka dan Polipropelina)

Fairuzdzah Ahmad Lothfy*, Asiah Mohd Nor, Syamsyir Akmal Senawi, Nur Sha'adah Zainuddin, Ermadasila Mohmad, Nur Aina Shuhada Norzeri, Nur Yasmin Sahira Saifful Bahri, Puteri Elyana Natasa Mohmad Azmi, Aliya Nuharissa Kamaruzaman

Faculty of Applied Sciences,
Universiti Teknologi MARA Pahang, 26400 Bandar Tun Razak Jengka, Pahang, Malaysia

**Corresponding author: fairuzdzah@pahang.uitm.edu.my*

Received: 4 December 2016; Accepted: 1 December 2017

Abstract

In this study, the bioplastic was successfully fabricated from jackfruit seed flour/polypropylene blend. Nowadays, the plastic used are originally from petroleum, in which is limited resources and non-degradable polymer that causes environmental problem. The jackfruit (*Artocarpus heterophyllus*) has been commercially produced in the farming industry. Approximately 8 to 15 % of jackfruit are mostly thrown after consumption. Thus it can be used as the value added product development for future demand. In this study, the jackfruit seeds flour was plasticized by using glycerol, and blended with different ratios of polypropylene. The mechanical properties such as tensile strength, strain at break, flexibility and water absorption of fabricated bioplastic were investigated. The tensile strength and strain at break decreased with increasing of jackfruit seed flour content, while Young's Modulus increased with the jackfruit seed flour content increased. Addition of polypropylene demonstrated higher water resistant ability. The jackfruit seed can be a new resource of bioplastic that could be preserved as a petrochemical resource and reduces the environmental impact.

Keyword: bioplastic, jackfruit seed, mechanical properties, polypropylene, water absorption

Abstrak

Dalam kajian ini, bioplastik berjaya dihasilkan dari campuran tepung biji nangka/polipropilena. Kini, plastik yang digunakan berasal daripada petroleum, di mana sumber yang terhad dan polimer yang tidak boleh degradasi yang menyebabkan masalah kepada alam sekitar. Buah nangka (*Artocarpus heterophyllus*) telah dihasilkan secara komersil dalam industri pertanian. Kira-kira 8 hingga 15% daripada nangka dibuang selepas penggunaan. Oleh itu, ia boleh digunakan sebagai nilai tambah produk untuk permintaan masa depan. Dalam kajian ini, tepung biji nangka telah diplastikkan dengan menggunakan gliserol, dan dicampur dengan polipropilena dengan nisbah yang berlainan. Sifat-sifat mekanik seperti kekuatan tegangan, ketegangan pada rehat, fleksibiliti dan penyerapan air bioplastik dikaji. Kekuatan tegangan dan ketegangan pada rehat menurun dengan peningkatan kandungan tepung biji nangka, sementara *Modulus Young* meningkat dengan kandungan tepung biji nangka meningkat. Penambahan polipropilena menunjukkan keupayaan tahan air yang lebih tinggi. Biji nangka dapat menjadi sumber bioplastik baru yang dapat dipelihara sebagai sumber petrokimia dan mengurangkan kesan kepada persekitaran.

Kata kunci: bioplastik, biji nangka, sifat mekanik, polipropilena, penyerapan air

Introduction

Bioplastics can be fabricated by whole or some parts from renewable biomass sources such as sugarcane and corn, or from microbe such as yeast [1]. According to European Bioplastics, bioplastic is defined if the plastic made of bio-based, biodegradable, or features both properties [2]. **The Future of Bioplastics for Packaging to 2020** examines the global market for bioplastic packaging and concludes with an assessment of the key challenges and opportunities that face suppliers in the wider commercialization of bioplastics for food and drink packaging [3]. Nowadays, bioplastics have become a necessity in many industrial applications such as food packaging, agriculture and horticulture, composting bags, and hygiene. With increasing demand for global plastic consumption in many branches, a lot of research is being dedicated toward exploring green materials and new ways to produce bioplastic [1].

The greater amount used for synthetic packaging films has led to a serious ecological problems due to their total non-biodegradability [4]. Commonly, synthetic thermoplastics are blended with starch or other biopolymer to enhance the potential biodegradability of polyolefin [5]. Polypropylene (PP), a synthetic polymer is an economical material that provides excellent physical, mechanical, thermal, and chemical properties that are not found in any other thermoplastic polymer [6]. According to Obasi et al., PP has good properties such as high strength and flexibility, good process ability, excellent resistance to acids, alcohols, bases and esters and dimensional stability [7]. Even so, PP wastes persist for many years after disposal and might be causing environmental hazards. The introduction of biodegradable polymers or natural fillers such as starch in PP based materials formulation might be considered as a credible alternative in the development of eco-friendly material and overcome non-degradability issue [7]. Obasi et al. concluded that the blend of PP/cassava starch increases the starch content, increases the surface area available for the microbial agents to 'attack and eat' the starch-PP blend, and increases the biodegradation rate [8]. Therefore, researchers have studied the incorporation of biodegradable polymers, such as jackfruit seed into the PP, which is justified by the presence of hydrolysable groups in the natural polymer that are able to induce the biodegradation of the PP and demonstrates significant potential in the bioplastic field.

Artocarpus heterophyllus Lam., or jackfruit, is a non-seasonal plant with many benefits [9]. Jackfruit (***Artocarpus heterophyllus*** L.) belongs to the family *Moraceae* and contributes to the value of agricultural production in Malaysia. According to Agrofood Statistics 2014, the production of jackfruit in Malaysia increases every year and achieves for 33,788 tonne at 2014 [10]. About 8 to 15% of the total fruit Jackfruit weight were seeds and it's have fairly high carbohydrate and protein contents [11]. Starch is a natural carbohydrate storage material accumulated by green plants in the form of granules. It is composed of linear polysaccharide molecules (amylose) and branched molecules (amylopectin) that are attractive raw material for use as barriers in packing materials [12]. The jackfruit seeds starch compositions are moisture 13.0%, fat (0.64%), protein (0.32%), ash (0.22%), and amylose (28.1%) [12]. Jackfruit's seeds comprise 90% of starch content [13]. Jackfruit seeds starch consists of two macromolecules: amylose (20–30%) and amylopectin (70–80%), which are associated with each other by hydrogen bonds [14]. Menzel et al. found that the increased amylose content and structural changes in amylopectin enhances film-forming behavior and improves barrier and tensile properties in starch films [15].

Materials and Methods

Jackfruits (*Artocarpus heterophyllus*) were chosen based on uniformity and visually free from defects were purchased at local market. At first, ripened fruit de-husked and their seeds were removed, cleaned, and rinsed thoroughly with sterile distilled water. The brown seed coats were removed. The fleshy white cotyledons were collected by scrubbing through water. Subsequently, the cleaned jackfruit seeds were chopped into small dimensions. Then, the seeds were dried by air circulation. By using Rotor Beater Mill SR 200, the chopped seeds were milled into flour. Then, the flour was sieved (100 mesh) and collected. Firstly, 20% of water was mixed into the jackfruit seed powder. Glycerol and hydrochloric acid 0.1 M were gradually added into the mixture. After that, the mixture was heated and stirred until almost boiling point. Sodium hydroxide 0.1 M were added and the mixture was poured into petri dish. The mixture was dried at room temperature. Subsequently, the sample was crushed by using crusher machine. After that, the crushed sample and polypropylene was blended into rheomixer at 170 $^{\circ}$C by ratio 9:1, 7:3, and 5:5. The blended sample was crushed again and poured into mold by using hot press machine at 170 $^{\circ}$C for 5 minutes and cold press at 0 $^{\circ}$C.

The mechanical properties of the fabricated bioplastic were determined from tensile stress, maximum strain, and Young's modulus by using Testometric Materials Testing machine. To obtain these values, 15 mm wide section and initial length 25 mm of the bioplastic sample was cut and attached to Testometric Materials Testing machine. Each end of the samples was clamped and the upper clamp of the sample was pulled up until it was broken. The information such as the tensile stress, maximum strain, and Young's modulus were measured.

The bioplastic samples were cut into 1 cm x 1 cm for water absorption test. Each sample was weighed prior to immersion in distilled water. Subsequently, the surfaces were wiped until it became dry, re-weighed, and calculated for the percentage of water absorption. Results were recorded every 5 days for 20 days. Three samples were used for each formulation and the average was determined. The percentage of water absorption, % M_t was calculated according to equation 1 below:

$$\% \, M_t = \frac{W_s - W_o}{W_o} \times 100 \quad (1)$$

whereas, M_t = total water absorption, W_s = weight of sample after immersion in water and W_o = original weight of sample before immersion.

Results and Discussion

Mechanical properties of the fabricated bioplastic were determined by calculating the maximum strain, tensile stress and Young's modulus values. Fundamentally, biological polymers show good biocompatibility, but their mechanical properties are often poor. Hence, the jackfruit seeds/ polypropylene blends in order to improve the mechanical properties of the fabricated bioplastic.

Figure 1 shows the variation of the tensile strength and strain percentage with the blend ratio of jackfruit seeds/PP. This figure showed that by increasing the amount of jackfruit seeds in the fabricated bioplastic, the tensile strength and the strain percentage of bioplastic decreased accordingly. It was clear that the tensile strength and elongation at break of jackfruit seeds/PP blends decreased from 12.07 M Pa to 8.16 M Pa and 10.3% to 7.03% respectively. Gupta (2014) studied that the tensile strength is 30.23 MPa [16]. From the results, it showed that more than 50% of the tensile strength and percentage of strain decreased after adding 50% of jackfruit seed into the blend. It is possible that the reduction of tensile strength and strain percentage is the amorphous nature of the jackfruit seed which has increased the brittleness. Similarly, the same observation occurred in the previous literatures [17, 18]. Shafiq et al. also found that the tensile strength and strain percentage decrease with increasing the percentage of corn starch in PVA/corn starch film [18]. The research concludes that the amorphous nature of starch increase the brittleness lead to decreasing of tensile strength and stain percentage. Research conducted by Parvin et al. the tensile strength of PVA/ starch decreased due to increasing of crystallization of the blend. The researcher observed the crystallization by using the micrograph analysis [17]. Rosa et al. observes the same behavior for high density polyethylene/polypropylene (HDPE/PP) starch blends [12]. These results are similarly shown in the previous work by Toh Wen et al. which finds the same trend of the graph for the study on poly vinyl alcohol)/sago pith waste (SPW) [5]. The tensile strength and elongation at break decreases with increasing SPW content and conclude the decreasing strength with increasing starch content contributed to the poor interfacial adhesion of the two components [5].

Figure 2 shows that Young's modulus increased from 1901.12 M Pa at 50 wt %, 2207.68 M Pa at 70 wt %, and 2598.38 M Pa at 90 wt %. Young's modulus increased because of the stiffening effect of the granules. The hydrogen bonding in starch of jackfruit seed gave higher modulus than that of a semi-crystalline polymer like PP, with no hydrogen bonding [7]. A similar result is shown in previous work by Toh Wen et al. where the incorporation of SPW fillers into PVA has led to an increase in the modulus of the composites. This condition is due to that starch granules are stiffer than the PVA matrix in which they are dispersed [5]. Another of probability for the high modulus was due to the fact that jack fruit seed granules were not melting and retain their shape as rigid filler during processing. As the jackfruit seed contents increased, particles were crowded and reduced the particle-matrix interaction. The fabricated bioplastic became more rigid and stiffer with increasing percentage of jackfruit seed.

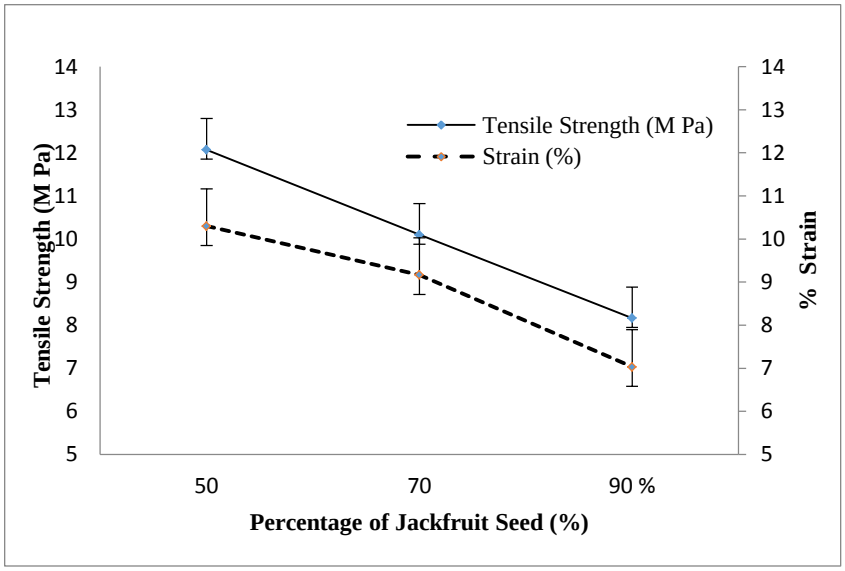


Figure 1. Variation of the tensile strength and percentage of strain with the percentage of jackfruit seeds in the blend

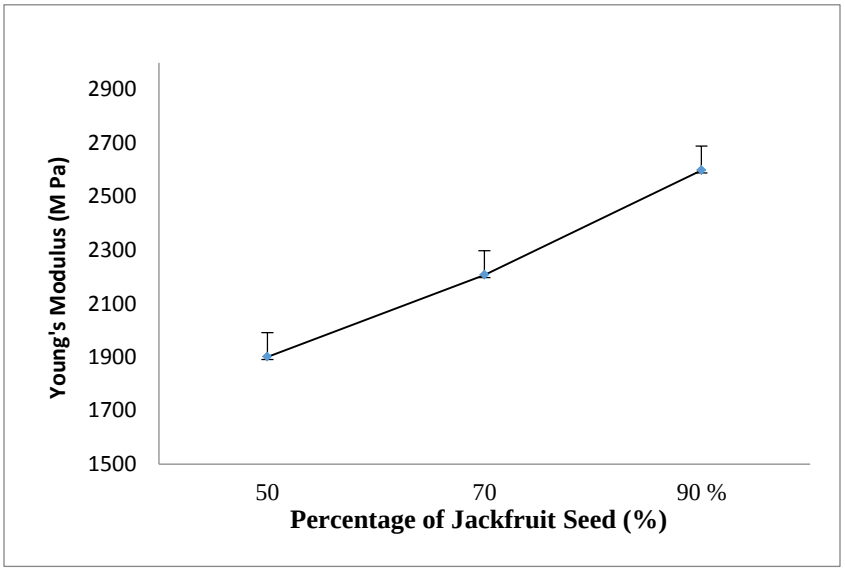


Figure 2. Variation of the Young's Modulus with the percentage of jackfruit seeds in the blend

Figure 3 shows the percentage of water absorbed by jackfruit seeds/PP blends bioplastic as a function of time. Water absorption increased with increasing immersion time and jackfruit seed content. This observation was due to the hydrophilic nature of jackfruit seed whereas have 25% to 40% of the quantity of starch was responsible for the water absorption in the blends. Hence, at higher jackfruit seed content, a higher amount of water was being absorbed. The increment of water absorption for jackfruit seed/PP blends was about 4.76%, 13.33% and 23.08% at 50 wt.%, 70 wt.% and 90 wt.% of the jackfruit seed contents. The higher percentage water absorption increment to

90 wt. % was due to the leaching away of jackfruit seed particles from the samples at high content with increasing time. By increasing the jackfruit seed content in the blends, it reduced interfacial compatibility of hydrophilic particles with hydrophobic polymer matrices (PP). Thereby, the blends would cause weaker adhesion between the composition and subsequently increase dispersion of water within the blends and enhance the moisture uptake rate [19].

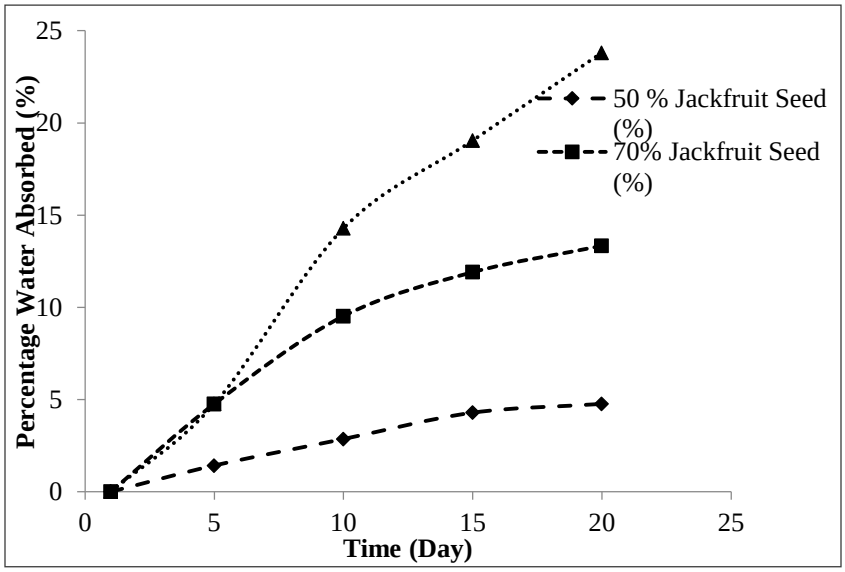


Figure 3. Percentage water absorption of jackfruit seeds/PP blend bioplastic

Conclusion

As conclusion, the results of mechanical strength show that all types' compositions in the blend have suitability properties for fabricating the bioplastic. The higher composition of jackfruit seeds in the blend will produce the bioplastic with the lower water resistance because the higher absorption rate. Although, all types composition show that the percentage of water absorption less than 25 %. Hence, the suitability for choosing the composition to fabricate the bioplastic depend on their own application.

Acknowledgement

Authors acknowledge the financial support for this research from the Universiti Teknologi MARA Pahang.

References

1. Ashter, S. A. (2016). New developments introduction to bioplastics engineering. Oxford: William Andrew Publishing, New York: pp. 251-274.
2. Gill, M. (2014). Bioplastic: A better alternative to plastics. *International Journal of Research in Applied, Natural and Social Sciences*, 2(8): 115-120.
3. The Future of Bioplastics for Packaging to 2020. (2015). United Kingdom: Smithers Pira.
4. Siracusa, V., Rocculi, P., Romani, S. and Dalla Rosa, M. (2008). Biodegradable polymers for food packaging: A review. *Trends in Food Science & Technology*, 19(12): 634–643.
5. Toh Wen, Y., Lai Jau, C. and Wan A. W. A. R. (2011). Mechanical and water absorption properties of poly(vinyl alcohol)/sago pith waste biocomposites. *Journal of Composite Materials*, 45(11): 1201-1207.
6. Rodriguez-Llamazares, S. (2013). Polypropylene/starch blends: Study of thermal and morphological properties. *Journal of the Chilean Chemical Society*, 58(1): 1643-1646.

7. Obasi, H. C. and Igwe, I. O. (2012). Cassava starch-mixed polypropylene bidegradable polymer: Preparation, characterization, and effect biodegradable products on growth of plants. *International Journal of Science and Research*, 3(7): 802-807.
8. Obasi, H., Onuoha, F., Eze, I., Nwanonenyi, S., Arukalam, I. and Uzoma, P. (2013). Effect of soil burial on properties of polypropylene (PP)/plasticized potato starch (PPS) blends. *The International Journal of Engineering and Science*, 2(8): 14-18.
9. Ismail, B. K. N. (2013). Consumer preference for jackfruit varieties in Malaysia. *Journal of Agribusiness Marketing*, 6: 37-51.
10. Ministry of Agriculture and Agro-Based Industry (2015). Agrofood Statistics 2014: Information Management and Statistics Section, Policy and Strategic Planning Division: pp. 39.
11. Tran, P. L., Nguyen, D. H. D., Do, V. H., Kim, Y.-L., Park, S., Yoo, S.-H. and Kim, Y.-R. (2015). Physicochemical properties of native and partially gelatinized high-amylose jackfruit (*Artocarpus heterophyllus* Lam.) seed starch. *LWT - Food Science and Technology*, 62(2): 1091-1098.
12. Rosa, D. S., Guedes, C. G. F. and Carvalho, C. L. (2007). Processing and thermal, mechanical and morphological characterization of post-consumer polyolefins/thermoplastic starch blends. *Journal of Materials Science*, 42(2): 551-557.
13. Madruga, M. S., de Albuquerque, F. S. M., Silva, I. R. A., do Amaral, D. S., Magnani, M. and Queiroga Neto, V. (2014). Chemical, morphological and functional properties of Brazilian jackfruit (*Artocarpus heterophyllus* L.) seeds starch. *Food Chemistry*, 143: 440-445.
14. Bobbio F. O., el Dash, A. A., Bobbio P. A. and Rodrigues L. R. (1978). Isolation and characterization of the physiochemical properties of the starch of jackfruit seeds (*Artocarpus heterophyllus*). *The American Association of Cereal Chemists*, 55(4): 505-511.
15. Menzel, C., Andersson, M., Andersson, R., Vazquez-Gutierrez, J. L., Daniel, G., Langton, M. and Koch, K. (2015). Improved material properties of solution-cast starch films: Effect of varying amylopectin structure and amylose content of starch from genetically modified potatoes. *Carbohydrate Polymers*, 130: 388-397.
16. Gupta A.P. and Alam, A. (2014). Study of flexural, tensile, impact properties and morphology of potato starch/polypropylene blends. *International Journal of Advanced Research*, 2(11): 599-604.
17. Shafik S. S., Majeed, K. J. and Kamil, M. I. (2014). Preparation of PVA/corn starch blend films and studying the influence of gamma irradiation on mechanical properties. *International Journal of Materials Science and Applications*, 3(2): 25-28.
18. Parvin, F., Rahman, M. A., Islam, J. M. M., Khan, M. A. and Saadat, A. H. M. (2010). Preparation and characterization of starch/PVA blend for biodegradable packaging material. *Advanced Materials Research*, 123-125: 351-354.
19. Visakh, P. M., L. Y. (2016). Starch-based blends, composites and nanocomposites. United Kingdom: Royal Society of Chemistry : pp 85-86.

Malaysian Journal of Analytical Sciences, Vol 22 No 3 (2018): 435 - 440
DOI: https://doi.org/10.17576/mjas-2018-2203-08

MALAYSIAN JOURNAL OF ANALYTICAL SCIENCES
Published by The Malaysian Analytical Sciences Society
ISSN 1394 - 2506

PREPARATION AND CHARACTERIZATION OF Ag NANOPARTICLES DECORATED WITH ZnO MICROSTRUCTURES FOR THE CATALYTIC PHOTODEGRADATION OF METHYLENE BLUE DYE UNDER UV LIGHT IRRADIATION

(Penyediaan dan Pencirian Ag Berstruktur Nanopartikel Diubahsuai dengan ZnO Berstruktur Mikro untuk Penurunan Fotokatalisis Pewarna Metilena Biru di bawah Sinar UV)

Hartini Ahmad Rafaie[1]*, Nur Azmina Mohemaed Safian[2], Roslan Md Nor[2], Yusof Mohd Amin[2]

[1]*Faculty of Applied Sciences,*
Universiti Teknologi MARA Pahang, 26400 Bandar Tun Abdul Razak Jengka, Pahang,Malaysia
[2]*Physics Department, Faculty of Science,*
Universiti Malaya, 50603 Kuala Lumpur, Malaysia

**Corresponding author: hartinirafaie@pahang.uitm.edu.my*

Received: 4 December 2016; Accepted: 1 December 2017

Abstract

Ag nanoparticles (AgNPs) decorated with ZnO microstructures was prepared by sol-gel method at different Ag concentration. The structures, composition and morphology of the samples were characterized by X-ray diffraction (XRD), electron dispersive X-ray spectroscopy (EDS) and field emission scanning electron microscope (FESEM). FESEM images shows that the samples were composed of Ag and ZnO with the particles size ranging from 100 to 500 nm. EDS analysis confirmed that atomic % increases as higher molar concentration applied with value of 5.6 at.% and 16.1 at.% for sample 0.05M and 0.1M AgNPs decorated ZnO microstructures. Methylene blue (MB) dye was used as a representative of dye pollutant to conduct the catalytic photodegradation activity. The AgNPs decorated with ZnO particles exhibited a better photocatalytic activity than the pure ZnO particles. The results show that an increasing of photodegradation rate constant, *k* was obtained when higher concentration of Ag was applied to the ZnO with value of 0.016, 0.026 and 0.032 min^{-1} for pure ZnO, 0.05M AgZnO and 0.1M AgZnO nanoparticles, respectively. The increased of *k* value in the presence of Ag was due to the prolonged lifetime of the photogenerated electron hole pairs in ZnO as a result of Ag nanoparticles acting as electron sink.

Keywords: Ag nanoparticles, zink oksida, sol-gel, photodegradation, methylene blue

Abstrak

Ag berstruktur nanopartikel (AgNPs) diubahsuai dengan ZnO berstruktur mikro pada kepekatan berbeza telah dibuat menggunakan teknik sol-gel. Sifat-sifat struktur, komposisi dan morfologi sampel diperincikan menggunakan pembelauan sinar-X (XRD), spektroskopi Sinar-X sebaran elektron (EDS) dan mikroskop elektron pancaran medan (FESEM). Analisis FESEM menunjukkan sampel terdiri daripada Ag dan ZnO yang mempunyai saiz partikel antara 100 – 500 nm. Analisis EDS pula membuktikan bahawa peratusan atomik meningkat apabila kepekatan Ag yang lebih tinggi digunakan dengan nilai 5.6 at.% dan 16.1 at.% bagi sampel 0.05 M dan 0.1 M ZnO berstruktur mikro diubahsuai dengan Ag berstruktur nanopartikel. Pewarna metilena biru (MB) digunakan sebagai contoh pencemaran warna untuk mengkaji aktiviti penurunan foto pemangkin. ZnO berstruktur mikro diubahsuai dengan Ag berstruktur nanopartikel menunjukkan aktiviti penurunan foto yang lebih baik daripada ZnO tulen. Keputusan menunjukkan bahawa peningkatan dalam pemalar kadar penurunan foto, *k* diperoleh apabila kepekatan Ag lebih tinggi digunakan pada ZnO dengan nilai 0.016, 0.026 dan 0.032 min^{-1} untuk ZnO tulen, 0.05 M dan 0.01 M ZnO berstruktur mikro diubahsuai dengan Ag berstruktur nanopartikel. Peningkatan nilai *k* dengan kehadiran Ag disebabkan oleh

jangka hayat berpanjangan penghasilan foto oleh pasangan lubang dan elektron di ZnO hasil daripada Ag nanopartikel yang bertindak sebagai penerima elektron.

Kata kunci: Ag berstruktur nanopartikel, zink oksida, sol-gel, penurunan foto, metilena biru

Introduction

Recently, Zinc Oxide (ZnO) has been widely investigated as one of the important material for photocatalytic applications due to its large initial rates of activities and having active sites with higher surface reactivity [1]. Combined with the advantages of non-toxicity, high sensitivity, stability, cost effective and environmental safety, ZnO has become a potential photocatalyst for remediation of environmental problem [2]. It is reported that, ZnO photocatalyst also presents some challenges such as fast recombination rate of the photogenerated electron-hole pair and low quantum efficiency, which resulting low photocatalytic efficiency reaction in the system [3, 4]. Therefore, in order to improve the photocatalytic activities, researchers have been found that doping is one of the alternative ways to improve the photocatalytic properties. For instance, Changle Wu et al. reported that Cu doped ZnO can enhance the photocatalytic efficiency of ZnO under visible light irradiation [5], and Jing Zhao et al. reported that Ni-doped ZnO nanorod exhibited higher photocatalytic activity than un-doped ZnO [6]. Incorporating and modifying silver in ZnO have been attract much interest in photocatalytic application due to more effective electron–hole separation of the Ag/ZnO composite and Ag will increase the electron transfer process [7 – 9]. In this work, the photocatalytic activities of the pure ZnO and AgNPs decorated microstructured ZnO act as photocatalyst prepared by sol-gel method were studied by the degradation of methylene blue (MB) under ultraviolet irradiation.

Materials and Methods

Synthesis of the photocatalyst

ZnO and Silver nitrate ($AgNO_3$) were used as the starting materials for the synthesis of AgNPs decorated with ZnO microstructures by sol-gel method. Methylene blue dye (MB) was used as a representative organic pollutant in water. All materials used were of analytical grade and were used without any further purification. The stock solution was prepared by dissolved 5 g of ZnO powder that mixed with $AgNO_3$ and HMTA at 0.05 M and 0.1 M concentration in 100 ml of deionized water. The stock solution was then heated at 95 °C for 6 hours. After completion, the obtained white-greyish precipitates were rinsed repeatedly with deionized water and finally dried at 300 °C for 2 hours.

Characterization methods

The structural properties of the prepared samples of AgNPs decorated with ZnO microstructures were characterized by X-ray diffraction (XRD) recorded by PANalytical diffractometer using Cu Kα (λ = 1.5406 Å), while the surface morphology of the samples was studied using field emission scanning electron microscope (FESEM). The composition analysis was performed by electron dispersive X-ray spectroscopy (EDS) attached to the FESEM. The optical absorbance properties of the catalyst were characterized by UV–Vis spectrophotometer.

Photocatalytic measurement

The photocatalytic activities of the samples were carried out by monitoring the photocatalytic degradation of MB dye in aqueous solution. 30 mg of pure ZnO, 0.05M and 0.1M AgNPs decorated microstructures ZnO act as a catalyst were placed into a beaker containing 10 mg/L MB dye solution. Prior to the irradiation, the mixture was stirred in the dark for 30 minutes to establish an adsorption/ desorption equilibrium. The solution then was irradiated under ultraviolet (UV) light (main wavelength: 254 nm). After irradiating for 10, 20, 30, 40, 50 and 60 minutes, a certain amount of solutions was collected and the concentration of residual MB was determined by the absorption of the reaction solution at the characteristic absorption wavelength 664 nm using UV–visible spectrophotometer.

Results and Discussion

Figure 1 shows the FESEM images of (a) pure ZnO, (b) 0.05 M AgNPs decorated microstructures ZnO, (c) 0.1 M AgNPs decorated microstructures ZnO and (d) the EDS spectra of selected area of all samples. The images clearly revealed that all samples composed of rod-like and cubic-like particles with average size about 100 - 500 nm. In addition, the morphology and size of the photocatalyst do not show significant changes when Ag was introduced.

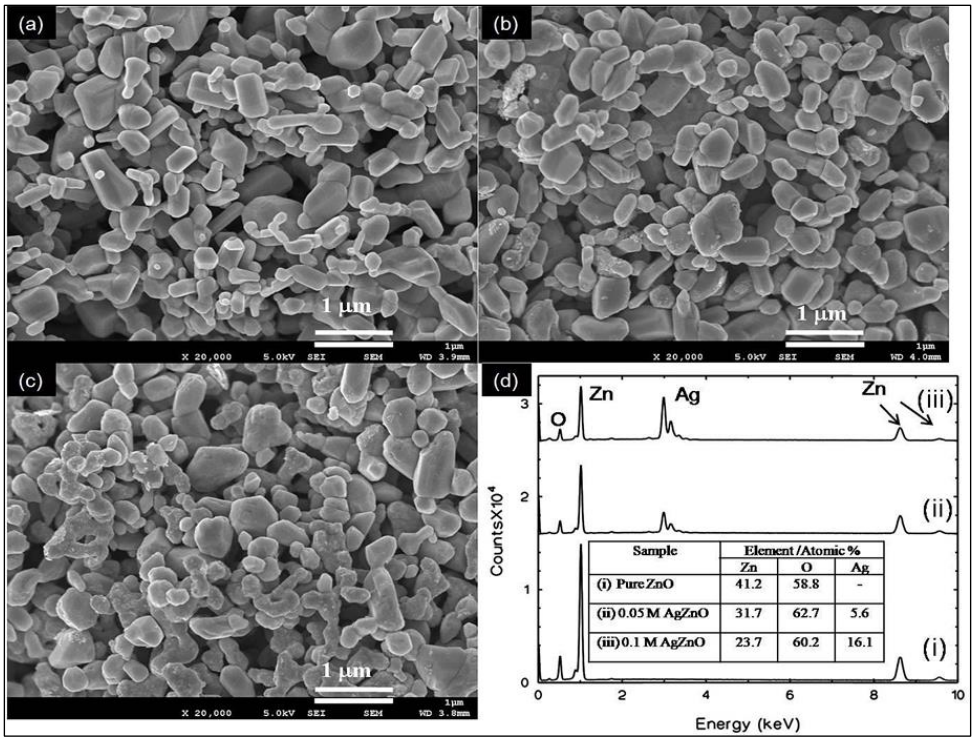


Figure 1. FESEM images of (a) pure ZnO, (b) 0.05M AgNPs decorated microstructures ZnO, (c) 0.1M AgNPs decorated microstructures ZnO and (d) the corresponding EDS analysis

However, from the EDS analysis confirmed that Ag element was detected in sample AgNPs decorated microstructures ZnO, shown in Figure 1 (b) and (c), respectively. As can be seen from the EDS graph, Ag was incorporated in the samples and the atomic percentage of Ag increased as higher concentration was applied with value of 5.6 at.% and 16.1 at.% for sample 0.05 M and 0.1 M AgNPs decorated microstructures ZnO. Besides, there was no other impurities was detected as EDS analysis of the sample only composed the element of Zn, O, and Ag.

Figure 2 shows the normalized XRD patterns for (a) pure ZnO, (b) 0.05 M AgNPs decorated microstructures ZnO and (c) 0.1 M AgNPs decorated microstructures ZnO. All the diffraction peaks are corresponding to the hexagonal wurtzite ZnO and cubic metallic Ag crystal structure (labelled as * in the graph) respectively. No other peak was detected and there was no significant shift for all diffraction peaks indicating that the silver did not substitutes for Zn^{2+} or interstitial atom [9] and suggested that the silver just decorated on the surface [10].

The photocatalytic degradation of the pure ZnO and AgNPs decorated microstructures ZnO in MB dye solution is shown in Figure 3 (a) – (d). From the time dependent absorbance spectra, the absorbance peak at 664 nm was reduced significantly, indicating the degradation of the dye molecule. It can be seen from Figure 3, AgNPs decorated microstructures ZnO showed a remarkable enhancement of photocatalytic activity compared with pure ZnO particles. Moreover, 0.1 M AgNPs decorated microstructures ZnO show the highest catalytic activity compared to 0.05 M AgNPs decorated microstructures ZnO and pure ZnO particles. The photocatalytic degradation of MB can be described to a linear pattern using pseudo-first kinetics model as stated in Equation (1):

$$\ln(C/C_0) = -kt \quad (1)$$

where *k* is the degradation rate constant, C_0 and C are the MB initial concentration and the concentration of solution after the degradation time of t, respectively.

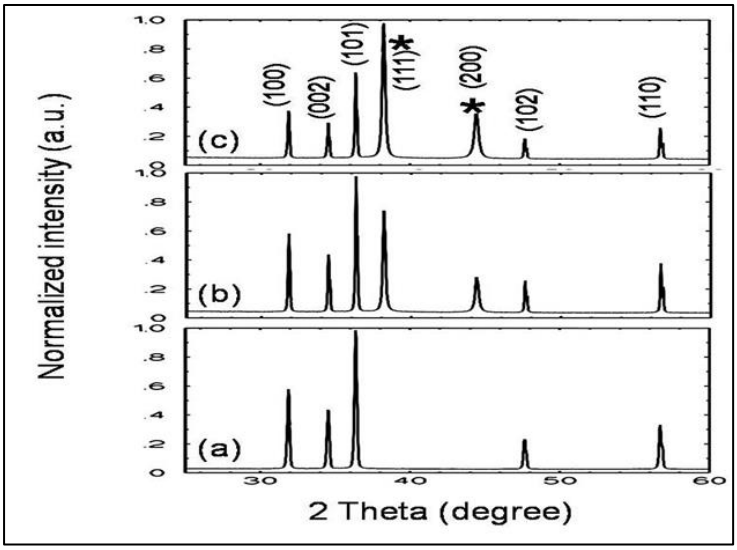


Figure 2. Normalized XRD patterns of the (a) pure ZnO, (b) 0.05M AgNPs decorated microstructures ZnO and (c) 0.1M AgNPs decorated microstructures ZnO, (Ag labelled as * in the graph)

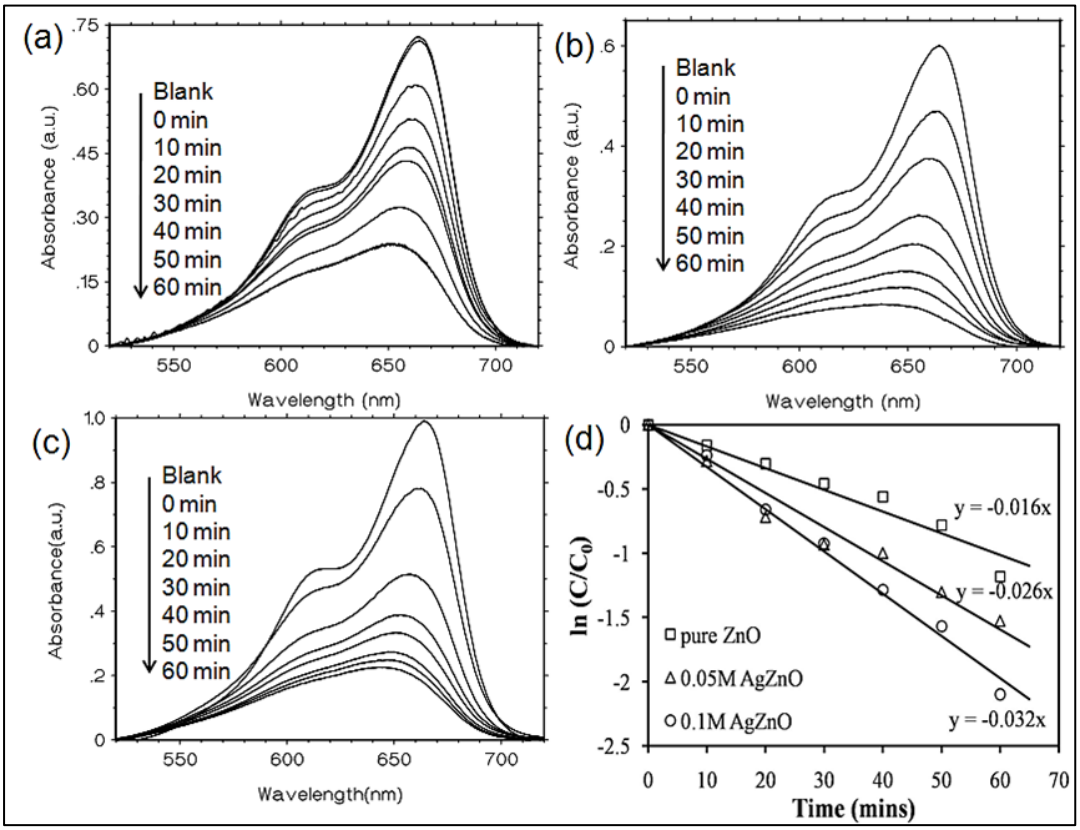


Figure 3. UV-Vis absorption spectral changes of MB under UV light irradiation by (a) pure ZnO, (b) 0.05M AgNPs decorated microstructures ZnO, (c) 0.1 M AgNPs decorated microstructures ZnO and (d) MB photodegradation curves of ln C/C_0 versus time for all photocatalyst

The obtained results are shown in Figure 3(d) where the photodegradation rate constant, *k* of different photocatalyst were 0.016, 0.026 and 0.032 min^{-1} for pure ZnO, 0.05 M and 0.1 M AgNPs decorated microstructures ZnO, respectively. Therefore, it can be seen that the photocatalytic activities efficiency of MB molecules increases in the following order: pure ZnO < 0.05 M AgNPs decorated microstructures ZnO < 0.1 M AgNPs decorated microstructures ZnO. In addition, the results showed that MB solution greatly degrade in the presence of AgNPs decorated microstructures ZnO and the rate constant is much higher using 0.1M AgNPs decorated microstructures ZnO. This significant effect of AgNPs decorated microstructures ZnO is possibly due to the efficient charge electron-hole separation of Ag and ZnO [11 – 13].

Generally, on semiconductor surface Ag having a characteristic like an electron sinks, which provide sites for the accumulation of photogenerated electrons, and then improve the separation of photogenerated electrons and holes [13, 14]. In addition, the electron pairs lifetime can be prolong and thus can enhance the photocatalytic activity of AgZnO photocatalyst [11]. Other than that, higher dispersity of Ag particles on the ZnO surfaces also gives higher photocatalytic activity of AgNPs decorated microstructures ZnO. Ag particles have a higher Fermi energy level compared to ZnO, caused a movement of electrons from Ag to the conduction band (CB) of ZnO in order to achieve Fermi energy level equilibrium (E_f).

Conclusion

The AgNPs decorated microstructures ZnO were successfully prepared by sol-gel method. After comparison with pure ZnO particles, AgNPs decorated microstructures ZnO exhibited better photocatalytic activity with photodegradation rate constant, *k* value of 0.016, 0.026 and 0.032 min^{-1} for pure ZnO, 0.05 M and 0.1M AgNPs decorated microstructures ZnO, respectively. The enhance performance of AgNPs decorated microstructures ZnO shows that it can be used as an alternative photocatalyst for remediation of environmental problem.

Acknowledgement

This work is funded by the University of Malaya under the UM Research Grant No. RG247-12AFR and PPP Grant No. PG068-2013A.

References

1. Chang, C.-W., Wu, H.-T., Huang, S.-H., Chen, C.-K., Un, I.-W. and Yen, T.-J. (2013). Single-crystalline heterostructure of ZnO nanowire arrays on large Ag microplates and its photocatalytic activity. *Acta Materialia*, 61(18): 6993–6999.
2. Stephen, J. P., David, P. N., Matt, P. I., Art, F. H., John, M. Z., Weimin, M. C. and Irina A. B. (2007). ZnO Doped With Transition Metal Ions. *IEEE Transactions on Electron Devices*, 54(5): 1040–1048.
3. Subash, B., Krishnakumar, B., Sreedhar, B., Swaminathan, M. and Shanthi, M. (2013). Superlattices and microstructures highly active WO_3–Ag–ZnO photocatalyst driven by day light illumination. *Superlattices and Microstructures,* 54: 155–171.
4. Han, Z., Ren, L., Cui, Z., Chen, C., Pan, H. and Chen, J. (2012). Applied Catalysis B : Environmental Ag/ZnO flower heterostructures as a visible-light driven photocatalyst via surface plasmon resonance. *Applied Catalysis B: Environmental,* 126: 298–305.
5. Wu, C., Shen, L., Zhang, Y.-C., Huang, Q. and Yu, H. (2011). Solvothermal synthesis of Cu-doped ZnO nanowires with visible light-driven photocatalytic activity. *Materials Letters*, 74(12): 236–238.
6. Zhao, J., Wang, L., Yan, X., Yang, Y., Lei, Y., Zhou, J., Huang, Y. and Gu, Y. (2011). Structure and photocatalytic activity of Ni-doped ZnO nanorods. *Materials Research Bulletin*, 46(8): 1207–1210.
7. Zhang, D., Liu, X. and Wang, X. (2011). Growth and photocatalytic activity of ZnO nanosheets stabilized by Ag nanoparticles. *Journal of Alloys and Compounds*, 509(15): 4972–4977.
8. Changdong, G., Chun, C., Haiyou, H., Tailun, W., Ning, W. and Tong-Yi, Z. (2009). Growth and photocatalytic activity of dendrite-like ZnO @ Ag. *Crystal Growth & Design*, 9(7): 3278–3285.
9. Georgekutty, R., Seery, M. K. and Pillai, S. C. (2008). A highly efficient Ag-ZnO photocatalyst: Synthesis, properties, and mechanism. *Journal of Physical Chemistry C*, 112(35): 13563–13570.
10. Yang, Z., Zhang, P., Ding, Y., Jiang, Y., Long, Z. and W. Dai. (2011). Facile synthesis of Ag/ZnO heterostructures assisted by UV irradiation: Highly photocatalytic property and enhanced photostability. *Materials Research Bulletin*, 46(10):1625–163.

11. Chai, B., Wang, X., Cheng, S., Zhou, H. and Zhang, F. (2014). One-pot triethanolamine-assisted hydrothermal synthesis of Ag/ZnO heterostructure microspheres with enhanced photocatalytic activity. *Ceramic International*, 40(1): 429–435.
12. Lin, D., Wu, H., Zhang, R. and Pan, W. (2009). Enhanced photocatalysis of electrospun Ag−ZnO heterostructured nanofibers. *Chemistry of Materials*, 21(15): 3479–3484.
13. Gao, S., Jia, X., Yang, S., Li, Z. and Jiang, K. (2011). Hierarchical Ag/ZnO micro/nanostructure: Green synthesis and enhanced photocatalytic performance. *Journal of Solid State Chemistry*, 184(4): 764–769.
14. Rezaei, M. and Habibi-yangjeh, A. (2013). Microwave-assisted preparation of Ce-doped ZnO nanostructures as an efficient photocatalyst. *Materials Letters*, 110: 53–56.

Malaysian Journal of Analytical Sciences, Vol 22 No 3 (2018): 441 - 445
DOI: https://doi.org/10.17576/mjas-2018-2203-09

MALAYSIAN JOURNAL OF ANALYTICAL SCIENCES
Published by The Malaysian Analytical Sciences Society
ISSN 1394 - 2506

SUPERCONDUCTING PROPERTIES OF $Y_2Ba_5Cu_8O_\delta$ (Y258) POROUS AND NON- POROUS STRUCTURE

(Sifat Superkonduktor $Y_2Ba_5Cu_8O_\delta$ (Y258) Struktur Berliang dan Tidak Berliang)

Suazlina Mat Ali[1], Syamsyir Akmal Senawi[2], Azhan Hashim[2]*, Azman Kasim[2], Wan Aizuddin Wan Razali[2], Hartini Ahmad Rafaie[2], Norihan Yahya[2]

[1]*Faculty of Applied Sciences,*
Universiti Teknologi MARA Shah Alam, 40450 Shah Alam, Selangor, Malaysia
[2]*Faculty of Applied Sciences,*
Universiti Teknologi MARA Pahang, 26400 Bandar Jengka, Pahang, Malaysia

**Corresponding author: dazhan@pahang.uitm.edu.my*

Received: 4 December 2016; Accepted: 1 December 2017

Abstract

Solid state reaction method was applied to produce porous and non-porous ceramic materials through a series of heating and grinding. This study revealed the distinguish properties of Y258 in terms of their porous and non-porous structure. The bulk material usually loses its high temperature features due to increase in critical current density. Therefore, it is essential to investigate the porous structure that influences the superconducting properties. The electrical properties of superconductor due to critical temperature, T_c and critical current density, J_c were determined using Resistivity Measurement System (RMS). The morphological structure of superconductor material was analysed by using Scanning Electron Microscopy (SEM). The grain boundary of porous structure is significant to induce higher conductivity without detriment the critical temperature of the superconductor. The higher J_c recorded for porous Y258 was 1.59 A/cm^2 at 50 K. The J_c value was higher compared to non-porous optimal structure which is 1.42 A/cm^2. The $T_{c\ zero}$ for porous and non-porous sample gives the same value which is 78 K for both samples. Results of Y247 doped with Ca were determined for comparison.

Keywords: porous, non-porous, critical temperature, current density, morphology

Abstrak

Kaedah tindak balas keadaan pepejal telah diaplikasikan bagi menghasilkan seramik berliang dan tidak berliang melalui siri-siri pembakaran dan kisaran. Kajian yang telah dilakukan adalah berkisar kepada perbandingan sifat superkonduktor Y258 berliang dan tidak berliang. Bahan pukal kebiasaannya hilang bersifat suhu tinggi disebabkan peningkatan dalam ketumpatan arus. Oleh yang demikian, adalah satu keperluan bagi mengkaji sifat struktur berliang dalam mempengaruhi sesuatu sifat superkonduktor. Sifat elektrik superkonduktor melalui suhu genting dan ketumpatan arus genting adalah ditentukan menggunakan Sistem Pengukuran Rintangan (RMS). Struktur permukaan superkonduktor dianalisis melalui Mikroskop Imbasan Elektron (SEM). Sempadan butiran bagi struktur berliang adalah penting bagi mempengaruhi kekonduksian yang lebih tinggi tanpa menjejaskan nilai suhu genting superkonduktor. Dapatan tertinggi J_c melibatkan Y258 berliang adalah 1.59 A/cm^2 pada suhu 50 K. Nilai J_c adalah tinggi dibandingkan dengan struktur optimum tidak berliang sekitar 1.42 A/cm^2. $T_{c\ sifar}$ bagi sampel berliang dan tidak berliang memberikan nilai suhu yang setara pada 78 K melibatkan kedua-dua sampel. Dapatan Y247 yang di dopkan Ca turut dijadikan sebagai rujukan serta perbandingan bagi teras kajian yang dilakukan.

Kata kunci: berliang, tidak berliang, suhu genting, ketumpatan arus, morfologi

Introduction

Materials in foam and porous structures can be considered as a novel class among bulks, films and single crystal since this materials have specific properties that has potentially high critical temperature as well as critical current density (J_c) [1]. A porous high temperature superconductor material can be considered as an aggregate of single crystals that are spatially separated and attach each other predominantly through their faces [2]. Materials containing tailored porosity exhibit special properties and features that usually cannot be achieved by their conventional dense counterparts [3]. The high specific surface of foam makes porous high temperature superconductor (HTSC) attractive for various practical applications. However, the influence of porosity on critical current is still unclear [4]. The porous structure also could be highly favourable for good oxygenation and better cooling for an efficient heat extraction from the superconducting element. This is used to overcome the typical hot-spot phenomena commonly observed in superconducting fault current limiters [5]. Moreover, many papers concerning the synthesis of bulk superconductor ceramics since fabrication of open-pores superconductive ceramics. It was found that crystalline sucrose was the best filler in order to obtain a homogeneous localization of free spaces [6]. Filling of crystalline sucrose does not destroy the superconductive properties yet it enables the fabrication of samples with good mechanical properties. Superconducting porous with small open porosity can be easily and continuously reinforced in order to improve their mechanical properties hence can overcome the forces encountered in levitation and quasi-permanent magnet applications [7].

Materials and Methods

Two distinguish structured porous and non-porous sample were prepared for Y258 and Ca doped Y247. Each series comprise four identical structures which were Y258 porous, Y258 non porous, Ca doped Y247 porous, and Ca doped Y247 non porous. Bulk samples were prepared by considering the relevant amount of high purity chemicals of Yttrium Oxide (Y_2O_3), Barium Carbonate ($BaCO_3$), Copper Oxide (CuO) and Calcium Carbonate ($CaCO_3$) for each series $Y_2CaBa_4Cu_7O_\delta$ and $Y_2Ba_5Cu_8O_\delta$ respectively. The powder and ethanol were mixed in alumina jar and milled about 24 hours in order to have homogeneous mixture. The mixture was dried in an oven at 120 ^oC for 6 hours. Then the mixture was pulverized using an agate mortar to ensure the chemicals were homogenously mixed and become fine powder. The powder was pre-sintered in the box furnace at 850 ^oC for 5 hours before pulverizing it again [11, 12]. For non-porous, 2g of powder was pressed to form a pellet while 1.8 g of powder and 0.2 g of sucrose was mixed together to obtain a porous pellet. The pellet and porous powder that mixed with sucrose was sintered at 400 ^oC for 2 hours before the execution of final sintering at 920 ^oC for 5 hours. The resistivity measurement system (RMS) was done to determine the critical temperature, T_c and critical current density, J_c. The crystallographic structures and lattice parameter were identified using X-Ray Diffraction (XRD). The surface morphology of the samples was observed by Scanning Electron Microscopy (SEM) [13]. Analysis of Y247 with Ca-doped was carried out for comparison.

Results and Discussion

The electrical resistivity analysis was performed to investigate the effect of porosity on superconducting properties of $Y_2Ba_5Cu_8O_\delta$ samples. The normalized resistance at room temperature as a function of temperature between 20 and 100 K with addition of crystalline sucrose as filler to Y258 and Y247 Ca-doped powders are shown in Figure 1(a). The curve indicated a metallic behaviour for all samples at normal state with a single step of superconducting transition. Both samples (porous and non-porous) for Y258 showed the same value of $T_{c\,zero}$ that is 78 K while sample of Y247 Ca-doped shows decreasing in $T_{c\,zero.}$ The Y258 for both structures possess highest T_c but for non -porous Ca doped Y247 has least T_c as shown in Table 1. The decline in T_c value is justified by the orthorhombicity properties of the samples. XRD results in Figure 2(b) shows that, the orthorhombicity of the system degraded varied to the doping level of Ca [8]. The porosity of Ca doped Y247 also indicates that the possibility of T_c reduction via orthorhombicity detrimental.

Table 1 also shows the critical current density, J_c value for the samples. The value of J_c was increased for samples with low density that has been created by introducing pores. This enhancement of J_c is due to the grain alignment of the porous structure [9]. In addition, the increase of J_c for porous sample might be due to the good electrical contact within the porous ceramic body rather than one just on the surface as in a dense sample [4].

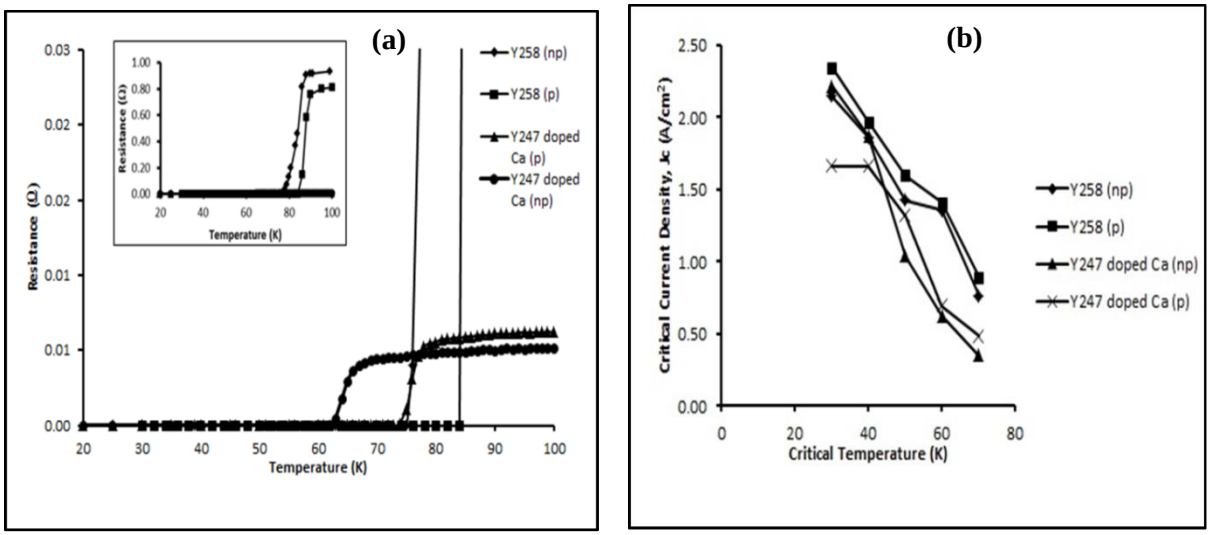


Figure 1. (a) Normalized resistance versus temperature of the samples (b) Critical current density versus temperature

Table 1. Lattice parameter, critical temperature and critical current density of the samples.

Sample	Lattice parameter (Å)			Volume $(Å)^3$	T_C (K)	Critical Current Density, J_C (A/cm^2)	
	a	b	c			50 K	60 K
$Y_2Ba_5Cu_8O_\delta$ non-porous	3.89	3.84	11.79	174.47	78.0	1.42	1.35
$Y_2Ba_5Cu_8O_\delta$ porous	3.89	3.84	11.79	174.47	78.0	1.59	1.41
$Y_2CaBa_4Cu_7O_\delta$ non-porous	3.83	3.88	50.80	754.51	75.0	0.62	0.35
$Y_2CaBa_4Cu_7O_\delta$ porous	3.90	3.88	49.81	752.84	62.9	0.69	0.48

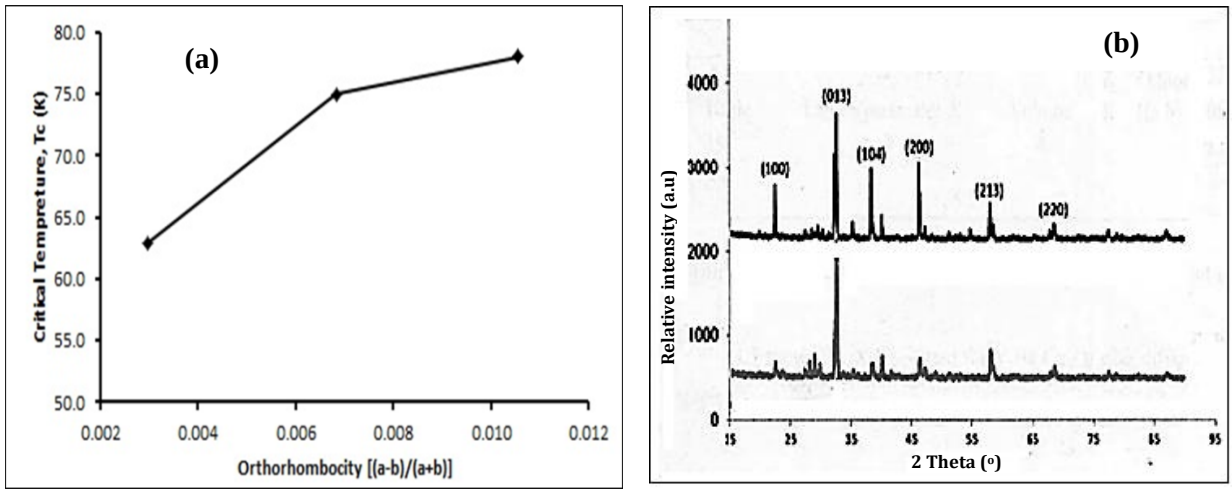


Figure 2. (a) Critical temperature versus orthorombicity (b) X-ray diffraction pattern of samples

Figure 3 shows the SEM micrograph of the samples. Morphology of the samples from SEM images revealed that the porous Y258 sample had the larger average grain size compared to non-porous structure. Larger grain size manifests the lessen of grain boundaries [8, 10]. The grain boundaries are significant to influence the current density in the polycrystalline form. Optimal sintering time is essential to increase the superconducting volume fraction as well as grains connectivity for better current transport. Short sintering period can produce smaller grain size, resulting in weak connectivity between grains. Longer sintering period possibly lead to phase decomposition but decreasing the superconducting phases can weaken the weak links [14]. Larger grain size will enhance the grains continuity, lessen the porosity thus-increased the J_c value. Smaller grain size and irregular grain shape in non-porous Y258 system decrease the J_c value.

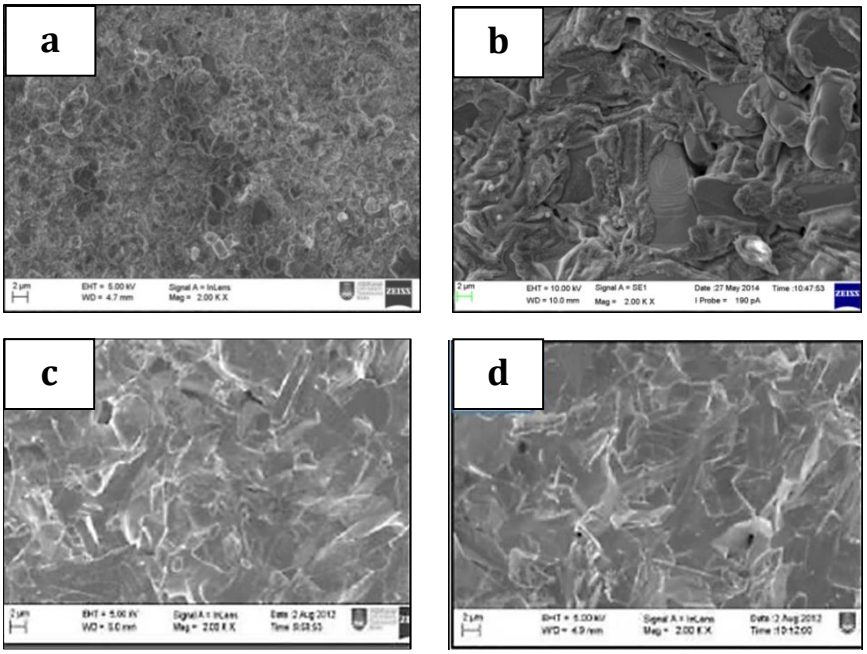


Figure 3. SEM photograph of samples (a) $Y_2Ba_5Cu_8O_\delta$non-porous (b)$Y_2Ba_5Cu_8O_\delta$porous (c)$Y_2CaBa_4Cu_7O_\delta$non-porous (d)$Y_2CaBa_4Cu_7O_\delta$ porous

Conclusion

The effect of porosity on the morphological of microstructure and the electrical resistance characteristics of Y258 porous structure were investigated in this study. The porous sample of YBCO 258 was successfully synthesized using solid state reaction method. It is found that the crystalline sucrose that used as filler does not affect the superconductive properties of the porous structure Y258 but changed the electrical properties which give lower critical current density, J_c than porous YBCO sample. Furthermore, it is found that the value of $T_{c\ zero}$ of porous Y258 is 78 K which is the same as non-porous sample.

Acknowledgement

The authors would like to thank the Ministry of Higher Education (MOHE), Malaysia for the financial support via Research Acculturation Grant Scheme (RAGS) no. 600-RMI/RAGS 5/3 (7/2013).

References

1. Petrov, M. I., Tetyeva, T. N., Kveglis, L. I., Efremov, A. A., Zeer, G. M., Balaev, D. A., Shaikhutdinov, K. A., Popkov S. I. and Ovchinnikov. S. G. (2005). The synthesis, microstructure, transport and magnetic properties of Bi-based low density HTSC. *Journal of Materials Processing Technology*, 161: 58–61.

2. Terent'ev, K. Yu., Gokhfel'd, D. M., Popkov, S. I., Shaikhutdinov K. A. and Petrov, M. I. (2011). Pinning in a porous high-temperature superconductor Bi-2223. *Physics of the Solid State,* 53(12): 2409–2414.
3. Studart, A. R., Gonzenbach, Urs T., Tervoort, E. and Gauckler, L. J. (2006). Processing routes to macroporous ceramics: A review. *Journal of the American Ceramic Society,* 89(6): 1771–1789.
4. Gokhfeld, D. M., Balaev, D. A., Popkov, S. I., Shaykhutdinov, K. A. and Petrov, M. I. (2006). Magnetization loop and critical current of porous Bi-based HTSC. *Physica C,* 434: 135-137.
5. Schwartz, R. W., Noudem, J. G. and Reddy, E. S. (2006). Single grain $YBa_2Cu_3O_y$, porous ceramic superconductors. *Electroceramic Materials and Applications: Ceramic Transactions Series,* 196: 33–43.
6. Fiertek, P. and Sadowski, W. (2006). Processing of porous structures of $YBa_2Cu_3O_{7-\delta}$ high-temperature superconductor. *Materials Science,* 24: 1103-1108.
7. Norazidah, A. W., Azhan, H., Azman, K., Hidayah, H. N. and Hawa, J. S. (2014). Effect of heat treatment on Ca substitution in a porous $Y(Ba_{1-x}Ca_x)_2Cu_3O_{7-\delta}$ superconductor. *Advanced Materials Research*, 895: 71–74.
8. Shlyk, L., Krabbes, G., Fuchs, G. and Nenkov, K. (2002). Melt-processed YBCO doped with Ca and Cd: Comparison of superconducting properties. *Physica C,* 383: 175-182.
9. Norazidah, A. W., Azhan, H., Azman, K., Hidayah, H. N. and Hawa, J. S. (2012). Superconducting properties of calcium substitution in barium site of porous $YBa_2Cu_3O_7$ ceramics. *Advanced Materials Research*, 501: 294–298.
10. Noel A. R., John, H. D., Sibe, H. M., Mark, G. B. and Judith, L. M. (2005). Transport properties of Ca-doped YBCO coated conductors. *IEEE Transactions on Applied Superconductivity,* 15: 2570-2573.
11. Roaa F. A. and Emad K. A. (2015). New high temperature superconductor phase of Y-Ba-Cu-O system. *International Journal of Advanced Research in Physical Science,* 2 (7): 33-39.
12. Pimentel Jr, J. L., Martinez Buitrago, D., Supelano, I., Parra Vargas, C. A., Mesquita, F. R. and Pureur, P. (2015). Synthesis and characterization of the superconductors $Y_3Ba_5Cu_{8-x}Fe_xO_{18}(0.0597 \leq x \leq 0.1255)$. *Journal of Superconductivity and Novel Magnetism,* 28: 509–512.
13. Khalida, S.. Fariesha, F.. Azhan, H. and Yusainee, S. Y. (2013). Influence of heat treatments on electrical properties and microstructure of 10% mass fraction of sucrose YBCO superconductor. *Malaysian Journal of Analytical Sciences,* 17(1): 1 – 10.
14. Shalaby, M. S., Hashem, H. M., Hammad, T. R., Wahab, L. A., Marzouk, K. H. and Soltan, S. (2016). Higher critical current density achieved in Bi-2223 High-T_C superconductors. *Journal of Radiation Research and Applied Sciences,* 9: 345–351.

Malaysian Journal of Analytical Sciences, Vol 22 No 3 (2018): 446 - 451
DOI: https://doi.org/10.17576/mjas-2018-2203-10

MALAYSIAN JOURNAL OF ANALYTICAL SCIENCES
Published by The Malaysian Analytical Sciences Society
ISSN 1394 - 2506

VENTILATION EFFECT ON THE RADON-222 ANNUAL EFFECTIVE DOSE INSIDE GUA GAJAH AND GUA PENYU CAVES, KOMPLEKS GUA KOTA GELANGGI, PAHANG, MALAYSIA

(Kesan Pengudaraan Kepada Dos Berkesan Tahunan Radon-222 dalam Gua Gajah dan Gua Penyu, Kompleks Gua Kota Gelanggi, Pahang, Malaysia)

Nazree Ahmad [1]*, Junaidah Md Sani[1], Nur Hafilah Muslim[1], Nur Amirah Alias[1], Ahmad Saat [2]

[1]*Faculty of Applied Sciences*
Universiti Teknologi MARA Pahang, 26400 Bandar Tun Abdul Razak Jengka, Pahang, Malaysia
[2]*Institute of Science,*
Universiti Teknologi MARA, 40450 Shah Alam, Selangor, Malaysia

**Corresponding author: nazreeahmad@pahang.uitm.edu.my*

Received: 4 December 2016; Accepted: 1 December 2017

Abstract

A study to determine the concentration and emanation rate of Radon-222 were done inside Gua Gajah and Gua Penyu limestone caves, Kompleks Gua Kota Gelanggi, Pahang, Malaysia to find the link between ventilation and annual effective dose. Gua Gajah has two major openings and features uneven earth surface unlike Gua Penyu which has single entrance and smooth passage way. Dosimeters with CR-39 solid state nuclear track detector (SSNTD) were distributed 15 m apart. For emanation rates, dosimeters were embedded about 5 cm into cave floor while for concentration measurements, they were placed 1 m above ground. The control samples were placed in front of the main entrance. The samples were left and collected after 30 days. Every CR-39 samples were etched with 6M NaOH solution with 70 ^{o}C for 6 hours in water bath and observed under microscope of 200x linear magnifications to calculate tracks densities. Results indicated that the average Radon-222 emanation rate inside Gua Gajah was higher than that of Gua Penyu. On the other hand, the average concentration of Radon-222 inside Gua Gajah was lower than that of Gua Penyu. The average annual effective dose of Radon-222 in Gua Gajah and Gua Penyu was 0.084 mSv yr^{-1} and 0.12 mSv yr^{-1}, respectively. These findings point out that ventilation contributed by cave openings plays an important role in reducing the indoor radon gas accumulation, thus lowering the annual effective dose.

Keywords: emanation rate, radon gas, radon concentration

Abstrak

Kajian bagi mengukur kepekatan dan kadar pemancaran Radon-222 telah dijalankan dalam gua-gua batu kapur Gua Gajah and Gua Penyu, Kompleks Gua Kota Gelanggi, Pahang, Malaysia untuk mencari hubungan di antara pengudaraan dengan dos berkesan tahunan. Gua Gajah dengan dua laluan utama menunjukkan mukabumi tidak sekata manakala Gua Penyu hanya mempunyai satu laluan masuk dan rata. Dosimeter dengan pengesan jejak nuklear keadaan pepejal CR-39 (SSNTD) diletakkan berjarak 15 m satu sama lain. Dosimeter untuk kadar pemancaran ditanam 5 cm ke dalam lantai gua manakala bagi pengukuran kepekatan, dosimeter diletakkan 1 m di atas lantai gua. Sampel kawalan diletakkan di hadapan laluan masuk utama. Kesemua sampel ditinggalkan dan dikutip selepas 30 hari. Setiap sampel CR-39 kemudiannya dicelup dalam rendaman panas larutan 6M NaOH pada 70 ^{o}C selama 6 jam sebelum dicerap di bawah microskop 200x pembesaran linear untuk menentukan kepadatan trek. Hasil menunjukkan purata kadar pemancaran Radon-222 dalam Gua Gajah lebih tinggi berbanding Gua Penyu. Sebaliknya, purata kepekatan Radon-222 dalam Gua Gajah lebih rendah berbanding Gua Penyu. Dos berkesan tahunan Radon-222 untuk Gua Gajah dan Gua Penyu masing-masing ialah 0.084 mSv yr^{-1} dan 0.12 mSv yr^{-1}. Penemuan ini menunjukkan kesan

pengudaraan daripada bukaan gua memainkan peranan penting dalam mengurangkan penumpukan radon gas dalaman seterusnya merendahkan nilai dos berkesan tahunan.

Kata kunci: kadar pemancaran, gas radon, kepekatan radon

Introduction

Radon is a naturally inert radioactive gas with a half-life of 3.824 days generated from the radioactive decay series of Uranium-238. It is the first decay product of Radium- 226 and a radioactive gas at room temperature. Radon is colorless, odorless and tasteless hence, does not give an immediate effect. However, if accumulated to higher levels in confined spaces radon gas may cause significant threat to human health especially when exposed in a long period of time [1], becoming the major contributor of radiation to the public [2]. The concentration of Radon-222 varies according to sites and geological materials [3] and its migration depends very much on the radioactivity concentration, porosity and permeability of the medium [4]. In addition, radon as a single atom gas easily diffuse through pores in soil, fractures in rocks and along other weak zone [5], such as shears, faults and thrust, increasing its migrating capability. In any air system, quantity of radon present depends upon the concentration of uranium in the local rock, atmospheric conditions and the extent of ventilation [6].

Gua Gajah and Gua Penyu caves at Kompleks Gua Kota Gelangi, are situated in Pahang, Malaysia located approximately at coordinate of 3°53'55.0"N 102°28'30.7"E. They are estimate 150 million years of age and mainly limestone marked by the internal formations of stalagmites and stalactites. These caves were about 100 meters long with inconsistence height between 20 to 30 m. Gua Gajah features a two openings tunnel, a main entrance and another opening at the end of the cave which leads to a hillside. Therefore, visitors to Gua Gajah could enter the cave through main entrance and leave *via* the second opening at the passage end. However, this cave has uneven rock-strewn cave floor towards the passage exit. Gua Penyu on the other hand, has one opening that is the main entrance and smooth passageway throughout the wave tunnel. Hence, the apparent dissimilarity between these two caves is on the aspect of air circulation contributed by the number of openings existing in the cave passage. Figure 1 illustrates the features of Gua Gajah and Gua Penyu caves respectively.

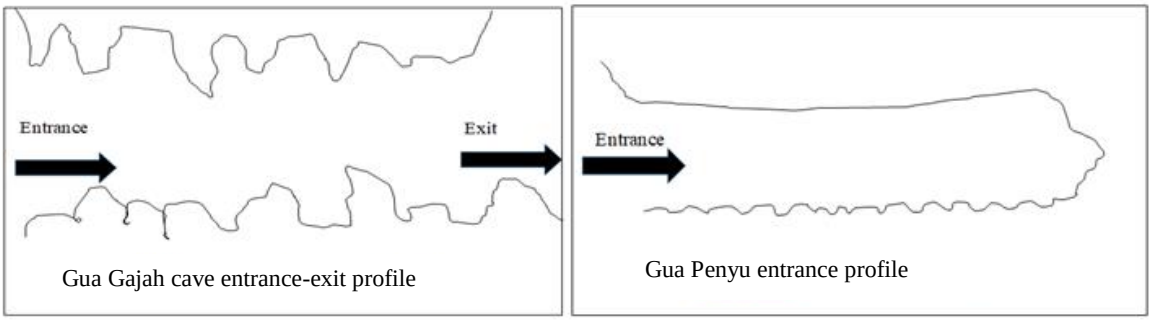


Figure 1. The sideview illustration of Gua Penyu and Gua Gajah caves entrance – exit profiles

In this investigation, the CR-39 solid-state nuclear track detector (SSNTD) used as the integrating detector of alpha particles from Radon-222.When an alpha particle struck the CR-39; the particle caused damage along its path that could be made visible by chemical etching [7]. These are called latent track that can be observed under a light transmission microscope with moderate magnification to calculate the track density. This was a passive technique which was very simple and economical, besides having ability for long term monitoring up to 12 months and has high registration sensitivity [8]. This research work aims to compare the emanation rates and concentration of Radon-222 as well as the annual effective dose between Gua Gajah and Gua Penyu caves. This finding will be used to verify the link between cave ventilation and accumulation of indoor radon gas as anticipated.

Materials and Methods

The dosimeter was composed of polymer cup 4 cm in height with a lid of 7.5 cm diameter. A small hole about 16 mm diameter was made at the middle of its lid. It was then covered by a 5 mm thick soft sponge. The dosimeter was designed as such to ensure that only radon gas would diffuse into the chamber [9]. The 1.5 cm by 1.5 cm rectangular CR-39 detector was fixed at the bottom of the can using double sided tape. The dosimeter was then sealed neatly. The schematic diagram of the dosimeter as shown in Figure 2.

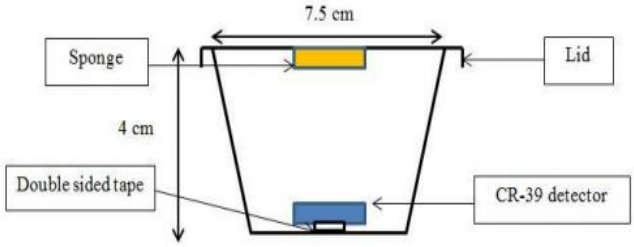


Figure 2. The schematic diagram of the radon dosimeter

Figure 3 shows the side view schematic diagram for sampling in each cave. Beginning at the main entrance, the sample locations were tagged L2 ascending to L12, consistently 15 m apart. A total of 22 dosimeters were placed inside each cave. For control experiment, a dosimeter for each cave was placed outdoor (L1) about 15 m from the main entrances. For determination of radon emanation rate, 11 units of dosimeter were embedded 5 cm in the soil while the remaining 11 dosimeters were placed 1m above cave floor for the purpose of measuring radon gas concentration. Dosimeters that were placed in ground floor were positioned in such a way that the CR-39 was facing down. On the other hand, the wall for sticking the dosimeter was rubbed meticulously to make sure that the dosimeter remains intact throughout the sampling period. Each point was also visual recorded to facilitate the recollection of dosimeters. All dosimeters were then left and collected after a period of 30 days.

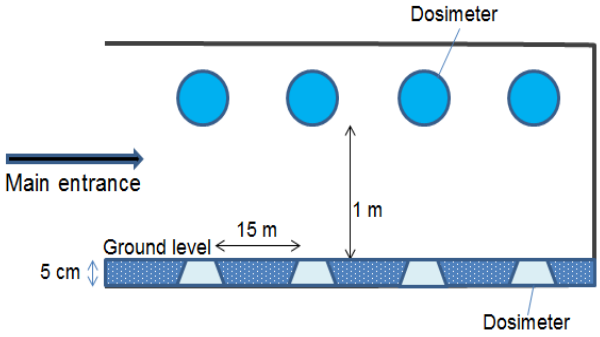


Figure 3. The side view illustration of the cave showing the method of sampling

During collection process, the dosimeters were kept in a container to secure the integrity of the samples. The CR-39 detectors underwent etching process by initially immersing them into a water bath containing 6 M sodium hydroxide (NaOH) solution at 70 °C for 6 hours. The detectors were then washed thoroughly with tap water for 1 hour before they were left to dry between tissue wipes and kept in airtight containers afterwards. The tracks were observed under the optical microscope with 200 times linear magnifications. The number of tracks of each detector was counted manually. Radon concentration was calculated according to Eq. (1) based on the number of visible spots on the CR-39 sheet. Only dark spots with diameter about 10 µm were reckoned for calculation.

$$C_{Rn} = \frac{D}{Ft} \quad (1)$$

C_{Rn} was the radon concentration, D was the track density (tracks.cm^{-2}), t was the exposure time (days) and F was the calibration factor (tracks m^3 cm^{-2} Bq^{-1} h^{-1}). The radon concentration in air was number of decays per second per cubic meter of air or Bq m^{-3}. According to [10], annual effective dose could be calculated using Eq. (2).

$$E = C \times H \times F \times T \times D \quad (2)$$

C was the radon concentration (Bq m^{-3}), F was the equilibrium factor, 0.4, H was the occupancy factor, 0.8, T was the number of hours in a year, 8760 h and D was the effective dose received by adults per unit Radon−222 or dose conversion factor (9.0 x 10^{-6} mSv h^{-1} Bq m^{-3}). The Radon−222 emanation rate was calculated using Eq. (3).

$$E_{Rn} = \frac{CV}{At} \quad (3)$$

E_{Rn} was the emanation rate (Bq m^{-2} day^{-1}), C was the Radon-222 concentration (Bq m^{-3}), V was the volume of the polymer container (m^3), A was the surface area (m^2) of the lid and t was the exposure time (days).

Results and Discussion

Radon emanation rate is defined as the decaying radon atoms that have been released through an area per day. Figure 4 indicates an uneven distribution of emanation rates for both caves. However, the emanation rates for Gua Gajah were of higher values at most of the locations except at sampling locations L6 and L9. This finding was anticipated because Gua Gajah cave has more rocky features throughout its passage compared to Gua Penyu cave. Due to the fact that Uranium-226 as the major source for Radon-222 depends very much on the type of rock concealed underneath the cave floor, it is suggested that granitic rocks are present in this cave. Previous study by Aljarallah [11] reported that granite was a significant source of radon emanation. The emanation rate at the exit point of Gua Gajah is unexplainable. Nonetheless, it might be attributed to the granitic type of rock exist. The Radon-222 concentration for Gua Gajah and Gua Penyu caves are compared in Figure 5. Radon concentration is the specific radon activity per unit volume in the atmosphere. It indirectly represents the amount of floating radon gas in the air.

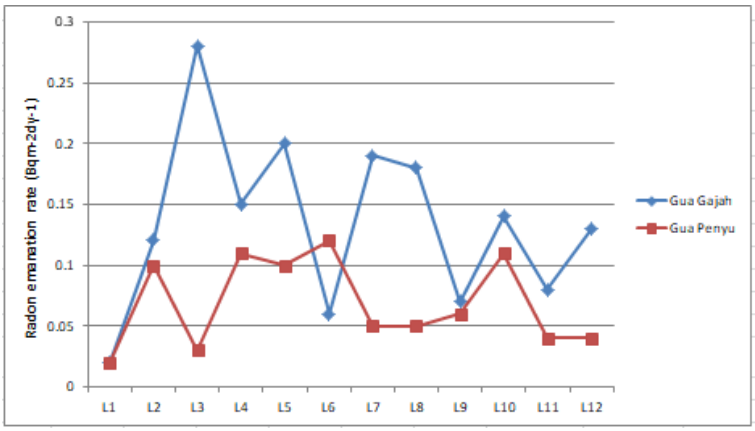


Figure 4. The Radon-222 emanation rates in Gua Gajah and Gua Penyu caves

The Radon-222 emanation rates between Gua Gajah and Gua Penyu caves are shown in Figure 5. The low concentration of radon at sampling point nearer to the main entrance of Gua Penyu was suggested a result of dilution and mixing of the gas with outdoor air. That near the end of its passage was suggested due to its poor ventilated feature. The lack of ventilation can permit high concentration of radon to build up in the trapped air. Gua Gajah on the other hand did not show apparent discrepancy between locations suggested due to the mixing of radon gas with air current between its two openings. Both caves indicated the value of Radon-222 concentrations lower than the indoor radon action level put forth by the International Commission on Radiological Protection (ICRP)

[12], which is 200 to 600 Bq m^{-3}. In average, the Gua Penyu cave which had only one opening showed noticeably higher concentration compared to that of Gua Gajah cave. This finding was dissimilar to that in Figure 4. It was suggested that the main reason for the differences was due to the variation in the natural ventilations. The average annual effective dose for Gua Penyu cave was 0.120 mSv yr^{-1} while Gua Gajah cave was 0.084 mSv yr^{-1}. The annual effective dose of Gua Gajah cave that has two openings was as anticipated, lower than that of Gua Penyu cave, which has single main entrance. This finding implies that ventilation plays an important part in reducing the average indoor radon gas content. The accumulation of indoor radon gas was hindered when there are ventilation holes, which allowed attenuation *via* dilution process.

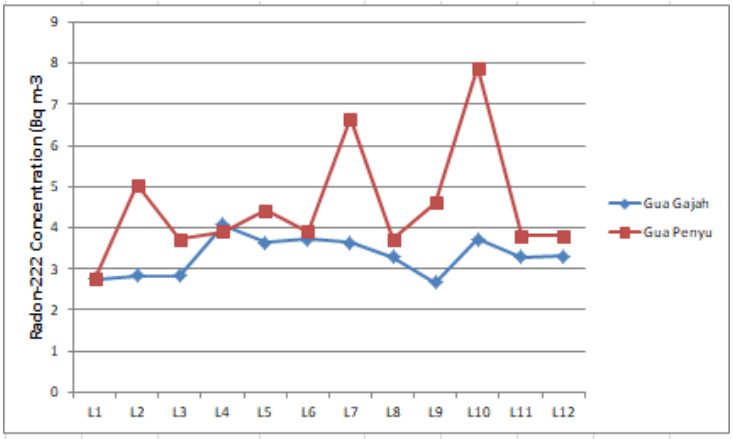


Figure 5. The concentrations of Radon-222 in Gua Gajah and Gua Penyu caves

Conclusion

From this study, it can be conclude that ventilation *via* cave openings plays an important role in reducing the indoor radon gas in a cave. Hence, more openings mean higher security in terms of breathing when occupying a cave. As far as human safety is concerned, it is very crucial for this study to be extend to other caves especially hotspot for tourism.

Acknowledgement

The writers would like to convey their greatest appreciation to the management of Tekam Felda Residence and Resort (Cave Division) and the Institute of Science, Universiti Teknologi MARA, Malaysia for their support and help during this study.

References

1. Field, M. S. (2007). Risks to cavers and cave workers from exposures to low-level ionizing α radiation from 222Rn decay in caves. *Journal of Cave and Karst Studies*, 69(1): 207–228.
2. Ahn, G. H. and Lee, J. K. (2005). Construction of an environmental radon monitoring system using CR-39 nuclear track detectors. *Nuclear Engineering and Technology*, 37(4): 395-400.
3. Mohamed, A. E. (2012). An overview on studying 222Rn exhalation rates using passive technique solid-state nuclear track detectors. *American Journal of Applied Sciences*, 9(10): 1653–1659.
4. Mansour, H. L., Tawfiq, N. F. and Karim, M. S. (2014). Indoor radon concentrations measurement in the dwellings of Thi-Qar governorate, Iraqi. *Journal of Natural Sciences*, 2(1): 19–26.
5. Alkhalifa, I. M., and Bakr, H. (2007). Determination of radon exhalation rates in Basrah Governorate (Iraq) using CR-39 solid state nuclear track detector (SSNTD's). *Basrah Journal of Science* (A), 25(2): 97–104.
6. British Caving Association on Working Party (2012). Radon exposure during underground trips: A set of guidelines for caving and mining exploration. British caving association, Buxton.
7. Kadhum, N. F., Jebur, L.A. and Ridha, A. A. (2016). Studying different etching methods using CR-39 nuclear track detector. *Scientific Research*, 4: 45–53.

8. Farid, S. M. (2012). A study on the radon concentrations in Tobacco in Jeddah (Saudi Arabia) and the associated health effects. *Medical Journal of Islamic World Academy of Sciences*, 20(3): 84–93.
9. Hussein, Z. A., Jaafar, M. S., and Ismail, A. H. (2013). Measurements of indoor Radon-222 concentration inside Iraqi Kurdistan: Case study in the summer season. *Journal of Nuclear Medicine & Radiation Therapy*, 4 (1):1–4.
10. Ahmad, S., Zaini, H., Zaharidah, A. B., Zuraidah, A. M., Siti, M. S and Misbah, H. (2010). Some remarks on diurnal radon concentration at various locations in Peninsular Malaysia. *Journal of Nuclear and Related Technologies*, 7(1): 49–57.
11. Aljarallah, M. I. (2001). Radon exhalation from granite used in Saudi Arabia. *Journal of Environmental Radioactivity*, 53(1): 91–98.
12. International Commission on Radiation Protection (1995). Protection against radon- 222 at home and at work. ICRP Publication, Pergamon, Oxford.

Malaysian Journal of Analytical Sciences, Vol 22 No 3 (2018): 452 - 457
DOI: https://doi.org/10.17576/mjas-2018-2203-11

MALAYSIAN JOURNAL OF ANALYTICAL SCIENCES
Published by The Malaysian Analytical Sciences Society
ISSN 1394 - 2506

PHYTOCHEMICAL SCREENING, ANTIFUNGAL AND ANTIBACTERIAL ACTIVITIES OF *Musa acuminata* PLANT

(Saringan Fitokimia, Antikulat dan Aktiviti Antibakteria Pokok *Musa acuminata*)

Siti Suhaila Harith*, Nur Hanis Mohd Yasim, Aiza Harun, Wan Siti Atikah Wan Omar, Mohd Supi Musa

Faculty of Applied Sciences,
Universiti Teknologi MARA Pahang, 26400 Bandar Tun Abdul Razak Jengka, Pahang,Malaysia

**Corresponding author: ssuhaila@pahang.uitm.edu.my*

Received: 4 December 2016; Accepted: 1 December 2017

Abstract

Musa acuminata plant is known for its edible fruits and the uses of its leaves as food wrapper in industries. Exploring it medicinal values will be an advantage because it can easily grow in Malaysia. The non-edible part which is the leaves of *Musa acuminata* 'Dwarf Cavendish' plant is analysed to determine the phytochemical constituents and antimicrobial properties. Two types of organic solvents used namely hexane and methanol. The antimicrobial properties of the extract produced were tested against *Staphylococcus epidermidis* and *Trichophyton mentagrophytes* by using disc-diffusion method. Phytochemical screening done on the sample showed that the methanolic extract contained bioactive components such as tannins, alkaloids, flavonoids, phenols, terpenoids and saponins whereas hexane extract indicated the presence of alkaloid. The methanolic extract of the leaves showed positive effects towards tested microorganisms whereas hexane extract showed vice versa. The best concentration of methanolic extract against *S. epidermidis* was 60 mg/ml and *T. mentagrophytes* were 40 mg/ml forming inhibition zone with diameter of 4.0 mm and 5.0 mm, respectively. Methanolic extract against *S. epidermidis* is comparable to ampicillin. Meanwhile, it is remarkable that methanolic extract of *M. acuminata* leaves showed stronger antifungal properties as compared to nystatin. As a conclusion, the methanolic extract of the leaves of *M. acuminata* 'Dwarf Cavendish' can be nominated as potential drug due to their antifungal properties.

Keywords: *Musa acuminata*, banana leaves, phytochemical screening, antimicrobial properties

Abstrak

Musa acuminata merupakan tumbuhan yang dikenali dengan buah yang boleh dimakan dan kegunaan daun sebagai pembungkus makanan dalam industri. Meneroka nilai perubatannya akan menjadi satu kelebihan kerana ia senang tumbuh di Malaysia. Bahagian yang tidak boleh dimakan iaitu daun tumbuhan *Musa acuminata* 'Dwarf Cavendish' dianalisis untuk menentukan juzuk fitokimia dan antimikrob. Dua jenis pelarut organik yang digunakan ialah heksana dan metanol. Sifat-sifat antimikrob ekstrak yang dihasilkan telah diuji terhadap *Staphylococcus epidermidis* dan *Tricophyton mentagrophytes* menggunakan kaedah cakera resapan. Penyaringan fitokimia dilakukan pada sampel menunjukkan bahawa ekstrak metanol mengandungi komponen bioaktif seperti tannin, alkaloid, flavonoid, fenol, terpenoid dan saponin manakala ekstrak heksana menunjukkan kehadiran alkaloid. Ekstrak metanol daun menunjukkan kesan positif terhadap mikroorganisma diuji manakala ekstrak heksana menunjukkan sebaliknya. Kepekatan terbaik ekstrak metanol terhadap *S. epidermidis* adalah 60 mg/ml dan *T. mentagrophytes* adalah 40 mg/ml membentuk zon perencatan dengan diameter masing-masing 4.0 mm dan 5.0 mm. Ekstrak metanol terhadap *S. epidermidis* adalah setanding dengan ampicillin. Sementara itu, ekstrak metanol daun *M. acuminata* jelas menunjukkan ciri-ciri antikulat lebih kuat berbanding nystatin. Kesimpulannya, ekstrak metanol daun *M. acuminata* 'Dwarf Cavendish' boleh dicalonkan sebagai ubat yang berpotensi berdasarkan sifat antikulatnya.

Kata kunci: *Musa acuminata*, daun pisang, penyaringan fitokimia, sifat antimikrob

Introduction

The uses of organic materials as the new source of drugs become more acknowledgeable day by day. According to Cowan [1], a large number of modern drugs have been isolated from natural sources such as plants. In the past decades, plants extracts are studied for their phytochemical contents such as alkaloids, flavonoids, amino acids and certain enzymes that make them valuable as medicinal source. Antimicrobial and antifungal are the properties of respective organisms to inhibit the growth of microorganisms such as bacteria, fungi or any pathogens. Usually, a plant contains chemicals that can act as an antimicrobial agent, which can protect it from fungal or bacterial infections. Plants are source of abundance bioactive secondary metabolites of wide variety such as tannins, terpenoids, saponins, alkaloids, flavonoids, and other compounds, reported to have *in vitro* antifungal properties [2].

Banana is the common name of the plant under genus *Musa*. *Musa acuminata* is the most widespread species and most diverse in Malaysia and Indonesia. This species is a hybrid of wild and cultivated bananas. Scientifically known as *M. acuminata* Colla (AAA Group) 'Dwarf Cavendish', the banana is a cultivar which descended from banana cultivar group of commercial produce, the Cavendish. Recently, this cultivar is the most important cultivar which represents approximate 50-60% of the total banana production [3]. The top individual producing countries are India, the Philippines, China, Ecuador and Brazil [4]. These species are usually grown as houseplants and produce slightly smaller edible bananas than other Cavendish cultivars. *M. acuminata* 'Dwarf Cavendish' is an evergreen perennial to 3 meters tall, with oblong leaves to 1.2 meters long; drooping spikes of yellow flowers with purple bracts open sporadically through the year, followed by edible yellow fruit. The shortness of the plants makes them become more stable, resistant against wind and easy to handle. These make them ideal for plantation cultivation besides their fast growth rate. The fruits of the 'Dwarf Cavendish' plants are thin-skinned and range from about 15 to 25 cm in length.

Some recent studies had proven that the extract of pseudostem from *M. acuminata* plants showed the antimicrobial and antifungal activities against *Klebsiella* sp. and *Streptococcus faecalis*, by the formation of inhibition zone around the discs containing the extract [5]. The evaluation of the antifungal activity against *Mycosphaerella fijiensis* of extracts obtained from healthy leaves banana plants of *M. acuminata* cv. Grand Nain showed significant activity [6]. An alcohol extract of banana peel of *Musa paradisiaca L.* has antimicrobial activity against *Porphyromonas gingivalis* and *Aggregatibacter actinomycetemcomitans*, which is proven through the formation of inhibition zone surround the discs containing the extract [7]. Thus, this study was aims to determine the phytochemical constituents and potential antimicrobial activity of *M. acuminata* 'Dwarf Cavendish' leaves.

Materials and Methods

Source of microorganisms

The bacterial culture used was the *S. epidermidis* and the fungal culture was *T. mentagrophytes*. These cultures were obtained from the culture stock of Universiti Teknologi MARA Pahang.

Chemicals and media

The list of chemicals used were methanol (MeOH), sodium hydroxide solution (NaOH), hydrochloric acid (HCl), sulphuric acid (H_2SO_4), ferric chloride solution ($FeCl_3$), hexane, Meyer's and Wagner's reagent, ampicillin, nystatin and ethanol. The bacteria were cultured in nutrient broth and maintained in nutrient agar at 37 °C throughout the study, where the fungi were cultured by using Tryptic Soy Broth and maintained in Potato Dextrose agar, also at 37 °C throughout the study.

Source of plant materials

The leaves of *Musa acuminata* 'Dwarf Cavendish' plant was collected from neighbourhood areas in Marang, Terengganu.

Preparation of leaves extract

The leaves were washed thoroughly and dried using an oven at 40 °C for about 3 days. The leaves then cut into small pieces and grinded using a grinder until fine powder produced. The extraction was done sequentially, in which

the extract soaked in hexane first before the methanol, both with the ratio of 1:3. The extract soaked in the hexane before was dried and weighed again, and then soaked in 95% methanol to produce the methanol extraction. The mixture was then filtered and evaporated until dry by using a rotary evaporator.

Phytochemical test

For qualitative phytochemical screening, standard methods as reported by Narendra et al. [8] and Tiwari et al. [9] were used. Froth test for detection of saponins, alkaline reagent test for flavonoids, Wagner's test for alkaloid, Ferric Chloride test for detections of tannins and phenols, and Salkowski test for detection of terpenoids were done. The antibacterial and antifungal activities of hexane and methanolic extract were tested using disc-diffusion method at different concentration.

Results and Discussion

The qualitative phytochemical screening showed most of the respective chemical contents presented in the leaves' methanol extract (Table 1). Methanol is an effective solvent that is used for extraction. In many studies, methanol extracts showed the greatest amount of phytochemicals which are important for medicinal purposes [10].

Table 1. Phytochemical analysis of different extracts of *M. acuminata* leaves

Test	Extraction	
	Hexane	Methanol
Alkaloids	+	+
Saponins	-	+
Terpenoids	-	+
Tannins	-	+
Phenols	-	+
Flavonoids	-	+

Antimicrobial assays

The antimicrobial activities of hexane extract and methanolic extracts of the banana leaves were tested against *S. epidermidis* and *T. mentagrophytes* by using disc-diffusion method. The data pertaining to the antimicrobial potential extract of the leaves of *Musa* sp. against *S. epidermidis* were presented in Table 2. The diameters of growth inhibition zone were in the range maximum of 4.0±0.33 mm and minimum of 2.0±0.58 mm whereas the standard drug, ampicillin had zones of inhibition of 4.0±0.33. The largest inhibition zone formed using 60 mg/ml and 80 mg/mL extract, while the smallest zone was formed using 20 mg/ml extract. Figure 1 illustrates zone of inhibition for both solvent against *S. epidermidis.*

Table 2. Antimicrobial activities of hexane and methanolic extracts against *S. epidermidis*

Concentration (mg/ml)	Average Inhibition Zone (mm)	
	Hexane Extract	Methanol Extract
20	-	2.0±0.58
40	-	3.0±0.33
60	-	4.0±0.33
80	-	4.0±0.33
100	-	3.0±0.33
Ampicillin	4.0±0.33	4.0±0.33

Data given are mean ± standard deviation

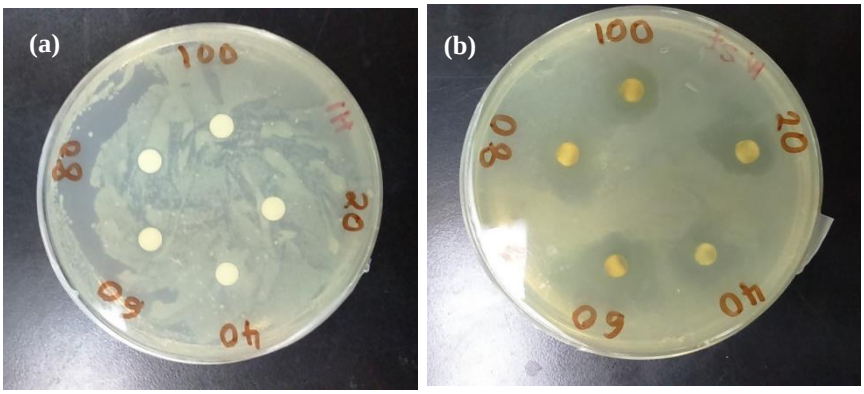


Figure 1. Disc-diffusion method of leaves extracts against *S. epidermidis*: (a) hexane extract and (b) methanol extract

Table 3 shows antimicrobial activities of hexane and methanol against *T. mentagrophytes*. For *T. mentagrophytes*, the best concentration were 40 mg/ml extract and 60 mg/ml extract, which showed the same diameter of inhibition zone of 5 mm (Figure 2). Nystatin, which was used as the positive control to act against the *T. mentagrophytes*, showed weak effects on the fungal colonies by forming 2 mm clear zone. This might be due to the inadequate dosage against the number of colonies. The observed antibacterial effects on the isolates are believed to exist, due to the presence of tannins, alkaloids and flavonoids which have been shown to possess antibacterial properties [11, 12].

Table 3. Antimicrobial activities of hexane and methanol extracts against *T. mentagrophytes*

Concentration (mg/ml)	**Average Inhibition Zone (mm)**	
	Hexane Extract	**Methanol Extract**
20	-	2.0±0.58
40	-	5.0±0.33
60	-	5.0±0.33
80	-	4.0±0.33
100	-	3.0±0.24
Nystatin	2.0±0.58	2.0±0.58

Data given are mean ± standard deviation

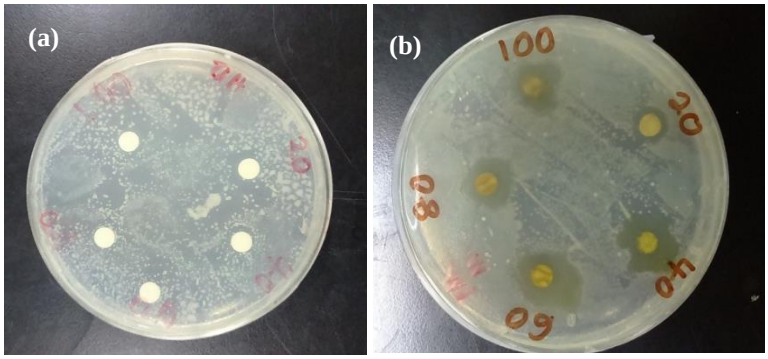


Figure 2. Disc-diffusion method of leaves extracts against *T. mentagrophytes*: (a) hexane extract and (b) methanol extract

Figure 3 shows the effect of methanol extract against different microorganisms *S. epidermidis* and *T. mentagrophytes.* For *T. mentagrophytes*, the inhibition zone showed decreasing trend as the concentration exceeded 60 mg/ml. According to Ibrahim and Osman [13], increasing the concentrations of the extracts gave the results of decreasing of the growth of dermatophytes. Based on the graph, the methanolic extract showed the best results against *T. mentagrophytes* at the concentration of 40 mg/ml whereas 60 mg/ml was needed to give the best size of inhibition zone for *S. epidermidis*. The result illustrated the possibility of banana leaves extract to become as potential drug based on its antifungal properties.

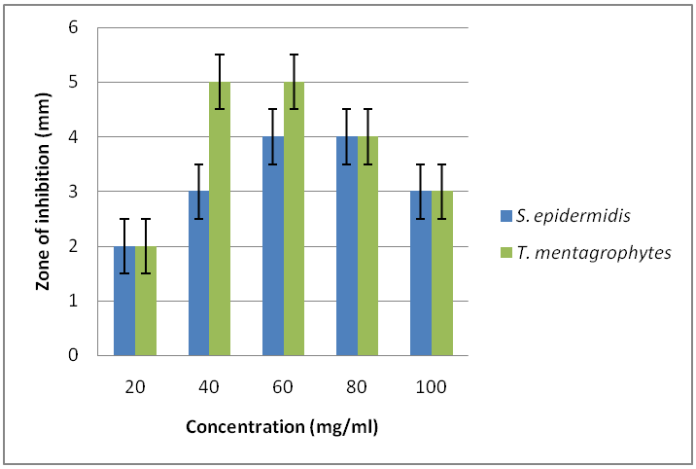


Figure 3. Effects of methanol extract against tested microorganisms

Conclusion

In the present study, the banana leaves were used to identify the phytochemical and antimicrobial properties. Among all the phytochemical constituents tested, only alkaloids were detected in hexane extract and all of the chemicals presents in methanol extract. For the antimicrobial activities, only methanol extract of *M. acuminata* 'Dwarf Cavendish' gave effects to both microorganisms tested. The results of the study have proven that the leaves of the banana contain medicinal properties, and thus can potentially be used in the antibacterial formulation in pharmaceutical industries such as in production of cream or other health care products.

References

1. Cowan, M. M. (1999). Plant products as antimicrobial agents. *American Society for Microbiology*, 12(4): 564-582.
2. Arif, T., Bhosale, J. D., Kumar, N., Mandal, T. K., Bendre, R. S., Lavekar, G. S. and Dabur, R. (2009). Natural products-antifungal agents derived from plants. *Journal of Asian Natural Products Research*, 11(7): 621-638.
3. Oliveira, L., Cordeiro, N., Evtuguin, D. V., Torres, I. C. and Silvestre, A. J. D. (2007). Chemical composition of different morphological parts from 'Dwarf cavendish' banana plant and their potential as a non-wood renewable source of natural products. *Industrial Crops and Products*, 26(2):163-172.
4. Evans, E. and Ballen, F. (2012). Banana market (FE901). UF Department of Food and Resource Economics: pp. 1-9.
5. Kumar, P. R., Srivastava, S., Singh, K. K., Mathad, C. and Thind, P. S. (2014). Study of antioxidant and antimicrobial properties, phytochemical screening and analysis of sap extracted from banana (*Musa acuminata*) pseudostem. *International Journal of Advanced Biotechnology and Research*, 5(4): 649-658.
6. Cruz-Cruz, C. A., Ramírez-Tec, G., García-Sosa, K., Escalante-Erosa, F., Hill, L., Osbourn, A. E. and Peña-Rodríguez, L. M. (2009). Phytoanticipins from banana (*Musa acuminata* Cv. Grande Naine) plants, with antifungal activity against *Mycosphaerella fijiensis*, the causal agent of black sigatoka. *European Journal of Plant Pathology*, 126(4): 459-463.

7. Kapadia, S., Pudakalkatti, P. and Shivanaikar, S. (2015). Detection of antimicrobial activity of banana peel (*Musa paradisiaca* L.) on *Porphyromonas gingivalis* and *Aggregatibacter actinomycetemcomitans*: An *in vitro* study (Health and Medicine Complete (Alumni Edition) ed. Vol. 6): Medknow Publications & Media Pvt. Ltd.
8. Narendra, K., Sowjanya, K. M., Swathi, J. and Satya, A. K. (2012). Phytochemical evaluation & antimicrobial efficiency of threatened medicinal plant of Andhra Pradesh *Pterospermum xylocarpum* (Thada Tree). *International Research Journal of Pharmacy*, 4(2): 155-160.
9. Tiwari, P., Kumar, B., Kaur, M., Kaur, G. and Kaur, H. (2011). Phytochemical screening and extraction - a review. *Internationale Pharmaceutical Sciencia*, 1(1): 98-104.
10. Shittu, G. A. and Akor, E. S. (2015). Phytochemical screening and antimicrobial activities of the leaf extract of *Entandrophragama angolense. African Journal of Biotechnology*, 14(3), 202-205.
11. Awoyinka, O. A., Balogun, I. O. and Ogunnowo, A. A. (2007). Phytochemical screening and *in vitro* bioactivity of *Cnidoscolus aconitifolius*. *Journal of Medicinal Plants Research*, 1(3): 63-65.
12. Thenmozhi, M. and Sivaraj, R. (2010). Phytochemical analysis and antimicrobial activity of *Polyalthia longifolia*. *International Journal of Pharma and Bio Sciences*, 1(3): 1-7.
13. Ibrahim, D., & Osman, H. (1995). Antimicrobial activity of *Cassia alata* from Malaysia. *Journal of Ethnopharmacology*, 45(3): 151-156.

Malaysian Journal of Analytical Sciences, Vol 22 No 3 (2018): 458 - 464
DOI: https://doi.org/10.17576/mjas-2018-2203-12

MALAYSIAN JOURNAL OF ANALYTICAL SCIENCES
Published by The Malaysian Analytical Sciences Society
ISSN 1394 - 2506

FABRICATION AND CHARACTERIZATION OF RUBY NANOPARTICLES

(Fabrikasi dan Pencirian Partikel Nano Delima)

Wan Aizuddin Wan Razali*, Azman Kasim , Syamsyir Akmal Senawi, Azhan Hashim, Norihan Yahya, Hartini Ahmad Rafaie

Faculty of Applied Sciences,
Universiti Teknologi MARA Pahang, 26400 Bandar Tun Abdul Razak Jengka, Pahang, Malaysia

**Corresponding author: wanaizuddin@pahang.uitm.edu.my*

Received: 4 December 2016; Accepted: 1 December 2017

Abstract

Numerous works have been done on finding nanoparticles (NPs) with excellent optical properties. In this work, ruby (chromium doped alumina) nanoparticles have been prepared using femtosecond laser ablation. The synthesized nanoparticles were characterised using dynamic light scattering (DLS), transmission electron microscopy (TEM) and fluorescence microscopy. DLS analysis indicates that the particles size is approximately 52 nm. TEM analysis gives smaller particles size with mean size of 38 nm compared to DLS analysis. Spherical shape of the particles was observed through TEM image. The synthesized NPs showed excellent stability in water with +55 mV zeta potential value. The most efficient wavelengths to excite the ruby NPs were determined as 405 nm and 554 nm. The emission peak for the ruby NPs was at 690 nm which is corresponds to ^2E-$^4A_2$ transition. The synthesized ruby NPs can be applied as a potential bioimaging label

Keywords: ruby nanoparticles, femtosecond laser ablation, emission, bioimaging

Abstrak

Pelbagai usaha telah dilakukan bagi mencari partikel nano yang mempunyai sifat optik yang baik. Dalam kajian yang dilakukan, partikel nano delima (kromium dop alumina) adalah dihasilkan melalui pelelasan laser femto saat. Pencirian sintesis partikel nano adalah berdasarkan serakan cahaya dinamik (DLS), Mikroskopi elektron terhantar (TEM) dan mikroskopi pendarfluor. Analisis DLS menunjukkan saiz partikel adalah dalam linkungan 52 nm. Analisis TEM menandakan kewujudan saiz partikel lebih kecil dengan saiz purata pada julat 38 nm berbanding analisis DLS. Bentuk sfera pada partikel-partikel berkenaan dicerap melalui imej TEM. Partikel nano yang dihasilkan memberikan bacaan tahap kestabilan yang amat baik di dalam air pada beza keupayaan zeta 55 mV. Panjang gelombang yang cekap bagi mengujakan partikel nano delima adalah sekitar julat 405 nm dan 554 nm. Puncak sinaran bagi partikel nano delima adalah 690 nm iaitu mewakili anjakan ^2E-$^4A_2$. Partikel nano delima yang dihasilkan berpotensi untuk digunakan bagi tujuan penandaan imbasanbio.

Kata kunci: partikel nano delima, pelelasan laser femto saat, sinaran, imbasanbio

Introduction

The fluorescence properties of ruby or Chromium doped Alumina ($Cr:Al_2O_3$) are very well known after the invention of first ruby laser by T. H. Maiman's in 1960 [1]. The ruby laser consisted of a single crystal rod of synthetic corundum with chromium ions substituted the aluminum ions. The rod was pumped using flashlamp in order to emit a single pulse of coherent and monochromatic radiation. The Cr^{3+} ion is very interesting because the ^2E-$^4A_2$ emission of Cr^{3+} is one of the best candidate for transitions in the optical spectroscopy of solids [2, 3] and it also have broad band luminescence properties at room temperature [4]. The two zero-phonon emission lines of bulk

ruby crystals are centred at 694.3 and 692.9 nm [5]. Previously, research has predominantly been focused on the properties of bulk ruby [6-10], whilst the properties of ruby in nanoparticles form has received less attention.

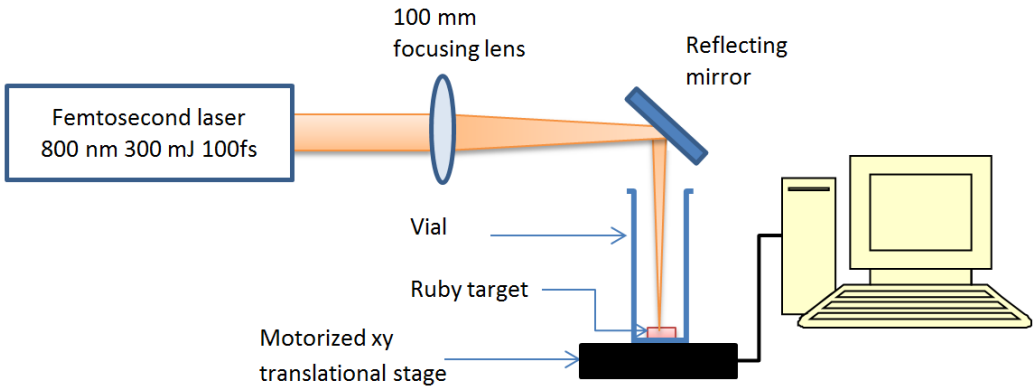
Since the development of the nanotechnology, ruby NPs have tremendous potential in photonic application. In nanosize form (known as nano-ruby) new applications have been discovered, due to their interesting properties such as long fluorescence lifetime, high colloidal stability and efficient luminescence [11]. Recently, ruby NPs show promising result to be applied as a fluorescence probe for bioimaging application.

A number of different methods have been investigated in order to produce nanoparticle such as sol gel, electrospraying, spray pyrolysis, reduction methods, chemical vapor deposition (CVD), and ball milling [12-17]. Nevertheless, laser ablation method attracts more attention since it can generate of nanoparticle colloids with outstanding purity compared to the conventional manufacturing routes [18]. In this research, a colloidal suspension of ruby NPs was prepared using femtosecond laser ablation. The nanoparticles size, zeta potential and luminescence properties of produced ruby NPs were analyzed using DLS, TEM and fluorescence spectroscopy.

Materials and Methods

A ruby crystal with dimension of 5 mm x 5 mm x 2 mm was ablated using femtosecond laser with 300 mJ power, 100 fs pulse duration with 1 kHz repetition rate. The beam spot was calculated using gaussian function derivation method and estimated to be approximately 100 µm. The laser fluence of the focused laser beam is 3 J/cm^2. The ablation procedure was done 1 hour per session in atmospheric environment and the particles were collected in distilled water. The laser scanning was set at 4 mm/s velocity and 4mm/s^2 acceleration. The target was moved during the ablation process in order to have fresh surface during laser ablation. The collected colloidal solution was centrifuged at 2000 rcf in 15 minutes in order to force larger particles to settle at the bottom of the tube. The entire upper section (the supernatant) was then collected.

Dynamic Light Scattering (DLS) analysis was used to determine the size distribution and zeta potential of the nanoparticles using a Malvern Nano ZS. The upper section was collected for further analysis. Transmission Electron Microscopy (TEM) analysis was performed using Philips CM10 to analyse the particles size and shape Fluorolog system from Jobin-Yvon-Horiba with 450 W Xe lamp excitation was employed for spectroscopic measurements. All data were collected at room temperature.



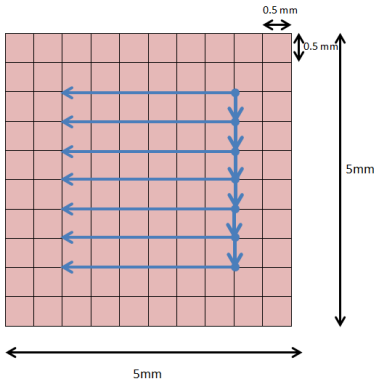


Figure 1. Schematics of experimental setup for laser ablation. Lower part describes the scanning track on ruby crystal surface

Results and Discussion

Initial investigations using the zeta sizer (see Figure 2a) shows that the size of the ruby NPs in term of hydrodynamics diameter was distributed from 50 nm to 120 nm centred at 52 nm. Smaller particles have also been observed which indicate the wide distribution in the size of the particles. Further centrifugation was done in order to fractionize the size of the particles. The particles can be considered as stable, when zeta potential value higher than +30 mV or lower than -30 mV [19]. In our work, the zeta potential of produced nanoparticles is +55 mV (Figure 2b), which indicates excellent stability in water.

Initial investigations using the zeta sizer (see Figure 2a) shows that the size of the ruby NPs in term of hydrodynamics diameter was distributed from 50 nm to 120 nm centred at 52 nm. Smaller particles have also been observed which indicate the wide distribution in the size of the particles. Further centrifugation was done in order to fractionize the size of the particles. The particles can be considered as stable, when zeta potential value higher than +30 mV or lower than -30 mV [19]. In our work, the zeta potential of produced nanoparticles is +55 mV (Figure 2b), which indicates excellent stability in water.

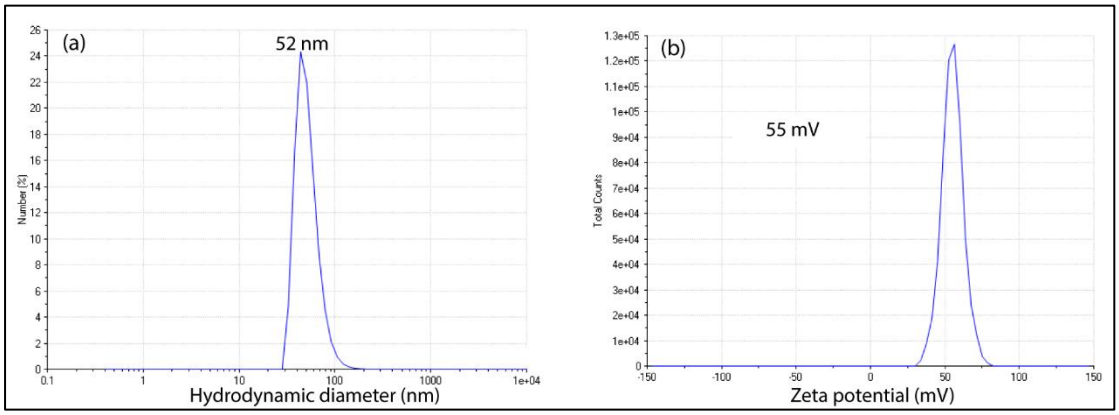


Figure 2. (a) DLS analysis for size distribution and (b) zeta potential of ruby NPs

The particles size and shape of the sample before and after centrifugation process was characterized by TEM. Figure 3 displays the TEM image after the centrifugation process. It can be seen that, more spherical ruby NPs were obtained after undergoing centrifugation process compared to those obtain without undergoing the centrifugation process. The formed nanoparticles disperse well in the solution and does not show any particle aggregation. Further analysis was done using histogram of particle distribution from TEM image as shown in Figure 4. The histogram

shows that the mean particle size is about 38 nm compared to DLS analysis with value of 52 nm. Small amount (approximately 10 %) of particles between 10 – 27 nm also have been observed.

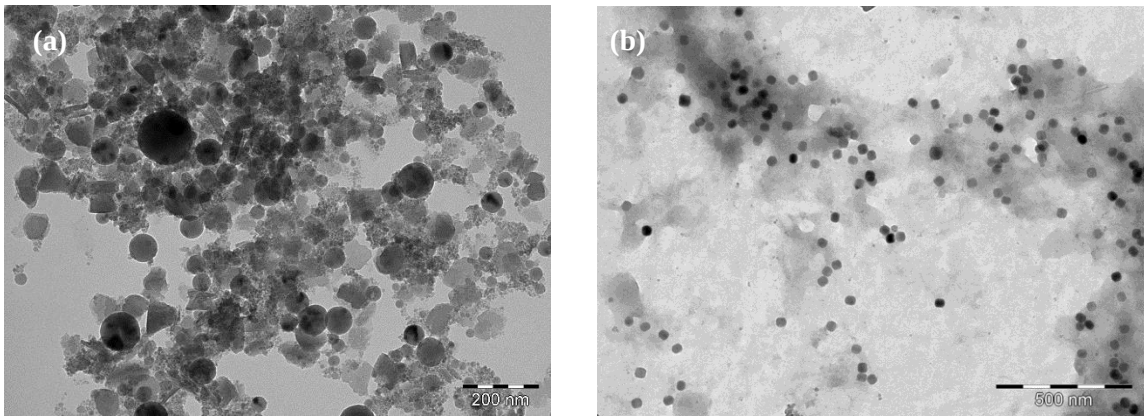


Figure 3. TEM image of ruby NPs before and after centrifugation

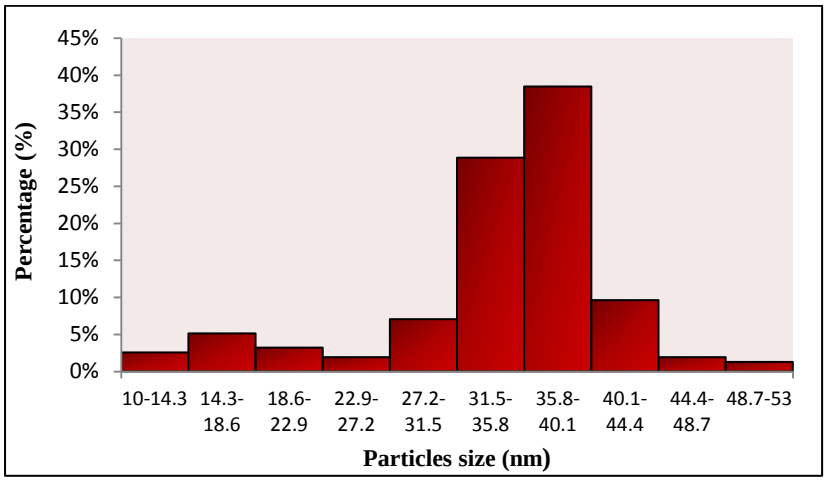


Figure 4. Histogram of particles size distribution from TEM image

Excitation spectrum analysis was carried out in order to determine the optimum excitation wavelength to excite the ruby NPs. As shown in Figure 5, two broad bands centred at 403 nm and 554 nm was detected. These peaks were correspond to the spin-allowed $^4A_2$ (^4F)-$^4T_1$and $^4A_2$ (^4F)-$^4T_2$ transitions [2, 19]. Peak at 403 nm shows higher intensity compared to peak at 554 nm, results in good excitation for the ruby NPs.

Figure 6 shows the emission spectra of the ruby NPs disperse in distilled water excited with 403 nm and 553 nm. Distilled water without ruby particles excited at 403 nm also been included as a reference. From the emission spectrum analysis for ruby NPs, the peak at 691.11 nm is observed which can be attributed to the transition of $\bar{E} \rightarrow {}^4A_2$and $2\bar{A} \rightarrow {}^4A_2$. However, the R_1 and R_2 lines cannot be seen here, this is could be due low resolution of spectrometer. The intensity of the emission spectrum excitation at 554 nm is lower compare to spectrum excitation at 405 nm due lower excitation spectra. There are also two less intensive and partially overlapped peaks at 671nm and 710 nm which could be corresponding to N-lines (zero-phonon lines) related to a coupling between Cr^{3+} state and lattice defects and to Cr^{3+}-Cr^{3+} pair interactions [4].

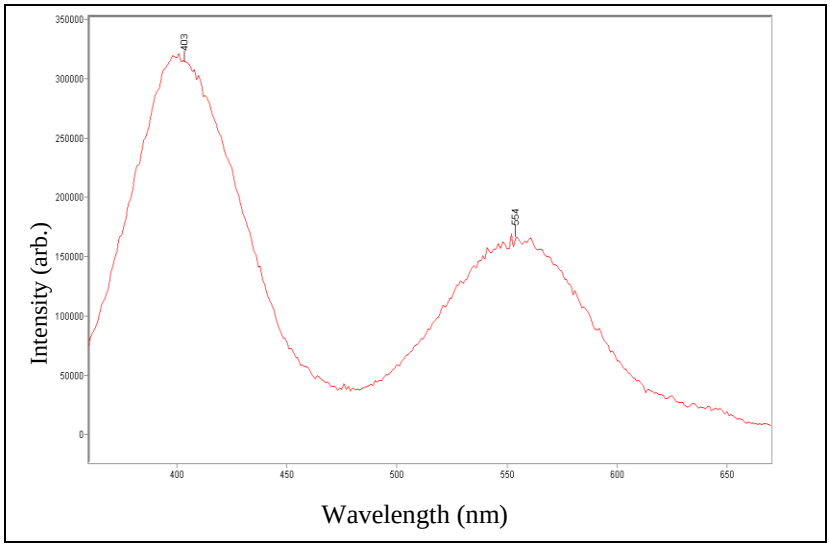


Figure 5. Excitation spectra of the ruby NPs

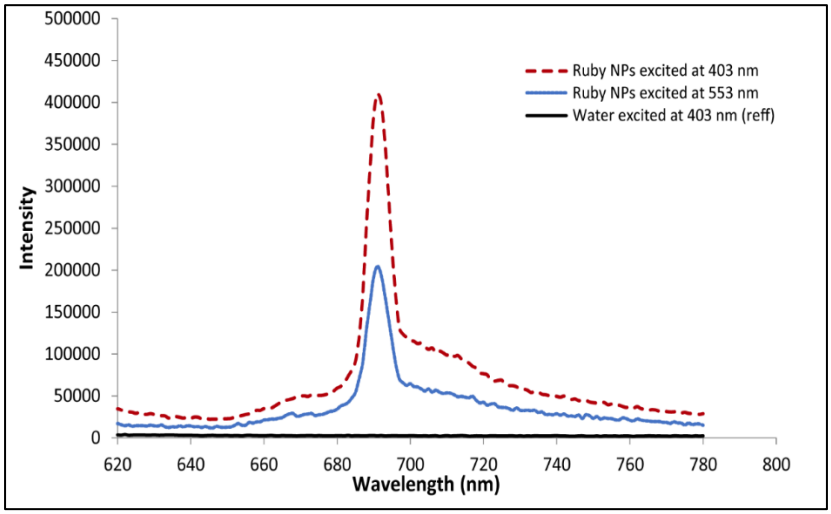


Figure 6. Emission spectrum of the ruby NPs colloid and distilled water

The image of Ruby NPs under 405 nm excitation is shown in Figure 6. Bright emission was observed using wide field microscope. These results clearly indicate the potential of the ruby NPs to be applied in bioimaging labelling in the future (Figure 7).

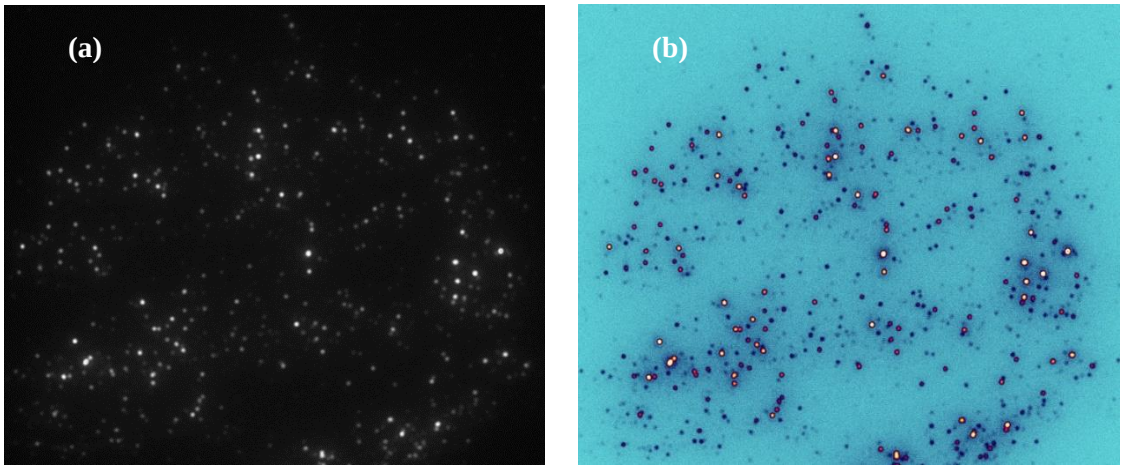


Figure 7. Image of ruby NPs under 405 nm excitation. Fluorescence image using wide field microscope (a) and (b) image after processing for clearer view

Conclusion

The physical and optical studies of prepared ruby NPs have been successfully discussed. The particle size was distributed from 50 nm to 120 nm centred at 52 nm. TEM image illustrates the spherical shape of the particles. The excitation spectra of the ruby colloid show that the strongest absorption for the sample occurs at 405 nm. Hence, the 554 nm excitation wavelength leads to the emission of red emission spectra centered at 690 nm which corresponding to the transitions of $\overline{E} \rightarrow {}^4A_2$ and $2\overline{A} \rightarrow {}^4A_2$. The outstanding properties of ruby NPs such as bright and sharp emission at 690 nm and excellent stability are potentially can be applied in biological labelling application.

Acknowledgement

The authors acknowledge financial support from Malaysian Government and University Teknologi MARA, and would like to acknowledge Macquarie University and University of Adelaide for their experimental equipment.

References

1. Maiman, T. H. (1960). Stimulated optical radiation in ruby. *Nature*, 187 (4736): 493-494.
2. Yang, L. Y., Dong, Y. J., Chen, D. P., Wang, C., Da, N., Jiang, X., Zhu, C. and Qiu, J. R. (2005). Upconversion luminescence from 2E state of Cr^{3+} in Al_2O_3 crystal by infrared femtosecond laser irradiation. *Optics Express*, 13 (20): 7893-7898.
3. Maiman, T. H. (1960). Optical and microwave-optical experiments in ruby. *Physical Review Letters*, 4 (11): 564-66.
4. Krizan, J., Mozina, J., Bajsic, I., and Mazaj, I. (2012). Synthesis and fluorescent properties of chromium-doped aluminate nanopowders. *Acta Chimica Slovenica*, 59(1):163-168.
5. Patra, A., Tallman, R. E. and Weinstein, B. A. (2005). Effect of crystal structure and dopant concentration on the luminescence of Cr^{3+} in Al_2O_3 nanocrystals. *Optical Materials*, 27(8): 1396-1401.
6. Schawlow, A. L., Wood, D. L. and Clogston, A. M. (1959). Electronic spectra of exchange-coupled ion pairs in crystals. *Physical Review Letters*, 3(6): 271-273.
7. Mollenauer, L. F. and Schawlow, A. L. (1968). Piezospectroscopic studies of exchange-coupled Cr^{3+} ion pairs in ruby. *Physical Review*, 168 (2): 309-317.
8. Kisliuk, P., Chang, N. C., Scott, P. L. and Pryce, M. H. L. (1969). Energy levels of chromium ion pairs in ruby. *Physical Review*, 184(2): 367-374.
9. Van der Ziel, J. P. (1974). Spectrum of first-nearest-neighbor Cr^{3+} pairs in ruby. *Physical Review B*, 9(7): 2846-2862.

10. Engstrom, H. and Mollenauer L. F. (1973). Chronospectroscopy of exchange-coupled Cr^{3+}-ion pairs in ruby. *Physical Review B*, 7 (4): 1616-1626.
11. Piriyawong, V., Thongpool, V., Asanithi, P. and Limsuwan, P. (2012). Effect of laser pulse energy on the formation of alumina nanoparticles synthesized by laser ablation in water. *Procedia Engineering*, 32: 1107-1112.
12. Rahman I. A. and Padavettan, V. (2012). Synthesis of silica nanoparticles by sol-gel: Size-dependent properties, surface modification, and applications in silica-polymer nanocomposites - a review. *Journal of Nanomaterials*, 2012 (8): 1-15.
13. Jaworek, A. (2007). Micro- and nanoparticle production by electrospraying. *Powder Technology*, 176(1): 18-35.
14. Mueller, R., Mädler, L. and Pratsinis, S. E. (2003). Nanoparticle synthesis at high production rates by flame spray pyrolysis. *Chemical Engineering Science*, 58(10): 1969-1976.
15. Iwamoto, M., Kuroda, K., Zaporojtchenko, V., Hayashi, S. and Faupel, F. (2003). Production of gold nanoparticles-polymer composite by quite simple method. *The European Physical Journal D - Atomic, Molecular, Optical and Plasma Physics*, 24(1): 365-367.
16. Nakaso, K., Han, B., Ahn, K. H., Choi, M. and Okuyama, K. (2003). Synthesis of non-agglomerated nanoparticles by an electrospray assisted chemical vapor deposition (ES-CVD) method. *Journal of Aerosol Science*, 34(7): 869-881.
17. Lam, C., Zhang, Y. F., Tang, Y. H., Lee, C. S., Bello, I. and Lee, S. T. (2000). Large-scale synthesis of ultrafine Si nanoparticles by ball milling. *Journal of Crystal Growth*, 220(4): 466-470.
18. Sajti, C., Sattari, R., Chichkov, B. and Barcikowski, S. (2010). Ablation efficiency of α-Al_2O_3 in liquid phase and ambient air by nanosecond laser irradiation. *Applied Physics A*, 100(1): 203-206.
19. Liu, D. (2013). Effects of Cr content and morphology on the luminescence properties of the Cr-doped alpha-Al_2O_3 powders. *Ceramics International*, 39(5): 4765-4769.

Malaysian Journal of Analytical Sciences, Vol 22 No 3 (2018): 465 - 470
DOI: https://doi.org/10.17576/mjas-2018-2203-13

MALAYSIAN JOURNAL OF ANALYTICAL SCIENCES
Published by The Malaysian Analytical Sciences Society
ISSN 1394 - 2506

SYNTHESIZED AND CHARACTERIZATION OF SODIUM COBALT OXIDE AS SODIUM-ION CATHODE BATTERIES USING SOL-GEL METHOD

(Sintesis dan Pencirian Sodium Kobalt Oksida Sebagai katod Bateri Ion-Sodium Menggunakan Kaedah Sol-Gel)

Sarah Laila Mohd Jan[1]*, Nur Athirah Mohd Azhar[1], Musfiroh Jani[2]

[1]*Faculty of Applied Sciences,*
Universiti Teknologi MARA Pahang, 26400 Bandar Tun Abdul Razak Jengka, Pahang, Malaysia
[2]*Faculty of Earth Science,*
Universiti Malaysia Kelantan, Kampus Jeli, 17600 Kelantan Malaysia

**Corresponding author: sarahlaila@pahang.uitm.edu.my*

Received: 4 December 2016; Accepted: 1 December 2017

Abstract

Sodium's chemical properties are like lithium and as batteries it has potential to be environmentally friendly, easier to recycle but five times much cheaper than lithium-ion batteries. Sodium cobalt oxide ($NaCoO_2$) cathode material in a sodium-ion battery was synthesized by a polyvinyl alcohol (PVA) assisted sol-gel method and its physical characterization was being analysed by using thermogravimetric analysis (TGA), attenuated total reflectance-fourier transform infrared (ATR-FTIR) spectroscopy, field emission scanning electron microscope (FESEM) and X-ray diffractometer (XRD). PVA was chosen as gelating agent as well as carbon source for the synthesized material in this study. The cathode material is observed to have smooth morphology and the particle sizes reach to sub-micrometre level which benefit for the high rate performance, although the shape of particles was irregular.

Keywords: sodium-ion batteries, cathode material, sol gel

Abstrak

Sifat kimia sodium menyerupai lithium dan sebagai bateri ia mempunyai potensi untuk mesra alam sekitar, mudah di kitar semular dan lima kali lebih murah berbanding bateri litium. Sodium kobalt oksida ($NaCoO_2$) iaitu bahan katod yang digunakan dalam ion-sodium bateri disintesiskan dengan kaedah sol- gel dibantu oleh polivinil alkohol (PVA) dan pencirian fizikal dianalisa menggunakan analisa termogravimetrik (TGA), spektroskopi inframerah transformasi fourier (ATR-FTIR), mikroskopi imbasan elektron pancaran medan (FESEM) dan teknik pembelauan sinar-X (XRD). PVA dipilih sebagai agen gelatin dan juga sebagai sumber karbon untuk mensintesiskan bahan kajian ini. Bahan katod yang dihasilkan menunjukkan morfologi permukaan yang rata dan saiz partikel yang mencecah sub-mikrometer memberi kelebihan dari segi kadar prestasi yang tinggi walaupun bentuk partikel tidak seragam.

Kata kunci: bateri ion-sodium, bahan katod, sol gel

Introduction

Over the past decade, electronic devices have boomed rapidly in the market. Smartphones especially have gained attention in the market and competition among producers are very high. These companies will always look for novel characteristic to sell to users. One of them is durability of the smartphone batteries. The performance of batteries relies on the characteristics and properties of their components materials [1]. Lithium-ion batteries have been widely

used as rechargeable batteries in electronic devices namely smartphones, laptops, cameras and even digital audio players. Its high-energy densities and long lifespan make it a perfect option as an energy storage for electronic devices especially portable electronic devices. However, the cost of lithium-ion batteries became debatable as a cheaper option for broader market application. It became limited and not enough to satisfy the needs in the market due to the high demand of lithium-ion batteries usage [2].

Therefore, an alternative to this problem have been investigated with the advances on sodium-ion batteries. High abundance and low cost of sodium-ion batteries offer an advantage compared to lithium-ion batteries. Electrochemical performance wise between these two types of batteries are similar and sodium ion batteries are expected to be an alternative especially in large-scale of energy reserve [2]. The aim of this paper is to synthesize cathode material for sodium-ion batteries using sol-gel method by utilizing the initial precursor of sodium nitrate ($NaNO_3$), cobalt nitrate hexahydrate ($Co(NO_3)_2.6H_2O$) and PVA. The synthesized material was then characterized using Thermogravimetric analysis (TGA), X-ray Diffraction (XRD), Attenuated Total-Reflectance Fourier Transform Infrared (ATR-FTIR) and Field Emission Scanning Electron Microscopy (FESEM).

Materials and Methods

Methods by previous researcher was used as a reference to synthesize sodium cobalt oxide cathode material by using sol-gel method with some modification [3]. A stoichiometric amount of $NaNO_3$ and $Co(NO_3)_2.6H_2O$ were weighed, mixed and dissolved in distilled water. Then, 5 wt.% of PVA was added to the solution as chelating agent. The solution was constantly stirred in water bath for 6 hours at 80 °C. The resulting gel was dried in the oven at 120 °C for 24 hours. Later, the dried gel was calcined at 800 °C in a furnace for 16 hours [3]. Characterization of cathode material were done using ATR-FTIR, (Perkin Elmer, Model 1600) and TGA, (Perkin Elmer, Thermal TGA Pyris 1) was conducted in the temperature range from 25 to 900 °C. The crystallographic structure and morphologies of the prepared sample were characterized by XRD and FESEM (JEOL, JSM-7800F).

Results and Discussion

Field emission scanning electron microscope

The morphology of sodium cobalt oxide cathode material observed under 1000x and 2000x magnification was heterogeneous particles with smooth surface as refer to Figure 1. Most flake-shaped particles were seen. By increasing the calcination temperature, the particle shape become clear and smooth surface, imply that the sample are well crystallized [4]. Under 2000x magnification, flakes-shaped particles were more clearly. In addition, there were some particles that agglomerate with each other. Research conducted done by previous researcher which is $Li_3V_2(PO_4)_3$ cathode materials that prepared by PVA assisted sol-gel method shown agglomerated particles and form larger secondary particles under observation of SEM [3]. The agglomeration will be useful in order to raise the density of the synthesized cathode material [5].

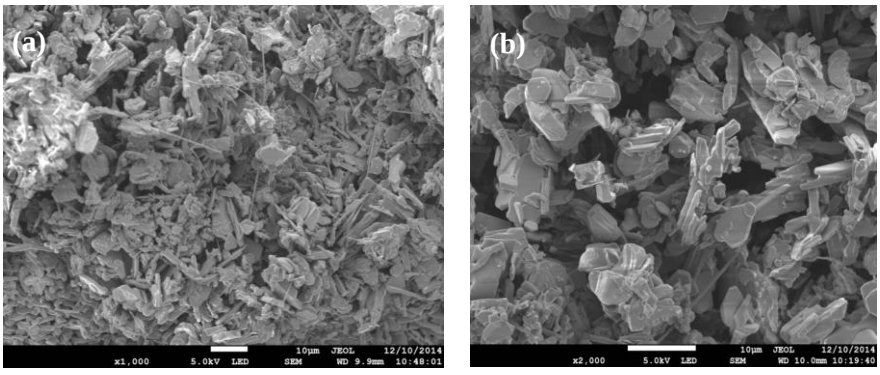


Figure 1. FESEM images of $NaCoO_2$ cathode material at magnification (a) 1000x and (b) 2000x

The morphology of $NaCoO_2$ cathode material under magnification of 3000x and 5000x are shown in Figure 2. Under 3000x magnification, some rough and round features were noticed on the surface of the particles. There were no pores present on the surface particles and the surface was smooth. These features are due to the presence of sodium carbonate ($NaCO_3$) [6]. Indeed, they can originate from the sodium being extracted from the structure by exposure to air. It was confirmed by ATR-FTIR spectrum, which shows peak at 861 cm^{-1} represents the carbonate peak. Based on such peak it was confirmed that there was $NaCO_3$ on the surface particles of the synthesized cathode material. Whereas, referring to Figure 2, the morphology of synthesized cathode material was obviously seen as inhomogeneous. There were flake-shaped particles, round particles scattered around and cylindrical needle-like particles. The inhomogeneous morphologies are related to the existence of impurity [7].

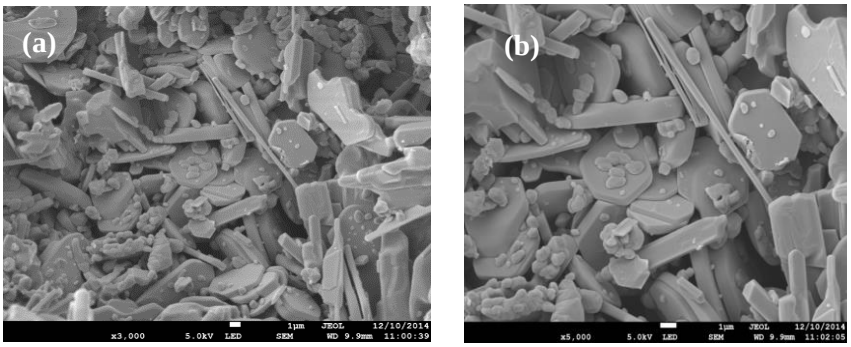


Figure 2. FESEM images of $NaCoO_2$ cathode material at magnification (a) 3000x and (b) 5000x

The FESEM image of the particle size under magnification 30,000x and 45,000x are shown in the Figure 3. Most of particles were distributed in the range of 731 nm to 1470 nm. The average particle size was measured to be 1100 nm. From the FESEM image, clearly observed that the $NaCoO_2$ sample had smooth morphology and the particle sizes reach to sub-micrometer level, although the shape of particles was irregular. This microstructure has a large specific surface area allowing the electrolyte to keep adequate contact with the active material, which is a benefit for the high rate performance [8].

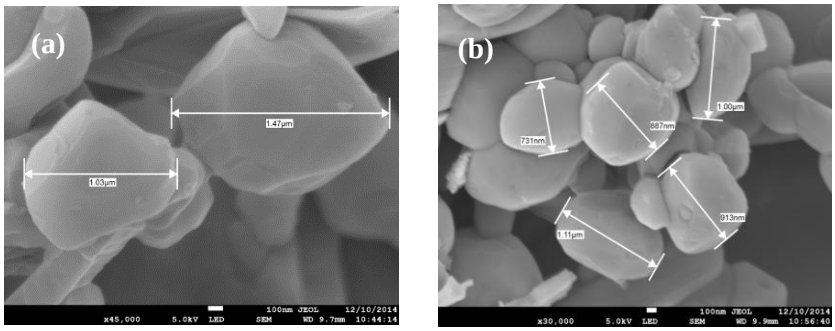


Figure 3. Particle size of $NaCoO_2$ cathode material at magnification (a) 30,000x and (b) 45,000x

Under 30,000x magnification, the round particles were seen to be agglomerated and there was space between the agglomerated particles. In this study, calcination temperature for synthesis of cathode material was set up at 800 °C. The agglomeration resulted in the particles in agreement with the finding of other researcher which is palpable agglomeration occurs when the temperature increase to 800 °C [8]. Others, under magnification of 45,000x of FESEM, the particles were seen to be sharp at the edges of round particles. Clearly, it shows that the synthesized $NaCoO_2$ cathode material was inhomogeneous and the shape of particles was irregular.

Attenuated total reflectance-fourier transform infrared spectroscopy

The ATR-FTIR spectrum of powdered $NaCoO_2$ cathode material after being calcined is shown in Figure 4. The peak appears at 567 cm^{-1} corresponding to the metal cobalt to oxygen bond (Co-O). These absorption bands at 616 and 539 cm^{-1} are represent the metal to oxygen (M-O) bond [9]. During preparation of $NaCoO_2$ cathode material, the sample may expose to the air. Therefore, initial precursor of sodium from $NaNO_3$ will react to the exposed air then form $NaCO_3$, thus carbonate peak (O-C-O) appeared at 861 cm^{-1}. Another peak that appears sharper and more intense is at 1356 cm^{-1}. This peak is known as NO_2 symmetric stretching. Whereas, peak for nitro (N=O) forms at 1407 cm^{-1}. Furthermore, a very intense peak at 1708 cm^{-1} is corresponding to the Co-NO_3^- bond. This peak is also known as anti-symmetric stretching peak. In this study, the initial precursors used were $NaNO_3$ and $Co(NO_3)_2.6H_2O$. In both chemicals contain NO_3^- ion bond, this is reason for the presence of NO_3^- peak in the ATR-FTIR spectrum. Studies of $Co(NO_3)_2.6H_2O$ by previous researcher stated that the stretch peak of anti-symmetric Co-NO_3^- bond is appeared at 1629 cm^{-1} [10].

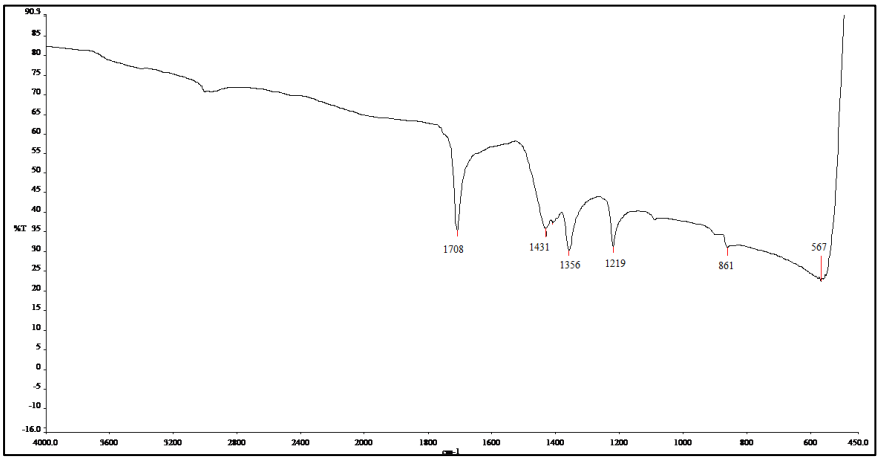


Figure 4. ATR-FTIR spectrum of powdered sodium cobalt oxide cathode material

Thermogravimetric analysis

The thermal property of synthesized $NaCoO_2$ cathode material was studied by thermogravimetric analysis (TGA). TGA curve of dried gel sodium cobalt oxide cathode material is shown in Figure 5. First mass loss was occurred from 26.82 to 139.25 °C is due to the removal of water content in that material. Researcher stated that, the weight loss before 220 °C is attributed by evaporation of water and ammonia from the precursor [3]. In addition, the slight weight loss from TGA curve appears around 102 °C due to the volatilization of residual water and the organic solvents [11]. Briefly, the weight loss in the next temperature region of 139.25–325.23 °C accompanied by a rapid chain-stripping elimination of water. In this region, one could observe melting of the precursor which caused the precursor to foam or intumesce [3]. Meanwhile, another 13.5% weight loss began at 130 °C with an endothermic peak at 194°C, might be the removal of crystalliferous water incorporated in the lattice of the material [4].

Furthermore, the TGA plot between 325.23 to 698.08 °C showed the pyrolysis process of PVA. The observance of multiple weight loss steps is attributed to the continuous elimination of H and O, leads to higher and higher carbon-to-hydrogen (C/H) ratios in the pyrolysis residue. Carbonization reaction also occurred in that temperature region [3]. Hence, the precursor is heat treated between 400 and 530 °C, polycrystalline carbon is formed due to the carbonization reaction that take place within the temperature range. The TGA curve becomes flat and no changes in the mass loss above 750 °C, indicating the completion of the entire reaction. Therefore, 800 °C was chosen as calcination temperature in order to obtain $NaCoO_2$ cathode material with high purity.

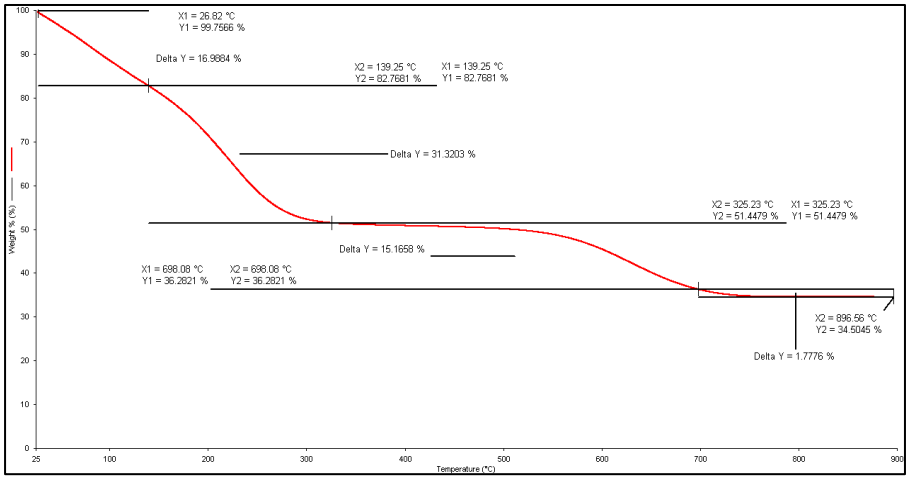


Figure 5. TGA curve of sodium cobalt oxide cathode material

X-Ray diffraction

The XRD analysis for synthesized material was conducted. From the diffractogram in Figure 6, the result shows that the sample was crystalline from two sharp peaks and high intensity diffraction pattern at 2 theta around 16° and 37°. This result also be supported from similar diffractograms obtained from previous researchers confirming the sodium cobalt oxides batteries [12, 13]

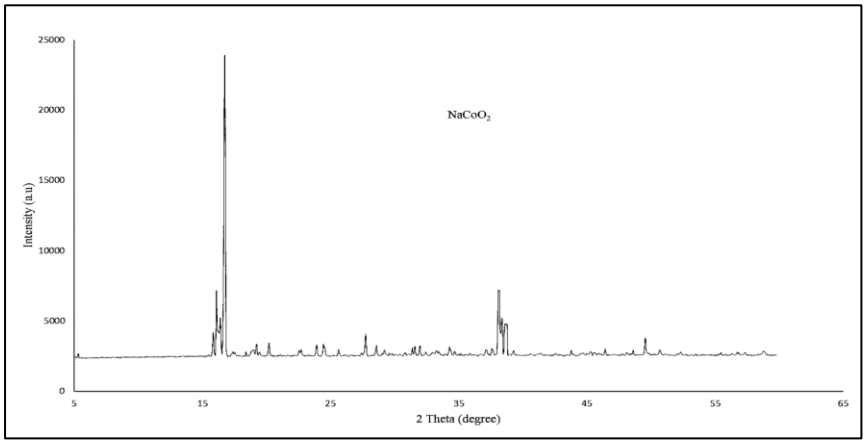


Figure 6. Sodium cobalt cathode material diffractogram from XRD analysis

Conclusion

In this research, the cathode material of sodium cobalt oxide as sodium-ion cathode battery was successfully synthesized by using sol-gel method. From the FESEM Analysis, the morphology of synthesized $NaCoO_2$ cathode material was heterogenous particles with smooth surface and agglomerated particles was present. Due to the agglomeration, the electrochemical performance of the synthesized cathode material might be lower if compared to the cathode material which has less agglomeration particles. However, electrochemical characterization was not being performed in this study, so the electrochemical performance of the synthesized cathode material cannot be confirmed. In general, low cost and environmental friendly cathode material will be possible to be produced hence can be used for electric storage applications.

Acknowledgement

Appreciation goes to all the staffs involved including the lab assistant from UiTM Cawangan Pahang, Universiti Malaysia Pahang (UMP) and Universiti Malaysia Kelantan (UMK) for their sincere assistance and help. This research was done without any national grant.

References

1. Islam, M. S. and Fisher, C. A. J. (2014). Lithium and sodium battery cathode materials: Computational insight into voltage, diffusion and nanostructural properties. *Chemical Society Reviews,* 43: 185-204.
2. Jian, Z., Yu, H. and Zhou, H. (2013). Designing high-capacity cathode materials for sodium-ion batteries. *Electrochemistry Communications,* 34: 215-218.
3. Jiang, T., Pan, W., Wang, J., Bie, X., Du, F., Wei, Y., Wang, C. and Chen, G. (2010). Carbon coated $Li_3V_2(PO_4)_3$ cathode material prepared by a PVA assisted sol-gel method. *Electrochimica Acta,* 55: 3864-3869.
4. Liu, Z., Jiang, Y., Zeng, X., Xiao, G., Song, H. and Liao, S. (2014). Two-step oxalate approach for the preparation of high performance $LiNi_{0.5}Mn_{1.5}O_4$ cathode material with high voltage. *Journal of Power Sources,* 247: 437-443.
5. Qiu, W., Liu, J., Yu, L., Zhang, G., Zhao, H. and Li, T. (2007). Studies on the low-heating solid-state reaction method to synthesize $LiNi_{1/3}Co_{1/3}Mn_{1/3}O_2$ cathode materials. *Journal of Power Sources*, 174: 701-704.
6. Doubaji, S., Valvo, M., Saadoune, I., Dahbi, M. and Edstrom, K. (2014). Synthesis and characterization of a new layered cathode material for sodium ion batteries. *Journal of Power Sources,* 266: 275-281.
7. Shun-yi, Y., Xian-you, W., Ying, W., Quan-qi, C., Jiao-jiao, L. and Xiu-kang, Y., (2010). Effects of Na content on structure and electrochemical performances of Na_xMnO_2 +δ cathode material. *Transactions of Nonferrous Metals Society of China*, 20: 1892-1898.
8. Yan, J, Yuan, W, Tang, Z, Sha, O, Wang, J, Mao, W and Ma, L (2012). Synthesis of $Li_3V_2(PO_4)_3$ cathode material *via* a fast sol-gel method based on spontaneous chemical reactions. *Journal of Power Sources*, 201: 301-306.
9. Zhang, M., Guo, S., Zheng, L., Zhang, G., Hao, Z., Kang, L. and Liu, Z., (2013). Preparation of $NiMn_2O_4$ with large specific surface area from an epoxide-driven sol-gel process and its capacitance. *Electrochimica Acta*, 87: 546-553.
10. Garry, P. G., Paul, W. J. and Manivannan, A. (2004). Formation of cobalt nitrate hydrate, cobalt oxide and cobalt nanoparticles using laser vaporization controlled condensation. *Journal of Physical Chemistry B,* 108 (28): 9604–9607.
11. Zhao, J., He, J., Ding, X., Jianhua, Z., Ma, Y., Wu, S. and Huang, R. (2010). A novel sol-gel synthesis route to $NaVPO_4F$ as cathode material for hybrid lithium ion batteries. *Journal of Power Sources,* 195: 6854-6859.
12. Lei, Y., Li, X., Liu, L. and Ceder, G. (2014). Synthesis and stoichiometry of different layered sodium cobalt oxides. *Chemistry of Materials*, 26(18): 5288-5296.
13. Wang, Y., Chou, S., Wexler, D., Liu, H. and Dou, S. X. (2014). High performance sodium-ion batteries and sodium-ion pseudocapacitors based on MoS_2 graphene composites. *Chemistry - A European Journal*, 20(31): 9607-9612.

Malaysian Journal of Analytical Sciences, Vol 22 No 3 (2018): 471 - 476
DOI: https://doi.org/10.17576/mjas-2018-2203-14

MALAYSIAN JOURNAL OF ANALYTICAL SCIENCES
Published by The Malaysian Analytical Sciences Society
ISSN 1394 - 2506

PHYTOCHEMICAL SCREENING AND LARVICIDAL ACTIVITY OF *Murraya koenigii* LEAVES EXTRACTS AGAINST MOSQUITO LARVAE

(Saringan Fitokimia dan Aktiviti Larvisid Ekstrak Daun *Murraya koenigii* Terhadap Larva Nyamuk)

Siti Suhaila Harith[1]*, Syarifah Nurul Akma Syed Mohd[1], Noorshilawati Abdul Aziz[2], Marlina Mohd Mydin[3], Nur Thabitah Shaikh Nasir[1]

[1]*Faculty of Applied Sciences*
[2]*Faculty of Plantation and Agrotechnology*
Universiti Teknologi MARA Pahang, 26400 Bandar Tun Abdul Razak Jengka, Pahang, Malaysia
[3]*Faculty of Applied Sciences,*
Universiti Teknologi MARA Cawangan Perak Kampus Tapah, 35400 Tapah, Perak, Malaysia

**Corresponding author: ssuhaila@pahang.uitm.edu.my*

Received: 4 December 2016; Accepted: 1 December 2017

Abstract

Exploring new use of aromatic leaves of *Murraya koenigii* lead us to test it as pesticide. Phytochemical screening of the extracts was conducted to determine the active compounds using hexane and methanol solvents. The LC_{50} and LT_{50} values for both extracts against mosquito larvae were determined. This study was comprised of several methods namely collection of leaves of *M. koenigii*, extraction *M. koenigii* leaves with hexane and methanol sequentially, phytochemical screening and larvicidal bioassay on third instar larvae using three different concentrations (250, 500 and 750 ppm). Phytochemical screening revealed the presence of alkaloids, saponins, tannins, flavonoids and glycoside for methanol extract meanwhile negative results were obtained for hexane. Larvicidal bioassay of methanol and hexane extraction crudes gave the lowest LC_{50} and LT_{50}, which were 250 ppm and 450 ppm with 36 hours, respectively. The plant extracts showed larvicidal activity against mosquito larvae at 0.05 level of significance in terms of concentration for hexane and duration for methanol. High larvicidal activity of *M. koenigii* leaves was supported by the presence of phytochemicals that shows synergistic effects in terms of larvicidal action to mosquito larvae. This study demonstrated that *M. koenigii* could be an effective mosquito larvicide.

Keywords: *Murraya koenigii*, phytochemical screening, mosquito larvicides

Abstrak

Menerokai kegunaan baru daun aromatik *Murraya koenigii* membimbing kami untuk mengujinya sebagai racun perosak. Saringan fitokimia ekstrak-ekstrak telah dikendalikan untuk menentukan sebatian aktif menggunakan pelarut heksana dan metanol. Nilai LC_{50} dan LT_{50} untuk kedua-dua ekstrak terhadap larva-larva nyamuk telah ditentukan. Kajian ini terdiri daripada beberapa kaedah iaitu pengumpulan daun *M. koenigii*, pengekstrakan daun *M. koenigii* menggunakan heksana dan metanol secara berturutan, saringan fitokimia dan biocerakin larva ke atas larva instar III menggunakan tiga jenis kepekatan (250, 500 dan 750 ppm). Saringan fitokimia mendedahkan kehadiran alkaloid, saponin, tannin, flavonoid dan glikosid untuk ekstrak metanol manakala hasil negatif telah didapati untuk heksana. Biocerakin larva hasil ekstrak mentah metanol dan heksana memberi nilai LC_{50} dan LT_{50} terendah iaitu masing-masing 250 ppm dan 450 ppm selama 36 jam. Ekstrak tumbuhan menunjukkan aktiviti larvisid terhadap larva nyamuk pada tahap signifikan 0.05 dari segi kepekatan untuk heksana dan tempoh untuk metanol. Aktiviti larvisid daun *M. koenigii* yang tinggi telah disokong oleh kehadiran fitokimia yang menunjukkan kesan sinergi dari segi tindakan larvisid kepada larva nyamuk. Kajian ini menunjukkan *M. koenigii* boleh menjadi larvisid nyamuk yang berkesan.

Kata kunci: *Murraya koenigii*, saringan fitokimia, larvisid nyamuk

Introduction

Murraya koenigii is a native plant of India, Sri Lanka, Bangladesh and the Andaman Islands [1]. According to Arivoli et al. [2], the common names for *M. koenigii* in South Asia are 'karivepu' or 'karuveppilai' in Tamil, 'karipatta' in Hindi, 'girinimba' in Sanskrit, 'karibevu' in Kannada, 'kariveppu' in Malayalam, 'kadhilimb' in Marathi and 'karepeku' in Telugu. *M. koenigii* are widely found around the world.

Lately, the global spread of arboviruses known as Zika by mosquitoes has been alarming the public of the damage these insects can cause. Mosquitoes can be simply considered as annoying pests due to the nuisance from their bites and they can transmit diseases to humans and domestic animals. Mosquitoes are one of the oldest human enemies that can cause diseases and affect human health. To date, mosquitoes are recognized to have more than 3,000 species all over the world. According to Vongsombath [3], all mosquitoes are small, long-legged flies, and have two wings that are classified in the Order Diptera (true flies) under the Family Culicidae. Mosquito control strategies have depended primarily on the use of synthetic chemical insecticides. The non-environmental friendly effect of most of these synthetic chemical insecticides has led to alternative ways of managing this problem and one of them is by focusing on safer and effective plant products as insecticides. Bioactive botanicals are promising alternatives for mosquito control because of low toxicity to non-target organisms and their innate biodegradation ability. The present study aims to explore the phytochemical constituents and larvicidal activity of the crude leaf extracts of *M. koenigii*.

Materials and Methods

Plant collection and preparation of crude extract

Murraya koenigii leaves were collected from botanical herb garden of Universiti Teknologi MARA Pahang Jengka Campus. A total of 2.6 kg of leaves was washed using water and dried in the oven. All the dried leaves were ground and weighted. A total mass of powder obtained was 850 gram. The powdered plant materials were sequentially extracted with hexane and methanol for 72 hours before they were filtered. The filtrates were then subjected to rotary evaporator until the solvents were completely evaporated. Both methanolic and hexane crude extracts obtained were stored in the universal bottles and maintained at 4 ^{o}C in a refrigerator until it is used.

Phytochemical screening test: Saponins test

0.2 g of extract was added to a half of test tube of distilled water. The solution was then shaken vigorously and left for 30 minutes. Creamy mist with small bubbles showed the presence of saponin [4].

Tannins test

Water was added to 0.1 g of extract, heated to boil and filtered. Then, ferric chloride was added into solution. Dark green colour of solution indicated the presence of tannins [5].

Glycoside test

Few drops of glacial acetic acid and 2-3 drops of ferric chloride were added to 2 ml of extracts along with 1 ml of concentrated sulfuric acid. The appearance of brown ring at the interface confirmed the cardiac glycoside [6].

Test for alkaloids

Few drops of HCI were added into 1 ml of each plant extract in test tubes. After that, the mixture was heated for 20 minutes and left for cooling process. Two drops of Wagner's reagents were added to 1 ml of the filtrate and reddish-brown precipitate observed had shown the presence of alkaloids [5].

Test for flavonoids

10 ml of distilled water was added to 0.5 g of each plant extract in a test tube and. Then, 5 ml of diluted ammonia solution was added to a portion of the aqueous filtrate of each plant extract followed by addition of 1 ml of concentrated H_2SO_4. Yellow colour showed the presence of flavonoids [7].

Larvicidal bioassay

Bioassay for the larvicidal activity was carried out according to WHO procedures with slight modifications. In each 250 ml glass beaker, ten healthy larvae were released. For positive control, the larvae were exposed to abate molecules/crystal (Abate 1.1 g, BASF). Control negative was prepared by using the mixture of hexane to dimethyl sulfoxide (DMSO). Three replicates were set up for each concentration at three different concentrations (250, 500, 750 ppm). Mortality was observed after 24 and 48 hours post-treatments. The observed percentage mortality was corrected by Abbott's formula (equation 1):

$$\text{Percent mortality} = \frac{\text{\% test mortality - \% control mortality}}{\text{100 - \% control mortality}} \times 100 \quad (1)$$

Statistical analysis

SPSS version 19.0 package was used for determination of lethal time (LT_{50}) and lethal concentration (LC_{50}). Both LT_{50} and LC_{50} refer to times or amount of substance that, when administered to a group of experimental animals, will kill 50 per cent of the group respectively. Data from mortality and effect of concentrations were subjected using Two-way ANOVA and the differences between the treatments were determined by Tukey's test ($p< 0.05$).

Results and Discussion

The results from phytochemical tests revealed that the *M. koenigii* methanol leaves extracts showed all positive results on alkaloids, saponin, tannins, glycoside and flavonoids whereas negative results were obtained for hexane extracts (Table 1). Mathur et al. [8] reported the presence of alkaloid, saponin and flavonoid in methanol *Murraya koenigii* leaves extracts. The polarity of the solvent determines the type of active biochemical form of plant extracts. The results confirmed that polar solvent like methanol is better than hexane solution. Several groups of phytochemicals such as alkaloids, steroids, terpenoids, essential oils and phenolics from different plants have been reported previously for their insecticidal activities [9]. Secondary metabolites in plant serve as a mean of defence mechanism of the plants to avoid from herbivore predators and other environmental factors.

Saponin is responsible in increasing mortality of insects, lowering food intake, causing instability and retardation in development and reproduction [10]. The presence of saponin in *M. koenigii* can be the reason of larvicidal activity. Besides being popular as anthelmintic, mosquito repellent, and antiseptic, tannin also functions as antidiarrheal and haemostatic [11, 12]. Glycosides presence in the plants is to increase the force of cardiac contraction. Through the history, alkaloids are the part of constitutive defence. Flavonoids play important roles in plants as insect feeding attractants or excitants, repellents or deterrents and as oviposition inhibitors. Flavonoids are believed to contribute to larvicidal activity through its toxicity.

Table 1. Phytochemical test of leaves extracts of *M. koenigii*

Phytochemicals	Compounds	Solvent	
		Hexane	Methanol
Alkaloids		-	+
Tannins		-	+
Glycoside		-	+
Saponins		-	+
Flavonoids		-	+

+ = present, - = absent

Vector control is facing a serious threat due to the emergence of resistance in vector mosquitoes to conventional synthetic insecticides or development of newer insecticides. Mosquitoes in the larval stages are attractive targets to pesticides because mosquitoes breed in water, thus, it is easy to deal with them in this habitat. However, the use of

conventional pesticides in the water sources introduces many risks to people and the environment. Natural pesticides, especially those derived from plants, are more promising in this aspect. A considerable number of plant derivatives have shown to be effective against mosquitoes in a safe manner. The results of the larvicidal bioassay are presented in Table 2 for hexane and Table 3 for methanol extracts. The larvae were considered dead when there was no movement detected if they were disturbed with a needle. Moribund larvae are those incapable to rise up to the water surface (within reasonable time) or show characteristic of diving reaction when water was disturbed. Table 2 indicates the number of larval death proportional to the level of concentration in hexane extract. The percentage of plant extracts used influenced the mortality rate of the larvae [13]. At 250 ppm and 500 ppm, the number of death larval was not significantly different. After 48 hours exposure with 750 ppm of crude hexane leaf extract, the mortality achieved was 100%. Abate 1.1 g; a standard insecticide achieved 100% mortality at much lower concentration, which was 110 ppm.

Table 2. Number of mosquito larval death by crude hexane leaf extract of *M. koenigii* after 24 and 48 hours of exposure

Concentration (ppm)	**No. of Larvae (24 hours)**	**No. of Larvae (48 hours)**
250	4.67 ± 3.79^{b}	5.33 ± 2.52^{b}
500	5.67 ± 1.53^{b}	7.68 ± 1.53^{b}
750	9.33 ± 0.58^{a}	10.00 ± 0.00^{a}
Control	0.0 ± 0.0^{c}	0.0 ± 0.0^{c}
Abate 1.1g (110)	10.00 ± 0.00^{a}	10.00 ± 0.00^{a}

Values are mean number of larval death of three replicates ± standard deviation. Different superscript alphabets indicate statistical significant difference at $p< 0.05$ levels by Two-way ANOVA followed by Tukey's test

Table 3 shows the significance between concentrations of *M. koenigii* methanolic leaves extract against mosquito larvae in both durations. Impressively, as low as 250 ppm, it has given high mortality rate that is 83.0% after 48 hours of exposure.

Table 3. Number of mosquito larval death by crude methanol leaf extract of *M. koenigii* after 24 and 48 hours of exposure

Concentation (ppm)	**No. of Larvae (24 hours)**	**No. of Larvae (48 hours)**
250	3.33 ± 0.578^{a}	8.33 ± 1.53^{a}
500	4.67 ± 1.16^{a}	7.00 ± 1.00^{a}
750	6.00 ± 3.464^{a}	8.67 ± 1.53^{a}
Control	0.00 ± 0.0^{b}	0.00 ± 0.0^{b}

Values are mean number of larvae death of three replicates ± standard deviation. Different superscript alphabets indicate statistical significant difference at $P<0.05$ levels by Two-way ANOVA followed by Tukey's test

Another experiment was conducted using 250, 300, 350, 400 and 450 ppm extractions to determine the exact value for LT_{50} and LC_{50}. Through the experiment, the results obtained were 450 ppm and 36 hours of LC_{50} and LT_{50} for hexane while 250 ppm with 36 hours for methanol, respectively. *Murraya koenigii* showed the highest potential of

larvicidal activity when methanol as solvent applied compared to hexane. Hexane crude extract shows low efficiency since it has higher LC_{50} compared to methanol crude extract. It is the evident that the phytochemical constituents contained in the crude extract are the main reason of the effect on mortality rate. Phytochemical screening test determined the reason why mortality rate is higher in methanol extract than hexane extract. The finding are in line with literature studies by Harvae and Kamath [14] that showed the percentage of mortality of *A. aegypti* in 50 ppm of polar acetone crude extract and 100 ppm in non-polar petroleum ether crude extract. The concept also applied to methanol and hexane as polar and non-polar solvents, respectively. The presence of saponins and tannins in methanol leaves extract contribute to the susceptibility of mosquito larvae and act as a killing agent. Contrarily, hexane extract's low mortality effect on mosquito larvae is because of the absence of saponin and tannin molecules [15, 13].

Conclusion

The use of plant extracts in insect control is an alternative method for minimizing the non-toxic effect of pesticide compounds. The results suggest future investigation on *M. koenigii* in becoming the best alternative medicine for other aspect of life.

Acknowledgement

The authors would like to express their gratitude to Universiti Teknologi MARA, Pahang for allowing them to conduct the experiment and supplying the raw materials.

References

1. Singh, S., More, P. K. and Mohan, M. S. (2014). Curry leaves (*Murraya koenigii* Linn. sprengal) - A miracle plant. *Indian Journal of Scientific Research*, 4(1): 46-52.
2. Arivoli, S., Ravindran, J. K. and Tennyson, S. (2012). Larvicidal efficacy of plant extracts against the malarial vector *Anopheles stephensi* liston (Diptera: Culicidae). *World Journal of Medical Sciences*, 7(2): 77-80.
3. Vongsombath, C. (2011). Botanical repellents and pesticides traditionally used against haematophagous invertebrates in Lao PDR. PhD dissertation. Uppsala Universiti, Sweden.
4. Bhandary, S. K., Suchetha Kumari, N., Bhat, V. S., Sharmila, K. P. and Bekal, M. P. (2012). Preliminary phytochemical screening of various extracts of *Punica granatum* peel, whole fruit and seeds. *Nitte University Journal of Health Science*, 2(4): 34-38.
5. Zohra, S. F., Meriem, B., Samira, S. and Alsayadi, M. M. S. (2012). Phytochemical screening and identification of some compounds from Mallow. *Journal of Natural Product and Plant Resources*, 2(4): 512-516.
6. Sharmila, S., Rebecca, L. J., Das, M. P., Saduzzaman, M. and Bala, S. (2013). A comparative study on phytochemical analysis of *Murraya koenigii* and *Manilkara zapota*. *Research Journal of Pharmaceutical, Biological and Chemical Sciences*, 4(2): 1104-1109.
7. Wadood, A., Ghufran, M., Jamal, S. B., Naeem, M., Khan, A., Ghaffar, R. and Asnad (2013). Phytochemical analysis of medicinal plants occurring in local area of Mardan. *Journal of Biochemistry & Analytical Biochemistry*, 2(4): 1-4.
8. Mathur, A., Dua, V. K. and Prasad, G. B. K. S. (2010). Antimicrobial activity of leaf extracts of *Murraya koenigii* against aerobic bacteria associated with bovine mastitis. *International Journal of Chemical, Environmental and Pharmaceutical Research*, 1(1): 12-16.
9. Ghosh, A., Chowdhury, N. and Chandra, G. (2012). Plant extracts as potential mosquito larvicides. *Indian Journal of Medical Research*, 135: 581-598.
10. Wina, E., Muetzel, S. and Becker, L. (2005). The impact of saponins or saponin-containing plant materials on ruminant productions - a review. *Journal of Agricultural and Food Chemistry*, 53(21): 8093-8105.
11. Ashok, P. K. and Upadhyaya, K. (2012). Tannins are astringent. *Journal of Pharmacognosy and Phytochemistry*, 1(3): 45-50.
12. Shruthi, S., Handra, H. K. and Pandith, A. (2012). A review on *Murraya koenigii*: Multipotential medicinal plant. *Asian Journal of Pharmaceutical and Clinical Research*, 5(4): 5-14.
13. Gutierrez, P. M., Antepuesto, A. N., Eugenio, B. A. L. and Santos, M. F. L. (2014). Larvicidal activity of selected plant extracts against the dengue vector *Aedes aegypti* mosquito. *International Research Journal of Biological Sciences*, 3(4): 23-32.

14. Harvae, G. and Kamath, V. (2004). Larvicidal activity of plant extracts used alone and in combination with known synthetic larvicidal agents against *Aedes aegypti*. *Indian Journal of Experiment Biology*, 42:1216-1219.
15. Abu Raihan, S. M. (2014). Effect of plant flavonoids on mosquito larvae. *National University Journal of Science*, 1(2): 26-30.

Malaysian Journal of Analytical Sciences, Vol 22 No 3 (2018): 477 - 482
DOI: https://doi.org/10.17576/mjas-2018-2203-15

MALAYSIAN JOURNAL OF ANALYTICAL SCIENCES
Published by The Malaysian Analytical Sciences Society
ISSN 1394 - 2506

THE EFFECTS OF FE-DOPING ON MECHANICAL PROPERTIES IN $Bi_{1.6}Pb_{0.4}Sr_2Ca_2Cu_{3-X}Fe_XO_Y$ SUPERCONDUCTOR

(Kesan Dop Ferum Terhadap Sifat Superkonduktor $Bi_{1.6}Pb_{0.4}Sr_2Ca_2Cu_{3-x}Fe_xO_y$)

Suazlina Mat Ali[1], Azhan Hashim[2]*, Syamsyir Akmal Senawi[2], Azman Kasim[2], Wan Aizuddin Wan Razali[2], Ruziana Mohamed[2], Fairuzdzah Ahmad Lothfy[2]

[1]*Faculty of Applied Sciences,*
Universiti Teknologi MARA Shah Alam, 40450 Shah Alam, Selangor, Malaysia
[2]*Faculty of Applied Sciences,*
Universiti Teknologi MARA Pahang, 26400 Bandar Jengka, Pahang, Malaysia

**Corresponding author: dazhan@pahang.uitm.edu.my*

Received: 4 December 2016; Accepted: 1 December 2017

Abstract

Bi-2223 superconductors doped with Fe_2O_3 at Cu-site were prepared in bulk form using high purity oxide powders via solid state reaction technique with intermediate grinding. The series of Fe stoichiometric ratio (x = 0.00, 0.02, 0.04, 0.06, 0.08 and 0.10) are systematically added to $Bi_{1.6}Pb_{0.4}Sr_2Ca_2Cu_{3-x}Fe_xO_y$ system to study the effect of Fe doping on mechanical and superconducting system properties. Vickers hardness, electrical resistivity, X-ray diffraction and Field Emission Scanning Electron Microscopy have been carried out to assess the effects of Fe doping. These measurements indicate that the Fe doping decreased the critical temperature and deteriorated formation of high T_c phase, compared to undoped sample. Grain size of the samples were also reduced by increasing the amount of Fe and the mechanical properties were found to be escalate with the increasing of Fe concentration.

Keywords: BSCCO superconductor, Fe-doped, critical current density, X-ray diffraction, microhardness

Abstrak

Superkonduktor Bi-2223 dop Fe_2O_3 dikawasan kuprum telah dihasilkan secara pukal menggunakan serbuk oksida tulin dengan kisaran perantara melalui kaedah tindak balas keadaan pepejal. Nisbah stokiometri bersiri (x = 0.00, 0.02, 0.04, 0.06, 0.08 and 0.10) ditambah secara sistematik terhadap sistem $Bi_{1.6}Pb_{0.4}Sr_2Ca_2Cu_{3-x}Fe_xO_y$ bagi mengkaji kesan dop Fe terhadap sifat mekanikal dan sistem superkonduktor. Ujian ketahanan Vickers, kerintangan arus, pembelauan Sinar-X dan mikroskopi imbasan elektron pancaran medan telah dilakukan bagi menilai kesan dop Fe. Pencirian ini menunjukkan bahawa kesan dop yang dilakukan mengurangkan suhu genting dan merencatkan pembentukan fasa suhu tinggi berbanding sampel tanpa dop. Saiz butiran sampel turut mengecil dengan penambahan jumlah kehadiran Fe dan sifat mekanikal didapati meningkat seiring dengan penambahan Fe.

Kata kunci: Superkonduktor BSCCO, dop-Fe, ketumpatan arus, pembelauan sinar-X, ketahanan mikro

Introduction

Bi-Sr-Ca-Cu-O compound has been extensively studied since the discovery of high superconducting temperature [1]. This system has been investigated by many research groups concerning the preparation, superconducting properties, effect of doping as well as the structure of these compounds [2-6]. Among the BSCCO system, Bi-2223 is both fundamental and technological subject of interest because of its higher critical temperature, *Tc* [7]. The grain

boundaries were essential as current transport factor in the polycrystalline form. Optimal sintering time is important to enhance the superconducting volume fraction and grains connectivity thus increases the critical sample current density. Short sintering time can produce smaller grain size, resulting in weak connectivity between grains. However, prolonging the sintering time may lead to phase decomposition, decreasing the superconducting phases and weakening the weak links. Bi-2223 is amenable for possible practical application as a conductor due to their large critical current density [8, 9].

However, it is difficult to obtain higher critical current density *Jc*, which is significant for promising superconductor system. The selective substitution studies are essential and interesting for superconductivity research area in order to improve the critical current density. Elemental substitution is one of the important roles to enhance the T_c and J_c by improving the phase formation or microstructure of the system [10, 11]. Practical applications, in terms of the BSCCO mechanical properties were also important for the studies since high temperature superconductors are generally restricted due to their brittleness in nature. The various substitutions have been investigated in order to improve the formation and stability of the 2223 phases and the most effective one is partial substitution of trivalent Bi with Pb. The 3d elements also embedded for substitution in Bi-2223 system.

In this paper, the effect of 3d elements (Fe) that has been substituted into Bi (Pb)-2223 superconductor through solid state reaction method was presented. The structural and transport properties of $Bi_{1.6}Pb_{0.4}Sr_2Ca_2Cu_{3-x}Fe_xO_y$ were characterized using X-ray diffraction (XRD) and electrical resistivity measurement respectively while mechanical properties was unveiled using Vickers hardness.

Materials and Methods

The high-T_c superconducting samples with nominal composition $Bi_{1.6}Pb_{0.4}Sr_2Ca_2Cu_{3-x}Fe_xO_y$ (where x = 0.00, 0.02, 0.04, 0.06, 0.08 and 0.10) ceramic superconductor were prepared using the solid state reaction method. The Bi_2O_3, PbO, $SrCO_3$, $CaCO_3$, Fe_2O_3 and CuO powders with 99.9% purity were used. The powders were weighed according to their stoichiometry ratio. The powders were ball-milled together with absolute ethanol in alumina crucible for 24 hours. After that, the homogenous mixture of the powders was dried out in the oven at the 120 °C for 6 hours. The powders were ground and pre-calcined at 800 °C for 15 hours. Then the mixture of the powder was again calcined at 820 °C for 15 hours to remove all oxides and carbonates. After that, the powders were pressed into pellet of 2 grams by applying a 30 MPa pressure. Finally, the pellets were sintered at 850 °C for 48 hours to form a high-T_c phase BSCCO superconductor. Results for T_c, I_c and J_c of the samples were measured by using four point probe machine. XRD analysis of the samples was carried out by using Cu (K_α) radiation. The surface morphologies of the samples were studies using FESEM machine, and the mechanical properties of the compounds have been investigated using Vickers hardness. All samples were denoted as sample *A*, *B*, *C*, *D*, *E*, and *F* for x = 0.00, 0.02, 0.04, 0.06, 0.08, and 0.10 respectively.

Results and Discussion

The normalized resistance at room temperature as a function of temperature between 30 K and 300 K with various concentration of Fe to Bi-2223 powder are shown in Figure 1. The curve indicated a metallic behaviour for all samples at normal state with a single leap of superconducting transition. The zero resistance temperature of the samples decreased with the addition of more dopant concentration into the system. Sample of Fe-doped with x = 0.10 shows that there is no any transition to the superconducting state due to no $T_{c\ zero}$. The highest $T_{c\ zero}$ was showed in pure sample is 93 K and decreases to 57 K for sample x = 0.08.

Figure. 2 shows the XRD patterns of samples. All samples consisted of the Bi-2223 and Bi-2212 phase with the increasing of Bi-2212 phase induction. No peaks belongs to Fe were detected, which implied that the Fe had incorporated into the crystal structure subjected to the low amount of Fe.

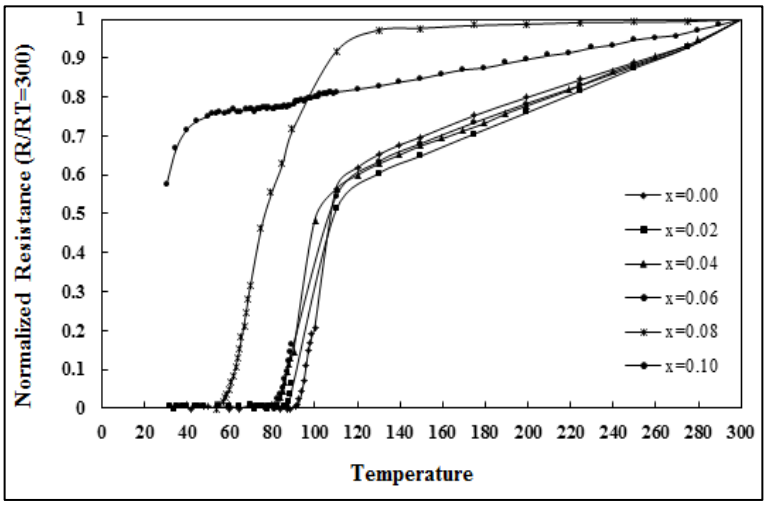


Figure 1. Normalized resistance as a function of temperature of the samples

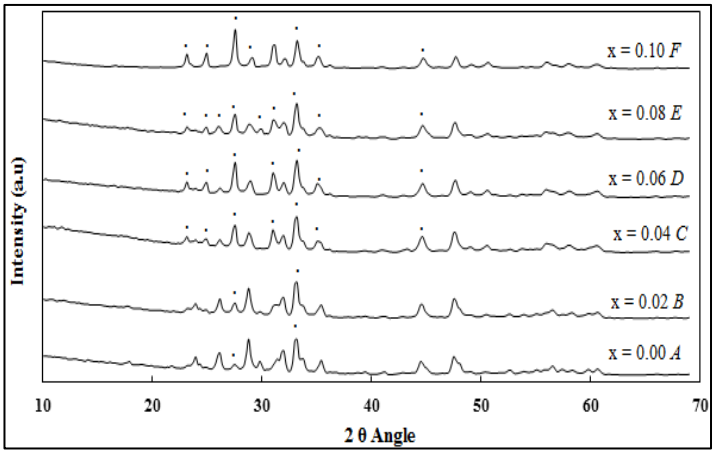


Figure 2. X-ray diffraction pattern of samples. The peaks indexed represent Bi-2212

Figure 3 shows the Vickers microhardness, Hv versus the concentration of Fe, *x* for all samples and the value of the Hv was tabulated in Table 1. It showed that the mechanical properties of the compounds were found to be linearly increased with the increasing of doping in Bi-2223 superconductors [12-15]. A sudden dropped was observed when $x = 0.08$ and this behaviour is might be due to the contribution of weak grain boundaries in the sample.

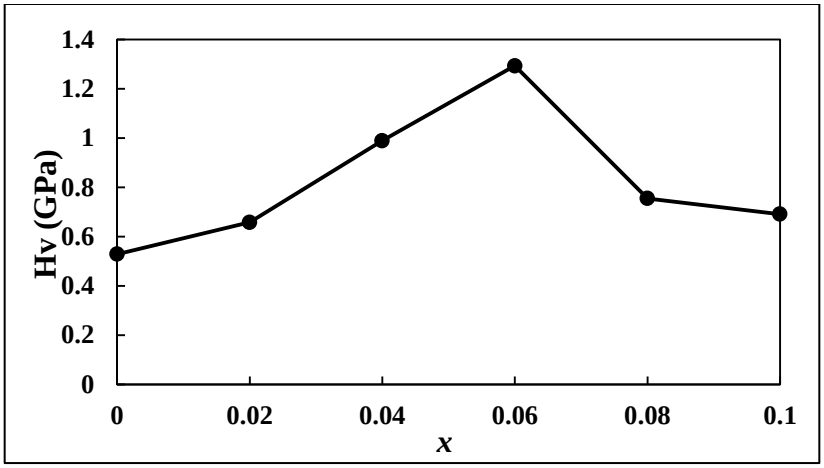
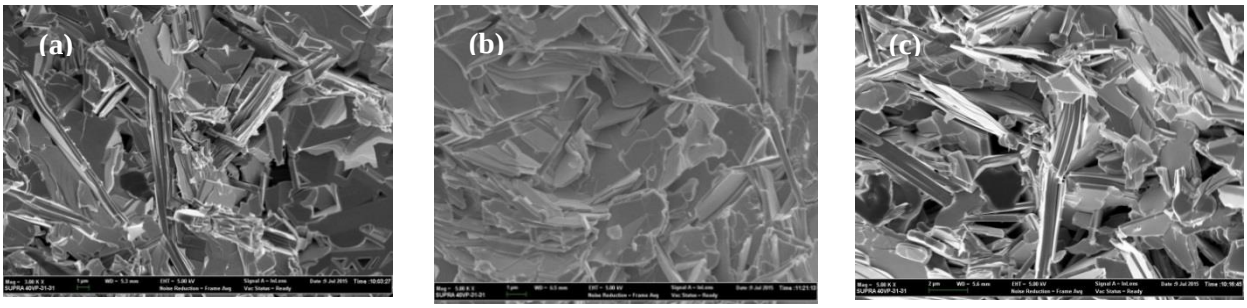


Figure 3. Vickers microhardness, Hv versus concentration of Fe, *x*

Table 1. Critical temperature (*Tc*), critical current density (*Jc*), lattice parameter *a*, *b* and *c*, volume fraction, and Vickers hardness (Hv) values for the samples

Sample	Tc_{zero} (K)	J_C (A/cm^2)	% V_{2223}	a	b	c	Hv (Gpa)
A	93	4.8728	78.46	5.3891	5.4036	36.5143	0.529
B	89	4.6180	75.06	5.3891	5.4036	36.5143	0.658
C	83	2.6225	66.13	5.3891	5.3434	33.9262	0.989
D	81	2.4026	29.64	5.3891	5.3582	33.8002	1.293
E	57	0.6197	24.48	5.3891	6.6780	30.6833	0.755
F	-	-	26.59	5.3891	5.5929	30.6201	0.691

The FESEM micrographs of all samples in Figure 4 consisted of plate-like grains with randomly distributed as the typical grain structure of the high-T_c phase (Bi-2223). It is observed that the grain connectivity is worsened greatly with increasing Fe concentration. The surface of the Fe-free sample is more uniform with better grains alignment. FESEM images of x = 0.00 and x = 0.02 show better crystallinity in comparison with the remaining two samples. Sample x = 0.10 has the worst appearance among these six samples. These results indicate that the surface morphology of the sample is worsened with increasing of Fe substitution.



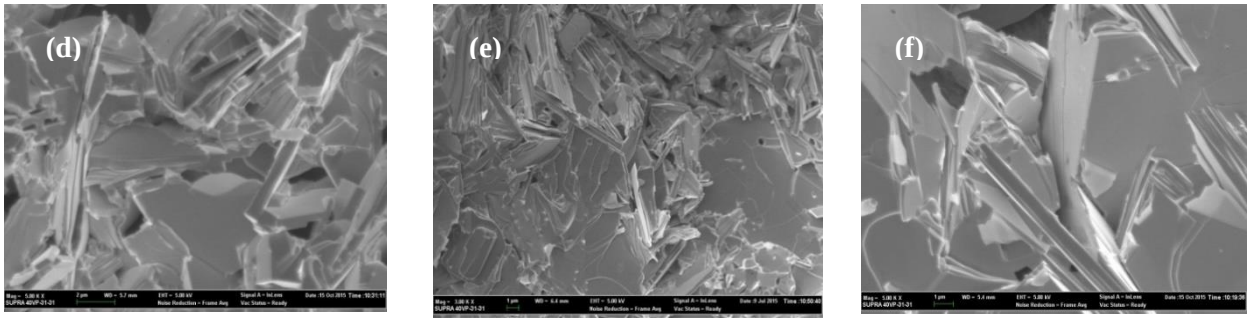


Figure 4. FESEM micrograph for the cross-section of the samples for a) x= 0.00, b) x= 0.02, c) x= 0.04, d) x= 0.06, e) x= 0.08 and f) x= 0.10

Conclusion

The influence of Fe doping on mechanical properties in $Bi_{1.6}Pb_{0.4}Sr_2Ca_2Cu_{3-x}Fe_xO_y$ system has been investigated. The results generally showed that the doping of Fe increased the mechanical properties of the samples until x = 0.06, and the value dropped when x = 0.08. The doping of Fe also does not favour the formation of high *Tc* phase. The samples exhibit the decrease values of T_c and J_c after further addition of dopant concentrations. XRD analysis showed that the volume fraction of the 2223 phases was decreased and the volume fraction of the 2212 phases was dominant with increasing of Fe doping. These measurements indicate that Fe doping decreased the critical temperature and degrade the formation of high-T_c phase of high temperature superconductor (HTS) compared with the undoped sample.

Acknowledgement

The authors would like to thank the Ministry of Higher Education (MOHE), Malaysia for the financial support via Research Acculturation Grant Scheme (RAGS) no. 600-RMI/RAGS 5/3 (7/2013).

References

1. Maeda, H., Tanaka, Y., Fukutomi, M. and Asano T. (1988). A new high-*Tc* oxide superconductor without a rare earth element. *Japanese Journal of Applied Physics*, 27: 209-210.
2. Trong On, D., Sato, O., Fujishima, A. and Hashimoto, K. (1999). Change of the critical temperature of high-*Tc* single (2223) phase Bi-Pb-Sr-Ca-Cu-O supercondcutors by intercalation process. *Journal of Physics and Chemistry of Solids*, 60: 883-890.
3. Mulay, V. N., Siva Prasad, P. V. L. N., Bhupal Reddy, K. and Jaleel M. A. (1990). Studies on the synthesis of $Bi_2CaSr_2Cu_2O_\delta$ by different chemical routes. *Journal of Materials Science Letter*, 9: 1284-1287.
4. Halim, S. A., Mohamed, S. B., Azhan, H., Khawaldeh, S. A. and Sidek, H. A. A. (1999). Effect of barium doping in Bi-Pb-Sr-Ca-Cu-O ceramics supercondcutors. *Physica C*, 312: 78-84.
5. Terzioglu, C., Yilmazlar, M., Ozturk, O. and Yanmaz, E. (2005). Structural and physical properties of Sm-doped $Bi_{1.6}Pb_{0.4}Sr_2Ca_{2-x}Sm_xCu_3O_y$ superonductors. *Physica C*, 423:119-126.
6. Suazlina, M. A., Yusainee, S. Y. S., Azhan, H., Abd-Shukor, R. and Mustaqim, R. M. (2014). The effects of nanoparticle addition in Bi-2212 superconductors. *Jurnal Teknologi*, 69(2): 49-52.
7. Gul, I. H., Anis-ur-Rehman, M. and Maqsood, A. (2006). Temperature dependence of thermal and electritrical conductivity of Bi-based high-Tc (2223) superconductor. *Physica C*, 450: 83-87.
8. Shalaby, M. S., Hashem, H. M., Hammad, T. R., Wahab, L. A., Marzouk, K. H. and Soltan, S. (2016). Higher critical current density achieved in Bi-2223 High-T_c superconductors. *Journal of Radiation Research and Applied Sciences*, 9: 345–351.
9. Godeke, A., Abraimov, D. V., Arroyo, E., Barret, N., Bird, M. D., Francis, A., Jaroszynski, J., Kurtev, D. V. and Markiewicz, W. D. (2017). A feasibility study of high-strength Bi-2223 conductor for high-field solenoids. *Superconductor Science and Technology*, 30(3), 035011.

10. Gul, I. H., Rehman, M. A., Ali, M. and Maqsood. A. (2005). Effect of vanadium and barium on the Bi-based (2223) superconductors. *Physica C,* 432: 71-80.
11. Sarun, P. M., Vinu, S., Shabna, R., Biju, A. and Syamaprasad, U. (2008). Highly enhanced superconducting properties of Eu-doped (Bi,Pb)-2212. *Materials Letter,* 62: 2725-2728.
12. Yilmazlar, M., Ozturk, O., Aydin, H., Akdogan, M. and Terzioglu, C. (2007). The effect of Sm→ Ca substitution on mechanical properties of BSCCO superconductors. *Chinese Journal of Physics,* 45: 128-134.
13. Khalil, S. M. (2001). Enhancement of superconducting and mechanical properties in BSCCO with Pb additions. *Journal of Physics and Chemistry of Solids,* 62: 457-466.
14. Bruneel, E., Degrieck, J., Van Driessche, I., Hoste, S. (2002). Mechanical properties of Bi-2223/Ag bulk composites. *Physica C,* 1063: 372-376.
15. Ling, H. C. and Yan, M. F. (1988). Microhardness measurements on dopant modified superconducting $YBa_2Cu_3O_7$ ceramics. *Journal of Applied Physics,* 64: 1307-1311.

Malaysian Journal of Analytical Sciences, Vol 22 No 3 (2018): 483 - 490
DOI: https://doi.org/10.17576/mjas-2018-2203-16

MALAYSIAN JOURNAL OF ANALYTICAL SCIENCES
Published by The Malaysian Analytical Sciences Society
ISSN 1394 - 2506

THE ASSESSMENT OF INDOOR RADON-222 CONCENTRATION AND EMANATION RATE AT GUA PENYU, PAHANG

(Penilaian Kepekatan dan Kadar Pancaran Dalaman Radon-222 di Gua Penyu, Pahang)

Junaidah Md Sani[1]*, Nuramirah Alias [1], Nazree Ahmad [1], Ahmad Saat [2]

[1]*Faculty of Applied Sciences,*
Universiti Teknologi MARA Cawangan Pahang, 26400 Bandar Tun Abdul Razak Jengka, Pahang, Malaysia
[2]*Institute of Science,*
Universiti Teknologi MARA, 40450 Shah Alam, Selangor, Malaysia

**Corresponding author: ajun@pahang.uitm.edu.my*

Received: 4 December 2016; Accepted: 1 December 2017

Abstract

The indoor Radon-222 concentration and emanation rate in Gua Penyu, Gua Gelanggi Complex, Pahang were measured using Solid State Nuclear Track Detector CR-39 (SSNTD CR-39) to evaluate the air quality and radiological exposure in this recreational cave. A total of 20 SSNTD CR-39 dosimeters were placed inside the cave at about 15 m apart each. 10 dosimeters were embedded 5 cm into cave floor to determine emanation rate, while the other 10 dosimeters were placed at one meter above the floor level for concentration measurement. The control samples were placed outside the cave 15 m from the main entrance. These SSNTD CR-39 samples were left for a month before undergone etching process with NaOH solution (6 M) at 70 °C for six hours. The radon concentration and emanation rate were both determined from the track density in each CR-39 (1cm × 1cm) sampling. The results showed that the radon emanation rates varied between 0.030 ± 0.004 $Bqm^{-2}day^{-1}$ and 0.120 ± 0.017 $Bqm^{-2}day^{-1}$ with the average rate of 0.080 $Bqm^{-2}day^{-1}$. The radon concentration was between 3.72 ± 1.60 Bqm^{-3} and 7.89 ± 2.10 Bqm^{-3} with the average of 4.8 Bqm^{-3}. These values were lower compared to indoor concentration allowed by the International Commission on Radiation Protection (ICRP) 2009 that is 200 – 300 Bqm^{-3}. The annual effective dose were found to range between 0.09 $mSv.y^{-1}$ and 0.20 $mSv.y^{-1}$ which was lower than recommended value 3 to 10 $mSv.y^{-1}$ put forth by the ICRP 1993. Hence, this recreational cave is safe to be visited by public.

Keywords: limestone cave, emanation rate, indoor radon

Abstrak

Kepekatan dan kadar pancaran dalaman Radon-222 dalam Gua Penyu, Kompleks Gua Gelanggi, Pahang telah diukur menggunakan Pengesan Jejak Nuklear Keadaan Pepejal CR-39 (SSNTD CR-39) untuk menilai kualiti udara dan pendedahan radiologi dalam gua rekreasi ini. Sejumlah 20 dosimeter SSNTD CR-39 telah ditempatkan dalam gua ini setiap satu berjarak kira-kira 15 m. 10 dosimeter telah dibenamkan 5 cm ke dalam lantai gua untuk penentuan kadar pancaran, manakala 10 dosimeter lain ditempatkan pada satu meter di atas aras lantai untuk pengukuran kepekatan. Sampel kawalan ditempatkan di luar gua 15 m hadapan pintu masuk utama. Sampel SSNTD CR-39 ini ditinggalkan selama sebulan sebelum melalui proses punaran dalam larutan NaOH (6M) pada 70 °C selama enam jam. Kepekatan dan kadar pancaran radon keduanya ditentukan dari ketumpatan jejak dalam setiap sampel (1 cm × 1cm) CR-39. Hasil kajian menunjukkan bahawa kadar pancaran radon berada antara 0.030 ± 0.004 $Bqm^{-2}hari^{-1}$ dan 0.120 ± 0.017 $Bqm^{-2}hari^{-1}$ dengan purata 0.080 $Bqm^{-2}hari^{-1}$. Kepekatan radon antara 3.72 ± 1.60 Bqm^{-3} and 7.89 ± 2.10 Bqm^{-3} dengan purata 4.8 Bqm^{-3}. Nilai-nilai ini lebih rendah berbanding nilai dalaman 200 – 300 Bqm^{-3} yang dibenarkan oleh Jawatankuasa Perlindungan Radiasi Antarabangsa (ICRP) 2009. Didapati dos berkesan tahunan berada antara 0.09 $mSv.tahun^{-1}$ dan 0.20 $mSv.tahun^{-1}$ lebih rendah berbanding dengan nilai tahunan yang disyorkan oleh ICRP 1993 iaitu 3 hingga 10 $mSv.tahun^{-1}$. Justeru, gua rekreasi ini adalah selamat dikunjungi oleh orang awam.

Kata kunci: gua batu kapur, kadar pancaran, radon dalaman

Introduction

Uranium-238 is a radionuclide which undergoes spontaneous decay chain through Radium-226 which then decays into Radon-222. This naturally occurring gas could be found everywhere on earth especially in rocky and mountainous areas such as mines and caves as well as soil and water. Radon is a radioactive gas that is colorless, odorless and tasteless. Being the heaviest noble gas, it is chemically inert and easily mobilizes in long distances through soil and rocks [1]. In addition, radon is a single atom gas. Thus, it can easily penetrate through fissures and cracks. The half-life of Radon-222 is 3.8 days makes it the most potential source of radiological exposure to the general public [2]. Radon gas from the soils escapes to the atmosphere through diffusion, evaporation of soil moisture and exhalation due to temperature or pressure changes. The gas suspends in the air which we breathe in. The fact that it is much denser than air makes it effortlessly inhaled by cave tourist. However, when radon is diluted to extremely low concentrations outdoor, the risk is very low. Nonetheless, radon content in indoor atmosphere typically contributes up to 50% to the background radiations [3]. Radon is a radiological poison associated with carcinogenic effect to human being [4]. In closed environment such as caves, mines and poor ventilated house, the inhalation of accumulated radon poses significant health hazards to human being [5]. International Atomic Energy Agency [6] and Yu et al. [7] reported that radon gas was the cause of lung cancer especially among underground miners. Furthermore, the ionizing alpha particles emitted by radon progenies (Polonium-218 and Polonium-214) may also lead to DNA damages in the respiratory system. According to the World Health Organization [8] which is also supported by Oufni et al. [9], the most notably health effect of radon is lung cancer. Likewise, the U.S Environmental Protection Agency in 1992, also reported an estimated 14,000 deaths per year due to Radon-222.

Caves are one of sought-after tourist recreational enthusiasm in Malaysia as well as interesting excavation sites for archeologist. The Gua Kota Gelanggi, which was chosen for radiological assessment, is a limestone cave located in Pahang state, Malaysia. It consists of a number of caves such as Gua Terang Bulan, Gua Bersanding, Gua Tongkat, Gua Balai, Gua Gajah, Gua Penyu, Gua Angin, Gua Tanggal 99, Gua Hijau and Gua Kelawat, which are open to public for cave exploration, rock climbing, abseiling, camping, jungle tracking and hiking. Visitors are ignorance about the existence of radon in the cave atmosphere and its radiological risk. Malaysia's tropical and humid nature provides the best trail for the migration of radon gas in caves which are greatly influenced by temperature difference, humidity, and rocks. The Gua Penyu cave that was chosen as a study site has no other opening except the main entrance. Consequently, there is a possibility for the radon gas to be enriched significantly due to the limited ventilation. Besides, this cave is frequented by the local visitors and tourist who is guest of the Tekam Plantation Resort. According to Koltai et al. [10], the radon concentration of caves air around the world ranges from 0.1 to 20 kBq m^{-3}. Thus, by assessing the indoor radon concentration and emanation rate in this recreational cave, information regarding the air quality and amount of radiological exposure can be used to develop certain precautions that could be adopted by its visitors.

The objective of this study is to measure the indoor Radon-222 concentrations and emanation rates in Gua Penyu cave using the Alpha Track Detector (ATD). ATD was chosen because it is a simple and efficient method for sampling period from one to 12 months. Moreover, it provides reliable data and inexpensive compared to the other detectors [1, 8]. The dosimeter that was used in this study is Solid State Nuclear Track Detector (SSNTD) CR-39 which is very sensitive to the alpha particles that strike its surface [11]. These alpha particles would strike the dielectric detector and produce a damage area that was called latent track. The latent track underwent etching process afterwards to be enlarged sufficiently making it visible under the optical microscope. The number of tracks is proportional to the concentration of radon and the period of exposure.

Materials and Methods

Preparation of dosimeters

The radon level measurements were performed using Solid State Nuclear Track Detector (SSNTD) CR-39 manufactured by Tastrak UK. The CR-39 track detector sheets were cut to 1cm x 1cm dimension. The CR-39 as the dosimeter was exposed to radon according to the can-mode configuration [12]. Each dosimeter was made of a

transparent polymer cup 6.7 cm in diameter and 4 cm in height. The lid of the cup was pierced in the centre to make a circular hole of 1 cm diameter. This hole was then sealed by mean of a domestic soft sponge 5 mm thick. The sponge would act as a filter that limited access to moisture as well as to block the entry of radon progeny daughters and to prevent contamination from impurities in the atmosphere. As a result, only the alpha particles emanated from radon would diffuse into the cup and strike the detector [13]. Another CR-39 sheet was attached to the inner bottom of the cup using a double sided tape. The tape helped to keep the CR-39 immobile so as to reduce error that might be caused by movement. The design of the dosimeter is shown in Figure 1.

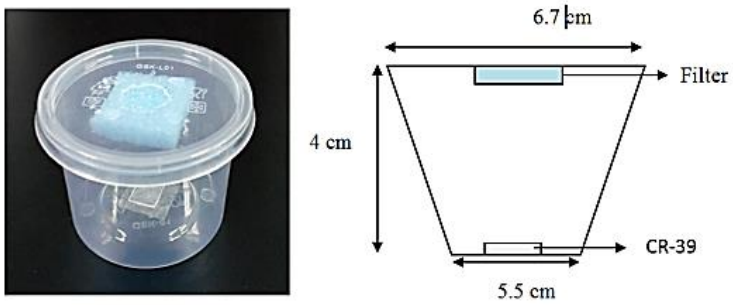


Figure 1. The schematic dosimeter for radon monitoring device

The sampling method

A total of 20 dosimeters which was 15 m apart from each other were placed inside the Gua Penyu cave. 10 units of dosimeters were embedded 5 cm depth on the cave floor while the other 10 units were placed at one meter above ground level by sticking the cups' bottom end to the cave wall. Two (2) dosimeters that were considered as control samples was placed 0.5 m outside the main entrance. For the purpose of measuring the radon emanation rate, dosimeters which were embedded in the ground were positioned in such a way that the CR-39 sheets were facing down. On the other hand, the dosimeters which were placed 1 m above ground would provide the data for determining the radon concentration. The wall must be rubbed prior to sticking the dosimeters to get rid of dust that might make it difficult to keep the dosimeters in position through its sampling periods. The radon concentration at 10 locations inside the cave was labeled ascending from L1 to L10 beginning from the entrance of the cave. L0 served as the control sample. Likewise, the dosimeters for radon emanation rate measurement were labeled ascending from L11 to L20 starting from the cave entrance. L00 served as the control sample for emanation rate measurement. The distributions of the dosimeters in the cave are illustrated in Figure 2. The locations of the dosimeters were tagged and visual recorded to avoid losing track of the samples. The samples were then left for 1 month.

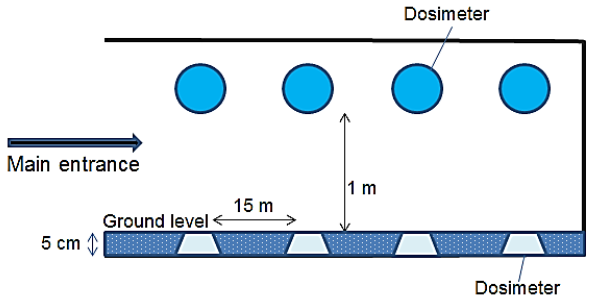


Figure 2. The side view illustration showing distributions of dosimeters inside the cave

Etching process

The exposed CR-39 sheet detector were removed from the polymer cup and etched in a 6M NaOH at 70 °C for six hours (constant temperature). During the etching process, the water was stirred once in a while to allow consistent thermal distribution so that the detector would fully etch. Next, the SSNTD sheets were washed in running water for 1 hour and left to dry between tissues wipes for 10 minutes to remove the residual of etchant from the surface of the detector. The track detector sheets were then observed under microscope with magnification of 400x for track density measurements. The tracks would appear as dark spots on a clear white background.

The determination of radon concentration rate

Radon concentration was calculated according to Equation 1 based on the number of visible spots on the CR-39 sheet. Only dark spots with diameter about 10 μm were reckoned for calculation.

$$C_{Rn} = \frac{D}{Ft} \quad (1)$$

where C_{Rn} is the radon concentration, D is the track density (tracks.cm^{-2}), t is the exposure time (days) and F is the calibration factor (tracks m^3 cm^{-2} Bq^{-1}h^{-1}). The radon concentration in air is defined as the number of decays per second per cubic meters of air or Bqm^{-3}.

The determination of annual effective dose

According to [3], annual effective dose could be calculated using the equation 2.

$$E = C \times H \times F \times T \times D \quad (2)$$

where, C is the radon concentration (Bqm^{-3}), F is the equilibrium factor, 0.4, H is the occupancy factor, 0.8, T is the number of hours in a year, 8760 h.y^{-1} and D is the effective dose received by adults per unit Radon–222 activities per unit volume, 9.0×10^{-6} mSv.h^{-1} Bqm^{-3}.

The determination of radon emanation rate

The Radon–222 emanation rate was calculated using equation 3.

$$E_{Rn} = \frac{CV}{At} \quad (3)$$

where, E_{Rn} is the emanation rate (Bqm^{-2}day^{-1}), C is the Radon-222 concentration (Bqm^{-3}), V is the volume of the polymer container (m^3), A is the surface area (m^2) of the lid and t is the exposure time (days).

Results and Discussion

Radon emanation rate is defined as the decaying radon atoms that have been released through an area per day. On the other hand, radon concentration is the specific radon activity per unit volume in the atmosphere. The spots on the CR-39 sheets that accounted for concentration measurement were seen as in Figure 3. The dark spot represented the site at which bombardment from the alpha particle that coexists with Radon-222 occurred.

The variation of Radon-222 concentration in Gua Penyu is presented in Figure 4. The average radon concentration was 4.77 Bq m^{-3} with the lowest reading recorded as 3.72 ± 1.6 Bqm^{-3} at location L2. There was a noticeable higher readings recorded as of 6.65 ± 2.1 and 8.90 ± 2.1 Bq m^{-3} at locations L6 and L9, respectively. As anticipated, location L9 as the less ventilated compound indicated the highest annual effective dose of 0.20 mSv.y^{-1} while that of location L2 recorded the lowest, which was 0.09 mSv.y^{-1}. The rest of sampling points gave consistent readings between 3.00 and 5.00 Bqm^{-3}. These results indicated that the radon gas was evenly distributed inside the cave. The fact that radon could travel through pores in soil, fractures in rocks and along other weak zone such as shears, faults and thrust [14] might fairly contributed to the occurrence of radon gas movement inside this cave.

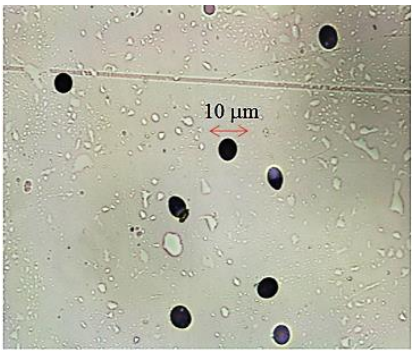


Figure 3. The track photo showing dark spots on the CR-39 sample at location L4

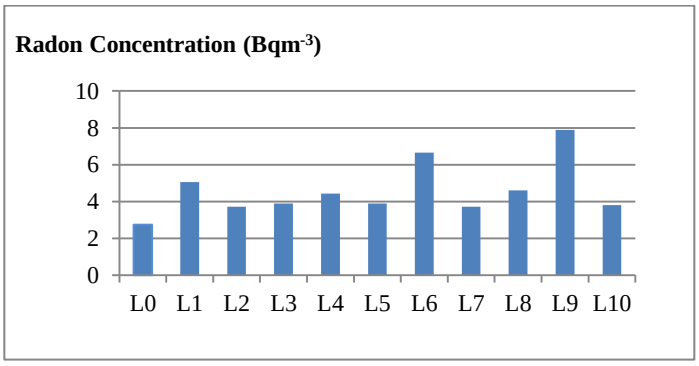


Figure 4. Radon concentrations at sampling locations L0 to L10 at Gua Penyu cave

The irregular high radon concentration at location L1 is unexplainable. Nevertheless, early presumption was that the opening of the cave might be a granitic type of rock which was a greater source of radon. Granite stones emit more radon compared to the other materials because of the existence of relatively high uranium content [15]. Granite samples are also reported as the main source of radon emanations. The effective annual dose of Radon-222 inside Gua Penyu cave is shown in Table 1. Note that the effective annual dose was derived from the radon concentration.

Table 1. The Radon-222 concentration and effective annual dose inside Gua Penyu cave

Location	Radon Concentration (Bqm^{-3})	Effective Annual Dose ($mSv.y^{-1}$)
L1	5.1 ± 2.2	0.13
L2	3.7 ± 1.8	0.09
L3	3.9 ± 1.3	0.10
L4	4.4 ± 1.5	0.11
L5	3.9 ± 1.2	0.10
L6	6.7 ± 2.1	0.17
L7	3.7 ± 1.6	0.09
L8	4.6 ± 1.8	0.12
L9	7.9 ± 2.1	0.20
L10	3.8 ± 1.3	0.10
Average	4.8 ± 0.6	0.12

Figure 5 shows the etched radon alpha track on sample at location L13. The sample was left for a period of one month for determination of radon emanation rate in Gua Penyu. The higher number of spots than in Figure 3 was a result of it being embedded closer to ground as the major source for Radon-222 after it decayed from Radium-226.

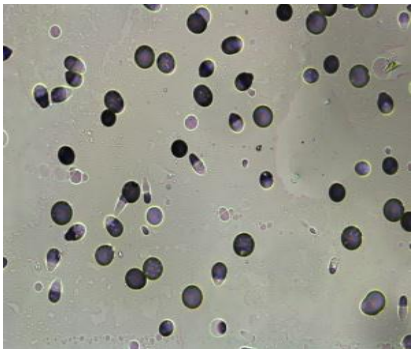


Figure 5. The track showing dark spots on the CR-39 sample at location L13

Radon-222 emanation rate of all study locations were presented in Figure 6. The radon emanation rate for the whole locations ranged between 0.030 ± 0.004 $Bqm^{-2}day^{-1}$ and 0.120 ± 0.017 $Bqm^{-2}day^{-1}$ with the average rate was 0.080 $Bqm^{-2}day^{-1}$.

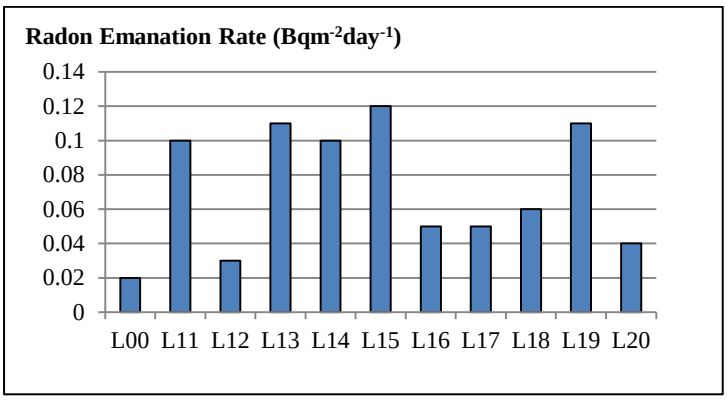


Figure 6. Radon emanation rates at sampling locations L00 to L20 at Gua Penyu cave

The variation in radon emanation rates according to locations indicated different amount of Uranium−238 that exist at sampling locations. This was expected as uranium concentration depends very much on the types of soil and rock. Figure 7 indicates the correlation between the indoor Radon-222 emanation rates and concentrations at sampling location beginning from the main entrance of the cave. This result infers the influence of radon emanation rate to its concentration in poor ventilated vicinity. It shows that higher emanation rates produced higher concentration of radon over time. More importantly, higher rate of emanation means higher level of uranium concentration in the cave ground [16]. As a result, more radon gas was emitted leading to the accumulation of this gas inside the cave. On the contrary, there was a dissimilar trend at sampling locations towards the center of the cave which could be attributed to the mixture and dilution of radon gas near the entrance whereas a consequence of none air ventilation towards the closed end. This was possible since radon gas emission depends on distribution of rocks underneath the cave floor as a major source of this gas.

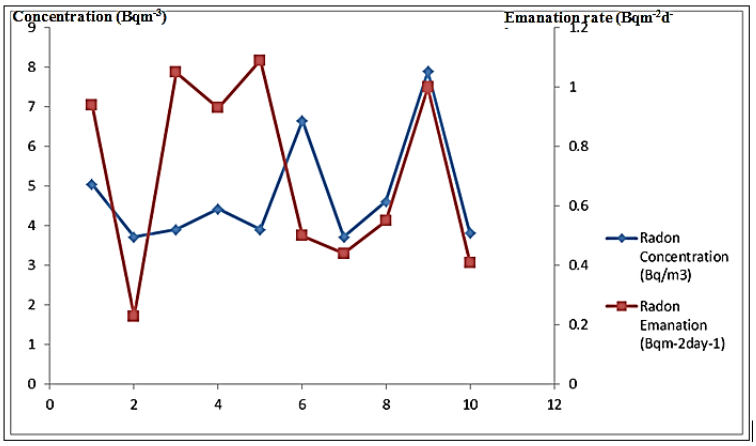


Figure 7. The relation between concentrations and emanation rates of Radon-222 according to sampling locations inside Gua Penyu cave

In this study, the Radon–222 concentration rates were found ranging from 3.7 ± 1.6 Bqm^{-3} to 7.9 ± 2.1 Bqm^{-3}. The average radon concentration was 4.77 Bqm^{-3}. This value was lower compared to other local places such as Puchong (6.6 Bqm^{-3}) and Johor Bharu (5.0 Bqm^{-3}) as reported by Saat and Hamzah [3]. Note that, as far as the quality of air was concerned, the value was much lower than the indoor concentration allowed by The International Commission on Radiation Protection 2009 [17]. The radon emanation rate on the other hand, ranged from 0.030 ± 0.004 $Bqm^{-2}day^{-1}$ to 0.120 ± 0.017 $Bq^{-2}day^{-1}$ with an average of 0.08 Bqm^{-2} day^{-1}. The effective annual dose ranged between 0.09 $mSv.y^{-1}$ and 0.20 $mSv.y^{-1}$, remained harmless if compared to the recommended effective annual dose by ICRP 1993 which was 3–10 $mSv.y^{-1}$.

Conclusion

The International Commission on Radiation Protection (ICRP) has recommended that remedial action against radon and its progeny is justified above a continued effective dose of 3 to 10 $mSv.y^{-1}$ [18]. The action level for radon activity should be in the range of 200–300 Bqm^{-3} [17]. The indoor Radon-222 concentrations, emanation rates and effective annual dose in Gua Penyu cave were all below the recommended ICRP action levels. In conclusion, Gua Penyu cave was harmless to be visited by holidaymakers.

Acknowledgement

The authors would like to sincerely thank the management of Tekam Plantation Resorts (Cave Division), Malaysia for helping and supporting this study and the Institute of Science, Universiti Teknologi MARA for allowing this work to be completed in their facility.

References

1. Elzaher, M. A. (2012). An overview on studying ^{222}Rn exhalation rates using passive technique solid-state nuclear track detectors. *American Journal of Applied Sciences*, 9 (10): 1653-1659.
2. Rowan, E. L., and Kraemer, T. F. (2012). Radon-222 content of natural gas samples from upper and middle Devonian sandstone and shale reservoirs in Pennsylvania: Preliminary data. U.S. Geological Survey Open-File Report 2012-1159: pp. 6.
3. Saat, A. and Hamzah, Z. (2012). Indoor and outdoor Radon-222 concentration at various locations in Peninsular Malaysia. *Proceedings-INTEC Academic Conference*, 2012: 48-54.
4. Sharma, J., Mahur, A. K., Kumar, R., Varshney, R, Sonkawade, R. G, Swarup, R., Singh, H. and Prasad, R. (2012). Comparative study of indoor radon, thoron with radon exhalation rate in soil samples in some historical places at Jaipur, Rajasthan, India. *Advances in Applied Science Research*, 3(2):1085-1091.
5. Najam, L. A, Tawfiq, N. F. and Mahmood, R. H. (2013). Radon concentration in some building in Iraq using CR-39 track detector. *International Journal of Physics*, 1(3): 73-76.

6. International Atomic Energy Agency (2003). Radiation protection against radon in workplaces other than mines. Safety reports series no. 33, IAEA, Vienna.
7. Yu, K. N., Nikezic, D., Ng, F. M. F. and Leung, J. K. C. (2005). Long-term measurements of radon progeny concentrations with solid-state nuclear track detectors. *Journal of Radiation Measurements,* 40: 560-568.
8. World Health Organization (2009). WHO handbook on indoor radon: A public health perspective. Avenue Appia, 1211 Geneva, Switzerland.
9. Oufni, L., Misdaq, M. A. and Amrane, A. (2005). Radon level and radon effective dose rate determination in Moroccan dwellings using SSNTDs. *Journal of Radiation Measurements,* 40: 118-123.
10. Koltai, G., Tegzes, Z. and Hulber, E. (2014). First results of the radon concentration monitoring in Abaliget and Kispaplika Caves. *Acta Climatologica et Chorologica,* 47-48: 71-76.
11. Ahn, G. H. and Lee, J. K. (2005). Construction of an environmental radon monitoring system using CR-39 nuclear track detectors. *Nuclear Engineering and Technology,* 37(4):395-400.
12. Maghrabi, A. M., Alzimami, K. and Abo-Elmagd, M. (2014). Estimation of the residential radon levels and the population annual effective dose in dwellings of Al-Kharj, Saudi Arabia. *Journal of Radiation Research and Applied Sciences,* 7: 577-582.
13. Sainz, C., Dinu, A., Dicu, T., Szacsvai, K., Cosma, C. and Quindos, L.S. (2009). Comparative risk assessment of residential radon exposures in two radon-prone areas, Stei (Romania) and Torrelodones (Spain). *Science of the Total Environment,* 407(15):4452-4460.
14. Mansour, H. L., Tawfiq, N. F., and Karim, M. S. (2014). Indoor radon concentrations measurement in the dwellings of Thi-Qar governorate, Iraqi. *Journal of Natural Sciences,* 2(1):19-26.
15. Nassiri, P., Ebrahimi, H. and Shalkouhi, J. P. (2011). Evaluation of radon exhalation rate from granite stone. *Journal of Scientific & Industrial Research,* 70: 230-231.
16. Bohus, L. S, Greaves, E. D, Palfalvi, J, Urbani, F. and Merlo, G. (1997). Radon concentration measurements in Venezuelan caves using SSNTDS. *Journal of Radiation Measurement,* 28(1-6): 725-728.
17. International Commission on Radiological Protection (2009), Statement on Radon. *Ref00/902/09,* 23(2): 1-44.
18. International Commission on Radiological Protection (1993). Protection against Radon-222 at home and at work, *ICRP Publication,* 23(2).

Malaysian Journal of Analytical Sciences, Vol 22 No 3 (2018): 491 - 498
DOI: https://doi.org/10.17576/mjas-2018-2203-17

MALAYSIAN JOURNAL OF ANALYTICAL SCIENCES
Published by The Malaysian Analytical Sciences Society
ISSN 1394 - 2506

ELECTROCHEMICAL PROPERTIES OF POLYMER ELECTROLYTES TREATED WITH 6PPD ON 30% POLY(METHYL METHACRYLATE) GRAFTED NATURAL RUBBER

(Sifat Elektrokimia Elektrolit Polimer 30% Poli(Metil Metakrilat) Cangkutan Getah Asli Terawat Dengan 6PPD)

Ahmad Fairoz Aziz[1], Khuzaimah Nazir[1]. Siti Fadzilah Ayub[1], Nurul Ilham Adam[2], Muhd Zu Azhan Yahya[3], Ab Malik Marwan Ali[1,4]*

[1]*Faculty of Applied Sciences,*
Universiti Teknologi MARA, 40450 Shah Alam, Malaysia
[2]*Faculty of Applied Sciences,*
Universiti Teknologi MARA, 35400 Tapah Road, Perak, Malaysia
[3]*Faculty of Defence Science and Technology,*
Universiti Pertahanan Nasional Malaysia, 57000 Kuala Lumpur, Malaysia
[4]*Institute of Science,*
Universiti Teknologi MARA, 40450 Shah Alam, Selangor, Malaysia

**Corresponding author: ammali@salam.uitm.edu.my*

Received: 4 December 2016; Accepted: 1 December 2017

Abstract

30% poly(methyl methacrylate) grafted natural rubber was treated with N-(1,3-dimethylbutyl)-N'-phenyl-p-phenylenediamine (6PPD) additive (TMG30) to retard its degradation before further used as electrolytes. The polymer electrolytes containing MG30-6PPD-LiTF were prepared by solution cast technique. X-ray diffraction studies show the electrolytes with the highest salt content are amorphous in nature. The TMG30-salt complexes were confirmed by using Fourier transformation infrared analysis. The highest ionic conductivity of the TMG30 polymer electrolytes containing 40 wt.% LiTF was found to be 1.5 x 10^{-2} S/cm at room temperature. Transference number studies show that the sample with highest ionic conductivity exhibits the charge transport species in this TMG30 polymer electrolyte film is predominantly due to ions.

Keywords: methyl-grafted natural rubber, n-(1,3-dimethylbutyl)-n'-phenyl-p-phenylenediamine, polymer electrolytes

Abstrak

30% poli(metil metakrilat) cangkutan getah asli telah terawat dengan bahan tambah N-(1,3-dimetilbutil)-N'-fenil-p-fenilindiamine (6PPD) (TMG) untuk melambatkan kemerosotan sebelum digunakan sebagai elektrolit. Elektrolit polimer yang mengandungi MG30-6PPD-LiTf telah disediakan melalui teknik pengacuan larutan. Kajian pembelauan sinar-X menunjukkan elektrolit dengan kandungan garam tertinggi berada dalam keadaan amorfus. Pengkompleksan TMG30-garam telah disahkan dengan menggunakan analisis spektroskopi inframerah transformasi Fourier. Elektrolit polimer TMG30 mengandungi 40 wt.% LiTF didapati menghasilkan kekonduksian ionik tertinggi pada 1.5 x 10^{-2} S/cm untuk di suhu bilik. Kajian nombor angkutan terhadap sampel filem elektrolit polimer TMG30 yang mempunyai kekonduksian ionik tertinggi menunjukkan pengangkutan cas dalam sampel tersebut adalah disebabkan oleh pergerakan ion.

Kata kunci: cangkutan metil-getah asli, n-(1,3-dimetilbutil)-n'-fenil-p-fenilindiamin, elektrolit polimer

Introduction

Researches on polymer electrolytes (PEs) have been progressively done in recent years. This type of electrolytes offer high ionic conductivity and can provide good electrode–electrolyte contact which make it suitable to be implemented in electrochemical devices. Modified natural rubber (MNR) has a low glass transition temperature (T_g), soft elastomer characteristics at room temperature, good elasticity and possess adhesive properties. Such characteristics fitted MNR to be used as PEs for further development. Since its ability to form PEs, various types of MNR based PEs have been produced by various techniques and additives. Ichino et al. [1] become the pioneer of using MNR electrolytes in the year 1993. In their studies they tried to overcome low mechanical stability of plasticized PEs. Their idea was utilizing the mechanically strong butadiene rubber to support polystyrene polymer electrolytes and declared the finding as dual-phase polymer electrolyte. Until today research has been geared to enhance the electrolytes properties of MNR particularly to obtain high ionic conductivity at room temperature with better mechanical properties. Various MNR has been used such as by using epoxidized natural rubber (ENR-25 and ENR-50) [2–5] and methyl grafted natural rubber (MG49 and MG30) [6–10] as a polymer host to produce PEs. The introduction of metal oxide inorganic filler such as TiO_2, SiO_2 and Al_2O_3 also was reported successfully enhanced the mechanical properties and improve ionic conductivity at room temperature [11–13].

Studied also goes to use the high dielectric constant plasticizer as additive like ethylene carbonate and propylene carbonate and showed an improvement in ionic conductivity [14,15]. However, all these type of electrolytes degrade with age. Report on retarding degradation problems based on MNR PEs is yet unpublished. The unsaturated C=C bond in natural rubber polymer backbone is considerably weak and easily breakdown with relatively low energy. The degradation process is more prone when MNR is being exposed to certain conditions such as ultra violet rays, high temperature and mechanical shear.

Nevertheless, studies has been done to retard the degradation of MNR by compromising N-(1,3-dimethylbutyl)-N'-phenyl-p-phenylenediamine (6PPD). It is a natural rubber antioxidant that was proven works onto rubber derivatives to retard the degradation [16, 17]. Our previous work have reported that by using 0.5 wt.% of 6PPD was reduce the 30% poly(methyl methacrylate) grafted natural rubber (MG30) degradation [18]. So, in this work, the same amount 6PPD additive will be used in order to enhance the ionic conductivity of the polymer electrolytes based on MNR in which the MG30 was treated with 0.5 wt.% 6PPD to form TMG30. Polymer electrolytes consisting TMG30 and lithium trifluoromethanesulfonate (LiTF) system was prepared. Several methods were employed to distinguish the physical and electrical properties of the prepared samples including X-ray diffraction (XRD), Fourier transform spectroscopy (FTIR), ac impedance spectroscopy (EIS) and transference number.

Materials and Methods

MG30 was obtained from Rubber Research Institute of Malaysia (RRIM) and lithium trifluoromethanesulfonate (LiTF) was obtained from Sigma Aldrich. N-(1,3-dimethylbutyl)-N'- phenyl-p-phenylenediamine (6PPD) antioxidant pallet was supplied by Centre West Industrial Supplies. All the materials were used without further purification. The samples comprising MG30 as host polymer, LiTF as doping salt, and 6PPD as antioxidant were prepared by the solution cast technique. MG30 was minced into smaller pieces and 0.5 wt.% 6PPD pellet was ground into powder before being dissolved in tetrahydrofuran (THF) solution (Mallinckrodt Baker Inc., USA) separately. LiTF solution was prepared separately in tetrahydrofuran solution and stirred for about 12 hours. MG30-6PPD-LiTF solution then mixed together and stirred for 24 hours at room temperature to form homogenous electrolytes solution. The electrolytes solution then poured into caped petri dish and left to slowly evaporate in fume hood. Electrolytes thin films were obtained then continue to dry in drying cabinet to remove all residual solvent before further used.

X-ray diffraction (XRD) studies were recorded at room temperature by using Philips X'Pert PRO diffractometer in the range of 2θ between 10^o and 80^o. Infrared studies were performed by using FTIR Perkin Elmer Spectrum 400 in wave region of 4000 to 500 cm^{-1}. Electrical measurements were done on a computer-controlled HIOKI 3532-50 LCR hi-tester in the frequency ranging from 100 Hz to 1 MHz at room temperature with stainless steel blocking electrode. Transference number (t_n) were tested on WonATech WBCS 3000 automatic battery cycler and evaluated by using Wagner's polarization technique. A constant dc potential (10 mV) was applied across the samples through

two symmetrical blocking electrode. The current was monitored as a function of time until it reached a constant value.

Results and Discussion

Figure 1 shows XRD plot of TMG30 polymer electrolyte with various concentration from 10^{o} to 80^{o}. A peak has spotted at around 18^{o} of all samples. The peak intensities are decreasing and broader with salt concentration suggested that the samples with more salt concentration are more amorphous in nature. This finding was contradict with MG30:LiTF polymer electrolytes system without 6PPD found by other researcher suggested that 6PPD had involved in the formation of amorphous nature in TMG30:LiTF [8]. The behaviour of 6PPD in TMG30 mimics the plasticizer-like behaviour in polymer electrolytes. The amorphous nature of polymer electrolytes has been reported increased upon the introduction of plasticizer and increase the ionic conductivity. Amorphous nature is very essential in polymer electrolytes for ion conduction mechanism that allows the ion movement easier by providing larger ionic path that lowering ion migration activation energy. Polymer electrolyte consist of 45 wt.% of LiTF are expected to have the highest ionic conductivity considering of it most amorphous nature state.

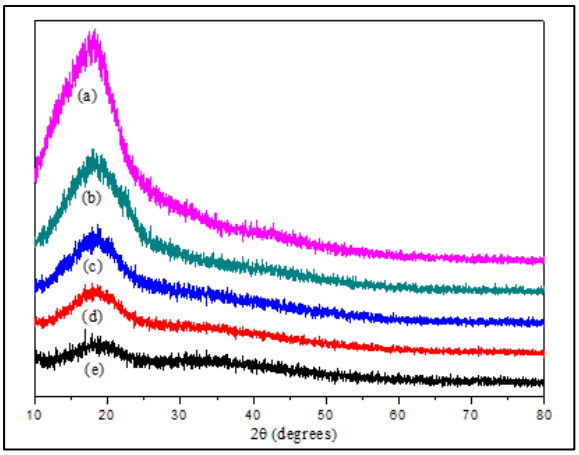


Figure 1. XRD pattern of TMG30 polymer electrolytes ranging between 10^{o} and 80^{o} with function of LiTF wt.% (a) 0, (b) 10, (c) 30, (d) 40 and (e) 45

FTIR spectroscopy was done to establish the interactions between the polymer and salt which identify any changes in the electronic levels of the atoms. In our previous studies it was observed that the oxygen atoms with lone pair of electron (C=O) from poly(methyl methacrylate) (PMMA) in MG30 play a vital role as electron donor in the polymer host. A dative bond between C=O and Li^{+} from the salt will form polymer-salt complex [19]. In MG30 FTIR spectra, the C=O symmetrical stretching frequency gives rise to an intense and sharp peak at 1729 cm^{-1}. The vibrational peaks at 1193 cm^{-1}, 1149 cm^{-1}, and 748 cm^{-1} are assigned to CH_2 in-plane bending mode of polyisoprene, CH_2 twisting mode of PMMA and CH_2 rocking mode of PMMA, respectively. Other MG30 peaks have presented and identified as observed in literature studies [15, 19, 20]. No significant peaks of 6PPD additive spotted throughout the FTIR spectra. This is maybe due to its small amounts of concentration at 0.5 wt.%.

Figure 2 depicts FTIR spectra of TMG30-LiTF complexes in the region between 1600 cm^{-1} and 1800 cm^{-1}. A sharp peak at 1729 cm^{-1} belong to C=O symmetrical stretching of PMMA were found to be shifted to lower wavenumber for sample TMG30-salt complexes. The C=O carbonyl stretching mode shifted to the lower wavenumber and reduced in intensity confirmed the polymer salt interactions take place and is in agreement with a previous report [14]. The peak at 1648 cm^{-1} become more obvious with salt incorporation suggested that LiTF is contributed to the peak growth. This peak is overshadowed the peak of C=C symmetric stretching of polyisoprene from MG30 at 1664 cm^{-1} [19].

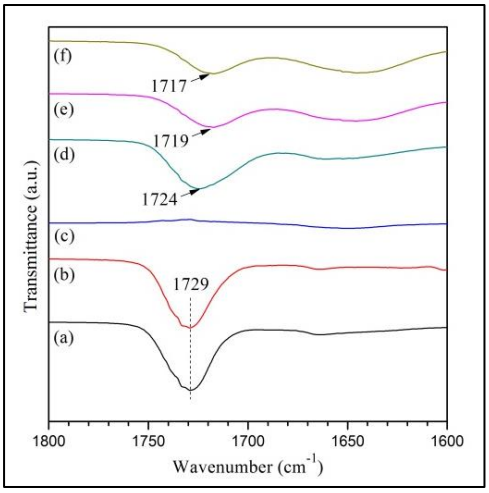


Figure 2. FTIR spectra region from 1600 cm-1 to 1800 cm-1 of (a) MG30, (b) TMG30, (c)LiT, (d) TMG30 + 10 wt.% LiTF, (e) TMG30 + 30 wt. % LiTF, (f) TMG30 + 40 wt.% LiTF

Several new peaks have been observed upon incorporating LiTF in the TMG30 at 1175 cm^{-1}, 1031 cm^{-1} and 765 cm^{-1}. These peaks were originally shifted from 1186 cm^{-1}, 1045 cm^{-1} and 776 cm^{-1} which belong to antisymmetric CF_3 stretching, symmetric SO_3 stretching and symmetric CF_3 deformation mode of LiTF. The band 1193 cm^{-1} of CH_2 in-plane bending mode of polyisoprene is shifted and totally disappeared at 40 wt.% salt incorporation. The peak 1149 cm^{-1} of CH_2 twisting mode of PMMA shifted to higher wavenumber and overlapped under the peak 1175 cm^{-1} as shown in Figure 3. The shifted peak of symmetric SO_3 stretching of LiTF in the TMG30 is shown in Figure 4. CH_2 rocking mode of PMMA at 748 cm^{-1} has been observed in all samples incorporating LiTF as shown in Figure 5. The shifting antisymmetric CF_3 stretching, symmetric SO_3 stretching and symmetric CF_3 deformation mode of LiTF upon the addition of LiTF in the TMG30 signify that Li^+ ions have been coordinated in TMG30.

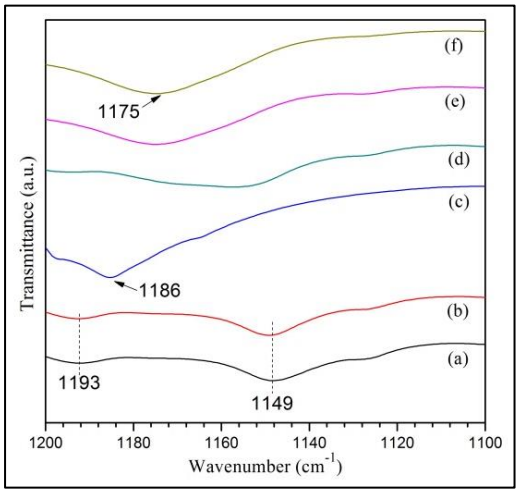


Figure 3. FTIR spectra region from 1100 cm^{-1} to 1200 cm^{-1} of (a) MG30, (b) TMG30, (c)LiTF, (d) TMG30 + 10 wt.% LiTF, (e) TMG30 + 30 wt.% LiTF, (f) TMG30 + 40wt.% LiTF

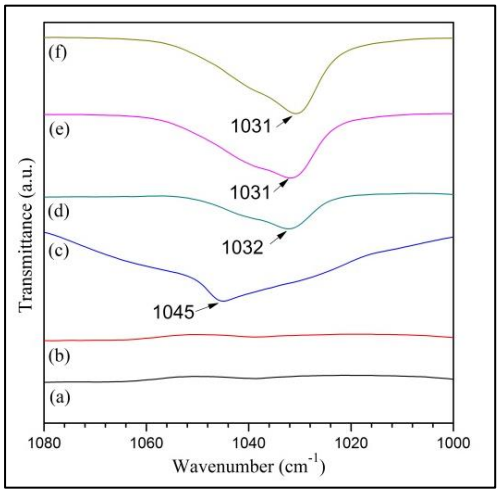


Figure 4. FTIR spectra region from 1000 cm^{-1} to 1080 cm^{-1} of (a) MG30, (b) TMG30, (c)LiTF, (d) TMG30 + 10 wt.% LiTF, (e) TMG30 + 30 wt.% LiTF, (f) TMG30 + 40 wt.% L

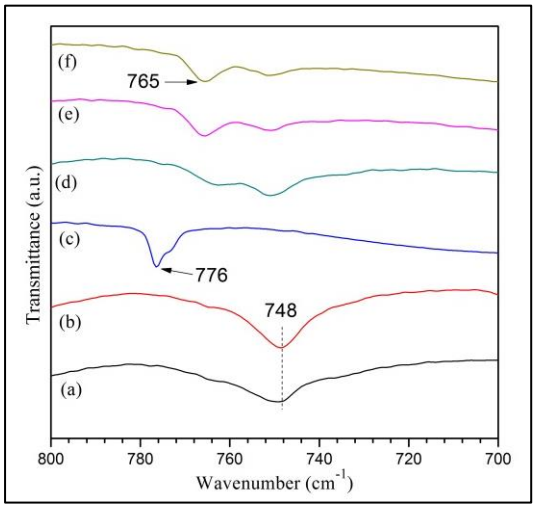


Figure 5. FTIR spectra region from 700 cm^{-1} to 800 cm^{-1} of (a) MG30, (b) TMG30, (c) LiTF, (d) TMG30 + 10 wt%LiTF, (e) TMG30+30wt% LiTF, (f) TMG30 + 40 wt.% LiTF

Figure 6 depicts the ionic conductivity of TMG30 in function of LiTF concentration. The ionic conductivity is increasing with the salt concentration. The ionic conductivity of the TMG30-salt complexes above 40 wt.% of LiTF was not measured due to undesired physical characteristic. This is in agreement with the XRD result in Figure 1 which shows that sample with higher salt concentration is tendency to have more amorphous state. This also explained the reason of the sample having higher ionic conductivity at higher salt concentration which can classify that TMG30-LiTF polymer complex have plasticized-like behaviour and unlike MG30-LiTF polymer salt complexes as reported in literatures [6, 21]. From Figure 6, it was observed the TMG30 with 40 wt.% of LiTF obtained an optimum ionic conductivity with the value of 1.5 x 10^{-2} S/cm at room temperature.

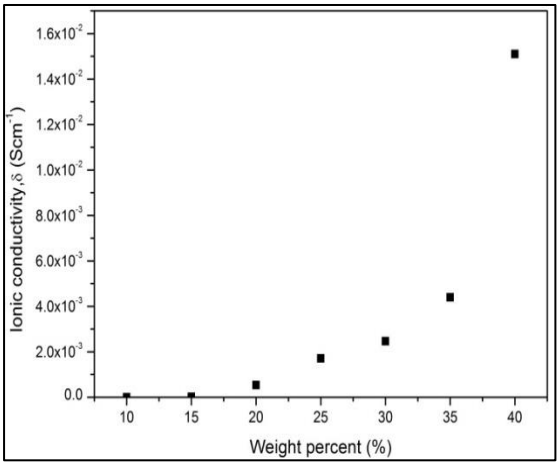


Figure 6. Ionic conductivity of TMG30 polymer electrolytes in function of LiTF concentration at 303 K

Figure 7 shows the current polarization versus time to evaluate the transference number (t_n). The value of t_n was calculated using the equation 1.

$$t_n = (I_i - I_{ss})/I_i \quad (1)$$

where I_i is the initial current and I_{ss} is the steady state current. The time variation of the current through the sample corresponds to the polarization at electrode/electrolyte interface. TMG30 with 40 wt.% LiTF was selected for the test is due to its highest ionic conductivity. The value of the ionic t_n is found to be 0.989 suggested that the ions is predominantly act as charge transport in TMG30 polymer electrolytes.

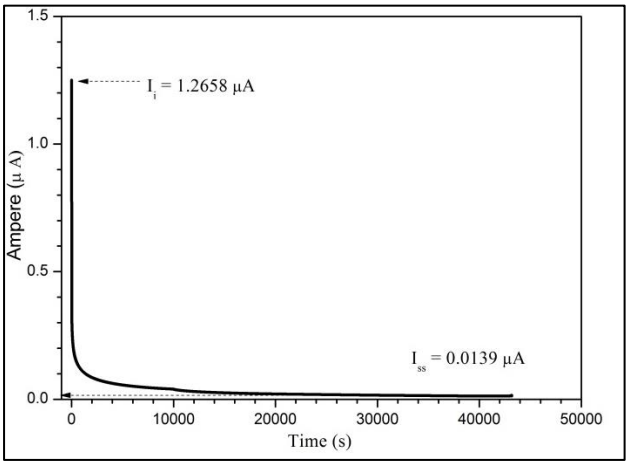


Figure 7. Transference number of TMG30 + 40 wt.% LiTF

Conclusion

FTIR studies confirmed TMG30-LiTF complexes occurred. 6PPD additive brings TMG30 polymer electrolytes to new dimension of polymer electrolytes by providing plasticized-like behaviour in physical and electrical properties. The highest ionic conductivity of TMG30 is obtain at 1.5 x 10^{-2} S/cm for sample with 40 wt.% of LiTF. Transference number confirmed the TMG30 electrolyte is predominately by ion conduction.

Acknowledgement

The authors wish to thank Universiti Teknologi MARA (UiTM) Shah Alam, Research Management Institute (RMI) UiTM and Ministry of Higher Education Malaysia (MOHE) for the financial support (ERGS/1/2013/STG02/UITM/02/01).

References

1. Ichino, T. and Matsumoto, M. (1993). New solid polymer electrolytes prepared from styrene–butadiene copolymer lattices. *Journal of Polymer Science Part A: Polymer Chemistry*, 31: 589-591.
2. Idris, R., Glasse, M. D., Latham, R. J., Linford, R. G. and Schlindwein, W. S. (2001). Polymer electrolytes based on modified natural rubber for used in rechargeable lithium batteries. *Journal of Power Sources*, 94: 206–211.
3. Latif, F., Aziz, M., Katun, N., Ali, A. M. M. and Yahya, M. Z. A. (2006). The role and impact of rubber in poly(methyl methacrylate)/lithium triflate electrolyte. *Journal of Power Sources*, 159: 1401–1404.
4. Mohamed, S. N., Johari, N. A., Ali, A. M. M., Harun, M. K. and Yahya, M. Z. A. (2008). Electrochemical studies on epoxidised natural rubber-based. *Journal of Power Sources*, 183: 351–354.
5. Nazir, K., Ayub, S. F., Aziz, A. F., Zakaria, R., Yahya, M. Z. A. and Ali, A. M. M. (2015). Conductivity and thermal behaviour of epoxidized-30% poly (methyl methacrylate)-grafted natural rubber-lithium triflate based solid polymer electrolytes, *Advanced Materials Research*, 1107: 175–180.
6. Ali, A. M. M., Subban, R. H. Y., Bahron, H., Yahya, M. Z. A. and Kamisan, A. S. (2013). Investigation on modified natural rubber gel polymer electrolytes for lithium polymer battery. *Journal of Power Sources*, 244: 636–640.
7. Kamisan, A. S., Kudin, T. I. T., Ali, A. M. M. and Yahya, M. Z. A. (2011). Electrical and physical studies on 49% methyl-grafted natural rubber-based composite polymer gel electrolytes. *Electrochimica Acta*, 57: 207–211.
8. Yap, K. S., Teo, L. P., Sim, L. N., Majid, S. R. and Arof, A. K. (2012). Investigation on dielectric relaxation of PMMA-grafted natural rubber incorporated with $LiCF_3SO_3$. *Physica B: Condensed Matter*, 407: 2421–2428.
9. Nazir, K., Ayub, S. F., Aziz, A. F., Ali, A. M. M. and Yahya, M. Z. A. (2014). Preparation and characterization of epoxidized-30% poly(methyl methacrylate)-grafted natural rubber polymer electrolyte, *Journal of Nano Research*, 28: 163–170.
10. Aziz, A. F., Nazir, K., Ayub, S. F., Zakaria, R., Yahya, M. Z. A. and Ali, A. M. M. (2015). Impedance behavior of treated methyl-grafted natural rubber polymer electrolytes. *Advanced Materials Research*, 1107: 217–222.
11. Tian Khoon, L., Hassan, N. H., Rahman, M. Y. A., Vedarajan, R., Matsumi, N. and Ahmad, A., (2015). One-pot synthesis nano-hybrid ZrO_2–TiO_2 fillers in 49% poly(methyl methacrylate) grafted natural rubber (MG49) based nano-composite polymer electrolyte for lithium ion battery application. *Solid State Ionics*, 276: 72–79.
12. Chew, K. W. and Tan, K. W. (2011). The effects of ceramic fillers on PMMA-based polymer electrolyte salted with lithium triflate, $LiCF_3SO_3$. *International Journal of Electrochemical Science*, 6: 5792–5801.
13. Kim, S. H., Choi, K. H., Cho, S. J., Kil, E. H. and Lee, S. Y. (2013). Mechanically compliant and lithium dendrite growth-suppressing composite polymer electrolytes for flexible lithium-ion batteries. *Journal of Materials Chemistry A*, 1: 4949-4955.
14. Ali, A. M. M., Yahya, M. Z. A., Bahron, H. and Subban, R. H. Y. (2006). Electrochemical studies on polymer electrolytes based on poly(methyl methacrylate)-grafted natural rubber for lithium polymer battery. *Ionics (Kiel)*, 12: 303–307.
15. Kumutha, K., Alias, Y. and Said, R. (2005). FTIR and thermal studies of modified natural rubber based polymer electrolytes. *Ionics (Kiel)*, 11: 472–476.
16. Cibulková, Z., Šimon, P., Lehocký, P. and Balko, J. (2005). Antioxidant activity of 6PPD derivatives in polyisoprene matrix studied by non-isothermal DSC measurements, *Journal of Thermal Analysis and Calorimetry*, 80: 357–361.
17. Breza, M., Kortišová, I. and Cibulková, Z. (2006). DFT study of the reaction sites of N,N-substituted P-phenylenediamine antioxidants. *Polymer Degradation and Stability*, 91: 2848–2852.
18. Aziz, A. F. and Ali, A. M. M. (2012). Thermal oxidation studies on methyl grafted natural rubber polymer electrolytes with paraphenylene diamine additive, *2012 IEEE Colloquium Humanity Science & Engineering:* pp. 719–723.

19. Kumutha, K. and Alias, Y. (2006). FTIR spectra of plasticized grafted natural rubber- $LiCF_3SO_3$ electrolytes. *Spectrochimica Acta Part A: Molecular and Biomolecular Spectroscopy*, 64: 442–447.
20. Ali, A. M. M., Subban, R. H. Y., Bahron, H., Winie, T., Latif, F. and Yahya, M. Z. A. (2008). Grafted natural rubber-based polymer electrolytes: ATR-FTIR and conductivity studies. *Ionics (Kiel)*, 14: 491–500.
21. Ali, A. M. M., Yahya, M. Z. A., Bahron, H., Subban, R. H. Y., Harun, M. K. and Atan, I. (2007). Impedance studies on plasticized PMMA-LiX [X: $CF_3SO_3^-$, $N(CF_3SO_2)_2^-$] polymer electrolytes. *Materials Letters*, 61: 2026–2029.

Malaysian Journal of Analytical Sciences, Vol 22 No 3 (2018): 499 - 507
DOI: https://doi.org/10.17576/mjas-2018-2203-18

MALAYSIAN JOURNAL OF ANALYTICAL SCIENCES
Published by The Malaysian Analytical Sciences Society
ISSN 1394 - 2506

COMPARATIVE STUDY OF MICROBIAL FUEL CELL'S PERFORMANCE USING THREE DIFFERENT ELECTRODES

(Kajian Perbandingan Bagi Prestasi Sel Bahan Bakar Mikrob Menggunakan Tiga Elektrod yang Berbeza)

Khairul Baqir Alkhair[1,3]*, Oskar Hasdinor Hassan[2], Sharifah Aminah Syed Mohamed[1],Yap Kian Chung Andrew[3], Zulkifli Ab. Rahman[3], Tunku Ishak Tunku Kudin[1],Ab. Malik Marwan Ali[1,4], Mohd Zu Azhan Yahya[5], Muhammad Haikal Zainal[1]

[1]*Faculty of Applied Science*
[2]*Faculty of Art and Design*
Universiti Teknologi MARA, 40450 Shah Alam, Selangor, Malaysia
[3]*Milling and Processing Unit, Enginering and Processing Research Division, Malaysian Palm Oil Board, 43000 Kajang, Selangor, Malaysia*
[4]*Institute of Science, Universiti Teknologi MARA, 40450 Shah Alam, Selangor, Malaysia*
[5]*Faculty of Defence Science and Technology, Universiti Pertahanan Nasional Malaysia, 57000 Sungai Besi, Kuala Lumpur, Malaysia*

**Corresponding author: oskar@salam.uitm.edu.my*

Received: 4 December 2016; Accepted: 1 December 2017

Abstract

Microbial Fuel Cell (MFC) is an alternative method of renewable energy which have gained considerable attention due to its capability to generate electricity and treat wastewater such as palm oil mill effluent (POME). MFC's mechanism on its electrochemical process is still lacking and further studies is needed. The objectives of this study are (1) to determine the compatibility of MFC device in generating electricity by using three different electrodes and (2) to study the effect of sodium hydroxide (NaOH) to MFC's performance. In this work, the MFC device is associated with 3 different electrodes which are carbon brush (CB), carbon cloth (CC) and pre-treated carbon cloth (PCC) on its anode chamber. There are 2 types of substrates used in this experiment which are POME with the presence of bacteria (POME+) and POME without bacteria in it (POME-). The experiment was carried out for 120 hours and its power generation was monitored. The experimental result shows that PCC with POME+ yielded the highest power density of 49.88 mW/m^2 at 27 hours as compared to the others. In addition, CC with POME- has the highest chemical oxygen demand (COD) deduction which indicates the POME treatment was deducted by 45.93%. NaOH affected the performance of MFC but is insignificant to influence the redox reaction of MFC.

Keywords: bio-electricity, fuel cell, wastewater treatment

Abstrak

Sel Bahan Bakar Mikrob (MFC) merupakan kaedah alternatif tenaga boleh diperbaharui yang mendapat perhatian yang baik kerana kemampuannya menjana elektrik dan merawat air kumbahan seperti sisa kilang minyak sawit (POME). Mekanisma MFC bagi proses elektrokimia masih kurang dan kajian lanjut diperlukan. Objektif kajian ini adalah (1) menentukan kesesuaian peranti MFC dalam menghasilkan elektrik dengan menggunakan tiga elektrod yang berbeza dan (2) untuk mengkaji kesan natrium hidroksida (NaOH) kepada prestasi MFC. Dalam kerja ini, peranti MFC dikaitkan dengan 3 elektroda yang berbeza iaitu berus karbon (CB), kain karbon (CC) dan pra rawatan kain karbon (PCC) di ruang anodnya. Terdapat 2 jenis substrat yang digunakan dalam eksperimen ini iaitu POME dengan kehadiran bakteria (POME+) dan POME tanpa bakteria di dalamnya (POME-).

Eksperimen ini dijalankan selama 120 jam dan penjanaan kuasanya dipantau. Keputusan eksperimen menunjukkan bahawa PCC dengan POME+ menghasilkan ketumpatan kuasa tertinggi 49.88 mW/m^2 pada 27 jam berbanding yang lain. Di samping itu, CC dengan POME- mempunyai permintaan oksigen kimia (COD) tertinggi yang menunjukkan rawatan POME berjaya sebanyak 45.93%. NaOH mempengaruhi prestasi MFC tetapi tidak signifikan untuk mempengaruhi tindak balas redoks MFC.

Kata kunci: bio-elektrik, sel bahan bakar, rawatan air kumbahan

Introduction

In Malaysia, POME is a highly polluted wastewater produced by palm oil processing mills, which was usually treated in open pond system consist of cooling ponds, acidification ponds, anaerobic ponds and facultative ponds until its biological oxygen demand (BOD) meets the limit set by Malaysian Department of Environment (DOE) which is 5,000 mg/1 [1] before discharging it into the water course [2]. POME anaerobic fermentation is a complex biochemical process in anaerobic condition where organic matters are degraded to methane and carbon dioxide in discrete steps involving the concerted action of myriad numbers of bacteria in several different metabolite groups of microorganism. The main pathways of anaerobic digestion are involved in 4 stages which are hydrolysis, acidogenesis, acetogenesis and methanogenesis [2].

Recently, the POME treatment process involving bacteria has gained some interest among many scientists and environmentalists, and usage of bacteria together in MFC is one of the alternatives for POME treatment. The application of MFC technologies is an alternative approach to wastewater treatment that uses by-product generated electricity [3]. In 2004, the relationship between electricity using MFCs and wastewater treatment was clearly forged when it was demonstrated that domestic wastewater could be treated to practical levels while simultaneously generating electricity [4]. Bioelectricity generation is a new approach for generating electricity from biomass using bacteria. Therefore, bacteria were further categorized by their ability to exogenously transfer electrons, called exoelectrogens that can produce power in an MFC [3]. Other names for exoelectrogens are electrogens, anode-respiring bacteria [5] and electrochemically active bacteria/microorganism [6]. Exogenously transfer electrons by bacteria are also known as e Extracellular Electron Transfer (EET) [5].

In the present study, the POME was autoclaved to eliminate any living microorganisms that potentially leading the experimental process to false result. The autoclaved POME was used as a substrate, there were two type of substrates that were used which is POME- and POME+. Each of the substrates was subjected with 3 different electrodes namely carbon brush (CB), carbon cloth (CC) and pre-treated carbon cloth (PCC). Mixed cultured exoelectorgens that was successfully isolated and cultured by our lab, was used in this experiment. NaOH was subjected in the MFC device and acted as reducing agent. The aims of this experiment were to determine the compatibility of MFC device in generating electricity by using three different electrodes, and also to study the effect of NaOH as reducing agent on 3 different electrodes that were used. The purpose to achieve the experiment's goals are to provide a basic understanding towards the electrochemical process of MFC device. By gaining this understanding, we could build a new MFC system that would enhance the power generation yields by the MFC devices and its performance.

Materials and Methods

The air cathode double-chambered MFC was made locally using acrylic fiber material with 100 mL of working volume for each component. The anode chamber (anaerobic) and cathode chamber (aerobic) were separated by a salt bridge compartment filled with molten 10% agarose with 4% potassium chloride salt [7] heated in a water bath which was allowed to be cooled and solidified in room temperature. The salt bridge assists in the proton transfer mechanism during the operational of MFC. The electrodes material used for anode and cathode were carbon cloth (Activated Carbon Fiber (ACF) Fabric, China) with the sizes of 3.0 x 3.0 cm (used in both chambers) with projected area of 9.0 cm^2 and carbon brush (Bosch Skil Dremel PG88, German) also with the sizes of 3.0 x 3.0 cm (used in both chambers) with projected area of anode was 9.0 cm^2, separately. The anode chamber is sealed to maintain its anaerobic condition. The electrodes close circuit was connected externally through copper wires to provide the permanent connection to external resistance of 1 kΩ resistor. The schematic diagram of MFC is shown in Figure 1.

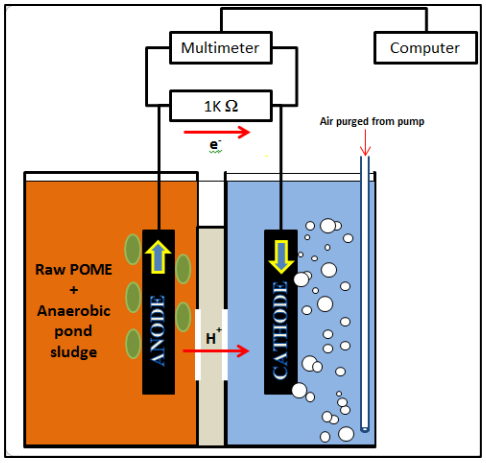


Figure 1. Schematic diagram of aqueous cathode double-chamber Microbial Fuel Cell (MFC)

The substrate used is autoclaved POME. A batch of 1.5 L raw POME was autoclaved for 15 minutes in temperature of 121 ^{o}C at 100 kPa to eliminate living microorganisms entirely. The substrates were introduced with inoculum (acetogenic mixed cultured bacteria) and were prepared in 250 mL borosilicate glass reagent bottles with a mixing ratio of 1:10 (20 mL of inoculum to 180 mL of autoclaved POME) with a total of 6 bottles. The pH of substrates was controlled by using sodium hydroxide (NaOH) that maintained pH 6.8 ± 0.2. Then, each 250 mL bottle transferred 100 mL of substrate into 100 mL borosilicate glass reagent bottles as controlled and calibrate sample. After 24 hours of fermentation process, the leftover substrates of 100 mL in each 250 mL bottle was used in MFC's operation.

In preparing PCC, the cloth was soaked in a pure acetone for 24 hours. After soaking overnight, the cloth was then soaked in ammonium peroxydisulfate (200g/mL) and concentrated sulfuric acid (100 mL/L) for 15 minutes. The furnace was set up to 450 $^{\circ}$C before the cloth was heat-treated for 30 minutes. This pretreated process was done as to increase the surface area of the carbon cloths that are used.

The electrode output voltage was recorded every 1 hour with digital multimeter with data logger (DM620, 50,000 Count Logger DMM and UT803, UNI-T). From these data, power generation was calculated using power density normalized by surface area ($\boldsymbol{P_A}$, Wm^{-2}) [8] using the equation 1 below;

$$P_{An} = \frac{V^2}{A_{An} R} \tag{1}$$

where $\boldsymbol{A}$ = total area of anode electrode (m^2), $\boldsymbol{An}$ = Anode, $\boldsymbol{P}$ = power (W), $\boldsymbol{V}$ = the potential (V) and $\boldsymbol{R}$ = external resistance (Ω). The data collection was analyzed and graphs were plotted based on the equation 1.

The COD of the anode substrates was determined by using COD cell test kit (20 - 1,500 mgL^{-1} range: Hach, USA), digested by using COD reactor (Hach DRB 200, USA) and measured using COD spectrophotometer (Hach DR2800, USA) where COD reading was taken. The initial COD reading was analyzed by taking 2 mL of substrate before filling it in MFC devices. The second COD reading was taken from the MFC anode chamber and the calibrate sample on the final day of the experiment. The COD reduction efficiency ($\boldsymbol{\eta}$) can be calculated as the ratio between the removed and initial effluent COD [8] using the following equation 2 as reported in [9].

$$\eta = \frac{\mathrm{COD_0} - \mathrm{COD_t}}{\mathrm{COD_0}} \tag{2}$$

where COD_o = initial COD of the effluent in the anode chamber, mgL^{-1} and COD_t = COD of the effluent in the anode chamber at measured time. The data is collected and analyzed.

Environmental Scanning Electron Microscopy (Quanta 450 FEG ESEM, USA) was used to observe the biofilm formed on the anodic carbon brush's (ACB) surface. A cut ACB was soaked for 4 hours in 4% glutaraldehyde phosphate buffer solution for fixation process. Then, the ACB was rinsed in distilled water before the sample was observed under ESEM at 20 kV.

Results and Discussion

The concept of MFC is the association of bacteria's metabolism activity as catalyst to enhance the redox process in the MFC, which means without the presence of bacteria in the fuel cell, there are still a small number of electrons will be transferred. The redox process, or dissolve of hydrogen and oxygen, between the electrodes used still occurred, although there are no bacteria subjected into the MFC. There are lots of studies regarding fuel cell without bacteria association that achieved a greater success such as polymer electrolyte membrane fuel cell (PEMFC) [10] and alkaline fuel cell (AFC) [11]. However, MFC is the most unique and versatile system amongst all fuel cells due to its ability to treat wastewater, although its power generation is low as compared to other fuel cell systems. Overall, the result of the experiment is parallel as the theory which are the association of bacteria in the MFC enhanced the power generation and the redox reaction between two electrodes showed some results and produced small amount of electricity.

Voltage reading was recorded, where power and current densities were calculated. From Figure 2, the highest voltage generated is by PCC2. As for CB1 and PCC1 are the lowest voltage generation compared to all the electrodes material used. In the graph, by comparing the materials that were introduced with bacteria (CB2, CC2 and PCC2) yielded higher voltage generations as compared to the materials that were not introduced (CB1, CC1 and PCC1) with the bacteria. If we compare the average power generated of 72 hours between the materials, the highest voltage generation that were produced by the materials that were not introduced by the bacteria is only 2.0 mW/m^2 at most on average. The highest power generated peak is produced by PCC2 at 26 hours, which is 49.55 mW/m^2. If we compare the materials in POME+ (straight line), the highest power generated is yielded by PCC2 and the lowest is CB2, with the average power generated of 38.38 mW/m^2 and 8.69 mW/m^2, respectively. If we compare the materials that subjected in POME- (dotted line), the highest power generated is yielded by CC1 and the lowest is PCC1, with the average power generated of 1.9 mW/m^2 and 0.28 mW/m^2, respectively as shown in Figure 2. It is proven that the association of exoelectrogens bacteria in MFC device enhanced the power generation of the MFC system. There is lack of studies that compares this factor of presence and absence of bacteria, due to vast studies which have proven the ability of MFC to generate electricity. This work is not entirely to test the ability of MFC to produce electricity but instead to determine whether the electricity that was produced is really the work of the bacteria metabolism activity, or it is actually produced by other factors. The result that is shown in Figure 2, it is proven that electricity that was produced is due to the activity of bacteria metabolism. This result aligns with most of the studies regarding MFC [12 – 14].

There are 3 types of exoelectrogens which are mediator, mediatorless and nano-wired [3]. Depending on the type of bacteria that is associated with the MFC, the result may be varied. In one case, in a single MFC device there may be only single type of exoelectrogens metabolize in the system, on the other hand, all types of exoelectrogens are working together and co-existing in a single MFC system to generate electricity. There are many types of mediator used in the previous studies, and most common mediator used was glucose [4, 15, 16].

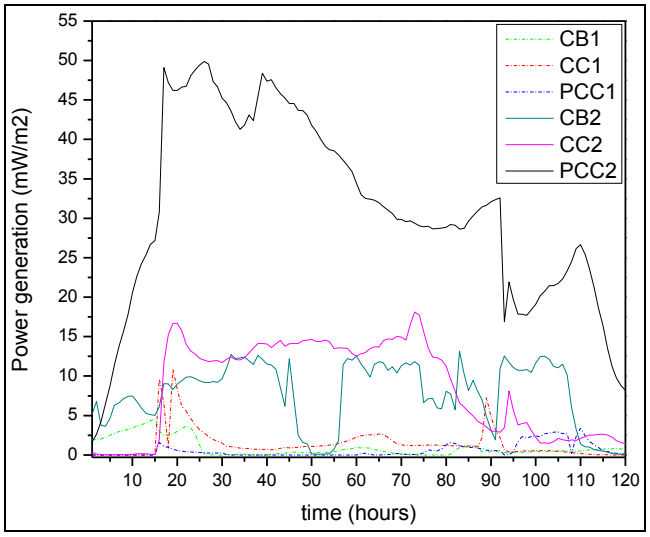


Figure 2. Power Generations with POME+ and POME- exoelectrogens on materials used

NaOH is commonly used in controlling the substrate's pH value [17 – 19]. The problem comes when NaOH itself may act as a reducing agent or mediator to the exoelectrogens that present in the MFC device. In different cases, a collaboration of NaOH which contributed in generating additional electrons is helpful in enhancing the power generation of the MFC system, but in this case, it is not, because this experiment is solely to determine the true potential of mediatorless exoelectrogens of yielding the highest power possible. This experiment was also conducted to determine whether the NaOH, that was used in maintaining the pH value of the substrate, may influence the result of power generation that generated by the exoelectrogens during the experimental process. From Figure 3 and Figure 4, there are two arrows aligned with the x-axis, these arrows represent the period of when the NaOH was inserted in the MFC's anode chamber. At 15 hours of the experiment, the substrate in the anode MFC chamber was introduced with 5 pellets of NaOH and the substrate was later introduced with another 1 pellet of NaOH at 88 hours. In the Figure 3, power generations by all electrodes were increased when the NaOH was first introduced, then the power generations started to decrease. The power generations continued to increase when the substrates were introduced with NaOH for the second time. Also in the graph, the power was only generated when the NaOH was introduced in the substrates, but after 1 day, the power generation dropped to almost 1 mW/m^2 which indicates no bacteria metabolism activity.

In Figure 4, power generations by all electrodes increased when the NaOH was first introduced, then the power generations started to maintain. As compared to power generations of POME- exoelectrogens, the power generated by POME+ exoelectrogens gradually decreased, but POME- exoelectrogens rapidly decreased, which proved the possibility of bacteria metabolism activity were taking place on the electrodes in POME+. Exoelectrogens' metabolism activity produced electrons and hydrogens. Both electrons and hydrogens travelled to the cathodic chamber through proton exchange membrane (salt bridge) and will reduce to water which led the circuit to complete [3]. The power generations continued to increase slowly when the substrates were introduced with NaOH for the second time, then the power generations decreased after a few hours. In the graph, if we compared all three electrodes' power generations, we can see a huge difference between PCC2 and both CC2 and CB2. The difference between them is around 35 mW/m^2 in average, which means 3 times higher. The difference between CC2 and CB2 are small but CC2 still produced higher power generation. If we compare Figure 3 and Figure 4, there were almost no power generated by POME- exoelectrogens, but it is clear in Figure 4, there are power that was generated by the POME+ exoelectrogens in the MFC device.

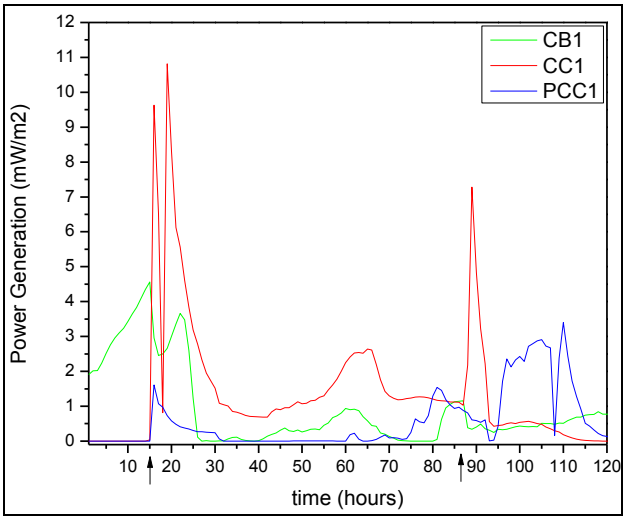


Figure 3. Effect of NaOH in POME- exoelectrogens' power generation CB1, CC1, and PCC1

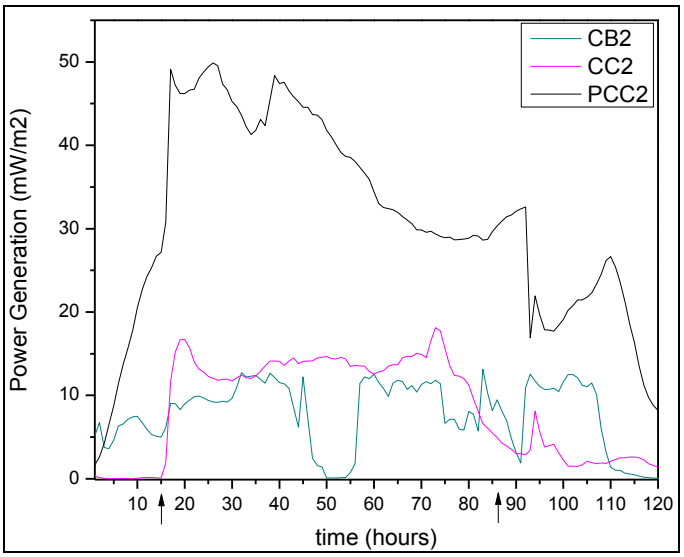


Figure 4. Effect of NaOH in POME+ exoelectrogens's power generation CB2, CC2, and PCC2

Most related MFC studies were using NaOH or $Ca(OH)_2$ as their pH controller but did not attend to study the interaction between the pH controller, that they were using, and the inoculum in the MFC device. A study done by Patil et al., 1N NaOH was used to control their substrate's pH value [19]. In another study, they did not just use the NaOH to control pH value of the substrates but also, they washed the electrodes that were used with NaOH and HCl [20]. In this work, NaOH also was used as a pH controller and from Figure 3 it shows a clear picture of the effect of NaOH to the power generated in MFC devices. However, the power peaked for a few hours then maintained back to its current power generation. It is proven that the use of NaOH, as pH controller, in MFC system affected the power generation as shown in Figure 3. In Figure 4, the NaOH affected the power generation, but as compared to Figure 3 the power that peaked maintained and decreased gradually. This strongly proved that the bacteria activity taken place after the effect of NaOH to the substrates wore off.

COD deduction done by POME-'s electrodes are relatively higher than POME+'s electrodes (Table 1). The highest COD deduction was done by CC1 with deduction of 45.93% and the lowest deduction is 22.73% by CB2. COD control, which is the POME sample that is not subjected in MFC device, of the experiment is 4.28%. There are a clear difference between COD deduction of control and both POME+ and POME- electrodes which proved the MFC's theory on its ability to increase the COD deduction in POME treatment [3]. Although there are no bacteria subjected in POME- but the COD deduction is better than POME+, which is due to the increment of COD in POME+ after the POME sample was fermented with bacteria after 24 hours. In "initial COD" column, an increment of 60% of COD on POME+ after it was fermented for 24 hours. This increment is the factor of why the COD deduction done by POME- is better than POME+, but in terms of amount (mg/L) of COD deduction, POME+ deducted more than POME-, relativity. The highest amount of COD that was deducted is 21166 mg/L which is done by PCC2 and the lowest amount of COD deduction is done by CB2 which is 15033 mg/L. In most MFC studies, they calculated the coulombic efficiency (CE) as to determine the performance of MFC [21], but in this work, CE is not calculated because the objective of this work is not to determine the performance of the MFC but to compare the material used in the MFC devices.

Table 1. COD deduction after 120 hours of MFC

Electrode	Initial COD (mg/L)	Final COD (mg/L)	Deduction (mg/L)	Deduction (%)
Control	38200	36566	1634	4.28
CB1		23633	16067	40.47
CC1	39700	21467	18233	45.93
PCC1		24033	15667	39.46
CB2		51100	15033	22.73
CC2	66133	46100	20033	30.29
PCC2		44967	21166	32.0

ESEM was used to observe the ACB's surface on both POME- and POME+. In ACB in POME- (Figure 5), there were a very small number of bacteria detected which did not contributed in generating electricity. In ACB in POME+ (Figure 5), there were lots of numbers of bacteria detected that formed a biofilm on the ACB which contributed in generating electricity. The comparison between both factors is clear and proven that the association of bacteria in MFC to generate electricity.

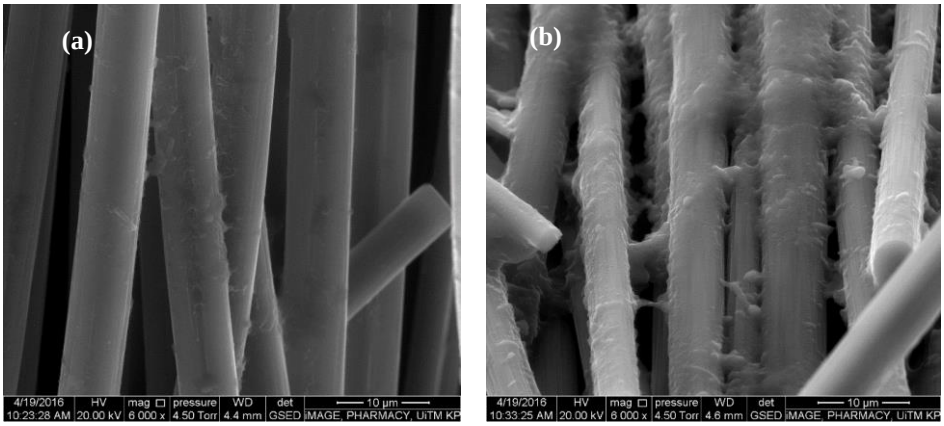


Figure 5. ESEM images of microorganisms' attachment on ACB's surface at day 5 (a) ACB from POME- (b) ACB from POME+

Conclusion

In conclusion, the result is as predicted. The comparison between two substrates used, which are POME- and POME+, shows a clear result that associations of bacteria in MFC devices generate a better power generation. On average, the highest power generated is 38.38 mW/m^2, which yielded by POME+ PCC2. There are only a small portion of power generated in all POME- substrates but the power that were generated is not significant. CC1 with POME- has the highest chemical oxygen demand (COD) deduction efficiency which indicates the POME treatment is deducted by 45.93%. The pH controller (NaOH) used did gave a kick start in power generations but in a few hours the effect of NaOH on the power generation decrease rapidly.

Acknowledgement

The authors would like to thank the Ministry of Education (MOE), Malaysia and University of Technology MARA (UiTM) and Malaysia Palm Oil Board (MPOB) for funding (ERGS (600-RMI/ERGS 5/3 (5/2013)) and GSAS) this project.

References

1. Malaysian Federal Subsidiary Legislation (1978). Environmental quality act 1974. Access from https://www.doe.gov.my/portalv1/wpcontent/uploads/2015/01/Environmental_Quality_Scheduled_Wastes Regulations_2005_-_P.U.A_294-2005.pdf
2. Andrew, Y. K. C. and Manaf, F. Y. A. (2013). Fermentation pathway for palm oil mill effluent. *Palm Oil Engineering Bulletin*, 109: 13-23.
3. Logan, B. E. (2008). Microbial fuel cells. John Wiley & Sons, Inc, United Kingdom: pp.200.
4. Liu, H. and Logan, B. E. (2004). Electricity generation using an air-cathode single chamber microbial fuel cell in the presence and absence of a proton exchange membrane. *Environmental Science and Technology*, 38(14): 4040–4046.
5. Torres, C. I., Marcus, A. K., Lee, H. S., Parameswaran, P., Krajmalnik-Brown, R. and Rittmann, B. E. (2010). A kinetic perspective on extracellular electron transfer by anode-respiring bacteria. *FEMS Microbiology. Reviews*, 34: 3–17.
6. Samir, K. K., Rao, Y. S., Zhang, T. C., Budhhi, P. L., Tyagi, R. D. and Kao, C. M. (2010). Bioenergy and biofuel from biowastes and biomass. *Institution American Society Civil Engineering*, 6: 116–126.
7. Nair, R., Renganathan, K., Barathi, S. and Venkatraman, K. (2013). Performance of salt-bridge microbial fuel cell at various agarose concentrations using hostel sewage waste as substrate. *International Journal of Advance Research Technology*, 2 (5): 326–330.
8. Logan, B. E., Hamelers, B., Rozendal, R., Schroder, U., Keller, J., Freguai, S., Aelterman, P., Verstraete, W. and Rabaey, K. (2006). Microbial fuel cells: Methodology and technology. *Environment Science and Technology*, 40(17): 5181–5192.
9. Baranitharan, E., Khan, M. R. and Prasad, D. (2013). Treatment of palm oil mill effluent in microbial fuel cell using polyacrylonitrile carbon felt as electrode. *Journal of Medical and Bioengineering*, 2(4): 252–256.
10. Garraín, D. (2011). Polymer electrolyte membrane fuel cells (PEMFC) in automotive applications: environmental relevance of the manufacturing stage. *Smart Grid Renewable Energy*, 2(2): 68–74.
11. Alhassan, M. and Garba, M. U. (2006). Design of an alkaline fuel cell. *Leonardo Electronic Journal of Practices and Technologies*, 9: 99–106.
12. Bond D. R. (2010) Electrodes as electron acceptors, and the bacteria who love them. In: Barton L., Mandl M., Loy A. (eds) Geomicrobiology: Molecular and environmental perspective. Springer, Dordrecht: pp. 385-399.
13. Logan, B. E. and Regan, J. M. (2006). Electricity-producing bacterial communities in microbial fuel cells. *Trends Microbiology*, 14(12): 512–518.
14. Gallert, C. and Winter, J. (2005). Bacterial metabolism in wastewater treatment systems. Wiley-VCH, Weinheim, Germany: pp. 1-48.
15. Alalayah, W. M., Kalil, M. S., Kadhum, A. A. H., Jahim, J. M. and Alauj, N. M. (2008). Hydrogen production using *Clostridium saccharoperbutylacetonicum* N1-4 (ATCC 13564). *International Journal Hydrogen Energy*, 33(1): 7392–7396.

16. Biffinger, J. C., Byrd, J. N., Dudley, B. L. and Ringeisen, B. R. (2008). Oxygen Exposure promotes fuel diversity for shewanella oneidensis microbial fuel cells. *Biosensors and Bioelectronics*, 23: 820–826.
17. Lang, L. Y. (2007). Treatability of palm oil mill effluent (POME) using black liquor in an anaerobic Treatment Process. Thesis Master of Science, Universiti Sains Malaysia, Malaysia.
18. Rajesh, J., Khac, U. Do, Adish, S., Ick-Tae, Y. and Kaliappan, S. (2012). A novel method of sludge pretreatment using the combination of alkali. *Journal of Enviromental Biology*, 33: 249–253.
19. Patil, S. A., Harnisch, F., Koch, C., Hübschmann, T., Fetzer, I., Carmona-Martínez, A. A., Müller, S. and Schröder, U. (2011). Electroactive mixed culture derived biofilms in microbial bioelectrochemical systems: The role of pH on biofilm formation, performance and composition. *Bioresources. Technology*, 102(20): 9683–9690.
20. Puig, S., Serra, M., Coma, M., Cabré, M., Balaguer, M. D. and Colprim, J. (2010). Effect of pH on nutrient dynamics and electricity production using microbial fuel cells. *BioresourcesTechnology*, 101: 9594–9599.
21. Zhang, X., He, W., Ren, L., Stager, J., Evans, P. J. and Logan, B. E. (2015). COD removal characteristics in air-cathode microbial fuel cells. *Bioresources Technology*, 176: 23–31.

Malaysian Journal of Analytical Sciences, Vol 22 No 3 (2018): 508 - 513
DOI: https://doi.org/10.17576/mjas-2018-2203-19

MALAYSIAN JOURNAL OF ANALYTICAL SCIENCES
Published by The Malaysian Analytical Sciences Society
ISSN 1394 - 2506

VARIATION OF PM_{10} AND HEAVY METALS CONCENTRATION OF SUB-URBAN AREA CAUSED BY HAZE EPISODE

(Variasi PM_{10} dan Kepekatan Logam Berat di Kawasan Separa-Bandar disebabkan oleh Episod Jerebu)

Mohd Zahari Abdullah* and Nurul Afirah Alias

Faculty of Applied Sciences,
Universiti Teknologi MARA Pahang, 26400 Bandar Tun Abdul Razak Jengka, Pahang, Malaysia

**Corresponding author: umizah@pahang.uitm.edu.my*

Received: 4 December 2016; Accepted: 1 December 2017

Abstract

A severe haze episode has swept across Malaysia in late June until October 2015 and has caused sharp rises of Air Pollution Index (API) across the country. This study was conducted to evaluate the effects of haze event on the API sub-indices during 10 days of the sampling period. The air particulate samples (PM_{10}) were collected at an open site in UiTM Jengka, Pahang by using high volume air sampler (HVAS). The standard acid digestion method was applied to dissolve the sample and the concentrations of heavy metals were analyzed by inductively coupled plasma – optical emission spectrometry (ICP–OES). The API sub-indices were calculated based on the standard method applied by Department of Environment (DOE) Malaysia. The results showed significant differences in PM_{10} mass between haze and non-haze days, which were ranged between 28.4 µg/m^3 to 132.9 µg/m^3 and 17.3 µg/m^3 to 34.7 µg/m^3 for the respective two sampling intervals, haze and non-haze days. The mass concentrations of the studied metals did not show any significant different between the two intervals which indicates other constituent of particulate has contributed to the different weight of PM_{10}. The highest API sub-indices during haze days was recorded as 89 which is classified as moderate level of air pollution. The overall results clearly showed that haze event has increased the PM_{10} mass of the surrounding air but not the concentration of heavy metals.

Keywords: API sub-indices, haze episode, high volume air sampler, particulate matter less than 10 µm

Abstrak

Episod jerebu yang teruk telah melanda Malaysia pada akhir bulan Jun hingga Oktober 2015 dan telah menyebabkan peningkatan mendadak Indeks Pencemaran Udara (API) di seluruh negara. Kajian ini dijalankan untuk menilai kesan daripada peristiwa jerebu kepada nilai sub-indeks API sepanjang 10 hari tempoh pensampelan. Sampel udara (PM_{10}) telah dikumpulkan di kawasan terbuka di UiTM Jengka, Pahang dengan menggunakan alat pensampel udara isipadu tinggi (HVAS). Kaedah pencernaan asid telah digunakan untuk melarutkan sampel dan kepekatan logam berat telah dianalisis menggunakan spektrometer pancaran optik plasma gandingan aruhan (ICP–OES). Sub-indeks API dikira berdasarkan kaedah piawai yang digunakan oleh Jabatan Alam Sekitar (JAS) Malaysia. Hasil kajian menunjukkan perbezaan yang signifikan bagi jisim PM_{10} antara hari berjerebu dan bukan jerebu, yang direkodkan antara 28.4 µg/m^3 hingga 132.9 µg/m^3 dan 17.3 µg/m^3 kepada 34.7 µg/m^3 bagi masing-dua selang pensampelan, hari jerebu dan hari tidak jerebu. Kepekatan jisim logam yang dikaji tidak menunjukkan sebarang perbezaan yang signifikan antara kedua-dua selang yang menunjukkan konstituen lain zarah telah menyumbang kepada berat PM_{10}. Sub-indeks API paling tinggi semasa hari jerebu telah direkodkan sebagai 89 yang diklasifikasikan sebagai pencemaran udara tahap sederhana. Keputusan keseluruhan jelas menunjukkan bahawa peristiwa jerebu telah meningkatkan jisim PM_{10} di udara sekitaran tetapi tidak bagi kepekatan logam berat.

Kata kunci: sub-indeks API, episod jerebu, alat pensampel udara isipadu tinggi, jirim partikel kurang daripada 10 µm

Introduction

Since a few decades ago until now, South East Asia has experienced severe air pollution phenomenon referred as haze [1]. Haze is caused by the emissions from biomass fires [2] and is formed when gaseous pollutants react in the atmosphere. Haze has been a continuing problem in the Southeast Asia's region, and Malaysia is one of the countries that have been badly affected by haze. A significant amount of particulate matters has been transported from a neighboring country, Indonesia due to the uncontrollable biomass fires [2]. The event increases fine particles concentration suspended in air and could give an adverse effect on human health. In September 2015, Malaysia had experienced deterioration of air quality due to massive land and forest fires in Sumatra and Kalimantan, Indonesia [3]. Thirty-four areas in the country recorded unhealthy air quality status for the first time in Malaysia's history since 1997. API reading has reached up to 200 which caused most of the schools to be closed.

The concentration of chemical composition of particulate matter (PM_{10}) has also been widely investigated in haze studies because it is directly connected to the potential human health risk [4]. The increases in respiratory diseases, cancer risk, cardiovascular mortality, hospital admissions and morbidity of human beings was due to the long-term exposure to the high concentration of PM_{10} in the ambient air [5, 6]. There was also a remarkable positive interaction between the concentrations of the total suspended particulate (TSP) and lung dysfunctional in children [7].

Studies relating the effects of air pollutants on human health are rarely conducted in rural or sub-urban areas because of many reasons which depend on the particular site. In general, it was related to cost, man-power and the benefit of the study outcome. This study was conducted specifically to measure the API based on the measured gravimetry sub-indices and to evaluate the metal concentration along the sampling intervals in sub-urban site during haze episode. It is hope that the outcome of this study could be used as a supporting data for the related local agencies to evaluate and observe the effect of haze event on the local sub-urban population.

Materials and Methods

Sampling site

PM_{10} levels was monitored for a period of 24-hours for 10 days during haze condition (17/09/15 to 3/10/15) and non-haze condition (1/3/16 to 13/03/16) at an open site in Universiti Teknologi MARA Pahang Campus. The specific latitude was at 3^o 46'6.50" N and 102^o 32'43.41" E. In general, the chosen studied location experiences an ambient temperature of 38 °C to 40 °C during daytime and gradually decreases along the night. The position was almost 200 meters away from the main road and no major industrial activities operated around the area.

Sample collection

Air particulate samples (PM_{10}) were collected on the pre-weight glass fiber filter with diameter 203 x 254 mm^2 (Advantec GA–55) using the high volume air sampler (Sibata HV – 1000F) instrument. The air particulate collector was operated with a constant flow rate at 1054 L/min. Samples were taken for 10 times (17 September to 3 October 2015). The loaded filters were conditioned in the desiccator for a week before the weight of the total gravimetrical mass was measured.

Sample treatment-wet digestion

The exposed filter (195 x 250 mm^2) was cut into 12 strips. For the purpose of acid extraction, the filter strips were cut into a smaller size. The selection and preparation of filters, extraction, and extraction of metals from filter strip were carried out based on the USEPA method (USEPA-Method IO-3.2, 1999).The exposed filter strip was dissolved in a mixture of 20 mL of 3% HNO_3 and 10 mL of 8% HCl solution. The mixture was heated using hot plate for 120 minutes at 150 °C until dryness and cooled at room temperature. The deionized water was added and filtered before bringing up to the final volume 100 ml. The metal concentrations in this study were analysed by using ICP – OES.

Assessment of soil contamination

Enrichment factor (EF) were evaluated to verify heavy metals in soil originate from geogenic or anthropogenic origins. It is frequently supposed that the contents of elements in a natural medium can be justified specially by crust or geogenic origin [8, 9]. The EF value was calculated based on the following formula in equation 1 below:

$$EF = (M/Fe)\ sample\ /\ (M/Fe)\ reference \quad (1)$$

where M is the metal in consideration and Fe is a reference metal. To develop the sensitivity of the EF to the iron mine influence, the soil at a reference site was utilized as a reference. According to Zhang and Liu [10], EF values between 0.05 and 1.5 reveal that the metal is exclusively from crustal origins or natural developments; however, EF values higher than 1.5 imply that the origins are more probable to be anthropogenic.

PM_{10} gravimetry mass distribution trend

The mass concentration of the suspended particulates with the size limited to 10 micron and below was calculated by using the following equation 2:

$$TSP = [(W_f - W_i) / Vt] \times 10^6 \quad (2)$$

where TSP is defined as concentration of particulate matter, $\mu g/m^3$, W_f is the final weight of the filter paper (grams), W_i is the initial weight of the filter paper (grams), V_t is the total volume of air sampling and 10^6 is conversion factor from grams to micrograms.

Variation of sub-air pollution indexes

The sub-indexes API reading in this study was calculated solely based on the mass concentrations of PM_{10} with the following equation 3:

$$Ii = (Ci / Si) \times 100 \quad (3)$$

where Ii is type of pollutant, Ci is concentration of pollutant and Si is reference value (attention state).

Heavy metal mass concentration in PM_{10} samples

The mass concentration of heavy metals contained in the PM_{10} samples was calculated using the following equation 4:

$$C = [(C_i \times V_f \times UFA)] / Vstd \quad (4)$$

where C is Concentration ($\mu g/m^3$), C_i is metal concentration determined ($\mu g/L$) – data obtained from ICP, V_f is total sample extraction volume from extraction procedure (L), UFA is usable filter area (8" x 9")] divide exposed area of one strip, and Vstd is standard air volume pulled through the filter (m^3).

Results and Discussion

The gravimetry mass of the PM_{10} measured during and after haze event was summarized in Table 1.

The average concentration of particulate samples (10 micron and below) observed during 10 days of haze event was 81.20 $\mu g/m^3$. The highest value of PM_{10} concentration was recorded on 30 September 2015 with 132.96 $\mu g/m^3$, while the lowest value was recorded as 28.40 $\mu g/m^3$, on 21st September 2015. The average daily PM_{10} level recommended in the Malaysian Ambient Air Quality Guidelines for PM_{10} is 150 $\mu g/m^3$ [11]. Concentration of PM_{10} above 150$\mu g/m^3$ in 24 hours is considered unhealthy to humans. The overall PM_{10} mass concentration measured during non-haze condition was lower compared to samples collected during haze days. The average mass concentration of PM_{10} during non-haze day was measured as 26.88 $\mu g/m^3$, which was 66.89% lower compared to the value during the haze event. The highest value of PM_{10} mass concentration recorded during non-haze days (34.72 $\mu g/m^3$) was recorded on the 10th of March 2015 while the lowest value of PM_{10} mass concentration

(17.26 µg/m^3) was recorded on the 7th of March 2015. The results of this study clearly showed that all the particulate mass during the haze days were higher compared to the non-haze days at least by 30%.

Table 1. Mass of Particulate Matter (PM_{10}) during and after the haze episode

Sampling Date (Haze day)	PM_{10} (µg/m^3)	Sampling Date (Non-Haze day)	PM_{10} (µg/m^3)	% Mass Difference
17/9/15	46.72	1/3/2016	25.57	45.26
18/9/15	117.28	2/3/2016	25.76	77.79
19/9/15	102.85	3/3/2016	26.09	74.51
21/9/15	28.40	7/3/2016	17.26	39.22
28/9/15	83.48	8/3/2016	21.81	74.63
29/9/15	95.61	9/3/2016	31.63	62.52
30/9/15	132.96	10/3/2016	34.72	73.48
1/10/15	66.42	11/3/2016	29.12	56.16
2/10/15	88.23	12/3/2016	22.20	74.84
3/10/15	50.08	13/3/2016	34.66	30.60
Average	81.20	Average	26.88	60.90
Minimum	28.40	Minimum	17.26	30.60
Maximum	132.96	Maximum	34.72	77.79

The strong and medium winds during September to November 2015 probably was created turbulent conditions which causes frequent dust storm and hazy condition in the study area [12]. The hazy condition has built up high particulate matter levels in the low altitude ambient air. The result obtained in this study clearly shows that the haze event has increased the PM_{10} gravimetry mass compared to the normal ambient condition. However, the average PM_{10} concentration measured in this study for haze and non-haze events not exceed the concentration limit as recommended by the Malaysian Ambient Air Quality Guidelines by DOE [13].

The sub-API data measured during the haze and non-haze days was summarized in Figure 1. The average sub-indices API during the haze days were observed at the level of 54. The highest sub-indices API during the ten days of haze was 87 which were recorded on 30 September 2015, and the lowest sub-indices API was at the level 19, on 21 September 2015. Based on the measured Air Pollution Indices level, the sub-indices API measured during haze episode were categorized at moderate level (index level below than 100). If the API readings exceed 100, it will cause long-term health problems to humans such as cancer risk, cardiovascular mortality, and respiratory diseases [6] which is not the case in our study.

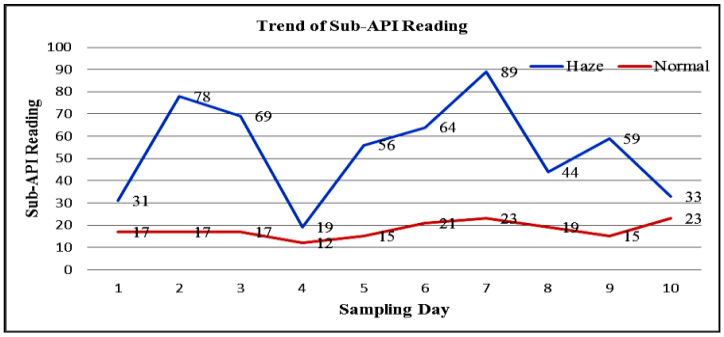


Figure 1. Sub-indices API during haze and non-haze days

In general, the sub-indices API observed along ten non-haze days were recorded at a lower index level compared to the haze days. The highest API level (at level 23) was observed on 13th of March 2016 and the lowest API reading (at level 12) was recorded on 7th of March 2016. All the API reading observed during non-haze days was not exceeded 50 in API reading which classified as good ambient air condition.

The average mass concentration of several atmospheric metal pollutants (Cu, Ni, Pb, Fe, Mn and Zn) during both haze and non-haze periods are presented in Table 2. The mean concentrations for the seven elements in PM_{10} samples follow the order of Zn, Fe, Cu, Pb, Mn, Cr and Ni during both haze and non-haze days. The average mass concentration of all studied elements contained in PM_{10} samples collected during haze period was only slightly different compared to the non-haze days (small ratio value). The low ratio of the mass concentration of Cu, Ni, Pb, Fe, Mn and Zn which were all below 1.5 ratio between haze and non-haze days clearly indicate that the haze particles has not affected the concentration levels of the studied elements in the PM_{10} samples.

Table 2. Average concentration of heavy metals during haze and normal ambient condition

Elements	**Haze Days (µg/m^3)**	**EF Value**	**Non- Haze Days (µg/m^3)**	**Haze/Non-Haze Ratio**	**Correlation Coefficient, r**						
					Cu	**Ni**	**Pb**	**Fe**	**Mn**	**Zn**	**Cr**
Cu	0.092	0.89	0.083	1.1	1	0.25	0.42	0.21	0.61	0.76	0.75
Ni	0.012	0.23	0.009	1.3		1	0.07	0.09	0.27	0.09	0.16
Pb	0.042	0.33	0.039	1.1			1	0.32	0.52	0.63	0.53
Fe	0.969		0.815	1.2				1	0.11	0.30	0.27
Mn	0.030	0.66	0.028	1.5					1	0.67	0.61
Zn	39.691	1.23	32.230	1.2						1	0.98
Cr	0.020	0.11	0.018	1.1							1

High correlations (0.76 – 0.98) were observed for the pair of Cu, Cr and Zn which indirectly indicates that the metals probably were contributed by the same sources. Furthermore, the moderate correlations were observed for Cu-Mn. Pb-Mn, Pb-Zn, PB-Cr, Zn-Mn and Mn-Cr which correlated with the r values within 0.52 to 0.67. The moderate correlation between the metals suggested there would be various emitters released the metals around the study area. The other pairs which recorded low correlation coefficients indicate that the metals were not originated from the same emitters. Based on the correlation analysis of the element pairs and the EF values measured, it would be suggested that all the studied metals were originated from lithogenic or geogenic sources. With the overall observation, this finding suggests a reasonable uniformity in the contribution of the different metal sources to PM_{10}. The high mass concentration of PM_{10} samples measured during haze days would probably be influenced by the other constituents such as hydrocarbon, biological matter, organic and inorganic compounds and acid aerosols [14].

Conclusion

Studies about the air quality in the sub-urban areas are rarely done because there are less economic activities carried out in these areas compared to the urban sites. The results obtained from the study clearly showed that the Air Pollution Index (API) readings are generally at a scale below the guidelines set by the Department of Environment Malaysia. Moreover, the concentrations of heavy metals contained in the PM_{10} samples were still in the safe zone. The concentration of PM_{10} also below the guidelines set by the Department of Environment. It could be concluded that the metal concentration in PM_{10} was not directly influenced by the increasing PM_{10} mass during haze episode.

Acknowledgements

The researchers would like to express their deep appreciation to Ministry of Higher Education of Malaysia (MOHE) and Research Management Unit (RMI) UiTM for the financial supports (FRGS Grant) and all individuals for their assistance and recommendations.

References

1. Muraleedharan, T. R., Radojevic, M., Waugh, A. and Caruana, A. (2000). Chemical characterisation of the haze in Brunei Darussalam during the 1998 episode. *Atmospheric Environment*, 34: 2725–2731.
2. Radojevic, M. (2003). Chemistry of forest fires and regional haze with emphasis on Southeast Asia. *Pure and Applied Geophysics*, 160: 157-187.
3. Department of Environment (2015). Chronology of haze episodes in Malaysia. Retrieved from http://www.doe.gov.my/portalv1/wp-content/uploads/2015/09/Chronology-of-Haze-Episodes-in Malaysia.pdf.
4. Billet, S., Garçon, G., Dagher, Z., Verdin, A., Ledoux, F., Cazier, F., Courcot, D., Aboukais, A. and Shirali, P. (2007). Ambient particulate matter ($PM_{2.5}$): Physicochemical characterization and metabolic activation of the organic fraction in human lung epithelial cells (A549). *Environmental Research*, 105(2): 212–223.
5. Jerrett, M., Buzzelli, M., Burnett, R. T. and DeLuca, P. F. (2005). Particulate air pollution, social confounders, and mortality in small areas of an industrial city. *Social Science & Medicine*, 60(12):2845–2863.
6. Finkelstein, M. M., Jerrett, M., Deluca, P., Finkelstein, N., Verma, D. K., Chapman, K. and Sears, M. R. (2003). A cohort study of income air pollution and mortality. *Canadian Medical Association Journal*, 169(5): 397–402.
7. Liu, L. and Zhang, J. (2009). Ambient air pollution and children's lung function in China. *Environment International*, 35(1): 178–186.
8. Jiang, J. B., Wang, J., Liu, S. Q., Lin, C. Y., He, M. C. and Liu X. T. (2013). Background, baseline, normalization, and contamination of heavy metals in the Liao River Watershed sediments of China. *Journal of Asian Earth Science*, 73: 87−94.
9. Li, P., Lin, C., Cheng, H., Duan, X. and Lei K. (2015). Contamination and health risks of soil heavy metals around a lead/zinc smelter in southwestern China. *Ecotoxicology and Environmental Safety*, 113: 391−399.
10. Zhang, J. and Liu C.L. (2000). Riverine composition and estuarine geochemistry of particulate metals in China weathering features, anthropogenic impact and chemical fluxes. *Estuarine, Coastal and Shelf Science*, 54:1051−1070.
11. Afroz, R, Hassan. M. N. and Ibrahim, N. M. (2003). Review of air pollution and health impacts in Malaysia. *Environmental Research*, 92: 71–77.
12. Varoujan K. S., Al-Ansari, N. and Knutsson, S. (2013). Sand and dust storm events in Iraq. *Natural Science*. 5(10): 1084-1094.
13. Department of Environment Malaysia (2000). A guide to Air Pollution Index (API) in Malaysia. Department of Environment: pp. 6 – 8.
14. Leili, M., Naddafi, K., Nabizadeh, R. Yunesian, M and Mesdaghinia, A. (2008). The study of TSP and PM10 concentration and their heavy metal content in central area of Tehran, Iran. *Air Quality, Atmosphere & Health*, 1(3): 159–166.

Malaysian Journal of Analytical Sciences, Vol 22 No 3 (2018): 514 - 521
DOI: https://doi.org/10.17576/mjas-2018-2203-20

MALAYSIAN JOURNAL OF ANALYTICAL SCIENCES
Published by The Malaysian Analytical Sciences Society
ISSN 1394 - 2506

PREPARATION, CHARACTERIZATION AND PERFORMANCE OF POLYVINYLIDENE FLUORIDE/TETRAOCTYL PHOSPHONIUM BROMIDE NANOCOMPOSITE ULTRAFILTRATION MEMBRANE

(Penyediaan, Pencirian dan Prestasi Membran Ultraturasan Nanokomposit Polivinilidena Flourida/Tetraoktil Fosfonium Bromida)

Asmadi Ali[1]*, Connie Ling Mee Yu[1], Nur Alyaa Mohd Sani[1], Mohd Aidil Adha Abdullah[2], Mohamad Awang[1], Nor Shalihan Mohamed[1], Mohd Azizi Che Yunus[3]

[1]*School of Ocean Engineering*
[2]*School of Fundamental Science*
Universiti Malaysia Terengganu, 21030 Kuala Nerus, Terengganu, Malaysia.
[3]*Centre of Lipid Engineering and Applied Research (CLEAR),*
Ibnu Sina Institute for Industrial and Scientific Research,
Universiti Teknologi Malaysia, 81310 UTM Johor Bahru, Johor, Malaysia

**Corresponding author: asmadi@umt.edu.my*

Received: 16 April 2017; Accepted: 7 March 2018

Abstract

Ultrafiltration (UF) membrane is widely used in many industrial areas and applications. Polyvinylidene fluoride (PVDF) is one of the commonly used materials for UF membrane fabrication due to its excellent properties. However, its hydrophobic nature causes the decrease of its demands and limits its applications. Hence, tetraoctyl phosphonium bromide (TOPBr) clay was used as a nanofiller material and was added into the PVDF matrix to decrease the hydrophobic surface through the antifouling properties of the PVDF/TOPBr nanocomposite membrane. The phase inversion process was employed for membrane fabrication which characterizes the water content and porosity of the PVDF/TOPBr nanocomposite UF membrane and to determine the performance of membrane in terms of pure water permeation, protein separation and fouling parameters. The results showed the increment of TOPBr dosage increases the water content and porosity, as well as enhances the porosity structure of PVDF/TOPBr nanocomposite membrane compared to the original PVDF membrane. The protein separation performance test revealed that after the addition of TOPBr, the flux increased from 2.06 L/m^2.h to 20.22 L/m^2.h with a 1.0 wt.% increase in protein separation as a result of the increase in the membrane hydrophilicity and porosity of the nanocomposite membrane. Moreover, PVDF/TOPBr1.0 nanocomposite showed the highest antifouling properties and flux recovery at 93% compared to other PVDF/TOPBr, as well as the native PVDF membrane.

Keywords: ultrafiltration**,** nanocomposite membrane, polyvinylidene fluoride, clay

Abstrak

Membran ultraturasan (UF) digunakan secara meluas dalam banyak industri dan aplikasinya. Polivinilidena fluorida (PVDF) adalah bahan yang biasanya digunakan untuk fabrikasi membran kerana mempunyai sifat yang cemerlang. Walaubagaimanapun, sifat asal yang hidrofobik menyebabkan penurunan permintaannya dan menghadkan penggunaannya. Maka, tanah liat tetraoktil fosfonium bromida (TOBr) telah digunakan sebagai bahan pengisi nano dan ditambah ke dalam matrik PVDF untuk mengurangkan permukaan hidrofobik melalui sifat antikotoran oleh membran nanokomposit PVDF/TOPBr. Proses fasa sonsangan digunakan untuk fabrikasi membran yang mencirikan kandungan air dan keliangan membran nanoomposit PVDF/TOPBr dan untuk menentukan prestasi membran dari segi penyerapan air tulen, pemisahan protein dan parameter pengotoran. Keputusan menunjukkan kenaikan dos TOPBr meningkatkan kandungan air dan keliangan, serta meningkatkan

struktur keliangan membran nanokomposit PVDF/TOPBr berbanding dengan membran PVDF asal. Ujian prestasi pemisahan protein menunjukkan bahawa selepas penambahan TOPBr, fluks meningkat dari 2.06 L/m^2.h kepada 20.22 L/m^2.h dengan kenaikan 1.0 wt.% dalam pemisahan protein akibat daripada peningkatan hidrofilik membran dan keliangan membran nanokomposit. Selain itu, nanokomposit PVDF/TOPBr1.0 menunjukkan sifat antikotoran yang tertinggi dan pemulihan fluks pada 93% berbanding dengan PVDF /TOPBr yang lain serta membran PVDF asli.

Kata kunci: ultraturasan**,** membran nanokomposit, polivinilidena fluorida, tanah liat

Introduction

Membrane technology has provided a good opportunity and presents an interesting approach to study separation processes in numerous applications, such as in water and wastewater treatment, gas purification, food processing, pharmaceutical industries and bio separation areas [1]. In recent years, the application of UF membrane in protein separation is growing rapidly as it is easy to operate, incurs a low operating cost and does not involve any phase change. In this light, producing membranes with better separation characteristics is important to the continued development of this technology. Most of the membranes used commercially based on polymeric materials and made from hydrophobic polymers such as polysulfone (PS), polyether sulfone (PES), polypropylene (PP), polyethylene (PE), and polyvinylidene fluoride (PVDF). Among of these various polymers, PVDF is a well-known polymeric membrane that has broadly been used in UF membrane separation process.

PVDF has been used in various applications, particularly in ultrafiltration processes due to its excellent chemical resistance, thermal stability and mechanical properties. However, PVDF membrane has a highly hydrophobic nature which leads to the deposition of solute or particle on a membrane surface or in membrane pores, causing serious fouling and a rapid decline in permeation flux [2]. The hydrophobicity of PVDF membrane has limited the application of the commercial PVDF membrane. Thus, it is necessary to improve the hydrophilicity of PVDF membrane through chemical or physical modifications,surface grafting polymerization, coating, or blending with a hydrophilic polymer [3]. Among these methods, blending with inorganic materials, especially nanoparticles has attracted much interest due to its simple operation and efficiency in enhancing the performance of the hydrophobic membranes in designing new materials [4]. In this regard, montmorillonite is one of the most familiar natural clay used in the preparation of polymer clay nanocomposite membrane because of its ability to be dispersed in the polymeric matrices at nanoscopic level [5] and only a small amount of this material is needed in the fabrication of nanocomposite membrane [6]. Thus, this study investigated the preparation of PVDF/Montmorillonite nanocomposite membrane using organically modified clay, tetraoctyl phosphonium bromide (TOPBr) by using the blending method.

To the best of our knowledge, there is no research conducted that focused on the use of clay materials in the nanocomposite membrane. The purpose of this research is to prepare flat sheet PVDF/TOPBr nanocomposite UF membranes by phase inversion method and to characterize its characteristics and performance by investigating the effect of clay dosage on water permeation and protein separation in detail.

Materials and Methods

Materials

All materials used were of analytical grade. The membranes were fabricated from the dope solution of polyvinylidene fluoride (PVDF) as the base polymer, tetraoctyl phosphonium bromide (TOPBr) clay, and N-methyl-2-pyrrolidone (NMP) as a solvent. All of these materials were supplied by Merck. The TOPBr clay was prepared via cation ion exchange between sodium ions of Na^+ MMT clay and tetraoctylphosphonium bromide (TOP-Br) surfactant ions. The modified clay was prepared according to Ali and his co-workers [3]. Distilled water was used as a coagulation medium in coagulation bath and was used in pure water permeation experiment. Bovine serum albumin (BSA) (Mw = 66kDa) purchased from Sigma was used for the evaluation of the protein separation performance test.

Membrane preparation

The membranes were prepared using the phase inversion method. Different TOPBr clay content (0.2, 0.4, 0.6, 0.8 and 1.0 weight %) were added into 17/83 wt.% of polymer/solvent solution and homogenous dispersion solutions

were prepared by mechanical stirring for 6 hours at 70 °C. The membranes were fabricated *via* phase inversion technique where the solution was cast on a glass plate with 150-µm thickness and immediately immersed into a coagulation bath. A flat sheet membrane was obtained and stored for 24 hours, in order to remove the excess solvent in the fabricated membrane. The membranes were stored in distilled water prior to usage.

Membrane characterization: Water content

The water content of each membrane was obtained after soaking the membranes in water for 24 hours at room temperature. The membranes were then dried in a vacuum drier at 75 °C for 48 hours befire the weight of each membrane was determined. The percentage of water content was calculated using equation 1:

$$\%\, Water\ content = \frac{(W_{wet} - W_{dry})}{W_{wet}} \times 100 \quad (1)$$

where W_{wet} is define as weight of is wet membrane (mg) and W_{dry} is a weight of dry membrane (mg).

Porosity

The porosity of each membrane was assessed by their holding ability for water absorption and was determined using the equation 2 below:

$$Porosity = \frac{(W_1 - W_2/d_{water})}{V} \times 100 \quad (2)$$

where $W_1$and W_2 are the mass of membrane in wet and dry states (mg), d_{water} is the density of water at room temperature (ml/mg) and V is the volume of the membrane in wet state (ml).

Pure water permeation

All of the permeation tests were carried out at room temperature using dead end permeation cell with the feed volume of 300 ml and area of membrane filtration was set at 14.6 cm^2. Distilled water was used for the feed solution in this experiment to earn pure water permeability and achieve membrane stability. Compaction tests were performed for each membrane, first at 5 bar between 30 minutes to 1 hour or until the pure water flux attained a steady state. After the compaction process, the distilled water was drawn through the membrane using compressed nitrogen gas with the operating pressure ranging from 1 to 5 bar. The equation 3 below was used to calculate pure water flux:

$$PWP(L/m^2.h) = \frac{Q}{A\,\Delta T} \quad (3)$$

where Q is a permeate collection quantity (L), A is area of the membrane (m^2) and ΔT time of sampling (hour).

Separation performance

For the BSA permeation, 0.1 mg/ml BSA solution were prepared in phosphate buffer at room temperature. The permeate solutions of the corresponding membranes were evaluated by using UV-Vis spectrophotometer at wavelength 280 nm. The value obtained from the absorbance of feed and concentration of permeate can be used to calculate the rejection percentage using the equation 4 below:

$$R\ (\%) = \left(1 - \frac{C_p}{C_f}\right) \times 100 \quad (4)$$

where C_p and C_f were concentrations of protein in the permeate and in the feed, respectively.

Fouling analysis test

Fouling can be measured by the resistance that occurred during the process of filtration and cleaning can be determined by the elimination of resistance. Pure water permeation was operated in pressure constant of 3 bars. The volume of permeated water was collected within 30 minutes and assumed as a pure water flux (J_0). It can be

calculated using equation (3). After measuring the water flux (J_0), the cell was unloaded and refilled with BSA solution. After 3 hour filtration, the permeate flux of BSA solution (J_{BSA}) was recorded and the membranes were cleaned by shaking in pure water for 30 minutes. The pure water flux (J_1) after cleaning was measured in a similar way as J_0. By comparing the value of J_0 and J_1, flux recovery ratio (FRR) can be determined using equation 5 below:

$$FRR\ (\%) = \left(\frac{J_1}{J_0}\right) \times 100 \quad (5)$$

The reversible fouling ratio (RRF) and irreversible fouling ratio (RIRF) were obtained by using the following equations:

$$R_{RF}\ (\%) = \left(\frac{J_1 - J_{BSA}}{J_0}\right) \times 100 \quad (6)$$

$$R_{IRF}(\%) = \left(\frac{J_0 - J_1}{J_0}\right) \times 100 \quad (7)$$

where J_o is define as the pure water flux before the BSA solution filtration, J_1 is the pure water flux after cleaning and J_{BSA} is the BSA solution flux after 3 hour of protein filtration.

Results and Discussion

Water content and porosity

Water content and porosity are two membrane characteristics which are indirectly linked to the hydrophilicity properties of the membrane. These two important parameters are involved in the membrane permeation and separation process and are closely linked to membranes morphology. The results of water content and membrane porosity with different clay contents are shown in Figure 1.

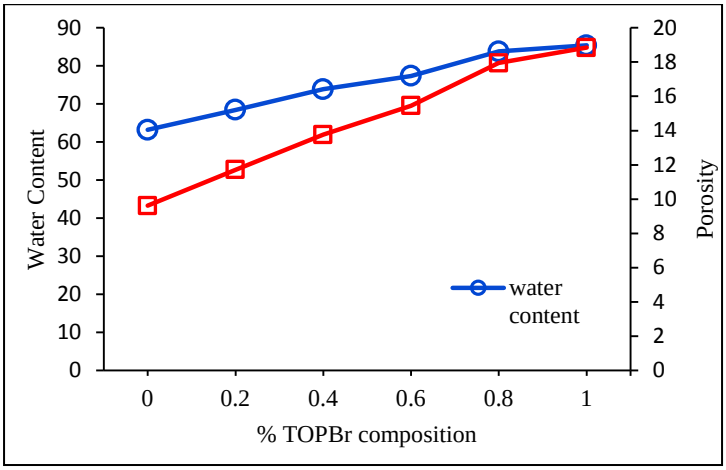


Figure 1. Water content and porosity of native PVDF membrane and PVDF/TOPBr nanocomposite membranes with different TOP-Br contents

It could be observed that the increase in water content is directly proportional to the increase in clay content. The water content of native membrane was 63% and increased to 68% after 0.2% of TOPBr clay were added. Meanwhile, for PVDF/TOPBr1.0, which contains 1wt.% of TOPBr clay, further addition of TOPBr clay in the PVDF/TOPBr nanocomposite membrane further increased the water content up to 85%. The increase in water content is due to the increment in void volume resulting in the formation of bigger pore size structure that consequently, increases the water uptake in the pores [7, 8].

A similar trend was observed on the porosity of PVDF/TOP-Br membranes. The increase in the clay content has increased the porosity of membranes where the hydrophilicity of the TOP-Br clay causes the increase in the exchanges of solvent and non-solvent that occur during the phase inversion process. This leads to the higher porosity in the membrane cross sectional area and the increase in the water uptake in the pores [7, 9]. Due to the low PVDF concentration of 17 wt.%, the compositions of the nanoclays were varied from 0.2-1.0 wt.% to overcome high dope viscosity and avoid the aggregation of nanoclays on the membrane surface. According to Ahmad et al. [10], the most suitable addition of nanoparticles into low polymer concentration in the range 15-17 wt.% is lower than 2.0 wt.% which consequently produces a product with low aggregation tendencies without blocking the membrane pores. This promises excellent final membrane hydrophilicity properties in terms of water content, porosity, permeability, as well as antifouling properties compared to the pure membranes.

Pure water permeation

In order to obtain the membrane permeability coefficient and membrane stability, all fabricated membranes were subjected to the pure water permeation process. The graph of pure water flux versus pressure is shown in Figure 2. All of the samples were measured at five different pressures ranging from 1 to 5 bar. It was observed that the pure water flux of all membranes increased linearly with the increase in the operating pressure. The native membrane recorded the lowest value of pure water flux which might be due to the hydrophobicity of the polymer itself. An increase of 0.2 % to 1.0% of TOPBr clay content has made the PVDF membranes to become more hydrophilic. PVDF/TOPBr1.0 showed the highest pure water flux compared to the other PVDF/TOPBr nanocomposite membranes. The increase of membrane porosity and hydrophilicity with the increase in the content of TOPBr clay can attract more water molecules inside the membrane matrix and promote the water molecules to pass through the membrane and enhance their permeability. This is due to the exchange process between the non-solvent in coagulation bath and solvent in the polymer dope that enhances the pore size of the membrane and increases the filtration area [9, 11, 12].

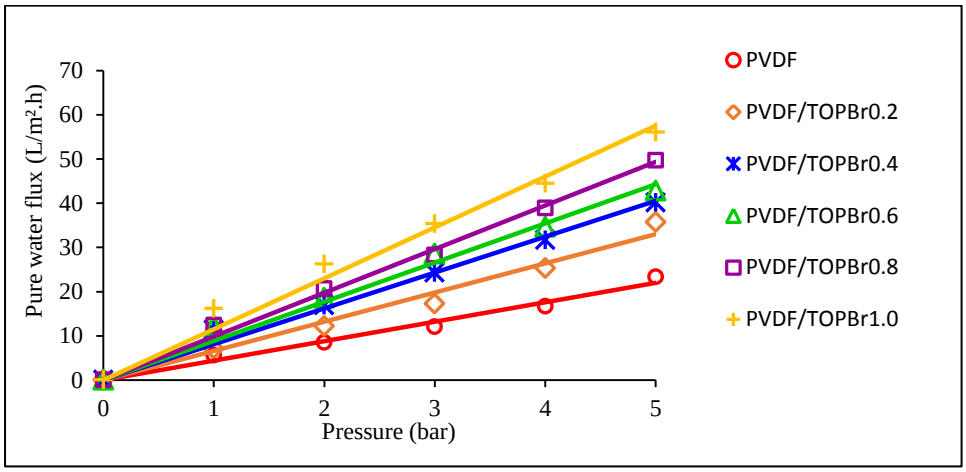


Figure 2. Pure water permeation (PWP) for native PVDF membrane and PVDF/TOPBr nanocomposite membranes with different TOP-Br contents

Table 1 shows the permeability and regression coefficient of native PVDF and PVDF/TOPBr nanocomposite membranes. Permeability coefficient also represents the porosity and as an indicator of its hydraulic resistance of UF membranes. The native PVDF membrane showed the lowest permeability coefficient while PVDF/TOPBr1.0 showed the highest permeability coefficient. This means that the lower permeability coefficient, the higher the membrane hydraulic resistance which represent membranes that are as less porous and dense. Table 1 clearly depicts that as the TOPBr clay content increases, the permeability coefficient also increase.

Table 1. Permeability coefficient and regression coefficient for native PVDF membrane and PVDF/TOPBr nanocomposite membrane with different clay composition

Membrane	Permeability Coefficient ($L/m^2.h.bar$)	Regression Coefficient (R^2)
Native	4.3996	0.9835
PVDF/TOPBr0.2	6.5985	0.9801
PVDF/TOPBr0.4	8.0997	0.9889
PVDF/TOPBr0.6	8.8646	0.9919
PVDF/TOPBr0.8	9.8673	0.9942
PVDF/TOPBr1.0	11.5060	0.9816

Protein separation performance

The prepared membranes were further evaluated by applying the separation of BSA solution. Figure 3 displays the graph of the permeate flux and solute rejection through PVDF/TOPBr nanocomposite membranes of different dosages of clay at the pressure level of 3 bar. It can be observed that the permeate flux has increased while the BSA rejection showed a fluctuated trend with the increase of the clay dosage. Only a slight increase of rejection was observed for the dosages of TOPBr clay ranging from 0.6% until 1.0%.The increase in the rejection values is due to the negative charges which are inherent in the silicate structure due to the homogeneity between the TOPBr clay in the polymer solution. Ali et al. [13] explained that the pore size on the membrane surface becomes smaller due to the close segmental gap between polymer chains for blend polymer membrane and consequently increased the protein rejection. A further increase of flux from 2.06 $L/m^2.h$ to 20.22 $L/m^2.h$ was observed when the dosage of TOPBr is at 1.0%. This may be due to the increase in porosity and the hydrophilicy of the membrane. In this light, membrane performance depends on the porosity, thickness, as well as the hydophilicy of the membrane. These properties improve the membrane resistance to fouling and allow better stability of the permeate flux [14].

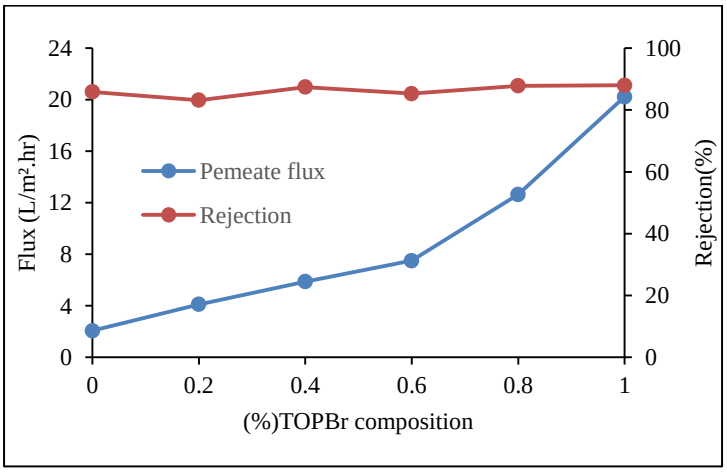


Figure 3. Permeate flux and solute rejection for native membrane and PVDF/TOPBr nanocomposite membrane with different dosage of clay

Fouling Analysis Test

The results of fouling analysis tests are shown in Figure 4. Theoretically, a better antifouling property in the membrane is related to the higher fouling ratio. Membrane fouling is associated with the adsorption of BSA protein on the surface of the membranes or inside the membrane pores which consist of reversible and irreversible fouling. Reversible fouling occurs from the building up of protein solutes on the membrane surface which can be easily

removed by simple hydraulic cleaning while irreversible fouling is caused by the strong deposition of protein molecules attached to the surface and the entrapment of protein molecules into the pores. These protein molecules remained and only a few would be removed even after the membranes were cleaned [15]. It can be observed that PVDF/TOPBr1.0 nanocomposite membrane shows the highest flux recovery ratio (FRR) value with 93% followed by PVDF/TOPBr0.8 with 88%. This result might be linked to the high porosity of both membranes which prevent the extensive accumulation of BSA on the membrane surface and membrane pores. A flux reduction will still appear due to the slightly irreversible fouling ratio (RIFR).

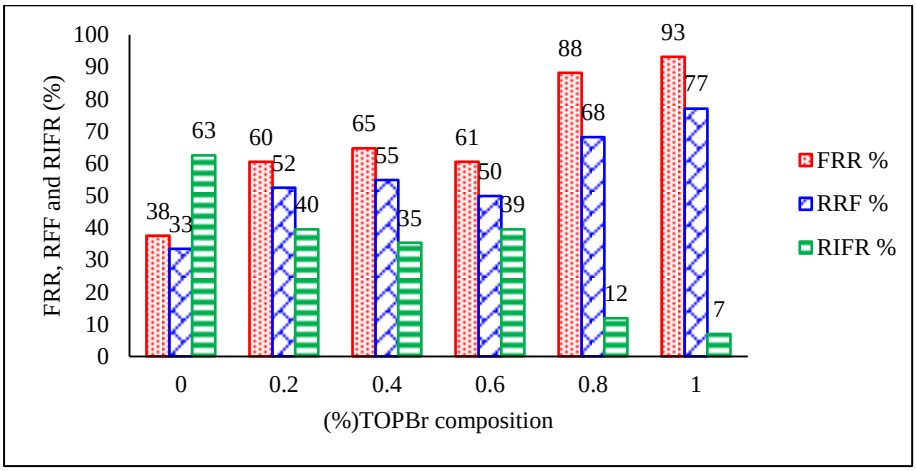


Figure 4. Flux recovery ratio (FRR), reversible fouling ratio (RRF) and irreversible fouling ratio (RIFR) of membranes

It was observed that native PVDF has the lowest value of flux recovery ratio with just 38% and a reduction of flux occurred when the irreversible fouling ratio is at highest value (63%). The fast blocking of membrane pores was caused by the low membrane porosity that occurred during the initial filtration stage since the cleaning membrane cleaning did not improve the membrane flux. The growth of cake layer on the membrane surface will form and reduce the flux permeation and consequently, decrease the value of FRR. This can be considered as the impact of membrane fouling which leads to an increase in hydraulic resistance and reduction of filtration efficiency [16-18].

Conclusion

This study has investigated the effect of the presence of TOPBr clay at different weight compositions on the properties of PVDF/TOPBr nanocomposite membrane focusing on its characteristics, pure water permeation, protein separation tests and fouling parameters. The results showed that varying the TOPBr clay composition in the PVDF polymer will produce membranes with different characteristics and performance. In this light, the presence of higher composition TOPBr clay in the nanocomposite membrane increased water content and porosity of PVDF/TOPBr nanocomposite membrane. The protein separation performance test revealed that after the addition of TOPBr, the flux increased from 2.06 $L/m^2.h$ to 20.22 $L/m^2.h$ with a 1.0 wt.% increase in protein separation as a result of the increase in the membrane hydrophilicity and porosity of the nanocomposite membrane. Moreover, PVDF/TOPBr1.0 nanocomposite showed the highest antifouling properties and flux recovery at 93% compared to other PVDF/TOPBr, as well as the native PVDF membrane. The addition of TOPBr clay showed a positive effect on membrane flux and hydrophilicity and has improved the membrane's surface resistance against protein fouling. Lastly, flux recovery and antifouling of all PVDF/TOPBr nanocomposite membranes have improved after TOPBr clay was blended into the membrane matrix.

Acknowledgement

The authors are grateful for research financial support by the Ministry of Higher Education, Malaysia under Fundamental Research Grant Scheme (FRGS) (Grant no.59351).

References

1. Kang, G. and Cao, Y. (2014). Application and modification of polyvinylidene flouride (PVDF) membranes – A review. *Journal of Membrane Science,* 463: 145-165.
2. Rajabi, H., Ghaemi, N., Madaeni, S. S., Daraei, P., Ali, M. and Falsafi, M. (2014). Nanoclay embedded mixed matrix PVDF nanocomposite membrane: preparation, characterization and biofouling resistance. *Applied Surface Science,* 313: 207-214.
3. Ismail, N. M., Ismail, A. F. and Mustaffa, A. (2014). Characterization of polyethersulfone/cloisite 15A mixed matrix membrane for CO_2/CH_4 separation. *Jurnal Teknologi,* 9: 83-87.
4. Wu, G., Gan, S., Cui, L. and Xu, Y. (2008). Preparation and characterization of PES/TiO_2 composite membranes. *Applied Surface Science,* 254(21): 7080-7086.
5. Zulhairun, A. K., Ismail, A. F., Matsuura, T., Abdullah, M. S. and Mustafa, A. (2014). Asymmetric mixed matrix membrane incorporating organically modified clay particle for gas separation. *Chemical Engineering Journal,* 241: 495-503.
6. Ali, A., Mohamed, N. S., Awang, M. and Mohd Sani, N. A. (2016). Preparation and characterization of alkylphosphonium modified montmorillonite. *International Journal of Applied Chemistry,* 12(1): 93-98.
7. Ali, A., Yunus, R. M., Awang, M., Johari, A. and Mat, R. (2014). Effect of cellulose acetate phthalate (CAP) on characterics and morphology of polysulfone/cellulose acetate phthalate (Psf/CAP) blend membranes. *Applied Mechanics and Materials,* 493: 640-644.
8. Ameduri, B. (2009). From vinylidene fluoride (PVDF) to the applications of VDF-containing polymers and copolymers: recent developments and future trends. *Chemical Reviews,* 109(12): 6632-6686.
9. Ali, A., Awang, M., Mat, R., Johari, A., Kamaruddin, M. J. and Sulaiman, W. R. W. (2014). Influence of hydrophilic polymer on pure water flux, permeability coefficient, and porosity of polysulfone blend membranes. *Advanced Materials Research,* 931–932: 168–172.
10. Ahmad, A. L., Abdulkarim, A. A., Ooi, B. S. and Ismail, S. (2013). Recent development in additives modifications of polyethersulfone membrane for flux enhancement. *Chemical Engineering Journal,* 223: 246–267.
11. Arthanareeswaran, A., Devi, T. K. S. and Raaajenthiren, M. (2008). Effect of silica particles on cellulose acetate blend ultrafiltration membranes: Part 1. *Separation and Purification Technology,* 64 (1): 38–47.
12. Arthanareeswaran, A. and Thanikaivelan, P. (2010). Fabrication of cellulose acetate-zirconia hybrid membranes for ultrafiltration applications: Performance, structure and fouling analysis. *Separation and Purification Technology,* 74(2): 230-235.
13. Ali, A., Yunus, M. R., Awang, M. and Yunus, C. M. A. (2015). Influence of hydrophilic polymer on proteins separation, molecular weight cut-off (MWCO) and average pore size of polysulfone blend Membrane. *Jurnal Teknologi,* 74(7): 53-56.
14. Anadão, P., Sato, L. F., Montes, R. R. and Santis, H. S. De. (2014). Polysulphone/montmorillonite nanocomposite membranes: Effect of clay addition and polysulphone molecular weight on the membrane properties. *Journal of Membrane Science*, 455: 187-199.
15. Monticelli, O., Bottino, A., Scandale, I., Capannelli, G. and Russo, S. (2006). Preparation and properties of polysulfone – clay composite membranes. *Journal of Applied Science*, 103(6): 3637-3644.
16. Daraei, P., Madaeni, S. S., Ghaemi, N., Khadivi, M. A., Astinchap, B. and Moradian, R. (2013). Enhancing antifouling capability of PES membrane via mixing with various type of polymer modified multi-walled carbon nanotube. *Journal of Membrane Science,* 444: 184-191.
17. Zularisam, A. W., Ismail, A. F., Salim, M. R., Sakinah, M. and Ozaki, H. (2007) The effects of natural organic matter (NOM) fractions on fouling characteristics and flux recovery of ultrafiltration membranes. *Desalination*: 212(1-3): 191-208.
18. Zulkali, M. M. D., Ahmad, A. L. and Derek, C. J. C. (2005). Membrane application in proteomic studies: preliminary studies on the effect of pH, ionic strength and pressure on protein fractionation. *Desalination*: 179(1-3): 381-390.

Malaysian Journal of Analytical Sciences, Vol 22 No 3 (2018): 522 - 531
DOI: https://doi.org/10.17576/mjas-2018-2203-21

MALAYSIAN JOURNAL OF ANALYTICAL SCIENCES
Published by The Malaysian Analytical Sciences Society
ISSN 1394 - 2506

ALGINATE AEROGELS DRIED BY SUPERCRITICAL CO_2 AS HERBAL DELIVERY CARRIER

(Pengeringan Gel Aero Alginat oleh CO_2 Supergenting Sebagai Pembawa Penghantaran Herba)

Ana Najwa Mustapa[1]*, Ángel Martín[1], María José Cocero[2]

[1]*Faculty of Chemical Engineering,*
Universiti Teknologi MARA, 40450 Shah Alam, Selangor, Malaysia
[2]*Department of Chemical Engineering and Environmental Technology,*
University of Valladolid, Calle Doctor Mergelina s/n, 47011 Valladolid, Spain

**Corresponding author: anajwa@salam.uitm.edu.my*

Received: 16 April 2017; Accepted: 7 March 2018

Abstract

Herbal medicinal plant have been recognized as alternative and natural drugs for therapeutic purposes due to their high content of phytocompounds with anti-bacterial, antioxidant and anti-inflammatory properties. Low solubility and poor absorption of medicinal compounds are seen as major challenges for herbal drugs. Impregnation of these substances into aerogels as a carrier is an innovative to improve poorly soluble compounds. In this work, alginate hydrogels were produced *via* sol-gel processing method and dried by supercritical CO_2 drying to obtain high porous structure of alginate aerogels. Alginate is a type of polysaccharides that is widely applied in biomedical, pharmaceuticals, cosmetics, and foods due to its nontoxic, stability and versatility properties. Plant extracts of *Clinacanthus nutans* Lindau (*C. nutans*) were impregnated into the alginate aerogels *via* liquid media followed by supercritical drying and *via* supercritical CO_2 assisted impregnation technique. Results exhibited that the initial concentration of polyphenols of the *C.nutans* extracts impregnated in the alginate aerogels is stable in the range of 0.796 to 0.745 mg/g in 6 month and drastically reduced after 9 month of storage duration. The herbal extract type *C.nutans-100* loaded *via* supercritical CO_2 impregnation has a comparable specific loading to the method of liquid media, range from 1.4 to 1.5 $\times 10^{-4}$ g/m^2 whereas the specific loading of *C.nutans-50* extract impregnated *via* liquid media showed higher compared with the loading by method of supercritical CO_2.

Keywords: supercritical, drying, alginate, aerogels, *Clinacanthus nutans* Lindau

Abstrak

Tumbuhan ubatan herba telah diiktiraf sebagai ubat-ubatan alternatif dan semula jadi untuk tujuan terapeutik kerana kandungan sebatian fito yang tinggi dengan ciri-ciri anti-bakteria, anti-pengoksidaan dan anti-radang, kelarutan dan penyerapan yang rendah sebatian perubatan dilihat sebagai cabaran besar untuk ubat-ubatan herba. Hal memberi bahan ke dalam gel aero sebagai pembawa adalah suatu tindakan yang inovatif untuk meningkatkan keterlarutan sebatian yang kurang larut dalam air. Dalam kajian ini, gel aero alginat telah dihasilkan melalui kaedah pemprosesan sol-gel dan dikeringkan melalui CO_2 supergenting untuk mendapatkan struktur berliang tinggi. Alginat adalah sejenis polisakarida yang sinonim dalam bioperubatan, farmaseutikal, kosmetik dan makanan disebabkan oleh sifatnya yang tidak toksik, kestabilan yang tinggi dan serba boleh dalam pelbagai bidang. Dalam kajian ini, ekstrak tumbuhan *Clinacanthus nutans* Lindau (*C. nutans*) yang diperolehi daripada teknik pengekstrakan gelombang mikro (MAE) telah diimpregnasi ke dalam gel aero alginat menggunakan kaedah penjerapan cecair diikuti dengan pengeringan menggunakan CO_2 supergenting dan juga impregnasi menggunakan CO_2 supergenting. Ekstrak herba *C. nutans-100* yang diimpregnasi menggunakan bendalir CO_2 supergenting menunjukkan kandungan spesifik yang hampir sama dengan kaedah media cecair iaitu dalam lingkungan 1.4 hingga 1.5 $\times 10^{-4}$ g/m^2 berat. Manakala, bagi ekstrak *C. nutans*-50, kandungan spesifiknya yang diimpregnasikan menggunakan kaedah media cecair adalah lebih tinggi berbanding dengan kaedah CO_2 supergenting iaitu , masing-masing. sebanyak 5.4 $\times 10^{-5}$ g/m^2 dan 4.9 $\times 10^{-6}$.

Kata kunci: supergenting, pengeringan, alginat, aerogel, *Clinacanthus nutans* Lindau

Introduction

Alginate aerogels is a class of biopolymer polysaccharides characterized by a combination of unique properties of aerogels and polysaccharides mainly high surface area, open porosity, good compatibility and biodegradable. Aerogels are porous structure materials derived either from synthetic inorganic precursor such as silica or from organic resources such as polysaccharides biopolymer *via* sol-gel method to obtain wet gels and dried by supercritical CO_2 drying. Nowadays, there is considerable growing attention on the use of biopolymer as aerogels for variety application. Numerous extensive works reported on the utilization of alginate aerogels contain desirable therapeutic properties as drug delivery application [1, 2]. Alginate is defined as natural polysaccharide biopolymer mainly recovered from brown algae. It contains of α-L-guluronic acid and β-D-mannuronic acid (M) residues, which linearly linked by 1,4-glycosidic linkage [3]. The natural biopolymer has been widely applied in several fields such as biomedical, pharmaceuticals, absorptions due to its biodegradable, biocompatible, non-toxic, low cost and stable.

Over many decades, herbs has been recognized as complementary and alternative supplement to modern drugs. In fact, World Health Organization (WHO) has estimated that about 80% of world population use herbal medicine in their primary healthcare. However, a systematic approach to measure their safety [4] and the poor compounds absorption remain as major challenges to extensively apply in the pharmaceutical industry [5]. There are many techniques have been introduced to improve the solubility and bioavailability of poorly soluble drugs or compounds such as production of drugs in nanoparticles [6, 7], incorporation in lipid based carrier such as micelles, liposomes, micro- and nanoemulsion [8, 9] and use of highly-soluble incipient such as β-cyclodextrin *via* formation of inclusion complex [10, 11]. Another promising way that has received considerable interest is by impregnating the compounds *via* supercritical CO_2 assisted technique in polymer or biopolymer materials [12, 13] and aerogels [14, 15].

The excellent characteristics of aerogels with large surface area and high pore volume make them attractive candidate for drugs delivery system to improve solubility of poorly soluble compounds [16]. In theory, high surface area and pore volume contribute to high compounds loading in the aerogels. The high loading capacity is very important as it provide large space for the compounds to be stored in pores of aerogels for drugs [14] and delivered to the target area with correct dosage or as absorbent for environmental issues [17]. However, these characteristics only can be obtained when the materials are dried by supercritical CO_2 ($SCCO_2$) to remove the liquid present in the solid pores. At supercritical condition, liquid-CO_2 present as a single phase and has zero surface tension avoid capillary forces on the mesopores of the aerogels. Furthermore, the unique properties of the CO_2 as the solvent such high diffusivity and low viscosity enables the penetration of the solvent into material pores and extract the liquid without deforming the structure of the material. On the other hand, in conventional method i.e. freeze and ambient pressure drying that are operated at sublimation pressure and by evaporation, respectively may lead to the formation of vapor-liquid phase that can create the capillary forces on the materials and cause high degree of shrinkage. As results, poor porosity and low specific surface area produced. Several studies have demonstrated that the $SCCO_2$ drying is more effective than freeze drying [18]. Density of aerogels dried by $SCCO_2$ showed higher density ranged from 0.08 to 0.24 g/cm^3 and porosity as high as 96.1% in comparison to those dried by ambient pressure drying technique [19].

This works focus on the production of alginate aerogels *via* sol-gel method and dried by $SCCO_2$ to be used as herbal carrier delivery. To the best our knowledge, to-date the use of biopolymer as a carrier for herbal delivery is very limited. The development of herbal or medicinal plant carrier is one of innovative technique to improve solubility and bioavailability of herbs in pharmaceutical industry. In this present study, medicinal plant extracts were impregnated into the alginate aerogels *via* liquid media and supercritical media i.e. $SCCO_2$ assisted method.

In the impregnation *via* $SCCO_2$ assisted, the substance solubilized in $SCCO_2$ at specified pressure and temperature in a vessel containing aerogels for a certain duration of time to allow equilibrium adsorption of the substance on the

aerogels pores. This technique is more attractive as the CO_2 is nontoxic, nonflammable and has been regarded as safe for food and pharmaceuticals application.

However, most of medicinal compounds have poor solubility in $SCCO_2$ that limits the application of the technique for wide range of compounds. On the other hand, *via* liquid media, the synthesized gels are contacted with the solution of substance for a certain time and followed by $SCCO_2$ drying to extract the organic solvent and leaves the substance precipitate in the pore of the aerogels. In principle, the substance must be soluble in an organic solvent and insoluble or poor solubility in $SCCO_2$. However, one of the drawbacks of the method is that the substance dissolved in an organic solvent may be co-extracted during the drying process due to effect co-solvent increase the solubility of the $SCCO_2$, hence reduced the extract content. In addition, the final product also may still contain some traces organic solvent which therefore need proper drying procedure to remove the solvent. Both methods offers their advantages but also have some drawbacks. Therefore, investigation on these methods for the impregnation of medicinal plant extracts is essential to determine the most promising method for future development.

Clinacanthus nutans Lindau (*C. nutans*) is a potential medicinal plant that has been traditionally applied to treat skin rashes, insect bites, gout, diabetes and to against herpes simplex virus [20]. The plant is widely grown in Southeast Asia countries such as Thailand, China, Indonesia and Malaysia. In this work, *Clinacanthus nutans* Lindau (*C. nutans*) extracts were impregnated into alginate aerogels by a conventional technique i.e. liquid media and more advance method that is $SCCO_2$ impregnation. The objectives of this study are to investigate the characteristics of alginate aerogels dried by supercritical CO_2 and to determine the specific loading of the alginate aerogels impregnated with the *C. nutans* extracts *via* liquid media and $SCCO_2$. The stability of the *C. nutans* extracts, particularly total phenols content (TPC) and physical color appearance was also evaluated. Eventually, *C. nutans* extracts dissolution was performed to determine the behavior of the extract releases from the alginate aerogels from both impregnation methods.

Materials and Methods

The *Clinacanthus nutans* Lindau (*C. nutans*) plant was supplied by a traditional practitioner from Kuala Lumpur, Malaysia. For the extraction of the *C. nutans* by microwave-assisted extraction (MAE), the plant was grinded and dried prior to the extraction process. The method of the extraction has been described in Mustapa et al. [21]. For the preparation of alginate aerogels, sodium alginate, calcium carbonate ($CaCO_3$), glucono-δ-lactone (GDL) and ethanol were purchased from Sigma Aldrich whereas double distilled water was purified by a Milli-Q water purifier system Millipore (Milford, MA, USA). All chemicals and materials used as received without any purification.

Preparation of alginate aerogels

Alginate aerogels were prepared *via* internal setting method. In this technique, the GDL was added to the solution of sodium alginate and $CaCO_3$ to lower the pH of the solution and initiate the gelation. Initially, the alginic sodium salt was dissolved in water (to obtain 1.5 to 2% w/w) followed by the addition of $CaCO_3$ and stirred until it completely dissolved. The GDL was then added to the solution with continuous stirring. The hydrogels were then transferred into molds and stored in refrigerator (4 ^{o}C) until they were completely gelled. Prior to the supercritical drying (SCD), the hydrogels undergone a successive solvent exchange (30, 50, 70, 90% v/v in 24 hours for each concentration, and finished by twice washing with pure ethanol) to remove water and its impurities. The alginate hydrogels are then called as alcogels after the solvent exchange procedures was completed.

Supercritical CO_2 drying and liquid media

To obtain blank alginate aerogels, the alcogels were subjected to the SCD which were conducted at 120 ± 5 bar and 40 ^{o}C for a duration of 4–5 hours. For the impregnation of *C. nutans* extracts *via* liquid media, the alcogels were soaked in solution of *C. nutans* in ethanol for maximum 3 days before the SCD, to allow maximum absorption of *C. nutans* extracts by the alginate alcogels. Previously, the *C. nutans* extracts were first extracted using microwave-assisted extraction [21]. Two types of *C. nutans* extracts were impregnated into the alginate aerogels i.e. *C. nutans-50* and *C. nutans-100*. Briefly, the *C. nutans* extracted using 50-50% ethanol/water content are called as *C. nutans-50* meanwhile the *C. nutans* extracted using absolute ethanol was named as *C. nutans-100*. After the duration was completed, the alcogels were dried by the supercritical CO_2 like has been done for the blank alginate aerogels.

Supercritical CO_2 assisted impregnation

For the supercritical impregnation, the *C.nutans* extracts were loaded into the alginate aerogels using supercritical CO_2 at 150 bar and 40 ^oC in 24 hours with small addition (10 wt.%) of absolute ethanol as a co-solvent to the $SCCO_2$. The setup of the supercritical impregnation are similar to the work presented in Mustapa et al. [22]. The amount of *C. nutans-50* and *C. nutans-100* placed in the supercritical impregnation was same to the amount of the extracts used in the liquid method. From our preliminary study, higher portion of ethanol, more than 10 wt.% caused a severe shrinkage on the alginate aerogels during the depressurization. The large amount of ethanol lead to the vapor-liquid interface caused capillary forces on the pores structure and deformed the alginate aerogels. Furthermore, the duration of 24 hours was chosen to allow equilibrium adsorption of the plant extracts on the alginate aerogels. A known amount of *C. nutans* extracts was placed in an autoclave while the aerogels were placed on top of the *C. nutans* extracts separated by a mesh metals to avoid direct contact between the extracts and the aerogels. After the 24 hours was completed, the system was depressurized slowly at rate of 2 bar/min to avoid the formation of liquid CO_2 in the autoclave. The presence of liquid CO_2 may shrink the aerogels due to the formation of two phases of liquid-gas in the pores of the aerogels.

Characterization of alginate aerogels

The textural properties of the alginate aerogels was characterized by nitrogen adsorption-desorption analysis using (Micrometer Analyzer, ASAP 2020 V4.02) at low temperature to determine the specific surface area, pore diameter and pore distribution. The alginate aerogels were degassed at 70 ^oC under vacuum prior to the analysis. The surface area was calculated based on the method of Brunauer, Emmett and Teller (BET) meanwhile the pore diameter and its distribution was calculated from the desorption isotherms. To determine thermal stability and residue decomposition of the alginate, differential scanning calorimetry (DSC) were carried out from 20 to 600 ^oC at a rate of 10 ^oC/min using DSC 822e Mettler Toledo SAE. All the analysis were repeated three times and the value was calculated as average and standard deviation. To examine the surface texture of the blank and impregnated alginate aerogels with *C.nutans* extracts were analyzed by using SEM JEOL JSM 820 and microanalysis (Bruker Quantax 2000). Before the analysis, the samples were splattered coated with gold layer and scanned at voltage of 2-4 kV.

Physical stability test

Stability analysis in terms of the physical appearance and color of the impregnated aerogels with the *C. nutans* extracts was also performed. This is to identify the quality of the product varies over a time period. To achieve this objective, alginate aerogels containing *C. nutans-50* and *C. nutans-100* were kept in glass *via*ls, sealed, covered properly with aluminum foil to protect the aerogels from light and stored in vacuum desiccator at room temperature. After 3 months, the appearance of the aerogels were observed and recorded. The measurement were made in each 3 months interval for total duration of 12 months. In each measurements of 3 month, the extract content were quantified by UV-Vis spectrophotometer to determine the changes of the extract concentration over time, particularly the total phenols content (TPC). Prior to the analysis, the alginate aerogels were ground and submerged in ethanol to dissolve the extracts. The aliquot were then filtered and subjected to the TPC analysis preparation as mentioned in Mustapa et al. [21] followed by UV-Vis measurement against 765nm wavelength. This physical stability test was repeated twice and calculated as average and standard deviation.

Dissolution test of *C. nutans* extracts

To determine the release kinetics behavior of the plant extracts impregnated in the alginate aerogels, dissolution tests were conducted in USP-certified Copley NE4-COPD dissolution tester equipment with saline phosphate buffer at pH 6.8. A known weight of the impregnated aerogels were placed in a basket and immersed in vessel containing the buffer solution. The system was maintained at a temperature of 37 ± 0.5 ^oC and kept stirred at 100 rpm. At each interval time, 2 ml of the aliquots was collected and replaced with 2 ml of fresh buffer solution that was maintained at 37 ^oC. The samples were analyzed by UV-Vis spectrophotometer at the wavelength with maximum absorption of the plant extract. The cumulative (%) amount of *C. nutans* released was calculated and plotted against time of the measurement.

Results and Discussion

The nitrogen-desorption analysis on the blank alginate aerogels showed that the specific surface area, pore volume and diameter of the alginate were found in range from 86.94 to 125.9 m^2/g, 0.42 to 0.8 cm3/g and 19.2 to 25.5 nm,

respectively. The textural surface properties of alginate was increased with the increases of alginate concentration ratio from 1 to 2% w/w. Higher alginate content increase the crosslinking and the specific surface area of the aerogels. This is because increasing the alginate concentration would provide more functional groups of alginate molecules to be interacted with calcium cross linker agent [23]. Veronovski et al. [24] also reported that increasing the alginate concentration result to more crosslinking of the alginate chains with the physical structure of the aerogels are more compact and stiff. High surface area of the aerogels is very important for the impregnation purposes. As a rule of thumb, higher specific surface area contribute to higher loading capacity. Nevertheless, other factors also may influence the aerogels capacity such as solubility of substance in solvent carrier, affinity interaction of aerogels material-solute and material-solvent.

For the thermal analysis, a DSC diagram of the alginate aerogels is presented in Figure 1. It can be observed that a broad endothermic peak occurred at 70 ^{o}C was may attributed to the loss of water from the alginate aerogels. As the temperature increased, an exothermic appeared at 240 ^{o}C corresponds to the decomposition of the biopolymer. This observation was apparently different from the result reported by Veronovski et al. [24] where they found the decomposition of the alginate occurred at from 330 to 450 ^{o}C.

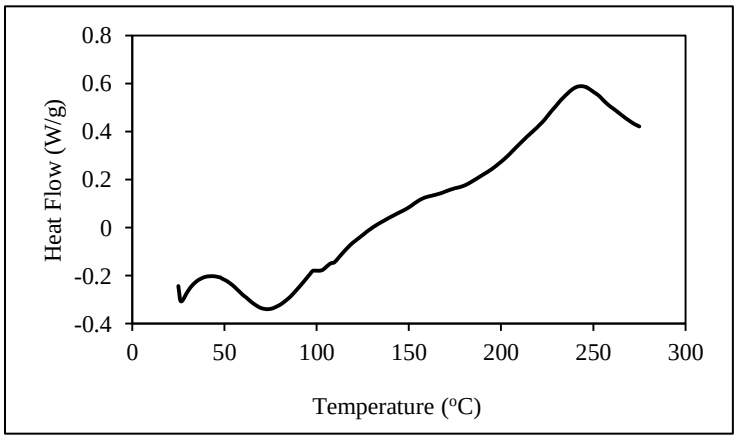


Figure 1. Thermal stability and residue decomposition of alginate aerogel by DSC measurement

Surface textures of blank and impregnated alginate aerogels with *C.nutans* extracts analyzed by SEM are presented in Figure 2. The images show that the textural of the blank alginate aerogels (Figure 2a) looks uniformly cross-linked and has smaller open pores in comparison to the texture of the alginate aerogels impregnated with the *C. nutans-100* extract (Figure 2b). The structure of the alginate impregnated with *C. nutans* extract appear to be slightly swollen and bigger compared with the blank alginate aerogels. This could be due to the interaction between ethanol and alginate material during the impregnation *via* liquid media and effect of CO_2 swell the material during the supercritical drying. In addition, longer impregnation time for 24 hours for this case also may lead to higher extent of swelling of the material matrix [25]. Eventually, higher swelling degree and high CO_2 sorption facilitated the diffusion of compounds solution into the material matrix [26]. Future thorough investigation on the interaction between multicomponent of *C. nutans* extracts and alginate materials in the presence of other solvent such as alcohol or CO_2 could interesting in order to understand the behavior of the impregnation using $SCCO_2$.

The physical stability test of the alginate aerogels impregnated with the *C. nutans-100* extracts are presented in Figure 3. It shows that at the first 3 month of the storage, the decreasing of the TPC content was insignificant from 0.796 to 0.745 mg/g. Meanwhile after 6 month, the TPC was started to decreased and found to be drastically reduced at month-12 to 0.332 mg/g of TPC. The decreasing of the TPC was continuously reduce until month-14 with 0.224 mg/g remained in the alginate aerogels. This result indicated that the reduction of the TPC still occur despite the samples were carefully covered and stored at room condition, due to the oxidation of some phenolic acid in the extract impregnated in the aerogels. However, the reduction of the TPC was slow could be due to minimal oxygen presence in the alginate pores [27]. As the duration continued until 12 month, the decreasing of the TPC

became remarkable from 0.612 to 0.332 mg/g as more empty pores are occupied with oxygen thus encourage the oxidation of the polyphenols. Few study on the stability polyphenols content impregnated into a material also showed that the TPC was lower at the end of the storage that due to the oxidation process [27].

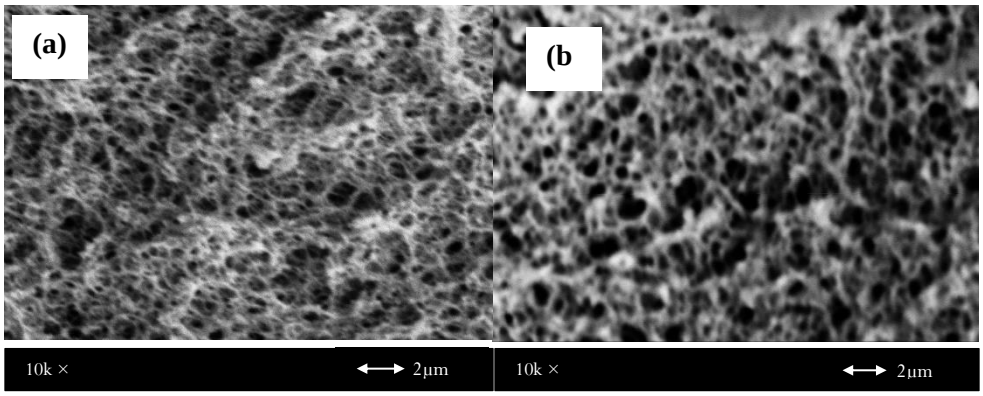


Figure 2. Textural surface of alginate aerogels: a) blank alginate (2 wt.%) and b) alginate aerogels (2 wt.%) impregnated with *C. nutans-100* extract by liquid media impregnation method

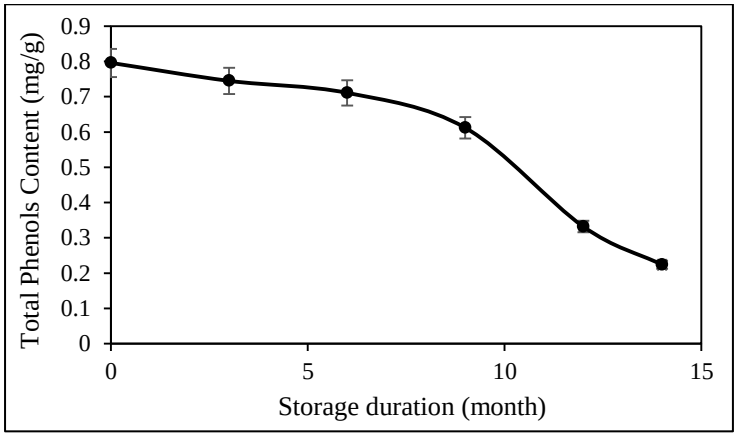


Figure 3. Variation of polyphenols content during storage

On the other hand, qualitative analysis on the color variations of the impregnated aerogels with *C. nutans* extracts are presented in Figure 4. As exhibited in Figure 4, the color of the alginate aerogels had faded away after 13 month in the storage. It was observed that the green color of the *C. nutans-100* extracts changed from green to yellow pale. This indicate that the chlorophyll was degraded with extension of storage duration. Theoretically, the degradation of chlorophyll can be influenced by environmental factors such as enzyme degradation and oxidation bleaching that caused by reactive oxygen [28]. Additional test was also observed for silica aerogels impregnated with *C. nutans-100*. The degree of decolorized of the *C. nutans* extracts was higher than the extracts impregnated into alginate aerogels. High opacity of the alginate aerogels may affects this observation.

The specific loading of *C. nutans* extracts into alginate aerogels were presented in Table 1. It is showed that the loading of the *C. nutans-50* extracts *via* liquid media impregnation was higher with 5.4×10^{-5} g/m^2 in comparison to the $SCCO_2$ technique that yielding 4.9×10^{-6} g/m^2. Poor solubility of phytocompounds in the *C. nutans-50* extracts in $SCCO_2$ that mainly comprises of large molecules compounds such as tannin, saponin and terpenoid was anticipated influenced the loading. Results also showed that the addition of 10 wt.% absolute ethanol in the $SCCO_2$-

impregnation did not enhanced the specific loading of *C. nutans-50* and *C. nutans*-100, relatively to the liquid media method. The specific loading of *C. nutans-100 via* liquid media was found to have comparable values to the loading obtained by $SCCO_2$ range from 1.4 to 1.5 × 10^{-4} g/m^2. This situation probably due to competitive of affinity of CO_2 sorption [29] and hydroxyl group on the alginate material may the loading of the extract. Thus, in this case, the selection of impregnation method for the *C.nutans-100* extract is anticipated not crucial, considering the extract loading in the alginate aerogels.

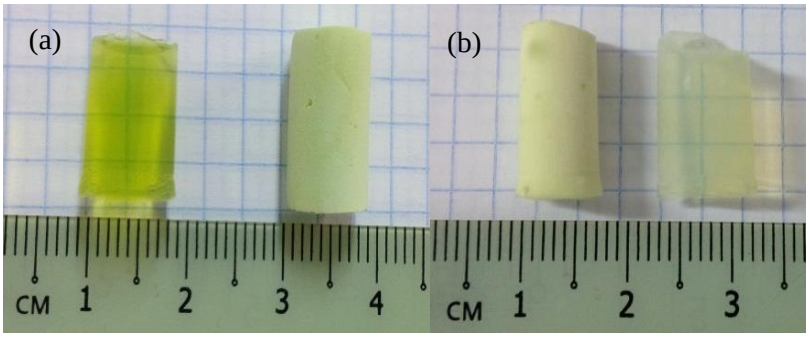


Figure 4. Sample of aerogels impregnated with *C.nutans-100* images in stability test a) month-1 and b) month-12

Table 1. Specific loading of *C.nutans* extracts by liquid media and supercritical CO_2 impregnation into alginate aerogels

Impregnation Technique	**Extracts**	**Specific Loading (g/m^2)**
Liquid media	*C.nutans-50*	$5.4 \times 10^{-5} \pm 1 \times 10^{-5}$
	C.nutans-100	$1.4 \times 10^{-4} \pm 2 \times 10^{-5}$
Supercritical CO_2 assisted	*C.nutans-50*	$4.9 \times 10^{-6} \pm 4 \times 10^{-5}$
	C.nutans-100	$1.5 \times 10^{-4} \pm 1 \times 10^{-5}$

***C.nutans* release kinetics**

C. nutans extracts release profile from the alginate aerogels are presented in Figure 5. The dissolution of the *C. nutans-50* extract impregnated *via* $SCCO_2$ is faster than the release from the alginate impregnated by liquid media; 70% of the *C. nutans-50* in 2 hours. Meanwhile for the *C. nutans-50* extract impregnated *via* liquid media, lower kinetic was observed i.e. 60% in 2 hours and tend to increase after 4 hours of the dissolution test. On the other hand, the release of the *C. nutans-50* that impregnated *via* $SCCO_2$ began to reduce after 3 hours and stabilize towards the end, with approximately 75% of total extract was released in 6 hours. The *C. nutans-100* extract impregnated by liquid media showed apparently slower kinetics than the release of *C. nutans-50*. It is anticipated that the slow release of *C. nutans-100* extract could be due to interaction between carboxyl groups on the alginate aerogels and hydroxyl groups that may present in some of multi-phytocompounds in the extract. This probably explain the extremely poor dissolution of *C. nutans-100* extract impregnated by $SCCO_2$, which only 3.5% (data not presented here) of the extract released after 8 hours of the duration. In contrast, high solubility of the phytocompounds present in the *C. nutans-50* extract in water is anticipated enhance good dissolution of the extract into the fluid test from the alginate aerogels.

These results indicated that, for the case of *C. nutans-50* extract, the compounds impregnated by $SCCO_2$ exhibited faster release from alginate biopolymer in comparison to the extracts impregnated by conventional technique i.e. liquid media method. Previous studies [30, 31] also have demonstrated that compounds loaded by $SCCO_2$ showed faster compounds release than the conventional impregnation.

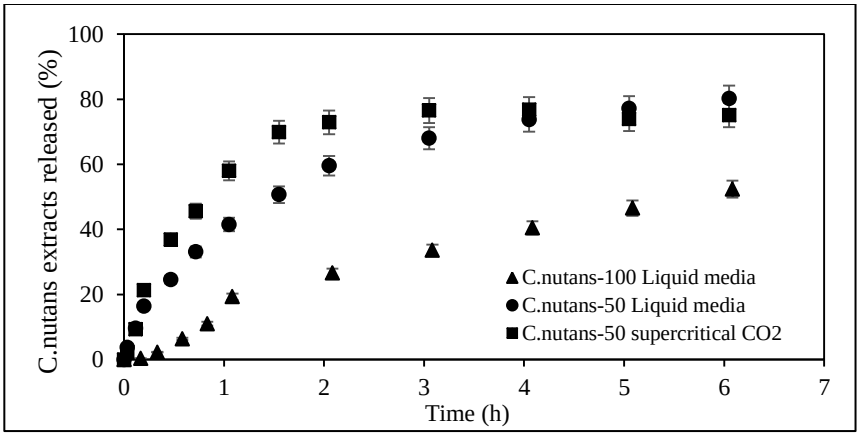


Figure 5. Release kinetics of *C.nutans* extracts from alginate aerogels (average ± standard deviation)

Conclusion

Impregnation of medicinal plant extracts, *C.nutans* results a variation of specific loading pattern, dependent on the type of *C. nutans* extracts and technique of impregnation. The selection of the most promising technique is based on the solubility of compounds and the target of the impregnation i.e. loading and release kinetics behavior. High loading of *C. nutans-50* extract can be achieved *via* liquid media impregnation but exhibits slower release. Meanwhile the *C. nutans-100* extract, liquid media and $SCCO_2$ shows a comparable loading values but the impregnation *via* liquid media exhibited faster kinetic release. The release kinetics study revealed that the impregnation of the plant extracts in the alginate might have different behavior depending on the solubility of the compounds, interaction between the compounds and alginate matrix as well as the method of impregnations. The physical stability test on the *C.nutans* extracts impregnated in the alginate aerogels deteriorate after 13 months loaded in the carrier material. This indicates that the shelf-life of the extracts in the aerogels can be maintained until 6-9 months considering the quality of the polyphenols content. A proper coating on alginate aerogels to protect the impregnated compounds or design micro- or nanoparticles carrier shape could be stimulating and enhanced for future development of new herbal carrier.

Acknowledgement

Ana Najwa Mustapa acknowledges a sponsorship of the program from Ministry of Education (MOE), Malaysia, supported together with Universiti Teknologi MARA. Ángel Martín thanks the Spanish Ministry of Economy and Competitiveness for a *Ramón y Cajal* research fellowship.

References

1. Mehling, T., Smirnova, I., Guenther, U. and Neubert, R. H. H. (2009). Polysaccharide-based aerogels as drug carriers. *Journal of Non-Crystal Solids*, 355(50-51): 1-7.
2. Veronovski, A., Knez, Ž. and Novak, Z. (2013). Preparation of multi-membrane alginate aerogels used for drug delivery. *Journal of Supercritical Fluids*, 79(1): 209-215.
3. Paques, J. P., Sagis, L. M. C., Van Rijn, C. J. M. and van der Linden, E. (2014). Nanospheres of alginate prepared through w/o emulsification and internal gelation with nanoparticles of $CaCO_3$. *Food Hydrocolloid*, 40(1): 182-188.
4. Wachtel-Galor, S. and Benzie, I. (2011). Herbal medicine: An introduction to its history, usage, regulation, current trends, and research needs. CRC Press/Taylor and Francis, Boca Raton.
5. Devi, V. K., Jain, N., and Valli, K. S. (2010). Importance of novel drug delivery systems in herbal medicines. *Pharmacognosy Reviews*, 4(7): 27-31.
6. Kalishwaralal, K., BarathManiKanth, S., Pandian, S. R. K., Deepak, V. and Gurunathan, S. (2010). Silver nanoparticles impede the biofilm formation by *Pseudomonas aeruginosa* and *Staphylococcus epidermidis*. *Colloids and Surfaces B: Biointerfaces*, 79(2): 340-344.

7. Shekunov, B. Y., Chattopadhyay, P., Seitzinger, J. and Huff, R. (2006). Nanoparticles of poorly water-soluble drugs prepared by supercritical fluid extraction of emulsions. *Pharmaceutical Research*, 23(1): 196-204.
8. de Paz, E., Martín, Á., Bartolomé, A., Largo, M. and Cocero, M. J. (2014). Development of water-soluble β-carotene formulations by high-temperature, high-pressure emulsification and antisolvent precipitation. *Food Hydrocolloid*, 37(1): 14-24.
9. Gonçalves, V. S. S., Rodríguez-Rojo, S., De Paz, E., Mato, C., Martín, Á. and Cocero, M. J. (2015). Production of water soluble quercetin formulations by pressurized ethyl acetate-in-water emulsion technique using natural origin surfactants. *Food Hydrocolloid*, 51(1): 295-304.
10. Abarca, R. L., Rodríguez, F. J., Guarda, A., Galotto, M. J. and Bruna, J. E. (2016). Characterization of beta-cyclodextrin inclusion complexes containing an essential oil component. *Food Chemistry*, 196(1): 968-975.
11. Chowdary, K. P. R. and Nalluri, B. N. (2000). Nimesulide and β-Cyclodextrin inclusion complexes: Physicochemical characterization and dissolution rate studies. *Drug Development and Industrial Pharmacy*, 26(11): 1217-1220.
12. Gong, K., Rehman, I. U. and Darr, J. A. (2007). synthesis of poly(sebacic anhydride)-indomethacin controlled release composites *via* supercritical carbon dioxide assisted impregnation. *International Journal of Pharmaceutics*, 338(1-2): 191-197.
13. Duarte, A. R. C., Casimiro, T., Aguiar-Ricardo, A., Simplício, A. L. and Duarte, C. M. M. (2006). Supercritical fluid polymerisation and impregnation of molecularly imprinted polymers for drug delivery. *Journal of Supercritical Fluids*, 39(1): 102-106.
14. Veres, P., López-Periago, A. M., Lázár, I., Saurina, J. and Domingo, C. (2015). Hybrid aerogel preparations as drug delivery matrices for low water-solubility drugs. *International Journal of Pharmaceutics*, 496(2): 360-370.
15. Pantić, M., Knez, Ž. and Novak, Z. (2016). Supercritical impregnation as a feasible technique for entrapment of fat-soluble vitamins into alginate aerogels. *Journal of Non-Crystal Solids*, 432: 516-526.
16. Arruebo, M. (2012). drug delivery from structured porous inorganic materials. *Wiley Interdisciplinary Reviews: Nanomedicine and Nanobiotechnology*, 40(1): 16-30.
17. Cheng, Y., Lu, L., Zhang, W., Shi, J. and Cao, Y. (2012). Reinforced low density alginate-based aerogels: preparation, hydrophobic modification and characterization. *Carbohydrate Polymers*, 88(3): 1093-1099.
18. Ciftci, D., Ubeyitogullari, A., Huerta, R. R., Ciftci, O. N., Flores, R. A. and Saldaña, M. D. A. (2017). Lupin hull cellulose nanofiber aerogel preparation by supercritical CO_2 and freeze drying. *Journal of Supercritical Fluids*, 127(1): 137-145.
19. Shahzamani, M., Bagheri, R., Masoomi, M., Haghgoo, M. and Dourani, A. (2017). Effect of drying method on the structure and porous texture of silica-polybutadiene hybrid gels: supercritical vs. ambient pressure drying. *Journal of Non-Crystalline Solids*, 460(1): 119-124.
20. Sakdarat, S., Shuyprom, A., Pientong, C., Ekalaksananan, T. and Thongchai, S. (2009). Bioactive constituents from the leaves of *Clinacanthus nutans* Lindau. *Bioorganic & Medicinal Chemistry*, 17(5): 1857-1860.
21. Mustapa, A. N., Martin, Á., Mato, R. B. and Cocero, M. J. (2015). Extraction of phytocompounds from the medicinal plant *Clinacanthus nutans* Lindau by microwave-assisted extraction and supercritical carbon dioxide extraction. *Industrial Crops and Products*, 74(1): 83-94.
22. Mustapa, A. N., Martin, A., Sanz-Moral, L. M., Rueda, M., & Cocero, M. J. (2016). Impregnation of medicinal plant phytochemical compounds into silica and alginate aerogels. *The Journal of Supercritical Fluids*, *116*, 251-263.
23. Daemi, H. and Barikani, M. (2012). Synthesis and characterization of calcium alginate nanoparticles, sodium homopolymannuronate salt and its calcium nanoparticles. *Scientia Iranica*, 19(6): 2023-2028.
24. Veronovski, A., Novak, Z. and Knez, Z. (2012). Synthesis and use of organic biodegradable aerogels as drug carriers. *Journal of Biomaterials Science Polymer Edition*, 23(7): 873-886.
25. Marizza, P., Pontoni, L., Rindzevicius, T., Alopaeus, J. F., Su, K., Zeitler, J. A., Keller, S. S., Kikic, I., Moneghini, M., De Zordi, N., Solinas, D., Cortesi, A. and Boisen, A. supercritical impregnation of polymer matrices spatially confined in microcontainers for oral drug delivery: Effect of temperature, pressure and time. *Journal of Supercritical Fluids*, 107(1): 145-152.
26. Champeau, M., Thomassin, J. M., Tassaing, T. and Jérôme, C. Drug loading of polymer implants by supercritical CO_2 assisted impregnation: A review. *Journal of Controlled Release*, 209(1): 248-259.

27. Tappi, S., Tylewicz, U., Romani, S., Dalla Rosa, M., Rizzi, F. and Rocculi, P. (2017). Study on the quality and stability of minimally processed apples impregnated with green tea polyphenols during storage. *Innovative Food Science and Emerging Technologies,* 39(1): 148-155.
28. Sun, Y. and Li, W. (2017). Effects the mechanism of micro-vacuum storage on broccoli chlorophyll degradation and builds prediction model of chlorophyll content based on the color parameter changes. *Scientia Horticulturae,* 224(1): 206-214.
29. Masmoudi, Y., Ben Azzouk, L., Forzano, O., Andre, J. M. and Badens, E. (2011). Supercritical impregnation of intraocular lenses. *Journal of Supercritical Fluids,* 60(1): 98-105.
30. Manna, L., Banchero, M., Sola, D., Ferri, A., Ronchetti, S. and Sicardi, S. (2007). Impregnation of PVP microparticles with ketoprofen in the presence of supercritical CO_2. *Journal of Supercritical Fluids,* 42(3): 378-384.
31. Marizza, P., Keller, S. S., Müllertz, A. and Boisen, A. (2014). Polymer-filled microcontainers for oral delivery loaded using supercritical impregnation. *Journal of Controlled Release,* 173(1): 1-9.

Malaysian Journal of Analytical Sciences, Vol 22 No 3 (2018): 532 - 541
DOI: https://doi.org/10.17576/mjas-2018-2203-22

MALAYSIAN JOURNAL OF ANALYTICAL SCIENCES
Published by The Malaysian Analytical Sciences Society
ISSN 1394 - 2506

MONOETHANOLAMINE WASTEWATER TREATMENT VIA ADSORPTION USING WOOD SAWDUST BASED ACTIVATED CARBON

(Rawatan Air Sisa Monoetanolamina Melalui Kaedah Penjerapan Menggunakan Karbon Habuk Kayu Yang Diaktifkan)

Azry Borhan[1]*, Tong Yeong Yit[1], Suzana Yusup[1], Normawati Mohd Yunus[2]

[1]*Department of Chemical Engineering*
[2]*Department of Fundamental and Applied Sciences*
Universiti Teknologi Petronas, 32610 Bandar Seri Iskandar, Perak, Malaysia

**Corresponding author: azrybo@utp.edu.my*

Received: 16 April 2017; Accepted: 7 March 2018

Abstract

In this work, sawdust, which is low cost and produced abundantly from wood industry, was tested as a precursor for the production of porous carbons in a chemical scheme using H_3PO_4. From synthesis parameters studied, F21 activated carbon with the largest surface area, total pore volume and diameter was obtained when sawdust is impregnated with ratio of 1:1 and treated with activation temperature of 500 °C for a period of 60 minutes. Through nitrogen adsorption-desorption isotherm analysis, existence of mesopores was proven when a combination of Type-I and Type-II isotherms were exhibited by the activated carbon produced. The results from adsorption test showed that under the effect of initial concentration, the optimum sample is capable of removing 96.8% of MEA at low concentration of 100 ppm, while under the effect of stirring rate, 99.7% of MEA is removed at highest stirring rate at 400 rpm. Finally under the effect of contact time, 99.7% of MEA removal is achieved at time of 45 minutes. The obtained results show that agriculture waste product from sawdust can be effectively used as an adsorption material in MEA wastewater treatment.

Keywords: wood sawdust, monoethanolamine, chemical activation, activated carbon, adsorption

Abstrak

Di dalam kajian ini, habuk papan, yang berkos rendah dan dihasilkan dengan banyak dari industri kayu, telah diuji sebagai pemula untuk pengeluaran karbon berliang dalam skim kimia menggunakan H_3PO_4. Dari parameter sintesis yang dikaji, F21 karbon yang diaktifkan menghasilkan luas permukaan, jumlah isi padu dan diameter berliang terbesar diperolehi apabila habuk papan diimpregnasikan dengan nisbah 1:1 dan dirawat dengan suhu pengaktifan 500 °C untuk tempoh 60 minit. Melalui analisis isoterma penjerapan nitrogen, kewujudan liang meso terbukti apabila gabungan isotem Jenis-I dan Jenis-II dipamerkan oleh karbon yang diaktifkan. Hasil daripada ujian penjerapan menunjukkan bahawa di bawah kesan kepekatan awal, sampel optimum mampu mengeluarkan 96.8% daripada monoetanolamina (MEA) pada kepekatan rendah 100 ppm, manakala di bawah kesan kadar kacau, 99.7% daripada MEA dikeluarkan pada kadar pengadukan tertinggi pada 400 rpm. Akhirnya di bawah kesan waktu hubungan, 99.7% penyingkiran MEA dicapai pada masa 45 minit. Hasil yang diperoleh menunjukkan bahawa produk sisa pertanian dari habuk papan boleh digunakan dengan berkesan sebagai bahan penjerap dalam rawatan air buangan MEA.

Kata kunci: habuk papan kayu, monoetanolamin, pengaktifan kimia, karbon diaktifkan, penjerapan

Introduction

In petrochemical industry, especially in natural gas processing plant, raw natural gas contains significant amount of carbon dioxide (CO_2). Prior to further processing activities, the gas stream needs to undergo treatment to remove CO_2 to meet specifications for successful liquefaction LNG process. The most important commercially applied technology for CO_2 removal is the absorption process by using amine-based solvent. One of the important amines is monoethanolamine (MEA) which is used in most acid gas recovery system as it provides sufficient alkalinity to absorb CO_2 [1]. However, during absorption-desorption, maintenance and transportation activities, amine may degrade over time and this corrosive by-products may be carried over and need to be removed as wastewater. Amines are known as toxic material and can have significant affect to human health and the aquatic ecosystem [2]. MEA is an organic matter and can upset the water stream by increasing the Chemical Oxygen Demand (COD). A high COD reading indicates oxygen deficiency in water. Decomposition of organic matter will consume the amount of water-dissolved oxygen, which in turns leads to lack of oxygen and ultimately destroy the aquatic ecosystem. It is common, in the range of 60 – 80 tons of MEA wastewater is generated per month [3]. In view of the fact that MEA wastewater is produced abundantly from petrochemical plants as well as other processing plants such as coal fired power station and ammonia synthesis plant, it is essential to identify the alternative route methods for treating MEA wastewater which is inexpensive, simple, economically viable and environmental friendly. One of the effective ways is by adsorption method using activated carbon (AC).

AC in its broadest definition includes a wide range of carbonaceous materials prepared to exhibit a high degree of porosity and an extended interparticulate surface area. The first-class features of high porosity and large surface area impart AC with excellent adsorptive characteristics, which make carbon very useful in many industrial processes such as filtration, separation, decolourization and purification [3, 4]. The versatility of this product is notably observed in the fact that it can be produced from a variety of raw materials. Among them, wood is by far the most common source of precursor, followed closely by coal, coconut shell and other biomass [5, 6]. In Malaysia, the growth of wood-based industry has been phenomenal over the past decades. Malaysia with its well-known tropical rainforest climate is considered as the most ideal climatic condition for cultivating timber, and this potential has been fully utilized and exploited. According to Malaysian Investment Development Authority (MIDA) [7], a total of 1025 sawmills operating in Malaysia has made it into becoming one of the major timber supplier in Southeast Asia region, with exports of saw logs and sawn timber in 2015 amounted to RM6.1 billion. However, the intense wood processing activities has led to generation of substantial amount of byproducts in the form of sawdust, offcut and wood barks [8]. Managing considerable quantities of residues in the form of sawdust and wood chips has become a challenge for the industry and the problem is indeed of great concern. To effectively manage the issue, waste minimization programs were carried out with the intent to reclaim this useful material. In line with the zero waste concept of viewing waste as a potential resource with value to be realized, sawdust has been shown to have potential as precursor material in the preparation of AC and is able to be transformed into value-added products rather than as a waste management problem to be dealt with.

High quality AC are manufactured through activation and carbonization of carbonaceous materials [9]. These carbon-based materials need to be activated and carbonized through a series of optimum processes to draw out and make full use of its enormous potential. The resultant products often have high adsorptive capacities, which are associated with their internal porosity and are related to properties such as surface area, pore volume and pore size distribution [10]. Basically, there are two different processes for preparing AC: physical and chemical activation. Physical activation involves the pyrolysis step followed by a stage of controlled oxidation to activate the carbon in the presence of steam or CO_2 [11]. Chemical activation, on the other hand, is a single step method consisting carbonization at a relatively low temperature in the presence of chemical activating agent. [5, 12]. Present study chose to employ chemical activation method due to numerous advantages over physical activation. In the process of chemical activation, the yield is relatively high, and activation temperature is low making the process more economical compared to physical activation [9, 13]. It is more common to use chemical activation when the material is of wood origin [14]. Zhang et al. [15] claim that AC in chemical activation usually has a relatively higher specific surface area and more mesopores than that in physical activation. The main chemical activating agents used include zinc chloride ($ZnCl_2$), phosphoric acid (H_3PO_4) and potassium hydroxide (KOH) solution. These chemical reagents generally act as the dehydrating agents and may promote the formation of cross-links. H_3PO_4 and $ZnCl_2$ are more suitable for activating a lignocellulosic material; whereas KOH is normally used for activation of coal

precursor or chars [12]. When compared with $ZnCl_2$, the use of H_3PO_4 is more favoured due to problems of environmental contamination with zinc compounds [7, 10].

In this study, chemical activation method by H_3PO_4 was selected due to its numerous advantages over physical activation method and favourable conditions compared to other chemical activating agents. The research study was set in the direction towards evaluating the potential of sawdust and to compare its effectiveness in adsorbing MEA from aqueous solution. Since chemical activation was adopted in this study, impregnation ratio, temperature and activation time would be the main factors affecting the extent of reaction. Therefore, these parameters were also investigated to assess the effects of operation conditions on pore development of activated carbon prepared from sawdust.

Materials and Methods

Sample preparation

Fresh sawdust produced from the process of converting the raw logs into sawn timber was collected from a local sawmill for experimental purpose. The type of sawdust acquired was originated from Nyatoh wood or scientifically known as *Sapotaceae spp.*, classified as species of light hardwood. The sawdust collected was sieved according to size of 250 µm. The sieved sawdust was then washed with distilled water several times to remove impurities and ashes that were collected together. After washing, the sawdust was dried in an oven overnight at 80 °C constant heating rate to preserve the samples [5]. The dried and cleaned sawdust was placed in a desiccator for further process. All chemicals were purchased from R & M Chemicals and were industrial reagent grade.

Carbonization and activation

The sawdust prepared was impregnated by mixing it with desired ratio (1:1, 1:2, and 1:3) of H_3PO_4 based on the dry weight of the sample. The impregnation ratio is given by:

$$\text{Impregnation ratio, IR} = \frac{W_{H3PO4}}{W_{sawdust}} \quad (1)$$

where W_{H3PO4} is the dry weight of phosphoric acid and $W_{sawdust}$ is the dry weight of sawdust [12]. The impregnation process was allowed to sit for overnight to ensure complete reaction takes place between the chemical reagent and raw material. The impregnated material was then carbonized in a fixed bed activation unit with heating temperature ranging from 400, 500, 600 to 700 °C and activation time of 30, 60, 90 and 120 minutes. The one-factor-at-a-time (OFAT) method was adopted in this study so that reduction of sample is achievable; it is a method of designing experiments involving the testing of factors one at a time instead of all simultaneously. Throughout the process, nitrogen gas, which acts as the carrier gas and promotes the pore formation in sawdust, was allowed to flow in the rotary kiln [5]. After the heat treatment, the material was left to cool to room temperature and subsequently washed with distilled water to remove the residual H_3PO_4 solution. The carbon sample produced was dried in an oven for overnight at 80°C and kept in a desiccator to prevent moisture.

Adsorption analysis

The batch experiment was carried out using UV-Vis Spectrophotometer set at wavelength of 195 nm to detect the concentration of MEA in synthetic MEA wastewater. Calibration was performed using standard solution of 100 ppm, 300 ppm and 500 ppm prepared by diluting MEA (analyte) with distilled water (solvent). The concentration range selected is based on reported MEA discharged into wastewater treatment plant [1]. Effect of initial concentrations (200, 300 and 400 ppm), stirring rate (100, 300 and 400 rpm) and contact time (15, 30 and 45 minutes) were studied to determine the optimum conditions of the sawdust AC sample prepared. All experiments were conducted at a room temperature of 32 °C and repeated twice for accuracy. Samples were extracted from the mixture and readings were taken at interval of 10 minutes. The graphs of % MEA removed versus the above three effects were plotted to study the effectiveness of AC in adsorbing MEA.

FESEM Analysis

To determine the best operating parameter for producing AC from sawdust, analytical technique used in material science for investigating the molecular surface structure was employed. A Zeiss EVO-50 Field Emission Scanning Electron Microscope (FESEM), model Supra 55 VP is an equipment designed for high resolution imaging at magnification of 10 – 100,000 times, and was used to compare the structural images of sawdust before and after activation by producing real space magnified images of its surface morphology.

Micrometrics ASAP 2020

Accurate and precise surface area and porosimetry measurements are essential to the determination of the effectiveness and quality of activated carbon samples. The pore size distribution, specific surface area (S_{BET}), porosity volume (V_T) and average pore diameter (D) of the AC samples are determined by nitrogen (N_2) adsorption-desorption isotherm isotherm whereby N_2 gas playing the role as adsorbate, was set to flow at 350 °C for 2 hours. The S_{BET} of samples are estimated using the Brunauer-Emmett-Teller (BET) method using N_2 gas adsorption isotherm data while the Barett-Joyner-Halenda (BJH) adsorption model is used for pore size distribution [11].

Results and Discussion

Characterization study and EDX spectroscopy

Table 1 below shows the preparation condition and results of AC samples produced from sawdust. Results showed that sample F21 which was prepared at IR of 1:1, T_{act} of 500 °C and t_{act} of 60 minutes yields the highest value of S_{BET} 1213.786 m^2/g with D equals 2.18 nm and V_T as high as 0.662 cm^3/g. Whereas sample D15 exhibit lowest characterization of S_{BET} (58.581 m^2/g), V_T (0.036 cm^3/g) and D (2.573 nm) were obtained at IR of 1:1, T_{act} of 700 °C and t_{act} of 30 minutes. In sample B9, B10 and B11, as the impregnation ratio increases, the samples show decreasing S_{BET} value with similar trend observed in sample A6, A7 and A8. Impregnation ratio (IR) is a critical parameter in formation of pores because it signifies the amount of ions available for intercalation to take place. An optimum IR of 1:1 to 1:3 has been reported to yield highest surface area carbon [17], and the result obtained shows that highest value is achieved at 1:1 IR. High IR favors more pore formation as it intensify the action of acid with more aggressive physico-chemical effect and dehydration which inhibits the contraction or collapse of the precursor particle. The washing after heat treatment will evacuate and free this internal porosity leaving behind an extensive microporous structure [18].

Table 1. Preparation condition and results of activated carbon samples

Sample	IR	Activation Temperature, T_{act} (°C)	Activation Time, t_{act} (min)	Specific Surface Area, S_{BET} (m^2/g)	Total Pore Volume, V_T (cm^3/g)	Average Pore Diameter, D (nm)
Raw	-	-	-	1.304	0.002	6.328
A6	1:1	400	30	474.483	0.253	2.134
A7	1:2	400	30	199.333	0.107	2.153
A8	1:3	400	30	1.161	-	-
B9	1:1	500	30	1135.624	0.565	1.992
B10	1:2	500	30	878.880	0.551	2.507
B11	1:3	500	30	399.013	0.261	2.616
C12	1:1	600	30	539.708	0.290	2.153
D15	1:1	700	30	58.581	0.036	2.573
F21	1:1	500	60	1213.786	0.662	2.180
J33	1:1	500	90	1176.079	0.634	2.158
N45	1:1	500	120	941.242	0.495	2.105

Nevertheless, the outcome of the analysis confirms that there is a maximum amount of ions that can be uptake beyond which would reduce pore development. The reason is because additional acid does not lead to further action and probably form an insulating layer (or skin) covering the particles, thus reducing the activation process and the contact with surrounding atmosphere. This phenomenon is particularly observed in sample A8 where most likely activation is hindered, resulting in negligible surface area and undetected pore. Similar trend was observed by Borhan et al. [5] using H_3PO_4 for banana peel activation when activated above 1:1 IR. As for activation temperature, the optimum temperatures have been reported to be between 400 to 700 °C by most of the earlier researchers [17]. Hence the experiments were conducted within the selected temperature range, and it turned out that the recommended temperature is reliable due to verification provided by sample B9 at 500 °C. The increase in temperature from 600 °C to 700 °C for Sample C12 and D15, clearly demonstrated the collapse of porous structure due to excessive heat energy intake, which results from knocking and breaking of some porous wall [12]. While maintaining a constant impregnation ratio at 1:1 and activation temperature at 500 °C, the influence of activation time is examined. The results obtained from sample B9, F21, J33 and N45 show that the optimum time for carbonization is 60 minutes. Prolonged heat exposure would only cause rupture in porous wall. Since the porous structure has already been well developed at temperature of 500 °C, the increase in activation time simply causes the break of the cross-links between carbon structures, with a consequent collapse of pores [16]. All the samples that have been analyzed show average pore diameter of around 2 nm, indicating formation of mesopores.

Aside from examining the surface morphology of the samples, FESEM is also equipped with EDX spectroscopy for detecting the elemental composition. Table 2 shows the comparison of elemental composition before and after activation. Two elements were detected on the sample before activation: carbon and oxygen. It was reported in specific that suitable range of carbon content should lie between 50 to 80% [6]. The result shows that *Nyatoh* wood species sawdust fulfills the criterion of producing AC. An additional element identified as phosphorus, P was detected in the sample after activation. Presence of phosphorus element is due to the use of H_3PO_4 as chemical activating agent during the impregnation process. Repetitive washing can further reduce the phosphorus element but complete elimination is hardly possible.

Table 2. Comparison of elemental composition before and after activation

Elements	**Before Activation**		**After activation**	
	Weight %	**Atomic %**	**Weight %**	**Atomic %**
Carbon, C	54.98	61.93	76.86	82.45
Oxygen, O	45.02	38.07	20.36	16.39
Phosphorus, P	0.00	0.00	2.78	1.16
Total	100.00		100.00	

N_2 adsorption – desorption isotherms

The existence of mesopores is further proven with the identified isotherms. The objective of this study is to categorize the right adsorption isotherm type based on IUPAC classification [19]. Figure 1 shows the N_2 adsorption-desorption isotherm of some selected samples. The isotherm is plotted as quantity of N_2 gas adsorbed against the relative pressure. Based on the six principal types of adsorption isotherms, it is stated that all isotherms produced should fit at least one or a combination of two or more of the shapes [12]. Referring to the graph in

From Figure 1, it can be seen that all selected samples exhibit trends with combination of Type-I and Type-II isotherms except Sample D15 which shows Type-I isotherm. Literature presents that Type-I isotherm is normally observed on microporous solid whose pore sizes are not exceedingly large when compare to the molecular diameter of the adsorbate, whereas Type-II isotherm is found in adsorbents with pore diameters larger than micropores. A combination of these two could be viewed as the effect of mixed micropores and mesopores structure.

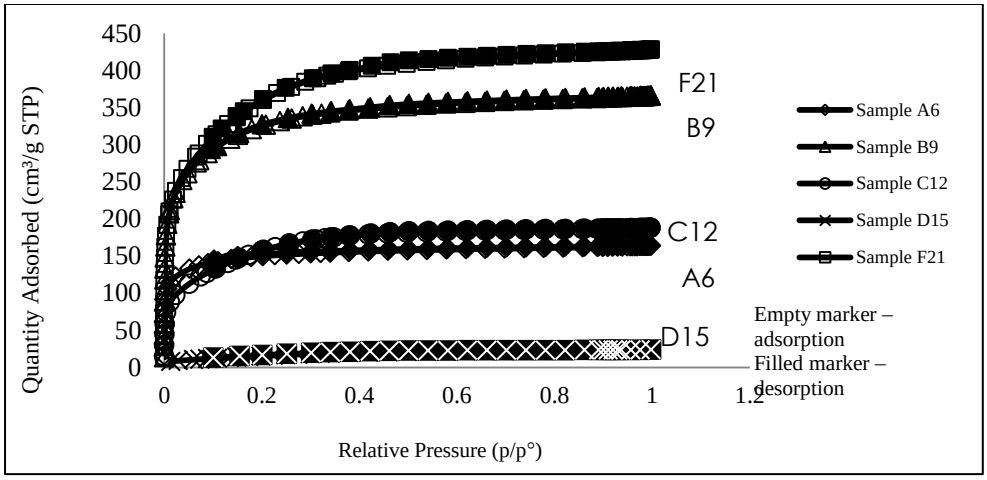
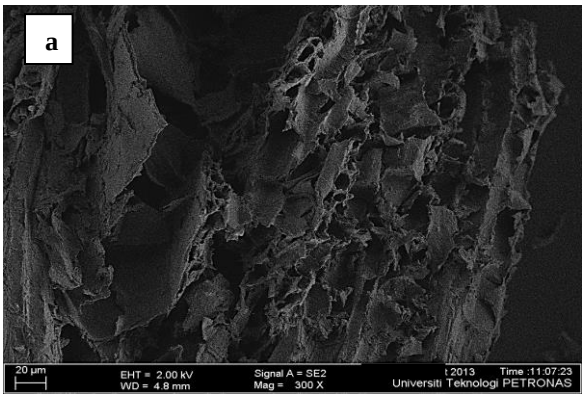
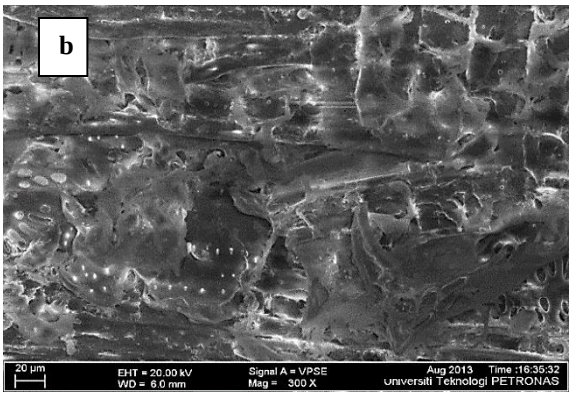


Figure 1. N_2 adsorption-desorption isotherms of selected samples

Morphology

Figure 2 shows the microscopic structure of the raw sawdust and some selected samples prepared at different activation parameters. By using FESEM, structural images with magnification up to 300 times are taken. The structural image of fresh sawdust in Figure 2(a) points up that the raw material before undergoing activation shows no noticeable pores. However, the image clearly shows the existence of fine pores on the surface, which is one of the important characteristics for manufacturing AC. After activation, a greater distribution of pores emerged to become active sites for adsorption to take place more readily. The difference in pore structure before activation and after activation is clearly illustrated through comparison made between Figure 2(a) with Figure 2(b) and 2(c). Sample A6 (Figure 2(b)) shows good canal structure for the AC, meaning that the carbonization and activation are taking place but still at early stages at temperature of 400 °C. Many new large pores were clearly observed on the surface of the AC. Sample F21 (Figure 2(c)) shows the most well developed porous structure among the three AC. This justified that sample F21 has the highest S_{BET}, V_T and D compared to other samples. On the other hand, collapse of porous wall due to excessive heat exposure is observed in Figure 2(d) with Sample D15 being activated at highest temperature.





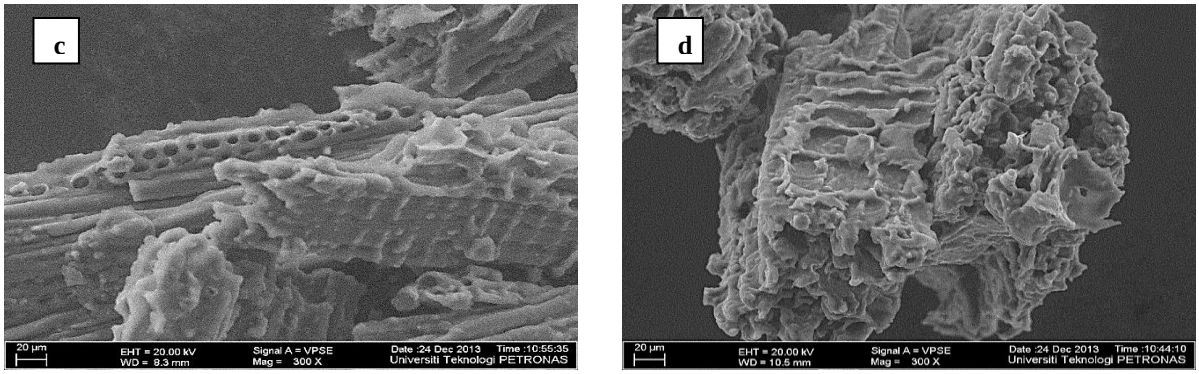


Figure 2. FESEM images of selected samples, (a) fresh sawdust, (b) sample A6, (c) sample F21 and (d) sample D15

Effect of initial concentration on MEA removal

The adsorption test on selected AC samples was conducted using synthetic MEA wastewater produced from diluting MEA with distilled water. Sample B9 and F21 having high value of S_{BET} and V_T, were selected as test subjects along with the fresh sawdust to show contrast. Figure 3 shows the plot of percentage removal against initial MEA concentration. It was revealed that at low concentration, the removal percentage was high and gradually decreased with the increase of MEA concentration. From Figure 3, MEA concentration prepared at 100 ppm, the removal percentage were 96.8, 92.7 and 4.6% for sample F21, B9 and raw sawdust, respectively. The low percentage MEA removal for raw sawdust without activation proved that the material is not capable of adsorbing MEA due to almost no noticeable pores. Sample B9 was able to remove up to 92.7% of MEA, nonetheless, the result was surpassed when Sample F21 which has relatively higher S_{BET} and V_T, exhibited higher adsorption capacity and higher rate of adsorption. On the other hand, the highest MEA concentration at 500 ppm led to the lowest removal percentage under test (86, 85.4 and 0% for samples F21, B9 and raw sawdust, respectively. The obtained results in the present work concerning MEA removal agreed with that obtained by Razali et al. [10] where the removal percentage of MEA was the highest at low concentration and decreased with the increase in its concentration. The reason behind this is due to the MEA molecules are no longer attached to the surface of the adsorbent since the adsorbent have reached their limited surface to adsorb. Further increase in concentrations brought no increase in adsorption, which was a result of overlapping of adsorption sites due to overcrowding of adsorbent particles.

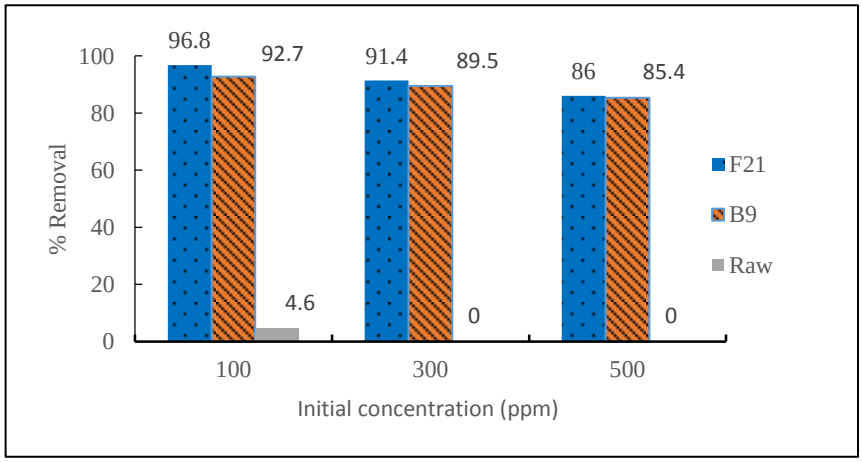


Figure 3. Effect of initial concentration on MEA removal

Effect of stirring rate on MEA removal

The effect of stirring rate on adsorption of MEA is shown in Figure 4. In general, it was observed that when the stirring rate is increased from 200 to 400 rpm, the percentage removal of MEA also increased for all samples. Sample F21 shows the highest percentage of removal followed with sample B9 and raw sawdust. At a stirring rate of 400 rpm, maximum recoveries obtained for MEA are, 99.7% removal for sample F21, 99.1% removal for sample B9 and 4.2% removal for raw sawdust. Due to the existence of pore volume on the surface of B9, therefore the percentage removal is high and comparable with sample F21. With the increasing of the stirring rate, the rate of diffusion of MEA from the bulk liquid to the liquid boundary layer surrounding the AC particle become higher because of an enhancement of the turbulence and a reduction in the thickness of the liquid boundary layer [20]. This effect may be additionally enhanced by the greater fragmentation of the adsorbent particles which accompanies the increased agitation speed. As for raw sawdust, effect of stirring rate did not improve on the amount of MEA adsorbed from the bulk solution.

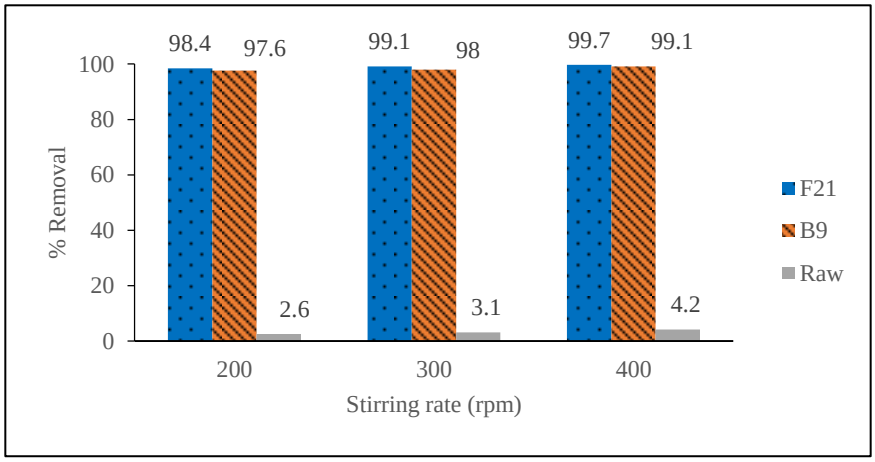


Figure 4. Effect of stirring rate on MEA removal

Effect of contact time on MEA removal

The relationship between contact time and the percentage removal of MEA with AC prepared from sawdust are shown in Figure 5. From the result obtained, it is evident that the removal of MEA increased as contact time increases. When MEA concentration prepared at 200 ppm and contact time of 45 minutes, the removal percentage were 99.7, 98.5 and 3.8% for samples F21, B9 and raw sawdust, respectively. This is the highest percentage removal compared than any other conditions specified. However, raw sawdust sample shows a constant MEA removal of 3.8% at contact time of 30 and 45 minutes of experiment. This is probably due to the adsorbent already achieved the optimum time to adsorb the MEA and equilibrium condition has been established [21, 22]. Increasing the contact time to promote removal of MEA will not bring any changes in the removal percentage, but probably resulted in desorption of the metal ions from the surface of the AC.

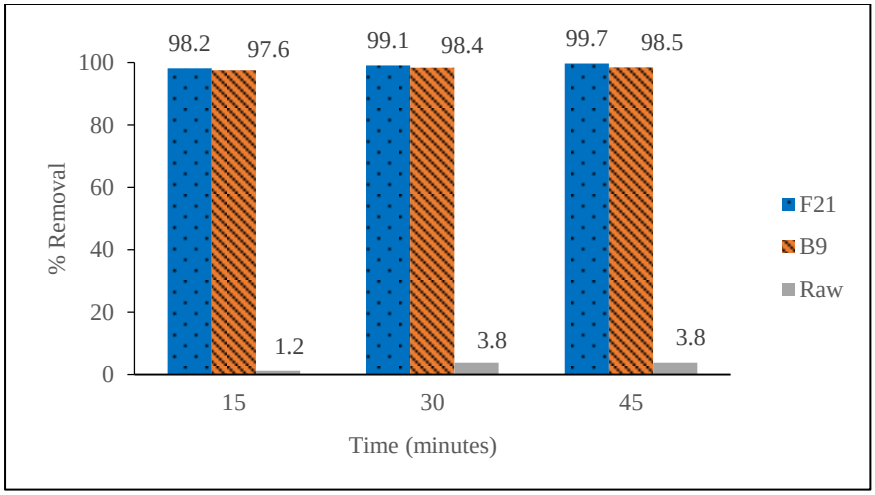


Figure 5. Effect of contact time on MEA removal

Conclusion

The result of this study clearly demonstrated that AC having high surface area and great distribution of microscopic pores can be prepared from sawdust by chemical activation with H_3PO_4. The optimal preparation process of AC from sawdust was successfully achieved by using one-factor-at-a-time (OFAT) method. With an IR of 1:1, T_{act} of 500°C and t_{act} of 60 minutes, AC with highest S_{BET} (1213.786 m^2/g), V_T (0.662 cm^3/g) and D (2.18 nm) can be produced. In addition, characterization analysis revealed that the range of pore diameter (2-6 nm) falls within mesopores group, indicating its suitability to be used for MEA adsorption. Results from batch experiments showed that sample F21 is capable of removing 96.8% of MEA at concentration of 200 ppm and 99.7% under effect of stirring rate at 400 rpm. While under the effect of contact time, 99.7% of MEA removal is achieved at time of 45 minutes. This study confirmed that sawdust is an effective remover of MEA from industrial wastewater and has the potential to be a promising precursor for the production of AC.

Acknowledgement

The authors gratefully thank Universiti Teknologi PETRONAS for providing financial support and laboratory facilities in carrying out this research work.

References

1. Luis, P. (2016). Use of monoethanolamine (MEA) for CO_2 capture in a global scenario: Consequences and alternatives. *Desalination*, 380: 93-99.
2. Zhang, Y., Chen, C. C., Plaza, J. M. and Rochelle, G. T. (2009). Rate-based process modelling study of CO_2 capture with aqueous monoethanolamine solution. *Industrial and Engineering Chemistry Research*, 48(20): 9233-9246.
3. Razali, M. N. (2011). Adsorption treatment of monoethanolamine wastewater from oil and gas industry. Master Thesis. Universiti Malaysia Pahang, Malaysia.
4. Hospido, A., Moriera, M. T., Fernandez, C. M. and Feijoo, G. (2004). Environment performance of a municipal wastewater treatment plant: LCA case-studies. *International Journal of Life Cycle Assessment*, 10: 336-345.
5. Borhan, A., Hoong, P. K. and Taha, M. F. (2014). Biosorption of heavy metal ions, oil and grease from industrial waste by banana peel. *Journal of Applied Mechanics and Materials*, 625: 749-752.
6. Jahagindar, A. A., Ahmed, M. N. Z. and Devi, B. V. (2012). Adsorption of chromium on activated carbon prepared from coconut shell. *International Journal of Engineering Research and Application*, 2: 364-370.
7. Malaysian Investment Development Authority (2016). Industries in Malaysia - Wood based industry. http://www.mida.gov.my/env3/index.php?page=wood-based-industry. [Access online 29 December 2016].
8. Prakash, K. B. G., Shivakamy, K., Miranda, L. R. and Velan, M. (2006). Preparation of steam activated carbon from rubberwood sawdust and its adsorption kinetics. *Journal of Hazardous Materials*, 136(3): 922-929.

9. Nur Izzati, A. G., Nur Yusra, M. Y., Wan Nor Roslam, W. I. and Mohd. S. M. (2017). Modification of active carbon from biomass Nypa and amine functional croups as carbon dioxide adsorbent. *Journal of Physical Science*, 28(1): 227-240.
10. Razali, M. N., Yunus, R. M., Jemaat Z. and Alias S. (2010). Monoethanolamine wastewater treatment *via* adsorption: A study on comparison of chitosan, activated carbon, alum and zeolite. *Journal of Applied Sciences*, 10(21): 2544-2550.
11. Mohammad, A. F. M., Yoshimitsu, U., Suzana, Y., Fathelrahman, E., Azhar, U. and Mitsuka, D. (2016). Activated carbon from rubber wood sawdust by CO_2 activation. *Procedia Engineering*, 148: 530-537.
12. Borhan, A., Taha, M. F. and Hamzah, A. A. (2014). Characterization of activated carbon from wood sawdust prepared *via* chemical activation using potassium hydroxide. *Advanced Materials Research*, 832: 132-137.
13. Muda, A. and Hidayu, A. R. (2016). Preparation and characterization of impregnated activated carbon from palm kernel shell and coconut shell for CO_2 capture. *Procedia Engineering*, 148: 106-113.
14. Zhang, T., Walawender, W. P., Fan, F. T., Fan, M. and Brown, R. C. (2004). Preparation of activated carbon from forest and agricultural residues through CO_2 activation. *Chemical Engineering Journal*, 105 (1-2): 53-59.
15. Zhang, H., Yan, Y. and Yang. L. (2010). Preparation of activated carbon from sawdust by zinc chloride activation. *Adsorption*, 16(3): 161-166.
16. Teng, H., Yeh, T. S. and Hsu, L.Y. (1998). Preparation of activated carbon from bituminous coal with phosphoric acid activation. *Carbon*, 36(9): 1387-1395.
17. Borhan, A. and Kamil, A. F. (2014). Preparation and characterization of activated carbon from rubber-seed shell by chemical activation. *Journal of Applied Sciences*, 11: 1124-1129.
18. Girgis, B. S. and El-Hendawy, A. A. (2002). Porosity development in activated carbons obtained from date pits under chemical activation with phosphoric acid. *Microporous and Mesoporous Materials*, 52 (2): 105-117.
19. Mays, T. J. (2007). A new classification pore sizes. *Studies in Surface Science Catalysis*, 160: 57-62.
20. Koumanova, B., Peeva, P. and Allen, J. S. (2003). Variation of intraparticle diffusion parameter during adsorption of p-chlorophenol onto activated carbon made from apricot stones. *Journal of Chemical Technology and Biotechnology*, 78: 582-587.
21. Bulut, Y. and Tex, Z. (2007). Removal of heavy metals from aqueous solution by sawdust adsorption. *Journal of Environmental Sciences*, 19: 160-166.
22. Gad, H. M. H. and El-Sayed, A. A. (2009). Activated carbon from agricultural by-products for the removal of Rhodamine-B from aqueous solution. *Journal of Hazardous Materials*, 168: 1070-1081.

Malaysian Journal of Analytical Sciences, Vol 22 No 3 (2018): 542 - 552
DOI: https://doi.org/10.17576/mjas-2018-2203-23

MALAYSIAN JOURNAL OF ANALYTICAL SCIENCES
Published by The Malaysian Analytical Sciences Society
ISSN 1394 - 2506

SURFACE MODIFICATION OF POLYETHERSULFONE MEMBRANE VIA UV-GRAFTING FOR FORWARD OSMOSIS TECHNOLOGY

(Modifikasi Permukaan Membran Polyetersulfon Melalui Cantuman-UV untuk Teknologi Osmosis ke Hadapan)

Ahmad Fikri Hadi Abdul Rahman* and Mazrul Nizam Abu Seman

Faculty of Chemical & Natural Resources Engineering,
Universiti Malaysia Pahang, 26300 Kuantan, Pahang, Malaysia

**Corresponding author: fikrihadi@gmail.com*

Received: 16 April 2017; Accepted: 7 March 2018

Abstract

In this study, UV-grafting was used in surface modification of polyethersulfone membrane (UFPES50) for forward osmosis (FO) application. Using two parameters, namely monomer concentration (acrylic acid) and grafting time, the modified membrane was characterised by attenuated total reflectance-Fourier transform infrared (ATR-FTIR), field emission scanning electron microscope (FESEM) and contact angle. The membrane was evaluated for its water permeability, solute permeability, and structural parameter. The water permeability increases as the grafting parameters increases; however, at the highest (50 g/L) of monomer concentration, a sudden drop occurred due to the thickening of the grafted layer. Focusing on this monomer concentration, the grafting time was increased up to 60 minutes and it was successfully demonstrated that the modification using UV-grafting on PES membrane involved both effective grafting and chain scission. In addition, negative rejection on the modified membrane was observed.

Keywords: forward osmosis, effective grafting, negative retention, structural parameter

Abstrak

Di dalam kajian ini, kaedah cantuman UV digunakan untuk mengubah membran polyetersulfon (UFPES50) untuk kegunaan aplikasi osmosis ke hadapan. Dua parameter digunakan iaitu kepekatan monomer (asid akrilik) dan masa cantuman. Pencirian bagi membran yang telah dimodifikasi dilakukan melalui spektroskopi transformasi infra merah Fourier- pantulan keseluruhan dikecilkan (ATR-FTIR), mikroskop imbasan elektron pancaran medan (FESEM) serta sudut sentuhan. Membran telah di nilai dari segi ketelapan air, ketelapan bahan larut dan struktur parameter. Ketelapan air meningkat dengan pertambahan percambahan parameter, tetapi pada kepekatan monomer yang tinggi (50g/L), telah berlaku perubahan yang mendadak. Dengan memberi fokus kepada kepekatan ini, masa cantuman ditingkatkan sehingga 60 minit. Hasil kajian berjaya membuktikan bahawa proses cantuman meliputi cantuman berkesan dan pemotongan rantaian. Selain daripada itu, di dapati terdapat penolakan negatif pada membran yang telah diubah suai.

Kata kunci: osmosis ke hadapan, cantuman berkesan, penolakan negatif, struktur parameter

Introduction

Access to clean water is crucial for all human being. As a result, advancement in water treatment technology is necessary. In the quest for a technology that can achieve better efficiency, longer life-cycle, limited operating area, as well as low capital and operating expenditure, forward osmosis (FO) was the breakthrough in replacing the conventional reverse osmosis (RO) process. In the FO process, it employs the natural osmotic pressure as its main

driving force. It purifies water by facilitating water diffusion through the membrane while rejecting almost all dissolved and suspended constituents [1]. Three parameters are commonly employed in measuring the performance of FO system, namely pure water permeability (A), solute permeability (B), and structural parameter (S) which governs the transport phenomena across the membrane support layer.

There are many methods available to modify FO membranes to make them ideal candidates for designated separation processes. Surface modification has been proven to increase the water flux and hydrophilicity, decrease solute permeability, and increase the resistivity towards natural organic matter and chlorine attack [2]. Grafting is a process to add new properties of functionalities into a polymer. The term grafting is defined as the covalent bond between carbon-carbon bond between monomer or polymer with a substrate [3]. The grafting techniques include chemical, ultraviolet, ozone, plasma and atmospheric pressure plasma [4]. Among surface modifications, UV-grafting has attracted various researchers as it provides advantages in terms of its simplicity, usefulness, versatility and low cost [5]. Modification *via* UV-grafting technology has been widely used in various industries especially in packaging and coating-related field [6]. The grafting process involves an optimal selection comprising irradiation intensity, duration, pH, and distance [7]. It is important to understand that in surface modification, hydrophilicity and roughness largely control the membrane fouling characteristics, while chemical, thermal, and mechanical stabilities determine the membrane durability under various environments [8]. This modification increases membrane surface hydrophilicity and shifts the membrane pore size distribution to a smaller size [9].

Polyethersulfone (PES) is one of the commonly used polymers in fabrication of ultrafiltration and microfiltration membranes. Advantages of this hydrophobic material are in its high mechanical, chemical and thermal stability due to the existence of aromatic hydrocarbon groups in the structure [10]. This polymer can generate several sites on the surface and on the pore wall because it is a photosensitive material. The aim of most previous researches involving UV-grafting technique was to add nanoparticle antifouling material [11], to add more layers using cross-linker [12, 13] and to focus on optimisation using response surface methodology (RSM) [14]. Most of the reported UV-grafted membranes are generally applied to pressure-based membranes (RO, NF, UF and MF) and they exhibited good performance. Therefore, this research paper reports on the potential use of UV-grafted in the FO application. It investigates the effect of grafting parameters (grafting time and monomer concentration) on the FO membrane.

Materials and Methods

The polyethersulfone ultrafiltration (UFPES50) membrane was purchased from AMFOR INC (China). Acrylic acid (Merck Chemicals) was used as monomer for UV-grafting. For membrane in the surface modification, the mercury lamp (UVP, 100W) was used as the UV-light source. Prior to surface modification, the membrane was immersed overnight and rinsed with pure water to remove its protective layer. Firstly, the membranes were immersed in 50 mL of different concentrations (5-50 g/L) of acrylic acid and left under gentle stirring for 15 minutes. Next, the membrane undergoes surface modification under UV light at predetermined time while it is still fully immersed. The membranes were later taken out and rinsed with pure water to remove the unreacted compound. Finally, all the modified membranes were stored in new DI water for at least 1 day prior to use. The membrane water permeability ($L/hr.m^2.bar$) and solute permeability were measured at different levels of pressure (1-8 bar) by using stirred cell (Sterlitech, HP4750). The water flux was calculated by using the following equation 1: (J_w= Permeate Volume/Area) where the water flux is ($L/h.m^2$); the permeate volume is (L); the effective membrane area is (m^2). For the solute permeability test, sodium chloride with 200 mg/L concentration was used. The concentration of the permeate and bulk solution was measured using conductivity meter. The pure water permeability, A, and solute permeability, B, was determined by using the following equations:

$$A = \frac{J_w}{\Delta P} \tag{1}$$

$$B = J_w \left(\frac{1-R}{R}\right) \exp\left(-\frac{J_w}{k}\right) \tag{2}$$

Rejection value was calculated from ($R=1-C_p/C_f$) where C_p is the concentration of permeate while C_f is the concentration of feed solution.

In addition, lab-scale forward osmosis system was also used to determine the structural parameter, S. In the FO experiment, 2000 mL of the draw solution (1M NaCl) and the feed solution of pure water were prepared and used to carry out the FO process. The initial mass of feed solution was recorded and further readings were determined at an interval of 5 min until the process was accomplished in one hour. Then, the structural parameter, S value was determined by using;

$$S = \frac{D_s}{J_w} ln\left(\frac{B + A\pi_{D,f}}{B + J_w + A\pi_{F,m}}\right) \quad (3)$$

where D_s is the feed solution diffusivity of the draw solute, $\pi_{D,f}$ is the feed osmotic pressure of the draw solution and $\pi_{F,m}$ is the osmotic pressure at the membrane surface on the feed side (zero for pure water feed). We assume a constant diffusion coefficient of NaCl for the stated concentration used.

The morphology structure of the modified membrane was observed *via* a Field Emission Scanning Electron Microscope, FESEM (Jeol, JSM7800F) where the sample was fractured after being immersed in liquid nitrogen to get the cross-section view. For the surface chemistry, the hydrophilicity of the membrane was measured using contact angle (Geniometer) while Attenuated Total Reflection-Fourier Transform Infrared Spectroscopy (ATR-FTIR) was used to detect the functional group.

Results and Discussion

ATR-FTIR, contact angle and FESEM analysis

The commercial ultrafiltration membrane was modified with different monomer concentration and irradiation time. The mechanism of surface modification starts when the phenoxyphenyl sulfone chromopores in the polyethersulfone chain absorb the UV-light. This results in the haemolytic cleavage of a carbon-sulphur bond at the sulfone linkage, yielding two radical sites at the end of the respective polymer chains [9]. These free radicals reacted with monomer solution to form chain of carboxylic group on the polymer trunk and leads to an increase in the hydrophilicity of the membrane [15]. To confirm the success of the modification via UV-grafting, the membrane was analysed using ATR-FTIR before and after modification as shown in Figure 1. New peaks appeared in ATR-FTIR spectra of the modified membranes in comparison with those obtained for the unmodified membrane. As can be seen clearly, for the modified membrane, a new peak is formed at 1721 cm^{-1} (shown in the circle) which could be assigned to the new carboxyl group.

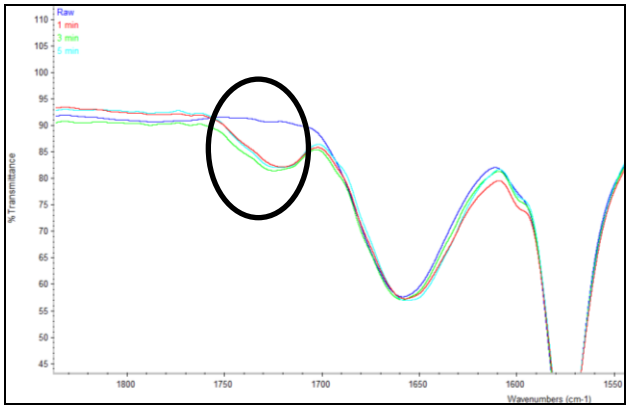


Figure 1. ATR-FTIR for modified and unmodified membranes at grafting time (1, 3 and 5 minutes)

Contact angle was commonly used to identify the hydrophilicity/hydrophobicity in membrane technology. Several factors affecting the morphology of a membrane, such as hydrophilicity, roughness, porosity, pore size, and its distribution affect the contact angle data [16]. The study on the hydrophobicity of PES is well documented by Zhao

et al. [17] who reported that in most cases, the modified membranes will become more hydrophilic after modification. In this experiment, the unmodified membrane with a 59^{o} contact angle and 50g/L monomer concentration of acrylic acid is used. From Figure 2, the value in contact angle does not clearly indicate whether there is an increase or a decrease trend in hydrophilicity. The hydrophilicity of the modified membrane is increased if the value obtained is lower than the unmodified. However, only two samples were successful: the membranes grafted at 20 minutes and 60 minutes. In the overall surface modification, the contact angle does not provide a clear picture to indicate that the addition of carboxylic group on the membrane surface will increase the membrane hydrophilicity.

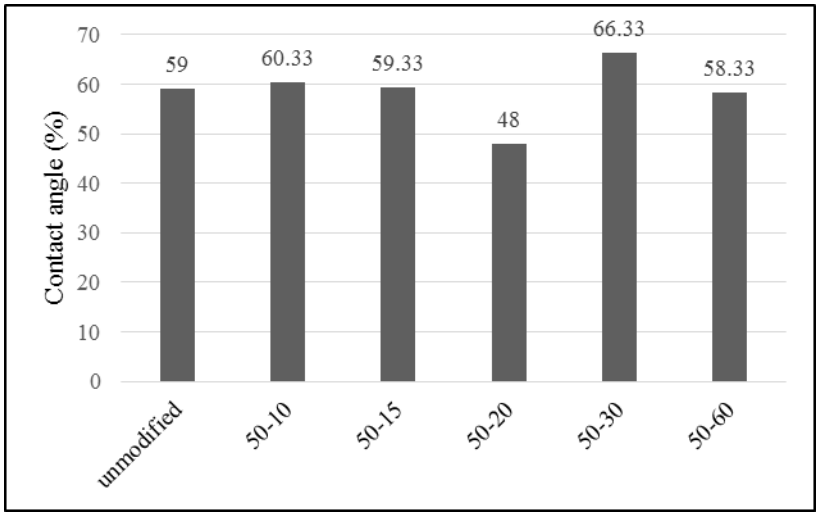
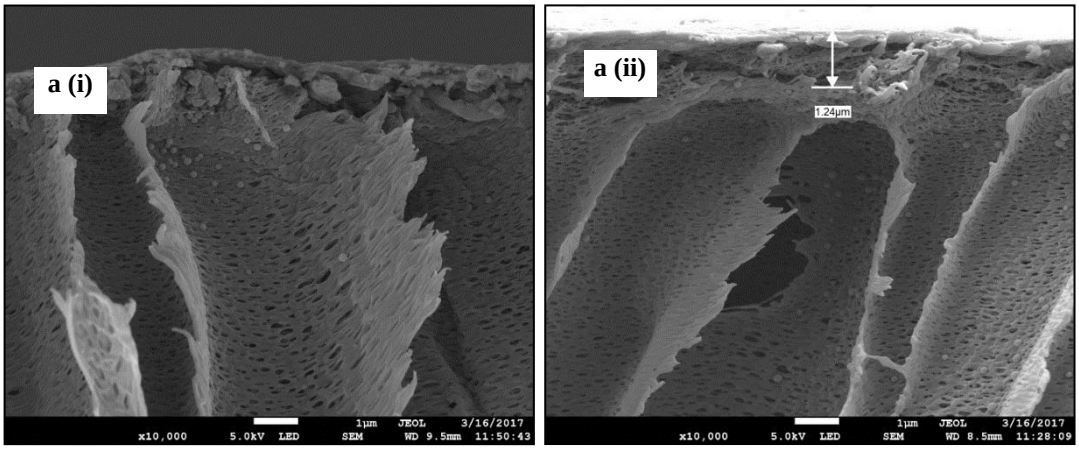


Figure 2. Hydrophilicity of the unmodified and modified membranes

The cross-section of the polyethersulfone membrane was characterised by FESEM as in Figure 3. One of the downsides in using the ultrafiltration to determine the cross section is that the support layer must be removed before any sample can be observed *via* FESEM. The support layer prevents the sample from getting fractured easily even after a prolonged time being immersed in liquid nitrogen. However, in this figure, the support layer is not visible as it is located at the bottom. In the unmodified membrane in (a), the active layer is 1.24 µm and is formed in the production process. Compared with the modified membrane of 50AA-15min, the active layer has increased to 4.51 µm. A uniform dense top layer is formed on the modified membrane and as can be observed, the uniform layer is made of interconnected holes and is restricting the initial pore size of the ultrafiltration membrane. It is believed to be the new polyacrylic layer with carboxyl functional group [18, 19]. This functional group provides negative charges and the hydrophilicity property of the modified membrane.



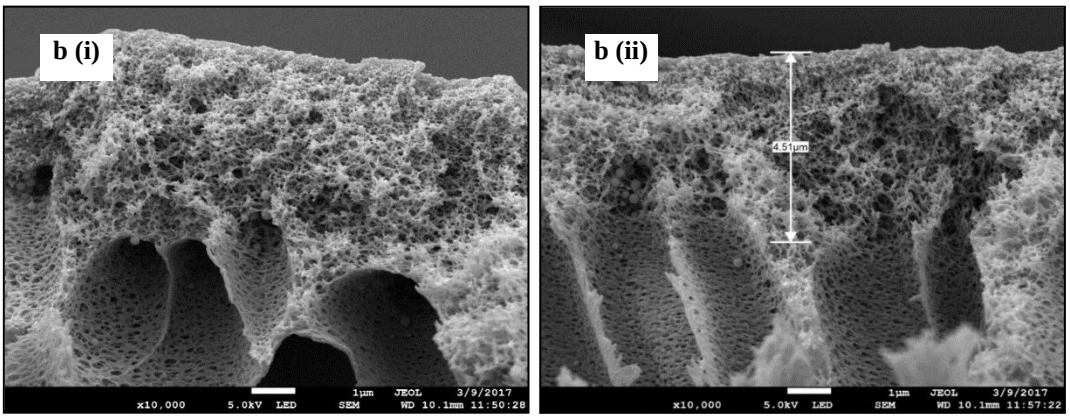


Figure 3. (a) unmodified and (b) modified membrane cross-section

Water permeability

The result of water permeability, A, is shown in Table 1. In the modification of the membrane, each of the monomer concentrations (5, 15, 30 and 50 g/L) was UV-grafted at different irradiation times (1, 3 and 5 minutes). The unmodified UFPES50 membrane has the value of A at 98.87 L/hr.m^2.bar. This value was obtained from the water flux and the pressure tested for up to 8 bars. In this paper, we use acrylic acid as the sole monomer, hence the effect of monomer size, chemical group, degree of polymerisation and surface coverage are remained constant [20]. This is with the assumption that the temperature during UV-grafting remains the same. From the Table 1, it can see that the water permeability increases with the increase in monomer concentration until it reaches a peak when monomer concentration used is at 30 g/L. A sudden drop in the water permeability can be observed when the monomer concentration used exceeds 30 g/L. The modified membranes have higher A value than the unmodified membranes except for 5AA/1min, 50AA/3min and 50AA/5min.

Table 1. Water permeability of the unmodified and modified membranes using different acrylic acid (AA) concentrations and different UV-irradiation times (T)

Membrane	**AA(g/L)**	**T(min)**	**A(L/hr.m^2.bar)**
Unmodified	-	-	98.87
5AA-1	5	1	97.97
5AA-3	5	3	108.48
5AA-5	5	5	122.31
15AA-1	15	1	131.66
15AA-3	15	3	152.21
15AA-5	15	5	121.83
30AA-1	30	1	161.16
30AA-3	30	3	171.23
30AA-5	30	5	182.65
50AA-1	50	1	114.16
50AA-3	50	3	93.40
50AA-5	50	5	97.85

Xi et al. [21] has also observed that the grafting yield increased with the increase in monomer concentration except at lower concentration. Acrylic acid is a strong acid and it provides negative charges to the modified membrane as the formation of carboxylic group in the functional group makes it more hydrophilic. The modified membrane 5AA-1min (97.97 L/m^2.hr.bar) is believed to have insufficient effective grafting as it was conducted in low monomer concentration and short grafting time. The original functional group at the membrane surface managed to either repel the negative charges from the monomer or the number of energy received by phenoxyphenyl sulfone chromopores was below the minimal energy to form free radicals. At 50g/L of monomer concentration, the water permeability shows a great decline in all tested grafting times. The highest monomer concentration might lead to a competitive effective grafting at the membrane surface. Similar trend is also observed by Bilongo et al. [22] where the effective grafting increases with the increase of monomer concentration. The author justifies the relationships of kinetic in photo-polymerisation where a good grafting condition must be derived from a high monomer concentration and strong dose of UV energy. This phenomenon leads to the thickening of the grafted layer.

Further experimental works has been conducted to evaluate the sudden drop in water permeability for monomer concentration of 50 g/L as shown in Figure 4 below. In general, the value of A shows a reduction with the increase of grafting time as shown by the trendline. The trendline was generated after the experiment was conducted under 8 different grafting times (minute). From the figure, A shows a decreasing value as the grafting time increases. However, as the grafting time exceeds 15 minutes, the water permeability shows an increasing value. The decrease in the water flux value does not correlate well with the progressive increase in the grafting time. Interestingly, the polymerisation mechanism in membrane surface involved both effective grafting and chain scission processes instead of a steady growth of polymer chain [23]. According to Mansourpah and Momeni Habili, the longer UV radiation period lead to the enhancement in the polymerisation degree before obtaining a denser thin layer [24]. Moreover, the reduction of water permeability after modification was also observed by Yu et al. [25]. The polyethersulfone membrane was modified *via* UV- grafting with the usage of an initiator to improve antifouling property. The authors claimed that the reduction in water permeability was due to the formation of grafted material which had narrowed down the pore size. Similar result was also obtained by Taniguchi and Belfort [26] which suggests that water permeability declines with the increase of grafting time. The formation of grafted material that leads to pore plugging implies a formation of gel layer on the modified surface. At grafting time of 15 minutes, the modified membrane impeded water movement. When a maximum pressure of 8 bar was used, however, the water permeability was only at 1.13 L/hr.m^2.bar. The trend of effective grafting increases with the increase of grafting time applied in the first 15 minutes.

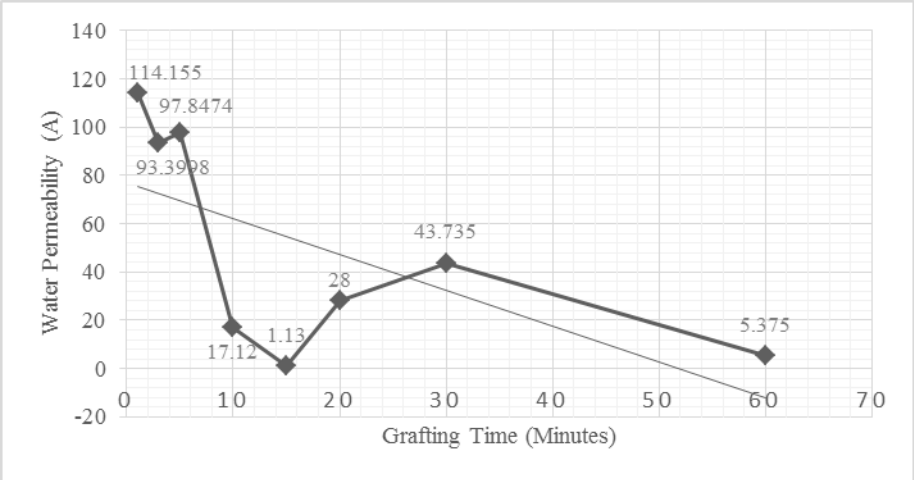


Figure 4. Water permeability for 50 g/L of monomer concentration

As the grafting time starts to increase from 15 minutes onwards, the water permeability starts to increase from 1.13 L/hr.m^2.bar, 28 L/hr.m^2.bar and 43 L/hr.m^2.bar. It is suggested that the mechanism that occurred between grafting time of 15 minutes and 30 minutes is chain scission. If chain scission is considered as the main reason for the increase in water permeability, the modified membrane with longer grafting time can be explained as in Figure 5.

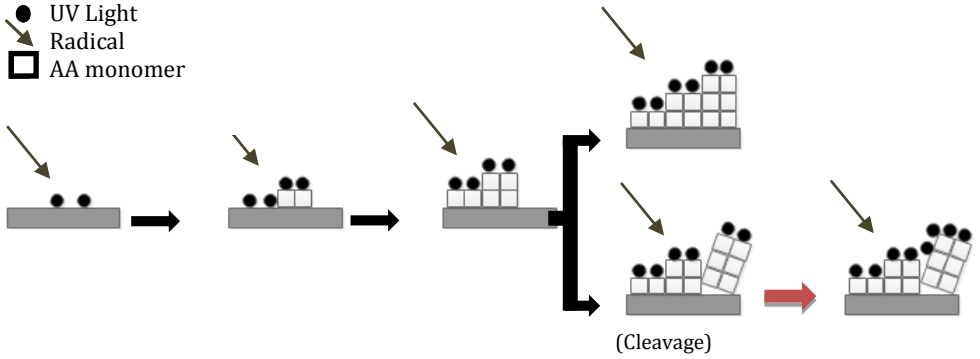


Figure 5. Proposed process on PES membrane surface. Modified from Taniguchi et al. [27].

At the area where the cleavage occurred, the membrane surface is exposed directly to the feed solution which leads to the increase in water permeability. Garcia et al. [5] defines this scenario as the deterioration of membrane after a membrane exceeds a certain grafting parameter. As the chain scission occurs more rapidly at 30 minutes of grafting time, the water permeability increases. The effect of degradation on PES due to irradiation is unavoidable. This evidence is supported by Taniguchi et al. [27] who has shown that the grafting time leads to an increase in pore size. This author identified the trends in effective grafting or chain scission by measuring the degree of grafting (DG) using ATR-FTIR. At 60 minutes of grafting time, the value of A reduces to 5.3 L/hr.m^2.bar. It is suggested that the grafting occurred at the cleavage of polymer chains to form a new layer. The phenomenon is relatively similar to the usage of a crosslinker such as glutaraldehyde (GA) in the formation of new layers on top of the previous layer. For example, Liu et al. [28] studied the usage of crosslinker and its effect on modified membrane that leads to reduction in pore size, increase in hydrophilicity and lowering of surface charge.

Solute permeability

Figure 6 shows the value of solute permeability using 50 g/L of acrylic acid against time. The experiment is conducted using 200 ppm of sodium chloride (NaCl). As can be seen, the solute permeability of the modified membrane allows a normal reaction only in the first 3 samples where the grafting time was at 1 minute, 3 minutes and 5 minutes, respectively. As the grafting time was increased from 10 minutes onwards, the solute permeability began to record negative values. The conductivity meter recorded a higher value in the permeate solution compared to the feed solution. To obtain a qualitative data, the salute permeability test was conducted using the samples that were previously used in water permeability analysis.

As the grafting time starts to increase from 10 minutes onwards, the solute permeability starts to decrease from -7.7 x 10^{-4} ms^{-1} and the values remain on the negative side as the grafting time reaches 60 minutes. This phenomenon is identified as negative retention. Negative retention is the existence of "preferable" material that can pass through the membrane layer [29] regardless of its size. In other words, the modified membranes have an interest in transporting selective material or in this research, transporting the monovalent salt; sodium chloride (NaCl). This halophile property was detected on the modified membrane and to the best of our knowledge this is the first-time negative retention is utilised in FO application. Similar trends have also been identified by Vatanpour et al. [30] by using NaCl, sodium sulphate (Na_2SO_4) and magnesium sulphate ($MgSO_4$). NaCl in the feed solution has high interaction with the membrane material and consequently, becomes preferential transport [29]. According to Schaep et al. [31]

back in 2001, NaCl is a single salt and this characteristic is suitable in determining the membrane charges. In the extended Nersk-Plack equation, the equation represents the transport mechanism involving diffusion, electric field gradient and convection. The existence of negative rejection in NaCl showed that the behaviour of the modified membranes could be classified by a combination of diffusion and Donnan exclusion mechanism [32]. Donnan exclusion in this context is defined as the reduction of ions in the feed solution due to the presence of fixed carboxylic group bearing the same sign as the mobile ions. The rejection of a charged solute depends on the pore radius of the effective membrane and the two electrical parameters, namely the effective membrane charge density and the dielectric exclusion energy barrier [33]. Furthermore, this charged solute is dependent on the ionic strength, the valence of the solutes and the concentration of the feed solution [31, 34]. It is quite impossible to differentiate which ions penetrate more in the modified membrane since the flux for Na^+ and Cl^- were nearly equimolar [35]. At a different angle, the interaction between carboxylic group on the membrane surface and the NaCl feed solution are either by dissociation of functional groups or adsorption of ions from the solutions [36], causing the ions in the feed solution to be attracted to the permeate solution.

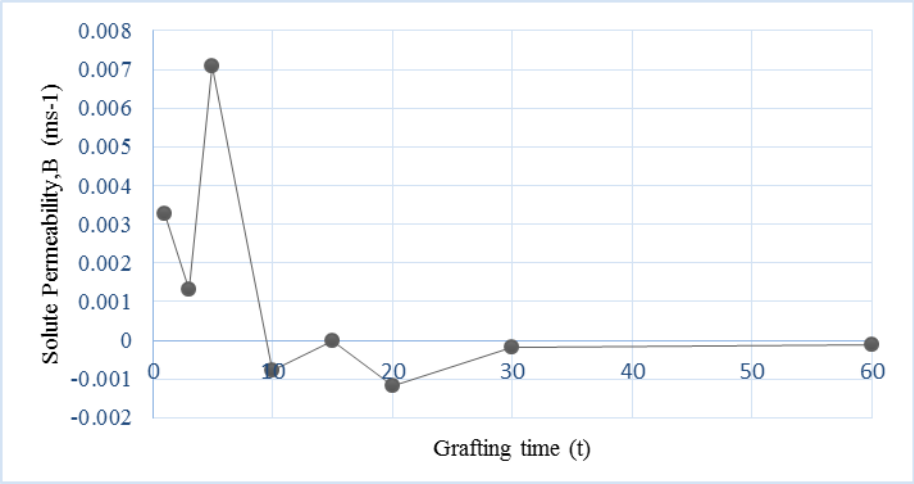


Figure 6. Solute permeability of the modified membrane at 50g/L of monomer concentration

Structural parameter

The membrane structural parameter, S, is an intrinsic membrane parameter used to determine the degree of internal concentration polarization (ICP) in the porous support of the membrane [38]. It is useful in quantifying the mass transport length scale across the membrane support layer [39]. Hence, the aim of having a surface modification is to lower the value of structural parameter. In the solute permeability, it was found that the carboxylic group on the membrane surface causes a negative rejection as the grafting time increases, which indicates that the diffusion transport of salts within the membrane plays a crucial role in regressing the FO processes. Since the negative rejection starts to develop as the grafting time increases from 10 minutes onwards, the measurement of structural parameter is only applicable with samples grafted at 1, 3 and 5 minutes. From Table 2, the highest value of S was observed for unmodified UFPES (54 x 10^{-4} m) while all the UV-grafted membranes exhibited a lower value of S. It is noted that under minimal modification (5AA-1min), the value decreases to 3.1 x 10^{-4} m which shows that surface modification on PES membrane via UV-grafting has great potential and is comparable with the commercial CTA membrane. However, the performance of the modified membrane in Table 2 contradicts the expected result. From the table, it is observed that as the grafting parameter increases, the value of S increases. For example, for the modification using 30g/L of monomer concentration, the values of S obtained are 1.5 x 10^{-4} m, 3.0 x 10^{-4} m and 12 x 10^{-4} m while at 5 minutes of grafting time, the values obtained are 2.7 x 10^{-4} m, 4.5 x 10^{-4} m, 12 x 10^{-4} m, and 13 x 10^{-4} m. The structural parameter value increases due to the decrease in water permeability and the low value of solute permeability. In general, the S values for most of our modified membranes are relatively in good agreement with the commercial CTA membrane (4.27 x 10^{-4} m).

Table 2. Performance characteristics of the prepared UFPES membranes. Structural parameter measured using FO setup while water permeability, A and solute permeability, B from RO setup

Sample		A ($Lm^{-2}hr^{-1}bar^{-1}$)	B ($x10^{-3}$ ms^{-1})	R (10^{-3})	$J_{w,FO}$ ($Lm^{-2}hr^{-1}$)	S ($10^{-4}m$)
AA Concentration (g/L)	**Grafting time (min)**					
-	-	98.87	7.4×10^{-3}	1.5	3.81	54
5	1	98.0	3.4	3.94	4.0	3.1
5	3	108.5	3.2	4.4	4.3	2.3
5	5	122.3	3.1	4.65	4.2	2.7
15	1	131.7	6.3	2.28	2.3	2.7
15	3	152.2	3.8	3.78	4.8	2.4
15	5	121.8	1.6	9.05	4.4	4.5
30	1	161.2	8.0	1.80	4.1	1.5
30	3	171.2	3.4	4.13	4.5	3.0
30	5	182.6	1.0	1.31	3.0	12
50	1	114.2	3.3	4.2	2.3	4.4
50	3	93.4	1.3	1.02	3.1	6.1
50	5	97.8	7.1	1.91	3.4	13
Commercial CTA membrane [37]						4.27

Conclusion

Surface modification via UV-grafting was successfully conducted as indicated by the new formation of carboxylic group on the polyethersulfone membrane. The addition of the hydrophilic material affects not only the water permeability and solute permeability but also the structural parameter. By lowering the structural parameter, it will eventually lower the internal concentration polarisation (ICP) which is one of the main problems faced in FO technology. The process of adding more hydrophilic layer onto the membrane surface will lead to the negative retention mechanism. It is suggested that this surface modification undergo optimisation process using response surface methodology (RSM) to achieve an optimal membrane in FO technology. Moreover, the interaction between carboxylic groups in a single layer is differentiated from those in a multilayer through the usage of photo initiator and cross linker.

Acknowledgement

The authors are grateful for the research financial support by Universiti Malaysia Pahang under the Postgraduate Research Grant Scheme (PGRS 160336) and the Ministry of Higher Education Malaysia for MyPhD and FRGS grant (RDU160127).

References

1. Cath, T., Childress, A. and Elimelech, M. (2006). Forward osmosis: Principles, applications, and recent developments. *Journal of Membrane Science*, 281(1-2): 70-87.
2. Kochkodan, V. and Hilal, N. (2015). A comprehensive review on surface modified polymer membranes for biofouling mitigation. *Desalination*, 356 (1): 187-207.

3. Ng, L. T., Garnett, J. L., Zilic, E. and Nguyen, D. (2001). Effect of monomer structure on radiation grafting of charge transfer complexes to synthetic and naturally occurring polymers. *Radiation Physics and Chemistry*, 62(1): 89-98.
4. Kim, S. M. (2013). Surface nanostructuring of polysulfone membranes by atmospheric pressure plasma-induced graft polymerization (APPIGP). Thesis of Master Degree, University of California, USA.
5. Garcia-Ivars, J., Iborra-Clar, M. I., Alcaina-Miranda, M. I. Mendoza-Roca, J. A. and Pastor-Alcañiz, L. (2016). Surface photomodification of flat-sheet PES membranes with improved antifouling properties by varying UV irradiation time and additive solution pH. *Chemical Engineering Journal*, 283(1): 231-242.
6. He, D., Susanto, H. and Ulbricht, M. (2009). Photo-irradiation for preparation, modification and stimulation of polymeric membranes. *Progress in Polymer Science*, 34(1): 62-98.
7. Zhao, C., Nie, S., Tang, M. and Sun, S. (2011). Polymeric pH-sensitive membranes—A review. *Progress in Polymer Science*, 36(11): 1499-1520.
8. Yin, J. and Deng, B. (2015). Polymer-matrix nanocomposite membranes for water treatment. *Journal of Membrane Science*, 479(1): 256-275.
9. Abu Seman, M. N., Khayet, M., Ali, Z. I. and Hilal, N. (2010). Reduction of nanofiltration membrane fouling by UV-initiated graft polymerization technique. *Journal of Membrane Science*, 355(1): 133-141.
10. Ng, L. Y., Ahmad, A. and Mohammad, A. W. (2013). Alteration of polyethersulphone membranes through UV-induced modification using various materials: A brief review. *Arabian Journal of Chemistry*, 10(2): 1821-1834.
11. Garcia-Ivars, J., Iborra-Clar, M. I., Alcaina-Miranda, M. I., Mendoza-Roca, J. A. and Pastor-Alcañiz, L. (2014). Development of fouling-resistant polyethersulfone ultrafiltration membranes via surface UV photografting with polyethylene glycol/aluminum oxide nanoparticles. *Separation and Purification Technology*, 135(1): 88-99.
12. Peeva, P. D., Pieper T. and Ulbricht, M. (2010). Tuning the ultrafiltration properties of anti-fouling thin-layer hydrogel polyethersulfone composite membranes by suited crosslinker monomers and photo-grafting conditions. *Journal of Membrane Science*, 362(1-2): 560-568.
13. Setiawan, L., Wang, R., Tan, S., Shi, L. and Fane, A. G. (2013). Fabrication of poly(amide-imide)-polyethersulfone dual layer hollow fiber membranes applied in forward osmosis by combined polyelectrolyte cross-linking and depositions. *Desalination*, 312(1): 99-106.
14. Chung, Y. T., Ng, L. Y. and Mohammad, A. W. (2014). Sulfonated-polysulfone membrane surface modification by employing methacrylic acid through UV-grafting: Optimization through response surface methodology approach. *Journal of Industrial and Engineering Chemistry*, 20(4): 1549-1557.
15. Deng, B., Li, J., Hou, Z., Yao, S., Shi, L., Liang, G. and Sheng, K. (2008). Microfiltration membranes prepared from polyethersulfone powder grafted with acrylic acid by simultaneous irradiation and their pH dependence. *Radiation Physics and Chemistry*, 77(7): 898-906.
16. Li, S. S., Xie, Y., Xiang, T., Ma, L., He, C., Sun, S. D. and Zhao, C. S. (2016). Heparin-mimicking polyethersulfone membranes – hemocompatibility, cytocompatibility, antifouling and antibacterial properties. *Journal of Membrane Science*, 498(1): 135-146.
17. Zhao, C., Xue, J., Ran, F. and Sun, S. (2013). Modification of polyethersulfone membranes – A review of methods. *Progress in Materials Science*, 58(1): 76-150.
18. Van der Bruggen, B. (2009). Chemical modification of polyethersulfone nanofiltration membranes: A review. *Journal of Applied Polymer Science*, 114(1): 630-642.
19. Wang, D., Zou, W., Li, L., Wei, Q., Sun, S. and Zhao, C. (2011). Preparation and characterization of functional carboxylic polyethersulfone membrane. *Journal of Membrane Science*, 374(1): 93-101.
20. Kato, K., Uchida, E., Kang, E. T., Uyama, Y. and Ikada, Y. (2003). Polymer surface with graft chains. *Progress in Polymer Science*, 28(2): 209-259.
21. Wei, X., Wang, R., Li, Z. and Fane, A. G. (2006). Development of a novel electrophoresis-UV grafting technique to modify PES UF membranes used for NOM removal. *Journal of Membrane Science*, 273(1): 47-57.
22. Bilongo, T. G., Remigy, J. C. and Clifton, M. (2010). Modification of hollow fibers by UV surface grafting. *Journal of Membrane Science*, 364(1): 304-308.
23. Kuroda, S. I., Nagura, A., Horie, K. and Mita, I. (1989). Degradation of aromatic polymers—III. Crosslinking and chain scission during photodegradation of polysulphones. *European Polymer Journal*, 25(6): 621-627.
24. Mansourpanah, Y. and Momeni Habili, E. (2013). Preparation and modification of thin film PA Membranes with improved antifouling property using acrylic acid and UV irradiation. *Journal of Membrane Science*, 342(1-2): 158-166.

25. Yu, H., Cao, Y., Kang, G., Liu, J., Li, M. and Yuan, Q. (2009). Enhancing antifouling property of polysulfone ultrafiltration membrane by grafting zwitterionic copolymer *via* UV-initiated polymerization. *Journal of Membrane Science,* 342(1-2): 6-13.
26. Taniguchi, M. and Belfort, G. (2004). Low protein fouling synthetic membranes by UV-assisted surface grafting modification: Varying monomer type. *Journal of Membrane Science,* 231(1-2): 147-157.
27. Taniguchi, M., Pieracci, J., Samsonoff, W. A. and Belfort, G. (2003). UV-assisted graft polymerization of synthetic membranes: Mechanistic studies. *Chemistry of Materials,* 15(20): 3805-3812.
28. Liu, C., Shi, L. and Wang, R. (2015). Crosslinked layer-by-layer polyelectrolyte nanofiltration hollow fiber membrane for low-pressure water softening with the presence of SO_4^{2-} in feed water. *Journal of Membrane Science,* 486(1): 169-176.
29. Volkov, A., Yushkin, A., Kachula, Y., Khotimsky, V. and Volkov, V. (2014). Application of negative retention in organic solvent nanofiltration for solutes fractionation. *Separation and Purification Technology,* 124(1): 43-48.
30. Vatanpour, V., Madaeni, S. S., Moradian, R., Zinadini, S. and Astinchap, B. (2011). Fabrication and characterization of novel antifouling nanofiltration membrane prepared from oxidized multiwalled carbon nanotube/polyethersulfone nanocomposite. *Journal of Membrane Science,* 375(1): 284-294.
31. Schaep, J., Vandecasteele, C., Wahab Mohammad, A. and Richard Bowen, W. (2001). Modelling the retention of ionic components for different nanofiltration membranes. *Separation and Purification Technology,* 22(1): 169-179.
32. Bhanushali, D., Kloos, S. and Bhattacharyya, D. (2002). Solute transport in solvent-resistant nanofiltration membranes for non-aqueous systems: Experimental results and the role of solute–solvent coupling. *Journal of Membrane Science,* 208(1): 343-359.
33. Qiu, C., Zhang, Q. T. N. L. and Ping, Z. (2006). Nanofiltration membrane preparation by photomodification of cardo polyetherketone ultrafiltration membrane. *Separation and Purification Technology,* 51(3): 325-331.
34. Nilsson, M., Trägårdh, G. and Östergren, K. (2008). The influence of pH, salt and temperature on nanofiltration performance. *Journal of Membrane Science,* 312(1): 97-106.
35. Phillip, W. A., Yong, J. S. and Elimelech, M. (2010). Reverse draw solute permeation in forward osmosis: Modeling and experiments. *Environmental Science and Technology,* 44(13): 5170-5176.
36. Elimelech, M., Chen, W. H. and Waypa, J. J. (1994). Measuring the zeta (electrokinetic) potential of reverse osmosis membranes by a streaming potential analyzer. *Desalination,* 95(3): 269-286.
37. Achilli, A., Cath, T. Y. and Childress, A. E. (2010). Selection of inorganic-based draw solutions for forward osmosis applications. *Journal of Membrane Science,* 364(1): 233-241.
38. Park, M., Lee, J. J., Lee, S. and Kim, J. H. (2011). Determination of a constant membrane structure parameter in forward osmosis processes. *Journal of Membrane Science,* 375 (1-2): 241-248.
39. Tiraferri, A., Yip, N. Y., Straub, A. P., Romero-Vargas Castrillon, S. and Elimelech, M. (2013). A method for the simultaneous determination of transport and structural parameters of forward osmosis membranes. *Journal of Membrane Science,* 444(1): 523-538.

Malaysian Journal of Analytical Sciences, Vol 22 No 3 (2018): 553 - 560
DOI: https://doi.org/10.17576/mjas-2018-2203-24

MALAYSIAN JOURNAL OF ANALYTICAL SCIENCES
Published by The Malaysian Analytical Sciences Society
ISSN 1394 - 2506

RAPID SYNTHESIS AND CHARACTERIZATION OF LEAF-LIKE ZEOLITIC IMIDAZOLATE FRAMEWORK

(Sintesis Cepat dan Pencirian Kerangka Seperti Daun Imidazolat Zeolitik)

Imran Ullah Khan[1, 2, 3], Mohd Hafiz Dzarfan Othman[1*], Juhana Jaafar[1], Haslenda Hashim[3], Ahmad Fauzi Ismail[1], Mukhlis A Rahman[1], Norafiqah Ismail[1]

[1]*Advance Membrane Technology Research Center (AMTEC), Faculty of Chemical and Energy Engineering, Universiti Teknologi Malaysia, 81310 Skudai, Johor, Malaysia*
[2]*School of Chemical and Material Engineering (SCME), National University of Science and Technology (NUST), H-12, Islamabad, Pakistan*
[3]*Process System Engineering Centre (PROSPECT), Faculty of Chemical and Energy Engineering, Universiti Teknologi Malaysia, 81310 Skudai, Johor, Malaysia*

**Corresponding author: hafiz@petroleum.utm.my*

Received: 16 April 2017; Accepted: 7 March 2018

Abstract

A two-dimensional zeolitic imidazolate framework with a leaf-like structure (ZIF-L) was synthesized in aqueous solution at room temperature with a molar ratio of Zn^{+2}/Hmim (1: 8). Various triethylamine (TEA) concentrations were also used for the rapid production of ZIF-L. Different characterization techniques like X-ray diffraction (XRD), field emission scanning electron microscopy (FESEM), transmission electron microscopy (TEM) and thermogravimetric analysis (TGA) were performed to investigate the effect of base type additive triethylamine (TEA) on the crystal morphology, crystallinity, particle size and thermal stability of ZIF-L particles. From the experimental results, it was found that ZIF-L with a particle size of 5.3 µm was formed at TEA/total mole ratio of 0, but particle size was decreased when TEA/total mole ratio was increased up to 0.0003. The smallest ZIF-L particles obtained were 3 µm that showed excellent thermal stability. It can be concluded that this promising synthesis method with base-type additive would provide the new insights in the development of ZIFs materials in economical ways.

Keywords: zeolitic imidazolate framework, leaf-like structure, base-type additive, characterization, particle size

Abstrak

Kerangka imidazolat zeolitik dua dimensi dengan struktur seperti daun (ZIF-L) telah disintesis dalam larutan akueus pada suhu bilik. Trietilamina (TEA) pelbagai kepekatan juga digunakan untuk penghasilan cepat ZIF-L. Teknik-teknik pencirian yang berbeza seperti pembelauan sinar-X (XRD), mikroskop imbasan elektron pancaran medan (FESEM), mikroskop transmisi elektron (TEM) dan analisis termogravimetri (TGA) telah dijalankan untuk menyiasat kesan jenis asas tambahan trietilamina (TEA) pada morfologi kristal, penghabluran, saiz zarah dan kestabilan haba zarah ZIF-L. Daripada keputusan eksperimen, ianya didapati bahawa ZIF-L dengan saiz zarah 5.3 µm terbentuk pada nisbah molekul TEA/jumlah 0, tetapi saiz zarah berkurangan apabila nisbah TEA/jumlah mol meningkat sehingga 0.0003. Partikel ZIF-L yang terkecil diperoleh adalah 3 µm yang menunjukkan kestabilan terma yang sangat baik. Sebagai kesimpulan, kaedah sintesis cepat ini berpotensi dengan bahan tambahan jenis asas akan memberikan gambaran baru dalam pembangunan bahan ZIF lebih ekonomik.

Kata kunci: kerangka imidazolat zeolitik, struktur seperti daun, asas-jenis bahan tambahan, pencirian, saiz zarah

Introduction

Zeolitic imidazolate frameworks (ZIFs), a sub class of metal-organic frameworks (MOFs) have created great research interest due to their unique advantages for a variety of applications such as gas storage [1], gas separation, and adsorption [2], catalysis [3], and chemical sensing [4]. They have permanent zeolitic porous structure with uniform microporosity, tunable crystal surface and having exhibit excellent thermal and chemical stability [5]. ZIFs are made up of tetrahedral metal ions (Zn or Co) bridged by 2-methyl imidazole (Hmim) as an organic linker and possess highly order porous structure [6]. ZIFs can be produced using various processes such as the solvothermal, the microwave assisted solvothermal and aqueous room temperature synthesis process [7].

Commonly solvothermal process and microwave-assisted solvothermal process are used to synthesize ZIFs as they produce better yield and smaller particle size [8-10]. A large variety of ZIFs with different crystal structure such as ZIF-21, ZIF-62, ZIF-11, ZIF-100, ZIF-95, ZIF-75 had been typically synthesized in organic solvents such as methanol (CH_3OH), diethylformamide (DMF) and diethylformamide (DEF) [1, 11]. Nevertheless, high-energy demand, time consumption, and expensive and pollutant organic solvents limit the utilization of these processes [12]. Therefore, cost effective and environmentally friendly synthesis approach for ZIFs is crucial and major challenge for researchers. To overcome the issues, an aqueous room temperature synthesis process has been explored.

Aqueous room temperature synthesis method had improved product yield with much shorter time compared to the synthesis processes developed in organic media. In addition, the product showed excellent thermal and chemical stabilities, and improved hydrothermal stability [8, 12]. The advantages of aqueous room temperature synthesis process such as low energy consumption, smaller particle size, shorter reaction time and higher yield have been successfully highlighted by various researchers [1, 2, 5, 7, 12-14]. Chen et al. [1], Low et al. [2], Zhong et al. [14] and Yao et al. [13] had successfully synthesized ZIF-L with a unique cushion-shaped cavity and leaf like structure from zinc nitrate hexahydrate and Hmim in deionized water at room temperature. They identified that molar ratio of Zn^{+2}/Hmim was the key synthesis parameter to produce leak like structure of ZIF. Although, they have produced leaf- like structure but particles size was bigger and longer time for synthesis was required.

Controlling crystal growth and morphology of synthesized ZIFs is also another important and research feature for large-scale productions. It is easy to fabricate thin mixed matrix membrane with smaller particle size and subsequently high adsorption capacity was achieved due to smaller pores [2]. Crystal growth is highly dependent on ligand to metal ratio as excess amount of ligand could limit the linkage with metal ions, subsequently reduce the yield [8, 12]. The amount of organic ligand can be significantly reduced by the addition of modulating agent (base-type additive) in the ZIF synthesis solution that can ease the ligand-metal interaction [11, 15, 16]. Subsequently, it gives rapid interaction between metal ion and ligand and produce smaller crystals in shorter time with low metal to ligand ratio. Among base type additives, triethylamine (TEA) has shown excellent compatibility with various organic ligands [7, 13, 17]. ZIF-8 nanoparticles were previously produced using TEA as a deprotonation agent at a relatively low ratio of Zn^{+2}/Hmim (1:16) [7]. To the best of our knowledge, no research has been reported to use TEA as an additive during synthesis of ZIF-L to reduce particle size, shorter synthesis time with lower cost and develop green synthesis process. Hence, the present work investigates the synthesis of ZIF-L at aqueous room temperature with various concentrations of TEA in the synthesis mixture. The effect of various concentration of TEA on the particle size, crystal growth and thermal stability were investigated and discussed in details. Such developments will undoubtedly lead to better understanding of ZIF crystallization mechanisms and facilitate the development of ZIF-L for large-scale applications.

Materials and Methods

Materials

Materials used to synthesize ZIF-L were zinc nitrate hexahydrate ($Zn(NO_3)_2.6H_2O$, 99% purity), Organic linker, 2-methylimidazole (Hmim, 99% purity), base-type additive triethylamine (TEA, 99.5% purity), purchased from Sigma-Aldrich. No further purification was needed for all chemicals.

Synthesis of ZIF-L

The molar ratio of Zn^{+2} and Hmim (1:8) was used during synthesis of ZIF-L in basic solution. The synthesis of ZIF-L was described in literature [1, 2, 7] but some changes were made to enhance the yield as well as reduce the time for synthesis. Typically, 2.95 g (1.98 mmol) of Zn $(NO_3)_2.6H_2O$ and 6.5 g (15.83 mmol) of Hmim was dissolved in 200 mL deionized water respectively. The appropriate amount of TEA was added to Hmim solution as a deprotonation agent (Table 1), and then the aqueous solution of zinc nitrate was added into the aqueous solution of Hmim under stirring. The mixture was stirred at room temperature for 60 minutes. The product was obtained by repeated centrifugation (10000 rpm for 10 minutes) and washed by deionized water to remove residual chemicals, and then dried in an oven at 60 ℃ for 12 hours. The yield of the product was calculated using equation (1).

$$\text{Yield}(\%) = \frac{\text{Mass of ZIF-L (obtained)}}{\text{Mass of ZIF-L (theoretical)}} \times 100 \quad (1)$$

Table 1. Different volume of TEA for synthesis of ZIF-L

Sample Name	TEA/Total Mole	TEA Volume (ml)
A0	0	0
A1	0.0002	0.5
A2	0.0003	1
A3	0.0004	1.5

Characterization

The field emission scanning electron microscopy (FESEM) images were taken using a Hitachi SU 8020 microscope. The X-ray diffraction (XRD) analysis was performed on a Rigaku smart lab diffractometer using CuKα radiation at 40 KV and 30 mA in the 2Θ range of 3-100°. Thermogravimetric analysis (TGA, Q 500, TA Instrument, USA) was used to check the thermal stability of the synthesized samples at different TEA loading. TGA records the weight changes of sample when heated from 30 to 900°C at the heating rate of 10°C/min under nitrogen atmosphere. The transmission electron microscopy (TEM) images were taken using Hitachi, HT7700 microscope. Samples were prepared by dispersing ZIF-L powder into concentrated ethanol solution. A drop of ethanol was used for the dispersion of ZIF-L onto carbon-coated copper grids operating at 120 KV. All the characterization were carried out at Central Lab UTM, Johor Bahru, Malaysia.

Results and Discussion

Figure 1 shows the XRD pattern of various synthesized samples of ZIF-L. The intensity of the peaks was in good agreement with the previous works [1,2]. In the first attempt (Figure 1, sample A0), ZIF-L was synthesized in zinc salt and Hmim aqueous solution at room temperature with no addition of TEA. After continues stirring the synthesis solution turned cloudy that shows the occurrence of reaction between reactants. FESEM image (Figure 2a) also confirm the leaf-like structure of ZIF-L. However, longer time of synthesis (4 hours) was required due to low reaction rate and insufficient deprotonation of Hmim. When the small amount of TEA (0.5 ml and 1ml) (TEA/total mole ratio = 0.0002, 0.0003) was added in the synthesis solution, surprisingly, ZIF-L particles were formed after 60 minutes (Figure 1, sample A1, A2). Furthermore, their FESEM images confirmed the leaf-like particles with 2D crystalline structure (Figure 2b, 2c). The possible reason was the fast deprotonation of Hmim to produce more reactive sites for reaction with Zn^{+2} [18–20]. Thus, ZIF-L was successfully synthesized in shorter time with high yield (Table 2).

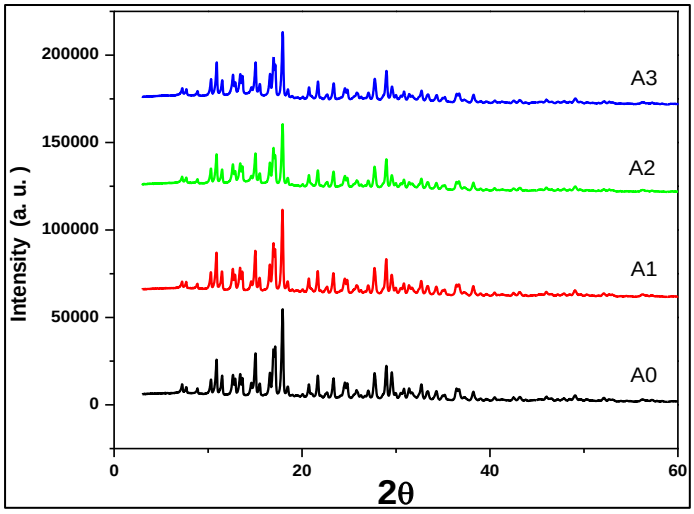
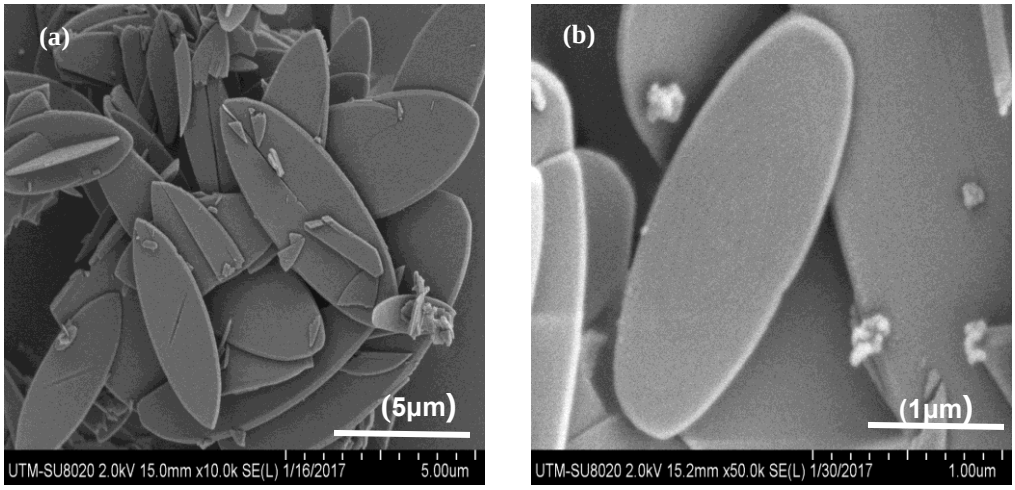


Figure 1. XRD pattern of synthesized ZIF-L samples with different TEA/total mole ratio: A0 (0), A1 (0.0002), A2 (0.0003) and A3 (0.0004)

Further increase in TEA/total mole ratio up to 0.0004 was not favorable for the formation of ZIF-L, as particles started to break up (Figure 2d). Higher TEA/total mole ratio increased the reaction rate by rapid deprotonation of Hmim, lead to break down the leaf-like structure. The series of FESEM images were used to estimate particle size. It was identified that particle size decreased from 5.3 to 3 µm when TEA/total mole ratio was increased from 0 to 0.0003 as shown in Table 2 and Figure 2a – c.

Table 2. Yield and particle size of ZIF-L

Sample Name	Yield (%)	Particle Size (µm)
A0	80	5.3
A1	90	3.2
A2	90	3



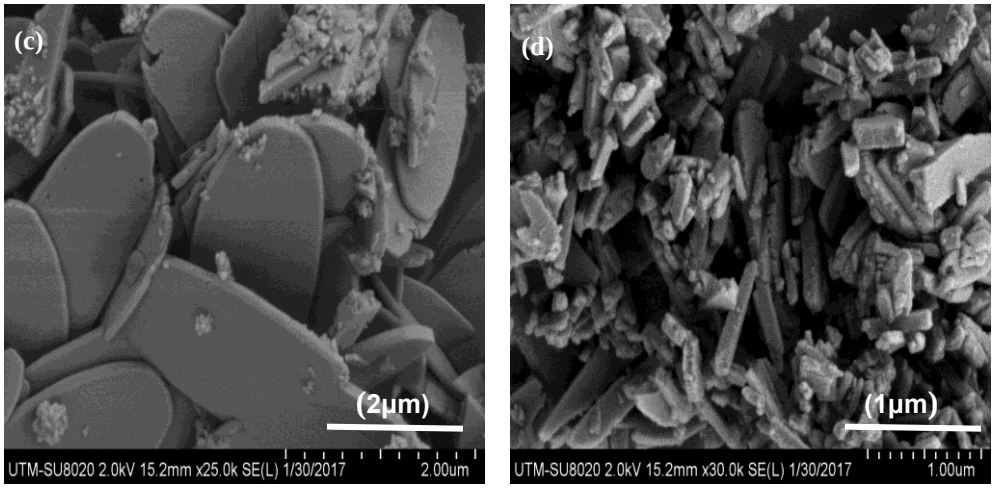


Figure 2. FESEM images of the synthesized ZIF-L samples at different TEA/total mole ratio: (a) A0 (0), (b) A1 (0.0002), (c) A2 (0.0003) and (d) A3 (0.0004)

The structure of ZIF-L was further confirmed by the transmission electron microscopy (TEM) images (Figure 3) that well agreed with the above FESEM images. Two samples of ZIF-L with maximum and minimum particle size were selected for this analysis. These TEM images clearly identified the 2D leaf-like structure of ZIF-L without TEA (Figure 3a, TEA/total mole = 0) and with the addition of TEA (Figure 3b, TEA/total mole = 0.0003).

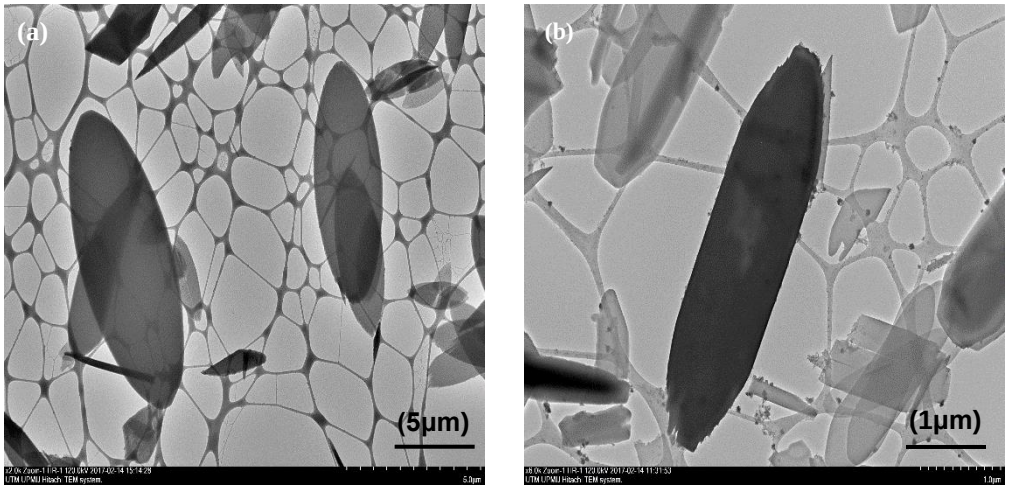


Figure 3. TEM images of the synthesized ZIF-L samples at different TEA/total mole ratio: (a) A0 (0) and (b) A2 (0.0003)

The thermal stability of the synthesized products of ZIF-L was also measured by thermogravimetric analysis (TGA) in which the mass of the product was monitored as a function of temperature as shown in Figure 4. We reported the higher thermal stability of products compared to previous work [1, 2]. Sudden weight loss started around 255°C was due to the decomposition of organic linkers and ZIF-L crystal structure.

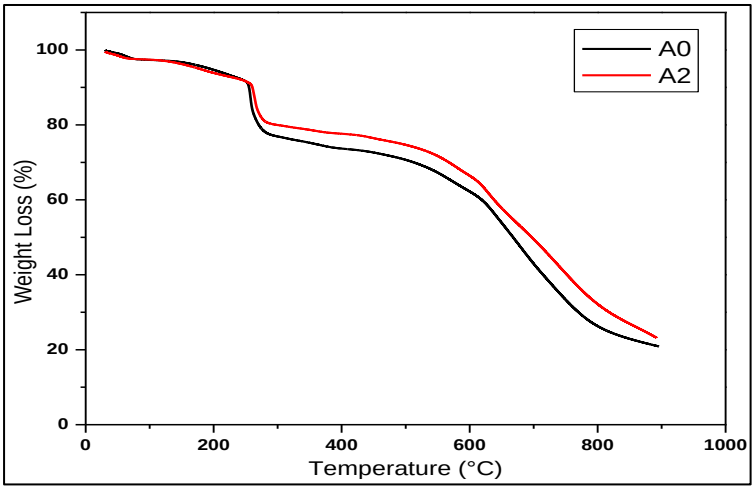


Figure 4. Thermal stability of synthesized ZIF-L samples with weight loss profile at different temperature and TEA/ total mole ratio: A0 (0) and A2 (0.0003)

Further confirmation of thermal stability was done by calculating the peaks at different temperature on derivative of the weight loss curves (Figure 5). The highest derivative peak was obtained around 255 °C indicated the point of greatest rate of change on the weight loss curve and was due to the structural decomposition ZIF-L. It could be concluded that thermal stability was not reduced due to the addition of TEA during synthesis process.

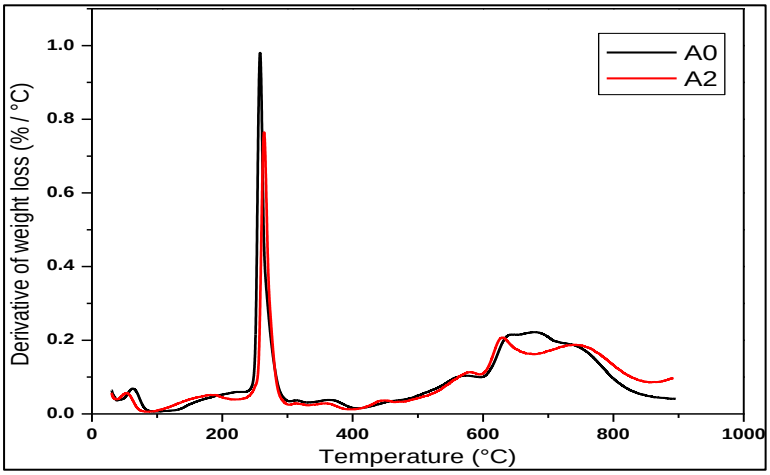


Figure 5. Thermal stability of synthesized ZIF-L samples with derivative of weight loss profile at different temperatures TEA/ total mole ratio: A0 (0) and A2 (0.0003)

Conclusion

In this study, ZIF-L with leaf like structure was rapidly synthesized in an aqueous solution at ambient temperature with smaller particle size and high thermal stability. The Zn^{+2}/Hmim ratio of 8 was used with various concentration of TEA. The addition of TEA was very important for the rapid synthesis of ZIF-L as it deprotonated the organic ligand. The particle size was also decreased from 5.3 to 3 μm as the TEA/total mole ratio increased from 0 to 0.0003. However, an excessive TEA would break down the particles due to more rapid reaction. In addition, ZIF-L particles showed excellent thermally stability around 255 °C. We expect this new synthesis approach with low

reagent ratio and base type additive will undoubtedly provide a better understanding of morphology control of ZIFs during synthesis and thus reduce the production cost for industrial applications.

Acknowledgement

The authors gratefully acknowledge financial support from the Universiti Teknologi Malaysia under the Research University Grant Tier 1 (Project number: Q. J130000.2546.12H25) and Nippon Sheet Glass Foundation for Materials Science and Engineering under Overseas Research Grant Scheme (Project number: R. J130000.7346.4B218). Lastly, the first author would also like to thank National University of Science and Technology (NUST), Pakistan for their scholarship under Faculty Development Programme (FDP).

References

1. Chen, R., Yao, J., Gu, Q., Smeets, S., Baerlocher, C. and Gu, H. (2013). A two-dimensional zeolitic imidazolate framework with a cushion-shaped cavity for CO_2 adsorption. *Chemical Communications*, 49 (1): 9500-9502.
2. Low, Z. X., Razmjou, A., Wang, K., Gray, S., Duke, M. and Wang, H. (2014). Effect of addition of two-dimensional ZIF-L nanoflakes on the properties of polyethersulfone ultrafiltration membrane. *Journal of Membrane Science*, 460: 9-17.
3. Lee, J., Farha, O. K., Roberts, J., Scheidt, K. A., Nguyen, S. T. and Hupp, J. T. (2009). Metal-organic framework materials as catalysts. *Chemical Society Reviews*, 38(5): 1450-1459.
4. Yao, J. and Wang, H. (2014). Zeolitic imidazolate framework composite membranes and thin films: Synthesis and applications. *Chemical Society Reviews*, 43(13): 4470-4493.
5. Low, Z. X., Yao, J., Liu, Q., He, M., Wang, Z., Suresh, A. K., Bellare, J. and Wang, H. (2014). Crystal transformation in zeolitic-imidazolate framework. *Crystal Growth and Design*, 14(12): 6589-6598.
6. Banerjee, R., Furukawa, H., Britt, D., Knobler, C., O'Keeffe, M. and Yaghi, O. M. (2009). Control of pore size and functionality in isoreticular zeolitic imidazolate frameworks and their carbon dioxide selective capture properties. *Journal of the American Chemical Society*, 131(11): 3875-3877.
7. Nordin, N. A. H. M., Ismail, A. F., Mustafa, A., Goh, P. S., Rana, D. and Matsuura, T. (2014). Aqueous room temperature synthesis of zeolitic imidazole framework 8 (ZIF-8) with various concentrations of triethylamine. *RSC Advances*, 4(63): 33292-33300.
8. Yamamoto, D., Maki, T., Watanabe, S., Tanaka, H., Miyahara, M. T. and Mae, K. (2013). Synthesis and adsorption properties of ZIF-8 nanoparticles using a micromixer. *Chemical Engineering Journal*, 227: 145-150.
9. Schlichte, K., Kratzke, T. and Kaskel, S. (2004). improved synthesis, thermal stability and catalytic properties of the metal-organic framework compound $Cu_3(BTC)_2$. *Microporous and Mesoporous Materials*, 73(1): 81-88.
10. Wen, L., Wang, D. E., Wang, C., Wang, F., Li, D. and Deng, K. (2009). A 3D porous zinc MOF constructed from a flexible tripodal ligand: synthesis, structure, and photoluminescence property. *Journal of Solid State Chemistry*, 182(3): 574-579.
11. Biemmi, E., Christian, S., Stock, N. and Bein, T. (2009). High-throughput screening of synthesis parameters in the formation of the metal-organic frameworks MOF-5 and HKUST-1. *Microporous and Mesoporous Materials*, 117(1): 111-117.
12. Pan, Y., Liu, Y., Zeng, G., Zhao, L. and Lai, Z. (2011). Rapid synthesis of zeolitic imidazolate framework-8 (ZIF-8) nanocrystals in an aqueous system. *Chemical Communications*, 47(7): 2071-2073.
13. Yao, J., He, M. and Wang, H. (2015). Strategies for controlling crystal structure and reducing usage of organic ligand and solvents in the synthesis of zeolitic imidazolate frameworks. *CrystEngComm*, 17(27): 4970-4976.
14. Zhong, Z., Yao, J., Low, Z. X., Chen, R., He, M. and Wang, H. (2014). Carbon composite membrane derived from a two-dimensional zeolitic imidazolate framework and its gas separation properties. *Carbon*, 72: 242-249.
15. Cravillon, J., Nayuk, R., Springer, S., Feldhoff, A., Huber, K. and Wiebcke, M. (2011). Controlling zeolitic imidazolate framework nano- and microcrystal formation: insight into crystal growth by time-resolved in situ static light scattering. *Chemistry of Materials*, 23(8): 2130-2141.
16. He, M., Yao, J., Li, L., Zhong, Z., Chen, F. and Wang, H. (2013). Aqueous solution synthesis of ZIF-8 films on a porous nylon substrate by contra-diffusion method. *Microporous and Mesoporous Materials*, 179: 10-16.
17. Pan, Y., Heryadi, D., Zhou, F., Zhao, L., Lestari, G., Su, H. and Lai, Z. (2011). Tuning the crystal morphology and size of zeolitic imidazolate framework-8 in aqueous solution by surfactants. *CrystEngComm*, 13(23): 6937-6940.

18. He, M., Yao, J., Liu, Q., Wang, K., Chen, F. and Wang, H. (2014). Facile synthesis of zeolitic imidazolate framework-8 from a concentrated aqueous solution. *Microporous and Mesoporous Materials,* 184: 55-60.
19. Hu, Y., Kazemian, H., Rohani, S., Huang, Y. and Song, Y. (2011). In situ high pressure study of ZIF-8 by FTIR spectroscopy. *Chemical Communications,* 47(47): 12694-12696.
20. Jian, M., Liu, B., Liu, R., Qu, J., Wang, H. and Zhang, X. (2015). Water-based synthesis of zeolitic imidazolate framework-8 with high morphology level at room temperature. *RSC Advances,* 5(60): 48433-48441.

Malaysian Journal of Analytical Sciences, Vol 22 No 3 (2018): 561 - 569
DOI: https://doi.org/10.17576/mjas-2018-2203-25

MALAYSIAN JOURNAL OF ANALYTICAL SCIENCES
Published by The Malaysian Analytical Sciences Society
ISSN 1394 - 2506

SEPARATION OF FATTY ACIDS FROM PALM OIL USING ORGANIC SOLVENT NANOFILTRATION

(Pemisahan Asid Lemak daripada Minyak Kelapa Sawit Menggunakan Penuras Nano Pelarut Organik)

Dayang Nur Fitrah Awang Ismail and Nazlee Faisal Ghazali*

Department of Bioprocess Engineering,
Faculty of Chemical and Energy Engineering,
Universiti Teknologi Malaysia, 81310 Skudai, Johor Bahru, Johor, Malaysia

**Corresponding author: nazlee@utm.my*

Received: 16 April 2017; Accepted: 7 March 2018

Abstract

Distillation of fatty acid from traditional recovery method consumes a lot of energy. Membrane process is more preferred because it reduces energy consumption. In this work, the possibility of separating free fatty acid (FFA) from palm oil using organic solvent nanofiltration was studied. Various commercial organic solvent nanofiltration membranes were tested using dead end filtration for their ability to remove free fatty acid from palm oil/acetone mixture. In all membranes, triglycerides (TAG) were preferentially retained at increasing pressure, while FFA were permeated through the membrane. All the three membranes showed selective permeation of FFA, with Solsep 030306 gave the highest selectivity of FFA over triglycerides. The best fatty acid separation performance was achieved using NF030306 membrane with acetone at pressure in the range of 30 to 40 bar and 3.6 g/L concentration of fatty acid. Using NF030306 membrane, 55% of low fatty acid and 87% of triglycerides were rejected from the system. Good separation was achieved at high pressure and concentration. We successfully demonstrated the separation of fatty acid separation from palm oil using organic solvent nanofiltration could be achieved.

Keywords: free fatty acid, palm oil, organic solvent nanofiltration, deacidification

Abstrak

Pemulihan tradisional asid lemak daripada minyak yang boleh dimakan menggunakan sejumlah besar tenaga. Jika penyulingan digantikan dengan proses membran, penggunaan tenaga boleh dikurangkan dengan banyak. Dalam kajian ini, kami akan mengkaji kemungkinan untuk memisahkan asid lemak bebas daripada minyak kelapa sawit dengan menggunakan penuras nano pelarut organik. Pelbagai pelarut organik membran penuras nano komersial telah diuji menggunakan penuras nano untuk keupayaan mereka untuk memisahkan asid lemak bebas daripada campuran kelapa sawit/aseton. Untuk semua membran, trigliserida adalah dikekalkan pada tekanan yang semakin meningkat, manakala asid lemak meresap melalui membran. Ketiga-tiga membran menunjukkan penyerapan terpilih asid lemak, bagaimanapun Solsep 030306 memberikan pemilihan tertinggi asid lemak/trigliserida. Pemisahan asid lemak yang terbaik dicapai dengan menggunakan membran NF030306 dengan aseton pada tekanan dalam lingkungan 30 hingga 40 bar dan 3.6 g/L kepekatan asid lemak. Penolakan asid lemak yang rendah iaitu 55% dan penolakan trigliserida yang tinggi sehingga 87% telah dicapai menggunakan membran NF030306. Pemisahan baik dicapai pada tekanan tinggi dan kepekatan tinggi. Ia menunjukkan pemisahan asid lemak daripada minyak kelapa sawit menggunakan penuras nano pelarut organik boleh dicapai.

Kata kunci: asid lemak bebas, minyak sawit, penuras nano pelarut organik, penyahasidan

Introduction

In palm oil processing, free fatty acid (FFA) has to be separated from crude palm oil because they adversely affect end-product quality. Currently free fatty acid removal from palm oil, a typical deacidification method for palm oil is steam distillation whereby the process is operated at 240-260 °C at of 1 to 3 mm Hg pressure [1]. However, this conventional process is energy-intensive and operated at high temperature which could destroy valuable thermal sensitive compounds. On the other hand, membrane separation offers several advantages over conventional process such as ambient temperature, less energy usage and reduction of thermal damage.

From the literature, researchers had tried the method of deacidification process of vegetable oil using membranes with and without the addition of solvent. Bhosle et al. used polymeric dense membranes to recover fatty acid from sunflower oil without any solvent but the selectivity between fatty acid and glycerides was low [2]. Some researchers used coupled extraction and membrane separation for fatty acid extraction from vegetable oil. For example, methanol was used to extract free fatty acids from soybean oil, where recovery the methanol was done using nanofiltration [3]. In addition, Kale et al uses methanol to extract free fatty acids from rice bran oil, and then to concentrate the free fatty acids and recover the methanol using reverse osmosis membranes [4]. Kumar and Bhowmick used membranes separation of FFA and glycerides from groundnut oil and showed that the selectivity between fatty acid and glycerides was low [5]. Firman et al. used commercial membrane and in-house fabrication PVDF membrane to deacidify soybean oil and solvent recovery by nanofiltration [6]. Currently, organic solvent nanofiltration (OSN) is becoming a great deal of attention for alternative molecular purification technology because of its low energy usage and ambient temperature operation [7, 8]. Organic solvent nanofiltration, it is sometimes called solvent resistant nanofiltration where a pressure driven membrane process that uses solvent resistant membranes to separate solutes of 100 to 1000 Da. The current applications of organic solvent nanofiltration (OSN) include solvent recovery [9, 10], catalyst recycling [11], enantiomer separation [12], peptide synthesis [13], and pharmaceutical purification [14].

The objective of this study was to remove free fatty acid from palm oil using organic solvent nanofiltration and to study the effects of pressure and concentration on the separation performance. This is the first time membrane was used to separate fatty acid from palm oil using OSN. To investigate the separation performance in deacidification of crude palm oil, various membranes were used in the experiments. A synthetic solution consists of palm oil and fatty acid was made. The molecular weight of palm oil is 847.78 g/mol and palmitic acid is 256.43 g/mol [15]. The performance is measured by the permeate flux and the rejection of solutes. The comparison of membrane performance was investigated through different pressure applied, and different concentration of free fatty acid contained in the oil feed.

Materials and Methods

Materials

Refined cooking oil was purchased from local store and the palmitic acid was purchased from Sigma-Aldrich. All membranes (NF030306, NF030306F, NF010206, and NF010306) were purchased from SOLSEP, Netherland. The properties of each membrane are shown in Table 1. The separation characteristics were measured by the rejection of solutes.

Membrane preparation

Each membrane was cut into circular disc with 20.43 cm^2 area and fitted in a dead-end nanofiltration set-up equipped to stainless steel feed tank under nitrogen atmosphere at 25 °C. NF030306 membrane was used in this experiment where it was tested using different solvents (acetone, hexane, isopropyl alcohol and ethyl acetate) at constant temperature, 25 °C, constant transmembrane pressure, 30 bar and stirred at 400 rpm.

Oil preparation

To represent as a crude palm oil, the feed sample was prepared by mixing the refined cooking palm oil with palmitic acid (4 wt.%). Solvent was added to the fatty acid-palm oil mixture due to high viscosity of the model solution. This solution was then filtered using dead end nanofiltration cell.

Measurement of free fatty acid concentration
The concentration of fatty acid in the feed, permeate and retentate was measured using GC. All experiments were performed in duplicate, the mean values were reported, and the differences between mean were statistically significant.

Table 1. Separation characteristics of SOLSEP membranes.

SOLSEP Membrane	Rejection of solutes R (Molecular Mass of Solutes)
NF010206	95% (*300 Da*)
NF010306	95% (*500 Da*)
NF030306F	95% (*300Da)*
NF 030306	95% (*500 Da*)

$$\text{Rejection} = 1 - (Cp/Cr)*100 \quad (1)$$

where Cp is the permeate concentration and Cr is the retentate concentration

Membrane preparation
Each membrane (NF030306, NF030306F, NF010206 and NF010306) was cut into circular disc with 20.43 cm^2 area and fitted in a dead-end nanofiltration set-up equipped to stainless steel feed tank under nitrogen atmosphere at 25 °C.

Optimization of membrane efficiency in the filtration process
The best membrane from membrane selection experiment was chosen. Filtration experiment was operated using different pressure; 10 bar, 20 bar, 30 bar, and 40 bar. The temperature and stirring speed was kept constant at 25 °C and 400 rpm, respectively. For the concentration variation experiment, The concentration of fatty acid (palmitic acid) in feed were 1.7 g/L, 3.6 g/L, 7.2 g/L and 14.4 g/L at constant pressure. For all filtration, the retentate and permeate was collected and analysed.

Analysis of free fatty acid and triglycerides
The fatty acid concentration was determined using gas chromatography (GC) AutoSystem XL (Shimadzu, Japan) while the analysis of triglycerides was done using evaporation method where 1 ml of sample was used and left to evaporate to remove solvents.

Optimisation of performance parameter
The important parameters that measure the performance of a membrane are flux and rejection. Flux J ($L/m^2.h$ = *LMH*) expressed as shown in equation 2:

$$J = \frac{V}{A \cdot t} \quad (2)$$

where *V* corresponds to the volume of accumulated permeate (L), *A* is the membrane effective area (m^2) and *t* is the filtration time (h).

The observed solute rejection R_i for a given species i is given by equation 3 below:

$$R_i = \left(1 - \frac{C_{ip}}{C_{ir}}\right) \times 100\% \quad (3)$$

where C_{ip} is the concentration in permeate while C_{ir} is the corresponding retentate concentration. An ideal membrane would allow all free fatty acids to pass through the membrane, while retaining all of triglycerides or in other hand, a high rejection for triglycerides and a low rejection of free fatty acids.

Results and Discussion

Selection of membrane

Figure 1 shows the permeate flux profile for each membranes tested. Permeate flux for NF010206 shown the highest (58.737 LMH) from the membranes tested while NF030306F was the lowest with 11.569 LMH permeate flux. A decline in permeate flux with time was observed in all samples. The decrease in flux permeation may be due to concentration polarization, membrane compaction, formation of gel layer and pore blocking of the membrane [16]. The best membrane in term of flux performance was NF010206. However, performance parameter such as rejection of free fatty acids and triglycerides along with the selectivity factor need to be taken into consideration too.

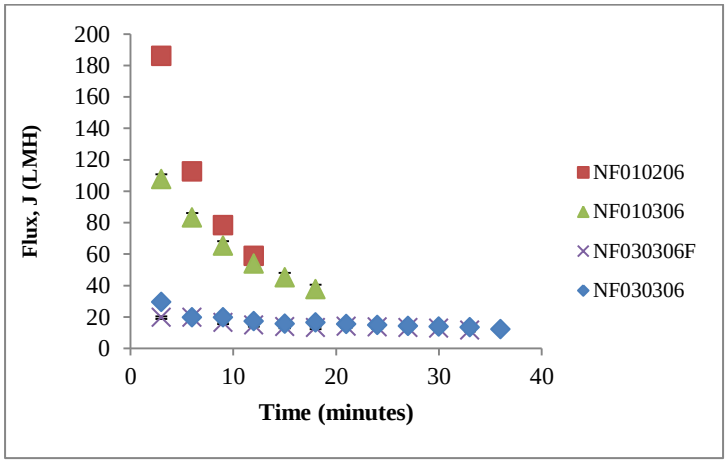


Figure 1. Flux profile for each membrane (Operation conditions: 30 bar, 25 °C and agitation 400 rpm with 100% pure acetone)

Figure 2 shows the rejections of free fatty acid and triglycerides for various membranes. It is desired to obtain the lowest possible percent of rejections of free fatty acids while the maximum possible rejection of triglycerides. From Figure 2, the lowest percent rejection of FFA was obtained by using NF010306 with 56.22% followed by NF030306 and NF030306 with 56.28%, respectively. Moreover, NF010206 and NF030306F were discarded for not presenting reasonable percent rejections, which were over 60% rejections of free fatty acids. The highest percent triglycerides rejection was obtained using NF010206 (R = 89.04%), however the rejections of fatty acid was also high (R = 86.41%) indicates that the separation was not efficient. This also applies with NF030306F which also gave high percent of free fatty acid rejection (R = 86.46%) This is expected since the molecular weight cutoff (MWCO) of NF010206 and NF030306F is around 300 Da. However, good separation was achieved using NF010306, and NF030306 since their values of percent rejections was quite high for rejection of triglycerides (R = 87.65%) and low percent for rejections of free fatty acid (R = 56.28%). As both membrane has 500 Da MWCO, it was expected for them to easily permeating free fatty acid while retaining the triglycerides.

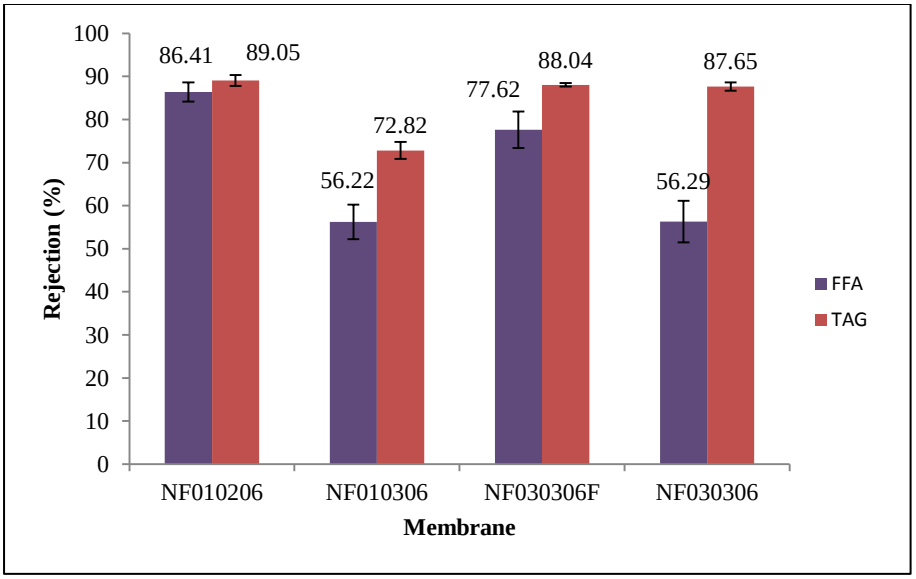


Figure 2. The effect of different type of membranes on the rejection of FFA and TAG at 30 bar, 25 °C and 400 rpm. FFA concentration of 3.6 g/L (4 wt.% FFA in 10 wt.% TAG).

Being the most permeable membrane to free fatty acid, with low free fatty acid rejection (56.29%), high percent rejection of triglycerides (87.65%), the NF030306 membrane was been selected for further optimization study.

The effects of transmembrane pressure

To evaluate the influence of transmembrane pressure towards the separation process, permeate flux was first evaluated. The permeate flux as a function of transmembrane pressure was shown in Figure 3. From Figure 3, the increase in pressure from 10 bar to 40 bar resulted in the increase of permeate flux from 18.4% to approximately 29.4%. This nonlinear behavior was probably caused by the build-up of rejected solute (palm oil) near the membrane surface. Shi et al. [17] suggested that in systems with retained solutes, concentration polarization becomes stronger as flux increases. This concentration polarization increased the osmotic pressure near the membrane surface and consequently lead to a lower effective driving pressure.

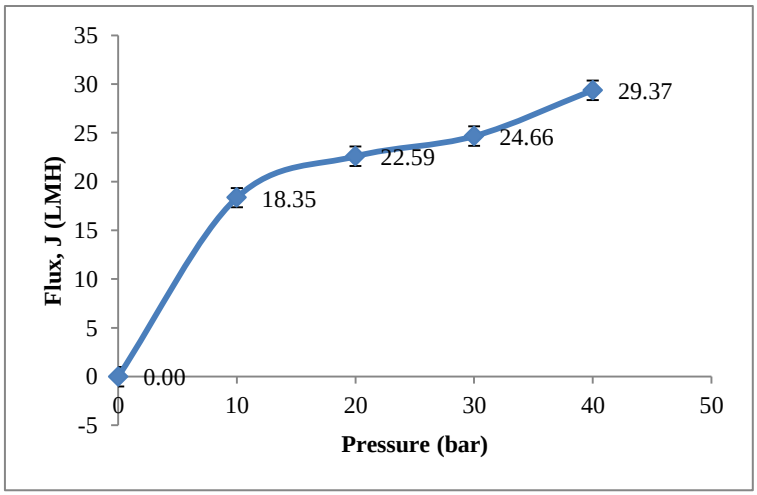


Figure 3. The effect of pressure towards flux (Operation conditions: 25 °C and agitation 400 rpm with FFA concentration of 3.6 g/L (4 wt.% FFA in 10 wt.% TAG) using NF030306 membrane)

The rejection of free fatty acid and rejection of triglycerides at different pressures were evaluated and shown in Figure 4 and Figure 5, respectively. The rejection of free fatty acid decreased from 68.8% to 54.51% at the pressure of 10 bar and 40 bar, while the rejection of triglyceride increased from 79.3 and 86.8%. It is postulated that the rejection of free fatty acid decreased probably due to affinity towards the membrane.

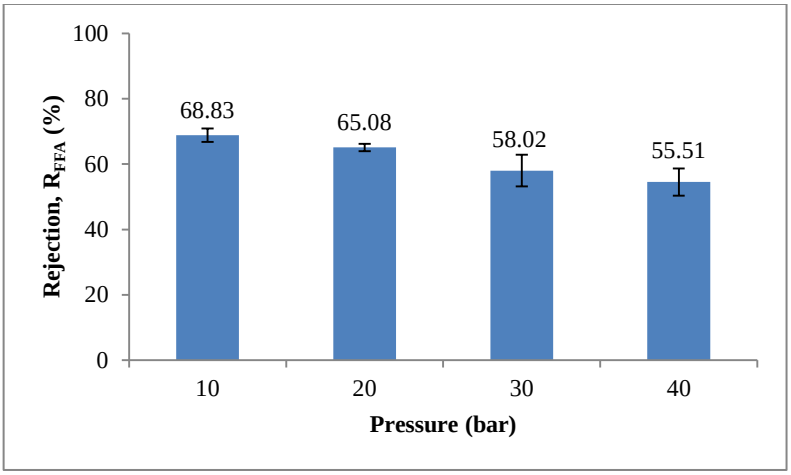


Figure 4. The effects of pressure towards rejections of FFA (Operation conditions: 25°C and agitation 400 rpm with FFA concentration of 3.6 g/L (4 wt.% FFA in 10 wt.% TAG) using NF030306 membrane)

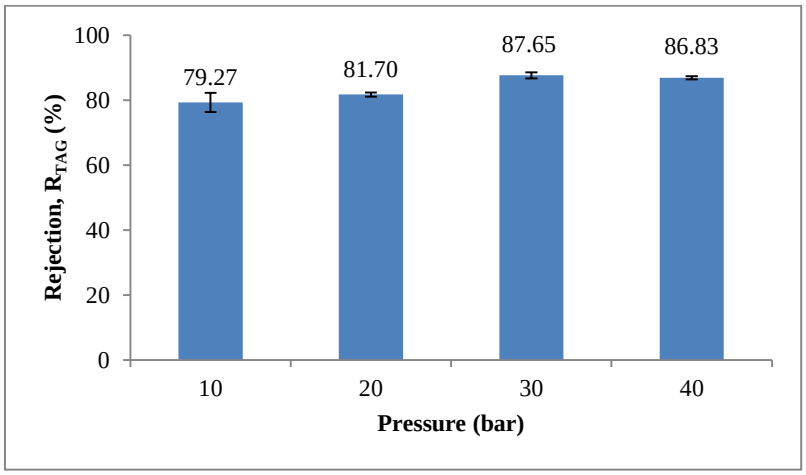


Figure 5. The effects of pressure towards rejection of TAG (Operation conditions: 25 °C and agitation 400 rpm with FFA concentration of 3.6 g/L (4 wt.% FFA in 10 wt.% TAG) using NF030306 membrane)

Effects of FFA concentrations

To evaluate the influence of fatty acid concentration towards the separation process, permeate flux was first evaluated. From Figure 6, the permeate flux decreased when the concentrations of feed increased. Permeate flux when the concentration of free fatty acid at 14.4 g/L was four times lower than that using 1.7 g/L concentration of free fatty acid. The decrease in flux was expected to occur especially with increasing viscosity due to high concentration of solutes.

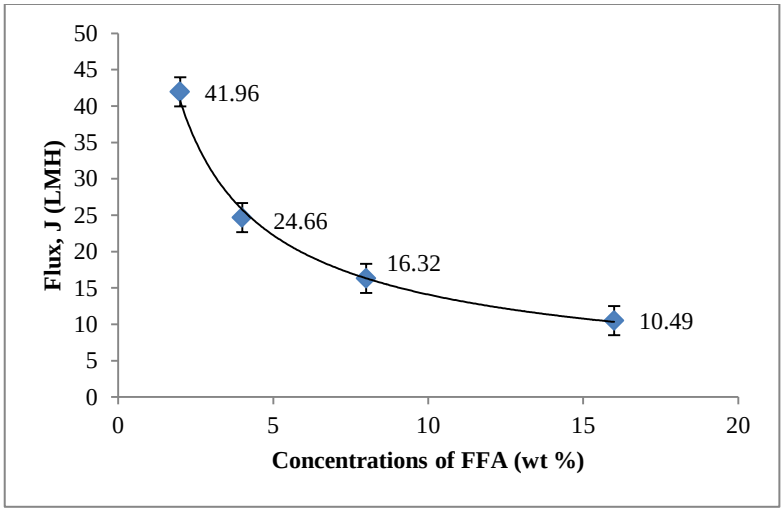


Figure 6. The effect of FFA concentration towards flux (Operation conditions: 30 bar 25°C and agitation 400 rpm using NF030306 membrane)

Next, the rejection of free fatty acid and triglycerides at different free fatty acid concentrations were evaluated. From Figure 7 and Figure 8, the rejection of free fatty acid decreased and triglycerides were constant as the concentration increased. According to Bhosle et al. [2], the increase in the concentration of free fatty acid results in increased diffusivity as they are concentration dependent, and resulted in lower rejection of free fatty acid. However, different observations are reported in OSN literature regarding the concentration effects on the rejection. Zwijnenberg et al. reported constant rejection [18] while Whu showed that the rejection increased with concentration of solutes [19]. Triglyceride rejection was constant probably due to its large molecular size compared to the apparent membrane MWCO cutoff, so most of the triglyceride was retained in the retentate at high rejection regardless of the concentration. It was concluded that the different observation of rejection was due to type of solutes and membranes involved and the interactions between them. It can be noted that the rejection profile depends not only on the molecular size of solute but also on the affinity of the solute towards the membrane.

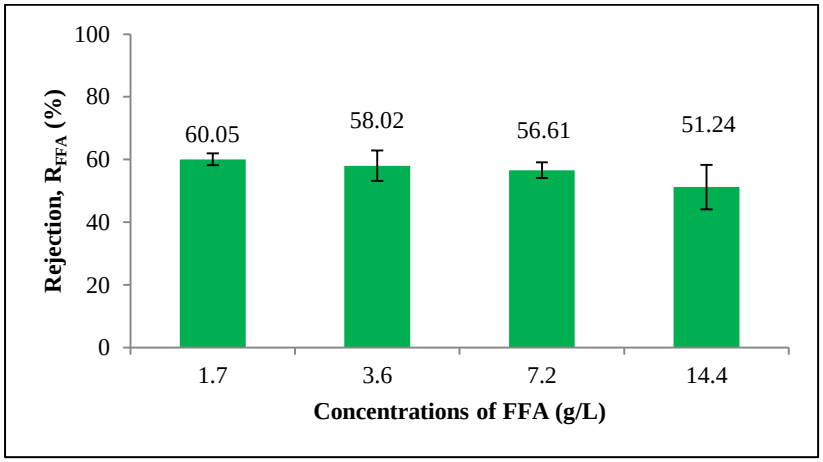


Figure 7. The effects of concentration of FFA towards rejection of FFA (Operation conditions: 30 bar 25°C and agitation 400 rpm using NF030306 membrane)

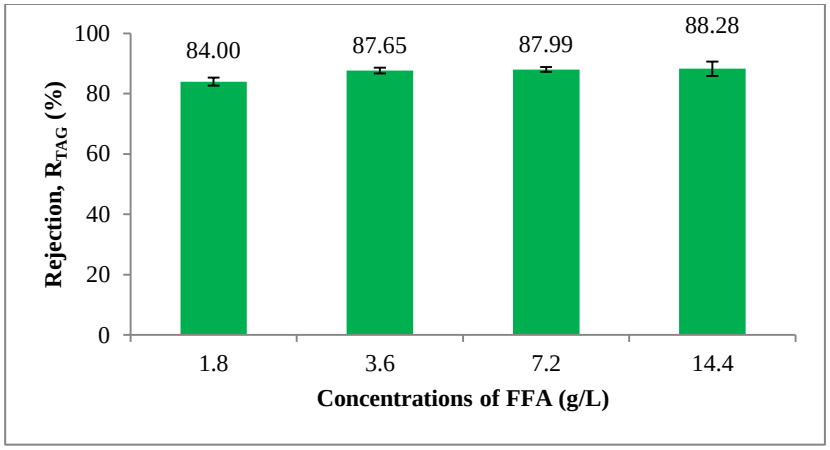


Figure 8. The effects of concentration of FFA towards rejection of TAG (Operation conditions: 30 bar 25 °C and agitation 400 rpm using NF030306 membrane)

Conclusion

The results successfully demonstrated the feasibility of fatty acid separation from palm oil using OSN. Based on results, the applied pressure increased the performance of the membrane. In all membranes, while FFA was permeated through them, the triglycerides (TAG) were found to predominantly retain. The best fatty acid separation performance was achieved using NF030306 membrane with acetone with the fatty acid rejection of 55%, and the triglycerides rejection of 87%. Good separation was achieved at high pressure (30 to 40 bar) and concentration (3.6 g/L). For these conditions, it is possible to deacidify palm oil/acetone mixture by using nanofiltration membranes. However, direct deacidification using nanofiltration membrane remains a challenge and in the need of more selective membranes for the maximum efficiency in fatty acid separation from crude palm oil.

Acknowledgment

The authors wish to thank UTM for support under GUP Tier 1 (14H20) and FRGS grant (4F616).

References

1. Rossi, M, Gianazza, M., Alamprese, C. and Stanga, F. (2001). The effect of bleaching and physical refining on color and minor components of palm oil. *Journal of the American Oil Chemists' Society,* 78 (10): 1051-1055.
2. Bhosle, B. M., Subramanian, R. and Ebert, K. (2005). Deacidification of model vegetable oils using polymeric membranes. *European Journal of Lipid Science and Technology*, 107: 746-753.
3. Raman, L. P., Cheryan, M. and Rajagopalan, N. (1996). Deacidification of soybean oil by membrane technology. *Journal of the American Oil Chemists' Society,* 73(2): 219-224.
4. Kale, V., Katikaneni, S. P. R. and Cheryan, M. (1999). Deacidification rice bran oil by solvent extraction and membrane technology. *Journal of the American Oil Chemists' Society,* 76(6): 723-727.
5. Kumar, N. S. and Bhowmick, D. N. (1996). Separation of fatty acids/triacylglycerol by membranes. *Journal of the American Oil Chemists' Society,* 73(3): 399-401.
6. Firman, L. R., Ochoa, N. A., Marchese, J. and Pagliero, C. L. (2013). Deacidification and solvent recovery of soybean oil by nanofiltration membranes. *Journal of Membrane Science*, 431: 187-196.
7. Vandezande, P., Gevers, L. E. M. and Vankelecom, I. F. J. (2008). Solvent resistant nanofiltration: Separating on a molecular level. *Chemical Society Reviews*, 37(2): 365-05.
8. Marchetti, P., Solomon, M. F. J, Szekely, G. and Livingston, A. G. (2014). Molecular separation with organic solvent nanofiltration: A critical review. *Chemical Review*, 114(21): 10735-10806.
9. Rundquist, E. M., Pink, C. J. and Livingston, A. G. (2012). Organic solvent nanofiltration: A potential alternative to distillation for solvent recovery from crystallisation mother liquors. *Green Chemistry*, 14(8): 2197-2205.

10. Schaepertoens, M., Didaskalou, C., Kim, J. F., Livingston, A. G. and Szekely, G. (2016). Solvent recycle with imperfect membranes: A semi-continuous workaround for diafiltration. *Journal of Membrane Science*, 514: 646-658.
11. Dreimann, J. M., Skiborowski, M., Behr, A. And Vorholt, A. J. (2016). Recycling homogeneous catalysts simply by organic solvent nanofiltration: new ways to efficient catalysis. *ChemCatChem*, 8(21): 3330-3333.
12. Ghazali, N. F., Ferreira, F. C., White, A. J. P. and Livingston, A. G. (2006). Chiral separation by enantioselective inclusion complexation-organic solvent nanofiltration. *Desalination*, 199: 398-400.
13. Kim, J. F., Gaffney, P. R. J., Valtcheva, I. B., Williams, G., Buswell, A. M., Anson, M. S. and Livingston, A.G. (2016). Organic solvent nanofiltration (OSN): A new technology platform for liquid-phase oligonucleotide synthesis (LPOS). *Organic Process Research and Development*, 20(8): 1439-1452.
14. Székely, G., Bandarra, J., Heggie, W., Sellergren, B. and Ferreira, F. C. (2011). Organic solvent nanofiltration: A platform for removal of genotoxins from active pharmaceutical ingredients. *Journal of Membrane Science*, 381(1): 21-33.
15. Goncalves, C. B. and Meirelles, A. J. A. (2004). Liquid-liquid equilibrium data for the system palm oil + fatty acid + ethanol + water at 318.2 K. *Fluid Phase Equilibria*, 221(1-2): 139-150.
16. Sablani, S. S., Goosen, M. F. A., Al-Belushi, R. and Wilf, M. (2001). Concentration polarization in ultrafiltration and reverse osmosis: A critical review. *Desalination*, 141(3): 269-289.
17. Shi, B., Marchetti, P., Peshev, D., Zhang, S. and Livingston, A. (2017). Will ultra-high permeance membranes lead to ultra-efficient processes? challenges for molecular separations in liquid systems. *Journal of Membrane Science*, 525: 35-47.
18. Zwijnenberg, H. J., Krosse, A. M., Ebert, K., Peinemeann, K. V. and Cuperus, F. P. (1999). Acetone-stable nanofiltration membranes in deacidifying vegetable oil. *Journal of the American Oil Chemist' Society,* 76(1): 83-87.
19. Whu, J. A., Baltzis, B. C. and Sirkar, K. K. (2000). Nanofiltration studies of larger organic microsolutes in methanol solutions. *Journal of Membrane Science*, 170(2): 159-172.

Malaysian Journal of Analytical Sciences Vol 22 No 4 2018

Articles 5-20 are selected papers from the "2nd International Conference on Separation Technology (ICOST 2017), 15 & 16 April 2017, Pulai Springs Resort, Johor Bahru, Malaysia; organised by Centre of Lipids Engineering and Applied Research, Universiti Teknologi Malaysia." Guest Editor: Norasikin Othman?

Page

1. MACRO, MICRO, AND NON-ESSENTIAL ELEMENTS IN DIFFERENT PARTS OF *Rhizophora apiculata* 570
(Makro, Mikro dan Elemen Tidak Perlu di dalam Pelbagai Bahagian *Rhizophora apiculata*)
Fathullah Abdullah, Hasrizal Shaari, Behara Satyanarayana, Wan Mohd Afiq Wan Mohd Khalik, Mohd. Zaidi Mohd. Jaafar

2. CHEMICAL CHARACTERIZATION OF *Berberis vulgaris* L. var. *asperma* EDIBLE BERRIES 579
(Pencirian Kimia Buah Beri Boleh di Makan *Berberis vulgaris* L. var. *asperma*)
Maria Carmen S. Tan, Irving D. Chiong, Mary Stephanie S. Carranza, Regina M. Salmasan, Glenn G. Oyong

3. FILLER AND POLYMER INTERACTIONS IN POLYMETHYL METHACRYLATE/50% EPOXIDIZED NATURAL RUBBER/SILICON DIOXIDE NANOCOMPOSITES 586
(Interaksi Pengisi Dan Polimer Dalam Nanokomposit Polimetil Metakrilat/Getah Asli Terepoksida 50%/Silikon Dioksida)
Sharil Fadli Mohamad Zamri, Famiza Abdul Latif, Ab Malik Marwan Ali, Ruhani Ibrahim, Siti Izzati Husna Mohd Azuan, Norashima Kamaluddin, Fitrah Hadip

4. ASSESSMENT OF METALS CONCENTRATION IN TILAPIA (*Oreochromis* sp.) AND ESTIMATION OF DAILY INTAKE BY MALAYSIAN 594
(Penilaian Kepekatan Logam dalam Tilapia (*Oreochromis* sp.) dan Anggaran Pengambilan Harian oleh Orang Malaysia)
Nurulnadia Mohd Yusoff, Siti NurTahirah Jaafar, Noor Azhar Mohamed Shazili, Nik Nurasyikin Nik Mohammad Azmi, Mohamad Sofi Abu Hassan

5. TETRABUTYLPHOSPHONIUM TRIFLUOROACETATE ($[P_{4444}]CF_3COO$) THERMORESPONSIVE IONIC LIQUID AS A DRAW SOLUTION FOR FORWARD OSMOSIS PROCESS 605
(Larutan Ionik Responsif Haba Tetrabutilfosfonium Trifluoroasetat ($[P_{4444}]CF_3COO$) sebagai Larutan Penarik untuk Proses Osmosis Kehadapan)
Phang Sook Nyan, Syed Mohd Saufi, Syamsul Bahari Abdullah, Mazrul Nizam Abu Seman, Malyanah Mohd Taib

6. PHYSICOCHEMICAL PROPERTIES OF ENCAPSULATED PURPLE SWEET POTATO EXTRACT; EFFECT OF MALTODEXTRIN CONCENTRATION, AND MICROWAVE DRYING POWER 612
(Sifat Fizikokimia Ekstrak Keledek Ungu yang Dikapsul; Kesan Kepekatan Maltodekstrin, dan Kuasa Pengeringan Gelombang Mikro)
Alyani Mohd Padzil, Azni A. Aziz, Ida Idayu Muhamad

7. EXTRACTION OF EICOSAPENTAENOIC ACID FROM *Nannochloropsis gaditana* USING SUB-CRITICAL WATER EXTRACTION 619

(Pengekstrakan Asid Eikosapentaenoik daripada *Nannochloropsis gaditana* dengan Menggunakan Kaedah Air Sub-kritikal)
Bernard Chon Han Ho, Siti Mazlina Mustapa Kamal, Mohd Razif Harun

8. SYNERGISTIC EXTRACTANT FOR EXTRACTION OF REMAZOL ORANGE 3R IN LIQUID MEMBRANE FORMULATION 626
(Pengekstrak Sinergistik untuk Pengekstrakan Remazol Orange 3R dalam Formulasi Membran Cecair)
Hilmi Abdul Rahman, Norasikin Othman, Muhammad Bukhari Rosly, Raja Norimie Raja Sulaiman, Norela Jusoh, Norul Fatiha Mohamed Noah

9. OLEIC ACID ENHANCEMENT IN USED FRYING PALM OIL VIA ENZYMATIC ACIDOLYSIS 633
(Peningkatan Kandungan Asid Oleik dalam Minyak Sawit Terpakai Melalui Kaedah Asidolisis Enzim)
Nor Athirah Zaharudin, Nurul Syafiqah binti Remzi, Roslina Rashid, Siti Marsilawati Mohamed Esivan, Ani Idris, Norasikin Othman

10. ADSORBENTS FROM THE BY-PRODUCT OF PALM OIL REFINERY FOR METHYLENE BLUE REMOVAL 642
(Penjerap daripada Produk Sampingan Penapisan Minyak Sawit untuk Penyingkiran Metilena Biru)
Hamzat Bashir Aderemi, Muhammad Abbas Ahmad Zaini, Noor Shawal Nasri

11. SYNERGISTIC EFFECT OF ADSORPTION-PHOTODEGRADATION OF COMPOSITE TiO_2/AC FOR DEGRADATION OF 1-BUTYL-3-METHYLIMIDAZOLIUM CHLORIDE 648
(Kesan Sinergistik Penjerapan-Fotopenguraian dari Bahan Komposit TiO_2/AC untuk Mengurai 1-Butil-3-Metillimidazolium Klorida)
Azhar Zawawi, Raihan Mahirah Ramli, Noorfidza Yub Harun

12. TOTAL PHENOLIC, FLAVONOID CONTENT AND ANTIOXIDANT ACTIVITY OF *Clinacanthus nutans* LEAVES BY WATER-BASED ULTRASONIC ASSISTED EXTRACTION 659
(Kandungan Fenolik, Flavonoid dan Aktiviti Antioksidan bagi *Clinacanthus nutans* Menggunakan Bantuan Pengekstrakan Ultrasonik Berasaskan Air)
Nurul Amila Fadhlin Baharuddin, Mariam Firdhaus Mad Nordin, Noor Azian Morad, Nor Ilia Anisa Aris, Mohd Azizi Che Yunus

13. EFFECT OF INCORPORATING PURPLE-FLESHED SWEET POTATO IN BISCUIT ON ANTIOXIDANT CONTENT, ANTIOXIDANT CAPACITY AND COLOUR CHARACTERISTICS 667
(Kesan Penambahan Keledek Ungu ke dalam Biskut Terhadap Kandungan Antioksida, Kapasiti Antioksidan dan Ciri-Ciri Warna)
Azni A. Aziz, Alyani Mohd Padzil, Ida Idayu Muhamad

14. BIOSYNTHESIS OF SILVER NANOPARTICLES USING *Citrus grandis* PEEL EXTRACT 676
(Biosintesis Nanopartikel Perak dengan Menggunakan Ekstrak Kulit *Citrus grandis*)
Nur Syazana Jalani, Wong Michell, Wong Ee Lin, Sharifah Zati Hanani, Uda Hashim, Rozaini Abdullah

15. PRODUCTION OF VOLATILE ORGANIC COMPOUNDS USING OIL PALM FROND JUICE AS A SOLE SUBSTRATE BY *Ceratocystis fimbriata* 684
(Penghasilan Sebatian Organik Meruap Menggunakan Jus Pelepah Kelapa Sawit Sebagai Substrat Tunggal oleh *Ceratocystis fimbriata*)
Nang Nor Azimah Long Nadzri, Mior Ahmad Khushairi Mohd Zahari, Saiful Nizam Tajuddin, Che Mohd Aizal Che Mohd

16. PHOTOCATALYTIC DEGRADATION OF INDUSTRIAL DYE WASTEWATER USING ZINC OXIDE-POLYVINYLPYRROLIDONE NANOPARTICLES 693
(Penguraian Fotopemangkinan Air Sisa Pewarna Industri Menggunakan Nanopartikel Zink Oksida-Polivinilpirolidon)
Dilaeleyana Abu Bakar Sidik, Nur Hanis Hayati Hairom, Nur Zarifah Zainuri, Amira Liyana Desa, Nurasyikin Misdan, Norhaniza Yusof, Chin Boon Ong, Abdul Wahab Mohammad, Nur Shahirah Mohd Aripen

17. LIQUID MEMBRANE COMPONENT SELECTION FOR REMOVAL OF PHENOL FROM SIMULATED AQUEOUS WASTE SOLUTION 702
(Pemilihan Komponen Cecair Membran untuk Pembuangan Fenol daripada Air Sisa)
Muhammad Bukhari Rosly, Norasikin Othman, Hilmi Abdul Rahman

18. ENZYMATIC HYDROLYSIS OF OIL PALM EMPTY FRUIT BUNCH AND ITS KINETICS 715
(Hidrolisis Enzim Tandan Buah Kelapa Sawit dan Sifat Kinetik)
Nazlee Faisal Ghazali and Nurul Aqilah Makhtar

19. ANALYSIS OF AMMONIUM ADSORPTION BEHAVIOR AND MASS TRANSFER RESISTANCE FROM AERATED LAGOON EFFLUENT ONTO ACTIVATED CARBON 723
(Analisis Sifat Penjerapan Amonium dan Rintangan Pemindahan Jisim dari Efluen Kolam Pengudaraan Terhadap Karbon Teraktif)
Mohd Hairul Khamidun, Shakila Abdullah, Umi Fazara Md.Ali, Mohamad Ali Fulazzaky

20. REMOVAL OF OIL AND GREASE AND ANIONIC SURFACTANTS IN SYNTHETIC CAR WASH WASTEWATER USING KAPOK FIBER: A BATCH-SCALE STUDY 735
(Penyingkiran Minyak dan Gris dan Anionik Surfaktan dalam Air Sisa Sintetik Basuhan Kereta Menggunakan Fiber Kapok: Kajian Skala-Kelompok)
Muhammad Shahrul Shafendy Ibrahim and Nor Haslina Hashim

Malaysian Journal of Analytical Sciences, Vol 22 No 4 (2018): 570 - 578
DOI: https://doi.org/10.17576/mjas-2018-2204-01

MALAYSIAN JOURNAL OF ANALYTICAL SCIENCES
Published by The Malaysian Analytical Sciences Society
ISSN 1394 - 2506

MACRO, MICRO, AND NON-ESSENTIAL ELEMENTS IN DIFFERENT PARTS OF *Rhizophora apiculata*

(Makro, Mikro dan Elemen Tidak Perlu di dalam Pelbagai Bahagian *Rhizophora apiculata*)

Fathullah Abdullah[1], Hasrizal Shaari[1,2]*, Behara Satyanarayana[2], Wan Mohd Afiq Wan Mohd Khalik[1], Mohd. Zaidi Mohd. Jaafar[1]

[1]*School of Marine and Environmental Science*
[2]*Institute of Oceanography and Environment*
Universiti Malaysia Terengganu, 21030 Kuala Nerus, Terengganu,Malaysia

**Corresponding author: riz@umt.edu.my*

Received: 26 August 2017; Accepted: 1 July 2018

Abstract

A total of 50 samples of different parts (roots, stem disks, barks, trunks, twigs, and leaves) from five individuals of 20-year-old *Rhizophora apiculata* were sampled at Matang Mangrove Forest, Kuala Sepetang, Perak. The aims of this study were to determine the concentration of selected macroelements (K, Mg, Na, and Ca), microelements (Al, Fe, Zn, Mn and Cu) and non-essential elements (Pb and Cd) in different parts of *R. apiculata*. The elemental analysis was conducted by using inductively coupled plasma-optical emission spectrometer (ICP-OES). The mean value of the studied elements was recorded in the decreasing order of Ca > Na > K > Mg > Mn > Al > Fe > Zn > Cu > Pb > Cd. The highest value of Ca compared to other elements in the major parts of *R. apiculata* is closely related to the role of this element in the cell wall formation. The variable concentration of elements in the different parts of *R. apiculata* is attributed to the absorption mechanism of the trees. High values of some macroelements than microelements suggest that a macroelement is more significant for the growth of *R. apiculata*. The lower mean values of Pb and Cd than other elements suggest that non-essential elements are not significantly involved in the major process of this mangrove species. This study is crucial in providing a preliminary data of the different types of elements in the different parts of the *R. apiculata* species, and its importance for the future development of the charcoal industry in Kuala Sepetang, Perak.

Keywords: Mangrove forest, *Rhizophora apiculata*, macroelement, microelement, non-essential element

Abstrak

Sebanyak 50 sampel terdiri daripada pelbagai bahagian (akar, batang pokok, kulit, dahan, ranting dan daun) daripada 5 batang pokok spesis *Rhizophora apiculata* berusia 20 tahun telah di ambil di Hutan Simpan Matang. Kuala Sepetang, Perak. Tujuan kajian ini adalah untuk mencari nilai kepekatan elemen yang terpilih daripada makroelemen (K, Mg, Na dan Ca), mikroelemen (Al, Fe, Zn, Mn and Cu) and elemen tidak perlu (Pb dan Cd) yang terdapat dalam pelbagai bahagian pokok *R. apiculata.* Kaedah mendapatkan elemen adalah dengan menggunakan spektrometer pancaran optikal- gandingan aruhan plasma (ICP-OES). Purata jumlah elemen dalam kajian ini dicatat dalam kedudukan menurun daripada Ca > Na > K > Mg > Mn > Al > Fe > Zn > Cu > Pb > Cd. Elemen Ca adalah tertinggi jika dibandingkan dengan elemen yang lain adalah disebabkan pokok *Rhizophora apiculata* memerlukan elemen ini untuk pembentukkan sel-sel dinding. Jumlah elemen yang pelbagai adalah disebabkan daripada cara mekanisma penyerapan pokok tersebut. Makroelemen tinggi dari mikroelemen adalah disebabkan makroelemen memerlukan sejumlah besar untuk proses tumbesaran pokok. Elemen Pb dan Cd dicatat rendah dibandingkan element lain disebabkan elemen ini tidak terlibat secara terus dalam proses utama tumbesaran pokok ini. Kajian ini dikaji adalah untuk rujukan bagi spesis *Rhizophora apiculata* dan ini adalah penting bagi pembuatan industri arang kayu di Kuala Sepetang, Perak.

Kata kunci: Hutan bakau, *Rhizophora apiculata*, makroelemen, mikroelemen, elemen tak perlu

Introduction

Mangrove is a dominant coastal vegetation community in tropical Asia where Malaysia-Indonesia is the centre of distribution [1]. There are over 15 million hectares of mangrove forest in over 121 countries [2, 3]. River deltas, lagoons, and estuaries are mostly preferred for the growth of mangrove plants due the special adaptation in saline environment. These areas are well adapted for the life in the tidal habitat [4]. Previous reports revealed that mangrove area is one of the most productive environments [5, 6]. The distribution of mangrove forest in Peninsular Malaysia is relatively dense in the west than the east coast. For example, Kuala Sepetang in Perak is known with its diversity of mangrove species and is very clear in forest zonation.

High density of mangrove trees helps in trapping sediments carried by rivers. This results in high sedimentation rate in mangrove forests and provides a good condition for elemental deposition with sediment deposits. The deposited elements will be absorbed by roots and distributed to the different parts of the mangrove tree. Consequently, a mangrove tree can be a suitable indicator of metal pollution because it has a high tolerance to metal accumulation and acts as long-term sinks for most metals [7, 8].

Studies on element contents in different parts of a mangrove tree in tropical environments, including Malaysia, are not well documented. To the best of our knowledge, there is only two published works in Malaysia, reported by Kamaruzaman and Ong [9] in Setiu Wetlands, Terengganu and Kamaruzzaman et al [10] in Balok, Pahang. However, their study is limited on some elements without focusing on the elemental content in the different parts of a mangrove tree. Thus, in this study, the concentration of macroelements (K, Mg, Na, and Ca), microelements (Al, Fe, Zn, Mn, and Cu), and non-essential elements (Pb and Cd) in roots, stem disks, barks, branches, twigs, and leaves of *Rhizophora apiculata* in the mangrove reserve forest of Kuala Sepetang was investigated.

Materials and Methods

Description of study area

Kuala Sepetang Reserved Forest, Perak is located near Kuala Larut and the intersection between Sangga Besar River and Sepetang River. The Forestry Department of Perak has implemented a systematic plantation and harvesting of mangrove tree from the species of *Rhizophora apiculata* and *Rhizophora mucronata* for charcoal industry. They divided this large forest area into several compartments in order to manage it appropriately. The study area is located far from human settlement and there is no development occurred within the gazetted area. There is a small river called Terusan Tima that is located near to the sampling location. The coordinate of each sampling location is tabulated in Table 1.

Table 1. The coordinate of each sampling locations

Sampling Point	Latitude (N)	Longitude (E)
1	04° 50' 38.076"	100° 37' 11.532"
2	04° 50' 38.760"	100° 37' 10.704"
3	04° 50' 38.760"	100° 37' 10.596"
4	04° 50' 38.184"	100° 37' 09.444"
5	04° 50' 37.464"	100° 37' 10.020"

Sample collection and preparation

Five individuals of 20-year-old *R. apiculata* were sampled at the Kuala Sepetang Reserve Forest in March 2016 with the help of logging contractors under the Forestry Department of Perak. The tree samples were cut and separated into six different parts of roots, stem disks, barks, branches, twigs, and leaves. The stem disk was divided into three segments: bottom, middle, and top. Each component of the trees was wrapped and stored in an icebox in order to avoid contamination from the environment. The samples were brought back to the laboratory and cleaned with distilled water. The samples were dried in oven at 65 °C for 72 hours. The dried samples were polished with

sandpaper to remove any metal effects during the cutting process. The samples were subjected to ultrasonic treatment and cleaned with distilled water in order to remove any impurity particles. Again, the samples were dried in oven at 65 °C for 72 hours. The dried samples were burned combustion in a furnace at 500 °C for 10 hours. The ashes of burned samples were stored in a glass container prior to further analysis.

Sample digestion and analysis

The analysis followed the proposed procedure by Wu et al. [11] with some modifications on the digesting time. An approximately 0.05 g of homogenised ashes sample was digested in 1.5 ml of nitric acid by using a microwave digestion oven (Advanced Microwave Digestion System, ETHOS One). The analysis of the selected elements was performed using inductively coupled plasma-optical emission spectrometry (ICP-OES) (Varian Vista-MPX). The concentration of the studied elements was reported as mg/kg. The accuracy of analysis was examined by analysing in duplicate the NIST-1547 Sigma-Aldrich standard research material (SRM) of peach leaves.

Results and Discussion

Method validation

The result of recovery analysis of the selected elements was compatible with the certified values of peach leaves (NIST-1547). The recovery percentage of the measured elements was found to be acceptable, ranging between 66.3 and 105.24% (Table 2). Only Ca showed the value lower than 70%.

Table 2. The value of accuracy of analysis for standard reference

Elements	Analysed Value (mg/kg)	Certified Value (mg/kg)	Recovery (%)
Ca	10334.81	15590	66.3
K	21188.53	24330	87.1
Mg	3671.85	4320	85.0
Al	241.84	248	97.5
Fe	227.09	219.8	103.3
Mn	89.02	97.8	91.0
Cu	3.85	3.75	102.7
Cd	0.03	0.0261	105.2

Concentration levels of macroelements

The mean value of each element is as follows: Ca > Na > K > Mg > Mn > Al > Fe > Zn > Cu > Pb > Cd. In general, the concentration of all macroelements shows a decreasing trend from barks to leaves. The concentration levels of macroelements ranged from 593.67 to 2973.28 mg/kg for Ca, 421.80 to 1525.04 mg/kg for Na, 958.56 to 2344.82 mg/kg for K, and 282.20 to 1163.32 mg/kg for Mg (Figure 1). Stem disks and leaves have low concentration of macroelements compared to other parts. Plants absorb nutrient through their roots or even *via* their stems and leaves, and accumulate them in their tissues; furthermore, plants take up elements selectively, which subsequently move through the biogeochemical cycle [12].

The high concentration of macroelements in *R. apiculata* is due to the high concentration of those elements in salt water. *R. apiculata* is a mangrove species that can adapt in saline environment. The salt tolerance of this plant can be defined as its capacity to endure the effects of salt excess in the medium of root growth [13]. This mangrove species may have the absorption mechanism [14], thus exhibits some restricted mobility *via* an obvious barrier to acropetal translocation process [15]. Halophytic plants like *R. apiculata* have special adaptation to grow in the area of high salt content [16]. Previous reports stated that every plant needs calcium for the growing process. This macroelement plays a very important role in the growth of a plant and cell wall deposition [17]. Thus, this explains the relatively high concentration of Ca in all parts of *R. apiculata*.

Potassium is the mineral required in huge amounts by plants for metabolic functions and growth [18]. Leigh and Jones [19] reported that potassium is required for maintaining the intracellular electric neutrality, osmotic regulation, enzyme activation, protein synthesis, and photosynthetic metabolism. In saline environment, potassium becomes a vital element for osmotic regulation [20] and facilitates water uptake against strong external salt gradient [21]. Thus, this is an advantage for *R. apiculata* to adsorb some abundant elements in saline environment. In comparison to other elements, Mg has the lowest micronutrient concentration in all parts of *R. apiculata*.

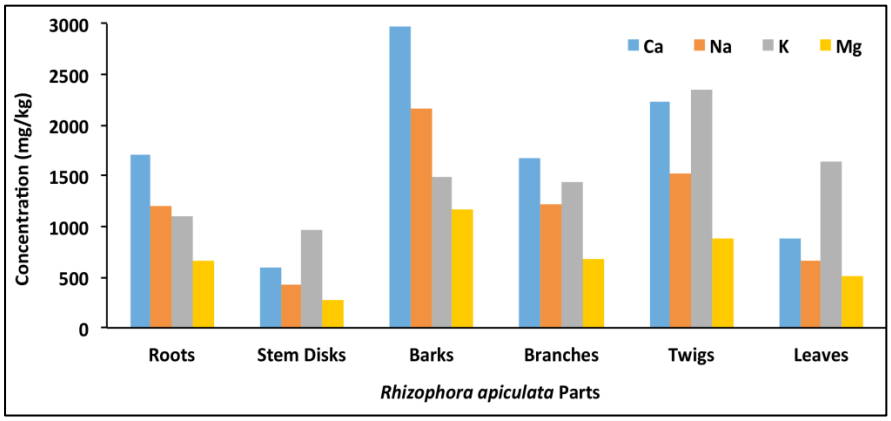
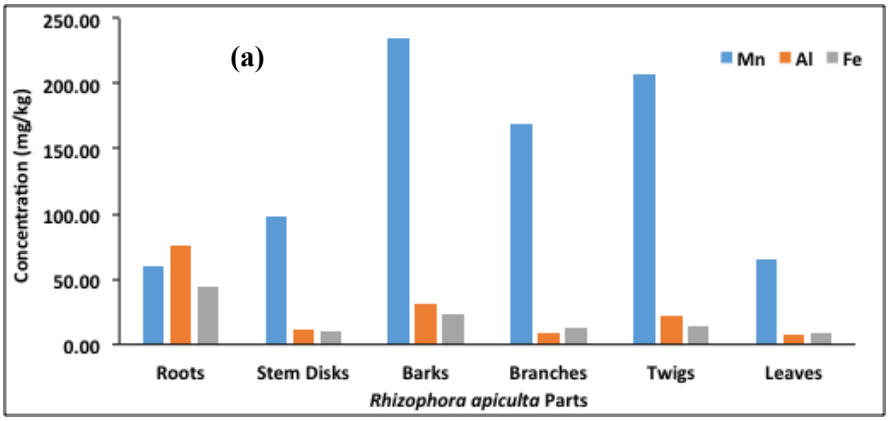


Figure 1. The concentration of macroelements in different parts of *Rhizophora apiculata*

Concentration levels of microelements

The concentration of microelements in the different parts of *R. apiculata* ranged from 59.99 to 235.09 mg/kg for Mn, 7.44 to 76.32 mg/kg for Al, 9.23 to 48.46 mg/kg for Fe, 1.14 to 3.60 mg/kg for Zn, and 0.53 to 1.40 mg/kg for Cu. From the results, Mn tends to be higher compared to another microelements. This indicates that Mn is the essential microelement for plant growth and involves in the reduction of nitrates in green plants [22]. There are reasons for high concentration of Mn at different parts. In Figure 2, Fe is high in roots because it is needed for the growth of *R. apiculata*. The importance of Fe is well known in the formation of chlorophyll, protein synthesis, and root growth [23]. Thus, high accumulation of Fe in roots indicates the importance of this element in the root cell formation. Another reason of high Mn and Fe concentrations in each part of *R. apiculata* is due to the oxygen released by the mangrove roots that creates geochemical oxidant [8]. Both elements in the form of Fe^{2+} and Mn^{2+} will be oxidized into the insoluble forms of $Fe(OH)_3$ and MnO_2 [24].



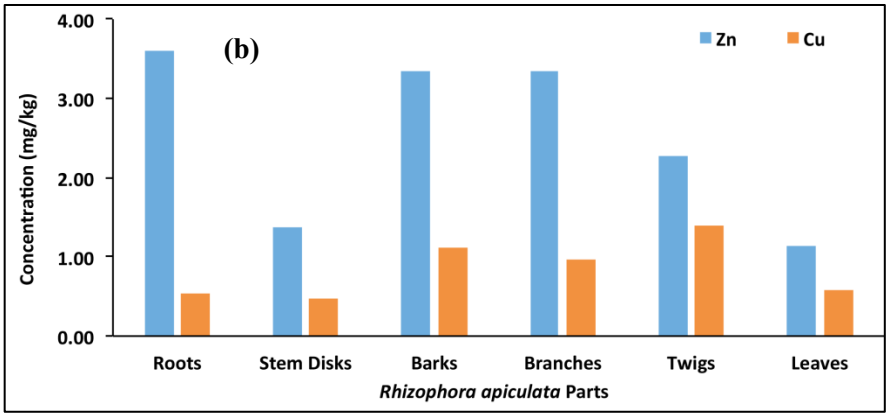


Figure 2. Concentration of microelements in different parts of *Rhizophora apiculata*

Figure 2b shows that Zn and Cu are present in the studied parts. The presence of both elements in plants is necessary for chloroplast reactions, enzyme systems, protein synthesis, and metabolism [25]. According to Anikwe et al. [26], mangrove trees are known with the capability to accumulate a considerable number of elements in roots and barks. However, the concentrations of microelements in each part of *R. apiculata* tend to be different due to the translocation and distribution process of the absorbed elements to other parts. Each element has different concentration in each component. This suggests that the element is immobilized and some elements are transported to the upper parts of the plant [27].

Concentration levels of non-essential elements

Concentrations of non-essential elements were recorded at the low range from 0.01 to 0.03 mg/kg for Cd and 0.08 to 0.35 mg/kg for Pb (Figure 3). The abundance of Cd may reflect from the natural background of the environment. The accumulation of Pb in *R. apiculata* in this research was at a normal range concentration (5.0–10.0 mg/kg) in plant material [28, 29]. Usman et al. [30] suggested that low concentration of Pb is due to the reaction with phosphates, hydroxides, carbonates, clays, and organic matters, which resulted in low solubility of Pb. This shows that Pb is immobile; besides, it has low solubility in low pH environment.

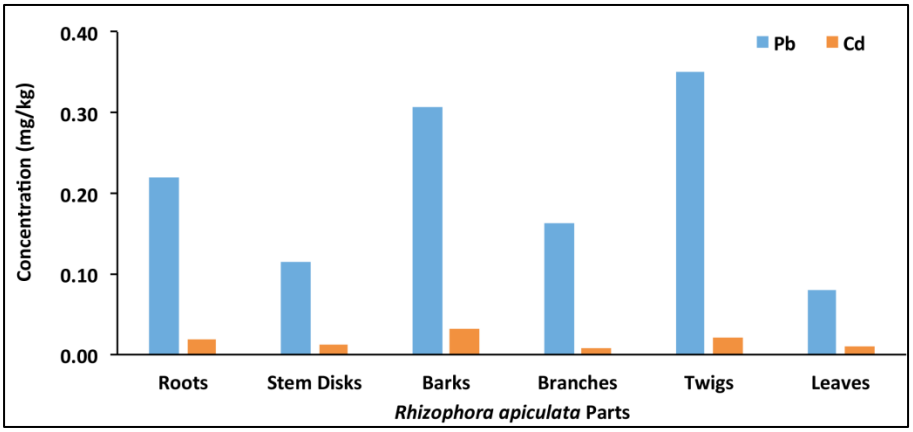


Figure 3. Concentration of non-essential elements in different parts of *Rhizophora apiculata*

Principal component analysis

The source of metal uptake was identified using principal component analysis through eigen-decomposition method. Principal components show pronounced change in the scree plot after 2 eigenvalues (6.72, 2.67). In this study, two

principal components rendered explained about 85.70% of the total variance in the data sets as illustrated in Figure 4. It is clearly shown that the metal uptake by *R. apiculata* tends to be dominant for barks. Both essential elements, Al and Fe, were higher in the roots of *R. apiculata*, thus giving an idea that negative impact is minimal since it is useful for plant growth. Despite the concentrations on non-essential elements (Pb and Cd) are still low, it is noteworthy to highlight that there is a potential of metal accumulation as similar observation was also recorded for the same species by Kamaruzzaman et al. with higher concentration [10].

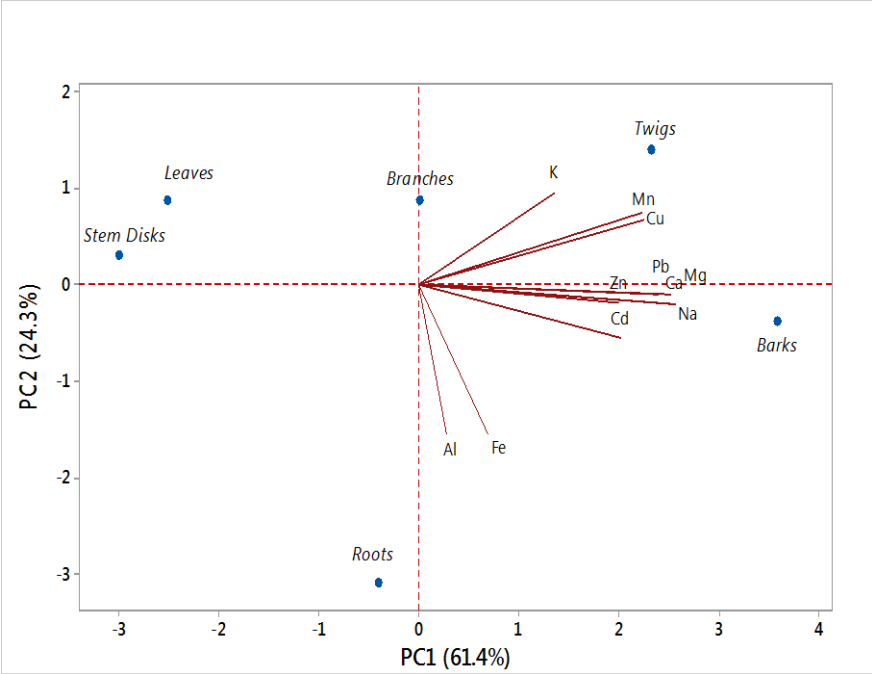


Figure 4. Biplot of principle component analysis

The concentration of elements in the present study was compared with the studies conducted in China [31, 32] and India [24, 33] (Table 3). Previous reports were based on the selected elements and did not divide them into different categories. Comparatively, the concentrations of micro and non-essential elements in the studied parts were lower than the other studies, except for Fe and Mn. The concentration of Mn was relatively higher than the values reported by Kathiresan et al. [24] in Cuddalore, India. The concentrations of Pb and Cd can be classified as low compared to other studies. It can be concluded that the concentration of the studied elements is low and Kuala Sepetang mangrove area is receiving the studied elements from the natural sources.

Table 3. A comparison of micro- and non-essential element in the different parts of mangrove species

Species	Ref.	Concentration (mg/kg)					
		Roots	Stem Disk	Bark	Branches	Twig	Leaves
Iron							
R. apiculata	This study	48.48±12.25	3.21±1.65	23.16±3.96	13.27±5.13	13.79±3.15	9.23±2.50
A. marina	[24]	1087.0±2.8	31.0±2.8	125.0±2.7	n.a.	n.a.	131.0±2.9
A. corniculatum	[32]	4619	n.a.	n.a.	n.a.	0.91	3.23
Copper							
R. apiculata	This study	0.53±0.13	0.21±0.12	1.11±0.36	0.97±0.60	1.40±0.96	0.58±0.15
A. marina	[24]	58.00±0.70	41.00±0.70	61.00±0.70	n.a.	n.a.	12.00±0.70
	[31]	30±2	n.a.	n.a.	n.a.	16±2	12±1
A. corniculatum	[32]	57.3	n.a.	n.a.	n.a.	6.71	5.28

Table 3 (cont'd). A comparison of micro- and non-essential element in the different parts of mangrove species

Species	Ref.	Concentration (mg/kg)					
		Roots	Stem Disk	Bark	Branches	Twig	Leaves
Manganese							
R. apiculata	This study	59.99±6.26	18.04±24.6	235.09±40.38	169.19±24.87	207.45±53.64	65.07±9.16
A. marina	[24]	21.00±0.30	11.00±0.4	28.00±0.10	n.a.	n.a.	5.00±0.30
A. corniculatum	[32]	740	n.a.	n.a.	n.a.	135	466
Zinc							
R. apiculata	This study	3.60±0.97	1.38±0.54	3.35±1.22	3.35±2.50	2.27±0.35	1.14±0.34
A. marina	[24]	21.0±0.8	12.00±0.2	17.0±0.9	n.a.	n.a.	9.0±0.4
	[31]	37±5	n.a.	n.a.	n.a.	15±1	17±1
A. corniculatum	[32]	82.8	n.a.	n.a.	n.a.	11	23.4
Cadmium							
R. apiculata	This study	0.02±0.01	0.01±0.01	0.03±0.01	0.01±0.001	0.02±0.01	0.01±0.006
A. marina	[24]	0.60±0.12	0.00±0.00	0.40±0.10	n.a.	n.a.	0.10±0.01
	[31]	0.15±0.01	n.a.	n.a.	n.a.	0.10±0.02	0.09±0.1
	[33]	4.05	1.83	n.a.	n.a.	n.a.	5.71
Lead							
R. apiculata	This study	0.22±0.13	0.11±0.06	0.31±0.13	0.16±0.05	0.35±0.11	0.08±0.04
	[9]	2.05	n.a.	1.05	n.a.	n.a.	1.43
A. marina	[24]	7.0±0.4	6.0±0.3	16.0±0.4	n.a.	n.a.	6.0±0.4
	[31]	4.4±0.4	n.a.	n.a.	n.a.	1.0±0.3	0.9±0.1
	[33]	1.57	0.38	n.a.	n.a.	n.a.	0.84
A. corniculatum	[32]	18.2	n.a.	n.a.	n.a.	0.91	3.23

* n.a. – not available

Conclusion

This study provides a baseline data of macroelements, microelements, and non-essential elements in different parts of 20-year-old *R. apiculata* at Kuala Sepetang Mangrove Reserve Forest. The average concentration of the studied elements is as follows: Ca > Na > K > Mg > Mn > Al > Fe > Zn > Cu > Pb > Cd. Macroelements were recorded high in all samples due to their abundance in salt water and are important for the mangrove tree growth in saline environment. Microelements may be supportive elements for plant growth and the concentration might not be as high as macronutrient elements. The low concentrations of Pb and Cd suggest that the study area is not strictly affected by the anthropogenic sources of non-essential elements. This study provides useful baseline data for the Perak Forestry Department and the charcoal industry in Kuala Sepetang, Perak, Malaysia.

Acknowledgements

This work was funded by the Research Acculturation Grant Scheme (RAGS) vot no. 57097 from Universiti Malaysia Terengganu (UMT). The authors would like to appreciate the Forestry Department of Malaysia especially Larut Matang District Forest Office for their cooperation and permission to collect samples from Kuala Sepetang Mangrove Reserve Forest. The authors acknowledge the School of Marine and Environmental Sciences, and Institute of Oceanography and Environment (INOS) for providing facilities to carry out this research.

References

1. Mazlan, A. G., Zaidi, C. C., Wan-Lotfi, W. M. and Othman, B. H. R. (2005). On the current status of marine bio-diversity in Malaysia. *Indian Journal of Marine Science,* 34: 76-87.
2. Agoramoorty, G., Chen, F. A. and Hsu, M. J. (2008). Threat of heavy metal pollution in halophytic and mangrove plants of Tamil Nadu, India. *Journal of Environmental Pollution,* 155: 320-326.

3. Lewis, M., Pryor, R. and Wilking, L. (2011). Fate and effects of anthropogenic chemical in mangrove ecosystem: A review. *Journal of Environmental Pollution,* 159: 2328-2346.
4. Sternberg, L. D. L., Teh, S. Y., Ewe, S. M. L., Miralles- Wilhelm, F. and DeAngelis, D. l. (2007). Competition between hardwood hammocks and mangrove. *Journal of Ecosystem*, 10: 648-660.
5. Kathiresan, K. and Qasim, S. Z. (2005). Biodiversity of mangrove ecosystem. New Delhi, India: Hindustan Publishing Corporation (India), New Delhi: pp. 251.
6. Rönnbäck, P., Troell, M., Kautsky, N. and Primavera, J. H. (1999). Distribution pattern of shrimps and fish among *Avicennia* and *Rhizophora* microhabitats in the Pagbilao mangrove, Philippines. *Journal of Estuarine, Coastal and Shelf Science,* 48: 223-234.
7. MacFarlane G. R. and Burchett M. D. (2002). Toxicity, growth and accumulation relationships of copper, lead and zinc in the grey mangrove *Avicennia marina* (Forsk.) Vierh. *Marine Environmental Research,* 54: 65–84.
8. Silva, C. A. R., Lacerda, L. D. and Rezende, C. E. (1990). Heavy metal reservoirs in a red mangrove forest. *Journal of Biotropica,* 22: 339–345.
9. Kamaruzzaman, B. Y. and Ong, M. C. (2009). Accumulation of lead and copper in *Rhizophora apiculata* from Setiu mangrove forest, Terengganu, Malaysia. *Journal of Environmental Biology,* 30: 821-824.
10. Kamaruzzaman, B. Y., Rina Sharlinda, M. Z., John, B. A. and Waznah, A. S. (2011). Accumulation and Distribution of lead and copper in *Avicennia marina* and *Rhizophora apiculata* from Balok mangrove forest, Pahang, Malaysia. *Sains Malaysiana*, 40(6): 555-560.
11. Wu, S., Feng, X. and Wittmeier, A. (1997). Microwave digestion of plant grain reference materials in nitric acid or mixture of nitric acid and hydrogen peroxide for the determination of multi-elements by inductively coupled plasma mass spectrometry. *Journal of Analytical Atomic Spectrometry,* 12: 797-806.
12. Ramos, S. C. A., da Silva, A. P. and de Oliveira. S. R. (2006). Concentration, stock and transport rate of heavy metals in a tropical red mangrove, Natal, Brazil. *Marine Chemistry,* 99: 2-11.
13. Teiz, L. and Zeiger, R. (1991). Plant physicology. The Benjamin-Cumming Publishing Company, Redwood City, CA, USA: pp. 565.
14. Qiu, Y. W., Yu, K. F., Zhang, G. and Wang, W. X. (2011). Accumulation and partitioning of seven trace elements in mangroves and sediment cores from three estuarine wetlands of Hanan Island, China. *Journal of Hazardous Materials,* 190: 631-638.
15. MacFarlane, G. R., Pulkownik, A. and Burchett M. D. (2003). Accumulation and distribution of heavy metals in the grey mangrove, *Avicennia marina* (Forsk.) Vierh: Biological indication potential. *Environmental Pollution,* 123: 139-151.
16. Glenn, E. P., Brown, J. J. and Blumwald, E. (1999). Salt tolerance and crop potential of halophytes. *Journal of Critical Review of Plant Sciences,* 18: 227-255.
17. Khalil, N. A., Al-Murshidy, W. A., Eman, A. M. and Badawy, R. A. (2015). Effect of plant density and calcium nutrition on growth and yield of some faba bean varieties under saline condition. *Journal of International Scientific Publications,* 3: 440-450.
18. Hsiao, T. C. and Lauchli, A. (1986). Role of potassium in plant-water relation. *Advanced Plant Nutrition,* 2: 28-31.
19. Leigh, R. A. and Wyn Jones, R. G. (1984). A hypothesis relating critical potassium concentrations for growth to the distribution and functions of this ion in the plant cell. *New Phytologist*, 97: 1-13.
20. Downton, W. J. S. (1982). Growth and osmotic relations of the mangrove *Avicennia marina*, as influenced by salinity. *Functional Plant Biology*, 9(5): 519-528.
21. Reef, R., Feller, I. C. and Lovelock, C. E. (2010). Nutrition of mangroves. *Tree Physiology*, 30(9): 1148-1160.
22. Chowdhury, R., Favas, P. J C., Pratas, J., Jonathan, M. P., Ganesh, P. S. and Sarkar, S. K. (2015). Accumulation of trace element by mangrove plants in Indian Sundarban Wetland: Prospects for phytoremediation. *International Journal of Phytoremediation,* 17(9): 885-894.
23. Jones, J. B., Wolf, B. and Mills, H. A. (1991). Plant analysis handbook: A practical sampling, preparation, analysis and interpretation guide. Micro and Macro Publishing, New York.
24. Kathiresan, K., Saravanankumar, K. and Mullai, P. (2014). Bioaccumulation of trace elements by *Avicennia marina*. *Journal of Coastal Life Medicine,* 2(11): 888-894.
25. Shaw, A. J. (1990). Heavy metal tolerance in plant: Evolutionary Aspects. CRC Press, Florida.

26. Anikwe, M. N. and Nwobodo, K. C. A. (2002). Long-term effect of municipal waste disposal on soil properties and productivity of sites used for urban agriculture in Abakaliki, Nigeria. *Bioresources Technology,* 83: 241-250.
27. Abohassan, R. A. (2013). Heavy metal pollution in *Avicennia marina* mangrove system on the Red Sea Coast of Saudi Arabia. *Journal of King Abdulaziz University; Meteorology, Environment and Arid Land Agriculture Science,* 24: 35-53.
28. Alloway, B. J. (1995) Soil processes and the behaviour of metals. In: Alloway BJ (ed). Heavy metals in soils. *Blackie Academic and Professional*, New York: pp. 11-50.
29. Bodin, N., Gom-Kâ, R., Thiaw, O. T., Tito de Morais, L., Le Loc´h, F. and Rozuel-Chartier, E. (2013). Assessment of trace metal contamination in mangrove ecosystem from Senegal, West Africa. *Chemosphere,* 90: 50-57.
30. Usman, A. R. A., Alkredaa, R. S. and Wabel, M. I. A. (2013). Heavy metal contamination in sediments and mangroves from the coast of Red Sea: *Avicennia marina* as potential metal bioaccumulator. *Ecotoxicology and Environmental Safety*, 97: 263-270.
31. Wang, Y., Qiu, Q., Xin, G., Yang, Z., Zheng J., Ye, Z. and Li, S. (2013). Heavy metal contamination in a vulnerable mangrove swamp in South China. *Environmental Monitoring Assessment*, 185(7): 5775-5787.
32. Yu, R. L., Hu, G. R., Zhang, W. F. and Liu B. X. (2015). Accumulation and transfer of heavy metals in the mangroves from Quanzhou Bay Wetland, South East Coast of China. *Journal of Residuals Science & Technology,* 12: 79-83.
33. Nirmal Kumar, I. J., Sajish, P. R., Nirmal Kumar, R., Basil, G. and Shailendra, V. (2011). An assessment of the accumulation potential of Pb, Zn and Cd by *Avicennia marina* (Forssk.) Vierh. in Vamleshwar Mangroves, Gujarat, India. *Notulae Scientia Biologicae*, 3(1): 36-40.

Malaysian Journal of Analytical Sciences, Vol 22 No 4 (2018): 579 - 585
DOI: https://doi.org/10.17576/mjas-2018-2204-02

MALAYSIAN JOURNAL OF ANALYTICAL SCIENCES
Published by The Malaysian Analytical Sciences Society
ISSN 1394 - 2506

CHEMICAL CHARACTERIZATION OF *Berberis vulgaris* L. var. *asperma* EDIBLE BERRIES

(Pencirian Kimia Buah Beri Boleh di Makan *Berberis vulgaris* L. var. *asperma*)

Maria Carmen S. Tan[1]*, Irving D. Chiong[1], Mary Stephanie S. Carranza[1], Regina M. Salmasan[1], Glenn G. Oyong[2]

[1]*Chemistry Department*
[2]*Molecular Science Unit Laboratory, Center for Natural Science and Environmental Research*
De La Salle University, 2401 Taft Avenue, Manila 1004, Philippines

**Corresponding author: maria.carmen.tan@dlsu.edu.ph*

Received: 11 January 2018; Accepted: 4 June 2018

Abstract

Berberis vulgaris L. var. *asperma* edible fruits have been found to have activity against several microbes and to be cytotoxic in certain immortalized cancer cell lines. In this study, the berries were analyzed to find the possible metabolites that could be the curative agents. Evaluations using an LC-UV/MS technique established the presence of chlorogenic acid, rutin, and berberine in ethanolic extracts of *B. vulgaris* berries. The ethanolic sample was found to have 47.1 mg/kg of 3-(3,4-dihydroxycinnamoyl) quinic acid, 0.02 mg/kg of rutin and 0.36 mg/kg of berberine. The free radical scavenging activity of the mixture of polyphenolics exhibited an IC_{50} at 34.48 µg/mL. An assessment of zinc and iron concentration using atomic absorbance spectrophotometry (AAS) was determined to be 45.3 and 198.1 mg/kg, respectively. The investigation of the volatile constituents through solid phase microextraction (SPME) and by dichloromethane extraction was explored using a gas chromatograph equipped with a mass spectrometer (GC-EI-MS). SPME analyses showed the presence of palmitic acid (C16:0), vaccenic acid (C18:1 Δ 11 trans) and stearic acid (C18:0). Three saturated fatty acids, SFAs (C14:0, C16:0, and C18:0), two methyl esters of the SFAs (C14:0 and C16:0), and one polyunsaturated fatty acid, PUFA (C18:2 Δ 9,12 cis) were detected in the dichloromethane extracts of the berries.

Keywords: atomic absorption spectroscopy, *Berberis vulgaris*, mass spectrometry

Abstrak

Buah yang boleh dimakan *Berberis vulgaris* L. var. *asperma* telah diketahui mempunyai aktiviti melawan beberapa jenis mikrob and menjadi sitotoksik di dalam sesetengah titisan sel kekal. Dalam kajian ini, buah beri dianalisis untuk mencari kebarangkalian metabolit yang boleh digunakan sebagai agen penawar. Penilaian menggunakan teknik LC-UV/MS dibangunkan untuk mengesan kehadiran asid klorogenik, rutin dan berberin di dalam ekstrak beri *B.vulgaris.* Sampel etanolik ditemui mengandungi 47.1 mg/kg 3- (3,4 – dihidroksisinamoil) asid quinik, 0.02 mg/kg rutin dan 0.36 mg/kg berberin. Pemerangkapan aktiviti radikal bebas bagi campuran polifenolik wujud pada IC_{50} 34.48 µg/mL. Penilaian kepekatan zink dan besi menggunakan spektrofotometri serapan atom (AAS) telah ditentukan dengan masing-masing ialah 45.3 dan 198.1 mg/kg. Penyiasatan terhadap jujukan sebatian merupa dilakukan menggunakan pengekstrakan mikro fasa pepejal (SPME) dan pengekstrakan diklorometana sebelum di analisis menggunakan kromatograf gas dilengkapi spektrometer jisim (GC-EI-MS). Analisis SPME menunjukkan kehadiran asid palmitik (C16:0), asid vasenik (C18:1 Δ 11 trans) dan asid stearik (C18:0). Tiga asid lemak tepu, SFAs (C14:0, C16:0, dan C18:0), dua metal ester SFAs (C14:0 and C16:0), and satu asid lemak politaktepu, PUFA (C18:2 Δ 9,12 cis) telah dikesan di dalam ekstrak diklorometana buah beri.

Kata kunci: spektroskopi serapan atom, *Berberis vulgaris*, spektrometri jisim

Introduction

Berberis vulgaris is a member of the Barberdaceae family and a common garden bush found in Europe and the British Isles. Barberry, as it is commonly known, has been used by herbalists since ancient times with its usage dating back to the Egyptians. Alkaloids and flavonoids have been reported in the root, stem, leaves and fruit of this bush. These two compound classes have been found to exhibit anti-diarrheal, anti-microbial, anti-inflammatory, anti-allergic, and anti-cancer effects. The edible fruit of *B. vulgaris* has been used in Asia and Europe especially in Iran as traditional medicine for various diseases which include malaria, dysentery and gall stones. Its antihistaminic and anticholinergic activity was found in the aqueous extracts of barberry on isolated guinea pig ileum [1]. Antioxidant activities of ethanolic extracts of roots, twigs, and leaves of the barberry plant were correlated with phenols and flavonols present in the plant tissue [2]. The fruit has been linked to diseases of the kidneys, urinary or gastrointestinal tract, liver, bronchial, and as a stimulant for the circulatory system [3].

In this work, ethanolic extracts of the barberry fruit were analyzed using a radical scavenging assay, high-performance liquid chromatography (HPLC), liquid chromatography-mass spectrometry (LC-ESI-MS), gas chromatography-mass spectrometry (GC-EI-MS), solid-phase microextraction (SPME) and dichloromethane extracts, and atomic absorption spectrometry (AAS). To the best of our knowledge, this is the first reported study using this methodology of chemical analyses on the extracts of *B. vulgaris* berries.

Materials and Methods

Fresh samples of *B. vulgaris* fruits were harvested from Mashhad, Khorasan Province, Iran and identified at the Mashhad Medical University of Sciences, Iran. The berries were lyophilized and extracted with ethanol for 10 hours, filtered (22 μm pore size), and concentrated in vacuo. The residue was reconstituted with ethanol (60 μg/μL) and was passed through a 0.45 μm cellulose acetate membrane before further analysis.

Free radical scavenging assay

The radical scavenging activity of *B. vulgaris* ethanolic fruit extracts was measured by 2,2-Diphenyl-1-picrylhydrazyl or DPPH (Sigma-Aldrich, Singapore) utilizing a modified version of the method by Sikder et al. [4]. An amount 10 mL of 60 mM of DPPH was added to each trial where the extracts were varied from 5 μL to 125 μL. The resulting reaction mixtures of 30.00 to 740.74 μL/mL were incubated at ambient temperatures in the dark for 30 minutes. A control sample which contained only DPPH solution and no fruit extract was also made. After incubation, changes in absorbance at 517 nm were analyzed using a Hitachi 2900 double beam UV-Visible spectrophotometer. Nonlinear regression and statistical analyses were done using GraphPad Prism 7.01 (GraphPad Software, Inc.) to extrapolate the half maximal inhibitory concentration, IC_{50} (50% reduction of absorbance as compared to the control).

RP-HPLC analyses

Fruit extracts (20 μL) were analyzed using an Agilent Technologies 1200 Series quaternary pump system with a variable wavelength detector and a 20-μL sample injector. Analytes were separated on a 250 mm × 4 mm, 5-μm particle RESTEK Pinnacle II ODS column (Supelco). Resolved compound peaks were identified by direct comparison of their retention times with reference standards. The columns were maintained at room temperature.

Optimization was conducted using a method developed by Hasler et al. [5] and Olszewska [6]. Solvent system consisted of 5% formic acid in distilled water (FA/H_2O) and acetonitrile (ACN) with a gradient of: 0-2 minutes at 95% (FA/H_2O) and 5% ACN; 5-7 minutes at 90% (FA/H_2O) and 10% ACN; 7-10 minutes at 90-85 % (FA/H_2O) and 10-15% ACN; 10-13 minutes at 85-80% (FA/H_2O) and 15-20% ACN; 13-23 minutes 80% (FA/H_2O) and 20% ACN; 23-25 minutes at 80-70% (FA/H_2O) and 20-30% ACN; 25-28 minutes at 70% (FA/H_2O) and 30% ACN; 30-32 minutes at 50% (FA/H_2O) and 50% ACN; 32-45 minutes at 50-95% (FA/H_2O) and 50-5% ACN. Flow rate was 1.00 mL/min, while the UV detector was set at 350 nm for all the trials. Standard stock solutions initially from 500 ppm of berberine (Sigma-Aldrich, Singapore), rutin (Sigma-Aldrich, Singapore), and chlorogenic acid (Sigma-Aldrich, Singapore) were freshly prepared in methanol and the goodness of fit generated from the absorbance per concentration on scatter charts confirmed whether the linear regression analysis ($R^2 > 0.97$) and external calibration were acceptable.

LC-ESI-MS analyses
Fruit extracts were analyzed using LC-MS system equipped with DIONEX Ultimate 3000 HPLC & Bruker micrOTOF-Q II MS with a C_{18} column (3 mm, 120 Å, 2.1 x 150 mm). Electrospray ionization positive mode was used and acquisition was at 50 m/z to 3000 m/z. The solvent gradient for RP-HPLC was used, with the last segment of the gradient extended for five minutes to account for the internal calibration (sodium formate) that was run simultaneously with the trials. Other parameters were as follows: capillary at 4500 V, end plate offset at -500 V, collision cell RF 500.0 VPP, nebulizer at 2.0 bar, dry heater at 180 °C, dry gas at 8.0 L/min. Mass spectra were calibrated internally during the trials and the background subtracted during data analysis.

SPME-GC-EI-MS analyses
Approximately 7 grams of lyophilized fruit extracts were placed in an Erlenmeyer flask covered with a septum. Samples for GC-MS analysis was collected using a polydimethylsiloxane (PDMS) fiber while heating the set-up at 40 °C for 30 minutes. The fiber was desorbed and analyzed manually in a Perkin–Elmer Clarus 500 gas chromatograph - mass spectrometer. Sampling rate was 1.56250 points/second. Temperature was set at 40 °C for 5 minutes then increased by 4 °C until it reached 230 °C where it was held for 5 minutes. Flow rate of the carrier gas was set at 2.0 mL/min while ionization was carried out using 70 eV (EI), and the masses were scanned from 50 m/z to 500 m/z.

GC-EI-MS analyses of DCM extracts
The freeze-dried *B. vulgaris* berries (9.37 g) were ground in an osterizer, soaked in CH_2Cl_2 (DCM) for one day, filtered, and concentrated over nitrogen gas to achieve the resultant crude residue (5.25 g) which was then redissolved in 1 mL of DCM. An Agilent GC MS 7890B, equipped with a HP-5ms (5% phenyl methylsiloxane) Ultra Inert column (30 m x 250 mm x 0.25 mm) with ultra-pure helium gas as the mobile phase, was used for the analysis of volatile constituents. The flow rate of helium gas was at 1 mL/min, pressure maintained at 8.2 psi, with an average velocity of 36.62 cm/sec and holdup time of 1.37 minutes. The split inlet, at 20:1 ratio, was held at 250 ºC, at 8.2 psi, total flow of 24 mL/min, with a septum purge flow rate of 3 mL/min. The temperature for the injector was held at 250 ºC and optimization of the temperature program was started at 50 ºC with a programmed linear ramp of 5 ºC/min until 220 ºC.

Compound identification was done using the NIST library 2.0 and peak areas were processed from the resultant total ion chromatograms. The resultant data was confirmed by the comparison of the compounds according to their elution order with their relative retention indices on a non-polar stationary phase. The retention indices were computed for all of the volatile constituents utilizing a homologous series of n-alkanes.

AAS analysis
Approximately 1 g of lyophilized fruit extract was pulverized and heated in a furnace at 200 °C to 250 °C for 30 minutes. Then, the sample was reduced to ashes by heating at 450 °C for 4 hours. After this, 2 mL of 5 M HNO_3 was added and the resulting mixture was evaporated to dryness in a sand bath. The sample was further dried at 400 °C for 15 minutes, then the ashes were dissolved in 5 mL of 20% HCl followed by dilution to 25 mL. The zinc and iron content of the sample were analyzed using a Shimadzu AA-6300 atomic absorption spectrophotometer.

Results and Discussion

Free radical scavenging activity
Through curve fitting or nonlinear regression of the data points of the varying volumes of barberry extract, the IC_{50} was found to be 34.48 μg/mL. The reaction mixture with 149.63 ppm of barberry extract caused the maximum decrease in absorbance and additional increments of the ethanolic extracts did not exhibit any significant variance ($p > 0.05$) at 95% CI of discrepancy. The extent of decrease in absorbance from the control correlates with the free radical scavenging potential of the antioxidant present in the plant extract [7].

Identification of alkaloids and flavonoids
Mass spectral analysis of *B. vulgaris* ethanolic fruit extracts resulted in the identification of three compounds (Figure 1). At a retention time of 9.9-10.2 minutes and a molecular weight of 355.1 m/z, the chemical formula $C_{16}H_{19}O_9$ with -0.1 err [mDa], -0.2 err [ppm], and 2.9 mSigma correlated with $[M]^{+1}$ of chlorogenic acid or

3-(3,4- dihydroxycinnamoyl) quinic acid. Rutin, $[M+H]^{+1}$, was found at a retention time of 14.2 - 14.9 minutes at 611.2 m/z, with the chemical formula $C_{27}H_{31}O_{16}$ and 1.4 err [mDa], 2.2 err [ppm] and mSigma 4.5. The $[M+H]^{+1}$ of berberine, $C_{20}H_{18}NO_4$, was found at 17.6 - 17.8 minutes.

Quantitative analysis of chlorogenic acid, berberine and rutin

From the chromatograms of the ethanolic extract and comparison of the retention times, it was found that chlorogenic acid (polyphenol), rutin (flavonoid) and berberine (alkaloid) were present. Analysis using chlorogenic acid, rutin, and berberine standards gave average retention times of 10.39, 18.58, and 33.81 minutes, respectively. The barberry extracts were found to contain 47.1 mg/kg of chlorogenic acid, 0.02 mg/kg of rutin and 0.36 mg/kg of berberine.

Chlorogenic acid has been found to be an activator of the Nrf2/antioxidant-response element pathway, which was initiated during oxidative stress [8]. The extensive range of therapeutic effects, such as antimutagenic, antiviral [9], anticarcinogenic [7], and free radical scavenging activity [10] has led many researchers to believe that this compound can have potential pharmaceutical applications. Rutin (vitamin P or rutoside) is considered a high value nutraceutical whose pharmacological action has been reported to benefit the central nervous system through its neuroprotective effect on brain ischemia by the upregulation of 'endogenous antioxidant defense enzymes' [11]. A significant attenuation in HL-60 cells in a murine model using a dose of 120 mg/kg of rutin displayed a high antileukemia capacity [12]. Berberine was found to inhibit gram-positive bacteria such as *Staphylococcus aureus* (X) with a MIC value of 250 mg/L [13]. Inhibition of mutant keratinocytes by berberine at IC_{50} = 30 μmol/L [14] and in HeLa cells at 100 and 150 mg/L [15] were observed.

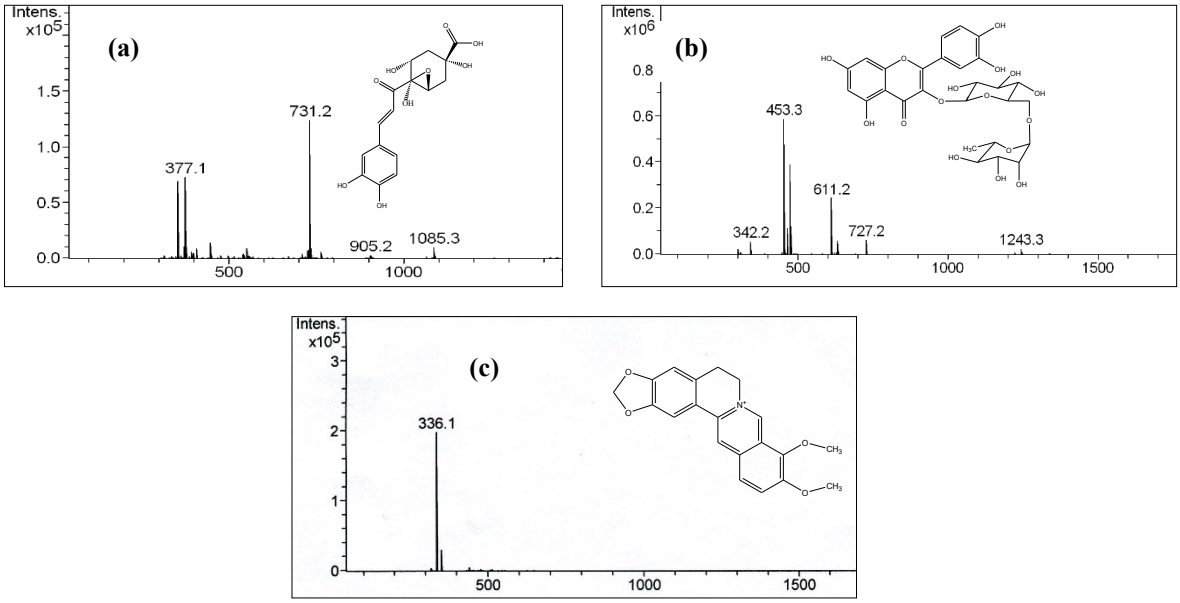


Figure 1. Mass spectra and structures of compounds (a) **1**, (b) **2**, and (c) **3** found in the LC-ESI-MS analyses

Concentration of zinc and iron

The barberry samples contained 45.3 and 198.1 mg/kg of zinc and iron respectively. *Streptococcus pyogenes, Staphylococcus aureus* and *Pseudomonas aeruginosa* were found to have physical damage on the bacterial cell membranes due the adhesion of zinc oxide rod structures on the sheaths [16]. Inorganic metal oxides such as iron(II) oxide can also act as operative antiseptics, owing to their innocuous profile, chemical stability and bioactivity against certain microbes. Composite nanoparticle structures oxides of Zn/Fe exhibited significant bacteriostatic activity on *Staphylococcus aureus* and minimally against *Escherichia coli* [17].

SPME-GC-EI-MS Analysis

Palmitic acid (256.0128 m/z, $[M]^+$) at 45.10 minutes was observed and the spectra showed the fragment $[(CH_2)_2CO_2H]^+$ with m/z = 72.9138. Fragments at 59.9186, 128.9987, 157.0768, 213.0133, and 227.0895 m/z also exhibited ions with the formula $[(CH_2)nCO_2H]^+$. Vaccenic acid was the most probable compound at 50.29 minutes which manifested a molecular ion peak at 282.1020 m/z and a base peak at 54.930 m/z which is presumed to be $[C_4H_7]^+$. The peak at 50.77 minutes gave a fragmentation pattern attributed to stearic acid 284.1314 m/z $[M]^+$; the base peak was also at 72.9138 m/z and exhibited a similar fragmentation pattern to that of palmitic acid. Olefinic fragments at approximately m/z: 69, 83, and 97 were also found in the three mass spectra (Figure 2).

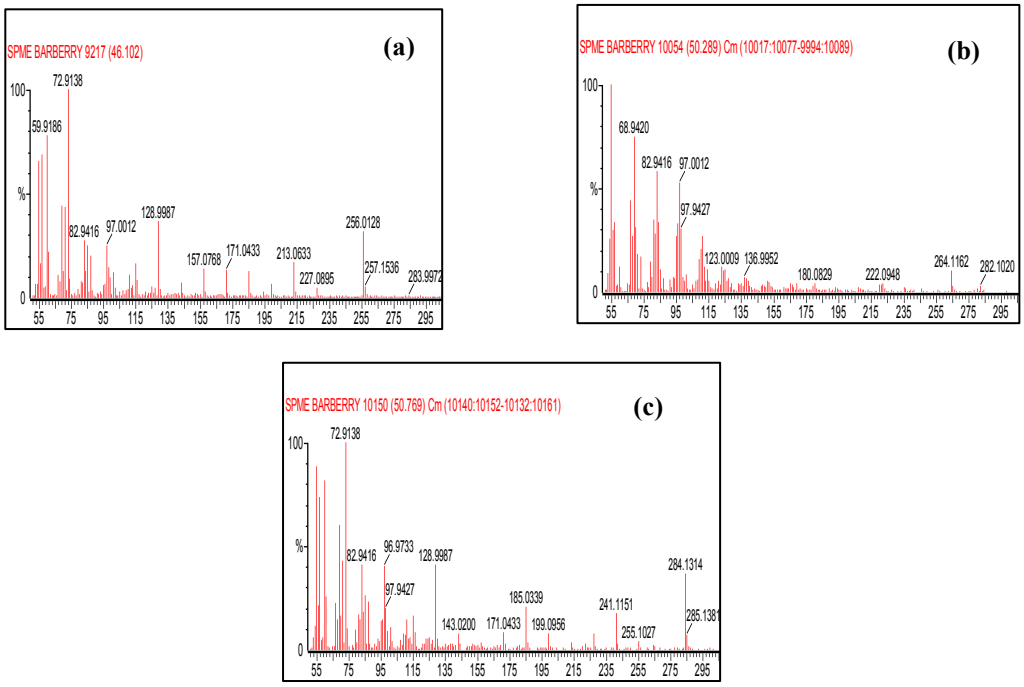


Figure 2. Mass spectra of (a) palmitic acid, (b) vaccenic acid, (c) stearic acid in the SPME-GC-EI-MS analyses

GC-EI-MS analyses of DCM extracts

GC-MS analyses of the dichloromethane extracts of *B. vulgaris* edible berries led to the identification of six constituents. The identified components of the low boiling point compounds of the crude extract were substantiated by retention index (RI) and structural class through the NIST library. The results are listed in Table 1 according to their elution order on a HP-5MS column. The sample consisted primarily of three SFAs (C14:0, C16:0, and C18:0), two methyl esters of the SFAs of C14:0 and C16:0, and one PUFA (C18:2 Δ 9,12 cis).

Antimicrobial function in human milk, skin and mucosal membranes have been linked to the presence of fatty acid in these food products which may have the capacity to be useful as microbicides against human pathogens that occur on the skin and mucosa [18, 19, 20]. Various concentrations of saturated fatty acids (SFAs) capric acid (C10:0), lauric acid (C12:0), myristic acid (C14:0), palmitoleic acid (C16:1), monocaprin (C10:0) monolaurin (C12:0) and monopalmitolein (C16:0) caused significant reduction in *H. pylori* cells [21]. The natural trans-fat vaccenic acid is the natural precursor of the polyunsaturated fatty acid (PUFAs) linoleic acid (C18:2 Δ 9,12 cis) and has been reported to have hypo-triglyceridemic action in JCR:LA-cp rats [22] and have anti-proliferative effects on the immortalized cell line MCF-7 (breast adenocarcinoma) by inhibiting the expression of Bcl-2 and procaspase-9 [23].

Table 1. The volatile constituents of the *B. vulgaris* DCM extracts

Peak Number	RT (minutes)	Compound[b]	RI[a]	Functionality
1	14.75	tetradecanoic acid	1766	saturated fatty acid
2	17.55	hexadecanoic acid methyl ester	2026	fatty acid methyl ester
3	20.08	n-hexadecanoic acid	1962	saturated fatty acid
4	20.66	9,12- octadecanoic acid (z, z)-	2068	polyunsaturated fatty acid
5	21.21	octadecanoic acid	2082	saturated fatty acid
6	21.33	tetracosanoic acid, methyl ester	2433	fatty acid methyl ester

[a] Retention Index (HP-5ms column), [b] Compounds listed in order of elution from a HP-5MS column

Conclusion

The bioactivity of *B. vulgaris*, which has been found to exhibit anti-microbial, anti-inflammatory, and anti-cancer effects, can be linked to the chemical constituents found inherently in the fruit. The edible berry was established to contain significant amounts of chlorogenic acid (47.1 mg/kg), rutin (0.02 mg/kg) and berberine (0.36 mg/kg) which have been observed to have medical applications and could be responsible for the observed high antioxidant potential in the DPPH assay (IC_{50} = 34.48 μg/mL crude extract). The bacteriostatic potential of these constituents could be linked to the ability of these entities to penetrate cell membranes, thereby affecting the integrity of the microbes, and to inhibit quorum-sensing. A substantial amount of zinc, iron, and medium to long chain free fatty acids were also detected in the samples which have been reported to induce the degradation of pathogens and malignant neoplasms. The pharmacognosy involved could be correlated to the translational capacity of these constituents to induce caspase-dependent apoptosis, quenching of reactive oxygen species, regulation of phase I or phase II enzymes, and the expression of anti-inflammatory agents.

Acknowledgement

A research grant from De La Salle University Science Foundation through the University Research Coordination Office is gratefully acknowledged.

References

1. Shamsa, F., Ahmadiani, A. and Khosrokhavar, R. (1999). Antihistaminic and anticholinergic activity of barberry fruit (*Berberis vulgaris*) in the guinea-pig ileum. *Journal of Ethnopharmacology*, 64(2):161-166.
2. Taheri, S., Zarei A., Ashtiyani, S. C., Rezaei, A. and Zaheiri, S. (2012). Evaluation of the effects of hydroalcoholic extract of *Berberis vulgaris* root on the activity of liver enzymes in male hypercholesterolemic rats. *Avicenna Journal of Phytomedicine*, 2(3): 153-161.
3. Koncic, M. Z., Kremer, D., Karlovic, K. and Kosalec, I. (2010). Evaluation of antioxidant activities and phenolic content of *Berberis vulgaris* L. and *Berberis croatica* Horvat. *Food and Chemical Toxicology*, 48: 2176-2180.
4. Sikder, A. A., Kuddus, R., Kasier, A. and Arshad, W. M. (2010). In vitro membrane stabilizing activity, total phenolic content, free radical scavenging and cytotoxic properties of *Aphanamixis polystachya* (Wall.). *Bangladesh Pharmaceutical Journal*, 13(2): 55-59.
5. Hasler, A., Sticher, O. and Meier, J. (1992). Identification and determination of the flavonoids from *Ginkgo biloba* by high-performance liquid chromatography. *Journal of Chromatography*, 605(1): 41–48.
6. Olszewska, M. (2007). Quantitative HPLC analysis of flavonoids and chlorogenic acid in the leaves and Inflorescences of *Prunus serotina* Ehrh. *Acta Chromatographica*, 19: 253-269.
7. Gordon, M. H. and Wishart, K. (2010). Effects of chlorogenic acid and bovine serum albumin on the oxidative stability of low density lipoproteins *in vitro*. *Journal of Agriculture Food Chemistry*, 58: 5828-5833.

8. Boettler, U., Volz Pahlke, N. G., Teller, N., Kotyczka, C., Somoza, V., Stiebitz, H., Bytof, G., Lantz, I., Lang, R., Hofmann, T. and Marko, D. (2011). Coffees rich in chlorogenic acid or N-methylpyridinium induce chemopreventive phase II-enzymes via the Nrf2/ARE pathway *in vitro* and *in vivo*. *Molecular Nutrition and Food Research*, 55: 798–802.
9. Wang, G. F., Shi, L. P., Ren, Y. D., Liu, Q. F., Liu, H. F., Zhang, R. J., Li, Z., Zhu, F. H., He, P. L., Tang, W., Tao, P. Z., Li, C., Zhao, W. M. and Zuo, J. P. (2009). Anti-hepatitis B virus activity of chlorogenic acid, quinic acid and caffeic acid *in vivo* and *in vitro*. *Antiviral Research*, 83: 186-190.
10. Sato, Y., Itagaki, S., Kurokawa, T., Ogura, J., Kobayashi, M., Hirano, T., Sugawara, M. and Iseki, K. (2011). *In vitro* and *in vivo* antioxidant properties of chlorogenic acid and caffeic acid. *International Journal of Pharmaceutics*, 403: 136–138.
11. Gordon, T., Perlstein, B., Houbara, O., Felner, I., Banin, E. and Margel, S. (2011). Synthesis and characterization of zinc/iron oxide composite nanoparticles and their antibacterial properties. *Colloids and Surfaces A: Physicochemical Engineering Aspects,* 374(1-3): 1-8.
12. Tang, Y. Z. and Liu, Z. Q. (2008). Chemical kinetic behavior of chlorogenic acid in protecting erythrocyte and DNA against radical-induced oxidation. *Journal of Agriculture and Food Chemistry*, 56: 11025–11029.
13. Khan, M. M., Ahmad, A., Ishrat, T., Khuwaja, G., Srivastawa, P., Khan, M. B., Raza, S. S., Javed, H., Vaibhav, K., Khan, A. and Islam, F. (2009). Rutin protects the neural damage induced by transient focal ischemia in rats. *Brain Research*, 1292: 123-135.
14. Lin, J. P., Yang, J. S., Lin, J. J., Lai, K. C., Lu, H. F., Ma, C. Y., Sai-Chuen W. R. Wu, K. C., Chueh, F. S., Gibson, W. and Chung, J. G. (2012). Rutin inhibits human leukemia tumor growth in a murine xenograft model in vivo. *Environmental Toxicology*, 27(8): 480-484.
15. Iawasa, K., Kamigauchi, M., Suguira, M., Nanba, H. (1997). Antimicrobial activity of some 13-alkyl a substituted protoberberinium salts. *Planta Medica*, 63(3): 196-198.
16. Muller, K., Ziereis, K. and Gawlik, I. (1995). The antisporatic *Mahonia aquifolium* and its active constituents; II. Antiproliferative against cell growth of human keratinocytes. *Planta Medica*, 61(1): 74-75.
17. Kettman, V., Kosfalova, D., Jantova, S., Cernakova, M. and Drimal, J. (2004). *In vitro* cytotoxicity of berberine against HeLa and L1210 cancer cell lines. *Pharmazie*, 59(7): 548-551.
18. Ling, C. A., Mahmud, S., Khadijah, S., Bakhori, M., Sirelkhatim, A., Mohamad, D., Hasan, H., Seeni, A. and Rahman, R. A. (2013). Antibacterial responses of zinc oxide structures against *Staphylococcus aureus*, *Pseudomonas aeruginosa* and *Streptococcus pyogenes*. *Ceramics International*, 40(2): 2993–3001.
19. Gordon, T., Perlstein, B., Houbara, O., Felner, I., Banin, E. and Margel, S. (2011). Synthesis and characterization of zinc/iron oxide composite nanoparticles and their antibacterial properties. *Colloids and Surfaces A: Physicochemical and Engineering Aspects*, 374(1-3): 1-8.
20. Isaacs, C. E., Kim, K. S. and Thormar, H. (1994). Inactivation of enveloped viruses in human bodily fluids by purified lipids. *Annals of the New York Academy of Sciences*, 724: 457–464.
21. Petschow, B. W., Batema, R. P. and Ford L. L. (1996). Susceptibility of *Helicobacter pylori* to bactericidal properties of medium-chain monoglycerides and free fatty acids. *Antimicrobial Agents and Chemotherapy*, 40: 302–306.
22. Isaacs, C. E., Litov, R. E. and Thormar, H. (1995). Antimicrobial activity of lipids added to human milk, infant formula, and bovine milk. *The Journal of Nutritional Biochemistry,* 6: 362–366.
23. Bergsson, G., Steingrímsson, O. and Thormar, H. (2002). Bactericidal effects of fatty acids and monoglycerides on *Helicobacter pylori. International Journal of Antimicrobial Agents*, 20(4): 258–262.
24. Wang, Y., Lu, J., Ruth, M. R., Goruk, S. D., Reaney, M. J., Glimm, D. R., Vine, D. F. and Field, C. J. (2008). Trans-11 vaccenic acid dietary supplementation induces hypolipidemic effects in JCR:LA-cp rats. *Journal of Nutrition*, 138(11): 2117-2122.
25. Lim,, J. N., Oh, J. J., Wang, T., Lee, J. S., Kim, S. H., Kim, Y. J. and Lee, H. G. (2014). Trans-11 18:1 vaccenic acid (TVA) has a direct anti-carcinogenic effect on MCF-7 human mammary adenocarcinoma cells. *Nutrients*, 6(2): 627-636.

Malaysian Journal of Analytical Sciences, Vol 22 No 4 (2018): 586 - 593
DOI: https://doi.org/10.17576/mjas-2018-2204-03

MALAYSIAN JOURNAL OF ANALYTICAL SCIENCES
Published by The Malaysian Analytical Sciences Society
ISSN 1394 - 2506

FILLER AND POLYMER INTERACTIONS IN POLYMETHYL METHACRYLATE/50% EPOXIDIZED NATURAL RUBBER/SILICON DIOXIDE NANOCOMPOSITES

(Interaksi Pengisi Dan Polimer Dalam Nanokomposit Polimetil Metakrilat/Getah Asli Terepoksida 50%/Silikon Dioksida)

Sharil Fadli Mohamad Zamri[1,2,3]*, Famiza Abdul Latif[1,2,3], Ab Malik Marwan Ali[1,3], Ruhani Ibrahim[1], Siti Izzati Husna Mohd Azuan[1], Norashima Kamaluddin[1], Fitrah Hadip[1]

[1]*Faculty of Applied Sciences*
[2]*Synthesis and Application of Conducting Polymer Research Group*
[3]*Frontier Materials & Industry Application*
Universiti Teknologi MARA, 40450 Shah Alam, Selangor, Malaysia

**Corresponding author: sharil7240@uitm.salam.edu.my*

Received: 13 April 2017; Accepted: 4 June 2018

Abstract

Polymethyl methacrylate/50% epoxidized natural rubber (PE) blend and polymethyl methacrylate/50% epoxidized natural rubber/silicon dioxide (PE15) nanocomposites were successfully prepared *via* solvent casting method with tetrahydrofuran (THF) as solvent. The interactions between silicon dioxide (SiO_2) particles with polymethyl methacrylate (PMMA) and 50% epoxidized natural rubber (ENR 50) in PE and PE15 films were investigated using Fourier transform infrared (FTIR) analysis. Meanwhile, the phase separation between PMMA and ENR 50 in PE and PE15 films was monitored using optical microscopy (OM) analysis. FTIR analysis shows the presence of hydrogen bonding between PMMA and ENR 50 in PE film and functional groups responsible to the hydrogen bonding was identified. FTIR analysis also revealed that interactions between SiO_2 with PMMA and ENR 50 were SiO_2 weight percent dependent. While, OM analysis confirmed that phase separation between PMMA and ENR 50 also influenced by weight percent of SiO_2.

Keywords: polymethyl methacrylate, 50% epoxidized natural rubber, silicon dioxide

Abstrak

Adunan polimetil metakrilat/getah asli terepoksida 50% (PE) dan nanokomposit polimetil metakrilat/getah asli terepoksida 50%/silikon dioksida (PE15) telah berjaya disediakan melalui kaedah acuan tuangan larutan dengan tetrahidrofuran (THF) sebagai pelarut. Interaksi antara zarah silikon dioksida (SiO_2) dengan polimetil metakrilat (PMMA) dan getah asli terepoksida 50% (ENR 50) dalam filem PE dan PE15 telah disiasat menggunakan analisis inframerah transformasi Fourier (FTIR). Sementara itu, fasa pemisahan antara PMMA dan ENR 50 dalam filem PE dan PE15 telah dipantau menggunakan analisis mikroskopi optik (OM). Analisis FTIR menunjukkan kewujudan ikatan hidrogen antara PMMA and ENR 50 dalam filem PE dan kumpulan berfungsi yang bertanggungjawab kepada ikatan hidrogen telah dikenalpasti. Analisis FTIR juga menunjukkan bahawa interaksi antara SiO_2 dengan PMMA dan ENR 50 adalah bergantung kepada peratusan berat SiO_2. Manakala, analisis OM mengesahkan bahawa fasa pemisahan antara PMMA dan ENR 50 juga dipengaruhi oleh peratusan berat SiO_2.

Kata kunci: polimetil metakrilat, 50% getah asli terepoksida, silikon dioksida

Introduction

PMMA is a transparent polymer with superior physical properties include resistance to chemical, corrosion and weathering, light weight and good insulating properties [1]. However, PMMA may not be able to provide some of the targeted polymer's properties necessary for curtain applications [1, 2]. This due to hard, brittle and rigid characteristics shown by PMMA [3]. Consequently, polymer blending is a simple, efficient and versatile modification approach that has been proposed to improve and tailor polymer properties [1]. It consists of two or more polymers mixed without involving new chemical bonding between its constituents [4]. In general, polymer blends show combination properties between both parent polymers that were mixed [5]. Previously, several polymer blends were investigated include polymethyl methacrylate-g-polyvinyl chloride/polymethyl methacrylate [2], polyethylene oxide/polymethyl methacrylate [3], polyethylene/polyamide [4], poly(2,6-dimethyl-1,4-phenylene ether)/poly(styrene-***co***-acrylonitrile) [5] and polypropylene/polyethylene [6]. Latif et al. reported that PMMA/ENR 50 blend with 10% ENR 50 composition lower the glass transition temperature (T_g) of PMMA and give a rubber-like characteristic to the PMMA/ENR 50 blend with excellent elasticity and adhesion properties [1]. Due to the rubbery properties of ENR 50.

Unfortunately, most polymer blends are not homogenized [1]. As result, polymer blends produced are inhomogeneous and cause phase separation [7, 8], thus performance of polymer blends may not be optimized [9, 10]. Interestingly, dispersion of inorganic filler in polymer blends were reported have the ability to improve the homogeneity and phase separation between polymers in the blending [11]. Besides, addition of inorganic fillers also has the ability to improve thermal stability [12] and mechanical stability [13] of the polymer nanocomposites. Among fillers were used in polymer blend include montmorillonite [4, 8], SiO_2 [11, 13] and titanium oxide [12, 13].

Solvent casting method is the most suitable method for preparation of polymer nanocomposites containing PMMA and ENR 50. This is due to the method can be carried out at room temperature, therefore, mixing polymers with different melting temperatures, thermal degradation of unstable polymer and evaporation of additives at high temperatures will be not concerned.

This study reports polymer nanocomposites were successfully prepared from PMMA, ENR 50 and SiO_2 *via* solvent casting method. The presence of hydrogen bonding between PMMA and ENR 50 in the polymer blend was identified and functional groups responsible to the hydrogen bonding was suggested. In addition, the ability of SiO_2 to occupy themselves in between PMMA and ENR 50 and manipulating the interaction between polymers and filler were discussed. The role of filler in improving miscibility and phase separation between PMMA and ENR 50 in PMMA/ENR 50 also was explained.

Materials and Methods

Preparation of stock solutions

10.0 g of PMMA (Aldrich Chemistry, USA), 5.0 g of ENR 50 (Malaysia Rubber Board, Malaysia) and 10.0 g of 15 nm SiO_2 (Aldrich Chemistry, USA) were dissolved separately in 500 mL of THF (J.T. Baker) in 1L screw cap bottles. The PMMA (2% (w/v)), ENR 50 (1% (w/v)), and SiO_2 (2% (w/v)) solutions were stirred for 24 hours using magnetic stirrers at room temperature. All solutions were kept in closed bottles and were stirred for an hour every time before use.

Preparation of PMMA/ENR 50 blend and PMMA/ENR 50/SiO_2 nanocomposites films

25.0 mL of PMMA and 5.0 mL of ENR 50 solutions were mixed and stirred to give PMMA:ENR 50 mass ratio of 90:10 in 100 mL screw cap bottles using magnetic stirrers for 24 hours. Then, SiO_2 solution was added to the polymer mixtures at specific ratios (Table 1) and continuously stirred for another 24 hours. The polymer solutions were casted in Teflon dish under nitrogen gas flow for 12 hours. The obtained thin films then were peeled off, dried in an oven at a temperature of 50 °C for 12 hours and kept in a desiccator.

Table 1. SiO_2 weight percent in the films

Weight Percent of SiO_2 (%)	**Designation**
0	PE
1	PE151
3	PE153
5	PE155
7	PE157

Characterization: Fourier transform infrared spectroscopy analysis
Perkin Elmer Spectrum One FTIR Spectrophotometer was used for FTIR analysis. The spectrum of all film samples were recorded at room temperature using the spectrophotometer that was equipped with Attenuated Total Reflectance (ATR) equipment. The scan wavenumber was fixed from 400 to 4000 cm^{-1} with resolution of 4 cm^{-1} and 16 times scan rate.

Optical microscopy
The surface of PE, PE151, PE153, PEl55 and PE157 films was observed under Nikon ECLISPE ME 600 optical microscopy. Samples were placed onto the microscope slide and the brightness, the contrast, the lens distance and the magnification of the optical microscope were adjusted in order to obtain the best micrograph.

Results and Discussion

Latif et al. claimed that PMMA and ENR 50 polymer chains in PMMA/ENR 50 blend can interact *via* hydrogen bonding [1]. However, the exact functional groups involve in the hydrogen bonding is not further investigated. Since, C=O and O-CH_3 groups of PMMA and C-O-C epoxy ring of ENR 50 are polar groups that have big potential to interact with any hydrogen atoms in ENR 50 and PMMA. Therefore, the effect of addition of SiO_2 on PMMA-ENR 50, PMMA-SiO_2 and ENR 50-SiO_2 interactions were monitored using FTIR analysis. Figure 1 shows that PE film possesses C=O, O-CH_3 and C-O-C peaks that recorded at 1723, 1380 and 1240 cm^{-1}, respectively.

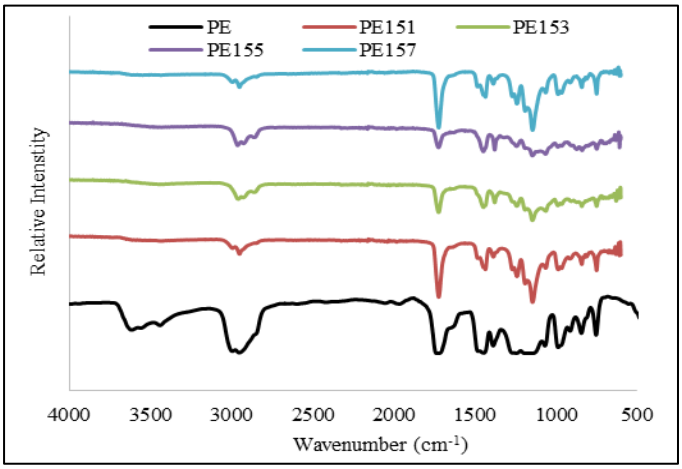


Figure 1. FTIR spectra corresponding to PE and PE15 films at various weight percent of SiO_2

Interestingly, a broad peak in PE FTIR spectrum recorded at 3640 cm^{-1} was probably due to hydrogen bonding between ENR 50 and PMMA, and the possible molecular interactions are illustrated in Figure 2. The formation of hydrogen bonds was probably due to the polarity of C=O, O-CH_3 and C-O-C groups. Similar observation was reported in other blend systems containing ENR 50 [7] and PMMA [14].

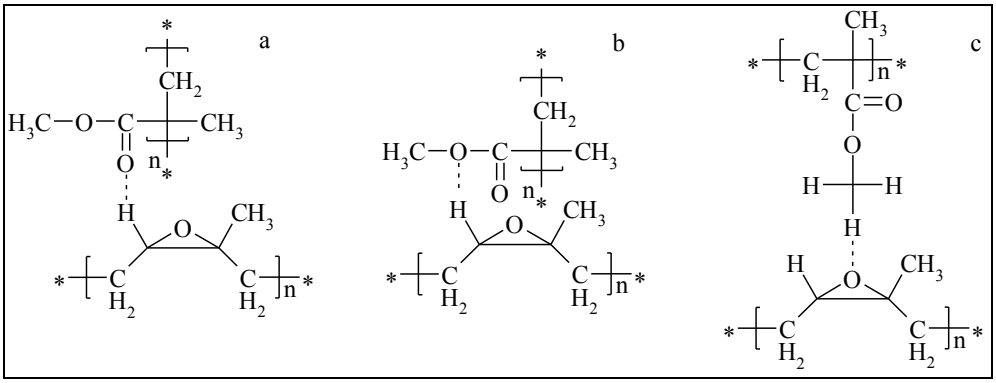


Figure 2. Possible hydrogen bonding between PMMA and ENR 50 in PMMA/ENR 50 blend

FTIR peaks comparison corresponding to C=O, O-CH_3 and C-O-C peaks of PMMA, ENR 50 and PE films was conducted to determine which among the functional groups in PMMA and ENR responsible for the hydrogen bond formed in PE film (Figure 3). It revealed that the intensity of C=O peak of PE film was broader compared to PMMA film (Figure 3 (a)), whereas, C-O-C peak of PE film was decreased compared to ENR 50 film (Figure 3 (c)). Indicated that C=O and C-O-C in PE film experienced strong interaction compared to PMMA and ENR 50 films. Meanwhile, O-CH_3 peak of PE film increased compared to PMMA film (Figure 3 (b)), thus, revealing that O-CH_3 was free. From the observation it may suggest that oxygen atoms in C-O-C and C=O group were responsible for the hydrogen bonding between PMMA and ENR 50 in PE film.

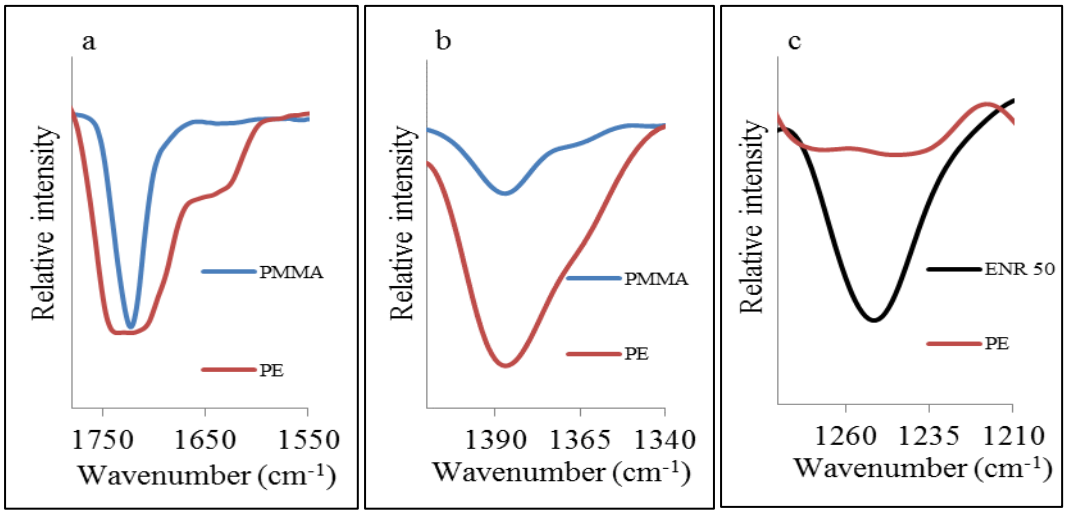


Figure 3. FTIR spectra corresponding a) C=O b) O-CH_3 and c) C-O-C for PMMA, ENR 50 and PE films

Interestingly, the O-H broad peak disappeared when SiO_2 was dispersed in PE151, PE153, PE155 and PE157 films. This phenomenon is due to the ability of SiO_2 particles to occupy itself in between polymeric chains and separate the polymer chains apart. As a result the number of hydrogen bonds reduced. This was further supported by an increase in intensity of C=O (Figure 4 (a)) and C-O-C (Figure 4 (c)) peaks of PE151 film. C=O and C-O-C groups in PE151 film were free since the number of hydrogen bonds between polymer chains in PE151 film was reduced when SiO_2 was added.

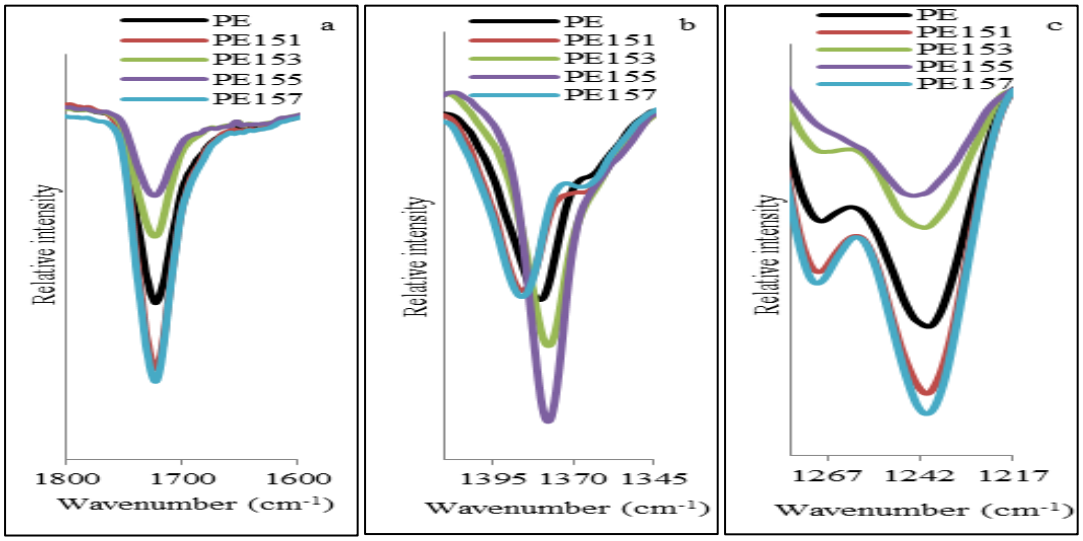


Figure 4. FTIR spectra corresponding to a) C=O b) O-CH_3 and c) C-O-C groups in PE and PE15 films

It was observed that O-CH_3 peak in PE151 film (Figure 4 (b)) slightly decreased compared to PE film. This indicates that a new polymer network was formed between oxygen atoms in O-CH_3 group and hydrogen atom in Si-OH group of SiO_2. The polymer network between PMMA and SiO_2 interaction is illustrated in Figure 5 (c). Interestingly, the intensity of C=O (Figure 4 (a)) and C-O-C (Figure 4 (c)) peaks in PE153 and PE155 films decreased when 3% and 5% of SiO_2 was added. This was probably due to the polymer network moving between oxygen atoms of C=O (Figure 5 (b)) and C-O-C (Figure 5 (c)) with hydrogen atom of Si-OH. Qu et al. also reported that Si-OH group of SiO_2 have the ability to interact with oxygen atom of polyamide [15]. In contrast, the intensity of O-CH_3 peak in PE153 and PE155 films increased when 3% and 5% of SiO_2 was added indicating O-CH_3 group does not take place in the polymer network with Si-OH in PE153 and PE155 films.

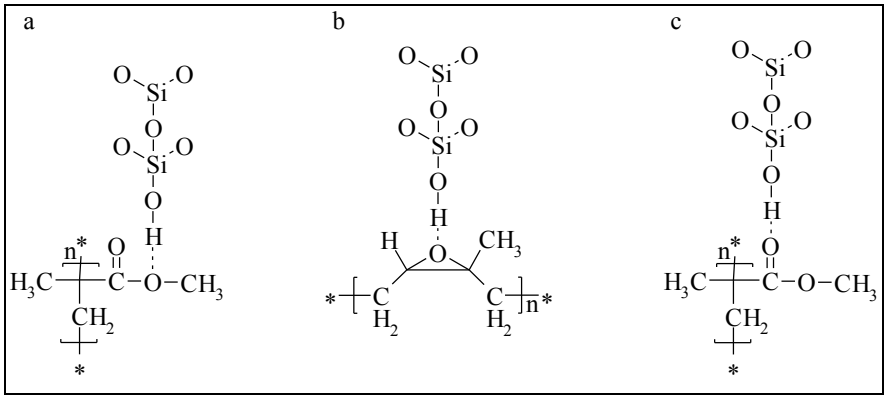


Figure 5. Possible polymer networks between SiO_2 with PMMA and ENR 50 in PE15 films

The phase separation between PMMA rich phase and ENR 50 rich phase were observed in PE film (Figure 6 (a). This observation confirmed that PMMA and ENR 50 in PE film was immiscible and was confirmed similar with our previous reports [11, 16]. Therefore, the PMMA rich phase was observed as brown continuous phase meanwhile ENR 50 rich phase as fine hairy lines when the polymer blend examined under OM. Interestingly, reduction on the size of ENR 50 rich phase when 1% of SiO_2 was added in PE151 (Figure 6 (b)) film indicated that the phase separation of PMMA and ENR 50 was improved. This probably due to the ability of SiO_2 to occupy space between PMMA and ENR 50 hence forcing ENR 50 to move into PMMA phase [16]. The role of SiO_2 as compatibilizer agent was also reported by Zhang et al. [17]. In their study, incompatible polypropylene/polystyrene (PP/PS) blend was successfully improved with addition of SiO_2 in which of PS has been well distributed in the blend upon from addition of SiO_2.

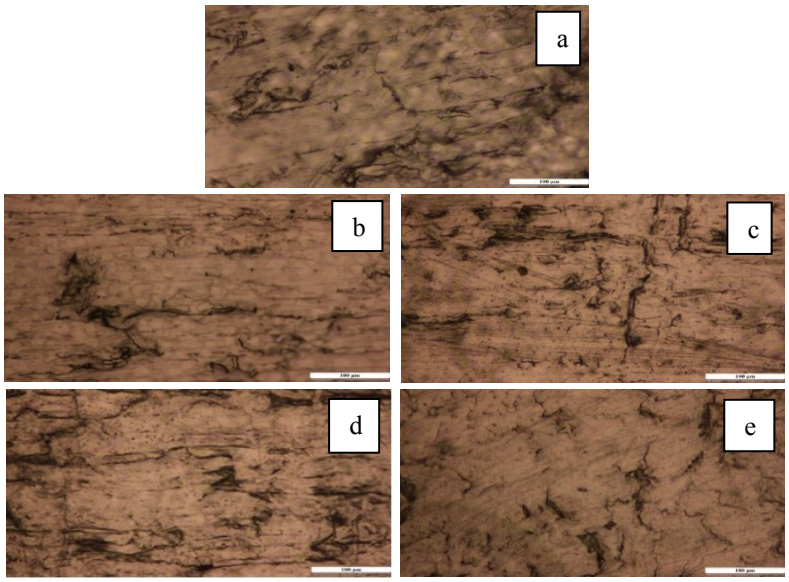


Figure 6. Optical micrographs for (a) PE, (b) PE151, (c) PE153, (d) PE155 and (e) PE157 films

Furthermore, the phase separation almost diminishing as the amount of SiO_2 filler was increased up to 7% in the blend system (Figure 6 (e)). The improvement of the phase separation probably due to more SiO_2 filler occupying space in the blend system. Similar observation was recorded by Du et al. when 5% of SiO_2 was added in PMMA/SAN [18]. Uniquely, the harry lines of ENR 50 phase was found to be orientated in one direction at 1, 3 and 3% of SiO_2 filler in PE151, PE153 and PE155 films, respectively. This was suggested that the interaction that occurred between the filler and the polymers as discussed previously.

In addition, as the amount of SiO_2 increased up to 5%, more SiO_2 were distributed into the blend system hence initiate the formation of polymer network between oxygen atom of C-O-C (Figure 5 (b)) and C=O (Figure 5 (c)) groups with hydrogen atom of the Si-OH. Since C=O and C-O-C are more polar than the $O-CH_3$, the filler seems to be attracted to these C=O and C-O-C groups like a “magnetic effect” and form a series of SiO_2 chain (Figure 7). This “magnetic effect” explained reason for the harry lines of ENR 50 phase and was observed to be orientated in one direction in its optical micrograph.



Figure 7. Propose magnetic effect of SiO_2 on PMMA and ENR 50 chain in PMMA/ENR 50 blend

Conclusion

PMMA/ENR 50 blend and PMMA/ENR 50/SiO_2 nanocomposites films were successfully prepared *via* solvent casting method. Hydrogen bonding between PMMA and ENR 50 in the polymer blend was determined and functional groups responsible for the hydrogen bond was determined. The interactions between filler and polymers films were SiO_2 weight percent dependent. PMMA and ENR 50 in PMMA/ENR 50 blend and PMMA/ENR 50/SiO_2 nanocomposites films were found immiscible. Interestingly, the miscibility between PMMA and ENR 50 improved when SiO_2 was added. This finding is crucial for further investigation on the effects of SiO_2 on physical, thermal and electrochemical properties of PMMA/ENR 50 electrolytes.

Acknowledgement

The authors would like to thanks Universiti Teknologi MARA for the technical support. Special thanks to the Ministry of Education (MOHE) of Malaysia for the financial support under Research Acculturation Grant Scheme (RAGS) (RAGS/2013/UiTM/SG06/1).

References

1. Latif, F. A., Aziz, M., Katun, K., Ali, M. A. M. and Yahya, M. Z. (2006). The role and impact of rubber in poly(methyl methacrylate)/lithium triflate electrolyte. *Journal of Power Sources*, 159: 1401-1404.
2. Yuan, W., Li, M. and Yang, M. (2006). Dual-phase polymer electrolyte with enhanced phase compatibility based on Poly(MMA-g-PVC)/PMMA. *European Polymer Journal,* 42: 1396-1402.
3. Sengwa, R. J., Dhatarwal, P. and Choudhary, S. (2014). Role of preparation methods on the structural and dielectric properties of plasticized polymer blend electrolytes: Correlation between ionic conductivity and dielectric parameters. *Electrochimica Acta,* 142: 359-370.
4. Huitric, J., Ville, J., Mederic, P. and Aubry, T. (2017). Solid-state morphology, structure, and tensile properties of polyethylene/polyamide/nanoclay blends: Effect of clay fraction. *Polymer Testing,* 58: 96-103.

5. Bahrami, R., Lobling, T. I., Schmalz, H., Müller, A. H. E. and Altstadt, V. (2017). Synergistic effects of Janus particles and triblock terpolymers on toughness of immiscible polymer blends. *Polymer,* 109: 229-237.
6. Wong, A. C. Y. and Lam, F. (2002). Study of selected thermal characteristics of polypropylene/polyethylene binary blends using DSC and TGA. *Polymer Testing,* 21(6): 691-696.
7. Noriman, N. Z., Ismail, H. and Rashid, A. A. (2010). Characterization of styrene butadiene rubber/recycled acrylonitrile-butadiene rubber (SBR/NBRr) blends: The effects of epoxidized natural rubber (ENR-50) as a compatibilizer. *Polymer Testing,* 29(2): 200-208.
8. Arroyo, M., Manchado, M. A. L., Valentín, J. L. and Carretero, J. (2007). Morphology/behaviour relationship of nanocomposites based on natural rubber/epoxidized natural rubber blends. *Composites Science and Technology*, 67: 1330-1339.
9. Ploypetchara, N., Suppakul, P., Atong, D. and Pechyen, C. (2014). Blend of polypropylene/poly(lactic acid) for medical packaging application: physicochemical, thermal, mechanical, and barrier properties. *Energy Procedia,* 56: 201-210.
10. Takayama, T., Todo, M. and Tsuji, H. (2011). Effect of annealing on the mechanical properties of PLA/PCL and PLA/PCL/LTI polymer blends. *Journal of the Mechanical Behavior of Biomedical Materials,* 4 (3): 255-260.
11. Zamri, S. F. M. and Latif, F. A. (2013). SiO_2 filler as interface modifier in PMMA/ENR 50 electrolytes. *Advanced Materials Research,* 812: 120-124.
12. Pradeepa, P., Raj, S. E and Prabhu, M. R. (2015). Effects of ceramic filler in poly(vinyl chloride)/poly(ethyl methacrylate) based polymer blend electrolytes. *Chinese Chemical Letters,* 26: 1191-1196.
13. Hema, M. and Tamilselvi, P. (2016). Lithium ion conducting PVA:PVdF polymer electrolytes doped with nano SiO_2 and TiO_2 filler. *Journal of Physics and Chemistry of Solids,* 96 – 97: 42-48.
14. Huang, C. F. and Chang, F. C. (2003). Comparison of hydrogen bonding interaction between PMMA/PMAA blends and PMMA-co-PMAA copolymers. *Polymer,* 44(10): 2965-2974.
15. Qu, C., Yang, H., Liang, D., Cao, W. and Fu, Q. (2007). Morphology and Properties of PET/PA-6/SiO_2 Ternary Composites. *Journal of Applied Polymer Science,* 104: 2288-2296.
16. Zamri, S. F. M., Latif, F. A., Ali, A. M. M., Ibrahim, R., Azuan, H. I. H. M, Kamaluddin, N. and Hadip, F. (2017). Exploration on effects of 15 nm SiO_2 filler on miscibility, thermal stability and ionic conductivity of PMMA/ENR 50 electrolytes. *AIP Conference Proceedings,* 1809: 020049.
17. Zhang, Q., Yang, H. and Fu, Q. (2004). Kinetics-controlled compatibilization of immiscible polypropylene /polystyrene blends using nano-SiO_2 particles. *Polymer,* 45(6): 1913-1922.
18. Du, M., Wu, Q., Zuo, M. and Zheng, Q. (2013) Filler effects on the phase separation behavior of poly (methyl methacrylate)/poly (styrene-co-acrylonitrile) binary polymer blends. *European Polymer Journal,* 49(9): 2721-2729.

Malaysian Journal of Analytical Sciences, Vol 22 No 4 (2018): 594 - 604
DOI: https://doi.org/10.17576/mjas-2018-2204-04

MALAYSIAN JOURNAL OF ANALYTICAL SCIENCES
Published by The Malaysian Analytical Sciences Society
ISSN 1394 - 2506

ASSESSMENT OF METALS CONCENTRATION IN TILAPIA (*Oreochromis* sp.) AND ESTIMATION OF DAILY INTAKE BY MALAYSIAN

(Penilaian Kepekatan Logam dalam Tilapia (*Oreochromis* sp.) dan Anggaran Pengambilan Harian oleh Orang Malaysia)

Nurulnadia Mohd Yusoff [1]*, Siti NurTahirah Jaafar[1], Noor Azhar Mohamed Shazili[2], Nik Nurasyikin Nik Mohammad Azmi[1], Mohamad Sofi Abu Hassan[2]

[1]*School of Marine and Environmental Sciences*
[2]*Institute of Oceanography and Environment*
Universiti Malaysia Terengganu, 21030 Kuala Nerus, Terengganu, Malaysia

**Corresponding author: nurulnadia@umt.edu.my*

Received: 13 December 2017; Accepted: 11 June 2018

Abstract

Aquaculture of tilapia is growing economically and nutritionally important in Malaysia. Fish is part of the human diet, the assessment of metals concentration in their tissues is compulsory. Cadmium (Cd), copper (Cu), lead (Pb) and zinc (Zn) concentrations were measured in the muscles, gills and liver tissue of tilapia, *Oreochromis* sp. Microwave digestion method was employed to extract the target metals followed by measurement of concentration by inductively coupled plasma-mass spectrometry (ICP-MS). The level of Cd, Cu and Pb were significantly high ($p < 0.05$) in the liver of tilapia from Tumpat lagoon with 0.359±0.129, 71.1±31.3 and 2.14±0.451 µg/g dry weight (dw), respectively compared to the fish liver from Terengganu River. However, Zn concentration was significantly high in muscle tissues with 15.2±3.75 µg/g dw. Daily intake of metals in human was also estimated and compared to established standards. The intake levels of Cd, Cu, Pb and Zn were lower than the standards. Hence, tilapia is safe for consumption if they do not ingest the liver. Lipid peroxidation (LPO) activity was measured in the same tissue but the correlation values between level of metals and malondialdehyde (MDA) were inconsistent. Thus, further investigation in controlled environment such as laboratory exposure experiment is necessary.

Keywords: metal, daily intake, Tumpat, Terengganu, lipid peroxidation

Abstrak

Kepentingan akuakultur tilapia dari segi ekonomi dan pemakanan semakin meningkat di Malaysia. Oleh kerana ikan adalah sebahagian daripada diet manusia, analisis kepekatan logam di dalam tisu tilapia perlu dilakukan. Kadmium (Cd), kuprum (Cu), plumbum (Pb) dan zink (Zn) telah diukur di dalam tisu otot, insang dan hati tilapia, *Oreochromis* sp. Kaedah pencernaan gelombang mikro telah digunakan untuk mengekstrak logam sasaran tersebut, dan diikuti dengan pengukuran kepekatan menggunakan spektrometri plasma-jisim berganding secara aruhan (ICP-MS). Tahap Cd, Cu dan Pb di dalam hati tilapia dari lagun Tumpat ternyata tinggi ($p < 0.05$) dengan bacaan masing-masing 0.359 ± 0.129, 71.1 ± 31.3 dan 2.14 ± 0.451 µg/g berat kering (dw) berbanding dengan hati ikan dari Sungai Terengganu. Walau bagaimanapun, kepekatan Zn ternyata tinggi ($p < 0.05$) di dalam tisu otot iaitu 15.2 ± 3.75 µg/g dw. Pengambilan logam harian oleh manusia juga telah dianggarkan dan dibandingkan dengan kadar piawaian yang ditetapkan. Kadar pengambilan Cd, Cu, Pb dan Zn didapati lebih rendah daripada piawaian, maka tilapia selamat untuk dimakan selagi mereka tidak memakan tisu hati. Aktiviti pemperoksidaan lipid (LPO) diukur dalam tisu yang sama tetapi nilai korelasi antara tahap logam dan malondialdehid (MDA) tidak konsisten. Oleh itu, kajian lanjut dalam persekitaran terkawal seperti eksperimen di makmal perlu dilakukan.

Kata kunci: logam, pengambilan harian, Tumpat, Terengganu, pemperoksidaan lipid

Introduction

Tilapia is the second most farmed fish group worldwide. The production has quadrupled over the past decades due to their promising characteristics for aquaculture purpose, high marketability and relatively stable market prices [1]. Tilapia farmed fish in the world reported yielding over 3 million metric tons in 2009. *Oreochromis* spp. is one of the most commercially important in aquaculture production contributing to the figures reported [2]. In 2012, aquaculture production in Malaysia contributed 163,757 tons valued at RM992 million and the main cultures species were black and red tilapia, *Oreochromis* spp. Department of Fisheries (DOF) Malaysia also predicted with a growing population and preference for fish, the annual demand will increase from 1.7 million tons in 2011 to 1.93 million in 2020 [3]. To comply with the demand, DOF initiated Aquaculture Industrial Zone (AIZ) including aquaculture farm in the Tumpat lagoon and Terengganu River.

Tilapia is known to have high tolerance to crowding, disease resistance and wide range of salt tolerance [2, 4]. Therefore, they can be cultured in both seawater (Tumpat lagoon) and freshwater ecosystem (Terengganu River). Tumpat lagoon located in the north-east of Peninsular Malaysia, bordering between Thailand and northern Malaysia. The estimated aquaculture area is 500 x 200 meters, along Seri Tujoh Beach. DOF of Tumpat had banned the locals to purchase and consume shellfish products in 2015 due to outbreak of bacteria and pollution in Tumpat lagoon. Terengganu River is the longest river in Terengganu (17 km) with a semi-enclosed breakwater near the river mouth. Following the existence of breakwater, sand dredging activity is continuously operated and potentially causing embedded pollutant to emerge in particulate form. Beside breakwater, a draw bridge construction that began in 2014 is still ongoing and predicted to disturb the ecology as well as contaminating Terengganu River. Tilapias in both sites were cultured in extended period (3 to 6 months, personal communication) prior to sell; hence they could be a good bioindicator of pollution such as metals.

Metals are ubiquitous pollutants which commonly found in water, sediment, as well as living organisms such as fish [5]. Metal pollution generally increases with the human's technological achievement including sand dredging, agriculture, sewage and motor vehicle industry [6]. Fish assimilate metals through ingestion of particulate in water across the gill, dietary uptake and absorption into muscle tissues [7]. Metals are known to disturb the physiological and biochemical functions in rainbow trout, zebrafish and tilapia [8]. Besides, they are toxic to human in high concentration that lead to various implications such as diarrhea, dysfunctions in the kidneys and impairment of reproduction [9, 10]. The increase demand of tilapia proportionally increases the quantity of consumption by local Malaysian, thus investigation of metals concentration in farmed tilapia is necessary.

Cheung et al. [11] and Wong et al. [12] have used tilapia tissues as biomarker of exposure to metal pollution in water which made tilapia a useful model fish species for ecotoxicological studies. Extraction of targeted elements was normally practiced in metals studies by using high-end instrument as measuring tools. However, these high-end instruments were both inefficiently time and cost consuming. Recently, the trend of monitoring the pollutant effects on animals was shifted towards molecular approach which represents better early signs of biological effects [13]. Metals can induce oxidative stress in aquatic animals by disturbing antioxidant efficiency, thus initiating DNA damage and lipid peroxidation [14]. Lipid peroxidation (LPO) of membrane lipids are normally detected by enhanced levels of malondialdehyde (MDA) [15], a byproduct of LPO. MDA has been used as a biomarker for LPO because of its facile reaction with thiobarbituric acid using colorimetric assay. If we managed to verify the level of MDA increment with metal concentrations, we can suggest LPO as another quick and easy approach for monitoring of metals in fishes.

The objectives of the present study are: 1) to determine the concentration of metals (Cd, Cu, Pb and Zn) in the tissues of tilapia, 2) to estimate the daily intake of metals by Malaysian, and 3) to determine the correlation between concentrations of metals and MDA levels in tissue as biomarker of lipid peroxidation due to metal pollution.

Materials and Methods

Water parameters

The water parameters in Tumpat lagoon and Terengganu River were measured using multiprobe Hydrolab Quanta. The temperature was found in the range of 30.9 to 32.6 °C, dissolved oxygen of 2.70 to 7.52 mg/L and pH of 6.30 to

7.41 in Tumpat lagoon. The smaller range of water parameter values was recorded in Terengganu River with temperature was in the range of 28.4 to 28.5 °C, and dissolved oxygen of 4.20 to 5.36 mg/L and pH of 7.52 to 8.55. The water depth was deeper in Terengganu River than Tumpat lagoon with 1.6 to 3.4 m compared to 0.3 to 1.5 m, respectively. Nevertheless, the major difference observed between these two sites was Tumpat lagoon has saline water with 29.7 to 30.4 ppt while Terengganu river was a freshwater with a constant salinity of 0.02 ppt.

Collection and preparation of tilapia

Twenty individual of tilapia samples were collected randomly from each aquaculture farms, Tumpat lagoon and Terengganu River (Figure 1) within June to August 2016.

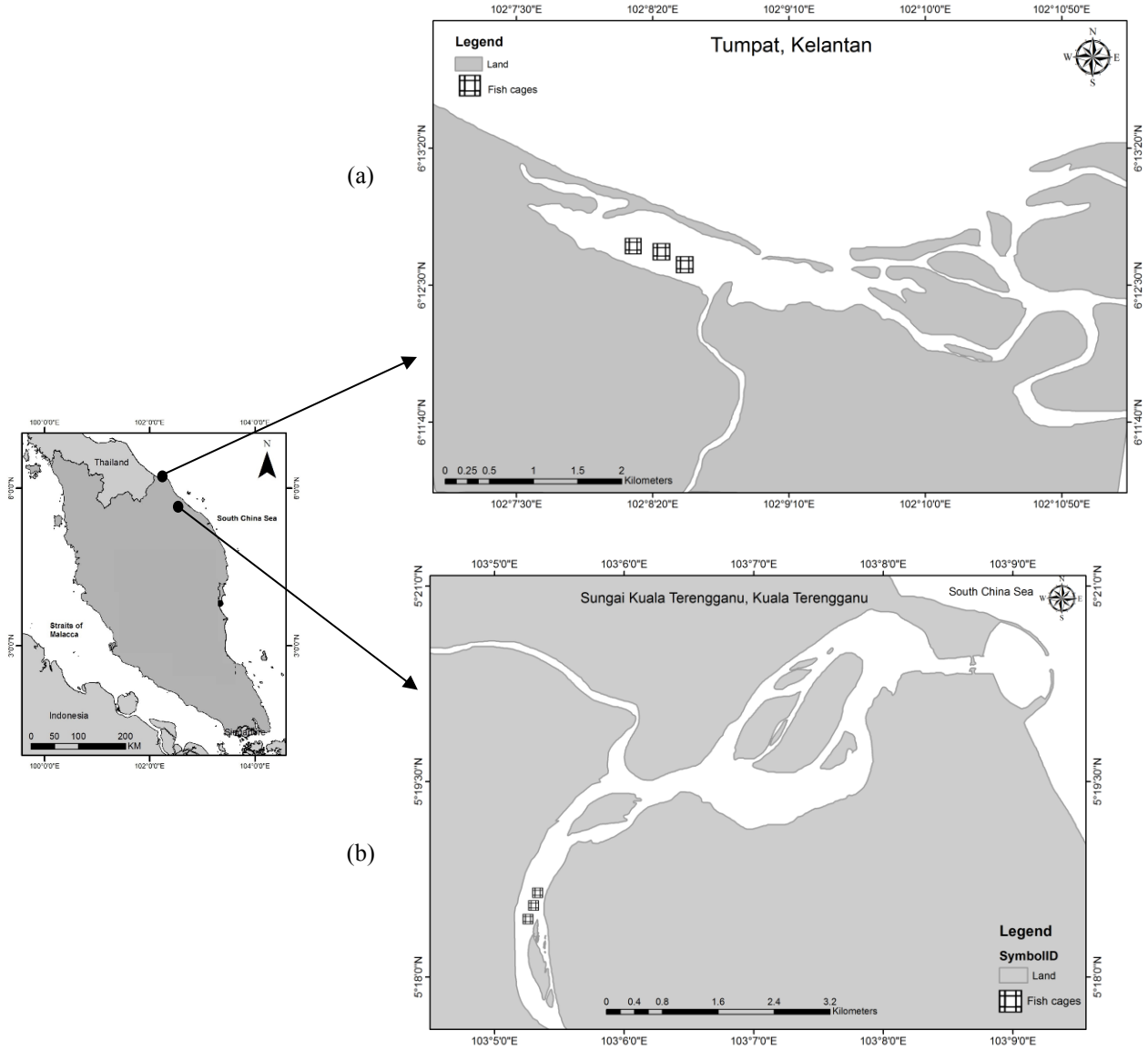


Figure 1. Twenty number of fresh tilapia were collected from (a) Tumpat lagoon, Kelantan and (b) Terengganu River, Terengganu

The fishes were purchased alive and in fresh condition to maintain the quality of flesh and tissues for LPO analysis. Samples were kept cold in ice, transported to the laboratory and prepared at the same day of collection date. The body length and weight were measured prior to dissection to collect muscle, gill and liver tissues. Each muscle, gill and liver tissue samples were divided for metals and LPO analysis. Tissue samples for LPO were immediately stored under -80 ºC temperature condition to prevent deterioration of oxidative activities in the tissue. Glassware and apparatus used for metals analysis were soaked in HNO_3 10% overnight and rinsed with double deionized water.

Metals analysis

Tissue samples for metal analysis were dried at 60 °C until constant weight was gained. Metal analysis was performed by using microwave system digestion as described in Türkmen [16] with some modifications. Targeted heavy metals in the tissues (50 mg) were digested in Teflon vessel with 7 mL nitric acid and 1 mL hydrogen peroxide in maximum pressure of 100 bar at 300 °C, closed digestion vessels (model – SK10, Milestone, Monroe, CT, USA). This device is able to extract ten samples simultaneously with high pressure rotor per batch. Upon completion of digestion (approximately 1 hour), the supernatant was thoroughly transferred into 10 mL polypropylene tube and meshed up to 10 mL with Milli-Q water. Samples were measured using inductively coupled plasma-mass spectrometry Perkin Elmer Elan 9000 (ICP-MS). The same procedures were applied to blank and standard reference material (SRM) samples, Dogfish Liver (DOLT-4). The detection limit for each heavy metal is shown in Table 1. The quality assurance test was performed using a standard reference material (Dogfish Liver, DOLT-4). Mean percentage recovery was calculated to be ranging from 81.3% to 98.7%. Analysis were performed in four replicates (n=6) with the error of all analysis within ±25%.

Table 1. Recovery test result of Dogfish Liver (DOLT-4) by ICP-MS in µg/g dw, n=6

Metal	Limit of Detection*	Certified value	Analysis value	Recovery (%)
Cd	0.001	24.3 ± 0.8	21.8 ± 0.03	89.7
Cu	0.650	31.2 ± 1.1	30.8 ± 6.19	98.7
Pb	0.068	0.16 ± 0.04	0.13 ± 0.02	81.3
Zn	9.090	116 ± 6	107 ± 55.0	92.2

*Detection limit were estimated from standard curve of metals standard solution

LPO analysis

LPO activity was measured using lipid peroxidation (MDA) assay kit from Sigma-Aldrich, USA. The homogenization started with 10 mg of respective tissue samples in 300 µL of MDA lysis buffer saline with 3 µL BHT (100x) on ice. The homogenized solution was then centrifuged at 13,000 x *g* for 10 minutes and the formed aliquot was transferred into micro centrifuge tube. The aliquot was added with 600 µL of TBA solution and incubated at 95 °C for 60 minutes in MDA-TBA adduct. The determination of MDA in samples was done in 96-well plates using ELISA plate spectrophotometer at 450 nm wavelength.

Data analysis

The condition factor of fish was calculated following Fulton's condition factor by dividing fish body weight (g) over [body length]^3 (cm) and multiplied to 100. The daily intake by Malaysian people was computed by the multiplication of measured concentration by 160 g of average weight of fish consumed daily [17]. Statistical analysis was conducted using IBM SPSS Statistics 24. T-test was used to determine the significant difference of metal concentrations in two study sites, while Pearson correlation was employed to determine the correlation between metals and MDA values.

Results and Discussion

The weight, length and condition factor of tilapia from Tumpat lagoon were in the range of 360 to 800 g, 23.5 to 35.0 cm and 2.23 to 2.98, respectively. The weight, length and condition factor of tilapia from Terengganu River

were found to be in the range of 250 to 498 g, 23.0 to 28.0 cm and 1.78 to 2.72, respectively. Condition factor values in these two sites were analysed but no significant difference was found ($p > 0.05$). Thus, environmental condition that influences the growth of tilapia in both sites was not much different from each other. The mean of moisture in respective muscle, gill and liver of tilapia were calculated as 63.5, 51.2 and 66.6% in Tumpat lagoon; and 74.1, 64.1 and 62.8%, in Terengganu River.

The concentration of Cd, Cu, Pb and Zn in respective muscles, gills and liver of tilapia is shown in Table 2. In general, the concentrations of all metals were found higher in gills and livers compared to muscles. The higher concentration in gills and livers could be explained by metallothionein's activities, a type of protein which has the ability to bind certain metals thus allowing these tissues to accumulate at a high degree [18]. The concentration of each metal was found significantly higher in Tumpat lagoon than Terengganu River (marked by asterisk) except for Cu in the liver. To our knowledge, no study has reported the level of pollutants in Tumpat lagoon. Therefore, no speculation could be made. From our observation, a sandbar has developed in front of the lagoon mouth, limiting the water movement especially during low tide. This was confirmed by the cage owner that some of the cultured fish normally died after this event. The limitation of water mixing and movement possibly retained metals in tilapia at extended period and higher level in Tumpat lagoon than Terengganu River. Copper concentration was extremely high in the liver of tilapia from both sites compared to muscles, suggested that liver as the best bioindicator of Cu accumulation.

The metals concentrations in this study are presented in both dry and wet weight in Table 2 to ease comparison with other reports. Cadmium concentrations in three different tissues from this study were lower than studies listed in Table 2. The concentration of Cu in muscles (1.49±0.749 and 1.60±0.736 µg/g dw) and gills (2.10±0.749 and 1.83±0.348 µg/g dw) in the current study was similar to values reported in River Benue with 1.65 and 2.98 µg/g dw, respectively [19]. The sampling location of River Benue received discharge wastes from various food industries such as Coca-cola PLC, Benue Breweries PLC plant and rice mills. This could attribute to the presence of such Cu level as the distance was only 12 km away from the sampling area. We could neither find distinguish food industry near Tumpat lagoon nor Terengganu River. The potential sources of metals were not investigated in the present study. However, we observed a small scale of scrap metal warehouse was located near Tumpat lagoon. Private motor vehicle workshop also operated near the lagoon where fishermen fix their boats engine and propeller potentially added the metals sources into the lagoon. A ship building dock and small jetties were found along Terengganu River, with boat wreck were left at the jetty without proper disposal. Hence, metals could potentially contribute from current boating activities as well as abandoned boat wreck [20]. Levels of Pb in the current study were higher than the concentrations reported in Shing Mun River, Hong Kong [21]. The Shing Mun River was claimed as one of the most contaminated river and estuarine region with two major industrial estates. However, no major industry could be traced either in Tumpat lagoon or Terengganu River. Therefore, Pb concentrations in tilapia in this study require further investigation as the levels were higher compared to the industrial area. However, Zn concentration in each tissue of this study was lower than the values reported in Jelebu, Malaysia [22]. The higher concentration reported in Jelebu was expected as that area was formerly a tin mining pool, and Zn was present since it is associated with Al [23].

Table 2. Comparison of metals concentration in muscle, gill and liver of tilapia, µg/g dw (unless noted as ww), to permissible level from established standards

Study Area	Tissue	Cd	Cu	Pb	Zn	Reference
Tumpat lagoon, Malaysia (n = 20)	Muscle	0.074±0.068 (ww = 0.047)	1.49±0.749 (ww = 0.946)	0.790±0.384 (ww = 0.502)	15.2±3.75* (ww = 9.65)	This study
	Gill	0.061±0.041 (ww = 0.031)	2.10±0.749 (ww = 1.08)	1.26±0.18* (ww = 0.645)	52.5±14.5 (ww = 26.9)	
	Liver	0.395±0.129* (ww = 0.263)	71.1±31.30* (ww = 47.4)	2.14±0.451* (ww = 1.43)	52.6±14.2 (ww = 35.0)	

Table 2 (cont'd). Comparison of metals concentration in muscle, gill and liver of tilapia, µg/g dw (unless noted as ww), to permissible level from established standards

Study Area	Tissue	Cd	Cu	Pb	Zn	Reference
Terengganu River, Malaysia (n = 20)	Muscle	0.048±0.036 (ww = 0.036)	1.60±0.736 (ww = 1.19)	0.567±0.319 (ww = 0.047)	11.5±1.58* (ww = 0.420)	This study
	Gill	0.040±0.034 (ww = 0.026)	1.83±0.348 (ww = 1.17)	0.673±0.336* (ww = 0.431)	41.5±25.5 (ww = 26.6)	
	Liver	0.078±0.051* (ww = 0.049)	219±91.3* (ww = 138)	0.671±0.453* (ww = 0.421)	43.7±17.3 (ww = 27.4)	
Jelebu, Malaysia	Muscle	na	1.20±0.100	0.048±0.007	17.5±0.800	[22]
	Gill	na	1.90±0.100	0.402±0.070	64.3±3.00	
	Liver	na	0.007±0.001	0.20±0.02	85.0±6.00	
River Benue, Nigeria	Muscle	0.306	1.65	1.18	5.24	[19]
	Gill	0.351	2.98	1.00	7.15	
Fo Tan River, Hong Kong	Muscle	0.540±0.190	2.09±0.56	1.53±0.55	22.4±1.50	[24]
	Gill	1.76±0.130	77.8±6.60	11.0±1.20	77.8±6.60	
Shing Mun River, Hong Kong (ww)	Muscle	0.016±0.009	0.240±0.090	0.247±0.163	17.8±3.60	[21]
	Gill	0.049±0.020	11.3±8.28	0.380±0.150	26.7±8.80	
	Liver	0.393±0.173	328±181	0.455±0.168	38.4±9.80	
Mguza Dam, Zimbabwe (ww)		0.120±0.020	0.130±0.040	0.430±0.040	1.23±0.140	[25]
Permissible level						
Department of Health, New Zealand		1.00	30.0	2.00	40.0	[26]
Department of Health, Australia		0.200	10.0	1.50	150	[26]
Turkish permissible limit (body weight)		0.100	20.0	1.00	50.0	[27]
World Health Organization		na	30.0	na	2.00	[28]
Malaysia Food Regulation (ww)		1.00	na	2.00	na	[29]

na = not available; dw = dry weight; ww = wet weight; The asterisk indicates the significant difference between two study sites ($p<0.05$).

The comparisons were made with several studies to provide us important information of status of metals accumulation in this study compared to other sites. However, this would not be enough to justify if the level is safe for human consumption. Therefore, permissible levels from several standards were referred. Comparing to the Malaysia Food Regulation [29], Cd and Pb in tilapia in this study were below the permissible level, suggesting that the fish is safe for consumption. Since the permissible values are not available for Cu and Zn in Malaysia Food Regulation, the other values were referred [26, 27, 28]. Copper level in the muscles and gills of tilapia were lower than all permissible values except for liver in both Tumpat lagoon and Terengganu River. Concerning with human consumption, livers are normally discarded prior to cooking. Hence, they will not impose any risk to humans.

Zinc concentration in all three tissues in this study extremely exceeded the permissible values of World Health Organization [28], but lower than permissible value of Department of Health Australia [26]. The concentration of Zn in gills and muscles from Tumpat lagoon exceeded Turkish permissible level [27] while Zn concentration in Terengganu River exceeded the Department of Health New Zealand [26]. Consequently, Zn content in tilapia should be monitored as the level has exceeded permissible level of these established standards. Zinc is one of the essential elements with the ability to function as an antioxidant and stabilize membranes especially in preventing free radical which induces injury during inflammatory processes [30]. However, the excess of Zn accumulation in human body can lead to local neuronal deficits, epigastric pain, diarrhea and elevated risk of prostate cancer [31].

Besides Malaysia Food Regulation, Malaysian government has not established the maximum permitted level of metals in fish. Therefore, standard values from Food Standards Australia and New Zealand (FSANZ) and Joint Expert Committee on Food Additives (JECFA) were referred to estimate the amount of daily consumption in humans [17] as shown in Table 3. The determination of seafood ingested per week is based on Laurenti [32] where author claimed the fish consumption in Malaysia is as high as 57.7 kg/year. This gives out an average estimation of 1.11 kg/week or approximately 160 g/day of fish consumed by Malaysian people. The daily intake by Malaysian people was computed by the multiplication of measured concentration by 160 g of average weight of fish consumed daily [17]. Comparing this to Malaysia Food Regulation, the daily intake of Cd and Pb were lower than the maximum permitted levels. The concentration level of Cu and Zn in this study was also lower than the standard value, except for Cu in the livers. Hence, as long as they do not ingest the livers, tilapia from this study are safe for consumption.

Table 3. Summary of dietary intakes for measured metals with daily consumption of 160 g of tilapia and comparison with food standards

		Cd	Cu	Pb	Zn
Standards	FSANZ RDI (mg/day)[a]	na	3.00	na	12
	FSANZ ML (mg/kg)[a]	na	5.00	0.500	130
	JECFA (mg/day)[a]	na	30.0	3.6	1000
	Malaysia Food Regulation[b]	0.159	na	0.317	na
Measured concentration (μg/g ww)	**Tumpat lagoon**				
	Muscle	0.047	0.946	0.502	9.65
	Gill	0.031	1.08	0.645	26.9
	Liver	0.263	47.4	1.43	35.0
	Terengganu River				
	Muscle	0.036	1.19	0.047	0.420
	Gill	0.026	1.17	0.431	26.6
	Liver	0.049	138	0.421	27.4
Intake (mg/day)	**Tumpat lagoon**				
	Muscle[a]	0.008	0.150	0.080	1.53
	Gill[a]	0.005	0.171	0.102	4.69
	Liver	0.042	7.52	0.227	5.55
	Terengganu River				
	Muscle[a]	0.006	0.189	0.008	0.067
	Gill[a]	0.004	0.186	0.068	4.22
	Liver[a]	0.008	21.9	0.067	4.35

na = not available; [a] Values referred from [27]; [b]calculated to daily consumption of 160 g tilapia; bold values indicate the value exceeding standards regulation

Biochemical endpoints have been employed to find the correlation between the metal bioaccumulation and stress level in fish [33, 34]. This technique is useful to recognize and identify subtle and early effects of contaminants [33, 35, 36]. LPO is one of the stress indicators formed from the oxidative deterioration of polyunsaturated lipids in the cell membranes and organelles. Malondialdehyde (MDA) is a LPO byproduct, generally used as a sign of cellular injuries [37]. Among these studied metals, Cu is most likely to enhance LPO as Cu will readily cycle between the cupric (Cu^{2+}) and the cuprous (Cu^{2+}) oxidation states, an activity that associated with the generation of hydroxyl radicals (**.**OH) [35, 38]. In the current study, LPO was measured in each tissue through the MDA values to see their correlation to metal concentrations. Since high concentrations of Cu were measured in the liver of tilapia from both sites, high concentrations of MDA in the liver was expected. The MDA values in the liver of tilapia from Tumpat lagoon results seem to support the assumption but the calculated values in Terengganu River was not as expected (Table 4).

Pearson correlation also justified low correlation between metals in tissues to the MDA values (Table 4). Despite of that, previous studies have reported increases in LPO with increasing metal exposure in fish [39, 40, 41]. Their investigation was performed in the laboratory exposure experiment, hence they can conclude in a better picture of metal concentrations and inductions of LPO. The measurement of LPO in the current study could be influenced by various factors such as tidal patterns, weather conditions, and sewage effluent as the fish was collected from the field and analysed right away in the laboratory. Therefore, in order to clearly identify the LPO as a bioindicator of metal pollution, a laboratory experiment should be conducted in the near future.

Table 4. Pearson correlation of metals and MDA in muscle, gill and liver of tilapia from Tumpat lagoon and Terengganu River

Tumpat Lagoon	**MDA Muscle (0.068±0.026 nmole/µL)**	**MDA gill (0.894±0.365 nmole/µL)**	**MDA liver (1.12±0.524 nmole/µL)**
Cd	-0.279	0.625	-0.597
Cu	0.106	0.304	-0.405
Pb	-0.123	0.052	0.122
Zn	0.037	0.002	0.363
Terengganu River	**MDA muscle (0.031±0.028 nmole/µL)**	**MDA gill (0.074±0.050 nmole/µL)**	**MDA liver (0.085±0.029 nmole/µL)**
Cd	0.699*	-0.006	-0.236
Cu	0.285	-0.038	-0.248
Pb	-0.074	0.003	0.582
Zn	-0.173	-0.007	0.740*

*Significant at $\alpha = 0.05$; bold font indicates moderate correlation

Conclusion

The concentration of Cd, Cu, Pb and Zn were consistently higher in the gills and livers than muscle tissues of tilapia from both Tumpat lagoon and Terengganu River. This indicates their ability to accumulate those metals. Compared to the established permissible level, the concentration of studied metals was low except for Zn concentration in the livers. However, liver normally discarded before cooking and not consumed by local people. The estimation of daily intake also concludes that tilapia is safe for consumption as long as liver is removed from their meal. Copper and Pb concentrations in tilapia were comparable to tilapia collected from industrial area, hence continuous monitoring should be done as part of environment and human safety. The LPO activity was measured in each tissue to represent biological effects in fish. Pearson correlation showed inconsistent correlation between MDA, byproduct of LPO to metals concentration, hence not a suitable indicator of metals concentrations in the current study. This could

possibly due to various factors that lead to oxidative stress in natural conditions. Therefore, to clearly justify the induction of LPO in fish due to metals accumulation, a control laboratory experiment should be carried out as it is previously proven as a good biomarker for metals.

Acknowledgements

The present study was funded by Research Acculturation Grant Scheme (***RAGS***), Ministry of Higher Education, Malaysia.

References

1. Ng, W. K., and Romano, N. (2013). A review of the nutrition and feeding management of farmed tilapia throughout the culture cycle. *Reviews in Aquaculture*, *5*(4): 220-254.
2. Food and Agriculture Organization of the United Nations (2011). FISHSTAT plus: Universal Software for Fishery Statistical Time Series, Version 2.3. FAO Fisheries Department, Fishery Information, Data and Statistical Unit, Rome.
3. Yusoff, A. (2015). Status of resource management and aquaculture in Malaysia. In M. R. R. Romana-Eguia, F. D. Parado-Estepa, N. D. Salayo and M. J. H. Lebata-Ramos (Eds.), Resource Enhancement and Sustainable Aquaculture Practices in Southeast Asia: Challenges in Responsible Production of Aquatic Species: Proceedings of the International Workshop on Resource Enhancement and Sustainable Aquaculture Practices in Southeast Asia 2014 (RESA) Tigbauan, Iloilo, Philippines: Aquaculture Dept., Southeast Asian Fisheries Development Center: pp. 53-65.
4. El-Sayed, A. F. M. (1999). Alternative dietary protein sources for farmed tilapia, *Oreochromis* spp. *Aquaculture,* 179: 149–168.
5. Ferreira, M., Caetano, M., Costa, J., Pousão-Ferreira, P., Vale, C. and Reis-Henriques, M. A. (2008). Metal accumulation and oxidative stress responses in, cultured and wild, white seabream from Northwest Atlantic. *Science of the Total Environment*, 407(1): 638-646.
6. Luoma, S. N., and Rainbow, P. S. (2008). Sources and cycles of trace metals. In: Metal Contamination in Aquatic Environments: Science and Lateral Management. Cambridge University Press, Cambridge: pp. 47-66.
7. Alam, M. G. M., Tanaka, A., Stagnitti, F., Allinson, G., and Maekawa, T. (2001). Observations on the effects of caged carp culture on water and sediment metal concentrations in Lake Kasumigaura, Japan. *Ecotoxicology and Environmental Safety*, 48: 107-115.
8. Pelgrom, S. M. G. J., Lamers, L. P. M., Garritsen, J. A. M., Pels, B. M., Lock, R. A. C., Balm, P. H. M., and Bonga, S. W. (1994). Interactions between copper and cadmium during single and combined exposure in juvenile tilapia *Oreochromis mossambicus*: Influence of feeding condition on whole body metal accumulation and the effect of the metals on tissue water and ion content. *Aquatic Toxicology*, 30(2): 117-135.
9. Young, R. A. (2005). Toxicity profiles: Toxicity summary for cadmium, risk assessment information system, RAIS, University of Tennessee. Access from rais.ornl.gov/tox/profiles/cadmium.shtml.
10. Nolan, K. R. (1983). Copper toxicity syndrome. *Journal of Orthomolecular Psychiatry*, 12(4): 270-282.
11. Cheung, A. P., Lam, T. H. J., and Chan, K. M. (2004). Regulation of Tilapia metallothionein gene expression by heavy metal ions. *Marine Environmental Research*, 58(2-5): 389-394.
12. Wong, C. K. C., Yeung, H. Y., Cheung, R. Y. H., Yung, K. K. L. and Wong, M. H. (2000). Ecotoxicological assessment of persistent organic and heavy metal contamination in Hong Kong coastal sediment. *Archives of Environmental Contamination and Toxicology*, 38(4): 486-493.
13. Souid, G., Souayed, N., Yaktiti, F. and Maaroufi, K. (2013). Effect of acute cadmium exposure on metal accumulation and oxidative stress biomarkers of *Sparusaurata*. *Ecotoxicology and Environmental Safety*, 89: 1-7.
14. Van der Oost, R., Beyer, J. and Vermeulen, N. P. E. (2003). Fish bioaccumulation and biomarkers in environmental risk assessment: A review. *Environmental Toxicology and Pharmacology,* 13: 57-149.
15. Gravato, C., Teles, M., Oliveira, M. and Santos, M. A. (2006). Oxidative stress, liver biotransformation and genotoxic effects induced by copper in *Anguilla anguilla* L. - the influence of pre-exposure to [beta]-naphthoflavone. *Chemosphere,* 65: 1821-1830.
16. Türkmen, A., Türkmen, M., Tepe, Y. and Akyurt, I. (2005). Heavy metals in three commercially valuable fish species from Iskenderun Bay, Northern East Mediterranean Sea, Turkey. *Food Chemistry*, 91(1): 167-172.

17. Allinson, G., Salzman, S. A., Turoczy, N., Nishikawa, M., Amarasinghe, U. S., Nirbadha, K. G. S. and De Silva, S. S. (2009). Trace metal concentrations in Nile tilapia (*Oreochromisniloticus*) in three catchments, Sri Lanka. *Bulletin of Environmental Contamination and Toxicology*, 82(3): 389-394.
18. Visnjic-Jeftic, Z., Jaric, I., Jovanovic, L., Skoric, S., Smederevac-Lalic, M., Nikcevic, M. and Lenhardt, M. (2010). Heavy metal and trace element accumulation in muscle, liver and gills of the Pontic shad (*Alosaimmaculata* Bennet 1835) from the Danube River (Serbia). *Microchemical Journal*, 95(2): 341-344.
19. Eneji, I. S., Sha'Ato, R. and Annune, P. A. (2011). Bioaccumulation of heavy metals in Fish (*Tilapia zilli and Clariasgariepinus*) organs from River Benue, North–Central Nigeria. *Pakistan Journal of Analytical and Environmental Chemistry*, 12: 1-8.
20. Reddy, M. S., Basha, S., Kumar, V. S., Joshi, H. V. and Ramachandraiah, G. (2004). Distribution, enrichment and accumulation of heavy metals in coastal sediments of Alang–Sosiya ship scrapping yard, India. *Marine Pollution Bulletin*, 48(11-12): 1055-1059.
21. Shen, L. H., Lam, K. L., Ko, P. W. and Chan, K. M. (1998). Metal concentrations and analysis of metal binding protein fractions from the liver of tilapia collected from Shing Mun River. *Marine Environmental Research*, 46(1-5): 597-600.
22. Low, K. H., Zain, S. M., and Abas, M. R. (2011). Evaluation of metal concentrations in red tilapia (*Oreochromis* spp) from three sampling sites in Jelebu, Malaysia using principal component analysis. *Food Analytical Methods*, 4(3): 276-285.
23. Wang, S., Ang, H. M., and Tadé, M. O. (2008). Novel applications of red mud as coagulant, adsorbent and catalyst for environmentally benign processes. *Chemosphere,* 72(11): 1621-1635.
24. Zhou, H. Y., Cheung, R. Y. H., Chan, K. M. and Wong, M. H. (1998). Metal concentrations in sediments and Tilapia collected from inland waters of Hong Kong. *Water Research*, 32(11): 3331-3340.
25. Siwela, A. H., Nyathi, C. B., and Naik, Y. S. (2009). Metal accumulation and antioxidant enzyme activity in *C. gariepinus*, Catfish, and *O. mossambicus*, tilapia, collected from lower Mguza and Wright Dams, Zimbabwe. *Bulletin of Environmental Contamination and Toxicology*, 83(5): 648.
26. Food and Agriculture Organization of the United Nations (1983). Food and Agriculture Organisation. Circular no. 764. Rome.
27. TKB, Central Fisheries Research Institute (2002). Fisheries laws and regulations. Ministry of Agriculture and Rural Affairs, Conservation and Control General Management. Ankara, Turkey.
28. World Health Organization (1989) Environment health criteria. Heavy metals environmental aspects. World Health Organization, Geneva.
29. Alina, M., Azrina, A., Mohd Yunus, A. S., Mohd Zakiuddin, S., Mohd Izuan Effendi, H. and Muhammad Rizal, R. (2012). Heavy metals (mercury, arsenic, cadmium, plumbum) in selected marine fish and shellfish along the Straits of Malacca. *International Food Research Journal*, 19(1): 135-140.
30. Prasad, A. S. (2008). Zinc in human health: effect of zinc on immune cells. *Molecular Medicine*, 14(5-6): 353.
31. Plum, L. M., Rink, L., and Haase, H. (2010). The essential toxin: impact of zinc on human health. *International Journal of Environmental Research and Public Health*, 7(4), 1342-1365.
32. Laurenti, G. (2002). Fish and fishery products: world apparent consumption statistics based on food balance sheets. FAO Fisheries Circular 2002 No. 821, rev. 6. 1961-1999.
33. Vasseur, P. and Cossu-Leguille, C. (2003). Biomarkers and community indices as complementary tools for environmental safety. *Environmental International,* 28: 711-717.
34. Giguère, A., Campbell, P. G., Hare, L., and Cossu-Leguille, C. (2005). Metal bioaccumulation and oxidative stress in yellow perch (*Percaflavescens*) collected from eight lakes along a metal contamination gradient (Cd, Cu, Zn, Ni). *Canadian Journal of Fisheries and Aquatic Sciences*, 62(3): 563-577.
35. Di Giulio, R. T., Washburn, P. C., Wenning, R. J., Winston, G. W. and Jewell, C. S. (1989). Biochemical responses in aquatic animals: A review of determinants of oxidative stress. *Environmental Toxicology and Chemistry*, 8(12): 1103-1123.
36. Stegeman, J. J., Brouwer, M., Di Giulio, R. T., Förlin, L., Fowler, B. A., Sanders, B. M. and Van Veld, P. A. (1989). Molecular responses to environmental contamination: enzyme and protein synthesis as indicators of chemical exposure and effect. In Biomarkers. Edited by R. J. Hugget, R. A. Kimerle, P. M. J. Mehrle, and H. L. Bergman. Lewis Publishers, Boca Raton. pp. 235-333.

37. Christie, N. T. and Costa, M. (1984). In vitro assessment of the toxicity of metal compounds. IV. Disposition of metals in cells: interactions with membranes, glutathione, metallothionein, and DNA. *Biological Trace Element Research,* 6: 139-158.
38. Halliwell B. and Gutteridge J. M. C. (1984) Oxygen toxicity, oxygen radicals, transition metals and disease. *Biochemical Journal,* 219: 1-14.
39. Chaurasia, S. S. and Kar, A. (1999). An oxidative mechanism for the inhibition of iodothyronine 5′-monodeiodinase activity by lead nitrate in the fish, *Heteropneustesfossilis*. *Water Air and Soil Pollution* 111: 417-423.
40. Romeo, M., Bennani, N., Gnassia-Barelli, M., Lafaurie, M. and Girard, J. P. (2000). Cadmium and copper display different responses towards oxidative stress in the kidney of the sea bass *Dicentrarchuslabrax*. *Aquatic Toxicology,* 48: 185-194.
41. Ptashynski, M. D., Pedlar, R. M., Evans, R. E., Wautier, K. G., Baron, C. L. and Klaverkamp, J. F. (2001). Accumulation, distribution and toxicology of dietary nickel in lake white fish (*Coregonusclupeaformis*) and lake trout (*Salvelinusnamaycush*). *Comparative Biochemistry and Physiology Part C: Toxicology and Pharmacology*, 130: 145-162.

Malaysian Journal of Analytical Sciences, Vol 22 No 4 (2018): 605 - 611
DOI: https://doi.org/10.17576/mjas-2018-2204-05

MALAYSIAN JOURNAL OF ANALYTICAL SCIENCES
Published by The Malaysian Analytical Sciences Society
ISSN 1394 - 2506

TETRABUTYLPHOSPHONIUM TRIFLUOROACETATE ($[P_{4444}]CF_3COO$) THERMORESPONSIVE IONIC LIQUID AS A DRAW SOLUTION FOR FORWARD OSMOSIS PROCESS

(Larutan Ionik Responsif Haba Tetrabutilfosfonium Trifluoroasetat ($[P_{4444}]CF_3COO$) sebagai Larutan Penarik untuk Proses Osmosis Kehadapan)

Phang Sook Nyan, Syed Mohd Saufi*, Syamsul Bahari Abdullah, Mazrul Nizam Abu Seman, Malyanah Mohd Taib

Faculty of Chemical & Natural Resources Engineering,
Universiti Malaysia Pahang, Lebuhraya Tun Razak, 26300 Gambang, Pahang, Malaysia

**Corresponding author: smsaufi@ump.edu.my*

Received: 16 April 2017; Accepted: 7 March 2018

Abstract

Forward osmosis (FO) is recognized as a potential membrane technology that utilizes low energy for water desalination. It is driven by natural osmotic pressure difference between feed solution and draw solution across semipermeable membrane. Pure water will permeate from the salinity feed water to the draw solution side. In order to produce pure water, it is necessary to find the best draw solute that exhibits high draw ability and can separate the permeated water efficiently from the draw solution. In the current study, lower critical solution temperature (LCST) thermoresponsive ionic liquid (IL) of tetrabutylphosphonium trifluoroacetate ($[P_{4444}]CF_3COO$) was synthesized as the draw solute for FO process. ($[P_{4444}]CF_3COO$) is dissolved in water below its critical temperature of 29°C and becomes two layered above this critical temperature. $[P_{4444}]CF_3COO$ IL showed high water flux of 0.44 ± 0.007 LMH compared to the water flux of 0.32 ± 0.049 LMH for the NaCl draw solute at the same draw solution concentration. Applying thermoresponsive IL as the draw solute in FO process has the potential to treat high salinity of feed stream with ease of water recovery and draw solute regeneration.

Keywords: forward osmosis, draw solution, thermoresponsive ionic liquid

Abstrak

Osmosis kehadapan (FO) diiktiraf sebagai teknologi membran berpotensi yang menggunakan tenaga yang rendah untuk penyahgaraman air. Ia didorong oleh perbezaan tekanan osmosis semula jadi antara larutan suapan dan larutan penarik merentasi membran separa telap. Air tulen akan meresap daripada air suapan ke bahagian larutan penarik. Dalam usaha untuk menghasilkan air tulen, ia adalah perlu untuk mencari bahan penarik terbaik yang mempamerkan keupayaan tarikan yang tinggi dan boleh memisahkan air yang telah meresap daripada larutan penarik dengan cekap. Dalam kajian semasa, suhu larutan kritikal rendah (LCST) larutan ionik (IL) responsif haba tetrabutilfosfonium trifluoroasetat ($[P_{4444}]$ CF_3COO) telah disintesis sebagai bahan penarik untuk proses FO. $[P_{4444}]$ CF_3COO) dilarutkan dalam air di bawahnya suhu kritikal 29 °C dan menjadi dua lapisan di atas suhu kritikal ini. $[P_{4444}]$ CF_3COO IL menunjukkan fluks air yang tinggi iaitu 0.44 ± 0.007 LMH berbanding fluks air 0.32 ± 0.049 LMH untuk bahan penarik NaCl pada kepekatan bahan penarik yang sama. Penggunaan larutan ionik responsif haba sebagai bahan penarik dalam proses FO mempunyai potensi untuk merawat air masin yang tinggi dengan lebih mudah untuk pemulihan semula air dan penjanaan semula bahan penarik.

Kata kunci: osmosis kehadapan, larutan penarik, larutan ionik responsif haba

Introduction

The rapid increment in world's population and industrialization resulted in high demand for fresh water. It has been recognized that water scarcity will be the global crisis faced in the future. Supply of fresh water and development of energy source are co-dependent and need to be managed and taken seriously in order to sustain the population. Reverse osmosis (RO) is widely applied for water desalination technology, but the high energy consumption and pressure are the drawbacks and unpreferred. Forward osmosis (FO) has been proposed as a potential energy-input-free desalination technology driven by natural osmosis instead of high hydraulic pressure. The osmotic pressure difference between the feed and draw solutions is used as a driving force across the semipermeable membrane. The selection of optimal draw solute and membrane plays a crucial role for superior FO performance. High reverse flux, concentration polarization, low water permeability flux, and high cost in water recovery are still under further studies for improvement in the FO technology [1].

Although the FO process is a natural process which do not require any external energy input, there is a concern on the energy requirement for the recovery of the permeated water from the draw solution side after the FO process. The selection and regeneration of draw solution is another key factor for advancing FO technology. Ge et al. [2] had summarized various types of draw solute used in FO process in his review paper. Inorganic and organic salts, glucose, polyelectrolytes, and hydroacid complexes can be classified as a non-responsive draw. They normally provide high osmotic pressure for water desalination but they are limited by high energy consumption in water recovery [2–4]. Synthetic materials such as thermoresponsive magnetic nanoparticles (MNPs) and stimuli-responsive polymer hydrogels had been proposed and used as a draw solute in the FO [5, 6]. Temperature stimulus was applied for the regeneration of thermoresponsive MNPs. When heating the thermoresponsive polymer coated on the nanoparticle surface above its critical temperature, agglomeration of nanoparticles occurred and eased the regeneration process using ultrafiltration or low strength magnetic field method [6]. However, nanoparticles possess large size and suspension state characteristic in water and cause low osmotic pressure and severe concentration polarization. Stimuli-responsive polymer hydrogels utilized either temperature or pressure, or light with the combination of light-absorbing carbon particles stimulus to extract or release water. However, the use of this polymer hydrogels as draw solute is restricted by poor performance at room temperature and the requirement of high hydraulic pressure in dewatering process [5].

Recently, thermoresponsive ionic liquid (IL) had been used as a new draw solute in FO process and showed a promising result. The solubility of this IL changed, depending on the critical solution temperature of the IL. There are two main types of thermoresponsive ILs, which are the upper critical solution temperature (UCST) and lower critical solution temperature (LCST) ILs. In LCST type IL, water will dissolve below its critical temperature and will be separated into two phases when heating above its critical temperature. Oppositely, in UCST IL, water will dissolve above its critical temperature. Cai et al. [7] had synthesized and tested three types of LCST ILs, which are tetrabutylphosphonium 2,4-dimethylbenzenesulfonate ($[P_{4444}]$DMBS), tetrabutylphosphonium mesitylenesulfonate ($[P_{4444}]$TMBS) and tributyloctylphosphonium bromide ($[P_{4444}]$Br). These ILs were able to draw water from feed solutions up to a 1.6 M salt concentration at room temperature. Betaine bis(trifluoromethylsulfonyl)imide ([Hbet][Tf2N]), a UCST type IL, was synthesized by Zhong et al. [8] and was able to draw up to 3.0 M NaCl feed solution. Water solubility of IL is mainly affected by anion and varies accordingly. It is important to synthesise the different types of thermoresponsive IL in order to find the best draw solute for FO process.

In this study, tetrabutylphosphonium trifluoroacetate ($[P_{4444}]CF_3COO$) IL was synthesized as draw solute for FO process. It is an LCST type of thermoresponsive IL with phase critical temperature of 29 °C. Using this IL, the FO process can be performed at room temperature and permeate water recovery, and the regeneration of draw solution can be easily done by heating the solution above 29 °C.

Materials and Methods

Materials

Cellulose acetate (CA) as the polymer for fabrication FO flat sheet membrane was purchased from Sigma-Aldrich. Dimethylformamide and acetone were used as solvents, which were purchased from Fisher Scientific and R & M Chemicals, respectively. Glycerol was purchased from Fisher Scientific. Tetrabutylphosphonium hydroxide and trifluoroacetic acid that were used to synthesize the IL draw solute were purchased from Acros Organics and Merck,

respectively. Dichloromethane was provided by Fisher Scientific. NaCl was purchased from Merck and used as feed and draw solutes in FO process.

Fabrication of cellulose acetate flat sheet membrane

Membrane dope solution was prepared based on the following weight composition: 20% CA, 31.66% dimethylformamide and 48.33% acetone. The CA powders were added slowly into the mixture of acetone and dimethylformamide solution under continuous stirring for about 24-48 hours until homogenous solution was obtained. The dope solution was poured onto a glass plate and casted evenly at ambient temperature using semi-automatic casting machine. The membrane thickness and casting speed were adjusted to 200 μm and 6.25 cm/s, respectively. The casted membrane film was immediately immersed into deionized water coagulation bath to form a thin membrane. Lastly, the membrane was washed and transferred into the deionized water bath for temporary storage before undergoing the next heat treatment step.

Heat treatment of cellulose acetate flat sheet membrane

The casted membrane was subjected to the heat treatment by immersing into a water bath at 60 °C for 60 minutes. After that, the membrane was cooled immediately to ambient temperature by pouring ice cube into the water bath. The membrane was then immersed into 50 wt.% glycerol aqueous solution for 48 hours, followed by drying in air at room temperature [9]. Heat treatment can be effectively used to shrink the membrane's mean pore radius until it is suitable for FO process.

Synthesis of ionic liquid

Tetrabutylphosphonium trifluoroacetate ($[P_{4444}]CF_3COO$) was synthesized by neutralization of tetrabutylphosphonium hydroxide and trifluoroacetic acid according to the method used by Kohno et al. [10]. The mixed solution was added to a dichloromethane/water biphasic system in separatory funnel for extraction process. The IL product was extracted with dichloromethane. The dichloromethane layer was washed several times with distilled water. Then, the solution was evaporated using rotary evaporator. After evaporation, the left solution was dried in vacuum oven at 70 °C for at least 24 hours.

Forward osmosis process

For the first part of the FO experiment, 500 mL feed solution of 0.6 M NaCl (equivalent to sea water concentration) and the draw solution of 2.0 M NaCl were used. This condition was selected in order to compare the performance of the CA membrane prepared during this study with the performance of commercial FO membrane used in the literature. The FO was run at room temperature. In the second FO experiment, the feed solution was reduced to 0.04 M NaCl and the draw solution was reduced to 0.087 M. The feed volume was reduced to 300 mL. Both feed and draw solutions concentration had to be reduced in order to accommodate the amount of IL synthesized. The performance of two types of draw solution, NaCl and $[P_{4444}]CF_3COO$, were compared in the second experiment. $[P_{4444}]CF_3COO$ draw solution was immersed in a cold bath to reduce the temperature below its critical temperature of 29°C during the FO process in the second experiment.

The FO experiment was conducted using Sterlitech CF042 acrylic FO membrane cell as shown in Figure 1. The membrane was placed vertically in the membrane cell between two compartments; one containing the feed solution and the other containing draw solution. Draw and feed solutions were flowed concurrently at the rate of 60.36 mL/min. The feed solution was placed on an electronic balance connected to the computer and monitor, and it recorded the change of mass in the feed solution. The initial and final conductivity of the feed solution was measured using conductivity meter. A standard calibration curve was constructed to obtain the NaCl concentration based on the conductivity value measured. The duration for the FO experiment was fixed at one hour.

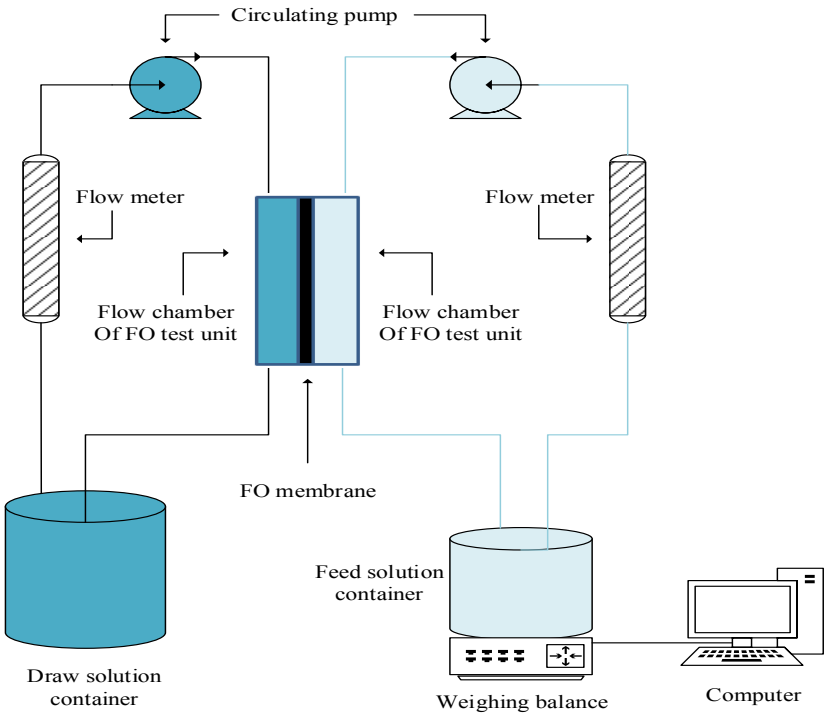


Figure 1. Schematic diagram of the lab-scale FO system

The water flux J_w ($Lm^{-2}h^{-1}$ or LMH) was calculated using equation (1)[11].

$$J_w = \frac{\Delta V}{A\Delta t} \quad (1)$$

where, ΔV is the volume change (in liter, L) of the feed solution over a time Δt (in hour, h) and A_m (in m^2) is the effective membrane surface area, which is 0.0042 m^2.

Thermally stimulated phase separation of ([P_{4444}]CF_3COO)

Thermally stimulated phase separation was employed in order to see the effectiveness of permeated water separated from the ([P_{4444}]CF_3COO) IL draw solution. Diluted ([P_{4444}]CF_3COO) draw solution around 28 mL was transferred into the centrifuge tube and placed in a water bath. The solution was heated at different temperatures of 40 °C, 50 °C and 60 °C. Time taken for complete phase separation at each temperature was determined. The same solution was used in each experiment by cooling the solution to room temperature to dissolve the IL back into the water. When IL has completely dissolved, it was then heated to the new heating temperature for another thermally phase separation.

Results and Discussion

Forward osmosis performances

In FO experiment using 0.6M NaCl feed solution and 2.0M NaCl draw solution, the CA membrane produced in this study showed a flux value of 1.83 ± 0.078 LMH. This value is acceptable compared to the CA hollow fiber membrane reported by Su et al. [9], which showed a value of 1.0 LMH at the same condition used during this study. The performance of FO using ([P_{4444}]CF_3COO) and NaCl draw solution was compared using the same draw solution concentration of 0.0087 M. The NaCl feed concentration of 0.040 M was used. As can be seen in Figure 2, water flux achieved by using ([P_{4444}]CF_3COO) draw solution is higher than that using NaCl draw solution. The water flux for ([P_{4444}]CF_3COO) and NaCl draw solution were 0.44 ± 0.007 LMH and 0.32 ± 0.049 LMH,

respectively. Although the water fluxes for both draw solutes were relatively low compared to the value found in the literature, however, it was demonstrated that ($[P_{4444}]CF_3COO$) had higher draw ability than the NaCl solution. The concept of using LCST type of thermoresponsive IL as draw solute in FO was successfully performed in this study.

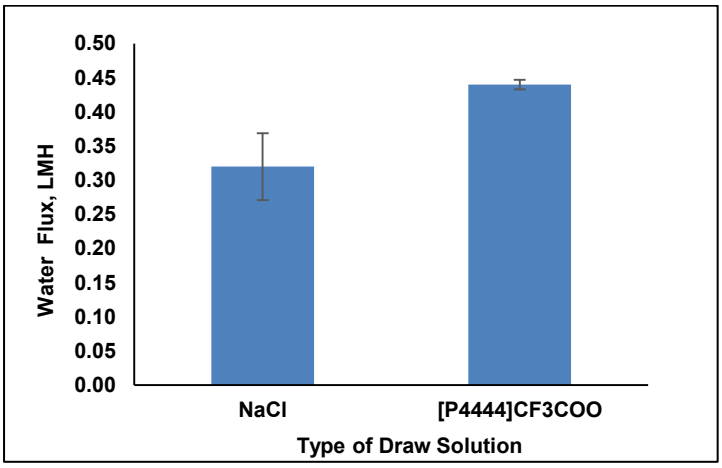


Figure 2. FO water flux using different draw solutions of NaCl and ($[P_{4444}]CF_3CO$). The feed concentrations used were 0.040 M NaCl and 0.087 M draw solute concentrations.

Thermally stimulated phase separation process of ionic liquid solution

After the FO process, the diluted ($[P_{4444}]CF_3COO$) draw solution was performed on the thermally stimulated phase separation by heating it above its critical temperature of 29 °C in a water bath. This phase change process of ($[P_{4444}]CF_3COO$) is reversible and fast. ($[P_{4444}]CF_3COO$) formed homogenous mixtures with water at low temperature. The phase separation temperature of the IL/water mixtures depended strongly on the hydrophobicity of the component ions as well as mixing ratio [10]. Upon gentle heating, it was observed that the clear and diluted IL draw solution turned turbid. When the draw solution was heated above its LCST, a clear liquid-liquid phase separation appeared, which formed an IL-rich phase and water-rich phase, as shown in Figure 3. The IL-rich phase was at the bottom due to its high density property.

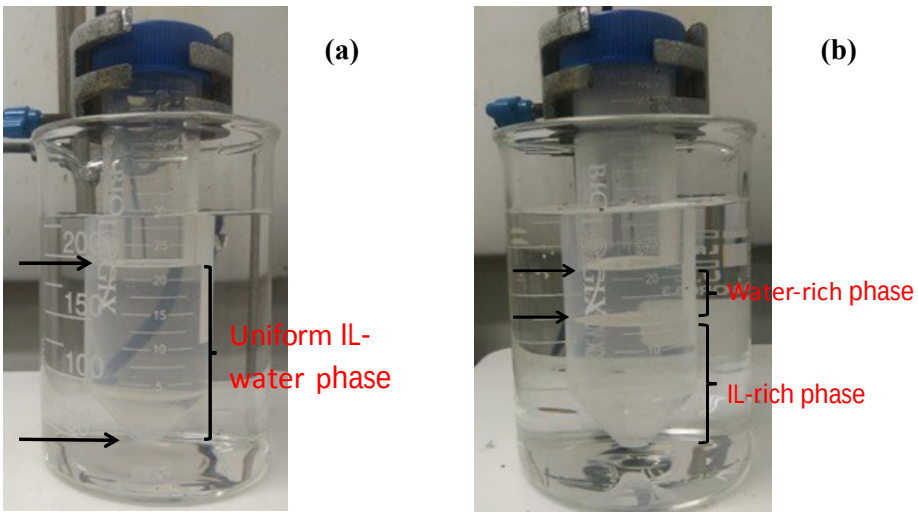


Figure 3. Water miscibility of ($[P_{4444}]CF_3COO$) at (a) room temperature, and (b) above the critical temperature of 29 °C during thermally stimulated phase separation process

The thermally stimulated phase separation behavior of draw solution with different heating temperatures was examined. The time taken used to complete the phase separation by heating at temperatures of 40 °C, 50 °C and 60 °C was shown in Figure 4. In fact, stable phase separation can be achieved readily with a mild temperature stimulus of 34 °C [10]. As the heating temperature increased, the time taken to complete phase separation decreased from 140 minutes to 40 minutes for heating temperatures of 40 °C to 60 °C. This allowed the IL to be efficiently regenerated and reused.

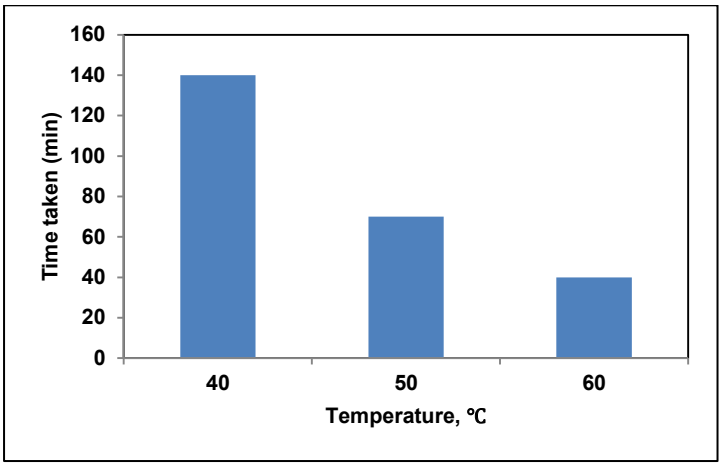


Figure 4. Time for phase separation of ([P_{4444}]CF_3COO)-water mixture at different heating temperature

Conclusion

([P_{4444}]CF_3COO) is an LCST type of thermoresponsive IL and can potentially be used as draw solute in FO. ([P_{4444}]CF_3COO) IL showed high water flux of 0.44 ± 0.007 LMH compared to the water flux of 0.32 ± 0.049 LMH for the NaCl draw solution at 0.087 M draw solution concentration. The regeneration and recovery of IL draw solution was achieved via an energy-efficient thermally stimulated phase separation process. The time for the phase separation of the ([P_{4444}]CF_3COO)-water mixture was 40 minutes by heating the mixture at a higher temperature of 60 °C.

Acknowledgement

The authors were grateful for the research financial support by the Ministry of Higher Education Malaysia under the Fundamental Research Grant Scheme (FRGS - RDU160128).

References

1. Thompson, N. A. and Nicoll, P. G. (2011). Forward osmosis desalination: A commercial reality. *IDA World Congress - Perth Convention and Exhibition Centre (PCEC), Perth, Western Australia.* pp. 16.
2. Ge, Q., Ling, M. and Chung, T. S. (2013). Draw solutions for forward osmosis processes: Developments, challenges, and prospects for the future. *Journal of Membrane Science,* 442: 225-237.
3. Stone, M. L., Wilson, A. D., Harrup, M. K. and Stewart, F. F. (2013). An initial study of hexavalent phosphazene salts as draw solutes in forward osmosis. *Desalination,* 312: 130-136.
4. Tan, C. H. and Ng, H. Y. (2010). A novel hybrid forward osmosis - nanofiltration (FO-NF) process for seawater desalination: Draw solution selection and system configuration. *Desalination and Water Treatment,* 13(1-3): 356-361.
5. Li, D., Zhang, X., Yao, J., Zeng, Y., Simon, G. P. and Wang, H. (2011). Composite polymer hydrogels as draw agents in forward osmosis and solar dewatering. *Soft Matter,* 7(21): 10048-10056.
6. Ling, M. M., Chung, T. S.and Lu, X. (2011). Facile synthesis of thermosensitive magnetic nanoparticles as smart draw solutes in forward osmosis. *Chemical Communications,* 47(38): 10788-10790.

7. Cai, Y., Shen, W., Wei, J., Chong, T. H., Wang, R., Krantz, W. B. and Hu, X. (2015). Energy-efficient desalination by forward osmosis using responsive ionic liquid draw solutes. *Environmental Science: Water Research and Technology,* 1(3): 341-347.
8. Zhong, Y., Feng, X., Chen, W., Wang, X., Huang, K.-W., Gnanou, Y. and Lai, Z. (2016). Using UCST ionic liquid as a draw solute in forward osmosis to treat high-salinity water. *Environmental Science and Technology,* 50(2): 1039-1045.
9. Su, J., Yang, Q., Teo, J. F. and Chung, T. S. S. (2010). Cellulose acetate nanofiltration hollow fiber membranes for forward osmosis processes. *Journal of Membrane Science,* 355(1-2): 36-44.
10. Kohno, Y., Arai, H., Saita, S. and Ohno, H. (2011). Material design of ionic liquids to show temperature-sensitive lcst-type phase transition after mixing with water. *Australian Journal of Chemistry,* 64(12): 1560-1567.
11. Kim, J., Kang, H., Choi, Y. S., Yu, Y. A. and Lee, J. C. (2016). Thermo-responsive oligomeric poly(tetrabutylphosphonium styrenesulfonate)s as draw solutes for forward osmosis (FO) applications. *Desalination,* 381: 84-94.

Malaysian Journal of Analytical Sciences, Vol 22 No 4 (2018): 612 - 618
DOI: https://doi.org/10.17576/mjas-2018-2204-06

MALAYSIAN JOURNAL OF ANALYTICAL SCIENCES
Published by The Malaysian Analytical Sciences Society
ISSN 1394 - 2506

PHYSICOCHEMICAL PROPERTIES OF ENCAPSULATED PURPLE SWEET POTATO EXTRACT; EFFECT OF MALTODEXTRIN CONCENTRATION, AND MICROWAVE DRYING POWER

(Sifat Fizikokimia Ekstrak Keledek Ungu yang Dikapsul; Kesan Kepekatan Maltodekstrin, dan Kuasa Pengeringan Gelombang Mikro)

Alyani Mohd Padzil[1]*, Azni A. Aziz[1], Ida Idayu Muhamad[1, 2]

[1]*Bioprocess and Polymer Engineering Department, Faculty of Chemical and Energy Engineering*
[2]*IJN-UTM Cardiovascular Engineering Center Level 2, Block B, Building V01, Faculty of Biomedical Engineering*
Universiti Teknologi Malaysia, 81310 Johor Bahru, Johor, Malaysia.

**Corresponding author: mpr.alyani@gmail.com*

Received: 16 April 2017; Accepted: 7 March 2018

Purple sweet potato (PSP) is rich with anthocyanin and has a great potential as natural food colorant. In this study, investigation on the effect of maltodextrin (MD, DE 4.0–7.0) concentration as wall material and various microwave drying powers towards physicochemical properties of microwave assisted encapsulation of purple sweet potato extract (PSPE) has been conducted. The effects of microwave power (550 W and 330W) and MD concentration (20%, 25%, and 30%) were analysed for moisture content, water activity, colour, and total monomeric anthocyanin content (TMA). Both moisture content and water activity of the encapsulated PSPE were significantly decreased ($p < 0.05$) as the MD concentration increased at 20% and 30%. With respect of anthocyanin content, increasing of MD concentration at 20% and 30% showed a statistically significant reduction ($p < 0.05$). PSPA with 20% concentration gave the highest TMA at both microwave drying power of 330 W and 550 W, with 385.93±10.81 mg/L and 419.28±10.89 mg/L respectively. However, moisture content, water activity, colour, and TMA were not significantly different with the changing of microwave drying power.

Keywords: purple sweet potato, anthocyanin, microwave-assisted encapsulation, natural colorants, maltodextrin

Abstrak

Ubi keledek ungu (PSP) kaya dengan antosianin dan berpotensi untuk digunakan sebagai pewarna makanan semula jadi. Dalam kajian ini, kajian tentang kesan kepekatan maltodekstrin (MD, DE 4,0-7,0) sebagai bahan pengkapsulan dan pelbagai kuasa gelombang mikro pengeringan terhadap sifat fizikokimia ekstrak keledek ungu yang dikapsul telah dijalankan. Kesan kuasa gelombang mikro pengeringan (550 W dan 330W) dan kepekatan maltodekstrin (MD) (20%, 25%, dan 30%) dianalisis untuk kandungan kelembapan, aktiviti air, warna, dan jumlah kandungan antosianin monomerik (TMA). Nilai kandungan kelembapan dan aktiviti air daripada ektsrak keledek ungu yang dikapsulkan ketara berkurangan ($p < 0.05$) dengan peningkatan kepekatan MD pada 20% dan 30%. Peningkatan kepekatan MD pada 20% dan 30% menunjukkan pengurangan TMA secara signifikan ($p < 0.05$). PSPA dengan 20% kepekatan MD menunjukkan kandungan tertinggi TMA pada kedua-dua kuasa pengeringan ketuhar mikro 330 W dan 550 W, dengan masing-masing 38593 ± 10.81 mg/L dan 41928 ± 10.89 mg/L. Walau bagaimanapun, kandungan kelembapan, aktiviti air, warna, dan kandungan TMA tidak berbeza signifikan dengan perubahan kuasa pengeringan ketuhar gelombang mikro.

Kata kunci: keledek ungu, antosianin, pengkapsulan dengan bantuan gelombang mikro, pewarna semulajadi, maltodekstrin

Introduction

Natural food colorants are derived into agricultural, biological, or mineral sources. They have a simple extraction process and long history of safe usage. Some of synthetic colours have a natural equivalent, although their substitute may vary with the application. Many researches claimed that synthetic colours and additives might affect human health. Eliminating or substituting synthetic colours as colorants, food and beverage industry can choose a wide array of natural alternatives. Independently, natural colours do not have the same colour intensity as synthetic, and some are less economical on a dosage basis. However, this performance gap has been reduced due to the research and development (R&D) initiatives. Furthermore, there are advantages in using natural colour. The side benefits such as natural antioxidant and sweetener can be carried out together during processing.

Purple Sweet Potato (PSP) was among the potential anthocyanin natural sources. PSP also known to have intense colour due to the high content of anthocyanin [1]. Research has been conducted on *Ipomoea batatas* also known as purple sweet potato (PSP) on its monomeric anthocyanin stability towards pH changes (pH 2.0, 2.5, 3.0, 3.5, 4.0 and 4.5) compared with *H. sabdariffa* (roselle), and *M. malabathricum* [2]. Results showed that PSP was not affected at all while roselle and *M. malabathricum* were slightly affected by pH and quite stable up to pH 4.5 due to its flexibility colour changing towards the pH value. They reported that; it could be used as a diagnostic device for detection of food spoilage. The stability of PSP anthocyanin also depends on temperature and solvent matrix [3]. Purple sweet potatoes are not the only food colourant. Choi et al. [4] had studied the development of a colometric pH indicator film packaging using colorant extracted from purple sweet potato.

Microwave is known as a common source of food heating. It also becomes an alternative drying method since it offers a shorter drying time and could improve the quality of a product [5]. Mohd Nawi et al. [6] agreed that microwave-assisted encapsulation can be categorised as an economical method for drying of natural colorant. Microwave-assisted encapsulation efficiency and product quality could be affected by several factors. Many studies proved that microwave drying capability is significantly affected by power variable [7]. Moreover, Zaidel et al. [5] showed that an optimum drying time is important to control the encapsulation process and prevent from degradation of anthocyanin content.

Encapsulation functions to coat an active compound or acts as a wall material which gives lots of advantages. It could be functioning as an effective barrier towards environmental parameters including oxygen, light, and free radicals. In food industry, encapsulation using spray drying method is the most commonly used approach. Ahmed et al. [1] reported that encapsulated purple sweet potato flour resulted in a higher total phenolic content, antioxidant capacity, and water solubility index compared to non-encapsulated purple sweet potatoes flour. Research has been done on encapsulation effect using different types of wall materials such as maltodextrin, gum arabic, and gelatin. The advantages of encapsulation application include allowing easier handling, split the compound of the material which might react with one another, and providing a concentration for a uniform dispersion of an active agent.

In general, there are 3 types of wall material that have been used; it is classified as polysaccharides (maltodextrin, starch, and gum), lipids (stearic acid), and proteins (gelatin, casein, soy and wheat) [9]. Some studies used maltodextrin with different dextrose equivalents as an encapsulation agent. Researchers have reported that maltodextrin with low dextrose equivalent (DE) has excellent nutrient binding properties [10]. Furthermore, presence of maltodextrin as an encapsulating agent could alter the surface stickiness of low molecular weight sugars, which consequently might improve the quality of a product. Maltodextrin as encapsulation agent able to protect the ingredient from oxidation except a water-soluble material [2].

The objective of this study is to determine the effect of maltodextrin (MD, DE 4.0 - 7.0) concentration as a wall material and various microwave drying powers towards physicochemical properties of encapsulated purple sweet potato anthocyanin extract (PSPE). The effects of microwave drying power (550 W and 330W) and maltodextrin (MD) concentration (20%, 25%, and 30%) were analysed for moisture content, water activity, colour, and total monomeric anthocyanin content (TMA).

Materials and Methods

Materials

Purple sweet potatoes (PSP) were obtained from fresh market located in Skudai, Johor. PSP were then peeled, washed, and sliced before the pre-treatment and extraction process. The PSP extract was then filtered and centrifuged (MPW 352, Poland) at 5000 rpm for 10 minutes to remove the fine suspended particles. PSP extract were then go through evaporation process using rotary evaporator (IKA RV 10, German) to achieve total solid 7°Brix. The physicochemical properties of PSP anthocyanin extract subjected to encapsulation process were analysed. Maltodextrin (MD) with dextrose equivalent (DE) of 4.0 -7.0 was purchased from Sigma, Aldrich (German) used as wall materials.

Encapsulation of purple sweet potato extract (PSPE)

Encapsulation of PSPA extract were prepared as follows:50% solution of maltodextrin (MD) were prepared with 70 °C distilled water under constant stirring at 120 rpm for 1 hour and kept overnight at 4 ± 2 °C. 50% solution of wall material was then mixed with PSPA extract (7°Brix). The mixtures were then homogenized at 30 °C and subjected to microwave-assisted drying. Different proportions of wall/core materials were tested (20%, 25% and 30%). A total of 25g of each sample were weighed and exposed to the microwave radiation in the following operational condition: Microwave power 550 W, and 330W, Drying time 300s. Samples were then ground, packed in the brown glass bottles, and stored over silica gel in desiccators at room temperature for further experiments.

Moisture content and water activity

Moisture content was carried out by weighing3 g of samples and dried in an oven at 105 °C until it reached a constant weight. Water activity values were measured using water activity meter (4TE, USA). Temperature was maintained at 25 °C during the test. Triplicate samples were analyzed and the mean was recorded.

Total monomeric anthocyanin

The total monomeric anthocyanin (TMA) was measured using the pH-differential method by Giusti and Wrolstad [11], using two buffer systems; 0.025M potassium chloride buffer, pH 1.0 and 0.4 M sodium acetate buffer, pH 4.5 [11]. Prepare two dilutions of PSPA using the two buffer systems (pH 1.0 & pH 4.5). Let the dilutions equilibrate for 15 minutes before measurement. Prolong standing times which may cause increase measured readings was avoided. Absorbance were measured for each dilution at 510 nm and 700 nm. Wavelength of 700 nm is to correct for haze. Absorbance (A) of dilutions was calculated using the following equation 1:

$$A = (A_{510} - A_{700})_{pH\ 1.0} - (A_{510} - A_{700})_{pH\ 4.5} \quad (1)$$

TMA content of PSP powder was calculated as cyanidin-3-glycoside using equation 2 as follows:

$$\text{Total Monomeric Anthocyanin Content (mg/L)} = (A \times MW \times DF \times 1000)/(\varepsilon \times 1) \quad (2)$$

where MW is the molecular weight, DF is the dilution factor, and ε is the molar absorptivity.

Colour

For the colour analysis, measurement of CIE L*(lightness), a*(red to green), b*(yellow to blue) values were done using Konica Minolta CR-400 Colorimeter. The samples were placed in glass plates and directly measured. Triplicate samples were analyzed and the mean was recorded.

Statistical analysis

In this research, multiple comparison methods (Tukey) along with One-way ANOVA were used to determine the statistical significance of the data ($p < 0.05$).

Results and Discussion

Physicochemical properties of PSPA extract prior drying

Table 1 shows the physicochemical properties of purple sweet potato extract (PSPE) subjected to encapsulation process. Total soluble solid of PSPE was fixed at 7.0°Brix before mixing it with maltodextrin 50% solution. The variety of total solid contents of feed prior to drying might affect the drying efficiency.

Table 1. Physicochemical properties of PSPE subjected to encapsulation process

Parameter	Value
Total Soluble solid (Brix)	7.0
pH	6.43 ± 0.01
Monomeric Anthocyanin content (mg/L)	121.07
Color Parameter	
L*	20.5 ± 0.4
a*	26.5 ± 1.2
b*	-3.6 ± 0.1
C*	26.3 ± 0.1
H	352.0 ± 0.2

All data are the mean of triplicate measurements ± standard deviation values

Moisture content and water activity

Moisture content is important in determining the amount of total water present in a product and can be used as a process monitoring. Lower moisture content limits the ability of water to act as plasticizer, and to prevent or reduce the capability of caking and agglomeration issue. The total solid content of feed prior to drying will affect the final moisture content of product. The addition of MD to the extract prior to drying process consequently increased the total solid content and reduced the amount of water for evaporation.

In this study, PSPA were encapsulated with maltodextrin (DE: 4.0 - 7.0).MD concentration of 20%, 25% and 30% were used and exposed to the microwave drying power of 330W and 550W. The results showed that the moisture content of encapsulated PSPE decreased when the maltodextrin added was increased. Encapsulated PSPE moisture contents are ranged from 3.76 ± 0.02 to 4.25 ± 0.04%. Significant decreased ($p < 0.05$) of moisture content results were showed at 20% and 30% of maltodextrin added at both 550 W and 330 W microwave power level. Researcher proves that additional MD percentage resulted in an increased of total solid which causing reduction of total moisture for evaporation [10, 12].

Shelf life of a powder product is greatly affected by its water activity value. Water activity value ranges from 0.20 - 0.40 for any dried foods is considered as microbiological stable [12] which might prolong the shelf life of product. Results from Table 2 show that encapsulated PSPE are in the ranges of 0.2588 ± 0.0049 to 0.3912 ± 0.0132. Increasing of maltodextrin significantly ($p <0.05$) decreased the water activity value.

Table 2. Effect of maltodextrin (MD) concentration and microwave power level on total monomeric anthocyanin content (TMA), of encapsulated PSPE

Microwave Power (W)	Maltodextrin Concentration (%)	Moisture Content (%)	Water Activity	TMA (mg/L)
550	20	3.98 ± 0.01^{a}	0.3428 ± 0.0177^{a}	385.93 ± 10.81^{a}
	25	3.83 ± 0.01^{b}	0.2924 ± 0.0079^{b}	285.73 ± 5.24^{b}
	30	3.76 ± 0.02^{b}	0.2636 ± 0.0079^{c}	263.53 ± 7.66^{b}
330	20	4.25 ± 0.04^{c}	0.3912 ± 0.0132^{a}	419.28 ± 10.89^{a}
	25	4.14 ± 0.04^{d}	0.3042 ± 0.0126^{b}	337.11 ± 8.47^{c}
	30	3.95 ± 0.01^{d}	0.2588 ± 0.0049^{c}	314.86 ± 6.41^{c}

All data are the mean of triplicate measurements ± standard deviation values. a, b, c, means with different letter(s) in the same column differed significantly ($p < 0.05$).

Total monomeric anthocyanin content

Total monomeric anthocyanin (TMA) of encapsulated PSPE has been measured and the results are shown in Table 2. TMA of PSPE range between 263.53 ± 7.66 to 419.28 ± 10.89 mg/L. PSPA with 20% concentration give the highest TMA at both microwave drying power 330 W and 550 W, with 385.93±10.81 mg/L and 419.28 ±10.89 mg/L, respectively. The addition of MD at 20%, 25% and 30% and different microwave power (550 W and 330W) was not significantly affect the TMA content of microwave-assisted encapsulated PSPE. However, a significant ($p < 0.05$) anthocyanin reduce can be seen between 20% and 30% of maltodextrin addition. A larger range of maltodextrin concentration and different drying time can be studied to see the significant changes of TMA. An optimum drying parameter and formulation of the encapsulation process could be achieved. In this study, time factor could be included because short drying time may cause insufficient drying and longer drying time may degrade the anthocyanin content in the capsule [5].

Colour

The colour (L*, a*, and b* values) values of the microwave-assisted encapsulated PSPA were measured with a Minolta CR-400 Colorimeter, Japan and the results were expressed in accordance with the CIE Lab. The L* value, is a measure of lightness which ranges between 0 and 100. Addition of wall material might cause the increases of L* values [9].

Table 3 shows a significance difference in L* values between control and encapsulated PSPA extract. L* value of encapsulated PSPE was increased due to the presence of maltodextrin, since the maltodextrin initially has white colour (L* = 98.18 ± 0.15). Furthermore, a significant difference of L* values was found with the increasing of maltodextrin content. This is supported by Ahmed et al. [1] where the increasing of maltodextrin concentration causing the L* value of spray dried purple sweet potato flour increased.

The redness (+a*) of encapsulated PSPE were significantly reduced with the increased of maltodextrin concentration while the blueness (-b*) is not significantly affected. Microwave power was not significantly affect the value for both redness (+a*) and blueness (-b*).

Table 3. Colometric results of encapsulated PSPE at different maltodextrin concentrations and microwave power levels

Microwave Power (W)	MD (%)	L*	a*	b*
Non-encapsulated (control)		20.1 ± 0.35	26.5 ± 1.2	-3.55 ± 0.05
550	20	49.83 ± 0.21[a]	35.30 ± 0.17[a]	-10.6 ± 0.20[a]
	25	52.7 ± .0.63[b]	33.47 ± 0.70[b]	-10.3 ± 0.21[b]
	30	54.63 ± 0.67[c]	32.37 ± 0.75[c]	-10.7 ± 0.26[a]
330	20	50.7 ± 0.37[d]	34.00 ± 0.56[d]	-10.3 ± 0.17[c]
	25	55.43 ± 0.61[b]	33.17 ± 0.71[b]	-10.6 ± 0.10[b]
	30	55.73 ± 0.84[c]	31.23 ± 0.47[e]	-10.8 ± 0.00[a]

All data are the mean of triplicate measurements ± standard deviation values. a, b, c, means with different letter(s) in the same column differed significantly ($p < 0.05$)

Conclusion

Maltodextrin (MD, DE= 4.0 - 7.0) is effective as drying aid for encapsulation of PSPE. The addition of various MD concentrations on physicochemical properties of encapsulated PSPE was investigated in this study. The results showed that MD concentrations at 20% and 30% significantly ($p < 0.05$) reduced moisture content, water activity, and TMA content of encapsulated PSPE. Furthermore, a significant difference of L* values was found with the increasing content of maltodextrin. However, microwave power levels of 550 W and 330W was not significantly affecting the TMA, moisture content, water activity, and colour value of microwave-assisted PSPA. This could be enhanced by widening the range of study parameters and including drying time factor so that an optimum parameter of encapsulation process could be determined.

Acknowledgement

The authors would like to thank Universiti Teknologi Malaysia (UTM), Ministry of Higher Education (MOHE), and Research Management Centre (RMC), UTM for their financial support of this work through the project number Q.J130000.3009.00M65.

References

1. Ahmed, M., Akter, M. S. and Eun, J. B. (2010). Impact of α-amylase and maltodextrin on physicochemical, functional and antioxidant capacity of spray-dried purple sweet potato flour. *Journal of the Science of Food and Agriculture,* 90(3): 494-502.
2. Aishah, B., Nursabrina, M., Noriham, A., Norizzah, A. R. and Mohamad Shahrimi, H. (2013). Anthocyanins from *Hibiscus sabdariffa*, *Melastoma malabathricum* and *Ipomoea batatas* and its color properties. *International Food Research Journal,* 20(2): 827-834.
3. Li, J., Li, X. D., Zhang, Y., Zheng, Z. D., Qu, Z. Y., Liu, M., Zhu, S. H., Liu, S., Wang, M. and Qu, L. (2013). Identification and thermal stability of purple-fleshed sweet potato anthocyanins in aqueous solutions with various pH values and fruit juices. *Food Chemistry,* 136(3): 1429-1434.
4. Choi, I., Lee, J. Y., Lacroix, M. and Han, J. (2017). Intelligent pH indicator film composed of agar/potato starch and anthocyanin extracts from purple sweet potato. *Food Chemistry,* 218 (Supplement C): 122-128.
5. Zaidel, D. N. A., Aqilah, N. and Mohd, Y. M. (2015). Efficiency and thermal stability of encapsulated anthocyanins from red dragon fruit (*Hylocereus polyrhizus* (Weber) Britton & Rose) using microwave-assisted technique. *Chemical Engineering Transactions,* 43: 127-132.
6. Mohd Nawi, N., Muhamad, I. I. and Mohd Marsin, A. (2015). The physicochemical properties of microwave-assisted encapsulated anthocyanins from *Ipomoea Batatas* as affected by different wall materials. *Food Science and Nutrition,* 3(2): 91-99.

7. Haghi, A. K. and Amanifard, N. (2008). Analysis of heat and mass transfer during microwave drying of food products. *Brazilian Journal of Chemical Engineering,* 25: 491-501.
8. Ahmed, M., Akter, M. S., Lee, J. C. and Eun, J. B. (2010). Encapsulation by spray drying of bioactive components, physicochemical and morphological properties from purple sweet potato. *LWT - Food Science and Technology,* 43(9): 1307-1312.
9. Peng, Z., Li, J., Guan, Y. and Zhao, G. (2013). Effect of carriers on physicochemical properties, antioxidant activities and biological components of spray-dried purple sweet potato flours. *LWT - Food Science and Technology,* 51(1): 348-355.
10. Quek, S. Y., Chok, N. K. and Swedlund, P. (2007). The physicochemical properties of spray-dried watermelon powders. *Chemical Engineering and Processing: Process Intensification,* 46(5): 386-392.
11. Giusti, M. M. and Wrolstad, R. E. (2001). Characterization and measurement of anthocyanins by UV-visible spectroscopy. *Current Protocols in Food Analytical Chemistry,* John Wiley & Sons, Inc, Hoboken, USA.
12. Caliskan, G. and Dirim, S. N. (2016). The effect of different drying processes and the amounts of maltodextrin addition on the powder properties of sumac extract powders. *Powder Technology,* 287 (Supplement C): 308-314.

Malaysian Journal of Analytical Sciences, Vol 22 No 4 (2018): 619 - 625
DOI: https://doi.org/10.17576/mjas-2018-2204-07

MALAYSIAN JOURNAL OF ANALYTICAL SCIENCES
Published by The Malaysian Analytical Sciences Society
ISSN 1394 - 2506

EXTRACTION OF EICOSAPENTAENOIC ACID FROM *Nannochloropsis gaditana* USING SUB-CRITICAL WATER EXTRACTION

(Pengekstrakan Asid Eikosapentaenoik daripada *Nannochloropsis gaditana* dengan Menggunakan Kaedah Air Sub-kritikal)

Bernard Chon Han Ho[1], Siti Mazlina Mustapa Kamal[2], Mohd Razif Harun[1]*

[1]*Department of Chemical and Environmental Engineering*
[2]*Department of Process and Food Engineering*
Universiti Putra Malaysia, 43400 Serdang, Selangor, Malaysia

**Corresponding author: mh_razif@upm.edu.my*

Received: 16 April 2017; Accepted: 7 March 2018

Abstract

Microalgae had been utilized for biofuel production due to the presence of high lipid concentrations in the past year. However, the current interest is to convert their lipids to produce value added products such as omega-3. Various types of microalgae are known to be rich in omega-3. Hence, a more sustainable and high efficiency extraction method is required to ensure its viability. Sub-critical water extraction (SWE) is an emerging extraction technique as the technique involves shorter period of extraction, high efficiency and most importantly uses green and environmentally friendly solvent (water). In this preliminary experiment, different process conditions of SWE include temperature (156 – 274 °C), biomass loading (33 – 117 g/L) and retention time (6.6 – 23.4 minutes) were investigated on microalga, *Nannochloropsis gaditana*. The maximum yields of lipid and eicosapentaenoic acid (EPA) extracted were 17.86 wt.% of biomass and 15.78 wt.% of total fatty acid methyl ester (FAME), respectively. This productivity level (~16 wt.%) which is in keeping or higher than that of current production systems endorses SWE as a promising extraction technique for microalgal EPA production. Future works on optimization of SWE parameters will be performed to achieve the highest EPA concentration.

Keywords: eicosapentaenoic acid, green extraction, microalgae, omega-3, sub-critical

Abstrak

Mikroalga telah digunakan secara menyeluruh menghasilkan bahan api bio kerana ia mempunyai kadar kepekatan minyak yang tinggi. Bagaimanapun, tarikan semasa tertumpu pada penukaran minyak untuk menghasilkan produk berharga seperti omega-3. Banyak jenis mikroalga adalah kaya dengan omega-3. Oleh sebab itu, kaedah pengekstrakan yang mapan dan efisien diperlukan untuk menjamin daya maju mikroalga dalam penghasilan omega-3. Kaedah pengekstrakan air sub-kritikal (SWE) merupakan kaedah baru yang memerlukan masa pengekstrakan yang pendek, efisien dan menggunakan air sahaja sebagai pelarut. Dalam eksperimen awal ini, keadaan proses yang berbeza termasuk suhu (156 – 274 °C), muatan biojisim (33 – 117 g/L) dan tempoh pengekstrakan (6.6 – 23.4 minit) telah dikaji dengan menggunakan mikroalga, *Nannochloropsis gaditana.* Kadar maksimum minyak dan asid eikosapentaenoik (EPA) di ekstrak masing-masing ialah 17.86 wt.% daripada jumlah biojisim dan 15.78 wt.% daripada jumlah asid lemak metil ester (FAME). Kadar pengekstrakan yang tinggi ini (~16 wt.%) berbanding dengan kaedah semasa menunjukkan bahawa SWE ini ialah kaedah pengekstrakan yang mempunyai harapan untuk menghasilkan EPA daripada mikroalga pada masa hadapan. Pengoptimuman bagi parameter SWE untuk mendapatkan kadar kepekatan EPA yang paling tinggi akan dilakukan pada masa hadapan.

Kata kunci: asid eikosapentaenoik, pengekstrakan hijau, mikroalga, omega-3, sub-kritikal

Introduction

In the past years, people are becoming more health conscious due to the many health related problems arising in the community. People are in search of better quality oil to be consumed. Many studies related to polyunsaturated fatty acid (PUFA) especially omega-3 have been widely reported. Recent studies had proven more on the benefits of omega-3 towards the health implications of human. Long chain omega-3 had been known to have neuroprotective capabilities [1]. Meanwhile, omega-3 is also related to the reduction of risk in developing cardiovascular diseases. Some researchers found that the intake of 2 g/day to 4g/day of omega-3 fatty acid could reduce the triglyceride level in the blood [2, 3]. Other health benefits of omega-3 include anti-inflammatory potential [4, 5], reduction in the effect of tumour cells [6, 7] and aiding in Alzheimer's disease [8]. Some of the health and government organizations have even recommended a significant daily intake of omega-3 to reduce the chances of cardiovascular diseases [9]. Many had incorporated the omega-3 oil in fortifying food and also pharmaceutical products [10, 11]

Microalgae are considered to be one of the promising supplies of biomass for value add bio-products production due to their adaptability to thrive on limited land space and also high biomass productivity [12]. While microalgae have been extensively studied on the usage in biodiesel production [13], there are other bio-products that are worth studying and discovering through the extraction from microalgae. Current paper focuses on omega-3 from microlgae. Many microalgae species are high in omega-3 content [14]. Lately, big algae companies shifted their focus on obtaining omega-3 from algae sources and some even developed algal based omega-3 pharmaceutical products, showing a significant effect on the level of blood nutrient [15, 16]. With such valuable material, the extraction method could be an important indicator to improve the yield while reducing the usage of harmful material as well.

Previous studies had extracted EPA from microalgae using solvent extraction in comparison with other new techniques. Supercritical fluid extraction had been proven surpass the extraction efficiency of solvent extraction using acetone and hexane [17]. Meanwhile, sub-critical water extraction (SWE) of microalgae had been proven to be able to recover high amount polyunsaturated fatty acid from the cell [18]. Extraction using harmful organic solvent had no significant effect to improve the extraction yield but the solvent itself will actually harm the end product and also the environment [19]. SWE is one of the green methods to overcome the issues wih solvent extraction method. This method mainly uses water as the solvent for extraction and the main principle is to change the properties of water under high temperature and pressure condition [20]. This method is known to be effective to extract products from microalgae such as *Nannochloropsis sp.* with high yield of lipid and omega-3 [21]. The strong cell wall of algae could be hydrolysed under this condition and the extraction of mainly non-polar content could be enhanced. Under sub-critical condition, this method is proven to allow shorter reaction time, lower operating cost and reduce or even omit the usage of harmful organic solvent [22]. Three parameters studied which are temperature, time and biomass loading are shown to have significant effect on the extraction yield [18].

Therefore, this article focuses on the preliminary study of the factors affecting the extraction yield which are extraction temperature, time and biomass loading on *Nannochloropsis ganditana*. This study is important towards the optimization of the process factors, targetting to improve the extraction yield while reducing the cost and time of the extraction.

Materials and Methods

Raw material and characterization

The 100% freeze dried biomass (*Nannochloropsis gaditana*) was purchased from Longevity Superfoods (Utah, USA). The powdered biomass was tightly sealed in the package and kept in dry condition to maintain the quality of the microalgae. The carbon, hydrogen, nitrogen and sulphur (CHNS) analysis were done in a CHNS628 analyzer. Ultimate analysis is important to characterize the biomass because each batch of cultivated biomass will be different. Soxhlet extraction method with hexane as the solvent was used to determine fat content of the biomass. Protein content was determined using the Kjeldahl method [23]. Moisture content was determined by the differences mass before and after the drying process in the oven at 105 °C followed by the incineration step at 550 °C to determine the ash content. Carbohydrate content was taken as the sum of residual after all other contents were determined.

Extraction equipment and procedures

The main components of the system consist of a salt bath, temperature controller unit and a stainless steel reactor (Swagelok 316 SS; 3/4 in. OD x 0.049 in. wall). The stainless steel reactor was filled with the desired amount of biomass (microalgae) and water (33 – 117 g algae/L) . The tightly screwed reactor then placed into the salt bath and run with the desired temperature (156.1 – 273.9 °C) and extraction time (6.6 – 23.4 minutes). All the parameters chosen were based on the range of parameters used by similar studies [18].

The reacted biomass in SWE was centrifuged at 4000 rpm for 10 minutes. The supernatant consists of oil layer was decanted by adding 10 mL of hexane and the process was repeated for 3-4 times to ensure the oil layer was completely recovered. The hexane and crude lipid mixture were then transferred to a rotary evaporator to recover the excess hexane. Meanwhile, the weight of the lipid was determined. The oil samples were tightly sealed in containers and kept in the freezer no longer than 6 months for further analysis.

Gas chromatography analysis

The dried crude lipid sample was mixed with 1 mL of hexane. 1 mL of sodium methoxide was added to the mixture of hexane and oil for transesterification reaction to take place. The mixture was then stirred for 10 seconds on a vortix stirrer. and the top layer of fatty acid methyl ester (FAME) was decanted for GC analysis.

The GC analysis was done on Hewlett-Packard 5890 Series II Plus GC with an automatic liquid sampler and flame ionization detector (FID). The stationary phase chosen was (50%-Cyanopropylphenyl)-dimethylpolysiloxane and the column used in this analysis was DB-225 (30 m × 0.25 mm × 0.25 µm). Splitless mode was used injecting 1.0 µL of sample to be analyzed. The carrier gas used was hydrogen with a set flowrate of 1.3 mL/min. Initial oven temperature was preset to 35 °C with holding time of 0.5 minute. Then the temperature was ramped up to 195 °C with heating rate of 25.0 °C/min. Then temperature was raised at 3.0 °C/min to 205 °C and then at 8.0 °C/min to 230 °C and held for 6.7 minutes. The total run time was 20.06 minutes. The detector temperature was set to 240 °C with nitrogen gas as make-up gas. The standard used for the analysis to compare all the peaks showing in the sample was Supelco® 37 Component FAME Mix standard.

Results and Discussion

Ultimate and proximate analysis

The biomass was characterized *via* CHNS and proximate analysis. The percentage of carbon, hydrogen, nitrogen and sulfur in the biomass were 47.91%, 6.83%, 7.56% and 0.63%, respectively. With the high carbon percentage, this microalgae biomass possesses a significant potential for biofuels and bio-products production. Meanwhile, potential products from the biomass can be developed from the proximate analysis in Table 1.

Table 1. Proximate analysis of *Nannochloropsis gaditana*

Content	Weight percent (wt.%)
Fat	10.2
Moisture	2.9
Ash	10.8
Carbohydrate	28.9
Crude Protein	47.2

High percentage of fat obtained from Soxhlet extraction showed that *Nannochloropsis gaditana* has potential to be used as omega-3 oil source. Also, the presence of carbohydrates and protein compositions in the biomass has potential for other bio-products (e.g. chemicals and feed) production.

Maximum lipid and EPA yield

The oil yield was calculated based on the final oil yield (g) extracted compared to the initial mass loading (g) of the biomass to the reactor. The maximum oil yield from both Soxhlet and SWE showed a significant difference as shown in Figure 1. It was found that oil yield of 10.2 wt.% was produced *via* Soxhlet extraction method whereas the SWE method produced higher oil yield of 17.86 wt.% using temperature at 215 °C for 15 minutes with 75 g algae/L as compared to Soxhlet extraction.

From GC analysis, the results showed a positive finding on the extraction of EPA from *Nannochloropsis gaditana*. The EPA compositions yielded the highest amount of up to 15.78 wt.% of total FAME using temperature at 215 ^{o}C for 6.6 minutes, with 75 g algae/L biomass loading. Meanwhile, the Soxhlet extraction yielded of 28.10 wt.% of total FAME. The lower amount of EPA yield obtained using SWE as compared to Soxhlet might be due to the degradation of some EPA during the extraction process as the process was not optimized [18]. Meanwhile, the Soxhlet extraction with a lower oil yield showed that oil was not fully recovered even though there might be a higher percentage of EPA in the oil. The oil yield is important as the lipids in microalgae mostly exist in the natural form with all the fatty acids attached to mainly glycerol, carbohydrates and phosphates [24]. Hence, high oil yield might increase the amount of EPA in the oil. These results proved that SWE is a safer and environmentally friendly process that can be used as an alternative method for EPA extraction in the future with further optimization.

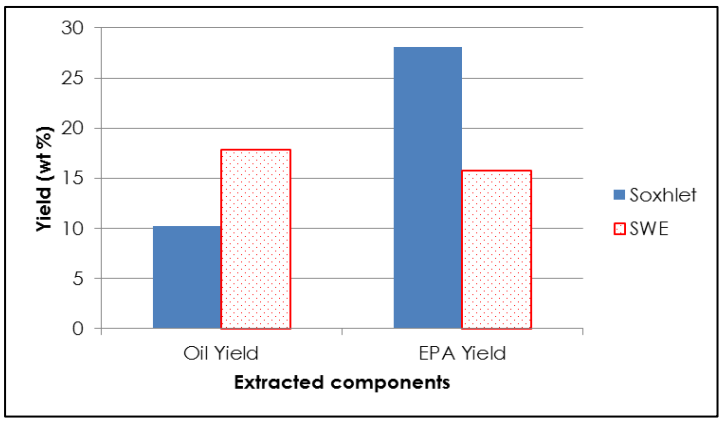


Figure 1. The maximum extraction yield for both Soxhlet and SWE

Effect of Temperature

Temperature is one of the signignificant parameters when dealing with SWE [20]. The findings on the effect of temperature for *Nannochloropsis gaditana* extraction using SWE are shown in Figure 2. The study found that the highest EPA (14.14 wt.% of total FAME) and oil (17.86 wt.% of biomass) yields were obtained at 215.0 °C.

The temperature setting affects the yield of the oil as the condition of the sub-critical water changes. As the water is heated up to a higher range of temperature, the water hydrolysis power will be higher [22]. Hydrolysis reaction is good in breaking up the cell wall of the microalgae. However, when the reaction is high in hydrolysis, degradation of oil occurs, hence, decreasing the oil yield as well as quality at high temperature. Meanwhile, the increase in temperature under SWE condition also increases the solubility of water to extract non-polar substrates such as triglycerides which holds the omega-3 [20].

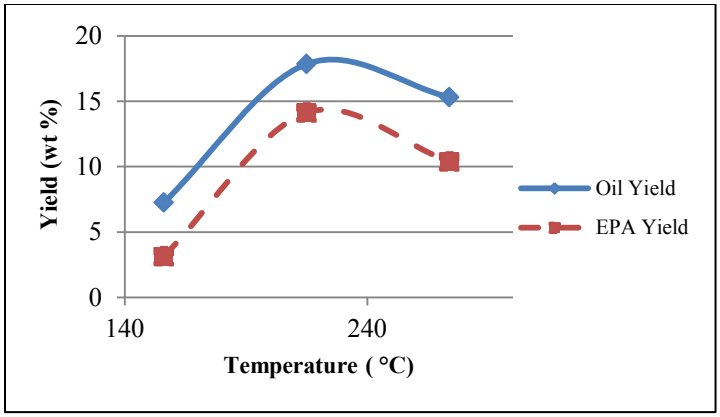


Figure 2. The effect of temperature on oil and EPA yield

Effect of extraction time

The extraction time is also one of the important factors to be considered when performing SWE. Although reducing the time of extraction might reduce the extraction cost, however, increasing the time of extraction could improve the yield of the bio-products as shown in Figure 3.

Figure 3 shows the effect of extraction time on the oil and EPA yields. The effect of reaction time affects the oil yield. From Figure 3, shorter reaction time is advantageous as it improves the EPA extraction to have lower denaturation effect. However, the shorter time of extraction does not allow a complete extraction process and leaving out most of the lipid in the microalgae. Meanwhile, at longer extraction time, due to the EPA is exposed under high temperature, the EPA will be denatured and there might be possibilities of secondary or tertiary reaction happening under SWE condition [25].

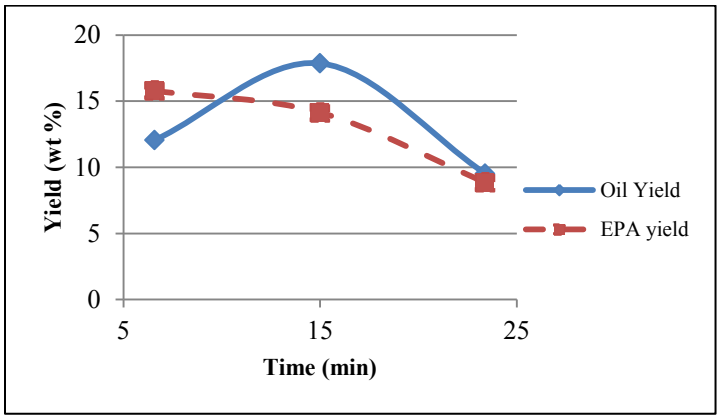


Figure 3. The effect of extraction time on oil and EPA yield

Effect of biomass loading

Dewatering and drying of microalgae involve high operational cost in the current microalgae harvesting industries [26]. Hence, low biomass loading or high water content extraction process would be favourable in reducing the initial cost of harvesting. Figure 4 shows the effect of biomass loading on oil and EPA yields.

From Figure 4, it was found that low biomass loading favoured the extraction of oil from the biomass. Lower biomass loading means more water could be used to extract the total lipid content in the biomass. However, the total

EPA was reduced at low biomass content. This might be due to the secondary or tertiary reaction happened at high water content, degrading the lipid quality in terms of omega-3 extraction. The reduction of EPA yield as compared to other FAME also showed that EPA is highly susceptible to oxidation due to its long chain of carbon as compared to other FAME [27].

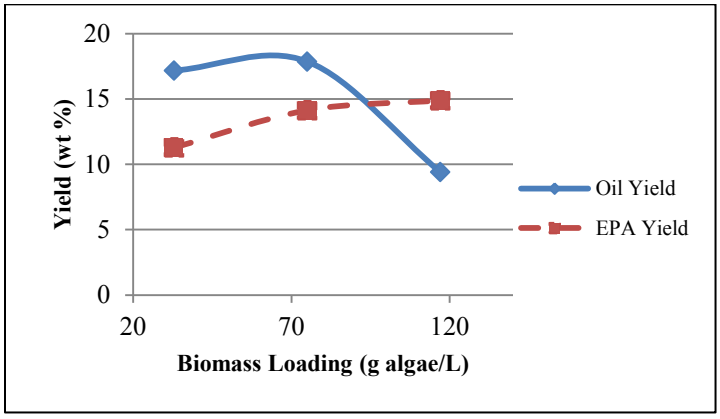


Figure 4. The effect of biomass loading on oil and EPA yield

Conclusion

This study discusses the preliminary results of using SWE to extract omega-3 from microalgae, *Nannochloropsis gaditana*. Utilizing SWE and microalgae as the source of omega-3 production are proven to be a sustainable and environmentally friendly as compared to harmful organic solvent usage. While the extraction yield of EPA might not be as high as conventional solvent extraction, this extraction process showed a significant extraction capability with the significantly high oil yield from SWE (17.86 wt.%). Hence, this study hopes to be a precursor of further optimization study on the extraction of omega-3 using SWE to improve the extraction process while making SWE possible to be scaled-up.

Acknowledgement

This work is technically assisted by the Department of Chemical and Environmental Engineering, UPM and funded by Putra Grant-Putra Group Initiative (IPB) (Grant Number: 94839032).

References

1. Dyall, S. C. (2015). Long-chain omega-3 fatty acids and the brain: A review of the independent and shared effects of EPA, DPA and DHA. *Frontiers in Aging Neuroscience,* 7(52): 1-15.
2. Kastelein, J. J. P., Maki, K. C., Susekov, A., Ezhov, M., Nordestgaard, B. G., Machielse, B. N., Kling, D. and Davidson, M. H. (2014). Omega-3 Free Fatty Acids for the Treatment of Severe Hypertriglyceridemia: The EpanoVa fOr Lowering Very high triglyceridEs (EVOLVE) trial. *Journal of Clinical Lipidology,* 8 (1): 94-106.
3. Maki, K. C., Orloff, D. G., Nicholls, S. J., Dunbar, R. L., Roth, E. M., Curcio, D., Johnson, J., Kling, D. and Davidson, M. H. (2013). A highly bioavailable omega-3 free fatty acid formulation improves the cardiovascular risk profile in high-risk, statin-treated patients with residual hypertriglyceridemia (the ESPRIT Trial). *Clinical Therapeutics,* 35 (9): 1400-1411.
4. Wall, R., Ross, R. P., Fitzgerald, G. F. and Stanton, C. (2010). Fatty acids from fish: The anti-inflammatory potential of long-chain omega-3 fatty acids. *Nutrition Reviews,* 68 (5): 280-289.
5. Weylandt, K. H., Chiu, C. Y., Gomolka, B., Waechter, S. F. and Wiedenmann, B. (2012). Omega-3 fatty acids and their lipid mediators: Towards an understanding of resolvin and protectin formation. *Prostaglandins and Other Lipid Mediators,* 97(3): 73-82.
6. Mandal, C. C., Ghosh-Choudhury, T., Yoneda, T., Choudhury, G. G. and Ghosh-Choudhury, N. (2010). Fish oil prevents breast cancer cell metastasis to bone. *Biochemical and Biophysical Research Communications,* 402(4): 602-607.

7. Murphy, R. A., Mourtzakis, M., Chu, Q. S., Baracos, V. E., Reiman, T. and Mazurak, V. C. (2011). Nutritional intervention with fish oil provides a benefit over standard of care for weight and skeletal muscle mass in patients with non-small cell lung cancer receiving chemotherapy. *Cancer,* 117(8): 1775-1782.
8. Swanson, D., Block, R. and Mousa, S. A. (2012). Omega-3 fatty acids EPA and DHA: Health benefits throughout life. *Advances in Nutrition: An International Review Journal,* 3(1): 1-7.
9. Turchini, G. M., Nichols, P. D., Barrow, C. and Sinclair, A. J. (2012). Jumping on the omega-3 Bandwagon: Distinguishing the role of long-chain and short-chain omega-3 fatty acids. *Critical Reviews in Food Science and Nutrition,* 52(9): 795-803.
10. Dawczynski, C., Martin, L., Wagner, A. and Jahreis, G. (2010). N-3 LC-PUFA-enriched dairy products are able to reduce cardiovascular risk factors: a double-blind, cross-over study. *Clinical Nutrition,* 29(5): 592-599.
11. Tur, J. A., Bibiloni, M. M., Sureda, A. and Pons, A. (2012). Dietary sources of omega 3 fatty acids: public health risks and benefits. *British Journal of Nutrition,* 107(Supplement 2): S23-52.
12. Zhou, W., Min, M., Li, Y., Hu, B., Ma, X., Cheng, Y., Liu, Y., Chen, P. and Ruan, R. (2012). A hetero-photoautotrophic two-stage cultivation process to improve wastewater nutrient removal and enhance algal lipid accumulation. *Bioresource Technology,* 110: 448-455.
13. Talebi, A. F., Mohtashami, S. K., Tabatabaei, M., Tohidfar, M., Bagheri, A., Zeinalabedini, M., Hadavand Mirzaei, H., Mirzajanzadeh, M., Malekzadeh Shafaroudi, S. and Bakhtiari, S. (2013). Fatty acids profiling: A selective criterion for screening microalgae strains for biodiesel production. *Algal Research,* 2(3): 258-267.
14. Griffiths, M. J., van Hille, R. P. and Harrison, S. T. L. (2012). Lipid productivity, settling potential and fatty acid profile of 11 microalgal species grown under nitrogen replete and limited conditions. *Journal of Applied Phycology,* 24(5): 989-1001.
15. Arterburn, L. M., Oken, H. A., Bailey Hall, E., Hamersley, J., Kuratko, C. N. and Hoffman, J. P. (2008). Algal-oil capsules and cooked salmon: nutritionally equivalent sources of docosahexaenoic acid. *Journal of the American Dietetic Association,* 108(7): 1204-1209.
16. Adarme-Vega, T. C., Lim, D. K. Y., Timmins, M., Vernen, F., Li, Y. and Schenk, P. M. (2012). Microalgal biofactories: A promising approach towards sustainable omega-3 fatty acid production. *Microbial Cell Factories,* 11(1): 96.
17. Treyvaud Amiguet, V., Kramp, K. L., Mao, J., McRae, C., Goulah, A., Kimpe, L. E., Blais, J. M. and Arnason, J. T. (2012). Supercritical carbon dioxide extraction of polyunsaturated fatty acids from northern shrimp (*Pandalus borealis* kreyer) processing by-products. *Food Chemistry,* 130(4): 853-858.
18. Reddy, H. K., Muppaneni, T., Sun, Y., Li, Y., Ponnusamy, S., Patil, P. D., Dailey, P., Schaub, T., Holguin, F. O., Dungan, B., Cooke, P., Lammers, P., Voorhies, W., Lu, X. and Deng, S. (2014). Subcritical water extraction of lipids from wet algae for biodiesel production. *Fuel,* 133: 73-81.
19. Griffiths, M. J., van Hille, R. P. and Harrison, S. T. (2010). Selection of direct transesterification as the preferred method for assay of fatty acid content of microalgae. *Lipids,* 45(11): 1053-1060.
20. Brunner, G. (2009). Near critical and supercritical water. part I. hydrolytic and hydrothermal processes. *The Journal of Supercritical Fluids,* 47(3): 373-381.
21. Lu, Y., Levine, R. B. and Savage, P. E. (2015). Fatty acids for nutraceuticals and biofuels from hydrothermal carbonization of microalgae. *Industrial & Engineering Chemistry Research,* 54(16): 4066-4071.
22. Toor, S. S., Rosendahl, L. and Rudolf, A. (2011). hydrothermal liquefaction of biomass: A review of subcritical water technologies. *Energy,* 36(5): 2328-2342.
23. Horwitz, W. (1990). Official methods of analysis of AOAC international. AOAC International, USA.
24. Ryckebosch, E., Bruneel, C., Termote-Verhalle, R., Goiris, K., Muylaert, K. and Foubert, I. (2014). Nutritional evaluation of microalgae oils rich in omega-3 long chain polyunsaturated fatty acids as an alternative for fish oil. *Food Chemistry,* 160: 393-400.
25. Akhtar, J. and Amin, N. A. S. (2011). A review on process conditions for optimum bio-oil yield in hydrothermal liquefaction of biomass. *Renewable and Sustainable Energy Reviews,* 15(3): 1615-1624.
26. Milledge, J. J. and Heaven, S. (2013). A review of the harvesting of micro-algae for biofuel production. *Reviews in Environmental Science and Bio/Technology,* 12(2): 165-178.
27. Kolanowski, W., Jaworska, D. and Weißbrodt, J. (2007). Importance of instrumental and sensory analysis in the assessment of oxidative deterioration of omega-3 long-chain polyunsaturated fatty acid-rich foods. *Journal of the Science of Food and Agriculture,* 87(2): 181-191.

Malaysian Journal of Analytical Sciences, Vol 22 No 4 (2018): 626 - 632
DOI: https://doi.org/10.17576/mjas-2018-2204-08

MALAYSIAN JOURNAL OF ANALYTICAL SCIENCES
Published by The Malaysian Analytical Sciences Society
ISSN 1394 - 2506

SYNERGISTIC EXTRACTANT FOR EXTRACTION OF REMAZOL ORANGE 3R IN LIQUID MEMBRANE FORMULATION

(Pengekstrak Sinergistik untuk Pengekstrakan Remazol Orange 3R dalam Formulasi Membran Cecair)

Hilmi Abdul Rahman[1], Norasikin Othman[1,2]*, Muhammad Bukhari Rosly[1], Raja Norimie Raja Sulaiman[1], Norela Jusoh[1], Norul Fatiha Mohamed Noah[1]

[1]*Department of Chemical Engineering, Faculty of Chemical and Energy Engineering,*
[2]*Centre of Lipids Engineering & Applied Research (CLEAR), Ibnu Sina Institute for Scientific and Industrial Research*
Universiti Teknologi Malaysia, 81310 UTM Johor Bahru, Johor, Malaysia

**Corresponding author: norasikin@cheme.utm.my*

Received: 16 April 2017; Accepted: 7 March 2018

Abstract

Currently, various synthetic dyes are used in the textile industry and a lot of non-bonded dyes are released into the wastewater; increasing its toxicity and carcinogenicity. Liquid membrane process is one of the potential methods to eliminate these unwanted particles from the wastewater. The most crucial part of the liquid membrane process is its formulation; especially the extractant or carrier. In order to find a suitable extractant, liquid-liquid extraction process was carried out. The effect of synergistic extractant to extract the Remazol Orange 3R reactive dyes in a shorter time and at a lower concentration of extractant was investigated in this study. Several parameters have been studied such as extractant type, extractant concentration, synergist extractant type and synergist extractant concentration. The results show that, Remazol Orange 3R reactive dyes were extracted by tridodecylamine (TDA) as a base and trioctylamine (TOA) as a synergist extractant. Meanwhile, the salicyclic acid (SA) was used to protonate the TDA and TOA, and cooking palm oil was used as a diluent. The performance of extraction of reactive dyes at the 0.1 M concentration of extractant was 70% when synergistic system was applied compared to single extractant which was only 50% of the dyes have been extracted. Therefore, the synergistic extractant has a potential to be further utilised in liquid membrane studies on the extraction of reactive dyes.

Keywords: liquid membrane, liquid-liquid extraction, synergistic extractant, synergist, extractant

Abstrak

Pada masa ini, pelbagai pewarna sintetik digunakan dalam industri tekstil dan banyak pewarna tanpa terikat dilepaskan ke dalam air sisa sehingga meningkatkan kadar toksik dan karsinogenik. Proses membran cecair adalah salah satu kaedah yang berpotensi untuk menghapuskan zarah-zarah yang tidak diingini dari air sisa. Formulasi membran adalah bahagian paling penting dalam proses membran cecair; terutamanya pengekstrak atau pembawa. Bagi mencari pengekstrak yang sesuai, proses pengekstrakan cecair-cecair telah dijalankan. Kesan sinergis pengekstrak untuk mengekstrak pewarna reaktif Remazol Orange 3R dalam masa yang lebih singkat dan pada kepekatan ekstrak yang lebih rendah telah dikaji. Beberapa parameter telah dikaji seperti jenis pengekstrak, kepekatan pengekstrak, jenis pengekstrak sinergis dan kepekatan pengekstrak sinergis. Keputusan menunjukkan bahawa, pewarna reaktif Remazol Orange 3R diekstrak oleh tridodekilamina (TDA) sebagai asas dan trioktilamina (TOA) sebagai sinergis. Sementara itu, asid salisiklik (SA) digunakan untuk protonate TDA dan TOA, dan minyak kelapa sawit digunakan sebagai pelarut. Prestasi pewarna reaktif yang diekstrak adalah sebanyak 70% apabila sistem sinergistik digunakan berbanding dengan hanya satu pengekstrak digunakan yang hanya 50% daripada pewarna telah diekstrak pada kepekatan 0.1M pengekstrak. Oleh itu, pengekstrak sinergis mempunyai potensi untuk digunakan dalam kajian membran cecair pada pengekstrakan pewarna reaktif dimasa hadapan.

Kata kunci: membran cecair, pengekstrakan cecair-cecair, pengekstrak sinergistik, sinergis, pengekstrak

Introduction

Textile wastewater has massively concerned by the public and the government due to the colour and toxic substances in dye wastewater [1]. It has been approximated that more than 100,000 commercial dyes with over 7 x 10^5 tons are produced annually [2]. Moreover, around 10-25% of textile dyes are lost during the colouring process and about 2-20% of them are directly discharged as an aqueous effluent [3]. The dyes lost in the textile industry pose a major threat to wastewater sources where these effluents contain high concentrations of both organic and inorganic compounds that can be considered as pollutants, which are mainly from chemical textile finishing processes [4].

Numerous conventional methods have been applied in the textile industry on the removal and recovery of dyes, such as biological [5], liquid-liquid extraction, adsorption, steam distillation and chemical oxidation [6]. Conventional methods possess their own disadvantages including high operating costs, time consuming, and production of secondary pollutants. At the present time, liquid membrane (LM) technology especially emulsion liquid membrane (ELM) technique is anticipated to be the promising method to encounter the drawbacks of conventional methods. This technology has been proven beneficial in various disciplines such as inorganic chemistry, chemical engineering, biomedical engineering, biotechnology, analytical chemistry, and physiology. Generally, a membrane may be defined as a semi permeable barrier which selectively allows a solute to pass through from the external to the internal phase which is dependent on the molecular weight, ionic charge, or type of extractant reacted on it, on top of preventing the mixing of external and internal phase [7]. They can be either an aqueous (W/O/W emulsion) or an organic solution (O/W/O emulsion). Ensuring an effective removal and recovery of dyes through LM process should take into account the suitable carrier, diluent and stripping agent. Previous studies indicated that various petroleum-based substances such as heptane [8], pentanol [9] and kerosene [10, 11] were used as diluent in LM formulation. However, petroleum based LM is non-environmental friendly and can potentially cause other pollutions. Benign based LMs such as coconut oil and palm oil have been proved as suitable diluents in the extraction of chromium performed by Othman et al. [12]. By following their footsteps, benign based ELM has been used in this study to replace the petroleum based ELM and its efficiency and stability on the extraction of reactive dyes have been studied.

Currently, single extractants have been used but they are famous to be time consuming. Thus, a synergistic extractant has been proposed to increase the extraction percentages, which is mixed up by two extractants at low concentration [13]. One molecule would transfer ions from aqueous to membrane phase in order to satisfy both solvation and co-ordination sites of the cation and neutralise charges, while another extractant would serve to replace the water. Synergistic extraction with a specified ration of extractants in the membrane will boost the efficiency of ions transport [14], selectivity [15] and extraction process [16]. The synergistic extractant can be synthesised through the following possible combinations of extractants such as acidic and neutral extractants, two acidic extractants, two neutral extractants, anionic and neutral extractant, cationic and ionic extractant and two anionic extractants [17]. The addition of two extractants into the membrane has had positive results on improving the rate of extraction and the selectivity of solute ions transport.

This paper presents a research to formulate the liquid membrane using synergistic extractant and to determine the optimum extractant concentration of the process. Thus, to fulfil this objective, several parameters such as type of base extractant, concentration of base extractant, type of synergist extractant and concentration of synergist extractant have been investigated.

Materials and Methods

Emulsion liquid membrane consists of four main components; diluents, extractant, surfactant and stripping phase. The membrane phase used is a homogeneous mixture of cooking palm oil (BURUH) as diluents, Tridodecylamine (TDA) (Merck), Trioctylamine (TOA) (Merck), Aliquat 336 (Merck), Trioctylephosphine oxide (TOPO) (Sigma-Aldrich) and Tributyl phosphate (TBP) (Sigma-Aldrich) as extractants or synergist extractants and salicylic acid (SA) for TDA and TOA protonation. The chemicals for all reagents have been obtained from the manufacturers.

Remazol Brilliant Orange 3R reactive dye has been obtained from NOZI Batik SDN BHD and has been used as an external phase solution. The dye solution is prepared by dissolving the dye in distilled water. All chemicals were of analytical grade and used without further purification.

Liquid membrane component selection

Liquid membrane formulation comprised of three main components; diluent, base and synergist extractant. The organic phase is a homogeneous mixture of diluents, base extractant phase, and synergist extractant. In this research, it has been decided that palm oil would be used as a diluent due to its non-toxic and biodegradable properties.

Single extractant extraction was conducted as a basis for the synergistic extractant. Liquid-liquid extraction experiment was started by mixing an equal volume (10 mL) of synthetic reactive dye solution and organic solution that consists of various concentrations of extractant in palm oil as a diluent in a 25 mL conical flask. The mixing process was carried out using a mechanical shaker at 320 rpm for 1 hour to perform the extraction. The mixture was then poured into a separating funnel which was then left for 15-30 minutes for phase separation. The treated aqueous phase was separated from the organic phase through gravity settling. The aqueous phase was analysed using a UV-spectrometer at 494 nm to measure the percentage of extraction.

Synergistic extractant of liquid membrane formulation

In order to formulate the synergistic extractant, the mixture of base extractant and synergist extractant was tested. The single extractant was mixed with another extractant as a synergist by the volume percentage (1-10 v/v%). The liquid-liquid extraction (LLE) process was conducted to determine the effect of synergistic extractant on extraction percentages. During the extraction process, a sample of aqueous solution underwent a UV absorbance test every 10 minutes for an hour to check the percentages of dye extraction.

The synergistic effect can be quantified through the synergistic coefficient (S.C) which can be defined using equation 1:

$$S.C = \frac{D_{mix}}{D_{synergist} + D_{extractant}} \quad (1)$$

where $D_{extractant}$ and $D_{synergist}$ are the distribution ratios obtained using each extractant separately, and D_{mix} represents the distribution ratio with the mixture. If the S.C is more than 1, the synergistic effect has occurred but if S.C is less than 1, there is no synergistic effect.

Results and Discussion

Effect of extractant type

The extraction performance of different types of extractant on Remazol Orange 3R extraction was studied and the results are presented in Figure 1. The results show that high percentages of extraction were obtained from basic extractants (TDA, TOA, Aliquat 336), and very low to negligible percentages were obtained from neutral extractants (TOPO and TBP) and acidic extractant (D2EHPA). This is because neutral extractants have no charges to extract dyes, and an acidic extractant has the same charge as the dye which makes them repel each other. Therefore, Remazol Orange 3R which is an acidic dye with a positive charge can be extracted using extractants of the opposite charge, which is the basic extractants.

The efficiency of basic extractant can be arranged in the following order: TOA>TDA>Aliquat 336. TOA has greater polarity [18, 19] compared to TDA solely due to the difference in the number of CH_2 attached to their respective nitrogen atoms. TDA has a higher number of CH_2 attached on its nitrogen atom $(CH_2)_{11}$ compared to that of TOA $(CH_2)_7$. This is due to the basicity of TOA that is stronger than that of TDA. Therefore, dyes can easily substitute the CH_2 group of TOA. As for Aliquat 336, Cl^- ions reacted with $Dyes^+$ to form a precipitate. The solid phase in the LLE process cannot be considered because it will affect the extraction phase. Hence, TOA was chosen as the most effective extractant for Orange 3R dye extraction. Figure 2 shows the chemical structure for TDA and TOA.

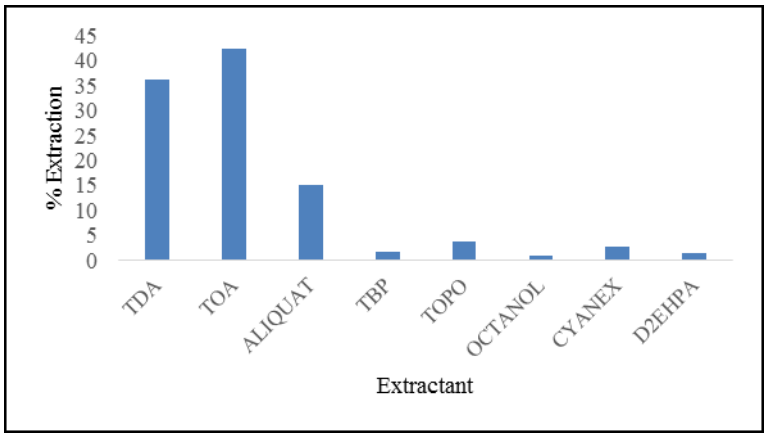
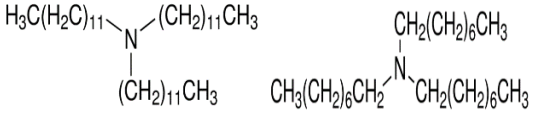


Figure 1. Effect of extractant type (experimental condition: concentration of each extractant = 0.1 M, shaker speed = 320 rpm, time = 1 hour, volume or organic = 10 mL, volume of dye = 10 mL)



(2a) TDA (2b) TOA

Figure 2. Chemical structure for TDA and TOA

Effect of extractant concentration

The extraction performance of different extractant concentrations was studied in the range of 0.04 to 0.2 M. Figure 3 (a and b) shows the effect of different concentrations of TDA and TOA on the extraction of Remazol Orange 3R in one hour. The results show that the percentage of extraction increased significantly as concentration increases. The maximum extraction percentages for both extractant were 51% at 0.16 M for TDA and 78% at 0.2 M for TOA.

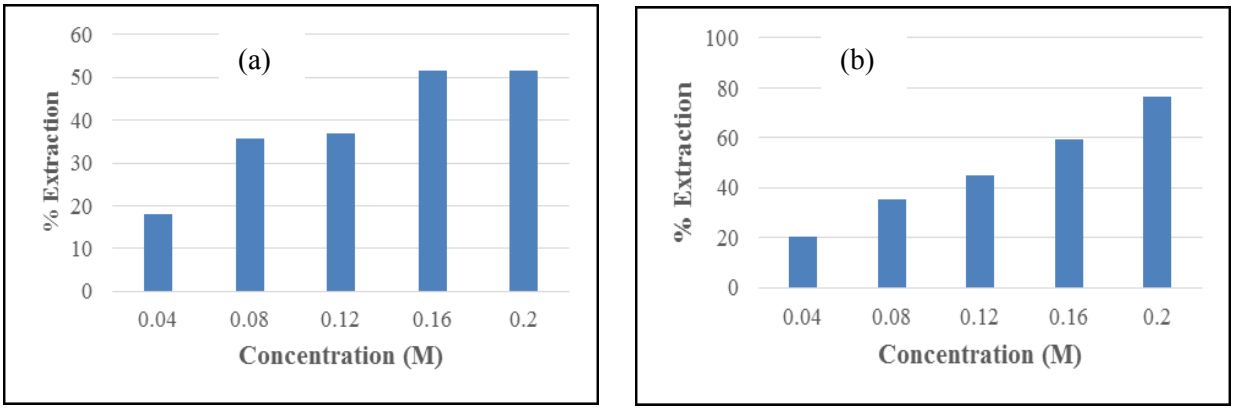


Figure 3. Effect of extractant concentration (experimental condition: extractant = (a) TDA and (b) TOA, shaker speed = 320 rpm, time = 1 hour, volume or organic = 10 mL, volume of dye= 10 mL)

According to Le Châtelier's principle, increasing the extractant concentration will increase the reaction rate by increasing the rate of collisions [20]. Based on the results obtained, the extraction percentage increased due to increasing extractant concentration. This condition created the potential gradient for both feed and organic phases which stimulated the complexation of dye-extractant [21]. TOA shows higher potential for the extraction of Remazol Orange 3R compared to TDA.

Selection of synergist extractant type

Synergistic extraction of Remazol Orange 3R was conducted in the binary extractant system by varying the synergist extractant (TDA and Aliquat 336 (basic), TBP and TOPO (neutral), and D2EHPA (acidic)) with TOA as the base extractant. The total volume of extractant and the concentration of base and synergist extractant were set at 10 mL and 0.1 M, respectively. As shown in Table 1, at 0.1 M mixture concentration, around 20% increment was obtained for TOA-TDA. Other combinations also showed the increasing of extraction performance.

Table 1. Effect of synergist extractant type

Extractant	% Extraction	Synergistic Coefficient
TDA	51	0.8
ALIQUAT	28	0.4
TBP	29	0.5
TOPO	9	0.1
D2EHPA	0	0

Experimental condition: base extractant = TOA, concentration of base and synergist extractant = 0.1 M, agitation speed = 320 rpm, time = 1 hour, volume of organic = 10 mL, volume ratio base: synergist = 1:1, volume of dye = 10 mL

In addition, the results also show that when 0.1 M TDA was used as a single extractant, 36% of dyes was extracted and when it was synergised with TOA, the extraction increased around 15%. As expected, there was a significant enhancement in dyes transport across the organic phase in the presence of a synergist extractant in the organic phase as compared to that without the synergist extractant. This shows that the combination of these two extractants have potential to be a synergistic system at the optimum ratio of its concentration.

Effect of synergist extractant concentration

Table 2 shows the extraction efficiency of TOA and synergist TDA with varied molar ratio on the extraction of Remazol Orange 3R. The experimental condition was set up at a total organic concentration of 0.2M, volume ratio of 1:1 and with TDA: TOA molar ratio of 0.04:0.16, 0.08:0.12, 0.12:0.08 and 0.16:0.04.

Table 2. Effect of synergist extractant concentration

Mole Percentage of TDA (%)	% Extraction	Synergistic Coefficient
20	51	0.63
40	50	0.73
60	49	0.85
80	69	1.7

Experimental condition, shaker speed = 320 rpm, time = 1 hour, volume of organic = 10 mL, volume of dye = 10 mL)

The results display that the percentage of dye extraction increased from 51 to 69% as the mole percentage of TDA increased from 20 to 80%. Ultimately, the synergist coefficient also increased, from 0.63 to 1.7. According to Guezzen and Didi [23], the synergistic coefficient should be greater than 1, then synergic effect will occur. If the synergistic coefficient is lower than 1, antagonistic effect will take place instead. In this experiment, only TDA at 80% mole percentage had a synergistic effect, while the rest experienced antagonistic effect. Compared to TDA as a single extractant, the percentage of extraction increased almost 20% with the presence of TOA. Therefore, it can be concluded that the TOA and TDA function as a synergist and base extractant, respectively.

Conclusion

Synergistic extractant for the extraction removal of Remazol Orange 3R was formulated using liquid-liquid extraction process. Base extractant, TDA and synergist extractant, TOA were chosen as a suitable combination of synergistic extractants. The extraction efficiency was improved from 51% to 69%. The results show that the synergistic extractant of TOA and TDA has potential to extract dyes under lower extraction time and concentration and would be usable in LM formulation for textile dye extraction.

Acknowledgements

The authors would like to acknowledge the Ministry of Higher Education (MOHE) and Universiti Teknologi Malaysia (RU Research Grant; GUP: Q.J130000.2546.18H33), Centre of Lipids Engineering and Applied Research (CLEAR), and Universiti Teknologi Malaysia (UTM) for facilities support to make this research possible.

References

1. Othman, N., Zailani, S. N. and Mili, N. (2011). Recovery of synthetic dye from simulated wastewater using emulsion liquid membrane process containing tri-dodecyl amine as a mobile carrier. *Journal of Hazardous Materials,* 198: 103-112.
2. Bahloul, L., Ismail, F. and Samar, M. E. H. (2013). Extraction and desextraction of a cationic dye using an emulsified liquid membrane in an aqueous solution. *Energy Procedia,* 36: 1232-1240.
3. Carmen, Z. and Daniela, S. (2010). Textile organic dyes – characteristics, polluting effects and separation/ elimination procedures from industrial effluents – a critical overview. Organic Pollutants Ten Years after the Stockholm Convention - Environmental and Analytical Update. pp. 55 – 86.
4. Zaharia, C., Suteu, D., Muresan, A., Muresan, R. and Popescu, A. (2009). Textile wastewater treatment by homogeneous oxidation with hydrogen peroxide. *Environmental Engineering and Management Journal*, 8(6): 1359-1369.
5. Daneshvar, N., Ayazloo, M., Khataee, A. R. and Pourhassan, M. (2007). Biological decolorization of dye solution containing malachite green by microalgae *Cosmarium sp. Bioresource Technology,* 98(6): 1176-1182.
6. Villegas, L. G. C., Mashhadi, N., Chen, M., Mukherjee, D., Taylor, K. E. and Biswas, N. (2016). A short review of techniques for phenol removal from wastewater. *Current Pollution Reports,* 2(3): 157-167.
7. Chakraborty, M., Bhattacharya, C. and Datta, S. (2010). Chapter 4 - emulsion liquid membranes: Definitions and classification, theories, module design, applications, new directions and perspectives A2 - Kislik, Vladimir S. BT - Liquid Membranes. Elsevier, Amsterdam: pp. 141–199.
8. Chanukya, B. S. and Rastogi, N. K. (2013). Extraction of alcohol from wine and color extracts using liquid emulsion membrane. *Separation and Purification Technology,* 105: 41-47.
9. Mokhtari, B. and Pourabdollah, K. (2013). Emulsion liquid membrane for selective extraction of bismuth from nitrate medium. *Korean Journal of Chemical Engineering,* 30(7): 1458-1465.
10. Othman, N., Ooi, Z. Y., Zailani, S.N., Zulkifli, E. Z. and Subramaniam, S. (2013). Extraction of Rhodamine 6G dye from liquid waste solution: Study on emulsion liquid membrane stability performance and recovery. *Journal of Separation Science and Technology,* 48(8): 1177-1183.
11. Othman, N., Mat, H. and Goto, M. (2005). Separation of silver from photographic wastes by emulsion liquid membrane system. *Journal of Membrane Science,* 282(1-2): 171-177.
12. Othman, N., Noah, N. F. M., Poh, K. W. and Yi, O. Z. (2016). High performance of chromium recovery from aqueous waste solution using mixture of palm-oil in emulsion liquid membrane. *Procedia Engineering,* 148(6): 765-773.
13. Sain, R. S., Ray, S. and Basu, S. (2014). Synergism in solvent extraction and solvent extraction kinetics. *Journal of Chemical, Biological and Physical Sciences,* 4(4): 3156-3181.

14. Wojciechowski, K., Kucharek, M. and Buffle, J. (2008). Mechanism of Cu(II) transport through permeation liquid membranes using azacrown ether and fatty acid as carrier. *Journal of Membrane Science,* 314(1-2): 152-162.
15. Darvishi, D., Haghshenas, D. F., Alamdari, E. K., Sadrnezhaad, S. K. and Halali, M. (2005). Synergistic effect of Cyanex 272 and Cyanex 302 on separation of cobalt and nickel by D2EHPA. *Hydrometallurgy,* 77(3-4): 227-238.
16. Biswas, S., Pathak, P. N. and Roy, S. B. (2012). Carrier facilitated transport of uranium across supported liquid membrane using dinonyl phenyl phosphoric acid and its mixture with neutral donors. *Desalination,* 290: 74-82.
17. Rajewski, J. and Religa, P. (2016). Synergistic extraction and separation of chromium(III) from acidic solution with a double-carrier supported liquid membrane. *Journal of Molecular Liquids,* 218:309-315.
18. Bruice, P. Y. (2006). Essential organic chemistry (1st ed). Pearson Prentice Hall, Upper Saddle River, New Jersey.
19. Solomons, T. W. G. and Fryhle, C. B. (2011). Organic chemistry (10th ed). John Wiley & Sons (Asia) Pte Ltd, Asia.
20. Homsirikamol, C., Sunsandee, N., Pancharoen, U. and Nootong, K. (2016). Synergistic extraction of amoxicillin from aqueous solution by using binary mixtures of Aliquat 336, D2EHPA and TBP. *Separation and Purification Technology,* 162: 30-26.
21. Kislik, V. S. (2010). Liquid membrane principles and applications in chemical separations and wastewater treatment (1st edition). Elsevier B.V, Linacre House, N.
22. Kim, J. S., Han, K. S., Kim, S. J., Kim, S. D., Lee, J. Y., Han, C. and Kumar, J. R. (2015). Synergistic extraction of uranium from korean black shale ore leach liquors using amine with phosphorous based extractant systems. *Journal of Radioanalytical and Nuclear Chemistry,* 307(2): 843-854.
23. Guezzen, B. and Didi, M. A. (2012). Removal of Zn(II) from aqueous acetate solution using di (2-ethylhexyl) phosphoric acid and tributylphosphate. *International Journal of Chemistry,* 4(3): 32-41.

Malaysian Journal of Analytical Sciences, Vol 22 No 4 (2018): 633 - 641
DOI: https://doi.org/10.17576/mjas-2018-2204-09

MALAYSIAN JOURNAL OF ANALYTICAL SCIENCES
Published by The Malaysian Analytical Sciences Society
ISSN 1394 - 2506

OLEIC ACID ENHANCEMENT IN USED FRYING PALM OIL VIA ENZYMATIC ACIDOLYSIS

(Peningkatan Kandungan Asid Oleik dalam Minyak Sawit Terpakai Melalui Kaedah Asidolisis Enzim)

Nor Athirah Zaharudin[1], Nurul Syafiqah binti Remzi[1], Roslina Rashid[1]*, Siti Marsilawati Mohamed Esivan[1], Ani Idris[1], Norasikin Othman[2]

[1]*Bioprocess and Polymer Engineering Department, School of Chemical and Energy, Faculty of Engineering*
[2]*Chemical Engineering Department, School of Chemical and Energy, Faculty of Engineering*
Universiti Teknologi Malaysia, 81310 Skudai, Johor, Malaysia

**Corresponding author: roslina@cheme.utm.my*

Received: 16 April 2017; Accepted: 7 March 2018

Abstract

The extensive amount of used frying palm oil (UFO) generated in Malaysia has caused serious environmental problems. Management of the waste faces a significant challenge especially on choosing the appropriate method by considering the possibilities of contaminating the environment. This study aims to add value to UFO by producing high oleic palm oil. Enzymatic acidolysis using lipase was employed to incorporate oleic acid in the UFO. This study also investigated the effect of enzymatic loading, reaction time and water content on the properties of modified UFO as to find the optimum condition for oleic acid incorporation. Oleic acid incorporation was quantified based on peroxide and iodine values. The optimum conditions for acidolysis process were obtained at enzyme loading of 30% (w/w), reaction time of 24 hours, and water content of 2% (w/w) with substrate mole ratio of 1:2 (UFO: oleic acid) and temperature of 50 °C. At optimum conditions, the modified used frying palm oil (MUFO) has peroxide and iodine values of 19.00 ± 0.99 meq/mg and 31.5 ± 0.42 mg/mg, respectively. After the acidolysis reaction, oleic acid concentration has increased from 27.00 ± 0.70% (v/v) to 62.34 ± 1.29% (v/v), demonstrating their feasibility as a substrate for structured lipid production.

Keywords: enzymatic acidolysis, used frying palm oil, oleic acid, high oleic palm oil, oleic acid incorporation

Abstrak

Lambakan minyak sawit terpakai (UFO) di Malaysia telah menyebabkan banyak masalah alam sekitar yang serius. Pengurusan sisa ini menempuh cabaran besar terutamanya dari espek pemilihan kaedah pelupusan yang mengambil kira kemungkinan-kemungkinan yang boleh mencemarkan alam sekitar. Kajian ini bertujuan menambah nilai UFO dengan menghasilkan minyak sawit tinggi asid oleik. Asidolsis enzimatik menggunakan lipase telah dijalankan untuk menggabungkan asid oleik ke dalam UFO. Kajian ini juga mengkaji kesan kepekatan enzim, masa tindak balas dan kandungan air pada sifat-sifat minyak sawit terubahsuai (MUFO) untuk mencari keadaan optimum peningkatan asid oleik. Peningkatan asid oleik dinilai berdasarkan nilai peroksida dan nilai iodin. Keadaan optimum untuk proses asidolisis yang diperoleh adalah pada kepekatan enzim 30% (w/w), masa tindak balas 24 jam dan kandungan air 2% (w/w) pada nisbah substrat 1:2 (UFO: asid oleik) serta suhu 50 °C. Pada keadaan optimum MUFO mempunyai nilai peroksida 19.00 ± 0.99 meq/mg dan nilai iodin 31.5 ± 0.42 mg/mg. Selepas tindak balas asiolisis enzim, kepekatan asid oleik telah meningkat dari 27.00 ± 0.70% (v/v) kepada 62.34 ± 1.29% (v/v), membuktikan UFO mampu menjadi substrat untuk penghasilan lipid berstruktur.

Kata kunci: asidolisis enzim, minyak terpakai, asid oleik, minyak sawit tinggi asid oleik, peningkatan asid oleik

Introduction

Structured lipids are defined as triacylglycerols (TAG) which have been chemically or enzymatically modified by altering the fatty acids composition and/or positional distribution in the glycerol backbone [1]. Products produced from TAG modification include cocoa butter equivalents, low-caloric fats, human milk substitutes, oil with enhanced essential fatty acids, margarines as well as plastic fats. The use of lipases as catalytic tools to alter fats and oils has attract many researches to produce wide range of structured lipids either for food or non-food purposes that offer excellent chemo-, region-, and stereo- selectivity properties.

The growth in human population has contributed to the extensive amount of used frying oil (UFO) generated and discharged to the environment. A greater quantity of UFO was produced from various sources including households, restaurants, catering establishment, as well as industrial kitchens. In Malaysia, approximately 50,000 tons of UFO was disposed without proper treatments [2]. Sebayang et al. [3] claimed that the total used-frying oil generated from fast food franchises all over Malaysia reached several thousand litres a day. It is believed that the actual amount of used-frying oil generated is far beyond the estimated value. Improper management of UFO will contribute to water pollution, marine life destruction, soil contamination, human health problems, septic and sewerage system failures, increase water and waste management cost and negative effects on the ecology. The availability of used-frying oil in Malaysia could provide a stable and constant feedstock for the demand on structured lipids production.

Production of structured lipid or tailor made fats provides an opportunity for cheap oils and fats to be utilized for the synthesis of high added value products. Utilization of UFO for biodiesel production is well explored. However, the utilization of used-frying oil still lacks of scientific investigation due to limited chemical and physical functionalities. Therefore, enhancement of used-frying oil into high quality oil offers an alternative route to a wide range of applications, thus reducing the environmental effect caused by its disposal problems.

Palm oil and palm olein have moderate contents of oleic acid [4, 5]. Vegetable oils with enhanced oleic acid content receive great attention for the use in a variety of industrial applications [6]. Oleic acid can be incorporated into oils to increase the oleic content of the mother oil, offer desirable properties related to both health benefits and stability characteristics [4]. According to Corbett [7], high oleic canola oil has twice the oxidative stability compared to regular canola oil. Besides stabilizing the oil, high oleic oils are also exploited in the preparation of snack food including potato chips frying as well as spraying to enhance mouth-feel and palatability. Not only restricted for food purposes, high oleic oils have been utilized for non-food applications. Vegetable-based high oleic oil can be further processed via transesterification to produce products such as polyurethane [8]. Ramli et al. [9] indicated that palm oil is among the vegetable source of monounsaturated fatty acids due to the abundant amount of palm oil available in Malaysia as compared to soybean and sunflower oils.

Acidolysis is a reaction where the fatty acyl group is exchanged through a combination of hydrolysis of a donor ester with esterification of released alcohol moiety with other free fatty acids [4]. Hypothetically, this reaction produces the mixtures of triacyglyceride (TAG) and targeted structured TAGs as well as fatty acids. Enzymatic acidolysis offers an easy, specific, fast, and cost friendly method for fatty acids enrichment of oils compared to time, energy and cost consuming of genetic engineering. Utilization of UFO provides an alternative method for cheap oil to be exploited for the production of high value added products where the cost of raw materials is much lower. Raw materials cost and the availability of fresh vegetable oil feedstocks are always major concern. In addition, most of the studies conducted on the enhancement of oil are using fresh cooking oil. The high cost of fresh vegetable oils could increase the total production cost up to 1.5% [10]. However, the price of UFO is 2 to 3 times cheaper than fresh vegetable oil. Hence, the production cost can be significantly reduced.

Rafael and Roberto [11] have emphasized the advantages of acidolysis process including the high positional selectivity and specificity, low cost and fewer side products, initiated by the inevitable existence of acyl migration which can be minimized by controlling the reaction conditions such as enzyme load, water content, substrate ratio, reaction temperature, and reaction time. Therefore, enzymatic acidolysis has been preferred as a suitable method to enrich vegetable oils with regard to the modification of oils rich in high value polyunsaturated fatty acids such as linoleic, oleic, arachidonic, eicosapentaenoic, and docosahexaenoic acids. The use of lipase for fats and oils

enhancement offers some benefits over conventional organic catalysts; increases the product purity, operates at mild reaction conditions, high substrate selectivity, and less or no unwanted side products [12]. *Candida rugosa* lipase is a non-specific lipase which catalyzes lipid at random position and successfully applied on the synthesis of oil hydrolysis, biodiesel, fatty acid ester, wax ester as well as monoesters and diesters [13, 14].

In this present study, effects of enzymatic loading, reaction time and water content on oleic acid incorporation degree were investigated. Oleic acid incorporation in UFO was quantified based on peroxide and iodine values. Oleic acid concentration in MUFO, fresh frying oil (FFO) and used frying oil (UFO) were compared.

Materials and Methods

Materials

Used frying palm oil (UFO) was obtained from the university cafeteria. Lipase from *Candida rugosa* was used as the catalysts and was immobilized on immobead 150. Pure oleic acid was purchased from Qrec Sdn. Bhd., Malaysia. Solvents including *n*-hexane, cyclohexane, acetone, and acetonitrile were purchased from a local supplier as well as other chemicals (phenolphthalein, sodium phosphate). All chemicals are analytical grade and were used without further purification.

Pre-treatment

Sample pre-treatment procedures were conducted based on the method proposed by Przybylski et al. [15], Pazouki et al. [16], and Hasnisa and Jumat [17]. UFO contains lot of impurities caused by continuous cooking and oxidation process. Therefore, pre-treatment was conducted to eliminate the indiscerptible impurities. Firstly, 50 ml of UFO was filtered by applying a reduced pressure system using a Whatman 42 filter paper [16]. The filtered UFO was stirred and heated to 100 °C for 15 minutes. Heating process was engaged as to eliminate excess water. Then, peroxide, iodine, and acid values were recorded.

Determination of peroxide value

Firstly, 10 ml of UFO and 50 ml of glacial acetic acid-isooctane mixture (3:2 v/v) were added into a 250 ml conical flask and stirred at low speed. Then, 1 ml of potassium iodide was added and continuously stirred at low speed for 1 minute. 100 ml of distilled water and 0.1 g thyodene indicator were added into the mixture. The mixture was mixed vigorously and immediately titrated with 0.1 N sodium thiosulfate (colour indication: from purple to a slight yellow or colourless endpoint). The blank determination was determined under the same condition. The peroxide value was calculated based on formula presented in equation 1 [18]:

$$POV = \frac{(V_1 - V_0) \times N \times 1000 \times T}{V_S \times 2} \quad (1)$$

where, *POV* is the peroxide value of UFO (mmol/L), V_1 is the sodium thiosulfate volume needed to neutralize UFO (ml), V_0 is the sodium thiosulfate volume needed to neutralize the blank solution (ml), *N* is the sodium thiosulfate normality (0.1 N), T is titre of sodium thiosulfate, and V_S is the volume portion of substance (ml).

Determination of iodine value

Approximately 0.1 g of UFO and 20 ml of carbon tetrachloride (CCl_3) were inserted and sealed in to 250 ml conical flask. The mixture was dissolved by applying high agitation speed. Then, 25 ml of Hanus solution was added and stirred for one minute. The mixture was sealed and leaved in a dark room at 20 ºC for 30 minutes. After that, 10 ml of 15% potassium iodide and 100 ml of water were added, sealed and shaken for 30 seconds. Lastly, the sample mixture was titrated with 0.1 N sodium thiosulfate in order to obtain the iodine value. The formula for calculating the iodine value is presented by equation 2 [19]:

$$IV = \frac{(V_1 - V_0) \times N \times 12.69}{W} \quad (2)$$

where; *IV* is the iodine value of UFO (I_2/g), V_1 is the sodium thiosulfate volume needed to neutralize UFO (ml), V_0 is the sodium thiosulfate volume needed to neutralize the blank solution (ml), *N* is the sodium thiosulfate normality (0.1 N), and *W* is the weight of UFO (g).

Determination of acid value

The acid value was determined by inserting 100 ml of neutralized ethanol-toluene (1:1 v/v) mixture and 4 g of treated UFO into a round bottom flask. The mixture was titrated with standard potassium hydroxide (KOH) in the presence of phenolphthalein (end point: pink colour). The acid value was calculated using the formula shown in equation 3 [19]:

$$AV = \frac{MW \times N \times V_1}{W} \quad (3)$$

where, AV is the acid value of UFO (mg KOH/g), MW is the molecular weight of KOH (56.1 g/mol), V_1 is KOH volume used to neutralize the sample solution (ml), N is the KOH normality (1.0 N), and W is the weight of UFO (g).

Acidolysis of UFO

Acidolysis of UFO with oleic acid and determination on effect of operating conditions upon oleic 1acid incorporation degree were conducted according to the method by Zou et al. [20], Siew and Saw [21], and Hasnisa and Jumat [17]. A mixture of treated UFO and oleic acid (1:2 mol/mol) were added to *n*-hexane (2 ml) followed by water (1 % w/w) and lipase (10 % w/w). The mixture was incubated at temperature of 50 °C, agitation speed of 250 rpm for 24 hours. The sample was titrated as to determine the peroxide and iodine value. Effect of operating conditions was determined by varying enzyme load (0-30% w/w), reaction time (0-36 hours), and water content (0-3% w/w). Enzymatic acidolysis using fresh frying palm oil was also conducted using the same optimum values gained in the acidolysis of UFO.

Separation of triacylglycerols

The separation of triacylglycerol was carried out based on method of Hasnisa and Jumat [17] and Senanayake and Shahidi [22]. Lipase was filtered from the reacted sample. The filtered sample was added to a mixture of acetone/ethanol (1:1 v/v) in 50 ml conical flask. Phenolphthalein indicator was added to the reaction mixture and titrated with 0.5 N NaOH (end point: pink). The mixture was added with 25 ml of hexane and transferred to a separatory funnel. The lower layer was separated and discarded. The upper layer (hexane and TAG) was passed through a bed of anhydrous sodium sulphate. The TAG fractionation was completed by hexane removal at 45 °C using a rotary evaporator (IKA RV 8) for 15 minutes.

GC Analysis

Determination of oleic acid concentration was conducted based on the method done by Hasnisa and Jumat [17]. Oleic acid content in the sample was determined by gas chromatography with flame ionization detector (Perkin Elmer XL-GC). One mL of the sample was diluted in 40 ml of isopropanol and filtered using a microfilter of 0.45 micropores before injecting into the GC-FID column. Then, 1 µl of diluted sample was injected into the GC-FID column at a flow rate of 1 µl/min. The TAG peaks were identified according to reference standards and were compared with fresh-frying oil, which was used as a benchmark. Quantification of oleic acid content was done based on the percentage of area.

Results and Discussion

Properties of fresh frying oil and used frying oil

Peroxide value (PV) indicates the quality of oil [9]. Peroxide value measures the oxidative and rancidity of the oil. Generally peroxide value increases with frying time [23]. The result shows that PV for UFO (38.8 ± 1.56 meq/kg) is higher than FFO (3.8 ± 1.27 meq/kg). UFO became rancid due to oxidation. Fan et al. [24] reported that the peroxide value of palm olein after 5 days of frying has increased from 3.40 to 34.55 meq/kg. The peroxide concentration, usually expressed as PV, is measured by oxidation or rancidity in its early stages and should be not more than 10 (milliequivalents peroxide/1000g sample) in cooking oil. It was observed that the measured iodine value (IV) value for FFO and UFO are 35.15 ± 1.06 mg/mg and 33.2 ± 1.41 mg/mg respectively. Lower IV indicates low degree of unsaturation which means higher oxidation rate. The result shows that UFO has similar stability as compared to FFO. Slightly lower unsaturation in UFO is due to oxidation and heating process. Talpur et al. [25] reported the decreasing trend of iodine value is caused by the increase in frying cycle. Iodine value

reflects the degree of unsaturation of the oil. As the oil undergoes continuous heating, double bond raptures will lead to the increase in saturation of fatty acids [26]. In other words, high iodine value is preferred. Acid number or acid value (AV) of an oil is corresponds to the ester amount present in the oil which indicates the quantity of free fatty acids. It was observed that, measured AV for FFO and UFO are 3.9 ± 0.99 mg KOH/g and 35.06 ± 1.47 mg KOH/g, respectively. UFO has a higher AV compared to fresh-frying oil. Higher AV for UFO compared to FFO is due to the increase in fatty acids content during frying process [27]. Aladedunye and Przybyliski [28] stated that the change in free fatty acids content is due to the double bond rapture during the frying process.

Effect of enzyme load

Increase in enzyme load will contribute towards the positive effect on fatty acids incorporation into targeted the TAG [17]. Commonly, the incorporation degree increases with enzyme loads until it reaches the optimum load. However further increase afterwards has no significant effect towards the incorporation degree. Zou et al. [20] indicated this trend is possibly due to the saturation of enzyme at the interface and aqueous phase. Hasnisa and Jumat [17] specified that at higher enzyme load the decrease in incorporation degree is significant due to insufficient amount of water in the reaction mixture. As the amount of enzyme increased the amount of water remains constant.

Result shows that the peroxide value decreased as the enzyme load increased. A low amount of peroxide value indicates a high degree of unsaturation that causes autoxidation (oxidative rancidity) [29]. Kaleem et al [30] stated that the double bond in fats and oils are responsible for autoxidation. Hence, oils with higher degree of unsaturation are extremely prone to autoxidation. However a different trend was observed in iodine value. The enzyme loads increased with iodine value. High amount of iodine value and low peroxide value were found at 30% of enzyme load. This indicates that more C=C bonds are present in the fats and oils. The increase in iodine value shows that oleic acid has successfully incorporated in triacylglycerol (TAG) [17]. Oleic acid in palm oil is predominantly located at sn-2 position in TAG [31]. Sufficient amount of enzyme promotes the incorporation of oleic acid at *sn-1, 3* positions in TAG. In addition, acyl migration from *sn-2* position of TAG should be considered as *Candida rugosa* lipase which is a non-stereoselective lipase and randomly catalyzed oleic acid at any position of TAG. Enzyme load of 30% (w/w) was selected as the optimum enzyme load with the highest iodine value of 16.40 ± 2.26 mg/mg and lower peroxide value of 6.40 ± 2.40 meq/mg. Effects of enzyme load towards peroxide and iodine values are presented in Figure 1.

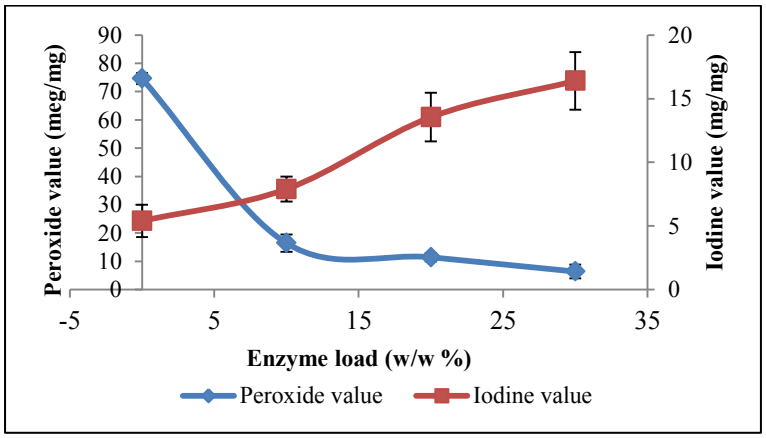


Figure 1. Effect of enzyme load on peroxide and iodine values. Conditions: substrate mol ratio (UFO: oleic acid) 2:1, 2 ml *n*-hexane, 1% (w/w) water, at constant temperature of 50 °C, and 250 rpm agitation speed for 24 hours

Effect of reaction time

Savaghebi et al. [32] indicated the effect of reaction time is crucial in order to determine the optimal rate of reaction as well as reduce the process cost. The incorporation degree increases with the reaction time [33]. In addition a

longer reaction time will result in the increase of acyl group migration especially in laboratory-scale continuous reactor [11]. A study conducted by Hasnisa and Jumat [17] showed incorporation of PUFA increased with reaction time, but decreased after 48 hours. Zhao et al. [34] obtained the highest incorporation of capric acid at 24 hours. A similar result was also obtained by Hamam and Shahidi [35].

The peroxide value of UFO is increased from 0 to 12 hour and slightly decreased until 36 hours. The results also showed that iodine value increased with reaction time. The increase in iodine value can be explained by the successful incorporation of oleic acid. However, the peroxide value is slightly decreased at reaction time of 24 hours. The decrease of peroxide value is due to the oxidation process during storage. At 24 hours, the iodine value shows the highest iodine value which indicated the highest amount of unsaturated fatty acid. Therefore, the optimum time for UFO acidolysis reaction is 24 hours with the highest iodine value (12.00 ± 1.27 mg/mg) and low peroxide (10.70 ± 2.55 meq/mg) value. Effect of reaction time towards peroxide and iodine values is presented in Figure 2.

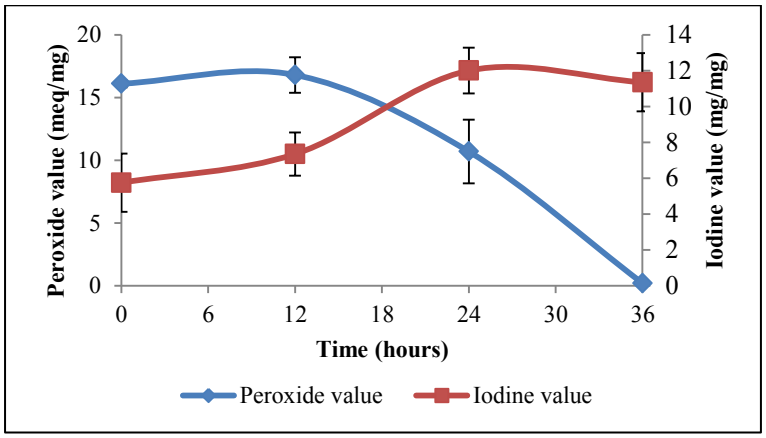


Figure 2. Effect of reaction time on peroxide and iodine values. Conditions: substrate mole ratio (UFO: oleic acid) 2:1, 30% (w/w) enzyme load, 2 ml *n*-hexane, 1% (w/w) water, 50 °C, and 250 rpm

Effect of water content

Lipase is generally activated by a small amount of water where it is vital for a first breaking of TAG [11]. Hence, water content in any quantity cannot be neglected. An optimum level of water in the reaction is essential to maintain the enzyme activity [17]. However, too much water will make the lipase unstable and promotes adverse impact on lipase activity, leading to an increase in amount of by-products. Conversely, a low water content will lead to the decrease in enzyme activity. Senanayake and Shahidi [22] reported that inadequate amount of added water may initiate the enzyme to be inactive as water is required to maintain the three-dimensional structure of enzyme.

An increase in water content was expected to have a positive effect in iodine value and negative effect in peroxide value. Both iodine and peroxide values indicated that as the water content increased from 0-2%, the iodine value is increased accordingly while the peroxide value decreased from 0-3%. The results showed that the higher the iodine value the higher the incorporation of oleic acid in UFO. However, at 3% of water content, there was a slight decrease of iodine value followed by the decrease of oleic acid incorporation in UFO. Excessive amount of water however resulted in poor incorporation of oleic acid in UFO. High amount of water will promote hydrolysis in the oil instead of acidolysis [22]. The optimum water content for UFO acidolysis was obtained at 2% (w/w) water content with 31.50 ± 0.42 mg/mg iodine value and 19.00 ± 0.99 meq/mg peroxide value. Effect of water content towards peroxide and iodine values is presented in Figure 3.

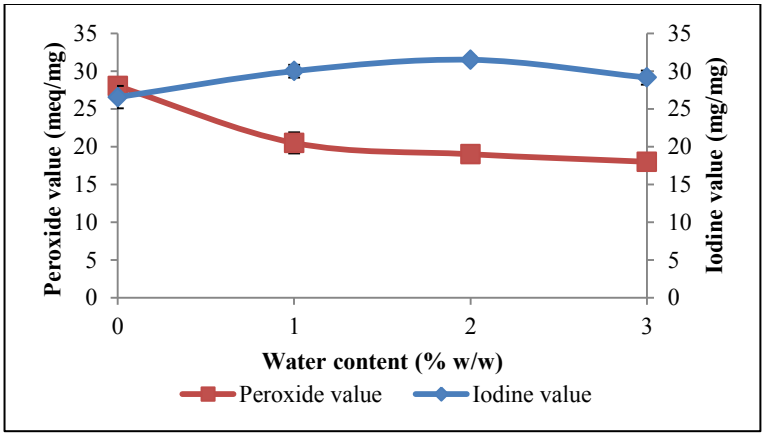


Figure 3. Effect of water content on peroxide and iodine values. Conditions: substrate mole ratio (UFO: oleic acid) 2:1, 30% (w/w) enzyme load, 2 ml *n*-hexane, 24 hours, 50 °C, and 250 rpm

GC analysis: Oleic acid content

Acidolysis of fresh frying oil (FFO) shows an increase in oleic acid concentration from 21.10 ± 1.40% (v/v) to 36.56 ± 1.29% (v/v). However, acidolysis of UFO shows a higher incorporation of oleic acid. The oleic acid content has increased from 27.00 ± 0.70% (v/v) to 62.34 ± 1.29% (v/v). The increase of the oleic acid concentration in both UFO and FFO is shown in Figure 4. Enzymes can improve the incorporation of fatty acids [11]. It shows that the enzyme load affects the amount of fatty acid concentration before and after acidolysis. Increase of enzyme load accelerated the reaction rate and improved the incorporation of acyl donors under given conditions [36]. Páez et al. [37] stated that the enzyme requires a certain level of water in the reaction medium to maintain a layer of water molecules around the enzyme and to maintain the enzyme activity for initiating the reaction. It showed that the enzyme plays an important role to lead off the reaction in order to achieve a high content of fatty acid.

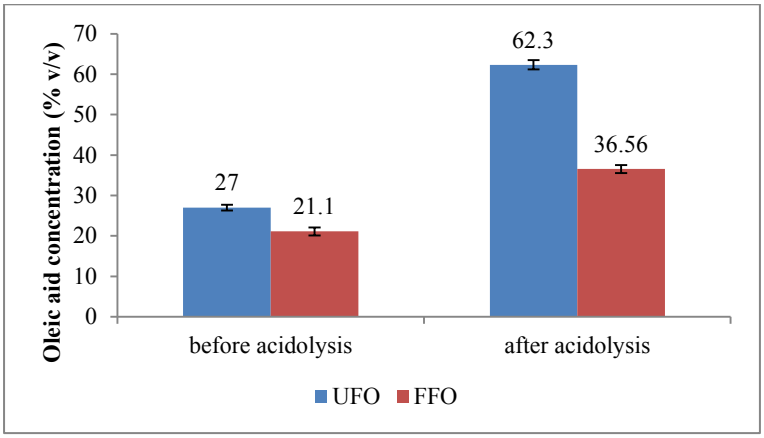


Figure 4. Oleic acid concentrations before and after acidolysis

Conclusion

In this study, UFO has a higher peroxide and acid values with lower iodine value when compared to FFO. The optimum conditions for the acidolysis process were obtained at enzyme loading of 30% (w/w), reaction time of 24 hours and water content of 2% (w/w). At the optimum conditions, the modified UFO has a peroxide value of 19 ± 0.99 meq/mg and iodine value of 31.5 ± 0.42 mg/mg. The modified UFO has higher oleic acid content, 62.34 ±

1.29% (v/v) compared to UFO before acidolysis reaction, 27.00 ± 0.70% (v/v). It can be concluded that oleic acid has been successfully incorporated into UFO.

Acknowledgement

This research is fully supported by RUG grant, Q.J130000.2546.12H37. The authors fully acknowledged the Ministry of Higher Education (MOHE) and Universiti Teknologi Malaysia for the approved fund which makes this important research viable and effective

References

1. Esteban, L., Jiménez, M. J., Hita, E., González, P. A., Martín, L. and Robles, A. (2011). Production of structured triacylglycerols rich in palmitic acid at sn-2 position and oleic acid at sn-1,3 positions as human milk fat substitutes by enzymatic acidolysis. *Biochemical Engineering Journal,* 54(1): 62-69.
2. Nurdin, S., Yunus, R. M., Nour, A. H., Gimbun, J., Azman, N. A. N. and Sivaguru, M. V. (2016). Restoration of waste cooking oil (WCO) using alkaline hydrolysis technique (ALHT) for future biodetergent. *ARPN Journal of Engineering and Applied Sciences,* 11: 6405-6410.
3. Sebayang, D., Agustian, E. and Praptijanto, A. (2010). Transesterification of biodiesel from waste cooking oil using ultrasonic technique. *International Conference on Environment*. 13-15 December. Penang, Malaysia: pp. 1 – 9.
4. Ferreira-Dias, S., Sandoval, G., Plou, F. and Valero, F. (2013). The potential use of lipases in the production of fatty acid derivatives for the food and nutraceutical industries. *Journal of Biotechnology,* 16(3): 1-36.
5. Xu, X. (2000). Production of specific structured-triacylglycerols by lipase-catalysed reactions: A review. *European Journal of Lipid Science and Technology,* 102(4): 287-303.
6. Kinney, A. J. and Clemente, T. (2005). Modifying soybean oil for enhanced performance in biodiesel blends. *Fuel Processing Technology,* 86(10): 1137-1147.
7. Corbett, P. (2003). It is time for an oil change: Opportunities for high-oleic vegetables oils. *Inform,* 14(8): 480-481.
8. Arniza, M. Z., Seng, S. H., Idris, Z., Shoot, K. Y., Abu Hassan, H, Din, A. K. and Yuen, M. C. (2015). Synthesis of transesterified palm olein-based polyol and rigid polyurethanes from this polyol. *Journal of American Oil Chemistry Society,* 92(2): 243-255.
9. Ramli, M. R., Siew W. L., Cheah, K. Y., Idris, N. A. and Mat Sahri, M. (2008). Physico-chemical properties and performance of high oleic and palm-based shortenings. *Journal of Oleo Science,* 57(11): 605-612.
10. Phan, A. N. and Phan, T. M. (2008). Biodiesel production from waste cooking oils. *Fuel,* 87: 3490-3496.
11. Rafael, C. R. and Roberto, F. L. (2010). Lipase from *Rhizomucor miehei* as a biocatalyst in fats and oils modifications. *Journal of Molecular Catalysis B-Enzymatic,* 66(1-2): 15-32.
12. Yigitoglu, M. and Temocin, Z. (2010). Immobilization of *C. rugosa* lipase on glutaraldehyde-activated polyester fiber and its application for hydrolysis of some vegetable oils. *Journal of Molecular Catalysis B: Enzymatic,* 66(1-2): 130-135.
13. Zhang, X., Niea,K., Zheng, Y., Wang,F., Deng, L. and Tan, T. (2016). Lipase Candida Sp. 99-125Coupled With-Cyclodextrin as Additive Synthesized the Human Milk Fat Substitutes. *Journal of Molecular Catalysis B: Enzymatic,* 125: 1-5.
14. BezbradicA, D., Karalazi, I., Ognjanovi, N., Mijin, D., Siler-Marinkovi, S. and Knezevic, Z. (2006). Studies on specificity of candida rugosa lipase catalyzed esterification reaction in organic media. *Journal of Serbian Chemical Society*, 71(1): 31-41.
15. Przybylski, R., Gruczynska, E. and Aladedunye, F. (2013). Performance of regular and modified canola and soybean oils in rotational frying. *Journal of American Oil Chemists' Society,* 90: 1271-1280.
16. Pazouki, M., Zamani, F., Zamzamian, A. H., Fahar, M. and Najafpour, G. (2010). Esterification of free fatty acids by *Rhizopus oryzae* as cell-catalysed from used cooking oil for biodiesel production. *World Applied Sciences Journal,* 8(6): 719-724.
17. Hasnisa, H. and Jumat, S. (2012). Enzymatic acidolysis of palm olein with PUFA to improve linoleic and α-linolenic acids ratio. *Journal of Tropical Agriculture and Food Science,* 40(1): 71-79.
18. IFRA. (2011). Analytical Method: Determination of the Peroxide Value. Access online www.ifraorg.org/view_document.aspx?docId=22291.

19. AOCS. (1989). Official methods and recommended practices of the American oil chemists' society. Ca 5a–40, Cd 1b–87 and Cd 8–53.4. Champaign IL, American Oil Chemists' Society.
20. Zou, X. G., Hu, J. N., Zhao, M. L., Zhu, X. M., Li, H. Y., Liu, X. R., Liu, R. and Deng, Z. Y. (2014). Lipozyme RM IM-catalysed acidolysis of cinnamomum camphora seed oil with oleic acid to produce human milk fat substitutes enriched in medium-chain fatty acids. *Journal of Agricultural and Food Chemistry,* 62(43): 10594-10603.
21. Siew, W. L. and Saw, M. H. (2009). High oleic enhancement of palm olein via enzymatic interesterification. *Journal of Oleo Science,* 58(11): 549-555.
22. Senanayake, S. P. J. and Shahidi, F. (2002). Structured lipids via lipase-catalysed incorporation of eicosapentaenoic acid into borage (*Borago officinalis* L.) and evening primrose (*Oenothera biennis* L.) oils. *Journal of Agricultural and Food Chemistry,* 50(3): 477-483.
23. Karakaya, S. and Simsek, S. (2011). Changes in total polar compounds, peroxide value, total phenols, and antioxidant activity of various oils used in deep fat frying. *Journal of American Oil Chemists' Society,* 88(9): 1361-1366.
24. Fan, H. Y., Sharifudin, M. S., Hasmadi, M. and Chew, H. M. (2013). Frying stability of rice bran oil and palm olein. *International Food Research Journal,* 20(1): 403-407.
25. Talpur, M. Y., Sherazi, S. T. H., Mahesar, S. A. and Kandhro, A. A. (2009). Effects of chicken frying on soybean, sunflower, and canola oils. *Pakistan Journal of Analytical and Environmental Chemistry,* 10(1-2): 59-66.
26. Kulkarni, M. G. and Dalai, A. K. (2006). Waste cooking oil-an economical source for biodiesel: A review. *Indian Journal of Chemical Engineering,* 45(9): 2901-2913.
27. Cvengros, J. and Cvengrosova, Z. (2004). Used frying oils and fats and their utilization in the production of methyl esters of higher fatty acids. *Biomass and Bioenergy,* 27(2): 173-181.
28. Aladedunye F. A. and Przybylski, R. (2009). Protecting oil during frying: A comparative study. *European Journal of Lipid Science and Technology,* 111(9): 893-901.
29. Majidi, M. I. H. A. L and Bader, A. T. (2015). Sciences physicochemical characteristics of some imported edible vegetable oils in Iraq. *Research Journal of Pharmaceutical, Biological and Chemical,* 6(5): 488-494.
30. Kaleem, A., Aziz, S., Iqtedar, M., Abdullah, R., Aftab, M., Rashid, F., Shakoori, F. R. and Naz, S. (2015). Investigating changes and effect of peroxide values in cooking oils subject to light and heat. *FUUAST Journal of Biology,* 5(2): 191-196.
31. Choo, Y. M. and Nesaretnam, K. (2014). Research advancement in palm oil nutrition. *European Journal of Lipid Scientific Technology,* 116(10): 1301-1315.
32. Savaghebi, D., Safari, M., Rezaei, K., Ashtari, P. and Farmani, J. (2012). Structured lipids produced through lipase-catalysed acidolysis of canola oil. *Journal of Agricultural Science Technology,* 14(6): 1297-1310.
33. Kocak, D., Keskin, H., Fadiloglu, S., Kowalski, B. and Gogus, F. (2011). Characterization of terebinth fruit oil and optimization of acidolysis reaction with caprylic and stearic acids. *Journal of American Oil Chemists' Society,* 88(10): 1531-1538.
34. Zhao, H., Lu, Z., Bie, X., Lu, F. and Liu, Z. (2007). Lipase catalysed acidolysis of lard with capric acid in organic solvent. *Journal of Food Engineering,* 78(1): 41-46.
35. Hamam, F. and Shahidi, F. (2004). Enzymatic acidolysis of an arachidonic acid single-cell oil with capric acid. *Journal of the American Oil Chemists' Society,* 81(9): 887-892.
36. Çiftçi, O.N., Fadiloğlu, S., Kowalski, B. and Göğüş, F. (2008). Synthesis of cocoa butter triacylglycerols using a model acidolysis system. *Grasas y Aceites,* 59(4): 316-320.
37. Páez, B. C., Medina, A. R., Rubio, F. C., Morenoa, P. G. and Grima, E. M. (2003). Modelling the effect of free water on enzyme activity in immobilized lipase-catalysed reactions in organic solvents. *Enzyme and Microbial Technology,* 33(6): 845-853.

Malaysian Journal of Analytical Sciences, Vol 22 No 4 (2018): 642 - 647
DOI: https://doi.org/10.17576/mjas-2018-2204-10

MALAYSIAN JOURNAL OF ANALYTICAL SCIENCES
Published by The Malaysian Analytical Sciences Society
ISSN 1394 - 2506

ADSORBENTS FROM THE BY-PRODUCT OF PALM OIL REFINERY FOR METHYLENE BLUE REMOVAL

(Penjerap daripada Produk Sampingan Penapisan Minyak Sawit untuk Penyingkiran Metilena Biru)

Hamzat Bashir Aderemi[1, 2], Muhammad Abbas Ahmad Zaini[1, 3]*, Noor Shawal Nasri[3, 4]

[1]*Centre of Lipids Engineering & Applied Research, Ibnu-Sina Institute for Scientific & Industrial Research*
Universiti Teknologi Malaysia, 81310 UTM Johor Bahru, Johor, Malaysia
[2]*Chemical Engineering Department,*
Kaduna Polytechnic, Kaduna, Nigeria
[3]*Faculty of Chemical & Energy Engineering*
[4]*UTM-MPRC Institute for Oil & Gas*
Universiti Teknologi Malaysia, 81310 UTM Johor Bahru, Johor, Malaysia

**Corresponding author: abbas@cheme.utm.my*

Received: 16 April 2017; Accepted: 7 March 2018

Abstract

The present work was aimed at evaluating the removal of methylene blue by palm fatty acid distillate-based adsorbents. The adsorbents at different weight ratios of palm fatty acid distillate (PFAD) to palm kernel shell (PKS) were prepared at 600 °C for 2 hours. Results show that the yield of adsorbent upon heat treatment decreased with increasing weight ratio, with yield as low as 0.53% was recorded by adsorbent derived by using only PFAD. The methylene blue adsorption data show a promising performance of PFAD-based adsorbents as compared to that of PKS-adsorbent (char) with q_e = 7.6 mg/g at C_o = 20.8 mg/L. To conclude, PFAD is a potential candidate of dye adsorbent.

Keyword: adsorbent, methylene blue, palm fatty acid distillate, palm kernel shell

Abstrak

Tujuan kajian ini adalah untuk menilai penyingkiran metilena biru oleh penjerap berasaskan distilat asid lemak sawit. Penjerap pada nisbah berat distilat asid lemak sawit (PFAD) kepada isirong sawit (PKS) disediakan pada 600 °C selama 2 jam. Keputusan menunjukkan bahawa hasil penjerap setelah rawatan haba berkurang dengan peningkatan nisbah berat, dengan hasil serendah 0.53% direkodkan oleh penjerap terbitan PFAD sahaja. Data penjerapan metilena biru menunjukkan prestasi menjanjikan oleh penjerap berasaskan PFAD berbanding penjerap berasaskan PKS (arang) dengan q_e = 7.6 mg/g pada C_o = 20.8 mg/L. Kesimpulannya, PFAD ialah calon berpotensi sebagai penjerap pencelup.

Kata kunci: penjerap, metilena biru, distilat asid lemak sawit, isirong sawit

Introduction

There has been an increasing interest to valorize industrial waste into value added commodity [1]. Waste that is high in carbon content is a promising candidate of carbonaceous char that can be further processed into porous adsorbent for wide range of applications in water and wastewater treatment. A promising candidate under this category is palm fatty acid distillate (PFAD) [2]. PFAD is a by-product of crude palm oil refining process. At room temperature it is in light brown, semi-solid form, and melts as brown liquid upon heating. PFAD comprises mainly of free fatty acid

(about 80%), in which palmitic acid and oleic acid are the major components, while the remainders are triglycerides, partial triglycerides and unsaponifiable matters [3].

PFAD is cheap and abundantly available [4]. It is generally used in low-grade soap, animal feed, and other oleo-chemical products such as candles, cosmetics and toiletries. Because of its substandard quality, PFAD is not usually blended and capitalized in high-end products. Hence, there is a need to exploit the inherent benefits associated with this by-product. Therefore, the present work was aimed at evaluating this material as adsorbent precursor for methylene blue adsorption.

Materials and Methods

Palm fatty acid distillate (PFAD) was supplied by IFFCO (M) Sdn Bhd. Palm kernel shell (PKS) was obtained from a local palm oil mill. PFAD and PKS were used as received. Methylene blue dye powder ($C_{16}H_{18}ClN_3S$, molecular weight = 319.85 g/mol, assay 98.5%) was supplied by HmbG Chemicals. The chemical structure of methylene blue is shown in Figure 1.

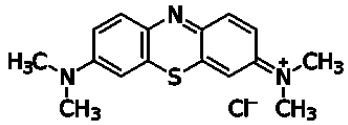


Figure 1. Molecular structure methylene blue

PFAD was mixed with PKS at different weight ratios (PFAD: PKS) of 2, 4, 5, 10 and 20. Then, the solid mixture was heated in furnace at 600 °C for 2 hours. The process is also known as carbonization. The same procedure was repeated for individual PFAD (0.5 hour) and PKS, respectively. All resultant adsorbents were used for methylene blue adsorption.

The working solution of desired methylene blue concentrations was prepared by diluting the stock solution. Thirty milligrams of solid adsorbent was brought into intimate contact with 30 mL of methylene blue solution of different concentrations. The solution mixture was allowed to equilibrate for 72 hours. After that, the residual concentration was measured using visible spectrophotometer (Halo Vis-10) at a wavelength of 615 nm. The adsorption capacity, q_e (mg/g) was calculated using equation 1:

$$q_e = (C_o - C_e) \times V/m \quad (1)$$

where C_o and C_e (mg/L) are the initial and equilibrium concentrations, respectively, V (L) is the volume of methylene blue solution, and m (g) is the weight of solid adsorbent.

Results and Discussion

Table 1 shows the yield of adsorbents derived from PFAD and PKS. The yield decreased from 10.6% to 0.53% with increasing PFAD-to-PKS ratio. It implies the oxidative effect of PFAD towards PKS, whereby PFAD in the presence of PKS could act as the oxidizing agent. The higher the amount of PFAD the more aggressive the oxidation process, consequently, the greater the weight loss. The role of PFAD is analogous to KOH, a commonly used activating/oxidizing agent for activated carbon preparation [5]. In the absence of PKS, PFAD displays a lower yield of 0.53% compared to 30% for only PKS (char) after the heat treatment. This signifies the feasibility of converting semi-solid PFAD into carbon-rich solid material and a promising adsorbent candidate although the yield is comparatively small. PKS alone exhibits a 30% yield. In the absence of activating agent, the carbonization of PKS at 600 °C normally produces rudimentary and partially clogged pores with undeveloped texture [6,7].

Table 1. Yield of adsorbents derived from PFAD and PKS

Sample ID	PFAD-to-PKS ratio	Yield (%)
C_1[a]	Only PFAD	0.53
C_2	2	10.6
C_3	4	6.18
C_4	5	5.34
C_5	10	3.0
C_6	20	2.0
C_7	Only PKS	30

[a] Pyrolysis at 600 °C for 0.5 hour

Figure 2 shows the removal of methylene blue by PKS- and PFD-derived adsorbents. All adsorbents demonstrate an increasing pattern of adsorption capacity with increasing methylene blue concentration. The concentration gradient is generally viewed as the driving force to overcome the adsorbent mass transfer resistance. The higher the solute concentration, the greater the adsorption capacity until the surface saturation is reached. In general, the adsorption of methylene blue onto adsorbent involved four steps. The first step is the liquid phase mass transfer in which the dye molecules shift from the bulk solution to the outer surface of adsorbent. This is followed by a second step that is diffusion of dye molecules through the interface surrounding the adsorbent (external diffusion step). The third step is the adhesion of dye molecules onto the active sites located on the outer layer of adsorbent (adsorption step). Finally, the fourth step is the intra-particle diffusion of dye molecules through the pores of adsorbents. In the adsorption-related wastewater treatment, the mass transfer step is considered as the rate determining process since the dye molecules adsorb onto active sites in a slow manner [8].

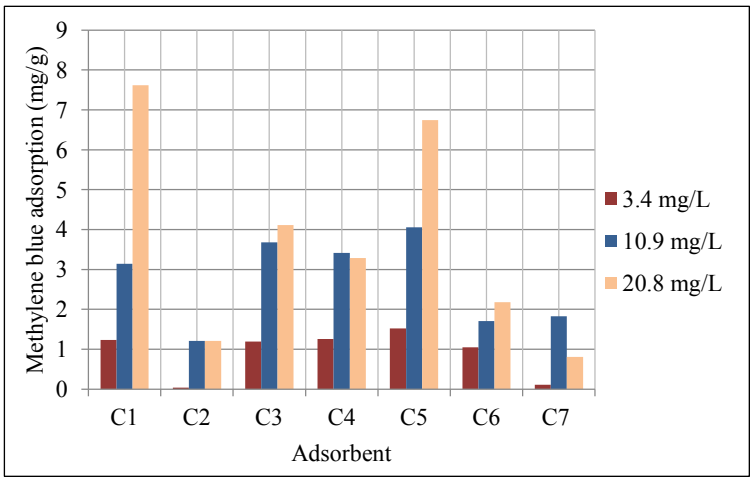


Figure 2. Methylene blue removal by adsorbents

Adsorbent derived from PFAD alone exhibits a better adsorption of methylene blue with q_e = 7.6 mg/g at C_o = 20.8 mg/L, compared to that prepared from PKS alone. It shows a good prospective of PFAD as adsorbent precursor or activating agent. This is true when compared with other PFAD-PKS mixed adsorbents as displayed in Figure 2. For adsorbents prepared at different PFAD-to-PKS ratios, C_5 (ratio 10) demonstrates a higher methylene blue removal, that is somewhat comparable to that of C_1. A bell-shaped distribution of adsorption capacity shown by C_2 to C_6 supported the comparability that PFAD can act as oxidizing agent, and most likely as an activating agent too for PKS. This pattern indicates the development of solid porous texture as the ratio of PFAD increases. However,

beyond the optimum point, the porous texture starts to collapse due to the broadening of existing pores because of excessive oxidizing/activating agent [5,9]. Nevertheless, more in-depth physico-chemical characterization of adsorbents would be needed as future works to confirm and establish the present findings.

Adsorption isotherm is crucial in comprehending the concept of adsorptive molecular distribution between the solid phase and the liquid phase at equilibrium. Equilibrium is attained when the rate of adsorption is equal to the rate of desorption for a given concentration. The fitting of experimental data into isotherm models is an indispensable step to analyze the adsorption behaviour for design purposes. The adsorption data were analyzed using two commonly used models, namely Langmuir and Freundlich equations [10,11].

The Langmuir model assumed monolayer coverage of adsorbate over a surface that holds a limited number of adsorption sites of uniform adsorption energy with no transmigration of adsorbate in the plane of surface. All sites are identical and energetically equivalent, and the adsorbent is structurally homogeneous. At surface saturation, no further adsorption can take place with increasing concentration, thus giving rise to the formation of a plateau graphically which also indicates a maximum adsorption capacity. The linearized form of Langmuir isotherm is expressed as equation 2:

$$C_e/q_e = 1/Q_m b + C_e/q_e \quad (2)$$

where b (L/mg) is the Langmuir isotherm constant and Q_m (mg/g) is the maximum monolayer coverage. By plotting C_e/q_e against C_e, the values of b and Q_m can be numerically determined from the gradient and y-intercept.

The Freundlich model assumed multilayer adsorption process on a heterogeneous surface. This isotherm model involves an exponential term of equilibrium concentration, suggesting that the adsorbate concentration on the adsorbent surface (q_e) increases exponentially along with the adsorbate concentration (C_e) in the solution. The linear form of Freundlich equation is given in equation 3:

$$\log q_e = \log K_F + (1/n) \log C_e \quad (3)$$

where K_F is the Freundlich constant related to the adsorption capacity and n is the adsorption intensity. A straight line can be elicited by plotting log q_e against log C_e to determine K_F and n. The surface heterogeneity or adsorption strength can be suggested using the gradient ranging between 0 and 1. The adsorption is more heterogeneous if the value is near to zero. The value which is less than 1 suggests the chemisorption process, while that of more than one implies the cooperative adsorption.

The Langmuir and Freundlich constants of methylene blue adsorption onto PKS and PFAD derived adsorbents are summarized in Table 2. The coefficient of determination, R^2 of 0.90 or greater reflects the acceptable fitting of Langmuir model with the adsorption data. The applicability of Langmuir model suggests that the adsorption of methylene blue onto the prepared adsorbents is monolayer and occurs over a surface with homogeneous energy sites accessible for interaction [12, 13]. Adsorbents C1, C3, C4, C5, and C6 gave R^2 values greater than 0.90, while that of C2 and C7 are lesser than 0.90. This could be associated with the poor removal performance of the latter adsorbents. Also, the calculated Q_m values are relatively close to the experimental ones (Figure 2).

The adsorption data were not adequately fitted to the Freundlich model as the R^2 values are lower, i.e. between 0.002 and 0.551 (Table 2). This implies that the model could not in any way be used to describe the methylene blue adsorption onto the adsorbents derived from PFAD, PKS and mixtures of both. The n constant supplies important information on the heterogeneous factor of the adsorbent which suggests that the adsorption system is linear when $n = 1$, chemical-type ($n < 1$) or physical-type ($n > 1$). Similarly, the adsorption intensity or the surface heterogeneity can be evaluated using $1/n$, whereby the surface is more heterogeneous when $1/n$ value approaches zero. Here, the $1/n$ values ranging from 0.0002 to 0.981 indicating the high surface heterogeneity of the adsorbents. While the corresponding n values signify that the process could be of physical-type adsorption (physisorption). However, this is somewhat in contradiction with the underlying notion of Langmuir model which stated that the process could be of chemical-type adsorption (chemisorption). The possible mechanisms of chemical-type adsorption between

methylene blue molecules and adsorbent surface include π-π interaction, π-cation interaction and the roles of acidic functional groups [14].

Table 2. Isotherm constants

Adsorbent	Langmuir isotherm			Freundlich isotherm		
	Q_m (mg/g)	b (L/g)	R^2	K_F (mg/g)(L/mg)$^{1/n}$	$1/n$	R^2
C1	5.87	0.461	0.989	1.314	0.369	0.551
C2	3.08	0.0079	0.039	0.235	0.981	0.470
C3	1.11	0.282	0.978	1.41	0.0002	0.002
C4	0.108	0.179	0.958	1.65	0.517	0.336
C5	2.76	0.656	0.994	1.53	0.140	0.214
C6	0.550	0	0.929	1.23	0.132	0.115
C7	0.970	0.106	0.805	0.467	0.490	0.261

Conclusion

Adsorbents were prepared using palm fatty acid distillate (PFAD) and palm kernel shell (PKS) at varying PFAD-to-PKS ratios. Adsorbent derived from PFAD alone shows a promising removal performance of methylene blue compared to PKS alone (char) even though the yield of the former is small. The removal of PFAD-based adsorbent was recorded as q_e = 7.6 mg/g at C_o = 20.8 mg/L. PFAD may act as oxidizing agent and activating agent in the presence of PKS. As such, the adsorbents produced display a bell-shaped distribution of adsorption capacity that is analogous to KOH activation. The adsorption data fitted well into Langmuir isotherm, suggesting monolayer coverage of methylene blue molecules, uniformly distributed onto homogeneous adsorbent surface. Also, the process could be that of chemisorption. The present findings concluded that PFAD is a promising candidate of dyes adsorbent.

Acknowledgement

Authors are grateful for the financial support by UTM-Flagship grants No. 03G70 and 14H19.

References

1. Garlapati, V. K., Shankar, U. and Budhiraja, A. (2016). bioconversion technologies of crude glycerol to value added industrial products. *Biotechnology Reports,* 9: 9-14.
2. Mahmood, W. M. F. W., Ariffin, M. A., Harun, Z., Ishak, N. A. I. Md., Ghani, J. A. and Rahman, M. N. Ab. (2015). Characterisation and potential use of biochar from gasified oil palm wastes. *Journal of Engineering Science and Technology,* 6: 45-54.
3. Ping, B. T. Y. and Yusof, M. (2009). Characteristics and properties of fatty acid distillates from palm oil. *Oil Palm Bulletin,* 59: 5-11.
4. Top, A. G. M. (2010) Production and utilization of palm fatty acid distillates (PFAD). *Lipid Technology,* 22(1): 11-13.
5. Shu-Hui, T. and Zaini, M. A. A. (2015). Potassium hydroxide activation of activated carbon: A commentary. *Carbon Letters,* 16(4): 275-280.
6. Zaini, M. A. A., Mohd-Setapar, S. H., Kamaruddin, M. J. and Yunus, M. A. C. (2013). In-depth studies of cattle-manure-compost activated carbons for Cu(II) ions removal. *Agricultural Research Updates,* 6: 247 – 265.
7. Hamza, U. D., Nasri, N. S., Amin, N. S., Mohammed, J. and Zain, H. M. (2016). Characteristics of oil palm shell biochar and activated carbon prepared at different carbonization times. *Desalination and Water Treatment,* 57(17): 7999-8006.
8. Pezoti Jr., O., Cazetta, A. L., Souza, I. P. A. F., Bedin, K. C., Martins, A. C., Silva, T. L. and Almeida, V. C. (2014). Adsorption studies of methylene blue onto $ZnCl_2$-activated carbon produced from buriti shells (*Mauritia flexuosa* L.). *Journal of Industrial and Engineering Chemistry,* 20(6): 4401-4407.

9. Zaini, M. A. A., Okayama, R. and Machida, M. (2009). Adsorption of aqueous metal ions on cattle-manure-compost based activated carbons. Journal of Hazardous Materials, 170(2-3): 1119-1124.
10. Langmuir, I. (1918). The adsorption of gases on plane surfaces of glass, mica and platinum. *Journal of American Chemical Society,* 40(9): 1361-1403.
11. Freundlich, H. M. F. (1906). Over the adsorption in solution. *The Journal of Physical Chemistry,* 57: 385-470.
12. Zhi, L. L. and Zaini, M. A. A. (2017). Adsorption properties of cationic rhodamine B dye onto metals chloride-activated castor bean residue carbons. *Water Science and Technology*, 75(4): 864-880.
13. Shu-Hui T. and Zaini, M. A. A. (2017). Malachite green adsorption by potassium salts-activated carbons derived from textile sludge: Equilibrium, kinetics and thermodynamics studies. *Asia-Pacific Journal of Chemical Engineering*, 12: 159-172.
14. Zaini, M. A. A. and Mohamad, N. A. (2015). Activated charcoal for oral medicinal purposes: Is it really activated? Journal of Applied Pharmaceutical Science, 5(10): 157-159.

Malaysian Journal of Analytical Sciences, Vol 22 No 4 (2018): 648 - 658
DOI: https://doi.org/10.17576/mjas-2018-2204-11

MALAYSIAN JOURNAL OF ANALYTICAL SCIENCES
Published by The Malaysian Analytical Sciences Society
ISSN 1394 - 2506

SYNERGISTIC EFFECT OF ADSORPTION-PHOTODEGRADATION OF COMPOSITE TiO_2/AC FOR DEGRADATION OF 1-BUTYL-3-METHYLIMIDAZOLIUM CHLORIDE

(Kesan Sinergistik Penjerapan-Fotopenguraian dari Bahan Komposit TiO_2/AC untuk Mengurai 1-Butil-3-Metillimidazolium Klorida)

Azhar Zawawi, Raihan Mahirah Ramli*, Noorfidza Yub Harun

Chemical Engineering Department,
Universiti Teknologi PETRONAS, 32610, Bandar Seri Iskandar, Perak, Malaysia

**Corresponding author: raihan.ramli@utp.edu.my*

Received: 16 April 2017; Accepted: 7 March 2018

Abstract

Most ionic liquids (ILs) were reported to be highly toxic and non-biodegradable such as ILs with imidazolium type cation. To overcome this problem, degradation of imidazolium based ILs via advance oxidation process is needed. In this research, photocatalytic study was employed in order to study the efficiency of the system for removal of ILs from wastewater. To introduce synergistic effect of adsorption-photodegradation, composite photocatalyst TiO_2/AC was synthesized using two steps (1) nano-TiO_2 was synthesized using microemulsion method and (2) it deposited onto functionalize (AC) activated carbon using impregnation method. The prepared composite photocatalyst was characterized using Thermo Gravimetric Analyzer (TGA), Brunauer-Emmet-Teller (BET) and Field Emission Scanning Electron Microscopic (FESEM). Photocatalytic study of 1-butyl-3-methylimidazolium chloride (bmimCl) was employed under visible light region. Increasing amount of AC as support increased the degradation rate of bmimCl. However, excess AC reduced the removal rate of bmimCl. Composite TiO_2/AC with 10 wt.% AC as support shows highest degradation rate with total removal 18.47%. Composite photocatalyst may enhance the diffusion rate between bmimCl and TiO_2 surface which increase the efficiency for overall systems.

Keywords: photodegradation, TiO_2, ionic liquid, activated carbon, synergistic

Abstrak

Penggunaan cecair ionik (ILs) dilaporkan sebagai sangat toksik dan tidak biodegradasi. Oleh itu, penguraian ILs dengan melalui proses pengoksidaan amat diperlukan. Dalam kajian ini, sistem fotopemangkin telah dilaksanakan untuk mengkaji kecekapan sistem ini dalam menyingkirkan ILs daripada air sisa. Komposit fotopemangkin TiO_2/AC telah dihasilkan untuk mencetuskan kesan sinergistik penjerapan-fotopenguraian untuk mengurai Ils melalui dua langkah (1) nano-TiO_2 telah dihasilkan melalui kaedah mikroemulsi dan (2) dicampurkan bersama karbon yang diaktifkan melalui kaedah pengisitepuan. Komposit fotopemangkin yang dihasilkan telah dihantar untuk proses pencirian bagi mengkaji ciri-ciri fizikal dan kimia fotopemangkin seperti analisis gravimetrik termo (TGA), Brenaeur-Emmet-Teller (BET) dan mikroskopi elektron pancaran medan (FESEM). Kajian fotopenguraian 1-butil-3-metilimidazolium klorida (bmimCl) sebagai rujukan ILs telah dilaksanakan di bawah sinar nampak. Penambahan bilangan AC sebagai sokongan telah meningkatkan kadar penguraian bmimCl. Walau bagaimanapun, sekiranya AC yang digunakan sebagai sokongan terlalu banyak, ianya telah mengurangkan kadar penguraian bmimCl. Komposit TiO_2/AC dengan bilangan 10 wt.% AC sebagai sokongan telah menunjukkan kadar penguraian yang paling tinggi. Komposit fotopemangkin akan meningkatkan kadar penyebaran antaran bmimCl and permukaan TiO_2 yang mana akan meningkatkan kecekapan sistem secara keseluruhannya.

Kata kunci: fotopenguraian, TiO_2, cecair ionik, karbon aktif, sinergistik

Introduction

Ionic liquids (ILs) have gained interest among researchers due to its tuneable properties that can be used in different application such as catalysis, separation and reaction processes [1]. ILs is regarded as a green solvent due to its negligible vapour pressure properties that can reduce the emission of chemicals to atmosphere. Imidazolium, quaternary ammonium and pyridinium are examples of cations that can be used to alter the physical and chemical properties of ILs [2] while halide groups (Cl^- and Br^-), tetrafluoroborate (BF_4^-) and tetracholoroaluminate ($AlCl_4^-$) are example of anions that have been used by researchers to tune the properties of ILs depending on its applications [1].

Aromatic ILs are known to be highly persistent in water, toxic and non-biodegradable. Advance oxidation processes (AOPs) such as electrochemical oxidation, Fenton systems and photocatalytic process under UV region [3-5] have been studied for removal of bmimCl from wastewater. Yet, there are several drawbacks of these systems such as high consumption of energy and formation of sludge. Photocatalytic process can be optimized by shifting the photoactivity of semiconductor towards the visible region since solar spectrum consist only 3-5% of UV region as compared to visible region up to 45% [6]. TiO_2 nanoparticles possess characteristics high photocatalytic activity, chemically stable and abundant [7]. However, major limitations of pristine TiO_2 that hinder its application in industry are high band gap energy and low diffusion rate between the targeted pollutant and TiO_2 surface [8, 9].

Nowadays, synthesis of nano-photocatalyst is mainly focusing on enhancing diffusion rate between pollutant and TiO_2 surface. Due to the hydrophilic nature of ILs, it is expected to diffuse slowly on TiO_2 surface, leading to low overall performance. The photodegradation study of bmimCl using TiO_2 as photocatalyst are still limited where based on the previous study, the research was mainly focusing on UV region as compared to visible region [10]. Hence, this study is focusing on the synthesis of activated carbon (AC) as support for TiO_2 with functionalize group to act as centre of accumulation. This process is to ensure high degradation rate of target pollutants onto TiO_2/AC surface leading to efficient overall system.

Materials and Methods

Materials

Titanium tetraisopropxide, TTIP ($C_{12}H_{28}O_4$, 97%), heptane (C_7H_{16}, 99%), hexanol ($C_6H_{14}O$, 98%), ferum nitrate nonahydrate ($Fe(NO_3)_3.9H_2O$), ethanol (C_2H_3OH, 95%) and 1-butyl-3-methylimidazolium chloride, bmimCl ($C_8H_{15}ClN_2$) were purchased from Merck (Germany). Triton X-100 ($C_{34}H_{62}O_{11}$, AR), nitric acid (HNO_3, 65%), potassium dihydrogen phosphate (KH_2PO_4) and triethylamine ($C_6H_{15}N$, AR) were purchased from R&M Chemicals (Malaysia). Meanwhile, phosphoric Acid (H_3PO_4, 85%) was purchased from QreC (New Zealand). All chemicals were used without further purification.

Methods

TiO_2 was prepared via microemulsion as reported from previous study [11]. Then, 1g of prepared TiO_2 was suspended in 10 ml of distilled water under continuous stirring. The solvent was removed at 80 $^{\circ}$C until white thick paste was formed. The resulting paste was dried in an oven at 80 $^{\circ}$C overnight prior to calcination at 400 $^{\circ}$C for 1.5 hours. Meanwhile, AC was prepared using bagasse as raw material and was carbonized in normal furnace at temperature 600 $^{\circ}$C for 1 hour. The produced biochar was then treated in a 1 M of nitric acid boiling solution. Then, resulting black powder was washed repeatedly with distilled water and dried in an oven for overnight at 80 $^{\circ}$C.

The synthesised TiO_2 was deposited onto AC using impregnation method. Pre-determined amount of TiO_2 and AC was mixed in a beaker and then 10 ml of distilled water was added. The mixture was stirred while heating until formation grey thick paste. The paste formed was dried overnight and then calcined at desired temperature. Samples are labelled following the format; TiO_2/nAC where n denotes the wt.% of AC i.e. TiO_2/5AC means 5wt.% of AC is used as support.

Characterization of photocatalyst

Synthesized photocatalyst were characterized using thermo gravimetric analysis (TGA) prior to calcination in order to determine the suitable temperature for calcination. The thermogram analysis was conducted using Perkin Elmer

TGA (Pyris 1) system under 20 ml/min N_2 flow, from 30–800 °C at ramp rate 20 °C /min. The morphology of photocatalyst was characterized using field emission scanning electron microscopic (FESEM) analysis. For FESEM analysis, model Zeiss Model Supra 35VP was used. Surface area and pore distribution was characterized using Brunauer-Emmet-Teller (BET) analysis. The characterization was done by using TriStar II 3020.

Photodegradation study

Photodegradation study was conducted in glass reactor at ambient condition. The reactor was placed under 500W halogen lamp with distance 15 cm. The initial concentration of bmimCl used was 5mM and 1g/L photocatalyst. The reactor was placed in dark for 30 minutes to allow for adsorption-desorption equilibrium prior to 4 hours photoreaction. The samples were analysed using Agilent 1100 high performance liquid chromatography (HPLC). Column used was Symmetry C-18 (250 x 4.6mm, 5µm) and mobile phase mixture of methanol (35 vol%) and 25 mM of phosphate buffer (KH_2PO_4/H_3PO_4) containing 0.5% of triethylamine were used to separate bmimCl. The analysis was conducted using injection 5 µl, temperature 30 °C and flow rate 0.8ml/min. UV detector with wavelength 212 nm was used to trace the BmimCl.

Results and Discussion

Thermo gravimetric analyser

Thermo gravimetric analyser (TGA) analysis was conducted to determine the thermal decomposition of the synthesized photocatalyst. From Figure 1(a), thermogram for TiO_2 shows significant weight loss from temperature 30-400 °C before the curve becomes constant. The significance weight loss may be due to loss of water from surface of sample and also elimination unhydrolyzed isopropoxide ligand as well as decomposition of organic entities that may present during synthesis steps [12, 13]. The derivative weight loss shows that the removal of water and organic entities from samples of photocatalyst was attributed by endothermic reaction.

Figure 1(b) shows the thermogram recorded for AC, the weight of compound increases from temperature 30 °C up to 500 °C. This is happened due to adsorption of N_2 gas at higher temperature to the surface of AC [14]. This is in agreement with finding reported by Kim et. al where AC has affinity towards adsorption of N_2[15]. At temperature 470 °C, the sample weight loss starts to decrease until 0.0 wt.% weight loss recorded at temperature 646 °C. This weight loss was due to the burning off the AC by endothermic process [16]. Figure 1(c) represent thermogram for TiO_2/AC where two significant weight losses recorded from temperature 30-400 °C (step 1) and 400-800 °C (step 2). Step 1 occurred due to endothermic reaction where the evaporation of adsorbed water vapour occurred at this temperature with main peak at 31°C. Second weight loss also occurred due endothermic reaction with broader main peak at 611°C.

Step 2 weight loss was due to the burn off the AC and only 15.4% weight loss was recorded compared to AC alone. The lower weight loss recorded was due to thermal persistent of composite photocatalyst containing synthesis TiO_2 at higher temperature [17]. Comparing to Figure 1(b), the increase in weight % due to adsorption of N_2 gas is not recorded for sample TiO_2/AC. This shows that the adsorption of N_2 gas during calcination treatment for composite photocatalyst did not occurred. From the previous study, adsorption of N_2 towards TiO_2 surface can only be done by specific complex cluster TiO_2 namely unsaturated Ti atom at the (110) surface of TiO_2. Hence due to specific formation of TiO_2 that can only adsorb N_2, the weight gain does not record in thermogram as negligible N_2 has been adsorbed during TGA analysis. From this finding also, we can conclude that synthesize bare TiO_2 and composite TiO_2/AC does not contain specific facets of TiO_2 that can be used to adsorb N_2 [18].

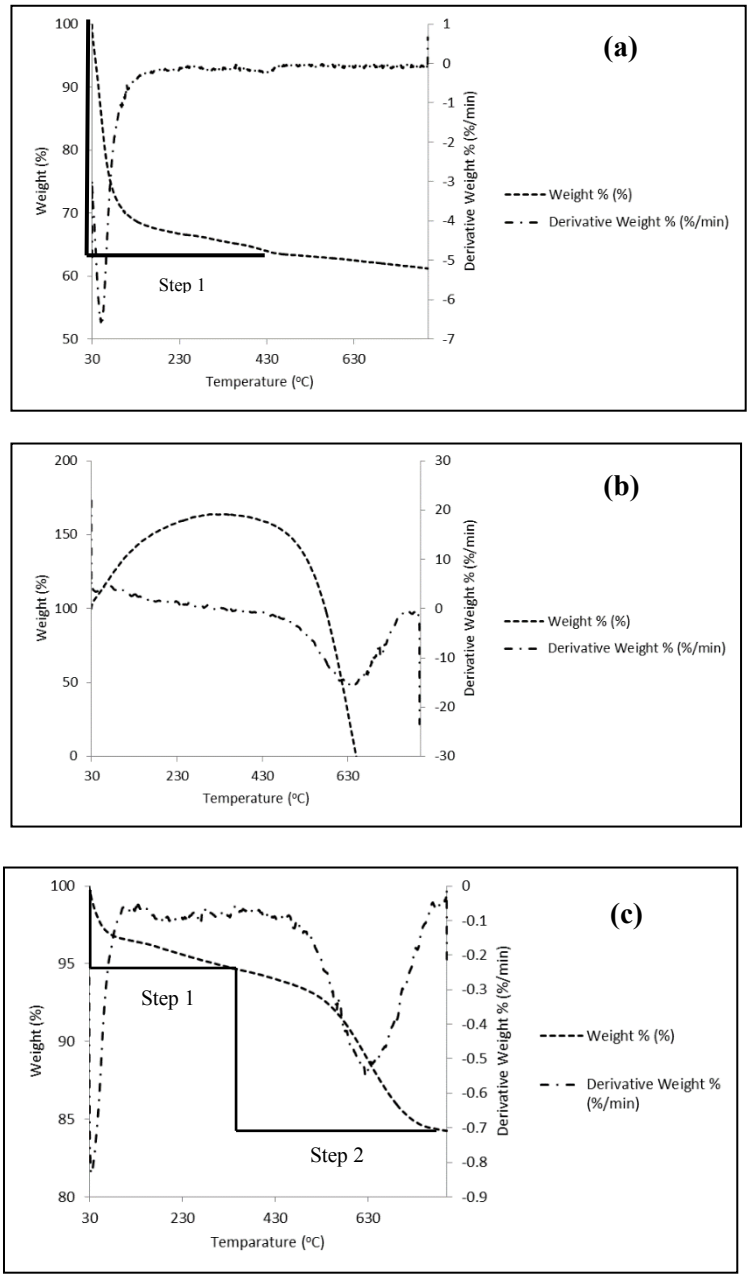


Figure 1. Thermogram analysis for (a) TiO_2, (b) AC and (c) TiO_2/AC

Surface area and pore distribution analyser

Figure 2 depicts the N_2 adsorption isotherms for TiO_2, AC and composite TiO_2/AC. TiO_2 and TiO_2/AC shows similar type of N_2 isotherm with type IV isotherm and hysteresis loop H3 type (Figure 2(a) and (c), respectively) meanwhile AC shows type I isotherm and hysteresis H4 type (Figure 2(b)) [16, 19]. TiO_2 and TiO_2/AC show a higher adsorption at relative P/P_o = 0.6-1.0 indicating the presence of mesoporous structure. The hysteresis loop was recorded due to aggregation of nanoparticles and this type of isotherm corresponds to lower porosity of material [20]. This phenomenon in agreement with BET surface area, (100.53 m^2/g). For AC, the adsorption uptake of N_2 occurring at pressure less than 0.1, followed by plateau at P/P_o more than 0.2 and indicating the microporosity of

AC. The hysteresis loops also confirm the presents of some mesoporous structure [16]. The pore distribution of TiO_2 and TiO_2/AC mainly distribute between 1.5-15.0 nm in agreement with isotherm result indicates the presence of microporous and mesoporous structure. Compare to TiO_2, AC pore volume distribute mainly around 1.5-2.0 nm represent the microporous structure of the sample [20].

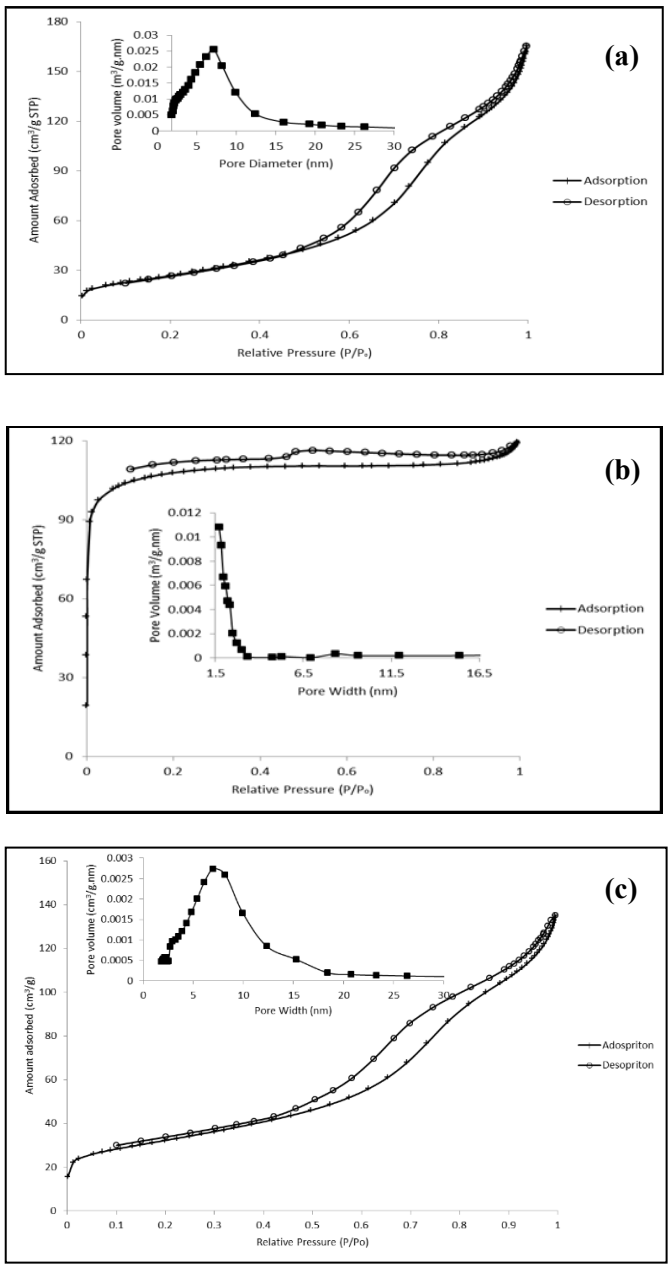


Figure 2. N_2 isotherm and pore distribution (inner graph) for (a) TiO_2, (b) AC and (c) TiO_2/10AC

Table 1 summarizes the surface area and pore size of synthesis TiO_2 and AC. From the table, it shows that AC has high surface area compared to synthesis TiO_2 and composite TiO_2/AC as AC was known to be highly surface area and porous structure. Reduction in surface area for composite photocatalyst compared to AC is mainly due to

blocking of the pores by TiO_2 that had been deposited on AC [16]. Interestingly, the V_{total} and pore size of the TiO_2 and composite photocatalyst is higher compared to synthesis AC and may lead to higher degradation rate of bmimCl. This is due to more adsorbate can be adsorbed in the pore structure of photocatalyst and enhance the diffusion rate between bmimCl and TiO_2 surface. This shows that synthesis TiO_2 via microemulsion produce highly porous structure of nanoparticles

Table 1. Specific surface area and pore diameters for the photocatalyst sample

Sample	S_{BET} (m^2/g)	V_{total} (cm^3/g)	Pore diameter (nm)
TiO_2	100.53	0.26	10.13
AC	335.25	0.18	7.98
TiO_2/10AC	96.29	0.21	8.67
TiO_2/20AC	111.97	0.20	7.28

Surface morphology

Morphological analysis was conducted using FESEM to investigate the surface structure of the samples. Micrographs in Figure 3 represent the imaging morphology for TiO_2, AC, TiO_2/10AC and TiO_2/20AC. AC image (Figure 2a) shows its spongy and porous structure similar to the report [21]. This is attributed to its high BET surface area (Table 1). While, the synthesized TiO_2 shows uniform spherical structure with particles size range between 15-18.00 nm, proving that the synthesis method produce small particle with high surface area as compared to commercialize TiO_2 P25 [22]. The spherical shape of TiO_2 provided higher surface area for photocatalyst that can be used to optimize the adsorption and absorption process which then enhance the degradation rate of ILs. The morphological of TiO_2 on surface of AC almost similar with morphology recorded for TiO_2 alone. In same time, agglomeration effect also could be observed from micrograph, with finer particles size could be observed for TiO_2 deposited onto AC (Figure 2c and d). This finding in agreement with discussion reported by Slimen et. al [23] where AC contain interfacial energy which can enhance and produce fine particle size of TiO_2. This theory was also supported by other researcher [19, 21].

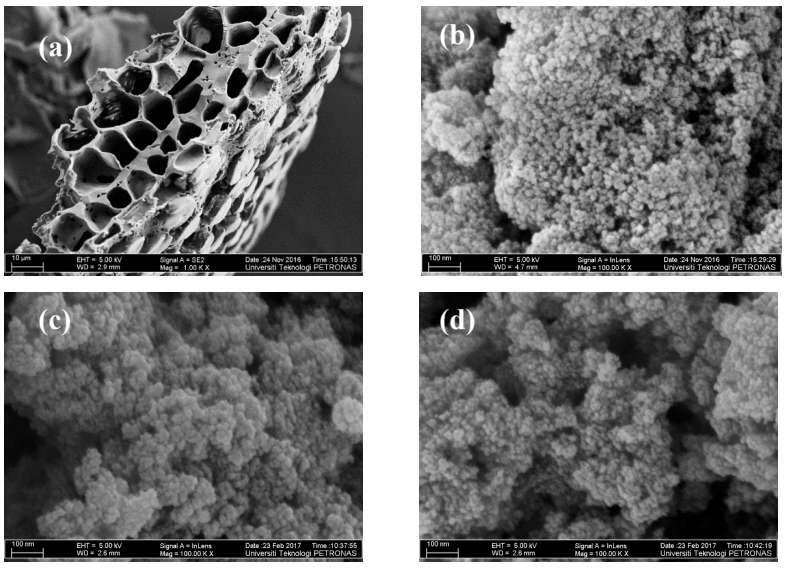


Figure 3. Imaging surface morphology of (a) AC (5 kX), (b) TiO_2 (100kX), (c) TiO_2/ 10AC (100kX) and (d) TiO_2/20AC (100kX)

Photodegradation analysis

Figure 4(a) depicts the concentration profile for AC treated with different type of acid. From the figure, the concentration of bmimCl started to increase after 30 minutes of adsorption study. Hence from this preliminary study, 30 minutes of dark reaction was selected prior to photodegradation under visible light to achieve equilibrium adsorption-photodegradation. Meanwhile Figure 4(b) shows the concentration profile for photodegradation process. From the figure, it shows that the concentration profile becomes plateau after 2 hours reaction. Based on the analysis, the photodegradation study will be done in 2 hours analysis for future study. Figure 4(c) presents the efficiency of bmimCl photodegradation process in different system and photocatalyst. In the photolysis process, bmimCl could not undergo self-destruction under visible light without the presence of photocatalyst. Meanwhile, the synthesized TiO_2 recorded 12% removal of bmimCl. However, significant increment of the photodegradation % was observed when the TiO_2 was deposited onto AC, with the highest removal was observed for 10 wt.% AC. When the amount of AC increase, total surface-active sites containing functionalized group increases and more interaction Van der Walls forces will occur between bmimCl and surface of AC [24]. Hence more bmimCl will be adsorbed on surface of AC and leading to increment in diffusion rate between bmimCl and surface of TiO_2. Hence direct oxidation of bmimCl occurred and increase in total degradation [25]. Compared to 5 wt.% of AC, the total removal of bmimCl was quite low. This is because, when less AC was used as support, the total surface of AC itself was blocked by TiO_2 leading to low active surface area which can be used to adsorb bmimCl. Moreover, generation of hydroxyl radical ($OH^{\bullet}$) as attacking agent in degradation study accumulate around surface of TiO_2. Production of $OH^{\bullet}$ can penetrate up to sub-millimeter distance from surface TiO_2. Interestingly, this radical also can penetrate into pore of AC to attack the pollutant that has been adsorbed deep into pore of AC. Hence, as bmimCl was accumulated on surface of AC, the molecules can be directly oxidized by $OH^{\bullet}$ thus increase the overall efficiency of the system [26].

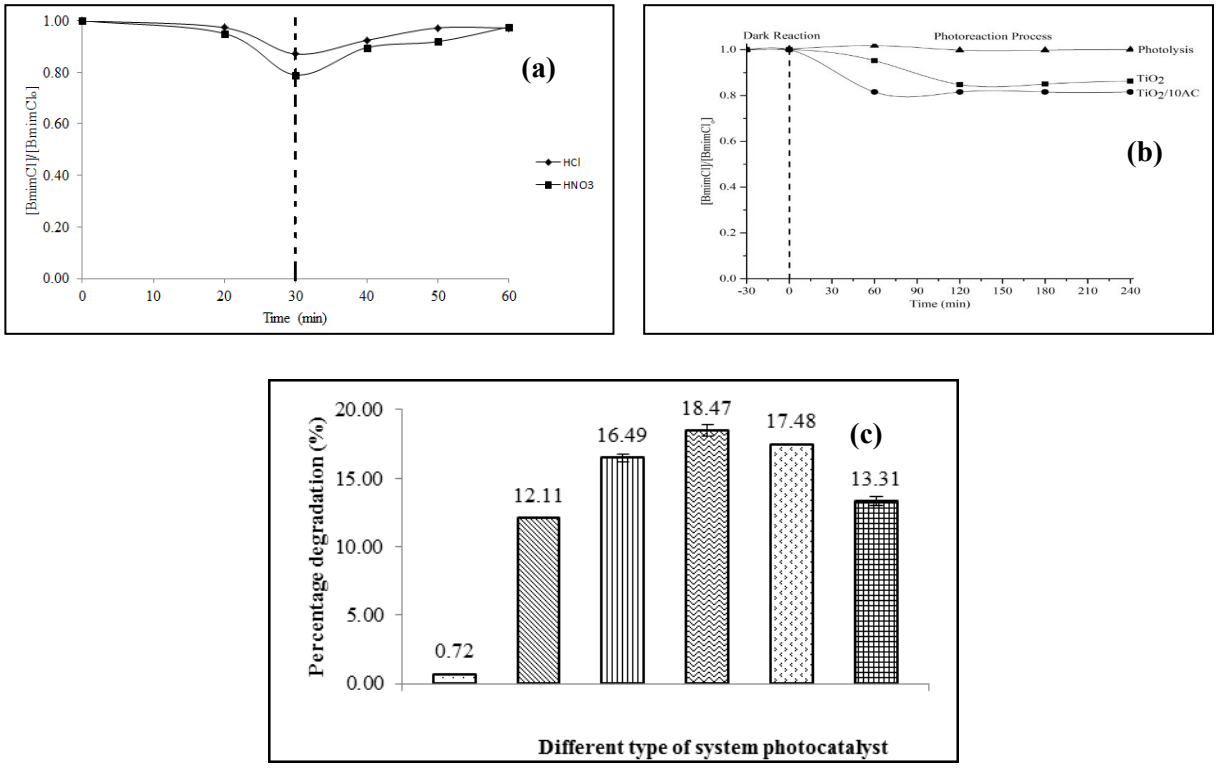


Figure 4. (a) Concentration profile for adsorption study of different type of AC, (b) concentration profile for photoreaction and (c) comparison photodegradation study for different type of photocatalyst

On the other hand, bare AC has been proved able to produce high water contact angle and leading to hydrophobic properties of AC. However, once AC was coated with TiO_2, the properties can be shifted to hydrophilic [27]. Hydrophilic composite materials could lead to increment in adsorption of organic molecule such as methylene blue (MB) [27] and Rhodamine-B [28] due to increase in the interaction of composite materials and targeted molecule itself. Hence degradation rate could increase.

The degradation reduced significantly when AC loading was increased from 10 to 20 wt.%. When the amount of AC used as support increased, more active site will be available for adsorption of bmimCl. Hence more bmimCl molecule will be accumulated on surface of AC. This phenomenon unfortunately, will block surface of TiO_2 and prevent the surface of TiO_2 from harvesting the light. Hence less charge carrier (e^-_{CB}/h^+_{VB}) could be generated and reduced the degradation rate. Similar phenomenon was recorded by other researchers [29]. In same time, TiO_2/20AC contains leas amount of TiO_2 based on synthesized procedure. Reduction in amount TiO_2 will reduce the active site TiO_2 surface that could be used to absorb photon for generation of charge carrier. Hence, less bmimCl molecule can be oxidized leading to reduction in total degradation rate.

The comparison of different types of AOP for degradation of ILs is presented in Table 2. From the table, all systems i.e. electrochemical oxidation, Fenton's oxidation and UV/TiO_2 systems show high degradation rate as compared to our current findings where only 18.47% total removal of bmimCl was recorded. The current finding is only focusing on the optimization of material development. The optimization of extrinsic factors such as initial pH of the solution, initial concentration of bmimCl, dosage of photocatalyst and the presence of oxidant are yet to be investigated. Apart from the optimization of material development, these factors also contribute significantly to the overall efficiency of the system [30]. In addition, major limitation of electrochemical oxidation is the dependency on electricity which relatively contributes to higher cost [31].

Table 2. Comparison study of AOP for degradation of ILs

AOP systems	Methodology	Findings	Ref.
Electrochemical Oxidation	Reaction run in electrolytic cell V = 100 ml, BDD as anode and stainless steel as cathode. Area and distance of electrode are 10 cm^2 and 1 cm respectively. Concentration of IL is 50 mg/l	100% of IL can be degrading in 120 minutes with optimum pH 3 and pH 6. Temperature of reactions was maintained at 40 °C. Degradation affected by IL used and imidazolium is more stable compare to pyridinium	[33, 34]
Fenton systems	Reaction run in reactor V = 300 ml, pH 3.5 and temperature maintained at 25 °C. Concentration of IL is 1.0 mM	IL with 100% degradation achieved in 60 minutes with presents of scavenger, [H_2O_2] = 400 mM and [Fe^{3+}] = 1 mM	[35-37]
UV/TiO_2 systems	Reactions run with 0.5 g/L of TiO_2 with 1 mM of IL and 1000 W Xenon arc lamp as light source	Almost 100% degradation can be achieved in 360 minutes	[10, 38]
TiO_2/AC	Reaction with 1g/L of TiO_2/AC with 5 mM of IL and 500W of Halogen lamp was used as source of light	Only 18.47% removal of bmimCl was achieved in 4 hours reactions without optimization of extrinsic factors	This study

On the other hand, the homogeneous nature of this process leads to the formation of ferric sludge during post-treatment prior to discharge which could cause another problem to the landfill management [32]. Though UV/TiO_2

system could be the solution to the problem faced by Fenton's oxidation process, limited capability of TiO_2 to adsorb visible light energy is not favoured since the solar spectrum consists only 4-5% of UV region as compared to visible region which is up to 45% [11]. The current finding shows the high potential of TiO_2/AC as photocatalyst to degrade bmimCl under visible light radiation, and provide options to overcome the limitation faced by the previously discussed processes. Further optimization work is anticipated to improve the overall efficiency of this photocatalytic system.

Conclusion

Degradation rate of bmimCl can be enhanced by employing activated carbon (AC) as the support for titania via the synergistic effect of adsorption-photodegradation of both materials. Positive effect of increasing AC amount further enhanced the diffusion rate of bmimCl from fluid phase to the surface of titania leading to direct oxidation of bmimCl by the titania. Optimum AC was found at 10 wt.% functionalized with 1M HNO_3 with maximum bmimCl removal of 18.47%. The synergistic effect of adsorption-photodegradation includes: (1) Interfacial energy on AC surface could prevent the transformation of anatase TiO_2 to rutile phase leading to the production of fine particle size. Hence more TiO_2 active site is available for the absorption of photon for generation of charge carrier, (2) functionalized group on AC could act as pollutant concentrator and enhanced the diffusion rate between bmimCl and TiO_2 surface leading to direct oxidation of bmimCl and (3) coating of TiO_2 with AC could shift the polarity of bare AC to become hydrophilic. This property then leads to the increase of interaction between composite materials and bmimCl and consequently increase the adsorption process. Hence more bmimCl can be directly oxidized by TiO_2.

Acknowledgement

Authors are grateful to Universiti Teknologi PETRONAS (UTP) for the research funding under I-Gen Grant (IGEN 0153 DA-162). Special thanks to Centralize Analytical Laboratory (CAL), UTP for the characterization analysis.

References

1. Olivier-Bourbigou, H., Magna, L. and Morvan, D. (2010). Ionic liquids and catalysis: Recent progress from knowledge to applications. *Applied Catalysis A: General,* 373(1-2): 1-56.
2. Pham, T. P., Cho, C. W. and Yun, Y. S. (2010). Environmental fate and toxicity of ionic liquids: A review. *Water Research,* 44(2): 352-372.
3. Siedlecka, E. M., Fabiańska, A., Stolte, S., Nienstedt, A., Ossowski, T., Stepnowski P. and Thöming, J. (2013). Electrocatalytic oxidation of 1-butyl-3-methylimidazolium chloride: Effect of the electrode material. *International Journal of Electrochemical Science,* 8(1): 5560-5574.
4. Munoz, M., Domínguez, C. M., de Pedro, Z. M., Quintanilla, A., Casas, J. A. and Rodriguez, J. J. (2015). Ionic liquids breakdown by fenton oxidation. *Catalysis Today,* 240(1): 16-21.
5. Zhou, H., Shen, Y., Lv, P., Wang, J. and Li, P. (2015). Degradation pathway and kinetics of 1-alkyl-3-methylimidazolium bromides oxidation in an ultrasonic nanoscale zero-valent iron/hydrogen peroxide system. *Journal of Hazardous Materials,* 284(1): 241-252.
6. Ramli, R. M., Chong, F. K. and Omar, A. A. (2013). Visible-light photodegradation of diisopropanolamine using bimetallic Cu-Fe/TiO_2 photocatalyst. *Advanced Materials Research,* 176(1): 451-458.
7. Saepurahman, Abdullah, M. A. and Chong, F. K. (2010). Preparation and characterization of tungsten-loaded titanium dioxide photocatalyst for enhanced dye degradation. *Journal of Hazardous Materials,* 176(1-3): 451-458.
8. Ramli, R. M., Kait, C. F. and Omar, A. A. (2014). Photodegradation of aqueous diisopropanolamine using Cu/TiO_2: Effect of calcination temperature and duration. *Applied Mechanics and Materials,* 625(1): 847-850.
9. Orha, C., Pode, R., Manea, F., Lazau, C. and Bandas, C. (2017). Titanium dioxide-modified activated carbon for advanced drinking water treatment. *Process Safety and Environmental Protection,* 108(1): 26-33.
10. Stepnowski, P., & Zaleska, A. (2005). Comparison of different advanced oxidation processes for the degradation of room temperature ionic liquids. *Journal of Photochemistry and Photobiology A: Chemistry,* 170(1): 45-50.
11. Ramli, R. M., Kait, C. F. and Omar, A. A. (2016). Remediation of DIPA contaminated wastewater using visible light active bimetallic Cu-Fe/TiO2 photocatalyst. *Procedia Engineering,* 148(1): 508-515.

12. Altın, İ., Sökmen, M. and Bıyıklıoğlu, Z. (2016). Sol gel synthesis of cobalt doped TiO_2 and its dye sensitization for efficient pollutant removal. *Materials Science in Semiconductor Processing,* 45(1): 36-44.
13. Mohd Zaid, H. F., Chong, F. K. and Abdul Mutalib, M. I. (2015). Photooxidative–extractive deep desulfurization of diesel using Cu–Fe/TiO_2 and eutectic ionic liquid. *Fuel,* 156(1): 54-62.
14. Al-Doghachi, F. A. J., Rashid, U. and Taufiq-Yap Y. H. (2016). Investigation of Ce(III) promoter effects on the tri-metallic Pt, Pd, Ni/MgO catalyst in dry-reforming of methane. *RSC Advances,* 6(1): 10372-10384.
15. Ho Kim, B., Reon Kim, B. and Seo, Y. G. (2005). A study on adsorption equilibrium for oxygen and nitrogen into carbon nanotubes. *Adsorption,* 11(1): 207-212.
16. Ouzzine, M., Romero-Anaya, A. J., Lillo-Ródenas, M. A. and Linares-Solano, A. (2014). Spherical activated carbon as an enhanced support for TiO_2/AC photocatalysts. *Carbon,* 67(1): 104-118.
17. Ganesh, I., Kumar, P. P., Annapoorna, I., Sumliner, J. M., Ramakrishna, M., Hebalkar, N. Y., Padmanabham, G. and Sundararajan, G. (2014). Preparation and characterization of Cu-Doped TiO_2 materials for electrochemical, photoelectrochemical, and photocatalytic applications. *Applied Surface Science,* 293(1): 229-247.
18. Rittner, F., Boddenberg, B., Fink, R. F. and Staemmler, V. (1999). Adsorption of nitrogen on rutile(110). 2. construction of a full five-dimensional potential energy surface. *Langmuir,* 15(4): 1449-1455.
19. Eliyas, A., Ljutzkanov, L., Stambolova, I., Blaskov, V., Vassilev, S., Razkazova-Velkova, E. and Mehandjiev, D. (2013). Visible light photocatalytic activity of TiO_2 deposited on activated carbon. *Open Chemistry,* 11(3): 464-470.
20. Xing, B., Shi, C., Zhang, C., Yi, G., Chen, L., Guo, H., Huang, G. and Cao, J. (2016). Preparation of TiO_2/activated carbon composites for photocatalytic degradation of RhB under UV light irradiation. *Journal of Nanomaterials,* 2016(1): 1-10.
21. Jamil, T. S., Ghaly, M. Y., Fathy, N. A., Abd el-halim, T. A. and Österlund, L. (2012). Enhancement of TiO_2 behavior on photocatalytic oxidation of MO dye using TiO_2/AC under visible irradiation and sunlight radiation. *Separation and Purification Technology,* 98(1): 270-279.
22. Raj, K. J. A. and Viswanathan, B. (2009). Effect of surface area, pore volume and particle size of P25 titania on the phase transformation of anatase to rutile. *Indian Journal of Chemistry,* 48(10): 1378-1382.
23. Slimen, H., Houas, A. and Nogier, J. P. (2011). Elaboration of stable anatase TiO_2 through activated carbon addition with high photocatalytic activity under visible light. *Journal of Photochemistry and Photobiology A: Chemistry,* 221(1): 13-21.
24. Lemus, J., Neves, C. M. S. S., Marques, C. F. C., Freire, M. G., Coutinho, J. A. P. and Palomar, J. (2013). Composition and structural effects on the adsorption of ionic liquids onto activated carbon. *Environmental Science: Processes & Impacts,* 15(9): 1752-1759.
25. Maneerung, T., Liew, J., Dai, Y., Kawi, S., Chong, C. and Wang, C. H. (2016). Activated carbon derived from carbon residue from biomass gasification and its application for dye adsorption: Kinetics, isotherms and thermodynamic studies. *Bioresource Technology,* 200(1): 350-359.
26. Huang, D., Miyamoto, Y., Matsumoto, T., Tojo, T., Fan, T., Ding, J., Guo, Q. and Zhang, D. (2011). Preparation and characterization of high-surface-area TiO_2/activated carbon by low-temperature impregnation. *Separation and Purification Technology,* 78(1): 9-15.
27. Zhou, W., Zhang, P. and Liu, W. (2012). Anatase TiO_2 nanospindle/activated carbon (AC) composite photocatalysts with enhanced activity in removal of organic contaminant. *International Journal of Photoenergy,* 2012: 1-7.
28. Li, Y., Zhou, X., Chen, W., Li, L., Zen, M., Qin, S. and Sun, S. (2012). Photodecolorization of Rhodamine B on tungsten-doped TiO_2/activated carbon under visible-light irradiation. *Journal of Hazardous Materials,* 227-228 (1): 25-33.
29. Sun, Z., He, X., Du, J. and Gong, W. (2016). Synergistic effect of photocatalysis and adsorption of nano-TiO_2 self-assembled onto sulfanyl/activated carbon composite. *Environmental Science and Pollution Research,* 23(21): 21733-21740.
30. Alkaim, A. F., Kandiel, T. A., Hussein, F. H., Dillert, R. and Bahnemann, D. W. (2013). Enhancing the photocatalytic activity of TiO_2 by pH Control: A case study for the degradation of EDTA. *Catalysis Science & Technology,* 3 (12): 3216-3222.
31. Siedlecka, E. M., Fabiańska, A., Stolte, S., Nienstedt, A., Ossowski, T., Stepnowski P. and Thöming, J. (2013). Electrocatalytic oxidation of 1-butyl-3-methylimidazolium chloride: Effect of the electrode material. *International Journal of Electrochemical Science,* 8(1): 5560-5574.

32. Ramli, R. M., Kait, C. F. and Omar, A. A. (2014). Photocatalytic degradation of diisopropanolamine in heterogeneous photo-fenton system. *Advanced Materials Research,* 917(1): 160-167.
33. Pieczyńska, A., Ofiarska, A., Borzyszkowska, A. F., Białk-Bielińska, A., Stepnowski, P., Stolte, S. and Siedlecka, E. M. (2015). A comparative study of electrochemical degradation of imidazolium and pyridinium ionic liquids: A reaction pathway and ecotoxicity evaluation. *Separation and Purification Technology,* 156 (Part 2): 522-534.
34. Fabiańska, A., Ossowski, T., Bogdanowicz, R., Czupryniak, J., Gnyba, M., Odzga, T., Janssens, S. D., Haenen, K. and Siedlecka, E. M. (2012). Electrochemical oxidation of ionic liquids at highly boron doped diamond electrodes. *Physica Status Solidi (A),* 209(9): 1797-1803.
35. Siedlecka, E. M., Gołębiowski, M., Kaczyński, Z., Czupryniak, J., Ossowski, T. and Stepnowski, P. (2009). Degradation of ionic liquids by fenton reaction; The effect of anions as counter and background ions. *Applied Catalysis B: Environmental,* 91(1-2): 573-579.
36. Siedlecka, E. M., Mrozik, W., Kaczyński, Z. and Stepnowski, P. (2008). Degradation of 1-butyl-3-methylimidazolium chloride ionic liquid in a fenton-like system. *Journal of Hazardous Materials,* 154(1): 893-900.
37. Siedlecka, E. M., Goêbiowski, M., Kumirska, J. and Stepnowski, P. (2008). Identification of 1-butyl-3-methylimidazolium chloride degradation products formed in Fe(III)/H_2O_2 oxidation system. *Journal of Analytical Chemistry,* 53(1): 943-951.
38. Czerwicka, M., Stolte, S., Müller, A., Siedlecka, E. M., Gołębiowski, M., Kumirska, J. and Stepnowski, P. (2009). Identification of ionic liquid breakdown products in an advanced oxidation system. *Journal of Hazardous Materials,* 171(1): 478-483.

Malaysian Journal of Analytical Sciences, Vol 22 No 4 (2018): 659 - 666
DOI: https://doi.org/10.17576/mjas-2018-2204-12

MALAYSIAN JOURNAL OF ANALYTICAL SCIENCES
Published by The Malaysian Analytical Sciences Society
ISSN 1394 - 2506

TOTAL PHENOLIC, FLAVONOID CONTENT AND ANTIOXIDANT ACTIVITY OF *Clinacanthus nutans* LEAVES BY WATER-BASED ULTRASONIC ASSISTED EXTRACTION

(Kandungan Fenolik, Flavonoid dan Aktiviti Antioksidan bagi *Clinacanthus nutans* Menggunakan Bantuan Pengekstrakan Ultrasonik Berasaskan Air)

Nurul Amila Fadhlin Baharuddin[1], Mariam Firdhaus Mad Nordin[1]*, Noor Azian Morad[1], Nor Ilia Anisa Aris[1], Mohd Azizi Che Yunus[2]

[1]*Shizen Conversion and Separation Technology (SHIZEN Ikohza),*
Malaysia-Japan International Institute of Technology (MJJIT)
Universiti Teknologi Malaysia, Jalan Sultan Yahya Petra, 54100 Kuala Lumpur
[2]*Centre of Lipid Engineering and Applied Research (CLEAR)*
Universiti Teknologi Malaysia, 81310 Johor Bharu, Johor, Malaysia

**Corresponding author: mariamfirdhaus@utm.my*

Received: 16 April 2017; Accepted: 7 March 2018

Abstract

Clinacanthus nutans (C. nutans) is a prominent herb species that widely cultivated in Southeast Asia region. The effect of water-based ultrasonic assisted extraction at various temperature (30 to 60 °C) and time (5 to 30 minutes) on the total phenolic, flavonoid content and antioxidant activity in *C. nutans* leaves extract was investigated. Acquired extract was quantified for its total phenolic, flavonoid content and antioxidant activity by Folin-Ciocalteu, aluminium chloride test and 2, 2-diphenyl-1-picrylhydrazyl (DPPH) assay, respectively. The result has revealed that the highest temperature led to the degradation of bioactive compound in *C. nutans* leaves. The highest phenolic content and antioxidant activity achieved at 55 °C and 25 minutes with 13.87 ± 0.15 mg gallic acid g^{-1} dry sample and 52.88 ± 3.91% inhibition, respectively. Meanwhile, greatest flavonoid content was obtained for 12.25 ± 1.01 mg quercetin g^{-1} of dry sample at 55 °C and 15 minutes of extraction. From this study, it was shown that *C. nutans* extraction has gained benefit from ultrasonic assisted extraction and has possibilities of being used for the herbs utilisation of beneficial food materials, nutraceuticals and pharmaceuticals at manufacturing industry.

Keywords: *Clinacanthus nutans*, ultrasonic assisted extraction, phenolic, flavonoid, antioxidant

Abstrak

Clinacanthus nutans (C. nutans) adalah spesies herba terkemuka yang ditanam secara meluas di rantau Asia Tenggara. Dalam kajian ini, kesan ultrasonik pada suhu (30 hingga 60 °C) dan masa (5 hingga 30 minit) yang berbeza terhadap kandungan fenolik, flavonoid dan aktiviti antioksida di dalam ekstrak daun *C. nutans* telah dikaji. Hasil pengekstrakan yang diperolehi telah dianalisa jumlah kandungan fenolik, flavonoid serta aktiviti antioksida setiapnya dengan menggunakan kaedah Folin-Ciocalteu, aluminium klorida dan ujian 2, 2-difenil-1-pikrilhidrazil (DPPH). Keputusan menunjukan bahawa, suhu yang tinggi menyebabkan penguraian sebatian bioaktif di dalam ekstrak *C. nutans*. Jumlah kandungan fenolik dan aktiviti antioksida yang tertinggi masing-masing telah didapati pada keadaan 55 °C dan 25 minit dengan nilai masing-masing adalah sebanyak 13.87 ± 0.15 mg asid galik g^{-1} sampel kering dan 52.88 ± 3.91% perencatan. Sementara itu, kandungan flavonoid pula telah diperolehi sebanyak 12.25 ± 1.01 mg quercetin g^{-1} sampel kering pada keadaan pengekstrakan 55 °C dan 15 minit. Hasil kajian ini menunjukan bahawa, kaedah pengekstrakan dengan bantuan ultrasonik amat berguna dalam pengekstrakan daun *C. nutans* dan mempunyai peluang yang tinggi dalam penggunaan herba yang bermanfaat di dalam industri pembuatan makanan, nutraseutikal serta farmaseutikal.

Kata kunci: *Clinacanthus nutans*, pengekstrakan bantuan ultrasonik, fenolik, flavonoid, antioksidan

Introduction

In recent times, there has been increasing consumer interest towards medicinal plants since it is healthier and free from side effects caused by synthetic products or drugs. Majority of the world population still rely upon plants and their extracts for primary health care and needs. The use of medicinal plants as herbal remedies still maintained their therapeutic effect in spite of overwhelming influence of modern medicine and tremendous advances made in the production of synthetic drugs. Their effectiveness, economical and less toxicity has made it popular and approved as a mode of treating diseases even in these modern times [1].

The pharmacological properties and phytoconstituents information in some herbal medicinal plants have offered a great potential to be used in medicinal research. *Clinacanthus nutans* is one of the herbs plant that belongs to the family of Acanthaceae and locally known as elephant's trunk leaves or Sabah snake grass in Malaysia. This plant has been widely cultivated throughout tropical regions including South East Asia and China [2]. *Clinacanthus nutans* leaves has been traditionally used to treat various diseases including skin rashes, insect and snake bites, lesions caused by herpes simplex virus, diabetes, and gout in Malaysia, Indonesia, Thailand and China [3]. In Malaysia, it is commonly used for its nourishing and antioxidant properties [4]. Antioxidant activity is very important in life as it helps to neutralise the oxidative damage caused by the production of free radicals in the body [5].

Natural antioxidant has more benefits, such as nontoxic and more easily decomposed by bodies than artificial antioxidant. *Clinacanthus nutans* leaves extract is rich in natural antioxidant due to the phytochemical compounds presence in the plants that provide the antioxidant properties including phenolic and flavonoid compounds [6]. Phenolic and flavonoid compounds have been known for their ability to scavenge free radical reaction redox reaction due to their properties that can act as reducing agents, hydrogen donors, singlet oxygen quenchers and also other biological effect that provide health benefits for human beings [7]. Many research have been done in quantification of the total phenolic, flavonoid content and antioxidant activity from *C. nutans* leaves using organic solvents in conventional and modern extraction methods [8]. Conventional extraction method includes maceration and Soxhlet extraction is typically carried out at a longer extraction temperature and time which can cause degradation of thermal-labile compound including phenolic compounds. This extraction method is also known for its low efficiency and potentially hazardous to the environment due to high amount of solvent used which is very toxic, carcinogenic and not easily decomposed [8, 9].

Recently, diverse extraction technology has been developed in providing a new and simpler sample preparation methods with high performance such as supercritical fluid extraction (SCFE), accelerated solvent extraction (ASE), subcritical water extraction (SWE) and ultrasound assisted extraction (UAE) [10]. Ultrasonic-assisted extraction (UAE) is an effective alternative for conventional extraction method that offers an inexpensive and environmental friendly extraction process. This process is based on the use of mechanical waves at a frequency above the threshold of human hearing (>16 kHz). The enhancement of solvent penetration into plants cells attributed by the mechanical effects that travel through the solvent media and production of acoustic cavitation bubbles which disrupts the plant cell wall resulting the release of desired bioactive compound into the solvent matrix [11]. UAE provides a high production yield, lower energy input and temperature used, shorter extraction time, low solvent consume and improve extraction of thermal-labile compound at low temperature [12, 13]. Previous studies have reported the extraction on the bioactive compounds of *C. nutans* by other extraction techniques, however, no information is available on the effect of ultrasound-assisted extraction using water as the solvent medium on phenolics content and antioxidant in *C. nutans* leaves. Therefore, the goal of present investigation was to study the effect of temperature and time in water based ultrasonic assisted extraction on total phenolic, flavonoid content and antioxidant activity from *C. nutans* leaves.

Materials and Methods

Sample preparation

The sources of fresh leaves of *C. nutans* were collected from a local supplier, Kiza Herbs farm which is located in Temerloh, Pahang. Initially, the *C. nutans* leaves was first separated from the stems and washed thoroughly to remove impurities. Then, the leaves were dried at 40 °C for overnight. The dried leaves was further grinded and sieved through 1.18 mm mesh size. The powdered leaves were kept stored in air-tight vacuum pack at room temperature prior to the extraction process.

Ultrasonic assisted extraction

Five grams of powdered sample in 85ml of distilled water was ultrasonicated at different temperatures of 30, 35, 45, 55 and 60 °C and times for 5, 15, 25 and 30 minutes using a 28 kHz ultrasonic water bath (CT-420B Digital Ultrasonic Cleaner). The residual was separated and centrifuged at 1500 rpm for 15 minutes. The extracts were filtered and used for further analysis. All extractions were done in triplicates.

Analysis of phenolic content

The phenolics was analysed using Folin-Ciocalteu method according to Susanti et al. [9] with some modification. About 0.5 mL of leaves extract (10%) was added into test tube containing 2.5 mL Folin-Ciocalteu reagent and the mixture was left to stand for 5 minutes before adding 2 mL of sodium carbonate solution (75g/L) and vortexed (Heidolph, Germany) for 30 s. Afterwards, the mixture was incubated for two hours at room temperature to allow the reaction to take place. The resulting blue complex indicated the presence of TPC which was measured spectrophotometrically using a UV-VIS spectrophotometer (SP-3000*nano*, Japan) at 765 nm of absorbance. Phenolic amount was quantified based on mg gallic acid equivalent (GAE) per gram of dry sample. All determination conducted in triplicates.

Analysis of flavonoid content

Total flavonoids were analysed using aluminium chloride method modified from Tan et al. [14]. Briefly, 0.5 mL of extracted aliquot leaves (10%) was mixed with 2 mL of distilled water and 0.15 mL of sodium nitrite (5%). Then, about 0.15 mL of aluminium chloride solution (10%) was added after incubated for 5 min. The mixture was mixed thoroughly and left again for 6 min. Subsequently, 2 mL of sodium hydroxide (4%) was added and topped up the volume of mixture to 5 mL with distilled water. Finally, the mixture was shaken vigorously using a vortex (Fisherbrand, Denmark) and left in a dark for 15 minutes. Flavonoid content was measured at absorbance of 510 nm using a UV-VIS spectrophotometer (SP-3000*nano*, Japan) and the result was demonstrated in term of mg quercetin equivalent (QE) per gram of dry sample. All determination performs in triplicates.

Analysis of antioxidant activity

The method for estimating antioxidant activity of the extracts was adapted from Sharifi et al. [15] with some changes. Concisely, 3.5 mL of (0.004%) ethanolic 2,2'-diphenyl-1-picrylhydrazyl (DPPH) was mixed with 0.5 mL ethanolic leaves extract (25%). Next, the mixture was allowed to stand for 30 minutes at room temperature before spectrophotometrically measured using a UV-VIS spectrophotometer (SP-3000*nano*, Japan) at 517 nm of absorbance. The antioxidant activity was evaluated by comparing the sample absorbance with the control. Each measurement was done in triplicate. The calculation of antioxidant activity was made based on following equation:

$$\text{Antioxidant Activity (\% inhibition)} = \frac{A_c - A_s}{A_c} \times 100 \quad (1)$$

where *Ac* is absorbance of control and *As* is absorbance of tested sample.

Statistical analysis

The data was computed and statistically analysed using the Microsoft Excel 2013 software. All experiments were performed in triplicates and results were expressed as mean ± standard deviation (S.D). Two-way analysis of variance (ANOVA) was established using Minitab Software 17 for estimating the outcome of time and temperature instantaneously. All parameters were measured to provide statistically significant different to the process and the significant value was considered as $p < 0.05$ regarding to 95% confidence level. Meanwhile, the higher f value would responded as high significant effect to the process.

Results and Discussion

Analysis of total phenolic content

Ultrasound-assisted extraction (UAE) is one promising alternative to traditional methods as it is easy, inexpensive and very environmental friendly. The major advantages of the process are noted when it produces higher yield and fast rate extraction process. Temperature and time are the two important parameters for the extraction process in optimising the bioactive compounds including phenolics and flavonoids from plant sample. In this study, the effect of different temperatures (30 to 60 °C) and time (5 to 30 minutes) in UAE on total phenolic content (TPC), total flavonoid content (TFC) and antioxidant activity of *C. nutans* were investigated and discussed.

Figure 1 shows an increasing trend of TPC of *C. nutans* leaves extracts within the range of 11.05 ± 0.71 to 13.87 ± 0.15 mg GAE/g dry sample as the increase in temperature from 30 to 55 °C. The highest TPC (13.87 ± 0.15 mg GAE/g dry sample) was achieved at 55 °C and 25 minutes of extraction. However, a further increase in temperature from 55 to 60 °C has resulted in decreasing of TPC. This finding was in agreement with Altemimi et al. [16] which indicated that the increase of ultrasonic temperature from 30 to 50 °C has increased the extraction of TPC in peach extracts and showed a reduction afterwards. The increase of TPC may be due to the increase of both solubility of solute and solvent diffusivity as the increase of temperature enhanced the efficiency of TPC extraction. Besides, the increase of extraction temperature with the aid of mechanical waves from sonication has increased the production of acoustic cavitation bubble that destroyed the plant cell wall resulting more phenolic compounds in plant cells that being released into the solvent matrix [16]. Yim et al. [17] also found that the TPC of *Schizophyllum commune* was increased when the temperature was raised from 30 to 42.5 °C. However, a decreasing of TPC from 42.5 to 55 °C was observed which probably due to the destruction of phenolic compounds. The increasing temperature enhances the extraction, but at beyond a certain extent, phenolic compounds could be destroyed [17]. Besides, the stability of compounds could be affected due to chemical and enzymatic degradation or losses by thermal decomposition which resulting in a decreasing of TPC [18].

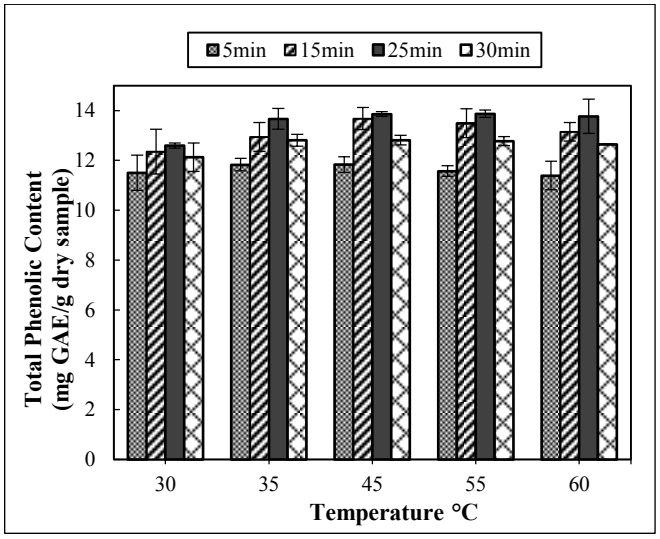


Figure 1. The total phenolic content of *C. nutans* extracts at different times and temperatures

Statistical evaluation of both extraction conditions (temperature and time) has demonstrated a high significant difference ($p < 0.05$) with time which indicated more significant effect on TPC than temperature with the highest f value of 55.10. This finding is parallel with those found by Gan and Latif [19], as the extraction of TPC from *Parkia speciosa* pod was shown as more likely to be significantly affected by the extraction of time than temperature. They suggested that increasing the temperature may enhance the internal reaction between phenols and other plants components which further hindered the extraction. Thus, extraction time becomes significant since

larger extraction periods might cause more extended polyphenol losses. Moreover, the increase of temperature enhances the contact time for the disintegration of plant cells by cavitation bubbles which also enhance the extraction of phenolics [20]. Nevertheless, prolonged extraction time over 30 min may cause more extended phenolics losses due to the thermal degradation or polymerisation reaction of various phenols which effects the analytical quantification [21].

Analysis of total flavonoid content

Figure 2 indicates a gradual increase of total flavonoid content (TFC) with increasing of temperature within 30 to 55 °C in ranging of 8.97 ± 0.68 to 12.25 ± 1.01 mg quercetin/g of dry sample and followed by a slight decrease when the temperature was above 55 °C. Increasing temperature in UAE might soften the plant tissue, weaken the cell wall integrity and enhance phenolic compounds solubility thus, resulting in a higher dissolution of phenolics in solvent [22]. However, the increase of ultrasonic temperature in this study gives only a slight increase of TFC. This finding was similar with Gan and Latif [19], who also found that the temperature ranges between 35 until 55 °C did not significantly affect the phenolic compounds (flavonoids) *Parkia speciosa* pod. This could be explained through the presence of thermal stability of flavonoid compounds in *C. nutans* leaves within the temperature range and the increase of TFC might be due to the disintegrating of *C. nutans* wall by ultrasonic waves that helps the release of flavonoids in the solvent which then increasing the TFC [23]. Nevertheless, a higher temperature of 60 °C significantly reduces TFC, possibly by denaturation of cell membranes. This finding was similar with Cacae et al. [24], which found that the degradation of flavonoids may occur when the temperatures exceeds 50 °C. Teh and Birch. [25], also reported that TFC from canola seed cake extracts rose with temperature from 40 to 50 °C, but decreases at 60 °C due to the decomposition of flavonoid compounds.

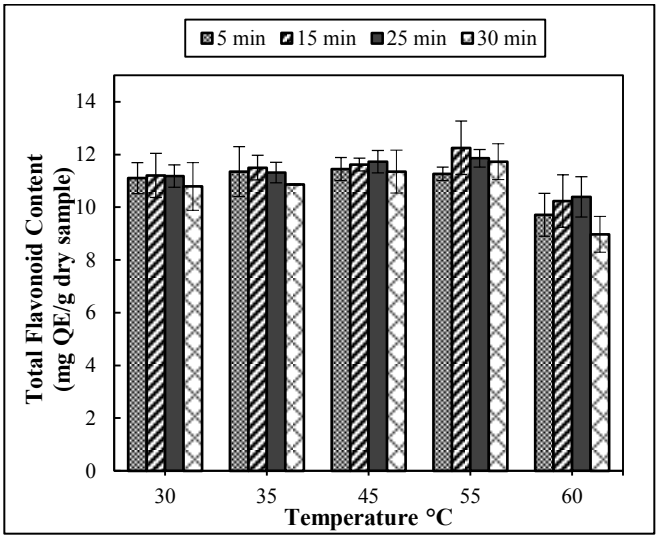


Figure 2. The total flavonoid content of *C. nutans* extracts at different times and temperatures

A significant difference ($p > 0.05$) between the temperature and extraction of flavonoids has been described statistically with little difference observed in the TFC in each time of extraction. This observation might be attributed to the presence of various degrees of polymerisation and interactions that occurred between flavonoid compounds in plant cell and the solvent at different extraction time which led to the final equilibrium constant to be attained [26]. Hence, prolonged extraction time in this study was unnecessary and degradation of flavonoid likely happened [27]. On top of that, Durling et al. [28] have proposed that the extraction time of 15 minutes in the ultrasonic assisted extraction is the best duration in extracting the flavonoid compounds. Therefore, it can be concluded that TFC has scored the highest (12.25 ± 1.01 mg quercetin/g of dry sample) at 55 °C and 15 minutes of extraction time.

Analysis of antioxidant activity

The changes of purple color of ethanolic 2,2'-diphenyl-1-picrylhydrazyl (DPPH) into yellowish indicates the reduction of DPPH as free stable radical to α, α-diphenyl-β-picryl hydrazine when reacted with compounds of antioxidant [29]. As displayed in Figure 3, the antioxidant activity increases with temperature from 30 to 55 °C in ranging of 35.56 to 52.88% inhibition at a given time and eventually decreases at further temperature. The highest antioxidant activity (52.88% inhibition) was determined at 55 °C and 25 minutes. Typically, the increasing extraction temperature has generated higher antioxidant activity which is similar to the finding by Pinelo et al. [30] where they found that the stability antioxidant compounds were affected at temperature above 50 °C and the disruption of the plant cells may affect the antioxidant capacity. Altemimi et.al [21] has revealed that there was reduction of antioxidant activity at temperature above 50 °C. Thus, the decrease of antioxidant activity as rising temperature beyond 55 °C region has been observed in this study and might conceivably due to the degradation of some thermally unstable antioxidative compounds.

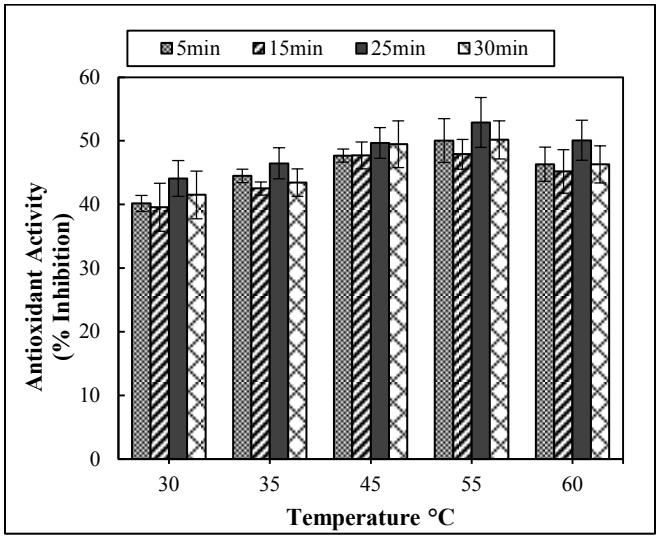


Figure 3. The antioxidant activity of *C. nutans* extracts at different times and temperatures

The result has determined the highest antioxidant activity (52.88% inhibition) during 55 °C and 25 minutes of extraction. There is a kind of fluctuation (increase and decrease) of antioxidant activity which was observed between 5 to 30 minutes of extraction. A slight decrease of antioxidant activity can be clearly seen at 15 minutes of extraction which probably explained by the presence of synergistic effect of other involved parameters. Besides, the decomposition of antioxidant compound may happen because of the thermal-based oxidation reaction that occurs during the extraction process [31]. Meanwhile, the statistical analysis has revealed that there was a significant effect of extraction temperature ($p < 0.05$) on antioxidant activity and there was no significant effect of extraction time ($p > 0.05$) on antioxidant activity. Extended extraction time has also led to an increase of adhesion of diffused particles (antioxidant compound) around the walls of the supporting material like glass or plastic tubes that may interrupt the process of extraction. Hence, this can be used to explain the insignificant effect of time on antioxidant activity in this study [31].

Conclusion

The present investigation also revealed that the total content of phenolic, flavonoid and antioxidant activity has been successfully extracted from *C. nutans* leaves at elevated temperature and time by water-based ultrasonic assisted extraction (UAE). All the extraction of the total content of phenolic and flavonoid with antioxidant activity were achieved highest at temperature 55 °C and subsequently degraded with further extraction temperature. Hence, this study showed that *C. nutans* extraction could have been benefited from UAE and promised the potential to be used for the herbs utilization of beneficial food materials, nutraceuticals and pharmaceuticals at manufacturing industry.

Acknowledgement

The financial support for this project was provided by Takasago, 4B264 and NRGS, 4H025 from MOE, Malaysia and Malaysia-Japan International Institute of technology (MJIIT), Universiti Teknologi Malaysia which is gratefully acknowledged.

References

1. Kumar Dash, G. and Deb, J. (2014). Pharmacognostical studies on stem bark of *Acacia ferruginea* DC. *Der Pharmacia Lettre,* 6(3): 61-66.
2. Aslam, M. S., Ahmad, M. S., Mamat, A. S., Ahmad, M. Z. and Salam, F. (2016). Antioxidant and wound healing activity of polyherbal fractions of *Clinacanthus nutanss* and *Elephantopus scaber*. *Evidence-based Complementary and Alternative Medicine,* 2016: 1-14.
3. Alam, A., Ferdosh, S., Ghafoor, K., Hakim, A., Juraimi, A. S., Khatib, A. and Sarker, Z. I. (2016). *Clinacanthus nutans*: A review of the medicinal uses, pharmacology and phytochemistry. *Asian Pacific Journal of Tropical Medicine,* 9(4): 402-409.
4. Yahaya, R., Dash, K., Abdullah, M. S. and Mathews, A. (2015). *Clinacanthus nutans* (burm. F.) Lindau: A useful medicinal plant of south-east Asia. *International Journal of Pharmacy and Pharmaceutical Research,* 7(6): 1244-1250.
5. Tee, L. H., Ramanan, R. N., Tey, B. T., Chan, E. S., Azrina, A., Amin, I., Bao, Y., Lau, C. Y. and Prasad, K. N. (2105). Phytochemicals and antioxidant capacities from *Dacryodes rostrata* fruits. *Medicinal Chemistry,* 5(1): 23-27.
6. Solibun, A. and Sivakumar, K. (2016). Sabah snake grass extract pre-processing: Preliminary studies in drying and fermentation. *IOP Conf. Series: Earth and Environmental Science,* 36: 1-7.
7. Gharekhani, M., Ghorbani, M. and Rasoulnejad, N. (2012). Microwave-assisted extraction of phenolic and flavonoid compounds from *Eucalyptus camaldulensis* Dehn leaves as compared with ultrasound-assisted extraction. *Latin American Application Research,* 42: 305-310.
8. Raya, K. B., Ahmad, S. H., Farhana, S. F., Mohammad, M., Tajidin, N. E. and Parvez, A. (2015). Changes in phytochemical contents in different parts of *Clinacanthus nutans* (Burm. f.) Lindau due to storage duration. *Bragantia,* 74: 445-452.
9. Susanti, R. F., Kurnia, K., Vania, A. and Reynaldo, I. J. (2015). Total phenol, flavonoid and antioxidant activity of *Physalis angulata* leaves extract by subcritical water extraction. *Modern Application Science,* 9(7): 190-198.
10. Pang, S. F., Yusoff, M. M., Abdullah. C. L. and Gimbun, J. (2015). Ultrasonic assisted extraction of phenolic and flavonoid content from *Orthosiphon stamineus* leaves. *Science Technology Progress,* 1: 10-13.
11. Picó, Y. (2013). Ultrasound-assisted extraction for food and environmental samples. *TrAC Trends in Analytical Chemistry,* 43: 84-99.
12. Dent, M., Dragović-Uzelac, V., Elez Garofulić, I., Bosiljkov, T., Ježek, D. and Brnčić, M. (2015). Comparison of conventional and ultrasound-assisted extraction techniques on mass fraction of phenolic compounds from sage (*Salvia officinalis* L.). *Chemical and Biochemistry,* 29: 475-484.
13. Vilkhu, K., Mawson, R., Simons, L. and Bates, D. (2008). Applications and opportunities for ultrasound assisted extraction in the food industry: A Review. *Innovative Food Science and Emerging Technologies,* 9(2): 161-169.
14. Tan, S. P., Parks, S. E., Stathopoulos, C. E. and Roach, P. D. (2014). Extraction of flavonoids from bitter melon. *Food and Nutrition Sciences*, 5(5): 458-465.
15. Sharifi, A., Mortazavi, S. A., Maskooki, A., Niakousari, M. and Elhamirad, A. H. (2013). Optimization of subcritical water extraction of bioactive compounds from barberry fruit (*Berberis vulgaris*) by using response surface methodology. *International Journal of Agriculture and Crop Sciences,* 6(2): 89-96.
16. Altemimi, A., Watson, D. G., Choudhary, R., Dasari, M. R. and Lightfoot, D. A. (2016). Ultrasound assisted extraction of phenolic compounds from peaches and pumpkins. *PLoS ONE,* 11(2): 1-20.
17. Yim, H. S., Chye, F. Y., Rao, V., Low, J. Y., Matanjun, P., How, S. E. and Ho, C. W. (2013). Optimization of extraction time and temperature on antioxidant activity of *Schizophyllum commune* aqueous extract using response surface methodology. *Journal of Food Science and Technology,* 50(2): 275-283.

18. Kiassos E., Mylonaki S., Makris D. P., Kiassos P. K. E, Mylonaki S., Makris D. P. and Kefalas P. (2009). Implementation of response surface methodology to optimise extraction of onion (*Allium cepa*) solid waste phenolics. *Innovative Food Science Emerging Technology,* 10: 246-252.
19. Gan, C. Y. and Latiff, A. A. (2011). Optimisation of the solvent extraction of bioactive compounds from *Parkia speciosa* pod using response surface methodology. *Food Chemistry,* 124: 1277-1283.
20. Wang, J., Sun, B., Cao, Y., Tian, Y. and Li, X. (2008). Optimisation of ultrasound-assisted extraction of phenolic compounds from wheat bran. *Food Chemistry,* 106: 804-810.
21. Gimbun, J., Ishak, N. F., Muhammad, N. I. S., Pang, S. F., Kadir, M. A. A., Ramli, H. and Khadisah, Z. (2014). Ultrasonic assisted extraction polyphenols and antioxidant from *Nigella sativa* seed. *Journal of Engineering and Technology,* 5(2): 17-26.
22. Tabaraki, R. and Nateghi, A. (2015). Optimization of ultrasonic-assisted extraction of natural antioxidants from rice bran using response surface methodology. *Ultrasonics Sonochemistry,* 18(6): 1279-1286.
23. Altemimi, A., Choudhary, R., Watson, D. G. and Lightfoot, D. A. (2015). Effects of ultrasonic treatments on the polyphenol and antioxidant content of spinach extracts. *Ultrasonic Sonochemistry,* 24: 247-255.
24. Cacace J. E. and Mazza G. (2003) Mass transfer process during extraction of phenolic compounds from milled berries. *Journal of Food Engineering,* 59: 379-389.
25. Teh, S. S. and Birch, E. J. (2014). Effect of ultrasonic treatment on the polyphenol content and antioxidant capacity of extract from defatted hemp, flax and canola seed cakes. *Ultrasonics Sonochemistry,* 21(1): 346-353.
26. Silva, A. J., Silva, J. R., de Souza, N. C. and Souto, P. C. (2014). Membranes from latex with propolis for biomedical applications. *Materials Letters,* 116: 235-238.
27. Wang, T., He, F. and Chen, G. (2014). Improving bio accessibility and bioavailability of phenolic compounds in cereal grains through processing technologies: A concise review. *Journal of Functional Foods,* 7: 101-111.
28. Durling, N. E., Catchpole, O. J., Grey, J. B., Webby, R. F., Mitchell, K. A., Foo, L. Y. and Perry, N. B. (2007). Extraction of phenolics and essential oil from dried sage (*Salvia officinalis*) using ethanol water mixtures. *Food Chemistry,* 101(4): 1417-1424.
29. Sharma, O. P. and Bhat, T. K. (2009). DPPH antioxidant assay revisited. *Food Chemistry,* 113(4): 1202-1205.
30. Pinelo, M., Rubilar, M., Jerez, M., Sineiro, J. and Núñez, M. J. (2005). Effect of solvent, temperature, and solvent-to-solid ratio on the total phenolic content and antiradical activity of extracts from different components of grape pomace. *Journal of Agricultural and Food Chemistry,* 53(6): 2111-2117.
31. Sathishkumar, T., Baskar, R., Aravind, M., Tilak, S., Deepthi, S. and Bharathikumar, V. M. (2013). Simultaneous extraction optimization and analysis of flavonoids from the flowers of *Tabernaemontana heyneana* by high performance liquid chromatography coupled to diode array detector and electron spray ionization/mass spectrometry. *International Scholarly Research Notices Biotechnology,* 13: 1-10.

Malaysian Journal of Analytical Sciences, Vol 22 No 4 (2018): 667 - 675
DOI: https://doi.org/10.17576/mjas-2018-2204-13

MALAYSIAN JOURNAL OF ANALYTICAL SCIENCES
Published by The Malaysian Analytical Sciences Society
ISSN 1394 - 2506

EFFECT OF INCORPORATING PURPLE-FLESHED SWEET POTATO IN BISCUIT ON ANTIOXIDANT CONTENT, ANTIOXIDANT CAPACITY AND COLOUR CHARACTERISTICS

(Kesan Penambahan Keledek Ungu ke dalam Biskut Terhadap Kandungan Antioksida, Kapasiti Antioksidan dan Ciri-Ciri Warna)

Azni A. Aziz[1,3], Alyani Mohd Padzil[1], Ida Idayu Muhamad[1,2]*

[1]*Bioprocess and Polymer Engineering Department, School of Chemical and Energy Engineering, Faculty of Engineering*
[2]*Cardiac Biomaterials Cluster, IJN-UTM Cardiovascular Engineering Center, School of Biomedical Engineering and Health Sciences, Faculty of Engineering*
Universiti Teknologi Malaysia, 81310 Johor Bahru, Johor, Malaysia
[3]*Technology and Natural Resources Department, Faculty of Applied Sciences and Technology,*
Universiti Tun Hussein Onn Malaysia, 86400 Batu Pahat, Johor, Malaysia

**Corresponding author: idaidayu@utm.my*

Received: 16 April 2017; Accepted: 7 April 2018

Abstract

Purple flesh sweet potato (PFSP) is considered to be a nutritionally rich crop. It also contain abundant amount of anthocyanin pigment which possess disease preventive properties. This work aims to study the effect of incorporating different form of processed PFSP, namely fresh, flour, and paste in biscuit formulation. Analysis was performed on the total phenolic, total anthocyanin content, antioxidant capacity, and colour characteristics. The analyses were made on samples, before and after the incorporation of PFSP in the biscuit. PFSP flour was prepared by directly using hot air-drying at 65 ºC for 18 hours while PFSP paste was steamed for 30 minutes at 100 ºC. The PFSP fresh contained total anthocyanin content at 21.40 mg CyE/100 g fw, and the content increased when processed into the form of flour and paste approximately at 38.90 mg CyE/100 g fw and 52.48 mg CyE/100 g fw, respectively. All forms of processed PFSP enhanced the purple colour when incorporated into the biscuit formulation. The experimental results showed that biscuit added with PFSP lost 15–36% of antioxidant capacity. Based on these findings, all forms of PFSP can be a natural colourant, a potential functional food ingredient, and can become a superior source for the production of foods with health benefits.

Keywords: purple-fleshed sweet potato, biscuit, phenolic, anthocyanin, antioxidant capacity, colour

Abstrak

Keledek ungu (PFSP) dianggap sebagai tanaman kaya khasiat. Ia juga mengandungi sejumlah besar pigmen antosianin yang mempunyai sifat pencegah penyakit. Kajian ini bertujuan untuk mengkaji kesan penambahan PFSP yang diproses dalam beberapa bentuk berbeza iaitu mentah, tepung, dan pes ke dalam formulasi biskut. Analisis dilakukan terhadap jumlah fenolik, jumlah kandungan antosianin, kapasiti antioksidan, dan ciri-ciri warna. Analisis kajian dijalankan terhadap sampel, sebelum dan selepas PFSP dimasukkan ke dalam biskut. Tepung PFSP disediakan dengan menggunakan pengeringan udara panas pada suhu 65 ºC selama 18 jam manakala pes PFSP dikukus selama 30 minit pada suhu 100 ºC. PFSP mentah mengandungi jumlah kandungan antosianin sebanyak 21.40 mg CyE/100 g fw, dan kandungannya meningkat apabila diproses ke dalam bentuk tepung dan pes iaitu masing-masing sebanyak 38.90 mg CyE/100g fw dan 52.48 mg CyE/100g fw. Kesemua bentuk PFSP yang diproses meningkatkan warna ungu apabila dimasukkan ke dalam formulasi biskut. Keputusan eksperimen menunjukkan biskut yang ditambah PFSP hilang kapasiti antioksidan sebanyak 15–36%. Berdasarkan dapatan ini, semua bentuk PFSP dapat menjadi

pewarna semula jadi, berpotensi sebagai bahan makanan berfungsi, dan boleh menjadi sumber penting untuk pengeluaran makanan dengan manfaat kesihatan.

Kata kunci: keledek ungu, biskut, fenolik, antosianin, kapasiti antioksidan, warna

Introduction

In recent years, interest on functional food or ingredients are increasing due to the rise in health conscious among consumers. Sweet potatoes are rich in vitamins B1, B2, C, and E; minerals such as calcium, magnesium, potassium and zinc; dietary fibre, and non-fibrous carbohydrates. There are many varieties of sweet potato available in the market. Sweet potato could be utilized in products to improve the colour, flavour, and nutrients content. In particular, anthocyanin can be found in abundant inside the purple-fleshed sweet potato varieties compared to other coloured-fleshed ones. The sweet potato roots exhibit the purple colour due to the build-up of anthocyanin as pigments. The sensory profiling for the purple sweet potatoes are characterized as fibrous visually and have chalky, dense, firm texture. The taste is characterised as of white baked potato flavour and vanilla aroma [1].

Previous research findings by Kim et al. [2] and Teow et al. [3] indicated that purple-fleshed sweet potato has higher antioxidant activities compared to other coloured-fleshed sweet potato. This is caused by the presence of anthocyanins and phenolic compounds in the storage roots. The anthocyanin is found to exhibit medical advantages, including reducing coronary illness and stroke, cancer-causing agent activity, anti-inflammatory effects, enhanced visual sharpness, and enhanced cognitive conduct [4, 5]. However, sweet potato is highly perishable and difficult to store. Thus, sweet potato can be processed into flour [6–8] and paste or puree [9–11], which could be incorporated into different appealing products for consumers, such as snacks, pasta, pancake, bread, and cookies.

Food can act as a vehicle to deliver bioactive and micronutrients at a suitable level. This is evidenced in a study by Chan et al. [12] which demonstrated an increment extraction yield, total phenolic substance, total flavonoid substance, and antioxidant capacity, showing that sweet potato flour bioactive compound could be stable in the gastrointestinal tract as their active component may be held and enhanced in the food. However, in creating a functional bakery product, it is essential to understand that a quality functional food not only to include the functional ingredients, but it must also meet consumers' necessities such as appearance, taste, and composition [13].

The main objectives of this study are (a) to determine the total phenolic, anthocyanin content, and antioxidant capacity of different PFSP forms, namely fresh, flour, and paste; (b) to compare the antioxidant content and capacity, before and after addition in biscuit formulation; and (c) to measure the colour characteristic of different PFSP forms and in biscuit, which will provide valuable information in utilizing PFSP in other formulated product.

Materials and Methods

Materials

The chemicals used in this study were of analytical grade, which includes acetone, chloroform, hydrochloric acid, Folin-Ciocalteu reagent, gallic acid, sodium carbonate, potassium chloride, sodium acetate, glacial acetic acid, methanol, 2,4,6-tri[2-pyridyl]-s-triazine (TPTZ), ferric chloride ($FeCl_3.6H_2O$), ferrous sulphate ($FeSO_4.7H_2O$), and 1,1-diphenyl-2-picrylhydrazyl (DPPH). The purple-fleshed sweet potato were purchased at a local market in Johor Bahru, Malaysia. Commercially available ingredients for biscuit formulation: wheat flour, butter, sugar, salt, and skim milk powder were purchased from a bakery shop in Johor Bahru.

Preparation of fresh, flour, and paste from purple-fleshed sweet potato

The three forms of PFSP were prepared by manually washing, peeling, and cutting into thin slices of 2 mm thick. PFSP fresh slices were further shredded into small pieces. PFSP flour was processed by directly using hot air-drying at 65 °C for 18 hours, finely ground using a commercial blender (Philips, Malaysia), and sieved through an 80-mesh (Retsch, Germany) screen to obtain uniform-size. The flours were then packed in polypropylene bags and stored at 5-10 °C until further use. Meanwhile, PFSP paste was made by steaming for 30 minutes at 100 °C, cooled, and mashed into paste.

Biscuit formulation
200 g wheat flour, 84 g sugar, 80 g butter, 2.5 g salt, and 2 g skim milk powder were used as the biscuit formulation. PFSP was incorporated at 30% flour weight basis. The butter and sugar was creamed, then salt, skim milk powder and water was added. Finally, the PFSP and wheat flour were mixed until uniform. The dough was rolled out at 5 mm thick and pressed using a 5 mm round cutter. The biscuit were then baked at 160 °C for 20 minutes in an electric oven (OT52R, Khind, Malaysia), cooled, and stored in a zip lock bag for further analysis. The analysis was performed on both conditions, before and after incorporation of PFSP in biscuit.

Extraction
Extraction of samples was performed as described by Rodriguez-Saona and Wrolstad [14]. The samples were freeze-dried (Alpha 1-2LD Plus, Martin Christ, Germany) at –50 °C for 12 hours. An amount of 50 g of the freeze-dried sample were weighed into a conical flask and mixed with 70% aqueous acetone 1:2 (w/v) by stirring for 15 minutes. The extract (filtrate) was obtained by filtering through Whatman No. 1 filter paper. The procedure was repeated thrice until a faintly coloured solution was attained. The filtrate was then transferred into a separating funnel and chloroform 1:2 (v/v) was added and gently mix until there is a clear partition between the two phases. The upper portion was then transferred into a rotary evaporator at 40 °C to remove the solvent residue and made up to 100 mL with acidified distilled water. The extraction was poured in a sample bottle and kept at 4 °C until further use. Duplicate extractions were made for each sample.

Total phenolic content
Total phenolic content was measured by Folin-Ciocalteu method [15]. Briefly, 20 µL of the sample extract was respectively mixed with 1.58 mL water, followed by 100 µL Folin-Ciocalteu reagent in a 1 cm, 2 mL plastic cuvette and incubated for 5 minutes. Then, 300 µL sodium carbonate solution was added, mixed, and incubated for 2 hours at room temperature. The sample was observed at 765 nm using a UV- Spectrophotometer (Jenway 7305 Spectrophotometer, USA). Gallic acid was used as a standard and the results was expressed as milligram of gallic acid equivalent (mg GAE/100g fw).

Total monomeric anthocyanin content
Total monomeric anthocyanin content was determined by using pH differential method [16]. Two 0.3 mL sample extracts were prepared for dilution. One was added with 2.7 mL potassium chloride buffer, pH 1.0 and another one was added with 2.7 mL sodium acetate buffer, pH 4.5. The sample was left to equilibrate for 15 minutes before using a UV-Spectrophotometer (Jenway 7305 Spectrophotometer, USA) to read the absorbance at 510 nm and 700 nm. Difference in absorbance between pH values and wavelengths were calculated using the following equation 1:

$$A = (A_{510nm} - A_{700nm})pH_{1.0} - (A_{510nm} - A_{700nm})pH_{4.5} \quad (1)$$

Meanwhile, concentration of monomeric anthocyanin pigment can be calculated as follows (equation 2):

$$\text{Monomeric anthocyanin pigment (mg/L)} = (A \times MW \times DF \times 1000) \div (\varepsilon \times 1) \quad (2)$$

where, MW is the molecular weight of Cyanidin-3-glucoside (MW = 449.2), ε is the molar absorptivity (ε = 26900), DF is the dilution factor, and 1 is for standard 1 cm path length. Results were expressed as mg cyanidin-3-glucoside equivalent (mg CyE/100g fw) because it is predominantly found in sweet potato.

Antioxidant capacity
Ferric Reducing Antioxidant Power (FRAP) was measured using a method adapted from Benzie and Strain [17]. In brief, 30 µL of sample extract was added into 1 mL of FRAP reagent (300 mM acetate buffer pH 3.6, 10 mM TPTZ in 40 mM HCl and 20 mM $FeCl_3$ at a ratio of 10:1:1). The mixture was left for 4 minutes and the absorbance was read at 593 nm using a UV-Visible spectrophotometer (Jenway 7305 Spectrophotometer, USA). Ferrous sulphate ($FeSO_4.7H_2O$) was used as a standard and FRAP was expressed as mg Fe/g fw.

The DPPH* radical scavenging assay was performed as described by Brand-Willams et al. [18] with a slight modification by mixing 0.2 mL of sample extract added with 1.8 mL of methanol and 2 mL DPPH (0.06 mM) in

methanol solution. The reaction mixtures were kept at room temperature in the dark for 30 minutes. The absorbance was measured at 517 nm using UV-Spectrophotometer (Jenway 7305 Spectrophotometer, USA). Antioxidant activity (%) by the DPPH free radical was calculated by using the following formula:

$$\text{Antioxidative activity (\%)} = \frac{A_b - A_s}{A_b} \times 100$$

where, A_b is the absorbance of blank (DPPH only) and A_s is the absorbance of sample.

Colour analysis

The colour of the samples was measured using a colorimeter (Konica Minolta, Japan) adopting CIE L*a*b* colour system and set with a D65 illuminant at 10º. The L* represents lightness, a* express (+) red or (-) green, and b* express (+) yellow or (-) blue. The chroma (C*) and hue angle (h*) was calculated by $[a^{*2} + b^{*2}]^{1/2}$ and arctan (b*/a*) respectively from the a* and b* values. C* represents the difference in saturation (+) brighter and (-) duller while h* indicates colour hue, where the units are in the form of degrees, ranging from 0° (red), 60° (yellow), 120° (green), 180° (cyan), 240° (blue), 300° (magenta), and back to 0°. The final data were averaged from six replications.

Statistical analysis

Analysis of variance (ANOVA) was carried out to determine and compare the significance of differences between means (comparison between means of samples). The results are shown as mean ± standard deviation of mean. The level of significance was set at $p < 0.05$.

Results and Discussion

Effect of different PFSP forms and its incorporation in biscuit on antioxidant content

As shown in Table 1, phenolic content in PFSP fresh is 76.70 mg GAE/100 g fw. After steaming into PFSP paste, the phenolic content increased nearly twice higher than the fresh sample. However, drying PFSP into flour did not show any significant difference compared to fresh sample. Cell structure was broken and ruptured during steaming which resulted in more components expressed from the tuber. Drying also released more bound phenolic from breakdown of cellular structure due to thermal treatment [19]. When incorporated in biscuit, the PFSP paste loss the most amount of total phenolic at 70%, while the PFSP fresh and flour at 46% and 33%, respectively. Substantial reduction in phenolic content was probable due to a cell rupture causing leaching into water, degradation from processing and oxidation by polyphenol oxidase [20].

Table 1. The total phenolic content and total anthocyanin content (means ± standard deviation) of different form of purple-fleshed sweet potato and its incorporation in biscuit

	Total Phenolic Content (mg GAE/100g fw)	**Total Anthocyanin Content (mg CyE/100g fw)**
PFSP Fresh	76.70 ± 1.24^{a}	21.40 ± 0.25^{a}
PFSP Flour	80.89 ± 1.58^{a}	38.90 ± 0.34^{b}
PFSP Paste	118.27 ± 2.77^{b}	52.48 ± 0.10^{c}
Incorporation in Biscuit		
Control	23.97 ± 0.14^{a}	-
PFSP Fresh	41.07 ± 0.28^{b}	3.55 ± 0.26^{a}
PFSP Flour	54.39 ± 0.88^{c}	10.81 ± 0.10^{b}
PFSP Paste	35.00 ± 0.29^{d}	4.14 ± 0.13^{c}

a, b, c means with different letter(s) in the same column differed significantly ($p < 0.05$)

PFSP paste had the highest total anthocyanin content at 52.48 mg CyE/100 g fw which was twice higher than the PFSP fresh. The results suggest that steaming of PFSP into paste inactivate enzymes that degrade anthocyanin pigments and other antioxidant compounds. This showed that PFSP fresh are a good source of anthocyanins and the level of these compounds increased when processed in different form. Anthocyanins found in this type of sweet potato exhibit more stability as compared to those in strawberry, raspberry, apple, and soybean with black seed coat with a low level of acylation [5]. Discoveries of acylated anthocyanins with better stability demonstrated that these colours may be more desirable in food product [21].

The antioxidant of a food matrix is likely to be enhanced when another functional ingredient is incorporated or substituted. As seen, after incorporation in biscuit formulation the anthocyanin content was still available where biscuit with PFSP flour (10.81 mg CyE/100 g fw) had the retention more than twice as compared to biscuit with PFSP fresh and paste. The stability of antioxidant compound anthocyanin in food processing could be seen in a study of biscuit production with added anthocyanin extract from red and black berries mix, sour cherries, grape, and pressed grape marc. The anthocyanin content in the baked cookies contained 103×10^{-3} g CyCl/ kg product. Considered that the mean weight of biscuits was about 8 g, five biscuits supply for about 4×10^{-3} g anthocyanins, similarly to the most marketed food supplements, that contain $2 \times 10^{-3} – 18 \times 10^{-3}$ g anthocyanins per dose [22].

Effect of different PFSP form and its incorporation in biscuit on antioxidant capacity

Ferric reducing power indicate the ability of natural antioxidant to donate electrons. Table 2 shows the FRAP values of the antioxidant extract of PFSP. PFSP paste had the highest reducing power (148.19 g Fe/g fw), while PFSP fresh exhibited the lowest power (85.97 g Fe/g fw) among all three forms. The PFSP flour and PFSP paste had significantly higher FRAP value 130.72 g Fe/g fw and 148.19 g Fe/g fw, respectively than the PFSP fresh samples, indicating that the reducing power in sweet potato was increased by thermal process [23]. Meanwhile, further thermal processing on biscuit causes the antioxidant capacity to be significantly reduced. The highest antioxidant capacity is biscuit with PFSP flour (28.64 g Fe/g fw), whereas the lowest is in biscuit with PFSP fresh (9.73 g Fe/g fw). However, all biscuits with PFSP incorporated showed a significant increase in antioxidant capacity as compared to control biscuit at 1.21 g Fe/g fw. This suggests that not only PFSP contribute to the colour of the biscuit, it also enhances the antioxidant capacity.

Table 2. The antioxidant capacity (means ± standard deviation) of different form purple-fleshed sweet potato incorporated in biscuit

	FRAP (mg Fe/g fw)	**DPPH (%)**
PFSP Fresh	85.97 ± 3.42^{a}	84.78 ± 0.37^{a}
PFSP Flour	130.72 ± 3.40^{b}	86.46 ± 0.26^{b}
PFSP Paste	148.19 ± 2.19^{c}	92.07 ± 0.65^{c}
Incorporation in Biscuit		
Control	1.21 ± 0.06^{a}	35.40 ± 1.05^{a}
PFSP Fresh	9.73 ± 0.04^{b}	54.12 ± 0.52^{b}
PFSP Flour	28.64 ± 0.27^{c}	73.82 ± 0.71^{c}
PFSP Paste	16.39 ± 0.16^{d}	64.12 ± 0.71^{d}

a, b, c, d means with different letter(s) in the same column differed significantly ($p < 0.05$)

There was significant difference in DPPH values among all forms of PFSP and when incorporated in biscuit as shown in Table 2. Obviously, the sample before being added in biscuit exhibits a higher radical scavenging activity between 84–92% in all forms. However, when incorporated in biscuit, PFSP paste suffered about 30% loss of antioxidant capacity. In comparison with PFSP flour in biscuit, only 15% lost in antioxidant capacity. PFSP fresh in biscuit has the lowest antioxidant capacity of 54.12% followed by PFSP paste 64.12%, and PFSP flour 73.82%. A study by previous researcher [24], showed that purple sweet potato demonstrated stronger DPPH radical-scavenging activities as compared to other commercial food pigments of the anthocyanidin family. DPPH radical scavenging activity can be contributed by the presence of anthocyanin or phenolic compound depending on the type of purple sweet potato cultivar. As demonstrated in a comparative study, the radical scavenger in cultivar Ayamurasaki and Kyushu-132 are dominantly contributed by anthocyanin while the cultivar of Miyanou-36 and Bise are from phenolic compounds [25]. This observation is supported by another study which showed that the antioxidant activity by sweet potato not only come from anthocyanins but also from an additive effect with hydroxycinnamic acids [26].

Effect of different PFSP form and its incorporation in biscuit on colour characteristics

The colour values are presented in Table 3 where PFSP fresh, flour, and paste exhibited hue angles of a purple (magenta) colour due to the rich accumulation of anthocyanins in the flesh of the storage roots. Analysis using HPLC-DAD/ESI-MS/MS on purple sweet potato concluded that the cyanidin and peonidin that contribute to the blue and red hue are the major contributor anthocyanin pigment colour found in purple-fleshed [27]. PFSP paste showed significantly lower L* value which is the darkest colour among all form. Inversely, when added in biscuit, PFSP flour had the lowest L* value. All forms of PFSP lost its negative b* value when incorporated in biscuit formulation. The difference in a* and b* values may be contributed to the amount of phenolic and anthocyanin content present [28]. When incorporated in biscuit, the hue angle was towards red colour and control biscuit exhibit a hue angle towards yellow colour as seen in a digital picture in Figure 1. The considerable changes of colour value in different forms of PFSP incorporated in biscuit was attributed to the degradation of anthocyanin during processing and baking [23].

Table 3. The colour characteristic (means ± standard deviation) of different form purple-fleshed sweet potato incorporated in biscuit

	L*	a*	b*	Chroma (C*)	Hue angle (h^*)
PFSP Fresh	32.77 ± 1.39^a	30.63 ± 1.71^a	-9.47 ± 1.07^a	32.06	342.82
PFSP Flour	61.22 ± 0.78^b	17.23 ± 0.31^b	-0.23 ± 0.16^b	17.23	359.24
PFSP Paste	27.08 ± 0.63^c	17.43 ± 0.40^b	-7.12 ± 0.19^c	18.83	337.78
Incorporation in Biscuit					
Control	75.40 ± 0.46^a	2.88 ± 0.34^a	31.03 ± 0.61^a	31.16	84.71
PFSP Fresh	62.93 ± 1.58^b	12.36 ± 1.16^b	15.45 ± 1.43^b	19.79	51.35
PFSP Flour	48.66 ± 0.68^c	20.94 ± 0.63^c	9.71 ± 0.69^c	23.08	24.89
PFSP Paste	59.46 ± 0.57^d	15.69 ± 0.88^d	11.09 ± 2.58^c	19.21	35.26

a, b, c, d Means with different letter(s) in the same column differed significantly ($p < 0.05$)

.

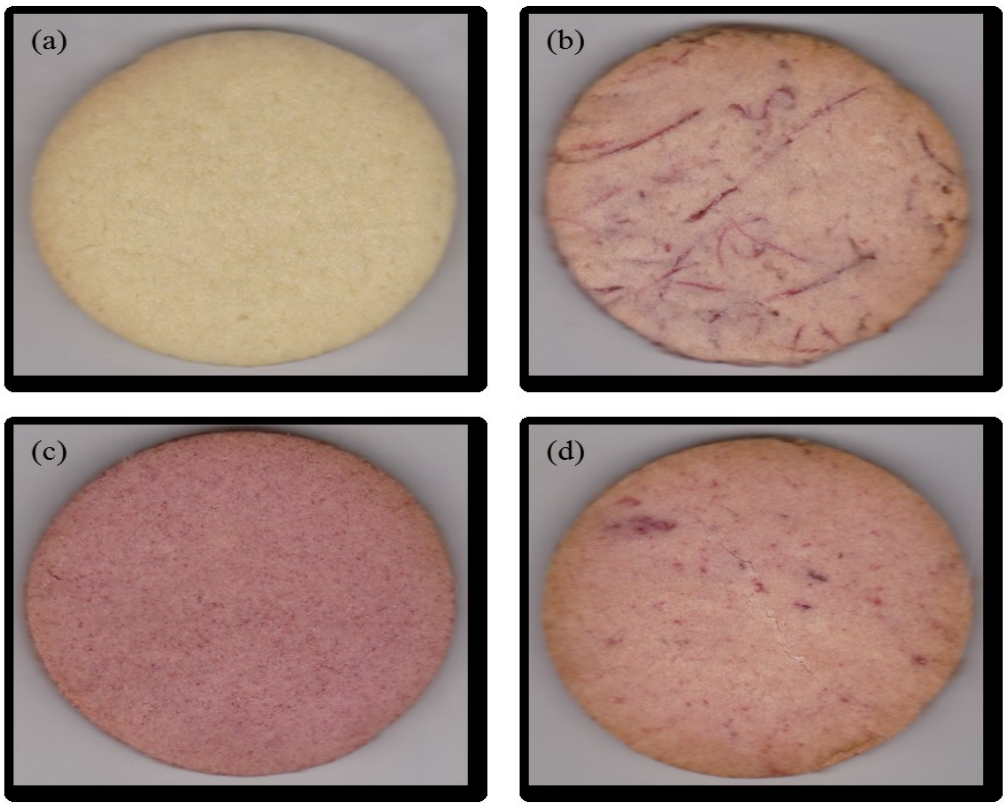


Figure 1. Biscuit incorporated with 30% different form PFSP. (a) Control, (b) PFSP fresh biscuit, (c) PFSP flour biscuit, (d) PFSP paste biscuit

Conclusion

Incorporation of any form of PFSP in biscuit not only produce a more attractive biscuit in terms of colour. It also add an additional content of phenolic and anthocyanin which significantly showed a higher antioxidant capacity compared to control biscuit, especially in PFSP flour form. Thus, more products utilizing purple flesh sweet potato could be commercialized in the near future and exert their health benefits by helping prevent lifestyle chronic disease.

Acknowledgement

The authors would like to thank Universiti Teknologi Malaysia (UTM), Universiti Tun Hussein Onn Malaysia (UTHM), Ministry of Higher Education (MOHE), Research Management Centre (RMC), UTM for their financial support of this work through the project number Q. J130000.3044.00M80 and R. J130000.7809.4F343 for their financial support of this work.

References

1. Leksrisompong, P. P., Whitson, M. E., Truong, V. D. and Drake, M. A. (2012). Sensory attributes and consumer acceptance of sweet potato cultivars with varying flesh colour. *Journal of Sensory Studies,* 27 (1): 59-69.
2. Kim, J. M., Park, S. J., Lee, C. S., Ren, C., Kim, S. S. and Shin, M. (2011). Functional properties of different korean sweet potato varieties. *Food Science and Biotechnology,* 20(6): 1501-1507.
3. Teow, C. C., Truong, V. D., McFeeters, R. F., Thompson, R. L., Pecota, K. V. and Yencho, G. C. (2007). Antioxidant activities, phenolic and β-carotene contents of sweet potato genotypes with varying flesh colours. *Food Chemistry,* 103(3): 829-838.

4. Wrolstad, R. (2006). Anthocyanin pigments-bioactivity and coloring properties. *Journal of Food Science,* 69(5): 419-425.
5. Suda, I., Oki, T., Masuda, M., Kobayashi, M., Nishiba, Y. and Furuta, S. (2003). Physiological functionality of purple-fleshed sweet potatoes containing anthocyanins and their utilization in foods. *Japan Agricultural Research Quarterly,* 37(3): 167-173.
6. Greene, J. L. and Bovell-Benjamin, A. C. (2004). Macroscopic and sensory evaluation of bread supplemented with sweet-potato flour. *Journal of Food Science,* 69(4): 167-173.
7. Huang, Y. C., Chang, Y. H. and Shao, Y. Y. (2006). Effects of genotype and treatment on the antioxidant activity of sweet potato in Taiwan. *Food Chemistry,* 98(3): 529-538.
8. Ruttarattanamongkol, K., Chittrakorn, S., Weerawatanakorn, M. and Dangpium, N. (2015). Effect of drying conditions on properties, pigments and antioxidant activity retentions of pretreated orange and purple-fleshed sweet potato flours. *Journal of Food Science and Technology,* 53(4): 1811-1822.
9. Wu, K. L., Sung, W. C. and Yang, C. H. (2009). Characteristics of dough and bread as affected by the incorporation of sweet potato paste in the formulation. *Journal of Marine Science and Technology,* 17(1): 13-22.
10. Steed, L. E. and Truong, V. D. (2008). Anthocyanin content, antioxidant activity, and selected physical properties of flowable purple-fleshed sweetpotato purees. *Journal of Food Science,* 73(5): 215-221.
11. Ginting, E. and Yulifianti, R. (2015). Characteristics of noodle prepared from orange-fleshed sweet potato, and domestic wheat flour. *Procedia Food Science,* 3: 289-302.
12. Chan, K. W., Khong, N. M. H., Iqbal, S., Umar, I. M. and Ismail, M. (2012). Antioxidant property enhancement of sweet potato flour under simulated gastrointestinal pH. *International Journal of Molecular Sciences,* 13: 8987 – 8997.
13. Siró, I., Kápolna, E., Kápolna, B. and Lugasi, A. (2008). Functional food. product development, marketing and consumer acceptance- A review. *Appetite,* 51(3): 456-467.
14. Rodriguez-Saona, L. E. and Wrolstad, R. E. (2001). Extraction, isolation, and purification of anthocyanins. In *Current Protocols in Food Analytical Chemistry*. Hoboken, NJ, USA: John Wiley & Sons, Inc. F1.1.1 – F1.1.11.
15. Waterhouse, A. L. (2003). Determination of total phenolics. In *Current Protocols in Food Analytical Chemistry*. Hoboken, NJ, USA: John Wiley & Sons, Inc. I1.1.1 – I1.1.8.
16. Giusti, M. M. and Wrolstad, R. E. (2001). Characterization and measurement of anthocyanins by UV-visible spectroscopy. In *Current Protocols in Food Analytical Chemistry*. Hoboken, NJ, USA: John Wiley & Sons, Inc. F1.2.1 – F1.2.13.
17. Benzie, I. F. F. and Strain, J. J. (1996). The ferric reducing ability of plasma (FRAP) as a measure of "antioxidant power": The FRAP assay. *Analytical Biochemistry,* 239 (1): 70-76.
18. Brand-Williams, W., Cuvelier, M. E. and Berset, C. (1995). Use of a free radical method to evaluate antioxidant activity. *LWT - Food Science and Technology,* 28(1): 25-30.
19. Yang, J., Chen, J., Zhao, Y. and Mao, L. (2010). Effects of drying processes on the antioxidant properties in sweet potatoes. *Agricultural Sciences in China,* 9(10): 1522-1529.
20. Takenaka, M., Nanayama, K., Isobe, S. and Murata, M. (2006). Changes in caffeic acid derivatives in sweet potato (*Ipomoea batatas L.*) during cooking and processing. *Bioscience, Biotechnology, and Biochemistry,* 70(1): 172-177.
21. Giusti, M. M. and Wrolstad, R. E. (2003). Acylated anthocyanins from edible sources and their applications in food systems. *Biochemical Engineering Journal,* 14(3): 217-225.
22. Pasqualone, A., Bianco, A. M., Paradiso, V. M., Summo, C., Gambacorta, G., Caponio, F. and Blanco, A. (2015). Production and characterization of functional biscuits obtained from purple wheat. *Food Chemistry,* 180: 64-70.
23. Tang, Y., Cai, W. and Xu, B. (2015). Profiles of phenolics, carotenoids and antioxidative capacities of thermal processed white, yellow, orange and purple sweet potatoes grown in Guilin, China. *Food Science and Human Wellness,* 4 (3): 123-132.
24. Kano, M., Takayanagi, T., Harada, K., Makino, K. and Ishikawa, F. (2005). Antioxidative activity of anthocyanins from purple sweet potato, *Ipomoera batatas* cultivar ayamurasaki. *Bioscience, Biotechnology, and Biochemistry,* 69(5): 979-988.

25. Oki, T., Masuda, M., Furuta, S., Nishiba, Y., Terahara, N. and Suda, I. (2002). Involvement of anthocyanins and other phenolic compounds in radical-scavenging activity of purple-fleshed sweet potato cultivars. *Journal of Food Science,* 67(5): 1752-1756.
26. Philpott, M., Gould, K. S., Lim, C. and Ferguson, L. R. (2004). *In situ* and *in vitro* antioxidant activity of sweetpotato anthocyanins. *Journal of Agricultural and Food Chemistry,* 52(6): 1511-1513.
27. Truong, V. D., Deighton, N., Thompson, R. T., McFeeters, R. F., Dean, L. O., Pecota, K. V. and Yencho, G. C. (2010). Characterization of anthocyanins and anthocyanidins in purple-fleshed sweetpotatoes by HPLC-DAD/ESI-MS/MS. *Journal of Agricultural and Food Chemistry*, 58(1): 404-410.
28. Yang, J. and Gadi, R. L. (2008). Effects of steaming and dehydration on anthocyanins, antioxidant activity, total phenols and color characteristics of purple-fleshed sweet potatoes (*Ipomoea batatas*). *American Journal of Food Technology*, 3(4): 224-234.

Malaysian Journal of Analytical Sciences, Vol 22 No 4 (2018): 676 - 683
DOI: https://doi.org/10.17576/mjas-2018-2204-14

MALAYSIAN JOURNAL OF ANALYTICAL SCIENCES
Published by The Malaysian Analytical Sciences Society
ISSN 1394 - 2506

BIOSYNTHESIS OF SILVER NANOPARTICLES USING *Citrus grandis* PEEL EXTRACT

(Biosintesis Nanopartikel Perak dengan Menggunakan Ekstrak Kulit *Citrus grandis*)

Nur Syazana Jalani[1], Wong Michell[1], Wong Ee Lin[1], Sharifah Zati Hanani[1]*, Uda Hashim[2], Rozaini Abdullah[1]

[1]*Department of Chemical Engineering, Faculty of Engineering Technology,*
Universiti Malaysia Perlis, Kampus UniCITI Alam, 02100 Sungai Chuchuh, Padang Besar, Perlis, Malaysia
[2]*Institute Nano Electronic Engineering,*
Universiti Malaysia Perlis, 01000 Kangar, Perlis, Malaysia

**Corresponding author: sharifahzati@unimap.edu.my*

Received: 16 April 2017; Accepted: 7 March 2018

Abstract

In this study, *Citrus grandis* or pomelo peel extract was used to synthesize silver nanoparticles (AgNPs). The effect of reaction time, amount of plant extract and concentration of silver nitrate which could influence the biosynthesis process were also studied. The synthesized AgNPs were then characterized by UV-Visible spectroscopy, Fourier transform infra-red spectroscopy (FTIR) and field emission scanning microscopy (FESEM) equipped with energy dispersive X-ray (EDX). The resulting UV-Vis spectra of synthesized AgNPs from pomelo peel extract showed standard surface plasmon resonance band in range of 401-433 nm which indicated the presence of AgNPs. FTIR spectra confirmed the existence of possible functional groups which might be responsible for the reduction of nanoparticles. Most of the synthesized AgNPs were observed in spherical shape which ranged between 20-30 nm under the Field Emission Scanning Electron microscope. The EDX analysis showed the strong signal at 3 keV from the silver atoms in the synthesized nanoparticles which confirmed that the synthesis of AgNPs was successful.

Keywords: silver nanoparticles, *Citrus grandis* peel extract, biosynthesis, surface plasmon resonance

Abstrak

Dalam kajian ini, ekstrak kulit *Citrus grandis* atau limau bali telah digunakan untuk menghasilkan nanopartikel perak. Pengaruh masa tindak balas, jumlah ekstrak kulit limau bali dan kepekatan perak nitrat ke atas biosintesis nanopartikel perak turut dikaji. Pencirian nanopartikel perak yang terbentuk kemudiannya dijalankan menggunakan spektroskopi sinar UV, spektroskopi infra merah transformasi Fourier (FTIR) dan mikroskopi imbasan pancaran medan (FESEM) dilengkapi dengan sinar-X tenaga serakan (EDX). Spektra UV-Vis nanopartikel perak dari ektrak kulit limau bali menunjukkan puncak resonansi plasmon sekitar 401-433 nm yang membuktikan pembentukan nanopartikel perak. Spektra FTIR membuktikan kewujudan beberapa kumpulan berfungsi yang mungkin terlibat dalam proses penurunan nanopartikel. Kebanyakan nanopartikel perak dilihat berbentuk sfera dan bersaiz di antara 20-30 nm melalui mikroskopi imbasan pancaran medan. Analisis EDX pula menunjukkan isyarat yang kuat daripada atom perak dalam nanopartikel yang telah disintesis dan ini membuktikan sintesis nanopartikel perak telah berjaya.

Kata kunci: nanopartikel perak, ekstrak kulit *Citrus grandis*, biosintesis, puncak resonansi plasmon

Introduction

Silver nanoparticles (AgNPs) have applications in various fields due to their unique optical, physical, electrical and medicinal properties. Silver nanoparticles can be incorporated into biosensor materials [1], antimicrobial applications [2], cosmetic products [3] and electronic components [4].

Commonly, AgNPs can be synthesized by physical, chemical and biological methods. Although physical and chemical methods may produce well-defined AgNPs, but these conventional methods have several disadvantages. These methods usually involve expensive equipment, high energy consumption and operation conditions such as temperature and pressure. Besides, utilizing hazardous chemicals as reducing agent in synthesizing AgNPs such as sodium borohydride, $NaBH_4$ gives an adverse effect to health due to the absorption of harmful chemicals on its surface. This concern has enhanced the researchers to develop safe consumption nanoparticles and environmentally friendly processes through other biological approaches.

Recently, biosynthesis of nanoparticles has been an emerging research area which offers an alternative to conventional chemical and physical methods. The biosynthesis of AgNPs employing either microorganisms or plant extract offers an environmentally friendly process by using less toxic chemicals. However, plants are preferred because it does not involve any process of maintaining cell culture. Moreover, use of plant extracts also reduces the cost of microorganism isolation and their culture media. The synthesizing AgNPs from plant extract such as *Azadirachta indica* [5], *Prosopis farcta* [6], *Peumus boldus* [7] and *Carica Papaya* [8] have been reported extensively. Different plant showed different morphology of synthesized nanoparticles. The spherical shaped AgNPs having size in range from 4.7-11.5 nm were achieved using *Azadirachta indica* extract as reducing and capping agent [5]. Meanwhile, spherical AgNPs with size 10.8 nm was successfully synthesized from *Prosopis farcta* extract [6]. The reaction conditions such as amount of plant extract, concentration of silver nitrate and reaction time is important to achieve maximum number of synthesized nanoparticles. These parameters also affected the shape and size of the synthesized nanoparticles [7, 8].

Even though AgNPs have been synthesized from various plants, the synthesis of AgNPs from *Citrus grandis* or pomelo peel waste has been not reported. In this study, pomelo peel extract was used as natural reducing agent for the synthesis of AgNPs. This pomelo peel extract has an ability to reduce and stabilize the metallic ions. Besides, the influence of reaction time, amount of plant extract and concentration of silver nitrate on the synthesis of AgNPs were also studied.

Materials and Methods

Materials

The fresh *Citrus grandis* fruit was purchased from nearest stall. Silver nitrate and all chemicals (analytical grade) were purchased from Bendosen Laboratory Chemicals, Norway. All the chemicals were used as received without further purification process.

Preparation of plant extract

The pomelo peels were dried in the oven at 60 °C for 16 hours. Then, the pomelo peels were blended into fine powder and sieved [9]. The preparation of plant extract was prepared following the modified procedure from [10]. An amount 1g of pomelo was dissolved in 50 ml of distilled water and then heated at 70 °C for 30 minutes in a water bath heater. After 30 minutes, the extract was removed from the water bath heater and filtered with a filter paper.

Biosynthesis of silver nanoparticles

The AgNPs were synthesized following the procedure by Nakhjiri et al. [11] with slight modification. In a typical experiment, 10 ml of pomelo peel extract was added to 30 ml of 1 mM silver nitrate solution and then kept in a water bath maintained at 70 °C for 2 hours. The formation of AgNPs were confirmed due to the colour changes of the solution. A series of experiments were conducted to investigate the effect of condition parameters including reaction time, amount of plant extract and concentration of silver nitrate. The effect of reaction time was evaluated by incubating the reaction mixtures for 1, 2, 3, 4 and 5 hours in a water bath. The amount of plant extract was varied to 2.5, 5.0, 7.5, 10.0 and 12.5 ml while the concentration of silver nitrate is constant at 1 mM. The effect of silver salt was determined by varying the concentration of silver nitrate (0.5, 2.0, 4.0, 6.0, 8.0, 10.0 and 12.0 mM).

Characterization of synthesized silver nanoparticles

The UV-Vis spectrometer (Shimadzu, Model UV-1800 spectrophotometer) was used to measure the absorption spectra of the synthesized AgNPs against distilled water as blank. The absorbance of solution was recorded after diluting a small aliquot (0.5 ml) of sample with 5 ml deionized water.

FTIR analysis was carried out after the removal of the free biomass residue or compound that was not absorbed by repeated centrifugation and redispersion in water. Thereafter, the purified suspension was dried in hot air oven at 60 °C for 10-15 minutes. Finally, the dried nanoparticles were analyzed by FTIR spectrophotometer (Perkin Elmer) and the spectra was scanned in the range of 4000 cm^{-1} to 650 cm^{-1}. The sample was dispersed uniformly in a matrix of dry KBr and then compressed to form a clear disc which then examined directly.

The morphology of the synthesized AgNPs was determined using FESEM-EDX (Model FEI Nova NanoSEM 450) at the NOR Laboratory in University Science Malaysia by coating the nanoparticles with a fine layer of platinum and placed in the FESEM-EDX to view its surface image.

Results and Discussion

Visual observation and UV-Vis spectroscopy

The early prediction of the AgNPs formation by reduction of silver nitrate and pomelo peel extract can be observed by colour change of the mixture. The change of colour from colourless to yellowish-brown solution as shown in Figure 1 indicates the presence of AgNPs in the reaction mixture. The increase in colour intensity of reaction mixture could be due to increasing number of nanoparticles formed because of reduction of silver ions present in the aqueous solution. It is known that AgNPs appear yellowish-brown colour due to the excitation of the surface plasmon vibrations [12]. The surface plasmon resonance (SPR) phenomenon occurs when noble metal nanoparticles emit strong electromagnetic fields on the particle surface thus enhancing its radiative properties [13]. This leads to a strong absorption band at about 400-500 nm in UV-Vis spectra of AgNPs [14].

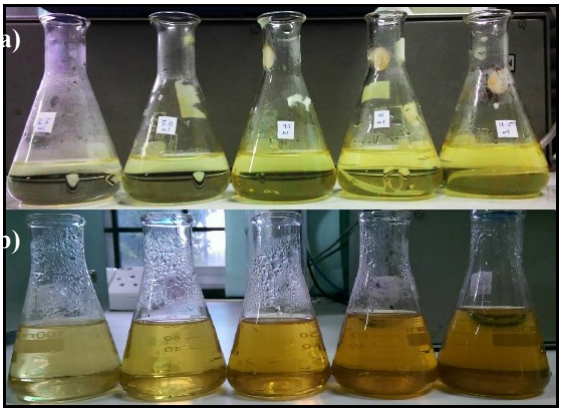


Figure 1. The colour of mixture reaction (a) before and (b) after the reaction

Effect of pomelo peel extract amount

Figure 2 shows the UV-Vis spectra of the synthesized AgNPs at different amount of pomelo peel extract from 2.5 ml to 12.5 ml. The UV-Vis spectra of synthesized AgNPs at pomelo peel extract from 5.0 ml to 12.5 ml showed the SPR peak obtained ranged from 401.6 nm to 407.6 nm as a result of silver plasmon resonance which confirmed the formation of AgNPs. The increase of pomelo peel extract results in increase of SPR intensity and the SPR band shifted to longer wavelength. The increase in intensity could be due to increasing number of nanoparticles formed because of reduction of silver ions present in the aqueous solution. Meanwhile the SPR band shifted to longer wavelength may be due to the amount of reducing agents found in the reaction mixture. As the amount of pomelo peel extract increases, more reducing agents are available. From Figure 2, the 12.5 ml of pomelo peels extract gave the highest SPR intensity where the reducing agent bounds itself to the surface of Ag^{+} and reduces it to Ag^{0} [15].

Meanwhile, no peak was observed at 2.5ml of pomelo peel extract. This is due to insufficient of reducing agent to complete the formation of AgNPs.

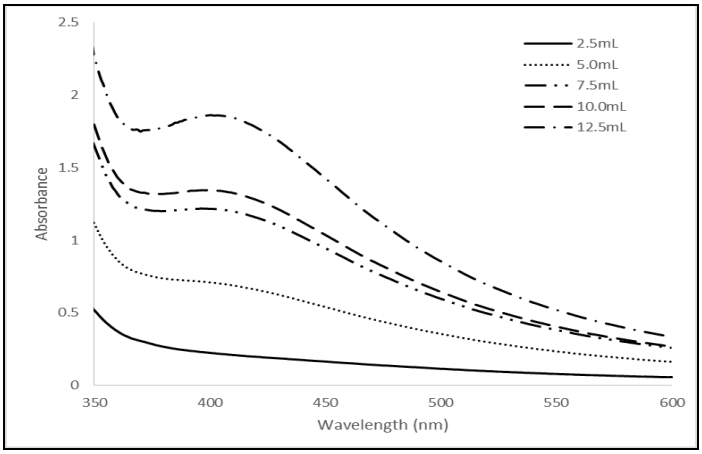


Figure 2. UV-Vis spectra of AgNPs synthesized at for various pomelo peel extract amount (Constant parameter: 1 mM $AgNO_3$, 70 ºC, 2 hours)

Effect of silver nitrate concentration

The UV-Vis spectra in Figure 3 shows the AgNPs were synthesized at different silver nitrate concentration. The SPR wavelengths vary from the range of 406 nm to 422 nm as the concentration silver nitrate increased from 1 mM to 5 mM. It was observed that as the concentration of silver nitrate increases, the SPR band shifts to the longer wavelength. This may suggest high concentrations of silver nitrate (3 mM to 5 mM) may cause the formation of large nanoparticles [16]. The highest SPR intensity can be observed at 2mM of silver nitrate. However, as the concentration further increase to 5 mM, the SPR intensity decreases. This phenomenon may occur due to the limited availability of functional groups in the pomelo peels extract to act as reducing agents [17]. Although the availability of silver ions for aggregation is high, the limited amount of reducing agent prevents the formation of AgNPs.

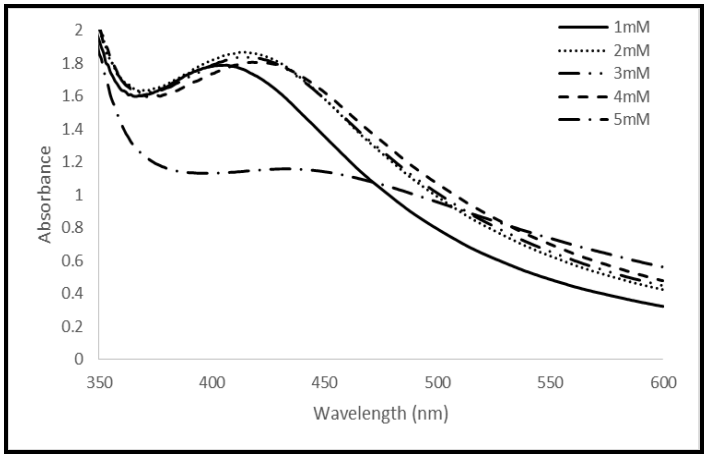


Figure 3. UV-Vis spectra of AgNPs at different concentration of silver nitrate (Constant parameter: 10 ml pomelo peel extract, 70 ºC, 2 hours)

Effect of reaction time

The UV-Vis spectra of synthesized AgNPs as shown in Figure 4 was synthesized at different reaction time. The SPR wavelength ranging from 401 nm to 415 nm as the reaction time increased from 1 hour to 5 hours. The SPR peak appeared at about 401 nm at the first hour and slowly shifts to the longer wavelength with increasing reaction time. The intensity of the SPR peak increased as the reaction time increased, which indicated the increased formation of the synthesized AgNPs. The increase in SPR intensity might be due to the transformation of OH groups to carbonyl groups because of silver ions reduction [18].

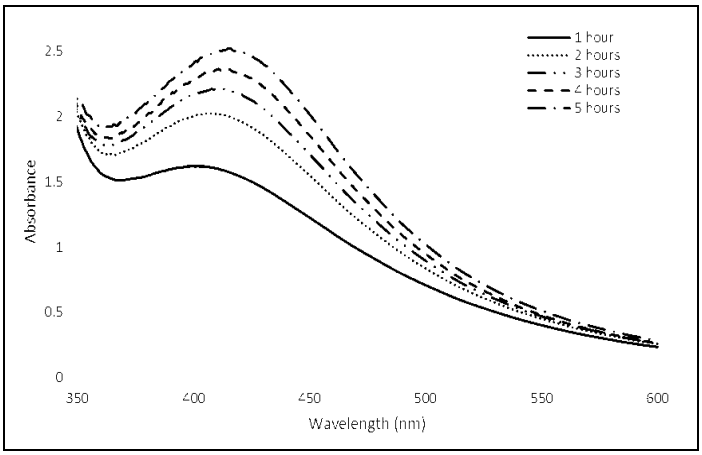


Figure 4. UV-Vis spectra of AgNPs at different reaction time (Constant parameter: 1 mM $AgNO_3$, 10 ml pomelo peel extract, 70 ºC)

FTIR analysis

The FTIR analysis was carried out to identify the major functional groups in pomelo peel and their possible involvement in AgNPs synthesis. Table 1 shows the shifting of peaks of peel extract which may suggest the involvement of the functional group in the formation of AgNPs. First, the shifting of the peak could be observed from 3357.90 cm^{-1} to 3380.21 cm^{-1} which is corresponds to H-bonded alcohols and phenols. Another shift is observed in peak from 1607.93 cm^{-1} to 1641.77 cm^{-1} which correspond to C=C of alkenes and C=N amine stretching. The shifting of these peaks indicates these functional groups might involve in the synthesis of AgNPs. Meanwhile, the observed peak at 1051.29 cm^{-1} denote –C-OC linkages and –C-O bonds which mainly attributed from flavonoids and terpenoids in pomelo peel extract [19]. The disappearance of these peaks in FTIR spectra of AgNPs suggest the involvement of these bioactive compounds in reducing silver ions to AgNPs.

Table 1. FTIR peak assignments of pomelo peel and synthesized AgNPs

Assignment	Pomelo Peel	AgNPs
H-bonded alcohols and phenols	3357.90 cm^{-1}	3380.21 cm^{-1}
C=C of alkenes and C=N amine stretching	1607.93 cm^{-1}	1641.77 cm^{-1}
C-N stretching and C-O stretching of amino and carboxyl groups	1051.29 cm^{-1}	-

Condition of synthesized AgNPs: 2 mM $AgNO_3$, 12.5 ml pomelo peel extract, 5 hours

FESEM-EDX analysis

The surface morphology of nanoparticles and their chemical composition was investigated using FESEM-EDX. Figure 5a and 5b show that most of the synthesized AgNPs are found to be in spherical shape and some are irregular which the size range between 20-30 nm. The aggregation of the synthesized AgNPs may be caused by cell

components present on the nanoparticles surface that acts as a capping agent [20]. The EDX profile in Figure 5c shows a spectral signal in silver region (Ag) approximately at 3 keV which corresponded to the absorption of metallic silver due to SPR of AgNPs [21]. The others signal from Cl, C, O, N and S atoms are also recorded which might be attributed to pomelo peel extract used.

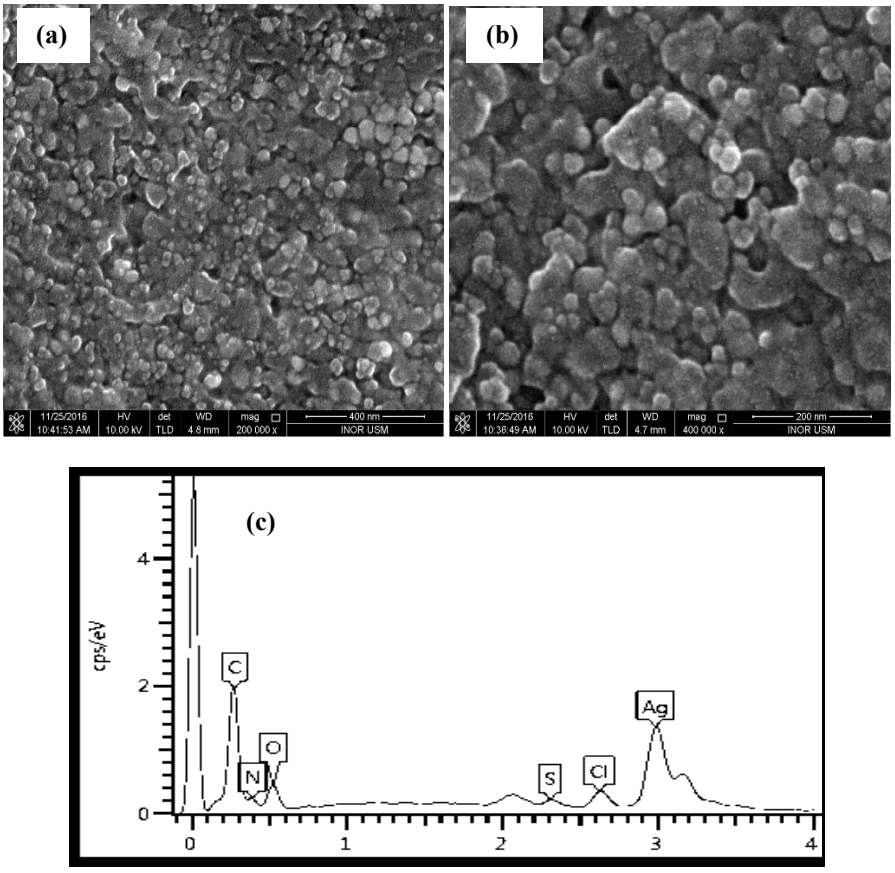


Figure 5. FESEM image of synthesized AgNPs at various resolutions (a) 200,000x, (b) 400,000x and (c) EDX profile showing the chemical composition (Condition of synthesized AgNPs: 2 mM $AgNO_3$, 12.5 ml pomelo peel extract, 5 hours)

Conclusion

The spherical and irregular AgNPs with size ranging from 20-30 nm were successfully synthesized using pomelo peel extract as reducing agent. The experiment done showed that parameters studied do affect the biosynthesis of AgNPs as the time and amount of peel extract was directly proportional to the number of AgNPs formed. In contrast, the number of AgNPs formed was inversely proportional to the concentration of silver nitrate.

Acknowledgement

This work has been supported by Ministry of Higher Education through research grant (FRGS 9003-00509). The authors were gratefully acknowledged Faculty of Engineering Technology and Institute of Sustainable Agrotechnology, Sungai Chuchuh for providing facilities to carry out this research. The author also appreciatively acknowledged Institute Nano Electronic Engineering for facilities and consultation support.

References

1. Ahmed, S., Ahmad, M., Swami, B. L. and Ikram, S. (2014). A review on plants extract mediated synthesis of silver nanoparticles for antimicrobial applications: A green expertise. *Journal of Advanced Research,* 7(1): 17-28.
2. Kotakadi, V. S., Rao, Y. S., Gaddam, S. A., Prasad, T. N. V. K. V, Reddy, A. V. and Gopal, S. V. R. S. (2013). Simple and rapid biosynthesis of stable silver nanoparticles using dried leaves of *Catharanthus roseus. Linn. G. Donn* and its antimicrobial activity. *Colloids and Surfaces B: Biointerfaces,* 105: 194-198.
3. Malik, P., Shankar, R., Malik, V., Sharma, N. and Mukherjee, T. K. (2014). Green chemistry based benign routes for nanoparticle synthesis. *Journal of Nanoparticles,* 2014: 1-14.
4. Sathyavathi, R., Krishna, M. B., Rao, S. V., Saritha, R. and Narayana Rao, D. (2010). Biosynthesis of silver nanoparticles using *Coriandrum sativum* leaf extract and their application in nonlinear optics. *Advanced Science Letters,* 3(2): 138-143.
5. Nazeruddin, G. M., Prasad, N. R., Waghmare, S. R., Garadkar, K. M. and Mulla, I. S. (2014). Extracellular biosynthesis of silver nanoparticle using *Azadirachta indica* leaf extract and its anti-microbial activity. *Journal of Alloys and Compounds,* 583: 272-277.
6. Miri, A., Sarani, M., Rezazade Bazaz, M. and Darroudi, M. (2015). Plant-mediated biosynthesis of silver nanoparticles using *Prosopis farcta* extract and its antibacterial properties. *Spectrochimica Acta - Part A: Molecular and Biomolecular Spectroscopy,* 141: 287-291.
7. Sanchez, G. R., Castilla, C. L., Gomez, N. B., Garcia, A., Marcos, R. and Carmona, E. R. (2016). Leaf extract from the endemic plant *Peumus boldus* as an effective bioproduct for the green synthesis of silver nanoparticles. *Materials Letters,* 183: 255-260.
8. Kokila, T., Ramesh, P. S. and Geetha, D. (2016). Biosynthesis of AgNPs using *Carica papaya* peel extract and evaluation of its antioxidant and antimicrobial activities. *Ecotoxicology and Environmental Safety,* 134: 467-473.
9. Zarina, Z. and Tan, S. Y. (2013). Determination of flavonoids in *Citrus grandis* (Pomelo) peels and their inhibition activity on lipid peroxidation in fish tissue. *International Food Research Journal,* 20(1): 313-317.
10. Nayak, D., Ashe, S., Rauta, P. R., Kumari, M. and Nayak, B. (2016). Bark extract mediated green synthesis of silver nanoparticles: Evaluation of antimicrobial activity and antiproliferative response against osteosarcoma. *Materials Science and Engineering C,* 58(1): 44-52.
11. Nakhjiri, F., Mirhosseini, M. and Mozaheb, M. A. (2013). Green synthesis of silver nanoparticles using olive leaf extract and its antibacterial activity. *Nanomedical Journal*, 4(2): 98-106.
12. Vasireddy, R., Paul, R. and Krishna, A. (2012). Green synthesis of silver nanoparticles and the study of optical properties. *Nanomaterial Nanotechnology,* 2: 1-6.
13. Huang, X. and El-Sayed, M, A. (2010). Gold nanoparticles: Optical properties and implementations in cancer diagnosis and photothermal therapy. *Journal of Advanced Research,* 1(1): 13-28.
14. Senthamilselvi, S., Kumar, P., Prabha, A. L. and Govindaraju, M. (2013). Green simplistic biosynthesis of anti-bacterial silver nanoparticles using *Annona Squamosa* leaf extract. *Nano Biomedical Engineering,* 5(2): 102-106.
15. Yang, N. and Li, W. (2013). Mango peel extract mediated novel route for synthesis of silver nanoparticles and antibacterial application of silver nanoparticles loaded onto non-woven fabrics. *Industrial Crops and Products,* 48: 81- 88.
16. Bar, H., Bhui, D. K., Sahoo, G. P., Sarkar, P., Pyne, S. and Misra, A. (2009). Green synthesis of silver nanoparticles using seed extract of *Jatropha curcas*. *Colloids and Surfaces A: Physicochemical and Engineering Aspects,* 348(1): 212-216.
17. Mansouri, S. S. and Ghader, S. (2009). Experimental study on effect of different parameters on size and shape of triangular silver nanoparticles prepared by a simple and rapid method in aqueous solution. *Arabian Journal of Chemistry***,** 2(1): 47-53.
18. Ahmad, B., Ali, J. and Bashir, S. (2013). Optimization and effects of different reaction conditions for the bioinspired synthesis of silver nanoparticles using *Hippophae rhamnoides Linn.* leaves aqueous extract. *World Applied Sciences Journal,* 22(6): 836-843.
19. Ahmed, S., Ullah, S., Ahmad, M. and Swami, B. L. (2015). Green synthesis of silver nanoparticles using *Azadirachta indica* aqueous leaf extract. *Journal of Radiation Research and Applied Sciences,* 9(1): 1-7.

20. Vanaja, M. and Annadurai, G. (2012). *Coleus aromaticus* leaf extract mediated synthesis of silver nanoparticles and its bactericidal activity. *Applied Nanoscience***,** 3(3): 217-223.
21. Prabakar, K., Sivalingam, P., Mohamed Rabeek, S. I., Muthuselvam, M., Devarajan, N., Arjunan, A. and Wembonyama, J. P. (2013). Evaluation of antibacterial efficacy of phyto fabricated silver nanoparticles using *Mukia scabrella* (Musumusukkai) against drug resistance nosocomial gram negative bacterial pathogens. *Colloids and Surfaces B: Biointerfaces,* 104: 282-288.

Malaysian Journal of Analytical Sciences, Vol 22 No 4 (2018): 684 - 692
DOI: https://doi.org/10.17576/mjas-2018-2204-15

MALAYSIAN JOURNAL OF ANALYTICAL SCIENCES
Published by The Malaysian Analytical Sciences Society
ISSN 1394 - 2506

PRODUCTION OF VOLATILE ORGANIC COMPOUNDS USING OIL PALM FROND JUICE AS A SOLE SUBSTRATE BY *Ceratocystis fimbriata*

(Penghasilan Sebatian Organik Meruap Menggunakan Jus Pelepah Kelapa Sawit Sebagai Substrat Tunggal oleh *Ceratocystis fimbriata*)

Nang Nor Azimah Long Nadzri[1], Mior Ahmad Khushairi Mohd Zahari[1]*, Saiful Nizam Tajuddin[2], Che Mohd Aizal Che Mohd [2]

[1]*Faculty of Chemical & Natural Resources Engineering*
[2]*Bio Aromatic Research Centre of Excellence*
Universiti Malaysia Pahang, Lebuhraya Tun Razak, 26300 Kuantan, Pahang, Malaysia

**Corresponding author: ahmadkhushairi@ump.edu.my*

Received: 16 April 2017; Accepted: 7 March 2018

Abstract

In this paper, the potential of oil palm frond (OPF) juice as an alternative and renewable carbon source to replace the function of glucose to produce volatile compounds by *Ceratocystis fimbriata* will be reported. The OPF juice was extracted using simple physical separation method. The growths of fungi were monitored by using cell dry weight (CDW) method whereby the characterization of sugar composition and consumption of the OPF juice by *Ceratocystis fimbriata* were carried out using high performance liquid chromatography (HPLC). The volatile organic compounds were separated and analyzed by gas chromatography-mass spectrometry (GC-MS) with solid phase micro extraction (SPME). On the fourth day, the biomass produced by *Ceratocystis fimbriata* increased significantly and produced the highest number of products comprising of 3 alcohols, 2 esters, 1 aldehyde, 1 fatty acid, 1 phenol and 1 ketone. Based on the GC-MS analysis, several volatile compounds namely aldehydes, alcohols, ketones, and esters could be produced from OPF juice supplemented with a mineral salt medium. This result shows the potential usage of OPF juice as substrates for the growth and production of volatile organic compounds by *Ceratocystis fimbriata*.

Keywords: oil palm frond juice, volatile organic compounds, *Ceratocystis fimbriata*

Abstrak

Dalam laporan ini, kajian mengenai kebolehan jus pelepah kelapa sawit (OPF) sebagai sumber karbon alternatif dan yang boleh diperbaharui telah dijalankan untuk menggantikan fungsi glukosa untuk pengeluaran sebatian meruap oleh kulat *Ceratocystis fimbriata*. Jus OPF diekstrak menggunakan kaedah pemisahan fizikal yang mudah. Pertumbuhan kulat dipantau menggunakan kaedah sel berat kering (CDW) manakala pencirian komposisi gula dan penggunaannya oleh *Ceratocystis fimbriata* di dalam jus ini telah dijalankan dengan menggunakan peralatan kromatografi cecair berprestasi tinggi (HPLC). Sebatian meruap pula dipisahkan dan dianalisis menggunakan kromatografi gas – spektrometri jisim (GC-MS) bersama pengekstrakan mikro fasa pepejal (SPME). Pada hari keempat, pengeluaran biojisim meningkat dengan ketara dan mengeluarkan produk yang paling tinggi, iaitu 3 alkohol, 2 ester, 1 aldehid, 1 asid lemak, 1 fenol dan 1 keton. Berdasarkan analisis daripada GC-MS, hasil fermentasi menunjukkan beberapa sebatian organik meruap seperti aldehid, alkohol, keton dan ester boleh dihasilkan daripada jus OPF ditambah dengan media garam mineral. Hasil daripada kajian ini menunjukkan bahawa jus OPF mempunyai potensi besar untuk digunakan sebagai substrat untuk pertumbuhan dan penghasilan sebatian organik meruap oleh *Ceratosystis fimbriata*.

Kata kunci: jus pelepah kelapa sawit, sebatian organik meruap, *Ceratocystis fimbriata*

Introduction

In Malaysia, oil palm plantations and the palm oil industries were the main contributors to the generation of agricultural waste. From previous studies, researches have studied the potential of utilizing the agricultural waste efficiently. For example, the conversion of the oil palm empty fruit brunch (OPEFB) into fermentable sugar [1-3], utilization of the OPEFB as a substrate for enzyme production [4] and pulp preparation from OPEFB [5]. The common substrate used during fermentation is glucose where it functions as a source of energy or carbon source. In this research, oil palm frond (OPF) juice is used to replace the role of glucose during fermentation. OPF juice is reported to contain renewable sugars such as glucose, sucrose and fructose [6]. In addition to that, it was suggested that OPF juice have high potential to be used as a fermentation feedstock for the production of various value-added products such as polyhydroxyalkanoates (PHA), bioethanol, biobutanol, lactic acid, and succinic acid as it contains high amount of sugars [7]. OPF juice is expected to address the environmental issues for the production of aromatic volatile compounds as OPF is abundantly available as a biomass and easily available throughout Malaysia.

The utilization and development of volatile organic compounds (VOCs) from microorganisms have been of increasing interest as they are naturally produced without chemical synthesis. VOCs are carbon-based solids and liquids that readily enter the gas phase by vaporizing at 0.01 kPa at a temperature of approximately 20 °C [8]. The identified VOCs generated by fungi and bacteria are mainly primary (from the synthesis of DNA, amino and fatty acids, etc.) and secondary metabolites (from intermediates of primary metabolism) [9].

Microorganisms are widely used role in the generation of natural compounds, particularly in the field of food aromas. From previous studies, filamentous fungi can be very useful in the flavor field because they are able to produce flavoring compounds and flavor related to enzyme [10]. *Ceratocystis fimbriata* is a mold which has the potential for synthesizing esters, it grows quickly and produces a variety of aromas (peach, pineapple, banana, citrus and rose) depending on the strain and culture conditions [11].

Therefore, in this study the ability of *Ceratocystis fimbriata* to produce aromatic volatile compounds by using OPF juice as a sole carbon source was investigated in the shake flask experiment. The head space-solid phase micro extraction (HS-SPME) technique combined with gas chromatography-mass spectrometry (GC–MS) was used to analyze the aromatic volatile compounds during the fermentation. To date, researches on the production of volatile compounds by *Ceratocystis fimbriata* from OPF juice as substrates has not been reported yet. Therefore, it is hope that this research will contribute for further investigation on the production of volatile compounds using this fungus at the commercial scale.

Materials and Methods

Microorganism and culture medium

The fungal strain *Ceratocystis fimbriata* (ATCC 12866) was obtained from freeze-dried microorganism purchased from American Type Culture Collection (ATCC), USA. The fungal was grown and transferred periodically onto the Potato Dextrose Agar (PDA). The seed culture was prepared after 7 days of growth at 30 °C. After 7 days, the spores were collected from the surface of the plate by adding distilled water containing a few drops of Tween 80 and some glass beads. The basal growth medium consisted of glucose, 20 g/L; urea, 0.75 g/L; ammonium sulfate ($(NH_4)_2SO_4$) 2.25 g/L; monopotassium phosphate (KH_2PO_4) 1 g/L; calcium nitrate tetrahydrate ($Ca(NO_3)_2.4H_2O$) 0.5 g/L; magnesium sulfate heptahydrate ($MgSO_4.7H_2O$) 0.5 g/L; trace element solution, 2 ml/L. The trace element solution comprised of: Iron(III) nitrate nonahydrate ($Fe(NO_3)_3.9H_2O$) 723.8 mg/L; zinc sulfate heptahydrate ($ZnSO_4.7H_2O$) 439.8 mg/L; manganese(II) sulfate tetrahydrate ($MnSO_4.4H_2O$) 203 mg/L. The medium was supplemented with chloramphenicol 0.5 g/L to inhibit bacterial contamination and the pH was adjusted to 6.0 with sodium hydroxide (NaOH) 0.5 N before autoclaved at 121 °C for 20 minutes. For the seed culture preparation, 1 mL of the spores were taken aseptically and transferred into 50 mL centrifuge tube containing 9 mL of basal growth medium. The seed cultures were then incubated at 27 °C for 9 days on a rotary shaker at (150 rpm).

Substrate preparation

The oil palm frond (OPF) juice used in this research were obtained from Lembaga Kemajuan Pertubuhan Peladang (LKPP) Oil Palm Plantation, Lepar Hilir, Gambang Pahang, Malaysia. The OPF juice was extracted by pressing the

frond using a conventional sugarcane press machine. The OPF juice was centrifuged at 10,000 rpm for 10 minutes at 4 °C. The sugar content in the OPF juice were determined by High Performance Liquid Chromatography (HPLC) (Agilent Series 1200, USA) using the Supelcosil LH-NH_2 column (Sigma Aldrich) (25 cm x 4.6 mm ID, 5 µm particles) with a RI detector operated at 30 °C. The mobile phase consisted of a ratio of acetonitrile: water (75%: 25%) at a flow rate of 1.0 mL/min.

Fermentation procedure

The experiments were done by using OPF juice containing 30 g/L of glucose using 250 mL flasks and were mixed with a mineral salt medium. This medium consisted of the following composition: urea, 0.9 g/L; $(NH_4)_2SO_4$, 2.7 g/L; KH_2PO_4, 1.2 g/L; $Ca(NO_3)_2.4H_2O$, 0.6 g/L; $MgSO_4.7H_2O$, 0.6 g/L; trace element solution, 2 ml/L; chloramphenicol 0.6 g/L and the pH was adjusted to 6.0 with NaOH 0.5 N before autoclaved. The flasks were covered with cotton and sterilized at 121 °C for 20 minutes. One mycelium cell from seed cultures was taken aseptically and introduced into a 250 mL Erlenmeyer flask containing 100 mL of the synthetic medium. The fermentation was carried out at 27 °C on a rotary shaker at 150 rpm for 8 days.

Growth determination

The mycelia were collected at every 24 hours for 8 days after centrifugation (10,000 rpm for 15 minutes at 4 °C). The mycelia were washed twice with distilled water. The biomass was measured by the dry weight determination (24 hours in a drying oven at 100 °C) method.

Analytical procedure

The samples were taken periodically from the culture medium and were centrifuged at 10,000 rpm for 15 minutes at 4 °C. The supernatants were filtered through a 0.22-µm pore filter (Millipore) prior to analysis. The volatile compounds were detected by gas chromatography-mass spectrometry-solid phase micro extraction (GC-MS SPME). In this study, the fibre DVB-CAR-PDMS (50/30 µm), which has been frequently employed for the extraction of the volatile fraction from natural products, was tested for the analysis of volatile compounds. The fibre was exposed to the head space (HS) for 45 minutes at 45 °C. After 45 minutes, the SPME fibre was immediately inserted into the GC injector for 46 minutes. The desorption time of 2 minutes at 230 °C was used in the splitless mode. Before sampling, the fibre was reconditioned for 45 minutes in the GC injector port at 230 °C.

Glucose consumption

The samples were taken periodically from the culture medium and the consumption of glucose by *Ceratocystis fimbriata* were determined by high performance liquid chromatography (HPLC) (Agilent Series 1200, USA) using the Supelcosil LH-NH_2 column (Sigma Aldrich) (25 cm x 4.6 mm ID, 5 µm particles) with a RI detector operated at 30 °C. The mobile phase comprised of acetonitrile: water (75%: 25%) at a flow rate of 1.0 mL/min.

Results and Discussion

The results of the biomass produced by *Ceratocystis fimbriata* in mineral salt medium supplemented with OPF juice is shown in Figure 1. The biomass production was calculated from the first day until the eighth day of fermentation. As shown in Figure 1, it was apparent that the *Ceratocystis fimbriata* biomass has increased sharply from the second day to the fourth day and increased slowly thereafter. Based on the growth profile, the lag phase for *Ceratocystis fimbriata* began from the first day until the second day. Then, followed by the exponential phase where the productions of biomass increased significantly up to the fourth day. After that, the stationary phase started to occur slowly from the fourth day until the end of the fermentation period. On the other hand, the results of the glucose consumption of *Ceratocystis fimbriata* in synthetic medium supplemented with OPF juice is shown in Figure 2. The glucose consumption was analysed from the first day of fermentation until the eighth day. In Figure 2, the glucose consumption of *Ceratocystis fimbriata* decreased sharply from second day to the fourth day of fermentation period and decrease slowly thereafter as it was consumed by the fungus. With reference to Figure 1 and Figure 2, it was shown that the biomass production profile is consistent with the glucose consumption profile by *Ceratocystis fimbriata*.

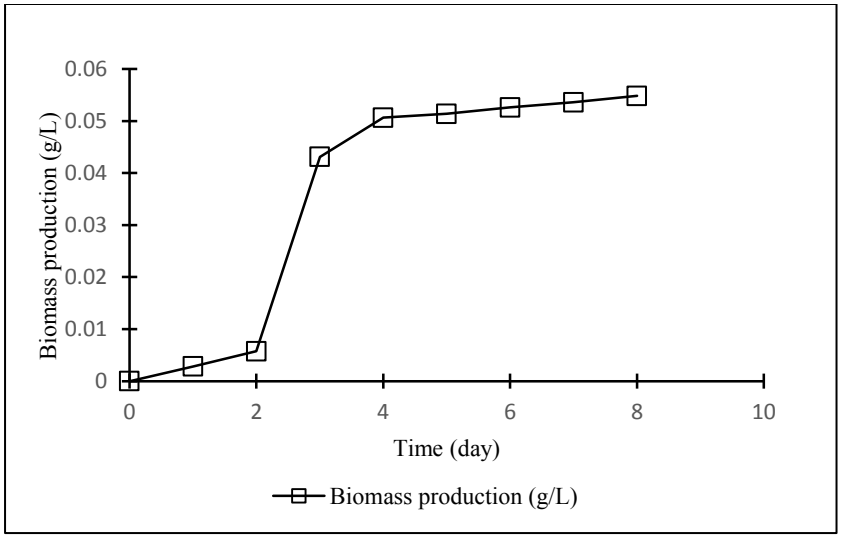


Figure 1. Biomass production of *Ceratocystis fimbriata* in mineral salt medium supplemented with OPF juices as a sole substrate for 8 days of fermentation

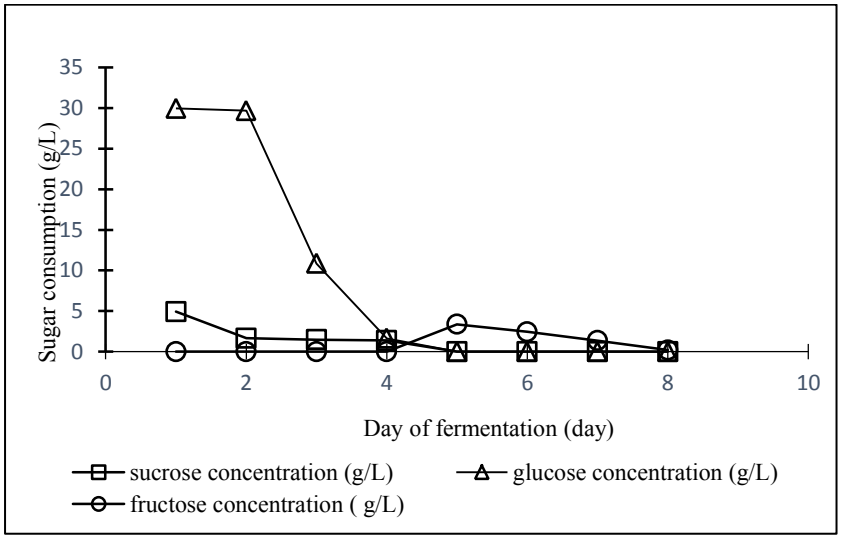


Figure 2. Glucose consumption profile for eight day of fermentation period by *Ceratocystis fimbriata* in mineral salt medium supplemented with OPF juice

In Figure 3(a), the seed culture was used as the inoculum in the fermentation of OPF juice. The seed culture was prepared at 27 °C on a rotary shaker (150 rpm) and incubated for eight (8) days. The inoculum was then transferred to the fermentation medium which consisted of 30 g/L glucose in OPF juice supplemented with a synthetic medium. Figure 3(b), shows that the flask had one cell of mycelia after the first day of fermentation. With reference to Figure 3(c), after two days of the fermentation period, the fungus germinated to two big mycelium followed by third days of fermentation, it had seven mycelium cells. On the fourth day until the end of fermentation, the fungus germinated and had grown into many myceliums of cells.

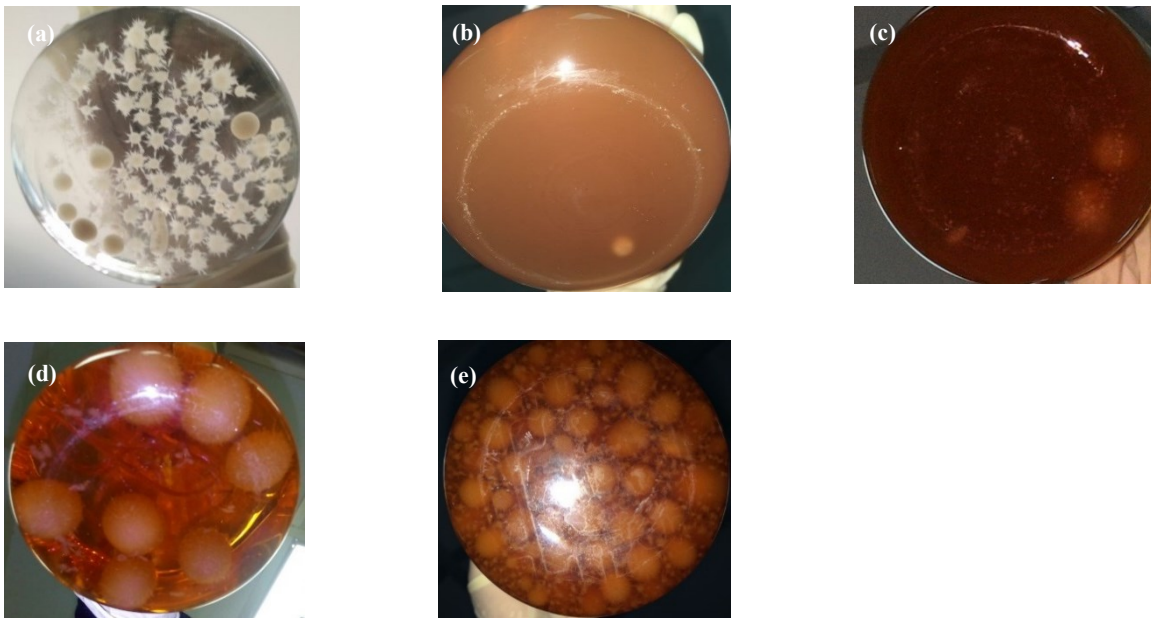


Figure 3. (a) Seed culture of *Ceratocystis fimbriata* in synthetic medium on the eight days of incubation. *Ceratocystis fimbriata* in 30 g/L of glucose in OPF juice supplemented with synthetic medium (b) on the first day of fermentation, (c) second day fermentation, (d) third day of fermentation, (e) on the fourth day of fermentation.

From the fermentation of *Ceratocystis fimbriata* using OPF juice (as the sole carbon source), it was found that at least 45 peaks of compounds were detected by GC-MS SPME. The compounds were shown in Figure 4 and Table 1. The volatile compounds identified from fermentation of *Ceratocystis fimbriata* were mostly alcohol, phenol, ester, aldehyde as the major compounds. While other compounds such as alkane, alkene, ketone, amide, fatty acid and others were also produced during fermentation.

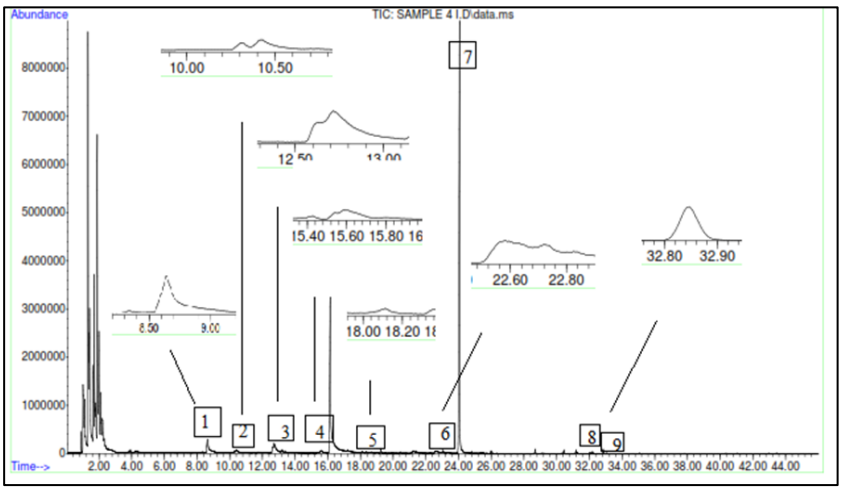


Figure 4. GC-MS with SPME analysis produced 9 peaks on the fourth day of fermentation. Peak (1) at the retention time 8.661, peak (2) at 10.421, peak (3) were the alcohol group at 12.732, peak (6) at the 22.643 and peak (9) at the 32.858 were the ester group, peak (4) at the 15.604 was the aldehyde group, peak (5) at the 18.107 was fatty acid, peak (7) at the 24.044 was the phenol group and peak (8) at the 32.174 was the ketone group.

Table 1. Volatile organic compounds produced by *Ceratocystis fimbriata* using OPF juice as the sole carbon source

Day	No	R_{time}	Area (%)	Volatile organic compounds
1	1	18.589	0.84	2-Methoxy-4-vinylphenol
	2	21.225	0.60	2-(4-ethoxyphenyl)-2-methyl-propanal,
	3	24.033	14.69	2,4-bis(1,1-dimethylethyl)- phenol,
	4	32.832	0.21	Methyl 3-(3,5-di-tert-butyl-4-hydroxyphenyl)propionate
2	1	15.582	0.58	3,4-dihydroxybenzyl alcohol, tris (trimethylsilyl)
	2	18.369	0.69	P-tert-butyl- phenol
	3	21.231	1.36	2-benzothiazolecarboxaldehyde
	4	23.621	0.31	2,4-bis(1,1-dimethylethyl)- phenol
3	1	8.688	2.47	1-Octen-3-ol
	2	12.774	1.49	Dimethyl(isopropyl)silyloxycyclohexane
	3	24.033	29.01	2,4-bis(1,1-dimethylethyl)- phenol
	4	31.184	0.09	2-(1-phenylethylidene)- hydrazinecarbothioamide
	5	32.826	0.16	Methyl 3-(3,5-di-tert-butyl-4-hydroxyphenyl)propionate
4	1	8.661	2.40	1-Octen-3-ol
	2	10.421	0.95	2-ethyl-1-hexanol
	3	12.732	2.50	Phenylethyl Alcohol
	4	15.604	0.47	3,4-dimethyl- benzaldehyde
	5	18.107	0.67	Nonanoic acid
	6	22.643	0.71	(Dimethylsilylene) bismethanol diacetate
	7	24.044	19.42	2,4-bis(1,1-dimethylethyl)- phenol
	8	32.174	0.08	7,9-di-tert-butyl-1-oxaspiro[4,5]deca-6,9-diene-2,8-dione
	9	32.858	0.15	Methyl 3-(3,5-di-tert-butyl-4-hydroxyphenyl)propionate
5	1	4.339	2.67	(Z)- 3-hexen-1-ol
	2	12.694	10.98	Phenylethyl Alcohol
	3	15.588	0.88	3,4-dimethyl- benzaldehyde
	4	21.241	0.70	Ethyltriethoxysilane
	5	24.022	27.09	2,4-bis(1,1-dimethylethyl)- phenol
	6	32.832	0.26	Methyl 3-(3,5-di-tert-butyl-4-hydroxyphenyl)propionate
6	1	8.682	2.06	1-Octen-3-ol
	2	12.694	8.45	Phenylethyl Alcohol
	3	15.593	0.78	3,5-dimethyl- benzaldehyde
	4	19.909	0.13	Oxalic acid, isobutyl nonyl ester
	5	24.038	35.54	2,4-bis(1,1-dimethylethyl)- phenol
	6	32.158	0.15	7,9-Di-tert-butyl-1-oxaspiro(4,5)deca-6,9-diene-2,8-dione
	7	32.826	0.22	Methyl 3-(3,5-di-tert-butyl-4-hydroxyphenyl)propionate
7	1	12.716	6.74	Phenylethyl Alcohol
	2	15.593	0.80	2,6-Dimethylbenzaldehyde
	3	19.899	0.18	2,6,10-trimethyl- dodecane
	4	24.039	42.11	2,4-bis(1,1-dimethylethyl)- phenol
8	1	8.693	2.43	1-Octen-3-ol
	2	11.737	1.56	cis-Linalool Oxide
	3	14.272	1.11	1,4-dimethoxy- benzene
	4	16.139	18.21	1,3,5-Trioxane
	5	19.968	0.36	1,2,4-Trimethoxybenzene
	6	24.033	37.05	2,4-bis(1,1-dimethylethyl)- phenol

Based on the GC-MS SPME analysis, eleven peaks were classified as alcohols from the second day until the eighth day. The compounds include 3,4-dihydroxybenzyl alcohol, tris (trimethylsilyl); 1-octen-3-ol; 2-ethyl-1-hexanol; phenylethyl alcohol and (Z)- 3-hexen-1-ol. As commonly known, alcohols do not play a predominant role in flavors but are known to contribute to the overall flavors quality and are precursors of fruit-like flavoring esters [12] In microorganisms, all alcohol, except ethanol is formed by the reduction of α-keto acids which are derived from amino acids metabolism [13].

Phenolic compounds were also detected consisting of 2-methoxy-4-vinylphenol; p-tert-butyl- phenol and 2,4-bis(1,1-dimethylethyl)- phenol on the first day until the eighth day of fermentation. Six peaks were recorded as ester between the first day until the sixth day of fermentation except for the second day.

The esters comprised of methyl 3-(3,5-di-tert-butyl-4-hydroxyphenyl) propionate; (dimethylsilylene) bismethanol diacetate and oxalic acid, isobutyl nonyl ester. On the fourth day of the fermentation period, there were two ester group was present, which are methyl 3-(3,5-di-tert-butyl-4-hydroxyphenyl) propionate and (dimethylsilylene) bismethanol diacetate. After six days of fermentation period, the ester group found are methyl 3-(3,5-di-tert-butyl-4-hydroxyphenyl) propionate and oxalic acid, isobutyl nonyl ester. The ester group plays a pivotal role in enhancing the different fruit fragrances such as methyl-butyrate (apple fragrance), methyl butanoate (pineapple), ethyl butyrate (orange), ethyl butanoate (pineapple), pentyl-butyrate (pear) and pentyl-butanoate (apricot) [14].

Four aldehydes were detected from the six peaks of compounds during the fermentation period except on the third day and the eighth day of fermentation. These aldehydes are methyl, 2-(4-ethoxyphenyl)-2- propanal; 2-benzothiazolecarboxaldehyde; 3,4-dimethyl-benzaldehyde; 3,5-dimethyl-benzaldehyde and 2,6-dimethyl-benzaldehyde. Three alkanes were recorded including dimethyl (isopropyl)silyloxycyclohexane on the third day; 2,6,10-trimethyl- dodecane on the seventh day and 1,3,5-trioxane on the eighth day.

Forty-five peaks were recorded during the fermentation which correspond to 11 alcohols, 10 phenols, 7 esters, 6 aldehydes, 3 alkanes, 2 ketones, 2 alkenes, 1 amide, 1 fatty acid and 2 others. During the fermentation process, the volatile compounds were produced from the first day until the eighth day of the fermentation period, however more volatile compounds were produced after the fourth day of fermentation period compared to the other day (Table 2). With reference to the past study which had used coffee husk as a substrate, the major compound produced by *Ceratocystis fimbriata* were ethyl acetate, ethanol and acetaldehyde [15]. Other compounds, including ethylpropionate, propylacetate, ethyl isobutyrate, butyl acetate was also produced during fermentation [15].

Table 2. Volatile organic compounds produced by *Ceratocystis fimbriata* using OPF juice as the sole carbon source for 8 days of fermentation (summarized from Table 1)

Fermentation Period (day)	**Alcohols**	**Esters**	**Aldehydes**	**Phenols**	**Alkanes**	**Alkenes**	**Ketones**	**Others**
1st		1	1	2				
2nd	1		1	2				
3rd	1	1		1	1			1
4th	3	2	1	1			1	1
5th	2	1	1	1				1
6th	2	2	1	1			1	
7th	1		1	1	1			
8th	1			1	1	2		1
Total no. of compounds	11	7	6	10	3	2	2	4

Another researcher found that nine volatile compounds were detected when citric pulp was used as the substrate in fermentation. These compounds are acetaldehyde, ethanol, ethyl acetate, propyl acetate, ethyl isobutyrate, 2-hexanone, 2-hexanol, isoamyl acetate and one unidentified compound [16].

Conclusion

Based on the results and discussion, it can be concluded that volatile organic compounds can be produced from the utilization of OPF juice as the carbon source by *Ceratocystis fimbriata*. With reference to the GC-MS SPME analysis, the highest number of VOCs (3 alcohols, 1 aldehyde, 1 fatty acid, 1 phenol, 1 ketone and 2 ester) were produced by *Ceratocystis fimbriata* on the fourth day of the fermentation period. For future work, further investigation on the parameters affecting volatile organic compounds production from OPF juice by *Ceratocystis fimbriata* will be look upon to improve the yield.

Acknowledgement

The author would like to be obliged to Universiti Malaysia Pahang (UMP) for providing laboratory facilities and financial assistance under UMP Grant Scheme project no. RDU 150315 and PGRS160324.

References

1. Ariffin, H., Abdullah, N., Umi Kalsom, M. S., Shirai, Y. and Hassan, M. A. (2006). Production and characterization of cellulase by *Bacillus pumilus* EB3. *International Journal of Engineering and Technology,* 3(1): 47-53.
2. Ariffin, H., Hassan, M. A., Umi Kalsom, M. S., Abdullah, N. and Shirai, Y. (2008). Effect of physical, chemical and thermal pretreatments on the enzymatic hydrolysis of oil palm empty fruit bunch (OPEFB). *Journal of Tropical Agriculture and Food Science,* 36(2): 259-268.
3. Roslan, A. M., Yee, P. L., Shah, U. K. M., Aziz, S. A. and Hassan, M. A. (2011). Production of bioethanol from rice straw using cellulase by local *Aspergillus* sp. *International Journal of Agricultural Research,* 6(2): 188-193.
4. Ariffin, H., Hassan, M. A., Umi Kalsom, M. S., Abdullah, N., Ghazali, F. N. and Shirai, Y. (2008). Production of bacterial endoglucanase from pretreated oil palm empty fruit bunch by *Bacillus pumilus* EB3. *Journal of Bioscience and Bioengineering,* 106(3): 231-236.
5. Rushdan, I. (2002). Chemical composition of alkaline pulps from oil palm empty fruit bunches. *Oil Palm Bulletin,* 44: 19-24.
6. Zahari, M. A. K. M., Zakaria, M. R., Ariffin, H., Mokhtar, M. N., Salihon, J., Shirai, Y. and Hassan, M. A. (2012). Renewable sugars from oil palm frond juice as an alternative novel fermentation feedstock for value-added products. *Biosource Technology,* 110: 566-571.
7. Maail, C. M. H. C., Ariffin, H., Hassan, M. A., Shah, U. K. M. and Shirai, Y. (2014). Oil palm frond juice as future fermentation substrate: A feasibility study. *BioMed Research International,* 2014: 1-8.
8. Morath, S. U., Hung, R. and Bennett, J.W. (2012). Fungal volatile organic compounds: A review with emphasis on their biotechnological potential. *Fungal Biology Reviews,* 26(2-3): 73-83.
9. Korpi, A., Järnberg, J. and Pasanen, A. L. (2009). Microbial volatile organic compounds. *Critical Reviews in Toxicology,* 39(2): 139-193.
10. Bigelis, R. (1992). Flavor metabolites and enzymes from filamentous fungi. *Food Technology,* 46: 151-161.
11. Medeiros, A. B. P., Pandey, A., Vandenberghe, L. P. S., Pastore, G. M. and Soccol, C. R. (2003). Coffee residues as substrates for aroma production by *Ceratocystis fimbriata* in solid state fermentation. *Brazilian Journal of Microbiology,* 34: 245-248.
12. Christen, P., Meza, J. C. and Revah, S. (1997). Fruity aroma production in solid state fermentation by *Ceratocystis Fimbriata*: Influence of the substrate type and the presence of precursors. *Mycological Research,* 101(8): 911-919.
13. Welsh, F. W., Murray, W. D. and Williams, R. E. (1989). Microbiological and enzymatic production of flavor and fragrance chemicals. *Critical Reviews in Biotechnology,* 9(2): 105-169.
14. Zawirska, W. R., Siwulski, M., Mildner, S. S. and Erwin, W. E. (2009). Studies on the aroma of different species and strains of *pleurotus* measured by GC/MS, sensory analysis and electronic nose. *Acta Scientiarum Polonorum : Technologia Alimentaria,* 8: 47-61.

15. Medeiros, A. B. P., Pandey, A., Vandenberghe, L. P. S., Pastore, G. M. and Soccol, C. R., (2006). Production and recovery of aroma compounds produced by solid-state fermentation using different adsorbents. *Food Technology and Biotechnology,* 44(1): 47-51.
16. Rossi, S. C., Vandenberghe, L. P. S., Pereira, B. M. P., Gago, F. D., Rizzolo, J. A., Soccol, C. R. and Medeiros, A. B. P. (2009). Improving Fruity Aroma Production by Fungi in SSF using Citric Pulp. *Food Research International,* 42 (4): 484 – 486.

Malaysian Journal of Analytical Sciences, Vol 22 No 4 (2018): 693 - 701
DOI: https://doi.org/10.17576/mjas-2018-2204-16

MALAYSIAN JOURNAL OF ANALYTICAL SCIENCES
Published by The Malaysian Analytical Sciences Society
ISSN 1394 - 2506

PHOTOCATALYTIC DEGRADATION OF INDUSTRIAL DYE WASTEWATER USING ZINC OXIDE-POLYVINYLPYRROLIDONE NANOPARTICLES

(Penguraian Fotopemangkinan Air Sisa Pewarna Industri Menggunakan Nanopartikel Zink Oksida-Polivinilpirolidon)

Dilaeleyana Abu Bakar Sidik[1,2], Nur Hanis Hayati Hairom[1]*, Nur Zarifah Zainuri[1], Amira Liyana Desa[1], Nurasyikin Misdan[3], Norhaniza Yusof[4], Chin Boon Ong[5], Abdul Wahab Mohammad[6], Nur Shahirah Mohd Aripen[2]

[1]*Department of Chemical Engineering Technology, Faculty of Engineering Technology*
[2] *Department of Science and Mathematics, Center of Diploma Studies*
[3]*Department of Mechanical Engineering Technology, Faculty of Engineering Technology*
Universiti Tun Hussein Onn Malaysia, 86400 Parit Raja, Batu Pahat, Johor, Malaysia
[4]*Advanced Membrane Technology Research Centre (AMTEC),*
Universiti Teknologi Malaysia, 81310 Skudai, Johor, Malaysia
[5]*Department of Chemical and Process Engineering, Faculty of Engineering and Built Environment*
[6]*Centre for Sustainable Process Technology (CESPRO), Faculty of Engineering and Built Environment*
Universiti Kebangsaan Malaysia, 43600 UKM Bangi, Selangor, Malaysia

**Corresponding author: nhanis@uthm.edu.my*

Received: 16 April 2017; Accepted: 7 March 2018

Abstract

Due to the lack of studies regarding the potential of polyvinylpyrrolidone (PVP) as capping agent in precipitation of zinc oxide (ZnO) nanoparticles, this research focused on the performance of ZnO nanoparticles with presence of PVP loading on photocatalytic degradation treatment for industrial dye wastewater. Three different samples of ZnO-PVP were successfully synthesized via precipitation method. The degradation rate of dye approached 90.61% under pH7 in the presence of ZnO-PVP (0.025g/L of PVP). The chemical bonds in ZnO-PVP was analysed using Fourier Transform Infrared Spectroscopy (FTIR).

Keywords: zinc oxide, polyvinylpyrrolidone, photocatalytic, nanoparticles, wastewater treatment

Abstrak

Oleh kerana kekurangan kajian mengenai potensi polivinilpirolidon (PVP) sebagai ejen penutup dalam mendakan nanopartikel zink oksida (ZnO), kajian ini memberi tumpuan kepada prestasi nanopartikel ZnO dengan kehadiran muatan PVP dalam rawatan penguaraian fotopemangkinan air sisa industri pewarna. Tiga sampel ZnO-PVP yang berlainan telah berjaya disintesis melalui kaedah pemendakan. Kadar degradasi pewarna menghampiri 90.61% di bawah pH 7 bagi ZnO-PVP (PVP sebanyak 0.025 g/L). Ikatan kimia ZnO-PVP telah dianalisis menggunakan spektroskopi inframerah transformasi Fourier (FTIR).

Kata kunci: zink oksida, polivinilpirolidon, fotopemangkinan, nanopartikel, rawatan air sisa

Introduction

In recent studies, zinc oxide (ZnO) nanoparticles have been prove as effective photocatalyst due to their properties such as strong excitation binding energy, higher reactivity, surface area, photosensitivity, non-toxic nature and

chemical stability [1-3]. Furthermore, ZnO nanoparticles have stable wurtzite structure and wide bandgap (3.4eV) which is suitable to act as catalyst, primarily for degradation of Congo red dyes [4].

To date, there are several methods have been implemented to synthesize ZnO including sonochemical [5, 6], sol gel process [7, 8], hydrothermal synthesis [9] and precipitation [1]. Since the synthesis method of nanoparticles is very sensitive and may influence their performance, precipitation is believed to be one of the promising method due to its simpler route, economic and operates at moderately low temperature [10]. However, there is severe drawback encounter in the synthesis of nanoparticles which is agglomeration. Agglomeration occurred due to Van der Waals and Ostwald ripening interactions which leads to the production of aggregation of the particles. In 2015, Hairom et al. [4] claimed that the agglomeration of ZnO nanoparticles could be stabilized by the addition of polyvinylpyrrolidone (PVP) in the precipitation method. Moreover, they also reported that the ZnO-PVP showed better photocatalytic activity in compared to absence of PVP, due to the less agglomeration of ZnO-PVP. Therefore, this study investigated the optimum loading of PVP on precipitation of ZnO nanoparticles and its photocatalytic activity in industrial dye wastewater treatment. These details are very useful as the preliminary study for the synthesis of nanoparticles in order to improve the performances of a photocatalyst in wastewater treatment.

Industrial dye wastewater is difficult to treat satisfactorily due to highly variable in compositions, flow and volume which contains various chemicals and coloring compounds. Therefore, a proper treatment is required before it was discharged into any water bodies. The industrial dye wastewater discharged is a major source which contributed wide range of pollutions on the earth. In terms of wastewater management, it does not favorable from a view of ecological point since the wastewater are heavily colored. It also cause severe health problem and toxic to the aquatic organisms by reducing photosynthetic activity due to less penetration of light. The influent of industrial dye wastewater is very important to be managed and degraded in order to prevent any diseases spread out over the world. Due to their toxic and recalcitrance properties, colored particles can also contribute to the failure of biological processes in wastewater treatment plants. Further, the regulations imposed for the discharged colored effluents have become more stringent and thus motivated the industries to improve their effluent de-colorization technology [11].Commonly, industrial dye wastewater has high degree chemical, highly variable in compositions and photolytic stability which is one of the sources of wastewater that give bad impacts to the environment [12].

There are many present methods are being used in these days for treating industrial dye wastewater. However, they only offered for phase transfer or partial degradation of water pollutants [13]. In recent years, photocatalysis process has been suggested as an alternative treatment for dye wastewater due to the completion degradation rate [14]. This method also involved the inexpensive photocatalyst, non-toxic photocatalyst and environmental safety compared to the other methods [1]. Photocatalytic degradation has great characteristics to investigate since it is essential and useful for decolorization of dye wastewater. This potential method has become research interest in order to create clean and fresh environment. Consequently, the other purpose of this study is to examine the optimum condition of several parameters including pH and ZnO-PVP loading on photodegradation efficiency (measured by color intensity, turbidity and dissolve oxygen (DO)) of industrial dye wastewater which collected from the newspaper printing factory.

Materials and Methods

Synthesis of ZnO nanoparticles

0.15 M solution of oxalic acid dehydrates (R&M Marketing, Essex, UK) was added slowly into 0.1M solution of zinc acetate dehydrated (R&M Marketing, Essex, UK) with molar ratio of 3:2 under room temperature (25 °C). Different loading of PVP (0.015g/L, 0.020g/L or 0.025g/L) was then added in each of the mixture after 5 minutes of the reactions. The mixture was stirred for 12 hours to increase the production of ZnO. The precipitate obtained will be filtered and consequently dried in oven under100 °C for 1 hour to remove water. Next, the precipitate was calcined in the furnace (Nabertherm model, Germany) under 550 °C for 3 hours to remove impurities. After calcination process, the white powder of ZnO-PVP has been formed and proceed for characterization.

Characterization of ZnO-PVP nanoparticles

The characterization has been conducted by using FTIR spectrophotometer was performed using a Perkin-Elmer FTIR (Spectrum RX-I) model (Nicolet FT-IR Avatar 360) in the wavelength range 400-6000 cm^{-1}. Chemical bonds

in the samples were analysed by producing an infrared absorption spectrum in order to ascertain the purity and nature of the ZnO-PVP.

Photocatalytic degradation

In this study, 500 mL of beaker used as the photocatalytic reactor in batch method. The photocatalysis process has been conducted under UV light (UV light source at 253 nm with definite power of 6 W) for activation of the photocatalyst as indicated in Figure 1. Then, ZnO-PVP nanoparticles (0.015, 0.020 and 0.025g/L of PVP) were added into the reactor which filled with 200 ml industrial dye wastewater which collected from newspaper printing industry located at Selangor, Malaysia. The mixture has been agitated at 150 rpm under room temperature (25 °C). The operation temperature was controlled by water recirculating in a water bath. At the interval of 5 minutes, 10 ml of degraded wastewater were sampled and the samples of domestic wastewater with ZnO were separated by using centrifuge for 20 minutes. Next the quality of samples were analysed after the separation process. For treated water quality analysis, color intensity of the samples has been determined by using UV-Vis Spectrophotometer (LABOMED, INC, Spectro UV-2650). Dissolve oxygen (DO) of the samples measured by using DO meter (HACH, H280G). While for turbidity was analysed by using turbidity meter (EUTECH Instrument, TN100, 1000NTU) respectively.

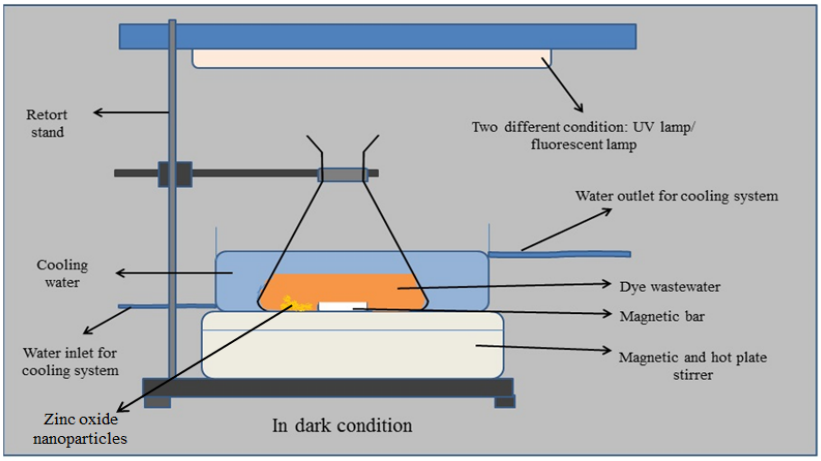


Figure 1. The schematic diagram of photocatalysis process

Results and Discussion

The findings presented in this research demonstrate the potential of the ZnO-PVP nanoparticles in photocatalytic degradation of dye wastewater. There are three different ZnO with the different loading of capping agent of PVP (0.015 g/L, 0.020 g/L and 0.025g/L) has been successfully synthesized via precipitation method. Figure 2 exhibits the FTIR spectra of ZnO-PVP nanoparticles with 0.025 g/L of PVP. The ZnO-PVP nanoparticles bands revealed several characteristics of the absorption bands in the range of 600-4000 cm^{-1}. The strong intensity of adsorption band from 1068 and 612 $cm^{-1}$was due to the larger magnitude of dipole change during the vibration process, which can be elucidated by the covalent bonds of PVP [15]. The peaks in the area from 1068 and 612 cm^{-1} were assigned to the C-C stretching of pyrrolidone. The result revealed that C=O bond existed in the range from 2327 until 2420 cm^{-1} was a group of carboxylic derivatives which may be present due to the residue of zinc acetate used in reaction. It may happened because of the precursor material and reaction product. The presence of absorption from 3000 to 4000 cm^{-1} related to O-H vibration of the moisture which make the bond arises and proved that ZnO-PVP samples has absorbed the existence water from surroundings [16].

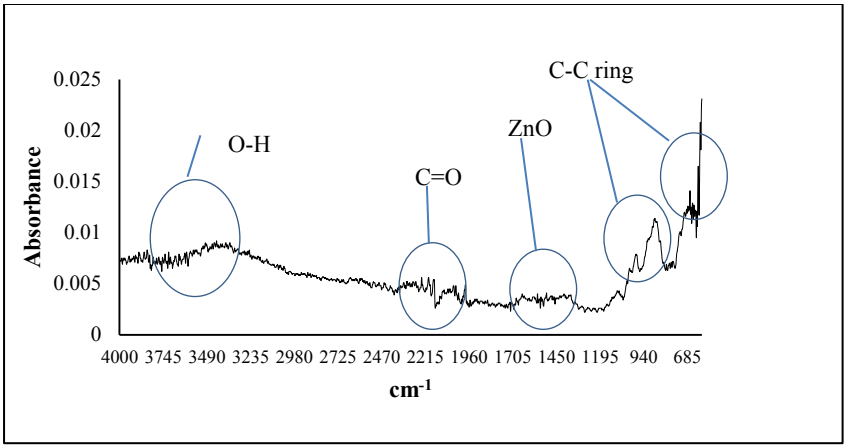


Figure 2. IR spectra of ZnO-PVP (0.025g/L)

Mechanism of photocatalytic degradation

According to Hairom et al. [10], mechanism of photocatalytic degradation for industrial dye wastewater has been started by the photo excitation of the ZnO which followed by the creation of an electron-hole pair on the nanoparticles surface. The high oxidative potential of the hole (hVB^+) in ZnO which leads the direct oxidation of dyes occurred. Through decomposition of water during the reaction between hydroxide ion and hole caused a formation of reactive hydroxyl radicals. Furthermore, due to the extremely unstable of hydroxyl radicals may lead to the degradation of organic chemicals. Then, the molecular oxygen continued for reduction to superoxide anion by electron in conduction band (eCB^-). The radical may formed into organic peroxides in the presence of organic scavengers or hydrogen peroxide (H_2O_2). Electrons in the conduction band are also included in the production of hydroxyl radicals, which have been indicated as the primary cause or organic matter mineralization.

Effect of photocatalytic activity of dye wastewater under different pH

Figure 3 shows the percentages of dye degradation in presence of ZnO-PVP (0.015 g/L of PVP) under three different pH condition which represented as acidic, neutral and alkaline wastewater. This can lead to obtain the ideal pH of the wastewater in order to ensure the best performance in treated wastewater. Based on the result, pH 7 was found as the optimum solution pH due to the higher percentage of dye degradation at 82.15% compared to pH 4 and pH 10 which are 54.84% and 71.76% respectively. In 2016, Mondal and Sharma [17] claimed that at certain concentration of dyes in both acidic and alkaline tends to lower degradation efficiency of some dye wastewater. The greater photodegradation at pH7 can be explained by the point of zero change (PZC) of the photocatalyst since the PZC value of ZnO has been found at pH 6.25 and pH 8.9. PZC refer to the condition which the surface charge of nanoparticles is zero or neutral. The impact of pH toward the performance of photocatalytic oxidation process can be explained through PZC. Where at PZC the interaction between nanoparticles and water contaminant is minimal due to the absence of electrostatic force. Consequently, the adsorption of dye wastewater is extremely good at pH7 and hence photocatalytic degradation activity is significant at neutral pH value.

Subsequently, the changes on dye degradation has been grown rapidly after 5 minutes of experiment conducted. The degradation rate of dye wastewater is very fast due to the involving PVP as capping agent in ZnO nanoparticles. It is correlative to Hairom et al. [1] statement in 2014 which stated that ZnO-PVP has good condition in morphology and smallest particle sizes which can lead to the faster degradation rate of dye wastewater. In 2013, Sudha and Rajarajan [18] claimed that the degradation efficiency by ZnO-PVP for Rhodamine B (RhB) increased with the increment of pH exhibiting maximum degradation efficiency at pH 8. Based on result obtained; the percentage of degradation at pH 10 rapidly increases from 23% to 45.88% and continued increases to 65.30% but it stay constant when it achieved at 71.76%. They also stated that the degradation rate found to be decreased when it was achieved at pH 8 beyond [18]. However, the reaction under alkaline conditions could be attributed to the increase of hydroxyl ions which leads to the formed of ·OH radicals. Thus, the degradation rate for condition of alkaline is much higher compared to the acidic but lower than neutral condition. As reported by Zahrim et al. [19] acidic and alkaline

condition would promote self-aggregation phenomena of nanoparticles in solution which caused the reduction of the dye degradation. The observed trend from this study correlated with electrostatic interaction between substract and photocatalyst surface which depending on the pH of wastewater. This phenomena caused by the effect of pH on the surface properties of photocatalyst and physical properties of dye solution including aggregation or dispersion of dye.

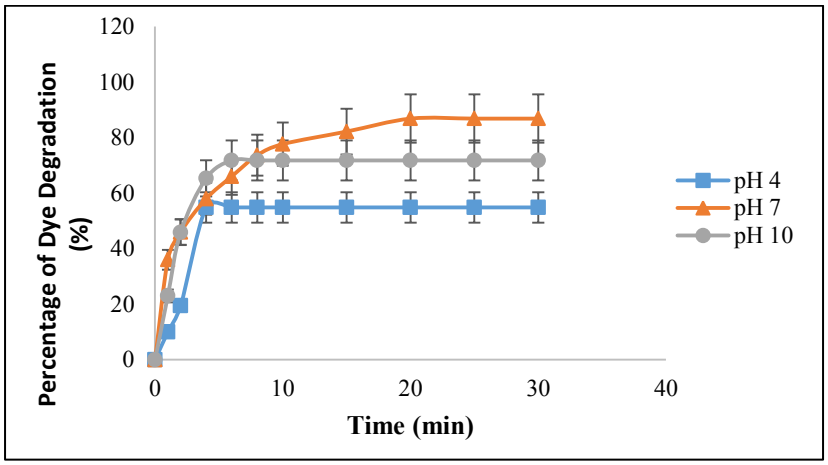


Figure 3. Percentages of dye degradation for photocatalysis process in the presence of ZnO-PVP (0.015 g/L of PVP)

Figure 4 shows the turbidity for three different pH of dye wastewater. It was observed that pH 7 is less cloudy at percentage of 54.49%, in comparison to the dye wastewater for pH4 and pH10 which has turbidity reduction at percentage of 36.67% and 52.17% respectively. The percentage different of the turbidity reduction between pH 4, 7 and 10 is minimal maybe due to varies of the real dye wastewater concentration. The percentage of dye degradation indicated in Figure 3 shows significance correlation with the turbidity reduction where the higher of degradation rate leads to the higher reduction of turbidity of the treated dye wastewater. According to Li et al. [20] revealed that photocatalytic degradation has ability to remove colours of dyeing effluent efficiently. In 2012, Huber and Carre [21] also claimed that UV photons excite ZnO, which then reacts with water molecules or hydroxide ion to produce hydroxyl radicals. Then, the dye molecules were degraded, and the degradation leads the breaking at least one of the conjugated bonds since the colour of dyes formed by conjugated molecules.

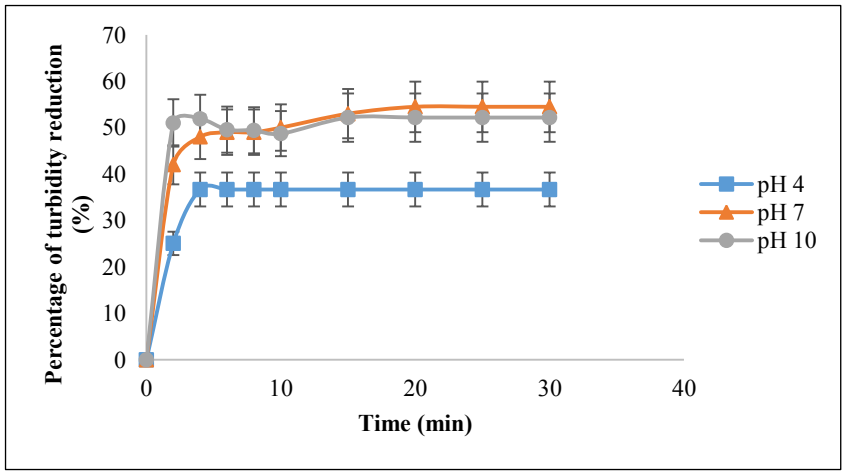


Figure 4. Percentage of turbidity reduction for photocatalysis process in presence of ZnO-PVP (0.015 g/L of PVP)

Based on Figure 4, pH 4 of wastewater was more turbid compared to others pH since the higher percentage of turbidity reduction that can be achieved at 36.67%. This was due to the photodegradation of the dye is retarded by the high concentration of proton, resulting in lower degradation efficiency [22]. Hence, the percentage of dye removal for pH 4 was lower compared to pH 7 and pH 10 of wastewater.

Figure 5 demonstrates the behavior of dissolved oxygen (DO) for different condition pH of wastewater after undergo the treatment. The results have been obviously stated that pH 4 lead for higher value of DO, followed by pH7 and continued by pH 10. It can be seen that certain value of DO shown to be decreased while the others has been increased than the initial value for DO of wastewater which is 3.36 ppm. The increment of DO occurred may be due to the presence of oxygen in photocatalytic degradation which acts as electron acceptor that used to trap the photo induced e^- [23]. According to the National Water Quality System (NWQS), the acceptable range of DO value after wastewater treatment is in the range 0.02 to 20 ppm. Therefore, the treated wastewater could be discharged to environment and safe to aquatic life. From the analyzed results, it could be deduced that the treated wastewater is safe to discharge to environment since their DO value is in the acceptable range.

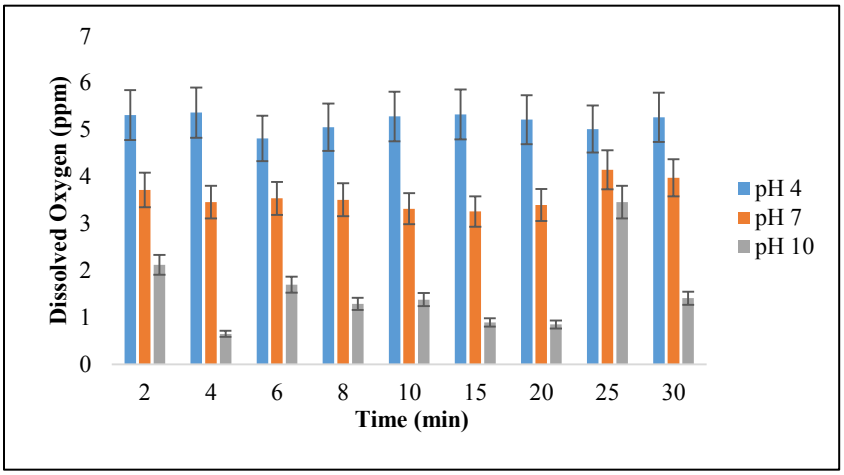


Figure 5. The amount of dissolve oxygen for photocatalysis process in the presence of ZnO-PVP (0.015 g/L of PVP

Photocatalytic activity under different loading of ZnO-PVP photocatalyst

The experiments were carried out with varying photocatalyst loading from 0.015, 0.020 and 0.025 g/L of PVP in precipitation of ZnO-PVP at pH 7. Figure 6 revealed that the ZnO-PVP (0.025 g/L of PVP) is the best performer regarding the highest degradation of dye which about 90.61% compared to the ZnO-PVP (0.015 and 0.020 g/L) were 86.81% and 86.75% respectively. PVP has been used to protect the nanoparticles from growing and agglomerating [24]. The introduction of optimum loading of PVP may leads to higher percentage of dye degradation due to the increasing of ZnO surface area which enhance the accessibility of photocatalyst sites [17,18]. Consequently, the number of hydroxyl radicals will increase and promote the increment of the degradation percentage of dye. In fact, the hydroxyl radicals is a powerful oxidizing agent and attacks to organic compounds and formed intermediates compounds [25].

Wang et al. also stated that the optimum loading of PVP may led to the modulation of viscosity and diffusion coefficient of the solvent which promote better dispersion of dye removal [24]. Thus, it can be deduced that the optimum loading of PVP in ZnO-PVP precipitation was 0.025 g/L of PVP. The efficiency of photocatalytic degradation rate was depend on the saturation of nanoparticles used. Chong et al. [26] reported that excess amount of nanoparticles operate in photocatalytic reactor will create a light screening effect which reduce the surface area of nanoparticle being expose to light illumination and subsequently will affect the photocatalytic efficiency.

The turbidity of treated wastewater is very relative to the percentage of dye degradation. It can be found as in Figure 6 and Figure 7 which are described that the higher of dye degradation may led to the less turbid of treated wastewater. Figure 7 shows the percentage of turbidity reduction on three different loading of PVP (0.015, 0.020 and 0.025 g/L of PVP) in the precipitation of ZnO-PVP. As illustrated, the treated wastewater by using ZnO-PVP (0.025 g/L of PVP) has less turbid as 58.99% of percentage for turbidity reduction than ZnO-PVP (0.020 and 0.015g/L of PVP) were 53.37% and 54.49%, respectively. The trend of sudden increment in the percentage of turbidity reduction for 0.015g/L of ZnO-PVP loading may be due to the tendency of the particles to aggregate in acidic condition. According to literature [1, 2], they claimed that the degradation efficiency increases along the catalyst dose of PVP due to the absorption of the maximum UV light and effective surface of ZnO-PVP. Hence, it could be concluded that ZnO-PVP (0.025 g/L of PVP) was the best photocatalyst for photocatalytic degradation of industrial dye wastewater due to the maximum adsorption of UV and less turbid of the treated wastewater.

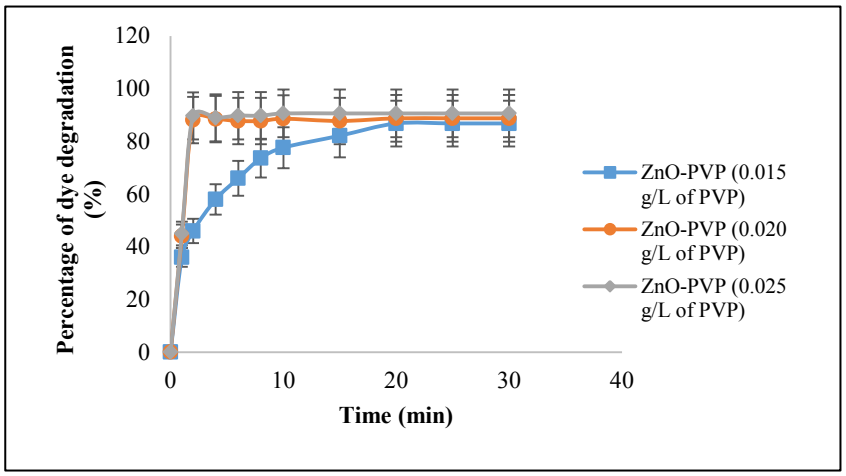


Figure 6. Percentages of dye degradation for photocatalysis process in presence of different loading PVP in ZnO-PVP

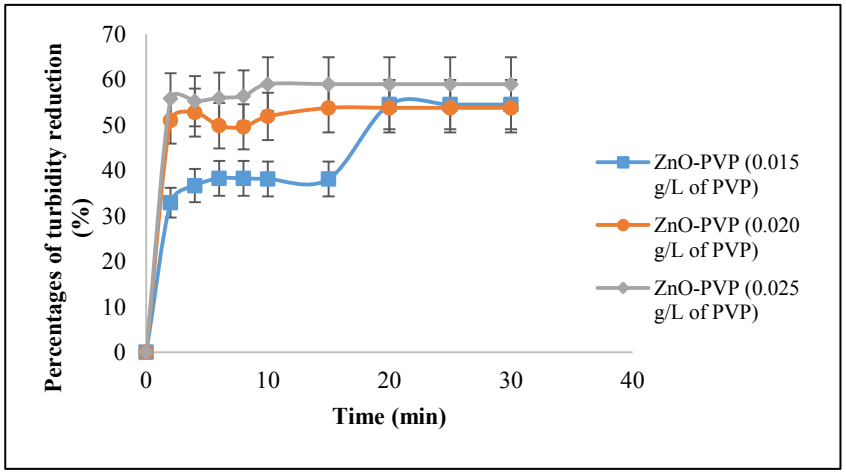


Figure 7. Percentage of turbidity reduction for photocatalysis process in presence of different loading PVP in ZnO-PVP

Based on the Figure 8, it obviously found that there is variation amount of DO that has been obtained by three different of photocatalyst. However, all the reading value of DO that has been obtained were lower to the initial amount of DO which is 3.36 ppm. This is due to the generated oxygen has been involved in the mineralization of dye wastewater since the presence of oxygen contributed to the photocatalytic degradation [23]. This might happen due to the exposure of treated wastewater to the environment.

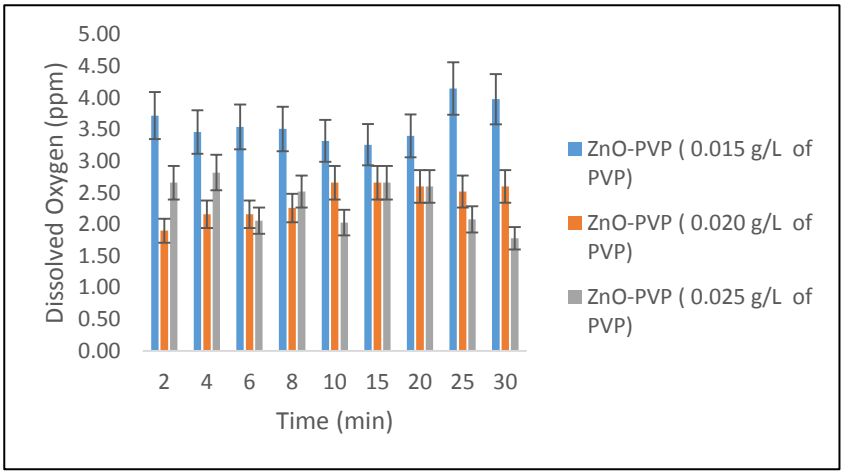


Figure 8. The amount of dissolved oxygen for photocatalysis process in presence of different loading PVP in ZnO-PVP

Conclusion

The optimum operational condition of photocatalytic degradation for the newspaper printing industrial dye wastewater was found under pH 7 of dye wastewater in the presence of ZnO-PVP (0.025 g/L of PVP) nanoparticles. This is due to the maximum dye degradation of 90.61% and turbidity reduction of 58.99%. It can be concluded that the photocatalytic degradation of industrial dye wastewater by ZnO-PVP nanoparticles has great potential as alternative treatment in order to preserve the potable water since it is an eco-friendly treatment due to the non-harmful by-products formed. Furthermore, this study demonstrates the feasibility of ZnO-PVP nanoparticles in photocatalytic treatment of newspaper printing wastewater

Acknowledgement

The authors gratefully acknowledge the financial support from Short Term Grant U659 Universiti Tun Hussein Onn Malaysia, Ministry of Higher Education Malaysia (MOHE) through FRGS grant Number 1616 and the sponsorship under MyBrain scholarship. The authors also would like to appreciate the newspaper printing factory in Selangor, Malaysia.

References

1. Hairom, N. H. H., Mohammad, A. W. and Kadhum, A. A. H. (2014). Effect of various zinc oxide nanoparticles in membrane photocatalytic reactor for Congo red dye treatment. *Separation and Purification Technology,* 137: 74-81.
2. Bandekar, G., Rajurkar, N. S., Mulla, I. S., Mulik, U. P., Amalnerkar, D. P. and Adhyapak, P. V. (2013). Synthesis, characterization and photocatalytic activity of PVP stabilized ZnO and modified ZnO nanostructures. *Applied Nanoscience,* 4(2): 199-208.
3. Satheeskumar, S., Ramesh, K. and Srinivasan, N. (2015). Synthesis and characterization of chitosan and polyvinylpyrrolidone (PVP) capped ZnO nanoparticles and their antibacterial activity against *Escherichia coli and Staphylococcus aurens*. *International Journal of ChemTech Research,* 7(5): 2478-2482.
4. Hairom, N. H. H., Mohammad, A. W. and Kadhum, A. A. H. (2015). Influence of zinc oxide nanoparticles in the nanofiltration of hazardous Congo red dyes. *Chemical Engineering Journal,* 260: 907-915.

5. Kandjani, A. E., Tabriz, M. F. and Pourabbas, B. (2008). Sonochemical synthesis of ZnO nanoparticles: The effect of temperature and sonication power. *Materials Research Bulletin,* 43(3): 645-654.
6. Yadav, R. S., Mishra, P. and Pandey, A. C. (2008). Growth mechanism and optical property of ZnO nanoparticles synthesized by sonochemical method. *Ultrasonics Sonochemistry,* 15(5): 863-868.
7. Vafaee, M. and Ghamsari, M. S. (2007). Preparation and characterization of ZnO nanoparticles by a novel sol-gel route. *Materials Letters,* 61(14-15): 3265-3268.
8. Jurablu, S., Farahmandjou, M. and Firoozabadi, T. P. (2015). Sol-gel synthesis of ZnO nanoparticles: Study of structural and optical properties. *Journal of Sciences, Islamic Republic of Iran,* 26(3): 281-285.
9. Baruwati, B., Kumar, D. K. and Manorama, S. V. (2006). Hydrothermal synthesis of highly crystalline ZnO nanoparticles: A competitive sensor for LPG and EtOH. *Sensors and Actuators, B: Chemical*, 119 (2): 676-682.
10. Hairom, N. H. H., Mohammad, A. W., Ng, L. Y. and Kadhum, A. A. H. (2014). Utilization of self-synthesized ZnO nanoparticles in MPR for industrial dye wastewater treatment using NF and UF membrane. *Desalination and Water Treatment* 54(4-5): 37-41.
11. Yaser, A. Z. and Pogaku, R. (2017). Recent trends for the removal of colored particles in industrial wastewaters. *Environmental Science and Pollution Research,* 24(19): 15861-15862.
12. Sowmyashree V. C., Tejaswini N. and Bhagwat, R. S. (2015). Removal of reactive blue dye from aqueous solution using neem leaves powder as an adsorbent. *International Journal of ChemTech Research,* 4(8): 117-120.
13. Chequer, F. M. D., Oliveira, G. A. R. De, Ferraz, E. R. A., Cardoso, J. C., Zanoni, M. V. B. and Oliveira, D. P. De. (2013). Textile dyes: Dyeing process and environmental impact. *Eco-Friendly Textile Dyeing and Finishing*: pp. 151-176.
14. Baruah, S., Pal, S. K. and Dutta, J. (2012). Nanostructured zinc oxide for water treatment. *Nanoscience and Nanotechnology,* 2(2): 90-102.
15. Sidik, D. A. B., Ngadi, N. and Amin, N. A. S. (2013). Optimization of lignin production from empty fruit bunch *via* liquefaction with ionic liquid. *Bioresource Technology,* 135: 690-696.
16. Lee, P. J., Saion, E., Al-hada, N. M. and Soltani, N. (2015). A simple up-scalable thermal treatment method for synthesis of ZnO nanoparticles. *Metals,* 5(4): 2383-2392.
17. Mondal, K. and Sharma, A. (2016). Photocatalytic oxidation of pollutant dyes in wastewater by TiO_2 and ZnO nano-materials – a mini-review. *Nanoscience & Technology for Mankind; The Academy of Sciences India* (NASI): Allahabad, India: pp. 36-72.
18. Sudha, M. and Rajarajan, M. (2013). Deactivation of photocatalytically active ZnO nanoparticle by surface capping with polyvinyl pyrrolidone. *IOSR Journal of Applied Chemistry*, 3(3): 45-53.
19. Zahrim, A. Y., Tizaoui, C. and Hilal, N. (2011). Coagulation with polymers for nanofiltration pre-treatment of highly concentrated dyes: A review. *Desalination,* 266(1-3): 1-16.
20. Li, Y., Zou, L. and Hu, E. (2004). Photocatalytic degradation of dye effluent by titanium dioxide pillar pellets in aqueous solution. *Journal of Environmental Sciences(China),* 16(3): 375-379.
21. Huber, P. and Carre, B. (2012). Decolorization of process waters in deinking mills and similar applications. *BioResources*, 7(1): 1366-1382.
22. Akpan, U. G. and Hameed, B. H. (2009). Parameters affecting the photocatalytic degradation of dyes using TiO_2-based photocatalysts: A review. *Journal of Hazardous Materials,* 170(2-3): 520-529.
23. Tseng, D. H., Juang, L. C. and Huang, H. H. (2012). Effect of oxygen and hydrogen peroxide on the photocatalytic degradation of monochlorobenzene in aqueous suspension. *International Journal of Photoenergy,* 2012: 1-9.
24. Wang, H., Qiao, X., Chen, J., Wang, X. and Ding, S. (2005). Mechanisms of PVP in the preparation of silver nanoparticles. *Materials Chemistry and Physics,* 94(2-3): 449-453.
25. Behnajady, M. A., Modirshahla, N. and Hamzavi, R. (2006). Kinetic study on photocatalytic degradation of Cl acid yellow 23 by ZnO photocatalyst. *Journal of Hazardous Materials,* 133(1-3): 226-232.
26. Chong, M. N., Jin, B., Chow, C. W. K. and Saint, C. (2010). Recent development in photocatalytic water treatment technology: A review. *Water Research,* 44(10): 2997-3027.

Malaysian Journal of Analytical Sciences, Vol 22 No 4 (2018): 702 - 714
DOI: https://doi.org/10.17576/mjas-2018-2204-17

MALAYSIAN JOURNAL OF ANALYTICAL SCIENCES
Published by The Malaysian Analytical Sciences Society
ISSN 1394 - 2506

LIQUID MEMBRANE COMPONENT SELECTION FOR REMOVAL OF PHENOL FROM SIMULATED AQUEOUS WASTE SOLUTION

(Pemilihan Komponen Cecair Membran untuk Pembuangan Fenol daripada Air Sisa)

Muhammad Bukhari Rosly[1], Norasikin Othman[1,2]*, Hilmi Abdul Rahman[1]

[1]*Department of Chemical Engineering, Faculty of Chemical and Energy Engineering*
[2]*Centre of Lipid Engineering and Applied Research, Ibnu Sina Institute of Scientific and Industrial Research*
Universiti Teknologi Malaysia, 81310 UTM Skudai, Johor, Malaysia

**Corresponding author: norasikin@cheme.utm.my*

Received: 16 April 2017; Accepted: 7 March 2018

Abstract

Phenol is considered as one of the environmental pollutants in various industrial effluents that needs to be removed. One of the potential methods for the removal and recovery of phenol is the emulsion liquid membrane (ELM) process. In order to prepare a stable and efficient emulsion liquid membrane, selecting the components of the membrane is crucial to the process development. This research was conducted to investigate the feasibility of palm oil as an organic solvent in liquid membrane (LM) formulation for phenol extraction and to study the effects of several parameters which affect the extraction and recovery performance of phenol using liquid-liquid extraction. The feasibility of palm oil was investigated by manipulating the organic solvent used, either palm oil or a mixture of palm oil and kerosene. Several parameters such as type of carrier, carrier concentration, type of stripping agent and stripping agent concentration were varied during LM component selection. The results showed that mixed palm oil and kerosene provides a high potential as an organic solvent for the extraction of phenol. About 71% of phenol was extracted at a palm oil to kerosene ratio of 70:30 and assisted with shorter time of phase separation between loaded organic and phenol feed phase. The addition of 0.1M of TBP (tributyl phosphate) as a carrier increased the extraction of phenol to 86% and prevented the third phase formation. Meanwhile, 2M of sodium hydroxide was able to act as a stripping agent to recover 81% of the phenol from the overall process. It can be concluded that palm oil has shown great potential in extracting phenol and could be applied in an ELM process as a green solvent for an emulsion liquid membrane process.

Keywords: phenol, wastewater, liquid membrane components selection, liquid-liquid extraction, organic solvent

Abstrak

Fenol dipertimbangkan sebagai salah satu bahan pencemar daripada air sisa buangan industri yang perlu dirawat. Salah satu kaedah yang berpotensi untuk penyingkiran dan pemulihan fenol adalah proses emulsi membran cecair (ELM). Pemilihan komponen membran adalah penting untuk membentuk emulsi membran cecair yang stabil dan cekap. Kajian ini dijalankan untuk mengkaji kebolehan minyak kelapa sawit sebagai pelarut organik dalam membran cecair (LM) untuk pengekstrakan fenol dan untuk mengkaji kesan terhadap beberapa parameter yang mempengaruhi pengekstrakan dan pemulihan fenol menggunakan pengekstrakan cecair-cecair. Kesesuaian minyak kelapa sawit dikaji dengan memanipulasi pelarut organik yang digunakan, sama ada minyak kelapa sawit atau campuran minyak kelapa sawit dan kerosin. Beberapa parameter seperti jenis pembawa, kepekatan pembawa, jenis agen pelucut dan kepekatan agen pelucut diubah semasa pemilihan komponen LM. Keputusan menunjukkan bahawa campuran minyak sawit dan kerosin berpotensi tinggi sebagai pelarut organik dalam pengekstrakan fenol. Kira-kira 71% fenol diekstrak oleh campuran minyak kelapa sawit dan kerosin yang bernisbah 70:30 dengan kadar masa pemisahan fasa yang lebih pendek di antara fasa organik yang mempunyai fenol dan fasa suapan. Penambahan 0.1M TBP (tributil fosfat) sebagai pembawa meningkatkan pengekstrakan fenol kepada 86% dan menghalang pembentukan fasa ketiga. Sementara itu, 2M natrium hidroksida mampu bertindak sebagai agen pelucutan untuk mendapatkan 81% daripada fenol daripada keseluruhan proses. Dapat

disimpulkan bahawa minyak sawit telah menunjukkan potensi yang besar dalam mengekstrak fenol dan boleh digunakan dalam proses ELM sebagai pelarut hijau untuk proses emulsi membran cecair.

Kata kunci: fenol, air sisa, pemilihan komponen membran cecair, pengekstrakan cecair-cecair, pelarut organik

Introduction

Phenol is a colourless crystalline aromatic alcohol which has a sweet odour. Due to its ability to form hydrogen bonds with other molecules, phenol is soluble in water and can dissolve in most organic solvents, such as aromatic hydrocarbons, halogenated hydrocarbons, ketones, ethers, alcohols and acids [1]. Thus, phenolic compounds are considered as valuable chemical products in various applications such as adhesives, dyes, germicides and chemical intermediates [2]. Unfortunately, phenol pollution can threaten the environment which includes the flora and fauna, and human health [3, 4]. Phenol is classified as corrosive and toxic and can be very dangerous if it is overexposed. Phenol exists in industrial effluents especially from petrochemical industries, refineries, paints and pharmaceuticals. The concentration of phenol present in wastewater from the industries is 6-500 mg/L for refineries, 28-3900 mg/L for coal processing and 2.8-1220 mg/L for petrochemical plants while pharmaceuticals, paints, plastics, pulp, wood products and paper industries contain 0.1-1600 mg/L of phenol [5]. Therefore, the treatment of wastewaters containing phenol before they are discharged has become the recent major concern.

There are various techniques of phenol removal and recovery which can be classified into traditional, and advanced techniques. The traditional techniques incorporate adsorption, liquid–liquid extraction (LLE), steam distillation, chemical oxidation, and biodegradation, while the advanced techniques incorporate photo oxidation processes and membrane separation technologies [2]. Basically, the feasibility of the separation techniques is revised according to the type of wastewater, wastewater composition, treatment efficiency, and operation costs. The most common process for phenol removal is adsorption [6]. A study shows that the use of one of the zeolitic imidazolate frameworks (ZIFs), as an absorbent in phenol removal promotes high adsorption capacity of phenol [7]. However, the difficulties in the recovering of the adsorbent such as activated carbon from treated water and high costs have become major disadvantages of the adsorption process. Besides, another technique in phenol removal and recovery, which is ultrafiltration has been studied by many researchers [8, 9]. The problem regarding this technique is it is incapable to remove small molecular weights of metal ions and organic solutes such as phenol where ultrafiltration systems with many tiny pore membrane size is required to remove small molecular weights metal ions or organic pollutants and this will significantly increase the capital and operating costs [8]. Liquid-liquid extraction is also one of the phenol removal techniques. However, the use of petroleum-based solvents such as kerosene, benzene and toluene are limited because of their high flammability and toxicity [10].

There are many advantages of the emulsion liquid membrane (ELM) process for the removal of phenolic compounds which is high selectivity, high flux ratio, recyclable organic solvents, promising green solvents or carriers, a single stage extraction process and treatment of multiple mixtures in the effluent [11]. In ELM, the emulsion droplets are formed through the emulsification of a stripping agent and a liquid organic solvent. The emulsion droplets are then dispersed into the feed phase for the permeation of solute to take place. The transfer of solute from the feed phase across the membrane phase into the receiving phase is a mass transfer process [12]. The accessibility of this technique basically depends on the emulsion's stability and the ability of solutes to transport across the membrane. Thus, LM component selection is crucial in determining the efficiency of solutes transport. Basically, the step was carried out using liquid-liquid extraction (LLE) for the selection of organic solvents (diluent), carriers and stripping agents [13, 14].

In this study, the efficiency of the combination of palm oil as an organic solvent and kerosene to extract phenol from simulated wastewater was investigated. The efficiency of extraction and the recovery performance were studied throughout the liquid-liquid extraction process.

Materials and Methods

Chemicals and reagents

All reagents used were of analytical grade and were used without further purification. Palm cooking oil was purchased from the supermarket, while kerosene and phenol were purchased from Sigma-Aldrich. For stripping

agents, acidic thiourea (assay: 99%) was obtained from Qrec, sodium hydroxide (assay: 99%) was obtained from Merck, hydrochloric and sulphuric acids (assay: 97%) were obtained from JT Baker.

Experimental procedures: Preparation of phenol solution

The phenol feed stock aqueous solution (300 ppm) was prepared by dissolving the required quantity of crystallized phenol in distilled water. For calibration, the 300 ppm phenol was diluted to 5, 10, 15, 20, 25 and 30 ppm. UV-spectrophotometer was used to measure the contents of phenol in wastewater at wavelength, λ of 270 nm.

***Extraction* and stripping process**

An equal volume of the feed phase of phenol waste and organic membrane solutions (100 ml) were mixed in a beaker and stirred at 150 rpm for 1 hour. After the extraction process, the solution was transferred into a separating funnel and was left for 15 minutes for phase separation. The treated aqueous phase was carefully separated from the organic phase and the concentration of phenol in the liquid phase was measured using the UV-spectrophotometer. The concentration of phenol extracted in the organic membrane phase was calculated based on mass balance principles. The organic solutions that were used in the process were in various ratio of palm oil to kerosene (10:0, 9:1, 8:2, 7:3, 6:4, 5:5 and 0:10).

The selection of carrier was conducted after finding the optimum composition of palm oil to kerosene. The liquid-liquid extraction process was repeated by adding a carrier into the diluent. The steps were repeated for different types of carrier such as TOA (trioctylamine), TDA (tridecylamine), TBP (tributylphosphate), D2EPHA (bis-2-ethylhexyl phosphate) and Cyanex 302. After the most suitable carrier was obtained, the extraction process was repeated by varying the concentrations of the selected carrier.

The stripping process was carried out after the extraction process. An equal volume of phenol loaded membrane phase and stripping agent at a specific concentration (100 ml) were stirred at 150 rpm for 1 hour and then the sample was slowly poured into a separating funnel and left for phase separation for 15 minutes. After that, the liquid phase was separated from the organic phase and the concentration of phenol stripped was measured. These procedures were repeated for other stripping agents and concentrations. The stripping agents used were hydrochloric acid, sodium hydroxide, sulphuric acid and thiourea. This study was conducted at room temperature (25±1 ˚C).

Emulsion liquid membrane (ELM) process

The ELM process was carried out after the selection of liquid membrane component completed. In this study, no carrier has been added in the organic phase because there was no significant result of phenol extraction during the LLE process. All optimum parameters for the ELM process were obtained from our previous work [15]. The w/o emulsion was prepared by mixing an organic liquid membrane containing 3% of Span 80 with a stripping agent. A 7.5 ml organic phase and a 2.5 ml stripping phase (ratio of solvent to stripping phase; 3: 1) were emulsified continuously using homogenizer at 8000 rpm for 5 minutes. Then, the 10 ml prepared w/o emulsion was dispersed into 100 ml of 100 ppm of phenol (treat ratio; 1:10). The solution was stirred at 500 rpm agitation speed using a digital mixer for 5 minutes. After the extraction process, the solution was immediately poured into a separating funnel and was left for 15 minutes for the phase separation of emulsion and external phase. The treated phenol solution (external phase) was taken for phenol content analysis using the UV-Spectrophotometer.

Analytical procedures

The percentage of extraction (E), percentage of stripping (S), percentage of recovery (R), and distribution ratio (D) were calculated using the following equations:

$$E(\%) = \frac{[phenol]i - [phenol]f}{[phenol]i} \times 100 \quad (1)$$

$$S(\%) = \frac{[phenol]strip}{[phenol]org} \times 100 \quad (2)$$

$$R(\%) = \frac{[phenol]strip}{[phenol]i} \times 100 \quad (3)$$

$$D = \frac{[phenol]org}{[phenol]f} \quad (4)$$

where $[phenol]_i$ is the initial phenol concentration in the aqueous phase (mg/L), $[phenol]_f$ is the phenol concentration in the aqueous phase after extraction (mg/L), $[phenol]_{org}$ is the phenol concentration in the organic phase (mg/L), and $[phenol]_{strip}$ is the phenol concentration in the stripping phase.

Results and Discussion

Effect of solvent type and composition on phenol extraction

Figure 1 shows the effect of the organic solvent used in the extraction of phenol. The results reveal that the highest extraction of phenol using a 100% of kerosene and palm oil were 21% and 79% respectively at 1 hour of extraction time. The results show that an aliphatic hydrocarbon such as kerosene contributes to the lower extraction of phenol. This is because aliphatic hydrocarbon structures form long carbon chains which have non-polar properties. This means that kerosene cannot form any chemical reaction with the polar phenol. The transport mechanism of phenol in kerosene is only through the diffusion of the solutes into the membrane [16]. Thus, the diffusivity of phenol into kerosene is restricted by the solubility of phenol in water. Based on the properties of phenol, phenol is more soluble in water due to the hydrogen bonds and is less soluble in aliphatic hydrocarbons such as kerosene [1]. The use of kerosene as a liquid membrane basically assisted the addition of carriers to form complexes with the selective solutes. Meanwhile, the result shows a potential extraction efficiency of phenol using palm oil as a solvent. Palm oil contains triglycerides that are formed from the reaction of glycerol and ester molecules. Even though palm oil has non-polar properties, the triglycerides present in palm oil could help with the formation of phenol-triglycerides complexes either through hydrogen bonding or through intermolecular interaction between the molecules [15]. The transport mechanism of phenol can be explained by partitioning (dissolving) and complexation [16]. Also, the hydrophobic property of oils can dissolve phenolic compounds and the emulsion stability can generally be increased as palm oil provides high viscosity [17].

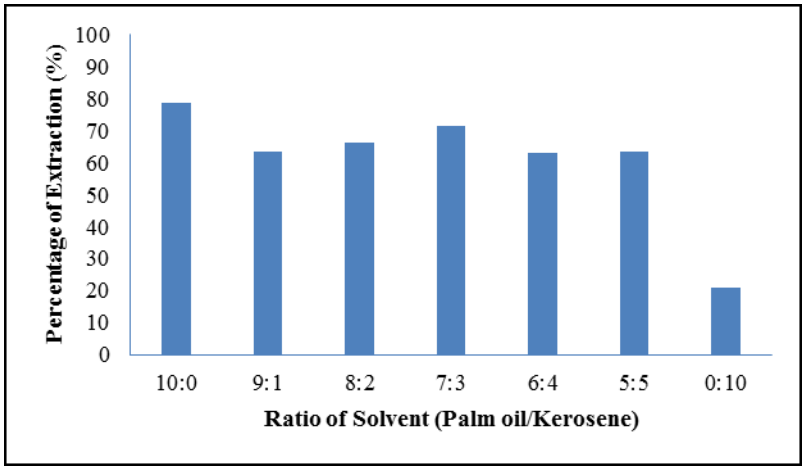


Figure 1. Extraction performance on difference ratio of palm oil to kerosene (Experiment conditions: [phenol] = 300ppm, rotation speed = 150rpm, duration = 1 hr, temperature = 25±1 ˚C, feed to solvent ratio =1:1)

However, the use of palm oil that resulted in the formation of a milky-like solution caused the phase separation of loaded organic and treated aqueous phase to become much slower. To improve the phase separation time, extractions using mixtures of palm oil and kerosene was carried out. The composition of the solvents that were investigated were in the ratio of 9:1, 8:2, 7:3, 6:4, and 5:5 of palm oil to kerosene. Based on Figure 1, 7:3 palm oil to kerosene ratio provided the highest phenol extraction compared to other ratio at 71% extraction efficiency. Also, it is observed that at this ratio the phase separation time of the mixed solution is significantly reduced. It is expected that by adding kerosene to palm oil, the viscosity of palm oil will be reduced hence it will increase the distribution

coefficient of solutes and will influence the solvent extraction kinetics [10]. This is because kerosene contains a higher number of carbon atoms, which resulted in higher hydrophobicity and it is much less soluble in water compared to palm oil [18]. Therefore, by mixing the solvents between palm oil and kerosene, the transport mechanism of the phenol into the mixture can be explained by subsequent dissolving, complexation, and diffusion. The lower extraction of phenol at ratio of palm oil to kerosene of 9:1 and 8:2 can be explained by the stable resonance of phenol in the system [19]. Meanwhile, the lower extraction of phenol at ratio of palm oil to kerosene of 6:4 and 5:5 can be explained by the non-polar aliphatic hydrocarbon of kerosene in the system. Furthermore, the performance of the solvent can be increased by adding modifiers such as carriers and ionic liquids to prevent the formation of a third phase, to improve the solvent properties and to enhance the extraction efficiency. The 7:3 ration was used further in the study.

Effect of carrier type on phenol extraction

Selective carrier toward the solute plays an important role to enhance the extraction efficiency of the system. To increase the extraction of phenol, the selection of carriers is important. The aqueous solute phenol molecules will bind to the selective carriers and form complexes, thus increasing the solubility of phenol in the organic solvent. Also, a suitable carrier will be able to prevent the formation of a third phase which is due to the reaction of triglycerides and phenol molecules. Five types of carriers were investigated to extract phenol from aqueous solutions such as TOA (trioctyl amine), TDA (tridecyl amine), TBP (tributyl phosphate), D2EPHA (bis-2-ethylhexyl phosphate) and Cyanex 302. Figure 2 shows the extraction efficiency of phenol using 0.05M carrier concentration. The results indicate that the highest extraction percentage of phenol was achieved when TBP was used as the carrier, which is at 77% and no third phase was observed. On the other hand, the extraction of phenol using TOA, TDA, D2EPHA and Cyanex 302 was lower due to weak molecular interactions. These results were in agreement with Zidi et al. [20] which reported that phenol can be efficiently extracted using various basic and solvating reagents due to the polarity of phenol.

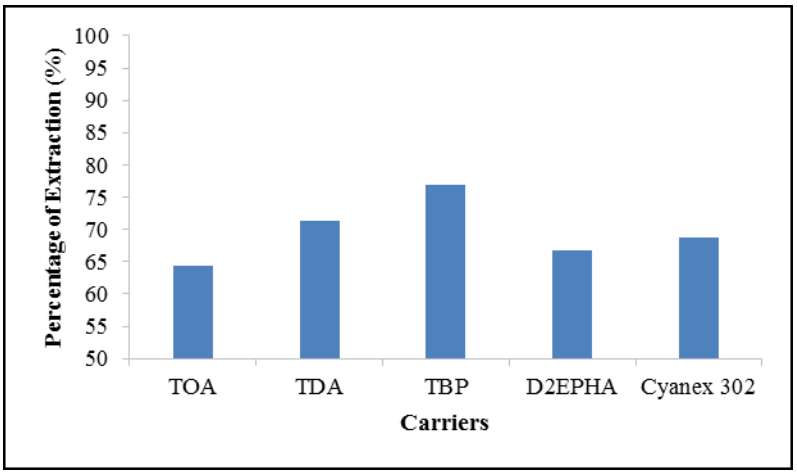


Figure 2. Liquid-liquid extraction of phenol using various carrier (experimental condition: Solvent= 7:3 of palm oil to kerosene ratio, [PhOH]= 300ppm, [carrier]= 0.05M, solvent= 7:3 palm oil to kerosene ratio, rotation speed= 150rpm, duration= 1 hour, T= 25±1 ˚C)

TBP as a solvating reagent has achieved the highest percentage of extraction due to its ability to react with polar phenol molecules and to be dissolved into solvents. This indicates that TBP has an ability to enhance the extraction of phenol using palm oil as a solvent. The extraction mechanism can be explained by the diffusion of phenol in aqueous solution from bulk to the interface where the reaction of phenol takes place with TBP present in the organic to form phenol-TBP complex by hydrogen bonding or intermolecular interactions between them. Zidi et al. [20] described the extraction of the phenol complex into the organic phase is based on the availability and the extractable phenol complex species formation due to transport flux. The presence of oxygen atoms in TBP (Figure 3) to form

strong hydrogen bonds with phenol molecules provided a synergistic effect, thus enhancing the extraction efficiency. The reaction of phenol and TBP is considered reversible throughout the process as described in equation 5 below [21].

$$PhOH_{(aq)} + TBP_{(org)} \leftrightarrow (PhOH.TBP)_{(org)} \quad (5)$$

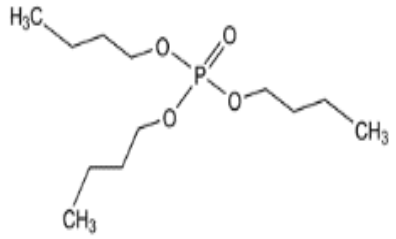


Figure 3. Molecular structure of tributyl phosphate (TBP)

Effect of carrier concentration

Figure 4 shows the result of phenol extraction in the range of 0.05M to 0.15M of TBP concentration. The result shows that the extraction percentage increases gradually and proportionally to carrier concentration from 0.05M to 0.1M. Basically, with the increase of TBP concentration, there are more phenol-TBP complexes that can be formed during the process. The highest extraction percentage of phenol is 86% at 0.1M of TBP concentration. Further increase of the concentration of TBP resulted in a plateau where the extraction was in excess of the carriers. It indicates that the saturation capacity of the solvent phase for the phenol-TBP complexes has reached its peak at 0.1M TBP concentration. There were no significant effects with further increments of carrier concentration. In this study, 0.1M TBP was chosen as the optimum concentration of carrier because any further increase of the carrier concentration is expected to increase the solvent viscosity, which in turn affect the transport mechanism of phenol molecules due to high viscosity.

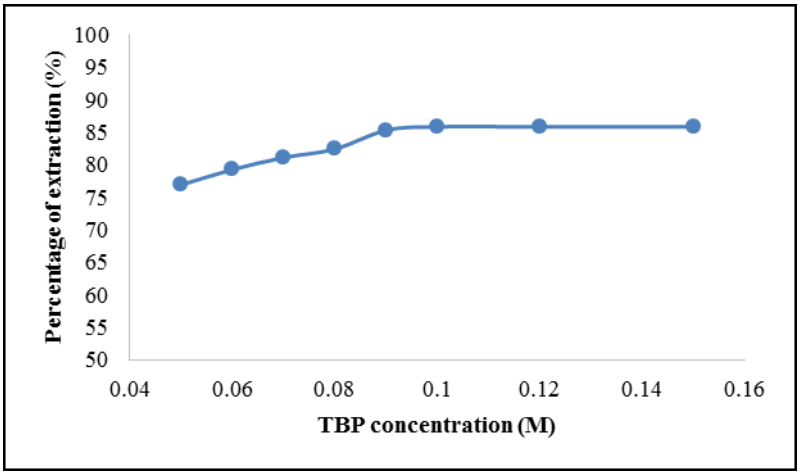


Figure 4. Effect of carrier concentration in liquid-liquid extraction of phenol (experimental condition: Solvent= 7:3 of palm oil to kerosene ratio, [PhOH]= 300ppm, carrier= TBP, rotation speed= 150rpm, duration= 1 hour, T= 25±1 ˚C)

According to Othman et al. [22], the nature of the extracted phenol was determined by plotting a graph of log D versus log [TBP] as shown in Figure 5. The slope of the line was used to determine the molar ratio of phenol reacting to TBP. The result shows that the distribution ratio of phenol increases with the carrier concentration in the

organic phase. The result gives a straight line with a slope value of 0.9 which is close to unity. Thus, the molar ratio of phenol to TBP can be assumed to be 1:1. This indicates that one mole of phenol requires one mole of TBP for the reaction to form phenol-TBP complexes in the extraction process. The result confirms that TBP is effective in extracting cationic phenols even though palm oil was used as a diluent. However, in this preliminary emulsion liquid membrane process, the addition of TBP as a carrier was not considered since there is no significant result in phenol extraction throughout the process.

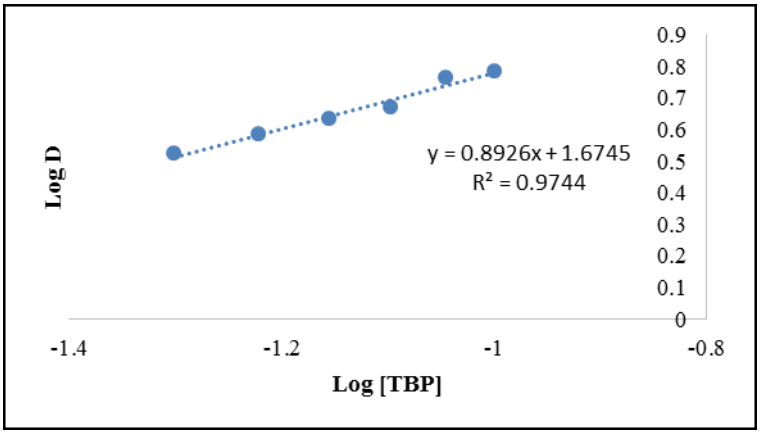


Figure 5. Stoichiometric plot for the equilibrium extraction of phenol using TBP as carrier

Effect of stripping agents type in stripping process

Stripping agents are a very important factor for solute recovery purposes. Various types of stripping agents at 0.5M concentration such as sodium hydroxide, sodium bicarbonate, hydrochloric acid, sulphuric acid and acidic thiourea were investigated during the stripping process. The stripping performance is illustrated in Figure 6. Sodium hydroxide shows the highest percentage of stripping which is 75%. It indicates that a strong base has the capability to form coordinate bonds with phenol and to strip the phenol molecules from the organic solvent effectively. This is in line with the work of Zidi et al. [20] where an aqueous sodium hydroxide solution effectively stripped the phenol molecules from the organic solvent due to the chemical reaction of phenol and sodium hydroxide. On the other hand, the stripping percentages of thiourea, $NaHCO_3$, HCl and H_2SO_4 have been found to be lower. This indicates that the phenol-triglyceride complexes' and the phenol-TBP complexes' bonding is strong enough to hinder the reaction of these stripping agents with phenol. Also, the same polarity between the stripping agents and phenol contributed to weak molecular interactions and van der Waal forces between the molecules. The basic reaction of phenol and sodium hydroxide can be described in equation 6 below [15]:

$$PhOH + NaOH \rightarrow PhONa + H_2O \quad (6)$$

In addition, sodium hydroxide, a strong base which provided sodium ions, Na attracted and reacted with the negative charges of phenol ions. The phenol molecules were converted into sodium phenolate at the organic solvent interface and were retained in the stripped solution [17]. The phenol-triglyceride complexes reacted with the aqueous sodium hydroxide solution, which lead to the formation of sodium phenolate and triglyceride molecules. Meanwhile, the phenol-TBP complexes reacted with the aqueous sodium hydroxide solution, leading to the formation of sodium phenolate, TBP molecules and water. Triglyceride and TBP molecules were expected to retain in the solvent to form complexes with excess phenols [10]. The sodium phenolates formed from the reaction are expected not to diffuse back into the solvent. The reaction is considered irreversible and instantaneous throughout the process as described in equation 7 below [20].

$$(PhOH.TBP)_{(org)} + NaOH_{(aq)} \leftrightarrow PhONa_{(aq)} + TBP_{(org)} + H_20 \quad (7)$$

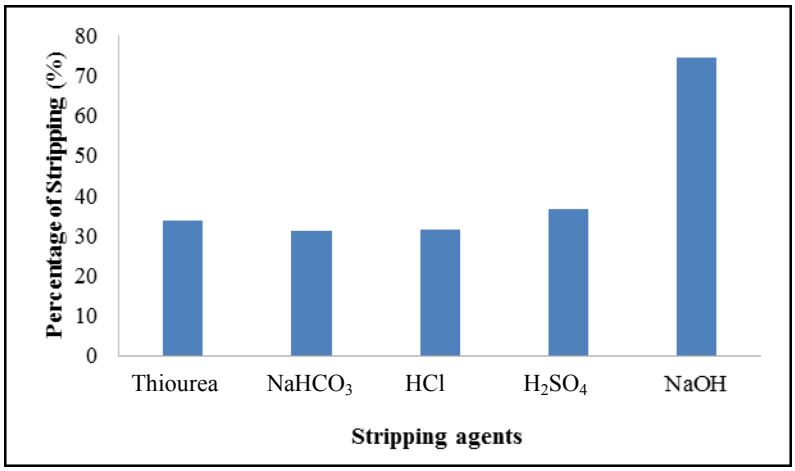


Figure 6. Effect of carrier different stripping agents in liquid-liquid extraction of phenol (experimental condition: [PhOH]= 300 ppm, [stripping agent]= 0.5M, rotation speed= 150 rpm, duration= 1hour, T= 25±1 ˚C)

Effect of stripping agent concentration

The performance of phenol recovery was studied by varying the stripping agent concentration. At the solvent strip interface, phenol reacts with sodium hydroxide to form sodium phenolate and is transported into the stripping phase. The sodium phenolate formed cannot permeate back to the solvent. The concentration of sodium hydroxide plays a crucial role in phenol recovery. The stripping efficiency of phenol was studied in the range of 0.5 – 2M of NaOH concentration. The results are shown in Figure 7.

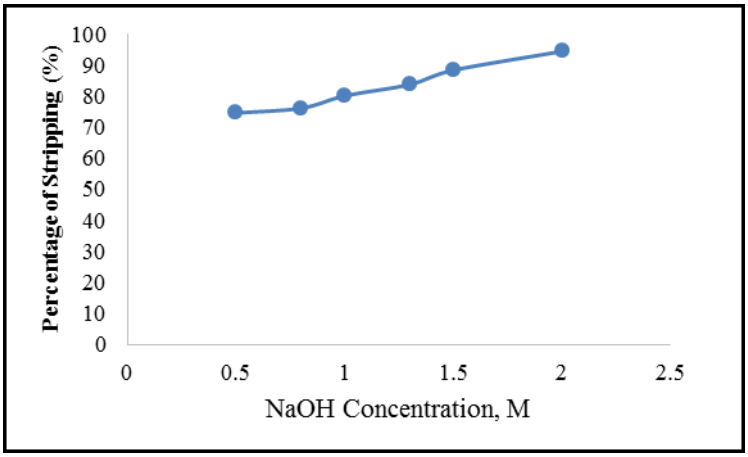


Figure 7. Effect of NaOH concentration in liquid-liquid extraction of phenol for stripping process (experimental condition: [PhOH]= 25.76 ppm, rotation speed= 150 rpm, duration= 1 hour, T= 25±1 ˚C)

Based on the results, the rate of phenol transfer is obviously dependent of the concentration of sodium hydroxide within the range studied. According to Venkateswaran and Palanivelu [17], the permeability of solutes depends on the strength of the receiving phase. Below the concentration of 0.5M, the concentration of phenol is insignificant due to the cloudiness of the stripping solution after the process. This problem might be due to the insufficiency of stripping agents to strip out the phenol into the stripping phase. Further increase of NaOH concentration enhances the stripping percentage of phenol which leads to a greater removal of phenol. It can be seen that by increasing the NaOH concentration from 0.5M to 2 M, the stripping percentage of phenol increases from 75% to 94%. Work by Sumalatha et al. [23] reported that the increase of NaOH concentration leads to an increase in NaOH to phenol

molar ratio. This is because a higher concentration of NaOH provides more Na^+ ions, thus more phenol ions in the form of complexes are able to be stripped. The more the phenol being stripped will significantly increase the phenol recovery throughout the process.

However, further increases of sodium hydroxide above 2M will lead to the formation of solid precipitates. It is believed that the solid formed is soap. This is because soap can be produced by hydrolysed fats or oils under basic conditions to form glycerol and a mixture of salts [24, 25]. The hydrolysis of an ester in a basic solution is called saponification. Basically, saponification can be carried out using a basic sodium or potassium solution. In an ELM process, a high concentration of NaOH might not be needed because there are various factors that could affect the stripping performance. Figure 8 shows the reaction of triglyceride with sodium hydroxide.

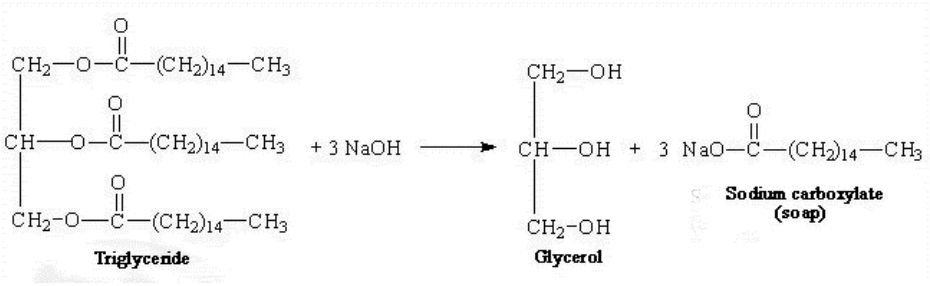


Figure 8. Saponification of triglyceride

By assuming that all sodium hydroxides have reacted with all phenol complexes, the nature of the stripped solute was evaluated by plotting the graph of log D versus log [NaOH] as shown in Figure 9. The results give a straight line with the line slope of 1.2 which is nearly 1. Thus, the molar ratio of phenol complex to sodium hydroxide can be assumed to be 1:1, which indicates that one mole of phenol complex requires one mole of sodium hydroxide for a stripping reaction.

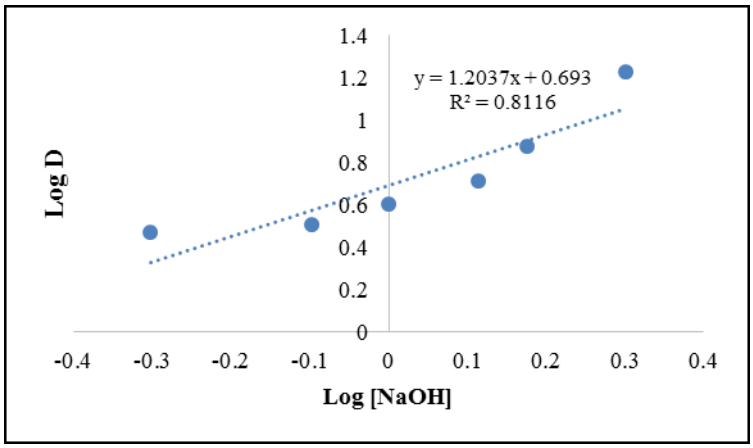


Figure 9. Stoichiometric plot for the equilibrium stripping of phenol using sodium hydroxide as stripping agent

Mechanism of phenol extraction and recovery

Table 1 shows the results of the liquid-liquid extraction with and without the addition of organic carriers and the recovery performance of phenol. In this research, the composition ratio of palm oil to kerosene (7:3) shows good extraction of phenol, which is 71% without using a carrier. This indicates that triglycerides present in the oil were able to react with phenol to form phenol-triglyceride complexes. Meanwhile, by adding the carrier (0.1M TBP), phenol extraction increases. This indicates the potential of carriers to enhance the extraction efficiency of phenol,

which is 86%. TBP is a basic solvating reagent, thus it can react with slightly acidic phenol and form phenol-TBP complex. The TBP structure which contains four oxygen atoms enables the formation of hydrogen bonds with phenol molecule.

In the phenol recovery process, sodium hydroxide shows good stripping performance with up to 94% of phenol stripped as shown in Figure 7. This proves that sodium hydroxide has the capability of forming stronger polar bonds with phenol molecules. Thus, from the mass balance calculated (Equation 3) based on the amount of phenol extracted and stripped into the stripping phase, the amount of phenol recovered is 81%. This is due to the polarity of phenol which is sufficiently acidic while sodium hydroxide which is known as strong basic compound thus the hydrogen ions of phenol can easily break away from the OH group and transfer to a base leaving a phenoxide ion. Phenoxide ions then reacted with sodium ions to give a colourless solution that contains sodium phenolate.

Table 1. Performance of phenol extraction and recovery at optimum conditions of component selection

Diluent (Phenol: Kerosene)	Carrier	Performance (%)
7:3	-	71% extraction
7:3	0.1M TBP	86% extraction

Based on results presented, the transfer of phenol through liquid membrane is by two transport mechanisms, which is simple diffusion through kerosene, and carrier-mediated transport through TBP and triglyceride as by functional carriers. Figures 10 and 11 shows the mass transfer mechanisms of phenol. Phenol reacts with the triglyceride present in palm oil to form a phenol-triglyceride complex. On the other hand, phenol reacts with TBP as a carrier to form a phenol-TBP complex. Both complexes react with sodium hydroxide to form sodium phenolate.

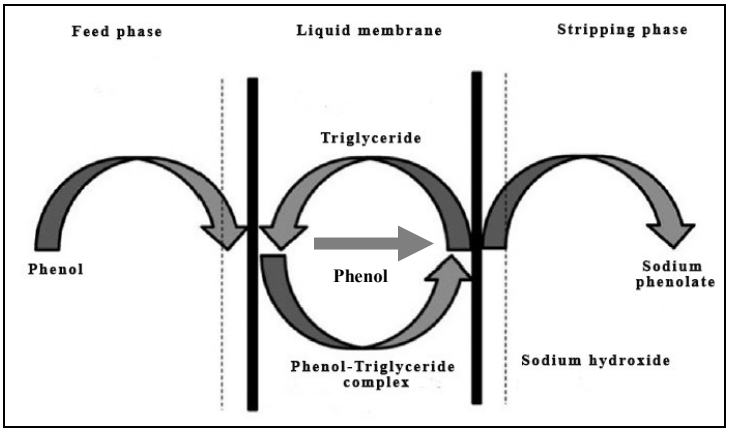


Figure 10. Mass transfer mechanism of phenol-triglyceride complex

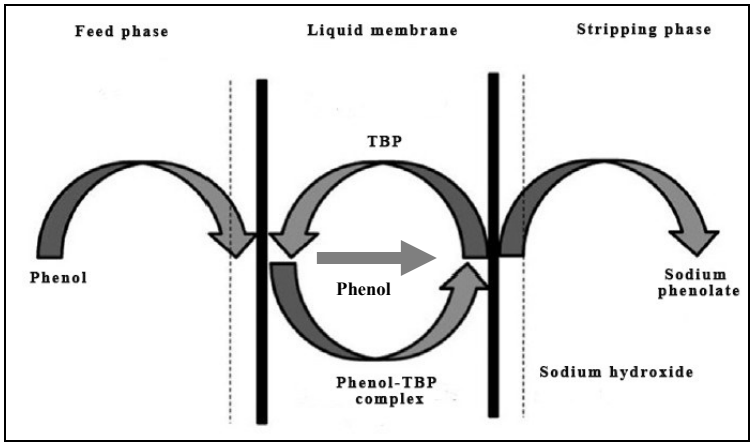


Figure 11. Mass transfer mechanism of phenol-TBP complex

Emulsion liquid membrane process

The extraction of phenol using ELM was studied after the selection of liquid membrane components had been completed. Figure 12 shows the effect of external feed phase concentration on phenol extraction by ELM process. The results show that the percentage of phenol extraction was highest at the lowest concentration of external feed concentration (100 ppm), where 73% of phenol was extracted. At lower concentrations, the extraction process was controlled by the external mass transfer that transported into the stripping phase continuously. However, by increasing the external feed concentration, the extraction decreases due to the limitation of triglycerides to form complexes with phenol. Also, the possible swelling and breakage behaviour of emulsion membrane due to osmotic pressure in the system might contribute to the decrement of phenol extraction [26].

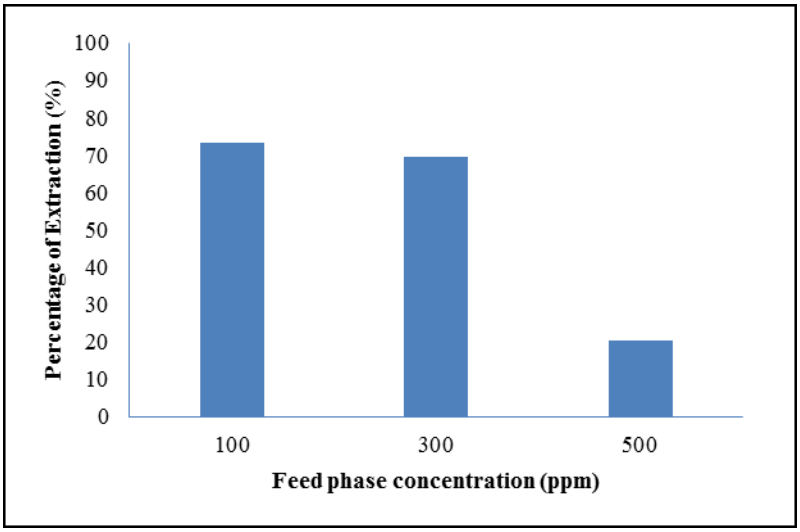


Figure 12. Effect of feed phase concentration in ELM process for phenol extraction (experimental condition: Solvent = 7:3 of palm oil to kerosene ratio, Span 80 = 3%, [NaOH] = 0.1M, homogenizer speed = 8000 rpm, emulsifying time = 5 minutes, agitation speed = 500 rpm, extraction time = 5 minutes, treat ratio = 1:3, T= 25±1 ˚C)

In addition, the transport rate of phenol solutes might decrease largely because of the small capacity of the stripping phase to strip the transported phenol. This attributed to the internal droplets that were readily saturated with the solutes and hindered the diffusion of phenol solutes across the membrane. In this study, the extraction process was conducted at a treat ratio of 1:3, where 10ml of emulsion (means that only 7.5 ml of organic solvent was used) was used to extract phenol from 100 ml of simulated waste solution. Results show that the ELM process was able to extract phenol without using a large amount of solvents and stripping agents. In this study, the extraction percentage during the LLE process using a 7:3 palm oil to kerosene ratio was 71% while the extraction percentage from the ELM process was 69%. It shows that almost 90% of organic solvents can be saved for other extraction cycles.

Conclusion

The liquid-liquid extraction of phenol offers one of the simplest methods as a preliminary study of the emulsion liquid membrane process. Palm oil to kerosene ratio of 70:30 was able to extract 71% of phenol from a simulated aqueous wastewater, which shows a great potential of palm oil as a green solvent. An addition of 0.1 M tributyl phosphate (TBP) increased the extraction efficiency to 86% and prevented the formation of a third phase during the experiment. Sodium hydroxide is a good stripping agent for phenol recovery and 2M of NaOH was able to recover more than 80% of phenol. The results also show the capability of ELM to extract phenol from wastewater with minimum usage of organic solvent.

Acknowledgements

The authors would like to acknowledge the Ministry of Higher Education (MOHE), Universiti Teknologi Malaysia (RU Research Grant; GUP: Q.J130000.2546.12H50), Ministry of Science Technology and Innovation (FRGS: R.J130000.7846.4F949), Centre of Lipids Engineering and Applied Research (CLEAR), Universiti Teknologi Malaysia (UTM) for the facilities supporting this research.

References

1. Rappoport, Z. (2003). The chemistry of phenols. John Wiley & Sons Ltd., Chichester.
2. Park, Y., Skelland, A. H. P., Forney, L. J. and Kim, J. H. (2006). Removal of phenol and substituted phenols by newly developed emulsion liquid membrane process. *Water Research,* 40 (9): 1763 – 1772.
3. Hori, T. S. F., Avilez, I. M., Inoe, K. L., Inoue, L. K. and Moraes, G. (2006). Metabolical changes induced by chronic phenol exposure in matrinxa brycon cephalus (*Teleostei chracidae*) juveniles. *Comparative Biochemistry and Physiology,* 143(1): 67-72.
4. Jiao, H., Peng, W., Zhao, J. and Xu, C. (2013). Extraction performance of bisphenol A from aqueous solutions by emulsion liquid membrane using response surface methodology. *Desalination,* 313: 36-43.
5. Mohammadi, S., Kargari, A., Sanaeepur, H., Abbassian, K., Najafi, A. and Mofarrah, E. (2015). Phenol removal from industrial wastewaters: A short review. *Desalination and Water Treatment,* 53(8): 2215-2234.
6. Mukherjee, S., Kumar, S., Misra, A. K. and Fan, M. (2007). Removal of phenols from water environment by activated carbon, bagasse ash and wood charcoal. *Chemical Engineering Journal,* 129(1-3): 133-142.
7. Pan, Y., Li, Z., Zhang, Z., Tong, X. S., Li, H., Jia, C. Z., Liu, B., Sun, C. Y., Yang, L. Y., Chen, G. J. and Ma, D. Y. (2016). Adsorptive removal of phenol from aqueous solution with zeolitic imidazolate framework-67. *Journal of Environmental Management,* 169: 167-173.
8. Tung, C. C., Yang, Y. M., Chang, C. H. and Maa, J. R. (2002). Removal of copper ions and dissolved phenol from water using micellar-enhanced ultrafiltration with mixed surfactants. *Waste Management,* 22(7): 695-701.
9. Witek, A., Kotuniewicz, A., Kurczewski, B., Radziejowska, M. and Hatalski, M. (2006). Simultaneous removal of phenols and Cr^{3+} using micellar-enhanced ultrafiltration process. *Desalination,* 19(1-3): 111-116.
10. Othman, N., Heng, L. C., Noah, N. F. M., Yi, O. Z., Nasruddin, N. A., Ali, N. and Hamzah, S. (2015). Removal of phenol from wastewater by supported liquid membrane process. *Jurnal Teknologi (Sciences & Engineering),* 74(7): 117-121.
11. Urtiaga, A., Gutierrez, R. and Ortiz, I. (2009). Phenol recovery from phenolic resin manufacturing: viability of the emulsion pertraction technology. *Desalination,* 245(1-3): 444-450.
12. Kislik, V. S. (2010). Liquid membrane: Principles and application in chemical separation and wastewater treatment. Elsevier, Amsterdam.

13. Othman, N., Mili, N., Idris, A. and Zailani, S. N. (2012). Removal of dyes from liquid waste solution: Study on liquid membrane component selection and stability. In *Sustainable Membrane Technology for Energy, Water, and Environment*. John Wiley and Sons, USA: pp. 221 – 229.
14. Othman, N., Mili, N. and Wong, y. M. (2011). Liquid-liquid extraction of black B dye from liquid waste solution using tridodecylamine. *Journal of Environmental and Technology,* 4(3): 324-331.
15. Othman, N., Noah, N. F. M., Shu, L. Y., Ooi, Z. Y., Jusoh, N., Idroas, M. and Goto, M. (2016). Easy removing of phenol from wastewater using vegetable oil-based organic solvent in emulsion liquid membrane process. *Chinese Journal of Chemical Engineering,* 25(1): 45-52.
16. Teng, T. T. and Talebi, A. (2012). Green liquid membrane: Development and challenges. *Journal of Membrane Science and Technology,* 2(3): 2-3.
17. Venkateswaran, P. and Palanivelu, K. (2006). Recovery of phenol from aqueous solution by supported liquid membrane using vegetable oils as liquid membrane. *Journal of Hazardous Materials,* 131(1-3): 146-152.
18. Othman, N., Mat, H. and Goto, M. (2006). Separation of silver from photographic wastes by emulsion liquid membrane system. *Journal of Membrane Science,* 282(1-2): 171-177.
19. Carey, A. F. (2008). Organic Chemistry. McGraw Hill, New York.
20. Zidi, C., Tayeb, R., Ali, M. B. S. and Dhahbi, M. (2010). Liquid–liquid extraction and transport across supported liquid membrane of phenol using tributyl phosphate. *Journal of Membrane Science,* 360(1-2): 334-340.
21. Cichy, W. and Szymanowski, J. (2002). Recovery of phenol from aqueous streams in hollow fiber modules. *Environmental Science & Technology,* 36(9): 2088-2093.
22. Othman, N., Noah, N. F. M., Sulaiman, R. N. R., Abdullah, N. A. and Bachok, S. K. (2014). Liquid-liquid extraction of palladium from simulated liquid waste using phosphinic acid as a carrier. *Jurnal Teknologi (Science & Engineering),* 68(5): 41-45.
23. Sumalatha, B., Narayana, A. V., Kumar, K. K., Babu, D. J., Venkateswarulu, T. C. (2016). Phenol removal from industrial effluent using emulsion liquid membranes. *Journal of Pharmaceutical Sciences and Research,* 8(5): 307-312.
24. Bruice, P. Y. (2006). Essential organic chemistry. Pearson Prentice Hall, Upper Saddle River, New Jersey.
25. Solomons, T. W. G. and Fryhle, C. B. (2011). Organic chemistry. John Wiley & Sons (Asia) Pte Ltd, Asia.
26. Goyal, R. K., Jayakumar, N. S. and Hashim, M. A. (2011). Chromiium removal by emulsion liquid membrane using $[BMIM]^{+}[NTF2]^{-}$ as stabilizer and TOMAC as extractant. *Desalination,* 278(1-3): 50-56.

Malaysian Journal of Analytical Sciences, Vol 22 No 4 (2018): 715 - 722
DOI: https://doi.org/10.17576/mjas-2018-2204-18

MALAYSIAN JOURNAL OF ANALYTICAL SCIENCES
Published by The Malaysian Analytical Sciences Society
ISSN 1394 - 2506

ENZYMATIC HYDROLYSIS OF OIL PALM EMPTY FRUIT BUNCH AND ITS KINETICS

(Hidrolisis Enzim Tandan Buah Kelapa Sawit dan Sifat Kinetik)

Nazlee Faisal Ghazali* and Nurul Aqilah Makhtar

Department of Bioprocess Engineering,
Faculty of Chemical and Energy Engineering,
Universiti Teknologi Malaysia, 81310 Skudai, Johor Bahru, Johor, Malaysia

**Corresponding author: nazlee@utm.my*

Received: 16 April 2017; Accepted: 7 March 2018

Abstract

Oil palm lignocellulosic biomass is a potential substrate for the production of renewable chemicals from agricultural wastes. Empty fruit bunch (EFB) is one of the biomass waste aside from the trunk and frond from oil palm plantation. Bioconversion of oil palm lignocellulose using enzymes to fermentable sugar could be used for the production of bioethanol. However, the bioconversion is challenging due to the complex interactions between substrate and enzymes. In order to utilize EFB as the feedstock, it is important to understand the effect of enzyme concentration and substrate concentration on the bioconversion of EFB. In this study, we investigated the effect of enzyme loading and substrate loading for the maximum conversion of oil palm lignocellulose. The results show that as the enzyme loading increased, the rate of reaction and also the yield of reducing sugar (RS) and glucose initially increased and then plateaued. High enzyme loading might lead to enzyme in excess and enzyme layering around the substrate. Similar pattern was also observed on the reaction rate as the substrate loading increased. However, the yield of RS and glucose decreased as the substrate loading increase. It could be explained by the substrate recalcitrance and product inhibition. The initial product formation rates were used to determine the kinetic parameters such as maximum rate constant V_{max} and the half saturation constant K_m. From this study, feasible amount of cellulase and EFB substrate could be identified for maximum conversion and facilitate bioethanol production.

Keywords: cellulase, oil palm lignocellulose, biomass, empty fruit bunch

Abstrak

Biojisim kelapa sawit lignoselulosa ialah substrat yang berpotensi untuk pengeluaran bahan kimia boleh diperbaharui daripada sisa pertanian. Tandan buah sawit (EFB) merupakan salah satu daripada sisa biojisim selain daripada batang dan pelepah dari ladang kelapa sawit. Penukaran biologi daripada lignoselulosa kelapa sawit menggunakan enzim untuk menghasilkan gula boleh digunakan untuk pengeluaran bioetanol. Walau bagaimanapun, penukaran biologi adalah mencabar berikutan interaksi kompleks antara substrat dan enzim. Dalam usaha untuk menggunakan EFB sebagai bahan mentah, ia adalah penting untuk memahami kesan kepekatan enzim dan substrat kepekatan pada penukaran EFB. Dalam kajian ini, kami telah menyiasat kesan enzim dan substrat untuk penukaran maksimum lignoselulosa kelapa sawit. Keputusan menunjukkan apabila muatan enzim meningkat, kadar tindak balas dan hasil gula (RS) dan glukosa pada awalnya meningkat tetapi kemudiannya mendatar. Muatan enzim tinggi mungkin membawa kepada enzim yang berlebihan dan enzim lapisan sekitar substrat. Corak yang sama berlaku pada kadar tindak balas apabila muatan substrat meningkat. Walau bagaimanapun, hasil RS dan glukosa menurun apabila muatan substrat meningkat. Ia boleh dijelaskan oleh kesusahan degradasi substrat dan perencatan oleh produk. Kadar pembentukan produk awal digunakan untuk menentukan parameter kinetik seperti kadar maksimum malar V_{max} dan pemalar separuh tepu K_m. Daripada kajian ini, jumlah celulase dan EFB substrat dapat dikenalpasti untuk penukaran maksimum dan memudahkan pengeluaran bioethanol.

Kata kunci: selulosa, lignoselulosa kelapa sawit, biojisim, tanda buah kelapa sawit

Introduction

Malaysia as one of the largest contributor of palm oil industry in the world is now facing a great environmental issues regarding the palm oil waste. To be able to convert this waste into product would be a great benefit to the country. Empty fruit bunch (EFB) is one of biomass waste aside from the trunk, frond and fruit mesocarp from oil palm plantation. It could be an alternative to renewable feedstock for the production of bioethanol. In order to utilize lignocellulose, it must be hydrolyze into its sugar components. The hydrolysis process can be achieved using chemically (acid) and biologically (enzyme). However, enzymatic process is milder, environmental friendly and allow better fermentability. Lignocellulose biomass consists of cellulose, hemicellulose, lignin and extractive. Cellulase attack the cellulose and the enzyme system consists of endoglucanase, cellobiohydrolase and β-glucosidase. These enzymes work in a synergistic manner in order to hydrolyze cellulose into sugars [1]. As the study on EFB hydrolysis by cellulase enzymes is still limited, we are taking an approach to provide more understanding in this hydrolysis. There are few factors affecting enzymatic hydrolysis such as pH, temperature [2], substrate concentration, enzyme concentration [3] and structure of lignocellulose [4]. In order to utilize EFB as the biofuel feedstock, it is important to understand the effect of enzyme concentration and substrate concentration on the bioconversion of EFB. Moreover, the significant cost in bioconversion is the enzymes and therefore the total amount of enzymes used in hydrolysis is important. Substrate loadings are also factor in creating economical enzymatic conversion and have to be high enough to achieve sufficient sugar levels for fermentation [5]. Therefore, the identification of the optimal enzyme and substrate loadings have to be made. In this study, we investigated the effect of enzyme loading and substrate loading for the maximum conversion of lignocellulose.

Materials and Methods

Materials

The lignocellulosic biomass used in this study was oil palm empty fruit bunch (EFB). This fibre was collected from Malaysia Palm Oil Berhad (MPOB) which located in Bangi, Selangor. After sampling the EFB was dried in an oven at 60 °C to avoid fungal growth and then followed by grinding process. The EFB was grounded into particles in size of 300-500 μm using grinder. Then, it was stored in an oven at 50 °C until the pre-treatment process. This pre-treatment includes hot water treatment and alkali treatment using method documented by Hamzah et al. [6]. Cellulase was purchased commercially from Novozymes Malaysia Sdn. Bhd. This cellulase is commercially known as Celluclast 1.5 L. It is cellulolytic system in brown solution with a slight fermentation odour with density 1.2 g/mL at 25 °C. It generally consisted of endoglucanase, exoglucanase and 1,4-β-glucosidase. This cellulase is produced by submerged fermentation of a selected strain of the fungus *Trichoderma reesei* and catalyzes the breakdown of cellulose into glucose, cellobiose and higher glucose polymers. The activity of Cellulclast 1.5 L was determined using filter paper assay and was found to be 137 FPU/mL.

Enzymatic hydrolysis of EFB

Enzymatic hydrolysis of EFB was carried out in a batch process using cellulase as the catalyst. Two parameters were investigated in this hydrolysis namely enzyme loading and substrate loading. The total reaction volume was 20 mL with citrate buffer of pH 5.0 as the reaction medium. For substrate loading, the hydrolysis experiments were carried out for 2.5 g/L, 5.0 g/L, 10.0 g/L, 20.0 g/L and 50.0 g/L treated EFB with 0.1 mL cellulase at 50 °C for 24 hours. For enzyme loading, the hydrolysis experiments were carried out for 10 g/L treated EFB with different cellulase amount (0.05 mL, 0.1 mL, 0.2 mL, 0.5 mL and 1.0 mL) at 50 °C for 24 hours. All samples were analysed for glucose and reducing sugar content at 1st and 24th hour using glucose analyser and dinitrosalicyclic acid (DNS) assay respectively. Adsorption was done at 50 for 24 hours using different enzyme loading at constant substrate concentration (10 g/L). The protein content in the supernatant was determined using Bradford reagent.

Analytical method

There are two important analysis that were carried out throughout this study which are determination of reducing sugar using dinitrosalicyclic acid (DNS) and determination of glucose concentration using glucose analyser. The main product of this lignocellulose hydrolysis is reducing sugar such as glucose, cellobiose and xylose. To determine the amount of reducing sugar released, dinitrosalicyclic acid (DNS) method by Miller [7] was used. Prior

to DNS method, all samples were heated at 90 °C for 10 minutes to stop the enzymatic reaction. After that the tubes were centrifuged for 5 minutes at 10000 rpm to separate the fibre. An amount of 3 mL of DNS reagent was added to 3 mL of sample in a capped test tube. Then, the mixture was heated in water bath at 90 °C for 5-15 minutes to develop the colour. After that, the mixture was taken out and 1 mL of 40% potassium sodium tartrate solution (Rochell salt) was added to stabilize the colour. The mixture was cooled in a cold water bath until it reaches room temperature. Then, the absorbance was recorded at wavelength 540 nm using UV-Vis spectrophotometer (Jenway, UK). Anhydrous glucose was used for standard curve and sugar calibration. As DNS method only determine the presence of reducing sugar in product, an accurate test of glucose concentration was needed. Thus remaining supernatant from centrifuged sample was isolated and tested for glucose content using biochemistry analyser (YSI Incorporated, USA) with standard glucose of 2.5 g/L.

Kinetic study

The kinetics of the hydrolysis were studied following Michalis-Menten (equation 1):

$$V = \frac{V_m[S]}{K_m + [S]} \tag{1}$$

where V is defined as enzymatic reaction rate (g/L.h), V_m is maximum rate of enzymatic reaction (g/L.h), K_m is Michaelis Menten constant (g/L) and S is substrate concentration (g/L).

The kinetic parameters were estimated by double reciprocal plot linearization of Lineweaver Burke plot.

$$\frac{1}{V} = \frac{1}{V_m} + \frac{K_m}{V_m}\frac{1}{[S]} \tag{2}$$

V_m *and* K_m were calculated from the slope and intercept of the double reciprocal plot.

Results and Discussion

The effect of substrate loading on EFB hydrolysis was carried out in batch reaction with the 0.1 mL (0.25 g/L) enzyme at 50 °C. The product was analysed for protein, glucose and reducing sugar content. The results were analysed for rate of reaction, yield of RS, yield of glucose and also percent of glucose in the product. Hydrolysis of EFB with respect to substrate loading shows that the rate of RS and glucose production initially increased rapidly and then slowed down as substrate loading increased, as shown in Figure 1. It seems that the rate is relatively linear below 10 g/L of substrate but the rate starts to plateau between 20 g/l to 50 g/L. This indicates that at 10 g/l, the enzyme to substrate ratio is not limiting, but at 20 to 50 g/l, the enzyme attaching to substrate start to becomes saturated (adsorption limiting). This might also cause by product inhibition and also noncellulosic interference which decelerated the reaction process [2].

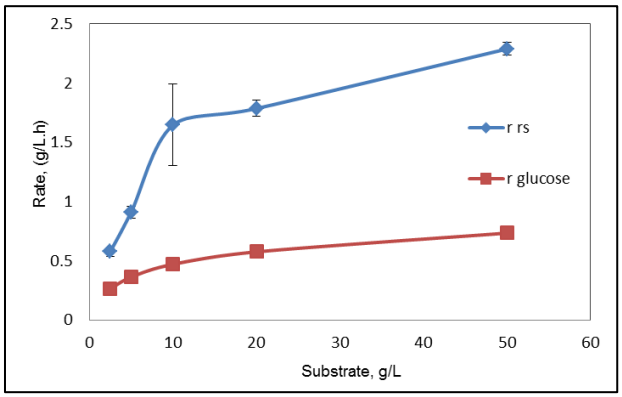


Figure 1. Rate of reducing sugar and glucose production for different substrate loading with 0.25 g/L cellulase at 50 °C

In contrast, Figure 2 shows that the percent yield of RS and glucose decreased as the substrate loading increased. This might happen as the substrate loading increased, cellulase was not sufficient to hydrolyse more substrate in the timeframe. Besides, the increase in substrate loading also increase the lignin components which create physical barrier for direct interaction between the enzyme and substrate thus lowering the hydrolysis yield. The yield of RS for 50 g/L and 10 g/L are around 40% and 70%, respectively. The lower yield of 50 g/L are probably due to mass transfer problem such as high viscosity and mixing and kinetic effects such as enzyme deficiency, product and substrate inhibition.

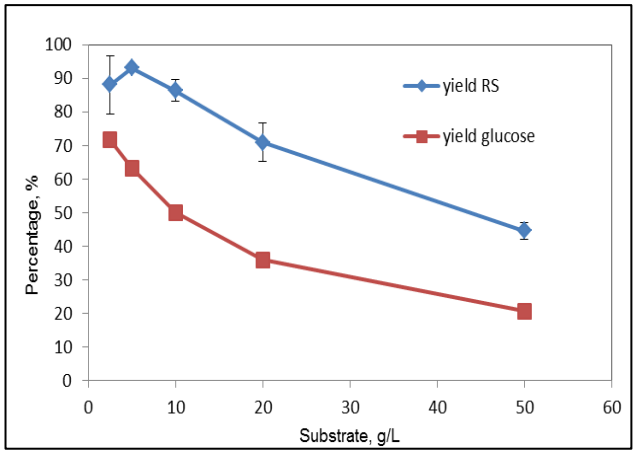


Figure 2. Yield of reducing sugar and glucose at 24th hour hydrolysis reaction for different substrate loading with 0.1 mL cellulase at 50 °C

In Figure 3, the percent of glucose decreased as the substrate loading increased at both 1st and 24th hour, respectively. The percent of glucose decreased as the substrate increased suggesting that available β-glucosidase is not enough to convert cellobiose to glucose as the substrate increased.

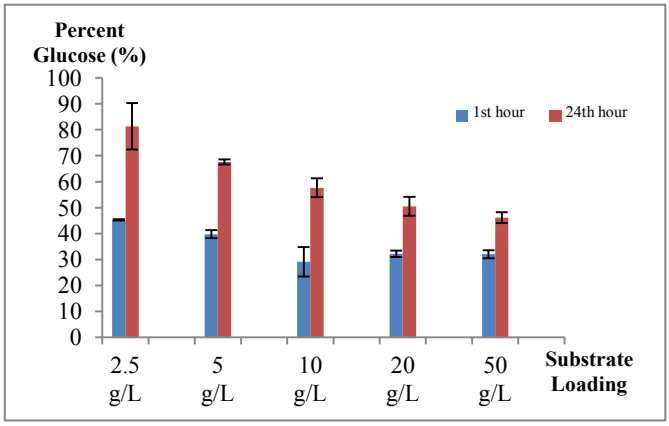


Figure 3. Percent of glucose at 1st and 24th hour hydrolysis reaction for different substrate loading with 0.1 mL cellulase at 50 °C

Figure 4 and 5 show that the rate of RS and glucose production and yield of RS and glucose initially increased then plateaued as enzyme loading increased. The reaction was initially increased as more enzymes were available to hydrolyse the fibres and then started to decelerate at one point as higher enzyme loading became in excess to the substrate. It also could be explained by Lee and Fan [8] that initially adsorbed enzyme on the substrate forms a

single layer where the excess enzyme adsorbed forms additional later. This has restricted diffusion process of the excess enzyme from to substrate surface. Based on Figure 5, the enzyme to substrate ratio (E/S) that give constant maximum yield is around 0.05 (0.5 g enzyme/10 g EFB). In terms of enzyme cost, putting more enzyme in the reaction would not be feasible because the yield has reached its maximum.

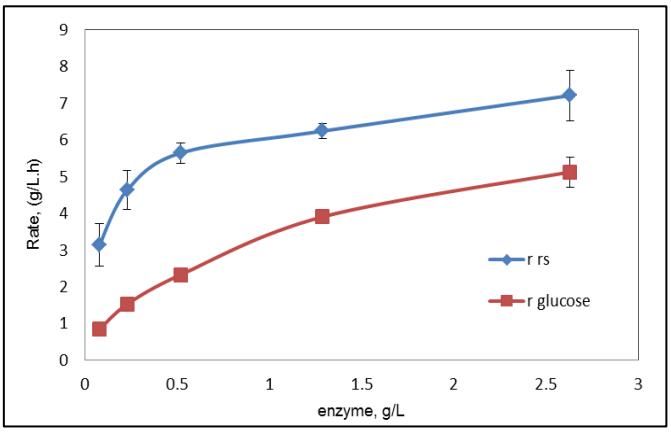


Figure 4. Rate of reducing sugar and glucose production for different enzyme loading with 10 g/L treated EFB at 50 °C

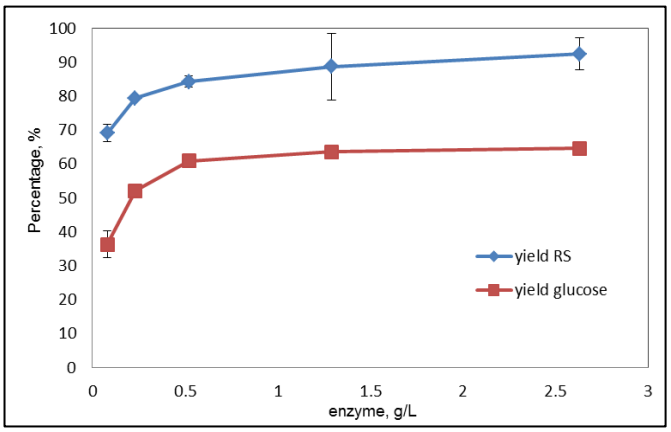


Figure 5. Yield of RS and glucose at 24th hour hydrolysis reaction for different enzyme loading with 10 g/L treated EFB at 50 °C

Adsorption of cellulase

The studies on the effect of enzyme loading on cellulase adsorption were carried out for 10 g/L treated EFB at different time frame. The product was analysed for the protein content in supernatant, adsorbed and percent of protein adsorbed to the substrate. In Figure 6 and 7, the protein concentration at supernatant and amount of protein adsorbed to the substrate increased as the enzyme loading increase after 30 minutes reaction. However, the percent of protein adsorbed to the substrate also decreased as the enzyme loading increase at 30 °C (Figure 8).

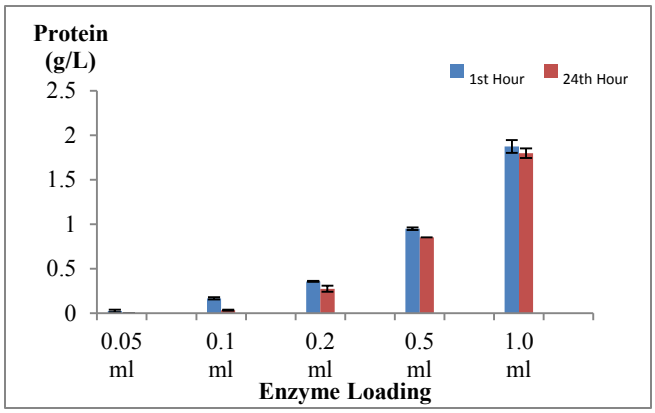


Figure 6. Concentration of protein at supernatant for 10 g/L treated EFB at 1st, 24th and 48th hours for different enzyme loading at 30 °C. (Note: 0.1 ml enzyme/20 mL solution = 0.25 g enzyme/L)

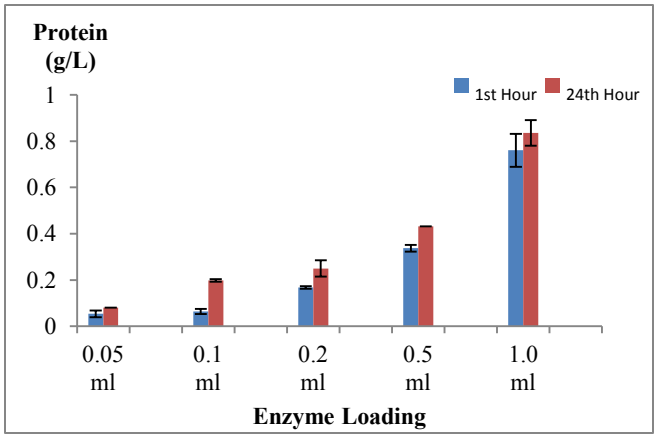


Figure 7. Concentration of protein adsorbed to 10 g/L treated EFB at 1st, 24th and 48th hours for different enzyme loading at 30 °C. (Note: 0.1 ml enzyme/20 mL solution = 0.25 g enzyme/L)

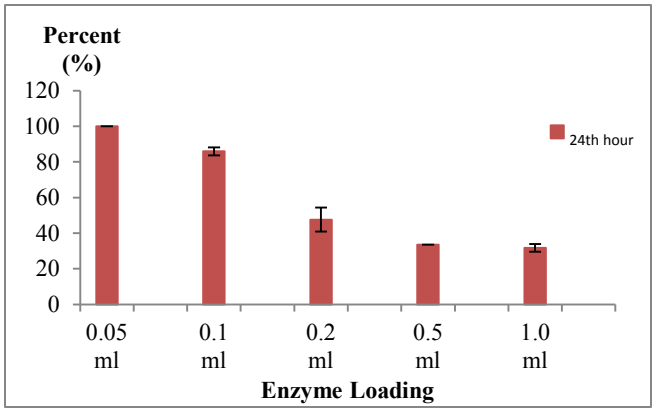


Figure 8. Percent of protein adsorbed to 10 g/L treated EFB at 24th for different enzyme loading at 30°C. (Note: 0.1 mL enzyme/20 mL solution = 0.25 g enzyme/L)

Figure 8 also shows that most of the cellulase is adsorbed at low concentration of enzyme (0.05 mL). Almost all of enzyme is absorbed in the substrate at low enzyme concentration however that high concentration (0.5 to 1.0 mL) with the percentage absorbed was around at 30%. In other words, at high concentration of enzyme, 70% of cellulase was in the liquid phase. This result also confirms the constant yield result at high enzyme concentration (Figure 5), the yield is almost constant at 4 g/L to 5g/L of enzyme. In an earlier study, Desphande and Erikson [9] showed that around 80% of endoglucanase were free in the liquid fraction after 24 hours of Avicel (crystalline cellulose) hydrolysis. However, this value decreased to less than 50% when lignin containing substrate is used. In a recent study, hydrolysis of wheat straw lignocellulose showed that proteins in supernatant increased from 30% to 65% when lignin substrate was decreased from 20% to 3.6% [10].

Based on adsorption, the substrate is saturated with enzyme at 4 g/L. Moreover based on the result, adding more enzyme to the reaction will not increase the yield. In terms of economics, this is significant, since enzyme is costly. Adding more enzyme will not be feasible since enzyme could denatured with time. Furthermore, Fox et al. [11] confirmed that rate of cellulose adsorption to substrate is important to determine the cellulose hydrolysis. Kumar et al. [12] observed that a positive correlation was found between adsorption and hydrolysis of cellulosic substrate at temperature below 60 °C.

Kinetic parameters

Kinetic parameters were determined using Michaelis-Menten approach. From the Lineweaver Burk plot, the value of the K_m and V_m are 9.866 g/L and 2.838 g/L.h. The reaction rate obtained from the experiment was well fitted with Michalis-Menten model describing by the high coefficient of R^2 which equal to 0.989. Therefore, it confirms the rate of EFB hydrolysis follows the Michalis-Menten model. The kinetic parameters offer quantitative information about the catalytic properties of the enzyme and maybe useful for reactor design. The higher value of Km means that the affinity of the substrate towards enzyme is low.

Conclusion

This study showed that as the enzyme loading increased, concentration of reducing sugar and glucose, yield of glucose and percent of glucose also increased. For substrate loading, reducing sugar and glucose concentration increased as the substrate loading increased. However, yield of RS, yield of glucose and percent of glucose decreased as the substrate loading increased. This could be due to substrate recalcitrance and product inhibition. The link between cellulase adsorption and hydrolysis rate and yield was elucidated. The influence of substrate concentration on the production of reducing sugar was studied by the Michaelis-Menten equation showing good correlation with experimental results. Our results show that substrate and enzyme loading are some of the key parameters in optimizing conversion of oil palm lignocellulose biomass to sugars using cellulase.

References

1. Kumar, R. and Wyman, C. E. (2009). Effects of cellulase and xylanase enzymes on the deconstruction of solids from pretreatment of poplar by leading technologies. *Biotechnology Progress,* 25(2): 302-314.
2. Jorgensen, H., Kristensen, J. B. and Felby, C. (2007). Enzymatic conversion of lignocellulose into fermentable sugars: challenges and opportunities. *Biofuels Bioproducts Biorefining,* 1(2): 119-134.
3. Tengborg, C., Galbe, M. and Zacchi, G. (2001). Influence of enzyme loading and physical parameters on the enzymatic hydrolysis of steam pretreated softwood. *Biotechnology Progress,* 17(1): 110-117.
4. Zhao, X., Song, Y. and Liu, D. (2011). Enzymatic hydrolysis and simultaneous saccharification and fermentation of alkali/peracetic acid-pretreated sugarcane bagasse for ethanol and 2, 3-butanediol production. *Enzyme and Microbial Technology,* 49(4): 413-419.
5. Van Dyk, J. S. and Pletschke, B. I. (2012). A review of lignocellulose bioconversion using enzymatic hydrolysis and synergistic cooperation between enzymes – factors affecting enzymes, conversion and synergy. *Biotechnology Advances,* 30(6): 1458-1480.
6. Hamzah, F., Idris, A. and Shuan, T. K. (2011). Preliminary study on enzymatic hydrolysis of treated oil palm (Elaies) empty fruit bunch fibre (EFB) by using combination of cellulose and β 1-4 glucosidase. *Biomass and Bioengineering,* 35(3): 1055-1059.
7. Miller, G. L. (1959). Use of dinitrosalicyclic acid reagent for determination of reducing sugar. *Analytical Chemistry,* 31(3): 426-428.

8. Lee Y. H. and Fan L. T. (1983). Kinetic studies of enzymatic hydrolysis of insoluble cellulose: (II). Analysis of extended hydrolysis times. *Biotechnology and Bioengineering,* 25(4): 939-966.
9. Desphande, M. V. and Erikson, K. E. (1984). Reutilization of enzymes for saccharification of lignocellulosic materials. *Enzyme and Microbial Technology,* 6(8): 338-340.
10. Qi, B., Chen, X., Su, Yi. and Wan, Y. (2011). Enzyme adsorption and recycle during hydrolysis of wheat straw lignocellulose. *Bioresource Technology,* 102(3): 2881-2889.
11. Fox, J. M., Levine, S. E., Clark, D. S. and Blanch, H. W. (2012). Initial-and processive-cut products reveal cellobiohydrolase rate limitations and the role of companion enzymes. *Biochemistry,* 51(1): 442-452.
12. Kumar, R., Singh, S. and Singh, O. V. (2008). Bioconversion of lignocellulosic biomass: Biochemical and molecular perspectives. *Journal of Industrial Microbiology & Biotechnology*, 35(5): 377-339.

Malaysian Journal of Analytical Sciences, Vol 22 No 4 (2018): 723 - 734
DOI: https://doi.org/10.17576/mjas-2018-2204-19

MALAYSIAN JOURNAL OF ANALYTICAL SCIENCES
Published by The Malaysian Analytical Sciences Society
ISSN 1394 - 2506

ANALYSIS OF AMMONIUM ADSORPTION BEHAVIOR AND MASS TRANSFER RESISTANCE FROM AERATED LAGOON EFFLUENT ONTO ACTIVATED CARBON

(Analisis Sifat Penjerapan Amonium dan Rintangan Pemindahan Jisim dari Efluen Kolam Pengudaraan Terhadap Karbon Teraktif)

Mohd Hairul Khamidun[1]*, Shakila Abdullah[2], Umi Fazara Md.Ali[3], Mohamad Ali Fulazzaky[4]

[1]*Micropollutant Research Centre, Faculty of Civil and Environmental Engineering*
[2]*Faculty of Science, Technology and Human Development*
Universiti Tun Hussein Onn Malaysia, 86400 Parit Raja, Batu Pahat, Malaysia
[3]*School of Environmental Engineering,*
Universiti Malaysia Perlis, Kompleks Pusat Pengajian Jejawi 3, 02600 Arau, Perlis, Malaysia
[4]*Directorate General of Water Resources,*
Ministry of Public Works and Housing, Jakarta, Indonesia

**Corresponding author: mhairulk@gmail.com*

Received: 16 April 2017; Accepted: 7 March 2018

Abstract

High concentration ammonium (NH_4^+) discharges from aerated lagoon effluent (ALE) correlated to eutrophication of receiving waters. This study presents the first attempt to scrutinise the mass transfer mechanism of NH_4^+ from ALE onto the granular activated carbon (GAC) in batch and plug-flow column (PFC) studies. The GAC was characterised by BET surface, X-ray fluorescence, scanning electron microscopy, X-ray diffraction and Fourier transform infrared spectroscopy. The kinetics and isotherm models were applied to experimental data to understand adsorption behaviour, while mass transfer factor (MTF) models was used to determine global, external, and internal mass transfer. The PFC was successfully applied for the removal of NH_4^+ from ALE. The results showed that the adsorption of NH_4^+ from ALE on the GAC followed the pseudo-second-order kinetic model and the Freundlich adsorption isotherm in batch study. The resistances of mass transfer for adsorption of NH_4^+ onto GAC from the PFC are verified. The use of these empirical models has been proved that the models were very suitable for PFC design and understanding mechanism of mass transfer of solutes from waters onto porous materials.

Keywords: adsorption, ammonium, isotherm, kinetics, mass transfer resistance

Abstrak

Kepekatan amonium (NH_4^+) yang tinggi di dalam efluen yang dilepaskan dari kolam pengudaraan (ALE) akan menyebabkan eutrofikasi pada saliran yang menerima efluen tersebut. Kajian ini dijalankan untuk meneliti mekanisma rintangan permindahan jisim NH_4^+ dari ALE ke seluruh karbon teraktif berbutir (GAC) menggunakan kaedah ujikaji berkelompok dan aliran penuh ruangan berongga (PFC). Sifat fizikal dan kimia GAC ditentukan dengan menggunakan ujikaji permukaan BET, pendarfluor sinar-X, mikroskopi elektron pengimbasan, pembelauan sinar-X dan spektroskopi inframerah transformasi Fourier. Sifat penjerapan GAC telah dianalisis dengan menggunakan model isoterma dan kinetik, manakala model faktor permindahan jisim (MTF) digunakan untuk menganalisis faktor permindahan jisim global, luaran dan dalaman. Penggunaan PFC telah diuji dan disahkan berkesan untuk menyingkirkan NH_4^+ dari ALE. Hasil ujikaji berkelompok menunjukkan penjerapan NH_4^+ dari ALE telah mematuhi prinsip model kinetik tertib kedua dan model penjerapan isorterma Freundlich. Rintangan permindahan jisim untuk penjerapan NH_4^+ ke seluruh GAC dari PFC telah disahihkan. Penggunaan semua model yang dinyatakan telah

membuktikan bahawa model tersebut sesuai digunakan untuk rekabentuk PFC dan juga untuk memahami mekanisma permindahan bahan terlarut dalam air ke seluruh bahan berliang.

Kata kunci: penjerapan, amonium, isorterma, kinetik, rintangan permindahan jisim

Introduction

Activated carbon (AC) is a material that has a porosity characterised by empty space within pore. Activation of AC increases the porosity and active sites on its surface to increase the adsorption capacity. The use of certain type of AC could be useful for the remove of ammonium (NH_4^+) from aqueous solutions. High amount of NH_4^+ present in aerated lagoon effluent can cause adverse effects on the environment when released into water body. An increase in NH_4^+ concentration released into the water bodies can cause the eutrophication. Note that eutrophication is an excess nutrient load of any waters, which is reflected by rapid growth of blue green algae. According to Fan et.al. [1], NH_4^+ is the primary nitrogen sources that cause the Choptank River bloom and the ambient uptake rates of NH^{4+} directly proportional with algae bloom progressed in Choptank River. Therefore, the algae bloom can be controlled by reducing the concentration of NH_4^+ in wastewater during the treatment process before discharging into water bodies.

The adsorption of NH_4^+ from leachate by the AC made up of coconut shells as reported by Halim et al. [2] can achieve approximately 6.08 mg g^{-1} of the adsorption capacity. The adsorption capacity of 2.30 mg g^{-1} to remove NH_4^+ from aqueous solution was verified by Boopathy et al. [3] in a batch experiment; therefore, physisorption could be more dominant. Many researchers have been focusing their investigations on physical or chemical properties of AC in order to improve the adsorption capacity [4-7]. Vassileva et al. [8] found that the coal activated carbon modified by nitric acid can significantly enhance the NH_4^+ removal from aqueous solutions. A mixture adsorbent of 45.94% zeolite, 15.31% limestone, 4.38% activated carbon and 4.38% rice husk carbon was used to adsorb NH_4^+ from a landfill leachate and verified that a high adsorption capacity can achieve approximately 24.39 mg g^{-1} of the adsorbent [9]. Even though many studies have been conducted to verify the efficiency of granular activated carbon (GAC) to remove NH_4^+ from aqueous solutions, the mechanism of mass transfer for the adsorption of NH_4^+ onto GAC from ALE is still not fully understood.

The mechanisms of adsorption consist of three successive steps in the transfer of solutes onto adsorbents in liquid, such that: (1) film mass transfer (referred also as external mass transfer) is the mechanism to transport an adsorbate from the bulk liquid to film zone exterior the grain immediately connecting the pores, (2) porous diffusion (referred also as internal mass transfer) is mechanism to diffuse an adsorbate from the film zone towards acceptor sites of the adsorbent, and (3) fixation (referred also as adsorption) is mechanism to attach the adsorbate onto acceptor sites of the adsorbent interior the grain [10, 11]. In spite of reducing the concentration of NH_4^+ can be achieved through adsorption process, the resistance of mass transfer of the adsorption in a plug-flow column needs to be verified. Therefore, the objectives of this study are to (i) to determine the kinetic and isotherm adsorption for the adsorption of NH_4^+ onto GAC based on the data of batch experiments and (ii) to analysis the variation of $[k_La]_g$, $[k_La]_f$ and $[k_La]_d$ for adsorption of NH_4^+ from ALE onto GAC in a PFC by using MTF models.

Materials and Methods

Characteristics of aerated lagoon effluent

This study monitored some important parameters of water quality over a period of 6 months for characterisation of the ALE. The average concentrations of NH_4^+, PO_4^{3-}, COD and SS were verified as high as 13.4, 9.5, 192 and 89 mg L^{-1}, respectively. The concentration of NH_4^+ was found to exceed highly above the admissible limits of the EU and USEPA effluent standards.

Adsorbent

The GAC made up of coconut shell was purchased from the Nikom Carbon Technology Sdn. Bhd. Klang, Selangor, Malaysia. Main characteristics of the GAC as provided by the supplier are listed in Table 1. The GAC was crushed and passed through a 2.13 mm mesh sieve and retained on 1.18 mm mesh sieve. Approximately 2 kg of the GAC was washed with distilled water and dried at 103 ^oC for 24 hours in an oven. The dried GAC used as adsorbent for the adsorption of NH_4^+ from ALE in batch and plug-flow column.

Table 1. Main characteristics of the granular activated carbon

Characteristic	Unit	Value
Origin (raw material)		Coconut shell
Bulk density	g cm^{-3}	0.49
Moisture contents	%	2.96
Hardness	%	98.17
Ash content	%	2.32
Mesh size 8 x 30	%	96.17
BET surface area	m^2g^{-1}	1076
pH		9.89

Instruments

The mineralogy of the GAC was identified by XRD pattern using Bruker D8 Advance X-ray powder Diffractometer (Bruker AXS, Germany). Fourier transform infrared (FTIR) analysis was performed on KBr pellets using a Spectrum One FT-IR Spectrometer (Perkin Elmer Instruments, USA) in the wavenumber range between 600 and 4000 cm^{-1}. Surface morphologies of GAC were observed by a scanning electron microscopy (SEM) using a JSM-638OLA instrument (JEOL Co., Ltd., Japan). The surface area of the GAC is determined by the Brunauer Emmet Teller (BET) method using a PulseChemiSorb 2705 apparatus (Micromeritics Instrument Co., USA).

The surface functional groups of GAC were identified using the Boehm titration method, where 2 g of GAC was placed in contact with 250 mL of NaOH, Na_2CO_3, $NaHCO_3$ or HCl solution with a concentration of 0.1 mol L^{-1} in an Erlenmeyer flask, separately. All the sample solutions in Erlenmeyer flask and their related blanks without filled with GAC in Erlenmeyer flask were sealed and shaken in an IKA KS 4000 I Control shaker for 24 hours at 225 rpm. Then, an aliquot of 10 mL was filtered and the excess of bases or acid was titrated with a 0.1 mol L^{-1} of HCl solution or a 0.1 mol L^{-1} of NaOH solution, respectively. The number of acidic sites was determined under the assumptions that NaOH neutralised carboxylic groups (-COOH), lactonic (C=O) and phenolic (-OH); Na_2CO_3 neutralised carboxyl groups and lactones, and $NaHCO_3$ neutralised carboxyl groups only. The number of basic sites was calculated based on the amount of HCl that reacted with the adsorbent [12]

Kinetics and isotherm studies

The batch experiments were conducted to determine adsorption isotherm and kinetic. The experiments of kinetic adsorption were conducted by adding 2, 6 and 10 g of the adsorbents into an Erlenmeyer flask of 250 mL. Each Erlenmeyer flask containing of 200 mL of ALE was shaken at 150 rpm. Then the concentration of NH_4^+ in each sample solution was monitored at appropriate time intervals until the adsorbent saturates. The pseudo-first-order and pseudo-second-order models were used to study the kinetics of the adsorption of NH_4^+ onto GAC from ALE.

The pseudo-first-order equation (or so called Lagergren equation) indeed is in line with the concept of linear driving force and is commonly expressed as equation 1 below [13]:

$$\frac{dq}{dt} = k_1 (q_e - q_t) \quad (1)$$

where q is the adsorption capacity (in mg g^{-1}), t is the adsorption time (in min), k_1 is a pseudo-first-order constant (in min^{-1}), q_e is the equilibrium amount of adsorbate adsorbed by per unit mass of adsorbent (in mg g^{-1}) and q_t is the amount of adsorbate adsorbed at adsorption time t (in mg g^{-1}). Integrating equation (1) with boundary values from $t = 0$ to $t = t$ and from $q_t = 0$ to $q_t = q_t$ yields (equation 2):

$$q_t = q_e(1 - e^{-k_1 t}) \quad (2)$$

The first-order rate equation its liner form can be expressed as equation 3 [14]:

$$\ln(q_e - q_t) = \ln(q_e) - k_1 t_i \quad (3)$$

where q_e is the equilibrium amount of adsorbate adsorbed by per unit mass of adsorbent (in mg g^{-1}) and q_t is the amount of adsorbate adsorbed at adsorption time t (in mg g^{-1}), k_1 is a pseudo-first-order constant (in min^{-1}) and t_i is the predetermined interval time (min).

Another model for the analysis of adsorption kinetics is pseudo-second-order (equation 4):

$$\frac{dq}{dt} = k_2 (q_e - q_t)^2 \quad (4)$$

where q is the adsorption capacity (in mg g^{-1}), t is the adsorption time (in min), k_2 is a pseudo-second-order constant (in min^{-1}), q_e is the equilibrium amount of adsorbate adsorbed by per unit mass of adsorbent (in mg g^{-1}) and q_t is the amount of adsorbate adsorbed at adsorption time t (in mg g^{-1}). Integrating equation (4) is given as

$$q_t = \frac{q_e^2 k_2 t}{1 + q_e k_2 t} \quad (5)$$

The application of pseudo-second-order model is suitable for the analysis of adsorption kinetics if the initial concentration of adsorbate is low. The second-order rate equation can be expressed in the linear form [15]:

$$\frac{t_i}{q_t} = \frac{1}{k_2 q_e^2} + \frac{t_i}{q_e} \quad (6)$$

where t_i is the predetermined interval time (min), q_t is the amount of adsorbate adsorbed at adsorption time t (in mg g^{-1}), k_2 is a pseudo-second-order constant (in min^{-1}) and q_e is the equilibrium amount of adsorbate adsorbed by per unit mass of adsorbent (in mg g^{-1}).

An appropriate kinetic model for the adsorption of NH_4^+ onto GAC to select either pseudo-first-order or pseudo-second-order, the error function (F_e) tests were performed using the values of q obtained from a batch experiment and those obtained from the calculation of using pseudo-first-order and pseudo-second-order models. The most appropriate model should have a smallest F_e value and highest correlation coefficient (R^2). The following equation can be used to calculate value of F_e [16]:

$$F_e = \sqrt{\left(\frac{1}{n-p}\right) \cdot \sum_i^n \left(q_{t(\text{exp})} - q_{t(\text{theo})}\right)^2} \quad (7)$$

where n is the number of measurements, p is the number of parameters in the kinetic equation, $q_{t(exp)}$ is the experimental q value obtained from the measurement during the experiments (in mg g^{-1}) and $q_{t(theo)}$ is the theoretical q value calculated by the model (in mg g^{-1}).

The isotherm experiments were carried out by adding 2, 4, 6, 8, and 10 g of the adsorbent into different Erlenmeyer flask containing 200 mL of ALE. Each sample solution was shaken ranged from 1 to 3 d, depending on time period of the isotherm equilibrium of NH_4^+. Then, the sample solutions were filtered using a 0.45 µm membrane filter and the residual concentration of NH_4^+ was analysed using the HACH DR 5000 UV–Vis Spectrophotometer. The Freundlich and Langmuir isotherm models were used to study the adsorption isotherm of NH_4^+ from the ALE.

The general form of the Freundlich equation is $q_e = K_F C^{1/n}$ where K_F and n are constants and $n > 1$. The Freundlich isotherm can be linearised by transforming the equation into the linear form (equation 8) [17, 18]:

$$\ln q_e = \ln K_F + \frac{1}{n} \ln C_e \quad (8)$$

where q_e is the equilibrium amount of adsorbate adsorbed by per unit mass of adsorbent (in mg g^{-1}), K_F is the Freundlich constant (in mg g^{-1}), n (dimensionless) is the heterogeneity factor which has a lower value for more heterogeneous surfaces, and C_e is the concentration of the adsorbate in the equilibrium solution (in mg L^{-1}).

The Langmuir isotherm is $q_e = QbC\ /(1 + bC)$ where b is a constant related to the energy of adsorption, and Q is the ultimate adsorption capacity (maximum value of q_b). The linear form of the Langmuir isotherm can be written as equation 9 [18, 19]:

$$\frac{1}{q_e} = \frac{1}{K_L q_{max} C_e} + \frac{1}{q_{max}} \tag{9}$$

where q_e is the equilibrium amount of adsorbate adsorbed by per unit mass of adsorbent (in mg g^{-1}), C_e is the concentration of the adsorbate in the equilibrium solution (in mg L^{-1}), q_{max} is the maximum adsorption capacity of the adsorbent (in mg g^{-1}) and K_L is the adsorption energy coefficient (in L mg^{-1}).

Plug-flow column studies

A schematic diagram for the laboratory scale plug-flow column is shown in Figure 1. The fixed-bed columns were made of acrylic tubes 2.1 cm internal diameter and 20 cm in height. The bed depths used in the experiments were 2, 4, 6, 9, 12 and 15 cm. In a typical experiment the known concentration of NH_4^+ in ALE was pumped using a Masterflex peristaltic pump at a fixed flow rate (Q = 0.11 L h^{-1}) to fill the packed-bed column heights. The concentration of NH_4^+ at inlet of the PFCR (storage tank), after passing the sand filter, and outlet of the PFCR treatment system were intermittently collected at defined time intervals and analysed based on Nesslerization method using HACH DR 5000 UV–Vis spectrophotometer at the maximum wavelength of 425 nm.

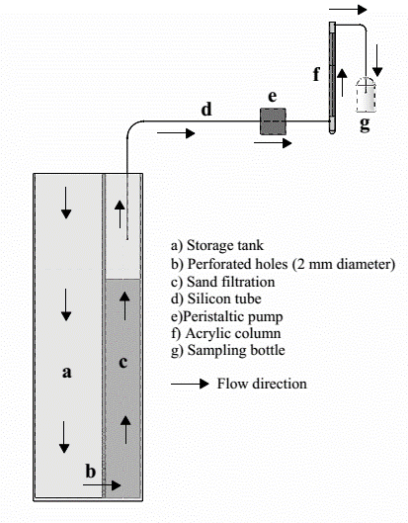


Figure 1. Experimental setup for plug-flow column operation

Data obtained from plug-flow column studies was analysed using the MTF models [11],[20] to understand the adsorption mechanisms of NH_4^+ from aqueous solution onto GAC. The MTF models are expressed in equation 10:

$$ln\left(\frac{C_o}{C_s}\right) = [k_L a]_g \times e^{-\beta \times ln(q)} \times t \tag{10}$$

where C_s is the concentration of the NH_4^+ to depart from the column (in mg L^{-1}), C_o is the concentration of the solute to enter into the column (in mg L^{-1}), $[k_L a]_g$ is the global mass transfer factor (in h^{-1}), β is the absorbent–adsorbent affinity parameter (in g h mg^{-1}); q is the cumulative quantity of the solute to adsorb onto GAC (in mg g^{-1}); and t is the accumulation time (in h). The mathematical deduction of the equation (10) can be simplified as equation 11:

$$\ln(q) = m\ln(t) + B \tag{11}$$

where $m = 1/\beta$ and B is the straight-line intercept of the plot ln(q) versus ln(t);

$$B = \frac{\ln([k_L a]_g) - \ln\left\{ln\left(\frac{C_0}{C_s}\right)\right\}}{\beta} \tag{12}$$

The value of $[k_L a]_g$ can be determined to use equation (12) since the index B and parameter β have been verified on a straight line. Using equation (13) permits to compute the values for $[k_L a]_f$, and equation (14) can be used to determine the $[k_L a]_d$.

$$[k_L a]_f = [k_L a]_g \times e^{-\beta \times ln(q)} \tag{13}$$

$$[k_L a]_d = [k_L a]_g - [k_L a]_f \tag{14}$$

where $[k_L a]_f$ is the film mass transfer factor (in h^{-1}) and $[k_L a]_d$ is the porous diffusion (in h^{-1}).

Results and Discussion

Physical and chemical characteristics of the GAC

The acidic and basic functional groups found on the surfaces of GAC were quantified using the Boehm's titration. It was found that a 1.35 mmol g^{-1} total acidic functional group consists of 0.63 mmol g^{-1} (46%) carboxylic, 0.44 mmol g^{-1} (33%) lactonic and 0.28 mmol g^{-1} (21%) phenolic group. A basic functional group (0.85 mmol g^{-1}) of less than total acidic functional group (1.35 mmol g^{-1}) was quantified for the GAC and could have more favourable to chemically attract more cations from a solution. The BET surface area of such GAC was measured using a Micromeritics Pulse Chemisorb 2705 apparatus to be 957 $m^2 g^{-1}$.

The surface morphology of GAC was investigated by SEM analysis and the SEM images are shown in Figure 2. Figure 2a shows that the SEM image of 500 times is wavy ripple morphology. Scanning the external surface of GAC with the high magnification images of 2,500 times (Figure 2b) and 5,000 times (Figure 2c) more specifically exhibit a rough surface with different sizes and shapes of the pores.

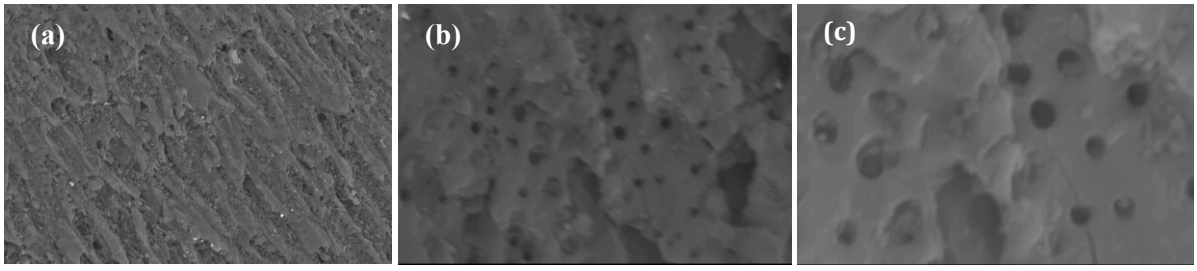


Figure 2. SEM photomicrograph of GAC: (a) overview 500 times magnification (b) 2,500 times magnification (c) overview 5,000 times magnification

The XRD analysis was performed to examine the mineralogy of the GAC sample, and the analysis result is depicted in Figure 3a. The XRD pattern of GAC has almost no diffraction lines; however, two broad peaks and one sharp peak have a diffraction maxima at diffraction angles 2θ of 23°, 2θ of 43° and 2θ of 81°, respectively. The peak 2θ of 23° denotes strong small angle indicating an amophorous structure with high porosity, and both the peaks 2θ of 23° and 2θ of 81° represent the graphitic basal plane [21]. These peaks pattern similar with mineralogy of activated carbon cloth [21] and coconut shell-activated carbon [3]. A peak at 2θ of 43° indicates the presence of minor phase of the quartz (SiO_2).

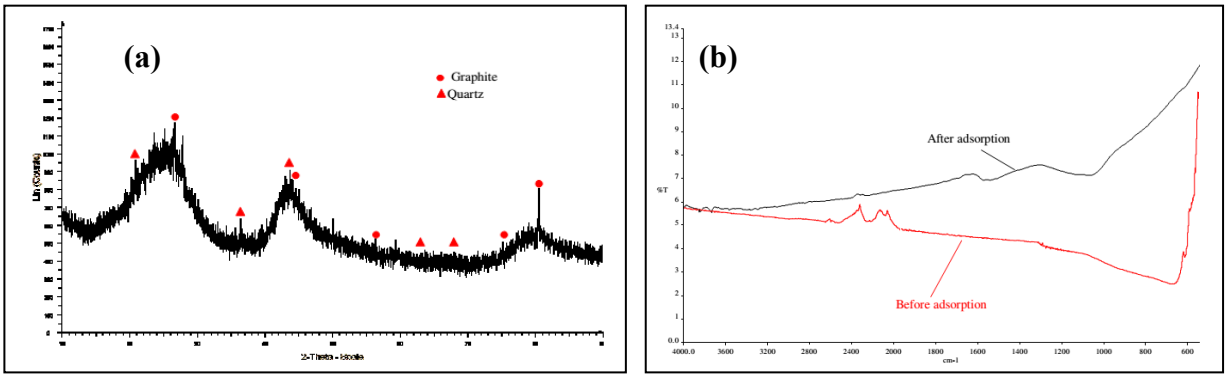


Figure 3. (a) XRD pattern of the GAC and (b)FTIR spectra of GAC of before and after NH_4^+ adsorption

The FTIR spectra of GAC (Figure 3b) shows weak and broad band in the spectra with the range of 676 – 2,581 cm^{-1} before and with the range of 1,075 – 3,600 cm^{-1} after the adsorption of NH_4^+. The presence of spectra peaks at 2,341; 2,110; 1,320; and 676 cm^{-1} would be assigned as C=O bonds; C≡C bonds; C–O stretch; and C–H bending, respectively [22, 23]. After the adsorption of NH_4^+, the FTIR spectra shows several new peaks within the range of 3,400–3,800 cm^{-1} to indicate the presence of O–H groups [24]. The new broad band appear at 1,572 and 1,075 cm^{-1} could be assigned as hydrogen-bonded asymmetric carbonyl stretching and C–H stretching, respectively, and would be caused by the adsorption of NH_4^+ attached on the surface of GAC [3],[25].

Adsorption kinetics of NH_4^+ onto the GAC

In this study, the linearised forms of pseudo-first-order (see $\ln(q_e\text{-}q_t)$ versus t in equation (3)) and pseudo-second-order (see t/q_t versus t in equation (6)) model were used to describe the adsorption kinetics of NH_4^+ from ALE. The non-linear regression analysis was used in solving the equations (2) and (5) with supported by Microsoft Office Excel program due to linear regression of pseudo-first-order model often results in incorrect determination of its constants. The kinetic parameters (k_1 and k_2) and theoretical equilibrium amount of NH_4^+ adsorbed per unit mass of GAC, q_e (theo), calculated by using these two linearised and non-linear models with their correlation coefficients are given in Table 2. The basis of selecting the best-fit kinetic model is that the value of R^2 is close to one and the value of F_e found should be lower. The experimental results of the adsorption kinetics data indicate that the pseudo-second-order kinetic model provides a best fit correlated value when compared with the pseudo-first-order kinetic model due to high R^2 and low F_e values were verified. As a conclusion, the adsorption phenomena could be leading to chemisorption rather than physisorption, suggesting that the chemisorption occurred to help the increased affinity of adsorbate-adsorbent could be caused by electron change and share between the NH_4^+ ions and the acidic functional groups [22]. The value of k_2 is proportional to the amount of GAC (Table 2), because of the rate of NH_4^+ adsorption can be increased by increasing the amount of GAC due to the availability of BET surface area and the number of active sites increase [26].

Table 2. Kinetic parameters obtained from the pseudo-first-order and pseudo second-order models for the adsorption of NH_4^+ onto GAC from ALE

	Linear regression								
Amount (g)	**Pseudo-first-order model**				**Pseudo-second-order model**				
	q_e (theo) (mg g^{-1})	**k_1 (min^{-1})**	**R^2**	**F_e**	**q_e (theo) (mg g^{-1})**	**k_2 (g mg^{-1} min^{-1})**	**R^2**	**F_e**	**q_e (exp) (mg g^{-1})**
2	0.48	0.0001	0.901	0.441	0.94	0.0075	0.986	0.115	0.89
6	0.32	0.0010	0.914	0.158	0.47	0.0101	0.979	0.048	0.46
10	0.21	0.0009	0.916	0.125	0.33	0.0155	0.994	0.025	0.32

Table 2 (cont'd). Kinetic parameters obtained from the pseudo-first-order and pseudo second-order models for the adsorption of NH_4^+ onto GAC from ALE

Amount (g)	Non-linear regression								
	Pseudo-first-order model				Pseudo-second-order model				
	q_e (theo) (mg g^{-1})	k_1 (min^{-1})	R^2	F_e	q_e (theo) (mg g^{-1})	k_2 (g mg^{-1} min^{-1})	R^2	F_e	q_e (exp) (mg g^{-1})
2	0.83	0.0080	0.966	0.007	0.87	0.0119	0.973	0.005	0.89
6	0.40	0.0056	0.974	0.0009	0.44	0.0152	0.978	0.0008	0.46
10	0.29	0.0050	0.987	0.0002	0.32	0.0174	0.991	0.0001	0.32

Adsorption isotherms of NH_4^+ onto the GAC

The curves obtained by plotting either $\ln(q_e)$ versus $\ln(C_e)$ in equation (8) or $1/q_e$ versus $1/C_e$ in equation (9) represent the Freundlich and Langmuir models; all the values for the parameters n, K_F, q_{max} and K_L calculated using these two models are depicted in Table 3. This study found that the curves in Figure 4a can have to fit the experimental data for Freundlich adsorption isotherm comparing to Langmuir adsorption isotherm as represented by Figure 4b due to the values of R^2 for the adsorption of NH_4^+ onto GAC from ALE are very close to one (Table 3). The surface of GAC covered by carboxylic, lactonic, phenolic and basic functional groups can allow the adsorption involved in the heterogeneous site progression with a multilayer mechanism of adsorption where the adsorbed NH_4^+ ions on the GAC surface can attract the NH_4^+ ions from bulk water [27].

Table 3. The parameters n, K_F, q_{max} and K_L for the adsorption of NH_4^+ onto GAC from ALE

Freundlich Model			Langmuir Model		
n	K_F (mg g^{-1})	R^2	q_{max} (mg g^{-1})	K_L (L mg^{-1})	R^2
0.485	0.003	0.990	0.40	0.007	0.961

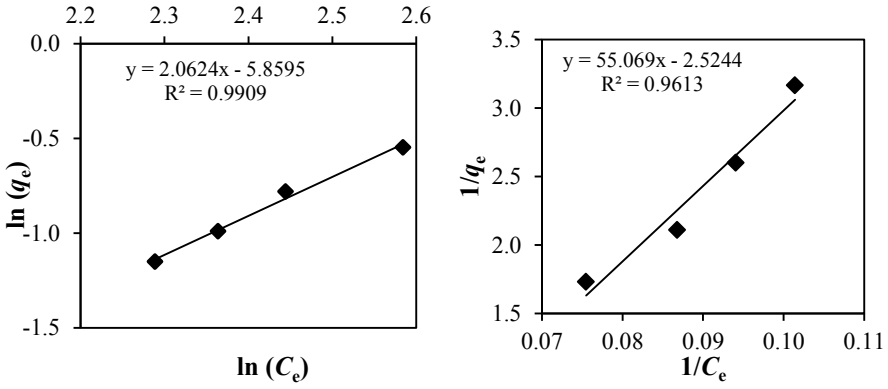


Figure 4. Linear line of plotting (a) $\ln(q_e)$ versus $\ln(C_e)$ and (b) $1/q_e$ versus $1/C_e$ for the adsorption of NH_4^+ onto GAC from WTPE

Resistance of mass transfer factor

A plot of ln(q) versus ln(t) in equation (11) gives us a straight line, intercept at B and β^{-1} is slope. The values for the parameters B and β for each curve are presented in Table 4. Correlation for all the parameters is very good ($R^2 >$ 0.97; see Table 4), meaning that both the index B and parameter β could be useful for scrutinising the mass transfer potential and the affinity of adsorbate–adsorbent for the adsorption of NH_4^+ onto GAC from ALE. The experimental data validation (Table 4) shows that the value of β decreases from 1.36 to 1.30 to 1.22 to 1.19 to 1.15 and to 1.14 g h mg^{-1} and the value of B also decreases from -1.16 to -2.22 to -2.55 to -2.93 to -3.171 and to -3.39 mg g^{-1} with increasing of the bed depth from 2 to 4 to 6 to 9 to 12 and to 15 cm, respectively. The parameter of β increased with increasing bed depth due to increases concentration of NH_4^+ in bulk water compared in film zone in short bed depth can increase driving force for adsorption of NH_4^+ that directly proportional with adsorbate-adsorbent affinity parameter.. The adsorption of NH_4^+ onto GAC is easily affected by both van der Waals force and chemical interaction and could have a strong affinity of the absorbate–adsorbent [28],[29]. The decreases in B value could be due to a high NH_4^+ concentration in the stagnant film on the water side of the interface, affecting the value of driving force reduces because of the difference in NH_4^+ concentration between the bulk water and film zone lowers.

Table 4. Results of determining the values of β and B for different GAC packed-bed column

h (cm)	β (g h mg^{-1})	B (mg g^{-1})	R^2
2	1.362	-1.610	0.972
4	1.295	-2.224	0.981
6	1.224	-2.559	0.985
9	1.186	-2.931	0.985
12	1.151	-3.171	0.989
15	1.145	-3.394	0.987

Analysis of $[k_La]_g$, $[k_La]_f$ and $[k_La]_d$

Using equation (11) permits us to determine the variations of $[k_La]_g$ pursuant to the percentage of outflow if the parameters B and β were verified. The percentage of outflow is ratio of effluent and influent concentration multiply by 100. Figure 5a shows the variations of $[k_La]_g$ decreased progressively from a high to low mass transfer potential with increasing of the percentage of outflow. The variation of $[k_La]_g$ value for a 2 cm of the packed-bed column is quite high when comparing to other packed-bed columns of 4, 6, 9, 12 and 15 cm. This could be due to a high rate of water flow passing through a packed-bed column can cause a rapid movement of NH_4^+ from the bulk water to acceptor sites at the surface of GAC.

Based on the curves in Figures 5b and 5c, the variations of $[k_La]_f$ and $[k_La]_d$ pursuant to the percentage of outflow can be used to determine the resistance of mass transfer for the adsorption of NH_4^+ onto GAC from ALE, which would be dependent on either film mass transfer or porous diffusion. Evidence shows that the variations of $[k_La]_f$ rapidly decrease, counterbalanced by the variations of $[k_La]_d$ rapidly increase, when the percentages of outflow are still less than 26.2, 24.3, 16.5, 14.6, 9.5 and 7.7% for the experimental runs with the packed-bed columns of 2, 4, 6, 9, 12, and 15 cm, respectively. The trends of $[k_La]_g$, $[k_La]_d$ and $[k_La]_f$ pursuant percentage of outflow is slightly similar with that reported by Fulazzaky et.al [10]. They found that the resistance mass transfer factors rate in short packed-bed column is high due to fast flow condition, which is the driving force increasing and has a strong movement of PO_4^{3-} molecules within bulk water toward the surface of granular laterites. As a conclusion, the application of the mass transfer factor models can determine that the resistance of mass transfer for the adsorption of NH_4^+ onto GAC from ALE could be dependent on porous diffusion due to lower $[k_La]_d$ value when percentage of outflow less than 30%.

Even though the physical characteristic of the GAC has a porosity of 957 m^2 g^{-1} of BET surface area, the movement of NH_4^+ ions from the bulk water towards acceptor sites within the pores could be still difficult. This is suggested that the different accessibilities of the pore structure areas within the GAC cannot always be entered equally easily

by all present inorganic and organic molecules in ALE [30]. The adsorption of NH_4^+ from ALE onto GAC would be mainly affected by surface chemical nature rather than the van der Waals forces. Two possible mechanisms of the adsorption of NH_4^+ onto GAC are suggested, such that: (1) the interaction between hydrogen of being composed of NH_4^+ molecules and oxygen of being composed of carboxylic (-COOH), lactonic (C=O) and phenolic (-OH) groups as the main acidic acceptor sites at the surface of GAC [24] and (2) the electrostatic interaction between the positive charges of NH4+ ions and the negative charges of carboxylic, phenolic, hydroxyl surface functional groups [31]. It is suggested that the modifications of the adsorbent properties by both physical treatments to increase the BET surface area and chemical treatment to increase the number of active acceptor sites can be recommended to improve the ability of the GAC to remove NH_4^+ from waters.

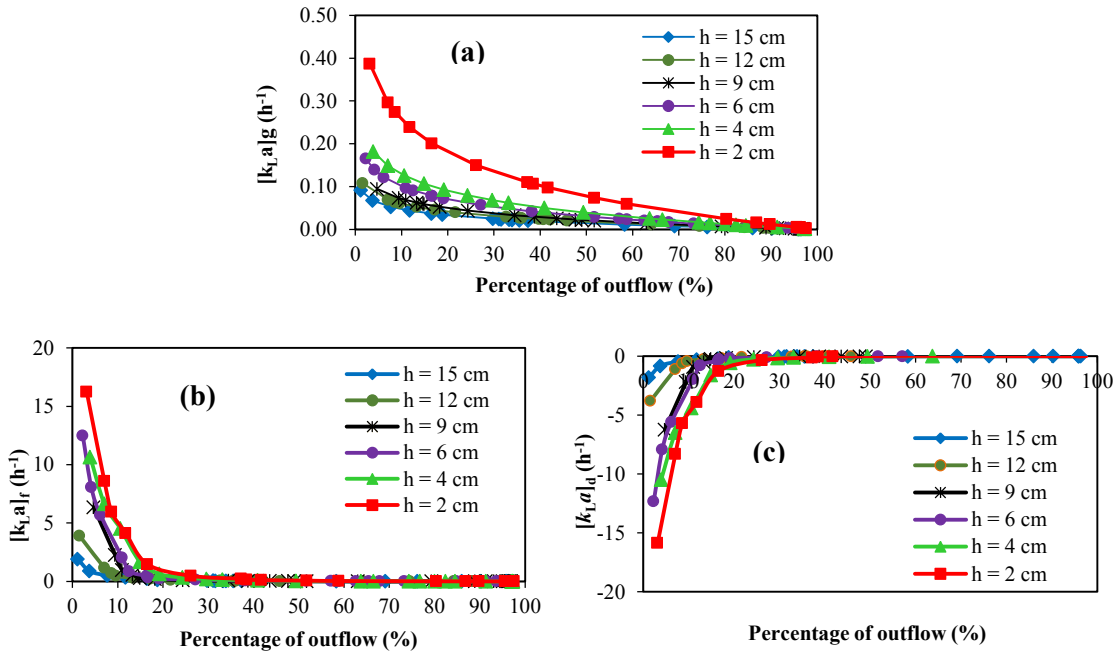


Figure 5. Variations of (a) $[k_La]_g$, (b) $[k_La]_d$ and (c) $[k_La]_f$ pursuant to the percentage of outflow for six different depths of GAC packed-bed column

Conclusion

In this study, the verification of the isotherm and kinetic models has been performed to understand the behavior of the adsorption of NH_4^+ from ALE onto GAC. The adsorption kinetic data were best described by pseudo-second order, suggesting that chemisorption would be involved during the adsorption process. The application of Freundlich models has best described the adsorption of NH_4^+ onto GAC, suggesting that the adsorption of NH_4^+ onto GAC would be occurred as multilayer. The variations of $[k_La]_g$, $[k_La]_f$ and $[k_La]_d$ versus percentage of outflow were found to be affected by bed depth of column and the resistance of mass transfer was dependent on porous diffusion. MTF models provide more information related to mechanism of mass transfer than the other models, which are more useful to understand the mechanisms of global, external and internal mass transfer for the adsorption of NH_4^+ from ALE onto GAC and to facilitate the performance and effectiveness of plug-flow column in removing pollutants from waters.

Acknowledgement

The author thanks the Universiti Tun Hussien Onn Malaysia, for short term grant under grant no Vot U635.

References

1. Fan, C., Glibert, P. M. and Burkholder, J. A. M. (2003). Characterization of the affinity for nitrogen, uptake kinetics, and environmental relationships for prorocentrum minimum in natural blooms and laboratory cultures. *Harmful Algae,* 2(4): 283-299.
2. Halim, A. A., Aziz, H. A., Johari, M. A. M. and Ariffin, K. S. (2010). Comparison study of ammonia and COD adsorption on zeolite, activated carbon and composite materials in landfill leachate treatment. *Desalination,* 262(1-3): 31-35.
3. Boopathy, R., Karthikeyan, S., Mandal, A. B. and Sekaran, G. (2013). Adsorption of ammonium ion by coconut shell-activated carbon from aqueous solution: Kinetic, isotherm, and thermodynamic studies. *Environmental Science and Pollution Research International,* 20(1): 533-542.
4. Gan, L., Zuo, J., Xie, B., Li, P. and Huang, X. (2012). Zeolite (Na) modified by nano-Fe particles adsorbing phosphate in rainwater runoff. *Journal of Environmental Sciences,* 24(11): 1929-1933.
5. Han, R., Zou, L., Zhao, X., Xu, Y., Xu, F., Li, Y. and Wang, Y. (2009). Characterization and properties of iron oxide-coated zeolite as adsorbent for removal of copper(II) from solution in fixed bed column. *Chemical Engineering Journal,* 149(1-3): 123-131.
6. Ruhl, A. S., Zietzschmann, F., Altmann, J., Meinel, F., Sperlich, A. and Jekel, M. (2015). Stratification of granular activated carbon filters for advanced wastewater treatment. *Water, Air, and Soil Pollution,* 226(11): 384-394.
7. Zayadi, N., Othman, N. and Hamdan, R. (2016). A potential waste to be selected as media for metal and nutrient removal. *IOP Conference Series: Materials Science and Engineering,* 136: 1-8.
8. Vassileva, P., Tzvetkova, P. and Nickolov, R. (2009). Removal of ammonium ions from aqueous solutions with coal-based activated carbons modified by oxidation. *Fuel,* 88(2): 387-390.
9. Halim, A. A., Aziz, H. A., Johari, M. A. M., Ariffin, K. S. and Adlan, M. N. (2010). Ammoniacal nitrogen and COD removal from semi-aerobic landfill leachate using a composite adsorbent: fixed bed column adsorption performance. *Journal of Hazardous Materials,* 175(1-3): 960-964.
10. Fulazzaky, M. A., Khamidun, M. H., Din, M. F. M. and Yusoff, A. R. M. (2014). Adsorption of phosphate from domestic wastewater treatment plant effluent onto the laterites in a hydrodynamic column. *Chemical Engineering Journal,* 258: 10-17.
11. Fulazzaky, M. A., Khamidun, M. H. and Omar, R. (2013). Understanding of mass transfer resistance for the adsorption of solute onto porous material from the modified mass transfer factor models. *Chemical Engineering Journal,* 228: 1023-1029.
12. Tazibet, S., Boucheffa, Y., Lodewyckx, P., Velasco, L. F. and Boutillara, Y. (2016). Microporous and mesoporous materials evidence for the effect of the cooling down step on activated carbon adsorption properties. *Microporous and Mesoporous Materials,* 221: 67-75.
13. Langmuir, I. (1916). The constitution and fundamental properties of solids and liquids. *Journal of the American Chemical Society,* 38 (11): 2221-2295.
14. Ho, Y. S. and Mckay, G. (1998). A comparison of chemisorption kinetic models applied to pollutant removal on various sorbents. *Trans IChemE,* 76: 332-340.
15. Ho, Y. S. (2006). Review of second-order models for adsorption systems. *Journal of Hazardous Materials,* 136(3): 681-689.
16. Ribas, M. C., Adebayo, M. A., Prola, L. D. T., Lima, E. C., Cataluña, R., Feris, L. A., and Calvete, T. (2014). Comparison of a homemade cocoa shell activated carbon with commercial activated carbon for the removal of reactive violet 5 dye from aqueous solutions. *Chemical Engineering Journal,* 248: 315-326.
17. Siu, P. C. C., Koong, L. F., Saleem, J., Barford, J. and McKay, G. (2015). Equilibrium and kinetics of copper ions removal from wastewater by ion exchange. *Chinese Journal of Chemical Engineering,* 24(1): 94-100.
18. Freundlich, H. M. F. (1906). Over the adsorption in solution. *The Journal of Physical Chemistry,* 57: 385-470.
19. Chan, L. S., Cheung, W. H., Allen, S. J. and McKay, G. (2012). Error analysis of adsorption isotherm models for acid dyes onto bamboo derived activated carbon. *Chinese Journal of Chemical Engineering,* 20 (3): 535-542.
20. Fulazzaky, M. A. (2011). Determining the resistance of mass transfer for adsorption of the surfactants onto granular activated carbons from hydrodynamic column. *Chemical Engineering Journal,* 166(3): 832-840.
21. Dhawan, R. and Meenakshi, K. K. B. (2015). Isotherms, kinetics and thermodynamics for adsorption of pyridine vapors on modified activated carbons. *Adsorption,* 21: 37-52.

22. Şencan, A., Karaboyaci, M. and Kiliç, M. (2015). Determination of lead(II) sorption capacity of hazelnut shell and activated carbon obtained from hazelnut shell activated with $ZnCl_2$. *Environmental Science and Pollution Research,* 22: 3238-3248.
23. Saha, P. Das, Chakraborty, S. and Chowdhury, S. (2012). Batch and continuous (fixed-bed column) biosorption of crystal violet by *Artocarpus heterophyllus* (jackfruit) leaf powder. *Colloids and Surfaces. B, Biointerfaces,* 92: 262 – 70.
24. Bandosz, T. J. and Petit, C. (2009). The reactive adsorption of ammonia on activated carbons modified by impregnation with inorganic compounds. *Journal of Colloid and Interface Science,* 338(2): 329-345.
25. Salman, J. M. (2014). Optimization of preparation conditions for activated carbon from palm oil fronds using response surface methodology on removal of pesticides from aqueous solution. *Arabian Journal of Chemistry,* 7(1): 101-108.
26. Chand, P. and Pakade, Y. B. (2015). Synthesis and characterization of hydroxyapatite nanoparticles impregnated on apple pomace to enhanced adsorption of Pb(II), Cd(II), and Ni(II) ions from aqueous solution. *Environmental Science and Pollution Research,* 22(14): 10919-10929.
27. Arshadi, M., Salimivahid, F., Salvacion, J. W. L. and Soleymanzadeh, M. (2014). Adsorption studies of methyl orange on an immobilized mn-nanoparticle: kinetic and thermodynamic. *RSC Advances,* 4: 16005-16017.
28. Fulazzaky, M. A. (2013). Calculation of the release of total organic matter and total mineral using the hydrodynamic equations applied to palm oil mill effluent treatment by cascaded anaerobic ponds. *Bioprocess and Biosystems Engineering,* 36(1): 11-21.
29. Khamidun, M. H., Fulazzaky, M. A., Md Din, M. F. and Mohd Yusoff, A. R. (2014). Resistance of mass transfer, kinetic and isotherm study of ammonium removal by using a hybrid plug-flow column reactor (HPFCR). In W. P. Sung, Jimmy C. M. Kao, and Ran Chen (Eds.), *Proceedings of the 2013 International Conference on Frontier of Energy and Environment Engineering, ICFEEE 2013*. Taylor & Francis Group, Xiam: pp. 555–559.
30. Zietzschmann, F., Worch, E., Altmann, J., Ruhl, A. S., Sperlich, A., Meinel, F. and Jekel, M. (2014). Impact of EfOM size on competition in activated carbon adsorption of organic micro-pollutants from treated wastewater. *Water Research,* 65: 297-306.
31. Foo, K. Y., Lee, L. K. and Hameed, B. H. (2013). Batch adsorption of semi-aerobic landfill leachate by granular activated carbon prepared by microwave heating. *Chemical Engineering Journal,* 222: 259-264.

Malaysian Journal of Analytical Sciences, Vol 22 No 4 (2018): 735 - 741
DOI: https://doi.org/10.17576/mjas-2018-2204-20

MALAYSIAN JOURNAL OF ANALYTICAL SCIENCES
Published by The Malaysian Analytical Sciences Society
ISSN 1394 - 2506

REMOVAL OF OIL AND GREASE AND ANIONIC SURFACTANTS IN SYNTHETIC CAR WASH WASTEWATER USING KAPOK FIBER: A BATCH-SCALE STUDY

(Penyingkiran Minyak dan Gris dan Anionik Surfaktan dalam Air Sisa Sintetik Basuhan Kereta Menggunakan Fiber Kapok: Kajian Skala-Kelompok)

Muhammad Shahrul Shafendy Ibrahim* and Nor Haslina Hashim

Department of Civil Engineering Technology,
Faculty of Engineering Technology,
Universiti Tun Hussein Onn Malaysia, 86400 Batu Pahat, Johor, Malaysia

**Corresponding author: msshafendy2@gmail.com*

Received: 16 April 2017; Accepted: 7 March 2018

Abstract

Kapok fiber (*Ceiba pentandra*) is a natural sorbent that exhibits excellent hydrophobic-oleophilic characteristics. The effects of dosage, and contact time were studied in a batch study. The initial and final concentration of the oil and grease and anionic surfactants in the synthetic car wash wastewater were evaluated to determine the removal efficiency of Kapok fiber. The results show excellent performance of Kapok fiber in removing oil and grease up to 100%, achieved using 0.1 g with 10 minutes contact time. Meanwhile, highest removal of anionic surfactants was up to 46%, achieved using 3.0 g of Kapok fiber with 10 minutes contact time. Overall, Kapok fiber showed great potential as an effective oil and grease, and anionic surfactants adsorbent.

Keywords: wastewater treatment, car wash wastewater, Kapok fiber, oil and grease, anionic surfactants

Abstrak

Serat Kapok (*Ceiba pentandra*) adalah penyerap semulajadi yang mempamerkan ciri-ciri hidrofobik-oleofilik cemerlang. Kesan dos, dan masa tindak balas dikaji dalam kajian skala kelompok. Kepekatan awal dan akhir kehadiran minyak dan gris surfaktan anionik dalam air kumbahan sintetik disediakan telah dinilai untuk menentukan kecekapan serat Kapok. Keputusan menunjukkan prestasi yang sangat baik serat Kapok dalam mengeluarkan minyak dan gris dan surfaktan anionik. Penyingkiran minyak dan gris sehingga 100% telah dicapai dengan menggunakan 0.1 g dengan masa tindak balas selama 10 minit, manakala penyingkiran surfaktan anionik sehingga 46% telah dicapai dengan menggunakan 3.0 g serat Kapok dengan masa 10 minit kenalan. Secara keseluruhan, serat Kapok berpotensi tinggi sebagai minyak dan gris yang berkesan dan penjerap surfaktan anionic yang berkesan.

Kata kunci: rawatan air sisa, air sisa basuhan kereta, serat Kapok, minyak dan gris, surfaktan anionik

Introduction

Car wash stations has been one of the many uprising service abundance in every city [1]. The car wash industry uses huge amount of water during the cleaning process. The usage of various chemical agents for cleaning and appealing efforts also contributes to deterioration of the environment. After the cleaning process, large quantities of surfactants are discharged into aquatic and terrestrial environments [2]. Oil and grease in car wash wastewater can originate from various kind of the petroleum-based products on the surface of vehicle or might also leaked out from

the motor engine [3]. Moreover, there is also a chance for the wastewater from the car wash station to contain hydraulic fluid and motor oil, which could have leaked out of the braking system and engine [4]. Generally, the composition of oil and grease is too complex due to the reason that it can contain lots of hazardous materials (such as phenols and polyaromatic hydrocarbons) which are carcinogenic to humans [3, 5, 6].

In addition, anionic surfactants were also produced in car wash cleaning processes [7]. Among the different type of surfactants, anionic surfactant can be considered as very important due to reason of it being responsible for 60% of the world soap production [8]. The anionic surfactants are known to have potential to cause skin irritation and it also shows obvious biological activity with various bioactive macromolecules such as starch [9] and proteins [10] or being introduced into various cell fragments thus causing malfunction as reported accordingly. Overall, the impacts of contaminants that originated from car wash wastewater can be as light as irritation to fatal (towards aquatic organisms). Thus, an efficient and cost-friendly treatment for the wastewater produced from car wash station should be established and practiced.

Among the natural fibres used in wastewater treatment, Kapok fiber is a natural hollow fiber which can be yielded from the seedpod of Kapok tree. Kapok trees belong to the family of *Bombaceae*, which can be cultivated in Asia, Africa and South America. Kapok fiber is composed of single-cell plant fibers that contains lignin and not attached to the seed grains. Visually, Kapok is a yellowish or light-brown silky fiber that covers the seeds of Kapok trees. In wastewater treatment industry, due to its unique properties (chemical and physical traits), Kapok fiber-based materials have offered potentials for new application as oil absorbent, thus highlighting Kapok fiber in recent years [11]. The wax layer exhibiting the surface of Kapok fiber enables the fiber to have excellent hydrophobic-oleophilic features and thus making Kapok fiber a fascinating medium for oil-sorbent application [12, 13]. The objectives of this work are to assess the potential of Kapok fiber for the removal of oil and grease, and anionic surfactants in synthetic car wash wastewater. Effects of adsorbent dosage, and contact time were studied.

Materials and Methods

Materials

In this work, natural Kapok fiber were screened (for impurities; dusts and lumps) and dried at 40 ^{0}C for a day before used [14]. To ensure freshness of the raw fiber, no further treatment was done on the Kapok fibers [12]. The Kapok fiber was obtained from a local supplier in Batu Pahat, Johor.

Chemicals

Sodium dodecyl sulphate (SDS), diesel oil, n-hexane, methyl-tert-butyl ether (MTBE), sodium sulphate anhydrous crystal, chloroform, and methylene blue.

Preparation of synthetic wastewater

Synthetic car wash wastewater was prepared based on the actual car wash wastewater was obtained from a local car wash station which was analysed for its oil and grease concentration (Average = 246.7 mg/L, Median = ~ 200 mg/L, n = 5) and anionic surfactants (Average = 115.3 mg/L, Median = ~ 100 mg/L, n = 5).

Oil and grease synthetic wastewater

An amount 200 mg/L of oil and grease synthetic wastewater was prepared by weighing 0.2 g of diesel oil and mixing it with 500 mL ultrapure water. The diesel oil was chosen to be used as the source of oil and grease for the synthetic wastewater due to its characteristics that can represents low viscosity oils such as light crude oil, kerosene and gasoline [15]. Next, the mixture was blended using a blender to form an emulsion. The mixture was then poured into a 1000 mL volumetric flask. The volumetric flask was top up with ultrapure water to the mark. Next, the pH of the solution was adjusted to 7.

Anionic surfactants synthetic wastewater

An amount 100 mg/L of anionic surfactants synthetic wastewater was prepared by dissolving 0.1 g of SDS powder in 100 mL ultrapure water in 1000 mL volumetric flask [16]. Then, the volumetric flask was top up with ultrapure water to the mark. Next, the pH value of the solution was adjusted to 7.

Evaluation of removal efficiency: Removals of oil and grease

An amount 150 mL of freshly prepared oil and grease synthetic wastewater was poured into a conical flask. Various dosage of dried Kapok fiber were added into the conical flask (0.1 g, 1.0 g and 3.0 g). Each conical flask containing the samples were shaken for 10, 30 and 60 minutes. The conical flasks containing the samples were shaken using orbital shaker at 120 rpm. Each set of experiment was done in triplicate to provide reliable data.

Removals of anionic surfactants

An amount 150 mL of freshly prepared SDS synthetic wastewater were poured into conical flasks separately. Various dosage of washed and dried Kapok fiber were added into the conical flask (0.1 g, 1.0 g and 3.0 g). Each sample were shaken for 10, 30 and 60 minutes. The conical flasks containing the samples were shaken using orbital shaker at 120 rpm. Each set were done in triplicates to provide reliable data.

Data analysis

The method used to determine the concentration of oil and grease in the treated and untreated samples was as according to the standard method APHA 2005 [17]. An amount 30 mL of each sample was pipetted into a separatory funnel. The oil and grease in the samples were then extracted using a mixture of n-hexane and MTBE (80% n-hexane: 20% MTBE). The organic layer was then filtered through a filter paper filled with sodium sulphate (to absorb water residue) into an empty beaker (previously weighed). The organic solvents were then evaporated in a water bath at 85 ^{0}C. The weight of the beaker with the oil residue were recorded. The concentration of oil and grease were calculated using equation 1:

$$\text{Oil and Grease, mg/L} = \frac{(A-B)\ x\ 1000}{Volume\ of\ sample\ (mL)} \quad (1)$$

where A is defined as final weight of beaker and B is initial weight of beaker

The method used to determine the concentration of anionic surfactants in the treated and untreated samples was the standard method APHA 2010 [17]. 10 mL of each sample was pipetted into the separatory funnel. The samples were mixed with methylene blue prior to chloroform extraction. The organic layer was then filtered through a phase separator filter paper (Whatman 1PS). The filtrates (chloroform + methylene blue) were then checked for their absorbances using a UV Spectrophotometer at the wavelength of 652 nm. A series of SDS solution at concentration of 10 ppm, 7 ppm, 5 ppm, 3 ppm, 2 ppm, and 1 ppm were prepared and extracted using the same method and the data obtained were used for plotting a calibration curve and to obtain a linear regression. The concentration of the samples was then calculated using the calibration curve.

Results and Discussion

Characterization of Kapok fiber

Kapok fiber used in this study was studied using FTIR instrument. Generally, plant wax consists of n-alkanes, smaller portion of alcohols, fatty acids, aldehydes, ketones and n-alkyl esters. The following primary absorption peaks can be observed, where 2915.80 cm^{-1}, corresponds to the asymmetric and symmetric aliphatic CH_2 and CH_3 stretching which can be associated with the presence of plant wax. The peaks around 1735.60 cm^{-1} is due to the presence of carbonyl group (C=O) in the ester bonds, which are alleged to be associated with the aliphatic aldehydes, esters and ketones of Kapok wax. The band around 1504 and 1592 cm^{-1} are corresponds to C-O stretching in lignin. Table 1 shows the characterization of Kapok fiber using FTIR instrument.

Table 1. FTIR absorption peaks of Kapok fiber used in the current study and those reported in literature

Non-free OH	Symmetric and Asymmetric CH_2 & CH_3	C=O: Ketone, Carboxylic, Ester in Lignin % Acetyl Ester in Xylan	Aromatic Ring Carbon Skeleton	C-H and C-O Bending	Reference
3410	2914	1740	1504 &1602	1373 & 1245	[18]
-	2891	1745 & 1234	-	1017	[12]
3350	2918	1738 & 1238	-	1037	[19]
3340	2906.59	1725.66	-	1366.28 & 1231.85	[20]
-	2915.80	1735.60	1504 & 1592	1369.19 & 1238.06	Current Study

Removals of oil and grease and anionic surfactants using Kapok fiber

Table 2, Figure 1 and Figure 2 shows the removal efficiency of anionic surfactants and oil and grease at pH 7.0 at room temperature using Kapok fiber. It was observed that for oil and grease, there was 100% removal using 0.1 g of Kapok at contact time of 10 minutes. This finding was also observed in another study using natural Kapok fiber [13]. On the other hand, the highest removal of anionic surfactants is 46%, using 3.0 g of Kapok fiber at a contact time of 10 minutes. The pattern shows that Kapok fiber does not need longer contact time to perform efficiently and discreetly remove oil and grease and anionic surfactants.

Table 2. Average concentration and average removals of samples

Sample Dosage (g)	Time (min)	Average Concentration (ppm)	Average Removals (%)
	10	33.3 (± 11.5)	61.5 (± 13.3)
	30	33.3 (± 11.5)	61.5 (± 13.3)
0.1 g	60	40.0 (± 0.0)	53.8 ((± 0.0)
	10	0.0 (± 0.0)	100.0 (± 0.0)
	30	13.3 (± 11.5)	84.6 (± 13.3)
1.0 g	60	26.7 (± 11.5)	69.2 (± 13.3)
	10	33.3 (± 11.5)	61.5 (± 13.3)
	30	13.3 (± 11.5)	84.6 (± 13.3)
3.0 g	60	26.7 (± 11.5)	69.2 (± 13.3)

Moreover, it was found that as the contact time increased, the efficiency for anionic surfactants removals decreased. This may be due to weak hydrophobic interactions between the waxy layers of Kapok fiber with the hydrocarbon tails of the anionic surfactants. Meanwhile, the efficiency for oil and grease removal does not differ much with time. In addition, the result shows that using shorter contact time will be preferable for Kapok fiber to perform efficiently.

In term of the removal efficiency, the hollow lumen structure of Kapok fiber and the waxy surface can be held responsible for its sorption capacity [15]. Moreover, for oil removal, the oil collected or entrapped in the fiber assembly can be due to the oil being retained in an internal lumen, and the oil entrapped in the voids between fibers (also known as inter-capillary fibers) [21]. On the other hand, for the absorption of anionic surfactants, it may be due to interaction of the alkyl groups of the surfactants with the waxy surface of Kapok fiber [22]. The interaction may mimic the hydrophobic interaction and van der Waals forces that may occur between the oils and the waxy

layer of the Kapok fibers in oil absorption onto Kapok [15] when the hydrocarbon chains of the SDS molecules are aligned with the hydrophobic waxy surface of the Kapok fibers.

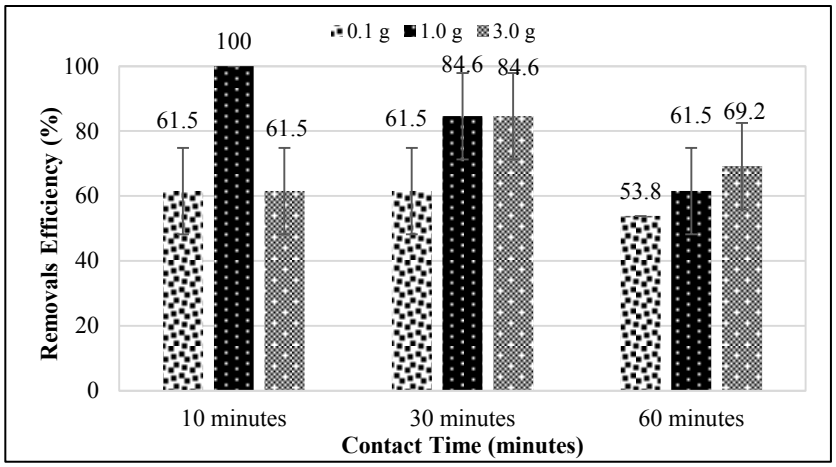


Figure 1. Removal efficiency of oil and grease using Kapok fiber

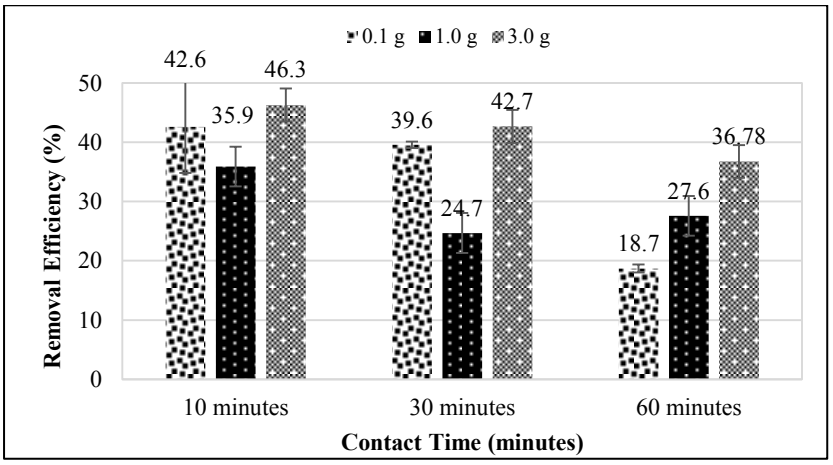


Figure 2. Removal efficiency of anionic surfactants using Kapok fiber

However, the results show that the removals of anionic surfactants were not as high as oil and grease removal. This may be due to weak interactions between the anionic surfactants and the waxy layers of the Kapok fibers as the hydrophobic interaction and van der Waals forces of attraction is rather weak and easily disturbed [23]. Moreover, the polar head of SDS molecule will be exposed to water. The forces of attraction between the negatively charged polar head of the anionic surfactants will pull the molecule back into the water, thus weakening and may destroy for the hydrophobic interaction of the alkyl group of SDS.

Conclusion

Kapok fiber as a natural sorbent shows high efficiency in oil and grease removals and promising application in anionic surfactants removal. The waxy layers of Kapok fiber are known to provide hydrophobic interaction with oil and grease. This work provides findings on the efficiency of the Kapok fibers in removing oil and grease and anionic surfactants. The new findings of Kapok fiber in removing anionic surfactants will provide new knowledge

of interactions between anionic surfactants and the Kapok fiber. The study is still ongoing, and further discussions will be shared in the future.

Acknowledgement

This work was funded by Ministry of Higher Education of Malaysia under the Fundamental Research Grant Scheme (FRGS), Vot No: 1565.

References

1. Bhatti, Z. A., Mahmood, Q., Raja, I. A., Malik, A. H., Khan, M. S. and Wu D. (2011). Chemical oxidation of carwash industry wastewater as an effort to decrease water pollution. *Physical Chemistry Earth,* 36(9-11): 465-469.
2. Shahbazi, R., Kasra-Kermanshahi, R., Gharavi, S., Moosavi- Nejad, Z. and Borzooee, F. (2013). Screening of SDS-degrading bacteria from car wash wastewater and study of the alkylsulfatase enzyme activity. *Iranian Journal of Microbiology,* 5(2): 153-158.
3. Lau, W. J., Ismail, A. F. and Firdaus, S. (2013). Car wash industry in Malaysia: Treatment of car wash effluent using ultrafiltration and nanofiltration membranes. *Separation Purification Technology,* 104: 26-31.
4. Jönsson, C., and Jönsson, A. S. (1995). The influence of degreasing agents used at car washes on the performance of ultrafiltration membranes. *Desalination,* 100(1-3): 115-123.
5. Kwach, B. O. and Lalah, J. O. (2009). High concentrations of polycyclic aromatic hydrocarbons found in water and sediments of car wash and kisat areas of Winam Gulf, Lake Victoria-Kenya. *Bulletin Environmental Contamination Toxicology,* 83(5): 727-733.
6. Wu, L., Ge, G. and Wan, J. (2009). Biodegradation of oil wastewater by free and immobilized Yarrowia Lipolytica W29. *Journal of Environmental Science,* 21(2): 237-242.
7. Perkowski, J., Bzdon, S. A., Bulska and Jóźwiak, W. K. (2006). Decomposition of detergents present in car-wash sewage by titania photo-assisted oxidation. *Polish Journal of Environmental Study,* 15(3): 457-465.
8. Aloui, F., Kchaou, S. and Sayadi, S. (2009). Physicochemical treatments of anionic surfactants wastewater: effect on aerobic biodegradability. *Journal of Hazardous Material,* 164(1): 353-359.
9. Merta, J. and Stenius, P. (1999). Interactions between cationic starch and mixed anionic surfactants. *Colloids Surfaces A Physicochem. Engineering Aspect,* 149(1-3): 367-377.
10. Nielsen, A. D. Borch, K. and Westh, P. (2000). Thermochemistry of the specific binding of C12 surfactants to bovine serum albumin. *Life Science,* 1479: 321-331.
11. Zheng, Y., Wang, J., Zhu, Y. and Wang, A. (2015). Research and application of kapok fiber as an absorbing material: A mini review. *Journal of Environmental Science,* 27: 21-32.
12. Abdullah, M. A., Rahmah, A. U. and Man, Z. (2010). Physicochemical and sorption characteristics of Malaysian *Ceiba pentandra* (L.) Gaertn. as a natural oil sorbent. *Journal of Hazardous Materials*, 177 (1-3): 683-691.
13. Rahmah, A. U. and Abdullah, M. A. (2011). Evaluation of Malaysian *Ceiba pentandra* (L.) Gaertn for oily water filtration using factorial design. *Desalination,* 266(1-3): 51-55.
14. Hori, S., Flavier, K. and Kuga, M. E. (2000). Excellent oil Absorbent Kapok *Ceiba pentandra* (L.) Gaertn fiber: Fiber structure, chemical characteristics, and application. *Japan Wood Resource Society,* 46: 401-404.
15. Lim, T. T. and Huang, X. (2007). Evaluation of Kapok (*Ceiba pentandra* (L.) Gaertn.) as a natural hollow hydrophobic–oleophilic fibrous sorbent for oil spill cleanup. *Chemosphere,* 66(5): 955-963.
16. Adak, A., Bandyopadhyay, M. and Pal, A. (2005). Removal of anionic surfactant from wastewater by alumina: A case study. *Colloids Surfaces A Physicochem. Engineering Aspect,* 254(1-3): 165-171.
17. APHA. (2005). Standard methods for the examination of water and wastewater. American Public Health Association ,Washington, D.C.
18. Wang, J., Zheng, Y. and Wang, A. (2012). Effect of Kapok fiber treated with various solvents on oil absorbency. *Industrial Crops Product,* 40(1): 178-184.
19. Rengasamy, R. S., Das, D. and Praba Karan, C. (2011). Study of oil sorption behavior of filled and structured fiber assemblies made from polypropylene, Kapok and Milkweed fibers. *Journal of Hazardous Materials,* 186(1): 526-532.
20. Ismail, Z. (2013). Comparative study on raw and modified Kapok fibers as sorbent materials for oil sorption. Thesis Universiti Teknologi PETRONAS, Malaysia.

21. Wang, J., Zheng, Y. and Wang, A. (2012). Superhydrophobic Kapok fiber oil-absorbent: Preparation and high oil absorbency. *Chemical Engineering Journal,* 213: 1-7.
22. Zhang, R. and Somasundaran, P. (2006). Advances in adsorption of surfactants and their mixtures at solid/solution interfaces. *Advance Colloid Interface Science,* 123: 213-229.
23. Stone, A. (2013). The theory of intermolecular forces. OUP Oxford.

Malaysian Journal of Analytical Sciences Vol 22 No 5 2018

Articles 11-15 are selected papers from the "2nd International Conference on Separation Technology (ICOST 2017), 15 & 16 April 2017, Pulai Springs Resort, Johor Bahru, Malaysia; organised by Centre of Lipids Engineering and Applied Research, Universiti Teknologi Malaysia."

Guest Editor: Norasikin Othman

Articles 16-20 are selected papers from the "Malaysia Polymer International Conference 2017 (MPIC 2017), 19 & 20 July 2017, Universiti Kebangsaan Malaysia, Bangi Campus, Selangor, Malaysia; organised by Polymer Research Center (PORCE), Universiti Kebangsaan Malaysia and co-organised by Mahatma Gandhi University, India and Gifu University, Japan."

Guest Editor: Siti Fairus Mohd Yusoff

Page

1. SYNTHESIS OF 2-AMINOBIARYL DERIVATIVES PROMOTED BY WATER EXTRACT OF ONION PEEL ASH 742
(Sintesis Terbitan 2-Aminobiaril Dimangkinkan oleh Ekstrak Air Abu Kulit Bawang)
Poh Wai Chia, Poh Seng Chee, Siti Nur Aqlili Riana Mohd Asseri, Fu Siong Julius Yong, Su-Yin Kan

2. EFFECT OF GOLD SOLUTION CONCENTRATION ON THE FORMATION AND PHOTOELECTROCHEMICAL PROPERTIES OF GOLD DEPOSITED TITANIUM DIOXIDE NANOTUBES 750
(Kesan Kepekatan Larutan Emas Terhadap Pembentukan dan Sifat-Sifat Fotoelektrokimia Nanotiub Titanium Dioksida Terendap Emas)
Siti Sarah Binti Ismail, Zainiharyati Mohd Zain, Asmaa Kadim Ayal, Lim Ying Chin

3. SYNTHESIS, CHARACTERISATION AND EFFECT OF TEMPERATURE ON CORROSION INHIBITION BY THIOSEMICARBAZONE DERIVATIVES AND ITS TIN(IV) COMPLEXES 758
(Sintesis, Pencirian dan Kesan Suhu Perencat Kakisan oleh Ligan Terbitan Tiosemikarbazon dan Kompleks Timah(IV))
Nur Nadira Hazani, Nur Nadia Dzulkifli, Sheikh Ahmad Izaddin Sheikh Mohd Ghazali, Yusairie Mohd, Yang Farina, Nurul 'Ain Jamion

4. SYNTHESIS AND PHYSICOCHEMICAL PROPERTIES OF MAGNETITE NANOPARTICLES (Fe_3O_4) AS POTENTIAL SOLID SUPPORT FOR HOMOGENEOUS CATALYSTS 768
(Sintesis dan Sifat Fizikokimia Nanopartikel Magnetit (Fe_3O_4) Sebagai Sokongan Padu Berpotensi Bagi Mangkin Homogen)
Wan Fatihah Khairunisa Wan Nor, Siti Kamilah Che Soh, Alyza Azzura Abd Rahman Azmi, Mohd Sukeri Mohd Yusof, Mustaffa Shamsuddin

5. PHYSICOCHEMICAL CHARACTERISTICS OF RECYCLED TYRE TREAD COMPOUNDS 775
(Ciri-Ciri Fizik-kimia Sebatian bagi Bunga Tayar Kitar Semula)
Muhammad Abbas Ahmad Zaini, Agus Arsad, Zainul Akmar Zakaria, Azhar Abdollah, Zaharrudin Abdul Wahid

6. SEPARATION OF L-ARGININE AND L-CITRULLINE IN RED AND YELLOW CRIMSON WATERMELON (*Citrullus lanatus*) JUICES EXTRACT USING HPLC GRADIENT MODE 785
(Pemisahan L-Arginina dan L-Sitrulina dalam Ekstrak Jus Tembikai (*Citrullus lanatus*) Merah dan Kuning Menggunakan Mod Cerun KCPT)
Rasdin Ridwan, Hairil Rashmizal Abdul Razak, Mohd Ilham Adenan, Wan Mazlina Md Saad

7. BIOACCESSIBILITY ASSESSMENT OF ^{232}Th AND ^{238}U FROM LANTHANIDE CONCENTRATE AND WATER LEACH PURIFICATION RESIDUE IN MALAYSIA 794
(Penilaian Bio-Kebolehcapaian bagi ^{232}Th Dan ^{238}U dalam Lantanida Pekat dan Residu Pemurnian Larut Resap Air di Malaysia)
Nur Shahidah Abdul Rashid, Um Wooyong, Yasmin Mohd Idris Perama, Amran Ab.Majid, Khoo Kok Siong

8. PHOTOCATALYTIC DEGRADATION OF PHENOL DERIVATIVES OVER SILVER SUPPORTED ON MESOPOROUS TITANIA NANOPARTICLES 807
(Degradasi Fotomangkin Daripada Terbitan Fenol Ke Atas Perak Disokong Pada Nanopartikel Titania Berliang Meso)
Nur Farhana Jaafar and Aishah Abdul Jalil

9. LIQUID CHROMATOGRAPHY TANDEM MASS SPECTROMETRY FOR THE DETECTION AND VALIDATION OF QUERCETIN-3-*O*-RUTINOSIDE AND MYRICETIN FROM FRACTIONATED *Labisia pumila* var. *alata* 817
(Kromatografi Cecair Spektrometri Jisim Tandem untuk Pengesanan dan Pengesahsahihan Kuersetin-3-*O*-Rutinosida dan Mirisetin daripada Pemeringkatan *Labisia pumila* var. *alata*)
Norliza Abdul Latiff, Chua Lee Suan, Mohammad Roji Sarmidi, Ismail Ware, Siti Nor Azlina Abdul Rashid, Nor Farahiyah Aman Noor, Maizatul Akmal Yahayu

10. DETERMINATION OF NATURAL RADIOACTIVITY AND HEAVY METALS AT THE FORMER MINING SITE OF KOLEJ UNIVERSITI ISLAM ANTARABANGSA SELANGOR (KUIS) LAKE 828
(Penentuan Keradioaktifan Tabii dan Logam Berat di Kawasan Bekas Lombong Tasik Kolej Universiti Islam Antarabangsa Selangor (KUIS))
Nur Ain Mohd Radzali, Norsyahidah Mohd Hidzir, Irman Abdul Rahman

11. CHITOSAN-BASED ADSORBENTS FOR THE REMOVAL OF METAL IONS FROM AQUEOUS SOLUTIONS 839
(Bahan Penjerap Berasaskan Kitosan untuk Penyingkiran Ion Logam dari Larutan Akueus)
Zetty Azalea Sutirman, Mohd Marsin Sanagi, Khairil Juhanni Abd Karim, Ahmedy Abu Naim, Wan Aini Wan Ibrahim

12. THE EFFECTS OF ZEOLITE ON MECHANICAL AND MORPHOLOGICAL PROPERTIES OF NR/ENR MEMBRANES 851
(Kesan Zeolit pada Sifat Mekanikal dan Morfologi Membran NR/ENR)
Kritsada Phatcharasit and Wirach Taweepreda

13. IMMOBILIZED METAL AFFINITY CHROMATOGRAPHIC MEMBRANE FOR TRYPSIN SEPARATION 857
(Kromatografi Membran Afiniti Logam Pegun untuk Pemisahan Tripsin)
Sofiah Hamzah, Nurul Hidayati Mat Alim, Nurul Fakhriah Ismail, Norhafiza Ilyana Yatim, Nur A'lya Mohd Sani

14. ENHANCEMENT AND OPTIMIZATION OF SINENSETIN EXTRACT FROM *Orthosiphon stamineus* USING SUPERCRTITICAL CARBON DIOXIDE EXTRACTION 867
(Peningkatan dan Pengoptimuman Ekstrak Sinensetin dari *Orthosiphon stamineus* Menggunakan Kaedah Pengekstrakan Bendalir Supergenting Karbon Dioksida)
Ahmad Hazim Abdul Aziz, Mohd Azizi Che Yunus, Lee Nian Yian, Zuhaili Idham, Fahim

Rithwan, Hafizah Mohd Hadzri, Ana Najwa Mustapha

15. TOTAL FLAVONOIDS AND PHENOLIC CONTENTS OF STICKY AND HARD PROPOLIS FROM 10 SPECIES OF INDO-MALAYAN STINGLESS BEES 877
(Jumlah Kandungan Flavonoid dan Fenolik dalam Propolis yang Melekit dan Keras daripada 10 Spesis Lebah Kelulut Indo-Malayan)
Norafiza Awang, Nora'aini Ali, Fadzilah Adibah Abd Majid, Sofiah Hamzah, Shamsul Bahri Abd Razak

16. LIQUID NATURAL RUBBER TOUGHENED POLY(LACTIC ACID) BLEND: EFFECTS OF COMPATIBILIZER TYPES AND LOADINGS ON THERMO-MECHANICAL PROPERTIES 885
(Adunan Asid Polilaktik Diperkuat Getah Asli Cecair: Kesan Jenis dan Kandungan Penserasi Terhadap Sifat Terma-Mekanik)
Mohd Farid Hakim Mohd Ruf, Sahrim Ahmad, Ruey Shan Chen, Dalila Shahdan, Farrah Diyana Zailan

17. THE EFFECTS OF GLYCEROL ADDITION TO THE MECHANICAL PROPERTIES OF THERMOPLASTIC FILMS BASED ON JACKFRUIT SEED STARCH 892
(Kesan Penambahan Gliserol pada Sifat Mekanik Filem Thermoplastik Berdasarkan Kanji Biji Nangka)
Nur'Aishah Ahmad Shahrim, Norshahida Sarifuddin, Hafizah Hanim Mohd Zaki, Ahmad Zahirani Ahmad Azhar

18. THERMAL, FLAMMABILITY, AND MORPHOLOGICAL PROPERTIES OF SEPIOLITE-FILLED ETHYLENE PROPYLENE DIENE MONOMER COMPOSITES 899
(Sifat Terma, Kemudahbakaran dan Morfologi bagi Komposit Etilena Propilena Monomer Diena Terisi Sepiolit)
Nurul Aizan Mohd Zaini, Hanafi Ismail, Arjulizan Rusli

19. MENGKUANG FIBER REINFORCED THERMOPLASTIC NATURAL RUBBER COMPOSITES: INFLUENCE OF RUBBER CONTENT ON MECHANICAL PROPERTIES AND MORPHOLOGY 906
(Komposit Termoplastik Getah Asli Diperkuat Serabut Mengkuang: Pengaruh Kandungan Getah ke atas Sifat Mekanik dan Morfologi)
Wan Zarina Wan Mohamed, Azizah Baharum, Ishak Ahmad, Ibrahim Abdullah, Nurzam Ezdiani Zakaria

20. FABRICATION OF CELLULOSE MICROSPHERES FROM MODIFIED COTTON LINTER AND OIL PALM TRUNK FIBRE VIA EMULSION METHOD 914
(Fabrikasi Mikrosfera Selulosa daripada Linter Kapas dan Gentian Batang Kelapa Sawit Termodifikasi Melalui Kaedah Emulsi)
Balqis Az-Zahraa, Nurul Shuhadah Mahadi, Nurul Nazatulatika Mohd Nizam, Sarani Zakaria, Muhammad Fauzi Daud, Sharifah Nabihah Syed Jaafar

Malaysian Journal of Analytical Sciences, Vol 22 No 5 (2018): 742 - 749
DOI: https://doi.org/10.17576/mjas-2018-2205-01

MALAYSIAN JOURNAL OF ANALYTICAL SCIENCES
Published by The Malaysian Analytical Sciences Society
ISSN 1394 - 2506

SYNTHESIS OF 2-AMINOBIARYL DERIVATIVES PROMOTED BY WATER EXTRACT OF ONION PEEL ASH

(Sintesis Terbitan 2-Aminobiaril Dimangkinkan oleh Ekstrak Air Abu Kulit Bawang)

Poh Wai Chia[1,2]*, Poh Seng Chee[1], Siti Nur Aqlili Riana Mohd Asseri[1], Fu Siong Julius Yong[2], Su-Yin Kan[3]

[1]School of Marine and Environmental Sciences
[2]Institute of Marine Biotechnology
Universiti Malaysia Terengganu, 21030 Kuala Nerus, Terengganu, Malaysia
[3]Faculty of Health Sciences,
Universiti Sultan Zainal Abidin, 21300 Kuala Nerus, Terengganu, Malaysia

**Corresponding author: pohwai@umt.edu.my*

Received: 17 March 2018; Accepted: 2 July 2018

Abstract

The biaryl and its derivatives are important organic compounds that possess various interesting applications, such as in the field of medicine, organic-light emitting materials, agrochemicals and other functional properties. Traditionally, radical arylation of arylhydrazines and anilines requires the use of metals, excess of base, flammable solvent and so on. Thus, a greener catalytic system for the synthesis of 2-aminobiaryls is highly sought after. In this work, a recyclable catalytic media has been developed for the synthesis of 2-aminobiaryl derivatives via a direct arylation of anilines with arylhydrazines in the presence of water extract of the burned-ash of onion peel waste (ash-water extract). This method provides numerous advantages, such as external base- and metal-free, recyclable catalytic system, inexpensive and the products were achieved in moderate to good yield. This sustainable synthesis is scientifically important, as it is capable of minimizing the use of toxic reagents and at the same time offers an alternative method to manage the abundant bio-waste.

Keywords: ash-water extract, 2-aminobiaryls, recyclable catalytic system, arylhydrazine, aniline

Abstrak

Biaril dan derivatifnya adalah sebatian organik yang penting dan didapati memiliki pelbagai aplikasi menarik, seperti dalam bidang perubatan, bahan pemancar cahaya organik, agrokimia dan sifat-sifat lain. Secara tradisional, arilasi radikal yang melibatkan arilhidrazin dan anilin memerlukan penggunaan logam, bes lebihan, pelarut mudah terbakar dan sebagainya. Oleh itu, sistem pemangkin yang lebih hijau untuk sintesis 2-aminobiaril sangat diperlukan. Dalam kerja ini, media pemangkin yang boleh dikitar semula telah dibangunkan untuk sintesis terbitan 2-aminobiaril melalui arilasi anilin dengan arilhidrazin dalam kehadiran ekstrak air abu bawang merah (ekstrak air-abu). Kaedah ini memberi pelbagai kelebihan termasuk mengelakkan penggunaan bes luaran, bebas logam, sistem pemangkin yang boleh dikitar semula, murah dan kuantiti produk yang dihasilkan dalam lingkungan sederhana hingga baik. Sintesis lestari ini adalah penting secara saintifik, kerana ia mampu meminimalkan penggunaan reagen beracun dan pada masa yang sama menawarkan satu kaedah alternatif untuk menguruskan sisa biologi.

Kata kunci: ekstrak air-abu, 2-aminobiaril, media pemangkin boleh kitar semula, arilhidrazin, anilin

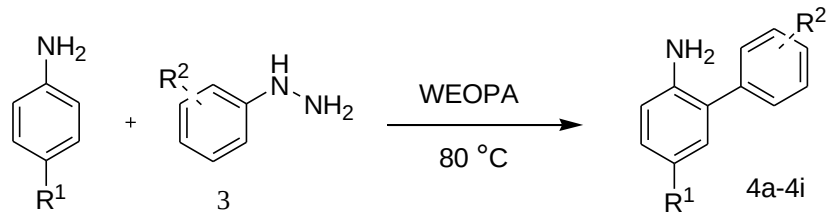
Introduction

In recent years, much attention has been devoted in both the industrial and academic communities to develop simple yet efficient green procedures in organic syntheses due to increasing environmental concern [1, 2]. The encouraging

use of environmentally acceptable chemicals, solvents and catalysts in recent times is scientifically significant to achieve both sustainable chemistry for synthesis and industrialization [3]. To that end, aqueous media have been highly regarded as a green solvent and has attracted the attention of the scientific community as they are environmentally friendly, inexpensive, non-toxic, have large dielectric constant, non-flammable and readily available, which are all desirable attributes in synthetic chemistry [4, 5]. Apart from meeting the benchmark of green chemistry, the use of water as solvent in organic synthesis has gained reputation as a catalyst [6-9].

The use of waste water, water extracts of fruits and vegetables juices have recently been reported to address and apply the concept of green chemistry in performing organic chemical processes [10]. Reactions promoted by these green catalytic systems and also other green media which utilize water as solvents are scientifically significant because of their biodegradable/recyclable nature and high solvating ability. As a result, the green aspect and recyclability of these non-classical solvents have been utilized in versatile organic reactions, such as the Suzuki-Miyaura reaction [11], Sonogashira reaction [12], green synthesis of 3-carboxycoumarins [13], Henry reaction [14] or Dakin reaction [15]. Bio-wastes are attractive resources from the perspective of green chemistry to achieve green chemical processes. According to a survey, the food processing factories and eateries generate millions of tonnes of bio-wastes monthly [16]. Furthermore, the amount of bio-wastes are expected to increase over time due to the increasing world population [17].

Onions (*Allium cepa* L.) are considered as one of the important vegetable crops grown globally for culinary, nutritional and other functional purposes [18]. Research has shown that more than 100,000 tonnes of onion wastes are generated annually from the United States of America and European countries [19]. These bio-wastes are disposed directly to the landfill which has seriously impacted our environment, wildlife and the human health [20]. In our continuous effort for developing new synthetic methodologies, herein we would like to report on a simple, and efficient procedure of synthesizing 2-aminobiaryls in the presence of a recyclable catalytic medium- Water Extract of Onion Peel Ash (WEOPA) (Scheme 1). The biaryls are important building blocks in various fields of application, such as drugs [21], organic chromophores [22], agrochemicals and other functional compounds [23]. In general, radical arylation involving the arylhydrazines and anilines required the use of metal [24], an excess of base [25], flammable solvent [26] and so on. The current work which employed the WEOPA catalytic system to facilitate the synthesis of 2-aminobiaryls is capable to reduce the environmental pressure by using environmental benign natural feedstock extract from waste onion peel and at the same time overcome the above mentioned drawbacks.



R^1 = F(1), ethyl (2)

Scheme 1. Synthesis of 2-aminobiaryls in the presence of WEOPA

Materials and Methods

All reagents and chemicals used in this research including ethyl acetate, 4-chlorophenylhydrazine, 3-bromo phenylhydrazine, 3-fluorophenylhydrazine, 4-fluorophenylhydrazine, 4-bromophenylhydrazine, 3-chlorophenyl hydrazine, 4-fluoroaniline, 4-ethylaniline, chloroform-d ($CDCl_3$) and silica gel 60 (0.063-0.200 mm) were purchased from Sigma-Aldrich and used without further purification. ^1H and ^{13}C-NMR spectra were recorded in $CDCl_3$ solvent on Bruker Avance III 400 spectrometer and chemical shifts were given in parts per million (ppm). The GC-MS spectra were recorded on a Shimadzu QP2010SE equipped with a Supelco fused silica capillary column (30 m × 0.25 mm i.d., 0.25 mm film thickness). The total carbon, hydrogen, nitrogen and sulphur (CHNS) of products was determined with a CHNS Analyser Flashea 1112 series. The FT-IR spectra were recorded using a

Perkin Elmer Spectrum 100 FT-IR Spectrometer. The metal content was studied using Varian Vista Pro inductive coupled plasma-optical emission spectroscopy (ICP-OES). The metal content analysis on ash-water extract was carried out in triplicates and the values were given as (mean ± standard deviation), in parts per billion (ppb).

Preparation of the water extract of onion peel ash (WEOPA)

The onion waste was sampled from a local disposal site in Kuala Terengganu, Malaysia in March 2018. The outer layer of onion peel was separated from the bulb, cleaned and washed twice with distilled water. Subsequently, the onion peels were cut into small pieces and sun-dried for two days. The WEOPA was prepared according to the method described by Boruah et al. [11]. Firstly, 2.5 g of dried peels were subjected to furnace at 500 °C for 1 hour. The resulted ash was collected and transferred to a 100 mL conical flask suspended with 30 mL of distilled water with continuous stirring for 1 hour. The mixture was filtered and the filtrate was termed as WEOPA.

Synthesis procedure for 2-aminobiaryls 4a-4i.

WEOPA (2 mL) was added into a 25 mL sample vial that was suspended with a mixture of anilines (1.00 mmol) and arylhydrazines (1.00 mmol). The reaction mixture was left for continuous stirring at 80 °C. The progress of the reaction was monitored by thin-layer chromatography (TLC). After the completion of the reaction, the aqueous layer was extracted with ethyl acetate (3 x 10 mL). The organic layer was subjected to silica gel column purification with ethyl acetate/hexane (1:9) as eluent. The aqueous WEOPA that was recovered was reused for the synthesis of other 2-aminobiaryls under the same condition.

Results and Discussion

Spectroscopic data of 2-aminobiaryls

3'-Chloro-5-fluoro-biphenyl-2-ylamine **4a** ^{1}H-NMR (400 MHz, $CDCl_3$): δ 3.62 (brs, 2H); 6.69 (dd, *J* = 4.9 Hz, *J* = 8.7 Hz, 1H); 6.84 (dd, *J* = 3.2 Hz, *J* = 9.2 Hz, 1H); 6.85 (m, 1H); 7.32-7.45 (m, 4H) ppm; ^{13}C NMR (100 MHz, $CDCl_3$) δ 115.36, 115.58, 116.42, 116.64, 116.72, 126.99, 127.77, 129.07, 130.20, 134.79, 139.52, 140.37, 155.01, 157.44 ppm; GC-MS: $C_{12}H_9ClFN$, m/z 221.05 $(M)^+$. Anal. calcd for $C_{12}H_9ClFN$: C 65.02, H 4.09, N 6.32; found C 65.00, H 4.02, N 6.29.

3'-Bromo-5-fluoro-biphenyl-2-ylamine **4b** ^{1}H-NMR (400 MHz, $CDCl_3$): δ 3.63 (brs, 2H); 6.70 (dd, *J* = 4.9 Hz, *J* = 8.3 Hz, 1H); 6.82 (dd, *J* = 2.8 Hz, J = 9.1 Hz, 1H); 6.88 (m, 1H); 7.26-7.59 (m, 4H) ppm; ^{13}C NMR (100 MHz, $CDCl_3$) δ 115.39, 115.66, 116.53, 123.00, 127.59, 130.45, 130.77, 132.01, 139.51, 140.59, 155.15, 157.42 ppm; GC-MS: $C_{12}H_9BrFN$, m/z 264.95 $(M)^+$. Anal. calcd for $C_{12}H_9BrFN$: C 54.16, H 3.41, N 5.26; found C 54.11, H 3.39, N 5.25.

3'-Fluoro-5-fluoro-biphenyl-2-ylamine **4c** ^{1}H-NMR (400 MHz, $CDCl_3$): δ 4.65 (brs, 2H); 6.66 (dd, *J* = 4.8 Hz, *J* = 8.6 Hz, 1H); 6.73-6.81 (m, 2H); 6.95-7.00 (m, 1H); 7.07-7.09 (m, 1H); 7.15-7.16 (m, 1H); 7.32-7.38 (m, 1H) ppm; ^{13}C NMR (100 MHz, $CDCl_3$) δ 113.31, 113.53, 114.43, 115.21, 115.44, 115.71, 115.78, 123.67, 123.68, 125.95, 129.52, 129.61, 139.01, 139.02, 139.90, 139.97, 153.91, 156.25, 166.79, 163.24 ppm; GC-MS: $C_{12}H_9F_2N$, m/z 205.05 $(M)^+$. Anal. calcd for $C_{12}H_9F_2N$: C 70.24, H 4.42, N 6.83; found C 70.21, H 4.39, N 6.80.

4'-Fluoro-5-fluoro-biphenyl-2-ylamine **4d** ^{1}H-NMR (400 MHz, $CDCl_3$): δ 3.58 (brs, 2H); 6.69 (dd, *J* = 4.6 Hz, *J* = 8.6 Hz, 1H); 6.81-6.90 (m, 2H); 7.12-7.16 (m, 2H); 7.39-7.42 (m, 2H) ppm; ^{13}C NMR (100 MHz, $CDCl_3$) δ 114.93, 115.15, 115.77, 115.98, 116.48, 116.56, 116.78, 127.56, 127.63, 130.62, 130.70, 134.43, 134.45, 139.66, 139.92, 155.11, 157.47, 161.01, 163.47 ppm; GC-MS: $C_{12}H_9F_2N$, m/z 205.05 $(M)^+$. Anal. calcd for $C_{12}H_9F_2N$: C 70.24, H 4.42, N 6.83; found C 70.22, H 4.38, N 6.81.

4'-Bromo-5-fluoro-biphenyl-2-ylamine **4e** ^{1}H-NMR (400 MHz, $CDCl_3$): δ 3.76 (brs, 2H); 6.71 (dd, *J* = 4.9 Hz, *J* = 8.7 Hz, 1H); 6.82-6.91 (m, 2H); 7.31-7.33 (m, 2H); 7.57-7.59 (m, 2H) ppm; ^{13}C NMR (100 MHz, $CDCl_3$) δ 115.21, 115.43, 116.38, 116.61, 116.81, 116.88, 121.78, 127.45, 127.52, 130.64, 132.16, 137.38, 139.14, 155.26, 157.61 ppm; GC-MS: $C_{12}H_9BrFN$, m/z 264.90 $(M)^+$. Anal. calcd for $C_{12}H_9BrFN$: C 54.16, H 3.41, N 5.26; found C 54.12, H 3.38, N 5.23.

3'-Chloro-5-ethyl-biphenyl-2-ylamine **4f** ^{1}H-NMR (400 MHz, $CDCl_3$): δ 1.21 (t, 3H); 2.57 (q, 2H); 3.65 (brs, 2H); 6.70 (d, *J* = 8.1 Hz, 1H); 6.94 (m, 1H); 7.00-7.02 (m, 1H); 7.30-7.36 (m, 3H); 7.46 (s, 1H) ppm; ^{13}C NMR (100 MHz, $CDCl_3$) δ 15.88, 27.92, 115.97, 126.17, 127.17, 127.27, 128.36, 129.21, 129.62, 129.96, 134.57, 134.65, 141.08, 141.63 ppm; GC-MS: $C_{14}H_{14}ClN$, m/z 231.08 $(M)^+$. Anal. calcd for $C_{14}H_{14}ClN$: C 72.57, H 6.09, N 6.04; found C 72.50, H 6.05, N 6.01.

3'-Bromo-5-ethyl-biphenyl-2-ylamine **4g** ^{1}H-NMR (400 MHz, $CDCl_3$): δ 1.22 (t, 3H); 2.58 (q, 2H); 3.61 (brs, 2H); 6.72 (d, *J* = 8.1 Hz, 1H); 6.94 (m, 1H); 7.01 (dd, *J* = 2.2 Hz, *J* = 8.1 Hz, 1H); 7.30 (m, 1H); 7.33-7.46 (m, 2H); 7.61 (m, 1H) ppm; ^{13}C NMR (100 MHz, $CDCl_3$) δ 15.88, 27.92, 115.97, 122.82, 126.08, 127.73, 128.39, 129.63, 130.10, 130.24, 132.11, 134.68, 141.07 ppm; GC-MS: $C_{14}H_{14}BrN$, m/z 275.05 $(M)^+$. Anal. calcd for $C_{14}H_{14}BrN$: C 60.89, H 5.11, N 5.07; found C 60.85, H 5.09, N 5.03.

4'-Fluoro-5-ethyl-biphenyl-2-ylamine **4h** ^{1}H-NMR (400 MHz, $CDCl_3$): δ 1.22 (t, 3H); 2.58 (q, 2H); 3.61 (brs, 2H); 6.73 (d, *J* = 8.1 Hz, 1H); 6.93 (m, 1H); 7.00 (m, 1H); 7.10-7.14 (m, 2H); 7.41-7.44 (m, 2H) ppm; ^{13}C NMR (100 MHz, $CDCl_3$) δ 15.89, 27.94, 115.51, 115.73, 115.87, 126.69, 127.96, 129.80, 130.71, 130.79, 134.64, 135.60, 135.63, 141.18, 160.77, 163.22 ppm; GC-MS: $C_{14}H_{14}FN$, m/z 215.10 $(M)^+$. Anal. calcd for $C_{14}H_{14}FN$: C 78.11, H 6.56, N 6.51; found C 78.08, H 6.53, N 6.49.

4'-Bromo-5-ethyl-biphenyl-2-ylamine **4i** ^{1}H-NMR (400 MHz, $CDCl_3$): δ 1.22 (t, 3H); 2.59 (q, 2H); 3.96 (brs, 2H); 6.74 (d, *J* = 8.0 Hz, 1H); 6.92 (d, *J* = 1.9 Hz, 1H); 7.02 (dd, *J* = 1.9 Hz, *J* = 8.0 Hz, 1H); 7.35 (m, 2H); 7.56 (m, 2H) ppm; ^{13}C NMR (100 MHz, $CDCl_3$) δ 15.86, 27.94, 116.24, 121.18, 126.66, 128.24, 129.61, 130.84, 131.88, 135.07, 138.54, 140.54 ppm; GC-MS: $C_{14}H_{14}BrN$, m/z 275.05 $(M)^+$. Anal. calcd for $C_{14}H_{14}BrN$: C 60.89, H 5.11, N 5.07; found C 60.86, H 5.08, N 5.05.

The FT-IR of onion peels obtained from a local grocery shop (Figure 1a) and the onion peels which was sampled from a local waste disposal site (Figure 1b) were compared. In Figure 1, a broad band centred at 3393 cm^{-1} is assignable to the stretching vibration of hydroxyl groups. The absorption band at 1637 cm^{-1} is attributed to the stretching frequency of carbonyl groups. Comparison of the two spectra showed that the relative intensity, shapes and the stretching frequencies of all signals shown by spectrum Figure 1b were well preserved as compared to that of FT-IR spectrum in Figure 1a. This indicated that no considerable changes were observed, in terms of the chemical structure (functional groups and hydrogen bonding network) on the onion peels which were obtained from the local grocery shop as compared to the recovered onion peels sampled from the local waste disposal site.

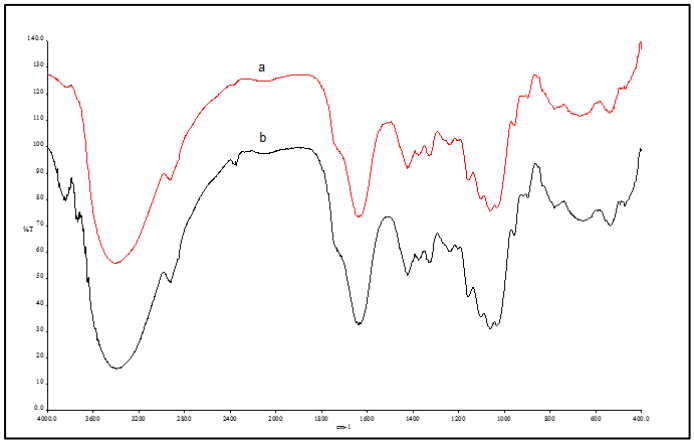


Figure 1. FTIR spectra of (a) onion peels obtained from a local grocery shop and (b) recovered onion peels from a local waste disposal site

In the optimisation study, we first examined the model reaction by using 4-fluroaniline **1a** as the model substrate. The arylation of **1a** (10 mmol) with 3-chlorophenylhydrazine **3a** in the presence of 0.5 mL of the WEOPA at 80 °C for 3 hours was investigated (Table 1). The regioselectivity of this reaction was found to produce **4a** in poor yield (Table 1, entry 1). Control reaction by employing pure water as solvent did not yield the product **4a**. (Table 1, entry 1) demonstrates the catalytic ability of WEOPA. As expected, a poor yield of **4a** was observed if the reaction time was short (Table 1, entry 6). The use of 2.0 mL of WEOPA produced the maximum isolated yield of **4a** (60 %) (Table 1, entry 4). When the reaction mixture was heated for a longer period of time by using 2 mL of WEOPA at 80 °C (Table 1, entry 7), this did not further improve the yield of **4a**. The same results were observed when the temperature of the reaction was altered, which did not result in a better yield (Table 1, entries 8-9). With all these information in mind, the optimised condition was determined (Table 1, entry 4).

Table 1. The optimization study using **1a** as the model substrate

Entry	Solvent (mL)	Time (h)	Temperature (°C)	Yield[a] (%)
1	H_2O (1.0)	3	50	0
2	WEOPA (0.5)	3	80	46
3	WEOPA (1.0)	3	80	50
4	WEOPA (2.0)	3	80	60
5	WEOPA (3.0)	3	80	58
6	WEOPA (2.0)	1	80	30
7	WEOPA (2.0)	4	80	56
8	WEOPA (2.0)	3	100	56
9	WEOPA (2.0)	3	60	45

[a]Isolated yield

Next, the general applicability of the WEOPA catalytic system to synthesise 2-aminobiaryls using different hydrazine's under the optimised condition was examined**.** In all the cases, the 2-aminobiaryls were obtained after silica gel column purification, with yields ranging from 47% to 60%. As indicated in Table 2, all arylation reactions of 4-fluoroaniline **1** with electron-withdrawing groups (Cl, Br and F) favoured the reactions by affording the corresponding 2-aminobiaryls **4a-4e** in moderate to good yields (Table 2, entries 1-5). 4-ethylaniline **2** was also subjected to the optimised reaction condition by reacting with electron-withdrawing groups (Cl, Br and F). The arylation employing **2** as the starting material proceeded smoothly to generate products in reasonably good yields within 3 h of reaction time (Table 2, entries 6-9). It is noteworthy that, compared to previous study, the catalytic performance of the WEOPA was regarded as unprecedented because of the fact that no solvents and additive were involved in the synthesis of 2-aminobiaryls [24-26]. In addition, all products were synthesised in a reasonable reaction time. The synthesized 2-aminobiaryls **4a-i** were characterised by NMR (^{1}H and ^{13}C) and further supported by GC-MS analyses.

Furthermore, the WEOPA catalytic system showed promising utility in line with sustainable chemistry due to its reusability in the synthesis of **4** model reaction. Upon the completion of arylation reaction between 4-fluonoaniline and 3-chlorophenylhydrazine, the WEOPA catalytic system was recovered and reused for up to five times, without significant losses of catalytic activity as shown in Figure 2.

Table 2. Isolated yields and the catalytic synthesis of 2-aminobiaryls **4**

Entry	Starting Materials	R^1	Product	Reaction Time (h)	Isolated Yield (%)
1	1	3-Cl	4a	3	60
2	1	3-Br	4b	3	55
3	1	3-F	4c	3	56
4	1	4-F	4d	3	50
5	1	4-Br	4e	3	49
6	2	3-Cl	4f	3	58
7	2	3-Br	4g	3	53
8	2	4-F	4h	3	51
9	2	4-Br	4i	3	47

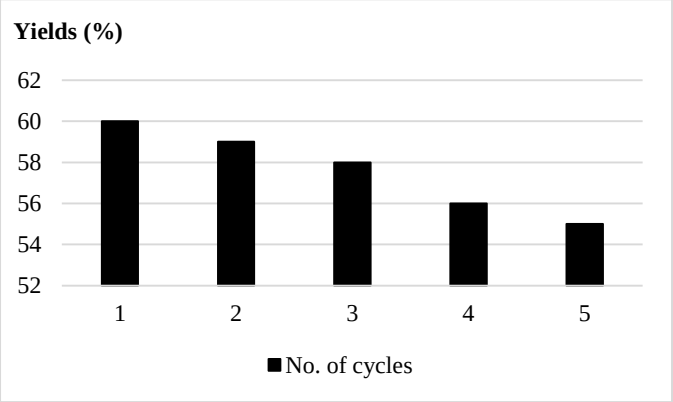


Figure 2. Recyclability of WEOPA in the synthesis of 2-aminobiaryls. Reaction conditions: 1 mmol of 3-chlorophenylhydrazine, 10 mmol of 4-fluoroaniline, 2 mL of WEOPA, 80 °C

Next, the characterisation of the ash-water extract with Inductively Coupled Plasma-Optical Emission Spectroscopy (ICP-OES) produced the following results (reported as mean value ± standard deviation) in parts per billion (ppb): potassium (11749.00 ± 227.00), sodium (92.00 ± 0.21), magnesium (528.00 ± 40.00), phosphorus (87.00 ± 5.00), yttrium (33.00 ± 0.02) and boron (32.00 ± 3.00). The data revealed that the ash-water extract primarily consisted of oxides, such as phosphorus, magnesium, zinc, manganese and sodium as major constituents along with other trace elements. We hypothesised that the alkali oxides, such as potassium, magnesium and calcium reacted with water to afford the hydroxides of these alkali and alkaline metals. These alkali and alkaline metals facilitated the formation of 2-aminobiaryls by acting as bases in the current investigated reaction, thus eliminated the use of external bases.

Conclusion

In the current study, we have demonstrated an efficient method of synthesizing 2-aminobiaryls catalyzed by the use of onion peel ash-water extract (WEOPA). There were several advantages of employing an ash-water extract catalytic system, including eliminating the use of additive, external bases and flammable solvent. Furthermore, the current catalytic system could be recovered and reused for up to five times, without significant losses of catalytic activity. We anticipate that the ash-water extract catalytic system could be used for the other organic transformations in the near future.

Acknowledgement

The authors would like to acknowledge the Ministry of Higher Education (MOHE) for the research grant (FRGS 59292) and financial assistance and Universiti Malaysia Terengganu for research facilities provided.

References

1. Polshettiwar, V., Luque, R., Fihri, A., Zhu, H., Bouhrara, M. and Basset, J.-M. (2011). Magnetically recoverable nanocatalysts. *Chemical Review*, 111(5): 3036-3075.
2. Simon, M.-O. and Li, C.-J. (2012). Green chemistry oriented organic synthesis in water. *Chemical Society Review*, 41(4): 1415-1427.
3. Waseem, M. A., Srivastava, A., Srivastava, A. and Siddiqui, I. (2015). Water and ionic liquid synergy: A novel approach for the synthesis of benzothiazole-2 (3H)-one. *Journal of Saudi Chemical Society*, 19(3): 334-339.
4. Li, C.-J. and Chen, L. (2006). Organic chemistry in water. *Chemical Society Review*, 35(1): 68-82.
5. Wagare, D. S., Netankar, P. D., Shaikh, M., Farooqui, M. and Durrani, A. (2017). Highly efficient microwave-assisted one-pot synthesis of 4-aryl-2-aminothiazoles in aqueous medium. *Environmental Chemistry Letters*, 15(3): 475-479.
6. Noshiranzadeh, N., Emami, M., Bikas, R. and Kozakiewicz, A. (2017). Green click synthesis of β-hydroxy-1, 2, 3-triazoles in water in the presence of a Cu (II)–azide catalyst: a new function for Cu (II)–azide complexes. *New Journal of Chemistry*, 41(7): 2658-2667.
7. Banerjee, B. (2017). Recent developments on ultrasound assisted catalyst-free organic synthesis. *Ultrasonics Sonochemistry*, 35(2017): 1-14.
8. Miklós, F. and Fülöp, F. (2016). A simple green protocol for the condensation of anthranilic hydrazide with cyclohexanone and n-benzylpiperidinone in water. *Journal of Heterocyclic Chemistry*, 53(1): 32-37.
9. Yang, Y., Bao, Y., Guan, Q., Sun, Q., Zha, Z. and Wang, Z. (2017). Copper-catalyzed S-methylation of sulfonyl hydrazides with TBHP for the synthesis of methyl sulfones in water. *Green Chemistry*, 19(1): 112-116.
10. Sarmah, M., Mondal, M. and Bora, U. (2017). Agro-waste extract based solvents: emergence of novel green solvent for the design of sustainable processes in catalysis and organic chemistry. *ChemistrySelect*, 2(18): 5180-5188.
11. RekhaáBoruah, P. and AzizáAli, A. (2015). Pd (OAc) 2 in WERSA: a novel green catalytic system for Suzuki–Miyaura cross-coupling reactions at room temperature. *Chemical Communications*, 51(57): 11489-11492.
12. Dewan, A., Sarmah, M., Bora, U. and Thakur, A. J. (2016). A green protocol for ligand, copper and base free Sonogashira cross-coupling reaction. *Tetrahedron Letters*, 57(33): 3760-3763.
13. Bagul, S. D., Rajput, J. D. and Bendre, R. S. (2017). Synthesis of 3-carboxycoumarins at room temperature in water extract of banana peels. *Environmental Chemistry Letters*, 15(4): 725-731.
14. Surneni, N., Barua, N. C. and Saikia, B. (2016). Application of natural feedstock extract: The Henry reaction. *Tetrahedron Letters*, 57(25): 2814-2817.
15. Saikia, B. and Borah, P. (2015). A new avenue to the Dakin reaction in H_2O_2–WERSA. *RSC Advances*, 5(128): 105583-105586.
16. Choi, I. S., Cho, E. J., Moon, J.-H. and Bae, H.-J. (2015). Onion skin waste as a valorization resource for the by-products quercetin and biosugar. *Food Chemistry*, 188: 537-542.
17. Marshall, R. E. and Farahbakhsh, K. (2013). Systems approaches to integrated solid waste management in developing countries. *Waste Managment*, 33(4): 988-1003.
18. Nile, S. H. and Park, S. W. (2013). Total phenolics, antioxidant and xanthine oxidase inhibitory activity of three colored onions (*Allium cepa* L.). *Frontier in Life Science*, 7(3-4): 224-228.
19. Sharma, K., Mahato, N., Nile, S. H., Lee, E. T. and Lee, Y. R. (2016). Economical and environmentally-friendly approaches for usage of onion (*Allium cepa* L.) waste. *Food & Function*, 7(8): 3354-3369.
20. Gao, S., Li, L., Geng, K., Wei, X. and Zhang, S. (2015). Recycling the biowaste to produce nitrogen and sulfur self-doped porous carbon as an efficient catalyst for oxygen reduction reaction. *Nano Energy*, 16: 408-418.
21. Costantino, L. and Barlocco, D. (2006). Privileged structures as leads in medicinal chemistry. *Current Medicinal Chemistry*, 13(1): 65-85.
22. Jiang, H., Sun, J. and Zhang, J. (2012). A review on synthesis of carbazole-based chromophores as organic light-emitting materials. *Current Organic Chemistry*, 16(17): 2014-2025.
23. McGlacken, G. P. and Bateman, L. M. (2009). Recent advances in aryl–aryl bond formation by direct arylation. *Chemical Society Review*, 38(8): 2447-2464.

24. Jiang, T., Chen, S.-Y., Zhang, G.-Y., Zeng, R.-S. and Zou, J.-P. (2014). CoPc-catalyzed selective radical arylation of anilines with arylhydrazines for synthesis of 2-aminobiaryls. *Organic & Biomolecular Chemistry*, 12(35): 6922-6926.
25. Jiang, T., Chen, S.-Y., Zhuang, H., Zeng, R.-S. and Zou, J.-P. (2014). Air-promoted direct radical arylation of anilines with arylhydrazines. *Tetrahedron Letters*, 55(33): 4549-4552.
26. Chen, Z.-X. and Wang, G.-W. (2005). One-pot sequential synthesis of acetoxylated [60] fullerene derivatives. *Journal of Organic Chemistry*, 70(6): 2380-2383.

Malaysian Journal of Analytical Sciences, Vol 22 No 5 (2018): 750 - 757
DOI: https://doi.org/10.17576/mjas-2018-2205-02

MALAYSIAN JOURNAL OF ANALYTICAL SCIENCES
Published by The Malaysian Analytical Sciences Society
ISSN 1394 - 2506

EFFECT OF GOLD SOLUTION CONCENTRATION ON THE FORMATION AND PHOTOELECTROCHEMICAL PROPERTIES OF GOLD DEPOSITED TITANIUM DIOXIDE NANOTUBES

(Kesan Kepekatan Larutan Emas Terhadap Pembentukan dan Sifat-Sifat Fotoelektrokimia Nanotiub Titanium Dioksida Terendap Emas)

Siti Sarah Binti Ismail[1], Zainiharyati Mohd Zain[1], Asmaa Kadim Ayal[2], Lim Ying Chin[1]*

[1]*School of Chemistry and Environment, Faculty of Applied Sciences, Universiti Teknologi MARA, 40450 Shah Alam, Selangor, Malaysia*
[2]*Department of Chemistry, College of Science for Women, University of Baghdad, Al-Jadriya Campus, Baghdad, Iraq*

**Corresponding author: limyi613@salam.uitm.edu.my*

Received: 29 August 2017; Accepted: 20 June 2018

Abstract

Solar photoelectrochemical (PEC) water splitting for hydrogen production is a clean, eco-friendly, and cost-effective technology that uses solar light as the energy source. Metal oxides, such as TiO_2, are preferable as a photoanode in PEC water splitting as they have relatively high reactivity, stable in aqueous solution, and cheaper than non-oxide semiconductors. However, TiO_2 has a large band gap (3.2 eV) that only allows it to be active upon irradiation with UV light. Thus, gold nanoparticles were deposited onto TiO_2 nanotubes (TNT) in this study to extend their spectral response to the visible region. Gold deposited titanium dioxide nanotubes (AuTNT) were synthesized by using pulse electrodeposition. Electrodeposition was carried out in 0.5 M H_2SO_4 that contained different concentrations (50, 100, 500, and 1,000 µM) of gold solution, with 75% duty cycle and an applied potential of -0.4 V for 20 minutes in a three-electrode electrochemical cell. The TNTs were annealed at 500 °C for 2 hours to induce crystallinity prior to gold deposition. The physicochemical properties of the AuTNT were characterised using a Field Emission Scanning Electron Microscope (FESEM), an Energy Dispersive X-ray (EDX), and an X-ray Diffractometer (XRD). Photoelectrochemical properties of AuTNT electrode was evaluated in 0.5 M Na_2SO_4 and 2 M C_2H_5OH under the illumination of a halogen lamp. The AuTNT electrode prepared with 500 µM gold solution demonstrated the highest photocurrent compared to other concentrations of gold.

Keywords: gold nanoparticles, titanium dioxide nanotube, pulse electrodeposition, photoelectrochemical properties

Abstrak

Pembelahan air secara fotoelektrokimia suria (PEC) untuk menghasilkan hidrogen merupakan teknologi yang bersih, mesra alam, dan kos efektif dengan memanfaatkan cahaya matahari sebagai sumber tenaga. Logam oksida, contohnya TiO_2, lebih digemari sebagai fotoanod dalam pembelahan air PEC kerana logam-logam ini mempunyai kereaktifan yang agak tinggi, stabil dalam larutan akueus, dan lebih murah berbanding semikonduktor bukan oksida. Walau bagaimanapun, TiO_2 mempunyai jurang jalur yang besar (3.2 eV) yang hanya membolehkan ia berfungsi di bawah sinaran cahaya ultralembayung. Oleh itu, nanopartikel emas diendap ke atas nanotiub TiO_2 (TNT) dalam kajian ini untuk mengembangkan tindak balas spektrum TNT ke kawasan cahaya nampak. Nanotiub titanium dioksida yang diendap emas (AuTNT) disintesis menggunakan kaedah nadi elektroendapan. Elektroendapan dilakukan dalam 0.5 M H_2SO_4 yang mengandungi kepekatan (50, 100, 500, dan 1,000 µM) larutan Au yang berbeza dengan 75% kitar tugas dan keupayaan dikenakan pada -0.4 V selama 20 minit menggunakan sel elektrokimia tiga elektrod. Pemanasan nanotiub titanium dioksida telah dilakukan pada suhu 500 °C selama 2 jam untuk meningkatkan struktur kristal TNT sebelum pengendapan emas. Sifat-sifat fizikokimia AuTNT dikaji menggunakan mikroskopi pengimbasan elektron

pancaran medan (FESEM), analisis penyerakan tanaga sinar-X (EDX), dan pembelauan sinar-X (XRD). Sifat-sifat fotoelektrokimia AuTNT telah dinilai dalam 0.5 M Na_2SO_4 dan 2 M C_2H_5OH di bawah pencahayaan lampu halogen. Elektrod AuTNT yang disediakan dengan kepekatan larutan Au pada 500 μM memberikan fotoarus yang tertinggi berbanding dengan kepekatan emas yang lain.

Kata kunci: nanopartikel emas, nanotiub titanium dioksida , nadi elektroendapan, sifat fotoelektrokimia

Introduction

Environmental pollution and energy crisis are getting worse day-by-day. Thus, renewable energy sources and environmentally friendly energy conversion methods are studied to overcome these raising issues. Photoelectrochemical (PEC) water splitting process is one of the promising technologies that provide clean and cost-effective energy conversion by exploiting the abundant sunlight irradiating the earth [1, 2]. The performance of a PEC photoanode can be influenced by the following factors: 1) light absorption efficiency; 2) charge separation; and 3) transport and surface reaction efficiency. An excellent PEC electrode should have the ability to harvest a large portion of the solar energy, is able to support charge separation and rapid transfer to the semiconductor, and have long-term stability [3].

A metal oxide, such as TiO_2, is favoured as it is stable in aqueous solutions, non-toxic, low cost, and shows efficient photoelectrocatalysis performance. TiO_2 nanotubes exhibit better PEC performance compared to TiO_2 nanoparticles due to their high aspect ratio, light trapping ability, and relatively efficient charge separation [4]. However, pristine TiO_2 suffers from a high band gap, reduced efficiency in light harvesting, and poor photogenerated charge carrier separation. Hence, metal/non-metal/noble metal doping is used to reduce the band gap of TiO_2 to extend its light absorption range into the visible region and improves the efficiency of the charge carriers [5]. In this study, TiO_2 nanotubes were deposited with gold nanoparticles to enhance the performance of PEC into visible light spectra. Gold nanoparticles are capable of increasing the stability of the electrode due to the chemical stability of gold as a noble metal [6]. The gold nanoparticles were deposited onto the nanotube using pulse electrodeposition technique. Subsequently, the effect of different gold solution concentrations on the morphology and PEC performance of the prepared samples were studied.

Materials and Methods

Materials

Ti foils (0.127 mm, 99.7% purity) for producing TNT substrate were purchased from Sigma Aldrich. The Ti foil was cleaned with acetone, isopropanol (R&M Chemicals), and deionized (DI) water (Millipore Alpha Q system, 18.2 MΩ). For the anodization and electrodeposition process, ethylene glycol, $C_2H_6O_2$ (Fisher, 99.8% p.a.) and ammonium fluoride, NH_4F (Fluka, 98.0%), gold(III) chloride trihydrate, $HAuCl_4{\cdot}3H_2O$ (Sigma Aldrich, 99.9%) and sulfuric acid (Fisher) were used without further purification for the preparation of electrolyte.

Preparation of titania nanotubes (TNTs)

The Ti foils were first cut into 1 × 2 cm rectangles and were ultrasonically cleaned with acetone, isopropanol, and DI water for 15 minutes each using an ultrasonicator (Analab Scientific Instruments). Then, the cleaned Ti foils were rinsed with DI water and dried at room temperature. The anodization process was conducted in a standard 2-electrode cell, with the Ti foil acting as the anode, while a high-density graphite rod served as the cathode, as shown in Figure 1. The distance between both electrodes was fixed at 2 cm, and the electrodes were immersed in electrolyte that comprised of 95% ethylene glycol, 5% DI water, and 0.5 wt.% NH_4F. The anodization process was conducted at room temperature with an applied potential of 40 V for 180 minutes with continuous stirring. Next, the anodized Ti substrate was rinsed with DI water and was ultrasonically cleaned with DI water for another 2 minutes to remove any surface debris. Then, the as-formed TNT substrate was calcined at 500 °C in a Thermolyne 21100 furnace for 120 minutes, with a heating rate of 2 °C/min. The calcination step was conducted to induce crystallinity in the TiO_2 nanotubes as they were initially amorphous.

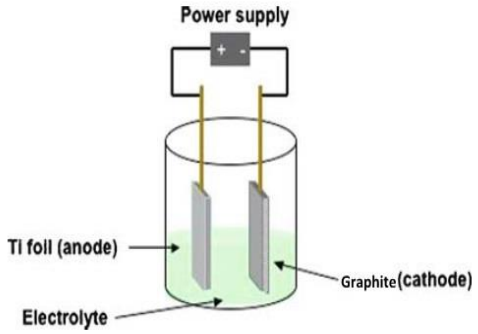


Figure 1. Setup of the anodization of Ti foil

Preparation of gold deposited titania nanotube (AuTNT)

The prepared TNTs were used as a substrate for the deposition of gold. The gold nanoparticles were deposited onto the calcined TNT using the pulse electrodeposition technique. Cyclic voltammetry was conducted prior to the deposition to determine the potential range for depositing the gold nanoparticles. Different concentrations of gold solution at 50, 100, 500, and 1,000 µM were prepared. Pulse electrodeposition was conducted in 0.5 M sulphuric acid (H_2SO_4), with various concentrations of gold(III) chloride solution in a three-electrode electrochemical cell. The prepared TNT substrate was used as the working electrode, while a platinum rod was used as the counter electrode and an Ag/AgCl as the reference electrode. The deposition was conducted with a fixed duty cycle of 75% at an applied potential of −0.4 V for 20 minutes. Subsequently, the resulting sample was rinsed with DI water and dried in air. Then, it was kept in a desiccator before proceeding with further characterisation.

Photoelectrochemical (PEC) test of gold deposited titania nanotube (AuTNT)

The PEC performance of the AuTNT was evaluated using a standard three-electrode cell connected to a potentiostat (AUTOLAB). The prepared AuTNT served as the working electrode, while a Pt wire was used as the counter electrode and an Ag/AgCl as the reference electrode in a mixed solution of 0.1 M Na_2SO_4 and 2 M C_2H_5OH. The cell was irradiated with a 120 V, 300 W halogen lamp, which acted as the visible light source *via* a quartz window. The irradiation was chopped intermittently at 20 s intervals to obtain both the dark and photocurrent readings in a single experiment.

Characterisation of AuTNT

The crystalline structure of AuTNT was determined using X-ray diffraction (XRD, Shimadzu D6000), with Cu K_α radiation (λ = 1.5406Å), operating at 30 kV and 40 mA. The surface morphology of the AuTNT substrate was studied using the Field Emission Scanning Electron Microscope (FESEM) (Zeiss, SUPRA 40 VP, Germany). Energy dispersive analysis of X-rays (EDX) was performed on Carl Zeiss Field Emission Scanning Microscope attached with Oxford INCA Energy 200 EDX to determine the elemental composition of the AuTNT samples.

Results and Discussion

Titanium dioxide nanotubes were prepared *via* electrochemical anodization of titanium in a standard two-electrode system. The oxide formation upon anodization and oxide dissolution by fluoride ions (F^-) would lead to the formation of the self-organised TiO_2 nanotubes [7, 8, 9]. TiO_2 layer was grown via electric field oxidation and chemical dissolution. The accumulation of electric charges at the interface between TiO_2 and Ti caused the Ti^{4+} to disrupt the TiO_2 layer, and eventually form nanoporous structures. Subsequently, the thickness of the TiO_2 layer would increase due to electric field oxidation [10] and chemical dissolution. The growth of the nanotubes involves the steps shown in equations 1-5:

$$Ti \rightarrow Ti^{4+} + 4e^- \quad (1)$$

$$H_2O \rightarrow 2H^+ + O^{2-} \quad (2)$$

$$Ti^{4+} + 2O^{2-} \rightarrow TiO_2 \quad (3)$$

$$NH_4F \rightarrow NH_4^+ + F^- \quad (4)$$

$$TiO_2 + 6F^- + 4H^+ \rightarrow [TiF_6]^{2-} + 2H_2O \quad (5)$$

Gold deposited titania nanotubes were prepared *via* pulsed electrodeposition, with a fixed duty cycle of 75% and applied potential of –0.4 V for 20 minutes. The effect of different Au solution concentrations on the morphology of TNT was determined using a field emission scanning electron microscope (FESEM). Figure 2 shows the morphology of AuTNT substrates prepared in different concentrations of gold solution; 50, 100, 500, and 1,000 µM, while bare TNT were used as the control. Based on the figure, the resulting nanotubes have an average diameter of 90-110 nm, and no discernible changes were observed on the size and diameter of the nanotubes upon deposition of Au nanoparticles.

However, upon deposition, the average size of the gold nanoparticles was found to increase with increasing gold solution concentration. The average nanoparticle size at 50 µM was 24 nm, at 100 µM was 40 nm, at 500 µM was 78-95 nm, and at 1,000 µM, the average nanoparticle size was 100-150 nm. The gold nanoparticles had increased in size because as the concentration of Au increases, the amount of Au nanoparticles had also increased. Thus, more Au nanoparticles were deposited onto TNT nanotubes, which tended to stack up on one another and produced larger sized nanoparticles. Based on Figure 2, small and round gold nanoparticles were obtained at a concentration range between 50 and 100 µM. It can also be seen that small amounts of gold nanoparticles were randomly distributed on the nanotubes at these concentrations. At 500-1,000 µM, bigger sized gold nanoparticles were observed to be deposited onto the nanotubes. Meanwhile, some of the smaller nanoparticles can be seen entering the TiO_2 nanotubes. In addition, the gold nanoparticles also appeared to be stacking up on one another, producing a big lump of gold deposit on the surface of the nanotubes. This indicates that gold nanoparticles were present on the TNT. This observation is supported by the EDX analysis, as will be discussed later.

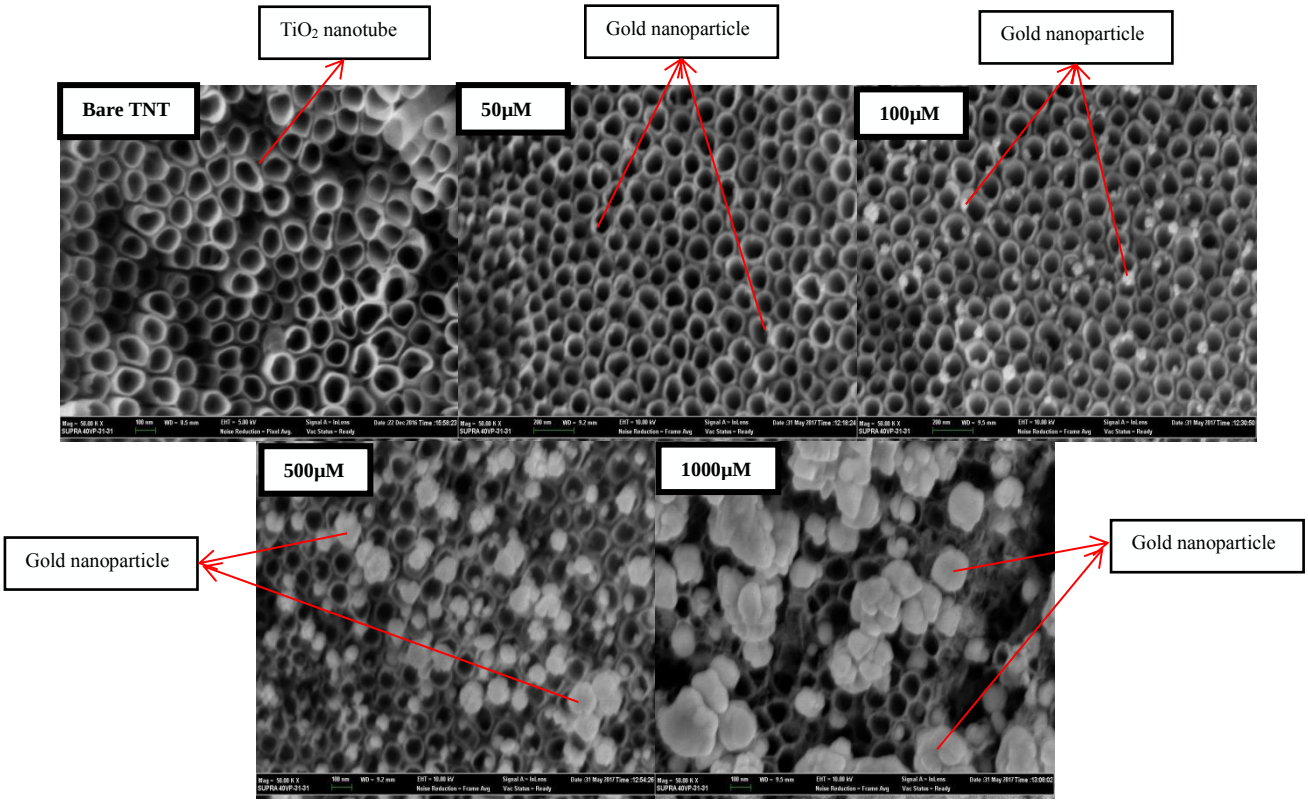


Figure 2. Morphology of AuTNT samples prepared with different concentrations of gold solution

Table 1 shows the elemental composition of AuTNT samples prepared using different concentrations of Au solution, with a bare TNT substrate as the reference. As expected, the amount of Au nanoparticles had increased with increasing gold solution concentration. From the table, only a small amount of gold nanoparticles was obtained using 50 µM and 100 µM gold solutions, with atomic percentage of 0.05% and 0.18%, respectively. At 500 µM, 3.70% of Au was detected, and the highest amount of gold nanoparticles at 31.19% was obtained using 1,000 µM. Higher concentrations of Au had provided more Au particles to be reduced and deposited onto the TiO_2 nanotubes. In addition, the presence of titanium and oxygen atoms were also confirmed using EDX. Titanium and oxygen atoms originated from the titanium foils and the nanotubes that formed on the titanium layer. No other impurities were detected for all AuTNT samples.

Table 1. Elemental composition of bare TNT and AuTNT samples

Element	Atomic %				
	Bare TNT	**50 µM**	**100 µM**	**500 µM**	**1,000 µM**
Ti	48.67	33.46	37.47	30.43	31.38
O	56.33	66.48	62.35	65.86	37.43
Au	ND	0.05	0.8	3.70	31.19

ND – not detected

The crystalline structure of the AuTNT was also studied and determined using XRD and the XRD patterns are shown in Figure 3. The XRD patterns are for the bare TiO_2 substrate, as-anodized TiO_2 substrate, calcined bare TiO_2 substrate, and AuTNT samples prepared with various Au concentrations. All substrates showed Ti peaks at 2θ = 38.5°, 35.3°, 40.3°, 53.2°, 70.8°, 76.40°, and 82.9° corresponding to the (100), (002), (101), (102), (103), (112), and (004) planes, respectively (JCPDS 00-044-1294). The bare TiO_2 and the as-anodized TNT showed similar XRD patterns, indicating that the as-anodized TNT were amorphous in nature. Upon calcination, anatase peaks at 2θ = 25.5° and 48.3° were observed, which corresponded to the (101) and (200) planes, respectively (JCPDS 00-021-1272), as the amorphous TNT began to crystallize. Upon deposition, Au peaks can be observed at 2θ = 44.6° and 65.3°, which corresponded to the (111) and (220) planes, respectively (JCPDS 00-004-0784). However, new Au peaks at 2θ = 44.6° and 65.3° were only observed for AuTNT samples synthesised with 500 µM and 1,000 µM gold solutions. This could be due to the presence of higher amount of gold nanoparticles at higher concentrations compared with at lower concentrations. No peak shift was observed for anatase phase at 2θ = 25.5° for all AuTNT samples, revealing that Au has not been incorporated into the TiO_2 lattice.

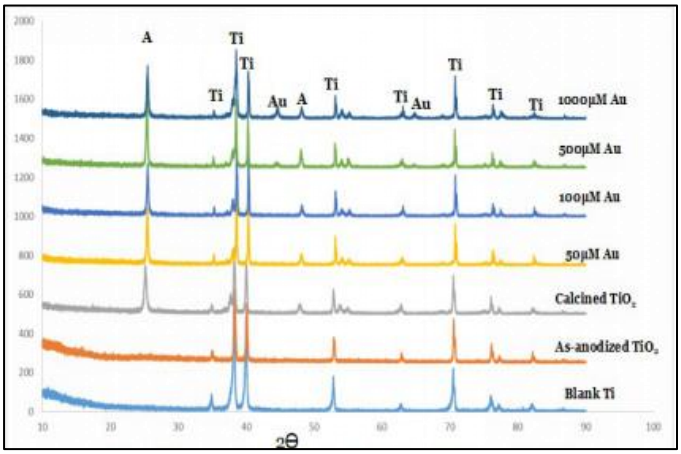


Figure 3. XRD patterns of AuTNT samples with different concentrations of gold solution

The effect of Au deposition on the photoactivity of AuTNT samples was measured using the photoelectrochemical test. In this study, the photocurrent responses were measured under halogen lamp radiation with fixed bias potential. The photoconversion efficiency, Ƞ(%), was measured using equation 6:

$$\eta = \frac{I_o(1.23 - V_{bias})}{J_{light}} \tag{6}$$

where I_o is the photocurrent density (A/m^2), 1.23 V is the theoretical potential required for water splitting, V_{bias} is the applied external potential (V), and J_{light} is the light irradiance (W/m^2). The efficiency of the gold deposited titania nanotubes was calculated and recorded in Figure 4. Upon illumination of light, prompt generation of photocurrent can be seen on both bare TiO_2 and AuTNT electrodes.

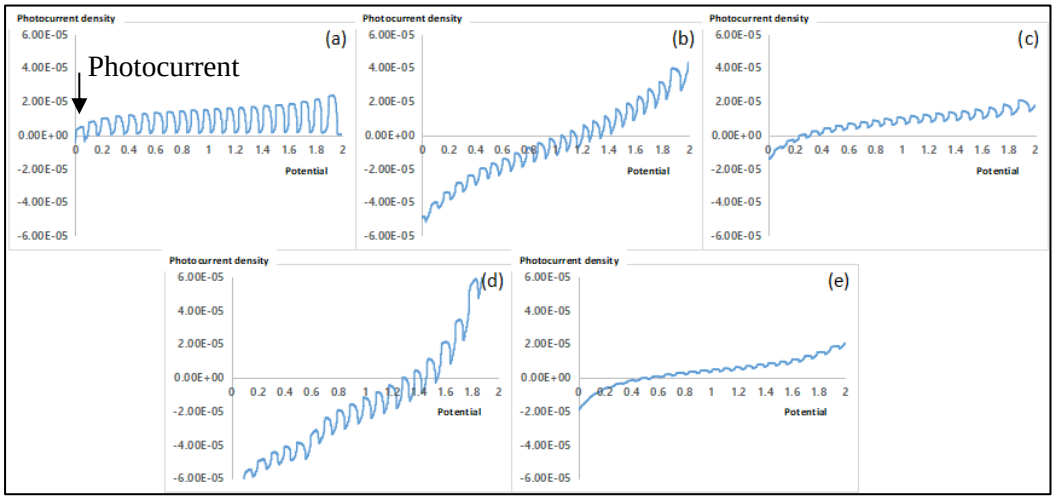


Figure 4. Photocurrent density spectra: (a) bare TNT and AuTNT samples, prepared using different concentrations: (b) 50 µM, (c) 100 µM, (d) 500 µM, and (e) 1,000 µM Au solution

Based on Figure 4, upon illumination, a sharp increase of photocurrent can be observed due to the charge generated by the gold nanoparticles. The charge was transferred to the TNT before it reached a steady value and a maximum charge transfer. The current was also seen to drop almost instantaneously when the light was turned off. Upon light illumination, electron-hole pairs were generated by the electric field in the space-charge region between the semiconductor and the electrolyte. This affected the bending of the conduction and valence band edges at the semiconductor surface and promoted the supply of free carriers to the electrode. The gold nanoparticles provided more free charges, which included both electrons and holes that improved the photocurrent of the bare TNT.

TiO_2 nanotubes possess the properties of an n-type semiconductor. Figure 4 shows that bare TNT can produce anodic current as an n-type semiconductor. However, upon the deposition of gold nanoparticles on the nanotubes, the prepared AuTNT sample began to produce cathodic current, which began with the anodic current. This observation suggests that the AuTNT sample also possessed the properties of a p-type semiconductor. It also indicates that the AuTNT sample has a combination of the n-type and p-type semiconductor as it was able to produce both anodic and cathodic currents.

The efficiency (Ƞ(%)) of all bare TNT and AuTNT samples were calculated from the PEC results. The highest efficiency was measured for TNT sample deposited with 500 µM Au solution at 0.64% compared with bare TNT at 0.42%, and other concentrations of Au solution. Au nanoparticles could have acted as the active sites that helped to increase the absorption in the visible spectrum. Hence, the photogenerated carrier transfer and separation were enhanced due to the plasmon resonance effect [8, 11]. Furthermore, the enhanced photocurrent can be attributed to

the enhanced light absorption and the potential difference generated on the metal-semiconductor interface due to the deposited Au. The potential difference accelerates the separation of the photogenerated hole-electron pairs, resulting in the enhanced photocurrent of the AuTNT sample [12]. However, when the concentration of Au solution was increased to 1,000 µM, the efficiency had decreased and had even produced a lower efficiency than the bare TNT. This result may be due to the larger sized Au nanoparticles deposited on the TiO_2 nanotubes, which blocked the overall surface of the nanotubes.

Conclusion

In this study, 500 µM Au had resulted in the highest photocurrent efficiency (Ƞ% = 0.64), which was higher than the efficiency of the bare TiO_2 (Ƞ% = 0.42). This study has proven that even a small amount of gold nanoparticles would be able to increase and enhance the photocurrent efficiency of titania nanotubes. However, when the concentration of Au was increased, the photocurrent efficiency had decreased and even produced a lower percentage of efficiency compared to the bare TNT. Furthermore, the pH of Au solution, duty cycle, and deposition duration of gold nanoparticles on titania nanotubes can be varied in the future to obtain a better photocurrent efficiency.

Acknowledgment

This material is based on a work supported by the Ministry of Higher Education (MOHE) Malaysia through FRGS grant number: 600-RMI/FRGS 5/3 (036/2017). The authors would also like to acknowledge the Faculty of Applied Sciences, Universiti Teknologi MARA (UiTM) for the facilities provided.

References

1. Chen, Z., Dinh, H. N. and Miller, E. (2013). Photoelectrochemical water splitting. *SpringerBriefs in Energy, New York*: pp. 49-61.
2. Ampelli, C., Centi, G., Passalacqua, R. and Perathoner, S. (2016). Electrolyte-less design of PEC cells for solar fuels: prospects and open issues in the development of cells and related catalytic electrodes. *Catalysis Today*, 259: 246-258.
3. Xu, F., Bai, D., Mei, J., Wu, D., Gao, Z., Jiang, K. and Liu, B. (2016). Enhanced photoelectrochemical performance with in-situ Au modified TiO_2 nanorod arrays as photoanode. *Journal of Alloys and Compounds*, 688: 914-920.
4. Xu, F., Mei, J., Zheng, M., Bai, D., Wu, D., Gao, Z. and Jiang, K. (2017). Au nanoparticles modified branched TiO_2 nanorod array arranged with ultrathin nanorods for enhanced photoelectrochemical water splitting. *Journal of Alloys and Compounds*, 693: 1124-1132.
5. Luo, J., Li, D., Yang, Y., Liu, H., Chen, J. and Wang, H. (2016). Preparation of Au/reduced graphene oxide/hydrogenated TiO_2 nanotube arrays ternary composites for visible-light-driven photoelectrochemical water splitting. *Journal of Alloys and Compounds*, 661: 380-388.
6. Mohite, V. S., Mahadik, M. A., Kumbhar, S. S., Hunge, Y. M., Kim, J. H., Moholkar, A. V. and Bhosale, C. H. (2015). Photoelectrocatalytic degradation of benzoic acid using Au doped TiO_2 thin films. *Journal of Photochemistry and Photobiology B: Biology*, 142: 204-211.
7. Yin, Y., Liu, E., Li, H., Wan, J., Fan, J., Hu, X. and Pu, C. (2016). Fabrication of plasmonic Au/TiO_2 nanotube arrays with enhanced photoelectrocatalytic activities. *Ceramics International*, 42(8): 9387-9395.
8. Notarianni, M., Vernon, K., Chou, A., Aljada, M., Liu, J. and Motta, N. (2014). Plasmonic effect of gold nanoparticles in organic solar cells. *Solar Energy*, 106: 23-37.
9. Chin, L. Y., Zainal, Z., Khusaimi, Z. and Ismail, S. S. (2016). Electrochemical synthesis of ordered titania nanotubes in mixture of ethylene glycol and glycerol electrolyte. *Malaysian Journal of Analytical Sciences*, 20(2): 373-381.
10. Nyein, N., Tan, W. K., Kawamura, G., Matsuda, A. and Lockman, Z. (2017). TiO_2 nanotube arrays formation in fluoride/ethylene glycol electrolyte containing LiOH or KOH as photoanode for dye-sensitized solar cell. *Journal of Photochemistry and Photobiology A: Chemistry*, 343: 33-39.
11. Pandikumar, A., Lim, S. P., Jayabal, S., Huang, N. M., Lim, H. N. and Ramaraj, R. (2016). Titania@ gold plasmonic nanoarchitectures: An ideal photoanode for dye-sensitized solar cells. *Renewable and Sustainable Energy Reviews*, 60: 408-420.

12. Moakhar, R. S., Masudy-Panah, S., Jalali, M., Goh, G. K. L., Dolati, A., Ghorbani, M. and Riahi-Noori, N. (2016). Sunlight driven photoelectrochemical light-to-electricity conversion of screen-printed surface nanostructured TiO_2 decorated with plasmonic Au nanoparticles. *Electrochimica Acta*, 219: 386-393.

Malaysian Journal of Analytical Sciences, Vol 22 No 5 (2018): 758 - 767
DOI: https://doi.org/10.17576/mjas-2018-2205-03

MALAYSIAN JOURNAL OF ANALYTICAL SCIENCES
Published by The Malaysian Analytical Sciences Society
ISSN 1394 - 2506

SYNTHESIS, CHARACTERISATION AND EFFECT OF TEMPERATURE ON CORROSION INHIBITION BY THIOSEMICARBAZONE DERIVATIVES AND ITS TIN(IV) COMPLEXES

(Sintesis, Pencirian dan Kesan Suhu Ke atas Perencatan Kakisan oleh Ligan Terbitan Tiosemikarbazon dan Kompleks Timah(IV))

Nur Nadira Hazani[1,2], Nur Nadia Dzulkifli[1]*, Sheikh Ahmad Izaddin Sheikh Mohd Ghazali[1], Yusairie Mohd[2], Yang Farina[3], Nurul 'Ain Jamion[1]

[1]*Faculty of Applied Sciences,*
Universiti Teknologi MARA, Kampus Kuala Pilah, 72000 Kuala Pilah, Negeri Sembilan, Malaysia
[2]*Faculty of Applied Sciences,*
Universiti Teknologi MARA, 40450 Shah Alam, Selangor, Malaysia
[3]*Faculty of Science and Technology,*
Universiti Kebangsaan Malaysia, 43600 UKM Bangi, Selangor, Malaysia

**Corresponding author: nurnadia@ns.uitm.edu.my*

Received: 29 August 2017; Accepted: 5 August 2018

Abstract

Thiosemicarbazone derivatives and its tin(IV) complexes used in this study were 2-acetylpyridine 4-ethyl-3-thiosemicarbazone (HAcETSc), 2-acetylpyridine 4-methyl-3-thiosemicarbazone (HAcMTSc), 2-acetylpyridine 4-ethyl-3-thiosemicarbazone dichlorophenyltin (Sn(HAcETSc)PhenCl$_2$), and 2-acetylpyridine 4-methyl-3-thiosemicarbazone dichlorophenyltin (Sn(HAcMTSc)PhenCl$_2$). All these title compounds were characterised using an elemental analyser, Fourier-transform infrared-attenuated total reflectance spectroscopy (FTIR-ATR), ultraviolet-visible spectroscopy (UV-Vis), and nuclear magnetic resonance (NMR). The efficiency of the synthesised compounds as a corrosion inhibitor of mild steel in 1.0 M HCl was investigated using weight loss technique at different concentrations, 1, 2, and 3 mM, and at a temperature range of 30–60 °C. The thiosemicarbazone ligand and its tin(IV) complexes affirmed the hypothesis where the inhibitor efficiency tends to increase as the inhibitor concentration increases, indicating their potential use as a corrosion inhibitor for mild steel. Moreover, inhibitor efficiency decreases when temperature increases.

Keywords: thiosemicarbazone, corrosion inhibitor, temperature, mild steel

Abstrak

Terbitan tiosemikarbazon dan kompleks timah(IV) yang digunakan dalam kajian ini adalah 2-asetilpiridina 4-etil-3-tiosemikarbazon (HAcETSc), 2-asetilpiridina 4-metil-3-tiosemikarbazon (HAcMTSc), 2-asetilpiridina 4-etil-3-tiosemikarbazon dikloridastanum (Sn(HAcETSc)PhenCl$_2$) and 2-asetilpiridina 4-metil-3-tiosemikarbazon dikloridastanum (Sn(HAcMTSc)PhenCl$_2$). Kesemua sebatian telah dicirikan menggunakan analisis unsur, spektroskopi inframerah transformasi Fourier-pantulan keseluruhan dikecilkan (FTIR-ATR), spektroskopi ultralembayung-sinar nampak (UV-Vis) dan resonans magnetik nuklear (NMR). Kecekapan sebatian yang telah disintesis dikaji sebagai perencat kakisan terhadap keluli lembut dalam 1.0 M HCl dengan kepekatan berbeza, 1, 2, dan 3 mM, serta suhu antara 30-60 °C menggunakan kaedah kesusutan berat. Ligan tiosemikarbazon dan kompleks timah(IV) membuktikan hipotesis di mana kecekapan perencat cenderung untuk meningkat apabila kepekatan perencat meningkat, menunjukkan ia berpotensi untuk digunakan sebagai perencat kakisan terhadap keluli lembut. Tambahan lagi, kecekapan perencat menurun apabila suhu meningkat.

Kata kunci: tiosemikarbazon, perencatan kakisan, suhu, keluli lembut

Introduction

Corrosion inhibitor is one of the methods used to prevent corrosion [1]. Inhibitors are compounds used in low concentration and applied in an aggressive environment to protect or slow down corrosion [2, 3]. Finding new corrosion inhibitors, which have high efficiency, are easy-to-make, and cheap, have attracted many researchers' attention [4]. In the industrial sector, building surface corrosion occurs from common activities such as acid pickling, acid descaling, and industrial acid cleaning, where an acid solution, such as hydrochloric acid, is used to remove undesirable scale or rust. This activity causes metal dissolution due to the attack of the aggressive media. A corrosion inhibitor containing heteroatoms of nitrogen (N), sulphur (S), and oxygen (O), as well as an aromatic group in its structure, is considered effective and has the potential as a corrosion inhibitor [5, 6]. Through adsorption process, the inhibitor forms a protective layer and offers a barrier from corrosive attack on the metal surface [7, 8].

Thiosemicarbazone (TSC) derivatives and tin complexes have been reported to be potential corrosion inhibitors due to the presence of nitrogen and sulphur atoms, which could increase inhibition efficiency [9]. Furthermore, tin complexes with thiosemicarbazone derivatives have received a great attention as a corrosion inhibitor, since organotin is recognised for its biocidal behaviour, friction and wear reducing properties, as well as corrosion-inhibiting characteristics [10,11]. Therefore, this study aims to synthesise and characterise new compounds for their expected anticorrosion activity. The synthesised ligands and complexes were tested as potential corrosion inhibitors in 1.0 M HCl. The compounds under investigation are listed in Table 1.

Table 1. Compounds under investigation

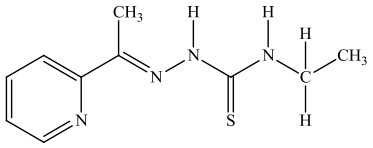
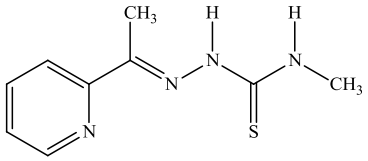
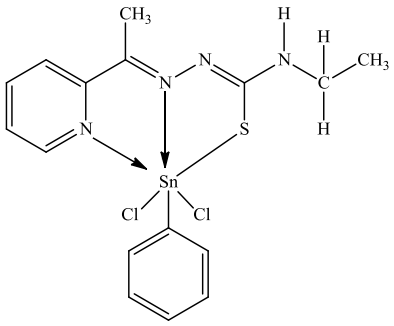
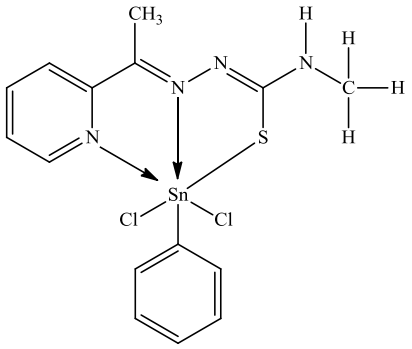
Inhibitor	Abbreviation	Structure	Molar Mass (g/mol)
2-acetylpyridine 4-ethyl-3-thiosemicarbazone	HAcETSc		222
2-acetylpyridine 4-methyl-3-thiosemicarbazone	HAcMTSc		208
2-acetylpyridine 4-ethyl-3-thiosemicarbazone dichlorophenyltin	Sn(HAcETSc)PhenCl$_2$		486

Table 1 (cont'd). Compounds under investigation

Inhibitor	Abbreviation	Structure	Molar Mass (g/mol)
2-acetylpyridine 4-methyl-3-thiosemicarbazone dichlorophenyltin	Sn(HAcMTSc)PhenCl_2		472

Materials and Methods

Material and measurement

All chemicals used were commercially purchased without further purification. The melting point was measured using a melting point apparatus (model SMP10 Stuart) and was taken in an open capillary tube. The elemental analysis of synthesised compounds was performed using CHNS/O Model Fision EA 1180 and Thermo Finnigan Flash EA 1112 Series. Meanwhile, the infrared spectra were recorded on Fourier-transform infrared-attenuated total reflectance (FTIR-ATR) Perkin Elmer spectrophotometer. The electronic absorption spectra were recorded on a PG Instrument T80/T80+ spectrophotometer in the 200–600 nm region using dimethyl sulfoxide (DMSO) as a solvent. ^{1}H and ^{13}C NMR spectra were measured on a Bruker spectrophotometer using deuterated dimethyl sulfoxide (DMSO-d_6) as a solvent and tetramethylsilane as an internal reference.

Synthesis of ligands

An ethanoic solution of 2-acetylpyridine (1 mmol) and ethanoic solution of 4-ethyl-3-thiosemicarbazide or 4-methyl-3-thiosemicarbazide (1 mmol) were mixed together, and then a few drops of acetic acid were added to the mixture. The mixture was refluxed for 2 h with a constant stirring rate of 400 rpm at a temperature between 60–70 °C. The product was cooled after 2 h and kept at room temperature to obtain a crystalline product. The crystalline product formed was filtered, washed with cold ethanol, and dried over silica gel.

Synthesis of tin(IV) complexes

The synthesised ligand (1 mmol) was dissolved in ethanol and the metal salt, phenyltin trichloride (1 mmol), was dissolved in distilled water. The metal salt was added dropwise to the ethanoic solution ligand with constant stirring at 400 rpm. The reaction mixture was continuously stirred for 4 hours. The precipitate was then filtered and washed with cold ethanol. The precipitate formed was left to dry over silica gel. The weight of the precipitate was recorded.

Corrosion inhibition study - weight loss technique

The aggressive solution, 1 M hydrochloric acid (HCl), 37% of analytical grade was prepared *via* dilution with distilled water. The inhibitor with concentrations of 1, 2, and 3 mM were also prepared by diluting the stock solution, 1 M HCl. The determination of weight loss on mild steel was tested for 24 hours at 30 °C. The experiment was conducted in triplicate and the average mass was calculated. The experiment was repeated at different temperatures of 40, 50, and 60 °C.

Results and Discussion

Physical measurement

The physical characteristics of the synthesised ligands and complexes, namely yield percentage, colour, melting point, molar conductivity, and elemental percentage are shown in Table 2. The complexes have a higher melting point compared to the ligands. The molar conductivities for both complexes are in the range of 4.0–12.5 $Scm^2.mol^{-1}$, which indicates non-electrolyte behaviour [12]. The elemental analysis of calculated and experimental data is in good agreement.

Table 2. Physical characteristics of synthesised ligands and complexes

Compound	Percentage Yield (%)	Colour	Melting Points (^oC)	Molar Conductivity ($Scm^2.mol^{-1}$)	Elemental Analysis (Experimental) (%)			
					C	H	N	S
HAcETSc	88.06	Light yellow	127-130	-	54.05 (53.34)	6.31 (7.41)	25.23 (24.50	14.42 (14.67)
HAcMTSc	71.61	Light yellow	176-177	-	51.56 (51.92)	5.88 (5.77)	28.06 (26.92)	14.55 (15.38)
$Sn(HAcETSc)PhenCl_2$	63.37	Yellow	232-235	7.5	39.51 (39.94)	3.70 (3.81)	11.52 (11.91)	6.58 (6.34)
$Sn(HAcMTSc)PhenCl_2$	56.14	Yellow	242-245	5.2	38.14 (37.59)	3.39 (3.39)	11.86 (11.83)	6.78 (6.28)

Infrared spectra

The tentative assignments to the significant IR spectral bands of ligands and complexes are presented in Table 3 and Table 4, respectively. The infrared spectra for compounds HAcETSc and $Sn(HAcETSc)PhenCl_2$ are shown in Figure 1, whereas the infrared spectra for compounds HAcMTSc and $Sn(HAcMTSc)PhenCl_2$ are shown in Figure 2. Thiosemicarbazone ligand contains thiomide, a C=S functional group, which is known to exist as a thione-thiol tautomerism. Nonetheless, the absence of S-H stretching band of 2500–2600 cm^{-1} indicates that the ligand is in a thione form [13]. Several significant changes in spectral complexes and ligands suggest the coordination of TSC ligands to metal ion through azomethine nitrogen and thiolate sulphur. In the spectra of ligands, the stretching bands at 3210 and 3240 cm^{-1} for compounds HAcETSc and HAcMTSc, respectively, correspond to the ν(N-H) group that disappeared, and a new stretching band appeared in the spectra of complexes, which is attributed to ν(C=N) stretching band due to thioenolisation of C=S [14].

Moreover, changes can be observed through the shifting of some bands. The shifting of $\nu(C=N_{py})$ stretching band to higher frequency from the spectra of ligand indicates the involvement of pyridine azomethine nitrogen in coordination with metal ion. Besides, ν(C=N) observed at 1527 and 1537 cm^{-1} in both ligands shifted to 1504 and 1557 cm^{-1}, respectively, in the spectra of complexes, indicating that the coordination occurred through azomethine nitrogen.

The stretching bands due to ν(C=S) at 1084 cm^{-1} [compound HAcETSc] and 1074 cm^{-1} [compound HAcMTSc] disappeared in the spectra of complexes and new stretching bands, C-S appeared at 1061 cm^{-1} [compound $Sn(HAcETSc)PhenCl_2$] and 1047 cm^{-1} [compound $Sn(HAcMTSc)PhenCl_2$], indicating that the coordination occurred through thiolate sulphur after enolisation of C=S functional group and followed by deprotonation on sulphur [15]. Nevertheless, the new stretching bands at 310–360 cm^{-1}, 258–327 cm^{-1}, and 330–354 cm^{-1} were assigned to ν(Sn-N), $\nu(Sn-N_{py})$, and ν(Sn-S), respectively, and the stretching band at 229–270 cm^{-1} range was assigned to ν(Sn-Cl) [16]. The existence of these new stretching bands indicates the coordination of ligands to metal ion.

Table 3. IR spectral data of the ligand and complexes (cm^{-1})

Compound	**ν(N-H)**	**ν(C=N_{py})**	**ν(C=N)**	**ν(N-N)**	**ν(C-N)**	**ν(C=S)**	**ν(C-S)**
HAcETSc	3349, 3210	1580	1527	1297	1221	1084	-
HAcMTSc	3288, 3240	1578	1537	1295	1230	1074	-
Sn(HAcETSc)$PhenCl_2$	3372	1601	1504, 1587	1283	1247	-	1061
Sn(HAcMTSc)$PhenCl_2$	3297	1601	1557, 1587	1290	1256	-	1047

Table 4. Far-IR spectral data of the complexes (cm^{-1})

Compound	**ν(Sn-N)**	**ν(Sn-S)**	**ν(Sn-N_{py})**	**ν(Sn-Cl)**
Sn(HAcETSc)$PhenCl_2$	331	354	289	267
Sn(HAcMTSc)$PhenCl_2$	328	357	289	265

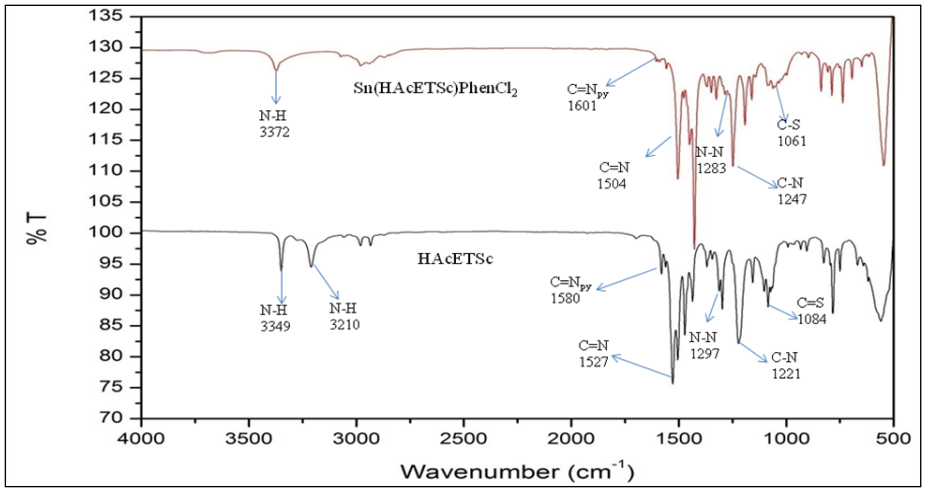


Figure 1. Infrared spectra for compound HAcETSc and Sn(HAcETSc)$PhenCl_2$

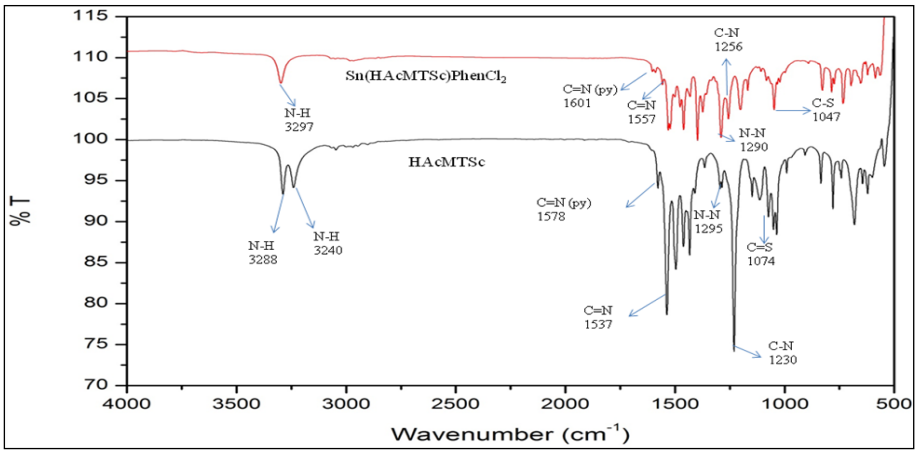


Figure 2. Infrared spectra for compound HAcMTSc and Sn(HAcMTSc)$PhenCl_2$

Electronic spectra

The UV-Visible (UV-Vis) absorption spectra for compounds HAcETSc and Sn(HAcETSc)PhenCl$_2$ are shown in Figure 3, whereas the UV-Vis absorption spectra for compounds HAcMTSc and Sn(HAcMTSc)PhenCl$_2$ are shown in Figure 4. For both ligands, there is only one absorption peak at 320 nm and assigned to n→π* transition. This band corresponds to the C=S and C=N groups. The absorption peak attributed to π→π* transition might not be observed in the ligand spectrum as n→π* transition in C=S and C=N has stronger absorption and might cover π→π* transition [17]. Upon complexation, two absorption peaks were observed at 315 and 400 nm [compound Sn(HAcETSc)PhenCl$_2$], as well as at 305 and 405 nm [compound Sn(HAcMTSc)PhenCl$_2$], which were appointed to n→π* transition and the ligand to metal charge transfer (LMCT), respectively. Moreover, both complexes underwent a hypsochromic shift. The spectra shifting shows the donation of electron lone pair from N or S to the metal ion [18].

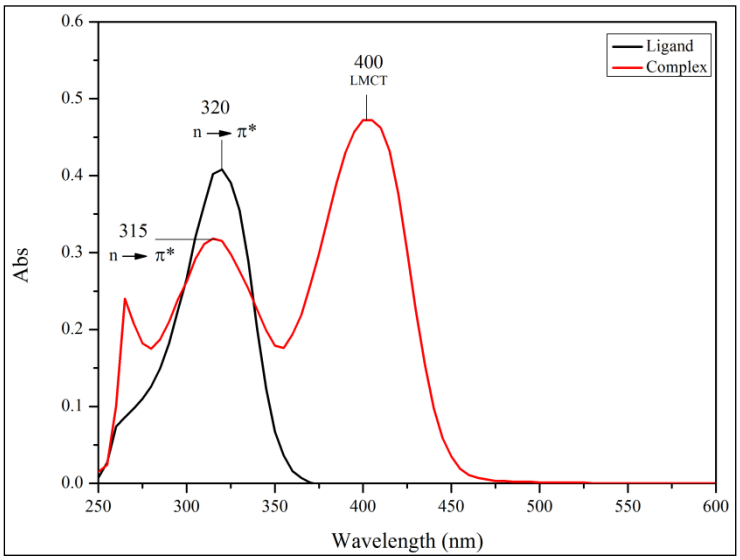


Figure 3. UV-Vis absorption spectra for compound HAcETSc and Sn(HAcETSc)PhenCl$_2$

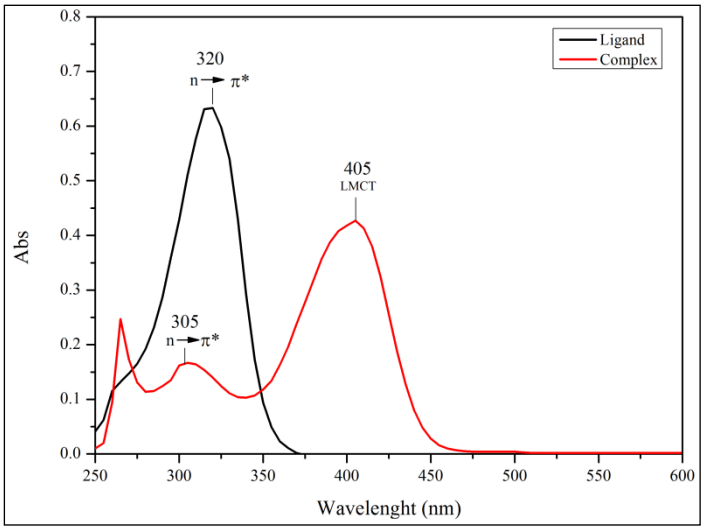


Figure 4. UV-Vis absorption spectra for compound HAcMTSc and Sn(HAcMTSc)PhenCl$_2$

^{1}H and ^{13}C NMR spectra

^{1}H and ^{13}C NMR spectral data of the ligands and complexes are tabulated in Table 5 and 6, respectively. For ligands HAcETSc and HAcMTSc, N(1)H signal appeared as a triplet at 8.68 and 8.62 ppm, respectively. Meanwhile, N(2)H signal appeared as a singlet at 10.25 ppm for both ligands. Upon complexation, the peak of N(1)H shifted downfield with a small shifting value and N(2)H signal disappeared due to deprotonation of the ligands when coordinated to the metal ion. Furthermore, CH_3-C=N signal of complexes showed about 0.4 ppm shift downfield as compared to the ligand, which revealed the involvement of an azomethine nitrogen in coordination to the metal ion. Multiplets signal were found for aromatic ring proton. The aromatic ring proton signals shifted downfield upon complexation with metal [19].

In ^{13}C NMR, the signal of C=S and C=N groups shifted to the upfield region in the complexes as compared to the ligands, which proved that the coordination occurred through N=C-S^- and nitrogen atom of pyridine group to the metal ion. Moreover, the coordination to metal ion occurred *via* an azomethine nitrogen was proven when the CH_3-C=N signal of the complexes shifted to downfield region, in comparison with the ligands. There were extra signals present, which are represented as a phenyl ring [20].

Table 5. ^{1}H NMR spectral data (ppm) of the ligands and complexes

Compound	Chemical shift, δ (ppm)					
	N(1)H	**N(2)H**	**-CH_3**	**CH_3-C=N**	**-CH_2**	**Aromatic**
HAcETSc	8.68	10.25	1.16	2.38	3.64	7.36 - 8.58
HAcMTSc	8.62	10.25	3.05	2.38	-	7.37 - 8.59
Sn(HAcETSc)PhenCl_2	8.70	-	1.22	2.78	3.55	7.52 – 8.70
Sn(HAcMTSc)PhenCl_2	8.68	-	3.02	2.79	-	7.51 – 8.68

Table 6. ^{13}C NMR spectral data (ppm) of the ligands complexes

Compound	Chemical shift, δ (ppm)					
	C=S	**C=N**	**-CH_3**	**CH_3C=N**	**-CH_2**	**Phenyl Ring**
HAcETSc	178.10	155.17	14.93	12.59	39.01	121.26 - 148.93
HAcMTSc	179.18	155.22	31.63	12.56	-	121.24 - 148.93
Sn(HAcETSc)PhenCl_2	168.76	135.77	15.05	14.46	37.80	142.24 – 144.87, 125.91 – 130.71
Sn(HAcMTSc)PhenCl_2	169.43	135,76	29.63	15.10	-	142.52 – 144.86, 125.96 – 130.73

Corrosion inhibition study

The inhibitor efficiency of mild steel in 1 M HCl at different temperatures and different concentrations was investigated by weight loss method, in the presence and absence of inhibitors. The values of inhibitor efficiency are given in Table 7. The results showed that the inhibition efficiency increased when the concentration of inhibitor increased. Apart from that, the title compounds showed a decreasing efficiency at higher temperature (60 °C). The results were different at certain temperatures for each compound. For instance, at concentration 3 mM, compound HAcETSc had better efficiency at 50 °C while other compounds worked better at 40 °C.

Table 7. Inhibitor efficiency at different concentrations in 1M HCl at different temperatures

Concentration	Compounds	Inhibitor Efficiency (%)			
		30 °C	40 °C	50 °C	60 °C
3 mM	HAcETSc	84.74	91.09	96.08	84.80
	HAcMTSc	84.32	95.91	83.80	80.48
	Sn(HAcETSc)$PhenCl_2$	86.44	89.88	81.61	73.32
	Sn(HAcMTSc)$PhenCl_2$	94.78	95.98	95.46	87.33
2 mM	HAcETSc	84.32	88.94	85.27	84.10
	HAcMTSc	78.67	78.00	81.06	76.10
	Sn(HAcETSc)$PhenCl_2$	79.52	87.32	71.84	40.95
	Sn(HAcMTSc)$PhenCl_2$	85.03	94.57	92.30	53.58
1 mM	HAcETSc	81.92	77.48	82.93	67.61
	HAcMTSc	42.51	66.03	72.32	61.56
	Sn(HAcETSc)$PhenCl_2$	54.52	80.14	57.58	34.76
	Sn(HAcMTSc)$PhenCl_2$	81.53	84.38	91.41	45.22

At 30 °C, the highest percentage of inhibitor efficiency is as follows: Sn(HAcMTSc)$PhenCl_2$ > Sn(HAcETSc) $PhenCl_2$ > HAcETSc > HAcMTSc. The efficiency for compound Sn(HAcMTSc)$PhenCl_2$ at 30 °C was 94.78%; the value increased slightly at 40 °C and started to decrease until 60 °C with the efficiency of 87.33%. Similarly, for compounds HAcMTSc and Sn(HAcETSc)$PhenCl_2$, its efficiency increased at 40 °C but became less efficient with increasing temperature. For compound HAcETSc, the efficiency kept increasing until the temperature was 50 °C and decreased at 60 °C. Even though the efficiency is low at higher temperature, it is still able to protect mild steel in the acid solution from corroding as compared to the blank of 1 M HCl [21].

Generally, the effects of a compound to provide better protection on mild steel surface are due to the presence of electron pairs, which are sulphur and nitrogen atoms, π-electrons on the aromatic rings, molecular size, and the formation of metallic complexes [22, 23]. Hence, it can be recommended that compound Sn(HAcMTSc)- $PhenCl_2$ is efficient in preventing mild steel dissolution as compared to other studied compounds

Conclusion

The thiosemicarbazone derivative ligands derived from 2-acetylpyridine and tin(IV) complexes have been successfully synthesised through condensation process. The ligands and complexes were characterised by using CHNS, FTIR, UV-Vis, and NMR. From the characterisation of the complexes, it has been determined that ligand acts as tridentate to metal ions, which coordinates through azomethine nitrogen and thiolate sulphur. The outcome for the corrosion study showed good inhibitive properties for mild steel corrosion and the inhibitor efficiency increased as the inhibitor concentration increased. For temperature effect, the inhibitor efficiency decreased at high temperature. This work suggests that the corrosion inhibition study should undergo further study using electrochemical impedance spectroscopy (EIS) and linear polarisation resistance (LPR) to confirm the corrosion efficiency based on the study done using weight loss technique.

Acknowledgement

The authors would like to thank the Faculty of Applied Sciences, Universiti Teknologi MARA, Negeri Sembilan, the Faculty of Science and Technology, Universiti Kebangsaan Malaysia, as well as the Centre of Research and Instrumentation (CRIM) for the research facilities. The authors are also grateful for the research grant from the Ministry of Higher Education with the grant number FRGS/1/2016/STG01/UITM/03/6.

References

1. Xu, B., Liu, Y., Yin, X., Yang, W. and Chen, Y. (2013). Experimental and theoretical study of corrosion inhibit ion of 3-pyridinecarbozalde thiosemicarbazone for mild steel in hydrochloric acid. *Corrosion Science*, 74: 206-213.
2. Dariva, C. and Galio, A. (2014). Corrosion Inhibitors–principles, Mechanisms and Applications. *Developments in Corrosion Protection*, 16: 365-378
3. Obot, I. B., Macdonald, D. D. and Gasem, Z. M. (2015). Density functional theory (DFT) as a powerful tool for designing new organic corrosion inhibitors: Part 1: An overview. *Corrosion Science*, 99: 1-30.
4. Saha, S. K., Ghosh, P., Hens, A., Murmu, N. C. and Banerjee, P. (2015). Density functional theory and molecul ar dynamics simulation study on corrosion inhibition performance of mild steel by mercapto-quinoline schiff ba se corrosion inhibitor. *Physica E: Low-Dimensional Systems and Nanostructures*, 66: 332-341.
5. Goulart, C. M., Esteves-Souza, A., Martinez-Huitle, C. A., Rodrigues, C. J. F., Maciel, M. A. M. and Echevarri a, A. (2013). Experimental and theoretical evaluation of semicarbazones and thiosemicarbazones as organic cor rosion inhibitors. *Corrosion Science*, 67: 281-291.
6. Kassim, K., Kamal, N. K. M. and Fadzil, A. H. (2016). Synthesis, characterization and electochemical studies o f 4-methoxybenzoylthiourea derivatives. *Malaysian Journal of Analytical Sciences*, 20(6): 1311-1317.
7. Yadav, M., Behera, D. and Kumar, S. (2014). Experimental and theoretical studies on corrosion inhibition of m ild steel in hydrochloric acid by thiosemicarbazone of schiff bases. *Canadian Metallurgical Quarterly*, 53(2): 2 20-231.
8. Daoud, D., Douadi, T., Hamani, H., Chafaa, S. and Al-noaimi, M. (2015). Corrosion inhibition of mild steel by two new *s*-heterocyclic compounds in 1 M HCl : Experimental and computational study. *Corrosion Science*, 94 : 21-37.
9. John, S., Jeevana, R., Aravindakshan, K. K. and Joseph, A. (2017). Corrosion inhibition of mild steel by N(4)-s ubstituted thiosemicarbazone in hydrochloric acid media. *Egyptian Journal of Petroleum*, 26(2): 405-412.
10. Rastogi, R. B., Singh, M. M., Singh, K. and Yadav, M. (2011). Organotin dithiobiurets as corrosion inhibitors f or mild steel- dimethyl sulfoxide containing HCl. *African Journal of Pure and Applied Chemistry*, 5(2): 19-33.
11. Kurniasih, H., Nurissalam, M., Iswantoro, B., Afriyani, H., Qudus, H. I., and Hadi, S. (2015). The synthesis, ch aracterization and comparative anticorrosion study of some organotin(IV). *Oriental Journal of Chemistry*, 31(4) : 2377-2383.
12. Rastogi, R. B., Singh, K. and Maurya, J. L. (2012). Synthesis and characterization of organotin(IV) thiobiurets. *Synthesis and Reactivity in Inorganic, Metal-Organic, and Nano-Metal Chemistry*, 42(4): 616–620.
13. Dzulkifli, N. N., Farina, Y. and Yamin, B. M. (2015). Dysprosium(III) isatin 2-methyl-3-thiosemicarbazone : S ynthesis, structural and characterization. *Malaysian Journal of Analytical Sciences*, 19(3): 541-549.
14. Netalkar, P. P., Netalkar, S. P., and Revankar, V. K. (2015). Transition metal complexes of thiosemicarbazone: Synthesis, structures and invitro antimicrobial studies. *Polyhedron*, 100: 215-222.
15. Sampath, K., Sathiyaraj, S., Raja, G. and Jayabalakrishnan, C. (2013). Mixed ligand ruthenium(III) complexes of benzaldehyde 4-methyl-3-thiosemicarbazones with triphenylphosphine/triphenylarsine co-ligands: Synthesis, DNA binding, DNA cleavage, antioxidative and cytotoxic activity. *Journal of Molecular Structure*, 1046: 82–91.
16. Parrilha, G. L., Da Silva, J. G., Gouveia, L. F., Gasparoto, A. K., Dias, R. P., Rocha, W. R., Santos, D. A., Spez iali, N. L. and Beraldo, H. (2011). Pyridine-derived thiosemicarbazones and their Tin(IV) complexes with antif ungal activity against *Candida spp*. *European Journal of Medicinal Chemistry*, 46(5): 1473-1482.
17. Affan, M. A., Wan, F. S., Ngaini, Z. and Shamsuddin, M. (2009). Synthesis, characterization and biological stu dies of organotin(iv) complexes of thiosemicarbazone ligand derived from pyruvic acid: X-ray crystal structure of [Me_2Sn(PAT)]. *Malaysian Journal of Analytical Sciences*, 13(1): 63-72.
18. Venkatesh, K., Rayam, P., Sekhar, K. B. C. and Mukkanti, K. (2016). Synthesis, characterization and biological activity of some new thiosemicarbazide derivatives and their transition metal complexes. *International Journal of Applied Biology and Pharmaceutical Technology*, 7(1): 258-267.
19. Abdalla, O., Farina, Y. and Ibrahim, N. (2015). Synthesis, characterization and antibacterial study of copper(II) complexes of thiosemicarbazones. *Malaysian Journal of Analytical Sciences*, 19(6): 1171-1178.
20. Singh, H. L., Singh, J. B. and Sharma, K. P. (2012). Synthetic, structural, and antimicrobial studies of organotin (iv) complexes of semicarbazone, thiosemicarbazone derived from 4-hydroxy-3- methoxybenzaldehyde. *Resear ch on Chemistry Intermediate*, 38: 53-65.

21. Hashim, N. N. Z. and Kassim, K. (2014). The effect of temperature on mild steel corrosion in 1 M HCl by schif f bases. *Malaysian Journal of Analytical Sciences,* 18(1): 28-36.
22. Badr, G. E. (2009). The role of some thiosemicarbazide derivatives as corrosion inhibitors for C-steel in acidic media. *Corrosion Science*, 51(11): 2529-2536.
23. Muralisankar, M., Sreedharan, R., Sujith, S., Bhuvanesh, N. S. P. and Sreekanth, A. (2017). *N*(1)-pentyl isatin-*N*(4)-methyl-*N*(4)-phenyl thiosemicarbazone (PITSc) as a corrosion inhibitor on mild steel in HCl. *Journal of A lloys and Compounds*, 695: 171-182.

Malaysian Journal of Analytical Sciences, Vol 22 No 5 (2018): 768 - 774
DOI: https://doi.org/10.17576/mjas-2018-2205-04

MALAYSIAN JOURNAL OF ANALYTICAL SCIENCES
Published by The Malaysian Analytical Sciences Society
ISSN 1394 - 2506

SYNTHESIS AND PHYSICOCHEMICAL PROPERTIES OF MAGNETITE NANOPARTICLES (Fe_3O_4) AS POTENTIAL SOLID SUPPORT FOR HOMOGENEOUS CATALYSTS

(Sintesis dan Sifat Fizikokimia Nanopartikel Magnetit (Fe_3O_4) Sebagai Penyokong Pepejal Bagi Mangkin Homogen)

Wan Fatihah Khairunisa Wan Nor[1], Siti Kamilah Che Soh[1]*, Alyza Azzura Abd Rahman Azmi[1], Mohd Sukeri Mohd Yusof [2], Mustaffa Shamsuddin[3]

[1]*School of Marine and Environmental Sciences*
[2]*School of Fundamental Sciences*
Universiti Malaysia Terengganu,21030 Kuala Nerus, Terengganu, Malaysia
[3]*Department of Chemistry, Faculty of Science,*
Universiti Teknologi Malaysia, 81310 Skudai, Johor Bahru, Johor, Malaysia

**Corresponding author: sitikamilah@umt.edu.my*

Received: 3 May 2018; Accepted: 13 September 2018

Abstract

Black and dark magnetite nanoparticles (MNPs) were successfully synthesised through a co-precipitation method as a crucial material to support palladium(II) complexes as they have the potential to become a stable solid support for homogeneous systems. The two-hour synthesis was done by mixing $FeCl_3.6H_2O$ and $FeCl_2.4H_2O$ in an alkaline medium. To improve the properties of iron oxide nanoparticles, the process was done under inert conditions. The physicochemical properties of this support was then characterised using various spectroscopic techniques such as Fourier Transform Infrared (FTIR) spectroscopy that shows the X-ray diffraction analysis (XRD), Thermogravimetric analysis (TGA), Field Emission Scanning Electron Microscope (FESEM), and Vibrating Sample Magnetometer (VSM). The pore size distribution and the specific BET surface area were measured by N_2 adsorption-desorption isotherms. The FTIR absorption spectroscopy was used to confirm the formation of Fe-O bond. The most intense peak correspond to the (311) crystallographic orientation of the spinel cubic phase of MNPs shown by XRD pattern result. The particle size of magnetite was successfully controlled in the range of 20-40 nm. All of the MNPs showed the superparamagnetic behaviour with high saturation magnetization.

Keywords: magnetite nanoparticles, catalyst support, homogeneous catalysis, heterogeneous catalysis

Abstrak

Nanopartikel magnetit hitam legap telah berjaya disintesis dengan kaedah pemendakan kerana ianya penting untuk menyokong kompleks paladium(II) dan berpotensi menjadi penyokong padu yang stabil bagi sistem homogen. Sintesis selama dua jam dilakukan dengan mencampurkan $FeCl_3.6H_2O$ dan $FeCl_2.4H_2O$ dalam medium beralkali. Bagi meningkatkan sifat nanopartikel oksida besi, persekitaran proses perlu dilakukan dalam keadaan lengai. Sifat fizikokimia penyokong ini telah dicirikan oleh pelbagai teknik spektroskopi seperti Spektroskopi Inframerah (FTIR), Pembelauan Sinar-X (XRD), Analisis Gravimetri Terma (TGA), Mikroskopi Elektron Pengimbasan Pancaran Medan (FESEM), dan Magnetometer Getaran Sampel (VSM). Sebaran saiz liang dan luas permukaan BET yang tertentu diukur menggunakan teknik penjerapan dan penyahjerapan N_2 isoterma. Serapan FTIR spektroskopi digunakan untuk menentukan pembentukan ikatan Fe-O. Puncak yang paling tinggi merujuk kepada fasa kubik spinel dengan orientasi kristalografik (311) ditunjukkan oleh keputusan corak XRD. Saiz zarah magnetit berjaya dikawal dalam linkungan 20-40 nm. Keseluruhan MNPs menunjukkan sifat ketepuan pemagnetan yang tinggi.

Kata kunci: nanopartikel magnetit, sokongan mangkin, pemangkinan homogen, pemangkinan heterogen

Introduction

Limitations on the catalyst separation becoming one of the drawbacks of homogeneous reaction systems, various approaches using solid materials as catalyst support have been extensively studied [1]. To date, considerable research attention has been paid to the usage of supported catalysts for organic synthesis. According to Lim and Lee, the heterogeneous catalytic system provides benefits as it can simply separate and purify organic reactions [2]. Nowadays, Fe_3O_4 magnetite nanoparticles (MNPs) have become a prominent support to catalyst due to its special properties including high surface area, super-paramagnetism, low toxicity and potential applications in various fields [3]. In huge industries, the usage of green catalysts are very crucial as economical catalysts can be re-used several times and produce low levels of contamination in the final products. In addition, the unique properties of Fe_3O_4 MNPs such as easy to separate using external magnets [4] and favorable in surface functionalisation promises excellent support as green catalysts. There are several methods to synthesise magnetic Fe_3O_4 nanoparticles such as hydrothermal synthesis, thermal decomposition, micro-emulsion and co-precipitation. However, the co-precipitation method is considered the ideal method as it is characterised by a low temperature, short reaction time and high reaction yield [5]. This paper is devoted to explaining the process of synthesising MNPs using the co-precipitation method and characterising the magnetite's behaviour using FTIR, XRD, FESEM, TGA, VSM and N_2 adsorption-desorption isotherms.

Materials and Methods

Reagents

The chemicals used in the experimental work-up are Iron(III) chloride hexahydrate, Iron(II) chloride tetrahydrate, tetraethyl orthosilicate (TEOS) and ammonia which were purchased from the standard chemical suppliers such as Sigma Aldrich and MERCK Chemical Co. Materials were used as received without any further purification or any special precautions during the experimental work-up.

Characterisation

The infrared (IR) spectrum was recorded on a Perkin Elmer 100 Fourier Transform Infrared Spectroscopy in the range of 4000-400 cm^{-1} using potassium bromide (KBr) pellets. The X-ray diffraction (XRD) pattern was recorded on a Rigaku MiniFlex II Advanced X-ray diffractometer with a Cu Kα radiation ($\gamma = 1.5418$) in the range of 15-80 ^{o} of a 2θ scale with a scanning speed of 0.03 ^{o}/s. The stability of compound was performed using a Perkin Elmer TGA Analyzer (Perkin Elmer Pyris 6 TGA) from 25 ^{o}C to 950 ^{o}C at a heating rate of 10 ^{o}C/min under a nitrogen atmosphere. The magnetisation of Fe_3O_4 was measured using a vibrating sample magnetometer (VSM) model LakeShore / 7404. The magnetisation curve consisted of 133 points taken at a scan speed of 8 s/point and was measured under a magnetic field strength of 14,000 Gauss (G) at room temperature. The morphological image was taken using a JEOL JSM-6701F Field Emission Scanning Electron Microscope (FESEM) at a 10kV acceleration voltage with magnifications n of 50000x and 100000x. The specific Brunauer-Emmett-Teller (BET) surface area and pore size measurements were performed using a Micromeritics ASAP 2020 instrument.

Synthesis of magnetite Fe_3O_4 nanoparticles (MNPs)

The co-precipitation method was used to synthesis the magnetite iron oxide nanoparticles [6,7,8] and its aqueous stabilisation [9]. The formation of nanoparticles was confirmed by the black color precipitate acquired by the mixture [10]. A mixture of $FeCl_2.4H_2O$ (1.0 g, 5.0 mmol) and $FeCl_3.6H_2O$ (2.6 g, 9.6 mmol) was prepared in 100 mL distilled water under vigorous stirring and in the presence of N_2 gas [11]. Then, the solution was added dropwise to 10 mL ammonia solution (NH_4OH 25 wt.%, excess). The reaction was heated at 70 ^{o}C for 2 hours. After cooling to room temperature, the black solid products were separated using a centrifuge. The precipitates were washed with deionised water and ethanol until it achieved a neutral pH reading. Finally, the magnetite Fe_3O_4 nanoparticles were dried in an oven for 24 hours at 80 ^{o}C.

Results and Discussion

The magnetite Fe_3O_4 nanoparticles were produced using the chemical co-precipitation of $FeCl_2.4H_2O$ and $FeCl_3.6H_2O$, using ammonium hydroxide as the precipitating agent [8]. This synthesis was carried out using

aqueous mixture Fe^{2+} and Fe^{3+} chloride at 1:2 molar ratio to produce Fe_3O_4 [12]. The overall chemical reaction is written as equation 1 below:

$$Fe^{2+} + 2Fe^{3+} + 8OH^{-1} \rightarrow Fe_3O_4 + 4H_2O \quad (1)$$

The FTIR spectrum and absorption bands of the synthesised magnetite iron oxide nanoparticles are shown in Figure 1. The infrared spectrum of these iron oxide nanoparticles revealed all the expected bands of interest which are ν(Fe-O) and ν(Fe-OH). For the magnetites, the band at the range of 579-635 cm^{-1} corresponds to the vibration of the Fe-O bonds. Additionally, two bands of ν(Fe-OH) were identified at 1609 and 3369 cm^{-1}, respectively, representing the stretching vibration of the hydroxyl groups on the surface of the MNPs which is in close agreement with previous reported [8, 13].

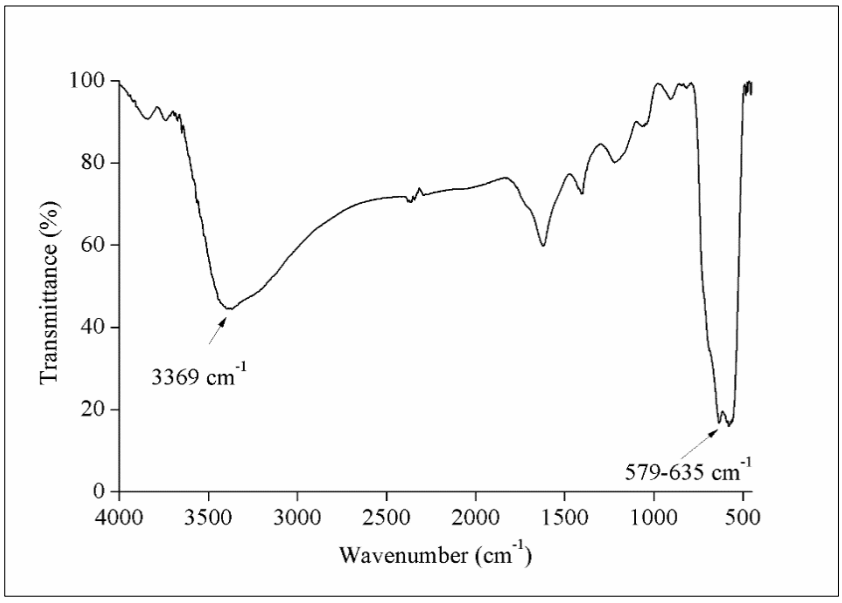


Figure 1. FT-IR spectrum of iron oxide (Fe_3O_4) nanoparticles

The phase identification and crystalline structure of the as-prepared black MNPs were determined using X-ray powder diffraction. As shown in Figure 2, the diffraction peaks of the sample could be readily assigned to Fe_3O_4 in accordance with the main characteristic peaks for magnetite reported in literature [11, 14, 15] and the standard values of Fe_3O_4 (PDF card 75-449). The diffraction peaks at (220), (311), (400), (422), (511) and (440) of the crystalline Fe_3O_4 nanoparticles reflect magnetite crystals with a cubic spinel structure [16]. The diffraction peaks obtained imply no other phase as impurities were detected in the sample. Generally, diffraction peaks were obtained for maghemite and hematite at (113), (210), (213) and (210), respectively [17]. However, these peaks do not appear in the XRD pattern.

An estimation of the magnetite Fe_3O_4 nanoparticles' size was performed using the Scherrer's formula. Particle size is calculated using the following equation 2 [18]:

$$d = \frac{k\lambda}{(\beta \cos\theta)} \quad (2)$$

where d is the particle size of magnetite; k is the shape parameter, also known as the Scherrer constant which is 0.9 for magnetite; λ is the X-ray wavelength (Cu Kα = 1.5418Å); β is the full width at half maximum (FWHM); and θ is

the corresponding Bragg diffraction [13]. Taking the highest intensity peak namely the (311) plane at $2\theta = 35.5^{o}$ and the half maximum intensity of the peak after accounting for instrument broadening, the calculated particle size is 12 nm.

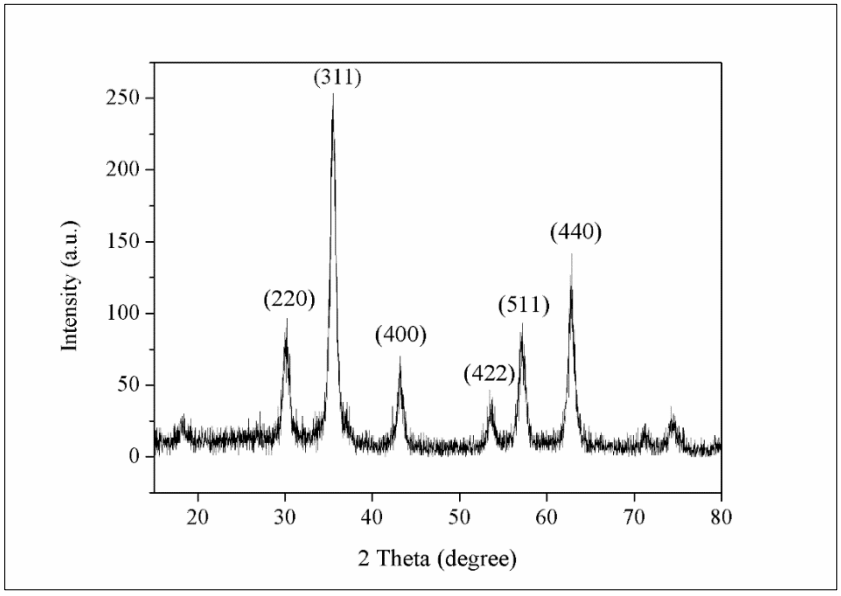


Figure 2. XRD pattern of Fe_3O_4 nanoparticles

The morphology of the magnetite Fe_3O_4 was identified using FESEM. As shown in Figure 3a, the morphology of the non-uniform distributed nanoparticles were observed. The FESEM image at higher magnification (Figure 3b) revealed that the resultant nanoparticles were measured to be 20-40 nm in average. Through observation, the particles have a larger size compared to the result obtained from the Scherrer equation due to aggregation between the particles [18].

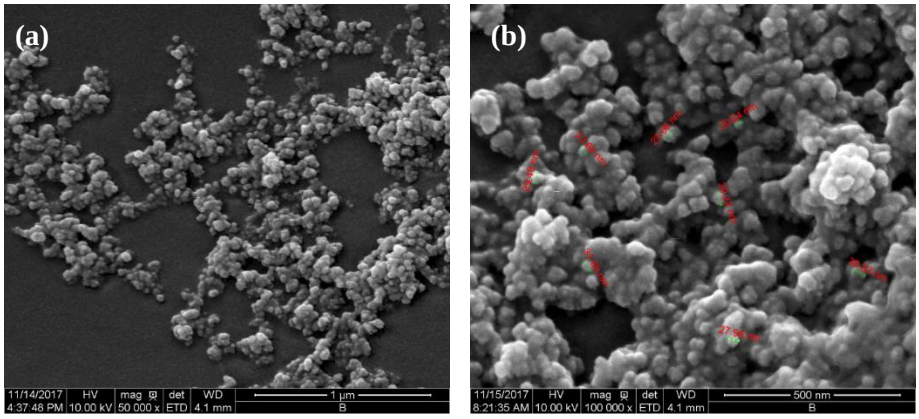


Figure 3. FESEM images of Fe_3O_4 nanoparticles. Scale bar (a) 1 μm and (b) 500 nm

The TGA curve of the magnetite Fe_3O_4 is shown in Figure 4. There are three mass losses in the TGA curve. The first degradation peak is at about 30-200 ^{o}C, which is around the boiling or evaporation point of absorbed water molecules [11]. The second peak is at the range of 250-400 ^{o}C and the percentage of mass loss is about 9%, which

confirms the physisorption and chemisorption processes occurring at the surface of the MNPs [19]. The third peak is at the range 500-750 °C where the percentage of mass loss is about 4% attributed to the phase transition from magnetite to hematite [20]. As seen in Figure 4, the thermal stability of the Fe_3O_4 nanoparticles was estimated at temperatures up to 250 °C.

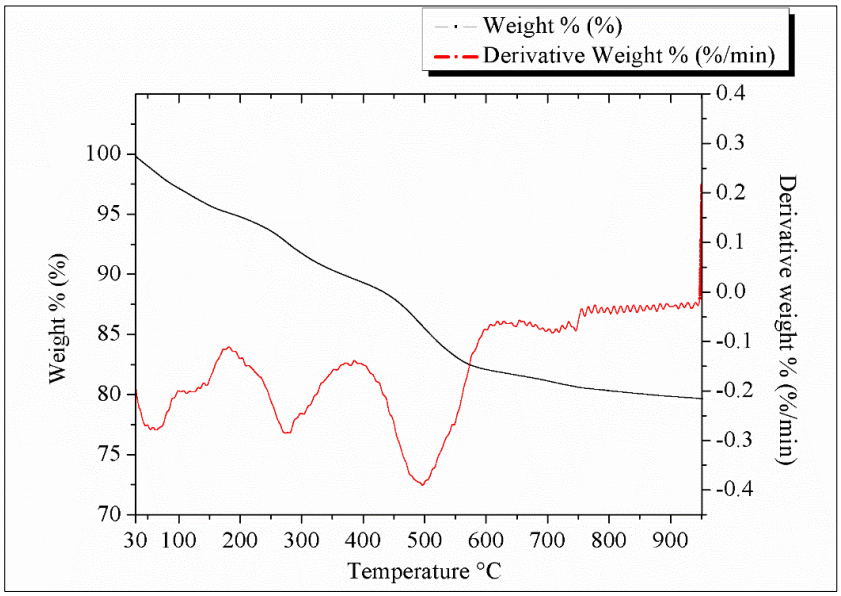


Figure 4. TGA curve of Fe_3O_4 nanoparticles

The magnetisation curve measured at room temperature for the synthesised magnetite Fe_3O_4 is given in Figure 5a. The curve indicates a superparamagnetic behaviour of the studied sample [8]. It is clear that the values of remanence (Mr) and coercivity (Hc) on the magnetisation loop which are close to zero verify the strong magnetic properties of synthesised Fe_3O_4 [21]. The saturation magnetisation (M_s) value was measured to be 54.85 emu g^{-1} for Fe_3O_4 which is consistent with the value reported in the literature [16]. Superparamagnetism is an important and crucial property for reusable catalysts which are responsive to an applied magnetic field without permanent magnetisation. The magnetic response of Fe_3O_4 was tested by placing a magnetic bar near the glass bottle (Figure 5b). The black particles were attracted towards the magnet; therefore the magnetite Fe_3O_4 can be easily separated from the catalytic reaction under an external magnetic field.

The specific Brunauer-Emmett-Teller (BET) surface area and the pore size distribution measurements of the sample were obtained from adsorption-desorption isotherms. The values dependent on the size and shape of the particles. The surface area and pore volume are crucial aspects as they can influence the distribution of active component for catalytic activity [22]. The effective surface area and high pore volume potentially increase the catalytic performance as the rising of the metal loading on the surface of catalyst [23]. The sample was found to possess a surface area of 93.67 m^2g^{-1} and a pore volume of 0.29 cm^3 g^{-1} with an average pore diameter of 12.34 nm (Table 2). The specific surface area and average pore diameter of synthesized magnetite Fe_3O_4 nanoparticles are lower than values corresponding to the reported iron oxide due to the agglomeration of particles [24]. In this study, the magnetite Fe_3O_4 nanoparticles obtained were surfactant free which affected the surface area as well as pore size of sample.

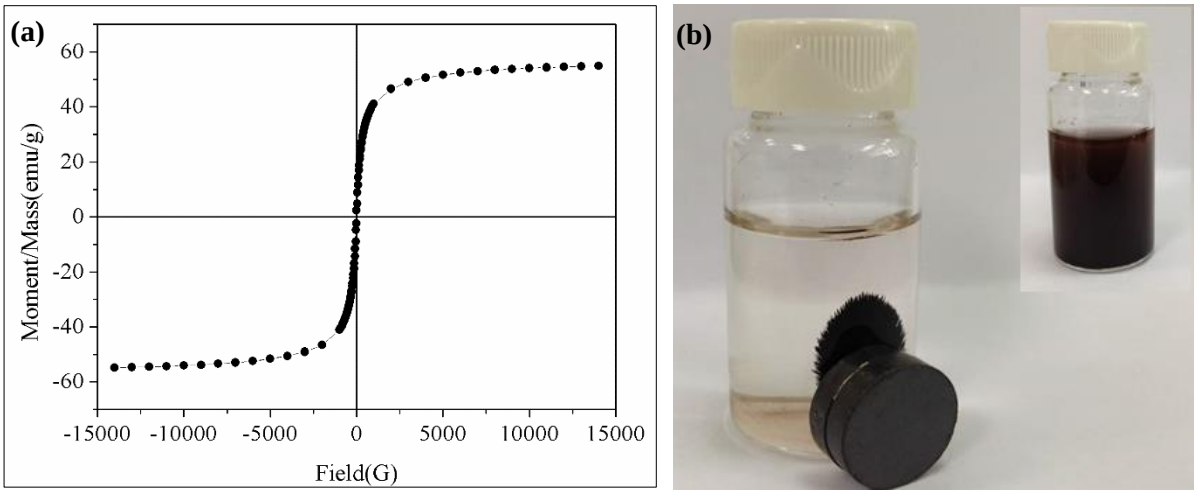


Figure 5. (a) VSM curve of Fe_3O_4, (b) Separation of Fe_3O_4 using an external magnet

Table 2. BET results of Fe_3O_4

Sample	Specific Surface Area (m^2/g)	Pore Volume (cm^3/g)	Average Pore Diameter (nm)
Fe_3O_4	93.67	0.29	12.34

Conclusion

This study investigated the synthesis of superparamagnetic Fe_3O_4 nanoparticles prepared using the co-precipitation method. The results show that the properties of the synthesised particles appear to be very promising as a solid support for heterogeneous catalysts. This is due to the thermal stability of the MNPs up to 250 °C, along with its high surface area and effective reclamation through the application of an external magnetic field. The synthesized supported material ease to recover from catalytic system as it can be reduced the formation of waste as well as economically.

Acknowledgement

The authors wish to thank the Ministry of Higher Education (FRGS) for grant no. 59456, Universiti Malaysia Terengganu (UMT) for the use of research facilities, and the Department of Chemistry, Universiti Teknologi Malaysia (UTM) who acted as our research collaborator.

References

1. Lv, D. and Zhang, M. (2017). O-carboxymethyl chitosan supported heterogeneous palladium and Ni catalysts for heck reaction. *Molecules*, 22:150.
2. Lim, C. W. and Lee, I. S. (2010). Magnetically recyclable nanocatalyst systems for the organic reactions. *Nano Today*, 5: 412-434.
3. Jin, X., Zhang, K., Sun, J., Wang, J., Dong, Z., and Li, R. (2012). Magnetite nanoparticles immobilized salen Pd(II) as a green catalyst for Suzuki reaction. *Catalysis Communications*, 26: 199-203.
4. Jusin, J. W., Aziz, M., Sean, G. P. and Jaafar, J. (2016). Preparation and characterization of graphene-based magnetic hybrid nanocomposite. *Malaysian Journal of Analytical Sciences*, 20(1): 149-156.
5. Alp, E. and Aydogan, N. (2016). A comparative study: Synthesis of superparamagnetic iron oxide nanoparticles in air and N_2 atmosphere. *Colloids and Surface a: Physicochem. Eng. Aspects*, 510: 205-212.

6. Peternele, W. S., Fuentes, V. M., Fascineli, M. L., Silva, J. R. D., Silva, R. C., Lucci, C. M. and Azevedo, R. B. D. (2014). Experimental investigation of the coprecipitation method: An approach to obtain magnetite and maghemite nanoparticles with improved properties. *Journal of Nanoparticles*, 2014:1-10.
7. Hariani, P. L., Faizal, M., Ridwan, M. and Setiabudidaya, D. (2013). Synthesis and properties of Fe_3O_4 nanoparticles by co-precipitation method to removal procion dye. *International Journal of Environmental Science and Development*, 4(3): 336-340.
8. Petcharoen, K. and Sirivat, A. (2012). Synthesis and characterization of magnetite nanoparticles via the chemical co-precipitation method. *Material Science and Engineering*, 177: 421-427.
9. Khalil, M. I. (2015). Co-precipitation in aqueous solution synthesis of magnetite nanoparticles using iron(III) salts as precursors. *Arabian Journal of Chemistry*, 8: 279-284.
10. Yazdani, F. and Seddigh, M. (2016). Magnetite nanoparticles synthesised by co-precipitation method: The effects of various iron anions on specifications. *Materials Chemistry and Physics*, 184: 318-323.
11. Miri, S. S., Khoobi, M., Ashouri, F., Jafarpour, F., Ranjar, P. R. and Shaffiee, A. (2015). Efficient C-C Cross-coupling reaction by (Isatin)-Schiff base functionalized magnetic nanoparticle-supported Cu(II) acetate as a magnetically recoverable catalyst. *Turkish Journal of Chemistry*, 39: 1232-1246.
12. Maity, D. and Agrawal, D. C. (2007). Synthesis of iron oxide nanoparticles under oxidizing environment and their stabilization in aqueous and non-aqueous media. *Journal of Magnetism and Magnetic Materials*, 308: 46-55.
13. Mahdavi, M., Namvar, F., Ahmad, M. B. and Mohamad, R. (2013). Green biosynthesis and characterization of magnetic iron oxide (Fe_3O_4) nanoparticles using seaweed (*Sargassum muticum*) aqueous extract. *Molecules*,18: 5954-5964.
14. Mamani, J. B., Costa-Filho, A. J., Cornejo, D. R., Vieira, E. D. and Gamarra, L. F. (2013). Synthesis and characterization of magnetite nanoparticles coated with lauric acid. *Materials Characterization*, 81: 28-36.
15. Ma, J., Wang, L., Wu, Y., Dong, X., Ma, Q., Qiao, C., Zhang, Q. and Zhang, J. (2014). Facile synthesis of Fe_3O_4 nanoparticles with a high specific surface area. *Materials Transactions*, 55(12): 1900-1902.
16. Liu, X., Kaminski, M.D., Guan, Y., Chen, H., Liu, H. and Rosengart, A.J. (2006). Preparation and characterization of hydrophobic superparamagnetic magnetite gel. *Journal of Magnetism and Magnetic Materials*, 306: 248-253.
17. Murbe, J., Rechtenbach, A. and Topfer, J. (2008). Synthesis and physical characterization of magnetite nanoparticles for biomedical applications. *Materials Chemistry and Physics*, 110: 426-433.
18. Urus, S. (2016). Synthesis of $Fe_3O_4@SiO_2@OSi(CH_2)_3NHRN(CH_2PPh_2)_2PdCl_2$ type nanocomposite complexes: Highly efficient and magnetically-recoverable catalysts in vitamin K_3 synthesis. *Food Chemistry*, 213: 336-343.
19. Shen, M., Yu, Y., Fan, G., Chen, G., Jin, Y. M., Tang, W. and Jia, W. (2014). The synthesis and characterization of monodispersed chitosan-coated Fe_3O_4 nanoparticles via a facile one-step solvothermal process for adsorption of bovine serum albumin. *Nanoscale Research Letters*, 9: 296.
20. Yuan, P., Fan, M., Yang, D., He, H., Liu, D., Yuan, A., Zhu, J.X. and Chen, T.H. (2009). Montmorillonite-supported magnetite nanoparticles for the removal of hexavalent chromium [Cr (VI)] from aqueous solutions. *Journal of Hazardous Materials*, 166: 821–829.
21. Esmaeilpour, M., Javidi, J., Dodeji, F. N. and Abarghoui M. M. (2014). Facile synthesis of 1- and 5-substituted 1H-tetrazoles catalyzed by recyclable ligand complex of copper(II) supported on superparamagnetic $Fe_3O_4@SiO_2$ nanoparticles. *Journal of Molecular Catalysis A: Chemical*, 393: 18-29.
22. Chen, S., Pan, X., Miao, C., Xie, H., Zhou, G., Jiao, Z., Zhang, X. (2017). Study of catalytic hydrodeoxygenation performance for the Ni/KIT-6 catalysts. *Journal of Saudi Chemical Society*, 22: 614-627.
23. Esmaeilpour, M., Javidi, J., Dodeji, F. N., Abarghoui, M. M. (2014). M(II) schiff base complexes (M= zinc, manganese, cadmium, cobalt, nickel, iron, and palladium) supported on superparamagnetic $Fe_3O_4@SiO_2$ nanoparticles: Synthesis, characterization and catalytic activity for Sonogashira-Hagihara coupling reactions. *Transition Metal Chemistry*, 39: 797-809.
24. Ruslimie, C. A., Razali, M. H. and Khairul, W. M. (2010). Effect of HTAB concentration on the synthesis of nanostructured TiO_2 towards its catalytic activities. *Malaysian Journal of Analytical Sciences*, 14(1): 41-49.

Malaysian Journal of Analytical Sciences, Vol 22 No 5 (2018): 775 - 784
DOI: https://doi.org/10.17576/mjas-2018-2205-05

MALAYSIAN JOURNAL OF ANALYTICAL SCIENCES
Published by The Malaysian Analytical Sciences Society
ISSN 1394 - 2506

PHYSICOCHEMICAL CHARACTERISTICS OF RECYCLED TYRE TREAD COMPOUNDS

(Ciri-Ciri Fizik-kimia Sebatian bagi Bunga Tayar Kitar Semula)

Muhammad Abbas Ahmad Zaini[1,2]*, Agus Arsad[2,3], Zainul Akmar Zakaria[2,4], Azhar Abdollah[5], Zaharrudin Abdul Wahid[5]

[1]*Centre of Lipids Engineering & Applied Research, Ibnu-Sina Institute for Scientific & Industrial Research*
[2]*School of Chemical & Energy Engineering*
[3]*UTM-MPRC Institute for Oil & Gas*
[4]*Institute of Bioproduct Development*
Universiti Teknologi Malaysia, 81310 UTM Johor Bahru, Johor, Malaysia
[5]*Revocomm Technologies Sdn Bhd,*
Bandar Pinggiran Subang, 40150 Shah Alam, Selangor, Malaysia

**Corresponding author: abbas@cheme.utm.my*

Received: 14 January 2018; Accepted: 26 July 2018

Abstract

The present work was aimed at evaluating the physicochemical characteristics of seven recycled tyre tread compounds. The materials were characterized for elemental composition, surface morphology, surface chemistry, oil content, ash content, thermal degradation and dielectric properties. Some of the materials were analyzed according to the Rubber Research Institute Malaysia (RRIM) in-house methods for comparison. Natural rubber, butadiene rubber and styrene-butadiene rubber were also employed to validate the thermal degradation profile. Results show that all materials exhibit comparable elemental composition, and dielectric and surface properties, but dissimilar composition of rubber compounds as revealed by the simple mass balance-thermogravimetric approach. The finding is consistent with the RRIM in-house methods. The proposed thermogravimetric approach is sufficient to assess the composition and quality of recycled tyre tread compounds.

Keywords: recycled tyre tread compound, physicochemical characteristic, mass balance-thermogravimetric approach

Abstrak

Kajian ini bertujuan untuk menilai ciri-ciri fizik-kimia tujuh sebatian bagi bunga tayar kitar semula. Bahan-bahan tersebut dicirikan berdasarkan komposisi unsur, morfologi permukaan, kimia permukaan, kandungan minyak, kandungan abu, kemerosotan terma dan sifat dielektrik. Beberapa bahan telah dianalisis mengikut kaedah dalaman Institut Penyelidikan Getah Malaysia (RRIM) untuk perbandingan. Getah semulajadi, getah butadiena dan getah stirena-butadiena juga digunakan untuk mengesahkan profil kemerosotan terma. Keputusan menunjukkan bahawa semua bahan mempamerkan komposisi elemen, dan sifat dielektrik dan permukaan yang hampir serupa, tetapi komposisi sebatian getah yang berbeza seperti didedahkan oleh pendekatan mudah termogravimetrik-imbangan jisim. Penemuan ini sejajar dengan kaedah dalaman RRIM. Pendekatan termogravimetrik yang dicadangkan ini memadai untuk menilai komposisi dan kualiti sebatian bagi bunga tayar kitar semula.

Kata kunci: sebatian bagi bunga tayar kitar semula, ciri fizik-kimia, pendekatan termogravimetrik-imbangan jisim

Introduction

There is an increasing concern over the quality of incoming recycled material for the manufacturing of tyre tread compounds. Often, the recycled material is a blend of different tyre segments [1]. The parts and segments of tyre generally contain varying composition of rubber constituents. Because of the similar physical appearance, the source and composition of this material are somewhat complicated to be differentiated, hence compromising the quality of the tyre treads produced.

In the manufacturing of tyre treads especially for heavy vehicles such as buses and trucks, the recycled material of sufficient quality should be used. The tread is normally composed of natural rubber and poly-butadiene rubber with the right proportion, as these two constituents offer high resistance to abrasion, resistance to cracking and low heat build-up [2]. Failure to attain the correct rubber composition would definitely lead to the inferior quality of tyre tread that may as well compromise the tyre safety. In the present practice, the readily formed tyre tread compound of unknown composition is tested for physicochemical and mechanical characteristics to ascertain its quality and suitability for heavy vehicles [3]. This trial-and-error approach is time-consuming and expensive, and commonly leads to unsatisfactorily outcomes. Consequently, the compound may end-up be rejected because of the quality and safety issues [3].

It is imperative to understand the nature and composition of the recycled materials beforehand. Therefore, the present work is aimed at evaluating the physicochemical characteristics of seven generic recycled materials of tyre treads to shed some light on fast and reliable quality estimation. The compounds were characterized for elemental composition, surface morphology, surface chemistry, oil content, ash content, thermal degradation and dielectric properties. A simple mass balance-thermogravimetric approach was proposed to ease the estimation of rubber constituents in these compounds. The results were compared and validated with the in-house method of Rubber Research Institute of Malaysia (RRIM).

Materials and Methods

Seven generic recycled materials to produce tyre tread compounds from anonymous sources, natural rubber (NR), butadiene rubber (BR), styrene-butadiene rubber (SBR) and Tube-X were supplied by Revocomm Technologies Sdn Bhd. The seven generic samples of unknown composition and quality were designated as SP40-X, SR-X, AP40, EcP40, Sh9(2), Sh8(2) and Sh-PT. A numeral 40 indicates 40-mesh recycled materials. Hexane was supplied by QReC (Malaysia), and is of analytical-grade reagent.

The materials were analyzed for elemental composition (CHNOS) using a VarioMICRO elementar. The surface functional groups were determined using a FTIR spectrometer (Perkin Elmer, Spectrum One). The thermal degradation profiles were obtained using a TGA equipment (Perkin Elmer, TGA 7) under N_2 flow with a heating rate of 10 °C/min. A FESEM-EDX (Hitachi, SU8020) was used to evaluate the surface morphology of materials. The dielectric properties of materials were determined using a vector network analyzer (Agilent, HP8720B) at varying frequencies. Some the compounds, namely SP40-X, AP40, EcP40 and Sh9(2) were tested by an in-house method of Rubber Research Institute of Malaysia (RRIM) for comparison and validation.

The materials were subjected to heating in a furnace at 850 °C for 2 hours. The residue, namely ash content was calculated as the residual mass over the original mass before heating. The oil extraction was performed by refluxing hexane using a Soxhlet apparatus. The solvent was recovered using a rotary evaporator and the oil content was calculated as the mass of oil over the mass of solid compound before extraction.

Results and Discussion

Table 1 shows the elemental composition and ash content of recycled tyre tread compounds. The ash content varies between 3.7% and 8.2%. Nevertheless, the composition of ash (carbon black or silica, and zinc oxide) and sulphur are still within the range allowed for truck tyre treads, i.e., 2.0% - 22% and 1.0% - 2.5%, respectively [1, 4]. Because the rubber materials are purely hydrocarbon, the presence of oxygen in the compounds could be attributed to the use of ZnO as filler. SP40-X exhibits a higher ash content, while SR-X shows a 2.2 times lower ash content than SP40-X. The finding suggests that, although these two materials are from the same anonymous source, their blended composition and the quality of compound produced are not uniform.

Table 1. Elemental composition and ash content

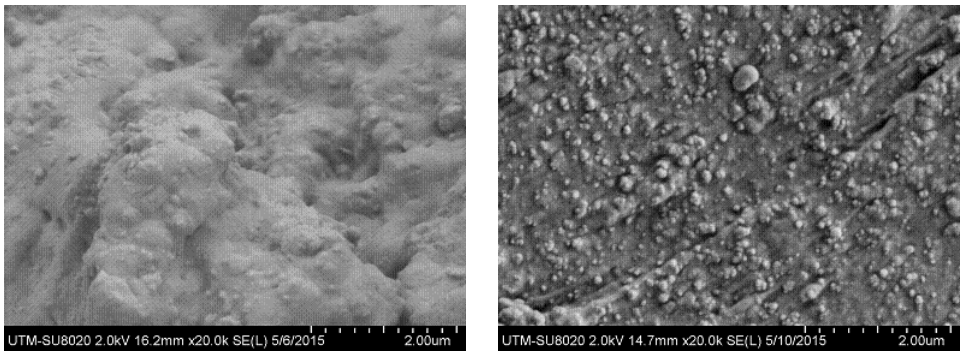
Generic ID	Ash Content (%)	Elemental Composition (%)				
		Carbon	Hydrogen	Nitrogen	Sulphur	Oxygen*
SP40-X	8.15	81.3	7.31	0.52	2.23	0.49
SR-X	3.67	83.8	7.40	0.33	1.67	3.13
AP40	6.93	81.5	7.48	0.48	2.07	1.54
EcP40	6.19	83.3	7.40	0.33	1.78	1.00
SH9(2)	5.09	82.1	7.74	0.43	2.19	2.45
SH8(2)	5.17	82.5	7.72	0.42	2.27	1.92
Sh-PT	5.02	82.4	7.68	0.43	2.10	2.37

*Calculated by difference

All ash samples show a common silver colour that probably indicates the presence of inorganic Zn metal (ZnO). In addition, the ash samples of AP40 and Sh-PT are slightly brownish. SP40-X and SR-X exhibit a trace carbon residue that remains even after the heating process. The finding implies that SP40-X and SR-X could contain some fraction of fixed carbon (probably carbon black powder) that can withstand a longer heating period at a higher temperature. Further, it should be noted that carbon black powder is rarely used as reinforcing filler in tyre treads [5]. This could be the reason for the absence of carbon residue in most of the tread samples studied.

From Table 1, all the studied materials demonstrate a comparable composition of elements. It signifies that all materials contain the right proportion of organic atoms for tyre treads. However, to differentiate the elements according to the specific constituents used in tread manufacturing, i.e., natural rubber, styrene-butadiene rubber, etc., is not possible by elemental analysis. The rubber constituents are common because of their identical atoms that building up the polymer although each of them having dissimilar molecular structures.

Figure 1 displays the SEM images of the recycled materials. The morphology varies according to the physical nature of the materials. For the slab compounds, Sh-PT reveals a smoother and uniform surface when compared to Sh8(2) and Sh9(2). This could be attributed to the process (operating conditions) from which the compound is made and/or the ratio of the constituents used in the blend. It is noted that both Sh8(2) and Sh9(2) are made from the whole tyre, and it is postulated that the cracks and rough surface are due to impurities, undesired substances and/or incorrect formulation that are associated with the use of the whole segments of recycled tyre. For 40-mesh powdered samples, AP40 exhibits a smoother surface as compared to the other similar counterparts. Accordingly, it is estimated that the quality of AP40 is comparable to that of Sh-PT.



SP40-X Sh9(2)

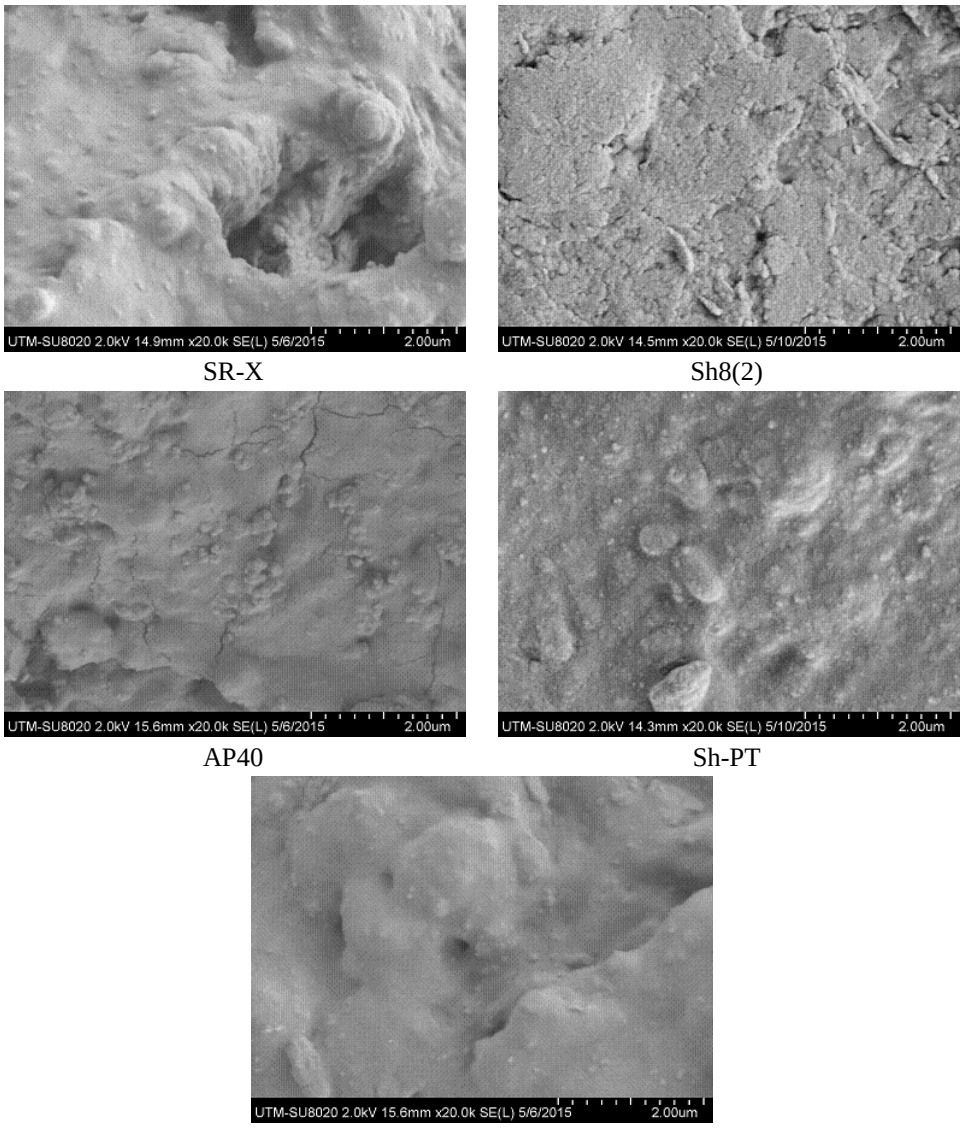


Figure 1. SEM images of tyre tread compounds

Table 2 summarizes the surface composition by EDX. In general, the data shown in Table 2 are in agreement with the elemental composition as reported in Table 1. The composition of carbon on the surface of each material varies from 75% to 100%. A 100% carbon content signifies the absence of other elements on the material surface. The EDX data also reveal that the possible constituents of ash are zinc and silica. The absence of oxygen and inorganic constituents in some of the tread compounds as detected by EDX as opposed to the data presented in Table 1 may indicate that the distribution of elements in tread compounds is not uniform throughout the material matrix.

Table 3 summarizes the oil content in the recycled materials. The values are ranging from 2% to 6%, i.e., the normal limit of oil amount used in conventional tyre to facilitate the processing of rubber compounds [6]. Oil is also used in tyre as an essential ingredient towards the technical performance, particularly for the road grip properties [2]. However, as far as the tyre tread is concern, the addition of oil should be kept minimum to meet the desirable proportion of natural rubber. In addition, the requirement to withstand overheating and wear resistance is more

important than wet grip [3]. The oil content obtained through this method was also compared with the approximate determination using a TGA at 350 °C.

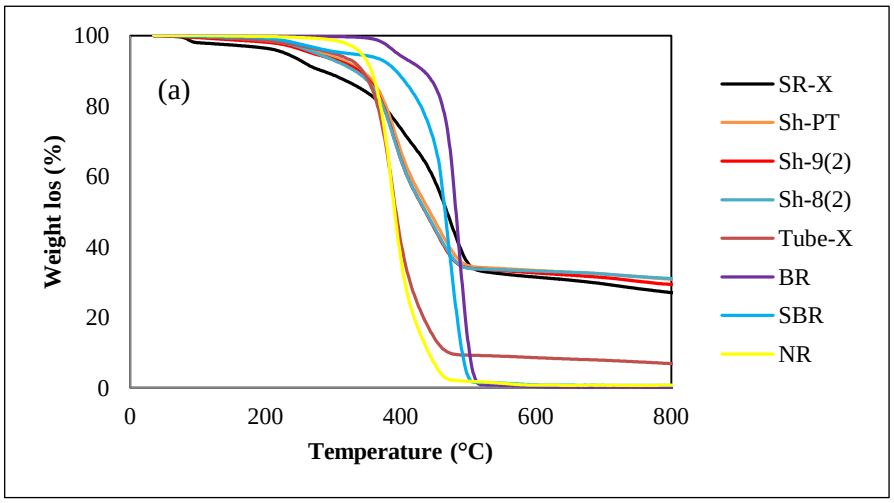
Table 2. Surface analysis by EDX

Generic ID	Carbon	Oxygen	Sulphur	Zinc	Silica
SP40-X	86.7	6.5	3.4	3.3	-
SR-X	97.1	-	2.9	-	-
AP40	100	-	-	-	-
EcP40	96.9	-	3.1	-	-
Sh9(2)	100	-	-	-	-
Sh8(2)	75.4	15.7	3.3	4.7	0.9
Sh-PT	100	-	-	-	-

Table 3. Oil content in the recycled tyre tread compounds

Generic ID	Oil Content (%)
SR-X	5.78
Sh-Pt	5.59
Sh-9(2)	3.67
Sh-8(2)	4.40
Tube-X	2.07
AP-40	2.63
ECP-40	4.30
SP40-X	2.55

Figure 2 shows the heating patterns of the recycled tyre tread compounds. The predicted breakdown of constituents is tabulated in Table 4.



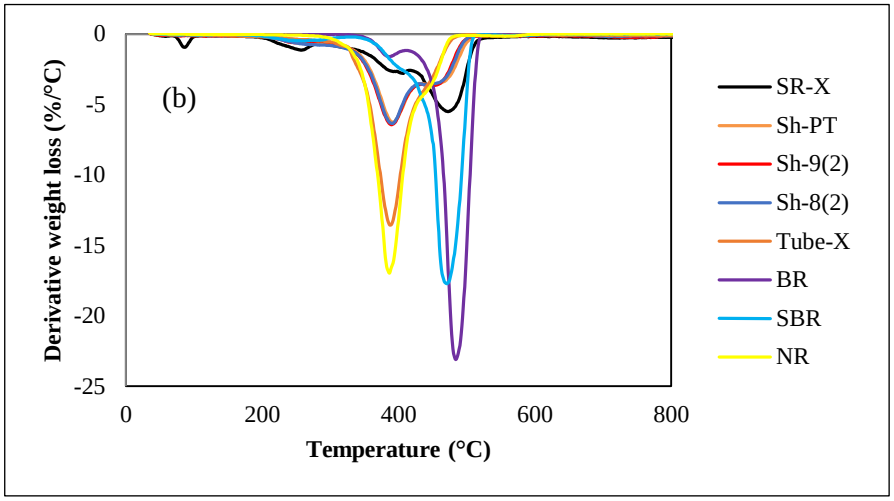


Figure 2. Thermogravimetric profiles: (a) TG and (b) DT curves

Table 4. Mass balance-thermogravimetric approach to estimate the composition of tread compounds

Generic ID	Oil wt.% at 350 °C	Carbon Black+Fillers wt.% at 515 °C	NR wt.% at 350-435 °C	NR wt.%	SBR wt.% (by diff.)	%NR Polymer	%SBR Polymer
NR	7.5	0.0	79.8	92.5	0.0	100.0	0.0
SBR	0.7	0.0	0.0	0.0	99.3	0.0	100.0
SR-X	16.2	33.3	19.5	22.6	27.9	44.7	55.3
Sh-Pt	11.2	34.2	36.1	41.8	12.8	76.6	23.4
Sh-9(2)	12.0	33.7	37.5	43.5	10.8	80.1	19.9
Sh-8(2)	12.9	33.7	36.5	42.3	11.1	79.2	20.8
Tube-X	12.0	9.2	68.6	79.5	0.0	100.0	0.0
AP40	11.2	37.3	42.8	49.6	1.9	96.3	3.7
EcP40	13.7	35.7	38.6	44.7	5.9	88.4	11.6
SP40-X	11.3	36.2	43.8	50.8	1.7	96.7	3.3

From Figure 2, it is obvious that each reference material (NR, BR and SBR) possesses distinct heat decomposition profile with sharp peak at different temperatures. Such dissimilarity can be used to predict the intrinsic composition of each rubber sample. As a matter of fact, oil is the first component that is released or decomposed upon heating at 300-350 °C [7]. Therefore, the first portion of weight loss in thermogravimetric profile at 350 °C is assumed to be that of oil. The oil content by this approximation method is nearly two to five times greater than that obtained using a conventional hexane extraction. It should be noted that oil readily exposed on the surface is most likely to be extracted, while certain amount of oil within the material matrix could be inaccessible to the solvent. Thus, the amount of oil obtained through solvent extraction is often inaccurate unless the compound has already been cut into small pieces to increase the contact area for extraction. While, the thermogravimetric relies on the boiling point of component, hence it is more reliable to represent the fraction of oil that is liberated upon heating. Nevertheless, cautions should be exercised as the given value could be misleading due to the small mass (30-100 mg) used in the TGA analysis.

SR-X exhibits some fraction of moisture, and a higher oil content that is easily vaporized at lower temperature as depicted by peaks at about 85 °C and 250 °C, respectively. The second portion of weight loss that generates sharp peak is due to the presence of natural rubber. The natural rubber (NR) displays a peak centred at 387 °C. Materials having a considerable fraction of NR (>70%) also display a similar peak but with different intensities depending on the amount of NR used in the tread compounds. It can be estimated that the weight loss from 350 °C to 435 °C directly corresponds to NR, and the value is then corrected to 100 % NR. For example, Tube-X that possesses similar intensity of peak as NR contains 79% NR, 12% oil and 9% carbon black and filler. The percentage of polymer in Tube-X is therefore 100% NR. The calculations are based on simple mass balance by integrating the peaks in the thermogravimetric profiles.

From Figure 2, there is a gradual weight loss for all recycled materials at temperature above 515 °C. The remaining weight could be assigned to the amount of carbon black and fillers (Zn and/or Si). It is evident that there is no amount of carbon black and filler in NR, BR and SBR, while Tube-X contains 9.2% carbon black and filler. On the other hand, other materials demonstrate a comparable amount of carbon black and filler, ranging between 34% and 37%. The difference between the amount of carbon black and filler can be established using BS EN 12879:2000 (heating at 850 °C for 2 h under air flow), i.e., the same method used to determine ash content. The TGA approach could also be used to determine the carbon black content through stepwise heating by switching the N_2 flow to air flow from 700 °C onwards [8, 9]. This is due to the fact that carbon black is somewhat resistant to heat and possesses slow degradation under N_2 flow as shown in Figure 2.

It is obvious from Figure 2 that most of the recycled materials display a secondary peak that is tallied with that of SBR. Hence, it is assumed that the remaining polymer in the tread compounds is SBR. The fraction of SBR in the compounds can be calculated by difference. From the mass balance calculation, SR-X demonstrates a considerable fraction of SBR of 55%. To validate the mass balance-thermogravimetric approach, some samples were analyzed using an in-house method of RRIM, and the findings are summarized in Table 5. The in-house method of RRIM yields a close agreement with the proposed mass balance-thermogravimetric approach (Table 4). It shows that the thermal degradation profiles could be sufficiently used to differentiate the types of rubber, and also to quantitatively estimate the composition of polymers used in the tyre tread compounds.

Table 5. Composition of tread compounds using an in-house method of RRIM

Composition	**SP40-X**	**AP40**	**EcP40**	**Sh9(2)**
NR (%)	90	90	70	70
BR (+SBR) (%)	10	10	30	30
Polymer (%)	57.5	57.8	54.2	60.3
Carbon black (%)	30.2	29.9	29.4	27.3
Ash (%)	5.6	5.6	5.3	5.3
Solvent extract (%)	6.7	6.7	11.1	7.1
Zinc oxide (%)	1.7	1.6	1.0	1.2
Total sulfur (%)	2.4	2.2	1.8	2.4
TMQ (%)	0.1	0.1	0.1	0.1

Figure 3 shows the FTIR spectra of the recycled tyre tread compounds, and the respective peaks assignments are summarized in Table 6. All tread compounds demonstrate a similar pattern of FTIR spectra. The peaks shown in Table 6 correspond to the common structure of rubber; long chain aliphatic (single bond) hydrocarbons, alkenes or aromatic (double bond), and sulfur groups (used in vulcanization). In addition, the presence of alkenes and aromatic could not be distinguished because both of them fall under the same wave number of 1300-1500 cm^{-1}. Thus, it is

rather difficult to identify as whether the tyre tread compounds contain either SBR or BR. Moreover, this approach is purely qualitative, and is only sufficient to estimate the surface functional groups.

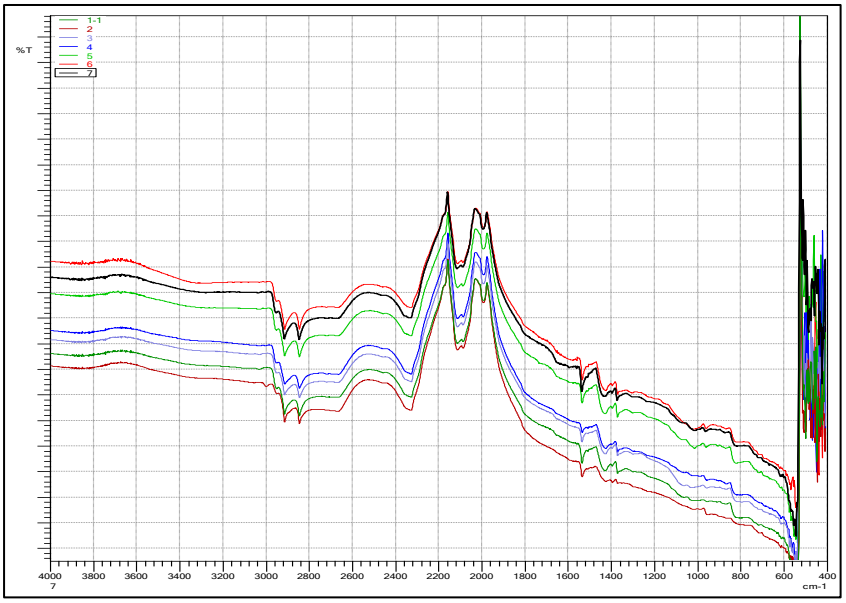


Figure 3. FTIR spectra of tread compounds

Table 6. Peaks assignments

Wavenumber (cm^{-1})	**Assignment**	**1. SP40-X**	**2. SR-X**	**3. AP40**	**4. EcP40**	**5. Sh9(2)**	**6. Sh8(2)**	**7. Sh-PT**
705-570	Disulfides, C—S stretch	548	556	542	548	538	542	538
1500-1300	C—H bending vibrations (alkenes)	1537, 1372, 1431	1537, 1396	1537, 1429, 1372	1535, 1427, 1371	1535, 1429, 1373	1535, 1425, 1371	1535, 1396, 1373
2150-1990	Isothiocyanate (—NCS)	2114, 1994	2116, 1991	2114, 1992	2114, 1990	2114, 1994	2116, 1990	2114, 1992
2700-2400	Thiols and sulfides (S—H)	2328	2328	2328	2328	2328	2326	2332
2865-2845	Methylene, C—H symmetric stretching vibrations	2847	2847	2847	2847	2847	2847	2847
2935-2915	Methylene, C—H asymmetric stretching vibrations	2916	2914	2914	2914	2914	2914	2914

Figure 4 shows the profiles of dielectric properties of tread compounds at varying frequencies. The values of dielectric constant, ε' and loss tangent, tan δ at 2.45 GHz are summarized in Table 7.

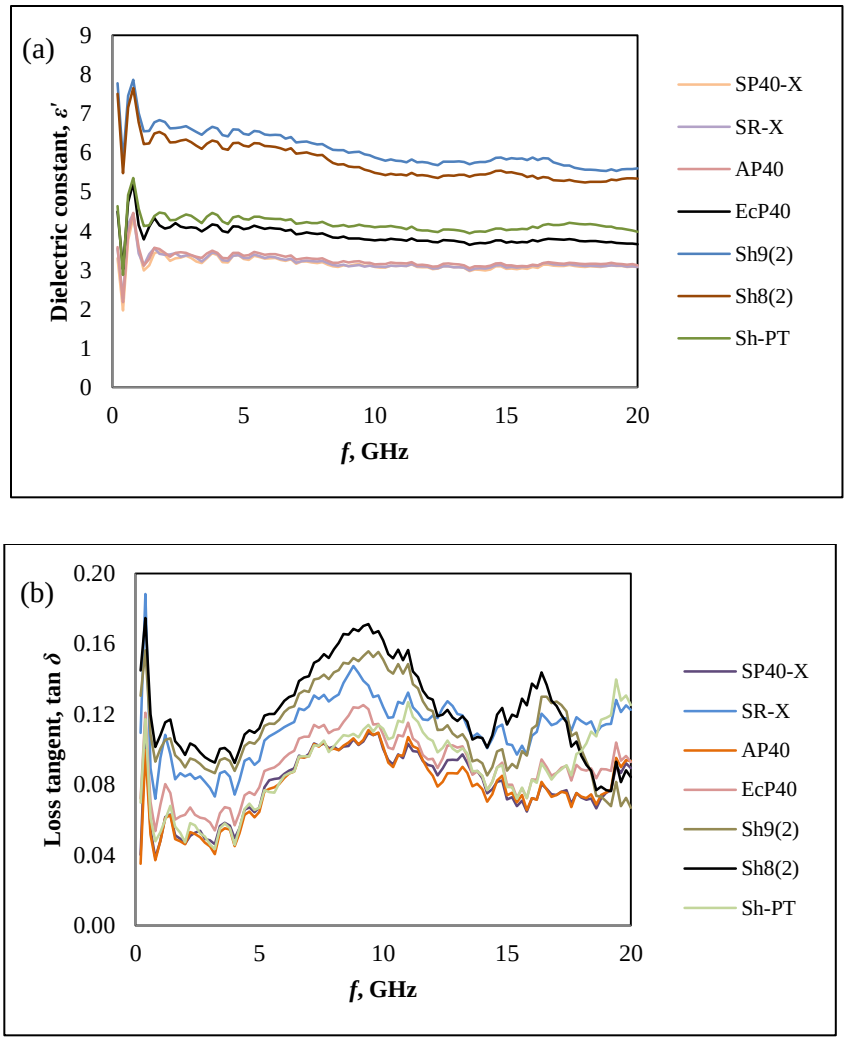


Figure 4. (a) Dielectric constant and (b) loss tangent of tread compounds at varying frequencies

Dielectric constant determines the behaviour of the material under microwave radiation. It includes how much energy is reflected from the material, as well as how efficient is the material to store the microwave energy. On the other hand, the loss tangent describes the efficiency of a material to dissipate the stored energy (microwaves) as heat [10]. In general, the compounds exhibit high dielectric constant and loss tangent compared to the pristine rubbers (Table 7). Although there are differences in the values of dielectric constant and loss tangent, all rubber samples display a comparable pattern of dielectric properties. It indicates that the materials are made from the same major constituents that are microwave-transparent [10]. Because rubber is not a dielectric material, the deviation in values could be attributed to the use of ionic salt (ZnO) in the material [11]. Nevertheless, this method seems unsuitable to distinguish the composition of polymers used in the compounds.

Table 7. Dielectric constant and loss tangent of tread compounds at 2.45 GHz

Sample	ε'	tan δ
BR	2.65	0.02
NR	2.18	0.02
SBR	2.17	0.02
SP40-X	3.30	0.05
SR-X	3.40	0.08
AP40	3.44	0.05
EcP40	4.11	0.06
Sh9(2)	6.63	0.09
Sh8(2)	6.26	0.10
Sh-PT	4.35	0.05

Conclusion

The recycled tyre treads were characterized to evaluate the composition, and to determine a suitable and quick approach to estimate the quality of the compounds. A simple mass balance-thermogravimetric approach was proposed to estimate the composition of oil, natural rubber and fillers, and that of SBR can be calculated by difference. The ash content can be obtained through heating at 850 °C for 2 hours, and its constituents can be predicted using EDX. The results were validated, and show a good agreement with the in-house methods of RRIM. Other characterization outcomes such as FTIR spectra and dielectric properties, however offer insufficient information towards the quality of tread compounds. The mass balance-thermogravimetric approach provides a quick and reliable assessment of the composition and quality of recycled tyre tread compounds.

Acknowledgement

This work was fully sponsored by Ministry of Higher Education Malaysia through a Demand-Driven Project of Public-Private Research Network (PPRN), No. 4L157.

References

1. Shulman, V. L. (2004). Tyre recycling. Rapra Technology Limited, iSmithers Rapra Publishing, 15: 3-26
2. Case, F. (2011). Tyres: Where the Rubber Meets the Road. *Chemistry World*: 52-55.
3. Lahti, J. (2012). Retreaded tyres: Quality, economy and eco-efficiency. Tyre Specialists of Finland, Helsinki.
4. Amari, T., Themelis, N. J. and Wernick, I. K. (1999). Resource recovery from used rubber tires. *Resources Policy*, 25: 179-188.
5. Ten-Brinke, J. W. (2002). Silica reinforced tyre rubbers. PhD Thesis. Twente University Press, Enschede.
6. Syamin, Y. M., Azemi, S. and Dzaraini, K. (2017). Evaluation of cooking oil as processing additive for natural rubber. *ASEAN Journal on Science and Technology for Development*, 34(1): 17-25.
7. Barneto, A. G., Carmona, J. A. and Barron, A. (2015). Thermogravimetric monitoring of crude oil and its cuts in an oil refinery. *Energy and Fuels*, 29(4): 2250-2260.
8. PerkinElmer (2009). Compositional analysis of tire elastomers using autostepwise TGA. Access from https://www.perkinelmer.com/CMSResources/Images/4474045APP_AutoStepwiseTGATireElastomers.pdf. [Access online 5 August 2017].
9. Kunioka, M., Taguchi, K., Ninomiya, F., Nakajima, M., Saito, A. and Araki, S. (2014). Biobased contents of natural rubber model compound and its separated constituents. *Polymers*, 6: 423-442.
10. Zaini, M. A. A. and Kamaruddin, M. J. (2013). Critical issues in microwave-assisted activated carbon preparation. *Journal of Analytical and Applied Pyrolysis*, 101: 238-241.
11. Alias, N. and Zaini, M. A. A. (2015). On the view of dielectric properties in microwave-assisted activated carbon preparation. *Asia-Pacific Journal of Chemical Engineering*, 10(6): 953-960.

Malaysian Journal of Analytical Sciences, Vol 22 No 5 (2018): 785 - 793
DOI: https://doi.org/10.17576/mjas-2018-2205-06

MALAYSIAN JOURNAL OF ANALYTICAL SCIENCES
Published by The Malaysian Analytical Sciences Society
ISSN 1394 - 2506

SEPARATION OF L-ARGININE AND L-CITRULLINE IN RED AND YELLOW CRIMSON WATERMELON (*Citrullus lanatus*) JUICES EXTRACT USING HPLC GRADIENT MODE

(Pemisahan L-Arginina dan L-Sitrulina dalam Ekstrak Jus Tembikai (*Citrullus lanatus*) Merah dan Kuning Menggunakan Mod Cerun KCPT)

Rasdin Ridwan[1], Hairil Rashmizal Abdul Razak[2], Mohd Ilham Adenan[3,4], Wan Mazlina Md Saad[1]*

[1]*Centre of Medical Laboratory Technology, Faculty of Health Sciences,*
Universiti Teknologi MARA Selangor, Puncak Alam Campus, 42300 Bandar Puncak Alam, Selangor, Malaysia
[2]*Centre for Diagnostic Nuclear Imaging, Faculty of Medicine & Health Sciences,*
Universiti Putra Malaysia, 43400 Serdang, Selangor, Malaysia
[3]*Faculty of Applied Sciences,*
Universiti Teknologi MARA, 40450 Shah Alam, Selangor, Malaysia
[4]*Atta-ur-Rahman Institute for Natural Product Discovery, Aras 9, Bangunan FF3,*
Universiti Teknologi MARA Selangor, Puncak Alam Campus, 42300 Bandar Puncak Alam, Selangor, Malaysia

**Corresponding author: wanmaz755@salam.edu.uitm.my*

Received: 29 August 2017; Accepted: 28 August 2018

Abstract

Watermelon (*Citrullus lanatus*) is a nutritious fruit that has attracted scientific interest due to its phytonutrient content including carotenoids and amino acids. Watermelon juice is the richest known source of amino acids including L-arginine and L-citrulline. For a complete separation of amino acids in watermelon juices, a gradient mode of reverse phase high performance liquid chromatography (RP-HPLC) with UV detection was utilised owing to its supremacy over isocratic mode. This present study was aimed at achieving good separation of chromatography profiles and baseline between L-arginine and L-citrulline in red and yellow crimson watermelon juice extract. The edible parts of watermelons were juiced, stored at – 80 ^{o}C and freeze dried to obtain dried juice powder. Samples were analysed by gradient mode of RP-HPLC using 0.1% orthophosphoric acid in water (v/v) and acetonitrile as mobile phase A and B. The chromatograph separation was performed using Gemini C_{18} column at a flow rate of 1.0 mL/min, maintained temperature at 25 ^{o}C while detection was made at four different wavelengths; 195 nm, 200 nm, 207 nm and 210 nm with total analysis time of 35 min. Excellent chromatographic separation was achieved at conditions of gradient elution (0%B - 95%B, 0-18 minutes and 95%B, 18-23 minutes, 95%B-0%B, 23-25 minutes, 0%B, 25-35 minutes) with baseline between L-arginine and L-citrulline in both watermelon juice extracts. The gradient mode used in this RP-HPLC successfully achieved efficient separation of chromatographic profile for amino acids, L-arginine and L-citrulline in the red and yellow crimson watermelon juice extracts.

Keywords: separation, L-arginine, L-citrulline, watermelon, juices extract

Abstrak

Tembikai (*Citrullus lanatus*) adalah buah yang berkhasiat yang menarik perhatian saintifik kerana kandungan fitonutriennya seperti karotenoid dan asid amino. Jus tembikai mempunyai asid amino yang tinggi termasuk L-arginina dan L-sitrulina. Untuk pemisahan lengkap asid amino dalam ekstrak jus tembikai, mod cerun fasa terbalik kromatografi cecair prestasi tinggi (FT-KCPT) dengan pengesanan UV dijalankan kerana kehebatannya berbanding mod isokratik. Kajian ini bertujuan mencapai pemisahan yang baik bagi profil kromatografi dan garis dasar antara L-arginina dan L-sitrulina dalam ekstrak jus tembikai merah dan tembikai kuning. Isi buah tembikai ditapis, disimpan di – 80 ^{o}C dan diletakkan dalam proses pengeringan-beku untuk

mendapatkan serbuk jus kering. Sampel dianalisis menggunakan mod cerun FT-KCPT dengan 0.1% asid ortofosforik dicairkan dalam air (v/v) dan asetonitril sebagai fasa bergerak A dan B. Pemisahan kromatografi dilakukan dengan menggunakan turus Gemini C_{18} pada kadar aliran 1.0 mL/min, suhu yang dikekalkan pada 25 ^{o}C dan pengesanan dibuat pada empat panjang gelombang yang berbeza; 195 nm, 200 nm, 207 nm dan 210 nm dengan 35 minit masa analisis keseluruhan. Pemisahan kromatografi yang cemerlang dicapai dengan keadaan elusi kecerunan (0% B - 95% B, 0-18 minit dan 95% B, 18-23 minit, 95% B-0% B, 23-25 minit, 0% B, 25-35 minit) dengan garis dasar antara L-arginina dan L-sitrulina dalam kedua-dua ekstrak jus tembikai. Mod cerun dalam FT-KCPT ini berjaya mencapai pemisahan profil kromatografi yang efisien untuk asid amino, L-arginina dan L-sitrulina dalam ekstrak jus tembikai merah dan kuning.

Kata kunci: pemisahan, L-arginina, L-sitrulina, tembikai, ekstrak jus

Introduction

Watermelon or scientifically known as *Citrullus lanatus* is categorised as a member of Cucurbitaceae family that incorporates several other important fruits such as muskmelon, cucumber, pumpkin, bottle ground and winter melon [1]. *Citrullus lanatus* is a vine-like flowering fruit mainly found worldwide in tropical and subtropical climates especially in Africa, Asia and Mediterranean [2]. Watermelon contains abundant carotenoid content that includes lycopene, β-carotene, lutein and neoxanthin, which are responsible for different watermelon flesh colours [3]. Red fleshed watermelon contains rich source of lycopene as the major carotenoid and secondarily, β-carotene [3]. Yellow crimson, a yellow fleshed watermelon contains major carotenoid known as neoxanthin that plays specific role in protection against photooxidative stress [3]. Recent report from previous studies have shown that both red and yellow crimson watermelon juices contain high concentration of amino acids especially L-arginine and L-citrulline [4, 5]. These amino acids are crucial in nitric oxide production for improving cardiovascular health, immune boosting, and sexual health benefits [6].

Amino acid profiling has been reported in numerous literatures using reverse phase high performance liquid chromatography (RP-HPLC) method following isocratic or gradient elution [7-10]. RP-HPLC has become the dominant mode for analytical analysis due to its excellent resolving power and versatile nature [11]. Previously, most RP-HPLC gradient methods for amino acid analysis including L-citrulline and L-arginine are performed along with pre- and post-column amino acid derivatisation using O-phthalaldehyde (OPA), but these methods require expensive equipments and tedious sample preparation [12]. Several derivatisation techniques using OPA in amino acid analysis have been conducted by isocratic HPLC, but the outcome was hampered by poor separation and overlapping of derivative peaks [13]. Recently, Jayaprakasha et al. [14] has successfully determined L-citrulline using isocratic elution method in reverse phase column, Gemini C_{18} with limitation for separation for single amino acid, L-citrulline. Therefore, the present study was aimed to achieve good separation of chromatography profiles and baseline between L-arginine and L-citrulline in two types of watermelon juices extract, the red and yellow crimson watermelons by gradient mode of RP-HPLC method.

Materials and Methods

Chemicals and reagents

Pure standards of L-arginine and L-citrulline were purchased from Sigma-Aldrich (St. Louis, MO). Phosphoric acid, ≥85% (Sigma-Aldrich) and HPLC grade deionised filtered water were used to prepare the mobile phase A. Acetonitrile, LiChrosolv gradient grade, was obtained from Merck (Darmstadt, Germany) as mobile phase B. All solutions were filtered by Durapore PVDF membrane, 0.45 µm (Merck, Germany) and degassed prior to the HPLC experiments. All chemicals and reagents used were of HPLC grade.

Sample and standard preparation

Locally harvested red and yellow crimson watermelons *(Citrullus lanatus*) were obtained from Selangor Fruit Valley, Rawang. Both watermelons were cleaned with filtered tap water, peeled to obtain the fleshes with the remaining seeds removed. Watermelons fleshes were chopped into small pieces. The fleshes were then processed with a commercial juice extractor (Panasonic, MY) that automatically separates the pulp and the juices. The juices were stored at – 80 ^{o}C and freeze-dried using Benchtop Freeze Dry System (Labconco, Kansas City, MO) to obtain dried juices powder. The freeze-dried juices were stored at – 80 ^{o}C until further analysis. An amount 5 mg of freeze-dried juices was dissolved in 1 mL deionised filtered water to yield 5 mg/mL of juice extract concentration.

Meanwhile, pure standard of L-arginine and L-citrulline were dissolved in deionised water to obtain 1 mg/mL stock solution. Fresh working standard and juices extracts were prepared daily and all solutions were filtered by nylon syringe filter (0.45 µm).

Instrumentation

Thermo Scientific™ UltiMate™ 3000 HPLC system was utilised for analysis. The system was equipped with an ultra-high pressure pump, column compartment, auto sampler, on-line degasser and diode array detector (DAD). The chromatographic profiles and integrated data were recorded using Chromeleon software version 7. The chromatographic separation was achieved using reverse phase column, Gemini C_{18}, 110 Å, 3 µm partial size, 250 x 4.6mm (Phenomenex, USA) in gradient mode.

RP-HPLC analysis

Chromatographic profiling of red and yellow watermelon juices extracts was performed on Thermo Scientific™ UltiMate™ 3000 HPLC system with diode array detector (DAD) and column temperature maintained at 25 ^{o}C. The Chromeleon chromatographic software was used for data collection and processing. A 20 µL of standard and juice extracts were automatically injected by the auto sampler. Elution was conducted using mobile phase A (0.1 % orthophosphoric acid in water (v/v)) and mobile phase B (100% acetonitrile) with a linear gradient elution programme (Table 1) at a flow rate of 1.0 mL/min. The following gradient was applied: 0%B – 95%B, 0-18 minutes and 95%B, 18-23 minutes, 95%B-0%B, 23-25 minutes, 0%B, 25-35 minutes with total analysis time of 35 minutes. Detection was monitored at four different wavelengths: 195 nm, 200 nm, 207 nm and 210 nm. Prior to analysis, the system was purged to remove bubbles from the line tubes. The column was conditioned for at least 30 minutes until flat baseline was achieved. In each chromatographic run, the column was flushed with 95% acetonitrile followed by 10 minutes at solvent composition for the next injection.

Table 1. Linear gradient elution

Time (minutes)	**% A (0.1% H_3PO_4)**	**% B (ACN)**
0	100	0
18	5	95
23	5	95
25	100	0
35	100	0

Results and Discussion

The present study has successfully achieved excellent chromatography profiles for separation two types of juice extract, red and yellow crimson watermelons, using gradient mode RP-HPLC. The linear gradient profile developed as shown in Figure 1 resulted in lowest baseline drift and provide excellent separation of amino acid, L-arginine and L-citrulline. The present result showed improvement from previous study conducted by Rao and Bitla [15] that demonstrated incomplete separation of L-arginine and L-citrulline without baseline resolve using gradient mode RP-HPLC. Gradient elution was confirmed to be performed in this analysis as the ratio in retention time, Δt, between the first, ta, and the last peak, tz, of compounds in linear gradient was > 0.25. This gradient programme was selected to achieve maximum separation and sensitivity. The linear gradient phase was performed by changing acetonitrile composition from the starting condition of 0% acetonitrile to 95% acetonitrile from 0 to 18 min. This phase is called as gradient time (tg) in which the solvent composition is changed to elute compounds of different polarity. The presence of acetonitrile in the starting solvent for the gradient elution is necessary to ensure the elution of both amino acids, L-arginine and L-citrulline, within a reasonable time. Acetonitrile was preferred as organic solvent due to lower viscosities and low UV cut off compared to methanol that often causes a higher baseline noise with electrochemical detection [16]. This can be confirmed by Abdullah et al. [17] study that stated the use of acetonitrile resulted in sharper peak shape and better resolution in a shorter analysis time than methanol.

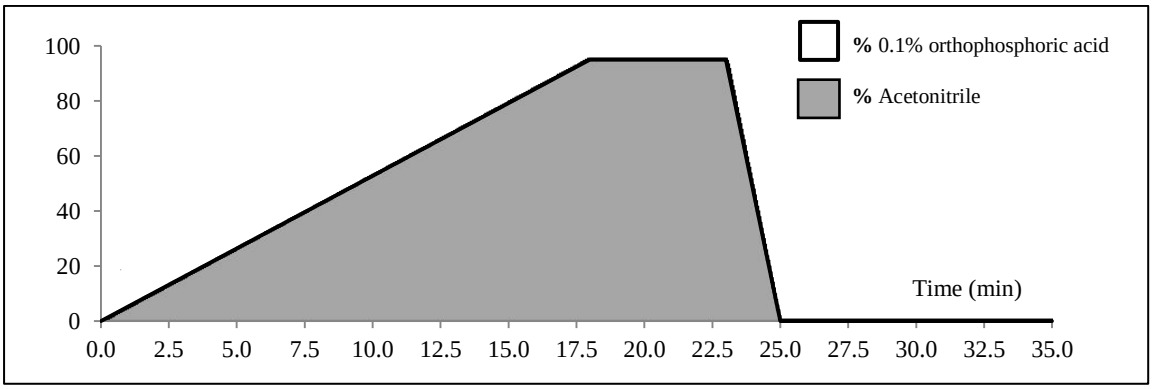


Figure 1. The linear gradient elution from 0 to 18 minutes; the graph represents the percentage of solvent A (0.1% phosphoric acid) and solvent B (acetonitrile

The chromatography separations of mixed standard, red and yellow crimson watermelon juice extracts at linear gradient phase were shown in Figure 2. The chromatographic profile of standard solution presented in Figure 2a showed that the standard mixture of L-arginine and L-citrulline was perfectly separated without any derivatisation. L-arginine was eluted first at retention time of 4.350 min followed by L-citrulline at 5.320 min. Excellent separation on chromatography profile in standard solution was achieved although additional minor peaks were observed, which might be due to reagent purity. The chromatography profiles of red and yellow crimson watermelon juice extracts showed well-separated peaks of 11 major compounds that were eluted including L-arginine and L-citrulline (Figures 2b and 2c). L-arginine and L-citrulline exhibited excellent baseline separation, good resolution and peak symmetry with increasing steepness under the gradient elution conditions. The finding was supported by Markowski et al. [18] and Mao et al. [19] that demonstrated successfully separation of L-arginine and L-citrulline with good baseline and resolution under gradient elution. Interestingly, only small minor additional peaks were observed on the chromatograph results even though simple extraction step was performed without sample clean-up. This simple extraction method provides convenient sample preparation and reduces instrumental requirements, hence less equipped laboratories are required to carry out this analysis [20].

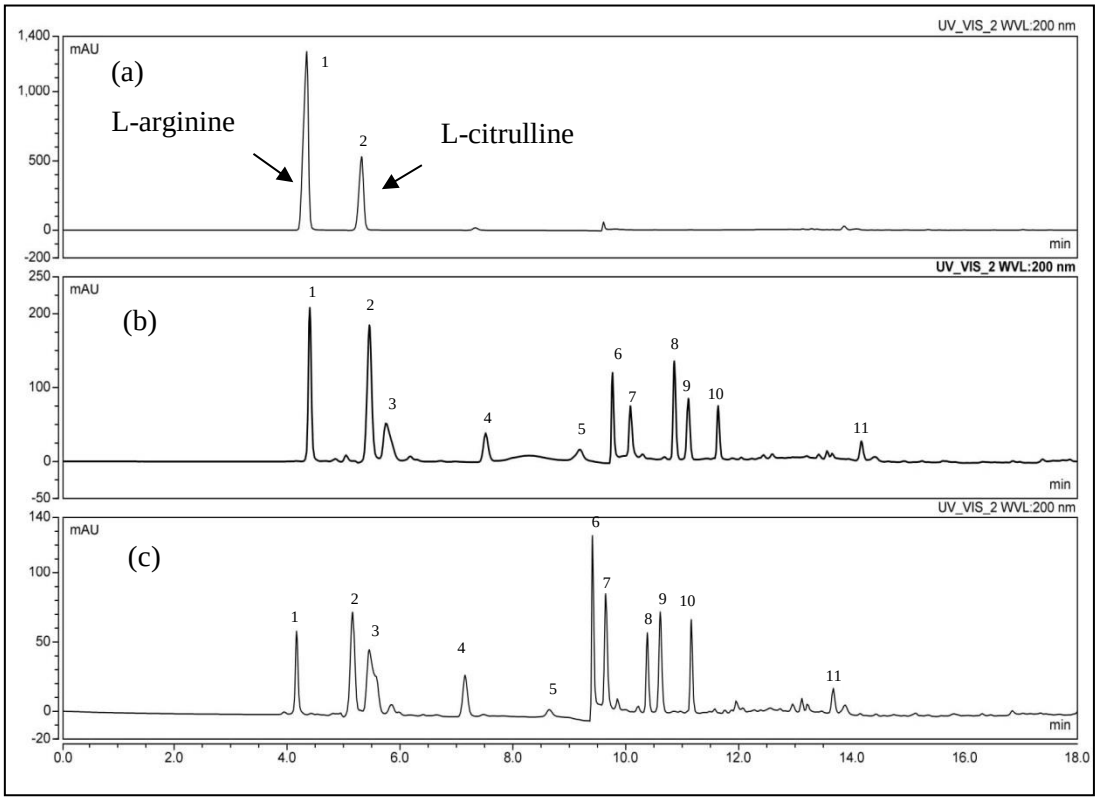


Figure 2. Comparison of RP-HPLC chromatographic profiles of (a) standard mixture solution (L-arginine, 1 mg/mL and L-citrulline, 1 mg/mL), (b) red watermelon juice extract (c) yellow crimson watermelon juice extract; 20 µL of mixed standard or samples were injected into the HPLC system; mobile phase flow of 1.000 mL/min; linear gradient (ACN: 0% to 95% in 18 minutes); UV/Vis detector wavelength of 200 nm; column oven maintained at 25 ^{o}C.

The effects of UV wavelengths on detection of L-arginine and L-citrulline were also determined within the range of 195 nm to 210 nm. The selection was done based on the previous literatures conducted by Ridwan et al. [5], Jayaprakasha et al. [14] and Sadji et al. [21] for underivatisation amino acid analysis. Comparison on chromatography profiles of red and yellow crimson watermelon juice extracts at four different wavelengths detection of 195 nm, 200 nm, 207 nm and 210 nm are showed in Figure 3 and 4, respectively. Detection of compounds at 200 nm yielded most stable and low baseline noise between peak of compounds in the chromatography profiles. Highest signal intensity of compounds was achieved at 195 nm but the chromatography baseline was less stable while the detection of signal intensity was decreased at 207 nm and 210 nm. This present finding is in agreement with Agrafiotou et al. [22] that showed high sensitivity detection of underivatised amino acids mixture at wavelength 200 nm compared to 190 nm and 210 nm. The lower wavelengths ranging from 195 nm to 210 nm were chosen in this study since most amino acids with appropriate functional group of carboxylic group (-COOH) including L-arginine and L-citrulline can only be detected at low UV wavelengths [5, 22]. Hesse and Weller [20] supported the notion that lower UV range provides high sensitivity, but interference of solvents, buffers, and other additives is often prohibitive. Thus, it is crucial to used proper mobile phases as there is only limited number of buffer components and electrolyte additives that can function optimally at low wavelengths. The employed mobile phase of 0.1% orthophosphoric acid and acetonitrile produced reproducible separation of L-arginine and L-citrulline in red and yellow crimson watermelon juice extracts at 200 nm.

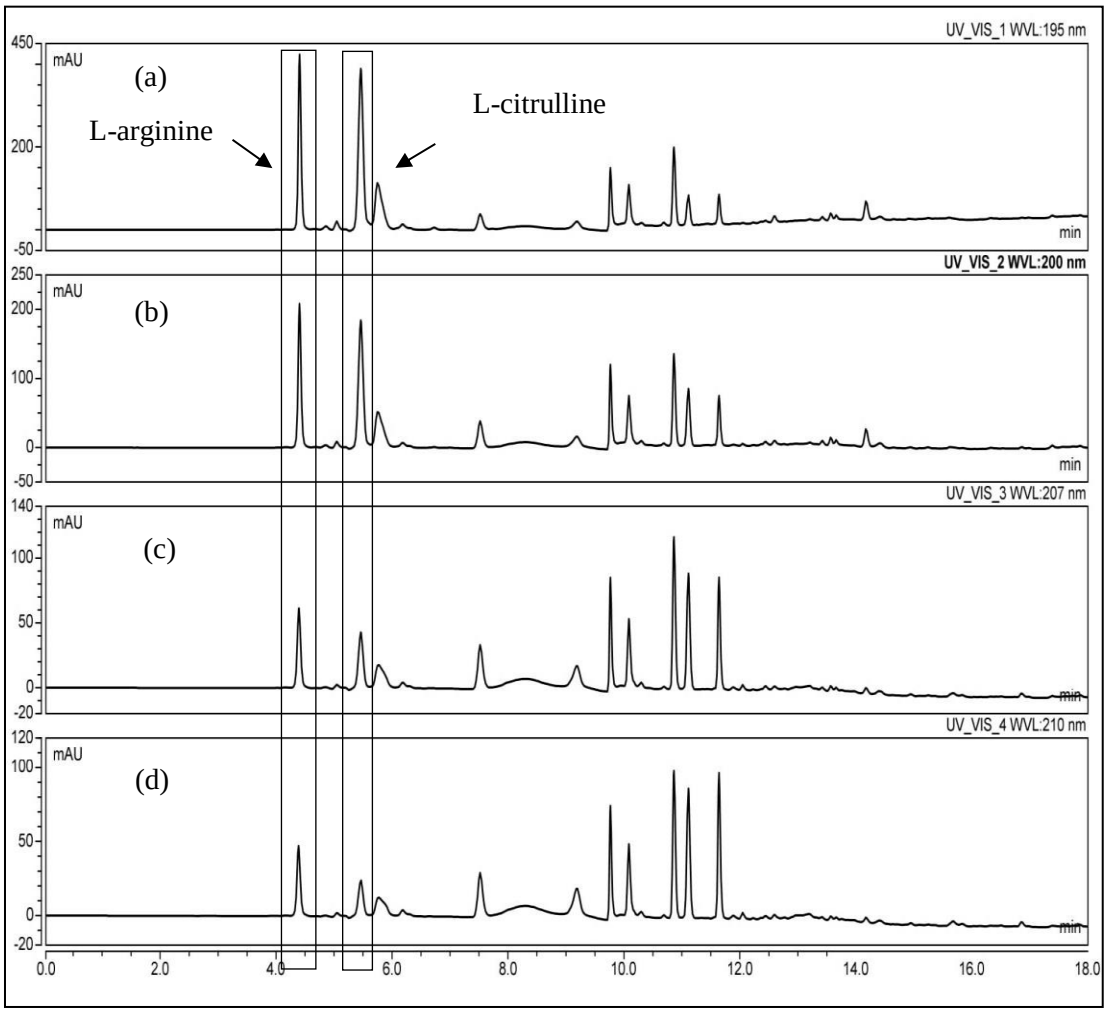


Figure 3. Comparison of chromatographic profiles obtained by gradient mode RP-HPLC in different wavelengths for red watermelon juice extract; (a) 195 nm (b) 200 nm (c) 207 nm (d) 210 nm; 20 µL of samples were injected into the HPLC system; mobile phase flow of 1.000 mL/min; linear gradient (ACN: 0% to 95% in 18 minutes); column oven was maintained at 25 ^{o}C.

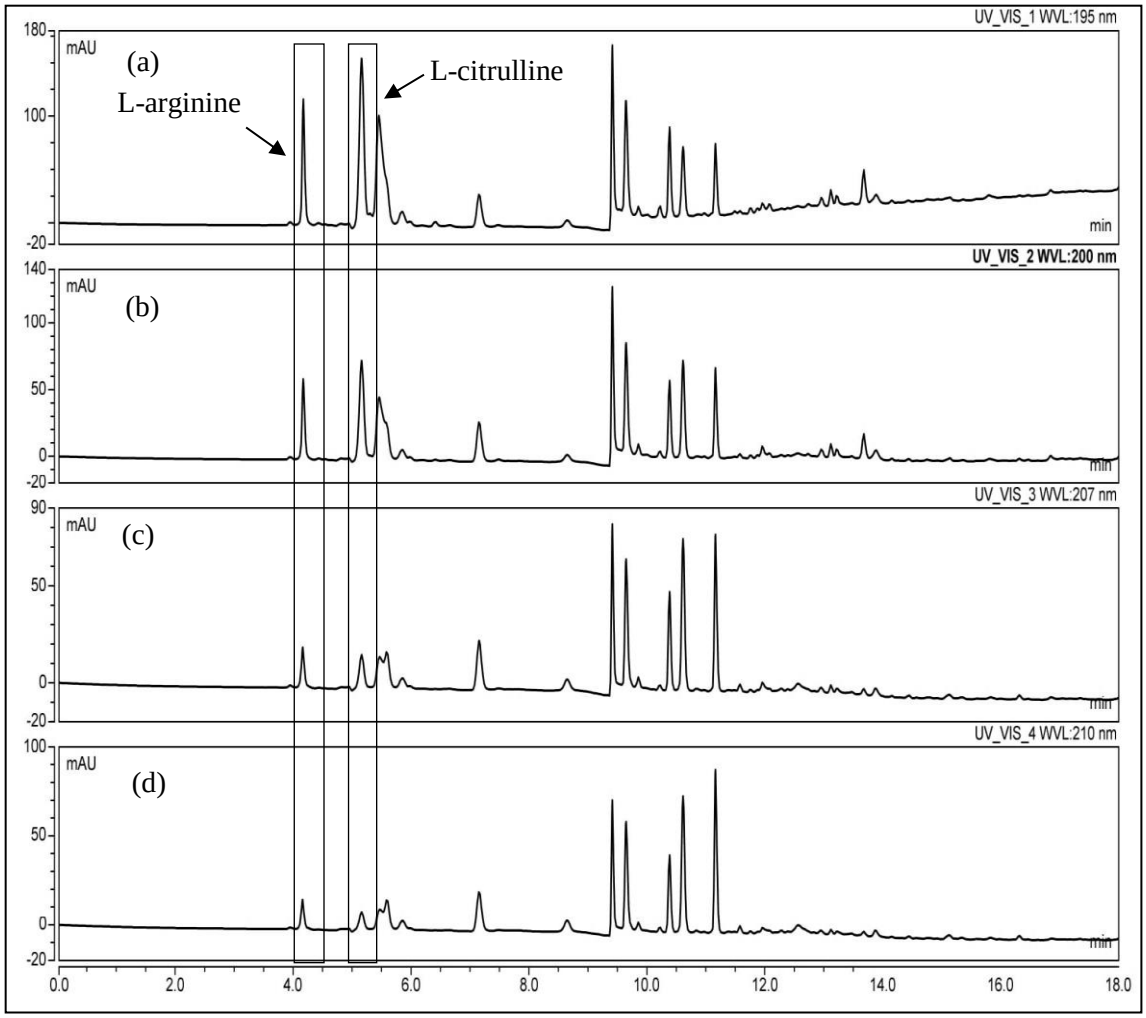


Figure 4. Comparison of chromatographic profiles obtained by gradient mode RP-HPLC in different wavelengths for yellow crimson watermelon juice extract; (a) 195 nm (b) 200 nm (c) 207 nm (d) 210 nm; 20 µL of samples were injected into the HPLC system; mobile phase flow of 1.000 mL/min; linear gradient (ACN: 0% to 95% in 18 minutes); column oven was maintained at 25 ^{o}C.

Conclusion

The gradient mode of RP-HPLC has successfully achieved efficient separation of chromatographic profile in linear gradient phase and baseline between L-arginine and L-citrulline in red and yellow watermelon juice extracts using Gemini C_{18} with 0.1% orthophosphoric acid in water (v/v) and acetonitrile as mobile phase at 200 nm. L-arginine and L-citrulline were excellently separated. The method is simple with minimum samples preparation without any derivatisation that could potentially solve the problems in derivatisation techniques for amino acid analysis. However, further study is warranted for a complete analysis of amino acid profiles using the gradient mode RP-HPLC and to quantify its content in local watermelon. It is also necessary to explore the roles of these bioactive constituents in watermelon as nutritional intervention for maintaining a healthy lifestyle.

Acknowledgement

The authors gratefully acknowledge financial support by the Ministry of Higher Education, Malaysia through Fundamental Research Grant Scheme (FRGS/1/2016/WAB01/UITM/02/3) and Institute of Research

Management and Innovation (IRMI), Universiti Teknologi MARA. The authors also would like to acknowledge Atta-ur-Rahman Institute (AuRIns), Centre of Medical Laboratory Technology, and Centre of Postgraduate Study of Faculty of Health Sciences, Universiti Teknologi MARA (UiTM) Selangor, Puncak Alam Campus for providing facilities throughout this study.

References

1. Mohammad, M. K. A., Mohamed, M. I., Zakaria, A. M., Abdul Razak, H. R. and Md Saad, W. M. (2014). Watermelon (*Citrullus lanatus* (Thunb.) Matsum. and Nakai) juice modulates oxidative damage induced by low dose X-ray in mice, *BioMed Research International*, 2014 :1-6.
2. Levi, A., Thomas, C.E., Keinath, A.P. and Wehner T.C. (2001). Genetic diversity among watermelon (*Citrullus lanatus* and *Citrullus colocynthis*) accessions. *Genetic Resources and Crop Evolution*, 48(6): 559-566.
3. Zhao, W., Lv, P. and Gu, H. (2013). Studies on carotenoids in watermelon flesh. *Agricultural Sciences*, 4(7): 13-20.
4. Rimando, A. M. and Perkins-Veazie, P. M. (2005). Determination of citrulline in watermelon rind. *Journal of Chromatography A*, 1078(1–2): 196-200.
5. Ridwan, R., Abdul Razak, H. R., Adenan, M. I. and Md Saad, W. M. (2018). Development of isocratic RP-HPLC method for separation and quantification of L-Citrulline and L-Arginine in watermelons. *International Journal of Analytical Chemistry*, 2018:1-9.
6. Egbuonu, A. C. C. (2015). Comparative assessment of some mineral, amino acid and vitamin compositions of watermelon (*Citrullus lanatus*) rind and seed. *Asian Journal of Biochemistry*, 10(5): 230-236.
7. Dimova, N. (2003). RP-HPLC analysis of amino acids with UV-detection. *Comptes Rendus de l'Academie Bulgare des Sciences*, 56(12): 12-75.
8. Shi, Z., Li, H., Li, Z., Hu, J. and Zhang, H. (2013). Pre-column derivatization RP-HPLC determination of amino acids in *Asparagi radix* before and after heating process. *IERI Procedia*, 5(2013): 351-356.
9. Sharma, V., Gulati, A. and Ravindranath, S. D. (2005). A simple and convenient method for analysis of tea biochemicals by reverse phase HPLC. *Journal of Food Composition and Analysis*, 18(6): 583-594.
10. Zafar, S., Naz, N., Nazir, S., Abbas, M. and Khan, A. M. (2014). Analysis of selected amino acids in different varieties of wheat available in Punjab, Pakistan. *Chromatography Research International*, 2014: 1-6.
11. Scott, R. P. W. (2003). Principles and practice of chromatography**.** Chrom-Ed Book Series, Library for Science Publishing, LCC, 1: pp 1 – 106.
12. Adegoke, O. (2012). An overview of applications of pre-column derivatization reactions for the liquid chromatographic analysis of pharmaceuticals and other compounds. *African Journal of Pure and Applied Chemistry*, 6(12): 129-140.
13. Fish, W. W. (2012). A reliable methodology for quantitative extraction of fruit and vegetable physiological amino acids and their subsequent analysis with commonly available HPLC systems. *Food and Nutrition Sciences*, 3(6): 863-871.
14. Jayaprakasha, G. K., Chidambara Murthy, K. N. and Patil, B. S. (2011). Rapid HPLC-UV method for quantification of L-citrulline in watermelon and its potential role on smooth muscle relaxation markers. *Food Chemistry*, 127(1): 240-248.
15. Rao, P. V. L. N. S. and Bitla A. R. (2017). Simultaneous determination of arginine, citrulline, and asymmetric dimethylarginine in plasma by reverse-phase high-performance liquid chromatography. *Journal of Laboratory Physicians*. 9(4): 243-248.
16. Matysova, L., Zahalkova, O., Klovrzova, S., Sklubalova, Z., Solich, P. and Zahalka, L. (2015). Development of a gradient HPLC method for the simultaneous determination of sotalol and sorbate in oral liquid preparations using solid core stationary phase. *Journal of Analytical Methods in Chemistry*, 2015: 1-6.
17. Abdullah, N. F., Anifah, W. and Hussain, R. M. (2015). Optimised method for purification of allylpyrocatechol from *Piper Betle L.* ethanolic extract using HPLC and H^1-NMR. *Journal of Pharmaceutical Sciences and Research*, 7(6): 292-301.
18. Markowski, P., Baranowska, I., and Baranowski, J. (2007). Simultaneous determination of L-arginine and 12 molecules participating in its metabolic cycle by gradient RP-HPLC method. Application to human urine samples. *Analytica Chimica Acta*, 605(2): 205-217.

19. Mao, H. M., Wei, W., Xiong, W. J., Lu, Y., Chen, B. G. and Liu, Z. (2010). Simultaneous determination of L-citrulline and L-arginine in plasma by high performance liquid chromatography. *Clinical Biochemistry*, 43(13–14): 1141-1147.
20. Hesse, A. and Weller, M. G. (2016). Protein quantification by derivatization-free high-performance liquid chromatography of aromatic amino acids. *Journal of Amino Acids*, 2016: 1-8.
21. Sadji, M., Perkins-Veazie, P.M., Ndiaye, N.F., Traore, D., MA, G., Zongo, C., Traore, Y,, Sal, M.D. and Traore, A. (2015) Enhanced L-citrulline in parboiled paddy rice with watermelon (*Citrullus lanatus*) juice for preventing sarcopenia: A preliminary Study. *African Journal of Food Science*, 9(10): 508-513.
22. Agrafiotou, P., Sotiropoulos, S. and Pappa-Louisi, A. (2009). Direct RP-HPLC determination of underivatized amino acids with online dual UV absorbance, fluorescence, and multiple electrochemical detection. *Journal of Separation Science*, 32(7): 949-954.

Malaysian Journal of Analytical Sciences, Vol 22 No 5 (2018): 794 - 806
DOI: https://doi.org/10.17576/mjas-2018-2205-07

MALAYSIAN JOURNAL OF ANALYTICAL SCIENCES
Published by The Malaysian Analytical Sciences Society
ISSN 1394 - 2506

BIOACCESSIBILITY ASSESSMENT OF ^{232}TH AND ^{238}U FROM LANTHANIDE CONCENTRATE AND WATER LEACH PURIFICATION RESIDUE IN MALAYSIA

(Penilaian Bio-Kebolehcapaian bagi ^{232}Th Dan ^{238}U dalam Lantanida Pekat dan Residu Permurnian Larut Resap Air di Malaysia)

Nur Shahidah Abdul Rashid[1]*, Um Wooyong[1], Yasmin Mohd Idris Perama[2], Amran Ab.Majid[2], Khoo Kok Siong[2]

[1]Division of Advanced Nuclear Engineering,
Pohang University of Science and Technology, Pohang, Republic of Korea
[2]School of Applied Physics, Faculty of Science and Technology,
Universiti Kebangsaan Malaysia, 43600 UKM Bangi, Selangor, Malaysia

**Corresponding Author : nurshahidah@postech.ac.kr*

Received: 28 September 2017; Accepted: 11 August 2018

Abstract

The aim of this case study was to estimate the bioaccessibility of ^{232}Th and ^{238}U from lanthanide concentrate (LC) and water leach purification (WLP) residue of Lynas Advanced Materials Plant by analysing the solubility of these radionuclides in synthetic gastrointestinal fluids. A DIN *in vitro* bioaccessibility method was applied to determine the targeted radionuclides from the LC and WLP residue, which were further evaluated through inductively coupled plasma mass spectrometry. ^{232}Th and ^{238}U concentrations in the gastrointestinal fluids portrayed the maximum amount of contaminants that were potentially available for intestinal absorption and transfer into the blood. The maximum concentrations of ^{232}Th in the LC and WLP residue were 0.1410 ± 0.0331 mg kg^{-1} and 0.1621 ± 0.1190 mg kg^{-1}, respectively. As for ^{238}U in the LC and WLP residue during the intestinal phase for high-risk cases, the maximum concentrations were 0.0558 ± 0.0164 mg kg^{-1} and 0.0480 ± 0.0213 mg kg^{-1}, respectively. The maximum bioaccessibility of ^{232}Th and ^{238}U was 0.14 % and 0.93 %, respectively. Based on the assessment, the committed equivalent dose and committed effective dose of ^{232}Th and ^{238}U were below the United Nations Scientific Committee on the Effects of Atomic Radiation reference values. Overall, the DIN *in vitro* bioaccessibility method is feasible to estimate the solubility of ^{232}Th and ^{238}U from LC and WLP residue, and is also useful for monitoring and risk assessment purposes for environmental, health, and contaminated samples.

Keywords: bioaccessibility, thorium, uranium, lanthanide concentrate, water leach purification

Abstrak

Tujuan kajian ini ialah mengkaji bio-kebolehcapaian ^{232}Th dan ^{238}U dari sampel lantanida pekat (LC) dan residu pemurnian larut resap air (WLP) yang terdapat di loji bahan termaju Lynas, dengan kaedah penentuan melalui kebolehlarutan radionuklid tersebut di dalam cecair sintetik gastrousus. Sampel LC dan residu WLP telah menjalani teknik bio-kebolehcapaian *in vitro* DIN, dan seterusnya sampel dianalisis menggunakan Spektrometer Jisim-Gandingan Plasma Teraruh. Kepekatan ^{232}Th dan ^{238}U dalam cecair gastrousus mewakili jumlah maksimum pencemaran radionuklid yang berpotensi diserap ke dalam badan melalui usus dan berpindah ke dalam darah. Kepekatan maksimum ^{232}Th dalam LC dan residu WLP ialah 0.1410 ± 0.0331 mg kg^{-1} dan 0.1621 ± 0.1190 mg kg^{-1}. Bagi ^{238}U dalam LC dan residu WLP semasa fasa usus bagi kes berisiko tinggi ialah 0.0558 ± 0.0164 mg kg^{-1} dan 0.0480 ± 0.0213 mg kg^{-1}. Nilai bio-kebolehcapaian maksimum bagi ^{232}Th dan ^{238}U ialah 0.14% dan 0.93%. Berdasarkan kajian, dos komited setara dan dos komited berkesan bagi ^{232}Th dan ^{238}U adalah di bawah nilai rujukan *United Nations Scientific Committee on the Effects of Atomic Radiation*. Kesimpulannya, teknik bio-kebolehcapaian *in vitro* DIN sangat berguna untuk

menganggar kelarutan ^{232}Th dan ^{238}U bagi tujuan pemantauan berterusan dan penilaian risiko terhadap alam sekitar, kesihatan manusia, dan sampel tercemar.

Kata kunci: bio-kebolehcapaian, torium, uranium, lantanida pekat, permurnian larut resap

Introduction

The world is currently facing intense demand and development of rare earth elements (REEs) for green and sustainable products in energy, armed forces, and manufacturing industries. Thus, to assist the global REEs market, the Lynas Advanced Materials Plant (LAMP) was built in the Gebeng Industrial Estate (GIE), Kuantan, Malaysia. This beneficial development brings investment profits in rare earth industry. About 0.03×10^6 t of rare earth ores production comes from Malaysia [1]. The LAMP processes lanthanide concentrate (LC) at an integrated processing site utilising physical and chemical treatment processes. Water leach purification (WLP) residue results from the leaching and purification of the water-soluble lanthanide components from the calcined and cracked concentrate. Radioactive elements, namely thorium dioxide (ThO_2) and uranium oxide (U_3O_8), are present in the rare earth concentrate that is processed by the LAMP. This plant is expected to yield approximately 65 000 t/a of rare earth concentrate with a rare earth oxide (REO) concentration of 40 %, a ThO_2 concentration of 0.17 %, and a concentration of U_3O_8 of 0.003 % [2]. According to United States Environmental Protection Agency (USEPA), the rare earth concentrate is classified as Technologically Enhanced Naturally Occurring Radioactive Material (TENORM) [3]. Even though REEs have been considered to be beneficial and profitable to Malaysia, the occupational, public safety, and health risks related to REEs should be addressed at their stages of mining, transportation, processing, and waste disposal, as well as decommissioning.

Internal irradiation can be triggered when radionuclides enter the human body by inhalation or ingestion [4, 5]. The most significant pathway for radionuclide ingestion is when radionuclides become integrated with food. Coincidental ingestion of soil material or soil dust is related to unusual soil ingestion called pica. The contaminated soil surface is transferred to hands, food and beverages, cigarettes, or other items that may cause ingestion of radioactive contaminants [6, 7]. Using *in vitro* bioaccessibility models, the digestion processes in the gastrointestinal tract can be imitated using a simplified technique. Bioaccessibility of compounds from their matrix during transit in the gastrointestinal tract can be examined as an aspect of oral internal exposure to the contaminant by applying an *in vitro* bioaccessibility model [8]. Bioaccessibility denotes the fragment of a contaminant that is propagated from soil into solution by digestive juices [9]. It constitutes the utmost number of contaminants that are available for intestinal absorption. This is the theoretical fraction convenient for adsorption through the gastrointestinal tract [10]. In this investigation, the sole medium for occupational exposure through radioactivity ingestion was when radionuclides became integrated with dust or other substances and were later exposed to food or other entities that were put into the mouth, for instance pens or fingers. Th and U cause concern for authorities as they may cause health hazards, particularly when they have been ingested. Th and U are both from chemical and radiological standpoints and their compounds are immensely toxic [11].

The *in vitro* bioaccessibility method was utilised to evaluate the LC and WLP residue radionuclide solubility potential or the ability of ^{232}Th and ^{238}U to be absorbed in the human digestive system. The study of ^{232}Th and ^{238}U solubility in synthetic gastrointestinal digestion liquid by applying a DIN *in vitro* bioaccessibility method is conducted outside the human digestive system in a system similar to the digestive systems of adults and children. Theoretically, if a fragment of discharged pollutants from soil entered the synthetic gastrointestinal fluids, then it could be implied as soluble. The absorption in the gut and transfer into the blood were represented by the maximum quantity of contaminants in the soil. This approach is also appropriate for bioaccessibility tests for allocating data in human health risk assessments. The objectives of this study were to determine the solubility level of ^{232}Th and ^{238}U in LC and WLP residue, and to analyse the effectiveness of ^{232}Th and ^{238}U solubility with synthetic gastrointestinal fluids using a DIN *in vitro* bioaccessibility method. Quantitative determination of ^{238}Th and ^{232}U in LC and WLP residue is of great interest and is vital for geological investigation. Bioaccessibility and oral bioavailability theories are significant to quantify the potential risks that are linked with oral exposure to environmental contaminants.

Materials and Methods

Sample collection and preparation

The LC and WLP residue samples used in this study were collected from the LAMP, Kuantan, Pahang. The samples were air-dried and passed through a 2 mm sieve for the later purpose of bioaccessibility assessment. The total initial concentrations of ^{232}Th and ^{238}U were analysed using a Bruker S8 Tiger X-Ray fluorescence spectrometer (XRF); the concentrations are shown in Table 1.

Table 1. Concentrations of ^{232}Th and ^{238}U before bioaccessibility method

	Concentration (mg kg^{-1})	
	^{232}Th	^{238}U
Lanthanide concentrate (LC)	18.0 – 101.0	2.0 – 6.0
Water leach purification (WLP) residue	27.0 – 155.1	2.0 – 6.9

DIN *in vitro* bioaccessibility method

The DIN *in vitro* bioaccessibility method was used to evaluate bioaccessibility. The German method E DIN 19738, which is also known as the Standardised German *In Vitro* Assay model, is a static gastrointestinal model that involves synthetic gastric fluids simulation followed by synthetic gastrointestinal fluids simulation [12]. The bioaccessibility method was started by suspending 2 g of LC or WLP residue samples in triplicate, where each sample was mixed with synthetic gastric fluids (solid to liquid ratio of 1:50) and later incubated for 2 hours at a pH of 1.4 ± 0.1. About 10 mL of the incubated gastric fluids were extracted, centrifuged at 3500 rpm for 15 minutes, and filtrated (0.45 µm filter paper) with a Rocker 400 laboratory vacuum pump. To fabricate the gastrointestinal fluids, the remaining volume of artificial gastric fluids was mixed with artificial intestinal fluids (solid to liquid ratio of 1:100). The artificial gastrointestinal fluids were further incubated for 6 hours at a pH of 7.5 ± 0.2. Then, 10 mL were extracted, centrifuged at 3500 rpm for 15 minutes, and filtrated. Both artificial fluids were incubated in a water bath that was kept at a constant temperature of 37 °C to simulate a normal human body temperature. The filtrated gastric and gastrointestinal fluids were sent for analysis with inductively coupled plasma mass spectrometry (ICP-MS) (Perkin Elmer ELAN 6000).

The elemental determination was conducted by irradiation of approximately 10 mL of each sample for 5 hours at the Malaysian Nuclear Agency, Bangi. Blanks of artificial gastric and gastrointestinal fluids without LC and WLP residue were run as controls. Table 2 portrays the preparation of artificial gastric and gastrointestinal fluids for the DIN *in vitro* bioaccessibility method. By analysing International Atomic Energy Agency (IAEA) standard reference materials (Soil-7 and 448), quality control of the analysis was conducted. The procedure was conducted to determine the concentrations of ^{232}Th and ^{238}U integrated in the gastrointestinal system at intervals of 5 hours.

Bioaccessibility of a particular radionuclide was calculated using the following equation 1:

$$\text{Bioaccessibility} = \frac{B_g}{B_s} \times 100\% \quad (1)$$

where B_q is the concentration of ^{232}Th or ^{238}U presented in artificial gastrointestinal fluids (mg kg^{-1}) and B_s is the concentration presented in samples before applying the *in vitro* bioaccessibility method (mg kg^{-1}).

The values of the committed effective dose and committed equivalent dose were calculated using the following equation 2:

$$H_A = \Sigma_j I_{Aj} h_{Aj} \quad (2)$$

where H_A is the committed effective dose or the committed equivalent dose (Sv) by ingestion, I_{Aj} is ^{232}Th or ^{238}U activity (Bq) in the samples (Bq kg^{-1}), and h_{Aj} is the ingestion dose coefficient (Sv Bq^{-1}) for the effective dose or the target organs for ^{232}Th or ^{238}U.

Table 2. Preparation for each sample (200 ml) in gastric fluid and (200 ml) in gastrointestinal fluid

	Gastric Fluid	Gastrointestinal Fluid
Bile Bovine	-	1.800 g
Calcium Chloride Dihydrate ($CaCl_2$ x $2H_2O$)	-	0.100 g
Hydrochloric acid (30% of HCl)	pH adjustment	-
Magnesium Chloride Hexahydrate ($MgCl_2$ x $6H_2O$)	-	0.040 g
Mucin	0.600 g	-
Pancreatin	-	1.800 g
Pepsin	0.200 g	-
Potassium Chloride (KCl)	0.140 g	0.060 g
Potassium Dihydrogen Phosphate (KH_2PO_4)	0.054 g	-
Sodium Bicarbonate ($NaHCO_3$ solid)	-	0.200 g
Sodium Chloride (NaCl)	0.580 g	pH adjustment
Trypsin	-	0.060 g
Urea (CH_4N_2O)	-	0.060 g
Final pH	2.0	7.5

\

Results and Discussion

^{232}Th and ^{238}U concentrations

The accuracy of the procedure used for determination of total concentrations of ^{232}Th and ^{238}U in the LC and WLP residue was verified. The results are shown in Table 1. The XRF analysis showed that the concentrations of ^{232}Th in the WLP residue and LC were 155.1 mg kg^{-1} and 101.0 mg kg^{-1}, respectively, where the former was the highest concentration overall. On the other hand, the concentrations of ^{238}U in the WLP residue and LC were 6.9 mg kg^{-1} and 6.0 mg kg^{-1}, respectively. The WLP residue is the major waste material resulting from water leaching and purification processes of the LC in the rare earth industry. This process utilises magnesium oxide and water, which produces WLP residue and is considered the most toxic due to its elevated levels of U, Th, associated radioactivity, and heavy metals compared with neutralisation underflow (NUF) and flue gas desulphurisation (FGD) waste [13, 14]. The concentration of ^{232}Th varied in the LC and WLP residue, which could have been due to the geological composition and the content of ^{232}Th and ^{238}U samples from each area where the soils originated. The original ^{232}Th and ^{238}U concentrations in rocks may have varied because of alteration or metamorphic processes [15]. The concentration of ^{232}Th was highest in the WLP residue, as the WLP residue undergoes refining processes that cause ^{232}Th to easily separate from the minerals inside the soil [16].

Heavy metals and radionuclide behaviours in soil are significantly related to soil properties. Soil determinants, such as pH, ferromanganese oxides, and organic matter, may be better predictors for metal mobility [17]. According to the National Toxics Network (NTN) report, the rare earths concentrate imported from Australia is expected to have ThO_2 concentrations of 1600 mg kg^{-1} and U_3O_8 concentrations of 28 mg kg^{-1}. These concentrations correspond to a ^{232}Th activity concentration of 5.7 Bq g^{-1} and a ^{238}U activity concentration of 0.28 Bq g^{-1}. The WLP residue is expected to have a ThO_2 content of 1655 mg kg^{-1} and a U_3O_8 content of 22.5 mg kg^{-1} [15]. Based on the International Atomic Energy Agency (IAEA) report, the rare earth, Th, and U contents of the ore are shown in Table 3 [18]. These concentrations correspond to a ^{232}Th activity concentration of 5.9 Bq g^{-1} and a ^{238}U activity concentration of 0.24 Bq g^{-1}.

In this study, ^{232}Th and ^{238}U concentrations were converted to specific activity using a radioelement conversion factor, where 1 mg kg^{-1} of Th in rock is equal to 4.06 Bq kg^{-1} ^{232}Th, and 1 mg kg^{-1} of U in rock is equal to 12.35 Bq kg^{-1} ^{238}U. The specific activities of ^{232}Th for the LC and WLP residue were 0.4101 Bq g^{-1} and 0.6297 Bq g^{-1}, respectively, while the specific activities of ^{238}U in the LC and WLP residue were 0.0741 Bq g^{-1} and 0.0852 Bq g^{-1},

respectively. The specific activities of ^{232}Th and ^{238}U before the DIN *in vitro* bioaccessibility method were lower than those in the NTN report.

Table 3. Rare earth, thorium and uranium contents of Mount Weld Ore

	Concentration (%)	
	Average	**Maximum**
Total REO	17 - 18	42
ThO_2	0.075	0.18
U_3O_8	0.003	0.006

By using ICP-MS, the occupational exposure of workers to ^{232}Th and ^{238}U was evaluated by determining both concentrations in the gastrointestinal tract. Table 4 and Table 5 show the solubility of ^{232}Th and ^{238}U in the LC and WLP residue within the first 5 hour interval. The general concentrations of ^{232}Th and ^{238}U during the gastric phase were in the range of 0.0580–0.0598 mg kg^{-1} for ^{232}Th and 0.0473–0.0554 mg kg^{-1} for ^{238}U in the LC, while they were 0.4793–0.5495 mg kg^{-1} for ^{232}Th and 0.7401–0.8731 mg kg^{-1} for ^{238}U in the WLP residue. The concentrations of ^{232}Th and ^{238}U during the gastrointestinal phase were in the range of 0.1167–0.1410 mg kg^{-1} for ^{232}Th and 0.0437–0.0558 mg kg^{-1} for ^{238}U in the LC, and 0.0407–0.0480 mg kg^{-1} for ^{238}U and 0.1621–0.0779 mg kg^{-1} for ^{232}Th in the WLP residue.

Table 4. Concentration of ^{232}Th after DIN *in vitro* bioaccessibility method

Time (h)	**Concentration of ^{232}Th (mg kg^{-1})**			
	Gastric Phase		**Gastrointestinal Phase**	
	Lanthanide Concentrate (LC)	**Water Leach Purification (WLP)**	**Lanthanide Concentrate (LC)**	**Water Leach Purification (WLP)**
1	0.0598 ± 0.017	0.4793 ± 0.0755	0.1175 ± 0.008	0.1621 ± 0.119
2	0.0597 ± 0.027	0.5495 ± 0.0422	0.1167 ± 0.0198	0.0779 ± 0.0352
3	0.0597 ± 0.0257	0.5461 ± 0.0414	0.1261 ± 0.0159	0.0844 ± 0.0414
4	0.0580 ± 0.0221	0.5402 ± 0.0551	0.1260 ± 0.0347	0.0889 ± 0.046
5	0.0583 ± 0.0220	0.5222 ± 0.0414	0.1410 ± 0.0331	0.0951 ± 0.0529

Table 5. Concentration of ^{238}U after DIN *in vitro* bioaccessibility method

Time (h)	**Concentration of ^{238}U (mg kg^{-1})**			
	Gastric Phase		**Gastrointestinal Phase**	
	Lanthanide Concentrate (LC)	**Water Leach Purification (WLP)**	**Lanthanide Concentrate (LC)**	**Water Leach Purification (WLP)**
1	0.0473 ± 0.0059	0.7401 ± 0.1038	0.0437 ± 0.0086	0.0467 ± 0.0257
2	0.0523 ± 0.0048	0.8294 ± 0.0676	0.0534 ± 0.0124	0.0407 ± 0.0189
3	0.0525 ± 0.0054	0.8731 ± 0.0548	0.0535 ± 0.0132	0.0422 ± 0.0191
4	0.0554 ± 0.0045	0.8134 ± 0.0773	0.0558 ± 0.0164	0.0480 ± 0.0213
5	0.0500 ± 0.0043	0.8671 ± 0.2252	0.0517 ± 0.0098	0.0430 ± 0.0198

The maximum concentrations of ^{232}Th in the LC and WLP residue during the intestinal phase were 0.1410 ± 0.0331 mg kg^{-1} and 0.1621 ± 0.1190 mg kg^{-1}, respectively. As seen in Figure 1, the solubility of ^{232}Th in the LC during the gastric phase slightly decreased at period 6 (7-hour mark), while the solubility of ^{232}Th in the LC increased gradually during the intestinal phase. The increasing solubility of ^{232}Th in the LC during the intestinal phase was due to its content of ThO_2, which is insoluble in acid and alkali. According to Langmuir and Herman [19], ThO_2 solubility with organic ligands present is increased by 5 orders of magnitude compared with the purely inorganic solubility at a pH of 5. The range in increased solubility extended up to a pH of 8, where inorganic ligands alone only significantly affected the solubility below a pH of 7. Thus, it was proven that ^{232}Th might exist in insoluble and refractory forms in LC. After treating the LC with concentrated sulphuric acid in the plant process, ^{232}Th was removed with other impurities into the WLP residue and remained in insoluble form, which was not dissolved by strong acids or alkali. Furthermore, the differences in pH in the content of the upper gastrointestinal tract between fed and fasted states may also influence the dissolution and absorption of weakly acidic and basic of ingestion soil. The fate and mobility of Th in environmental media are governed by its chemical and biological behaviours. The quadrivalent Th compounds are very stable towards reducing agents. Because of its low solubility, Th, which is discharged as ThO_2 on water surfaces from mining, milling, and processing, is present as suspended particles or sediments in water [20]. The International Commission on Radiological Protection (ICRP) has proposed a human gastrointestinal absorption value of 0.02 % for all forms of Th [21]. Based on Johnson and Lamothe's review of literature, a human gastrointestinal absorption value of 0.1 % to 1 % was calculated [22]. Meanwhile, the United State Environmental Protection Agency (USEPA) highlighted that the average person ingests about 2 µg of U in food and water every day, but only a very minor fraction of 1 % or 2 % is absorbed into the body [23].

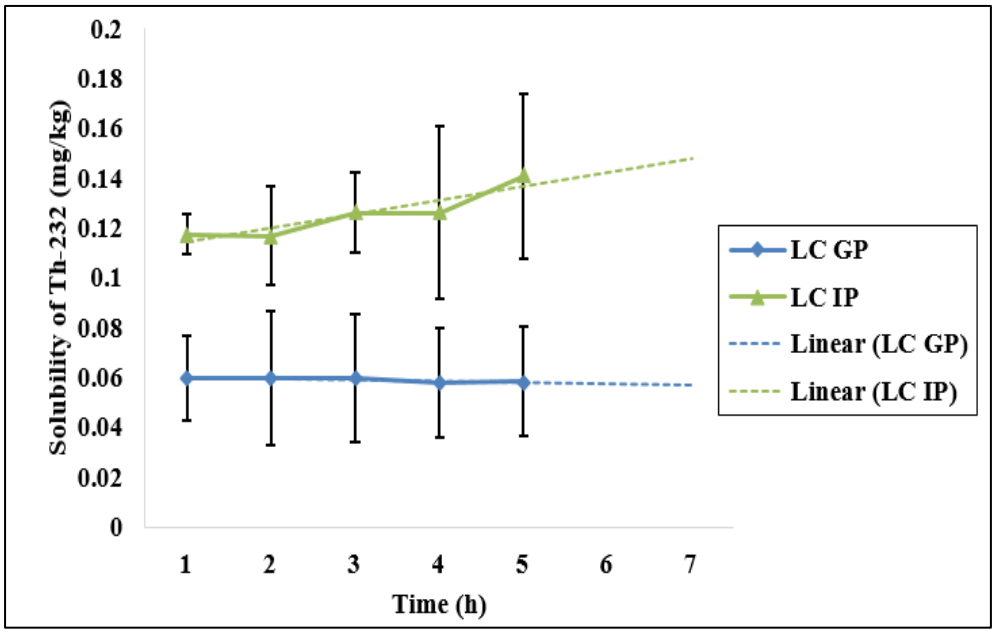


Figure 1. ^{232}Th solubility in lanthanide concentrate and water leach purification residue during gastric phase

Figure 2 shows that the solubility of ^{232}Th in the WLP residue during the gastric phase gradually increased. Contrastingly, the solubility of ^{232}Th in the WLP residue during the intestinal phase decreased. The decrease in ^{232}Th in the WLP residue could have been due to chemical precipitation at a pH of 7.5, while the solubility of ^{232}Th decreased due to adsorption in mineral soils, organic material, and other suspended solids because absorption of metals by soil is known to increase with pH [24]. Increasing pH intensifies ^{232}Th adsorption into clays, oxides, and organic matter, which is almost accomplished at a pH of 6.5 [25]. Soil properties, particularly pH and existing organic matter, influenced the absorption of radionuclides in soil [26]. Th in the tetravalent oxidation state forms insoluble crystalline or hydrous oxides that can perpetuate in low aqueous concentrations in natural waters and

waste repository environments [27]. Hydroxide and carbonate are the two dominant ligands in the groundwater system. Hydrous Th(IV) oxides are soluble at low pH values, but the solubility decreases significantly at pH values higher than 3–4. Therefore, it was practical to use amorphous hydrous Th(IV) oxide in this study, as it is the initial solid phase precipitated under oversaturation conditions and equilibrates with the aqueous phase more rapidly [28].

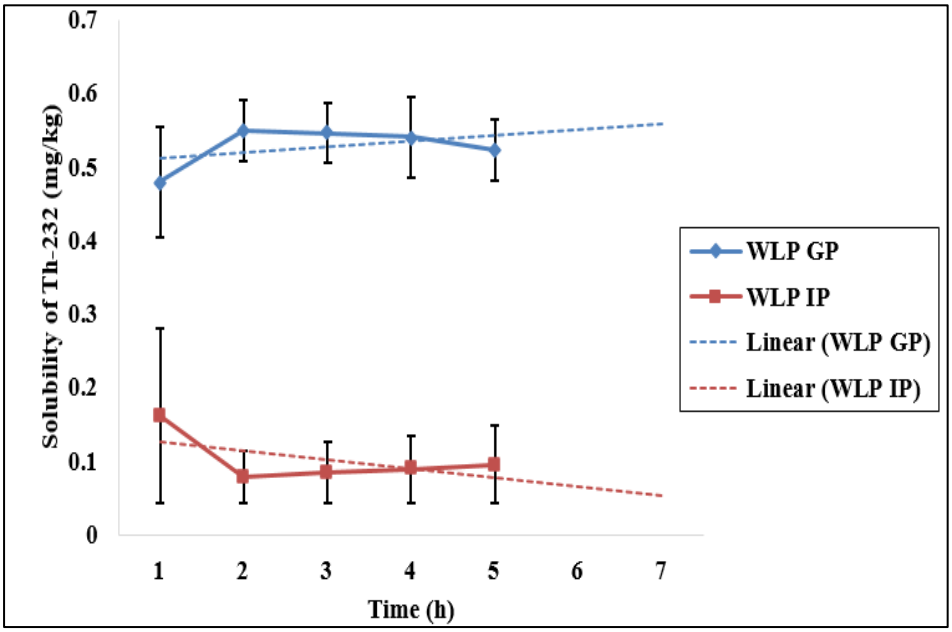


Figure 2. ^{232}Th solubility in lanthanide concentrate and water leach purification residue during gastrointestinal phase

The solubility of ^{238}U in the LC and WLP residue during the gastrointestinal phase is presented in Figure 3 and Figure 4. The results in Figure 3 show that based on the trendline pattern at 6 and 7 hours, the solubility of ^{238}U in the LC during the gastric phase and gastrointestinal phase increased with respect to time. Comparing Figure 3 with Figure 4, the following results depicted that the solubility of ^{238}U in the WLP residue increased during the gastric phase and was consistent when entering the intestinal phase. The solubility of ^{238}U in the WLP residue was higher than that in the LC during the gastric phase. The maximum solubility of ^{238}U in the LC and WLP residue was 0.8731 ± 0.0548 mg kg^{-1} during the gastric phase and 0.0558 ± 0.0164 mg kg^{-1} during the gastrointestinal phase. The overall result showed that the solubility of ^{238}U in the LC and WLP residue during the gastric phase was higher than that in the intestinal phase due to the more acidic pH in the gastric phase. As stated by Oliver et al., the solubility of trace elements can be improved by lowering the pH of stomach synthetic gastric fluid [29]. This results in ^{238}U being dissolved with acid in a chemical reaction. It can be said that ^{238}U reacts chemically under acidic conditions compared to alkaline conditions.

Lynas' report documented that over 99 % of ^{238}U in the feed LC is eliminated to WLP residue and by calcination at temperatures up to 600 °C, and ^{238}U is transformed into refractory and insoluble forms and later discarded into the WLP residue [15, 30]. The solubility of ^{238}U is very minimal when the pH surpasses 1. Contrarily, ^{238}U solubility is elevated by lowering the pH value. This affects the dissolution of ^{238}U with acid in chemical reactions [31, 32]. ^{238}U concentrations rely on the intake amount of the soil samples, volume of gastric fluid, and volume of intestinal fluid [33]. In addition, the solubility of ^{238}U shows the amount of ^{238}U that is dissolvable in gastrointestinal fluids, and it shows an association between concentration and solubility. Table 5 exhibits the maximum concentration of ^{238}U in the gastrointestinal phase for high-risk cases, which was 0.0558 ± 0.0164 mg kg^{-1}.

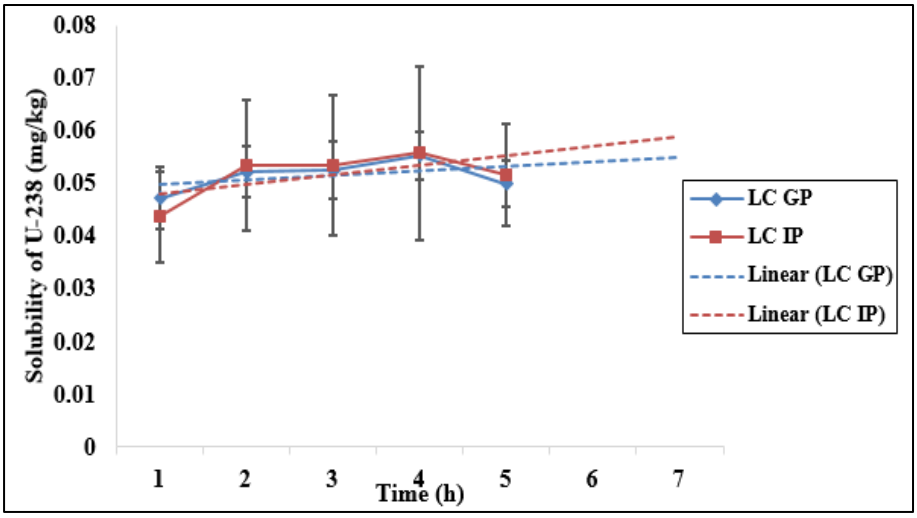


Figure 3. Solubility of ^{238}U in lanthanide concentrate and water leach purification residue during gastric phase

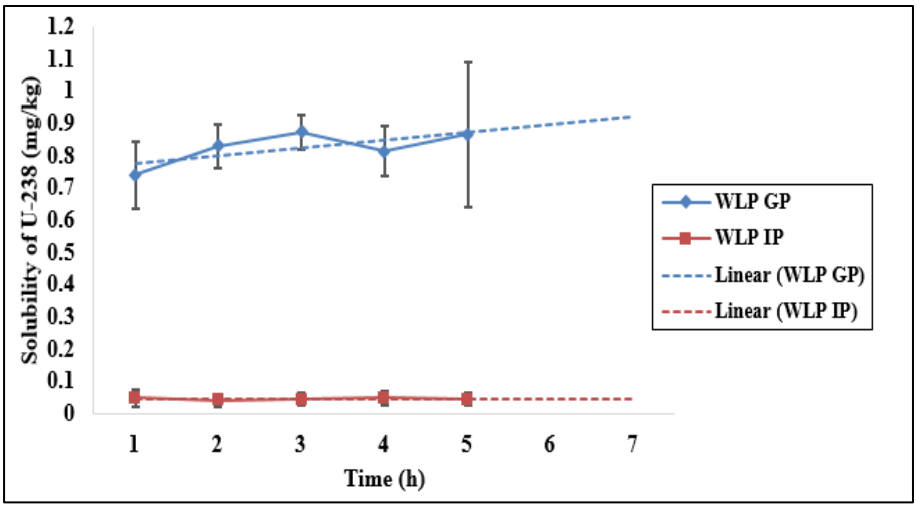


Figure 4. Solubility of ^{238}U in lanthanide concentrate and water leach purification residue during gastrointestinal phase

Specific activity of ^{232}Th and ^{238}U in the samples

Correspondingly, the maximal concentrations of ^{232}Th in the LC and WLP residue during the intestinal phase for high-risk cases were 0.1410 ± 0.0331 mg kg^{-1} and 0.1621 ± 0.1190 mg kg^{-1}, respectively. Meanwhile, the maximum concentrations of ^{238}U in the LC and WLP residue were 0.0558 ± 0.0164 mg kg^{-1} and 0.0480 ± 0.0213 mg kg^{-1}, respectively, during the intestinal phase for high-risk cases. During this study, maximum values of ^{232}Th and ^{238}U solubility were recorded to diagnose high-risk cases. Table 6 and Table 7 present the daily and annual intakes, as well as the daily and annual specific activities of ^{232}Th and ^{238}U in the LC and WLP residue during the gastrointestinal phase. In the report of the Agency for Toxic Substances and Disease Registry (ATSDR) of 1990, the daily intake of Th from food and water ingestion was 0.0023 µg kg^{-1}. Based on Table 6, it can be seen that the daily intake of ^{232}Th was lower than the ATSDR reference level [34]. The ^{238}U day-to-day intake was below the minimal risk level for intermediate-duration ingestion where the recommended oral uptakes are 0.0020 mg kg^{-1} day^{-1} [35], 0.0007 mg kg^{-1} day^{-1} [36], 0.0006 mg kg^{-1} day^{-1} [37, 38], and 0.0002 mg kg^{-1} day^{-1} [39].

Table 6. The daily concentration intakes, annual concentration intakes, daily specific activity intakes, and the annual specific activity intakes of ^{232}Th in the samples

	Maximum intake of ^{232}Th			
	Daily		**Annual**	
	(mg kg^{-1} day^{-1})	**(Bq kg^{-1} day^{-1})**	**(mg kg^{-1} year^{-1})**	**(Bq kg^{-1} year^{-1})**
Lanthanide concentrate (LC)	0.260	1.057	95.012	385.750
Water leach purification (WLP)	0.432	1.755	157.777	640.576

Table 7. The daily concentration intakes, the annual concentration intakes, the daily specific activity intakes and the annual specific activity intakes of ^{238}U in the samples

	Maximum intake of ^{238}U			
	Daily		**Annual**	
	(mg kg^{-1} day^{-1})	**(Bq kg^{-1} day^{-1})**	**(mg kg^{-1} year^{-1})**	**(Bq kg^{-1} year^{-1})**
Lanthanide concentrate (LC)	0.112	1.3783	40.734	503.065
Water leach purification (WLP)	0.096	1.186	35.040	432.749

Bioaccessibility of ^{232}Th and ^{238}U

A compound moving from its matrix (bioaccessibility) in the gastrointestinal tract is a dynamic process with constant changes in physiological conditions. By making use of *in vitro* bioaccessibility models, the digestion process in the gastrointestinal tract is imitated in a more intelligible manner by using physiological-based conditions, namely the chemical composition of digestive fluids, pH, and the usual residence times for each movement.

The gastrointestinal bioaccessibility of ^{232}Th and ^{238}U are summarised in Table 8. Based on these observations, the values of ^{232}Th radionuclide bioaccessibility in the LC and WLP residue were 0.14% and 0.10%, respectively. Concurrently, ^{238}U bioaccessibility in the WLP residue during the gastric phase was significantly higher than other values. As highlighted by Oomen et al. [9, 40], pH is probably the main factor that influences the final outcome; low pH during the stomach phase causes higher bioaccessibility values. Aside from stomach pH as a digestion parameter, residence time and bile salt concentrations also influence the bioaccessibility measurements [41]. The contaminant bioaccessibility can be determined in each compartment; however, compound absorption predominantly occurs in the small intestine, which is also known as the gastrointestinal phase. Therefore, bioaccessibility is only determined in the gastrointestinal chyme [42]. Thus, the value for the gastrointestinal phase was appraised in this study. Bioaccessibility illustrates the fraction of a chemical that desorbs from the soil matrix and is accessible for intestinal absorption.

The ^{238}U radionuclide in the LC had the highest bioaccessibility value (0.93%), whereas the ^{238}U in the WLP residue yielded lower values, which was 0.70% in the gastrointestinal phase. As specified by Morrow et al. [43], solubility in the body fluids is the best predictor of U compounds that are absorbed in the human body, rather than their water solubility [44]. The maximum bioaccessibility values for ^{232}Th and ^{238}U were 0.14% and 0.93%, respectively, which were lower than the bioaccessible fraction, i.e. $F_B < 1$. This verified that the value had lower internal exposure. The maximum amount of a contaminant available for absorption inside the human body is represented by F_B; therefore, the oral bioavailability may not be higher than the bioaccessibility. Thus, a bioaccessibility of lower than 100 % suggested that the internal exposure to the contaminant was lower compared to the external exposure, and that the internal exposure to the contaminants was overestimated [9, 40].

Table 8. Bioaccessibility of ^{232}Th and ^{238}U in lanthanide concentrate and water leach purification residue by DIN *in vitro* bioaccessibility model

	Bioaccessibility (%)	
	^{232}Th	**^{238}U**
Lanthanide concentrate (LC)	0.14	0.93
Water leach purification (WLP)	0.10	0.70

Equivalent dose and effective dose

According to International Atomic Energy Agency (IAEA) [45], the committed equivalent tissue dose per unit activity for ^{232}Th ingested by adults is 70 µSv Bq^{-1} for bone surfaces, 0.78 µSv Bq^{-1} for the kidneys, 0.74 µSv Bq^{-1} for the liver, and 2.0 µSv Bq^{-1} for red marrow. According to the ICRP [21], the committed effective dose coefficients of ^{232}Th for workers and the public are 0.22 µSv Bq^{-1} and 0.23 µSv Bq^{-1}, respectively. In contrast, the dose coefficient committed equivalent tissue dose per unit activity for ^{238}U ingested by adults is 0.71 µSv Bq^{-1} for bone surfaces, 0.25 µSv Bq^{-1} for the kidneys, 0.096 µSv Bq^{-1} for the liver, and 0.075 µSv Bq^{-1} for red marrow. Based on the ICRP 60, the committed effective doses of ^{238}U for workers and the public are 0.44 µSv Bq^{-1} and 0.45 µSv Bq^{-1}, respectively. High committed equivalent doses and committed effective doses of ^{232}Th and ^{238}U that were found in the LC and WLP residue are presented in Table 9 and Table 10, respectively. The committed equivalent doses and committed effective doses of ^{232}Th and ^{238}U in Table 9 and Table 10 were below the United Nations Scientific Committee on the Effects of Atomic Radiation (UNSCEAR) reference values.[46].

Table 9. Committed equivalent doses and committed effective doses of ^{232}Th

	^{232}Th (µSv)					
	Committed Equivalent Doses				**Committed Effective Doses**	
	Kidneys	**Liver**	**Bone Surfaces**	**Red Marrow**	**Public**	**Workers**
Lanthanide Concentrate (LC)	1.204	1.142	108.009	3.086	0.355	0.339
Water Leach Purification (WLP)	1.999	1.896	17.936	5.125	0.589	0.564

Table 10. Committed equivalent doses and committed effective doses of ^{238}U

	^{238}U (µSv)					
	Committed Equivalent Doses				**Committed Effective Doses**	
	Kidneys	**Liver**	**Bone Surfaces**	**Red Marrow**	**Public**	**Workers**
Lanthanide Concentrate (LC)	0.503	0.193	1.429	0.151	0.091	0.089
Water Leach Purification (WLP)	0.433	0.166	1.229	0.130	0.078	0.076

Conclusion

In summary, the present study illustrated that bioaccessibility of ^{232}Th and ^{238}U in the gastric phase is higher than that in the gastrointestinal phase; the values were acquired using DIN *in vitro* bioaccessibility methodology. Health risk assessments depicted the estimated daily intake, committed equivalent, and effective doses of LC and WLP residue through ingestion as significantly lower than the acceptable reference level. Therefore, there were no health

effects related to the radiotoxicity of the incorporated nuclides. Finally, future research is required in order to differentiate ^{232}Th and ^{238}U by *in vivo* bioavailability values measured using different biomarkers and non-identical animal models.

Acknowledgement

The authors would like to thank Universiti Kebangsaan Malaysia for financial support under the project code DLP/2014/011.

References

1. Charalampides, G. and Vatalis, K. I. (2015). Global production estimation of rare earth elements and their environmental impacts on soils. *Journal of Geoscience and Environment Protection*, 3(8): 66.
2. Schmidt, G. (2013). Description and critical environmental evaluation of the REE refining plant LAMP near Kuantan/Malaysia. Radiological and non-radiological environmental consequences of the plant's operation and its wastes.
3. O'Brien, R., S. and Cooper, M. B. (1998). Technologically enhanced naturally occurring radioactive material (NORM): Pathway analysis and radiological impact. *Applied Radiation and Isotopes.* 49(3):227-239.
4. Sowby, F., D. (1965). Radiation protection. *Canadian Medical Association Journal*, 92(19): 1039.
5. World Health Organization (2012). Ionizing radiation, health effects and protective measures. Access online http://www.who.int/news-room/fact-sheets/detail/ionizing-radiation-health-effects-and-protectiv-measures [Access online 20 April 2016].
6. Chaney, R. L., Mielke, H.W. and Sterrett, S. B. (1989). Speciation, mobility and bioavailability of soil lead. *Environmental Geochemistry Health*, 11: 105-129.
7. Calabrese, E. J. and Stanek, E. J. (1994). Soil ingest ion issues and recommendations. *Journal of Environmental Science & Health Part A*, 29(3): 517-530.
8. Omar, N. A., Praveena, S., Mohd, A., Ahmad, Z. and Hashim, Z. (2013). Bioavailability of heavy metal in rice using *in vitro* digestion model. *International Food Research Journal*, 20(6): 2979-2985.
9. Oomen, A. G., Rompelberg, C. J. M., Bruil, M. A., Dobbe, C. J. G., Pereboom, D. P. K. H. and Sips, A. J. A. M. (2003). Development of an *in vitro* digestion model for estimating the bioaccessibility of soil contaminants. *Archives of Environmental Contamination and Toxicology*, 44(3): 0281-0287.
10. Monachese, M., Burton, J. P. and Reid, G. (2012). Bioremediation and tolerance of humans to heavy metals through microbial processes: A potential role for probiotics. *Applied and Environmental Microbiology*, 78(18): 6397-6404.
11. Al-Jundi, J., Werner, E., Roth, P., Höllriegl, V., Wendler, I. and Schramel, P. (2004). Thorium and uranium contents in human urine: Influence of age and residential area. *Journal of Environmental Radioactivity*, 71(1): 61-70.
12. Van, D., W., Tom, R., Oomen, A., G., Wragg, J., Cave, Mark, Minekus, Mans, Hack, Alfons and Klinck, B. (2007). Comparison of five *in vitro* digestion models to in vivo experimental results: Lead bioaccessibility in the human gastrointestinal tract. *Journal of Environmental Science and Health Part A*, 42(9): 1203-1211.
13. Kolo, M. T., Aziz, Siti, A. A., Khandaker, M., Uddin, A., Khandoker and Amin, Y. M. (2015). Evaluation of radiological risks due to natural radioactivity around Lynas Advanced Material Plant environment, Kuantan, Pahang, Malaysia. *Environmental Science and Pollution Research*, 22(17): 13127-13136.
14. Wragg, J. and Cave, M. In-vitro methods for the measurement of the oral bioaccessibility of selected metals and metalloids in soils: A critical review. R&D Technical Report P5-062/TR/01 Environment Agency: pp. 1-28.
15. National Toxics Network (2012). Rare earth and radioactive waste a preliminary waste stream assessment of the Lynas Advanced Materials Plant, Gebeng, Malaysia.
16. Pasquale, V., Verdoya, M. and Chiozzi, P. (2001). Radioactive heat generation and its thermal effects in the Alps–Apennines boundary zone. *Tectonophysics*, 331(3): 269-283.
17. Guo, P., Duan, T., Song, X., Xu, J. and Chen, H. (2008). Effects of soil pH and organic matter on distribution of thorium fractions in soil contaminated by rare-earth industries. *Talanta*, 77(2): 624-627.
18. International Atomic Energy Agency (2011). Radiation protection and NORM residue management in the production of rare earths from thorium containing minerals. Safety Reports Series No. 68.
19. Langmuir, D. and Herman, J. S. (1980). The mobility of thorium in natural waters at low temperatures. *Geochimica et Cosmochimica Acta*, 44(11):1753-1766.

20. Platford, R. F. and Joshi, S. R. (1989). Radionuclide partitioning across Great Lakes natural interfaces. *Environmental Geology and Water Sciences*, 14(3):183-186.
21. International Commission on Radiological Protection (2012). ICRP Publication 119: Compendium of Dose Coefficients Based On ICRP Publication 60. *Annal ICRP*, 42(4): 2013.
22. Johnson, J. R. and Lamothe, E. S. (1989). A review of the dietary uptake of Th. *Health Physics*, 56(2): 165-168.
23. United States Environmental Protection Agency (2015). Radionuclide basics: Uranium. Access from https://www.epa.gov/radiation/radionuclide-basics-uranium [Access online 11 Jan 2018].
24. Hooda, P. S., Henry, C. J. K., Seyoum, T. A., Armstrong, L., D. M. and Fowler, M. B. (2004). The potential impact of soil ingestion on human mineral nutrition. *Science of the Total Environment*, 333(1): 75-87.
25. Bondietti, E.A. (1974). Adsorption of U (+ 4) and Th (+ 4) by soil colloids. In *Agronomy Abstracts*, 23.
26. Guo, P., Duan, T., Song, X. and Chen, H. (2007). Evaluation of a sequential extraction for the speciation of thorium in soils from Baotou area, Inner Mongolia. *Talanta*, 71(2):778-783.
27. Reiller, P., Moulin, V., Casanova, F. and Dautel, C. (2002). Retention behaviour of humic substances onto mineral surfaces and consequences upon thorium(IV) mobility: Case of iron oxides. *Applied Geochemistry*, 17(12): 1551-1562.
28. Rand, M., H., Mompean, F., J., Perrone, J. and Illemassène, M. (2008). Chemical thermodynamics of thorium. OECD Publishing, 11: 1-393
29. Oliver, D. P., McLaughlin, M. J., Naidu, R., Smith, L. H., Maynard, E. J. and Calder, I. C. (1999). Measuring Pb bioavailability from household dusts using an *in vitro* model. *Environmental Science & Technology*, 33(24): 4434-4439.
30. Golev, A., Scott, M., Erskine, P. D., Ali, S. H. and Ballantyne, G. R. (2014). Rare earths supply chains: Current status, constraints and opportunities. *Resources Policy*. 41: 52-59.
31. Adams, W. H., Buchholz, J. R., Christenson, C. W., Johnson, G. L. and Fowler, E. B. (1974). Studies of plutonium, americium, and uranium in environmental matrices: Los Alamos Scientific Lab., North Mexico.
32. Träber, S. C., Höllriegl, V., Li, W. B., Czeslik, U., Rühm, W., Oeh, U. and Michalke, B. (2014). Estimating the absorption of soil-derived uranium in humans. *Environmental Science & Technology*, 48(24): 14721-14727.
33. Rashid, N. S. A., Sarmani, S., Majid, A. A., Mohamed, F. and Siong, K. K. (2015). Solubility of 238U radionuclide from various types of soil in synthetic gastrointestinal fluids using "USP *in vitro*" digestion method. *Proceedings of the Nuclear Science, Technology, and Engineering Conference 2014* (NuSTEC2014).
34. Agency for Toxic Substances and Disease Registry (1990). Public health statement for Thorium. Access from https://www.atsdr.cdc.gov/phs/phs.asp?id=658&tid=121 (21 January 2018).
35. Agency for Toxic Substances and Disease Registry (1999). Toxicological profile: Uranium. Access from https://www.atsdr.cdc.gov/toxprofiles/TP.asp?id=440&tid=77 (21 January 2018).
36. Jacob, P., Pröhl, G., Schneider, K. and Voß, J. U. (1997). Machbarkeitsstudie zur Verknüpfung der Bewertung radiologischer und chemisch-toxischer Wirkungen von Altlasten: Inst. für Strahlenschutz.
37. World Health Organization (1998). Guidelines for drinking-water quality, Second edition, Addendum to Volume 2: Health Criteria and Other Supporting Information, WHO/EOS/98.1, Geneva 1998: pp. 283.
38. World Health Organization. (2003). Guidelines for Drinking Water Quality, Third edition. Volume 1 – Recommendations Incorporating first and second addenda: pp. 1-668.
39. Konietzka, R., Dieter, H. H. and Voss, J. U. (2005). Vorschlag für einen gesundheitlichen Leitwert für Uran in Trinkwasser. *Umweltmed Forsch Prax*, 10(2):133-143.
40. Oomen, A., G., Hack, A., Minekus, M., Zeijdner, E., Cornelis, C., Schoeters, G. and Rompelberg, C., J., M. (2002). Comparison of five *in vitro* digestion models to study the bioaccessibility of soil contaminants. *Environmental Science & Technology*, 36(15): 3326-3334.
41. Jadán, P., Carlos, C., P., Marie, J., Devesa, V. and Vélez, D. (2016). Influence of physiological gastrointestinal parameters on the bioaccessibility of mercury and selenium from swordfish. *Journal of Agricultural and Food Chemistry*, 64(3): 690-698.
42. Vázquez, M., Calatayud, M., Piedra, C. J., Chiocchetti, G. M., Vélez, D. and Devesa, V. (2015). Toxic trace elements at gastrointestinal level. *Food and Chemical Toxicology*. 86:163-175.
43. Morrow, P. E., Gibb, F. R. and Beiter, H. D. (1972). Inhalation studies of uranium trioxide. *Health Physics*, 23(3): 273-280.
44. Leggett, R. W. and Harrison, J. D. (1995). Fractional absorption of ingested uranium in humans. *Health Physics*, 68(4): 484-498.

45. International Atomic Energy Agency (1999). Assessment for doses to the public from ingested radionuclides. IAEA Publishing, Safety Reports Series No. 14.
46. United Nations Scientific Committee on the Effects of Atomic Radiation (2000). Sources and effects of ionizing radiation: sources. United Nations Publications, 1: 1-17.

Malaysian Journal of Analytical Sciences, Vol 22 No 5 (2018): 807 - 816
DOI: https://doi.org/10.17576/mjas-2018-2205-08

MALAYSIAN JOURNAL OF ANALYTICAL SCIENCES
Published by The Malaysian Analytical Sciences Society
ISSN 1394 - 2506

PHOTOCATALYTIC DEGRADATION OF PHENOL DERIVATIVES OVER SILVER SUPPORTED ON MESOPOROUS TITANIA NANOPARTICLES

(Degradasi Fotomangkinan Terbitan Fenol Ke Atas Perak Disokong Pada Titania Nanopartikel Berliang Meso)

Nur Farhana Jaafar[1]* and Aishah Abdul Jalil[2,3]

[1]*School of Chemical Sciences,*
Universiti Sains Malaysia, 11800 USM Penang, Malaysia
[2]*Centre for Hydrogen Energy, Institute of Future Energy*
[3]*Department of Chemical Engineering, Faculty of Chemical and Energy Engineering*
Universiti Teknologi Malaysia, 81310 UTM Johor Bahru, Johor, Malaysia

**Corresponding author: nurfarhana@usm.my*

Received: 15 May 2018; Accepted: 23 July 2018

Abstract

In this study, the potential of silver supported on mesoporous titania nanoparticles (Ag-MTN) as visible-light-driven photocatalyst was investigated for the degradation of phenol derivatives. Characterisation results illustrated that the presence of Ag reduced the band gap of MTN and increased the number of oxygen vacancies (OV) and Ti^{3+} site defect (TSD). The presence of both properties is among the important factors that need to be considered for catalyst properties in order to achieve effective photocatalytic degradation under visible light. The photoactivity of the catalyst was also significantly influenced by the presence of Ag, which acted as an electron trap that enhanced electron-hole separation. The ability of Ag-MTN to degrade phenol derivatives [phenol (Ph), 2-chlorophenol (2-CP), 2,4-dichlorophenol (2,4-diCP), and 4-acetamidophenol (4-AcePh)] was compared with commercial TiO_2 and MTN. The percentage degradation of phenol derivatives was in the following order: TiO_2 < MTN < Ag-MTN. This indicated that the presence of Ag in MTN effectively enhanced the photoactivity of MTN towards the degradation of phenol derivatives.

Keywords: Ag-MTN catalyst, electron trapper, visible light, phenol derivatives

Abstrak

Dalam kajian ini, potensi perak disokong pada nanopartikel titania berliang meso (Ag-MTN) sebagai fotomangkin-pemacu-cahaya nampak telah disiasat bagi degradasi terbitan fenol. Keputusan pencirian menunjukkan kehadiran Ag mengurangkan luang jalur MTN dan meningkatkan bilangan kekosongan oksigen (OV) dan permukaan Ti^{3+} cacat (TSD). Kehadiran kedua-dua sifat adalah antara faktor penting yang perlu dipertimbangkan bagi sifat mangkin bagi mencapai degradasi fotomangkin yang efektif di bawah cahaya nampak. Fotoaktiviti bagi mangkin juga sangat dipengaruhi dengan kehadiran Ag di mana bertindak sebagai perangkap elektron yang meningkatkan pemisahan elektron-lubang. Keupayaan Ag-MTN untuk degradasi terbitan fenol [fenol (Ph), 2-klorofenol (2-CP), 2,4-diklorofenol (2,4-diCP) dan 4-asetamidofenol (4-AcePh)] telah dibandingkan dengan TiO_2 komersial dan MTN. Peratusan degradasi bagi terbitan fenol telah mengikuti susunan: TiO_2 < MTN < Ag-MTN. Ini menunjukkan kehadiran Ag dalam MTN berkesan meningkatan fotoaktiviti bagi MTN terhadap degradasi terbitan fenol.

Kata kunci: mangkin Ag-MTN, perangkap elektron, cahaya nampak, terbitan fenol

Introduction

Phenol derivatives are widely used as intermediates in pulp, paper, biocides, cleaning agents, dyes, preservatives, and pesticides industries [1]. However, the release of phenol derivatives into aqueous environmental systems has raised concerns due to their high toxicity, high stability, and potentially carcinogenic [2]. The carbon-halogen bond causes recalcitrance of phenol derivatives, which is cleaved with great difficulty and the stability of their aromatic structure, resulting in their growth in nature. As a result, the Department of Environment (DOE) Malaysia has gazetted the allowable limits as in Environmental Quality (Sewage and Industrial Effluent) Regulations, 1979, that this pollutant should be treated to be less than 1 mg L^{-1} before being discharged to water bodies.

There are ongoing studies on the appropriate methods for eliminating these toxic organic compounds from aqueous systems due to the adverse effect caused by phenol derivatives on the environment and humans. Several removal techniques including ion exchange, adsorption, and solvent extraction have been proposed for removing or treating phenol derivatives [3]. However, these techniques incur high cost, is time consuming, and can be responsible for generation of secondary pollutants [4]. Heterogeneous photocatalysts such as TiO_2, FeOOH, ZnO, CuO, and ZrO_2 are commonly used in advanced oxidation process (AOP) for removal of this recalcitrant pollutant. Among them, TiO_2 shows superior performance due to its strong oxidising power and chemical inertness [5]. However, photocatalytic application of TiO_2 has been limited by its high photogenerated electron-hole recombination rate caused by the rapid transfer of electrons generated from the semiconductors to the metal particles and can only be excited by UV-light irradiation [6]. Hence, many approaches have been reported to overcome this problem such as varying the synthesis method in order to obtain a mesoporous structure for enhancing its efficiency and modification with other semiconductors or noble metals.

Nowadays, self-modified mesoporous titania nanoparticles (MTN) containing oxygen vacancies (OV) and Ti^{3+} site defects (TSD) are one of the approaches in light-absorption modification for TiO_2 to increase its photocatalytic performance [7]. Microwave (MW)-assisted method is one of the efficient methods that have been studied to synthesise MTN since it could provide a uniform and fast reaction environment to produce mesoporous materials [8]. Besides, Ag^0 is one of the potential photocatalysts to be used in the doping with TiO_2 due to its properties that delay the recombination of photogenerated electron-hole pairs by acting as an electron trap [9]. Various methods have been used to activate Ag^+ to Ag^0 for synthesising Ag-MTN including electrochemical method, which is a simple activation of Ag^0 onto MTN without the need of high temperature or longer time. Therefore, we reported the synergistic effect between Ag^0 and MTN towards the degradation of phenol derivatives under visible light.

Materials and Methods

Reagents, material and apparatus

TiO_2 powder catalyst, JRC-TiO_2-2, was supplied by the Catalysis Society of Japan and titanium (IV) isopropoxide (TTIP) was bought from Sigma Aldrich. Ag and Pt plates of greater than 99% purity were used as electrodes and were obtained from Nilaco, Japan. *N*,*N*-dimethylformamide (DMF), cetyltrimethylammonium bromide (CTAB), propanol, phenol (Ph), 2-chlorophenol (2-CP), 2,4-dichlorophenol (2,4-diCP), 4-acetamidophenol (4-AcePh), and perchloric acid were purchased from MERCK, Malaysia. Naphthalene and tetraethylammonium bromide solution were obtained from Fluka Chemical and acetone was purchased from HmbG Chemical. Sodium hydroxide (NaOH), ammonium hydroxide (NH_4OH), and hydrochloric acid (HCl) were purchased from QREC^{TM} and methanol was purchased from RPE Reagent Pure Erba. Tetraethylammonium perchlorate (TEAP), which was used as a supporting electrolyte in the electrolysis, was prepared in accordance with the procedure reported in the literature [10].

Preparation of catalyst: Synthesis of mesoporous titania nanoparticles

Mesoporous titania nanoparticles (MTN) was synthesised by dissolving 4.68 g of CTAB in 720 ml of distilled water, 120 ml of propanol, and 29 ml of 28% ammonia solution. The mixture was stirred continuously for 30 minutes at 323 K in water bath. Then, the temperature of water bath was increased to 353 K, followed by the addition of 5.7 mL TTIP, and the mixture was stirred for another 2 hours. The white solution was transferred into a beaker after 2 hours of stirring and placed in a microwave. The heating continued under 0.56 Wg^{-1} as the power density of microwave until a sol-gel of TiO_2 was formed. The obtained product was collected and dried overnight in an oven before calcination at 873 K for 3 hours.

Synthesis of silver supported on mesoporous titania nanoparticles

The synthesis of Ag-MTN was carried out using a simple electrochemical method in accordance with procedure in the literature [11]. A closed-system electrolysis cell was fitted with a magnetic stirrer and a platinum plate cathode facing a silver plate anode. Then, MTN and TEAP were added to DMF. The electrolysis was conducted at a constant current of 240 mA cm^{-2} and 273 K under air atmosphere to load 5 wt.% Ag on MTN. The sample was evaporated and dried at 383 K for 12 hours before calcination at 873 K for 3 hours to yield a grey powder catalyst donated Ag-MTN that is ready for characterisation and photocatalytic testing.

Characterisation

The crystalline structures of the catalysts were examined using a Bruker Advance D8 X-ray powder diffractometer (XRD) with Cu Kα radiation of λ=1.5418 Å at 2θ angle ranging from 22º to 66º. The phases were identified with the aid of the Joint Committee on Powder Diffraction Standards (JCPDS) files. The chemical functional groups present in the catalysts were identified by Fourier transform infrared (FTIR) spectroscopy (Perkin Elmer Spectrum GX FTIR spectrometer). IR absorbance data were obtained over a range of wavenumbers from 390 to 3700 cm^{-1}. The morphological properties of the catalysts were examined by transmission electron microscopy (TEM, JEOL JEM-2100F). Nitrogen adsorption-desorption isotherms were used to determine the textural properties at liquid nitrogen temperatures using a, SA 3100 Surface Analyzer (Beckman Coulter). The Brunauer-Emmett-Teller (BET) and non-local density functional theory (NLDFT) methods were used to calculate surface area and pore distribution, respectively. Prior to measurement, all samples were degassed at 300 ºC and 0.1 Pa. The X-ray photoelectron spectroscopy (XPS) was conducted in the range 0–800 eV using a Kratos Ultra spectrometer equipped with Mg K_α radiation source (10 mA, 15 kV). A small Inox cylinder was used to press the powdered sample prior to analysis inside an analysis chamber pressure at about 1×10^{-10} Pa to obtain the data. The binding energy of the C (1s) at peak 284.5 ± 0.1 eV was taken as the internal standard or reference as the solution to correct the energy shift. A JEOL JES-FA100 ESR spectrometer was used for the determination of surface defect Ti^{3+} and oxygen vacancy, where the sample was placed at about 2 cm height inside the glass vessel followed by the electron spin resonance (ESR) measurement to identify the g-value at room temperature. UV-Vis diffuse reflectance spectroscopy (UV-Vis DRS) was recorded in air at room temperature using a Perkin Elmer Lambda 900 UV/Vis/NIR spectrometer with an integrating sphere.

Photodegradation of phenol derivatives

The photoactivity of the catalysts was tested for the degradation of phenol derivatives. Four types of phenol derivatives were used: Ph, 2-CP, 2,4-diCP, and 4-AcePh. The stock solutions of the phenol derivatives were prepared with the initial concentration of each derivative of 50 mgL^{-1}. The stock solutions of the phenol derivatives were mixed in the ratio of 1:1:1:1. The photocatalytic experiments were performed in a batch reactor fixed with a cooling system. A 39 W metal halide lamp (400 nm) was used as a visible light source.

For photoactivity evaluation, 0.375 gL^{-1} of MTN was added to the phenol derivatives solution (200 ml) and stirred for 1 hour in the dark to achieve adsorption-desorption equilibrium. The initial pH of the solution was pH 5 and the reaction was carried out at 30 °C. Then, the reaction was carried out for another 6 hours under light irradiation under continuous stirring. The concentration of the sample was measured using UV-Vis spectrometer at the absorption bands of 270, 274, 285, and 248 nm for Ph, 2-CP, 2,4-diCP, and 4-AcePh, respectively. Similar procedure was used for TiO_2 and Ag-MTN.

Results and Discussion

Figure 1 shows the XRD patterns of TiO_2, MTN, and Ag-MTN in the range of 2θ = 22-66°. A series of characteristic peaks was observed for TiO_2 (Fig. 1a) with peaks at 25° (101), 36.8° (103), 37.5° (004), 39° (112), 47.5° (200), 54° (105), 56° (211), and 63° (204) that was consistent with the TiO_2 anatase phase (JCPDS file no. 00-004-0477). The XRD pattern of MTN was similar to TiO_2. However, the peak intensity of MTN (Fig. 1b) seemed to be more intense compared with TiO_2, which indicated that the crystallinity of MTN is better than TiO_2. The XRD pattern of Ag-MTN catalyst (Fig. 1c) was similar to MTN (Fig.1b), which illustrated that the loading of Ag did not intrude the structure of MTN [12]. However, the peak intensity of MTN seemed to decrease with the addition of Ag, which indicated the degree of orderliness in MTN and mesoporous uniformity decreased but did not remarkably

intrude the structure of catalyst [13]. Meanwhile, new diffraction peaks were observed at 32.35° (200), 33.15° ($\bar{1}11$), and 57.2° ($\bar{1}13$) after the Ag loading due to the plane of Ag for AgO moieties in Ag-MTN [14]. In addition, another two diffraction peaks at 27.5° and 46.3° showed the presence of traces of rutile and brookite. The crystallite size of the catalysts was calculated by the Debye-Scherrer equation based on the major peak 2θ = 25° as follows:

$$\tau = \frac{k\lambda}{\beta \cos \theta} \quad (1)$$

where τ is the particle size, λ is the wavelength of X-ray radiation (Cu K_α = 0.1542 nm), k is the shape factor (k = 0.94), β is the line width at half-maximum height, and θ is the angular position of the peak maximum. It was found that the size of TiO_2 and MTN were 30.0 and 11.3 nm, respectively. However, the addition of Ag onto MTN demonstrated the decrease in the crystallite size from 11.3 to 7.21 nm, possibly due to the interaction of Ag and MTN. A similar observation was reported by Das et al., which revealed that the interaction of titania species with ZrP and TiP was the reason for the decrease in crystallite size of catalysts [15].

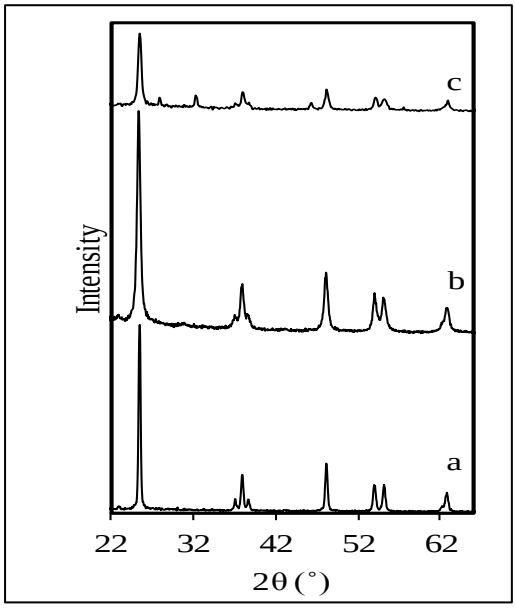


Figure 1. XRD diffractograms of (a) TiO_2 (b) MTN and (c) Ag-MTN

The textural properties for all catalysts are summarised in Table 1. The results showed that MTN has higher surface area and pore volume compared to TiO_2. This phenomenon indicates that the balance of heat distribution by microwave during the synthesis for hydrolysis and condensation may contribute to the framework cross-linking for better growth of smaller pores [16]. In contrast, the introduction of Ag onto MTN shows a decrease in surface area and pore volume probably due to the aggregation of Ag nanoparticles that blocks the pore surface of MTN. In addition, the introduction of Ag onto MTN also decreased the band gap from 3.11 to 3.05 eV. This result demonstrates that the anchoring of Ag to MTN surface helps to reduce the band gap of Ag-MTN catalyst. A similar trend was also observed by Khan et al. for the synthesis of Ag@TiO_2 composite, in which the band gap of TiO_2 decreased after the introduction of Ag from 3.33 to 2.86 eV [17].

The morphology of the catalysts was then examined by TEM analyses and the images are shown in Figure 2. The TEM images of TiO_2 (Fig. 2a) and MTN (Fig. 2b) show translucent property with irregular shaped particles. Then, the TEM image of MTN (Fig. 2b) was compared with Ag-MTN (Fig. 2c) to study their morphology properties. The original morphology of MTN was interrupted by the introduction of Ag but by comparing with the translucent image of MTN, the distribution of Ag was clearly observed in Ag-MTN. This result confirmed that Ag nanoparticles dispersed well on the surface of MTN.

Table 1. Textural properties of catalysts

Catalyst	Surface Area (m^2g^{-1})	Pore Volume (cm^3g^{-1})	[a]Band Gap (eV)
TiO_2	12.5	0.22	3.31
MTN	181	0.35	3.11
Ag-MTN	100	0.31	3.05

[a] Band gap calculated using $E_g=1240/\lambda$

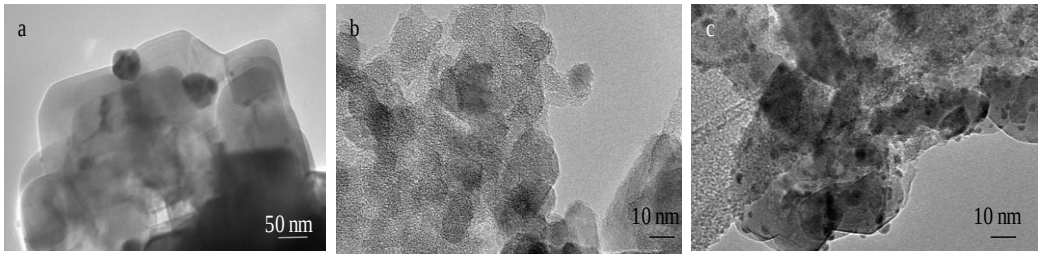


Figure 2. TEM images of (a) TiO_2 (b) MTN and (c) Ag-MTN

Figure 3 shows the FTIR spectroscopy in the range of 2000–390 cm^{-1} for all the catalysts. All catalysts showed a band at 1625 cm^{-1} that corresponded to OH vibration of the surface-adsorbed water [18]. The bands observed at 1100 and 455 cm^{-1} for MTN (Fig. 3b) and Ag-MTN (Fig. 3c) were assigned to Ti-O-Ti asymmetric stretching and bending vibration modes, respectively [19]. However, TiO_2 (Fig. 3a) illustrated that both of the bands were absent but a sharp band could be detected at 530 cm^{-1}, which was attributed to the Ti-O-Ti bond of TiO_2 anatase phase [20]. Besides, another new peak was also observed for Ag-MTN at 650 cm^{-1} attributed to the Ag-O bond, which illustrated that Ag nanoparticles were successfully introduced on MTN.

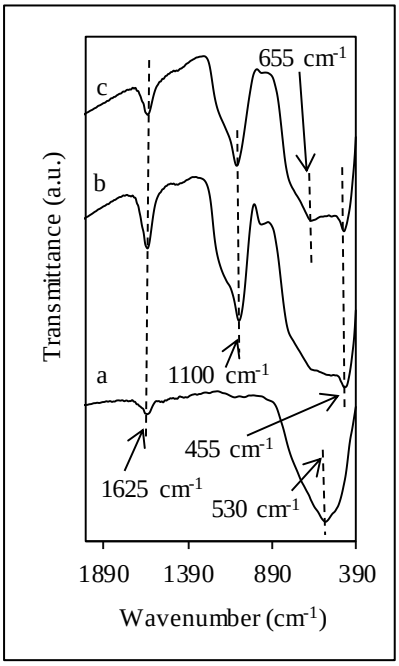


Figure 3. FTIR spectra in region 2000-390 cm^{-1} of (a) TiO_2 (b) MTN and (c) Ag-MTN

Chemical states of MTN and Ag-MTN were determined using XPS analysis as shown in Figure 4. Fig. 4A shows the wide scan for MTN and Ag-MTN. Titanium (Ti) and oxygen (O) were detected for both catalysts, while Ag could only be detected in Ag-MTN, as indexed in both catalysts. Fig. 4B(a) displays the region of Ti $2p_{3/2}$ with Ti^{3+} were observed at 457.7 and 458.9 eV while the binding energies at 458.3 and 459.3 eV were assigned to Ti^{4+} for MTN [21]. The region O 1s of MTN (Fig. 4C(a)) illustrated the existence of Ti^{3+}-O at 530.8 and 532.5 eV, whereas the binding energies at 529.5 and 534.5 eV were attributed to Ti^{4+}-O and OH or OH^-, respectively [22]. These results confirmed the presence of TSD in MTN. The XPS analysis of Ag-MTN showed that new regions were observed other than Ti $2p_{3/2}$ (Fig. 4B(b)) and O 1s (Fig. 4C(b)), which were Ti $2p_{1/2}$ (Fig. 4B(b)) and Ag 3d (Fig. 4D) prior to the introduction of Ag onto MTN. Fig. 4B(b) illustrated four binding energies in the region of Ti $2p_{3/2}$ at 458 (Ti^{3+}), 459 (Ti^{3+}), 458.4 (Ti^{4+}), and 459.5 eV (Ti^{4+}), with two binding energies at 462.8 (Ti^{4+}) and 464.7 eV (Ti^{4+}) for the region of Ti $2p_{1/2}$ [17]. Meanwhile, O 1s (Fig. 4C(b)) region showed the binding energies at 530.4 and 532.7 eV for peak Ti^{3+}-O, whereas the peaks at Ti^{4+}-O and OH or OH^- were observed at 529.5 and 534.5 eV, respectively. The presence of Ag nanoparticles was confirmed in Fig. 4D by the presence of binding energies at 368 and 374 eV, which were attributed to Ag $3d_{5/2}$ and Ag $3d_{3/2}$, respectively [23]. This result agrees with XRD (Fig. 1c) and FTIR (Fig. 3) analysis where Ag and AgO were detected.

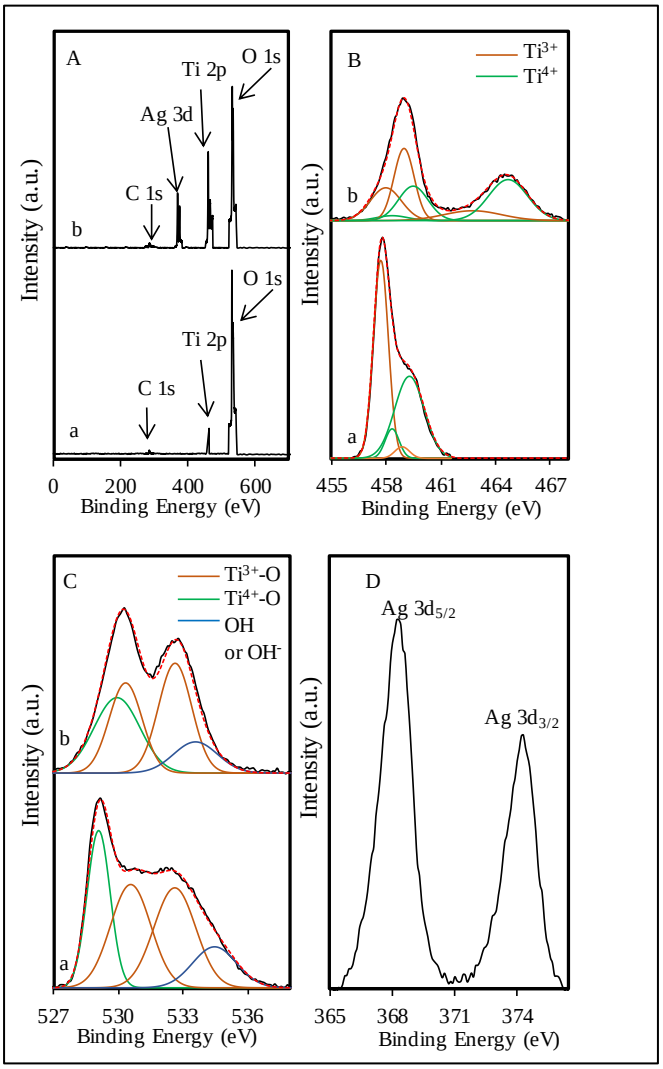


Figure 4. XPS spectra of (A) wide scan; (B) Ti 2p; (C) O 1s of (a) MTN and (b) Ag-MTN; and (D) Ag 3d of Ag-MTN

In addition, ESR also further confirmed the presence of TSD and oxygen vacancies (OV) for the catalysts and the results are shown in Figure 5. Two signals corresponded to OV and TSD sites were observed at g=1.99 and g=1.96, respectively. The signal intensity of Ag-MTN (Fig. 5c) was the highest for both OV and TSD prior to the introduction of Ag onto MTN compared to MTN. However, the signal intensities of MTN (Fig. 5b) were higher compared to TiO_2 (Fig. 5a). These results signify the presence of OV and TSD in all catalysts where these species are important elements in the photocatalytic process since this process mainly depends on OV and TSD [24].

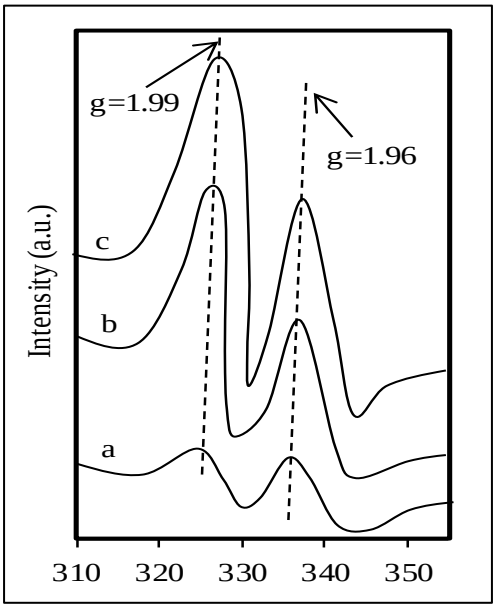


Figure 5. ESR of (a) TiO_2 (b) MTN and (c) Ag-MTN

Figure 6 demonstrates the photocatalytic activities of the catalysts on the degradation of phenol derivatives. It could be observed that MTN showed higher performance on the degradation of phenol derivatives compared to TiO_2. Photocatalytic degradation of phenol derivatives using MTN successfully degraded 80, 92, 70, and 75% of Ph, 2-CP, 2,4-diCP, and 4-AcePh, respectively. In contrast, TiO_2 only managed to degrade 15, 20, 25, and 13% of Ph, 2-CP, 2,4-diCP, and 4-AcePh, respectively. This phenomenon occurs may be due to numbers of OV and TSD for TiO_2 that are lower than MTN, where the larger values of both species, the higher the photoactivity. These two species could act as the electron acceptor in order to decrease the electron-hole recombination, as well as the promoter in the oxidation of phenol derivatives since it could also adsorb O_2 [25].

Meanwhile, Ag-MTN showed the highest degradation of phenol derivatives compared to TiO_2 and MTN, in which Ag-MTN successfully degraded 85, 95, 80, and 79% of Ph, 2-CP, 2,4-diCP, and 4-AcePh, respectively. This result is probably because Ag-MTN has the highest number of OV and TSD according to the ESR result (Fig. 5), which benefits the photocatalytic process by reducing the band gap energy of the catalyst. The decrease in the band gap of Ag-MTN could also improve photoactivity because it is expected that Ag nanoparticles will act as the electron acceptor after the visible light irradiation on MTN that leads to electron excitation from the valence band (V_B) to the existing OV and TSD before reaching the conduction band (C_B). Consequently, this increases the concentration of photogenerated holes that play an important role at the catalyst surface. Besides, this result also illustrated the role of Ag as the electron trapper, which is attributed to the Schottky energy barrier formed between the interaction of Ag and MTN and plasmonic sensitizer to suppress the electron-hole recombination, where the synergistic effect between Ag and MTN plays an important role in the system.

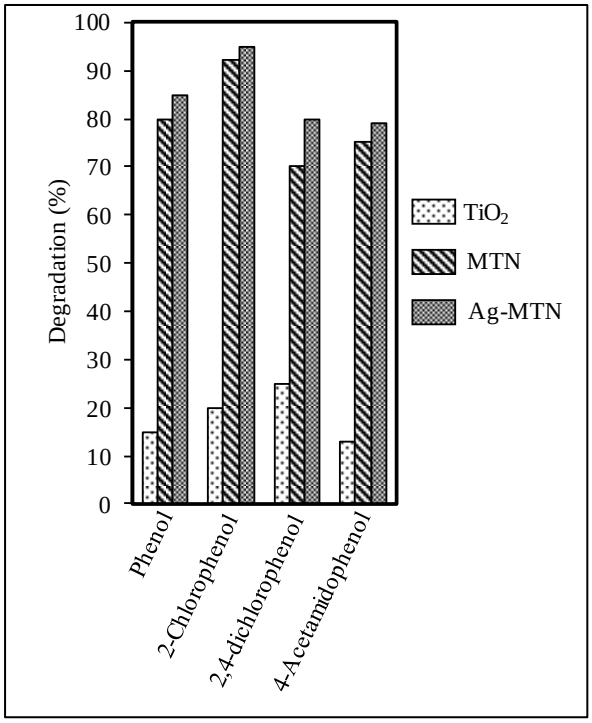


Figure 6. Photodegradation activity of TiO_2, MTN and Ag-MTN for degradation of simulated phenol derivatives [$C_{Phenol\ derivatives}$=50 mg L^{-1}, pH=5, W= 0.375 g L^{-1}, t=6 hours, 303 K]

Conclusion

The introduction of Ag onto MTN demonstrated that it can be used as an effective photocatalyst for the degradation of phenol derivatives under visible light. The physicochemical properties of the catalysts were studied using XRD, TEM, FTIR, ESR, N_2 adsorption desorption, UV-Vis DRS, and XPS. The analyses of UV-Vis DRS, ESR, and XPS verified that the introduction of Ag reduced the band gap of MTN and increased the number of OV and TSD, which seemed to play important roles for application under visible light. Ag-MTN gave the highest percentage degradation of phenol derivatives followed by MTN, while TiO_2 showed the lowest degradation. The presence of Ag not only improved the properties of MTN to be applied under visible light but also acted as electron trapper and plasmonic sensitizer to enhance the photoactivity of catalyst. Thus, this modified catalyst has a great potential to be extended for degradation of various pollutants such as heavy metal, organic pollutants, and pharmaceutical wastes. Besides, by using the reported techniques (microwave-assisted method and electrochemical method), it is believed that further modification of other semiconductors can be also carried out to create various properties for various applications.

Acknowledgement

The authors are grateful for the financial support by the Ministry of Education Malaysia for Fundamental Research Grant (203.PKIMIA.6711607) and Universiti Sains Malaysia for Short Term Grant (304/PKIMIA/6315055). A special dedication to our late supervisor, Professor Sugeng Triwahyono for his endless advice. Thank you very much for everything.

References

1. Lindholm-Lehto, P. C., Knuutinen, J. S., Ahkola, H. S. and Herve, S. H. (2015). Refractory organic pollutants and toxicity in pulp and paper mill wastewaters. *Environmental Science and Pollution Research*, 22(9): 6473-6499.

2. Gryglik, D., Miller, J. S. and Ledakowicz, S. (2007). Singlet molecular oxygen application for 2-chlorophenol removal. *Journal of Hazardous Materials*, 146(3): 502-507.
3. Wang, S. L., Tzou, Y. M., Lu, Y. H. and Sheng, G. (2007). Removal of 3-chlorophenol from water using rice-straw-based carbon. *Journal of Hazardous Materials*, 147(1-2): 313-318.
4. Khan, M. Z., Mondal, P. K. and Sabir, S. (2011). Bioremediation of 2-cholorophenol containing wastewater by aerobic granules-kinetics and toxicity. *Journal of Hazardous Materials*, 190(1-3): 222-228.
5. Lee, J. S., You, K. H. and Park, C. B. (2012). Highly photoactive, low bandgap TiO_2 nanoparticles wrapped by graphene. *Advanced Materials*, 24(8): 1084-1088.
6. Jaafar, N. F., Jalil, A. A. and Triwahyono, S. (2017). Visible-light photoactivity of plasmonic silver supported on mesoporous TiO_2 nanoparticles (Ag-MTN) for enhanced degradation of 2-chlorophenol: Limitation of Ag-Ti interaction. *Applied Surface Science*, 392: 1068-1077.
7. Xie, Y., Li, Y., and Zhao, X. (2007). Low-temperature preparation and visible-light-induced catalytic activity of anatase F-N-codoped TiO_2. *Journal of Molecular Catalysis A: Chemical*, 277(1): 119-126.
8. Jaafar, N. F., Jalil, A. A., Triwahyono, S. and Shamsuddin, N. (2015). New insights into self-modification of mesoporous titania nanoparticles for enhanced photoactivity: effect of microwave power density on formation of oxygen vacancies and Ti^{3+} defects. *RSC Advances*, 5(110): 90991-91000.
9. Tian, J., Liu, R., Wang, G., Xu, Y., Wang, X. and Yu, H. (2014). Dependence of metallic Ag on the photocatalytic activity and photoinduced stability of Ag/AgCl photocatalyst. Applied Surface Science, 319: 324-331.
10. Jalil, A. A., Triwahyono, S., Razali, N. A. M. Hairom, N. H. H., Idris, A., Muhid, M. N. M., Ismail, A., Yahaya, N. A. M., Ahmad, N. A. L. and Dzinun, H. (2010). Complete electrochemical dechlorination of chlorobenzenes in the presence of various arene mediators. *Journal of Hazardous Materials*, 174: 581–585.
11. Jalil, A. A., Kurono, N. and Tokuda, M. (2002). Facile synthesis of ethyl 2-arylpropenoates by cross-coupling reaction using electrogenerated highly reactive zinc. *Tetrahedron*, 58: 7477-7484.
12. Jaafar, N. F., Jalil, A. A., Triwahyono, S., Muhid, M. N. M., Sapawe, N., Satar, M. A. H. and Asaari, H. (2012). Photodecolorization of methyl orange over α-Fe_2O_3-supported HY catalysts: The effects of catalyst preparation and dealumination. *Chemical Engineering Journal*, 191:112-122.
13. Kao, K. C. and Mou, C.Y. (2013). Pore-expanded mesoporous silica nanoparticles with alkanes/ethanol as pore expanding agent. *Microporous and Mesoporous Materials*, 169: 7-15.
14. Priyadharshini, R. I., Prasannaraj, G., Geetha, N. and Venkatachalam, P. (2014). Microwave-mediated extracellular synthesis of metallic silver and zinc oxide nanoparticles using macro-algae (*Gracilaria edulis*) extracts and its anticancer activity against human PC3 cell lines. *Applied Biochemistry and Biotechnology*, 174(8): 2777-2790.
15. Das, D. P., Baliarsingh, N. and Parida, K. M. (2007). Photocatalytic decolorisation of methylene blue (MB) over titania pillared zirconium phosphate (ZrP) and titanium phosphate (TiP) under solar radiation. *Journal of Molecular Catalysis A: Chemical*, 261(2): 254-261.
16. Mori, Y. and Pinnavaia, T.J. (2001). Optimizing organic functionality in mesostructured silica: Direct assembly of mercaptopropyl groups in wormhole framework structures. *Chemistry of Materials*, 13(6): 2173-2178.
17. Khan, M. M., Ansari, S. A., Pradhan, D., Ansari, M. O., Lee, J. and Cho, M. H. (2014). Band gap engineered TiO_2 nanoparticles for visible light induced photoelectrochemical and photocatalytic studies. *Journal of Materials Chemistry A*, 2(3): 637-644.
18. Mazinani, B., Masrom, A. K., Beitollahi, A. and Luque, R. (2014). Photocatalytic activity, surface area and phase modification of mesoporous SiO_2-TiO_2 prepared by a one-step hydrothermal procedure. *Ceramics International*, 40(8): 11525-11532.
19. Todan, L., Dascalescu, T., Preda, S., Andronescu, C., Munteanu, C., Culita, D.C., Rusu, A., State, R. and Zaharescu, M. (2014). Porous nanosized oxide powders in the MgO-TiO_2 binary system obtained by sol-gel method. *Ceramics International*, 40(10): 15693-15701.
20. Jaafar N. F., Jalil A. A., Triwahyono S., Ripin A. and Ali M. W. (2016) Significant effect of pH on photocatalytic degradation of organic pollutants using semiconductor catalysts. Jurnal Teknologi (Sciences & Engineering), 78(8-4): 7-12.
21. Yan, X. M., Kang, J., Gao, L., Xiong, L. and Mei, P. (2013). Solvothermal synthesis of carbon coated N-doped TiO_2 nanostructures with enhanced visible light catalytic activity. *Applied Surface Science*, 265: 778-783.

22. Huang, C. N., Bow, J. S., Zheng, Y., Chen, S.Y., Ho, N. J. and Shen, P. (2010). Nonstoichiometric titanium oxides via pulsed laser ablation in water. *Nanoscale Research Letters*, 5(6): 972-985.
23. Cheng, B. Le, Y. and Yu, J. (2010). Preparation and enhanced photocatalytic activity of Ag@TiO_2 core-shell nanocomposite nanowires. *Journal of Hazardous Materials*, 177(1): 971–977.
24. Liu, H., Ma, H. T., Li, X. Z., Li, W. Z., Wu, M. and Bao, X. H. (2003). The enhancement of TiO_2 photocatalytic activity by hydrogen thermal treatment. *Chemosphere*, 50(1): 39-46.
25. Neppolian, B., Wang, Q., Yamashita, H. and Choi, H. (2007). Synthesis and characterization of ZrO_2-TiO_2 binary oxide semiconductor nanoparticles: Application and interparticle electron transfer process. *Applied Catalysis A: General*, 333(2): 264-271.

Malaysian Journal of Analytical Sciences, Vol 22 No 5 (2018): 817 - 827
DOI: https://doi.org/10.17576/mjas-2018-2205-09

MALAYSIAN JOURNAL OF ANALYTICAL SCIENCES
Published by The Malaysian Analytical Sciences Society
ISSN 1394 - 2506

LIQUID CHROMATOGRAPHY TANDEM MASS SPECTROMETRY FOR THE DETECTION AND VALIDATION OF QUERCETIN-3-*O*-RUTINOSIDE AND MYRICETIN FROM FRACTIONATED *Labisia pumila* var. *alata*

(Kromatografi Cecair Spektrometri Jisim Tandem untuk Pengesanan dan Pengesahsahihan Kuersetin-3-*O*-Rutinosida dan Mirisetin daripada Pemeringkatan *Labisia pumila* var. *alata*)

Norliza Abdul Latiff[1,3]*, Chua Lee Suan[2], Mohammad Roji Sarmidi[3], Ismail Ware[1], Siti Nur Azlina Abdul Rashid[1,3], Maizatulakmal Yahayu[1]

[1]*Institute of Bioproduct Development*
[2]*Faculty of Chemical and Energy*
Universiti Teknologi Malaysia, 81310 Johor Bahru, Johor, Malaysia
[3]*Innovation Centre in Agritechnology for Advanced Bioprocessing,*
Universiti Teknologi Malaysia, 84600 Pagoh, Johor, Malaysia

**Corresponding author: norliza@ibd.utm.my*

Received: 6 August 2018; Accepted: 24 September 2018

Abstract

Quercetin-3-*O*-rutinoside and myricetin was reported to be important secondary metabolites in *Labisia pumila* (*L. pumila*). The reliability of the instrument, its sensitivity and methodology are the key in the analysis of a specific metabolite and liquid chromatography tandem mass spectrometry (LC-MS/MS) provides better accuracy and faster separation in detecting of such chemical compound. Therefore, this study aims to detect and validate the presence of quercetin-3-*O*-rutinoside and myricetin from fractionated extract of *L. pumila* (40% MeOH: water). The plant material was fractionated using octadecyl (C_{18}) silica solid phase and eluent with a ratio of 40% MeOH: water. The separation of compounds was carried out using a C_{18} reversed phase column (Acquity, 150mm × 4.6mm × 1.7 µm). Negative ionization was utilized to fragment the precursor ion of *m/z* 609 for quercetin-3-*O*-rutinoside and *m/z* 317 for myricetin. Three fragments ions; *m/z* 447, 463, 301 was recognized as quercetin-3-*O*-rutinoside product ions within 3.3 minutes. Meanwhile, *m/z* 271,137 and 151 represented characteristics ions for myricetin were recognized within 3.9 minutes. The concentration of quercetin-3-*O*-rutinoside and myricetin was 0.007 mg/g and 0.009 mg/g respectively. The linearity was found between 0.991-0.998. Detection based on (limit of detection) LOD and (limit of quantification) LOQ were found in the ranged of 0.03-0.04 µg/mL and 0.11-0.13 µg/mL, respectively. Both compounds showed good recovery of above 87%. Intra-day and inter-day (RSD) study was in the acceptable range (below 10%). Based on the result of this study, the LC-MS/MS was shown to be the best selective, fast and sensitive method to determine quercetin-3-*O*-rutinoside and myricetin in the plant fraction. These findings could be used as a guideline for the detection of the compounds and suitable for quality controls of *L. pumila* this and another medicinal herb containing quercetin-3-*O*-rutinoside and myricetin.

Keywords: *Labisia pumila*, quercetin-3-*O*-rutinoside, myricetin, validation

Abstrak

Kuersetin-3-*O*-rutinosida dan mirisetin telah dilaporkan sebagai metabolit sekunder yang penting dalam *Labisia pumila* (*L. pumila*). Kebolehpercayaan instrumen, kepekaan dan kaedah pembangunan menjadi aspek penting dalam analisis yang disasarkan kepada metabolit tertentu dan kromatografi cecair spektrometri jisim tandem (KC-SJ/SJ) menyediakan pengasingan lebih cepat dan tepat bagi pengesanan sebatian kimia. Oleh itu, kajian ini adalah bertujuan untuk mengesan dan menentusahkan kehadiran kuersetin-3-*O*-rutinosida dan mirisetin daripada pemeringkatan *L. pumila* (40% metanol:air). Bahan tumbuhan ini

diperingkatkan menggunakan fasa pepejal oktadesil silika (C_{18}) dengan kadar 40% metanol: air. Pengasingan komponen dicapai menggunakan fasa turus berbalik C_{18} (Acquity, 150 mm × 4.6 mm × 1.7 µm). Pengionan negatif telah digunakan untuk mengasingkan pencetus ion *m/z* 609 untuk kuersetin-3-*O*-rutinosida dan *m/z* 317 untuk mirisetin. Tiga pecahan ion; *m/z* 447, 463, 301 dikenal pasti sebagai produk molekul ion dari kuersetin-3-*O*-rutinosida dalam selang masa 3.3 minit. Manakala *m/z* 271, 137 and 151 mewakili ciri ion untuk mirisetin telah dikenalpasti dalam selang masa 3.9 minit. Kepekatan kuersetin-3-*O*-rutinosida dan mirisetin masing-masing ialah 0.007 mg/g dan 0.009 mg/g. Kelinearan adalah di antara 0.991-0.998. Had pengesanan (LOD) dan had pengkuantitian (LOQ) adalah masing-masing dalam julat 0.03-0.04 µg/mL dan 0.11-0.13 µg/mL. Kedua-dua sebatian menunjukkan penghasilan yang baik, lebih daripada 87%. Kajian dalam-hari dan antara-hari (RSD) adalah dalam julat yang boleh diterima (bawah 10%). Berdasarkan keputusan melalui kajian ini, KC-SJ/SJ ditunjukkan sebagai kaedah terpilih, cepat dan sensitif bagi menentukan kuersetin-3-*O*-rutinosida dan mirisetin di dalam pemeringkat tumbuhan ini. Penemuan ini boleh digunakan sebagai panduan untuk pengesanan sebatian dan sesuai sebagai kawalan kualiti untuk *L. pumila* dan herba perubatan yang lain yang mengandungi kuersetin-3-*O*-rutinosida and mirisetin.

Kata kunci: *Labisia pumila*, kuersetin-3-*O*-rutinosida, mirisetin, pengesahsahihan

Introduction

Labisia pumila (L. pumila) is known as the best Malaysian herbal recognized in various medical benefits especially for women. Locally known as *Kacip Fatimah* (Myrsinaceae), it is a traditional herbal plant widely used by peoples from the Asian region, especially in Malaysia and Indonesia. This plant is exclusive for women's health due to the presence of phytoestrogen. It can relief menopausal syndrome as well as health booster during post-delivery and it is also suitable to be used during pregnancy [1-6]. Furthermore, it was reported earlier that the aqueous plant extract could assist in modulating the post-menopause adiposity in ovariotamized rats and the result was comparable to the estrogenic receptor replacement therapy (ERT) [7]. There was also no acute toxicity reported for the treatment of post-menopausal symptom based on the clinical studies conducted [8]. Additionally, the plant's root aqueous extract was also found to be effective in osteoporosis treatment [9] as it showed significant modulation effect in pharmacokinetic and pharmacodynamics properties [10]. Interestingly, the value of anti-aging and antioxidant property of the *L. pumila* has surged its application as acosmeceutical agent [11-14]. The plant aqueous extract also showed a prospective application as anticancer, anti-inflammatory and anti-fungal agent [13, 15]. The three types of *L. pumila* variety were recognized worldwide as *alata*, *pumila* and *lanceolata* [16] and the former two varieties were selected as most important valued sources due to its significant medicinal properties [3].

Recently, many types of phytochemicals have been identified from the leaves, roots and whole plant parts of *L. pumila* [13-15, 17-21]. Based on the analytical studies using various detection techniques, it was shown that the plant extract contained significant amount of polyphenols and the sub-group of polyphenols; flavonoids was the major constituents. In our initial work, qualitative analysis of *L. pumila* var. *alata* from the methanolic extract using LC-MS/MS in profiling 20 polyphenols constituents has been achieved [22]. Quercetin-3-*O*-rutinoside and myricetin have shown by its significant peaks in the chromatogram. In other related publication, the presence of these compounds was also detected in leaves and roots of the same plant variety [13, 14, 17, 18]. These compounds were the most beneficial flavonoids and commonly used in food and beverages and it was used and registered in over 130 medicinal formulations for its therapeutic effect [23]. In addition, the pharmacological properties of quercetin-3-*O*-rutinoside as anti-cancer, antioxidant, antidiabetic and anti-inflammatory agent were also studied [23]. From cosmeceutical view, quercetin-3-*O*-rutinoside has the sun light blocking properties as well as the ability to prevent skin diseases such as redness and skin lesions [24]. Myricetin were also used as a chemotaxonomic marker in *Chrysobalanaceae* family [25]. Relevant pharmacological activity from this compound has been reported earlier [25-26].

From the literature review, analytical procedure that has been developed to identify and quantify the quercetin-3-*O*-rutinoside and myricetin was using HPLC [13, 17]. However, high sensitivity and resolution with accurate mass can only be achieved using mass spectrum. Still, analysing complex matrices have become a challenge to create consistent signal in every sample injection. The use of LC-MS/MS with triple quadrupoles ion trap for quantitation offer faster and accurate results. Hence, it is essential to developed new analytical procedures that provide good compound resolution and sensitivity to identify quercetin-3-*O*-rutinoside and myricetin from plant. This analytical technique could be used together with chemical and biological assays of natural products.

The aim of this study was to develop a LC-MS/MS method to identify quercetin-3-*O*-rutinoside and myricetin. The quantitative results were further validated in this study for quality control purposes. Prior to analysis, to reduce sample matrix in the complex mixture, preparative fractionation by using packed C_{18} column bed in the solid phase extraction (SPE) technique were used after the extraction process [22-27].The analytical method developed could be essential for the discovery of natural product especially to identify quercetin-3-*O*-rutinoside and myricetin from *L. pumila* and other herbal plants.

Materials and Methods

Chemicals

Reagent grade methanol (MeOH) was purchased from Fisher Scientific (Pittsburgh, PA). HPLC grade methanol and acetonitrile were obtained from Merck (Darmstadt, Germany). Ultra-pure water was from a Barnstead Nano-pure Diamond water purification system (Thermo, Waltham, MA). The deionized water was produced from Barnstead E-pure water system (Thermo, Waltham, MA). The chemical standards of quercetin-3-*O*-rutinoside and myricetin were procured from Sigma-Aldrich (St Louis, MO) and the SPE cartridge, Strata™-X, (8B-S029 FBJ, 200 mg) was purchased from the local supplier (Phenomenex, Torrance, CA).

Plant material: Sources and preparation

L. pumila var. *alata* which was labeled as FRI 59810 was freshly taken from the herbal farm at Forest Research Institute Malaysia (FRIM), Selangor. After harvesting, the leaves were dried using conventional drying oven at 40 °C for 24 hours. The dried leaves were ground (mesh size approximate 200 micron) by using a warring blender and kept in seal plastic before storage at -20 °C, prior to further analysis.

Fractionation of *L. pumila* by solid phase extraction

The extraction and fractionation method were done based on method established by Chua et al. [22]. The fractionation of *L. pumila* was done by using C_{18} sorbent type material. The SPE cartridge, Strata™-X, (8B-S029 FBJ, 200 mg) was procured from local supplier (Phenomenex, Torrance, CA). In this procedure, 40% MeOH-water mixture was used as the eluting solvent. The crude extract (50 mg) was suspended in 5 mL MeOH. The mixture was vortexed to allow homogenization. The homogenized mixture (2 mL) was further diluted with 3 mL of deionized water. The fractionation process was started by conditioning the cartridges with 15 mL of 100% MeOH and followed by 15 mL of deionized water, at a control flow rate of 10 mL/min, under vacuum. This procedure is important to remove the air bubbles trapped inside the cartridge. The sample (2 mL) was then added to the SPE cartridge at slow flow rate of 1 mL/min. An amount 5 mL of 5:95 MeOH: water in ratio 5:95 was loaded into the cartridge to remove the impurities. The fraction was then collected upon elution with 40% MeOH-water (15 mL). The fraction was dried using rotary evaporator and finally weighed and stored in the refrigerator before further analysis.

LC-MS/MS analysis

The method is referred from established method by Chua et al. [22] with minor changes for improvement. The plant fraction (10 mg) was diluted with 10 mL 40% MeOH-water. The sample was vortexed to homogenise and filtered using 0.20 µm syringe filters (Nylon membrane, Titan, Thermo Scientific, Germany). The filtered solution (1 mL) was inserted into HPLC vial to be injected into LC-MS/MS system. Chromatographic separation was done by using an Acquity, system (Waters Corporation, Milford, MA) and an Acquity reversed phase C_{18} column (150 mm × 4.6 mm × 1.7 µm particle size) from Waters (Milford, MA). The detection was done *via* mass spectrometry 4000 QTRAP (Applied Biosystems-AB Sciex, Life Technologies Corporation, Carlsbad, CA). The analysis of the fraction was performed using the Analyst software (version 1.4.2). Gradient system was used to elute the sample before entering the mass spectrometry system. The mobile phase A consists of 0.1% formic acid in water and 0.1% formic acid in acetonitrile for mobile phase B. The mobile phase was developed using gradient system at 0-5 minutes, 10% B; 5-15 minutes, 10-90% B; 15-20 minutes, 90%B; 20-25 minutes, 90-10% B; 25-30 minutes, 10% B for the final wash and column equilibration before the next injection. The injection volume was 5 µL. The mobile phase was filtered using 0.2 µm nylon membrane filter. The flow rate was set at 0.25 mL/min and system was run at 15 minutes.

The mass spectrometry (MS/MS) was done by using electrospray ionization (ESI) in negative and positive ion mode. The mass spectra were acquired with the ranges molecular weight (*m/z*) of 100-1500 with 20 mass ion accumulations. The capillary and voltage of the ESI source were maintained at 400 °C and 4.5 kV, respectively (both negative and negative mode). The ESI parameters used were as follows: nitrogen was used as ion source gas for nebulization at 40 psi; solvent drying at 40 psi; nitrogen gas was set at 10 psi; collision gas was set at high; declustering potential of 30-50 V, and collision exit energy, 10-20 V. The scan rate was 100 amu/s. A low energy collision dissociation (CID) was used in quantitative by multiple reactions monitoring (MRM) mode. The MRM mode was used to generate the standard curve from a standard compound of aglycone. To develop the mass spectrum from targeted compounds, the compounds were directly delivered into ESI source. This procedure was called as the direct infusion where the sample was directly injected to the mass detector. Manual injection was done by using syringe pump and the injection flow rate was 0.5 mL/min at 1 μg/mL.

Validation of the quercetin-3-*O*-rutinoside and Myricetin

According to European Analytical Chemistry (EURACHEM) guideline for method validation, the fundamental of validation includes accuracy, precision, recovery, selectivity, calibration curve and stability [28]. This fundamental work can be applied todetermine the quantity of metabolites from the complex matrices. The EURACHEM guidance provides general references on the best practice of chemical analysis and its criteria can be selected depending on the specific test and analytical method applied. The validation of the quercetin-3-*O*-rutinoside and myricetin was selected based on four criteria which are the calibration curve, sensitivity, accuracy, and precision, as suggested [28, 29].

Linearity

Linearity was evaluated through the determination of six standards working solutions containing 0.1-100 μg/mL of the standard compounds in triplicate preparations. The peak area and concentration were subjected to least-squares linear regression analysis to calculate the calibration equation and correlation coefficients.

Accuracy

The accuracy was calculated through the recovery studies by adding a known amount of the solution of each standard compound into triplicate aliquots of extract. The sample and the spiking solutions were followed by the fractionation process before subjected to LCMS/MS analysis. The recovery of the standard compounds was calculated in the percentage unit. Recovery of the standard compounds was calculated in percentage as follows:

$$\text{Recovery (\%)} = \frac{C1 - C2}{C3} \quad (1)$$

where C1 is define as concentration of spiked sample, C2 is concentration of sample and C3 is concentration of the standard solution.

Sensitivity

The sensitivity of the method was evaluated by utilizing the limit of detection (LOD) and limit of quantitation (LOQ) analysis. The LOD was described as the minimum detection (signal) of instrument response a significant difference between background, blank and analyte signals [28]. LOQ was described as the quantitative result which can be reported at a high degree of confidence. The LOD and LOQ of the LCMS/MS method for the standards were established at a standard deviation of the average value of 3 and 10, respectively, which were experimentally verified by six injections of each of the substances at the LOQ concentrations.

Precision

To study the precision, the analysis was carried out in intra-day and inter-day with the aim to produce reproducibility. The aliquots were subjected to LCMS/MS injection. For intra-day studies, aliquots were injected at four different times on the same day. The peak area was analyzed and compared between injection samples at 4 different times. The percentage of the relative standard deviation (% RSD) was calculated. The inter-day studies were evaluated by injecting the aliquots on the first day, second day, after 1 week and after 1 month. The good reproducibility for the investigated compounds was observed, which is evident by the RSD value which was less than 10%.

Results and Discussion

Optimization of LC-MS/MS

The 40% MeOH-water fraction of *L. pumila* was found having glycosides which include quercetin-3-*O*-rutinoside [22]. Further detection of quercetin-3-*O*-rutinoside and myricetin to improved quantitative analysis is necessary. In this study, several parameters were considered for compound optimization which basically signalled by the chromatographic separation as well as the mass spectra that was used for the compound characterisation. The parameter of the mobile phase was investigated using both isocratic and gradient separation. The isocratic separation was done *via* a combination of mobile phase A and mobile phase B consisting of mixtures of water: acetonitrile and water-methanol. The compound resolution using water: methanol (90:10) mixture was found to be lower when compared with the water-acetonitrile (90:10) mixture using isocratic separation system. The gradient system employed could improve the compounds resolution and eliminate the effect of peak tailing. The addition of low concentration, of 0.1% formic acid was able to improve the chromatographic feature and the mass spectra quality. Therefore, 0.1% formic acid was added into water as mobile phase A and into acetonitrile as mobile phase B in the gradient system with the system set at a fast flow rate; 0.25 mL/min. Fast separation was obtained between 10 minutes for both quercetin-3-*O*-rutinoside and myricetin. The ratio of mobile phase A and B was 90:10 for the first elution and was changed to 10:90 after 3 minutes and stay to equilibrate in the system for the next 6 minutes before return to the initial ratio in 8.10 to 10 minutes in a total runtime.

The MS/MS detection method for product ion characterisation was designated to acquire the mass signal. In this study, the mass was set up to render the mass of interest. The identification of product ion for compound verification was done by enhancing the product ion (EPI) scan mode. Different energy was used to produce ion from the electro-spray ionisation (ESI) source. The parameter included studying entering declustering potential (DP, Volt, V) and collision exit energy (CE, Volt, V) before it was identified. Meanwhile, the quantification of quercetin-3-*O*-rutinoside and myricetin were done using the multiple reaction monitoring (MRM) scan mode. This MRM scan mode is the best operational mode to localize the accuracy with specific ion fragmentation from the precursor ion (by mean parent ion) to its specific fragmentation ion (by mean daughter ion). The DP energy was set up from 30-50 V which is from high to lower energy. Meanwhile, CE was acquired from 10-20 V. Negative fragmentation produced better sensitivity detection signal for quercetin-3-O-rutinoside. The optimized DP energy for EPI scan mode was achieved at 40 V, while CE at 10 V. The optimized DP and CE for MRM scan mode were accomplished at 50V and 20V, correspondingly for both mass of interests.

Figure 1 showed the molecular ion *m/z* 609 at two different DP energy which produce characteristics ions of *m/z* 463, 447, 301, 271, 285, 179 and 151. The presence of four ions, *m/z* 271,285,179 and 151 were attributed to the major characteristics of quercetin [30]. The mass spectra showed an intense peak with clear characteristics ions at DP 40 V rather than DP 55 V with reference to the Figure 1. However, by increasing the DP energy, the product of quercetin was fragmented to intense quercetin peaks, however, the other three peaks of *m/z* 463, 447 and 609 had disappeared from the mass spectrum. From the EPI mass spectral, the loss of 146 Da (rhamnoside residual) from *m/z* 609 formed the *m/z* 463, and occurrence of *m/z* 447 was due to the cleavage of glucoside unit (162 Da) from the main quercetin structure. It was reported that *m/z* 609 was quercetin-3-*O*-rutinoside [31]. The loss of galactose, glucose or mannose from *m/z* 609 showed a significant peak at *m/z* 463 which was similar with previous article reported by Abad and his team [31]. The peak corresponding to *m/z* 463 was identified as quercetin-3-*O*-galactoside [30, 32]. The presence of *m/z* 447 was designated as quercitrin or commonly known as a quercetin-3-rhamnoside where one type of sugar was attached to its basic aromatic rings. The *m/z* 447 corresponded to the loss of one-unit sugar (146 Da) to form the quercetin *m/z* 301 together with the product ion *m/z* 179 and *m/z* 151 [30, 33]. The rhamnose unit was easily deprotonated with the loss of 146 Da, resulting in fragments at *m/z* 301, 179 and 151 (Figure 1). Pikulski and Brodbelt [33] reported that the deprotonation of quercitrin apparently by homolytic bond cleavage. This compound was commonly found in Brazilian cherry and South America berries fruits [32, 34].

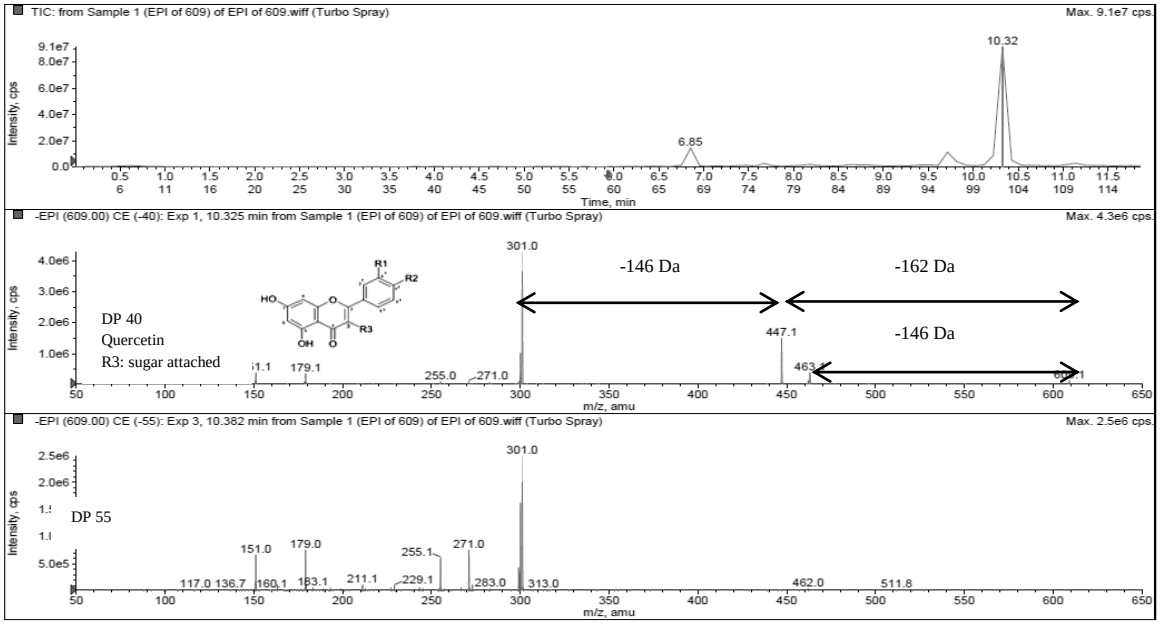


Figure 1. EPI mass spectra of quercetin-3-O-rutinoside from *L. pumila* fraction (40% MeOH: water) at different DP energy (DP 40 V and DP 55 V)

Identification of quercetin-3-*O*-rutinoside and myricetin from the fraction

Identification of quercetin-3-*O*-rutinoside and myricetin were carried out in negative and positive ionisation mode by comparing the MS/MS spectra in EPI scan. The $[M-H]^-$ was selected because it produces extensive MS/MS fragmentation compare to $[M+H]^+$. Quercetin-3-*O*-rutinoside (*m/z* 610) has loss 1-unit hydrogen in $[M-H]^-$ producing *m/z* 609 as shown in Figure 1. Myricetin (*m/z* 318) has also loss 1 unit of hydrogen to formed molecular ion, *m/z* 317 (Figure 2). The structure of quercetin-3-*O*-rutinoside and myricetin were shown in Figure 3.

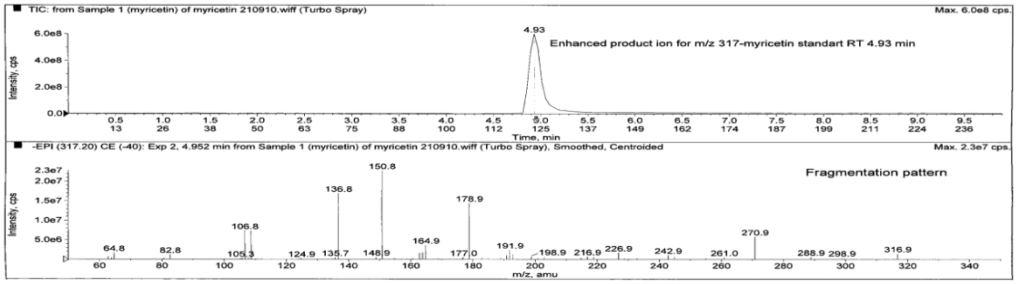
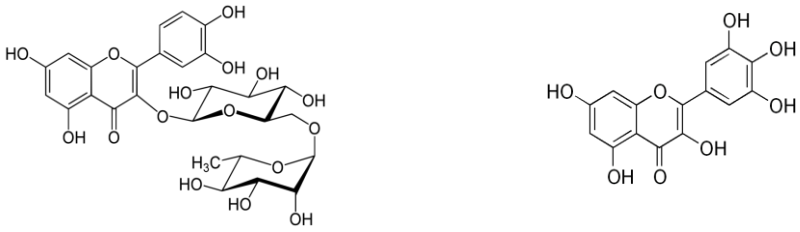


Figure 2. The EPI mass spectra of myricetin *L. pumila* fraction (40% MeOH: water) at different DP energy (DP 40 V and DP 55 V)



Quercetin-3-O-rutinoside Myricetin

Figure 3. Structure of quercetin-3-O-rutinoside and myricetin

Myricetin with molecular ion *m/z*318 was ionised leading to loss 1 unit of hydrogen to generate negative ion $[M-H]^-$ *m/z* 317 which was then fragmented to four characteristics ion of *m/z* 271, 179, 151, 137 (Figure 1) that is similar to the aglycone of quercetin. This occurrence was due to the breakdown of the aglycone myricetin structure, with the loss of 92 Da, 28 Da ($2CH_2$) and 14 Da (CH_2) with reference to the formation of peaks of *m/z* 179, 151 and 137, respectively. The presence of two peaks of *m/z* 179 and 151 were attributed to the major characteristics ion of myricetin [35, 36]. These four product ions were then confirmed by MRM scan, where consistent fragment ions matched to the standard myricetin. Myricetin is a flavonol-type which consists of three hydroxyl groups located at the B ring at position 3, 4 and 5. The sugar unit was attached to its basic aromatic ring to form a myricetin glycosides. This compound was also presence in fruits such as cherry, grapes and cranberry [25, 32, 37]. Our experiments showed that the best DP energy to generate the product ion was 40 V and the CE was at 40 V.

From the study, 40% MeOH fraction contained quercetin-3-*O*-rutinoside and myricetin and the presence of product ion is essential for the characterisation of these compounds. The generated DP energy at 40V was the most optimum energy to generate the product ion for both compounds in the enhance product ion scan mode (EPI).

Quantification and validation

The quantification step was done by using MRM scan to generate peaks from the precursor ion to product ion. Fragment of *m/z* 301 is the dominant product ion over quercetin-3-*O*-rutinoside. Meanwhile, *m/z* 137 was selected for myricetin in MRM scan mode. Using fast and accurate MRM scan mode, chromatographic data for both compounds including retention time, peak area, and peak height were monitored. As a requirement to verify and quantify the presence of these compounds, a standard working solution of quercetin-3-*O*-rutinoside and myricetin (99% purity) was used to build a standard calibration curve.

The peak of quercetin-3-*O*-rutinoside was detected at 3.3 minutes with a total running time of 10 minutes (Figure 4). The concentration of quercetin-3-*O*-rutinoside was determined to be at 0.007 mg/g in the plant fraction. Meanwhile, myricetin was detected at 3.9 minutes with the total running time set at 10 minutes (Figure 5). Significantly, myricetin was found to be higher in this plant fraction as compared to quercetin-3-*O*-rutinoside which was at 0.009 mg/g in the plant fraction.

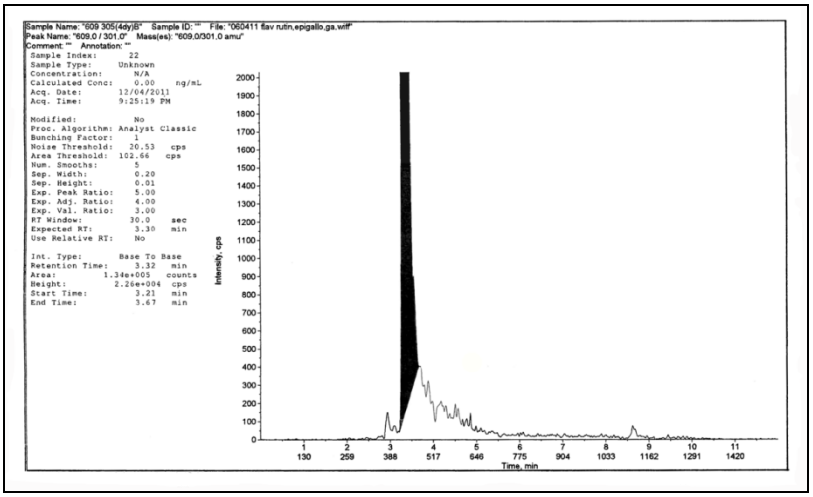


Figure 4. The MRM peak of quercetin-3-*O*-rutinoside from the *L. pumila* in 40% MeOH: water fraction

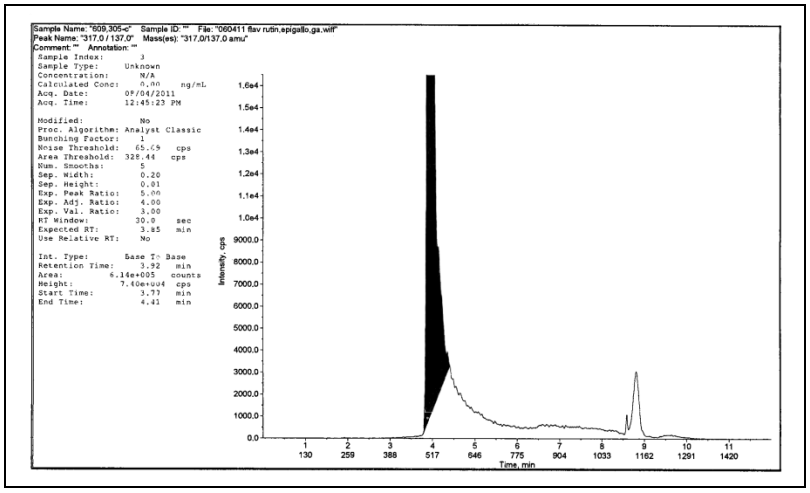


Figure 5. The MRM peak of myricetin from the *L. pumila* in 40% MeOH: water fraction

The LC-MS/MS validated method was determined based on its linearity, LOD, LOQ, precision and accuracy according to the guideline [28] suitable for quality control (Table 1). The response of quercetin-3-*O*-rutinoside in the range of 0.1-100 µg/mL produced linearity result with good regression equation and correlation coefficient (r^2= 0.998 with the following equation; y = 99956x – 89337). The detection limit, LOD and LOQ for the quercetin-3-*O*-rutinoside were 0.04 µg/mL and 0.13 µg/mL, respectively. The developed LC-MS/MS method had successfully achieved high sensitivity detection of quercetin-3-*O*-rutinoside based on the LOD and LOQ which were comparable to the signal noise to ratio (S/N). This method was found fit for quantitation purpose. The recovery for quercetin-3-*O*-rutinoside was measured at 87% and most probably the 13% loss was probably due to the steps involved during the sample preparation. However, it can be considered as a good compound recovery since the percentage was above 80%. Good precision was expressed by the RSD (%) value, which is required to be less than 10%. The intra-day and inter-day for quercetin-3-*O*-rutinoside were found to be 5.01% and 9.18%, respectively. These two values showed that quercetin-3-*O*-rutinoside was stable for at least a month, but it is recommended to prepare the extract fresh for analysis to avoid any deterioration.

The detection method for myricetin was described based on the optimal detection condition (not shown). The calibration curve in order to obtain the linearity of myricetin was found to be straight linear concentration ranged from 0.1 to 100 µg/mL and had a linear regression of $r^2 = 0.991$ with the following equation; y = 35125x – 13273. The LOD and LOQ for myricetin were found to be at 0.03 µg/mL and 0.11 µg/mL, respectively. Analysis of the spiked myricetin standard for recovery study had showed an average recovery of 88.2%. The analysis of the compound in the solution on the same day had shown good reproducibility at 3.14%. The study on the different days (inter-day) also showed good precision of 3.18%. Therefore, the robustness of the method indicated that myricetin is possibly consistent for at least 1 month of storage based on these results. Table 1 summarises the results from the study.

Table 1. Linearity, LOD, LOD, recovery, intra-day and inter-day data of quercetin-3-*O*-rutinoside and myricetin in *L. pumila* fraction (40% MeOH: water) by LC-MS/M

Flavonoids	**Linear Equations**	**LOD (µg/mL)**	**LOQ (µg/mL)**	**Recovery (%)**	**Intra-day (RSD) %**	**Inter-day (RSD) %**	**Concentration (mg/g)**
Quercetin-3-*O*-rutinoside	Y = 99956x – 89337	0.04	0.13	87.00	5.01	9.18	0.007
Myricetin	Y = 35125x – 13273	0.03	0.11	88.20	3.14	3.18	0.009

Conclusion

The present work describes the application of LC-MS/MS procedure to analysed quercetin-3-*O*-rutinoside and myricetin in *L. pumila* fraction which was obtained from 40% MeOH: water. The validated method indicated that lower concentration of quercetin-3-*O*-rutinoside and myricetin can be identified and quantified in the plant fraction by using high throughput analytical technique via electrospray ionisation (ESI). Valuable information can be provided including mass identity together with characteristics fragmentation ion. This method is applicable for the analysis of plant containing quercetin-3-*O*-rutinoside and myricetin as well as for quality control and routine analysis purposes.

Acknowledgment

The authors would like to express Universiti Teknologi Malaysia for the financial assistant under Research University Grant (GUP) Q.J130000.2609.11J53 and Institute of Bioproduct Development for facilities provided.

References

1. Ezumi, M. F. W., Siti Amrah, S., Suhaimi, A. W. M. and Mohsin, S. S. J. (2007). Evaluation of female reproductive toxicity of aqueous extract of *Labisia pumila* var. alata in rats. *Indian Journal of Pharmacology*, 39(1): 30-32.
2. Burkill, I. H. (1935). A dictionary of the economic products of Malay peninsula, Crown Agent, London, UK.
3. Jamal, J. A., Houghton P. J., Milingan S. R. and Ibrahim, J. (2003). The estrogenic and cytotoxic effects of the extracts of *Labisia pumila* var. alata and *Labisia pumila* var. *pumila* in vitro. *Malaysian Journal of Medicine and Health Sciences*, 1: 53-60.
4. Institute for Medical Research (2002). Estrogenic and androgenic activities of Kacip Fatimah (*Labisia pumila*). Ministry of Health Malaysia, Kuala Lumpur: pp. 8.
5. Bhathena, S. J. and Velasquez, M. T. (2002). Beneficial role of dietary phytoestrogens in obesity and diabetes. *The American Journal of Clinical Nutrition*, 76(6): 1191–1201.
6. Ayida, A. W., Wan Norzaimoon, W. M., Farihan, H. S. and Azian, A. L. (2007). Effect of ovariectomy, *L. pumila* var. alata treatment and estrogen replacement therapy on the morphology of adipose tissue in ovariectomized Sparague Dawley rats. *Journal of Medicine*, (1): 1-7.
7. Al-Wahaibi, A., Wan Nazaimoon W. N. Norsyam, W. N., Farihah, H. S. and Azian, A. L. (2008). Effect of water extracts of *Labisia pumila* var. alata on aorta of ovariectomized Sprague-Dawley rats. *Pakistan Journal of Nutrition*, 7: 208-213.

8. Singh, R. P., Murthy, C. K. N. and Jayaprakasha, G. K. (2002). Studies on the antioxidant activity of pomegranate (*Punicagranatum*) peel and seed extracts using in vitro models. *Journal of Agricultural and Food Chemistry*, 50: 81–86.
9. Fathilah, S. N., Mohamed, N., Muhammad, N., Mohamed, I. S., Soelaiman, I. N. and Shuid, A. N. (2013). *Labisia pumila* regulates bone-related genes expressions in postmenopausal osteoporosis model. *BMC Complementary and Alternative Medicine*, 13: 217.
10. Manda, V. K., Dale, O. R., Awortwe, C., Ali, Z., Khan, I. A., Walker, L. A. and Khan, S. I. (2014). Evaluation of drug interaction potential of *Labisia pumila* (Kacip Fatimah) and its constituents. *Frontiers in Pharmacology*, 5: 178.
11. Choi, H. K, Kim, D. H., Kim, J. W., Ngadiran, S., Sarmidi, M. R. and Park, C. S. (2010). *Labisia pumila* extract protects skin cells from photoaging caused by UVB irradiation. *Journal of Bioscience. Bioengineering*, 109: 291–296.
12. Chua, L. S., Lee S. Y., Abdullah., N., Sarmidi. M. R. (2012). Review on *Labisia pumila* (Kacip Fatimah): Bioactive phytochemicals and skin collagen synthesis promoting herb. *Fitoterapia*, 83(8): 1322-1335.
13. Karimi, E., Jaafar, H. Z. E. and Ahmad, S. (2011). Phytochemical analysis and antimicrobial activities of methanolic extracts of leaf stem and root from different varieties of *Labisia pumila Benth*. *Molecules*, 16: 4438-4450.
14. Ibrahim, M. H and Jaafar, H. Z. E. (2011). Enhancement of leaf gas exchange and primary metabolites under carbon dioxide enrichment up-regulate the production of secondary metabolites in *Labisia pumila* seedlings. *Molecules*, 16: 3761-3777.
15. Ali, Z. and Khan, I. A. (2011). Alkyl phenols and saponins from the roots of *Labisia pumila* (Kacip Fatimah). *Phytochemistry*, 72: 2075-2080.
16. Stone, B. C. (1988). Notes on the genus *Labisia Lindl* (Myrsinaceae). *Malayan Nature Journal*, 42: 43–51.
17. Karimi, E. and Jaafar, H. Z. E. (2011). HPLC and GC-MS determination of bioactive compounds in microwave obtained extracts of three varieties of *Labisia pumila Benth*. *Molecules*, 16: 6791-6805.
18. Avula, B., Wang Y. H., Ali Z., Smillie, T. J. and Khan, I.A. (2011). Quantitative determination of triterpene saponins and alkenated-phenolics from *Labisia pumila* using LC-UV/ELSD method and confirmation by LC-ESI-TOF. *Planta Medica*, 77: 1742-1748.
19. Al-Mekhlafi, N. A., Shaari, K., Abas, F, Kneer, R., Jayaseela Jeyaray, E. and Stanslas, J. (2012). Alkenylresorcinols and chytotoxic activity of constituents isolated from *Labisia pumila*. *Phytochemistry*, 80: 42-49.
20. Mohd Nazrul Hisham, D., Mohd Lip, J., Mohd Noh, A., Normah, F. and Nurul Nabilah, M. F. (2011). Identification and isolation of methyl gallate as a polar chemical marker for *Labisia pumila Benth*. *Journal of Tropical Agriculture and Food Science*, 39: 279-284.
21. Abdullah, F., Sui K. L., Man, S., Tan, A. I., Tan, H. P. and Abdullah, Z. (2012). Characterization and identification of *Labisia Pumila* by multi-steps infrared spectroscopy. *Vibrational Spectroscopy*, 62: 200-206.
22. Chua, L. S., Norliza, A. L., Lee, S. Y., Lee, C. T. and Sarmidi, M. R. (2011). Flavonoids and phenolic acids from *Labisa pumila* (Kacip Fatimah). *Food Chemistry*, 127: 1186-1192.
23. Chua, L. S. (2013). A review on plant-based rutin extraction methods and its pharmacological activities. *Journal of Ethnopharmacology*, 150(3): 805–817.
24. Anelwew (2014). The use of rutin in anti-aging cosmetics. Retrieved from http://www.articlesnatch.com/ article//3702816#.U6PlHfmSxqW [14 June 2014,]
25. Mendez, J., Bilia A. R and Morelli, I. (1995). Phytochemical, investigations of *Licania* genus, flavonoids and triterpenoids from *Licaniapittieri*. *Pharmaceutica Acta Helvetiae*, 70: 223-226.
26. Aherne, S. A. and O'Brien. (1999). The flavonoids, myricetin, quercetin and rutin, protect against cholestan-3p, 5cr, 6p-triol- induced toxicity in Chinese hamster ovary cells *in vitro*. *Nutrition Research*, (19)5: 749-760.
27. Abdah, M. S. N., Sarmidi, M. R., Yaakob, H. and Ware, I. (2014). Fractionation of *Labisia pumila* using solid-phase extraction for extraction of gallic acid. *Jurnal Teknologi*, 69:465-468.
28. Barwick, V. (2016). Eurachem/CITAC Guide: Guide to quality in analytical chemistry: An aid to accreditation (3rd edition). Available from www.eurachem.org.
29. Armbruster, D. A., Tillman M. D. and Hubbs, L. M. (1994). Limit of detection (LQD)/limit of quantitation (LOQ): Comparison of the empirical and the statistical methods exemplified with GC-MS assays of abused drugs. *Clinical Chemistry*, 40(7): 1233-1238.

30. Hollecker, L., Maurizio P. M., Filippino, G., Scruglia, S., Pinnab, B., Argiolas, F. and Mariano M. M. (2009). Simultaneous determination of polyphenolic compounds in red and white grapes grown in Sardinia by high performance liquid chromatography–electron spray ionisation-mass spectrometry. *Journal of Chromatography A*, 1216: 3402-3408.
31. Abad Garcia, B., Berrueta, L. A., Garmon-Lobato, S., Gallo, B. and Vicente, F. (2009). A general analytical strategy for the characterization of phenolic compounds in fruit juices by high-performance liquid chromatography with diode array detection coupled to electrospray ionization and triple quadrupole mass spectrometry. *Journal of Chromatography A*, 1216: 5398-5415.
32. Celli, G. B., Pereira-Netto, A. B. and Beta, T. (2010). Comparative analysis of total phenolic content, antioxidant activity, and flavonoids profile of fruits from two varieties of Brazilian cherry (*Eugenia uniflora* L.) throughout the fruit developmental stages. *Food Research International*, 44(2011): 2442-2245.
33. Pikulski, M. and Brodbelt, J. S. (2003). Differentiation of flavonoid glycoside isomers by using metal complexation and electrospray ionization mass spectrometry. *Journal American Society Mass Spectrometry*, 14: 1437–1453.
34. Simirgiotis, M. J., Bórqueza, J. and Schmeda-Hirschmannb, G. (2013). Antioxidant capacity, polyphenolic content and tandem HPLC–DAD–ESI/MS profiling of phenolic compounds from the South American berries *Lumaapiculata* and *L. chequén*, *Food Chemistry*, 139(1-4): 289-299.
35. Yun, L., Bin, W., Zhixiong, L., Ting, H., Mingcang, C., Yingzi, T., Jian, J. and Chenggang, H. (2012). Metabolite identification of myricetin in rats using HPLC coupled with ESI-MS. *Chromatographia*, 75(11): 655-660.
36. Saldanha, L. L.,Vilegas, W. and Dokkedal, A. L. (2013). Characterization of flavonoids and phenolic acids in *Myrciabella cambess* using FIA-ESI-IT-MSn and HPLC-PAD-ESI-IT-MS combined with NMR. *Molecules*, 18: 8402-8416.
37. Koponen, J. M., Happonen, A. M., Auriola, S., Kontkanen, H., Buchert, J. and Poutanen, K. S. (2008). Characterization and fate of black currant and bilberry flavonols in enzyme-aided processing. *Journal of Agriculture and Food Chemistry*, 56(9): 3136-3144.

Malaysian Journal of Analytical Sciences, Vol 22 No 5 (2018): 828 - 838
DOI: https://doi.org/10.17576/mjas-2018-2205-10

MALAYSIAN JOURNAL OF ANALYTICAL SCIENCES
Published by The Malaysian Analytical Sciences Society
ISSN 1394 - 2506

DETERMINATION OF NATURAL RADIOACTIVITY AND HEAVY METALS AT THE FORMER MINING SITE OF KOLEJ UNIVERSITI ISLAM ANTARABANGSA SELANGOR (KUIS) LAKE

(Penentuan Keradioaktifan Tabii dan Logam Berat di Kawasan Bekas Lombong Tasik Kolej Universiti Islam Antarabangsa Selangor (KUIS))

Nur Ain Mohd Radzali, Norsyahidah Mohd Hidzir*, Irman Abdul Rahman

Nuclear Technology Research Centre, School of Applied Physics,
Faculty of Science and Technology,
Universiti Kebangsaan Malaysia, 43600 UKM Bangi, Selangor, Malaysia

**Corresponding author:* syahidah@ukm.edu.my

Received: 29 August 2017; Accepted: 15 August 2018

Abstract

An ex-mining site has created an undesirable effect on the environment, such as the destruction of plants and contamination. Thus, this study was conducted to determine the natural radioactivity and heavy metal presence in the ex-mining site at Kolej University Islam Antarabangsa Selangor (KUIS) lake. Both parameters were measured using gamma spectrometry and inductively coupled plasma-mass spectrometry (ICP-MS). The results showed that the concentrations of ^{238}U (0.44 ± 0.31 Bq/L), ^{232}Th (0.04 ± 0.02 Bq/L), ^{226} Ra (0.19 ± 0.11 Bq/L), and ^{40}K (0.62 ± 0.37 Bq/L) in water samples were below the recommended values by the World Health Organization (WHO) for drinking water source, which implied the safe consumption of the water. However, the presence of ^{238}U, ^{232}Th, ^{226} Ra, and ^{40}K in sediment samples exceeded the limit proposed by UNSCEAR, with the radioactivity of 49.1 ± 18.8 Bq/kg, 102.3 ± 3.3 Bq/kg, 133.2 ± 18.8 Bq/kg, and 297.1 ± 25.7 Bq/kg, respectively. For heavy metal determination, zinc was found in the sediment with the highest concentration (17.34 ± 15.79 mg/kg) compared to other heavy metals, while the concentration of arsenic was highest in water with 0.58 ± 0.26 µg/L. All hazard indices were found to be below the safety limit except for the gamma index of 1.6 ± 0.7 Bq/kg and 104.1 ± 48.4 nGy/h for the gamma dose rate.

Keywords: radioactivity, heavy metals, water, sediment, gamma spectrometry

Abstrak

Tapak bekas lombong telah meninggalkan impak yang tidak diingini kepada alam sekitar seperti pemusnahan tanaman dan pencemaran. Oleh itu, kajian ini dijalankan untuk menentukan kehadiran radionuklid tabii dan logam berat di tapak bekas perlombongan di tasik Kolej Universiti Islam Antarabangsa Selangor (KUIS). Kedua-dua parameter ini diukur menggunakan spektrometri gama dan spektometer jisim-gandingan plasma teraruh (ICP-MS). Hasil kajian menunjukkan kepekatan ^{238}U (0.44 ± 0.31 Bq/L), ^{232}Th (0.04 ± 0.02 Bq/L), ^{226}Ra (0.19 ± 0.11 Bq/L) dan ^{40}K (0.62 ± 0.37 Bq/L) berada di bawah nilai yang disyorkan oleh WHO untuk sumber air minuman, menunjukkan air berada ditahap selamat untuk diminum. Walau bagaimanapun, kehadiran ^{238}U, ^{232}Th, ^{226}Ra and ^{40}K dalam sampel sedimen melebihi had yang dicadangkan oleh UNSCEAR, dengan kepekatan 49.1 ± 18.8 Bq/kg, 102.3 ± 3.3 Bq/kg, 133.2 ± 18.8 Bq/kg dan 297.1 ± 25.7 Bq/kg. Bagi penentuan logam berat, didapati zink menunjukkan kepekatan tertinggi dalam sedimen (17.34 ± 15.79 mg/kg) berbanding dengan logam berat lain, manakala kepekatan arsenik adalah tertinggi dalam air dengan 0.58 ± 0.26 µg/L. Semua indeks bahaya didapati berada di bawah had keselamatan kecuali indeks gamma iaitu 1.6 ± 0.7 Bq/kg dan 104.1 ± 48.4 nGy/h untuk kadar dos gama.

Kata kunci: radioaktiviti, logam berat, air, sedimen, spektrometri gama

Introduction

Exposure to either natural radiation or manufactured radiation sources can be dramatically enhanced through human practices. For example, fertilizer production and mining activities can result in the increase of natural radiation exposure. Uranium-238 (^{238}U), thorium-232 (^{232}Th), and potassium-40 (^{40}K) are the examples of primordial elements that naturally exist in the earth's crust, while radium-226 (^{226}Ra) is the progeny of ^{238}U and ^{232}Th. Radionuclides can be transferred from the soil to the human body in various pathways and have a greater potential to damage the cells once they enter the body. Based on the amount of radiation exposure, many unwanted biological effects may occur, such as cell alteration [1]. One of the radionuclides that is well known to be chemically toxic is ^{226}Ra. In addition, ^{226}Ra tends to be collected in the bones if ingested into the body, which later may result in either leukaemia or bone cancer [2].

Recently, many abandoned mining lakes in Malaysia have been converted into more economical areas, such as recreational and residential areas. Human-made activities around the ex-mining lake can result in the enrichments of radionuclides and heavy metals surrounding the lake. Kolej University Islam Antarabangsa Selangor (KUIS) lake is an ex-mining lake with an estimated area of 0.09 km^2, located at Bangi Lama, Selangor. Many recreational activities have been conducted around the lake, such as canoeing and fishing competitions. The determination of concentration of naturally occurring radioactive materials (NORM) present in water and sediments around the KUIS lake is an effort of better understanding the spatial distribution of the radionuclides and their associated health hazards [3]. In addition to being the main source of radiation exposure to humans, the soil acts as a medium of migration for transfer of radionuclides to the biological systems; hence, it is the basic indicator of radiological contamination in the environment [4, 5]. Therefore, research on the intake of NORM and heavy metals in KUIS lake is performed to evaluate the safety aspect of the people surrounding the lake. The concentration of radionuclides ^{238}U, ^{232}Th, ^{226}Ra, and ^{40}K and heavy metals in water and sediment is a good indicator of the presence of hazards in that area. The main objective is to evaluate the safety level of the former mining area because research has shown that exposure to radiation could lead to lung, pancreas, skin, and kidney cancer [6]. Knowledge of natural radioactivity present in sediment and water is important to assess any possible radiological hazard indices associated with exposure to humans.

Materials and Methods

Materials

Water and sediment samples were taken at four different locations around KUIS lake; represented as K1, K2, K3, and K4 (refer to Figure 1). The average reading of sample at K1 to K4 were taken to represent the activity presence at KUIS lake with the label of K^w for average concentration of radionuclides and heavy metals in water, whereas K^s represents the average concentration of radionuclides and heavy metals in sediment. Controlled sample was taken along Semenyih river and labelled as S^w for concentration of radionuclides and heavy metals in water, whereas S^s represents concentration of radionuclides and heavy metals in sediment. Hydrochloride acid (purity 36.5-38%) and nitric acid (purity 69%-70%) were obtained from JT Baker.

Pre-treatment of samples

About 6 L of water sample and 3 kg of sediment sample were collected with three replicates in single sampling from each station (K1 to K4, S^w, and S^s). The water sample was collected based on the standard procedure for water analysis study [7]. For water sample, four parameters: pH, conductivity, dissolved oxygen and temperature, were determined using a pH meter (WITEG W 100), a conductivity meter (YSI SCT Model 33), and an oxygen meter (HANNA instruments HI 91942), respectively [8]. About a 2-L sample of water was concentrated to 200 mL by heating the water at 60°C. For NORM analysis, the water sample was filled inside the polyethylene container to a height of 4 cm and kept for 30 days to reach the secular equilibrium before being analysed by a highly pure germanium (HPGe) detector (Canberra Model GC1018). For heavy metal analysis, approximately a 100-mL sample of water was filtered using filter paper and kept in a bottle before being analysed by inductively coupled plasma-mass spectrometry (ICP-MS) model (ELAN® DRC-E, Perkin Elmer Elan 9000) [8]. For NORM analysis of the sediment sample, the sediment was first weighed and dried in the oven before sieved through 500 micrometer sieve to obtain a uniform distribution of sediment [9]. Then, the sample was kept for 30 days inside a polyethylene container (4 cm height) to reach a secular equilibrium before being analysed by the HPGe detector. For heavy metal

analysis, the digestion method was used with approximately 0.1 g of sediment sample placed in the solution containing a mixture of 6 mL of hydrochloric acid and 4 mL of nitric acid. Then, the solution mixture was digested using the microwave digestive system for two hours until a clear solution formed [8] before further analysis by ICP-MS.

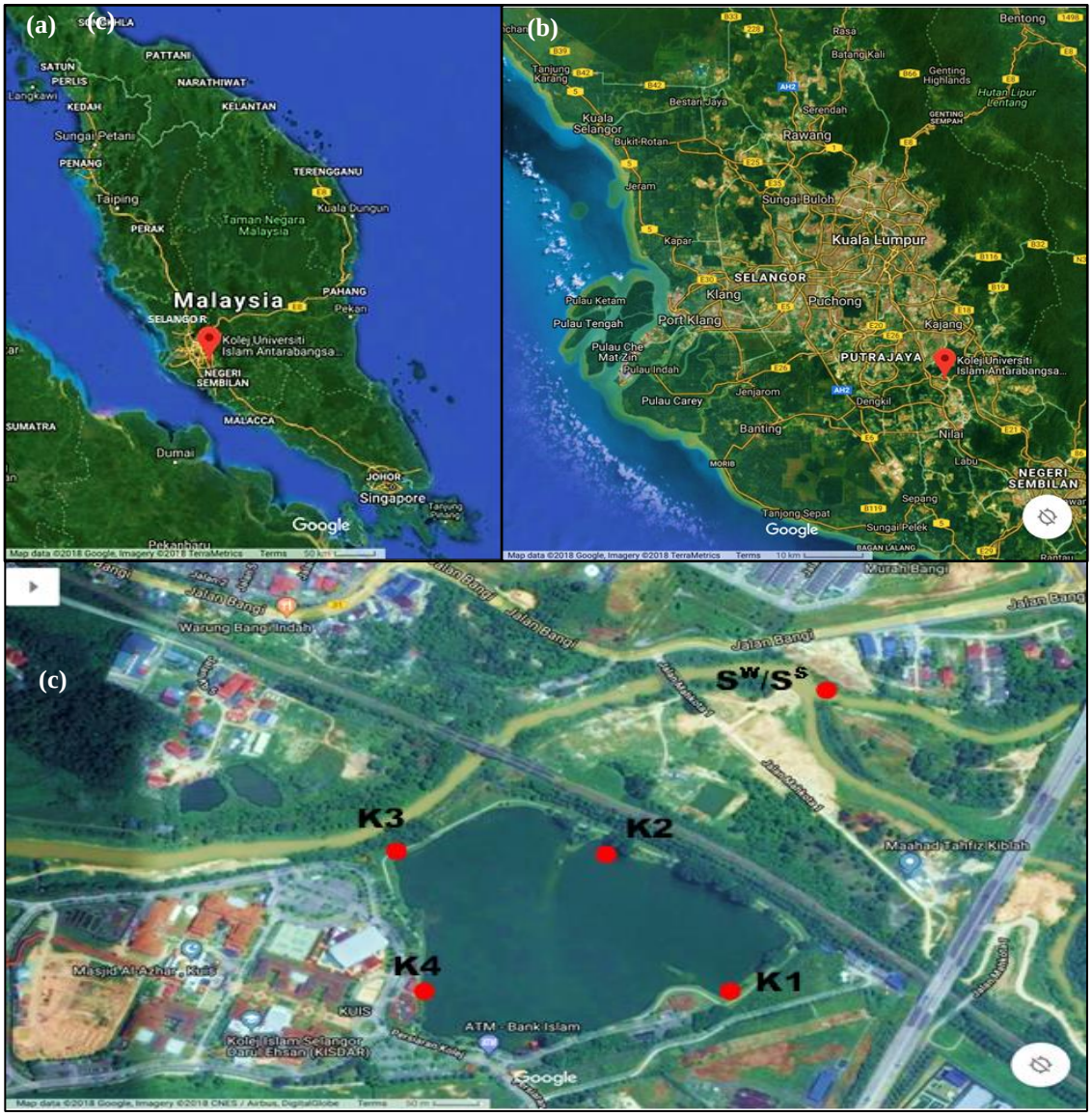


Figure 1. Geographical map of (a) peninsular Malaysia, (b) Selangor state and (c) location of the sampling site.

Characterisation

The concentration of radionuclides in water and sediment samples was determined using the HPGe detector (Canberra Model GC1018) at Nuclear Science Laboratory at UKM. The calibration of the machine was made using a standard source. Both samples and background were counted for 12 hours. The concentration of radionuclide in the water sample was determined by plotting the efficiency curve of the multi-nuclide standard solution. The specific activity (A_s) of radionuclides in the water sample was determined using the formula in equation 1 [10]:

$$A_s\left(\frac{Bq}{L}\right)=\frac{N}{\mathcal{E}\times P\gamma\times V}, \quad (1)$$

where N is the corrected net peak area background (cps), $\mathcal{E}$ is the efficiency of the detector for a γ-ray interest (cps/Bq), $P\gamma$ is the branching ratio of elements (%), and V is the volume of the water sample (L). The concentration of radionuclides in the sample was determined from the net counts of the sample obtained using the multichannel analyser (Software Genie 2000) by referring to the peak energy of 1764 keV for ^{238}U, 1460 keV for ^{40}K, 2614 keV for ^{232}Th, and 609 keV for ^{226}Ra.

The concentration of radionuclides in the sediment sample (W_s) was determined using a comparison technique in which the activity of the sample was compared with the standard of IAEA-375. The concentration was calculated using the formula in equation 2 [11]:

$$W_s\left(\frac{Bq}{kg}\right)=\frac{M_P}{M_s}\times\frac{A_s}{A_p}\times W_p\,, \quad (2)$$

where M_p and M_s are the mass of the standard and sample (kg), respectively, and A_p and A_s are the activity of the standard and sample (cps), respectively, while W_p is the concentration of radionuclides in the standard (Bq/kg).

The concentration of heavy metals in the water and sediment samples was determined using ICP-MS model (ELAN® DRC-E, Perkin Elmer Elan 9000) at Environmental Science Laboratory UKM. The total count technique was used and heavy elements, such as arsenic (As), barium (Ba), cadmium (Cd), copper (Cu), mercury (Hg), manganese (Mn), antimony (Sb), strontium (Sn), and zinc (Zn), were chosen in these studies based on their toxicity, which can result in hazards to the environment. The concentration of heavy metals (C) in the sediment sample was calculated using the formula in equation 3 [12]:

$$C\left(\frac{Bq}{kg}\right)=\frac{N\times V}{M}, \quad (3)$$

where N is the concentration of radionuclides (μg/L), V is the volume of solution (L), and M is the mass of dried sample used during digestion process (g).

Statistical analysis

All statistical tests were performed using the Statistical Package for the Social Sciences (SPSS) software package (IBM SPSS Statistic 22). The T-test was performed and significances were defined as $p < 0.05$, if not stated otherwise [13].

Radiological hazard

Radium equivalent activity index (Ra_{eq}) was introduced to compare the specific activity of a sample, which have different concentrations of ^{232}Th, ^{226} Ra, and ^{40}K [14]. Moreover, Ra_{eq} is defined as the total activity of the three radionuclides based on the estimation that 370 Bq/kg of ^{226} Ra, 259/kg of ^{232}Th, and 4810 Bq/kg of ^{40}K produced the same dose rates. The Ra_{eq} is related to the external and internal γ-dose due to radon and its daughter. The maximum value of Ra_{eq} for a safe limit is 370 Bq/kg [15]. In addition, Ra_{eq} was determined using the formula in equation (4).

The Gamma Index (I_γ) was used to estimate the gamma radiation hazard levels associated with natural radionuclides. These indexes can be determined using the formula in equation (5), derived by the Nuclear Energy Agency-Organisation for Economic Co-operation and Development (NEA-OECD) 1979 [15]. The safe value for I_γ is ≤ 1 [16].

The External Hazard Index (H_{ex}) was determined to estimate the external hazard received by the people. The H_{ex} was calculated using the formula in equation (6). The safe value of this index was ≤ 1 [17].

The total exposure was also donated by the internal exposure from radionuclide, such as radon, which can affect the respiratory organs. Therefore, the Internal Hazard Index (H_{in}) was determined in this study. The value for H_{in} was calculated using the formula in equation (7). The value for H_{in} must be ≤ 1 for the radiation hazard to be negligible [17].

Absorb dose rate (*D*) was determined in this study. In addition, *D* is defined as the average activity concentration of ^{40}K, ^{226} Ra, and ^{232}Th in the air at the height of 1.0 m above the surface [18]. According to UNSCEAR (2000) [19], *D* can be calculated using formula in equation (8).

$$Ra_{eq}(\frac{Bq}{kg}) = A_{Ra} + 1.43A_{Th} + 0.077A_K, \quad (4)$$

$$I_\gamma = \frac{ARa}{150} + \frac{A_{Th}}{100} + \frac{A_K}{1500} \leq 1, \quad (5)$$

$$H_{ex} = \frac{ARa}{370} + \frac{A_{Th}}{259} + \frac{A_K}{4810} \leq 1, \quad (6)$$

$$H_{in} = \frac{ARa}{185} + \frac{A_{Th}}{259} + \frac{A_K}{4810} \leq 1, \quad (7)$$

$$D(\frac{nGy}{h}) = 0.462A_{Ra} + 0.621A_{Th} + 0.0417A_K, \quad (8)$$

where $A_{Ra,}$ A_{Th}, and A_k in the formulas in equations (4) to (8) are specific activity concentrations in Bq.kg^{-1} of ^{226} Ra, ^{232}Th, and ^{40}K, respectively.

The estimated annual effective dose rate (D_{eff}) was calculated in this study using the formula in equation (9) [19].

$$D_{eff}(\frac{mSv}{t}) = D(\frac{nGy}{h}) \times 8760(\frac{h}{t}) \times 0.2 \times 0.7(\frac{Sv}{Gy}) \times 10^{-6}, \quad (9)$$

where 0.7 Sv/Gy was taken as the conversion coefficient from the absorbed dose in the air, and the outdoor occupancy factor (0.2) was taken from UNSCEAR 2000 [19].

Results and Discussion

Physical parameter of water

The physical parameters of water, including pH, conductivity, dissolved oxygen (DO), and temperature, at each station were determined in this study. The results are presented in Table 1. The pH level of water can influence the solubility of the radionuclides and heavy metals in water [20]. From this study, an average pH of 6 was recorded for the water sample in the KUIS lake (K^w) and a pH of 6.2 was found in the control sample (S^w), which indicated that both water samples were slightly acidic and that no significant difference was found between those two locations (p = 0.44). A previous study by Ashraf et al. [21] found a similar trend for the acidic water parameter with a pH level of 5.71 ± 0.52 at an ex-mining area in Bestari Jaya, Kuala Selangor. A similar observation was also reported by Al-Badaii et al. [22] in the Semenyih River (similar river at S^w) with a pH between 5.23 and 6.55, which was in the range of the current study. According to National Lake Water Quality Criteria and Standards (NLWQS), the pH value range between 6 and 9 is classified as category C [23]. Thus, KUIS lake in this study fell into this category (category C) from NLWQS, which indicated that the pH of the lake is good for the preservation of aquatic living and biodiversity [23]. An average temperature in the K^w was recorded at 30.7°C similar to S^w (29.5°C ± 0.2°C) and statistical differences were not found between those two locations (p = 0.5).

Table 1. Physical parameters of water

Sample	Location	pH	Conductivity (µS/cm)	Temperature (˚C)	Dissolved Oxygen (mg/L)
K^w	KUIS lake	6.0 ± 0.1	13.8 ± 5.8	30.7 ± 1.2	5.6 ± 0.5
S^w	Semenyih River (control)	6.2	52.8 ± 0.2	29.5 ± 0.2	6.1 ± 0.1

K^w Average value for K1, K2, K3, and K4 in water sample

Dissolved oxygen in water is essential for the metabolism of all aquatic organisms. An average of dissolved oxygen in the K^w was lower (5.6 ± 0.5 mg/L) compared to the S^w (6.1 ± 0.1 mg/L). The dissolved oxygen in K^w was lower compared to the control sample (S^w) possibly because of a large amount of dissolved organic matter present near the

surface of K^w, which causes undersaturated dissolved oxygen [24]. An aquatic organism process, such as photosynthesis of the algae in S^w, might result in the increase of oxygen concentration at S^w compared to K^w. Referring to NLWQS Malaysia, the dissolved oxygen in water in the current study was classified as category B or C (dissolved oxygen ranged from 5.5-8.7 mg/L for category B and 4.5-10.3 mg/L for category C), in which the dissolved oxygen for class B indicates that the lake is also suitable for secondary body contact recreational purposes, such as boating, but is not suitable for swimming activities [23]. The capability of water to pass the electrical flow (conductivity of water) was measured through a conductivity meter. The conductivity of the water for K^w was 13.8 µS/cm, which is significantly lower that that of S^w (2.8 ± 0.2 µS/cm) (p = 0.01). Generally, most of the freshwater conductivity ranges from 10 to 1000 µS/cm but may also exceeded 1000 µS/cm for polluted water or places with land run-off [25]. The conductivity of water in both of the samples (K^w and S^w) indicates that the water was clean and free from any pollution.

Radionuclides concentration

The concentration of ^{238}U, ^{232}Th, ^{226}Ra, and ^{40}K in water samples were calculated using equation (1) and presented in Table 2. The current study showed that all radionuclides (^{40}K, ^{226}Ra, ^{232}Th, and ^{238}U) were detected in the water sample of KUIS lake (K^w). The highest concentration of ^{40}K (0.62± 0.37 Bq/L) was observed in the water sample compared to other radionuclides, possibly due to the natural existence of ^{40}K in the rocks and on the earth's crust [26, 27]. However, all radionuclides were not detected in the control sample (S^w), except for ^{232}Th (0.13 ± 0.01 Bq/L). The presence of all radionuclides in K^w compared to S^w might possibly prove that the mining activity in the past in K^w can result in the enhancement of natural radionuclides in the water sample. The concentration of ^{238}U in K^w was higher compared to ^{232}Th, possibly due to the higher solubility of ^{238}U in water compared to ^{232}Th in an acidic condition (current study with pH of 6) [28]. In addition, the lower concentration of ^{232}Th in the water samples of K^w compared to ^{238}U could possibly be due to the transportation of ^{232}Th with particulate matter and subsequent deposit in the sediment. Therefore, the concentration of ^{232}Th in the sediment samples (K^s) was significantly higher compared to ^{232}Th in the water samples (K^w) (refer to Table 2).

Table 2. Concentration of NORM in water and sediment samples

Type of Sample	Sample	Concentration of Radionuclides (Bq/L)* or (Bq/kg)**			
		^{40}K	^{226}Ra	^{232}Th	^{238}U
Water	K^w (KUIS's lake)	0.62± 0.37	0.19 ± 0.1	0.04 ± 0.02	0.44 ± 0.31
	S^w (control)	bdl	bdl	0.13 ± 0.01	Bdl
	Taman Dengkil Jaya Lake [11]	11.44± 2.04	0.76 ± 0.07	1.57 ± 0.33	1.4 ± 0.15
	Amang processing plant pool [29]	-	-	29.59 – 36.16	28.98 – 35.42
	Kapal 7 Lake, Kampung Gajah [1]	12.8 ± 2.26	1.66 ± 0.30	-	-
	WHO [30]	-	1	1	10
Sediment	K^s (KUIS lake)	297.1±25.7	133.2±18.8	102.3 ± 3.3	49.1±18.8
	S^s (control)	199.1±30.5	46.5±21.6	48.9±36.9	30.3±21.6
	Amang processing plant pool [29]	-	-	154.4–1966.6	262.9-1110.5
	Chini lake [31]	618.3	-	160.3	191
	Kapal 7 Lake, Kampung Gajah [1]	1782±201	249.8±19.5	-	-
	UNSCEAR [19]	310	67	82	66

*Unit for water sample, ** Unit for sediment sample, bdl is below detection limit, K^s is average value for K1, K2, K3, and K4 in sediment sample

The concentration of NORM (^{40}K, ^{226}Ra, ^{232}Th, and ^{238}U) in the water sample (K^w) in the current study was lowered compared to the study reported in the ex-mining area at Taman Dengkil Jaya Lake [11]. The higher concentration of NORM in Taman Dengkil Jaya Lake could be contributed from the tailing processing plant, which is located nearby

studied area. A higher concentration of NORM was also reported from the study by Yasir et al. [29] at the Amang processing plant in Perak with 30–36 Bq/L for ^{232}Th and ^{238}U, compared to 0.04 and 0.44 Bq/L for ^{232}Th and ^{238}U in the current study. A lower concentration of NORM in the current study compared to other studies, including the study reported by Saat et al. [1], indicates that the concentration of NORM at KUIS lake was considered not highly contaminated for the public.

The concentration of NORM obtained from the water sample was also compared with the guidelines for drinking water quality from the World Health Organization. The standard value for the concentration of radionuclides stated by WHO in ^{238}U, ^{232}Th, and ^{226}Ra drinking water were 10 Bq/L, 1 Bq/L, and 1 Bq/L, respectively [30]. Based on Table 2, the results showed that the concentrations of ^{238}U (0.44 ± 0.31 Bq/L), ^{232}Th (0.04 ± 0.02 Bq/L), and ^{226} Ra (0.19 ± 0.11 Bq/L) in water samples were below the recommended values by WHO for drinking water sources, which implied the safe consumption of the water. A previous study by Sharip et al. [32] applied the National Quality Water Standard (NQWS) Malaysia to classify water quality at 15 lakes in Malaysia. In the study, the lake pH was between class II and III and the dissolved oxygen was in class II, according to NQWS [33]. However, based on NQWS, these lakes need to be treated before consumption, as other parameters involved, such as the pH and dissolved oxygen, must be considered to fulfil the standard requirements [33].

All radionuclides (^{40}K, ^{226}Ra, ^{232}Th, and ^{238}U) were detected in the sediment sample in this study (K^s) with the highest concentration of ^{40}K (199.1 ± 30.5 Bq/kg) compared to other radionuclides, which is similar to the trend observed in water samples. In general, all radionuclides (^{40}K, ^{226}Ra, ^{232}Th, and ^{238}U) in the sediment of K^s were significantly higher compared to the control sample (S^s). The higher concentration of radionuclides obtained in both water and sediment samples compared to the control sample is possibly due to the enhancement of the radionuclide concentration from the former mining activities in that area.

The concentration of ^{232}Th and ^{238}U in the sediment in this study was lowered compared to the Amang processing plant pool [29] in Perak and Chini lake [31]. The higher concentration of ^{232}Th and ^{238}U in Chini lake compared to the current study is possibly due to the development in that area [34], the geological condition, tourism activities, and logging activities, which affect the distribution and enrichment of the natural radionuclides in the sediment. Similar factors might also contribute to the higher concentration of ^{40}K and ^{226}Ra in Kapal 7 Lake, Kampung Gajah (former mining site). Overall, all radionuclides in sediments were found to be below the safe value reported by UNSCEAR except for ^{226}Ra. The higher concentration of ^{226}Ra in this study compared to UNSCEAR might be due to the desorption process occurring on the suspended sediment [34].

Heavy metals

Based on Table 3, the toxic heavy metal Ba was detected in both water and sediment samples (K^w and K^s); however, the concentration of Ba was below the standard value for drinking water reported by United States Environmental Protection Agency (US EPA) [35] and WHO [30]. Other heavy metals, such as As, Cu, Sb, and Sn, were detected in the water sample at K^w. These heavy metals were classified as very toxic and relatively accessible. However, these heavy metals were present in very low concentrations (0.004–0.58 µg/L), and most of these heavy metals did not exceed the recommended value by the Ministry of Health (MOH) [36] , US EPA [35] and WHO [30] as shown in Table 3.

The concentration of heavy metals in this study was higher in sediment compared to water samples. In addition, Zn was found to have the highest concentration compared to other heavy metals in the sediment with an average of 17 mg/kg. According to Moore et al., the concentration of heavy metals that does not show toxicity was in the range of 5-15 mg/kg [37]. The concentration of heavy metals depends on the types of sediment, and size of the sediment plays an important role to determine the ability of the sediment to absorb metals [38]. This is due to the properties of the sediment, which is composed of fine sand and silt; thus, heavy metals can be easily trapped in sediment due to its stable condition [39]. Singh et al. also showed that the concentration of heavy metals in sediment was higher than in water in their previous research at Gonti river [40]. The higher concentration of heavy metals in sediment compared to water is possibly due to the heavy metals in the water deposited in the sediment.

The results obtained from this study were also compared to the previous study on Bera Lake [41] and Antartuk Lake [42] in which both lakes reported higher concentrations of heavy metals present compared to the current study, possibly due to the different geological characteristics. Bera Lake is a natural freshwater lake [41], while Antaturk Lake is a dam that is the largest on earth and a rock embankment [42].The concentration of heavy metals in sediment was also compared with the US EPA standard. Referring to the Table 3, all heavy metals were below the standard value for freshwater sediment provided by the US EPA [43].

Table 3. Concentration of heavy metals in water and sediment

Sample	Location	Concentration of Heavy Metal (µg/L)* or (mg/kg)**						
		Ba	As	Cu	Mn	Sb	Sn	Zn
Water	K^w (lake area)	0.29±0.02	0.58±0.26	0.49±0.10	bdl	0.01	0.004	bdl
	S^w (control)	0.62±0.21	bdl	1.03±0.32	0.03	0.47	0.01	bdl
	Bestari Jaya Lake [21]	-	79±9.8	125±9.94	85±6.92	-	404±53.46	115±10.24
	MOH [36]	-	10	1000	200	-	-	300
	US EPA [35]	200	10	-	-	6	-	-
	WHO [30]	700	10	2000	-	20	-	-
Sediment	K^s (lake area)	1.30±0.37	2.06±1.03	0.99	9.74±1.90	0.04±0.02	0.41±0.14	17.34±15.79
	S^s (control)	0.73±0.66	4.37±0.57	2.54	30.37	0.03	0.41±0.58	12.83±5.5
	Peninsular Malaysia (ex-tin mining lake) [44]	-	48.9±9.6	19.24±0.89	407.9± 68.3	-	-	199.1±17.6
	Bera Lake [41]	-	139.0	2312	449	-	-	94
	Gonti River [40]	-	-	5.0	148.13	-	-	41.67
	Ataturk Lake [42]	-	-	14.57	514.07	-	-	59.24
	US EPA [43]	-	9.8	31.6	460	2	-	121

* Unit for water sample, ** Unit for sediment sample, bdl is below detection limit

Radiological hazards

The radiological hazards, which include a Radium-equivalent Activity Index (Ra_{eq}), Gamma Index (I_γ), External Hazard Index (H_{ex}), Internal Hazard Index (H_{in}), absorbed dose (D), and effective dose (D_{eff}) in this study were presented in Table 4. The Ra_{eq} in K^s was 225.5 Bq/kg, less than the recommended maximum levels by NEA-OECD (370 Bq/kg) [16]. Similar trends were recorded for the H_{ex} and H_{in} with the values of (0.6) and (0.9), less than the unity value of 1 [17]. In addition, the D_{eff} (0.10 mSv/y) was lowered compared to the range proposed by UNSCEAR 2000 (1-10 mSv/y) [19], whereas I_γ was measured at ≥ 1. In general, the values for Ra_{eq}, H_{ex}, H_{in}, D, and D_{eff} in both the control and KUIS lake (S^s and K^s) were below the recommended value, thus indicating a safe environment around KUIS lake for any recreational activities.

Table 4 also summarized the radiation hazard in sediment obtained in some of the regions around Malaysia. For example, Ra_{eq}, I_γ, H_{ex}, H_{in}, D, and D_{eff} that were measured in this study were approximately similar to the results

obtained in the northern peninsular area [10] but were slightly higher than the value reported in Jengka 15 [5], Pahang and in the east coast peninsular area [45].

Table 4. Comparison radiation hazard indices in this study and other studies in some regions in Malaysia

Location	Ra_{eq} (Bq/kg)	I_γ (Bq/kg)	H_{ex}	H_{in}	D (nGy/h)	D_{eff} (mSv/y)
K^s (lake area)	225.5	1.6	0.6	0.9	104.1	0.1
S^s (control)	90.9	0.7	0.2	0.4	42.4	0.1
Jengka 15, Pahang [5]	-	-	0.08-0.31	-	13-50	-
Northern Peninsular [10]	63-414	-	0.17-1.1	0.21-1.61	29-188	0.036-0.231
East Coast Peninsular [45]	143.1	-	0.4	-	-	-

Conclusion

This study represents the comprehensive investigation on the determination of the concentrations of natural radionuclides, heavy metals, and radiological hazards at the former mining area of KUIS lake. Results showed that the concentration of ^{40}K was the highest, followed by ^{238}U, ^{226}Ra, and ^{232}Th in the water samples. Similarly, the concentration of ^{40}K was found to be the highest in the sediment sample, followed by ^{226}Ra, ^{238}U, and ^{232}Th. The radionuclides concentration in water obtained in this study was still in the safe limit to become a source of drinking water. In the sediment matrix, the highest heavy metal reading was Zn whereas the highest heavy metal reading was As in the water sample. Based on the radiation hazard index level in the current study, KUIS Lake was found to be safe for the public to perform any activities; however, occasional monitoring still needs to be considered in the future. For future prospects, the study of concentrations of natural radionuclides and heavy metals in biotic samples, such as fish and plants surrounding the lake area can provide a very good indicator of the complete transfer factor of the lake ecosystem.

Acknowledgements

The authors wish to thank the School of Applied Physics, UKM, especially the Nuclear Science Programme, GGPM-2015-038, and GUP-2017-085 for the funds. The authors acknowledge Mr Azman, Senior Assistant Architect Landscape of Kolej University Islam Antarabangsa Selangor (KUIS) for his cooperation throughout the research. The authors also acknowledge the facilities of the School of Environmental Science, UKM for assistance with the ICP-MS analysis.

References

1. Saat, A., Isak, N. M., Hamzah, Z. and Wood, A. K. (2014). Study of radionuclides linkage between fish, water and sediment in former tin mining lake in Kampung Gajah, Perak. *Malaysian Journal of Analytical Sciences*, 18(1): 170-177.
2. Irvin, T. R. and Cruz-Batres, C. (1996). Naturally occurring radioactive material:Principles and practices. St. Lucoe Press, Delray Beach, Florida: pp. 2-3.
3. Avwiri, G. O., Ononugbo, C. P. and Nwokeoji, I. E. (2014). Radiation hazard indices and excess lifetime cancer risk in soil, sediment and water around Mini-Okoro/Oginigba Creek, Port Harcourt, River State, Nigeria. *Journal of Environment and Earth Sciences*, 3(1): 38-50
4. Al-Hamarneh, I. F. and Awadallah, M. I. (2009). Soil radioactivity levels and radiation hazard assessment in the highlands of northern Jordan. *Radiation Measurements*, 44(1): 102-110.
5. Alias, M., Hamzah, Z., Saat, A., Omar, M. and Wood, A.K. (2008). An assessment of absorbed dose and radiation hazard index from natural radioactivity. *Malaysian Journal of Analytical Sciences*, 12(1): 195-204.
6. Taskin, H., Karavus, M., Ay, P., Topuzoglu, A., Hidiroglu, S. and Karahan, G. (2009). Radionuclide concentrations in soil and lifetime cancer risk due to gamma radioactivity in Kirklareli, Turkey. *Journal of Environmental Radioactivity*, 100(1): 49-53.

7. Erickson, A. J., Weiss, P. T. and Gulliver, J. S. (2013). Water sampling methods: pp. 163-192.
8. Yasir, M. S., Kabir, N. A., Yahaya, R. and Majid, A. A. (2008). Kandungan logam berat dan radionuklid tabii dalam ikan, air, tumbuhan dan sedimen.*Malaysian Journal of Analytical Sciences*, 12 (1): 172-178.
9. Nasirian, M., Bahari, I. and Abdullah, P. (2008). Assessment of natural radioactivity in water and sediment from amang (tin tailing) processing ponds. *Malaysia Journal of Analytical Sciences*, 12(1): 150-159.
10. Almayahi, B. A., Tajuddin, A. A. and Jaafar, M. S. (2012). Radiation hazard indices of soil and water samples in Northern Malaysian Peninsula. *Applied Radiation and Isotopes*, 70(11): 2652-2660.
11. Yasir, M. S., Ab. Majid, A., Ibrahim, F., Tap, S. Q. M. and Abidin, M. R. Z. (2006). Analisis ^{238}U, ^{232}Th dan ^{40}K dalam sampel amang, tanah dan air di Dengkil, Selangor menggunakan spektrometri gama. *Malaysian Journal of Analytical Sciences*, 10(1): 35-40.
12. United States Environmental Protection Agency (2014). Method 6020B: Inductively coupled plasma - mass spectrometry, part of test methods for evaluating solid waste, physical/chemical methods. Washington DC: pp. 1-33.
13. Talib, O. (2015). SPSS: Analissis data kuantitatif untuk penyelidik muda. MPWS Rich Publication Sdn Bhd, Bangi, Selangor: pp. 4-215.
14. Harb, S., El-Kamel, A.H., El-Mageed, A.I.A., Abbady, A. and Rashed, W. (2008). Concentration of U-238, Ra-226 Th-232 and K-40 for some granite samples in Eastern Desert of Egypt. *Proceedings of the 3rd Environmental Physics Conference*, Aswan, Egypt: 109-117.
15. Organisation for Economic Cooperation and Development. (1979). Exposure to radiation from natural radioactivity in building materials. France: pp. 1-40.
16. Guptaa, M., Chauhana, R. P., Gargb, A., Kumarc, S. and Sonkawaded, R. G. (2010). Estimation of radioactivity in some sand and soil samples. *Indian Journal of Pure & Applied Physics*, 48: 482-485.
17. Diab, H. M., Nouh, S. A., Hamdy, A. and El-Fiki, S. A. (2008). Evaluation of natural radioactivity in a cultivated area around a fertiliser factory. *Journal of Nuclear and Radiation Physics*, 3(1): 53-62.
18. United Nations Scientific Committee on the Effects of Atomic Radiation (1977). Sources and effects of ionizing radiation. Annex A:Concepts and quantities in the assessment of human exposures. New York.
19. United Nations Scientific Committee on the Effects of Atomic Radiation (2000). Annex B-exposures from natural radiation sources. New York.
20. Hirner, A.V. (2016). Environmental impacts of metallic elements: Speciation, bioavailability and remediation, in *Environmental Earth Sciences*, Sarfraz M. Ashraf M. A., Naureen R., Gharibreza M, Editor. Springer, Berlin: pp. 1183.
21. Ashraf, M. A., Maah, M. J. and Yusoff, I. B. (2010). Study of water quality and heavy metals in soil & water of ex-mining area Bestari Jaya, Peninsular Malaysia. *International Journal of Basic & Applied Sciences*, 10(03): 7-23.
22. Al-Badaii, F., Shuhaimi-Othman, M. and Gasim, M. B. (2013). Water quality assessment of the Semenyih River, Selangor, Malaysia. *Journal of Chemistry*, 2013: 1-10.
23. National Hydraulic Research Institute of Malaysia and Ministry of Natural Resources and Environment. (2015). National Lake Water Quality Criteria and Standards. Malaysia. Access from http://www.nahrim.gov.my/en/publications/listofpublications/1195-national-lake-water-quality-criteria-and-standards.html.
24. Wetzel, R. G. (2001). Limnology, lake and river ecosystem. Elsvier, United States.
25. Chapman D. (1996). Water quality assessments - A guide to use of biota, sediments and water in environmental monitoring. University Press, Cambridge. Great Britain: pp. 1-609.
26. Schmus, W. R. V. (1995). Global earth geophysics: A handbook of physical constants. American Geophysical Union, USA: pp. 1-376.
27. Kathren, R. L. (1998). NORM sources and their origins. *Applied Radiation and Isotopes*, 49(3): 149-168.
28. Boyle, R.W. (1982). Geochemical prospecting for thorium and uranium - Hydrochemical Surveys. Elsevier: pp. 277-315.
29. Yasir, M. S., Majid, A. A., Yahaya, R., Bahari, I. and Kim, W. S. (2007). Impak aktiviti pemprosesan amang sistem tertutup ke atas kualiti air dan sedimen setempat. *Malaysian Journal of Analytical Sciences*, 11(2): 370 - 378.
30. World Health Organisation (2011). Guidelines for drinking-water quality. (4th) WHO Press. Switzerland: pp. 1-564.

31. Majid, A., Umar, S. R., Yahaya, R., Yasir, M. S. and Othman, M. S. (2008). Analisis unsur dan keradioaktifan dalam sampel sedimen Tasik Chini, Pahang Darul Makmur. *Malaysian Journal of Analytical Sciences*, 12(1): 167-171.
32. Sharip, Z., Zaki, A. T. A., Shapai, M. A. H. M., Suratman, S. and Shaaban, A. J. (2014). Lakes of Malaysia: Water quality, eutrophication and management. *Lakes and Reservoirs: Research and Management,*19(2): 130-141.
33. Water Environment Partnership in Asia. (2008). National water quality standards for Malaysia. Access from http://wepa-db.net/3rd/jp/topic/waterstandard/Malaysia_1_surface.pdf.
34. Mohamed, C. A. R., Ahmad, Z. and Mon, G. C. (2006). Aktiviti Ra^{226} dalam sistem aliran sungai lembangan Langat, Selangor. *Malaysian Journal of Analytical Sciences*, 10(2): 295-302.
35. United States Environmental Protection Agency (2009). National Primary Drinking Water Regulations. Access from https://www.epa.gov/ground-water-and-drinking-water/national-primary-drinking-water-regulations.
36. Ministry of Health Malaysia (2000). National water quality standards for Malaysia.Access from https://environment.com.my/wp-content/uploads/2016/05/Drinking-Water-MOH.pdf.
37. Moore, J.W. and Ramamoorthy, S. (1984). Heavy Metals in Natural Waters: Applied Monitoring and Impact Assessment. Springer-Verlag New York Inc: 1-269.
38. Greaney, K. M. (2005). An assessment of heavy metal contamination in the marine sediments of Las Perlas Archipelago, Gulf of Panama. Thesis of Master Degree. Heriot-Watt University, Edinburgh, UK.
39. Hamzah, Z., Saat, A., Bakar, Z. A. and Wood, A. K. (2011). Anthropogenic heavy metals, U-238 and Th-232 profiles in sediments from an abandoned tin mining lake in Malaysia. *3rd International Conference on Chemical, Biological and Environmental Engineering*, 2011:75-79.
40. Singh, K. P., Mohan, D., Singh, V. K. and Malik, A. (2005). Studies on distribution and fractionation of heavy metals in Gomti river sediments—a tributary of the Ganges, India. *Journal of Hydrology*, 312 (1-4): 14-27.
41. Gharibreza, M., Ashraf, M. A., Yusoff, I. and Raj, J. K. (2013). An evaluation of Bera Lake (Malaysia) sediment contamination using sediment quality guidelines. *Journal of Chemistry*, 2013: 1-13.
42. Karadede, H. and Unlu, E. (2000). Concentrations of some heavy metals in water, sediment and fish species from the Atatürk Dam Lake (Euphrates). *Chemosphere*, 41: 1371-1376.
43. United States Environmental Protection Agency (2006). Freshwater Sediment Screening Benchmarks. Access from https://www.epa.gov/sites/production/files/2015-09/documents/r3_btag_fw_sediment_ benchmarks_8-06.pdf
44. Hamzah, Z., Saat, A., Wood, A. K. and Bakar, Z. A. (2011). Sedimentation, heavy metals profiles and cluster analysis of a former tin mining lake. *International Journal of Environmental Science and Development*, 2(6): 448-453.
45. Mei-Wo, Y., Jaffary, N. A. M. and Ahmad, Z. (2011). Radiation hazard from natural radioactivity in the sediment of the East Coast Peninsular Malaysia Exclusive Economic Zone (EEZ). *Malaysian Journal of Analytical Sciences*, 15(2): 202-121.

Malaysian Journal of Analytical Sciences, Vol 22 No 5 (2018): 839 - 850
DOI: https://doi.org/10.17576/mjas-2018-2205-11

MALAYSIAN JOURNAL OF ANALYTICAL SCIENCES
Published by The Malaysian Analytical Sciences Society
ISSN 1394 - 2506

CHITOSAN-BASED ADSORBENTS FOR THE REMOVAL OF METAL IONS FROM AQUEOUS SOLUTIONS

(Bahan Penjerap Berasaskan Kitosan untuk Penyingkiran Ion Logam dari Larutan Akueus)

Zetty Azalea Sutirman[1], Mohd Marsin Sanagi[1,2]*, Khairil Juhanni Abd Karim[1], Ahmedy Abu Naim[1], Wan Aini Wan Ibrahim[1,2]

[1]*Department of Chemistry, Faculty of Science*
[2]*Centre for Sustainable Nanomaterials, Ibnu Sina Institute for Scientific and Industrial Research*
Universiti Teknologi Malaysia, 81310 UTM Johor Bahru, Johor, Malaysia

**Corresponding author: marsin@kimia.fs.utm.my*

Received: 16 April 2017; Accepted: 7 March 2018

Abstract

Wastewater containing heavy metal ions is one of the most serious environmental concerns. Exposure to elevated levels of heavy metals can adversely affect water resources, endangering the ecosystems and human health. Among the various treatment technologies, adsorption using biopolymer seems a promising alternative method. Chitosan is a natural polymer produced from chitin with excellent properties such as biocompatibility, biodegradability and non-toxicity. Moreover, chitosan is known as an effective sorbent due to the presence of amino and hydroxyl groups in its molecules which can serve as attachment sites towards metal ions. Recently, chitosan derivatives as metal ion sorbents have gained considerable attention. These derivatives are prepared by either physical or chemical modifications or both in order to improve chitosan properties in adsorption. This paper discusses recent developments in the modifications of chitosan and the application of the derived materials in the removal of metal ions from aqueous solutions. The mechanisms of adsorption, metal sorption capacities, effect of pH, isotherm and kinetic models are also described.

Keywords: chitosan, modification, sorption, metal ions

Abstrak

Air sisa yang mengandungi logam berat merupakan salah satu isu alam sekitar yang serius. Pendedahan yang tidak terkawal kepada logam berat boleh menyebabkan kesan negatif terhadap sumber air, membahayakan ekosistem dan kesihatan manusia. Di antara pelbagai teknologi rawatan, penjerapan menggunakan biopolimer menunjukkan kaedah alternatif yang menjaminkan. Kitosan ialah polimer semula jadi yang dihasilkan daripada kitin dengan ciri-ciri seperti biokompatibiliti, biopenguraian dan bukan toksik. Tambahan pula, kitosan dikenali sebagai penjerap yang efektif kerana mempunyai kumpulan amina dan hidrosil dalam molekulnya yang bertindak sebagai tapak penghubung terhadap ion logam. Baru-baru ini, derivatif kitosan sebagai penjerap ion logam telah menerima perhatian yang luas. Derivatif-derivatif ini dihasilkan sama ada melalui pengubahsuaian fizikal atau kimia atau kedua-duanya untuk menambah baik ciri-ciri kitosan dalam penjerapan. Kertas ini membincangkan pengembangan yang terbaru dalam pengubahsuaian kitosan serta aplikasi daripada bahan derivatif dalam penyingkiran ion logam dari larutan akues. Mekanisma penjerapan, kapasiti penjerapan logam, kesan pH, model dan kinetik juga diterangkan.

Kata kunci: kitosan, pengubahsuaian, penjerapan, ion logam

Introduction

Heavy metals such as cadmium (Cd), mercury (Hg), lead (Pb), zinc (Zn), arsenic (As), nickel (Ni) and chromium

(Cr) are elements with atomic density of at least five times the specific gravity of water [1]. They are also known as trace elements due to their presence at low concentrations (<1000 ppm) in environmental matrices. In fact, some of them have been recognized as essential nutrients for organisms (i.e. Cu and Zn).

Even though heavy metals are natural components of the Earth's crust, most of environmental pollution and human exposure to heavy metals are caused by various anthropogenic activities such as military, industrial and agricultural processes and waste disposal. Heavy metals are also released to the ecosystem through natural processes like weathering of rocks and volcanic eruptions [2, 3]. Most heavy metals are highly toxic to living organisms especially when their concentrations exceed the allowable limits in the ecosystem. These pollutants are non-biodegradable and can be absorbed by marine life. Once high concentrations of heavy metals enter the food chain, they tend to accumulate in living tissues and thus, dysfunction the system of the human bodies [4]. Hence, it is important to decontaminate or minimize these heavy metals from water sources in the interest of public health and the environment.

Up to now, various treatment methods have been developed to remove heavy metals, which include chemical precipitation, solvent extraction, ion exchange, evaporation, reverse osmosis, electrolysis and adsorption. However, most of these methods tend to show some economical and technical disadvantages [5]. For example, chemical precipitation has been widely used to remove dyes or heavy metals from inorganic effluent by increasing the pH of the solution to convert the soluble substances into an insoluble form. Even though the process is simple, it generates a large quantity of sludge which requires further treatment and high cost. Chemical precipitation is also not effective to remove trace level of pollutants from aqueous solutions. Meanwhile, in ion exchange method, the resin, either synthetic or natural solid, exchanges its cations with the unwanted substance in the wastewater. The problem is drawn when the ion exchanger is quickly polluted and thus, reducing the exchange capacity. In addition, this method usually consumes high capital and operational costs. Coagulation-flocculation has been capable of removing pollutants from solution, but the process can destabilize colloidal particles by adding a chemical agent (coagulant) which results in sedimentation [6, 7]. Adsorption is established as the most effective method for water decontamination applications and analytical separation purposes. It offers advantages over the other options such as simplicity in terms of design and operation, uses less chemicals, requires low initial costs and can remove different types of pollutants [4, 8].

Chitosan, an amino polysaccharide produced from chitin are found naturally in some fungi. It is the most versatile biopolymer for a broad range of applications due to its biocompatibility, biodegradability and antibacterial property. Furthermore, this material is regarded as an ideal adsorbent. The presence of $–NH_2$ and –OH groups on the polymeric backbone can serve as chelating and reaction sites [9].

Several methods have been employed to modify chitosan either physically or chemically to enhance adsorption capacity. Crosslinking is one of the common modifications performed on chitosan mainly to prevent its dissolution in acidic media [10]. This technique involves the formation of covalent bonds between two polymer chains by using bifunctional reagents containing reactive end groups that react with functional groups of chitosan (i.e. NH_2). Therefore, it must be taken into account that crosslinking can reduce the adsorption capacity as it diminishes the number of free amino on chitosan, but this loss is worth to increase the stability of the polymer [11].

Another important modification is graft copolymerization. This approach has gained considerable interest among researchers and has become a vital technique in polymer chemistry. Grafting reaction provides various molecular designs leading to novel types of hybrid materials, which are composed of bio- and synthetic-polymers [12]. Chitosan has two types of reactive groups; hydroxyl and amine groups for grafting to occur. Different functional groups have been successfully grafted onto chitosan by covalent bond onto the chitosan backbone.

Several reviews on chitosan modifications have been reported particularly on metal ions removal from water of wastewater [10, 13-16]. Other works on chitosan and its derivatives not limited to metal sorption have also been reviewed [17-21]. However, to the best of our knowledge, no detail review has been reported on different modifications of chitosan such as beading, crosslinking and grafting and their adsorption potential for various metal ions. In this paper, we present updated relevant information on the current modifications techniques employed on

chitosan to enhance its properties in metal ions adsorption. The adsorption performances of chitosan-based adsorbents are also compared.

Chitosan

Chitosan, a main derivative of chitin, can be prepared by deacetylation of chitin under alkaline conditions (Figure 1). It was first discovered by Professor C. Rouget in 1859. Chitosan only occurs naturally in some fungi such as *Mucor rouxii* and *Choanephora cucurbitarum*. This polysaccharide is mainly composed of a linear of β (1→4)-linked 2-amino-2-deoxy-β-D-glucopyranose. Since complete deacetylation of chitin is practically impossible, the molar ratio of *N*-acetyl-2-amino-2-deoxy-D-glucose (GlcNAc) is often expressed as a degree of *N*-acetylation (DA), which defines the average number of GlcNAc units per 100 monomers. Meanwhile, the deacetylation degree (DD) is used for 2-amino-2-deoxy-D-glucose (GlcN) residue [22].

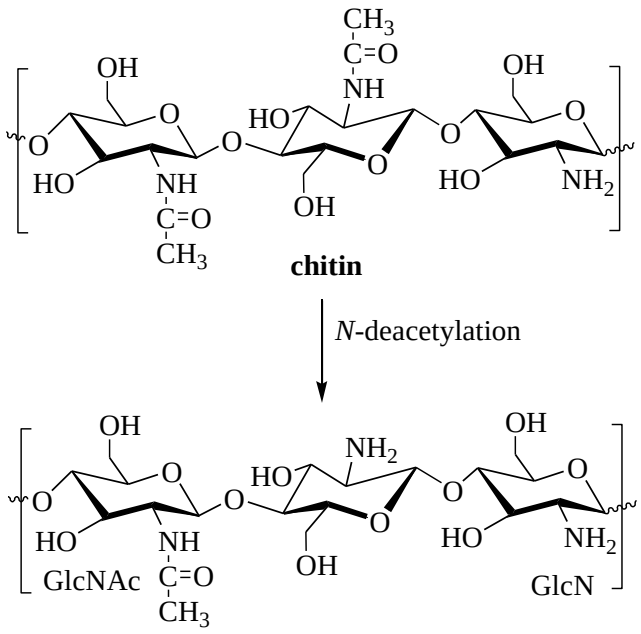


Figure 1. Chemical structures of chitin and chitosan

Chitosan is named by the content of DD in the polymer. The DD for commercial chitosan is usually 70-95%. Some researchers believe that chitosan is built up of at least 50% DD and soluble in aqueous acidic media [23, 24]. The solubility of chitosan occurs when the amino group, $–NH_2$ on the GlcN repeated unit is protonated, converting the polysaccharide to polyelectrolyte (pK_a=6.5). However, an exact nomenclature with respect to DD ratio between chitin and chitosan has not been clearly defined because it may vary depending on the production process, natural source and other factors [22].

The effectiveness of chitosan and its derivatives to interact with metal ions from aqueous solution has been studied by many workers. It is important to note that the adsorption capacities of these adsorbents depend on the experiment conditions such as pH, initial concentration, contact time, adsorbent dosage, presence of competitive ions, etc.

Modified chitosan

Although chitosan shows a great potential as sorbent, it has severe drawbacks that restrict its application in water treatment and purification. Chitosan is commonly available in powder or flake form as the end product in the production process. It has crystallized structure due to strong inter- and intra-molecular hydrogen bonding in the

structure, presents poor acid resistance and low porosity. In view of these limitations, raw chitosan is not suitable to be used in adsorption process without further modifications [25].

Modification of chitosan in adsorption study has two main goals. The first goal is to increase the chemical stability of the polymer in wide pH-range aqueous media. The second goal is to improve the sorption performance such as sorption capacity and pollutant selectivity [13]. The modification of chitosan can be carried out by either physical or chemical techniques or both.

Physical modification

The selection of physical modification of chitosan depends mainly on the system configuration to be used for applications. In this manner, several techniques have been employed to mold chitosan into different morphologies such as powder, microspheres, hydrogels, membranes and fibers [26].

Solid chitosan can be obtained when chitosan in acidic aqueous solution is mixed with alkali. This method is usually used to prepare membranes, fibers and foremost, spherical gel beads of different sizes and porosities. Adarsh and Madhu [27] have prepared the beads by spraying chitosan solution into a precipitation bath containing 1 M NaOH. In order to obtain membrane, chitosan solution was spread on a petri dish and dried. The membranes were then immersed in NaOH solution for neutralization [28]. Chitosan membrane or film can also be fabricated by the solvent evaporation method.

Furthermore, porous three-dimensional sponges can be prepared by freeze–drying. In this method, chitosan solutions or gels are frozen followed by lyophilization. The porosity and morphology of the material produced depends on the chitosan molecular weight and on the composition and concentration of the starting solution, and most importantly on the freezing temperature and freezing rate [29].

Chemical modification

Chitosan bears a large number of free hydroxyl and amino groups distributed along the backbone, which are an ideal candidate for chemical modification. The main aim of modifying chitosan is to vary properties such as solubility, water sorbency, adsorptive capability and thermal resistance. Chemical modification, however, would not change the fundamental skeleton of chitosan, yet affords a wide range of derivatives with desired properties for specific use and applications in various areas mainly of pharmaceutical, biomedical and biotechnological fields [10]. Derivatization by incorporating functional groups to chitosan may involve the $–NH_2$ group at the C-2 position (specific reactions) or –OH groups at the C-3 and C-6 positions (non-specific reactions) [30].

Preparation of new chitosan-based materials may include impregnation, crosslinking, graft polymerization and composite formation [18]. The use of chitosan in relatively low pH solution is not feasible because it tends to form gel or dissolve. Thus, one way to overcome this problem is by inducing crosslinking on chitosan. Crosslinking agents or crosslinkers are generally bifunctional compounds with various forms such as straight chains, branch chains and rings. These crosslinking agents are classified upon their nature and interaction with biopolymer (i.e. chemical or physical crosslinking). Chemical crosslinking occurs when the crosslinker forms intermolecular covalent bond between the polymer chains. The reaction often involves the $-NH_2$ and -OH functional groups on the biopolymer. Chemical crosslinking is commonly accomplished using crosslinker such as glutaraldehyde, epichlorohydrin, ethylene glycol diglycidyl ether, genepin, glyoxal, cylclodextrins, etc. [10, 31]. Meanwhile, physical crosslinking results from non-covalent linkages between polymer chains. The reaction is weaker than chemical crosslinking since it relates to physical attractive forces such as ionic interaction, hydrophobic and hydrogen bonding. Pentasodium tripolyphosphate and calcium chloride are the two established examples of physical crosslinker. In a general way, crosslinking decreases the adsorption capacity slightly because amine groups of chitosan, which is known to be the main sites for target analytes, are usually bound with the crosslink agent to form a stable covalent bond (i.e. imine group).

Grafting copolymerization is another common way to improve adsorption capacity and increase chelating or complexation properties by introducing functional groups onto chitosan. During grafting reaction, side chains are covalently bonded to the main polymer backbone to give a branched structure copolymer. Until today, many

research works have been carried out to synthesize graft copolymers by polymerization reaction of chitosan with monomer using free radical initiation. There are two main kinds of free radical initiating systems employed. The first type of initiation is called conventional or chemical initiation. In this system, the initiators used are usually thermal initiator and redox initiator. Meanwhile, the second type of initiation is free radical initiation by irradiation with either high energy (i.e. γ-ray) or low energy (i.e. microwave, UV light) [32].

Chitosan beads and membranes

Many studies have reported that the efficiency of adsorption strongly depends on the physicochemical properties of adsorbents including crystallinity, surface area, porosity and particle size. Therefore, chitosan flake or powder is not considered to be used as adsorbent due to its high crystallinity, resistance to mass transfer, low adsorption capacity and very low porosity. Small particle is also inappropriate for a fixed bed column system especially in industrial scale because they can increase their resistance to mass transfer rate, lead to clogging effect as well as hydrodynamic limitations [17]. Conversion of chitosan flake into bead has been reported to be essential as it allows the expansion of the polymer network, thus increasing access to internal sorption sites and enhancing diffusion mechanism.

Chitosan, in its native state, is characterized as a crystallized polymer. Since adsorption process usually occurs only at the amorphous region of the crystal, chitosan is usually subjected to physical modification by converting it into gel beads in order to reduce its crystallinity, thus enhancing the adsorption capacity. Cahyaningrum *et al.* reported the comparison between chitosan powder and chitosan beads for the removal of Hg(II) ions [33]. The results revealed that the adsorption capacity of the metallic ion by chitosan beads (17.39×10^{-4} mol g^{-1}) was much higher than that of chitosan powder (7.20×10^{-4} mol g^{-1}).

Wan Ngah et al. compared the adsorption capacity of chitosan flakes and beads as sorbents for removing Pb(II) ions from aqueous solution [34]. They found that the maximum adsorption capacity of chitosan beads was higher than that of chitosan flakes because the structure of the beads slightly changed because of reducing the crystallinity of chitosan. The adsorption of Cu(II) ions onto flake- and bead-type chitosan derived from shrimp was compared by Wu et al. [35]. The results showed that chitosan flakes possessed higher uptake for Cu(II) ions than that of chitosan flakes.

Crosslinked chitosan

As afore-mentioned, raw chitosan has a major limitation of being highly soluble in most dilute mineral and organic acid solutions by protonation of the amine groups. This makes it even more difficult to evaluate its application as sorbent in the treatment of industrial effluents. Crosslinking process has been found to be an effective method to reinforce chemical stability of chitosan under acidic conditions. Several common chemical crosslinking agents such as glutaraldehyde (GA), epichlorohydrin (EPC), triphosphate (TPP) and ethylene glycol diglycidyl ether (EDGE) have been used for this purpose. Results on metal ions adsorption onto crosslinked chitosan using different crosslinking agent are shown in Table 1. It is important to note that the adsorption capacities of the adsorbents cited in this paper depend on the experiment conditions such as pH, initial concentration, contact time, adsorbent dosage, presence of competitive ions, etc.

Wan Ngah and Fatinathan successfully crosslinked chitosan beads with GA for removal of Cu(II) ions in aqueous solution [9]. The crosslinked chitosan was insoluble in acetic acid solution, showing crosslinking reaction enhanced the resistance of the polymer against acid. The researchers also investigated the effect of GA content in adsorption. An increase in the density of crosslinking lowered the adsorption capacity of chitosan because the number of amino groups that serve as binding sites for metal ions was reduced.

In another work, a batch experiment was carried out to study the adsorption of Fe(II) and Fe(III) ions by chitosan and crosslinked chitosan beads [43]. The chitosan beads were crosslinked with GA, EPC and EDGE in order to improve its chemical resistance and mechanical strength. The maximum adsorption capacity was in the sequence of chitosan > chitosan-EPC > chitosan-GA > chitosan-EDGE.

Table 1. Removal of different metal ions from aqueous solutions by crosslinked chitosan

Crosslinking Agent	Metal Ion	q_{max} (mg g^{-1})	pH	Isotherm	Reference
TPP	Cu(II)	200.0	4-5	L	[36]
GA	Pb(II)	24.2	5-7	L	[37]
	Cd(II)	23.9		L	
GA crown ether	Cd(II)	-	2	-	[38]
	Hg(II)	126.4	6	-	[39]
	Pb(II)	96.8	6	-	
GA 2-aminopyridine glyoxal Schiff's base	Pd(II)	166.7	8	L	[40]
	Cu(II)	124	5	L	[41]
	Cd(II)	84	5	L	
	Ni(II)	67	5	L	
Adipic acid dihydrazide	Cu(II)	200.1	5	L	[42]

L = Langmuir

Chitosan film was crosslinked using two different crosslinkers; GA and EPC for the adsorption of Cu(II), Hg(II) and Cr(II) [44]. In this work, X-ray photoelectron spectroscopy (XPS) confirmed the crosslinking of chitosan with GA and EPC occurred preferentially on hydroxyl and amino groups thus forming final structures with different functional groups. The uptake of Cu(II) and Cd(II) ions by chitosan crosslinked EPC subsequently treated with TPP was studied by Laus and Fevere [45]. The results for binary solutions showed the adsorbent has great affinity towards Cu(II) rather than Cd(II) due to a significant competition effect.

Grafting of chitosan

Grafting of chitosan allows the formation of functional derivatives by covalent binding of molecules onto chitosan backbone. This kind of modification can lead to increasing functional sides which involve in metal complexation. The adsorption capacities of grafting chitosan for the removal of different metal ions from aqueous solutions are listed in Table 2.

Table 2. Removal of different metal ions from aqueous solutions by grafted chitosan

Graft Copolymer	Metal Ion	q_{max} (mg g^{-1})	pH	Isotherm	Reference
Polyaniline grafted chitosan	Pb(II)	16.1	6	L	[46]
	Cd(II)	14.3	6	L	
Silane grafted chitosan	As(V)	11.8		L	[47]
Succinyl-grafted chitosan	Zn(II)	1401	5	T	[48]
Poly(methacrylic acid)-grafted chitosan	Cd(II)	146.1	5	L	[49]
Ethylacrylate grafted chitosan	Pb(II)	613	6	L	
N-butylacrylate grafted chitosan	Cd(II)	573	6	L	[50]
Amidoximated chitosan-grafted polyacrylonitrile	Zn(II)	653	6	L	
	Cr(II)	17.2	3.5	L/F	[51]
	U(IV)	312.1	~7	L	[52]

L = Langmuir, T = Tóth and F = Freundlich

Graft copolymer of chitosan with acrylamide was prepared using gamma radiation and used for the adsorption of copper(II) and nickel(II) from aqueous solutions [53]. The adsorption of both metal ions increases with increasing pH and polymer concentration. At lower pH, hydrogen ions occupy most of the adsorption sites of the adsorbent and this leads to a very low adsorption due to electrostatic repulsion. Lalita et al. was grafted chitosan with *N*-isopropylacrylamide with the presence of azoisobutrylnitrile (AIBN) as an initiator [54]. Chitosan and the graft copolymer were characterized by different techniques such as by FTIR, TGA/DTA, XRD and SEM. The graft copolymer showed good adsorption capacity towards Cr(VI), Cu(II) and Fe(II) ions.

Some researchers reported the enhancement of adsorption capacity after grafting due to introducing of new functional group onto chitosan chain. Galhoum et al. found that grafting of aspartic acid onto chitosan significantly increased the sorption properties for Nd(III) [55]. The adsorption capacity was two times higher compared to that of chitosan and GA-crosslinked chitosan. Similarly, the adsorption capacities of chitosan for several metal ions (Pb(II), Hg(II), Cd(II), Ni(II), Mn(II), Co(II), As(V) and Se(VI)) were increased after grafting with acrylic acid [56].

Grafting of crosslinked chitosan

Grafting copolymerization on crosslinked chitosan beads with vinyl monomers is necessary to increase the number of adsorption sites and thereby, the adsorption capacity. For example, adsorption of Pb(II) and Cd(II) was carried out by Benamer et al. on chitosan beads grafted with acrylic acid [57]. Chitosan was first crosslinked with glutaraldehyde and then grafted with monomers using ^{60}Co gamma radiation technique. The graft copolymer presented greater ability to adsorb Cd and Pb ions compared to unmodified chitosan. The adsorption capacity of the graft copolymer also increased with the increasing degree of grafting.

Our research group utilized ammonium persulfate as free radical initiator for grafting methacrylamide onto crosslinked chitosan beads. Several characterization techniques such as FTIR, TGA, SEM and ^{13}C NMR were used to confirm the successful modifications. The efficiency of the beads as adsorbent was studied to remove Pb(II) ions in batch experiment [58]. On the other hand, we successfully grafted *N*-vinyl-2-pyrrolidone (NVP) onto crosslinked chitosan by using the same technique (unrevealed data). The beads have shown a good adsorption capacity towards several metal ions such as Pb(II), Cu(II) and Cd(II). The interaction between adsorbent and Cu(II) ions is also proposed according to XPS analysis (Figure 2).

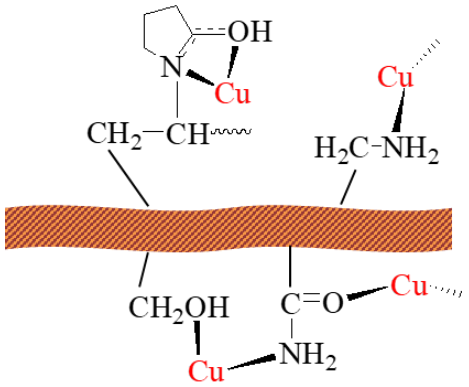


Figure 2. Possible interactions between Cu(II) ion and crosslinked chitosan-*g*-poly(NVP)

The effect of experimental conditions on the adsorption and desorption behavior of Cd(II) and Pb(II) on polyaniline grafted cross-linked chitosan beads was studied by Igberasa and Osifo [59]. The study showed that the binding of metal ions was highly dependent on factors such as pH, adsorbent dosage, contact time, initial concentration and point of zero charge.

Novel chitosan-based adsorbent was synthesized for Fe(II) adsorption by Liu et al. from TPP and GA-crosslinked chitosan, followed by grafting with five phenolic acid derivatives (Gallic acid (GA), protocatechuic acid (PA),

caffeic acid (CA), p-hydroxybenzoic acid (HA), vanillic acid (VA)) [60]. Results showed that the graft copolymerization occurred at amino groups (C2), hydroxyl groups (C3 and C6) of chitosan and incorporation of carboxyl groups from phenolic acids decreased in crystallinity of the polymer. In addition to the above-stated examples, several other grafting crosslinked chitosan sorbents are presented in Table 3.

Table 3. Removal of different metal ions from aqueous solutions by grafting crosslinked chitosan

Chitosan Derivative	**CA**	**Metal ion**	q_{max} **(mg g^{-1})**	**pH**	**Isotherm**	**Ref.**
Crosslinked chitosan-*g*-acrylonitrile	GA	Cu(II)	230.8	5	L	[61]
Itaconic acid grafted crosslinked chitosan beads	EPC	Cu(II)	19.6	6	F	[62]
Crotonic acid grafted crosslinked chitosan beads			15.9		F	
Chitosan beads grafted with acrylic acid	GA	Pb(II)	217.4	7	L	[63]
Poly(acrylic acid) grafted and crosslinked chitosan	GA	Cu(II)	224.7	4	L	
Poly (itaconic acid)-grafted crosslinked chitosan nanoadsorbent	GA	Pb(II)	734.3	5	L	[64]
Poly(maleic acid)-grafted crosslinked chitosan	GA	Hg(II)	870.1	6	L	[65]
		Pb(II)	1320	5	L	
Triethylene-tetramine grafted magnetic chitosan	EPC	Hg(II)	1044	6	L	[66]
		Pb(II)	370.3	6	L	[67]

CA= crosslinking agent, L = Langmuir and F = Freundlich

Conclusion and Future Perspective

Recent years have seen increasing developments and works carried out to find alternatives in view of economic adsorbents for water treatment. Natural polymers, in particular chitosan, have high potential as sorbent in removing a wide range of contaminants, yet this material presents significant limitations which require appropriate developments. Raw chitosan (powder or flakes form) has crystalline structure, consequently limit its adsorption capacity as adsorption merely takes place on the amorphous of the crystal region. This problem is solved by converting chitosan into hydrogel beads through gel formation process. However, chitosan beads tend to dissolve in acidic medium. The stability of the beads can be enhanced by crosslinking reaction. Crosslinking agent is usually prone to react with the amine group in chitosan which known to be main chelating sites for metal ions. Therefore, grafting of functional groups onto chitosan backbone is necessary to increase selectivity and capacities. Grafting appears to be a convenient approach for improving the intrinsic properties of natural polymers or bring them with new properties.

Modifications of chitosan by crosslinking and grafting represent good alternatives for new potential adsorption system. Yet, there are still few factors that need to be considered to transfer the process to industrial scale. The influence of crosslinker content on the reaction or the properties of chitosan (i.e. crystallinity, solubility) could be investigated in future study to prepare a better adsorbent. Developing adsorbents that can remove variety of pollutants from industrial effluents is preferable. It would also be of interest to investigate other type of modified adsorbents and their capable in treating wastewater.

Acknowledgement

The authors would like to thank Universiti Teknologi Malaysia for facilitations and the Ministry of Higher Education Malaysia (MOHE) and Organization for the Prohibition of Chemical Weapon for financial supports through vote numbers Q.J130000.2509.09H84 and R.J130000.7309.4B222, respectively.

References

1. Duruibe, J. O., Ogwuegbu, M. O. C. and Egwurugwu, J. N. (2007). Heavy metal pollution and human biotoxic effects. *International Journal of Physical Sciences*, 2(5): 112-118.
2. Wang, X., Guo, Y., Yang, L., Han, M., Zhao, J. and Cheng, X. (2012). Nanomaterials as sorbents to remove heavy metal ions in wastewater treatment. *Environmental and Analytical Toxicology*, 2(7): 1-7.
3. Okoya, A., Akinyele, A., Amuda, O. and Ofoezie, I. (2016). Chitosan-grafted carbon for the sequestration of heavy metals in aqueous solution. American Chemical Science Journal, 11 (3): 1 – 14.
4. Fu, F. and Wang, Q. (2011). Removal of heavy metal ions from wastewaters: A review. *Journal of Environmental Management*, 92(3): 407-418.
5. Mehdinia, A., Shegefti, S. and Shemirani, F. (2015). Removal of lead(II), copper(II) and zinc(II) ions from aqueous solutions using magnetic amine-functionalized mesoporous silica nanocomposites. *Journal of the Brazilian Chemical Society*, 26(11): 2249-2257.
6. O'Connell, D. W., Birkinshaw, C. and O'Dwyer, T. F. (2008) Heavy metal adsorbents prepared from the modification of cellulose: A review. *Bioresource Technology*, 99(15): 6709-6724.
7. Abas, S. A., Ismail, M. H. S., Lias, K. and Izhar, S. (2013). Adsorption process of heavy metals by low-cost adsorbent: A review. *World Applied Sciences Journal*, 28(11): 1518-1530.
8. Bhatnagar, A. and Minocha, A. K. (2006). Conventional and non-conventional adsorbents for removal of pollutants from water-a review. *Indian Journal of Chemical Technology*, 13(3): 203-217.
9. Wan Ngah, W. S. and Fatinathan, S. (2008). Adsorption of Cu(II) ions in aqueous solution using chitosan beads, chitosan-GLA beads and chitosan-alginate beads. *Chemical Engineering Journal*, 143 (1-3): 62-72.
10. Miretzky, P. and Cirelli, A. F. (2009). Hg(II) removal from water by chitosan and chitosan derivatives: A review. *Journal of Hazardous Materials*, 167(1-3): 10-23.
11. Vakili, M., Rafatullah, M., Salamatinia, B., Ibrahim, M. H., and Abdullah, A. Z. (2015). Elimination of reactive blue 4 from aqueous solutions using 3-aminopropyl triethoxysilane modified chitosan beads. *Carbohydrate Polymers*, 132: 89-96.
12. Zohuriaan-mehr, M. J. (2005). Advances in chitin and chitosan modification through graft copolymerization: A comprehensive review. *Iranian Polymer Journal*, 14 (3): 235-265.
13. Wang, J. and Chen, C. (2014). Chitosan-based biosorbents: Modification and application for biosorption of heavy metals and radionuclides. *Bioresource Technology*, 160: 129-141.
14. Wan Ngah, W. S., Teong, L. C. and Hanafiah, M. A. K. M. (2011). Adsorption of dyes and heavy metal ions by chitosan composites: A review. *Carbohydrate Polymers*, 83(4): 1446-1456.
15. Muzzarelli, R. A. A. (2011). Potential of chitin/chitosan-bearing materials for uranium recovery: An *Interdisciplinary Review. Carbohydrate Polymers*, 84(1): 54-63.
16. Zhang, L., Zeng, Y. and Cheng, Z. (2016). Removal of heavy metal ions using chitosan and modified chitosan: A review. *Journal of Molecular Liquids*, 214: 175-191.
17. Crini, G. and Badot, P. M. (2008). Application of chitosan, a natural amino polysaccharide, for dye removal from aqueous solutions by adsorption processes using batch studies: a review of recent literature. *Progress in Polymer Science*, 33: 399-447.
18. Vakili, M., Rafatullah, M., Salamatinia, B., Abdullah, A.Z., Ibrahim, M.H., Tan, K.B., Gholami, Z. and Amouzgar, P. (2014). Application of chitosan and its derivatives as adsorbents for dye removal from water and wastewater: A review. *Carbohydrate Polymers*, 113: 115-130.
19. Kumirska, J., Czerwicka, M., Kaczynski, Z., Bychowska, A., Brzozowski, K., Thoming, J. and Stepnowski, P. (2010) Application of spectroscopic methods for structural analysis of chitin and chitosan. *Marine Drugs*, 8(5): 1567-1636.
20. Bhatnagar, A. and Sillanpaa, M. (2009). Applications of chitin- and chitosan-derivatives for the detoxification of water and wastewater - a short review. *Advances in Colloid and Interface Science*, 152 (1-2): 26-38.
21. Azlan, K., Wan Ngah, W. S. and Lai Ken, L. (2009) Chitosan and chemically modified chitosan beads for acid dyes sorption. *Journal of Environmental Sciences*, 21(3): 296-302.
22. Kumirska, J., Weinhold, M. X., Thoming, J. and Stepnowski, P. (2011). Biomedical activity of chitin/chitosan based materials- influence of physicochemical properties apart from molecular weight and degree of n-acetylation. *Polymers*, 3(4): 1875-1901.
23. Pillai, C. K. S., Paul, W. and Sharma, C.P. (2009). Chitin and chitosan polymers: Chemistry, solubility and fiber formation. *Progress in Polymer Science*, 34(7): 641-678.

24. Yuan, Y., Chesnutt, B. M., Haggard, W. O. and Bumgardner, J. D. (2011). Deacetylation of chitosan: Material characterization and in vitro evaluation via albumin adorption and pre-osteoblastic cell Cultures. *Materials*, 4(8): 1399-1416.
25. Poon, L., Wilson, L. D. and Headley, J. V. (2014). Chitosan-glutaraldehyde copolymers and their sorption properties. *Carbohydrate Polymers*, 109: 92-101.
26. El-hefian, E. A., Nasef, M. M. and Yahaya, A. H. (2011). Chitosan physical forms: A short review. *Australian Journal of Basic and Applied Sciences*, 5(5): 670-677.
27. Adarsh, K. J. and Madhu, G. (2014). A comparative study on metal adsorption properties of different forms of chitosan. *International journal of Innovative Research in Science Engineering and Technology*, 3(2): 9609-9617.
28. Vieira, R. S. and Beppu, M. M. (2005). Mercury ion recovery using natural and crosslinked chitosan membranes. Adsorption, 11(1): 731-736.
29. Krajewska, B. (2005). Membrane-based processes performed with use of chitin/chitosan materials. *Separation and Purification Technology*, 41(3): 305-312.
30. Rinaudo, M. (2006). Chitin and chitosan: Properties and applications. *Progress in Polymer Science*, 31 (7): 603-632.
31. Mane, S., Ponrathnam, S. and Chavan, N. (2016). Effect of chemical crosslinking on properties of polymer microbeads: A review. *Canadian Chemical Transactions*, 3 (4): 473-485.
32. Bhattacharya, A. and Misra, B. N. (2004). Grafting: A versatile means to modify polymers: techniques, factors and applications. *Progress in Polymer Science*, 29(8): 767-814.
33. Cahyaningrum, S. E., Narsito, Santoso, S. J. and Agustini, R. (2010). Adsorption of Mg(II) ion from aqueous solution on chitosan beads and chitosan powder. *Journal of Coastal Development*, 13(3): 179-184.
34. Wan Ngah, W. S., Ab Ghani and Hoon, L. L. (2002). Comparative adsorption of Lead(ll) on flake and bead-types of chitosan. *Journal of the Chinese Chemical Society*, 49(4): 625-628.
35. Wu, F. C., Tseng, R. L. and Juang, R. S. (2000). Comparative adsorption of metal and dye on flake- and bead-types of chitosans prepared from fishery wastes. *Journal of Hazardous Materials*, 73(1): 63-75.
36. Lee, S., Mi, F., Shen, Y. and Shyu, S. (2011). Equilibrium and kinetic studies of copper(II) ion uptake by chitosan-tripolyphosphate chelating resin. *Polymer*, 42(5): 1879-1892.
37. Manasi, Rajesh, V. and Rajesh, N. (2015). An indigenous halomonas BVR1 strain immobilized in crosslinked chitosan for adsorption of lead and cadmium. *International Journal of Biological Macromolecules*, 79: 300-308.
38. Hsien, T. and Liu, Y. (2012). Desorption of cadmium from porous chitosan beads. *Advancing Desalination*: pp. 163-180.
39. Radwan, A. A., Alanazi, F. K. and Alsarra, I. A. (2010). Microwave irradiation-assisted synthesis of a novel crown ether crosslinked chitosan as a chelating agent for heavy metal ions. *Molecules*, 15(9): 6257-6268.
40. Nagireddi, S., Katiyar, V. and Uppaluri, R. (2017). Pd(II) adsorption characteristics of glutaraldehyde cross-linked chitosan copolymer resin. *International Journal of Biological Macromolecules*, 94(Part A): 72-84.
41. Monier, M., Ayad, D. M. and Abdel-Latif, D. A. (2012). Adsorption of Cu(II), Cd(II) and Ni(II) ions by cross-linked magnetic chitosan-2-aminopyridine glyoxal Schiff's base. *Colloids and Surfaces B*: *Biointerfaces*, 94: 250-258.
42. Zheng, E., Dang, Q., Liu, C., Fan, B., Yan, J., Yu, Z. and Zhang, H. (2016). Preparation and evaluation of adipic acid dihydrazide cross-linked carboxymethyl chitosan microspheres for copper ion adsorption. *Colloids and Surfaces A: Physicochemical and Engineering Aspects*, 502: 34-43.
43. Wan Ngah, W. S., Ab Ghani, S. and Kamari, A. (2005). Adsorption behaviour of Fe(II) and Fe(III) ions in aqueous solution on chitosan and cross-linked chitosan beads. *Bioresource Technology*, 96(4): 443-450.
44. Vieira, R .S., Oliveira, M. L. M., Guibal, E., Rodriguez-Castellon, E. and Beppu, M. M. (2011). Copper, mercury and chromium adsorption on natural and crosslinked chitosan films: an XPS investigation of mechanism. *Colloids and Surfaces A: Physicochemical and Engineering Aspects*, 374(1-3): 108-114.
45. Laus, R. and Favere, V. T. (2011). Competitive adsorption of Cu(II) and Cd(II) ions by chitosan crosslinked with epichlorohydrin–triphosphate. *Bioresource Technology*, 102(19): 8769-8776.
46. Karthik, R. and Meenakshi, S. (2015). Removal of Pb(II) and Cd(II) ions from aqueous solution using polyaniline grafted chitosan. *Chemical Engineering Journal*, 263: 168-177.

47. Lalhmunsiama, Lalchhingpuii, Nautiyal, B. P., Tiwari, D., Choi, S. I., Kong, S. H. and Lee, S. M. (2016). Silane grafted chitosan for the efficient remediation of aquatic environment contaminated with arsenic(V). *Journal of Colloid and Interface Science*, 467: 203-212.
48. Kyzas, G. Z., Siafaka, P. I., Pavlidou, E. G., Chrissafis, K. J. and Bikiaris, D. N. (2015). Synthesis and adsorption application of succinyl-grafted chitosan for the simultaneous removal of zinc and cationic dye from binary hazardous mixtures. *Chemical Engineering Journal*, 259: 438-448.
49. Huang, L., Yuan, S., Lv, L., Tan, G., Liang, B. and Pehkonen, S. O. (2013). Poly(methacrylic acid)-grafted chitosan microspheres via surface-initiated ATRP for enhanced removal of Cd(II) ions from aqueous solution. *Journal of Colloid and Interface Science*, 405: 171-182.
50. Maleki, A., Pajootan, E. and Hayati, B. (2015). Ethyl acrylate grafted chitosan for heavy metal removal from wastewater: Equilibrium, kinetic and thermodynamic studies. *Journal of the Taiwan Institute of Chemical Engineers*, 51: 127-134.
51. Santhana Krishna Kumar, A., Uday Kumar, C., Rajesh, V. and Rajesh, N. (2014). Microwave assisted preparation of n-butylacrylate grafted chitosan and its application for Cr(VI) adsorption. *International Journal of Biological Macromolecules*, 66: 135-143.
52. Xu, C., Wang, J., Yang, T., Chen, X., Liu, X. and Ding, X. (2015). Adsorption of uranium by amidoximated chitosan-grafted polyacrylonitrile using response surface methodology. *Carbohydrate Polymers*, 121: 79-85.
53. Saleh, A. S., Ibrahim, A. G., Abdelhai, F., Elsharma, E. M., Metwally, E. and Siyam, T. (2017). Preparation of poly(chitosan-acrylamide) flocculant using gamma radiation for adsorption of Cu(II) and Ni(II) ions. *Radiation Physics and Chemistry*, 134: 33-39.
54. Lalita, Singh, A. P. and Sharma, R. K. (2017). Synthesis and characterization of graft copolymers of chitosan with NIPAM and binary monomers for removal of Cr(VI), Cu(II) and Fe(II) metal ions from aqueous solutions. *International Journal of Biological Macromolecules*, 99: 409-426.
55. Galhoum, A. A., Hassan, K. M., Desouky, O. A., Masoud, A. M., Akashi, T., Sakai, Y. and Guibal, E. (2017). Aspartic acid grafting on cellulose and chitosan for enhanced Nd(III) sorption. *Reactive and Functional Polymers*, 113: 13 – 22.
56. Hong, T. T., Hai, L., Man, N. T., Tam, T. T., Thi, P. and Ha, L. (2012). Preparation of poly(acrylic acid)-chitosan hydrogels by gamma irradiation for metal ions sorption. The Annual Report 2012, VINATOM: pp. 286-294.
57. Benamer, S., Mahlous, M., Tahtat, D., Nacer-Khodja, A., Arabi, M., Lounici, H. and Mameri, N. (2011). Radiation synthesis of chitosan beads grafted with acrylic acid for metal ions sorption. *Radiation Physics and Chemistry*, 80(12): 1391-1397.
58. Sutirman, Z. A., Sanagi, M. M., Abd Karim, K. J. and Wan Ibrahim, W. A. (2016). Preparation of methacrylamide-functionalized crosslinked chitosan by free radical polymerization for the removal of lead ions. *Carbohydrate Polymers*, 151: 1091-1099.
59. Igberase, E. and Osifo, P. (2015). Equilibrium, kinetic, thermodynamic and desorption studies of cadmium and lead by polyaniline grafted cross-linked chitosan beads from aqueous solution. *Journal of Industrial and Engineering Chemistry*, 26: 340-347.
60. Liu, J., Wu, H. T., Lu, J. Feng, Wen, X. Yuan, Kan, J. and Jin, C. Hai. (2015). Preparation and characterization of novel phenolic acid (hydroxybenzoic and hydroxycinnamic acid derivatives) grafted chitosan microspheres with enhanced adsorption properties for Fe(II). *Chemical Engineering Journal*, 262: 803-812.
61. Ramya, R., Sankar, P., Anbalagan, S. and Sudha, P.N. (2011). Adsorption of Cu(II) and Ni(II) ions from metal solution using crosslinked chitosan-g-acrylonitrile copolymer. *International Journal of Environmental Sciences*, 1(6): 1323-1338.
62. Bal, A., Özkahraman, B., Acar, I., Özyürek, M. and Güçlü, G. (2013). Study on adsorption, regeneration, and reuse of crosslinked chitosan graft copolymers for Cu(II) ion removal from aqueous solutions. *Desalination and Water Treatment*, 52(16-18): 3246-3255.
63. Benamer, S., Mahlous, M., Tahtat, D., Nacer-Khodja, A., Arabi, M., Lounici, H. and Mameri, N. (2011). Radiation synthesis of chitosan beads grafted with acrylic acid for metal ions sorption. *Radiation Physics and Chemistry*, 80(12): 1391-1397.
64. Ge, H., Hua, T. and Chen, X. (2016). Selective adsorption of lead on grafted and crosslinked chitosan nanoparticles prepared by using Pb^{2+} as template. *Journal of Hazardous Materials*, 308: 225-232.

65. Ge, H., Hua, T. and Wang, J. (2016). Preparation and characterization of poly(itaconic acid)-grafted crosslinked chitosan nanoadsorbent for high uptake of Hg^{2+} and Pb^{2+}. *International Journal of Biological Macromolecules,* 95: 954-961.
66. Ge, H. and Hua, T. (2016). Synthesis and characterization of poly(maleic acid)-grafted crosslinked chitosan nanomaterial with high uptake and selectivity for Hg(II) sorption. *Carbohydrate Polymers*, 154: 446-452.
67. Kuang, S. P., Wang, Z. Z., Liu, J. and Wu, Z. C. (2013). Preparation of triethylene-tetramine grafted magnetic chitosan for adsorption of Pb(II) ion from aqueous solutions. *Journal of Hazardous Materials,* 260(1): 210-219.

Malaysian Journal of Analytical Sciences, Vol 22 No 5 (2018): 851 - 856
DOI: https://doi.org/10.17576/mjas-2018-2205-12

MALAYSIAN JOURNAL OF ANALYTICAL SCIENCES
Published by The Malaysian Analytical Sciences Society
ISSN 1394 - 2506

THE EFFECTS OF ZEOLITE ON MECHANICAL AND MORPHOLOGICAL PROPERTIES OF NR/ENR MEMBRANES

(Kesan Zeolit pada Sifat Mekanikal dan Morfologi Membran NR/ENR)

Kritsada Phatcharasit[1]* and Wirach Taweepreda[2]

[1] *Department of Rubber and Polymer Engineering, Faculty of Engineering, Thaksin University, 93110 Phatthalung, Thailand*
[2] *Department of Materials Science and Technology, Faculty of Science, Prince of Songkla University, 90110 Songkla, Thailand*

**Corresponding author: krit_off@hotmail.com*

Received: 16 April 2017; Accepted: 7 March 2018

Abstract

The main focus of this research is on the organic-inorganic membranes. In this study, the effects of zeolite on natural rubber (NR)/epoxidized natural rubber (ENR) membranes properties were investigated. NR/ENR blends were combined with zeolite in various contents at 0-50 phr by the two-roll mill. The rubber compounds were produced by compression molding at 150 ºC to form membranes with thickness of not more than 0.4 mm. NR/ENR blends with zeolite were characterized according to cure characteristics, mechanical properties, swelling properties and scanning electron microscope (SEM). It was found that the mechanical properties of the blends increased with the addition of zeolite for 10 phr while the cure time (t_{c90}) increased with increasing zeolite content. Membranes swelling increased with increasing amount of zeolite (zeolite at 30 phr produced the best results). Meanwhile, the micrograph showed a surface filled with pores-like small holes with the addition of zeolite in the NR/ENR membranes.

Keywords: natural rubber, epoxidized natural rubber, zeolite, membrane

Abstrak

Membran organik-bukan organik hibrid merupakan fokus utama dalam kajian ini. Kesan zeolit ke atas sifat-sifat getah asli (NR)/getah asli terepoksida(ENR) telah dikaji di dalam eksperimen ini. Campuran NR/ENR dengan zeolit dalam pelbagai kandungan pada 0-50 phr telah dijalankan oleh pengisar dua gulung. Sebatian getah asli tersebut telah dihasilkan melalui pengacuan mampatan pada 150 ºC untuk membentuk membran pada ketebalan tidak melebihi 0.4 mm. Campuran NR/ENR dan zeolit ini telah dikaji berdasarkan beberapa aspek iaitu sifat-sifat perawatan, mekanikal, pembengkakan dan pengimbasan mikroskop elektron (SEM). Kajian ini mendapati bahawa sifat mekanikal campuran ini meningkat dengan pertambahan zeolit pada 10 phr manakala masa rawatan (t_{c90}) juga meningkat dengan peningkatan kandungan zeolit. Pembengkakan membran juga meningkat dengan peningkatan jumlah zeolit (zeolit pada 30 phr adalah yang terbaik). Mikrograf menunjukkan permukaan yang dipenuhi dengan lubang kecil seperti liang dengan pertambahan zeolit dalam NR/ENR membran.

Kata kunci: getah asli, getah asli terepoksida, zeolit, membran

Introduction

Membrane technologies have developed as a workable and cost effective treatment alternative to wastewater, treat water, and air pollution. Membrane process is favored over conventional techniques because process less, consumes low energy and very effective and selective [1]. In addition, membrane can also be made from organic (natural rubber and polymer) and inorganic (ceramic, carbon, silica, zeolite and other) can be classified into 2 main groups based on its structure: porous and dense (non-porous) inorganic membranes. Nowadays, hybrid organic-inorganic membranes have been growing rapidly. Compared to certain inorganic membranes, polymeric membranes have relatively low separation performance. However, the processing flexibility and low cost of polymers still makes them highly attractive for many applications [2].

Natural rubber (NR) has been applied for a long time in several industrial and medicinal segments. More recently, NR compounds and membranes have attracted attention due to their great potential for biological and technological applications [3]. The NR can employ to produce transdermal drug delivery systems where it is the controlling layer membrane. Epoxidized natural rubber (ENR) is a unique elastomeric polymer derived from the chemical modification of natural rubber with epoxidized group randomly with 25% and 50% (ENR-25 and ENR-50). ENR is miscible with more polar rubber, good oil resistance, highly damping and low gas permeability [4]. Zeolites are very potential membrane materials because of their resulting pore sizes with zeolite mixed into natural rubber, effect to mechanical properties and vulcanizates of natural rubber [5].

In this study, the NR/ENR/Zeolite membrane was prepared by two-roll mill and the influence of zeolite as filler on the cure characteristics of the vulcanizates, mechanical properties, swelling properties and scanning electron microscope (SEM) and compared.

Materials and Methods

Materials

The natural rubber used in this study was STR 5L and ENR-50 were manufactured by Union Rubber Product Corporation Co., Ltd. and Muang Mai Guthrie Public Co., Ltd. Thailand., respectively. Zinc oxide (ZnO), stearic acid, wingstay L, sulphur and 2-mercaptobenzothiazole (MBT) were obtained from Kij Paiboon Chemical Ltd., Thailand. Zeolite type Sodium alumosilicate has a structural formula (Na_{12} $[Al_{12}Si_{12}O_{48}]$ $\cdot 27H_2O$) was purchased from Sigma-Aldrich Co., Ltd.

Preparation of membranes

The membrane compound composition used in the present study is given in Table 1. The compound was prepared by mixing NR/ENR blends loaded with zeolite as filler using two-roll mill for 13 minutes and then the mixes were kept at room temperature for 24 hours before testing. Thereafter, the membrane compound was compressed and vulcanized at 150 ˚C to formed sheet with thickness approximately not over than 0.4 mm. The cure time determined using a moving die rheometer (Alpha, MDR-2000).

Characterization of membranes

The mechanical properties of membranes were carried out using a LLOYD instrument tensile tester. The test was done according to ASTM D412. Across head speed of 500 mm/min with load cell of 100 N. The swelling test was carried out according to ISO 1817. The cured specimens, with dimensions of 30 mm x 5 mm x 2 mm, followed by immersion in a deionized water for 72 hours at room temperature (25 ˚C) and the phase morphology of the membranes was studied using scanning electron microscopy (SEM, JEOL JSM-5800 LV).

Table 1. The compounds composition of NR/ENR blends with zeolite

Ingredients	phr (part per hundred of rubber)				
	1	**2**	**3**	**4**	**5**
STR 5L	50	50	50	50	50
ENR-50	50	50	50	50	50
ZnO	2.5	2.5	2.5	2.5	2.5
Stearic acid	1	1	1	1	1
MBT	1.5	1.5	1.5	1.5	1.5
Wingstay L	1	1	1	1	1
Sulphur	2	2	2	2	2
Zeolite	vary (0, 5, 10, 20, 30 and 50)				

Results and Discussion

Cure characteristics

The scorch time (t_{s2}), Optimum cure time (t_{c90}), Minimum torque (M_L), Maximum torque (M_H) and the torque difference between the Minimum and Maximum torque (ΔM) of NR/ENR/Zeolite compounds are summarized in Table 2 and Figure 1. It was found that ΔM is related to the crosslink density of the compound, the value of M_H and the torque difference of the compound increased with increasing zeolite loading.

The measured torque is proportional to the system elasticity, viscosity and the crosslinking process is expected to increase the torque along with the period of vulcanization. Torque value of the rubber compound is increased due to the rigidity of the filler. That is, when the amount of fill increases, the rigidity increases, resulting in higher torque value. In other words, when increasing the amount of zeolite, the viscosity increases [11-13]. The cause of viscosity increase may be due to interactions between zeolites [12, 13]. The t_{s2} decreased with increasing zeolite composition due to the interaction between the zeolite surfaces. The t_{c90} increased with increasing zeolite composition due to the acidity effect of zeolite [7]. Because the filler-filler interactions occurred because silica has a number of hydroxyl groups on its surface and there was accelerated adsorption on the silica surface [6].

Table 2. Cure characteristics of the NR/ENR/Zeolite compounds

NR/ENR/Zeolite	Minimum Torque M_L (dN m)	Maximum Torque M_H (dN m)	ΔM (dN m)	Scorch Time t_{s2} (min)	Optimum Cure Time t_{c90} (min)
50/50	0.36	7.34	6.98	0.32	4.05
50/50/5	0.33	7.03	6.70	0.40	3.10
50/50/10	0.34	7.63	7.29	0.37	3.31
50/50/30	0.35	8.34	7.99	0.34	4.25
50/50/50	0.34	9.82	9.48	0.36	5.37

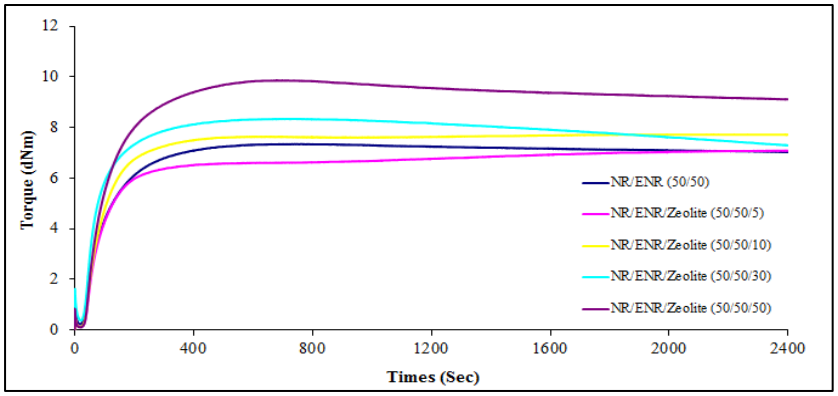


Figure 1. The curing characteristics of the NR/ENR/Zeolite compounds

Mechanical properties

Figure 2 presents the mechanical properties of the NR/ENR/Zeolite compounds. The change in tensile strength and elongation at break is related to the crosslinking density of the compounds, it was found that tensile strength improved with increasing zeolite loading up to 10 phr (15.25 MPa). The zeolite containing at beyond 10 phr, the mechanical properties reduced, because of the inability of the filler to support the stresses [6] and there may have been poor dispersion or agglomerations of the filler in the rubber [8, 11]. The elongation at break decreased with increasing zeolite content (from 950.36% at 5 phr to 777.20 at 50 phr).

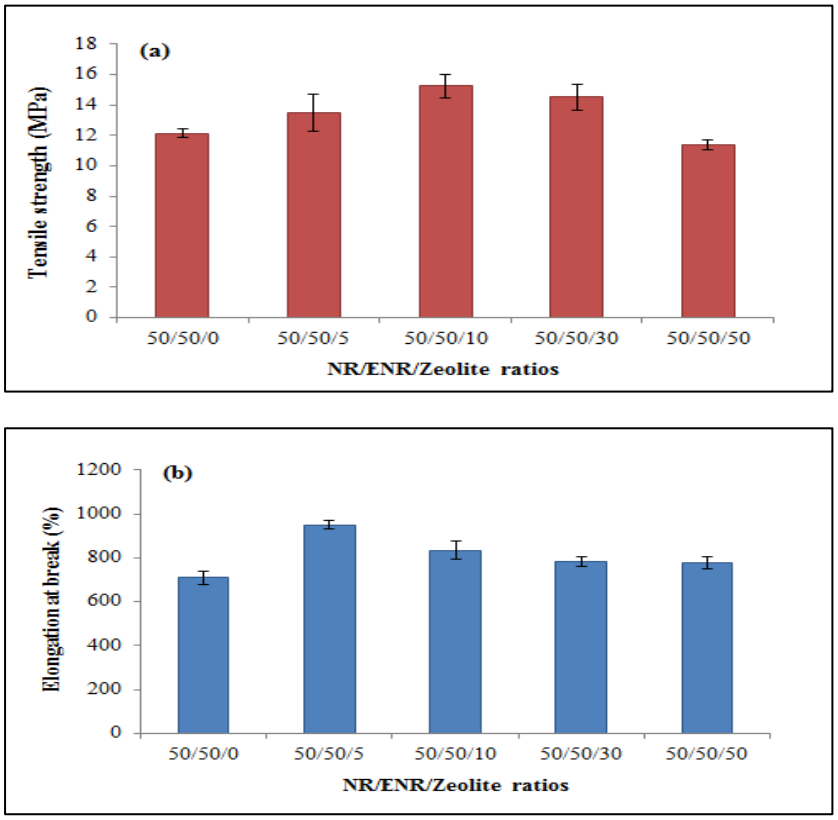


Figure 2. Effect of composition on the tensile strength (a) and elongation at break (b) for the NR/ENR/Zeolite

Swelling behavior

Figure 3 shows the swelling of NR/ENR/Zeolite, the addition zeolite into the NR/ENR blends exhibited higher degrees of swelling than the loading of without zeolite filled NR/ENR blends. Addition of zeolite increased the swelling ratio with increasing content of zeolite due to good dispersion of zeolite and strong interactions between zeolite and rubber matrix. In addition, NR/ENR/Zeolite (50/50/50) swelling ratio decreased due to agglomerations of zeolite [10].

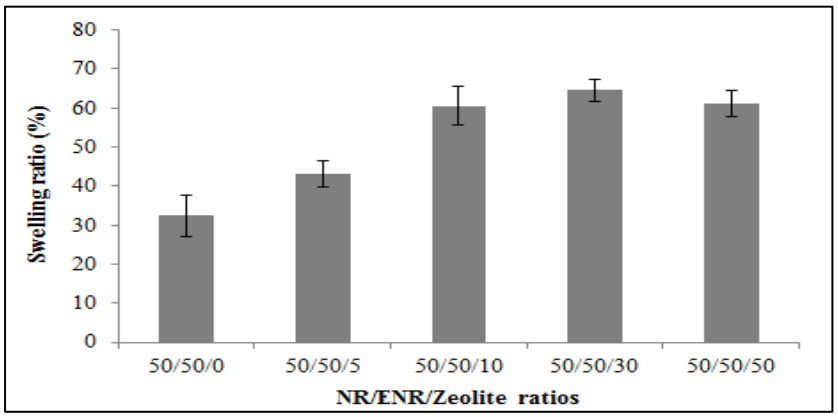


Figure 3. The swelling of the NR/ENR/Zeolite

Membrane morphology

Figure 4 presents the SEM micrographs of the surface of the membranes. The pores increased with the increasing of zeolite loading. The porosity results in the molecules are adsorbed on porous surfaces. It has the ability to permeable membrane well. The pore development is clearly seen and gave smooth surface in NR/ENR/Zeolite (50/50/30) [Figure 4(b)] and NR/ENR/Zeolite (50/50/50) [Figure 4(c)] membranes. Interestingly, zeolite is not just as reinforcing filler but also has potential as pore former on the membranes. The pore size was determined via visual investigation using scanning electron microscopy. It was found that the average pore size of the NR/ENR/Zeolite was in the range of 2-5 µm. However, the more pore developed can deduced the weak interaction between zeolite and NR/ENR which may affect the mechanical properties of the membrane because formation agglomerations of zeolite [3].

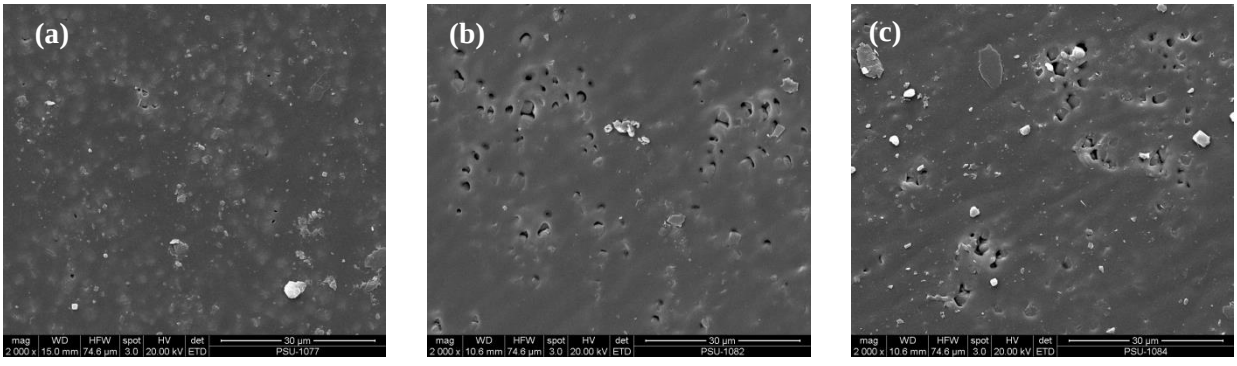


Figure 4. SEM micrographs of (a) NR/ENR/Zeolite (50/50/10), (b) NR/ENR/Zeolite (50/50/30) and (c) NR/ENR/Zeolite (50/50/50)

Conclusion

The NR/ENR/Zeolite membranes were prepared by two-roll mill. As the amount of zeolite in the membrane increased, swelling property increased due to adsorption on the surface and the cure time (tc_{90}) increased due to incorporation of natural zeolite in the rubber matrix produced a better crosslink density. The mechanical properties of the membranes improved with the incorporation of zeolite with NR/ENR/Zeolite (50/50/10) membrane exhibited better mechanical properties as compared to NR/ENR/Zeolite (50/50/30) and NR/ENR/Zeolite (50/50/50) membranes has the lowest mechanical properties because agglomerations of zeolite. SEM micrographs were found that the pores increased with the increasing of zeolite loading.

Acknowledgement

The authors would like to thank Department of Rubber and Polymer Engineering, Faculty of Engineering, Thaksin University and Department of Materials Science and Technology, Faculty of Science, Prince of Songkla University.

References

1. Jon, N., Samad, N., Abdullah, N. A., Abdullah, I. and Othaman, R. (2013). Influence of silica addition on the properties of epoxidised natural rubber/polyvinyl chloride composite membrane. *Journal of Applied Polymer Science,* 129(5): 2789-2795.
2. Faita, F. L., Dotto, M. E. R., Franca, L. G., Cabrera, F. C., Job, A. E. and Bechtold, I. H. (2014). Characterization of natural rubber membranes using scaling laws analysis. *European Polymer Journal,* 50: 249-254.
3. Samad, N. A., Othaman, R. and Abdullah, I. (2014). Preparation and characterization of epoxidised natural rubber/polyvinyl chloride/rice husk (ENR/PVC/RH) thin film composite by solution casting technique. *International Journal Materials Engineering Innovation,* 5(1): 61-69.
4. Chantara, T. R., Sabariah, K., Yaganaidu, S., Marina T. and Norzawani, Y. (2006). Radiation crosslinking of rubber phase in poly(vinyl chloride)/epoxidized natural rubber blend: Effect on mechanical properties. *Polymer Testing,* 25(4): 475-480.
5. Barbosa, G. P., Debone, H. S., Severino, P., Souto, E. B. and da Silva, C. F. (2016). Design and characterization of chitosan/zeolite composite films-effect of zeolite type and zeolite dose on the film properties. *Materials Science and Engineering: C,* 60: 246-254.
6. Siriyong, T. and Keawwattana, W. (2012). Utilization of different curing systems and natural zeolite as filler and absorbent for natural rubber/nitrile rubber blend. *Kasetsart Journal (Natural Science),* 46(6): 918-930.
7. López–Manchado, M. A., Arroyo, M., Herrero, B. and Biagiotti, J. (2003). Vulcanization kinetics of natural rubber-organoclay nanocomposites. *Journal of Applied Polymer Science,* 89(1): 1-15.
8. Cuong, M. V., Huong, T. V. and Hyoung, J. C. (2015). Fabrication of natural rubber/epoxidized natural rubber/nanosilica nanocomposites and their physical characteristics. *Macromolecular Research*, 23(3): 284-290.
9. Hazwani, S. A., Hanafi, I. and Azura, A. R. (2016). Tensile Properties and Morphology of Epoxidized Natural Rubber/Recycled Acrylonitrile-Butadiene Rubber (ENR 50/NBRr) Blends. *Procedia Chemistry,* 19: 359 – 365.
10. Gopakumar, S. and Gopinathan Nair, M. R. (2005). Swelling characteristics of NR/PU block copolymers and the effect of NCO/OH ratio on swelling behavior. *Polymer,* 46: 10419-10430.
11. Soney, C. G., Manfred, K. and Sabu, T. (1999). Effect of nature and extent of crosslinking on swelling and mechanical behavior of styrene-butadiene rubber membranes. *Journal of Membrane Science,* 163: 1-17.
12. Ansarifar, M. A. and Nijhawan, R. (2000). Effects of silane on properties of silica filled natural rubber compounds. *Journal* of *Rubber Research,* 3(3): 169-184.
13. Tan, E. H., Wolff, S., Haddeman, M., Grewatta, H. P. and Wang, M. J. (1993). Filler-elastomer interactions. Part IX. Performance of silicas in polar elastomers. *Rubber Chemistry and Technology,* 66 (4): 594-604.

Malaysian Journal of Analytical Sciences, Vol 22 No 5 (2018): 857 - 866
DOI: https://doi.org/10.17576/mjas-2018-2205-13

MALAYSIAN JOURNAL OF ANALYTICAL SCIENCES
Published by The Malaysian Analytical Sciences Society
ISSN 1394 - 2506

IMMOBILIZED METAL AFFINITY CHROMATOGRAPHIC MEMBRANE FOR TRYPSIN SEPARATION

(Membran Kromatografi Afiniti Logam Dipegun untuk Pemisahan Tripsin)

Sofiah Hamzah[1]*, Nurul Hidayati Mat Alim[1], Nurul Fakhriah Ismail[1], Norhafiza Ilyana Yatim[2], Nur A'lya Mohd Sani[1]

[1]School of Ocean Engineering
[2]School of Marine and Environmental Sciences
Universiti Malaysia Terengganu, 21030 Kuala Nerus, Terengganu, Malaysia

**Corresponding author: sofiah@umt.edu.my*

Received: 16 April 2017; Accepted: 7 March 2018

Abstract

As a new technology, Immobilized Metal Affinity Chromatographic Membrane (IMAC) has proven its efficiency for protein purification. It is also a separation technique that use covalently bound chelating compounds on the membrane supports to immobilize metal ions, which serve as affinity ligands for various proteins. This study aims to prepare and characterize highly specific IMAC for trypsin separation. Chitosan and polyethylene glycol were used as modification solutions to impart the membrane porosity and flux recovery ratio (FRR) of IMAC matrix. The modified PSf with chitosan improved its FRR up to 82.11% which indicated that PSf/Chitosan was a suitable matrix for the affinity membrane. Glutaraldehyde and Cu^{2+} served as crosslinker agents and affinity ligands respectively. Maximum immobilization capacity of Cu^{2+} occurred at 120 ppm within 60 minutes' incubation time. The optimum capacity of trypsin adsorption (12.67 mg/cm^2) onto IMAC membrane occurred when 0.3 M ionic strength of trypsin solution was used. Desorption of the enzyme by displacing salt of potassium chloride showed the highest trypsin recovery at 72.3%.

Keywords: affinity, chitosan, membrane, trypsin, ultrafiltration

Abstrak

Sebagai teknologi baru, Membran Kromatografi Afiniti Logam Dipegun (IMAC) telah membuktikan kecekapannya untuk penulenan protein. Ia juga merupakan teknik pemisahan yang menggunakan sebatian pelekat yang terikat secara kovalen pada membran sokongan untuk pegunkan ion logam, yang berfungsi sebagai ligan afiniti untuk pelbagai protein. Kajian ini bertujuan untuk menyediakan dan mencirikan IMAC yang sangat spesifik untuk pemisahan trypsin. Kitosan dan polietilen glikol digunakan sebagai larutan pengubahsuai bagi meningkatkan keliangan membran dan nisbah pemulihan fluks (FRR) matriks IMAC. PSf yang telah diubah suai dengan kitosan telah meningkatkan FRR sehingga 82.11 % yang menunjukkan bahawa PSf/kitosan adalah matrik yang sesuai untuk membran afiniti. Glutaraldehid dan Cu^{2+} masing-masing berfungsi sebagai agen silangan dan ligan afiniti. Kapasiti imobilisasi maksimum Cu^{2+} berlaku pada 120 ppm dalam masa inkubasi selama 60 minit. Kapasiti jerapan trypsin paling optimum (12.67 mg / cm^2) ke atas membran IMAC berlaku apabila 0.3M larutan tripsin digunakan. Penyerapan enzim dengan menggunakan garam gantian kalium klorida menunjukkan dapatan tripsin paling tinggi iaitu kira-kira 72.3%.

Kata kunci: afiniti, kitosan, membran, tripsin, penurasan-ultra

Introduction

There is a growing trend of widening the use of proteolytic enzymes as precursors in their production and commercialization in the fields of food, biopharmaceuticals and biotechnology. There are many methods for enzyme separation and purification in order to achieve good selectivity which includes ion exchange chromatography, affinity chromatography and centrifugation. Those separation techniques have their limitations and the best technique is determined as achieving the best technology of enzyme purification. Affinity chromatography has been considered as one of the essential alternatives and has been utilized many years ago in the aspect of separating and of purifying a wide variety of proteins. Indeed, affinity chromatography is a well-established method for the identification, purification, and separation of macromolecules based on highly specific molecular recognition. Immobilized metal affinity (IMA) absorbents provide moderate affinity to macromolecules by covalently coupling chelating compounds on solid supports to entrap metal ions.

In affinity chromatography, the matrix could affect the activity and stability of the biomolecules, such as proteins and enzymes attached to the matrix [1]. Thus, selection of the supporting matrix is the first important consideration in affinity systems. The matrix must show extremely low nonspecific adsorption, which may be due to charged or hydrophobic groups on its surface, which compromise the specificity of the affinity sorbent. This is essential because the power of affinity sorption relies on specific interaction between the immobilized ligand and the target molecules within the adsorption medium. The matrix must have functional surface groups such as hydroxyl, carboxyl, or amide for further derivation and immobilization of ligands.

Classical matrices for IMAC are based on soft-gels, such as cross-linked dextran and agarose which are compressible and restricted to low flow rate in chromatography operations. Besides, there are many drawbacks by utilizing soft gels such as cross-linked dextran and agarose used in affinity chromatography. It requires the process to apply only low flow rates as to prevent gel deformation and allow mass transfer. The sample must also be clarified before being loaded onto the column. Such traditional multistage protocols may span several days, resulting in large yield loss, contributing to protein sample "aging" and denaturation, as well as involve high operational costs.

Therefore, polymeric membranes such as polysulfone can serve as an excellent matrix for IMAC. This is due to the concern that the membrane process can offer many advantages such as no intra-particle diffusion, short axial-diffusion path, low pressure drops, no bed compaction, and easier scale up. It is highly expected to provide an alternative to the conventional packed-column systems [2-5]. Although this polymer membrane material is proven to have good chemical, thermal and mechanical stability, unfortunately it is lack of reactive functional groups on the polymer backbones [6-7]. Furthermore, the hydrophobic nature of polysulfone results in the adsorption and deposition of hydrophobic solutes on the membrane surface [8] which consequently causes severe membrane fouling, during enzyme production. A thick gel layer forms on the surface, which blocks the membrane's pores, reduces flux and shortens the life of the membrane. This phenomenon deteriorates the membrane and diminishes its separation performance, thereby reducing production efficiency and increasing operating costs. Modified PSf membranes have been widely explored, including both surface modifications (e.g. hydrophilicity improvement) [9, 10] and material modifications (e.g. polymer blends) [11]. Most of the techniques introduced have still not overcome the problems regarding separation performance, process complexity, manufacturing costs and membrane stability. Therefore, the fabricated membrane from polysulfone needs to be modified to eliminate the non-specific type of adsorption as well as to enhance the separation efficiency through improved adsorptive surfaces, especially for biomolecules such as proteins.

The modification of fabricated membrane using hydrophobic material (polysulfone) with hydrophilic material (chitosan) is vital because it can improve membrane performance and is bio-fouling resistant. This is because membrane fouling is still a major problem in spite of much research devoted to its reduction and elimination [8]. There are some reports that have stated that the chitosan has been used as a membrane forming material in preventing any membrane fouling because of its hydrophilic nature and very high affinity for water.

Chitosan (CS), a biopolymer widely available from seafood processing waste, has been increasingly studied as an adsorptive material for a wide range of applications; starting from the dietary regime constituents, food packaging

materials, drug release components and for environmental pollutants among others [12-14]. Chitosan is an important biomass prepared by the de-acetylation of chitin mainly obtained from crab and shrimp shell and is an amino polysaccharide that is useful in chemical modifications because it has reactive amino and hydroxyl groups [15]. Chitosan has been considered as a potential chromatographic matrix for the presence of free amino and hydroxyl groups on its polysaccharide chain, which provides active reaction sites for the easily coupling of various affinity ligands or ion exchange ligands. Chitosan has many useful features such as hydrophilicity, biocompatibility and anti-bacterial property. This biopolymer is also a well-known adsorbent and is effective in the adsorption of proteins and metal ions since the amino ($–NH_2$) and hydroxyl (–OH) groups on chitosan chains can serve as electrostatic interaction and coordination sites, respectively [16]. Moreover, the biomaterials have been proven to possess high performance as a matrix for enzyme separation [17].

In this study, ultrafiltration membrane was fabricated using polysulfone membrane and modified by chitosan and polyethylene glycol to improve its properties. Immobilization capacity of metal ion (Cu^{2+}) at different concentrations onto the selected IMAC Matrix was also studied to determine the optimum ligand concentration for IMAC membrane. Trypsin which was dissolved in different ionic strength buffers was used as model protein to evaluate the performance of the prepared IMAC membrane. While, the final stage focused on the effect of displacing salt in elution buffer which affected the trypsin recovery.

Materials and Methods

Materials

All materials used in this research are of analytical grade. In this research, the polymer polysulfone (PSf) was used to develop the affinity membrane. The polymer was mixed together with solvent, N-methyl-2-pyrrolidone (NMP) supplied by Merck and ultrapure water (H_2O), which acts as non-solvent and provides a coagulation medium. Chitosan (CH) low molecular weight used to modify the affinity membrane was supplied from Aldrich. Polyethylene glycol (PEG) with molecular weight (20,000) was obtained from UMT Research Laboratory, Department of Engineering Science. Acetic acids ($C_2H_4O_2$), ethanol (C_2H_60), sodium hydroxide (NaOH), sodium chloride (NaCl, ammonia (NH_3) and distilled water were used for the preparation of affinity membrane for IMAC matrix e.g. NaCl.

Membrane fabrication

The materials used in ternary dope preparation are the same with the materials used in the binary dope preparation: polysulfone (PSf) as the polymer, N-methyl-2-Pyrrolidone (NMP) as the solvent and water (H_2O) as the non-solvent. The initial stage of preparation is also similar with binary dope preparations; the only difference is the formulation used. Water was added when all the polymers had dissolved, and its amount determined by cloud point. A stirrer was used as to completely dissolve all materials. The polymer must be prepared without any damage. By that, during the dope preparation, the temperature of electrical heating mantel was controlled not to exceed 60 ^oC. After 8 hours, the polymer solution was placed into an ultrasonic bath to remove trapped air bubbles. The prepared dope solution was stored in Schott bottle.

Membrane surface modification, membrane activation and IMAC membrane preparation

The modification of the asymmetric PSf membrane is necessary as to enhance the performance of the membrane as well as to reduce the fouling. Membranes were fabricated via simple dry/wet phase inversion technique. The fabrication membranes were done by using the electrically casting machine at shear rate 200 ms^{-1} and then immersed directly into a coagulation bath for 24 hours. Membrane surface modification was employed using modification solution containing 50% w/v chitosan and 50% v/v polyethylene glycol. The dipped time of native PSf membrane was at the optimum time of 60 minutes. This stage was performed as to deposit the chitosan and PEG particles onto the membrane surface. After the dipped time was over, the membrane was dried at room temperature. The membrane was then neutralized with NaOH solution (0.1 M in 50% water-ethanol mixture) for 30 minutes, rinsed with 50% ethanol solution 3 times and followed by washing with distilled water. PSf/CH/PEG was served as IMAC matrix for further study.

For membrane activation, the prepared matrix was immersed in 100 mL buffer (0.1 M sodium chloride and 0.1 M sodium acetate-acetic acid pH 7.4) and 100 mL of 25% v/v glutaraldehyde aqueous solution. The system was

occasionally stirred and allowed to react for 150 minutes at 30 °C. After the reaction, the excess of glutaraldehyde was removed by washing the membranes three times with a 2 M acetic acid solution.

The metal ion used was copper(II) sulfate anhydrous ($CuSO_4$) and all procedures were carried out based on different concentrations of 30 ppm, 60 ppm, 90 ppm, 120 ppm and 150 ppm and was prepared in distilled water. The modified PSf chitosan membranes were placed in the metal ion solution with stirring 100 rpm at room temperature and were immobilized onto the activated membrane for 150 minutes immobilization time. The adsorption capacity was determined for every 30-minute interval.

Membrane characterization

Membrane characterization studies were performed in terms of pure water permeability, membrane morphology using scanning electron microscopy (SEM), and functional groups on the membrane surface assessed using Fourier-transform infrared spectroscopy equipped with attenuated total reflection (ATR-FTIR). In SEM studies, membranes samples were first immersed in liquid nitrogen and then fractured membranes for preparing samples. The SEM samples were then deposited with gold using an Auto Fine Coater before scanning. The chemical functional groups of membrane surface were determined using Fourier Transform Infra-Red Spectroscopy (FTIR). FTIR spectra of the modified membrane were obtained using the FTIR spectrophotometer at Physic Laboratory, University Malaysia Terengganu. The dry membranes of about 0.1 g were thoroughly mixed with KBr and pressed into pellet form. The FTIR spectrum was recorded.

Adsorption of trypsin onto IMAC membrane

Trypsin was used as a model protein. 0.5 mg/mL of trypsin solution was prepared by dissolving trypsin in 0.1 M phosphate buffer solution at pH 8 at room temperature. Ionic strength studies were carried out by the adding different concentrations of NaCl (0.01 M, 0.05 M, 0.1 M, 0.3 M and 0.5 M). This experiment was conducted in triplicates for 150 minutes with stirring 100 rpm at room temperature and was started after immersion of membrane disk in the trypsin solution. The concentration of trypsin was measured at 595 nm by using UV-Vis spectrophotometer. The amount of adsorbed trypsin on the affinity membranes were obtained by using the following equation 1:

$$q = \frac{(C_o - C)V_s}{A} \quad (1)$$

where q is the amount of trypsin adsorbed onto membranes (mg/cm^2), C_o and C are the concentration of the total protein in the initial and final solutions after adsorption (mg/mL) respectively. V_s is the volume of aqueous solution (mL) and A is the area of the membranes in the adsorption medium (cm^2).

Results and Discussion

Properties of IMAC matrix

Native PSf and modified PSf, which served as IMAC matrices, were characterized in terms of permeability coefficient, membrane porosity, fouling quantification, surface morphology and FTIR analysis.

Table 1. Permeability Coefficient of Native and Modified PSf

Membrane ID	Permeability Coefficient ($L/m^2.h.bar$)	Regression Coefficient (R^2)	Membrane Porosity (%)	Flux Recovery Ratio (%)
PSf 15	75.932	0.9931	82.67	53.03
CH-50/PEG-50/PSf	70.445	0.9968	77.06	82.11

There are only slightly decreased in permeability coefficient and membrane porosity between native and modified PSf. However, modification of PSf with chitosan and PEG successfully improved the flux recovery ratio (FRR) of the modified membrane by 29.1%. This result indicates that the modified PSf membrane was more suitable to serve as IMAC matrix since it has a low tendency for fouling phenomenon due to the high percentage of FRR and high porosity membrane. Chitosan or its derivatives are known as excellent antifouling agents, and surface coating is the simplest method for the modification of membranes to achieve a good antifouling property. Besides, PEG also has been introduced to improve the anti-fouling properties of PSf membrane. Moreover, PEG can increase the hydrophilicity of the membrane and this has been supported by Rana et al. [18] which states that the improvement in hydrophilicity of the membrane surface is confirmed as an effective and popular method for fouling resistance.

Characteristics of IMAC membrane

The asymmetric membrane can be seen clearly with the presence of the active layer and the support layer. The active layer of the membrane consists of a thin skin while the supporting structure is the layer below the skin due to the rapid solvent precipitation during the phase inversion process. The morphology of membrane surface and cross section for the IMAC membrane are shown in Figure 1. Figure 1(a) represents the surface morphology of IMAC membrane. The IMAC membrane shows a rough and porous surface structure which can provide a high adsorption capacity of the enzyme. Trypsin inhibitors were successfully immobilized onto the PSf/chitosan membrane using the activation with glutaraldehyde.

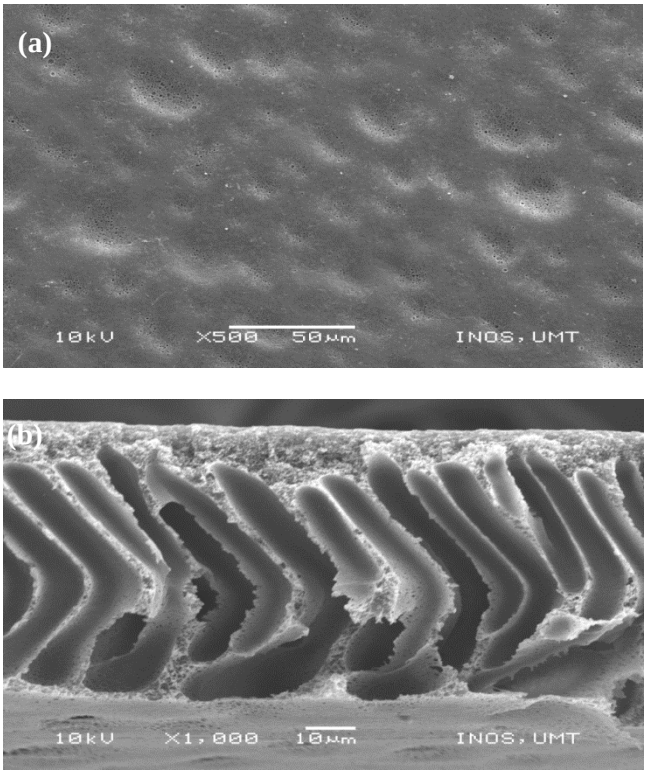


Figure 1. Morphology of (a) IMAC surface and (b) IMAC cross section

The cross section of developed pores and finger-like structures were observed from the thin skin until the support layer for all cases. The affinity membrane with immersion method shows a relative thick skin layer on the membrane skin due the remains of metal ion ligands that bound on the skin surface. To verify the functional group of membrane surface, IMAC membrane was also characterized by using ATR-FTIR and the result shows in Figure 2.

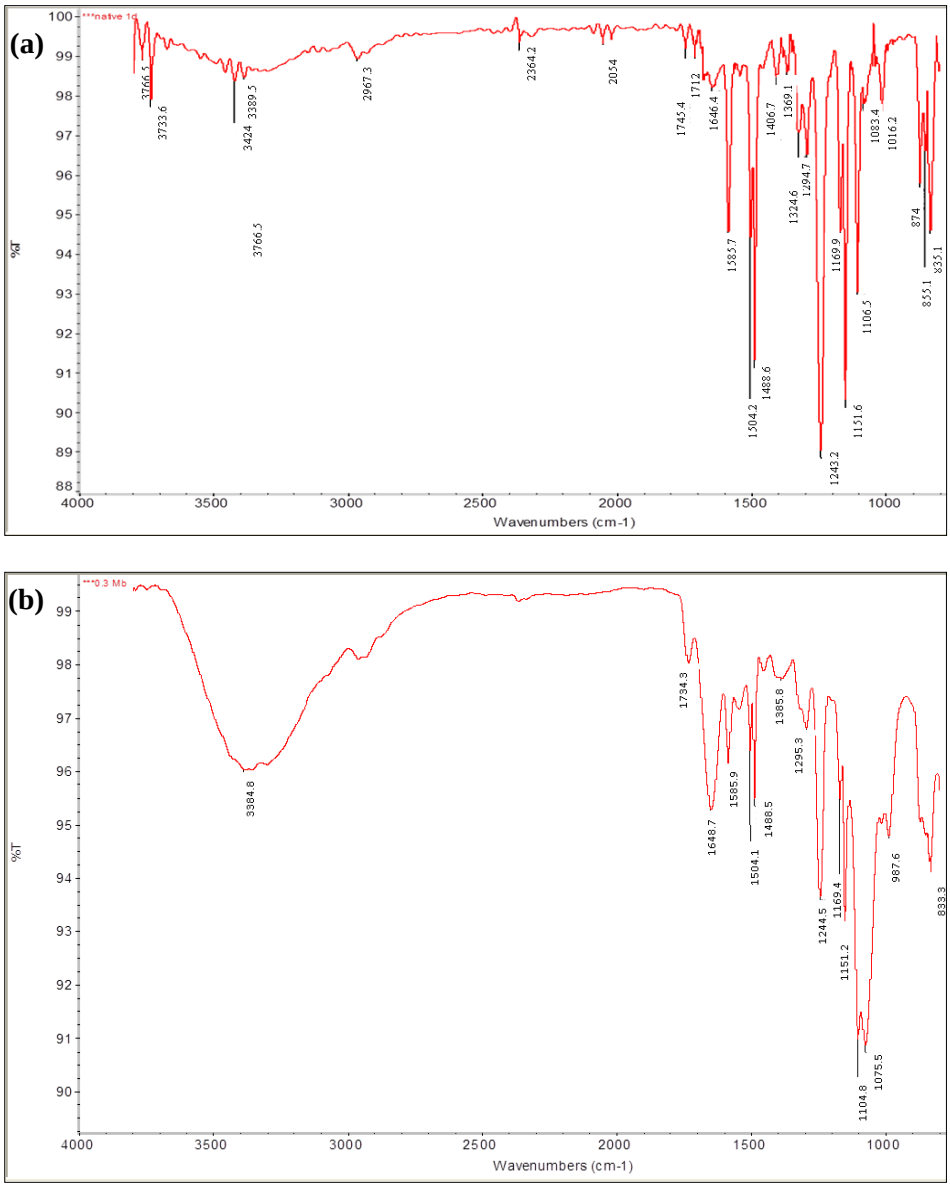


Figure 2. ATR – FTIR spectra of (a) Native PSf15 and (b) IMAC membrane

The new bands coming after membrane modification indicates the presence of a thin layer deposited on top of the PSf15 membrane. For the unmodified membrane, the absorption peaks at 1504 cm^{-1} are characteristic of polysulfone membrane. This shows that the weak bands are due to methyl groups and they present exclusively on the spectrum of polysulfone. The band range from 3424–3733 cm^{-1} shows the presence of the amine groups occurring in the polymer polysulfone. The band appearing at 3389 cm^{-1} is attributed to NH_2 and O-H of the N-acetyl group in chitosan particle where it ranges from 3200–3600 of spectra. This may be due to the slight hydrolysis of the sulfone group of the pristine PSf membrane by NaOH which occurs during the membrane neutralization process. The band at 1743 cm^{-1} in the spectra were due to ethylenic chain and this explains the presence of the aldehyde peaks in the developed affinity membrane. The presence of saccharide of chitosan in the affinity membrane around 987.6 cm^{-1} indicates that the surface of membrane was coated by the chitosan.

Immobilization capacity of metal ion Cu^{2+}onto IMAC matrix

Metal ion concentration is one of the most important factors to influence adsorption behavior. As observed in Figure 3, an increase in the ligand concentration has led to an increase of immobilization capacity up to 120 ppm ligand. Rapid adsorption can be seen within the first 30 min and afterwards. In all cases, the interactions slowed down, approached equilibrium and began to decrease in nearly 60 to 90 min under the given set of experimental conditions. The maximum capacity for the metal ion immobilization was 0.875 mg/cm^2 using 120 ppm concentration. This shows that the high concentration of ligand could provide more surface available sites for enzyme binding and better adsorption can be performed.

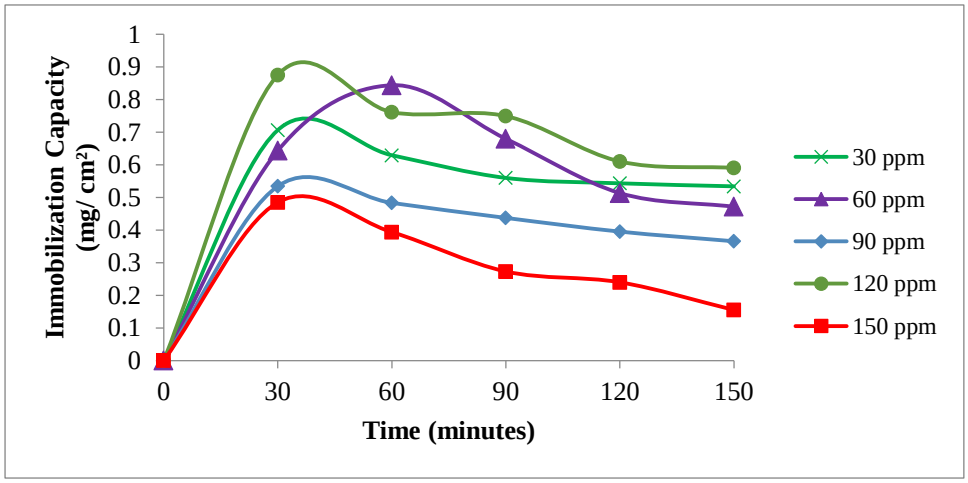


Figure 3. The effect of different concentrations of copper on its immobilization capacity onto IMAC matrix

However, for the higher concentration of metal ion which was 150 ppm, the efficiency of immobilization was reduced due to the excess of metal ions that cannot be bound with the membrane. The decrease of adsorption capacity was most likely to be caused by the precipitation of excess Cu(II) and free Cu(II) inhibiting the protein by forming a complex compound.

Trypsin adsorption onto IMAC membrane at different ionic strength

The effect of ionic strength on the adsorption of trypsin onto IMAC membrane was studied by using different concentrations of NaCl, ranging from 0.01 M until 0.5 M in a buffer solution (pH 8). The amount of trypsin adsorbed was measured with enzyme concentrations determined before and after adsorption. The result obtained is shown in Figure 4.

The adsorption behavior of IMAC membrane is suppressed in the presence of salt. As seen in Figure 4, the value of the immobilization capacity for each trypsin adsorption was reduced with increasing salt concentration. The maximum trypsin adsorption was obtained at 0.3 M in 120 minutes with 12.67 mg/cm^2 adsorption capacity. In all cases, the adsorption slowed down and started to decrease in about 90 to 120 minutes under the given set of experimental conditions. The adsorption behavior in this study occurred mostly by electrostatic interactions between the trypsin molecules and membranes. The electrostatic interaction between protein molecules and metal chelated affinity system are reduced by the presence of salt due to the screening charge on protein surfaces [17]. This is the reason why the experiment was performed at pH 8, as to ensure that the electrostatic attraction between the surface and the metal chelated was high.

An increase in ionic strength also causes a change in the interaction mechanism due to more contributions from hydrophobic and protein-protein interactions [4]. In the higher salt concentration range, enzyme solubility generally decreases due to the reduced activity of water and the neutralization of surface charge. At higher ionic strength, the

protein will be dehydrated due to the hydrated effect of salt molecules surrounding the protein allowing the hydrophobic interactions to contribute.

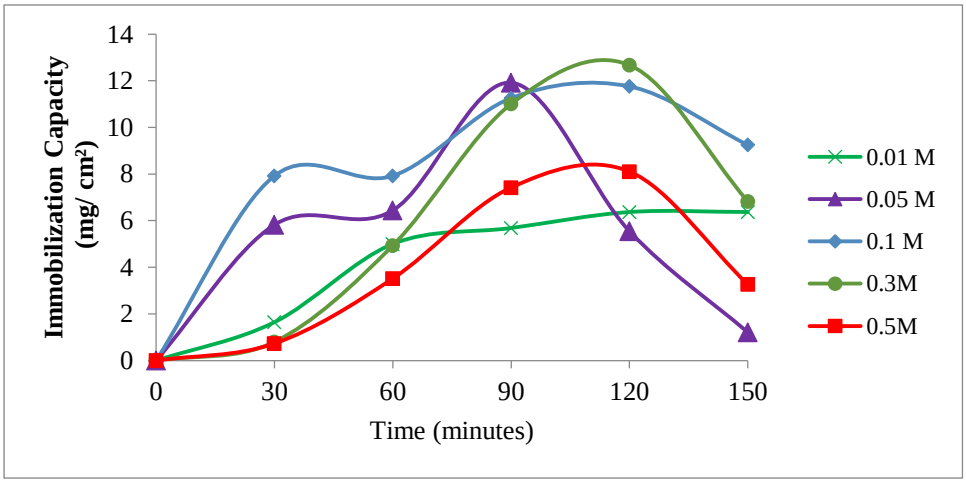


Figure 4. The effect of ionic strength on the adsorption capacity of trypsin onto IMAC

The influence of displacing salt in elution buffer

The elution strength of an eluent is the ability to elute solutes from the affinity membrane and is determined by the concentration and type of ionic species in the eluent. Different salts used give different elution strength. Therefore, the prospective salts to be used had to fulfill several conditions to qualify for evaluation in this study. These conditions are essentially demands that have to be met for a salt to make it useful in practice. In this study, four types of displacing salt were used, including KCl, NaCl, ZnCl and CaCl with 0.05 M ionic strength. Figure 5 shows the total protein, total activity and purity of trypsin obtained after affinity ultrafiltration process and Figure 6 shows the trypsin recovery.

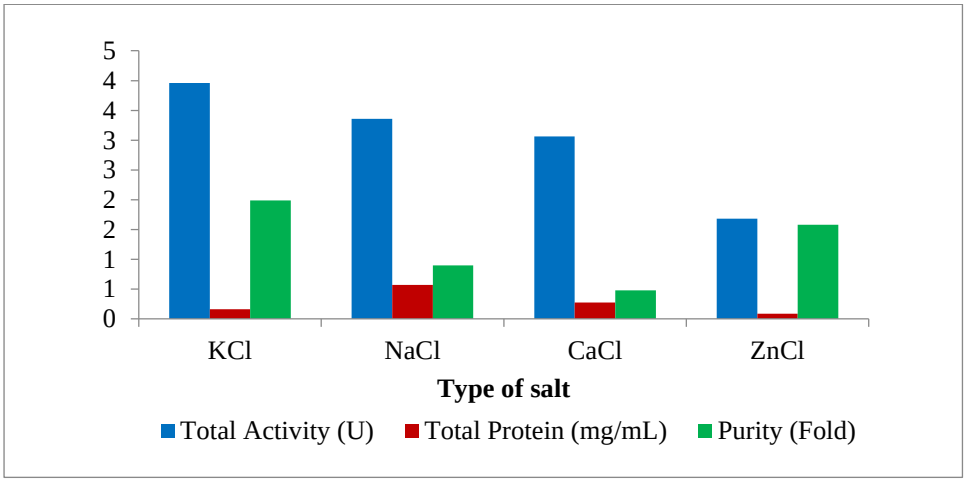


Figure 5. Total protein, total activity and purity of trypsin after affinity ultrafiltration with different type of displacing salt

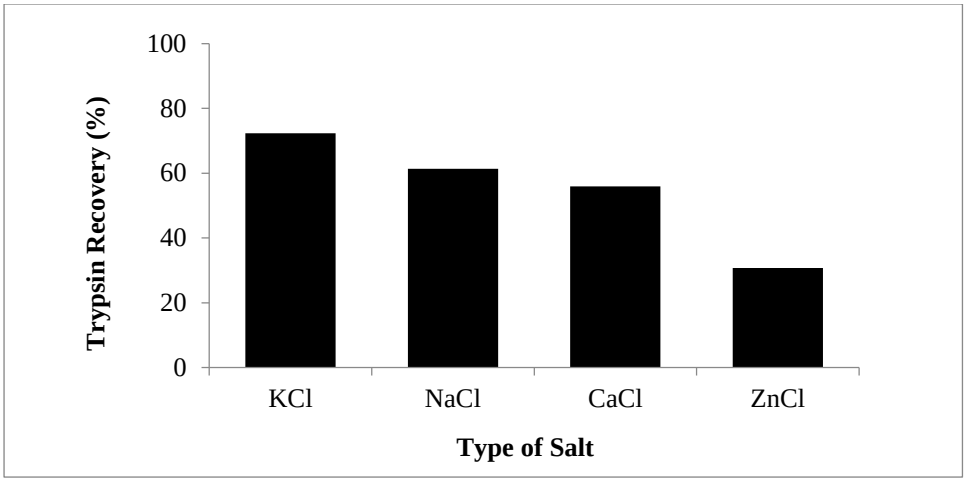


Figure 6. Trypsin recovery using affinity ultrafiltration membrane with different displacing salt

The results show that the different salts added give a major effect on trypsin recovery. Potassium chloride has the highest trypsin recovery for about 72.3% with 1.99 purification fold. Sodium chloride only recovered 61.4% trypsin. The ionized salts in this study are classified as chaotropes and kosmotropes. The term kosmotrope refers to salts that stabilize protein structure while chaotropes are salts that destabilize protein structures. The potassium has been expected to be the highest since it is one of the chaotropes ion. Besides that, the cationic properties also affect the experimental values. Since potassium and sodium are in group 1 in the periodic table, they are alkali metals and are among the most reactive metals. They tend to donate their electrons in reactions and have oxidation state of +1. Since the position of potassium in periodic table is below the sodium, where the activity increases down the group, potassium is more reactive, oxidizes easily and is able to separate the bonding between the trypsin and its ligand, allowing for higher amount of trypsin to be passed through the affinity membrane.

The least significant trypsin recovery was observed when zinc chloride was used as additional salt in the elution buffer which is at 30.7% only. As observed, the addition of zinc chloride to the elution buffer caused the solution to become cloudy due to incomplete ionization and had affected the reading of total protein. Moreover, zinc is a kosmotropes which promotes hydrophobic reaction. Zinc is in the transition metal group on the periodic table and is less reactive than other ions used, which can be ranked in descending order as K > Na > Ca > Zn. This results in the difficulty of breaking the bond between the trypsin and its ligand and reducing the transmission during the elution process.

Conclusion

In this study, the preparation and characterization of immobilized metal affinity chromatography (IMAC) matrix for trypsin separation and purification had been successfully developed. The most significant changes in membrane properties and separation performance had been performed by CH-50/PEG-50/PSf membrane and is considered as an optimum condition for membrane surface modification. This membrane is modified with the self-assembly of 50% of chitosan and 50% PEG in the modifying formulation. Combination of chitosan and PEG had improved the hydrophilicity of membranes and flux recovery ratio at about 29.01%. In addition, high porosity and excellent performance during trypsin permeation had promoted this membrane as a good matrix for affinity membrane development. Optimum ligand concentration for maximum immobilization capacity was 120 ppm Cu^{2+}. The highest trypsin adsorption obtained was 12.67 mg/cm^2 by using 0.3 M ionic strength of trypsin solution. Desorption of the enzyme by using displacing salt of potassium chloride was successfully recovered about 72.3% trypsin. Hence, it can be concluded that objectives in this study had been successfully achieved. The outcome from this study is a part of the contribution for further development in affinity membrane development.

Acknowledgement

Authors want to express a high gratitude to Ministry of Higher Education Malaysia for the funding of this research (ERGS 55097) and University Malaysia Terengganu for all supports and contributions.

References

1. Jianmin, W., Fengna, X. and Qingfu, Y. (2005). Separation and purification of Cry1Ab protein expressed from Bt transgenic plants. *Chinese Journal of Analytical Chemistry,* 33(7): 927-930.
2. Yang, P., Chen, C., Wang, Z., Fan, B. and Chen, Z. (1999). A pathogen- and salicylic acid-induced WRKY DNA-binding activity recognizes the elicitor response element to the tobacco class I chitinase gene promoter. *The Plant Journal,* 18(3): 141-149.
3. Zou, H., Luo, Q. and Zhou, D. (2001). Affinity membrane chromatography for the analysis and purification of proteins. *Journal of Biochemical and Biophysical Methods,* 49(1-3): 199-240.
4. Wu, C. Y., Suen, S. Y., Chen, S. C. and Tzeng, J. H. (2003). Analysis of protein adsorption on regenerated cellulose-based immobilized metal affinity membranes. *Journal of Chromatography A,* 996 (1-2): 53-70.
5. Hu, H. L., Wang, M. Y., Chung, C. H. and Suen, S. Y. (2006). Purification of VP3 protein of infectious bursal disease virus using nickel ion immobilized regenerated cellulose-based membranes. *Journal of Chromatography B,* 840(2): 76-84.
6. Jiraratananon, R., Chanachai, A. and Huang, R. Y. M. (2002). Pervaporation dehydration of ethanol–water mixtures with chitosan/hydroxyethylcellulose (CS/HEC) composite membranes: II. Analysis of mass transport. *Journal of Membrane Science,* 199(1-2): 211-222.
7. Liu, C. X. and Bai, R. B. (2005). Preparation of chitosan/cellulose acetate blend hollow fibers for adsorptive performance. *Journal of Membrane Science,* 267(1-2): 68-77.
8. Ramesh, B. P. and Gaikar, V. G. (2001). Membrane characteristics as determinant in fouling of UF membranes. *Separation Purification Technology,* 24(1-2): 23-34.
9. Gancarz, I., Zniak, G. P., Bryjak, M. and Tylus, W. (2002). Modification of polysulfone membranes. Effect of n-butylamine and allylamine plasma. *European Polymer Journal,* 38(10): 1937-1946.
10. Hamzah, S., Ali, N., Mohammad, A. W., Ariffin, M. A. and Ali, A. (2012). Design of Chitosan /PSf self-assembly membrane to mitigate fouling and enhance performance in trypsin separation. *Journal of Chemical Technology and Biotechnology,* 87(8): 1157-1166.
11. Ali, A., Yunus, M. R, Awang, M. and Mat, R. (2015). Effect of shear rate on characteristics, performance and morphology of polysulfone blend membranes. *Applied Mechanics and Materials,* 699: 305-310.
12. Arvanitoyannis, I., Nakayama, A. and Aiba, S. (1998). Chitosan and gelatin based edible films: State diagrams, mechanical and permeation properties. *Carbohydrate Polymer,* 37(4): 371-382.
13. Arvanitoyannis, I. (1999). Totally and partially biodegradable polymer blends based on natural and synthetic macromolecules: preparation, physical properties, and potential as food packaging materials. *Journal of Macromolecular Science, Part C,* 39(2):205-271.
14. Sashiwa H. and Aiba S. (2004). Chemically modified chitin and chitosan as biomaterials. *Progress in Polymer Science (Oxford),* 29(9): 887-908.
15. Sashiwa, H., Fujishima, S. and Yamano, N. (2003). Enzymatic production of *n*-acetyl-d-glucosamine from chitin. degradation study of *n*-acetylchitooligosaccharide and the effect of mixing of crude enzymes. *Carbohydrate Polymer,* 51(4): 391-395.
16. Saxena, S., Gupta, B., Arora, A. and Alam, M. S. (2006). Chitosan-polyetylene glycol coated cotton membranes for wound dressings. *Indian Journal of Fibre and Textile Research,* 36(3): 272-280.
17. Bayramoğlu, G. and Yakup, A. M. (2002). Procion green H-4G immobilized on a new IPN hydrogel membrane composed of poly (2-hydroxyethylmethacrylate)/chitosan: preparation and its application to the adsorption of lysozyme. *Colloids and Surfaces A: Physicochemical and Engineering Aspects,* 202 (1): 41-52.
18. Rana, T. M. (1994). Artificial proteolysis by a metal chelate: Methodology and mechanism. *Advanced Inorganic Biochemical,* 10: 177-200.

Malaysian Journal of Analytical Sciences, Vol 22 No 5 (2018): 867 - 876
DOI: https://doi.org/10.17576/mjas-2018-2205-14

MALAYSIAN JOURNAL OF ANALYTICAL SCIENCES
Published by The Malaysian Analytical Sciences Society
ISSN 1394 - 2506

ENHANCEMENT AND OPTIMIZATION OF SINENSETIN EXTRACT FROM *Orthosiphon stamineus* USING SUPERCRTITICAL CARBON DIOXIDE EXTRACTION

(Peningkatan dan Pengoptimuman Ekstrak Sinensetin dari *Orthosiphon stamineus* Menggunakan Kaedah Pengekstrakan Bendalir Supergenting Karbon Dioksida)

Ahmad Hazim Abdul Aziz[1], Mohd Azizi Che Yunus[2]*, Lee Nian Yian[1], Zuhaili Idham[1], Fahim Rithwan[3], Hafizah Mohd Hadzri[4], Ana Najwa Mustapha[5]

[1]*Centre of Lipids Engineering and Applied Research (CLEAR), Ibnu Sina Institute for Scientific and Industrial Research*
[2]*Faculty of Chemical and Energy Engineering*
Universiti Teknologi Malaysia, 81310 UTM Johor Bahru, Johor, Malaysia
[3]*NF Marketing, 41050 Meru, Selangor, Malaysia*
[4]*Mukjizat International Sdn Bhd., 40100 Shah Alam, Selangor, Malaysia*
[5]*Faculty of Chemical Engineering,*
Universiti Teknologi MARA,40450 Shah Alam, Selangor, Malaysia

**Corresponding author: azizi@cheme.utm.my*

Received: 16 April 2017; Accepted: 7 March 2018

Abstract

Sinensetin is a rare valuable flavonoid compound that contains 5 methoxy groups attached on the flavone backbone. This compound is abundantly established in citrus peel and can also be found in medicinal herb, 'misai kucing'. Scientifically, 'misai kucing' is known as *Orthosiphon stamineus*; mostly used to treat kidney stones by old folks. *Orthosiphon stamineus* was listed in National Key Economic Area (NKEA) as contributor towards the Malaysian Economic Growth. Thus, this study was conducted with objectives to determine suitable modifier for supercritical carbon dioxide (SC-CO_2) extraction and to optimize the SC-CO_2 extraction condition (pressure, temperature and average particle size) on the concentration of sinensetin. Water, methanol and acetone were used on the determination of modifier for SC-CO_2 extraction by using water bath extraction at 40 °C in 8 hours. The results showed that acetone gave the highest percentage of sinensetin extract of 0.11%. Therefore, acetone was used as a modifier to enhance the extraction of sinensetin. The concentration of sinensetin was increased and the highest percentage of sinensetin obtained was 6.99%. Response surface methodology (RSM) through Box-Behnken design via Design Expert Software was applied to optimize the SC-CO_2 conditions. The first-order polynomial was used to express the percentage of sinensetin with R^2 value of 0.542. The optimum SC-CO_2 operating condition was 30 MPa, 40 °C and 308.24 µm with sinensetin percentage of 4.35%. Hence, SC-CO_2 with small amount of modifier was the best method to extract sinensetin as compared to water bath extraction method.

Keywords: sinensetin, supercritical carbon dioxide, orthosiphon stamineus, misai kucing, optimization

Abstrak

Sinensetin merupakan sebatian flavonoid yang jarang ditemui dan sangat berharga terdiri daripada 5 kumpulan metoksi yang terikat pada struktur flavone. Sebatian ini banyak dijumpai dalam kulit limau dan juga boleh didapati dalam herba 'misai kucing'. Secara saintifik, 'misai kucing' dikenali sebagai *Orthosiphon stamineus*; di mana '*misai kucing*' digunakan untuk merawat batu karang oleh orang-orang tua. *Orthosiphon stamineus* telah disenaraikan dalam Kawasan Ekonomi Utama Negara (NKEA) sebagai penyumbang kepada pertumbuhan ekonomi negara. Oleh itu, kajian ini dijalankan dengan objektif untuk menentukan pelarut tambahan yang sesuai untuk pengekstrakan bendalir supergenting karbon dioksida (SC-CO_2) dan mengoptimumkan

pemboleh ubah SC-CO_2 (tekanan, suhu dan purata saiz zarah) terhadap kepekatan sinensetin. Air, metanol dan aseton telah digunakan untuk menentukan pelarut tambahan untuk pengekstrakan SC-CO_2 dengan menggunakan pengekstrakan rendaman air pada suhu 40 °C dalam masa 8 jam. Keputusan menunjukkan bahawa aseton memberikan peratusan sinensetin tertinggi sebanyak 0.11%. Oleh itu, aseton digunakan sebagai pelarut tambahan untuk meningkatkan pengekstrakan sinensetin dalam SC-CO_2. Kepekatan sinensetin meningkat dan peratusan tertinggi sinensetin diperoleh ialah 6.99%. Kaedah gerak balas permukaan (RSM) melalui rekabentuk Box-Behnken menggunakan perisian Design Expert untuk mengoptimumkan pemboleh ubah SC-CO_2. Polinomial tertib pertama digunakan untuk menyatakan peratusan sinensetin dengan nilai regrasi R^2 ialah 0.542. Keadaan optimum bagi SC-CO_2 adalah 30 MPa, 40 ° C dan 308.24 μm dengan peratusan sinensetin sebanyak 4.35%. Oleh itu, SC-CO_2 dengan sedikit pelarut tambahan adalah kaedah terbaik untuk mengekstrak sinensetin berbanding kaedah pengekstrakan rendaman air.

Kata kunci: sinensetin, bendalir supergenting karbon dioksida, orthosiphon stamineus, misai kucing, pengoptimuman

Introduction

By 2020, Malaysian government targeted Malaysia to become a developed and high-income country comparable with Japan, Korea and other developed countries. Economic Transformation Programme (ETP) was introduced by Malaysian government on 2010 as an approach to increase growth gross national income (GNI) per capita of USD 15,000 and create million new jobs. In the program, agriculture sector is one of the main sector listed in the National Key Economic Areas (NKEAs) with other 11 sectors. The 16 Entry Point Projects (EPPs) have been pointed out to urge growth in this sector and one of them is high-value herbal products. The first phase of this EPP focused on five main local herbs which are *tongkat ali*, *misai kucing*, *hempedu bumi*, *dukung anak* and *kacip fatimah* while ensuring the supply for research and development (R&D) is sufficient.

Orthosiphon stamineus, generally known as *misai kucing*, is a traditional herb that is mostly used as tea beverage and herb medicine in Malaysia and Indonesia. People consume the herb to treat kidney stones, urinary tract infections, diabetes and high blood pressure. Recent studies revealed that approximately 116 chemical compounds were isolated from O. stamineus, providing medicinal benefit to human health [1]. In addition, researchers also found scientific evidences on health benefits of O. stamineus extract such as diuretic and hypouricemic effect [2], anti-infective activity [3], anti-hyperglycemic activity [4] and anti-diabetic activity [5]. These evidences are associated with the presence of main secondary metabolites in O. stamineus extract such as rosmarinic acid, eupatorin, 5-hydroxy-3',4',6,7-tetramethoxyflavone (TMF) and sinensetin [6].

Sinensetin is the most potent compound in *O. stamineus* because it is a rare polymethoxylated flavone which abundantly found in citrus peel [7]. Sinensetin has antiagiogenesis activity. Angiogenesis is the formation of a mature blood vessel network through expansion and remodeling of the pre-existing vascular primordium. It plays a crucial role in the development of cancer [8, 9]. In addition, sinensetin has chemo-sensitizing effect that can reverse P-glycoprotein as mediated multidrug resistance (MDR) by increasing the intracellular accumulation of drugs [10].

Extraction of plant materials like *O. stamineus* could be done by various procedures. Conventional method of extraction like Soxhlet and water bath extraction method commonly used massive amount of organic solvent associates with long extraction regime and high temperature. These approaches however, risk the degradation of interest bioactive compounds. This disadvantage gives rise to non-conventional method such as supercritical fluid extraction (SFE) which is more environmentally friendly, shorter extraction regime and give better quality of extract. Carbon dioxide is believed to be an ideal solvent for SFE because of its critical temperature (31.1 °C) which is relatively ambient, and moderate critical pressure of 7.38 MPa. However, low polarity of carbon dioxide limits the solubility exhibited by polar compound. This has becomes the main problem in SFE because most of the bioactive compounds in plant materials are polar. Nevertheless, this can be overcome by introducing a small amount of organic solvent (e.g., ethanol, methanol, and acetone) that can act as modifier in the system to increase the range of solvating strength to extract more polar compounds and significantly enhance the polarity of carbon dioxide [11]. In this study, supercritical carbon dioxide (SC-CO_2) extraction was introduced to attain a better yield extract of O. stamineus leaves compared with other extraction methods. Moreover, few studies have proved that SC-CO_2 extraction gave better yield of extraction on plant matrices such as *manjakani* [12], *dukung anak* [13], *jering* [14] and rubber seed [15] compared to conventional extraction method.

Response surface methodology (RSM) is widely used to optimize the operating parameters of SC-CO_2 extraction based on experimentally-fitted empirical model that described the response of the affecting parameters. The response can be represented graphically either in 3-D space or as contour plot that help visualize the shape of the response. There are different softwares that can be used to perform RSM such as Statistica, Design Expert, Minitab, and SPSS. Design Expert software widely used because it is more user friendly than others [16-19].

In this study, selection of the most effective solvent as modifier in SC-CO_2 to enhance the quality of the sinensetin in the extract was conducted using water bath extraction method. Meanwhile, optimization of SC-CO_2 extraction parameters (pressure, temperature and average particle size) was conducted using RSM to obtain high percentage of sinensetin from *O. stamineus* leaves.

Materials and Methods

Sample preparation

Dried leaves of *O. stamineus* were purchased from Herbagus Trading, Penang. The leaves were ground in several sizes of 300, 500 and 700 µm. The ground leaves were sealed in a plastic seal bag and kept in a freezer at −20 °C to keep the freshness of the leaves.

Water bath extraction

Polarity of sinensetin was not known. Hence, various concentrations of solvents were used in this study to investigate. A total of 10 grams *O. stamineus* ground leaf was extracted using water, methanol (100% and 50%) and acetone (100% and 70%) for 8 hours at 40 °C in water bath [20].

Supercritical fluid extraction

A schematic diagram of the fabricated SC-CO_2 rig used in this study is shown in Figure 1. The fabricated SC-CO_2 unit was consisted of a 50 mL extraction vessel, high-pressure pump (Supercritical 24, Lab Alliance), modifier pump (Series II Pump, Lab Alliance), automated back pressure regulator (Jasco, BP-2080 Plus) and oven (U10, Mermert) as extraction chamber. Total flowrate of 4 mL/min with 5% modifier was used, where 3.8 mL/min of 99.99% pure carbon dioxide (Kras, Instrument and Services, Johor, Malaysia) were pumped in the system with 0.2 mL/min of 99.5% analytical grade acetone (Merck Millipore) [21]. A total of 5 g samples were required for 90 minutes extraction regime under these conditions: temperature (40–80 °C) and pressure (10–30 MPa) for various average particle sizes (300, 500 and >500 µm).

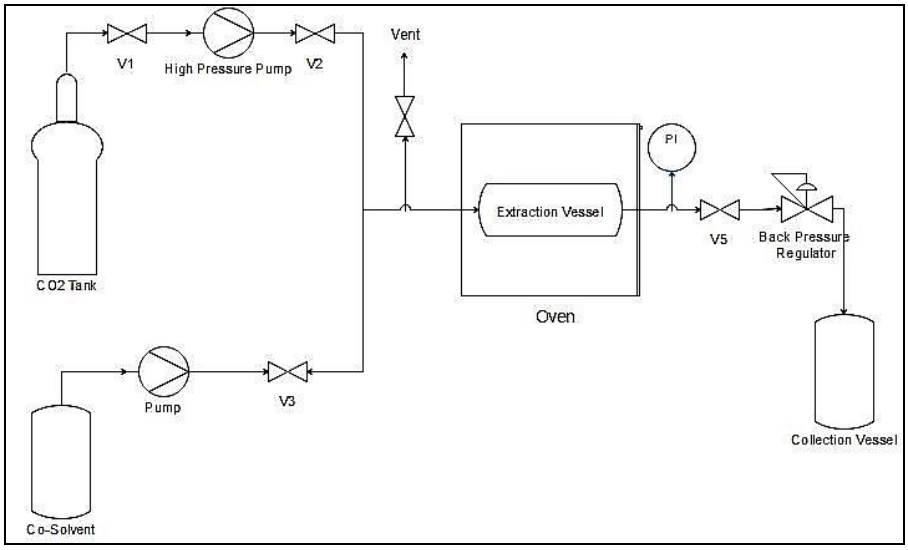


Figure 1. Schematic diagram of SC-CO_2 extraction unit

Enhancement of the sinensetin recovery from *O. stamineus* was performed using SC-CO_2. However, SC-CO_2 has disadvantage on the polar compound extract because carbon dioxide is a nonpolar compound. Hence, addition of modifier in small amount into the process could enhance the amount of sinensetin recovery. Acetone was selected as a modifier in this study based on the highest percentage of sinensetin (0.11%) in the extract during water bath extraction compared to the other solvents as shown in Figure 2.

High performance liquid chromatography

The extract of *O. stamineus* was filtered using a 0.45 µm filter paper prior to use. HPLC analysis was performed using an Agilent Technologies series 1100 system/series equipped with an automatic injector, a column oven, and a diode array UV detector. A LiChrosorb RP-18 (250 mm × 4.6 i.d. mm, 5 µm particle size) (Merck Darmstadt, Germany) was used. The temperature was maintained at 25 °C, with injection volume of 20 µL and flow rate of 1 mL/min. Sinensetin was separated using methanol: water: tetrahydrofuran (45:50:5 v/v) as mobile phase for 30 minutes [20]. The peaks were detected at 340 nm and identified by standard substance. Sinensetin standard was purchased from ChromaDex. The amount of sinensetin found in the extract (µg/g) was calculated by using equation 1 as follows and expressed in percentage of sample used:

$$Q\ (\mu g/g) = (A - C)/S * (V/W) \quad (1)$$

where as Q is defined as amount of sinensetin in the sample, A is peak area of chromatogram, V is dilution volume (mL), S is slope of calibration curve, C is intercept of the calibration curve and W is weight of the sample (g).

Optimization

Design Expert software version 6 was used in this study to determine the optimum condition of SC-CO_2 process. The ranges of pressure, temperature and average particle size were 10 - 30 MPa, 40 - 80 °C and 300 - 500 µm respectively. 15 runs were conducted in optimization process with responses of sinensetin percentage in the extract of *O. stamineus* as shown in Table 1. The experimental data were fitted with response surface model generated by the Design Expert software using Box-Behnken design. Box-Behnken is better compared to central composite design because it avoids experiments at extreme conditions and more economical [22]. The analysis of variance (ANOVA) was also used to evaluate the quality of the fitted model through calculation of the correlation factor, R^2 and F-test. The F value calculated should be higher than F value tabulated (from F table), indicating that the response surface model is significant.

Table 1. Experimental design

Run	Pressure	Temperature	Average Particle Size	Sinensetin
1	10	40	500	3.20
2	30	40	500	6.99
3	10	80	500	1.03
4	30	80	500	1.68
5	10	60	300	1.51
6	30	60	300	2.67
7	10	60	700	1.74
8	30	60	700	2.24
9	20	40	300	2.24
10	20	80	300	1.76

Table 1 (cont'd). Experimental design

Run	Pressure	Temperature	Average Particle Size	Sinensetin
11	20	40	700	2.52
12	20	80	700	1.61
13	20	60	500	2.65
14	20	60	500	2.35
15	20	60	500	2.91

Results and Discussion

Enhancement of the sinensetin extract

By analyzing the area of the chromatograms and compare it with calibration curve graph, it was possible to estimate the percentage of sinensetin in the extract. Water bath extraction method with various solvent showed that different solvent gave different percentage of sinensetin extract. Figure 2 shows that 100% acetone give the highest percentage of sinensetin (0.11%), followed by 70% acetone (0.10%), 100% methanol (0.08%), 50% methanol (0.03%), and water (0.03%). Similar result was reported by Akowuah et al., where acetone gave the highest percentage of sinensetin (0.32%) compared to methanol (0.15%), chloroform (0.18%) and ethyl acetate (0.21%) from 1 g of dry powder methanol extract [20].

This phenomenon can be explained according to "like dissolve like" principle, where solvents would extract and attract compounds of similar polarity. In this case, sinensetin was the target compound and was mostly obtained in acetone. Hence, it can be concluded that sinensetin is a polar compound based on the result shows in Figure 2.

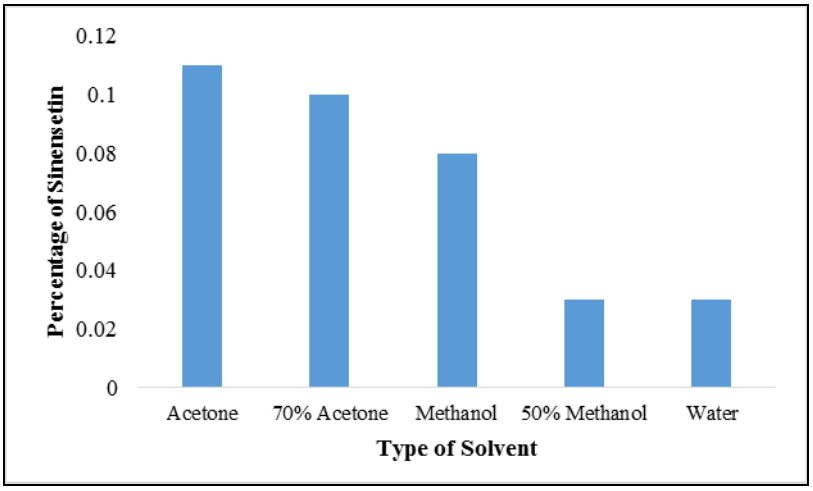


Figure 2. Effect of various solvents on the percentage yield of sinensetin

Therefore, acetone was selected to be used as modifier in the SC-CO_2 extraction, where, binary-solvent system gave high quality of extract compared with mono-solvent system [23]. Table 1 indicates that SC-CO_2 extraction enhanced the percentage of sinensetin in the *O. stamineus* extract. The highest percentage of sinensetin extract was 6.99% at 30 MPa, 40 °C and 500 µm. This is because high pressure of 30 MPa and low temperature of 40 °C increase the solvent density; hence improved the solubility of sinensetin and enhanced the percentage of sinensetin extract.

Optimization of the sinensetin extract

Evaluation of the response surface model and analysis of variance (ANOVA) were performed using data in Table 1 by using Design Expert software version 6.0. Based on the ANOVA test presented in Table 2, it is possible to evaluate the influence of extraction conditions analyzed regarding the response percentage of sinensetin.

Table 2. Descriptive of ANOVA test

Source	Df	Sum of Square	Mean Square	F calculated	F Table
Regression	3	14.49	4.83	4.35	3.59
Residual	11	12.26	1.11		
Total	14	26.75			

According to the ANOVA data, only temperature is statistically significant ($p < 0.05$) considering a significance level of 95% (α=0.05). The average particle size did not show a significant influence in the percentage of sinensetin in the extract according to descriptive index (p value) of 98.17%. Therefore, in the present conditions, assumption that there is a relationship between the average particle size and the percentage of sinensetin should be rejected. Other parameters should be considered to replace the average particle size such as solvent flowrate, extraction time and concentration of modifier.

The analysis also elucidates that the regression is statistically significant, so it can be applied to the model to describe the variation of sinensetin percentage in the extract. With p value of 0.0302 for linear regression, linear model should be adopted. The F calculated value that is larger than F tabulated value indicates that the model is accepted. Thus, the regression coefficients of response surface were estimated for the linear model resulting in equation 2 without interaction of the parameters.

$$\% \text{ Sinensetin} = 4.296 + 0.076X_1 - 0.055X_2 - 4.375E\text{-}05X_3 \quad (2)$$

From the analysis, coefficient of determination, R^2 was equal to 0.542 and the adjusted coefficient of determination, R^2 adjusted was equal to 0.417. The coefficient of determination value was quite low but still acceptable. The validity of the model was further confirmed by non-significant value of ($p > 0.05$) for lack of fit, which indicates a linear model without interaction as statistically significant for the response.

By using equation 2, response surface graph was generated as shown in Figure 3. From Figure 3(a), as pressure increase the density of the solvent increased, and decreased the distance between molecules; hence strengthening the interaction between the solvent into the system and enhance the amount of sinensetin. In contrast, as temperature increase, the amount of sinensetin extract decrease. This effect can be attributed to the decomposition of heat-sensitive component (sinensetin) during extraction at higher temperature. As can be seen in Figure 3(b) and (c), particle size of the sample did not affect the extraction of the sinensetin. Therefore, the optimum SC-CO_2 extraction conditions to extract sinensetin based on the equation 2 are 30 MPa, 40 °C and 308.24 µm with the sinensetin percentage as 4.35%.

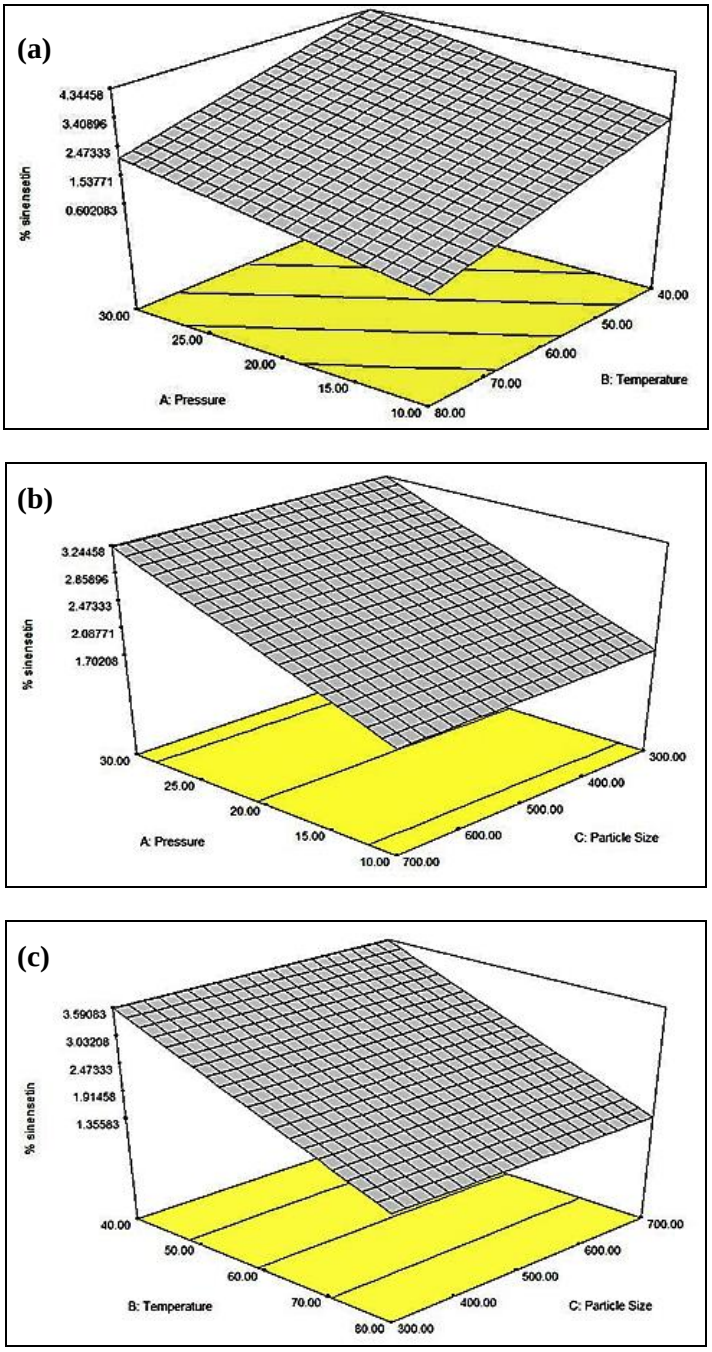


Figure 3. Response surface plot for two independent variables effect on percentage of snensetin: (a) pressure and temperature; (b) pressure and average particle size; (c) temperature and average particle size

Determination of sinensetin

The sinensetin standard was diluted into different concentrations to develop a calibration curve and gave an equation of $Y = 63.99X - 794.02$ with R^2 value is 0.9711. The peak of sinensetin from the extract was validated by comparing the retention time with standard. Figure 4(a) indicates a chromatogram of sinensetin standard at 20 ppm

and Figure 4(b) indicates the chromatogram of the *O. stamineus* extract. Both the standard and sinensetin from the extract resolved and eluted at 3.9 minutes.

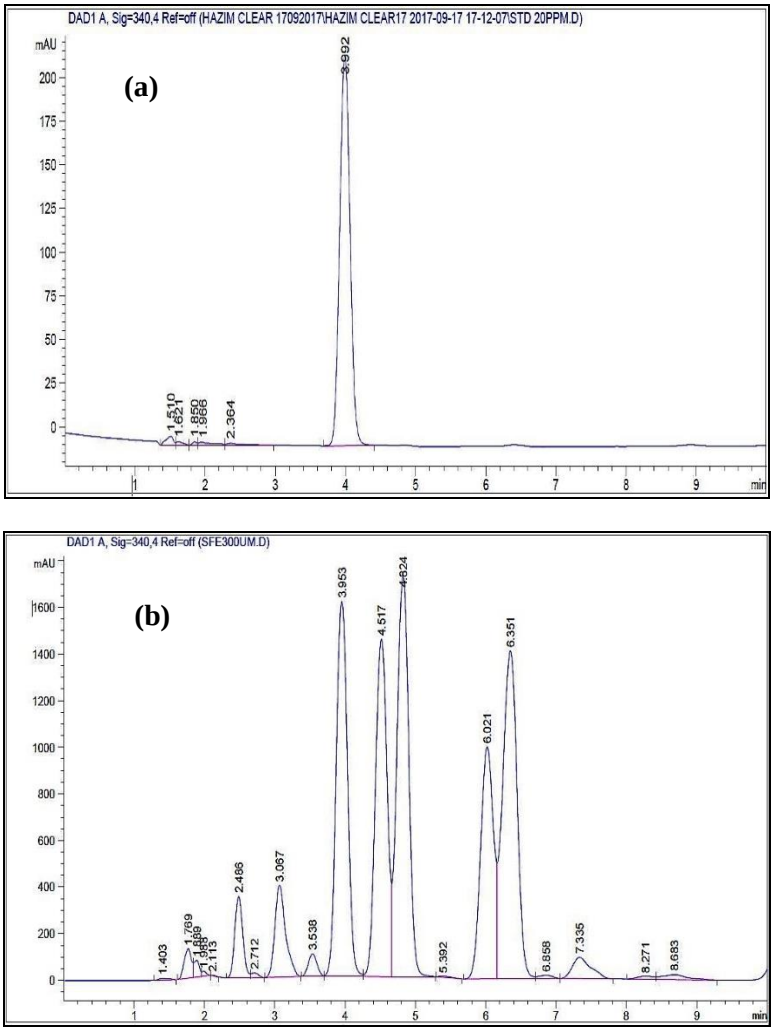


Figure 4. Chromatogram of sinensetin: (a) standard at 20 ppm and (b) extract of *O. stamineus* using SC-CO_2 extraction

Conclusion

SC-CO_2 is the best extraction technique that can be used to extract sinensetin from *O. stamineus* leaves compared with conventional technique. This is due to the high selectivity properties of SC-CO_2 method. It was proved that SC-CO_2 could enhance the amount of sinensetin extract from 0.11% to 6.99% in short extraction regime using small amount of organic solvent. At pressure of 30 MPa at 40 °C, and 308.24 µm particle size, the highest sinensetin amount (4.35%) was obtained by using response surface methodology. Even though the coefficient of determination (R^2) value was low (0.542), the model is still acceptable and significant, and the average particle size of the sample can be neglected. In addition, retention time of sinensetin in chromatogram was observed at 3.9 minutes.

Acknowledgement

This research is fully supported by Universiti Teknologi Malaysia and Johor State Government Fund (R.J130000.7709.4J260). The authors fully acknowledged Johor State Government and Universiti Teknologi Malaysia for the approved fund which makes this important research viable and effective.

References

1. Adnyana, I. K., Setiawan, F. and Insanu, M. (2013). From ethnopharmacology to clinical study of *Orthosiphon stamineus* Benth. *International Journal of Pharmacy and Pharmaceutical Sciences*, 5: 66-73.
2. Arafat, O. M., Tham, S. Y., Sadikun, A., Zhari, I., Haughton, P. J. and Asmawi, M. Z. (2008). Studies on diuretic and hypouricemic effects of *Orthosiphon stamineus* methanol extracts in rats. *Journal of Ethnopharmacology*, 118(3): 354-360.
3. Kong, C., Tan, M. W. and Nathan, S. (2014). *Orthosiphon stamineus* protects *Caenorhabditis elegans* against *Staphylococcus aureus* infection through immunomodulation. *Biology Open*, 3(7): 644-655.
4. Mohamed, E. A. H., Mohamed, A. J., Asmawi, M. Z., Sadikun, A., Ebrika, O. S. and Yam, M. F. (2011). Antihyperglycemic effect of *Orthosiphon stamineus* benth leaves extract and its bioassay-guided fractions. *Molecules*, 16(5): 3787–3801.
5. Mohamed, E. A., Ahmad, M., Ang, L. F., Asmawi, M. Z. and Yam, M. F. (2015). Evaluation of α-glucosidase inhibitory effect of 50% ethanolic standardized extract of *Orthosiphon stamineus* benth in normal and streptozotocin-induced diabetic rats. *Evidence-Based Complementary and Alternative Medicine*, 2015: 1-6.
6. Singh, M. K., Gidwani, B., Gupta, A., Dhongade, H., Kaur, C. D., Kashyap, P. P. and Tripathi, D. K. (2015). A review of the medicinal plants of genus orthosiphon (Lamiaceae). *International Journal of Biological Chemistry*, 9(6): 318-331.
7. Gaydou, E. M., Bianchini, J. P. and Randriamiharisoa, R. P. (1987). Orange and mandarin peel oils differentiation using polymethoxylated flavone composition. *Journal of Agricultural and Food Chemistry*, 35(4): 525-529.
8. Lam, I. K., Alex, D., Wang, Y. H., Liu, P., Liu, A. L., Du, G. H. and Yuen Lee, S. M. (2012). In vitro and in vivo structure and activity relationship analysis of polymethoxylated flavonoids: Identifying sinensetin as a novel antiangiogenesis agent. *Molecular Nutrition and Food Research*, 56(6): 945-956.
9. Sahib, H. B., Aisha, A. F., Yam, M. F., Asmawi, M. Z., Ismail, Z., Salhimi, S. M., Othman, N. H. and Majid A. M. S. A. (2009). Anti-angiogenic and antioxidant properties of *Orthosiphon stamineus* benth. methanolic leaves extract. *International Journal of Pharmacology*, 5(2): 162-167.
10. Choi, C. H., Sun, K. H., An, C. S., Yoo, J. C., Hahm, K. S., Lee, I. H., Sohng, J. K. and Kim, Y. C. (2002). Reversal of p-glycoprotein-mediated multidrug resistance by 5,6,7,3',4'-pentamethoxyflavone (Sinensetin). *Biochemical and Biophysical Research Communications*, 295(4): 832-840.
11. Edward, R., Qiubai, S. U. N., Zhiqiang, Z., Chongmin, Z. and Wei, G. O. U. (2009). Mini-review: Green sustainable processes using supercritical fluid carbon dioxide. *Journal of Environmental Sciences*, 21(6): 720–726.
12. Nasir, N. H. M., Salleh, L. M., Nur Syukriah, A. R., Ya'akob, H., Yunus, M. A. C. and Majid, F. A. A. (2015). Total phenolic content and antioxidant activity of *Quercus infectoria* galls using supercritical CO_2 extraction technique and its comparison with Soxhlet extraction. *Pertanika Journal of Science and Technology*, 23(2): 287-295.
13. Hadzri, H. M., Yunus, M. A. C., Zhari, S. and Rithwan, F. (2014). The effects of solvents and extraction methods on the antioxidant activity of *P. niruri. Jurnal Teknologi (Sciences and Engineering)*, 68(5): 47-52.
14. Yunus, M. A. C., Zhari, S., Haron, S., Arsad, N. H., Idham, Z. and Ruslan, M. S. H. (2015). Extraction and identification of Vitamin E from *Pithecellobium jiringan* seeds using supercritical carbon dioxide. *Jurnal Teknologi*, 74(7): 29-33.
15. Yian, L., N., Setapar, S. H. M., Sharif, N. S. M., Ahmad, A., Khatoon, A., Yunus, M. A. C. and Muhamad I. I. (2013). Extraction of rubber (*Hevea brasiliensis*) seed oil using supercritical carbon dioxide and Soxhlet extraction. *Research Journal of Chemistry and Environment*, 17(10): 46-52.
16. Hartati, S. L. M., Yunus, M. A. C. and Aziz, A. A. (2014). Optimization of supercritical CO_2 extraction of *Swietenia mahagoni* seed by response surface methodology. *Jurnal Teknologi (Sciences and Engineering)*, 67(1): 15-20.
17. Aziz, A. H. A., Yunus, M. A. C., Arsad, N. H., Yian, L. N., Idham, Z. and Razak, A. Q. A. (2016). Optimization of supercritical carbon dioxide extraction of *Piper betel* Linn leaves oil and total phenolic content. *IOP Conference Series: Materials Science and Engineering*, 162(1): 1-7.
18. Yunus, M. A. C., Idham, Z. and Morad, N. A. (2015). Optimisation of squalene from palm oil mesocarp using supercritical carbon dioxide. *10th Asian Control Conference (ASCC)*, 1-6.

19. Danlami, J. M., Zaini, M. A. A., Arsad, A. and Yunus, M. A. C. (2015). A parametric investigation of castor oil (*Ricinus comminis* L) extraction using supercritical carbon dioxide *via* response surface optimization. *Journal of the Taiwan Institute of Chemical Engineers*, 53: 32-39.
20. Akowuah, G. A., Ismail, Z., Norhayati, I. and Sadikun, A. (2005). The effects of different extraction solvents of varying polarities on polyphenols of *Orthosiphon stamineus* and evaluation of the free radical-scavenging activity. *Food Chemistry*, 93(2): 311-317.
21. Rithwan, F., Zhari, S., Yunus, M. A. C. and Hadzri, H. M. (2014). Efficacy of biological activity of *Andrographis paniculata* extracted by using supercritical carbon dioxide ($SC\text{-}CO_2$) extraction. *Jurnal Teknologi (Sciences and Engineering)*, 69(4): 61-64.
22. Sharif, K. M., Rahman, M. M., Azmir, J., Mohamed, A., Jahurul, M. H. A., Sahena, F. and Zaidul, I. S. M. (2014). Experimental design of supercritical fluid extraction – A review. *Journal of Food Engineering*, 124: 105-116.
23. Turkmen, N., Sari, F. and Velioglu, Y. S. (2006). Effects of extraction solvents on concentration and antioxidant activity of black and black mate tea polyphenols determined by ferrous tartrate and Folin–Ciocalteu methods. *Food Chemistry*, 99(4): 835-841.

Malaysian Journal of Analytical Sciences, Vol 22 No 5 (2018): 877 - 884
DOI: https://doi.org/10.17576/mjas-2018-2205-15

MALAYSIAN JOURNAL OF ANALYTICAL SCIENCES
Published by The Malaysian Analytical Sciences Society
ISSN 1394 - 2506

TOTAL FLAVONOIDS AND PHENOLIC CONTENTS OF STICKY AND HARD PROPOLIS FROM 10 SPECIES OF INDO-MALAYAN STINGLESS BEES

(Jumlah Kandungan Flavonoid dan Fenolik dalam Propolis yang Melekit dan Keras daripada 10 Spesis Lebah Kelulut Indo-Malayan)

Norafiza Awang[1], Nora'aini Ali[1]*, Fadzilah Adibah Abd Majid[2], Sofiah Hamzah[1], Shamsul Bahri Abd Razak[3]

[1]*School of Ocean Engineering*
[2]*Institute Marine Biotechnology*
[3]*School of Food Science and Technology*
Universiti Malaysia Terengganu, 21030 Kuala Nerus, Terengganu, Malaysia

**Corresponding author: noraaini@umt.edu.my*

Received: 16 April 2017; Accepted: 7 March 2018

Abstract

The present works aimed to identify the total flavonoids content (TFC), total phenolic content (TPC) and antioxidant activities of sticky and hard propolis of 10 species of Indo-Malayan stingless bee's namely *Heterotrigona itama (H. itama), Geniotrigona thoracica (G. thoracica), Homotrigona aliceae (H. aliceae), Homotrigona fimbriata (H. fimbriata), Tetrigona apicalis (T. apicalis), Tetrigona vidua (T. vidua), Tetrigona peninsularis (T. peninsularis), Lophotrigona canifrons (L. canifrons), Tetrigona melanoleuca (T. melanoleuca),* and *Tetrogona binghami (T. binghami).* The ethanolic extracts of these propolis (EEP) were prepared and analysed for the determination of TFC using aluminium chloride method, TPC and antioxidant activity using the 1,1-diphenyl-2-picrylhydrazyl (DPPH) free radical-scavenging assay system. The sticky propolis showed 91% of TFC and 49% of TPC higher than the hard propolis. Interestingly, the sticky propolis had stronger antioxidant activities than hard propolis for all species. The highest antioxidant activities were found in sticky propolis of *H. itama* which is 85% of DPPH degradation while the lowest antioxidant activity was found in the hard propolis of *L. conifrons* which is 5% of DPPH degradation. In conclusion, the data gathered in this study revealed that propolis from all 10 types of stingless bees' species are biologically active. The selection of propolis for further development can be based on its biological activities, which vary according to the species of stingless bees.

Keywords: stingless bees, propolis, total flavonoids content, total phenolic content

Abstrak

Kajian ini bertujuan untuk mengenal pasti jumlah kandungan flavonoid, jumlah kandungan fenolik dan aktiviti antioksidan dalam propolis yang melekit dan keras daripada 10 spesis lebah kelulut Indo-Malayan iaitu *Heterotrigona itama (H. itama), Geniotrigona thoracica (G. thoracica), Homotrigona aliceae (H. aliceae), Homotrigona fimbriata (H. fimbriata), Tetrigona apicalis (T. apicalis), Tetrigona vidua (T. vidua), Tetrigona peninsularis (T. peninsularis), Lophotrigona canifrons (L. canifrons), Tetrigona melanoleuca (T. melanoleuca),* dan *Tetrogona binghami (T. binghami).* Ekstrak etanolik propolis ini (EEP) telah disediakan dan dianalisis bagi menentukan jumlah kandungan flavonoid (TFC) dengan menggunakan kaedah aluminium klorida, jumlah kandungan fenolik (TPC) dan aktiviti antioksidan menggunakan 1,1-difenil-2-pikrilhidrazil (DPPH) sistem ujian berasaskan radikal bebas. Propolis yang melekit menunjukkan TFC 91% dan TPC 49% lebih tinggi daripada propolis keras. Menariknya, propolis yang melekit mempunyai aktiviti antioksidan yang lebih kuat daripada propolis keras untuk semua spesies. Aktiviti antioksidan tertinggi didapati dalam propolis yang melekat *H. itama* 85% degradasi DPPH manakala aktiviti antioksidan paling rendah didapati dalam propolis keras *L.conifrons* 5% degradasi DPPH. Kesimpulannya, data yang dikumpul dalam kajian

ini mendedahkan bahawa propolis dari semua 10 jenis lebah adalah spesies biologi aktif. Pemilihan propolis untuk pembangunan selanjutnya boleh berdasarkan aktiviti biologinya, yang bervariasi mengikut spesies lebah tanpa ragu-ragu.

Kata kunci: lebah kelulut, propolis, jumlah kandungan flavonoid, jumlah kandungan fenolik

Introduction

According to EPU (2009), Malaysia is one of the world's 12-mega biodiversity countries, with a highly rich natural and environmental resources [1, 2]. One of these natural sources is the species of stingless bees. Stingless bees reap resins from different types of plant and take them back to the hive where they are then used as propolis (propolis is an apicultural term for the resins when utilized by stingless honey bees inside a hive) [3, 4].

Propolis is an important material, which is used by stingless bees to protect their hive and also to support their honey pot. The glue-like propolis is composed of various types of plant resins, waxes and pollens. Propolis contains a classification of chemical compounds, for example, polyphenols like flavonoid aglycones, phenolic acids and their esters, phenolic aldehydes, alcohols and ketones, sesquiterpene quinones, coumarins, steroids, amino acids and inorganic compounds. Moreover, propolis samples contain more than 160 constituents, and their structure contrasts incredibly because of the varieties of their topographical and natural birthplace [5-7]. The presence of different types of plants will also influence the types of physical and chemical properties in the propolis.

Malaysian stingless bees produce two types of propolis, the sticky and hard propolis. Figure 1 (a) and (b) shows the difference between sticky and hard propolis of stingless bees. The most common domesticated species in Malaysia are *Heterotrigona itama (H. itama)* and *Geniotrigona thoracica (G. thoracica)* producing sticky propolis. The stingless bees that produce hard propolis are *Homotrigona aliceae (H. aliceae), Homotrigona fimbriata (H. fimbriata), Tetrigona apicalis (T. apicalis), Tetrigona vidua (T. vidua), Tetrigona peninsularis (T. peninsularis), Lophotrigona canifrons (L. canifrons), Tetrigona melanoleuca (T. melanoleuca),* and *Tetrogona binghami (T. binghami)* (refer Table 1).

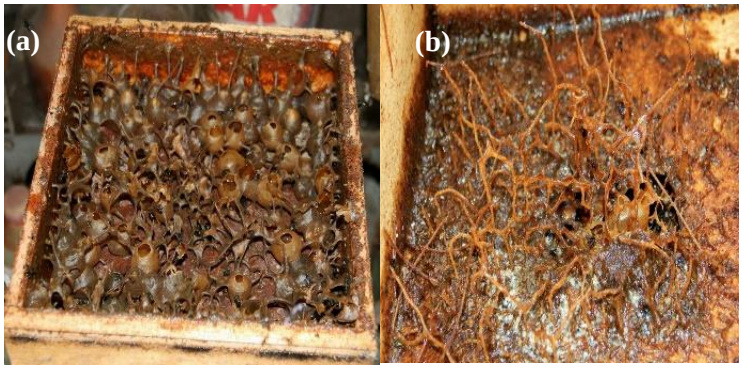


Figure 1. Types of propolis (a) sticky propolis (b) hard propolis

Propolis was found to have different types of medicinal activities such as anti-septic, anti-bacterial, anti-cancer, anti-mycotic, anti-inflammatory, anti-protozoan, astringent, and anti-viral [8-10]. Consequently, propolis based health products are claimed to have high amount of nutrients and antioxidants and are beneficial for health and wellbeing. It is proposed that the propolis biological activities mainly depend on the presence of a large amount of flavonoids [8-10].

The biological activities of stingless bee propolis in Malaysia are not yet well studied. Some of activities, such as antioxidant properties have been found in the ethanolic extracts of propolis, and recently, *H. itama* propolis was reported to have the highest inhibition percentage of anti-radical activity (DPPH), followed closely by *G. thoracica* propolis [11]. At present, hardly any available literature reports the studies on the antioxidant property or chemical

constituents of hard propolis. Therefore, this study was conducted to initiate the screening of nutraceutical properties of sticky and hard propolis from the different stingless bees' species in Malaysia.

In this study, the scavenging of diphenyl picrylhydrazyl (DPPH) was conducted through colorimetric method for determining free radical-scavenging activity. The aluminium nitrate method was conducted to identify the total flavonoid content, and the Folin-Ciocalteu method was used to determine the total phenolic content. It is expected that there will be variations in the nutraceutical values of the propolis from different species of stingless bees.

Materials and Methods

Chemicals and reagents

Aluminium chloride ($AlCl_3$) and all solvents were purchased from Merck, Germany. 1,1-diphenyl-2-picrylhydrazyl (DPPH) and Folin Ciocalteu's reagent were purchased from Sigma-Aldrich, USA. All chemicals and reagents used were analytical grade.

Collection and preparation of propolis

The propolis samples from ten species of Indo-Malayan stingless bees collected from Taman Pertanian Sekayu, Terengganu in April 2016. Each sample was freezing in -10 ºC, then ground to powder and kept desiccated up to their processing.

Extraction

Crude propolis (10 g) was extracted with 70% ethanol (100 ml) through mixing for 24 hours at room temperature. The crude extract was recovered by centrifugation at 27 000 x g for 20 minutes. The insoluble portion was then separated by filtration using filter paper and the filtrates were kept in a freezer at -10 ºC overnight. Then, they are filtered again to reduce the wax content of the extracts. The solvent was evaporated off in a vacuum oven at a temperature of 60 ºC to obtain dry ethanolic extract.

Preparation of standard solution

Gallic acid and Quercetin 10 mg were accurately weighed into a 10 ml volumetric flask, and were dissolved in 10 ml ethanol. The solution was made up to 10 ml with the same solvent [1 mg/ml].

Determination of total phenolic content

Total Phenolic Content (TPC) in EEP were determined according to the Folin-Ciocalteu colorimetric method [12-13]. Gallic acid was used as a standard, and the total phenolics were expressed as mg/g Gallic Acid equivalents (GAE). Consequently, 1 ml of standard solution of concentration 1.95, 3.9, 7.8, 15.63, 31.25 and 62.5 mg/ml of gallic acid were prepared in ethanol. 1 mg/ml propolis extracts with concentration of 1:10 (0.1) were also prepared in ethanol and 0.5 ml of each sample were introduced into the test tubes and mixed with 0.5 ml of the Folin-Ciocalteu reagent and 0.5 ml of 7.5% sodium carbonate, Na_2CO_3. The absorbance was read at 760 nm after 2 hours of incubation in the dark at room temperature.

Determination of total flavonoids content

Aluminium chloride method was used for flavonoids determination. In this method, Quercetin was used as standard and flavonoid contents were measured as Quercetin equivalent. 1 ml of standard solution of concentration 1.95, 3.9, 7.8, 15.63, 31.25, 62.5 and 125 mg/ml of Quercetin were prepared in ethanol. 1 mg/ml of propolis extracts, with the concentration of 1:10 (0.1) were also prepared in ethanol and 0.5 ml of each sample were introduced into the test tubes and mixed with 0.5 ml of fresh 2% of Aluminium chloride, $AlCl_3$ ethanol solution. After being placed in the dark at room temperature for one hour, the absorbance was measured at 420 nm [14].

DPPH radical scavenging activity

The DPPH free radical scavenging activity was evaluated using Blois method with slight modification [15]. The DPPH solution (0.2 mM) was prepared in methanol and 100 µl to 100 µl of the sample extracts, 5.0, 2.5, 1.25, 0.6, 0.3, 0.16, 0.08, 0.04, 0.02, 0.01, 0.005 (mg/ml). The resulting extracts solutions were kept at room temperature in a dark place for 30 minutes. The absorbance was measured at 515 nm. Moreover, the radical scavenging activity was

expressed as the inhibition percentage, and was calculated using the following formula, while Ascorbic acid was used as a positive control:

$$\%\text{Radical scavenging activity} = [(\text{Abs Control} - \text{Abs Sample})/ (\text{Abs Control}] \times 100\% \quad (1)$$

Results and Discussion

Physical evaluation of 10 species of Indo-Malayan stingless bees

Stingless bees produce propolis as part of their defense system to protect their hives from invaders and microbial attacks. In this study, propolis produced by 10 species of stingless bees were collected and each different species of stingless bee has different physical attributes, such as their types of propolis base. Table 1 shows the different species of Indo-Malayan stingless bees propolis and their propolis physical base.

Table 1. Types of physical base propolis of stingless bee

Sticky Propolis	Hard Propolis
Heterotrigona itama (H. itama) and *Geniotrigona thoracica (G. thoracica)*	*Homotrigona aliceae (H. aliceae), Homotrigona fimbriata (H. fimbriata), Tetrigona apicalis (T. apicalis),Tetrigona vidua (T. vidua),Tetrigona peninsularis (T. peninsularis), Lophotrigona canifrons (L. canifrons), Tetrigona melanoleuca (T. melanoleuca),* and *Tetrogona binghami (T. binghami).*

TFC and TPC of propolis stingless bees

The TFC was calculated from the regression equation of the standard plot ($y = 0.016x - 0.0171$, $r^2=0.997$) and is expressed as quercetin equivalents (QE). The flavonoid contents can be determined in the sample extract by using aluminium chloride method at wavelength of 415 nm [16]. Several studies reported that the total flavonoids content that present in propolis extract significantly contributed to their antioxidant activities [7, 17-18]. It has been shown to be good scavengers of most oxidizing molecules, including single oxygen and various free radicals.

The TPC was determined using the Folin-Ciocalteu reagent. The result of TPC was calculated from the regression equation of the standard plot ($y = 0.0417x + 0.0299$, $r^2 = 0.999$). The TPC in propolis play the key role as primary antioxidants or free radical scavengers. The antioxidant activity of the TPC is mainly due to their redox properties, which an important role in absorbing and neutralizing free radicals, quenching singlet and triplet oxygen or decomposing peroxides [19]. In this regard, the bioactivity of phenolics may be related to their ability to chelate metals, inhibit. lipoxygenase and scavenge free radicals [20-21]. TFC and TPC of each stingless bee species are summarized in Figure 2 and Table 2.

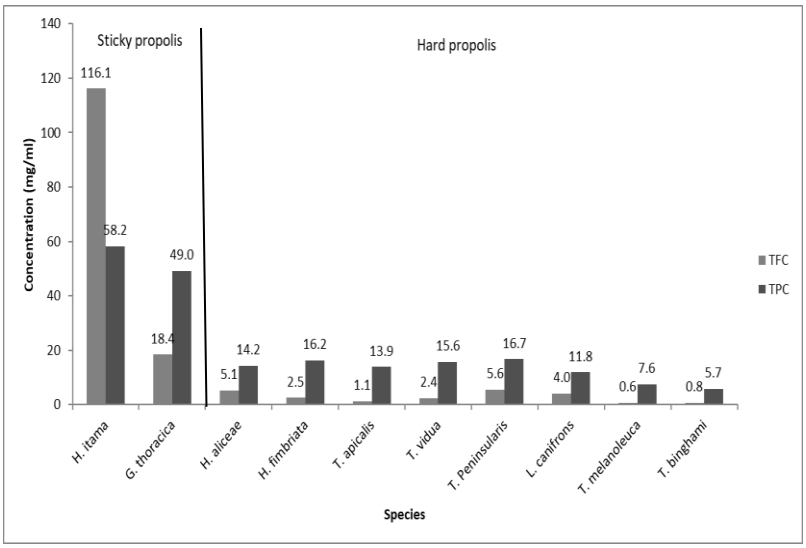


Figure 2. Total flavonoids content and total phenolic content of stingless bees' species

Table 2. Mean values and standard deviations of TFC and TPC found in sticky and hard propolis extracts

Samples Extracts	TFC (mg/ml)	TPC (mg/ml)
H. itama	116.1 ± 3.93	58.2 ± 2.97
G. thoracica	18.4 ± 0.69	49.0 ± 1.03
H. aliceae	5.1 ± 0.32	14.2 ± 0.52
H. fimbriata	2.5 ± 0.47	16.2 ± 1.24
T. apicalis	1.1 ± 0.29	13.9 ± 1.05
T. vidua	2.4 ± 0.45	15.6 ± 0.61
T. Peninsularis	5.6 ± 0.30	16.7 ± 0.32
L. canifrons	4.0 ± 0.20	11.8 ± 1.12
T. melanoleuca	0.6 ± 0.06	7.6 ± 0.35
T. binghami	0.8 ± 0.34	5.7 ± 0.45

The maximum concentration of TFC found in the ethanolic extract of propolis was 116.1 mg/ml from the *H. itama* species, while the lowest comes from the *T. melanoleuca* species with 0.6 mg/ml. The amount of TPC was found to be high in *H. itama* propolis extract (58.2 mg/ml), compared to the TPC, which was lower in the sample of *T. binghami* propolis extract (5.7 mg/ml). Meanwhile, for both the sticky base propolis of *H. itama* propolis extract and *G. thoracica* propolis extract, the *H. itama* propolis extract contains high amount of flavonoids content, compared to *G. thoracica* propolis extract which were 116.1 mg/ml and 18.4 mg/ml, respectively. Similarly, the *H. itama* propolis extract possesses large quantities of phenolic content compared to *G. thoracica* propolis extract, which were 58.2 mg/ml and 18.4 mg/ml, respectively. The results obtained from the present study show that the propolis extract of *H. itama* species, which contains the highest amount of TFC and TPC, followed by propolis extract of *G. thoracica* species, exhibited the greatest antioxidant activity. The sticky propolis showed 91% of TFC and 49% of TPC higher than the hard propolis. Previous study has been reported that TPC and TFC of *H. itama* was higher than *G. thoracica* [21]. Thus, both sticky base propolis of *H. itama* and *G. thoracica* species have more potential to be developed as part of new drugs, compared to harden base propolis of *H. aliceae, H. fimbriata, T. apicalis, T. vidua, T. peninsularis, L. canifrons, T. melanoleuca*, and *T. binghami*. Moreover, it is clearly understood that the phenolic compounds and flavonoids are the chief components of propolis and account for

antioxidant properties. The variation in the TFC of propolis is mainly attributable to the difference in the preferred regional plants pollinated by the stingless bees. In this regard, the content of flavonoids and other phenolic substances are suggested as able to prevent cancer and heart diseases [22].

Free radical-scavenging activity

In order to evaluate the dose-response curve for the free radical-scavenging activity of ethanol extract of propolis, a method based on the reduction of DPPH a stable free radical, was used. The use of DPPH to scavenge radicals has advantages, including being easy to use, highly sensitive and able to analyze of large numbers of samples in a short time. The DPPH is a free radical compound that has been widely used to analyze the free radical scavenging ability of various samples [23]. It is approved that the DPPH free radical scavenging through antioxidants is caused by their hydrogen-donating ability [24]. To evaluate the scavenging effect of DPPH on ethanol extract of propolis, DPPH inhibition was investigated and the results are shown as relative activities against control, as well as the variation of inhibition percentage. As shown in Figure 3, ascorbic acid has the highest inhibition percentage (antiradical activity), closely followed by *H. itama* and the *L. canifrons* has the lowest and the defenses are statistically significant. Meanwhile, although ascorbic acid showed higher scavenging activity for all tested samples, ethanol extracts of propolis of sticky propolis still showed good free radical scavenging activity compared to ethanol extracts of propolis of harden propolis.

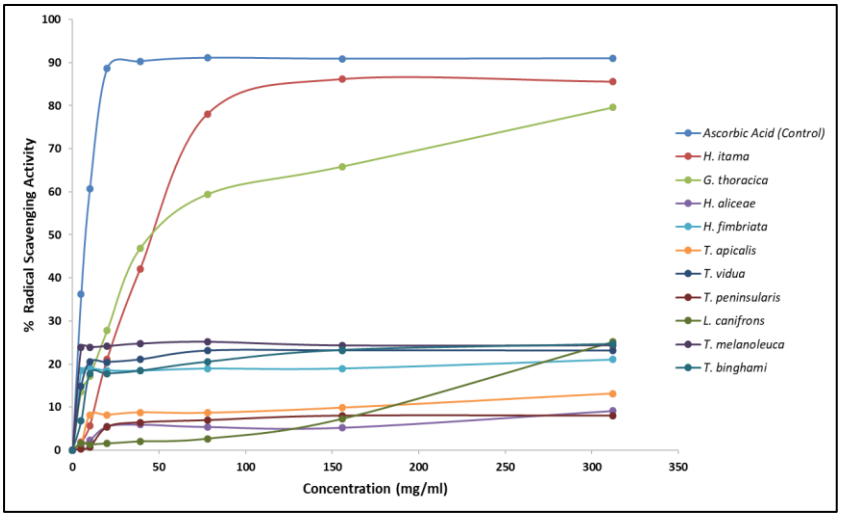


Figure 3. Free radical-scavenging activity of propolis stingless bees

In general, these findings demonstrate that the antioxidant activity was correlated with total polyphenol contents in propolis samples. In this light, the antioxidant activity of propolis is due to the presence of phenolic acids and flavonoid compounds, which have ability to reduce free radical formation, scavenge free radicals and chelate metal ions [18]. The highest antioxidant activities were found in sticky propolis of *H. itama* which is 85% of DPPH degradation while the lowest antioxidant activity was found in the hard propolis of *L. conifrons* which is 5% of DPPH degradation. The results showed that the sticky propolis extract from the *H. itama* and *G. thoracica* species possess higher free radical-scavenging activity which shows it suitability to be used as a source of natural antioxidants, compared to hard propolis [25]. The reasons behind the marked higher radical scavenging activity exhibited by different types of propolis are probably due to their resin plant origin, climate, and resin collection time by the stingless bees.

Conclusion

This study shows that stingless bees species play a role in determining the phytochemical and antioxidant activity. This is the first report on the antioxidant activity of Malaysian propolis which, presents the comparison between sticky and hard propolis, particularly two commonly sticky propolis produced by *H. itama* and *G. thoracica* species

and the other hard propolis of *H. aliceae, H. fimbriata, T. apicalis, T. vidua, T. peninsularis, L. canifrons, T. melanoleuca,* and *T. binghami* species. In this regard, the propolis samples have strong antioxidant activities, and the strongest activity was found in the *H. itama* propolis which was came from sticky propolis. Consequently, the data presented in this study will shed some light on the potential of propolis produced by stingless bees in Malaysia. In this light, further investigations on the identification of marker compounds should be carried out to be use in propolis standardization.

Acknowledgement

This paper is fully supported by Fundamental Research Grant Scheme (Vot 59438), Ministry of Higher Education (MOHE) and University Malaysia Terengganu by the approved fund.

References

1. Prime Minister's Department, Malaysia (2009). Economic planning unit. Access from http://www.epu.gov.my/web [Online 18 November 2009].
2. Talaat, W. I. A. W., Tahir N. M. and Mohd L. H. (2012). Sustainable management of forest biodiversity and the present Malaysian policy and legal framework. *Journal of Sustainable Development*, 5(3): 76-83.
3. Bankova, V., Trusheva, B. and Popova M. (2008). new developments in propolis chemical diversity studies. *Transworld Research Network*: pp. 1-13.
4. Banskota A. H., Tezuka Y. and Kadota S. (2001). Recent progress in pharmacological research of propolis. *Phytotherapy Research*, 15(7): 561-571.
5. Ghisalberti, E. L. (1979). Propolis: A review. *Bee World*, 60: 59-84.
6. Greenaway, W., May, J., Scaysbrook, T. and Whatley, F. R. (1991). identification by gas chromatography-mass spectrometry of 150 compounds in propolis. *Zeitschrift für Naturforschung,* 46(1-2): 111-121.
7. Bonvehí Josep, S. and Coll Francesc, V. (1994). Phenolic composition of propolis from China and from South America. *Zeitschrift für Naturforschung,* 49(11-12): 712-718.
8. Bankova, V., Dyulgerov, A., Popov, S. and Marekov, N. (1987). A GC/MS study of the propolis phenolic constituents. *Zeitschrift für Naturforschung,* 42(1-2): 147-151.
9. Bonvehí, J. S., Coll, F. V. and Jordà, R. E. (1994). The composition, active components and bacteriostatic activity of propolis in dietetics. *Journal of the American Oil Chemists' Society,* 71(5): 529-532.
10. Vennat, B., Arvouet-Grand, A., Gross, D. and Pourrat, A. (1995). Qualitative and quantitative analysis of flavonoids and identification of phenolic acids from a propolis extract. *Journal De Pharmacie De Belgique*, 50: 438-444.
11. Ibrahim, N., Farah Shakila Mohd Niza, N., Rodi, M., Jamil Zakaria, A., Ismail, Z. and Mohd, K. (2016). Chemical and biological analyses of Malaysian stingless bee propolis extracts. *Malaysian Journal of Analytical Sciences*, 20(2): 413-422.
12. Singleton, V. L., Orthofer, R. and Lamuela-Raventós, R. M. (1999). Analysis of total phenols and other oxidation substrates and antioxidants by means of Folin-Ciocalteu reagent. *Methods in Enzymology*, 299: 152-178.
13. Kumazawa, S., Taniguchi, M., Suzuki, Y., Shimura, M., Kwon, M. S. and Nakayama, T. (2002). Antioxidant activity of polyphenols in carob pods. *Journal of Agricultural and Food Chemistry*, 50(2): 373-377.
14. Chang, C., Yang, M. and Wen, H. (2002). Estimation of total flavonoid content in propolis by two complementary colorimetric methods. *Journal of Food Drug Analysis*, 10(3): 178-182.
15. Blois, M. S. (1958). Antioxidant determinations by the use of a stable free radical. *Nature*, 181: 1199-1200.
16. Abu Bakar, M. F., Mohamed, M., Rahmat, A. and Fry, J. (2009). Phytochemicals and antioxidant activity of different parts of bambangan (*Mangifera pajang*) and Tarap (*Artocarpus odoratissimus*). *Food Chemistry*, 113(2): 479-483.
17. Isla, M. I., Nieva Moreno, M. I., Sampietro, A. R. and Vattuone, M. A. (2001). Antioxidant activity of argentine propolis extracts. *Journal of Ethnopharmacology*, 76(2): 165-170.
18. Kumazawa, S., Hamasaka, T. and Nakayama, T. (2004). Antioxidant activity of propolis of various geographic origins. *Food Chemistry*, 84(3): 329-339.
19. Osawa, T. (1994). Novel natural antioxidants for utilization in food and biological systems. postharvest biochemistry of plant food-materials in the tropics. Japan Scientific Press, Tokyo, Japan: pp. 241-251.

20. Mallavadhani, U. V., Sudhakar, A. V. S., Satyanarayana, K. V. S., Mahapatra, A., Li, W. and vanBreemen, R. B. (2006). Chemical and analytical screening of some edible mushrooms. *Food Chemistry*, 95(1): 58-64.
21. Ibrahim, N., Zakaria, A. J., Ismail, Z. and Mohd, K. (2016). Antibacterial and phenolic content of propolis produced by two Malaysian stingless bees, *Heterotrigona itama* and *Geniotrigona thoracica*. *International Journal of Pharmacognosy and Phytochemical Research*, 8(1): 156-161.
22. Lin, S. Y., Liu, H. Y., Lu, Y. L. and Hou, W. C. (2005). Antioxidant activities of mucilages from different Taiwanese yam cultivars. *Botanical Bulletin of Academia Sinica*, 46: 183-188.
23. Kahkonen, M. P., Hopia, A. I., Vuorela, H. J., Rauha, J. P., Pihlaja, K., Kujala, T. S. and Heinonen, M. (1999). Antioxidant activity of plant extracts containing phenolic compounds. *Journal of Agricultural and Food Chemistry*, 47(10): 3954-3962.
24. Hatano, T., Takagi, M., Ito, H. and Yoshida, T. (1997). Phenolic constituents of liquorice. VII. A new chalcone with a potent radical scavenging activity and accompanying phenolics from liquorice. *Chemical and Pharmaceutical Bulletin*, 45(9): 1485-1492.
25. Tang, S. Z., Kerry, J. P., Sheehan, D. and Buckley, D. J. (2002). Antioxidative mechanisms of tea catechins in chicken meat systems. *Food Chemistry*, 76(1): 45-51.

Malaysian Journal of Analytical Sciences, Vol 22 No 5 (2018): 885 - 891
DOI: https://doi.org/10.17576/mjas-2018-2205-16

MALAYSIAN JOURNAL OF ANALYTICAL SCIENCES
Published by The Malaysian Analytical Sciences Society
ISSN 1394 - 2506

LIQUID NATURAL RUBBER TOUGHENED POLY(LACTIC ACID) BLEND: EFFECTS OF COMPATIBILIZER TYPES AND LOADINGS ON THERMO-MECHANICAL PROPERTIES

(Adunan Asid Polilaktik Diperkuat Getah Asli Cecair: Kesan Jenis dan Kandungan Penserasi Terhadap Sifat Terma-Mekanik)

Mohd Farid Hakim Mohd Ruf, Sahrim Ahmad, Ruey Shan Chen*, Dalila Shahdan, Farrah Diyana Zailan

School of Applied Physics,
Faculty of Science and Technology,
Universiti Kebangsaan Malaysia, 43600 UKM Bangi, Selangor, Malaysia

**Corresponding author: chen@ukm.edu.my*

Received: 20 July 2017; Accepted: 28 April 2018

Abstract

This research was carried out to investigate the addition of grafted copolymers of maleic anhydride grafted-polylactic acid (PLA-g-MA) and maleic anhydride grafted-natural rubber (NR-g-MA) on the mechanical and thermal properties of polylactic acid/ liquid natural rubber (PLA/LNR) blends. Prior to blend preparation, the PLA-g-MA and NR-g-MA were the first self-synthesized by mixing maleic anhydride (MA) and dicumyl peroxide (DCP) which acted as initiator with the PLA and natural rubber (NR), respectively. The PLA/LNR, PLA/LNR/PLA-g-MA and PLA/LNR/NR-g-MA blends were prepared *via* melt-blending method. The loading of PLA-g-MA and NR-g-MA was varied between 5, 10 and 15%, respectively. By comparing to the control sample (neat PLA/LNR blend), the addition of PLA-g-MA with 5 and 10% led to increment in tensile strength up to 22 MPa, whereas NR-g-MA promoted a negative trend of tensile properties to the blends. Differential scanning calorimetry (DSC) and thermogravimetry analysis (TGA) results showed the enhanced thermal stability for PLA/LNR/PLA-g-MA blend. Fourier transform infrared (FTIR) analysis confirmed the chemical interaction between the PLA and NR components where the grafted copolymers were successfully grafted onto PLA backbone and bonded with NR.

Keywords: polymer blend, polylactic acid, toughening agent, compatibilizer, thermal

Abstrak

Kajian ini dijalankan bagi mengkaji kesan penambahan kopolimer maleik anhidrida cantuman-asid polilaktik (PLA-g-MA) dan maleik anhidrida cantuman-getah asli (NR-g-MA) terhadap sifat mekanik and terma polimer adunan asid polilaktik/cecair getah asli (PLA/CGA). Sebelum penyediaan adunan, PLA-g-MA dan NR-g-MA terlebih dahulu disintesiskan dengan mengadun maleik anhidrida (MA) dan dikumil peroksida (DCP) yang bertindak sebagai pemula bersama dengan PLA dan getah asli (GA). Adunan PLA/LNR, PLA/LNR/PLA-g-MA dan PLA/LNR/NR-g-MA disediakan dengan menggunakan kaedah pengadunan dalaman. Kandungan PLA-g-MA dan NR-g-MA masing-masing divariasikan kepada 5, 10 dan 15%. Berbanding dengan sampel kawalan (adunan PLA/LNR), penambahan PLA-g-MA sebanyak 5 dan 10% memberikan peningkatan terhadap kekuatan tegangan sehingga 22 MPa manakala NR-g-MA memberikan corak penurunan terhadap adunan. Keputusan kalorimeter pemgimbasan pembezaan (DSC) dan analisa termogravimetri (TGA) menunjukkan peningkatan kestabilan terma adunan PLA/LNR/PLA-g-MA. Analisa spektroskopi inframerah transformasi Fourier (FTIR) membuktikan interaksi kimia berlaku antara komponen PLA dan NR di mana kopolimer cantuman berjaya dicantum pada tulang belakang PLA dan diikat dengan NR.

Kata kunci: polimer adunan, asid polilaktik, agen penguat, penserasi, terma

Introduction

Polymer blending is well known as an effective method for improving nature physical properties of one or both individual components. Unfortunately, polymer blends are mostly not miscible. To solve this immiscibility issue, the utilization of coupling agent or compatibilizer is required to improve the interfacial adhesion between the inherently immiscible polymeric components, which subsequently increasing the mechanical and other properties of blends. For instance, previous study reported that the incorporation of ethylene-glycidyl methacrylate (E-GMA) as compatibilizer had improved the compatibility of the recycled high-density polyethylene/polyethylene terephthalate (HDPE/PET) blend which subsequently resulted in the increase of mechanical properties [1]. The improvement of polymer blending properties can be achieved by the addition of toughening agent like co-polymer block and liquid natural rubber (LNR) [2]. LNR has been synthesized via a photodegradation method by cutting natural rubber (NR) into small cubes prior to mixing in the solution containing toluene solvent, methylene blue, rose Bengal and methanol. LNR was formed after the exposure under ultraviolet for approximately 12-20 days [3]. The addition of LNR has successfully increased the mechanical properties such as tensile and impact strength in polymer blends and composites [2, 3].

In order to obtain better adhesion between the blending components, some modification are required [4]. One of the cheapest and simplest methods is by using the self-synthesized compatibilizer. The synthesis of compatibilizer usually involves a free radical grafting polymerization in which the monomers are often grafted onto polar polymer backbones. Maleic anhydride (MA) was selected as the main functional group for compatibilizing/coupling agent and the maleic copolymers have been extensively used for grafting onto the binary immiscible polymer blends in the previous research works [5, 6]. By adding the MA, the properties and interfacial adhesion of the blends were enhanced [7]. As reported by Orozco and his coworkers, the blending of PLA grafted with starch led to the better interaction as compared to the blend without the addition of MA as compatibilizer [5]. Besides, the incorporation of NR-g-MA promoted compatibilization for various blends and composites such as natural rubber/short nylon fiber composites and acrylonitrile-butadiene copolymer (NBR) [8, 9], thereby has resulted in the increase of modulus and tensile strength. Rui and his coworkers also reported that the incorporation of grafted MA compatibilizer gave better tensile property and improved interfacial adhesion of PLA/soy protein concentrate (SPC) composites [10].

Numerous published research works have been reported on the use of PLA or PLA/LNR as the matrix in the composites, such as PLA/PP blends [11], PLA/LNR/NiZn ferrite [12], and etc. Nevertheless, the shortcomings of these matrices should be highlighted which are the brittleness of PLA but the toughening effect on PLA can be imparted by LNR (PLA/LNR). However, the PLA/LNR somehow showed the incompatibility problem which thereby restricting the properties. In this aspect, the modification of PLA/LNR matrix is required. The aim of this research was to investigate the effect of adding different types of self-synthesized compatibilizers (PLA-g-MA or NR-g-MA) into the PLA/LNR blends and the compatibilizer loadings on the mechanical, thermal and chemical properties of the blends.

Materials and Methods

Materials

Polylactic acid (PLA) was purchased from Nature Works LLC, UNIC Technology (SUZHOU) LTD with average molecular weight 5.5 x 10^4 g/mol, relative viscosity of 2.5, melt flow index of 35 g/10min and melting point of 160-170 ^oC . SMR-L grade natural rubber (NR) with molecular weight 2.5 x 10^6 g/mol was obtained from Malaysian Rubber Board (MRB). Maleic Anhydride (MA) with 99% purity, molecular weight of 98.06 g/mol and dicumyl peroxide (DCP) were purchased from Aldrich Chemistry company.

Preparation of liquid natural rubber

The liquid natural rubber (LNR) was synthesized using photochemical degradation or an oxidation technique of NR [13]. About 1.5 kg of NR were cut into small pieces and soaked in 60 cm^3 glass flask that filled with approximately 4000 ml of toluene for 24 hours. After that, 0.3 g of methylene blue, 0.39 g of rose Bengal and 15 ml of methanol were added to the mixture. The mixture was stirred continuously by a mechanical stirrer at 10 rpm under the exposure to visible light for 10 days.

Preparation of maleic anhydride grafted - polylactic acid and - natural rubber

Before use, PLA pellets were dried for 24 hours at 60 ^{o}C in an oven to eliminate the moisture. The DCP was used asan initiator. The composition of MA and DCP was fixed at 3.6 and 9 phr, respectively [4, 14]. The grafting of MA onto PLA was carried out by using the internal mixer. Firstly, PLA pellets were fed into internal mixer until it was fully melted before adding DCP. For the next 3 min, MA was added and left for 15 min. The temperature of internal mixer was set at 190 ^{o}C and the screw speed was set at 80 rpm. The obtained grafted copolymers were then cut into small pieces to be used in the blending with PLA and LNR.

Blending preparation

In the presence and absence of compatibilizer, PLA/LNR blends were prepared using an internal mixer (Haake Rheomix 600P) with a processing mixing temperature at 190 ºC, a rotor speed of 80 rpm and mixing time of 15 min. The PLA/LNR was fixed at the ratio of 90:10 (wt:wt), whereas PLA-g-MA and NR-g-MA were added at 5, 10 and 15%, respectively. PLA was first placed into the mixer and allowed to melt for about 4 minutes, followed by the introduction of LNR which took another 3 minutes. Finally, the grafted copolymers were added into the mixing and it was completed in 15 minutes. After blending process, the samples were prepared *via* compression moulding using a hot press machine (LABTECH Engineering Company LTD) under pressure 6.9 MPa at 190 °C. A 3 mm dumb bell shape mould was used for moulding process. The periods for compression moulding were set as 4 minutes for pre-heating and venting process, 5 minutes for full pressing and 3 minutes for cool pressing.

Characterization

The tensile test of the samples was conducted using tensile machine (model Testometric M500-50CT) with 10 kN load cell at a crosshead speed of 5 mm/min according the standard ASTM D638-03. At least five samples were tested for each composition. The thermal tests were carried out using Thermogravimetric Analyzer (model Shimadzu DSC-60 Plus Series) and Differential Scanning Calorimetry (model Shimadzu DTG-60). A chemical analysis was conducted by using FTIR-Near infrared instrument (model Perkin Elmer Spectrum 400 FT-IR). The samples were scanned from 650 to 4000 cm^{-1}.

Results and Discussion

Tensile properties

Figure 1 shows the effect of PLA-g-MA loading on the (a) tensile strength and (b) Youngs modulus of the blends. By adding 5% of PLA-g-MA, it showed a slight increment in tensile strength, which increased about 2%. The optimum tensile strength was achieved at 10% PLA-g-MA (~22 MPa), which increased by approximately 15%. The great improvement in the blend properties suggests that the presence of PLA-g-MA has promoted a better compatibility and stronger adhesion between the PLA and LNR components and thus promoting a more homogeneous blend. As the loading of PLA-g-MA increased up to 15%, the tensile strength showed a significant reduction. The reduction in tensile properties was due to the less uniform and weak adhesion of the components in the blends. For NR-g-MA, the tensile strength showed a gradual reduction upon the increase of NR-g-MA loading from 5 to 15%. The reduction could be due to rubbery nature of NR [15].

On the other hand, the presence of PLA-g-MA resulted in a lower Young's modulus value, which decreased about 12% than that of PLA/LNR blend (Figure 1(b)). This reduction in Young's modulus was expected and the similar trends have been reported in the previous studies [1, 16]. For both compatibilizers at the loadings of 10 and 15%, the Young's Modulus of both blends was found to be constant as the compatibilizer achieved the optimum loading at 10%. Therefore, it was believed that the ability to withstand the tension has achieved the same level since the compatibilizer was saturated along the interface area in the blends at 15%.

For the elongation at break shown in Figure 1(c), the addition of compatibilizer did not provide positive effect on PLA/LNR blends, as observed by the lower values than that of PLA/LNR, irrespective to the compatibilizer types. The reduction in elongation at break implies the increased brittleness of the blends. By comparing the effectiveness of PLA-g-MA and NR-g-MA, the earlier compatibilizer with 10% (optimum loading) was shown to be more suitable than the latter one.

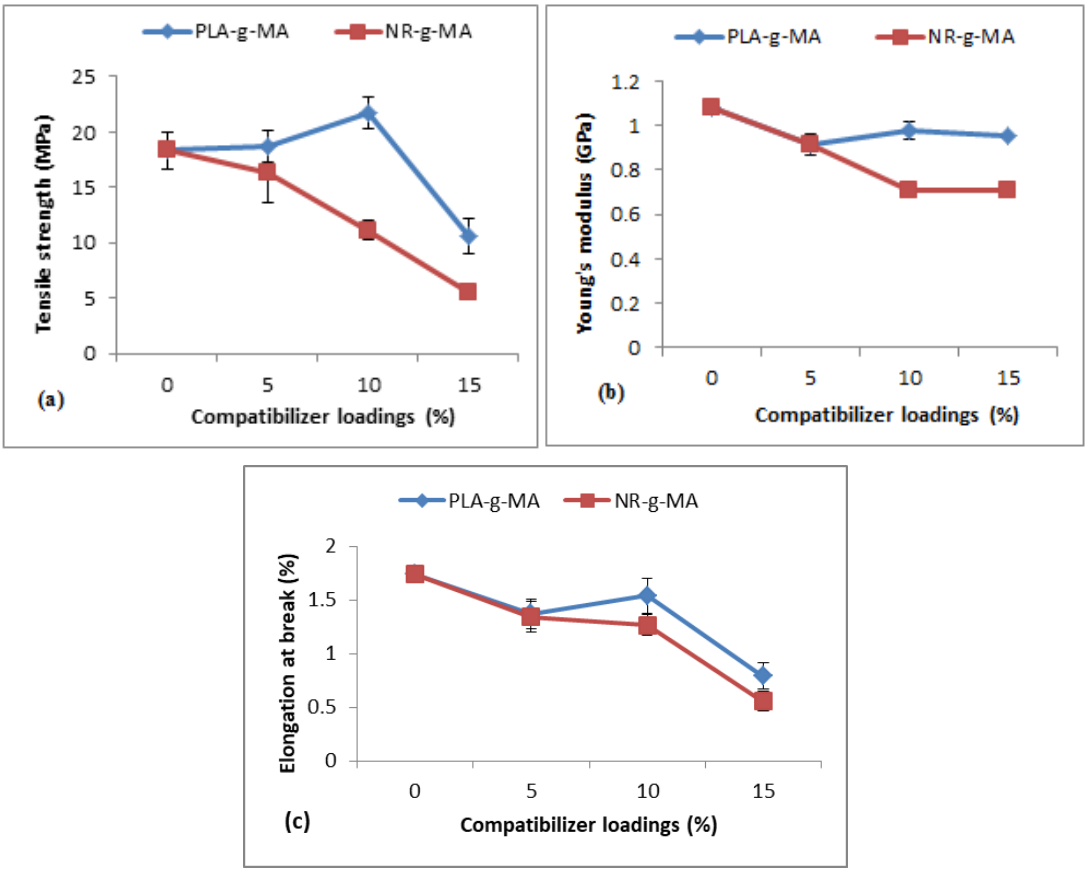


Figure 1. The effect of compatibilizer loadings on (a) tensile strength, (b) Young's modulus and (c) elongation at break of the blends

Thermogravimetric (TGA) Analysis

Figure 2 shows TGA results of PLA/LNR, PLA/LNR/10% PLA-g-MA and PLA/LNR/5% NR-g-MA blends. It can be seen that the TGA curves of the PLA/LNR samples containing compatibilizers delayed the degradation process as compared to that of PLA/LNR without compatibilizer, as shown in inset image over the temperature of 180 - 330 ºC where the weight loss of PLA/LNR occurred before the PLA/LNR/compatibilizer samples. At fixed temperature of about 280 ºC, PLA/LNR exhibited a greater amount of weight loss than those containing compatibilizer, irrespective of the compatibilizer types. This implies that the thermal stability of the blends incorporated with the compatibilizer was improved. These results are in the agreement with the previous studies [15]. Upon heating to the temperature of 400 ºC, the decomposition of PLA/LNR was almost completed with only approximately 0.26% of residues. The PLA/LNR with compatibilizers, especially NR-g-MA exhibited lesser residues than that of neat PLA/LNR. This was attributed to the greater interaction of the compatibilizer with the matrix, which giving a less carbon residue [15].

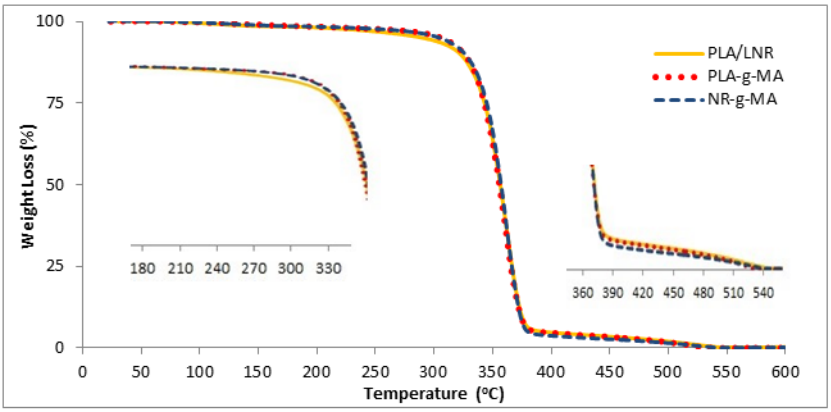


Figure 2. TGA curve of PLA/LNR, PLA/LNR/PLA-g-MA and PLA/LNR/NR-g-MA

Differential scanning calorimetry analysis

Figure 3 shows the DSC curves of the blends which consist of glass transition temperature (T_g), crystallization temperature (T_c) and melting temperature (T_m). The first endothermic peak at around 50 - 60 ºC indicated T_g, T_c was at 85 ºC and T_m took place at around 168 ºC. As can be seen from the curves, PLA/LNR blend exhibited T_g at around 58 ºC, whereas the incorporation of compatibilizer into the blends slightly shifted the curve to the right. For the T_c, it was shown at approximately 85 ºC for PLA/LNR. By incorporating PLA-g-MA, the T_c of the blends shifted to the right with a slight increment by approximately 3 ºC. However, NR-g-MA showed a similar peak with the PLA/LNR. These changes in PLA-g-MA indicate that the incorporation of compatibilizer increased the thermal stability of the blends. Meanwhile, the T_m peak showed a tiny right shift for the compatibilized blend. These phenomena imply that a positive effect on the thermal stability has been induced by the incorporation of compatibilizer into the PLA/LNR blend, and higher effectiveness was achieved by PLA-g-MA. This is attributed to which the grafted copolymers may prohibit the crystal formation and delay the T_c [6].

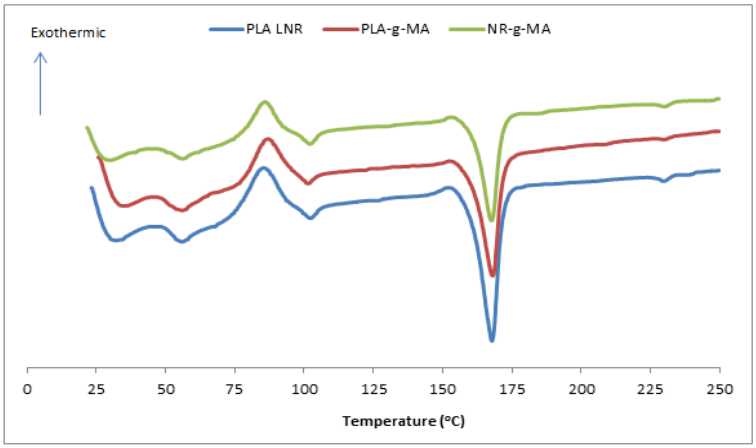


Figure 3. DSC curve of PLA/LNR, PLA/LNR/PLA-g-MA and PLA/LNR/NR-g-MA

Fourier transform infrared analysis

Figure 4 shows IR-spectra of PLA, PLA/LNR, PLA/LNR/PLA-g-MA and PLA/LNR/NR-g-MA blends. For the neat PLA, the peaks that located at 765, 881, 1096, 1191, 1462 and 1755 cm^{-1} are assigned to the stretching vibration of C=O while the peaks at 2858, 2930 and 3316 cm^{-1} are representing the CH_3 stretching of PLA component. PLA exhibited a strong absorption band at 1755 cm^{-1} which corresponds to the C=O stretching of ester

bond. For comparison, the addition of compatibilizer into PLA/LNR exhibits similar spectrum with that of the neat PLA/LNR. By adding the compatibilizer (PLA-g-MA and NR-g-MA) and toughening agent (LNR), a higher intensity of the peak can be observed as compared with PLA itself, exception for the absorption band of 1500-1650 cm^{-1}, 2800-3000 cm^{-1}, 3316 cm^{-1}. For the blends with PLA-g-MA and NR-g-MA compatibilizer, peak at 1755 cm^{-1} had a more intense absorption band as compared to neat PLA and this indicates that the reaction was taken place between MA and PLA backbone [14]. Several peaks at 1579, 1645 and 3316 cm^{-1} which assigned for stretching of PLA were invisible in the spectra of compatibilized blends, and this indicates the chemical reaction occurred between the PLA and grafted MA group. Another small shoulder peak emerged at 1277 cm^{-1} which corresponds to the C=O stretching of carbonyl group of PLA in the PLA-g-MA spectrum. Since the amount of MA used in the blends was relatively small, the C=O stretching of MA or anhydride peak was very weak and may overlap with the carbonyl band of PLA [5].

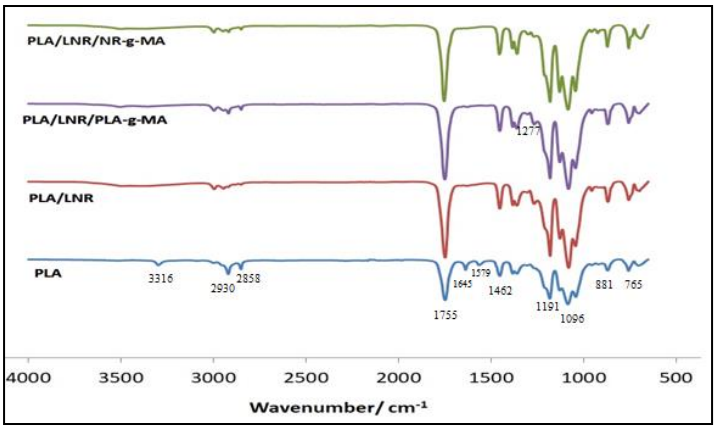


Figure 4. FTIR spectra of PLA, PLA/LNR, PLA/LNR/PLA-g-MA and PLA/LNR/NR-g-MA

Conclusion

The tensile test showed that the PLA-g-MA was more suitable to be a compatibilizer for PLA/LNR blend as compared to NR-g-MA, and the optimum loading of PLA-g-MA was 10% PLA-g-MA. The addition of 10% PLA-g-MA into PLA/LNR blend promoted the tensile strength from the PLA/LNR which acted as the control sample. In TGA and DSC, the incorporation of PLA-g-MA into PLA/LNR blends delayed the T_g and degradation temperature, hence, the thermal stability of the blend was increased. From FTIR analysis, the difference in the spectra between PLA/LNR and compatibilized PLA/LNR blend showed that MA was successfully grafted to PLA backbone.

Acknowledgement

The authors gratefully thank the financial support provided by Universiti Kebangsaan Malaysia (UKM) and under grant of DIP-2016-023. We also appreciate the cooperation given by the staff of Materials Science laboratory (FST), and Electron Microscopy Unit, UKM during the SEM viewing.

References

1. Chen, R. S., Ab Ghani, M. H., Salleh, M. N., Ahmad, S. and Gan, S. (2014). Influence of blend composition and compatibilizer on mecahnical and morphological properties of recycled HDPE/PET blends. *Material Sciences and Applications*, 5: 943-952.
2. Ahmad, S., Ibrahim, A., Che Som, S., Kohjiya, S. and Yoon, J. R. (1994). Natural rubber-HDPE blends with liquid natural rubber as a compatibilizer: thermal and mechanical properties. *Journal of Applied Polymer Science*, 51: 1357- 1363.
3. Lee, Y. S., Ahmad, S. Rasid, R., Se Yong, E. N., Yew, C. H. and Tarawneh, M. A. (2011). Effects of liquid natural rubber (LNR) on the mechanical properties of LNR toughened epoxy composite. *Sains Malaysiana*, 40(7): 679-683.

4. Tsou, C. H., Hung, W. S., Wu, C. S., Chen, J. C., Huang, C. Y., Chiu, S. H., Tsou, C. Y., Yao, W. H., Lin, S. M., Chu, C. K., Hu, C. C., Lee K. R. and Suen, M. C. (2014). New composition of maleic-anhydride-grafted poly(Lactic Acid)/rice husk with methylenediphenyl diisocyanate. *Material Science*, 20: 446-451.
5. Orozco, V. H., Brostow, W., Chonkaew, W. and Lopez, B. L. (2009). Preparation and characterization of poly(lactic acid)-g-maleic anhydride + starch blends. *Maromol Symposium*, 277: 69-80.
6. Mohammad, N. N. B., Arsad, A., Abdullah Sani, N. S. and Basri, M. H. (2017). Effect of compatibilisers on thermal and morphological properties of polylactic acid/natural rubber blends. *Chemical Engineering Transactions*, 56: 1027- 1032.
7. Ma, P., Jiang, L., Ye, T., Dong, W. and Chen, M. (2014). Melt free-radical grafting of maleic anhydride onto biodegradable poly(lactic acid) by using styrene as a comonomer. *Polymers*, 6: 1528-1543.
8. Afifi, H. and El-Wakil, A. A. (2008). Study of the effect of natural rubber-graft-maleic anhydride (NR-g-MA) on the compatibility of NR-NBR blends using the ultrasonic technique. *Polymer-Plastic Technology and Engineering*, 47: 1032-1039.
9. Dong, Z. X., Liu, M. X., Jia, D. M. and Zhou, Y. H. (2013). Synthesis of natural rubber-g-maleic anhydride and its use as a compatibilizer in natural rubber/short nylon fiber composites. *Chinese Journal of Polymer Science*, 31: 1127-1138.
10. Rui, Z., Hongzhi, L. and Jinwen, Z. (2012). Compatibilizing effects of maleated poly(lactic acid) on properties of PLA/soy protein composites. *American Chemical Society*, 51(22): 7786-7792.
11. Bijarimi, M., Ahmad, S. and Rasid, R. (2012). Mechanical, thermal and morphological properties of PLA/PP melt blends. *International Conference on Agriculture, Chemical And Environmental Sciences*: pp. 115-117.
12. Shahdan, D., Ahmad, S. and Flaifel, M. H. (2014). Effect of ultrasonic treatment on tensile properties of PLA/LNR/NiZn ferrite nanocomposite. *AIP Conference Proceedings*, 1571: 75-82.
13. Abdullah, I. (1992). Liquid natural rubber as a compatibilizer in the blending of natural rubber with polypropylene. *Materials Forum*, 16: 353-357.
14. Abdullah Sani, N. S., Arsad, A. and Rahmat, A. R. (2014). Synthesis of a compatibilizer and the effects of monomer concentration. *Applied Mechanics and Materials*, 554: 96-100.
15. Abdullah Sani, N. S., Arsad, A., Rahmat, A. R. and Mohammad N. N. B. (2015). Effects of compatibilizer on thermal and mechanical properties of PLA/NR belnds. *Material Science Forum*, 819: 241-245.
16. Yi, X., Xu, L., Wang, Y. L., Zhong, G. J., Ji, X. and Li, Z. M. (2010). Morphology and properties of isotactic polypropylene/poly(ethyleneterepthalate) in situ microfibrillar reinforced blends: influence of viscosity ratio. *European Polymer Journal*, 46: 719-730.

Malaysian Journal of Analytical Sciences, Vol 22 No 5 (2018): 892 - 898
DOI: https://doi.org/10.17576/mjas-2018-2205-17

MALAYSIAN JOURNAL OF ANALYTICAL SCIENCES
Published by The Malaysian Analytical Sciences Society
ISSN 1394 - 2506

THE EFFECTS OF GLYCEROL ADDITION TO THE MECHANICAL PROPERTIES OF THERMOPLASTIC FILMS BASED ON JACKFRUIT SEED STARCH

(Kesan Penambahan Gliserol pada Sifat Mekanik Filem Thermoplastik Berdasarkan Kanji Biji Nangka)

Nur'Aishah Ahmad Shahrim*, Norshahida Sarifuddin, Hafizah Hanim Mohd Zaki, Ahmad Zahirani Ahmad Azhar

Department of Manufacturing and Materials Engineering,
International Islamic University Malaysia, 53100 Kuala Lumpur, Malaysia

**Corresponding author: aisydahlia@gmail.com*

Received: 20 July 2017; Accepted: 28 April 2018

Abstract

Thermoplastic films based on 3 wt.% jackfruit seed starch were prepared using 5 to 30 wt.% glycerol as plasticizer *via* solution casting method. The aim of this study is to investigate the effect of glycerol on the mechanical properties of films. According to the analysis, the optimum tensile strength of the film was obtained at 4.40 MPa, which revealed that the native starch granules were converted into a continuous phase in the presence of glycerol as indicated by scanning electron microscopy. The incorporation of glycerol in starch also showed the formation of hydrogen bond evidenced by Fourier transform infrared spectroscopy.

Keywords: starch, jackfruit, glycerol, thermoplastic film

Abstrak

Filem thermoplastik berdasarkan 3 wt.% kanji biji nangka telah disediakan dengan menggunakan 5 ke 30 wt.% gliserol sebagai pemplastik melalui kaedah penuangan larutan. Tujuan kajian ini dijalankan adalah untuk menyiasat kesan penambahan gliserol terhadap sifat mekanik filem. Analisis kajian menunjukkan kekuatan tegangan optimum filem diperoleh pada 4.40 MPa, yang menunjukkan butir-butir kanji bertukar ke fasa berterusan dengan kehadiran gliserol seperti yang ditunjuk oleh mikroskop imbasan elektron (SEM). Penggabungan gliserol dalam kanji turut menunjukkan pembentukan ikatan hidrogen seperti yang dibuktikan oleh spektroskopi inframerah transformasi Fourier (FTIR).

Kata kunci: kanji, nangka, gliserol, filem thermoplastik

Introduction

Starch, a natural renewable polysaccharide from numerous diversities of plants, as a raw material to produce biodegradable and eco-friendly plastics has been a topic of interest in many researches. This is driven by the global environmental concern resulted from petroleum-derived plastics, which continue to be prevalent over time [1]. Previously, many researchers concentrated on starches from different sources, such as corn, tapioca, potato, and wheat. So far, there have been very few works reported on starch from non-conventional sources such as jackfruit seed. Hence, in this study, jackfruit seed (*Artocarpus heterophyllus*) is utilized as a source of starch to develop starch-based films. Jackfruit is one of the most popular tropical fruits that grows abundantly in Asia. In Malaysia, jackfruit seeds are usually thrown away as waste even though the seeds are a potential source of nutrition [2].

Moreover, jackfruit seeds have a high starch content; seeds content in a jackfruit are about 100 to 500 or approximately 8 to 15% by weight of a jackfruit [3]. However, this type of starch is classified as a native starch, or in other words, it is not in thermoplastic form.

Starch-based thermoplastic films have a variety of industrial uses, such as for food packaging, compost bags, and coatings [4]. Plasticizer such as polyol should be added to starch since it is natural, inexpensive, and renewable so that the final product is both biodegradable and cost-effective [5]. The incorporation of jackfruit seed starch with glycerol as plasticizer will overcome the native starch drawbacks such as brittleness and high moisture sensitivity and at the same time will enhance the product flexibility and workability, in developing a potential and ecological alternative to the synthetic products [6]. For this reason, it is expected that the modification of jackfruit seed starch with the addition of glycerol as plasticizer will result in high tensile strength and elongation at break of the film due to the reduction of intermolecular forces and an increase in polymer chain mobility as reported elsewhere [7]. However, the optimum amount of glycerol in the jackfruit seed starch has not been reported as yet.
Therefore, the aim of this study is to develop glycerol-plasticized jackfruit seed starch (GTPS) film *via* solution casting method and to evaluate the effect of glycerol content on the mechanical and physical properties of jackfruit seed starch film.

Materials and Methods

Materials

Jackfruit seeds were obtained from Tropical Fruit Farm, Penang, and glycerol (85% purity) was purchased from Merck Sdn. Bhd. (Selangor, Malaysia).

Preparation of jackfruit seed powder

Jackfruit seeds were cleaned, peeled, and sliced into thin pieces. Then, the seeds were dried in the oven for 24 hours. The dried seeds were grounded with an electronic kitchen blender for 20 minutes followed by milling (Fritsch, Planetary Ball Mill) at a ratio of 1 g powder:5 balls for about 1 hour to obtain micro-meter scale size of seeds. Finally, the powder was sieved using 100 µm mesh, packed and sealed in a plastic bag, then stored in a refrigerator (<5 ℃) until further use.

Extraction of starch from jackfruit seed

The extraction of jackfruit seed starch (JFSS) was carried out as per the method mentioned by Noor et al. [3] with a slight modification. About 100 ml distilled water was poured into 5 g of jackfruit seed powder and stirred constantly for 6 to 8 hours at room temperature. The slurry produced was then filtered using 212 mesh sieve and the remaining residues were washed three times with distilled water. Finally, the filtrate wet starches were precipitated overnight at 4 ℃ and dried in the oven at 40 ℃ for 24 hours. The dry starches obtained were filled in a plastic bag and kept at room temperature until further use.

Preparation of thermoplastic starch film with glycerol

The fabrication of TPS incorporation with glycerol was carried out via solution casting as proposed by Seligra et al. [8] and Reddy and Yang [9] with a minor modification. Total mass of the system is 100 g where starch content was fixed at 3 wt.% and the amount of glycerol varied from 5 to 30 wt.%. The materials' abbreviations and corresponding sample compositions are listed in Table 1. The starch and distilled water were mixed and heated up to 90 ℃ on a hot plate and held for 20 minutes with a constant stirring speed at 250 rpm. Then, the solution was cooled to 65 ℃ and glycerol was added to the mixture while stirring continuously for 5 minutes. The film forming solution was casted on acrylic plates and dried for 24 hours in the oven. Later, the thermoplastic film was peeled from the plates and stored in the desiccator maintained at 23 ℃ and 30% relative humidity prior to characterization.

Table 1. Used symbols and corresponding compositions of each sample

Materials	Abbreviations	Samples (Weight Proportions, gram)		
		Starch	Glycerol	Distilled Water
GTPS1	G05	3	0.5	96.5
GTPS2	G10	3	1.0	96.0
GTPS3	G15	3	1.5	95.5
GTPS4	G20	3	2.0	95.0
GTPS5	G25	3	2.5	94.5
GTPS6	G30	3	3.0	94.0

X-ray diffraction test
The diffraction pattern of the JFSS powder was analysed with an X-ray diffractometer (Shimadzu; XRD-6000). The scanning region of the diffraction angle (2θ) was set from 5 to 40° at a rate of 3°/min of scan speed and the diffractometer was operated at a power of 40 kV and 20 mA.

Mechanical test
The mechanical properties of the starch films were determined in accordance with ASTM standard D882-02 by using MTS tensile tester (Shimadzu; Material Testing System) with 20 mm/min of speed and 5 kN of load. The test was carried out on five samples that were cut manually into strips with a dimension of 70 mm x 10 mm from the cast films based on the standard ISO–527.

Scanning electron microscopy
The surface structure of JFSS powder and TPS films were examined using a scanning electron microscope (JEOL, JSM 5600 SEM; JEOL Ltd., Tokyo, Japan). The samples were sputter coated with carbon (Polaron SC515) and observed under SEM at a voltage of 8 kV.

Fourier transform infrared spectroscopy analysis
The infrared (IR) spectra of the JFSS powder and GTPS2 film was recorded on FTIR spectrometer (Spectrum 100 FTIR; PerkinElmer, United States). Measurements were taken in the average of 32 scans per sample between 4000 cm^{-1} to 600 cm^{-1} with a resolution of 4 cm^{-1}.

Results and Discussion

X-ray diffraction analysis
The XRD pattern obtained with the JFSS granules is shown in Figure 1. The broad diffraction peaks can be related to the amorphous characteristic of starch. The appearances of peaks of 2θ at 15.37°, 22.97°, and 23.57° indicating the presence of type-A starch in jackfruit seed since there is no peak in the range of 5°– 6°. In fact, jackfruit seed contains a high amount of starch and the amylose content is about 32% as reported by Theivasanthi and Alagar [10].

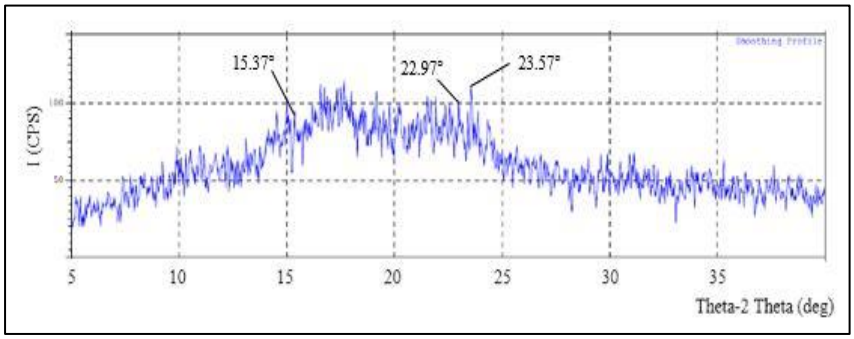


Figure 1. XRD diffractogram of jackfruit seed starch powder

Mechanical properties

The addition of glycerol greatly affects the tensile strength (TS) and elongation at break (E%) of TPS films. Figure 2 and Figure 3 show the effect of increasing the glycerol content of TPS films on tensile properties.

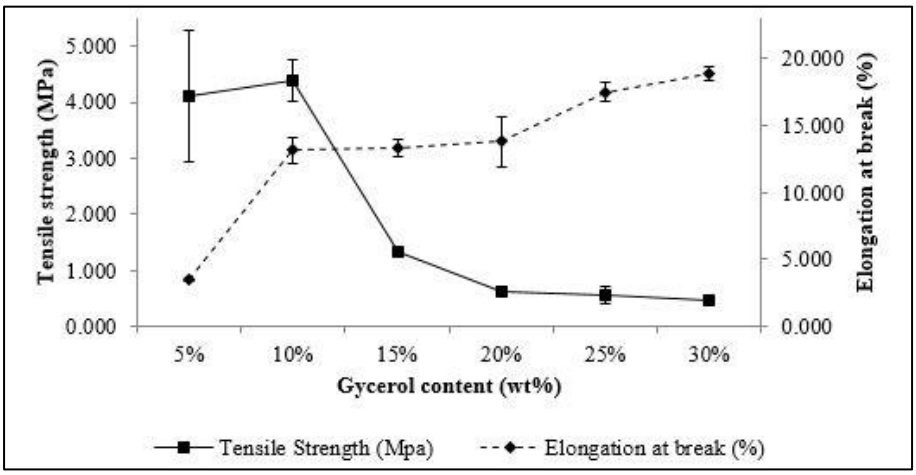


Figure 2. Effect of increasing glycerol content on the tensile properties of starch films

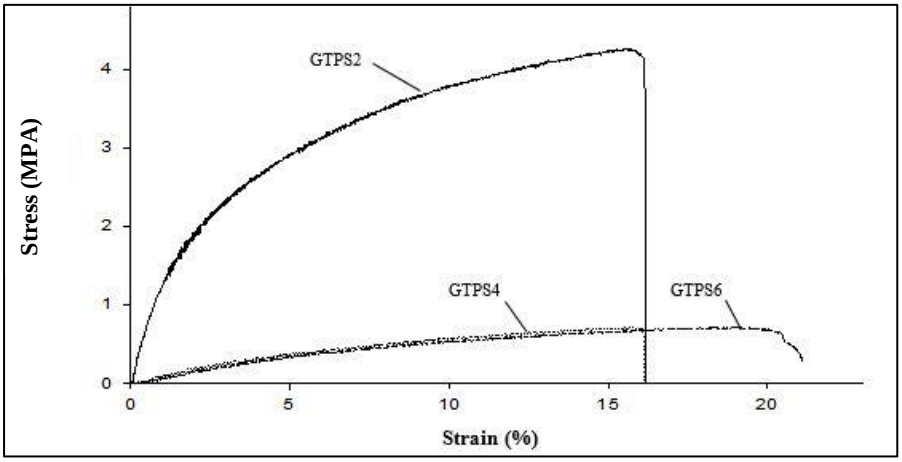


Figure 3. Effect of increasing the glycerol content on stress-strain curve of starch films

Starch film with less than 5% glycerol was ignored due to brittleness. Starch film with the addition of 5% glycerol showed a tensile strength of 4.12 MPa. The addition of 10% glycerol increased the TS of GTPS1 by 7%, indicating that there is enough plasticizing effect. However, the addition of 15% of glycerol to GTPS2 reduced the TS by almost 70% due to the plasticizing effect that is too prominent. On the other hand, the E% of the films increased gradually by adding more concentration of glycerol into the starch. The results showed that with the increase in glycerol content from 5% to 30% in the blend, the E% increased to a large extent: 3.47%-18.88%. In short, increasing glycerol concentration more than 10% on the JFSS will produce films that are more extendible as well as less rigid and stiff. This is depicted in Figure 2, which show a decrease of TS and an increase of the E% of the films, respectively. These trends are probably due to the reduction in interactions between the starch chains, which caused the expansion of distance between starch molecules to allow the plasticizers to be embedded between them, thus forming a hydrogen bond between the glycerol and starch molecules.

Furthermore, the tensile failure stress-strain curves in Figure 3 shows a more ductile character of the films with the increase in glycerol concentration. This was shown by the decrease of the film TS and an increase in flexibility as the glycerol concentration increased from 10% to 30%. GTPS2 indicated high stress coupled with low strain, thus, were considered brittle. Increasing the concentration of glycerol improved the ductility of GTPS4 and GTPS6 films, which is revealed by their significant deformation before fracture. Sanyang et al. [6] also reported a similar trend based on the results obtained from using glycerol in sugar palm starch films. In fact, 10% glycerol delivered the highest TS of 4.40 MPa to the JFSS films, which can be associated with its homogeneous surface structure revealed by SEM and the formation of hydrogen bond evidenced by FTIR.

Morphological structure

The morphology of jackfruit seed starch granules and glycerol-plasticized starch films (magnification of 500x) were presented in Figure 4. Figure 4(a) shows that the starch granules have varied round shape with a smooth surface. As a result of the plasticization of jackfruit seed starch with 5% and 10% glycerol, less coarse granules were observed in Figure 4(b) – 4(c), probably due to the starch granule fusing into homogeneous phase. It is revealed that the surface of starch with 10% glycerol is clear and smooth without gross defects. This indicates that the starch molecules were well dispersed as not many granules were exposed to low glycerol content. Reddy and Yang [9] also found a similar morphology in glycerol-plasticized corn starch films. Increasing the glycerol content to more than 10% resulted in a rougher surface and the phase separation between glycerol and starch in blend films were clearly observed in Figure 4(d) – 4(g). The fact that the blend with 10% glycerol was very strong and has lower elongation compared to the blend with 30% glycerol may account for the appearance of such voids and cracks. It should be noted that the surface structure of thermoplastics is corroborated with the mechanical properties finding as discussed previously.

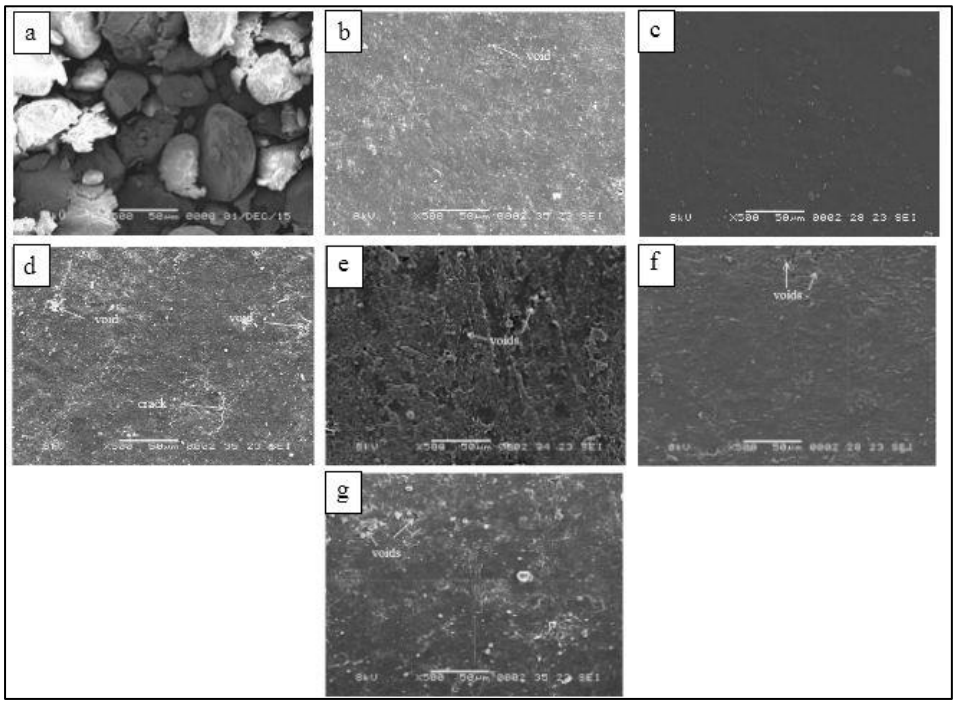


Figure 4. SEM micrographs of (a) JFSS powder, (b) 5 wt.% glycerol (GTPS1), (c) 10 wt.% glycerol (GTPS2), (d) 15 wt.% glycerol (GTPS3), (e) 20 wt.% glycerol (GTPS4), (f) 25 wt.% glycerol (GTPS5), and (g) 30 wt.% glycerol (GTPS6) films

FTIR analysis

The FTIR spectra of the jackfruit seed starch granules and 10% glycerol-plasticized starch films are shown in Figure 5(a) and 5(b).

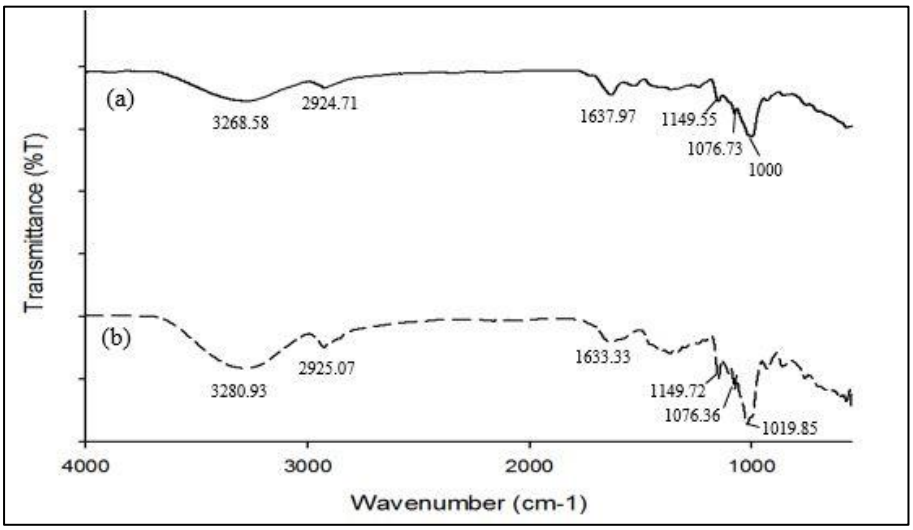


Figure 5. FTIR spectra for (a) JFSS powder and (b) GTPS2 film

The analysis of FTIR spectra of the 10% glycerol-plasticized film enabled the hydrogen bond interaction to be recognized compared to the native JFSS powder. For GTPS2, the characteristic peaks that were attributed to C-O bond stretching of C-O-H group were found to be shifted from 1076.73 cm^{-1} to 1076.36 cm^{-1} and 1149.55 cm^{-1} to 1149.72 cm^{-1}. This indicates that the O-H group of starch was encompassed in the hydrogen bond formation. Another peak, that was related to C-O bond stretching of C-O-C group at 1000 cm^{-1} became more prominent and presented a displacement to 1019.85 cm^{-1}, could be regarded as the structure changes of JFSS from an amorphous to semi-crystalline state [11]. In sum, the appearance of characteristic peaks proved that glycerol could form hydrogen bond interaction with starch molecules. It is also believed that the formation of hydrogen bond in thermoplastic contributed to the improvement of mechanical properties as discussed earlier.

Conclusion

The difference in the amount of glycerol incorporated with jackfruit seed starch has been shown to have a substantial effect on the physical and mechanical properties of casted films. The increase in the glycerol content of more than 10% in jackfruit seed starch films improved its flexibility but reduced the strength. Starch film plasticized with 10% glycerol achieved the highest strength, 4.40 MPa, and formed stable hydrogen bond interactions with the starch molecules. In addition, TPS produced from the native JFSS has homogeneous structure.

Acknowledgement

The authors would like to acknowledge the Research Management Centre, International Islamic University Malaysia for the research grant RIGS16-072-0236.

References

1. Nafchi, A. M., Moradpour, M., Saeidi, M. and Alias, A. K. (2013). Thermoplastic starches : Properties, challenges, and prospects. *Starch/Stärke*, 65(1 – 2): 61-72.
2. Noor, F., Rahman, J., Mahomud, S., Akter, M. S., Talukder, A. I. and Ahmed, M. (2014). Physicochemical properties of flour and extraction of starch from jackfruit seed. *International Journal of Nutrition and Food Sciences*, 3(4): 347-354.

3. Hansen, M. C., Krylov, A. and Tyukavina, A. (2017). Utilization starch of jackfruit seed (*Artocarpus heterophyllus*) as raw material for bioplastics manufacturing using sorbitol as plasticizer and chitosan as filler. *IOP Conference Series: Journal of Physics*, 801(1): 012014.
4. Han, J. H. (2013). Innovations in food packaging. Academic Press, Canada: pp. 391-412.
5. Khan, B. Bilal, M., Niazi, K., Samin, G. and Jahan, Z. (2016). Thermoplastic starch : A possible biodegradable food packaging material – a review. *Journal of Food Process Engineering*, 40(3): 12447- 12452.
6. Sanyang, M. L., Sapuan, S. M., Jawaid, M., Ishak, M. R. and Sahari, J. (2015). Effect of plasticizer type and concentration on tensile, thermal and barrier properties of biodegradable films based on sugar palm (*Arenga pinnata*) starch. *Polymers*, 7(6): 1106-1124.
7. Retnowati, D. S., Ratnawati, R. and Purbasari, A. (2015). A biodegradable film from jackfruit (*Artocarpus heterophyllus*) and Durian (*Durio zibethinus*) seed flours. *Scientific Study and Research*, 16(4): 395-404.
8. Seligra, P. G., Jaramillo, C. M., Fama, L. and Goyanes, S. (2016). Biodegradable and non-retrogradable eco-films based on starch-glycerol with citric acid as crosslinking agent. *Carbohydrate Polymers*, 138: 66–74.
9. Reddy, N. and Yang, Y. (2010). Citric acid cross-linking of starch films. *Food Chemistry*, 118(3): 702-711.
10. Theivasanthi, T. and Alagar, M. (2011). An insight analysis of nano sized powder of jackfruit seed. *Nano Biomedicine Engineering*, 3(3): 163-168.
11. Ahmad, Z., Anuar, H. and Yusof, Y. (2011). The study of biodegradable thermoplastics sago starch. *Key Engineering Materials*, 471 – 472: 397-402.

Malaysian Journal of Analytical Sciences, Vol 22 No 5 (2018): 899 - 905
DOI: https://doi.org/10.17576/mjas-2018-2205-18

MALAYSIAN JOURNAL OF ANALYTICAL SCIENCES
Published by The Malaysian Analytical Sciences Society
ISSN 1394 - 2506

THERMAL, FLAMMABILITY, AND MORPHOLOGICAL PROPERTIES OF SEPIOLITE-FILLED ETHYLENE PROPYLENE DIENE MONOMER COMPOSITES

(Sifat Terma, Kemudahbakaran dan Morfologi bagi Komposit Etilena Propilena Monomer Diena Terisi Sepiolit)

Nurul Aizan Mohd Zaini, Hanafi Ismail*, Arjulizan Rusli

School of Materials and Mineral Resources Engineering, Engineering Campus, Universiti Sains Malaysia,14300 Nibong Tebal, Pulau Pinang, Malaysia

**Corresponding author: ihanafi@usm.my*

Received: 20 July 2017; Accepted: 28 April 2018

Abstract

The effects of different sepiolite contents on the thermal stability, flammability, and morphological properties of sepiolite-filled ethylene-propylene-diene monomer composites were studied. These sepiolite-filled composites, containing 0-70 parts per hundred rubber (phr) of sepiolite fillers, were prepared through the conventional processing method of using a two-roll mill. The results demonstrated a significant increase in the thermal stability of the composites when sepiolite loading was increased compared to unfilled composites. The results also showed a decrease in the linear rate of burning of the composites with increasing sepiolite loading. The morphological study confirmed the presence of unburned sepiolite, which increased the flammability resistance of the composites.

Keywords: sepiolite, flammability, rubber, thermal stability, morphology

Abstrak

Kesan kandungan sepiolit yang berbeza terhadap kestabilan terma, kemudahbakaran, dan ciri-ciri morfologi bagi komposit etilena-propilena-monomer diena terisi sepiolit telah dikaji. Komposit terisi sepiolit yang mengandungi 0 hingga 70 bahagian per seratus getah (bsg) telah disediakan melalui kaedah lazim menggunakan mesin pengisar bergulung dua. Keputusan menunjukkan peningkatan ketara pada kestabilan terma komposit apabila kandungan sepiolit ditambah berbanding dengan komposit tidak terisi. Hasil kajian turut menunjukkan penurunan kadar pembakaran selari komposit ini dengan penambahan kandungan sepiolit. Kajian morfologi mengesahkan kehadiran sepiolit yang tidak terbakar yang telah meningkatkan ketahanan kemudahbakaran komposit ini.

Kata kunci: sepiolit, kemudahbakaran, getah, kestabilan terma, morfologi

Introduction

The demand for clay minerals expands through various applications and their role has undoubtedly become more profound since the discovery of clay varieties at the end of the last century. Clay minerals are produced through the weathering process, in which the clay species experience changes through sedimentation and burial courses [1]. Clay minerals have long been incorporated in plastics or elastomer matrix as fillers. Clay-based materials have been most widely investigated among other potential nanocomposite alternatives, possibly due to the abundant sources of clay materials and because the study of their intercalation chemistry is already established [2]. Currently, the most

intensive researches have been focused on layered silicates based on the smectite class of aluminum silicate clays, especially on montmorillonites (MMT) as the reinforcing phase [3]. However, these nanofillers are not the only type of nanoclays that can be incorporated into polymer matrices. Recently, several studies have focused on the use of sepiolite, a nanofiller with a needle-like morphology, to reinforce nanocomposites [4].

Sepiolite can be expressed as $Si_{12}O_{30}Mg_8(OH)_4(OH_2)_4.(H_2O)_8$ [5, 6], and it is also chemically known as the hydrated magnesium silicate [7]. This compound belongs to the 2:1 phyllosilicate structure; one octahedral sheet is sandwiched between two tetrahedral sheets. It is microfibrous, with 2-10 mm particles and exhibits nanosized tunnel structures [8, 9]. The fibrous-like structure of sepiolite is believed to be more easily dispersed in the polymer matrix compared to platelet-like minerals, such as MMT [10]. Moreover, sepiolite can prevent flocculation when it is distributed within the network of a polymer and reduce filler agglomeration [5]. The presence of clay particles within a polymer matrix could enhance fire retardant properties. These particles can contribute to the formation of a char layer at the silicate surface, behaving as a barrier that reduces the oxygen transmission rate, retards the spread of flames, and help to keep the structural integrity of the burned sample [11]. As a potential filler, sepiolite offers promising advantages that could improve the mechanical, thermal, and flammability properties of the composites as well as reduce cost.

Polymer matrices, such as natural rubber [12, 13], nitrile rubber [14], styrene butadiene rubber [15, 16], silicone rubber [17], acrylonitrile butadiene styrene [18], polyether imide [19], and polyamide 6 [20] have been filled with sepiolite to improve their properties. However, little attention has been paid to the properties of sepiolite in ethylene-propylene-diene monomer (EPDM). Wang et al. [21] conducted several preliminary investigations based on the surface free energy of EPDM/Sepiolite nanocomposites. However, they had only reported a limited number of properties of the EPDM/Sepiolite composites. Therefore, further studies are necessary to generate positive results from the various properties of the sepiolite-filled EPDM composites.

Based on a literature survey, none of the previous reports have dealt with the effects of sepiolite on the thermal stability, flammability, and morphology of the char residue of EPDM/Sepiolite composites. Thus, this study has focused on investigating the potential effects of using sepiolite as fillers on the thermal stability, flammability, and morphological properties of EPDM/Sepiolite composites at various loadings.

Materials and Methods

Materials

The EPDM used in this study was Vistalon 2504N that contained 54% ethylene, with 3.6% of ethylidene norbornene (ENB) and Mooney viscosity [ML (1+4) at 125 °C] of 26.8 (Mooney Unit), which was purchased from ExxonMobil. The density of the EPDM was 0.818 g/cm^3 as measured using an analytical balance (Precisa, model XB 220A). The sepiolite clay was purchased from Hebei DFL Minmet Refractories Corp., China. Meanwhile, other compounding ingredients were purchased from Bayer (M) Ltd., namely, zinc oxide, stearic acid, tetramethyl thiuram disulphide (TMTD), mercaptobenzothiazole (MBT), and sulphur.

Sample preparation

The sepiolite was dried in an oven for 24 hours at 80 °C before mixing to remove any existing moisture. Table 1 lists the compounding formulations for EPDM/Sepiolite composites, in which each compound was prepared using a laboratory scale (160 × 320 mm^2) and a two-roll mill (model XK-160). All composites were mixed for 21 minutes according to the ASTM D3568. The optimum cure time (t_{90}) and scorch time (t_{s2}) were obtained by utilising the Monsanto Moving Die Rheometer (model MDR2000) at 160 °C. Based on their respective t_{90} values, the compounds were compression moulded into 3 mm rectangular sheets, with a dimension of 125 mm × 13 mm × 3 mm using the KAO-Tieh GO Tech Compression Moulding Machine, at 160 °C with a force of 10 MPa.

Table 1. Compounding formulations for EPDM/Sepiolite Composites (phr)

Materials	Content (phr)
EPDM	100
Zinc Oxide	5
Stearic Acid	1.5
TMTD[a]	1.5
MBT[b]	0.8
Sulphur	1.5
Sepiolite	0,10,20,30,70

[a] Tetramethyl thiuram disulphide,
[b] Mercaptobenzothiazole

Thermal analysis
Thermogravimetric analysis (TGA) was performed on 10 mg samples that were heated from 30 to 600 °C at a ramp rate of 20 °C/min, under nitrogen flow (50 mL/min) using a Perkin Elmer Pyris 6 thermogravimetric analyser. The analysis involved measuring weight loss as a function of temperature where the TGA curve was recorded.

Flammability test
The samples' flammability was tested using the horizontal burning test in accordance with ASTM D635. Initially, samples with a dimension of 125 mm × 13 mm × 3 mm were prepared. The flame was ignited on one end of the sample using natural gas. The burnt length and the time for the flame front to reach the 25 mm reference mark, and travel to the 100 mm reference mark were recorded. Equation (1) was used to calculate the linear rate of the burning samples.

$$V = 60L/t \quad (1)$$

where V is the linear burning rate, L is the burnt length, and t is the time in minutes [22].

Morphological study
The morphology of the charred surfaces of the EPDM/Sepiolite composites was examined under the Zeiss Supra 35-VP field emission scanning electron microscope (FESEM) at 1,000x magnification. The test specimens were first coated with a thin layer of gold-palladium. The coating was necessary to eliminate any electrostatic charges during the examination.

Results and Discussion

Thermal stability analysis
Figure 1 and Table 2 present the thermal degradation properties of EPDM/Sepiolite composites in comparison with unfilled EPDM compound. In general, weight loss is used to determine the thermal stability of the polymer composites. The heating process will prompt the production of volatile products, hence reducing the weight of the compound [23].

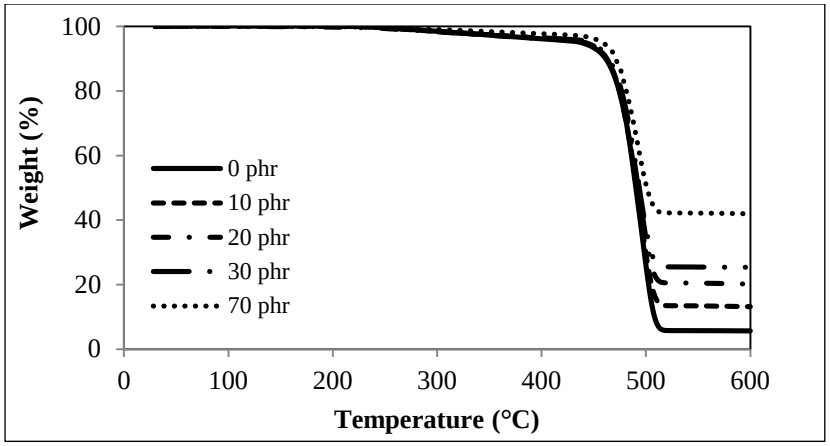


Figure 1. TGA curves for unfilled EPDM and sepiolite-filled EPDM composites

Table 2. Thermal properties of unfilled EPDM and sepiolite-filled EPDM composites

Sepiolite Content (phr)	Temp at 5% wt. Loss (°C)	Temp at 50% wt. Loss (°C)	Max wt. Loss (%)	Char Residue at 600 °C (%)
0	432	489	56.4	5.7
10	438	491	52.3	13.2
20	440	492	44.1	20.2
30	446	494	42.3	25.4
70	458	500	34.5	41.9

Overall, all sepiolite-filled EPDM composites exhibited improved thermal stability. The data showed that the incorporation of sepiolite into the EPDM matrix had increased the overall thermal stability of the composites because sepiolite acted as a thermal insulator [24]. For instance, the temperature at 5% of weight loss of unfilled EPDM compound was at 432 °C, while 70 phr of sepiolite in the EPDM had increased the temperature up to 458 °C. The char residue at 600 °C was increased from 5 to 41%, with sepiolite clay loadings that ranged between 0 to 70 phr. This result indicated that sepiolite was the mass transport barrier [17]. Reduction in the thermal energy transfer had halted the thermal degradation process, while the decomposition process was hindered by the fibrous structure of the sepiolite. These deterrents had resulted in the reduced rate of volatility loss, and higher amount of residues. Additionally, the well-dispersed sepiolite may have restricted the mobility of the polymer chains, which led to the delayed heating.

Flammability analysis

Figure 2 displays the effect of different sepiolite loadings on the flammability of EPDM/Sepiolite composites, as determined by the linear rate of burning. The linear rate of burning was reduced when sepiolite concentration was increased. The EPDM composite with 70 phr sepiolite exhibited the longest burnout time compared to the unfilled composites and subsequently, exhibited the lowest linear rate of burning. The linear rate of burning agreed with the thermal properties of the composites, as previously discussed. The fibrous structure of the sepiolite and the formation of carbonaceous char layers during the burning process had contributed to the fire resistance nature of these composites [25]. During the burning process, sepiolite had formed a protective layer of char on the matrix surface, by acting as an insulating barrier against oxygen, and preventing heat from reaching the underlying matrix. Therefore, the amount of decomposed volatiles that escaped from the interior polymer matrix was reduced, which resulted in a longer time to burn, and subsequently, reduced the linear rate of burning. This process was further inhibited by the formation of char at higher filler loadings, which shielded

the underlying EPDM matrix from heat.

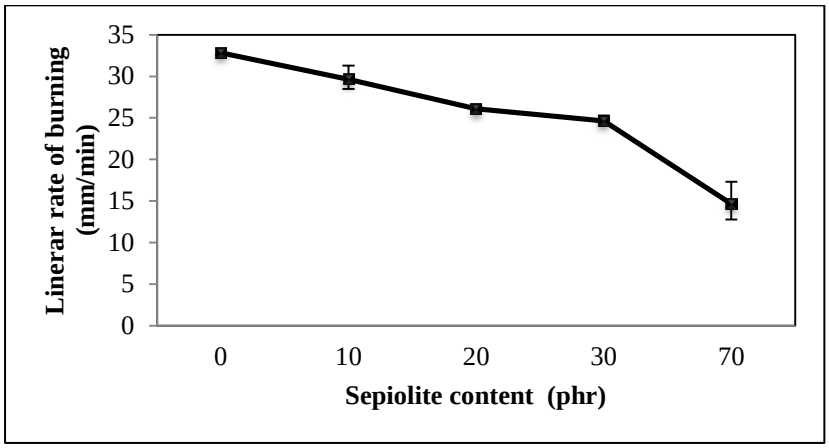


Figure 2. The effect of different sepiolite loadings on the flammability of EPDM/Sepiolite composites

Morphologies of charred surfaces

Figures 3(a) and (b) show the charred surfaces of EPDM/Sepiolite composites at 30 and 70 phr of sepiolite loadings, respectively. The 30 phr sepiolite, as observed in Figure 3(a), had delayed the burning time of the composite due to the presence of unburned sepiolite. The unburned sepiolite had impeded the transport of flammable vapour, thus reducing the flammability rate of the EPDM/Sepiolite composite. This observation confirmed the reduction of the linear rate of burning and the increment of char residues of the EPDM/Sepiolite composites, as shown by the TGA results when the sepiolite loadings were increased.

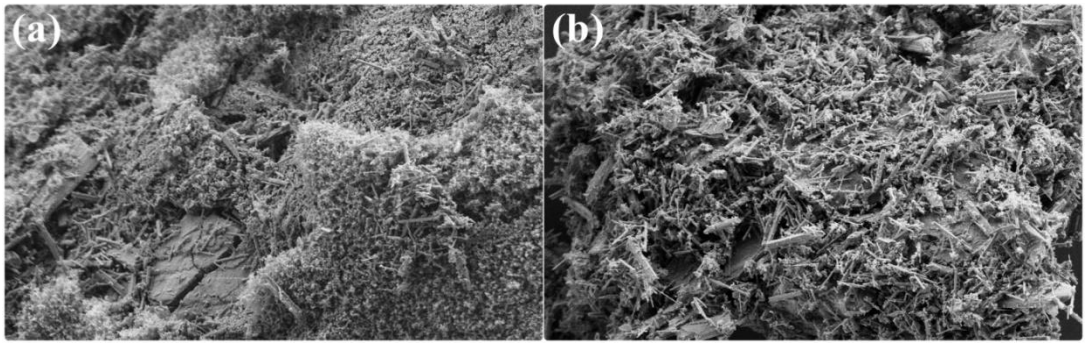


Figure 3. Char residues collected following the flammability test of EPDM/Sepiolite composites, with sepiolite loadings of: (a) 30 phr; and (b) 70 phr at 1,000× magnification

Conclusion

The thermal stability of the EPDM/Sepiolite composites was remarkably improved with increased clay loadings compared to the thermal stability of the unfilled compound. Sepiolite had acted as a thermal insulator by reducing the transfer of thermal energy through the composites. The presence of unburned sepiolite had reduced the linear rate of burning of the EPDM/Sepiolite composites. FESEM micrographs confirmed that the unburned sepiolite particles had created a protective barrier, which reduced the linear rate of burning.

Acknowledgement

The authors wish to thank the management and staff members at the Department of Materials and Mineral Resources Engineering, Universiti Sains Malaysia (USM) for providing the research facilities that made this

research project possible. One of the authors is grateful to the Ministry of Higher Education Malaysia (KPT(BS)821115065540) and Universiti Teknologi Mara (UiTM) (600-BPD(PKH.1/2/9946) for the financial support under their scholarships.

References

1. Velde, B. (1992). Introduction to clay minerals- chemistry, origin, uses and environmental significance. First edition. Chapman and Hall, London.
2. Pavlidou, S. and Papaspyrides, C.D., (2008). A review on polymer-layered silicate nanocomposites. *Progress in Polymer Science*, 33(11): 1119-1198.
3. Nguyen, Q. T. and Baird, D. G. (2006). Preparation of polymer–clay nanocomposites and their properties. *Advances in Polymer Technology*, 25(4): 270-285.
4. Zaini, N. A. M., Ismail, H. and Rusli, A. (2017). Short review on sepiolite filled polymer nanocomposites. *Polymer- Plastics Technology and Engineering*, 56(15): 1665-1679.
5. Olivato, J. B., Marini, J. and Yamashita, F. (2017). Sepiolite as a promising nanoclay for nano-biocomposites based on starch and biodegradable polyester. *Materials Science and Engineering C*, 70: 296-302.
6. Zotti, A., Borriello, A. and Ricciardi, M., (2015). Effects of sepiolite clay on degradation and fire behaviour of a bisphenol A-based epoxy. *Composites Part B Engineering*, 73: 139-148.
7. Tartaglione, G., Tabuani, D., Camino, G. and Moisio, M. (2008). PP and PBT composites filled with sepiolite: Morphology and thermal behaviour. *Composites Science and Technology*, 68(2) :451-460.
8. Kotal, M and Bhowmick, A. K. (2015). Polymer nanocomposites from modified clays: Recent advances and challenges. *Progress in Polymer Science*, 51: 127-187.
9. Chen, H., Lu, H. and Zhou, Y., (2012). Study on thermal properties of polyurethane nanocomposites based on organo-sepiolite. *Polymer Degradation and Stability*, 97(3): 242-247.
10. Liu, M., Pu, M. and Ma, H. (2012). Preparation, structure and thermal properties of polylactide/sepiolite nanocomposites with and without organic modifiers. *Composites Science and Technology*, 72(13): 1508-1514.
11. Darder, M., Matos, C. R. S. and Aranda, P., (2016). Bionanocomposite foams based on the assembly of starch and alginate with sepiolite fibrous clay. *Carbohydrate Polymers*, 157: 1933-1939.
12. Lowe, D. J., Chapman, A. V., Cook, S. and Busfield, J. J. C. (2011). Natural rubber nanocomposites by in situ modification of clay. *Macromolecular Materials and Engineering*, 296(8): 693-702.
13. Bhattacharya, M. and Bhowmick, A.K. (2010). Synergy in carbon black-filled natural rubber nanocomposites. Part I: Mechanical, dynamic mechanical properties, and morphology. *Journal of Materials Science*, 45(22): 6126-6138.
14. Takei, T., Oda, R. and Miura, A. (2013). Effect of dispersion of sepiolite in sepiolite-NBR composite on the tensile strength. *Composites Part B Engineering*, 44(1): 260-265.
15. Bhattacharya, M., Maiti, M. and Bhowmick, A. K. (2009). Tailoring properties of styrene butadiene rubber nanocomposite by various nanofillers and their dispersion. *Polymer Engineering and Science*, 49(1): 81-98.
16. Bokobza, L., Leroy, E. and Lalanne, V. (2009). Effect of filling mixtures of sepiolite and a surface modified fumed silica on the mechanical and swelling behavior of a styrene-butadiene rubber. *European Polymer Journal*, 45(4): 996-1001.
17. Roy, N. and Bhowmick, A. K. (2010). Novel in situ polydimethylsiloxane-sepiolite nanocomposites: Structure-property relationship. *Polymer*, 51(22):5172-5185.
18. Basurto, F. C., García-López, D. and Villarreal-Bastardo, N. (2012). Nanocomposites of ABS and sepiolite: Study of different clay modification processes. *Composites Part B Engineering*, 43(5): 2222-2229.
19. Tabatabaei-Yazdi Z. and Mehdipour-Ataei S. (2015). Poly(ether-imide) and related sepiolite nanocomposites: investigation of physical, thermal, and mechanical properties. *Polymer for Advanced Technologies*, 26(4): 308-314.
20. Bilotti, E., Duquesne, E. and Deng, H. (2014). In situ polymerised polyamide 6/sepiolite nanocomposites: Effect of different interphases. *European Polymer Journal*, 56(1): 131–139.
21. Wang, F, Tang, Q.G. and Chen, C. (2013). Effect of Sepiolite Nanofibers on Properties of EPDM Nanocomposites. *Applied Mechanics and Materials*, 320: 595–598.
22. America Society for Testing and Materials (2010). Standard Test Method for Rate of Burning and/or Extent and Time of Burning of Plastics in Horizontal Position. ASTM D635-10.

23. Bidsorkhi, H. C., Adelnia, H. and Naderi, N. (2015). Ethylene vinyl acetate copolymer nanocomposites based on (un)modified sepiolite: Flame retardancy, thermal, and mechanical properties. *Polymer Composites*, 38(7): 1302-1310.
24. Chen, H., Zheng, M., Sun, H. and Jia, Q. (2007). Characterization and properties of sepiolite/polyurethane nanocomposites. *Materials Science Engineering:A*, 445–446 (25): 725-730.
25. Munusamy, Y., Ismail, H., Mariatti, M. and Ratnam, C. T. (2009). Effects of different preparation methods on the properties of poly[ethylene-co-(vinyl acetate)]/(Standard Malaysian natural rubber)/organoclay nanocomposites. *Journal of Vinyl Additive and Technology*, 15: 244-251.

Malaysian Journal of Analytical Sciences, Vol 22 No 5 (2018): 906 - 913
DOI: https://doi.org/10.17576/mjas-2018-2205-19

MALAYSIAN JOURNAL OF ANALYTICAL SCIENCES
Published by The Malaysian Analytical Sciences Society
ISSN 1394 - 2506

MENGKUANG FIBER REINFORCED THERMOPLASTIC NATURAL RUBBER COMPOSITES: INFLUENCE OF RUBBER CONTENT ON MECHANICAL PROPERTIES AND MORPHOLOGY

(Komposit Termoplastik Getah Asli Diperkuat Serabut Mengkuang: Pengaruh Kandungan Getah ke atas Sifat Mekanik dan Morfologi)

Wan Zarina Wan Mohamed[1, 2], Azizah Baharum[1, 3]*, Ishak Ahmad[1, 3], Ibrahim Abdullah[4], Nurzam Ezdiani Zakaria[1]

[1]*School of Chemical Sciences and Food Technology, Faculty of Sciences and Technology, Universiti Kebangsaan Malaysia, 43600 UKM Bangi Selangor, Malaysia*
[2]*Faculty of Engineering and Life Sciences, Universiti Selangor, 45600 Bestari Jaya Selangor, Malaysia*
[3]*Polymer Research Center, Faculty of Science and Technology, Universiti Kebangsaan Malaysia, 43600 UKM Bangi Selangor, Malaysia*
[4]*Academy Sciences of Malaysia, 50480 Kuala Lumpur, Malaysia*

**Corresponding email: azeiss@ukm.edu.my*

Received: 20 July 2017; Accepted: 28 April 2018

Abstract

This paper presents the influence of rubber on mengkuang (MK) reinforced thermoplastic composites as the rubber content appeared to increase at low fibre loading of 10% MK and high fibre loading of 30% MK. The MK fibre was blended with high density polyethylene (HDPE) and natural rubber (NR) through melt blending *via* internal mixer. The MK composites at 10% MK fibre loading exhibited higher tensile strength, tensile strain at break, and impact strength; but lower tensile modulus than MK composites at 30% fibre loading. Both fibre contents showed that the tensile strength and the tensile modulus decreased, while tensile strain at break and impact strength seemed to increase as the rubber content increased up to 40%. Field emission scanning electron microscopy (FESEM) micrograph was employed to observe the fibre dispersion, as well as physical interactions between the fibre and the matrix. This study showed that the effects of MK fibre loading on mechanical properties and morphology were influenced by rubber content.

Keywords: rubber, polymer composites, mengkuang fibre, mechanical properties, morphology

Abstrak

Kertas kerja ini membentangkan pengaruh getah ke atas komposit termoplastik diperkuat serabut mengkuang (MK) dengan peningkatan kandungan getah pada muatan serabut rendah MK 10% dan muatan serabut tinggi MK 30%. Serabut MK telah diadun bersama polietilena berketumpatan tinggi (HDPE) dan getah asli (NR) melalui pengadunan lebur dengan pencampur dalaman. Komposit MK pada muatan serabut 10% menunjukkan kekuatan regangan, kekuatan terikan pada takat putus, dan kekuatan hentaman yang lebih tinggi; tetapi modulus regangan yang rendah berbanding komposit MK pada muatan serabut 30%. Kedua-dua muatan serabut menunjukkan kekuatan regangan dan modulus regangan menurun, sementara kekuatan terikan regangan takat putus dan kekuatan hentaman seperti meningkat dengan pertambahan kandungan getah sehingga 40%. Sebaran serabut MK dan interaksi fizikal antara serabut dan matrik telah diperhati menerusi mikroskop elektron imbasan pancaran medan (FESEM). Kajian telah menunjukkan kesan muatan serabut MK terhadap sifat mekanikal dan morfologi komposit mengkuang dipengaruhi oleh kandungan getah.

Kata kunci: getah, komposit polimer, serabut mengkuang, sifat mekanik, morfologi

Introduction

The global economic growth has generated new ideas, new technologies, innovative approaches, as well as new requirements and demands in many fields. Similar circumstances occur in the polymer composites world. The growing demands for polymer composites in many areas seem to replace the use of metals, glass, wood, and other materials [1, 2]. The shortage of these materials is an advantage to the polymer composites to extend its applications. Polymer composites offer advantages of a wide range of properties from hard to soft, cheap to expensive, and low temperature to high temperature applications [3, 4]. Polymer composites can also be divided into semi biodegradable and fully biodegradable [5]. The combination of Natural Rubber (NR) and Mengkuang (MK) fibre as biodegradable materials with high density polyethylene (HDPE) as non-biodegradable material has found its use in polymer composites.

Selecting polymer matrices and fillers from the polymer composite blends is important to select a favourable polymer composite property. Each component in the polymer blends contributes its attributes in polymer composites. Polymer composites heavily depend on materials selection to cater to the necessity and the performance to be developed. The correct material selection and the suitable ratio used in the polymer composite blending, in terms of polymer matrix, reinforcement, and interphase, may produce extraordinary results for certain applications. In fact, polymer matrices have always dominated the properties of polymer [6]. Polymer matrix supports the reinforcement fibres, binds the fibres, and grasps the stress transferred. Besides, several plant fibres have been used as reinforcement filler in polymer composites. According to Monteiro et al. [7] and Fortea-Verdejo et al. [8], the mechanical properties of different types of plant fibres differ significantly due to dissimilar percentages of components in the fibres. Meanwhile, several studies that have looked into polymer matrix, reinforcement, and interface, have developed advance technologies in polymer composites. The relationships between each component, behaviour, and the responses after blending have been investigated with unlimited aspects [9–11].

Furthermore, the mechanical properties and the morphology of polymer composites are strongly influenced by fibre shape, chemical structure of fibre, fibre size, fibre concentration, fibre orientation and dispersion, as well as interactions of matrix-matrix, matrix-fibre, and fibre-fibre. The interaction of matrix-matrix is referred as miscibility of polymers, while the interaction of matrix-fibre is the compatibility of polymers. In addition, Van Der Waals forces and hydrogen bonding reflect the fibre-fibre physical interactions. In fact, many kinds of chemicals have been used as interphase for immiscible polymer blends, such maleic anhydride, dicumyl peroxide, N,N'-m-phenyl dimaleimide (HVA-2), and silane.

HDPE and NR are immiscible polymer blends. Therefore, the incorporation of NR in the blend form suggests significant physical interactions. A research study carried out by Ahmad et al. [12] indicated that the HDPE/NR blend gave the best properties at 40/60 composition. However, the addition of MK fibre to the polymer HDPE/NR blends exhibits varying effects upon the polymer composite blends. Therefore, this study focused on the influence of rubber upon MK composites, at low MK fibre loading and high MK fibre loading. This study excluded other additives or compatibilizer to serve as a preliminary study for further researches.

Materials and Methods

Materials

In this study, HDPE and NR were used as the polymer matrices. HDPE with a density of 0.95 g/cm^3, melt flow rate (MFR) of 1.1 g/10 min, and T_m at 135 °C had been supplied by Polyethylene Malaysia Sdn Bhd (Malaysia). Meanwhile, NR with Standard Malaysia Rubber grade SMR-L was obtained from Felda Rubber Industries Sdn Bhd (Malaysia). The mengkuang leaves were harvested in Bangi (Selangor, Malaysia), while the MK fibre had been prepared in the laboratory of Universiti Kebangsaan Malaysia.

Fibre preparation

The dried mengkuang leaves were ground with a universal cutting mill (Model-Pulverisette 19, Fritsch) (Germany). The fibres were immersed in tap water for another 3 days with the water changed frequently. Next, the fibres were dried at room temperature for 3 days, and then, oven-dried at 80 °C for 24 hours to remove moisture by using

Universal Oven (Memmert, Model UFB400, Germany). After that, the fibres were sieved at size 125 - 250 µm using a sieve (Retsch Test Sieve, Model ZM200).

Composite Preparation

The HDPE and the NR had been melt blended using an internal mixer (Model-Haake Rheomix R600) (Germany). The processing temperature was set at 135 °C, while the rotation speed was fixed at 50 rpm for 15 min. Prior to blending, the fibre was oven-dried for 2 h at 105 °C to eliminate moisture. After blending, the first fibre was added after 3 min, followed by NR, and then, HDPE was added after 5 min. The samples were compressed for 10 min at 145 °C under 8 GPa pressure using a hot press to produce 1-mm and 3-mm thick sheets for tensile and impact testing, respectively. The experimental design of polymer blends is as shown in Table 1.

Mechanical Characterisation

Ten specimens for tensile test were cut with dumbbell cutter JIS K-6251-6 (Model DMK-1000-D) (Japan). The tensile properties were measured by using a universal testing machine (Instron, Model-5566) (USA) with a 1 kN load cell at 50.0 mm/min crosshead speed, in accordance to ASTM 412-98a type B (2004). Notched impact strength was measured by using a pendulum digital universal fractoscope machine (Tinius Olsen, Model - IT 504), (United Kingdom), by adhering to ASTM D 256-04 (2004). On the other hand, five specimens were cut at dimensions of 65 × 12.7 × 3.0 (length × width × thickness) mm^3 with 0.25 mm depth notch for each specimen. The impact test energy was performed at 2 joules. The impact specimens were drenched in liquid nitrogen for 1 min before performing the test in such a manner so as to completely break the specimens.

Table 1. The experimental design of polymer blends

Polymer Matrix /MK Fibre 90/10						
MK Fibre: 10%		10	10	10	10	10
Polymer Matrix: 90%	HDPE	100	90	80	70	60
	NR	0	10	20	30	40
Polymer Matrix /MK Fibre 70/30						
MK Fibre: 30%		30	30	30	30	30
Polymer Matrix: 70%	HDPE	100	90	80	70	60
	NR	0	10	20	30	40

Morphology

The morphology of the impact fracture surfaces of the specimens was examined and analysed by using a SUPRA 55VP Model field emission scanning electron microscope (FESEM) (Germany). Cross-sections of the fractured surfaces of specimens were coated with platinum to prevent the generation of electrical charges during investigation. The specimens were observed at 100x magnification.

Results and Discussion

Tensile properties

The tensile strengths of polymer composites at 10% MK fibre and 30% MK fibre are shown in Figure 1. 10% of MK fibre represents low filler loading, whereas 30% fibre loading represents high filler loading. In general, the tensile result for 10% MK fibre was higher than that for 30% MK fibre. The blends at 10% MK fibre loading had more polymer matrices, when compared to 30% of MK fibre loading. Hence, it can be considered that the tensile strength at 10% MK fibre was dominated by the matrix HDPE in the blends. In fact, Rozman et al. and Jamil et al. [13, 14] found that increment in fibre loading did not necessarily increase tensile strength. The composite blends system without any compatibilizer suggested poor interaction between MK fibre and polymer matrices, as well as

the agglomeration of the fibres. However, the addition of rubber in the blends appeared to promote physical interactions between the blends.

The tensile strength for composite blends with only HDPE and without rubber exhibited MK fibre was 18.6% higher for 10% than 30% MK fibre loading. It showed that tensile strength for both blend compositions was influenced by the properties of HDPE. The stiffness of the HDPE was further increased due to dominance of HDPE matrix in the blends with higher tensile strength.

When rubber was added into the composite blends at 10% MK fibre loading and 30% MK fibre loading, the results of tensile strength seemed to slowly decrease. The composite blends lost their stiffness as the content of rubber was increased. The increasing rubber content dropped the tensile strength for both polymer blends. When less MK fibre existed in the composite blends, the tensile strength was dominated by the matrices. The increasing rubber content at low loading of MK fibre caused more dilution effect by the volume taken out as the fibre entered into the composite blends. The increasing rubber content supported the tensile strength from the sudden drop at higher fibre loading; 30% MK fibre. The elasticity property of rubber held the large amount of fibres in the composites.

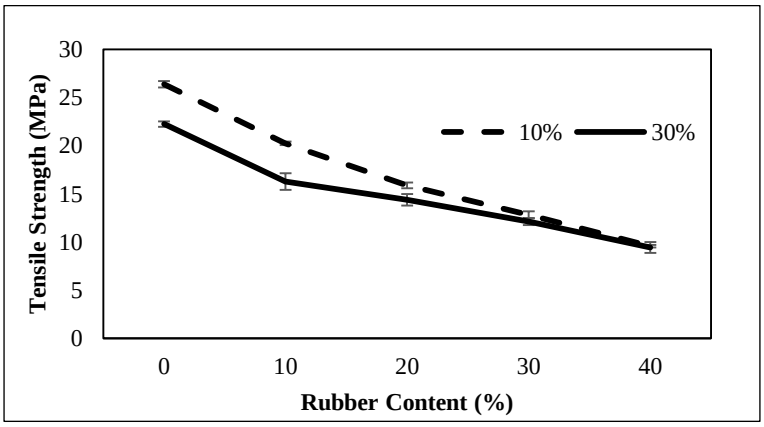


Figure 1. Tensile strength of MK composites at 10% MK and 30%MK

Figure 2 represents the tensile modulus of MK composites at 10% MK fibre loading and 30% MK fibre loading. Stiffness of natural fibre reinforced thermoplastic elastomer depends heavily on the fibre behaviour and the fibre loading. Tensile modulus of the MK composites was attributed from the fibre in the blends. Relatively, the increasing fibre increased the stiffness of the polymer composites and the tensile modulus. The graphs further display that tensile modulus of 30% of MK fibre was higher than polymer composites with 10% MK fibre for all compositions. The tensile modulus for both systems of low fibre loading and high fibre loading appeared to drop with increment in rubber content. The presence of rubber softened the composite blends and decreased the stiffness of the polymer composites. In fact, the trend of tensile modulus seemed to be similar with the pattern of tensile strength. Both fibre loading at 10% MK and 30% MK showed the two curves were getting closer when the rubber content was increased. Hence, rich rubber component hindered the effect of fibre loading.

Next, the wettability of the matrix on the fibre was also an additional factor that increased the stiffness in the composite blends. Similar results were reported by Zahari et al. [15], whereby increment in tensile modulus displayed better fibre dispersion in the composites.

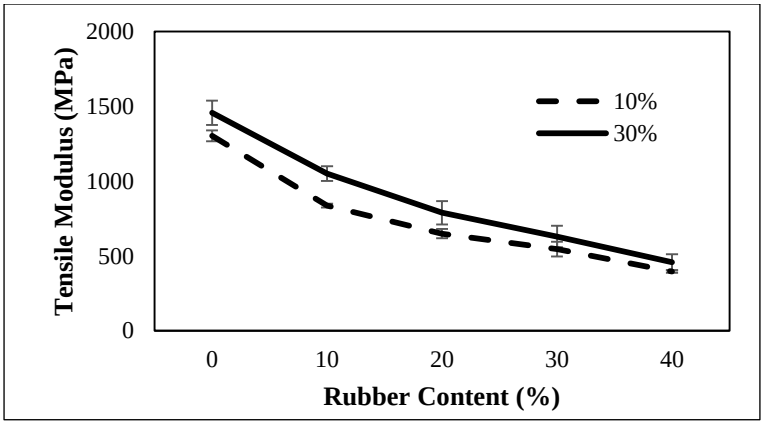


Figure 2. Tensile modulus of MK composites at 10% MK fibre and 30%MK fibre

The outcomes of tensile strain at break are illustrated in Figure 3. The MK composites at 10% MK fibre exhibited a sharp increase with the presence of rubber content in the blends. It reached the highest point at 40% rubber with 262% improvement, when compared to the blend without rubber at the same amount of fibre content. Moreover, the polymer matrices seemed to boost their properties at low concentration of fibre. In fact, at low concentration of fibre, the MK composites were less influenced by the MK fibre, thus resulting in lower rigidity. The polymer chain of the matrix could move freely due to lower obstacles in the blends. Furthermore, the rubber matrix dominated the tensile strain at break properties at low concentration of fibre.

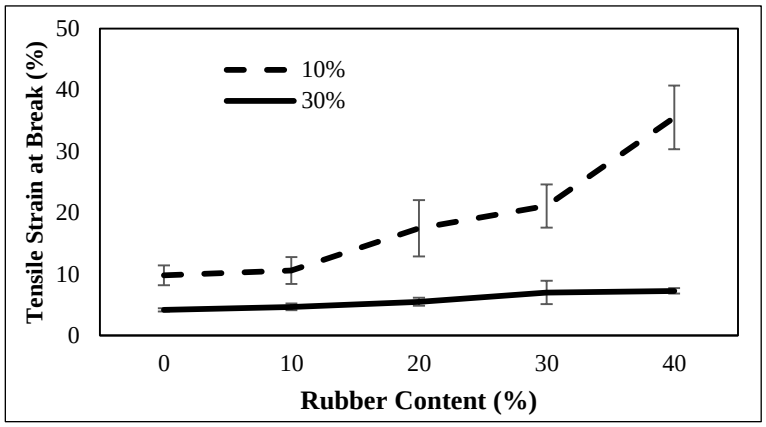


Figure 3. Tensile strain of MK composites at 10% MK and 30% MK

Meanwhile, at 30% of MK fibre loading, the increased rubber content had less effect on elasticity. The composites lost their elasticity as the fibre content was increased. The results showed that as the rubber content was increased, the tensile strain at break increased slightly as well. Besides, the large amount of fibre content hindered the stress that was transferred from the matrix to the fibre. The reduction of the amount of rubber matrix as the MK fibre amount was increased also caused MK composites to be more rigid. Similar results have been reported [15–17], as the presence of fibres in the polymer matrix enhanced the aspect of rigidity in the polymer composites.

Impact strength

An elastomer material, such as rubber, is well-known as a good impact absorber [12, 18]. The effect of rubber content for both polymer blends on impact strength is shown in Figure 4. The composite blends with 10% MK fibre loading exhibited a higher impact strength, as compared to 30% MK fibre for all compositions, with and without the presence of rubber content. Low concentration of fibre caused the polymer matrices to expose its role to absorb the

immediate energy given. Besides, the presence of more matrix component increased the ability of the polymer composites to absorb energy. Hence, more matrix offers more toughness in the polymer composites.

The impact strength of 30% MK fibre loading seemed to slowly increase with the increasing rubber content in the composite blends. Similar result is also reported by El-Shekeil et al. [19] in their research on kenaf composites. The existence of fibre decreases the local motion of polymer chain. A large number of fibre initiates more crack propagation between the matrix and the fibre. However, the presence of rubber matrix appeared to reduce all those effects and supported the weak interaction between the MK fibre and the matrices. Furthermore, due to polarity factors, the tendency for the interaction between fibre and fibre is more likely to occur, when compared to the interaction between the polymer matrices. This phenomenon provides more probability for fibres agglomeration, aside from reducing the ability of composites to absorb the energy given.

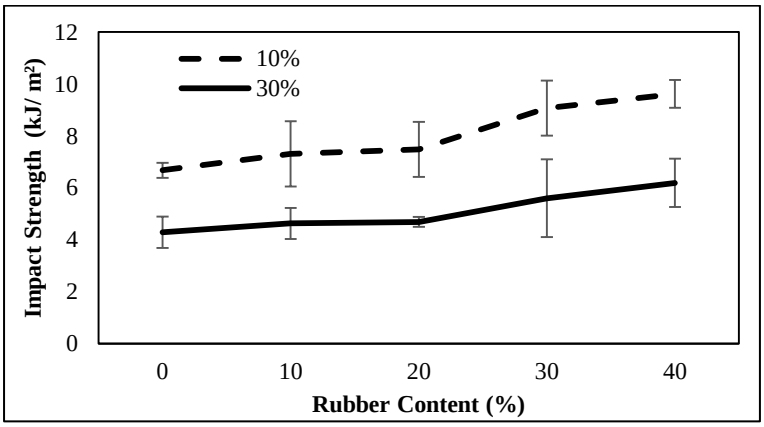


Figure 4. Impact strength of MK composites at 10% MK and 30%MK

Morphology

Figure 5(a) presents the FESEM micrograph images of fracture surface impact test performed upon MK composites with the presence of 10% NR at 10% MK fibre loading at 100x magnification, whereby a rough surface is observed with broken fibres and fibre sites. More fibres appear to disperse throughout the matrices. Next, Figure 5(b) illustrates the FESEM micrograph images of fracture surface impact test performed on MK composites with the presence of 10% NR at 30% MK fibre loading at 100x magnification, in which more MK fibre is noted throughout the matrices. Moreover, a lot of fibre agglomeration had been detected with vast fibre bundles. The tensile strength also dropped due to fibre agglomeration [20]. Meanwhile, Figure 6(a) shows the FESEM micrograph images of fracture surface impact test performed on MK composites with 40% NR at 10% MK fibre loading at 100x magnification. The MK fibres were found to be well-dispersed in the composite blends. Figure 6(b) displays the FESEM micrograph images of fracture surface impact test performed on MK composites with 40% NR at 30% MK fibre loading at 100x magnification. This resulted in more MK fibre with a lot of fibres in bundles that were well-dispersed in the matrices. Uneven fracture surface indicates the effect of rubber holding the MK fibre. The rubber phase was also obviously deposited on the surface of MK fibre, which signified physical interactions between MK fibre and rubber phase at high rubber content.

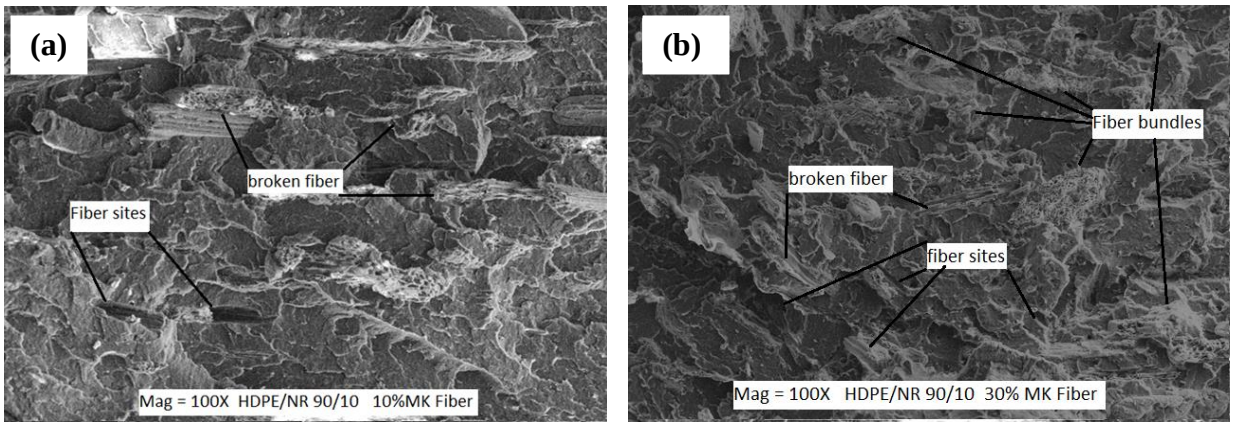


Figure 5. FESEM micrograph images of impact fracture surface on MK composites a) 10% rubber content and 10% MK fibre at 100× magnification, b) 10% rubber content and 30% MK fibre at 100× magnification

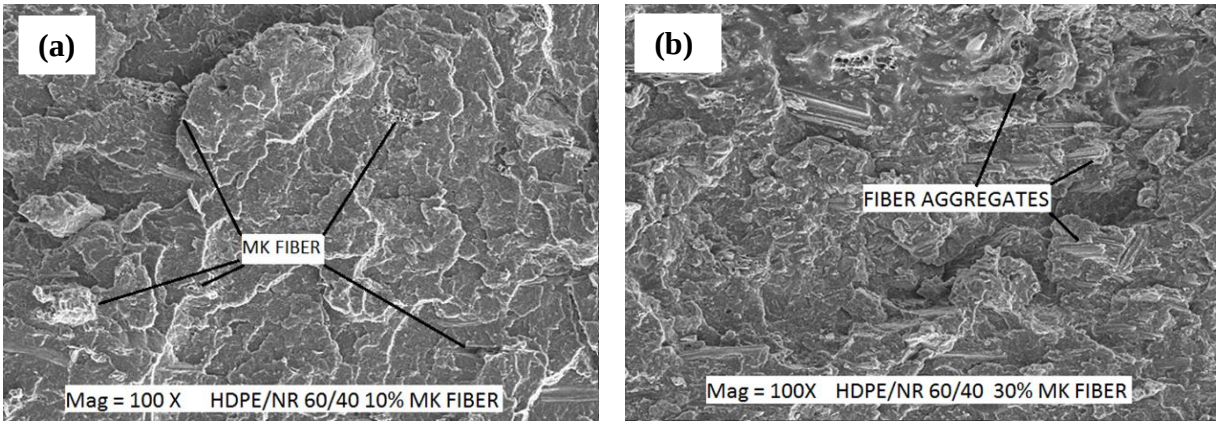


Figure 6. FESEM micrograph images of impact fracture surface on MK composites a) 40% rubber content and 10% MK fibre at 100× magnification, b) 40% rubber content and 30% MK fibre at 100× magnification

Conclusion

Based on the results of this study, NR content strongly influenced the mechanical properties and the morphology of MK composites. The increasing rubber content in the composite blends improved their elasticity and toughness attributes. The influence of MK fibre loading upon tensile strength and tensile modulus of MK composite blends slowly diminished at high rubber content, while the morphology displayed physical interactions between fibre and matrices for the composite blends.

Acknowledgement

The authors wish to acknowledge Universiti Kebangsaan Malaysia (UKM), Universiti Selangor (UNISEL), as well as the Malaysian Ministry of Science, Technology, and Environment, for sponsoring the research under the IRPA scheme 03-01-02-SF1000, Fundamental Research Grant Scheme (FRGS/2/2014/TK04/UKM/02/1), including Selangor State Government, PORCE UKM, and CRIM UKM for the technical support and facilities extended.

References

1. Saheb, N. D. and Jog, J. P. (1999). Natural fiber polymer composites: A review. *Advance Polymer Technology*, 18(4): 351-363.
2. Joshi, S., Drzal, L., Mohanty, A. and Arora, S. (2004). Are natural fiber composites environmentally superior to glass fiber reinforced composites?. *Composite Part A: Applied Science and Manufacturing*, 35(3): 371-376.
3. Alves, F. M. E., Pereira, T. V. C. and Gomes, O. D. F. M. (2013). The effect of fiber morphology on the tensile strength of natural fibers. *Journal of Materials Research and Technology*, 2(2): 149-157.
4. Tezara, C., Siregar, J. P., Lim, H. Y., Fauzi, F. A., Yazdi, M. H., Moey, L. K. and Lim, J. W. (2016). Factors that affect the mechanical properties of kenaf fiber reinforced polymer: A review. *Journal of Mechanical Engineering and Sciences*, 10(2): 2159-2175.
5. John, M. J., Varughese, K. T. and Thomas, S. (2008). Green composites from natural fibers and natural rubber: effect of fiber ratio on mechanical and swelling characteristics. *Journal of Natural Fibers*, 5(1): 47-60.
6. Thakur, V. K., Thakur, M. K. and Gupta, R. K. (2014). Review: Raw natural fiber–based polymer composites. *Internatinal Journal of Polymer Analysis and Characterization*, 19(3): 256-271.
7. Monteiro, S. N., Lopes, F. P. D., Ferreira, A. S. and Nascimento, D. C. O. (2009). Natural-fiber polymer-matrix composites: Cheaper, tougher, and environmentally friendly. *Polymer-Matrix Composites*, 61(1): 17-22.
8. Fortea-Verdejo, M., Bumbaris, C., E., Burgstaller, C., Bismark, A. and Lee, K. Y. (2017). Plant fibre-reinforced polymers: Where do we stand in terms of tensile properties?. *International Materials Reviews*, 62(8): 441-464.
9. Hassaini, L., Kaci, M., Touati, N., Pillin, S., Kervoelen, A. and Bruzaud, S. (2017). Valorization of olive husk flour as a filler for biocomposites based on poly(3-hydroxybutyrate-co-3-hydroxyvalerate): Effects of silane treatment. *Polymer Testing*, 59: 430-440.
10. Puglia, D., Sarasini, F., Santulli, C. and Kenny, J. M. (2017). Manufacturing of natural fiber/agrowaste based polymer composites. *Green Biocomposites, Springer*: pp. 125–147.
11. Preet Singh, J. I., Dhawan, V., Singh, S. and Jangid, K. (2017). Study of effect of surface treatment on mechanical properties of natural fiber reinforced composites. *Material Today Proceeding*, 4(2):2793-2799.
12. Ahmad, S., Abdullah, I., Sulaiman, C. S. and Kohjiya, S. (1994). Natural rubber-hdpe blends with liquid natural-rubber as a compatibilizer. I. thermal and mechanical-properties. *Journal of Applied Polymer Science*, 51:1357-1363.
13. Rozman, H. D., Tan, K. W., Kumar, R. N., Abubakar, A., Mohd Ishak, Z. A. and Ismail, H. (2000). The effect of lignin as a compatibilizer on the physical properties of coconut fiber- polypropylene composites. *European Polymer Journal*, 36: 1483-1494.
14. Jamil, M. S., Ahmad, I. and Abdullah, I. (2006). Effects of rice husk filler on the mechanical and thermal properties of liquid natural rubber compatibilized high-density polyethylene/natural rubber blends. *Journal of Polymer Research*, 13(4):315-321.
15. Zahari, W. Z. W., Badri, R. N. R. L., Ardyananta, H., Kurniawan, D. and Nor, F. M. (2015) Mechanical properties and water absorption behavior of polypropylene / ijuk fiber composite by using silane treatment. *Procedia Manufacturing*, 2: 573-578.
16. Stelescu, M-D., Manaila, E., Craciun, G. and Dumitrascu, M. (2014). New green polymeric composites based on hemp and natural rubber processed by electron beam irradiation. *The Scientific World Journal*, 2014: 1-13.
17. Chen, R. S., Ahmad, S. and Gan, S. (2016). Characterization of rice husk-incorporated recycled thermoplastic blend composites. *BioResources*, 11(4): 8470-8482.
18. Ibrahim, A. and Dahlan, M. (1998). Thermoplastic natural rubber blends. *Progress in Polymer Science*, 23: 665-706.
19. El-Shekeil, Y. A., Sapuan, S. M., Khalina, A., Zainudin, E. S. and Al-Shuja'a, O. M. (2012). Influence of fiber content on the mechanical and thermal properties of Kenaf fiber reinforced thermoplastic polyurethane composites. *Journal of Thermal Analysis and Calorimetry*, 109: 299-303.
20. Syafri, R., Ahmad, I. and Abdullah, I. (2011). Effect of rice husk surface modification by LENR the on mechanical properties of NR/HDPE reinforced rice husk composite. *Sains Malaysiana*, 40(7): 749-756.

Malaysian Journal of Analytical Sciences, Vol 22 No 5 (2018): 914 - 920
DOI: https://doi.org/10.17576/mjas-2018-2205-20

MALAYSIAN JOURNAL OF ANALYTICAL SCIENCES
Published by The Malaysian Analytical Sciences Society
ISSN 1394 - 2506

FABRICATION OF CELLULOSE MICROSPHERES FROM MODIFIED COTTON LINTER AND OIL PALM TRUNK FIBRE VIA EMULSION METHOD

(Fabrikasi Mikrosfera Selulosa daripada Linter Kapas dan Gentian Batang Kelapa Sawit Termodifikasi Melalui Kaedah Emulsi)

Balqis Az-Zahraa Norizan[1], Nurul Shuhadah Mahadi[1], Nurul Nazatulatika Mohd Nizam[1], Sarani Zakaria[1], Muhammad Fauzi Daud [2], Sharifah Nabihah Syed Jaafar[1]*

[1]*School of Applied Physics, Faculty of Science and Technology, Universiti Kebangsaan Malaysia, 43600 UKM Bangi, Selangor, Malaysia*
[2]*Institute of Medical Science Technology, Universiti Kuala Lumpur Malaysia, 43000 Kajang, Selangor, Malaysia*

**Corresponding author: nabihah@ukm.edu.my*

Received: 20 July 2017; Accepted: 28 April 2018

Abstract

In this study, cellulose microspheres from modified cotton linter (CL) and oil palm trunk fibre (OPTF) were fabricated by using simple emulsion method. The cellulose was obtained from the CL and OPTF through the alkaline pre-treatment and acid hydrolysis processes. The emulsion method was performed using polyvinyl alcohol (PVA) as an emulsifying agent. The characterization of the cellulose from CL and OPTF were analysed using Fourier transform infrared spectroscopy (FTIR) and X-ray diffraction (XRD), and the morphological characterizations of cellulose microspheres were later observed under optical microscopy (OM) and field emission-scanning electron microscopy (FE-SEM). Based on the results, FTIR spectra displayed the lignin and hemicellulose had removed after treatments, while XRD revealed that the crystallinity index of OPTF and CL was increased after the treatments. The microspheres, formed with different ranges of size between 80 to 150 µm under OM and FE-SEM, showed the formation of pores on the surface of the microspheres.

Keywords: emulsification, lignin, porous, field emission scanning electron microscopy

Abstrak

Kajian ini dijalankan bagi menghasilkan mikrosfera selulosa daripada linter kapas (LK) dan gentian batang kelapa sawit (GBKS) melalui kaedah emulsi. Selulosa didapati daripada LK dan gentian GBKS selepas proses pra-rawatan alkali dan hidrolisis asid. Manakala, kaedah emulsi dijalankan dengan menggunakan polivinil alkohol (PVA) sebagai agen pengemulsi. Pencirian selulosa daripada LK dan GBKS akan dianalisa menggunakan analisis transformasi inframerah Fourier (FTIR) dan pembelauan sinar-X (XRD) dan pencirian morfologi bagi mikrosfera selulosa dijalankan oleh mikroskopi optik (OM) dan mikroskop elektron-imbasan pancaran medan (FE-SEM). Berdasarkan keputusan FTIR yang diperoleh, lignin dan hemiselulosa telah berjaya dibuang selepas rawatan, sementara itu, keputusan XRD menunjukkan terdapat peningkatan pada indeks kehabluran bagi GBKS dan LK selepas rawatan. Mikrosfera yang terbentuk juga dapat diperhatikan melalui OM dengan saiz berjulat 80 hingga 150 µm dan FE-SEM pula menunjukkan penghasilan liang pada permukaan kedua-dua mikrosfera.

Kata kunci: pengemulsi, lignin, berliang, mikroskop elektron imbasan pancaran medan

Introduction

Microspheres are mostly produced from polymers and ceramics such as poly(D,L, -lactide-co-glycolide) (PLG), poly(ε-caprolactone) (PCL), poly(lactic-co-glycolic acid) (PLGA), calcium phosphate, and hydroxyapatite (HA) [1]. Today, the number of medical applications for natural and synthetic biomaterial continues to expand. The material selection is important due to their chemical, physical, and geometrical effects on the microcarriers. The porosity of the microspheres are one of the important properties needed in medical applications as porosity helps in cell proliferation, viability, and differentiation compared to non-porous microspheres. Furthermore, porous microspheres are preferred due to its high surface area, low density, low thermal conductivity, and good flow ability [2].

Cellulose and its derivatives are natural and low-cost polymer with renewable and biodegradable properties [3]. All of these properties make cellulose as one of the attractive materials in biomedical applications. For example, cellulose-based materials are excellent in prevention of excessive bleeding due to hemostatic agent, wound healing, implantation on connective tissue due to biocompatibility and long lasting stability [4]. As cellulose is known as the polymer with pores, it is suitable for the formation of porous microspheres.

The production of microspheres by thermal phase separation, emulsion polymerization, and spray drying possess a difficulty in maintaining the uniformity and homogeneity in particle size distribution. The most common technique in microspheres fabrication is emulsion method, where the polymer and the solvent are mixed together to appear in one phase under high speed rotation with the addition of emulsifier [5].

In Malaysia, oil palm trunk fibre (OPTF) has been underutilised, producing 8.2 million tonnes of waste annually [6]. Usually, the felled oil palm trunk (OPT) is used as compost or burned on the field. Consequently, carbon dioxide, carbon monoxide, and suspended particles of unburned carbon are released to the atmosphere which contributes to global warming and greenhouse effect. In this paper, the objective was to study the effect of microspheres microstructure on different modified cellulose (cotton linter (CL) and OPTF) by using emulsion method. Perhaps, the OPTF has a potential to be used as starting materials in microspheres fabrication.

Materials and Methods

Materials

Oil palm trunk fibre (OPTF) was provided by Leong Brothers Earthworks Construction, Kluang, Johor while cotton linter (CL) was purchased from Hubei Chemical Fibre, ammonium hydroxide (NH_4OH) (28%-30%), hydrochloric acid (HCl) (36%-38%), sulphuric acid (H_2SO_4) (95%-98%), dichloromethane (DCM) (89.34 g/mol), and polyvinyl alcohol (PVA) (87%-89%), acetone (99.9%) were purchased from Sigma-Aldrich.

Preparation of cellulose from CL and OPTF

The CL was ground and dissolved in 0.5% HCl at a ratio of 1:2 (w/v) for 4 hours at 120 ºC. Then, the hydrolyzed CL was filtered and washed until pH became neutral and dried in an oven for 24 hours at 60 ºC. OPTF was washed to remove dust and dried in oven for 24 hours at 60 ºC. The OPTF was then ground to form powder. 100 g of OPTF powder was dissolved in 1 L 10% NH_4OH to remove lignin for 24 hours at 25 ºC. After lignin was removed, the remaining solid was hydrolyzed by 0.5% HCl at 120 ºC for 4 hours. The hydrolyzed powder was filtered and washed until pH became neutral and dried in an oven for 24 hours at 60 ºC.

Preparation of cellulose microspheres (CM)

Cellulose microspheres (CM) were prepared by undergoing emulsion method, where 0.002 g cellulose powder from OPTF and CL were dissolved in 2 mL DCM for 30 s. 50 mL of 5% PVA (10 ºC) was added to the mixture and stirred for 2 hours at 500 rpm. The emulsion was then subjected to another 500 mL of 1% PVA (10 ºC) and stirred for 6 hours at 500 rpm. Lastly, the microspheres produced were dried under ambient conditions. The microspheres were kept in a dry box prior to analyses.

Characterization: X-ray diffraction (XRD)

Phase and crystallinity index (CrI) of cellulose samples were characterized using X-ray diffraction (XRD) (Bruker D8 Advance Madison, WI, USA). The XRD was performed using radiation of Cu Kα = 1.5458 Å at a diffraction angle (2θ) range from 10 to 80°. Diffraction profiles were carried out with a Gaussian function to determine the CrI

of the samples. The CrI of the samples were examined by using Bruker Advanced X-Ray Solutions software, DIFFRAC^{PLUS} Evaluation (EVA) with the following equation 1 with slight modifications:

$$\text{CrI (\%)} = A_{Cystal}/A_{Total} \text{ x } 100 \quad (1)$$

where $A_{Crystal}$ is the sum of the areas under the crystalline diffraction peaks and A_{Total} represents the total area under the diffraction curve between $2\theta = 10^{o}$-80^{o}.

Fourier transform infrared spectroscopy

The FTIR spectra of 3 mg CL and OPTF cellulose were recorded using Fourier transform infrared spectroscopy (FTIR) spectrometer (Perkin Elmer Spectrum 400) to observe the functional groups before and after chemical treatments. The transmittance mode and 16 s scanning number were selected ranging from 4000 cm^{-1} to 600 cm^{-1}.

Optical microscope (OM)

The size and distribution of CM was analysed by optical microscope (OM) (Axiolab A1.MAT). A small sample was dispersed in water and placed between two glass slides and then observed under OM. The dimensions of CM were determined using digital image analyses with 10x magnifications.

Field emission scanning electron microscope (FE-SEM)

The morphology of CM from CL and OPTF cellulose were observed by using field emission scanning electron microscope (FE-SEM, Zeiss/Supra 55VP). Platinum was used to coat all samples in order to enhance the quality of images and prevent charging with 10x magnification at 1.0 kV.

Results and Discussion

Crystallinity analysis of cellulose from CL and OPTF

XRD diffractogram of OPTF, modified OPTF, CL and modified CL were observed in Figure 1. The spectra shows the changes happened in diffraction pattern of OPTF and CL after undergoing the chemical treatments. The peak intensity (Figure 1) which was observed at $2\theta = 15^{o}$, 16^{o}, 22^{o}, and 35^{o} confirmed the modified cellulose was type I [7]. Moreover, the peaks corresponded to the crystallographic planes of 110, $1\bar{1}0$, 200, and 004, respectively. This result was comparable to Lamaming et al. [8] for OPTF and for CL [9]. The CrI of 22.4%, 33.2%, 61.8%, and 60.8% were determined for OPTF, modified OPTF, CL and modified CL, respectively. Based on the findings, CrI of OPTF was lower as compared to CL due to high number of extractives and thick wall owned by OPTF which gives strength to the plant [10]. In addition, the CrI result for the CL suggested that there was no adverse effect of acid hydrolysis on crystalline structure of CL, whereas the CrI of OPTF greatly increased after the hydrolysis due to the elimination of amorphous substances such as hemicellulose and lignin [11].

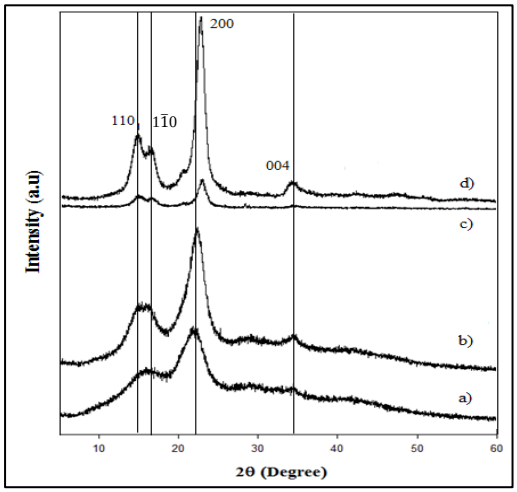


Figure 1. X-ray diffraction spectra of (a) OPTF, (b) modified OPTF, (c) CL, and (d) modified CL

Spectroscopic analysis

Figure 2 represents the FTIR spectra of OPTF, modified OPTF, CL and modified CL. Basically, the spectra look alike with slight differences on the intensity of certain peaks. All spectra showed a peak at ~3400 cm^{-1}. According to Salim and Sorya [12], the stretching vibration of O–H performed at 3200 cm^{-1} to 3700 cm^{-1} was due to the lignocellulosic materials in the fibre, consisting of hemicellulose and cellulose. From the spectra, all samples appeared peaks at 2800 cm^{-1} to 2900 cm^{-1} which contributed to C–H stretching vibrations. Meanwhile, the absorption of water by cellulose can be indicated by a peak at 1500 cm^{-1} to 1600 cm^{-1} [13]. The difference of certain peaks can be seen between spectra of CL and OPTF. Peaks at 1000 cm^{-1} to 1100 cm^{-1} which corresponded to the deformation of C–H in cellulose were observed less prominent on OPTF as compared to CL due to the removal of lignin and hemicellulose [14].

Besides that, the effect of treatment on OPTF had caused the absence of peak at ~1700 cm^{-1} on modified OPTF which fit to the elimination of hemicellulose on the samples [15]. The peaks at ~1200 cm^{-1} on the spectra which correlated with the C=O bonding in lignin could be observed at OPTF but changed slightly after chemical treatment on modified OPTF [16], but no indication on CL samples due to high crystallinity. Another peak at 800 cm^{-1} to 900 cm^{-1} was appointed as amorphous region on the samples [17].

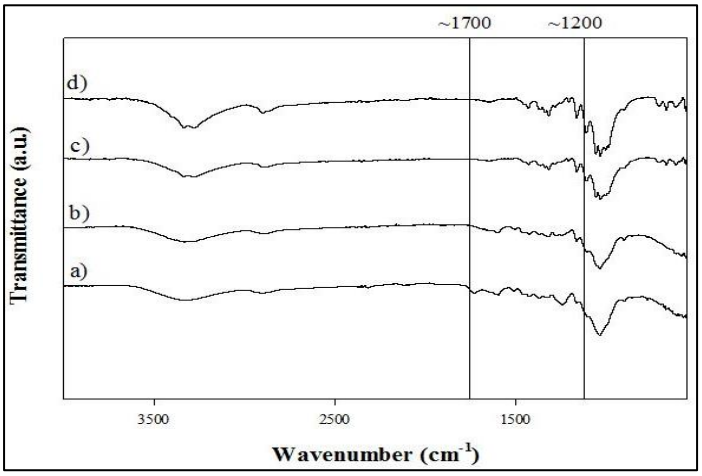


Figure 2. FTIR spectra of (a) OPTF, (b) modified OPTF, (c) CL, and (d) modified CL

Microstructural analysis

Based on Figure 3, spherical shape of CM shows size of 80 to 150 µm in diameter for CL and OPTF microspheres. The result also showed that the CL microspheres exhibited smaller size as compared to OPTF microspheres. This might be due to the high crystalline region of CL which contributed to more hydrogen bond networks that made cellulose rigid and resistant to solvent and emulsifier reactions than OPTF. Furthermore, difference in size of the microspheres could be related to the stability of the emulsion in the solution. According to Mi et al. [18], the stability of the emulsion was related to the interface energy between the polymer and the emulsifier. Flocculation between the microspheres can be avoided by reducing the interface energy. Besides that, different sizes of microspheres also resulted from the increasing temperature as the solution was stirred for 6 hours after addition of emulsifier. This resulted in increase of temperature which gave effect to the interfacial strength of emulsion where the interfacial strength reduced and destabilised the emulsion, hence causing flocculation [19].

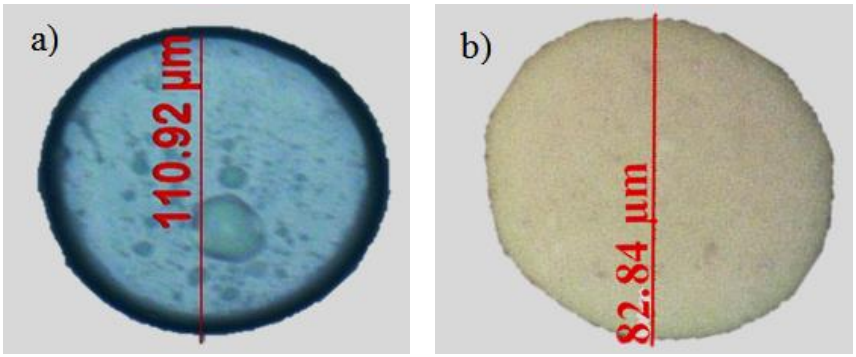


Figure 3. Optical micrographs of cellulose microspheres fabricated from (a) modified OPTF and (b) modified CL

Surface morphology analysis

Figure 4 shows a formation of porous structure on the surface of microspheres. The pores were formed due to the complete evaporation of solvent that occurred during processing [20]. Besides, the solvent used in this research, i.e., DCM has low solubility towards the water, thus prevents the water to penetrate into the droplet hence supresses the pore formation. This property favours the microspheres to be used as carriers due to the pores that provide maximum surface area for the attachment of substances. In addition, the diameter of the pores < 20 µm was said to be ideal as carriers [21].

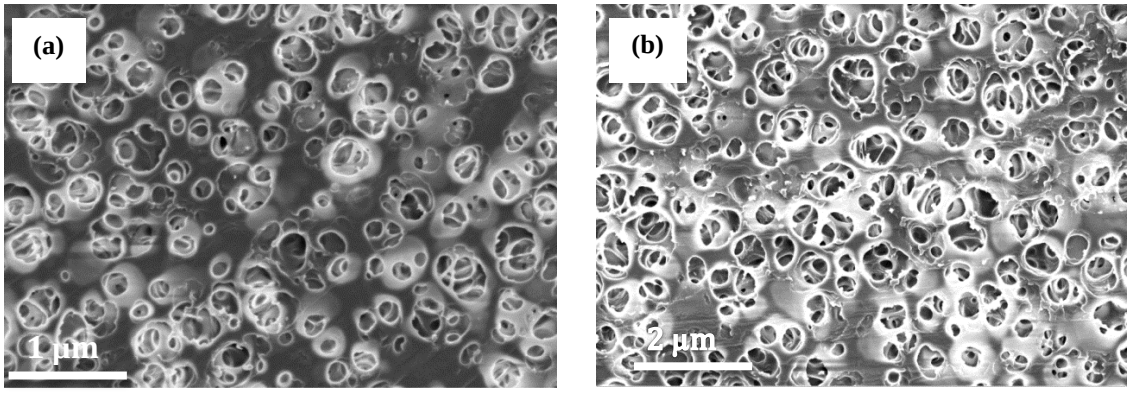


Figure 4. Pore size of cellulose microspheres from (a) modified OPTF and (b) modified CL

Conclusion

In conclusion, cellulose microspheres from modified OPTF and CL were successfully prepared using emulsion method. The microspheres from CL and OPTF revealed the size of 80 to 150 µm in diameter and showed a porous structure. The FTIR spectra displayed that non-cellulosic components were removed after treatments, while XRD revealed that there was an increase in crystallinity index after treatment, which were 22.4%, 33.2%, 61.8%, and 60.8% for OPTF, modified OPTF, CL and modified CL, respectively.

Acknowledgement

We would like to acknowledge the financial support from the Industrial and Malaysian Ministry of Higher Education through the GUP-2017-114, LRGS/TD/2012/USM-UKM/PT/04, and Centre for Research and Instrumentation (CRIM), UKM for the testing services.

References

1. Xiao, Q., Zhou, K., Chen, C., Jiang, M., Zhang, Y., Luo, H. and Zhang, D. (2016). Hollow and porous hydroxyapatite microspheres prepared with an O/W emulsion by spray freezing method. *Materials Science & Engineering C,* 69: 1068-1674.
2. Yang, H., Xie, Y., Hao, G., Cai, W. and Guo, X. (2015). Preparation of porous alumina microspheres via n oil-in-water emulsion method accompanied by a sol–gel process. *New Journal of Chemistry*, 40: 589-595.
3. Dong, S., Bortner, M. J. and Roman, M. (2016). Analysis of the sulfuric acid hydrolysis of wood pulp for cellulose nanocrystal production: a central composite design study. *Industrial Crops and Products*, 93: 76-87.
4. Czaja, W. K., Young, D. J., Kawecki, M. and Jr., R. M. (2007). The future prospects of microbial cellulose in biomedical applications. *Biomacromolecules*, 8: 1-12.
5. Kemala, T., Budianto, E. and Soegiyono, B. (2012). preparation and characterization of microspheres based on blend of poly(lactic acid) and poly(ε-caprolactone) with poly(vinyl alcohol) as emulsifier. *Arabian Journal of Chemistry*, 5: 103-108.
6. Suhaily, S. S., Jawaid, M., Abdul Khalil, H., Mohamed, A. and Ibrahim, F. (2012). A review of oil palm biocomposites for furniture design and applications: potential and challenges. *BioResources*, 7(3): 4400-4423.
7. Tang, Y., Shen, X., Zhang, J., Guo, D., Kong, F. and Zhang, N. (2015). Extraction of cellulose nano-crystals from old corrugated container fibre using phosphoric acid and enzymatic hydrolysis followed by sonication. *Carbohydrate Polymers*, 125: 360-366.
8. Lamaming, J., Hashim, R., Sulaiman, O., Leh, C. P., Sugimoto, T. and Nordin, N. A. (2015). Cellulose nanocrystals isolated from oil palm trunk. *Carbohydrate Polymers*, 127: 202-208.
9. Gan, S., Padzil, F. N. M., Zakaria, S., Chia, C. H., Jaafar, S. N. S. and Chen, R. S. (2015). Synthesis of liquid hot water cotton linter to prepare cellulose membrane using NaOH/Urea or LiOH/Urea. *BioResources*, 10: 2244-255.
10. Lamaming, J., Hashim, R., Leh, C. P., Sulaiman, O., Sugimoto, T. and Nasir, M. (2015). Isolation and characterization of cellulose nanocrystals from parenchyma and vascular bundle of oil palm trunk (*Elaeis Guineensis*). *Carbohydrate Polymers*, 134: 534-540.
11. Ramli, R., Junadi, N., Beg, M. D. and Yunus, R. M. (2015). Microcrystalline cellulose (MCC) from oil palm empty fruit bunch (EFB) fibre via simultaneous ultrasonic and alkali treatment. *International Journal of Chemical, Nuclear, Materials and Metallurgical Engineering*, 9: 8-11.
12. Salim, B. and Sorya, N. (2015). Effects of chemical treatments on the structural, mechanical and morphological properties of poly(vinylchloride)/spartium junceum fibre composites. *Cellulose Chemistry and Technology*, 49: 375-385.
13. Rhim, J.-W., Reddy, J. P. and Luo, X. (2014). Isolation of cellulose nanocrystals from onion skin and their utilization for the preparation of agar-based bio-nano composites films. *Cellulose*, 22: 407-420.
14. Mohamad Haafiz, M., Hassan, A., Zakaria, Z. and Inuwa, I. (2014). Isolation and characterization of cellulose nanowhiskers from oil palm biomass microcrystalline cellulose. *Carbohydrate Polymers*, 103: 119-125.
15. Nazir, M. S., Wahjoedi, B. A., Yussof, A. W. and Abdullah, M. A. (2013). Eco-friendly extraction and characterization of cellulose from oil palm empty fruit bunches. *BioResources*, 8: 2161-2172.
16. Owolabi, A. F., Mohamad Haafiz, M., Hossain, M. S., Hussin, M. H. and Nurul Fazita, M. (2017). Influence of alkaline hydrogen peroxide pre-hydrolysis on the isolation of microcrystalline cellulose from oil palm fronds. *International Journal of Biological Macromolecules*, 95: 1228-1234.
17. Lamaming, J., Hashim, R., Leh, C. P. and Sulaiman, O. (2017). Properties of cellulose nanocrystals from oil palm trunk isolated by total chlorine free method. *Carbohydrate Polymers*, 156: 409-416.
18. Mi, Y., Li, J., Zhou, W., Zhang, R., Ma, G. and Su, Z. (2016). Improved stability of emulsions in preparation of uniform small-sized konjac glucomanna (KGM) microspheres with epoxy-based polymer membrane by premix membrane emulsification. *Polymers*, 8: 1-13.
19. Parida, P., Mishra, S. C., Sahoo, S., Behera, A. and Nayak, B. P. (2016). Development and characterization of ethylcellulose based microspheres for sustained release of nifedipine. *Journal of Pharmaceutical Analysis*, 6: 341-344.
20. Murakami, M., Matsumoto, A., Watanabe, C., Kurumado, Y. and Takama, M. (2015). Fabrication of porous ethyl cellulose microspheres based on the acetone-glycerin-water ternary system: Controlling porosity via the solvent-removal mode. *Drug Discoveries & Therapeutics*, 9: 303-309.

21. Qutachi, O., Vetsch, J., Gill, D., Cox, H., Scurr, D. and Hofmann, S. (2014). Injectable and porous PLGA microspheres that form highly porous scaffolds at body temperature. *Acta Biomaterialia,* 10: 5090-5098.

Malaysian Journal of Analytical Sciences Vol 22 No 6 2018

Articles 9-17 are selected papers from the "Malaysia Polymer International Conference 2017 (MPIC 2017), 19 & 20 July 2017, Universiti Kebangsaan Malaysia, Bangi Campus, Selangor, Malaysia; organised by Polymer Research Center (PORCE), Universiti Kebangsaan Malaysia and co-organised by Mahatma Gandhi University, India and Gifu University, Japan."

Guest Editor: Siti Fairus Mohd Yusoff

Articles 18-20 are selected papers from the "3rd International Conference on Science and Natural Resource (ICSNR 2018), 1 & 2 April 2018, Grand Borneo Hotel, Sabah, Malaysia; organised by United Scientists and Engineers International (UniSE International), in collaboration with e-VIBS and Faculty of Science and Natural Resources of the Universiti Malaysia Sabah."

Guest Editor: Chong Khim Phin

		Page
1.	THE PHYSICAL AND ELECTROCHEMICAL CHARACTERISTIC OF GOLD NANOPARTICLES SUPPORTED PEDOT/GRAPHENE COMPOSITE AS POTENTIAL CATHODE MATERIAL IN FUEL CELLS (Pencirian Fizikal dan Elektrokimia Komposit Zarah Nano Aurum Disokong PEDOT/Grafin sebagai Bahan Katod Berpotensi dalam Sel Bahan Api) *Nurul'ain Basyirah Muhamad and Farhanini Yusoff*	921
2.	ENHANCED CORROSION INHIBITION USING PURIFIED TANNIN IN HCl MEDIUM (Peningkatan Perencat Kakisan Menggunakan Tanin Tertulen dalam Medium HCl) *Hatika Kaco, Nur Atiqah Abu Talib, Sarani Zakaria, Sharifah Nabihah Syed Jaafar, Norinsan Kamil Othman, Chin Hua Chia, Sinyee Gan*	931
3.	FORMATION OF VANILLIN AND VANILLIC ACID FROM KRAFT LIGNIN THROUGH GREEN CHEMICAL OXIDATION (Pembentukan Vanillin dan Asid Vanillik dari Kraft Lignin melalui Proses Pengoksidaan Kimia Hijau) *Nabilah Ismail and Leonard James Wright*	943
4.	CORROSION INHIBITIVE EFFECT OF THIOUREA ON 1100 ALUMINIUM ALLOY SHEET IN HYDROCHLORIC ACID SOLUTION (Kesan Perencatan Kakisan Thiourea Terhadap kepingan Aloi Aluminium 1100 Dalam Larutan Asid Hidroklorik) *Maria Fazira Mohd Fekeri, Chan Kok Sheng, Lee Hou Yi*	950
5.	CHEMICAL COMPOUNDS AND ANTIMICROBIAL ACTIVITY OF ACETONE *Musa acuminate* AA/AAA LEAF STALK EXTRACTS ON SELECTIVE GRAM-NEGATIVE BACTERIA (Sebatian Kimia dan Aktiviti Antimikrob dari Ekstrak Aseton Pelepah Daun *Musa acuminate* AA/AAA pada Bakteria Jenis Gram Negatif Terpilih) *Tuan Nadrah Ismail, Raja Azman Awang, Suharni Mohamad, Wan Nazatul Shima Shahidan*	957
6.	MODIFIED LEACHING OF ^{238}U AND ^{232}TH FROM WATER LEACH PURIFICATION (WLP)	965

RESIDUE
(Modifikasi Larut Lesap Bagi ^{238}U dan ^{232}TH dari Residu Pemurnian Larut Lesap Air (WLP))
Nur Shahidah Abdul Rashid, Zetty Izzaty Saleh, Nurul Syiffa Mahzan, Siti Nur Ain Sulaiman, Khoo Kok Siong, Mohd. Idzat Idris, Syazwani Mohd Fadzil

7. EXTRACTION OF SQUALENE FROM *Aquilaria malaccensis* LEAVES USING DIFFERENT EXTRACTION METHODS 973
(Pengekstrakan Skualena daripada Daun *Aquilaria malaccensis* Menggunakan Kaedah Pengekstrakan yang Berlainan)
Wan Nurul Diyana Ramli, Mohd Azizi Che Yunus, Lee Nian Yian, Zuhaili Idham, Ahmad Hazim Abdul Aziz, Noor Aiysah Aris, Nicky Rahmana Putra, Shahid Kamar Sham

8. EFFECT OF GRAPHENE OXIDE AND CELLULOSE NANOFIBER TOWARDS MECHANICAL PROPERTIES OF POLYLACTIC ACID BASED ACTIVE PACKAGING USING RESPONSE SURFACE METHODOLOGY 984
(Kesan Grafin Oksida dan Gentian Fibril Selulosa Terhadap Kekuatan Mekanikal Pembungkus Aktif Menggunakan Kaedah Gerak Balas Permukaan)
Mohd Harfiz Salehudin and Ida Idayu Muhamad

9. BLENDS OF LINEAR LOW-DENSITY POLYETHYLENE, NATURAL RUBBER AND POLYANILINE: TENSILE PROPERTIES AND THERMAL STABILITY 999
(Adunan Polimer Polietilena Linear Berketumpatan Rendah, Getah Asli dan Polianilina: Sifat Regangan dan Kestabilan Terma)
Farrah Diyana Zailan, Ruey Shan Chen, Sahrim Ahmad, Dalila Shahdan, Adilah Mat Ali, Mohd Farid Hakim Mohd Ruf

10. COMBINED MECHANICAL-CHEMICAL PRE-TREATMENT OF OIL PALM EMPTY FRUIT BUNCH (EFB) FIBERS FOR ADSORPTION OF METHYLENE BLUE (MB) IN AQUEOUS SOLUTION 1007
(Gabungan Rawatan Mekanik-Kimia ke atas Gentian Tandan Kosong Kelapa Sawit untuk Penjerapan Metilena Biru dalam Larutan Akues)
Chee Mun Chan, Siew Xian Chin, Soon Wei Chook, Chin Hua Chia, Sarani Zakaria

11. EFFECT OF EPOXIDISED NATURAL RUBBERS ON CALCIUM CARBONATE-FILLED NATURAL RUBBER COMPOUNDS 1014
(Kesan Getah Asli Terepoksida Terhadap Sebatian Getah Asli Terisi Kalsium Karbonat)
Indra Surya, Seri Maulina, Hanafi Ismail

12. DIIMIDE REDUCTION OF LIQUID NATURAL RUBBER IN HYDRAZINE HYDRATE/HYDROGEN PEROXIDE SYSTEM: A SIDE REACTION STUDY 1023
(Penurunan Diimida Getah Asli Cecair dalam Sistem Hidrazin Hidrat/Hydrogen Peroksida: Kajian Tindak Balas Sampingan)
Muhammad Jefri Mohd Yusof, Nur Aidasyakirah Mohd Tahir, Fazira Firdaus, Siti Fairus M. Yusoff

13. AN ACOUSTIC STUDY OF *Shorea leprosula* WOOD FIBER FILLED POLYURETHANE COMPOSITE FOAM 1031
(Kajian Akustik Busa Komposit Poliuretana Terisi Serat Kayu *Shorea leprosula*)
Muhammad Shafiq Mohd Azahari, Anika Zafiah M. Rus, Shaharuddin Kormin, M. Taufiq Zaliran

14. POLYURETHANE MEMBRANE AS AN ADSORBENT FOR METHYL ORANGE AND ETHYL VIOLET DYES 1040
(Membran Poliuretana Sebagai Penjerap untuk Pewarna Metil Oren dan Etil Ungu Lembayung)
Khairiah Haji Badri, Fatem Hamimie Ismail, Amira Shakim Abdul Shakir, Sharifah Mohamad,

Hawa Aqilah Hamuzan, Nur Syakilla Hassan

15. DETERMINATION OF GLUCOSE CONTENTS IN KENAF 1048
(Penentuan Kandungan Glukosa dalam Kenaf)
Fatin Afifah Ahmad Kuthi, Nurulhuda Mohd Yunus, Goh Kae Horng, Khairiah Haji Badri

16. EFFECTS OF FIBRE SIZE ON *Sansevieria trifasciata*/NATURAL RUBBER/ HIGH DENSITY POLYETHYLENE BIOCOMPOSITES 1057
(Kesan Saiz Serat Terhadap Biokomposit *Sansevieria trifasciata*/Getah Asli/ Polietilena Berketumpatan Tinggi)
Nurzam Ezdiani Zakaria, Ishak Ahmad, Wan Zarina Wan Mohamad, Azizah Baharum

17. OPTIMIZATION OF ACID DOPED POLYBENZIMIDAZOLE ELECTROLYTE MEMBRANE FOR HIGH-TEMPERATURE PEM FUEL CELL 1065
(Pengoptimuman Asid Didopkan Membran Elektrolit Polibenzimidazol untuk Sel Bahan Api PEM Suhu Tinggi)
Md Ahsanul Haque, Abu Bakar Sulong, Edy Herianto Majlan, Kee Shyuan Loh, Teuku Husaini, Rosemilia Rosli

18. *In-vitro* PHOTOPROTECTIVE ACTIVITIES OF DIFFERENT SOLVENT EXTRACTION OF *Hibiscus sabdariffa* 1078
(*In-vitro* Aktiviti Foto Perlindungan Bagi Ekstrak Pelarut yang Berbeza dari *Hibiscus sabdariffa*)
Nur Royhaila Mohamad, Siti Salwa Abd Gani, Roswanira Abdul Wahab, Uswatun Hasanah Zaidan

19. THE INFLUENCE OF GROWTH TEMPERATURE ON THE PROPERTIES OF ZINC OXIDE BY THERMAL OXIDATION 1084
(Kesan Pertumbuhan Suhu Ke Atas Sifat-Sifat Zink Oksida Menggunakan Pengoksidaan Haba)
Nuraini Abdullah, Noor Mazni Ismail, Dewan Muhammad Nuruzzaman

20. EXTRACTION OF SUCCINIC ACID FROM REAL FERMENTATION BROTH BY USING EMULSION LIQUID MEMBRANE PROCESS 1090
(Pengekstrakan Asid Suksinik daripada Larutan Penapaian Sebenar dengan Menggunakan Proses Membran Cecair Emulsi)
Norasikin Othman, Norela Jusoh, Mariah Syafiqah Mohar, Muhammad Bukhari Rosly, Norul Fatiha Mohamed Noah

Malaysian Journal of Analytical Sciences, Vol 22 No 6 (2018): 921 - 930
DOI: https://doi.org/10.17576/mjas-2018-2206-01

MALAYSIAN JOURNAL OF ANALYTICAL SCIENCES
Published by The Malaysian Analytical Sciences Society
ISSN 1394 - 2506

THE PHYSICAL AND ELECTROCHEMICAL CHARACTERISTIC OF GOLD NANOPARTICLES SUPPORTED PEDOT/GRAPHENE COMPOSITE AS POTENTIAL CATHODE MATERIAL IN FUEL CELLS

(Pencirian Fizikal dan Elektrokimia Komposit Zarah Nano Aurum Disokong PEDOT/Grafin sebagai Bahan Katod Berpotensi dalam Sel Bahan Api)

Nurul'ain Basyirah Muhamad and Farhanini Yusoff*

School of Marine and Environmental Sciences,
Universiti Malaysia Terengganu, 21030 Kuala Nerus, Terengganu, Malaysia

**Corresponding author: farhanini@umt.edu.my*

Received: 2 August 2018; Accepted: 13 November 2018

Abstract

Gold nanoparticles/poly(3,4-ethylenedioxythiophene)/reduced graphene oxide (denoted as AuNPs/PEDOT/rGO) was synthesized as an electrocatalyst of cathode materials for used in fuel cells. The AuNPs/PEDOT/rGO catalyst was prepared by chemical deposition of AuNPs/PEDOT onto rGO sheets. The physical properties of composite were characterized by X-ray diffraction (XRD), scanning electron microscopy (SEM), Brunauer-Emmett-Teller (BET) and thermogravimetric analysis (TGA). The SEM results confirm the AuNPs is successfully attached on PEDOT/rGO sheets, while the XRD pattern confirmed the existence of crystallographic structure of composite. Analysis of thermogravimetry revealed the decomposition of synthesized composite is below 100 °C, where it is suitable for cathode material in fuel cells. For the fabrication of modified electrode, 10 µL of composite suspension was drop-casted on glassy carbon electrode (GCE) surface. Meanwhile, cyclic voltammetry and electrochemical impedance spectroscopy were used to study the electrochemical behaviour of modified electrode in in 1.0 M KCl solution with a reference to 5.0 mM $K_4[Fe(CN)_6]$ redox system. The result demonstrates that AuNPs/PEDOT/rGO catalyst enhance the high conductivity and charge transfer where it is useful as a material for cathode catalyst in fuel cells.

Keywords: gold nanoparticles, poly(3,4-ethylenedioxythiophene), reduced graphene oxide, cathode catalyst, fuel cells

Abstrak

Zarah nano aurum/poli(3,4-etilenadioxitiopena)/grafin oksida terturun (dilabel sebagai AuNPs/PEDOT/rGO) telah disintesis sebagai elektropemangkin bahan katod untuk digunakan dalam sel bahan api. Pemangkin AuNPs/PEDOT/rGO telah disediakan melalui pemendapan kimia AuNPs/PEDOT ke dalam lembaran rGO. Sifat fizikal komposit telah dicirikan oleh pembelauan sinar-X (XRD), mikroskop imbasan elektron (SEM), Brunauer-Emmett-Teller (BET) dan analisis termogravimetrik (TGA). Hasil SEM telah mengesahkan AuNPs telah berjaya melekat di lembaran PEDOT/rGO, sementara corak XRD mengesahkan kehadiran struktur kristalografi komposit. Analisis termogravimetrik telah membuktikan penguraian komposit yang telah disintesis di bawah 100 °C dimana ia sesuai digunakan sebagai bahan katod untuk sel bahan api. Untuk fabrikasi elektrod diubahsuai, setiap 10µL pemendapan komposit telah dititik alas pada permukaan elektrod karbon berkaca (GCE). Sementara itu, voltametri berkitar dan spektroskopi elektrokimia impedans telah digunakan untuk mengkaji sifat elektrokimia elektrod diubahsuai di dalam cecair 1.0 M KCl merujuk kepada sistem redoks 5.0 mM $K_4[Fe(CN)_6]$. Keputusan menunjukkan pemangkin AuNPs/PEDOT/rGO/GCE meningkatkan konduktiviti yang tinggi dan pemindahan cas dimana ia berguna sebagai bahan untuk pemangkin katod dalam sel bahan api.

Kata kunci: zarah nano aurum, poli(3,4-etilenadioxitiopena), grafin oksida terturun, pemangkin katod, sel bahan api

Introduction

As the world moves towards renewable and sustainable energy, fuel cells (FCs) technology gained attention as a source to replace a combustion engine in vehicles. The good performance of FCs such as high reliability, quite operation and low maintenance capability making it has a capability used in wide application such as power generation, power transportation and portable power generation. In spite of FCs has an attraction as a green technology, the development of FCs still low due to the high cost and lack of suitable materials, especially for cathode electrode [1]. At the current stage technology of FCs, the Platinum (Pt) based electrode is used as a main cathode catalyst in FCs, however, the cost of Pt catalyst is extremely expensive and it is not stable yet [2].

Recent researches have been active in development of novel low cost electrocatalyst to replace high cost of commercial Pt-based electrode [3-5]. In order to replace Pt-based catalyst, gold nanoparticle (AuNPs) is promising a good metal catalyst compared to other metallic catalyst. The characteristic of AuNPs such as high stability and good resistant for oxidation making it is suitable as greener catalyst material. Additionally, the fabrication of AuNPs with others material can be considered for electrochemical applications, which is high catalytic activity of AuNPs in many reaction such as CO oxidation, methanol oxidation and redox reaction of oxygen [6].

Metal nanoparticles (NPs) decorated graphene sheets gained attracted in order to improve efficiency and stability of electrode materials. Up to date, numerous studies have been focused on the hybridization of graphene with AuNPs in electrochemical application [7-11]. Recent work has been reported that graphene sheets has an ability to decrease Pt particle size and existence a binding sites that provide strong interaction between Pt particles and graphene sheets [12]. Furthermore, the 2-dimensional carbon structure of graphene oxide (GO) with electrical and mechanical properties can be used effectively as electrocatalytic support materials. Meanwhile, reduced graphene oxide (rGO) with less oxygen functional group provide an active binding site for NPs and minimizing poisoning of electrocatalyst [13].

Indeed, conducting polymer/NPs hybrids has an ability as a novel composite materials with a synergetic and behaviour [14]. In addition, conjugated polymer with high conductivity such as poly(3,4-ethylenedioxythiophene) (PEDOT) as a substrate for deposition of NPs on graphene has a possibilities to achieve uniform dispersion and enhance a stability of NPs. The unique properties of PEDOT such as high electrochemical stability and catalytic activity making them excellent and high efficiency as a catalyst support [15]. PEDOT decorated graphene composite can be a good adhesion with NPs and improve the adsorption, catalytic and conductive properties leading for good performance for cathode catalyst materials.

Herein, the purpose of this work is to prepare AuNPs/PEDOT/rGO composite as a potential material for cathode electrode in FCs. For the comparison, rGO and PEDOT/rGO composite were also prepared by one-pot chemical method. For the physical and electrochemical characteristic, the composites were characterized *via* several instruments and electrochemical technique.

Materials and Methods

Chemicals and reagents

Graphite powder, chloroauric acid ($HAuCl_4$), sodium nitrate ($NaNO_3$), 3,4-ethylenedioxythiophene (EDOT) monomer and sodium borohydride ($NaBH_4$) were purchased form Sigma Aldrich, USA. Sulphuric acid (H_2SO_4, 95-98%), potassium permanganate ($KMnO_4$), hydrochloric acid (HCl, 5%), ethanol absolute, potassium chloride (KCl) and potassium ferrocyanide ($K_4[Fe(CN)_6]$) were supplied from Hamburg, German. Alumina powder supplied by Bendosen and was used for the clean of electrode's surface.

Physical characterization

The surface morphology of catalyst was determined using scanning electron microscopy (SEM) JEOL JSM 6360LA at the operational voltage of 5 kV. X-ray diffraction (XRD) pattern was conducted using X-ray Diffractometer, Rigaku Miniflex II using CuKα line (λ = 1.540598 Å) as radiation source. Brunauer-Emmett-Teller (BET) surface area analyzer with a heating rate of 10 ºC over a temperature range of 20ºC-800ºC in a nitrogen atmosphere was

performed by ASAP 2020 Micrometrics, USA.Thermogravimetric analyses (TGA) was carried out using Mettler Toledo thermal analysis system TGA/DSC 1 with a heating temperature over a range of 20 ºC – 800 ºC.

Electrochemical characterization

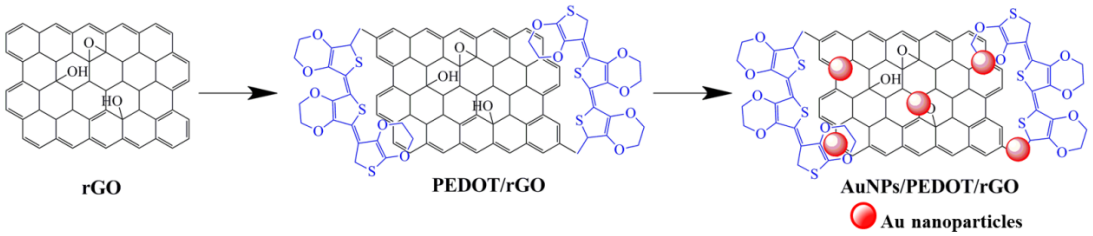
The electrocatalytic activity of modified electrode was determined using cyclic voltammetry (CV) technique performed by Potentiostat/Galvanostat Autolab PGSTAT302N controlled with NOVA 1.10 software. The cyclic voltammogram was scanned in the potential range of -0.2 V to 0.8 V at the 100 mV/s of scan rate. Glassy carbon electrode (GCE) with or without catalyst, platinum wire electrode and Ag/AgCl (3.0 M KCl) were served as working electrode, counter electrode and reference electrode, respectively. Electrochemical impedance spectroscopy (EIS) measurement was conducted using Autolab FRA32M with the frequency range of 1 Hz to 100,00 Hz and AC voltage 0.20 V.

Preparation of GO

GO was prepared according to modified Hummers method [16]. In a typical synthesis, 3 g of graphite powder and 1.5 g of $NaNO_3$ was poured into 23 ml of H_2SO_4 under rapid stirring. After 30 minutes, 4 g of $KMnO_4$ was slowly added into mixture solution. The solution was kept under 10 ºC. Next, the mixture solution was transferred into 35±5 ºC water bath and kept stirring for 30 minutes, then the mixture solution was diluted with 46 ml of deionized water and the temperature was raised up to 98 ºC. The mixture solution was diluted again with 140 ml of deionized water and left it stirred for 30 minutes. Finally, the mixture solution was treated with 10 ml of H_2O_2 to stop the reaction. Further, the mixture solution was washed with 5% of HCl and repeated centrifuging with deionized water. The synthesized product was dried in oven at 60 ºC.

Preparation of AuNPs/PEDOT/rGO

To synthesis AuNPs/PEDOT/rGO, 25 ml of EDOT in ethanol solution (22.5 mM) was poured into 350 ml of $HAuCl_4$ solution (0.65 mM) under a rapid stirring (750 rpm). The solution was immediately turned into dark blue solution. After 4 hours, 25 ml of GO suspension (0.5 mg/ml) was added into mixture solution, and then the AuNPs/PEDOT/GO was sonicated for 2 hours until homogenous. After that, 27.5 ml of $NaBH_4$ (0.16 M) was added drop by drop into mixture solution under rapid stirring. The reaction was continuously stirring for 6 hours. Finally, the AuNPs/PEDOT/rGO (Scheme 1) composite was obtained by washing a mixture solution using centrifugation with methanol and deionized water for several times, then dried it in an oven at 60 ºC. For comparison, rGO and PEDOT/rGO were prepared under a same condition.



Scheme 1. Schematic diagram for the formation of AuNPs/PEDOT/rGO

Electrode fabrication

A bare GCE was pre-polished with alumina slurry and then rinsed with deionized water before and after use. For prepare catalyst suspension, 1 mg of each catalyst was dissolved in 1 ml of deionized water and was sonicated for 30 minutes. Then, 10 µL of each suspension is casted on the GCE surface and allowing excessive water to evaporate at room temperature. The modified electrode was carefully rinsed with deionized water before and after an electrochemical experiment.

Results and Discussion

Physical characterization

The SEM images were recorded to determine the morphology of graphene sheets before and after modified with AuNPs and PEDOT as presented in Figure 1. The 2-dimenisonal of rGO surface (Figure 1(a)) is wrinkle with fold structure and rGO layers are restacked together. This appearance is might be due to the interlocking between nanoscale and GO sheets, which have led to the increasing of surface area and decreasing of surface energy [17]. In Figure 1(b), the surface of rGO with modified PEDOT has produced more rough wrinkles due to the PEDOT embedded on the rGO sheets. It is also evident that PEDOT/rGO catalyst can provide a sufficient surface area for the attachment of AuNPs and enhance an electron transfer for modified electrode [18]. In addition, the morphology of AuNPs/PEDOT/rGO surface clearly shows AuNPs was agglomerated on PEDOT/rGO sheets. It is clear the wrinkle surface of PEDOT/rGO sheet providing attachment sites and increase dispersity of AuNPs [19].

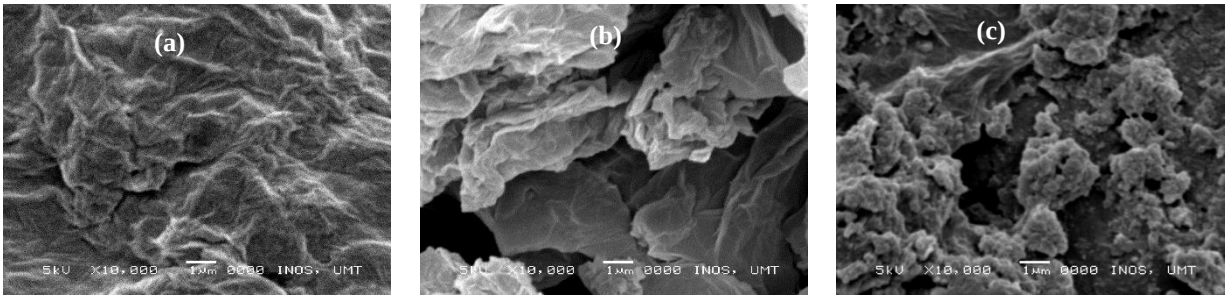


Figure 1. SEM results of (a) rGO; (b) PEDOT/rGO and (c) AuNPs/PEDOT/rGO at 10x magnification.

The XRD pattern of the phase structure for synthesized catalyst is depicted in Figure 2. The XRD pattern of GO in Figure 2(a) shows a sharp peak (001) at 2θ = 10.62º, suggesting the existing of oxygen functional group attached at edge of GO sheets [20]. After chemical reduction of GO, the (001) diffraction peak of GO is disappear and shifted to 2θ = 23.01º indicating the oxygen functional group successfully removed and restoration of C-C bonding in rGO (Figure 2(b)) [21]. Furthermore, the XRD pattern of PEDOT/rGO in Figure 2(c) exhibits a broad peak at 2θ = 28.04º attributed from polymeric amorphous of PEDOT [22]. XRD pattern of AuNPs/PEDOT/rGO in Figure 2 (d) shows a broad peak at 2θ = 25.0º belongs to C of PEDOT and rGO and five sharp peaks appearing at 2θ as 38.05º, 44.17º, 64.52º, 77.30º and 81.84º that correspond to the Au(111), Au(200), Au(220),Au (311) and Au(222), respectively. Therefore, it reveals that the Au has been successfully reduced and growth on PEDOT/rGO sheets.

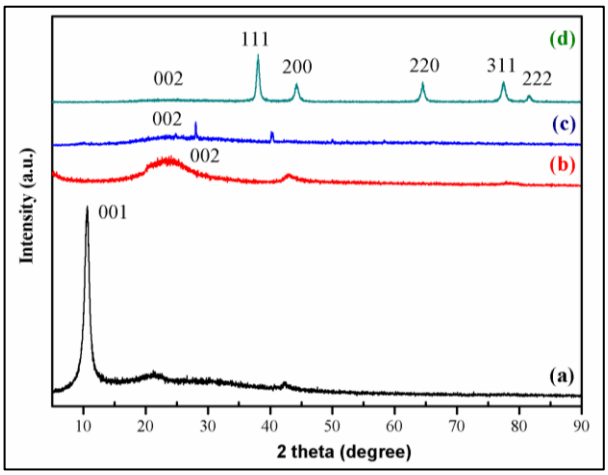


Figure 2. XRD results of (a) GO; (b) rGO; (c) PEDOT/rGO and (d) AuNPs/PEDOT/rGO.

From Table 1, the interlayer spacing ($\boldsymbol{d}$) is calculated using Bragg's formula (Eq. 1) [22]:

$$\boldsymbol{d}=\frac{\lambda}{2\sin\theta} \quad (1)$$

where $\boldsymbol{d}$ is interlayer spacing, λ is the wavelength of Cu Kα radiation (λ = 1.54 *Å*) and θ is the Bragg angle from highest value of FWHM (full width at half maximum), respectively. From the Eq.1, the value of GO (0.83 nm) is slightly higher due to the formation of oxygen group between graphene layer. The $\boldsymbol{d}$ value of rGO (0.39 nm) is much lower than GO signifying to the removal of oxygen group and restoration of conjugation of π-π interaction in rGO sheets [23]. The layer distance of PEDOT/rGO is 0.32 nm reflects to the closer packing of polymer matrix with graphene sheets [24], while the distance of AuNPs/PEDOT/rGO (0.21 nm) is much closer due to the AuNPs bind to PEDOT/rGO surface. The average of crystallite is obtained from Debye-Scherrer formula, and they were about GO (9.27 nm), rGO (0.97 nm), PEDOT/rGO (71.30 nm) and AuNPs/PEDOT/rGO (12.80 nm).

Table 1. Various parameter of catalyst obtained from XRD results

Composites	***2θ*** **(degree)**	**FWHM (degree)**	***d*** **(nm)**	**D (nm)**
GO	10.62	0.89	0.83	9.27
rGO	23.01	8.74	0.39	0.97
PEDOT/rGO	28.04	0.15	0.32	71.30
AuNPs/PEDOT/rGO	44.17	0.70	0.21	12.80

The surface area of synthesized composites was recorded using Brunauer-Emmett-Teller (BET) is listed in Table 2. The properties BET surface area of GO was measured is 400.58 m^2g^{-1}, which is far lower than theoretical value of graphene (~2620 m^2g^{-1}) which may be due to the incomplete oxidation of graphite and agglomeration of graphene sheet upon reduction [25]. However, the properties surface area of rGO is lower surface area compared to GO due to the removal of oxygen functional group which leading to rearrangement of spatial carbon atom. The deposition of PEDOT on rGO sheets resulted to the lowering BET surface area because of covering of polymeric structure of PEDOT on rGO sheets. Meanwhile, the specific surface area of AuNPs/PEDOT/rGO was increased twice than PEDOT/rGO corresponding to the incorporation of AuNPs has increased the surface area of composite.

Table 2. Surface area of GO, rGO, DOT/rGO and AuNPs/PEDOT/rGO

Composites	**Properties BET surface area/ m^2g^{-1}**
GO	400.58
rGO	211.27
PEDOT/rGO	8.18
AuNPs/PEDOT/rGO	21.07

Figure 3 shows TGA curves of rGO, PEDOT/rGO and AuNPs/PEDOT/rGO under argon atmosphere at rate 10 ºC/min. The thermogram of rGO shows a two decomposition steps; the first step located at 57 ºC with 3.29% weight loss due to the loss of adsorbed water. The second decomposition step at 518 ºC, where 17.13% catalyst was decomposed corresponding to the pyrolysis of a carbon material in rGO. There is small amount of weight loss by rGO because of it does not contain a large amount of oxygen group [20]. Meanwhile, PEDOT/rGO catalyst also shows two decomposition steps. The first decomposition step takes places at 75 ºC due to the decomposition of oxygen group contain in rGO, then the second mass loss in range 300 ºC – 600 ºC, corresponding to 44.87%

decomposition of PEDOT material [26]. The thermogram of AuNPs/PEDOT/rGO also has two decomposition steps, the first step weight loss at 96 ºC due to the loss of water molecule adsorbed catalyst during catalyst preparation. The second step located at 493 ºC attributed to decomposition of PEDOT. The residual mass loss is about 49.76 % corresponding to AuNPs that it is more stable [27]. Therefore, the result suggests that the synthesize catalyst start to decompose below 100 ºC, where it is stable for material in FCs.

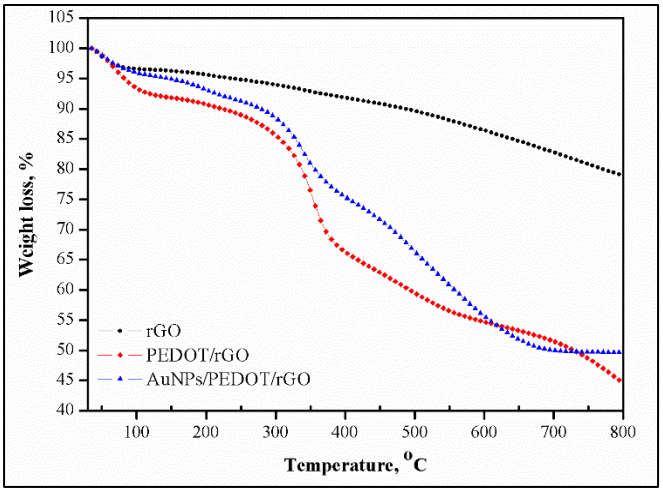


Figure 3. TGA curves of rGO, PEDOT/rGO and AuNPs/PEDOT/rGO

Electrochemical behavior of modified electrode

CV technique was performed to study the performance of modified electrode toward electrocatalytic activity. As shown in Figure 4(a), all the cyclic voltammogram of modified electrodes are well—defined peak quasi-reversible redox peak attributed to the stability of electron transfer between electrode surface and electrolyte. Specifically, rGO/GCE and PEDOT/rGO/GCE have a higher redox peak current and smaller peak separation compared to bare GCE. The increasing of the peak current is likely due to the electrical conductivity and electroactive surface area of rGO and PEDOT. However, the cyclic voltammogram of AuNPs/PEDOT/rGO/GCE shows the largest redox peak current, which probably due to the AuNPs provide a reaction sites for enhance larger effective surface area to facilitate transfer of $[Fe(CN)]^{-3/-4}$ electron [28].

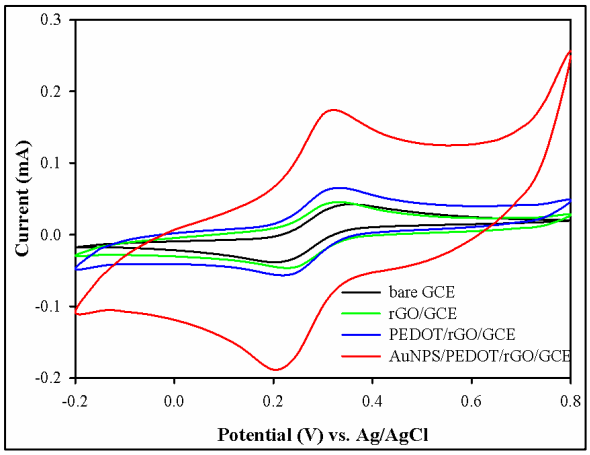


Figure 4. Cyclic voltammogram of bare GCE, rGO/GCE, PEDOT/rGO and AuNPs/PEDOT/rGO in 5.0 mM $K_4[Fe(CN)_6]$ of 1.0 M KCl solution at a scan rate of 100 mV/s

The effect of potential scan rate was studied on the AuNPs/PEDOT/rGO/GCE (Figure 5(a)). From the graph, the anodic and cathodic peaks are shifted to higher and lower current with the increasing of scan rate, respectively. This result revealed the AuNPs/PEDOT/rGO modified electrode has a fast electron transfer on the surface electrode indicating it has a good diffusion process and good rate capability [29]. In addition, the cyclic voltammogram of redox peaks show a similar shape for all scan rates means that the modified electrode is reversible. The specific capacitances (C) on the scan rate of modified electrodes were calculated by using Eq. 2 [30]:

$$C = \frac{I}{2.V.S.m} \tag{2}$$

where C is the specific capacitance (F/g), *I* is the integrated area of cyclic voltammogram (V A), S is the scan rate (V/s) and m is the mass (g) of composite. Figure 5(b) shows the dependence of capacitance of scan rate for all modified electrode. As can be seen, the trend of specific capacitance for all modified electrode is decrease with the increasing of scan rate where the highest specific capacitance is obtained at slower scan rate may be due to the better ion penetration on the surface of modified electrode. The highest potential window of AuNPs/PEDOT/rGO/GCE gives the largest capacitive value compared to others indicating the hybridization of AuNPs with PEDOT/rGO has a better contact between modified electrode and electrolyte.

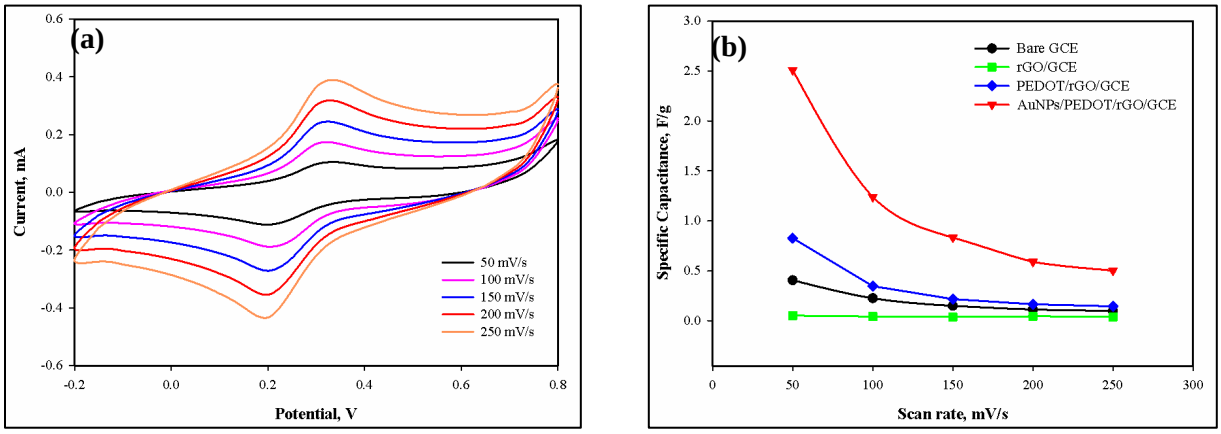


Figure 5. (a) Effect of scan rate on AuNPs/PEDOT/rGO/GCE and (b) plot of specific capacitance vs. scan rate of modified electrode. (Electrolyte solution: 5.0 mM $K_4[Fe(CN)_6]$ in 1.0 M KCl)

The charge-transfer resistance (R_{ct}) and double layer capacitance (C_{dl}) characteristic of modified electrode were conducted by EIS. The Nyquist plot typically presents a semicircle of R_{ct} occur at electrode surface at high frequency and the linearly part of diffusion-controlled process (Z_w) at low frequency. In Figure 6(a), the R_{ct} is only exhibit in bare GCE, but as the catalyst was casted on bare GCE, the R_{ct} is decreased. This could be attributed to the positive charge from catalyst has an ability to attract a negative charge of $[Fe(CN)]^{-3/-4}$ ion and enhance electron transfer on electrode surface [31]. However, AuNPs/PEDOT/rGO/GCE exhibits the characteristic of kinetic and diffusion process at low frequencies indicating high conductive and capacitive behaviour due to the AuNPs as a modifier.

Figure 6(b) shows an elements proposed in modified Randles circuit were extracted from Nyquist plot. To obtained best fitting for Nyquist Plot, the R[C(RW)] Randles circuit for bare GCE is changed to R[(RW)C]Q for modified electrode. It can be seen from Table 3, the solution resistance (R_s) is decrease with the addition of catalyst on bare GCE. Meanwhile, the modified electrodes exhibit double capacitance processes, where the value of *n* is near to ideal capacitor. The apparent electron transfer rate constant (K_{app}) for modified electrodes were obtained from Eq. 3;

$$K_{app} = RT/F^2R_{ct}C \tag{3}$$

where R is the gas constant, T is temperature of system, F is Faraday constant, C is concentration of $[Fe(CN)]^{-3/-4}$. The value of K_{app} is higher as the R_{ct} is lower for AuNPs/PEDOT/rGO/GCE reveals this electrode is fastest electron transfer process compared to others as supported from CV result [32].

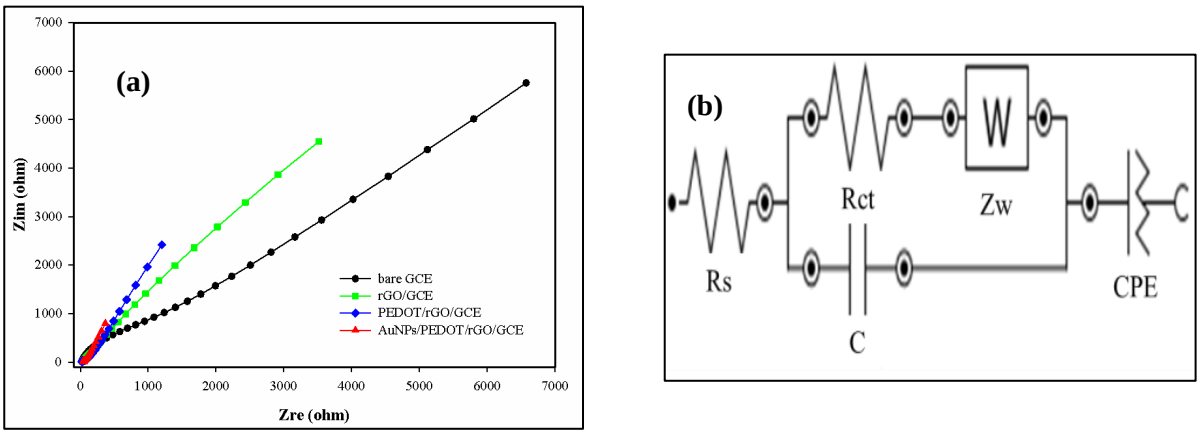


Figure 6. (a) Nyquist plot of modified electrode in 5.0 mM $K_4[Fe(CN)_6]$ and 1.0 M KCl solution and (b) Modified Randles equivalent circuit.

Table 3. Parameter's value of modified Randles equivalent circuit for all modified electrode

Modified Electrode	**R_s (Ωcm^2)**	**R_{ct} (Ωcm^2)**	***n***	**K_{app} (cms^{-1})**
Bare GCE	73.0	815	0.280	6.53×10^{-5}
rGO/GCE	61.0	63.8	0.788	8.34×10^{-4}
PEDOT/rGO/GCE	55.0	49.2	0.745	1.08×10^{-3}
AuNPs/PEDOT/rGO/GCE	43.7	6.85	0.832	7.77×10^{-3}

Conclusion

In this work, AuNPs/PEDOT/rGO is successfully synthesized by facile chemical method as a new catalyst for cathode material in FCs. This study found that AuNPs as a modifier on PEDOT/rGO sheet has improved the performance of catalyst in terms of conductivity, capacity and charge transfer. The stability, thermal decomposition and sensitivity of AuNPs/PEDOT/rGO are recommended for a new catalyst in cathode materials of FCs. Future work would attempt to study the kinetic analysis and electrocatalytic activity of modified electrode on oxygen reduction reaction.

Acknowledgements

The authors are grateful to Ministry of Education Research Acculturation Grant Scheme (RAGS) RAGS/1/20215/ST01/UMT/03/2 and Fundamental Research Grant Scheme (FRGS) FRGS/1/2017/STG01/ UMT/02/2 for financial support as well as Universiti Malaysia Terengganu for providing facilities for undertaking this research.

References

1. Shao, M. (2015). Electrocatalysis in fuel cells. *Catalysts*, 5 (4): 2115-2121.
2. Holton, O. T. and Stevenson, J. W. (2013). The role of platinum in proton exchange membrane fuel cells. *Platinum Metals Review*, 57(4): 259-271.

3. Peera, S. G., Tintula, K. K., Sahu, A. K., Shanmugam, S., Sridhar, P. and Pitchumani, S. (2013). Catalytic activity of Pt anchored onto graphite nanofiber-poly (3, 4-ethylenedioxythiophene) composite toward oxygen reduction reaction in polymer electrolyte fuel cells. *Electrochimica Acta*, 108: 95-103.
4. Ferreira, P. J., Shao-Horn, Y., Morgan, D., Makharia, R., Kocha, S. and Gasteiger, H. A. (2005). Instability of Pt/C electrocatalysts in proton exchange membrane fuel cells a mechanistic investigation. *Journal of The Electrochemical Society*, 152(11): 2256-2271.
5. Zhang, L. and Xia, Z. (2011). Mechanisms of oxygen reduction reaction on nitrogen-doped graphene for fuel cells. *The Journal of Physical Chemistry C*, 115(22): 11170-11176.
6. Rad, A. G., Abbasi, H. and Afzali, M. H. (2011). Gold nanoparticles: Synthesizing, characterizing and reviewing novel application in recent years. *Physics Procedia*, 22: 203-208.
7. Choi, Y., Gu, M., Park, J., Song, H. K. and Kim, B. S. (2012). Graphene multilayer supported gold nanoparticles for efficient electrocatalysts toward methanol oxidation. *Advanced Energy Materials*, 2 (12): 1510-1518.
8. Hu, Y., Jin, J., Wu, P., Zhang, H. and Cai, C. (2010). Graphene–gold nanostructure composites fabricated by electrodeposition and their electrocatalytic activity toward the oxygen reduction and glucose oxidation. *Electrochimica Acta*, 56(1): 491-500.
9. Chen, J., Jia, C. and Wan, Z. (2014). Novel hybrid nanocomposite based on poly (3,4-ethylenedioxythiophene)/multiwalled carbon nanotubes/graphene as electrode material for supercapacitor. *Synthetic Metals*, 18: 69-76.
10. Shervedani, R. K. and Amini, A. (2014). Novel graphene-gold hybrid nanostructures constructed via sulfur modified graphene: preparation and characterization by surface and electrochemical techniques. *Electrochimica Acta*, 121: 376-385.
11. Ali, A., Zhang, Y., Jamal, R. and Abdiryim, T. (2017). Solid-state heating synthesis of poly(3,4-ethylenedioxythiophene)/gold/graphene composite and its application for amperometric determination of nitrite and iodate. *Nanoscale Research Letters*, 12(1): 568.
12. Fortunato, G. V., de Lima, F. and Maia, G. (2016). Oxygen-reduction reaction strongly electrocatalyzed by Pt electrodeposited onto graphene or graphene nanoribbons. *Journal of Power Sources*, 302: 247-258.
13. Dinesh, B. and Saraswathi, R. (2016). Enhanced performance of Pt and Pt–Ru supported PEDOT–RGO nanocomposite towards methanol oxidation. *International Journal of Hydrogen Energy*, 41(31): 13448-13458.
14. Rao, H., Chen, M., Ge, H., Lu, Z., Liu, X., Zou, P., Wang, X., He, H., Zeng, X. and Wang, Y. (2017). A novel electrochemical sensor based on Au@ PANI composites film modified glassy carbon electrode binding molecular imprinting technique for the determination of melamine. *Biosensors and Bioelectronics*, 87: 1029-1035.
15. Groenendaal, L., Zotti, G., Aubert, P. H., Waybright, S. M. and Reynolds, J. R. (2003). Electrochemistry of poly (3, 4-alkylenedioxythiophene) derivatives. *Advanced Materials*, 15(11): 855-879.
16. Hummers Jr, W. S. and Offeman, R. E. (1958). Preparation of graphitic oxide. *Journal of The American Chemical Society*, 80(6): 1339-1339.
17. Yang, J. and Gunasekaran, S. (2013). Electrochemically reduced graphene oxide sheets for use in high performance supercapacitors. *Carbon*, 51: 36-44.
18. Mao, X., Yang, W., He, X., Chen, Y., Zhao, Y., Zhou, Y., Yang, Y. and Xu, J. (2017). The preparation and characteristic of poly (3, 4-ethylenedioxythiophene)/reduced graphene oxide nanocomposite and its application for supercapacitor electrode. *Materials Science and Engineering: B*, 216: 16-22.
19. Liu, Z., Xu, J., Yue, R., Yang, T. and Gao, L. (2016). Facile one-pot synthesis of Au–PEDOT/rGO nanocomposite for highly sensitive detection of caffeic acid in red wine sample. *Electrochimica Acta*, 196: 1-12.
20. Park, S., An, J., Potts, J. R., Velamakanni, A., Murali, S. and Ruoff, R. S. (2011). Hydrazine-reduction of graphite-and graphene oxide. *Carbon*, 49(9): 3019-3023.
21. Zhang, X., Zhang, D., Chen, Y., Sun, X. and Ma, Y. (2012). Electrochemical reduction of graphene oxide films: preparation, characterization and their electrochemical properties. *Chinese Science Bulletin*, 57(23): 3045-3050.
22. Selvaganesh, S. V., Mathiyarasu, J., Phani, K. L. N. and Yegnaraman, V. (2007). Chemical synthesis of PEDOT–Au nanocomposite. *Nanoscale Research Letters*, 2(11): 546.

23. Saini, P., Sharma, R. and Chadha, N. (2017). Determination of defect density, crystallite size and number of graphene layers in graphene analogues using X-ray diffraction and raman spectroscopy. *Indian Journal of Pure & Applied Physics*, 55(9): 625-629.
24. Chen, L., Liu, W., Su, X., Xiao, S., Xie, H., Uher, C. and Tang, X. (2017). Chemical synthesis and enhanced electrical properties of bulk poly (3, 4-ethylenedioxythiophene)/reduced graphene oxide nanocomposites. *Synthetic Metals*, 229: 65-71.
25. Dreyer, D. R., Park, S., Bielawski. C. W. and Ruoff, R. S. (2010) The chemistry of graphene oxide. *Chemical Society Reviews*, 39: 228-240.
26. Li, Y. and Ni, X. (2016). One-step preparation of graphene oxide–poly(3,4-ethylenedioxythiophene) composite films for nonvolatile rewritable memory devices. *RSC Advances*, 6(20): 16340-16347.
27. Felix-Navarro, R. M., Beltran-Gastelum, M., Reynoso-Soto, E. A., Paraguay-Delgado, F., Alonso-Nuñez, G. and Flores-Hernandez, J. R. (2016). Bimetallic Pt–Au nanoparticles supported on multi-wall carbon nanotubes as electrocatalysts for oxygen reduction. *Renewable Energy*, 87: 31-41.
28. Yusoff, F., Mohamed, N., Aziz, A. and Ab Ghani, S. (2014). electrocatalytic reduction of oxygen at perovskite (BSCF)-MWCNT composite electrodes. *Materials Sciences and Applications*, 5(4): 199-211.
29. Azman, N. H. N., Lim, H. N. and Sulaiman, Y. (2016). Effect of electropolymerization potential on the preparation of PEDOT/graphene oxide hybrid material for supercapacitor application. *Electrochimica Acta*, 188: 785-792.
30. Dar, F. I., Moonoosawmy, K. R. and Es-Souni, M. (2013). Morphology and property control of Nio nanostructures for supercapacitor applications. *Nanoscale Research Letters*, 8(1): 363.
31. Zhang, Z., Zhu, H., Wang, X. and Yang, X. (2011). Sensitive electrochemical sensor for hydrogen peroxide using Fe_3O_4 magnetic nanoparticles as a mimic for peroxidase. *Microchimica Acta*, 174(1-2): 183-189.
32. Yusoff, F., Aziz, A., Mohamed, N. and Ab Ghani, S. (2013). Synthesis and characterizations of BSCF at different pH as future cathode materials for fuel cell. *International Journal of Electrochemical Science*, 8(8): 10672-10687.

Malaysian Journal of Analytical Sciences, Vol 22 No 6 (2018): 931 - 942
DOI: https://doi.org/10.17576/mjas-2018-2206-02

MALAYSIAN JOURNAL OF ANALYTICAL SCIENCES
Published by The Malaysian Analytical Sciences Society
ISSN 1394 - 2506

ENHANCED CORROSION INHIBITION USING PURIFIED TANNIN IN HCl MEDIUM

(Peningkatan Perencat Kakisan Menggunakan Tanin Tertulen dalam Medium HCl)

Hatika Kaco[1], Nur Atiqah Abu Talib[2], Sarani Zakaria[2]*, Sharifah Nabihah Syed Jaafar[2], Norinsan Kamil Othman[3], Chin Hua Chia[2], Sinyee Gan[2]

[1]*Kolej PERMATA Insan,*
Universiti Sains Islam Malaysia, PERMATA Insan Complex,Bandar Baru Nilai, 71800 UKM Nilai, Negeri Sembilan, Malaysia
[2]*Bioresources and Biorefinery Laboratory, Faculty of Science and Technology*
[3]*School of Applied Physics, Faculty of Science and Technology*
Universiti Kebangsaan Malaysia, 43600 UKM Bangi, Selangor, Malaysia

**Corresponding author: szakaria@ukm.edu.my*

Received: 4 June 2018; Accepted: 7 November 2018

Abstract

Tannin was successfully extracted from Gelam bark using acetone as the solvent as natural alternatives. The extracted tannin was then used as corrosion inhibitor for mild steel under acidic medium. The gravimetric and electrochemical potentiodynamic corrosion tests were executed at different purified and unpurified tannin concentrations (200-800 ppm) to test the ability to inhibit mild steel corrosion. The results showed that the corrosion rate decreased as tannin concentration increased while the inhibition efficiency increased. The isotherm adsorption found that the Langmuir model was the best model to represent the interaction of tannin inhibitor and the active sites on mild steel surface. The SEM analysis showed that the mild steel morphology changed after the addition of tannin. The presence of blue-black color on the mild steel surface indicated the formation of ferric tannate to protect the surface of mild steel. In conclusion, purified tannin was a better inhibitor compared to unpurified tannin on mild steel in 1 M HCl.

Keywords: corrosion rate, extraction, gelam bark, green inhibitor, Langmuir

Abstrak

Tanin telah berjaya diekstrak daripada kulit Gelam menggunakan aseton sebagai pelarut. Tanin yang diekstrak kemudian digunakan sebagai perencat kakisan untuk keluli lembut dalam medium berasid. Ujian kakisan gravimetrik dan potensiodinamik elektrokimia dikaji pada kepekatan tanin tulen dan tidak tulen yang berbeza (200-800 ppm) ke atas kebolehan untuk merencat kekisan keluli lembut. Ia menunjukkan bahawa kadar kakisan berkurang dengan peningkatan kepekatan tanin manakala kecekapan perencatan meningkat. Lengkung suhu penjerapan mendapati bahawa model Langmuir merupakan model terbaik untuk menjelaskan interaksi perencat tanin dan tapak aktif permukaan keluli lembut. Morfologi keluli lembut berubah selepas penambahan tanin seperti dalam analisis SEM. Kehadiran warna biru hitam pada permukaan keluli lembut menunjukkan pembentukan ferik tanat untuk melindungi permukaan keluli lembut. Sebagai kesimpulan, tanin tertulen menunjukkan perencatan yang lebih baik berbanding tannin tak tulen keatas keluli lembut dalam 1 M HCl.

Kata kunci: kadar kakisan, pengekstrakan, kulit gelam, perencat hijau, Langmuir

Introduction

Corrosion inhibitor is defined as a material or chemical compound used to delay and/or control the corrosion process especially in iron-based material such as steel and alloy [1, 2]. Previous studies have shown that corrosion inhibitor is able to hinder the corrosion attack which damages and degrades mild steel surfaces [3−5]. Particularly, organic compound heteroatom, such as nitrogen, sulphur, oxygen, and heterocyclic compound has the potential to be used as a corrosion inhibitor [2, 3, 6]. The sequence of the heteroatom coordination bond (O < N < S < P) corresponds to its efficiency as the corrosion inhibitor [7,8] due to the compound's higher electron density acting as the reaction centre [6]. These compounds adsorb onto the surface of metal and prevent corrosion active sites to be attacked by the corrosive environment [3].

However, most of synthetic corrosion inhibitors are toxic, expensive, and non-biodegradable [3, 6]. Consequently, the use of natural inhibitors derived from plants is environmentally friendly, attractive, and important [1, 8, 9]. Natural inhibitors have been derived from plants like mangrove [5, 10−12], *Azadirachta indica* [4], black wattle [13], *Chamaerops humilis* [1], *Pterocarpus soyaux* [3], and *Thevetia peruviana* [14]. These natural inhibitors mostly contain various types of components such as alkaloids, tannins, flavonoids, saponins, and volatile oil which are analogous with synthetic inhibitor and being proven to work as efficiently as their synthetic counterpart [9].

Tannin can be obtained from plant tissue particularly bark, leaves, and fruits through extraction process using organic solvents such as acetone, ethanol and methanol [15]. Many researchers successfully extracted tannin from mangrove bark, acacia, and black wattle [11−13]. Generally, tannin can be found as hydrolysable and condensed tannin polyphenolic compounds [16, 17]. Condensed tannins are a group of phenolic polymers consisting of flavan-3-ol units linked together through C4–C6 or C4–C8 bonds. These polyflavonoids contain (−)-robinetinidol, (+)-catechin, and (+)-gallocatechin units [12]. The hydrolysed tannin is derived from glucose and categorized into two types: gallotannins or gallic acids and ellagitannins or digallic acids which are frequently esterified to polyols [13, 16].

Therefore, owing to the hydroxyl group in the ortho position on the aromatic rings, tannins are capable to chelate iron and other metallic cations such as copper [13]. The highly soluble ferric tannate is a blue-black complex formed during the reaction between Fe^{+3} ion, which comes mostly from the metallic compound, and the hydroxyl group in the ortho position in a oxygenate aqueous solution [13]. Tannin molecules having hydroxyl groups can reach to the metal surface and adsorb onto the surface of corroded metal by electronic interaction. Thus, they form protective layers to repel water molecules and inhibit ingression of destructive species like Cl^-, SO_4^{-2} and CO_2 which are responsible for the de-passivation of metal [5,18].

In this study, we aim to identify the ability and performance of tannin and purified tannin extracted from a local plant, gelam (*Melaleuca cajuputi*) in 1 M HCl. Different concentrations of tannin were applied on mild steel. We subsequently measured the weight loss of the mild steel and the potentiodynamic test result to obtain the corrosion rate and inhibitor efficiency value of the tannin inhibitor. The mild steel samples before and after undergoing corrosion test were analysed using optical metallurgy microscopy and scanning electron microscopy (SEM).

Materials and Methods

Materials

The bark of 10-year-old gelam plant was obtained from Pulau Duyung Terengganu. For the extraction, purification, and corrosion control processes, the chemicals used were acetone, methanol, ethanol, and hydrochloric acid purchased from Sigma Aldrich without any further purification.

Tannin extraction and purification

Tannin from the gelam bark was extracted using acetone: 20 g of gelam bark was immersed in a mixture of acetone and distilled water at 7:3 ratio (v/v) for 72 h at room temperature. The extracted yield was filtered and evaporated using a rotary evaporator to remove the acetone. The extract was freeze-dried, producing a dark brown powder which was the extracted tannin [19]. Then, the extracted tannin was purified: 40 g of Sephadex LH-20 powder was mixed into 400 ml methanol/water solution at 1:1 ratio. The mixed solvent was stirred and 2 g of the extracted

tannin was dissolved. The mixed solvent was removed using rotary evaporator. The purified tannin was freeze-dried and placed in a dry bottle for further use.

Preparation of mild steel

Mild steel was cut into 16 mm × 3 mm specimens in cylinder shape. A 1.5 mm small hole was punched on the top of the mild steel to facilitate the sample suspension during the weight loss test. The sample was then polished and ground using a disc grinding machine with different grade silicon carbide paper (240, 400, 600, 800, 1000 and 1200 mesh). The sample was rinsed using acetone, followed by distilled water, and later kept in a desiccator to prevent oxidation until all the excess grounded materials have been removed.

Preparation of corrosion medium

The mild steel specimens were immersed in HCl medium at different tannin concentrations at room temperature for 6 h. The corrosion test at different tannin concentrations was repeated three times to obtain an average reading. The concentration of tannin was summarized in Table 1.

Corrosion inhibition - gravimetric methods

The mild steel specimens were rinsed using acetone to ensure that the samples were free from chemicals or impurities that can disturb the results on weight loss test. The specimens were weighed before immersing for 6 hours in 25 ml HCl mixed with 5 ml ethanol and tannin at different concentration as shown in Table 1. The specimens were lifted and washed to remove the oxide formed on the surface following the ASTM standard G1-03 and rinsed using distilled water and acetone, and then dried. The dried samples were weighed to calculate the weight after immersing in corrosive medium. The percentage of inhibition efficiency (IE) was calculated using equation 1 [8]:

$$IE = 1 - \frac{Wi}{Wo} \times 100 \quad (1)$$

where W_o is the weight loss of mild steel without inhibitor and W_i is the weight loss of mild steel with inhibitor.

Table 1. Preparation of corrosion medium for gravimetric test and electrochemical potentiodynamic test

Tannin Concentration (ppm)	Medium
Control medium	Ethanol + HCl
200	Ethanol + HCl + tannin powder
400	Ethanol + HCl + tannin powder
600	Ethanol + HCl + tannin powder
800	Ethanol + HCl + tannin powder

Potentiodynamic electrochemical test

Polarization test was performed using three electrodes: saturated calomel electrode (SCE) as reference electrode, platinum plate (1 cm × 1 cm) as counter electrode, and the sample as working electrode with 1 cm2 sample surface area. The sample was immersed in the corrosive medium for 30 s to achieve the stability phase before starting the potentiodynamic electrochemical test. A potentiodynamic slope required a scanning capability from −0.25 to +0.25 mV. This electrochemical analysis involved a computer-controlled potentiostat model K47 Gamry at the scanning rate of 1.0 mVs^{-1}. Each experiment was repeated three times.

This analysis yielded constant Tafel anode (βa), cathode (βc), and polarization resistance value (Rp). The polarization slope would give the value of corrosion inhibitor efficiency (% IE) and corrosion rate. The % IE can be calculated using the following equation [20]:

$$\% \text{ IE} = [(\text{Icorr}(0) - \text{Icorr}(i))/\text{Icorr}(0)] \times 100 \quad (2)$$

where, Icorr(0) = corrosion current density of uninhibited system (mA cm^2) and Icorr(i) = corrosion current density of inhibited system (mA cm^2).

Morphological analysis

The microstructure and morphology of mild steel before and after the corrosion test were analysed under an optical microscopy metallurgy (model Carl Ziees AXIOLAB A1) and a scanning electron microscope (SEM) (model ZEISS model 55VP).

Results and Discussion

Fourier transform infrared spectroscopy (FTIR) of extracted and purified tannin

Surface functional groups of the extracted tannin (TN) and purified tannin (PTN) were investigated by using FTIR. The FTIR spectrums of the extracted tannin from gelam bark using acetone as solvent is shown in Figure 1. The FTIR spectrum of TN sample was the same as the commercial tannin. The wide range of 3100-3700 cm^{-1} intensity peak showed that the extracted tannin contained high amount of hydroxyl group due to the moisture in the tannin and hydroxyl group coming from lignin, cellulose, and hemicellulose [21]. These hydroxyl groups are necessary for tannin to inhibit corrosion of mild steel [13, 22]. The peaks at 2938 cm^{-1} and 2934 cm^{-1} represented the C-H group; the peak ranging at 1455-1516 cm^{-1} exhibited the stretch of aromatic ring groups; and 1036 cm^{-1} was the peak for aliphatic C-O group [22]. The other main peaks for tannin were at wavenumber of 1618, 1619, 1423 and 1420 cm^{-1} which signaled the presence of aromatic groups [13, 22]. For the purified tannin (PTN), some peaks were reduced while others increased in intensity. The intensity peak at 2930 cm^{-1} of C-H group for PTN is lower compared to TN, indicating that the PTN contained lower amount of C-H due to the purification process. However, the 1036 cm^{-1} peak, corresponding to the aliphatic group, has increased for the PTN sample compared to TN. Moreover, the aromatic group intensity of TN at 1400 to 1600 cm^{-1} range has reduced after the purification process.

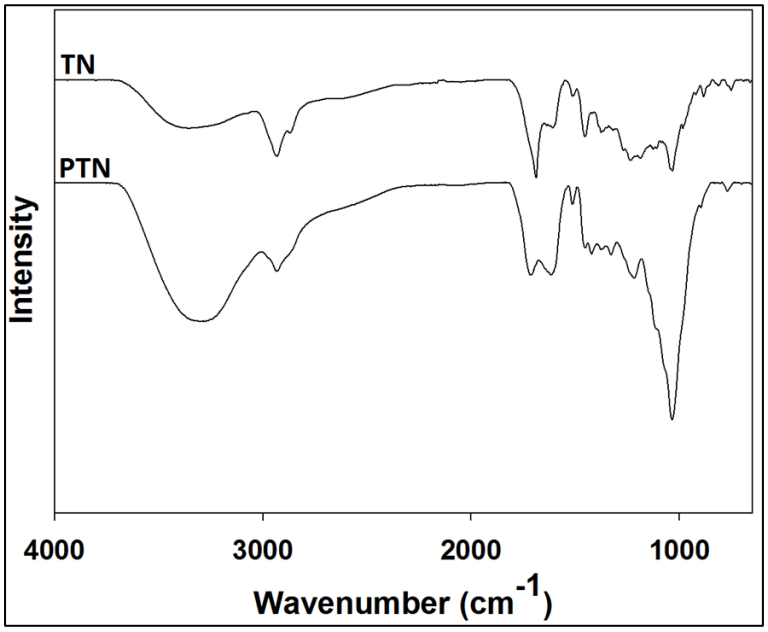


Figure 1. FTIR spectrum of tannin (TN) and purified tannin (PTN)

Corrosion inhibition analysis: Gravimetric test

Figure 2 shows the effect of concentration on the corrosion rate (mpy) of mild steel in 1 M HCl at room temperature. At first (blank sample), the weight loss of mild steel in corrosive medium of 1 M HCl is high but the addition of tannin has decreased its weight loss. Additionally, increasing the concentration of tannin on the mild steel surface has further decreased its weight loss for both tannin (TN) and purified tannin (PTN) samples. The corrosion rate followed the same pattern as weight loss, decreasing at higher concentration of tannin for both TN and PTN under the same medium. The decreasing corrosion rate was due to the increase of chemical reaction as a result of increasing concentration of the corrosive medium [3]. Corrosion rate of mild steel without the inhibitor was 40.49 mpy which was higher compared to corrosion rate of mild steel with TN and PTN as inhibitor which were 13.85 mpy and 6.93 mpy, respectively, showing that TN was more efficient as corrosion inhibitor for mild steel compared to PTN.

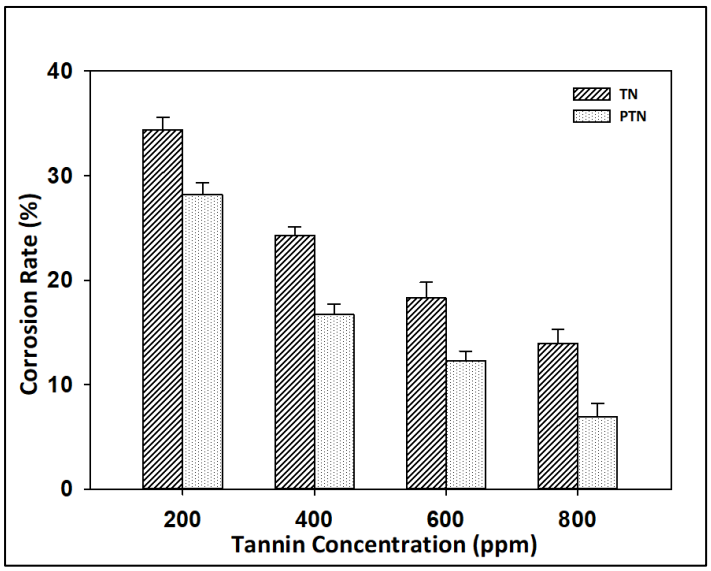


Figure 2. Effect of tannin concentration on corrosion rate of mild steel using TN and PTN as green inhibitor

Figure 3 shows the inhibition efficiency (%IE) for both TN and PTN at tannin concentration of 200, 400, 600 and 800 ppm based on Icorr from the Tafel curves and Rp values. Both TN and PTN showed the highest IE (65.8 % and 83 %) with the inhibitor concentration of 800 ppm at 300 K due to the aromatic group that gave some advantages in corrosion inhibition process [23]. Tannin as inhibitor possesses the ability to inhibit corrosion on mild steel due to the presence of functional groups such as hydroxyl (OH), methoxyl (-OCH) and methyl (-CH3) which act as electron donor groups [10]. In aqueous medium, these functional groups release their electron and bond at the d-orbital which exists on mild steel. Hence, by increasing the concentration of tannin, the adsorption rate increases, thus protecting the mild steel from corrosion agent [10]. However, the PTN samples still had some impurities such as carbohydrates, polysaccharides, and sugars which occurred alongside tannin during the gravimetric test.

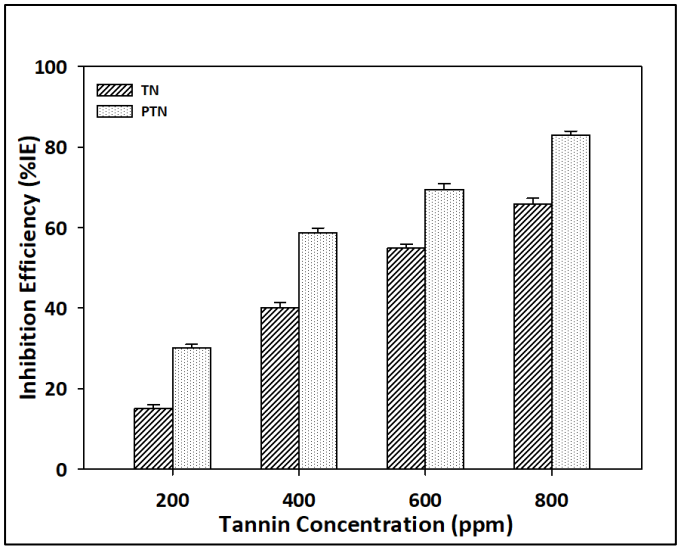


Figure 3. Effect of tannin concentration on inhibition efficiency of mild steel using TN and PTN as green inhibitor

Electrochemical potentiodynamic test

The determination of potentiodynamic polarization on TN and PTN samples was performed to investigate the kinetics of the cathodic and anodic reactions [24]. The polarization profile of mild steel in 1.0 M HCl is shown in Figure 4 and 5. The values of the variation of corrosion current density (Icorr), corrosion potential (Ecorr), anodic Tafel slope (βa), and cathodic Tafel slope (βc) at various concentrations of the TN and PTN inhibitors were obtained from the polarization profiles (Tables 2 and 3).

Figure 4 and 5 show the polarization curve for mild steel at different concentration of TN and PTN in 1 M HCl, displaying the effects of TN and PTN inhibition on cathodic and anodic reactions. Both changes in the slope of cathodic and anodic current-potential lines revealed that both reactions restrained with the presence of inhibitor; further restrictions occurred when the concentration of inhibitor increased [24]. The Tafel plot showed that the gradient of cathodic Tafel slope (βc) value was higher than that of the anodic Tafel slope (βa), demonstrating that the tannin molecules successfully inhibited the corrosive activities on the mild steel. A compound can be categorized as anodic- or cathodic-type inhibitor when the shifted value of Ecorr is more than 85 mV. Therefore, from Table 2 and 3, tannin can be indicated as a mixed corrosion inhibitor; it was able to inhibit via anodic and cathodic reactions [20, 25]. Therefore, the anodic dissolution reactions and the hydrogen evolution reactions on the cathodic sites had been inhibited by both inhibitors [7].

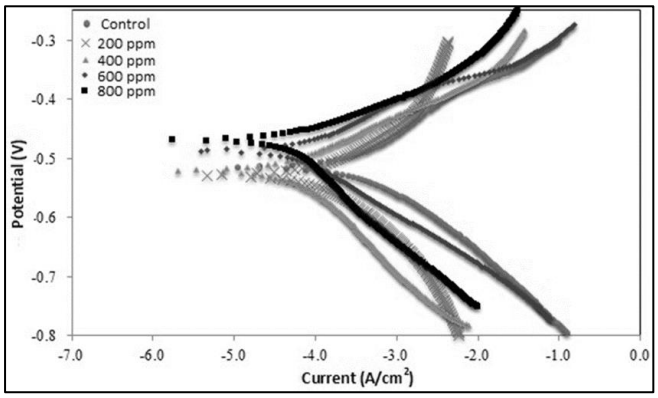


Figure 4. Polarization curve of mild steel at different concentration of TN in 1 M HCl at room temperature

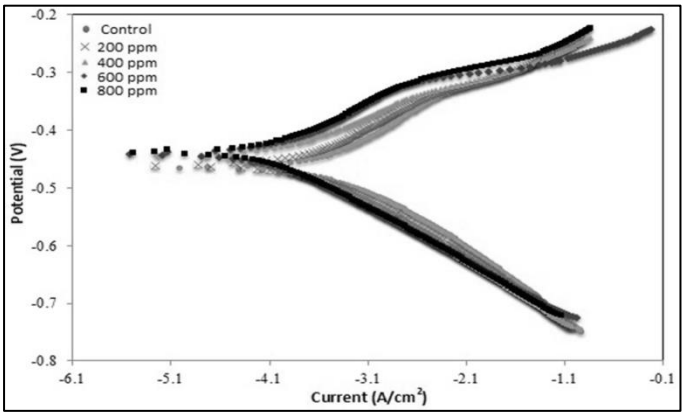


Figure 5. Polarization curve of mild steel at different concentration of PTN in 1 M HCl at room temperature

From Table 2 and 3, the current density value (Icorr) decreased but the inhibition efficiency increased with the increase of the inhibitor concentration from 200 to 800 ppm. This phenomenon can be explained by the increasing adsorption of inhibitor onto the mild steel surface with the increasing inhibitor concentration. Thus, higher mild steel surface area was protected by the acidic medium and the metal dissolution rate decreased, leading to the increased inhibition efficiency which was determined by the Icorr value [7, 24]. The increasing trend in the percentage of inhibition efficiency for PTN was higher compared to TN due to less impurity such as simple sugar, glycoside, polyphenol monomer, and carbohydrate which acted as barriers to the formation of ferric tannate [12].

Table 2. Electrochemical polarization potentiodynamic data for mild steel at different concentration of TN in 1 M HCl at 300 K

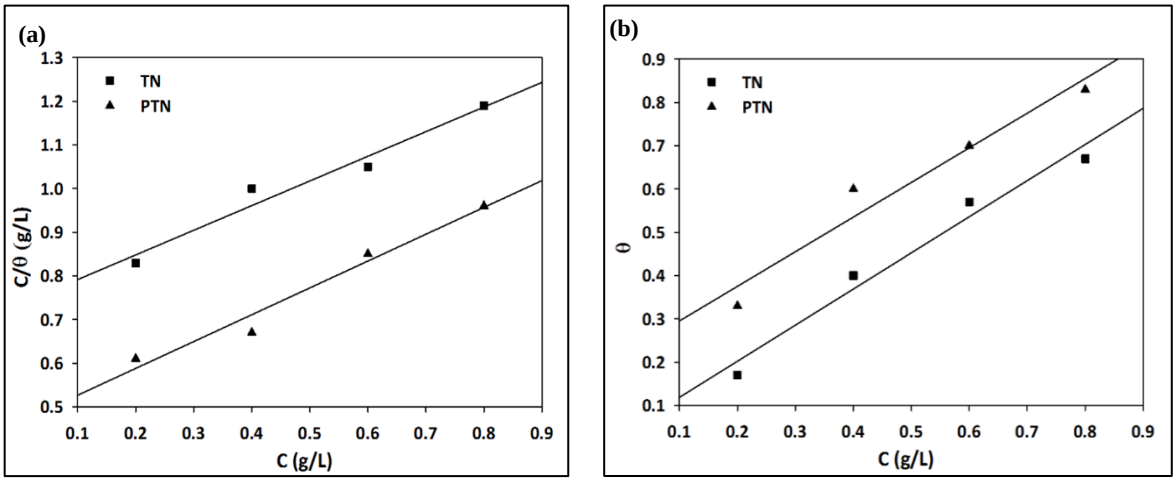
Inhibitor Concentration (ppm)	**Corrosion Potential E_{corr} (mV)**	**Corrosion Current Density I_{corr} (mA/cm^2)**	**Gradient Anode β_a (mV)**	**Gradient Cathode β_c (mV)**	**Corrosion Rate (mm/y)**	**Inhibitor Efficiency Percentage *(%IE)***
0	-467.00	4.051^{-4}	121.3	100.50	4.777	-
200	-479.70	1.287^{-4}	94.50	118.00	1.516	68.23
400	-470.20	5.101^{-5}	68.60	131.80	0.606	87.41
600	-437.60	5.074^{-5}	60.30	83.60	0.597	87.47
800	-421.30	4.751^{-5}	51.80	130.50	0.559	88.27

Table 3. Electrochemical polarization potentiodynamic data for mild steel at different concentration of PTN in 1 M HCl at room temperature

Inhibitor Concentration (ppm)	Corrosion Potential E_{corr} (mV)	Corrosion Current Density I_{corr} (mA/cm^2)	Gradient Anode β_a (mV)	Gradient Cathode β_c (mV)	Corrosion Rate (mm/y)	Inhibitor Efficiency Percentage *(%IE)*
0	-467.00	4.051^{-4}	121.30	100.5	4.770	-
200	-460.70	2.387^{-4}	105.00	99.10	2.811	41.15
400	-443.60	1.287^{-4}	75.90	100.1	1.487	68.23
600	-442.00	9.100^{-5}	84.50	92.80	1.071	77.54
800	-439.30	8.777^{-5}	83.60	93.50	1.0333	89.66

Adsorption isotherm analysis

Langmuir, Freundlich and Temkim models were used as adsorption isotherms models to investigate the molecular interactions between the inhibitor molecules and the active sites on the mild steel surface [25]. These models provided more intuitiveness towards the corrosion inhibition mechanism [26]. The plots of these models are shown in Figure 6. From the plots, Langmuir isotherm showed a strong R^2 correlation value which indicated that the model was the most suitable model to explain the adsorption isotherm mechanism on mild steel [23]. Langmuir model stated that the tannin molecules adsorbed on mild steel surface was strongly bound and unable to move. The tannin molecules adsorbed on the surface of mild steel possessed a specific active site and the adsorbed tannin molecule did not interact with each other. Therefore, the adsorption of tannin molecules only happened at one layer [27]. Langmuir model was also the common model to describe the interaction occurred during the corrosion inhibition process. The free energy of adsorption (ΔG_{ads}) value for Langmuir, Temkin and Freundlich models using TN and PTN as inhibitor is shown in Table 4. If the ΔG_{ads} value was less than -20 kJ/mol, it involved an electrostatic adsorption; the energy of charged metal and charged molecule interacted with the mild steel surface. On the other hand, if the ΔG_{ads} value was greater than -40 kJ/mol, the charge transfer or electron sharing from the inhibitor molecule to the metal surface formed coordination bond of chemical adsorption [28]. However, according to the Table 4, ΔG_{ads} value for Langmuir and Temkin was less than -20 kJ/mol (between 10.22 and 20.53 kJ/mol), illustrating that both TN and PTN followed the electrostatic adsorption.



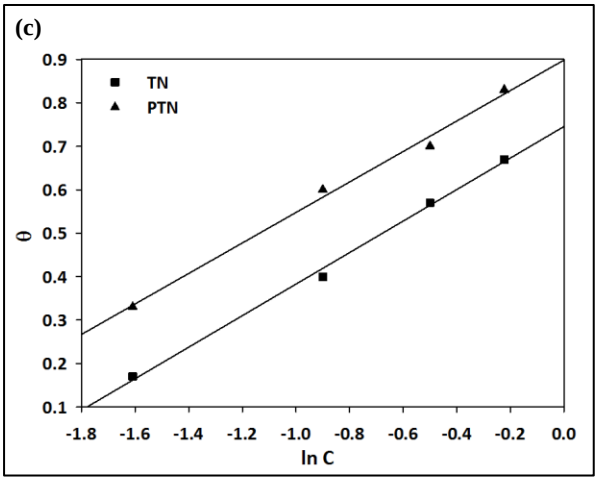


Figure 6. Adsorption mechanism of (a) Langmuir, (b) Freundlich and (c) Temkin isothermal for mild steel in 1 M HCl medium containing TN and PTN corrosion inhibitor

Table 4. Adsorption isotherm data model for Langmuir, Freundlich and Temkim in 1 M HCl medium at 300 K

Isotherm	**Inhibitor**	**R^2**	**K_{ads}**	**G_{ads} (kJ/mol^{-1})**
Langmuir	TN	0.96330	1.36	-10.79
	PTN	0.96880	2.1505	-11.93
Temkin	TN	0.99828	7.80	-15.14
	PTN	0.99220	12.94	-16.40
Freundlich	TN	0.97056	1.09	-10.22
	PTN	0.94095	8.73	-17.12

Morphological analysis: Optical microscope analysis

The circle in Figure 7(a) shows that there are tiny holes present on the surface of mild steel. These holes were formed due to the aggressive chloride ion that eroded the surface of mild steel, leading to the dissolving process also known as pitting corrosion. The dark brown on the sample's surface showed that the corrosion process had happened. Figure 7(b), (c) and (d) show the microscope images of mild steel immersed in 1 M HCl solution containing tannin at different concentration. Dark blue formation was found shrouding the mild steel, indicating that the tannin has been adsorbed onto the surface of mild steel and combined with the iron ion to form ferric tannate which was blue-black in colour [10−12]. The formed ferric tannate acted as a thin layer or film to protect the mild steel from further corrosion [13].

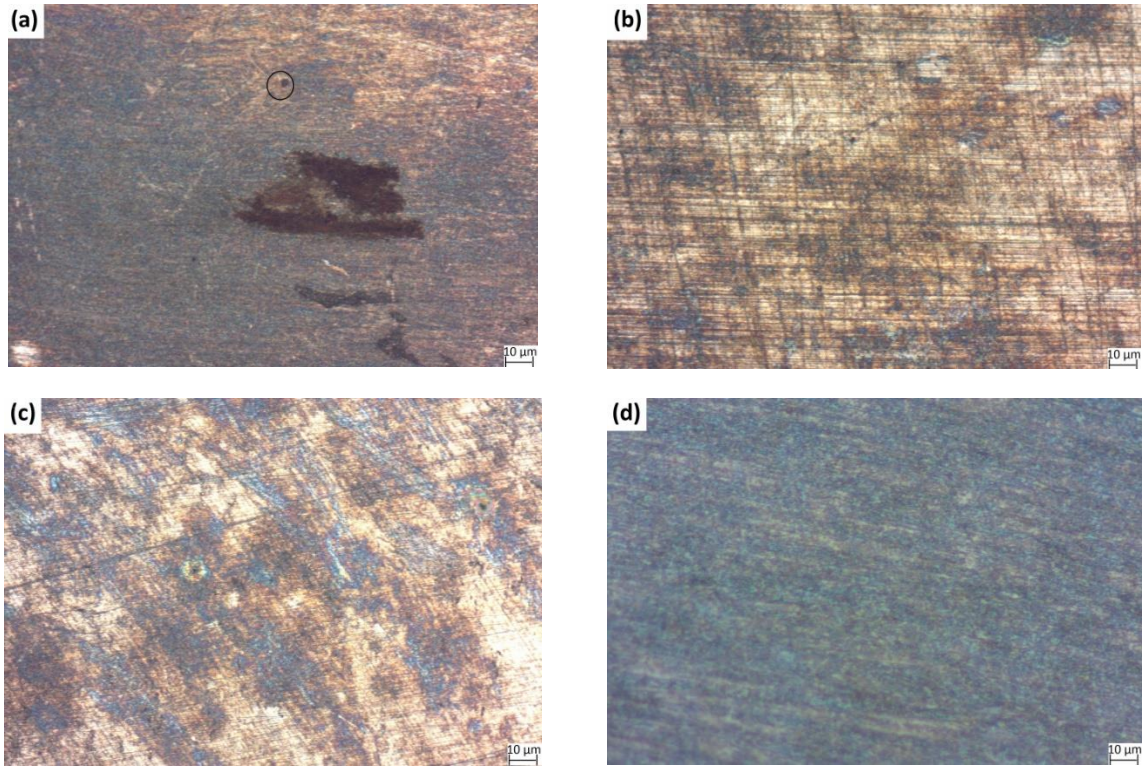


Figure 7. Microscopy images of mild steel after gravimetric test at room temperature for (a) without inhibitor and TN at concentration of (b) 200 ppm, (c) 400 ppm and (d) 600 ppm

Scanning electron microscope (SEM)

Figure 8 shows the SEM images of mild steel before and after corrosion test. It can be seen that mild steel immersed in 1 M HCl containing tannin inhibitor presence a white layer (tannin inhibitor) on the surface of the mild steel (Figure 8(b)). This layer could be observed as a coating which acted as a passive layer adsorbed on the mild steel surface. It also could protect the mild steel from chloride ion attacks that corroded the mild steel surface [10−12].

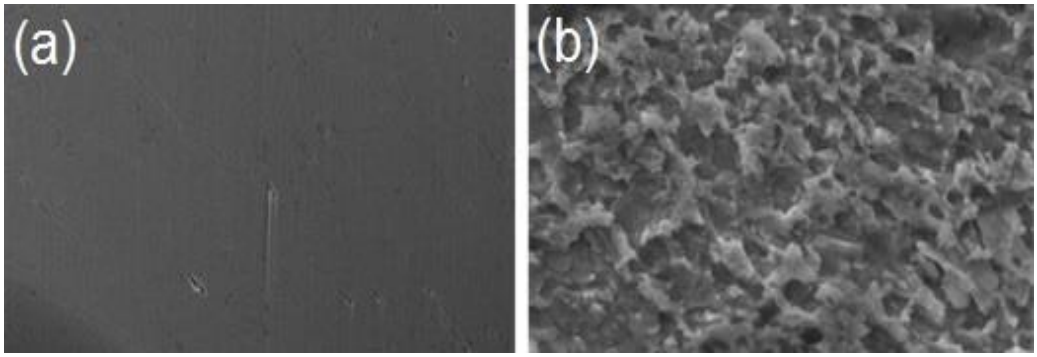


Figure 8. SEM images of (a) mild steel surface before corrosion test performed and (b) mild steel immersed in 1 M HCl containing 800 ppm concentration of TN

Conclusion

Tannin from gelam bark was successfully extracted using acetone. From the FTIR analysis, the presence of aromatic groups can be found in tannin (TN) and purified (PTN) tannin compound. The intensity peak of these aromatic groups decreased after being purified, indicating that the purification process had eliminated some of the tannin's aromatic groups. The weight loss test revealed that at higher concentration of inhibitor, the corrosion rate decreased, and inhibition efficiency increased. Both inhibitors exhibited excellent inhibition performance as a mixed-type inhibitor. The Langmuir isotherm was the best model to describe the adsorption isotherm of tannin on mild steel, giving the highest R^2 value (R^2>0.9). Microscopy analysis showed the formation of ferric tannate as indicated by the blue-black colour on the surface of the mild steel. This complex compound protected the mild steel from corrosion attacks in the presence of tannin as a green corrosion inhibitor. Hence, the natural tannin from gelam bark can be used as an alternative to replace other sources based on the observed corrosion inhibitor property.

Acknowledgement

The authors gratefully acknowledge the Ministry of Higher Education Malaysia for the financial support via the research project PRGS/1/2015/SG06/UKM/01/1. The authors also acknowledge support from the Centre for Research and Instrumentation (CRIM) for providing the instrument for analysis purposes.

References

1. Benali, O., Benmehdi, H., Hasnaoui, O., Selles, C. and Salghi, R. (2013). Green corrosion inhibitor: Inhibitive action of tannin extract of chamaerops humilis plant for the corrosion of mild steel in 0.5M H_2SO_4. *Journal of Materials and Environmental Science*, 4:127-138.
2. Tan, K. W. and Kassim, M. J. (2011). A correlation study on the phenolic profiles and corrosion inhibition properties of mangrove tannins (*Rhizophora apiculata*) as affected by extraction solvents. *Corrosion Science*, 53: 569-574.
3. Iloamaeke, I. M., Onuegbu, T. U., Ajiwe, V. I. E. and Umeobika, U. C. (2012). Corrosion inhibition of mild steel by *Pterocarpus soyauxi* leaves extract in HCl medium. *International Journal of Plant, Animal and Environmental Sciences*, 2: 22-28.
4. Okafor, P. C., Ebenso, E. E. and Ekpe, E. J. (2010). *Azadirachta indica* extracts as corrosion inhibitor for mild steel in acid medium. *International Journal of Electrochemical Science*, 5: 978-993.
5. Oki, M., Charles, E. Alaka, C. and Oki, T. K. (2011). Corrosion inhibition of mild steel in hydrochloric acid by tannins from *Rhizophora racemose*. *Materials Sciences and Applications*, 2: 592-595.
6. Umoren, S. A., Ogbobe, O., Igwe, I. O. and Ebenso E. E. (2008). Inhibition of mild steel in acidic medium using synthetic and naturally occurring polymers and synergistic halide additives. *Corrosion Science*, 50: 1998-2006.
7. Al-Amiery, A. A., Kassim, F. A., Kadhum, A. A. H. and Mohamad A. B. (2016). Synthesis and characterization of a novel eco-friendly corrosion inhibition for mild steel in 1 M hydrochloric acid. *Scientific Reports*, 6:19890-19912.
8. Shah, A. M., Rahim, A. A., Hamid, S. A. and Yahya, S. (2013). Green inhibitors for copper corrosion by mangrove tannin. *International Journal of Electrochemical Science*, 8: 2140-2153.
9. Chigondo, M. and Chigondo, F. (2016). Recent natural corrosion inhibitors for mild steel: an overview. *Journal of Chemistry*, 2016: 1-7.
10. Rahim, A. A., Rocca, E. and Steinmetz, J. (2007). Mangrove tannins and their flavanoid monomers as alternative steel corrosion inhibitors in acidic medium. *Corrosion Science*, 49: 402-417.
11. Rahim, A. A. and Kassim, J. (2008). Recent development of vegetal tannins in corrosion protection of iron and steel. *Recent Patents on Materials Science*, 1: 223-231.
12. Rahim, A. A., Rocca, E., Steinmetz, J., Kassim, M. J., Adnan, R. and Sani Ibrahim, M. (2008). Inhibitive action of mangrove tannins and phosphoric acid on pre-rusted steel via electrochemical methods. *Corrosion Science*. 50: 1546-1550.
13. Peres, R. S., Cassel, E. and Azambuja, D. S. (2012). Black wattle tannin as steel corrosion inhibitor. *ISRN Corrosion*, :1−9.
14. Fouda, A. S., Megahed, H. E., Fouad, N. and Elbahrawi, N.M. (2016). Corrosion inhibition of carbon steel in 1 M hydrochloric acid solution by aqueous extract of *Thevetia peruviana*. *Journal of Bio- and Tribo-Corrosion*, 2(3): 16.

15. Barbosa, V., Ramires, E. C., Razera, I. A. T. and Frollini, E. (2010). Biobased composites from tannin–phenolic polymers reinforced with coir fibers. *Industrial Crops and Products*, 32: 305-312.
16. Elgailani, I. E. H. and Ishak, C. Y. (2016). Methods for extraction and characterization of tannins from some acacia species of Sudan. *Pakistan Journal of Analytical & Environmental Chemistry*. 17: 43-49.
17. Mailoa, M. N., Mahendradatta, M., Laga, M. and Djide, N. (2013). Tannin extract of guava leaves (*Psidium Guajava L*) variation with concentration organic solvents. *International Journal of Scientific & Technology Research*, 2:106-110.
18. Kundu, M., Prasad, S. K. and Kumar, V. (2016). A review article on green inhibitors of reinforcement concrete corrosion. *International Journal of Emerging Research in Management &Technology*, 5: 42-46.
19. Oo, C. W., Kassim, M. J. and Pizzi, A. (2009). Characterization and performance of *Rhizophora apiculata* mangrove polyflavonoid tannins in the adsorption of copper(II) and lead(II). *Industrial Crops and Products*, 30: 152-161.
20. Behpour, M., Ghoreishi, S. M., Mohammadi, N., Soltani, N. and Salavati-Niasari, M. (2010). Investigation of some Schiff base compounds containing disulfide bond as HCl corrosion inhibitors for mild steel. *Corrosion Science*, 52: 4046-4057.
21. Bakarudin, S. B., Zakaria, S., Chia, C. H. and Jani, S. M. (2012). Liquefied residue of kenaf core wood produced at different phenol-kenaf ratio. *Sains Malaysiana*, 41: 225-231.
22. Li, J., Li, C., Wang, W., Zhang, W. and Li, J. (2016). Reactivity of larch and valonia tannins in synthesis of tannin-formaldehyde resins. *Bioresources*, 11: 2256-2268.
23. Manimegalai, S. and Manjula, P. (2015). Thermodynamic and adsorption studies for corrosion inhibition of mild steel in aqueous media by *Sargasam swartzii* (brown algae). *Journal of Materials and Environmental Science*, 6: 1629-1637.
24. Shukla, S. K, Singh, A. K. and Quraishi, M. A. (2011). Corrosion inhibition and adsorption properties of n-phenylhydrazine-1,2-dicarbothioamide on mild steel in hydrochloric acid. *International Journal of Electrochemical Science*, 6: 5779-5791.
25. Peme, T., Olasunkanmi, L. O., Bahadur, I., Adekunle, A. S., Kabanda, M. M. and Ebenso, E. E. (2015). Adsorption and corrosion inhibition studies of some selected dyes as corrosion inhibitors for mild steel in acidic medium: gravimetric, electrochemical, quantum chemical studies and synergistic effect with iodide ions. *Molecules*, 20: 16004-16029.
26. Emregul, K. C. and Hayvali, M. (2006). Studies on the effect of a newly synthesized Schiff base compound from phenazone and vanillin on the corrosion of steel in 2 M HCl. *Corrosion Science*, 48: 797-812.
27. Chia, C. H., Razali, N. F., Sajab, M. S., Zakaria, S., Huang, N. M. and Lim, H. N. (2013). Methylene blue adsorption on graphene oxide. *Sains Malaysiana*, 42: 819-826.
28. Singh, A., Pramanik, T., Kumar, A. and Gupta, M. (2013). Phenobarbital: A new and effective corrosion inhibitor for mild steel in 1M HCl solution. *Asian Journal of Chemistry*. 25(17): 9808-9812.

Malaysian Journal of Analytical Sciences, Vol 22 No 6 (2018): 943 - 949
DOI: https://doi.org/10.17576/mjas-2018-2206-03

MALAYSIAN JOURNAL OF ANALYTICAL SCIENCES
Published by The Malaysian Analytical Sciences Society
ISSN 1394 - 2506

FORMATION OF VANILLIN AND VANILLIC ACID FROM KRAFT LIGNIN THROUGH GREEN CHEMICAL OXIDATION

(Pembentukan Vanillin dan Asid Vanillik dari Kraft Lignin melalui Proses Pengoksidaan Kimia Hijau)

Nabilah Ismail[1]* and Leonard James Wright[2]

[1]*School of Fundamental Sciences,*
Universiti Malaysia Terengganu, 21030 Kuala Terengganu, Terengganu, Malaysia
[2]*Centre for Green Chemical Sciences,*
University of Auckland, 23 Symonds St, Private Bag 92019, Auckland, New Zealand

**Corresponding author: nabilah.i@umt.edu.my*

Received: 16 September 2018; Accepted: 22 November 2018

Abstract

The development of efficient methods to produce useful small molecules such as vanillin and vanillic acid from kraft lignin is an important goal for a sustainable production of fine chemicals. It is generally known that oxidative treatments of kraft lignin can cause partial oxidative depolymerization to produce vanillin, but the conditions required are usually harsh and the yields are low. Therefore, the possibility of achieving the same reaction at 25 °C using an alternative green chemical catalytic oxidation process involving hydrogen peroxide and an Fe(TAML®) oxidation catalyst was investigated. Preliminary experiments using this method at 25 °C with kraft lignin resulted in the formation of small amounts of vanillin (ca. 5%) as well as vanillic acid (<1%). The influence of key parameters including the concentrations of the catalyst (2.0-4.0 µM) and H_2O_2 (0.5-2.0 mM) on the amount of these compounds formed were reported.

Keywords: Fe(TAML®), hydrogen peroxide, kraft lignin, vanillin, vanillic acid

Abstrak

Pembangunan kaedah yang berkesan untuk menghasilkan molekul kecil yang berguna seperti vanillin dan asid vanillik dari kraft lignin adalah penting bagi penghasilan bahan kimia yang mampan. Adalah diketahui bahawa pengoksidaan kraft lignin mampu mengakibatkan depolimerisasi oksidatif separa untuk memberikan vanilin, tetapi kondisi yang diperlukan biasanya kasar dan hasilnya rendah. Oleh itu, kemungkinan untuk mencapai tindak balas yang sama pada 25 °C menggunakan proses pengoksidaan pemangkin kimia alternatif yang melibatkan hidrogen peroksida dan pemangkin pengoksidaan Fe (TAML®) disiasat. Eksperimen awal menggunakan kaedah ini pada 25 °C dengan kraft lignin mengakibatkan pembentukan sejumlah kecil vanillin (sekitar 5%) serta asid vanillik(<1%). Pengaruh parameter utama termasuk kepekatan pemangkin (2.0-4.0 µM) dan H_2O_2 (0.5-2.0 mM), keatas jumlah pembentukan sebatian ini dilaporkan.

Kata kunci: Fe(TAML®), hidrogen peroksida, kraft lignin, vanillin, asid vanillik

Introduction

There is an increasing worldwide drive to develop sustainable alternatives in the use of fossil carbon (coal, oil and gas) as fuels and feedstock for the chemical industry. Lignin is the second-most abundant renewable polymer on earth next to cellulose and can contribute up to 30% of the weight of lignocellulosic biomass. Furthermore, lignin represents one of the very few abundant natural resources that, in principle, could serve as a renewable source of

small aromatic building blocks for other more complex organic molecules [1 – 4]. However, the production of smaller organic molecules from lignin is generally hampered by the nature of lignin as an insoluble, complex three-dimensional amorphous polymer, which is formed by the radical polymerization of three types of hydroxycinnamyl alcohol precursors (*p*-coumaryl, coniferyl, and sinapyl alcohols) known as monolignols, and the resulting polymer contains numerous types of ether (C-O-C) as well as carbon-carbon (C-C) linkages that connect the monomer units. Therefore, unlike many other polymers, lignin does not have a simple repeating chemical structure. Furthermore, many connecting groups are not easily cleaved. Consequently, it is very difficult to obtain high yield of simple, useful organic molecules through the depolymerization of lignin [2].

Kraft lignin, on the other hand, is lignin that has been partially broken down and solubilized. It is produced during the pulping of wood to obtain cellulose fibers for making paper. Globally, more than 72 million tons of kraft lignin are annually produced this way. During kraft pulping, strong alkali and sulfide solution at high temperatures partially break down and solubilize the lignin. After removing the cellulose by filtration, the highly modified, soluble kraft lignin is usually burnt in the recovery boiler to produce heat. However, it has long been recognized that the enormous amounts of kraft lignin produced this way could be much better utilized if an efficient method is found to break it down into small molecules that either were of intrinsic commercial value or could be used as platform compounds for producing fine chemicals [5, 6].

Numerous methods for the depolymerization of kraft lignin to produce fine chemicals have been investigated including hydrolysis, reduction, oxidation and pyrolysis. Among these, oxidation has been the most studied as it tends to give better yield of usefully functionalized molecules. Oxygen is by far the most common oxidant that has been utilized although high temperatures and high oxygen pressures are needed to obtain moderate yield of aromatic compounds [7, 8]. Remarkably, there are very few studies in which hydrogen peroxide has been used for the oxidative depolymerization of kraft lignin [9]. Notably, it has been reported that in the presence of catalytic amounts of simple transition metal salts namely $MnSO_4$, $FeSO_4$ or Na_2WO_4, very small amounts of aromatic compounds including vanillin can be produced on treatment with hydrogen peroxide under mild conditions, but the yields are ≤ 0.51 wt.% [7].

This study has a long-standing interest in the use of the Fe(TAML®) complex, FeB* (see Figure 1) to catalyze the H_2O_2 bleaching (oxidation) of residual lignin on cellulose fibers obtained from the kraft pulping process [10 – 13]. The use of hydrogen peroxide as the oxidant for this purpose is particularly attractive as it is readily available, inexpensive and unlike chlorine-based bleaches, it does not form organo-chlorine by-products, which led this study to consider whether or not the same catalytic oxidation system could be adapted to oxidatively depolymerize kraft lignin and produce aromatic compounds like vanillin under mild conditions if very limited amounts of hydrogen peroxide were employed. The oxidation catalyst, FeB*, is non-toxic and comprises elements commonly found in the biological systems. It is water-soluble and is a very potent and efficient activator of hydrogen peroxide, even at nanomolar concentrations [14, 15]. When the catalyst is eventually degraded, it is transformed into environmentally benign byproducts. Importantly, the hydrogen peroxide oxidation of organic compounds catalyzed by FeB* occurred rapidly at 25 °C [14, 15]. In this paper, a small amount of vanillin (up to 5%) as well as vanillic acid (ca. 1%) was observed upon the treatment of kraft lignin with the FeB*/H_2O_2 system at 25 °C. The results showed that partial depolymerization of kraft lignin occurred under these conditions. The influence of key parameters such as the concentrations of the catalyst and H_2O_2, on the amounts of these compounds formed was also presented.

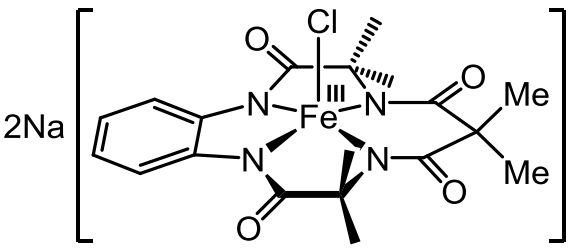


Figure 1. Molecular structure of the Fe(TAML®) compound FeB*

Materials and Methods

Generals procedures

All chemical reagents were analytical grade and used without purification. Softwood kraft lignin samples were obtained from Sigma Aldrich (37,095-9) (SAKL) while hardwood kraft lignin was obtained from Scion Ltd. NZ (*Eucalyptus regnans*) (SCKL). The iron TAML catalyst FeB* was collected from GreenOx Catalysts, Inc. 4400 Fifth Ave, Suite 713 Pittsburgh, PA 15213, USA and used without further purification. The effective M_r of 667.32 g mol^{-1} supplied by the manufacturer was used to calculate catalyst concentrations of the solutions prepared. The catalyst solutions were prepared in deionized water and used within three days. Meanwhile, the Na_2CO_3/$NaHCO_3$ buffer solutions (pH 9.5, 0.010 mol L^{-1}) were prepared using a standard literature procedure [16]. The pH of each buffer solution prepared was checked using a Sartorius PB-10 pH meter fitted with a Sartorius pH/ATC electrode. Hydrogen peroxide stock solutions were made by diluting a commercial solution (~30% w/v) to approximately 1% w/v with deionised water. The solutions were then standardized by UV-Vis absorbance measurement in quartz cuvette cells at 230 nm using $\varepsilon = 72.8$ mol^{-1} L cm^{-1} [17]. UV-Vis measurements were made using a double beam Perkin Elmer Lamda 35 UV-Visible spectrophotometer with a slit width of 1.0 nm and a scan speed of 480 nm/min. Concentrations were determined from the average of three triplicate measurements. The results were confirmed by titration with standard thiosulphate solution (ca. 0.1M concentration accurately determined by iodometric titration [18].

To prepare the standard calibration curves for the analysis of both vanillin and vanillic acid by HPLC, a set of solutions of pure compounds with concentrations of 1.00×10^{-5}, 3.00×10^{-5}, 6.00×10^{-5}, 9.00×10^{-5} and 1.20×10^{-4} mol L^{-1} were prepared in Na_2CO_3/$NaHCO_3$ buffer solution (pH 9.5, 0.010 mol L^{-1}). To an aliquot (10.0 mL) of each solution, acetic acid (1.50 mL of 0.10 mol L^{-1} solution) was added to reduce the pH to ~5.5. After filtration through a small membrane filter, the resulting solution was analyzed by HPLC (injection volume 100 µL, UV-Vis detector set at 270 nm) using the same conditions detailed below for analyzing the lignin samples.

Lignin oxidative depolymerization reactions

In this typical experiment with the temperature maintained at 25 °C, a sample of lignin (12.5 mg) was placed in a 100 mL beaker and Na_2CO_3/$NaHCO_3$ buffer solution (40 mL of a 0.010 mol L^{-1} solution, pH 9.5) was added. While stirring with a magnetic stir bar, aliquots of standard FeB* solution and standard H_2O_2 solution were then added so that the overall concentrations of FeB* and H_2O_2 would be 2.00 µM and 1.00 mM, respectively, once the total solution volume had reached 50 mL by the addition of more buffer solution. The additional buffer solution was added as soon as possible after the adding the FeB* and H_2O_2. The resulting mixture (50 mL) was then stirred at 25 °C for 1 hour. After this time, catalase was added to destroy the remaining hydrogen peroxide and stop the reaction. After one hour, the solution was checked with a peroxide test strip to confirm that all the hydrogen peroxides have been destroyed. An aliquot (10.0 mL) of the solution was removed and acetic acid (1.50 mL of 0.10 mol L^{-1} solution) was added to acidify the solution to pH ~5.5. After filtration through a small membrane filter of 0.4 nm, the resulting solution was analyzed by HPLC using the conditions detailed below. Experiments were carried out using the two different lignins (SAKL and SCKL) with different concentrations of FeB* and hydrogen peroxide.

HPLC analysis

Measurements were made on a Shimadzu LC-20AT HPLC with an SPL-20A UV-Vis detector. The column used was a ProntoSIL EPS column-W RP C18 reverse-phase HPLC column (25 x 0.46 cm, 10 µm). The column temperature was 25 °C, while the diode array detector was set to measure absorbance at 270 with a flow rate of 1.0 mL/min and injection volume of 100 µL. The mobile phases were; Solvent A comprising milli-Q water acidified with 1.25% (v/v) acetic acid and Solvent B that contains pure methanol. Samples were eluted using the following conditions; t = 0, Solvent A 95%; t = 5 min, Solvent A 90% (linear gradient); t = 10 minutes, Solvent A 90% (isocratic); t = 40 minutes, Solvent A 65% (linear gradient); t = 50 minutes Solvent A 65% (isocratic). Between each analysis, the column was eluted with Solvent B (100%) for 15 minutes followed by elution with Solvent A (95%) for 5 minutes [19].

Results and Discussion

The production of vanillin and vanillic acid from Kraft lignin through a catalytic oxidative treatment at 25°C was investigated. The formation of these two products was studied since preliminary experiments indicated that they were the major water-soluble products formed under the conditions used. The catalytic oxidation system employed was hydrogen peroxide in the presence of FeB* at 25 °C in alkaline (pH 9.5) solution. The rates at which FeB* catalyzes hydrogen peroxide oxidations of organic substrates were very rapid at 25 °C in the basic solution and reached a maximum at pH *ca.*10.8. At pH 9.5, the rates of oxidation were slower by more than an order of magnitude. Since it was anticipated that catalytic oxidation and/or polymerization of the vanillin produced could occur in unwanted side-reactions, this study opted to carry out the reactions at this lower pH to minimize the rates of these reactions. In a further attempt to limit unwanted oxidation of the products, this study also restricted the amount of hydrogen peroxide used to 1.36 mg per 10.0 mg lignin. There have been no previous reports on the use of this catalytic oxidation system for vanillin and vanillic acid production from kraft lignin.

In the blank reactions in which neither hydrogen peroxide nor the FeB* catalyst was present, only a very small amount of vanillin was obtained from each kraft lignin (Entry 1, Table 1). The other two blank reactions in which only the FeB* catalyst or only hydrogen peroxide was added (entries 2 and 3, Table 1) provided some unexpected results. In the reactions to which only FeB* (4.00 µM) was added (entry 2, Table 1), the amount of vanillin produced from the SCKL lignin had increased from 0.46% to 1.47% (a factor of 3.2). For the SAKL lignin, an increase was also observed, which was much smaller from 0.87% to 1.07% (a factor of 1.23). There was no clear evidence as to why the increased amounts of vanillin were produced in both cases. However, one possibility is that FeB* had utilized atmospheric oxygen as an oxidant for these reactions. Oxidation reactions using oxygen and the catalyst FeB* have been reported previously [20]. The other blank reactions in which the kraft lignin samples were stirred in alkaline buffer with hydrogen peroxide alone at 20 °C resulted in unexpectedly large amounts of vanillin formed (Entry 3, Table 1). Under these conditions, similar amounts (5.19% and 5.48%) of vanillin were obtained from both lignin samples.

The reaction of the two kraft lignins with hydrogen peroxide and catalyst FeB* (entries 4-7, Table 1) produced vanillin, but the amounts varied considerably depending on the amounts of hydrogen peroxide and catalyst used. In all cases, the amounts of vanillin were less than 1%, except for Entry 6 in which the concentrations of FeB* and H_2O_2 were 4.00 µM and 1.00 mM, respectively. With the SCKL lignin, a considerable amount of vanillin (4.27%) was produced, which was slightly less than the amount formed by hydrogen peroxide alone (5.18%). However, for the SAKL lignin, the results were very different. Although this ratio also produced the largest amount of vanillin from all the FeB*/H_2O_2 reactions (entries 4-7, Table 1), the amount was only 1.07%, which was considerably less than the amount formed by hydrogen peroxide alone (5.48%). Again, this underscores how differently sourced kraft lignins can display very different reactivity.

Table 1. Formation of vanillin from SCKL and SAKL kraft lignins after treatment with different concentrations of hydrogen peroxide and the oxidation catalyst FeB* at 25 °C and pH 9.5 for one hour

Entry Number	Concentrations of Reagents		Kraft Lignin Source			
			SCKL		SAKL	
	[FeB*] (µM)	[H_2O_2] (mM)	[Vanillin] (mg/L)	% Vanillin (by wt.)	[Vanillin] (mg/L)	% Vanillin (by wt.)
1	0	0	1.15	0.46	2.18	0.87
2	4.00	0	3.67	1.47	2.68	1.07
3	0	1.00	13.0	5.19	13.7	5.48
4	2.00	1.00	1.67	0.67	0.51	0.22
5	2.00	2.00	1.81	0.72	1.59	0.64
6	4.00	1.00	10.7	4.27	2.67	1.07
7	4.00	0.50	1.75	0.70	1.01	0.40

The amounts of vanillic acid formed during each of the oxidative reactions are presented in Table 2. In each case, the amounts of vanillic acid were much less than the amounts of vanillin obtained. Interestingly, the same conditions that produced the largest amounts of vanillin also produced the largest amounts of vanillic acid. Thus, upon treatment with hydrogen peroxide alone (Entry 3, Table 2) 0.46% and 0.75% of vanillic acid were obtained from the SCKL and SAKL lignins, respectively. For the other two blank reactions (entries 1 and 2, Table 2) relatively larger amounts of vanillic acid were formed from the SAKL lignin than that of the SCKL lignin. In all cases, the FeB*/H_2O_2 oxidation system produced less vanillic acid than the amount obtained using hydrogen peroxide alone (entries 4-7, Table 2). For the FeB* catalyzed reactions, it was again when the concentrations of FeB* and H_2O_2 were 4.00 µM and 1.00 mM, respectively, that the maximum amount of vanillic acid was formed (Entry 6, Table 2).

Table 2. Formation of vanillic acid from SCKL and SAKL kraft lignins after treatment with different concentrations of hydrogen peroxide and the oxidation catalyst FeB* at 25 °C and pH 9.5 for one hour

Entry Number	**Concentrations of Reagents**		**Kraft Lignin Source**			
			SCKL		**SAKL**	
	[FeB*] (µM)	**[H_2O_2] (mM)**	**[Vanillic Acid] (mg/L)**	**% Vanillic Acid (by wt.)**	**[Vanillic acid] (mg/L)**	**% Vanillic Acid (by wt.)**
1	0	0	0.05	0.02	0.86	0.34
2	4.00	0	0.40	0.16	1.30	0.52
3	0	1.00	1.15	0.46	1.88	0.75
4	2.00	1.00	0.15	0.06	0.12	0.05
5	2.00	2.00	0.04	0.01	0.53	0.21
6	4.00	1.00	0.79	0.32	0.68	0.27
7	4.00	0.50	0.18	0.07	0.32	0.13

Meanwhile, the SCKL lignin started to approach the amount of vanillic acid formed by hydrogen peroxide alone (0.32% vs 0.46%), whereas it was considerably less in the case of the SAKL lignin (0.27% vs 0.75%). The results in tables 1 and 2 provide no evidence that catalytic oxidation of vanillin produced vanillic acid. Thus, although relatively small amounts of vanillin were obtained from the catalytic reactions as represented in entries 4, 5 and 7 of Table 1, there were no corresponding increase in vanillic acid formation under these same conditions (Table 2). Besides, although considerably more vanillin was formed from the SCKL lignin (4.27%) than the SAKL lignin (1.07%) (Entry 6 Table 1), almost the same amount of vanillic acid (0.32 and 0.27%, respectively) was formed in each case under these conditions (Entry 6, Table 2). A possible further complication is that the FeB*/H_2O_2 system could initiate some oxidative polymerization of several formed vanillin and/or vanillic acid. It was shown that this catalytic system can cause the oligomerization/polymerization of phenolic compounds including bisphenol A [21].

Conclusion

The treatment of kraft lignins with the FeB*/H_2O_2 catalytic oxidation system at 25 °C for one hour has resulted in oxidative depolymerization to form small amounts of vanillin (up to 4.27%) and vanillic acid (up to 0.32%). The amounts of these products formed were highly dependent on the source of the kraft lignin and the conditions used. Surprisingly, it has been found that the treatment of these kraft lignins with hydrogen peroxide alone under the same mild conditions resulted in the formation of slightly more of each of these two products (5.48% and 0.75%, respectively). It is possible that during the FeB*/H_2O_2 oxidation reactions, competing non-productive oxidations utilized some of the hydrogen peroxide and therefore reducing the amount of vanillin and vanillic acid produced. Furthermore, oxidative polymerization of vanillin and vanillic acid may also occur under these conditions, which

further reduced the yield of these compounds. The amounts of vanillin obtained by these hydrogen peroxide oxidative depolymerization reactions all fall within the range (3.5 – 10% by weight) previously reported for different kraft lignins upon the treatment with oxygen (9 bar) at 130-150 °C for several hours. Further refinement of the oxidative reactions described in this study could therefore lead to a more efficient method of vanillin production from kraft lignin. The intriguing observation was that the treatment of kraft lignin with FeB* under aerobic conditions had produced some vanillin and vanillic acid, which also merits further investigation.

Acknowledgement

Nabilah Ismail would like to acknowledge the scholarship received from Majlis Amanah Rakyat (MARA), an agency under the Malaysian Government for master studies.

References

1. Mahmood, N., Yuan, Z., Schmidt, J. and Xu, C. C. (2016). Depolymerization of lignins and their applications for the preparation of polyols and rigid polyurethane foams: A review. *Renewable and Sustainable Energy Reviews*, 60: 317-329.
2. Lange, H., Decina, S. and Crestini, C. (2013). Oxidative upgrade of lignin–Recent routes reviewed. *European Polymer Journal*, 49(6): 1151-1173.
3. Zakzeski, J., Bruijnincx, P. C., Jongerius, A. L., & Weckhuysen, B. M. (2010). The catalytic valorization of lignin for the production of renewable chemicals. *Chemical Reviews*, 110(6): 3552-3599.
4. Bjørsvik, H. R. and Liguori, L. (2002). Organic processes to pharmaceutical chemicals based on fine chemicals from lignosulfonates. *Organic Process Research & Development*, 6(3): 279-290.
5. Pinto, P. C. R., Costa, C. E. and Rodrigues, A. E. (2013). Oxidation of lignin from *Eucalyptus globulus* pulping liquors to produce syringaldehyde and vanillin. *Industrial & Engineering Chemistry Research*, 52(12): 4421-4428.
6. Voitl, T. and Rohr, P. R. V. (2009). Demonstration of a process for the conversion of kraft lignin into vanillin and methyl vanillate by acidic oxidation in aqueous methanol. *Industrial & Engineering Chemistry Research*, 49(2): 520-525.
7. Napoly, F., Kardos, N., Jean-Gérard, L., Goux-Henry, C., Andrioletti, B. and Draye, M. (2015). H_2O_2-mediated kraft lignin oxidation with readily available metal salts: What about the effect of ultrasound?. *Industrial & Engineering Chemistry Research*, 54(22): 6046-6051.
8. Voitl, T., Nagel, M. V. and von Rohr, P. R. (2010). Analysis of products from the oxidation of technical lignins by oxygen and H3PMo12O40 in water and aqueous methanol by size-exclusion chromatography. *Holzforschung*, 64(1): 13-19.
9. Ouyang, X., Ruan, T. and Qiu, X. (2016). Effect of solvent on hydrothermal oxidation depolymerization of lignin for the production of monophenolic compounds. *Fuel Processing Technology*, 144: 181-185.
10. Wingate, K. G., Stuthridge, T. R., Wright, L. J., Horwitz, C. P. and Collins, T. J. (2004). Application of TAML® catalysts to remove colour from pulp and paper mill effluents. *Water Science and Technology*, 49(4): 255-260.
11. Horwitz, C. P., Collins, T. J., Spatz, J., Smith, H. J., Wright, L. J., Stuthridge, T. R., Wingate, K. G & McGrouther, K. (2006). Iron-TAML® catalysts in the pulp and paper industry. *ACS Symposium Series*, 921: 156-169
12. Collins, T. J., Horwitz, C. P., Ryabov, A. D., Vuocolo, L. D., Gupta, S. S., Ghosh, A., Fattaleh, N. L., Handgun, Y., Steinhoff, B., Noser, C. A. and Beach, E. (2002). Tetraamido macrocyclic ligand catalytic oxidant activators in the pulp and paper industry. *Advancing Sustainability through Green Chemistry and Engineering*, 823: 47-60.
13. Collins, T. J., Hall, J. A., Vuocolo, L. D., Fattaleh, N. L., Suckling, I., Horwitz, C. P., Gordon-Wylie, S. W., Allison, R. W. Fullerton, T. J., Wright, L. J., (2000). The activation of hydrogen peroxide for selective, e. w. p. b.; In "Green Chemistry: Challenging Perspectives P. T., ed., Oxford University Press, Oxford, pp. 79-105
14. Bartos, M. J., Gordon-Wylie, S. W., Fox, B. G., Wright, L. J., Weintraub, S. T., Kauffmann, K. E., Münck, E., Kostka, K.L., Uffelman, E.S., Rickard, C.E. and Noon, K. R. (1998). Designing ligands to achieve robust oxidation catalysts. Iron based systems. *Coordination Chemistry Reviews*, 174(1): 361-390.
15. Ryabov, A. D. and Collins, T. J. (2009). Mechanistic considerations on the reactivity of green FeIII-TAML activators of peroxides. *Advances in Inorganic Chemistry*, 61: 471-521.

16. Delory, G. E. and King, E. J. (1945). A sodium carbonate-bicarbonate buffer for alkaline phosphatases. *Biochemical Journal*, 39(3): 245.
17. Chahbane, N., Popescu, D. L., Mitchell, D. A., Chanda, A., Lenoir, D., Ryabov, A. D., Schramm, K.W. and Collins, T. J. (2007). Fe III–TAML-catalyzed green oxidative degradation of the azo dye Orange II by H_2O_2 and organic peroxides: products, toxicity, kinetics, and mechanisms. *Green Chemistry*, 9(1): 49-57.
18. Kingzett, C. T. (1888). On the estimation of peroxide of hydrogen. *Analyst*, 13: 62-63.
19. Voisine, R., Carmichael, L., Chalier, P., Cormier, F. and Morin, A. (1995). Determination of glucovanillin and vanillin in cured vanilla pods. *Journal of Agricultural and Food Chemistry*, 43(10): 2658-2661.
20. Tang, L. L., Gunderson, W. A., Weitz, A. C., Hendrich, M. P., Ryabov, A. D. and Collins, T. J. (2015). Activation of dioxygen by a TAML activator in reverse Micelles: characterization of an $Fe^{III}Fe^{IV}$ dimer and associated catalytic chemistry. *Journal of the American Chemical Society*, 137(30): 9704-9715.
21. Onundi, Y., Drake, B. A., Malecky, R. T., DeNardo, M. A., Mills, M. R., Kundu, S. and Truong, L. (2017). A multidisciplinary investigation of the technical and environmental performances of TAML/peroxide elimination of Bisphenol A compounds from water. *Green Chemistry*, 19(18): 4234-4262.

Malaysian Journal of Analytical Sciences, Vol 22 No 6 (2018): 950 - 956
DOI: https://doi.org/10.17576/mjas-2018-2206-04

MALAYSIAN JOURNAL OF ANALYTICAL SCIENCES
Published by The Malaysian Analytical Sciences Society
ISSN 1394 - 2506

CORROSION INHIBITIVE EFFECT OF THIOUREA ON 1100 ALUMINIUM ALLOY SHEET IN HYDROCHLORIC ACID SOLUTION

(Kesan Perencatan Kakisan Thiourea Terhadap kepingan Aloi Aluminium 1100 Dalam Larutan Asid Hidroklorik)

Maria Fazira Mohd Fekeri[1], Chan Kok Sheng[2]*, Lee Hou Yi[1]

[1]*School of Ocean Engineering*
[2]*School of Fundamental Science*
Universiti Malaysia Terengganu, 21030 Kuala Nerus, Terengganu, Malaysia

**Corresponding author: chankoksheng@umt.edu.my*

Received: 2 September 2018; Accepted: 3 October 2018

Abstract

Corrosion is the degradation of material properties or mass over time due to environmental effects. It cannot be avoided but can be prevented using appropriate inhibitor for corrosion resistant. In this work, the beneficial role of thiourea as organic inhibitor for the 1100 aluminium (Al) alloy sheet corrosion in hydrochloric (HCl) acid solution was first investigated in detail by a simple gravimetric method. The result showed that increasing concentration of thiourea reduced the weight loss percentage and corrosion rate of Al. Meanwhile, the inhibition efficiency increased up to 52.54% with the increase of thiourea concentration for 30 days of immersion time. The surface morphology of the samples was characterized by metallurgical microscope. It can be observed that the number of corrosion pits distributed on Al surface became fewer as the concentration of thiourea increased, proving the effective retardation of corrosion on Al sheet.

Keywords: thiourea, aluminium, hydrochloric acid, corrosion rate, inhibition efficiency

Abstrak

Kakisan adalah degradasi ciri-ciri bahan dari semasa ke semasa disebabakan oleh kesan alam sekitar. Kakisan tidak dapat dielakkan tetapi boleh dicegah dengan menggunakan perencat kakisan yang sesuai. Dalam kajian ini, peranan tiourea sebagai perencat organik atas kakisan kepingan 1100 aloi aluminium (Al) dalam larutan asid hidroklorik (HCl) telah dikaji secara terperinci dengan menggunakan kaedah gravimetrik yang mudah. Hasil kajian menunjukkan peningkatan kepekatan tiourea telah mengurangkan peratus kehilangan jisim dan seterusnya kadar kakisan Al. Sementara itu, kecekapan perencatan meningkat kepada 52.54% dengan penambahan kepekatan tiourea dalam larutan HCl. Morfologi permukaan spesimen telah dicirikan melalui mikroskop metalorgikal. Bilangan pit kakisan yang bertaburan pada permukaan Al berkurangan apabila kepekatan tiourea meningkat membuktikan keberkesanan perencatan kakisan pada kepingan Al.

Kata kunci: tiourea, aluminium, hidroklorik asid, kadar kakisan, kecekapan perencatan

Introduction

Corrosion is an electrochemical process by which metallic structures are destroyed gradually through anodic dissolution. It is one of the main concerns in the durability of materials and structures; as a result, studies are continuously carried out to develop an effective corrosion control. This phenomenon necessitates the continuous search for better corrosion inhibitors, due to vast differences in the media encountered in industry which remains a focal point in corrosion control as the inhibitors slow down the corrosion process on metals [1, 2].

Inhibitor use has become one of the most practical methods for protection against corrosion in acidic media. Generally, the first stage in the action mechanism of the inhibitors in aggressive acid media is the adsorption of the inhibitors on the metal surface, where acid is used for the pickling of metal for its chemical or electrochemical etching. An effective inhibitor must also transfer water from the metal surface, interact with anodic or cathodic reaction sites to retard the oxidation and reduce corrosion reaction, and further prevent transportation of water and corrosion-active species on the metal surface [2 - 4]. Recently, the use of organic compounds to inhibit corrosion has great significance due to their application in preventing corrosion under various corrosive environments. These compounds have shown great effectiveness for inhibiting aqueous corrosion due to film formation on the metal surface [4 - 6].

Organic compounds containing nitrogen (N) and sulphur (S) have also been proven to be good inhibitors for the prevention of corrosion under acidic condition [5]. Therefore, thiourea [$S(NH_2)_2$] and its derivatives have been extensively investigated as corrosion inhibitors in acidic medium. The corrosion inhibition of thiourea is superior to the metal surface due to its strong polar coordinate. S compounds, such as thiourea and amine-based inhibitors in acidic media can simultaneously act in both anodic and cathodic media. The multiple bonds in the thiourea molecules that facilitate adsorption are very effective inhibitors for metal corrosion in acidic medium because the S atom is easily protonated in acidic solution and a stronger electron donor than N, therefore S atom is more strongly adsorbed to the metal surface [5 - 10]. Also, it has been reported by Loto et al. [5] that S-containing and N-containing inhibitors exert their best efficiencies in the acid solution.

Aluminum (Al) is one of the best metals used in construction, packaging and transportation because of its unique mechanical strength and electrical conductivity. It is also used in electronics as an anodic material for power sources with high energy density due to its superior purity. Although Al has an adhesive protective passivating oxide film, this film also has an amphoteric susceptibility, leading the metal to dissolve readily in acidic and basic solutions concentrated above and below pH (4-9) [3]. In our efforts to mitigate the electrochemical corrosion of Al, the main solution is to isolate the metal from corrosive agents and this can be achieved by using corrosion inhibitors which prevent the adsorption of the aggressive anions or by the formation of a more resistance oxide film on the metal surface [4].

Recently, there are plenty of published studies using organic inhibitors such as sodium benzoate [1], thiadiazole derivatives [5] and triazole derivative [10] for corrosion control of metal. However, studies based on the inhibition effect on Al in acidic solution utilizing the thiourea as an organic inhibitor are very limited. Hence, in this study, we presented a detailed investigation on the effect of thiourea as an organic inhibitor for the 1100 Al alloy corrosion in 5 wt.% dilute HCl solution. The corrosion rate and inhibition efficiency were determined by the gravimetric method for 6-day interval until 30 days of immersion duration. The surface morphology of the specimens was then observed under a metallurgical optical microscope.

Materials and Methods

Al alloy 1100 (99.0% Al) was used as received. Firstly, the Al was cut into a rectangular dimension of 25 mm x 35 mm x 2 mm. It was then mechanically polished with 1200 emery paper, lubricated with 50 ml of distilled water and acetone to remove the oxide layer, and further dried at room temperature for one day. After weighing, the Al was immersed in 5 wt. % HCl solution with different concentrations of thiourea (i.e. 0 wt.%, 5 wt.%, 10 wt.%, 15 wt.%, 20 wt.% and 25 wt.%) for an immersion duration of 6-day intervals until 30 days. Meanwhile, a typical sample immersed in HCl without the presence of thiourea was used as reference. After immersion, the Al was removed from the solution and immersed in nitric acid for 2-3 minutes to remove the corrosion residues. The specimen was then rinsed with distilled water, dried in air and weighted to determine the final weight. The weight loss percentage was determined by the gravimetric method as:

$$WL = \frac{W_I - W_F}{W_I} \times 100\% \quad (1)$$

where WL is the weight loss percentage, W_I is the initial weight before corrosion and W_F indicates the final weight after corrosion. The corrosion rate was then determined from the following expression [11]:

$$CR = \frac{87.6\ \Delta wt}{\rho_A t} \quad (2)$$

where CR is the corrosion rate in mm/year, Δwt is the weight loss, ρ_A is the density of Al in g/cm^3, and t is the exposure time. Lastly, the inhibition efficiency (IE) was determined from corrosion rate values by the following equation [12]:

$$IE\,(\%) = \frac{CR_o - CR_1}{CR_o} \times 100\% \quad (3)$$

where CR_0 and CR_1 are corrosion rates without and in the presence of inhibitor, respectively. TM-1000 Hitachi tabletop metallurgical microscope was used to examine the specimen surface before and after the immersion in HCl at 20x magnification for a clear surface imaging.

Results and Discussion

The gravimetric method for corrosion studies is a time-tested and reliable technique with good correlation between impedance and polarization techniques [11, 12]. Figure 1 shows the weight loss percentage (%) against time for the Al immersed in HCl solution with different concentration of thiourea. From the figure, it shows that the weight loss of Al increased gradually with immersion time. A clear difference was noticed between the Al exposed to thiourea as compared to the one without thiourea with the highest weight loss, which indicated that the thiourea is effective to protect the Al from corrosion. The weight loss also decreased with the increase of thiourea concentration, which means a higher concentration of inhibitor reduced the corrosion effect by protecting the Al surface at longer immersion time. This inhibition effect agrees with the work reported by Ahmad and Hassan [10], in which the adding of the desired concentration of triazole derivative as organic corrosion inhibitor into the hydrochloric acid solution would substantially reduce the corrosion rate. The highest and lowest weight losses of Al in HCl were determined respectively as 18.52% and 3.50% for the samples without inhibitor and for the specimens with 25 wt.% of thiourea concentration at 30 days of immersion time. This result shows that thiourea is an appropriate inhibitor for Al corrosion in HCl acid that can retard the corrosion process.

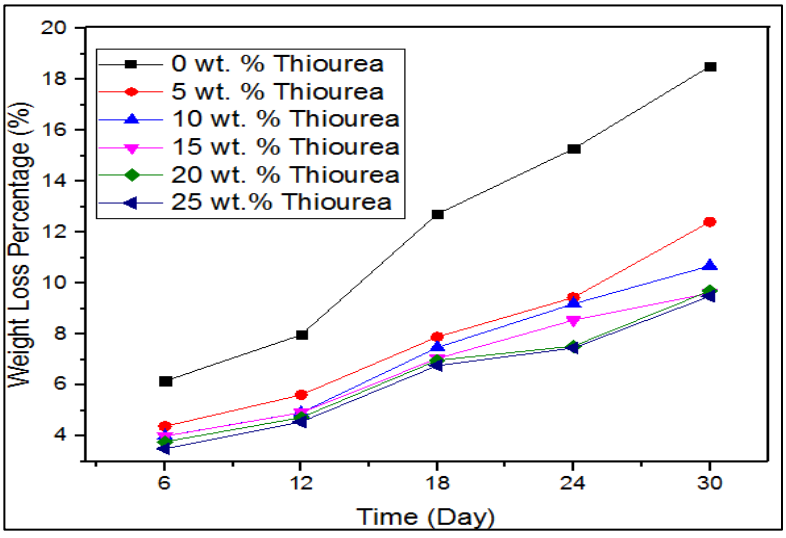


Figure 1. The weight loss percentage (%) of the Al immersed in HCl solution against immersion time

Subsequently, the corrosion rate of the present samples was calculated by equation (2). Figure 2 depicts the plot of corrosion rate versus the immersion time of the Al with different concentrations of thiourea. As can be seen from the figure, the corrosion rate showed a significant decrease from days 6 to days 12, and afterwards, it showed only a slight variation with immersion time until days 30. Furthermore, the Al immersed in thiourea solution gave a lower corrosion rate as compared to the one without inhibitor since there was protection provided by thiourea on the specimen from being attacked by chloride ions. This result also indicated that the corrosion rate has been remarkably reduced after thiourea was added into the solution. As stated by Rosliza [13], corrosion inhibitor is a substance which, when added in small amount to a medium normally corrosive to a metal or alloy in contact with it, can effectively reduce the corrosion rate as it protects the metal surface from being further attacked by chloride ion. The lowest corrosion rate obtained in this study was for the Al immersed in 25 wt.% of thiourea followed sequentially by 20 wt.%, 15 wt.%, 10 wt.% and 5 wt.% of thiourea. Again, this result gave evidence that higher thiourea concentration and longer immersion time will protect the samples from undergoing further corrosion.

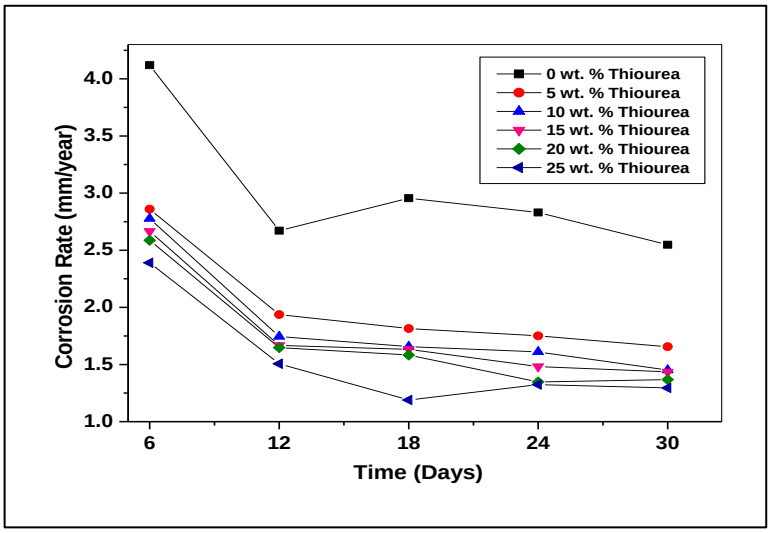


Figure 2. The corrosion rate of the Al against immersion time at different thiourea concentrations

The inhibition efficiency (%) was calculated by equation (3). Table 1 shows the inhibition efficiency for Al immersed in HCl with different thiourea concentrations from days 6 until days 30. The plot of inhibition efficiency versus immersion time for different concentrations of thiourea is shown in Figure 3.

Table 1. The inhibition efficiency of Al corrosion at different immersion durations and thiourea concentrations.

Samples (5 wt.% HCl)	**Inhibition Efficiency (%)**				
	Day 6	**Day 12**	**Day 18**	**Day 24**	**Day 30**
5 wt.% thiourea	28.59	30.87	31.55	35.57	39.33
10 wt.% thiourea	35.28	37.10	37.50	37.32	46.85
15 wt.% thiourea	36.85	40.09	40.86	43.90	47.40
20 wt.% thiourea	39.59	39.06	41.28	47.54	49.87
25 wt.% thiourea	40.31	42.02	45.32	51.31	52.54

From the figure, it can be seen that the inhibition efficiency increased with the increasing of thiourea concentration and immersion time. This again indicated that thiourea can be utilized to retard the Al corrosion in HCl for a prolonged time. The inhibitors will react with and remove the active corrosive species from the metal surface by creating a barrier between the metal and their environment to decrease the attack of chloride ion [13]. Hence, we can elucidate that the role of thiourea as an inhibitor becomes more effective when the concentration of thiourea increases. This effect is in agreement with the work reported by Prabhu and Rao [14], in which a corrosion inhibitor is a chemical substance that, when a small concentration is added into the environmental medium would effectively increases the inhibition efficiency. Also, the inhibition efficiency range obtained in this work is comparable with those obtained by Ahmad and Hassan [10], Rosliza [13], and Prabhu and Rao [14], in which the thiourea can provide an alternative and better solution to metal corrosion in an acidic med

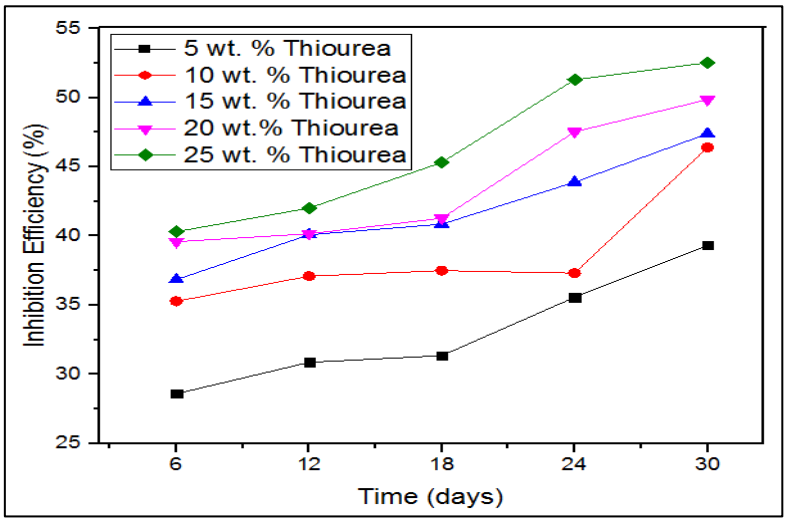


Figure 3. The inhibition efficiency of the Al corrosion against immersion time for different thiourea concentrations

Pitting is a particular characteristic of chloride ion (Cl^-) attacks and is considered to be autocatalytic in nature; once a pit starts to grow, the local conditions are altered such that further pit growth is promoted [15]. Figure 4 illustrates the microstructure surface images of pure Al and the Al immersed in 5 wt.% and 25 wt.% thiourea concentrations for 6 days and 30 days of immersion duration. As shown in Figure 4(a), the surface of the Al before corrosion was homogeneous without any pitting or crack. However, the Al after immersing in the HCl solution had the irregular mixtures of conical, hemisphere and cylindrical pits on the surface. Corrosion of Al appeared to occur principally at flaws or grain boundaries within the surface film and at sites where the film was damaged mechanically under conditions in which self-repair will not occur. This acidic chloride environment is aggressive to most metals and tends to prevent re-passivation and promote continued propagation of the pit. As a result, pitting will occur during active dissolution if certain regions of the samples are susceptible and dissolve faster than the rest of the surface. In practice, pits have a tendency to form an irregular geometry associated with increasing size [15, 16].

From Figure 4, the corrosion pits observed on the Al surface as indicated by the dark region became wider when the immersion time increased. However, the number of pits decreased with the increasing of thiourea concentration. This is due to the role of thiourea inhibitor to protect the surface from further corrosion. Nevertheless, the corrosion cannot be avoided from occurring on Al, even when there an inhibitor is present in the solutions, but the corrosion can be retarded from getting worse for a prolonged time. Consequently, this finding proved the coverage of thiourea as a corrosion inhibitor on the Al surface and significantly decreased the corrosion attack in HCl solution.

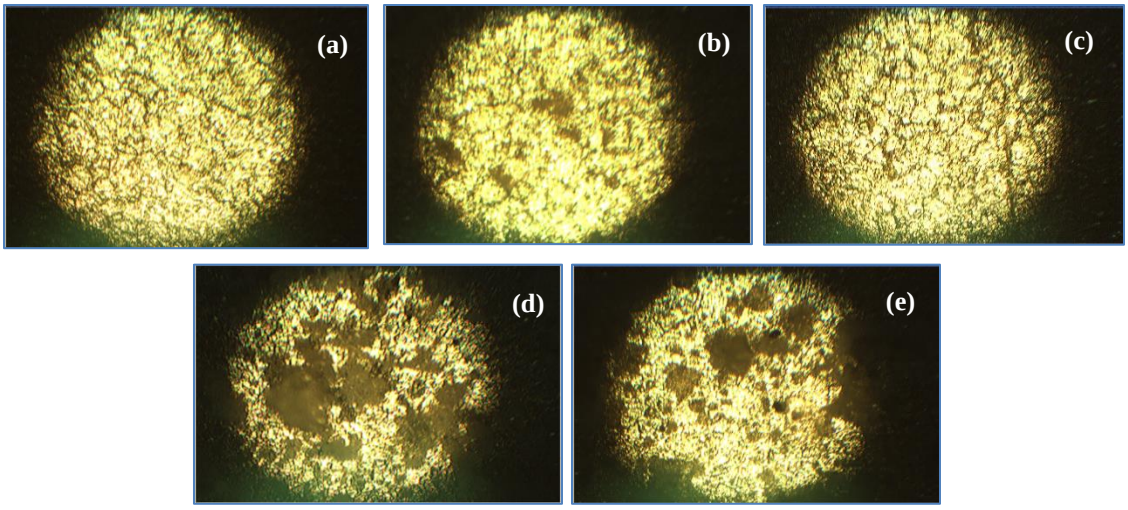


Figure 4. Surface morphology (50X) of (a) pure Al, (b) Al immersed with 5 wt. % thiourea for 6 days; (c) 25 wt.% thiourea for 6 days; (d) 5 wt.% thiourea for 30 days and (e) 25 wt.% thiourea for 30 days in HCl solution

Conclusion

In this work, the beneficial role of thiourea as an organic inhibitor on 1100 Al alloy corrosion in HCl acid solution was successfully investigated in detail by a simple gravimetric method. The results showed that increasing the concentration of thiourea has reduced the weight loss percentage and corrosion rate of Al specimens in HCl, thereby increasing the inhibition efficiency. Microstructure images showed that the number of pits distributed on the Al surface became fewer as the concentration of thiourea increased, which evidences the prevention of corrosion attacked on Al surface by thiourea. Based on this finding, further study on the corrosion inhibition effect by thiourea may be carried out in the future with different types of etchant mediums and applied metals to meet multiple commercialization purposes.

Acknowledgements

The authors would like to thank the School of Fundamental Science, School of Ocean Engineering, Universiti Malaysia Terengganu and the Malaysian Government for the assistance and support in conducting this work.

References

1. Nik, W. B. W., Sulaiman, O., Giap, S. G. E. and Rosliza, R. (2010). Evaluation of inhibitive action of sodium benzoate on corrosion behaviour of AA6063 in seawater. *International Journal of Technology*, 1: 20–28.
2. Palou, R. M., Xomelt, O. O., and Likhanova, N. V. (2014). Environmentally friendly corrosion inhibitors. *Developments in Corrosion Protection*, 431-464.
3. Meena, S. L. and Verma, P. S. (2014). Effect of inhibitors on corrosion of aluminum in acidic medium. *Indian Journal of Chemical Technology*, 21: 220-223.
4. Fouda, A. S., Shalabi, K. and Mohamed N. H. (2014). Corrosion inhibition of aluminum in hydrochloric acid solutions using some chalcone derivatives. *International Journal of Innovative Research in Science, Engineering and Technology*, 3(3): 9861-9875.
5. Loto, C. A., Loto, R. T. and Popoola, A. P. I. (2012). Corrosion inhibition of thiourea and thiadiazole derivatives: A review. *Journal of Materials and Environmental Science*, 3(5): 885-894.
6. Dariva, C. G. and Galio, A. F. (2014). Corrosion inhibitors–principles, mechanisms and applications. *Developments in Corrosion Protection*, 365-379.
7. Shettya, S. D. and Shetty, P. (2008). Inhibition of mild steel corrosion in acid media by N-benzyl-N′phenyl thiourea. *Indian Journal of Chemical Technology*, 15: 216-220.
8. Yaro, A. S. and Abdulaaima, D. A. (2012). Phenyl thiourea as corrosion inhibitor for mild steel in strong hydrochloric acid. *Iraqi Journal of Chemical and Petroleum Engineering*, 13(2): 1-9.

9. Ali, A. I., and Foaud, N. (2012). Inhibition of aluminum corrosion in hydrochloric acid solution using black mulberry extract. *Journal of Material Environmental Science*, 3(5): 917-924.
10. Ahmad, Y. H. and Hassan, W. M. (2012). Corrosion inhibition of steel in hydrochloric acid solution using a triazole derivative: Electrochemical and computational studies. *International Journal of Electrochemical Science*, 7:12456-12469.
11. Kingsley, O. O. and Gideon C. O. (2014). Comparison of percentage weight loss and corrosion rate trends in different metal coupons from two soil environments. *International Journal of Environmental Bioremediation & Biodegradation*, 2(5):243-249.
12. Eldwaib, K. A. (2013). Corrosion behavior of Al-alloy in NaCl contains some inhibitors. *International Journal of Chemical, Environmental & Biological Sciences*, 1(3): 524–527.
13. Rosliza, R. (2012). Improvement of corrosion resistance of aluminium alloy by natural products. *Corrosion Resistance*, 377-396.
14. Prabhu, D. and Rao, P. (2017). Coriandrum sativum L.—A novel green inhibitor for the corrosion inhibition of aluminium in 1.0 M phosphoric acid solution. *Journal of Environmental Chemical Engineering*, 1: 676-683.
15. Leygraf, C. and Graedel, T. E. (2000). Atmospheric Corrosion. New York: John Wiley & Sons, Inc.
16. Pereira, M. C., Silva, J. W., Acciari, H. A., Codaro, E. N. and Hein, L. R. (2012). Morphology characterization and kinetics evaluation of pitting corrosion of commercially pure aluminium by digital image analysis. *Materials Sciences and Applications*, 3: 287-2

Malaysian Journal of Analytical Sciences, Vol 22 No 6 (2018): 957 - 964
DOI: https://doi.org/10.17576/mjas-2018-2206-05

MALAYSIAN JOURNAL OF ANALYTICAL SCIENCES
Published by The Malaysian Analytical Sciences Society
ISSN 1394 - 2506

CHEMICAL COMPOUNDS AND ANTIMICROBIAL ACTIVITY OF ACETONE *Musa acuminate AA/AAA* LEAF STALK EXTRACTS ON SELECTIVE GRAM-NEGATIVE BACTERIA

(Sebatian Kimia dan Aktiviti Antimikrob dari Ekstrak Aseton Pelepah Daun *Musa acuminate AA/AAA* pada Bakteria Jenis Gram Negatif Terpilih)

Tuan Nadrah Ismail, Raja Azman Awang, Suharni Mohamad, Wan Nazatul Shima Shahidan*

School of Dental Sciences, Health Campus,
Universiti Sains Malaysia, 16150 Kubang Kerian, Kelantan, Malaysia

**Corresponding author: shima@usm.my*

Received: 3 May 2017; Accepted: 29 October 2018

Abstract

Banana is a familiar tropical fruit and is acclaimed for its therapeutic uses. A previous study has found that acetone banana leaf stalk extract of the Cavendish group (*Musa acuminate AA/AAA*) have antibacterial properties on selected Gram-negative bacteria using the agar disc diffusion method. Hence, this study is aimed to evaluate the phytochemical analysis and antibacterial activities *Musa acuminate AA/AAA*. The chemical composition of *Musa acuminate AA/AAA* leaf stalk extract was analysed using gas chromatography–mass spectrometry (GC-MS) and the mass spectra library was used to identify an unknown chemical in the sample mixture. The minimum inhibitory concentration (MIC) and minimum bactericidal concentration (MBC) of *Musa acuminate AA/AAA* leaf stalk extract was investigated using macrobroth dilution on *Pseudomonas aeruginosa* and *Escherichia coli*. The GC/MS analysis revealed the presence of more than forty individual compounds and a significant difference in the percentage composition of leaf stalk parts was observed. The extract inhibited bacterial growth at an MIC of 125 mg/ml and 250 mg/ml against *Pseudomonas aeruginosa* and *Escherichia coli* respectively, while the MBC was 500 mg/ml against both organisms with comparable effects to chlorhexidine. *Musa acuminate AA/AAA* leaf stalk extract possesses good antibacterial activities against the tested bacteria. The results indicate that *Musa acuminate AA/AAA* leaf stalk can be used against other Gram-negative bacteria.

Keywords: phytochemical, *Musa acuminate AA/AAA* leaf stalk, acetone extract, Gram-negative bacteria

Abstrak

Pisang adalah buah tropika yang biasa dan telah diiktiraf untuk kegunaan terapeutiknya. Kajian kami sebelum ini telah mendapati bahawa ekstrak tangkai daun pisang berangan (*Musa acuminate AA/AAA*) menggunakan aseton mempunyai ciri-ciri antibakteria terhadap bakteria gram-negatif terpilih dengan menggunakan kaedah penyebaran cakera agar. Oleh itu, objektif utama kajian ini adalah untuk menganalisa fitokimia dan aktiviti antibakterianya. Komposisi kimia ekstrak tangkai daun *Musa acuminate AA/AAA* dianalisa menggunakan GC/MS dan perpustakaan spektrum jisim telah digunakan untuk mengenal pasti bahan kimia yang tidak diketahui dalam campuran sampel. Aktiviti antibakteria ekstrak telah disiasat oleh MIC dan MBC menggunakan pencairan macrobroth terhadap strain patogen *Pseudomonas aeruginosa* dan *Escherichia coli*. GC/MS analisis menunjukkan kehadiran lebih daripada empat puluh sebatian individu dan perbezaan yang signifikan dalam komposisi peratusan bahagian tangkai daun dapat dilihat. Ekstrak menghalang pertumbuhan bakteria pada MIC 125 mg/ml terhadap *Pseudomonas aeruginosa* dan 250 mg/ml terhadap *Escherichia coli*, manakala MBC adalah 500 mg/ml terhadap kedua-dua organisma dengan kesan setanding klorheksidina. Perbezaan ketara dalam komposisi peratusan bahagian tangkai daun dilihat. Keseluruhan ekstrak dalam kajian ini memiliki aktiviti antibakteria yang baik terhadap bakteria yang diuji. Keputusan menunjukkan bahawa kajian terhadap tangkai daun pisang boleh diteruskan terhadap beberapa bakteria Gram-negatif.

Kata kunci: fitokimia, pelepah daun pisang *Musa acuminate AA/AAA*, ekstrak aseton, bakteria gram-negatif

Introduction

Banana plant extracts derived from their parts (roots, stem, leave, and fruits) are now increasingly used in research due to their availability and cheap cost. They also have potential medicinal properties as a therapeutic agent and the ability to manage certain health conditions [1]. In past studies, various parts of banana have been shown to have an inhibitory effect on pathogens, making them excellent candidates for antimicrobial as well as being a good antitumoral, antimutagenic, antihelminthic, and antiulcerogenic source [2-4]. The phytochemical compounds present in banana include sterol, terpenoids, fatty acids, phenolic compound, and tocopherol [5-7]. A recent study done by Ehiowemwenguan [8] has reported that ethanol extract of *Musa sapientum* peels had significant *in-vitro* broad-spectrum antimicrobial activity. Thus, they concluded that the extract from banana peel could be used to control infections caused by both Gram-positive and Gram-negative bacteria. ~~A~~ study conducted by Fairus Fadhilah [9] has reported that acetone banana leaf stalk extracted from three different banana species, including Cavendish group (*Musa acuminate AA/AAA*), has antibacterial properties on selected Gram-negative bacteria when tested using the agar diffusion method. However, the phytochemical analysis and antimicrobial activity of this banana leaf stalk extract against these selected Gram-negative bacteria has not been investigated yet. Hence, this study aims to screen its phytochemical compound. The minimum inhibitory concentration (MIC) and minimum bactericidal concentration (MBC) of acetone extract of *Musa acuminate AA/AAA* against pathogenic strains *Pseudomonas aeruginosa* (*P. aeruginosa*) and *Escherichia coli* (*E. coli*) were also determined to maximise its therapeutic effects.

Materials and Methods

Collection and preparation of plant extracts

Banana leaf stalks of *Musa acuminate AA/AAA*) were obtained from the district of Kubang Kerian, Kelantan, Malaysia (Figure 1). The banana leaf stalks were washed thoroughly using tap water and wiped using a clean cloth. The succulent parts of the banana leaf stalk were cut into two-centimetre thickness. Next, the cut leaf stalk was allowed to dry in the oven at 50 °C for three days. The dried leaf stalk was powdered using an electric blending machine and kept at 4 °C in a tight-capped bottle.

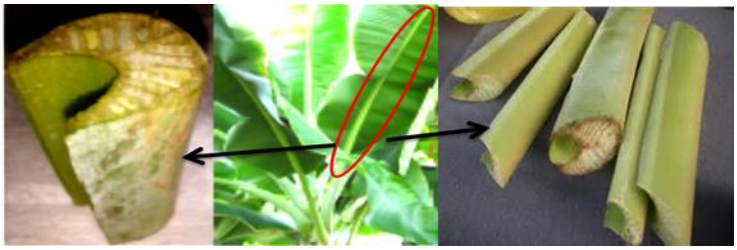


Figure 1. Leaf stalk of *Musa acuminate AA/AAA* which was used for extraction

Preparation of extracts

Soxhlet apparatus technique was used to extract the crude compound from the banana leaf stalk using acetone as its extraction solvent. Twenty grams of each banana pulp powder was placed inside a thimble made from thick filter paper. The thimble was loaded into the middle chamber of the Soxhlet extractor. Three hundred millilitres of extraction solvent were added into a distillation flask and the rest of the Soxhlet apparatus consisting of a condenser and a middle chamber, with thimble, was attached to the flask. The solvent was heated to begin the distillation process and the cycle was allowed to stand for three days. Next, the extract was filtered using No 1 (11 µm) Whatman filter paper and transferred into a 50 ml falcon tube. The solvents were removed using a Concentrator Plus machine yielding the extracted compound.

GC-MS analysis

The analysis was carried out using a Hewlett Packard 789A Gas Chromatograph with 5975C Mass Selective Detector. The column was a fused silica capillary, HP-5 column (30 m x 0.25 mm i.d. x 0.25 µm film thickness) (Agilent Technologies, USA). The carrier gas was helium with a flow rate of 1.0 ml/min with oven temperature programmed at 50 °C (held for 5 minutes) to 300 °C (held for 10 minutes) at a rate of 25 °C/min. The injection and interface temperatures were set at 250 °C and 280 °C, respectively. One microlitre of the sample was injected *via* GC auto sampler (7693 Auto sampler, Agilent Technologies, USA) in split-less mode and was analysed in MS full scan mode (m/z 40-650). The electron ionisation was fixed at 70 eV. The mass spectra library was used to identify an unknown chemical in the sample mixture. The banana leaf stalk compounds were identified by matching their mass spectra with NIST02 and WILEY275 libraries.

Bacterial strains

The bacterial species used in this study were obtained from the Medical Microbiology and Parasitology Laboratory, School of Medical Sciences, Universiti Sains Malaysia. Malaysia comprises of two types of Gram-negative bacteria, P. aeruginosa and E. coli. All bacterial strains were grown and maintained by sub-culturing on MacConkey agar (Oxoid, UK). All agar plates were incubated for 24 hours at 37 °C and maintained at 4 °C.

Determination of minimum inhibitory concentration (MIC)

The determination MIC of the extract was carried out using the macro-dilution technique as described by a double-fold serial dilution using Muller Hinton broth (Oxoid, UK). The following concentrations were used: 500 mg/ml, 250 mg/ml, 125 mg/ml and 62.5mg/ml. Concentration was based on a previous study's results [9]. Colonies from the plates were suspended into sterile Mueller Hinton broth to form turbidity of 0.5 McFarland standards using a densitometer (DEN-1, Grant Instruments, Cambridge) and further diluted into 1x106 CFU/ml. Then, equal volumes of extract and bacterial suspension were dispensed into sterilised test tubes, which were incubated aerobically at 37 ^{o}C for 24 hours. A tube containing broth and inoculums without extract served as organism control. The tube with broth and extract without inoculums served as extract control. Chlorhexidine digluconate (C-9394, Sigma Chemical Co., St. Louis, MO, USA) diluted to 0.12% was used as a positive control. The experiment was performed in triplicates for each concentration and organism. The lowest concentration of the extracts which inhibited microbial growth (no turbidity) was recorded as the MIC [10].

Determination of minimum bactericidal concentration (MBC)

Sterile Mueller Hinton agar plates were inoculated with samples from each of the test tubes that showed no visible growth from the MIC test. The plates were then incubated at 37 ^{o}C for 24 hours. Chlorhexidine digluconate (C-9394, Sigma Chemical Co., St. Louis, MO, USA) diluted to 0.12% was used as a positive control. The experiment was performed in triplicates for each concentrations and organisms. The highest dilution that yielded no single bacterial colony was taken as the MBC [11]

Data analysis

The MIC and MBC were expressed as means ± SE.

Results and Discussion

The GC-MS analysis shows that the classes of compounds identified in *Musa acuminate AA/AAA* leaf stalk were terpenoids, phytosterol, phenolic compounds, fatty acids, hydrocarbon, and tocopherol. More than forty individual compounds were identified as shown in Table 1. The main classes of compounds identified were phytosterol (18.53%), terpenoids (15.86%), fatty acids (6.61%) and tocopherol (5.54%). The major identified phytosterol was gamma-sitosterol (8.26%) followed by stigmasterol (6.3%). Seven terpenoids compounds were identified and squalene (12.02%) was found most abundant in banana leaf stalk. Palmitic acid was the highest fatty acid (4.38%) and alpha-tocopherol was the highest tocopherol found in banana leaf stalk.

Table 1. Chemical compound banana leaf stalk extract from *Musa acuminate AA/AAA*

Compounds	**% of Total Ion Chromatogram**
Terpenoids	(15.86)
(-)-Loliolide	0.15
Phytol	0.78
Farnesol	0.19
Cycloeucanol	0.97
Cycloartenol	1.19
3-o-acetyl-delta24-cycloartenol	0.56
Squalene	12.02
Phytosterols	(18.53)
Campesterol	3.97
Stigmasterol	6.30
Gamma-sitosterol	8.26
Phenolic	(0.33)
2-methoxy-4vinylphenol	0.10
Pradox 146	0.23
Fatty acids	(6.61)
Lauric acid	0.30
Pentadecanoic acid	0.29
Palmitic acid	4.38
Margaric acid	0.61
Stearic acid	0.86
Nonadecanoic acid	0.17
Hydrocarbon	(3.33)
Tridecane	0.29
2-methyl-z-4-tetradecane	0.61
Cyclopentadecane	0.13
Eicosane	0.16
Cyclotetracosane	0.17
Heptacosane	0.89
Cyclooctasane	0.56
Tetratetracontane	0.52
Tocopherol	(5.54)
Alpha-tocopherol	5.08
Gamma-tocopherol	0.46

Table 1 (cont'd). Chemical compound banana leaf stalk extract from *Musa acuminate AA/AAA*

Compounds	**% of Total Ion Chromatogram**
Others	(5.01)
2-Pentanone,4-hydroxy-4-methyl	0.13
6-Methyl-5-Hepten-2-One	0.06
4-Methyl-1,5-Heptadiene	0.04
Decanoic acid, methyl ester	0.07
Palmitic acid, (2,2-dimethyl-1,3-dioxolan-4-yl) methyl ester	0.23
Tricosanoic acid, methyl ester	0.12
6,11-Dimethyl-2,6,10-dodecatrien-1-ol	0.22
9,12,15-octadecatrienoic acid, methyl ester, (Z, Z, Z)	0.67
9,12,15-Octadecatrien-1-ol, (Z, Z, Z)	0.45
9,12,15-Octadecatrienoic acid, (Z, Z, Z)	2.99
Trans-Geranyl acetone	0.11
Cis-Geranylacetone	0.11
Cyclopentane, -1-ethyl-2-methyl-cis	0.04

The MIC and MBC of the acetone extract of *Musa acuminate AA/AAA* leaf stalk are shown in Table 2. The acetone extract of the pulp had MIC values ranged from 125 mg/ml to 250 mg/ml. The acetone extract of the leaf stalk had MIC values of 125 mg/ml against *P. aeruginosa* and 250 mg/ml against *E. coli*, respectively. The MBC of acetone extract of *Musa acuminate AA/AAA* leaf stalk for both organisms was 500 mg/ml.

Table 2. The minimum inhibitory and bactericidal concentrations of acetone extract of *Musa acuminate AA/AAA* leaf stalk

Bacterial Strain	**MIC[a] (mg/ml)**	**MBC[b] (mg/ml)**
Pseudomonas aeruginosa	125 ± 1.0	500 ± 1.0
Escherichia coli	250 ± 1.0	500 ± 1.0

[a]MIC and [b]MBC are presented as the mean value of triplicate values ± SE in mg/ml; all tested bacteria showed inhibitory and bactericidal effects against chlorhexidine digluconate (0.12%)

The search for antimicrobial compounds for the benefit of humanity is necessitated by the inherent ability of pathogens to develop and adopt mechanisms of resistance against antibiotics. The present work demonstrates that the composition of volatile leaf stalk extract of *Musa acuminate AA/AAA* is a complex mixture of several classes of components, mainly terpenoids, phytosterol, phenolic compounds, fatty acids, hydrocarbon, tocopherol and other minor compounds, which is in agreement with other banana parts (peel, pulp, flowers, petioles/midrib, leaf blades/sheaths, floral stalk and rachis) and species reported [5, 12]. Phytosterol was the major class of compounds identified and this finding was similar with previous studies of other parts and varieties of banana [5, 7]. Dikshit [7] found that methanol extract of a banana's stem from *Musa sapientum* is rich in sterol and has antihypercholesterolemic and antioxidant effects in cholesterol-fed wistar rats. Other studies found that phytosterol has antibacterial [13], anticancer [14], and antidiabetic [15] properties. Tocopherol was also identified in this banana leaf stalk and concordant with previous findings of another Musa spp. [6].

Tocopherol is a potent antioxidant and recent findings showed that it reduces inflammatory responses in type 2 diabetes patients [16]. The terpenoids were found abundantly in this banana leaf stalk compared to the previous study of the unripe peel [5] and ripe pulp of *Musa acuminate AA/AAA* [17]. Squalene (12.02%) is the major identified compound in the terpenoids class and recent studies found that it has antibacterial [18], anticancer [19], and anti-inflammatory [20] activities. Palmitic acid (hexadecanoic acid) is the most abundant fatty acid (4.38%) identified and this finding is similar with previous studies of other Musa varieties [5]. Interestingly, a recent study by Nagata [21] showed that palmitic acid has anti-multiple myeloma activity. Low phenolic compounds in this banana leaf extract were in agreement with previously published results obtained from other Musa varieties [5].

The present work demonstrates that leaf stalk extract of *Musa acuminate AA/AAA* possessed antibacterial properties against two strains of Gram-negative bacteria (*E. coli* and *P. aeruginosa*) which is in agreement with the previous study [9] which used agar disc-diffusion method. To date, only Gram-negative bacteria (*E. coli* and *P. aeruginosa*) are susceptible to this stalk extract of *Musa acuminate AA/AAA* compared to previous studies using Gram-positive bacteria namely *Staphylococcus aureus* and *Streptococcus mutans* [9]. In addition, there is no other similar antimicrobial study reported on a specific leaf stalk extract of *Musa acuminate AA/AAA* on a specific Gram-negative bacterium. This finding could be correlated with identified compounds found in this study that has antibacterial property. The antimicrobial effects of acetone extract against these organisms may be due to the ability of the acetone to extract some of the active properties of these plants such as phenolic compounds, saponin, bryophyllin and other secondary metabolites which are reported to be antimicrobial [22].

Microorganisms vary widely in their degree of susceptibility to antimicrobial agents [3]. Based on the results, it is suggested that both bacteria are susceptible to the extract of the leaf stalk. *Musa acuminate AA/AAA* leaf stalk acetone extract showed MIC at 125 mg/ml for *P. aeruginosa* and 250 mg/mL for *E. coli*. The relatively higher MIC and MBC values against *P. aeruginosa* and *E. coli* might be contributed to their cell wall properties. Gram-negative bacteria are protected by their lipopolysaccharide layer (LPS), hindering the direct exposure of the inner membrane layer to the natural antibacterial activities [23, 24]. It has been reported that Gram-negative bacteria are usually more resistant to the plant-origin antimicrobials and even show no effects, compared to gram-positive bacteria [25]. Moreover, it was also suggested that the crude extract might contain compounds that inhibited the antibacterial activity of the effective compounds.

Conclusion

Based on the results obtained in this investigation, it can be concluded that acetone extract of *Musa acuminate AA/AAA* leaf stalk possesses antimicrobial activities against *P. aeruginosa* and *E. coli*. Thus, extracts from this plant possess the capabilities of being a candidate to control infections and/or diseases caused by these Gram-negative bacteria. However, the *in-vivo* experiment and pharmacological research of the identified compounds are very limited. Therefore, future work should be focused on *in-vivo* and pharmacological assays of known compounds, especially phytosterol and squalene that have antimicrobial properties. A better understanding of the antimicrobial compounds from *Musa acuminate AA/AAA* leaf stalk is crucial to identify the potential side effects and trace out the new host target and molecular mechanisms, which will provide evidence to further clinical applications of these compounds.

Acknowledgement

We thank the School of Dental Sciences, USM for the facilities and reagents, year 5 undergraduate students; Adibah Husna Ali, Mas Amira Mustaffa, Kow Hui Xuan and Nor Akmar Zamri, postgraduate student Nik Yusliyana Nik Yusoff from the School of Dental Sciences, Mrs. Khairiena, and all Staff members of the Craniofacial Science Laboratory, School of Dental Sciences, USM, and Mrs. Roslina and Mr. Mohammad Amin from the School of Health Sciences for their assistance and for making data collected available. This study was supported by a short-term grant awarded to Universiti Sains Malaysia (304/PPSG/61313028).

References

1. Venkatesh, K.V., Girish, K. K., Pradeep, A. K. and Santosh Kumar, S. R. (2013). Antibacterial activity of ethanol extract of *Musa paradisiaca* CV. puttable and *Musa acuminate AA/AAA* CV. grand naine. *Asian Journal of Pharmaceutical and Clinical Research*, 62: 169-172.

2. Kumar, K. P. S., Bhowmik, D., Duraivel, S. and Umadevi, M. (2012). Traditional and medicinal uses of banana. *Journal of Pharmacognosy and Phytochemistry*, 1:51-63.
3. Karuppiah, P. and Mustaffa, M. (2013). Antibacterial and antioxidant activites of Musa sp. leaf extracts against multidrug resistant clinical pathogens causing nasocomial infection. *Asian Pacific Journal of Tropical Biomedicine*, 3: 737-742.
4. Zainab, A. G. C., Alaa, H. A., Nada, K. K. H. and Shatha, K. K. H. (2013). Antimicrobial effects of aqueous banana peel extracts, Iraq. *Pharmaceutical Sciences*, 1: 73-75.
5. Villaverde, J. J., Oliveira, L., Vilela, C., Domingues, R. R. M., Freitas, N. I., Cordeiro, N., Freire, C. S. R. and Silvestre, A. J. D. (2013). High valuable compounds from the unripe peel of several Musa species cultivated in Madeira Island (Portugal). *Industrial Crops and Products*, 42: 507-512.
6. Vilela, C., Santos, S. N. A., Villaverde, J. J., Oliveira, L. C., Nunes, A., Cordeiro, N., Freire, C. S. and Silvestre, A. J. (2014). Lipophilic phytochemicals from banana fruits of several Musa species. *Food Chemistry*, 162: 247-252.
7. Dikshit, P., Tyagi, M. K., Shukla, K., Gambhir, J. K. and Shukla, R. (2015). Antihypercholesterolemic and antioxidant effect of sterol rich methanol extract of stem of *Musa sapientum* (banana) in cholesterol-fed wistar rats. *Journal of Food Science and Technology*, 53: 1690-1697.
8. Ehiowemwenguan, G., Emoghene, A. O. and Inetianbor, J. E. (2014). Antibacterial and phytochemical analysis of banana fruit peel. *Journal of Pharmacy*, 4:18-25.
9. Fairus, F. M. J., Suharni, M. and Wan Nazatul Shima, S. (2014). Antibacterial effects of banana pulp extracts based on different extraction methods against selected microorganisms. *Asian Journal of Biomedical and Pharmaceutical Sciences*, 4: 14-19.
10. Shahidi, B. G. H. (2004). Evaluation of antibacterial properties of iranian medicinal plants against *Micrococcus aureus, Serratia marcescens, Klebsiella pneumoniae and Bordella bronchoseptica. Asian Journal of Sciences,* 3: 82-86.
11. Akinyemi, K. O., Oladapo, O., Okwara, C. E., Ibe, C. C. and Fasure, K. A. (2005). Screening of crude extracts of six medicinal plants used in southwest Nigerian unorthodox medicine for antimethicillin resistant *Staphylococcus aureus* activity. *BMC Complementary and Alternative Medicine*, 5(1): 1-7.
12. Oliveira, L., Freire, C., Silvestre, A. and Cordeiro, N. (2008). Lipophilic extracts from banana fruit residues: A source of valuable phytosterols. *Journal of Agricultural and Food Chemistry*, 56: 9520-9524.
13. Woldeyes, S., Adane, L., Tariku, Y., Muleta, D. and Begashaw, T. (2016). Evaluation of antibacterial activities of compounds isolated from *Sida rhombifolia Linn*. (Malvaceae). *Natural Products Chemistry & Research*, 1: 101. doi:10.4172/npcr.1000101.
14. Mahaddalkar, T., Suri, C., Naik, P. K. and Lopus, M. (2015). Biochemical characterization and molecular dynamic simulation of B-sitosterol as a tubulin-binding anticancer agent. *European Journal of Pharmacology*, 760: 154-162.
15. Karan, S. K., Mishra, S. K., Pal, D. and Mondal, A. (2012). Isolation of-sitosterol and evaluation of antidiabetic activity of *Aristolochia indica* in alloxan-induced diabetic mice with a reference to in-vitro antioxidant activity. *Journal of Medicinal Plants Research*, 6: 1219-1223.
16. Jamalan, M., Rezazadeh, M., Zeinali, M. and Ghaffari, M. A. (2015). Effect of ascorbic acid and alpha-tocopherol supplementations on serum leptin, tumor necrosis factor alpha, and serum amyloid A levels in individuals with type 2 diabetes mellitus. *Avicenna Journal of Phytomedicine*, 5: 531-539.
17. Oliveira, L., Freire, C., Silvestre, A., Cordeiro, N., Torres, I. and Evtuguin, D. (2006). Lipophilic extractives from different morphological parts of banana plant "Dwarf Cavendish". *Industrial Crops and Products*, 23: 201-211.
18. Bindu, B. S. C., Mishra, D. P. and Narayan, B. (2015). Inhibition of virulence of *Staphylococcus aureus* "a food borne pathogen "by squalene, a functional lipid. *Journal of Functional Foods*, 18: 224-234.
19. Rao, C.V., Newmark, H. L. and Reddy, B, S. (1998). Chemopreventive effect of squalene on colon cancer. *Carcinogenesis*, 19: 287-290.
20. Cárdeno, A., Aparicio-Soto, M., Montserrat-de la Paz, S., Bermudez, B., Muriana, F. J., Alarcón-de-la-Lastra, C. (2015). Squalene targets pro-and anti-inflammatory mediators and pathways to modulate over-activation of neutrophils, monocytes and macrophages. *Journal of Functional Foods*, 14:779-790.

21. Nagata, Y., Ishizaki, I., Waki, M., Ide, Y., Hossen, M.A., Ohnishi, K., Miyayama, T. and Setou, M. (2015). Palmitic acid, verified by lipid profiling using secondary ion mass spectrometry, demonstrates anti-multiple myeloma activity. *Leukemia Research*, 39: 638-645.
22. Okwu, D. E. and Josiah, C. (2006). Evaluation of the chemical composition of two Nigerian medicinal plants. *African Journal of Biotechnology*, 5: 357-361.
23. Munyendo, W. L. L., Orwa, J. A., Rukunga, G. M. and Bii, C. C. (2011). Bacteriostatic and bactericidal activities of *Aspilia mossambicensis*, *Ocimum gratissimum* and *Toddalia asiatica* extracts on selected pathogenic bacteria. *Research Journal of Medical Plants*, 5: 717-727.
24. Mellisa, K. (2000). The problem with gram-negative bacteria. The Merck Manual, Home Edition, Bacillary Infections, Section 17 Chapter 177 http://www.anapsid.org/gramnegative.html [Access online 27 December 2016].
25. Bipul, B., Kimberly, R., Fredrick, M., Dwayne, D. and Anand, Y. (2013). Antimicrobial activities of leaf extracts of guava (*Psidium guajava L*.) on two Gram-negative and Gram-positive bacteria. *International Journal of Microbiology*, 2013: 1-7.

Malaysian Journal of Analytical Sciences, Vol 22 No 6 (2018): 965 - 972
DOI: https://doi.org/10.17576/mjas-2018-2206-06

MALAYSIAN JOURNAL OF ANALYTICAL SCIENCES
Published by The Malaysian Analytical Sciences Society
ISSN 1394 - 2506

MODIFIED LEACHING OF ^{238}U AND ^{232}Th FROM WATER LEACH PURIFICATION (WLP) RESIDUE

(Modifikasi Larut Lesap Bagi ^{238}U dan ^{232}Th dari Residu Pemurnian Larut Lesap Air (WLP))

Nur Shahidah Abdul Rashid[1], Zetty Izzaty Saleh[2], Nurul Syiffa Mahzan[2], Siti Nur Ain Sulaiman[2], Khoo Kok Siong[2], Mohd. Idzat Idris[2], Syazwani Mohd Fadzil[2]*

[1]Division of Advanced Nuclear Engineering,
Pohang University of Science and Technology, 790784 Pohang, Gyeongsangbuk, South Korea
[2]School of Applied Physics, Faculty of Science and Technology,
Universiti Kebangsaan Malaysia, 43600 UKM Bangi, Selangor, Malaysia

**Corresponding author: syazwanimf@ukm.edu.my*

Received: 29 August 2017; Accepted: 29 October 2018

Abstract

In recent years, the importance of actinide element mobile fractions in risk assessment evaluation of contaminated sites has increased. The knowledge of the sorption kinetics of ^{238}U and ^{232}Th and the thermodynamics behind the sorption process on radioactive waste is important to understand their mobility. In this study, the leaching process of ^{238}U and ^{232}Th from water leach purification (WLP) residue of Lynas Advanced Materials Plant was investigated to obtain the optimum leaching conditions by combining synthetic precipitation leaching procedure and batch method for the simulation of acid rain and heavy flooding, correspondingly. The initial ^{238}U and ^{232}Th concentrations, and the concentration at varies pH and contact time of ^{238}U and ^{232}Th from the WLP residue were studied. Results show that the initial concentrations of ^{238}U and ^{232}Th in the WLP residue are 6.6 and 206.1 mg/kg, respectively. In general, the highest values of the concentration after the leaching process of ^{238}U and ^{232}Th are 0.363 and 8.288 mg/kg, correspondingly. These results show the maximum potential remobilisation of ^{238}U and ^{232}Th at pH 4 with the same contact time of 14 days. At a similar duration, the maximum percentages of leaching are 5.50% and 3.99% for ^{238}U and ^{232}Th, respectively. Moreover, at pH 7, the minimum leaching percentages of ^{238}U and ^{232}Th are 4.7% and 3.61%, correspondingly. Thus, remobilising ^{238}U and ^{232}Th shows that the rate of leaching is influenced by the pH of leachant used. The maximum concentrations of ^{238}U and ^{232}Th are obtained at low pH such as pH 4. At pH 7 and 8, the leached amounts of ^{238}U and ^{232}Th are minimum. Therefore, combining the SPLP and batch method is practical for estimating the leaching and remobilisation of ^{232}Th and ^{238}U from WLP residues. The combined method may be useful for monitoring and risk assessment in environmental studies.

Keywords: leaching, WLP residue, uranium, thorium

Abstrak

Dalam tahun-tahun kebelakangan ini, kepentingan pergerakan unsur aktinida menjadi perhatian semasa penilaian risiko tapak-tapak yang tercemar. Pengetahuan tentang penyerapan kinetik dan termodinamik di sebalik proses penyerapan sisa radioaktif adalah penting untuk memahami pergerakan ^{238}U dan ^{232}Th. Dalam kajian ini, proses kelarut lesapan ^{238}U dan ^{232}Th dari residu pemurniaan larut lesap air (WLP) dari Lynas Advanced Materials Plant telah dikaji untuk mendapatkan keadaan kelarut lesapan yang optimum menggunakan gabungan prosedur larut lesap pemendapan sintetik dan kaedah kelompok, masing-masing sebagai simulasi semasa keadaan hujan asid dan banjir. Kepekatan awal ^{238}U dan ^{232}Th, dan kepekatan ^{238}U dan ^{232}Th terhadap pH dan masa berbeza dari residu WLP turut dilihat. Keputusan menunjukkan kepekatan awal ^{238}U dan ^{232}Th dalam residu WLP masing-masing adalah 6.6 mg/kg dan 206.1 mg/kg. Secara amnya, nilai tertinggi kepekatan selepas proses larut lesap bagi ^{238}U dan ^{232}Th masing-masing adalah 0.363 mg/kg dan 8.288 mg/kg. Kedua-dua hasil menunjukkan bahawa potensi pergerakan maksimum adalah pada pH 4 bagi ^{238}U dan ^{232}Th dalam masa 14 hari. Dalam tempoh masa yang sama, peratusan kelarut lesapan maksimum

dicatatkan sebanyak 5.50% dan 3.99% masing-masing bagi ^{238}U dan ^{232}Th. Selain itu, pada pH 7, peratusan larut lesap minimum bagi ^{238}U dan ^{232}Th masing-masing adalah 4.7% dan 3.61%. Oleh itu, pergerakan ^{238}U dan ^{232}Th menunjukkan ia dipengaruhi oleh pH pelarut yang digunakan. Kepekatan maksimum ^{238}U dan ^{232}Th diperoleh pada pH yang lebih rendah seperti pH 4. Pada nilai pH 7 dan 8 mencatatkan kepekatan larut lesap ^{238}U dan ^{232}Th yang minimum. Kesimpulannya, gabungan kaedah SPLP dan kaedah kelompok adalah praktikal untuk menganggar larut lesap dan pergerakan ^{238}U dan ^{232}Th dari residu WLP. Gabungan kaedah ini boleh digunakan sebagai tujuan pemantauan dan penilaian risiko terhadap kajian alam sekitar.

Kata kunci: larut lesap, residu WLP, uranium, torium

Introduction

Demands for rare earth elements (REEs) have been increasing in many new energy technologies and systems that contribute to reduced greenhouse gas (GHG) emission and fossil fuel depletion [1]. However, producing REEs is far from being environmentally sustainable because it requires significant material and energy consumption whilst generating considerable air/water emissions and solid waste. Although many REEs are critically important for sustainable mobility and energy supply, producing REEs incurs serious environmental damages [2].

The Mount Weld mine is operated by Lynas Corporation Ltd. which is involved in mining and concentrating REE ore. On average, the ore contains 0.075% ThO_2 and 0.003% U_3O_8; these contents correspond to the average activity concentrations of 2.7 Bq g^{-1} of ^{232}Th and 0.3 Bq g^{-1} of ^{238}U [3]. The mining and processing concentrations of REE ore at Mount Weld is followed by a shipment of the concentrate to an REE processing facility, that is, Lynas Advanced Materials Plant (LAMP) at Gebeng, Pahang State, Malaysia, where further processing is conducted to produce high-purity REE compounds [3]. LAMP processes lanthanide concentrates at an integrated processing site which utilises physical and chemical treatment processes. Water leach purification (WLP) residues resulted from the leaching and purification of water-soluble lanthanide components from the calcined, cracked concentrate. According to the United States Environmental Protection Agency, rare earth concentrate is classified as a Technologically Enhanced Naturally Occurring Radioactive Material (TENORM) [4]. REEs have been considered beneficial and profitable in Malaysia, but occupational, public safety and health risks related to REEs may be addressed at their mining, transportation, processing, waste disposal and decommissioning stages [5]. Thorium is a waste product in REE mining; it is mainly eliminated during the leaching process of the desired metals. Furthermore, thorium which denotes a radioactive impact of REE mining in addition to uranium and their decay products has raised environmental concerns for the last several years [6].

In addition to WLP residues, LAMP produces flue gas desulphurisation (FGD) and neutralised underflow (NUF) residues. Among the residues, the WLP is considered the most toxic given its elevated levels of uranium, thorium, associated radioactivity and heavy metals [7]. The WLP residue process generates the most radioactive and contaminated tailings. The WLP residue contains most of uranium and thorium separated from the REE products during the refining process. The concentrate used as feedstock for the refining process contains uranium (30 ppm) and thorium (approximately 1700 ppm) generated between 3.5 and 8 Bq g^{-1} of a specific activity. Theoretically, all the radioactive elements are removed during the refining process and are expected to be transferred to waste streams and disposed of in the tailing pond.

Leaching is a process in which contaminants are transferred from a stabilised matrix to liquid media, such as water or other solutions. Chemical reagents, such as acids, bases and chelating agents, are used to create a leaching solution to investigate the mobilisation of heavy metals from the soils [8]. Previous researchers have used leaching test to investigate the leachability of environmental contaminants from oil sludge to assess potential environmental impact [9, 10]. Then, results from leaching have been extrapolated to assess the long-term release of toxic elements from the oil sludge [10, 11]. Similar studies that used modification and combination of leaching tests have also been conducted for ^{238}U and ^{232}Th in WLP samples and have been discussed elsewhere [12, 13]. A leaching test has similar concepts adopted for soil washing.

Soil washing is frequently used in soil remediation because this process (i) completely removes contaminants, thus ensuring the rapid clean-up of a contaminated site, (ii) satisfies specific criteria, (iii) reduces or eliminates long-term liability, (iv) may be the most cost-effective solution and (v) may produce recyclable materials or energies.

Chemical reagents must be added to the washing water because washing the soils with water alone will remove the low amount of cations in the leachates [14-17]. Generally, soil washing with acids relies on ion exchange and dissolution of soil components or discrete metal compounds to extract metals [8]. Strong acids attack and degrade the soil crystalline structure at extended contact times [18]. Many research studies have mentioned different types of acids used as leaching agents, thereby resulting in different metal removal efficiencies [19]. The effectiveness of soil washing is closely related to the ability of the extracting solution to dissolve the metal contaminants in soils. However, the strong bonds between the soil and metals complicate the cleaning process [18]. Moreover, efficiency is affected by extraction time with chemical reagents because the rate of metal extraction is a factor of time [8]. Although many studies on soil washing which uses different chemical reagents have been conducted, the number of reports that focused on leaching process kinetically and thermodynamically have remained insufficient in literature.

This study aims to simulate the potential remobilisation of ^{238}U and ^{232}Th that leach from the WLP residue over a range of pH with different contact time. Synthetic precipitation leaching procedure (SPLP) experiments have been performed to provide information on ^{238}U and ^{232}Th release, thus simulating the acid rain condition.

Materials and Methods

Sample preparation

The WLP residue samples were collected from LAMP, Kuantan, Malaysia. The sample was dried and sieved using a mechanical sieve to separate <2 mm particles from a coarse material. Then, the samples were transformed into pellets with a ratio of 1:6, that is, 1.0 g of WLP residue and 6.0 g of boric acid. The initial concentration of ^{238}U and ^{232}Th was determined using X-ray fluorescence spectrometer (XRF) Bruker/S8 Tiger/2009 at the Centre for Research and Instrumentation, Universiti Kebangsaan Malaysia (UKM), Bangi. The leaching test was applied to the sample to eliminate any possibility of redistributing actinides between different phases given air oxidation.

Leaching experiments

The SPLP test (Method 1312) is designed in accordance with the procedure of Solid Waste Manual 846 [20] to determine the mobility of organic and inorganic analytes present in liquids, soils and wastes. The SPLP test is used to simulate the effect of acid rain on land-disposed wastes. However, the leaching experiment is modified from the SPLP by adding pH 7 and 8, thereby simulating groundwater pH. It can also be used to determine the concentration of a contaminant that will leach from the soil. The method uses a diluted sulphuric and nitric acids (with a pH of 4.2) as the leaching solution. This method can simulate weathering for 100 years of exposure to acid rain [21] and has been studied with other leaching tools [10, 11]. This single-batch extraction method is used to assess the leaching potential of a waste exposed to rainfall. The procedure is performed using the same equipment used to perform the toxicity characteristic leaching procedure and requires using one of two leaching fluids depending on the location of the waste disposal site. A 20:1 liquid-to-solid (L/S) ratio and an extraction time of 18 ± 2 hours were used in this test. The leachate fluid consists of slightly acidified deionised water that is formulated to simulate natural precipitation. A mixture of 60:40 (H_2SO_4:HNO_3; by weight) is used to achieve the appropriate pH for the extraction fluid [20].

Combined with the previous procedure, 10 g of WLP residue was equilibrated with 200 mL of leaching solution at a 20:1 ratio with various pH values (4, 5, 7 and 8) as a function of time. Additional information on batch leaching test can be found elsewhere [9-13]. The pH of the solution was adjusted prior to the experiments, thus simulating the potential remobilisation of ^{238}U and ^{232}Th after heavy flooding of the catchment area. The meter was calibrated prior to each set of measurements, and checks were obtained on other buffers between readings to ensure that all buffers are read and recorded at ±0.05 pH units. The pH analysis did not require a sample treatment but the sample solution should be measured immediately. The agitation was held at 200 rpm using a stirrer at a fixed temperature (27 °C) for 18 hours. Then, the samples were left in the room with different contact time. This approach presents the correlation between leachates and contact time. All the samples were then observed on the 1^{st}, 2^{nd}, 7^{th} and 14^{th} day. Then, the solid/liquid slurry is filtered and analysed by using inductively coupled plasma–mass spectrometer (ICP-MS) ELAN 9000 PerkinElmer SCIEX at the Malaysia Nuclear Agency, Bangi. Data were recorded, and each extraction method was prepared in duplicate. Blanks of leaching solutions (pH 4, 5, 7 and 8) without WLP were run as controls.

Percent of contaminant mass in the SPLP leachate also known as percentage uptake was calculated as equation 1:

$$\frac{(C_L \times V_L)}{(C_T \times M_S)} \times 100, \quad (1)$$

where C_L is the leachate concentration (mg/L), V_L is the volume of leachate in litres (0.2 L), C_T is the total sample concentration (mg/kg) and M_S is the mass of the sample in kilograms (0.01 kg) [22].

Results and Discussion

The initial concentration of ^{238}U and ^{232}Th in WLP residue samples was analysed using the XRF. The analysis finding shows that the concentration of ^{238}U and ^{232}Th is 6.6 and 206.1 mg/kg, respectively [12, 13]. According to the Malaysia Nuclear Agency [23], the WLP residue with a production of approximately 32,000 tonnes per year contains 1655 ppm ^{232}Th and 22.5 ppm ^{238}U. The radioactive residue is stored in retention ponds which are built with impermeable soil and are lined with a high-density polyethylene cover to prevent any seepage. WLP residue was also classified as a radioactive residue in accordance with the preview of Act 304 and regulations [24]. The treated effluent was analysed for its thorium radionuclide contents, ^{226}Ra and ^{228}Ra, but the concentrations did not reach the detection limit of 0.5 Bq/L during a test run. Thorium is assumed to be completely precipitated as thorium pyrophosphate (ThP_2O_7) during the separation with MgO at pH 3.5 and discharged in the WLP. The WLP residues contain abundant compounds in addition to ThP_2O_7, such as iron, barium, calcium or silica species. The composition of WLP residue affects the elemental solubility in an aqueous phase. ThP_2O_7 is water-insoluble formed by converting the sulphate of thorium, whereas the rare earth sulphates remain stable in sulphate solution [24,25].

The leaching process depends on several physical and chemical factors and occurs whenever a liquid phase percolates or is in contact with a solid material, thereby dissolving inorganic or organic substances [26]. The most important physical factors are size, shape and porosity of the particles, homogeneity of mineral phases, temperature, time frame, flow rate or liquid amount of leachant and degree of saturation and wet/dry cycles. The most important chemical aspects are related to pH and redox conditions, control mechanisms (kinetic or equilibrium), availability for leaching, complexation and sorption processes [27]. The leaching processes may involve precipitation/dissolution, diffusion, sorption, surface coating or wash-off which may be controlled kinetically or by equilibrium conditions [28]. Numerous tests, such as identifying leachable constituents [29], may be used depending on the objectives to evaluate the leaching processes. The present study focuses on ^{238}U and ^{232}Th. The most important variables that must be established for a specific leaching test are the sample preparation, leachant composition (pH, redox conditions), method of contact, L/S ratio, contact time, temperature and leachant separation method [28].

The pH values of leachate used in modified SPLP method are illustrated in Figure 1. The pH is selected to simulate acid rain (pH = 4 ± 0.05 and pH = 5 ± 0.05) because air includes several acidic emissions such as hydrogen fluoride (HF) and sulphuric acid (H_2SO_4) [7]. The modified SPLP was adjusted to pH = 7 ± 0.05 and pH = 8 ± 0.05 to simulate groundwater condition. Soil and water contaminants may be released by natural processes, such as weathering or human mismanagement, when constructing defective impoundment areas which may break or leak. Environmental effects of acid gases are popular and can lead to localised ‘acid rain’ which can damage crops and acidify freshwater bodies such as lakes and streams [30]. LAMP which is situated on the east coast peninsula of Malaysia receives considerable rains during monsoon season. These climates would lead to heavy flash floods and might cause several dams to overflow, thereby dispersing the WLP residue by wind and rain. The leaching of ^{238}U, ^{232}Th and other metals may contribute to increased groundwater contamination.

Figure 1 demonstrates that the average ^{238}U concentration leached from the WLP residue is in the ranges of 0.271–0.363 mg/kg (pH 4), 0.256–0.349 mg/kg (pH 5), 0.283–0.31 mg/kg (pH 7) and 0.235–0.323 mg/kg (pH 8), whereas that of the ^{232}Th concentration is in the ranges of 2.078–8.228 mg/kg (pH 4), 2.054–8.08 mg/kg (pH 5), 2.139–7.44 mg/kg (pH 7) and 1.827–8.026 mg/kg (pH 8). At low pH, the concentration of ^{238}U and ^{232}Th is the maximum. The maximum concentration value is frequently reported as the availability for leaching. For both radionuclides, at pH 7 and 8, the leached amount is minimum. The mixture of two concentrated acid solutions does not have a buffering characteristic. Thus, the solution mixture does not resist changes in the concentrations of hydronium and hydroxide

ions, as well as the pH. The resistance of a buffer solution to pH change is based on Le Chatelier's principle and the common ion effect [31].

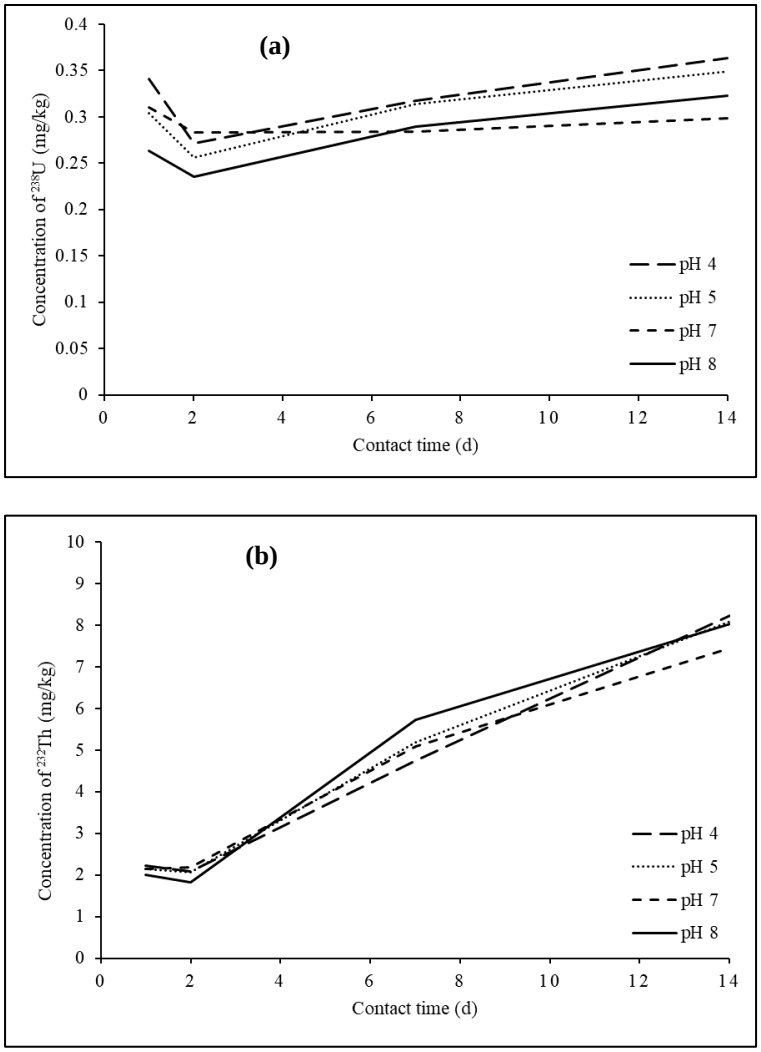


Figure 1. Effect of contact time and pH on the leaching concentrations of (a) ^{238}U and (b) ^{232}Th.

Figure 1 exhibits that the highest values of the concentration of ^{238}U and ^{232}Th are 0.363 and 8.228 mg/kg, correspondingly [12, 13]. The concentration of ^{232}Th is higher than ^{238}U probably due to the ^{232}Th chemical and physical characteristics, namely, strong sorption to solid matrices, thereby resulting in an extremely low bioavailability and mobility. Thorium (Th^{+4}) is highly insoluble in water. Under acidic conditions below pH 4, the solubility increases, and complexation with carbonates, sulphates or organic substances enhances its solubility [32]. Al-Areqi et al. [24] found that the maximum recovery and concentration of ^{232}Th are obtained by HNO_3 and H_2SO_4 in comparison with NaOH. Thorium is mostly available as an insoluble material during the physical beneficiation process, but it is transformed during the chemical processes into extra soluble species, such as $Th(NO_3)_4$, $Th(OH)_4$, Th-oxalate and other species [32]. In soils, humic substances are considered particularly important in adsorbing thorium. In most cases, sediment resuspension and mixing may control the transportation of particle-sorbed thorium in water; however, in several cases, the concentration of dissolved thorium in waters may increase due to formation of soluble complexes with carbonate, humic materials or other ligands in the water [33]. The contamination of

groundwater by transporting thorium from soil to groundwater does not occur in most soils, except those with low sorption characteristics and the capability to form soluble complexes. Chelating agents produced by certain microorganisms (*Pseudomonas aeruginosa*) present in soils may enhance the dissolution of thorium in soils [32].

Contact intervals of 1–14 days were applied to evaluate leaching as a function of contact time. This approach is different from previous studies [10, 11] which have extended intervals based on a different standard leaching procedure. This period was selected because it was reported as a period of flooding on the east coast peninsula of Malaysia which receives abundant rain during the monsoon season. In Figure 1(a), the concentration of ^{238}U slightly increased with contact time, whereas Figure 1(b) displays that the concentration of ^{238}Th rapidly increased with contact time. Moreover, Figure 2 depicts the average percentage release for ^{238}U and ^{232}Th. The patterned release for ^{238}U and ^{232}Th was presented in a log scale line to represent the release behaviour on the basis of the calculated percentage release using Eq. (1). The maximum percentages of leaching are 5.50% and 3.99% for ^{238}U and ^{232}Th, respectively. These results show the maximum potential remobilisation of ^{238}U and ^{232}Th at low pH (pH=4) during the end of the duration test at 14 days. By contrast, the minimum leaching efficiencies at pH 7 were recorded for ^{238}U and ^{232}Th at 4.7% and 3.61%, correspondingly.

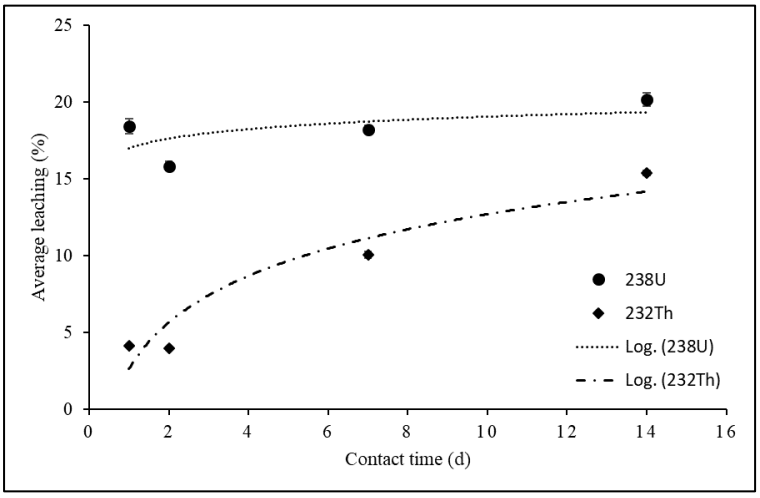


Figure 2. Percentage of average ^{238}U and ^{232}Th release as function of time

Conclusion

In summary, the effect of ^{238}U and ^{232}Th leaching release was moderately influenced by the pH of the solution used. The findings indicate that the maximum potential remobilisation percentages of ^{238}U and ^{232}Th at pH 4 at the final-day testing interval (14 days) are 5.50% and 3.99%, respectively. By contrast, at pH 7, the minimum leaching release was found for both waste products. Potential mobilisation of ^{238}U and ^{232}Th was observed from the WLP in the aqueous medium during the monsoon and flooding seasons.

Acknowledgement

The authors are grateful to the Centre for Research and Instrumentation (CRIM) for the facility and Universiti Kebangsaan Malaysia for the financial support under the project code GGPM-2016-040.

References

1. Alonso, E., Sherman, A. M., Wallington, T. J., Everson, M. P., Field, F. R., Roth, R. and Kirchain, R. E. (2012). Evaluating rare earth element availability: A case with revolutionary demand from clean technologies. *Environmental Science & Technology,* 46(6): 3406-3414.
2. Navarro, J. and Zhao, F. (2014). Life-cycle assessment of the production of rare-earth elements for energy applications: A review. *Frontiers in Energy Research,* 2: 45.

3. IAEA (2011). Report of the international review mission on the radiation safety aspects of a proposed rare earths processing facility (the Lynas project). International Atomic Energy Agency (IAEA).
4. O'Brien, R. and Cooper, M. (1998). Technologically enhanced naturally occurring radioactive material (NORM): pathway analysis and radiological impact. *Applied Radiation and Isotopes,* 49(3): 227-239.
5. Zhang L. (2014). Towards sustainable rare earth mining: a study of occupational & community health issues. Thesis of Master Degree, University of British Columbia.
6. IAEA (2011). Radiation protection and NORM residue management in the production of rare earths from thorium containing minerals. International Atomic Energy Agency (IAEA).
7. National Toxics Network (2012). Rare earth and radioactive waste a preliminary waste stream assessment of the Lynas Advanced Materials Plant, Gebeng, Malaysia. National Toxics Network (NTN).
8. Alghanmi, S. I., Al Sulami, A. F., El-Zayat, T. A., Alhogbi, B. G. and Salam, M. A. (2015). Acid leaching of heavy metals from contaminated soil collected from Jeddah, Saudi Arabia: kinetic and thermodynamics studies. *International Soil and Water Conservation Research,* 3(3): 196-208.
9. Fadzil, S. M., Sarmani, S., Ab. Majid, A., Khoo, K. S. And Hamzah, A. (2011). k_0-INAA measurement of levels of toxic elements in oil sludge and their leachability. *Journal of Radioanalytical and Nuclear Chemistry* 287: 41-47.
10. Mohd Fadzil, S. (2011). Penentuan kepekatan dan penilaian jangka masa panjang pelepasan unsur As, Co, Cr, dan Zn dari enap cemar minyak. Thesis of Master Degree, Universiti Kebangsaan Malaysia.
11. Mohd Fadzil, S., Sarmani, S., Ab. Majid, A., Hamzah A. and Khoo, K.S. (2013). Modeling of cumulative release on long term leaching behaviour of selected oil sludge from crude oil terminal and petroleum refining plant. *Journal of Radioanalytical and Nuclear Chemistry* 297: 265-270.
12. Mahzan, N. S. (2017). Menentukan tahap kelarutlesapan radionuklid ^{238}U dari sampel residu pemurnian larut lesap air (WLP) terhadap medium akues. Thesis of Bachelor Degree, Universiti Kebangsaan Malaysia.
13. Saleh, Z. I. (2017). Penentuan kelarutlesapan radionuklid ^{232}Th dalam sampel pemurnian larut lesap air (WLP). Thesis of Bachelor Degree, Universiti Kebangsaan Malaysia.
14. Government of Canada (2003). Site remediation technologies: A reference manual. Contaminated Sites Working Group, Government of Canada, Ontario, Canada.
15. Fawzy, E. (2008). Soil remediation using in situ immobilisation techniques. *Chemistry and Ecology*, 24(2): 147-156.
16. Nouri, J., Khorasani, N., Lorestani, B., Karami, M., Hassani, A. and Yousefi, N. (2009). Accumulation of heavy metals in soil and uptake by plant species with phytoremediation potential. *Environmental Earth Sciences*, 59(2): 315-323.
17. Kord, B., Mataji, A. and Babaie, S. (2010). Pine (*Pinus Eldarica Medw.*) needles as indicator for heavy metals pollution. *International Journal of Environmental Science & Technology,* 7(1): 79-84.
18. Wuana, R., Okieimen, F. and Imborvungu, J. (2010). Removal of heavy metals from a contaminated soil using organic chelating acids. *International Journal of Environmental Science & Technology,* 7(3): 485-496.
19. Moutsatsou, A., Gregou, M., Matsas, D. and Protonotarios, V. (2006). Washing as a remediation technology applicable in soils heavily polluted by mining–metallurgical activities. *Chemosphere*, 63(10): 1632-1640.
20. USEPA (1994). Method 1312: Synthetic Precipitation Leaching Procedure, part of test methods for evaluating solid waste, physical/chemical methods. United States Environmental Protection Agency (USEPA).
21. Townsend, T., Jang, Y.-C. and Tolaymat, T. (2003). A guide to the use of leaching tests in solid waste management decision making. University of Florida, Florida.
22. New Jersey Department of Environmental Protection (2013). Development of Site-Specific Impact to Ground Water Soil Remediation Standards Using the Synthethic Precipitation Leaching Procedure. New Jersey Department of Environmental Protection.
23. Malaysia Nuclear Agency (2010). Radiological impact assessment of advanced materials plant Gebeng Industrial Estate, Kuantan, Pahang. Malaysia Nuclear Agency.
24. Al-Areqi, W. M., Majid, A. A., Sarmani, S. (2014). Digestion study of water leach purification (WLP) residue for possibility of thorium extraction. *Malaysian Journal of Analytical Sciences*, 18(1): 221-225.
25. IAEA. (2014). Report of international post-review on the radiation safety aspects of the operation of a rare earth processing facility and assessment of the implementation of the 2011 mission recommendations. International Atomic Energy Agency (IAEA).

26. Quina, M. J., Bordado, J. C. and Quinta-Ferreira, R. M. (2009). The influence of pH on the leaching behaviour of inorganic components from municipal solid waste APC residues. *Waste Management,* 29(9): 2483-2493.
27. Van der Sloot, H. and Dijkstra, J. (2004). Development of horizontally standardized leaching tests for construction materials: A material based or release based approach? Identical leaching mechanisms for different materials, (ECN-C-04-060). https://www.ecn.nl/publications/PdfFetch.aspx?nr=ECN-C--04-060. [Accessed online 15 February 2017].
28. Pendowski, J. (2003). An assessment of laboratory leaching tests for predicting the impacts of fill material on ground water and surface water quality-Report to the legislature. Washington State Department of Ecology. https://fortress.wa.gov/ecy/publications/documents/0309107.pdf. [Accessed online 8 March 2017].
29. Guo, P., Duan, T., Song, X., Xu, J. and Chen, H. (2008). Effects of soil pH and organic matter on distribution of thorium fractions in soil contaminated by rare-earth industries. *Talanta,* 77(2): 624-27.
30. Wright, R. and Schindler, D. (1995). Interaction of acid rain and global changes: effects on terrestrial and aquatic ecosystems. *Water, Air, and Soil Pollution,* 85(1): 89-99.
31. Treptow, R. S. (1980). Le Châtelier's principle: A reexamination and method of graphic illustration. *Journal of Chemical Education*, 57(6): 417.
32. Langmuir, D. and Herman, J. S. (1980). The mobility of thorium in natural waters at low temperatures. *Geochimica et Cosmochimica Acta*, 44(11): 1753-1766.
33. Mernagh, T. P. and Miezitis, Y. (2008). A review of the geochemical processes controlling the distribution of thorium in the earth's crust and Australia's thorium resources. Geoscience Australia, Canberra: pp. 48.

Malaysian Journal of Analytical Sciences, Vol 22 No 6 (2018): 973- 983
DOI: https://doi.org/10.17576/mjas-2018-2206-07

MALAYSIAN JOURNAL OF ANALYTICAL SCIENCES
Published by The Malaysian Analytical Sciences Society
ISSN 1394 - 2506

EXTRACTION OF SQUALENE FROM *Aquilaria malaccensis* LEAVES USING DIFFERENT EXTRACTION METHODS

(Pengekstrakan Skualena daripada Daun *Aquilaria malaccensis* Menggunakan Kaedah Pengekstrakan yang Berlainan)

Wan Nurul Diyana Ramli[1,2], Mohd Azizi Che Yunus[1,2]*, Lee Nian Yian[1], Zuhaili Idham[1], Ahmad Hazim Abdul Aziz[1,2], Noor Aiysah Aris[1,2], Nicky Rahmana Putra[1,2], Shahid Kamar Sham[2]

[1]*Centre of Lipids Engineering (CLEAR) & Applied Research, Ibnu Sina Institute for Scientific and Industrial Research*
[2]*Faculty of Chemical and Energy Engineering*
Universiti Teknologi Malaysia, 81310 UTM Johor Bahru, Johor, Malaysia

**Corresponding author: azizi@cheme.utm.my*

Received: 16 April 2017; Accepted: 18 November 2018

Abstract

Nowadays deep sea sharks species have been hunted for its liver oil as the major source of squalene because of its importance in medical field especially as an antioxidant and anticancer compound. Studies have proved the existence of squalene compound in the *Aquilaria malaccensis* leaves. Supercritical carbon dioxide (SC-CO_2) extraction was done to study the effect of SC-CO_2 operating parameters (pressure and temperature) on the oil yield as well as percentage yield of squalene compound in the oil extracted from the leaves. Both the oil yield and the squalene percentage obtained by using SC-CO_2 extraction method were compared with conventional Soxhlet extraction technique. For SC-CO_2 extraction, the temperature used were 45 °C, 60 °C and 75 °C while the operating pressures were 100 bar, 200 bar and 300 bar. Each extraction process was carried out for 60 minutes with carbon dioxide flow rate of 8 g/min. Meanwhile for Soxhlet extraction, six types of solvents were used (methanol, ethanol, ethyl acetate, n-hexane, acetone and water). Soxhlet extraction gave higher oil yield (45.66%) by using ethanol as solvent compared to SC-CO_2 (13.22%) at 300 bar and 60 °C. However, Soxhlet gave lower squalene percentage in the oil extract (0.78%) by using n-hexane as solvent when compare with SC-CO_2 (3.97%) at 200 bar and 60 °C. These findings reveal that SC-CO_2 extraction is a preferable technique used to extract oil with high percentage of squalene compared to conventional Soxhlet extraction technique with shorter extraction time and higher selectivity on squalene.

Keywords: *Aquilaria malaccensis*, supercritical carbon dioxide, squalene, gas chromatography analysis

Abstrak

Pada masa kini spesies jerung laut dalam diburu kerana minyak hatinya sebagai sumber utama skualena disebabkan kepentingannya dalam bidang perubatan terutama sekali sebagai sebatian antioksida dan antikanser. Kajian telah membuktikan kewujudan sebatian skualena di dalam daun *Aquilaria malaccensis.* Pengekstrakan karbon dioksida lampau genting (SC-CO_2) telah dijalankan untuk mengkaji kesan parameter operasi SC-CO_2 (tekanan dan suhu) terhadap hasil minyak bersama peratusan hasil sebatian skualena di dalam minyak yang diekstrak daripada daun tersebut. Kedua-dua hasil minyak dan peratusan skualena yang didapati menggunakan kaedah pengekstrakan SC-CO_2 telah dibandingkan dengan kaedah pengekstrakan Soxhlet konvensional. Untuk pengekstrakan SC-CO_2, suhu yang digunakan adalah 45 °C, 60 °C dan 75 °C manakala tekanan operasi pula adalah 100 bar, 200 bar dan 300 bar. Setiap proses pengekstrakan telah dijalankan selama 60 minit dengan kadar aliran karbon dioksida sebanyak 8 g/min. Manakala bagi pengekstrakan Soxhlet, enam jenis pelarut telah digunakan (metanol, etanol, etil asetat, n-heksana, aseton dan air suling). Pengekstrakan Soxhlet memberikan hasil minyak yang lebih tinggi (45.66%) dengan menggunakan etanol sebagai pelarut berbanding pengekstrakan SC-CO_2 (13.22%) pada 300 bar dan 60 °C. Walau bagaimanapun, Soxhlet dengan menggunakan n-heksana sebagai pelarut memberikan peratusan skualena yang lebih rendah di dalam ekstrak minyak (0.78%) apabila dibandingkan dengan SC-CO_2 (3.97%) pada 200 bar dan 60 °C. Hasil penemuan ini

mendedahkan bahawa pengekstrakan SC-CO_2 adalah kaedah yang lebih baik untuk mengekstrak minyak dengan peratusan skualena yang tinggi dengan masa pengekstrakan yang lebih singkat dan pemilihan yang lebih tinggi terhadap skualena berbanding kaedah pengekstrakan Soxhlet konvensional.

Kata kunci: *Aquilaria malaccensis*, karbon dioksida lampau genting, skualena, analisis kromatografi gas

Introduction

Squalene production or manufacture is typically from shark liver oil. In the case of deep-sea sharks, the liver is the main organ for lipids storage, being in the same time an energy source and means for adjusting the buoyancy. In their case, the unsaponifiable matter represents 50–80% of the liver, the great majority there of being squalene. *Centrophorus artomarginatus* deep-sea sharks which live in waters at 600 to 1000 m depth, without sunlight, manage to survive where pressure is consistently high and the oxygen supply is very poor, due to this compound from their liver, which accounts for 25% to 30% of their total body weight. The liver of the shark *Centrophorus squamosus* represents 18.1% from the body mass; 77.2% by weight of the liver composition is oil and the squalene concentration in this oil is 79.6%. Similar values have been obtained for *Centroscymnus crepidater* [3].

Aquilaria are genera of tropical trees that produces a valuable resinous wood called agarwood. The aromatic properties of agarwood when burned or distilled are extraordinary and there is high demand for the resinous wood to make incense, perfume and as traditional medicine [1]. History of trading agarwood internationally was started as early as the thirteenth century, with India as one of the first origin of agarwood for overseas markets. Ordinarily, agarwood is exported in bulky quantities. In 1997 report, over 700 tons of agarwood from *Aquilaria malaccensis* species were involved in international trade. From these data almost among 20 reported countries, export or re-export were from Indonesia and Malaysia [2]. The leaves of *Aquilaria malaccensis* tree is being discarded as waste due to large consumption of the barks and woods. As the leaves are good sources of natural antioxidants and bioactive compounds, it can be utilized and used as ingredients of healthcare products.

As the world becomes more advanced, many researchers have explored the novel usage of these nature. Plants and plant extracts have been used as medicine, culinary spice, dye and general cosmetic since ancient times. Plant extracts are seen as a way of meeting the demanding requirements of the modern industry. In the past two decades, much attention has been directed particularly in the food pharmaceutical and perfume industries [4]. Chemical compounds originated from plants assist their effect on the human body over manners similar to the chemical compounds in man-made drugs. Therefore, herbal medicines do not have much difference from conventional drugs in terms of mechanism. This feature not only qualifies herbal medicines to have valuable pharmacology, but also gives them the same ability as conventional medicinal drugs that have dangerous side effects [5].

Rapid development of technology and knowledge has revealed another source of squalene compound in natural plant which is Agarwood plant. Based on previous research [6] done on the leaves of *Aquilaria crassna Pierre* (Gaharu), it is found that the sample contained 5-hydroxy-7-methoxy-2-(4-methoxyPhenyl)-4H-I-benzopyran-4-on, squalene and epifriedelanol. Another research done [7] also found 12 compounds that appeared in the characterization of methanolic extracts of Agarwood leaves which one of them is squalene (Table 1).

Table 1. Chemical components of agarwood leaves

Component	**Molecular formula**
n-hexadecanoic acid	$C_{16}H_{32}O_2$
Glycerine	$C_3H_8O_3$
2-propanone,1,3 dihydroxy	$C_3H_6O_3$
3,7,11,15-tetramethyl-2-hexadecen-1-ol (Phytol)	$C_{20}H_{40}O$
Dodecyl acrylate	$C_{15}H_{28}O_2$
2,3-dihydro-3,5-dihydroxy-6-methyl-4H-pyran-4-one	$C_6H_8O_4$

Table 1 (cont'd). Chemical components of agarwood leaves

Component	Molecular formula
6-ethyl-5-hydroxy-2,3n,7-trimethoxynaphthoquinone	$C_{15}H_{16}O_6$
9,12,15-octadecatrienoic acid, (z,z,z)-	$C_{18}H_{30}O_2$
Squalene	$C_{30}H_{50}$
Octaethylene glycol monodecyl ether	$C_{28}H_{58}O_9$
1-tetradecanol	$C_{14}H_{30}O$

Currently, in order to improve product yields and quality of certain material used, many innovative technologies have been developed such as microwave assisted extraction (MAE), accelerated solvent extraction (ASE), subcritical water extraction (SWE), ultrasound extraction (Sonication), supercritical fluid extraction (SFE) and phytonics process. For this study, it is focused on the supercritical fluid extraction technology using carbon dioxide as solvent. For comparison purpose, Soxhlet extraction method was carried out too besides of SFE method.

Supercritical fluid extraction (SFE) is a substitute method in sample preparation to lessen the use of organic solvents and escalate production. The factors to be considered are pressure temperature, modifier addition, sample volume, analyte collection, flow rate and pressure control and restrictors. There are many benefits in using carbon dioxide as the extracting fluid not only to its encouraging physical properties, carbon dioxide is also economical, safe and copious. Other important properties of this solvent is that it has low surface tension, low viscosities and moderately high diffusion coefficients [8]. Besides, the extraction of product at low temperature which can avoid damages from heat and for some organic solvents, carbon dioxide does not have solvent remains and also practices natural friendly extraction procedure.

This research was done in order to investigate the effects of the operating condition of SC-CO_2 extraction such as temperature and pressure on the oil yield and percentage of squalene extracted from the *Aquilaria malaccensis* leaves as the leaves is claimed to be contained high quantity of squalene. It was also done by comparing the oil yield and the percentage of squalene obtained from *Aquilaria malaccensis* leaves by using SC-CO_2 and Soxhlet extraction.

Materials and Methods

Sample preparation

Fresh, green, healthy and matured *Aquilaria Malaccensis* leaves were selected and obtained from Gaharu Plantation in Segamat in a large quantity to ensure its same properties. The leaves were washed first using tap water to remove dirt's and unwanted substance from the surface of the leaves. The leaves were dried under sun continuously every day until the percentage humidity loss achieved 65% weight in dry basis. The dried leaves were then dried powdered using grinder (Waring, U.S) into small pieces. In order to get a particle size of 355µm, the powdered leaves were then sieved by using sieve tray (Endecotts Octagon 2000 Digital Sieve Shaker). For preserving and storing purposes, the sealed plastic bag was kept in freezer at -20 °C.

Extraction using supercritical carbon dioxide extraction

15g of sample was placed into the vessel, with glass beads and methanol as modifier. 30 glass beads (4.76g) were used to prevent clogging during the run with mixture configuration. 10% of methanol used as the modifier (10 mL) was calculated using volume basis of the vessel (1L). The experiment was conducted with pressure range (100-300 bar) and temperature range of (45-75 °C) and each set of extraction processes were run for 1 hours. Next, 99.9% pure CO_2 gas (Mega Mount Industrial Gases Sdn Bhd, Malaysia) were supplied into the system (SEPAREX Equipment, France, Unit 4397- XUO32) continuously with pump at flow rate of 8 g/min so that it is fed through high pressure. Back pressure regulator (Tescom Corp., USA) with temperature of 65 °C was adjusted to apply the pressure according to the desired value while the temperatures were adjusted by setting the oven temperature. After the pressure and temperature inside the vessel have achieved the desired value, the start time was recorded. The extracted oil in the vessel was then collected for every 15 minutes by opening the collection valve at each interval

and the weights of oil extracted were recorded. The extracted oil collected was automatically separated from the CO_2 as the solvent is in gas state at back pressure regulator temperature of 65 °C and some were purged out from the system. Each run was replicated 3 times to ensure reliability of the data gained.

Extraction using Soxhlet extraction

50g of the dried powder was placed in the Soxhlet tea bag and was loaded into Soxhlet extractor chamber. The Soxhlet extractor was placed onto the round bottomed flask which contains 500 mL of analytical graded solvent. Sample to solvent ratio of 1:10 was constant for each type of solvent used. The Soxhlet extractors were set in series for simultaneous extraction by using six different types of solvents used (methanol, ethanol, ethyl acetate, n-hexane, acetone and water). The main chamber of the Soxhlet extractor was equipped with a condenser. The flow of water in the condenser was set co-currently with the flow of vapor. The water flows in from the bottom inlet and going out the top outlet of the condenser. The solvent is then heated up to its boiling point until reflux. Next, rotary evaporator (Heidolph, German) was used to remove the solvent from the mixture of oil and solvent by evaporation. After most of the solvent was removed from the mixture and only the oil left which is 5% from the initial weight, the oil was put into sample beaker and then was dried in oven for 6 consecutive days at 40 °C for further evaporation of solvent. Due to squalene high boiling point (429 °C) which is the target compound, the length of oven drying does not destroy the compound targeted. The weight of dried extract obtained was weigh and recorded.

Analysis of oil yield percentage

The comparison of oil yield percentage of *Aquilaria malaccensis* leaves extract was made in terms of mass percentage of the samples. The extracted oil obtained was placed in the collection vessel, sealed and stored in chiller at 2.7 °C after each extract to prevent any possible degradation of the product for further analysis using gas chromatography.

$$\text{Extract yield (\%)} = \frac{mass\ of\ oil\ extracted\ (g)}{mass\ of\ sample\ (g)} \times 100\% \quad (1)$$

GC-analysis of squalene

For the condition of gas chromatography, separations were performed on a 5% diphenyl/95% dimethyl polysiloxane fused silica column (30m x 0.250 mm internal diameter, 0.25-*ím* film thickness, Sugelabor, Madrid, Spain) with helium as the carrier gas. The GC temperature was programmed at a rate of 20°C/min from 130 to 230 °C (2 minutes) and then to 290°C (30 minutes) at 3°C /min. In all analyses, the detector temperature was set at 320 °C and the 2600 Chromatography software (Perkin-Elmer Nelson Systems) was used for data acquisition [9].

Results and Discussion

Oil yield percentage

Each set of temperature and pressure was conducted for one hour of four fractions. Each fraction is equivalent to 15 minutes. The percentage of oil yield was calculated using equation 1 and the results obtained were tabulated in Table 2.

Based on the result tabulated in Table 2, the average oil yield obtained is 3.161%. It can be seen clearly that the highest percentage of oil yield obtained is at 300 bar and 60 °C which is 13.222%. The lowest yield percentage obtained is at 100 bar and 75 °C which is 0.102% *Aquilaria malaccensis* oil.

Table 2. Oil yield obtained by using SC-CO_2 extraction

Pressure (bar)	Temperature (°C)	Extraction Time (minutes)			
		15	30	45	60
		Oil Yield (%)			
100	45	0.0367	0.1693	0.2013	0.2360
	60	0.2240	0.2500	0.2793	0.3113
	75	0.0200	0.0687	0.0860	0.1020
200	45	0.1667	0.1820	0.2007	0.3433
	60	3.1853	3.2227	3.2640	3.2907
	75	3.5707	3.7093	3.7240	3.7513
300	45	0.4167	0.6153	0.7227	0.8513
	60	13.0880	13.1753	13.1960	13.2227
	75	6.0520	6.2893	6.3093	6.3407

Effect of temperature at constant pressure

It can be observed that increases in temperature does not affect the oil yield obtained at 100 bar. The highest oil yield was obtained at moderate temperature of 60 °C. Meanwhile, lowest oil yield was obtained at highest temperature which is 75 °C. It can be seen that the oil yield increases as the temperature increases. From Figure 1(b), the highest oil yield was obtained at an operating temperature of 75 °C followed by temperature at 60 °C and 45 °C. From Figure 1(b) and (c), it was shown that the lowest oil yields were obtained at 45 °C, the lowest operating temperature. It can be observed that the oil yield was low at low temperature, and increases as the temperature increases. This is due to the decrease in the CO_2 density when the temperature increases at constant pressure, hence reduced the extractability of the oil into the $SCCO_2$.

On the other hand, it is anticipated that increase in solute vapor of oil occurred as the temperature increase that contributed to the high oil extraction yield. This phenomenon is similar with other studies reported [10]. The solvent approached the gas-like properties as temperature increases and this facilitate the extraction rate and produced asymptotic yield [11]. However, in Figure 1(a) the higher temperature resulted in lower oil yield percentage. This phenomenon happened due to the decrease in fluid density at increasing temperature, leading to the reduction in the fluid solvent power, eventually reducing the extraction efficiency [12]. Because of this reason, the oil yield decreases as the temperature increases from range 60 °C and above as can be seen in Figure 1 (a) and Figure 1 (c). The reduction of oil yield happened when the temperature increased from 60 °C to 75 °C, showed in Figure 1(a) and (c), while in Figure 1(b), the yield was increased as temperature increased from 40 °C to 75 °C. Although the oil yield obtained was the highest at highest temperature of 75 °C as shown in Figure 1(b), the difference was not significantly large when compared to the oil yield obtained at 60 °C.

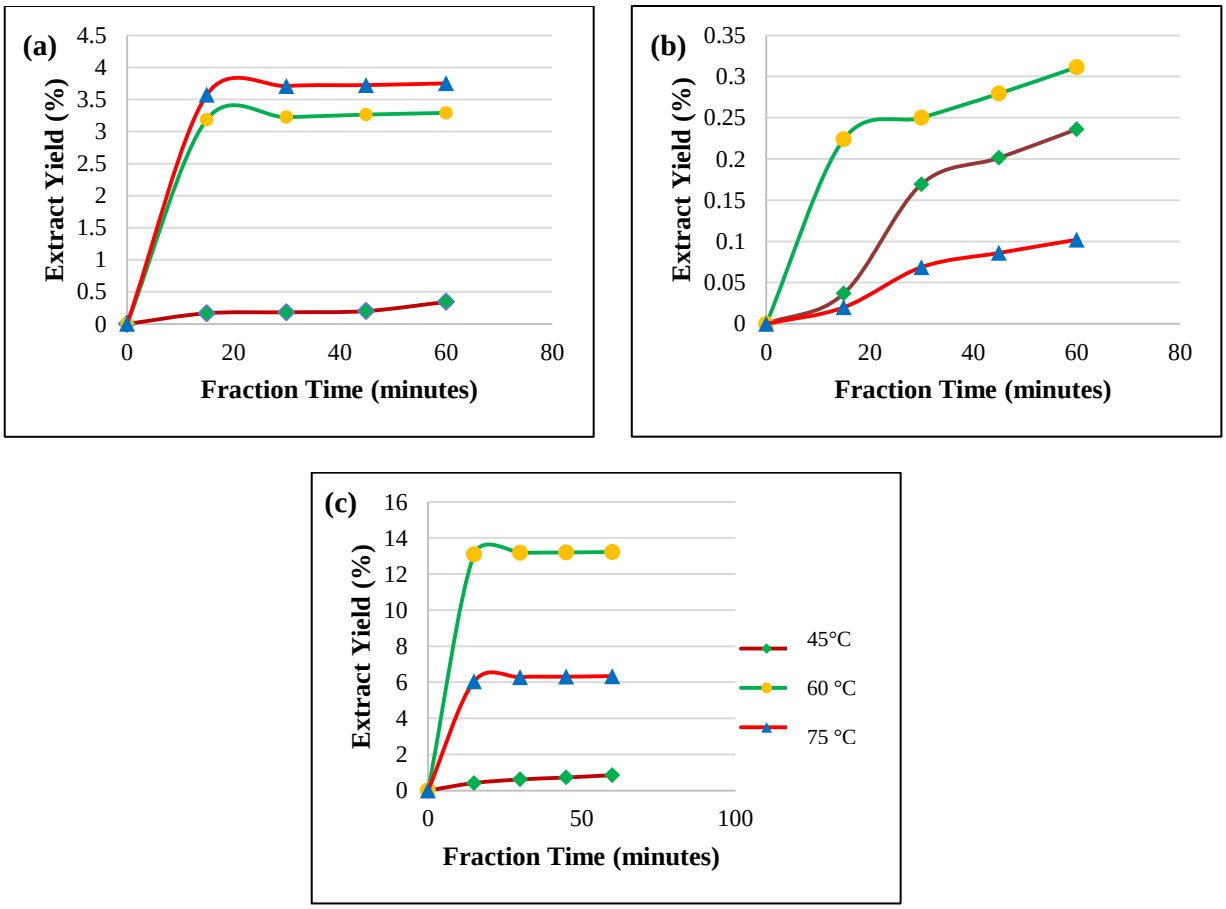


Figure 1. Percentage of oil yield at (a) 100 bar, (b) 200 bar, and (c) 300 bar

Effect of pressure at constant temperature

The highest percentage of oil yield obtained was collected at pressure 300 bar as shown in Figure 2. Meanwhile, the lowest percentage of oil yield is at pressure of 100 bar. The results represented have shown that the effect of pressure at constant temperature is noticeable. As the pressure increases, the oil yield obtained increases as well. This can be explained because some compounds appeared at certain pressure and disappeared at other pressure. The phenomenon existed because there are competition between solvent density and solute pressure. The density of solvent used increases with an increase in pressure at constant temperature, while the vapor pressure of the solute decreases as pressure decreases [13]. The increase in pressure at constant temperature will increase the solvent density and the solubility of oil components and enhance the extraction yield [14]. In addition, this was also due to the effect of diffusion rates of the extracted compounds from the matrix to the supercritical fluid medium [15]. Thus, it can be concluded that the pressure resulted in the highest oil yield of 13.222% was obtained at the highest pressure of 300 bar.

Increasing temperature also can improve the mass transfer coefficient, which is quite significant for the extracted experiments. According to the phenomenon, it shows that the oil yield increases with increasing pressures, however this characteristic has a little similarity with the effect of extraction temperature which reveals that the oil yield increases with increasing temperature [16]. Thus, it can be concluded that the increase in temperature increases the oil yield obtained to a certain level, but might decreases despite of the temperature increase. In conclusion, the best operating temperature for the oil yield is 60 °C.

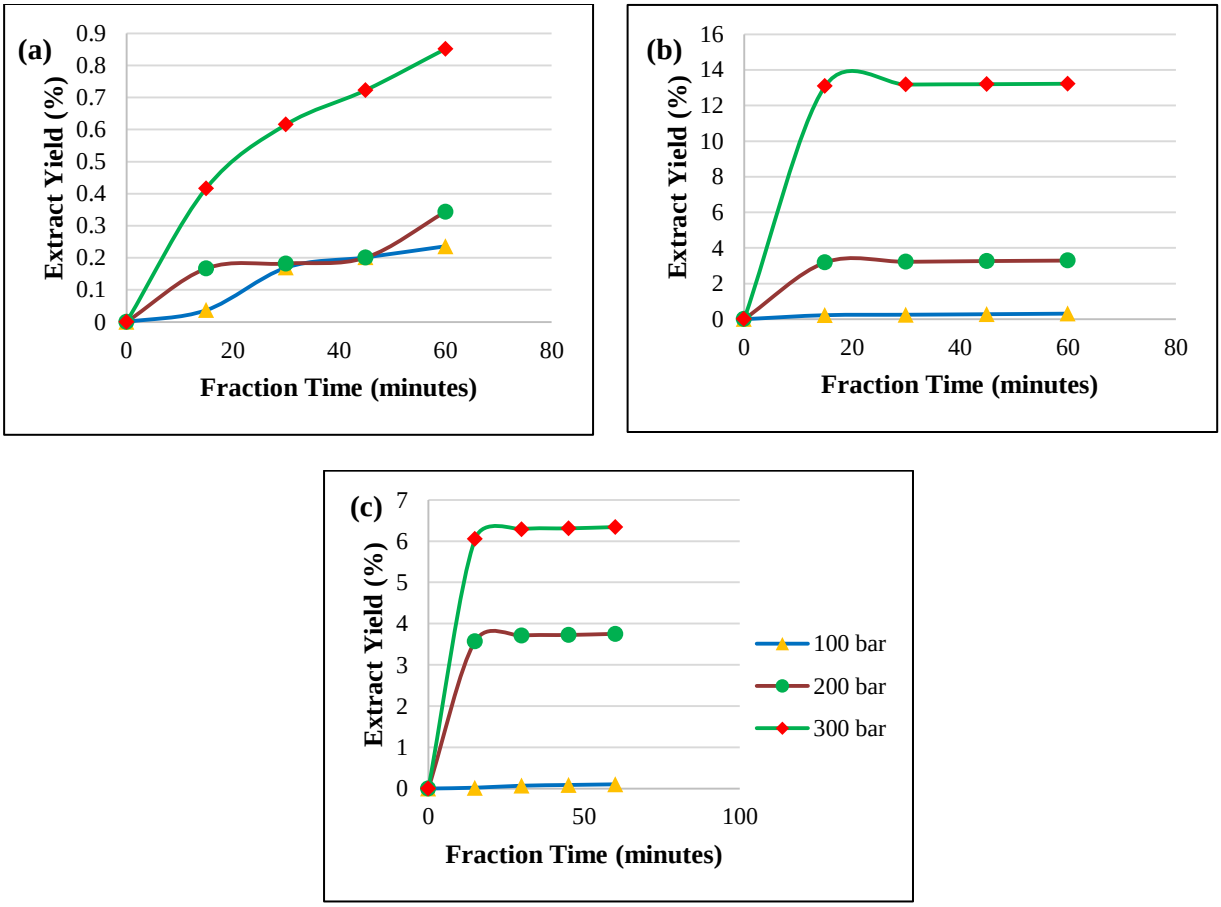


Figure 2. Percentage of oil yield at (a) 45 ^{o}C, (b) 60 ^{o}C, and (c) 75 ^{o}C

Soxhlet extraction

For Soxhlet extraction method, the polarity of the solvent is the most significant factor because it will influence the extraction result overwhelmingly [16]. Thus, different types of solvent were used to investigate which solvent could obtain the highest yield of oil as well as squalene from *Aquilaria malaccensis* leaves.

From the results obtained, we can see that the highest oil yield obtained by using this method is by using solvent ethanol which gave 45.66% oil yield. In contrast, the lowest oil yield was obtained by using n-hexane as solvent which gave 14.06% oil yield. Generally speaking, polar molecules are soluble in water while non-polar molecules are soluble in fat or organic substances. From Figure 3 above, methanol gives the second highest oil yield percentage which is 38.16%. Both methanol and ethanol are bipolar because they own hydroxyl group. Bipolar solvents can dissolve in a large number of oils because of the hydrogen bonds, and can dissolve in water because they possess an ionic end on the molecule [17].

Since ethanol and methanol is considerably highly in polarity and have bipolar properties, thus higher oil yield percentages were obtained. Then, water gives moderate percentage of oil yield which is 25.12%. Water is polar while the oil is non-polar. Oil is not soluble in water thus give lower oil yield when water is compared to bipolar solvents which are ethanol and methanol. The structure of oil is made up of long hydrocarbon chain and has lack of charge to attract the molecules of water [18]. Moreover, oil is non-polar while water is a polar compound. This makes oil immiscible with water and insoluble in water. This phenomenon follows the principle 'like dissolves like' which means that polar substances will only be dissolved in polar substance while non-polar substances only dissolves in non-polar substances.

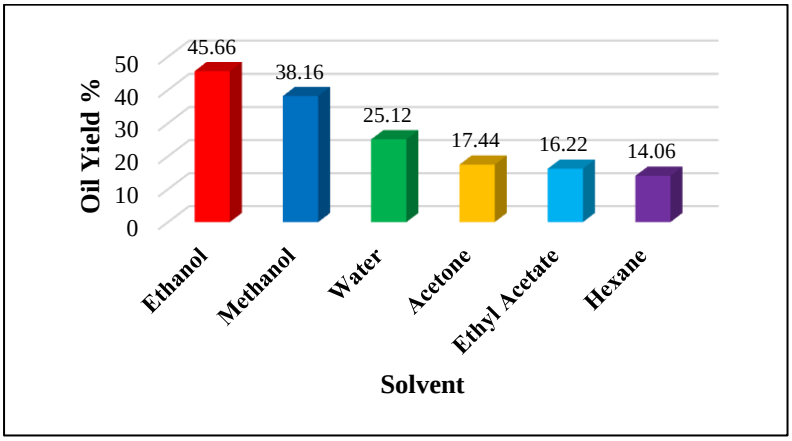
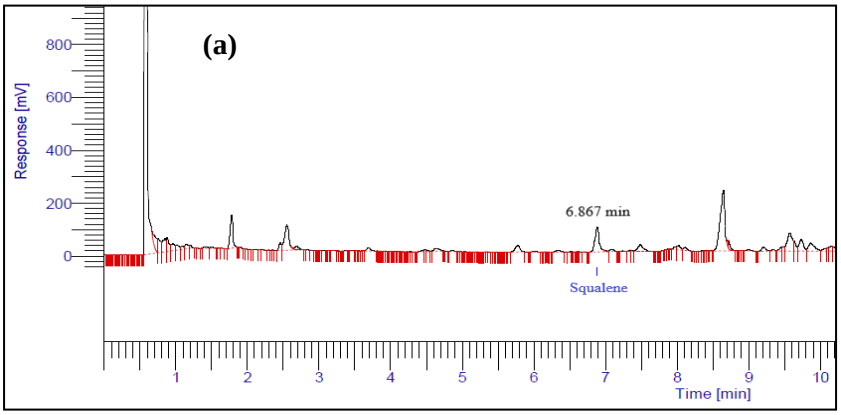


Figure 3. Percentage of oil yield obtained for different types of solvents used

The other three solvents which are acetone, ethyl acetate and n-hexane extracted relatively lower percentage of oil yield which are 17.44%, 16.22% and 14.06%, respectively. The oil yield obtained is lower compared to other solvents mentioned before because it is non-polar thus only extract non-polar components. Although oil is non-polar, the low oil yield shows that there are low numbers of nonpolar components per weight of sample during the extraction process. In conclusion, the percentage of oil yield obtained is based on the polarity of the solvent used. The polarity is the main factor contributing to the difference in the oil yield according to the principle 'like dissolves like'.

Gas chromatography analysis

During the extraction process, the vapor pressure of other compounds in the sample increases with increasing temperature. In addition, since the polarity of solvent CO_2 changes with the change in temperature and pressure, this might be the reason to the decrease in percentage of squalene yield even though both the temperature and pressure increases. The polarity of solvent supercritical CO_2 varies with variation of temperature and pressure [19]. Moreover, since the extraction process is dependent on the conditions of solubility and diffusely, competitive extraction of substances will occur [17]. Thus, it can be concluded that the highest percentage of squalene yield is 3.97% which was obtained at moderate temperature and pressure at 60 °C and 200 bar. Figure 4 shows the chromatogram of both extraction where squalene appears at retention time of 6.867 minutes.



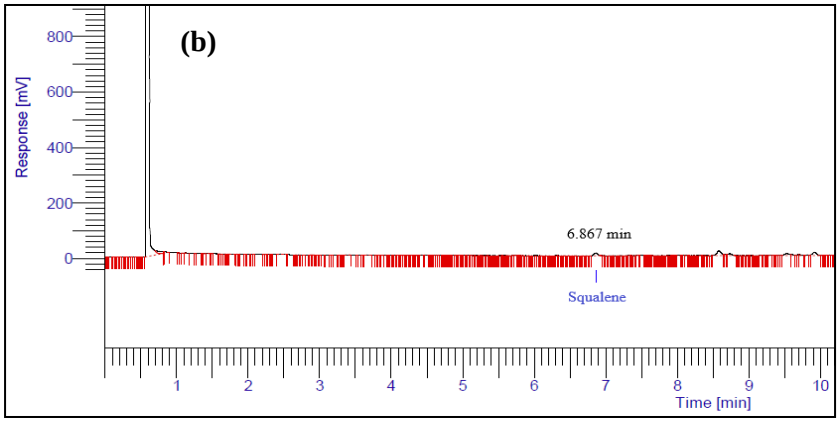


Figure 4. GC chromatogram of (a) SC-CO_2 extract at 200 bar, 60 °C and (b) Soxhlet extract using solvent n-hexane

The highest percentage of squalene obtained from Soxhlet extraction was by using n-hexane as extracting solvent with percentage of 0.78% of the total components in the extracted oil. This is reasonably true because n-hexane is the most non-polar compound thus it favors to extract squalene and most of the non-polar component from the sample. The polarity of squalene is reasonably low which almost zero and it is categorized as non-polar compound [20]. This phenomenon obeys the principle of 'like dissolves like'. The percentage of squalene yield decreases as the polarity of the solvent increases from ethyl acetate to acetone with percentage of 0.5% and 0.33%respectively. As the polarity increases, the solvent becomes least favor to extract the squalene which is a non-polar compound.

Result shows moderately high percentage of squalene in the extract by using solvent ethanol and methanol which are 0.52% and 0.26% respectively even though both compounds are high in polarity. This can be explained because of the bipolar properties of the solvents makes it possible to dissolve non-polar as well as polar compound. Squalene is slightly soluble in ethanol and methanol and thus was able to be extracted. However, the percentage is not as high as non-polar solvents such as n-hexane. In conclusion, the result shown that non-polar solvent which is n-hexane was able to easily extract highest percentage of squalene by Soxhlet extraction from Aquilaria Malaccensis leaves.

Comparison of extraction

It was observed that the highest reading of 13.22% oil yield extracted by SC-CO_2 extraction was lower than the highest oil yield of 45.66% extracted by using Soxhlet extraction by using solvent ethanol. In general, when we compare the oil yield obtained by both methods, Soxhlet extraction will give higher percentage of oil yield compared to that by using SC-CO_2 extraction. The same result was observed in the previous researcher that the extracted oil yield obtained by SC-CO_2 extraction was lower than Soxhlet extraction. The properties of solvents such as the solubility ability used in Soxhlet extraction affect the oil yield percentage. The phenomenon where the oil yield obtained is higher is most probably due to the high oil solubilization capability of solvent used as well as to the extraction of waxes and resin-like materials [21]. However, this phenomenon cannot illustrate that Soxhlet extraction is better than SC-CO_2 extraction in terms of selectivity. Since CO_2 is non-polar solvent, supercritical extraction will extract only non-polar components from *Aquilaria malaccensis* leaves, and moreover squalene is a non-polar compound. Thus, this makes SC-CO_2 extraction is better to be used as the purification and separation of squalene from other components when comparing with Soxhlet extraction [17].

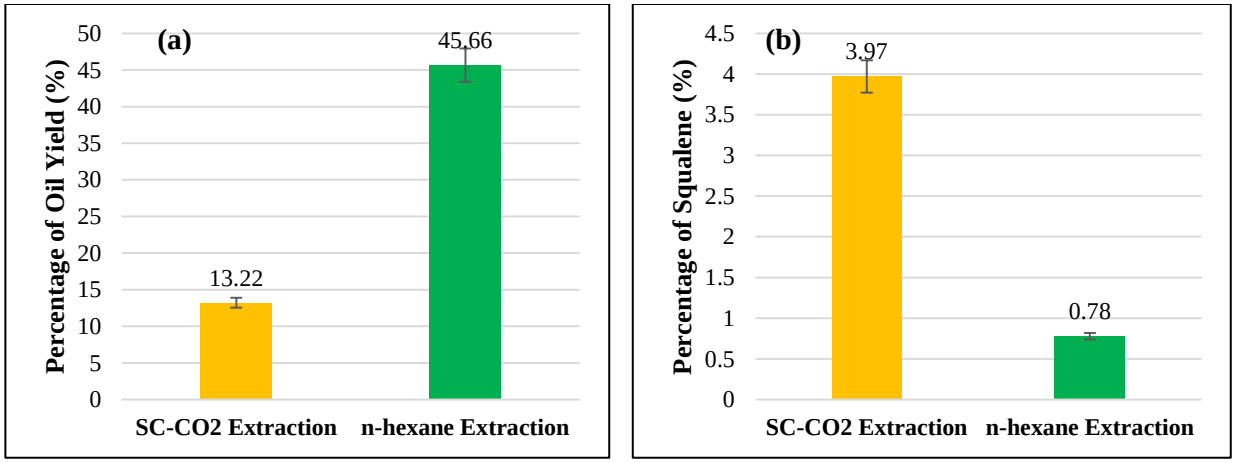


Figure 5. (a) Percentage of oil yield and (b) percentage of squalene obtained by both methods of extraction

From Figure 5, it can be seen that the SC-CO_2 extraction method successfully extract a significantly high percentage of squalene per extract compared to that of by using Soxhlet extraction method. It shows a huge difference where the highest percentage of squalene in the oil yield for SC-CO_2 is 3.97% which was obtained at 200 bar and 60 °C while Soxhlet extraction gave highest squalene percentage of 0.78% by using n-hexane as solvent. The lowest percentages of squalene in the extract yield were same for both methods which is 0.01% at condition of 100 bar and 45 °C for SC-CO_2 and solvent water for Soxhlet. The same result was proven in a previous research where the extraction of vitamin E where the percentage yield extracted by SC-CO_2 is higher compared to Soxhlet extraction method [16]. This is because CO_2 is non-polar solvent and thus it targets the compound squalene which is also a non-polar component, based on the principle 'like dissolves like', thus SC-CO_2 extraction extract more non-polar substance compared to Soxhlet extraction method [22]. Moreover, the variation of polarity of CO_2 based on the variation of temperature and pressure makes it possible for the SC-CO_2 solvent to have a high selectivity on squalene compound at the correct temperature and pressure. In conclusion, SC-CO_2 extraction method extract higher percentage of squalene compared to Soxhlet extraction method.

Conclusion

The highest oil yield obtained from Soxhlet extraction is 45.66% by using ethanol as a solvent. However, n-hexane solvent shows the highest squalene percentage of 0.78% in Soxhlet extraction. For SC-CO_2 extraction the highest oil yield obtained was 13.222% at operating condition of 300 bar and 60 °C but the highest squalene percentage was obtained at 200 bar and 60 °C (3.97%). SC-CO_2 extraction was more selective to the squalene compound compared to Soxhlet extraction as higher percentage of squalene was extracted by using SC-CO_2 (3.97%) compared to Soxhlet extraction (0.78%). Hence, it can be concluded that extraction using SC-CO_2 is more preferred and better compared to extraction using Soxhlet in getting higher percentage of target compound squalene.

Acknowledgement

The author would like to thank Ministry of Higher Education, Malaysia for Fundamental Research Grant Scheme Number R.J130000.7809.4F766 and Centre of Lipids Engineering and Applied Research (CLEAR), Universiti Teknologi Malaysia for the laboratory facilities in carrying out this research work.

References

1. Robert, A. B., Jurgens J. A. and Heuveling van Beek H. (2015). Growing aquilaria and production of agarwood in hill agro-ecosystems. Akansha Publishing House, Delhi: pp. 66-82.
2. Angela, B., Anak, N. A., Mulliken, T. and Song, M. (2000). Heart of the matter: Agarwood use and trade and CITES implementation for *Aquilaria malaccensis*. Unpublished note. Cambridge, TRAFFIC.
3. Popa, O., Babeanu, N. E., Popa,I., Nita, S. and Dinu-Pârvu, C. E. (2015). Methods for obtaining and determination of squalene from natural sources. *BioMed Research International*, 2015: 1-16.

4. Simandi, B., Kery, A., Lemberkovics, E., Oszagyan, M., Ronyai, E., Mathe, I., Fekete, J. and Hethelyi, E. (1996). Supercritical fluid extraction of medicinal plants. *High Pressure Chemical Engineering*, 12: 357-362.
5. Tapsell, L. C., Hemphill, I., Cobiac, L., Patch, C. S., Sullivan, D. R., Fenech, M., Roodenrys, S., Keogh, J. B., Clifton, P. M., Williams, P. G., Fazio, V. A. and Inge, K. E. (2006). Health benefits of herbs and spices: The past, the present, the future. *The Medical Journal of Australia*, 185(4): 4-24.
6. Norzafneza, M. A., Saripa, S. S. A. A., Hasimah, A., Ramli, I., Mohd, A. H. M. S., Mat, R. M. and Abdul, H. A. H. (2010). Chemical constituents of leaves from *Aquilaria Crassna Pierre* (Karas) and their biological activities. *Proceedings of the Seminar on Medicinal and Aromatic Plants:* pp. 111-120.
7. Khalil, A. S., Rahim, A. A., Taha, K. K. and Abdallah, K. B. (2013). Characterization of methanolic extracts of agarwood leaves. *Journal of Applied and Industrial Sciences*, 1(3): 78-88.
8. Selva, M. and Perosa, A. (2008). Green chemistry metrics: A comparative evaluation of dimethyl carbonate, methyl iodide, dimethyl sulfate and methanol as methylating agents. *Green Chemistry*, 10(4): 457-464.
9. Villén, J., Blanch, G. P., Ruiz del Castillo, M. L. and Herraiz, M. (1998). Rapid and simultaneous analysis of free sterols, tocopherols, and squalene in edible oils by coupled reversed-phase liquid chromatography-gas chromatography. *Journal of Agricultural and Food Chemistry*, 46(4): 1419-1422.
10. Özkal, S., Salgın, U. and Yener, M. (2005). Supercritical carbon dioxide extraction of hazelnut oil. *Journal of Food Engineering*, 69(2): 217-223.
11. Yunus, M. A. C., Zhari, S., Haron, S., Arsad, N. H., Idham, Z. and Ruslan, M. S. H. (2015). Extraction and identification of vitamin E from *Pithecellobium jiringan* seeds using supercritical carbon dioxide. *Jurnal Teknologi*, 74(7): 29-33.
12. Xiao, J. B., Chen, J. W. and Xu, M. (2007). Supercritical fluid CO_2 extraction of essential oil from *Marchantia convoluta*: Global yields and extract chemical composition. *Electronic Journal of Biotechnology*, 10(1): 141-148.
13. Peterson, A., Machmudah, S., Roy, B. C., Goto, M., Sasaki, M. and Hirose, T. (2006). Extraction of essential oil from geranium (*Pelargonium graveolens*) with supercritical carbon dioxide. *Journal of Chemical Technology and Biotechnology*, 81(2): 167-172.
14. Ibrahim, A., Al-Rawi, S., Majid, A. A., Rahman, N. A., Abo-Salah, K. and Ab Kadir, M. (2011). Separation and fractionation of *Aquilaria malaccensis* oil using supercritical fluid extraction and the cytotoxic properties of the extracted oil. *Procedia Food Science*, 1: 1953-1959.
15. Rezaei, K. and Temelli, F. (2000). Using supercritical fluid chromatography to determine diffusion coefficients of lipids in supercritical CO_2. *The Journal of Supercritical Fluids*, 17(1): 35-44.
16. Mohd Azizi, C. Y. (2007). Extraction, identification and separation of vitamin E and djenkolic acid from *Pithecellobium jiringan* (jack) prain seeds using supercritical carbon dioxide. PhD Thesis. Universiti Sains Malaysia.
17. Long, C. X. (2014). Extraction of squalene from palm oil mesocarp using supercritical carbon dioxide. Thesis of Master Degree. Universiti Teknologi Malaysia.
18. Blanks, R. F. and Prausnitz, J. (1964). Thermodynamics of polymer solubility in polar and nonpolar systems. *Industrial and Engineering Chemistry Fundamentals*, 3(1): 1-8.
19. Ikushima, Y., Saito, N., Arai, M. and Arai, K. (1991). Solvent polarity parameters of supercritical carbon dioxide as measured by infrared spectroscopy. *Bulletin of the Chemical Society of Japan*, 64(7): 2224-2229.
20. Vieillescazes, C., Sierra, I. and Morante-Zarcero, S. (2012). Separation techniques. In conservation science for the cultural heritage Springer: pp. 15-35.
21. Mohd, A. C. Y., Nur, H. A., Salman, Z., Zuhaili, I., Siti, H. S. and Ana, N. M. (2012). Effect of Supercritical carbon dioxide condition on oil yield and solubility of *Pithecellobium jiringan* (Jack) prain seeds. *Jurnal Teknologi*, 60: 45-50.
22. Yunus, M. A. C., Idham, Z. and Morad, N. A. (2015). Optimisation of squalene from palm oil mesocarp using supercritical carbon dioxide. *10th Asian Control Conference:* pp.1-6.

Malaysian Journal of Analytical Sciences, Vol 22 No 6 (2018): 984 - 998
DOI: https://doi.org/10.17576/mjas-2018-2206-08

MALAYSIAN JOURNAL OF ANALYTICAL SCIENCES
Published by The Malaysian Analytical Sciences Society
ISSN 1394 - 2506

EFFECT OF GRAPHENE OXIDE AND CELLULOSE NANOFIBER TOWARDS MECHANICAL PROPERTIES OF POLYLACTIC ACID BASED ACTIVE PACKAGING USING RESPONSE SURFACE METHODOLOGY

(Kesan Grafin Oksida dan Gentian Fibril Selulosa Terhadap Kekuatan Mekanikal Pembungkus Aktif Menggunakan Kaedah Gerak Balas Permukaan)

Mohd Harfiz Salehudin[1] and Ida Idayu Muhamad [1,2]*

[1]*Bioprocess and Polymer Engineering Department, School of Chemical and Energy Engineering, Faculty of Engineering*
[2]*Cardiac Biomaterials Cluster, IJN-UTM Cardiovascular Engineering Center Level 2, Block B, Building V01, School of Biomedical Engineering, Faculty of Engineering*
Universiti Teknologi Malaysia, 81310 Johor Bahru, Johor, Malaysia

**Corresponding author: idaidayu@utm.my*

Received: 16 April 2017; Accepted: 18 November 2018

Abstract

A simple preparation of functional nanoscale graphene oxide (GO) *via* synthetic route was done using modified Hummer's Method whilst cellulose nanofiber from oil palm empty fruit bunch fiber was prepared using acid hydrolysis method. An active polylactide based nanocomposite film was prepared by incorporation of cellulose nanofiber (CNF), graphene oxide (GO) and essential oil (EO). In determining of factor influences the mechanical properties (tensile strength, elongation percentage and Young's modulus), the response surface methodology (RSM) Box Behnken Design (BBD) were used. The factors considered were the ratio (wt.%) of GO and CNF as an additive and 5 wt.% of EO was set as minimum. The mechanical properties that interpreted as tensile strength, percent elongation and Young's modulus were the response variables investigated. The ratio of EO wt.% (C) is found to be the most significant factor that influences the tensile strength of the nanocomposite. In the case of elongation percentage (%E) the percentage of cellulose nanofiber CNF (A) gave the most significant effect, where in Young's modulus, EO wt.% (C) is the most significant effect, followed by wt.% of GO (B). Validation of optimization by carrying out the confirmation run high degree of prognostic ability of response surface methodology. The results showed that the optimized formulation provided a mechanical strength (tensile strength, percentage elongation and Young's Modulus) pattern that is similar to the predicted curve, which indicated that the optimal formulation could be obtained using RSM.

Keywords: cellulose nanofiber, graphene oxide, mechanical properties, active packaging, essential oil

Abstrak

Penyediaan sintetik serphihan nano grafin oksida telah dilakukan melalui kaedah terubahsuai Hummer. Selulosa nanofiber dari tandan kelapa sawit telah disediakan dengan menggunakan kaedah hidrolisis asid. Filem komposit aktif nano polilaktik disediakan melalui penggabungan selulosa nanofiber, grafin oksida dan minyak pati. Dalam mengenal pasti faktor nisbah bahan penambah ke atas sifat-sifat mekanik, reka bentuk eksperimen yang sistematik berdasarkan kaedah gerak balas permukaan (RSM), rekabentuk Box-Behnken (BBD) telah digunakan. Faktor yang dikaji adalah nisbah (wt.%) daripada GO dan nanofibril selulosa (CNF) sebagai bahan tambahan dan minimum berat 5 wt.% sebagai berat minyak pati (EO) telah ditetapkan. Sifat-sifat mekanik yang terdiri daripada kekuatan tegangan, peratus pemanjangan dan modulus Young's adalah respon yang ditetapkan. Nisbah peratusan berat (wt.%) EO didapati menjadi faktor yang paling penting yang mempengaruhi kekuatan tegangan filem. Dalam kes peratusan pemanjangan (%E), CNF (A) didapati menjadi faktor utama yang mempegaruhi peratus pemanjangan, dimana dalam modulus Young's, EO wt.% (C) menjadi faktor utama dituruti peratus GO (B). Pengesahan pengoptimuman dijalankan untuk menguji tahap kemampuan respon prognostik keadah gerak balas permukaan. Hasil kajian menunjukkan

bahawa pengoptimaan untuk kekuatan mekanikal (kekuatan tegangan, peratus tegangan dan modulus Young's) menyerupai corak yang seperti diramalkan, menunjukkan bahawa pengoptimaan boleh didapati menggunakan RSM.

Kata kunci: gentian nanosellulosa, grafin oksida, sifat mekanikal, pembungkusan aktif, minyak pati

Introduction

In general, polylactic (PLA) biopolymers are naturally brittle and poorer mechanical properties than the conventional non-biodegradable plastic films used in the food packaging industries [1]. However, PLA a type of biopolymer can be designed and casted as thin film for various purpose by incorporation of different filler and additives. Polymer/nanofiber/nanosheet nanocomposites have significantly established attention compared to conventional composites because they often exhibit substantial improvement in term of physical, mechanical, barrier, thermal and optical properties [2]. Those improvements mentioned can be achieved by incorporating low filler or additives into the PLA based polymer as reported by previous studies; 0.1-1% cellulose nanofiber and 0.1-1 graphene oxide [3], 1-5 wt.% nanocellulose/nanoclay [2], 1%-10% cellulose nanowhiskers/ montromorillonite and others. In making PLA based active film for application in food packaging, an active compound need to be incorporated either by coating or applied directly into the packaging during film formation. The active compound in the packaging will then release to the food surrounding to kill pathogen/microbes hat responsible for food spoilage. The most natural and safer choice of antimicrobials is a volatile and phenolic compound that can be found in essential oil [4]. However, the addition of essential oil or oil-based antimicrobial into the polymer packaging decrease the tensile strength and Young's modulus [5]. It was found that the tensile strength of the film added with clove and thyme essential oil were lower than neat film. It was also reported that the results attributed by the breakup of film network that caused by essential oil addition [6-7].

The usages of cellulose nanofiber and graphene oxide on the other hand are quite new. Its potential in active packaging and controlled release are not fully explored. With the better insight of both nanomaterials in term of its functional properties, chemical and physical properties, the PLA film can be modified to serve specific purpose. As a result, the incorporation of cellulose nanofiber and graphene oxide into the bio plastic may enhance the physical characteristics of the film and able to control the release of active agents (such as pesticide and repellent). It is important in food packaging applications as well as food commodity and related sector. This finding may solve or at least reduce numerous species of insects and mites attack on the plant during the period of cultivation and also storage that known as a major reason of dreadful economic loss. Cellulose nanofiber, one form of nanomaterial has attracted massive attention because of its small size that interacts better with biodegradable polymer matrix. It is also more compatible when applied in flexible thin film. Cellulose nanofiber (CNF) could give excellent mechanical properties to the biodegradable plastic as it may exhibits comparable strength to petroleum-based plastic.

In its crystal region, cellulose nanofiber has high Young's modulus approximately at 138Gpa [8] also gives a very low coefficient of thermal expansion along longitudinal direction [9]. This expounds that nano-size cellulose has a big potential in the development of new and enhanced biopolymers. Graphene oxide is newly emerged nanomaterial with unique dimensional structure (one to two atom sheet) that might provide new functionality (controlled release of pesticide). Graphene sheet possesses numerous oxygen-containing groups on the surface, such as hydroxyls, epoxides, carbonyls, and carboxyls [10, 11]. These available oxygen containing group can facilitates the interaction between polymer hosts and graphene oxide, also between graphene oxide and active compound (repellant) via covalent or non-covalent bonds [11]. Hence, the addition of both nanomaterial serves different purpose. Cellulose nanofiber is found to be an approach to enhance the mechanical and physical properties of the PLA based packaging. The graphene oxide (GO) in PLA on the other hand may provide more efficient pesticide delivery hence reduce pesticide usage & adverse effect. In term of formulation and experimental design procedure, previous research on nanocomposite packaging involves the use of one-factor-at-a-time experimental approach. It is known as time consuming approach, cost higher, and also neglects the effect of interaction between factors.

Thus, this study attempts to investigate the percentage addition (wt.%) of nanofiller used on the mechanical characteristics of active nanocomposite film using response surface method (RSM). The RSM enables the prediction of the optimum composition of CNF, GO and EO to the production PLA nanocomposite film. This study covered the effect of GO, CNF and EO towards the mechanical properties of the active film formed. The statistical

analysis using respond surface methodology was used to compute the optimal additive (CNF/GO/EO) to be added into an active film to provide the optimum mechanical properties.

Materials and Methods

Materials

Oil palm empty fruit bunch (OPEFB) fiber was retrieved from Universiti Kebangsaan Malaysia - Malaysia Palm Oil Board (UKM-MPOB) research center, Bangi, Malaysia. Sulfuric acid (Sigma Aldrich®), graphite fine powder (VChem ®), sodium nitrate (Qrec), hydrogen peroxide (GCE) were used to synthesize graphene oxide. Polylactic acid (Natureworks), chloroform (Fischer Scientific), and thyme essential oil (Sigma-Aldrich) were used as based film.

Nanomaterials preparation and characterization

Cellulose nanofiber (CNF) from oil palm empty fruit bunch (OPEFB) was prepared and characterized as described in previous method [12]. Graphene oxide nanosheet was synthesized *via* modified Hummer's method. Physical and chemical characterization of graphene nanosheet was done through field emission scanning electron microscope (FESEM) with energy dispersive X-ray spectroscopy (EDX), Fourier transform infrared spectroscopy (FTIR), and Fourier Atomic-Force Microscopy (AFM).

Polylactic acid based active nanocomposite film

In nanocomposite film making, CNF and GO were dispersed in chloroform to known concentration, the same solvent that used to dissolve PLA in this experiment. The dispersion takes place *via* solvent exchange, where the graphene oxide and cellulose nanofiber was first dispersed into acetone then into chloroform. Next, PLA pellet, CNF, GO and EO was dispersed in chloroform at temperature 60 ◦C in water bath for two hours. The mixture was cast on 19cm x 10cm acrylic plate and dried at room temperature overnight. The formed film was conditioned in desiccator for 48 hours.

Mechanical strength evaluation

Referring to method ASTM D 882-02, the mechanical strength Young modulus (Y) tensile strength (TS), and percentage elongation (%E) of prepared nanocomposite was evaluated using texture analyzer CT3 (Brookfield, USA). TA-DGA fixture accessories for packaging and thin sheet polymer was specifically used. The gauge length was set to 5 cm with crosshead speed 0.5 mm/min. In sampling preparation, films were cut into rectangular shape (8cm x 1cm). Total average of five specimens will be recorded for each test. The purpose of this test is to investigate the effect of cellulose nanofiber and graphene oxide incorporation percentage to the mechanical strength of the film that is being formed.

Experimental design

The response surface design is developed based on three factors, three level Box-Behnken. The design consists of a replicated center point and a set of points lying at the midpoint of each edge of the multidimensional cube that defines the region of interest. The processing material, independent and dependent variables involved in the design are listed in Table 1. The experimental design generated using the Design Expert Version 6.0 software. The 3-D response surface plots were also drawn using this software. The design involved 17 runs with five replications and the response variables measured were the tensile strength and elongation percentage (%E) as shown in Table 2. The nonlinear, quadratic model is given as:

$$Y = b0 + b1(CNF) + b2(GO) + b3(EO) + b12(CNF)(GO) + b13(CNF)(EO) + b23(GOEO) + b11(CNF)^2 + b22(GO)^2 + b33(EO)^2 \quad (1)$$

where y is the measured response associated with each factor level combination; b0 is an intercept; b1 to b33 are regression coefficients computed from the observed experimental values of Y; and CNF, GO and EO are the coded levels of independent variables and E is the error term. The statistical validity of the polynomials was established on the basis of ANOVA provision in the Design Expert Software. Finally, the feasibility and grid searches were performed to locate the composition of optimum formulations.

Table 1. Variables in Box-Behnken design

Factor	Levels		
	Low	Medium	High
CNF = Cellulose Nanofiber	0	0.75	1.5
GO = Graphene Oxide	0	0.75	1.5
EO = Essential oil	5	10	15

Table 2. Design layout and experimental results for Box-Behnken design

Run	Independent Factor			Response		
	X1	X2	X3	Y1 (Tensile)	Y2 (%E)	Y3 (YM)
1	0.75	1.50	15.00	12.48	134.27	6.76
2	0.00	0.75	5.00	20.69	235.93	9.544
3	0.75	0.75	10.00	14.38	210.22	8.642
4	0.00	1.50	10.00	15.36	179.16	7.406
5	0.75	1.50	5.00	26.38	45.16	6.144
6	1.50	1.50	10.00	26.50	7.84	7.711
7	1.50	0.75	5.00	37.90	2.93	8.187
8	0.75	0.75	10.00	12.54	247.95	9.898
9	0.75	0.75	10.00	14.27	211.63	9.07
10	0.00	0.75	15.00	12.41	130.34	2.891
11	1.50	0.00	10.00	23.27	7.78	4.719
12	0.75	0.00	5.00	22.39	3.22	6.971
13	0.75	0.00	15.00	9.44	108.31	1.587
14	1.50	0.75	15.00	16.38	11.10	4.623
15	0.75	0.75	10.00	13.23	231.96	9.738
16	0.00	0.00	10.00	20.62	4.15	2.459
17	0.75	0.75	10.00	13.52	222.86	9.102

All check points performed over the entire experimental domain to validate the chosen experimental design and polynomial equations. The formulations corresponding to these check points were prepared and evaluated for various response properties

Results and Discussion

The neat PLA based film was prepared without the addition of CNF, GO and EO was evaluated for its mechanical properties. The tensile strength, elongation percentage, and Young's modulus of neat PLA based packaging obtained was 18.51 ± 0.2 MPa, 87.54 ± 0.1%, and 4.5 GPa that is on par with the result obtained by Arjmandi et al. [13] and Chen et al. [3]. Both researchers stated that the tensile and Young's modulus were at range 17-20 Mpa, and 3-4.5 GPa, respectively. The nanocomposite packaging produced was evaluated and per experimental plan are shown in Table 2. The tensile strength, elongation percentage (%E), and Young's modulus results were input into the Design Expert software for further analysis. Examination of the fit summary output revealed that the quadratic model is statistically significant for the tensile, elongation percentage and Young's modulus. Therefore, both these models for tensile and elongation were used to represent each of the responses for further analysis.

ANOVA analysis

For the response surface methodology based on Box – Behnken design, 17 experiments were required. The experimental runs and the observed responses for the 17 formulations are given in Table 2. In evaluation of a good optimization model, test for significance of regression model, test for significance on individual model coefficients and test for lack-of-fit need to be performed. An ANOVA table is commonly used in summarized the tests performed. In general, at 5% level of significance, a model is considered statistically significant if the p – value is less than 0.05. The ANOVA analysis for the response surface, quadratic model for tensile strength is shown in Table 3.

Table 3. ANOVA table (sum of square) for quadratic model (Response: Tensile strength)

Source	Sum of Square	DF	Mean Square	F	Prob > F	
Block	37.73	2	18.86			
Model	790.85	9	87.87	32.94	0.0006	significant
A	152.86	1	152.86	57.31	0.0006	
B	5.96	1	5.96	2.23	0.1953	
C	399.4	1	399.4	149.74	< 0.0001	
A2	151.23	1	151.23	56.7	0.0007	
B2	0.42	1	0.42	0.16	0.7068	
C2	14.82	1	14.82	5.56	0.065	
AB	24.42	1	24.42	9.15	0.0292	
AC	50.98	1	50.98	19.11	0.0072	
BC	0.23	1	0.23	0.085	0.7829	
Residual	13.34	5	2.67			
Lack of Fit	11.61	3	3.87	4.48	0.1879	not significant
Pure Error	1.73	2	0.86			
Cor Total	841.92	16				
Standard Deviation	1.73					
Mean	18.34		R^2 =	0.9834		
			Adjusted R^2 =	0.9536		
			Predicted R^2 =	N/A		
			Adequate precision =	19.839		

In Table 3, the values of "prob>F" for the model is less than 0.05; which indicates that the model is significant. It is desired as it indicates that the model has a significant effect on the response. In a similar manner, the main effect of essential oil EO (C), cellulose nanofiber CNF (A), and the quadratic interaction of CNF (A) with EO (C) designated as (AC) and CNF (A) with graphene oxide (GO) designated by (AB) are significant model terms. Other model terms can be classified as insignificant. An improved model otherwise, can be developed by eliminating the insignificant model. The lack-of-fit in the model shows as insignificant. Insignificant model term in lack-of-fit is desirable as we want a model that fits. The regressive elimination procedure was performed to automatically reduce the insignificant terms. As a result, the ANOVA table for the reduced quadratic model is tabulated in Table 4. The results designated that the model remains significant. The significant model terms are still the same as mentioned in Table 3. The significant factors were ranked based on the value of F-ratio. The larger the magnitude of F-value and correspondingly the smaller the "prob>F" value, the more significant is the corresponding coefficient [14, 15].

Thus, in this study, the ranking is as follows**:** C> A> AC> AB> B. The R-squared (R^2)-value calculated is 0.98. The value is close to 1 which is reasonably acceptable. that close to 1. It signifies that about 98.3% of the variability in the data is explained by the model. Adequate precision on the other hand compares the range of the predicted values at the design points to the average prediction error. Ratios greater than 4 indicate adequate model discrimination. In this case, the value is well above 4. The exact same method is also applied to the other response, percentage elongation (%E) and Young's modulus. The ANOVA analysis of the quadratic model of elongation (%E) and Young's modulus was tabulated in Table 5 and Table 6, respectively. In response variable on of elongation percentage (%E), it's shown that cellulose nanofiber (CNF), second order of effect of cellulose nanofiber CNF (A^2), and effect of ratio CNF to GO (AB) are the significant model terms. The R^2 value for percentage elongation is 0.92486 that adjacent to 1 which shows the desirable characteristic for a good model. The ANOVA for Young's modulus as shown in Table 6, indicates that the model is significant as the "prob>F" is less than 0.05. It also indicates that the terms in the model have a significant effect on the response. In Young's modulus the ranking of significant factor that affecting Young's modulus is as follows; C> B> A^2> BC> C^2> B^2> AC. The other model on the other hand are said to be not significant.

Table 4. ANOVA table for reduced quadratic model (response: Tensile strength)

Source	**Sum of Squares**	**DF**	**Mean Square**	**F Value**	**Prob > F**	
Block	37.73	2	18.86			
Model	790.63	8	98.83	43.72	< 0.0001	significant
A	152.86	1	152.86	67.63	0.0002	
B	5.96	1	5.96	2.63	0.1557	
C	399.40	1	399.40	176.70	< 0.0001	
A2	151.23	1	151.23	66.90	0.0002	
B2	0.42	1	0.42	0.19	0.6803	
C2	14.82	1	14.82	6.56	0.0429	
AB	24.42	1	24.42	10.80	0.0167	
AC	50.98	1	50.98	22.55	0.0032	
Residual	13.56	6	2.26			
Lack of Fit	11.83	4	2.96	3.42	0.2386	not significant
Pure Error	1.73	2	0.86			
Cor Total	841.92	16				
Std. Deviation	1.50					
Mean	18.34		R^2 =	0.98		
			Adjusted R^2 =	0.96		
			Predicted R^2 =	N/A		
			Adequate precision =	22.71		

Table 5. ANOVA table (sum of square) for quadratic model (Response: Percentage elongation)

Source	Sum of Square	DF	Mean Square	F	Prob > F	
Block	33475.71	2	16737.85			
Model	1.14E+05	9	12661.41	6.84	0.0238	significant
A	33790.9	1	33790.9	18.25	0.0079	
B	3325.7	1	3325.7	1.8	0.2379	
C	3333.73	1	3333.73	1.8	0.2374	
A^2	28292.38	1	28292.38	15.28	0.0113	
B^2	5560.15	1	5560.15	3	0.1437	
C^2	7614.1	1	7614.1	4.11	0.0984	
AB	13195.11	1	13195.11	7.13	0.0444	
AC	7489.95	1	7489.95	4.05	0.1005	
BC	63.84	1	63.84	0.034	0.86	
Residual	9258.06	5	1851.61			
Lack of Fit	8540.77	3	2846.92	7.94	0.1139	not significant
Pure Error	717.29	2	358.64			
Cor Total	1.57E+05	16				
Standard Deviation	43.03					
Mean	117.34		R^2 =	0.92		
			Adjusted R^2 =	0.79		
			Predicted R^2 =	N/A		
			Adequate precision =	7.28		

Table 6. ANOVA table (sum of square) for quadratic model (Response: Young's modulus)

Source	Sum of Square	DF	Mean Square	F	Prob > F	
Block	31.49	2	15.75			
Model	77.63	9	8.63	9.73	0.0110	significant
A	1.08	1	1.08	1.22	0.3199	
B	13.93	1	13.93	15.71	0.0107	
C	21.62	1	21.62	24.38	0.0043	
A^2	9.48	1	9.48	10.69	0.0222	
B^2	4.67	1	4.67	5.27	0.0702	
C^2	8.13	1	8.13	9.17	0.0292	
AB	2.27	1	2.27	2.56	0.1708	
AC	4.12	1	4.12	4.65	0.0836	
BC	9.00	1	9.00	10.15	0.0244	
Residual	4.43	5	0.89			

Table 6 (cont'd). ANOVA table (sum of square) for quadratic model (Response: Young's modulus)

Source	Sum of Square	DF	Mean Square	F	Prob > F	
Lack of Fit	3.50	3	1.17	2.49	0.2990	not significant
Pure Error	0.93	2	0.47			
Cor Total	113.55	16				
Standard Deviation	0.94					
Mean	6.79		R^2 =	0.95		
			Adjusted R^2 =	0.85		
			Predicted R^2 =	N/A		
			Adequate precision =	11.25		

The final empirical models in terms of coded factors were presented as follows (equation 2-4):

$$Y^1(\text{Tensile}) = 13.94 + 4.37A + 0.90B - 7.35C + 6.28A^2 + 0.46B^2 + 1.96C^2 + 2.67AB - 3.86AC - 0.24BC \quad (2)$$

$$Y^2(\%\ \text{Elongation}) = 212.38 - 64.99A + 21.22B + 21.25C - 85.84A^2 - 53.27B^2 - 44.53C^2 - 62.04AB + 46.74AC - 3.99BC \quad (3)$$

$$Y^3(\text{Young's Modulus}) = 9.04 + 0.37A + 1.37B - 1.71C - 1.57A^2 - 1.54B^2 - 1.45C^2 - 0.81AB - 1.10AC + 1.50BC \quad (4)$$

In actual factor terminology, the final experimental models are presented as equation 5-7:

$$Y^1(\text{Tensile}) = 32.45976 - 4.18167CNF - 2.96708GO - 2.22373EO + 11.15648CNF^2 + 0.82648GO^2 + 0.078579EO^2 - 4.74407(CNF)(GO) - 1.02828(CNF)(EO) - 0.063333(GO)(EO) \quad (5)$$

$$Y^2(\%\ \text{Elongation}) = -80.12 + 100.32CNF + 263.73GO + 31.32EO - 152.60CNF^2 - 94.71GO^2 - 1.78EO^2 - 110.29(CNF)(GO) + 12.46(CNF)(EO) - 1.07(GO)(EO) \quad (6)$$

$$Y^3(\text{Young's Modulus}) = 6.16877 + 2.83900CNF + 3.03308GO + 0.30246EO - 2.79256CNF^2 - 2.74522GO^2 - 0.058198EO^2 - 1.44511(CNF)(EO) - 0.29237(CNF)(EO) + 0.4(GO)(EO) \quad (7)$$

Within the limits of the experiment, the tensile strength, percentage elongation and Young's modulus can be predicting by using this model. Figures 1 (a-f) shown the normal probability plot of the residuals and the plot of the residuals versus the predicted response for tensile strength, percentage elongation and Young's modulus.

Plot pattern on the Figures 1 (a, c, e) revealed that the residuals mostly fall on a straight line inferring that errors are distributed normally, and thus, support adequacy of the least-square fit [16]. Figures 1 (b, d, and f) presented that they have no obvious pattern and unusual structure. The point also scattered equally above and below the x-axis. This suggests that the models proposed are satisfactory and there is no reason to suspect any violation of the independence or constant variance assumption.

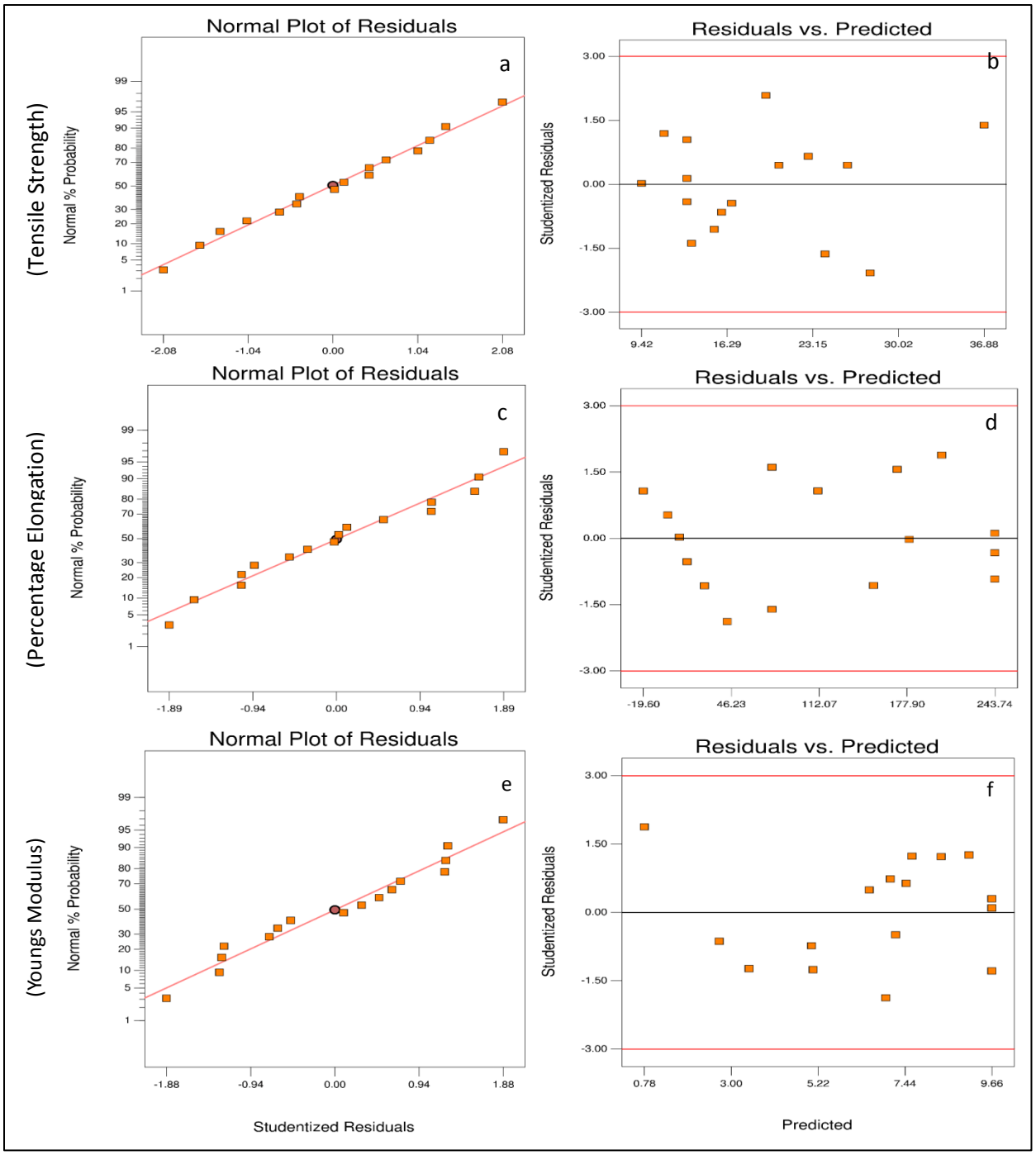


Figure 1. Normal probability plot of residual for tensile strength (a), percentage elongation (c), and Young's modulus (e) respectively, and plot of residual *vs* predicted response for strength (b), percentage elongation (d), and Young's modulus (f)

Effect of factor variables on tensile, elongation and Young's modulus

The effect of different factor variables on tensile strength, percentage elongation and Young's modulus are demonstrated by three-dimensional surface, and contour plate as depicted in Figure 2, 3 and 4, respectively. The 3D surface graph for the tensile strength has a hyperbolic profile in accordance to the quadratic model and is shown in Figure 2(a). The contour plot for the response surface for tensile strength is shown in Figure 2(b). In a condition where the essential oil is keeping at the middle level (10), the effect of the ratio of CNF (A) and GO (B) can be clearly seen in Figure 2(a). At the lowest level of CNF and GO, the tensile was 18.08 MPa. The increase and decrease of tensile strength are dependent on amount of GO and CNF. The maximum tensile strength was determined at 38.0617 Mpa when the ratio of CNF was at 1.5% and G.O at 0.82 as interpreted by numerical optimization on Figure 2(c).

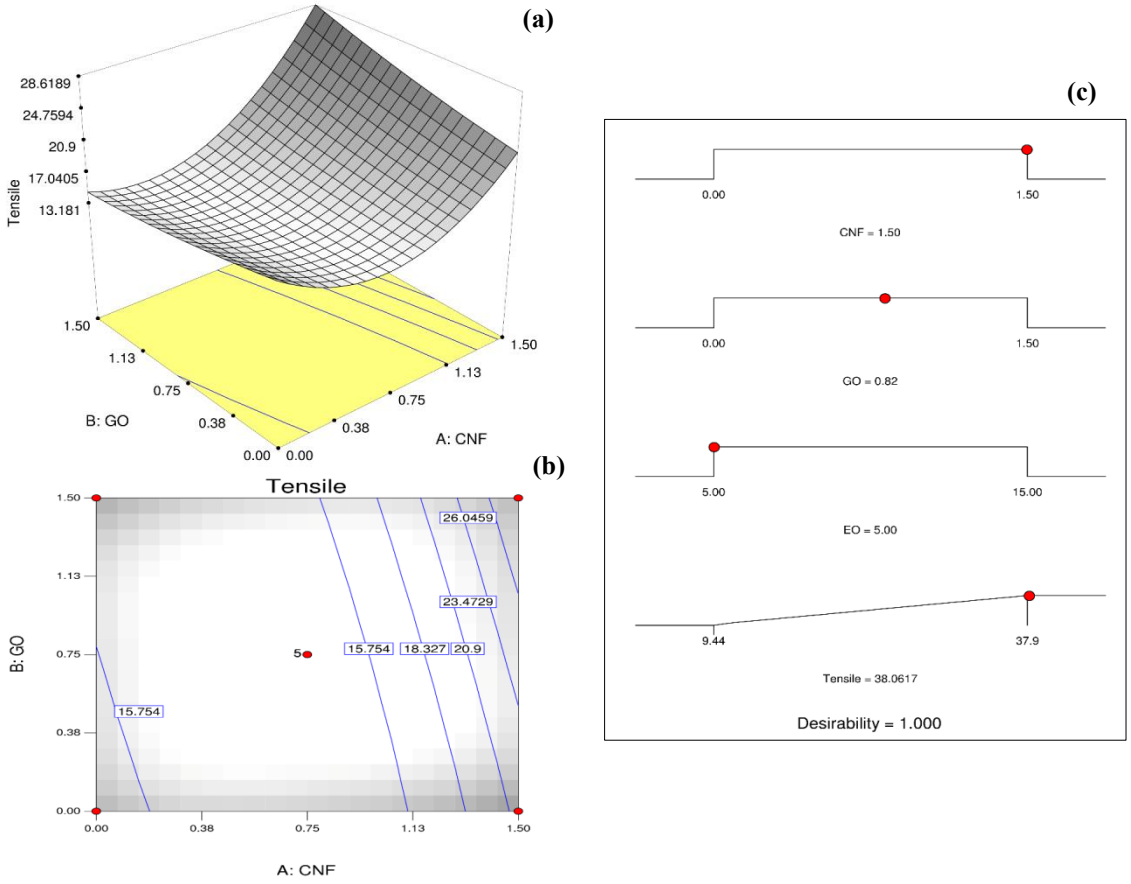


Figure 2. Surface (a) and contour (b) plot on tensile of CNF and GO (c) numerical optimization

The surface and contour plots of the ratio of CNF versus GO on the percentage elongation are presented in Figure 3. At fixed GO and EO concentration, the elongation increased with the increase of CNF ratio that is until 0.59% then decreased with the increase of CNF in the rest of region. Similar pattern shown when the EO and CNF were kept at minimum of addition percentage. The elongation increased with the increment of GO ratio until 0.89% addition and the elongation was decreased in the rest of the region. Numerical optimization of the elongation percentage was depicted in Figure 3(c). The effect of factor CNF and GO on the response Young's modulus represented in Figure 4. From the 3D surface diagram (Figure 4a), the maximum Young's modulus 9.62 GPa can be achieved when the amount of CNF and GO were at 0.66% and 0.92%, respectively. Any addition of CNF and GO after that point, can cause the decrement of Young's modulus.

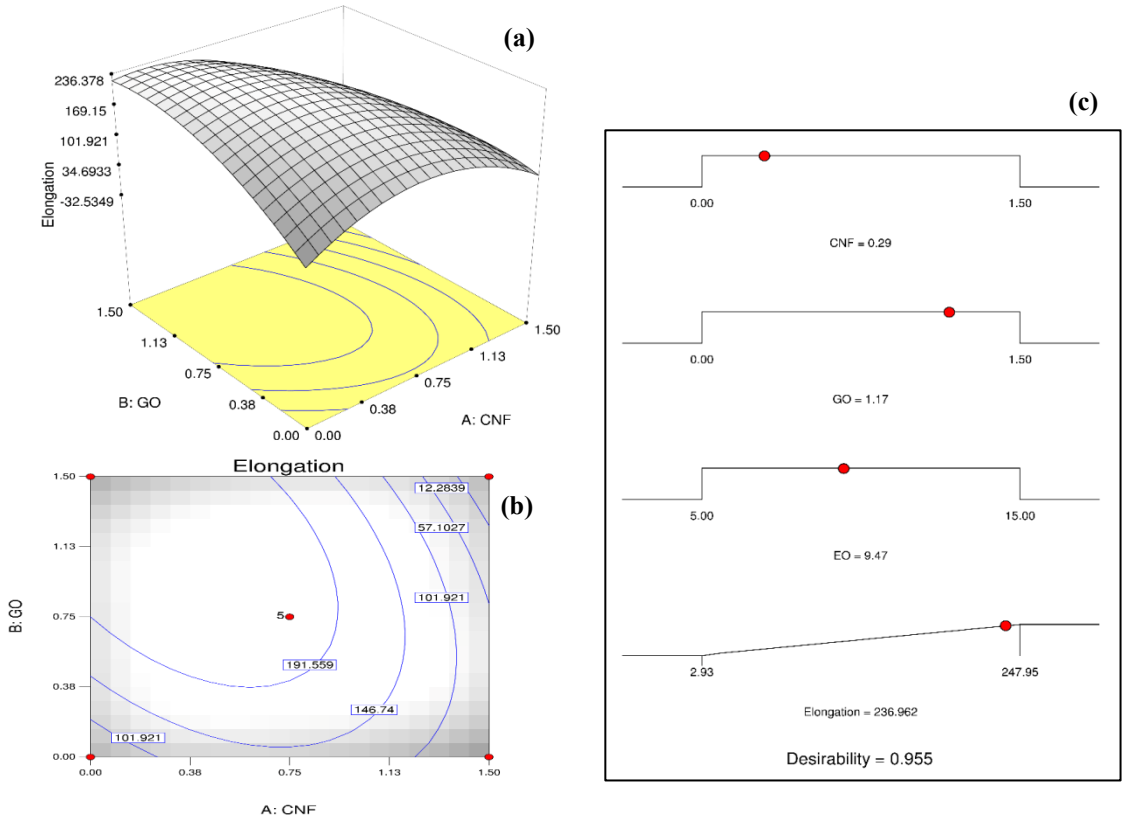


Figure 3. Surface (a) and contour (b) plot on percentage elongation of CNF and GO (c) numerical optimization

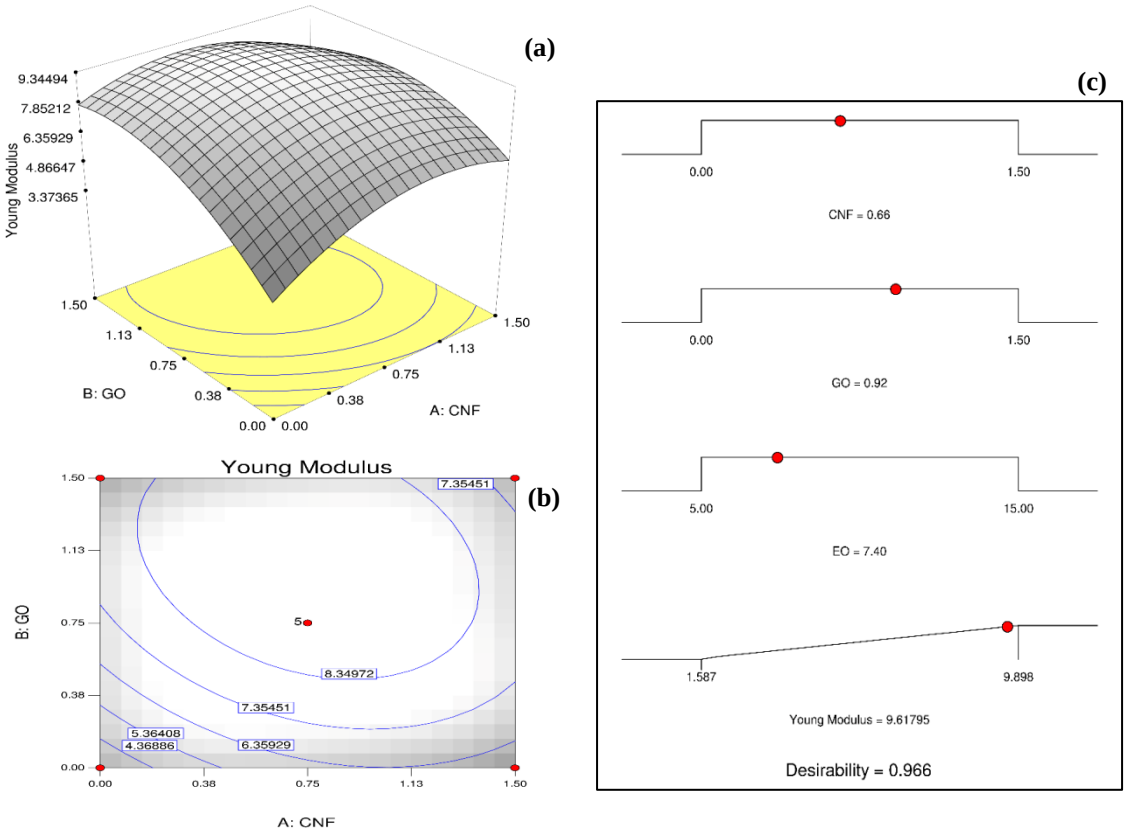


Figure 4. Surface (a) and contour (b) plot on Young's modulus of CNF and GO (c) numerical optimization

From the results obtained, it shows that increment of percentage additives (CNF, GO and EO) positively affects the mechanical properties (tensile strength, elongation percentage and Young's Modulus) until a certain point that lies within the limits of the factors being investigated. Typically with many nanocomposite systems, adding 1% and 2% by weight of graphene oxide showed slightly decreased mechanical properties due to aggregation of graphene oxide at this point [17]. Similar pattern was reported by Ionita et al. who found that the modulus and tensile strength increased at low concentration of graphene oxide but the mechanical properties decreased when the GO reached 2 wt.% [18]. These studies lead to the conclusion that generally GO has poor dispersion at high loading in most polymer matrices hence reduce the mechanical properties. The addition of CNF and EO also exhibits the same pattern that shows improvement on mechanical properties with the addition of low filler concentration that varied between 0-1 wt.% [19]. The effect of both nanofiller addition in packaging polymer towards the mechanical properties are not widely studied. However, this RSM study can be used to primarily visualizing or predict the behavior of the mechanical properties. It gives an insight to researcher to identify the significant effect of the addition of nanofiller percentage (wt.%) in this research and provides a framework for further investigation.

Confirmation run

Eight random check point formulations for which the results of all the dependent variables were found to be within the limits. Using experimental data, regression equations can be obtained in order to predict the tensile strength percentage elongation and Young's modulus at any particular ratio of CNF, GO and EO that lie in the limits tested. The predicted values and the actual experimental values were compared, the residual and the percentage error calculated. Table 7 lists the actual and predicted values of the check formulations among with the % prediction error in order to validate the model adequacy.

Table 7. Actual experimental value, predicted value, and error percentage of tensile, percentage elongation, and Young's modulus

Ratio of CNF, GO and EO			Tensile			Elongation			Young's Modulus		
CNF	**GO**	**EO**	**Actual Value**	**Predicted Value**	**Error**	**Actual Value**	**Predicted Value**	**Error**	**Actual Value**	**Predicted Value**	**Error**
0	0	10	20.62	19.38	1.24	4.15	13.17	-9.02	2.46	2.7	-0.24
1.5	0	10	23.27	22.79	0.48	7.78	7.26	0.52	4.72	5.06	-0.34
0	1.5	10	15.36	15.84	-0.48	179.16	179.68	-0.52	7.41	7.07	0.34
1.5	1.5	10	26.5	27.74	-1.24	7.84	-1.18	9.02	7.71	7.47	0.24
1.5	0.75	5	37.9	36.88	1.02	2.93	-19.60	22.53	8.19	7.62	0.57
0.75	1.5	15	12.48	10.98	1.50	134.27	111.21	23.06	6.76	6.53	0.23
0.75	0.75	10	13.52	13.52	0.00	222.86	222.86	0.00	9.1	9.1	0
0.75	0.75	10	12.54	13.06	-0.52	247.95	243.74	4.21	9.9	9.66	0.24

Correlation plot of linearity between the actual (experimental) value and predicted values are shown in Figure 5 (a), (b), and (c). The correlation obtained exhibits high R^2 values, 0.988, 0.9891, 0.9711 for tensile, percentage elongation, and Young's Modulus respectively. Thus, it can be said that the empirical models developed were reasonably accurate, for tensile, elongation % and young's modulus as all actual values for the confirmation runs are within the 95% prediction interval.

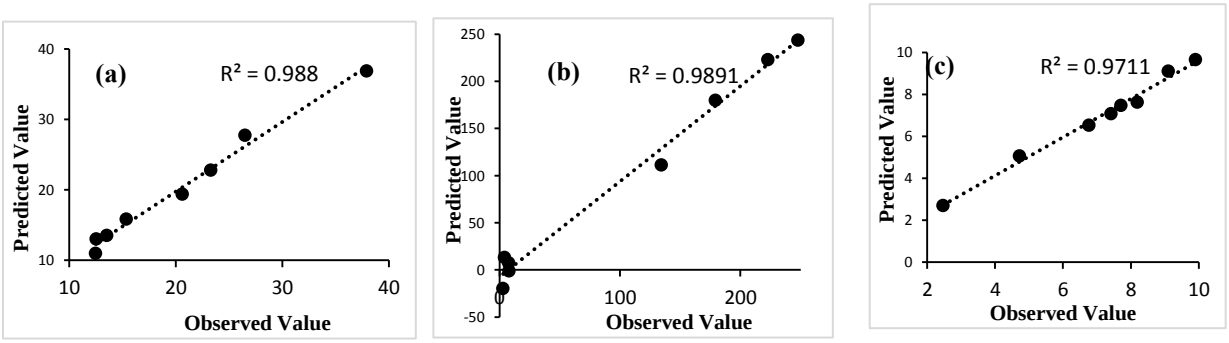


Figure 5. Linear correlation of predicted value *vs* observed value for (a) tensile strength (b) percentage elongation, and (c) Young's modulus

Multiple responses optimization

In packaging field, it is desirable if the packaging material exhibits certain mechanical characteristic by means high tensile strength, high percentage elongation (elasticity) and high Young's modulus. Multiple responses using the desirability approach is a procedure involves the optimization of more than one response. Once the optimization comprises multiple response (more than one), it is impossible to optimize each one separately because number of solutions equal to the variables under study, which are the amount of CNF, GO and EO would be gathered. The optimum level of the response variables was determined by desirability with the scale 0 to 1.0. As stated by Derringer and Suich [20], different desirability functions can be used, depending on the partial response that is required to be maximized, minimized or assigned target value. In this study, all the partial response, tensile, percentage elongation and Young's modulus were maximized. The factors (CNF, GO and EO % ratio) were set to within the range of limit of factors to be studied. Finally, one compromise solution was found for this multiple optimization and numerical ramp solution is shown in Figure 6. It shown the maximum response for tensile strength, percentage elongation and Young's modulus were interpolated to 21.39 Mpa, 182.68 % and 9.26 GPa,

respectively. The overall desirability on the other hand was calculated as the geometric average of the partial desirability functions of individual components. The overall desirability for this solution is 0.652. It shows that all responses are predicted to be within the desired limits. The possible solution was stated in the figure where CNF, GO and EO needed to be at the ratio of 0.51:0.99:5.00 weight percent respectively in order to reach maximum response.

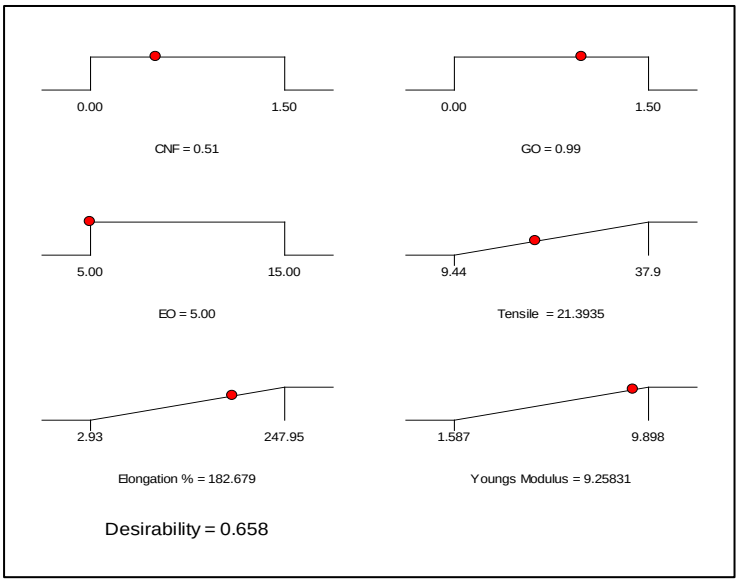


Figure 6. Multiple response using numerical ramp and desirability

Conclusion

The mechanical performance in term of tensile strength, percentage elongation (%E) and Young's modulus were analyzed using RSM method. The results from the analysis of variance (ANOVA) revealed that essential oil (EO) is the most significant factor that influences the tensile strength and it's followed by CNF (A), second order of CNF (A^2), interaction of CNF to EO (AC), and then followed by interaction of CNF to GO (AB). In the case of elongation percentage (%E), CNF (A) gave the most significant effect followed by second order effect of CNF (A^2), and then followed by the interaction of CNF to GO (AB). In Young's modulus, wt.% of EO (C) give the most significant effect followed by wt.% of GO (B). The ranking for the Young's modulus is as follows C> B> A^2> BC> C^2> B^2> AC. The multiple optimization for three responses; tensile, percentage elongation and Young's Modulus that were set to maximum yield one possible solution. The maximum tensile, elongation percentage and Young's modulus can be optimized up to 21.39 MPa, 182.68%, and 9.26 GPa, respectively that can be achieved by keeping the ratio of CNF, GO and GO at 0.51:0.99:5.00 (%), respectively. Overall, the validation of optimization technique demonstrated the reliability of the model. The experimental values of the response variables obtained from the optimized formulations were closed and in linear with the predicted values. Thus, the models developed using RSM were reasonably accurate and enabled the formulation of active packaging with desirable mechanical strength. The use of RSM approach also enable to identify the significant factor (the percentage of additives; CNF, GO, and EO) that affects the mechanical properties (tensile strength, elongation percentage and Young's Modulus). It was concluded that the appropriate statistical design and optimization techniques can be successfully used in the development of active packaging with predictable mechanical properties. The use of RSM approach enables the identification of significant factors for the wt.% of nanofiller addition in this research and finally provides a framework for further investigation.

Acknowledgement

The authors would like to thank Universiti Teknologi Malaysia (UTM), Ministry of Higher Education (MOHE), and Research Management Centre (RMC), UTM for their financial support of this work through the project number Q.J130000.7846.4F726.

References

1. Abdul Khalil, H. P. S., Bhat, I. U. H., Jawaid, M., Zaidon, A., Hermawan, D. and Hadi, Y. S. (2012). Bamboo fibre reinforced biocomposites: A review. *Materials and Design,* 42: 353-368.
2. Trifol, J., Plackett, D., Sillard, C., Szabo, P., Bras, J. and Daugaard, A. E. (2016). Hybrid poly(lactic acid)/nanocellulose/nanoclay composites with synergistically enhanced barrier properties and improved thermomechanical resistance. *Polymer International,* 65(8): 988-995.
3. Chan, C. H., Chia, C. H., Zakaria, S., Ahmad, I., Dufresne, A. and Tshai, K. Y. (2014). Low filler content cellulose nanocrystal and graphene oxide reinforced polylactic acid film composites. *Polymers Research Journal,* 9(1): 165-176.
4. Del Nobile, M. A., Lucera, A., Costa, C. and Conte, A. (2012). Food applications of natural antimicrobial compounds. *Frontiers in Microbiology,* 3(287): 1-13.
5. Silverajah, V. S., Ibrahim, N. A., Zainuddin, N., Yunus, W. M. and Hassan, H. A. (2012). Mechanical, thermal and morphological properties of poly(lactic acid)/epoxidized palm olein blend. *Molecules,* 17 (10): 11729-47.
6. Hosseini, M. H., Razavi, S. H. and Mousavi, M. A. (2009). Antimicrobial, physical and mechanical properties of chitosan-based films incorporated with thyme, clove and cinnamon essential oils. *Journal of Food Processing and Preservation,* 33: 727-743.
7. Pranoto, Y., Rakshit, S. K. and Salokhe, V. M. (2005). Enhancing antimicrobial activity of chitosan films by incorporating garlic oil, potassium sorbate and nisin. *Lebensmittel-Wissenschaft and Technologie,* 38(8): 859-865.
8. Sakurada, I., Nukushina, Y. and Ito, T. (1962). Experimental determination of the elastic modulus of crystalline regions in oriented polymers. *Journal of Polymer Science,* 57(165): 651-660.
9. Nishino, T., Matsuda, I. and Hirao, K. (2004). All-cellulose composite. *Macromolecules,* 37(29): 7683-7687.
10. Chen, J., Yao, B., Li, C. and Shi, G. (2013). An improved Hummers method for eco-friendly synthesis of graphene oxide. *Carbon,* 64: 225-229.
11. Tao, C. A., Wang, J., Qin, S., Lv, Y., Long, Y., Zhu, H. and Jiang, Z. (2012). Fabrication of pH-sensitive graphene oxide–drug supramolecular hydrogels as controlled release systems. *Journal of Materials Chemistry,* 22(47): 24856-24861.
12. Salehudin, M. H., Salleh, E., Muhamad, I. I. and Mamat, S. N. H. (2014). Starch-based biofilm reinforced with empty fruit bunch cellulose nanofibre. *Materials Research Innovations,* 18(S6): 322- 325.
13. Arjmandi, R., Hassan, A., Eichhorn, S., Mohamad Haafiz, M. K., Zakaria, Z. and Tanjung, F. (2015). Enhanced ductility and tensile properties of hybrid montmorillonite/cellulose nanowhiskers reinforced polylactic acid nanocomposites. *Journal of Materials Science,* 50(8): 3118-3130.
14. Cochran, W. G. and Cox, G. M. (1992). Experimental Designs, 2nd Edition. John Wiley & Sons, Inc, Canada.
15. Myers, R. H., Montgomery, D. C. and Anderson-Cook, C. M. (2009) Response surface methodology: Process and product optimization using designed experiments. Wiley, Hoboken, New Jersey.
16. Idris, A., Kormin, F. and Noordin, M. (2006). Application of response surface methodology in describing the performance of thin film composite membrane. *Separation and Purification Technology,* 49(3): 271-280.
17. Ammar, A., Al-Enizi, A. M., AlMaadeed, M. A. and Karim, A. (2016). Influence of graphene oxide on mechanical, morphological, barrier, and electrical properties of polymer membranes. *Arabian Journal of Chemistry,* 9(2): 274-286.
18. Ionita, M., Pandele, A. M., Crica, L. and Pilan, L. (2014). Improving the thermal and mechanical properties of polysulfone by incorporation of graphene oxide. *Composites Part B: Engineering,* 59: 133-139.
19. Lavoine, N., Desloges, I., Dufresne, A., Bras, J. (2012). Microfibrillated cellulose - its barrier properties and applications in cellulosic materials: A review. *Carbohydrate Polymer,* 90(2): 735-64.
20. Derringer, G. and Suich, R. (1980). Simultaneous optimization of several response variables. *Journal of Quality Technology,* 12: 214-219.

Malaysian Journal of Analytical Sciences, Vol 22 No 6 (2018): 999 - 1006
DOI: https://doi.org/10.17576/mjas-2018-2206-09

MALAYSIAN JOURNAL OF ANALYTICAL SCIENCES
Published by The Malaysian Analytical Sciences Society
ISSN 1394 - 2506

BLENDS OF LINEAR LOW-DENSITY POLYETHYLENE, NATURAL RUBBER AND POLYANILINE: TENSILE PROPERTIES AND THERMAL STABILITY

(Adunan Polimer Polietilena Linear Berketumpatan Rendah, Getah Asli dan Polianilina: Sifat Regangan dan Kestabilan Terma)

Farrah Diyana Zailan, Ruey Shan Chen*, Sahrim Ahmad, Dalila Shahdan, Adilah Mat Ali, Mohd Farid Hakim Mohd Ruf

School of Physics and Materials Novel, Faculty of Science and Technology
Universiti Kebangsaan Malaysia, 43600 UKM Bangi, Selangor, Malaysia

**Corresponding author: rueyshanchen@hotmail.com*

Received: 27 July 2017; Accepted: 28 April 2018

Abstract

The thermoplastic natural rubber (TPNR) blends made up of linear low-density polyethylene (LLDPE) and natural rubber (NR) were mixed using internal mixer at 130 °C, 30 rpm and for 13 minutes. Liquid natural rubber (LNR) was added as a compatibilizer for an immiscible blend of TPNR. The effect of polyaniline (PANI) content (1–5 wt.%) on the tensile and thermal properties of TPNR blend was investigated. The mechanical property results showed that the tensile strength increased 21% as compared to TPNR. Thermogravimetric analysis (TGA) measurement proved that the incorporation of PANI, even though in low content, had enhanced the thermal stability of TPNR blend. The glass transition temperature (T_g) and melting temperature (T_m) of the TPNR and TPNR/PANI blends were studied by differential scanning calorimeter (DSC) analysis. Scanning electron microscopy (SEM) micrograph confirmed the good dispersion of PANI within the TPNR phases and the well interaction among the components in TPNR/PANI blends.

Keywords: polymer blend, thermoplastic natural rubber, liquid natural rubber, morphology

Abstrak

Adunan getah asli termoplastik (TPNR) yang terdiri daripada campuran polietilena linear berketumpatan rendah (LLDPE) dan getah asli (NR) telah diadun dengan menggunakan mesin pengadun dalaman pada suhu 130 °C, 30 ppm dan selama 13 minit. Cecair getah asli (LNR) telah ditambah sebagai pengserasi terhadap adunan TPNR yang tak terlarutcampur. Kesan kandungan polianilina (PANI) (1-5 %bt.) terhadap sifat regangan dan terma bagi adunan TPNR/PANI telah dikaji. Keputusan sifat mekanik menunjukkan bahawa kekuatan regangan telah ditambahbaik sebanyak 21% berbanding dengan TPNR. Analisis termogravimetri (TGA) membuktikan bahawa penggabungan PANI, walaupun pada kandungan yang rendah, dapat meningkatkan kestabilan terma adunan TPNR/PANI. Suhu peralihan kaca (T_g) dan suhu peleburan (T_m) bagi adunan TPNR dan TPNR/PANI telah dikaji melalui analisis kalorimetri imbasan perbezaan (DSC). Mikrograf mikroskop elektron pengimbas mengesahkan penyebaran PANI yang baik dalam fasa TPNR serta interaksi yang baik antara komponen-komponen dalam adunan TPNR/PANI.

Kata kunci: polimer adunan, getah asli termoplastik, cecair getah asli, morfologi

Introduction

The development of rubber industry has attracted high interests from many researchers in the use of natural rubber (NR) as main material. Thermoplastic natural rubber (TPNR) is classified as a new class material with the combined

properties via blending of vulcanized rubbers with the ease processable thermoplastics [1, 2]. NR has been used to mix with various types of polyethylene (PE), for instance, linear low-density polyethylene (LLDPE) exhibits the most prominent properties by having a good compatibility with NR [3, 4, 5], owing to its low melting temperature. In which this can prevent the thermal degradation of rubber [5]. In this context, the intention of NR/PE blend preparation was to recycle rubber wastes or NR, thereby overcome global wastage problems of rubber and severe environmental problems [6]. In decades, TPNR has been studied by blending the NR and thermoplastic polyolefins, such as the blends of NR/LLDPE [7], NR/LLDPE/liquid natural rubber (LNR) [8], NR/polypropylene (PP) [1], or etc. The fabricated TPNR blend with certain composition improves the overall mechanical properties and are widely used for different applications (i.e. film packaging) [9, 10]. However, TPNR is lack of conductive properties. As for that, a conductive material can be made from the insulating polymer matrix by filling with conductive filler such as carbon- or metal-based materials. Besides that, conducting polymers such as polyaniline (PANI) and polypyrole are now an alternative sources to promote the excellent electrical and mechanical properties [11, 12].

Polyaniline (PANI) is one of conductive polymer materials which is also known as a conductive additive. PANI is considered as a potential candidate to produce new conductive blends because of its high conductivity, stability, easy to synthesize and low-cost. A number of research works have been published on electrically conductive PANI/elastomer blends such as PANI doped with dodecyl-benzene sulfonic acid (PANI-DBSA)/NR [1], PANI/nitrile rubber (NBR) [8], PANI/NR [2], PANI coated with nylon fiber/NR [3] and etc. However, there was a lack of scientific papers reported in mechanical properties of the PANI/elastomer blends. As reported by Sukitpaneenit et al., PANI/NR doped in hydrochloric acid exhibited poor mechanical properties which was due to the inhomogeneous distribution of PANI in NR matrix [2].

The blending of PANI with those thermoplastics has led to the positive effect on the resultant blends' properties. For instance, Annala et al. studied the blend of low-density polyethylene (LDPE)/PANI with different contents of functionalized metallocane PE which acted as a compatibilizer, and the findings showed that the mechanical properties of the blend were improved but the electrical conductivity remained the same [4]. Cote et al. proved that LDPE/PANI blend promoted the improvement in the mechanical properties [5]. The concentration of PANI is one of the most important factors that influences the mechanical properties and electrical conductivity [5]. Due to the high difference in the polarity of PANI (polar) and PE matrix (non-polar), the increasing content of PANI can lead to the reduction of elongation and brittle fracture of LLDPE as there is a lack of adhesion between both phases. In contrast, Youngs Modulus was found to increase with the PANI content in blends as PANI was expected to positively contribute in the stiffness of the blend [10]. From the aspect of thermal stability, it was proved that the existence of PANI in NR/PANI blend did not change the thermal stability in which the NR degraded before PANI [12]. According to Kazimi et al. who investigated on LDPE/PANI blend, it was claimed that the increasing of PANI caused an increment in the thermal stability of LDPE which was due to uniform integration of PANI within the matrix [9].

In this context, the direction of the current research was to fabricate PANI-filled NR/LLDPE/LNR blend with the combined mechanical properties and ease of processibility (obtained from LLDPE and NR) as well as the electrical properties (imparted by PANI, conductive polymer). Particular emphasis was placed on investigating the effect of PANI content on the tensile, electrical conductivity and thermal behaviour of TPNR/PANI blend.

Materials and Methods

Raw materials

Natural rubber (NR) SMR-L grade was obtained from Malaysian Rubber Board (MRB) and used to prepare liquid natural rubber (LNR). Linear low-density polyethylene (LLDPE) was used as thermoplastic resin in this study. It was purchased from Exxon Mobile Chemical Corporation. It has density of 0.918 g/cm^3, melt flow index of 1.0g/10 min and the melting temperature in the range between 120-160 ºC. Emeraldine oxidation state of polyaniline (PANI), needle-like green powders, the half oxidized form, was purchased from E-TEK Co.Ltd , Kyengki-Do, Korea.

Preparation of liquid natural rubber (LNR)

LNR was synthesized via photochemical degradation or oxidation technique on the NR. Approximately 1.5 kg of NR was cut into small pieces and soaked in a glass flask filled with toluene, 0.3 g methylene blue, 0.39 g rose Bengal and 15 ml methanol for 24 hours. The mixture in glass flask was then stirred continuously with a mechanical stirrer rod at 10 rpm under the exposure of fluorescent light for 10 days.

Preparation of blends

Indirect mixing technique (IDT) was applied to prepare the blends where it involved a manual pre-mixing of PANI powders with LNR using a glass rod prior to the melt blending process. The NR was first placed into the mixer and allowed to melt for about 3 minutes, the pre-mixture of LNR and PANI was then added into the mixer. Lastly, the LLDPE pellets were added into the mixture after 5 minutes and the whole mixing process took about 13 minutes. The TPNR (based on composition of NR/LLDPE/LNR at 50:40:10) and 1-5 wt.% PANI powders were compounded using an internal mixer (Haake Rheomix 600P) with the processing parameter as follows: processing temperature of 130 °C, rotor speed of 30 rpm and processing time of 13 minutes. The addition of PANI powders was varied in the range of 1 – 5 wt.% PANI. After the blending process, the samples were prepared by compression moulding *via* hot and cold pressing (LP50, LABTECH Engineering Company LTD) under the pressure of 6.9 MPa at 130 °C.

Characterization

The mechanical property of TPNR/PANI samples was tested using a tensile machine (model Testometric M350-10CT) with a 5 kN load cell. The tensile test was carried out according to ISO 37-2 standard specification procedure. In which the test samples were cut in the thickness of 1 mm and a crosshead speed of 50 mm min^{-1} was applied during the test. Differential scanning calorimetry (DSC) was conducted to study the effect of different PANI content (0-4 wt.% PANI) on the glass transition temperature (T_g) and melting temperature (T_m) of TPNR-based blend. The samples were scanned from the temperature of -120 to 200 ºC. The morphology characterization of TPNR/PANI blends sample was examined under the scanning electron microscope (SEM) using the tensile-fractured surfaces of blend sample. Before the examination, the samples were sputter-coated with a thin layer of gold to avoid electrostatic charging during the morphology examination.

Results and Discussion

Figure 1 shows the effect of PANI content (1 – 5 wt.%) on the tensile properties of TPNR blend. As can be seen in the Figure 1(a), the highest tensile strength (1.92 MPa) was achieved at 3 wt.% of PANI where this content can be considered as the optimal level of PANI in this TPNR blend. The increment was recorded for about 28% as compared to the control sample, TPNR without PANI. This could be due to which the inclusion of PANI aided in the increase of the crosslinking interaction within the polymeric chains by increasing the amount of hydrogen bonding between polymer and PANI component [14]. Fabio et al. reported that the incorporation of 40 wt.% PANI into the LLDPE blend had promoted a positive effect on the composite strength [10]. Based on the previous research by Nehad et al. who investigated the immiscibility of polystyrene (PS)/polymethyl methacrylate (PMMA) blend, the tensile strength was improved by the addition of PANI (1, 3, 5, 10, 15, 20 wt.%) with 3% pluronic, and this was because of the well dispersion of PANI in polymers that filled the voids and interface position as well as could act as cross-linking centre between the molecules [15]. Thus, the interaction between the polymer molecules was improved due to the increase of the interfacial surface area.

However, the tensile strength of TPNR blend reduced gradually by increasing the PANI up to 4-5 wt.%. This is attributed to the PANI aggregation within the polymer matrix. This trend was similarly observed in the study by Nehad et al. who reported that the initial reduction of tensile strength was occurred after 1 wt.% PANI was added in PS/PMMA blend [15]. As the PANI content increased in the blend, the brittle fracture occurred [10, 11], as shown in Figure 1(c). The large deviation in polarity of PANI and LLDPE was negatively affecting the adhesion behaviour between the phases, thereby resulted in a downward trend in the mechanical properties. This phenomenon was obvious to be revealed as the added PANI exceeded the optimum PANI content, which was 3 wt.% in this case. Figure 1(b) shows that the Young modulus of TPNR blend increased drastically as the PANI was incorporated in the blend. This is attributed to the contribution of PANI in increasing the blend stiffness [10].

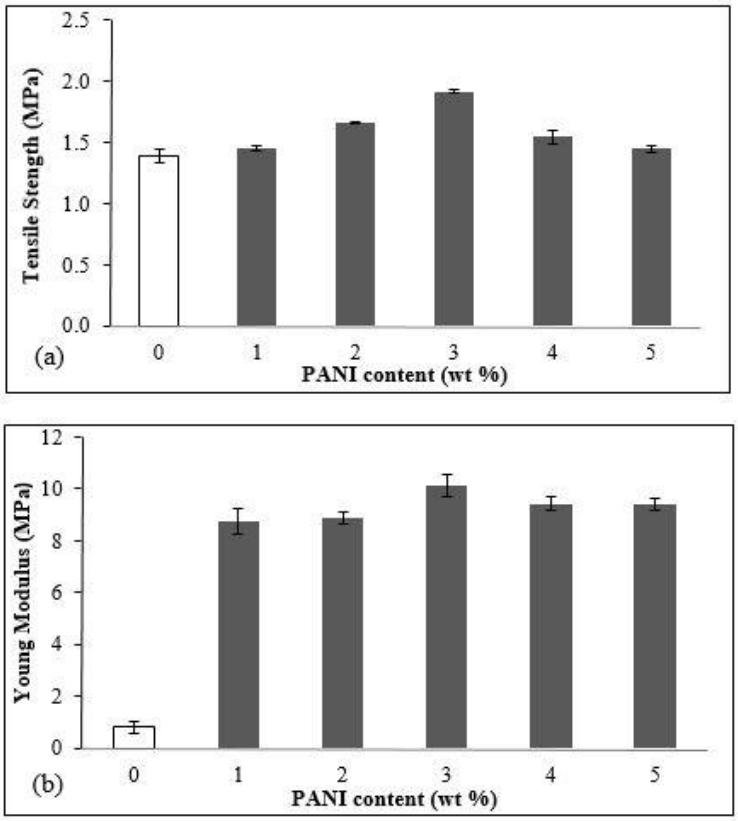


Figure 1. Effect of PANI content in TPNR blend on a) tensile strength and b) Young modulus

Figure 2 shows DSC thermogram curves for all tested samples. The existence of two endothermic peaks was observed in Figure 2. The first small shallow peak was displayed at approximately -60 °C, which refers to the glass transition temperature (T_g) of natural rubber component where herein the amorphous regions become rubbery. This is in agreement with the previous report [2, 11]. As the heating temperature further increased to reach melting temperature (T_m), a transition from a crystalline or semi-crystalline phase to a solid amorphous phase occurred. The T_m of the TPNR / PANI blend was recorded at 126 ºC, as shown in Figure 2. With the exception of slightly higher T_m for TPNR containing 2 and 3 wt.% PANI (which supported the tensile strength trend), the other T_g and T_m values for the blends containing various loadings of PANI showed insignificant changes. This was possibly because of the relatively small range of loadings was involved in the investigation. The similar finding has been reported by Fabio et al. who studied on the LLDPE blend with PANI [10].

The thermal stability of blends was analyzed using thermogravimetric analysis (TGA) measurement. The TGA curves of TPNR/PANI with various PANI contents are illustrated in Figure 3. By increasing the temperature, the weight loss changed when the degradation of materials occurred. Figure 3 displays two steps of degradation process for TPNR/PANI blends with various PANI content (1-5 wt.%) and TPNR as control sample.

The first degradation step occurred in the temperature range between 330 °C and 350 °C, which corresponding to the degradation of NR component. According to Dwi Puryanti et al. who carried out research on TPNR filled with Ni-Co-Zn Ferrite, it was reported that the degradation temperature of NR occurred at 340 °C [16]. Jonas da Silva et al. stated that in NR/ PANI-DBSA, the evaporation and degradation of DBSA and the oxidation of PANI structure occurred in the temperature range of 200 – 350 °C [1]. In this study, this degradation peak of the PLA/LNR/PANI samples was found to shift to the right with higher degradation temperature as PANI loading increased, and the increasing trend was as follows: from 363 °C (TPNR) to 369 °C (TPNR/ 1 wt.% PANI), 369 °C (TPNR/ 2 wt.%

PANI), 370 °C (TPNR/ 3 wt.% PANI), 375 °C (TPNR/ 4 wt.% PANI) and 375 °C (TPNR/ 5 wt.% PANI). This suggests an enhancement of thermal stability of the blends is due to the uniform integration of PANI nanofiber in the matrix as agreed by the previous study on LDPE/PANI [9].

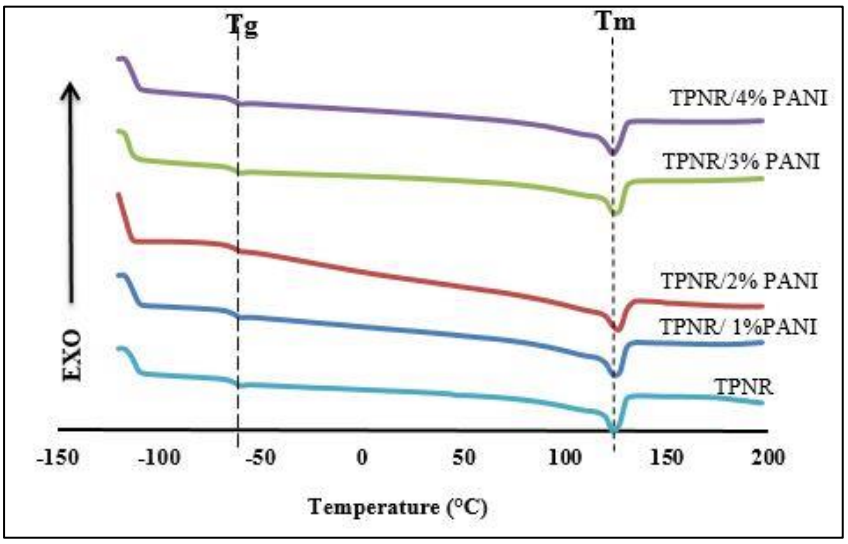


Figure 2. DSC thermogram for different of PANI content in TPNR/PANI blend

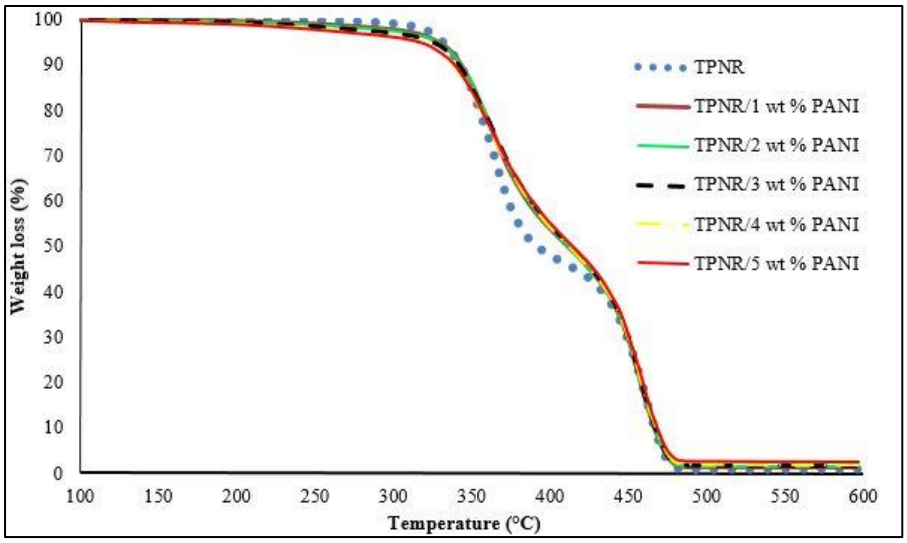


Figure 3. TGA curves of TPNR/PANI with various PANI content

The second degradation step occured at around 380 - 460 °C which corresponds to PANI degradation. Interestingly, this degradation temperature peak displayed an inverted trend as compared to the first degradation peak, which was shifted to the lower temperature with the increasing PANI content, as follows: from 456 °C (TPNR) to 450 °C (TPNR/ 1 wt.% PANI and TPNR/ 2 wt.% PANI), 446 °C (TPNR/ 3 wt.% PANI), 445 °C (TPNR/ 4 wt.% PANI) and 445 °C (TPNR/ 5 wt.% PANI). This degradation temperature range was similarly reported by da Silva et al. which that the degradation of the bound PANI-DBSA and the decomposition of PANI occurred in 400 – 500 °C [1]. This was also reported by Saritha et al. who investigated on PANI-nylon fiber with NR which the degradation temperature of PANI started at ~415 °C and ended at 581 °C [3].

Table 1 summarizes the data obtained from TGA curve, the temperature of weight loss at 3% (T_3), 50% (T_{50}) and residue level left after 500 °C. As compared to neat TPNR blend (T_3 = 316 °C and T_{50} = 386 °C), the TPNR/ 1 wt.% PANI blend (T_3 = 305 °C and T_{50} = 398 °C), TPNR/ 2 wt.% PANI blend (T_3 = 299 °C and T_{50} = 401 °C), TPNR/ 3 wt.% PANI blend (T_3 = 277 °C and T_{50} = 404 °C), TPNR/ 4 wt.% PANI blend (T_3 = 258 °C and T_{50} = 410 °C) and TPNR/5 wt.% PANI (T_3 = 252 °C and T_{50} = 415 °C). These phenomena showed that the late degradation of PANI and the uniform integration of PANI in TPNR blend played roles in improving the thermal stability [12, 16].

Table 1. TGA data of TPNR/PANI with different PANI content

Sample	**T_3 (°C)**	**T_{50} (°C)**	**Residue (%)**
TPNR	316	386	0.85
TPNR/1 wt % PANI	305	398	1.47
TPNR/2 wt % PANI	299	401	1.63
TPNR/3 w % PANI	277	404	1.77
TPNR/4 wt % PANI	258	410	1.89
TPNR/5 wt % PANI	252	415	2.55

Note: T_3 means the temperature of weight loss at 3 %; T_{50} means the temperature of weight loss at 50%

The residues of the samples upon heating of 600 °C are shown in percentages (%). From the Table 1, the TPNR exhibited 0.85% of residues. This amount of residues increased gradually as the PANI content increased from 1 to 5 wt.%, which increased up to 2.55%.

The SEM micrographs in Figure 4(a) and (b) show the morphological views for the tensile fractured surfaces of the samples. For the control sample in Figure 4(a), the large voids can be clearly seen on the rough surface which was induced by the rubbery material as compared to the TPNR/PANI sample in Figure 4(b). In Figure 4 (b), the morphology showed lower roughness of surface area with the presence of small voids and this indicates a good interaction of PANI propagation through rubber domain matrix phases and the efficient stress transfer within the rubber blend [16]. As compared to Figure 4(a), the morphology for the TPNR/3 wt.% PANI in Figure 4(b) displays a more compact structure which suggesting the filling of holes by PANI component [7, 10] and this led to a good blending and the increased mechanical properties. As the PANI content exceeded the optimum level (3 wt.%), that was for TPNR/4 wt.% PANI, the morphology in Figure 4(c) shows an existence of agglomeration of PANI particles and large voids within the polymer matrix. This indicates the non-uniform distribution and a lack of adhesion between different phase because of the great polarity difference between PANI and LLDPE [10], as discussed earlier, and thus resulted in the brittleness property, as proven in the deteriorated tensile properties at this composition.

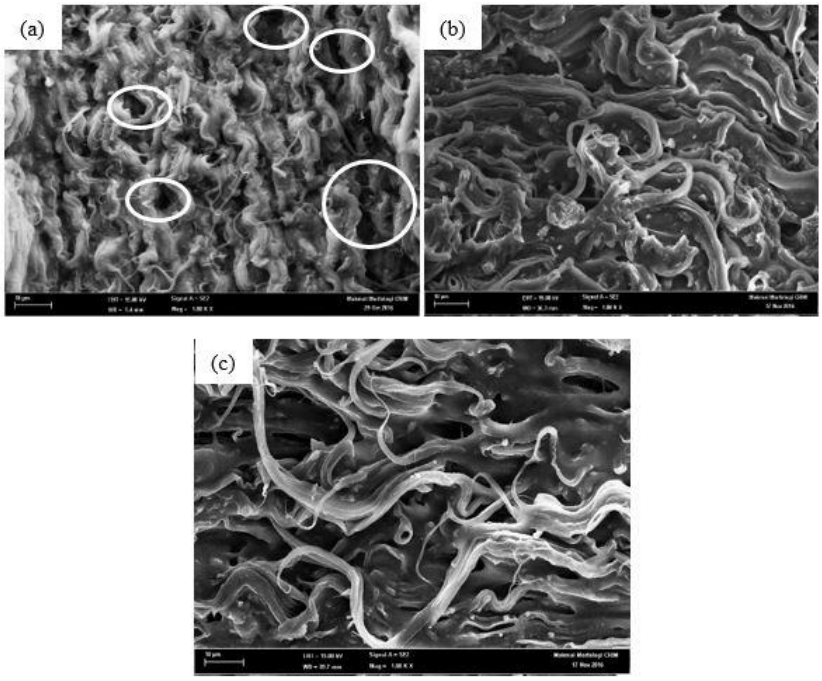


Figure 4. SEM micrograph of (a) TPNR, (b) TPNR/3 wt.% PANI blends and (c) TPNR/4 wt.% PANI blend

Conclusion

TPNR blends with various loadings of PANI were fabricated *via* melt blending method. The mechanical and thermal analysis results showed that the optimum PANI content for the fabrication of TPNR/PANI was 3 wt.%. The thermal stability of the TPNR/PANI blend was improved significantly by the incorporation of PANI, irrespective of PANI content. SEM micrograph showed a good dispersion of PANI within the TPNR matrix and a good interfacial interaction among the components. From the aspect of the improved mechanical and thermal properties, the fabricated TPNR/PANI blend acts as a potential candidate in the future application such as sensors, electromagnetic shielding, light emitting diodes and field-effect transistors.

Acknowledgement

The authors would like to be obliged to Universiti Kebangsaan Malaysia (UKM) for providing laboratory facilities at Materials Science laboratory (FST), Electron Microscopy Unit and financial assistance under project no. DIP-2016-023.

References

1. Silva, M. J., Sanches, A. O., Malmonge, L. F. and Malmonge, J. A. (2014). Electrical, mechanical and thermal analysis of NR-PANI-DBSA composites. *Materials Research Bulletin*, 17(1): 59-63.
2. Sukitpaneenit, P., Thanpitcha, T., Sirivat, A., Weder, C. and Rujiravanit, R. (2007). Electrical conductivity and mechanical properties of polyaniline/natural rubber fomposite fibers. *Journal of Applied Polymer Sciences*, 106(6): 4038-4046.
3. Saritha, C. A. and Sunil, K. N. (2011). Polyaniline-coated short nylon fiber/natural rubber conducting composites. *Polymer Plastics Technology Engineering*, 50(5): 443-452
4. Annala, M. and Lofgren, B. (2006). Compatibilization of conductive polyethylene/polyaniline blends. *Macromolecules Materials Engineering*, 291(7): 848-857.
5. Cote, M., Cortes, M. T., Bletran, D. and Ortiz, P. (2009). PANI-LDPE composites: Effect of blending conditions. *Polymer Composites*, 30(1): 22-28.

6. Dahlan, H. M., Khairul Zaman, M. D. and Ibrahim, A. (2002). The morphology and thermal properties liquid natural rubber (LNR)-compatibilized 60/40 NR/LLDPE blends. *Polymer Testing*, 21(8): 905-911.
7. Hassan, N. A., Hassan, N., Ahmad, S. H., Rasid, R., Hazleen, A., Najmi, B. N. and Surip, S. N. (2012). Physical and mechanical properties of thermoplastic natural rubber (TPNR) nanocomposites. *Advanced Materials Research*, 576: 394-397.
8. Camillo, E. C., Constantino, C. J. L., Teruya, M. Y., Alves, N., Mattoso, L. H.C. and Job, A. E. (2005). Dependence of the electrical conductivity and elastomeric properties on sample preparation of blends of polyaniline and natural rubber. *Journal of Applied Polymer Sciences*, 97(4): 1498-1503.
9. Kazimi, M. R., Tahir, S., Shima, J. and Faizal, C. K. M. (2014). Characterization of functionalized LDPE/PANI nanofiber composite. *Journal of Medical Bioengineering*, 3(4): 307-310.
10. Fabio, R. P., Patrick V., d. F., Eduardo, H. B., Larissa, S. M., Simone, d. S. P., Luiz, A. P. and Mirabel C. R. (2017). Thermal, mechanical and electromagnetic properties of LLDPE/PANI composites. *Polymer Bulletin*, 74(7): 2701-2717.
11. Abdullah, I., Ahmad, S. and Sulaiman, C. S. (1995). Blending of natural rubber with linear low-density polyethylene. *Journal of Applied Polymer Sciences*, 58(7): 1125-1133.
12. Ahmad. S., Abdullah, I., Sulaiman, C. S., Kohjiya, S. and Yoon, J. R (1994). Natural rubber-HDPE blends with liquid natural rubber as compatibilizer on thermal and mechanical properties. *Journal of Applied Polymer Sciences*, 51(8): 1357-1363.
13. Ozturk, A., Kaynak, C. and Tincer, T. (2001). Effects of liquid rubber modification on the epoxy resin. *European Polymer Journal*, 37(12): 2353-2363.
14. Dopico-Garcia, M. S., Ares, A., Lasagabaster-Latorre, A. and Garcia, X. (2014). Extruder polyaniline/EVA blends: Enhancing electrical conductivity using gallate compatibilizers. *Synthetic Metals*, 189: 193-202.
15. Nehad, N. R., Aman, I. K. and Azza, A. W. (2016). Studies the behavior of polyaniline on the properties of PS/PMMA blends. *Journal of Materials Design and Application*, 230(2): 526-536.
16. Dwi, P., Ahmad, S., Abdullah, H. M. and Yusoff, H. A. N. (2007). Effect of nickel-cobalt-zinc-ferrite filler on magnetic and thermal properties of thermoplastic natural rubber composites. *International Journal of Polymeric Materials and Polymeric Biomaterials*, 56(3): 327-338.

Malaysian Journal of Analytical Sciences, Vol 22 No 6 (2018): 1007 - 1013
DOI: https://doi.org/10.17576/mjas-2018-2206-10

MALAYSIAN JOURNAL OF ANALYTICAL SCIENCES
Published by The Malaysian Analytical Sciences Society
ISSN 1394 - 2506

COMBINED MECHANICAL-CHEMICAL PRE-TREATMENT OF OIL PALM EMPTY FRUIT BUNCH (EFB) FIBERS FOR ADSORPTION OF METHYLENE BLUE (MB) IN AQUEOUS SOLUTION

(Gabungan Rawatan Mekanik-Kimia ke atas Gentian Tandan Kosong Kelapa Sawit untuk Penjerapan Metilena Biru dalam Larutan Akues)

Chee Mun Chan[1], Siew Xian Chin[1,2]*, Soon Wei Chook[2], Chin Hua Chia[2], Sarani Zakaria[2]

[1]*ASASIpintar Programme UKM, Pusat Permata Pintar Negara*
[2]*Bioreousrces and Biorefinery Laboratory, Faculty of Science and Technology*
Universiti Kebangsaan Malaysia, 43600 UKM Bangi, Selangor, Malaysia

**Corresponding author: chinsiewxian@ukm.edu.my*

Received: 27 July 2017; Accepted: 28 April 2018

Abstract

The effectiveness of combined mechanical-chemical pre-treatment on oil palm empty fruit bunch (EFB) fibers in removing organic dye from aqueous solution was studied. The efficiency of dye adsorption in aqueous solution using natural fibers is generally affected by several factors, such as pH, temperature, and the concentration of dye. However, the effect of the size of the fibers (adsorbent) has rarely been investigated. Prior to any MB adsorption process, mechanical-chemical pre-treatment was performed on EFB fibers *via* a high-shear process using a Silverson mixer. Shearing duration and the introduction of sodium hydroxide (NaOH) influenced the rate of adsorption, due to the changes in fiber size and accessible surface after the treatment process. From these results, it was found that smaller EFB fibers enhanced the rate and adsorption capacity of MB. However, this was not a linear relationship, as the rate of adsorption decreased when the shearing duration was prolonged to 30 minutes. Meanwhile, treatment with 0.1 M NaOH also improved the adsorption performance of the fibers. Hence, combined mechanical-chemical pre-treatment of EFB fibers can increase the adsorption rate and capacity of the fibers. This study may provide useful information on a practical pre-treatment approach for natural fibers as dye adsorbent in wastewater treatment.

Keywords: adsorption, oil palm empty fruit bunch fibres, methylene blue, pre-treatment

Abstrak

Keberkesanan proses pra-rawatan gabungan mekanik-kimia ke atas gentian tandan kosong kelapa sawit (TKKS) untuk penyingkiran pewaran organik telah dikaji. Kajian lepas membuktikan bahawa tahap keberkesanan proses penjerapan pewarna dalam larutan akues adalah bergantung pada beberapa faktor penting, seperti suhu, keasidan dan kepekatan pewarna. Namun, faktor saiz gentian (bahan jerapan) dalam proses penjerapan jarang dikaji. Sebelum proses penjerapan, pra-rawatan secara mekanik-kimia telah dilakukan pada gentian TKKS dengan menggunakan pengacau Silverson. Didapati bahawa jangka masa pra-rawatan yang berbeza dan penambahan NaOH akan mempengaruhi kadar penjerapan MB ekoran daripada perubahan saiz dan permukaan terdedah gentian selepas proses pra-rawatan. Malahan, saiz gentian TKKS yang lebih kecil berupaya untuk meningkatkan kadar dan kapasiti penjerapan MB. Akan tetapi, keputusan kajian ini adalah tidak linear kerana kadar penjerapan gentian TKKS didapati menurun apabila masa pra-rawatan mekanikal dipanjangkan 30 minit dan ke atas. Sehubungan itu, modifikasi gentian TKKS dengan menggunakan 0.1 M NaOH dapat meningkatkan prestasi kadar dan kapasiti penjerapan MB. Kesimpulannya, pra-rawatan gabungan mekanik-kimia terhadap gentian TKKS dapat meningkatkan kadar dan kapasiti gentian. Kajian ini dapat memberi maklumat penting bagi kaedah pra-rawatan yang praktikal kepada gentian semula jadi sebagai bahan penjerap pewarna dalam rawatan air buangan.

Kata kunci: penjerapan, gentian tandan kosong kelapa sawit, metilena biru, pra-rawatan

Introduction

Dye industries, such as textile, paper, printing, and cosmetics, produce water pollutants that have caused environmental problems. Currently, there are about 10,000 different commercial dyes and pigments in existence and over 7×10^5 tonnes of synthetic dyes produced worldwide [1]. Among all industries, the textile industry was the first to use dyes for the coloration of fibers [2]. The release of dye compounds into water systems without proper treatment will harm aquatic life [3]. Also, these dyes can cause several health issues, such as allergies, infections, and dysfunction of systems in humans [4]. For example, upon inhalation, it can give rise to a short period of rapid and difficult breathing, while ingestion through the mouth results in a burning sensation and may even cause nausea, vomiting, profuse sweating, mental confusion, and *methemoglobinemia* [5]. Methylene blue (MB) is one of the most common dyes that is used and is abundant in the effluent that is discharged into water. Therefore, the treatment of effluent containing such a dye is paramount due to its harmful impacts on receiving water [6].

Chemical and physical adsorption processes are some of the most effective techniques for color removal from wastewater [4]. Adsorbents, such as activated carbon, have been reported to be the most promising material for adsorption of MB due to its high adsorption efficiency, based on its large surface area, micro-porosity structure, and high surface reactivity. However, several number of problems arise with the regeneration of activated carbon, because it is a tedious and costly procedure [1]. Therefore, as an alternative approach, there is growing research interest in the production of alternative sources to replace the activated carbons from renewable and cheaper precursors, mainly industrial and agricultural polymers, such as oil palm fibers, rice hulls, natural clay, corn hubs, wood chips, silica ash, and coal [6, 7].

Natural cellulosic materials, such as oil palm fibers, are some of the most renewable sources of environmentally friendly raw material. Lignocellulose fibers can be obtained from the tree trunk, frond, fruit mesocarp, and empty fruit bunch (EFB) [8]. EFB is the fibrous mass that is extracted from the seed hair of the oil palm [9]. Based on a review by Shinoj et al. [8], EFB has the potential to yield up to 73% fibers and is thus preferable in terms of availability and cost. Malaysia is the world's second largest palm oil exporter, and about 3.0 million tons of oil palm EFB fibers are produced every year [5, 10]. To make better use of this cellulosic material, it has been suggested that EFB fibers be converted into an alternative adsorbent in light to replace the high cost of activated carbon [6].

To enhance the adsorption process, the fiber surface has functional groups, such as hydroxyl groups, that increase its hydrophilic property, reducing their affinity to bind to hydrophobic molecules. Also, pre-treatment of EFB fibers is essential to alter the structure of cellulosic biomass to increase the accessibility of the pores and surface of the cellulose. This can be achieved by unsealing the lignin and disrupting the crystalline structure of the cellulose. As a result, EFB fibers are more efficient in removing MB from wastewater [8, 11].

The aim of this study is to investigate the efficiency of combined mechanical-chemical pre-treatment of oil palm EFB fibers for the removal of MB in aqueous solution *via* an adsorption approach, in which the size of the fibers can be correlated with the rate of adsorption of MB. Smaller EFB fibers are predicted to increase the rate of adsorption of MB [12]. Also, chemical modification with alkali, such as sodium hydroxide (NaOH), will also enhance the adsorption capacity of the EFB fibers, thus increasing the rate of adsorption of MB [1]. Alkali pre-treatment increases the physical and adhesion properties and reduces water absorption of EFB fibers. Also, the removal of lignin (which holds the cellulose and hemicellulose tightly by adhesion forces) by alkali increases the surface area of porous pores that are exposed for adsorption [9]. The data obtained from the experiment were then fitted to a calibration curve for studying the adsorption rate and adsorption capacity. This study can benefit the country by proving the potential of EFB fibers in treating one of the most serious problems in Malaysia: wastewater.

Materials and Methods

Oil palm EFB fibers were obtained from Szetech Engineering Sdn. Bhd. (Malaysia). The fibers were sieved into sizes ranging from 150–500 μm and dried at 105 °C before the pretreatment process. The sodium hydroxide

(NaOH) (Sigma-Aldrich), hydrochloric acid (Sigma-Aldrich), and methylene blue (MB) (Mallinckrodt >99%) were analytical-grade.

Pre-treatment of EFB fibers

Briefly, 10 g of EFB fibers (in 500 mL deionized) was sheared at 8000 rpm using a Silverson homogenizer (L5M-A) for various durations (ranging from 15 to 60 minutes). The homogenizer was fitted with a square-hole high-shear screen to provide high-shear mixing to defibrillate the fibers. The pre-treated EFB fibers were rinsed with deionized water until the pH of the fibers decreased to pH 7. The same procedure was repeated using 0.1 M NaOH.

Preparation of MB solution

Methylene blue (MB) solutions were prepared and diluted according to the required initial concentration i.e. 100 mg/L. The concentration of the MB was determined using a UV-visible spectrometer (Jenway 7315 Spectrometer) at 665 nm in a quartz cuvette.

Adsorption of MB using pre-treated EFB fibers

Adsorption experiments were performed to determine the effect of mechanical-chemical modification on the adsorption performance of the pre-treated fibers. Briefly, 0.5 g of EFB fibers from different samples was added to a beaker containing 100 ml of diluted MB solution (50 mg/L). The mixture was stirred at 250 rpm until equilibrium readings were achieved. The MB concentration of the supernatant solution was measured at various intervals, ranging from 5 to 30 minutes, using the UV-visible spectrophotometer. Prior to that, the mixture was centrifuged for 2 minutes at 250 rpm to fully separate the fibers. The amount of dye that adsorbed onto the fibers was calculated using the following equation:

$$q_e = \frac{(C_0 - C_e)}{C_0} \times 100\% \quad (1)$$

where C_o and C_e are initial and subsequent concentrations of dye (mg/L), respectively.

Scanning electron microscope (SEM)

The morphology of the raw and pretreated EFB fibers was observed using a scanning electron microscope (Phenom ProX SEM).

Results and Discussion

The morphology of the raw and pretreated EFB fibers is shown in Figure 1(a-e). As observed in Figure 1a, the surface of the raw untreated EFB fibers was smooth and rigid with the presence of embedded silica particles. The surface of the fibers became rougher after the pre-treatment process and homogenized in water for 15 minutes, as shown in Figure 1b. Hence, the presence of silica and empty craters was also observed. As the shearing duration was prolonged to 60 minutes, as shown in Figure1c, the structure of fibers was disrupted and opened up. The size of the fibers decreased, and the existence of microfibrils could be clearly seen. In the comparison between Figure 1b and Figure 1d with the same shearing duration (15 minutes), the EFB fibers in Figure 1d had a more disrupted cellulosic structure, and a larger surface area of the fibers was exposed. This was due to the alkali modification, which swelled and delignified the fibers during the shearing process [13]. Similarly, the EFB fibers in Figure 1e were completely disrupted and were the smallest, resulting in a rougher and larger surface than EFB fibers that were sheared with water in Figure 1c. The differences in its morphology show that a longer shearing duration and incorporation with NaOH as the shearing medium may reduce the size of EFB fibers efficiently and enhance the removal of impurities from the fibers.

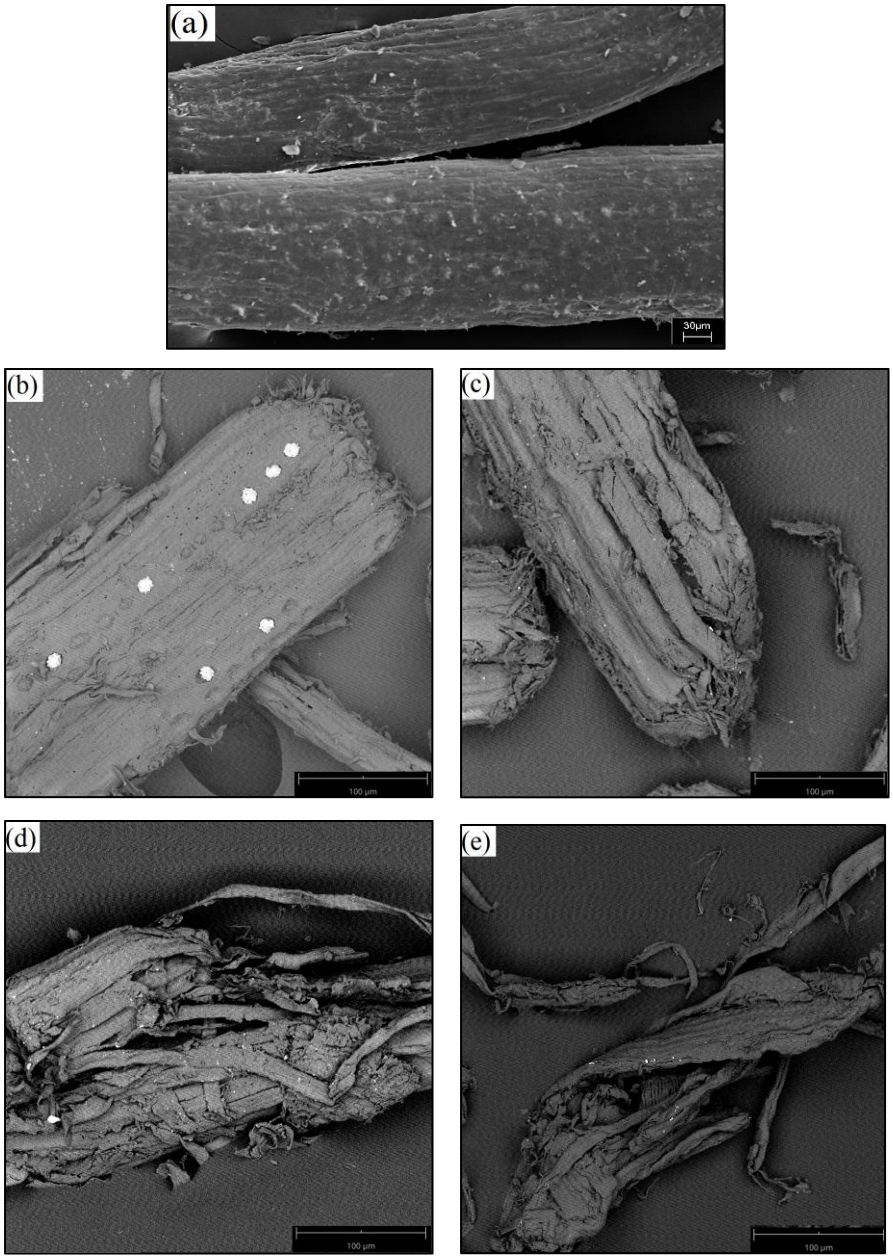


Figure 1. SEM micrographs of (a) raw EFB fibers, (b) EFB fibers sheared with H_2O for 15 minutes (H_2O-15), (c) EFB fibers sheared with H_2O for 60 minutes (H_2O-60), (d) EFB fibers sheared with 0.1 M NaOH for 15 minutes (NaOH-15), and (e) EFB fibers sheared with 0.1 M NaOH for 60 minutes (NaOH-60)

The rates of removal of MB *via* adsorption using different pretreated fibers are shown in Figure 2. The adsorption curves were characterized by an initial step with an increase in adsorption capacity assuming a convex shape. The initial rate had a steep slope due to the peak rate of MB adsorption.

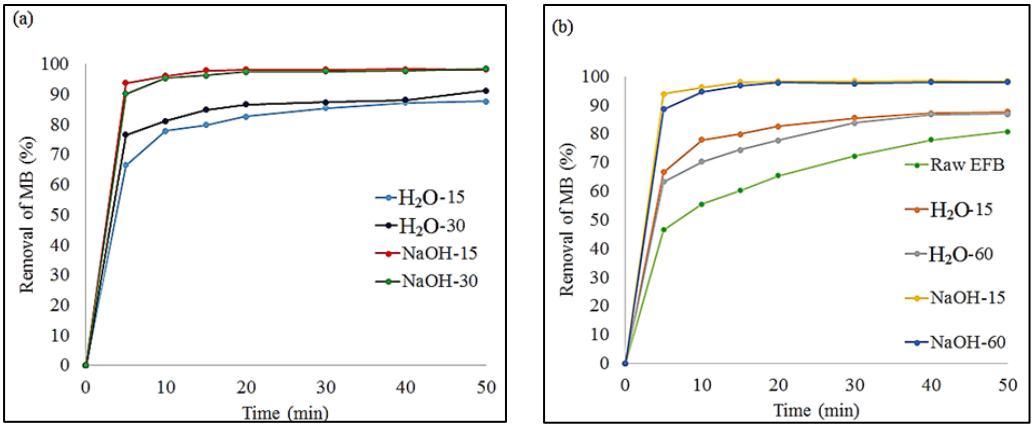


Figure 2. Rate removal of MB using (a) EFB fibers sheared with H_2O for 15 and 30 minutes (H_2O-15, H_2O-30) and EFB fibers sheared with 0.1 M NaOH for 15 and 30 minutes (NaOH-15, NaOH-30). (b) Raw EFB fibers (Raw EFB), EFB fibers sheared with H_2O for 15 and 60 minutes (H_2O-15, H_2O-60) and with 0.1 M NaOH for 15 and 30 minutes (NaOH-15, NaOH-30)

To study the effect of duration of the combined mechanical-chemical pretreatment of EFB fibers on MB adsorption, a control sample (raw EFB) was used to adsorb MB. From Figure 2b, it can be seen that the control sample had the lowest initial rate of removal of MB, while alkali pre-treated fibers (NaOH-15 and NaOH-60) yielded highest initial removal rate of MB. The results also suggested that there is no significant difference between (H_2O-15 and H_2O-30) and (NaOH-15 and NaOH-30), as shown in Figure 2a. This may be due to the short shearing duration, effecting insignificant changes in fibers size. Therefore, the result is not reported in Figure 2b.

It can be seen that the rate of removal of MB and adsorption capacity of MB using EFB fibers that were sheared with 0.1 M NaOH were higher than those of EFB fibers that were sheared with water. According to a review by Shweta and Jha [14], fibers are bonded tightly in a complex matrix, thus closing most of the porous pores on the cellulose. Hence, it is difficult for MB molecules to diffuse into the fibers. Alkali may swell and remove some of the lignin and impurities in the fibers, thus exposing the pores of the rigid fibers and increasing the surface area, which correlate with the micrograph images in Figure 1d and e. Therefore, this enhances the diffusion of MB molecules. The obtained result is consistent with the analysis by Oh and co-workers, in which alkali pre-treatment increased the hydrogen bond intensity (HBI) of EFB fibers, thus increasing the rate of adsorption of MB molecules [15].

It was predicted that as the shearing duration increases, the rate of MB adsorption will also rise due to the smaller size of the fibers (Figure 1 b-e). However, from the obtained result, the rate of removal of MB decreased when the shearing duration was prolonged to 30 and 60 minutes. Based on Kim and co-workers, the effect of pre-treatment on the structure of EFB is quite complex and not fully understood. The Crystalline Index (CI) of EFB is increased by the removal of lignin but not by the disruption of its structure. In other words, smaller EFB fibers do not expose their porous pores or increase their number of microfibrils [16]. Hence, this factor might decrease the rate of removal and adsorption capacity of MB as the pre-treatment duration increases. Yet, as the shearing duration increases, the removal of lignin, impurities, and hemicellulose from the fibers also increases. This is due to the decrease in the size of the EFB fibers during shearing and their incorporation with NaOH. As in a previous study, alkali pre-treatment will remove some of the hemicellulose in fibers [17, 18]. Hemicellulose in EFB is composed of a xylan backbone with O-acetyls and 4-O-methylglucuronic acid side chains. These can serve as functional groups to attract MB *via* electrostatic attraction [19]. However, as the duration of shearing with NaOH increases, the hemicellulose content will be reduced. Therefore, prolonged shearing of EFB fibers did not increase the rate of adsorption/adsorption of MB any further, as shown in Figure 2b.

Figure 3 shows the rate of MB removal by fibers that underwent shearing with H_2O and NaOH (H_2O-30 and NaOH-30) and control EFB fibers (stirred with 0.1 M NaOH for 30 minutes, without shearing) (Control-30). EFB fibers that were subjected to the shearing process were able to adsorb MB at a higher rate as compared with the Control-30 sample. This is consistent with the SEM results, where shearing reduced the size of the EFB effectively, providing a larger surface area of porous pores that were exposed; thus, more MB molecules could diffuse into the pores at an earlier stage. Control-30 resulted in a higher adsorption capacity than H_2O-30 due to surface and mechanical modifications that were made by the alkali, even though the size of the fibers was not reduced by shearing. Hence, we can conclude that chemical modification plays a larger role in affecting the rate of MB adsorption than the size of the EFB fibers. NaOH-30 induced the highest rate of MB adsorption compared with the H_2O-30 and Control-30 samples. In conclusion, mechanical-chemical pretreatment of EFB fibers has a synergistic effect in MB removal *via* the absorption by pretreated EFB fibers.

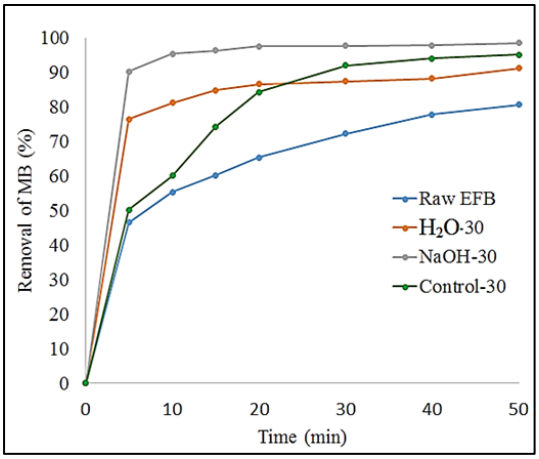


Figure 3. Removal rate of MB using raw EFB fibers (Raw EFB), sheared with H_2O for 30 minutes (H_2O-30), shearing with 0.1M NaOH for 30 minutes (NaOH-30) and EFB fibers without shearing but stirred with 0.1 M NaOH for 30 minutes (Control 30)

Conclusion

Oil palm EFB fibers were used to remove MB *via* an adsorption process. The rate of adsorption was faster with high adsorption capacity using pretreated EFB fibers *via* combined mechanical-chemical pre-treatment. Up to 98.4% of MB could be removed. This may be attributed to the increase in accessible pores and microfibrils in EFB fibers, as well as the hydroxyl functional groups, thus enhancing the rate of adsorption of MB. Pre-treatment of EFB fibers in the presence of NaOH effected the highest rate of MB adsorption compared with water pre-treated EFB fibers, suggesting that alkali can help swell the fibers and remove impurities and lignin during the shearing process.

Acknowledgments

The authors acknowledge the financial support provided by the research grants GGPM-2017-089 and FRGS/1/2016/STG01/UKM/02/3.

References

1. Sajab, M. S., Chia, C. H., Zakaria, S. and Khiew, P. S. (2013). Cationic and anionic modifications of oil palm empty fruit bunch fibers for the removal of dyes from aqueous solutions. *Bioresource Technology*, 128: 571-577.
2. Saad, S. A., Daud, S. D., Kasim, F. H. and Saleh, M. N. (2007). Methylene blue removal from simulated wastewater by adsorption using treated oil palm empty fruit bunch. *International Conference on Sustainable Materials*: pp. 293-296.

3. Almeida, C. A., Debacher, N. A., Downs, A. J., Cottet, L. and Mello, C. A. (2009). Removal of methylene blue from colored effluents by adsorption on montmorillonite clay. *Journal Colloid and Interface Science*, 332: 46-53.
4. Mohammed, M. A., Shitu, A. and Ibrahim, A. (January 2014). Removal of methylene blue using low cost adsorbent: A review *Research Journal of Chemical Sciences*, 4(1): 91-102.
5. Rebitanima, N. Z., Ghani, W. A. W. A. K., Mahmoud, D. K., Rebitanim, N. A. and Salleh, M. A. M. (2012). Adsorption of methylene blue by agricultural solid waste of pyrolyzed EFB biochar. *Journal of Purity, Utility Reaction and Environment*, 1(7): 376-390.
6. Tan, I. A. W. and Hameed, B. H. (2010). Adsorption isotherm, kinetics, thermodynamics and desorption of studies of basic dye on activated carbon derived from oil palm empty fruit bunch. *Journal of Applied Sciences*, 10(21): 2565-2571.
7. Robinson, T., McMullan, G., Marchant, R. and Nigam, P. (2001). Remediation of dyes in textile effluent: A critical review on current treatment technologies with a proposed alternative. *Bioresource Technology*, 77: 247-255.
8. Shinoj, S., Visvanathan, R., Panigrahi, S. and Kochubabu, M. (2011). Oil palm (OPF) and its composites: A review. *Industrial Crops and Products*, 33(1): 7-22.
9. Thakur, V. K. and Thakur, M. K. (2014). Processing and characterization of natural cellulose fibres/themoset polymer composites. *Carbohydrate Polymers*, 109: 102-117.
10. Mohammed, M. A., Salmiaton, A., Wan Azlina, W. A. and Mohamad Amran, M. S. (2012). Gasification of oil palm empty fruit bunches: A characterization and kinetic study. *Bioresource Technology*, 110: 628-636.
11. Mosier, N., Wyman, C., Dale, B., Elander, R., Lee, Y. Y., Holtzapple, M. and Ladisch, M. (2005). Features of promising technologies for pretreatment of lignocellulosic biomass. *Bioresource Technology*, 96(6): 673-686.
12. Cherifi, H., Fatiha, B. and Salah, H. (2013). Kinetic studies on the adsorption of methylene blue onto vegetal fiber activated carbons. *Applied Surface Science*, 282: 52-59.
13. Rollin, J. A., Zhu, Z., Sathitsuksanoh, N. and Zhang, Y. H. (2011). Increasing cellulose accessibility is more important than removing lignin: A comparison of cellulose solvent-based lignocellulose fractionation and soaking in aqueous ammonia. *Biotechnology and Bioengineering*, 108(1): 22-30.
14. Shweta, K. and Jha, H. (2015). Rice husk extracted lignin-TEOS biocomposites: Effects of acetylation and silane surface treatments for application in nickle removal. *Biotechnology Reports*, 7: 95-106.
15. Oh, S. Y., Yoo, D. I., Shin, Y., Kim, H. C., Kim, H. Y., Chung, Y. S., Park, W. H. and Youk, J. H. (2005). Crystalline structure analysis of cellulose treated with sodium hydroxide and carbon dioxide by means of X-ray diffraction and FTIR spectroscopy. *Carbohydrate Research*, 340(15): 2376-2391.
16. Kim, T. H., Kim, J. S., Sunwoo, C. and Lee, Y. Y. (2003). Pre-treatment of corn stover by aqueous ammonia. *Bioresource Technology*, 90(1): 39-47.
17. Jung, Y. H., Kim, I. J., Han, J. I., Choi, I. G. and Kim, K. H. (2011). Aqueous ammonia pretreatment of oil palm empty fruit bunches for ethanol production. *Bioresource Technology*, 102(20): 9806-9809.
18. Chin, S. X., Chia, C. H. and Zakaria, S. (2014). Green liquor pretreatment of oil palm empty fruit bunch (EFB) fibers for high yield of reducing sugars. *Journal of Biobased Materials and Bioenergy*, 8(3): 352-357.
19. Gong, R., Sun, Y., Chen, J., Liu, H. and Yang, C. (2005). Effect of chemical mmodification on dye adsorption capacity of peanut hull. *Dyes and Pigments*, 67(3): 175-181.

Malaysian Journal of Analytical Sciences, Vol 22 No 6 (2018): 1014 - 1022
DOI: https://doi.org/10.17576/mjas-2018-2206-11

MALAYSIAN JOURNAL OF ANALYTICAL SCIENCES
Published by The Malaysian Analytical Sciences Society
ISSN 1394 - 2506

EFFECT OF EPOXIDISED NATURAL RUBBERS ON CALCIUM CARBONATE-FILLED NATURAL RUBBER COMPOUNDS

(Kesan Getah Asli Terepoksida Terhadap Sebatian Getah Asli Terisi Kalsium Karbonat)

Indra Surya[1]*, Seri Maulina[1], Hanafi Ismail[2]

[1]*Department of Chemical Engineering,*
Universitas Sumatera Utara, Medan, 20155, Indonesia
[2]*School of Materials and Mineral Resources Engineering,*
Universiti Sains Malaysia, Engineering Campus, Nibong Tebal, 14300, Penang, Malaysia

**Corresponding author: indradanas@yahoo.com*

Received: 27 July 2017; Accepted: 28 April 2018

Abstract

By using a semi-efficient vulcanisation system, two grades of epoxidised natural rubbers (ENR 25 and ENR 50) were incorporated separately into calcium carbonate ($CaCO_3$) filled natural rubber (NR) compounds at 5.0, 10.0, 15.0, 20.0 and 25.0 phr. An investigation was carried out to examine the effects of the ENRs on cure characteristics, rubber - filler interaction and crosslink density of the $CaCO_3$ filled NR compounds. Results revealed that both ENR 25 and ENR 50 functioned as curatives and compatibilizers. They decreased the scorch time, cure time and minimum torque; increased torque difference, crosslink density and degree of rubber - filler interaction. The higher the ENRs loadings; the lower were the scorch and cure times and the higher were the torque difference, crosslink density and degree of rubber - filler interaction. At a similar loading, ENR 50 exhibited a more pronounced curative and compatibilization effects than ENR 25.

Keywords: epoxidised natural rubber, calcium carbonate, cure characteristics, natural rubber, rubber - filler interaction

Abstrak

Dua gred getah asli terepoksida (ENR 25 dan ENR 50) dimasukkan secara berasingan ke dalam sebatian getah asli terisi kalsium karbonat pada 5.0, 10.0, 15.0, 20.0 dan 25.0 phr dengan menggunakan kaedah pemvulkanan separa cekap (semi-EV). Kajian terhadap sebatian untuk mengkaji kesan ENR terhadap ciri-ciri pematangan, interaksi getah-pengisi dan ketumpatan sambung-silang telah dijalankan. Hasil kajian menunjukkan kedua-dua gred ENR berfungsi sebagai kuratif dan pengserasi. ENR 25 dan ENR 50 memberikan kesan penurunan terhadap masa pembakaran, masa pematangan dan tork minima; peningkatan perbezaan tork, ketumpatan sambung-silang dan darjah interaksi pengisi-getah. Semakin meningkat jumlah kedua-dua ENR, semakin rendah nilai masa pembakaran dan pematangan dan semakin tinggi nilai perbezaan tork, ketumpatan sambung-silang dan darjah interaksi pengisi-getah. Pada nilai muatan yang sama, ENR 50 menunjukkan kesan yang lebih baik sebagai kuratif dan pengserasi berbanding ENR 25.

Kata kunci: getah asli terepoksida, kalsium karbonat, ciri-ciri pematangan, getah asli, interaksi getah-pengisi

Introduction

In rubber science and technology, fillers can be divided into black and non-black fillers. The black filler is carbon black (CB), and non-black fillers are calcium carbonate ($CaCO_3$), kaolin clay, precipitated silica, talc, barite, wollastonite, mica, precipitated silicates, fumed kaolin and diatomite. Of these, the three most widely utilised, by volume and by functionality, are $CaCO_3$, precipitated silica and kaolin.

Due to their inadequate reinforcement levels, $CaCO_3$ and the other non-black fillers are not satisfactory alternatives to CB when it comes to numerous applications [1]. The fundamental problem is their surface chemistry which is more polar and hydrated than CB. It can be considered as a deficiency which causes them to be difficult to wet, disperse and interact with non-polar rubbers such as natural rubber (NR) and styrene butadiene rubber [2]. Numerous methods have been carried on to improve the reactivity of the non-black fillers with the rubber phases. One of them is the utilising of a silane-coupling agent. The coupling agent modifies the surface of the filler. The modified polar-filler provides chemically active surfaces that can participate in vulcanisation, providing coupling bonds between silane and both the polar-filler and the rubber phases [3]. Those rubber products/vulcanisates show a significant improvement in performance compared to their base materials.

The $CaCO_3$, a type of polar-fillers, can be easily dispersed in polar rubbers than in non-polar ones, like NR. Therefore, recipes or formulations of the $CaCO_3$ – NR system must contain a compatibilizer which promotes a greater rubber – filler interaction. In order to overcome the deficiency of $CaCO_3$, this research work incorporates epoxidised natural rubber (ENR) into $CaCO_3$ filled NR compounds. ENR is a polar-rubber and is a product of chemical modification on NR. As the NR is epoxidised, its chemical and physical properties change according to the extent to which the mole % of modification is introduced [4-5]. The higher the epoxidation degree, the higher is the degree of polarity [6].

In this work, the effects of the incorporation of ENRs on cure characteristics, rubber - filler interaction and crosslink density of $CaCO_3$ filled NR compounds were investigated. Two grades of ENRs; ENR 25 and ENR 50 having 25 and 50 mol of epoxidation were utilized as additive ingredients.

Materials and Methods

Materials

NR grade SMR-L was obtained from Guthrie (M) Sdn. Bhd., Seremban, Malaysia. ENR 25 and ENR 50 were supplied by the Rubber Research Institute Malaysia (RRIM). Other compounding ingredients such as sulphur (S), zinc oxide (ZnO), stearic acid, N-isopropyl-N'-phenyl-p-phenylenediamine (IPPD), Mercapto benzothiazolyl disulphide (MBTS) and $CaCO_3$ were supplied by Bayer Co. (M) Sdn. Bhd., Petaling Jaya, Selangor, Malaysia. All materials were used as supplied. The molecular structure of ENR is presented in Figure 1.

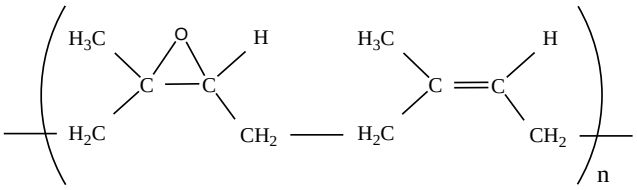


Figure 1. The molecular structure of epoxidized natural rubber.

Compounding

A semi-efficient vulcanisation system was used for the rubber compounding. The compounding procedure was done in accordance with the American Society for Testing and Material (ASTM) – Designation D 3184 – 80. The compounding was performed on a two-roll mill (Model XK-160). Table 1 displays the compound formulation of $CaCO_3$ filled NR compounds with various ENRs loading.

Table 1. The composition of the $CaCO_3$ filled NR compounds

Ingrediants	Content (phr)[a]
SMR-L	100.0
ZnO	5.0
Stearic acid	2.0
IPPD	2.0
MBTS	1.5
S	1.5
$CaCO_3$	30.0
ENRs[b]	0.0; 5.0; 10.0; 15.0; 20.0 and 25.0

[a] *parts per hundred part of SMR-L,* [b] *ENR 25 or ENR 50*

Cure characteristics

The cure characteristics of the $CaCO_3$ filled NR compounds with and without ENRs were obtained using a Monsanto Moving Die Rheometer (MDR 2000) which was employed to determine the scorch time (ts_2), cure time (t_{90}), minimum torque (M_L), maximum torque (M_H) and torque difference (M_H—M_L) according to ASTM D2084-11. Samples of the respective compounds were tested at 150 ^oC.

Measurement of Crosslink Density

Swelling tests on the $CaCO_3$ filled NR vulcanisates were performed in toluene in accordance with ASTM D471-12a. The cured test pieces (30 mm × 5 mm × 2 mm) were weighed using an electric balance and swollen in toluene until equilibrium, which took 72 hours at room temperature. The samples were taken out from the liquid, the toluene was removed from the sample surfaces and the weight was determined. The samples were then dried in the oven at 70^oC until constant weights were obtained. The swelling results were used to calculate the molecular weight between two crosslinks (M_c) by applying the Flory-Rehner equation [7-8].

$$M_C = \frac{-\rho_r V_s V_r^{1/3}}{\ln(1-V_r) + V_r + \chi V_r^2} \quad (1)$$

$$V_r = \frac{1}{1+Q_m} \quad (2)$$

where ρ_r is the rubber density (ρ_r of SMR-L = 0.92 g/cm^3), V_s is the molar volume of the toluene (V_s = 106.4 cm^3/mol), V_r is the volume fraction of the rubber in the swollen specimen, Q_m is the weight increase of the vulcanisate in toluene and χ is the interaction parameter of the rubber network−solvent (χ of SMR-L = 0.393). The crosslink density is given in equation 3:

$$V_C = \frac{1}{2M_C} \quad (3)$$

where V_c is the crosslink density in mol per cubic centimetre.

Measurement of rubber - filler interaction

The rubber - filler interaction was determined by swelling the cured $CaCO_3$ filled NR compounds with and without ENRs in toluene, according to ISO 1817. Test pieces with dimensions of (30mm x 5mm x 2mm) were prepared from the moulded sheets. The initial weights were recorded prior to testing. The test pieces were then immersed in toluene and conditioned at room temperature in a dark environment for 72 hours. After the conditioning period, the weights of the swollen test pieces were recorded. The swollen test pieces were then dried in the oven at 70 ^oC for 15 minutes and were allowed to cool at room temperature for another 15 minutes before the final weights were

recorded. The Lorenz and Park's equation [9-10] was applied in this study. The swelling index was calculated according to equation 4.

$$Qf/Qg = ae^{-z} + b \quad (4)$$

where the subscripts f and g referred to filled and gum vulcanisates, respectively; z was the ratio by weight of filler to hydrocarbon rubber in the vulcanizate; while a and b were constants. The lower the Qf/Qg value, the greater the rubber - filler interaction is [10]. In this study, the weight of the toluene uptake per gram of hydrocarbon rubber (Q) was calculated based on equation 5.

$$Q = [\text{Swollen} - \text{Dried weight}]/[\text{Initial weight} \times 100/\text{Formula weight}] \quad (5)$$

Results and Discussion

The cure characteristics

The effects of ENRs on the cure characteristics of the $CaCO_3$ filled NR compounds are shown in Figures 2-6. The cure characteristics were measured at 150 ^oC including scorch time, cure time, minimum torque, maximum torque and torque differences. As shown in Figure 2, the scorch times (ts_2) of $CaCO_3$ filled NR compounds with ENRs were lower than those of without ENRs (control compounds). In this case, ENRs functioned as curative ingredients which facilitated the starting point of vulcanisation or curing reaction. Curative ingredients play an important role in determining the cure characteristics of rubber compounds [11]. They affect the rate and nature of the curing process.

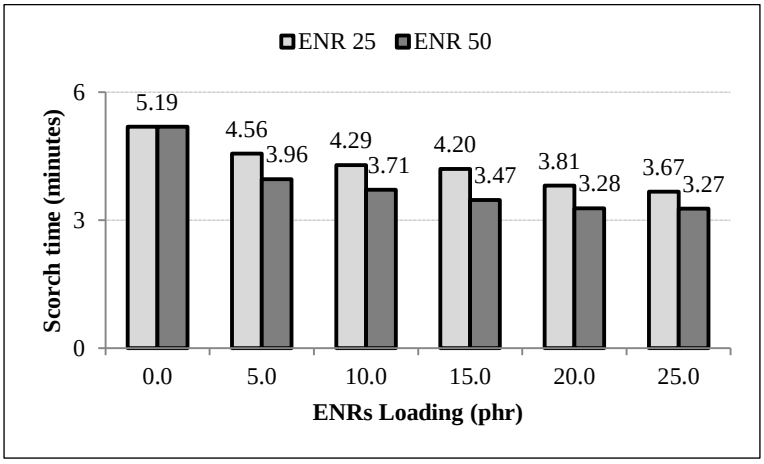


Figure 2. The effect of ENRs loading on scorch time (ts_2) of the $CaCO_3$ filled NR compounds

Figure 3 shows that the addition of each 5.0 phr of ENR 25 or ENR 50 into the control compounds decreased the cure time (t_{90}). A decreasing cure time means an enhancement in cure rate. Again, this indicates that ENRs functioned as curative ingredients which enhanced the cure rate. The cure enhancement was attributed to the epoxide groups of ENRs which played an important role in the curing of the $CaCO_3$ filled NR compounds. The epoxide groups activated the adjacent double bonds of the rubbers and hence, a faster cure rate was observed [12].

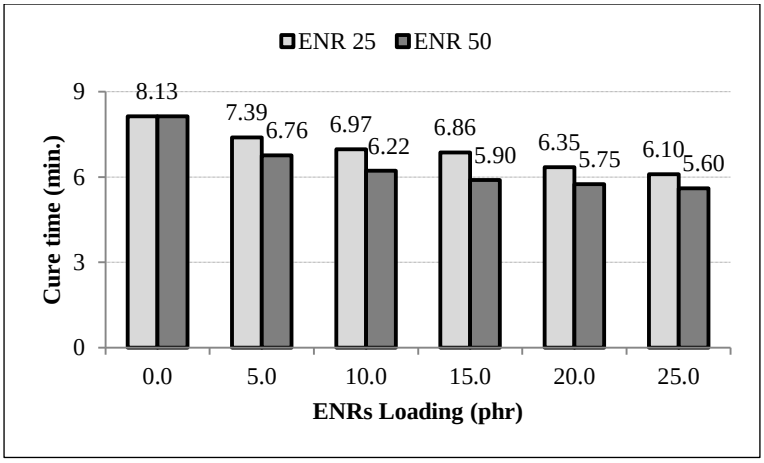


Figure 3. The effect of ENRs loading on cure time (t_{90}) of the $CaCO_3$ filled NR compounds

It can be seen from Figures 2 and 3 that the higher the ENRs loading, the lower were the scorch and cure times. It was attributed to the more and more epoxide groups presented in $CaCO_3$ filled NR compounds. At a similar ENR loading, the scorch and cure times of ENR 50 were shorter than those of ENR 25. It was simply attributed to the degree of epoxidation of ENRs; ENR 50 has more epoxide groups than ENR 25.

Figure 4 shows that the addition of each 5.0 phr of ENR 25 or ENR 50 into the control compounds decreased the minimum torque; however, the minimum torque was constant with further increases of ENRs loadings. The minimum torque indicates qualitatively the filler-filler inter agglomeration [13] and it can also be used to measure the relative viscosity of a rubber compound [1]. The lower the value, the weaker the filler - filler interaction is; resulting in a lower viscosity of a rubber compound. Actually, the incorporation of ENRs into the filled NR compounds, its effect was the same as an increase in total rubber content of the filled NR compound. This affected in an increase in the concentration of rubber phases and a decrease in viscosity of the filled NR compounds. As a consequent, the processability or degree of $CaCO_3$ or filler dispersion in the rubbers systems was improved.

The same minimum torque observed at 5 – 25 phr ENR loading for both NR25 and ENR50 was due to the almost equal of viscosity of both ENRs. ENRs are less viscous than NR and, the viscosity of ENR 25 is quite equal to the viscosity of ENR 50.

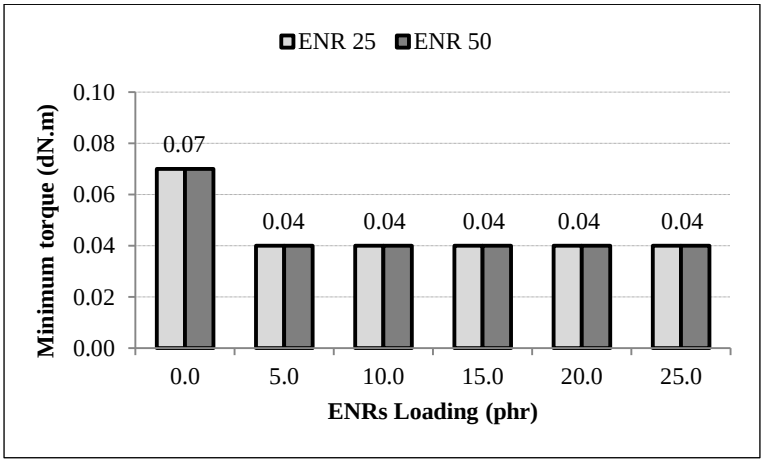


Figure 4. The effect of ENRs loading on minimum torque of the $CaCO_3$ filled NR compounds

Figure 5 shows that the additions of 5.0 phr of each type of the ENRs slightly increased the maximum torque. The maximum torque corresponds with measurement of stock modulus which was increased in this case. It was attributed to the nature of rubber - filler interaction including intercalation and exfoliation [14]. The increases in maximum torque were more pronounced whenever the ENRs loadings were further increased up to 25.0 phr. The intercalation, exfoliation and rubber - filler interaction was further increased. In this case, the ENRs might be considered as compatibilizers in the $CaCO_3$ filled NR compounds.

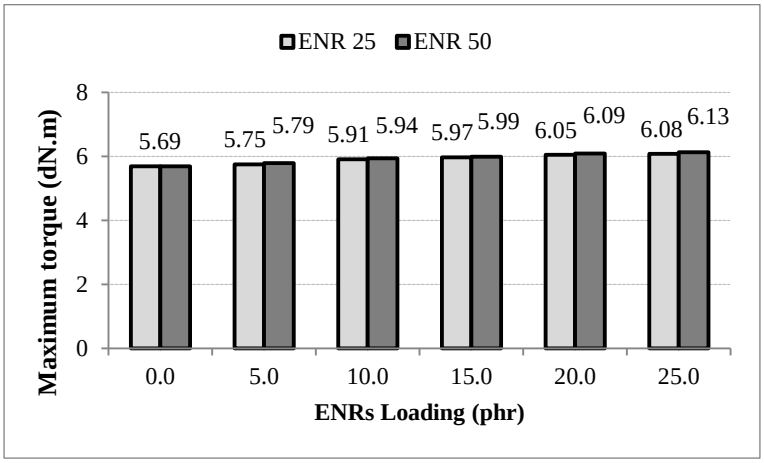


Figure 5. The effect of ENRs loading on maximum torque of the $CaCO_3$ filled NR compounds

Figure 6 shows the effect of ENRs on the torque difference (M_H—M_L) of the $CaCO_3$ filled NR compounds. It is believed that torque difference indicates the total crosslink density of a rubber compound [14-16]. The greater the torque difference, the higher is the total crosslink density. Generally, the total crosslink density of a rubber compound contains sulphide and physical crosslinks [17, 18]. ENRs can undergo acid catalyst ring-opening reactions *via* ether crosslinks during curing, resulting in an increase in crosslink density [4]. Therefore, the total crosslink density of the $CaCO_3$ filled NR compounds might contain sulphide, ether and physical crosslinks due to the presence of ENR.

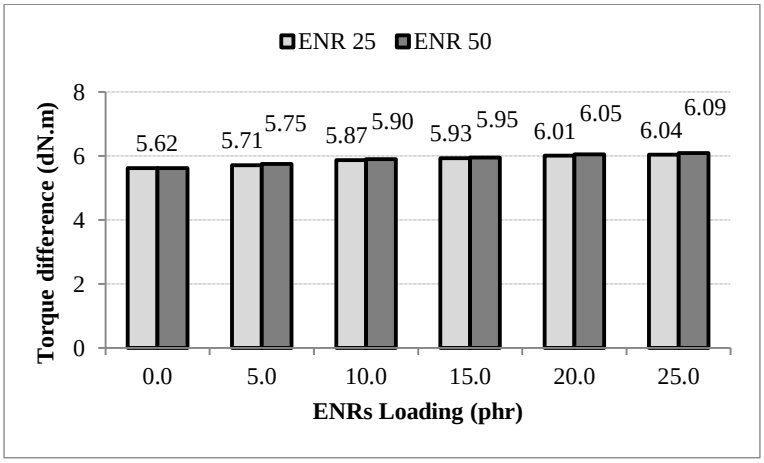


Figure 6. The effect of ENRs loading on torque difference of the $CaCO_3$ filled NR compounds

As shown in Figure 6, the addition of 5.0 phr of ENR 25 or ENR 50 increased the torque difference (M_H—M_L) of the control compound. The higher the ENRs loadings, the higher were the torque differences. It was attributed to the functions of ENRs not only as curative ingredients but also as compatibilizers. During curing, the curatives ENRs enhanced the rate and state/degree of the formations of sulphide and ether crosslinks. Simultaneously, they reduced filler – filler agglomeration and improved rubber – filler interaction, respectively. The rubber – filler interaction is defined as physical crosslinks [18, 19].

At a similar ENR loading, the torque differences of ENR 50 were higher than those of ENR 25. Again, it showed that the degree of epoxidation has played an important role in the curing process of the filled NR compounds. ENR 50 systems with more epoxide groups produced a higher degree of additional ether crosslinks than ENR 25 systems.

The rubber - filler interaction

The rubber - filler interaction, based on the Lorenz and Park's equation is shown in Figure 7. For both ENRs systems, it can be seen that the Qf/Qg values were decreased by increasing the ENRs loadings from 5.0 to 25.0 phr. A lower Qf/Qg value indicates a greater rubber - filler interaction [8, 10]. A greater degree of rubber - filler interaction of the filled compounds with ENRs was attributed not only to the additional rubber phase amount (as discussed earlier) but also to the polarity of ENRs. Due to the presence of epoxide groups, ENRs are polar rubbers and they are relatively compatible with polar fillers such as $CaCO_3$ and silica compared NR. Surely, such compatibility should produce a greater rubber - filler interaction.

At a similar ENR loading, the rubber - filler interactions of ENR 50 were greater than those of ENR 25. It was simply attributed polarity degree of those ENRs. Compared to ENR 25, ENR 50 has more epoxide groups and hence, makes it more polar and it has a stronger interaction with $CaCO_3$.

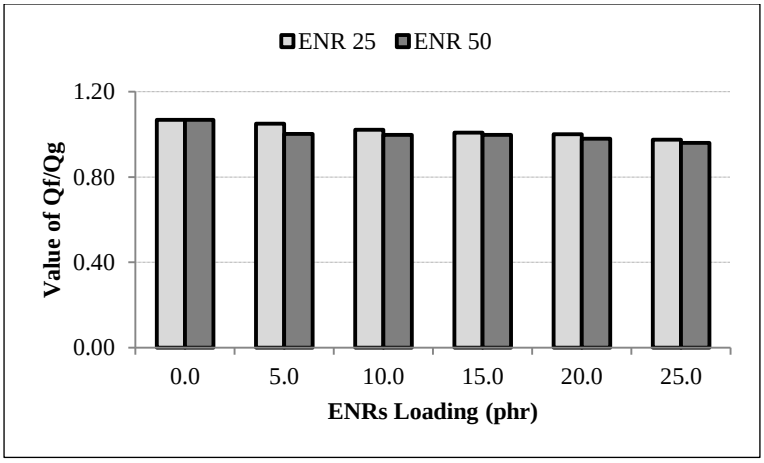


Figure 7. The effect of ENRs loading on Qf/Qg values of the $CaCO_3$ filled NR compounds

The total crosslink density

The effect of ENRs on the total crosslink density of the $CaCO_3$ filled NR vulcanisates is shown in Figure 8. The total crosslink density was determined by the Flory—Rehner approach. The additions of 5.0 phr of each ENRs into the $CaCO_3$ filled NR compound increased the total crosslink density and further increases the ENRs loadings increased the total crosslink density. This observation is in line with the result of the torque difference as presented in Figure 6. This surely confirms that torque difference indicates the degree of crosslink density of the filled NR compounds. At a similar ENR loading, the total crosslink density of ENR 50 systems was higher than that of ENR 25 systems. It was attributed a higher degree of sulphide, ether and physical crosslinks altogether of ENR 50 systems compared to ENR 25 systems.

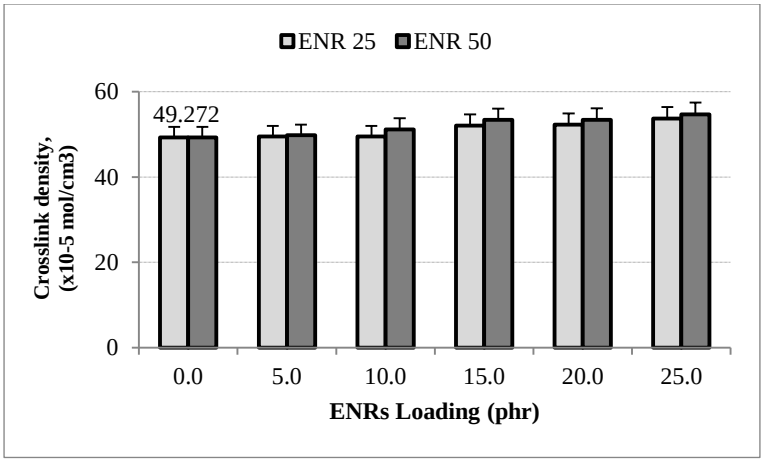


Figure 8. The effect of ENRs loading on crosslink density of the $CaCO_3$ filled NR compounds

Conclusion

Epoxidized natural rubbers functioned as curatives ingredients in calcium carbonate filled natural rubber compounds. They decreased the scorch and cure times; increased the maximum torque and torque difference of calcium carbonate filled natural rubber compounds. Epoxidized natural rubbers also functioned as compatibilizers. They improved the filler dispersion, rubber - filler interaction and crosslink density of calcium carbonate filled natural rubber compounds. The higher the loading of epoxidized natural rubber in the calcium carbonate filled natural rubber compounds; the more pronounced were the curative and compatibilization effects. At a similar loading, the curative and compatibilization effects of epoxidized natural rubber with 50 mol epoxidation were higher than those of epoxidized natural rubber with 25 mol epoxidation.

Acknowledgement

The authors would like to thank the Directorate General of Higher Education Ministry of Education and Culture of Republic Indonesia for a research grant (Penelitian Fundamental, 1608/UN5.1.R/KEU/2012) and Universiti Sains Malaysia for providing the materials and research facilities.

References

1. Surya, I., Ismail, H. and Azura, A. (2013). Alkanolamide as an accelerator, filler-dispersant and a plasticizer in silica-filled natural rubber compounds. *Polymer Testing*, 32(8): 1313-1321.
2. Fetterman, M. Q. (1984). The unique properties of precipitated silica in the design of high performance rubber. *Elastomerics*, 116(9): 18-31.
3. Ranney, M. and Pagano, C. (1971). Silane coupling agent effects in ethylene propylene diene terpolymers. *Rubber Chemistry and Technology*, 44(4): 1080-1092.
4. Ismail, H. and Chia, H. (1998). The effects of multifunctional additive and epoxidation in silica filled natural rubber compounds. *Polymer Testing*, 17(3): 199-210.
5. Ismail, H. and Suzaimah, S. (2000). Styrene butadiene rubber/epoxidized natural rubber blends: Dynamic properties, curing characteristics and swelling studies. *Polymer Testing*, 19 (8): 879 - 888.
6. Baker, C., Gelling, I. and Newell, R. (1985). Epoxidized natural rubber. *Rubber Chemistry and Technology*, 58(1): 67-85.
7. Flory, P. J. and Rehner Jr., J. (1943). Statistical mechanics of crosslinked polymer networks II. Swelling. *Journal of Chemical Physics*, 11: 521-526.
8. Surya, I. and Ismail, H. (2016). The effect of the addition of alkanolamide on properties of carbon black-filled natural rubber (SMR-L) compounds cured using various curing systems. *Polymer Testing*, 50: 276-282.
9. Lorenz, O. and Parks, C. (1961). The crosslinking efficiency of some vulcanizing agents in natural rubber. *Journal of Polymer Science*, 50(154): 299-312.

10. Ismail, H., Shaari, S. and Othman, N. (2011). The effect of chitosan loading on the curing characteristics, mechanical and morphological properties of chitosan-filled natural rubber (NR), epoxidised natural rubber (ENR) and styrene-butadiene rubber (SBR) compounds. *Polymer Testing*, 30(7): 784-790.
11. Rodgers, B. (2004). *Rubber* compounding: Chemistry and applications: CRC Press.
12. Poh, B., Ismail, H., Quah, E. and Chin, P. (2001). Cure and mechanical properties of filled SMR L/ENR 25 and SMR L/SBR blends. *Journal of Applied Polymer Science*, 81(1): 47-52.
13. Manna, A. K., De, P., Tripathy, D., De, S. and Peiffer, D. G. (1999). Bonding between precipitated silica and epoxidized natural rubber in the presence of silane coupling agent. *Journal of Applied Polymer Science*, 74(2): 389-398.
14. Teh, P., Mohd Ishak, Z., Hashim, A., Karger-Kocsis, J. and Ishiaku, U. (2004). Effects of epoxidized natural rubber as a compatibilizer in melt compounded natural rubber–organoclay nanocomposites. *European Polymer Journal*, 40(11): 2513-2521.
15. Ramesan, M., Mathew, G., Kuriakose, B. and Alex, R. (2001). Role of dichlorocarbene modified styrene butadiene rubber in compatibilisation of styrene butadiene rubber and chloroprene rubber blends. *European Polymer Journal*, 37(4): 719-728.
16. Surya, I. and Ismail, H. (2016). Alkanolamide as a novel accelerator and vulcanising agent in carbon black-filled polychloroprene rubber compounds. *Plastics, Rubber and Composites*, 45(7): 287-293.
17. Polmanteer, K. and Lentz, C. (1975). Reinforcement studies-effect of silica structure on properties and crosslink density. *Rubber Chemistry and Technology*, 48(5): 795-809.
18. Surya, I., Ismail, H. and Azura, A. (2015). The effect of alkanolamide loading on properties of carbon black-filled natural rubber (SMR-L), epoxidised natural rubber (ENR), and styrene-butadiene rubber (SBR) compounds. *Polymer Testing*, 42: 208-214.
19. Nunes, R., Fonseca, J. and Pereira, M. (2000). Polymer–filler interactions and mechanical properties of a polyurethane elastomer. *Polymer Testing*, 19(1): 93-103.

Malaysian Journal of Analytical Sciences, Vol 22 No 6 (2018): 1023 - 1030
DOI: https://doi.org/10.17576/mjas-2018-2206-11

MALAYSIAN JOURNAL OF ANALYTICAL SCIENCES
Published by The Malaysian Analytical Sciences Society
ISSN 1394 - 2506

DIIMIDE REDUCTION OF LIQUID NATURAL RUBBER IN HYDRAZINE HYDRATE/HYDROGEN PEROXIDE SYSTEM: A SIDE REACTION STUDY

(Penurunan Diimida Getah Asli Cecair dalam Sistem Hidrazin Hidrat/Hidrogen Peroksida: Kajian Tindak Balas Sampingan)

Muhammad Jefri Mohd Yusof[1], Nur Aidasyakirah Mohd Tahir[1], Fazira Firdaus[1], Siti Fairus M. Yusoff[1,2]*

[1]*School of Chemical Sciences and Food Technology, Faculty of Science and Technology*
[2]*Polymer Research Centre, Faculty of Science and Technology*
Universiti Kebangsaan Malaysia, 43600 UKM Bangi, Selangor, Malaysia

**Corresponding author: sitifairus@ukm.edu.my*

Received: 27 July 2017; Accepted: 28 April 2018

Abstract

Hydrogenation of liquid natural rubber (LNR) has been successfully accomplished via diimide reduction using hydrazine hydrate/hydrogen peroxide (HH/H_2O_2) system. Each parameter in the system was optimized to obtain maximum hydrogenation degree such as the mass of boric acid, mole ratio of HH: H_2O_2, reaction time and reaction temperature. As a result, the highest degree of hydrogenation was achieved at 91.2% using a molar ratio HH: H_2O_2 of 2:3, in the presence of boric acid as a promoter at 60 °C for 8 hours. In this research, we report on possible side reactions that led to lowering the hydrogenated rubber product. Reactivity of diimide species as well as decomposition of hydrogen peroxide were postulated based on literature reviews to be one of the factors hindering hydrogenation of LNR. The presence of side reactions such as degradation, cyclization, and crosslinking had been confirmed by gel permeation chromatography (GPC), ^{1}H nuclear magnetic resonance (^{1}H NMR), and swelling test, respectively.

Keywords: hydrogenation, liquid natural rubber, side reactions, hydrazine hydrate, hydrogen peroxide

Abstrak

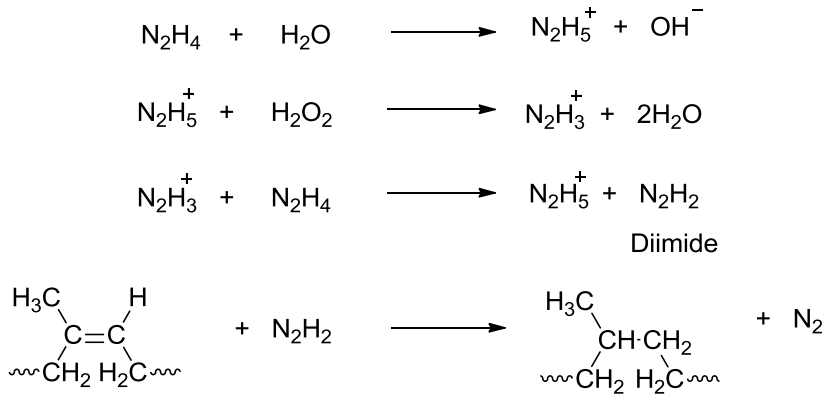
Penghidrogenan getah asli cecair (LNR) telah berjaya dijalankan menggunakan sistem hidrazin hidrat/hidrogen peroksida (HH/H_2O_2). Setiap parameter dalam sistem tersebut dioptimumkan bagi mendapatkan darjah penghidrogenan yang maksimum seperti jisim asid borik, nisbah mol HH: H_2O_2, masa dan suhu tindak balas. Hasilnya, peratus penghidrogenan sebanyak 91.2% diperolehi apabila menggunakan nisbah molar HH: H_2O_2 sebanyak 2:3, dalam kehadiran asid borik sebagai penggalak pada suhu 60 °C selama 8 jam. Dalam kajian ini, kami melaporkan tindak balas sampingan yang berkemungkinan berlaku yang menyebabkan pengurangan hasil getah terhidrogen. Berdasarkan kajian-kajian lepas, kereaktifan spesis diimida dan penguraian hidrogen peroksida dipercayai merupakan antara faktor yang merencatkan penghidrogenan LNR. Kehadiran tindak balas balas sampingan seperti degradasi, pengkitaran, dan taut silang telah dikenal pasti masing-masing melalui kromatografi penelapan gel (GPC), resonans magnetik nuklear proton, dan ujian bengkakan.

Kata kunci: penghidrogenan, getah asli cecair, tindak balas sampingan, hidrazin hidrat, hidrogen peroksida

Introduction

Hydrogenation is a method for chemical modification that reduces the degree of C=C unsaturation. Previously, many researchers focused on decomposition of *p*-TSH in toluene as diimide source for non-catalytic hydrogenation [2]. However, hydrazine hydrate/hydrogen peroxide (HH/H_2O_2) system was introduced by Wideman in 1984 as one

of the non-catalytic methods to hydrogenate unsaturated polymers [1]. This HH/H_2O_2 system was developed as an alternative for diimide supply due to its conventional preparation in aqueous medium and economical value with simple apparatus set up [3]. Simma et al. applied similar system on their hydrogenation of styrene-butadiene latex resulting in production of thermoplastic elastomer that was stable at high temperature and pressure [4].
Hydrogenation using diimide reduction involves reaction between HH with H_2O_2 to produce diimide species before it can be used to reduce the unsaturated units [5]. Scheme 1 shows the reaction mechanism for the formation of diimide species followed by its action on unsaturated unit reduction. Hydrazine in aqueous medium will dissociate into hydrazinium and hydroxyl ion. The hydrazinium ion then reacts with hydrogen peroxide to produce hydrazinylium ion, and water molecule. Subsequently, hydrazine and hydrazinylium will react to produce diiimide that are needed to hydrogenate the unsaturated units of LNR.



Scheme 1. Formation of diimide species and its action on unsaturated units [6]

Due to *in situ* nature of this reaction, several side reactions are prone to happen and affect the hydrogenation process as reported by past researches [3, 7]. Typical side reactions for non-catalytic hydrogenation would be chain-scissoring, cyclization, crosslinking, gel formation and *cis-trans* isomerism [8].

Wang et al. in 2013 studied on hydrogenation of styrene-butadiene rubber (SBR) using this system. In their work, they discovered that the hydrogenation percentage was decreased when larger particle size of SBR has been used. They suspected that larger particle size provided further penetration surface for the diimide species to inefficiently hydrogenate the double bond units [9]. Meanwhile, Simma et al. demonstrated that HH/H_2O_2 system would promote crosslinking that affected the yields of their hydrogenated acrylonitrile-butadiene rubber (NBR) as proven by gel fractioning of the products [4]. Han et al. also found out that their hydrogenated SBR were high in gel content (89.8% - 98.6%) prior to this reaction [10].

In this paper, we report on a number of side reactions that occurred throughout our hydrogenation of LNR using HH/H_2O_2 system. This information would be useful to explain variation of yield percentages of hydrogenated products as well as providing synthetic route to produce chemically and physically modified LNR. Based on our results, the products have been identified to contain gel, possess shorter chain, and bear cyclization group. These remarks are useful for applications development. Materials with gel content are used as lubricant (low gel content) or adhesive (high gel content) [11] as polymers with shorter polymeric chain can act as compatibilizer in polymer blends [12]. Meanwhile, cyclic polymers are widely synthesized in bio-related properties and applications [13].

Materials and Methods

Materials

Natural rubber from Rubber Research Institute of Malaysia (RRIM) has been used as starting material. Hydrazine hydrate 80% was purchased from R&M Chemicals. A 30% aqueous solution of hydrogen peroxide (90% purity) was obtained from Sigma Aldrich. Sodium dodecyl sulfate (98%) and boric acid (≥99.5%) were purchased from Systerm.

Diimide reduction of LNR

The emulsion of LNR (5 g), sodium dodecyl sulphate (0.00035 mol, 0.10 g) as a surfactant, few drops of silicone oil, and distilled water (50 mL) were added in the three-neck round-bottom flask. After stirring for 30 minutes, hydrazine hydrate was added and continued stirring for another 30 minutes at 60 °C while stirring. The solution of hydrogen peroxide and boric acid was prepared by dissolving 1.5 g of boric acid (0.024 mol) in 40 ml of hydrogen peroxide. Then, the mixture was added drop wise for 8 hours. The product obtained was coagulated in ethanol and dried in vacuum oven for at least 12 hours.

^{1}H-NMR characterization

NMR spectroscopy was used to examine the microstructure of the product. In addition, integration of signals from proton NMR (^{1}H-NMR) was used to estimate the percentage of conversion from LNR to HLNR. Peak areas of aliphatic region (a) and olefinic region (b) were used to calculate the percentage of hydrogenation using the formula in equation 2:

$$Percentage\ of\ hydrogenation, \% = \frac{a-5b}{a+3b} \quad (1)$$

Samples were dissolved in deuterated chloroform ($CDCl_3$) for measurements with NMR spectrometer (JNM-ECP 400 MHz).

Swelling Test

Swelling test was performed to determine the degree of crosslinking of the samples. It can be obtained by the change in weight using the following method. The samples with weight of 0.5-1.0 g (M_I) were weighed and immersed in 20 ml toluene for 2 hours at room temperature. Samples were removed and weighed (M_{II}). The percentage of weight change was calculated by the following formula in equation 2.

$$Change\ in\ weight, \% = \left(\frac{M_{II}}{M_I} - 1\right) \times\ 100 \quad (2)$$

GPC analysis

The Waters Model 1515/2414 gel permeation chromatograph has been used to study the average molecular weights (Mw) and polydispersity index (PDI) of LNR and HLNR. About 5 mg of the samples were dissolved in 5 mL tetrahydrofuran (THF) before scanning. The analysis was carried out using three Styragel HR columns. Measurements were made at column temperature of 40 °C using THF as eluent at a flow rate of 1 mL min^{-1}, and the samples were monitored by Breeze™ system.

Results and Discussion

The conversion percentages of hydrogenated products from this reaction ranged from 15.9% to 91.2%. Table 1 shows the degree of hydrogenation with respective parameters optimization. The differences in hydrogenation degree when the reaction parameters were manipulated could be explained by the occurrence of these following side reactions.

Table 1. Degree of hydrogenation with respective parameters optimization

Mole of Acid Boric (mol)	Molar Ratio of HH:H_2O2	Reaction Time (hours)	Reaction Temperature (^{o}C)	Hydrogenation Degree (%)
0	1:1	6	40	15.9
0.008	1:1	6	40	34.8
0.016	1:1	6	40	35.2
0.024	1:1	6	40	38.5

Table 1 (cont'd). Degree of hydrogenation with respective parameters optimization

Mole of Acid Boric (mol)	Molar Ratio of HH:H_2O2	Reaction Time (hours)	Reaction Temperature (^oC)	Hydrogenation Degree (%)
0.08	1:1	6	40	34.9
0.024	1:2	6	40	56.2
0.024	1:3	6	40	71.2
0.024	1:4	6	40	73.0
0.024	1:5	6	40	56.3
0.024	2:1	6	40	61.5
0.024	3:1	6	40	51.5
0.024	2:3	6	40	78.0
0.024	2:3	2	40	45.6
0.024	2:3	4	40	65.1
0.024	2:3	6	40	68.0
0.024	2:3	8	40	82.9
0.024	2:3	10	40	67.0
0.024	2:3	8	27	43.4
0.024	2:3	8	50	53.6
0.024	2:3	8	60	91.2
0.024	2:3	8	70	56.5

Reactivity of diimide species

At mole ratio of 3:1 (HH: H_2O_2), the hydrogenation degree was found to be at 51.5%. The amount was reduced from 61.5% at 2:1 of HH: H_2O_2. Highly excessive HH signified with prolonged reaction time increased amounts of diimide molecules that could lead to self-reaction of diimide. Equation 3 shows the diimide self-reaction [9]. Besides, excess diimide species were reported to penetrate aqueous phase instead of rubbery phase of the reaction [14]. This would reduce the addition of hydrogen into LNR unsaturated units [9].

$$NH{=}NH + NH{=}NH \longrightarrow N_2H_4 + N_2 \quad (3)$$

De Sarkar et al. proposed the reaction scheme of diimide decomposition when the reaction time was extended (equation 4 and 5) [7]. Longer reaction time in this study (10 h) showed decrement in percentage of hydrogen due to unavailability of diimide species that were needed to hydrogenate the unsaturated units [7].

$$NH{=}NH \longrightarrow N_2 + H_2 \quad (4)$$

$$2NH{=}NH \longrightarrow N_2H_4 + N_2 \quad (5)$$

Decomposition of Hydrogen Peroxide

The percentage of hydrogenation dropped from 73.0% to 56.0% when the mole ratio of H_2O_2 to HH was increased from 4:1 to 5:1. De Sarkar et al. in 1997 suggested side reactions of H_2O_2 that prevented the formation of diimide species (equation 6-8) [15]. Consequently, the amounts of diimide were insufficient to yield more hydrogenated products.

$$2H_2O_2 + N_2H_4 \longrightarrow N_2 + 4H_2O \quad (6)$$

$$H_2O_2 + N_2H_2 \longrightarrow N_2 + 2H_2O \quad (7)$$

$$2H_2O_2 \longrightarrow O_2 + 2H_2O \quad (8)$$

At high H_2O_2 concentration, hydroxyl radicals were formed that could attack the polymeric chains of LNR. This would cause chain-scissoring and crosslinking reaction [16]. The mole ratio of HH: H_2O_2 should be at right amount to produce sufficient diimide species for maximum hydrogenation. It was reported that Kongsinlark et al. used ratio of 1:3 to hydrogenate their latex at maximum degree (89%) [17].

Cyclization

The decomposition of H_2O_2 gives acidic medium which increases the tendency of reaction to undergo Markovnikov addition [18]. The product of the hydrogenation reaction at 50 ^oC for 6 hours with mole ratio HH: H_2O_2 = 1:2, boric acid ($2x10^{-4}$ mmol) underwent cyclization reaction as can be seen from the ^1H NMR spectrum (Figure 1).

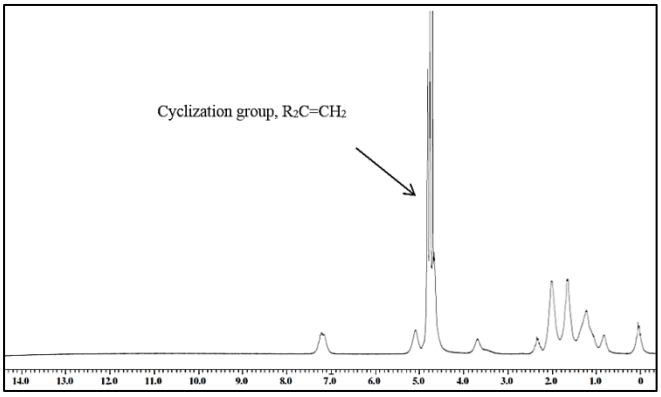


Figure 1. ^1H-NMR for detection of cyclization group in hydrogenated product

In cyclization reaction, the addition of acidic reagent causes the formation of carbonium ion which leads to formation of polycyclic ring structure of polymeric chain (mono-, bi-, and tricyclic) [19]. These cyclic structures would prevent penetration of diimide species to hydrogenate unsaturated units of LNR. Figure 2 shows that the cyclization reaction that starts when the carbonium ion attacks on an adjacent double bond, forming a ring structure.

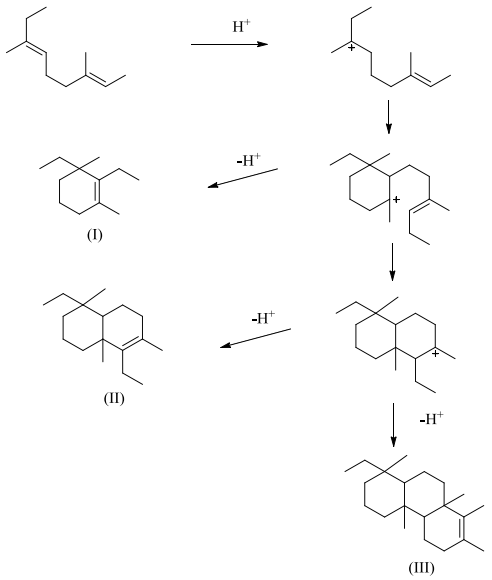


Figure 2. Mechanisms of cyclization reaction [6]

Crosslinking

The presence of H_2O_2 in the system can also contributes to crosslinking reaction. H_2O_2 prone to be dissociated into hydroxyl radicals that attacks the allylic proton of the *cis*-1,4-poliisoprene unit, forming macroradical units [20]. The macroradical can interact with each other to produce a cross-linked product. Figure 3 shows the mechanism for crosslinking reaction. Next, swelling test was performed to determine the degree of crosslinking of the samples.

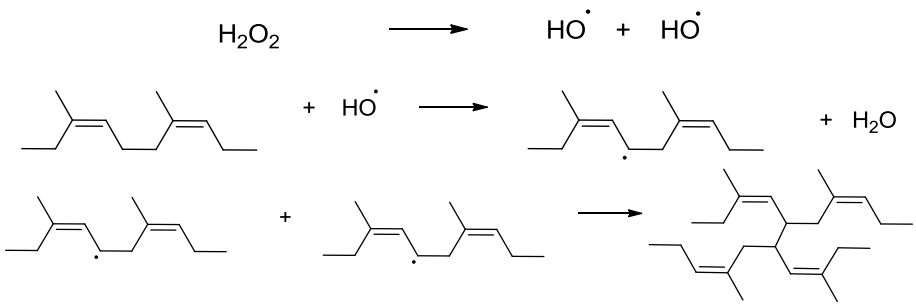


Figure 3. Mechanisms of crosslinking reaction [6]

Swelling test

Swelling test is carried out to determine the degree of crosslink in the samples after hydrogenation. The aim of this method is to identify the solvent (water) uptake into the polymer matrix which is expected to decrease with an increase of crosslinking [21]. Table 2 shows the outcomes of the swelling test on selected samples.

The weight increases with the decrease in degree of crosslinking [22]. From this study, lower value of crosslinking ratio indicated high degree of crosslinking (lower percentage of hydrogenation). Similarly, samples with highest hydrogenation percentage (91%) showed higher crosslinking ratio as a result of efficient hydrogenation due to less formation of hydroxyl radicals that triggered crosslinking reaction.

Table 2. Swelling test data

Samples	Initial Weight W_1 (g)	Final Weight W_2 (g)	% Weight Increment	Crosslinking Ratio
34% HLNR	1.06	11.52	1020.00	9.86
42% HLNR	0.30	3.55	1084.13	10.87
50% HLNR	0.17	2.56	1393.57	13.97
68% HLNR	0.25	3.70	1378.80	14.03
91% HLNR	0.20	3.06	1428.57	14.27

Degradation

Changes in molecular weight and its distribution during hydrogenation reaction can be determined by using GPC. Table 3 shows the comparison of polydispersity index, Đ for each sample. Hydrogenated products had lower molecular weight than LNR. It can be said that degradation process occurred during hydrogenation reaction in which causing the breakage of polymer chain and increasing the dispersity of polymer chain. These changes might happen as the results of thermal or acid degradation in the system related to effects of HH: H_2O_2 ratio [10].

Table 3. GPC analysis data

Samples	% Hydrogenation	M_w	M_n	Đ
LNR	-	96 400	10 800	8.93
HLNRi	50.1	9 500	7 400	1.28
HLNRii	71.3	9 500	7 200	1.32
HLNRiii	91.2	6 700	5 500	1.21

Conclusion

LNR has been successfully hydrogenated using HH: H_2O_2 system at various percentages of hydrogenation with respond to parameter optimization. The radicals formed in this system through reactivity of diimide species and decomposition of hydrogen peroxide have contributed to the manifestation of several side reactions such as cyclization, crosslinking, and degradation. Those identifications were based on spectrum analysis of NMR and GPC as well as swelling test.

Acknowledgement

The authors would like to acknowledge Universiti Kebangsaan Malaysia (UKM) for the research grants (GUP-2015-020 and FRGS/1/2016/STG01/UKM/02/4) and Centre for Research and Instrumentation (CRIM) at UKM for their facilities.

References

1. Zhou, S., Bai, H. and Wang, J. (2004). Hydrogenation of acrylonitrile–butadiene rubber latexes. *Journal of Applied Polymer Science*, 91(4): 2072-2078.
2. Jamaluddin N., Mohd Yusof M. J., Abdullah I. and M. Yusoff S.F. (2016). Synthesis, characterization, and properties of hydrogenated liquid natural rubber. *Rubber Chemical Technology*, 89(2): 227-239.
3. Lin X., Pan Q. and Rempel G. L. (2004). Cupric ion catalyzed diimide production from the reaction between hydrazine and hydrogen peroxide. *Applied Catalysis A: General*, 263 (1): 27 – 32.
4. Simma K., Rempel G. L. and Prasassarakich P. (2009). Improving thermal and ozone stability of skim natural rubber by diimide reduction. *Polymer Degradation and Stability*, 94(11): 1914-1923.
5. Yusof M. J. M., Jamaluddin N., Abdullah I. and Yusoff, S. F. M. (2015). Hydrogenation of liquid natural rubber via diimide reduction in hydrazine hydrate/hydrogen peroxide system. *AIP Conference Proceeding*, 1678: 050001
6. Samran J., Phinyocheep P., Daniel P. and Kittipoom S. (2005). Hydrogenation of unsaturated rubbers using diimide as a reducing agent. *Journal of Applied Polymer Science*, 95(1): 16-27.
7. De Sarkar M., De P. P. and Bhowmick A. K. (2000). Diimide reduction of carboxylated styrene–butadiene rubber in latex stage. *Polymer*, 41(3): 907-915.
8. Kongparakul S., Prasassarakich P. and Rempel G. L. (2008). Effect of grafted methyl methacrylate on the catalytic hydrogenation of natural rubber. *European Polymer Journal*, 44(6): 1915-1920.
9. Wang, X., Zhang, L., Han, Y., Shi, X., Wang, W. and Yue, D. (2013). New method for hydrogenating NBR latex. *Journal of Applied Polymer Science*, 127(6), 4764-4768.
10. Han Y., Su L. and Mao L. (2014). Self-cross-Linking hydrogenated nitrile-butadiene rubber latex/polyvinyl chloride emulsion composite film and its properties. *Polymer-Plastics Technology and Engineering*, 53(3): 306-311.
11. Huang G., Yu Q. and Cai M. (2016). Highlighting the effect of interfacial interaction on tribological properties of supramolecular gel lubricants. *Advanced Materials Interfaces*, 3(3): 1500489.
12. Sojoudiasli H., Heuzey M. C. and Carreau P. J. (2014). Rheological, morphological and mechanical properties of flax fiber polypropylene composites: influence of compatibilizers. *Cellulose*, 21(5): 3797-3812.
13. Tu X., Liu M. and Wei H. (2016). Recent progress on cyclic polymers: Synthesis, bioproperties, and biomedical applications. *Journal of Polymer Science Part A: Polymer Chemistry*, 54(11): 1447-1458.
14. Pisuttisap, A., Hinchiranan, N., Rempel, G. L. and Prasassarakich, P. (2013). ABS modified with hydrogenated polystyrene-grafted-natural rubber. *Journal of Applied Polymer Science*, 129 : 94-104.

15. De Sarkar M., De P. P. and Bhowmick A. K. (1997) Thermoplastic elastomeric hydrogenated styrene-butadiene elastomer: Optimization of reaction conditions, thermodynamics, and kinetics. *Journal of Applied Polymer Science*, 66(6) : 1151-1162.
16. Lin X., Pan Q. and Rempel G. L. (2005). Gel formation in diimide-hydrogenated polymers. *Journal of Applied Polymer Science*, 96(4): 1122-1125.
17. Kongsinlark A., Rempel G. L. and Prasassarakich P. (2013). Synthesis of nanosized ethylene-propylene rubber latex via polyisoprene hydrogenation. *Journal of Applied Polymer Science*, 127(5): 3622-3632.
18. Lenko D., Schlögl S. and Temel A. (2013) Dual crosslinking of carboxylated nitrile butadiene rubber latex employing the thiol-ene photoreaction. *Journal of Applied Polymer Science*, 129(5) : 2735-2743.
19. Dinçalp H. and Içli S. (2006). Photoinduced electron transfer-catalyzed processes of sulfoamino perylene diimide under concentrated sun light. *Solar Energy*, 80(3): 332-346.
20. Jiang D. D., Levchik G. F. and Levchik S. V. (2000). Thermal degradation of cross-linked polyisoprene and polychloroprene. *Polymer Degradation and Stability*, 68(1): 75-82.
21. Hirschl C., Biebl–Rydlo M. and DeBiasio M. (2013). Determining the degree of crosslinking of ethylene vinyl acetate photovoltaic module encapsulants—a comparative study. *Solar Energy Materials and Solar Cells*, 116 : 203-218.
22. Khan .F, Kwek D., Kronfli E. and Ahmad S.R. (2007). Crosslinking of ethylene–propylene (–diene) terpolymer elastomer initiated by an excimer laser. *Polymer Degradation and Stability*, 92(8): 1640-1644.

Malaysian Journal of Analytical Sciences, Vol 22 No 6 (2018): 1031 - 1039
DOI: https://doi.org/10.17576/mjas-2018-2206-13

MALAYSIAN JOURNAL OF ANALYTICAL SCIENCES
Published by The Malaysian Analytical Sciences Society
ISSN 1394 - 2506

AN ACOUSTIC STUDY OF *Shorea leprosula* WOOD FIBER FILLED POLYURETHANE COMPOSITE FOAM

(Kajian Akustik Busa Komposit Poliuretana Terisi Serat Kayu *Shorea leprosula*)

Muhammad Shafiq Mohd Azahari, Anika Zafiah M. Rus*, Shaharuddin Kormin, M. Taufiq Zaliran

Sustainable Polymer Engineering, Advanced Manufacturing and Material Center (SPEN-AMMC),
Faculty of Mechanical and Manufacturing Engineering,
Universiti Tun Hussein Onn Malaysia, 86400 Parit Raja, Batu Pahat, Johor, Malaysia

**Corresponding author: zafiah@uthm.edu.my*

Received: 27 July 2017; Accepted: 28 April 2018

Abstract

Polyurethane foam is an excellent material for sound absorbing materials. This material is produced by mixing crosslinker, and polyol to produce foams with the presence of blowing agent. This study consists of an experimental study on acoustics properties enhancement of polyurethane foam by mixing different weight percentage of *Shorea leprosula* wood fiber into the polymer matrix. An optimal percent of 5-20% wood fiber was used to obtain a homogeneous mixture. The polymer foam composites acoustic properties were measured by using impedance tube test to obtain the sound absorption coefficient. The polymer foam composites UF_{80} produced have a better sound absorption coefficient, α of 0.9507. UF_{80} gives a higher density of 865.5 kg/m^3 and smallest pore size of 413.4 µm which is determined by using Mettler Toledo Density kit and Scanning Electron Microscope (SEM) respectively compared to UF. The noise reduction coefficient (NRC) of the polymer foam composites UF_{80} is twice as high as UF. This studies proved that *Shorea Leprosula* wood fiber influenced the acoustic properties of polymer foam composites.

Keywords: polyurethane foam, wood fiber, acoustic properties, sound absorption coefficient, noise reduction coefficient

Abstrak

Busa poliuretana adalah bahan yang sangat baik untuk bahan menyerap bunyi. Bahan ini dihasilkan dengan mencampurkan penghubung silang, dan poliol untuk menghasilkan busa dengan kehadiran ejen meniup. Kajian ini terdiri daripada kajian mengenai sifat-sifat akustik penambahbaikan busa poliuretana dengan mencampurkan peratusan berat serat kayu *Shorea leprosula* berbeza ke dalam matriks polimer. Peratus optimum serat kayu 5-20% digunakan untuk mendapatkan campuran homogen. Sifat akustik polimer komposit diukur dengan menggunakan ujian tiub impedans untuk mendapatkan pekali penyerapan bunyi. Polimer komposit UF_{80} yang dihasilkan mempunyai pekali penyerapan bunyi, α yang lebih baik dengan 0.9507. UF_{80} memberikan ketumpatan yang lebih tinggi dengan 865.5 kg/m^3 dan saiz liang yang lebih kecil dengan 413.4 µm masing-masing ditentukan menggunakan kit ketumpatan Mettler Toledo dan Mikroskopi Pengimbas Elektron (SEM) berbanding UF. Pekali pengurangan hingar (NRC) daripada polimer komposit UF_{80} adalah dua kali lebih tinggi daripada UF. Kajian ini membuktikan bahawa serat kayu Meranti Merah mempengaruhi sifat akustik busa poliuretana.

Kata kunci: busa poliuretana, serat kayu, sifat akustik, pekali penyerapan bunyi, pekali pengurangan hingar

Introduction

As the industrial waste gradually expands, it is slowly turned to be a major concern for the surroundings as well as human well-being. Another surroundings issue, which is changing into an undeniably major concern because of its

negative effect on human well-being, is noise pollution [1]. Hence, innovative development of effective and environmentally friendly sound absorbing materials is essential [2,3]. Polymer foams are incorporate interconnected cells in a polymer matrix. Polymer foam can have an open, partially open, or a closed cell structure. Closed pores are usually much less efficient than open pores in absorbing sound energy. This is due to the fact that open pores have a continuous channel of communication with the external surface of the frame, and they have a tremendous effect on the absorption of sound [4].

Polymer foam needs less material than a sturdy polymer having a similar volume, consequently material expenses are decreased in several applications [5]. Polyurethane foams are generally used as a part of the industry for their thermal, mechanical, electrical, and acoustic properties [6, 7]. Polyurethane foam is a good sound absorbing material due to its generally low density and high porosity. When acoustic waves propagate within the foams porosity, energy is reduced. The air friction loss within the cores and then converted into heat [8]. This energy absorption is enclosed by the polymer foam morphology, which is an inherent property of the foam and is defined by using the gradual decrease in energy in the dissemination of the acoustic wave propagation [9]. The addition of polyurethane foam with various waste materials produces development composites materials with vital applications [5, 10]. Many researches proved that the feasibility to strengthen polymer foams with waste materials is to improve their mechanical; acoustic properties. Hence, researchers have utilized and considered fibrous waste with several characteristics to get sound absorbing materials: cotton [11], hemp strands [12], coconut coir fiber [11], and tea-leaf strands [13].

In Malaysia, wood plantation industries dispose and burned all the wood waste in the incinerators for each year and caused environmental pollution [14, 15]. Only a few wood wastes materials are reused by farmers and industrials enterprises. The leftover wood waste goes to landfills or to metropolitan waste incinerators [16] and used in several applications. This wood waste may result from the sawdust of furniture manufacturing or may simply come from building construction industries that are no longer used [14, 15, 17]. Wood waste is biodegradable, lightweight, cheaper, nontoxic, and has nonabrasive qualities with environmental and economic advantages

The target of this study is to study the acoustic properties of polymer foam composites which are used to utilize the wood waste materials by making new materials and also reduce the noise. The aims of this studies are to test the acoustic properties of polyurethane foam with various percent of wood fiber (*Shorea leprosula*) polymer foam composites as sound absorbing materials.

Materials and Methods

Raw materials

Figure 1 show the *Shorea leprosula* wood fiber which is used to enhance acoustic properties of polyurethane foam, origins from the manufacture of furniture manufacturing. The wood fiber was sun dried for a day to remove the humidity and then being ground and sieved into fine wood by using heavy duty blender to get desired fine particle size (<300 μm). The matrix of composite materials produced in this study is polymer foam composites.



Figure 1. *Shorea leprosula* wood fiber

Foam preparation

Polymer foam composites samples were prepared by adding wood fiber with a polyurethane formulation consist of polymethane polyphenyl isocyanate (Modified Polymeric-MDI) and polyol. The polyurethane foams were prepared by mixing by the polyol and water (blowing agent) with isocyanate ratio of 1.0:0.1:0.5. This polymerization reaction is exothermic when reactions between alcohols with two or more reactive hydroxyls (-OH) groups per molecule (diols, triols, polyols) and isocyanates that have more than one reactive isocyanate group (-NCO) per molecule (diisocyanates, polyisocyanates). At the beginning of the procedures, different weight percentage (wt.%) of *Shorea leprosula* wood fiber into polyurethane foam were produced. Table 1 shows the weight percentage range of wood fiber used varies less or equal to 20% wt/wt of polyol.

Polyol and isocyanate were mixed with wood fiber at pre-determined weight ratios. The mixture in the mold is continuously stirred until it reaches homogenous composition and left to cure at room temperature for 24 hours [14, 15, 17]. Upon curing, the sample is cut to get 10 mm in thickness of each sample with 100 mm and 28 mm in diameter for sound absorption coefficient measurement using impedance tube testing as referred to Figure 2.

Table 1. Polymer foam composites composition ratios

Samples	Flexible Polyurethane Foam (wt.%)	Wood Fiber (wt.%)	Sample Thickness (mm)
UF	100	0	10
UF_{95}	95	5	10
UF_{90}	90	10	10
UF_{85}	85	15	10
UF_{80}	80	20	10



Figure 2. Polymer foam composites prepared for sound absorption coefficient measurement using impedance tube testing

Density of polymer foam composite

The densities of the polymer foam composites were measured by using Buoyancy method according to European Standard EN 993-1 which automatically determined the density by using Mettler Toledo Density Kit. Each sample with 10 × 10 × 10 mm size (length × width × thickness) was cut from the polymer foam composites and average value from five different samples were recorded.

Scanning electron microscope

Scanning electron microscopy (SEM) analyses were performed in a JEOL-JSM6380LA for polymer foam composites after vacuum-coating with gold (Auto Fined Coater of JEOL-JFC1600). This coated procedure for each sample is to avoid electrostatic charging during testing and at accelerating voltage of 10.0 kV [14, 15, 17]. Average pore size was obtained by measuring at least 10 pore size on the surface of each polymer foam composites.

Impedance tube testing

A sound wave incident on a material can be absorbed, reflected as well as transmitted by the material. These three processes are whole feasible relying on the characteristics of the material. The incident sound wave absorption is a practical approach to reduce noise. Sound absorption coefficient examined the acoustic property of the sound absorbing material.

It comprises of an adjustable filter, propagation tube, large sample tube 100 mm diameter (0-1500 Hz), small sample tube 28 mm diameter (1500-6000 Hz) and two-microphone technique and a digital frequency analysis system for the estimation of the normal incidence sound absorption coefficient and normal specific acoustic impedance proportion of materials [14, 15, 17]. The sample is analyzed by using impedance tube test according to ASTM E1050 for evenly mounted orientation materials for the frequency range of 100-6000 Hz.

Results and Discussion

The influences of material density on acoustic properties

Density difference plot of sound absorbing polymer foam composites used in this research, relying on the percentage of added wood fiber as shown in Figure 3. The highest density is 865.5 kg/m^3 for UF_{80} samples, follows by 850.8 kg/m^3 for UF_{85} sample, then, 835.1 kg/m^3 for UF_{90} sample, and 814.7 kg/m^3 for UF_{95} sample. Meanwhile, the smallest density is 807.0 kg/m^3 for UF sample. As the wood waste fiber percentage used increases, the density of the material also increases.

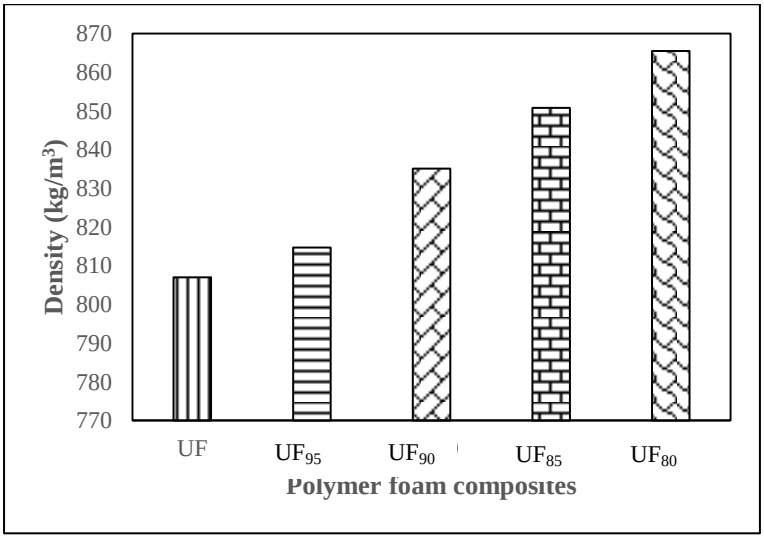


Figure 3. Density of polymer foam composites, kg/m^3

The influences of type and pore size of materials on acoustic properties

Type and size of pores are among important factors to be considered in porous sound absorbing material. In Figure 4, the overall polymer foam composites samples show open pores. Open pores with continuous channels give better sound absorption, because of the multiple reactions between the sound wave and the walls of the pores [2, 18]. As a result, more energy will be transformed into heat energy resulting in high sound wave absorption.

From Figure 4, the average pore size was calculated and presented in Figure 5. It can be observed that, as the weight percentage of wood fiber is increased, the average pore size will decreases. In Figure 5, UF gives the largest average pore size with 578.4 μm, follows by UF_{95} with 574.4 μm, UF_{90} with 568.2 μm and UF_{85} with 504.4 μm. The smallest average pore size shows by UF_{80} with 413.4 μm. The influence of pore size on sound absorption can be understood by the difference in the converted energy from sound energy to thermal energy through friction with the inner wall of air and pores. As cross-referring to Figure 6, the smaller the pore size, the more the collision happens among sound wave and cell wall, the longer the path of reflection and refraction and the more the absorption energy, the greater the sound absorption coefficient [19].

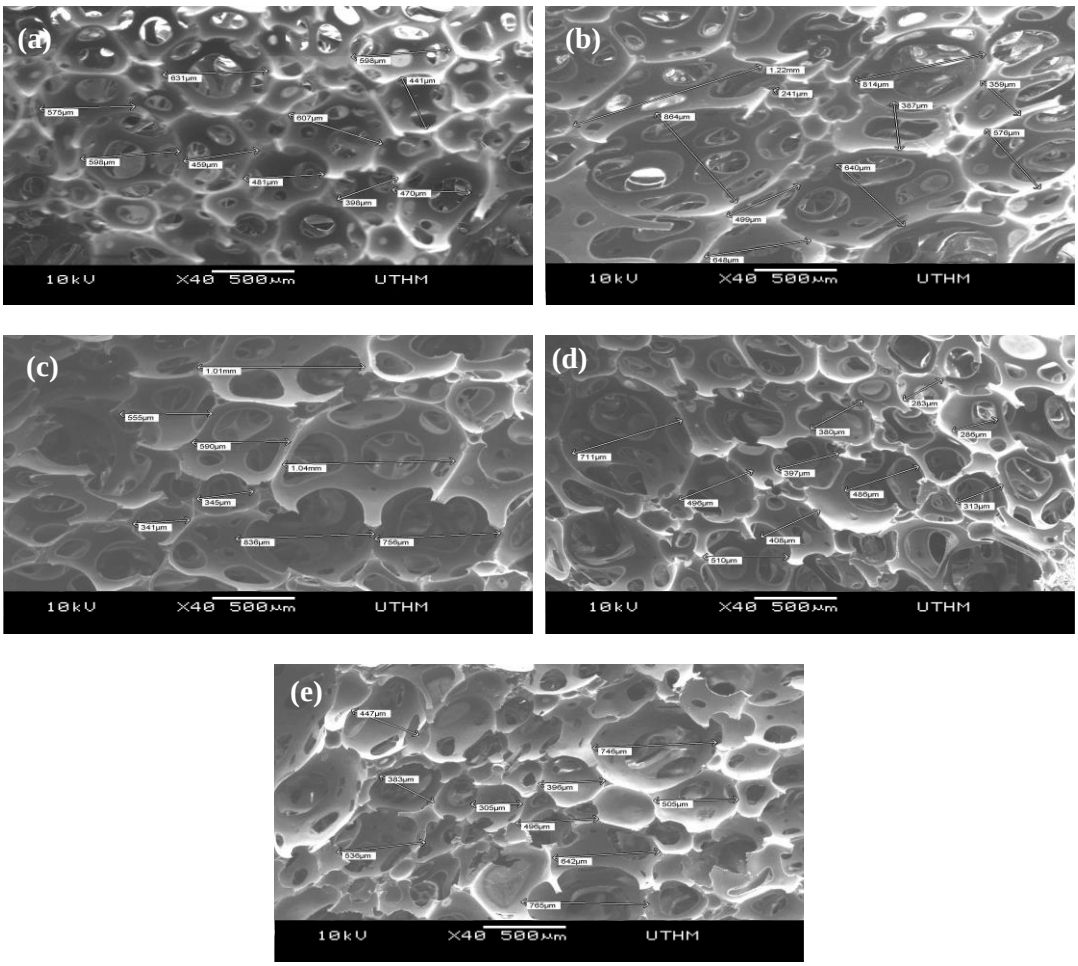


Figure 4. SEM image of polymer foam composites for: (a) UF, (b) UF_{95}, (c) UF_{90}, (d) UF_{85} and (e) UF_{80}

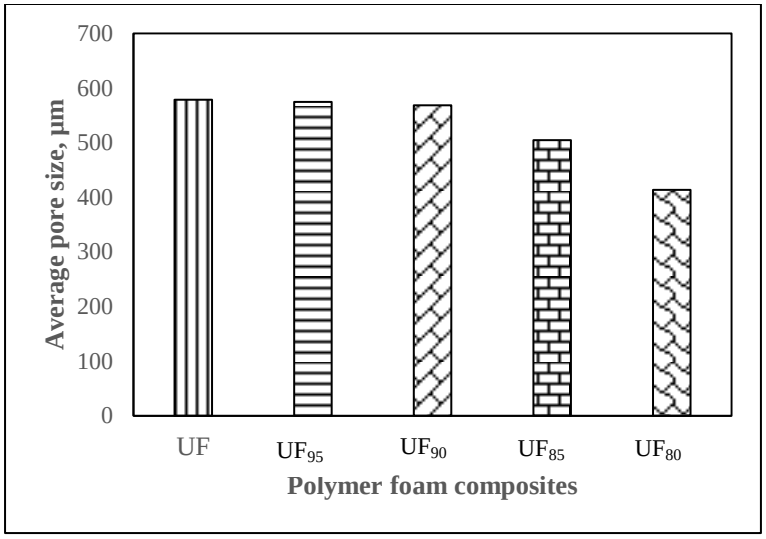


Figure 5. Average pore size, μm of polymer foam composites for: (a) UF; (b) UF_{95}; (c) UF_{90}; (d) UF_{85} and; (e) UF_{80}

The influences of wood fiber percentage on acoustic properties

The influences of wood fiber percentage used in producing polymer foam composites on the sound absorption coefficient are shown in Figure 6. Polymer foam composites with wood waste fiber have better sound absorption properties in comparison to the UF that gives sound absorption coefficient, α is 0.1606 and 0.7737 at low (0 – 1500 Hz) and high (1501- 6000 Hz) absorption frequency level in the overall frequency range analyzed. The UF_{80} gives α, 0.2355 and 0.9507 at the low and high absorption frequency level respectively. The UF_{85} shows at the low and high absorption frequency level; α is 0.2210 and 0.9211, respectively. At the low and high absorption frequency level, UF_{90} α is 0.1700 and 0.8994, respectively. The UF_{95} shows that at the low and high absorption frequency level, α is 0.2355 and 0.9507, respectively. The maximum value of α is achieved by sample material UF_{80} at high absorption frequency level. Thus, the sound absorption coefficient has a strong connection with the amount of percentage wood fiber added in the polymer foam composites [16, 20].

The increase in sound absorption coefficient due to the large surface area of fillers on the polymer foam composites interface in which the acoustic energy can be dissipated as heat energy [2]. Sound propagation takes place in a network of interconnected pores where viscous and thermal interaction causes the acoustic energy to be dissipated and converted into heat energy. At low frequencies, polymer foam composites absorb sound by energy loss caused by heat exchange. This is an isothermal process. The absorbed energy moves within the cells by friction with air. This friction is converted into heat. Formation of fine morphology by fillers creates more paths for passing of sound waves into foam structure and as a consequence, polymer foam composites absorb more sound [2, 17].

As cross-referring in the previous page, in Figure 3, the density of polymer foam composites influences the sound absorption coefficient. Thus, by referring to Figure 6, as the density of the polymer foam composites increased, the sound absorption value at high frequency absorption level (1501 - 6000 Hz) also increases. When the wood fiber percentage per unit area increases, the apparent density becomes increases. Materials with higher density normally will absorb more sound energy caused by more surface frictional between the sound wave and the fiber elements [4, 21]. Hence, the sound absorption coefficient increases when energy loss increases as the surface friction increases. From Figure 6, less dense and more open structure absorbs sound at low absorption level frequencies (500 Hz) while, denser polymer foam composites absorb better at frequencies above than 2000 Hz.

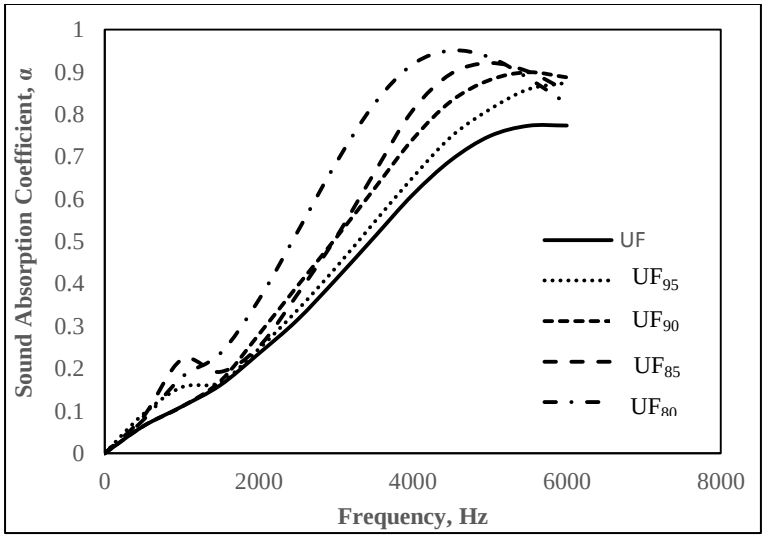


Figure 6. Sound absorption coefficient of polymer foam composites at low and high frequency absorption level

Further interest in acoustic analysis properties of polymer foam composites of the sound absorption coefficient, α values at different frequency ranges is calculated by using a single value; which is the noise reduction coefficient (NRC). The noise reduction coefficient (NRC) is the average of sound absorption coefficients, α at a specified set of frequencies, typically 250 Hz, 500 Hz, 1000 Hz, and 2000 Hz in accordance with the type of tube and acoustic measuring instrument used for the tests. The NRC can be calculated by using the formula in equation 1:

$$NRC = \frac{(\propto_{250} + \propto_{500} + \propto_{1000} + \propto_{2000})}{4} \quad (1)$$

Interpretation of acoustic properties of flexible polyurethane foam by adding wood fiber can be gained from the values of noise reduction coefficient in Figure 7, which is higher in the case of polymer foam composites. As the percentage of wood fiber increase, the value of noise reduction coefficient (NRC) also increases [1, 22]. The UF_{80} has the maximum NRC value of 0.3140, which is twice as UF.

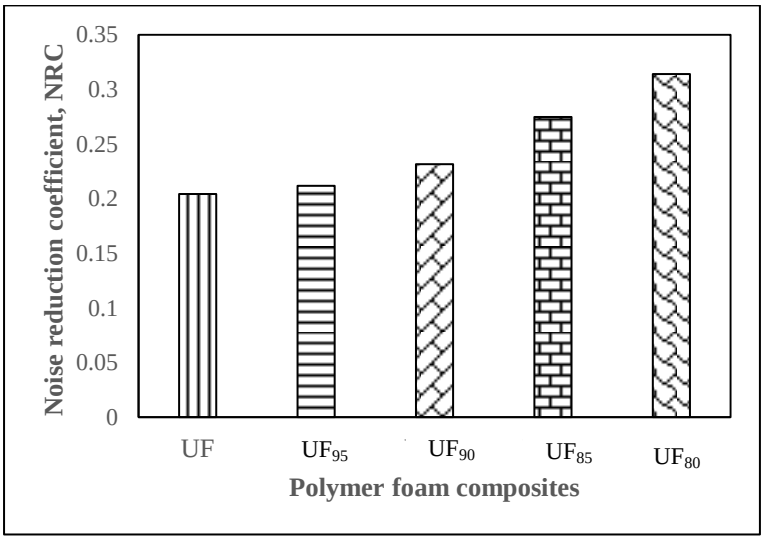


Figure 7. Noise reduction coefficient of polymer foam composites

Conclusion

Acoustic properties of polymer foam composites show a great influence to improve the current materials properties and producing advanced materials with better sound absorption properties. These sound absorbing materials can lessen the cost as well as beneficial to sound absorbing material by producing materials from reused and natural resources. Polymer foam composites produced by mixing the *Shorea leprosula* wood fiber in flexible polyurethane foam matrix revealed excellent acoustic properties with better improvement compared to UF foam. The UF_{80} polymer foam composite was found to be the best composite used in noise reduction application with a maximum sound absorption coefficient of 0.9507 and noise reduction coefficient of 0.3140. Furthermore, the microstructural morphology shows an open pore and smallest pore size with 413.4 µm with a maximum density of 865.5 kg/m^3. Consequently, the produced polymer foam composites are best to use both for outdoor and indoor sound absorption applications.

Acknowledgement

The author would like to thank Sustainable Polymer Engineering, Advanced Manufacturing and Materials Center (SPEN-AMMC), Universiti Tun Hussein Onn Malaysia (UTHM), Johor and Malaysian Government for supporting this research under Postgraduate Incentive Research Grant (GIPS U832) and Fundamental Research Grant Scheme (FRGS), vot 1481.

References

1. Chathurangani, O. S., Perera, W. J. M. K., Kumari, H. M. N. S., Subashi, G. H. M. J. and De Silva, G. S. Y. (2013). Utilization of sawdust and coconut coir fibre as noise reducing wall surface materials. http://dl.lib.mrt.ac.lk/handle/123/8928. [Access online 27 March 2018].
2. Gayathri, R., Vasanthakumari, R. and Padmanabhan, C. (2013). Sound absorption, thermal and mechanical behavior of polyurethane foam modified with nano silica, nano clay and crumb rubber fillers. *International Journal of Scientific & Engineering Research*, 4(5): 301-308.
3. Peng, L., Song, B., Wang, J. and Wang, D. (2015). Mechanic and acoustic properties of the sound-absorbing material made from natural fiber and polyester. *Advances in Materials Science and Engineering*, 2015: 1-5.
4. Zhu, X., Kim, B. J., Wang, Q. and Wu, Q. (2013). Recent advances in the sound insulation properties of bio-based materials. *BioResources*, 9(1): 1764-1786.
5. Maderuelo-Sanz, R., Nadal-Gisbert, A. V., Crespo-Amorós, J. E. and Parres-García, F. (2012). A novel sound absorber with recycled fibers coming from end of life tires (ELTs). *Applied Acoustics*, 73(4): 402-408.
6. Gu, R., Sain, M. M. and Konar, S. K. (2013). A feasibility study of polyurethane composite foam with added hardwood pulp. *Industrial Crops and Products*, 42: 273-279.
7. Luo, X., Mohanty, A. and Misra, M. (2013). Lignin as a reactive reinforcing filler for water-blown rigid biofoam composites from soy oil-based polyurethane. *Industrial Crops and Products*, 47: 13-19.
8. Mamtaz, H., Fouladi, M. H., Al-Atabi, M. and Namasivayam, S. N. (2016). Acoustic absorption of natural fiber composites. *Journal of Engineering*, 2016: 1-11.
9. Chen, S., Jiang, Y., Chen, J. and Wang, D. (2015). The effects of various additive components on the sound absorption performances of polyurethane foams. *Advances in Materials Science and Engineering*, 2015: 1-9.
10. Lacoste, C., Basso, M. C., Pizzi, A., Celzard, A., Ella Ebang, E., Gallon, N. and Charrier, B. (2015). Pine *(P. pinaster*) and Quebracho (*S. lorentzii*) tannin-based foams as green acoustic absorbers. *Industrial Crops and Products*, 67: 70-73.
11. Zulkifli, R., Zulkarnain and Nor, M. J. M. (2010). Noise control using coconut coir fiber sound absorber with porous layer backing and perforated panel. *American Journal of Applied Sciences*, 7(2): 260-264.
12. Youneung, L. and *Changwhan* J. (2003). Sound absorption properties of recycled polyester fibrous assembly absorbers. *AUTEX Research Journal*, 3(2): 78-84.
13. Ekici, B., Kentli, A. and Küçük, H. (2012). Improving sound absorption property of polyurethane foams by adding tea-leaf fibers. *Archives of Acoustics*, 37(4): 515-520.
14. Azahari, M. S. M., Rus, A. Z. M., Kormin, S. and Zaliran, M. T. (2017). Acoustic properties of polymer foam composites blended with different percentage loadings of natural fiber. *IOP Conference Series: Materials Science and Engineering*, 244(1): 012009.

15. Azahari, M. S. M., Rus, A. Z. M., Zaliran, M. T. and Kormin, S. (2017). Improving sound absorption property of polyurethane foams doped with natural fiber. *IOP Conference Series: Materials Science and Engineering*, 226(1): 012009.
16. Rus, A. Z. M. and Shafizah, S. (2015). Acoustic behavior of polymer foam composite of *Shorea leprosula* after UV-irradiation exposure. *International Journal of Mechanical, Aerospace, Industrial and Mechatronics and Manufacturing Engineering*, 9(1): 188-192.
17. Rus, A. Z. M., Azahari, M. S. M., Kormin, S., Soon, L. B., Zaliran, M. T. and Ahraz Sadrina M. F. L. (2017). Hybrid waste filler filled bio-polymer foam composites for sound absorbent materials. *AIP Conference Proceedings*, 1877(1): 060004.
18. Berardi, U. and Iannace, G. (2015). Acoustic characterization of natural fibers for sound absorption applications. *Building and Environment***,** 94: 840-852.
19. Soto, G., Castro, A., Vechiatti, N., Iasi, F., Armas, A., Marcovich, N. E. and Mosiewicki, M. (2017). Biobased porous acoustical absorbers made from polyurethane and waste tire particles. *Polymer Testing*, 57: 42-51.
20. Sa'adon, S. and Rus, A. Z. M. (2013). Utilization of treated red meranti wood dust as polymer foam composite for acoustic study. *Key Engineering Materials*, 594-595: 760-764.
21. Nandanwar, A., Kiran, M. C. and Varadarajulu, K. C. (2017). Influence of density on sound absorption coefficient of fibre board. *Open Journal of Acoustics*, 7: 1-9.
22. Sa'adon, S. and Rus, A. Z. M. (2014). Acoustical behavior of treated wood dust-filler for polymer foam composite. *Applied Mechanics and Materials*, 465-466: 1039-1043.

Malaysian Journal of Analytical Sciences, Vol 22 No 6 (2018): 1040 - 1047
DOI: https://doi.org/10.17576/mjas-2018-2206-14

MALAYSIAN JOURNAL OF ANALYTICAL SCIENCES
Published by The Malaysian Analytical Sciences Society
ISSN 1394 - 2506

POLYURETHANE MEMBRANE AS AN ADSORBENT FOR METHYL ORANGE AND ETHYL VIOLET DYES

(Membran Poliuretana Sebagai Penjerap untuk Pewarna Metil Oren dan Etil Ungu Lembayung)

Khairiah Haji Badri[1,2]*, Fatem Hamimie Ismail[1], Amira Shakim Abdul Shakir[1], Sharifah Mohamad[3], Hawa Aqilah Hamuzan[1], Nur Syakilla Hassan[1]

[1]*Polymer Research Center, Faculty of Science and Technology*
[2]*School of Chemical Sciences and Food Technology, Faculty of Science and Technology*
Universiti Kebangsaan Malaysia, 43600 UKM Bangi, Selangor, Malaysia
[3]*Department of Chemistry, Faculty of Science,*
Universiti Malaya, 50603 Kuala Lumpur, Malaysia

**Corressponding author: kaybadri@ukm.edu.my*

Received: 27 July 2017; Accepted: 28 April 2018

Abstract

Ethyl violet (EV) and methyl orange (MO) are commercial dyes used in a large number of industries. Due to their complex chemical structures and synthetic nature, these dyes are highly stable to light and oxidation, making them non-biodegradable, highly toxic, carcinogenic and mutagenic in nature. Among all techniques, adsorption continues to attract considerable attention due to its simplistic approach and numerous benefits such as greater efficiency, capacity to remove dyes on a large scale, ease of recovery, and recyclability of adsorbents. A palm-based polyurethane (PU) membrane has been synthesised into adsorbent and its ability to adsorb the dye molecules was investigated. The PU membrane was produced *via* condensation polymerisation between palm-based monoester (PKOp) and 4,4-methylene diphenyl diisocyanate (MDI) with acetone as the solvent. The FTIR spectrum has confirmed the formation of urethane linkage (HN-(C)O) through the presence of N-H, C-NH, C-O-C and C=O urethane peaks which were observed at 3293 cm^{-1}, 1602cm^{-1}, 1221 cm^{-1} dan 1716 cm^{-1}, respectively. Tensile testing has demonstrated that as the thickness of membrane is increased, the elasticity also increased proportionally with increasing tensile strain ranging from 6.7 MPa to 7.42 MPa. Various adsorption parameters such as initial concentration of dyes, effect of pH, effect of adsorbent dosage and contact time were studied and optimised. The adsorption study revealed that approximately 99% of EV and 25% of MO was adsorbed by the PU membrane within a short duration of 30 minutes. The parameters were determined from Langmuir, Freundlich and Temkin adsorption isotherm models. The isotherm studies specified that the adsorption of PU membrane towards EV and MO dyes is well fitted to the Langmuir model with the value of the maximum adsorption capacities for monolayer adsorption at 9.461 mg/g for EV and 4.340 mg/g for MO.

Keywords: polyurethane membrane, adsorption, ethyl violet, methyl orange, adsorption isotherm

Abstrak

Etil ungu lembayung (EUL) dan metil oren (MO) adalah pewarna komersial yang digunakan dengan banyaknya dalam industri. Pewarna ini adalah sangat stabil di bawah dedahan cahaya dan pengoksidaan disebabkan oleh struktur kimianya yang komplek dan sifat sintetiknya menjadikannya tidak terbiodegradasi, sangat bertoksik, karsinogenik dan mutagenik. Penjerapan adalah kaedah yang semakin mendapat perhatian disebabkan pendekatannya yang ringkas dan kepentingan lain seperti keberkesanan yang tinggi, kemampuan menyingkirkan pewarna pada skala besar, perolehan semula yang mudah dan kitar-semula penjerap. Membran PU telah dihasilkan melalui tindak balas pra-pempolimeran antara monoester berasaskan poliol sawit (PKO-p) dan 4,4-metilena difenil diisosianat (MDI). Pencirian membran PU dijalankan melalui analisis spektroskopi FTIR, FESEM serta ujian regangan. Kehadiran tulang belakang uretana dikenalpasti dalam spektrum FTIR membran PU dengan kehadiran puncak N-H, CNH, C-O-C dan C=O masing-masing dikesan pada nombor gelombang 3293 cm^{-1}, 1602cm^{-1}, 1221 cm^{-1} dan 1716 cm^{-1}.

Ujian regangan menunjukkan pertambahan dalam ketebalan membran meningkatkan terikan regangan dalam julat 6.7 MPa sehingga 7.42 MPa. Beberapa parameter penjerapan seperti kepekatan awal pewarna, kesan pH, kesan dos penjerap dan masa sentuhan telah dikaji dan dioptimumkan. Kajian penjerapan mendapati kira-kira 99% EUL dan 25% MO telah dijerap oleh membran PU dalam tempoh yang singkat iaitu 30 minit. Parameter ini ditentukan melalui model penjerapan isoterma Langmuir, Freundlich dan Temkin. Kajian isoterma ini mendapati penjerapan membran PU terhadap EUL dan MO adalah bertepatan dengan model Langmuir dengan nilai maksima kapasiti penjerapan sebanyak 9.461 mg/g untuk EUL dan 4.340 mg/g untuk MO.

Kata kunci: membran poliuretana, penjerapan, etil ungu lembayung, metil oren, isoterma penjerapan

Introduction

Rapid growth in industrial and manufacturing activities not only led to economic development but it has increased pollution by releasing toxic materials to the environment. An increasing concern on releasing of dye effluents from the textile industry into the aquatic ecosystems has initiated this study. It has become a major problem due to non-biodegradable nature of dyes which permanently pollute the environment [1-4]. Furthermore, bright coloured effluent containing toxic dyes may adversely affect aquatic life by lowering the penetration rate of sunlight entering the water and causing harm to living organisms [5-7]. Ethyl violet (EV) and methyl orange (MO) are commercial dyes used in a large number of industries, not only textile but also the food industry. Due to their complex chemical structures and synthetic nature, these dyes are highly stable to light and oxidation, making them non-biodegradable, highly toxic, carcinogenic and mutagenic in nature.

Thus, effective approaches are necessary to reduce this problem. Solid adsorbent has been increasingly used recently for the removal of chemical substance from industrial waste water. The adsorption method using polymeric membranes is one of the interesting methods that can be studied. Polymeric membrane has the ability to remove dye in a short time and polymer has high resistance to chemical and thermal stability. Polymers such as polyurethane (PU) is one of the polymers that can be used to study membrane adsorption levels based on the elastomer characteristics of PU and its ability to act as membranes. Besides that, PU is elastic and has good adsorption properties [8-10]. In this research, PU membrane was prepared and adsorptions of dyes on PU membrane were examined.

Materials and Methods

Materials

Palm-based polyol (PKO-p) was supplied by UKM Technology Sdn Bhd directly from the pilot plant stationed at UKM/MPOB Station, Pekan Bangi Lama, Selangor, Malaysia. 4,4-diphenylmethane diisocyanate (MDI) was obtained from Behn Meyer Agricare (M) Sdn. Bhd Subang Jaya Selangor, Malaysia. Industrial grade acetone was supplied by Saintifik Gemilang Sdn. Bhd. Polyethylene glycol (PEG; MW 200 Da) and hydrochloric acid (HCl, 98%) were purchased from Merck (M) Sdn Bhd. Selangor, Malaysia. Sodium hydroxide pellet (NaOH, ~98% purity) was supplied by Systerm Sdn Bhd, Shah Alam, Selangor, Malaysia. Ethyl violet (cationic triarylmethane dye) and methyl orange (anionic dye) were purchased from Sigma Aldrich (M) Sdn. Bhd. Both dyes were used without further purification.

Method

Pre-polymerisation method was used to produce the palm-based PU membrane. Polyurethane membrane involved the reaction between PKO-p and MDI in the presence of PEG as the chain extender and acetone as the solvent. Initially, 100 wt.% PKO-p, 40 wt.% PEG and 30 wt.% acetone were mixed together and then reacted with the mixture consisting of 100 wt.% MDI and 30 wt.% acetone at a ratio of 1:1 and stirred for 30 s until a homogeneous mixture was obtained. The mixture was casted on a Teflon plate and left at room temperature for the curing process.

Characterisation

Fourier transform infrared spectroscopy (FTIR) analysis was conducted using a Perkin Elmer Spectrum 400 model spectrophotometer. Each spectrum was recorded in a frequency ranging from 4000 to 650 cm^{-1} *via* the ATR-FTIR technique. The tensile test was performed using Instron Universal Testing Machine model 2716 Series in accordance with ASTM D882-10 standard. The PU membrane was cut into dumbbell-shape with the dimension of 180 mm x 25 mm (length x width). The surface morphology of the PU membrane was examined using a Field

Emission Scanning Electron Microscope (FESEM) model JEOL JSM-7600F. PU membrane was cut into cube shape with the dimension of 2 mm x 2 mm x 2 mm for the adsorption experiment.

Adsorption experiments

For the effect of contact time study, 250 ml of dye solution was prepared and 0.6 g adsorbent was added and shaken using an electronic shaker at 180 rpm. The temperature was maintained at 30 °C. Initial concentrations of dyes were studied by preparing five different concentrations which were 5, 10, 15, 20, 25 and 30 ppm dye solutions. About 0.6 g of adsorbent was added into 250 ml dye solution and left for 40 min at 30 °C. The solutions were filtered and further examination was carried out using UV-vis spectrometer. In the pH study, a constant amount of adsorbent (0.6 g) was added into a constant volume of dye (250 ml). The initial concentration used was 10 ppm with different pH. The pH of dyes was adjusted to 2.5, 4.5, 5.5, 7.5, 8.5 and 12.5 by adding 0.01 M NaOH and 0.01 M HCl. The flask was shaken at 180 rpm using the electronic shaker at 30 ° C. In order to investigate the effect of adsorbent dose, different amounts of adsorbent (0.2 g, 0.4 g, 0.6 g, 0.8 g, 1.0 g and 1.2 g) were added into the 250 ml dye solution at 30 °C, pH 7 with 30 minutes contact time.

Results and Discussion

Fourier transform infrared spectroscopy

The FTIR spectrum exhibited the presence of several peaks related to the functional group in PU membrane. PU was formed from the reaction between isocyanate group (-N=C=O) with hydroxyl group (OH) from PKO-p to produce urethane linkage. The presence of C-NH, -OH, CNH dan C=O peaks were observed in FTIR spectrum of PU membrane. Table 1 summarises several important peaks observed in the FTIR spectra of the PU membrane, MDI and PKO-p.

Table 1. Data analysis from the FTIR spectrum of the PU membrane, MDI and PKO-p

Functional Group	Wavenumber, cm^{-1}		
	PU	MDI	PKO-p
N-H	3293	-	-
CH_2	2923	2914	2853
CH_3	2853	-	2922
C=O	1716	1717	1737
C-N	1602	1608	-
N-H	1534	-	-
C-O-C	1221	-	1048
N=C=O	-	2246	
-OH	-	-	3359

The peak at 3293 cm^{-1} indicated the presence of NH group. The peaks at 2923 and 2853 cm^{-1} are attributed to the stretching vibration of $-CH_2$ and CH_3. The absorption peaks at 1716 cm^{-1}, 1602 cm^{-1} and 1221 cm^{-1} are assigned to carbonyl urethane group (C=O), carbamate (C-NH) and ether (-C-O-C-) respectively. These peaks showed the presence of the urethane bond which is the main chain in the PU structure. The disappearance of isocyanate group in MDI and hydroxyl group in PKO-p from the PU spectra showed that MDI and PKO-p have completely reacted to form PU [11].

Field emission scanning electron microscope analysis

FESEM analysis provides information about surface morphology and pore distribution of the PU membrane. This information is used to study on the porosity property of the PU membrane and its effect on adsorption of the dyes. Basically, PU membrane has a flat surface and is transparent. However, the clear colour of PU membrane changed to yellowish for a thicker PU membrane. Figure 1 shows the FESEM micrographs obtained at three different

magnifications which are (a) 5,000x, (b) 10,000x, (c) 20,000x and (d) 25,000x. The FESEM micrographs show the porosity and the hollow structure on the surface of the PU membrane. Membranes with pores indicate excellent potential in the adsorption study. Presence of pores is important for an adsorbent to effectively work in the adsorption process.

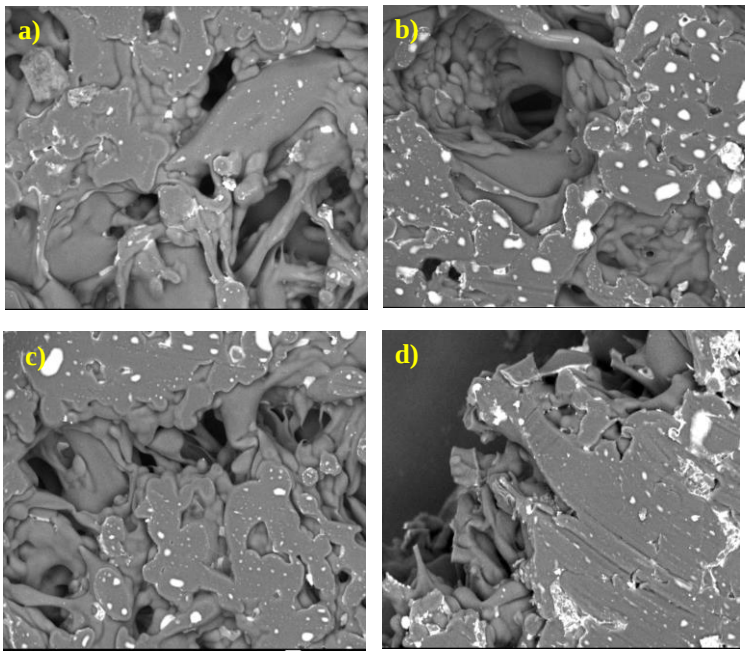


Figure 1. FESEM micrographs at magnifications of (a) 5,000x, (b) 10,000x, (c) 20,000x and (d) 25,000x

Tensile properties

Figure 2 shows the graph of tensile strain at break and tensile stress against thickness of the PU membrane. The percentage of tensile strain at break increased from 418 % to 543% with increasing thickness from 0.8 mm to 2.5 mm (Figure 2a). However, the percentage of tensile strain at break reduced for PU membrane at 2.5 mm thickness. The same trend is observed in Figure 2b where increasing thickness of the PU membrane from 0.8 mm to 2.5 mm increased the tensile stress from 6.70 MPa to 7.42 MPa. Based on the graph, the PU membrane with 2.0 mm thickness has been selected for adsorption studies. This is because it shows the highest tensile strain capability, indicating the highest elasticity and tensile strength.

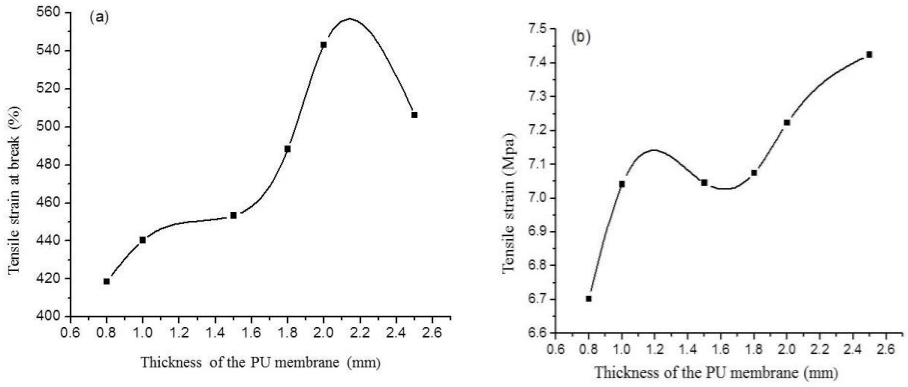


Figure 2. (a) Tensile strain at break and (b) tensile strain trends with increasing thickness of the PU membrane

Adsorption study

The pH of the aqueous medium is an important factor in the adsorption process. In order to investigate the effect of pH on dye removal, studies were carried out at the pH range of 2.5-12.5 at the dye concentration of 10 mg/L, adsorbent dosage of 0.6 g in 250 ml and 60 min contact time at room temperature. As shown in Figure 3(a), the maximum removal percentage of MO was observed at pH 7 (neutral) and at higher than pH 7, the removal percentages reduced. For MO, the percent removal of dyes increased with the increasing pH from acidic condition (more than pH 7) to the maximum state at base condition (pH 8.5). MO has a pKa value of 3.4 [12]. If the pH value is less that the *pKa* value, MO that exists in anionic state will become protonated.

Effect of absorbent dosage on the absorption of EV and MO was investigated using six different masses of PU membrane as shown in Figure 3(b). As we can see, the removal percentage increased significantly at low dosage of PU membrane up to a point where the removal percentage remained constant. Optimum dosage of PU membrane for removal percentage was 0.6 g for both EV and MO. At 0.6 g dosage, PU membranes had adsorbed 98% of EV and 25% of MO.

In this study, adsorption of dyes on PU membrane at different contact time has been studied for 3 hours with the constant initial concentration of 10 mg/L, temperature of 30 °C, adsorbent dosage of 0.6 g/250 ml and pH 7. The effect of contact time on removal percentages of dyes by PU membrane is presented in Figure 3 (c). For the first 40 min, the removal percentage of EV was rapid but after that it remained constant. Meanwhile, the removal percentage of MO increased slowly up to 50 minutes and then remained constant. Removal percentages for both dyes were constant at certain times due to the fact that absorption equilibrium has been achieved. The removal percentages of dyes were higher at the beginning because the absorbent provided a large surface area for adsorption until it accumulated or formed flux.

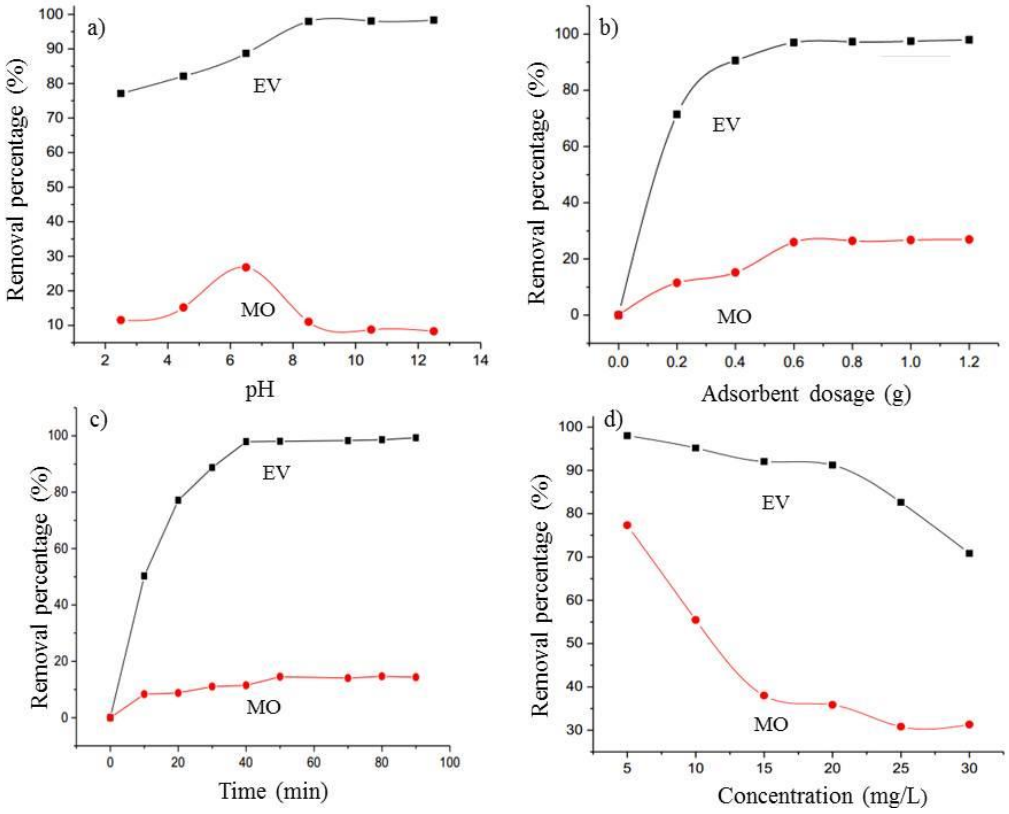


Figure 3. (a) Effect of pH, (b) amount of adsorbent, (c) contact time and (d) initial concentration on removal percentage of dyes

Dye concentrations were varied to 5, 10, 15, 20, 25 dan 30 ppm with constant weight of adsorbent at 0.6 g in 250 ml at pH 7 (Figure 4). The adsorption was monitored at 30 °C with 40 and 50 min contact time for EV and MO respectively. Figure 3(d) shows the effect of initial concentration of dye solution. As can be seen from the figure, both dyes showed higher removal percentage at 5 ppm concentration at about 98% and 78% for EV and MO respectively. At increasing dye concentrations, the removal percentage of both dyes decreased. This can be attributed to the fact that at lower concentrations, the availability of adsorption sites increased; thus, adsorption of dyes occurred immediately.

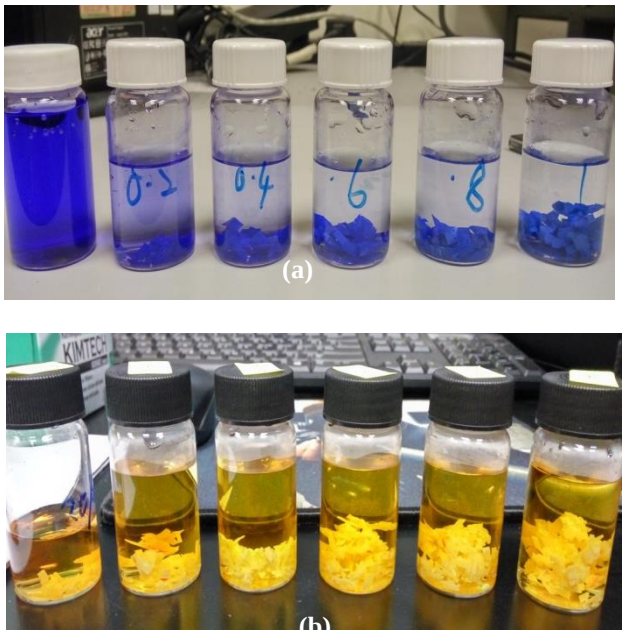


Figure 4. Physical changes on the dye-containing effluent upon removal of (a) EV and (b) MO dyes using the PU membranes at varying concentrations of the dyes

Adsorption isotherms

The isotherm parameters were explored to study the adsorption process by using Langmuir, Freundlich and Temkin adsorption isotherm models. In this study, Langmuir isotherm was employed to describe the adsorption isotherm. The linear form of Langmuir equation is as follows:

$$\frac{C_e}{q_e} = \frac{1}{Q_0 b} + \frac{C_e}{Q_0} \quad (1)$$

where C_e (mg/L) is the concentration of the dye solution at equilibrium (mg/L), q_e is the amount of dye adsorbed per mass of adsorbent (mg/g), Q_o and b is the Langmuir constant related to capacity and adsorption rate. The linear plot of C_e/q_e versus C_e (Figure 5) shows that the adsorption followed the Langmuir model with the value of the maximum adsorption capacity for monolayer adsorption at 9.461 mg/g for EV and 4.340 mg/g for MO respectively.

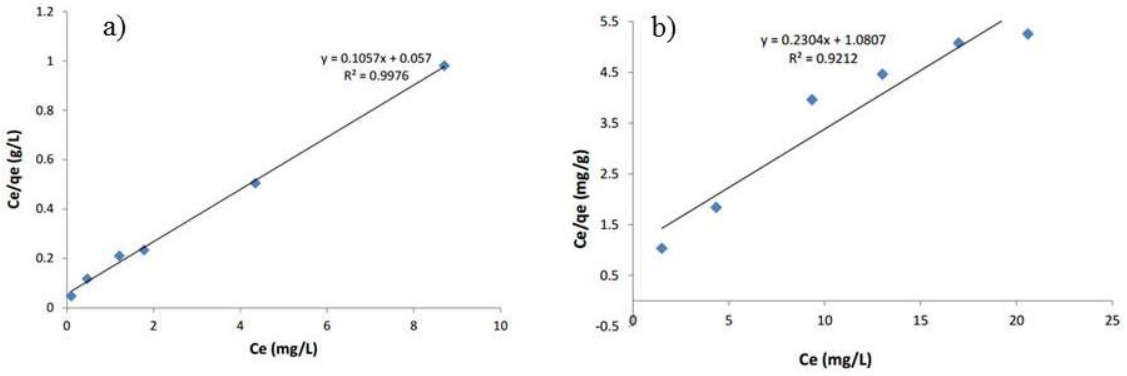


Figure 5. Langmuir adsorption isotherms for adsorption of (a) EV dye and (b) MO dye

Conclusion

Palm-based PU membrane has proven to be a promising adsorbent for the removal of EV and MO from aqueous medium. The removal percentage of dyes was found to be dependent on pH, adsorbent dosage, contact time and initial dye concentration. The adsorption study indicated that EV dye shows excellent absorption percentages on PU membrane compared to MO dye because the molecule size of EV is smaller than MO. Thus, the adsorption of EV dye molecules was more effective and quick. The adsorption data fitted very well in the Langmuir isotherm equation.

Acknowledgements

The authors would like to thank the Polymer Research Centre and School of Chemical Sciences and Food Technology, Faculty of Science and Technology, Universiti Kebangsaan Malaysia for providing the working area, Ministry of Higher Education and Centre for Research Instrumentation Management (CRIM), Universiti Kebangsaan Malaysia for the instruments provided for sample analysis throughout the study**.** This research has been funded by the Universiti Kebangsaan Malaysia through its Publication Grant Scheme DLP-2014-020.

References

1. Beydilli, M., Pavlostathis, S. and Tincher, W. (1998). Decolorization and toxicity screening of selected reactive azo dyes under methanogenic conditions. *Water Science and Technology*, **38**(4-5): 225-232.
2. Bayramoğlu, G. and Arica, M. Y. (2007). Kinetics of mercury ions removal from synthetic aqueous solutions using by novel magnetic p (GMA-MMA-EGDMA) beads. *Journal of Hazardous Materials*, 144(1): 449-457.
3. Bechtold, T., Burtscher, E. and Turcanu, A. (2001). Cathodic decolourisation of textile waste water containing reactive dyes using a multi- cathode electrolyser. *Journal of Chemical Technology and Biotechnology*, 76(3): 303-311.
4. Salleh, M. A. M., Mahmoud, D. K., Karim, W. A. and A. Idris. (2011). Cationic and anionic dye adsorption by agricultural solid wastes: A comprehensive review. *Desalination*, 280(1): 1-13.
5. Culp, S. J. and Beland, F. A. (1996). Malachite green: a toxicological review. *International Journal of Toxicology*, 15(3): 219-238.
6. Srivastava, S., Sinha, R. and Roy, D. (2004). Toxicological effects of malachite green. *Aquatic Toxicology*, 66(3): 319-329.
7. Attia, A. A., Girgis, B. S. and Fathy, N. A. (2008). Removal of methylene blue by carbons derived from peach stones by H_3PO_4 activation: batch and column studies. *Dyes and Pigments*, 76(1): 282-289
8. Queiroz, D. P. and De Pinho, M. N. (2005). Structural characteristics and gas permeation properties of polydimethylsiloxane/poly (propylene oxide) urethane/urea bi-soft segment membranes. *Polymer*, 46(7): 2346-2353.

9. Sadeghi, M., Semsarzadeh, M. A., Barikani, M. and Ghalei, B. (2010). The effect of urethane and urea content on the gas permeation properties of poly (urethane-urea) membranes. *Journal of Membrane Science,* 354(1): 40-47.
10. Li, H., Freeman, B. D. and Ekiner, O. M. (2011). Gas permeation properties of poly (urethaneurea) s containing different polyethers. *Journal of Membrane Science*, 369(1): 49-58.
11. Clemitson, I. (2011). Polyurethane casting prime edition. CRC Press, New York.
12. Shahabuddin, S., Sarih, N. M., Mohamad, S. and Baharin, S. N. A. (2016). Synthesis and characterization of Co_3O_4 nanocube-doped polyaniline nanocomposites with enhanced methyl orange adsorption from aqueous solution. *RSC Advances,* **6**(49): 43388-43400.

Malaysian Journal of Analytical Sciences, Vol 22 No 6 (2018): 1048 - 1056
DOI: https://doi.org/10.17576/mjas-2018-2206-15

MALAYSIAN JOURNAL OF ANALYTICAL SCIENCES
Published by The Malaysian Analytical Sciences Society
ISSN 1394 - 2506

DETERMINATION OF GLUCOSE CONTENTS IN KENAF

(Penentuan Kandungan Glukosa dalam Kenaf)

Fatin Afifah Ahmad Kuthi[1], Nurulhuda Mohd Yunus[1], Goh Kae Horng[1], Khairiah Haji Badri[1,2]*

[1]*School of Chemical Sciences and Food Technology, Faculty of Science and Technology*
[2]*Polymer Research Center, Faculty of Science and Technology*
Universiti Kebangsaan Malaysia, 43600 UKM Bangi, Selangor, Malaysia

**Corresponding author: kaybadri@ukm.edu.my*

Received: 27 July 2017; Accepted: 28 April 2018

Abstract

Kenaf is one of the potential plant fibres used in research on the extraction and recovery of glucose. Kenaf fiber is comprised of a kenaf core (KC) and kenaf bast (KB). This study was performed to explore a hot water pre-treatment (HWP) using boiling water immersion for 2 hours on both KC and KB. Alkaline treatment using 6% (w/v) sodium hydroxide (NaOH) aqueous solution was subsequently performed for 3 hours at room temperature. The percentages of α-cellulose and hemicellulose in both KC and KB were found to increase after HWP. On the contrary, the percentages of α-cellulose and hemicellulose decreased upon NaOH treatment. The percentage of Klason lignin was reduced when KC and KB had undergone the HWP and NaOH treatments. A Fourier transform infrared spectroscopy analysis (FTIR) revealed the removal of lignin from both parts of kenaf fibre after the NaOH treatment. This was confirmed when the peaks at 1735 cm^{-1} and 1246 cm^{-1} disappeared after the treatment. Glucose as part of carbohydrates was determined in the fibre and filtrate using phenol sulfuric (PS) and dinitrosalicylic acid (DNS) analyses respectively. PS analysis indicated that the amount of glucose in KC-HWP (0.17 mg/g) was higher than in untreated KC (0.13 mg/g) and KC-NaOH (0.09 mg/g). The untreated KB showed the highest glucose content (0.36 mg/g), followed by KB-HWP (0.29 mg/g) and KB-NaOH (0.18 mg/g). Meanwhile, DNS analysis disclosed that the glucose concentrations in the KC filtrate for both treatments were 0.05 mg/mL. In contrast, the DNS analysis for KB showed a slightly lower glucose concentration in the KB-HWP filtrate (0.062 mg/mL) compared to the KB-NaOH (0.064 mg/mL). The glucose production was highly related to the composition of α-cellulose in the kenaf fibers.

Keywords: carbohydrate, kenaf fibre, compositional analysis, phenol sulfuric, dinitrosalicylic acid

Abstrak

Kenaf merupakam salah satu serabut tumbuhan yang berpotensi dalam penyelidikan yang melibatkan pengestrakan dan perolehan glukosa. Serabut kenaf terdiri daripada dua bahagian iaitu teras (KC) dan kulit (KB). Kajian ini meneroka pra-rawatan rendaman air mendidih (HWP) selama 2 jam bagi kedua-dua KC dan KB. Seterusnya, rawatan alkali menggunakan 6% (w/v) larutan akues natrium hidroksida (NaOH) dijalankan selama 3 jam pada suhu bilik. Peratus kandungan α-selulosa dan hemiselulosa bagi KC dan KB didapati meningkat selepas pra-rawatan air panas. Sebaliknya, peratusan α-selulosa dan hemiselulosa menurun selepas rawatan NaOH. Peratus kandungan lignin Klason berkurang apabila KC dan KB menjalani rawatan HWP dan NaOH. Analisis spektroskopi inframerah transformasi Fourier (FTIR) menunjukkan bahawa berlaku penyingkiran lignin pada kedua-dua bahagian kenaf yang dirawat NaOH. Ia dapat dibuktikan apabila puncak pada nombor gelombang 1735 cm^{-1} dan 1246 cm^{-1} hilang selepas rawatan NaOH dijalankan. Glukosa yang merupakan sebahagian daripada karbohidrat ditentukan kandungannya di dalam serabut dan filtrat masing-masing menggunakan kaedah fenol sulfurik (PS) dan asid dinitrosalisilik (DNS). Berdasarkan analisis PS, kandungan glukosa dalam KC-HWP (0.17 mg/g) adalah lebih tinggi berbanding sampel KC tidak terawat (0.13 mg/g) dan KC-NaOH (0.09 mg/g). Berbeza dengan serabut KB di mana sampel KB tidak terawat menunjukkan kandungan glukosa yang tinggi iaitu 0.36 mg/g diikuti dengan KB-HWP (0.29 mg/g) dan KB-NaOH (0.18 mg/g). Analisis DNS menunjukkan kepekatan filtrat KC-HWP dan KC-NaOH adalah sama iaitu 0.05 mg/mL. Sebaliknya,

analisis DNS bagi KB mempamerkan kepekatan glukosa yang sedikit rendah dalam filtrat KB-HWP (0.062 mg/mL) berbanding filtrat KB-NaOH (0.064 mg/mL). Perolehan glukosa sangat bergantung kepasa kandungan komposisi α-selulosa serabut kenaf.

Kata kunci: serabut kenaf, analisis komposisi, karbohidrat, fenol sulfurik, asid dinitrosalisilik

Introduction

Kenaf (*Hibiscus cannabinus, L. family Malvacae*) has been planted intensively to replace tobacco plantations in Malaysia. Kenaf is a non-wood lignocellulosic material that originated from Africa [1]. Kenaf contains two parts, i.e. the outer part, which is known as the bast and the inner part called the core. The percentages of lignocellulosic material are different in both kenaf core and bast as shown in Table 1 [2]. Kenaf core (KC) is used as a source of pulp for the paper industry [3], cosmetics, industrial chemicals and biopolymers [4]. Meanwhile, kenaf bast (KB) is used to produce ropes, canvas, bags and carpets [5, 6].

Table 1. Chemical composition of kenaf core and bast [2]

Constituent (%)	Kenaf Bast	Kenaf Core
Holocelluose	76.9	77.6
α-cellulose	69.8	45.3
Lignin	9.2	19.0
Alcohol-benzene extractives	3.4	3.0
Hot water solubilty	15.9	7.5

Cellulose is a homopolysaccharide composed of β-D-glucopyranose, $C_6H_{10}O_5$ units which are linked together by (1→4)-glycosidic bonds with a molecular weight between 50,000 to one million kDa [7, 8]. Cellulose molecules are completely linear and have a strong tendency to form intra- and intermolecular hydrogen bonds. Bundles of cellulose molecules are thus aggregated together in the form of microfibrils in which crystalline regions alternate with amorphous regions [9].

Hemicelluloses are heterogeneous polysaccharides. Like cellulose, most hemicelluloses function as supporting materials in cell walls. The main feature that differentiates hemicellulose from the cellulose is that hemicellulose has branches with short leteral chains consisting of different sugars. Due to its branching sructure, hemicellulose lacks crystalline regions. Hemicellulose mainly consists of five carbon sugar monomers, xylose and six carbon sugar monomers such as glucose. In contrast to cellulose, the polymers present in hemicellulose are hydrloysable [10, 11].
Lignin can be divided into klason lignin (acid insoluble lignin) and acid soluble lignin. Lignin has a complex and large molecular structure containing cross-linked polymers of phenolic monomers. It is present in the primary cell wall and is resistant to microbial attack [12]. Lignin consists of three main C6-C3 (phenypropanoid) units known as syringyl alcohol, guaiacyl alcohol and p-coumaryl alcohol [13].

Measurements of carbohydrate content is one of the basic analytical operations. The most common methods used for measurement are the phenol sulfuric (PS) analysis and dinitrosalisylic (DNS) analysis. The phenol sulfuric method is widely used due to its sensitivity and simplicity [14]. The analytical method that can be used in determining the reduction in sugar usually involves colorimetric detection based on the oxidation of the carbonyl group. In a DNS analysis, dinitrosalicylic acid will react with the free carbonyl group in the reducing sugar under an alkaline environment. This will allow the formation of an aromatic compound (3-amino-5-nitrosalicylic acid) with the highest absorption at 540 nm [15].

In this paper, we focus on the compositional analysis of the kenaf core and bast before and after treatment by comparing the determination method of glucose content using either the phenol sulfuric analysis or the DNS assay analysis. The fibre was first pre-treated with hot water, followed by treatment with sodium hydroxide (NaOH) at 6%

(w/v). There are numerous methods that can be used to determine glucose content. In this study, the PS and DNS methods were chosen because they can provide a quick check on the sugar content [16]. These methods are not only reliable but also time and cost efficient [15].

Materials and Methods

Materials

The kenaf fibre used was generously supplied by Kenaf Natural Fibre Industry Sdn Bhd (KFI), Kelantan, Malaysia. The kenaf core (KC) and kenaf bast (KB) were refined to a size of 100 to 160 μm and 125-250 μm respectively. The chemicals used for α-cellulose, hemicellulose and lignin extraction and acid hydrolysis were ethanol, C_2H_5OH (John Kollin Chemicals, United Kingdom), sodium chlorite, $NaClO_2$ (Sigma Aldrich, USA) and hydrogen peroxide, H_2O_2 (Friendemann Schmidt Chemical, Germany). Acetic acid (CH_3COOH), sodium hydroxide pellet (NaOH), sulfuric acid (H_2SO_4) and toluene (C_7H_8) were purchased from Systerm Sdn Bhd, Selangor, Malaysia. The chemicals used for phenol sulphuric analysis, hydrochloric acid (HCl) and sodium carbonate ($NaCO_3$) were obtained from Systerm Sdn Bhd, Selangor, Malaysia. Chemicals used for the dinitrosalicylic (DNS) assay such as 3,5-dinitrosalicylic acid ($C_7H_4N_2O_7$), phenol crystal (C_6H_6O) were supplied by Fluka Analytical, Subang Jaya, Selangor, Malaysia, while sodium bisulfate ($NaHSO_3$) and potassium sodium tartrate ($KNaC_4H_4O_6{\cdot}4H_2O$) were purchased from Systerm Sdn Bhd, Selangor, Malaysia.

Method

The kenaf core (KC) and kenaf bast (KB) fibres were dried at 105 °C until a constant weight was obtained. Hot water pre-treatment (HWP) was carried out at a boiling temperature for 2 hours with a fibre to hot water ration of 1:20 [17, 18]. The sample was filtered and dried at 105 °C until it reached a constant weight. The pre-treated sample was then soaked in 6% (w/v) NaOH aqueous solution for 3 hours at room temperature. The ratio of fibre to NaOH aqueous solution was 1:20 [19, 20]. The sample was filtered and rinsed with distilled water for several times until it reached pH 7. The filtered cake was dried at 105°C for 24 h in a conventional oven until a constant weight was obtained. These steps were followed and repeated for KB fibre.

Characterisation: Chemical composition analysis

The untreated and treated kenaf fibres (KB and KC) were analysed to determine their moisture content, solubility and composition [21-26]. Standard methods of moisture content was followed, where the samples were dried in a conventional oven for 24 hours at the temperature of 105 °C (TAPPI T208 om-84). Hot water solubility (TAPPI T 207 om-81) was carried out by soaked the samples in a boiling water for 3 hours. Alcohol-benzene solubility was carried out to remove the extractives materials such as oil, wax and inorganic substances according to TAPPI T204 cm-97. Holocellulose content was determined according to Wise et al. [25] where the sample was bleached with natrium chlorite ($NaClO_2$) and and acetic acid (CH_3COOH) alternately. The α-cellulose content was determined via treatment of holocellulose sample with 17.5% (w/v) NaOH to removed hemicellulose from the fibres under 20 °C water bath (TAPPI T203 om-83). The KC and KB fibres was treated with 72% (v/v) H_2SO_4 for 1 hour followed by dilution of the acid to 3% (v/v) by addition of distilled water. Subsequently, the solution was heated at boiling temperature for 4 hours to determine the Klason-lignin content (TAPPI T222 om-83).

Fourier transform infrared spectrophotometer

The FTIR spectroscopy analysis was conducted on a spectrophotometer model Perkin Elmer Spectrum BX using the KBr pellet method. The functional group was analysed at wavenumbers ranging from 4000 to 400 cm^{-1} for the untreated, pre-treated and treated samples.

Phenol sulfuric analysis

100 mg of the untreated KC and KB were put into separate test tubes. Each sample was hydrolysed with 5 mL 2.5 N hydrochloric acid for 3 hours at 100 °C. The solution was cooled to room temperature and neutralised with 10% (w/v) sodium carbonate ($NaCO_3$) solution. Deionised water was added to a final volume of 100 mL. The solution was centrifuged and 0.1 mL of supernatant was placed into the test tube. Deionised water was added until the final volume reached 1 mL. 1 mL of 5% (w/v) of phenol solution was added, followed by 5 mL of 96% (v/v) sulfuric acid. The test tubes were placed in a water bath at 30 °C for 20 minutes. The colour was read at 490 nm on a UV-Vis Spectrophotometer (model Secomam Prim Advanced Visible Spectrophotometer) and 1 mL of deionised water

was set as the blank. A standard calibration curve was prepared using a glucose solution at concentration of 0.00 – 0.02 mg/mL. The absorbance reading was recorded. These steps were repeated for the HWP and NaOH samples.

Dinitrosalicylic acid assay: Preparation of dinitrosalicylic acid reagent

This reagent was prepared by dissolving 10 g of 3, 5-dinitrosalicylic acid and 10 g NaOH in deionised water. After a homogenous mixture was produced, 2 g of crystal phenol and 1 g $NaHSO_3$ were added in order to avoid the dinitrosalicylic acid from getting oxidised. Then, 133 g of $KNaC_4H_4O_6{\cdot}4H_2O$ was added, followed by deionised water until the total DNS reagent reached up to 1 L. The solution was mixed well until the entire reagent dissolved, and it was then stored in a dark place [27].

Determination of reducing sugar

300 µL of filtrate from the HWP pre-treated samples and 900 µL DNS solution were mixed using a vortex mixer in an Eppendorf tube. A blank solution was prepared by mixing 300 µL distilled water with 900 µL DNS reagent. These solutions were heated using a heating block at 95 °C for 5 min. After the solutions were cooled, a dilution process was carried out by adding 50 µL of each solution to 950 µL distilled water. These samples were analysed using a UV-vis spectrophotometer at 540 nm. The concentration of each sample was calculated using a standard D-glucose calibration curve at 0.05-1.00 mg/mL [28]. The absorbance was measured on a UV-Vis Spectrophotometer (model Secomam Prim Advanced Visible Spectrophotometer) at a fixed wavelength of 540 nm. These steps were repeated for filtrates obtained from the NaOH treatment of both KC and KB.

Results and Discussion

Compositional analysis

Table 2 shows the changes in the chemical compositions of KC and KB before and after treatment. The percentage of α-cellulose and hemicellulose increased upon pre-treatment with hot water. The hot water pre-treatment also showed a decrement in the percentage of lignin. According to Farm et al. [29], hot water pre-treatment helps in dissociating lignin and this then increases the cellulose content. The HWP caused the structure of KC and KB to open up or swell (Figure 1).

Table 2. Chemical composition of KC and KB

Constituent	Kenaf Core (KC), (%)			Kenaf Bast (KB), (%)		
	Untreated	HWP	NaOH	Untreated	HWP	NaOH
α-cellulose	30.2	30.5	22.9	56.5	57.8	66.8
Hemicellulose	31.9	42.3	17.2	28.0	28.3	11.8
Klason Lignin	22.0	20.5	14.0	10.9	10.7	9.40
Moisture content	5.80	4.80	6.30	8.00	2.20	7.20
Hot water solubility	11.8	13.0	33.5	14.8	10.5	11.5
Alcohol-benzene extractives	7.90	11.6	13.7	9.50	10.5	12.7

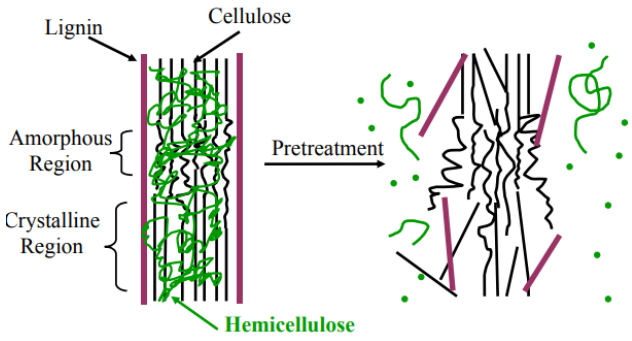


Figure 1. Pre-treatment effect on minimizing degradation of the fiber [30]

The composition of lignocellulosic materials decreased after the NaOH treatment. Hydrolysis via alkaline treatment resulted in the hydrogen bonding of the structure being disturbed, which leads to surface roughness [32, 33]. In this treatment, the extractive materials that covered the outer surface of the fibre such as wax and oils were removed. NaOH treatment causes the degradation in the ester linkage of lignin with carbohydrate chains (glycosidic linkages). During this treatment, there will be an alteration of lignin structure along with a partial decrystallisation of cellulose and hemicellulose [10, 33]. According to Trivedi et al. [34], alkaline treatment is also known as a delignification process as it can also solubilise some amount of hemicellulose. A saponification reaction occurred, leading to the disturbance of intermolecular ester bonds that cross-link xylan in hemicellulose.

The percentage of moisture content had decreased after HWP and increased after NaOH treatment. Cellulose is hydrophilic in nature, whereas lignin is hydrophobic [34]. According to Pettersen [35], wood materials absorb water, causing its cell walls to swell and become saturated with water. Kenaf fibre swells when exposed to moisture. Once the fibre swells, micro-cracking occurs and at later stage, wrecks the fibre. Thus, the hydrophilicity of kenaf fibre further contributes to major water penetration into the micro cracks. Theoretically, fibre with higher lignin content is expected to exhibit the lowest values of water absorption. This is due to the fact that lignin is hydrophobic, thus can provide resistance against the hydro-degradation (or hydrolysis) of kenaf fibre. The delignification process during alkaline treatment makes the water molecules to be easily absorbed by the fibre. As the NaOH solution penetrates into the kenaf fibre, the degradation of cellulose becomes active. The proposed mechanism of cellulose in alkaline media as shown in Figure 2 is also supported by Nosbi et al. [36].

Hot water solubility estimates the external components such as inorganic compounds, gum, sugar and coloring wood present [37]. In this analysis, the percentage of hot water solubility in NaOH samples was much higher compared to the HWP samples. When kenaf fibre was treated with alkaline solution, lignin was removed and water molecules were absorbed easily through the cellulose fibre [38].

Alcohol-benzene solubility indicated the presence of components such as wax, fats, resin, non-volatile hydrocarbons, carbohydrates with low molecular weight, salts and other water soluble materials [18, 37]. From the analysis, the percentage solubility in alcohol-benzene increased when treated with hot water and NaOH solution. This might be due to the increasing solvent absorption of the sample upon delignification of the fibres.

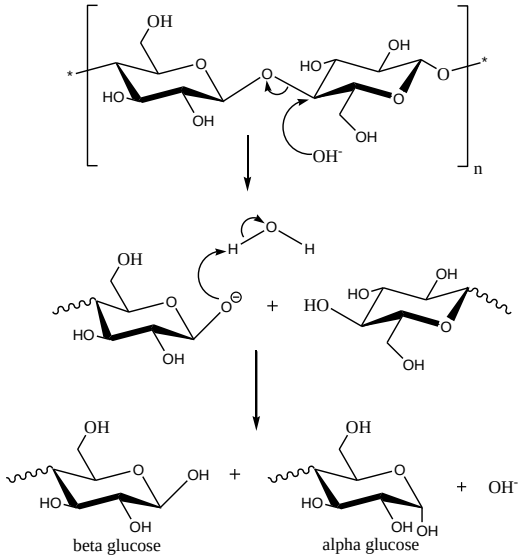


Figure 2. Hydrolysis of cellulose linkage in alkaline medium

Identification of functional group

Figures 3 and 4 shows the FTIR spectra for untreated and treated KC and KB, respectively. Peaks at 3400 and 2927 cm^{-1} represent the hydroxyl (OH) group and C-H stretching, respectively. These peaks belong to the cellulose, hemicellulose and lignin [39-41]. The peak at 1731 cm^{-1} indicates the presence of acetyl group (C=O) in the hemicellulose and lignin, while the peak at 1242 cm^{-1} is the stretching of the aryl group (C-O) in lignin [31, 42, 43]. The peak at 1650-1590 cm^{-1} is associated to the vibration of the C=C in the aromatic ring. The guaiacyl unit and syringyl units in lignin are present at 1245 cm^{-1} and 1375 cm^{-1} respectively. The guaiacyl unit comprises of two methoxy groups, whereas syringyl unit has one methoxy group [44, 45]. Upon alkaline hydrolysis, the peak of acetyl group (C=O) and peak of aryl group (C-O) disappeared. This indicates that the alkaline treatment has a greater tendency in removing lignin [33]. The absorption band around 897 to 898 cm^{-1} refers to the C-O-C stretching of β-glycosidic linkages [46, 47].

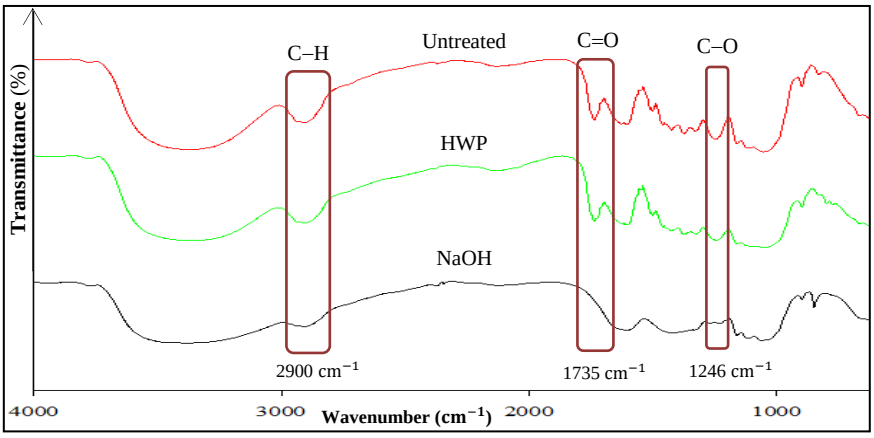


Figure 3. FTIR spectra of untreated and treated kenaf core (KC) fibre

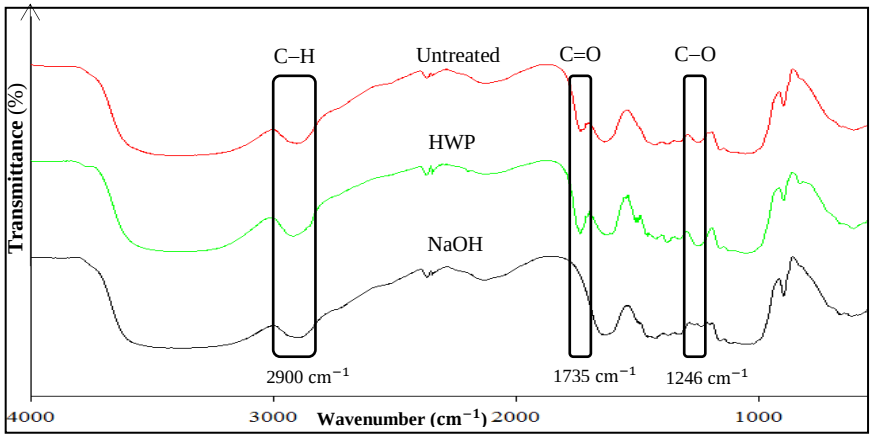


Figure 4. FTIR spectra of untreated and treated kenaf bast (KB) fibre

Examination of glucose content in kenaf fibres via phenol sulfuric analysis

The glucose concentration was determined based on the calibration curve. The increment of glucose concentration of KC after HWP are due to the dissociating of lignin and the increment of cellulose content by the treatment [29]. The HWP caused the structure of KC to swell and this aid the scissoring of the α-cellulose into glucose. Through this analysis (Table 3), the glucose recovery for KC and KB showed decrements after NaOH treatment. The reduction in glucose content is probably due to the possible formation of furfural during the acid hydrolysis. When

acid hydrolysis is running at a high temperature and high concentration, it will further degrade the glucose to furfural [48].

Table 3. Glucose concentration of untreated, HWP and NaOH treated KC and KB obtained from phenol sulfuric analysis

Fibre Sample	Glucose Concentration (mg/g)	
	KC	KB
Untreated	0.13	0.36
HWP	0.17	0.29
NaOH treated	0.09	0.18

Glucose content of kenaf treated filtrate *via* dinitrosalicylic acid assay

Table 4 shows that the reduced sugar resulting from hot water treatment is similar to the one obtained from the NaOH treatment. The result showed that the cellulose in fibres are readily hydrolysed in alkaline medium compared to HWP. During the NaOH treatment, the phenolic benzyl ether bonds in lignin were easily hydrolysed in the alkaline solution [49]. This would inhibit the reading of glucose in the filtrate from the NaOH treatment.

Table 4. Glucose concentration of untreated, HWP and NaOH treated KC and KB obtained from DNS assay analysis

Sample	Glucose Concentration (mg/mL)	
	KC	KB
HWP filtrate	0.050	0.062
NaOH filtrate	0.050	0.064

Conclusion

The percentage of α-cellulose and hemicellulose increased upon hot water pre-treatment and decreased after NaOH aqueous solution treatment for KC. Meanwhile, the α-cellulose content in KB increased from untreated to HWP to NaOH, and hemicellulose increased upon hot water pre-treatment and decreased after NaOH treatment. The percentage of Klason lignin reduced when the kenaf fibres undergone HWP and NaOH treatments. The Fourier Transform Infrared Spectroscopy analysis (FTIR) revealed the removal of lignin from KC and KB after NaOH treatment. These were confirmed when the peaks at 1735 cm^{-1} and 1246 cm^{-1} disappeared after the treatments. Phenol sulfuric analysis showed a decrement in glucose concentration on fibres after NaOH treatment. The DNS analysis showed no significant changes on the filtrate after NaOH treatment due to hindrance from the furfural and lignin in the liquid sample. The experimental investigation showed that hot water pre-treatment (HWP) enhances sugar recovery compared to alkaline treatment.

Acknowledgement

The author would like to thank Polymer Research Centre and School of Chemical Sciences and Food Technology, Faculty of Science and Technology, Universiti Kebangsaan Malaysia for providing the working space and instrument for sample analysis throughout the study. This research has been funded by the Ministry of Education through its Exploratory Research Grant Scheme ERGS/1/2013/STG01/UKM/02/2.

References

1. Ashori, A. (2006). Pulp and paper from kenaf bast fibers. *Fibers and Polymers*, 7(1): 26-29.
2. Ohtani, Y., Mazumder. B. and Sameshima, K. (2001). Influence of the chemical composition of kenaf bast and core on the alkaline pulping response. *Journal of Wood Science*, 47(1): 30-35.

3. Pande H. and Roy, D. N. (1996). Delignification kinetics of soda pulping of kenaf. *Journal of Wood Chemistry and Technology,* 16:311-325.
4. Juhaida, M. F., Paridah, M. T., Mohd Hilmi, M., Sarani, Z., Mohamad Zaki, A. R., and Jalaluddin, A. 2009. Production of polyurethane from liquefied kenaf (*Hisbiscuis cannabinus* L.) core for wood laminating adhesive. Master Thesis, Universiti Putra Malaysia.
5. Kaldor, A. F., Brasher, B. S. and Fuller, M. J. 1992. A strategy for the development of a kenaf-based pulp and paper industry. *Tappi Journal*, 75(1): 87-91.
6. Li D. (1980). Theory and technology of fiber crops. Chinese: Shanghai: Scientific and Technological Press.
7. Wolfgang, D. B., Talmadge, K. W., Keegstra, K. and Albresheim, P. (1973). The structure of plant cell walls. *Plant Physiology,* 51: 174-187.
8. Kuthi, F. A. A., Norzali, N. R. A. A. and Badri, K. H. (2016). Thermal characteristics of microcrystalline cellulose from oil palm biomass. *Malaysian Journal of Analytical Sciences*, 20(5): 1112-1122.
9. Li, X. (2004). Physical, chemical, and mechanical properties of bamboo and its utilization potential for fiberboard manufacturing. Masters Thesis, Louisiana State University.
10. Kumar, P., Barrett, D. M., Delwiche, J. M. and Streove, P. (2009). Method for pretreatment of lignicellulosic biomass for efficient hydrolysis and biofuel production. *Industrial and Engineering Chemistry,* 48(8), 3713-3729.
11. Harmsen, P. F. H., Huijgen, W., Bermudez, L. and Bakker, R. (2010). Literature review of physical and chemical pretreatment processes for lignocellulosic biomass. *Wageningen UR Food & Biobased Research* (No. 1184).
12. Agbor, V. B., Cicek, N., Sparling, R., Berlin, A. and Levin, D. B. (2011). Biomass pretreatment: Fundamentals toward application. *Biotechnology Advances,* 29: 675-685.
13. She, D., Xu, F., Geng, Z. C., Sun, R. C., Jones, G. L. and Baird, M. S. (2010). Physicochemical characterization of extracted lignin from sweet sorghum stem. *Industrial Crops and Products*, 32:21-28.
14. Masuko, T., Minami, A., Iwasaki, N., Majima, T., Nishimura, S., Lee, Y. C. (2005). Carbohydrates analysis by a phenol-sulfuric acid method in microplate format. *Analytical Biochemistry,* 339: 69-72.
15. Negrulescu, A., Patrulea, V., Mincea, M. M., Ionascu, C., Vlad-Oros, B. A. and Ostafe, V. (2012). Adapting the reducing sugars method with dinitrosalicylic acid to microtiter plates and microwave heating. *Journal of Brazilian Chemical Society*, 23(12):2176-2182.
16. Hu, R., Lin, L., Liu, T., Ouyong, P., He, B. and Liu, S. (2008). Reducing sugar content in hemicellulose hydrolysate by DNS method: A revisit. *Journal of Biobased Materials and Bioenergy*, 2: 156-161.
17. Hasegawa, I., Kazuhide, T., Osamu, O. and Kazuhiro, M. (2004). New pretreatment methods combining a hot water treatment and water/acetone extraction for thermo-chemical conversion of biomass. *Energy and Fuel,* 18(3): 755-760.
18. Sun, R. C., Fang, J. M. and Tomkinson. J. (2000). Delignication of rye straw using hydrogen peroxide. *Industrial Crops and Product,* 12: 71-83.
19. Edeerozey, A. M. M., Akil, H. M., Azhar, A. B. and Ariffin, M. I. Z. (2007). Chemical modification of kenaf fibers. *Materials Letters*, 61(10): 2023-2025.
20. Bachtiar, D., Mohd, S. S., Edisyam, Z., Khalina, A. and Khairul, Z. H. M. D. (2011). Effect of alkali treatment and a compatibilizing agent on tensile properties of sugar palm fibre-reinforced high impact polystyrene composites. *Bioresource,* 6(4); 4815-4823.
21. Anon. (1984). Moisture in wood paper and paperboard. TAPPI *Testing Procedure* (TAPPI T207 om-81). USA.
22. Anon. (1981). Water solubility of wood and pulp. TAPPI *Testing Procedure* (TAPPI T207 om-81). USA.
23. Anon. (1997). Alcohol-benzene solubility of pulp. TAPPI *Testing Procedure* (TAPPI T204 om-97). USA.
24. Anon. (1983). Alpha-, beta-, and gamma-cellulose of pulp. TAPPI *Testing Procedure* (TAPPI T203 om-83). USA.
25. Anon. (1983). Klason lignin of pulp. TAPPI *Testing Procedure* (TAPPI T222 om-83). USA.
26. Wise, L. D., Murphy, M. and D'addiego, A. (1946). Chlorite hollocellulose, its fractionation and bearing on summative wood analysis and on studies on hemicellulose. *Journal of Paper Trade,* 112(2): 35-43.
27. Ibrahim, S. M. (2012). Hidrolisis berenzim ke atas serabut tandan kosong sawit terawat gliserol akues bagi perolehan glukosa dan xilosa. Thesis of Master Degree, Universiti Kebangsaan Malaysia.
28. Ling, T. P. (2013). Penghasilan gula yang boleh difermentasikan melalui dekonstruksi dan degradasi serat tandan kosong kelapa sawit. Thesis of Master Degree, Universiti Kebangsaan Malaysia.

29. Farm, Y. Y., Duduku, K., Ranjin, M. and Bono, A. (2009). Cellulose extraction from palm karnel oil using liquid phase oxidation. *Journal of Engineering and Technology* 4(1): 57-68.
30. Mosier, N., Wyman, C., Dale, B., Elander, R., Lee, Y. Y., Holtzapple, M. and Ladisch, M. (2005). Features of promising technologies for pretreatment of lignocellulosic biomass. *Bioresource Technology*, 96(6): 673-686.
31. Jonoobi, M., Jalaludin, H., Alireza, S., Manjusri., M. and Kristiina, O. (2009). Chemical composition, cystallinity, and thermal degration of bleached and unbleached kenaf bast (*Hibiscus cannabinus*) pulp and nanofibers. *Bioresource,* 4(2) 626-639.
32. Xue L., Tabil, L. G. and Panigrahi, S. (2007). Chemical treatments of natural fiber for use in natural fiber-reinforced composites: A review. *Journal of Polymer Environment*, 15: 25-33.
33. Ioelovich, M. and Morag, E. (2012). Study of enzymatic hydrolysis of mild pretreated lignocellulosic biomasses. *Bioresource*, 7(1): 1040-1052.
34. Trivedi, N., Gupta, V., Reddy, C. R. K. and Jha, B. (2013). Enzymatic hydrolysis and production of bioethanol from common macrophytic green alga *Ulva fasciata* Delile. *Bioresource Technology*, 150: 106-112.
35. Pettersen, C. R. (1984). The chemical composition of wood. *Advances in Chemistry,* 207: 57-126.
36. Nosbi, N., Akil, H. M., Ishak, Z. M. and Bakar, A. A. (2010). Degradation of compressive properties of pultruded kenaf fiber reinforced composites after immersion in various solutions. *Materials and Design*, 31(10): 4960-4964.
37. Shakhes, J., Morteza. A. B. M., Farhad, Z., Ahmadreza, S. and Tayebe, S. (2011). Tobacco residuals as promising lignocellulosic materials for pulp and paper industry. *Bioresource Technology*, 6(4): 4481-4493.
38. Nosbi, N., Hazizan, M. A., Ishak, Z. A., and Abu, B. A. (2011). Behavior of kenaf after immerion in several water conditions. *Bioresource*, 6(2): 950-960.
39. Pandey, K. K. (1998). A study of chemical structure of softwood and hardwood and wood polymers by FTIR spectroscopy. *Journal of Applied Polymer Science*, 71: 1969-1975.
40. Schwanninger, M., Rodrigues, R. C., Pereira, H. and Hinterstoisser, B. (2004). Effects of short-time vibratory ball milling on the shape of FT-IR spectra of wood and cellulose. *Vibrational Spectroscopy,* 36: 23-40.
41. Abdul Khalil, H. P. S., Yusra, A. F. I., Bhat, A. H. and Jawaid, M. (2010). Cell wall ultrastructure, anatomy, lignin distribution, and chemical composition of Malaysian cultivated kenaf fiber. *Industrial Crops and Products*, 31(1):113-121.
42. Kuthi, F. A. B. A. and Badri, K. H. (2014). Effect of cooking temperature on the crystallinity of acid hydrolysed-oil palm cellulose. *AIP Conference Proceedings*, 1614(1): 456-462.
43. Kuthi, A. F. A., Haji Badri, K. and Mohmad Azman, A. (2015). X-ray diffraction patterns of oil palm empty fruit bunch fibers with varying crystallinity. *Advanced Materials Research*, 1087: 321-328.
44. He, W., Li, Y., Si, H., Dong, Y., Sheng, F., Yao, X. and Hu, Z. (2006). Molecular modeling and spectroscopic studies on the binding of guaiacol to human serum albumin. *Journal of Photochemistry and Photobiology A: Chemistry*, 182(2): 158-167.
45. Chang, J. L. and Thompson. J. E. (2010). Characterization of colored products formed during irradiation of aqueous solutions containing H_2O_2 and phenolic compounds. *Atmospheric Environment* 44(4): 541-551.
46. Ciolacu, D., Ciolacu F. and Popa, V. I. (2011). Amorphous cellulose- structure and characterization, *Cellulose Chemistry Technology,* 45: 13-21.
47. Mahato, D. N., Mathur, B. K. and Bhattacherjee, S. (2013). DSC and IR methods for determination of accessibility of cellulosic coir fibre and thermal degradation under mercerization. *Indian Journal of Fibre & Textile Research*, 38: 96-100.
48. Wenzl, H. F. J. (1970). The acid hydrolysis of wood. *The Chemical Technology of Wood*, Academic Press Inc., New York: pp. 157-252.
49. Takahashi, N. and Koshijima, T. (1986). Molecular properties of lignin-carbohydrate complexes from beech (*Fagus crenata*) and pine (*Pinus densiflora*) woods. *Wood Science and Technology*, 22: 177-189.

Malaysian Journal of Analytical Sciences, Vol 22 No 6 (2018): 1057 - 1064
DOI: https://doi.org/10.17576/mjas-2018-2206-16

MALAYSIAN JOURNAL OF ANALYTICAL SCIENCES
Published by The Malaysian Analytical Sciences Society
ISSN 1394 - 2506

EFFECTS OF FIBRE SIZE ON *Sansevieria trifasciata*/NATURAL RUBBER/ HIGH DENSITY POLYETHYLENE BIOCOMPOSITES

(Kesan Saiz Serat Terhadap Biokomposit *Sansevieria trifasciata*/Getah Asli/ Polietilena Berketumpatan Tinggi)

Nurzam Ezdiani Zakaria[1,2], Ishak Ahmad[1,3], Wan Zarina Wan Mohamad[2], Azizah Baharum[1,3]*

[1]*School of Chemical Sciences and Food Technology, Faculty of Science and Technology, Universiti Kebangsaan Malaysia, 43600 UKM Bangi, Selangor, Malaysia*
[2]*Food Processing and Packaging Programme, Food Science Technology Research Centre, Malaysian Agricultural Research and Development Institute,P.O Box 12301 General Post Office, 50774 Kuala Lumpur, Malaysia*
[3]*Polymer Research Centre, Faculty of Science and Technology, Universiti Kebangsaan Malaysia, 43600 UKM Bangi, Selangor, Malaysia*

**Corresponding author: azeiss@ukm.edu.my*

Received: 27 July 2017; Accepted: 28 April 2018

Abstract

This research was done to study the effects of different fibre sizes (1 mm, 500 µm, 250 µm and 125 µm) on the mechanical, morphological and thermal properties of *Sansevieria trifasciata* fibre/natural rubber/high density polyethylene (STF/NR/HDPE) composites. Processing of STF/NR/HDPE composites was done by using an internal mixer machine. The processing parameters used were 135 °C for temperature and a mixing rotor speed of 55 rpm for 15 minutes. Filler loading was varied from 10% to 40% of STF. The composite blends obtained were pressed with a hot press machine to get test samples of 1 mm and 3 mm in thickness. Samples were evaluated *via* tensile tests, Izod impact test and differential scanning calorimeter (DSC). Morphological studies were carried out *via* scanning electron microscope (SEM). Results showed that tensile strength and impact strength decreased while tensile modulus increased when filler loading increased. Smaller particle size will give more interfacial interaction between fibre and matrix. Adding a higher amount of filler will also increase the viscosity and the stiffness of the materials. Overall, it showed that 125 µm of fibre size has given higher values/stable results of tensile strength and modulus. Thermal behaviour of the materials was not affected much by fibre size.

Keywords: polymer composites, fibre size, natural fibre, mechanical properties, thermal properties

Abstrak

Kajian ini dilakukan untuk mengkaji kesan perbezaan saiz serat (1 mm, 500 µm, 250 µm and 125 µm) ke atas sifat mekanikal, morfologi dan terma komposit *Sansevieria trifasciata*/getah asli/polietilena ketumpatan tinggi (STF/NR/HDPE). Pemprosesan komposit STF/NR/HDPE dilakukan dengan menggunakan mesin pengadun dalaman. Parameter pemprosesan yang digunakan adalah 135°C untuk suhu dan kelajuan rotor pada 55 rpm selama 15 minit. Penambahan pengisi telah divariasikan antara 10% hingga 40% STF. Adunan komposit yang terhasil ditekan dengan mesin penekan panas untuk mendapatkan sampel ujian berketebalan 1 mm dan 3 mm. Sampel dinilai melalui ujian regangan, ujian hentaman Izod dan kalorimetri pengimbasan berbeza (DSC). Kajian morfologi dijalankan dengan menggunakan SEM. Keputusan menunjukkan bahawa kekuatan regangan dan kekuatan hentaman menurun manakala modulus regangan meningkat dengan penambahan pengisi. Saiz partikel pengisi yang lebih kecil akan memberi interaksi antaramuka yang lebih baik antara serat dan matriks. Penambahan pengisi juga akan meningkatkan kelikatan dan kekakuan bahan. Secara keseluruhannya, keputusan menunjukkan bahawa saiz serat 125 µm telah memberikan nilai yang lebih tinggi atau keputusan yang lebih stabil bagi kekuatan regangan dan modulus. Sifat terma bahan pula didapati tidak banyak dipengaruhi oleh perbezaan saiz serat yang digunakan.

Kata kunci: komposit polimer, saiz serat, serat semula jadi, sifat mekanik, sifat terma

Introduction

The world is facing a serious problem developing new technologies and methods to treat solid wastes, especially for non-naturally-reversible polymers. Decomposing process of those wastes is usually not cost-effective and will produce harmful chemicals [1]. Incorporating natural filler into polymer matrix has gained a lot of attention nowadays. Many types of filler have been used in the plastic industry, either to cut the production costs or to tailor the mechanical properties of the materials. Environmental awareness research groups all over the world have focused their attention on the use of natural fibres to reinforce polymer matrixes. The attractive features of using natural fibres include light weight, low density, recyclable, moderate strength, high specific modulus, renewable, biodegradable, lack of health hazards, eco-friendly material, amenability to chemical modification and can be obtained at low cost [1, 2, 3]. Natural fibres also possess better electrical resistance, higher resistance to fracture, and good thermal and acoustic insulation properties [4].

There are many types of natural fibre from plant resources. Most of them are agrowaste. Natural fibres like flax, hemp, jute, sisal, kenaf, coir, kapok, banana, henequen, rice husk, pineapple leaf, oil palm, wood pulp and many more are commonly used as reinforcement in polymer matrixes [1, 2, 5]. Thus, new fibre resources should be explored. *Sansevieria trifasciata* (ST) are usually used as decoration plants in parks or homes. Sansevieria plants can also grow in wild environments [2]. Common names for ST are snake's tongue, devil's tongue, mother in laws' tongue, bow string hemp or snake's plant. Current research showed that utilising the *Sansevieria trifasciata* fibre (STF) as reinforcement filler in composites is still at the preliminary stage. STF has a lot of potentials to be explored. Therefore, the effect of fibre size is important to characterise the composites. Fibre length will play an important role in a homogenous distribution of mechanical strength in a composite system [6, 7]. It is observed that *Sansevieria trifasciata* fibres have good mechanical and thermal insulation properties [8]. A study by NASA found that ST is one of the best plants for improving indoor air quality by absorbing toxins [4]. This plant also offers properties that are similar to pineapple leaf fibre with lower lignin content [9].

Adding natural rubber (NR) into the composite blend will also modify its characteristic. It was reported that better tensile properties were obtained when NR and thermoplastics were combined in the system due to some structure similarity, compatibility and phase interaction [10]. The objectives of this research are to produce STF/NR/HDPE biocomposites, to evaluate the performance of the composites obtained and to study the effect of fibre size to the composite system. Fibre size plays an important role in the determination of strength and properties of composites.

Materials and Methods

Materials

High density polyethylene (HDPE) Etilinas HD5301AA grade was obtained from Polyethylene (M) Sdn. Bhd. Natural rubber (NR) SMR-L grade was bought from Chemolab Supplies. *Sansevieria trifasciata* trees, aged more than 2 years were bought from Sungai Buloh Nursery. The leaves were cut and washed in order to remove dirt and adhering soil. The leaves were then chopped by using a slicer machine (Emura, Japan), dried by using a drum dryer at 60 °C for 5 hours and ground to produce smaller sized fibres. The fibres were then sieved to the sizes of 1 mm, 500 µm, 250 µm and 125 µm.

Composite blending was done by using an internal mixer (Brabender W50EHT, Germany). Processing parameters used were 135 °C for temperature and rotor speed at 55 rpm for 15 minutes. These are the optimum processing parameters obtained from a previous experiment. NR/HDPE composition of 40/60 was used in the system while filler loading was 10-40% of STF. HDPE was added into the internal mixer, followed by NR. After 8 minutes, STF was added into the mixer's chamber. Composites obtained were pressed in a hot press machine (Labtech, Sweden) at 145 °C to produce samples with 1 mm and 3 mm of thickness. The total pressing time was 12 minutes.

Testing: Tensile test

Tensile tests were carried out according to ASTM D412 on an Instron Universal Testing Machine (model 5567, United Kingdom). Dumb-bell specimens of 1 mm thickness were cut from the hot press sheets by using a die cutter. A crosshead speed of 50 mm/min was used and the test was performed at 25±3 °C. Seven specimens were used and the average was calculated respectively.

Impact test

Izod impact test was done according to ASTM D256 by using a Tinius Olsen Impact Tester (model 104, USA). Specimens of 64 x 12.7 x 3 mm were cut by using a Hollow Die Punch cutter. Notched samples (1 mm) were clamped into the pendulum impact test fixture with the notched side facing the striking edge of the pendulum. The test was done at 25 ± 3 °C. Five specimens were used and the average was calculated respectively.

Differential scanning calorimeter analysis

Thermal analysis of the samples was done *via* the Mettler Toledo differential scanning calorimeter machine (model 823e, USA). Differential scanning calorimeter (DSC) was used to measure the crystallisation and melting temperatures (T_c and T_m, respectively) of STF-NR-HDPE composites. Analysis was done on the samples used for the tensile tests. Around 12 mg of samples were placed on aluminium pans and hermetically sealed. Each sample was first heated for 1 minute at 200 °C, then cooled at 10 °C per minutes until the temperature reached -40 °C and finally heated from -40 °C to 200 °C at a heating rate of 10 °C min $^{-1}$. The thermogram obtained from the analysis displayed the variation of heat flow per gram of samples (W g^{-1}) towards temperature (°C).

Morphological study

Morphological study was done by using a scanning electron microscopy (Zeiss LEO1450VP, Germany). Fractured samples from the impact test were used in this study. Samples were mounted on an aluminium stub and sputter-coated with a thin layer of gold before analysis.

Results and Discussion

Mechanical properties

Figure 1 shows the value of tensile stress at 10-40% of STF composition in the matrix with a variation of fibre sizes (1 mm, 500 µm, 250 µm and 125 µm). Adding STF into the composites decreased the value of tensile strength for all of fibre sizes. Tensile strength decreased as STF composition increased due to weaker interaction between hydrophilic fibre (contains OH group) and hydrophobic matrix (hydrocarbons). From the results obtained, it is shown that STF at 125 µm gave the highest value of tensile strength compared to all other sizes. Tensile properties are strongly influenced by the fibre length [2]. Smaller size of fibre will increase interfacial interaction between fibre and matrix. It will also improve fibre orientation.

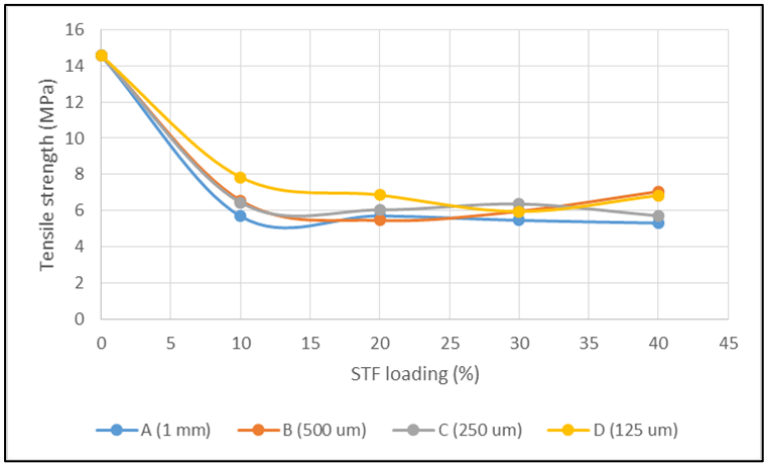


Figure 1. Tensile strength with filler loading from 0-40% of STF

Figure 2 shows the value of tensile modulus at 10-40% of STF composition in the matrix with a variation of fibre sizes (1 mm, 500 µm, 250 µm and 125 µm). Overall, tensile modulus increased as STF composition increased because of material rigidity that also increased when more fillers were incorporated into the composite system. At 10% of filler loading, an unstable trend was observed due to the amount of filler content. Results showed that the fibre size of 125 µm can contribute to the stiffness effect, even at 10% of filler loading. Modulus is slightly decreased at 20% of STF composition but kept increasing after 30% onwards for fibre size of 125 µm. Young's modulus is closely related to particle loading and particle size [11]. But at 20% of filler loading, tensile modulus has given a similar reading for all sizes. This showed that at 20% incorporation of STF into 80% of matrix (40/60 of NR and HDPE), the rigidity and stiffness of the materials were not affected much by different fibre sizes (range from 1mm to 125 µm). It also showed that at 20% of STF composition, the fibre-matrix interaction in the composites' system has been saturated with the amount of 40% NR in 60% HDPE. From the graph, it shows that 125 µm has given the highest value of tensile modulus compared to other sizes.

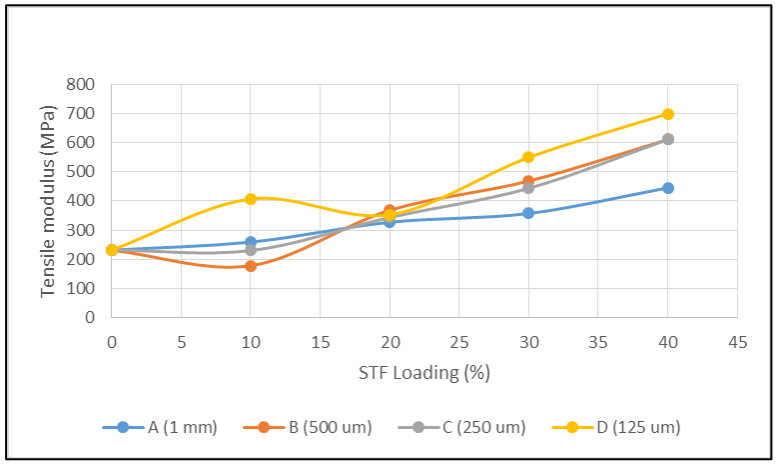


Figure 2. Tensile modulus with filler loading from 0-40% of STF

Figure 3 shows the value of impact strength at 10-40% of STF composition in the matrix with a variation of fibre sizes (1 mm, 500 µm, 250 µm and 125 µm). Impact strength is an important parameter to measure the plasticity of materials. The impact values are the reflection of the ability of materials to absorb the energy transferred from the pendulum [12]. Notched samples were used in this test. Sudden droppage was observed when 10% of STF was added into the composites' system for all sizes. However, impact strength began to increase at 20% of filler loading before starting to decrease afterwards. At 10%, STF tended to interact more with NR, therefore the values of impact strength decreased. NR is a natural polymer compared to HDPE which is a synthetic polymer. The degree of hydrophobicity of NR is lower than HDPE [13]. Therefore, at lower amount of filler, it tends to interact more with NR compared to HDPE. After 20% onwards, the amount of filler for all sizes was increased and impact value decreased because the amount of 40% NR in the matrix was unable to absorb the energy transferred from the pendulum. Thus, the physical interaction between fibre and matrix became weaker due to the hydrophilic properties of fibre and hydrophobicity properties of the matrix. Composite with the fibre size of 1 mm gave the highest value of impact strength.

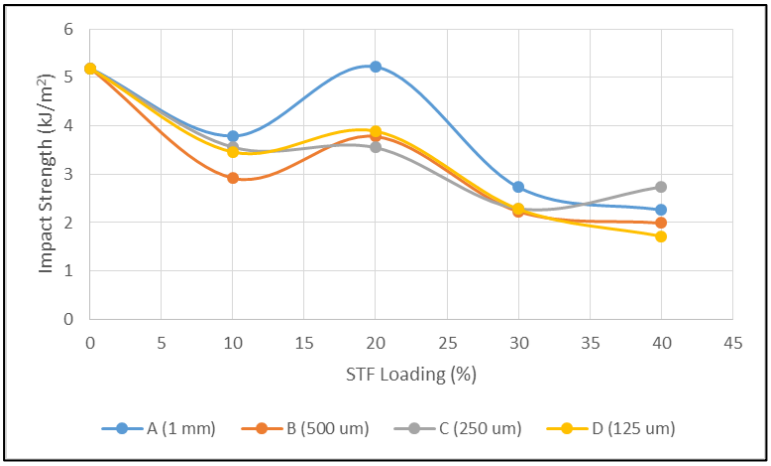
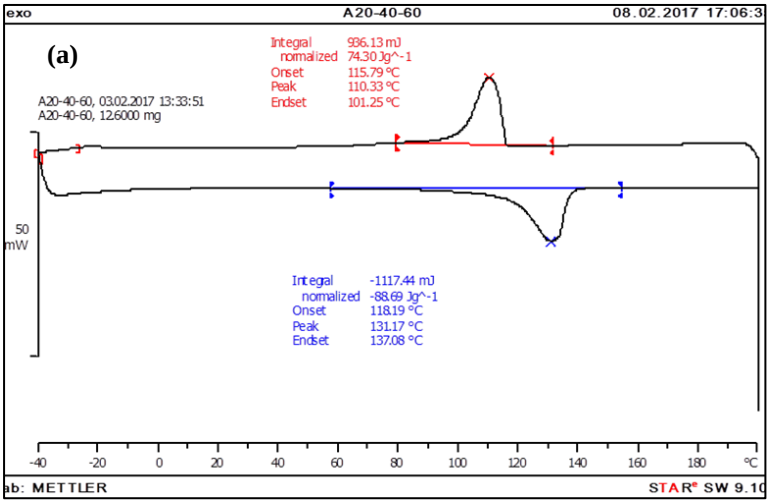


Figure 3. Impact strength value with filler loading from 0-40% of STF

Thermal properties

Figure 4 shows the DSC curves for all sizes (1 mm, 500 µm, 250 µm and 125 µm). Composition of 20% STF was used in this analysis. It is shown that thermal properties were not affected much by different fibre sizes. No significant changes were observed for melting temperature of materials obtained. No appearance of crystallinity peak in the thermograms was observed. This showed that HDPE become more amorphous by adding NR and STF (all sizes) in the system.



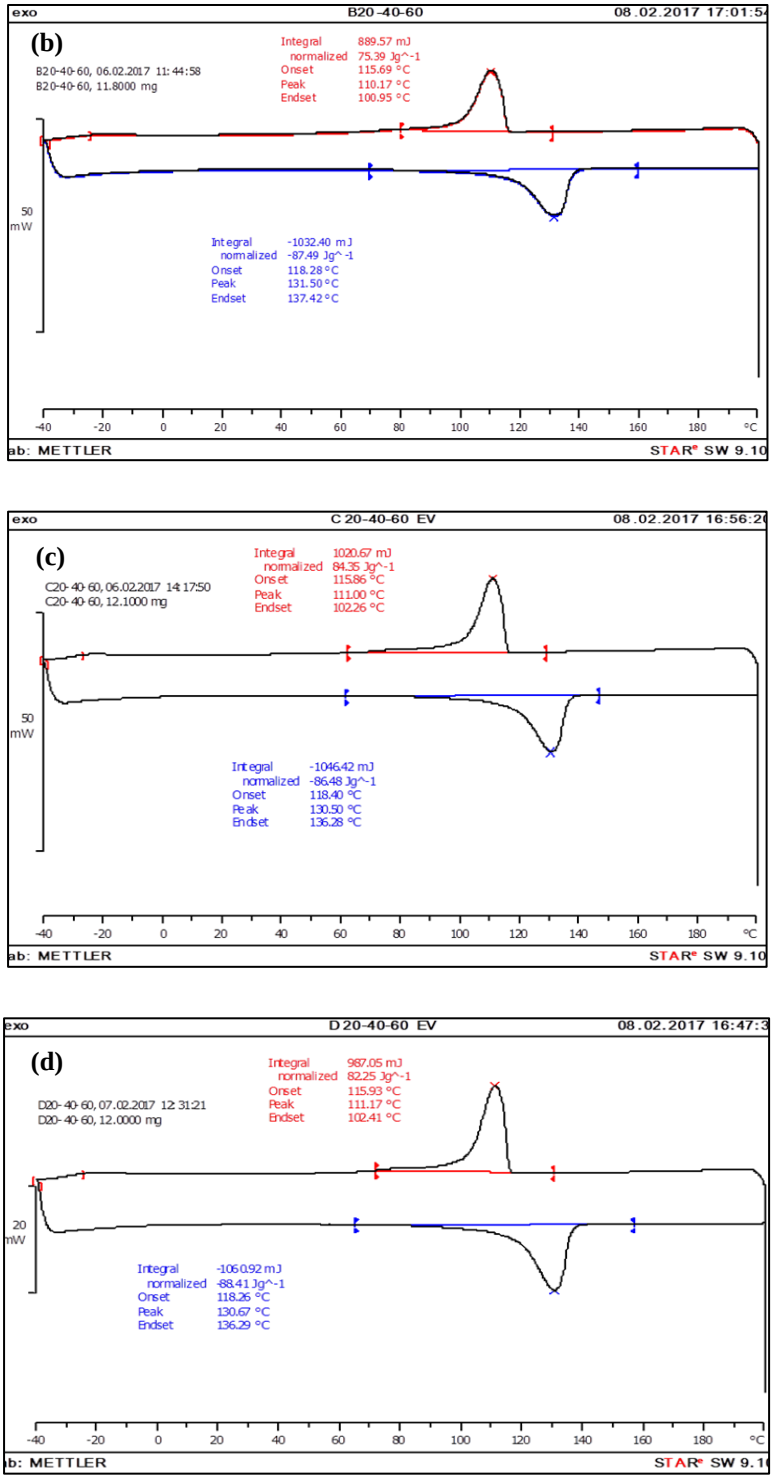


Figure 4. DSC curves of STF/NR/HDPE at different sizes of fibre (a) 1 mm, (b) 500 µm, (c) 250 µm and (d) 125 µm

Morphological study

Figure 5 shows the SEM micrograph of composites for all fibre sizes (1 mm, 500 µm, 250 µm and 125 µm) at 500 times magnification. Composition of 20% STF was used in this analysis, with a matrix combination of 40% NR and 60% HDPE. Good interaction between fibre and matrix was observed from the fractured samples. This clearly indicates that the filler distribution was homogeneous with less voids and pull-outs as the filler size was decreased.

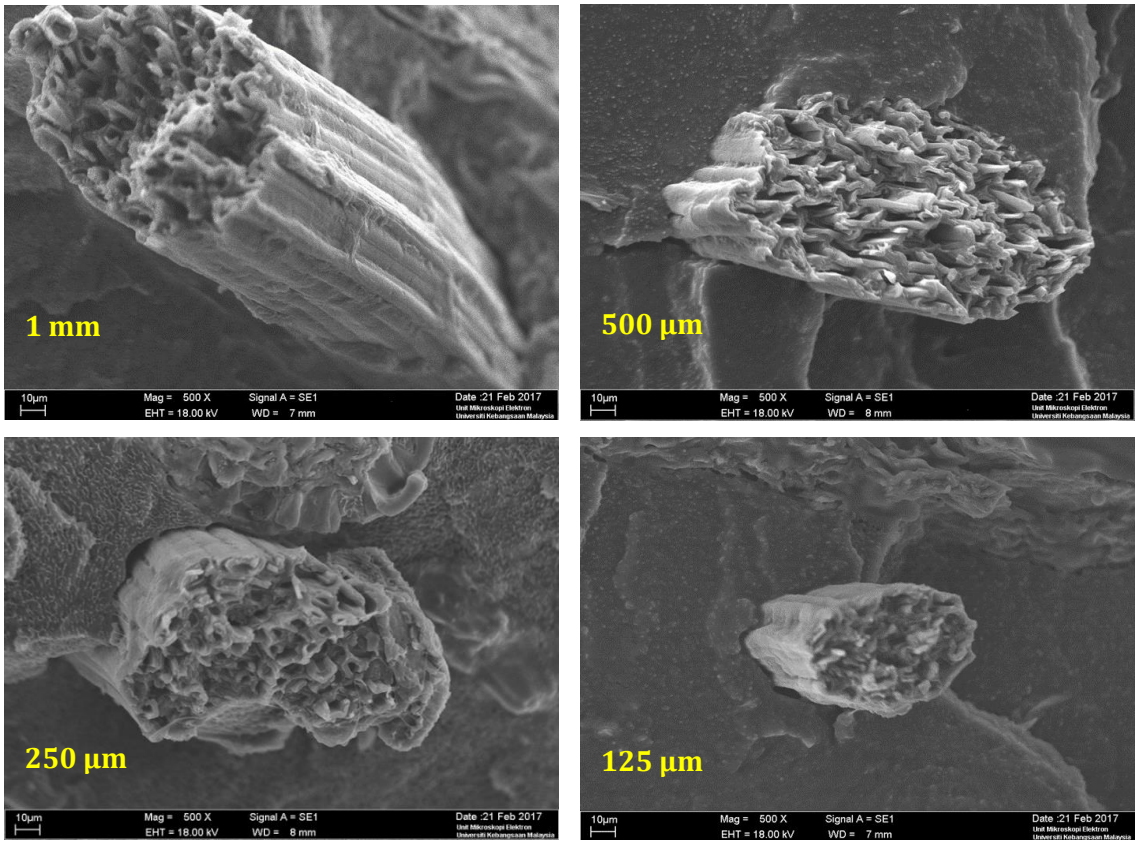


Figure 5. SEM micrographs of STF/NR/HDPE at different sizes of fibre

Conclusion

The samples obtained showed that blending STF/NR/HDPE together has produced homogenous composites at all level of fibre sizes. Adding NR to the composite system has produced a less rigid and softer surface composite. Overall, it is shown that 125 µm of fibre size has given higher values/stable results for tensile strength and tensile modulus. Different fibre sizes with a range from 1mm to 125 µm did not give a significant effect to the thermal behaviour of the composites. Morphological study done on the composites has supported the results from mechanical testing.

Acknowledgments

The authors would like to thank the Ministry of Higher Education (MHE) for providing the research grant (FRGS/2/2014/TK04/UKM/02/1), Universiti Kebangsaan Malaysia (GUP-2017-123) and the Malaysian Agricultural Research and Development Institute for making this research work possible.

References

1. Ku, H., Wang, H., Pattarachaiyakoop, N. and Trada, M. (2011). A review on the tensile properties of natural fiber reinforced polymer composites. *Composites: Part B*, 42: 856-873.
2. Sreenivasan, V. S., Ravindran, D., Manikandan, V. and Narayanasamy R. (2011). Mechanical properties of randomly oriented short *Sansevieria cylindrica* fiber/polyester composites. *Materials and Design*, 32: 2444-2455.
3. Faruk, O., Bledzki, A. K., Fink, H. P. and Sain, M. (2012). Biocomposites reinforced with natural fibers: 2000-2010. *Progress in Polymer Science*, 37: 1552-1596.
4. Sameer, B. R. K., Kumar, M. A, Murthy, V. N. and Karthikeyan N. (2015). Development of *Sansevieria trifasciata*-carbon fiber reinforced polymer hybrid nanocomposites. *International Letters of Chemistry, Physics and Astronomy*, 50: 179-187.
5. Sreenivasan, V. S., Somasundaram, S., Ravindran, D., Manikandan, V. and Narayanasamy, R. (2011). Microstructural, physico-chemical and mechanical characterization of *Sansevieria cylindrica* fibres – An exploratory investigation. *Materials and Design*, 32: 453-461.
6. Singha, A. S. and Rana, R. K. (2012). Natural fiber reinforced polystyrene composites: Effect of fiber loading, fiber dimensions and surface modification on mechanical properties. *Materials and Design*, 41: 289-297.
7. Sreenivasan, V. S., Rajini, N., Alvudeen, A. and Arumugaprabu, V. (2015). Dynamic mechanical and thermo-gravimetric analysis of *Sansevieria cylindrica*/polyester composite: Effect of fiber length, fiber loading and chemical treatment. *Composites: Part B*, 69: 76-86.
8. Ramanaiah, K., Prasad, A. R. and Reddy, K. H. C. (2013). Mechanical, thermophysical and fire properties of sansevieria fiber-reinforced polyester composites. *Materials & Design*, 49: 986-991.
9. Kanimozhi M. (2011). Investigating the physical characteristics of *Sansevieria trifasciata* fibre. *International Journal of Scientific and Research Publications*, 1: 1-4.
10. Hanafi, I., Nizam, J. M. and Abdul Khalil, H. P. S. (2001). The effect of a compatibilizer on the mechanical properties and mass swell of white rice husk ash filled natural rubber/linear low density polyethylene blends. *Polymer Testing*, 20: 125-133.
11. Fu, S. Y., Feng, X. Q, Lauke, B. and Mai Y. W. (2008). Effect of particle size, particle/matrix interface adhesion and particle loading on mechanical properties of particulate-polymer composites. *Composites: Part B*, 39: 933-961.
12. Sahin, S. and Yayla P. (2005). Effects of testing parameters on the mechanical properties of polypropylene random copolymer. *Polymer Testing*, 24: 613-619.
13. Goosey, M. (1999). Plastics for electronics. Springer-Science-Business Media, United Kingdom: pp. 19-21.

Malaysian Journal of Analytical Sciences, Vol 22 No 6 (2018): 1065 - 1077
DOI: https://doi.org/10.17576/mjas-2018-2206-17

MALAYSIAN JOURNAL OF ANALYTICAL SCIENCES
Published by The Malaysian Analytical Sciences Society
ISSN 1394 - 2506

OPTIMIZATION OF ACID DOPED POLYBENZIMIDAZOLE ELECTROLYTE MEMBRANE FOR HIGH-TEMPERATURE PEM FUEL CELL

(Pengoptimuman Asid Didopkan Membran Elektrolit Polibenzimidazol untuk Sel Bahan Api PEM Suhu Tinggi)

Md Ahsanul Haque[1, 2], Abu Bakar Sulong[1, 3]*, Edy Herianto Majlan[1], Kee Shyuan Loh[1], Teuku Husaini[1], Rosemilia Rosli[1]

[1]*Fuel Cell Institute,*
Universiti Kebangsaan Malaysia, 43600 UKM Bangi, Selangor, Malaysia
[2]*Department of Applied Chemistry and Chemical Engineering,*
Islamic University, Kushtia-7003, Bangladesh
[3]*Department of Mechanical and Materials Engineering,*
Universiti Kebangsaan Malaysia, 43600 UKM Bangi, Selangor, Malaysia

**Corresponding author: abubakar@ukm.edu.my*

Received: 27 July 2017; Accepted: 28 April 2018

Abstract

This study optimized the H_3PO_4 acid doping level (ADL) of polybenzimidazole (PBI) polymer electrolyte membranes using Taguchi method and characterized their ionic conductivity, contour plot and performed statistical regression analysis. Electrochemical impedance spectroscopic (EIS) analysis revealed that PBI copolymer-1 exposed better ionic conductivity among other membranes used. The maximum proton conductivity of PBI copolymer-1was recorded as 6.30 mS/cm at a doping temperature of 130 °C, doping time of 6 hours, and an operating temperature of 160 °C whereby, the optimum parameters were driven from the contour plot and signal to noise ratios effect of variable factors. The ionic conductivity showed differentiable dependency on the ADL and required high operating temperature for maximum conductivity. Therefore, the data recommends that the PBI copolymer-1 may be applicable as a proton exchange membrane for the high-temperature polymer electrolyte membranes fuel cell.

Keywords: acid doping level, polybenzimidazole, Taguchi method, contour plot, proton conductivity

Abstrak

Kajian ini mengoptimumkan tahap pendopan asid H_3PO_4 bagi membran polimer elektrolit polibenzimidazol (PBI) menggunakan kaedah Taguchi dan mencirikan kekonduksian elektronik, plot kontur dan melakukan analisis prestasi regresi statistik. Analisis spektroskopi elektrokimia impedans (EIS) membuktikan bahawa kopolimer-1 PBI mendedahkan ionik konduktiviti yang lebih baik berbanding membran lain yang digunakan. Proton konduktiviti maksimum kopolimer-1 PBI direkodkan pada 6.30 mS/cm pada suhu pendopan pada 130 °C, masa pendopan 6 jam, dan masa suhu operasi 160 °C, manakala parameter optimum didorong dari plot kontur dan isyarat kepada kesan nisbah hingar dari faktor variasi. Ionik konduktiviti menunjukkan perbezaan kebergantungan terhadap ADL dan memerlukan suhu operasi yang tinggi untuk konduktiviti yang maksimum. Oleh itu, data mencadangkan bahawa kopolimer-1 PBI berkemungkinan boleh diaplikasi sebagai membran penukaran proton untuk membran polimer elektrolit sel fuel bersuhu tinggi.

Kata kunci: tahap pendopan asid, polibenzimidazol, kaedah Taguchi, plot kontur, konduktiviti proton

Introduction

Today, green energy is considered to be the most desirable energy source for near future across countries. As such this energy approach not only challenges the use of CO_2 emission technique that has a major role for the global warming but also poses a concern on the limited reserve of the fossil fuel for future use. To address these issues, Sopian et al. [1] have suggested that the PEMFC is going to be the most popular and attractive alternative clean energy conversion devices in the near future applications for automotive, stationary, and portable sectors. In PEMFC, the proton exchange membrane remains separated from the anode and cathode, and thus required conduction of protons from one side to the other electrode side. Therefore, the expected proton conduction rate through the membrane is very important for the overall cell performance. Currently, many researchers are involving membrane development for a demonstration in PEMFC applications [2-4].

In a low operating temperature (usually < 80 °C) PEMFC, the perfluoro sulfonic acid (PFSA, Nafion) polymer membrane is commonly used as the electrolyte membrane due to its low ionic conductive resistance. Lufrano et al. [5] have mentioned some potential challenges of this technique. The challenges are, for example, it is expensive, and having a limited working temperature, dependent on humidity, and inadequate for longer cell operations. Additionally, during operation at high temperatures (usually 120–180 °C), the Nafion membrane acts like a nonconductive substance, because of the dryness in the conductive medium of the membrane at this high temperature ranges. To solve these complexities, Wieser et al. [6] and Zhang et al. [7] have introduced high thermo-chemical resistant alternative polymeric membranes such as polyimides, polysulfones, polybenzoxazoles, poly(ether, ether ketones), PBI (polybenzimidazole), AB-PBI, poly(2,5-benzimidazole), poly(2,2-m-(phenylene)-5,5 bibenzimidazole), pyridine-based PBI, and sulfo-based PBI, to preferable use in high temperature PEMFC applications. Figure 1 depicts the chemical structure of PBI membrane.

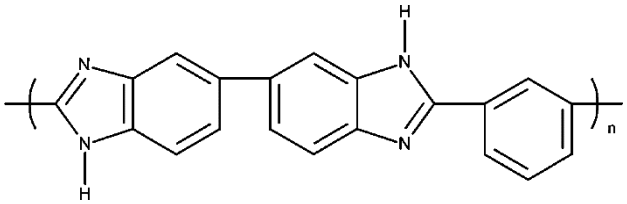


Figure 1. The chemical structure of polybenzimidazole.

PBI-based membranes have some potential advantages over Nafion in terms of price, thermal, mechanical, and chemical properties. However, the pristine PBI membrane has a low ionic conductivity due to lack of conduction media for proton transportation. It is only able to manage a high proton conduction system inside the membrane with the required amount of acid doping level (ADL). Jouanneau et al. [8] have shown that the PBI membranes are basic in nature because of having the N-H sites in the imidazole group. Therefore, this type of membrane could easily be modified by the treatment of strong acids such as H_3PO_4, H_2SO_4, HCl, HNO_3, $HClO_4$, and so on in order to enhance the proton conductivity [9]. However, the excess acid doping might be counter intuitive on the mechanical and thermal properties of the PBI membrane. Therefore, it would also be effective for the ADL of the PBI membrane to retain the prior criteria. In this study, we emphasized an optimum use of H_3PO_4 doping level of proton exchange membrane using Taguchi method. Additionally, we studied the relationship among variable factors using regression analysis and contour plot of PBI membrane.

Materials and Methods

We used pristine PBI copolymer-1 and PBI copolymer-2 electrolyte membrane (Fumatech BWT Group, Germany), the Nafion 212 membrane (DuPont, USA) and the chemical reagents, such as orthophosphoric acid, H_2O_2, and $FeSO_4$ (Sigma Aldrich, USA). All chemicals were used in laboratory analyzed grade.

Pristine PBI copolymer-1 and PBI copolymer-2 electrolyte membranes are ionic conductive and electronic nonconductive, despite their different molecular weight and thickness, although both are PBI based copolymer. In addition, Nafion 212 is commonly used PEM fuel cell application in the low working temperature range. In this

study, we compared PBI AM, PBI AP and Nafion 212 in terms of proton conductivity under high temperature. For proton conduction, it needs a less volatile solvent and high boiling point to support the conduction media, which increases the hoping of hydrogen bonds inside the membrane (Grothious mechanism) that is most likely to favor of proton transportation through the membrane [10]. PBI copolymer-1 and PBI copolymer-2 membranes were cut into small pieces that submerged in the orthophosphoric acid bath (85% concentration H_3PO_4) to get the expected proton conductivity. Prior to the acid doping, the PBI membrane was dried in a vacuum oven at 110 °C until a constant weight was reached, and the membrane thickness was recorded by the Mitutoyo-7321 (Japan) thickness gauge. Later on, the membrane was dipped into the acid bath for a certain period of time with a desirable temperature. The membrane thickness was increased due to gradually penetration of acid molecules. Next, the acid doped membrane was gently swept by a lab tissue to remove any unexpected residue or solvent, which was finally dried at 70 °C for 24 hours.

The proton conductivity of acid doped PBI copolymer-1, PBI copolymer-2, and Nafion 212 membranes was measured by the Autolab Potentiostat AUT84976 in context to the electrochemical impedance spectroscopic (EIS) analysis. The frequency ranges set were from 0.10 Hz to 1MHz, amplitude was 0.01, and the applied current ranged from 100 nA to 1 A. Using those parameters, we performed a Nyquist plot that helps find out the ionic resistance of that membrane. In this case, two Pt mesh probes were used to measure the proton conductivity through the membrane, according to the following equation (1) [11-12].

$$\alpha = L/RA \tag{1}$$

whereas σ is proton conductivity (S/cm), L is thickness of membrane (cm), R is = resistance of membrane (Ω) and A is membrane area πr^2 (cm^2); r is the radius of sample specimen.

The acid doping level (ADL) of the doped PBI membranes were determined on the basis of the ion exchange capacity (IEC). In addition, acid doped membranes were immersed in 2.0 M NaCl solution and kept overnight for H^+ ion exchange from the doped membrane. The resultant NaCl solution was titrated by a 0.02 M NaOH solution. The Phenolphthalein indicator was used to detect the endpoint. The membranes were protonated using 1.0 M HCl solution for several hours. After that, it was dried in an oven at 105°C until getting the constant weight. Therefore, the ADL of the doped membrane was calculated according to the following equation (2) [13-16].

$$\mathrm{ADL} = \frac{V_{NaOH} * S_{NaOH}}{W_{PBI}} \tag{2}$$

V_{NaoH} is volume of NaOH in ml, S_{NaoH} strength of NaOH in molarity, and W_{PBI} is dry weight of PBI membrane

Taguchi method is one of the well-known techniques, which can be used in a systematic optimization and efficient methodology process for a design of experiment (DoE) [17]. According to this method, L9 orthogonal array created the DoE as shown in Table 1. The acid doped PBI copolymer-1 membrane optimized the maximum ADL and the highest proton conductivity. In this case, three factors were considered doping time, doping temperature, and operating temperature at three levels. To get the optimum conditions, we made sure of the narrow and sharp analysis during the screening of all factors. Signal to noise ratios and orthogonal arrays are two major tools that were used to analyze the responses of DoE. In this study, "Larger is better" of S/N ratio was determined the steps according to the following equation (3) [18].

$$\frac{S}{N} = -10log\frac{1}{n}\sum y^2 \tag{3}$$

where, $\frac{S}{N}$ is signal to noise ratio, n is number of observations, and y is response.

Table 1. Taguchi design of experiment based on L9 orthogonal array

Exp. No	Doping Temperature	Doping Time	Operating Temperature
1	1	1	1
2	1	2	2
3	1	3	3
4	2	1	2
5	2	2	3
6	2	3	1
7	3	1	3
8	3	2	1
9	3	3	2

Responses comprised the statistical analysis of variances based on the regression analysis of the ADL and proton conductivity were performed in MINITAB 17 (software). The regression analysis refers to the correlation and interaction effect between the responses of ADL, as well as of proton conductivity.

Results and Discussion

Membrane selection

The proton conductivity is the most selective criterion of high temperature proton exchange membrane (PEM) fuel cell. The Nyquist plot that was introduced to measure the ionic conductivity of the membrane confirms the concurrency of the curve according to the $[R_S(C[R_{CT}Q])W]$ as an equivalent circuit that is shown in Figure 2(a and b). Figure 2(b) shows that the phase angle is close to zero at high frequency range. Therefore, the conductance C, and constant phase element Q are negligible impedance, since the impedance is inversely proportional to frequency [19, 20]. Whereas R_S represents the electrolyte resistance that was needed in the analysis of the membrane, R_{CT} refers the charge transfer resistance. However, the symbol of W indicates the infinite diffusion that was further confirmed by the Nyquist plot. During the conductivity measurement, the proton remained in diffusion throughout the membrane. The proton conductivity of each membrane was calculated by putting the value of electrolyte (polymer membrane) resistance (R_S), with their corresponding electrolyte membrane area (A), and thickness of electrolyte membrane (L) in equation (1). In case of the PBI copolymer-1, PBI copolymer-1, and Nafion 212 electrolyte membranes, the recorded proton conductivities were 5.83, 4.85, and 3.34 mS/cm respectively, at 120 °C temperature. Table 2 shows the values of proton conductivity and equivalent circuit elements. Among of them, the PBI copolymer-1 membrane exhibits the maximum proton conductivity. Since the PBI copolymer-1 membrane absorbed the high ADL content compared to the PBI copolymer-2 membrane which can accelerate the conduction medium at a high temperature. In addition, greater thickness and different molecular weight can explain for high acid absorbing affinity [21]. In contrast, the Nafion 212 membrane exhibits relatively lower conductivity compared to the both PBI membranes at high temperature. Since the Nafion 212 was dehydrated at 120 °C temperature (over the water boiling point), this was insufficient to support the conduction media for proton conduction. Taken together, it may be concluded that the PBI copolymer-1 membrane is the most promising candidate for high temperature PEM fuel cell.

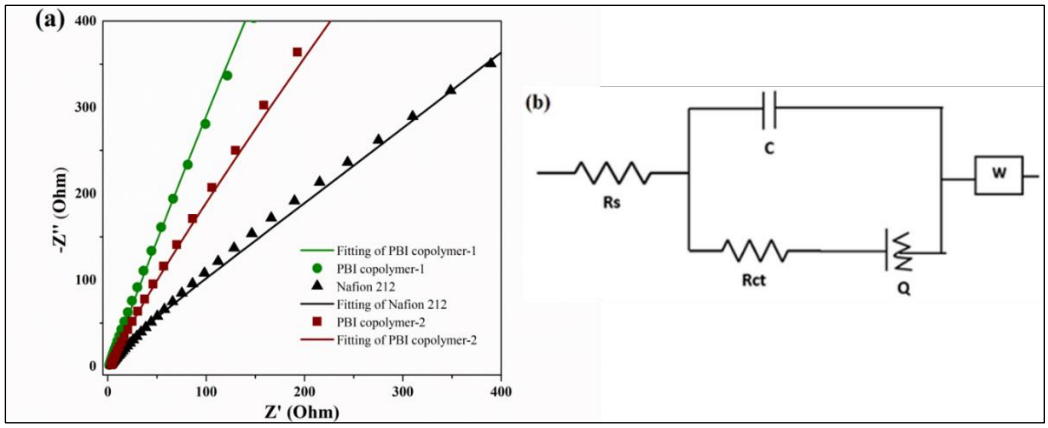


Figure 2. (a) Nyquist plot with fitting curve of membranes and (b) equivalent circuit

Table 2. Proton conductivity and equivalent circuit report

Items	Thickness L (cm)	Area A (cm^2)	Resistance R_s (Ohm)	Conductance (C)	Constant Phase Element (Q)	Chi-Square (x^2)	Conductivity (mS/cm)	Estimate Error (%)
Nafion 212	0.0036	0.64	1.687	1.2E-06	4.4E-05	< 0.01	3.34	1.33
PBI copolymer-1	0.0052	0.64	1.394	1.6E-06	2.0E-05	< 0.01	5.83	1.78
PBI copolymer-2	0.0051	0.64	1.642	2.2E-06	5.0E-05	< 0.01	4.85	1.56

Factor screening

The Nyquist plot depicts that the proton conductivity increases due to the lowering of membrane resistance at high doping temperature as shown in Figure 3(a). Figure 3(b) clearly shows that the conductivity and ADL gradually increase as a function of doping temperature, and the maximum outcomes occur doping temperature of 120 °C. Because of the acid absorbing power of membranes are increased under high doping temperature. Furthermore, the factor screening for narrow and sharp analysis was performed such a way so that one variable was varied while other two variables were kept constant. For example, the doping temperature was increased by 20 °C started from 80 °C to 120 °C while the doping time of 6 h and operating temperature of 120 °C were kept constant. In these preparations, the maximum conductivity and ADL were recorded at 4.36 mS/cm and 10.6 (mol/repeating unit), respectively.

Figure 4(a) shows that the doping time of 6 h screen out in terms of proton conductivity and ADL responses. Figure 4(b) shows that ADL and conductivity increase abruptly at the beginning stages. ADL content does not appreciably increase as a function of doping time increment, because of the membrane has saturated by acid doping. Similarly, the conductivity does not show significant improvement to further progress of doping time.

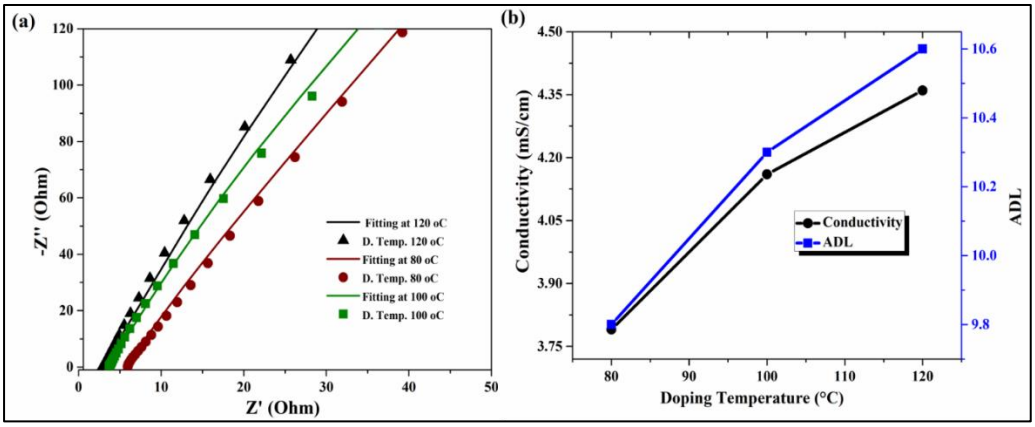


Figure 3. (a) Nyquist plot with fitting curve of PBI copolymer-1 at different doping temperatures and (b) corresponding proton conductivity and ADL

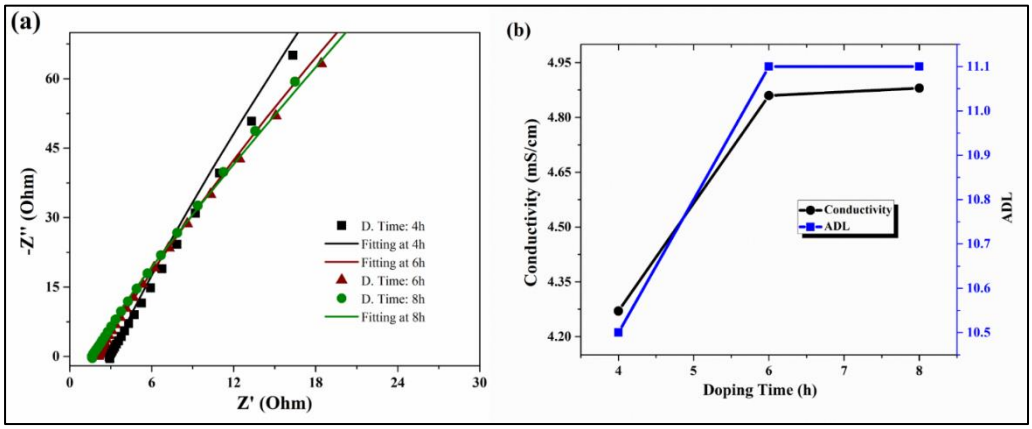


Figure 4. (a) Nyquist plot with fitting curve of PBI copolymer-1 at different doping time and (b) corresponding proton conductivity and ADL

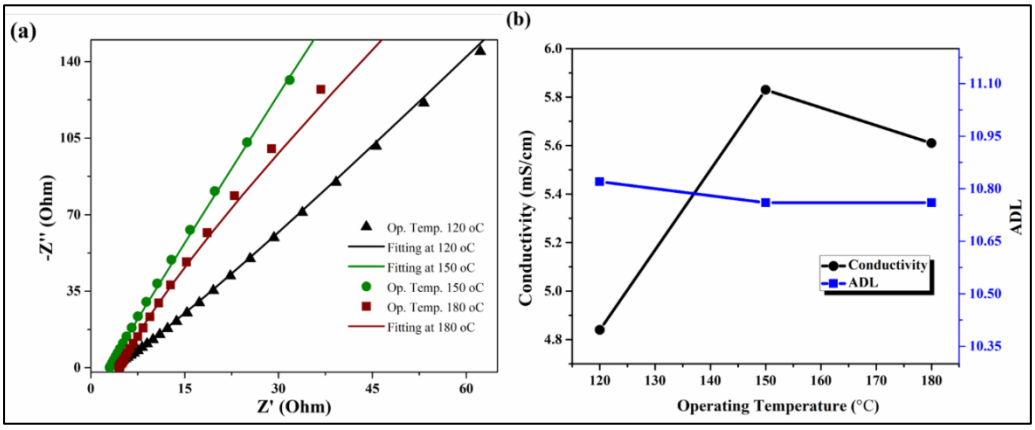


Figure 5. (a) Nyquist plot with fitting curve of PBI copolymer-1 at different operating temperatures and (b) corresponding proton conductivity and ADL

Operating temperature is the most significant factor in terms of proton conductivity due to its huge impact on the impedance, i.e. the conductivity of the membrane as shown in Figure 5(a). At the beginning stage, the conductivity increases as a function of operating temperature. Figure 5(b) reflects that the maximum conductivity recorded at 5.83 mS/cm under 150 °C operating temperature can be considered as a screening level for further analysis. The conductivity again decreases at high operating temperature. This is because it may fairly be changing tendency from phosphoric acid (H_3PO_4) to pyrophosphoric acid ($H_4P_2O_7$) which is less conductive than phosphoric acid [22]. In contrast, ADL content shows the steady state during different operating temperatures that were used. It is possible because the operating temperature of ADL refers the heat treatment of acid doped membrane and hence observes the effect of ADL content (like acid leaching, dryness etc.) of the membrane.

Taguchi optimization

Based on DoE, the outcomes of ADL, conductivity and their analyzed data were tabulated in Table 3, along three variable factors such as doping temperature, doping time, and operating temperature. Figure 6 demonstrations the Nyquist plot to measure the conductivity for all respective observations. Among of them, Obs-5 represents the maximum conductivity as 6.31 (mS/cm) under doping temperature 120 ℃, doping time 6 hours and operating temperature 160 ℃. Moreover, outcomes of ADL and conductivity were transformed into the signal to noise (S/N) ratios using equation (3) to select the optimum parameters. In this case, it has been considered that the "larger is the best". The main effects have been plotted for the ADL and conductivity of the S/N ratios that is shown in Figure 7(a) and 7(b).

Table 3. Optimization of ADL and conductivity based on DoE

Exp. No	Doping Temp. (°C)	Doping Time (h)	O. Temp. (°C)	ADL	S/N-1 Ratio of ADL	Conductivity (mS/cm)	S/N-2 Ratio of Conductivity
Obs-1	110	5	140	10.3	20.2567	5.07	14.1002
Obs-2	110	6	150	10.7	20.5061	5.72	15.1479
Obs-3	110	7	160	10.6	20.5877	5.80	15.2686
Obs-4	120	5	150	10.7	20.6685	5.56	14.9015
Obs-5	120	6	160	11.1	20.9065	6.31	16.0006
Obs-6	120	7	140	11.2	20.9065	5.69	15.1022
Obs-7	130	5	160	10.7	20.6685	5.93	15.4611
Obs-8	130	6	140	11.2	21.0616	5.74	15.1782
Obs-9	130	7	150	11.2	20.9844	6.11	15.7208

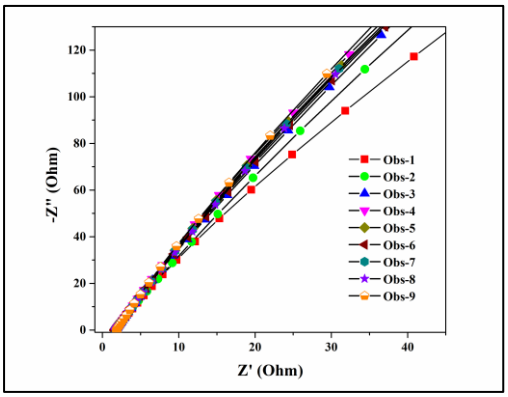


Figure 6. Nyquist plot of membrane for different observation of DoE

Figure 7(a) and Table 4 exhibit that the doping temperature and doping time great influencing factors on the ADL outcome. For ADL, the optimum factors were considered the doping temperature of 130 °C (level 3) and doping time of 6 hours (level 2). These values were obtained from the main effect plot of S/N ratios. In fact, the operating temperature is no appreciable effect on ADL outcome, and therefore it has no more significant effect on the S/N ratios. Similarly, Figure 7(b) and Table 5 reveal that the effect of factors on the conductivity responses to select optimum conditions. In this case, optimum conditions were obtained, such as doping temperature at 130 °C (level 3), doping time at 6 hours (level 2), and operating temperature at 160 °C (level 3).

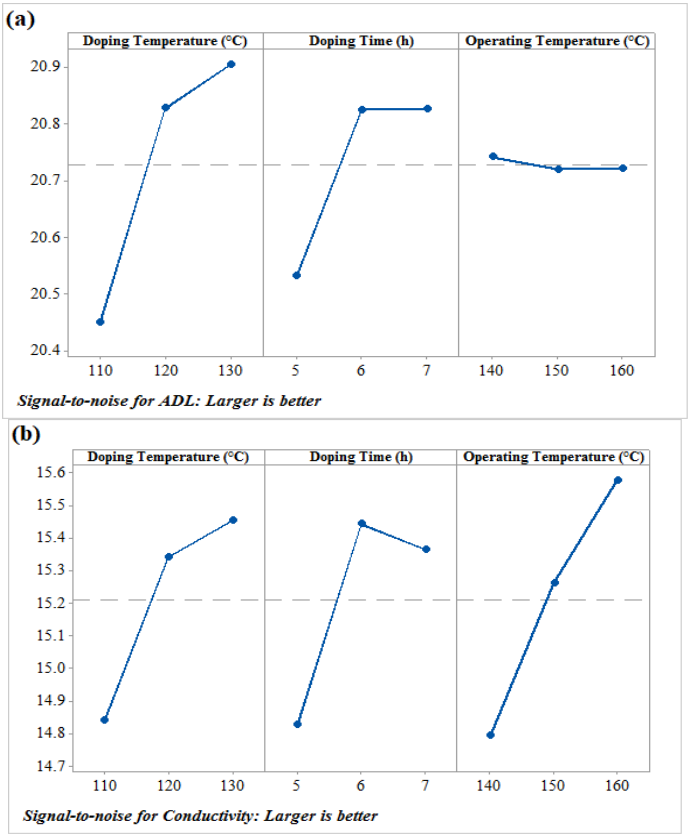


Figure 7. The main effect plot for S/N ratios of (a) ADL and (b) proton conductivity

Table 4. Signal-to-Noise (S/N) responses table for ADL

Level	Doping Temp. (°C)	Doping Time (h)	O. Temp. (°C)
1	20.45	20.53	20.74
2	20.83	20.82	20.72
3	20.90	20.83	20.72
Delta	0.45	0.29	0.02
Rank	1	2	3

Table 5. Signal-to-Noise (S/N) responses table for conductivity

Level	Doping Temp. (°C)	Doping Time (h)	O. Temp. (°C)
1	14.84	14.82	14.79
2	15.33	15.44	15.26
3	15.45	1536	15.58
Delta	0.61	0.62	0.78
Rank	3	2	1

Regression analysis

The regression equation has expressed the relationship among the variable parameters in a bid to evaluate the ADL and conductivity for any combination of factors at a level in a particular range. Based on the regression model, the error factors of ADL and conductivity were measured 1.33% and 1.34% using the optimum factors level through regression equations (4) and (5), respectively [23]. These results express the responses of ADL and conductivity that were measured in a systematic and scientific way. The multiple linear regression equations (4) and (5) were formulated for the ADL and conductivity using the MINITAB 17 software as following as [24, 25].

$$ADL = 6.63 + 0.02833\ D_{Temp} + 0.1833\ D_{Time} - 0.00167\ O_{Temp} \quad (4)$$

$$Conductivity = -1.49 + 0.01983\ D_{Temp} + 0.1717\ D_{Time} + 0.02567\ O_{Temp} \quad (5)$$

ADL regression results were tabulated in Table 6. It shows the different P values of different factors such as doping temperature, doping time, and operating temperature are 0.026 (<0.05), 0.010 (<0.05), and 0.823 (>0.05), respectively. It is very important in terms of lower (<0.05) P values that have a significant effect on the outcome. However, large P values (>0.05) have no significant effect on the results. Based on the P value, it is clear that the doping temperature and doping time have a huge effect on ADL outcome. Furthermore, it was studied the contour plot of ADL *vs.* respective factors that shown in Figure 8 (a-c), whereas; green colour represents the more reactive factorial effect on ADL and the blue colour represents the less reactive factors. Based on the contour plot, it may easily be concluded that the doping temperature and doping time are the influencing factors on ADL.

Table 6. Analysis of variance for ADL

Source	DF	Adj SS	Adj MS	F-Value	P-Value
Regression	3	0.685000	0.228333	7.58	0.026
Doping Temp. (°C)	1	0.481667	0.481667	16.00	0.010
Doping Time (h)	1	0.201667	0.201667	6.70	0.049
O. Temp. (°C)	1	0.001667	0.001667	0.06	0.823
Error	5	0.150556	0.030111		
Total	8	0.835556			

Similarly, it may also explain the effect P of values on the conductivity responses. Table 7 shows the P values for the doping temperature, doping time, and operating temperature such as 0.044, 0.069, and 0.018, respectively. In this case, all factors have a significant effect on the conductivity due to their low P values which are less than 0.50. In addition, the contour plot of conductivity depicts in Figure 8 (d-f), whereas; doping temperature and doping time had an approximately analogous effect on conductivity. However, the operating temperature was a higher impact on conductivity. Therefore, conductivity is dependent on factors according to priorities such as operating temperature>doping time>doping temperature.

Table 7. Analysis of variance for conductivity

Source	DF	Adj SS	Adj MS	F-Value	P-Value
Regression	3	0.8081	0.26937	8.14	0.023
Doping Temp. (°C)	1	0.2360	0.23602	7.14	0.044
Doping Time (h)	1	0.17682	0.17682	5.35	0.069
O. Temp. (°C)	1	0.3953	0.39527	11.95	0.018
Error	5	0.1654	0.03308		
Total	8	0.9735			

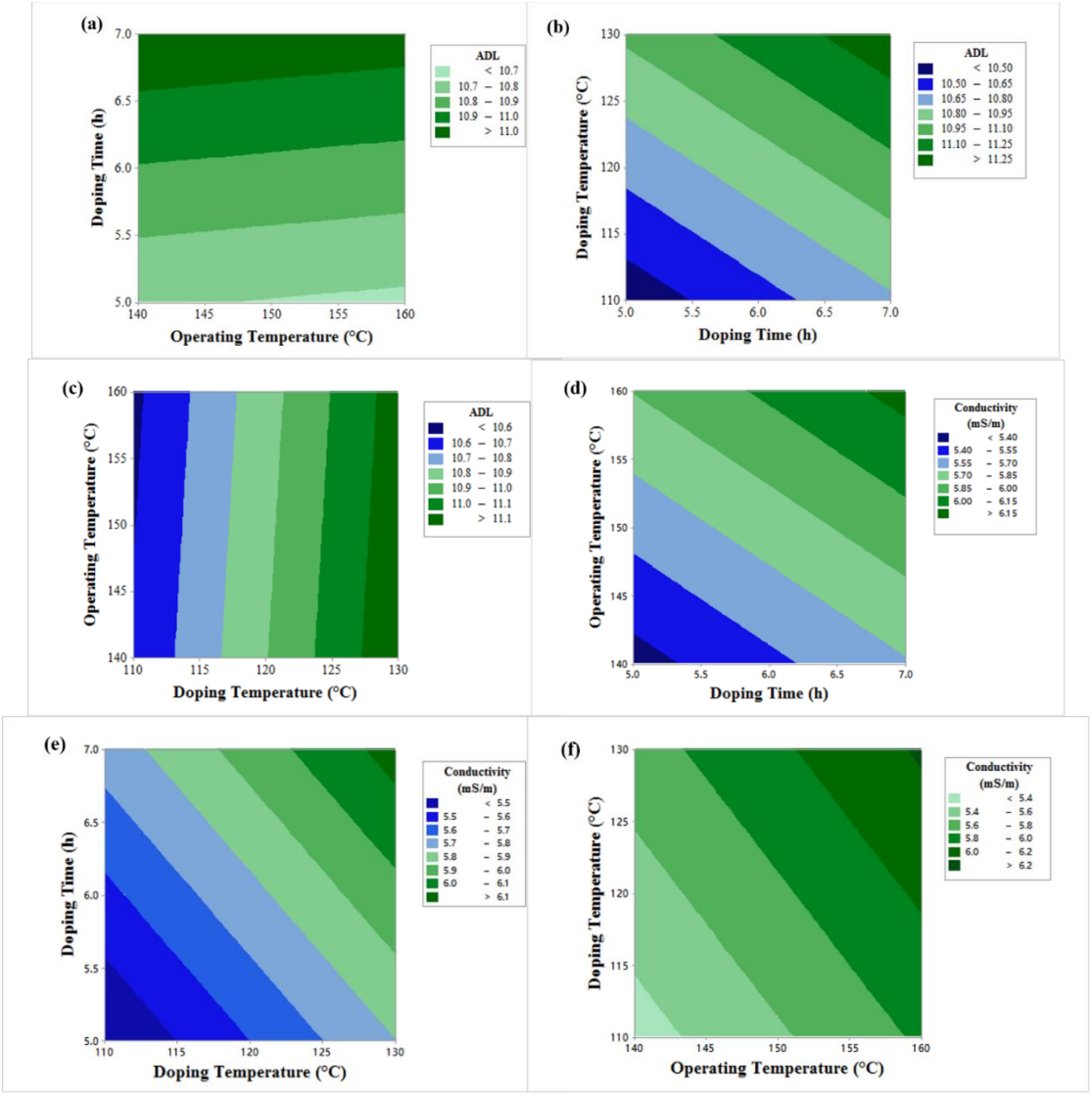


Figure 8. The contour plot of ADL at considering factors between (a) operating temperature *vs* doping time, (b) doping time *vs* doping temperature and (c) doping temperature *vs* operating temperature. The contour plot of proton conductivity for (d) operating temperature *vs* doping time, (e) doping temperature *vs* doping time and (f) doping temperature *vs* operating temperature

Confirmation test

The confirmation test is used to verify the experimental results with the predicted value. If the optimal combination of parameters and their levels coincidently match with one of the experiments of the DoE, then a confirmatory test is not required. In this study, the confirmation test is required due to the optimum combination of factors and their levels are not available to any individual observation in the DoE. The predicted value of the ADL and conductivity at optimum conditions were measured by adding the average performance to the contribution of each parameter at the optimum level for ADL and conductivity using the following equations (6) & (7), respectively [26-28].

$$Y_{ADL} = T_{avg} + (D.\ Time_{opt} - T_{avg}) + (D.\ Temp_{opt} - T_{avg}) \quad (6)$$

$$Y_{con} = T_{avg} + (D.\ Time_{opt} - T_{avg}) + (D.\ Temp_{opt} - T_{avg}) + (O.\ Temp_{opt} - T_{avg}) \quad (7)$$

whereas, Y_{ADL} is the predicted value of ADL, Y_{con} is the predicted value of conductivity, T_{avg} is the grand total average performance, D. $Time_{opt}$ is the doping time factor average at optimum level, D. $Temp_{opt}$ is the doping temperature factor average at optimum level, and O. $Temp_{opt}$ is the operating temperature factor average at optimum level. During the calculation of the predicted value of ADL and conductivity, it was substituted the respective values in above equations. The experimental and predicted results are shown in Table 8 and Table 9 for the confirmation of ADL and conductivity, respectively.

Table 8. Confirmation test for ADL

Opt. Level	Exp. Level	Predicted	Experimental Value			
			Obs-1	Obs-2	Obs-3	Average
A3, B2 (excluded C3)	A3, B2 (excluded C3)	11.2	11.1	11.4	11.3	11.3

Table 9. Confirmation test for conductivity

Opt. Level	Exp. Level	Predicted	Experimental Value			
			Obs-1	Obs-2	Obs-3	Average
A3, B2, C3	A3, B2, C3	6.19	6.36	6.25	6.29	6.30

Conclusion

This study suggested that PBI copolymer-1 is the most promising candidate for high-temperature PEM fuel cell application compared with PBI copolymer-2 and Nafion 212 due to convenient proton conductivity and acid absorbing capacity. The variable factors such as doping temperature, doping time, and operating temperature including three levels were considered for the Taguchi optimization of ADL and conductivity responses. The maximum ADL and ionic conductivity have measured 11.3 and 6.30 mS/cm under optimized conditions respectively. In addition, proton conductivity increases with increasing ADL. However, ADL depends on acid doping time and doping temperature. The contour plot is suggested that the variable factors of conductivity can be arranged high to low priorities as operating temperature>doping time>doping temperature.

Acknowledgement

This work has been financially supported by the Universiti Kebangsaan Malaysia under the Grant AP-2013-010 and TRGS/2/3014/UKM/02/4/1. The authors would like to thanks the university administration for the financial support.

References

1. Sopian, K. and Daud, W. R. W. (2006). Challenges and future developments in proton exchange membrane fuel cells. *Renewable Energy*, 31(5): 719-727.
2. Haque, M. A., Sulong, A. B., Rosli, R. E., Majlan, E. H., Shyuan, L. K. and Mashud, M. A. A. (2015). Measurement of hydrogen ion conductivity through proton exchange membrane. *IEEE International WIE* Conference: pp. 552-555.

3. Tang, Z., Ng, H. Y., Lin, J., Wee, A. T. and Chua, D. H. (2010). Pt/CNT-based electrodes with high electrochemical activity and stability for proton exchange membrane fuel cells. *Journal of The Electrochemical Society*, 157(2): 245-250.
4. Shao, Y., Yin, G., Gao, Y. and Shi, P. (2006). Durability study of Pt/C and Pt/CNTs catalysts under simulated PEM fuel cell conditions. *Journal of the Electrochemical Society*, 153(6): 1093-1097.
5. Lufrano, F., Baglio, V., Staiti, P., Arico, A. S. and Antonucci, V. (2006). Development and characterization of sulfonated polysulfone membranes for direct methanol fuel cells. *Desalination*, 199(1-3): 283-285.
6. Wieser, C. (2004). Novel polymer electrolyte membranes for automotive applications–requirements and benefits. *Fuel Cells*, 4(4): 245-250.
7. Zhang, H. and Shen, P. K. (2012). Recent development of polymer electrolyte membranes for fuel cells. *Chemical Reviews*, 112(5): 2780-2832.
8. Jouanneau, J., Mercier, R., Gonon, L. and Gebel, G. (2007). Synthesis of sulfonated polybenzimidazoles from functionalized monomers: Preparation of ionic conducting membranes. *Macromolecules*, 40(4): 983-990.
9. Xing, B., and Savadogo, O. (1999). The effect of acid doping on the conductivity of polybenzimidazole (PBI). *Journal of New Materials for Electrochemical Systems*, 2: 95-102.
10. Haque, M. A., Sulong, A. B., Loh, K. S., Majlan, E. H., Husaini, T. and Rosli, R. E. (2017). Acid doped polybenzimidazoles based membrane electrode assembly for high temperature proton exchange membrane fuel cell: A review. *International Journal of Hydrogen Energy*, 42(14): 9156-9179.
11. Chang, H. Y., and Lin, C. W. (2003). Proton conducting membranes based on PEG/SiO_2 nanocomposites for direct methanol fuel cells. *Journal of Membrane Science*, 218(1): 295-306.
12. Chang, H. Y., Thangamuthu, R. and Lin, C. W. (2004). Structure–property relationships in PEG/SiO_2 based proton conducting hybrid membranes—A^{29} Si CP/MAS solid-state NMR study. *Journal of membrane science*, 228(2): 217-226.
13. Navessin, T., Eikerling, M., Wang, Q., Song, D., Liu, Z., Horsfall, J., and Holdcroft, S. (2005). Influence of membrane ion exchange capacity on the catalyst layer performance in an operating PEM fuel cell. *Journal of the Electrochemical Society*, 152 (4): 796-805.
14. Thiam, H. S., Daud, W. R. W., Kamarudin, S. K., Mohamad, A. B., Kadhum, A. A. H., Loh, K. S. and Majlan, E. H. (2013). Nafion/Pd–SiO_2 nanofiber composite membranes for direct methanol fuel cell applications. *International Journal of Hydrogen Energy*, 38(22): 9474-9483.
15. Wang, J., Zhang, H., Jiang, Z., Yang, X. and Xiao, L. (2009). Tuning the performance of direct methanol fuel cell membranes by embedding multifunctional inorganic submicrospheres into polymer matrix. *Journal of Power Sources*, 188(1): 64-74.
16. Kang, S., Zhang, C., Xiao, G., Yan, D., and Sun, G. (2009). Synthesis and properties of soluble sulfonated polybenzimidazoles from 3,3′-disulfonate-4,4′-dicarboxylbiphenyl as proton exchange membranes. *Journal of Membrane Science*, 334(1): 91-100.
17. Phadke, M. S. (1995). Quality engineering using robust design. Prentice Hall PTR.
18. Vankanti, V. K. and Ganta, V. (2014). Optimization of process parameters in drilling of GFRP composite using Taguchi method. *Journal of Materials Research and Technology*, 3(1): 35-41.
19. Leong, J. X., Daud, W. R. W., Ghasemi, M., Ahmad, A., Ismail, M., and Liew, K. B. (2015). Composite membrane containing graphene oxide in sulfonated polyether ether ketone in microbial fuel cell applications. *International Journal of Hydrogen Energy*, 40(35): 11604-11614.
20. Song, X., Ren, S., Yang, Y., Guo, Y., Jing, H., Mao, Q., and Hao, C. (2017). Polyaniline-based electrocatalysts through emulsion polymerization: Electrochemical and electrocatalytic performances. *Journal of Energy Chemistry*, 26(1): 182-192.
21. Yang, J. S., Cleemann, L. N., Steenberg, T., Terkelsen, C., Li, Q. F., Jensen, J. O., Hjuler, H. A., Bjerrum, N. A. and He, R. H. (2014). High molecular weight polybenzimidazole membranes for high temperature PEMFC. *Fuel Cells*, 14(1): 7-15.
22. Cobridge, D. E. C. (1995). Phosphorus: an outline of chemistry, biochemistry and uses. *Studies in Inorganic Chemistry*: pp. 20.
23. Gopalsamy, B. M., Mondal, B., and Ghosh, S. (2009). Taguchi method and ANOVA: An approach for process parameters optimization ofhard machining while machining hardened steel. *Journal of Scientific and Industrial Research,* 68(8): 686-695.

24. Sousa, S. I. V., Martins, F. G., Alvim-Ferraz, M. C. M. and Pereira, M. C. (2007). Multiple linear regression and artificial neural networks based on principal components to predict ozone concentrations. *Environmental Modelling & Software*, 22(1): 97-103.
25. Andrews, D. F. (1974). A robust method for multiple linear regression. *Technometrics*, 16(4): 523-531.
26. Suherman, H. (2017). Optimization of internal mixing parameter on the electrical conductivity of multiwall carbon nanotubes/synthetic graphite/epoxy nanocomposites for conductive polymer composites using Taguchi method. *Jurnal Kejuruteraan*, 29(2): 79-85.
27. Mahapatra, S. S. and Patnaik, A. (2006). Parametric optimization of wire electrical discharge machining (WEDM) process using Taguchi method. *Journal of the Brazilian Society of Mechanical Sciences and Engineering*, 28(4): 422-429.
28. Kamaruddin, S., Khan, Z. A. and Foong, S. H. (2010). Application of Taguchi method in the optimization of injection moulding parameters for manufacturing products from plastic blend. *International Journal of Engineering and Technology*, 2(6): 574-530.

Malaysian Journal of Analytical Sciences, Vol 22 No 6 (2018): 1078 - 1083
DOI: https://doi.org/10.17576/mjas-2018-2206-18

MALAYSIAN JOURNAL OF ANALYTICAL SCIENCES
Published by The Malaysian Analytical Sciences Society
ISSN 1394 - 2506

In-vitro PHOTOPROTECTIVE ACTIVITIES OF DIFFERENT SOLVENT EXTRACTION OF *Hibiscus sabdariffa*

(*In-vitro* Aktiviti Foto Perlindungan Bagi Ekstrak Pelarut yang Berbeza dari *Hibiscus sabdariffa*)

Nur Royhaila Mohamad[1], Siti Salwa Abd Gani[1,2]*, Roswanira Abdul Wahab[3], Uswatun Hasanah Zaidan[4]

[1]*Halal Product Research Institute (HPRI), Putra Infoport*
[2]*Department of Agriculture Technology, Faculty of Agriculture*
Universiti Putra Malaysia, 43400 Serdang, Selangor, Malaysia
[3]*Department of Chemistry, Faculty of Science,*
Universiti Teknologi Malaysia, 81310 Johor Bahru, Johor, Malaysia
[4]*Department of Biochemistry, Faculty of Biotechnology & Biomolecular Sciences,*
Universiti Putra Malaysia, 43400 Serdang, Selangor, Malaysia

**Corresponding author: ssalwaag@upm.edu.my*

Received: 2 April 2018; Accepted: 31 July 2018

Abstract

In recent years, plant extracts have been considered as potential sunscreen resources owing to their antioxidant activity as well as capability to absorb ultraviolet (UV) rays in the UVA region. In the present study, the UV protective factor of three different extracts of *Hibiscus sabdariffa* (HS) namely ethanol (HS-ETOH), ethyl acetate (HS-EA), and hexane (HS-HEX), all of which are rich in flavonoids and other phenolic components were assessed by using UV-Vis spectrophotometer to estimate their corresponding *in-vitro* Sun Protection Factors (SPF). The results revealed that both extracts of HS-ETOH and HS-EA showed characteristic absorption bands in the UVA and UVB regions, while the HS-HEX extract was observed to absorb in the UVB and UVC regions under similar concentration. Pertinently, the highest SPF (17.53±0.22) was obtained in the HS-ETOH extract, inferring its potential as an active component for sunscreen in pharmaceutical and cosmeceutical preparations.

Keywords: *Hibiscus sabdariffa*, sun protection factor, sunscreen, UV-spectrophotometry

Abstrak

Bahan-bahan semulajadi yang telah diekstrak daripada tumbuh-tumbuhan baru-baru ini telah dipertimbangkan potensinya untuk menjadi sumber perlindungan matahari bagi penyerapan sinar ultraviolet dalam lingkungan UVA dan aktiviti antioksidan. Dalam kajian ini, faktor perlindungan UV bagi tiga ekstrak yang berbeza iaitu ekstrak etanol (HS-ETOH), ekstrak etil asetat (HS-EA), dan ekstrak heksana (HS-HEX) daripada *Hibiscus sabdariffa* (HS) yang kaya dengan komponen seperti flavonoid dan fenolik telah dinilai dengan menggunakan spektrofotometer UV-Vis dan dikira dengan Faktor Perlindungan Matahari (SPF). *In-vitro* SPF daripada ekstrak HS telah dianalisis dengan menggunakan pengukuran penjerapan terhadap pelarut yang berbeza semasa proses pengekstrakan. HS-ETOH dan HS-EA telah menunjukkan ciri jalur penyerapan bagi kawasan UVB dan UVA manakala HS-HEX di kawasan UVC dan UVB pada kepekatan yang sama. HS-ETOH mencapai faktor perlindungan matahari yang paling tinggi SPF (17.53±0.22). Ia menunjukkan kemungkinan untuk menggunakan ekstrak ini sebagai perlindungan matahari dalam persediaan farmaseutikal dan kosmeseutikal.

Kata kunci: *Hibiscus sabdariffa*, faktor perlindungan matahari, pelindung matahari, UV-spektrofotometri

Introduction

Oxidative stress and inflammatory responses induced by ultraviolet radiation (UV) can result in a variety of harmful effects on skin, which include premature photoaging, induction of immunosuppression, skin carcinogenesis [1] and even skin cancer [2]. The harmful effects of UV rays on humans can be divided into three regions: ultraviolet A (UVA – from 320 nm to 400 nm); ultraviolet B (UVB – from 290 nm to 320 nm) and ultraviolet C (UVC – from 200 nm to 290 nm). UVC radiation is filtered by the atmosphere before reaching Earth but radiation from UVB may still pass through the ozone layer and is responsible for skin damage through sunburn. Furthermore, UVA radiation can reach the deeper layers of epidermis and dermis, and the damaging effects provoke premature skin aging [2]. The problem has been further exacerbated by the fact that the ozone layer surrounding the Earth's atmosphere, which shields us from the harmful effects of UV, has become considerably thinner than it was 50 years ago. This has resulted in higher penetration of all types of UV radiation. The unfortunate outcome has been associated with increased hazardous compound emissions, i.e., chlorofluorocarbons into the atmosphere, which is brought about by increased industrialization activities. In view of such circumstances, skin protection by using creams with high sun protection factor (SPF) [1] may prove to be essential for reducing the harmful effects of UV exposure. Therefore, concerted efforts in developing sunscreen formulations that effectively protect the human skin against UVA-induced and UVB-induced damages have merit scientific and commercial pertinence.

Among the active compound sources described to exhibit sun-protective properties against UV-induced damages are those extracted from plants. It has been indicated that plants produce various antioxidants as well as compounds that quench and protect against molecular damage caused by reactive oxygen species (ROS). The most important group of compounds includes flavonoids which are known for their ability to scavenge UV-induced radicals, a feature which also indicates that flavonoids make excellent UV-absorbing screens [3]. *Hibiscus sabdariffa* (HS), also known as Roselle from the Malvaceae family [4], is among the many plants known for being high in polyphenols [5] and the calyces are inherently rich in antioxidants. So far, HS calyce extracts were mainly studied to combat degenerative diseases and act as local herbal medicines for their diuretic, choleretic, febrifugal and hypotensive, blood thinning effects as well as stimulating intestinal peristalsis [6]. Studies utilizing extracts of HS as active ingredients in sunscreen preparations have yet to be reported and the feasibility of using HS for such purpose remains to be seen.

To date, only a limited number of plant extracts and oils exhibiting photo-protective action were used in formulations to manufacture sunscreens [1]. However, the current selection of plant extracts, containing sun-protective ingredients for preparing sunscreens, are rather limited and insufficient to satisfy the increased consumer demands for cosmetics formulated by using products obtained from natural resources. Herein, the study aims to evaluate another potential source of sun-protective compounds, i.e. HS, extracted by using solvents, ethanol, ethyl acetate and hexane. The extracts of HS were evaluated for their photo-protective potential by using a UV-Vis spectrophotometer.

Materials and Methods

Hibiscus sabdariffa L.

Roselle (*Hibiscus sabdariffa)* was purchased in February, 2017 from the Federal Agricultural Marketing Authority (FAMA) in Rengit, Malaysia. The plant was authenticated by an expert and deposited at the Herbarium Unit of Institute of Bioscience, in Universiti Putra Malaysia.

Chemicals and reagents

All reagents used were of analytical grade and used as-received without further purification. Distilled water was used for preparing solutions. Solvents, ethanol, methanol and ethyl acetate were purchased from Sigma Aldrich (Milwaukee, WI, USA).

Preparation of HS extracts

The calyces were washed with tap water three times and air-dried for 7 days prior to being grinded into coarse powder. HS extracts, containing high quantities of antioxidant rich compounds, were prepared according to the method by Zhen et al. with some minor modifications [8]. HS powder (10 g) was transferred into a 200 mL round-bottom flask, containing 100 mL of solvent (ethanol, ethyl acetate and hexane) and shaken by using an orbital

shaker for 12 hours at temperature 40 °C. The mixture was filtered through a Whatman filter paper (No. 4) and the residues were further extracted with a fresh batch of solvents (100 mL) and filtered once again. The supernatants of the extracts were combined and concentrated in a rotary evaporator (IKA RV 10 Digital V, German) at 45 °C and lyophilized.

Screening of potential of UV-protective effect and sun protection factor value *in-vitro*

For determining of the maximum absorption wavelength (λ_{max}), the dried extracts were diluted in the extraction solvent, to have the final concentration as 1 mg/mL. Subsequently, the spectrophotometric scanning was performed at wavelengths between 260-400 nm, with intervals of 5 nm. The readings were performed using 1 cm quartz cell, and ethanol used as blank [7]. Meanwhile the calculation of SPF was obtained according to the equation 1 developed by Mansur [9]:

$$SPF_{spectrophotometric} = CF \times \Sigma EE(\lambda) \times I(\lambda) \times Abs(\lambda) \quad (1)$$

where EE (λ) is defined as erythemal effect spectrum, I (λ) is solar intensity spectrum, Abs (λ) is absorbance of sunscreen product, CF is correction factor (= 10). The values of EE x I are constants. The value was determined by Sayre et al. [10] and shown in Table 1.

Table 1. Normalized product function used in the calculation of SPF

Wavelength (nm)	EE x I (normalized)
290	0.0150
295	0.0817
300	0.2874
305	0.3278
310	0.1864
315	0.0839
320	0.0180
Total	1.0000

Results and Discussion

SPF is a quantitative measurement of sunscreen formulation effectiveness. To be effective in preventing sunburn and other skin damages, a sunscreen product should have a wide range of absorbance between 290 nm and 400 nm. The potential of HS-EtOH, HS-EA, and HS-HEX extracts as UV-sunscreen agents was measured by the extract and solution absorbance in UVA range and UVB range. Figure 1 shows the spectrophotometric absorption profile of the HS extracts with different solvent extractions. From the data analysis, HS-EtOH and HS-EA showed characteristic absorption bands in both regions, UVB (290 nm – 320 nm) and UVA (320 nm – 400 nm) at 1 mg/mL concentration, suggesting a possible photo-protective potential. Furthermore, HS-EtOH extracts showed a higher absorbance at UVA wavelength of 330 nm at 1.73 and 355 nm at 1.01. The effect of different solvents, in which the extracts are dissolved and emollients have upon the wavelength of maximum absorbance and upon the UV absorbance of several sunscreen chemicals, alone or in combination; thus, interfering those of UVA and UVB regions is well known and documented [11, 12]. This protective effect against sunrays could be advantageous to an extract as it could enhance the effect of anti-wrinkles activity.

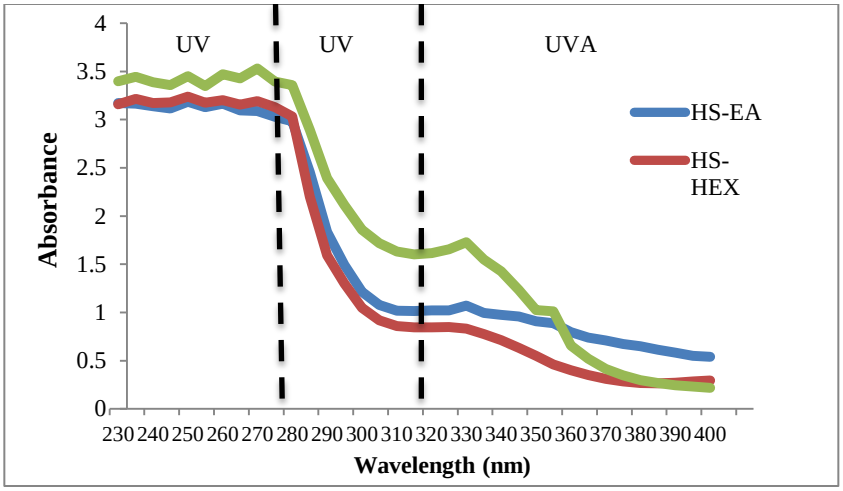


Figure 1. UV-Spectrum Profile of ethanol (HS-ETOH), ethyl acetate (HS-EA) and hexane (HS-HEX) extracts of *Hibiscus sabdariffa* (230-400 nm)

The SPF in vitro value was determined by the spectrophotometric method developed by Mansur et al. through using the UVB region [9], which was considered to be the region of greatest incidence during the day in which people are exposed longer [2]. This in vitro assay is a simple, reliable, quick, inexpensive and a validated technique, which has been widely used to determine the sunscreen potential of several, natural and synthetic products or formulations [13, 14]. In Figure 2, it can be observed that HS-EtOH extract showed 4 higher SPF value (17.53±0.22), followed by HS-EA extract (12.26±0.15). The lowest SPF value was obtained with HS-HEX extract at 10.74±0.13, respectively, with same concentration (1 mg/mL). This may due to the presence of flavonoids, flavones, phenolics acids as well as other phytoconstituents in the HS-EtOH and HS-EA extracts. Flavonoids and phenolic compounds were reported as functional components in plant and fruits, which play an important role in the management of inflammation and erythema, due to solar radiations [15]; thus, it can be concluded that high amount of phenolic compound and flavonoids could be the cause for their high SPF [16]. The antioxidant property of the flavonoids and phenolic compounds further potentiates the UV protection or photo-protection activity. Antioxidants provide endogenous photo-protective activity and are essential for the protection and maintenance of skin health. Further, flavonoids can also modulate enzyme activity and effect cell division [17].

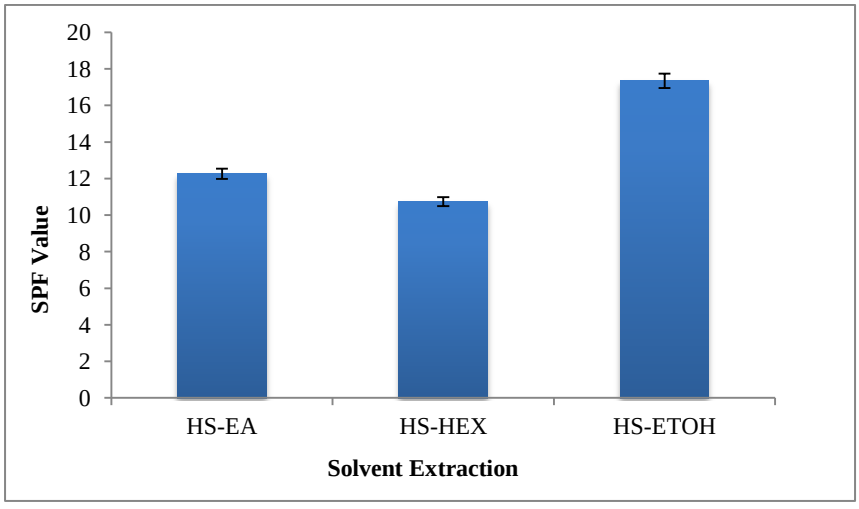


Figure 2. Sun Protection Factor (SPF) value of ethanol (HS-ETOH), ethyl acetate (HS-EA) and hexane (HS-HEX) extracts of *Hibiscus sabdariffa*

Conclusion

The study demonstrated the ethanolic and ethyl acetate extracts of *Hibiscus sabdariffa* have photoprotective properties, suggesting that these solvents were efficient in extracting high concentrations of photoprotective active compounds in HS calyces. The high SPF values obtained for HS-EtOH extracts (17.53±0.22), as well as strong absorptions in UVA region for HS-EtOH (330 nm and 355 nm), were good indications that HS-EtOH extracts would be beneficial as photo-protective additives in sunscreen formulations. Considering the favorable results for the HS- EtOH extracts, *in-vivo* experiments to validate efficacy of both extracts for application in sunscreen formulations may prove necessary.

Acknowledgement

The author would like to acknowledge the valuable help and suggestions provided by Universiti Putra Malaysia and Ministry of Higher Education (MoHE) for the MyBrain15 (MyPhD) fund.

References

1. Vinay, K. G., Rajbir, K., Ramit, S. and Vikas, J. (2016). Photoprotective, antioxidant screening and new ester from dry root extracts of *Potentilla atrosanguinea* (Himalayan cinquefoil). *South African Journal of Botany*, 103: 49-53.
2. Dutra, E. A., Oliveira, D. A., Kedor-Hackmann, E. R. and Santoro, M. I. (2004). Determination of sun protection factor (SPF) of sunscreens by ultraviolet spectrophotometry. *Brazilian Journal of Pharmaceutical Science*, 40: 381-385.
3. Mambro, V. M. D. and Fonseca, M. J. V. (2005). Assays of physical stability and antioxidant activity of a topical formulation added with different plant extracts. *Journal of Pharmaceutical and Biomedical Analysis*, 37: 287-295.
4. Mohamed, R., Fernandez, J., Pineda, M. and Aguilar, M. (2007). Roselle (*Hibiscus sabdariffa*) seed oil is a rich source of gamma-tocopherol. *Journal of Food Science*, 72(3): 207-211.
5. Mourtzinos, I., Makris, D. P., Yannakopoulou, K., Kalogeropoulos, N., Michali, I. and Karathsnos, V. T. (2008). Thermal stability of anthocyanin extract of *Hibiscus sabdariffa* L. in the presence of β-cyclodextrin. *Journal of Agricultural and Food Chemistry*, 56: 10303-10310.
6. Da-Costa-Rocha, I., Bernd, B., Hartwig, S., Ivo, P. and Micheal, H. (2014). *Hibiscus Sabdariffa* L- a phytochemical and pharmacological review. *Food Chemistry*, 165: 424-443.
7. Violante, I. M. P., Souza, I. M., Venturini, C. L., Ramalho, A. F. S., Santos, R. A. N. and Ferrari, M. (2009). Avaliação *in vitro* da atividade fotoprotetora de extratos vegetais do cerrado de Mato Grosso. *Brazilian Journal of Pharmacognsosy*,19: 452-457.
8. Zhen, J., Villani, T. S., Guo, Y. Q. Y., Chin, K., Min-Hsiung, P., Chi-Tang, H., James, E. S. and Qingli W. (2016). Phytochemistry, antioxidant capacity, total phenolic content and anti-inflammatory activity of *Hibiscus sabdariffa* leaves. *Food Chemistry*, 190: 673-680.
9. Mansur, J. S., Breder, M. V. R., Mansur, M. C. A. and Azulay, R. D. (1986). Determinação do fator de proteção solar por espectrofotometria. *Anais Brasileiros de Dermatologia*, 61: 121-124.
10. Sayre, R. M., Agin, P. P., Levee, G. J. and Marlowe, E. (1979). Comparison of *in vivo* and *in vitro* testing of sun screening formulas. *Photochemistry and Photobiology*, 29: 559-566.
11. Riegelman, S. and Penna, R. P. (1960). Effect of vehicle components on the absorption characteristics of sunscreens compounds. *Journal of Society Cosmetic Chemist*, 11: 280-291.
12. Agrapidis-Paloympis, L. E., Nash, R. B. and Shaath, N. A. (1987). The effect of solvents on the ultraviolet absorbance of sunscreens. *Journal of Society Cosmetic Chemist*, 38: 209-221.
13. Suva, M. A. (2014). Evaluation of sun protection factor of *Zingiber officinale* roscoe extract by ultraviolet spectroscopy method. *Journal of Pharmaceutical Science and Technology*, 3: 95-97.
14. Roy, A., Sahu, R. K., Matlam, M., Deshmukh, V. K., Dwivedi, J. and Jha, A. K. (2013). *In vitro* techniques to assess the proficiency of skin care cosmetic formulations. *Pharmacognosy Reviews*, 7: 97-106.
15. Treichel, H., De Oliveira, D. A., Mazutti, M., Di Luccio, M. and Oliveira, J. V. (2010) A review on microbial lipases production. *Food Bioprocess Technology*, 3: 182-196.
16. Kaur, C. D. and Saraf, S. (2011). Photochemprotective activity of alcoholic extracts of *Camellia sinensis*. *International Journal of Pharmacology*, 7(3): 400-404.

17. Imam, S., Azhar, I. and Mahmood, Z. A. (2015). *In-vitro* evaluation of sun protection factors of a cream formulation prepared from extracts of *Musa accuminata* (L.), *Psidium gujava* (L.) and *Pyrus communis* (L.). *Asian Journal of Pharmaceutical and Clinical Research*, 8(3); 234-237.

Malaysian Journal of Analytical Sciences, Vol 22 No 6 (2018): 1084 - 1089
DOI: https://doi.org/10.17576/mjas-2018-2206-19

MALAYSIAN JOURNAL OF ANALYTICAL SCIENCES
Published by The Malaysian Analytical Sciences Society
ISSN 1394 - 2506

THE INFLUENCE OF GROWTH TEMPERATURE ON THE PROPERTIES OF ZINC OXIDE BY THERMAL OXIDATION

(Kesan Suhu Pertumbuhan Ke Atas Sifat-Sifat Zink Oksida Menggunakan Pengoksidaan Haba)

Nuraini Abdullah*, Noor Mazni Ismail, Dewan Muhammad Nuruzzaman

Faculty of Manufacturing Engineering,
Universiti Malaysia Pahang, 26600 Pekan, Pahang, Malaysia

**Corresponding author: nuraini.abdullah89@yahoo.com*

Received: 2 April 2018; Accepted: 31 July 2018

Abstract

Zinc thin films were successfully deposited on Si substrate by thermal evaporation method under constant base pressure of 1.604 x10^{-4} Pa. Thermal oxidation of the deposited film was carried out at two different growth temperatures of 300 ^{o}C and 500 ^{o}C. The effects of growth temperature on the properties of zinc oxide were investigated. Thermal oxidation was carried out in a horizontal tube furnace in air condition for constant time one hour. After thermal oxidation at temperature 500 ^{o}C, the white-silver zinc thin films were changed to black-brown zinc oxide. FESEM results show that the zinc particles were almost round shape with nanostructures in size. ZnO nanocrystals were successfully obtained at low growth temperature of 300 ^{o}C and the size of nanowires decreased as the growth temperature was increased to 500 ^{o}C. The XRD results confirmed that ZnO started to oxidize at growth temperature of 300 ^{o}C with the sharpest peak obtained indexed to ZnO(101). However, the oxidation of Zn was not fully completed while Zn peaks appeared at this temperature. At growth temperature 500 ^{o}C, all the peaks were indexed to ZnO with the sharpest peak was ZnO(101) meaning that the oxidation was completed. The calculated crystallite sizes were varied from 27.841 nm to 36.788 nm for ZnO at 300 °C and 0.697 nm to 161.18 nm for ZnO at 500 °C.

Keywords: zinc oxide, silicon, thermal evaporation, thermal oxidation

Abstrak

Filem nipis zink telah berjaya didepositkan pada substrak Si oleh kaedah penyejatan haba di bawah tekanan asas tetap 1.604x10^{-4} Pa. Pengoksidaan termal telah dijalankan ke atas filem yang telah didepositkan pada dua suhu yang berbeza iaitu 300 ^{o}C dan 500 ^{o}C. Kesan suhu pertumbuhan pengoksidaan telah disiasat terhadap sifat zink oksida. Pengoksidaan termal untuk masa malar 1 jam dalam relau tiub mendatar dalam kehadiran udara telah dijalankan. Filem nipis zink putih diubah menjadi zink oksida hitam coklat selepas pengoksidaan haba pada suhu 500 ^{o}C. Keputusan FESEM menunjukkan bahawa zarah zink hampir membentuk bulat dengan saiz nanostruktur. Nanokristal ZnO telah berjaya diperoleh pada suhu pertumbuhan yang rendah iaitu 300 ^{o}C dan saiz nanowayar menjadi berkurangan apabila suhu pertumbuhan meningkat kepada 500 ^{o}C. Hasil XRD mengesahkan bahawa ZnO mula teroksida pada suhu pertumbuhan 300 ^{o}C dengan puncak paling ketara yang diperoleh diindeks ke ZnO(101). Walau bagaimanapun, pengoksidaan Zn tidak siap sepenuhnya kerana masih terdapat puncak Zn muncul pada suhu ini. Pada suhu pertumbuhan 500 ^{o}C, semua puncak diindeks kepada ZnO dengan puncak paling ketara ialah ZnO(101) yang bermaksud pengoksidaan telah berlaku sepenuhnya. Saiz kristal yang dikira berbeza bermula dari 27.841 nm hingga 36.788 nm untuk ZnO pada 300 °C dan 0.6966 nm hingga 161.18 nm untuk ZnO 500 °C.

Kata kunci: zink oksida, silikon, pengewapan haba, pengoksidaan haba

Introduction

Recently zinc oxide (ZnO) thin film has been listed as one of the most interesting semiconductor oxides due to its special characteristics. Other than its wide band gap of 3.27eV, it also has a large excitation energy bonding of 60 meV [1]. It has attracted much attention in order for many applications such as solar cells, gas sensor, nanolaser and other photoluminescent devices. There are several techniques that can be used to synthesize ZnO thin films for example sputtering, spray pyrolysis, sol-gel, chemical vapor deposition, RF magnetron sputtering, pulsed laser deposition, etc. Besides, one of the simplest methods is thermal oxidation that has been paid less attention. Thermal oxidation method also requires a relatively simple and low-cost procedure that does not need any catalyst or higher temperature growth [2]. By comparing to the catalyst-assisted growth, direct oxidation of metallic zinc can produce ZnO nanostructures with a large-scale growth capabilities and high purity owing to the elimination of intermediaries involved in catalytic chemical synthesis of oxide nanostructures [3]. The oxidation of Zn foils or powders under oxygen gas flow results the variation of ZnO nanostructures morphologies [1]. There have been a few reports of synthesizing zinc oxide by thermal oxidation methods [1-10]. Based on some reports, ZnO nanostructures were formed at growth temperature (420 ^{o}C) and boiling temperature (907 ^{o}C) of Zn while decomposition of ZnO was reported at a temperature up to ~1400 ^{o}C [3]. As prevention, the growth of ZnO nanostructures should stop below the decomposition temperature of Zn.

In this study, we have reported the growth temperature effect on the properties of ZnO by thermal oxidation. The deposited Zn thin films on Si substrates resulted white color of thin films and changed to silver-grey at low oxidation temperature of 300 ^{o}C and was changed to black-brown at temperature 500 ^{o}C. The characterizations of ZnO were conducted by FESEM, EDX and XRD. This research was focused to investigate the difference between the physical characteristics of ZnO at two different conditions i.e. partially oxidized and fully oxidized states that were obtained at 300 and 500 °C, respectively.

Materials and Methods

High purity (99.99%) Zn powders (purchased from Permula Sdn Bhd) were used in thermal evaporation experiments. Silicon (Si) with a dimension of 4inch diameter was used as a substrate. The cleaning process of Si substrate was conducted by using Piranha method. A solution of acid sulphuric (H_2SO_4) 3:1 hydrogen peroxide (H_2S_2) was freshly prepared. The cleaning process was conducted in an ultrasonic bath at temperature 65 ^{o}C for 30 minutes to remove the contaminant on the surface. After that, the Si substrate was rinsed with distilled water and dried by air gun. Next, the thermal evaporation was started with filled Zn powder (0.05g) in the tungsten boat and placed the Si substrate in the thermal evaporator. The base pressure in thermal evaporator was set at 1.60 x 10^{-4} Pa with target-substrate distance of 10.5 mm at room temperature, voltage 0.9V and current 20-25A. The deposition time was constant for 30 minutes for each sample.

Then, the deposited Zn thin films were characterized by FESEM JEOL, JSM-7800F with EDX analysis. The oxidation of Zn was performed in a tube furnace in closed air condition at growth temperature of 300 ^{o}C and 500 ^{o}C at constant heating rate of 5 ^{o}C/min for 1h. After oxidation process, the tube furnace was naturally cooled down to room temperature and the samples were unloaded. The ZnO films were then characterized by FESEM JEOL, JSM-7800F with EDX analysis and X-ray Diffraction (XRD) pattern was collected on a XRD Bruker D8 Advance with CuKα radiation ($\lambda = 0.1546$ nm).

The average crystallite size (D) was determined using the Sherrer's equation [10]:

$$D=k\lambda/\beta_{20}\cos\theta \quad (1)$$

where k denotes the Scherrer constant (the shape factor of the average crystallite and can be considered k = 0.9 [10]; $\lambda = 1.54060$Å is the wavelength of the incident Cukα radiation; β_{20} represents the full-width at half maximum of the respective peak and θ is the Bragg diffraction angle.

Results and Discussion

Figures 1(a-d) show the characterization results using FESEM and EDX. Figure 1(a) shows the average particle size of the Zn thin film using 10000 x magnifications. The measured particle size varies from 101nm to 176nm with the

particles almost round shape. The obtained results also showed that the sizes of particles are almost uniform which means that the evaporation process was uniformly distributed over the surface. Figure 1(b) shows the cross section of the Zn thin films. The obtained results showed that measured thickness of the deposited Zn thin film varies from around 0.6µm to 1.1µm. Figures 1(c)-(d) show the EDX results of the Zn film and the elements consist of Si, C, O and Zn meaning that Zn was successfully grown on the Si substrate.

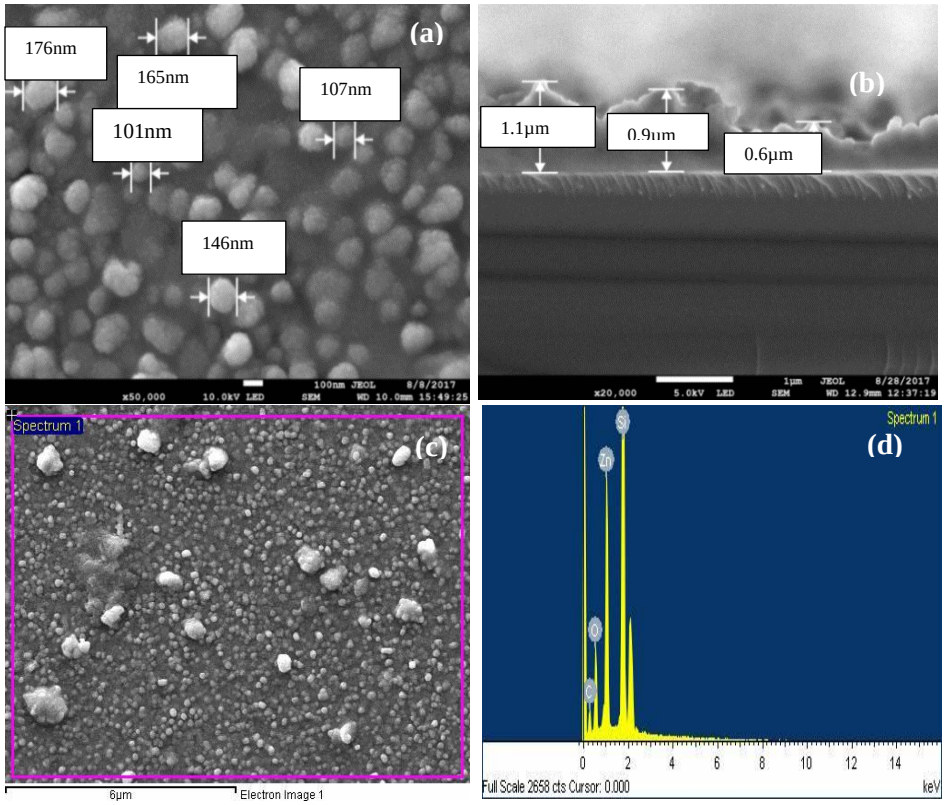


Figure 1. FESEM image of Zn thin film after thermal evaporation and (b)cross section of Zn layer on the Si substrate (c) EDX point surface of Zn layer on Si and (d) EDX spectrum of Zn thin film

Figures 2(a-f) show representative of FESEM images and EDX spectrum of the surfaces of ZnO oxidized at different temperatures. The uniform hexagonal nanocrystals at 300 ^{o}C and nanowires of ZnO at 500 ^{o}C were observed. Figure 2(a) shows the top view of the ZnO films at growth temperature 300 ^{o}C and ZnO nanocrystals are uniformly distributed over the surface. These results of hexagonal nanocrystals of ZnO on Si substrate are the same results using low temperature hydrothermal method [11] and thermal oxidation of Zn films at 600 ^{o}C deposited in Ar+O_2/10mTorr [8].

The ZnO nanocrystals sizes were measured 75 nm, 99.7 nm and 104 nm. The formation of ZnO nanowires strongly depended on the thermal oxidation temperature. The optimal temperature range for the ZnO nanowires are in between 300 ^{o}C and 400 ^{o}C and below the melting points of Zn and ZnO (Zn: 419.58 ^{o}C, ZnO:1975 ^{o}C). However, there are some results claimed that the ZnO nanowires became less and gradually vanished at higher temperature such as 500 ^{o}C and 600 ^{o}C [12]. The results of ZnO nanowires have been studied by the other researcher at oxidation temperature 400 ^{o}C and the formation became much higher surface density, larger diameter and long length at 500 ^{o}C [3]. In this study, we found that the size of nanowires became smaller by increased oxidation temperature at 500 ^{o}C as shown in Figure 2(b) and the image of uniform ZnO nanowires distributed over the surface at 500 ^{o}C. The measured nanowires sizes decreased to 20.6 nm, 21.4 nm and 24.6 nm. Liu et al. [7] also claimed that when the temperature increased over 400 ^{o}C, the density of the nanowires was decreased with few nanowires.

Figures 2(c-d) and Figures 2(e-f) show the EDX spectrum of ZnO thin films at growth temperature 300 ^{o}C and 500 ^{o}C, respectively. The results show that at these two different temperatures, the highest element of the sample consists of Zn and the other elements are Si, C and O.

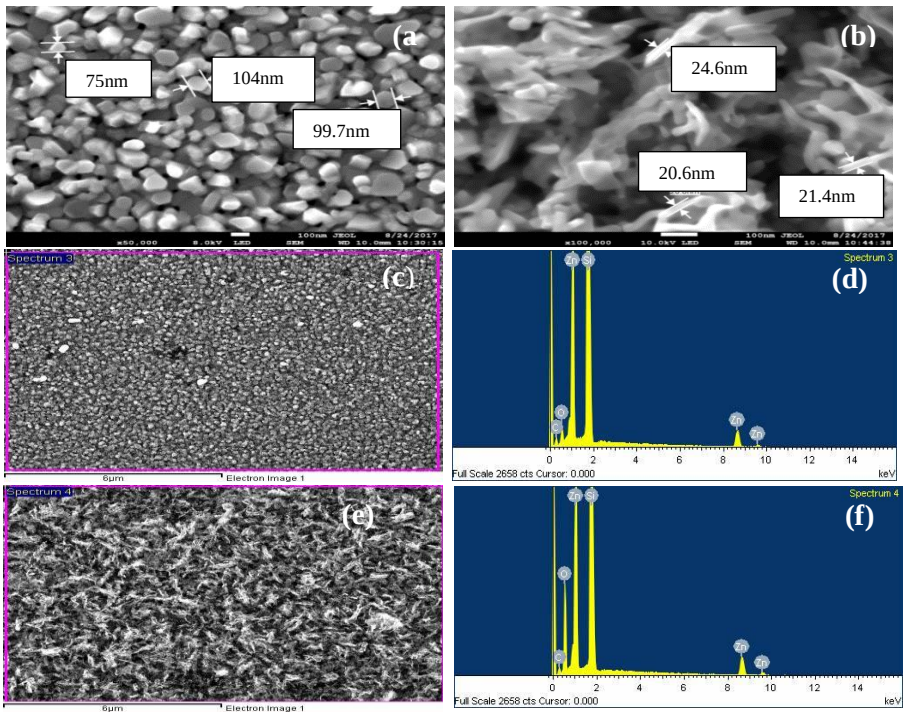


Figure 2. FESEM and EDX images of ZnO thin film after thermal oxidation (a) the surface and particle size of ZnO at 300 ^{o}C, (b) the surface and average particle of ZnO at 500 ^{o}C, (c) EDX point surface of ZnO nanocrystals layer on Si at 300 ^{o}C, (d) EDX spectrum of ZnO nanocrystals at 300 ^{o}C (e) EDX point surface of ZnO nanowires layer on Si at 500 ^{o}C and (f) EDX spectrum of ZnO nanowires at 500 ^{o}C

The identification of crystallite phases and microstructural analysis for ZnO thin films was studied by XRD. Figures 3(a) and (b) show the representative XRD patterns of ZnO thin film at growth temperature 300 ^{o}C and 500 ^{o}C, respectively. From Figure 3(a), it can be observed that those ZnO thin films are polycrystalline and have a hexagonal close-packed structure. M.S Aida et al. claimed that the oxidation started at a temperature equal to 250^{o}C and the total oxidation was achieved at 300^{o}C leading to stoichiometric ZnO films [1]. Within their research, preparation of ZnO thin films was carried out by direct thermal evaporation of ZnO powder and then followed by annealing in oxygen/air atmosphere using an open horizontal furnace. They also demonstrated that the oxidation mechanism was achieved by diffusion of oxygen ions. But in our work, Zn was not fully oxidized at this temperature because the oxidation method and the mechanism were different as compared to Aida et al. [1]. The XRD pattern was indexed to ZnO (zincite) according to PDF card 01-089-7102 with lattice parameter a=3.250Å and c=5.207Å. The most intense peak was indexed to ZnO(101) at 2θ = 36.2554°. However, there are still have other peaks corresponding to Zn hexagonal structure according to PDF card 01-087-0713 with lattice parameter a = 2.665Å and c = 4.947Å. From the obtained results, we can say that Zn was not fully oxidized at this growth oxidation temperature since the melting point of Zn is 419.58 °C. Further information of studied structural characteristics of ZnO at 300 °C are presented in Table 1. Figure 3(b) shows the XRD pattern of ZnO films at growth temperature 500 °C and the results claimed that all the peaks were indexed to hexagonal ZnO according to PDF card 01-082-3143 with lattice parameter a = 3.245Å and c = 5.220Å. The sharpest peak was indexed to ZnO(101) plane and the other peaks of ZnO were indexed to (100), (002), (102), (110), (103) and (112) plane as reported in Rusu et al. [5] and Li et al. [8] at 600 °C. At this growth temperature, Zn thin film was completely oxidized with increasing the intensity of ZnO peaks compared to ZnO at 300 °C. Yuvaraj et al. [6] also stated that

the intensity of the ZnO peaks increased with the increase in the oxidation temperature. The further information of structural characteristics of ZnO films at 500 °C are presented in Table 2. The average crystallite size varied from 27.841 nm to 36.788 nm for ZnO at 300 °C and 0.6966 nm to 161.18 nm for ZnO at 500 °C. These values indicate that a nanocrystalline structure of the ZnO films was obtained. Other researchers reported the improvement of the quality of the ZnO films with increase of the annealing temperature [2].

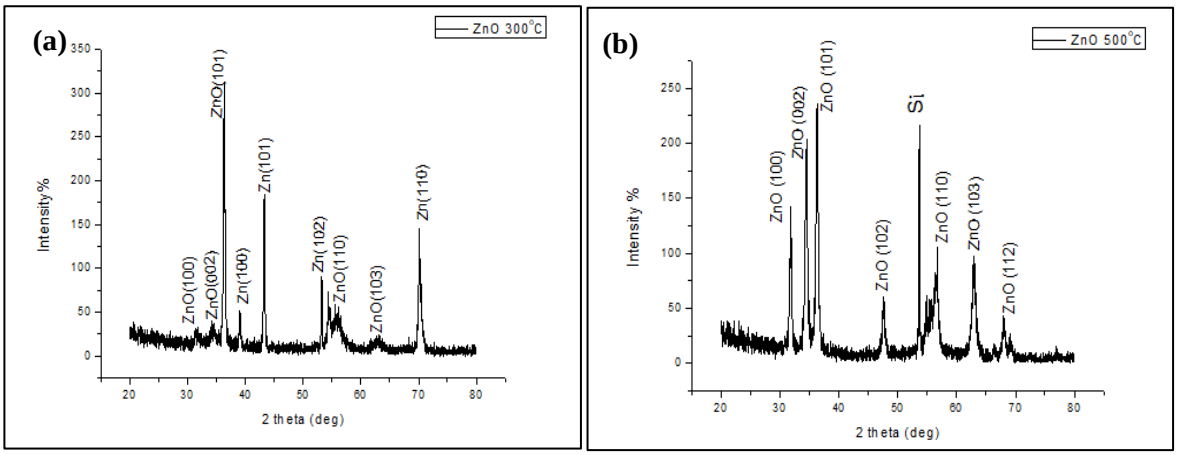


Figure 3. XRD pattern for ZnO films on Si substrate prepared by thermal oxidation (a) ZnO films at growth temperature 300 ^{o}C and (b) ZnO films at growth temperature 500 ^{o}C.

Table 1. Structural parameters of the investigated ZnO thin film at 300 ^{o}C

	ZnO(101)	**Zn(101)**	**ZnO(110)**	**Zn(110)**
D crystallite size (nm)	36.788	35.232	35.263	27.841
2θ	36.2554	43.2196	56.6004	70.6300
d (Å)	2.47570	2.09154	1.62475	1.33250

Table 2. Structural parameters of the investigated ZnO thin film at 500 ^{o}C

	(100)	**(002)**	**(101)**	**(102)**	**(110)**	**(103)**	**(112)**
D crystallite size (nm)	23.0	161.1	25.83	8.51	3.06	16.7	0.69
2θ	31.82	34.33	36.27	47.5	56.69	62.7	67.97
d (Å)	2.81	2.61	2.47	1.91	1.62	1.48	1.38

Conclusion

The FESEM and EDX spectrum results we can say that Zn was successfully deposited on the Si substrate by using thermal evaporation method. The FESEM of Zn thin film shows that the particles were almost round shape with uniform distribution over the Si surface. Zn particles were in nanoparticles size and the thickness of Zn layer showed by cross section of Zn film was in micrometer. For thermal oxidation process, we obtained ZnO nanocrystals with hexagonal shape from the top view of FESEM image at low growth temperature of 300 ^{o}C. The size of nanowires was decreasing with increasing the growth temperature to 500 ^{o}C. The EDX spectrum of ZnO at 300 ^{o}C and ZnO of 500 ^{o}C confirmed that the highest peaks were Zn and O meaning that oxidation was occurred. The XRD pattern of ZnO at growth temperature 300 ^{o}C obtained that the oxidation of Zn was started at 300 ^{o}C since

the sharpest peak was indexed to ZnO(101) plane but the oxidation was not fully completed by considering other peaks of Zn. However, all the peaks of ZnO at 500 ^{o}C were indexed to ZnO (100), (002), (102), (110), (103) and (112) planes meaning that the oxidation was completely occurred. The intensity was increased with the increase in growth temperature from 300 ^{o}C to 500 ^{o}C. The crystallite size, D of ZnO particles was calculated from 27.841 nm to 36.788 nm for ZnO at 300 °C and 0.697 nm to 161.18 nm for ZnO at 500 °C.

Acknowledgement

The authors are grateful to the RAGS grant #RDU 151410 for financial support to carry out this work. The authors also wish to extend their sincere thanks to all the technical staffs of Faculty of Manufacturing Engineering, University Malaysia Pahang involved related to this research work.

References

1. Aida, M. S., Tomasella, E., Cellier, J., Jacquet, M., Bouhssira, N., Abed, S. and Mosbah, A. (2006). Annealing and oxidation mechanism of evaporated zinc thin films from zinc oxide powder. *Thin Solid Films,* 515 1494-99.
2. Rusu, G. G., Girtan, M. and Rusu, S. (2007). Preparation and characterization of ZnO thin films prepared by thermal oxidation of evaporated Zn thin films. *Superlattices and Microstructures,* 42: 116-22.
3. Yuan, L., Wang, C., Cai, R., Wang, Y. and Zhou, G. (2014). Temperature-dependent growth mechanism and microstructure of ZnO nanostructures grown from the thermal oxidation of zinc. *Journal of Crystal Growth,* 390:101-108.
4. Girtan, M., Rusu, G.G., Dabos-Seignon, S. and Rusu, M. (2008). Structural and electrical properties of zinc oxides thin films prepared by thermal oxidation. *Applied Surface Science,* 254: 4179-4185.
5. Rusu, G. G., Rusu, M. and Apetroaei, N. (2007). On the structural changes during thermal oxidation of evaporated Zn thin films. *Thin Solid Films,* 515: 8699-8704.
6. Yuvaraj, D. and Rao, K. N. (2009). Selective growth of ZnO nanoneedles by thermal oxidation of Zn microstructures. *Materials Science and Engineering B,* 164:195-99.
7. Liu, Y., Pan, C., Dai, Y. and Chen, W. (2008). Synthesis of one-dimensional ZnO nanoneedles using thermal oxidation process in the air and its application as filed emitters. *Materials Letters,* 62: 2783-2786.
8. Li, Z. W., Gao, W. and Reeves, R. J. (2005). Zinc oxide films by thermal oxidation of zinc thin films. *Surface & Coatings Technology,* 198: 319-323.
9. Dhananjay., Nagaraju, J. and Krupanidhi, S. B. (2007). Investigations on zinc oxide thin films grown on Si(100) by thermal oxidation. *Materials Science and Engineering B,* 137: 126-130.
10. Rusu, D. I., Rusu, G. G. and Luca, D. (2011). Structural characteristics and optical properties of thermally oxidized zinc films. *Acta Physica Polonica A,* 119: 850-856.
11. Pietruska, R., Witkowski, B.S., Gieraltowska, S., Caban, P., Wachnicki, L., Zielony, E., Gwozdz, K., Bieganski, P., Placzek-Popko, E. and Godlewski, M. (2015). New efficient solar cell structures based on zinc oxide nanorods. *Solar Energy Materials & Solar Cells,* 143: 99-104.
12. Yu, W. and Pan, C. (2009). Low temperature thermal oxidation synthesis of ZnO nanoneedles and the growth mechanism. *Materials Chemistry and Physics,* 115: 74-79.

Malaysian Journal of Analytical Sciences, Vol 22 No 6 (2018): 1090 - 1101
DOI: https://doi.org/10.17576/mjas-2018-2206-20

MALAYSIAN JOURNAL OF ANALYTICAL SCIENCES
Published by The Malaysian Analytical Sciences Society
ISSN 1394 - 2506

EXTRACTION OF SUCCINIC ACID FROM REAL FERMENTATION BROTH BY USING EMULSION LIQUID MEMBRANE PROCESS

(Pengekstrakan Asid Suksinik daripada Larutan Penapaian Sebenar dengan Menggunakan Proses Membran Cecair Emulsi)

Norasikin Othman[1,2]*, Norela Jusoh[1], Mariah Syafiqah Mohar[1], Muhammad Bukhari Rosly[1], Norul Fatiha Mohamed Noah[1]

[1]*Department of Chemical Engineering, Faculty of Chemical and Energy Engineering*
[2]*Centre of Lipids Engineering and Applied Research, Ibnu Sina Institute for Scientific and Industrial Research*
Universiti Teknologi Malaysia, 81310 UTM Johor Bahru, Johor, Malaysia

**Corresponding author: norasikin@cheme.utm.my*

Received: 2 April 2018; Accepted: 31 July 2018

Abstract

Succinic acid is listed as one of the twelve building block chemicals based on the ease of production through a biotechnological approach and potential to derive various chemicals. The application of bio-based succinic acid is still limited due to high downstream processing costs. One of the potential methods to recover succinic acid is emulsion liquid membrane (ELM). The ELM system consists of three main liquid phases; external feed, membrane, and internal. In this study, the membrane phase was prepared by dissolving Amberlite LA2 as a carrier, sorbitan monooleate (Span 80) and polyoxyethylenesorbitan monooleate (Tween 80) as surfactants in commercial grade palm oil, while the internal phase comprised of sodium carbonate solution, Na_2CO_3. The influence of emulsifying time, agitation speed, and agitation time on the water-in-oil-in-water (W/O/W) emulsion stability were studied. The most stable condition was implemented on various external phase concentrations to study the extraction and recovery performances. The results showed that the most stable emulsion was obtained at 5 minutes of emulsifying time, 300 rpm of agitation speed and 3 minutes of agitation time. The emulsion produced was able to provide a balanced result between stability and ELM performance as it was able to extract almost 100% of succinic acid with 98% recovery. The finding of this study showed ELM process as the potential technology to extract succinic acid produced from fermentation.

Keywords: succinic acid, fermentation broth, emulsion liquid membrane, stability, extraction

Abstrak

Asid suksinik telah disenaraikan sebagai salah satu daripada dua belas bahan kimia asas berdasarkan kepada kemudahan pengeluaran melalui pendekatan bioteknologi dan berpotensi untuk menerbitkan pelbagai bahan kimia. Penggunaan asid bio-suksinik masih terhad disebabkan oleh kos pemprosesan hiliran yang tinggi. Salah satu daripada kaedah yang berpotensi untuk memperoleh asid suksinik ialah proses membran cecair emulsi (ELM). Sistem ELM terdiri daripada tiga fasa cecair utama; suapan luaran, membran, dan dalaman. Dalam kajian ini, fasa membran telah disediakan dengan melarutkan pembawa Amberlite LA2, surfaktan Span 80 dan Tween 80 di dalam minyak kelapa sawit komersial, manakala fasa dalaman terdiri daripada larutan natrium karbonat, Na_2CO_3. Kesan masa pengemulsian, kelajuan pengadukan, dan masa pengadukan ke atas kestabilan air-dalam-minyak-dalam air (W/O/W) telah dikaji. Keadaan emulsi yang paling stabil telah digunakan pada pelbagai kepekatan fasa luaran untuk mengkaji prestasi pengekstrakan dan perolehan. Keputusan menunjukkan keadaan emulsi yang paling stabil didapati pada 5 minit masa pengemulsian, pada 300 rpm kelajuan pengadukan, dan 3 minit masa pengadukan. Emulsi yang dihasilkan dapat memberikan hasil yang seimbang di antara kestabilan dan prestasi ELM kerana ia dapat mengekstrak hampir 100% asid suksinik dengan perolehan sebanyak 98%. Hasil daripada kajian ini menunjukkan bahawa proses ELM adalah teknologi yang berpotensi untuk mengekstrak asid suksinik yang dihasilkan daripada proses penapaian.

Kata kunci: asid suksinik, larutan penapaian, membran cecair emulsi, kestabilan, pengekstrakan

Introduction

Succinic acid is a C4 di-carboxylic acid with the IUPAC name of butanedioic acid. It is recognised as one of top twelve building block chemicals that can be produced through biological processes [1]. Succinic acid is a key compound in producing numerous important chemicals, such as the raw materials of pharmaceutical and food products, as the intermediate of chemical synthesis of biodegradable plastics, green solvents, detergents, and surfactants, and also as an ingredient to stimulate animal and plant growth [2, 3]. Most of the commercial succinic acid is currently produced through petrochemical process, which causes environmental pollution and the concerns of sustainable developments [4]. As to preserve the environment, studies are directed towards producing succinic acid by fermentation. Many anaerobic and facultative anaerobic microbes, for instance *Actinobacillus succinogenes*, *Mannheimia succiniciproducens*, and *Escherichia coli*, produce succinic acid as the fermentation end product [5, 6]. It is well known that there are contaminants such as acetic and formic acids by-product, unconsumed carbon source, and protein, which reduce the yield of succinic acid and cause difficult purification process. Therefore, an effective and economical separation process is required to recover succinic acid from fermentation broth.

Various separation methods were developed for the separation and purification of succinic acid, including crystallization, precipitation, solvent extraction, and membrane filtration [5, 7, 8]. In direct crystallization, the desired product can be obtained without a complicated unit operation, but it is constrained by low product yield. Precipitation comprises a simple operation where calcium hydroxide, $Ca(OH)_{2,}$ is added to precipitate succinate. However, a large dosage of $Ca(OH)_2$ is required, thus contributes to high operating cost. Solvent extraction offers high product yield and low energy consumption, yet is still lacking due to large quantity of extractant is required. While membrane filtration produces high product purity, the membrane pollution and high costs of the device are the disadvantages.

One of the promising methods to extract succinic acid from fermentation broth is emulsion liquid membrane (ELM). It is a very unique separation method that provides various advantages, including large mass transfer area, ease of operation, low energy consumption, efficient for low solute concentration, and low energy requirement [9, 10]. In principal, ELM involves the dispersion of the primary emulsion that contains the internal and membrane phases, into the external phase that holds the desired solute. The solute from the external phase diffuses through the membrane phase and chemically reacts with the stripping agent, then remains confined in the internal phase. In most cases, a carrier is added into the membrane phase to facilitate solute transport. The success of ELM applications is widely reported in the extraction of metal ions, dyes contaminant, organic and inorganic compounds, and pharmaceutical compounds [11-14].

However, the industrial application of ELM is limited due to emulsion stability problem which affects the extraction efficiency. Unstable emulsion occurs in the form of breakage or swelling. Emulsion breakage causes the release of internal stripping solution and extracted solute, which reduce the extraction performance [15]. During swelling, water molecules from the external phase are transferred into the internal phase and the extracted solute concentration in the internal phase is diluted. Emulsion swells are the results of emulsion volume increment and consequently trigger the emulsion globules and reduce the extraction efficiency [16]. The emulsion is considered stable when neither breakage nor swelling phenomenon occurs.

In this study, the effect of several parameters on the emulsion stability of succinic acid extraction system is presented. The formulation of ELM was described by Jusoh et al. [17] where, Amberlite LA2 was used as the carrier, palm oil as the diluent, Span 80 and Tween 80 as surfactants, and Na_2CO_3 as the stripping agent. In addition, research on ELM extraction of succinic acid mostly covers the extraction from simulated solution, but very limited from real fermentation broth [18]. Therefore, the performance of ELM in the present study was evaluated for succinic acid extraction and recovery from real fermentation broth.

Materials and Methods

Materials

Palm oil as the diluent is a commercial cooking oil (BURUH) from Lam Soon Edible Oils. Amberlite LA2 as the carrier was procured from MERCK. Solid sodium carbonate (Na_2CO_3) (99% assay) used as the internal solution was purchased from Merck. Sorbitan monooleate (Span 80) and polyoxyethylenesorbitan monooleate (Tween 80) were used as surfactants and obtained from Sigma Aldrich. Succinic acid (SA) (99.0% assay) was also acquired from Sigma Aldrich. The reagents and solutions were used directly as- received without further purification.

Emulsion stability study

A two-step emulsification procedure, consisting of primary emulsion preparation and dispersion process, was implemented to investigate the stability of emulsion. The internal and membrane phases (0.05 M Amberlite LA2 and 3% (w/v) Span 80 in palm oil) were emulsified by using a motor driven homogeniser (Heidolph Silent Crusher M, Germany) at 7000 rpm for 3 min to 9 min. The emulsion was then dispersed into succinic acid external solution containing 1% (w/v) Tween 80 and agitated at 200 rpm to 500 rpm for 1 minute to 7 minutes by using a digital mixer system (Cole-Parmer EW-50006-00, Germany). Upon completion, the solution was transferred into a separation funnel and allowed to settle. A small drop of emulsion was taken and placed under a microscope (Olympus CX31, Japan) to access the state of aggregation of the emulsion globules. The external solution volume was measured to determine the emulsion stability *via* Equation 1.

$$\text{Breakage/Swelling (\%)} = \frac{V_{e,f} - V_{e,i}}{V_{int}} x100 \quad (1)$$

where $V_{e,f}$ is the volume of external phase after extraction, $V_{e,i}$ is the volume of external phase before extraction, and V_{int} is the volume of internal phase.

Extraction and recovery performance

Emulsion, prepared at the most stable condition, was dispersed in real succinic acid fermentation broth produced by using *E. coli* AFP184 strain containing 1.4 g/L of succinic acid [19]. Prior to fermentation, the strain was stored in 30% (v/v) glycerol at -80 ^{o}C. The inoculum and production medium used were Luria Broth (LB) containing 1.4 g/L of K_2HPO_4, 0.6 g/L of KH_2PO_4, 3.3 g/L of $(NH_4)_2SO_4$, 0.4 g/L of $MgSO_4.7H_2O$, and 15 g/L of yeast extract in distilled water. The prepared medium was sterilised in an autoclave (HIRAYAMA, Model HVE 50) at 121 °C for 20 minutes. An amount 0.2 mL of glycerol stock culture was added into a 40 mL of LB medium in a 100 mL flask, in which the cells were aerobically incubated at 37 °C and 200 rpm for 24 hours by using an incubator shaker (SASTEC, Model ST 100C). Then, the succinic acid production was done in batch fermentations. An amount 40 ml of fermentation medium was prepared in a 100 mL shake flask, while 10 mL of glucose as carbon source was prepared in a universal bottle. The prepared medium and carbon source were sterilised at 121 °C for 20 minutes. After that, the carbon source with 5 mL of inoculum was added into the fermentation medium. The final solution was then incubated at 200 rpm for 24 hours. During the whole process, the temperature was maintained at 37 °C and pH was controlled between 6.6 and 6.7 with the addition of NaOH.

In order to investigate the performance of ELM, the succinic acid concentration was adjusted (5-50 g/L) with the addition of pure succinic acid. After dispersion, the solution was allowed to settle in a separation funnel. The external phase at the bottom of the funnel was taken for concentration measurement. For recovery purpose, heat induced demulsification method was applied to break the emulsion at the top of the separation funnel. The emulsion was placed in a water bath and assisted with ultrasonic vibration (LIR Biotech 020S) for 10 minutes to initiate the demulsification process. After that, it was heated at 70 °C for 24 hours for phase separation [20]. The separated aqueous phase was collected for succinic acid concentration analysis. The performance of extraction, recovery, and enrichment ratio were calculated by using Equations 2 to 4:

$$\text{Extraction (\%)} = \frac{[SA]_i - [SA]_f}{[SA]_i} x100 \quad (2)$$

$$\text{Recovery (\%)} = \frac{[SA]_{int}}{4TR[SA]_i} x100 \quad (3)$$

$$\text{Enrichment ratio} = \frac{[SA]_{int}}{[SA]_i} \quad (4)$$

where $[SA]_i$ is the initial succinic acid concentration in the external phase, $[SA]_f$ is the final acid concentration in the external phase, $[SA]_{int}$ is the acid concentration in the internal phase, and TR is the treat ratio.

Analytical procedures

A Mettler Toledo pH meter was used for pH measurement of the succinic acid fermentation broth. Meanwhile, succinic acid concentration was determined by using the high performance liquid chromatography (HPLC) (Agilent 1260 Infinity, Germany) with an ion exchange column (Aminex HPX-87H, 300 mm x 7.8 mm, brand X). A five-point calibration curve for succinic acid was prepared by using a known concentration of succinic acid standard. This step also helped to determine the retention time (time required to go off the column) of succinic acid, which was around 16 minutes in this study. The concentration of succinic acid in the sample was determined by comparing the peak areas with those of the standard curves. The measurement was performed *via* UV detection at 210 nm. Prior to analysis, each sample was filtred through 0.45 µm Whatman puradisc syringe filter into 2 mL of HPLC vials. 0.005 M of sulphuric acid (H_2SO_4) at a flow rate of 0.5 mL/ min was used as the mobile phase.

Emulsion droplets and globule size were measured by using an optical microscope (Olympus CX31) equipped with a camera that was connected to a computer. A small drop of emulsion was placed on a glass slide which was later being placed on the microscope stage. The focus of the microscope was adjusted accordingly so as to obtain a clear emulsion image. Each image was captured at the magnification of 400 times within 10 minutes after the sample preparation process. The size of the emulsion was determined by taking the average size of 40 droplets by using the VImage 2014 software and expressed as the Sauter mean diameter (D_{32}) as defined in Equation 5 [21].

$$D_{32} = \frac{\sum(n_i . d_i^3)}{\sum(n_i . d_i^2)} \quad (5)$$

where n_i represents the number of drops of the class i of the droplet diameter, d_i.

Results and Discussion

Analysis of succinic acid fermentation broth

Succinic acid was characterized by using HPLC. The concentration of succinic acid measured was 1.4 g/L from the fermentation of glucose by *E. coli*. The yield of succinic acid obtained is considered very low as a higher amount can be produced through fermentation condition optimization. It was discovered that, under optimum condition, the fermentation process was capable of producing succinic acid up to 50 g/L [22]. Meanwhile, the interest of this study is to obtain the fermentation broth, regardless of the succinic acid yield. In order to investigate the performance of ELM extraction, pure succinic acid was added into the solution up to the desired concentration. Other compounds, such as unconsumed glucose, and small amount of by-products also existed in the fermentation solution as shown in Figure 1. In addition, the pH of the broth was slightly acidic at 5.6. Basically, the accumulation of succinic acid in the fermentation broth inevitably led to the lowering of the pH in the fermentation medium. Maintaining the pH of the fermentation in a suitable range for the microorganism is one of the significant factors that affect the yield of succinic acid.

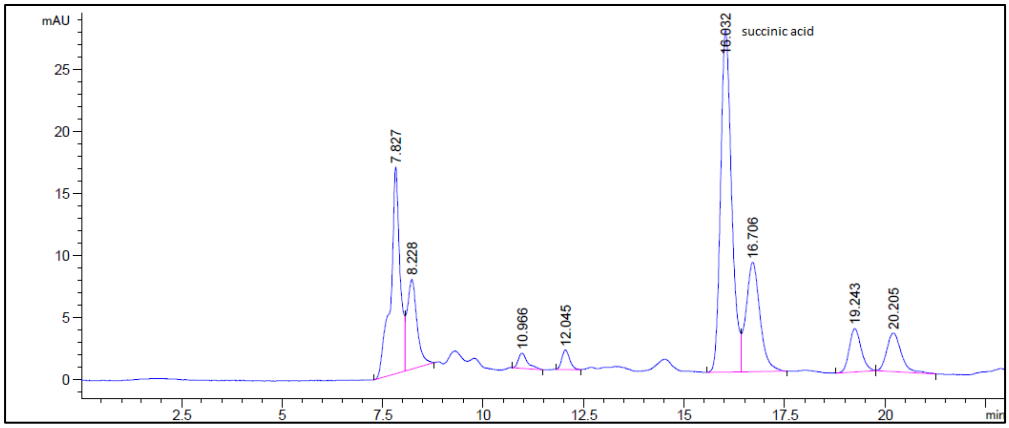


Figure 1. HPLC chromatogram of succinic acid fermentation broth

Emulsion stability study

Table 1 presents the effect of emulsification time, as well as agitation speed and time on the emulsion breakage. The experiments were performed in duplicates and the investigation was carried out one factor at a time with the best condition of each factor was used in the subsequent experiment.

Table 1. Effect of parameters on emulsion breakage. [diluent: palm oil; [Amberlite LA2]: 0.05M; Octanol: 10%; [Na_2CO_3]: 0.5M; O/I: 3/1; homogenizer speed: 7000 rpm; Tween 80: 1%; Span 80: 3%]

Parameters	**Condition**	**Emulsion Breakage (%)**
Emulsification time (minute)	3	40
	5	0
	7	40
	9	40
Agitation speed (rpm)	200	40
	300	0
	400	40
	500	60
Text C	1	40
	3	0
	5	40
	7	60

The influence of emulsification time was studied in the range of 3 to 9 minutes. It was found that the most stable emulsion was at 5 minutes of emulsification time where no breakage was observed. Meanwhile, emulsification time of both shorter and longer than 5 minutes resulted in higher breakage which was 40%. A higher breakage at short emulsification time happened because the time provided was insufficient to disperse the internal in the membrane phase. The configuration of surfactant at the interfacial area was unorganized and the interfacial tension was slightly reduced. This led to poor droplet formation with unbalanced size distribution obtained, as shown in Figure 2(a). Consequently, the emulsion broke easily when dispersed in the external phase. This is in agreement with the study by Gaikwad and Pandit [23] which indicated that a short emulsification time is insufficient to produce desirable emulsion droplet and leads to high breakage percentage. The intensity of the solution was enhanced at a longer

emulsification time with more internal phase entrapped in the membrane phase. Besides that, greater surface tension was reduced at 5 minutes of emulsification time, which contributed to uniform droplet distribution with smaller size at 1.33 µm as presented in Figure 2(b) and Table 2. A study by Sabry et al. [24] stated that when the droplets are smaller, they will take a longer time to coalesce. Therefore, the emulsion is more stable and the breakage phenomenon is hindered during emulsion dispersion. However, a further increase in the emulsification time (7 and 9 minutes) will damage the emulsion stability with 40% breakage. Intense emulsification leads to the formation of higher number of small emulsion droplets, as displayed in Figure 2(c) and Figure 2(d). The droplets tend to coalesce with one another and form larger sizes, such as 1.41 µm and 1.66 µm as listed in Table 2. This is in accordance with another study by Djenouhat et al. [25] that observed coalescence of internal droplets at a prolonged emulsification time. In this study, 5 minutes was chosen as the best emulsification time to form a stable emulsion.

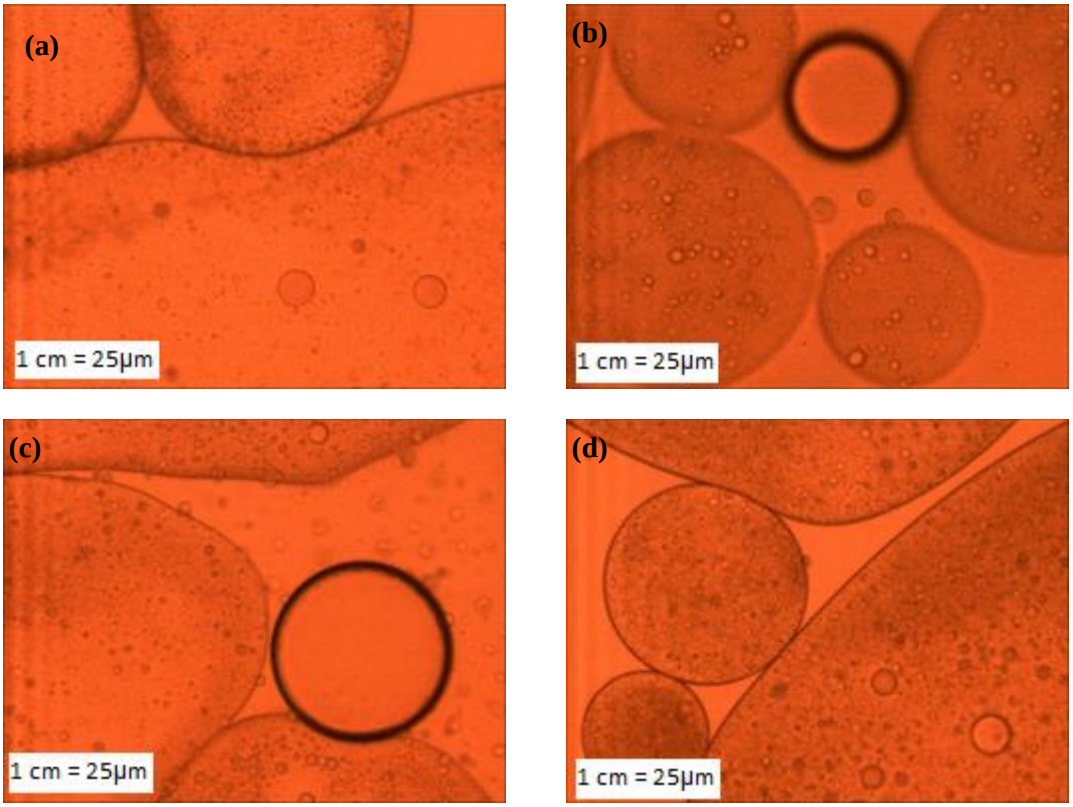


Figure 2. Microscopic images of emulsion at different emulsification time (a) 3 minutes, (b) 5 minutes, (c) 7 minutes and (d) 9 minutes (magnification 400x)

Table 2. Effect of emulsification time on emulsion droplets size

Agitation Time (minutes)	Diameter of Droplets (µm)
1	1.35
3	1.33
5	1.41
7	1.66

Besides that, Table 1 displays the results of the effect of agitation speed from 200 rpm to 500 rpm. It is apparent from this table that the most stable emulsion happens at 300 rpm. The emulsion was found unstable at lower agitation speed, where 40% of emulsion breakage was recorded. The result can be explained by the fact that the shear energy provided was insufficient to disperse the emulsion in the external phase. Consequently, larger globules were formed and they tended to coalesce with one another [23]. As can be seen in Figure 3(a) and Table 3, the size of emulsion globules formed at 200 rpm is larger (52.67 µm) compared to other agitation speeds. This result reflects those of Othman et al. [26] who also found that large globules were formed when low agitation speed was applied. Apart from that, larger emulsion globules could also reduce extraction performance since they increase the membrane thickness together with the small mass transfer area. Looking at Figure 3(b), it can be seen that smaller size of emulsion globules was formed at 36.48 µm. This can hinder the coalescence phenomenon between the emulsion globules that contributes to a more stable system. A further increase in agitation speed (400 rpm and 500 rpm) produced smaller emulsion globules at 24.42 µm and 17.66 µm, respectively. Unfortunately, the emulsion was found unstable where 40% and 60% of breakage were observed. This result could be attributed to the thinning of interfacial film and favored rapid coalescence of emulsion globules. Furthermore, the application of higher speed beyond a certain limit exposed the emulsion to high shear and led to globules rupture. These results seem to be consistent with another research which found that high agitation speed could damage the emulsion [12, 16]. Taken together, 300 rpm of agitation speed was chosen as the best condition in this study.

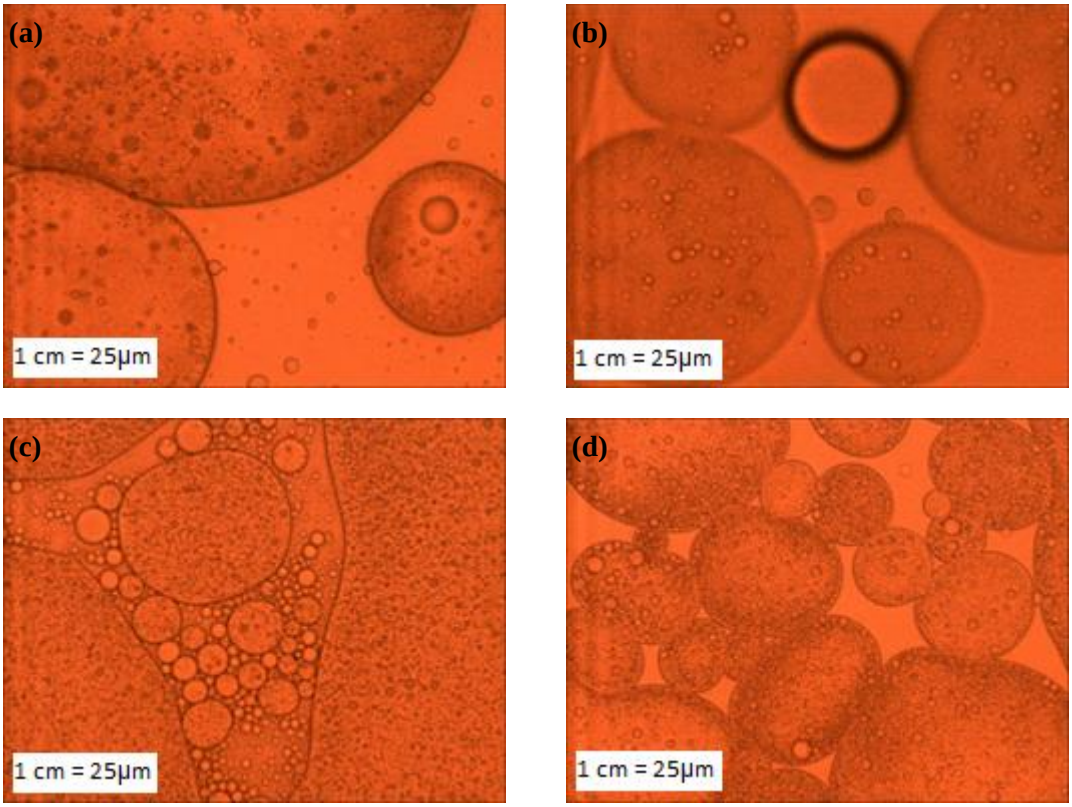
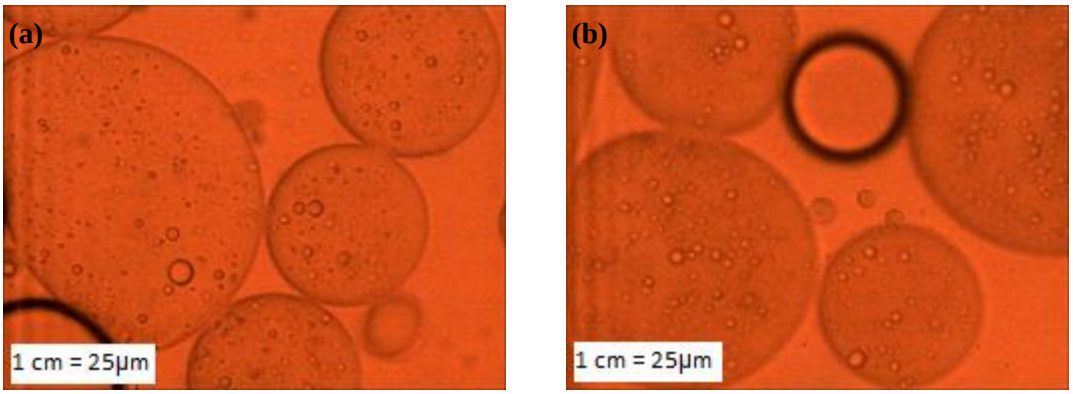


Figure 3. Microscopic images of emulsion at different agitation speed (a) 200, (b) 300, (c) 400 and (d) 500 (magnification 400x)

Table 3. Effect of agitation speed on size of emulsion globules

Agitation Speed (rpm)	Diameter of Globules (µm)
200	52.67
300	36.48
400	24.42
500	17.66

In addition, the effect of agitation time from 1 to 7 minutes was investigated. As can be seen from Table 1, emulsion stability improves when the agitation time is increased from 1 to 3 minutes, where 40% and no breakage can be observed, respectively. This happens because the shorter agitation time is insufficient to disperse primary emulsion in the external phase. As a consequence, a larger size of emulsion globules (42.77 µm) is formed as depicted in Figure 4(a). Consequently, coalescence phenomenon could occur within a short time [24]. As mentioned previously, large size of emulsion globules is also undesirable since it could decrease the extraction performance. A further increase in the agitation time (3 minutes) revealed that a stable emulsion was obtained with smaller globule size of 36.48 µm. The interface between the primary emulsion and external phase was basically deformed to the extent that large globules were formed. These large globules were subsequently broken up into smaller ones with time. As a result, the emulsion produced was more stable owing to smaller globules that will take more time to coalesce. A further increment in the agitation time (5 and 7 minutes) had worsen the emulsion stability, where 40% and 60% of emulsion breakage were recorded, respectively. As indicated earlier, longer agitation time favored the dispersion of smaller emulsion globules. Unfortunately, this condition led to rapid coalescence of small globules which later caused breakage. While Table 4 shows that smaller sizes of emulsion globules are obtained at 34.19 µm and 33.18 µm, Figure 4(c) and Figure 4 (d) demonstrate that larger globule size distribution is the result of coalescence. The findings are consistent with that of Kulkarni and Mahajani [27] who reported emulsion breakage at a prolonged time in the ELM process of molybdenum extraction. Thus, 3 min of agitation time was selected as the best condition.



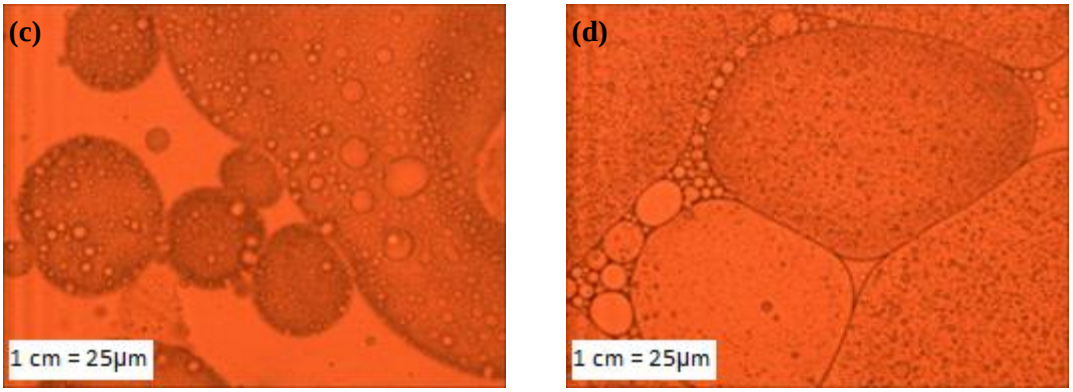


Figure 4. Microscopic images of emulsion at different emulsification time (a) 1 minute, (b) 3 minute, (c) 5 minute and (d) 7 minute (magnification 400x)

Table 4. Effect of agitation time on size of emulsion globules

Agitation Time (minutes)	Diameter of Globules (µm)
1	42.77
3	36.48
5	34.19
7	33.18

Succinic acid extraction and recovery performance

In order to determine ELM performance on succinic acid, the primary emulsion was dispersed in the fermentation broth at the best stability condition. The transport of succinic acid is governed by non-equilibrium mass transfer, which is due to the chemical concentration gradient [28]. The transfer of succinic acid through the liquid membrane consisted of two steps, which involved the reaction at the external and internal interfaces [29]. At the external interface, the succinic acid reacted with Amberlite LA2 and formed a complex. Following the reaction, the complex diffused through the membrane phase into the internal phase. The succinic acid was then released into the internal phase by stripping reaction with Na_2CO_3. Once completed, Amberlite LA2 was freed and diffused back to the external interface.

The effect of succinic acid concentration on the extraction (by varying it from 5 to 50 g/L) and the recovery performance were investigated and the results are shown in Figure 5. The graph shows that when the external concentration is increased, a marked decline can be seen in both extraction and recovery. It can also be seen that, by far the best condition is at 5 g/L of initial external feed concentration, where almost 100% of extraction and 94% of recovery are achieved. At this condition, the concentration of succinic acid recovered in the internal phase is 11.3 enrichment compared to the initial concentration in the external phase, as shown in Table 5. This intriguing result can be described by the fact that the concentration of solute is low compared to the larger amount of carrier. Another possible explanation is the concentration of the stripping agent in the internal phase is sufficient to strip succinic acid from the complex. This leads to the release of free carrier that reacts with another solute at the external interface. Moreover, the sufficient stripping agent could also delay the accumulation of succinic acid complex in the membrane phase that may obstruct the ELM process. These are consistent with those reported by Lee [30] and Noah et al. [31].

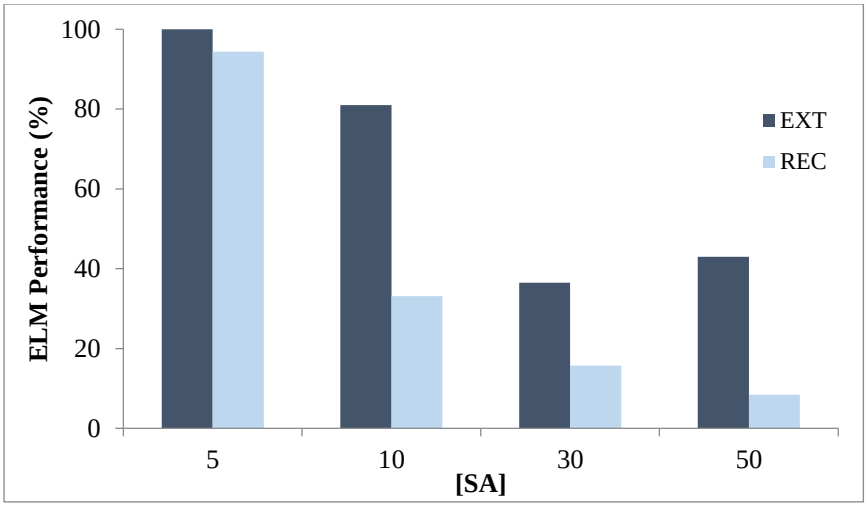


Figure 5. Succinic acid extraction and recovery performance at different initial concentration. [diluent: palm oil; [Amberlite LA2]: 0.05M; Octanol: 10%; [Na_2CO_3]: 0.5M; O/I: 3/1; homogenizer speed: 7000 rpm; emulsification time: 5 minutes; Tween 80: 1%; Span 80: 3%; agitation speed: 300 rpm; agitation time: 3 minutes]

Table 5. Enrichment of the recovered succinic acid

Initial Concentration of Succinic Acid in External Phase (g/L)	Final Concentration of Succinic Acid in Internal Phase (g/L)	Enrichment Ratio
5	58.98	11.3
10	39.7	4.0
30	62.87	1.9
50	56.21	1.0

When the initial concentration was increased to 10 g/L, the degree of extraction decreased slightly to 81%. After that, there was a significant decrease in the performance of ELM when the initial concentration was raised up to 50 g/L, where only around 40% of succinic acid extraction was attained. The result was likely to be coherent with the required amount of carrier to transport the higher amount of succinic acid. This result also could be related to the complex formation that controlled the external mass transfer of low solute concentration [32]. Hence, the extraction rate at high concentration was lower than that at low initial succinic acid concentration. On the other hand, a clear reduction of the recovery performance to only 33% with four times enrichment was identified at 10 g/L of initial feed concentration in this analysis. Less than 16% of recovery with enrichment ratio lower than 2 of succinic acid was recovered when the initial concentration was raised to 50 g/L. An important concept that emerged at high initial concentration was the transport of solute could decrease largely owing to the reduced capacity of internal phase to strip the transported solute. Moreover, the internal droplets in the peripheral emulsion region were readily saturated with solute. Therefore, succinic acid complex must diffuse into a deeper region inside the emulsion globule to release solute in the internal phase. Once all the internal droplets were saturated, the succinic acid-carrier complex accumulated in the membrane phase and prevented the carrier to react with another solute. These results are in agreement with those obtained by Chakraborty et al. [33] and Ammar et al. [34]. In this study, it can be concluded that 5 g/L is the best condition for recovery of succinic acid from fermentation broth.

Conclusion

This study presented the feasibility of succinic acid recovery by using ELM from real fermentation broth. The best operating conditions for emulsion stability were 5 minutes of emulsification time, 300 rpm of agitation speed, and 3 minutes of agitation time. The ELM performance from 5 g/L of succinic acid in fermentation broth was almost 100% extraction, 94% recovery, and 11 times enrichment. Thus, the ELM process is very promising to be applied in downstream processing of bio-based succinic acid production.

Acknowledgement

The authors would like to acknowledge the Ministry of Higher Education (MOHE) (Research University Grant: Vot 18H33), Centre of Lipids Engineering and Applied Research (CLEAR), and Universiti Teknologi Malaysia (UTM) for the assistance and facilities provided to make this research possible.

References

1. Werpy, T., Holladay, J. and White, J. (2004). Top value added chemicals from biomass: I. Results of screening for potential candidates from sugars and synthesis gas. DOE Scientific and Technical Information.
2. Isar, J., Agarwal, L., Saran, S. and Saxena, R. K. (2006). Succinic acid production from *Bacteroides fragilis*: Process optimization and scale up in a bioreactor. *Anaerobe*, 12(5): 231-237.
3. Wang, C., Li, Q., Tang, H., Zhou, W., Yan, D., Xing, J. and Wan, Y. (2013). Clarification of succinic acid fermentation broth by ultrafiltration in succinic acid bio–refinery. *Journal of Chemical Technology & Biotechnology*, 88(3): 444-448.
4. Jiang, M., Ma, J., Wu, M., Liu, R., Liang, L., Xin, F., Zhang, W., Jia, H. and Dong, W. (2017). Progress of succinic acid production from renewable resources: Metabolic and fermentative strategies. *Bioresource Technology*, 245: 1710-1717.
5. Huh, Y. S., Jun, Y. S., Hong, Y. K., Song, H., Lee, S. Y. and Hong, W. H. (2006). Effective purification of succinic acid from fermentation broth produced by *Mannheimia succiniciproducens*. *Process Biochemistry*, 41(6): 1461-1465.
6. Andersson, C., Helmerius, J., Hodge, D., Berglund, K. A. and Rova, U. (2009). Inhibition of succinic acid production in metabolically engineered *Escherichia coli* by neutralizing agent, organic acids, and osmolarity. *Biotechnology Progress*, 25(1): 116-123.
7. Li, Q., Wang, D., Wu, Y., Li, W., Zhang, Y., Xing, J. and Su, Z. (2010). One step recovery of succinic acid from fermentation broths by crystallization. *Separation and Purification Technology*, 72(3): 294- 300.
8. Hatti-Kaul, R. (2010). Downstream processing in industrial biotechnology. In W. Soetaert and E. J. Vandamme (Eds.), Industrial Biotechnology. Wiley-VCH Verlag GmbH & Co. KGaA: pp. 279 – 321.
9. Jusoh, N. and Othman, N. (2016). Stability of water-in-oil emulsion in liquid membrane prospect. *Malaysian Journal of Fundamental and Applied Sciences*, 12(3): 114-116.
10. Othman, N., Noah, N. F. M., Shu, L. Y., Ooi, Z. Y., Jusoh, N., Idroas, M. and Goto, M. (2017). Easy removing of phenol from wastewater using vegetable oil-based organic solvent in emulsion liquid membrane process. *Chinese Journal of Chemical Engineering*, 25(1): 45-52.
11. Othman, N., Mili, N., Idris, A. and Zailani, S. N. (2012). Removal of dyes from liquid waste solution: Study on liquid membrane component selection and stability. In A. F. Ismail and T. Matsuura Eds.), Sustainable Membrane Technology for Energy, Water, and Environment. John Wiley & Sons, Inc., Canada: pp. 221-229.
12. Chaouchi, S. and Hamdaoui, O. (2014). Acetaminophen extraction by emulsion liquid membrane using Aliquat 336 as extractant. *Separation and Purification Technology*, 129: 32-40.
13. Ooi, Z. Y., Harruddin, N. and Othman, N. (2015). Recovery of kraft lignin from pulping wastewater via emulsion liquid membrane process. *Biotechnology Progress*, 31(5): 1305-1314.
14. Noah, N. F. M., Othman, N. and Jusoh, N. (2016). Highly selective transport of palladium from electroplating wastewater using emulsion liquid membrane process. *Journal of the Taiwan Institute of Chemical Engineers*, 64: 134-141.
15. Jusoh, N., Othman, N. and Nasruddin, N. A. (2016). Emulsion liquid membrane technology in organic acid purification. *Malaysian Journal of Analytical Sciences*, 20(2): 436-443.
16. Sulaiman, R. N. R., Othman, N. and Amin, N. A. S. (2014). Emulsion liquid membrane stability in the extraction of ionized nanosilver from wash water. *Journal of Industrial and Engineering Chemistry*, 20 (5): 3243-3250.

17. Jusoh, N., Othman, N. and Nasruddin, N. (2015). Liquid membrane formulation for succinic acid extraction from simulated aqueous waste solution. In M. A. Hashim (Ed.), ICGSCE 2014. Springer Singapore: pp. 51-59.
18. Lee, S. C. and Hyun, K. S. (2010). Development of an emulsion liquid membrane system for separation of acetic acid from succinic acid. *Journal of Membrane Science*, 350(1–2): 333-339.
19. Jusoh, N., Othman, N., Idris, A. and Nasruddin, A. (2014). Characterization of liquid pineapple waste as carbon source for production of succinic acid. *Jurnal Teknologi (Sciences and Engineering)*, 69(4): 11- 13.
20. Peng, W., Jiao, H., Shi, H. and Xu, C. (2012). The application of emulsion liquid membrane process and heat-induced demulsification for removal of pyridine from aqueous solutions. *Desalination*, 286: 372-378.
21. Noah, N. F. M. (2015). Emulsion liquid membrane extraction of palladium from simulated electroplating wastewater. Thesis of Master Degree, Universiti Teknologi Malaysia.
22. Nghiem, N., Kleff, S. and Schwegmann, S. (2017). Succinic Acid: Technology development and commercialization. *Fermentation*, 3(2): 1-14.
23. Gaikwad, S. G. and Pandit, A. B. (2008). Ultrasound emulsification: Effect of ultrasonic and physicochemical properties on dispersed phase volume and droplet size. *Ultrasonics Sonochemistry*, 15 (4): 554-563.
24. Sabry, R., Hafez, A., Khedr, M. and El-Hassanin, A. (2007). Removal of lead by an emulsion liquid membrane: Part I. *Desalination*, 212 (1–3): 165-175.
25. Djenouhat, M., Hamdaoui, O., Chiha, M. and Samar, M. H. (2008). Ultrasonication-assisted preparation of water-in-oil emulsions and application to the removal of cationic dyes from water by emulsion liquid membrane: Part 2. Permeation and Stripping. *Separation and Purification Technology*, 63 (1): 231 – 238.
26. Othman, N., Noah, N. F. M., Poh, K. W. and Yi, O. Z. (2016). High performance of chromium recovery from aqueous waste solution using mixture of palm-oil in emulsion liquid membrane. *Procedia Engineering*, 148: 765-773.
27. Kulkarni, P. S. and Mahajani, V. V. (2002). Application of liquid emulsion membrane (LEM) process for enrichment of molybdenum from aqueous solutions. *Journal of Membrane Science*, 201(1–2): 123-135.
28. León, G. and Guzmán, M. A. (2005). Kinetic study of the effect of carrier and stripping agent concentrations on the facilitated transport of cobalt through bulk liquid membranes. *Desalination*, 184 (1): 79-87.
29. Jusoh, N. (2017). Palm oil based emulsion liquid membrane formulation for succinic acid extraction performance. PhD Thesis, Universiti Teknologi Malaysia.
30. Lee, S. C. (2011). Extraction of succinic acid from simulated media by emulsion liquid membranes. *Journal of Membrane Science*, 381(1–2): 237-243.
31. Noah, N. F. M., Othman, N. and Jusoh, N. (2016). Highly selective transport of palladium from electroplating wastewater using emulsion liquid membrane process. *Journal of the Taiwan Institute of Chemical Engineers*, 64: 134-141.
32. Chakraborty, M., Bhattacharya, C. and Datta, S. (2010). Emulsion liquid membranes: Definitions and classification, theories, module design, applications, new directions and perspectives. In V. S. Kislik (Ed.), Liquid Membranes. Elsevier, Amsterdam: pp. 141-199.
33. Chakraborty, M., Bhattacharya, C. and Datta, S. (2002). Studies on transport mechanism of nickel(II) from an acidic solution using emulsion liquid membranes. *Journal of Energy Heat and Mass Transfer*, 24: 75-88.
34. Ammar, S. H., Attia, H. G. and Affat, A. K. D. (2012). Extraction of metal ions mixture cadmium, iron, zinc and copper from aqueous solutions using emulsion liquid membrane technique. *2012 First National Conference for Engineering Sciences*: pp. 1-10.